Vol. 71, No. 3 / 2023

e: ISSN 2068 – 2239
p: ISSN 2068 – 4215

INMATEH – AGRICULTURAL ENGINEERING

SEPTEMBER - DECEMBER

No liability is assumed by the editorial staff for the content of scientific papers and opinions published in this volume. They represent the author's point of view

Managing Editorial Board - INMA Bucharest

Editor in Chief

Lucian-Ionel CIOCA, Professor, PhD.Eng., "Lucian Blaga" University of Sibiu

Executive Editor

Lucreţia POPA
PhD.Eng, SR I

Assistant Editor

Nicolae-Valentin VLADUŢ
PhD.Eng, SR I
Mihai-Gabriel MATACHE
PhD.Eng, SR I

Logistic support, database

Virgil MURARU
PhD.Eng, SR I

Scientific Secretary

Cârdei Petre, math.

Official translator

RADU Daniela-Cristina, English

Editorial Board

- *QUENDLER Elisabeth – Austria, Vienna, Univ. of Natural Resources & Applied Life Sciences;*
- *Ir. HUYGHEBAERT Bruno – Belgia, Walloon Agricultural Research Center CRA-W;*
- *Van IMPE F.M. Jan – Belgia, KU Leuven University*
- *FABBRO Dal Inacio Maria - Brazil, Campinas State University;*
- *ATANASOV Atanas – Bulgaria, "Angel Kanchev" University of Rousse*
- *MOLINOS-SENANTE María – Chile, Pontificia Universidad Católica - Vicedecana, Escuela de Ingeniería UC*
- *BILANDZIJA Nikola – Croatia, Zagreb University, Faculty of Agriculture;*
- *KOSUTIC Silvio – Croatia, Zagreb University, Faculty of Agriculture;*
- *KOVACEV Igor - Croatia, Zagreb University, Faculty of Agriculture;*
- *GONZÁLEZ Omar – Republic of Cuba, Central University "Marta Abreu" de las Villas;*
- *KATHIJOTES Nicholas – Cyprus, University of Nicosia;*
- *HERAK David - Czech Republic, Czech University of Agriculture Prague;*
- *BORCHARD Nils – Finland, Natural Resources Institute Finland (Luke);*
- *SAUER Johannes – Germany, Technical University Munich;*
- *FENYVESI László – Hungary, Hungarian Institute of Agricultural Engineering Godolo;*
- *PEEYUSH Soni - India, Indian Institute of Technology, Kharagpur;*
- *MOHAMMADREZA Alizadeh – Iran, Department of Agricultural Engineering, Rice Research Institute of Iran (RRII);*
- *De WRACHIEN Daniele - Italy, State University of Milan;*
- *BIOCCA Marcello - Italy, Agricultural Research Council, Agricultural Engineering Research Unit;*
- *COLANTONI Andrea – Italy, University Viterbo;*
- *SARAUSSKIS Egidijus – Lithuania, Vytautas Magnus University, Faculty of Agricultural Engineering;*
- *KRIAUCIUNIENE Zita - Lithuania, Vytautas Magnus University;*
- *DUKE Mike – New Zealand, University of Waikato, Faculty of Science and Engineering;*
- *EWEMOJE Temitayo Abayomy – Nigeria, University of Ibadan, Faculty of Technology, Department of Agricultural and Environmental Engineering;*
- *SKIERUCHA Wojciech – Poland, Institute of Agro-physics Polish Academy of Sciences, Lublin;*
- *EKIELSKI Adam - Poland, Warsaw University of Life Sciences;*
- *KOT Sebastian - Poland, Czestochowa University of Technology*
- *SAVIN Lazar– Serbia, University of Novi Sad, Faculty of Agriculture, Department of Agricultural Engineering;*
- *SIMIKIC Mirko– Serbia, University of Novi Sad, Faculty of Agriculture, Department of Agricultural Engineering;*
- *MARTINOV Milan - Serbia, Faculty of Agriculture, Department of Agricultural Engineering,*
- *TURAN Jan – Slovakia, Technical University Kosice, Dept Elect & Multimedia Commun, Kosice;*
- *MADYIRA M. Daniel - South Africa, University of Johannesburg, Mechanical Engineering Science Department*
- *COZ FERNANDEZ Alberto – Spain, University of Cantabria, School of Nautical Studies, Department of Chemistry and Process & Resource Engineering;*
- *ERTEKIN Can - Turkey, Akdeniz University Antalia;*
- *KABAŞ Önder –Turkey, Antalia, Agricultural Scientific Research Institute of Batı Akdeniz;*
- *SELVİ Kemal Çağatay - Turkey, Samsun, University of Ondokuz Mayıs, Faculty of Agriculture, Department of Machines for Agriculture;*
- *ÖTLEŞ Semih - Turkey, Ege University, Engineering Faculty, Food Engineering Department;*
- *MARUSCHAK Pavlo - Ukraine, Ternopil Ivan Pul'uj National Technical University, Department of Technical Mechanics and Agricultural Engineering;*
- *BULGAKOV Volodymyr – Ukraine, National University of Life and Environmental Sciences of Ukraine;*
- *PARASCHIV Gigel - Romania, Politehnica University of Bucharest;*
- *VOICU Gheorghe - Romania, Politehnica University of Bucharest;*
- *BIRIŞ Sorin - Romania, Politehnica University of Bucharest;*
- *MAICAN Edmond - Romania, Politehnica University of Bucharest;*
- *FILIP Nicolae - Romania, Technical University Cluj Napoca;*
- *COZAR Onuc-Romania, „Babes-Bolyai" University of Cluj-Napoca Romania, Faculty of Physics;*
- *VLASE Sorin - Romania, "Transilvania" University of Braşov;*
- *ŢENU Ioan - Romania, USAMV Iaşi;*
- *HERIŞANU Nicolae - Romania, Politehnica University of Timisoara;*
- *MARSAVINA Liviu - Romania, Politehnica University of Timisoara*
- *MARINCA Vasile - Romania, Politehnica University of Timisoara*
- *GERGEN Iosif - Romania, USAMVB Timişoara;*
- *BORDEAN Despina-Maria - Romania, USAMVB Timişoara;*
- *BUNGESCU Sorin - Romania, USAMVB Timişoara;*
- *VOICEA Iulian - Romania, INMA Bucharest*
- *DEAK Gyorgy - Romania, INCDPM;*
- *BELC Nastasia - Romania, IBA Bucharest;*
- *BUŢU Alina - Romania, INCDSB Bucharest;*
- *PAUN Mihaela - Romania, National Institute of Research and Development for Biological Sciences, INCDSB*

INMATEH - Agricultural Engineering **journal is indexed in the next international databases:**
ELSEVIER /SciVerse SCOPUS, CLARIVATE - WEB of SCIENCE- Emerging Sources Citation Index (ESCI), ULRICHS Web: Global Serials Directory, CABI, SCIPIO, Index COPERNICUS International, EBSCO Publishing, Elektronische Zeitschriftenbibliothek

INMATEH - Agricultural Engineering
vol. 71, no.3 / 2023
e-ISSN: 2068 – 2239; p: ISSN: 2068 – 4215

https://inmateh.eu/ *E-mail: inmatehjournal@gmail.com*

Edited by: INMA Bucharest
Copyright: INMA Bucharest / Romania
National Institute for Research-Development of Machines and Installations
Designed for Agriculture and Food Industry - INMA Bucharest
6, Ion Ionescu de la Brad Bvd., sector 1, Bucharest, ROMANIA

CONTENT

		Page(s)
1.	THE PECULIARITIES OF SEEDS AND THE QUALITY OF THE GREEN MASS OF SOME NON-TRADITIONAL CROPS IN THE REPUBLIC OF MOLDOVA **Valerian CEREMPEI[1)], Victor ȚÎȚEI[2)], Nicolae-Valentin VLĂDUT[3)], Oana-Diana CRISTEA[*3)]** [1)] Technical University of Moldova, Chisinau/ Republic of Moldova; [2)] „Alexandru Ciubotaru" National Botanical Garden (Institute) of Moldova State University, Chisinau Republic of Moldova; [3)] INMA Bucharest/ Romania	11
2.	DESIGN AND EXPERIMENT OF COMBINED CAVITY-TYPE PRECISION HOLE-DROP SEED-METERING DEVICE FOR RICE **Wenwen SONG[1)], Yu WAN[1)], Bo ZHOU [1)], Fuming KUANG[1)], Wei XIONG [1)], Juan LIAO [1)], Dequan ZHU[1)], Shun ZHANG [*1, 2)]** [1)] College of Engineering, Anhui Agricultural University, Hefei, Anhui, China [2)] Engineering Laboratory of Intelligent Agricultural Machinery Equipment, Anhui, Hefei, China	25
3.	DETECTION OF EATING BEHAVIOUR IN PIGS BASED ON MODIFIED YOLOX **LI Yanwen, LI Juxia*), DUAN Lei, NA Tengxiao, ZHANG Pengpeng, ZHI Qingyu** College of Information Science and Engineering, Shanxi Agricultural University / China	44
4.	DESIGN AND ANALYSIS OF INDEPENDENT STRUT TYPE AIR SUSPENSION APPLIED TO HIGH CLEARANCE SELF-PROPELLED SPRAYER **Chenwei HU [1)], Jiayu CAO [1)], Shuo ZHANG[1)], Yu CHEN[*1)], Liquan LU [1)]** [1)] Northwest A&F University, Yangling, China	53
5.	ANALYSIS ON ROOT CUTTING MECHANISM OF SELF-PROPELLED CHINESE CABBAGE HARVESTER AND OPTIMISATION OF DEVICE PARAMETERS **Liming ZHOU [*1,2)], Yifan ZENG [1,2)], Kang NIU [2)], Yanwei YUAN [2)], Shenghe BAI[2)] and Kaikang CHEN [2)]** [1)] College of Mechanical and Electrical Engineering, Qingdao Agricultural University, Qingdao, China; [2)] Chinese Academy of Agricultural Mechanization Sciences Group Co., Ltd, Beijing, China	70
6.	STUDY OF THE PROCESS OF THRESHING LEGUMINOUS GRASS SEEDS WITH A DRUM-TYPE THRESHING DEVICE **Mykhailo ANELIAK, Alvian KUZMYCH, Serhii STEPANENKO*), Viktor LYSANIUK** Institute of Mechanics and Automatics of Agroindustrial Production / Ukraine	83
7.	DESIGN AND TESTING OF MODERN APPLE ORCHARD PRUNING MACHINERY **Yuliang WANG[1,2)], Zhiqiao WANG [1,2)], Zhaoying CHEN[1,2)], Guoqiang FAN[1,2)], Rui SU[1,2)], Peijun YIN[1,2)], Jinxing WNAG [*1,2)]** [1)]College of Mechanical and Electronic Engineering, Shandong Agricultural University, Tai an / China; [2)]Shandong Provincial Key Laboratory of Horticultural Machinery and Equipment, Tai an / China	93
8.	DETECTION OF DEFECTS OF *CERASUS HUMILIS* FRUITS BASED ON HYPERSPECTRAL IMAGING AND CONVOLUTIONAL NEURAL NETWORKS **Bin WANG [1)], Lili LI [*1)]** [1)] College of Information Science and Engineering, Shanxi Agricultural University, Taigu / China	103
9.	NON-DESTRUCTIVE ESTIMATION OF MATURITY LEVEL OF 'CRYSTAL' GUAVA FRUIT BY MEANS OF FLUORESCENCE SPECTROSCOPY **Setyo PERTIWI *[1)], Alexander Salvatoris Febrian HUTOMO [2)], Slamet WIDODO [1)]** [1)] Faculty of Agricultural Engineering and Technology, IPB University, Indonesia; [2)] Agricultural and Biosystem Engineering Study Program, Faculty of Agricultural Engineering and Technology, IPB University, Indonesia	115
10.	STUDY ON ARTIFICAL INTELLIGENCE RECOGNITION METHODS FOR MAIZE LEAF LESION IMAGE **Linwei LI[1)], Yanbo SONG[2)], Jie SUN[1)], Yuanyuan LU[2)], Lili NIE[1)], Fumin MA[3)], Xinyu HOU[4)], Juxia LI[1)], Yanwen LI[1)], Zhenyu LIU[5,6 *)]** [1)]Shanxi Agricultural University, Taigu, China; [2)] Shanxi Agricultural University, Taigu, China; [3)] Lanzhou University of Technology, Lanzhou, China; [4)] Hainan University, Meilan, China; [5)] Shanxi Agricultural University, Taigu, China; [6)] Dryland Farm Machinery Key Technology and Equipment Key Laboratory of Shanxi Province, Taigu, China	124
11.	DESIGN AND EXPERIMENT OF POTATO SEEDLING FILM-BREAKING DEVICE BASED ON MACHINE VISION **Zhaoqin LV[1)], Zhuangzhuang GUO[2,3)], Wanzhi ZHANG[*2,3)], Xiang ZENG[2,3)], Yuelin HAN[2,3)]** [1)] College of Intelligent Manufacturing, Qingdao Huanghai University / China; [2)] College of Mechanical and Electronic Engineering, Shandong Agricultural University / China; [3)] Shandong Provincial Key Laboratory of Horticultural Machinery and Equipment / China	136
12.	SUPERIOR INFERENTIAL STATISTICS OF THE EXPERIMENTAL DATA OF A COMPLEX EXPERIMENTAL CULTIVATOR **Petru CARDEI[1)], Nicolae CONSTANTIN[1)], Cătălin PERSU[1)], Vergil MURARU[1)], Raluca SFÎRU[1*)], Maria IAMANDEI[2)*], Daniel LATES[3)]** [1)]INMA Bucharest / Romania; [2)]Research Development Institute for Plant Protection Bucharest / Romania [3)] "George Emil Palade" University of Medicine, Pharmacy, Târgu Mureș / Romania	147
13.	COMPARATIVE STUDY ON WATER USE CHARACTERISTICS AND PRODUCTIVITY OF SOYBEAN AND MAIZE INTERCROPPING SYSTEM UNDER DRY FARMING CONDITIONS **Yaoyu LI[2)], Tengteng QU [3)], Qixin ZHAO [3)], Yuzhi WANG [3)], Zizheng DENG [2)], Wuping ZHANG [3)], Xiaoying ZHANG [4)]Lili SUN [1)], Fuzhong LI [3,*)]** [1)] Shanxi Agricultural University, Taigu, Shanxi / China; [2)] China Agricultural University, Beijing / China [3)] Shanxi Agricultural University, Taigu, Shanxi / China; [4)] Shanxi Agricultural University, Taigu, Shanxi / China	164
14.	RELIABILITY ANALYSIS OF FMECA THRESHING AND CLEANING SYSTEM BASED ON FUZZY COMPREHENSIVE EVALUATION **Qian DONG, Guohai ZHANG*, Yuqian ZHAO, Fukang ZHOU, Peng LIU, Yihu WANG, Xipeng QIAN [1]** School of Agricultural Engineering and Food Science, Shandong University of Technology, Zibo, China	173

		Page(s)
15.	DEPOSITION PERFORMANCE OF HYDRODYNAMIC ULTRASONIC ATOMISING NOZZLES WITH DIFFERENT SPRAY PARAMETERS **Zengqiang SONG [1)], Jinliang GONG [2*)], Yanfei ZHANG [1*)]** [1)]School of Agricultural Engineering and Food Science, Shandong University of Technology, Zibo / China [2)]School of Mechanical Engineering, Shandong University of Technology, Zibo / China	185
16.	DISCRETE ELEMENT METHOD (EDEM) SIMULATION AND PARAMETER OPTIMIZATION: DESIGN AND TESTING OF A LOW-LOSS AND HIGH-EFFICIENCY CORN THRESHING DEVICE **Yaxiu HOU[1)], Shuqi SHANG, Xiang LI, Xiaoning HE, Haifeng ZHENG, Tongtong DONG, Xu LI, Zhixin LIU, Shuai YANG, Dongwei WANG*** [1)] Qingdao Agricultural University, College of Mechanical and Electrical Engineering / China	194
17.	PRELIMINARY RESEARCH REGARDING THE CREATION OF A CATEGORY OF COMPOSITE MATERIAL BASED ON A MUD MATRIX AND AGRICULTURAL WASTE AS FILLER MATERIALS **Dana-Claudia FARCAȘ-FLAMAROPOL[1)], Elena SURDU[1*)], Radu I. IATAN[1)], Petru CÂRDEI[2*)], Ramona MARE[1)]** [1)]U.N.S.T "POLITEHNICA" of Bucharest / Romania; [2)] INMA Bucharest / Romania	205
18.	CALIBRATION OF WHITE RICE SIMULATION PARAMETERS BASED ON DISCRETE ELEMENT METHOD **Biao XIE, Jinyin BAI, Jiagang YAN, Shibo ZHAO, Nian LIU, Qiang ZHANG*)** College of Engineering, Huazhong Agricultural University, Wuhan/ China; Key Laboratory of Agricultural Equipment in Mid-lower Yangtze River, Ministry of Agriculture, Wuhan / China	215
19.	DESIGN AND TEST OF INTELLIGENT YIELD MONITORING SYSTEM FOR PLOT COMBINE HARVESTER **Xiaoxiang ZHANG, Yingmei WANG, Renjie CHANG, Luxi ZHAO, Xin LI, Yinxing YAN, Wendong NIU, Shixing MA, Haiyan SONG*** College of Agricultural Engineering, Shanxi Agricultural University, Taigu / China	225
20.	RESEARCH ON DYNAMIC CHARACTERISTICS OF A DOUBLE-PENDULUM SUSPENSION FOR A BOOM SPRAYER **Fang LI[1)], Xiaohu BAI*[2)]** [1)] School of Information and Control Engineering, Liaoning Petrochemical University, Fushun/China; [2)] College of Engineering, Shenyang Agricultural University, Shenyang/China	237
21.	CALIBRATION OF DISCRETE ELEMENT PARAMETER OF SOIL IN HIGH-SPEED TILLAGE **Shaochuan LI, Peisong DIAO*, Yongli ZHAO, Hequan MIAO, Xianghao LI, Hongda ZHAO** Shandong University of Technology, Collage of Agricultural Engineering and Food Science, ZiBo, China	248
22.	DESIGN AND EXPERIMENT OF CLAMPING-PULL-OFF APPLE PICKING ROBOT **Shike GUO, Min FU*, Xiaoman CUI, Zijan WANG, Chengmeng WANG** Northeast Forestry University, College of Mechanical and Electrical Engineering, Harbin / China	259
23.	DESIGN AND EXPERIMENT OF AN END-EFFECTOR FOR HARVESTING SWEET PEPPER IN COMPLIANT OBSTACLE ENVIRONMENT **Yunting HUI[1#)], Yangyang LIAO[1#)], Decheng WANG[1*)], Xinxing LI[2*)], Zhiheng LU[3)], Yong YOU[1)], Hanchu JIA[1)]** [1)]College of Engineering, China Agricultural University, Beijing, China; [2)]College of Information and Electrical Engineering, China Agricultural University, Beijing, China [3)]Guangxi University, Nanning, China	271
24.	HEAT ENVIRONMENT STUDY OF PASSIVE SOLAR GREENHOUSE **Zhouhua LIU [*1)] , Xin YOU [2)] , Penghui QIAO[2)], Mengjun CHEN[2)], Weiwei CHEGN[1)])** [1)] Shanxi Agricultural University, College of Urban and Rural Construction, Taigu / China [2)] Shanxi Agricultural University, College of Agricultural Engineering, Taigu / China	282
25.	THE ELECTRIC TRACTION MOTORS BALANCING FOR LOAD TRANSFER EFFECTS COMPENSATION **Mihail ANDREI [1)], Gabriel POPA[2)], Emil TUDOR [3*)], Paula ANGHELIȚA[3)], Mihai-Gabriel MATACHE[4*)])** [1)] National University of Science and Technology POLITEHNICA of Bucharest / Romania; [2)] N.U.S.T. POLITEHNICA of Bucharest / Romania; [3)] National Institute for Research and Development in Electrical Engineering ICPE-CA, Bucharest / Romania; [4)] National Institute of Research – Development for Machines and Installations Designed for Agriculture and Food Industry – INMA Bucharest / Romania	290
26.	POROUS HOT AIR TEA DE-ENZYMING AND CARDING MACHINE UNDER GAS–SOLID COUPLING CONDITIONS: NUMERICAL SIMULATIONS AND PERFORMANCE TESTING **Haijun BI[*1, 2)], Pengcheng JIA[1,2)], Kuan QIN[3,4)], Lei YU[5)], Chengmao CAO[3,4)], Dongsong XIA[3,4)], Xinliang GUO[1,2)], Yang LIU[3,4)], Bin CHEN[3,4)], Yuzhen BI[1,2)]** [1)] Anhui Agricultural University, Hefei, China; [2)] Anhui Agricultural University, Hefei, China; [3)] Anhui Agricultural University, Hefei, China; [4)] Anhui Agricultural University, Hefei, China [5)] Anji Yuanfeng Tea Machinery Co. Ltd, Huzhou, China	301
27.	DESIGN AND MANUFACTURE OF A SUPERCRITICAL CO_2 LIQUID EXTRACTION MACHINE FOR EXTRACTING BIOACTIVE COMPOUNDS **Bambang DWI ARGO*[1,2)], Adam SYECH[1)], Avial YOSUA RIJADI[1)], Mochamad BAGUS HERMANTO[1,2)], Wahyunanto AGUNG NUGROHO[1,2)]** [1)] Faculty of Agricultural Engineering, Brawijaya University, Malang/ Indonesia [2)] Faculty of Agricultural Engineering, Brawijaya University, Malang / Indonesia	319
28.	NUMERICAL SIMULATION AND TEST OF HOT AIR FAN **Guoliang YOU[1,2)], Yaoming LI[*1,2)], Hanhao WANG[1,2)]** [1)]Key Laboratory of Modern Agricultural Equipment and Technology, Jiangsu University, Zhenjiang / China [2)]School of agricultural equipment engineering, Jiangsu University, Zhenjiang / China	327

		Page(s)
29.	OPTIMIZING AND INTEGRATING ELECTROMECHANICAL ACTUATORS IN AGRICULTURAL EXCAVATOR BOOMS FOR ENHANCED EFFICIENCY AND BATTERY LONGEVITY **Ioan Mihail SAVANIU[1)], Alexandru-Polifron CHIRIȚĂ[*2)], Ioana Aristia POPOVICI[1)], Oana TONCIU[1)], Magdalena CULCEA[1)], Ancuța NEAGU[1)], Robert BLEJAN[2,3)], Vasilica ȘTEFAN [4)]** [1)] Technical University of Civil Engineering Bucharest / Romania; [2)] National Institute of Research & Development for Optoelectronics/ INOE 2000, Subsidiary Hydraulics and Pneumatics Research Institute / IHP / Romania; [3)]National University of Science and Technology Politehnica Bucharest, Doctoral School of Power Engineering / Romania; [4)] INMA Bucharest / Romania	335
30.	DISCRETE ELEMENT METHOD IS USED TO ANALYZE THE OPERATING PARAMETERS OF THE CUTTING TABLE OF CRAWLER SELF-PROPELLED REED HARVESTER **Kuizhou JI [1)], Yaoming LI[1*)], Binbin JI[1,2)], Zhenwei LIANG[1)], Tuo DU[1)]** [1)]School of Agricultural Engineering, Jiangsu University, Zhenjiang, China [2)]School of Mechanical Engineering, Nantong University, Nantong, China	345
31.	TRIZ-AIDED DESIGN AND EXPERIMENT OF KIWIFRUIT PICKING END-EFFECTOR **Min FU*, Shike GUO, Jianan CAI, Jiacheng ZHOU, Xiaoyi LIU** Northeast Forestry University, College of Mechanical and Electrical Engineering, Harbin / China	356
32.	ENERGETICS OF PULLING FLAX STALKS WITH A DISC-BELT FLAX-PULLING APPARATUS **Svitlana YUKHYMCHUK, Serhii YUKHYMCHUK*), Mykola TOLSTUSHKO, Igor TSIZ, Nataliya TOLSTUSHKO** Lutsk National Technical University, 75, Lvivska str., Lutsk, Ukraine	367
33.	EVALUATION OF TRACTION CHARACTERISTICS OF TRACTOR TIRES ON LOOSE SOILS: SIMULATION AND EXPERIMENTAL RESEARCH **Jie WANG[1)], Lili SHANG[1)], Liangyuan XU[1,2)], Qiansheng TANG[1,2*)]** [1)] School of Engineering, Anhui Agricultural University, Hefei / China; [2)] Anhui Intelligent Agricultural Machinery Equipment Engineering Laboratory, Hefei / China	379
34.	DESIGN AND OPTIMIZATION OF AN INTEGRATED EXCAVATION AND TRANSPLANTING DEVICE FOR TOBACCO **Zhiguo PAN[1)], Tianfeng SUN[1)], Xiaomeng WANG[*2)], Qiuqiang HOU[2)], Shiting LV[1)], Luming ZHANG[2)], Zhenfei YANG[2)], Xuehui ZHANG[2)]** [1)]College of Mechanical and Electrical Engineering, Qingdao Agricultural University, Qingdao, China; [2)]Yunnan Tobacco Company Honghezhou Company, Honghezhou, China	391
35.	STUDY ON VIBRATION ADSORPTION CHARACTERISTICS OF SMALL-PARTICLE-SIZE SEEDS BASED ON DEM **Wenxue DONG[1)], Na LI[1)], Fei LIU[*1)], Xuan ZHAO[1)], Lihe WANG[1)], Dezheng XUAN[1)], Wendong ZHONG[1)], Hengtong HU[1)], Xiang KONG[1)], Xinyu MENG[1)], Mingyi LI[1)], Zhijiang DUAN[1)]** [1)] College of Mechanical and Electrical Engineering, Inner Mongolia Agricultural University, Hohhot, China;	406
36.	DESIGN AND EXPERIMENT OF NO-TILLAGE PLANTER FOR HIGH AND LOW BORDERS WHEAT **Shandong YANG[1)], Chuang MA[1)], Baochang ZHANG[*1)], Yinping ZHANG[1)], Jinchang YANG[2)]** [1)]School of Agricultural and Food Science, Shandong University of Technology, Zibo, China; [2)]Shandong Qingyun Yiyuan Agricultural Machinery Manufacturing Co., Ltd, Zibo, China	419
37.	HARVEST LOSS TEST AND OPTIMISATION OF KEY COMPONENTS OF OILSEED RAPE CUTTING TABLES **Jia YAO, Guohai ZHANG*), Xin WANG, Jitan LIAN, Minghao LIU, Xipeng QIAN, Yihu WANG, Peng LIU** College of Agricultural Engineering and Food Science, Shandong University of Technology, Zibo, China	429
38.	HOT AIR DRYING, IMPACT OF INFRARED DRYING, AND COMBINED HOT AIR-INFRARED DRYING ON ALFALFA DRYING QUALITY AND PERFORMANCE **Xihang SUN, Ziwen GUO, Guanghui WANG*), Chen CAI, Zhiqin WANG** Department of Agricultural Engineering, College of Engineering, China Agricultural University, Beijing, China	441
39.	CRYOGENIC FREEZING OF SOME BERRY SPECIES USING AN EXPERIMENTAL MODEL OF MULTI-FUNCTIONAL QUICK-FREEZING EQUIPMENT **Cristian Marian SORICĂ[1*)], Nicolae-Valentin VLĂDUȚ[1)], Andreea Iulia GRIGORE[1)], Mario CRISTEA[1)], Elena SORICĂ[1)], Remus OPRESCU[1)], Alexandru IONESCU[1)], Laurențiu VLĂDUȚOIU[1)], Lucian DUMITRESCU[2)]** [1)]INMA Bucharest, 6 Ion Ionescu de la Brad Blvd., Bucharest, Romania; [2)] ICDIMPH HORTING Bucharest/Romania	451
40.	THREE-DIMENSIONAL PATH PLANNING OF APPLE HARVESTING ROBOT BASED ON IMPROVED GENETIC ALGORITHM **Zeyuan YAN[1)] *, Ming SUN[1)]** [1)] Xinxiang Vocational and Technical College, Xinxiang, Henan, China	459
41.	PATH PLANNING OF FRUIT AND VEGETABLE PICKING ROBOTS BASED ON IMPROVED A* ALGORITHM AND PARTICLE SWARM OPTIMIZATION ALGORITHM **Li CHEN*** School of Applied Technology, Zhumadian Preschool Education College, Zhumadian, Henan, China	470
42.	AUTOMATED QUALITY ASSESSMENT OF APPLES USING CONVOLUTIONAL NEURAL NETWORKS **Adrian IOSIF [1)], Edmond MAICAN[1)], Sorin BIRIȘ[1)], Lucretia POPA[2)]** [1)] U.N.S.T POLITEHNICA of Bucharest / Romania; [2)] INMA Bucharest / Romania	483
43.	IMPROVED YOLOv8-BASED AUTOMATED DETECTION OF WHEAT LEAF DISEASES **Na MA, Yanwen LI, Miao XU, Hongwen YAN*)** College of Information Science and Engineering, Shanxi Agricultural University, Taigu / China	499
44.	LIGNIN UTILIZATION FOR THE REMOVAL OF MICROPLASTIC PARTICLES FROM WATER **Iuliana GĂGEANU[1)]; Florbela CARVALHEIRO[*2)]; Adam EKIELSKI[*3)]; Luis C. DUARTE[2)]** [1)] INMA Bucharest / Romania; [2)]LNEG – Laboratório Nacional de Energia e Geologia, Unidade de Bioenergia e Biorrefinarias, Lisboa / Portugal; [3)] Warsaw University of Life Sciences / Poland	511

		Page(s)
45.	EXPERIMENTAL STUDY ON NAVIGATION FOR WHEAT SEEDLING ROOT CUTTING BASED ON DEEP LEARNING **HaiBo LIN [*1,2)], Chenhe XU [1,2)], Yuandong LU [3)]** [1)] School of Mechanical & Automotive Engineering, Qingdao University of Technology, Qingda, China [2)] Key Lab of Industrial Fluid Energy Conservation and Pollution Control, Ministry of Education, Qingda, China [3)] Shandong Lingong Construction Machinery Co., Ltd., Shandon, China	522
46.	SIMULATION TEST AND VERIFICATION OF MATERIAL CONVEYING FOR SMALL AND MEDIUM-SIZED AIR SUCTION JUJUBE PICKING MACHINE BASED ON CFD-DEM COUPLING **Fengkui ZHANG[1,2,3)], Wenxi SHAO[1)], Shijie ZHAO[1,2,3)], Jikui ZHU[1,2,3)], Ping LI [1,2,3*]** [1)] College of Mechanical and Electrical Engineering, Tarim University, Alar, Xinjiang, China; [2)] Modern Agricultural Engineering Key Laboratory at Universities of Education Department of Xinjiang Uygur Autonomous Region, Tarim University, Alar, Xinjiang, China [3)] Key Laboratory of Tarim Oasis Agriculture (Tarim University), Ministry of Education, Tarim University, Xinjiang, China	535
47.	ANALYSIS ON PATH OPTIMIZATION OF AGRICULTURAL HANDLING ROBOTS BASED ON ANT COLONY-IMPROVED ARTIFICIAL POTENTIAL FIELD METHOD **Hexia CHU*** Department of Mathematics Education, Zhumadian Preschool Education College, Zhumadian, Henan, China	548
48.	EVALUATION OF THE THERMAL BEHAVIOR OF PLANTS IN THE MICROGREENHOUSE WITH MICROBOLOMETRIC IMAGE SENSORS **George IPATE [*1)], Constantin Daniel COTICI[1)], Alina-Daiana IONESCU [1)], Viorel FATU[1)], Iuliana GAGEANU[2)], Dan CUJBESCU[2)], Ana Maria NICOLAU[3)]** [1)] National University of Science and Technology "POLITEHNICA" of Bucharest / Romania. [2)] National Institute of Agricultural Machinery Bucharest / Romania [3)] National University of Science and Technology "POLITEHNICA" of Bucharest	558
49.	STUDY ON THE INFLUENCE OF MOISTURE CONTENT AND COMPRESSION RESISTANCE CHARACTERISTICS OF CORN GRAIN ON THRESHED BREAKAGE RATE **Yinping ZHANG[1)], Zehua HAO[1)], Lihang JIAO[1)], Qinghua LUAN[*2)], Hua ZHOU[*1)], Meizhou CHEN[1)]** [1)]School of Agricultural and Food Science, Shandong University of Technology, Zibo, China; [2)]Agricultural machinery business service center of Zichuan, Zibo, China	566
50.	EFFECTS OF INSULATION COVER MEASURES ON THE TEMPERATURE ENVIRONMENT OF CHINESE SOLAR GREENHOUSE **Qian SUN [1)], Yang SONG [1)], Zhigang YANG [2)], Xiaorui LIU [2)], Shimao CUI *[1)]** [1)] Inner Mongolia Agricultural University, College of Horticulture and Plant Protection, Huhhot / China [2)] Inner Mongolia Academy of Agricultural and Animal Husbandry Sciences, Huhhot / China	573
51.	RESEARCH ON DAMPING PERFORMANCE OF ORCHARD FRUIT THREE-STAGE DAMPING TRAILER BASED ON ADAMS **Yifan WANG[1)], Nan AN[1)], Jiaxin LU[1)], Zhihong ZHAO[1)], Xiahui FU[1)], Qingliang CUI[1,2)], Juxia WANG*[1,2)]** [1)]College of Agricultural Engineering, Shanxi Agricultural University, Shanxi Taigu / China [2)]Key Technology and Equipment of dry farming agricultural machinery Shanxi Key Laboratory, Shanxi Taigu / China	583
52.	DESIGN AND EXPERIMENT OF OVERLOAD PROTECTION AND AUTOMATIC OBSTACLE AVOIDANCE MECHANISM FOR BIDIRECTIONAL PLOUGHING EQUIPMENT **Jinbao LIU[1)] , Xuan ZHENG[*1)] , Yanhui ZHANG[2)], Yuying SONG[2)], Zhihui TANG[1)]** [1)] Xinjiang Academy of Agricultural and Reclamation Science, Shihezi, China [2)]College of Sciences, Shihezi University, Shihezi, China	599
53.	DISTRIBUTION ROUTE OPTIMIZATION FOR MULTI-VEHICLE AGRICULTURAL MATERIALS CONSIDERING CARBON EMISSION COST **Li LI [1,2)], Xuesong YANG [1)*]** [1)] School of Urban Design, Wuhan University, Wuhan, Hubei, China; [2)] Teaching Affairs Department, Hubei Engineering University, Xiaogan, Hubei, China	611
54.	AGRICULTURAL UAV CROP SPRAYING PATH PLANNING BASED ON PSO-A* ALGORITHM **Lijuan FAN** Xinxiang Vocational and Technical College, Xinxiang, Henan, China	625
55.	CONSTRUCTION AND EVALUATION OF SIMULATION MODEL FOR THE GROWTH AND DEVELOPMENT OF MILLET IN ARID AREAS **Yuzhi WANG [1)], Yaoyu LI [1)], Tengteng QU [1)], Siyu WANG [1)], Lili SUN [2)], Wuping ZHANG [1*)], Fuzhong LI [1*)]** [1)] College of Software, Shanxi Agricultural University, Taigu, Shanxi / China [2)] College of Agricultural Engineering, Shanxi Agricultural University, Taigu, Shanxi / China	637
56.	TOWARDS SUSTAINABLE SUBSISTENCE AGRICULTURE IN ROMANIA WITH LOW-COST IoT MODULES AND SOLUTIONS – PROOF OF CONCEPT **Ştefania-Adriana HOŢEI[1)], Cristina Ioana MARGHESCU[2*)], Rodica Cristina NEGROIU[2)], Andrei DRUMEA[2)]** [1)] Faculty of Electronics, Telecommunication and Information Technology, National University of Science and Technology POLITEHNICA of Bucharest; [2)] Electronic Technology and Reliability Department, Faculty of Electronics, Telecommunication and Information Technology, N.U.S.T. POLITEHNICA of Bucharest / Romania	647

		Page(s)
57.	EFFECT OF LOW-VOLTAGE -ELECTROSTATIC-FIELD (LVEF) ASSISTING REFRIGERATION ON PRESERVATION QUALITY OF STRAWBERRY **Huaming HOU[1,2,3], Shuai CUI[1], Dengming LI[1], Zhigang LI [1], Yisheng CHEN *[1]** [1] College of Food Science and Engineering, Shanxi Agricultural University, Taigu / China; [2] College of Agricultural Engineering, Shanxi Agricultural University, Taigu / China; [3] Dryland Farm Machinery Key Technology and Equipment Key Laboratory of Shanxi Province, Taigu / China	657
58.	ESTIMATION OF THE RANDOM INTENSITY OF THE SOIL TILLAGE DRAFT FORCES IN THE SUPPORTS OF THE WORKING BODIES OF A CULTIVATOR **Petru CARDEI[1], Nicolae CONSTANTIN[1], Vergil MURARU[1], Catalin PERSU[1], Raluca SFIRU *[1], Daniel LATEŞ[2]** [1] INMA Bucharest / Romania; [2] "George Emil Palade" University of Medicine, Pharmacy, Sciences and Technology from Târgu Mureș / Romania	667
59.	RESEARCH ON THE PROCESS OF OBTAINING BUTTER IN LABORATORY CONDITIONS **Iuliana STANA[1], Paula TUDOR*[1], Alexandru CIRIC*[1], Mihaela BEGEA*[1], Gheorghe VOICU*[1], Vasilica STEFAN[2]** [1] National University of Science and Technology Politehnica Bucharest, Faculty of Biotechnical Systems Engineering / Romania; [2] INMA Bucharest / Romania	681
60.	DESIGN AND EXPERIMENTAL OPTIMIZATION OF ROTARY CUTTING SAFFLOWER HARVESTING END EFFECTOR **Puhang LI, Xinyue ZHANG, Hao ZHANG, Zeyu WANG, Shiwei WEN, Jun CHEN*** College of Mechanical and Electronic Engineering, Northwest A&F University, Yangling /China	690
61.	THE EVOLUTION OF ROMANIAN AGRICULTURE MECHANIZATION DEGREE **Ancuta MARIN, Vili DRAGOMIR*, Ruxandra POP, Marian BUTU** Institute of Research for Agriculture Economy and Rural Development, Bucharest / Romania	703
62.	MECHANICAL PROPERTIES AND CONSTRUCTION OF CONSTITUTIVE MODEL FOR COMPRESSION AND STRESS RELAXATION OF CATTLE MANURE **Weisong ZHAO[1,3], Yongsheng CHEN[1,3], Weiqiang LIN[2], Zhenwei WANG[1,3], Qimin GAO[1], Hu XIE[1], Biao MA[1], Mingjiang CHEN*[1], Jingjing FU*[1,3]** [1] Nanjing Institute of Agricultural Mechanization, Ministry of Agriculture and Rural Affairs, Nanjing, China; [2] Zhongnong Guoke (Nanjing) Planning and Design Co., Ltd，Nanjing, China; [3] Western Research Institute, CAAS, Changji, China	713
63.	STUDY ON THE CHARACTERISTICS OF *CERASUS HUMILIS* FREE FALLING IMPACT **Shilei KANG[1,2], Yanshun XU[1], Jingpu ZHOU[1], Bin TONG[1], Junlin HE*[1,2]** [1]College of Agricultural Engineering, Shanxi Agricultural University, Taigu, China; [2]Dryland Farm Machinery Key Technology and Equipment Key Laboratory of Shanxi Province, Taigu, China	725
64.	DESIGN AND EXPERIMENT OF IMPELLER TYPE VARIABLE FERTILIZER DISCHARGER BASED ON EDEM SIMULATION **Bai-wei Wang [1,2], Gang Che*[1,2], Lin Wan *[1,2], Nai-chen Zhao [1], Zhan-nan Guan [1]** [1]College of Engineering, Heilongjiang Bayi Agricultural University, Daqing / P.R.China [2]Key Laboratory of Intelligent Agricultural Machinery Equipment in Heilongjiang Province, Daqing / P.R.China	734
65.	RESEARCH ON SEMANTIC SEGMENTATION OF GREENHOUSE ROAD IMAGE **YongZheng YANG, HongBo WANG*, ZhiCheng XIE, JunMao LI, ZiLu HUANG** College of Mechanical and Electronic Engineering, Inner Mongolia Agricultural University, Hohhot / China	745
66.	DESIGN AND SIMULATION OF THREE-DEGREE-OF-FREEDOM WRIST STRUCTURE OF PICKING MANIPULATOR **Junhui SUN [1], Jinliang GONG [2*], Yanfei ZHANG [1*]** [1]School of Agricultural Engineering and Food Science, Shandong University of Technology, Zibo/China [2]School of Mechanical Engineering, Shandong University of Technology, Zibo/China	755
67.	CLOUD-SIDE COLLABORATION-BASED TASK ALLOCATION STRATEGY FOR AGRICULTURAL MACHINE FLEET **Junzheng ZHAO[1], Jinliang GONG [2*], Yanfei ZHANG[1*]** [1]School of Agricultural Engineering and Food Science, Shandong University of Technology, Zibo/China [2]School of Mechanical Engineering, Shandong University of Technology, Zibo/China	765
68.	VIBRATION ASSESSMENT OF TRACTOR OPERATOR BASED ON VIBRATION SIGNALS **Christos I. DIMITRIADIS*[1], Dimitrios KATERIS[2], Panagiotis XYRADAKIS[3], Aspasia GIALAMA[4], Theodoros GIALAMAS[4]** [1] International Hellenic University, Thessaloniki, Greece; [2] Institute for Bio-Economy and Agri-Technology (iBO), Thessaloniki, Greece; [3] University of Thessaly, Volos, Greece; [4] Department of Agriculture – Agrotechnology, University of Thessaly, Larissa, Greece	776
69.	STUDY OF THE KEY COMPONENT PARAMETERS OF THE WINGED CHISEL PLOW ON SOIL-STRAW DISTURBANCE PATTERN **Kun CHEN[1], Xianliang WANG*[1], Xiangcai ZHANG, Xiupei CHENG[1], Hua ZHOU[1], Zhongcai WEI[1], Lei LIU[1], Mingyue BAI[1], Shang GAO[1],** [1]School of Agricultural Engineering and Food Science, Shandong University of Technology, Zibo, China	785

		Page(s)
70.	USING STATISTICAL ANALYSIS TO ASSESS THE EFFECTS OF FEEDING PELLETS ON FISH DIETARY PREFERENCES IN AN INTENSIVE POLYCULTURE SYSTEM **Iulian VOICEA[1)], Petru CÂRDEI [1)], Vlad-Nicolae ARSENOAIA [2)], Nicoleta UNGUREANU [3)], Florin NENCIU [1)], Nicoleta VANGHELE *[1)]** [1)] INMA Bucharest, Romania; [2)] "Ion Ionescu de la Brad" University of Agricultural Sciences and Veterinary Medicine, Iasi, Romania; [3)] National University of Science and Technology "POLITEHNICA" Bucharest, Romania	798
71.	RESEARCH ON DETACHMENT PROCESS AND SEPARATION OF FROZEN SEA-BUCKTHORN FRUITS FROM BRANCHES **Radu CIUPERCĂ[1*)], Ana ZAICA[1)], Vasilica STEFAN[1)], Petruţa-PETCU[2)], Lucian DUMITRESCU[3)], Oana Cristea[1)]** [1)]National Institute of Research- Development for Machines and Installations for Agriculture and Food Industry - INMA Bucharest/ Romania; [2)] National University of Science and Technology "POLITEHNICA" of Bucharest, Faculty of Aerospace Engineering / Romania; [3)] ICDIMPH HORTING Bucharest/Romania	808
72.	INVESTIGATION OF THE ENERGY INDICATORS FOR THE SURFACE TILLAGE OF SOIL BY A HARROW WITH A SCREW-TYPE WORKING BODY **Volodymyr BULGAKOV[1)], Hryhorij KALETNIK[2)], Oleksandra TROKHANIAK[1)], Svitlana LUTKOVSKA[2)], Mykola KLENDII[3)], Semjons IVANOVS[4)], Lucretia POPA[5)], Vitalii YAROPUD[2)]** [1)]National University of Life and Environmental Sciences of Ukraine; [2)]Vinnytsia National Agrarian University, Ukraine; [3)]Separated Subdivision of National University of Life and Environmental Sciences of Ukraine, Berezhany Agrotechnical Institute, Ukraine; [4)]Latvia University of Life Sciences and Technologies, Latvia; [5)] INMA Bucharest / Romania	818
73.	DESIGN AND TEST OF HIGH-SPEED FERTILIZER POINT-APPLIED DEVICE **Xin DU, Tong WANG, Shufa CHEN, Qixin SUN, Zhihao XU, Changqing LIU*** School of Mechanical Engineering, Jiangsu Ocean University, Lianyungang / China	834
74.	CONSIDERATIONS REGARDING THE EFFECTS OF SHOCKS AND VIBRATIONS ON OPERATORS OF SELF-PROPELLED AGRICULTURAL EQUIPMENT **Valentin VLĂDUŢ[1)], Sorin-Ștefan BIRIŞ[2)], Gigel PARASCHIV [2)], Nicoleta UNGUREANU[2*)], Sorin Tiberiu BUNGESCU[3)], Iulian VOICEA[1)], Dan CUJBESCU[1)], Iuliana GĂGEANU[1)], Evelin LAZA[1)], Lorena-Diana POPA[4)], Gheorghe MATEI[5)], Atanas ATANASOV[6)]** [1)]INMA Bucharest / Romania; [2)]NUST Politehnica Bucharest / Romania; [3)]USV "King Mihai I" Timişoara / Romania; [4)]ARDS Secuieni / Romania; [5)]University of Craiova / Romania; [6)]University of Ruse / Bulgaria	843
75.	STUDIES ON THE DEVELOPMENT OF A RELIABILITY DIAGNOSIS FOR AGRICULTURAL TRACTORS GEARBOXES **Alexandru-Vlad HELLER *); Nicolae FILIP; Teodora DEAC** Technical University of Cluj-Napoca, Department of Road Vehicles and Transport, Cluj-Napoca / Romania	857
76.	THE RELATIONSHIP BETWEEN ENVIRONMENTAL PUBLIC PERCEPTION AND GREEN PRODUCT TRADE. THE MODERATING ROLE OF POLICIES AND LEGAL TEXT **Guoli HAN *[1)]; Shuming MA [2)]** [1)] College of Humanity and Law, Xinxiang Institute of Engineering, Xinxiang, Henan / China; [2)] Commercial College, Henan Normal University, Xinxiang, Henan / China	865
77.	ROMANIAN BIOMASS PELLET MARKET – TECHNO-ECONOMIC ANALYSIS **Georgiana MOICEANU[1)], Mirela - Nicoleta DINCĂ*[1)], Mihai CHIȚOIU[2)], Gigel PARASCHIV[1)], Oana-Diana CRISTEA[3)]** [1)] National University of Science and Technology POLITEHNICA Bucharest / Romania; [2)] CENIT SRL / Romania; [3)] National Institute for Research-Development of Machines and Installations Designed for Agriculture and Food Industry – INMA Bucharest/ Romania	882
78.	EXPERIMENTAL RESEARCH ON REED HARVESTING WITH "ERBA" ELECTRIC BOAT **Vasilica ȘTEFAN[1)], Radu CIUPERCĂ[1)], Emil TUDOR[2)], Mihai MATACHE[1)], Ionuț VASILE[2)], Ion Cătălin SBURLAN[2)], Ana ZAICA[1)]** [1)] INMA Bucharest/ Romania; [2)] National Institute for Research and Development in Electrical Engineering, ICPE-CA Bucharest, Romania	891

THE PECULIARITIES OF SEEDS AND THE QUALITY OF THE GREEN MASS OF SOME NON-TRADITIONAL CROPS IN THE REPUBLIC OF MOLDOVA
/
PARTICULARITĂŢILE SEMINȚELOR ŞI CALITATEA MASEI VERZI LA UNELE CULTURI NETRADIȚIONALE ÎN REPUBLICA MOLDOVA

Valerian CEREMPEI[1)], Victor ȚÎȚEI[2)], Nicolae-Valentin VLĂDUT[3)], Oana-Diana CRISTEA[*3)]

[1)] Technical University of Moldova, Chisinau/ Republic of Moldova;

[2)] „Alexandru Ciubotaru" National Botanical Garden (Institute) of Moldova State University, Chisinau/ Republic of Moldova;

[3)] INMA Bucharest/ Romania;

*Tel.: 0761052624, *E-mail: diana10.cristea@gmail.com*

DOI: https://doi.org/10.35633/inmateh-71-01

Keywords: *biochemical methane potential, green mass, non-traditional crops, nutritive value, seed peculiarities*

ABSTRACT

The article presents the results of the studies on the peculiarities of the seeds and the quality indices of the green mass, obtained from the non-traditional crops Amaranthus hypochondriacus, Raphanus sativus var. olifera, Sinapsis alba, Linum usitatissimum, Sesamum indicum and the hybrid Rumex tianschanicus × Rumex patientia. The results reflect the values of dimensional parameters, friability, seed structure and quality indices of the harvested green mass (nutritive value, biochemical potential to obtain biomethane). It has been demonstrated that the criterion of dimensional proportionality K_{dp}, used in the present research, shows the real structure of the seeds. The harvested green mass from non-traditional crops has the optimal content of protein and carbohydrates for animal feed and biomethane production.

REZUMAT

Sunt prezentate rezultatele studiilor privind particularitățile semințelor și indicilor de calitate a masei vegetale, obținute din culturi de plante netradiţionale în Republica Moldova: Amaranthus hypochondriacus, Raphanus sativus, Sinapis alba, Linum usitatissimum, Sesamum indicum, hibridul Rumex patientia. Rezultatele obținute reflectă valorile parametrilor dimensionali, de friabilitate, de structură a semințelor și indicii de calitate a masei verzi recoltate (valoarea nutritivă, potențialul biochimic de obținere a biometanului). S-a demonstrat că criteriul de proporționalitate dimensională K_{dp}, utilizat în prezenta lucrare, redă structura reală. Masa recoltată din culturi de plante netradiţionale investigate are conținutul optim de substanțe proteice și carbohidrați necesari pentru alimentația animalelor și producerea biometanului.

INTRODUCTION

According to the information presented by specialized international organizations (*U.S. Census Bureau, 2023; U.S. Energy Information Administration, 2023; United Nations, 2023),* in 1950, world population reached 2.5 billion people, over fifty years – in 1999 – 5.98 billion (population growth rate in the period 1950-1999: 69.6 million/year). In August 2023, Earth's population is estimated at 7.99 billion *(population growth rate in the period 2000-08.2023: 85.5 million/year).* According to the above-mentioned sources, the global population is expected to keep growing, reaching 8.9÷9.55 billion in 2050 (the average expected growth rate in 08.2023-2050: 48.5 million/year). Simultaneously with population growth, the total energy consumption has also increased. In 1950-1999, the world population increased 2.4 times, but energy consumption increased 4 times. At the same time, during the mentioned period, the production of cereals increased 3 times and the indicators of economic development increased 5 times (*International Energy Agency, 2023; United Nations, 2023; FAO, 2016*). The analysis of statistical data and the forecast of the development of human society prove that the world population is constantly rising, requiring urgent measures to maintain the quality of people's lives.

Managing these interdependent trends in the development of human society is possible only by strengthening food and energy security, as well as by improving the ecological situation. The studies carried out demonstrate, that the achievement of these complex objectives of vital importance in the development of human society can be achieved by protecting biodiversity, mobilizing plant genetic resources, making use of the fodder and energy potential of non-traditional plants and implementing them in the bioeconomic circuit (*FAO, 2016; Bojariu et al., 2021; Cerempei, 2016; Kshnikatkina et al., 2005; Rakhmetov, 2011, 2018; Roman et al., 2016; Țiței, 2015, 2020b, 2023; Țiței and Roșca, 2021; Teleuţă and Ţîţei, 2016; Von Cossel, 2019)*.

In the Republic of Moldova and in other countries, theoretical and practical results have been achieved on implementing the potential of non-traditional plants of several botanical families, including the following *Asteraceae* (*Cynara cardunculus, Silphium perfoliatum*), *Fabaceae* (*Galega orientalis*, *Onobrychis arenaria*), *Hydrophylaceae* (*Phacelia tanacetifolia*), *Malvaceae* (*Malva crispa*, *Sida hermaphrodita*), *Poaceae* (*Pennisetum glaucum, Sorghum almum*). These results indicate, in particular, the physico-chemical and technological properties of the seeds and the green mass of these plants (*Cerempei et al., 2022, 2023; Coşman et al., 2017; Cumplido-Marin et al., 2020; Kaliniewicz, et al., 2015; Peni et al., 2020; Rakhmetov, 2011, 2018; Schäfer et al., 2017; Teleuţă and Ţîţei, 2016; Von Cossel, 2019; Zarczynski et al., 2021*).

The analysis of the situation in the given field of research demonstrates that it is possible, under the soil-climatic conditions of the Republic of Moldova, to make full use of the potential of a number of non-traditional plants from the families *Amaranthaceae, Brassicaceae, Linaceae, Pedaliaceae, Polygonaceae*, which are studied to a lesser extent by the international scientific community *(Abbasi et al., 2018; Alekksha Kudos, Chandan, 2018; Amorim et al., 2019; Biel et al., 2017; Bhat et al., 2018; Das, 2016; Elleuch et al., 2007; Gautam et al., 2016; Herrmann et al., 2016; Kshnikatkina et al., 2005; Kukusheva and Stepanov, 2016; Mursec et al., 2009; Peiretti, 2018; Póti et al., 2014; Rahnama, Safaeie, 2017; Rakhmetov, 2011, 2018; Rakhmetov and Rakhmetova, 2006; 2011; Rakhmetov et al., 2004; Seppälä, 2013; Słomka and Wójcik Oliveira, 2021; Ustak et al., 2011; Uteush, 1990; Von Cossel, 2019)* and the one from the Republic of Moldova *(Chisnicean et al., 2011; Teleuţă and Ţîţei, 2016; Teleuță et al., 2008; Țîței, 2015, 2020, 2023; Țîței and Roșca, 2021; Teleuţă and Ţîţei, 2016).*

Therefore, the goal of our work has been to contribute to the exploitation of the fodder and energy biomass potential of the non-traditional plant species from the families *Amaranthaceae, Brassicaceae, Linaceae, Pedaliaceae, Polygonaceae* by conducting studies on the seed peculiarities and the quality indices of the phytomass produced from these species under the conditions of the Republic of Moldova.

MATERIALS AND METHODS

To achieve the goal, the following objectives were set:

1. To measure the physical-mechanical and technological features of seeds;
2. To determine the biochemical composition and the nutritional value of the feed, also the biomethane potential of phytomass substrates.

Based on the goal and objectives of the research, the following species from the collections "Alexandru Ciubotaru" National Botanical Garden (Institute) of Moldova State University, Chisinau were studied.

The seeds and the phytomass collected from taxa of the following families served as research objects:

A. *Amaranthaceae* (*Amaranthus sp.,* prince's-feather *Amaranthus hypochondriacus);*
B. *Brassicaceae (*fodder radish *Raphanus sativus* var. *oleifera,* white mustard *Sinapis alba);*
C. *Linaceae (*flax *Linum usitatissimum);*
D. *Pedaliaceae (*sesame *Sesamum indicum);*
E. *Polygonaceae (*hybrid sorrel *Rumex tianschanicus*× *Rumex patientia);*
F. *Fabaceae* (alfalfa *Medicago sativa* – control).

Methods of measuring the physico-mechanical properties of seeds

It is known that the correct selection of parameters for facilities, machines and equipment, as well as operating regimes of technological processes in the agri-food sector largely depends on the dimensional characteristics and morphological structure of the seeds (*Ene and Mocanu, 2016; Matei and Feher, 2010*).

As dimensional parameters, the length *L*, the width *W* and the thickness *T* of seeds were considered, being measured according to the recommendations ((*Mohsenin, 2020*) using a mechanical calliper ST-I-125-0.05 (GOST 166-89) with the error limit ± 0.05 mm. The accuracy of the results was ensured by measuring, for each plant species, at least 25 grains taken from the average sample, sampled at predetermined intervals by the four-quarter method.

The determined values of the dimensional parameters (length *L*, the width *W* and the thickness *T*) of seeds, served as a basis for calculating their geometric parameters:

- geometric mean diameter

$$D_g = (LWT)^{1/3}, \text{ [mm]} \quad (1)$$

- sphericity

$$S = (D_g/L) \times 100, \text{ [\%]} \quad (2)$$

Along with the geometrical parameters D_g, S, calculated according to the formulas (1, 2), it was elaborated and applied, for a more detailed appreciation of the shape of the seeds, the criterion of dimensional proportionality K_{dp}, which was determined based on the ratio of the main dimensions L, W, T:

$$K_{dp}=(L/T)/(W/T)/(T/T) = (L/T)/(W/T)/1 \quad (3)$$

The morphological structure of the seeds was established based on the objective parameters, taking into account the calculated values of the K_{dp} criterion and the requirements of the classification, which divides the seeds into 5 distinct types, resulting from the relationships of the L, W, T parameters of seeds, which are specific for each type:

1. *Spheroidal*, which have almost equal values of seed dimensions
$L \backsimeq W \backsimeq T$, characteristic of peas, soybeans, etc.;
2. *Flattened*: seed width is approximately equal to the length, and the thickness index is much smaller
$L \backsimeq W >> T$ (lentil);
3. *Elliptical*: the thickness and the width are equal, while the length is bigger $L > W \backsimeq T$ (legumes);
4. *Elongated*: all the dimensions differ from each other, with length having the greatest value:
$L >> W \neq T$ (cereals);
5. *Pyramidal*: with triangular sides (buckwheat).

The friability (flow capacity) of seeds was evaluated based on a detailed study, which included measuring the values of the angle of repose α and of the flow angle α_1 on surfaces of different materials (steel, wood, enamel). In order to make sure that the results of measuring seed friability were accurate, the values of angle α were determined by 2 methods:

1. *The general method*, which is currently widely used by researchers (*Ene and Mocanu, 2016; Alekksha Kudos and Chandan, 2018; Cerempei et al., 2023*). In this case, this method was implemented by pouring the seeds through a funnel and letting them fall freely on a horizontal surface, thus forming a conical pile of seeds.
2. *The local method* was proposed and used in the present work, by applying the digital inclinometer on the tilted surface of the cone of seeds formed by free flow.

To form a conical seed pile, samples were taken from the majority fractions obtained after sieving. The volume of samples varied between 200 and 250 ml. The following instruments were used for the measurements: general method - depth calliper SG 0-250, instrumental ruler 0-400 mm; b) local method - digital inclinometer 360° with accuracy ± 0.2°. The measurement of the angle α was performed by the local method, by applying successively the inclinometer on 4 cone generators, in 2 perpendicular planes. To apply the general method, the parameters of the cone were measured in 2 perpendicular planes – the height h and the diameter of the base D. The value of the angle of repose was calculated according to the following formula:

$$\text{tg } \alpha = 2h \cdot D^{-1} \quad (4)$$

The second criterion of seed friability, the flow angle α_1, was determined using a table with a vertically rotating upper surface. On the rotating surface of the table, plates made of steel 10 with low carbon content, GOST 16 523-97, C10, EN 10083-2:2006, enamelled steel and wood, were fixed successively. The flow angle α_1 was determined by applying the digital inclinometer when the seeds started moving on the inclined surface. To verify the accuracy of the results of measuring the friability parameters, the measurements were repeated as follows: when determining the values of the angle α, experiments were repeated 10 times, and for the angle α_1 – 5 times. The obtained results allowed the calculation of statistical parameters: the confidence interval and the standard deviation.

The detailed description of the methods and materials used in measuring the physical-mechanical and technological properties of the seeds (dimensional parameters, friability etc.) is given in the paper (*Cerempei et al., 2022*). The results of measurements were processed by applying the facilities of the MATHLAB and Microsoft Office Excel programs.

Methods of evaluation of the biochemical composition, nutritional value of feed and biomethane production potential

The green mass from non-traditional plant species was harvested in the budding - flowering stage, the control variant *Medicago sativa* in second growing seasons from for the first cut. For biochemical analyses, the harvested whole plants were cut into small pieces and dried in an oven with forced ventilation at a temperature of 60°C, at the end of the fixation, the biological material was finely ground in a laboratory ball mill.

The dry matter (*DM*) or total solid (*TS*) content was detected by drying samples up to constant weight at 105°C, crude protein (*CP*) – by Kjeldahl method; crude fat (*EE*) – by Soxhlet method, crude cellulose (*CF*) – by Van Soest method; ash – in muffle furnace at 550°C, nitrogen-free extract *(NFE*) was mathematically appreciated. The calcium (Ca) concentration of the samples was determined by using atomic absorption spectrometry method, phosphorus (P) concentration – by spectrophotometric method.

The gross energy (*GE*), metabolizable energy (*ME*), net energy for lactation (NEl) were calculated according to standard procedures:

$$GE = 23.9 \times CP + 39.8 \times EE + 20.1 \times CF + 17.5 \times NFE \quad (5)$$

$$ME = 14.07 + 0.0206 \times EE - 0.0147 \times CF - 0.0114 \times CP \quad (6)$$

$$NEl = 9.10 + 0.0098 \times EE - 0.0109 \times CF - 0.073 \times CP \quad (7)$$

where: *CP* is the crude protein, [g/kg]**;**
CF is the crude fibre, [g/kg];
EE is the crude fat, [g/kg];
NFE is the nitrogen-free extract, [g/kg].

The carbon (C) content of the substrates was calculated using an empirical equation indicated by *Badger et al. (1979)*:

$$C = OM/1.8 \quad (8)$$

where *OM* is the organic matter [g/kg].

The biogas (*BP*) and the biomethane potential (*MP*), litre per kg of organic dry matter, were calculated using the gas forming potential of nutrients according to Baserga (1998), corrected by the nutrient digestibility:

$$BP = 1250 \times DEE + 700 \times DP + 790 \times DCH \quad (9)$$

$$MP = 850 \times DEE + 490 \times DP + 395 \times DCH \quad (10)$$

where *DEE* is the digestible fats, [g/kg];
DP is the digestible protein, [g/kg];
DCH is digestible carbohydrates, [g/kg].

RESULTS

Physico-mechanical properties of seeds. The results of the investigations demonstrate that the studied seeds have different dimensional characteristics and morphological structure, geometric mean diameter varying in a limited range: from the minimal value D_g=0.68 mm in *Amaranthus* seeds, to maximal values D_g=2.59 mm in the seeds of radish *Raphanus sativus.* The seeds of alfalfa (control crop) from the family Fabaceae have the following dimensional characteristics (Table 1): *LWT*=2.17×1.2×1.07 mm (D_g=1.48 mm). In the case of alfalfa seeds (*S*=68.2%) the criterion of dimensional proportionality (K_{dp}=2.03/1.12/1) has values that show convincingly that these seeds belong to the type 3. *Elliptical* (*L*>*W*≃*T*), which is common for legume crops. The seeds of the Brassicaceae family have the same morphological structure, *Elliptical*: the white mustard *Sinapis alba* with the dimensional characteristics *LWT*=1.98×1.67×1.67 mm (D_g=1.77 mm) and radish *Raphanus sativus* – *LWT*= 3.50×2.43×2.05 mm (D_g=2.59 mm). The seeds of the three species mentioned above, of the families *Fabaceae* and *Brassicaceae* are named in the preceding text with increasing sizes: from the value D_g=1.48 mm (alfalfa seeds) to D_g=2.59 mm (radish seeds).

The values of the criterion of dimensional proportionality K_{dp}=1.19/1/1 of white mustard (*S*=89.4%) and K_{dp}=1.71/1.19/1 of fodder radish (*S*=74.0%) serve as evidence that the seeds of the species of the *Brassicaceae* family have an *Elliptical* structure. It is important that the more the values of the component elements in the proposed criterion approach the value equal to one (K_{dp}→1/1/1) the more the values of sphericity *S* approach 100%, close to the spherical shape. This phenomenon indicates the fact that the appropriate K_{dp} dimensional proportionality criterion reflects the morphological structure of the seeds.

The analysis of the outward appearance of the seeds of the families *Fabaceae* and *Brassicaceae* (Fig. 1, a-c) confirms the veracity of the conclusions made based on the dimensional characteristics of *LWT*, *S* and K_{dp}. The seeds of alfalfa and white mustard have a smooth integument (Fig. 1, a, b), and on the seeds of fodder radish, longitudinal grooves are observed.

The seeds of the *Amaranthaceae* family are *1. Spheroidal* in shape with the following dimensional characteristics (Table 1): *Amaranthus*- *LWT*=0.68×0.68×0.68 mm (D_g=0.68 mm) and white amaranthus – *LWT*=1.0×1.0×1.0 mm (D_g=1.0 mm). It is natural that in seeds of both species the criteria of proportionality and sphericity have equal values: K_{dp}=1/1/1 and *S*=100%. The integument of the above-mentioned seeds is smooth (Fig. 1, d).

Table 1

The values of the dimensional parameters of the seeds

Families, species	Dimensional parameters			Criterion K_{dp}	Geometric parameters	
	L	*W*	*T*		D_g	*S*
	[mm]				[mm]	[%]
Fabaceae						
Medicago sativa (control)	2.17± 0.10	1.20±0.06	1.07 ± 0.06	2.03/1.12/1	1.48	68.2
Amaranthaceae						
Amaranthus sp.	0.68 ±0.06	0.68 ±0.06	0.68 ±0.06	1/1/1	0.68	100
Amaranthus hypochondriacus	1.00±0.08	1.00±0.08	1.00±0.08	1/1/1	1.00	100
Brassicaceae						
Raphanus sativus var. oleifera	3.50±0.24	2.43±0.21	2.05± 0.04	1.71/1.19/1	2.59	74.0
Sinapis alba	1.98±0.11	1.67±0.03	1.67±0.03	1.19/1/1	1.77	89.4
Linaceae						
Linum usitatissimum	4.08±0.07	2.0±0.08	0.65±0.08	6.28/3.08/1	1.74	42.7
Pedaliaceae						
Sesamum indicum	2.97±0.04	1.38±0.07	0.5± 0.1	5.94/2.76/1	1.27	42.8
Polygonaceae						
Rumex tianschanicus × Rumex patientia	3.1±0.28	1.72±0.25	1.72± 0.26	1.8/1/1	2.09	67.4

The dimensional characteristics of the seeds of the *Pedaliaceae* and *Linaceae* families have the following values (Table 1): sesame – *LWT*=2.97×1.38×0.5 mm (D_g=1.27 mm) and flax – *LWT*=4.08×2.0×0.65 mm (D_g=1.74 mm), respectively. Seeds from both families demonstrated similar values of proportionality criterion and sphericity: sesame – K_{dp}=5.94/2.76/1, *S*= 42.8% and flax – K_{dp}=6.28/3.08/1, *S*= 42.7%, respectively.

The analysis of the geometric parameters and the external shape (Fig. 1, e, f) demonstrates that the sesame and flax seeds belong to type 4. *Elongated (L>>W≠T)* according to their morphological structure. The integument of these seeds is smooth.

The analysis of the properties of the seeds of the representative of the family *Polygonaceae*, *Rumex tianschanicus* × *Rumex patientia*, resulted in obtaining the following dimensional characteristics: *LWT*=3.1×1.72×1.72mm (D_g=2.09mm). The particularity of these seeds consists in the fact that they have the shape of type 5. *Pyramidal*, which can be seen from the joint analysis of the values of the proportionality criterion (K_{dp}=1.8/1/1) and the external shape of these seeds (Fig.1, g).

In our previous research *(Cerempei et al., 2022)* it has been established that a range of factors influence the flow ability of the seeds: a) the particularities of the seeds (size and morphological structure, integument surface condition, humidity and physical purity); b) the condition of the working surface of the machine on which the seeds flow (material, roughness).

The highest flow capacity is characteristic of the seeds with a shape close to the spherical one (type 1), with a smooth surface of the integument, low humidity and with a small number of impurities. The studied seeds from the six families (Table 2) were conditioned at the initial stage according to humidity U and physical purity *P*. Surfaces on which the flow angle α_1 was studied were identical for all seeds: steel C10, wood, enamel.

That is why the friability of the seeds (values of the angles α and α_1) was studied according to the morphological structure and the state of the surface of their integument.

As mentioned in the research methodology, the angle of repose α was measured by two methods: general and local. Because there is a relatively small difference between the values of the angle α, determined by the general and the local methods (Table 2), in the following will be used the average value of the angle α to simplify the analysis of the friability of the seeds, and, if necessary, will be used the α values obtained by both methods.



Fig. 1 - The images of the studied seeds
a) Medicago sativa; b) Sinapsis alba; c) Raphanus sativus; d) Amaranthus hypochondriacus; e) Sesamum indicum; f) Linum usitatissimum; g) Rumex tianschanicus × Rumex patientia.

In the *Fabaceae* family, alfalfa seeds, the control, had the following values of friability (Table 2): the angle of repose α=30.9° and flow angle α_1=27.3° (on steel), α_1=33.6° (on wood), α_1=26.7° (on enamelled surface). The alfalfa seeds were chosen as control in our studies because, in the specialized literature, there are many sources of information regarding the friability of these seeds. For example, according to one source (*Togo et al., 2018*), for alfalfa seeds, the angle of repose varies in the range α=27.05°-33.21°.

The seeds of non-traditional plant species in the Republic of Moldova had, in most cases, higher flow capacity than alfalfa seeds. The seeds with the highest friability are from the families *Linaceae* (flax) and *Amaranthaceae* (*Amaranthus*, white amaranthus). As a result of the measurements, the following parameters were identified for flax seeds (the angle of repose α=21.9° and flow angle: on steel- α_1= 19.0°, on wood- α_1= 20.4°, on enamelled surface– α_1=19.7°), for *Amaranthus* seeds (the angle of repose α=22.3° and flow angle: on steel- α_1= 19.7°, on wood- α_1= 22.8°, on enamelled surface – α_1=20.7°) and white amaranthus seeds (the angle of repose α=24.6° and flow angle: on steel- α_1= 22.9°, on wood- α_1= 27.2°, on enamelled surface – α_1=26.1°).

The high level of friability of flax seeds (type 4. *Elongated*) is due to the outer surface that is smooth, shiny and with little roughness *(Fig.1, f),* and – of the seeds of the Amaranthaceae family (*Amaranthus*, white amaranthus) – due to the morphological structure 1. *Spheroidal* (*Table 1; Fig.1, d)*. The seeds of representatives of other three families *Brassicaceae* (fodder radish, white mustard), *Pedaliaceae* (sesame) and *Polygonaceae* (the hybrid *Rumex tianschanicus*× *R. patientia*) had values of the angle of repose α and flow angle α_1 in the range of the respective angles for the seeds of alfalfa and the seeds of the families *Linaceae*, *Amaranthaceae*: the angle of repose α=24.15°- 28.2° and flow angle on steel α_1= 21.3°- 27.0°, on wood α_1= 26.0°- 31.6°, on enamelled surface α_1=22.7°- 28.2°. The highest flow capacities on the studied surfaces (steel, wood, enamel) are characteristic of the fodder radish seeds that have the 3. *Elliptical* type structure (Fig.1, c) and geometric mean diameter with the highest value D_g= 2.59 mm.

Table 2

Values of seed friability parameters

Families, species	Angle of repose α, methods			Flow angle α_1, surfaces		
	general	local	average	steel	wood	enamel
	[degrees]			[degrees]		
Fabaceae						
Medicago sativa	30.2±0.3	31.5±0.4	30.9	27.3 ± 0.4	33.6 ± 0.9	26.7 ± 0.2
Amaranthaceae						
Amaranthus sp.	20.6±0.5	24.0±1.0	22.3	19.7±0.4	22,8±0,2	20,7±0,3
Amaranthus hypochondriacus	24.1±0.1	25.1±0.9	24.6	22.9±0.3	27,2±0,8	26,1±0,1
Brassicaceae						
Raphanus sativus *var. oleifera*	27.4±0.4	28.9±1.6	28.2	21.3±0.3	26.0±0.8	22.7±0.2
Sinapsis alba	25.3±0.5	29.3±1.3	27.3	22.0±0.6	27.4±1.5	24.7±0.3
Linaceae						
Linum usitatissimum	20.0 ±0.45	23.8±0.7	21.9	19.0±0,1	20.4±0,3	19.7±0.25
Pedaliaceae						
Sesamum indicum	24.0± 0.3	24.3±1.1	24.15	27.0± 0,8	31.6±0,4	28.2± 0.5
Polygonaceae						
Rumex tianschanicus × Rumex ***patientia***	27.3±1.0	29.0±1.1	28.2	23.0±0,1	31.2±0,8	27.4±0.6

The results of the measurements (Table 2) indicate that in the studied seeds, usually, the coefficient of internal friction between the seeds f_i, characterized by angle of repose α, has higher values than the coefficient of external friction f_e between the seeds and the sliding surface, characterized by flow angle α_1, that is $\alpha > \alpha_1$. The exception is mainly the values of the angle α_1 in the case of flow on a wooden surface.

Data on seeds parameters of studied botanical family are presented in other publications (*Bhat et al. 2018; Cagatay Selvi et al. 2006; Coşkuner and Karababa, 2007; Elleuch et al. 2007; Gautam et al. 2016; Kaliniewicz et al. 2015; Rakhmetov and Rakhmetova, 2006, 2011; Togo et al. 2018; Tunde-Akintunde and Akintunde, 2004; Uteush,1990*).

Biochemical composition, nutritional value of feed and biomethane production potential. The forage yield and seasonal distribution may be of great importance to the livestock breeders. Sometimes the balance of nutrients in the forage will have positive or negative effects on animal health and production indices. The quality indices of the harvested green mass from studied species, is presented in Table 3. It was found that, in forage dry matter the crude protein varied from 144.3 to 198.1 g/kg, crude fats - from 18.5 to 65.2 g/kg, crude cellulose – from 254.8 to 324.3 g/kg, nitrogen free extract - from 375.8 to 425.5 g/kg, ash - from 70.1 to 137.4 g/kg, calcium - from 6.3 to 19.0 g/kg, phosphorus - from 2.8 to 5.2 g/kg. We would like to mention that fodder from *Raphanus sativus*, hibrid *Rumex* and *Sinapis alba* was characterised by a significantly higher content of proteins, as compared with *Medicago sativa*. The concentrations of crude fats in fodder from *Sesamum indicum*, *Sinapsis alba*, *Raphanus sativus*, *Linum usitatissimum* and *Amaranthus hypochondriacus* also were very high. The level of crude cellulose in fodder from studied species is optimal and low as compared with *Medicago sativa.* The nitrogen free extract content in *Sesamum indicum, Linum usitatissimum, Amaranthus hypochondriacus* and hibrid *Rumex* fodders reached 40.00-42.55%, which were higher than in *Medicago sativa* green mass. The fodder from *Brassicaceae* species contained a low amount of nitrogen free extract. The concentrations of ash in fodder from the studied species were higher as compared with *Medicago sativa,* except *Linum usitatissimum* green mass, where this index was lower (7.01%). It was found that the concentrations of phosphorus in the investigated fodders also were significantly high.

The concentration of nutrients and their digestibility influence the energy value of fodder. It should be mentioned that the concentrations of metabolizable energy and net energy for lactation were high in fodder from studied species as compared with *Medicago sativa,* very higher energy level in fodder from *Sesamum indicum*, *Amaranthus hypochondriacus* and *Sinapis alba*.

Several literature sources describe the biochemical composition and nutritional performance of fodder from investigated species. Also, *Medvedev and Smetannikova (1981)* mentioned that nutrient content of dry matter white mustard plants was 19.8% crude protein, 2.3% crude fats, 28.1% crude cellulose, 36.6% nitrogen free extract and 13.1% ash; oil radish - 15.0-25.9% crude protein, 2.0-4.5% crude fats, 19.0-24.0% crude cellulose, 35.5-57.0% nitrogen free extract and 14.7-23.6% ash; sorrel-11.9-26.2% crude protein, 0.8-1.8% crude fats, 14.5-24.5% crude cellulose, 40.8-49.4% nitrogen free extract and 8.1-11.4% ash.

Kshnikatkina et al. (2005) reported that the dry matter from *Sinapis alba* forage 21.26-22.18% crude protein, 1.60-3.31% crude fats, 19.45- 34.00% crude cellulose, 14.82-15.80% ash, 0.58-0.90% Ca, 0.06-0.10% P, but *Raphanus sativus* -16.0-19.0% crude protein, 19.0-24.0% crude cellulose, 10.0-14.0% ash, 0.8-0.9% Ca, 0.9-1.1% P. *Póti et al. (2014)* reported that the nutritive and energy value of white mustard was 154 g/kg dry matter, 20.6% crude protein, 2.9% crude fats, 19.4% crude cellulose, 8.9% ash, 48.2% nitrogen free extract, 629 g/kg TDN, 11.61 MJ/kg DE, 9.52 MJ/kg ME and 5.88 MJ/kg net energy for maintenance, but oil radish fodder contained, respectively, 135 g/kg dry matter, 14.8% crude protein, 3.1% crude fats, 14.1% crude cellulose, 13.0% ash, 55.0% nitrogen free extract, 616 g/kg TDN, 11.31 MJ/kg DE, 9.32 MJ/kg ME and 5.70 MJ/kg net energy for maintenance.

Heuze et al. (2015), reported the average dry matter content and feed value of *Linum usitatissimum* aerial part was: 219 g/kg dry matter, 13.6% crude protein, 3.6% crude fats, 57.0% NDF, 46.7% ADF, 12.1% lignin, 6.6% ash, 65.9% DOM, 18.7 MJ/kg GE. Leukebandara et al. (2015) mentioned that the *Amaranthus hypochondriacus* plants harvested the mid-bloom stage contained 132.0 g/kg dry matter, 18.43 crude protein, 3.17% crude fats, 24.50% crude cellulose, 16.83% ash. *Țîței and Țeleuță (2015)* found that depending on cut period the dry matter content and biochemical composition of fodder from the hybrid *Rumex* was 107.5-206.7 g/kg dry matter, 9.71-24.88% crude protein, 1.03-2.86% crude fats, 15.03-44.43% crude cellulose, 6.28-15.62% ash and 36.82-41.56% nitrogen free extract, but *Medicago sativa* fodder first cut - 243.0 g/kg dry matter, 16.66% crude protein, 1.88% crude fats, 34.24% crude cellulose, 10.0% ash and 37.22% nitrogen free extract. *Biel et al. (2017)* mentioned that biochemical composition and nutritive value of *Amaranthus hypochondriacus* aerial part was 101 g/kg crude protein, 17.6 g/kg crude fats, 240 g/kg crude cellulose, 440 g/kg NDF, 332 g/kg ADF, 63.1 g/kg lignin, 269 g/kg Cel, 109 g/kg HC, 144 g/kg ash, 13.7 g/kg Ca and 6.8 g/kg P, 63.8% DMD, 10.8 MJ/kg DE and 8.7 MJ/kg ME.

Rahnama and Safaeie (2017) revealed that *Amaranthus hypochondriacus* can produce 75.86-90.30 t/ha fresh forage or 11.0-13.05 t/ha dry matter with 11.5-12.00% crude protein, 2.1-2.4% crude fats, 67.4-69.1% DMD, RFV= 157.1-171.5, RFQ =158-174.6. *Abbasi et al. (2018)* reported that harvested amaranth forage contained 233 g/kg dry matter with 18.7% crude protein, 42.0 %NDFom, 27.5 %ADFom, 4.46 %ADL, 5.7 %EE, 6.25 %WSC, 14.5 %ash, 1.11% Ca, 0.66 % P and 8.4 MJ/kg ME.

Rolinec et al. (2018) reported that hybrid sorrel Rumex OK 2 depends on growth phase contained 74.2-169.1 g/kg dry matter with 10.09-26.17% crude protein, 1.16-2.23% crude fats, 14.48-39.48% crude cellulose, 43.82-55.38% nitrogen free extract, 1.36-6.46% ash, 21.6-51.1% NDF, 17.2-45.2% ADF, 1.84-11.5% ADL, 4.4-6.0% HC, 15.3-33.7%Cel.

Amorim et al. (2018) remarked the dry matter content and chemical composition of forage from *Sesamum indicum* plans was: 233 g/kg dry matter with 11.7% crude protein, 10.54% crude fats, 6.08% ash, 56.24% NDF, 36.29% ADF, 3.14% ADL, 19.25% HC, 33.85%Cel and 56.41% TDN.

Țîței (2020a, 2022) found that biochemical composition and nutritive value of *Amaranthus hypochondriacus* whole plant was 17.2 % crude protein, 33.0 % ADF, 46.2 %NDF, 5.5 %ADL, 6.8 %TSS, 8.8 % ash, RFV = 127, 12.44 MJ/kg DE, 10.22 MJ/kg ME and 6.23 MJ/kg NEl and *Sinapis alba* whole plant respectively 18.3-22.9% crude protein, 9.2-10.9% ash, 43.9-51.8% NDF, 28.3-34.7% ADF, 4.8-5.6% ADL, 23.5-29.1 % Cel, 15.6- 17.1 % HC, 6.3-8.7% TSS, 63.3-75.9% DMD, 57.3-66.1% DOM, RFV=111-142, 12.22-13.08 MJ/kg DE, 10.03-10.74 MJ/kg ME and 6.04- 6.77 MJ/kg NEl.

Table 3

Biochemical composition and fodder value of the green mass from studied species

Indices	Species						
	Medicago sativa	***Amaran-thus hypocho ndriacus***	***Raphanus sativus var. oleifera***	***Sinapsis alba***	***Linum usitatissi-mum***	***Sesamum indicum***	**Rumex**
Crude protein, [% DM]	16.28	16.08	19.81	18.94	14.62	14.43	19.22
Crude fats, [% DM]	2.75	4.09	5.03	5.54	4.54	6.52	1.85

Indices	Species						
	Medicago sativa	*Amaranthus hypochondriacus*	*Raphanus sativus var. oleifera*	*Sinapsis alba*	*Linum usitatissimum*	*Sesamum indicum*	Rumex
Crude cellulose, [% DM]	33.25	26.04	27.89	27.93	32.43	25.48	26.02
Nitrogen free extract, [% DM]	39.50	40.05	38.98	37.58	41.40	42.55	40.00
Ash, [% DM]	8.22	13.74	12.40	10.01	7.01	11.02	13.00
Gross energy, [MJ/kg]	18.56	19.71	19.39	18.92	19.06	18.61	17.56
Metabolizable energy, [MJ/kg]	8.26	9.67	9.14	9.34	8.95	10.46	8.82
Net energy for lactation, [MJ/kg]	4.57	5.50	5.11	5.22	4.94	5.91	5.04
Calcium, [g/kg DM]	14.3	19.0	14.9	15.9	6.3	10.4	14.4
Phosphorus, [g/kg DM]	2.2	4.0	3.6	2.9	3.9	4.3	5.2

Phytomass is an important source for renewable energy production. The production of biomethane gas via anaerobic digestion using lignocellulosic phytomass as a renewable energy source is both sustainable and environmentally friendly. The stability and the productivity of biogas digesters are mostly influenced by nutrient concentration and rhythm biodegradability, ratio of carbon and nitrogen (C/N) of substrate. It is known the optimal C/N ratio in substrate should range from 10 to 30, which does not affect the development of bacteria involved in anaerobic digestion. The quality indices of the substrate and its biochemical methane potential from the investigated species are shown in Table 4.

Table 4

The biochemical biomethane production potential of the green mass substrates from the studied species

Indices	Species						
	Medicago sativa	*Amaranthus hypochondriacus*	*Raphanus sativus var. oleifera*	*Sinapsis alba*	*Linum usitatissimum*	*Sesamum indicum*	*Rumex*
Digestible protein, g/kg DM	122.1	119.0	170.4	153.4	108.2	106.8	148.0
Digestible fats, g/kg DM	12.7	24.1	28.2	42.1	26.8	25.1	10.0
Digestible carbohydrates, g/kg DM	446.1	439.9	557.8	405.4	483.5	449.0	430.3
Nitrogen, g/kg DM	26.0	25.7	31.7	30.3	23.4	23.1	30.8
Carbon, g/kg DM	509.8	479.2	486.7	500.0	516.6	494.3	483.3
Carbon/ Nitrogen	19.6	18.6	15.4	16.5	22.1	21.4	15.7
Biogas, l/kg ODM	453	457	591	480	507	461	456
Biomethane, l/kg ODM	246	251	328	271	267	251	251
Methane content, %	54.4	54.8	55.5	56.5	52.6	54.4	55.0

It should be mentioned that in the investigated substrates from non-traditional crops, the carbon and nitrogen ratio varied from 15.4 to 22.1, but in *Medicago sativa* substrates C/N = 19.6. The calculated biochemical biomethane potential of the non-traditional crops substrates varied from 251 l/kg to 328 l/kg, but *Medicago sativa* green mass substrates reached 246 l/kg. The best biomethane potential was achieved in Brassicaceae plants *Raphanus sativus* and *Sinapis alba*.

Several publications have documented the biomethane potential of substrates from studied species. Also, *Zubr (1986)* reported the methane potential of *Sinapis alba* was 300 l/kg VS. *Murphy et al. (2011)* reported that methane yield in *Raphanus sativus* var. *oleifera* substrate achieved 240-340 m^3/t VS.

Ust'ak et al. (2011, 2021) remarked that the specific methane yield of hybrid *Rumex* green mass substrate was 362 l /kg DM, but in ensiled substrate 284 l/kg DM, the total methane yield varied from 2500 to 3600 m^3/ha.

Molinuevo-Salces et al. (2013), reported that the methane potential of white mustard substrates ranged between 251 and 379 l/kg VS and from fodder radish 356- 474 l/kg VS. *Seppälä (2013)* found that under boreal conditions the methane yield from amaranth biomass reached 290 l/kg VS or 2 700 m3 /ha.

Eberl et al., (2014), reported that the specific methane yield of amaranth substrate was 270 l/kg compared to maize substrate 350 l/kg. *Ahlberg & Nilsson (2015)* found that the specific methane yield for the intermediate crops after 30 days BMP tests ranged from 278 to 290 l/kg VS in the *Sinapis alba* and 297-304 l/kg VS in *Raphanus sativus* substrates.

Herrmann et al., (2016), reported that the tested amaranth substrate had C/N = 27, and biochemical methane potential 278.4 l/kg VS; the *Raphanus sativus* substrate had C/N=17 and biochemical methane potential 29l.0 l/kg VS, but alfalfa grass mixtures silage: C/N=18 and biochemical methane potential 280.0 l/kg VS.

According to *Von Cossel, (2019)*, the specific methane yield of Amaranthus hypochondriacus substrate was on average 266 l/kg VS, which was negatively affected by the high contents of ash (13.6%), lignin (6.5%) and cellulose (32.9%). *Słomka and Wójcik Oliveira, (2021),* mentioned that in the white mustard substrate C/N=15.5-19.9, whereas its biogas potential amounted to 350–440 m3 /t DM. *Țiței, (2020a, 2022),* found that *Amaranthus hypochondriacus* green mass substrate had C/N = 18.4 and biochemical methane potential 278 l/kg VS; the *Sinapis alba* green mass substrates have C/N=13.5-17.2 and biochemical methane potential 281-2950 l/kg VS, but the Medicago sativa green mass substrate C/N = 18.4 and biochemical methane potential 270 l/kg VS.

CONCLUSIONS

The obtained results indicate the fact that the criterion of dimensional proportionality K_{dp}, chosen and used in our research, has values that correlate with those of the sphericity *S* of seeds, objectively reflecting their morphological structure. Therefore, the following types of seeds have been identified: 1. *Spheroidal* (*L≃W≃T,* the seeds of *Amaranthaceae species);* 3. *Elliptical* (L>W≃T, alfalfa, family *Fabaceae*; white mustard and fodder radish, family *Brassicaceae*); 4. *Elongated* (*L>>W≠T*, sesame, family *Pedaliaceae*, and flax, family *Linaceae*); 5. *Pyramidal* (with triangular sides, the seeds of *hybrid Rumex tianschanicus* × *R. patientia,* family *Polygonaceae*). Besides, a correlation between the values of the criterion K_{dp} and sphericity *S* was identified.

The seeds of the non-traditional plant species, included in this study, have high friability in comparison with the seeds of alfalfa, the traditional control crop: angle of repose $\alpha \leq 28.2^0$ and flow angle- $\alpha_1 \leq 27.8°$ (on steel), $\alpha_1 \leq 31.6°$ (on wood), $\alpha_1 \leq 28.2°$ (on enamelled surface). These features are due to the appropriate morphological structure and the low roughness of the seed coat. The dimensional characteristics of seeds from non-traditional plant species are characterized by relatively small sizes, the geometric mean diameter value varying within the range D_g= 0.68- 2.59 mm.

The analysis of the physico-mechanical and technological properties of the studied seeds confirms that it is possible to use the facilities and technical means, available in the agro-food sector, to transport, process and store these seeds, which is a great advantage in making good use of the biological potential of these crops with minimal expenses.

The harvested green mass from non-traditional crops has the optimal content of nutrients: protein 14.43-19.81 % crude protein, 25.48-32.43 % crude cellulose, 37.58-42.55 % nitrogen free extract, 0.63-1.9% Ca, 0.28 -0.52% P with nutritive energy values 8.82-9.67 MJ/kg ME and 4.94-5.91 MJ/kg NEl.

The biochemical methane potential of the studied green mass substrates from studied non-traditional crops reaches 251-328 l/kg VS. The studied non-traditional crops can be used as a source of nutrients in livestock nutrition, or as a source of biomass for biomethane production.

ACKNOWLEDGEMENT

The study has been carried out in the framework of the project 20.80009.5107.02 “Mobilization of Plant Genetic Resources, Plant Breeding and as Forage, Melliferous and Energy Crop in Bioeconomy” 20.80009.5107.02.

REFERENCES

[1] Abbasi M., Rouzbehan Y., Rezaei J., Jacobsen S.E. (2018). The effect of lactic acid bacteria inoculation, molasses, or wilting on the fermentation quality and nutritive value of amaranth (*Amaranthus hypochondriaus*) silage. *Journal of Animal Science*, 96, 3983–3992.

[2] Ahlberg I., Nilsson T.L.S. (2015). *Investigation on the use of intermediate crops for anaerobic digestion as a renewable source of energy.* Lund University. https://lup.lub.lu.se/luur/download?func=downloadFile&recordOId=5472252&fileOId=5472409

[3] Alekksha Kudos S.K., Chandan S. (2018). Evaluation of physical properties of amaranth grain (*Amaranthus paniculatus*) *International Journal of Chemical Studies*, 6(2), 2197-2201.

[4] Amorim D.S., Edvan R.L., Nascimento R.R., Bezerra L.R., Araújo M.J., Silva A.L., Diogénes L.V., Oliveira R.L. (2019). Sesame production and composition compared with conventional forages. *Chilean journal of agricultural research*, *79*(4), 586-595. https://dx.doi.org/10.4067/S0718-58392019000400586

[5] Badger C.M., Bogue M.J., Stewart D.J. (1979). Biogas production from crops and organic wastes. *New Zealand Journal of Science*, 22, 11-20.

[6] Baserga U., 1998. Agricultural co-digestion biogas plants – biogas from organic residues and energy grass (Landwirtschaftliche Co-Vergärungs-Biogasanlagen – Biogas aus organischen Reststoffen und Energiegras). FAT Reports, 512: 1-11.

[7] Biel W., Jendrzejczak E., Jaroszewska A., Witkowicz R., Piatkowska E., Telesinski A. (2017). Nutritional content and antioxidant properties of selected species of *Amaranthus* L. *Italian Journal of Food Science*, 29(4), 728–740.

[8] Bhat V., Madhusudhan B. Naik N.J. (2018). Studies on physical properties and chemical make-up of hybrid and native varieties of flaxseeds. *International Journal of Advanced Research*, 6, 369-373.

[9] Bojariu R., Nedealcov M., Boincean B., Bejan I., Rurac M., Pîntea M., Caisîn L., Cerempei V., Hurmuzachi I., Baltag G., Zaharia N. (2021). *Best practice guide to adapting to climate change and implementing climate change mitigation measures in the agricultural sector. (Ghid de bune practici întru adaptarea la schimbările climatice și implementarea măsurilor de atenuare a schimbărilor climatice în sectorul agricol)*. UCIP IFAD. Print-Caro, Chișinău. 120p. *(in Romanian) http://dspace.uasm.md/bitstream /handle/123456789/6570/Ghid_agricultura_web.pdf?sequence=1&isAllowed=y*

[10] Cagatay Selvi, K., Pinar Y., Yesiloglu E. (2006). Some physical properties of linseed. *Biosystems Engineering,* 95, 607-612.

[11] Cerempei V., Țîței V., Guțu A., Cârlig N., Gadibadi M. (2022). Some physical and technological properties of seeds of non-traditional plant species in the Republic of Moldova. *Scientific Papers. Series A. Agronomy*, 65 (1), 643-654, http://agronomyjournal.usamv.ro/pdf/2022/issue_1/Art91.pdf

[12] Cerempei V., Țîței V., Vlăduț V., Moiceanu G. A. (2023). Comparative study on the characteristics of seeds and phytomass of new high-potential fodder and energy crops. *Agriculture, 13,1112., https://doi.org/10.3390/agriculture13061112*

[13] Cerempei V. (2016). *Technology and technical means of production and use of biofuels based on monoatomic alcohols:* [Doctoral dissertation. ITA Mecagro-UASM, Chisinau] (Tehnologia și mijloacele tehnice de producere și utilizare a biocombustibililor în baza alcoolilor monoatomici: [Tz. de doct. habilitat în tehnică. ITA Mecagro-UASM, Chișinău]. 239 p., http://www.cnaa.md/files/theses/2016/50722/valerian_cerempei_thesis.pdf. *(in Romanian)*

[14] Chisnicean L., Ţîţei V., Teleuţă A., Colțun M. (2011). Cultivation of aromatic plants (guide) (*Cultivarea plantelor condimentar – aromatice* (îndrumar). Chişinău, Moldpres, 24 p. *(in Romanian)*.

[15] Coşkuner Y., Karababa E. (2007). Some physical properties of flaxseed (*Linum usitatissimum* L.). *Journal of Food Engineering*, 78, 1067-1073. 10.1016/j.jfoodeng.2005.12.017.

[16] Coşman S., Ciopată A.C., Coşman V., Bahcivanji M., Ţîţei V. (2017). Study on the chemical composition and nutritional value of the *Galega orientalis* Lam. and the prospects of its valorification in the Republic of Moldova. *Scientific papers, series D, Animal Science*, 60, 75-80, http://animalsciencejournal.usamv.ro/pdf/2017/Art12.pdf .

[17] Cumplido-Marin L., Graves A.R., Burgess P.J., Morhart C., Paris P., Jablonowski N.D., Facciotto G., Bury M., Martens R., Nahm M. (2020). Two novel energy crops: *Sida hermaphrodita* (L.) Rusby and *Silphium perfoliatum* L.—State of knowledge. Agronomy 2020, 10, 67. https://doi.org/10.3390/agronomy10070928.

[18] Das S. (2016). *Amaranthus: A promising crop of future*. Springer. 208p. https://doi.org/10.1007/978-981-10- 1469-7.

[19] Dubrovskis V., Adamovics A. (2015). Anaerobic digestion of hemp, sunflower silage and amaranth silage with catalyst metaferm. 23rd European Biomass Conference and Exhibition, 845–850 DOI: 10.5071/23rdEUBCE2015-2DV.1.45

[20] Elleuch M., Besbes S., Roiseux O., Blecker C., Attia H. (2007). Quality characteristics of sesame seeds and by-products. *Food Chemistry*, 103, 641–650.

[21] Eberl V., Fahlbusch W., Fritz M., Sauer B. (2014). *Screening and selection of amaranth varieties and lines as a biogas substrate rich in trace elements* (No.37), *Screening und Selektion von Amarantsorten und - linien als spurenelementreiches Biogassubstrat*, reports from the TFZ. Technology and support centre in the Competence Centre for Renewable Raw Materials, Straubing, 114 p.

[22] Ene T. A., Mocanu V. (2016). Production, conditioning and storage of seeds of perennial grassland grasses and legumes – Technologies, equipment and facilities (Producerea, condiționarea și stocarea semințelor de graminee și leguminoase perene de pajiști – Tehnologii, echipamente și instalații). Brașov, 116p. http://www.madr.ro/attachments/article/224/ADER-1112-ghid.pdf (in Romanian)

[23] Gautam A. Khurana R., Manes G.S., Dixit A.K. (2016). Studies on physical properties of pelleted radish (*Raphanus sativus*) seeds. *Research in Environment and Life Sciences*, 9(4), 473-476.

[24] Herrmann C., Idler C., Heiermann M. (2016). Biogas crops grown in energy crop rotations: linking chemical composition and methane production characteristics. *Bioresource Technology*, 206, 23-35. https:// doi.org/10.1016/j.biortech.2016.01.058

[25] Heuzé V., Tran G., Lebas F. (2015). Flax straw and flax crop by-products. *Feedipedia*, a programme by INRAE, CIRAD, AFZ and FAO. https://www.feedipedia.org/node/132 .

[26] Kaliniewicz Z., Markowski P., Anders A., Jadwisienczak K. (2015). Frictional properties of selected seeds. *Tech. Sci.,* 18(2), 85–101.

[27] Kshnikatkina, A.N., Gushchina, V.A., Galiullin, A.A., Varlamov, V.A., Kshnikatkin, S.A. (2005). Nontraditional fodder crops. RIO PGSKHA, Penza. 240 p. (in Russian).

[28] Kukusheva, A., Stepanov, A. (2016). Effect of mowing term on biometrics, yield and nutritional properties of hybrid (*Rumex patientia* x *Rumex tianschanicus*). *Bulgarian Journal of Agricultural Science*, *22*(6), 948–954.

[29] Leukebandara I.K., Premaratne S., Peiris B.L. (2015). Nutritive quality of thampala (*Amaranthus* spp.) as a forage crop in Sri Lanka. *Tropical Agricultural Research*, 26(4), 624–631.

[30] Matei, G., Feher, E. (2010). Conditioning and preservation of agricultural products (*Condiționarea și conservarea produselor agricole). Universitaria, Craiova*, 168p, (in Romanian).

[31] Medvedev P.F., Smetannikova A.I. (1981). *The forage crops of European part of the USSR*. Leningrad, Kolos. (in Russian).

[32] Mohsenin N. N. (2020). Physical properties of plant and animal materials: structure, physical characteristics and mechanical properties. *New York, Imprint Routledge*, 758p. e-Book ISBN 9781003062325, DOI https://doi.org/10.4324/9781003062325 .

[33] Molinuevo-Salces B., Ahring B.K., Uellendahl H. (2013). Catch crops as an alternative biomass feedstock for biogas plants. In Proceedings of the International Anaerobic Digestion Symposium on "Dry Fermentation, Substrate Treatment and Digestate Treatment" within the BioGasWorld 2013. Berlín (pp. 92-98). FNBB. http://ibbk.fachgruppe-biogas.de/index.php?id=32&L=1&eventId=91.

[34] Mursec B., Vindis P., Janzekovic M., Brus M., Cus F. (2009). Analysis of different substrates for processing into biogas. *Journal of Achievements in Materials and Manufacturing Engineering*, 37(2), 652–659.

[35] Peiretti P.G. (2018). *Amaranth* in animal nutrition: A review. *Livestock Research for Rural Development*. 30. http://www.lrrd.org/lrrd30/5/peir30088.html.

[36] Peni D., Stolarski M.J., Bordiean A., Krzyzaniak M., Debowski M. (2020). *Silphium perfoliatum*—a herbaceous crop with increased interest in recent years for multi-purpose use. *Agriculture*, 10, 640. https://doi.org/10.3390/agriculture10120640.

[37] Pisaoikova B., Peterka J., Trakova M., Moudr J., Zral Z., Herzig I. (2006). Chemical composition of the above-ground biomass of *Amaranthus cruentus* and *A. hypochondriacus*. *Acta Veterinaria Brno*, 75, 133–138.

[38] Pospisil A., Pospisil M., Macesic D., Svecnjak Z. (2009). Yield and quality of forage sorghum and different amaranth species (*Amaranthus* spp.) biomass. *Agriculturae Conspectus Scientificus*, 74(2), 85–89.

[39] Póti P., Pajor F., Bodnár Á., Penksza K., Tőzsér J., Gyuricza C. (2014). Potential of second crops of oil radish and white mustard as fall grazing pasture for German mutton merino sheep. *Notulae Botanicae Horti Agrobotanici*, 42(1), 286–288.

[40] Rahnama A., Safaeie A.R. (2017). Performance comparison of three varieties of amaranth (*Amaranthus hypochondriacus* L.) at different harvest time. *Journal of Asian Scientific Research*, 7(6), 224– 230.
[41] Rakhmetov D. (2018). *Non-traditional plant species for bioenergetics*. Nitra: Slovak University of Agriculture in Nitra, 103 p. https://doi.org/10.15414/2018.fe-9788055218557 (in Russian).
[42] Rakhmetov D.B. (2011). *Theoretical and practical aspects of plant introduction in Ukraine*. Ed. Agrar Media Grup, Kyiv, 398 p. (in Ukrainian).
[43] Rakhmetov D.B., Rakhmetova S.O. (2006). Varietal diversification of shchavnat (*Rumex patientia* L. × R. *tianschanicus* Losinsk) and directions of its use. *Plant Introduction*, 1, 11-16. http://www.nbg.kiev.ua/upload/introd/Intr-N1-06.pdf (in Ukrainian).
[44] Rakhmetov D.B., Rakhmetova S.O. (2011) Shchavnat: both fruit, and feed and biofuels. *Cereal*, 3, 8-10. http://www.zerno-ua.com/journals/2011/mart-2011-god/shchavnat-i-ovoshch-ikorm-i-fitotoplivo (in Russian).
[45] Rakhmetov D., Ust'ak S., Ust'aková M. (2004). Perennial spinach-sorrel hybrid– schavnat as a new perspective multipurpose crop. *VIII ESA Congress*, Copenhagen, p. 86-94.
[46] Rolinec M., Rakhmetov D., Bíro D., Juráček M., Šimko M., Gálik B., Hanušovský O. (2018). Nutritional value of hybrid *Rumex patientia* L.× *Rumex tianschanicus* A. Los (Rumex OK 2) in different periods. *Acta fytotechn zootechn*, *21*(4), 197-200.
[47] Roman Gh. V., Ion V., Epure L.I., Băşă A. Gh. (2016). *Biomass. Alternative Energy Source* (*Biomasa. Sursă alternativă de energie).* București, *432 p. DOI: 10.5682/978-606-28-0506-7* (in Romanian).
[48] Schäfer A., Damerow L., Schulze Lammers P. (2017). Determination of the seed geometry of cup plant as requirement for precision seeding. *Landtechnik*, 72, 122–128, https://www.landtechnik-online.eu/landtechnik/article/view/2017-72-3-122-129.
[49] Seppälä M. (2013). Biogas production from high yielding energy crops in boreal conditions. Jyväskylä University Printing House. 92p.
[50] Słomka A., Wójcik Oliveira K. (2021). Assessment of the biogas yield of white mustard (*Sinapis alba*) cultivated as intercrops. *Journal of Ecological Engineering*, 22(7), 67–72.
[51] Tunde-Akintunde, T. Y., Akintunde, B. O. (2004). Some physical properties of sesame seeds. *Biosystems Engineering*, 88, 127– 129.
[52] Teleuță A., Colțun M., Mihailescu C., Ciocarlan N. (2008). Medicinal herbs (*Plante medicinale)*. Chişinău. 335 p. (in Romanian).
[53] Teleuţă A., Ţîţei V. (2016). Mobilization, acclimatization and use of fodder and energy crops. *Journal of Botany*. 1(12), 112-120. https://ibn.idsi.md/en/vizualizare_articol/48812 .
[54] Titei V. (2015). Plant species for renewable energy production in the Republic of Moldova. *Scientific Papers. Series A. Agronomy*, 58, 425-431. www.agronomyjournal.usamv.ro/pdf/2015/vol.LVIII/art77.pdf.
[55] Ţîţei, V. (2020a). The quality of green mass and silage from *Amaranthus hypochondriacus* growing under the conditions of the Republic of Moldova. *Scientific Papers. Series A. Agronomy*, 63 (1), 594-601. http://agronomyjournal.usamv.ro/pdf/2020/issue_1/Art83.pdf.
[56] Ţîţei V. (2020b) The mobilization and use of plant genetic resources with high potential as fodder, honey and energy crops: achievements and prospects. (Mobilizarea și valorificarea resurselor genetice vegetale cu potențial furajer, melifer și biomasă energetică: realizări și perspective). *Journal of Bot*any, 2 (21), 92-105. DOI: https://doi.org/10.52240/1857-2367.2020.2(21).9 (in Romanian).
[57] Ţîţei V. (2023). The mobilization of energy crop resources in Moldova. *Romanian Agricultural Research*, 40, 646-654. https://www.incda-fundulea.ro/rar/nr40/rar40.3.pdf .
[58] Ţîţei V., Roșca I. (2021). *Good practices for the use of degraded lands in the cultivation of crops with energy biomass potential* (*Bunele practici de utilizare a terenurilor degradate în cultivarea culturilor cu potenţial de biomasă energetică).* Chișinău: S. n., 80p. (in Romanian).
[59] Ţîţei V., Teleuţă, A. (2015). The perspective of cultivation and utilization of the hybrid *Rumex tianschanicus* × *Rumex patientia* in Moldova. *Scientific papers*, series *Agronomy*, 58 (2),163-168.
[60] Togo J.M., Decheng W., Wenpeng M., Changbin H. (2018). Effects of moisture content on selected physical and mechanical properties of alfalfa seeds. *Journal of Biology, Agriculture and Healthcare*, 8, 8-18. https://www.iiste.org/Journals/index.php/JBAH/article/view/43338.
[61] Ustak S., Šinko J., Muňoz J. (2021). Hybrid sorrel: cultivation potential and use as a novel non-food multipurpose crop. *Biofuels Bioproducts and Biorefining*. 15(1). https://doi.org/10.1002/bbb.2157.

[62] Usťak S., Váňa J., Petříková V. (2011). Non-traditional fodder sorrel as suitable raw material for biogas production (Netradiční pícnina šťovík krmný jako vhodná surovina pro výrobu bioplynu). *Agritech Science*, 11, 1-7. (in Czech).
[63] Uteush Y.A. (1990). *New promising forage crops*. Edit. Naukova dumka, Kyiv. 192. (in Russian).
[64] Von Cossel, M. (2019). Agricultural diversification of biogas crop cultivation. Dissertation, University of Hohenheim, Stuttgart, Germany. https://opus.unihohenheim.de/volltexte/2019/1600/.
[65] Zarczynski P., Sienkiewicz S., Wierzbowska J., Krzebietke S. (2021). Fodder galega—a versatile plant. Agronomy 2021, 11, 1797. https://doi.org/10.3390/agronomy11091797 .
[66] Zubr J. (1986). Methanogenic fermentation of fresh and ensiled plant materials. *Biomass*, 11. 156–171,
[67] ***"Key World Energy Statistics" (PDF). International Energy Agency. 2023, https://www.eia.gov/international /data/world, (accessed on 17 August 2023).
[68] *** Strategy the European Environment Agency EEA–Eionet 2021–2030, Luxemburg: Publications Office of the European Union, 2021 ISBN 978-92-9480-360-3 Doi:10.2800/92395, https://www.eea.europa.eu/ro /publications/strategia-aem2013eionet-202120132030 (accessed on 18 August 2023).
[69] *** FAO. (2016). The State of Food and Agriculture: Climate change, Agriculture and Food security Food and Agriculture Organization of the United Nations (FAO), Rome, 194p. ISBN 978-92-5-109374-0, ISSN 0081-4539, http://www.fao.org/3/a-i6030e.pdf .
[70] *** The World at un.org.: https://www.un.org/en/site-index (accessed on 12 August 2023).
[71] *** U.S. Census Bureau – World POP Clock Projection. https://www.census.gov/popclock/ (accessed on 17 August 2023).
[72] *** World population prospects: The 2023 Revision Population Database. https://www.un.org/esa/population/publications/ (accessed on 15 August 2023).

DESIGN AND EXPERIMENT OF COMBINED CAVITY-TYPE PRECISION HOLE-DROP SEED-METERING DEVICE FOR RICE

/

组合腔道式水稻精量穴播排种器设计与试验

Wenwen SONG [1)], Yu WAN [1)], Bo ZHOU [1)], Fuming KUANG [1)], Wei XIONG [1)], Juan LIAO [1)], Dequan ZHU [1)], Shun ZHANG *[1, 2)]

[1)] College of Engineering, Anhui Agricultural University, Hefei, Anhui, 230036, China

[2)] Engineering Laboratory of Intelligent Agricultural Machinery Equipment, Anhui, Hefei, 230036, China

Tel: +86 18856922971; E-mail addresses: shunzhang@ahau.edu.cn

DOI: https://doi.org/10.35633/inmateh-71-02

Keywords: *precision hole-drop seed-metering; adjust the seeding quantity; seed-inlet width; metering hole slope angle; cavity outer angle*

ABSTRACT

In order to solve the problems of unstable seeding quantity and poor applicability of traditional lightweight simplification mechanical seed-metering device, a combined cavity-type rice precision hole-drop seed-metering was developed. According to the material characteristics of rice seed and the requirements of seeding quantity, the innovative metering hole structure achieves the purpose of accurate filling of rice seed. In order to adapt to the demands of different rice seeds and improve the accuracy and convenience of the adjustment of the seeding quantity, the number of cavities involved in seeding operation was simply adjusted. Bench tests are carried out on the effects of the seed-inlet width, the metering hole slope angle, and the cavity outer angle on the precision seeding performance of the seed-metering device. The test results show that when the outer and middle seed-inlets width both are 3.8 mm, the innermost seed-inlet width is 5.4 mm, and the metering hole slope angle is 35 °, and the cavity outer angle is 85 °, the performance of the three kinds of rice was better. Opening outermost seed-inlet to seeding super hybrid rice, the qualified rate is 90.67%, the miss-seeding rate is 3.77%. Opening outer and middle seed-inlets to seeding hybrid rice, the qualified rate is 90.80%, the miss-seeding rate is 3.73%. Opening all three seed-inlets to seeding conventional rice, the qualified rate is 90.67%, the miss-seeding rate is 3.53%. The field test shows the seed-metering device can also meet the requires of these kinds of rice seeding.

摘 要

为解决传统水稻轻简机械式排种器穴播量稳定性差、精确调节困难，导致品种适用性差的问题，研制了一种组合腔道式精量穴播排种器。根据稻种的物料特性及穴播量要求，创新异形量孔结构达到稻种精量充种的目的；提出通过简单调节参与排种作业的腔道个数调节排种器的穴播量，以适应不同品种水稻不同穴播量的需求，提高排种器播量调节的精确性与便捷性。先后采用单因素与全因素试验方法，研究了量孔的进种口宽度、斜面倾角、腔道外侧角对排种器穴播量的影响。明确了外层与中间腔道进种口宽度均为3.8mm、内侧腔道进种口宽度为5.4mm，量孔斜面倾角均为35°，且腔道外侧角均为85°时，排种器排种三种水稻的穴播排种性能均较优.单个进种口排种超级稻时，漏播率为3.77%，合格率为90.67%；两个进种口排种杂交稻时，漏播率为3.73%，合格率为90.80%；三个进种口排种常规稻漏播率为3.53%，合格率为90.67%。田间试验表明排种器能满足水稻精量穴直播的种植要求。

INTRODUCTION

Rice holds the status of being China's primary food crop. Its yield per area exceeds that of wheat by 22.4% and corn by 13.1% (*China Statistics Press, 2022*). Thus, the promotion of rice cultivation plays a critical role in ensuring the nutritional security of the populace in the region (*Tian et al., 2022; Jat et al., 2022*). Mechanized transplantation and direct seeding are the two primary modes of rice planting in the region.

Wenwen Song, M.S. Stud.; Yu Wan, M.S. Stud.; Bo Zhou, M.S. Stud.; Fuming Kuang, Assoc. Prof; Wei Xiong, Lecturer; Juan Liao, Assoc. Prof; Dequan Zhu, Prof.; Shun Zhang, Assoc. Prof

Among these, precision cavity direct seeding of rice through seed-metering device offers the benefits of time and labor savings, as well as accuracy and efficiency. (*Yamauchi, 2017; Zhang et al., 2018; Farooq et al., 2011*).

The critical component in the rice precision hole direct seeding technology is the seed-metering device. The component structure and working principle of rice precision hole direct seeding device were studied (*Van et al., 2020*). The seed-meter device is mainly mechanical and robust. The mechanical type is highly adaptable to seed shape and can withstand field vibration, dust, and high humidity. Its structure is simple and easy to repair. However, it requires stable gas and a gas source are prone to clogging of pores. It is a primary method to achieve lightweight simplification of rice mechanization equipment for seed-meter device (*Zhang et al., 2015; Li et al., 2021; Cheamuangphan et al., 2018*).

There are three types of rice: super hybrid, hybrid, and conventional. Their diligence capabilities have decreased in that order. Therefore, direct seeding of rice at essential points must consider the growth characteristics of each rice category (*Liu et al., 2016*). Typically, super hybrid rice, hybrid rice, and conventional rice are sown with 1-3 seeds, 2-5 seeds, and 5-10 seeds, respectively (*Xing et al., 2022; Zeng, 2013*). Due to the difference requirements of seeding quantity between the conventional and hybrid rice, the seeding quantity is difficult to be controlled accurately for the seed-metering device. Wang, Z. et al. designed a rice precision metering device with seeding quantity stepless adjusting. The precision metering device has advantages of wide adjustment range, good adaptation, simple and quick stepless adjustment show that this device is practical. Nonetheless, this device is only able to respond to the seeding demands of hybrid and conventional rice (*Wang et al., 2018*). Li Hanqing and his team have designed a rice seed-metering device that by the variable capacity roller-wheel managed to adjust the quantity of hole seeding. Because the direct seed-metering device for rice cannot continuously adjust the quantity of seeding, it has a small adjustment range and low accuracy. They designed and verified variable capacity roller-wheel. The variable capacity method achieves a stepless adjustment of the seeding quantity, and results in high accuracy (*Li et al., 2022*). Tang H and others designed the multi-grain cluster air suction type rice hole direct seed metering device. A multi grain cluster air suction type rice hole direct seed metering device was developed to solve the problem of high reseeding rates and miss-seeding rates in the rice multi-grain hole direct seeding process (*Tang et al., 2022*). Rajaiah et al. designed a precision planter for paddy rice direct seeding, its seeding plate can only hold 1-2 rice seeds in each groove and the hole seeding rate cannot be adjusted (*Rajaiah et al., 2020*). Hensh et al. designed a precision hole drop seed metering mechanism of rice, the opening time of its outlet is precisely controlled by an inductive proximity sensor. However, it is not easy for the device to adjust the seeding quantity (*Hensh et al., 2022*). Because of the lack of the light and simple mechanical direct seed-metering device that can be used for the three major types of rice, the utilization rate of precision direct seeding equipment for rice is reduced and the application of precision direct seeding technology is hindered.

In response to the issue of accurate regulation of seeding quantity stability and precision regulation of the traditional rice mechanical precision hole-drop seed-metering device, this article proposes the combined cavity-type rice precision hole-drop seed-metering device which can adjust the seeding quantity. This innovative design offers a simplified mechanical structure and allows for accurate adjustment of the measuring instrument's quantity, providing a new avenue for experimentation and advancement.

MATERIALS AND METHODS

Configuration and Working Principle

The combined cavity-type rice precision hole-drop seed-metering device is mainly composed of shells, discharge plate, as shown in Fig. 1, seeding quantity adjustment disk, seeding shafts, bolts, etc. The seeding quantity adjustment disk is embedded in the grooves installed in the discharge plate, and the two form the discharge plate. There are multiple cavities in the discharge plate, and each group of cavities consist of 3 cavities. A single cavity is composed of the metering hole part and the curve transfusion cavity. The metering hole include metering hole slope, seed-limiting plate, inner and outer side of the cavity and other side of the cavity, as shown in Fig. 3(f). The three cavities have a variety seed-inlet each, and meet at the same outlet. The seeding quantity adjustment disk can rotate relative to the discharge plate. By adjusting the relative position of the seeding quantity adjustment disk and the discharge plate, the number of opened seed-inlet is controlled. When the seeding quantity adjustment disk covers the innermost and the middle seed-inlet of the discharge plate, the seed-metering device opens the outermost seed-inlet of the discharge plate and it is used for the seeding of each hole (1-3) with the super hybrid rice.

The seeding quantity adjustment disk only covers the innermost seed-inlet, the seed-metering device opens two seed-inlets, and it is used for the seeding of each hole (2-5) with the hybrid rice.

When the seeding quantity adjustment disk does not cover the seed-inlet of the discharge plate, the seed-metering device opens all three seed-inlets and it is used for the seeding of each hole (5-10) with the conventional rice.

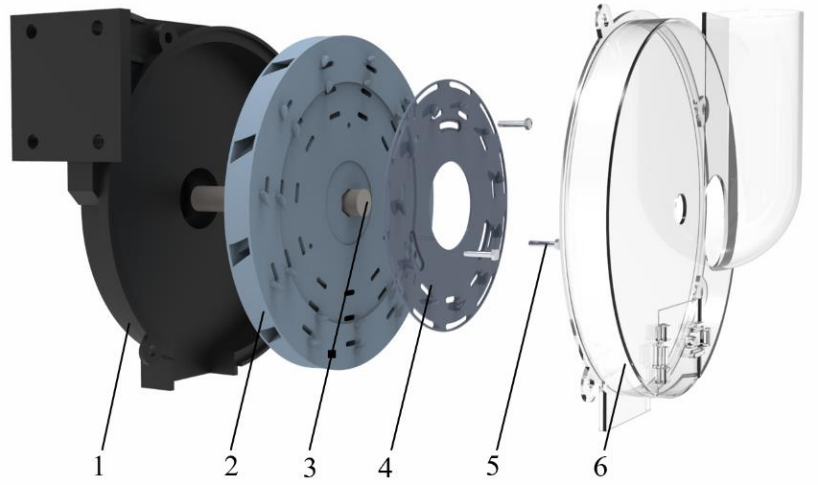


Fig. 1 - Display diagram of the seed-metering device

1. Left shell; 2. The discharge plate; 3. Shaft; 4. The seeding quantity adjustment disk; 5. Bolts; 6. Right shell.

The seeding process of the seeder is mainly formed by the three links of filling, carrying, and dropping, as shown in Fig. 2.

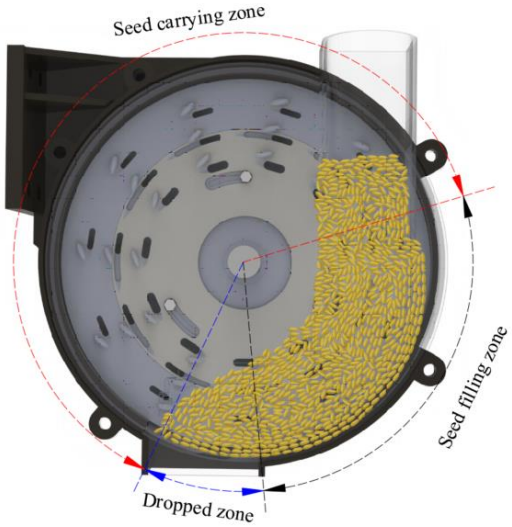


Fig. 2 - The diagram of working zone

Before the seeding, according to the requirements of the quantity of rice varieties, rotate the seeding quantity adjustment disk to adjust the number of openings of each group of cavities into the variety. After the discharge plate is rotated, the rice seeds are charged into the metering hole through the influence of their own gravity and population side pressure.

When the sector is transferred to the filling zone, the rice seeds in the metering hole will be under the constraints of its own gravity and the bottom plate and the top plate, lying on the metering hole, and under the blockage of the limit rice species board, the bottom rice is stranded in the metering hole, and the upper excess rice will drop out from holes under their own gravity, and return to the filling zone. As the discharge plate continues to rotate, the rice in the metering holes declines along the transfusion curve cavity and converges at the exit. When the outlet which is equipped with rice seeds arrive at the dropping zone, rice is discharged. The seedlings of multiple metering holes in a group of cavities do not interfere with each other. Before the outlets move to the dropping zone, the rice seeds in multiple curves gather at the outlet, as shown in Fig.3 (a).

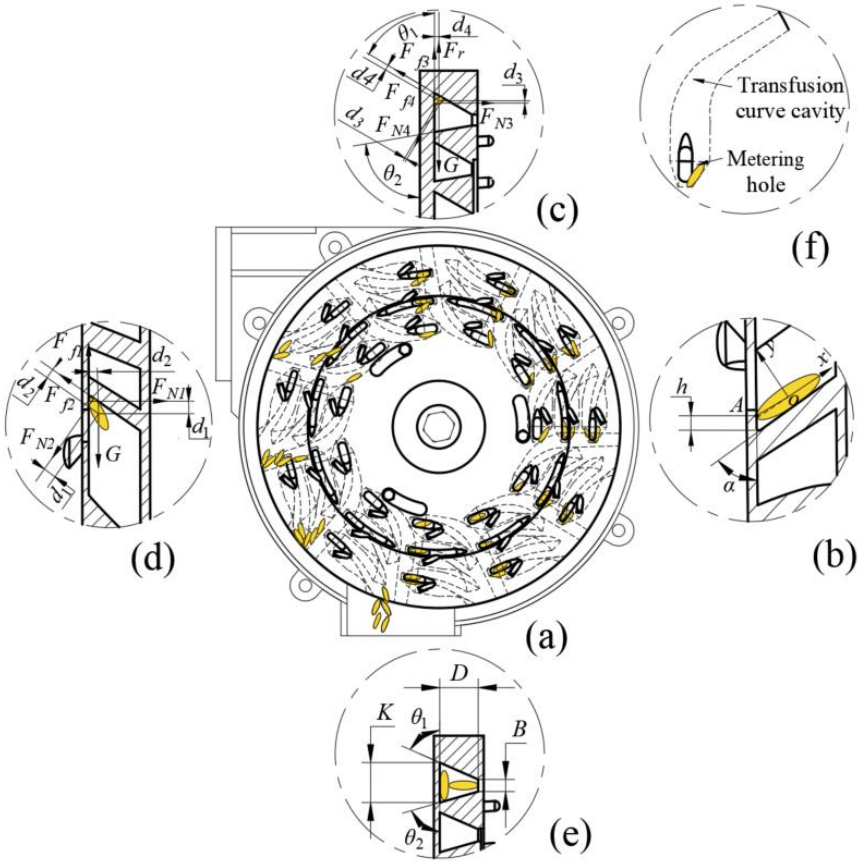


Fig. 3 - The diagram of seeding process.

(a) The seeding process; (b) The diagram of metering hole slope angle; (c) The status chart of cavity outer plane pick up rice seed; (d) The status chart of metering hole slope and seed-limiting plate pick up rice seed; (e) The sectional schematic diagram of transfusion curve cavity; (f)The diagram of the cavity composition.

The shape and size of seed-inlets

The shape and size of rice seeds are the main basis of the design parameters of the seed-inlets. The shape of rice seeds is similar with the spindle body. It is commonly used in three axial sizes of length, width, and thickness. The average three-axis size of the familiar rice species were counted, as shown in Fig. 4.

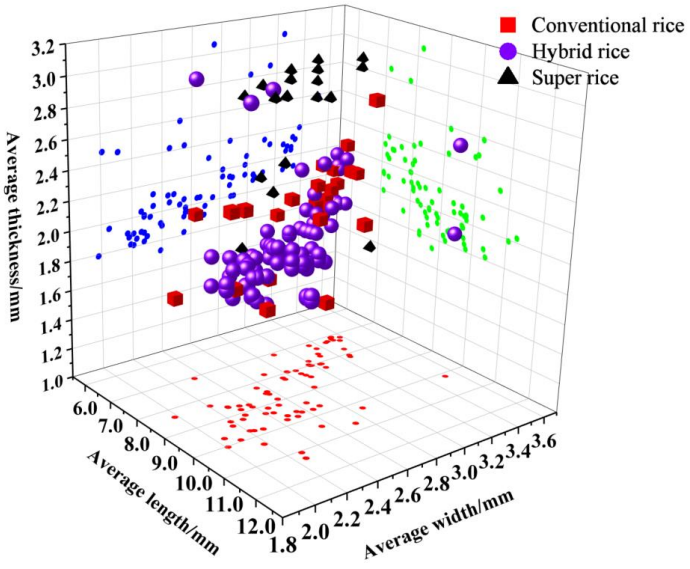


Fig. 4 - Familiar rice species three-axis size distribution map

It can be seen from the Fig. 4 that the average three-axis size distribution of super hybrid rice, hybrid rice and conventional rice does not have a significant distinction, as it is intertwined. However, regardless of variety, the length of the rice species is large, mainly distributed between 6.5-11.5 mm.

The range of the width size and thickness size is relatively concentrated, and the range of distribution is 2-3.5 mm and 1.5-3.1 mm, respectively. The three-axis size of common rice species is shown in Table 1. The rice seeds have obvious length and width structural characteristics. Therefore, the distribution way of rice seeds in the filling zone is also an important reference for the shape of seed-inlets.

Table 1

Three axis size of the frequent rice species

	Three axis median value (Length × width × thickness)	Maximum length	Maximum width	Minimum thickness
Size / mm	8.75×2.69×2.07	11.29	3.52	1.50

Studies have shown that rice seeds are distributed in the same consistent way in the direction of their long shafts and the rotation lines in the seed filling zone (*Zhang et al., 2023*). Therefore, the shape of seed-inlets is designed as round waist shape, and the horizontal direction of the seed-inlet is distributed in the direction of the discharge plates' cut line, as shown in Fig. 5. The structure size of the seed-inlets are mainly length and width size. Based on super hybrid rice, hybrid rice and conventional rice, the appropriate quantity of hole seeding, the regulation of the adjusting hole seeding quantity and the distribution posture of rice seeds in the filling zone, the width size of each seed-inlets of the combination cavity can be adjusted to adapt to the quantity of hole seeding of different rice varieties, and the length size of each seed-inlet should be consistent (*Rajaiah et al., 2015*), and should meet the formula (1).

$$L > a_{max} + l' \tag{1}$$

where:

a_{max} is the maximum length size of rice seeds, (mm);

l' is the bud length of rice seeds, (mm).

When the seed-metering device is opened only on the outermost side of the seed to adapt to the super hybrid rice requirement for the (1-3) grains per hole, the seed-inlet width B should meet the formula (2):

$$b_{max} < B < 4c_{min} \tag{2}$$

where:

$b_{\max}$ is the maximum width size of rice seeds, (mm);

$c_{\min}$ is the minimum thickness size of rice seeds, (mm), as shown in Fig. 5.

When the discharge plate is opened for two seed-inlets of the outer side to adapt to the hybrid rice requirement for the (2-5) grains per hole, the width size of the middle seed-inlet should be consistent with the outer seed-inlet. When the discharge plate is opened for three seed-inlets to adapt to the conventional rice requirement for the (5-10) grains per hole, the width size of the inner seed-inlet should be appropriately enlarged, and it also needs to be determined through the later seeding performance test.

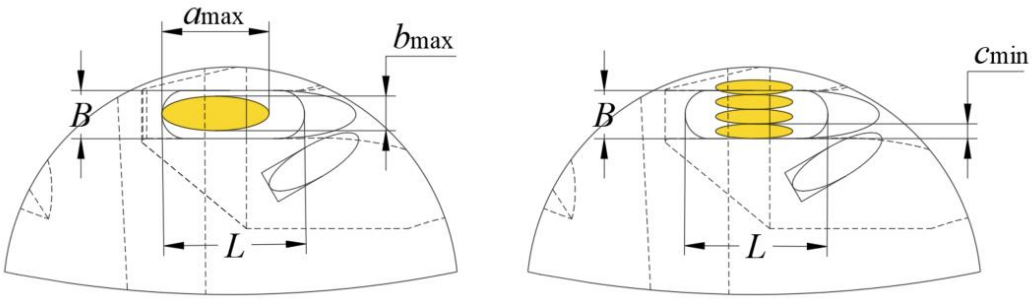


Fig. 5 - The diagram of the seed-inlet size

In order to avoid the entanglement of rice germination and affect normal seeding, the rice buds are generally not more than 2 mm after the rice is soaked in germination. Based on formula (1) and formula (2), combined with Table 1, the length size L of the seed-inlet should be larger than 13.29 mm, and this article takes 14 mm. The width size of the seed-inlet should be between 3.52-6 mm.

The metering hole slope angle

According to the working principle of the seed dispenser, the metering hole is an important part that determines the number of seed particles filled in a single cavity. The metering hole slope angle affects the successfully cleared excess rice seeds on the upper layer within the cavity. Therefore, the metering hole slope angle α should satisfy formula (3).

$$\alpha \geq arctan\,\mu \tag{3}$$

where:

μ represents the sliding friction coefficient between rice seeds, which is taken as 0.55 (*Jiang, 2021*);

α is the metering hole slope angle, (°).

It is not advisable for the metering hole slope angle to be too large, as it may result in a small angle between the metering hole inclined plane and the seed-limiting plate, causing the rice seeds to get stuck. This means that the rice seeds cannot successfully detach from the metering hole and slide into the transfusion curve cavity. If the rice seeds get stuck in the metering hole, there will be deformation due to the compression between the metering hole inclined plane and the seed-limiting plate. Therefore, the maximum value of the metering hole slope angle can be determined by considering the critical state where the rice seeds are in contact with the metering hole inclined plane but not subjected to compression. The spindle-shaped rice seeds were simplified into homogeneous and regular ellipsoids, and the force analysis was carried out, as shown in Figure 3(d).

Establish the force balance formula for rice seed, that is:

$$\begin{cases} \sum F_x = 0 & F_{N_1} - F_{f_2}\cos\alpha - F_{N_2}\sin\alpha = 0 \\ \sum F_y = 0 & F_{f_1} + F_{f_2}\sin\alpha - F_{N_2}\cos\alpha - mg = 0 \\ \sum M = 0 & F_{N_2}d_1 + F_{f_2}d_2 - F_{N_1}d_1 - F_{f_1}d_2 = 0 \end{cases} \tag{4}$$

$$\begin{cases} F_{f_1} = \mu F_{N_1} \\ F_{f_2} = \mu F_{N_2} \end{cases} \tag{5}$$

where: F_{N1} is the supporting force of rice seed for seed-limiting plate, (N);

F_{N2} is the supporting force of the rice seed for metering hole slope, (N);

F_{f1} is the friction force of rice seed for seed-limiting plate, (N);

F_{f2} is the friction force of rice seed for metering hole slope, (N);

G is the gravity of rice seed, (N);

d_1 is the supporting force lever, (m);

d_2 is the friction force lever, (m);

μ_1 is the friction coefficient of the discharge plate and the rice seed, which is 0.46 in this article;

From formula (4) formula (5), it can be seen that:

$$\left(F_{N_2} - F_{N_1}\right)d_1 + \left(F_{f_2} - F_{f_1}\right)d_2 = 0 \tag{6}$$

After sorting out the formula:

$$\left(F_{N_2} - F_{N_1}\right) + \left(d_1 + \mu d_2\right) = 0 \tag{7}$$

$$\begin{cases} F_{N_1} = F_{N_2} = F_N \\ F_{f_1} = F_{f_2} = \mu F_N \end{cases} \tag{8}$$

By substituting in formula (4), it can be obtained:

$$\begin{cases} \mu\cos\alpha + \sin\alpha = 1 \\ F_N\left(\mu + \mu\sin\alpha - \cos\alpha\right) - mg = 0 \end{cases} \tag{9}$$

It can be seen from the formula that if the rice seed is in the equilibrium state at this position and the gravity of the rice seed is constant, the supporting force on the slope decreases with the increase of the

metering hole slope angle; when the metering hole slope angle increases to a certain value, the equilibrium state breaks with the operation of the seed-metering device, and the resultant force along the vertical direction refers to the metering hole inclined plane, and the rice seed is clamped by metering hole, and the metering hole slope angle is the pinch angle.

Also know that: (10)

$$\sin^2\alpha+\cos^2\alpha=1$$

By substituting in formula (9) can be calculated

$$\alpha=\arccos\left(\frac{2\mu}{1+\mu^2}\right) \quad (11)$$

Diameter calculation α=40.60°. Therefore, the value range of the inclination angle of the metering hole should be 28.81° < α < 40.60°.

The height of seed-limiting plate

In order to ensure that the metering hole can "pocket" the bottom rice seeds, it is necessary to design a suitable height seed-limiting plate. Since the bottom rice seeds lie on it under the guidance of the metering hole inclined plane, the geometric relationship model between any single lying rice seed and the seed-limiting plate was established, as shown in Fig. 3(b). The cartesian coordinate system *xoy* was established by taking the centroid of rice seed as the coordinate origin.

Let (x_0, y_0) represent the coordinates of the intersection point A between the rice seeds and the seed-limiting plate. According to Fig. 3(b), the geometric expression for the height of the seed-limiting plate is:

$$h=\frac{y_0}{\cos\alpha}+\frac{c}{2\cos\alpha} \quad (1)$$

where: c is the average thickness of rice seed, (mm);

In the coordinate system *xoy*, the slope equation for seed-limiting plate projection is:

$$k=-\frac{c^2x_0}{a^2y_0} \quad (13)$$

where:

a is the average length of rice seed, (mm);

It can also be expressed by metering hole slope angle α: (14)

$$k=\tan\left(90°-\alpha\right)$$

By substituting in formula (12) and (13) can be calculated:

$$x_0=-\frac{a^2y_0\tan\left(90°-\alpha\right)}{c^2} \quad (15)$$

Because tangent point A satisfies the elliptic equation:

$$\frac{4x_0^2}{a^2}+\frac{4y_0^2}{c^2}=1 \quad (16)$$

Substituting equations (14) and (15) into equation (11) and rearranging, is obtained

$$h=\frac{c^2}{2\cos\alpha\sqrt{c^2+a^2\cot^2\alpha}}+\frac{c}{2\cos\alpha} \quad (17)$$

Substituting the average length and thickness dimensions of the rice seed from Table 1 into the equation, the relationship curve between the seed-limiting plate height h and the metering hole slope angle α, can be plotted as shown in Fig. 6. The seed-limiting plate height h increases with the increase in the metering hole slope angle α. When the metering hole slope angle α is determined, the value of the seed-limiting plate height h is also determined.

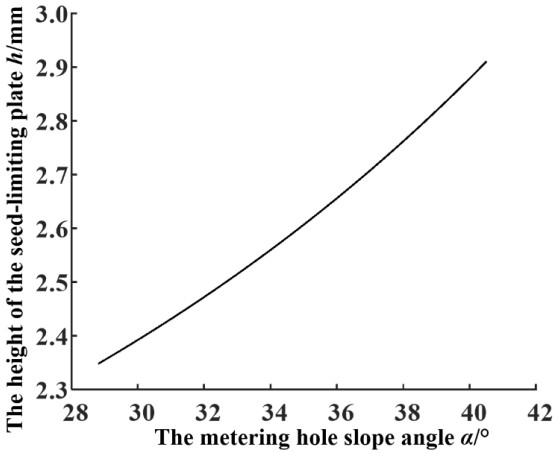


Fig. 6 - The diagram of h and α relationship

The cavity outer angle

Due to the small width of the seed-inlet of the metering hole, in order to ensure that the rice seed filling into the metering hole can move smoothly in the curved cavity, the section of the cavity is designed as a trapezoid expanded from one side of the seed-inlet, as shown in Fig. 3(c). The cavity outer angle is composed of the inner side, the outer and the bottom side of the cavity, which is divided into the outer angle and the inner angle. In order to ensure that the rice seeds filling into the metering hole do not get stuck into the cavity outer plane, ensure the smooth transportation of rice seed and the subsequent filling into the metering hole, and perform a force analysis on the rice seed at the cavity outer plane when they reach the top during motion.

The force equilibrium equation of rice seed being clamped in the cavity outer plane is:

$$\begin{cases} \sum F_x = 0 & F_{N_4}\cos\theta_1 + F_{f_4}\sin\theta_1 - F_{N_3} = 0 \\ \sum F_y = 0 & F_r + F_{f_3} + F_{f_4}\cos\theta_1 - F_{N_4}\sin\theta_1 - G = 0 \\ \sum M = 0 & F_{N_3}d_3 + F_{f_3}d_4 - F_{N_4}d_3 - F_{f_4}d_4 = 0 \end{cases} \tag{18}$$

$$\begin{cases} F_{f_3} = \mu F_{N_3} \\ F_{f_4} = \mu F_{N_4} \end{cases} \tag{19}$$

where:

F_{N3} is the supporting force of rice seed for cavity plane, (N);

F_{N4} is the supporting force of the rice seed for cavity outer plane, (N);

F_{f3} is the friction force of rice seed for cavity plane, (N);

F_{f4} is the friction force of rice seed for cavity outer plane, (N);

θ_1 is the cavity outer angle, (°);

θ_2 is the cavity inner angle, (°);

d_3 is the supporting force lever, (m);

d_4 is the friction force lever, (m).

From formula (18) and formula (19) can be obtained

$$\begin{cases} F_{N_3} = F_{N_4} = F_N^{'} \\ F_{f_3} = F_{f_4} = \mu F_N^{'} \\ \cos\theta_1 + \mu\sin\theta_1 = 1 \end{cases} \tag{20}$$

By substituting in formula (20) can be calculated

$$\theta_1 = \arcsin\left(\frac{2\mu}{1+\mu^2}\right) \tag{21}$$

After calculation, θ_1 is found to be 49.40°, which means that the angle between the inner and outer sides of the curved cavity should not be less than 49.40° in order to avoid the rice seed clamping by the plane of cavity.

The depth of the cavity

According to Fig. 3(e), in order to ensure that the rice seed do not get stuck in the cavity, the depth of the cavity D should satisfy formula (22):

$$D > a_{max} + l' + b_{max} \tag{22}$$

Based on Table 1, the depth of the curved cavity D is 16 mm.

The expression for the width K of the curved cavity bottom is as follows:

$$K > a_{\max} + \frac{b_{\max}}{\tan\theta_1} + \frac{b_{\max}}{\tan\theta_2} \tag{23}$$

When both the inner and outer angles are taken as the minimum value, the width range of curved cavity bottom is K > 14.31 mm, and it is set to 16 mm.

There exists the following geometric relationship between the cavity inner angle θ_2 and the depth of cavity D, the width of curved cavity bottom K, the width of seed-inlet B, cavity outer angle, as shown in Fig. 3(e). After other parameters are determined, the cavity inner angle θ_2 can be determined.

$$\theta_2 = \arctan\left(\frac{\sqrt{D^2 + \frac{D^2}{\cot^2\alpha}}}{K - B - \left(\frac{D}{\tan\theta_1}\right)}\right) \tag{24}$$

The equation of the transfusion curve cavities

When multiple cavities are involved in the seeding operation at the same time, the rice seeds in each cavity need to quickly gather at the seed outlet in the seed carrying link (*Kulaev et al., 2020; Laryushin et al., 2021*). Therefore, the trajectory of the transfusion cavities is designed as a brachistochrone curve in order to achieve the precision seeding of rice seeds, as shown in Fig. 3(a).

The curve equation is as follows:

$$\begin{cases} x_i = e_i t - e_i sin(t) - \pi e_i + f \\ y_j = -e_i cos(t) - g_i \end{cases} \tag{25}$$

where: i =1, 2, 3, 1 represents the outermost cavity of the discharge plate, e_1 is 12.88, 2 represents the middle cavity, e_2 is 10.30, 3 represents the innermost cavity, e_3 is 7.92, f, g_i respectively are the horizontal and vertical deviation distance between the starting point of the brachistochrone curve and the center of the discharge plate. Based on the principle of distributing the combined cavities as much as possible on the discharge plate, comprehensively referring to the diameter of the discharge plate and the length of the rice seeds, set f as 7mm, g_1 as 112.88mm, g_2 as 92.88 mm, g_3 as 71.88 mm.

RESULTS AND ANALYSIS

The performance testing of the seeding system on the test stand

The experimental apparatus and materials

The experimental apparatus for performance testing of the seeding system on the test bench is shown in Fig. 7.

The seed-metering device is driven by a three-phase asynchronous motor. A high-speed video camera (i-Speed 3, Olympus) is used to record the number of rice seeds discharged per hole during the seeding performance testing. The camera has a capture rate of 240 (f/s) and a resolution of 1280×1024 pixels.

The testing rice seeds include Wan Dao 153, Hybrid Rice II You 346, and Conventional Rice Te Sanai. Before the experiment, all rice seeds were under soaking and germination treatment to break the seed dormancy (*Hensh et al., 2022*). They were then placed in a cool and well-ventilated area to air-dry until the population became loose and free of clumps. This ensured the optimal conditions for mechanical direct seeding.

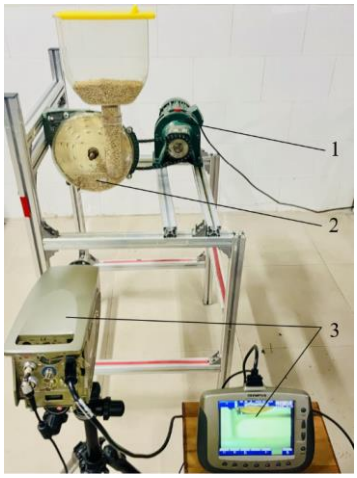


Fig. 7 - The diagram of seeding performance testing bench

1. The three-phase asynchronous motor; 2. The discharge plate; 3. The high-speed video camera;

The experimental method

According to the reference national standard GB-T25418-2022 (Rice direct seeder), the number of grains from 250 rice seed holes is continuously counted during stable seeding of the seed dispenser in each experimental group. For a set of experimental groups, the experiment is repeated three times, and the average value is obtained. The experimental evaluation indicators is given by calculation formula (26).

$$\begin{cases} M_j = \dfrac{n_{M_j}}{N} \times 100\% \\ Q_j = \dfrac{n_{Q_j}}{N} \times 100\% \\ R_j = \dfrac{n_{R_j}}{N} \times 100\% \\ P = \dfrac{m_P}{M_n} \times 100\% \end{cases} \tag{26}$$

In the formula, M represents the miss-seeding rate, (%); Q represents the qualified rate, (%); R represents the replay rate, (%); and N represents the total number of seed holes in a set of experimental groups. And, j=1, 2, and 3 respectively represent the number of openings of the seed-inlet for the discharge plate of each curved cavities set. When only one seed-inlet works, j=1, in this case, n_{M1} is the total number of holes which dropped out less than 1 seed, n_{Q1} is the total number of holes which dropped 1-3 seeds, and n_{R1} is the total number of holes which dropped out more than 3 seeds. When there are two seed-inlets opening on the outer side of the discharge plate, j=2, at this time, n_{M2} is the total number of holes which dropped out less than 2 seeds, n_{Q2} is the total number of holes which dropped 2-5 seeds, and n_{R2} is the total number of holes which dropped out more than 5 seeds. When all three seed-inlets opening simultaneously, j=3, at this time, n_{M3} is the total number of holes which dropped out less than 5 seeds, n_{Q3} is the total number of holes which dropped 5-10 seeds, n_{R3} is the total number of holes which dropped out more than 10 seeds. P represents the seed breakage rate in percentage (%). M_n represents the weight of seeds discharged during stable seeding for 1 minute, (kg). m_P represents the weight of damaged seeds among the discharged seeds, (kg). During the experiment, the speed of the discharge is set according to formula (27) (*Zha et al., 2020*).

$$n = \frac{60 v_d}{ks(1-q)} \tag{27}$$

where: v_d is the advance speed of the direct seeding machine, m/s, and 0.75 m/s is taken according to the general advance speed of the paddy field direct seeding machine;

k represents the number of curved cavities in the discharge plate, and in this case, the discharge plate has 11 groups.

s is seeding hole distance, mm,

q is the slip coefficient (Here, choose as 0.05).

Due to the difference in suitable seeding hole distance between super hybrid rice, hybrid rice and conventional rice, the distance is 180 mm, 150 mm and 140 mm respectively (*Zhang et al., 2020*). Therefore, the corresponding seeding speeds are 23.9 r/min, 28.7 r/min, and 30.8 r/min

The experimental design

Based on the previous theoretical analysis, the main parameters of metering hole structure which affect the performance of seeding device are the seed-inlet width B, the metering hole slope angle α, and curved cavity outer angle θ_1. To clarify the impact of the above structural parameters on seeding performance, a single-factor experiment will be conducted using Super Hybrid Rice Wan Dao 153 as the test crop, and the miss-seeding rate, qualified rate, and replay rate as the evaluation indicators. Test experimental factors and level setting refer to the results of the previous theoretical analysis, as shown in Table 2.

Table 2

Single factor test factors and levels

Test number No.	Factors		
	Seed-inlet width /mm	Metering hole slope angle /%	Curved cavity outer angle /%
1	3.6	30	55.0
2	3.8	32	62.5
3	4.0	34	70.0
4	4.2	36	77.5
5	4.4	38	85.0
6	-	-	92.5

In order to determine the optimal combination of metering hole structure parameters, a full-factor test refer to the single factor test results, with the miss-seeding rate, qualified rate, and replay rate as the evaluation indicators. The test level was set as shown in Table 3.

Table 3

Factors and levels in experiments

Test number No.	Factors	
	Seed-inlet width / mm	Metering hole slope angle / °
1	3.6	32
2	3.8	34
3	4.0	36

Based on the results of the single-factor and full-factor experiments, as well as the relationship between the results of seeding performance test of three types of rice—super hybrid rice, hybrid rice, and conventional rice—a variety compatibility experiment is performed by seeding different rice varieties with different numbers of seed-inlets on the discharge plate to ascertain the appropriate hole size for seeding super hybrid rice and conventional rice.

The experimental results and analysis

The effect of seed-inlet width on seeding performance

During the single factor test of seed-inlet width, the metering hole slope angle α and the cavity outer angle θ_1 were respectively maintained at 34° and 77.5°, the experimental results are as shown in Fig. 8.

According to Fig. 8, it can be observed that as the seed-inlet width increases, the miss-seeding rate of the seed-metering device decreases significantly at first and then gradually decreases, the replay rate increases slowly at first and then rapidly increases, and the qualified rate initially increases and then decreases. When the seed-inlet width is relatively small, it becomes difficult for the seeds to filling into the seed-inlet, resulting in a higher miss-seeding rate and a lower replay rate. As the seed-inlet width increases, the rice seed can fill into the seed-inlet smoothly, resulting in a significant decrease in miss-seeding rate, a slight increase in replay rate, and an overall increase in the qualified rate. When the seed-inlet width is too large, an excessive quantity of rice seeds is filled into the seed-inlet, resulting in a significant increase in replay rate and a gradual decrease in miss-seeding rate. As a result of the increased replay rate, the overall qualified rate decreases noticeably. It can be observed that the suitable seed-inlet width for the discharge plate should be in the range of 3.6-4.0 mm. At this range, the seed-metering device achieves a qualified rate of 85% or higher.

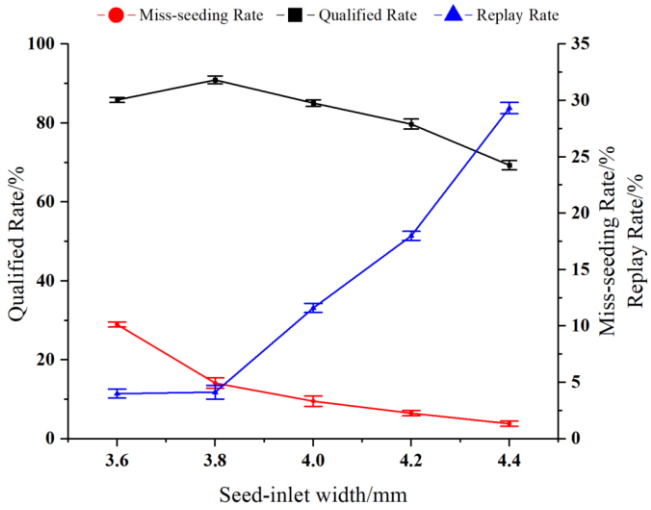


Fig. 8 - Test results of seed-inlet width

The effect of metering hole slope angle on seeding performance

In the single-factor experiment of the metering hole slope angle, the seed-inlet width *B* and the curved cavity outer angle θ_1 were respectively maintained at 3.8 mm and 77.5°. The experimental results as shown in Fig. 9.

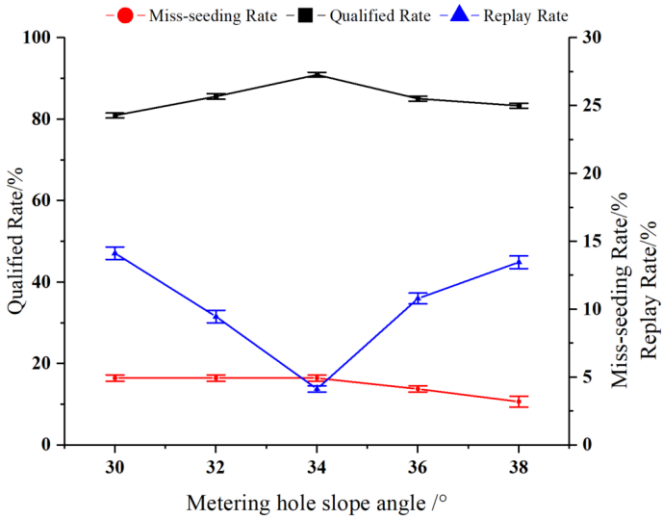


Fig. 9 - Test results of metering hole slope angle

From Fig. 9, it can be observed that as the metering hole slope angle increases, the miss-seeding rate of the seed-metering device decreases slowly, the replay rate decreases significantly at first and then increases significantly, and the qualified rate first increases and then decreases. When the metering hole slope angle is smaller, the height of seed-limiting plate is lower. As the angle increases, the height of seed-limiting plate increases, which lead to the metering hole inclined plane gradually becomes steeper. When the metering hole slope angle is small, the metering hole inclined plane is gentle, and the height of seed-limiting plate has a lesser impact on seeding performance. However, as the metering hole slope angle increases, the height of seed-limiting plate also increases, resulting in a phenomenon where the miss-seeding rate remains basically unchanged while the replay rate decreases significantly. In the later stage, when the metering hole inclined plane is steeper, the height of seed-limiting plate has a significant impact on the seeding performance. As the metering hole slope angle increases, the height of seed-limiting plate also increases. In this case, it is difficult for the seed-metering device to clear the superfluous seeds, resulting in a decrease in miss-seeding rate and an increase in replay rate.

The effect of cavity outer angle on seeding performance

In the single-factor experiment of the cavity outer angle, the seed-inlet width *B* and the metering hole slope angle α were respectively maintained at 3.8 mm and 34°. The experimental results as shown in Fig.10.

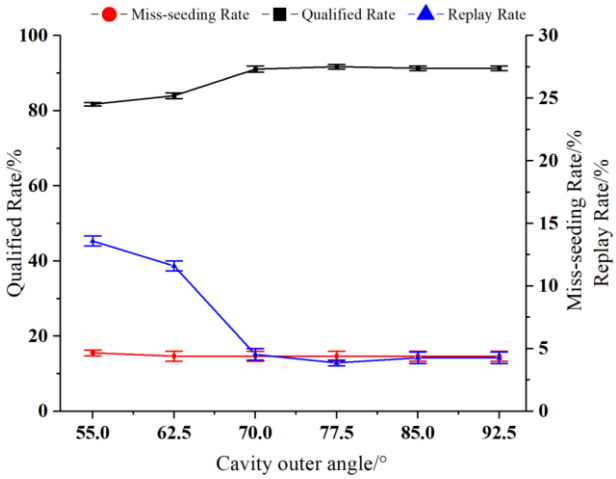


Fig. 10 – Test results of cavity outer angle

According to Fig. 10, it can be observed that as the cavity outer angle increases, the miss-seeding rate remains basically unchanged, while the qualified rate initially increases and then stabilizes. On the other hand, the replay rate initially decreases and then stabilizes. When the cavity outer angle is smaller, the cavity outer plane is steeper, making it easier for the rice seed to enter the seed-inlet. Additionally, it can accommodate more rice seeds and is not easily cleared out. This results in a higher replay rate. As the cavity outer angle increases, the cavity outer plane becomes flatter, which improves the phenomenon of overfilling with rice seed. And, the superfluous seeds are easily cleared out from the seed-inlet. As a result, the replay rate significantly decreases, and the qualified rate increases. When the cavity outer angle increases to 70° or above, the cavity outer plane becomes flatter. This prevents excessive accumulation of rice seeds at the cavity outer angle, it becomes easier to clear out superfluous seeds, resulting in all the evaluation indicators stabilizing and maintaining at a good level of seeding performance. The qualified rate consistently floats above 90%, and the miss-seeding rate remains below 5%.

The full factor experiment

The results of the full factor experiment are shown in Fig. 11.

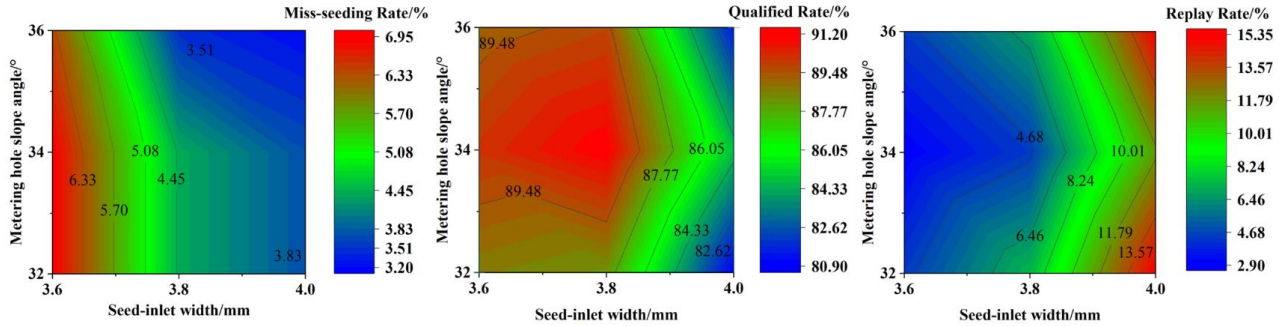


Fig. 11 - Test results of the full factor experiment

In order to analyze the impact of various experimental factors on the evaluation indicators, a two-dimensional contour plot depicting the influence of experimental factors on the evaluation indicators can be constructed based on the data of the full factor experiment. According to Fig. 11, it can be observed that the color distribution in the plot shows distinct levels of change with the variation in the seed-inlet width. This indicates that the evaluation indicators exhibit significant variations with the changing in the seed-inlet width. Within the range of the experiment for the metering hole slope angle, it can be observed that the results of experiment for intermediate horizontal experimental factors are better than the two sides' horizontal experimental factors, with lower incidences of missing and replay rates. Therefore, it can be concluded that the seed-inlet width has a more significant impact on the seeding performance. As the seed-inlet width increases, the miss-seeding rate decreases while the replay rate increases, and the qualified rate initially remains stable, but later decreases. As the metering hole slope angle increases, the miss-seeding rate remains unchanged at first and then decreases, the replay rate initially decreases and then increases, and the qualified rate initially increases and then decreases. The results of the full factor experiment are consistent with those of the single-factor experiment.

Minitab 21 software was used for regression analysis of the test results, and regression equations (28) were established between each evaluation indicators of seeding performance and the seed-inlet width and the metering hole slope angle. The results of the analysis of variance are shown in Table 4.

$$\begin{cases} M = 1.57 - 2.095\,A + 0.0914\,B + 0.2712\,A^2 - 0.000775\,B^2 - 0.00081\,A \bullet B \\ Q = -30.30 + 7.22\,A + 0.639\,B - 0.972\,A^2 - 0.00572\,B^2 - 0.0001\,A \bullet B \\ R = 29.72 - 5.11\,A - 0.731\,B + 0.700\,A^2 + 0.00650\,B^2 + 0.00081\,A \bullet B \end{cases} \quad (28)$$

Table 4

The table of analysis of variance

	M				Q				R			
R^2	99.46%				98.27%				99.09%			
S	0.0018				0.0082				0.0075			
Source of variance	DF	SS	F	P	DF	SS	F	P	DF	SS	F	P
Model	5	0.0018	111.22	**	5	0.0115	34.13	**	5	0.0183	65.38	**
A	1	0.0002	58.82	**	1	0.0023	33.73	**	1	0.0011	20.30	**
B	1	0.0000	6.20	*	1	0.0010	14.63	*	1	0.0013	22.95	**
A*A	1	0.0002	72.44	**	1	0.0030	44.95	**	1	0.0016	27.96	**
B*B	1	0.0000	5.91	*	1	0.0011	15.57	*	1	0.0017	24.11	**
A*B	1	0.0000	0.13	0.742	1	0.0000	0.000	0.996	1	0.0000	0.010	*
Error	3	0.0000			3	0.0002			3	0.0002		
Total	8	0.0018			8	0.0117			8	0.0185		

(is significant effects, $P < 0.05$; ** is extremely significant effects, $P < 0.01$)*

According to Table 4, the regression models for the miss-seeding rate, qualified rate, and replay rate of the seed-metering device are all extremely significant. The correlation coefficients R^2 for each regression models respectively are 99.46%, 98.27%, and 99.09% for the miss-seeding rate, qualified rate, and replay rate, which are very close to 100%. The standard error of regression S is less than 0.01, which indicates that the equation of quadratic regression models fit very well with the actual situation. It can accurately reflect the relationship between the performance of the seed discharge and the seed-inlet width and the metering hole slope angle, and can better predict the test results.

In addition, seed-inlet width has significant effects on the miss-seeding, qualified and replay rate of seed-metering device. The metering hole slope angle has significant effects on the qualified rate and replay rate, but not on the miss-seeding rate. The reason may be that the metering hole inclined plane gradually becomes steeper and the height of seed-limiting plate is higher within the range of the parameter for the metering hole slope angle, so the seeds which filled into the metering hole is difficult to clear. Therefore, with the increase of metering hole slope angle, the miss-seeding rate does not change much, only decreases slightly. As a result, the influence of metering hole slope angle on the miss-seeding rate of seed-metering device is not significant.

In order to clarify the optimal combination of the seed-inlet width and the metering hole slope angle, a multi-objective optimization model is established based on the regression models of each evaluation indicators of seeding.

$$\begin{cases} \min M \\ \max Q \\ \min R \\ 3.6 \le A \le 4.0 \\ 32 \le B \le 36 \end{cases} \quad (29)$$

The response optimizer in Minitab 21 software was used to solve the optimization model. The optimal combination of structural parameter predicted that seed-inlet width was 3.79 mm and metering hole slope angle was 35.07°. In the predictor, the miss-seeding rate was 3.88%, the qualified rate was 90.39%, and the replay rate was 5.73%.

To verify the reliability of the optimization results, the seed-inlet width and the metering hole slope angle were respectively set to 3.80 mm and 35°. And the discharge plate was processed to carry out seeding validation experiments, the experimental results are shown in Table 5. From Table 5, it can be observed that the results of the optimization model are consistent with the results of seeding validation experiments, which indicates that the optimization results are reliable. The results indicated that the appropriate seed-inlet width is 3.80 mm and the metering hole slope angle is 35° for super hybrid rice.

Table 5

Results of validation experiment

Test number No.	Test results		
	Miss-seeding Rate/%	Qualified Rate/%	Replay Rate/%
1	4.00	90.80	5.20
2	3.60	90.80	5.60
3	4.00	90.40	5.60
Average	3.87	90.67	5.46

The hybrid rice seeding experiment

Based on the appropriate structure parameters of metering hole for super hybrid rice and the required hole-seeding quantity what have multiplied relationship between super hybrid rice and hybrid rice, the hole-seeding quantity of hybrid rice is approximately double that of super hybrid rice. Therefore, the structure of metering hole for seed-inlet width of 3.8 mm and metering hole slope angle of 35° were adopted. Two rows of inlets were opened on the outer circumference of the discharge plate to conduct hybrid rice seeding experiments, repeated three times, with the experimental results shown in Table 6.

Table 6

Results of seeding experiment of hybrid rice

Test number No.	Test results		
	Miss-seeding Rate / %	**Qualified Rate / %**	**Replay Rate / %**
1	3.60	91.20	5.20
2	3.60	90.40	6.00
3	4.00	90.80	5.20
Average	3.73	90.80	5.47

As shown in Table 6, when the dimensions of the two rows of metering holes on the outer circumference of the discharge plate are the same (seed-inlet width of 3.8 mm and metering hole slope angle of 35°), the results of the experiments was miss-seeding rate of 3.73%, qualified rate of 90.80%, and replay rate of 5.47%. This meets the agronomic requirements for precise hole-seeding of hybrid rice.

The conventional rice seeding experiment

Based on the two-factor full factorial experiment results of the seed-inlet width and the metering hole slope angle, there was a significant impact of the seed-inlet width on the miss-seeding rate, qualified rate, and replay rate, while the metering hole slope angle had no significant impact on the miss-seeding rate. Based on the principle of "prefer to be replay rather than missing" in direct seeding of rice, where the metering hole slope angle can be maintained, the quantity of seeding can be adjusted only by changing the seed-inlet width. Strive for a higher qualified rate while maintaining a low miss-seeding rate. Based on the experimental results of hybrid rice and the relationship between the required hole-seeding quantity conventional rice and hybrid rice, it is observed that the required hole-seeding quantity for conventional rice is approximately twice that of hybrid rice. To meet the planting requirements of 5-10 seeds per hole for conventional rice, three seed-inlet must be opened of the combined cavity. In addition, the outer two circles of the seed-inlet should maintain suitable dimensions for hybrid rice seeding. This means that the seed-inlet width is 3.8 mm and the metering hole slope angle is 35°. An experiment for the innermost seed-inlet width can be conducted. Due to the stacking shape of the rice seeds inside the seed-metering device, the filling area of the inner-side inlet is smaller than the two outer-side inlets. This leads to a difference in the optimal seeding width between the outer-side inlets and the inner-side inlet when using the same structural parameters. Based on the reference dimensions for suitable seed-inlet width for super hybrid rice and hybrid rice, three different levels can be set for the innermost seed-inlet width: 5.2 mm, 5.4 mm and 5.6 mm. The experimental results are shown in Fig. 12.

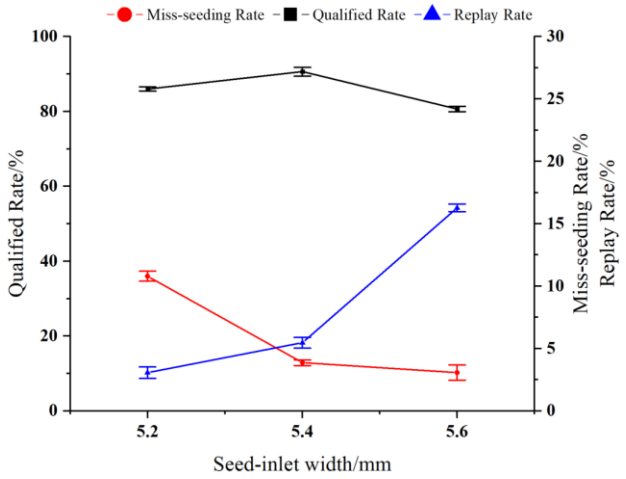


Fig. 12 – Test results of the conventional rice seeding experiment

According to Fig. 12, it can be observed that as the innermost seed-inlet width for the discharge plate increases, the miss-seeding rate decreases significantly at first and then decreases slightly. Meanwhile, the replay rate increases slightly at first and then increases significantly. The qualified rate initially increases and then decreases. These patterns of change are consistent with the results of the single-factor experiment on seed-inlet width. Based on the analysis, it can be concluded that when the innermost seed-inlet width for the discharge plate is set to 5.4 mm, the seeding performance is optimal.

At this width, the miss-seeding rate is 3.53%, the qualified rate is 90.67%, and the replay rate is 5.80%. It can meet the required hole-seeding quantity of conventional rice precision hole. If the seed-inlet width is too small, the miss-seeding rate will increase sharply. If it is too large, the replay rate will increase sharply, and the miss-seeding rate does not change much. Therefore, the optimal for the innermost seed-inlet width of conventional rice planting is determined to be 5.4 mm.

The seed breakage rate experiment

According to the reference national standard GB-T25418-2022 (Rice direct seeder), experiments were conducted with suitable seed-metering device apparatus structural parameters for three types of rice. The experiments focused on the seed breakage rate during rice seeding, and were repeated 5 times. The results of the experiments are shown in Table 7.

Table 7

Results of seed breakage rate

Test number No.	Test results of seed breakage rate		
	Wan Dao 153/%	Ⅱ You 346/%	Te Sanai /%
1	0.20	0.14	0.32
2	0.20	0.24	0.49
3	0.17	0.34	0.47
4	0.18	0.28	0.38
5	0.20	0.22	0.44
Average	0.19	0.24	0.42

From Table 7, it can be observed that the seed breakage rates for all three types of rice which are used by the seed-metering device are less than 0.5%. These are all below the standard requirement of 0.8% for seed breakage rate. This indicates that the design of the seed-metering device is reasonable and meets the planting agronomic requirements for precise hole-seeding.

The field validation test

In order to test the field seeding performance of the combined cavity-type rice precision hole-drop seed-metering device, a field seeding experiment was carried out in June 2023.

Before experiment, a rotary tiller was used to plough the experimental field, then irrigate and bubble the field, ensuring a smooth surface without crop residues and weeds. Taking filed experiment after the field was allowed to static precipitation for 2 days, and there was no standing water on the surface.

Install the seed-metering device on the rice direct seeding machine. The seed-metering device is driven by the ride-on chassis of the direct seeding machine. Adjust the discharge plate to the required state for seeding the rice seeds. The seeding operation is shown in Fig. 13.



Fig. 13 - The diagram of the seed-metering device works

During the experiment, the speed of the direct seeding machine was kept stable at 0.75 m/s, and the discharge plate speed was adjusted to match the required speed for the rice seeds. Every 250 holes were regarded as a group, the number of hole seeding, the hole diameter, and the hole distance were counted. Each variety was repeated three times for experimentation and the average values were obtained. The experimental results are shown in Table 8.

Table 8

Results of field validation test

Species	Test results of field validation test				
	Miss-seeding Rate %	Qualified Rate %	Replay Rate %	Hole diameter mm	Hole distance mm
Wan Dao 153	2.67	86.33	11.00	19.82	175.77
Ⅱ You 346	2.53	86.34	11.13	25.43	146.87
Te Sanai	2.33	90.33	7.34	33.3	140.91

As shown in Table 8, for seeding super rice Wan Dao 153 using outermost seed-inlets, the miss-seeding rate is 2.67%, the qualified rate (1-3 grains per hole) is 86.33%, average hole diameter is 19.82 mm, average hole distance is 175.77 mm, the requirement of hole distance is 180 mm. For seeding hybrid rice II You 346 using outer two seed-inlets, the miss-seeding rate is 2.53%, the qualified rate (2-5 grains per hole) is 86.34%, average hole diameter is 25.43 mm, average hole distance is 146.87 mm, the requirement of hole distance is 150 mm. For seeding conventional rice Te Sanai using all three seed-inlets, the miss-seeding rate is 2.33%, the qualified rate (5-10 grains per hole) is 90.33%, average hole diameter is 33.31 mm, average hole distance is 140.91 mm, the requirement of hole distance is 140 mm. The seeding requirements are met for the three varieties of rice seeds. Compared with bench test, field test had lower miss-seeding rate, higher replay rate and slightly lower qualified rate. The reason is that in the field test, due to the vibration of the machine, the number of seeds filling into the seed-metering device increases, resulting in a higher replay rate and a lower miss-seeding rate.

CONCLUSIONS

(1) In order to meet the different seeding requirement quantity of super rice, hybrid rice, and conventional rice, a seeding quantities selectable combined cavity-type precision hole-drop seed-metering device was designed which used an innovative combined seeding method. By adjusting the number of metering holes involved in seeding, it could realize the adjustment of the seeding quantity. This design shows promising practical prospect.

(2) Single factor and full factor bench seeding tests were carried out on the structural parameters of the seed-inlet width, the metering hole slope angle, and cavity outer angle, which affected the seeding performance of the seed-metering device. Under the appropriate structural parameters, that is, when the width of outer and middle seed-inlets is 3.8 mm, the innermost seed-inlet width is 5.4 mm, the metering hole slope angle is 35°, the cavity outer angle is 85°, the precision filling function can adapt to different seeding quantity of different varieties of rice, and has been verified by bench and field seeding tests.

ACKNOWLEDGEMENT

This work was supported by the National Natural Science Foundation of China, China (Grant numbers 51805005), Major Project of Natural Science Research in Universities of Anhui Province (Grant numbers KJ2021ZD0012), Key research and Development Project of Anhui Province (Grant numbers 202204c06020024) and Key programs of outstanding young talents in universities (Grant numbers gxyqZD2022016)

REFERENCES

[1] Cheamuangphan, A., Singhavara, M., & Phaoumnuaywit, A. (2018). Cost and Benefit Analysis of Rice Production between Transplanting and Direct Seeded Method for Rice in Upper Northern Region. *International Journal of Business and Economic Affairs*, 3(5), 227-236. 10.24088/IJBEA-2018-35005

[2] Farooq, M., Siddique, KHM., Rehman, H., Aziz, T., Lee, D., & Wahid, A. (2011). Rice direct seeding: Experiences, challenges and opportunities. *Soil & Tillage Research*, 111(2), 87-98. https://doi.org/10.1016/j.still.2010.10.008

[3] Hensh, S., & Raheman, H. (2022). Laboratory evaluation of a solenoid-operated hole dropping seed metering mechanism for pre-germinated paddy seeds. *Journal of Biosystems Engineering*, 47(1), 1-12. 10.1007/s42853-021-00124-8

[4] Hensh, S., & Raheman, H. (2022). An unmanned wetland paddy seeder with mechatronic seed metering mechanism for precise seeding. *Computers and Electronics in Agriculture*, 203, 107463. https://doi.org/10.1016/j.compag.2022.107463

[5] Jat, R K., Vijay S. M., Manish K., Vijay S. J., Illathur R. R., & Avinash C. P. (2022). Direct Seeded Rice: Strategies to Improve Crop Resilience and Food Security under Adverse Climatic Conditions. *Land*, 11 (3), 382. https://doi.org/10.3390/land11030382

[6] Kulaev, E. V., Danilov, M. V., Vysochkina, L. I., Kalugin, D. S., & Maliev, V. K. (2020, June). Improvement of the process of dosing sugar beet seeds using a cone-shaped sowing apparatus. In *IOP Conference Series: Materials Science and Engineering*, 873(1), 012034. 10.1088/1757-899X/873/1/012034

[7] Li, B., Ahmad, R., Qi, X., Li, H., Nyambura, S.M., Wang, J., Chen, X., & Li, S. (2021). Design Evaluation and Performance Analysis of a Double-Row Pneumatic Precision Metering Device for Brassica chinensis. *Sustainability*, 13(3), 1374. https://doi.org/10.3390/su13031374

[8] Li, H., Zhao, C., Yan, B., Ling, L., & Meng, Z. (2022). Design and Verification of the Variable Capacity Roller-Wheel Precision Rice Direct Seed-Metering Device. *Agronomy*, 12(8), 1798. https://doi.org/10.3390/agronomy12081798

[9] Liu, Y., Dokohely, M.E., Fan, C., Li, Q., Zhang, X., Zhao, H., & Xiong, Z. (2016). Influence of Different Seedling-Nursing Methods on Methane and Nitrous Oxide Emissions in the Double Rice Cropping System of South China. *Clean Soil Air Water*, 44(12), 1733-1738. https://doi.org/10.1002/clen.201400479

[10] Laryushin, N. P., Shukov, A. V., Kiryukhina, T. A., & Yashin, A. V. (2022). Innovative seed planter implements for resource-saving sowing technologies. In *IOP Conference Series: Earth and Environmental Science* 953(1), 012012. https://doi.org/10.1088/1755-1315/953/1/012012

[11] Rajaiah, P., Mani, I. N. D. R. A., Kumar, A., & Singh, A. K. (2015). Role of physical and engineering properties of rice (Oryza sativa) cultivars for designing of precision planter. *The Indian Journal of Agricultural Sciences*, 85(12), 1602-1608. https://www.researchgate.net/publication/292843868

[12] Rajaiah, P., Mani, I., Parray, R. A., Lande, S. D., Kumar, A., & Vergese, C. (2020). Design and development of precision planter for paddy direct seeding. *Journal of Agricultural Engineering*, 57(4), 302-314. https://www.researchgate.net/publication/349059316

[13] Tang, H., Xu, C., Guo, F., Yao, Z., Jiang, Y., Guan, R., Sun, X., & Wang, J. (2022). Analysis and Experiment on the Seed Metering Mechanism of Multi-Grain Cluster Air Suction Type Rice (*Oryza sativa L.*) Hole Direct Seed Metering Device. *Agriculture*, 12(8), 1094. https://doi.org/10.3390/agriculture12081094

[14] Tian, L., Ding, Z., Su, Z., Li, L., & Wang, Z. (2022). Design and experiment of rotary precision hole direct seed-metering device for rice. *INMATEH Agricultural Engineering*, 66(1), 311-320. https://doi.org/10.35633/inmateh-66-31

[15] Van Loon, J., Krupnik, T.J., López-Gómez, J.A., Timsina, J., & Govaerts, B.A. (2020). Standard Methodology for Evaluation of Mechanical Maize Seed Meters for Smallholder Farmers Comparing

Devices from Latin America, Sub-Saharan Africa, and Asia. *Agronomy*, 10(8), 1091. https://doi.org/10.3390/agronomy10081091

[16] Wang, Z., Huang, Y, Wang, B., Zhang, M.; Ma, Y.; Ke, X.; & Luo, X. (2018). Design and experiment of rice precision metering device with seeding quantity stepless adjusting (播量无级调节水稻精量排种装置设计与试验). *Transactions of the Chinese Society of Agricultural Engineering*, 34(11), 9-16. (in Chinese) https://doi.org/10.11975/j.issn.1002-6819.2018.11.002

[17] Xing, H., Wang, Z., Luo, X., Zang, Y., He, S., Xu, P., & Liu, S. (2022). Design and experimental analysis of rice pneumatic seeder with adjustable seeding rate. *International Journal of Agricultural and Biological Engineering*, 14(4), 113-122. https://doi.org/10.25165/j.ijabe.20211404.5658

[18] Yamauchi, M. (2017). A review of iron-coating technology to stabilize rice direct seeding onto puddled soil. *Agronomy Journal*, 109(3), 739-750. https://doi.org/10.2134/agronj2016.10.0569

[19] Zeng, X. (2013). *The research in mechanization planting ways and seeding ratios at different early direct seeding rice (不同早稻品种的机直播方式和播种量研究)* [Unpublished doctoral dissertation]. Nanchang: Jiangxi Agricultural University. (in Chinese)

[20] Zhai, J., Xia, J., Zhou, J., Zhou, Y., & Zhan, P. (2017). Design and field trials of pneumatic precision drilling planter of rice budded seed in dry land (气力式杂交稻精量穴直播排种器设计与试验). *Journal of Huazhong Agricultural University*, 36(1), 110-116. (in Chinese) https://doi.org/10.13300/j.cnki.hnlkxb.2017.01.017

[21] Zha, X., Zhang, G., Zhang, S., Hou, Q., Wang, Y., & Zhou, Y. (2020). Design and experiment of centralized pneumatic deep precision fertilization device for rice transplanter. *International Journal of Agricultural and Biological Engineering*, 13(6), 109-117. 10.25165/j.ijabe.20201306.5479

[22] Zhang, M., Wang, Z., Luo, X., Zang, Y., Yang, W., Xing, H., & Dai, Y. (2018). Review of precision rice hole-drop drilling technology and machine for paddy. *International Journal of Agricultural and Biological Engineering*, 11(3), 1-11. https://doi.org/10.25165/j.ijabe.20181103.4249

[23] Zhang S, He H L, Yuan Y W, Kuang F M, Xiong W, Li Z D, & Zhu, D Q. (2023). Optimization of hole-groove combined hole-type of guide filling precision Hole-drop seed-metering device for rice (导向充填式水稻精量穴播排种器孔-槽组合型孔设计与试验). *Transactions of the Chinese Society of Agricultural Engineering*, 39(12), 39-50. (in Chinese) 10.11975/j.issn.1002-6819.202302154

[24] Zhang S., Li Y., Wang H., Liao J, Li Z, & Zhu D. (2020). Design and Experiment of U-shaped Cavity Type Precision Hole-drop Seed-metering Device for Rice (U 型腔道式水稻精量穴播排种器设计与试验). *Transactions of the Chinese Society of Agricultural Machinery*, 51(10),98-108. (in Chinese) 10.6041/j.issn.1000-1298.2020.10.012

[25] Zhang S., Xia J., Zhou Y., Zhai J., Guo Y., Zhang X., & Wu H. (2015). Design and experiment of pneumatic cylinder-type precision direct seed-metering device for rice(气力滚筒式水稻直播精量排种器的设计与试验). *Transactions of the CSAE*, 31(1), 11-19. (in Chinese) https://doi.org/10.3969/j.issn.1002-6819.2015.01.002

[26] *** *China Statistical Yearbook* (中国统计年鉴) (2022). Beijing: China Statistics Press. (in Chinese)

[27] *** GB/T 25418-2022. (2022). *Rice direct seeder* (水稻直播机). National Standard of the People's Republic of China. (in Chinese)

DETECTION OF EATING BEHAVIOUR IN PIGS BASED ON MODIFIED YOLOX
/
基于改进的 YOLOX 猪只饮食行为检测

Yanwen LI, Juxia LI *), Lei DUAN, Tengxiao NA, Pengpeng ZHANG, Qingyu ZHI
College of Information Science and Engineering, Shanxi Agricultural University/China
Tel: +86-15803446486; E-mail: lijxsn@126.com
DOI: https://doi.org/10.35633/inmateh-71-03

Keywords: *deep learning, behavior detection, YOLOX, attentional mechanism, pig*

ABSTRACT
Due to the complex environment of pig farms and the diversity of pig behaviors, the existing methods based on deep learning cannot meet the requirements of high accuracy and real-time detection of pig eating behavior. In this paper, a SE-YOLOX model for detecting pig diet and drinking behaviors was designed. In this model, a Squeeze-and-Excitation (SE) attention module is introduced between the neck layer and the prediction layer of YOLOX, and the input feature map is compressed into a vector through global average pooling operation, and then mapped to a smaller vector through a fully connected layer. A sigmoid function is also used to compress each element in this vector to between 0 and 1 and multiply it with the original input feature map to get the weighted feature map. Through SE attention mechanism, the model can learn the importance of each channel adaptively, thus improving the detection accuracy. The experimental results show that the mean Average Prediction (mAP) of the SE-YOLOX model is 88.03%, which is higher than 13.11% of the original YOLOX model. SE-YOLOX can ensure real-time performance, it also can effectively improve the accuracy of pig diet and drinking water behavior detection.

摘要
由于养猪场环境的复杂和猪行为的多样性，现有的基于深度学习的方法难以满足猪食用行为检测的高精度和实时性要求，本文提出了一种 SE-YOLOX 猪只饮食饮水检测模型。该模型在 YOLOX 的 Neck 层和 Prediction 层之间引入 Squeeze-and-Excitation (SE)注意力模块，通过全局平均池化操作将输入特征图压缩成一个向量，然后通过一个全连接层将其映射到一个较小的向量；同时使用一个 sigmoid 函数将这个向量中的每个元素压缩到 0 到 1 之间，并将其与原始输入特征图相乘，得到加权后的特征图。通过 SE 注意力机制，该模型可以自适应地学习到每个通道的重要特征，从而提高检测精度。实验结果表明，SE-YOLOX 模型的平均检测精度(mAP)为 88.03%，高于原 YOLOX 模型 13.11%。SE-YOLOX 在保证实时性的同时，能有效提高猪饮食饮水行为检测的准确性。

INTRODUCTION

The eating behavior of pigs can often reflect the health and emotional problems of pigs and is an important basis for judging the health of pigs. Through monitoring, the dietary behavior rules of pigs can be extracted, and feed amount, water consumption, and other resources can be allocated rationally according to different times and seasons. Artificial monitoring of pigs' dietary behavior requires a large amount of manpower and is difficult to achieve long-term and sustained observation. Meanwhile, errors in judgment will inevitably occur. Automatic monitoring of pig-eating behavior has become a hot topic in recent years. It not only improves the level of automatic pig breeding but also has great significance to master the health status of pigs and improve their growth welfare (*Chen et al., 2022; Statham et al., 2020; Shen et al., 2014*).

At present, the commonly used methods to detect pig eating behavior include radio frequency identification technology and machine vision technology. RFID technology is mainly used to identify the eating behavior of pigs by wearing electronic ear tag sensors. In addition, RFID receivers are installed next to drinking water and eating utensils. When pigs are close to drinking and eating utensils, the receiver reads the corresponding information, thereby recording pig eating behavior and pig health problems (*Maselyne et al., 2014; Li et al., 2021; Wang, 2021*). Although RFID technology has high accuracy and can complete real-time monitoring of pigs' dietary behavior, each pig needs to wear ear tags, which leads to increased costs. At the same time, the sensor is damaged or lost due to abnormal behavior such as ear biting.

Nowadays, Machine vision technology based on deep learning can not only accurately identify pig behavior, but also has the advantages of convenience and low cost, and has been widely used in the current pig-raising process (*Qin et al., 2021)*. Yang Qiumei achieved pig detection through image segmentation, and the accuracy rate of pig drinking behavior recognition reached 92.11% (*Yang et al., 2018*). Wu Shihai used convolutional neural networks to extract the depth features of pig images, and the accuracy of pig behavior recognition in sequence images reached 94% (*Wu et al., 2020*). The above target detection model mainly adopts the setting of a priori frame, which cannot well solve the influence of factors such as the size of the target in the image and the mutual occlusion of the target on the detection result during model detection.

In order to ensure the real-time detection of the pig dietary behavior detection model, the detection accuracy is improved as much as possible. In this paper, a targeted method for pig diet behavior detection based on the SE-YOLOX model is proposed. This model ensures the accuracy of real-time detection and can be ported to various devices, which can be applied to various aquaculture farms.

MATERIALS AND METHODS

Data Acquisition and Preprocessing

The experimental data in this paper were collected from the pig breeding base in Fenxi County, Linfen City, Shanxi Province. In order to obtain the diet images of pigs in different environments, four adult pigs were selected and placed in a captive environment of 3.0m×3.0m×2.0m from July 2, 2020. 3h videos were filmed in the morning, afternoon, and night for 7 consecutive days. The total video length is 63h. Allied Vision Technologies' Manta G-282C camera was used. In order to clearly check the eating and drinking situation of pigs during the day, a stationary camera is one meter high from the ground and forms a 35° angle to the wall which is mounted on the wall to the right of the pig feed trough. In order to prevent unsupervised shooting at night and reduce the difficulty of shooting, another camera with a height of 3 meters and forms a 45° angle to the wall was placed on the roof of the piggery for night shooting.

KMPlayer software was used for video interception of the collected data, and JPG images were extracted according to 1F/s for the captured video, and then the obtained images were screened. In order to enrich the training data of the model, the selected samples included samples of different time periods, different lighting intensities and different shooting angles, and finally 1615 images were selected as the training and test sample data. The sample size was uniformly adjusted to 640 *640 pixels to improve the training speed of the model.

After selecting appropriate samples, LabelImg image labeling tool was used to label the eating behavior of pigs, as shown in Fig. 1.



Fig. 1 - Data annotation

SE-YOLOX algorithm

YOLOX is a new high-performance detector based on YOLOv3, which improved the Anchor free mechanism, the Decoupled Head, and the label distribution strategy SimOTA. It achieved significant performance improvements while still maintaining the efficient reasoning characteristics of the YOLO series. Its network structure is shown in Fig. 2.

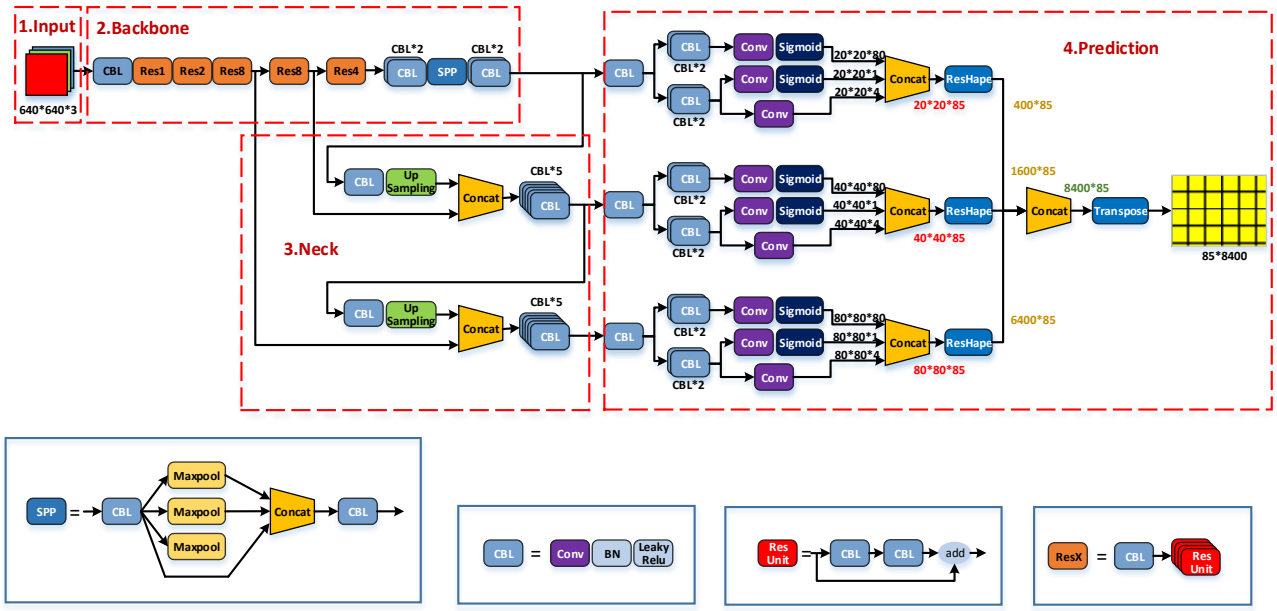


Fig. 2 - YOLOX network structure

The backbone network of YOLOX network structure is Darknet53, in which neck layer and prediction layer are updated and strengthened. YOLOX adopts Mosaic and MixUp data enhancement methods on the input side. For neck layer, YOLOX still adopts the structure of Feature Parymid Network (FPN) for fusion, and transmits and fuses the feature information of high level through up-sampling from top to bottom, so as to obtain the feature graph for prediction. YOLOX achieves a better balance in terms of speed and accuracy than any other model of YOLO series.

In order to obtain more detailed information about the target of attention from different sources and suppress other useless information, the Squeeze and Excitation (SE) Networks attention mechanism was introduced. SE attention mechanism is a channel type of attention mechanism. It's main content is squeeze and excitation. Through automatic learning, another new neural network is used to obtain the importance of each channel of the feature map and then use this importance to assign a weight value to each feature, so that the neural network can focus on certain feature channels. Promote the feature graph channels that are useful to the current task, and suppress the feature channels that are not useful to the current task. The main innovation of the network is that the model can automatically learn the importance of different channel features by focusing on the relationship between channels. The SE attention mechanism mainly includes operations through squeezes and excitation. The squeeze operation uses global averaging pooling to encode the entire spatial features on the channel as local features.

The calculation method is shown in (1) :

$$z_C = \frac{1}{H \times W} \sum_{i=1}^{H} \sum_{j=1}^{w} u_C(i, j) \tag{1}$$

In this formula, the second two-dimensional matrix in the convolution 3d matrix represents the result of the squeeze operation, and the subscript represents the number of channels. After the squeeze operation gets the channel information, use two full connection layers to form the gate mechanism and activate it with Sigmoid function. The calculation method is shown in (2) :

$$s = F_{ex}(z, W) = \sigma(g(z, W)) = \sigma(W_2 \delta(W_1 z)) \tag{2}$$

Where:

δ is ReLU activation function, σ is Sigmoid function, W_1 and W_2 are the weights used by the two fully connected layers to reduce and increase dimensions, respectively equal to $\frac{C}{\mathrm{r}} \times C$ and $\frac{C}{\mathrm{r}} \times C$, and r is the scaling parameter to limit model complexity and improve model capability. s represents the weight set of feature graphs obtained through the fully connected layer and nonlinear layer. Finally, the weight of the output is assigned to the original feature. The calculation formula is shown in (3):

$$\tilde{x}_c = s_c \times u_c \tag{3}$$

where, $\tilde{x}_c$ is the feature graph of the feature channel of x, s_c is the weight, and u_c is a two-dimensional matrix. As shown in Figure 3:

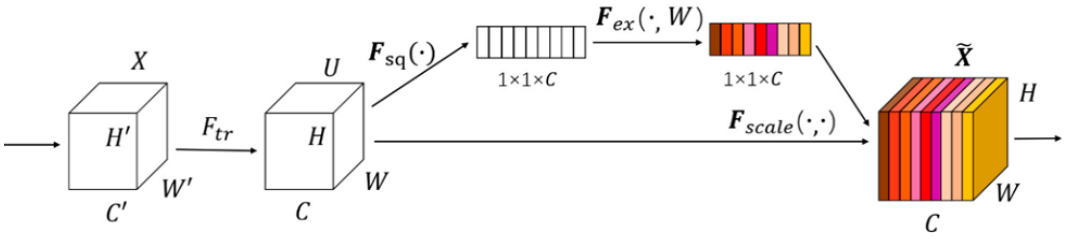


Fig. 3 - The structure of SE attention mechanism

This example inserts SE attention mechanism in the YOLOX. The network structure name is defined as SE-YOLOX. The SE-YOLOX network structure is shown in Fig.4.

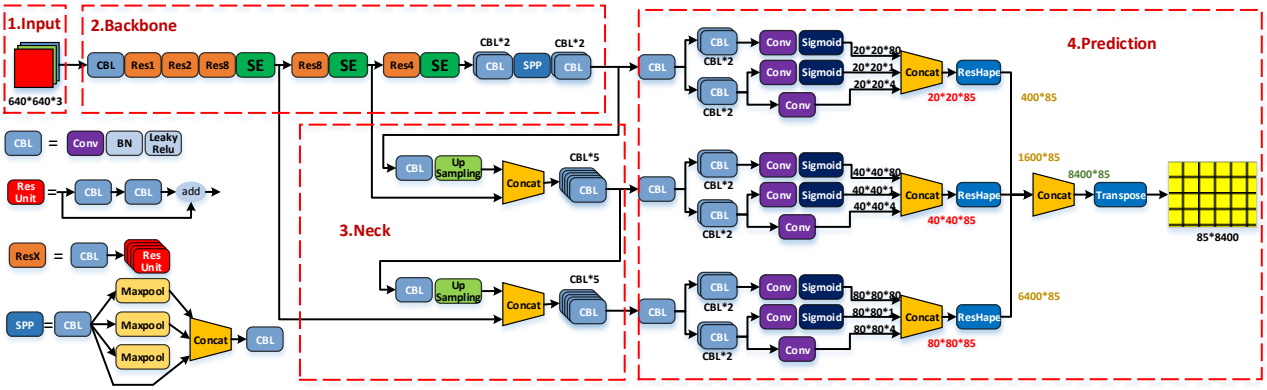


Fig. 4 - SE-YOLOX network structure

Evaluation indexes of the model

In this paper, commonly used evaluation indexes in target detection field include IoU, Precision, Recall, P-R curve, AP value and mAP value.

When evaluating the target detection model, IoU is used to quantify the degree of fitting, that is, to judge the quality of detection from the degree of fitting between the prediction frame and the real frame. The calculation formula is shown in (4) :

$$IoU = \frac{S_A \cap S_B}{S_A \cup S_B} \tag{4}$$

where S_A represents the collection of pixels in the prediction frame area, S_B represents the collection of pixels in the real frame area.

Precision and Recall are used to evaluate the quality of an information retrieval system. Precision stands for detection prediction, representing the proportion of targets detected by the model to be real target objects. Recall stands for detection recall rate, representing the proportion of all real targets effectively detected by the model. Precision and Recall formulas are shown in (5) and (6) :

$$Precision = \frac{TP}{TP + FP} \tag{5}$$

$$Recall = \frac{TP}{TP + FN} \tag{6}$$

TP (True Positive) refers to the number of samples whose IoU is greater than the threshold and whose category label is consistent with the actual label. FP (False Positive) represents the number of samples predicted by the model as individual boxes of pigs and whose category label is inconsistent with the actual label. FN (False Negative) indicates the number of samples for which no individual pig is detected.

The Average Precision (AP) of the model detection target is the area under the P-R curve, and the average precision can be used to evaluate the overall performance of the model for target detection and classification. The mean of average accuracy represents the average of the average accuracy of all classes. Compared with the mean of average accuracy, the mean of average accuracy can more accurately reflect the overall performance of the model to detect various targets. AP is the measure of the area formed by P–R curve and coordinate axis and is given as Formula (7):

$$AP = \int_0^1 p(r)dr \tag{7}$$

where p is the abbreviation of Precision and r is the abbreviation of Recall.

The mAP value can be calculated by

$$mAP = \frac{\sum_{i=1}^{N} AP_i}{N} \tag{8}$$

where N is the number of images in the test set. The mAP represents the mean average precision of the model. It can evaluate the overall detection effect of the model on the test set.

Considering that the selection of different IoU thresholds directly affects TP and FP values and thus causes the fluctuation of mAP index values, in this paper, three IoU thresholds of 0.5, 0.75, and 0.5:0.05:0.95 (where 0.05 represents the growth step) were denoted as $mAP_{0.5}$, $mAP_{0.75}$, and $mAP_{0.5:0.95}$ respectively to measure the model detection under different conditions. At the same time, considering the accurate detection performance of the model, the median and maximum of mAP under 10 thresholds with IoU of 0.5~0.95 are $mAP_{0.5:0.95\text{-medium}}$ and $mAP_{0.5:0.95\text{-large}}$.

Model Parameters

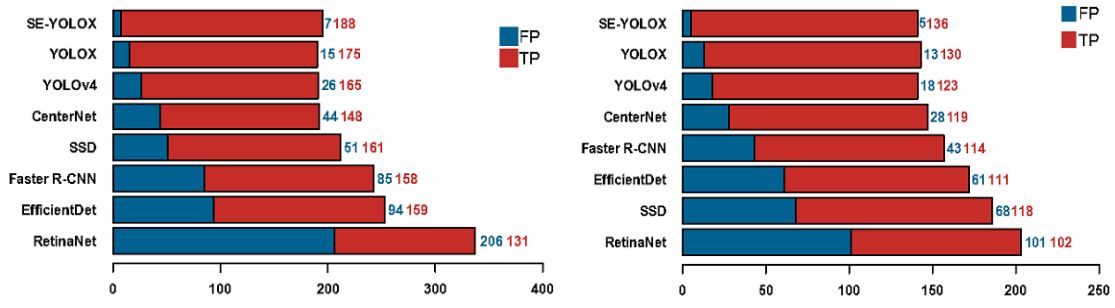
In this experiment, PyTorch deep learning framework was adopted, the operating system was Windows 10, and THE GPU was RTX2080Ti. The data set of eating and drinking images involved in this paper includes 1615 images. The collected 1615 image data sets were divided into training sets and test sets according to the ratio of 8:2, including 884 training sets and 221 test sets.

In this experiment, eight target detection models of SE-YOLOX, YOLOX (*Ge et al., 2021*), YOLOv4 (*Bochkovskiy et al., 2020*), RetinaNet (*Lin et al., 2017*), EfficientDet (*Tan et al., 2019*), Faster R-CNN (*Ren et al., 2017*), CenterNet (*Duan et al., 2019*) and SSD (*Liu et al., 2016*) were used to detect the dietary behavior of pigs on the same training set. Relevant parameters need to be set before the training of the model. In this paper, the epoch is set to 200, momentum is 0.9, and regularization coefficient for weight decay is 0.005. The experiment adopts a learning rate decay mechanism, and the initial learning rate is 0.0001. Once learning stagnates, the model learning rate usually decays at a rate of 2-10 times, and the attenuation times are set as 80% and 90% of the maximum number of iterations.

Results and analysis

In order to better evaluate the performance of the eight models involved in this paper, the same experimental data training set and test set were used for training and testing, and the results were compared and analyzed. The specific results are as follows.

TP and FP values were calculated for eight models to identify pig eating and drinking behavior. The higher the TP value, the better the model. The lower the FP value, the better the model. The results for the 8 models are presented in bar graphs, as shown in Figure 5.



a - Drink behavior **b - Eat behavior**

Fig. 5 - TP and FP values predicted by eight models

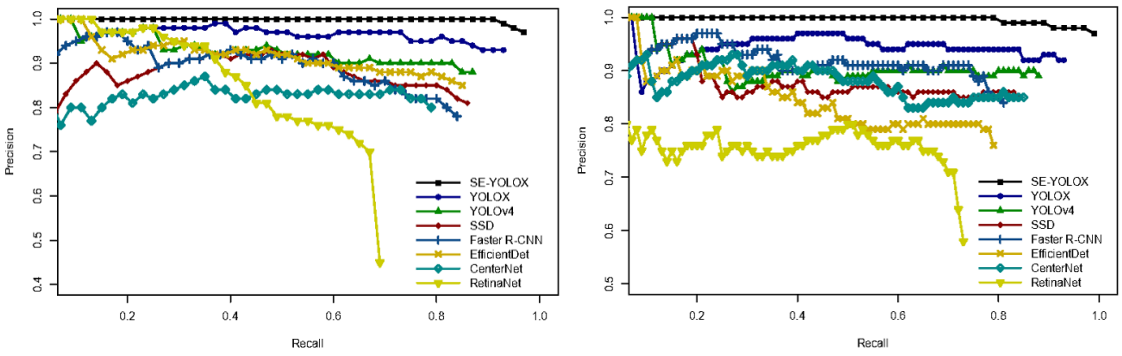
The experimental results show that:

1) As shown in Figure 5a, for the drinking behavior of pigs, the TP value of the SE-YOLOX model was significantly higher than that of the other seven models. For FP values, SE-YOLOX model detected FP values significantly lower than the other seven models. The order of FP values of the eight models was SE-YOLOX < YOLOX < YOLOv4 < CenterNet < Faster RCNN < EfficientDet < RetinaNet < SSD. The FP values of SE-YOLOX were 8 less than those of YOLOX, and 19-199 less than those of other models of the same type.

2) Figure 5b shows that for TP value, SE-YOLOX model is significantly higher than that of the other seven models. The predicted FP values of SE-YOLOX model were lower than those of the other seven models, and the order of the predicted FP values of the eight models was SE-YOLOX < YOLOX < YOLOv4 < SSD < RetinaNet < Faster RCNN < EfficientDet < CenterNet. The FP values of SE-YOLOX decreased by 8 compared with YOLOX, and significantly decreased by 13-96 compared with other models of the same type.

In conclusion, under the same experimental conditions, SE-YOLOX model is superior to other seven models in terms of TP and FP performance. Compared with the increase of TP index value, the increase of FP is much higher than that of TP, so FP is preferred in overall prediction performance to reduce the loss of detection performance caused by the large increase of FP value. It can also be seen that the improved anchor-free mode and label allocation strategy of SE-YOLOX model significantly reduced its FP value compared with other models. Therefore, SE-YOLOX model is more suitable for the detection of TP and FP values of pigs' eating and drinking behavior.

The P-R curves of the seven models for pig eating and drinking behavior recognition are shown in Figure 1. The area below the P-R curve is the AP value of the corresponding model in the eating and drinking behavior of pigs. The closer the curve is to the upper right corner, the better the model effect is. Where the black line represents the SE-YOLOX model, the dark blue line represents YOLOX model, the green line represents YOLOv4 model, the yellow line represents RetinaNet model, the orange line represents EfficientDet model, the blue line represents Faster RCNN model, the light blue line represents CenterNet model and the red line represents SSD model.



(a) drink **(b) eat**

Fig. 6 - P-R curve

The experimental results show that:

In the P-R curve prediction of pigs' drinking behavior, the P-R curve of SE-YOLOX model was always at the top, and the prediction accuracy of the model remained between 0.9 and 1.0 with the increase of Recall. The Precision of SSD model decreases rapidly when Recall is between 0.5-0.6, and the Precision of RetinaNet model decreases rapidly when Recall is between 0.6-0.7. YOLOv4, EfficientDet, Faster RCNN and CenterNet models gradually decreased with Recall of 0.8-0.9.

In the prediction of P-R curve of pig-eating behavior, the P-R curve of SE-YOLOX model was also always above other models, and the Precision value remained 1.0 between Recall and 0.8, and remained between 0.95 and 1.0 even though it decreased slightly after that. The P-R curve of SSD model decreased the fastest, and the Precision decreased rapidly when Recall was 0.4-0.5, while the Precision of the other five models decreased gradually when Recall was 0.7-0.9.

In conclusion, compared with the other six models, the P-R curves of eating and drinking of SE-YOLOX model are always at the top with stable changes, which is better than the other six models. The results indicated that the SE-YOLOX model had better stability and better detection performance for pigs' eating and drinking behaviors.

In order to explore the detection effects of different models on the eating and drinking behaviors of pigs, this paper compared the detection effects of eight models on the eating behaviors of pigs by calculating the mAP of each model. Table 1 shows the comparison of mAP of the eight models.

Table 1

Comparison of mAP values of eight models

Model	$mAP_{0.5}$	$mAP_{0.75}$	$mAP_{0.5:0.95}$	$mAP_{0.5:0.95\text{-medium}}$	$mAP_{0.5:0.95\text{-large}}$
SE-YOLOX	99.86%	98.36%	88.03%	98.36%	99.86%
YOLOX	99.95%	90.01%	74.92%	92.10%	99.95%
YOLOv4	99.88%	81.64%	68.51%	87.85%	99.88%
CenterNet	97.33%	71.99%	61.10%	76.87%	97.33%
Faster RCNN	98.71%	76.08%	63.40%	81.49%	98.71%
EfficientDet	98.79%	73.47%	61.89%	78.81%	98.79%
RetinaNet	95.50%	59.18%	54.20%	67.53%	95.50%
SSD	80.78%	45.54%	45.89%	52.63%	80.78%

The experimental results show that:

1) Different models have different detection effects on eating and drinking behavior of pigs. As can be seen from the Table 1, the detection results of SE-YOLOX model are always higher than other models and remain in the best state. $mAP_{0.5:0.95\text{-large}}$ is 99.86%, which is only 0.09% higher than the maximum value and 1.07%-19.08% higher than other models. The $mAP_{0.5:0.95}$ of SE-YOLOX model was 13.11% higher than that of YOLOX model, 19.52% higher than that of YOLOv4 model, and higher than CenterNet and Faster RCNN, EfficientDet, RetinaNet and SSD models were 26.93%, 24.63%, 26.14%, 33.83% and 42.14%. The mAP0.5:0.95-medium of SE-YOLOX model is 98.36%, only 1.50% different from the $mAP_{0.5:0.95\text{-large}}$, while the difference between the $mAP_{0.5:0.95\text{-medium}}$ of other models and the $mAP_{0.5:0.95\text{-large}}$ is 7.85% ~ 28.85%.

2) Because the same model has different detection accuracy under different thresholds. Therefore, in the process of increasing the IoU threshold from 0.5 to 0.95, the mAP values of the eight models gradually decreased. However, the mAP value of SE-YOLOX model when IoU threshold is 0.75 is only 1.50% lower than that when IoU threshold is 0.5. YOLOX, YOLOv4, CenterNet, Faster RCNN, EfficientDet, RetinaNet and SSD models decreased 9.94%, 18.24%, 25.34%, 22.43%, 25.32%, 36.32%, 35.24%. Thus, YOLOX model is more stable in detecting the eating behavior of pigs.

In summary, it can be seen that the SE-YOLOX model has a faster convergence rate and better effect after improving the decoupling head, which not only greatly improves the detection accuracy of the experiment but also makes it more stable than other models. It can accurately predict the eating and drinking behavior of pigs at a faster speed. Therefore, SE-YOLOX model is more suitable for the detection of eating and drinking behavior of pigs.

To better evaluate the performance of the detection model, this study visualizes the results of eight detections, as shown in Figure 7. Figure 7a shows the detection results of eating behavior of pigs from a side view angle under sufficient light. Figure 7b shows the test results of drinking behavior of pigs from a side view angle under sufficient light. Figure 7c shows the detection results of the simultaneous eating and drinking behaviors of pigs from a vertical angle under the condition of insufficient light. Figure 7d shows the detection results of eating and drinking behaviors of pigs in the condition of overlooking angle adhesion under insufficient light. Part of the test results are shown in Figure 7, with the green box representing eating behavior and the red box representing drinking behavior.

SE-YOLOX

YOLOX



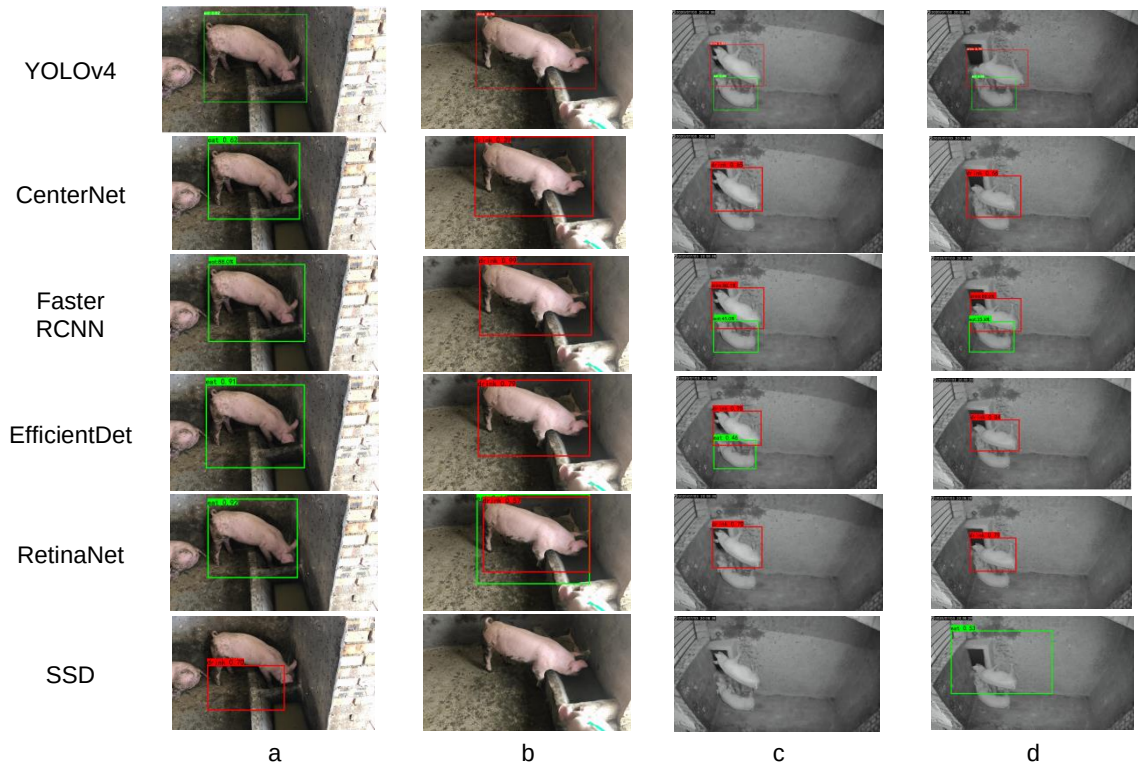


Fig. 7 - Some forecast results

Through the tests of all models, it can be seen from Fig. 7a and 7b that the eight models can detect the eating and drinking behaviors of pigs correctly under sufficient light. Among the detection results of pig eating behavior, SE-YOLOX model had the highest confidence.

Fig.7c shows that CenterNet model and RetinaNet model have errors in the detection of eating status and SSD model has errors in the detection of eating status and drinking status in the condition of insufficient light and simultaneous eating and drinking behavior. The SE-YOLOX, YOLOX, YOLOv4, Faster RCNN and EfficientDet models were all able to correctly detect drinking behavior and eating behavior, and the SE-YOLOX model had the highest confidence.

Fig.7d shows that SE-YOLOX, YOLOX, YOLOv4 and Faster RCNN models can correctly detect the eating and drinking behaviors of pigs in the sticky state under insufficient light. CenterNet, EfficientDet and RetinaNet models failed to detect the eating behavior of the pigs under the condition of adhesion, while SSD model failed to detect the eating and drinking behavior of the pigs under the condition of adhesion.

In conclusion, the SE-YOLOX model can accurately detect the eating and drinking behaviors of pigs under any circumstances, and the confidence degree is always the best compared with other models. The results showed that the SE-YOLOX model improved the input data enhancement and label allocation, and maintained the best stable state while improving the detection rate. Compared with other models, the SE-YOLOX model was more suitable for dietary detection of pigs.

CONCLUSIONS

This paper integrates the SE attention module into the YOLOX model, improves the YOLOX model, and establishes the detection model SE-YOLOX, which is used to detect the drinking and eating behavior of pigs in the pig house environment. The main conclusions are as follows:

1) Compared with the other seven deep learning detection models, the YOLOX model has better detection performance of pig drinking and eating behavior, and the model detection accuracy is improved after adding the SE attention mechanism.

2) The SE-YOLOX model outperforms the other seven models on various indicators of mAP. It indicated that the SE-YOLOX model had better stability in the detection of pigs' eating drinking behavior.

3) The SE-YOLOX model can effectively detect the eating behavior of pigs under the condition of side view, top view, adhesion state and insufficient light in real-time. While efficiently and accurately detecting the eating and drinking behavior of pigs, it does not affect the normal living order of pigs and is more easily accepted by farms. It is of great significance to the management of pig farms and the improvement of breeding welfare.

ACKNOWLEDGEMENT

This research, titled 'Detection of Eating Behavior in Pigs Based on Modified YOLOX', was funded by the Basic Research Program of Shanxi Province (202103021223141).

REFERENCES

[1] Bochkovskiy A., Wang C Y., Liao H Y M., (2020). Yolov4: Optimal speed and accuracy of object detection. *arXiv preprint arXiv*: 156,107552, India.

[2] Chen C J., Gota M., Kiho L., Zhiwu Z., Hao C., (2022). VTag: a semi-supervised pipeline for tracking pig activity with a single top-view camera. *Journal of Animal Science*, 100(6), skac147, United States.

[3] Duan K., Bai S., Xie L., et al. (2019). Centernet: Keypoint triplets for object detection. *Proceedings of the IEEE/CVF international conference on computer vision,* pp. 6569-6578, United States.

[4] Ge Z., Liu S., Wang F., Li Z., Sun J., (2021). Yolox: Exceeding yolo series in 2021. *arXiv preprint arXiv*:2107.08430, Japan.

[5] Li R., Huang Y., Wei L., Qin R., Li M., (2021). Design of large-scale intelligent pig system based on RFID (基于 RFID 的规模化智能养猪系统设计). *Modern Agricultural Equipment*. 42(04): 60-63, Guangxi/China.

[6] Lin T Y., Goyal P., Girshick R., He K., Dollár P., (2017). Focal loss for dense object detection. *Proceedings of the IEEE international conference on computer vision,* pp. 2980-2988, United States.

[7] Liu W., Anguelov D., Erhan D., Szegedy C., Reed S., Fu C Y., Berg A C., (2016). SSD: Single shot multibox detector. *European conference on computer vision,* pp. 21-37, Germany.

[8] Maselyne J., Nuffel A V., BD Ketelaere., Bart D K., Jürgen V., Engel F. Hessel C., Bart S., Wouter S., (2014). Range measurements of a high frequency radio frequency identification (HF RFID) system for registering eating patterns of growing-finishing pigs. *Computers & Electronics in Agriculture,* 108 (10): 209-220, Beijing/China.

[9] Qin Q., Liu Z., Zhao C., Zhang C., Dai D., Sun J., Wang Z., Li J., (2021). Application of machine vision technology in animal husbandry (机器视觉技术在畜牧业中的应用). *Agricultural Engineering,* 11(7): 27-33, Neimenggu/China.

[10] Ren S., He K., Girshick R., Sun J., (2017). Faster R-CNN: towards real-time object detection with region proposal networks. *IEEE Transactions on Pattern Analysis & Machine Intelligence,* 39(6): 1137-1149, United States.

[11] Statham P., Hannuna S., Jones S., Campbell N., Mendl M., (2020). Quantifying defence cascade responses as indicators of pig affect and welfare using computer vision methods. *Scientific Reports,* 10(1), United States.

[12] Shen M., Liu L., Yan L., Lu M., Yao W., Yang X., (2014). Review of Monitoring Technology for Animal Individual in Animal Husbandry (畜禽养殖个体信息监测技术研究进展). *Transactions of the Chinese Society for Agricultural Machinery,* 45(10): 245-251, Nanjing/China.

[13] Tan M., Pang R., Le Q V., (2020). Efficientdet: Scalable and efficient object detection. *Proceedings of the IEEE/CVF conference on computer vision and pattern recognition,* pp. 10781-10790, Germany.

[14] Wang L., (2021). Design of Intelligent and Precise Livestock Breeding Management System—Taking Pig Breeding as an example (智能精准畜禽养殖管理系统设计——以猪的养殖为例). *Journal of Shandong Institute of Commerce and Technology,* 21(02): 107-110, Shandong/China.

[15] Wu S., Bao Y., Chen G., Chen Q., (2020). Contactless Identification System for Pig Behavior Based on Machine Vision (基于机器视觉技术的猪行为活动无接触识别系统). *Computer Systems and Applications,* 29(04): 113-117, Guizhou/China.

[16] Yang Q., Xiao D., Zhang G., (2018). Automatic Pig Drinking Behavior Recognition with Machine Vision (猪只饮水行为机器视觉自动识别). Transactions of the Chinese Society for Agricultural Machinery, 49(06): 232-238, Guangdong/China.

DESIGN AND ANALYSIS OF INDEPENDENT STRUT TYPE AIR SUSPENSION APPLIED TO HIGH CLEARANCE SELF-PROPELLED SPRAYER
/
应用于高地隙自走式喷雾机的独立式立轴空气悬架设计与分析

Chenwei HU [1)], Jiayu CAO [1)], Shuo ZHANG[1)], Yu CHEN*[1)], Liquan LU [1)]
[1)] Northwest A&F University, Yangling 712100, China;
Tel: +86 17795759790; E-mail: jdxy73@nwafu.edu.cn
DOI: https://doi.org/10.35633/inmateh-71-04

Keywords: *high clearance self-propelled sprayer, air suspension, design, simulation, analysis*

ABSTRACT
As an important plant protection machinery for spraying and fertilizing crops, high clearance self-propelled sprayer is of great significance to promote food security production and stable development of agriculture. Aiming at the complex operating conditions and unique operating requirements of large high clearance self-propelled sprayer, this paper analyzes and determines the main components of the sprayer suspension, such as elastic components, guiding devices, buffer devices, damping components, etc., and designs a stand-alone vertical shaft air suspension system structure suitable for high clearance sprayers. The stress of the sprayer chassis under different extreme conditions such as side slip, emergency braking and uneven road driving is analyzed, and the vertical shaft is designed and checked in detail. Based on the stress analysis results of the sprayer chassis, the finite element analysis software HyperMesh 10.0 was used to analyze the statics of the key components of the suspension, such as the vertical shaft, the motor protection shell, the steering arm, and the spring top support. According to the results of force analysis and finite element analysis, combined with the requirements of process production, the suspension structure in the design scheme is improved, and the final suspension form and the whole structure scheme of the sprayer are obtained. Through this study, it provides a basis for the design and development of large high clearance self-propelled sprayer.

摘要
作为对农作物进行喷药、施肥等作业的重要植保机械，高地隙自走式喷雾机对促进粮食安全生产和农业稳定发展具有非常重要的意义。本文针对大型高地隙自走式喷雾机复杂的运行工况和独特的作业要求，分析确定喷雾机悬架的弹性元件、导向装置、缓冲装置、阻尼元件等主要部件，设计了适用于高地隙喷雾机的独立式立轴空气悬架系统结构方案。分析喷雾机底盘在侧滑、紧急制动、不平路面行驶等不同极限工况下的受力情况，并对立轴进行了详细设计与校核。基于喷雾机底盘受力情况分析结果，应用有限元分析软件 HyperMesh 10.0，对悬架关键零部件立轴、马达保护壳体、转向臂、弹簧顶部支撑等进行了静力学分析。根据受力分析与有限元分析结果，结合工艺生产要求，对设计方案中的悬架结构形式进行改进，得到最终的悬架形式和喷雾机整机结构方案。通过本文研究，为大型高地隙自走式喷雾机设计与研发提供基础。

INTRODUCTION

High clearance self-propelled sprayer is a kind of large and high-end agricultural equipment (*Sánchez-Hermosilla J. et al., 2022; Hu Y. et al., 2022*), which is characterized by high intelligence, wide operation width, high ground clearance and fast driving speed (*Li W. et al., 2022*). At present, the maximum speed of sprayer has reached 60 km/h. The large ground clearance and high driving speed make it necessary to be equipped with a special suspension system to buffer the vibration. On the one hand, the ride comfort of the driver is improved by vibration reduction. On the other hand, the vibration, swing and rotation of the boom are prevented and reduced, so that it is kept at a constant height, so that the spraying is more uniform, and the drift is reduced. During the operation of the sprayer, the sprung mass changes with the change of the amount of Chinese medicine in the medicine box, which requires the suspension to have a wide adaptability. At the same time, due to the complex and changeable field working environment, the suspension also needs to ensure the balance of the frame and the traction of the whole vehicle. In the process of driving on the road, the speed is high, and the suspension is needed to improve the ride comfort and handling stability of the sprayer. Mainstream agricultural machinery enterprises in the world have developed a variety of sprayer chassis suspensions, and formed the following two characteristics in structure and function:

(1) The suspension with helical spring as elastic element has been applied in sprayer (*Press R.U., 2012; Buschena J., 2012*). For example, the four-wheel independent damping system installed on the Patriot series sprayer produced by Case New Holland and the shock absorber and spiral spring damping system installed on the 3WZG-3000 sprayer produced by modern agricultural equipment. The advantage of this suspension form is that the structure is simple, and the semi-active control of the suspension is realized by using the adjustable damping shock absorber. However, because the spiral spring and the shock absorber are mostly in parallel, it is not convenient to realize the body height stability and load balance control of the sprayer due to the small spring stroke and weak load capacity adjustability.

(2) Independent nonlinear spring suspension, especially air suspension has become the mainstream (*Hung T.M., 2022; Jiang X. et al., 2022; Zhou Y. et al., 2022*). The air spring is widely used in foreign sprayers because of its good nonlinear elastic characteristics, large suspension stroke and adjustable load capacity. Sprayer companies such as John Deere (*Carlson B.C. et al., 2011; Wubben T.M. et al., 2007*), AGCO (*Slawson J., 2013; Steffensen C, et al., 2012)*, HAGIE (*Schaffer J.A., 2002; Schaffer J.A., 2002*), and AgriFac (*Blaauw D., 1999; Ehlen V. et al., 2011*) have applied for patents on air suspensions, and their new generation sprayers are also equipped with air suspension systems. For example, the Miller sprayer uses an air suspension system with a vibration reduction stroke of up to 20 inches. The multi-link guiding device ensures that the air spring is only subjected to vertical force. The John Deere 4000 series sprayer and the sprayer independently developed by our team adopt a four-wheel independent vertical air suspension system (*Chen Yu et al., 2021; Yu Chen et al., 2020*). There is a vertical shaft between the hub and the bottom of the airbag. The top of the airbag is fixed on the sleeve connected to the frame through the gantry. When the sprayer passes through the uneven road surface, the wheel squeezes and stretches the air spring to cushion the vibration. The sprayer equipped with independent vertical shaft air suspension has simple structure, high ground clearance, large vibration reduction range, easy track adjustment and four-wheel steering. It has been widely used in the products of well-known sprayer manufacturers such as HAGIE, AGCO and AGRIFAC. However, the independent sprayer chassis air suspension system is not equipped with a damper due to structural and space constraints, and only relies on the tire and spring self-damping and mechanical structure friction damping to attenuate vibration. When the sprayer is running at a higher speed or on poor road conditions, the vibration reduction effect will be affected.

(3) The research of active and semi-active chassis suspension system has been paid more and more attention. In order to better adapt to the complex working conditions of the sprayer, some manufacturers began to actively develop active and semi-active suspension systems (*Chen, Y et al., 2020; Li, W et al., 2018*). For example, John Deere and HAGIE equipped the mechanical body height adjustment system on their R40 series and STS series sprayer suspensions, respectively. The system ensures that the chassis of the sprayer is always stable in a certain height range when the charge ratio of the tank changes, thus ensuring the vibration reduction performance of the suspension and the stability of the body. AGCO is equipped with a hydro-pneumatic suspension system that integrates ground clearance adjustment and wheelbase adjustment on its Challenger RG600 series sprayers (*Hiddema J., 2013; Zatrieb J. et al., 2012)*. A variable orifice is connected between the accumulator and the hydraulic cylinder, and the system damping can be adjusted by changing the size of the orifice. One end of the double-acting hydraulic cylinder in the hydro-pneumatic suspension is connected to the motor shell, and the other end is connected to the frame. Through the expansion of the hydraulic cylinder, the sprayer 's ground clearance can be changed steplessly between 75 cm and 120 cm. At the same time, there are two four-way solenoid valves between the inlet and outlet of the oil cylinder of the left and right hydro-pneumatic suspensions. During normal driving, the solenoid valve is in the left position, the left and right cylinders are not connected, and the hydro-pneumatic suspension is independently supported and damped; when the sprayer rolls seriously, the solenoid valve is in the right position, and the rodless cavity of the left cylinder is connected with rod cavity of the right cylinder. At this time, the roll stiffness increases, which can effectively reduce the roll of the whole machine.

In summary, world-renowned agricultural equipment companies such as AGCO, John Deere, HAGIE, AgriFac, etc. have designed and developed a series of suspension systems with air springs as elastic elements for the operation characteristics of high-clearance sprayers. However, due to structural and space constraints, fewer suspensions are equipped with dampers, and most sprayers rely only on tires and spring damping to attenuate vibration. When the sprayer is running at a higher speed or on poor road conditions, the vibration reduction effect will be greatly affected. Therefore, how to design a large high clearance self-propelled sprayer suspension system that can meet the requirements of high ground clearance, large vibration reduction stroke, convenient four-wheel steering and wheel track adjustment is a problem to be

solved on the basis of combining the existing suspension system according to the characteristics of large high clearance self-propelled sprayer, such as fast driving speed, high working efficiency, and the change of sprung mass with the change of liquid volume (*Wei Z. et al., 2023; Han J. et al., 2022; Rondelli V. et al., 2022*). Based on this, aiming at the complex operating conditions and unique operating characteristics of large high clearance self-propelled sprayer, this paper designs a stand-alone vertical shaft air suspension system suitable for high-clearance sprayers, and selects and analyzes the main components. Through this study, it provides a basis for the design and development of large high clearance self-propelled sprayer.

MATERIALS AND METHODS

Structural element selection and analysis

According to the design condition requirements of the chassis suspension system of the spray, the main components of the suspension such as elastic elements, guiding devices, buffer devices, damping elements and the structural form of the suspension system of the spray are analyzed and determined.

- **Elastic elements**

The air spring is selected as the elastic element of the suspension system of the spray, which can meet the design requirements of the suspension system such as simple structure, large damping travel, automatic height stability, load balancing capacity, sufficient strength and life (*Chen Y. et al., 2020; Chen Y. et al., 2021*).

Membrane air springs have a small effective area change rate, a compact structure and smaller stiffness under the same load carrying capacity, and are widely used in trucks, buses, and agricultural vehicles. When selecting an air spring, ensuring that its design height is within the recommended range can achieve the best service life and vibration damping performance. The pressure p_{10}, stiffness k_0, and bias frequency f_0 of the membrane air spring at the load W_1 and design height can be calculated from Equations (1) to (3).

$$p_{10} = \frac{m_1 p_{20}}{m_2} \tag{1}$$

$$k_0 = p_{10}\frac{\mathrm{d}A_e}{\mathrm{d}x} + n\left(p_{10} + p_a\right)\frac{A_{e0}^{\ 2}}{V_0} \tag{2}$$

$$f_0 = \frac{1}{2\pi}\sqrt{\frac{k_0}{m}} \tag{3}$$

According to the overall design requirements of the high clearance sprayer, the vehicle is fully loaded with a sprung mass of 12,000 kg, that is, the load distributed on each spring is 3,000 kg. Therefore, the selected air spring needs to be able to output no less than 29.4 KN at the design height and within the pressure range of 4~6 bar. Based on the above requirements, the 1T19L-7 diaphragm air spring produced by Firestone is selected. Its design height is 380 mm, and the static data curve of the spring is shown in Fig.1.

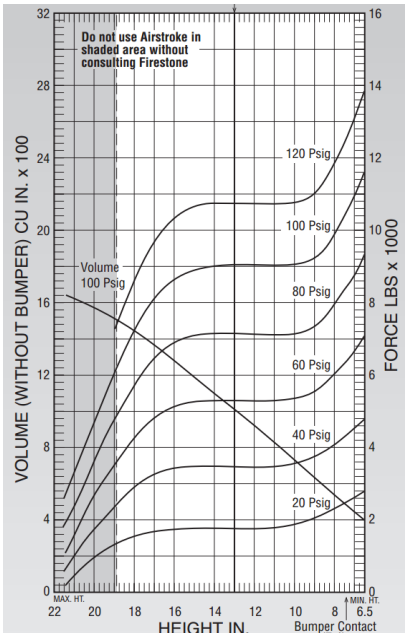


Fig. 1 – Offering of 1T19L-7 reversible sleeve style air spring static data curve by Firestone

By fitting the displacement-load curve and displacement-volume curve under 5 bar in Fig. 1, the effective area and volume formula of the spring are obtained as follows:

$$A_e = \begin{cases} 1.6786(x-0.38)^2 + 0.3761(x-0.38) + 0.0775 & (0.18 \le x \le 0.24) \\ 0.0567 & (0.24 < x < 0.38) \\ -1.4583(x-0.38)^2 - 0.0294(x-0.38) + 0.0565 & (0.38 \le x \le 0.56) \end{cases} \quad (4)$$

$$V = 0.0564(x-0.38) + 0.01914 \quad (0.18 \le x \le 0.56) \quad (5)$$

As described in formulas (4) and (5), the effective area change rate A_e' and volume change rate V_1' of the spring change with the height *h* of the spring, and are less affected by the internal pressure and temperature, which can be ignored. The basic parameters of the spring under the load of 29.4KN and the design height of 380 mm can be calculated from Eqs. (1) to (5), as shown in Tab. 1.

Table 1

Essential parameters of 1T19L-7 reversible sleeve style air spring in 380 mm design height and 29.4 KN load

Load	Gauge pressure	Effective sectional area	Volume	Stiffness	Natural frequency
29.4 KN	5.18 bar	567.5 cm^2	19140 cm^3	163 KN/m	1.17 Hz

- **Buffer device**

The buffer device is mainly to prevent the direct impact between the suspension and the frame, absorb the impact load transmitted from the wheel to the frame, and limit the maximum stroke of the suspension. It can be seen from the static data curve of 1T19L-7 film air spring that the spring height can change in the range of 167~545 mm without buffer device. It is necessary to limit the stroke of air spring in the range of ±100 mm through buffer device to meet the overall design requirements of sprayer. The commonly used buffer device is composed of different materials such as rubber or porous polyurethane. Fig. 2 shows the rubber buffer block structure. The steel plate and rubber are connected by vulcanization, and then the buffer block is fixed and installed on the frame or other parts by the screws on the welded steel plate, which plays the role of limit and protection.

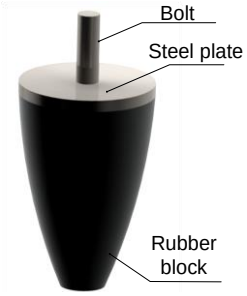
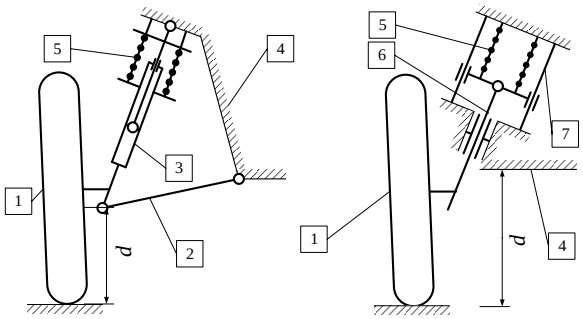


Fig. 2 – Rubber bumper

- **Guiding device**

The guiding device is used to transmit various forces and moments except the vertical force, which determines the motion characteristics of the wheel relative to the frame. In view of the advantages of the McPherson independent suspension system, the structure is appropriately deformed to form an independent vertical shaft suspension system suitable for large high clearance self-propelled sprayer, as shown in Fig. 3.

In Fig. 3(a), the shock absorber in the McPherson independent suspension not only provides damping force, but also supports the body. Its advantage is that the structure is compact and the space is small. The disadvantage is that it cannot bear large lateral force, and additional guide rods such as yaw arm and anti-tilt connecting rod are needed to increase the lateral stiffness and roll stiffness of the suspension. However, the existence of the guide rod system makes it unable to meet the requirements of high clearance of the sprayer. Replace the shock absorber 3 with the vertical shaft 5, remove the guide rod 2, and install the guide shaft 7 on both sides of the spring (to ensure that the spring only bears the vertical force), and obtain the independent vertical shaft suspension system shown in Fig. 3(b). Compared with the McPherson suspension, the ground clearance of the vertical shaft suspension is significantly increased, and the ground clearance can be changed by replacing the vertical shaft with different lengths under the premise of satisfying the stiffness and strength. Since the shock absorber is replaced by the vertical shaft, the vertical shaft suspension needs to be equipped with other forms of damping devices, such as friction dampers or additional air chambers, to attenuate vibration.



(a) McPherson suspension structure *(b) Independent strut type air suspension structure*

Fig. 3 – Structural sketch of suspension

1. Wheel; 2. Track arm; 3. Shock absorber; 4. Frame; 5. Spring; 6. Strut; 7. Guide shaft; d. Clearance value

- **Damping elements**

A suitable damping device is very important to improve the ride comfort performance of the sprayer. In this paper, according to the structure of the independent vertical shaft air suspension, the additional air chamber air damping suitable for the sprayer suspension is designed. Compared with other damping, the air damping generated by the gas exchange between the air spring and the auxiliary chamber (*Giuseppe Quaglia et al., 2001; Zheng Y et al., 2022; Zheng Y et al., 2023*) has the advantages of less heating, better vibration isolation effect in the frequency band (4~8Hz) which is most sensitive to low frequency and high amplitude vibration and human body. Based on the air spring, an additional air chamber is added, and a throttle valve hole is set between the main and auxiliary air chambers. Throttle valve is a key component to realize air damping, which can adjust the gas mass flow between the spring and the auxiliary chamber. When the air flows through the throttle valve hole A_k from the cross section A_1, the pressure difference ($p_1 \neq p_2$) will be generated at both ends of the throttle valve, which will cause the air to generate damping when passing through the throttle valve (see Fig. 4). By adjusting the aperture size of the throttle valve hole to change the damping of the suspension, the semi-active control of the damping of the sprayer suspension system is realized. In addition, since the arrangement of the additional chamber is not limited by the structure and space, the additional chamber can be placed at any position of the chassis.

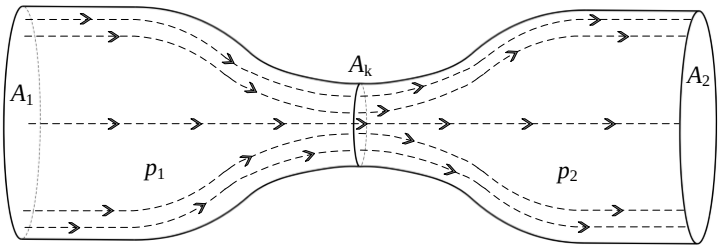
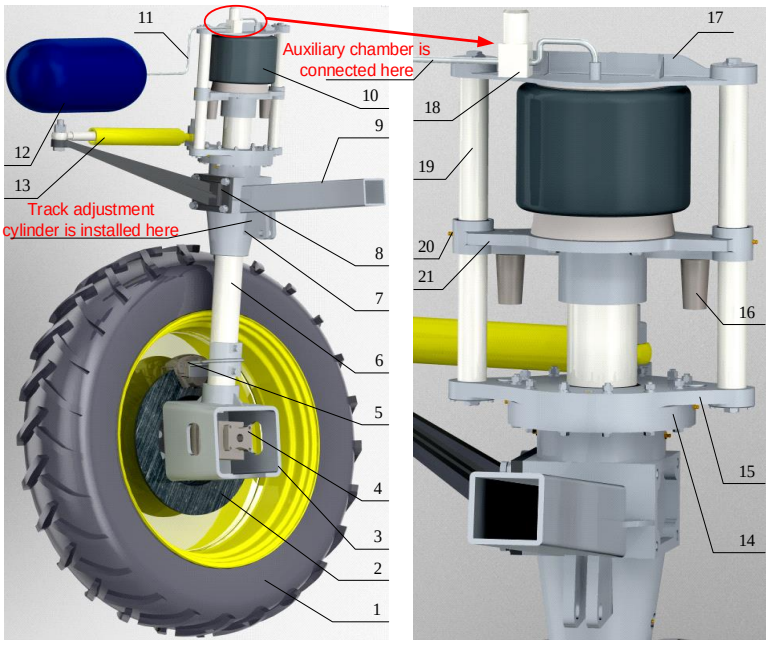


Fig. 4 – Schematic diagram of air flowing through the throttle orifice

Structural design

Based on the McPherson independent suspension, this study designed an independent vertical air suspension system suitable for large high clearance self-propelled sprayer through appropriate deformation and air damping principle.

Fig. 5 shows the preliminary design of the independent vertical air suspension structure assembly based on air damping. Among them, 1~5 form tire assembly T, 7 and 9 form frame connection assembly F, 8, 13 and 15 form steering assembly Z, 10~12, 14~21 and 6 form suspension damping assembly S; the same as Fig. 2-7, the elastic element uses the 1T19L-7 air spring produced by Firestone, and the damping range is about ±100 mm by the internal buffer block and the limit block 16 of the spring. Throttle valve 18 is an important part of air damping device. It can use the gas-specific electromagnetic proportional flow control valve designed and manufactured by iQValves company. It has the advantages of low hysteresis, high frequency response, high pressure resistance and long life.



(a) Overall structure *(b) Local large map*

Fig. 5 – Instruction diagram of independent strut type air suspension system based on air damper

1. Wheel; 2. Brake disc; 3. Motor protection housing; 4. Hydraulic motor; 5. Brake caliper installation; 6. Strut; 7. Beam support column; 8. Steering cylinder support arm; 9. Beam; 10. Air spring; 11. Compressed air hose; 12. Auxiliary chamber; 13. Steering cylinder; 14. Positioning ring; 15. Steering arm; 16. Rubber limit block; 17. Spring top support; 18. Variable throttle valve; 19. Guide post; 20. Lubrication mouth; 21. Spring bottom support

Sprayer chassis force analysis

The working conditions of the sprayer are complex. During the operation of the whole machine, it is necessary to bear the effects of vertical, longitudinal, lateral and other forces. Through the force analysis of different extreme conditions (side slip, emergency braking, uneven road driving) of the sprayer chassis, the main structural parameters of the key components are obtained. For the convenience of analysis, it is assumed that the centroid G of the sprayer is located at the center of the whole machine, that is, in the transverse direction, the centroid distance is equal to the distance between the left and right wheels; longitudinally, the distance from the front and rear bridges is equal. On this basis, the following variables and positions are defined: G_m is the full load half vehicle weight, N; GB_1 and GB_2 are the reaction forces on the left and right wheels of the front axle when driving on uneven roads, N; GC_1 and GC_2 are the reaction forces on the left and right wheels of the front axle during sideslip, N; GZ_1 and GZ_2 are the ground reaction forces on the left wheels of the front and rear axles during braking, N; GX_1 and GX_2 are the ground reaction forces on the left wheels of the front and rear axles during climbing, N; FC_1 and FC_2 are the lateral forces on the left and right wheels of the front axle during sideslip, N; FZ_1 and FZ_2 are the braking force of the left wheel of the front and rear axle respectively, N; F_b is the additional load transferred by the braking inertia force, N; F_c is the additional load transferred by sideslip centrifugal force, N; a and b are the distances from the top and bottom joints of the vertical shaft to the axle joints, m; r is the tire rolling radius, m; l is the distance between the axle joint (point O) and the center surface of the tire, m; h is the height of mass center, m; c is the wheel track, m; L is the wheelbase, m; d is the distance from the center surface of the tire to the center surface (O_2 point) of the mounting shaft sleeve, m; w is the length of the axle, m; s is the distance from the contact point under the vertical shaft to the cross section of the tire, m; β is the vertical axis inclination, 8°; θ is the slope angle, 12°; δ is the dynamic load coefficient when passing through the uneven road surface, generally taking 2.5; φ is the peak adhesion coefficient between tire and ground, take 0.7; φ' is the lateral peak adhesion coefficient, take 0.7; G is the center of mass, O_L and O_R are the intersections of the left wheel and the right wheel with the ground, O_F and O_B are the intersections of the front and rear axle center lines with the ground, O is the intersection of the front axle housing support and the left vertical shaft, O_2 and O_3 are the intersections of the vertical shaft with the ground clearance adjustment mechanism and the bottom support of the air spring.

When the sprayer passes through the uneven road surface, the wheels mainly bear the dynamic load. Currently,

$$G_{B1} = G_{B2} = \delta \frac{G_m}{2} \tag{6}$$

When turning, the wheel should bear the lateral force generated by the sprayer (see Fig. 6). When the sideslip occurs, the lateral force reaches the maximum.

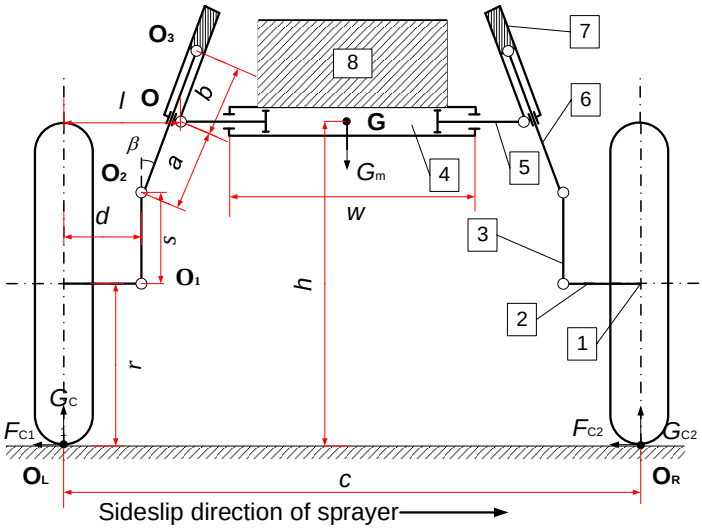


Fig. 6 – Stress analysis diagram of sprayer passing through uneven road and skidding

1. Wheel; 2. Motor; 3. Motor protection housing welding; 4. Axle; 5. Beam; 6. Strut; 7. Air spring; 8. Sprayer body;

Assuming that the sprayer slides to the left side, the left wheel is subjected to the combined action of the vertical load G_L and the additional load F_c transferred by the side slip centrifugal force. Taking the moment of the centroid G in Fig. 6, it can be obtained:

$$G_{C1}\frac{c}{2} = G_{C2}\frac{c}{2} + F_{C1}h + F_{C2}h \tag{7}$$

due to

$$F_{C1} = \varphi' G_{C1} \tag{8}$$

$$F_{C2} = \varphi' G_{C2} \tag{9}$$

$$G_{C1} = \frac{G_m}{2} + F_c \tag{10}$$

$$G_{C2} = \frac{G_m}{2} - F_c \tag{11}$$

The formula (2-8)~(2-11) into formula (2-7), the following is obtained:

$$F_c = \frac{h}{c}\varphi' G_m \tag{12}$$

Then:

$$G_{C1} = (\frac{1}{2} + \frac{h}{c}\varphi')G_m \tag{13}$$

$$G_{C2} = (\frac{1}{2} - \frac{h}{c}\varphi')G_m \tag{14}$$

When the sprayer brakes urgently, the front axle is subjected to the combined action of vertical load G_m and braking inertia force F_b, as shown in Fig. 7.

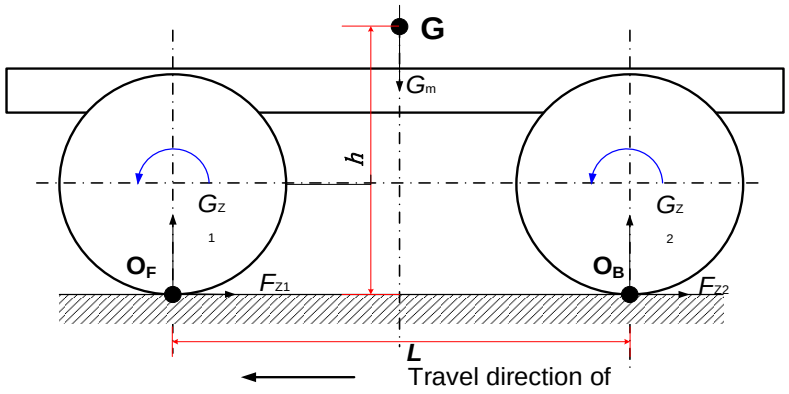


Fig. 7 – Stress analysis diagram of sprayer emergency braking

During the braking process, under the action of negative acceleration, the vertical load is transferred to the front axle. At this time, the moment of the centroid G in Fig. 7 is taken, then:

$$G_{Z1}\frac{L}{2} = G_{Z2}\frac{L}{2} + F_{Z1}h + F_{Z2}h \tag{15}$$

due to

$$F_{Z1} = \varphi G_{Z1} \tag{16}$$

$$F_{Z2} = \varphi G_{Z2} \tag{17}$$

$$G_{Z1} = \frac{G_m}{2} + F_b \tag{18}$$

$$G_{Z2} = \frac{G_m}{2} - F_b \tag{19}$$

The formula (15)~(19) can be obtained:

$$G_{Z1} = \left(\frac{1}{2} + \frac{\varphi h}{L}\right)G_m \tag{20}$$

$$G_{Z2} = \left(\frac{1}{2} - \frac{\varphi h}{L}\right)G_m \tag{21}$$

When the sprayer is climbing, part of the mass of the vehicle will transfer to the rear axle, as shown in Fig. 8. The moments of O_F and O_B are taken respectively, and the reaction force of the left wheel of the front and rear axles can be obtained as shown in Formulas (22) and (23). where θ is the slope angle, rad.

$$G_{X1} = \left(\frac{\cos\theta}{2} - \frac{h}{L}\sin\theta\right)G_m \tag{22}$$

$$G_{X2} = \left(\frac{\cos\theta}{2} + \frac{h}{L}\sin\theta\right)G_m \tag{23}$$

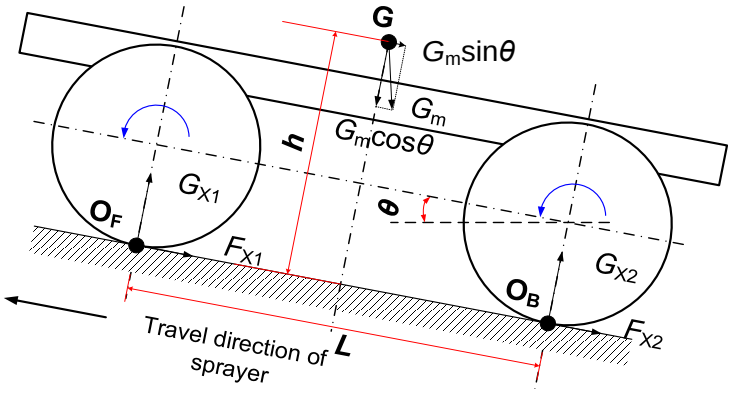


Fig. 8 – Stress analysis diagram of sprayer running on the slope

The following takes the vertical shaft as an example to analyze its stress under different working conditions. In order to simplify the analysis, the backward inclination of the vertical shaft and the camber of the tire are not considered, and it is assumed that the action point of the force is located at the midpoint O_3

and O_2 of the connection between the upper and lower ends of the vertical shaft and the bottom support of the air spring and the support plate on the motor protection shell.

When passing through uneven pavement, the vertical shaft bears dynamic load. Suppose that the forces acting on O_2 and O_3 are F_{BD} and F_{BU}, respectively. According to the moment balance, the moments of O_2 and O_3 are taken respectively.

$$F_{BU} = \delta \frac{G_m}{2} \frac{(l - a\sin\beta)}{a+b} \tag{24}$$

$$F_{BD} = \delta \frac{G_m}{2} \frac{(l + b\sin\beta)}{a+b} \tag{25}$$

When climbing, the forces acting on O_2 and O_3 are set to F_{XD} and F_{XU}, respectively.

$$F_{XU} = \left(\frac{\cos a}{2} + \frac{h}{L}\sin a\right)\frac{(l - a\sin\beta)}{a+b} G_m \tag{26}$$

$$F_{XD} = \left(\frac{\cos a}{2} + \frac{h}{L}\sin a\right)\frac{(l + b\sin\beta)}{a+b} G_m \tag{27}$$

The force analysis of the vertical shaft is shown in Fig. 9. The supporting force G_{C1} generates two opposite forces on the vertical axis, which are F_{CU} and F_{CD} respectively. According to the moment balance, the moments of O_2 and O_3 are taken respectively. From the moment balance, it can be obtained that:

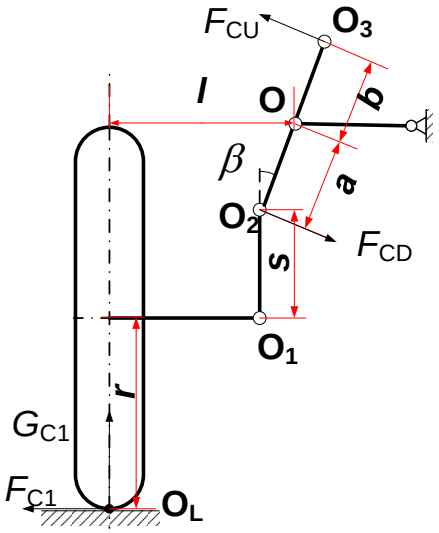


Fig. 9 – Stress analysis schematic diagram of strut under sideslip working condition

$$F_{CU}(a+b) = G_{C1}(l - a\sin\beta) + F_{C1}(r+s) \tag{28}$$

$$F_{CD}(a+b) = G_{C1}(l + b\sin\beta) + F_{C1}(r+s) \tag{29}$$

Bring (8), (13) into (26) and (27):

$$F_{CU} = \frac{(l - a\sin\beta + \varphi' r + \varphi' s)}{2c(a+b)}(c + 2h\varphi')G_m \tag{30}$$

$$F_{CD} = \frac{(l + b\sin\beta + \varphi' r + \varphi' s)}{2c(a+b)}(c + 2h\varphi')G_m \tag{31}$$

Fig. 10 shows the force analysis diagram of the vertical shaft during braking. The supporting force G_{Z1} generates two opposite forces on the vertical shaft, which are F_{ZU1} and F_{ZD1}, respectively.

The braking force F_{Z1} generates two co-directional forces F_{ZU2} and F_{ZD2} on the vertical shaft support. In addition, under the action of braking force F_{Z1}, the axle housing support on the wheel has a tendency to rotate around the vertical axis, which is stopped by the steering cylinder on the steering arm.

At this time, the thrust F_u acting on the steering arm by the steering cylinder produces two co-directional forces F_{ZU3} and F_{ZD3} on the vertical axis support.

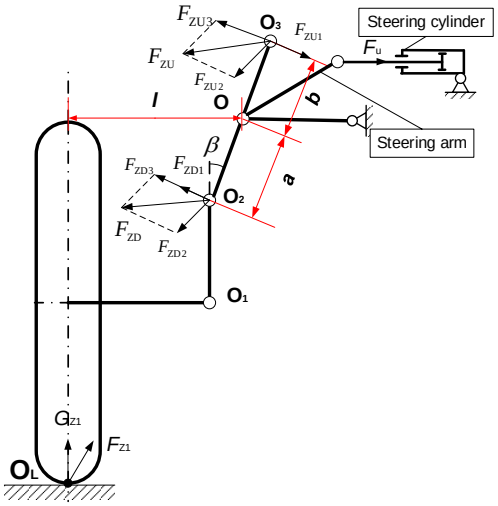


Fig. 10 – Stress analysis schematic diagram of strut under emergency braking working condition.

During braking, the support force G_{Z1} generates two opposite forces on the left front vertical shaft, which are F_{ZU1} and F_{ZD1} respectively. According to the vertical shaft torque balance relationship, it is obtained that:

$$F_{ZU1} = G_{Z1}\frac{(l - a\sin\beta)}{(a+b)} \tag{32}$$

$$F_{ZD1} = G_{Z1}\frac{(l + b\sin\beta)}{(a+b)} \tag{33}$$

The braking force F_{Z1} generates two co-directional forces F_{ZU2} and F_{ZD2} on the vertical shaft support, which are balanced with the thrust F_u acting on the steering arm by the steering cylinder.

$$F_u = \frac{F_{Z1}l}{2\,l'} \tag{34}$$

The two forces F_{ZU2} and F_{ZD2} of F_u on the vertical shaft support are:

$$F_{ZU2} = \frac{F_{Z1}l}{2\,l'}\frac{a}{a+b} \tag{35}$$

$$F_{ZD2} = \frac{F_{Z1}l}{2\,l'}\frac{b}{a+b} \tag{36}$$

The thrust of the steering cylinder acting on the steering arm F_u produces two co-directional forces F_{ZU2} and F_{ZD2} on the vertical shaft:

$$F_{ZU3} = \frac{F_{Z1}l}{2\,l'}\frac{l'' - b\sin\beta}{a+b} \tag{37}$$

$$F_{ZD3} = \frac{F_{Z1}l}{2\,l'}\frac{l'' + a\sin\beta}{a+b} \tag{38}$$

From Fig. 10:

$$F_{ZU} = \sqrt{(F_{ZU1} - F_{ZU3})^2 + F_{ZU2}^{\,2}} \tag{39}$$

$$F_{ZD} = \sqrt{(F_{ZD1} + F_{ZD3})^2 + F_{ZD2}^{\,2}} \tag{40}$$

In the formula, l' is the radius of the steering arm of the sprayer, and l'' is the distance from the end point of the steering arm to O_2.

Bring Eqs. (16), (20), (32)-(38) into Eqs. (39) and (40), the following is obtained:

$$F_{ZU} = \frac{L + 2\varphi h}{4l'L(a+b)}G_m\sqrt{\left(2\,l'(l - a\sin\beta) - l\varphi(l'' - b\sin\beta)\right)^2 + (la\varphi)^2} \tag{41}$$

$$F_{ZD} = \frac{L + 2\varphi h}{4l'L(a+b)}G_m\sqrt{\left(2\,l'(l + b\sin\beta) + l\varphi(l'' + a\sin\beta)\right)^2 + (lb\varphi)^2} \tag{42}$$

From the formula (24)~(27),(30),(31),(41),(42), it can be seen that the force on the lower end of the vertical shaft is greater than that on the upper end.

Therefore, the maximum value in F_{BD}, F_{XD}, F_{CD} and F_{ZD} is taken as the calculation load F_{max} of the vertical shaft. The bending stress, shear stress and extrusion stress of the vertical shaft are calculated as follows:

$$\begin{cases} \sigma_F = \dfrac{32e}{\pi d^3} F_{max} \\ \tau_T = \dfrac{4}{\pi d^2} F_{max} \\ \sigma_C = \dfrac{F_{max}}{de} \end{cases} \quad (2\text{-}43)$$

where e is the contact length between the vertical shaft and the upper and lower connectors, m.

According to the force analysis results of the vertical shaft, combined with the force diagram of the sprayer suspension in Figs. 6~10 and the relationship between the force and the reaction force, the force of other main components of the suspension is obtained, which provides the necessary basis for further finite element analysis and structural improvement of the components.

Finite element analysis of main parts

Compared with other CAE analysis software, HyperMesh has the advantages of high-performance finite element preprocessor and postprocessor, and has a good interface with a variety of CAD software. It can accurately and quickly establish finite element and finite difference models of various complex models, and has been widely used in many manufacturing enterprises and scientific research institutes around the world. In this paper, HyperMesh 10.0 software is used to analyze the key components of the designed independent vertical shaft air suspension system, including spring top support, vertical shaft, motor protection shell and steering arm. Combined with the results of mechanical analysis, the suspension system structure is improved design.

Open HyperMesh 10.0, set the working path, and save the 3D model format as *.stp. In order to ensure the success of HyperMesh 10.0 meshing, the model needs to be simplified in Creo. The simplified parts are mainly chamfering, chamfering and small holes. By meshing, the finite element model is established, and the parameters such as density, elastic modulus and Poisson 's ratio of the model material are set. The stress and strain state of each component is analyzed by adding constraints to the stress analysis results of each component. The parameters of the key components of the designed vertical air suspension are shown in Tab. 2.

Table 2

Material property parameters of key suspension components

Part name	Material	Density (g/cm^3)	Elastic modulus (GPa)	Poisson's ratio
Strut	45	7.85	210	0.31
Motor protection housing	Q345	7.89	135	0.269
Steering arm	Q345	7.89	135	0.269
Spring top support	Q345	7.89	135	0.269

RESULTS AND DISCUSSION

Key parts force analysis results and discussion

Based on the structural size of the whole machine, the variable values shown in Tab. 3 are taken, and the known quantities are brought into Section 2.4 to obtain the chassis force under different working conditions as shown in Tab. 3. The meaning of each symbol in Tab. 3 is known from Section 2.4. According to Tab. 3, the chassis force is closely related to the size of the wheelbase, and increasing the wheelbase can reduce the force of some parts. And the relationship between the size of the force is F_{CD}>F_{ZD}>F_{BD}>F_{XD}, select F_{max}=F_{CD}, according to Formula (2-43), known 45 steel allowable bending stress σ_F=120 MPa, allowable shear stress τ_T=30 MPa, allowable extrusion stress σ_C=50 MPa, check the vertical shaft diameter D≥106 mm. Considering that the selection of some parameters in the preliminary design is not necessarily consistent with the actual situation, some of the limit conditions may not be taken into account. At the same time, the influence of the keyway and cone surface on the spindle is calculated, and the minimum diameter of the vertical shaft is 120 mm. According to the relationship between the force and the reaction force, the force of the motor protection shell is calculated to be 85750 N. The force on the bottom of the steering arm is 34300 N, and the thrust of the steering cylinder is 40004 N; The reaction force of the spring top support is 57291 N. The direction and position of the force are shown in Fig. 11.

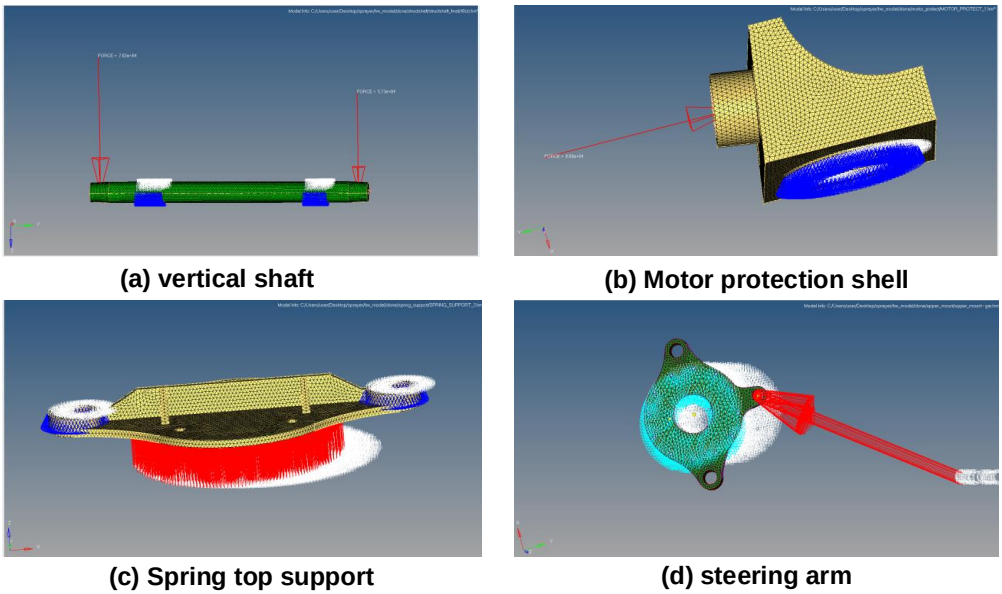
Table 3

Mechanical analysis and calculation results of chassis

Known variables		Calculation results		
Variables / measure unit	**Value**	**Force symbol / measure unit**	**When the wheel track is 3.0 m**	**When the wheel track is 3.8 m**
G_m / N	68600	Uneven road excitation condition		
G_b / N	58800	G_{B1} / N	85750	85750
a / m	0.45	G_{B2} / N	85750	85750
b / m	1.05	Sideslip condition		
r / m	0.93	G_{C1} / N	74316.7	65892.1
l / m	0.3	F_{C1} / N	52021.7	46124.5
h / m	2.5	Emergency braking condition		
c / m	3.0~3.8	G_{Z1} / N	74793.1	74793.1
L / m	3.6	F_{Z1} / N	63574.1	63574.1
S / m	0.24	Ramp driving condition		
w / m	1.8	G_{X1} / N	43455.1	43455.1
β / °	8	F_{X1} / N	36936.9	36936.9
Θ / °	12	Stress results of strut		
δ	2.5	F_{BU} / N	13569.8	13569.8
ψ	0.85	F_{BD} / N	25503.9	25503.9
ψ'	0.7	F_{XU} / N	6876.7	6876.7
g / m·s^{-2}	9.8	F_{XD} / N	12924.5	12924.5
l' / m	0.23	F_{CU} / N	52337.4	46404.4
l'' / m	1.3	F_{CD} / N	66256.1	58745.3
B / m	0.38	F_{ZU} / N	23601.7	23601.7
e / m	0.078	F_{ZD} / N	61482.2	61482.2

Simulation results and discussion

The mesh size is defined as 10 mm, and the tetrahedral method is used for meshing. According to the force analysis results of Tab. 3 and the material properties of Tab. 2, the constraints and loads are applied to the parts, and the finite element analysis model of the key parts is obtained as shown in Fig. 11.

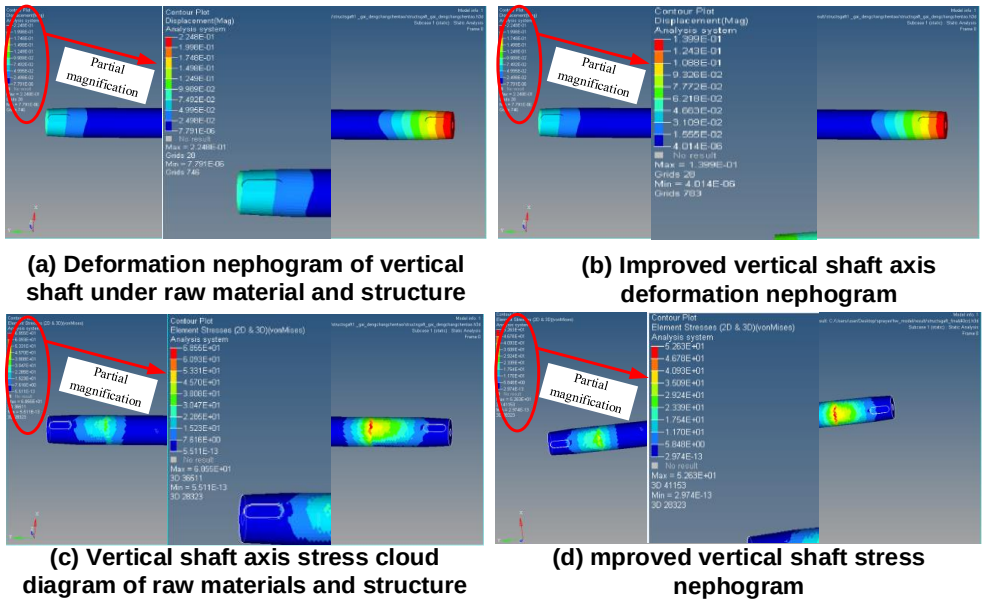


(a) vertical shaft **(b) Motor protection shell**

(c) Spring top support **(d) steering arm**

Fig. 11 – Finite element analytical model of suspension key components

According to the finite element model of the vertical shaft, the stress and strain analysis of the vertical shaft is shown in Fig. 12.



(a) Deformation nephogram of vertical shaft under raw material and structure

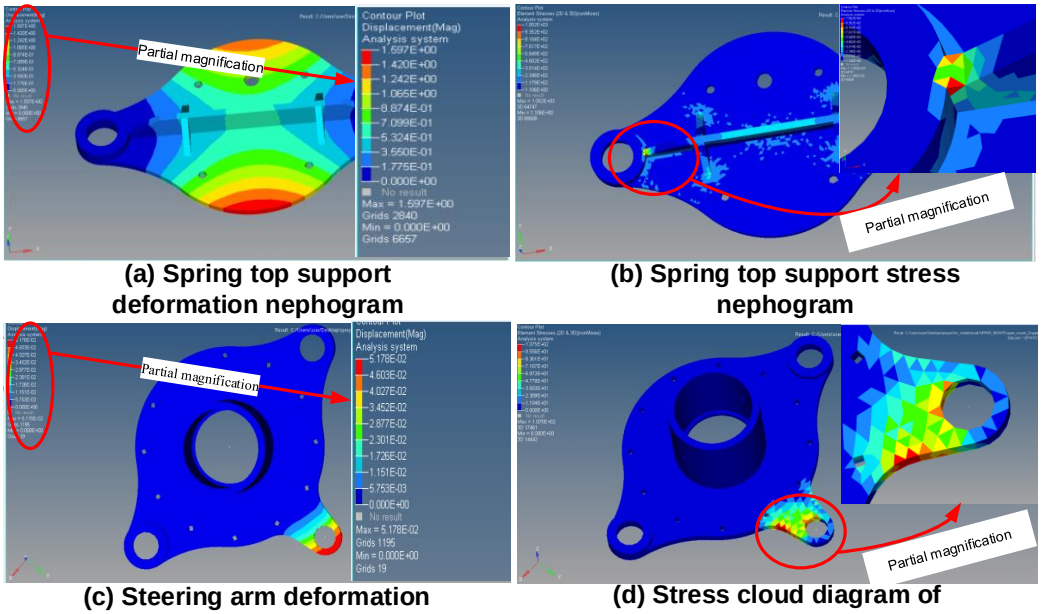
(b) Improved vertical shaft axis deformation nephogram

(c) Vertical shaft axis stress cloud diagram of raw materials and structure

(d) mproved vertical shaft stress nephogram

Fig. 12 – Stress and strain nephogram of strut before and after improvement

Fig. 12 (a) and (c) are shown as the stress-strain cloud diagram under the premise that the vertical shaft material is 45 steel, the outer diameter is 100 mm, and the inner diameter is 60 mm. The maximum deformation and stress are 0.224 mm and 68.666 MPa, respectively, which does not meet the allowable stress requirements of the selected material. The outer diameter of the vertical shaft is 120 mm, the inner diameter is 60 mm, and the length of the beam support column is 100 mm. The maximum deformation and stress are 0.1399 mm and 52.6 MPa, respectively, as shown in Fig. 12(b) and (d), which meet the allowable requirements. The improved vertical shaft size by simulation is consistent with the vertical shaft size of the mechanical check, indicating the effectiveness of the mechanical analysis and the accuracy of the simulation structure. Similarly, the finite element analysis of the spring top support, motor protection shell and steering arm is carried out, and the final stress and strain cloud diagram is shown in Fig. 13. The maximum deformation of each part is 1.597 mm, 0.05178 mm and 0.5091 mm respectively, and the maximum stress is 105.2 MPa, 107.5 MPa and 137 MPa respectively. The maximum deformation of the top support of the spring is too large, and the deformation displacement can be reduced by increasing the welding reinforcement. In addition, the maximum stress of each part is too large, which exceeds the allowable stress requirement of Q345, but these maximum values are located at the corners and sharp corners, and stress concentration occurs. Therefore, in the actual machining process, these corners and sharp corners need to be chamfered to eliminate stress concentration.



(a) Spring top support deformation nephogram

(b) Spring top support stress nephogram

(c) Steering arm deformation nephogram

(d) Stress cloud diagram of steering arm



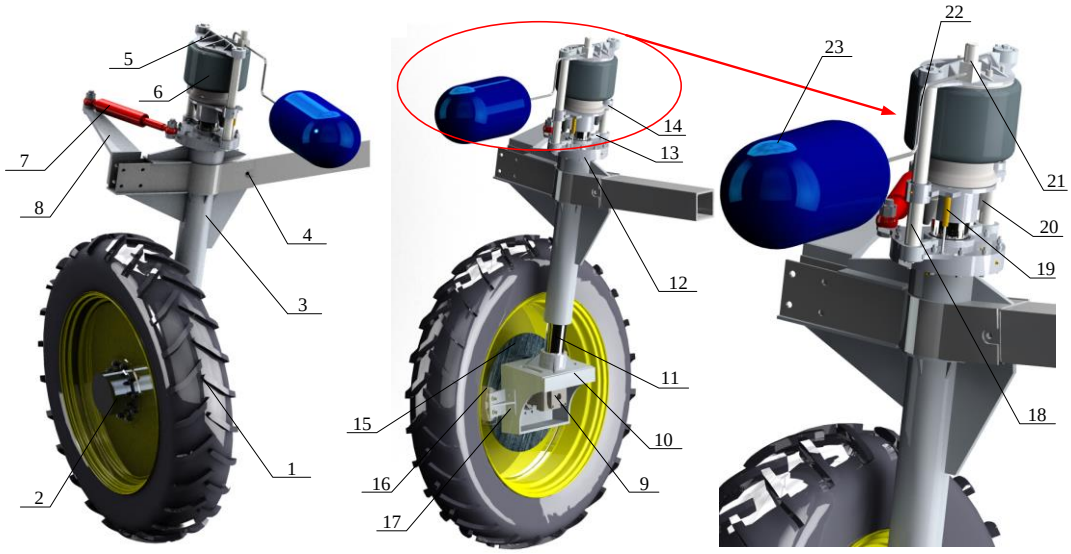
(e) Deformation cloud diagram of motor protection shell **(f) Motor protection shell stress nephogram**

Fig. 13 – Stress and strain nephogram of suspension key components

According to the finite element analysis method of the key parts of the suspension, the finite element model of the remaining parts is established. According to the results of the finite element analysis, the final structure of the suspension is improved.

Analysis of the final structure of the sprayer

According to the results of force analysis and finite element analysis, combined with the requirements of process production, the suspension structure in the design scheme is improved, and the final suspension structure is obtained as shown in Fig. 14.



(a) Exterior view *(b) Inner view* *(c) Partial magnification*

Fig. 14 – Final structure form of independent strut type air suspension system

1. Wheel; 2. Reducer; 3. Beam support column; 4. Track adjustment cylinder mounting hole; 5. Spring top support; 6. Air spring; 7. Steer cylinder; 8. Steer cylinder support arm; 9. Hydraulic motor; 10. Motor protection housing; 11. Strut; 12. Positioning ring; 13. Steering arm; 14. Spring bottom support; 15. Brake disc; 16. Brake caliper; 17. Brake caliper installation; 18. Guide post; 19. Height sensor; 20. Rubber limit block; 21. Variable throttle valve; 22. Compressed air hose; 23. Auxiliary chamber.

As shown in Fig. 14, in the process of suspension vibration reduction, the vibration caused by the road surface is first transmitted to the tire assembly, and then transmitted to the motor protection shell welding body by the tire assembly, and then reaches the vertical shaft. Under the guidance of the inner sleeve of the frame connection assembly, the vertical shaft passes the vibration transmitted by the motor protection shell welding through the spring bottom support welding body, air spring, guide column, spring top support welding, steering arm welding body, positioning ring and frame connection assembly, and finally passes it to the body. Compared with the existing sprayer suspension system, the independent vertical shaft air suspension designed in this paper has the following advantages:

(1) The structure is simple and easy to process. The adjustment of the ground clearance of the sprayer can be realized by replacing the vertical shaft with different lengths. The main structural components such as motor protection shell, steering arm, steering cylinder support arm and frame connection device are welded by welding process, which reduces the manufacturing cost.

(2) The air suspension adopts the active independent suspension structure, so that the suspension can adjust the air volume in the air spring according to the different working conditions of the sprayer to achieve the best vibration reduction performance.

(3) Through the damping adjustment device composed of additional air chamber, variable throttle valve and additional air chamber, the suspension damping can be automatically adjusted according to the driving condition of the sprayer, so as to absorb the impact load transmitted from the ground to the body more effectively and ensure the ride comfort of the driver. In addition, the additional air chamber is arranged flexibly and is not limited by the suspension structure and space.

The suspension system designed in Fig. 14 is assembled on the sprayer to obtain a large high clearance self-propelled sprayer layout as shown in Fig. 15.

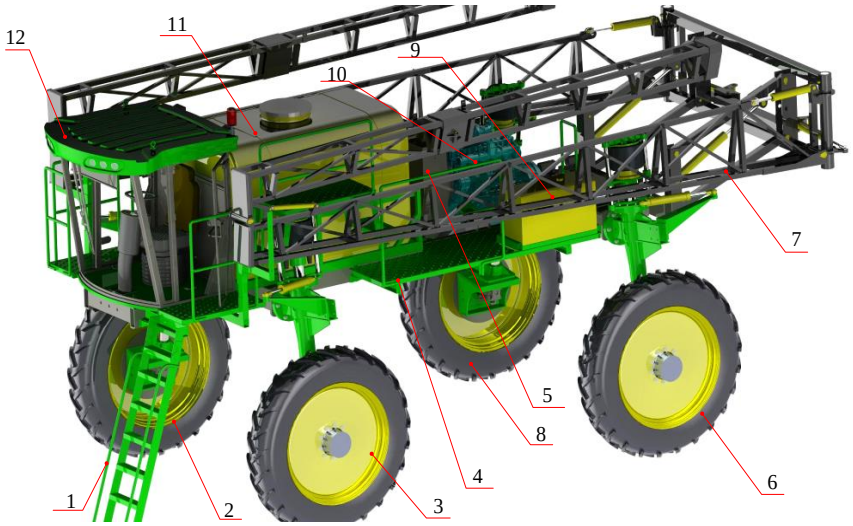


Fig. 15 – Overall structure and layout of sprayer

1. Ladder; 2. Right front suspension system; 3. Front left suspension system; 4. Walkways and handrails; 5. Radiator; 6. Rear left suspension system; 7. Spray boom; 8. Right rear suspension system; 9. Fuel tank; 10. Engine; 11. Medicine tank; 12. Cab

CONCLUSIONS

(1) According to the operating conditions and operating characteristics of the sprayer, the basic requirements of the sprayer suspension design are proposed. On this basis, the basic structural components of the suspension system, including elastic components, buffer devices, guiding devices and damping components, are analyzed and selected. A scheme of independent vertical shaft air suspension system based on air damping for high clearance sprayer is designed.

(2) Aiming at the complex mechanical action of vertical, longitudinal and lateral during the operation of the sprayer, the stress analysis of different extreme working conditions such as sideslip, emergency braking and uneven road driving of the sprayer is carried out. It is concluded that the force of the chassis is closely related to the size of the wheel track, and increasing the wheel track can reduce the force of some parts. The vertical shaft is analyzed and checked in detail, and the diameter of the vertical shaft is determined to be 120 mm. According to the relationship between the force and the reaction force, the force of the motor protection shell is calculated to be 85750 N. The force on the bottom of the steering arm is 34300 N, and the thrust of the steering cylinder is 40004 N. The reaction force of the spring top support is 57291N.

(3) According to the results of mechanical analysis, the finite element analysis of the main components of the suspension is carried out by using HyperMesh 10.0 software. Based on the analysis results, the final suspension structure is determined. The simulation results show that the size of the improved parts is consistent with the size of the mechanical check, indicating the validity of the mechanical analysis and the accuracy of the simulation structure.

ACKNOWLEDGMENT

This research was funded by the National Natural Science Foundation of China (32001428), the Key R&D projects in Shaanxi Province (2022NY-205) and the Shaanxi Provincial Key Industry Innovation Chain (Cluster) Project (2023-DLNY-62).

REFERENCES

[1] Blaauw D. (1999). *Spring-mounted spreading device*. EP, 0919124 A1[P], 1999-06-02.

[2] Buschena J. (2012). *Combination drive and suspension system for a vehicle*. US, 8172032[P], 2012-05-08.

[3] Carlson B C, Young D E, Baxter G E, et al. (2011). *Suspended axle for sprayer*. US, 7938415[P], 2011-05-10.

[4] Chen Y., Chen J., Li W., Zhang S., Xia H., Zhu Y., Wang J., (2020), Research on design and hybrid sliding mode control of high clearance self-propelled sprayer chassis air suspension, *INMATEH-Agriculture engineering*, vol.61, pp. 115-126. DOI: https://doi.org/10.35633/inmateh-61-13

[5] Chen Y., Wu J., Zhang S., Chen J., Xia H., Zhu Y., Wang J., (2021), Auto load-leveling control of a large sprayer chassis using the sliding mode method, *INMATEH-Agriculture engineering*, vol.64, pp. 65-80. DOI: https://doi.org/10.35633/inmateh-64-06

[6] Chen, Y., Mao, E., Li, W., Zhang, S., Song, Z., Yang, S., Chen, J. (2020). Design and experiment of a high-clearance self-propelled sprayer chassis. *Int J Agric & Biol Eng*, 13(2): 71-80.

[7] Chen, Y., Zhang, S., Mao, E., Du, Y., Chen, J., Yang, S. (2020). Height stability control of a large sprayer body based on air suspension using the sliding mode approach. *Information Processing in Agriculture*, 7: 20-29.

[8] Ehlen V., Voth R. (2011). *Suspension for self-propelled spreading machine*. EP, 2388157 A1[P].

[9] Giuseppe Quaglia, Massimo Sorli. Air Suspension Dimensionless Analysis and Design Procedure[J]. Vehicle System Dynamics: *International Journal of Vehicle Mechanics & Mobility*, 2001, 35(6): 443~475.

[10] Han, J.H; Park, C.H.; Jang, Y.Y. (2022). Development of a Moving Baseline RTK/Motion Sensor-Integrated Positioning-Based Autonomous Driving Algorithm for a Speed Sprayer. *Sensors,* 22, 9881.

[11] Hiddema J. (2013). Agricultural application machine with variable width track. US, 8376078 B2[P], 2013-02-19.

[12] Hu Y, Yang H, Hou B, et al. (2022). Influence of Spray Control Parameters on the Performance of an Air-Blast Sprayer[J]. *Agriculture*, 12(8): 1260.

[13] Hung T.M. (2022). Optimal selection for an air suspension system on buses through a unique high level parameter in genetic algorithms[J]. *Heliyon*, 8(3): e09059.

[14] Jiang X., Xu X., Shan H. (2022). Model-Based Fault Diagnosis of Actuators in Electronically Controlled Air Suspension System[J]. *World Electric Vehicle Journal*, 13(11): 219.

[15] Li W., Yang F., Mao E. et al. (2022). Design and Verification of Crab Steering System for High Clearance Self-Propelled Sprayer[J]. *Agriculture*, 12(11): 1893.

[16] Li W., Chen Y., Zhang S., Mao E., Du Y., Wen H. (2018). Damping Characteristic Analysis and Experiment of Air Suspension with Auxiliary Chamber. *IFAC-PapersOnLine*, 51(17): 166-172.

[17] Press R U. Raised axle and suspension system. US, 8162335 B1[P], 2012-04-24.

[18] Rondelli, V.; Capacci, E.; Franceschetti, B. (2022). Evaluation of the Stability Behavior of an Agricultural Unmanned Ground Vehicle. *Sustainability,* 14, 15561.

[19] Sánchez-Hermosilla J., Pérez-Alonso J., Martínez-Carricondo P. et al. (2022). Evaluation of Electrostatic Spraying Equipment in a Greenhouse Pepper Crop[J]. *Horticulturae*, 8(6): 541.

[20] Schaffer J A. (2002). Steering system for variable height agricultural sprayer. US, 6371237 B1[P].2002-04-16.

[21] Schaffer J A. (2002). Wheel support system for agricultural sprayer. US, 6491306 B2[P], 2002-12-10.

[22] Slawson J. (2002). Independent strut suspension. US, 8534686[P], 2013-09-17.

[23] Steffensen C., Michels E., Kleven J.E. (2012). Suspension assemblies with bump steer control, US, 8136824[P], 2012-03-20.

[24] Wei Z., Xue X., Salcedo R., Zhang Z., Gil E., Sun Y., Li Q., Shen J., He Q., Dou Q., Zhang Y. (2023). Key Technologies for an Orchard Variable-Rate Sprayer: Current Status and Future Prospects. *Agronomy,* 13, 59.

[25] Wubben T.M., Maiwald M.A., Carlson B.C. et al. (2007). High clearance vehicle suspension with twin spindles for transferring steering torque. US, 7168717 B2[P], 2007-01-30.

[26] Yu Chen, Jun Chen, Wei Li, et al. (2020). Research on design and hybrid sliding mode control of high clearance self-propelled sprayer chassis air suspension[J]. *INMATEH-Agricultural Engineering,* 61(2):115-126.

[27] Zatrieb J., Kasler R. (2012). New generation of hydro-pneumatic suspension systems with adaptive damping[R], *SAE Technical Paper*,
[28] Zheng Y., Shangguan W.B., Rakheja S. (2022), Modeling and analysis of time-domain nonlinear characteristics of air spring with an auxiliary chamber[J]. *Mechanical Systems and Signal Processing*, 176: 109161.
[29] Zheng Y., Shangguan W.B. (2023). A combined analytical model for orifice-type and pipe-type air springs with auxiliary chambers in dynamic characteristic prediction[J]. *Mechanical Systems and Signal Processing*, 185: 109830.
[30] Zhou Y., Li Z., Yu W. et al. (2022), Cooperative Control of Interconnected Air Suspension Based on Model Predictive Control[J]. *Applied Sciences*, 12(19): 9886.

ANALYSIS ON ROOT CUTTING MECHANISM OF SELF-PROPELLED CHINESE CABBAGE HARVESTER AND OPTIMISATION OF DEVICE PARAMETERS
/
自走式大白菜收获机切根机理分析及装置参数优化

Liming ZHOU [*1,2)], Yifan ZENG [1,2)], Kang NIU [2)], Yanwei YUAN [2)], Shenghe BAI[2)] and Kaikang CHEN [2)]
[1)] College of Mechanical and Electrical Engineering, Qingdao Agricultural University, Qingdao 266109, China;
[2)] Chinese Academy of Agricultural Mechanization Sciences Group Co., Ltd,
National Key Laboratory of Agricultural Equipment Technology, Beijing 100083, China
Tel: +86-17860737771; E-mail: zengyifan@stu.qau.edu.cn
DOI: https://doi.org/10.35633/inmateh-71-05

Keywords: *root; Chinese cabbage; parameter optimization; mechanical harvesting*

ABSTRACT
For Chinese cabbage cutting device in the harvesting process, the problem of cutting resistance and low cutting root qualification rate will occur. This paper takes the Chinese cabbage root as the research object, analyses the root-cutting mechanism of Chinese cabbage, and determines that the main factors affecting its cutting effect are the cutter's inclination angle, rotational speed and its working speed. The finite element method is adopted to establish a rigid-flexible coupling model between the cutting device and the cabbage root, and the Response Surface Method (RSM) central composite design method is used to investigate the relationship among the cutter inclination angle, the cutter rotational speed as well as the working speed and Maximum root-cutting reaction force (MRF) of the cabbage and to further obtain the optimal combination of parameters. Field test results show that in the optimal combination of parameters, which means cutter inclination angle of 11°, cutter rotating speed of 216 r/min and working speed of 0.28 m/s, the root cutting effect is perfect. At this time, the root-cutting qualification rate of 92.81% and field productivity of 0.12 hm²/h, meet the requirements of the standard of Chinese cabbage harvesting mechanization. The results of the study can provide reference for optimization of Chinese cabbage harvesting equipment design.

摘 要
针对大白菜切割装置在收获过程中存在切割阻力大、切根合格率低的问题。本文以大白菜根部为研究对象，分析大白菜切根机理，确定影响其切割效果的主要因素为割刀倾角、割刀转速和工作速度。利用有限元法建立切割装置与大白菜根部刚柔耦合模型，采用响应面（RSM）中心复合设计方法，探究割刀倾角、割刀转速和工作速度与大白菜最大切根反作用力（MRF）影响关系，并获得最优参数组合。田间试验验证结果表明，在最优参数组合割刀倾角为 11°、割刀转速为 216r/min 和工作速度为 0.28m/s 时，切根效果较好，此时切根合格率为 92.81%，田间生产率为 0.12hm²/h，满足大白菜收获机械化标准的要求。研究结果为大白菜收获装备设计优化提供参考。

INTRODUCTION[1]
Originated in China, Chinese Cabbage is a cruciferous Brassica biennial herbaceous plant, with high yield per unit area, convenient storage, richness in nutritional value and other advantages [1]. The Chinese Cabbage, whose planting area has reached 1.8 million hm^2, accounting for 15% of the total vegetable planting area, has ranked the second largest vegetable in China [2]. With the increasing area of cabbage planting, traditional manual harvesting has been unable to meet the needs of cabbage industrialization [3]. Therefore, the research and development of Chinese cabbage mechanical harvesting equipment is of great significance to improve operational efficiency and promote the development of vegetable mechanization.

Scholars at home and abroad have carried out research on Chinese cabbage harvesting: Kanamitsu [4] and others developed a walk-behind self-propelled cabbage harvester, which realizes the combined harvesting of cabbage, focusing on the design of the root-cutting device and the extraction device, but when harvesting different varieties of cabbage, there are problems such as poor root-cutting effect and greater damage.

Yanmar and Osada Nouki company jointly developed a crawler self-propelled cabbage harvester, which realized the first extraction and backward conveying, and at the same time clamped the cut root during

Liming ZHOU, Prof. Ph.D. Eng.; Yifan ZENG, Ph.D. Stud. Eng.; Kang NIU, Prof. Ph.D. Eng.;*
Yanwei YUAN, Prof. Ph.D. Eng.; Shenghe BAI, Ph.D. Stud. Eng.; Kaikang CHEN, Ph.D. Stud. Eng.

conveying to ensure the stability of the cut root, but the structure is complicated, the cost is high, and the requirements for planting mode are strict [5]. Kim et al developed a small crawler self-propelled cabbage harvester, which focuses on the optimization of extraction mechanism, and has a better extraction effect, but the damage rate of the plant is higher, and the adaptability is poor [6]. Yao Huiling of China Agricultural University designed a double screw plucking harvesting device to provide reference for the design and optimization of root cutting device, but no prototype was developed [7]. Zhao Tusen et al. of Heilongjiang University designed a two-row cabbage harvester, using the first extraction and then cut the root method, but the harvest cut loss rate is high, the performance needs to be improved [8]. In summary, the domestic and foreign cabbage harvester is mainly pulling first and then cut, although the pulling efficiency is high, but the plant damage is large and the demands for position of the root cutting and attitude are strict, at the same time there are problems including cutting operation resistance and low cabbage root-cutting qualification rate, which restrict the standardization of harvesting and planting of Chinese cabbage to improve the economic benefits. Therefore, there is an urgent need to study and develop cutting device with stable performance, and good root-cutting effect, which is meaningful to accelerate the development of mechanized cabbage harvesting.

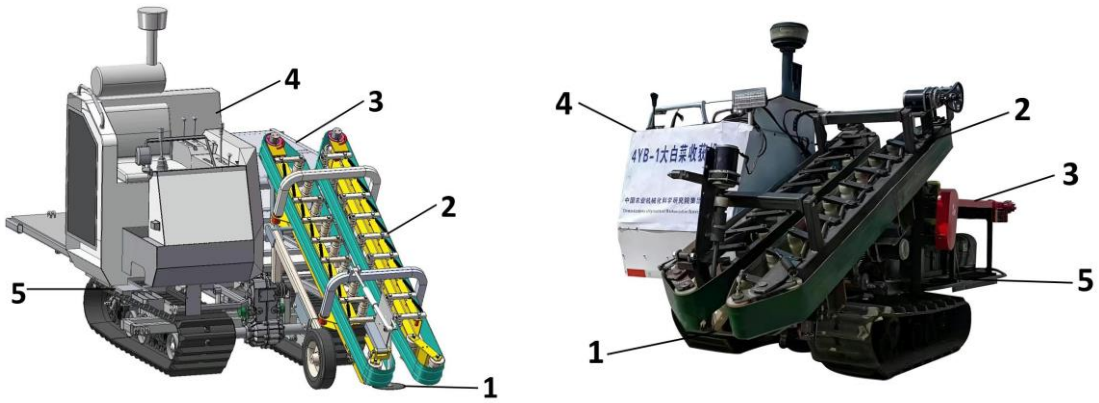
For the problem of large cutting resistance and low qualified rate of root cutting in the process of cabbage harvesting, this paper analyzes the main contributing factors affecting the cutting effect of cabbage root based on the mechanism of cabbage root cutting, uses the finite element method to establish a rigid-flexible coupling model of the cutting device and the root of the cabbage [9], and virtually simulates the process of cutting the root of the cabbage to seek for the optimal combination of the cutting device and obtains a better combination of the parameters of the cutting device through the verification of the field test.

MATERIALS AND METHODS

Structure design

- **Complete machine structure**

The whole structure of a crawler self-propelled Chinese Cabbage harvester is shown in Figure 1. Mainly composed of a cutting device, clamp conveying device, transverse conveying device, console, and automatic chassis, it can complete the root cutting, clamp transportation, transverse conveying, and manual basket loading at one time, to realize the joint harvesting of Chinese Cabbage. When running, its clamp conveying device is first adjusted by the console to incline 20°~30° from the ground. In that case, the ring cutter of the cutting device is tightly closed to the ground and aligned with the Chinese Cabbage. As the machine advances, the cutting device is driven by the motor to complete the root cutting of the Chinese Cabbage, and then the root-cut cabbage will be transported into the transverse conveying device at the top of the machine by the clamp conveying device. After that, cabbages will be selected and packaged artificially, which marks the completion of the harvest. The cutting device and clamp conveying device are designed to be adjustable to ensure that the machine can adapt to different situations. The main technical parameters of the harvesting machine are presented in Table 1.



(a) Three-dimensional diagram *(b) Actual diagram*

Fig. 1 - A crawler self-propelled Chinese Cabbage harvester

1. cutting device; 2. clamp conveying device; 3. transverse conveying device; 4. console; 5. self-propelled carrier

Table 1

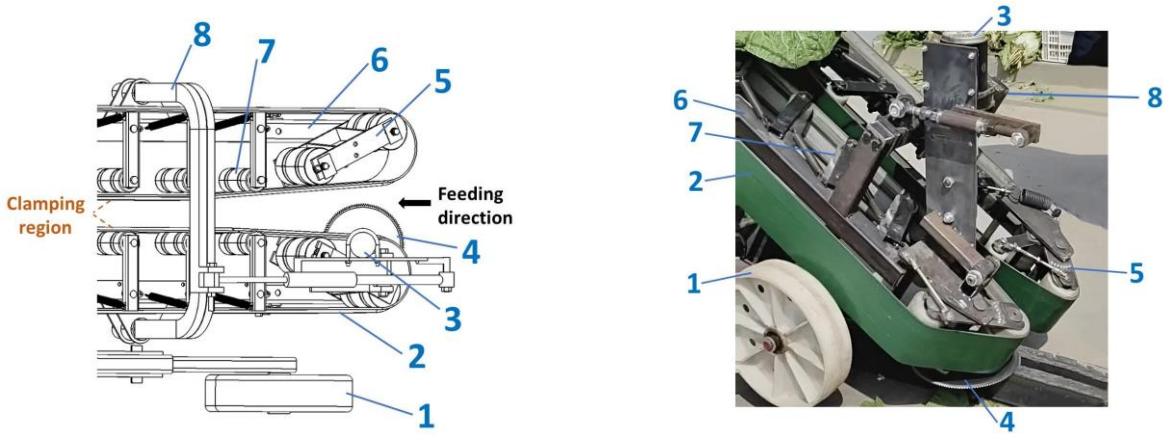
Technical characteristics of the crawler self-propelled Chinese Cabbage harvester

Parameter	Value

External dimensions(L×W×H) / m	4.1×2.0×2.3
Overall Weight / kg	1520
Auxiliary Power / kW	52
Walking Speed / m/s	0.2~1.8
No. of Rows Harvested / -	1
Appropriate Cabbage Ball Diameter / mm	150~200

- **Cutting device structure**

The cutting device is one of the key components of the Chinese cabbage harvester, as shown in Figure 2. It is designed to be placed at the front end of the clamp conveying device, mainly consisting of a profiling wheel, a follower pulley set, a front-end clamping belt, a drive motor, and a serrated disc cutter. The serrated disc cutter is mounted between the sets of driven wheels near the end of the profiling wheel, with the drive motor located at the top of it. The front clamping belt is powered by the motor of the conveyor unit, which can effectively clamp the cabbage and convey it upward through the follower pulley set and tensioner pulley. When the cutting device is aligned with the cabbage, the serrated disc cutting knife rotates at high speed in the opposite direction, in collection with the follower pulley set and the front clamping belt to complete the root-cutting of the Chinese Cabbage. The inclination, rotating speed, and front clamping angle of the serrated disc cutter are all adjustable to match different working environments, thus improving the adaptability and operability of the machine.



(a) Structure of the Cutting Device *(b) Actual diagram of the Cutting Device*

Fig. 2 - Cutting Device

1.Profiling wheel; 2. Front-end clamping belt; 3. Drive motor; 4. The serrated disc cutter; 5.Follower pulley set; 6. Rackmount; 7. Tensioner pulley; 8. Joint beam.

Analysis of root cutting mechanism

The cutting device is powered by a servo motor, as shown in Figure 3a. Analyzed from the starting point of the cut, the cabbage root is subjected to the *X*, *Y*, and *Z* direction of the cutting force of F_1, F_2, and F_3, respectively; The projection components of F_1 and F_3 in the *XY* plane are F_{1xy} and F_{3xy}, respectively; the projection components of F_{1xy} in the *X*-axis and *Y*-axis are F_{1x} and F_{1y}, respectively; the projection components of F_{3xy} in the *X*-axis and *Y*-axis are F_{3x} and F_{3y}, respectively; θ is the angle between F_{1xy} and the force F_1; γ is the angle between F_{3xy} and F_3; β and φ are the angles of the projected components F_{1xy} and F_{3xy}, respectively, concerning the *X*-axis direction. Due to the inclination angle of the cutting disc cutter and the disc cutter serrations, there still exists a certain cutting force in the *X*-axis and *Z*-axis directions (F_2). The X-axis direction is subjected to two opposite directions of the cutting force F_{1x} and F_{3x}, and their value of them is so high that the cutting disc cutter is seriously worn. Under the joint action of the cutting friction in the forward direction and the component cutting forces F_{1z} and F_{3z} in the Z-axis direction, the cabbage can be subjected to a large longitudinal component force, which helps to extract the roots of the cabbage. Setting the actual operation situation γ to zero [*10]* only the effect of pitch angle θ is taken into consideration. For the angle of θ is adjustable, it will help to find the optimal cutting combination parameters.

When working, the serrated mouth on the edge of the serrated disc cutter will clamp and shear the cabbage root [11], and the related process is shown in Figure 3b.

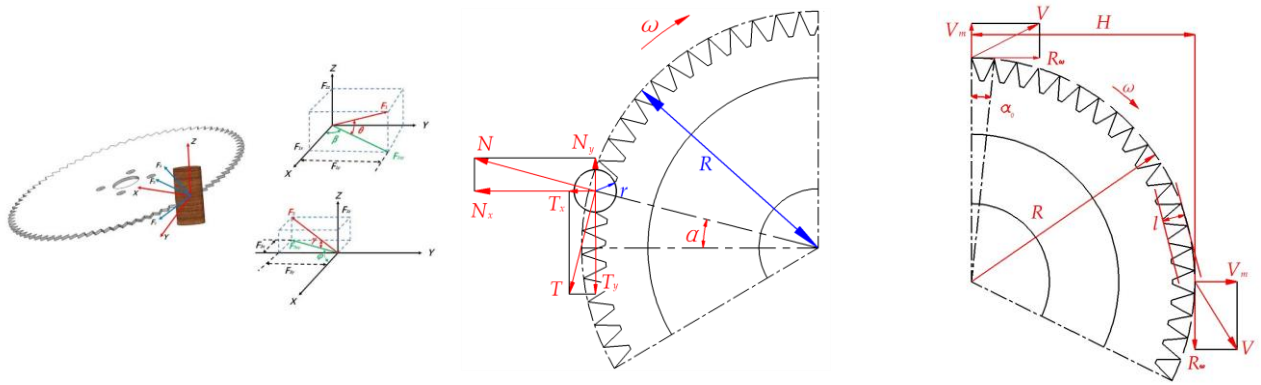


Fig. 3 - Root cutting mechanism analysis diagram

(a) Spatial analysis of root-cutting force; (b) Force Analysis Diagram of the Cut-root when cut; (c)The Analysis of Disc Cutter Motion

During the root-cutting process, if analyzing from the starting point of root cutting, it suggests that the cabbage root is subjected to cutting force F_X and clamping force F_Y, which is:

$$\begin{cases} F_X = T_X + N_X \\ F_Y = T_Y - N_Y \end{cases} \quad (1)$$

where:

N is the normal reaction force on the disc cutter during the cutting process, (N);

N_X is the component forces in the *X* directions, (N);

N_Y is the component forces in the *Y* directions, (N);

T is the friction force on the serrated disc cutter during the cutting process, (N);

T_X is the component forces in the *X* directions, (N);

T_Y is the component forces in the *Y* directions, (N).

The conditions under which the serrated disc cutter can clamp on the roots of the cabbage are [12]:

$$F_Y > 0 \quad (2)$$

It can be referred that $TY>NY$, and $F=Nf$, which means:

$$N \cdot f \cos\alpha > N \cdot \sin\alpha \quad (3)$$

At this time, when $f>tan\alpha$, the serrated disc cutter can clamp well:

$$\alpha = \arccos\frac{R}{R+r} \quad (4)$$

where:

R is the radius of the serrated disc cutter, (mm);

r is the radius of the cabbage root, (mm);

f is the friction between the cutting disc cutter and the cabbage root, generally taking 0.4~0.7;

α is the angle between the cutting disc cutter and the X-axis for the reaction force on the cabbage root, (°).

To ensure that the cabbage root can be cut off smoothly, the working area of the cutting device should be larger than the width of the cabbage ridge. Inside the working area, the direction of the combined speed of the forward speed of the cabbage harvester is opposite to the direction of the absolute speed of the cutting disk knife, and the absolute speed component of the forward direction of the machine should not be less than the forward speed of the machine. The working area of the cutting device and the analysis of the disc cutter motion are shown in Figure 3c. Therefore, the width of the working area of the cutting device is calculated as:

$$\begin{cases} H \le 2R(1-\sin\alpha_0) \\ \sin\alpha_0 = \dfrac{30v_{max}}{\pi Rn} \end{cases} \quad (5)$$

where:

H is the working width of the disc cutter, (mm);

R is the radius of the disc cutter, (mm);

v_{max} is the maximum working speed of the machine, (m/s);

α_0 is the horizontal angle of the cutter relative to the forward direction of the machine, (°);

n is the rotational speed of the disc cutter, (r/min).

To keep the working disc cutter away from the adjacent rows of cabbage, the trajectory of the cutter teeth's top center should be separated from the adjacent rows of cabbage for a certain distance, the expression is:

$$S \geq 2R + \Delta l + \frac{d_c}{2} \tag{6}$$

where:

S is the row spacing of cabbage planting, (mm);

R is the radius of the disc cutter, (mm);

Δl is the spacing between the movement track of tooth top center and the adjacent rows of cabbage, (mm);

d_c stands for the middle diameter of cabbage, (mm).

According to the actual measurement and reference to literature related to cabbage and sugar cane cutting [13] [14], Δl is taken as 100 mm, d_c (the average diameter of cabbage) is 200 mm, and cabbage planting row spacing is 450 mm, so as to determine R (the radius of the disc cutter) should not be longer than 125 mm. Considering that the cutter is installed with the ground into a certain angle of inclination, the range of R values can be appropriately increased. Studies on root-cutting of vegetables, such as Chinese broccoli, suggest that as the rotating speed increases, the more unstable the cutter is, the more vibration there will be [12]. Therefore, to ensure the quality of root cutting, a low rotational speed of root cutting is often chosen. Bringing R into the cutting device working area width calculation formula, taking v_m max as 1.6 m/s, n (disc cutter maximum speed) as 400 r/min, at this time the calculation of H (the working area width) is no more than 0.14 m.

However, to avoid disc cutter leakage, S_m (disc cutter's leading distance) must be less than or equal to l (the cutter's working distance); at the same time to ensure the root of the cabbage must be completely cut off, l must be greater than or equal to the maximum diameter of the cabbage root d_{max}, then the expression is:

$$\begin{cases} S_m \leq l \\ S_m = \dfrac{60 v_m}{Zn} \\ l \geq d_{\max} \end{cases} \tag{7}$$

where:

S_m is the disc cutter's leading distance, (m);

l is the maximum working distance of the disc cutter, (m);

v_m is the working speed of the machine, (m/s);

Z is the number of teeth of the disc cutter, (piece);

n is the rotational speed of the disc cutter, (r/min);

d_{max} is the maximum diameter of the cabbage root, (m).

The serrated cutting disc cutter is equipped with several continuous serrations, and in theory, the more teeth are, the root cutting process can be approximately continuous cutting. According to the cabbage physical parameters of the test, the maximum diameter of the cabbage root d_{max} value is taken as 30 mm, which is regarded as the minimum working distance of the disc cutter. Based on the design requirements of the cabbage harvester, v_m should be 1.2 m/s when it can work smoothly; Z (the maximum number of teeth) is 80 when R (the radius of the disc cutter) is taken as 125 mm. Taking them into account, n (the rotating speed of the disc cutter) should be no less than 30 r/min without cut missing and its value range is 30 up to 400 r/min.

In summary, the stability of root-cutting can be ensured by adjusting appropriate working parameters through the design of reasonable cutting disc cutter structure parameters. From equation (5), the main factors affecting the stability of root cutting can be confirmed: cutter inclination angle, cutter rotating speed, and forward speed. Combined with the relevant literature and the analysis of principle, the structural parameters of the cutting disc cutter and other data are preliminarily determined: the diameter of the cutting disc cutter is 250 mm, the thickness is 3 mm, the material is 65Mn, the inclination angle of the cutter is 5^{o}~15^{o}, the rotational speed of the cutter is 100~300 r/min, and the forward speed is 0.2~0.4 m/s. The above structural and working parameters will be verified in the simulation test and will be further verified through the field test.

Design of Cabbage Root-cutting Simulation Experiment

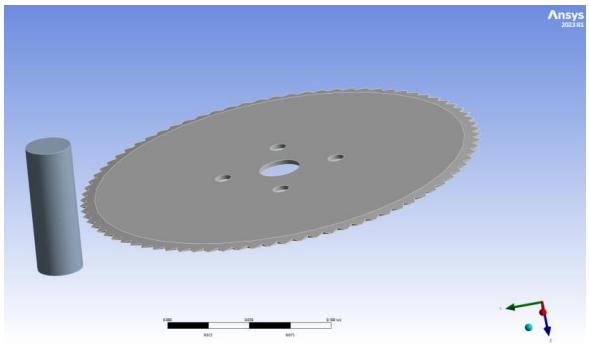
Based on ANSYS/LS-DYNA, a rigid-flexible coupling model related to the interaction between the cabbage root and the cutting disc cutter was constructed. The cabbage root was assigned the soft body characteristics while the cutter was assigned the rigid body characteristics [15]. The optimal combination parameters of the cutting device are obtained through dynamic analysis by performing simulation tests and parameter optimization by the central composite design method of response surface (RSM), which can be used for the study of cabbage harvesting prototype field trials.

- **Modeling of Cabbage Roots and Cutting Disc Cutter**

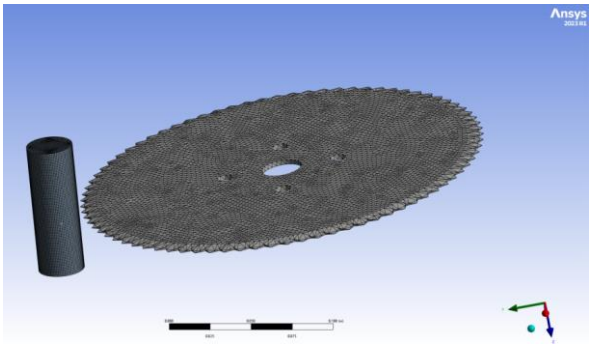
Cabbage roots are divided into main roots and lateral roots, and the main roots also have different lengths and diameters. To simplify, the site where the upper part of the underground root of the soil combines with the foliar root immediately above it is selected as the cutting part in this study. In this part, the root structure has a fibrous layer outside and a matrix inside. For simulation and calculation, the cabbage root model was designated as a solid cylinder and the material was considered homogeneous. According to the mechanical properties of cabbage roots, due to the existence of fibers along the axial direction, the mechanical properties of the material along the axial and radial directions of the root are quite different, while the mechanical properties are consistent along the radial direction and in all directions in the plane where they are located, hence they can be regarded as linearly elastic radially isotropic materials [16], ignoring micro-defects and micro-discontinuities [17].

Based on the previous physical measurements of the cabbage root, the average diameter of the root is 28.78 mm and the average length is 103.76 mm. In this chapter, the model of the cabbage root is regarded as a cylinder with a diameter of 28 mm and a length of 80 mm, and the cutting disc cutter is modeled with a diameter of 250 mm, a thickness of 3 mm, and an army of teeth of 80 as shown in Figure 4a.

Since only meshes and nodes can be computed and analyzed when performing finite element analysis, meshing the cabbage root and the cutting disc cutter is needed. A slightly coarser mesh size can be selected to shorten the calculation time and reduce the analysis effort. After the division, the cabbage root became a hexahedral cell, the number of its grid is 78,489, and the number of cells is 73,920; cutting the disc cutter the tetrahedral cell, the number of its grid is 90,724, the number of cells is 114,436. Figure 4b shows the effect of cutting the model after meshing.



(a) Geometric model of cabbage root and cutting disc cutter



(b) Cutting model effect after mesh division

Fig. 4 - Modelling diagram

- **Setting of model material properties**

Through the above analysis, the cabbage root is a typical anisotropic material, hence being set up as a flexible body. According to the material model provided by ANSYS/LS-DYNA, orthotropic linear-elastic orthotropic anisotropic materials adapt for modeling Chinese cabbage root materials.

Thus, by adding failure parameters to the file, the root material model can be disabled and can be used to simulate the root-cutting process [18]. The model material parameters of Chinese cabbage root include density DENS, Poisson's ratio uXY, Poisson's ratio uXZ (uYZ), radial modulus of elasticity Ex (Ey) or axial modulus of elasticity Ez, radial shear modulus Gxz (Gyz), and axial shear modulus Gxy. Based on the tests of the mechanical properties of Chinese cabbage root and the reference to the related literature [8] [19] , it was determined that the material parameters of the Chinese cabbage root were as shown in Table 2.

Table 2

The material parameters of the cabbage root model

Parameter	Value
DENS / kg·m^{-3}	880
uXY	0.06
uXZ	0.30
uYZ	0.30
Ex / MPa	398
Ey / MPa	398
Ez / MPa	140
Gxz / MPa	29.7
Gyz / MPa	29.7
Gxy / MPa	15.3

The cutting disk cutter is set as a rigid body, which will not be deformed during the simulation process and the strength and hardness of it is much larger than that of the cabbage root. To reduce the amount of calculation to shorten the simulation time, the material of the cutting disc cutter is 65Mn. The cutter takes 65Mn, a rigid body material for reference, whose density is 7.85 × 103 kg/m^3, modulus of elasticity is 210 GPa, Young's modulus is 2 × 10^5 MPa, and the Poisson's ratio is 0.3 [20].

The cabbage root and the disk cutter interact with each other, and the contact type is friction. Due to the destruction of the cabbage root material during the cutting process, the contact characteristics are set to "erosion", i.e., the face-to-face erosion contact algorithm ESTS. The dynamic and static friction coefficients of the defined contact surfaces are 0.15 and 0.23 respectively. Since the Chinese cabbage is clamped by the front-end gripping device at the moment of root-cutting, the fixed constraints are added at the upper end of the root to achieve the real effect. The cutting disc cutter is adjusted to rotate around the Z-axis to move along the X-axis, and the angle between the disc cutter and the horizontal forward direction is adjusted, i.e., the direction of movement of the cut root.

- **Response Surface Experimental Designs**

During the harvesting process of Chinese cabbage, the cabbage root is affected by the soil and the cutting device. Combined with the results of the stress analysis of the cabbage root, the MRF directly affects the damage of the cabbage and acts as an important index to measure the effect of cabbage harvesting. Based on the theoretical analysis, the cutter inclination angle, cutter rotational speed, and machine forwarding speed were selected as the test factors, which were expressed as X_1, X_2, and X_3 respectively. MRF was chosen as the test index, denoted by y. To adapt to different working conditions and soil types, the value range of α was determined to be 5°~15° regarding the range of commonly used cutting angles [10].

Based on the preliminary test and theoretical analysis, the rotational speed of the serrated disc cutter was selected to be 100~300 r/min, and the forward speed of the machine was selected to be 0.2~0.4 m/s. Response surface testing was performed by using a centralized composite design method.

The factor and level coding is shown in Table 3.

Table 3

Code	Experimental factors		
	Cutter Inclination Angle X_1/(°)	Cutter Rotational Speed X_2/(r/min)	Machine Forwarding Speed X_3/(m/s)
-1.682	1.6	32	0.13
-1	5	100	0.2
0	10	200	0.3
1	15	300	0.4
1.682	18.4	368	0.47

Test Equipment and Methods

- **Experimental Arrangement**

On March 29th, 2023, the developed 4YB-1 cabbage harvester prototype, in Shandong Dezhou Yucheng Vegetable Professional Cooperative cabbage planting base, was used to carry out field trials on the test cabbage varieties Significant ("Si Jin" in Chinese). Rows of multi-row open-air planting were adopted, the soil type was clay, the top of the row width was 500~550 mm, plant spacing was 390~430 mm and row spacing of 800~850 mm. The soil type was clay soil, the width of the top of the row was 500~550 mm, and the plant spacing was 390~430 mm. Row spacing was 800~850mm, and the cabbage was elliptical, with an average height of 380 mm. The ball diameter was about 170 mm, and the total weight of a single cabbage was an average of about 2.3 kg, with a root diameter of about 31 mm and a root length of about 90 mm.

The test randomly selected five rows of cabbage with basically the same growth condition and 20 m as the test area with a total of five replicated tests. According to the optimization results of the root-cutting simulation test, the structural parameters and working parameters of the cutting device of the cabbage harvester were pre-adjusted before the test, and after the devices of the prototype were stabilized, the cabbage root-cutting and harvesting test were conducted.

- **Evaluation Indicators**

Due to the lack of relevant standards and specifications for mechanized harvesting of cabbage, this experiment refers to the relevant test methods of Test Methods for Sugar Beet Harvesting Machinery (JB/T 6276-2007) and Specification for Production of Knotty Kale (GB/Z 26582-2011) as well as the operational standards. Taking the field productivity and root-cutting qualification rate as the mechanical performance of the cabbage harvester-cutting device, indexes are evaluated. Each index is defined as follows:

Field productivity refers to the actual harvested area completed by the cabbage harvester per unit of time. The actual operating width is estimated in terms of the row spacing of the cabbage, and the expression:

$$E = 3.6Bv \tag{8}$$

where:

E is the field productivity, (hm^2/h);

B is the operating width of the cabbage harvester, (m);

v is the operating speed of the cabbage harvester, (m/s).

Root-cutting qualification rate refers to the proportion of the total number of harvested cabbages that have passed root-cutting. The evaluation criteria for qualified root cutting are that the location of cut root should locate in a better area and the cutting device should not cause damage to the cabbage bulb, etc., and its expression is:

$$Q_c = \frac{N_c}{N} \times 100 \tag{9}$$

where:

Q_c is the qualified rate of root cutting, (%);

N_c is the number of qualified cabbages with cut roots, (tree);

N is the total number of harvested cabbages, (tree).

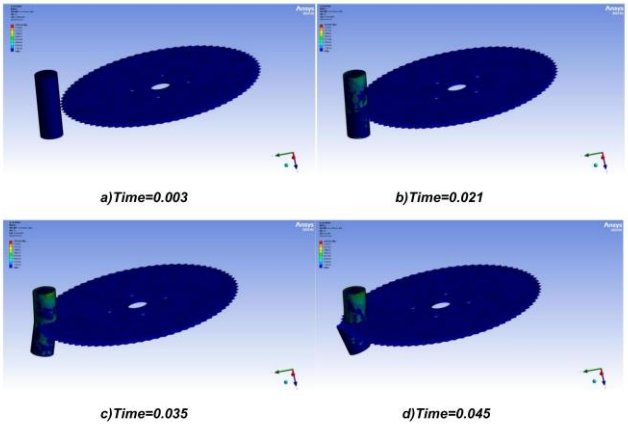
RESULTS AND DISCUSSION

Cutting Simulation Modeling Process and Results

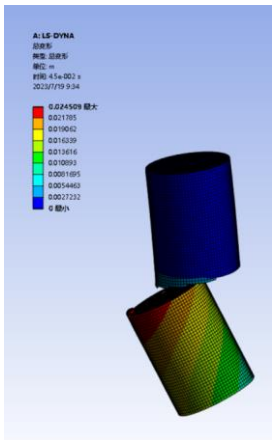
- **Cutting Simulation Modeling Process**

The factors and levels are designed according to the central composite design method of response surface (RSM), and each parameter of each group of root-cutting models is set separately for simulation and calculation of results. The stress cloud displacement process of the cutting simulation is obtained by reading the resultant file calculated by the LS-DYNA program as shown in Figure 5a.

The total simulation time is set to 0.045 s, the inclination angle of the cutting disk cutter and the horizontal forwarding direction is 5°, and the rotational speed and horizontal speed are set to 300 r/min and 0.4 m/s respectively. It can be seen from the pictures that the disc cutter cuts into the Chinese cabbage root in the time of 0~0.021 s, but the root does not fracture; in the time of 0.035 s, the disk cutter continues to cut, and the root of Chinese cabbage began to fracture, until 0.045 s, the cabbage root completely fractured. The final orthogonal test results are shown in Table 4. The root fracture model is shown in Figure 5b, with the red part representing the maximum stress on the cabbage root.



(a) Simulation process of root-cutting cloud displacement map



(b) Total deformations of cabbage roots

Fig. 5 - Simulation of root cutting process

Table 4

Orthogonal test results of root-cutting models

Serial number	Experimental factors			Y / N
	X_1 / (°)	X_2 / (r/min)	X_3 / (m/s)	
1	10	368	0.3	213.22
2	5	100	0.4	214.55
3	10	200	0.3	100.44
4	5	300	0.4	176.76
5	18.4	200	0.3	147.95
6	10	200	0.3	99.91
7	10	200	0.3	109.32
8	10	200	0.3	98.34
9	15	300	0.4	158.53
10	15	100	0.2	175.34
11	10	200	0.3	96.56
12	5	100	0.2	192.94
13	10	200	0.47	191.16
14	10	200	0.13	146.14
15	10	200	0.3	110.62
16	5	300	0.2	171.36
17	15	100	0.4	219.82
18	15	300	0.2	159.21
19	1.6	200	0.3	183.96
20	10	32	0.3	255.49

The MRF variation curve for the root-cutting process is shown in Figure 6, with the first peak due to the initial contact of the disk cutter with the root. The maximum peak occurs between 0.030 s and 0.035 s when the disk cutter cuts the deepest part of the root and its multiple teeth are in contact.

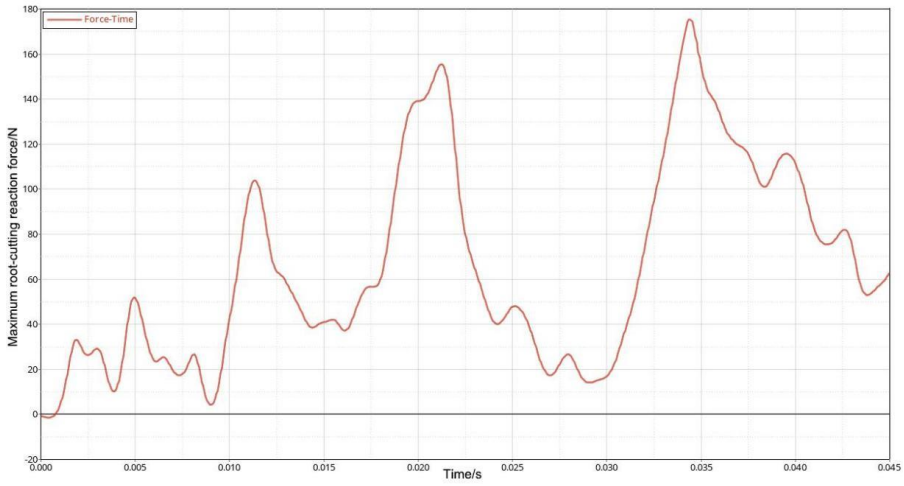


Fig. 6 - Plot of MRF variation during root-cutting simulation

- **Establishment of the regression equation and variance analysis**

The multivariate regression analysis and fitting of the experimental results using Design-Expert 12 software yielded the multivariate regression quadratic equations for the cutter inclination, cutter rotational speed, forward speed, and MRF:

$$Y_1 = 102.90 - 7.56X_1 - 15.22X_2 + 10.73X_3 - 2.26X_1X_2 + 2.10X_1X_3 - 7.67X_2X_3 + 20.02X_1^2 + 44.21X_2^2 + 20.98X_3^2 \quad (10)$$

The analysis of variance (ANOVA) is shown in Table 5. A P-value of the MRF y model is less than 0.0001, indicating the validity of this model. The p-values of the cutter inclination X_1, cutter rotation speed X_2, and forward speed X_3 on MRF are less than 0.05, suggesting that X_1, X_2, and X_3 have a significant effect on MRF. From the F-value, it can be seen that the magnitude of the effect of X_1, X_2, and X_3 of the clamped carrier on MRF is X_2, X_3, and X_1 in that order.

Table 5

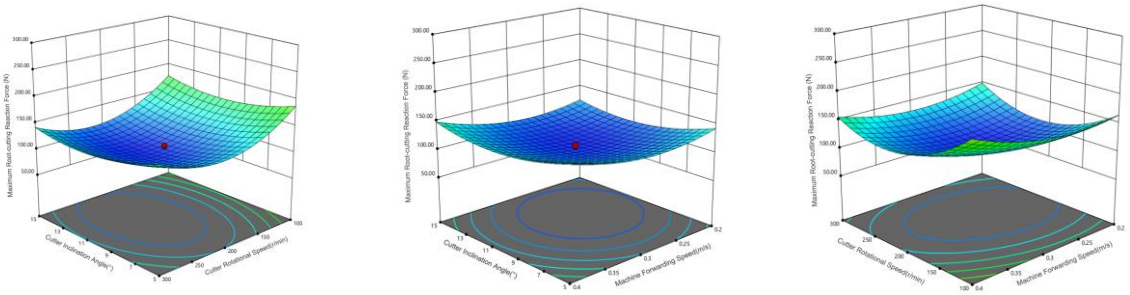
The analysis results of variance (ANOVA)

Source	Maximum Root-cutting Reaction Force / N			
	Sum of squares	Mean square	F	p
Model	41162.98	4573.66	49.42	< 0.0001
X_1	780.92	780.92	8.44	0.0157
X_2	3164.26	3164.26	34.19	0.0002
X_3	1572.06	1572.06	16.99	0.0021
X_1X_2	40.73	40.73	0.4400	0.5221
X_1X_3	35.24	35.24	0.3807	0.5510
X_2X_3	470.78	470.78	5.09	0.0477
X_1^2	5777.93	5777.93	62.43	< 0.0001
X_2^2	28162.52	28162.52	304.28	< 0.0001
X_3^2	6340.91	6340.91	68.51	< 0.0001
Residual error	925.55	92.55		
Misfit term	749.56	149.91	4.26	0.0689
Pure error	175.98	35.20		
Total difference	42088.53			

- **Analysis of the influence law of interaction terms on test indexes**

The response surface is shown in Figure 7. From Fig. 7a, when the forward speed X_3 is the center level, i.e., X_3=0.3 m/s, it can be seen that the MRF decreases and then increases with the increase of X_1 and X_2.

From Fig. 7b, it can be seen that when the cutter speed X_2 is the center level, i.e., X_2=200 r/min, the interaction between X_1 and X_3 is relatively smooth, which indicates that X_1 and X_3 have the least influence among the interaction factors. From Fig. 7c, it can be seen that when the cutter inclination X_1 is center level, i.e., X_1=10°, the value of MRF decreases and then increases with the increase of X_2; and with the decrease of X_3, the MRF also decreases gradually.



(a) *(b)* *(c)*

Fig. 7 - Influence response surface of test factors on test indexes

- **Optimization of parameters**

The minimum value of the maximum root-cutting reaction force (MRF) of the cabbage root is selected as the optimization objective, and the objective function expression is as follows:

$$\begin{cases} \min\ Y(X_1, X_2, X_3) \\ 5^o \le X_1 \le 15^o \\ 100r/\min\ \le X_2 \le 300r/\min \\ 0.2m/s \le X_3 \le 0.4m/s \end{cases} \tag{11}$$

According to the optimization calculation results of DesignExpert software, the minimum value of MRF was 99.636 N. At this time, the optimal parameter combinations were a cutter inclination angle of 11.055°, cutter rotational speed of 215.669 r/min, and working speed of 0.276 m/s. Considering the cost of the optimized parameter combinations and the feasibility of the field test, the above values were rounded up to the closest integer, which was 11°, 216 r/min, and 0.28 m/s respectively. Validation tests were conducted based on the optimized cutting device and the optimum MRF was determined to be 102.785 N, which was comparable to the original values within an acceptable percentage range (3.16%). The optimal parameter combinations optimized by the root-cutting simulation test set the basis for subsequent field tests of the prototype.

Cutting device field test results

Before the test, the optimal combination of parameters was selected, the forward speed of the prototype was adjusted to 0.28 m/s, and the rotational speed of the cutting disc cutter was adjusted to 216 r/min and adjusted to an angle of 11° with the ground to verify the results of the root-cutting simulation test. Field tests show that the overall performance of the prototype is stable, the cutting device works smoothly, the overall damage to the cabbage plant is little, and the prototype has a high degree of harvest integrity which meets the requirements of single-row cabbage harvest (Figure 8), the average field productivity of the cabbage harvester is about 0.12 hm^2/h. In the cabbage-cutting process, due to soil unevenness, the prototype is easy to harvest inaccurately, it needs the driver to correct, resulting in a reduction in the qualified rate of cut roots. However, the overall qualification rate is still high, the average value is about 92.81%.

There is no leakage of cuts, which verifies the reliability of the design of the cutting device, and further explains the importance of the cutting device in the mechanized harvesting of Chinese cabbage operations.



Fig. 8 - Harvesting Process and Cutting Effect of the 4YB-1 Cabbage Harvester Prototype in the Field

Discussion

In this study, the effects of cutter inclination angle, cutter speed, and forward speed on MRF were analyzed by dynamic simulation of root cutting. The MRF was minimal when the cutter inclination angle, the cutter speed, and the forward speed were 11°, 216 r/min, 0.28 m/s respectively. At the same time, a high root-cutting qualification rate could be obtained in the field test. The effects of blade thickness, blade shape, and cutting position on MRF will be further studied in the future.

From the field test, it was found that due to the uneven soil, the prototype was not aligned when harvesting, and there were cases of incomplete cutting of roots or cutting damage to the cabbage, resulting in a decrease in the qualification rate of root cutting. As the cabbage is affected by the interaction of plant, soil, and cutting device in the actual process, the possible vibration of the cabbage plant during harvesting and the complexity of soil conditions also could affect the interaction during the root-cutting process. In the root-cutting simulation test, the soil and cabbage vibration in the cutting process was not considered, so there are some limitations. Therefore, it can be considered to further study the complex simulation model of cabbage plant-soil-cutting device interaction mutual influence, improving the reliability of the cutting device.

CONCLUSIONS

Based on the cabbage root cutting mechanism, this paper analyzes the main factors affecting the root cutting effect of cabbage and optimizes the parameters of the cutting device by using the central composite design method of finite element method and Response Surface Method (RSM). This device of cutter inclination angle and cutter speed is adjustable. The optimized cutting device effectively reduces cabbage root cutting resistance and improves cabbage field productivity and root cutting qualification rate. The main research conclusions are as follows:

(1) The optimized parameter combination of the cutting device is the key to lower resistance and damage on Chinese cabbage. Through the analysis of the root-cutting process and the construction of the cabbage root-cutting model, the cutter inclination angle, cutter rotational speed, and machine forward speed were identified as the key factors affecting the maximum root-cutting reaction force (MRF) of the cabbage.

(2) According to the key parameters of the cabbage and the cutting device, the dynamic simulation model of the cabbage root-disc cutting knife was established. Through the virtual simulation test of the cabbage root-cutting process, the multiple regression equations of the influence of the inclination angle, the rotational speed, and the forward speed of the cutter on the MRF were obtained. The degree of influence of each factor on MRF was determined, which was the cutter rotational speed, forward speed, and cutter inclination angle in descending order. The optimal combination of cutting device parameters was determined by using Design-Expert 12 software: when the cutter inclination angle was 11.055°, the cutter rotational speed was 215.669 r/min, and the working speed was 0.276 m/s, the MRF was 99.636N. According to the feasibility of the optimal parameters verified by the field test, the rounded-up parameters 11°, 216 r/min and 0.28 m/s were determined to further validate the optimized cutting device and working parameters. Based on the optimized parameter verification test, the optimum MRF was measured as 102.785 N, which is comparable to the original value within the acceptable percentage range (3.16%).

(3) Through the field test, the cutting device was verified in the optimal combination of cutting root parameters under the cabbage harvesting effect. The test results show that the field productivity of the cabbage harvester is 0.12 hm^2/h, and the qualified rate of root cutting is 92.81%, which meets the requirements of mechanized cabbage harvesting.

ACKNOWLEDGEMENT

This work was supported by the R&D and Demonstration of Key Technical Equipment for Intelligent Agricultural Machinery for Mountain Fruits and Vegetables (Project No. 2022YFD2001803).

REFERENCES

[1] Wang, J.J. (2020) Production Status and Development Countermeasures of Chinese Cabbage in China[J]. *China Fruit & Vegetable*, 40(07): 80-82+106;

[2] Yang, Y.T., et al. (2020). The current situation and development suggestions of mechanized production of Chinese cabbage in China[J]. *China Veg*, (11): 9-16;

[3] El Didamony, M.I. et al. (2020). Fabrication and Evaluation of a Cabbage Harvester Prototype. *Agriculture*, 10(12): 631. https://doi.org/10.3390/agriculture10120631;

[4] Kanamitsu M., et al. (1994) Development of a Chinese cabbage harvester (Part 3): development of height controller and field test of harvester[J]. *Japan Agricultural Research Quarterly*, 56(2): 127-133;

[5] Zhang, J., et al. (2019) Research Status of Key Technology and Equipment of Corm Leaf Vegetable Harvester[J]. *Xinjiang Agricultural Mechanization*, (02): 29-34;

[6] Kim, H.J., et al. (2020) Pulling performance of a self-propelled Chinese cabbage harvester and design of a preprocessing unit[J]. *Journal of Agriculture Life Science*, 54(1): 99-108;

[7] Yao, H.L. (2007) *Study on key parts of Chinese cabbage harvester* [D], China Agricultural University, Beijing;

[8] Zhao, T.S. (2020) *Study on the design and key technology of cabbage harvester*[D]. Heilongiang University, Harbin;

[9] Cui, T., et al. (2012) Flexible Body Simulation for Corn Stem Based on ANSYS and ADAMS[J]. *Trans. Chin. Soc. Agric*. Mach, 43(S1): 112-115;

[10] Li, T.H., et al. (2020) Mechanical analysis and parameter optimization of cabbage root cutting operation[J]. *Trans. CSAE*, 36(07): 63-72;

[11] Zhang, J.F., et al. (2022) Parameter Optimization and Testing of a Self-Propelled Combine Cabbage Harvester. *Agriculture*. 12(10): 1610. https://doi.org/10.3390/agriculture12101610;

[12] Li, X.Q., et al. (2013) Analysis of influencing factors on cutting force of cabbage rhizomes[J]. *Trans. CSAE*, 29(10): 42-48;

[13] Zhang, J. (2022). *Research on physical and mechanical properties of headed Chinese cabbage and its crawler self-propelled harvesting equipment* [D]. Zhejiang University, Hangzhou;

[14] Xie, L.X. (2019) *Design and parameter optimization of stalk chopping, leaf stripping and top breaking devices for sugarcane harvester* [D]. Zhejiang University, Hangzhou;

[15] Tang, J.H., et al. (2023) An ANSYS/LS-DYNA Simulation and Experimental Study of Sectional Hob Type Laver Harvesting Device. *Agriculture*, 13(2): 361. https://doi.org/10.3390/agriculture13020361;

[16] Huang, H.D., et al. (2011) Finite element simulation of sugarcane cutting [J]. *Trans. CSAE*, 27(02):161-166;

[17] Shi, N. (2018) *Peeling method of cotton stalk and development of rubbing peeling machine* [D]. Northwest AF University, Xianyang;

[18] Jiang, L.Q. (2013) *Simulation study of circular saw cutting process based on ANSYS/LS-DYNA* [D]. Guangxi University, Nanning;

[19] Zheng, J.M., et al. (2023) Parameter Calibration of Cabbages (*Brassica oleracea L.*) Based on the Discrete Element Method. *Agriculture*, 13(3): 555. https://doi.org/10.3390/agriculture13030555;

[20] Dun, G.Q., et al. (2015) Effect of rotation direction of knife teeth configuration on clearing straw unit performance for no-tillage and straw mulching precision seeder [J]. *Trans. CSAE*, 31(12):48-56;

STUDY OF THE PROCESS OF THRESHING LEGUMINOUS GRASS SEEDS WITH A DRUM-TYPE THRESHING DEVICE
/
ДОСЛІДЖЕННЯ ПРОЦЕСУ ВИТИРАННЯ НАСІННЯ БОБОВИХ ТРАВ МОЛОТИЛЬНИМ ПРИСТРОЄМ БАРАБАННОГО ТИПУ

Mykhailo ANELIAK, Alvian KUZMYCH, Serhii STEPANENKO*), Viktor LYSANIUK
Institute of Mechanics and Automatics of Agroindustrial Production / Ukraine
Tel: +38 050 457 22 47; E-mail: stepanenko_s@ukr.net
DOI: https://doi.org/10.35633/inmateh-71-06

Keywords: *drum-type threshing device, leguminous grass seeds, completeness of threshing, seed damage.*

ABSTRACT

The article presents the results of studies of the process of threshing leguminous grass seeds with a drum-type threshing device. The process of material movement in the working gap of the drum deck was modelled and the intensity of the action of the working on the material under optimal operating conditions was substantiated. The dependence of the completeness of threshing alfalfa seeds on the number of rasp bar actions on the material on pendulum copra and in a threshing device was obtained based on the results of laboratory research. The influence of the design and technological parameters of the threshing device on the efficiency of threshing alfalfa seeds, as well as on the energy indicators of their operation, has been determined. The rational parameters of the threshing device are substantiated, which ensure complete threshing of seeds at the level of 96.5-98.2%, and damage to no more than 0.8% of seeds.

РЕЗЮМЕ

У статті наведено результати досліджень процесу витирання насіння бобових трав терковим пристроєм барабанного типу. Проведено моделювання процесу руху матеріалу в робочому зазорі бич-дека та обґрунтовано інтенсивність дії робочих органів на матеріал при оптимальних режимах їх роботи. За результатами лабораторних досліджень отримано залежності повноти витирання насіння люцерни від кількості дій бичів по матеріалу на маятниковому копрі і в терковому пристрої. Визначено вплив конструктивно-технологічних параметрів теркового пристрою на ефективність витирання насіння люцерни, також на енергетичні показники його роботи. Обґрунтовано раціональні параметри теркового пристрою за яких забезпечується повнота витирання насіння на рівні 96,5-98,2%, та пошкодження не більше 0,8% насіння.

INTRODUCTION

To harvest seeds of leguminous grass such as clover, alfalfa and melilotus, grain harvesters are mainly used. Therefore, all known technologies are based on the use of combine harvesters (*Sheichenko et al., 2019*). As an object of processing, legumes grass seed plants have a number of specific features different from grain crops in the structure of plants, inflorescences and seeds, which causes significant differences in the physical, mechanical and technological properties of the processed material (Moss *et al., 2021*). Significant differences in the physical and mechanical properties of the biological mass of legumes grass seed plants from cereal crops complicate the process of seed harvesting, and especially the operations of thrashing and separating seeds with a combine harvester (*Ivan, 2016*).

Special adapters are used for harvesting grass seeds by combine harvesters, which are more suitable for working with such material as unthreshed inflorescence of leguminous grass seeds. This allows reducing seed losses, but still they remain significant and make up 20-30% of the grown crop.

The problematic issue in the operation of threshing unit of combine harvesters is the process of threshing seeds from legume. The percentage of threshing seeds after passing them through the threshing unit is only 45-55%.

Therefore, for threshing the rest of the seeds from the beans, the fraction of unthreshed seeds is re-fed to the threshing unit or to the stand-alone after-threshing devices of the combine, the efficiency of which is too low (*Liao, et al., 2021*). In one pass of the material through the after-threshing devices, only 10-15% of the seeds are threshed off. In addition, due to the low adaptation of the air-sieve cleaning unit to work with a heap of legume grass seeds, a significant part of straw and chaff impurities is fed into the after-threshing devices with unthreshed seeds.

Repeated feeding of the same material into the threshing device leads to recirculation of the material in the thresher of the combine and damage to the seeds (*Chu et al., 2022*). This leads to an overload of the working bodies of the combine thresher and an even greater deterioration in the operation of the air-screen cleaning unit and, accordingly, an increase in the loss of seeds by the thresher of the combine (*Pari et al., 2020*). Significant losses of seeds during the harvesting of leguminous grass seed plants prompt the need to search for and develop new technological and technical solutions for the processes of field and stationary threshing and seed separation.

Studies of the qualitative indicators of the operation of special shelling devices have shown that the use of these devices on combine harvesters for threshing seeds of legumes grass allows increasing the percentage of seeds in the bunker by only 10-15%. But it is not possible to solve the problem of complete threshing of seeds with the thresher of the combine harvester. This produces only up to an increase in the circulation load on the working bodies of the combine thresher and, first of all, the cleaning unit (*Miu & Kutzbach, 2008*).

Another technological solution for harvesting grass seeds may be the option of harvesting the seed part of the material in the field, followed by threshing and separating the seeds in stationary conditions. (*Spirin et al., 2023*). In this case, it is possible to reduce the loss of seeds in the field, but there is a need to justify the degree of contamination of the seed and chaff mixture, both with straw impurities and the content of unthreshed seeds in it. Depending on the clogging of the seed and chaff mixture, the loss of seeds behind the combine will change, as well as the conditions for processing it in stationary conditions (*Stefanoni et al., 2022*). Significant losses of seeds were noted during the harvesting of seed plants of perennial legumes, primarily due to the low quality of work and the low productivity of threshing devices. (*Clifford & McCartin, 1985*).

An analysis of the operation of drum-type devices for threshing grass seeds shows that the main factors affecting the completeness of seed extraction are the exposure of the heap processing and the operating modes of the device (*Khawaja & Khan, 2022*). However, one should take into account the possibility of injury to seeds due to fatigue load with an increase in threshing exposure (*Wang et al., 2023*). The percentage of seed damage also increases with increasing impact energy (*Delfan et al., 2023*).

The absence of machines for dosing and loading material into technical means, as well as the absence of special machines for working with clogged seed heaps, leads to a significant increase in the labor intensity of work and a decrease in the productivity of machines during threshing and separating leguminous seeds. In addition, the efficiency of the machines that can be used in these operations is low, both in terms of quality indicators of work and the reliability of the process.

An analysis of known methods and technical means for threshing seeds of grasses and other crops revealed the advantages of drum-type devices with axial material movement over other types of devices (*Fu et al., 2018*). However, the well-known drum-type threshing devices have a number of design and technological drawbacks, only if they are eliminated, they can be effectively used for threshing seed and chaff mixture of leguminous grass seeds (*Ji et al., 2020*).

The purpose of the research is to intensify the process of legume seeds threshing with drum-type device. This can be achieved due to the intensity of action of the working bodies under optimal operating conditions, increasing the exposure of material processing in the working gap of the device when developing a technical mean.

MATERIALS AND METHODS

The intensity of the seed threshing process and energy consumption depending on the number of actions of the rasp bars on the material was determined using a pendulum tester and an experimental threshing device (Berry et al., 2014). The energy intensity of the process of threshing alfalfa seeds and the necessary number of actions of the rasp bars to completely thresh the seeds from the hook with unthreshed beans were determined on the MK pendulum copra according to the method, which provides for the manufacture of working elements of the rasp bars and the concave similar to the working bodies of the threshing device.

A 50 mm long bar with a grooved surface similar to the threshing rasp bars was attached to the copra pendulum. The deck 60 mm wide and 250 mm long with a corrugated surface was installed with special fasteners on the supporting surface of the copra.

A sample of material with unthreshed alfalfa beans was poured onto the deck, from which the seeds were separated by repeated actions of a pendulum with a bar installed on it. After each action of the bar, energy consumption for the process of releasing seeds and the amount of threshed seeds were determined. Energy consumption was determined based on:

$$A = G \cdot r \cdot (\cos\alpha - \cos\beta) \quad (1)$$

where G is the weight of the pendulum with the rasp bars installed on it, [N];

r is the distance from the axis of suspension of the pendulum to the center of its gravity, [m];

α and β are the angles of rise of the pendulum after the working and idle strokes, respectively.

The threshing of the seeds from the sample was carried out by repeated actions of the bar until the seeds were completely threshed from the sample.

Most of the existing studies on the threshing process in combine harvesters assume a constant mass, which contradicts the phenomenon of separation of grains and short stems in the actual threshing process (Zhong et al., 2013). To describe the movement of unthreshed beans in the working gap of the drum-deck, a model of a particle with a decrease in its mass is used. In the working gap (Fig. 1) the particle is affected by: compression force *N*; friction force on the surface of the deck sheet F_1; friction force on the drum (bar) F_2.

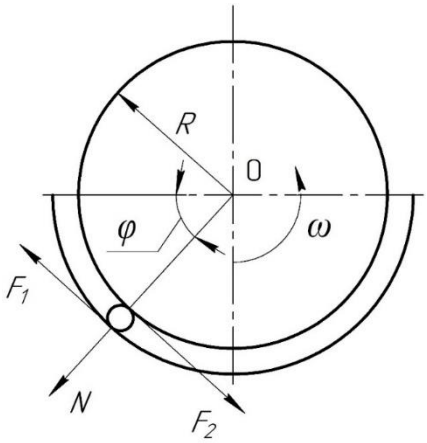


Fig. 1 – The action of forces on a particle in the working gap of the drum-deck

A particle of mass m_0 moves in the working gap Δl between the tray and the drum, rotating with an angular velocity ω_0. The radius of the drum is R. Under the action of the rasp bar on the particle, its mass decreases according to a linear law:

$$m(t) = m_0(1 - k \cdot t) \quad (2)$$

where m and m_0 are the initial and final mass of the particle, [kg];

k is the coefficient of particle mass reduction depending on time *t*.

Considering that the rasp bar of the drum acts impulsively on the particle, the graph of the change in the mass of the particle will have a stepped shape. When rotating, the drum pulls the particle, but due to its sliding along the drum, the particle will have a speed less than the speed of the drum.

Assume that the particle has the shape of a sphere with a radius r. At $r > \Delta l$, the particle is deformed. The particle compression force occurs according to Hooke's law:

$$N = E(r - \Delta l) \quad (3)$$

where E is Young's modulus.

The forces of friction of the particle on the surface of the tray and drum are:

$$F_1 = k_1 \cdot N; \quad F_2 = k_2 \cdot N\,, \quad (4)$$

where k_1 and k_2 is mass friction coefficients on the deck and drum surface.

According to the theorem on the change in the momentum of a particle:

$$R\frac{d}{dt}\left(m\frac{d\varphi}{dt}\right) = F_2 - F_1 = E(k_2 - k_1)(r - \Delta l) \quad (5)$$

Taking into account the formula for the sphere volume, the following equation is obtained:

$$\varphi'' + \frac{1}{x}\varphi' = \frac{E(k_2 - k_1)}{R \cdot m_0 \cdot k^2}\left[\Delta l - \sqrt[3]{\frac{3m_0(1 - k \cdot t)}{4\pi \cdot \rho}}\right] \quad (6)$$

The solution of equation (6) with the initial conditions $\varphi_0 = 0$; $\varphi'_0 = \omega_0$ allows us to determine the value of $\varphi'(t)$.

Let us consider the process of changing the particle mass in the working gap. To do this, consider the motion of a particle (Fig. 2) first in the interval $0 - t_1$, then in the intervals $t_1 - t_2$ and $t_2 - t_3$, replacing m_0 with $m_0 - \Delta m$. The amount of particle mass reduction Δm can be determined by assuming that the gap between the rasp bar and the deck is *δ*:

$$\Delta m = \frac{4\pi \cdot \rho}{3} r^3 [\, 1 - \frac{3}{4} \cdot \frac{\delta^2}{r^2} - \frac{1}{4} \cdot \frac{\delta^3}{r^3} \,] \tag{7}$$

When the rasp bars act on the particle, the ribs of the rasp bars displace it in the axial and radial directions relative to the axis of the drum. The value of the axial displacement of a particle can be determined from the following assumptions that when a rasp bar acts on a particle, it is displaced along the axis of the axial-tangential drum by a value Δx equal to $b \cdot \tan \alpha_1$. Then the axial displacement of the particle according to the k' action of the rasp bars during one pass in the zone of placement of the deck, taking into account the friction coefficient f, is equal to:

$$h_1 = f \cdot k' \cdot b \cdot tan \propto_1 \tag{8}$$

where: k' is the number of actions of rasp bar per particle;

b - the width of the rasp bar, [m];

$\propto_1$- angle of inclination of rasp bar ribs.

The axial movement of the particle in one pass in the upper part of the threshing device casing will be:

$$h_2 = 2\varphi \cdot R \cdot sin \propto_2, \tag{9}$$

where h_2 is the displacement of the particle in the upper part of the threshing device, [m];

R - the casing radius, [m];

φ - the angle of the sector of the casing on which the spiral ribs are installed;

$\propto_2$ - the angle of inclination of the spiral ribs relative to the casing axis

Then the axial displacement of the particle with one turn of displacement around the drum is:

$$h = f \cdot k' \cdot b \cdot tan \propto_1 + 2\varphi \cdot R \cdot sin \propto_2. \tag{10}$$

If m rasp bars are placed on the drum along its perimeter, then it is possible to determine the number of rasp bar actions on the particle during the time t when it moves in the working gap between the rasp bar and the deck. The linear velocity of the particle relative to the drum is:

$$\vec{V}_r = R \cdot (\omega_0 - \varphi'), \tag{11}$$

where: $\varphi'(t)$ is determined by the solution of equation (6).

During the time t the particle receives k' actions with rasp bar

$$k' = \frac{t}{\Delta t}, \tag{12}$$

where k' is the number of rasp bar actions per particle;

Δt - the time interval after which the action of the rasp bar on the particle occurs, [s].

$$\Delta t = \frac{2\pi \cdot R}{P \cdot V_r}. \tag{13}$$

Then the number of actions of rasp bars per particle is:

$$k' = \frac{t \cdot P \cdot V_r}{4\pi \cdot R} = \frac{t \cdot P}{4\pi} (\omega_0 - \varphi'). \tag{14}$$

If the length of the deck is L, then the particle in the working gap between the deck and the drum passes n turns

$$n = \frac{L}{f \cdot k' \cdot b \cdot tan \propto_1 + 2\varphi \cdot R \cdot sin \propto_2} \tag{15}$$

Studies of the influence of structural and kinematic parameters on the quality parameters of leguminous grass threshing were carried out on an experimental devise consisting of a drum-type tangential-axial threshing device (Fig. 2), a feeding conveyor, and a drive station.

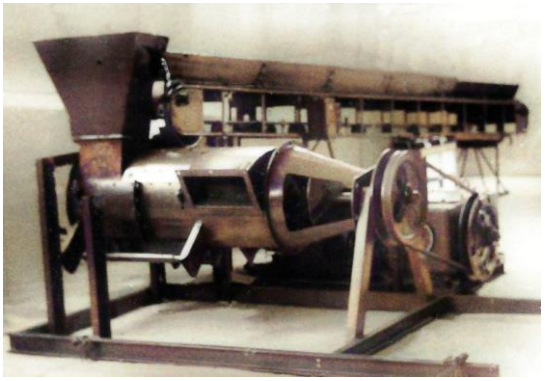


Fig. 2 – General view of a drum-type tangential-axial threshing device

The design of the threshing device is shown in Fig. 3. The threshing device consists of a cylindrical casing 1 with inlet and outlet pipes, in which a drum 3 is placed on bearing units. Drum 3 is made in the form of a supporting cylindrical tube on which rasp bars 15 are placed evenly around the perimeter. Spiral ribs 2 are located on the inner surface in the upper part of the casing 1. Sections 12 and 16 of decks are placed in the lower part of casing 1. Sections of the desk 12 and 16 are articulated connected to the cylindrical casing.

The deck sections have brackets that go out through the holes in the casing 1 and serve for articulated fastening of the sections 12 and 16 with the casing. All gaps between the brackets and the casing are sealed with pads. The gaps between the casing and deck sections are covered with shields.

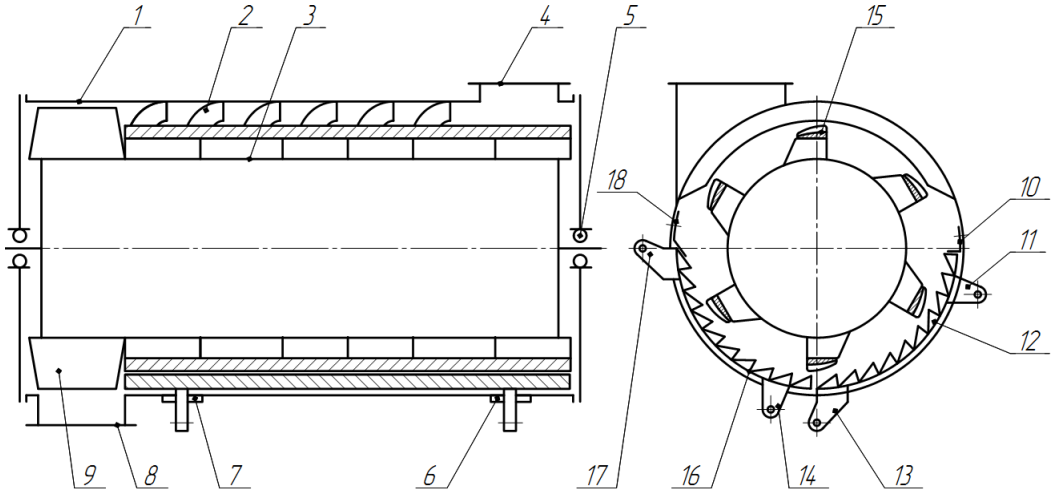


Fig. 3 – Scheme of the drum-type tangential-axial threshing device

1 – casing; 2 – spiral ribs; 3 – drum; 4 - inlet pipe; 5 - bearing; 6, 7 – seal linings; 8 - outlet pipe; 9 - unloading blades; 10, 18 - seal; 11, 13, 14, 17 - deck mounting brackets; 12, 16 - deck sections; 15 - rasp bars

Studies of the threshing process using laboratory equipment were carried out as follows. A heap with unthreshed alfalfa seeds was placed out on the conveyor belt. Turning on the electric motor of the drive station caused the drum of the threshing device to rotate. After that, the engine of the inquiring conveyor was turned on. The material placed on the belt was fed into the inlet pipe of the threshing device. The material threshed in the experimental device at the exit from the outlet pipe was taken into the sampler.

The feed rate of seed heap to the threshing device varied within 1.0-2.0 kg/s with the speed of the feed conveyor belt. As an object of processing, a non-threshed seed heap of alfalfa, obtained by harvesting with a combine in the form of under threshing, was used. In the process of research, the size of the working gaps between the rasp bars of the drum and sections of the decks was changed within 1.0-3.0 mm, at the exit from the deck. The rotation speed of the drum was changed by the variator drive in the range of 80-120 rad/s.

Several variants of decks with different working surfaces were used. The operation of a threshing device with a different number of rasp bars was studied. The design of the upper part of the cylindrical casing was designed in such a way that it made it possible to shift the inlet pipe along the length of the device, thereby changing the length of the deck.

In addition, it is possible to change the angle of inclination of the spiral ribs relative to the axis of the drum within 45-75 degrees. The heap processing exposure was determined depending on the length of the deck, which varies in the range L = 200-800 mm and the angle of inclination of the spiral ribs to the drum axis.

The material from the threshing device was taken into a sampler. The sampler had a five-section frame with suspended sleeves. The frame moved in the grooves of the threshing device's unloading pipe, which made it possible to take three samples of the material in the steady state mode.

The studies were planned and carried out according to the methodology of a single-factor and multifactor experiments. The experiments were carried out according to the plan-matrix or the plan of single-factor studies under the appropriate modes and operating parameters of the threshing device. The main levels and intervals of variation of all factors were taken on the basis of preliminary experiments (Table 1). The optimization criterion by which the operation of the threshing device was evaluated is the completeness of seeds threshing from the beans and crushing the seeds during the operation of the device.

Table 1

Variable factors and limits of their variation for determining the percentage of unthreshed and injured seed when threshing alfalfa beans at the experimental device

Factor	Value	Encoded value	Limits of variation	Levels of variation		
				lower	middle	upper
Angular velocity of the drum, rad/s	ω	X_1	40	80	100	120
Material feed rate, kg/s	Q	X_2	1.0	1.0	1.5	2.0
Gap between bar and deck, mm	δ	X_3	2.0	1.0	2.0	3.0
Number of bars on the drum	m	X_4	4	2	4	6
Content of threshed seeds in the starting material, %	C	X_5	6.0	0	3.0	6.0

RESULTS

As a result of experimental studies and statistical processing, dependences were obtained for the completeness of threshing alfalfa seeds depending on the number of rasp bar actions on a material on a pendulum impact tester and an experimental threshing device (Fig. 4). In the course of experiments on a pendulum tester, elements of a rasp bar and a deck of an experimental threshing device were used.

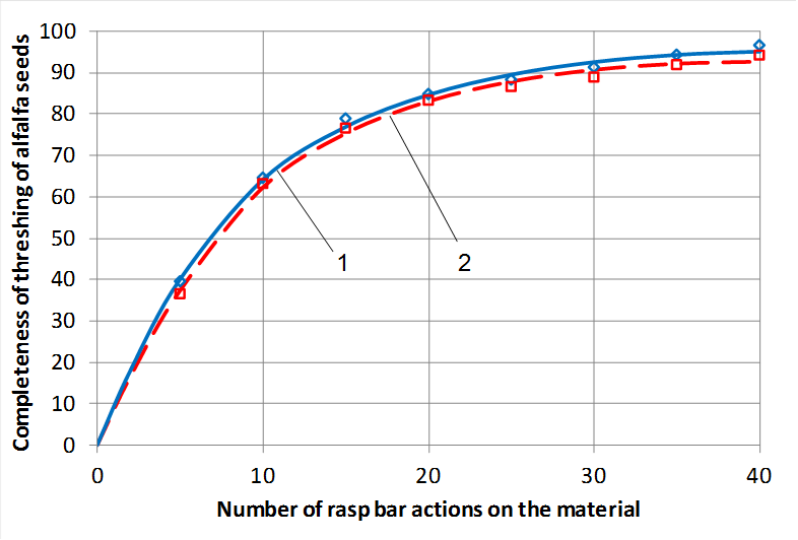


Fig. 4 - Dependences of the completeness of threshing of alfalfa seeds depending on the number of rasp bar actions on the material

1 – studies carried out with a pendulum impact tester; 2 – studies carried out with an experimental device

It has been established that the intensity of threshing of alfalfa seeds on a pendulum impact tester decreases with an increase in the number of actions of the rasp bar on a material, which has a significant impact on energy consumption.

So, during the first ten actions of the rasp bar, about 60% of the seeds from the beans are threshed off. The energy consumption for threshing one seed from a bean averages 0.2^{-10} J. To threshing out 20% of the residue of unthreshed seeds in beans, it is necessary to double the number of rasp bar actions over the material, compared to the number of the rasp bar actions that was spent at the beginning process for threshing 60% of the seeds. At the same time, the energy consumption for the process increases significantly. So after 33-34 actions of the rasp bar, the energy consumption for threshing one seed increases ten or more times and reaches 2.8^{-10} J.

The completeness of threshing seeds and the number of actions of rasp bars over a material in the working gap of the experimental threshing device, depending on the exposure of its processing, were determined. The number of rasp bar actions per particle was determined by formula (14).

Dependence 2 (Fig. 4) of the completeness of threshing of alfalfa seeds on the number of actions of rasp bars on the material was obtained, which with a 90% probability is adequate to dependence 1. It has been established that in an experimental threshing device, the completeness of seed extraction at the level of 96.5-99.1% of alfalfa is ensured by the duration of processing the heap of 0.39-0.40 s, with forty actions of rasp bars on the material. The results of the study allow us to determine the rational length of the deck. With a deck radius and curvature of 236 mm, with a wrapping angle of the drum deck of 180° and with an angle of inclination of the spiral ribs to the drum axis of 75°, the length of the deck is 800 mm.

As a result of studies influence of structural and kinematic parameters on the quality parameters of leguminous grass threshing and statistical processing of experimental data, regression mathematical models were obtained that adequately reflect the dependences of percentage of unthreshed seed Y_1 and percentage of injured seed Y_2:

$$Y_1 = 51.807 + 40.999 \cdot m + 133.432 \cdot Q - 3.485 \cdot \omega - 3.052 \cdot m^2 - 0.481 \cdot m \cdot \delta - 3.245 \cdot m \cdot Q - \\ -0.1149 \cdot m \cdot \omega - 2.794 \cdot \delta \cdot Q + 0.09134 \cdot \delta \cdot \omega - 29.608 \cdot Q^2 - 0.2046 \cdot Q \cdot \omega + 0.01739 \cdot \omega^2; \quad (16)$$

$$Y_2 = 0.678 + \frac{0.777}{m} + \frac{1.042}{\delta} + \frac{0.971}{Q} - \frac{93.80}{\omega} - \frac{0.005}{C}. \quad (17)$$

The analysis of the regression equations showed that they are adequate to the experimental data for the 5% significance level. The graphic dependence of percentage of unthreshed seed on material feed rate and angular velocity of the drum is shown in Fig. 5.

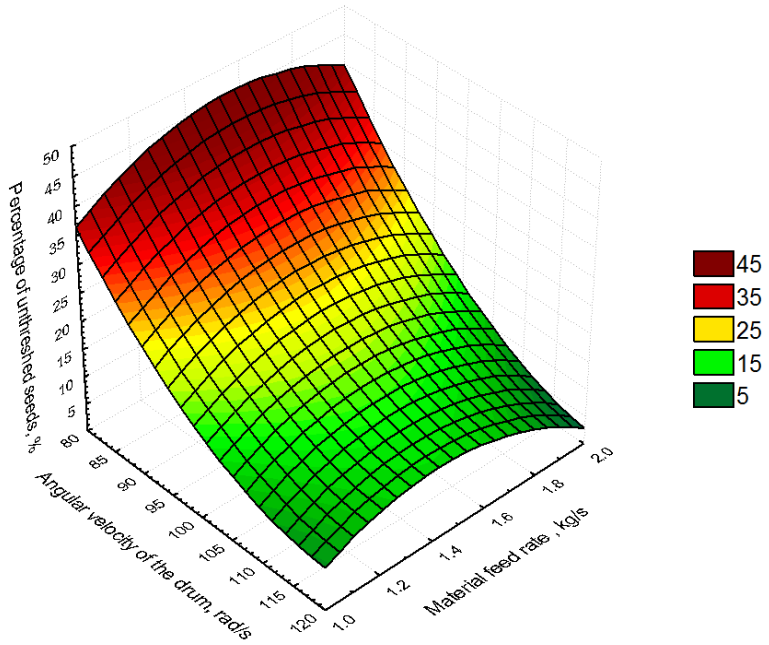


Fig. 5 - Dependence of percentage of unthreshed seed on material feed rate and angular velocity of the drum at the number of bars on the drum m = 6 and gap between bar and deck δ = 2 mm

The graphic dependences of percentage of injured seed on structural and kinematic parameters of experimental threshing device are shown in Fig. 6 and Fig. 7.

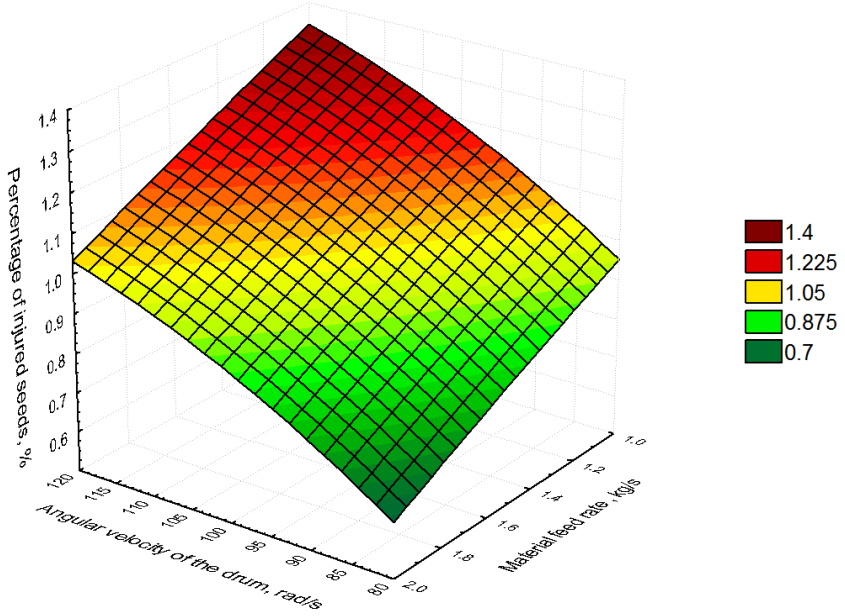


Fig. 6 - Dependences of percentage of injured seed on material feed rate and angular velocity of the drum at the number of bars on the drum m = 6 and gap between bar and deck δ = 2 mm

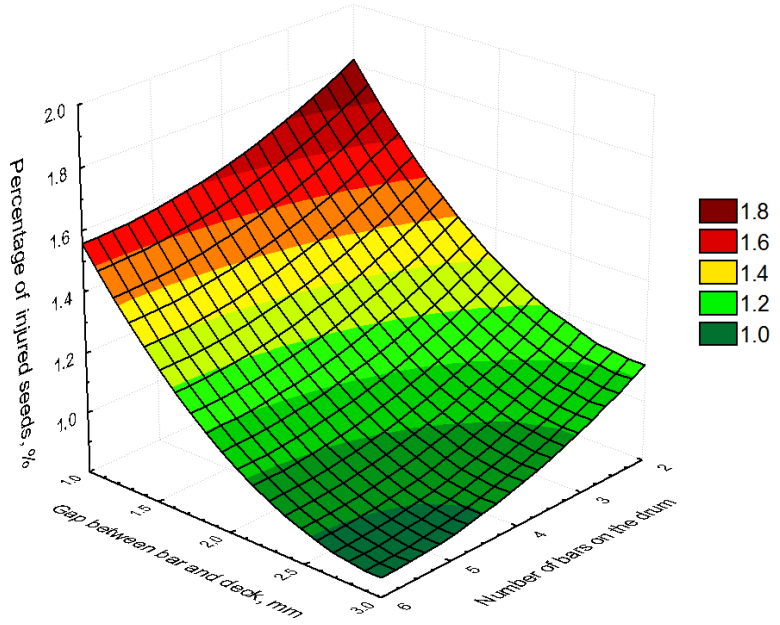


Fig. 7 - Dependences of percentage of injured seed on gap between bar and deck and the number of bars on the drum at material feed rate Q = 1.5 kg/s and angular velocity of the drum ω = 100 rad/s

By analyzing the two-dimensional sections of the response surfaces, described by equations (16) and (17), the rational parameters of the experimental threshing device are determined: the angular speed of rotation of the drum n = 105-110 rad/s; the number of rasp bar on the drum m = 6; material feed rate Q = 1.5-2.0 kg/s; the gap between bar and deck δ = 2.0 mm. An experimental threshing device with above-defined rational parameters provides 96.5% 98.2% completeness of threshing the seeds, while damaging no more than 0.8% of the seeds.

According to the research results, a prototype drum-type tangential-axial threshing device was developed. A study of the developed device in the field with combine and stationary technologies for harvesting seed plants of perennial legumes was carried out. The influence of the material moisture on the quality indicators of the device operation was studied (Fig. 8).

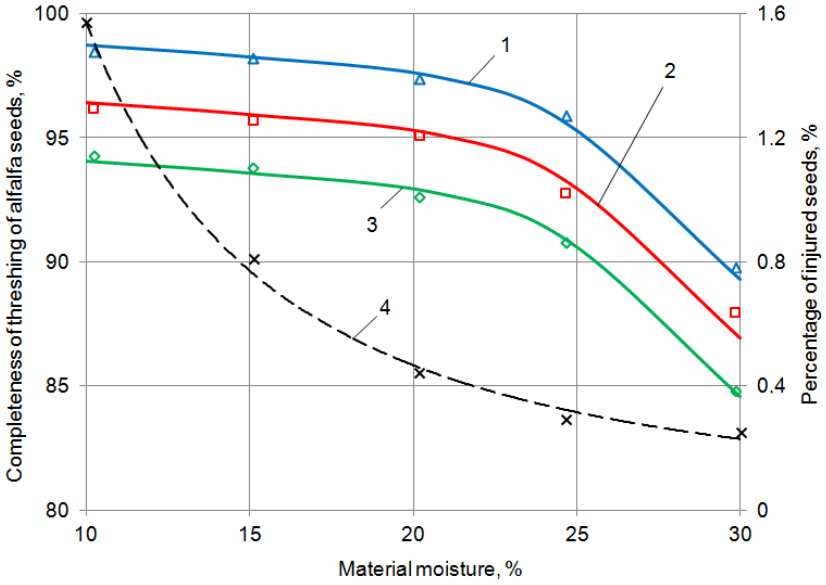


Fig. 8 - Dependences of the completeness of threshing (1-3) and seed injury (4) on the moisture content of the threshing material

1 – Q = 2.0 kg/s; 2 – Q = 1.5 kg/s; 3 – Q = 1.0 kg/s

An analysis of the results of studies of the influence of the moisture content of an unthreshed material of alfalfa on the completeness of threshing seeds showed that with an increase in the moisture content from 10 to 20%, the completeness of threshing seeds decreases slightly from 98.2 to 97.2%, or by 0.7%. Only with a further increase in the moisture content of the material from 20 to 30%, the effectiveness of the threshing process significantly decreases, since the flower shell of the seeds becomes softer and more elastic, it becomes more and more difficult to destroy it.

CONCLUSIONS

The probability of alfalfa beans threshing in the working gap between the drum and the deck is considered as the process of the action of the rasp bars on the particle with a decrease in its mass in the process of its movement. Dependence of the completeness of threshing of alfalfa seeds on the number of actions of rasp bars on the material in the experimental threshing device was obtained, which with a 90% probability is adequate to dependence obtained on the pendulum impact tester.

According to the research results the rational parameters are determined and a prototype drum-type tangential-axial threshing device is developed. A developed threshing device provides 96.5-98.2% completeness of threshing the seeds, while damaging no more than 0.8% of the seeds at moisture content of unthreshed alfalfa material is within 10-20%.

REFERENCES

[1] Berry, N.K., Fielke, J.M., & Saunders, C. (2014). Determination of impact energy to devitalise annual ryegrass (Lolium rigidum) seed from one impact using double and single sided impacts. *Biosystems Engineering*, 118 (1), 138-146. https://doi:10.1016/j.biosystemseng.2013.11.010

[2] Chu, Y., Han, Y., Jia, F., Wang, Y., Chen, P., Meng, X., Zhang, J., & Li, A. (2022). Analysis of the impact hulling behaviour of paddy grains. *Biosystems Engineering*, 220, 243-257. https://doi:10.1016/j.biosystemseng.2022.06.005

[3] Clifford, P. T. P. & S. McCartin, J. M. (1985). Effects of pre-harvest treatment and mower and header types on seed loss and hard seed content at mowing, recovery, and separation when harvesting a white clover seed crop., *New Zealand Journal of Experimental Agriculture*, 13:4, 307-316. https://doi:10.1080/03015521.1985.10426099

[4] Shvidia, V.O., Stepanenko, S.P., Kotov B.I., Spirin A.V., & Kucheruk V.Yu. (2022) Influence of vacuum on drying of seeds of grain crops Herald of Karaganda University. "Physics" series. № 3(107)/2022– p. 90-98. https://doi:10.31489/2022PH3/90-98

[5] Delfan, F., Shahbazi, F., & Esvand, H.R. (2023). Impact damage to chickpea seeds during free fall. *International Agrophysics*, 37 (1), 41-49. https://doi:10.31545/intagr/156049

[6] Fu, J., Chen, Z., Han, L.J., & Ren, L.Q. (2018). Review of grain threshing theory and technology. *International Journal of Agricultural and Biological Engineering*, 11 (3), 12-20, https://doi:10.25165/j.ijabe.20181103.3432

[7] Ivan, Gh. (2016). Mathematical modelling of the threshing process made by the threshing systems with multiple rotors. *INMATEH - Agricultural Engineering*, 49 (2), 83-90.

[8] Ji, J.T., Hu, J.P., Wang, S.S., Zhang, R.H., & Pang, J. (2020). Vibration and impact detection of axial-flow threshing unit under dynamic threshing conditions. *INMATEH-Agricultural Engineering*, 60(1), 183-192. https://*doi:10.35633/inmateh-60-21*

[9] Khawaja, A.N., & Khan, Z.M. (2022). DEM study on threshing performance of "compression–oscillation" thresher. *Computational Particle Mechanics*, 9 (6), 1233-1248. https://doi:10.1007/s40571-021-00456-4

[10] Liao, Q., Wang, C., He, K., Yuan, J., & Wan, X. (2021). Design and experiment on re-cleaning machine for rapeseed after combine harvesting. *Nongye Jixie Xuebao/Transactions of the Chinese Society for Agricultural Machinery*, 52(10), 175-185. https://doi:10.6041/j.issn.1000-1298.2021.10.018

[11] Miu, P. & Kutzbach, H.-D. (2008). Modeling and simulation of grain threshing and separation in threshing units—Part I. *Computers and Electronics in Agriculture*, 60, 96-104. https://doi:10.1016/j.compag.2007.07.003.

[12] Moss, W. M., Guzzomi, A. L., Foster, K. J., Ryan M. H., & Nichols P. G. H. (2021) Harvesting subterranean clover seed – current practices, technology and issues. *Crop and Pasture Science,* 72, 223-235. https://doi.org/10.1071/CP20269

[13] Stepanenko, S., Kotov, B., Kuzmych, A., Kalinichenko, R., & Hryshchenko V. (2023) Research of the process of air separation of grain material in a vertical zigzag channel Journal of Central European Agriculture, 2023, 24(1), p.225-235**.** https://doi:10.5513/JCEA01/24.1.3732

[14] Pari, L., Latterini, F., & Stefanoni, W. (2020). Herbaceous oil crops, a review on mechanical harvesting state of the art. *Agriculture (Switzerland)*, 10(8), 1-25. https://doi:10.3390/agriculture10080309

[15] Sheychenko, V.O., Kuzmych, A.Y., Shevchuk, M.V., Shevchuk, V.V., & Belovod, O.I. (2019). Research of quality indicators of wheat seeds separated by pre-threshing device. *INMATEH - Agricultural Engineering*, 57 (1), 157-164.

[16] Spirin, A., Borysiuk, D., Tsurkan, O., Tverdokhlib, I., Veselovska, N. & Edl, M. (2023). Ways of intensification of grass seed production. *Journal of Engineering Sciences*. 10. F11-F19. https://doi:10.21272/jes.2023.10(1).f3.

[17] Stefanoni, W., Latterini, F., Malkogiannidis, V., Salpiggidis, V., Alexopoulou, E., & Pari, L. (2022). Mechanical harvesting of castor bean (ricinus communis L.) with a combine harvester equipped with two different headers: *A comparison of working performance. Energies*, 15(9). https://doi:10.3390/en15092999

[18] Stepanenko, S., Aneliak, M., Kuzmych, A., Kustov, S., & Lysaniuk V. (2022). Improving the Efficiency of Harvesting Sunflower Seed Crops INMATEH - Agricultural Engineering. Vol. 67, No. 2/2022, p331-340. 9p. https://doi:10.35633/inmateh-67-34

[19] Wang, B., Lin, Z., Gao, M., Zhang, G., Geng, D., & Shi, Z. (2023). Statistical analysis of fatigue damage life of corn kernels. *INMATEH - Agricultural Engineering*, 69 (1), 589-596, https://doi:10.35633/inmateh-69-56

[20] Zhong, T., Yaoming, L. & Chenghong, W. (2013). Experiments on variable-mass threshing of rice in the tangential-longitudinal-flow combine harvester. *Journal of Agricultural Science and Technology*. 15. 1319-1334.

DESIGN AND TESTING OF MODERN APPLE ORCHARD PRUNING MACHINERY
/
现代苹果园修剪机械的设计与试验

Yuliang WANG [1,2], Zhiqiao WANG [1,2], Zhaoying CHEN[1,2], Guoqiang FAN[1,2], Rui SU[1,2], Peijun YIN[1,2], Jinxing WANG [*1,2]
[1)]College of Mechanical and Electronic Engineering, Shandong Agricultural University, Tai an 271018 / China;
[2)]Shandong Provincial Key Laboratory of Horticultural Machinery and Equipment, Tai an 271018 / China;
Tel: +86 05388246826; E-mail: jinxingw@163.com
DOI: https://doi.org/10.35633/inmateh-71-07

Keywords: *Apple pruners, Branch sawing simulation, Sawing parameters, Orthogonal tests*

ABSTRACT
In response to the problems of low efficiency and difficulty of pruning operations in modern dwarf dense orchards, an adjustable position saw blade pruning machine was designed, mainly consisting of a pruning device, a regulating device and a hydraulic system. Through the mechanical and modal analysis of the circular saw blade, the limit speed of the circular saw blade was derived. A finite element model of the sawing process was established, and a single-factor simulation analysis was conducted for three important parameters: feed rate, circular saw blade speed and branch diameter, and a three-factor, three-level quadratic regression orthogonal test was designed to derive the best matching sawing parameters, which was verified in field tests. The test results showed that the average passing rate was 92.8% at the feed rate of 4 km/h under the circular saw blade speed of 2800 rpm, which was higher than 88.8% at 3 km/h and 88.9% at 5 km/h. The optimum sawing parameters were: the circular saw blade speed of 2800 rpm and feed rate of 4 km/h, which were consistent with the simulation results, and the passing rate of the cut was high at this time, meeting the technical requirements of orchard pruning.

摘要
针对现代矮砧密植果园修剪作业效率低、操作难度大等问题，设计了一种姿态可调节的锯片式修剪机械，主要由修剪装置、调节装置和液压系统组成。通过圆锯片的力学和模态分析，得出圆锯片极限转速。建立锯切过程的有限元模型，对进给速度、圆锯片转速和枝条直径三个重要参数进行单因素仿真分析，以此设计三因素三水平的二次回归正交试验，得出配合最佳的锯切参数，并进行田间试验验证。试验结果表明：在圆锯片转速 2800rpm 的情况下，进给速度 4km/h 时的平均合格率为 92.8%，高于 3km/h 时的 88.8%和 5km/h 的 88.9%，得出配合最佳的锯切参数为：圆锯片转速 2800rpm，进给速度 4km/h，与仿真结果一致，此时切口的合格率高，满足果园修剪的技术要求。

INTRODUCTION

At present, the planting area and production of apples in China are among the highest in the world *(Zheng et al., 2020; Zhang et al., 2021),* and with the increasing area of orchard planting, the traditional planting methods can no longer meet the requirements of apple farming industry. For this reason, China had started to adopt the dwarf anvil dense planting method to improve the yield and quality of apples, which has the advantages of fast fruiting, high yield, high fruit quality and easy management *(Shi L.., 2018)*.

For various orchard pruning machines, scholars at home and abroad had conducted a lot of research. Shu Yu et al. designed a sawing apple pruner with a clamping mechanism, which added a clamping mechanism to the traditional sawing method to improve the stability of the cutting process *(Shu Y. et al., 2018)*. Wang Zheng et al. conducted a kinetic simulation analysis and experiment on the sawing process of apple trees to study the mechanism of the effect of saw blade speed, work-in speed and branch diameter on the quality of the cut *(Wang Z. et al., 2017)*. Zhang Jiaxi et al. designed a single motor reciprocating grape pruner, which was driven by a single hydraulic motor and can prune the branches on one side and the top of the grape at the same time *(Zhang J. X. et al., 2021).*

Yuliang Wang, Assoc. Prof. Ph.D. Eng.; Zhiqiao Wang, M.S. Stud. Eng.; Zhaoying Chen, Ph.D. Stud. Eng.; Guoqiang Fan, Assoc. Prof. Ph.D. Eng.; Rui Su, M.S. Stud. Eng.; Peijun Yin, M.S. Stud. Eng.; Jinxing Wang, Prof. Ph.D. Eng.

Liu Xuechuan et al. designed a combined profiling pruner, which can be adjusted according to different tree shapes, with high applicability and reduced pruning costs *(Liu X.C. et al., 2020).* Meng Y et al. analysed the sawing force magnitude of a small mulberry cutter under different sawing parameters based on orthogonal tests. The optimum sawing parameters were obtained *(Meng Y. et al.,2019).* At present, most apple orchards in China are still pruned manually or with simple machinery, which has problems such as high operation technology requirements, low automation and low pruning efficiency, and the traditional pruning methods such as heavy pruning, strong tree shaping and short cutting are not suitable for modern dwarf dense orchards.

In response to the above problems, this paper designed a saw blade apple tree pruning machine to meet the pruning requirements of dwarf dense orchards with high spindle shape. The design of the pruning device and adjusting device was analysed according to the tree shape of the dense apple orchard, and the final size was determined by constructing a mathematical model; mechanical and dynamics analysis and orthogonal test were conducted to determine the best-fit sawing parameters, and field performance test was carried out to realize the efficient pruning operation of dwarf dense apple orchards.

MATERIALS AND METHODS

Structure and working mechanism

In order to meet the requirements of simultaneous pruning of unilateral and top branches, a saw blade pruning machine was designed, as shown in Fig 1.

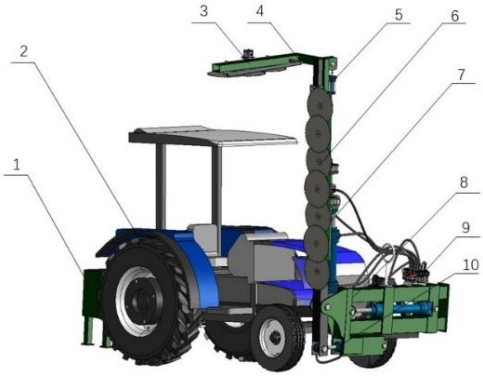


Fig. 1 - Schematic diagram of the trimming machine

1 - Hydraulic Station; 2 - Tractors; 3 - Horizontal trimming device; 4 - Automatic obstacle avoidance device; 5 - Horizontal angle adjustment device;6 - Vertical trimming device; 7 - Vertical expansion device; 8 - Solenoid Valve; 9 - Vertical angle adjustment device; 10 - Horizontal expansion device

The working principle of the pruning machinery is: the circular saw blade is driven by the hydraulic motor to rotate at high speed, and the circular saw blade is driven by the synchronous belt to realize the staggered distribution of saw blades rotating in the same direction; the adjustment device is controlled by solenoid valve to carry out tilting and telescoping action to realize the pruning of apple trees of different shapes; the pruning machinery is installed in the front of the tractor, and the tractor provides the power to work

The trimming device mainly includes the horizontal trimming device and the vertical trimming device. Vertical trimming device uses a hydraulic motor to drive seven staggered circular saw blades, relying on a timing belt drive, to complete the vertical section trimming operation, with a required effective working length of 2200mm, as shown in Fig 2.

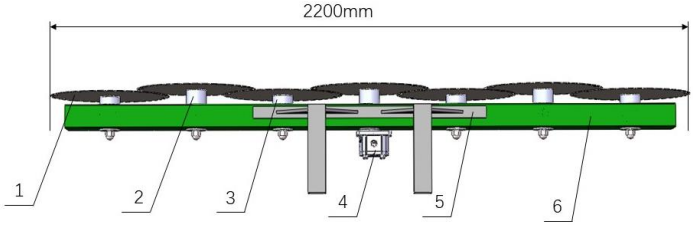


Fig. 2 - Vertical trimming device

1 - Circular saw blades; 2 - Long saw blade holder; 3 - Short saw blade holders; 4 - Hydraulic Motor; 5 - Saw base hook up square steel; 6 - Saw base support square tube;

The number of circular saw blades of the horizontal trimming device is three, and the working principle is the same as that of the vertical section, requiring an effective working length of 1000 mm and installing gas springs for obstacle avoidance, as shown in Fig. 3.

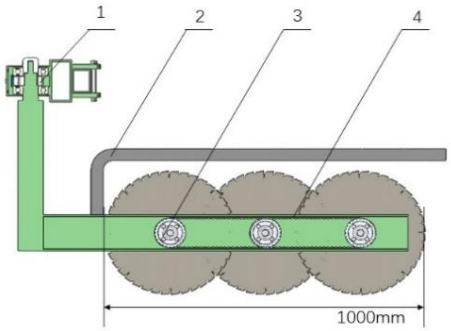


Fig. 3 - Horizontal trimming device

1 - Connecting gear;2 - Automatic obstacle avoidance device;3 - Timing pulleys;4 - Synchronous belts

The adjustment device includes horizontal angle adjustment device, horizontal telescopic adjustment device, vertical angle adjustment device and vertical telescopic adjustment device, as shown in Fig 4. Each adjusting device controls the hydraulic cylinder through a solenoid valve to achieve adjustment.

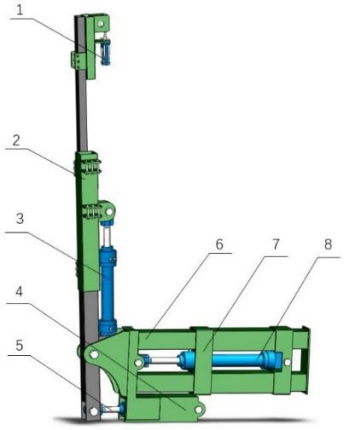


Fig.4 - Adjustment device

1 - Horizontal angle adjustment device; 2 - Square tube outside the vertical beam; 3 - Vertical telescopic adjustment device; 4 - Bottom hydraulic cylinder support beam; 5 - Vertical angle adjustment device; 6 - Horizontal telescopic beam; 7 - Base beam; 8 - Horizontal telescopic adjustment device;

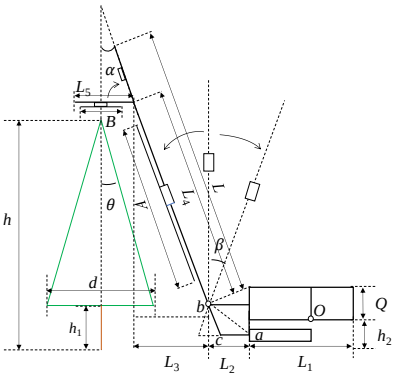


Fig. 5 - Schematic diagram of the pruning mechanism

According to the standard, a dwarf rootstock densely planted with tall spindle apple trees, with a height '*h*' of 4 meters, the height '*h1*' of the tree trunk is 0.7 meters, and the tree canopy diameter, denoted as '*d*', is 1.2 meters. The geometric relationship between pruning machinery and fruit trees, as shown in Fig 5, requires pruning machinery to form a certain angle with the fruit tree during operation, which was approximately equal to the angle between the crown and the main trunk, then it was:

$$\tan\alpha \approx \tan\theta = \frac{d/2}{h - h_1} \quad (1)$$

α - the angle between the main trunk of the fruit tree and the pruning machinery, [°];

θ - the angle between the main trunk and the crown of the fruit tree, [°];

The angle of inclination of the vertical pruning device was found to be $\alpha = 17°$. The height of the pruning machine should be greater than the tree height, therefore:

$$(L + l_{4\max})\cos\alpha + h_2 + Q/2 > h \quad (2)$$

h_2 - the distance between the installation position of the trimming device and the ground, [m];

l_{4max} - maximum extension of vertical telescopic hydraulic cylinder, [m];

Q - width of horizontal telescopic adjustment device, [m];

In formula (2), h_2 = 0.4 m, l_{4max}=0.5 m, the total length L needs to be greater than 3.1 m, considering the actual working condition, the final design was L = 3.4 m, horizontal section length L_5 = 1.1 m, effective sawing length B =1 m; length of vertical section L_4 = 2.3 m, effective sawing length A = 2.2 m; inclination angle 22°, camber angle 17°. When the length adjustment hydraulic cylinder was telescoped to the design maximum l_{1max} = 0.5 m, l_{4max} = 0.5 m; at this time the camber angle was 17 °, then $\angle acb$ = 107 °, the length of ab, bc can be measured directly, the length of L_2 can be based on the cosine theorem (3) to find, L_2 = 139 mm.

$$\cos\angle acb = \frac{{L_2}^2 + {L_{bc}}^2 - {L_{ab}}^2}{2L_2 \cdot L_{bc}} \quad (3)$$

When the state of the adjusting device was: the horizontal trimming device was parallel to the ground, and the vertical angle adjusting device was at the maximum camber angle, the mathematical model was constructed based on the designed data with the point O as the coordinate origin, as shown in formula (4).

$$\begin{cases} X_o = l_{1\max} + L_2 + L_3 + L_5 \\ Y_o = (L_4 + l_{4\max})\cos\alpha + Q/2 \end{cases} \quad (4)$$

$$L_3 = (L_4 + l_{4\max})\sin\alpha \quad (5)$$

l_{1max} - maximum extension of horizontal telescopic hydraulic cylinder, [m];

L_2 - vertical angle adjustment of hydraulic cylinder extension, [m];

The trajectory in the horizontal direction X_o = 2404 mm, which was also smaller than the planted row spacing under the consideration of the tractor width, so the adjustment amount of the pruning device was sufficient; the trajectory in the vertical direction Y_o = 2932 mm, which was smaller than the tree height of 4 m.

When the state of the adjusting device was: the horizontal trimming device and the vertical angle adjusting device were at the same time at the maximum camber angle of 17°, the mathematical model was constructed with the point O as the coordinate origin according to the designed data:

$$\begin{cases} X_o = l_{1\max} + L_2 + (L_4 + L_5 + l_{4\max})\sin\alpha \\ Y_o = (L_4 + L_5 + l_{4\max})\cos\alpha + Q/2 \end{cases} \quad (6)$$

The horizontal trajectory X_o = 1779 mm, can work normally; the vertical trajectory Y_o = 3985 mm, slightly less than the tree height of 4m, can complete the pruning of the top of the apple tree, so the design meets the requirements.

Circular saw blade analysis

In the trimming operation, the circular saw blade had a feed rate along the *X*-axis and rotated around the *Z*-axis. The sawing force was mainly composed of tangential force F_t, radial force F_n and axial force F_a, as shown in Fig. 6. Radial force was the main force of the trimming operation, acting in the direction of the radius of the circular saw blade; tangential force acted in the direction perpendicular to the radial force; axial force acted in the direction perpendicular to the surface of the saw blade, causing lateral vibration of the saw blade *(Wang Z et al., 2017)*.

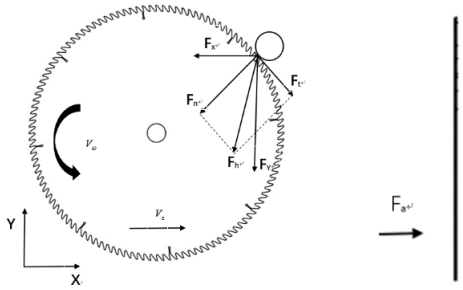


Fig. 6 - Force diagram of circular saw blade

Due to the woody properties of apple branches, which were anisotropic materials, and the influence of many external factors during sawing, it was a complex nonlinear process, so, in order to simplify the calculation of sawing forces, dynamics need to be constructed for the whole system for analysis. The constructed kinetic model can have multiple variables and applies to nonlinear problems, which could be verified by kinetic simulation later *(Meng Y. et al, 2020)*. To facilitate the calculation, decompose the combined tangential and radial forces in X and Y directions respectively and perform force analysis, as shown in Fig. 6.

In the X direction:

$$F_x = F_t \cos\beta - F_n \sin\beta - c\frac{dx}{dt} - kx \tag{7}$$

In the Y direction:

$$F_y = -F_n \cos\beta - F_t \sin\beta - c\frac{dy}{dt} - ky \tag{8}$$

The force in the Z direction was equivalent to the axial force:

$$F_z = F_a \tag{9}$$

β - angle of radial force to *Y*-axis, [°];

c - damping of apple tree branches, [Nm/s];

k - stiffness of apple tree branches, [N/m];

x,y - displacement of circular saw blade in X-direction and Y-direction, [m];

According to the spatial mechanic's relationship the sawing force F was:

$$F = \sqrt{F_x^2 + F_y^2 + F_z^2} \tag{10}$$

According to the research, the main factor affecting the sawing force is the feed per tooth, calculated by the formula (11) *(Zhang B et al., 2022)*, and the feed per tooth was directly proportional to the feed speed and inversely proportional to the speed and number of teeth.

$$V_z = \frac{1000 \cdot V_C}{n \cdot z} \tag{11}$$

V_z - feeds per tooth, [mm];

V_c - linear feed speed, [m/min];

n - circular saw blade speed, [rpm];

z - number of teeth of circular saw blade.

The branch sawing process in the orchard was an unsupported cutting method, and studies had shown that the working line speed for unsupported cutting must not be less than 30 m/s *(Liu J et al., 2021)*, bringing in the data, the minimum speed of a circular saw blade with a diameter of 400 mm was found to be 1433 rpm.

$$n = \frac{60V_a}{\pi D} \tag{12}$$

V_a - linear speed of saw blade, [m/s]; D - circular saw blade outer diameter, [m];

A three-dimensional model of the circular saw blade was created using the dimensions given in Table 1, and then modal analysis was performed on the established model.

Table 1

Circular saw blade size parameters

Outer diameter / (mm)	Inner diameter / (mm)	Thickness / (mm)	Number of teeth	Front corner / °	Rear corner / °	Materials
400	30	3	120	15	15	65Mn

According to Table 2 *(Wu Q.B. et al., 2020)*, the material parameters of the circular saw blade were assigned and meshing was performed. The mesh cell size of the circular saw blade mesh was 2.0 mm.

Table 2

Circular saw blade material parameters

Poisson's ratio	Modulus of elasticity / (MPa)	Density / (kg/m^3)	Yield limit / (MPa)	Shear modulus / (MPa)
0.3	2.06e^5	7850	440	80000

Sixth-order modal analysis of the circular saw blade was performed by Workbench, and the inherent frequency and maximum displacement of the circular saw blade was obtained, as shown in Table 3, as well as the first six-order modal vibration diagram, as shown in Fig 7.

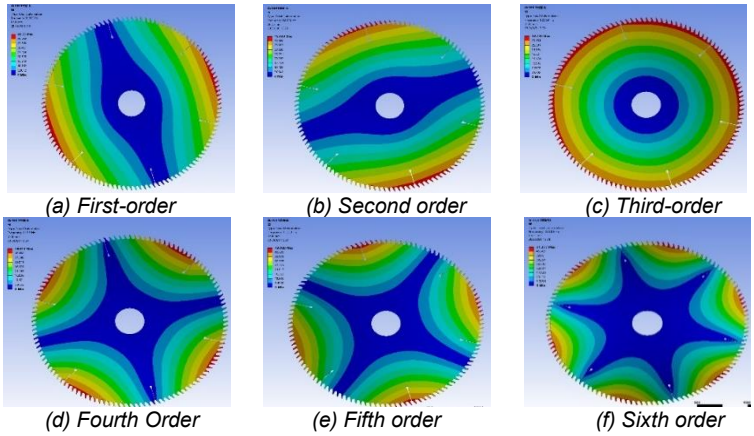


Fig. 7 - Sixth-order modal diagram of circular saw blade

Table 3

The first six natural frequencies and the maximum displacement

Mode order	1	2	3	4	5	6
Frequency / (Hz)	82.99	83.12	92.37	113.50	113.53	222.06
Displacement / (mm)	45.73	45.49	32.80	48.02	49.09	51.38

According to the vibration diagram of the first six orders of modes, it was obtained that the circular saw blade mainly oscillates or deforms reciprocally along the X-axis, Y-axis, Z-axis and the blade teeth around the circular saw blade. From Table 3, the first-order intrinsic frequency of the circular saw blade was 82.99 Hz, and according to the speed and frequency equation (13) *(An R., 2019)*, the critical speed of the circular saw blade was 4980 rpm, and the stable speed of the circular saw blade was better than 15% of its critical speed, so the critical speed was 4233 rpm.

$$n = 60 \cdot f \tag{13}$$

f – frequency, [Hz].

Finite element modeling and simulation analysis of sawing process

Circular saw blade sawing of branches belongs to the contact nonlinear type material impact dynamics problem *(Wang X.C. et al., 2015; Sun et al., 2022)*, and the process is relatively complex. In order to facilitate the calculation, it is necessary to simplify the whole sawing model while ensuring the simulation results are as close to the real situation as possible. Then, the branch was defined as a Solid unit and its material was set to *MAT_ORTHOTROPIC_ELASTIC. Since the apple branch will break when it was sawed, for this reason, it was necessary to add the keyword *MAT_ADD_EROSION. material parameters, as in Table 4 *(Jiang L Q, 2013)*.

Table 4

Branch material parameters

Parameter Name	Parameter Value
Density / (kg/m^3)	550
Paramagnetic modulus of elasticity / (MPa)	29.8
Horizontal radial modulus of elasticity / (MPa)	439.8
Horizontal chordal modulus of elasticity / (MPa)	15.5
Parallel grain shear modulus of elasticity / (MPa)	26.7
Horizontal radial shear modulus of elasticity / (MPa)	18.3
Horizontal chordal shear modulus of elasticity / (MPa)	1.8
Parallel Poisson's ratio / (MPa)	0.46
Horizontal radial Poisson's ratio / (MPa)	0.031
Horizontal chordal Poisson's ratio / (MPa)	0.015

The circular saw blade was defined as a Solid unit, set the material as *MAT_RIGID, material parameters as shown in Table 2. Set the contact to *CONTACT_ERODING_SURFACE_TO_SURFACE, applied a fixed constraint to the bottom of the branch, gave the circular saw blade a feed speed of 3 km/h along the X-axis and a rotation speed of 3000 rpm around the Y-axis, and constrained the tool Y and Z direction movement and rotation around the X and Y axis.

RESULTS AND ANALYSIS

Single factor test

The branch diameter was selected to be 20 mm at a feed speed of 3 km/h. The rotational speeds of 500 rpm, 1000 rpm, 2000 rpm, 3000 rpm and 4000 rpm were selected for the test. The obtained trend of sawing force with speed was shown in Fig 8. At low speed, the sawing force was very large and difficult to say, with the increase of speed, the sawing force decreased rapidly and tended to be stable gradually, when the speed reached 3000 rpm, the sawing force started to increase slowly. According to the formula (11), the smaller the rotational speed, the larger the feed per tooth, and the more cutting volume would increase, resulting in an increase in sawing force. When the rotational speed exceeds the allowed range, the saw blade will vibrate significantly, so the rotational speed should be selected from 2000 to 3000 rpm.

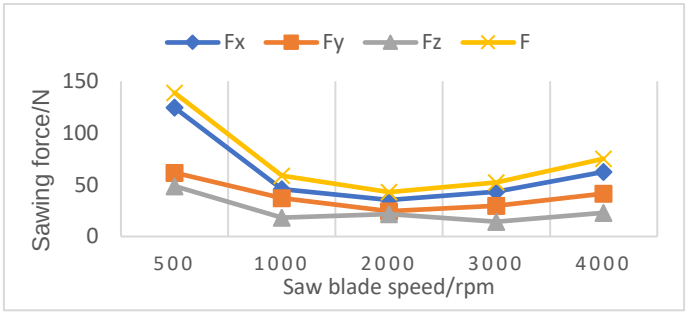


Fig. 8 - Relationship between saw blade speed and sawing force

Selecting the diameter as 20 mm and saw blade speed as 3000 rpm, the simulation was carried out for the feed speed of 1~5 km/h respectively, and the data obtained is shown in Fig 9. From equation (11), it can be seen that the increase in feed speed would lead to an increase in sawing difficulty, so the sawing force had been increasing. As can be seen from Fig 11, the feed speed increased faster after 3 km/h. Taking into account the efficiency and sawing difficulty and other factors, the feed speed of 3~5 km/h was selected.

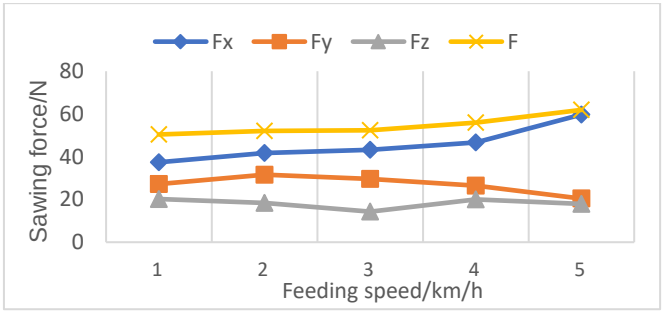


Fig. 9 - Relationship between feed rate and sawing force

The speed of 3000 rpm and feed rate of 3 km/h were chosen to simulate the branch diameter of 10~40 mm respectively, and the test results are shown in Fig 10. The circular saw blade was easier to cut branches below 20 mm in diameter, when the diameter exceeded 20 mm, the growth rate of the sawing force required for cutting was greatly accelerated, especially the axial force, which may lead to the deformation of the circular saw blade when cutting large diameter branches.

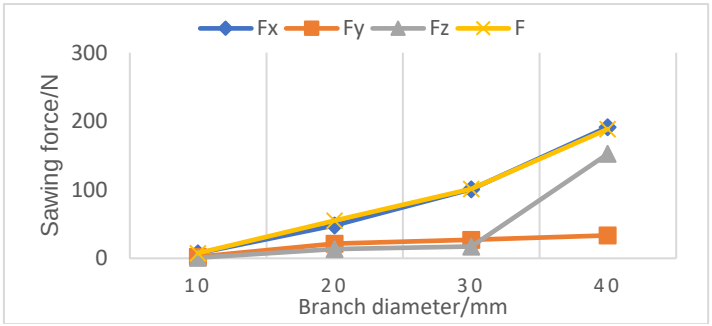


Fig. 10 - Relationship between branch diameter and sawing force

Orthogonal test

A three-factor, three-level quadratic orthogonal test was designed according to the Box-Behnken principle to analyse the effect on sawing force when multiple factors acted simultaneously on the basis of a single factor and to seek the optimal parameter fit *(Kang F et al.,2020)*, with the parameters shown in Table 5.

Table 5

Orthogonal test element level table

Branch diameter (A) /(mm)	Saw blade speed (B) /(rpm)	Feeding speed (C) /(km/h)
10	2600	3
20	2800	4
30	3000	5

The quadratic polynomial regression was fitted to the test data using Design-Expert 8.0.6, and the resulting regression equation (14), and the regression equation ANOVA was performed on the results of the central combination test, and the results were shown in Table 6.

$$F = 48.76 + 44.49A + 2.57B + 5.29C - 1.95AB + 2.18AC - 1.95BC + 4.53A^2 + 3.16B^2 + 1.08C^2 \quad (14)$$

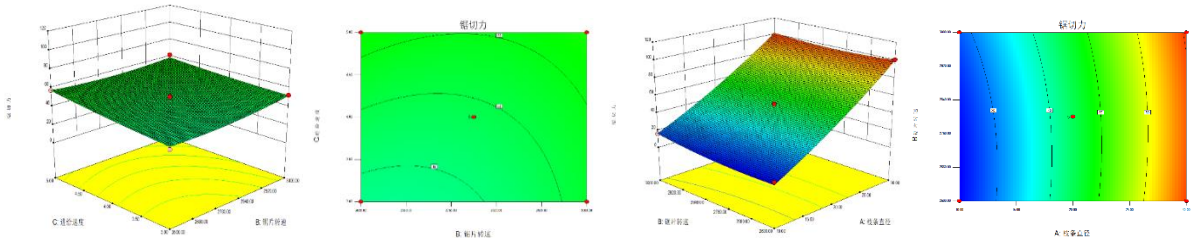
Table 6

Regression equation analysis of variance

Source	Squares	DF	MS	F value	P value
Models	16304.00	9	1811.56	211.63	< 0.0001
A	15833.10	1	15833.10	1849.68	< 0.0001
B	53.05	1	53.05	6.20	0.0416
C	223.66	1	223.66	26.13	0.0014
AB	15.21	1	15.21	1.78	0.2243
AC	18.92	1	18.92	2.21	0.1807
BC	15.21	1	15.21	1.78	0.2243
A²	86.50	1	86.50	10.11	0.0155
B²	41.98	1	41.98	4.90	0.0624
C²	4.93	1	4.93	0.58	0.4725
Residual	59.92	7	8.56		
Lack of Fit	45.27	3	15.09	4.12	0.1025
Pure Error	14.65	4	3.66		
Cor Total	16363.92	16			

*Note:P<0.01(extremely significant,**), P<0.5(significant,*)*

As shown in Fig.11 (a), the feed speed and branch diameter are positively correlated with the sawing force when the branch diameter is constant, and the correlation between the two is close; the effect of the saw blade speed on the sawing force is more significant than the feed speed; when the feed speed is certain, the sawing force increases with the increase of the saw blade speed. As shown in Fig.11 (b), the correlation between branch diameter and sawing force is extremely significant at a certain feed speed, while the correlation between saw blade speed and sawing force is negative and increases with the increase of feed speed. The influence of branch diameter on the sawing force is much more significant than the saw blade speed, when the saw blade speed is certain, the sawing force increases with the increase of branch diameter.



(a) branches of a certain diameter, F=f(0,B,C) *(b) certain feed rate, F=f(A,B,0)*

Fig. 11 - Response surfaces of sawing forces under different conditions

The optimal solution derived from the orthogonal test was 2800 rpm for the saw blade speed and 4 km/h for the feed speed at a branch diameter of 20 mm, but the actual working conditions need to be considered, so field performance tests need to be conducted for further verification.

Prototyping and field trials

To verify the functionality and reliability of the apple pruning machinery and the degree of fit of the designed sawing parameters, the overall prototype was tried and field trials were conducted as shown in Fig.12. The test was conducted in March 2022 at the test base of Gaomi Yifeng Machinery Co.

The test conditions included: Dongfanghong X700 tractor with a calibrated power of 51.5 kW; the orchard was planted with standardized dwarf anvil and dense planting; the pruning machine prototype with circular saw blade speed selected at 2800 rpm.



Fig. 12 - Prototype trial production and field test

During the test, the pruning machinery was sensitive to action, and the automatic obstacle avoidance function was good. The position adjustment process was smooth and fluid. The apple pruning machine was mainly used for pruning dwarf dense orchards with short anvils, so the main test was the qualified rate of pruning. 9 areas were selected as test points, each area includes about 20 branches, and the qualified rate was tested under different feeding speeds, the test data was shown in Table 7.

Table 7

Experimental data statistics

Test site	1	2	3	4	5	6	7	8	9
Feeding speed/ (km/h)	3	3	3	4	4	4	5	5	5
Passing Rate/ (%)	89.5	86.8	90.2	92.1	97.5	88.9	88.3	91.2	87.1

The main criteria for passing rate are: branches missed cut, not cut and extremely rough cut surface covered with burrs are considered as failing, while other cases are considered as passing (*Chang J X., 2019*). The cut quality is mainly influenced by the saw blade speed, feed rate and branch diameter. At the saw blade speed of 2800 rpm, most of the branches could reach the passing standard, and the average passing rate at the feed speed of 4 km/h was 92.8% higher than 88.8% at 3 km/h and 88.9% at 5 km/h, and the overall average passing rate reached 90.2%. When the saw blade speed is reduced, the quality of the section decreases, the burr increases and the passing rate decreases. After the test, the best sawing parameters were obtained to match the saw blade speed of 2800 rpm and the feed speed of 4 km/h.

CONCLUSIONS

(1) This pruning machine is suspended from the front of the tractor and uses a hydraulic motor to drive a circular saw blade for pruning operations. The dimensions of the pruning device are determined according to the planting requirements of dense apple orchards with dwarf anvils: horizontal section length L_5 = 1.1 m, vertical section length L_4 = 2.3 m, inclination angle 22° and inclination angle 17°.

(2) Sawing process analysis and modal analysis were carried out for the saw blade, and the limit speed of the circular saw blade was determined. Through finite element simulation analysis, a reasonable range of circular saw blade speed, branch diameter and feed speed was derived, and a three-factor, three-level quadratic orthogonal test was designed according to the Box-Behnken principle. The experiment showed that when the diameter of the cut branch was 20 mm, the best cutting effect was achieved with a saw blade speed of 2800 rpm and a tractor feed speed of 4 km/h.

(3) The prototype and field test was carried out, and the test results showed that the low saw blade speed would lead to an increase in the cut burr, and the fast tractor feed speed would lead to incomplete cutting of the branch and tearing of the epidermis of the branch. The test results showed that when the saw blade speed was 2800 rpm and the tractor was at 4 km/h, the sawing effect was the best and the average passing rate reached 92.8%, which was consistent with the simulation results and the cutting quality met the pruning requirements of the new orchard.

ACKNOWLEDGEMENT

This work was supported by “Shandong Province Key Research and Development Plan (2022CXGC0 20706) and China Agriculture Research System of MOF and MARA (CARS-27)”.

REFERENCES

[1] An R. (2019). Design and experimental research of edible rose pruner in Yunnan *(Master's thesis, Kunming University of Technology)*.

[2] Chang, J.X., Zhang, Y.L., Li, S.J., Zhang W. & Ma P.Y., (2019). Design of double-sided flush-cut citrus pruner. *Journal of Huazhong Agricultural University* (03), 104-111.

[3] Jiang L.Q., (2013). Simulation study of circular saw blade sawing process based on ANSYS/LS-DYNA *(Master's thesis, Guangxi University)*.

[4] Kang F., Tong, S.Y., Zhang, H.S., Li, W.B., Chen, Z.G. & Zheng, Y.J. (2020). Analysis and experiments on the parameters of reciprocating cutting pruning of apple branches. *Journal of Agricultural Engineering* (16), 9-16.

[5] Liu J., Deng Y.J., Wang C., Dai J.J., Zhao P., Shu R. & Liu Z. (2021). Design and experiment of self-propelled bilateral mulberry pruner. *Agricultural Mechanization Research* (06), 105-110+120.

[6] Liu X.C., Liu X.F., Zhang L.F., Min L.Q., Chu Y.H. & Ren D.M., (2020). Design and research of a new type of orchard wide-width combined profiling pruning machine. *Chinese Journal of Agricultural Machinery* (08), 65-71. doi: 10.13733/j. jcam.issn.2095-5553.2020.08.010.

[7] Meng Y.M., Wei J.D., Wei J., Chen H., & Cui Y.S., (2019). An ANSYS/LS-DYNA simulation and experimental study of circular saw blade cutting system of mulberry cutting machine. *Computers and Electronics in Agriculture*,157, 38-48.

[8] Shi L., (2018). Ideas and methods of summer pruning in modern dwarf rootstock dense apple orchards. *Northwest Horticulture (Fruit Tree)* (04), 16-17.

[9] Shu Y., Geng X. Y., Song Y.P., Gao D.S., Liu H.J. & Wang Z., (2018). Design of sawing type apple pruner with clamping mechanism. *Chinese Journal of Agricultural Chemistry* (08), 9-16.

[10] Sun, J.F., Xing, K.F., Yang Z. & Duan, J.L., (2011) A new species of the genus Phyllostachys (Hymenoptera, Braconidae) from China. (2022). Simulation and experimental study of fruit pruning process based on ANSYS/LS-DYNA. *Journal of South China Agricultural University* (04), 113-124.

[11] Wang S.C., Wang J.Y., & Jiang L.Q., (2015). ANSYS/LS-DYNA modeling and simulation study of high-speed hedge trimming process. *Mechanical Design and Manufacture* (08), 267-269

[12] Wang Z, Song Y.P., Gao D.S., Liu H.J., Fan G.J & Zhang T., (2017). Simulation analysis and experiments on the kinetics of apple tree branch sawing process. *Chinese Journal of Agricultural Chemistry* (09), 44-50.

[13] Wu, Q.B., Jin, Y., Hou, L.J. & Zhao, X.Y., (2020). Design and modal analysis of disc knife type cutting device. *Journal of Henan University of Technology* (02),6-8+62.

[14] Zhang B., Liu Y., Zhang H., Shen C., & Fu W. (2022). Design and Evaluation of a Shaping and Pruning Machine for Dwarf and Densely Planted Jujube Trees. *Applied Sciences*, *12*(5), 2699.

[15] Zhang D.X., Qin X.T., Liu X.F., Li Q.J., Min L.Q. & Ren D.M., (2021). Research process and supporting equipment for branch pruning in orchards at home and abroad. *China Fruit Tree* (02), 6-12.

[16] Zhang, J.X., Huang, T & Wang, M.B., (2011) A new species of the genus Phyllostachys (Hymenoptera, Braconidae) from China. (2021). Design and experiment of single motor reciprocating grape pruner. *Journal of Agricultural Machinery* (08), 106-116.

[17] Zhang, H.S. (2020). Simulation and investigation of apple branch sawing mechanics test *(Master's thesis, Beijing Forestry University)*.

[18] Zheng Y.J., Jiang S.J., Chen B.T., Lu H.T., Wan, C. & Kang, F., (2020). Research progress on mechanization technology and equipment for orchards in hilly mountainous areas. *Journal of Agricultural Machinery* (11), 1-20.

DETECTION OF DEFECTS OF *CERASUS HUMILIS* FRUITS BASED ON HYPERSPECTRAL IMAGING AND CONVOLUTIONAL NEURAL NETWORKS
/
基于高光谱成像和卷积神经网络的欧李果实缺陷检测

Bin WANG [1], Lili LI [*1]
[1] College of Information Science and Engineering, Shanxi Agricultural University, Taigu 030800 / China
Tel: 18306832356; E-mail: lilycqdxyjs@163.com
DOI: https://doi.org/10.35633/inmateh-71-08

Keywords: *cerasus humilis fruits, natural defects, convolutional neural networks, hyperspectral imaging technology*

ABSTRACT
In order to perform highly effective identification of external defects and increase the additional value of Cerasus Humilis fruits, this study used hyperspectral imaging technology to collect information on intact and defective Cerasus Humilis fruits. Based on the full transition spectrum, partial least squares discriminant analysis (PLS-DA) and back propagation neural networks (BPNN) were used to establish a discriminative model. The competitive adaptive reweighted sampling (CARS) was used to extract feature wavelengths, principal component analysis was used for data compression of single band images, BPNN and convolutional neural networks (CNN) were used for defect Cerasus Humilis fruits recognition of principal component images. The results showed that the overall detection accuracy of PLS-DA and BPNN models based on wavelength spectral information were 83.81% and 85.71%, respectively. BPNN was used to establish the calibration model based on the selected characteristic wavelengths by CARS, the accuracy rate was 90.47%. The classified accuracy of CNN model based on principal component images was 93.33%, which was obviously better than that of BPNN model at 83.81%. The research shows that the CNN model was successfully applied to the detection of Cerasus Humilis fruits defects using hyperspectral imaging. This study provides a theoretical basis for the development of fruit grading and sorting equipment.

摘要
为实现欧李果缺陷特征的识别，提高欧李果附加价值，采用高光谱成像技术采集了完好和缺陷欧李果的信息。基于全渡段光谱，采用偏最小二乘判别分析 (Partial Least Squares-Discriminant Analysis, PLS-DA) 和误差反向传播神经网络 (Back Propagation Neural Networks, BPNN) 建立判别模型。采用竞争自适应加权(CARS)提取特征波长，并利用主成分分析进行单波段图像的数据压缩，针对主成分图像采用BPNN和卷积神经网络(Convolutional Neural Networks, CNN) 进行缺陷欧李果识别。结果表明，基于全波段光谱建立的PLS-DA、BPNN模型的整体判别正确率分别为83.81％和85.71%；采用CARS提取样本的特征波长后所建BPNN判别模型的正确率为90.47%；基于主成分图像建立的BPNN和CNN模型的判别正确率分别为83.81%和93.33%。研究表明，CNN可成功应用于基于高光谱技术的鲜枣黑斑特征识别中，该研究为开发水果的分级分选设备提供了理论基础。

INTRODUCTION

Cerasus Humilis fruits not only have a unique flavor, but is also rich in sugars, amino acids, proteins, vitamins, flavonoids, and other components. However, external defects such as rust spots, insect pests, and cracks on the surface of *Cerasus Humilis* fruits not only reduce the quality and price of the fruit but also easily cause fungi to infect other intact fruits, causing serious economic losses *(Wang et al., 2023)*.

Defect detection is an important aspect of fruit safety testing. At present, the detection of *Cerasus Humilis* fruits mainly relies on manual sorting, which involves manually sorting out irregular and damaged fruits, and then using existing grading equipment for size grading before being packaged and sold. Due to the low efficiency and accuracy of manual sorting, it is also difficult to sort *Cerasus Humilis* fruits with natural defects. Hyperspectral imaging technology has the advantages of being fast, non-destructive, and real-time, and has been successfully applied in the detection of fruit diseases such as pears *(Zhang et al., 2022)*, apples *(Gao et al., 2022)*, *Cerasus humilis* fruits *(Wang et al., 2023)*, and winter jujubes *(Jiang et al., 2023)*. In the external quality inspection of fruits, relevant research has been mainly focused on insect pests *(Liu et al., 2016)*, cracks *(Yu et al., 2014)*, and black spots *(Ye et al., 2022)* to achieve the classification of various defects and intact samples.

In modeling methods, convolutional neural networks, as a typical deep learning technique, can extract more abstract features and have been well applied in image processing and other fields *(Khaw et al., 2017; Fazari et al., 2021; Gai et al., 2022)*. In hyperspectral imaging, there are many spectral channels with high spatial variability. *Chen et al. (2018)* used convolutional neural networks (CNN) for hyperspectral classification, providing a feasible basis for fruit CNN hyperspectral detection. *Xue et al. (2020)* proposed using the GoogLeNet deep transfer model to detect apple defects and compared it with traditional machine learning methods. The results showed that the GoogLeNet deep transfer model has better generalization ability and robustness. *Zhu et al. (2019)* used near-infrared hyperspectral imaging technology to obtain spectral data for three soybean varieties and established a 1D-CNN model to distinguish soybean varieties. Research has shown that the classification accuracy of this model for each variety is above 90%. *Singh et al. (2021)* used a hyperspectral imaging system (900-1700 nm) to collect hyperspectral reflectance images of the ventral and dorsal sides of barley seeds, and the constructed CNN model had an accuracy of more than 98% in the test set.

This study aims to explore the feasibility of Hyperspectral imaging (HSI) combined with CNN for the identification of *Cerasus Humilis* fruit defects. The objectives of this study are as follows: (1) Collect hyperspectral images of intact and defective *Cerasus Humilis* fruit samples, extract average spectral data of regions of interest (ROI), and partial least squares discriminant analysis (PLS-DA) and back propagation neural networks (BPNN) discriminative models were established based on the full wavelength spectral information. By comparison, the optimal discriminant model was obtained; (2) Characteristic wavelength was extracted by competitive adaptive reweighting sampling (CARS), and BPNN discriminant model was established; (3) The data compression of the single band images was carried out by principal component analysis, and the *Cerasus Humilis* fruit defects was discriminated using the principal component image of both BPNN and a CNN; (4) By comparing the classification results of different methods, select the best model for identifying defects in *Cerasus Humilis* fruit.

MATERIALS AND METHODS

Experimental Sample

The "Nongda No. 6" *Cerasus Humilis* fruit samples were collected from the *Cerasus Humilis* planting base in the agricultural high-tech industry demonstration zone of Jinzhong, China. To ensure the consistency of the samples and reduce the impact of sample differences on the study, the principles of picking were similar shapes, uniform size (9.0-13.0g per fruit), and complete defect types (intact, rust spots, insect damage, cracks) are followed.

On the day of harvest, the samples were transported to the laboratory and screened. A total of 420 samples were selected and divided into intact and defective groups. Among them, 160 were intact *Cerasus Humilis* fruits, while the defective group included 92 rust spot fruits, 84 insect damage fruits, and 84 crack fruits. The intact and three types of defective samples were shown in Fig. 1.



a) Intact sample *b) Rust spot sample* *c) Insect damage sample* *d) Crack sample*

Fig. 1 - Figure of intact and defective samples of *Cerasus Humilis* fruit

Rust spots are the spots formed on the surface of fruits after being damaged by pests and diseases. Cracked fruit is a type of fruit that encounters rainy weather during its ripening period. With the rapid expansion of the flesh, the skin of the fruit will crack in different sizes and shapes, exposing the flesh tissue and causing the fruit to begin to decay. Insect damage fruit refers to its larvae often drilling holes on the surface of the fruit to feed inside, resulting in low fruit yield and loss of commercial value.

Reasonable and effective sample set partitioning is of great significance for the model establishment and can improve model discrimination accuracy. Collect hyperspectral images of each sample and assign values of 1, 2, 3, and 4 to four types of data (rust spot fruit, cracked fruit, insect damage fruit, and intact fruit).

Using the SPXY algorithm, each type of sample was randomly divided into a correction set and a prediction set according to the ratio of 3:1 *(Galvao et al., 2005)*, with 315 samples as the correction set and 105 samples as the prediction set. The statistical results of sample set partitioning were shown in Table 1.

Table 1

The sample set results were divided by the SPXY algorithm

Type	No. of samples	Correction set	Prediction set
Rust spot	92	69	23
Crack	84	63	21
Insect damage	84	63	21
Intact	160	120	40
Total	420	315	105

Instruments and Equipment

The "Gaia" hyperspectral imaging system developed by Beijing Zhuoli Hanguang Company was used in this study, with a wavelength range of 900~1700 nm, and the schematic of the system was shown in Fig. 2. It mainly consists of an Image-k-N17E spectral camera, four 35 W bromide tungsten lamps, a computer, an electric mobile platform, and a dark box. To avoid information oversaturation and imaging distortion, after multiple experiments, it was finally determined that the exposure time t=150 ms, the distance between the sample and the lens h=280 mm, and the conveyor belt movement speed v=8.0 mm/s. When obtaining hyperspectral images, a self-made perforated carrier plate was placed on the platform, and the tested sample was placed horizontally on the carrier platform. For the tested samples with defects, the defect area was manually oriented and the target area was oriented towards the camera. The images of the samples obtained in the hyperspectral imaging system was shown in Fig. 3.

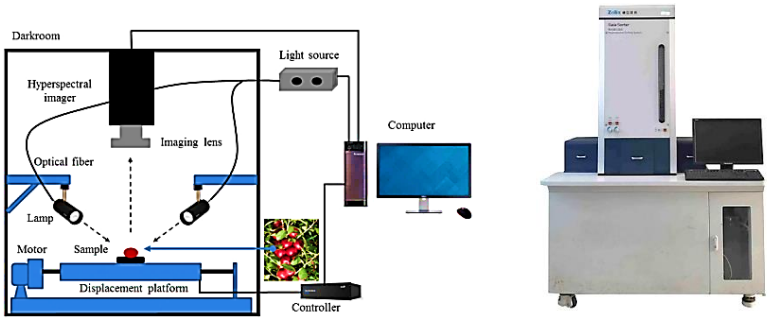


Fig. 2 - Experiment platform of the hyperspectral imaging system



a) Intact sample *b) Rust spot sample* *c) Insect damage sample* *d) Crack sample*

Fig. 3 - Hyperspectral Images of *Cerasus Humilis* fruit Samples

Correction Method of Hyperspectral Image

In order to eliminate the influence of changes in light intensity and dark currents in the lens on imaging, as well as to calculate the relative reflection spectrum value of the scanned object, it is necessary to perform black and white board correction before the spectral acquisition *(Baranowski et al., 2012)*. The calculation formula is shown in Equation (1):

$$I_C = \frac{I_R - I_D}{I_W - I_D} \times 100\% \quad (1)$$

where I_C represents the corrected image, I_R represents the original image, I_D represents the black reference image, and I_W represents the white reference image.

Statistical Analysis

This study used the CARS algorithm to extract characteristic wavelengths and modeled them using PLSDA, BPNN, and CNN. CARS is a new variable optimization method *(Ma et al., 2019)*, which imitates the principle of "survival of the fittest" in Darwin's evolution theory. Using adaptive reweighted sampling (ARS) technology, each wavelength was treated as a separate individual, and variables with large absolute values of regression coefficients are selected from the PLS model. Variables with small absolute values of regression coefficients are eliminated, and a series of wavelength variable subsets were obtained through multiple repeated screenings. The subset of variables with the smallest root mean square error in the PLS model was selected through cross-validation with ten folds, which was the optimal wavelength variable quantum set *(Wieme et al., 2022).*

PLS-DA is a multivariable statistical analysis method combining the partial least squares method and linear discriminant analysis method *(Yan et al., 2020)*. It uses cross-validation to obtain the optimal number of principal components, and then carries out linear discriminant analysis to solve the problem of independent variable multicollinearity in regression analysis. In this study, principal components were selected based on interaction testing, with a maximum principal component score of 10, and a 10-fold interaction test was performed.

BPNN is a multi-layer feedforward neural network trained according to the error backpropagation algorithm *(Li et al., 2017)*. It can arbitrarily complex pattern classification and excellent multidimensional function mapping and solves the XOR and other problems that cannot be solved by simple perceptron. In this study, the activation function of the hidden layer and output layer of the network was set as tansing and purelin functions, respectively. The network training function was trainlm function, and the number of neurons in the hidden layer was set as 6. The number of network iterations was 2500, an expected error of 0.001, and a learning rate of 0.1.

The basic structure of CNN includes a feature extraction layer and a feature mapping layer, which is an improvement based on BP neural network *(Xu et al., 2020)*. In CNN, the perception area of a neural unit comes from the part of the upper neural units. The same feature plane realizes weight sharing, which reduces the complexity of the network and the risk of overfitting. In this study, the structure of CNN includes an input layer, a 2-layer convolution layer, a down-sampling layer, a full connection layer, and an output layer. See Fig. 4 for the basic structure.

The input image size is 36×36, the feature mapping structure uses the sigmoid function with a small influence function kernel as the activation function of the convolution network. The number of feature maps of the first convolution is 4, the number of feature maps of the second convolution is 8, the size of the convolution kernel is 5×5, the size of the convolution kernel for down-sampling layer was 2×2, with a learning efficiency of 0.1. The number of training samples in each batch was 10, and the number of iterations in each batch was 720.

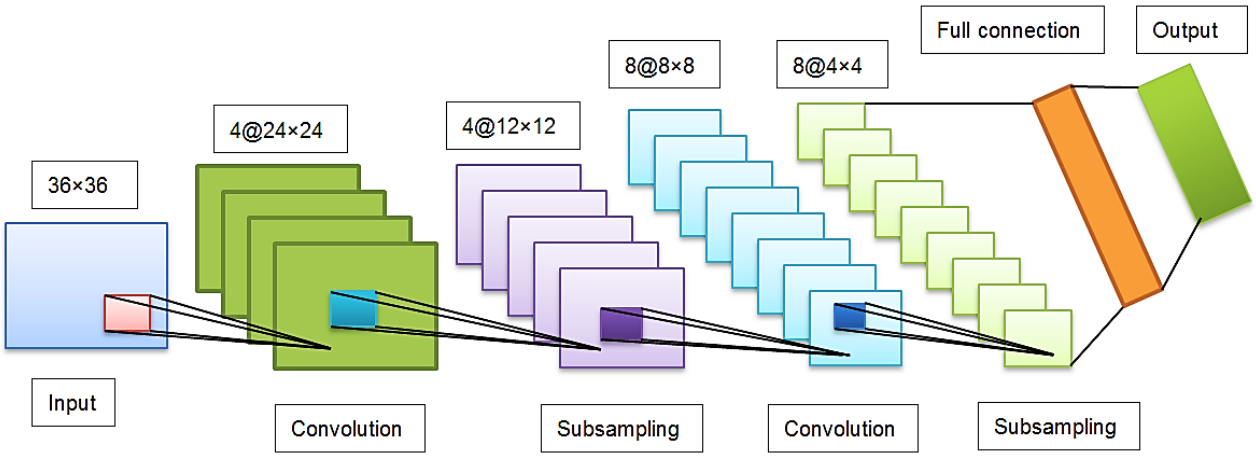
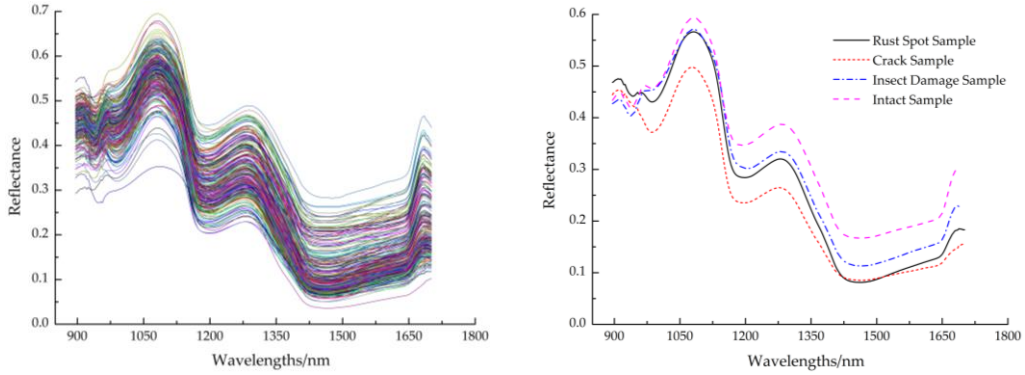


Fig. 4 - CNN structure

EXPERIMENTAL RESULTS AND ANALYSIS

Spectral Characteristics and Analysis

Using ENVI software to extract spectral information of the region of interest of the samples, the original spectral curves of 420 samples were shown in Fig. 5(a). Then calculate the average spectra of each sample as spectral information, as shown in Fig. 5 (b). Remove the bands containing a large amount of noise and only retain the wavelength range of 945-1675 nm (230 bands) for subsequent research.



a) Original spectral curve *b) Average raw spectra curve*

Fig. 5 - Spectral curves of four different *Cerasus Humilis* fruit samples

From the spectrogram Fig. 5, it can be seen that the spectra of all four types of samples exhibit similar spectral features and curve shapes. From Fig. 5(a), it can be seen that the absorption peaks at 980 nm and 1195 nm are related to the second overtone of O-H stretching and the second overtone of C-H stretching, respectively *(Liu et al., 2010)*. There is a clear absorption peak at about 1460 nm, which was related to the first overtone of bond O-H *(Osborne et al., 2006)*. From Fig. 5(b), it can be seen that the spectral reflectance values of all defective samples are significantly lower than those of intact samples. This may be because the gray value of defective regions is usually lower, reducing the reflection of incident light *(Li et al., 2012)*.

Discriminative Model Based on Full Wavelengths Spectral Information

Linear (PLS-DA) and nonlinear (BPNN) discriminative models were established based on the full wavelength spectral information. When the discriminative model was established to discriminate the type of samples if the correct prediction value of the rust blotch is within the threshold value [0.5, 1.5], it is determined that the prediction category is consistent with the assumed category, that is, it is determined as the rust spotted fruit. By analogy, the threshold range for cracked fruit was (1.5, 2.5], the threshold range for insect-infested fruit was (2.5, 3.5], and the threshold range for intact fruits was (3.5, 4.5]. Compare and analyze the discriminant classification performance of the established models.

PLS-DA Discriminative Model

With the full wavelength spectral data as the input of the PLS-DA model, a PLS-DA prediction discriminative model was established to discriminate the prediction set of *Cerasus Humilis* fruit samples. During the modeling process, 10 times of cross-validation was selected to prevent overfitting, and the latent variables (Lvs) value was within the range of 2~20. When Lvs was 12, the PLS-DA model had the highest discrimination accuracy, as shown in Table 2.

Table 2

Discrimination results for defect types of *Cerasus Humilis* fruits by PLS-DA model

Type	Number of predicted samples	Misjudgment samples	Accuracy (%)
Rust spot	23	6	73.91
Crack	21	5	76.19
Insect damage	21	5	76.19
Intact	40	1	97.50

Total	105	17	83.81

From Table 2, it can be seen that the PLS-DA model had a good discrimination effect on the prediction set. The discrimination accuracy of this model for rust spot fruit, cracked fruit, insect damage fruit, and intact fruit was 73.91%, 76.19%, 76.19%, and 97.50%, respectively, with an overall accuracy of 83.81%. The total number of misjudged samples in the prediction set by this model was 17. Among them, 6 rust spot fruit were misjudged as intact due to their small rust area, 5 cracked fruits were misjudged as insect damage fruit due to their small cracks, 5 insect damage fruit were misjudged as intact due to their small insect damage area, and 1 intact fruit was not detected.

BPNN Discriminative Model

A BPNN discriminative model for the defect types of *Cerasus Humilis* fruits was established by using Matlab software. The number of input nodes of the model was determined by the data dimension of the full spectrum input, and the number of output nodes was determined by the defect types of *Cerasus Humilis* fruits, that is, the number of model output nodes was 4. Normalize the input data matrix to distribute the data within the range of [-1, 1]. The discrimination results of this model for four types of *Cerasus Humilis* fruit defect samples were shown in Table 3.

Table 3

Discrimination results for defect types of *Cerasus Humilis* fruits by BPNN model

Type	Predicted samples	Misjudgment	Accuracy (%)
Rust spot	23	6	73.91
Crack	21	4	80.95
Insect damage	21	4	80.95
Intact	40	1	97.50
Total	105	15	85.71

From Table 3, it can be seen that the BPNN model had a good discrimination effect on the prediction set, but the model required a longer training time. The discrimination accuracy of this model for rust spot fruit, cracked fruit, insect damage fruit, and intact fruit was 73.91%, 80.95%, 80.95%, and 97.50%, respectively, with an overall correct discrimination rate of 85.71%. The total number of misjudged samples in the prediction set by this model was 15. Among them, 6 rust spot fruit were misjudged as intact due to their small rusty area, 4 cracked fruits were misjudged as insect damage fruit due to their small cracks, 4 insect damage fruit was misjudged as intact due to their small insect damaged area, and 1 intact fruit was not detected.

Characteristic Wavelength Extraction

The purpose of feature extraction is to extract effective information from the original standard sample spectrums, overcome the linear correlation, singularity, and instability of the original spectrum data, and improve prediction reliability. When extracting feature spectra, it is necessary to minimize the dimensionality of the data or the number of variables, while also minimizing the omission of useful explanatory information.

The results of the CARS algorithm (with Monte Carlo sampling number N=50) running in Matlab R2014b software were shown in Fig. 6, where Fig. 6(a) reflected a continuous decrease in the number of wavelength variables filtered as the sampling number increases, and the rate of decrease from fast to slow. In Fig. 6(b), it can be seen that during the 1~43 sampling process, RMSECV showed a downward trend, reflecting that the eliminated variables in this process were information unrelated to the identification of defect features of *Cerasus Humilis* fruits. Starting from the 44th sampling, RMSECV gradually increased, reflecting that this screening process began to eliminate useful information related to the identification of defect features of *Cerasus Humilis* fruits. Fig. 6(c) showed the trend of the regression coefficients of each wavelength variable during the process of wavelength variable optimization. The vertical line position marked with "*" in the figure indicated that when the number of sampling runs was 43, the RMSECV reached the minimum value of 0.4298.

At this time, the eight characteristic wavelengths selected by CARS were 950, 994, 1071, 1263, 1336, 1457, 1542, and 1628 nm, respectively.

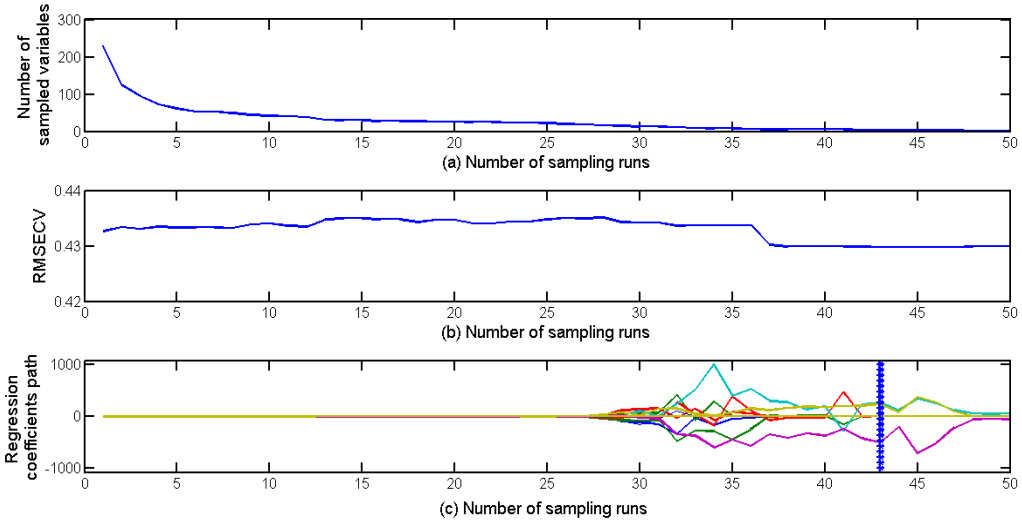


Fig. 6 - Process of selecting characteristic wavelength by CARS method

Based on the characteristic wavelength extracted by the CARS algorithm, a BPNN discriminative model was established. When the mean square error was 0.0028 and the number of iterations was 12, the discrimination accuracy of the CARS-BPNN model was 90.47%. This indicated that the characteristic wavelength had a better modeling effect than the full wavelength, and there was some noise in the full wavelength of this study. Therefore, the selection of effective variable information, the improvement of computational speed, and the stability and reliability of algorithms were also important influencing factors for model stability.

The CNN Recognition Model Based on Image Information

Principal component analysis (PCA) is a widely used method for data dimensionality reduction and feature extraction, which helps to enhance target area information and remove noise. PCA converts raw data into linearly independent variables, known as principal components (PCs). Perform principal component analysis on the images corresponding to the 8 characteristic wavelengths extracted by CARS and obtain the cumulative principal component contribution values of intact and defective *Cerasus Humilis* fruit samples, as shown in Table 4. From Table 4, it can be concluded that the cumulative contribution rate of the first six PCs had reached 99.82%, which can effectively explain the sample information variables. Therefore, the first six principal components were selected for analysis.

Table 4

The cumulative contribution rate of the first eight principal components of the image

PCs	Characteristic Value	Contribution Rate (%)
1	28924.1723	81.78
2	8847.3621	93.62
3	1035.3651	95.35
4	753.5245	96.92
5	186.7485	98.62
6	70.7625	99.82
7	9.6372	99.99
8	1.8674	100.00

Fig. 7 showed the first eight PC images based on intact and defective *Cerasus Humilis* fruits in the feature band. Different PC images reflect different *Cerasus Humilis* fruit defect features. These PC images

were sorted according to the degree of decreasing variance, with the first PC image having the highest proportion of variance and containing the most original information.

From Fig. 7, it can be seen that the top 6 PC images (PC-1 to PC-6) of four different defect types of *Cerasus Humilis* fruit had the most original image information, while PC-7 to PC-8 images contain more noise and no longer have meaningful information for detecting surface defect features of *Cerasus Humilis* fruit. Through rapid visual inspection of the top 6 PC images, it was found that in some converted partial PC images, the main defect features became more prominent, indicating that PCA can extract useful features. Therefore, PC-3 images of cracked fruits, PC-5 images of insect-infested fruits, PC-6 images of rusty fruits, and PC-6 images of intact fruits were selected for analysis. Simultaneously extract the grayscale values of each sample PC image and normalize the data, and establish a classification model using BPNN and CNN.

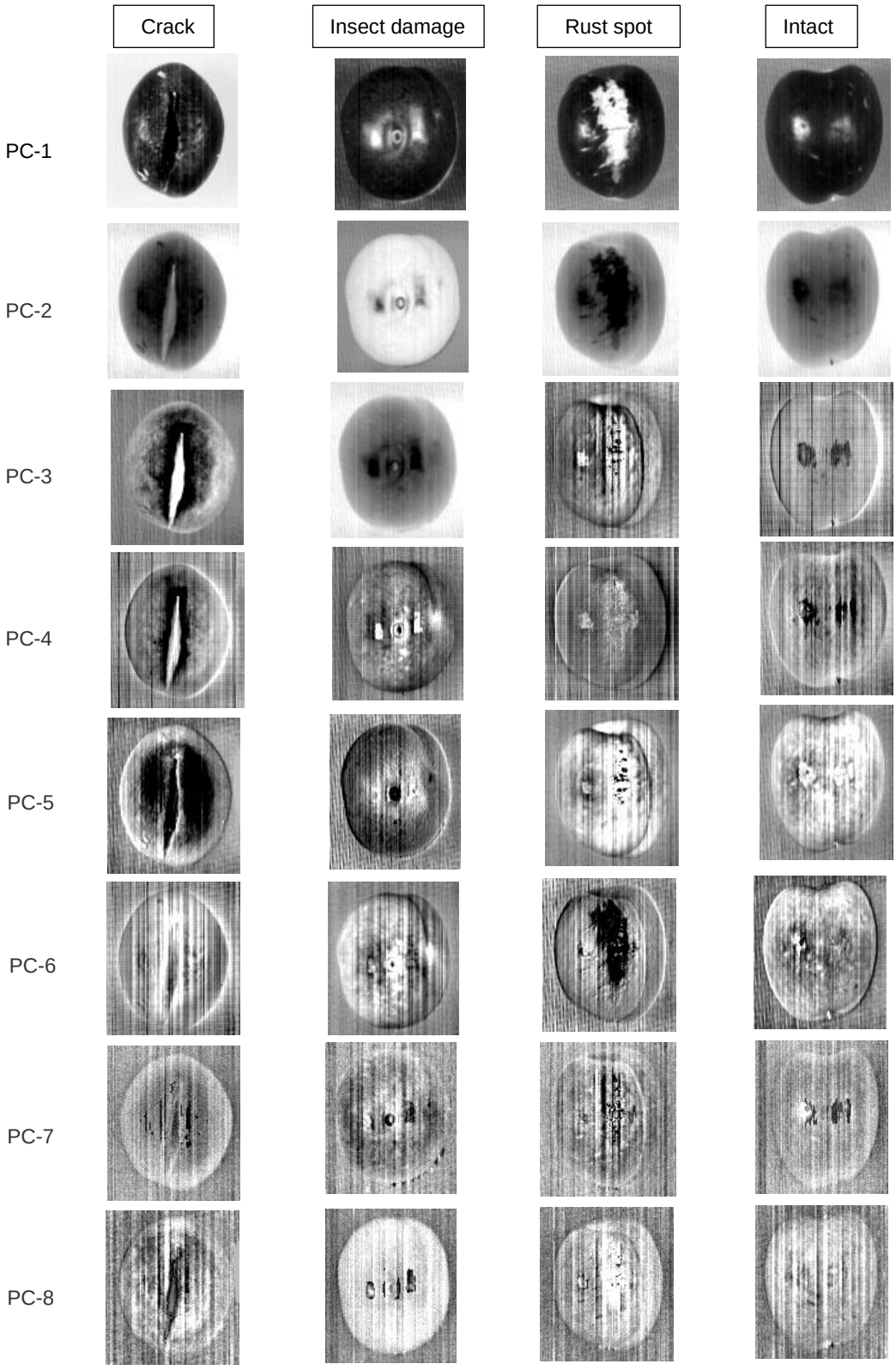


Fig. 7 - The first eight PCs grayscale images of *Cerasus Humilis* fruit based on the special bands

The discrimination results of the BPNN and CNN models established based on principal component images were shown in Table 5. When the root mean square error of the BPNN model was 0.97 and the number of iterations was 5, the discrimination accuracy reached 83.81%. Four intact fruits were misclassified as rust spot fruits, five rust spot fruits were identified as intact fruits, four insect damage fruits were misclassified as intact fruits, and four cracked fruits were not detected. In CNN discriminative model, with the increase of learning times, the mean square error showed a downward trend on the whole and converges to a stable value when the number of iterations was 14226.

When the number of iterations is 23610 and the mean square error is 0.0063, the discrimination accuracy was 93.33%. Two intact fruits were misclassified as rust spot fruits, three rust spot fruits were misclassified as intact fruits, one insect damage fruit was misclassified as intact fruit, and one cracked fruit was not detected. The discrimination accuracy of the CNN model was significantly better than that of BPNN, and it had good application prospects in agricultural product quality detection based on hyperspectral imaging technology. The CARS-BPNN defect recognition based on spectral information and the CNN recognition based on image information has achieved good results.

Based on this, future research will establish a stable model suitable for online sorting in industrial production.

Table 5

The results of BPNN and CNN models

Models	Epochs	Mean square error	Accuracy (%)
BPNN	5	0.97	83.81
CNN	23610	0.0063	93.33

DISCUSSION

In this study, hyperspectral technology combined with convolutional neural network was used to identify the defective *Cerasus Humilis* fruit. Different detection models were established from two angles of spectral information and image information, and the optimal detection model was determined by comparison. Both CARS-BPNN based on spectral information and CNN based on image information has achieved good results in identifying defective *Cerasus Humilis* fruit. When the number of iterations is 23610 and the mean square error is 0.0063, the discrimination accuracy of the CNN model was 93.33%. *Sun et al. (2018)* detected black spot disease in fresh jujube based on hyperspectral and convolutional neural networks, and collected the information of intact and black spot fresh jujube in different years.

The results show that the discrimination accuracy of the CNN model based on principal component images was 90.0%. *Liu et al. (2018)* collected hyperspectral image information of 5 types of cucumbers (normal, watery, split/hollow, shrivel, and surface defect) and developed a classification algorithm that the SSAE combined with convolutional neural network (CNN-SSAE) learning.

The results showed that the overall classification accuracy of CNN- SSAE for defective cucumbers was 91.1%. *Chen et al. (2023)* combined hyperspectral imaging technology with convolutional neural network to conduct real-time detection of egg defects and freshness. The research results indicate that the overall accuracy of one-dimensional convolutional neural networks (1D-CNN) for egg freshness and defect detection were 99% and 100%, respectively. *Pham et al. (2022)* proposed to combine convolutional neural networks with hyperspectral image information to classify the surface defect types of red jujube. The results show that, compared with the traditional machine learning method, the detection accuracy of CNN was 94.5%, and the classification time was reduced to 16.6 s. Compared with the above research results, this study also achieved good results in the identification of *Cerasus Humilis* fruit defects, but there are still missing detection phenomena.

Finally, the research shows that CNN could better detect the defect types of fruits and vegetables. However, compared with relevant researchers *(Chen et al., 2023)*, the detection accuracy of the results was slightly lower of this study (93.33%). This may be due to the small size and the irregular defect area on the fruit surface of this study object, resulting in a slightly lower recognition rate. The subsequent research will improve the image recognition algorithm to improve the recognition rate.

CONCLUSIONS

This study was based on hyperspectral imaging technology for identifying defective *Cerasus Humilis* fruit. PLS-DA and BPNN were used to establish a full band recognition model, and the discrimination accuracy of PLS-DA and BPNN models was above 83.00%. CARS were used to extract feature wavelengths and a CARS-BPNN model was established, with a recognition accuracy of 90.47%, which was significantly better than the models built for all bands. Based on the feature wavelengths extracted by CARS, principal component images were obtained, and recognition models were established using BPNN and CNN, with discrimination

accuracy rates of 83.81% and 93.33%, respectively. Both CARS-BPNN based on spectral information and CNN based on image information have achieved good results in identifying defective *Cerasus Humilis* fruit. Therefore, the combination of hyperspectral imaging technology and CNN had good application prospects in the classification of agricultural products, providing a theoretical basis for further designing classification devices and achieving real-time online sorting in industrial production.

However, the *Cerasus Humilis* fruits of similar weight and size were selected as research objects in this study, and the influence of different sizes and varieties, growing environment, and more defect types of *Cerasus Humilis* fruit on the identification accuracy was not considered. In the later stage, hyperspectral image information of various types of *Cerasus Humilis* fruit will be collected considering the influence of the above factors, and combined with deep learning algorithm, the optimal model will be found by adjusting model parameters, and its defects and varieties will be identified.

ACKNOWLEDGEMENT

This work was funded by Basic Research Project of Shanxi Province (Free Exploration) (Project No. 202203021212426), "Introduction of Talents and Scientific Research Initiation Project" of Shanxi Agricultural University (Project No. 2023BQ42).

REFERENCES

[1] Baranowski, P., Mazurek, W., Wozniak, J., & Majewska, U. (2012). Detection of early bruises in apples using hyperspectral data and thermal imaging. *Journal of Food Engineering*, *110*(3), 345-355. https://doi.org/10.1016/j.jfoodeng.2011.12.038

[2] Chen, C., Jiang, F., Yang, C., Rho, S., Shen, W., Liu, S., & Liu, Z. (2018). Hyperspectral classification based on spectral–spatial convolutional neural networks. *Engineering Applications of Artificial Intelligence*, *68*, 165-171. https://doi.org/10.1016/j.engappai.2017.10.015

[3] Chen, S. Y., Hsu, S. H., Ko, C. Y., & Hsu, K. H. (2023). Real-time defect and freshness inspection on chicken eggs using hyperspectral imaging. *Food Control*, *150*, 109716. https://doi.org/10.1016/j.foodcont.2023.109716

[4] Fazari, A., Pellicer-Valero, O. J., Gómez-Sanchıs, J., Bernardi, B., Cubero, S., Benalia, S., ... & Blasco, J. (2021). Application of deep convolutional neural networks for the detection of anthracnose in olives using VIS/NIR hyperspectral images. *Computers and Electronics in Agriculture*, *187*, 106252. https://doi.org/10.1016/j.compag.2021.106252

[5] Fu, L., Feng, Y., Liu, Z., Li, R., & Cui, Y. (2018). Image recognition method of multi-cluster kiwifruit in field based on convolutional neural networks. *Transactions of the Chinese Society of Agricultural Engineering*, *34*(2), 205-211. https://doi.org/10.11975/j.issn.1002-6819.2018.02.028

[6] Gai, Z., Sun, L., Bai, H., Li, X., Wang, J., & Bai, S. (2022). Convolutional neural network for apple bruise detection based on hyperspectral. *Spectrochimica Acta Part A: Molecular and Biomolecular Spectroscopy*, *279*, 121432. https://doi.org/10.1016/j.saa.2022.121432

[7] Galvao, R. K. H., Araujo, M. C. U., José, G. E., Pontes, M. J. C., Silva, E. C., & Saldanha, T. C. B. (2005). A method for calibration and validation subset partitioning. *Talanta*, *67*(4), 736-740. https://doi.org/10.1016/j.talanta.2005.03.025

[8] Gao, Q., Wang, P., Niu, T., He, D., & Zhao, X. (2022). Soluble solid content and firmness index assessment and maturity discrimination of Malus micromalus Makino based on near-infrared hyperspectral imaging. *Food Chemistry*, *370*, 131013. https://doi.org/10.1016/j.foodchem.2021.131013

[9] Jiang, M., Li, Y., Song, J., Wang, Z., Zhang, L., Song, L., & Pan, L. (2023). Study on Black Spot Disease Detection and Pathogenic Process Visualization on Winter Jujubes Using Hyperspectral Imaging System. *Foods*, *12*(3), 435. https://doi.org/10.3390/foods12030435

[10] Khaw, H.Y., Soon, F.C., Chuah, J.H., & Chow, C.O. (2017). Image noise types recognition using convolutional neural network with principal components analysis. *IET Image Processing*, *11*(12), 1238-1245. https://doi.org/10.1049/iet-ipr.2017.0374

[11] Li, J., Rao, X., & Ying, Y. (2012). Development of algorithms for detecting citrus canker based on hyperspectral reflectance imaging. *Journal of the Science of Food and Agriculture*, *92*(1), 125-134. https://doi.org/10.1002/jsfa.4550

[12] Li, Y., Lu, W., Zhao, J., Feng, G., Wei, D., Lu, J., & Lu, Z. (2017). Detection of caloric value of coal using laser-induced breakdown spectroscopy combined with bp neural networks. *Spectroscopy and Spectral Analysis*, *37*(08), 2575-2579. https://doi.org/10.3964/j.issn.1000-0593(2017)08-2575-05

[13] Liu, G., He, J., Wang, S., Luo, Y., Wang, W., Wu, L., & He, X. (2016). Application of near-infrared hyperspectral imaging for detection of external insect infestations on jujube fruit. *International Journal of Food Properties*, *19*(1), 41-52. https://doi.org/10.1080/10942912.2014.923439

[14] Liu, Y., Sun, X., Zhang, H., & Aiguo, O. (2010). Nondestructive measurement of internal quality of Nanfeng mandarin fruit by charge coupled device near infrared spectroscopy. *Computers and Electronics in Agriculture*, *71*, S10-S14. https://doi.org/10.1016/j.compag.2009.09.005

[15] Liu, Z., He, Y., Cen, H., & Lu, R. (2018). Deep feature representation with stacked sparse auto-encoder and convolutional neural network for hyperspectral imaging-based detection of cucumber defects. *Transactions of the ASABE*, *61*(2), 425-436. https://doi.org/10.13031/trans.12214

[16] Ma, W., Zhang, M., Li, Y., Yang, L., Zhu, Z., & Cui, K. (2019). Non-destructive Detection for Fat Content of Walnut Kernels by Near Infrared Spectroscopy. *Transactions of the Chinese Society for Agricultur*al Machinery, 50(3), 374-379. https://doi.org/10.6041/j.issn.1000-1298.2019.S0.057

[17] Osborne, B. G. (2006). Near-infrared spectroscopy in food analysis. Encyclopedia of analytical chemistry: applications, theory and instrumentation. https://doi.org/10.1002/9780470027318.a1018

[18] Pham, Q. T., & Liou, N. S. (2022). The development of on-line surface defect detection system for jujubes based on hyperspectral images. *Computers and Electronics in Agriculture*, *194*, 106743. https://doi.org/10.1016/j.compag.2022.106743

[19] Singh, T., Garg, N. M., & Iyengar, S. R. (2021). Nondestructive identification of barley seeds variety using near-infrared hyperspectral imaging coupled with convolutional neural network. *Journal of Food Process Engineering*, *44*(10), e13821. https://doi.org/10.1111/jfpe.13821

[20] Sun, H., Zhang, S., Liu, J., Chen, C., & Xing, S. (2018). Detection of black rot of fresh jujube fruits using hyperspectral imaging and a convolutional neural network. *Journal of Shanxi Agricultural University*, *38*(11), 15-19. https://doi.org/10.13842/j.cnki.issnl671-8151.201807021

[21] Wang, B., Yang, H., & Li, L. (2023). Discrimination of cerasus humilis fruit maturity based on hyperspectral imaging technology. *INMATEH-Agricultural Engineering*, *70*(2), 107-116. https://doi.org/10.35633/inmateh-70-10

[22] Wang, B., Yang, H., Zhang, S., & Li, L. (2023). Detection of Defective Features in Cerasus Humilis Fruit Based on Hyperspectral Imaging Technology. *Applied Sciences, 13*(5), 3279. https://doi.org/10.3390/app13053279

[23] Wieme, J., Mollazade, K., Malounas, I., Zude-Sasse, M., Zhao, M., Gowen, A., ... & Van Beek, J. (2022). Application of hyperspectral imaging systems and artificial intelligence for quality assessment of fruit, vegetables and mushrooms: A review. *Biosystems Engineerin*g, *222*, 156-176. https://doi.org/10.1016/j.biosystemseng.2022.07.013

[24] Xu, J., Shao, M., Wang, Y., & Han, W. (2020). Recognition of corn leaf spot and rust based on transfer learning with convolutional neural network. *Transactions of the Chinese Society for Agricultural Machinery*, *51*(2), 230-236+253. https://doi.org/10.6041/j.issn.1000-1298.2020.02.025

[25] Xue, Y., Wang, L., Zhang, Y., & Shen, Q. (2020). Defect detection method of apples based on GoogLeNet deep transfer learning. *Transactions of the Chinese Society for Agricultural Machinery*, *51*(7), 30-35. 10.6041/j.issn.1000-1298.2020.07.004

[26] Yan, L., Pang, L., Wang, H., & Xiao, J. (2020). Recognition of different Longjing fresh tea varieties using hyperspectral imaging technology and chemometrics. *Journal of Food Process Engineering*, *43*(4), e13378. https://doi.org/10.1111/jfpe.13378

[27] Ye, S., & Weng, H. (2022). Identification of Grapefruit Black Spot Based on Hyperspectral Imaging using Naïve-Bayes Classifier. Agricultural Mechanization, *Electrification and Automation*, *1*(1), 1-9. https://doi.org/10.23977/hyde.2022.010101

[28] Yu, K., Zhao, Y., Li, X., Shao, Y., Zhu, F., & He, Y. (2014). Identification of crack features in fresh jujube using Vis/NIR hyperspectral imaging combined with image processing. *Computers and Electronics in Agriculture*, *103*, 1-10. https://doi.org/10.1016/j.compag.2014.01.016

[29] Zhang, Y., Wang, W., Zhang, F., Ma, Q., Gao, S., Wang, J., & Liu, Y. (2022). Rapid and non-destructive decay detection of Yali pears using hyperspectral imaging coupled with 2D correlation spectroscopy. *International Journal of Agricultural and Biological Engineering*, *15*(5), 236-244. https://doi.org/10.25165/j.ijabe.20221505.7313

[30] Zhu, S., Zhou, L., Zhang, C., Bao, Y., Wu, B., Chu, H., & Feng, L. (2019). Identification of soybean varieties using hyperspectral imaging coupled with convolutional neural network. *Sensors*, *19*(19), 4065. https://doi.org/10.3390/s19194065

NON-DESTRUCTIVE ESTIMATION OF MATURITY LEVEL OF 'CRYSTAL' GUAVA FRUIT BY MEANS OF FLUORESCENCE SPECTROSCOPY
/
PENDUGAAN TINGKAT KEMATANGAN BUAH JAMBU KRISTAL SECARA NON DESTRUKTIF DENGAN SPEKTROSKOPI FLUORESENSI

Setyo PERTIWI *[1)], Alexander Salvatoris Febrian HUTOMO [2)], Slamet WIDODO [1)]
[1] Department of Mechanical and Biosystem Engineering, Faculty of Agricultural Engineering and Technology, IPB University, Indonesia
[2] Agricultural and Biosystem Engineering Study Program, Faculty of Agricultural Engineering and Technology, IPB University, Indonesia
Tel: +62-251-8623026; E-mail: pertiwi@apps.ipb.ac.id
DOI: https://doi.org/10.35633/inmateh-71-09

Keywords: *Crystal guava, fluorescence, physicochemical properties, maturity level*

ABSTRACT

This research aims to explore the potential use of fluorescence spectroscopy combined with chemometrics for predicting the maturity level of crystal guava fruits non-destructively. The physicochemical properties including total soluble solids (TSS), water content, firmness, and pH were obtained from laboratory tests and used as a reference in developing the predictive model. The fluorescence emission spectra under excitation of 365 nm UV LED were used as predictors. The fluorescence spectra were acquired and recorded using a miniaturized UV-Vis spectrophotometer with an effective 340 – 800 nm range. In total, 240 sets of data from crystal guava fruit samples with varying ages of 90-106 DAA (days after anthesis) were used for calibration and validation. A multivariate analysis using Partial Least Squared Regression (PLSR) was used to develop the predictive models. Several data preprocessing methods were applied to enhance the information contained in the spectral data to find the best predictive model. Analysis results showed that the developed model could accurately predict water content with r_{cal}=0.94; SEC=0.08%, r_{val}=0.84; SEP=0.08%; RPD=2.59, followed by TSS with r_{cal} =0.91; SEC = 0.47%Brix, r_{val} =0.79; SEP=0.48%Brix; RPD=2.13. Although with lower accuracy, it also could predict firmness with r_{cal} =0.86; SEC=0.43 kgf, r_{val} =0.74; SEP=0.43 kgf; RPD=1.82 and pH with r_{cal} =0.81; SEC=0.10, r_{val} =0.79; SEP=0.09; RPD=1.76. The results indicate that fluorescence spectroscopy could be used as an alternative method for non-destructive estimation of physicochemical properties as indicators of the maturity level of crystal guava fruits.

ABSTRAK

Penelitian ini bertujuan untuk mengeksplorasi potensi penggunaan spektroskopi fluoresensi dikombinasikan dengan kemometri untuk memprediksi tingkat kematangan buah jambu kristal secara non-destruktif. Sifat fisikokimia meliputi total padatan terlarut (TPT), kadar air, kekerasan, dan pH diperoleh dari uji laboratorium dan digunakan sebagai acuan dalam pengembangan model prediktif. Spektrum emisi fluoresensi di bawah eksitasi LED UV 365 nm digunakan sebagai prediktor. Spektrum fluoresensi diperoleh dan direkam menggunakan spektrofotometer UV-Vis mini dengan rentang efektif 340 – 800 nm. Total sebanyak 240 set data sampel buah jambu kristal dengan variasi umur 90-106 HSA (hari setelah bunga mekar) digunakan untuk kalibrasi dan validasi. Analisis multivariat menggunakan Partial Least Squared Regression (PLSR) digunakan untuk mengembangkan model prediktif. Beberapa metode pra-pemrosesan data diterapkan untuk menyempurnakan informasi yang terkandung dalam data spektral untuk menemukan model prediksi terbaik. Hasil analisis menunjukkan bahwa model yang dikembangkan mampu memprediksi kadar air secara akurat dengan rcal=0,94; SEC=0,08%, rval=0,84; SEP=0,08%; RPD=2,59, diikuti TPT dengan rcal =0,91; SEC = 0,47%Brix, rval =0,79; SEP=0,48%Brix; RPD=2.13. Meskipun dengan akurasi yang lebih rendah, namun juga dapat memprediksi kekerasan dengan rcal =0,86; SEC=0,43 kgf, rval =0,74; SEP=0,43 kgf; RPD=1,82 dan pH dengan rcal =0,81; SEC=0,10, rval =0,79; SEP=0,09; RPD=1,76. Hasil penelitian menunjukkan bahwa spektroskopi fluoresensi dapat digunakan sebagai metode alternatif untuk estimasi sifat fisikokimia secara non-destruktif sebagai indikator tingkat kematangan buah jambu kristal.

INTRODUCTION

Guava (*Psidium guajava* L.) is well known for its abundant nutritional and functional ingredients, such as various vitamins, minerals, phenolics, and dietary fibers *(Jamieson et al.,2021; Sahu et al., 2020)*. It is also known as a good source of ascorbic acid, and even its ascorbic acid content is almost three times higher than oranges *(Hassimoto et al., 2005; Jawaheer et al., 2003)*.

There are various varieties of guava fruits, and one of them is crystal guava. This variety was first introduced to Indonesia through the Taiwan Technical Mission in Indonesia under the International Cooperation and Development Fund (ICDF) program and recently has been cultivated in many areas in Indonesia, especially in Java and Sumatra Islands. Crystal guava is known for its superior characteristics, making it one of important and desirable fruits. Some of these include fresh sweet fruit flavors, crisp fruit texture, fewer seeds (less than 3 % parts of fruit or even seedless), relatively large size, thick and hard skins which allow them to last longer than other guava varieties, good storage ability, fast growth rate, and high yielding *(Susanto et al., 2019; Herdiat et al., 2019)*.

Crystal guava fruit (*Psidium guajava* L.) is a non-climacteric fruit because it has a stable respiration pattern, or in other words, it cannot ripen after being picked. This condition requires farmers to harvest crystal guava fruit exactly when it is fully ripe so that it is in accordance with consumer desires. Usually, farmers estimate the level of fruit maturity based on their experience, however, they potentially harvest fruits that are not optimally ripe. According to *Patel et al. (2015)*, the time needed for guava fruit from flower anthesis until ready for harvest ranges from 110 to 120 days, depending on the cultivar. A better predictor of maturity level is to perform laboratory tests but it will take time to get the result and make the measurement not real-time. Therefore, a fast and accurate way is needed to estimate the ripeness level of the guava fruit.

A comprehensive review of advances in the non-destructive assessment of fruit ripeness toward defining optimal time of harvest and yield prediction has been undertaken in *Li et al. (2018)*, from which it was learned that a variety of non-destructive techniques have been introduced to estimate the ripeness or maturity including colorimetry, visible imaging, visible and near-infrared (Vis-NIR) spectroscopy, hyperspectral imaging, multispectral imaging, fluorescence imaging, acoustic impulse technique, acoustical vibration technique, Computed Tomography (CT) scan, Magnetic Resonance Imaging (MRI), and the electronic nose technique, but not all of them are applicable for in situ assessment. In a more specific topic, there are various studies on non-destructive methods for estimating the maturity level and/or physicochemical of guava fruits. A machine vision system was introduced to estimate the ripeness level of guava (green, ripe, overripe, and spoiled) *(Kanade and Shaligram, 2015)*. Using color information (RGB, CIE1931 standard-based tristimulus value, chromaticity coordinates, and average) combined with Principal Component Analysis (PCA) and Artificial Neural Network (ANN) the system could classify the ripening stages with 100% accuracy. The thermal imaging method has been used by *Widodo et al. (2021)*. The result indicated that fruit temperature had some correlation with the physical characteristics (firmness) and chemical characteristics (TSS, free acids, sucrose, and starch) of crystal guava fruit. Resonant frequency and elasticity index (EI) to estimate fruit firmness have been reported to be inversely correlated to its maturity *(Mayorga-Martínez et al., 2016)*. Visible/near-infrared (Vis-NIR) spectroscopy was applied to detect the sugar content and hardness of pearl guava *(Hsieh and Lee, 2005)*. Using three different calibration models, the proposed method could estimate the sugar content and hardness with a validation accuracy of 94%. Near-infrared spectroscopy (NIRS) with an effective range of 1000-2500 nm could be used to predict total soluble solids and moisture content with good accuracy, while they were less viable to predict the flesh hardness of the guava fruit *(Ahmad et al., 2018)*. Computer vision combined with Convolutional Neural Networks (CNN) with LeNet architecture was successfully applied to identify the maturity of guava fruit with 100% accuracy *(Sunarya et al., 2019)*.

Another non-destructive method that has also potential to be used for estimating the maturity level and physicochemical properties of guava is fluorescence spectroscopy. Fluorescence is a light emission phenomenon that arises after the absorption of light at a certain wavelength by fluorescence molecules or a substructure known as a fluorophore. Fluorophore absorbs energy in the form of light with a certain wavelength and releases energy in the form of light emission with longer wavelengths *(Lakowicz, 2006)*. As indicated by *Krishnamoorthy (2018)*, the power of fluorescence spectroscopy in comparison to other types of spectroscopies is as follows: (i) high sensitivity and selectivity, in which a single molecule can be tracked from its fluorescence; (ii) high level of environmental sensitivity of a fluorescent molecule used as a probe and (iii) feasibility of monitoring wide timescale (femtoseconds to seconds) of dynamic processes.

UV-induced fluorescence spectroscopy that utilized UV lamps for excitation is one of the most used in various studies. Previous studies had shown that UV light at certain wavelengths could produce fluorescence emissions which contain information about the physicochemical changes of the fruit. *Li et al. (2011)* reported that the excitation of UV light onto navel orange fruit at a wavelength of 365 nm was able to produce emissions identified at wavelengths 385–414 nm. Fluorescence spectroscopy could be developed for non-destructive measurement of the fruit maturity index of satsuma mandarin (*Citrus unshiu* Marc) *(Muharfiza et al., 2017)*.

Other research also reported that excitation at a wavelength of 365 nm resulted in a better fluorescence spectrum in several varieties of citrus in Indonesia *(Siregar et al., 2018)*. A study on the ability to predict fruit maturity of four yellow peach 'August Flame', 'O'Henry', 'Redhaven', and 'September Sun' cultivars using a prototype non-destructive fluorescence spectrometer has been undertaken *(Scalisi et al., 2020)*. Collected spectra were analyzed to predict, among others, flesh firmness (FF) and soluble solids content (SSC). It was found that except for 'September Sun', a good prediction of FF and SSC was observed. Fruit maturity classes were reliably predicted with a high likelihood (F1-score = 0.85) when samples from the four cultivars were pooled together.

Das et al. (2016) utilized the smartphone spectrometer to rapidly evaluate the ripeness of different varieties of apples using chlorophyll (ChlF) emissions when excited using UV light. It was observed that there is a satisfactory correlation between the ripeness that was measured by a penetrometer and by ChlF emission using the proposed device. This study aims to explore the potential use of UV-induced spectroscopy in determining the maturity level of crystal guava fruit. There is no such study reported yet previously.

MATERIALS AND METHODS

Sample material

Sample materials used in this research were crystal guava fruits harvested directly from the farmer at Cidahu, Sukabumi, Indonesia. In order to get a representative variation of the ripening stage, the samples were harvested at four age categories, starting from 90 DAA, 95 DAA, 100 DAA, and 106 DAA. For this purpose, all crystal guava samples were marked using a colored string during anthesis. Guava crystals were collected and labeled with the identity of the sample, then they were transported to the laboratory for measurement on the same day. Prior to in-lab measurement, the crystal guavas were cleaned of impurities using running water and then dried using a cloth. Next, the measurement points for the fluorescence spectrum and destructive test are marked on the crystal guava fruit in three main parts, top, middle, and bottom. In total, 240 samples were collected and then divided into two groups of datasets for calibration and validation during predictive model development.

Fluorescence spectra and physicochemical parameter measurements

Fluorescence spectra were acquired using a simple Do It Yourself (DIY) instrument which is similar to that used by *Das et al. (2016*). A UV LED with an effective wavelength of 365 nm was used for excitation and a UV-Vis mini-spectrometer C1266280MA (Hamamatsu, Japan) was used to capture the emission spectra. For each sample, fruit spectra measurement was done at three different points, and the spectra obtained were the average value of five scans. The process is then followed by destructive measurements including total soluble solids (TSS), firmness, pH, and water content. The measurement of total soluble solids (TSS) was carried out using a digital pocket refractometer (Atago, Japan), firmness level was measured using a rheometer (Sun Rheometer CR 500-DX, USA), pH was measured using a handheld pH meter (Extech, USA) and water content of crystal guava was measured by the oven method following AOAC standard *(AOAC, 2018)*.

Data analysis

A multivariate analysis using Partial Least Squares Regression (PLSR) was selected to develop the predictive model. In many cases, PLSR can provide better prediction results compared to other linear regression approaches such as Multiple Linear Regression (MLR) and Principal Component Regression (PCR). PLSR algorithm considered and modeled both the predictor and response simultaneously to determine the latent variables in the predictor data that will best predict the response *(Kusumiyati et al., 2021)*. From a total of 240 sets of data, it was then divided into two groups, about 2/3 of the data was used for calibration (n=159) and 1/3 for validation (n=81). The obtained raw fluorescence spectrum data as well as the pre-processed data were used in the model development. Data pretreatment was usually needed to reduce or eliminate noise in the fluorescence spectra data and enhance the information in the spectra data. Data pretreatment was carried out by using six methods, namely, Standard Normal Variate (SNV), Multiplicative Scatter Correction (MSC), Smoothing Savitzky-Golay (SSG), baseline correction, normalization, and Detrending (DT). The data analysis was done using Microsoft Excel and The Unscrambler X 10.4 software (CAMO, Norway).

The results of the calibration and validation model of the maturity level of guava crystals were evaluated based on several parameters, namely, *R* (correlation coefficient), SEC (standard error of calibration), SEP (standard error of prediction), RPD (ratio of the standard error of prediction to deviation), and consistency.

A good model should have an *R* value close to 1, SEC and SEP value close to 0. An RPD between 1.5 and 2 means that the model can discriminate low from high values of the response variable; a value between 2 and 2.5 indicates that coarse quantitative predictions are possible, and a value between 2.5 and 3 or above corresponds to good and excellent prediction accuracy, respectively *(Nicolai et al., 2007)*. The consistency value is a ratio or value that shows the closeness between SEC and SEP. This value should be in the range of 80-110% for the model with good predictability to avoid overfitting or underfitting during model development (*Cantor et al., 2011*).

RESULTS AND DISCUSSION

Physicochemical properties of crystal guava samples

The physicochemical properties of crystal guava fruit obtained from destructive measurements showed different TSS, water content, firmness, and pH values at each harvest age (Table 1). The data showed that the TSS values fluctuate at each harvest age. It seems to be uncommon because generally there is a positive linear correlation between TSS and fruit age. The more the fruit was aged, the TSS value would increase. However, Bashir et al. *(2003)* indicated that when the fruit has reached a certain level of maturity, the fruit will experience a decrease in TSS because the carbohydrates and sucrose in the fruit are used as an energy source. The increase in TSS was caused by the degradation of starch into simple sugars while the decrease in TSS was due to the sugar being used as a respiration substrate to produce energy. The growing conditions such as soil, climate, or other factors that were not measured in this research could also influence the TSS. The value of water content did not change significantly but did increase with harvest age. The firmness level of the fruit appeared to decrease with the increasing harvest age. According to Zainal et al. (2012), the softening of the fruit was caused by the breakdown of insoluble protopectin into soluble pectin or starch or by fat hydrolysis. In fruits, there is a cell wall consisting of cellulose, hemicellulose, pectin, and lignin. Fruit softening is caused by the degradation of hemicellulose and protopectin. The pH value obtained showed a change that is not linear with the age of the fruit, although it has an increasing trend. The increase in pH value with age was caused by acid hydrolysis that occurs during the fruit ripening process (*Rachmayati et al., 2017*). The riper the fruit, the pH value will increase because the total sugar in the fruit also increases. During the ripening process, the fruit becomes sweeter after the organic acids are converted into sugar. Acid hydrolyzed into simple sugars causes the H+ ions in the fruit to decrease so that the pH value becomes higher as the fruit ripens. The obtained destructive measurement data was then used as reference data in developing the predictive model.

Table 1

Physicochemical properties of crystal guava with different harvest age

Harvest Age	Number of Samples	TSS (ºBrix)	Water Content (%)	Firmness (kgf)	pH
90	60	5.971 ±0.729	87.78 ± 0.013	3.29± 1.07	3.97± 0.18
95	60	7.022± 1.191	88.53 ± 0.029	3.32± 0.49	3.88± 0.17
100	60	5.725± 0.710	89.56 ± 0.017	2.75± 0.50	3.98± 0.11
106	60	6.143± 0.933	90.10 ± 0.011	2.30± 1.08	4.04± 0.11

Fluorescence Emission Spectra

The fluorescence emission spectrum of all samples under excitation of UV-LED at 365 nm is shown in Figure 1. There were two peaks observed at around 550 nm and 690 nm. Although it was not obvious, a small peak was also observed at the range of 730 nm. The first peak was likely emission from flavonoid substances such as poly-methoxylated flavone (PMF) substances *(Muharfiza, 2017; Siregar, 2018)*. Guava fruit contains high phenolic and flavonoid compounds and hence traditionally is used for curing several diseases *(Gutiérrez, 2018).* This has been confirmed by the study of Sanches et al. (2005) as well as Gull et al. *(2012)* which also stated that the UV (270, 331, 392 nm) spectra data were typical of flavonoids. The second and third peaks were likely emissions from chlorophyll substances (*Muharfiza, 2017; Kusumiyati et al., 2019)*.

Flavonoids are a class of polyphenolic compounds that are widely present in nature and have grown to be an important part of the human diet *(Mutha et al., 2021).*

TSS is the function of several factors of which total sugars and organic acids constitute the major part with minor contributions from other small components (phenolics, amino acids, vitamins, and minerals) (*Bexiga et al., 2017*). TSS also correlates with the pH value because changes in the value of TSS are followed by changes in the amount of sugar and other compounds that will affect the pH value. Therefore, it is hypothesized that the estimation of the parameter value of the maturity level of the guava fruit could be done indirectly by utilizing the spectrum information showing the levels of flavonoids and chlorophyll. The spectrum intensity data of 450-800 nm was chosen to be used to develop the predictive model of physicochemical properties (i.e., TSS, water content, firmness, and pH) as indicators of the maturity level of crystal guava fruits.

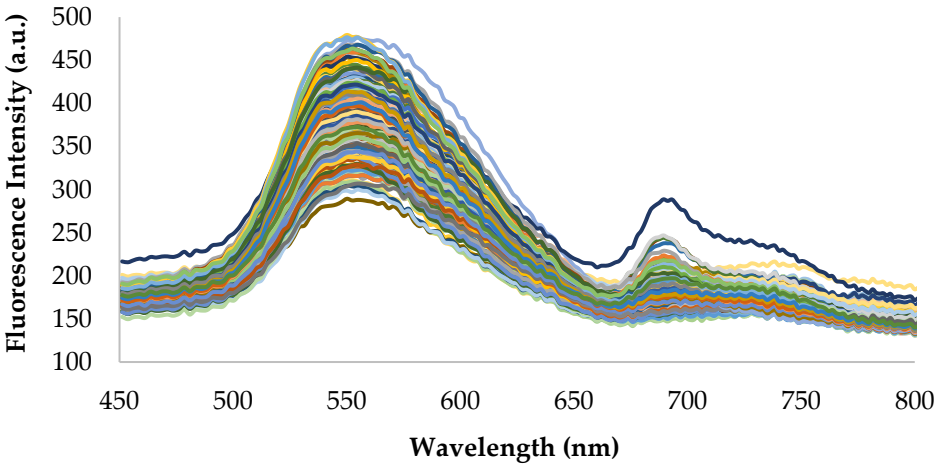


Fig. 1 - The fluorescence emission spectrum of crystal guava

Prediction of physicochemical properties of crystal guava fruits

This study used fluorescence spectroscopy combined with chemometrics to non-destructively predict some of the physicochemical properties as indicators of crystal guava fruit maturity. These physicochemical properties can be used to determine the maturity level of the fruit more accurately as an alternative to conventional methods which are only based on the age or external appearance of the fruit. Table 2 shows the calibration and validation results of crystal guava's physicochemical properties prediction using the PLSR method with original/raw and several pre-processed data.

The results indicate that each parameter requires a different pre-processing method to produce the best model. This study's normalization treatment provides a better prediction for TSS and pH, baseline correction for water content, and MSC for firmness. The best developed model could accurately predict water content with r_{cal}=0.94; SEC=0.08%, r_{val}=0.84; SEP=0.08%; RPD=2.59; consistency=99.05%, followed by TSS with r_{cal}=0.91; SEC = 0.47%Brix, r_{val}=0.79; SEP=0.48%Brix; RPD=2.13; consistency=97.67%. Although with lower accuracy, it also could predict firmness with r_{cal}=0.86; SEC=0.43 kgf, r_{val}=0.74; SEP=0.43 kgf; RPD=1.82; consistency=100.47% and pH with r_{cal}=0.81; SEC=0.10, r_{val}=0.79; SEP=0.09; RPD=1.76; consistency=109.65%.

Based on the RPD value, the pH and firmness parameters were above 1.5, indicating that the estimation model for these parameters was feasible, while the moisture content and TSS parameters were at a value of 2-3 indicating that the prediction model for these parameters was good for rough screening. Furthermore, the consistency value of each parameter was between 80% - 110%, indicating that the model was neither under-fitted nor over-fitted. Scatter plots between reference and predicted values for all parameters are shown in Figure 2. The data distribution for the calibration and validation stages seems acceptable and represents the entire data population.

Figure 3 shows the plot of the regression coefficient of Factor-1 of PLSR for all parameters. From the regression coefficient profile, the variables that contributed most to the predictive model for TSS were similar to firmness, although with the opposite trend. Meanwhile, the variables and trends for water content tend to be similar to pH. In the TSS and firmness estimation, the flavonoid content appears to be more dominant, while for the water content and pH estimation both the flavonoids and chlorophyll have a comparable contribution.

Figure 3 also indicates that in the 500-650 nm range, there is likely more than one fluorescence component, although this needs further investigation.

Table 2

The results of physicochemical prediction of crystal guava fruit using the PLSR

Pre-processing	PLS Factor	Calibration		Validation		RPD	Consistency (%)
		r_{cal}	SEC	r_{val}	SEP		
Total Soluble Solid -TSS (%Brix)							
Original/raw	13	0.90	0.50	0.78	0.51	2.03	98.77
SNV	12	0.90	0.48	0.77	0.50	2.07	97.47
MSC	12	0.90	0.49	0.75	0.52	2.00	94.87
SSG 1	20	0.85	0.59	0.62	0.61	1.69	97.26
SSG 2	20	0.87	0.57	0.70	0.55	1.87	103.39
Baseline	13	0.90	0.48	0.78	0.50	2.08	97.48
Peak Normalize	**13**	**0.91**	**0.47**	**0.79**	**0.48**	**2.13**	**97.67**
Max Normalize	13	0.91	0.48	0.77	0.50	2.07	96.51
DT 1	12	0.90	0.50	0.76	0.51	2.02	98.80
DT 2	12	0.90	0.49	0.75	0.53	1.94	92.14
Firmness (kgf)							
Original/raw	12	0.86	0.43	0.72	0.45	1.74	95.54
SNV	10	0.86	0.43	0.78	0.44	1.79	98.18
MSC	10	0.86	0.43	0.77	0.44	1.77	96.89
SSG 1	20	0.80	0.51	0.67	0.49	1.59	102.67
SSG 2	20	0.83	0.48	0.78	0.46	1.70	103.03
Baseline	**10**	**0.86**	**0.43**	**0.74**	**0.43**	**1.82**	**100.47**
Peak Normalize	10	0.80	0.50	0.66	0.48	1.64	104.87
Max Normalize	11	0.85	0.45	0.72	0.44	1.76	100.71
DT 1	4	0.85	0.45	0.70	0.45	1.74	98.51
DT 2	10	0.86	0.43	0.74	0.43	1.82	100.47
Water Content (%)							
Original/raw	17	0.93	0.08	0.84	0.08	2.61	103.85
SNV	16	0.93	0.08	0.84	0.08	2.56	102.07
MSC	**16**	**0.94**	**0.08**	**0.84**	**0.08**	**2.59**	**99.05**
SSG 1	20	0.79	0.15	0.62	0.12	1.82	125.33
SSG 2	20	0.81	0.14	0.62	0.12	1.81	117.80
Baseline	16	0.93	0.09	0.82	0.09	2.48	103.20
Peak Normalize	16	0.93	0.09	0.82	0.09	2.47	102.31
Max Normalize	16	0.93	0.09	0.81	0.09	2.39	98.80
DT 1	15	0.93	0.09	0.82	0.09	2.41	98.14
DT 2	14	0.92	0.09	0.82	0.09	2.41	102.71
pH							
Original/raw	13	0.79	0.10	0.80	0.09	1.78	98.77
SNV	11	0.79	0.10	0.75	0.10	1.63	105.19
MSC	11	0.78	0.10	0.79	0.09	1.73	117.59
SSG 1	20	0.67	0.12	0.67	0.10	1.44	116.39
SSG 2	20	0.72	0.11	0.74	0.10	1.53	117.30
Baseline	12	0.77	0.11	0.78	0.09	1.72	118.77
Peak Normalize	12	0.79	0.10	0.74	0.10	1.56	104.11
Max Normalize	**13**	**0.81**	**0.10**	**0.79**	**0.09**	**1.76**	**109.65**
DT 1	11	0.78	0.10	0.78	0.09	1.69	113.44
DT 2	11	0.78	0.10	0.81	0.10	1.59	104.26

In general, it was found from this study that flavonoid and chlorophyll fluorescence were strongly correlated and could be used to indirectly estimate some physicochemical properties of crystal guava. Furthermore, those physicochemical properties could be used to calculate the maturity index of crystal guava. Such an approach has been applied by *Khumaidi et al. (2022)* to determine the maturity index of intake mango. This method is also considered to be more objective, standardized, and free from bias that may arise due to subjectivity. Overall, based on the performance evaluation of the developed predictive model, the results of this study suggested that fluorescence spectroscopy combined with chemo-metrics could be used as an alternative method for non-destructive estimation of physicochemical properties of crystal guava fruits as indicators of the maturity level of crystal guava fruits.

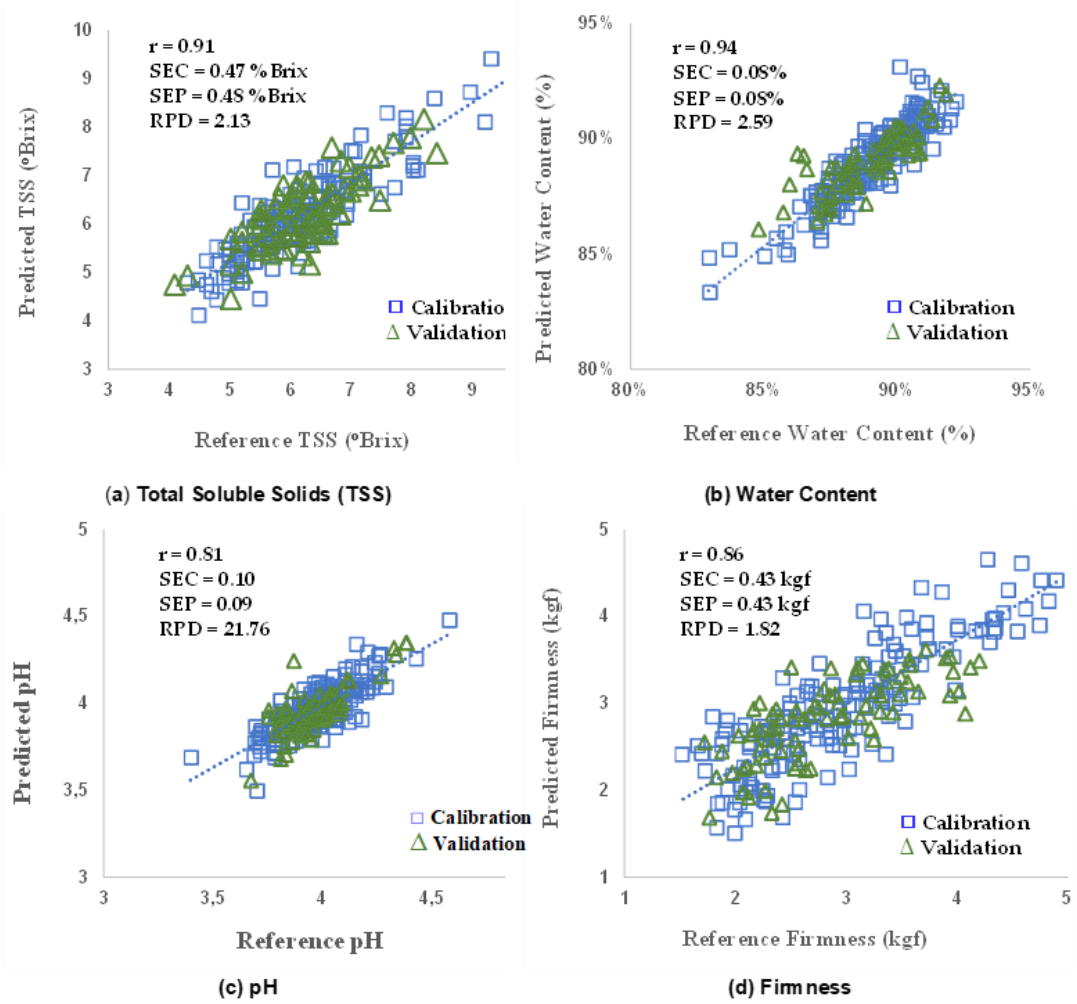


Fig. 2 - Prediction and reference value of each maturity parameter

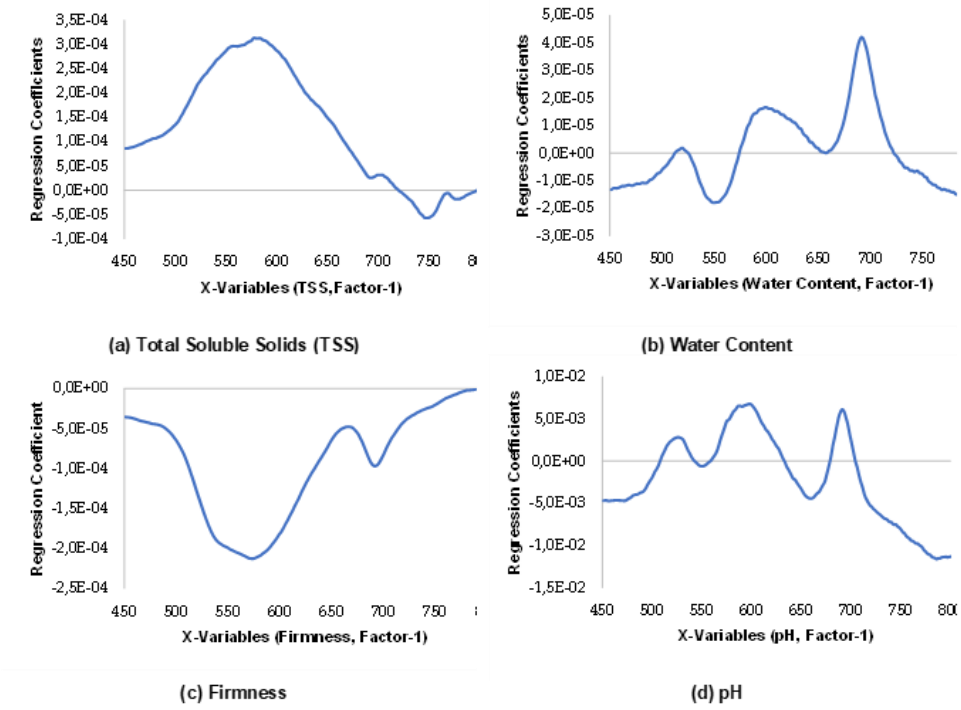


Fig. 3 - The regression coefficient of Factor-1 PLSR

CONCLUSIONS

This study explored an alternative method for non-destructive estimation of the physicochemical properties of crystal guava fruit using fluorescence spectroscopy combined with chemometrics. Using fluorescence emission spectra at 450-800 nm under excitation of a 365 nm UV LED combined with PLSR, the developed models were able to accurately predict water content (r=0.94; SEP=0.08%; RPD=2.59; consistency=99.05%) and TSS (r=0.91; SEP=0.48; RPD=2.13; consistency=97.67%). Although with lower accuracy, it also could predict firmness (r=0.86; SEP=0.43; RPD=1.82; consistency=100.47%) and pH (r=0.81; SEP=0.09; RPD=1.76; consistency=109.65%). The results indicate that fluorescence spectroscopy could be used as an alternative method for non-destructive estimation of physicochemical properties as indicators of the maturity level of crystal guava fruits.

REFERENCES

[1] *** AOAC, (2005), *Official Methods of Analysis 18th edition,* Association of Official Analytical Chemists, Arlington, VA, USA. 2005.

[2] Ahmad, U., Purwanto, Y.A., Cahyo, L.D., (2018), Study on measuring the ripeness level of the 'Crystal' guava fruit using NIR (near infrared) spectroscopy. *Proceeding of IV Asia Symposium on Quality Management in Postharvest System, Acta Horticultura,* 1210, ISHS. https://doi.org/10.17660/ActaHortic.2018.1210.6

[3] Bashir, H.A. and Abu-Goukh, A.B.A., (2003), Compositional changes during guava fruit ripening, *Food Chemistry*, *80*(4), 557-563.

[4] Bexiga, F., Rodrigues, D., Guerra, R., Brazio, A., Balegas, T., Cavaco, A. M., Antunes, M. D., Oliveira, J. V., (2017), A TSS classification study of 'Rocha'pear (Pyrus communis L.) based on non-invasive visible/near infra-red reflectance spectra, *Postharvest Biology and Technology*, 132, 23-30.

[5] Cantor, S.L., Hoag, S.W., Ellison, C.D., Khan, M.A., Lyon, R.C., (2011), NIR Spectroscopy Applications in the Development of a Compacted Multiparticulate System for Modified Release, AAPS PharmSciTech, vol. 12, 262-278. https://doi.org/10.1208/s12249-010-9580-z

[6] Das, A.J., Wahi, A., Kothari, I., Raskar, R., (2016), Ultra-portable, wireless smartphone spectrometer for rapid, non-destructive testing of fruit ripeness, *Scientific Report,* vol. 6, Article ID 32504. https://doi.org/10.1038/srep32504

[7] Gull, J., Sultana, B., Anwar, F., Naseer, R., Ashraf, M., Ashrafuzzaman, M., (2012), Variation in Antioxidant Attributes at Three Ripening Stages of Guava (*Psidium guajava* L.) Fruit from Different Geographical Regions of Pakistan, *Molecules,* no 17, Article ID 7033165, 3165-3180. https://doi.org/10.3390/molecules17033165

[8] Gutiérrez, R.M.P., Mitchell, S., Solis, R.V., (2018), Psidium guajava: A review of its traditional uses, phytochemistry and pharmacology, *Journal of Ethnopharmacology,* vol. 117, no. 1, 1-27. https://doi.org/10.1016/j.jep.2008.01.025

[9] Hassimotto, N.M.A., Genovese, M.I., Lajolo, F.M., (2005), Antioxidant activity of dietary fruits, vegetables, and commercial frozen fruit pulps, *Journal of Agricultural and Food Chemistry,* vol. 53, no. 8, 2928–2935.

[10] Herdiat, I., Dwiratna, S.N.P., Kendarto, D.R., (2019), Conformity Evaluation of Crystal Guava Plant Land as an Expansion Effort for Land in Sumedang Regency (Evaluasi Kesesuaian Lahan Tanaman Jambu Kristal Sebagai Upaya Perluasan Lahan di Kabupaten Sumedang), *Jurnal Keteknikan Pertanian Tropis dan Biosistem,* vol. 7, no. 1, 43-54.

[11] Hsieh, C. and Lee, Y., (2005), Applied Visible/Near-Infrared Spectroscopy on Detecting the Sugar Content and Hardness of Pearl Guava, *Applied Engineering in Agriculture,* vol. 21, no. 6, 1039–1046. https://doi.org/10.13031/2013.20020

[12] Lakowicz J.R. (Ed.), (2006), *Principles of Fluorescence Spectroscopy,* Boston, MA: Springer US.

[13] Jamieson, S., Wallace, C. E., Das, N., Bhattacharyya, P., Bishayee, A. (2021), Guava (*Psidium guajava* L.): A glorious plant with cancer-preventive and therapeutic potential, *Critical Reviews in Food Science and Nutrition,* vol. 63, no. 2, 192-223. https://doi.org/10.1080/10408398.2021.1945531

[14] Jawaheer, B., Goburdhun, D., Ruggoo, A., (2003), Effect of processing and storage of guava into jam and juice on the ascorbic acid content, *Plant Foods for Human Nutrition,* no. 58, 1–12.

[15] Kanade, A. and Shaligram, A., (2015), Development of machine vision-based system for classification of Guava fruits on the basis of CIE1931 chromaticity coordinates, *2nd International Symposium on Physics and Technology of Sensors (ISPTS).* https://doi.org/10.1109/ispts.2015.7220107

[16] Khumaidi, A., Purwanto, Y. A., Sukoco, H., Wijaya, S. H., (2022), Using Fuzzy Logic to Increase Accuracy in Mango Maturity Index Classification: Approach for Developing a Portable Near-Infrared Spectroscopy Device, *Sensors,* vol. 22, Article ID 9704. https://doi.org/10.3390/s22249704

[17] Krishnamoorthy, G., (2018), Fluorescence spectroscopy for revealing mechanisms in biology: Strengths and pitfalls, *Journal of Biosciences,* vol. 43, 555–567. https://doi.org/10.1007/s12038-018-9763-4

[18] Kusumiyati, Munawar, A.A., Suhandy, D., (2021), Fast, simultaneous and contactless assessment of intact mango fruit by means of near infrared spectroscopy, *AIMS Agriculture and Food,* vol. 6 no. 1, 172-184. https://doi.org/10.3934/ agrfood.2021011

[19] Kusumiyati, Sutari, W., Farida, Mubarok, S., Hamdani, J. S., (2019), Prediction of surface color of 'crystal' guava using UV-Vis-NIR spectroscopy and multivariate analysis, *IOP Conference Series: Earth and Environmental Science* 365, Article ID 012026.

[20] Li, B., Lecourt, J., Bishop, G., (2018), Advances in Non-Destructive Early Assessment of Fruit Ripeness towards Defining Optimal Time of Harvest and Yield Prediction—A Review, *Plants,* vol. 7, no. 1, 3.

[21] Li, J., Xue, L., Liu, M. H., Wang, X., Luo, C. S., (2011), Study of fluorescence spectrum for measurement of soluble solids content in navel orange, Advanced Materials Research, vol. 186, 126-130.

[22] Mayorga-Martínez, A. A., Olvera-Trejo, D., Elías-Zúñiga, A., (2016), Non-destructive Assessment of Guava (*Psidium guajava* L.) Maturity and Firmness Based on Mechanical Vibration Response. *Food and Bioprocess Technology,* no. 9, 1471–1480. https://doi.org/10.1007/s11947-016-1736-8

[23] Muharfiza, Riza, D. F. A., Saito, Y., Itakura, K., Kohno, Y., Suzuki T., Kuramoto, M., Kondo, N., (2017), Monitoring of fluorescence characteristics of satsuma mandarin (*Citrus unshiu* Marc.) during the maturation period, *Horticulturae,* vol. 3, no. 4, 51.

[24] Mutha, R. E., Tatiya, A. U., and Surana, S. J., (2021), Flavonoids as natural phenolic compounds and their role in therapeutics: An overview, *Future Journal of Pharmaceutical Sciences*, *7*, 1-13.

[25] Nicolai, B. M., Beullens, K., Bobelyn, E., Peirs, A., Saeys, W., Theron, K. I., Lammertyna, J., (2007), Nondestructive measurement of fruit and vegetable quality by means of NIR spectroscopy: A review, *Postharvest Biology and Technology*, no 46, 99–118.

[26] Patel, R. K., Maiti, C. S., Deka, B. C., Deshmukh, N. A., Verma, V. K., Nath, A., (2015), Physical and biochemical changes in guava (*Psidium guajava* L.) during various stages of fruit growth and development, *International Journal of Agriculture, Environment and Biotechnology*, vol. 8, no. 1, 75-82.

[27] Rachmayati, H., Susanto, W. H., Jaya, M. M., (2017), The Influence of Ripeness Level of Starfruit *(Averrhoa carambola L.)* and Addition of Sugar Proportion on Physical, Chemical and Organoleptic Properties of Starfruit Jelly Drink Containing Carrageenan (Pengaruh Tingkat Kematangan Buah Belimbing *(Averrhoa carambola L.)* dan Proporsi Penambahan Gula Terhadap Karakteristik Fisik, Kimia dan Organoleptik Jelly Drink Menggunakan Karaginan), *Jurnal Pangan dan Agroindustri,* vol. 5, no.1, 49-60.

[28] Sahu, S. K., Barman, K., Singh, A. K., (2020), Nitric oxide application for postharvest quality retention of guava fruits, *Acta Physiologiae Plantarum,* no. 42, 1-11.

[29] Sanches, N. R., Cortez, D. A. G., Schiavini, M. S., Nakamura, C. V., Filho, B.P.D., (2005), An Evaluation of Antibacterial Activities of *Psidium guajava (L.)*, *Brazilian Archive of Biology and Technology,* vol. 48, no. 3, 429-436.

[30] Scalisi, A., Pelliccia, D., O'Connell, M. G., (2020), Maturity Prediction in Yellow Peach (*Prunus persica* L.) Cultivars Using a Fluorescence Spectrometer, *Sensors*, vol. 20, Article ID 6555.

[31] Siregar, T. H., Ahmad, U., Sutrisno, Maddu, A., (2018), Fluorescence spectroscopy characteristics of Indonesian citrus, *Journal of Physics: Conference Series*, no. 1057, Article ID 012011.

[32] Sunarya, P. A., Mutiara, A. B., Refianti, R., Huda, M., (2019), Identification of Guava Fruit Maturity using Deep Learning with Convolutional Neural Network Method, *Journal of Theoretical and Applied Information Technology,* vol. 97, no. 19, 5126-5137.

[33] Susanto, S., Melati, M., Aziz, S. A., (2019), Pruning to Improve Flowering and Fruiting of 'Crystal' Guava, *AGRIVITA Journal of Agricultural Science,* vol. 41, no. 1, 48–54.

[34] Widodo, S. E., Putri, R. A., Waluyo, S., Zulferiyenni, (2021), Detection of the Maturity Level of Guava (*Psidium Guajava* L.) Kristal Non-Destructively Using Thermal Image Method (Deteksi Tingkat Kematangan Buah Jambu Biji (Psidium Guajava L.) Kristal Secara Tak Merusak Dengan Metode Thermal Image), *Proceedings of National Seminar of PERHORTI*.

[35] Zainal, P. W., Ahmad, U., Purwanto, Y. A., (2012), Detection of chilling injury on gedong gincu using near infrared spectroscopy (Deteksi Chilling Injury pada Buah Mangga Gedong Gincu dengan Menggunakan Near Infrared Spectroscopy), *Jurnal Keteknikan Pertanian,* vol. 26, no. 1, 61-68.

STUDY ON ARTIFICAL INTELLIGENCE RECOGNITION METHODS FOR MAIZE LEAF LESION IMAGE
/
针对玉米叶片病斑图像的人工智能识别方法研究

Linwei LI[1)], Yanbo SONG[2)], Jie SUN[1)], Yuanyuan LU[2)], Lili NIE[1)], Fumin MA[3)], Xinyu HOU[4)], Juxia LI[1)], Yanwen LI[1)], Zhenyu LIU[5,6 *)]

[1)] College of Information Science and Engineering, Shanxi Agricultural University, Taigu 030801, China;
[2)] College of Life Sciences, Shanxi Agricultural University, Shanxi Agricultural University, Taigu 030801, China;
[3)] College of Energy and Power Engineering, Lanzhou University of Technology, Lanzhou 730050, China;
[4)] School of Information and Communication Engineering, Hainan University, Meilan 570228, China;
[5)] College of Agricultural Engineering, Shanxi Agricultural University, Taigu 030801, China;
[6)] Dryland Farm Machinery Key Technology and Equipment Key Laboratory of Shanxi Province, Taigu 030801, China;
Tel: 0354-6285940; E-mail: lzysyb@126.com. Corresponding author: Liu Zhenyu
DOI: https://doi.org/10.35633/inmateh-71-10

Keywords: *Maize lesion leaf spot, maize eyespot, image classification, neural network, AlexNet architecture*

ABSTRACT
Maize eyespot and maize curvularia leaf spot *are two diseases that often occur on maize leaves. Because of the similarity of the shape and structure, it is difficult to identify the two diseases just relying on the observation of the growers. For the harmfulness and prevention methods are different, it would cause great loss if the disease can't be identified accurately. To address this issue, this paper first employs a connected region feature recognition method to design an automated lesion cropping process after acquiring leaf images with several lesions. Subsequently, a lesion recognition model based on the AlexNet architecture is built and subjected to five-fold cross-validation experiments. The results indicate that the model achieves a comprehensive recognition accuracy exceeding 99%. To further comprehend model characteristics, an analysis of the recognition accuracy and its fluctuations is conducted, revealing that the fractal growth and biological characteristics of the lesions may influence the recognition results. Moreover, the distribution of model parameters could be a potential reason for fluctuations in recognition accuracy rates with increasing number of iterations. This paper could offer valuable reference and support for the intelligent identification and diagnosis of maize and other plant diseases.*

摘要
玉米北方炭疽病和玉米弯孢菌叶斑病是常见于玉米叶片的两种疾病，由于病斑外形结构和形状特征相似，传统的神经网络和图像识别方法较难识别两者，而两者危害程度和防治方法不同，因此误识别会造成较大损失。为此，本文首先基于连通域特征识别实现了对带病叶片图像中病斑的自动裁切。之后，基于 AlexNet 架构构建了病斑识别模型，并采用五折交叉验证法进行试验。试验结果显示，模型的综合识别准确率超过了 99%。为了进一步理解模型特性，本文还对模型的识别准确率及其波动性进行分析，分析结果显示，病斑的分形生长和生物学特性会影响识别结果，模型参数的分布可能是导致识别率随迭代次数增加而波动的潜在原因。本文研究可为玉米及其他植物病害的智能化识别诊断提供有效参考和支持。

INTRODUCTION
Maize eyespot and maize curvularia leaf spot are serious leaf diseases that pose significant threat to maize industry *(Dai et al., 1998; Fu et al., 2016)*. Both the two disease lesions can cover the whole plant leaves, which could lead to the photosynthesis loss of leaves and even cause withering of the plant. Though both the two diseases have different causes and hazards, and maize curvularia leaf spot does not infect the midrib and lacks gray or black mould layer on the surface of the lesion in the later stage in humid environment *(Xu et al., 2000)*, hardness still exists in identifying the two diseases based on intuitive phenotypic observation of lesions of various development stages *(Zhang, 2014)*.

First author. Mail address: sxrllw@126.com. Mailing address: No.1, Mingxian South Road, Taigu District, Jinzhong City, Shanxi Province, China. Tel:0354-6288587.
** Corresponding author. Mail address: lzysyb@126.com. Mailing address: No.1, Mingxian South Road, Taigu District, Jinzhong City, Shanxi Province, China. Tel:0354-6285940*

The lesions of the two diseases are initially small and always would gradually expand into a circular, oval or oblong spot in the late stage. At that time, mature curvularia leaf spot would have the size of (0.5 – 2.0) mm × (0.5 – 1.5) mm, the phenotype would be milky white core surrounded by a brown ring *(Wang et al., 2006; Zhang et al., 2010),* and there would be a translucent light yellow ring with intermittent pattern surrounding the edge of the brown ring *(Shi et al., 2000; Zhang et al., 2017).* As for the leaf spot of maize eyespot in the late stage, the size would be (2.0 – 5.0) mm × (1.0 – 2.0) mm, the core would also be milky white as well as the edge would be a brown ring, and there would be narrow ring or halo with the colour of green surrounding the brown ring's periphery *(Sun et al., 2016; Wang et al., 2010; Chen et al., 2015).* The two kinds of lesions share many similar phenotype *(Sun et al., 2015)*, so using traditional observations to distinguish the two types of lesions always results in misclassification. For the disposition schemes of maize eyespot and maize curvularia leaf spot are different, the misjudgement would lead to improper treatment, which may result in large reduction in maize production and even affect farming in the next years.

Recent advances in computer vision and image processing have provided great opportunities for intelligent identification and assessment of plant diseases *(Shi et al., 2023; Weng et al., 2019; Joseph et al., 2023; Meng et al., 2017; Toda & Okura, 2019). Ahila Priyadharshini et al (2019*) propose a maize leaf disease classification model based on CNN architecture. The architecture is trained to identify four different classes with an average accuracy of 97.89%. *Nagaraju and Chawla (2023)* propose a model named NPNet-19 based on CNN architecture to determine maize crop infections. The model's accuracy and robustness are tested by using a dataset of 15,960 images on six disease classes and one healthy class. Moreover, current researches also attempt to generate unified multi-crop-diseases models to tackle complex tasks. *Picon et al (2019)* introduce a challenging dataset containing almost equally distributed disease stages of seventeen diseases and five crops. This paper proposes three different CNN architectures with contextual non-image meta-data (such as crop information) incorporated onto the image. In addition, to increase the recognizable types of lesions and the accuracy in natural scenes with complex background noise, attention mechanisms which might add model parameters have been proven to be an essential technique *(Guo et al.,2022; Niu et al., 2021)*. *Fang et al (2022)* propose a network model named HCA-MFFNet for maize leaf disease recognition in a complex background. To reduce the influence of complex backgrounds, hard coordinated attention (HCA) in HCA-MFFNet is employed at different spatial scales to extract features from maize leaf disease images. The average recognition accuracy of the model is 97.75%. To reduce the impact of optical noise and background interference, *Li et al (2022)* propose a maize disease identification model based on wavelet threshold-guided bilateral filtering, multi-channel ResNet and attenuation factor. *Albahli et al (2022)* introduce a spatial-channel attention mechanism to focus on infected locations of maize leaf datasets which are taken under diverse and challenging environmental conditions. The approach recognizes multiple maize leaf diseases with an accuracy of 99.89%. *Li et al (2023)* propose an effective data augmentation method of auxiliary classifier GAN (ACGAN) to solve the problem of insufficient data volume. Then to extract multi-scale information on the images of infected maize leaves that are collected from the field of complex background, the DenseNet-based CNN model is developed by integrating multiple expansion modules and Convolutional Block Attention Module (CBAM). Furthermore, small and irregular lesions characterize maize leaf disease in natural scene, which increases identification difficulties of identification models *(Liu & Wang, 2021)*. *Zeng et al (2022)* enhance the model's ability to extract features from leaves with small and irregularly shaped points by replacing the convolutional kernels and activation functions. *Chen et al (2022)* propose a convolutional ensemble network to improve the capability of the model for identifying minute plant lesion features. The method attains an average accuracy of 99.37% on the local dataset and an average accuracy of 99.61% on the open-source PlantVillage dataset.

Although the models mentioned previously have achieved significant results in the identification of maize diseases, their designs focus on recognition challenges in intricate scenarios by studying comprehensive network, which consequently results in higher model complexity and parameter volume. Heavyweight networks need higher performance for equipment, while farmers always prefer to use terminal equipment to take photographs directly of diseased leaves, and human-controlled photographs do not always have too much disturbing factors such as complex lighting, so on the basis of ensuring accuracy, this paper concentrates on the model design of lightweight for image identification of common maize lesions with significant self-similarity. Firstly, automatic cropping process is investigated for lesion images to minimize the impact of subsequent recognition; then recognition model based on the AlexNet architecture is designed and the accuracy is compared to the model based on the architecture of CNN; finally, accuracy and volatility of the model as well as their possible formation mechanisms are analysed for better understanding of the recognition model.

MATERIALS AND METHODS

Image acquisition and processing

Image source

In this paper, the maize variety of Shen 135 is used as an identification host. Then *Kabatiella zeae* which causes maize eyespot and *Curvularia lunata* that causes maize curvularia leaf spot are inoculated onto the leaves of different maize plants separately. The infected maize plants are then placed in an incubator at the temperature 25 °C and the humidity of 75%. After five days of cultivation, images of the infected leaves are captured by the camera of Canon EOS2000D.

Automatic cropping of source images

During the process of image collection, grayscale and median filtering are performed to decrease the possible impact from external optical noise. In addition, the entire diseased leaf is collected by the camera, which would take too much time and manpower to crop the lesions manually. Therefore, this paper automatically cuts the lesions individually by means of the connected domain feature extraction. The automatic cropping process of lesion images is shown in Fig.1.

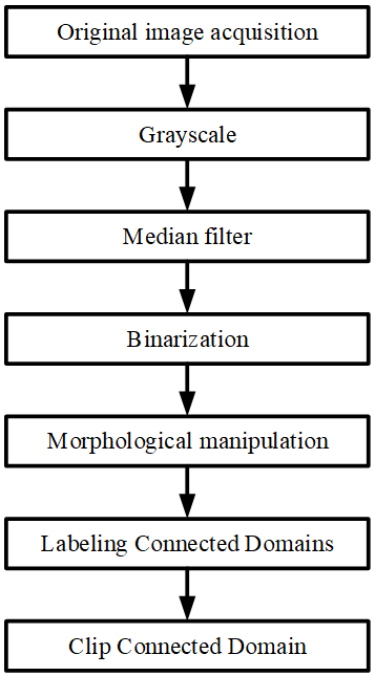


Fig. 1 – Automatic cropping process for lesion images

(1) Pre-processing before cropping

1) Grayscale conversion. Grayscale conversion can eliminate redundant information in the original colour image and simplify the image matrix. In this paper, the average of the R, G, and B parameters in the input image is utilized to determine the output image's grayscale value 'Gray':

$$\text{Gray} = (\text{R} + \text{G} + \text{B})/3 \quad (1)$$

2) Optical noise reduction. The image captured by the camera is susceptible to noise interference. Therefore, Gaussian noise in small pixel area could be eliminated by employing median filtering and the noise in larger pixel area could be reduced by applying dilation-erosion algorithm.

① Median filtering. Median filtering that can suppress noise effectively is a nonlinear signal processing technique based on ranking statistics theory. The basic principle is to replace the disturbed pixel value with the median value which is closer to the real value. The median value is chosen from the neighbourhood of the disturbed point. In this way, the isolated noise point could be eliminated. In this paper, the median filter of 3×3 window is selected for smoothing, which is:

$$f(x,y) = media_{(s,t\in S_{xy})} g\{s,t\} \quad (2)$$

where:

$f(x,y)$ - the image processed by median filtering;

S_{xy} - point (x,y) as the centre of the square field;

$g\{s,t\}$ - Input image.

② Dilation-erosion treatment. The median filtering algorithm has no obvious effect on optical noise in a large area. The erosion algorithm utilizes a specific structuring element to identify the fitted regions. Dilation algorithm serves as the dual operation of erosion to conduct the complement operation of the image.

Image erosion is denoted as $g\{s,t\} \ominus B$, which is defined as:

$$g\{s,t\} \ominus B = \{x: B + x \subset g\{s,t\}\} \quad (3)$$

where:

$g\{s,t\}$ - Input image;

B - structural elements;

$g\{s,t\} \ominus B$ - Consists of translating *B* by x but still including all points x within *g*{s,t}.

Image dilation is expressed as $g\{s,t\} \oplus B$, which is defined as:

$$g\{s,t\} \oplus B = [g\{s,t\}^c \ominus (-B)]^c \quad (4)$$

$g\{s,t\}^c$ - The complement of $g\{s,t\}$.

(2) Lesion identification

1) Recognizing connected domains. The collection of several pixels which conform to the characteristics of the lesions should obey the rules, including: ① All gray values of the pixels are less than or equal to the threshold of the connected domain. ② Pixels within the same connected domain exists in pairs, which means that there exists a path between any two of the pixels.

2) Marking the image. This paper uses pipelined fast labelling method for connected domains based on zigzag and pixel-by-pixel scanning. The determining basis for the start and end in the line run is: when the value of the target pixel and the previous pixel constitutes "01", it means that the start of the run is found; when the value of the target pixel and the previous pixel constitutes "10", it means that the end of the run is determined. For 8-neighborhood connected situation, the relational expression for judging whether the run length of the current row and the run length of the previous row are connected is as follows:

$$Y_0 \leq y_1 + 1 \text{ or } Y_1 \leq y_0 - 1 \quad (5)$$

where:

Y_0, Y_1——The column coordinates of the start and end in the current line run;

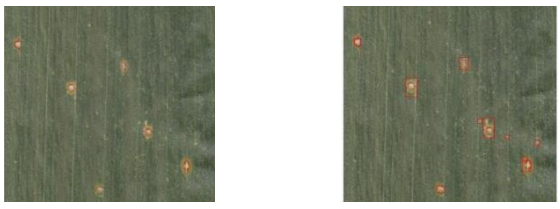
y_0, y_1——The column coordinates of the start and end in the previous line run.

When the two runs are determined as connected, the algorithm usually marks the two runs as equivalent pairs and stores the equivalence relationship in the temporary mark table. Unification of the equivalent pairs will be marked by traversing the temporary mark table. This paper uses the 8-neighborhood connectivity rule to count the pixels which meet the lesions conditions. In the pixel matrix of 3×3, compared with the 4 points of the upper, lower, left and right of the 4-neighborhood, the 8-neighborhood includes 4 extra points of the upper-left, upper-right, lower-left and lower-right. The connectivity is more comprehensive and the versatility is better. The pixels of the multiple lesions connected domains can be grouped together by using the 8-domain connectivity rule.

In this paper, the area containing lesions is extracted as a candidate, and then the grayscale image of the candidate area is gradually removed by changing the threshold value. According to a certain evaluation standard, it would be judged whether the result of each treatment is acceptable. The pixels in the image that conform to a certain connectivity rule (8-neighborhood connectivity) are marked with the same label, and only the binary image that is marked accurately can be used for quantitative extraction of the lesions.

(3) Automatic cropping of lesions

This paper adds external connected rectangle to lesion domains. The comparison between the original identification image and marked image is shown in Fig.2.



a) Before marking *b) After marking*

Fig. 2 – Comparison of the original image and the marked image

One lesion image on maize leaves would be generated by cropping directly through the size of all external connected rectangles. Cycle the operation of the cropping following the labelled numbers and writing them to specific folder will automate the creation of the database, which could replace manpower for faster extraction. Parts of the cropping image in connected domain are shown in Fig.3. In this paper, 24 leaves with lesions are collected, and 23 of the leaves are found to have diseased lesions and the lesions are extracted to form the database.

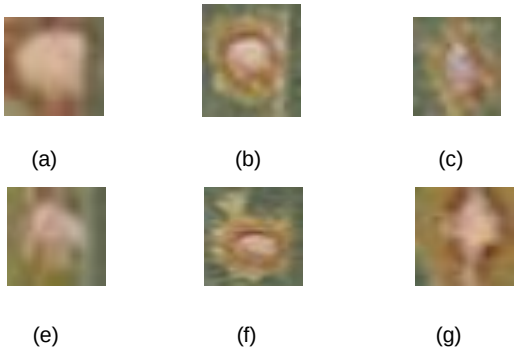
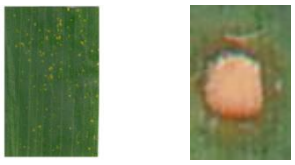


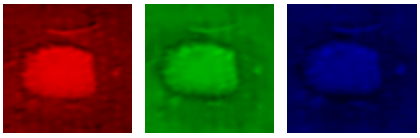
Fig. 3 – Parts of cropping image of selected region in connected domain

Data Preprocessing

After the automatic cropping process, 700 images of the lesions are obtained. Further processing is performed on these 700 images with the following specific steps: (1) All of images are reconstructed into a size of 64 × 64 × 3 (64 pixels in length, 64 pixels in width, 3 channels). Images before and after the treatment are shown in Fig.4 and Fig.5. (2) To reduce the required calculation amount and reduce overflow value which prevents the training or calculation, each pixel value that corresponds to each channel of the image is normalized. (3) In order to eliminate the potential impact of their sequence information on image recognition, the images are shuffled randomly.

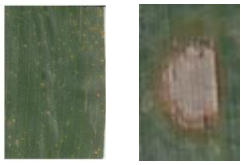


(a)Image of infected leaves (b) The captured lesion image

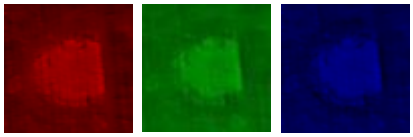


(c)The captured lesion image is reconstructed to 64 × 64 × 3

Fig. 4 – Contrast before and after preprocessing of maize eyespot



(a) Image of infected leaves (b) The captured lesion image



(c) The captured lesion image is reconstructed to 64 × 64 × 3

Fig. 5 – Contrast before and after preprocessing of maize curvularia leaf spot

Model structure

The images in the local dataset are all adjusted to a standard size of 64 × 64 × 3 and all pixel values are normalized to floating-point numbers between 0 and 1. The resized and normalized data tensors are used as the input of the neural network. The data stream passes through 3 convolutional layers and a fully connected layer, and is finally expelled by an output layer containing two neurons. The model structure is shown in Fig.6.

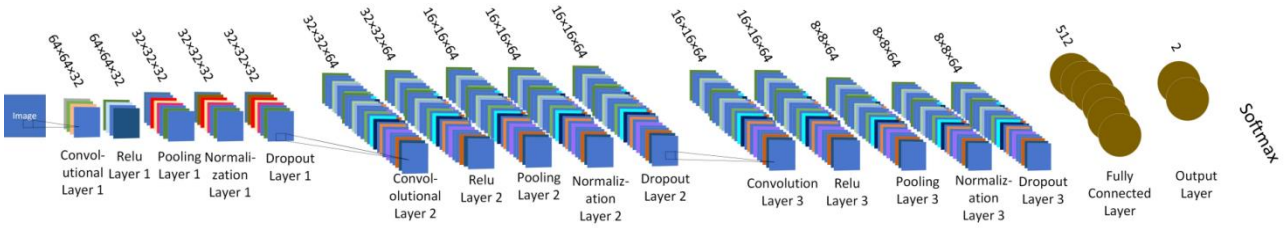


Fig. 6 – Model structure

(1) The first convolutional layer uses 32 convolution kernels of size 3 × 3 × 32 and convolution stride of 1 to perform convolution on each input image, which would extract its local texture and colour features as well as derive a tensor of 32-channel. During the convolution, the edge information of the input tensor is retained by filling in zero.

(2) By applying non-linear correction unit (ReLU) as activation function, the output of the previous convolution layer is used as an input and is mapped into the next max-pooling layer. The filter size of the pooling layer and the step size are set to 2 × 2 and 2, respectively. As a result, the magnitudes of the first and second dimensions (length and width) of the output tensor in the previous layer are reduced by half, which compresses the size of the data stream. The number of parameters required in the subsequent convolution layer and the risk of over fitting will also be reduced. The pooling layer will export an output three-dimensional tensor of size 32 × 32 × 32.

(3) The pooling layer is followed by a local response normalization layer (LRN), through which a competitive mechanism is created based on Eq. 1 *(Krizhevsky et al., 2017)*. Competitive mechanism is used for the activity of local neurons.

After processed by Eq. 1, values with larger feedback can be relatively consumed, while neurons with smaller feedback can be inhibited.

$$b^{i}_{x,\,y} = \frac{a^{i}_{x,\,y}}{\left(k + \alpha \sum_{j=\max(0,\, i-\frac{n}{2})}^{\min(N-1,\, i+\frac{n}{2})} (a^{j}_{x,\,y})^{2}\right)^{\beta}} \tag{1}$$

Where k, α, n and β are hyperparameters, $a^{i}_{x,\,y}$ represents the current activation value, N denotes the total number of feature maps generated by the previous convolution layer, and $b^{i}_{x,\,y}$ is the value of $a^{i}_{x,\,y}$, after being processed by local normalization.

(4) To prevent the possible overfitting and gradient vanishing in the neural network, a random dropout layer is added after the LRN layer. By randomly resetting 20% of the output from the previous layer to zero, the response of these neurons is discarded. The remaining 80% output continues to propagate forward. This processing realizes the neural network regularization and reduces structural risks.

(5) After the first dropout layer, the second convolutional layer follows. In the entire neural network, there are a total of three convolutional layers. The ReLU layer, max-pooling layer, LRN layer, and dropout layer also follow each convolutional layer in sequence.

Each of the second and third convolution layers contains 64 convolution kernels with one convolution step. The filter size of each pooling layer and the step size are set to 2 × 2 and 2, respectively. Each LRN layer is parameterized by setting bias to 1.0, alpha to $1.11e^{-4}$ and beta to 0.75. The drop ratio of each dropout layer is set to 0.2 during the training.

(6) The third dropout layer is connected to a fully connected layer of 512 neurons. A three-dimensional tensor of size 8 × 8 × 64 obtained after the 3 convolutions is expanded into a one-dimensional tensor containing 4,096 values. There are 2 neurons in the output layer. The activation function is set to Softmax. The output layer would export probabilities of the lesion on maize eyespot or maize curvularia leaf spot.

The whole model comprises 2,155,010 parameters, with 896 in the first, 18,496 in the second, and 36,928 in the third convolution layer. There are 2,097,664 parameters in the fully connected layer.

Furthermore, by removing all three LRN layers from the above AlexNet model, a classical CNN model is generated. The CNN model is used to compare the recognition convergence and accuracy of the model based on the AlexNet architecture.

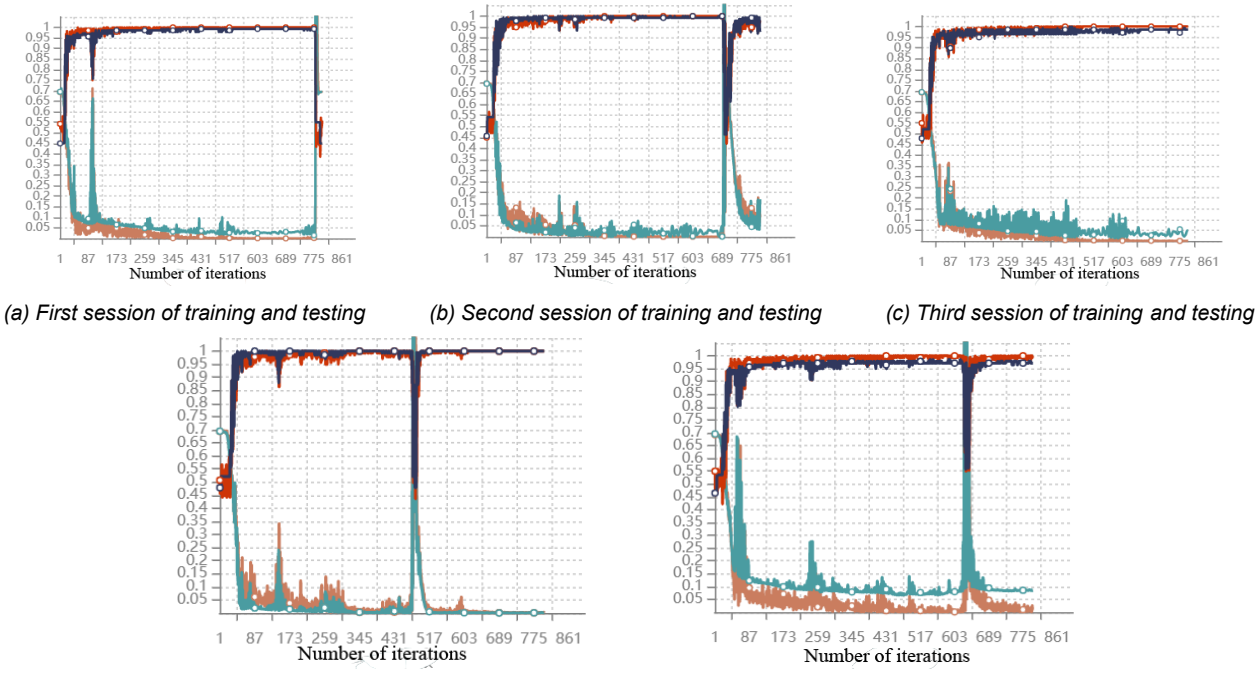
Model training

This paper employs a five-fold cross-validation experiments. Specifically, 700 preprocessed images are randomly assigned to five equal-sized groups with 140 images in the test set and 560 images in the training set. In total, AlexNet and CNN are trained at 800 iterations and then the results on convergence accuracy would be obtained. The process showed above would be conducted 5 times independently and each time the test set and training set is totally different. At the beginning of each training session, the weights and biases are initialized to 32-bit random numbers that follow a normal distribution with a standard deviation of 0.01. For both AlexNet and CNN, the cost function is set as cross entropy and Adam optimizer is used during the training process. The adjustable gradient descent method is used to adjust the parameters of the model. In every iteration of each session, the accuracy and loss values on the training and test sets as well as the maximum, minimum, mean, standard deviation, and parameter distribution of each layer are saved.

RESULTS AND ANALYSIS

Results of model training

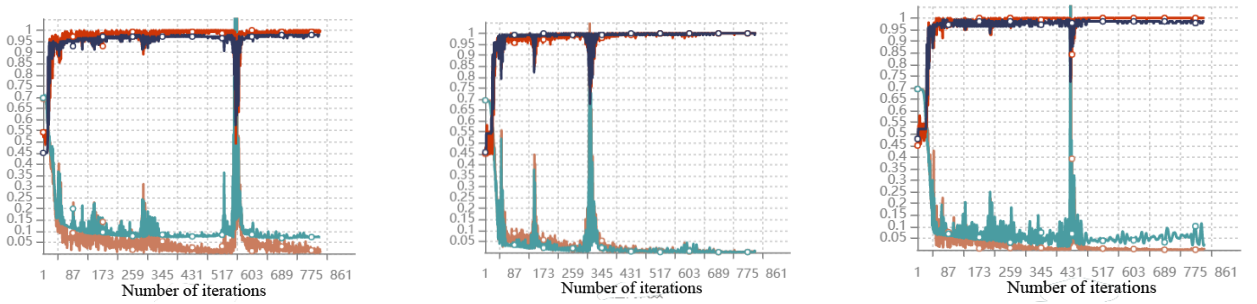
Each iteration of AlexNet or CNN would generate one model. To evaluate the generalization ability of the trained model, 800 iterations in each session is saved, so there would be 800 models for AlexNet or CNN architecture in each session. After each model is produced, it would be used to classify the 140 images in the test dataset. The best-performing model in the last 800 iterations in each time is selected as representative. The maize eyespot is treated as positive example and maize curvularia leaf spot is treated as negative example. If the maize eyespot is erroneously identified as maize curvularia leaf spot, or vice versa, the results will be wrong and will be considered a loss. The accuracy/loss results of the optimization model after each training session are summarized in Fig.7 and Fig.8, where the abscissa and ordinate represent the number of iterations and accuracy/loss value, respectively.



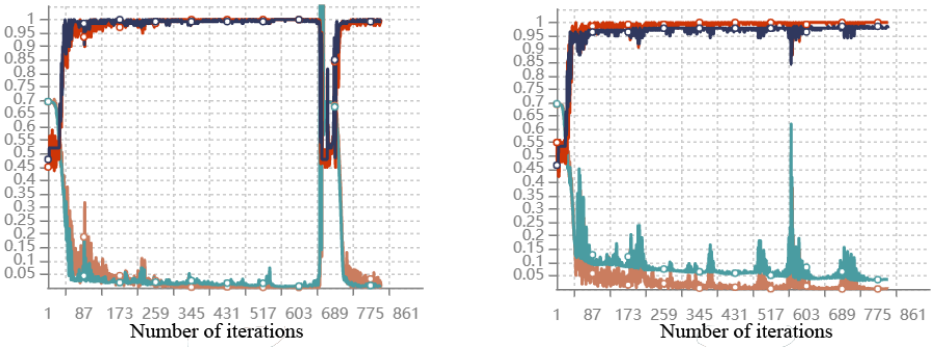
(a) First session of training and testing *(b) Second session of training and testing* *(c) Third session of training and testing*

(d) Fourth session of training and testing *(e) Fifth session of training and testing*

Fig. 7 –Training and testing results of CNN



(a) First session of training and testing *(b) Second session of training and testing* *(c) Third session of training and testing*



(d) Fourth session of training and testing *(e) Fifth session of training and testing*

Fig. 8 –Training and testing results of AlexNet

Evaluation of model generalization

The generalization ability of both models is assessed with the evaluation index shown in Eq. 2, consisting of three formulas to determine the accuracy rate P, recall rate R and F1 score, which are in turn calculated from real example number TP, false negative number FN, false positive number FP, and true negative number TN (Li Tianqi, 2019). The best-performing models produced independently in the 800 iterations of the 5 training sessions are used to calculate the P, recall rate R and F1 score.

The confusion matrices of CNN and AlexNet are shown in Table 1 and Table 2, respectively.

$$\begin{cases} P=TP/(TP+FP) \\ R=TP/(TP+FN) \\ F1=2P\bullet R/(P+R) \end{cases} \quad (2)$$

Table 1

Confusion matrix for CNN

Model number	TP	TN	FP	FN	P	R	F1
1	76	63	0	1	0.992857	0.993506	0.993182
2	63	76	0	1	0.992857	0.992188	0.992522
3	67	72	1	0	0.992857	0.993151	0.993004
4	67	73	0	0	1	1	1
5	63	73	2	2	0.971429	0.971282	0.971355

Table 2

Confusion matrix for AlexNet

Model number	TP	TN	FP	FN	P	R	F1
1	76	60	3	1	0.971429	0.969697	0.970562
2	64	76	0	0	1	1	1
3	67	72	1	0	0.992857	0.993151	0.993004
4	67	73	0	0	1	1	1
5	64	74	1	1	0.985714	0.985641	0.985678

Comparison and analysis of model accuracy

Accuracy comparison and analysis

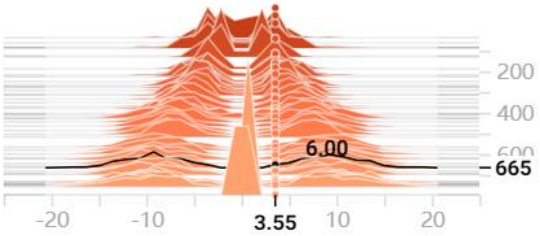
From Tab.1 and Tab.2, it could be observed that both models could achieve 100% on recognition accuracy, recall ratio and F1 score. CNN gets 100% recognition accuracy in the fourth training session, and AlexNet gets 100% recognition accuracy in the first and fourth training session. The recognition accuracy of AlexNet and CNN for maize eyespot and maize curvularia leaf spot are almost same. Though the average recall ratio and F1 score of CNN is slightly higher than AlexNet, AlexNet is obviously easier to show higher performance.

Both models demonstrate outstanding performance in recognizing lesions. This paper would analyse the appearance of 100% on recognition accuracy from the perspective of the biological characteristics and fractal theory. The formation of lesions is determined by the interactions between pathogens and host plants *(Scholthof, 2007)*. Consequently, when the same pathogen infects the same host plant (especially the same leaf), it typically leads to similar morphological and characteristics of the disease lesions. Additionally, the expansion of disease lesions follows fractal patterns over time, resulting in the emergence of similar morphological features in space *(Gong & Zhang, 2002)*. The strong similarity in morphological features in lesions of the same type enables the models to effectively learn the lesion characteristics, and then adapt to the test dataset perfectly, which leads to achieve excellent recognition performance on the test set.

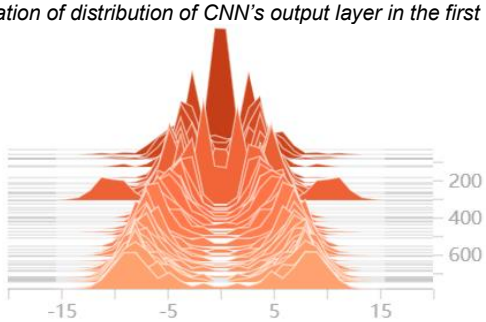
Parameter characteristic and analysis

Fig.7 and Fig.8 illustrate intuitively that during the 10 training sessions, the accuracy-iteration curve of the model generally shows a gradual increase on stability. There is also some fluctuation which is especially evident at some specific points. Taking Fig.8(b) as an example, it shows three distinct spikes where the accuracy sharply transforms from an increasing trend to a rapid decline, and then the accuracy-iteration curve is followed by a quickly increasing trend again. To better understand the reasons and implications of these dramatic fluctuations, it might be useful to analyse the phenomenon from two perspectives: parameter distribution and model principles.

(1) The parameter distribution of each iteration can be obtained as shown in Fig.9 where the X, Y and Z axis represent the parameter range for each iteration, the number of parameter, and the number of iterations, respectively.



(a) Weight variation of distribution of CNN's output layer in the first training session



(b) Weight variation of distribution of AlexNet's output layer in the second training session

Fig. 9 – Weight variation of distribution of the two models with increasement of iterations

Fig.9 demonstrates the changing trend of the variance in the output layer with the increasing iterations. From a holistic perspective, with the increasing number of iterations, the weight distribution in the output layer becomes more dispersed. Not only the output layer but also each layer in the neural network shows the similar trend that the weight values would show dispersed distributions as the number of training iterations increases.

For further analysis on model characteristics, variance was used to describe the dispersion and obtain variance-iteration curve shown in Fig.10. In Fig.10, it can be observed that the variance of the weight distribution shows increasing trend until it stabilizes in terms of the overall iterative process, which aligns with the overall changing trend in the Fig.9(b). At the same time, at certain specific number of iterations, the curve in Fig.10 exhibits clear inflection points indicated by the arrows in the image. By comparing Fig.10 with Fig.8(b), it is evident that these inflection points correspond to the positions where the model's accuracy shows dramatic fluctuations. This result might reveal an inherent connection between the abrupt fluctuations in model accuracy and the weight distribution.

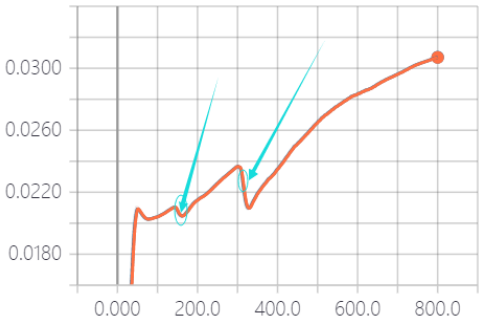


Fig. 10 – Variance-iteration curve of AlexNet *in the second training session*

(2) Besides, from the aspect of the distribution changing of activation values of the fully connected layer shown in Fig.11, the activation values are closer to zero as the number of iterations increases. For the activation function is ReLU, when the activation value of the neuron is updated to zero, it would not be updated to other numbers in subsequent iterations, which means that the node would be inactivated and would not be valid. As the number of iterations increases, more and more neurons become inactivated in the neural network. After the number of iterations exceeds the threshold, the neural network might collapse, which might lead to the corresponding decrease in modeling ability of the features and predictive ability of the neural network. After the collapse, the parameters of the model might be in the unstable state. As training proceeds, the network parameters may gradually move to more appropriate regions through adaptive adjustments on learning rate again, thus improving the performance of the model.

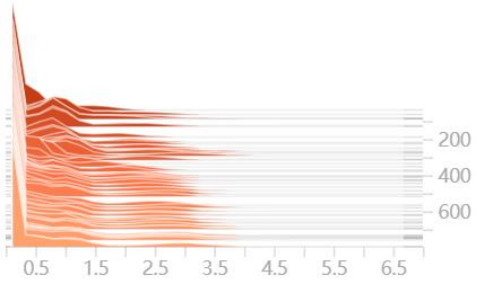


Fig. 11 – Distribution of activation values of the fully connected layer of AlexNet in the second training session

CONCLUSIONS

Misidentification of maize eyespot and maize curvularia leaf spot are found commonly on maize leaves and would lead to invalid operation of farming, which would result in large economic losses. In this paper:

(1) The automatic segmentation theory based on connectivity is utilized and the connected component labelling algorithm is employed. This methodology efficiently separates numerous concentrated lesions from maize leaves, ensuring their accurate extraction and automatic labelling.

(2) Based on AlexNet architecture, neural network model on image recognition is developed. Recognition effect of the model is also compared to image recognition model based on CNN architecture. The result shows outstanding performance on identifying the two kinds of lesions. The evaluation of generalization ability shows achieving 100% accuracy two times of the five training sessions.

(3) From perspective of the accuracy, leaf similarity in disease spots which is resulted from biological and fractal characteristics might lead to the accuracy of 100%. At the same time, from the perspective of fluctuation, activation values and weight distribution might lead to model accuracy's jitter on the way up as the iteration proceeds. This paper constructs a maize lesion recognition model and conducts an analysis of its characteristics, which will lay the groundwork for a portable intelligent lesion recognition system, subsequently contributing to advancements in smart cultivation practices.

ACKNOWLEDGEMENTS

This project is financially supported by the Basic Research Programme (Free Exploration Category) Fund of Shanxi Province, China (20210302124497), Shanxi Agricultural University, China (2021BQ113), Key Laboratory of Equipment and Informatization in Environment Controlled Agriculture, Ministry of Agriculture and Rural Affairs, China (2011NYZD2202) and Shanxi Agricultural University, China (2018023). The authors declare no competing interests.

REFERENCES

[1] Ahila Priyadharshini, R., Arivazhagan, S., Arun, M., & Mirnalini, A. (2019). Maize Leaf Disease Classification Using Deep Convolutional Neural Networks. *Neural Computing and Applications*, 31(12), 8887-8895.

[2] Albahli, S., & Masood, M. (2022). Efficient Attention-based CNN Network (EANet) for Multi-class Maize Crop Disease Classification. *Frontiers in Plant Science*, 13, 1003152.

[3] Chen, G., Chen, Z., Zheng, T., Ma, S., Yan, Z., & Liu, G. (2015). The Diagnosis and Identification of Three Fungal Leaf Spot Disease of Maize Leaf in the Hexi Corridor *(*河西走廊制种玉米 3 种真菌性叶斑病的诊断与识别*). Seed,* 34(3), 94-96.

[4] Chen, J., Zeb, A., Nanehkaran, Y. A., & Zhang, D. (2022). Stacking Ensemble Model of Deep Learning for Plant Disease Recognition. *Journal of Ambient Intelligence and Humanized Computing*, 14(9), 12359-12372.

[5] Dai, F., Wang, X., Zhu, Z., Gao, W., Huo, N., & Jin, X. (1998). Curvularia Leaf Spot of Maize: Pathogens and Varietal Resistance (玉米弯孢菌叶斑病研究). *ACTA Phytopathologica Sinica*, 28(2), 123-129.

[6] Fu, J., Jing, D., Liu, Z., & Zhou, R. (2016). Review of Epidemic Dynamics and Forecasting and Warning of Maize Leaf Disease (玉米叶部病害流行动态及预测预警研究进展). *Journal of Jilin Agricultural University,* 38(6), 651-655.

[7] Fang, S., Wang, Y., Zhou, G., Chen, A., Cai, W., & Wang, Q. (2022). Multi-channel Feature Fusion Networks with Hard Coordinate Attention Mechanism for Maize Disease Identification under Complex Backgrounds. *Computers and Electronics in Agriculture*, 203, 107486.

[8] Gong, G., & Zhang, S. (2002). Fractal analysis of patch patterns on plant diseases (植物病害病斑形状的分形研究). *Plant Protection*, 28(6), 9-12.

[9] Guo, M., Xu, T., Liu, J. , Liu, Z., Jiang, P., & Mu, T., et al. (2022). Attention Mechanisms in Computer Vision: A Survey. *Computational Visual Media*, 8(3), 331-368.

[10] Joseph, D. S., Pawar, P. M., & Pramanik, R. (2023). Intelligent Plant Disease Diagnosis Using Convolutional Neural Network: A Review. *Multimedia Tools and Applications*, 82(14), 21415-21481.

[11] Krizhevsky, A., Sutskever, I., & Hinton, G. E. (2017). ImageNet Classification with Deep Convolutional Neural Networks. *Communications of the ACM*, 60(6), 84-90.

[12] Li, E., Wang, L., Xie, Q., Gao, R., Su, Z., & Li, Y. (2023). A Novel Deep Learning Method for Maize Disease Identification Based on Small Sample-size and Complex Background Datasets. *Ecological Informatics*, 75, 102011.

[13] Liu, J., & Wang, X. (2021). Plant Diseases and Pests Detection Based on Deep Learning: a Review. *Plant Methods*, 17, 1-18.

[14] Li, Z., Zhou, G., Hu, Y., Chen, A., Lu, C., & He, M. (2022). Maize Leaf Disease Identification Based on WG-MARNet. *PLoS One*, 17(4), e0267650.

[15] Meng, Y., Chen, G., Lu, J., & Xu, R. (2017). Simulink Platform in Video Image Real-time Diagnosis of Maize Disease (Simulink 平台在玉米病害视频图像中的实时诊断). *Journal of Jilin Agricultural University*, 39(4), 483-487.

[16] Nagaraju, M., & Chawla, P. (2023). Maize Crop Disease Detection Using NPNet-19 Convolutional Neural Network. *Neural Computing and Applications*, 35(4), 3075-3099.

[17] Niu, Z., Zhong, G., & Yu, H. (2021). A Review on the Attention Mechanism of Deep Learning. *Neurocomputing*, 452, 48-62.

[18] Picon, A., Seitz, M., Alvarez-Gila, A., Mohnke, P., Ortiz-Barredo, A., & Echazarra, J. (2019). Crop Conditional Convolutional Neural Networks for Massive Multi-crop Plant Disease Classification over Cell Phone Acquired Images Taken on Real Field Conditions. *Computers and Electronics in Agriculture*, 167, 105093.

[19] Shi, J., Liu, Y., & Wei, L. (2000). On Pathogens of Maize Curvularia Leaf Spot (玉米弯孢菌叶斑病病原菌的研究). *Journal of Shenyang Agricultural University,* 31(5), 479-481.

[20] Sun, J., Xiao, S., Xu, J., Liu, K., Ma, C., Xue, C., & Chen, J. (2016). Occurrence Condition and Chemical Control of Maize Eyespot in Liaoning Province (辽宁省玉米北方炭疽病发生条件与药剂防治). J*ournal of Maize Sciences, 24*(5), 147-151.

[21] Sun, J., Xiao, S., Lu, Y., Tu, G., Xue, C., & Chen, J. (2015). Isolation Identification and Biological Characteristics of Aureobasidium Zeae in Liaoning Province (辽宁省玉米北方炭疽病菌的分离鉴定及生物学特性). *Journal of Plant Protection,* 42(6), 927-934.

[22] Scholthof, K. B. G. (2007). The Disease Triangle: Pathogens, the Environment and Society. *Nature Reviews Microbiology*, 5(2), 152-156.

[23] Shi, T., Liu, Y., Zheng, X., Hu, K., Huang, H., Liu, H., & Huang, H. (2023). Recent Advances in Plant Disease Severity Assessment Using Convolutional Neural Networks. *Scientific Reports*, 13(1), 2336-2349.

[24] Toda, Y., & Okura, F. (2019). How Convolutional Neural Networks Diagnose Plant Disease. *Plant Phenomics*, 2019, 9237136.

[25] Wang, C., Chen, L., Guo, X., Lu, Z., & Gao, J. (2006). Study on Some Problems of Maize Curvularia Leaf Spot Caused by Curvularia Lunata (玉米弯孢菌叶斑病发生和防治若干问题研究). *Journal of Maize Sciences, 14(2),* 144-146+149.

[26] Wang, X., Shi, J., Jin, Q., Li, X., & Sun, S. (2010). Field Manual of Corn Pests and Diseases (玉米病虫害田间手册). Beijing/*China: China Agricultural Science and Technology Press.*

[27] Weng, Y., Zeng, R., Wu, C., Wang, M., Wang, X., & Liu, Y. (2019). A Survey on Deep-learning-based Plant Phenotype Research in Agriculture (基于深度学习的农业植物表型研究综述). *Scientia Sinica Vitae,* 49(6), 698-716.

[28] Xu, X., Dong, H., Jiang, Y., Qiao, Y., Liu, Z., & Sun, J. (2000). Preliminary Studies on the Northern Anthracnose Disease in Maize (辽宁省玉米新病害——北方炭疽病研究初报). *Journal of Shenyang Agricultural University,* 31(5), 507-510.

[29] Zhang, S., & Zhang, C. (2014). Maize Disease Recognition based on Local Discriminant Algorithm (基于局部判别映射算法的玉米病害识别方法). *Transactions of the Chinese Society of Agricultural Engineering*, 30(11), 167-172.

[30] Zeng, W., Li, H., Hu, G., & Dong, L. (2022). Identification of Maize Leaf Diseases by Using the SKPSNet-50 Convolutional Neural Network Model. *Sustainable Computing: Informatics and Systems*, 35, 100695.

[31] Zhang, X., Su, Q., Song, S., Du, J., Liu, Y., Zhang, W., Li, H., & Jin, Q. (2010). Pathogenicity Differentiation and RAPD Analysis of Curvularia Lunata in Northeast China (东北地区玉米弯孢菌致病性分化与 RAPD 分析). *Journal of Maize Sciences,* 18(6), 122-126.

[32] Zhang, Y., Zhang, S., Yang, S., Zhou, Y., & Zhao, W. (2017). Pathogen Identification of Curvularia Leaf Spot of Maize in Heilongjiang Province (黑龙江省玉米弯孢霉叶斑病病原鉴定). *Journal of Northeast Agricultural University,* 48(6), 17-23.

DESIGN AND EXPERIMENT OF POTATO SEEDLING FILM-BREAKING DEVICE BASED ON MACHINE VISION

/

基于机器视觉的马铃薯幼苗破膜装置设计与试验

Zhaoqin LV [1)], Zhuangzhuang GUO[2,3)], Wanzhi ZHANG*[2,3)], Xiang ZENG[2,3)], Yuelin HAN[2,3)]

[1)] College of Intelligent Manufacturing, Qingdao Huanghai University / China;

[2)] College of Mechanical and Electronic Engineering, Shandong Agricultural University / China;

[3)] Shandong Provincial Key Laboratory of Horticultural Machinery and Equipment / China

Tel: +86-0538-8249830; E-mail: zhangwanzhi@163.com

DOI: https://doi.org/10.35633/inmateh-71-11

***Keywords**: potato, film-breaking, machine vision, improved YOLOv5s, motion control*

ABSTRACT

An automatic potato seedling film-breaking device based on machine vision was designed to reduce the labor intensity of potato film-breaking. The device mainly consisted of a motion mechanism, a seedling recognition mechanism, a film-breaking mechanism, etc. Based on single-ridge and single-row potato planting agronomy, the whole structure and key component dimensions of the film-breaking device were determined, the YOLOv5s model was improved to build a potato seedling recognition system, and the film-breaking mechanism based on the parallel CoreXY structure was designed. Potato seedlings at the emerging stage were used as research objects for field film-breaking tests. The results showed that the recognition rate of potato seedlings was 89.7%, the qualified rate of film-breaking was 83.5%, and the damage rate was 2.3%. This paper could provide technical support for the development of intelligent film-breaking equipment for potato seedlings.

摘要

为减轻马铃薯人工破膜劳动强度，设计了一种基于机器视觉的马铃薯幼苗自动破膜装置。该装置主要由运动机构、幼苗识别机构、破膜机构等组成。基于单垄单行马铃薯种植农艺，确定破膜装置的整体结构和关键部件尺寸，改进 YOLOv5s 模型搭建马铃薯幼苗识别系统，设计基于并联 CoreXY 结构的破膜机构。以出苗期马铃薯幼苗为研究对象进行田间破膜试验，结果表明：马铃薯幼苗识别率为 89.7%，破膜合格率为 83.5%，幼苗损伤率为 2.3%。本文可为马铃薯幼苗智能化破膜装备研制提供技术支持。

INTRODUCTION

Potato is a food crop with high nutritional value and good production efficiency. At present, China's potato planting area and output are ranked first in the world (*Xu et al., 2021; Li et al., 2019*). Plastic film mulching cultivation is a widely used technology in the potato planting industry. It has the functions of increasing temperature, water retention, fertilizer retention, and inhibiting the growth of weeds, which can effectively improve the yield and quality of potatoes. However, if the mulching time is too long, the potato seedlings are easy to be burned or grow in a bent state under the film, which will affect the normal growth of potatoes in the later period. Seedling film-breaking is an important link in the normal growth and yield increase of potatoes. At present, artificial film-breaking is mainly used in production. Artificial film-breaking is to use fingers or iron hooks to dig or cut through the plastic film so that potato seedlings are exposed, but this operation process requires manual squatting or bending to operate, and the labor intensity is very high. Therefore, the realization of mechanized film-breaking of potato seedlings is of great significance to the sustainable and healthy development of the potato industry.

Owing to differences in geographical environment and planting patterns, there was almost no research on potato seedling film-breaking machines abroad (*Escuredo et al., 2019; Rahaman et al., 2019*). In order to meet market demand, China had actively promoted facilities for potato planting in recent years. This planting mode mostly adopted single-ridge and single-row potato planting agronomy, with a ridge distance of about 650 mm, and the furrow width was about 150 mm. It could not only improve potato yield and quality but is also conducive to resource protection.

[1] *Zhaoqin Lv, Prof. Ph.D. Eng.; Zhuangzhuang Guo, M.S. Stud. Eng.; Wanzhi Zhang, Prof. Ph.D. Eng.; Xiang Zeng, M.S. Stud. Eng.; Yuelin Han, M.S. Stud. Eng.*

However, due to the lack of corresponding machinery for potato seedling film-breaking, it was necessary to manually break the film, which greatly increased labor intensity. Therefore, with the aim of improving work efficiency and reducing labor costs, many scholars had conducted research on potato seedling film-breaking, which mainly includes: Zhang proposed a potato seedling cultivation technology of natural rupture of the covering soil on high ridge film, referring to the soil pressing soil covering technology, through the cultivation of soil on the ridge surface, and covering the soil layer on the mulch to form a high ridge, so as to achieve natural emergence and irrigation and water prevention. Although this method could produce seedlings naturally, the covering soil on the film affected the light transmittance and thermal insulation of the film (*Zhang et al., 2019*). Hou proposed a potato seeding machine with manual punching on the film, which used manual mode to break the film (*Hou et al., 2021*). Li invented a film-breaking seedling machine applied to potato black film, which used an infrared spectrum to identify potato seedlings covered with black film, performed film-breaking operations, and was equipped with a waste film recycling device. This machine is currently in the research and development stage, and the actual operation effect has not been verified (*Li et al., 2021*).

The research on film-breaking of other crops includes: *Mustaqimah* designed a plastic mulch punching machine for punching and recycling plastic mulch during pepper planting (*Mustaqimah et al., 2022*). *Tadeo* designed a nylon rope film-breaking mechanism for paddy field operations (*Tadeo et al., 2000*). Wang used wet felt film-breaking to break the film of garlic buds. Compared with artificial film-breaking, the film-breaking efficiency was improved, but it would cause a higher damage rate to garlic buds (*Wang et al., 2019*). Chen proposed a cultivation technique for the natural emergence of yam without breaking film (*Chen et al., 2018*). Liu designed a small electric film-breaking soil covering machine for flue-cured tobacco under film planting technology, which used 3D laser scanning to locate the position of the tobacco seedlings, and then broke the film, but it was only a theoretical study and lacked the test of the whole machine (*Liu et al., 2019*). Cheng designed a garlic seedling film-breaking machine based on the Delta robotic arm, which used the YOLOv5 network to recognize the unbroken garlic seedlings, and then used the Delta robotic arm to break the film of the garlic seedlings (*Cheng, 2019*).

In recent years, technologies such as machine vision and deep learning have developed rapidly and have been widely used in the field of agriculture. These research results provide methods and ideas for solving the problems raised in this paper *(Fu et al., 2020; Han et al., 2023; Li et al., 2020; Yang et al., 2022; Zong et al., 2021*). Aiming at the labor-intensive problem of artificial film-breaking, this paper designs an automatic film-breaking device for potato seedlings based on machine vision to realize the recognition and positioning of potato seedlings and the motion control of the film-breaking mechanism.

MATERIALS AND METHODS

GENERAL DESIGN

Whole structure

The structure of the potato seedling automatic film-breaking device was shown in Fig. 1, which was mainly composed of a frame, a motion mechanism, a seedling recognition mechanism, and a film-breaking mechanism. The frame was composed of aluminum profiles, fixing parts, etc. The seedling recognition mechanism was composed of a computer and an industrial camera, which was installed in the middle of the frame.

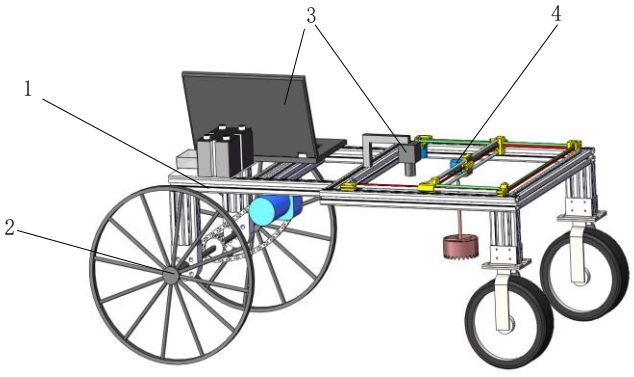


Fig. 1 -Schematic diagram of the whole structure

1-Frame; 2-Motion mechanism; 3-Seedling recognition mechanism; 4-Film-breaking mechanism

Working principle

The film-breaking mechanism was installed at the rear of the frame, the DC geared motor was powered by the battery, and the whole machine was driven forward through the transmission shaft, chain sprocket, and other components. The height of the whole machine was adjusted according to the potato seedling ridge height before work to ensure that the distance between the seedlings and the film-breaking mechanism was within the working range of the film-breaking device. The working process of the film-breaking device was divided into three stages: image acquisition, recognition and positioning, and mobile film-breaking. The industrial camera in the seedling recognition mechanism completed the collection of potato seedling images during the forward process; the potato seedling recognition and control system in the upper computer identified and located the potato seedlings in the image. After receiving the positioning information, lower single chip microcontroller controlled the film-breaking mechanism to move the film-breaking knife quickly to the position directly above the potato seedlings. Then it moved downward to pierce the film to complete the film-breaking work.

DESIGN OF KEY COMPONENTS

Design of film-breaking mechanism

The film-breaking mechanism was mainly composed of stepping motors, timing belts, timing pulleys, optical axes, linear bearings, 3D printing fixed parts, a film-breaking knife, etc. The structure was shown in Fig 2. M1 and M2 motors were X and Y axis drive motors respectively, and 2-phase 4-wire 42 stepping motors were selected, and the model was 17HD4800-22B. The Z-axis motor was a fixed screw motor with a stroke of 63.5 mm. Because the stepping motor started too fast, it would stall or lose steps, and if it stopped too fast, it would overstep. Therefore, the trapezoidal model algorithm was used in this paper to control the stepping motor's acceleration and deceleration. The schematic diagram of the algorithm model was shown in Fig. 3. The trapezoidal acceleration and deceleration were divided into three stages: the acceleration stage OA, the constant speed stage AB and the deceleration stage BC. In the acceleration phase, started with a frequency lower than that of the stepping motor, and increased the speed to the target value with constant acceleration; in the constant speed phase, moved at a constant speed at the maximum speed; in the deceleration phase, decelerated to 0 with a constant deceleration.

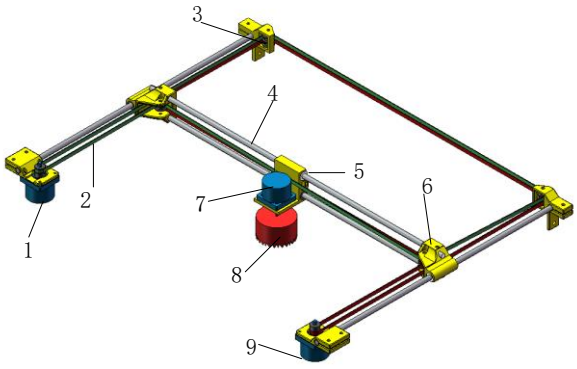


Fig. 2 - Schematic diagram of the film-breaking mechanism

1-M1 stepping motor; 2-Timing belt; 3-Timing pulley; 4-Optical axis; 5-Linear bearing; 6-3D printing fixed part; 7-Z-axis stepping motor 8-Film-breaking knife; 9-M2 stepping motor

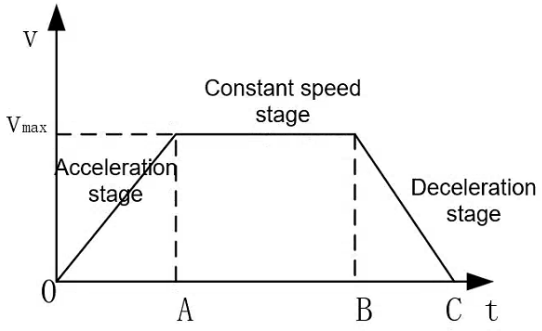


Fig. 3 - Schematic diagram of stepping motor trapezoidal algorithm

The film-breaking mechanism adopted a parallel CoreXY structure, its schematic diagram was shown in Fig. 4, and its kinematic relationship was:

$$\Delta X = \frac{1}{2}(\Delta A + \Delta B) \qquad \Delta Y = \frac{1}{2}(\Delta A - \Delta B) \tag{1}$$

where:

$\Delta A, \Delta B$ is the linear displacement of the stepping motors M1 and M2, clockwise is negative and counterclockwise is positive; $\Delta X, \Delta Y$ is the displacement of the film-breaking mechanism along the positive direction of the X-axis and Y-axis respectively.

Since the emerging diameter of potato seedlings was about 30-50 mm, in order not to cause damage to potato seedlings, the diameter of the film-breaking knife was designed to be 60 mm, and its end structure was serrated. The distance between the potato planting ridge was 650 mm, and the maximum stroke of the designed film-breaking mechanism was 650 × 600 × 63.5 mm, which could cover the potato planting ridge surface and realize the film-breaking operation in all aspects.

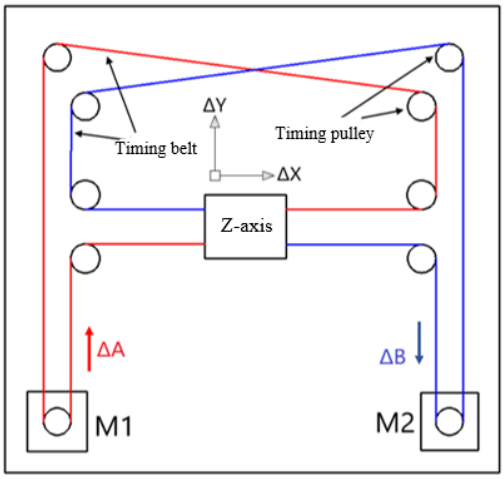


Fig. 4 - Schematic diagram of CoreXY structure

Design of motion Mechanism

The motion mechanism was mainly composed of batteries, DC geared motors, relays, governors, proximity switches, driving wheels, driven wheels, etc., as shown in Fig. 5. The model of the DC geared motor was XD6D300-24GU21S, the reduction ratio was 1:1.75, and the maximum load was 5.2 N.m; the battery specification was 12V20AH, and the DC geared motor was powered by connecting two batteries in series. When working, the DC geared motor drove the driving wheel to rotate through the gear and chain, and the motor speed was adjusted through the governor to control the forward speed of the motion mechanism.

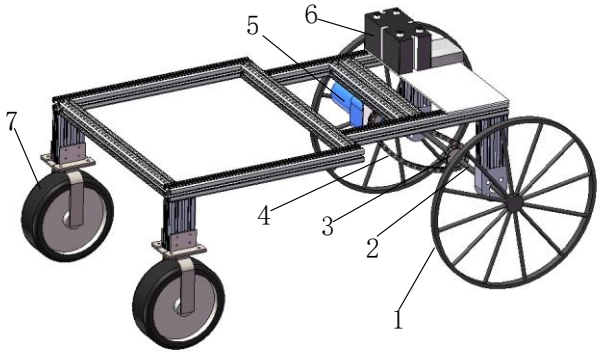


Fig. 5 - Motion mechanism

1-Driving wheel; 2-Driving shaft; 3-Gear; 4- Chain; 5- DC geared motor; 6-Battery; 7-Driven wheel

Design of other components

HF868_2.8-12 industrial camera was used for image acquisition of potato seedlings. The highest image resolution was 1920 pixels × 1080 pixels, and the maximum frame rate was 30fps. It was connected to the computer through the USB Type-c interface.

The upper computer used a computer to recognize and position seedlings; the lower computer used Arduino UNO single chip microcomputer and Arduino CNC expansion board to receive signals from the upper computer. The external circuit was powered by 12V DC, and UART was used for communication between the upper and lower bits. The development board was connected to the USB port of the upper computer to transmit signals through the USB interface. At the same time, the parallel data was converted into serial data for transmission. The baud rate was set to 115200b/ s.

POTATO SEEDLING RECOGNITION AND COORDINATE TRANSFORMATION

Potato seedling recognition

Improved YOLOv5s seedling recognition model

Among the existing target recognition algorithms, YOLOv5 has the advantages of fast recognition speed and high accuracy, and has a wide range of applications (*Huang et al., 2022; Sami et al. 2023*). Therefore, this paper improved the potato seedling recognition algorithm based on the original model of YOLOv5s, mainly through the fusion of Coordinate Attention Mechanism, replaced the Coupled Head with a Decoupled Head and replaced the loss function with Focal-EIOU Loss to strengthen the learning ability of the network model for seedlings and reduce false detection and missed detection (*Liu et al., 2020; Xiu et al. 2022*). Specifically, improvements were made in the following three aspects:

1) Coordinate Attention Mechanism

To obtain the key feature information of potato seedlings from complex features, and considering that water vapor and weeds under the film would interfere with seedling recognition, this paper introduced a Coordinate Attention Mechanism to strengthen the target information of potato seedlings and suppress redundant features. Compared with the traditional channel attention, the CA attention mechanism integrated the location information into the attention, used the acquired location information to locate the target location faster, and improved the algorithm's performance without consuming additional computing resources.

The CA attention mechanism divided two channels of attention into two parallel one-dimensional features, which were aggregated along the two spatial directions respectively. Its module structure was shown in Fig. 6.

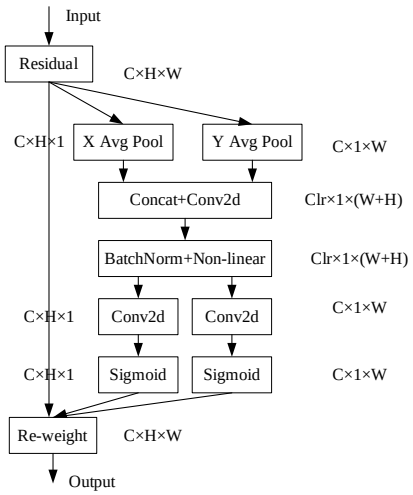


Fig. 6 - CA attention mechanism structure

2) Decoupled Head

To solve the conflict between the seedling recognition and classification problem and the regression task, accelerate the convergence speed of the model, and improve the overall performance, this paper introduced the Decoupled Head to replace the Coupled Head in YOLOv5s. Considering that the classification problem of the target recognition algorithm and the regression task were mutually exclusive, the focus of classification and regression were different. Classification paid more attention to the texture content of the target, and regression paid more attention to the edge information of the target. The Coupled Head combined the classification problem and the regression task for calculation, and the classification and regression branches shared parameters, which could not balance positioning and recognition, causing the problem of slow convergence in the training process. The Decoupled Head was introduced to separate the classification problem and the regression task as two branches, so that the focus of the two tasks was clearer and the convergence speed was accelerated. Its structure was shown in Fig.7.

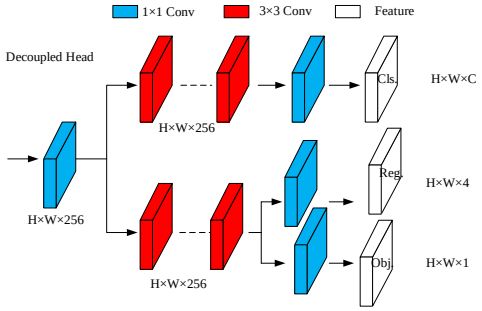


Fig. 7- Decoupled Head structure diagram

3) Focal-EIOU loss function

Aiming at the CIOU Loss function in YOLOv5 could not deal with the optimization similarity problem of the model well, this paper proposed to improve the penalty item based on CIOU, and disassembled the influence factor of aspect ratio based on CIOU's penalty item to calculate the length and width of the anchor box respectively, and then became EIOU Loss, the calculation formula was shown in formula (2).

$$Loss_E = 1 - IOU + \frac{\rho^2\left(b, b^{gt}\right)}{c^2} + \frac{\rho^2\left(w, w^{gt}\right)}{c_w^2} + \frac{\rho^2\left(h, h^{gt}\right)}{c_h^2} \quad (2)$$

where: IOU represents the intersection ratio between the predicted box and the real box, b, b^{gt} respectively represents the center point of the predicted box and the real box; ρ represents the calculation of the Euclidean distance between the two center points; c represents the diagonal distance of the minimum closure area that can contain both the predicted box and the real box ; w, w^{gt} represents the width of the predicted box and the real box, respectively; c_w is the width of the minimum bounding box covering the predicted box and the ground truth box; h, h^{gt} representing the width of the predicted box and the real box, respectively; c_h is the height of the minimum bounding box covering the predicted box and the ground truth box. Combining Focal Loss based on f EIOU to synthesize a new type of Focal-EIOU Loss, the calculation formula is:

$$Loss_F = IUO^{\gamma} Loss_E \quad (3)$$

Where: γ is a parameter to control the degree of outlier suppression. According to the above formula, the higher the IOU, the greater the loss, which was equivalent to the weighting effect, and the better the regression target, the greater the loss, which helped to improve the regression accuracy and strengthen the sensitivity of the network to information such as the direction and position of potato seedlings.

The improved overall network architecture was shown in Fig. 8.

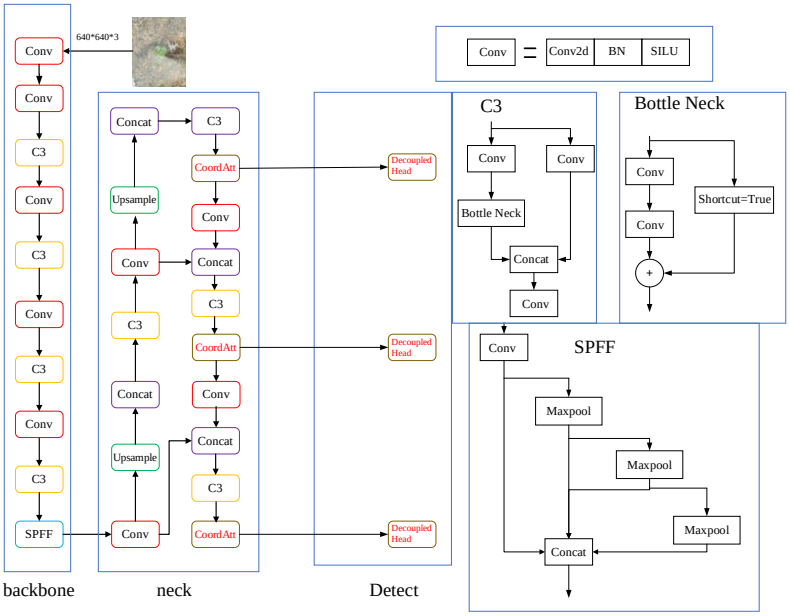


Fig. 8 - Improved YOLOv5s framework diagram

Potato seedling recognition test

(1) Dataset making

The collection location of potato seedlings was Qixiang Potato Planting Cooperative in Tengzhou City, Shandong Province. The collection time of the dataset was set into three stages, namely 6:30-7:30, 12:00-1:00, 4:00-5: 00. The collected dataset had 800 potato images in total after manually eliminating redundant and poor pixel quality images. To avoid too few samples in the dataset from affecting its model training effect and generalization performance, this paper used mirroring, rotation, brightness adjustment, and adding noise to enhance data. After expansion and processing, the dataset had a total of 2,400 images. Some sample images as shown in Fig. 9. The images of potato seedlings were labeled using LabelImg software. The labeled dataset was divided into a training set (2160 images) and a verification set (240 images) at a ratio of 9:1.

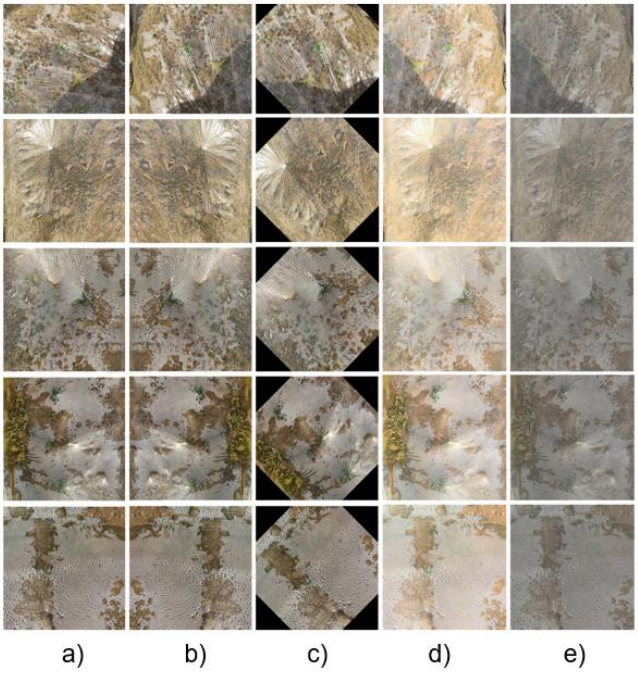


Fig. 9 -Some seedling image enhancement samples

a) Original image; b) Mirror; c) Rotation; d) Brightness adjustment; e) Add noise

(2) Test environment and evaluation indicators

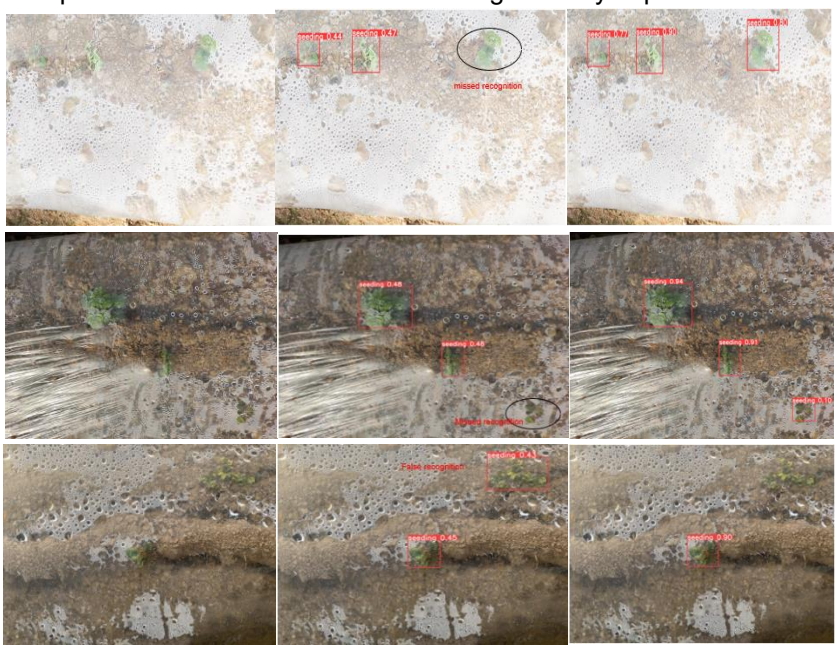
The model training process was carried out under the Win11 operating system, the computer processor was 2nd Gen Intel(R) Core(TM) i7-12700K 3.60 GHz, the graphics card model was Nvidia GeForce RTX 3080Ti, the deep learning framework was Pytorch, and CUDA11.6 was installed in parallel Computing framework and acceleration library of CUDNN8.0.5, using Python3.9.13 programming language. To evaluate the recognition performance of the model for potato seedlings, recognition accuracy (P, Precision), recall rate (R, Recall), mean average precision (mean Average Precision, mAP) were used as evaluation indexes *(Kim et al., 2022).*

(3) Test results and analysis

To test the recognition effect of the model, the verification sets were recognized by YOLOv5s and the improved YOLOv5s algorithm respectively. The results showed that the P, R and mAP of the improved YOLOv5s model were 93.2%, 92.7%, and 95.5%, which were 3.5 percentage points higher than the original model mAP, while P and R were increased by 1.5 and 1.7 percentage points, respectively. The above results showed that the improved model introduces the CA coordinate attention mechanism, which could strengthen the model's attention to potato seedlings and effectively avoid the influence of redundant features such as water vapor and weeds under the film; the improved model Coupled Head was replaced by a Decoupled head, which could solve the conflict between the seedling recognition classification problem and the regression task, and speed up the convergence speed of the model; the improved model loss function was changed to the Focal-EIOU Loss function, which could optimize the sample imbalance problem in the bounding box regression task and strengthen the sensitivity of the network to information such as direction and position.

Partial results of potato seedlings were shown in Fig. 10. From top to bottom, the recognition effect was compared under strong exposure, water vapor occlusion and weed interference respectively. For the seedling

recognition in the three special environments, the YOLOv5s model had missed or false detections, but the recognition effect of the improved YOLOv5s model had been significantly improved.



a) b) c)

Fig. 10 - Comparison of recognition results

a) Original image; b) YOLOv5s; c) Improved YOLOv5s

Potato seedling coordinate transformation

The seedling coordinates of potato seedlings were given under camera coordinates, which needed to be converted to the film-breaking mechanism coordinate system. The height of the potato planting ridge was relatively fixed, and the potato seedlings could be regarded as being in the two-dimensional plane of the ridge surface. Therefore, the transformation between the pixel coordinates of the potato seedlings in the camera coordinate system and the coordinate system of the film-breaking mechanism could be expressed by affine transformation. That is, the conversion from the camera coordinate system to the film-breaking mechanism coordinate system could be regarded as the translation of the film-breaking mechanism coordinate system by x0 units along the X direction, the translation of y0 units along the Y direction, and the transformation of the rotation angle around the Z axis to the camera coordinate system, which the conversion matrix could express:

$$H=\begin{bmatrix}1&0&x_0\\0&1&0\\0&0&1\end{bmatrix}\begin{bmatrix}1&0&0\\0&1&y_0\\0&0&1\end{bmatrix}\begin{bmatrix}\cos\theta&-\sin\theta&0\\\sin\theta&\cos\theta&0\\0&0&1\end{bmatrix}=\begin{bmatrix}\cos\theta&-\sin\theta&x_0\\\sin\theta&\cos\theta&y_0\\0&0&1\end{bmatrix} \quad (4)$$

where:

H is the transformation matrix. The coordinates of the point $p(u,v)$ in the plane of the camera coordinate system in the coordinate system of the film-breaking mechanism could be expressed as:

$$\begin{bmatrix}x\\y\\1\end{bmatrix}=\begin{bmatrix}\cos\theta&-\sin\theta&x_0\\\sin\theta&\cos\theta&y_0\\0&0&1\end{bmatrix}\begin{bmatrix}u\cdot\alpha_x\\v\cdot\alpha_y\\1\end{bmatrix} \quad (5)$$

where: (x,y) is the point in the coordinate system of the film-breaking mechanism; α_x,α_y is the scale factor of the camera coordinate system. According to formula (6), the affine transformation equation could be obtained as:

$$\begin{cases}x=a_2\cdot u+b_1\cdot v+x_0\\y=a_1\cdot u+b_2\cdot v+y_0\end{cases} \quad (6)$$

Where:

$a_1=\alpha_x\cdot\sin\theta$, $a_2=\alpha_x\cdot\cos\theta$, $b_1=\alpha_y\cdot\sin\theta$, $b_2=\alpha_y\cdot\cos\theta$. In this paper, the nine-point calibration method was used to solve the parameters of the affine transformation equation (*Zhang et al., 2021*), and the

transformation matrix H could be obtained, In the actual film-breaking process, the potato seedling coordinates in the film-breaking mechanism coordinate system could be obtained in the camera coordinate system through the transformation matrix H, as shown in Fig.11. Fig.11(a) was the result of potato seedling recognition, and Fig.11(b) was the result of coordinate transformation.

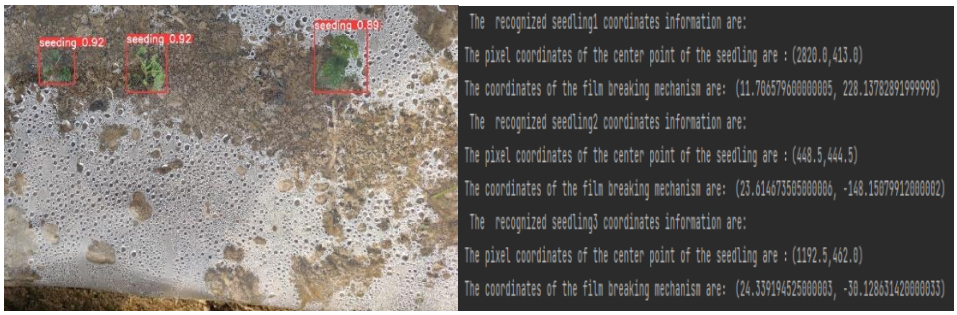


Fig.11 - Potato seedling recognition results and coordinate transformation

a) Potato seedling recognition results *b) Coordinate transformation results*

RESULTS

FIELD TESTS

Test conditions and methods

To verify the operating performance of the film-breaking device, a field test was conducted at the potato planting base of Shandong Agricultural University in March 2023. The potato planting mode was single-ridge and single-row, the ridge distance was 650 mm, the ridge height was 250 mm, the ridge top width was 300 mm, the ridge bottom width was 500 mm, and the film thickness was 0.008 mm. Before the start of the test, the vertical distance between the seedling recognition camera and the plastic film was adjusted to 250 mm to ensure that the recognition range covered the entire ridge top. The initial height of the film-breaking knife from the ridge surface was 30 mm, and the forward speed of the motion mechanism was set to 0.2 m/s. Three ridges were randomly selected, and 200 potato seedlings were selected from each ridge for film-breaking test. The test process was shown in Fig.12.



Fig.12 - Field test and film-breaking results

In the experiment, the seedling recognition rate, film-breaking qualified rate, and seedling damage rate were selected as evaluation indicators, and the calculation formula was as follows

$$Q = \frac{q}{M} \times 100\% \tag{7}$$

$$I = \frac{F}{M} \times 100\% \tag{8}$$

$$K = \frac{N}{M} \times 100\% \tag{9}$$

where: Q is the seedling recognition rate q is the number of potato seedlings correctly recognized; I is the qualified rate of film-breaking; F is the number of completed film-breaking; K is the damage rate of seedlings, N is the number of potato seedlings damaged by film-breaking knife, M is the total number of potato seedlings.

Test results

The results of film-breaking of potato seedlings were shown in Table 1. It could be seen that the recognition rate of potato seedlings was 89.7%, the qualified rate of film-breaking was 83.5%, and the seedling damage rate was 2.3%. The results showed that the film-breaking device designed in this paper could complete the film-breaking work of potato seedlings well.

Table 1

Test results

Line number	Number of potato seedlings	The number of potato seedlings correctly recognized	The number of completed film-breaking	The seedling recognition rate /%	Film-breaking qualified rate /%	Seedling damage rate /%
1	200	183	170	91.5	85.0	2.5
2	200	176	165	88.0	82.5	2.5
3	200	179	166	89.5	83.0	2.0

CONCLUSIONS

An automatic film-breaking device for potato seedlings based on machine vision was designed. Based on the single-ridge and single-row potato planting agronomy, the film-breaking device's whole structure and key component sizes were determined. The potato seedling recognition system was built using the improved YOLOv5s model, and the film-breaking mechanism based on the parallel CoreXY structure was designed.

The field film-breaking tests were carried out on potato seedlings at the emerging stage. The results showed that the recognition rate of potato seedlings was 89.7%, the qualified rate of film-breaking was 83.5%, and the seedling damage rate was 2.3%. The film-breaking device designed in this paper could complete the film-breaking work of potato seedlings well. It can provide technical support for the development of intelligent film-breaking equipment for potato seedlings in the next step.

ACKNOWLEDGEMENT

This work was supported by Shandong Province Potato Industry Technology System Agricultural Machinery Post Expert Project (SDAIT-16-10) and Shandong Province Key R&D Plan (Major Scientific and Technological Innovation Project) Project (No. 2022CXGC020703).

REFERENCES

[1] Chen, X., Zhao, X., Chen, L., et al., (2018) Simplified seedling emergence and non-breaking film cultivation techniques of yam (山药简化出苗免破膜栽培技术), *Hebei Agriculture*, Issue 05 pp. 25-26, Hebei/China.

[2] Cheng, M., (2022), *Design and experiment of garlic seedling film breaker based on delta manipulator* (基于 Delta 机械臂的大蒜幼苗破膜机设计与试验), Master dissertation, Shandong Agricultural University/China.

[3] Escuredo, O., Seijo, R., Ana, G., et al., (2019), Seasonal Dynamics of Alternaria during the Potato Growing Cycle and the Influence of Weather on the Early Blight Disease in North-West Spain, *American Journal of Potato Research*, Vol. 96, Issue 6, pp. 532-540, Spain.

[4] Fu, L., Song, Z., Zhang, X., et al., (2022), Applications and research progress of deep learning in agriculture (深度学习方法在农业信息中的研究进展与应用现状), *Journal of China Agricultural University*, Vol. 25, Issue 02, pp. 105-120, Shaanxi /China.

[5] Hou, J., Zhang, G., Zhang, X., et al., (2021), *A potato seeder for manually punching holes on a film*. Patent, No. CN212660552U, China.

[6] Huang, T., Huang, H., LI., et al., (2022), Citrus fruit recognition method based on the improved model of YOLOv5 (基于 YOLOv5 改进模型的柑橘果实识别方法), *Journal of Huazhong Agricultural University*, Vol. 41 Issue 04, pp. 170-177, Guangdong/China.

[7] Han, C., Yan, C., Chou, S., et al., (2023), Design and Experiment of Double Disc Cotton Topping Device Based on Machine Vision (基于机器视觉的双圆盘式棉花打顶装置设计与试验), *Transactions of the Chinese Society for Agricultural Machinery*, Vol. 54, Issue 05, pp. 36-46 Xinjiang/China.

[8] Kim, M., Kim, Y., (2022), Parcel Classification and Positioning of Intelligent Parcel Storage System Based on YOLOv5, *Applied Sciences*, Vol. 13, Issue 1, South Korea.

[9] Li, Z., Wen, X., Lyu, J., et al., (2019), Analysis and Prospect of Research Progress on Key Technology and Equipment of Mechanization of Potato Planting (马铃薯种植机械化关键技术与装备研究进展分析与展望), *Transactions of the Chinese Society for Agricultural Machinery*, Vol. 50 Issue 3, pp. 1-16, Heilongjiang/China.

[10] Liu, F., Liu, Y., Lin, S., et al., (2020), Fast Recognition Method for Tomatoes under Complex Environments Based on Improved YOLO (基于改进型 YOLO 的复杂环境下番茄果实快速识别方法), *Transactions of the Chinese Society for Agricultural Machinery*, Vol. 51, Issue 6, pp. 229-237, Beijing/China.

[11] Li, T., Yang, M., Zhang, X., et al., (2020), Potato Production Technology and Difference of Mechanization Level in Northwest China (西北地区马铃薯机械化生产技术与差异性研究), *Transactions of the Chinese Society for Agricultural Machinery*, Vol. 51, Issue s1, pp. 307-313, Beijing/China.

[12] Li, L., Li, S., Wang, S., et al., (2021), *A film-breaking seedling introduction machine applied to potato black film.* Patent, No. CN113396760A, China.

[13] Mustaqimah, M., Anas mufti, M., Bulan, R., et al., (2022), Analysis of the performance of a plastic mulch punching machine (Analisis kinerja mesin pelubang mulsa plastik), *INMATEH - Agricultural Engineering*, Vol. 68 Issue 3, pp. 729-734, Indonesia.

[14] Rahaman, M., Shehab, M., (2019) Water consumption, land use and production patterns of rice, wheat and potato in South Asia during 1988–2012, *Sustainable Water Resources Management*, Vol. 5, Issue 4, pp. 1677-1694, Dhaka/Bangladesh.

[15] Sami, A., Sakib, S., Deb, K., et al., (2023), Improved YOLOv5-Based Real-Time Road Pavement Damage Detection in Road Infrastructure Management, *Algorithms*, Vol. 16, Issue 9, Bangladesh.

[16] Tadeo, B., Nagata, M., Mitarai, M., et al., (2000), Study on mechanization of mulching cultivation using biodegradable film for early season culture rice, *Piping/equipment/plant technology*, Vol. 62 Issue 2, pp. 154-166, Japan.

[17] Wang, C., Sun, B., Wang, Z., et al., (2019), Effect of wet felt film-breaking method on the film-breaking rate and yield of garlic (湿毡破膜法对大蒜破膜率及产量的影响), *China Cucurbits and Vegetables*, Vol. 32, Issue 12 pp. 37-40, Henan/China.

[18] Xu, N., Zhang, H., Zhang, R., et al., (2021), Current Situation and Prospect of Potato Planting in China (中国马铃薯种植业现状与展望), *Chinese Potato Journa*l, Vol. 35, Issue 1 pp. 81-96, Heilongjiang/China.

[19] Xiu, C., Sun, L., (2022), Potato Leaf Bud Detection Method Based on Improved YOLO v4 Network (基于改进 YOLO v4 网络的马铃薯自动育苗叶芽检测方法), *Transactions of the Chinese Society for Agricultural Machinery*, Vol. 53, Issue 06 pp. 265-273, Tianjin/China.

[20] Yang, K., Hu, Z., Yu, Z., et al., (2022), Design and Experiment of Garlic Harvesting and Root Cutting Device Based on Deep Learning Target Determination (基于深度学习目标测定的大蒜收获切根装置设计与试验), *Transactions of the Chinese Society for Agricultural Machinery*, Vol. 53 Issue 01, pp. 123-132, Jiangsu/China.

[21] Zhang, W., Zhang, X., Qi, F., (2019), Potato Industry Development Advantages in Dongxiang County and Cultivation Techniques for Natural Membrane Breaking and Emergence of High Ridge Mulch Covering Soil (东乡县马铃薯产业发展优势及高垄膜上覆土自然破膜出苗栽培技术), *Modern Agricultural Science and Technology*, Issue 07, pp. 69-70, Gansu /China.

[22] Zhang, G., Yang, M., Jin, M., et al., (2021), Robot board throwing algorithm based on improved nine-point calibration (基于改进九点标定的机器人投板方法), *Manufacturing Technology and Machine Tool*, Issue 12, pp. 7-14, Hebei/China.

[23] Zong, Z., Liu, G., (2021), Design and Experiment of Maize Fertilization Control System Based on Machine Vision(基于机器视觉的玉米定位施肥控制系统设计与试验), *Transactions of the Chinese Society for Agricultural Machinery*, Vol. 52, Issue s1, pp. 66-73, Beijing/China.

SUPERIOR INFERENTIAL STATISTICS OF THE EXPERIMENTAL DATA OF A COMPLEX EXPERIMENTAL CULTIVATOR
/
STATISTICA INFERENȚIALĂ SUPERIOARĂ A DATELOR EXPERIMENTALE ALE UNUI CULTIVATOR EXPERIMENTAL COMPLEX

Petru CARDEI[1)], Nicolae CONSTANTIN[1)], Cătălin PERSU[1)], Vergil MURARU[1)], Raluca SFÎRU[1*)], Maria IAMANDEI[2)*], Daniel LATES[3)]

[1)]INMA Bucharest / Romania; [2)]Research Development Institute for Plant Protection Bucharest / Romania;
[3)] "George Emil Palade" University of Medicine, Pharmacy, Sciences and Technology from Târgu Mureș / Romania
Tel: 0040723333159; E-mail: raluca_sfiru@yahoo.com; maria_iamandei@yahoo.com
DOI: https://doi.org/10.35633/inmateh-71-12

Keywords: *statistical tools, statistical modelling, complex agricultural cultivator, agricultural aggregate speed, predictors, Artificial neural networks, multivariate analysis*

ABSTRACT

The aim of the research is to highlight some statistical tools that favour extracting the components of the dynamic process that are dependent on the forward speed of some agricultural aggregates. The main objectives are: (I) identification of a minimum number of components in a multitude of random variables, with the help of which the other random variables can be calculated, and the application of this result to the strain gauge measurements; (II) establishing the connection between the synthetic results that partially solve the first objective and the forward speed of the agricultural aggregate. The second objective is used to obtain indications in search of the parameters' dependencies on the forward speed of the aggregate. The first objective seeks to determine a group of three signals from the twelve, with the help of which the best multivariate linear interpolation is obtained for the other nine signals, which in physical terms means the reduction to a quarter of the measurement points and of the strain sensors used. A result associated with the first objective refers to the estimation of information loss due to the limited number of deformation sensors mounted on the tested structure. The article also presents attempts to use the results of the theory of neural networks and statistical interaction. In order to capitalise on the experimental data in this complex statistical framework, it is necessary to monitor at least the working speed (not only the average speed per experiment), fuel consumption, working depth (continuously monitored), soil moisture etc.

REZUMAT

Scopul cercetării este de a evidenția unele instrumente statistice care favorizează extragerea componentelor procesului dinamic care sunt dependente de viteza de avans a unor agregate agricole. Principalele obiective sunt: (I) identificarea unui număr minim de componente într-o multitudine de variabile aleatoare, cu ajutorul cărora pot fi calculate celelalte variabile aleatoare și aplicarea acestui rezultat la măsurătorile extensometrice; (II) stabilirea legăturii dintre rezultatele sintetice care rezolvă parțial primul obiectiv și viteza de avans a agregatului agricol. Al doilea obiectiv este utilizat pentru a obține indicații în căutarea dependențelor parametrilor de viteza de avans a agregatului. Primul obiectiv urmărește determinarea unui grup de trei semnale din cele douăsprezece, cu ajutorul cărora se obține cea mai bună interpolare liniară multivariată pentru celelalte nouă semnale, ceea ce în termeni fizici înseamnă reducerea la un sfert a punctelor de măsurare și a senzorilor de deformare utilizați. Un rezultat asociat primului obiectiv se referă la estimarea pierderii de informații din cauza numărului limitat de senzori de deformare montați pe structura testată. Articolul prezintă, de asemenea, încercări de utilizare a rezultatelor teoriei rețelelor neuronale și a interacțiunii statistice. Pentru a valorifica datele experimentale din acest cadru statistic complex, este necesar să se monitorizeze cel puțin viteza de lucru (nu doar viteza medie pe experiment), consumul de combustibil, adâncimea de lucru (monitorizată continuu), umiditatea solului etc.

INTRODUCTION

The results presented in this article are the last of the series of those presented by *Cardei and collaborators* (*Cardei et al., 2023a*; *Cardei et al., 2023b*; *Cardei et al., 2023c*) regarding the numerical data obtained in the field with a complex structure of experimental cultivator MCLS.

The dependence of some parameters of the dynamics of agricultural aggregates on the forward speed has been studied for many decades, with various solutions appearing in many publications (*Letosnev, 1959; Moenifa et al., 2014; Cardei et al., 2019; Cardei et al., 2020; Ranjbar et al., 2013; Naderloo et al., 2009; ASAE, 2003 and 2017; McKyes, 1985; Owen 1989; Larson, 1964; Fechete-Tutunaru et al., 2019; Cardei et al., 2023b; Shafei et al., 2018; Damanauskas, Janulevicius, 2022; Dizaji, 2022; Karmarkar, Gilke, 2021; Askari et al., 2017; Al-Suhaibani, Ghaly, 2010; Elsheika et al., 2021; Deshpande, Shirwal, 2017; Saleh et al., 2021; Rashidi et al., 2013*), for example. In general, the draft force depending on the main parameters that define the soil, the geometry of the working bodies, the mass of the machine, the forward speed, the working depth, and the working width was studied and modelled. At first, simple models were proposed, for example *Letosnev* (*1959*), then the models were gradually complicated with geometric components, for example (*McKyes, 1985; Owen 1989; Al-Neama, Hertzilius, 2017*). Later, generalisations appeared relative to the components that contain work speed, in *ASAE* (*2003*) or *Moenifar et al.* (*2014*). In search of more precise approximations of the draft force, the research became theoretical-experimental. The experimental data were directly transformed into formulas through various interpolation procedures. Since experimental research has taken place on a large scale, statistics have been increasingly used for the processing of experimental data, as shown in *Da Silva et al.* (*2020*) or *Gomez and Gomez* (*1984*), referring to modern agriculture. Having as an objective the rationalisation of fuel consumption, the authors *Mamkagh*(*2018*) and *Singh et al.* (*2018*) carried out some review of the main influencing factors: forward speed, tractor ballast, and tyre pressure. Finally, the authors *Sadek et al*. (*2021*) determine, using experimental data, a linear regression equation in which the forward speed, gang angle, inclination angle, working depth, and disc diameter appear. The authors *Ahmed and Al_Sayed* (*2022*) obtained results regarding the influence of forward speed and soil type on the performance of the Massey Ferguson tractor (model 290). Analysis of variance, or ANOVA tests, are used, for example in *Deshpande and Shirwal*(*2017*), to determine the influence of the forward speed and the shape of the working bodies on the draft force. Statistical modelling has become a tool often used to make predictions of draft force. For this purpose, speed and working depth are used as predictors, as are others (*Afify et al.,2020; Kim et al., 2020; Rashidi, 2013a and 2013b; Saleh et al., 2021*). Artificial neural networks have started to be used in the last decades to obtain predictions of the parameters targeted in the field of agricultural soil processing (*Shafei et al., 2018; Çarman et al., 2021; El Wahed, Aboukarima, 2007; Al-Dosary et al., 2020; Carman et al., 2019; Askari, Abbaspour-Gilandeh, 2020*). Also, nonlinear regression formulas for the problem of predicting the draft tillage force are used in *Shafei et al.* (*2018*) and *Almaliki et al*. (*2019*), in the case of a disc plough. The use of neural networks in the case of measuring several parameters, including fuel consumption, allowed highlighting the decrease in this consumption with the increase in forward speed (*Çarman et al., 2019*).

Proceeding in this way, the generality of the solution is deeply affected due to the dependence on the soil and the environmental conditions in which the experiments were made. Not only the generality was affected, but also the cost of research. Experimental research, however satisfactory, is expensive and beyond the reach of any research team.

The research whose results are described in this work also uses experimental data in the statistical framework, both descriptive and inferential. Within the descriptive statistics, it was sought to highlight some estimators that are well correlated with the forward speed. Inferential statistics were used to investigate the possibilities of reducing the number of measurements or measurement points with minimal loss of information. For this purpose, linear multivariate analysis techniques were used, which are also used in PCA analyses or in neural networks. Due to the small data structure, the statistical analysis of the networks, which can provide very important results, could not be applied in these studies (*Brinkmeier, Schank, 2005; Avrachenkov, Dreveton, 2022*). Instead, it was possible to estimate some of the structural data needed for modelling, which must be collected in future experiments to effectively use such statistical tools.

Regarding the first objective of our research, namely that of studying the relationships between the randomvariables that describe each recording within an experiment, modern statistics provides a specific notion calledinteraction (statistics), defined in *Dodge* (*2003*); *Cox* (*1984*); *https://en.wikipedia.org/wiki/Interaction_(statistics)*. According to these sources, in statistics, an interaction can occur when considering the relationship between three or more variables and describing a situation where the effect of one causal variable on an outcome depends on the state of a second causal variable (i.e., when the effects of the two causes are not additive). Interactions are often considered in regression analyses or factorial experiments. Non-linear relationships with interaction have been proposed since the beginning of modelling the phenomenon of soil processing in agriculture (*Cardei et al., 2019*).

Also, in a research done by *Dodge* (*2003*), it was stated that the presence of interactions can have important implications for the interpretation of statistical models. If two variables of interest interact, the relationship between each of the interacting variables and a third "dependent variable" depends on the value of the other interacting variable. In practice, this makes it more difficult to predict the consequences of changing the value of a variable, especially if the variables it interacts with are difficult to measure or control.

The notion of interaction is closely related to that of moderation, which is common in social and health science research. The interaction between an explanatory variable and an environmental variable suggests that the effect of the explanatory variable was moderated or modified by the environmental variable (*Dodge, 2003*). This framework of statistical interaction is probably the best description of our research framework for achieving, the first goal. The link between the notions of interaction and influence is strong, as the dictionary also shows (*https://dexonline.ro/definitie/interacțiune;https://dictionary.cambridge.org/dictionary/english/interaction*).

The efficiency of some modern scientific tools is evaluated in the problem of forecasting traction parameters in soil works, such as the neuro-fuzzy strategy (*Shafei et al., 2018*). The method of optimising the combination of channels that, through multivariate analysis, can generate the best linear approximations of the other channels considered unmonitored, presented in subchapter 2.3 and whose results are summarised in table 3, is part of the working techniques of inferential statistical analysis described in the last paragraphs. The method is simple and logical, and it only needs knowledge of the definitions of the notions to be worked with. Calculation algorithms can be easily developed without the need for software specialists. The calculation volume increases a lot with the number of basic channels (monitored and unmonitored) and with the number of experiments. The dependence on the working speed of the optimal predictor channel combinations is insignificant, remaining in the field of randomness.

MATERIALS AND METHODS

The working material of the research whose results are presented in this article is made up of the strain gauge measurement recordings made in experiments carried out in 2022, presented in detail in *Cardei et al.* (*2023a and 2023b*).

The research, the results of which are described in this article, proposed the analysis of experimental recordings as sets of parametrized random variables. Concretely, the sets of random variables are the experimental records (converted into draft force) grouped into 12 numerical strings each, with different lengths between 2000 and 4000 samples (real numbers). Seven such groups of random variables were examined and parameterized according to the timed average speed corresponding to each experiment.

Our investigations tried to highlight the characterization efficiency of some statistical tools, the detection of possible links between the random variables of each group or the non-existence of these links, the correlation of some characteristics with the values of the characterization parameters of the groups (forwarded speed), or the non-correlation. Therefore, the investigations are open to any conclusions and do not follow a fixed orientation, such as, for example, the optimisation of some work regimes. The aim is only to obtain information that can be used in the research activities that will be developed.



Fig. 1 - The tractor unit (45 HP)-MCLS, the version with a working width of 1 m (left), and the locations of the deformation sensors on the supports of the working bodies of the MCLS (right)

2.1. The average signal

In this chapter, the average signal of the twelve signals collected from the supports of the working bodies of the MCLS, the version with a working width of 1 m, will be defined according to equation (2). Definition (1) was considered.

$$A = \{x_{i,j}, i = 0, \dots n, j = 0, \dots, 11\} \quad (1)$$

Where: A is the matrix of numerical recordings converted into forces obtained from the twelve deformation sensors (fig. 1, right). An average signal will be defined according to the natural definition given in (2).

$$xm_i = \frac{\sum_{k=0}^{11} x_{i,k}}{12} \quad (2)$$

For each moment of time (sample), the average signal represents the arithmetic mean of the values of the twelve signals at that moment (sample).

For the study of the dependence of the force on the traction resistance, a quantity dependent on the variation compared to the average of the signals that form the columns of the matrix A namely the matrix of standardized signals, is defined:

$$AS = \{xs_{i,j}, i = 0 \dots n, j = 0, \dots, 11\} \quad (3)$$

where:

$$xs_{i,j} = \frac{x_{i,j} - \mu_j}{\sigma_j} \quad (4)$$

and:

$$\mu_j = \frac{\sum_{k=0}^{n} x_{k,j}}{n}, \sigma_j = \sqrt{\frac{\sum_{k=0}^{n} (x_{k,j} - \mu_j)^2}{n-1}}, j = 0, \dots 11. \quad (5)$$

are the mean and standard deviation of the signal j. To give a measure of the representativeness of the average signal, (2), for the signals collected during an experiment, it was used the formula of a given distance as in (6).

$$dmed_j = \sqrt{\sum_{k=0}^{n-1} ((A^{\langle j \rangle})_k - xm_k)^2} \quad (6)$$

The coding of the recording channels, according to the notations in Fig. 1 (right), is listed in Table 1.

Table 1

Coding of signals stored in matrix A

$ch4$	$A^{\langle 0 \rangle}$	$x_{i,3}, i = 0, \dots, n$	$ch23$	$A^{\langle 10 \rangle}$	$x_{i,10}, i = 0, \dots, n$	$ch24$	$A^{\langle 11 \rangle}$	$x_{i,11}, i = 0, \dots, n$
$ch21$	$A^{\langle 8 \rangle}$	$x_{i,8}, i = 0, \dots, n$	$ch3$	$A^{\langle 2 \rangle}$	$x_{i,2}, i = 0, \dots, n$	$ch22$	$A^{\langle 9 \rangle}$	$x_{i,9}, i = 0, \dots, n$
$ch19$	$A^{\langle 6 \rangle}$	$x_{i,6}, i = 0, \dots, n$	$ch20$	$A^{\langle 7 \rangle}$	$x_{i,7}, i = 0, \dots, n$	$ch2$	$A^{\langle 1 \rangle}$	$x_{i,1}, i = 0, \dots, n$
$ch1$	$A^{\langle 0 \rangle}$	$x_{i,0}, i = 0, \dots, n$	$ch17$	$A^{\langle 4 \rangle}$	$x_{i,4}, i = 0, \dots, n$	$ch18$	$A^{\langle 5 \rangle}$	$x_{i,5}, i = 0, \dots, n$

In Table 1, by $A^{\langle j \rangle}$, was symbolised the column j of the data matrix A, which contains the signal $j = 0, \dots, 11$. Table 1 contains notations valid for each of the seven experiments, corresponding to six different values of the average forward speed (two experiments were carried out with the same speed). The experiment codes, corresponding average forward speed, and data file sizes are listed in Table 2.

Table 2

The codes, the average speeds, and the sizes of the data files corresponding to the experiments

Experiment code	Rows	Cols	Forward speed, m/s
T2_R2_1500rpmtxt	4001	13	0.781
T1_R2_2400rpmtxt	4001	13	0.789
T1_R3_1500rpmtxt	2501	13	1.095
T2_R2_2700rpmtxt	1501	13	1.613
T2_R3_1500rpmtxt	2501	13	1.613
T3_R2_1500rpmtxt	2201	13	2.158
T2_R3_2000rpmtxt	1701	13	2.256

2.2. The statistical estimators calculated for the evaluation of the link with the forward speed

To evaluate the link between the draft force and the forward speed of the aggregate, the most frequently used descriptive statistical estimators were used: the average value, the median, the variance, the standard deviation, the asymmetry coefficient, and the vaulting for all the signals of each experiment and for the average experiment of each experiment, both for the original signals (1) and for the standardised signals (3). The results are given in Table 3.

2.3. Determination of essential components for signal interpolation

The estimators whose method of calculation is explained in this chapter are not part of the category of descriptive statistics but are elements of inferential statistical analysis. These estimators are developed for the purpose of finding the "best channel combinations" (of channel recordings). The optimal meaning of this combination of random variables (experimental records) is that, with their help, a linear multivariate interpolation formula can be obtained, which produces a matrix of the coefficients of determination with the largest sum of elements or produces signals of interpolation with the smallest variation compared to the original signals.

To achieve this goal, several channels are conventionally used. Any number of channels between 1 and the maximum number of registered channels can be taken. Obviously, the interest is to reproduce as much information as possible (see 2.4) with as few physical records as possible. If the interests of the experimenter and the operator who processes the data are considered, then the smallest possible number of sensors that generate a quantity of information that can be generalised to the entire studied structure would be taken into account. In the case of the version with a working width of 1 m of the MCLS (fig. 1), the maximum number of recorded channels is 12. For the optimisation analysis of the linear multivariate interpolation, the number of three basic channels was taken inspired by the number of channels on a line of working body perpendicular to the forward axis of the aggregate. Obviously, one, two, four, or more channels could be used. Increasing the number of channels makes the operation more expensive (when processing only for calculation but when experimenting with all sensor mounting operations, calibration, and recording, in addition to the optimal selections for eliminating transient areas or recording accidents). If fewer basic channels are taken, then obviously the precision decreases and the loss of information becomes important (see 2.4).

If three basic channels are taken, the number of possible combinations between the 12 channels is 220 (for a number N of basic channels, $C_{12}^{N}, N = 1, \dots, 12$ possible combinations of channels that each generate a linear multivariate interpolation must be estimated for N variables). In this case, N=3 was taken, and for each of the seven experiments, 220 interpolations were made. Then, for each interpolation, the coefficient of determination and the variance were selected. There were two objectives. The first was the global coefficient of determination (the sum of the coefficients of determination corresponding to the interpolation with the combination of channels used, including the basic channels, so the maximum value would be 12). The second objective function was the sum of variances achieved with each interpolation over all signals in an experiment (global variance). The optimisation consisted of maximising the global coefficient of determination objective function and minimising the global variance objective function. The results for each experiment are listed in Table 3.

The calculations presented in subsection 2.3 are related to the notion of *statistical interaction*, to which references were made in the introduction of the article.

2.4. Loss of information due to survey measurement

In general, in practise, strain sensors are mounted on a small number of measurement points. In this way, information loss occurs. In this subchapter, it was intended to give the reader an idea of the size of the information loss.

First, the term "information loss" must be rigorously defined because the calculation depends on the definition. For simplicity, an information loss will be defined relative to the arithmetic mean of the random variables (the twelve numerical strings collected on the measurement channels, fig. 1, right), because it is simpler to calculate. Therefore, the information loss is defined relative to the average value of the random variables by formula (7).

$$I_l = \min_{k=0,\dots,219} \sum_{j=0}^{11} \frac{|\mu 3_k - \mu_j|}{12 \cdot \mu_j} \tag{7}$$

In Eq.7, $\mu 3_k$ is the arithmetic mean of the basic channel signals, μ_j is the arithmetic mean of the recording on channel j. The minimum value is taken after all 220 combinations of three channels out of the 12 possible.

Practically, for each of the combinations of channels (random variables) generated by the combinations of twelve taken in threes (see 2.3), the arithmetic mean of the three channels is calculated. From this, the mean corresponding to each channel is subtracted in absolute value, after which it is summed up, averaged over the number of channels, and relativized to the true average (measured in this experiment). After this, the combination with the minimum value of information loss from the 220 results is taken. The third set of channels realises the minimum loss of information and retains the amount of this loss. With these specifications, the combinations and values of the minimum information loss are obtained for each of the seven experiments listed in Table 2. These combinations and the corresponding information loss values are listed in Table 3.

Obviously, instead of three basic channels, any number between 1 and the number of channels (random variables) contained in the data file can be used. With the increase in the number of basic channels considered for the calculation of the average value (or other comparison criteria), the precision increases, but the measurements with a larger number of basic channels are more expensive.

Instead of the average value criterion for choosing a satisfactory base combination of the measurement channels, the global option can be chosen for the optimisation criterion, as defined in 2.3. The calculation becomes much more complex. Also, the calculation becomes more complex, and when we choose a larger number of basic channels, for example, taking the number of combinations for four basic channels, 495 combinationsthat must be evaluated are obtained.

RESULTS

The numerical results obtained using the methods described above are given in this chapter. For a better understanding, fig. 2 gives the graphic representation of the signals of a data file recorded in one of the seven experiments, namely the one with the code T3_R2_1500rpmtxt, corresponding to the average forward speed of the aggregate with a value of 2.158 m/s. In order to make the discrete curves and the average curve more easily observable, only 1000 samples were represented from 2201 of the selected recording (to eliminate transient passages). In Fig. 3, the same type of graphs is given but for standardised signals, according to formulas (3), (4), and (5).

Graphic representations like those in Figs. 2 and 3 are obtained for each of the seven data files recorded in the seven experiments. The channels in the legends of Figs. 2 and 3 correspond to the labels of the deformation sensors mounted on the structure according to Fig. 1 (right). Using formulas 2, 3, 4, and 5, it is observed that the average value of the standardised signal and the average value of the average standardised signal are zero. For this reason, they were not included in Table 3 because their correlation with the speed of travel is meaningless. In the same situation are the variance of all the signals and the standard deviation for the standardised signals, which give a constant value of 1.1.

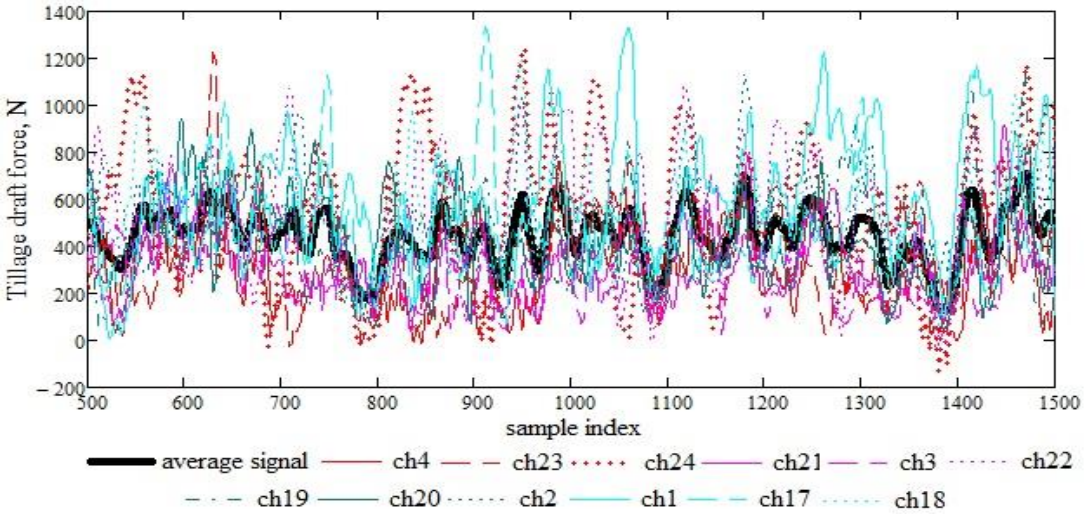


Fig. 2 - Graphic representation of the recorded signals and the average signal for the experiment, working at a forward speed of 2.158 m/s

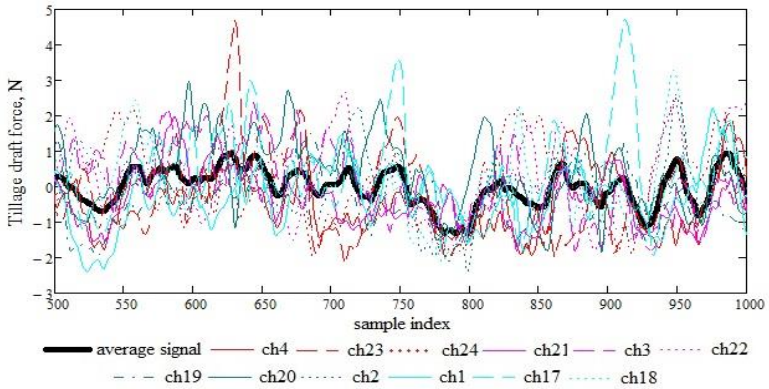


Fig. 3 - Graphic representation of the recorded signals and the average signal for the experiment (detail), working at a forward speed of 2.158 m/s

The values of the statistical estimators calculated for each signal and experimental recording and their correlations with the forward speed

The values of the main statistical estimators of the signals, in the original and standardised versions, as well as the optimal interpolation performances using as a basis three signals from each experimental data file, are listed in Table 3.

Table 3

Descriptive statistics estimators of the data recorded in the experiments carried out with the 1 m working width variant of MCLS and estimators of the optimal channels for generating the other recordings

Experiment code	T2_R2_ 1500rpmtxt	T1_R2_ 2400rpmtxt	T1_R3_ 1500rpmtxt	T2_R2_ 2700rpmtxt	T2_R3_ 1500rpmtxt	T3_R2_ 1500rpmtxt	T2_R3_ 2000rpmtxt	Correlation with speed
Speed, m/s	**0.781**	**0.789**	**1.095**	**1.613**	**1.613**	**2.158**	**2.256**	1
Minimum value, N	16.342	23.03	30.952	-51.566	28.041	-130.612	-65.466	-0.805
Maximum value, N	1110.303	1086.078	1432.804	1345.208	1250.377	1343.686	1468.57	0.715
Mean value, N	478.413	518.448	491.532	508.53	495.54	448.719	452.695	-0.6842359
Mean value of the mean signal, N	478.413	518.448	491.532	508.53	495.54	448.719	452.695	-0.6842359
Median, N	474.97	517.684	480.54	494.14	474.473	423.896	441.37	-0.7870628
Median of the mean signal, N	484.086	520.204	495.332	502.667	492.819	453.272	461.094	-0.7554842
Variance of all signals	30764.988	24291.887	27717.492	38210.409	31887.955	49279.026	46055.503	0.9188198
Average signal variance	5318.869	4600.255	6822.551	9501.582	5120.232	13059.114	12081.83	0.8738812
Standard deviation (A)	175.4	155.859	166.486	195.475	178.572	221.989	214.605	0.9197003
Standard deviation (xm)	72.931	67.825	82.599	97.476	71.556	114.276	109.917	0.8679225
Skew (A)	0.126	0.127	0.39	0.405	0.503	0.572	0.399	0.8141647
Skew (xm)	-0.699	-0.192	-0.127	0.112	0.26	-0.334	-0.146	0.329507
Kurt (A)	-0.223	-0.187	0.377	0.364	-0.026	0.166	0.222	0.5266001
Kurt (xm)	0.864	-0.03	-0.015	-0.417	0.255	-0.069	-0.338	-0.5818835
Median*, N	-0.017	-0.004	-0.053	-0.11	-0.069	-0.079	-0.068	-0.7393499
Medium signal median*, N	0.036	0.019	0.029	-0.028	-0.017	0.017	0.043	-0.1001057
Medium signal variance*	0.252	0.253	0.297	0.309	0.299	0.314	0.321	0.9077523
Standard deviation (xm)*	0.502	0.503	0.545	0.556	0.547	0.56	0.567	0.9031289
Skew (A)*	0.091	0.076	0.353	0.46	0.46	0.481	0.43	0.8496965
Skew (xm)*	-0.7	-0.201	-0.08	0.082	0.243	-0.295	-0.165	0.3347382
Kurt (A)*	0.022	-0.198	0.467	0.291	0.529	0.147	0.239	0.3787685
Kurt (xm)*	0.959	-0.056	0.007	-0.391	0.282	-0.14	-0.298	-0.5859633

Experiment code	T2_R2_ 1500rpmtxt	T1_R2_ 2400rpmtxt	T1_R3_ 1500rpmtxt	T2_R2_ 2700rpmtxt	T2_R3_ 1500rpmtxt	T3_R2_ 1500rpmtxt	T2_R3_ 2000rpmtxt	Correlation with speed
Maximum component of the correlation Matrix of the original signals	0.645	0.645	0.585	0.749	0.653	0.586	0.628	-0.0767691
Maximum component of the correlation of the original signals with the average signal	0.7	0.683	0.709	0.754	0.636	0.658	0.733	0.0258697
Minimum component of the correlation matrix of the original signals	-0.207	-0.157	-0.042	-0.115	-0.11	-0.105	-0.319	-0.267858
Minimum value of the correlation of the original signals with the average signal	0.289	0.354	0.389	0.272	0.357	0.429	0.395	0.501923
Sum of the distances between the signals and the average signal	20.534	16.801	14.57	12.7	15.786	19.55	16.545	-0.0783404
Optimal combination of channels for maximum R	ch2 ch3 ch19	ch3 ch22 ch23	ch1 ch3 ch18	ch19 ch20 ch22	ch2 ch21 ch24	ch3 ch18 ch19	ch1 ch4 ch22	-
Maximum total R	0.4072	0.4041	0.4408	0.5526	0.4658	0.4714	0.4919	0.6835293
Optimal combination of channels for minimum variance	ch18 ch20 ch22	ch3 ch22 ch23	ch1 ch3 ch18	ch19 ch21 ch24	ch2 ch21 ch24	ch3 ch18 ch19	ch1 ch4 ch22	-
Minimum total variance	4.536	42.13	32.35	22.32	31.57	29.49	25.39	0.0849382
Combination of channels that gives the minimum information loss	ch4 ch18 ch23	ch2 ch19 ch22	ch19 ch20 ch211	ch4 ch18 ch21	ch4 ch19 ch20	ch1 ch3 ch23	ch4 ch20 ch22	-
I_1 minimum, %	19.35	12.163	11.454	15.229	18.997	14.021	15.354	0.042
SMD minimum, %	6.061	13.636	9.091	6.061	7.576	9.091	7.576	-0.299

**For standardised signals.*

Also, Table 3 lists the combinations of channels that achieve the minimum information loss relative to the average of the random variables and the value of this loss in percentages. The value of the Pearson correlation coefficient corresponding to the series of information losses and average forward speeds for the seven analysed experiments is also given.

The main observations from Table 3 are:

- the most intensively correlated statistical estimators with the forward speed of the aggregate are: standard deviation and variance (slightly higher for the original signals than for the average signal);
- an intense descriptive statistical estimator related to the forward speed is, according to the results in Table 2, asymmetry (skew);
- remarkable for future tests are the inverse correlations with the forward speed of the averages and medians of the original signals and the average signal;
- remarkable is also the correlation of the series of the best interpolations made with three channels each if the determination coefficient is taken as a performance criterion; the variance, as a performance criterion of the interpolation, is not correlated with the forward speed.

The last statements are also supported by the linear regression tests, which indicate, for example, a value of 0.92 for the dependence between the standard deviation of the draft force and the work speed and a value of 0.846 for the adjusted coefficient of determination, according to https://jasp-stats.org/. The probability of rejecting the linear model with zero free terms is p=0.003, so the hypothesis of linear dependence is accepted. The proposed linear model is given by relation (8).

$$\sigma_F = 131.871 + 37.388v \quad (8)$$

In (8), σ_F is the standard deviation of the average resistance force per experiment, and v is the average forward speed in the same experiment.

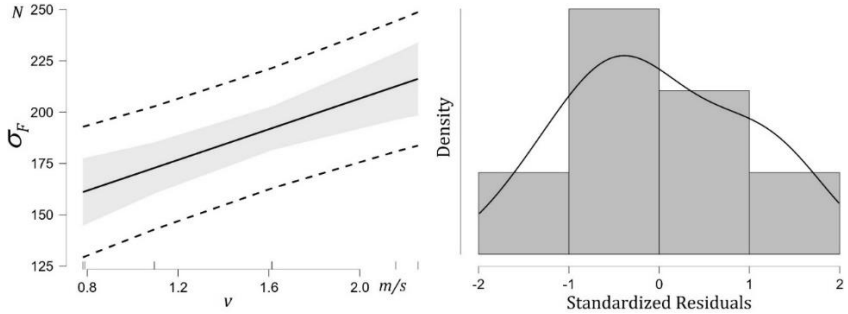


Fig. 4 - Edge effects of forward speed on the standard deviation of the draft force (left) and histogram of standardised residuals (right)

Connection tests between random variables and relationships with work speed values

A PCA analysis, carried out with the help of the JASP programme (*https://jasp-stats.org*), shows that the principal components detected for each of the twelve random variables obtained in each of the seven physical experiments are different in each of the seven experiments both in structure and in number. The main components detected for each work speed differ in number and structure between the seven sets of twelve random variables, and there is no parameter that links the number and structure of the main components to the average forward speed of the experiment. On the other hand, the number and structure of the main components depend on a series of parameters of the programme and the choice of some work options.

Another test on the link between the signals (random variables) of a data file and between their synthetic indicators and the series of forward speeds was obtained using the standardised mean differences (SMD)(*https://cran.rproject.org/web/packages/TOSTER/vignettes/SMD_calcs.html;https://towardsdatascience.com /how-tocompare-two-or-more-distributions-9b06ee4d30bf; https://statisticaloddsandends.wordpress.com/2021/ 10/31/standardized-mean-difference-smd-in-causal-inference*).

An absolute value of SMD below the threshold of 0.1 is conventionally considered the small one between two random variables (*https://towardsdatascience.com/how-to-compare-two-or-more-distributions-9b06ee4d30bf*; *https://statisticaloddsandends.wordpress.com/2021/10/31/standardized-mean-difference-smd-in-causal-inference*). Discussions on the threshold value for separating small differences between random variables and the effects on percentage overlap can be found in *https://www.psychiatrist.com/jcp/psychiatry/mean-difference-standardized-mean-difference-smd-and-their-use-in-meta-analysis*, for example. The online calculation of SMD can be checked at: *https://www.campbellcollaboration.org/escalc/html/EffectSizeCalculator-SMD1.php*. For the seven data sets corresponding to the working speeds realised in our experiments, the percentages of SMDs below the 0.1 threshold (so with small differences between random variables) are listed in Table 3. The maximum percentage of signal pairs with small differences between them is 13,636% in the case of the experiment with an average working speed of 0.789 m/s. This means that most pairs of signals in all seven experiments differ greatly from each other, which is an argument in favour of the random character of the draft force.

Structuring data files with the help of statistical network techniques

In search of the expression or representation of some of the measured channels, depending on the base of channels used as independent variables in the multiple regression calculation, the neural network technique was also used, according to the programme from: *https://jasp-stats.org/*. As dependent variables, three random variables out of the twelve were used, corresponding to the deformation sensors mounted on the supports of the first line of bodies behind the tractor: ch4, ch23, and ch24. For the experiment with the code T2_R2_1500rpmtxt, carried out with an average speed of 0.781 m/s, the network is shown in Fig. 5.

On this network, one can read the weights of the relationships between the dependent variables (the other nine channels, whose labels are written on the network). The programme also provides many other tabulated or graphical data sources. For more information *https://ro.wikipedia.org/wiki/Re%C8%9Bea_neural%C4%83* and the literature included in this source are recommended. The network from Fig. 5 shows the links between the random variables (recordings on each of the twelve channels) and the intensity of these links. The model introduced in the programme data tried to obtain a forecast of the approximation of the signals from the nine channels in the diagram given in Fig. 5, using only the data from the channels on the first line of bodies after the tractor, respectively ch4, ch23, and ch24 (see Fig. 1, right). As it was seen from the analysis in 2.4, the three channels do not give the best result in the interpolation of the other nine channels.

According to the reasoning in 2.4, a neural network analysis should be done for each of the 220 cases highlighted for the three-channel model used for interpolation. For a larger number of interpolation channels (the non-economic case), the number of analyses increases. Practically, this neural network is the precursor of an e-learning network, with three nodes as input, nine nodes consisting of the interpolated channels, and several nodes for validation, as well as many estimators of the interpolation performance that are used. After covering all possible cases, the most favourable case or cases are selected.

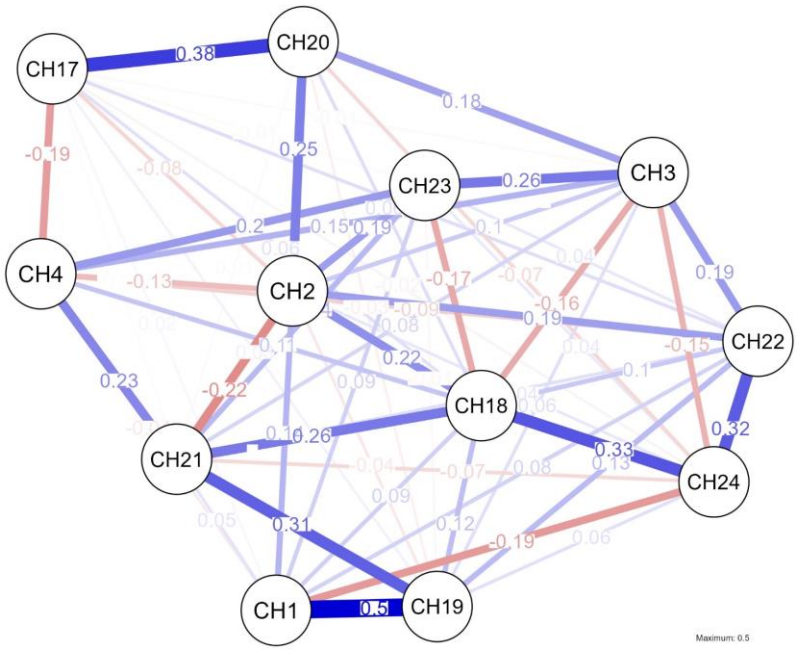


Fig. 5 - The neural network corresponding to the R2_T2_1500rpmtxt experiment, carried out with the average speed having a value of 0.781 m/s, considering all channels as dependent variables

Figs. 6 and 7 show the structure of the network of random variables formed by the data files of the experiments with the codes T2_R2_1500rpmtxt and T2_R2_2700rpmtxt. The network structures of the other five experiments are not given because it is established that there are no constant groupings and a fixed number of main components (it can be seen in Figs. 6 and 7, experiments with four and three main components, under similar setting conditions of the calculation programme) to help us choose the supports for mounting a small number of deformation sensors so that the loss of information during interpolation is minimal. It is possible to force a constant number of main components with special settings in the calculation, but these have hard-to-appreciate consequences on the interpolation errors (under conditions of the uniform set of the calculation programme, the number of main components has no significant relationship with the value of the forward speed of the aggregate). As a result, principal component analysis is not appropriate for our purposes. Similarly, the use of neural networks or machine learning techniques is not beneficial for our purposes since there is little physical data, which does not allow us to formulate calculation models in which to impose inputs and outputs.

Working techniques with PCA analysis, neural networks, or machine learning would have made sense if there was a complete monitoring of working depth, speed, fuel consumption, etc. Among the parameters listed previously, the dependent variables could have been chosen, while the forward speed and the forces would have become predictors, for example.

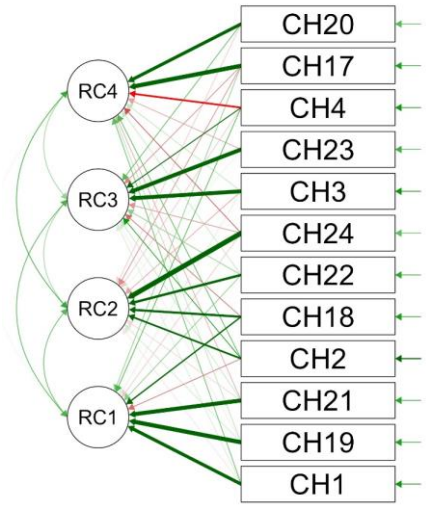


Fig. 6 - Diagram of the main components highlighted in the data file of the experiment T2_R2_1500rpmtxt

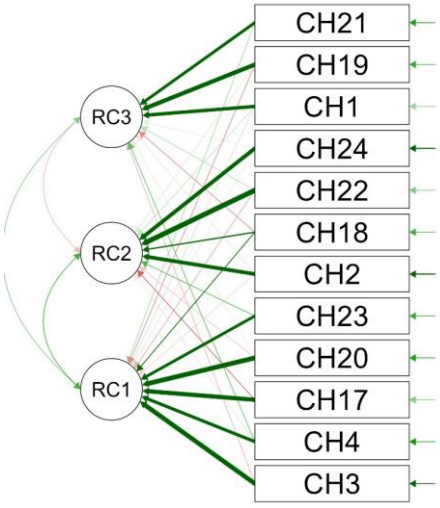


Fig. 7 - Diagram of the main components highlighted in the data file of the experiment T2_R2_2700rpmtxt

COMMENTS

The physical structure whose characteristics were analysed in the research described in this article and in the related precedents (*Cardei et al., 2023a, 2023b, 2023c*) is a working variant of a cultivator, equipped with working bodies whose supports allow vibrations of an appreciable amplitude of assemblies formed by bodies and supports. Moreover, the vibrations are transmitted to the supporting structure, leading to errors in the working depth. For this reason, such soil processing tools are not intended for work that requires high precision in the working depth. Tools of this type have other advantages, as shown, for example, in *Gheorghita et al.* (*2017*) and *Abbaspour-Gilandeh et al.* (*2020*): reducing energy consumption in the execution of agricultural works; improving the quality of agricultural technological processes; increasing the productivity of agricultural machines; and universalizing certain assemblies or subassemblies of agricultural machines.

Complex mathematical models confirm the operation in the vibration mode of cultivators equipped with working bodies used in the experiments of the MCLS variant analysed in this article (*Cardei et al., 2015a and 2015b*). According to some previous works, the search for optimal working speeds is related to crossing certain speed thresholds (*Cardei et al., 2019; Cardei et al., 2021*), which cannot always be reached. One of the observed effects is that, in the absence of rigorous control of the working depth, the increase in the forward speed implies a decrease in the working depth (*Cardei et al., 2023b; Chehaibi et al., 2008*). The authors *Singh et al*. (*2018*) confirmed two clear phenomena: increasing draft force with working speed and with working depth. It is also important to note that the increase in draft force due to the increase in working depth is much more significant than the increase in the same force due to the increase in work speed, which is also shown in *Dizaji et al.* (*2022*); *Karmarkar and Gilke* (*2021*). However, the authors *Singh et al.* (*2018*) do not specify whether increasing the working speed affects the precision of the working depth. *Kim et al.* (*2022*) finds the well-known conclusions also noted by the authors *Singh et al.* (*2018*), but, in addition, they also find a decrease in the working depth with the increase of the working speed (for each of the three types of soil they worked on). The attempt to maintain or increase the working depth results in an increase in the slippage of the tractor, a phenomenon noticed by *Chenarbon* (*2022*), and implicitly affects the increase in the working speed. Experimental research with statistical processing of the results regarding the skidding (or sliding) of traction wheels and the effect of loading these wheels is published in *Taghavifar and Mrdani* (*2015*). For more in-depth studies on the traction performance of tractors, one can consult the work of *Zoz and Grisso* (*2003*). For electric tractors, the results of similar research, also using inferential statistical analysis techniques, are published in *Baek et al.* (*2022*). Similar conclusions are obtained by the authors *Al-Suhaibani and Ghaly* (*2010*), who make additional specifications on the vertical component of traction and on the unit of horizontal and vertical draft. The authors *Al-Suhaibani and Ghaly* (*2010*) also do not refer to the influence of the forward speed on the precision of the working depth. Monitoring the working depth is a difficult problem; this may be the reason why it is rarely performed. A solution for monitoring the working depth is presented by the authors *Kim et al.* (*2020*).

The authors *Damanauskas and Janulevicius* (*2022*) find the same conclusions relative to the dependence of the traction resistance force on the forward speed and on the working depth, their work focusing on other very important and less common aspects, namely the dependence of the quality of soil processing on the speed and depth of work in two types of soil. The authors *Askari et al.* (*2017*) also find an increasing dependence of the draft force on working depth and speed. In *Askari et al.* (*2017*), it is also shown that, under the specified experimental conditions, the increase in draft force decreases, in general (with some exceptions), depending on the working speed; that is, the force increases, but its derivative in relation to the speed decreases. Similar conclusions are reached by the authors *Becker et al.* (*2019*) for operations of cutting plant residues in cultivation systems without ploughing (no-tillage systems). The authors *Becker et al.* (*2019*) use the tools of experimental research and statistical processing of the results, including inferential analysis (box-plot representations, statistical tests, interpolations, etc.). According to the results of *Becker et al.* (*2019*), the traction force increases non-linearly with the working speed, which leads to the same type of increase in the hourly fuel consumption.

Descriptive and inferential statistical tools and the technique of random functions are not new techniques; they have been frequently used in the field of motor vehicle research since the second half of the 20th century (*Sireteanu, 1981; Harris and Crede, 1969; Negrus et al., 1983*). Moreover, in *Myalo et al.* (*2019*), Marius Iosifescu drew attention to the delay in the introduction of these tools into education: "However, we cannot overlook the fact that, in a striking discrepancy with the role they play today, the theory of probabilities and mathematical statistics have not find their place and the appropriate weight in the study programmes of technical and economic influence on the ability of our technical and economic specialists to successfully solve the complex problems of tomorrow's world". This is what it was found in *Cardei et al.* (*2023b*). In addition, these appreciations also refer today to the research activity, where the limits of purely theoretical models are becoming more and more visible.

Regarding the objective of finding possible relationships between the random variables that are part of the recordings of some experiments, the literature is poor in such attempts, if not completely devoid of examples. Somewhat more complex statistical tools, such as ANOVA-type analyses, were used to highlight the effect of soil moisture, working depth, and forward speed on the forward resistance force (*Deshpande, Shirwal S., 2017; Saleh et al., 2021; Rashidi et al., 2013; Shafei et al., 2018*), for example. Multivariate regression analysis is used by the authors *Sadek et al*. (*2021*) to estimate the effects of forward speed and working depth on the longitudinal and vertical components of the draft force. Regression analysis is used by the authors *Sadek et al.* (*2021*) together with DEM (discrete element method, available at https://en.wikipedia.org/wiki/Discrete_element_method) analysis of the working process of a disc in soil. The authors *Sadek et al.* (*2021*) show that increasing the forward speed and/or the working depth contributes to the increase of the longitudinal component (soil draft force) and to the decrease of the vertical component. In *Myalo et al.* (*2019*), it is shown that the elastic systems of some cultivators increase the traction resistance force, but the whole of the working bodies is not studied, but only an individual working body. The authors *Babitsky et al*. (*2021*) use the shape of the scarab as a source of inspiration for the design of the working bodies of a cultivator, but they still limit themselves to an individual working body; they do not address the whole, the relationships between the bodies, or the degree of randomness of their movements. Only at the theoretical level (mathematical modelling) was an initial approach to the problem of the interaction of the working bodies of cultivators made (*Cardei et al., 2015b*). Modern experiments are done on problems that interact deeply with the problem of the effect of the interaction of the working bodies of the cultivators (*Fanigliulo et al., 2023*). Multiple regression prediction models are used by the authors *Askari et al.* (*2017*) for the prediction of the traction resistance force depending on the forward speed, working depth, and working width of a working body wing for three types of bodies: subsoiler, paraplow, and bentleg. The conclusions are like those in the published literature and those found in this paper. The authors *Saleh et al.* (*2021*) proceed in the same way, relative to a characteristic soil for an area of Nigeria. Again, the same conclusions apply: the increase in draft force is associated both with the increase in forward speed and with the working depth. From the results presented in graphic form, the non-linear trend of these relationships can be observed. For the study of the non-linear aspect of the dependence of the draft force on the forward speed and working depth (but also on other parameters such as soil moisture, working width, etc.), more data (and therefore more experiences) are needed to satisfy the calculation needs of the nonlinear multivariate analysis programmes, at least of the second degree. Similar results (increasing draft force with forward speed and working depth, as well as the non-linear aspect) are obtained by more complicated statistical methods in the paper of *Shafei et al.* (*2018*), together with the evaluation of the prediction procedure that uses the neuro-fuzzy modelling method.

CONCLUSIONS

The obtained results allow drawing some conclusions linked to their possible practical application. As for example, the triplets of strain sensors that perform the interpolation of all the signals in the processed experiments do not at the same time maximise the coefficient of determination *R*, minimise the variance, and minimise the loss of information relative to the average value of the signal. As a result, the statistical results show that working with only three deformation sensors, all three optimisation objectives cannot be simultaneously achieved. Optimal compromise criteria can be developed. The correlation of the synthetic characteristics of the experiments with the forward speeds has high values for the variance over all signals (0.9188), the standard deviation (0.9197), the variance of the average signal (0.87388), and the standard deviation of the average signal (0.8679). Also interesting are the values of 0.739 for the median of the average signal, 0.68 for the coefficient of determination, and -0.68 for the average value of the signal and the average signal. As a result, the influence of feed (or work) speed on draft force is most easily found using the standard deviation or variance. Also, it appears that the minimum and maximum values of the force on the set of the twelve channels of each recording correlate well with the forward speed: the maximum value is in direct correlation with the value 0.715, and the minimum in inverse correlation with the value -0.805. The twelve signals corresponding to each of the seven experiments with different forward speeds (yet two with the same speed value) do not show connections between them and do not show signs of influence, which provides an additional reason to characterise the vibrations in the work of the cultivator's bodies as predominantly random. The use in the analysis of some complex inferential statistical tools (non-linear multivariate analysis, factor analyses, variance analyses, statistical interaction analyses, etc.) can bring new data and knowledge only for data collections containing the monitoring of many parameters of the experienced and modelled system (input, output, control, and adjustment parameters). The data collections analysed in this article and in the previous ones contain only one continuously monitored parameter (soil tillage draft force, measured indirectly through strain gauge measurement), the forward speed is estimated as an average per experiment, and the working depth is estimated only through a few surveys as a number and is ineffective. That is why complete statistical analyses are useless and even impossible in this case. Practically, in common experiments and in exploitation, the forward speed, and the working depth (even the working width) are random parameters obtained from the interaction of the soil processing machine and the entire aggregate with the soil and vegetation. These parameters must be permanently monitored and recorded at the values they take; their exact programming has no meaning in such a random framework as that of the soil processing phenomenon. It is sufficient to maintain these parameters within the desired limits.

REFERENCES

[1] Abbaspour-Gilandeh Y., Fazeli M., Roshanianfard A., Hernandez-Hernandez J.L., Penna A.F., Herrera-Miranda I., (2020), Effect of Different Working and Tool Parameters on Performance of Several Types of Cultivators, *Agriculture*, MDPI, Basel/Switzerland, Vol.10, no.5, 145, ISSN:2077-0472, https://doi.org/10.3390/agriculture10050145

[2] Afify M.T., El-Haddad Z.A., Lamia A.A.D., (2020), Modeling the Effect of Soil-Tool Interaction on Draft Force Using Visual Basic, *Annals of Agricultural Sciences, Moshtohor* ***(***AASJM***),*** Benha University / Egypt, Vol. 58, No. 3, pp. 223-232; DOI: 10.21608/ASSJM.2020.112746

[3] Ahmed M.A.A, Al_Sayed A.B., (2022), Effect of Forward Speed and Soil Type in Massey Ferguson Tractor (Model 290) Performance, *Diyala Agricultural Sciences Journal (DASJ)*, College of Agriculture/University of Diyala/Iraq, Vol.14, No 2, ISSN**:** 2310-8746 (Online), pp. 33-42; doi:10.52951/dasj.22140204

[4] Al-Dosary N.M.N., Al-Hamed S.A., Aboukarima A.M., (2020), Application of adaptive neuro-fuzzy inference system to predict draft and energy requirements of a disk plow, *International Journal of Agriculture and Biological Engineering (IJABE)*, Chinese Academy of Agricultural Engineering, Vol.13, No. 2, ISSN 1934-6344 and eISSN 1934-6352, pp. 198-207, DOI: 10.25165/j.ijabe.20201302.4077

[5] Almaliki S., Himoud M.S., Muhsin S.J., (2019), A Stepwise Algorithm for Prognostication Draft Requirements of Disk Plough, *Journal of Engineering and Applied Sciences*, Medwell Publications, Vol. 14, No. 8, ISSN: 1818-7803 (Online), pp. 10335-10340; DOI: 10.36478/jeasci.2019.10335.10340

[6] Al-Neama A.K.A., Hertzilius T., (2017), Draft forces prediction model for standard single tines by using principles of soil mechanics and soil profile evaluation, *Landtechnik*, Vol. 72, no. 3, pp. 157–164, DOI:10.15150/lt.2017.3161

[7] Al-Suhaibani S.A., Ghaly A.E., (2010), Effect of Plowing Depth of Tillage and Forward Speed on the Performance of a Medium Size Chisel Plow Operating in a Sandy Soil, *American Journal of Agricultural and Biological Sciences*, Vol 5, no. 3, ISSN 1557-4989, pp. 247-255, https://www.thescipub.com/pdf/ajabssp.2010.247.255.pdf

[8] American Society of Agricultural Engineers, (2003), *Agricultural machinery management data*, ASAE standards, D497.4, pp. 373-380, In: ASAE. ASAE standards 2003. ASAE, St. Joseph, MI, USA

[9] Askari M., Abbaspour-Gilandeh Y., (2020), Predicting the Imposed Forces on the Tines, and Tractor Fuel Consumption during Subsoiling Operation Using Adaptive Neuro-Fuzzy Inference System (ANFIS), *Agricultural Mechanization and System Research*, Vol. 21, No. 47, pp. 47-66; https://doi.org/10.22092/amsr.2023.361037.1435

[10] Askari M., Shahgholi G., Abbaspour-Gilandeh Y., (2017), The effect of tine, wing, operating depth, and speed on the draft requirement of subsoil tillage tines, *Research Agricultural Engineering*, ISSN 1805-9376 (ON-LINE), vol. 63, no. 4, pp. 160-167

[11] Avrachenkov K., Dreveton M., (2022), Statistical Analysis of Networks, Boston–Delft: Now Publishers;

[12] Babitsky L.F., Sobolevsky I.V., Kuklin V.A., (2021), Methodology for designing tillage working bodies of a stubble cultivator-flat-cutter based on agricultural biomechanics, *IOP Conf. Series: Earth and Environmental Science* Vol. 868, International Conference on Agricultural Engineering and Green Infrastructure Solutions (AEGIS 2021) 12th-14th May 2021, Tashkent, Uzbekistan, DOI 10.1088/1755-1315/868/1/012007

[13] Baek S.-Y., Baek S.-M., Jeon H.-H., Kim W.-S., Kim Y.-S., Sim T.-Y., Choi K.-H., Hong S.-J., Kim H., Kim Y.-J., (2022), Traction Performance Evaluation of the Electric All-Wheel-Drive Tractor, *Sensors*, MDPI, Basel/Switzerland, vol. 22, no. 3; https://doi.org/10.3390/s22030785

[14] Becker R.S., Alonço A.dS., Francetto T.R., Carpes D.P., Zart B.C.C.R., Moreira A.R., (2019), Operational performance of crop residue cutting discs in the no-tillage system, *Agricultural Engineering International: The CIGCR e-journal*, ISSN: 1682-1130, vol 21, no. 2, pp. 78-85;

[15] Brinkmeier M., Schank T., (2005), Network Statistics, Network Analysis (Brandes U., Erlebach T., Eds.), LNCS 3418, pp. 293-317, Springer-Verlag Berlin Heidelberg;

[16] Cardei P., Rigon L., Muraru V.M., Muraru-Ionel C., Constantin N., David A., (2015a), A method of calculating the optimal speed of operation for vibrocultivators, *Proceedings of the 43rd International Symposium on Agricultural Engineering*; Opatija, Croatia, ISSN 1848-4425, pp. 395-404.

[17] Cardei P., Muraru V., Constantin N., Muraru C., Cilan T., Hodre C. D., Matache M., (2015b), Mathematical modeling and comparative simulation of the vibrations of vibro-cultivators and agricultural cultivators, *Proceedings of International Symposium ISB-INMA-TEH, Bucharest, Romania,* eISSN 2068-4215, pp. 53-58.

[18] Cardei, P., Muraru S.L., Sfiru R., Muraru V., (2019), General structure of tillage draft force. Consequences in experimental and applicative researches, *INMATEH Agricultural Engineering*, vol. 59, no.3, e: ISSN 2068 – 2239, pp. 253-262; DOI: https://doi.org/10.35633/inmateh-59-28

[19] Cardei, P., Condruz P., Sfiru R., Muraru C., (2020), Tests for physical laws of the draft force generated in the tillage operations, *Proceedings of 19th International Scientific Conference Engineering for Rural Development*, Jelgava/Latvia, 2020, vol. 19, pp. 1262-1269,

[20] Cardei P., Nutescu C., Matache M., Cristea O., (2021), Optimum working conditions for variable width ploughs, *INMATEH-Agricultural Engineering*, vol. 65, no. 3, 2021, pp. 248-254; DOI: 10.35633/inmateh-65-26

[21] Cardei P., N. Constantin, V. Muraru, C. Persu, R. Sfiru, (2023a), Estimation of the random intensity of the soil tillage draft forces in the supports of the working bodies of a cultivator, *Preprint*, DOI:10.13140/RG.2.2.34201.49760

[22] Cardei P., N. Constantin, V. Muraru, C. Persu, R. Sfiru, (2023b), The random vibrations of the active body of the cultivators, Agriculture 2023, Vol.13,no.8, 1565, https://doi.org/10.3390/ agriculture13081565

[23] Cardei P., N. Constantin, C. Persu, V. Muraru, R. Sfiru,(2023c), Analysis of the dependence of traction resistance force on forward speed for tractor-cultivator aggregates, *Preprint*, https://www.researchgate.net/publication/370636572_Analysis_of_the_dependence_of_traction_resistance_force_on_forward_speed_for_tractor-cultivator_aggregates

[24] Çarman K., Çitil E., Taner A., (2019), Artificial Neural Network Model for Predicting Specific Draft Force and Fuel Consumption Requirement of a Mouldboard Plough, *Selcuk Journal of Agriculture and Food Sciences*, Vol. 33, No. 3, ISSN 2458-8377, pp. 241-247

[25] Çarman K., Marakoğlu T., Taner A., Çıtıl E., (2021), Prediction of Draft Force and Disturbed Soil Area of a Chisel Tine in Soil Bin Conditions Using Draft Force and Its Comparison with Regression Model, *Selcuk Journal of Agriculture and Food Sciences*, Vol. 35, No. 1, ISSN 2458-8377, pp. 56-64

[26] Chehaibi S., Hannachi C., Pieters J.G., Verschoore R.A., (2008), Impact de la Vitesse d'avancement du tracteur sur la structure du sol et le rendementd'une culture de pomme de terre, *Tropicultura*, vol. 26, no. 3, eISSN 2295-8010, pp. 195-199

[27] Chenarbon H, A., (2022), Effect of moldboardplow share age and tillage depth on slippage and fuel consumption of Tractor (MF399) in Varamin region, *Idesia*, vol. 40, no. 2, ISSN 0718-3429, 113-122

[28] Cox, D.R., (1984), "Interaction". *International Statistical Review*. Vol. 52, no.1, pp. 1–25. Published by: International Statistical Institute (ISI), doi:10.2307/1403235. JSTOR 1403235.

[29] Da Silva R.P., dos Santos A. F., de Oliveira B.R., Souza J. B. C., de Oliveira D.T., Carneiro F.M., (2020), Potential of using statistical quality control in agriculture 4.0, *Revista Ciência Agronômica*, Vol.51, 2020, pp. 1-15, https://doi.org/10.5935/1806-6690.20200105

[30] Damanauskas V., Janulevicius A., (2022), Effect of tillage implement (spring tine cultivator, disc harrow), soil texture, forward speed, and tillage depth on fuel consumption and tillage quality, *Journal of Agricultural Engineering*; Vol, 53, no. 3, doi: 10.4081/jae.2022.1371

[31] Deshpande S., Shirwal S., (2017), Effect of Operational Parameters of Selected Tillage Tools in Soil Bin, *International Journal of Current Microbiology and Applied Sciences*, Vol. 6, No. 6, Excellent Publishers, ISSN: 2319-7706, pp. 1051-1061, DOI: https://doi.org/10.20546/ijcmas.2017.606.121

[32] Dizaji H.Z., Khorasani M.E., Nategh N.A., Sheikhdavoodi M., Adekaiezadeh K., (2022) Specific draft modeling for combined and simple tillage implements, *AgrEngInt: CIGR Journal Open access*, vol. 24, no. 4, pp. 41-56

[33] Dodge, Y., (2003), *The Oxford Dictionary of Statistical Terms*. Oxford University Press. ISBN 978-0-19-920613-1

[34] El Wahed A., Aboukarima M., (2007), Draft models of chisel plow based on simulation using artificial neural networks, *Misr Journal of Agricultural Engineering*, Vol. 24, No. 1, pp. 42-61

[35] Elsheika, A.M., Al-Rajihi M.A., El Shabasy T.M., (2021), Effect of Coating Chisel Plow Shares with Some Materials on Draft Force Requirement, *Journal of Soil Sciences and Agricultural Engineering*, vol 12, no. 9, pp. 611-614, DOI: 10.21608/JSSAE.2021.201484

[36] Fanigliulo R., Biocca M., Grilli R., Fornaciari L., Gallo P., (2023), Assessment of the Performance of Agricultural Tires Using a Mobile Test Bench, *Agriculture; Basel*, vol 13., No. 1, DOI: https://doi.org/10.3390/agriculture13010087

[37] Fechete-Tutunaru L.V., Gaspar F., Gyorgy Z., (2019) Soil-tool interaction of a simple tillage tool in sand, *E3S Web of Conference s 85*, 0.8007; https://doi.org/10.1051/e3sconf/20198508007

[38] Gheorghita N.E., Biris S.S., Ungureanu N., Ionescu M., (2017), Aspects regarding the construction and operation of agricultural cultivators with vibratory working tools, *Proceedings of International Symposium ISB-INMA-TEH, Bucharest, Romania 2017*; pp. 753-756

[39] Gomez K.A., Gomez A.A., (1984), *Statistical procedures for agricultural research*, second edition,

John Wiley & Sons, (first edition, 1976)

[40] Harris C.M., Crede C.E., (1969), *Shocks and Vibrations (SocurisiVibratii)*, Technical Publishing House (EdituraTehnica), Bucharest / Romania

[41] Karmarkar A.U., Gilke N.R., (2021), Embodiment design of a soil bin for soil-tool interaction study, *Journal of Physics: Conference Series, IOP Publishing*, ICAPSM, doi:10.1088/1742-6596/2070/1/012229

[42] Kim Y.S., Kim T.J., Kim Y.J., Lee S.D., Park S.U., Kim W.S., (2020), Development of a Real-Time Tillage Depth Measurement System for Agricultural Tractors: Application to the Effect Analysis of Tillage Depth on Draft Force during Plow Tillage, *Sensors,* MDPI, Basel/Switzerland, Vol. 20, No. 3, 912

[43] Kim Y-S., Lee S-D., Baek S-M., Baek S-Y., Jeon H-H., Lee J-H., Kim W-S., Shim J-Y., Kim Y-J., (2022), Analysis of the Effect of Tillage Depth on the Working Performance of Tractor-Moldboard Plow System under Various Field Environments, *Sensors*, MDPI, Basel/Switzerland, vol. 22, no. 7

[44] Larson L.W., (1964), Predicting draft forces using model moldboard, plows in agricultural soils, Retrospective Theses and Dissertations. *Iowa State University of Science and Technology*, USA

[45] Letosnev, M. N., (1959), *Agricultural Machinery*. (S. Agro-Forestry, Ed.) Bucharest, Romania: Ministry of Agriculture and Forestry

[46] Mamkagh A.M., (2018), Effect of Tillage Speed, Depth, Ballast Weight, and Tire Inflation Pressure on the Fuel Consumption of the Agricultural Tractor: A Review, *Journal of Engineering Research and Reports*, Vol. 3, No. 2, pp. 1-7

[47] McKyes E., (1985), Soil Cutting and Tillage, vol. 7, *Elsevier Science*, eBook ISBN: 9780444601049

[48] Moenifar, A., Mousavi-Seyedi, S., Kalantari, D., (2014), Influence of tillage depth, penetration angle and forward speed on the soil/thin-blade interaction force, *Agricultural Engineering International: CIGR*, Vol 16, no. 1, ISSN 1682-1130, pp. 69-74

[49] Myalo V.V., Myalo O.V., Demchuk E.V., Mazyrov V.V., (2019), *Basic Parameters Substantiation of the Cultivator Working Body for the Continuous Tillage* in the System of Ecologically Safe Resource-Saving Agriculture, IOP Conf. Series: Earth and Environmental Science 224 012023

[50] Naderloo, L., Alimadani, R., Akram, A., Javadikia, P., Khanghah, H. Z., (2009), Tillage depth and forward speed effects on draft of three primary tillage implements in clay loam soil, *Journal of Food, Agriculture& Environment*, Vol. 7, no. 3&4, pp. 382-385

[51] Negrus E., Soare I., Tanase F., Bejan N., (1983), *Testing of vehicles (Incercareaautovehiculelor)*, Didactic and Pedagogical Publishing House (Editura Didactica si Pedagogica), Bucharest / Romania

[52] Owen G.T., (1985), Subsoiling forces and tool speed in compact soils, vol. 31, no. 1, *Canadian Society for Bioengineering*, Canada

[53] Ranjbar, I., Rashidi, M., Najjarzadeh, I., Niyazadeh, M., (2013), Modeling of Moldboard Plow Draft Force Based on Tillage Depth and Operation Speed, *Middle-East Journal of Scientific Research*, vol. 17, no. 7, pp: 891-897

[54] Rashidi M., Lehmali H.F., Beni M.S., Malekshahi M., Namin S.T., (2013a), Prediction of Disc Harrow Draft Force Based on Soil Moisture Content, Tillage Depth and Forward Speed, *Middle-East Journal of Scientific Research*, Vol. 15, No. 2, pp. 260-265

[55] Rashidi M., Lehmali H.F., Fayyazi M., Akbari H., Jaberinasab B., (2013b), Effect of Soil Moisture Content, Tillage Depth and Forward Speed on Draft Force of Double Action Disc Harrow, *American-Eurasian J. Agric. & Environ. Sci.*, vol. 13, no. 8, pp. 1124-1128

[56] Sadek M.A., Chen Y., Zeng Z., (2021), Draft force prediction for a high-speed disc implement using discrete element modelling, *Biosystem Engineering*, 202, pp. 133-141;

[57] Saleh A., Sani M.T., Suleiman M.L., (2021), Effects of Speed on Draft for Selected Tractor-Driven Tillage Implements in Samaru Soil, Zaria, Nigeria, *Journal of Applied Sciences Environmental Management*, vol. 25, no. 5, pp.751-757

[58] Shafei S.M., Loghavi M., Kamgar S., (2018), A comparative study between mathematical models and the ANN data mining technique in draft force prediction of disk plow implement in clay loam soil, *Agricultural Engineering International: CIGR Journal*, Vol.20, No. 2, pp. 71–79

[59] Shafei S.M., Loghavi M., Kamgar S., Raoufat M.H., (2018), Potential assessment of neuro-fuzzy strategy in prognostication of draft parameters of primary tillage implement, *Annals of Agrarian Science*, vol. 16, pp. 257-266

[60] Singh J., Chatha S.S., Sidhu B.S., (2018), Influence of Tillage Depth and Plough Speed on Performance ofPrimary Tillage Tools, *Asian Journal of Engineering and Applied Technology*, vol. 7, no. S2, pp. 138-142

[61] Sireteanu T., Gündisch O., Pârâian S., (1981), *The random vibrations of automobiles (Vibratiilealeatoare ale automobilelor)*, Technical Publishing House (EdituraTehnica), Bucharest / Romania

[62] Taghavifar H., Mrdani A., (2015), Net traction of a driven wheel as affected by slippage, velocity and wheel load, *Journal of the Saudi Society of Agricultural Sciences*, vol. 14, no. 2, pp. 161-171

[63] Zoz F.M., Grisso R.D., (2003), Traction and Tractor Performance, *ASAE Publication* Number 913C0403, 49 p. ASAE, St. Joseph, MI, USA

[64] https://cran.r-project.org/web/packages/TOSTER/vignettes/SMD_calcs.html, last accessed 30/05/2023

[65] https://dexonline.ro/definitie/interacțiune, last accessed 02/06/2023

[66] https://dictionary.cambridge.org/dictionary/english/interaction, last accessed 02/06/2023

[67] https://en.wikipedia.org/wiki/Discrete_element_method, last accessed 02/06/2023

[68] https://en.wikipedia.org/wiki/Interaction_(statistics), last accessed 02/06/2023

[69] https://jasp-stats.org/, last accessed 30/05/2023

[70] https://ro.wikipedia.org/wiki/Re%C8%9Bea_neural%C4%83, last accessed 30/05/2023

[71] https://statisticaloddsandends.wordpress.com/2021/10/31/standardized-mean-difference-smd-in-causal-inference/, last accessed 30/05/2023

[72] https://towardsdatascience.com/how-to-compare-two-or-more-distributions-9b06ee4d30bf, last accessed 30/05/2023

[73] https://www.campbellcollaboration.org/escalc/html/EffectSizeCalculator-SMD1.php, last accessed 30/05/2023

[74] https://www.psychiatrist.com/jcp/psychiatry/mean-difference-standardized-mean-difference-smd-and-their-use-in-meta-analysis/, last accessed 30/05/2023

COMPARATIVE STUDY ON WATER USE CHARACTERISTICS AND PRODUCTIVITY OF SOYBEAN AND MAIZE INTERCROPPING SYSTEM UNDER DRY FARMING CONDITIONS

/

旱作条件下大豆玉米复合种植系统水分利用特征和生产力的比较研究

Yaoyu LI[1)], Tengteng QU [3)], Qixin ZHAO [3)], Yuzhi WANG [3)], Zizheng DENG [2)], Wuping ZHANG [3)], Xiaoying ZHANG [4)], Lili SUN [1)], Fuzhong LI [3,*)]

[1)] College of Agricultural Engineering, Shanxi Agricultural University, Taigu, Shanxi / China
[2)] College of Land Science and Technology, China Agricultural University, Beijing / China
[3)] College of Software, Shanxi Agricultural University, Taigu, Shanxi / China
[4)] Department of Basic, Shanxi Agricultural University, Taigu, Shanxi / China
Tel: +8603546287093; E-mail: sxaulfz@126.com
Corresponding author: Li Fuzhong
DOI: https://doi.org/10.35633/inmateh-71-13

Keywords: *soybean maize intercropping planting, water demand, Penman-Monteith formula, productivity*

ABSTRACT

Quantitative investigation of the utilization characteristics of precipitation resources and the production capacity of the intercropping production system under the soybean maize intercropping mode in northern China is of great significance for improving the resource utilization rate of dryland agriculture and regional sustainable development. This study adopted a completely randomized block design, and six planting modes were set up: soybean monoculture, maize monoculture, and four soybean maize intercropping modes. Plant height and grain yield data were observed, and precipitation resource utilization efficiency was calculated. Based on the FAO-56 recommended crop coefficients, the crop coefficients were corrected according to the actual growth of crops in the experimental area; combined with meteorological data, the crop water demand under different planting modes was estimated based on the Penman-Monteith principle. The results showed that crops' daily growth water demand under different planting modes was generally deficient in water in the early and middle stages of growth, and surplus in the later stages. Compared with the monoculture mode, there were significant differences in precipitation resource utilization efficiency under different intercropping modes (P < 0.05), with soybeans reduced by 67.50% ~ 89.56%, and maize reduced by 43.99% ~ 61.05%. Based on the semi-humid and semi-arid area of the eastern Loess Plateau, an appropriate irrigation system needs to be designated for soybean and maize intercropping systems in the early and middle stages of crop growth. Under a certain proportion of water resource supply, different modes have different water resource utilization efficiency and final production capacity for the intercropping system.

摘要

定量化探究中国北方大豆玉米复合种植方式下降水资源的利用特征及复合生产系统的生产能力对提升旱作农业资源利用率和区域可续发展具有重要意义。本研究采用完全随机区组设计，布设六种种植模式，即大豆单作、玉米单作、以及四种大豆玉米复合种植模式，观测株高、籽粒产量数据，计算降水资源利用效率。基于 FAO-56 推荐作物系数，根据试验区作物实际长势进行作物系数矫正；结合气象数据，基于 Penman-Monteith 原理，估算不同种植模式下作物需水量。结果表明：不同种植模式下作物逐日生长需水量，整体呈生育前、中期水分亏缺严重，生育后期水分盈余；与单作模式相比，不同复合种植模式下降水资源利用效率存在显著差异（P < 0.05），大豆降低了 67.50% ~ 89.56%、玉米降低了 43.99 % ~ 61.05%。基于黄土高原东缘半湿润偏旱区，大豆、玉米复合种植系统下，在作物生长前、中期需要指定适宜的灌溉制度。比例水分资源供应一定下，不同的模式对复合系统的水资源利用效率及最终的生产能力是不同的。

Yaoyu Li, Ph.D. Eng.; Tengteng Qu, M.S. Stud. Agr.; Qixin Zhao, M.S. Stud. Agr.; Yuzhi Wang, M.S. Stud. Eng.; Zizheng Deng, Ph.D. Agr.; Wuping Zhang, Prof. Ph.D. Agr.; Xiaoying Zhang, Prof. Ph.D. Eng.; Lili Sun, Ph.D. Eng.; Fuzhong Li, Prof. Ph.D. Eng.

INTRODUCTION

Against the backdrop of global climate change and increasing water scarcity, effective water management and enhancing agricultural productivity have become crucial topics in contemporary agricultural research *(Scanlon et al., 2023; Walter et al., 2023)*. Particularly in rainfed agricultural conditions, addressing the urgent and complex challenge of efficiently utilizing limited water resources to ensure food security is paramount. In recent years, the composite planting system of soybeans and maize has garnered widespread attention due to its potential advantages in water utilization and productivity.

A study conducted in the Punjab Province, Pakistan, indicates that under rainfed conditions, the strip intercropping system of maize and soybeans may be a productive and sustainable strategy to improve water use efficiency and land productivity under irrigated conditions *(Muhammad et al., 2021).* Similarly, in Egypt, a study emphasizes the importance of intercropping in improving water use efficiency and increasing land utilization efficiency for legumes and maize *(Metwally et al., 2019)*. In northern Nigeria, a study was made on maize and soybean intercropping systems, aiming to achieve sustainable intensification of cereal-legume intercropping. The study suggests that overall, monoculture of maize and soybeans is superior to intercropping, with land equivalent ratios for all intercropping treatments greater than 1, indicating the advantage of intercropping maize and soybeans over monoculture *(Kamara et al., 2019)*. Results from a study in Serra Talhada, Pernambuco, Brazil, examining intercropping and mulching techniques in semi-arid areas for prickly pear and millet production suggest that adopting intercropping techniques can reduce water loss due to evaporation compared to sole cultivation *(George et al., 2023).* In northwest China it is also confirmed the potential of mixed planting systems in improving water use efficiency in dryland areas *(Falong Hu's et al., 2017)*. In another study from southwestern Japan *(Azizi et al., 2021)*, the yield and protein variation in intercropped soybeans and maize of different varieties were investigated, providing practical information for agricultural production in subtropical regions. Additionally, a study from Nebraska USA, by establishing water productivity benchmarks, further deepens the understanding of water use efficiency for maize and soybeans under different water resource management conditions *(Mekonnen et al., 2020)*. It reveals the impact of maize and soybean intercropping systems on water resource utilization efficiency, contributing to narrowing water productivity gaps and improving water sustainability goals for the state, providing important insights for the sustainable development of global agricultural production.

In summary, research on the soybean-maize intercropping system under rainfed conditions in different regions worldwide indicates a significant advantage of intercropping systems in improving water use efficiency and productivity. However, it is important to note that the applicability of these research findings may be influenced by specific geographical, climatic, and soil conditions.

Therefore, the main objective of this case study was to explore the water requirement patterns for soybeans and maize in a composite planting system based on the semi-humid to semi-arid conditions on the eastern edge of the Loess Plateau. Under a fixed proportional water supply, this study aims to investigate the impact of different planting patterns on the water resource utilization efficiency and the final production capacity of the composite system, with the goal of providing more precise guidance for achieving sustainable agricultural production.

MATERIALS AND METHODS

Experimental Area Overview and Experimental Material

The experimental base is located in the National Agricultural High-tech Zone of Jinzhong (112°36'E, 37°25'N, 786.7 m), situated in the northeastern part of the Jinzhong Basin. The area belongs to a warm temperate continental climate, with an annual average precipitation of about 450 mm, an annual average temperature of about 10°C, an average frost-free period of 160 ~ 190 days, abundant sunshine, and high evaporation. The soil in the experimental area is brown soil, and the basic soil fertility is shown in Table 1.

Table 1

Soil composition content at the test site

Depth	Alkaline hydrolysable nitrogen	Total nitrogen	Total phosphorous	Organic matter
[cm]	[mg/kg]	[g/kg]	[g/kg]	[g/kg]
0~20	43.30	1.02	1.13	15.65
20~40	22.10	0.61	0.83	8.19

On May 22, 2022, a completely randomized block design was adopted, with a plot area of 85 m^2 (10 m x 8.5 m). Maize "Qiangsheng 199" and soybean "Tiefeng 31" were selected as experimental materials. Six planting modes were set up, including soybean monoculture (S), maize monoculture (M), and four soybean-maize intercropping modes (S3M3, S4M2, S6M3, S4M3, with the row ratios of soybeans to maize being 3:3, 4:2, 6:3, and 4:3, respectively). Each planting mode was repeated three times (Figure 1). The planting density for each mode is shown in Table 2.

Table 2

Planting density table of soybean maize intercropping system

Planting pattern	S	M	S3M3		S4M2		S6M3		S4M3	
			Soybean	Maize	Soybean	Maize	Soybean	Maize	Soybean	Maize
Density [plants/hm^2]	1846	575	1272	720	1696	616	1692	520	1504	549

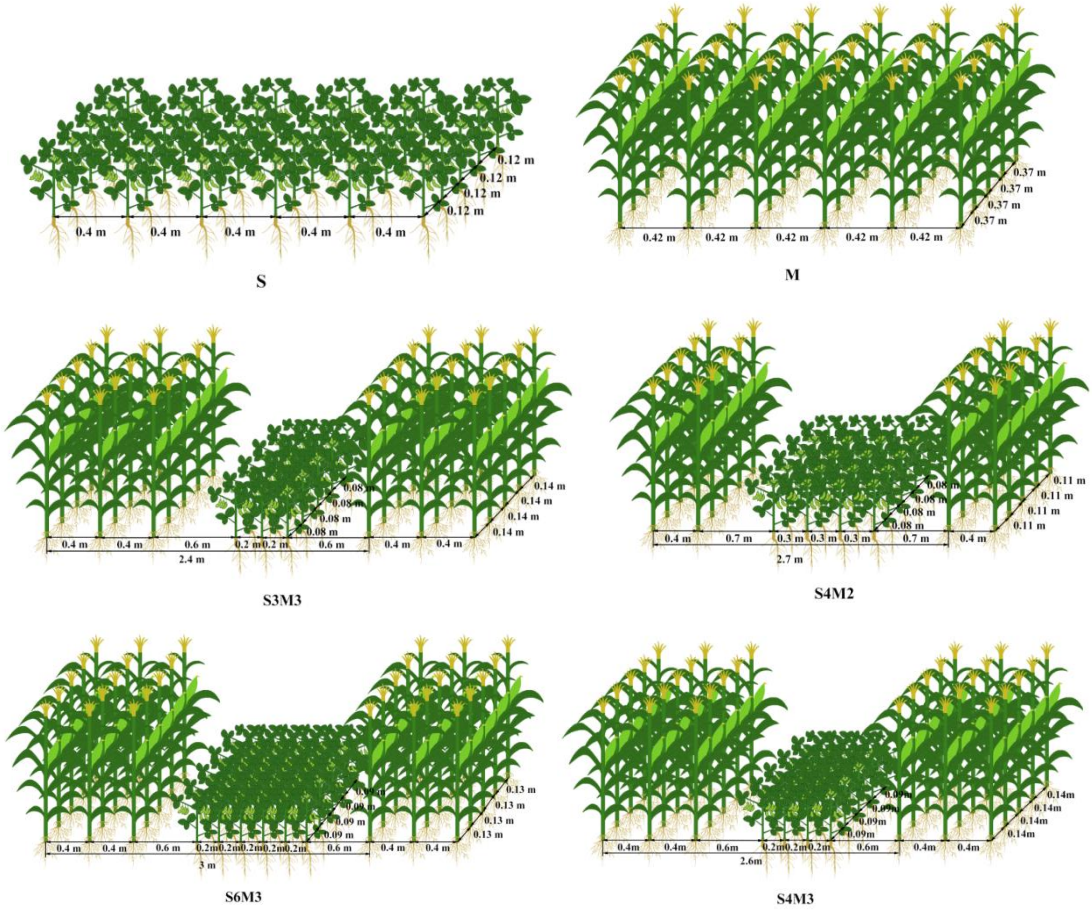


Fig. 1 - Schematic diagram of planting mode of soybean maize intercropping system

Test method

(1) Meteorological data

In the experimental area, daily observations of six meteorological elements are conducted through a small weather station, including average temperature, maximum temperature, minimum temperature, relative humidity, average wind speed, and rainfall amount, as well as sunshine duration. The small weather station comprises a platinum resistance temperature sensor, a capacitive humidity sensor, a spiral-type wind direction and speed sensor, a single tipping bucket rain gauge, and an automatic sunshine recording sensor. All these sensors are integrated into a louvered box and are programmed to automatically record and store hourly data from each sensor into its internal memory *(Central Meteorological Bureau, 2003)*.

(2) Crop coefficient

According to the FAO classification standards *(Allen et al., 1998)*, the growth period of soybeans and maize is divided into the early, middle, and late stages (Table 3).

Table 3

Soybean and maize growth stage division

Crop plant	Initial period [d]	Middle stage [d]	Late stage [d]	Whole growth period
Soybean	31	37	65	2022-05-22 to 2022-10-01(133 d)
Maize	36	58	36	2022-05-22 to 2022-09-28(130 d)

The FAO recommended values for soybean and maize at the early, middle and late stages were 0.50, 1.15, 0.50, and 0.51, 1.20, 0.60, respectively. The crop coefficients at the middle and late stages were corrected by formula (1).

$$K_c = K_{ctable} + [0.04(u_2 - 2) - 0.004(RH_{\min} - 45)][\frac{h}{3}]^{0.3} \quad (1)$$

where:

K_{ctable} is the recommended value for FAO-56 *(Allen et al., 1998)*, $RH_{\min}$ is the daily average minimum relative humidity, u_2 is 2 m high daily average wind speed, h is the average plant height of each growth stage.

(3) Crop water requirement

The Penman-Monteith formula recommended by FAO *(Allen et al. 1998)* was used to calculate the reference crop evapotranspiration, and the formula (2) was used to calculate the crop water storage.

$$ET_c = K_c \cdot ET_0 \quad [\text{mm/d}] \quad (2)$$

where:

ET_c is crop water requirement, ET_0 is reference crop evapotranspiration, K_c is the crop coefficient.

(4) Plant height

In the key growth stages of soybean and maize, the plant height of soybean and maize was obtained by manual measurement.

(5) Yield of soybean and maize under different planting patterns

Maize yield measurement. For each sampling point, measure 3 production units (e.g., each unit consisting of 2 rows of maize, totaling 6 row spaces) to calculate the average row spacing. In these 6 rows, select a representative 4 meters of double rows (avoiding the edge rows), count the number of plants and ears, and calculate the number of ears per acre. In each measured sample section, harvest one ear of maize for every two ears, totaling 10 ears as a sample to measure the number of grains per ear.

The formula for calculating yield is as follows:

Theoretical yield (kg/acre) = Number of ears per acre × Number of grains per ear × Average 100-grain weight (average of the past three years for the measured variety) × 85% (3)

Soybean Yield Measurement: Based on the number of soybean rows in each strip of strip compound planting, measure the distance of 3 production units (e.g., 6 rows for 2 rows per strip of soybeans, 9 rows for 3 rows per strip) or more at the sampling points, and divide by 6 or 9 (3 production units), to calculate the average row spacing (meters). Randomly determine the number of effective soybean plants in 4 meters within a strip, calculate the average plant spacing, and then calculate the number of effective plants per acre based on the average row spacing. Investigate the number of grains per plant for 10 consecutive plants in each row within the soybean strip, and then calculate the average number of grains per plant within the sampling point based on the number of rows per strip. The formula for calculating yield is as follows:

Theoretical yield (kg/acre) = 0.85 × Number of effective plants per acre × Number of grains per plant × Average 100-grain weight (grams) / 100 / 1000 (4)

(6) Calculation of precipitation resource utilization efficiency

Rainfall utilization efficiency can comprehensively reflect the change characteristics of land production capacity. The formula of precipitation resource utilization efficiency is (*Deng et al. 2023*):

$$RUE = \frac{Y}{PG}[kg/(ha*mm)] \quad (5)$$

RUE is the utilization efficiency of precipitation resources, Y is crop grain yield, PG is precipitation during growth period. Perform one-way mean analysis on RUE using SPSS Data Analysis software.

RESULTS AND DISCUSSION

Water requirement rule of soybean monoculture

According to the actual situation of the experiment and the analysis of the soil moisture cycle process, the annual rainfall in Shanxi Province fluctuates around 450 mm, and the frequency of heavy rainstorms in meteorology occurs five times a year. Therefore, there is no rainfall recharge to groundwater and the formation of surface runoff. If the buried depth of groundwater is more than 5 m, groundwater has no supplementary effect on crop growth water demand.

The minimum relative average humidity during the middle growth stage of soybean and maize was 47.61% and 48.58%, respectively, and the daily average wind speed at 2 m height was 1.62 m/s and 1.61 m/s, respectively. The minimum relative average humidity in the late growth stage was 31.66% and 35.47%, respectively, and the daily average wind speed at 2 m height was 1.71 m/s and 1.68 m/s, respectively. The average plant height in the middle and late stages of crops under different planting patterns is shown in table 4.

Table 4

The average plant height of crops in different planting patterns in the middle and late growth stages

Repro-ductive period	S [m]	M [m]	S3M3		S4M2		S6M3		S4M3	
			Soybean [m]	Maize [m]	Soybean [m]	Maize [m]	Soybean [m]	Maize [m]	Soybean [m]	Maize [m]
Mid- stage	0.466	1.855	0.415	1.953	0.554	2.102	0.354	1.655	0.520	2.132
Late stage	0.720	3.280	0.844	2.884	0.854	2.909	0.766	2.923	0.883	3.103

Based on the FAO-56 recommended crop coefficient as the basis of localized correction crop coefficient, the climatic factors in the test area are used as the influencing factors to localize the crop coefficient. The results of crop coefficient correction of different planting patterns are shown in table 5.

Table 5

Crop coefficients of different intercropping and planting stages

Reproductive period	S	M	S3M3		S4M2		S6M3		S4M3	
			Soybean	Maize	Soybean	Maize	Soybean	Maize	Soybean	Maize
Mid-stage	1.135	1.174	1.136	1.180	1.135	1.179	1.136	1.180	1.135	1.179
Late stage	0.527	0.626	0.529	0.625	0.529	0.625	0.528	0.625	0.529	0.626

The P-M formula was used to calculate the daily growth water demand of crops according to the six meteorological elements in the experimental area and the actual growth status of soybean monoculture. The estimated water requirement during the whole growth period was 369.60 mm. The estimated water requirements before, during and after growth were 93.98 mm, 168.80 mm and 106.82 mm, respectively. The rainfall during the whole growth period of soybean monoculture was 329.27 mm, and the rainfall before, during and after the growth period was 25.42 mm, 120.95 mm and 182.90 mm, respectively. 24 mm irrigation was carried out in each treatment area in the early stage of crop growth on June 5 in order to ensure the emergence rate of crop growth because of soil drought and atmospheric drought in the early stage of crop growth.

Therefore, the actual water supply in the early stage of crop growth was 49.42 mm. The water deficit under the condition of no irrigation in the whole growth cycle of soybean monoculture was 40.33 mm, corresponding to the water deficit of 68.56 mm and 47.85 mm in the early and middle stages of crop growth. The water surplus in the late growth stage was 76.08 mm.

There is a mismatch between water demand and water supply according to the analysis of different growth stages of soybean. The water deficit is serious in the early and middle stages of soybean growth. The water surplus occurs in the late stage of growth.

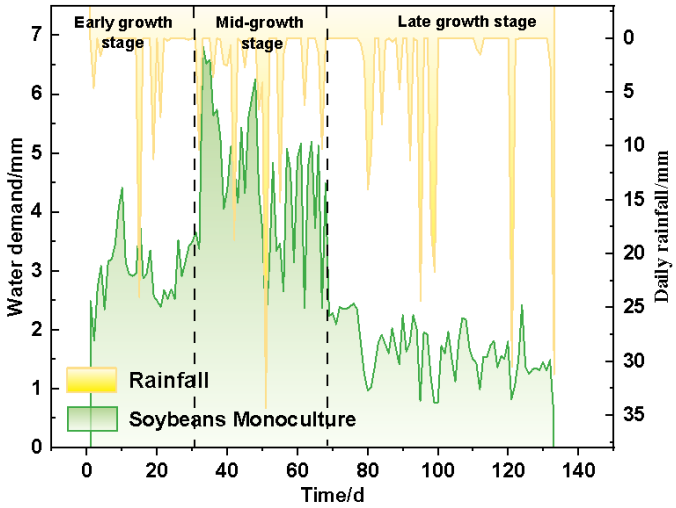


Fig. 2 - The actual water demand and daily precipitation of a single soybean species

Water requirement rule of maize monoculture

Figure 3 indicates that, in the study of water requirements for monoculture maize, the water requirement curve follows a basic pattern consistent with monoculture soybeans, represented by the equation:

$$y = -0.0006x^2 + 0.0686x + 2.3553[mm] \quad (6)$$

Where: y is water demand, x is time.

The difference is that the middle growth period of maize is longer, and the water demand is larger. The estimated water demand during the whole growth period is 427.82 mm. The estimated water demands before, during and after growth were 108.89 mm, 254.90 mm and 64.03 mm, respectively. The rainfall in the whole growth cycle of maize monoculture was 295.27 mm. The rainfalls before, during and after the growth period were 39.39 mm, 158.88 mm and 97 mm, respectively. The soil drought and atmospheric drought occurred in the early stage of maize monoculture. In order to ensure the emergence rate of maize monoculture, 24 mm irrigation was performed in each treatment area at the early stage of crop growth on June 5. Therefore, the actual water supply in the early stage of crop growth was 63.39 mm. The water deficit under the condition of no irrigation in the whole growth cycle of maize monoculture was 132.55 mm, corresponding to the water deficit of 69.5 mm and 96.02 mm in the early and middle stages of crop growth. The water surplus in the late growth stage was 32.97 mm.

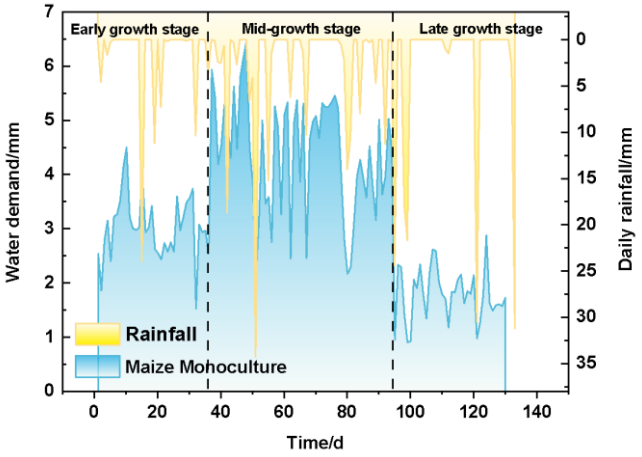


Fig. 3 - Actual water demand and daily precipitation of a single species of maize

The water demand and water supply of maize monoculture also appeared mismatch according to the analysis of three different growth periods. The water deficit was serious in the early and middle stages of maize monoculture. The water surplus appeared in the later stage of maize monoculture. Therefore, according to the rainfall situation of the test area and the estimated water demand of the crop, the irrigation system suitable for the water demand of the maize is formulated in ten days or weeks, which has achieved the maximization of resource utilization.

Water requirement law of soybean-maize intercropping

In different intercropping systems of soybean and maize, the estimated water requirements of soybean and maize during the whole growth period were 370.15 mm and 429.02 mm under intercropping S3M3. Under intercropping S4M2, the estimated water requirements of soybean and maize during the whole growth period were 370.00 mm and 428.81 mm, respectively. Under intercropping S6M3, the estimated water requirements of soybean and maize during the whole growth period were 369.94 mm and 429.02 mm, respectively. Under intercropping S4M3, the actual water requirements of soybean and maize during the whole growth period were 370.15 mm and 428.91 mm, respectively. The estimated water demand and water deficit of soybean and maize under different intercropping patterns in each growth period are shown in Table 6.

Table 6

Estimation of water demand and water gain and deficit at different growth stages under different intercropping modes

Reproductive period			Early stage	Middle stage	Late stage
S3M3	Soybean	Estimate water demand [mm]	93.98	168.94	107.23
		water deficit [mm]	-68.56	-47.99	75.67
	Maize	Estimate water demand [mm]	108.89	256.2	63.93
		water deficit[mm]	-69.5	-97.32	33.07
S4M2	Soybean	Estimate water demand [mm]	93.98	168.79	107.23
		water deficit [mm]	-68.56	-47.99	75.67
	Maize	Estimate water demand [mm]	108.89	255.99	63.93
		water deficit [mm]	-69.5	-97.11	33.07
S6M3	Soybean	Estimate water demand [mm]	93.98	168.94	107.02
		water deficit [mm]	-69.5	-97.11	32.97
	Maize	Estimate water demand [mm]	108.89	256.2	63.93
		water deficit [mm]	-69.5	-97.32	33.07
S4M3	Soybean	Estimate water demand [mm]	93.89	168.94	107.23
		water deficit [mm]	-68.56	-47.99	75.67
	Maize	Estimate water demand [mm]	108.89	255.99	64.03
		water deficit [mm]	-69.5	-97.11	32.97

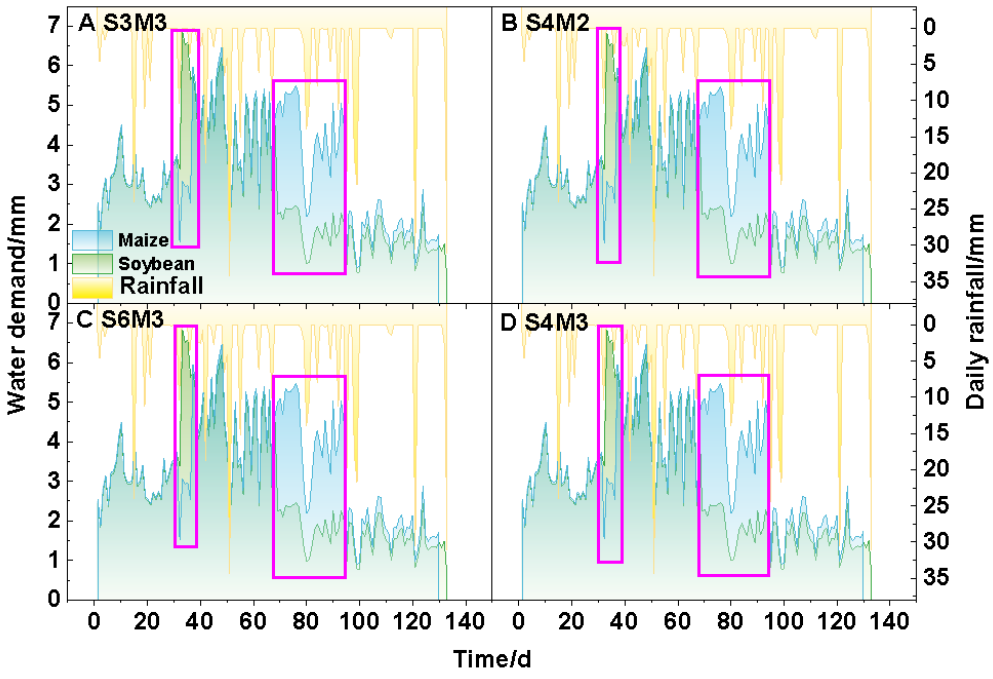


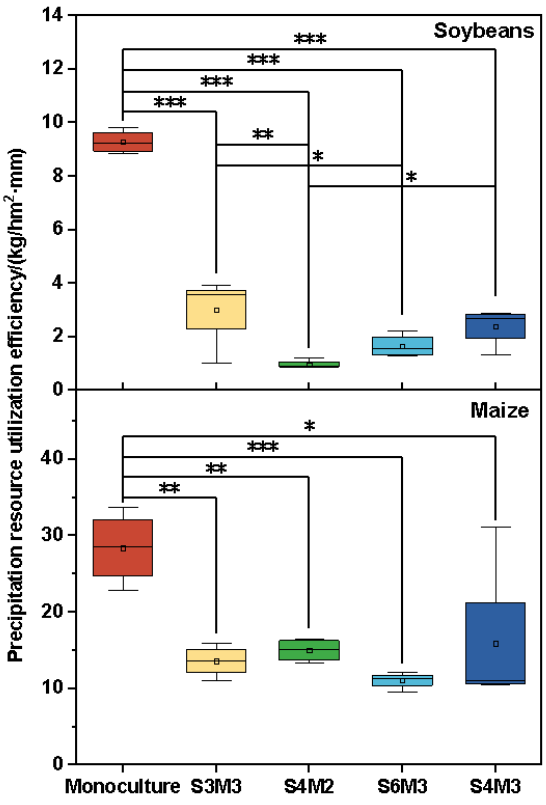
Fig. 4 - Estimation of water requirement and daily precipitation of soybean and maize intercropping planting

Figure 4 shows that the vigorous water demand period of soybean is maintained for 37 days. The

vigorous water demand period of maize is maintained for 58 days. In addition, the vigorous water demand period of soybeans was about 5 days earlier than that of maize. After the end of the vigorous water demand period of soybeans, the vigorous water demand period for maize remained for 26 days. The coexistence period of water demand in the soybean-maize intercropping system was 32 days. It is possible to select in the early stage of crop growth less irrigation or no irrigation in the four intercropping patterns of soybean and maize without affecting the emergence rate. The period of vigorous water demand enters quickly in the middle stage of crop growth. It is necessary to make scientific irrigation decisions in combination with soil moisture in order to ensure the growth of crops under stress.

Precipitation use the efficiency of different planting patterns

The difference between different planting ratios was analyzed by one-way analysis of variance (ANOVA), and the significant level was set at $P < 0.05$. Soybean monoculture (S) and maize monoculture (M) were 9.29 and 33.89 kg ha^{-1} mm, respectively. In S3M3 mode, soybean and maize were 3.01 and 16.22 kg ha^{-1} mm, respectively. The RUE of soybean and maize under S4M2 were 0.96 and 17.89 kg ha^{-1} mm, respectively. In S6M3 mode, soybean and maize were 1.66 and 13.20 kg ha^{-1} mm, respectively. Under S4M3, the yield of soybean and maize were 2.40 and 18.98 kg ha^{-1} mm, respectively. Compared with soybean and maize monoculture, the utilization efficiency of crop precipitation resources under different intercropping patterns decreased significantly ($P < 0.05$). The utilization efficiency of soybean and maize decreased by 67.50 % - 89.56 % and 43.99 % - 61.05 %, respectively. Compared with S4M2 mode, S3M3 mode soybean increased by 211.38 %, compared with S6M3 increased by 82.04 %, and S4M3 mode increased by 147.52 % compared with S4M2 mode. The decrease of crop precipitation resource utilization efficiency in intercropping mode is mainly due to the large decrease of yield. There are two reasons: (1) planting time is too late. (2) Some seedlings of supplementary inoculation did not grow out.



*The t-test is used to test the significance of RUE * P < 0.05, ** P < 0.01, *** P < 0.001*

Fig. 5 - Different planting methods reduce the efficiency of water use

CONCLUSIONS

A comparison of water resource utilization efficiency and yield in the mixed planting mode revealed that the reduction in precipitation resource utilization efficiency for soybean and maize ranged from 67.50% to 89.56% and 43.99% to 61.05%, respectively.

The intercropping of soybeans and maize essentially involves the competition and mutual

supplementation of resources between grass crops and legumes, such as sunlight and groundwater resources.

Due to the complex relationship between crop root development and water resources, future efforts will require the use of partial differential equation models and the laws of soil water movement to model and analyze the water requirements of crops in intercropping systems accurately, particularly focusing on understanding the water characteristics of soybeans and maize.

As intercropping systems are conducted in field experiments, they are susceptible to external factors such as climate and regional differences, which may lead to unstable productivity. In the future, employing principles of resistance to interference for data modeling is necessary to obtain a crop interaction model under intercropping conditions. This research aims to investigate the mechanisms that stabilize and increase productivity in intercropping systems.

ACKNOWLEDGEMENT

The authors were funded for this project by the Major research and development Projects of Shanxi Province, China (202202140601021), the National Key Research and Development Program of China (No. 2021YFD1901101–5), and the Basic Research Project of Shanxi Province (202103021224123).

REFERENCE

[1] Allan R.G., Pereira L.S., Raes D., Smith M. (1998). Crop evapotranspiration guidelines for computing crop requirements. FAO Irrig. Drain. Report modeling and application. *Journal of Hydrology*, vol. 300(9): D05109, Netherlands.

[2] Azizi A.S., Kobayashi I., Chuuka J., & Ishigaki G. (2021). Evaluation of corn-soybean inter-cropping systems in southwestern Japan. *Tropical Grasslands-Forrajes Tropicales*, 9(3), 307–314, Japan.

[3] ***Central Meteorological Bureau, (2003), *Ground meteorological observation specifications*, China Meteorological Press, 9787502936907, China.

[4] Deng Z., Huang M, Zhang W, Wang G, Huang X, Liang G, et al. (2023) Effects of five years conservation tillage for hedging against drought, stabilizing maize yield, and improving soil environment in the drylands of northern China (中国北方旱地五年年保护性耕作抗旱、稳定玉米产量、改善土壤环境的效果). *PLoS ONE* 18(3): e0282359, China.

[5] Falong H., Fuxue F., Cai Z. et al. (2017). Integration of wheat-maize intercropping with conservation practices reduces CO2 emissions and enhances water use in dry areas (小麦-玉米间作与保护措施相结合可减少二氧化碳排放并提高干旱地区的用水量), *Soil and Tillage Research*, Volume 169, 2017, 44-53, China.

[6] George do Nascimento Araújo Júnior, José Edson Florentino de Morais. et al. (2023). Use of intercropping and mulch to improve the water and natural resources use efficiencies of forage cactus and millet production in a semiarid region, *Field Crops Research*, Volume 304, 2023, 109171, ISSN 0378-4290, Brazil.

[7] Kamara, A., Tofa, A., Ademulegun, T. et al. (2019). Maize–Soybean Intercropping for Sustainable Intensification of Cereal–Legume Cropping Systems in Northern Nigeria. *Experimental Agriculture*, 55(1), 73-87. Nigeria.

[8] Metwally AA, Abdel-Wahab TI, Abdel-Wahab ShI. (2019). Increasing land and water use efficiencies by intercropping summer legumes with corn in Egypt. *AGBIR*, December-2019; 35(2): 6-12, Egypt.

[9] Mesfin M. Mekonnen, Arjen Y., et al. (2020), Water productivity benchmarks: The case of maize and soybean in Nebraska, *Agricultural Water Management*, Volume 234, 2020, 106122, ISSN 0378-3774, USA.

[10] Muhammad Ali Raza, Hina G. et al. (2021). Land productivity and water use efficiency of maize-soybean strip intercropping systems in semi-arid areas: A case study in Punjab Province, Pakistan, *Journal of Cleaner Production*, Volume 308, 2021, 127282, ISSN 0959-6526, Pakistan.

[11] Scanlon B.R., Fakhreddine S., Rateb A. et al. (2023) Global water resources and the role of groundwater in a resilient water future. *Nat Rev Earth Environ* 4, 87–101, USA.

[12] Leal Filho W., Nagy G., Freitas Setti A.F., Sharifi A., et al., (2023), Handling the impacts of climate change on soil biodiversity, *Science of The Total Environment*, Volume 869, 2023, 161671, ISSN 0048-9697, UK.

RELIABILITY ANALYSIS OF FMECA THRESHING AND CLEANING SYSTEM BASED ON FUZZY COMPREHENSIVE EVALUATION

/

基于模糊综合评判的 FMECA 脱粒清选系统可靠性分析

Qian DONG, Guohai ZHANG*, Yuqian ZHAO, Fukang ZHOU, Peng LIU, Yihu WANG, Xipeng QIAN [1)]
School of Agricultural Engineering and Food Science, Shandong University of Technology, Zibo 255000, China
Tel: +86-15965534882; E-mail: guohaizhang@163.com
DOI: https://doi.org/10.35633/inmateh-71-14

Keywords: *Fuzzy FMECA; Analytic Hierarchy Process; System reliability*

ABSTRACT

Aiming at the traditional FMECA (Failure Modes, Effect and Criticality Analysis) results of the threshing and cleaning system, which are strongly influenced by subjective factors, imprecise and easy to repeat, the fuzzy comprehensive evaluation method is introduced to quantify the results of the expert evaluation and reduce the subjective influence. Analytic Hierarchy Process (AHP) is used to assign weights to each influencing factor, and by calculating the comprehensive hazard level index, the hazard ranking of each failure mode is carried out, from which the critical failure modes are identified as the focus of improvement, so as to improve the reliability of the system. Comparison shows that the improved method effectively makes up for the shortcomings of the traditional FMECA analysis method, and it is easier to find out the critical failure modes, which provides a theoretical basis for practical application.

摘要

针对脱粒清选系统传统 FMECA(Failure Modes, Effect and Criticality Analysis)分析结果受主观因素影响强烈、取值不精确且易重复等问题，引入模糊综合评判方法，量化专家评价的结果，降低主观影响；采用层次分析法（AHP）对各个影响因素进行权重分配，并通过计算综合危害度等级指数，对各个故障模式进行危害度排序，从中找出关键故障模式作为改进的重点，以此来提高系统的可靠性。通过对比表明，改进后的方法有效弥补了传统 FMECA 分析方法的不足，更易找出关键故障模式，为实际应用提供理论依据。

INTRODUCTION

The reliability of agricultural machinery has an important impact on the quality of agricultural operations, production efficiency, maintenance costs, and user benefits. With the increasing degree of digitisation, automation and intelligence of agricultural machinery, the system structure tends to be complex, resulting in the possibility of potential failures be also increasing, and the reliability of agricultural machinery products has also attracted attention *(Yang et al., 2021)*. In 2022, the Department of Agricultural Mechanisation Management of the Ministry of Agriculture and Rural Development organised a quality survey of some in-use grain combine harvesters for harvesting wheat, and the results of the survey showed that fatal failures and serious failures of these implements in the course of their work mainly occurred in the threshing and clearing system, the engine system, and the travelling undercarriage system, with the highest frequency of failures occurring in the threshing and clearing system.

Threshing and cleaning system is the key part of combine harvester to complete crop harvesting, and its working stability and working effect directly affect the quality of crop harvesting. With the improvement of agricultural production level, people's threshing performance requirements for combine harvester is also higher and higher, its structure is more and more complex, the reliability is more unstable. Therefore, it is of great significance to analyse the reliability of the threshing and cleaning system, grasp its working status, analyse its weak links and optimise it to improve the working quality of the whole machine.

Failure Mode, Effects and Criticality Analysis (FMECA) is a common method of product reliability analysis, by analysing all potential failure modes and their possible impact on the system of each constituent unit of the product (components, assemblies, sub-systems, systems) and classifying each failure mode according to its severity, detection difficulty and probability of occurrence. The weak links and key components in the design can be identified, and the corresponding measures can be taken to prevent or improve them, in order to reduce or eliminate the probability of failures, and thus improve the reliability of the product *(Zhu, 2022; Zhang et al., 2019)*.

Currently, the FMECA analysis method is widely used in aerospace, automotive, machinery and other fields. Shao Weigui draws the hazard matrix diagram of the failure modes of the aircraft front landing gear system through the FMECA analysis method, combines with fuzzy mathematical theory, determines the hazard degree level of each failure mode, finds the weakness of the system, and proposes the corresponding maintenance measures in order to reduce the failure rate *(Shao, 2019)*. Brahim I.B. et al constructs the Bayesian network structure through the FMECA method, and the automobile industry Example analysis is carried out to verify the applicability of the method in the industrial environment *(Brahim et al., 2020)*. Zou Jinglian carried out failure mode impact and hazard analysis of diesel engine subsystems through FMECA analysis method, effectively identified the weak links in the process of diesel engine use, and proposed corresponding optimization methods *(Zou, 2011)*. Hu Qiguo et al analysed the reliability of the hydraulic system of amphibious armoured vehicle by improving the FMECA method, and the analysis results show that the reasonable use of FMECA method can effectively find out the key failure modes of the hydraulic system *(Hu et al., 2017)*.

Reliability analysis through the traditional FMECA method can find the weak links in product design or use in a timely manner, but with the continuous development of reliability analysis methods, people would like to get quantitative assessment results through the analysis, and then the traditional FMECA method would show its shortcomings.

Traditional FMECA analysis defines the risk level of each failure mode by using the Risk Priority Number (RPN), where the higher the RPN value, the higher the risk level of the failure (*Singh et al., 2019*). The RPN of a particular failure mode is equal to the product of the Effect Severity Rating (ESR) of the failure, the Occurrence Probability Rating (OPR) of the failure, and the Difficulty of Detection Rating (DDR) of the failure, that is:

$$RPN=ESR\times OPR\times DDR \tag{1}$$

ESR, OPR, and DDR are classified according to levels, and their levels are usually described qualitatively using fuzzy language such as high, low, size, and difficulty, and the assignment of levels is not fuzzified, so it is highly subjective. In addition, traditional FMECA has the following problems *(Liu et al., 2013; Yu & Zhang, 2022; Hu et al., 2018)*.

(1) There is no consideration of the relative importance between the severity of the fault, the probability of occurrence, and the difficulty of detection.
(2) Different combinations of ESR, OPR, and DDR may produce exactly the same RPN value, at which point the risk priority number is the same, but the potential risk posed by the different combinations will vary.

In order to overcome the above problems of traditional FMECA, scholars at home and abroad adopt various methods such as Fuzzy Mathematics, Grey Theory, Analytic Hierarchy Process (AHP) and so on to improve traditional FMECA *(Xu et al., 2022)*. Dai Chengguo et al. cited the fuzzy comprehensive evaluation method to improve the traditional FMECA, and analysed it by establishing the factor set, evaluation set, and weight set to give more relevant assessment results *(Dai et al., 2011)*. Taking into account the interactions between different factors, Chen Yuan used AHP to determine the distribution of weights among factors based on the citation of fuzzy comprehensive evaluation. Wang Hao et al. based on the FMECA analysis method, combined with the third-order conversion function, and modified on the traditional hazard degree calculation method *(Wang et al., 2017)*. Zhang Haoran et al. introduced "Trapezoidal Fuzzy Number" to transform the evaluation language into fuzzy probability, and the fuzzy probability was homogenised, defuzzified and normalised to obtain specific values, and then ranked the hazards of each failure mode *(Zhang et al., 2020)*. Zhu Xiaocui Application of gray theory to comprehensive cluster assessment of reliability and repairability of CNC machine tools as a way to reduce the subjectivity of expert assessment results *(Zhu, 2013)*. HA Khorshidi aggregates subjective data on failure modes and causes through the system to develop an Overall Failure Index (OFI), which is used to represent the reliability behaviour of the system and prioritize the adoption of corrective actions (*Khorshidi et al., 2016*). Shoaib Ahmed et al. developed a fuzzy logic system using a rule-based fuzzy set approach, which was modelled and tested using different types of membership function in order to compute the corresponding risk values for assessing their potential failure impact *(Ahmed, 2020)*.

Fuzzy comprehensive evaluation method is a comprehensive evaluation method based on fuzzy mathematics, which transforms qualitative evaluation into quantitative evaluation according to the relevant theories of fuzzy mathematics.

It is characterised by clear and systematic results and can effectively solve problems that are difficult to quantify *(Zhang & Wang, 2016; Chai et al., 2011)*. Therefore, combining the two methods to form the FMECA analysis method based on fuzzy comprehensive evaluation can quantify the evaluation opinions of experts, reduce the subjectivity of personal evaluation, and determine the weights between the factors through AHP, so as to make the evaluation results more objective and practical, and effectively improve the shortcomings of the traditional FMECA method.

This paper mainly focuses on the reliability analysis of corn harvester threshing and cleaning system by introducing the fuzzy comprehensive evaluation method on the basis of the traditional FMECA method, and effectively identifies the weak links in the design by calculating the hazard level coefficient to rank the hazard degree of each failure mode. The results show that this method effectively makes up for the shortcomings of the traditional FMECA method. In practical application, it has practical application value for the design and maintenance of the components of combine harvester threshing and cleaning system, and provides theoretical reference for improving the reliability of combine harvester.

MATERIALS AND METHODS

Traditional FMECA for threshing and cleaning system

Fuzzy FMECA is the introduction of the idea of fuzzy mathematics on the basis of traditional FMECA, so the threshing and cleaning system is first analysed by traditional FMECA. The steps of the traditional FMECA analysis method are shown in Figure 1.

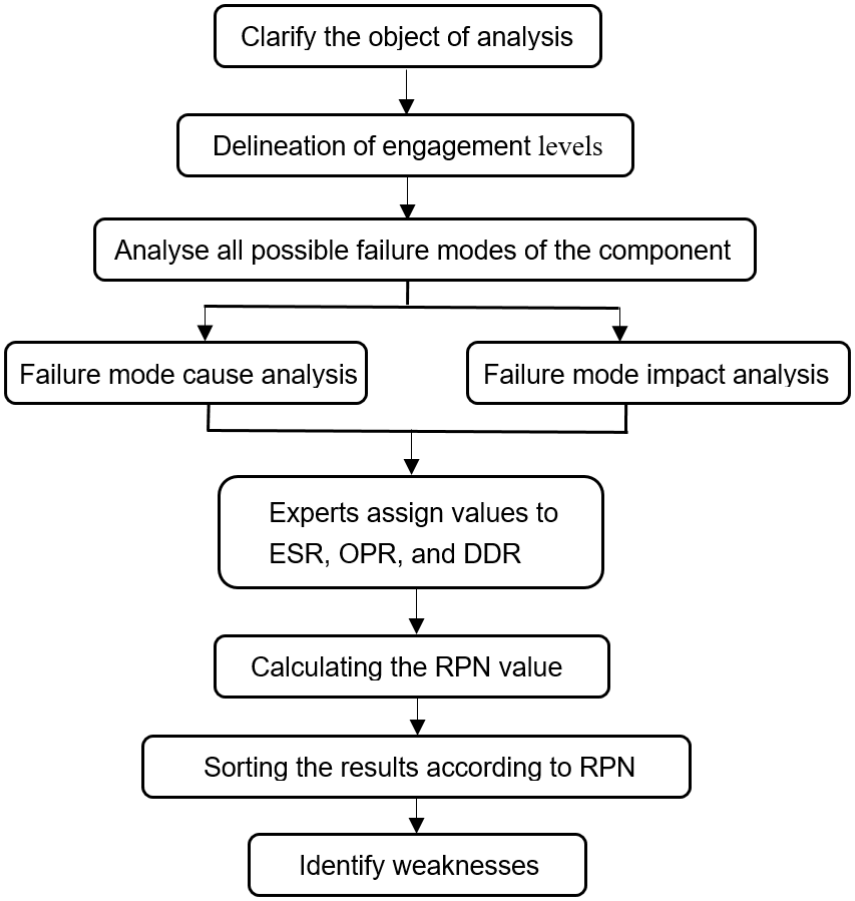


Fig. 1 – The Steps of Traditional FMECA

Wheat combine harvester threshing and sorting system contains threshing separation and sorting two parts, the main components are threshing drum, concave plate sieve, sorting fan, sorting sieve, shaking plate, etc. The FMECA method analysis is based on the smallest unit of the system, bottom up to analyse the potential failure modes of the units and their possible impact on the system, so first of all, the threshing and sorting system is divided into the agreed level, the results of the division are shown in Figure 1. According to the lowest level of agreement in Figure 2, the faults are analysed, the causes and effects of the faults are explored, and the FMECA analysis table is finally obtained, as shown in Table 1.

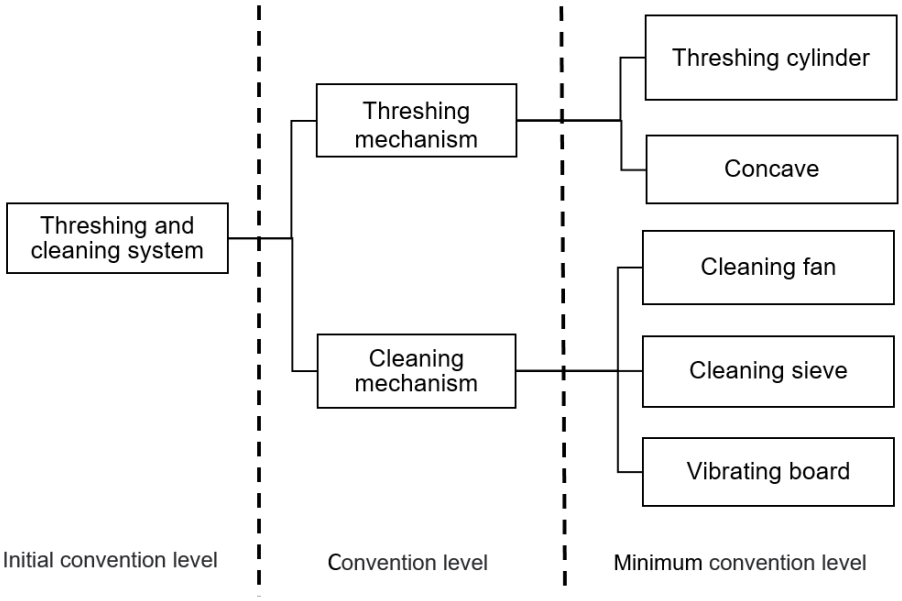


Fig. 2 - Conventional layer classification (Part)

Table 1

FMECA analysis of threshing cleaning system (Part)

Minimum convention level	Serial number	Failure mode	Failure cause	Failure effect		
				Local effect	Higher level influence	Ultimate effect
Threshing cylinder	1	Threshing failure (Threshing is not clean)	The roller speed is low, the grain rod is seriously worn, the grain feeding amount and the threshing gap is too large.	Functional decline	Functional decline	Threshing is not clean
	2	Clogging	The crop moisture content is high, the engine speed is low, the crop feeding amount is too large, the threshing gap is too small, and the transmission belt is slipping.	Loss of function	Loss of function	Cannot work
	3	High seed breakage rate	The roller speed is too high and the threshing gap is too small	Functional decline	Functional decline	Threshing effect descend
	4	Threshing drum abnormal sound	Uneven feeding, bolt loosening or falling off, foreign matter into the roller.	Functional decline	Functional decline	Abnormal work
Concave	5	Abrasion and distortion	Excessive feeding	Functional decline	Functional decline	Abnormal work
Cleaning fan	6	Large fan vibration	Fan and foundation connection is not strong, fan hub wear.	Functional decline	Functional decline	Abnormal work
Cleaning sieve	7	Screen clogging	The opening of the screen is small, the amplitude or inclination does not meet the requirements, and the fan air volume is small.	Loss of function	Loss of function	Cannot work
Vibrating board	8	Breakage	Excessive feeding	Loss of function	Loss of function	Cannot work

Based on ESR, OPR, and DDR scoring guidelines *(Tang et al., 2022)*, combined with the combine harvester threshing and cleaning system failure modes, failure causes and failure impacts in Table 1, 10 relevant experts were invited to assess and assign values to the severity, occurrence probability, and detection difficulty level of each failure mode, and the RPN value was obtained from the product of these three influencing factors, and the calculation results are shown in Table 2.

Table 2

RPN values for each failure mode in traditional FMECA

Minimum convention level	Failure mode	ESR	OPR	DDR	RPN
Threshing cylinder	Threshing failure （Threshing is not clean）	4	3	6	72
	Clogging	6	3	5	90
	High seed breakage rate	5	3	6	90
	Threshing drum abnormal sound	1	5	2	10
Concave	Abrasion and distortion	4	2	6	48
Cleaning fan	Large fan vibration	2	5	3	30
Cleaning sieve	Screen clogging	6	5	6	180
Vibrating board	Breakage	5	1	6	30

As can be seen from Table 2, the traditional FMECA analysis method has a large human subjectivity in the weight allocation of ESR, OPR and DDR, and the calculated RPN values of failure mode 2 and failure mode 3 are both 90, and the RPN values of failure mode 6 and failure mode 8 are both 30, and for such cases with the same RPN values, it is then impossible to correctly rank their specific hazard levels. At this point, the risk priority order of each failure mode cannot be obtained by the traditional FMECA analysis method, which also proves that the traditional FMECA analysis has the problem of low accuracy.

Fuzzy FMECA for threshing and cleaning system

Fuzzy comprehensive evaluation refers to the process of applying fuzzy mathematical ideas to judge complex systems that are not easy to quantify through survey sampling and accumulation of relevant data *(Wang et al., 2021; Zhao et al., 2018)*.

In order to make the evaluation results more scientific and accurate, the fuzzy comprehensive evaluation method is introduced to analyse the reliability of the threshing and cleaning system. On the basis of the traditional FMECA analysis of threshing and cleaning, fuzzy comprehensive evaluation is carried out for each failure mode, and the evaluation results are quantified to rank the hazard level of the failure modes.

The steps of fuzzy FMECA are shown in Figure 3, and the steps of fuzzy comprehensive evaluation are shown in Figure 4.

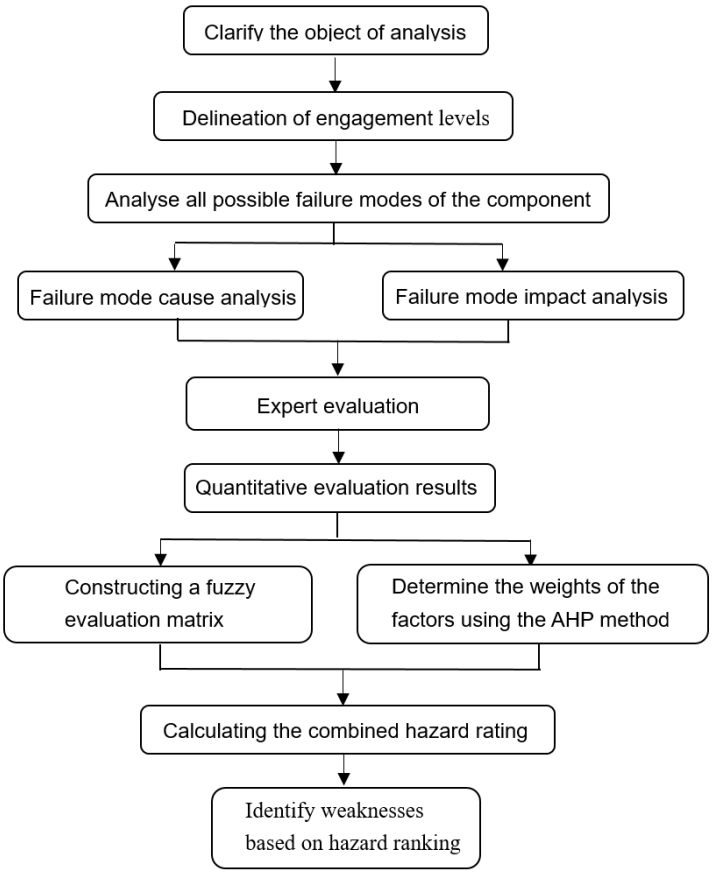


Fig. 3 – The steps of Fuzzy FMECA

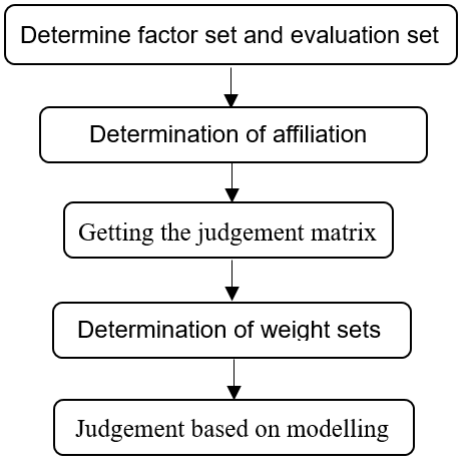


Fig. 4 – The steps of Fuzzy Comprehensive Evaluation

Build a factor set U

A factor set is a collection of factors that affect the object of evaluation, with different elements within the set representing different influences. Factors affecting the reliability of the threshing and cleaning system are the frequency of faults, the degree of fault impact, the difficulty of fault detection, and the difficulty of fault maintenance, so the set of factors U is constructed, that is, U = {Fault frequency (u_1), Fault influence degree (u_2), Fault detection difficulty (u_3), Fault maintenance difficulty (u_4)}.

Create an evaluation set V

The evaluation set is a collection of expert evaluation results, and each element in the set represents the grade of the evaluation results, which is represented by V, that is, $V=\{ v_1, v_2, v_3, v_4, v_5 \}=\{1,3,5,7,9\}$, and the specific grading and assignment of each influence factor is shown in Table 3.

Table 3

Grade definition of each influencing factor

Factor	Grade				
	1	2	3	4	5
Fault frequency	Very low frequency	Lower frequency	Medium frequency	High frequency	Very high frequency
Fault influence degree	Slight effect	Lower impact	Medium impact	Have a great effect	Influence seriously
Fault detection difficulty	Easy to detect	Easier to detect	Moderate detection difficulty	Harder to detect	Cannot detect
Fault maintenance difficulty	Easy to maintain	Easier to maintain	Moderate maintenance difficulty	Harder to maintain	Cannot repair

The fuzzy evaluation matrix is established

(1) Single factor evaluation

Before carrying out the comprehensive evaluation, a single-factor evaluation is carried out to determine the single-factor evaluation set. In the fuzzy comprehensive evaluation of a certain failure mode, let the i^{th} influencing factor u_i in the factor set have an affiliation degree of r_{ij} to the evaluation level v_j. The single-factor evaluation set of influencing factor u_i is:

$$r_i=\{r_{i1},r_{i2},\cdots,r_{im}\} \tag{2}$$

In carrying out the evaluation, "a" experts are usually invited to form an evaluation group, and each member of the evaluation group evaluates each failure mode separately, and determines the evaluation level v_j of the influence factor u_i. If there are a_{ij} people among the a experts who evaluate u_i to be subordinate to v_j, then the set of experts' evaluations R_i is obtained, that is:

$$R_i=\{\frac{a_{i1}}{a},\frac{a_{i2}}{a},\cdots,\frac{a_{ij}}{a},\cdots,\frac{a_{im}}{a}\}=\{r_{i1},r_{i2},\cdots,r_{ij},\cdots,r_{im}\} \tag{3}$$

where: $\sum_{j=1}^{m}\frac{a_{ij}}{a}=1$

(2) Establish a fuzzy comprehensive evaluation matrix

The single-factor evaluation set for each failure mode is used as the rows in the matrix to construct a fuzzy comprehensive evaluation matrix of the influencing factors, denoted by R, that is:

$$R=[R_1R_2,\ \ldots,\ R_n]^T=\begin{bmatrix} r_{11} & r_{12} & \cdots & r_{1n} \\ r_{21} & r_{22} & \cdots & r_{2n} \\ \vdots & \vdots & \ddots & \vdots \\ r_{m1} & r_{m2} & \cdots & r_{mn} \end{bmatrix} \tag{4}$$

Taking the drum threshing fault as an example, from equation (3), it can be seen that the evaluation results of the expert group for this fault mode can be obtained after the fuzzification process, and the fuzzy comprehensive evaluation matrix of the fault mode 1 can be obtained as:

$$R_1=\begin{bmatrix} 0.2 & 0.3 & 0.5 & 0 & 0 \\ 0 & 0 & 0.3 & 0.7 & 0 \\ 0 & 0.4 & 0.5 & 0.1 & 0 \\ 0 & 0 & 0.4 & 0.6 & 0 \end{bmatrix}$$

Establishment of factor weight sets W based on AHP

The weights reflect the relative importance of an influencing factor in the overall evaluation, and since the relative importance of each influencing factor is different, it is necessary to assign different weights to each factor in order to establish the factor weight set W.

There are many methods to determine weight distribution, mainly including expert scoring method, entropy weight method, AHP etc. *(Dai et al., 2023)*. This paper uses the AHP method. AHP divides the problem into different factors according to its own knowledge or experience and the overall goal, build a pairwise comparison matrix of different levels for each factor, and make pairwise comparison, and grades the factors according to their importance *(Hu et al., 2021)*, the importance of which is defined in Table 4.

Table 4

Grade definition of each influencing factor

Scale a_{ij}	Meaning
1	Equally important
3	Slightly important
5	Obviously important
7	Strongly important
9	Extremely Important
2,4,6,8	Between the above two adjacent scale values

The analysis process of this method is as follows:

(1) Construct the judgement matrix A. The element a_{ij} in the matrix is the value indicating the relative importance of u_i to u_j, namely:

$$A=\begin{bmatrix} a_{11} & a_{12} & \cdots & a_{1n} \\ a_{21} & a_{22} & \cdots & a_{2n} \\ \vdots & \vdots & \ddots & \vdots \\ a_{n1} & a_{n2} & \cdots & a_{nn} \end{bmatrix} \quad (5)$$

The judgement matrix A is normalised to obtain the eigenvector ω and the maximum eigenvalue λ_{max} is calculated, that is:

$$\lambda_{max}=\sum_{i=1}^{n}\frac{(AW)_i}{W_i} \quad (6)$$

(2) The consistency test was then performed and the consistency indicator CI value was calculated, that is:

$$CI=\frac{(\lambda_{max}-n)}{(n-1)} \quad (7)$$

The RI value is the average stochastic consistency index of the judgement matrix, which is the standard value, and the RI values of the 1st to 13th order judgement matrices are shown in Table 5.

Table 5

The standard value of average random consistency index RI

Order of matrix	1	2	3	4	5	6	7	8	9	10	11	12	13
Value of RI	0	0	0.58	0.90	1.12	1.24	1.32	1.41	1.45	1.49	1.52	1.54	1.56

Based on the equation (7) and table 5, the consistency ratio CR is calculated, that is:

$$CR=\frac{CI}{RI} \quad (8)$$

Finally, the calculated CR value is compared with 0.1, if CR < 0.1, it proves that the consistency test of the judgement matrix passes, otherwise the judgement matrix should be modified. When the consistency test of the judgement matrix passes, the ω obtained after the normalisation process is used as the weighting coefficient W_k of the factor set, that is:

$$W_k=\{\omega_1, \omega_2, \cdots, \omega_n\} \quad (9)$$

The drum threshing fault is illustrated as an example of the process of determining the weights through AHP. According to the expert group assessment, the relative importance of each influencing factor of the drum threshing fault can be obtained, which is shown in Table 6.

Table 6

Relative importance of each influencing factor

Influence factor	u_1	u_2	u_3	u_4
u_1	1	$\frac{1}{3}$	5	6
u_2	3	1	7	9
u_3	$\frac{1}{5}$	$\frac{1}{7}$	1	1
u_4	$\frac{1}{6}$	$\frac{1}{9}$	1	1

After normalisation, the final fuzzy judgement matrix and weights can be obtained, as shown in Table 7.

Table 7

Relative importance and weight of each influencing factor

Influence factor	u_1	u_2	u_3	u_4	w_i	Aw_i
u_1	0.23	0.21	0.36	0.35	0.2873	1.1777
u_2	0.68	0.63	0.50	0.53	0.5849	2.4561
u_3	0.05	0.09	0.07	0.06	0.0676	0.2682
u_4	0.04	0.07	0.07	0.06	0.0596	0.2400

The maximum eigenvalue λ_{max} can be calculated from equation (6) as 4.07, and the consistency index CI is 0.02 from equation (7), and by checking table 5, it can be seen that the RI is 0.89 in this paper.

Finally, the consistency ratio CR is calculated as 0.0276 by equation (8), and this value is less than 0.1 and the consistency test is passed. Therefore, the set of factor weights for drum threshing failure is as follows:

$$W_1 = \{0.2873,\ 0.5849,\ 0.0676,\ 0.0596\}$$

First-level fuzzy comprehensive evaluation

The fuzzy comprehensive evaluation matrix B_k for failure mode k is the multiplication of the factor weight vector W_k for failure mode k with the level evaluation matrix R_k for failure mode k, that is:

$$B_k = W_k R_k \tag{10}$$

This shows that the first level fuzzy comprehensive evaluation matrix for drum threshing faults is as follows:

$$B_1 = W_1 R_1 = [0.0575,\ 0.1132,\ 0.3768,\ 0.4520,\ 0] \tag{11}$$

Calculation of comprehensive hazard grade index

The comprehensive hazard grade index C_k of failure mode k is equal to its composite fuzzy evaluation matrix B_k multiplied by the evaluation set V^T, namely:

$$C_k = B_k V^T \tag{12}$$

where: V^T is the evaluation matrix.

In the case of drum threshing failure, for example, the combined hazard rating is:

$$C_1 = B_1 V^T = 5.4446 \tag{13}$$

The same procedure was used to determine the fuzzy evaluation matrix for failure modes 2 to 8, respectively:

$$R_2=\begin{bmatrix}0.1 & 0.2 & 0.6 & 0.1 & 0\\ 0 & 0 & 0.1 & 0.6 & 0.3\\ 0 & 0.3 & 0.6 & 0.1 & 0\\ 0 & 0 & 0.3 & 0.7 & 0\end{bmatrix}$$

$$R_3=\begin{bmatrix}0 & 0.2 & 0.5 & 0.3 & 0\\ 0 & 0.1 & 0.3 & 0.6 & 0\\ 0.1 & 0.4 & 0.5 & 0 & 0\\ 0 & 0.1 & 0.4 & 0.5 & 0\end{bmatrix}$$

$$R_4=\begin{bmatrix}0 & 0.1 & 0.3 & 0.5 & 0.1\\ 0 & 0.3 & 0.7 & 0 & 0\\ 0.1 & 0.6 & 0.3 & 0 & 0\\ 0 & 0.2 & 0.4 & 0.4 & 0\end{bmatrix}$$

$$R_5=\begin{bmatrix}0.2 & 0.5 & 0.3 & 0 & 0\\ 0 & 0.2 & 0.5 & 0.3 & 0\\ 0 & 0.2 & 0.5 & 0.3 & 0\\ 0 & 0.4 & 0.4 & 0.2 & 0\end{bmatrix}$$

$$R_6=\begin{bmatrix}0 & 0.1 & 0.4 & 0.5 & 0\\ 0 & 0.3 & 0.6 & 0.1 & 0\\ 0.1 & 0.5 & 0.4 & 0 & 0\\ 0 & 0.3 & 0.4 & 0.3 & 0\end{bmatrix}$$

$$R_7=\begin{bmatrix}0 & 0 & 0.2 & 0.7 & 0.1\\ 0 & 0 & 0.2 & 0.7 & 0.1\\ 0 & 0.3 & 0.5 & 0.2 & 0\\ 0 & 0 & 0.3 & 0.6 & 0.1\end{bmatrix}$$

$$R_8=\begin{bmatrix}0.1 & 0.6 & 0.3 & 0 & 0\\ 0 & 0.2 & 0.4 & 0.4 & 0\\ 0 & 0.2 & 0.4 & 0.4 & 0\\ 0 & 0.1 & 0.5 & 0.4 & 0\end{bmatrix}$$

In this paper, since the relative importance of the factors affecting each failure mode is the same, the same set of weights W is used, that is:

$$W=\{0.2873,0.5849,\ 0.0676,0.0596\}$$

According to formula (10) and formula (12), the fuzzy comprehensive evaluation matrix B_k and the comprehensive hazard coefficient C_k can be calculated for failure modes 2 to 8, respectively:

$$B_2=[0.0287\quad 0.0777\quad 0.2893\quad 0.4282\quad 0.1755]$$

$$C_2=6.2848$$

$$B_3=[0.0068\quad 0.1490\quad 0.3768\quad 0.4669\quad 0]$$

$$C_3=5.6059$$

$$B_4=[0.0068\quad 0.2567\quad 0.5397\quad 0.1675\quad 0.0287]$$

$$C_4=4.9065$$

$$B_5=[0.0575\quad 0.2980\quad 0.4363\quad 0.2077\quad 0]$$

$$C_5=4.5865$$

$$B_6=[0.0068\quad 0.2559\quad 0.5167\quad 0.2200\quad 0]$$

$$C_6=4.8982$$

$$B_7=[0\quad 0.0203\quad 0.2261\quad 0.6598\quad 0.0932]$$

$$C_7=6.65$$

$$B_8=[0.0287\quad 0.3088\quad 0.3770\quad 0.2848\quad 0]$$

$$C_8=4.8340$$

According to the comprehensive hazard index, the hazards of failure modes 1 to 8 are, in descending order, as follows: failure mode 5, failure mode 8, failure mode 6, failure mode 4, failure mode 1, failure mode 3, failure mode 2, and failure mode 7. By analysing the historical failure data, it is found that the results of this judgement are in line with the situation in actual use.

RESULTS

By comparing the results of traditional FMECA analysis with the results of fuzzy FMECA analysis, it can be seen that in the traditional FMECA analysis method, the relative importance of the three influencing factors of ESR, OPR and DDR is not considered, and the assignment of the value is not fuzzy, so that different failure modes get the same RPN value, and then it is not possible to rank them in terms of their hazard degree. After the introduction of fuzzy comprehensive evaluation, the weights of each influencing factor are assigned and the expert scores are processed using fuzzy mathematical methods to obtain more accurate hazard level coefficients, which can effectively rank the risk level of each failure mode, so as to find out the weaknesses and make up for the shortcomings in the traditional FMECA analysis.

CONCLUSIONS

(1) In this paper, on the basis of traditional FMECA, the fuzzy comprehensive evaluation method is introduced to quantify and analyse the evaluation results and reduce the influence of subjective evaluation of experts on the results. At the same time, AHP is used for weight allocation, two-by-two comparisons are made between the influencing factors of the failure modes, a judgement matrix is constructed to determine the relative importance of the factors, and the failure modes are ranked by calculating the hazard level index, which effectively compensates for the shortcomings of the traditional FMECA, and makes the evaluation results more scientific and in line with the reality.

(2) This paper takes the threshing and cleaning system of wheat combine harvester as an example, and carries out reliability analysis based on the improved FMECA method, and finally concludes that failure mode 7 has the greatest degree of harm, followed by failure mode 2, which can be used as the focus of reliability improvement and provide a theoretical basis for practical production application. According to the results of reliability analysis, the weak links of the system can be identified, and the system can be checked before operation to reduce the failure rate during operation, thus improving the reliability of the system as well as the service life of the whole machine.

ACKNOWLEDGEMENT

The work was supported by the High Efficiency and Low Loss Single Longitudinal Axial Flow Threshing and Separation Technology and Development of Intelligent Flexible Threshing Device, (Grant No.2021YFD200050204), and the Development of Intelligent Multifunctional Wheat Corn Grain Combine Harvester, (Grant No.2016YF026).

REFERENCES

[1] Ahmed, S. (2020). Risk *Assessment of Failure Modes Related to Marine Boiler Using Fuzzy Expert System* [Master Dissertation], Shanghai Jiao Tong University.

[2] Brahim, I. B., Addouche, S. A., Mhamedi, A. E. et al. (2020). Build a Bayesian Network from FMECA in the Production of Automotive Parts: Diagnosis and Prediction. *IFAC Conference on Manufacturing Modelling, Management and Control.*

[3] Chai, B. M., Li, W. X., Wang, Z. T. et al. (2011). Fuzzy Mathematics in Mechanical Fault Diagnosis（模糊数学在机械设备故障诊断中的应用）. *Coal Mine Machinery*, Vol. 32, No.03, 261-262.

[4] Chen, Y. (2011). *Reliability analysis of aircraft power supply system based on fuzzy FMECA method*（基于模糊 FMECA 方法的飞机供电系统可靠性分析研究） [Master Dissertation], University of Electronic Science and Technology of China.

[5] Dai, C. G., Wang, X. H., Zhang, X. et al. (2011). Fuzzy comprehensive evaluation in FMECA of electro-hydraulic servo valve (基于模糊综合评判的电液伺服阀 FMECA). *Journal of Beijing University of Aeronautics and Astronautics.* Vol. 37, No. 12, 1575-1578.

[6] Dai, M., Chen, C., Zhou, L. et al. (2023). A reliability allocation method for agricultural machinery based on AHP-IFM. *Qual Reliab Eng Int,* Vol. 39, 687– 705.

[7] Hu, N., Zhang, T. Q., Wang, Y. H. et al. (2021). Failure Modes and Effect Analysis of Ship Reducer Based

on Analytic Hierarchy Process. (基于层次分析法的船舶减速器故障模式影响分析). *Electronic Product Reliability and Environmental Testing,* Vol. 39, No. 03, 35-39.

[8] Hu, Q. G., & Shen, X. X. (2017). Reliability Analysis on Hydraulic System of Amphibious Armored Vehicle Based on Fuzzy FMECA. (基于模糊 FMECA 的两栖装甲车液压系统可靠性分析). *Machine Tool & Hydraulics,* Vol. 45, No. 13, 168-173.

[9] Hu, W. Z., He, K., Jin, C. Q. et al. (2018). FMECA Method Based on Fuzzy Comprehensive Evaluation. (基于模糊综合评判的农业机械 FMECA 方法研究). *Transactions of the Chinese Society for Agricultural Machinery,* Vol. 49, No. S1, 332-337.

[10] Khorshidi, H. A., Gunawan, I., Ibrahim, M.Y. (2016). Data-Driven System Reliability and Failure Behavior Modeling Using FMECA. *IEEE Transactions on Industrial Informatics,* Vol.12, No.3, 1253-1260.

[11] Liu, H. C., Liu, L., & Liu, N. (2013). Risk evaluation approaches in failure mode and effects analysis: a literature review. *Expert Systems with Applications,* Vol. 40, No. 2, 828-838.

[12] Singh, J., Singh, S., & Singh, A. (2019). Distribution transformer failure modes, effects and criticality analysis (FMECA). *Engineering Failure Analysis,* 99, 180-191.

[13] Shao, W. G. (2019). *Research on the FMECA and FTA of the Landing Gear System for A Certain Type of Aircraft in Failure Analysis* (FMECA 和 FTA 在某型飞机起落架系统故障分析中的应用研究) [Master Dissertation], Xihua University.

[14] Tang, S. B., Wang, T. Y., Wen, Y. K., (2022). Product Reliability Analysis Method Based on FMECA (基于 FMECA 的产品可靠性分析方法). *Electronic Product Reliability and Environmental Testing*, Vol. 40, No.05, 61-63.

[15] Wang, H., Zhang, Y. M., Yang, Z. et al. (2017). Multi-factor reliability allocation method of CNC lathes considering failure correlation (考虑相关性的数控车床多因素可靠性分配法). *Journal of Harbin Institute of Technology*, Vol. 49, No. 07, 93-99.

[16] Wang, H. J., Bian, X. D., Deng, X. W. et al. (2021). Suitability Evaluation of Underground Space Development and Utilization of Coal Mine Based on Fuzzy Mathematics Theory-Taking Baiyuan Coal Mine as an Example (基于模糊数学理论的煤矿地下空间开发利用适宜性评价——以白源煤矿为例). *Northwestern Geology*, Vol. 54, No.04, 156-170.

[17] Xu, B., Pan, W. J., Luo, Y. M. et al. (2022). Failure Mode Effect and Criticality Analysis of Airport Remote Tower System (机场远程塔台系统故障模式影响及危害性分析). *Ship Electronic Engineering,* Vol.42, No. 02, 115-119.

[18] Yu, H., & Zhang, H. S. (2022). Improved FMECA for Traction Transmission System of EMU Based on Fuzzy Comprehensive Evaluation (基于模糊综合评价的动车组牵引传动系统改进). *Journal of the China Railway Society,* Vol. 44, No. 09, 33-41.

[19] Yang, L., Dang, M., Dong, C.Q. et al. (2021). Reliability Status Analysis and Development Suggestions of Agricultural Machinery Equipment (农机装备可靠性现状分析及发展建议). *Electronic Product Reliability and Environmental Testing,* Vol. 39, No. 02, 1-6.

[20] Zhang, H., Kang, J. M., Zhang, G.H. et al. (2019). Reliability analysis of air suction duckbill type seed metering device based on improved FMECA method (基于改进 FMECA 方法气吸鸭嘴滚筒式排种器的可靠性分析). *Journal of Shihezi University (Natural Science),* Vol. 37, No. 05, 543-548.

[21] Zhang, H. R., Hong, R. J., Chen, F. X. et al. (2020). Reliability analysis method of CNC machine tools on FMECA and fuzzy evaluation. (基于 FMECA 和模糊评判的数控机床可靠性分析方法). *Manufacturing Technology & Machine Tool,* No. 11, 125-129.

[22] Zou, J. L. (2011). *A Study on Diesel Engines' Reliability and FMECA for Engineering Machinery* (工程机械柴油机可靠性及 FMECA 研究) [Master Dissertation], Nanjing Forestry University].

[23] Zhang, Q., & Wang, X. P. (2016). The Comparison of Some Fuzzy Operators Used in Fuzzy Comprehensive Evaluation Models (模糊综合评价中几类模糊算子的比较). *Fuzzy Systems and Mathematics,* Vol. 30, No.03,165-171.

[24] Zhu, T. (2022). Failure Mode, Effects and Criticality Analysis of Aero-derivative Gas Turbine Combustor (航改燃气轮机燃烧室故障模式、影响及危害性分析). *Aeroengine,* Vol. 48, No. 01, 33-39.

[25] Zhu, X. C. (2013). *Study on Reliability and Maintainability Analysis of CNC Machine Tools Based on Grey System Theory (*基于灰色理论的数控机床可靠性及维修性分析技术*).* [Doctoral dissertation], Jilin University.

[26] Zhao, Y. D., Sun, T., Zhou, C. M. et al. (2018). Study on Evaluation Method of Energy Consumption of Centrifugal Pump Based on Fuzzy Mathematics (基于模糊数学的离心泵系统能耗评价方法研究). *Journal of Liaoning Petrochemical University*, Vol. 38, No.04, 77-81.

DEPOSITION PERFORMANCE OF HYDRODYNAMIC ULTRASONIC ATOMISING NOZZLES WITH DIFFERENT SPRAY PARAMETERS
/
不同喷雾参数对流体动力式超声雾化喷嘴的沉积性能研究

Zengqiang SONG [1)], Jinliang GONG [2*)], Yanfei ZHANG [1*)]
[1)]School of Agricultural Engineering and Food Science, Shandong University of Technology, Zibo/China
[2)]School of Mechanical Engineering, Shandong University of Technology, Zibo/China
Tel: +8618265338441; E-mail: 1392076@sina.com; gjlwing@sdut.edu.cn
DOI: https://doi.org/10.35633/inmateh-71-15

Keywords: *Ultrasonic atomization, Droplet size, Atomization angle, Deposition coverage, Data fitting*

ABSTRACT
In order to study the spraying effect of hydrodynamic ultrasonic atomizing nozzle under different spraying methods, and to investigate the practical application effect of hydrodynamic ultrasonic atomizing nozzle in agriculture, the atomization angle test and droplet size test under different spraying conditions were designed. Different spraying conditions atomization angle test and droplet size test were designed, the test results data were recorded, the pattern of change of the data was observed, and the data were fit to give the data changes in line with the functional equation; different spraying conditions and different corn leaf position droplet deposition coverage test were designed and the value of the deposition coverage of each position was recorded. The results showed that: the maximum value of the variation of atomization angle under different spraying conditions was 75.49°, and the minimum value was 14.49°; the maximum value of the variation of droplet size was 18.23 μm, and the minimum value was 4.78 μm; and the droplet deposition coverage was the highest in the mid-leaf position of the upper and lower leaves of the maize when the input air pressure was 0.3 MPa, which was 86.98% and 46.97%, respectively. Fitting the atomization angle data and droplet size data, the R^2 of the binomial fit was 0.85 and 0.94, respectively, and the Adjusted R^2 was 0.87 and 0.88, respectively, which made the fitting function meaningful and the fitting accuracy high. The hydrodynamic ultrasonic atomizing nozzle has a great advantage in generating small droplet sizes and performs well in deposition effect, and the experimental results can provide a reference for the research of hydrodynamic nozzles in the application technology.

摘要
为研究流体动力式超声雾化喷嘴在不同喷雾方式下喷雾效果，探究流体动力式超声雾化喷嘴在农业中实际应用效果。设计不同喷雾条件下雾化角试验和雾滴粒径试验，对试验结果数据进行记录，观测数据变化规律，并对数据进行拟合，给出符合数据变化的函数关系式；设计不同喷雾条件及不同玉米叶位置雾滴沉积覆盖率试验并对各位置的沉积覆盖率值进行记录。试验结果表明：不同喷雾条件下雾化角变化最大值为 75.49°，最小值为 14.49°；雾滴粒径变化最大值为 18.23μm，最小值为 4.78μm；在输入气压为 0.3MPa 时，玉米上、下叶的叶中位置雾滴沉积覆盖率最高，分别为 86.98%和 46.97%。对雾化角数据和雾滴粒径数据进行拟合，二项式拟合的 R^2 分别为 0.85 和 0.94，Adjusted R^2 分别为 0.87 和 0.88，拟合函数有意义且拟合精度较高。流体动力式超声雾化喷嘴在产生小雾滴粒径有着很大优势并在沉积效果上表现优异，试验结果可为流体动力式喷嘴在施药技术方面的研究提供参考。

INTRODUCTION
During plant protection application, *Hewitta J et al., (2008),* pointed out that ideally all the droplets of the liquid should be effectively deposited in the target area. However, *Allan S. Felsot et al., (2010),* state that it is not possible to avoid spray drift completely but it can be minimized by using best-management practices. *Hiltz et al., (2013),* showed that in the actual operation process due to the main factors such as spraying parameters (e.g., spraying pressure, atomisation angle, droplet size) and environmental and meteorological conditions (e.g., wind speed) will affect the droplet drift.

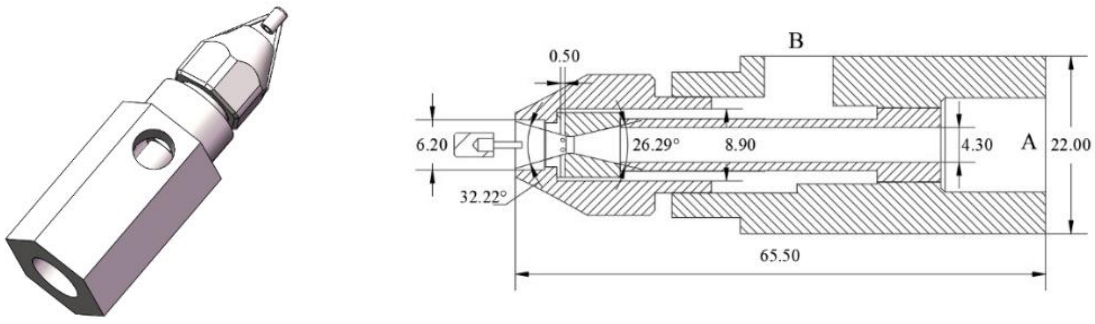
[1] *Zengqiang SONG, M.S. Eng..; Jinliang GONG, A. Prof. Ph.D. Eng.; Yanfei ZHANG, Prof. Ph.D. Eng.*

Huang Y.B. et al., (2013), pointed out that the droplet drift will cause the phenomena of soil environment pollution, part of the pesticide loss and pesticide utilisation rate reduction. *Maghsoudi H. et al., (2015),* pointed out that ultra-low volume spraying can improve the utilisation rate of pesticides, reduce the cost of pesticide use and pollution to the environment, and is a kind of application technology that is strongly promoted in the field of plant protection operations. *Wen S. et al., (2016), Yan X.J. et al., (2021),* found that compared to the conventional way of applying pesticides, 30% of pesticides can be saved. At this stage, the main way to achieve this technology is mostly pressure atomisation, centrifugal atomisation and electrostatic atomisation, or a combination of one or more atomisation methods, *Zhang J.T. et al., (2016),* showed that the above methods are complicated in structure and high in cost. Ultrasonic atomisation method generates small and uniform droplets and its application in agriculture has been explored by *Gao J.M. et al., (2017). Lu D.P. et al., (2017),* pointed out that ultrasonic atomisation technology is mechanically divided into piezoelectric and hydrodynamic, and the former has a complex structure, high cost and energy consumption and low atomisation capacity, which is difficult to meet the actual needs of agriculture despite the innovation and improvement made by *Wu C.Q. et al. (2021). Wu G.G. et al., (2021),* pointed out that the latter has excellent atomisation performance, *Park J. et al., (2022),* showed that wind field can affect the deposition coverage of droplets, *Tian Z. et al., (2022),* showed that the presence of a wind field can increase the penetration of droplets between the blades, *Liu C. et al., (2023),* showed that a conical wind field can increase the deposition coverage of droplets, and *Butler M.C. et al., (2017),* showed that downwind field reduces the drift of droplets. Therefore, *He R. et al., (2019) and Jiang C. et al., (2019),* pointed out that the hydrodynamic ultrasonic atomisation technology has great potential to achieve ultra-low-volume spraying in facility agriculture and ground plant protection operations. In order to investigate the application effect of hydrodynamic ultrasonic atomising nozzles in pesticide spraying and the influence of its spraying parameters on the deposition performance, this paper investigates the distribution of droplet size and the droplet deposition on corn seedlings by hydrodynamic nozzles under different operating parameters through experimental means, with a view to providing a reference to the research of hydrodynamic nozzles in the application technology, and to promote the technology in the agricultural plant protection operation. The results of this study are summarised as follows.

MATERIALS AND METHODS

Test equipment

The test was carried out in the atomisation laboratory of Shandong University of Technology, and the nozzle used was a hydrodynamic ultrasonic atomisation nozzle, which has the shape and parameters as shown in Fig. 1(a) and 1(b). A is the gas entry point, i.e. the input air pressure, and B is the liquid entry point; Peristaltic pump (XA01, input voltage 12V-24V, Changzhou); Laser particle size analyser (Omeco, DP-02, Beijing, China); Adjustable DC Regulated Power Supply (Myson, MS305D, Guangdong Province); High-speed camera (PHOTRON, AX100-8G, Japan); Air compressor (DA5001, measuring output range 0-0.5MPa, Zhejiang).



(a) Nozzle model drawing (b) Nozzle parameter diagram

Fig. 1 - Ultrasonic atomizing nozzle

Experimental design

The test is divided into three parts, respectively, for different spraying conditions under the atomisation angle measurement test, droplet size test, droplet deposition test on corn seedlings, each test using its own control test method. Firstly, test the peristaltic pump to determine the volumetric flow rates produced under different input voltages. It is observed that the peristaltic pump operates effectively at an input current of 0.4A and an input voltage of 12V. However, it fails to function when the current or voltage drops below this threshold. To ensure proper operation of the peristaltic pump, maintain a fixed current of 0.4A during testing.

Fogging Atomisation angle test, droplet particle size test, and maize seedling deposition test were designed separately.

(1) *Atomisation angle test*

Atomisation angle measurement test used high-speed camera shooting, nozzle height from the ground 1500 mm, high-speed camera from the atomisation nozzle 2000 mm. The test was carried out indoors and there was indoor dark light treatment, in order to improve the shooting effect of high-speed digital camera. The test site is shown in Fig. 2(a). The test was conducted by adjusting the peristaltic pump input voltage to regulate the water intake of the ultrasonic atomising nozzle, and adjusting the output air pressure of the air compressor to regulate the input air pressure of the ultrasonic atomising nozzle. The gas pressure of the input gas was gradually increased from 0.1 MPa to 0.4M Pa at intervals of 0.1 MPa, and the fog shape sprayed from the atomising nozzle was photographed and recorded each time. The test results were analysed uniformly at a later stage and the corresponding conclusions were drawn.

(2) *Droplet size test*

Droplet particle size is one of the key factors affecting pesticide drift and settling. Under the condition of the same spray volume, the finer the droplet size, the higher the number of droplets, the more uniformly distributed on the target and the larger the coverage area. *Ding S.M. et al.* pointed out that it is a close factor affecting the value of spray droplet size. The nozzle used in this experiment is a hydrodynamic ultrasonic atomising nozzle, which requires a certain gas pressure and a certain amount of water intake in order to produce droplets, so in the droplet size test, a low intake volume of 500 mL/min was chosen, the gas pressure from 0.1 MPa to 0.4 MPa gradually increasing, the pressure interval of 0.1 MPa, ultrasonic atomising nozzle and the laser beam of the laser particle sizing instrument. The distance between the ultrasonic atomising nozzle and the laser beam of the laser particle sizer was gradually increased from 100 mm to 500 mm, and the size of the droplets under each gas pressure was measured using the laser particle sizer and the corresponding conclusions were drawn, and the droplet size detection system is shown in Fig. 2(b).

(3) *Maize seedling deposition test*

In order to investigate how effective ultrasonic atomising nozzles are in practical application in agriculture, this experiment was conducted using maize seedlings at the four to six leaf stage, with water-sensitive test strips placed at the tips, middle and roots of the broad upper and lower leaves of the maize on the seedlings. Corn seedlings were placed according to the standard corn field, row spacing of 600 mm, plant spacing of 250 mm, the test for the simulation of real corn field application scenarios, the ultrasonic atomisation nozzle is fixed in a certain speed of uniform movement of the trolley, ultrasonic atomisation nozzle distance from the crop canopy is 500 mm, the trolley travelling speed is set at 4.3 Km/h, select the low feed volume of 500 mL/min, before the start of each test until the fog pattern is stable, the test variable is the gas input pressure, the input pressure from 0.1 MPa gradually increasing to 0.4 MPa at intervals of 0.1 MPa. Before the start of each test, the robot moves forward at a constant speed after the fog is stabilised, the test variable is the input pressure of the gas, the input pressure gradually increases from 0.1 MPa to 0.4 MPa, with an interval of 0.1 MPa, and the water-sensitive test paper is replaced at the same position after each spraying in the next test, and after each test, the water-sensitive test paper is removed and placed in a standby position, and the test scenario is shown in Fig. 2(c), and all the tests are completed later. After all the tests were done, the water-sensitive test paper was analysed and the corresponding conclusions were drawn.



(a)Atomization Angle measurement system

(b)Droplet particle size detection system

(c)Droplet Deposition Test System

Fig. 2- Test site map

1. Ultrasonic atomizing nozzle；2. Fill light；3. Air compressor;4. Air compressor; 5. Peristaltic pump; 6. Laser particle size analyser 7. Water sensitive test paper; 8. Corn seedlings; 9 Sports car

RESULTS AND ANALYSES

The test results of the peristaltic pump in terms of the feed volume it can provide at different input voltages are shown in Table 1.

Table 1

Values of flow rates available for peristaltic pumps at different input voltages

Input Voltage	Input Current	Flow rate	Input Voltage	Input Current	Flow rate
V	A	mL·min^{-1}	V	A	mL·min^{-1}
12	0.4	450	19	0.4	750
13	0.4	500	20	0.4	800
14	0.4	550	21	0.4	850
15	0.4	600	22	0.4	870
16	0.4	650	23	0.4	900
17	0.4	700	24	0.4	950
18	0.4	720			

Size of atomisation angle under different spraying conditions

Test results

Under different experimental conditions, the test results of the atomization angle of the fluid dynamic ultrasonic atomizer nozzle are shown in Table 2. The experimental results can provide a basis for selecting different spraying schemes. Calibration of the atomisation angle is calculated by taking a picture of the stable fog pattern at the same height of the tip of the nozzle; drawing a horizontal reference line at a distance of 250 mm from the nozzle outlet, obtaining two intersections between the reference line and the atomisation boundary, and connecting the two points and the centre of the nozzle outlet to the angle obtained as the atomisation angle of the spray application, which is the conditional atomisation angle.

Table 2

Results of atomization angle test under different test conditions

Input Air Pressure	Feed volume	Fogging angle	Input Air Pressure	Feed volume	Fogging angle
MPa	mL·min^{-1}	°	MPa	mL·min^{-1}	°
0.1	450	31.89	0.3	450	70.17
0.1	500	21.43	0.3	500	69.91
0.1	550	18.90	0.3	550	70.29
0.1	600	19.97	0.3	600	67.88
0.1	650	20.08	0.3	650	66.10
0.1	700	18.78	0.3	700	64.37
0.1	750	18.72	0.3	750	54.86
0.1	800	21.29	0.3	800	55.13
0.1	850	18.93	0.3	850	51.18
0.1	900	18.63	0.3	900	40.99
0.1	950	17.40	0.3	950	35.91
0.2	450	28.02	0.4	450	107.38
0.2	500	25.35	0.4	500	104.11
0.2	550	25.08	0.4	550	90.98
0.2	600	24.83	0.4	600	89.75
0.2	650	23.48	0.4	650	77.87
0.2	700	24.51	0.4	700	72.27
0.2	750	24.17	0.4	750	54.32
0.2	800	23.73	0.4	800	46.12
0.2	850	23.54	0.4	850	45.32
0.2	900	23.20	0.4	900	43.2
0.2	950	22.22	0.4	950	42.70

Analysis of results

In order to more intuitively analyse the influence of the input air pressure and the liquid feed volume on the size of the atomization angle, establish a binary function with the input air pressure and the liquid feed volume as the independent variables, and the atomization angle as the dependent variable, and then use Origin2019 to plot the spatial surface distribution of the influence of the input air pressure and the liquid feed volume on the atomization angle, as shown in Fig.3.

As can be seen from Fig. 3, the atomization angle increases significantly with the increase of input air pressure at low inlet volume, which is due to the fact that the increase of input air pressure accelerates the impact of high-speed gas flow on the liquid stream broken, resulting in greater droplet dispersion force and gas shear force, which makes the liquid droplets to form more fine droplets, thus expanding the atomisation angle; at low input air pressures, the variation in liquid intake does not significantly alter the size of the atomization angle. This is because the lower pressure hinders the airflow from effectively dispersing the liquid into smaller droplets, resulting in shorter distances traveled by the droplets during the spraying process and a reduced level of collision and breakup. Larger droplets are more stable and less prone to further dispersion under low pressure, thus maintaining their shape and leading to a smaller atomization angle.

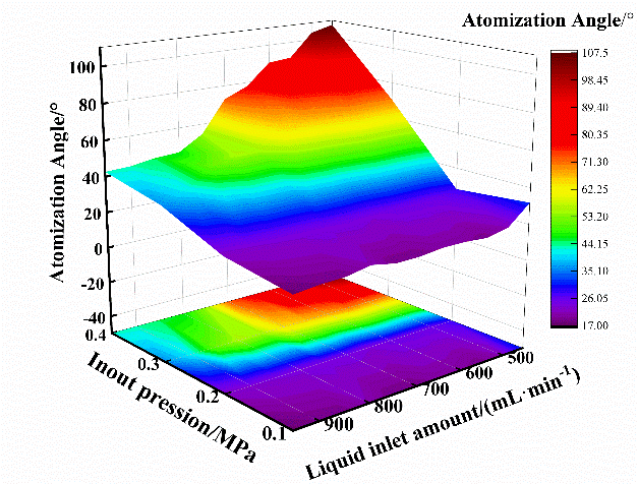


Fig. 3 - Atomization Angle diagram under different test conditions

Fitting of atomisation angle data under different spraying conditions

In order to further analyse the accuracy and reference value of the experimental data, Origin2019 was used to fit the polynomials to the atomisation angle data under different spraying conditions using the nonlinear surface fitting function, and the fitted model was Equation 1, where *x* represents the input air pressure, *y* represents the liquid inlet volume, *z* represents the atomisation angle, z_0 represents the zero offset, and A_i and B_i are the coefficients of *x* and *y*, respectively (i=1, 2, ……5). Table 3 shows the parameters of the fitted model for the atomisation angle, the coefficient of determination R^2 for the polynomial fit is 0.85 and the Adjusted R^2 for the adjusted coefficient of determination is 0.81, which indicates that the fitted function is meaningful.

$$z = z_0 + A_1 \bullet X + A_2 \bullet pow(x,2) + A_3 \bullet pow(x,3) + A_4 \bullet pow(x,4) + A_5 \bullet pow(x,5) + B_1 y + B_2 \bullet pow(y,2) + B_3 \bullet pow(y,3) + B_4 \bullet pow(y,4) + B_5 \bullet pow(y,5) \quad (1)$$

Table 3

Polynomial fitting model parameters

Parameters	z_0	A_1	A_2	A_3	A_4	A_5	B_1	B_2	B_3	B_4	B_5
Value	5.84	-1.11	6.32	-8.96	-1.96	4.39	-14.19	0.04	-6.02E-5	4.28E-8	-1.19E-11
Error	4. 9E+6	1.29	1.07	2.03E9	-	-	38.72	0.12	1.71E-4	1.24E-7	3.53E-11

Droplet size under different spraying conditions

Test results

The droplet size value is the average value of 3 tests of the droplet size in each position of the axial direction of the ultrasonic atomising nozzle under different air pressures, and the results of the droplet size distribution tests with different input air pressures and different heights are shown in Table 4, which provides a basis for selecting the optimal input air pressures and optimal spraying heights of the fluid-dynamic ultrasonic atomising nozzles through the test results.

Table 4

Test results of droplet size under different spraying conditions

Input Air Pressure	Distance	Droplet size	Input Air Pressure	Distance	Droplet size
MPa	mm	μm	MPa	mm	μm
0.1	100	35.79	0.3	100	26.09
0.1	200	40.73	0.3	200	27.35
0.1	300	43.44	0.3	300	29.15
0.1	400	45.82	0.3	400	30.87
0.1	500	51.86	0.3	500	32.64
0.2	100	28.38	0.4	100	24.69
0.2	200	32.35	0.4	200	24.54
0.2	300	33.77	0.4	300	25.20
0.2	400	35.07	0.4	400	25.44
0.2	500	37.08	0.4	500	25.75

Analysis of results

It can be seen from Fig. 4 that the droplet particle size decreases significantly with the increase of input air pressure at a certain spraying height, and the droplet particle size increases with the increase of spraying distance at a certain input air pressure.

(1) Effect of Input Air Pressure on Droplet Size Distribution

As can be seen from Figure 4, the droplet size decreases significantly with the increase of air pressure. With the increase of the input air pressure, the speed of the airflow will be larger and larger, the impact on the liquid will be stronger, making it easier for the liquid to rupture the formation of smaller droplets, but the droplet size increases gradually with the axial distance. The larger the inlet air pressure, the droplet size in the axial position of the degree of change of the droplet size is smaller, and the distribution of the droplets is also more stable.

(2) Influence of different heights on droplet size distribution

As can be seen from Fig. 4, when the spraying air pressure is certain, with the spraying height increasing, the size of the droplet size is gradually increasing, this is because the farther away from the ultrasonic atomisation nozzle, the droplets themselves have a greater loss of kinetic energy, so the farther away from the nozzle the droplet condensation occurs, resulting in the droplet size of the droplet group increases.

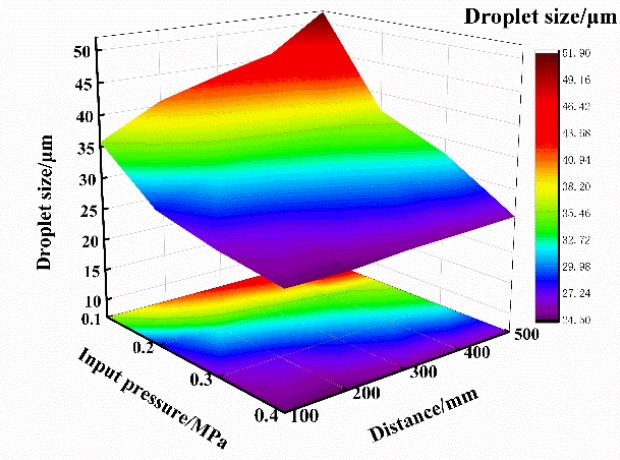


Fig. 4 - Particle size of droplets under different test conditions

Fitting of droplet size under different spraying conditions

In order to visually analyse the variation of droplet size, the polynomial fitting of the droplet size values under different spraying conditions was performed with reference to the data fitting method in the above chapters, and the fitting model was Eq. (2), in which x' indicated the input air pressure, y' indicated the spraying height, and z' indicated the atomization angle, z_0' denotes the zero offset, A′ and B′ are the coefficients of x' and y', respectively. Table 5 shows the parameters of the droplet size fitting model, and the coefficient of determination of the polynomial fit, R^2, is 0.94, and the adjusted coefficient of determination, Adjusted R^2, is 0.94. Adjusted R^2 is 0.88, which indicates that the fitting function is meaningful.

$$z' = z_0' + A_1' \bullet x' + A_2' \bullet pow(x',2) + A_3' \bullet pow(x',3) + A_4' \bullet pow(x',4) + A_5' \bullet pow(x',5) + B_1' y' + B_2' \bullet pow(y',2) + B_3' \bullet pow(y',3) + B_4' \bullet pow(y',4) + B_5' \bullet pow(y',5) \quad (2)$$

Table 5

Polynomial fitting model parameters

Parameters	z_0'	A_1'	A_2'	A_3'	A_4'	A_5'	B_1'	B_2'	B_3'	B_4'	B_5'
Value	-5.79E14	1.04E16	-5.06E16	4.48E15	4.35E17	-6.77E17	0.62	0.004	1.45E-5	-2.27E-8	1.34E-11
Error	4.81E6	6.58E7	4.6E8	7.69E8	-	-	5.31E4	4.36E2	1.65	0.002	1.93E-6

Evaluation of droplet deposition characteristics under different spraying conditions

Test results

The results of the droplet deposition measurements under different input air pressures are shown in Table 6, through which the test results can be verified for the pre-selected spraying conditions.

Table 6

Results of depositional coverage at each position of upper and lower leaves of maize

Placement	Input Air Pressure	Sedimentation coverage	Placement	Input Air Pressure	Sedimentation coverage
	MPa	%		MPa	%
tip of the upper leaf blade	0.1	10.41	tip of the lower leaf blade	0.1	11.60
	0.2	28.26		0.2	17.89
	0.3	35.60		0.3	22.75
	0.4	20.17		0.4	13.41
middle portion of the upper leaf blade	0.1	27.30	middle portion of the lower leaf blade	0.1	24.55
	0.2	54.69		0.2	34.87
	0.3	86.98		0.3	46.97
	0.4	66.79		0.4	40.85
root base of the upper leaf blade	0.1	3.60	root base of the lower leaf blade	0.1	1.87
	0.2	8.26		0.2	7.07
	0.3	16.84		0.3	14.10
	0.4	11.59		0.4	6.73

Analysis of results

The variation patterns of fog droplet deposition coverage under different test conditions are shown in Fig. 5, and the highest density of deposition coverage was found in the leaf among all positions. In addition, the highest droplet deposition coverage was found at 0.3 MPa air pressure, while the same results were obtained regardless of the position at which the test was conducted. However, at 0.4 MPa air pressure, the droplet deposition coverage was, on the contrary, less than that at 0.3 MPa, a phenomenon that can be explained by the interference of the high-speed airflow on the corn leaves, which resulted in some of the droplets not being able to be fully deposited on the target surface.

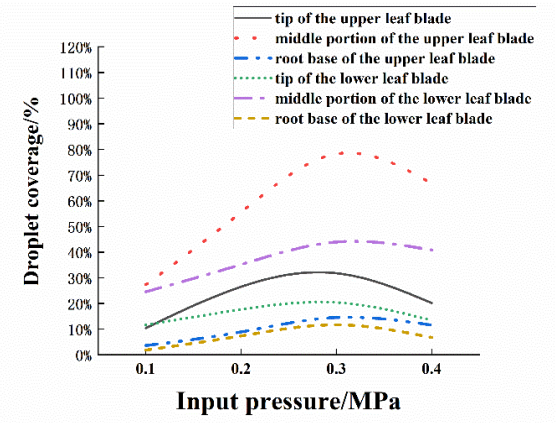


Fig. 5 - Results of droplet deposition coverage without test

CONCLUSIONS

(1) The atomisation angle will change with the change of input air pressure and liquid feed volume, in the liquid feed volume of 450 mL/min, the atomisation angle increases significantly with the increase of input air pressure, and the value of the angle of the atomisation angle ranges from 31.89° to 107.38°; in the input air pressure of 0.1 MPa, the value of the change of the size of the atomisation angle is not much affected by the change of the liquid feed volume, and the value of the change of the angle of the atomisation angle is only 14.49°.

(2) The change of input air pressure can obviously cause the change of droplet size, in the spraying height of 300 mm, the droplet size by the input air pressure size change value of 18.23 μm; in the input air pressure of 0.3 MPa, with the increase of spraying height, the droplet size will gradually become bigger, the droplet size change value of 4.78 μm, the further the distance from the nozzle, the droplets will be coagulated and phenomenon leads to the increase of the droplet size. The larger the distance from the nozzle, the more the droplets will be condensed, resulting in a large increase in droplet size.

(3) The potential of ultrasonic atomising nozzles in agriculture was explored through deposition test experiments on maize. The results show that the hydrodynamic ultrasonic atomising nozzle exhibits excellent deposition performance, with 86.98% of the middle part of the maize leaf being covered by a highspeed airflow, and 46.97% of the lower part of the maize leaf being covered by a leaf, resulting in a high deposition coverage. The results can provide a reference for the research of hydrodynamic nozzles in application technology and promote the in-depth application of this technology in agricultural plant protection operations.

ACKNOWEDGEMENT

This work was funded by the Top Talents Program for One Case One Discussion of Shandong Province, the Key Research and Development Program of Shandong Province (Major Innovative Project in Science and Technology) (2020CXGC010804), Shandong Provincial Natural Science Foundation (ZR2021MC026).

REFERENCES

[1] Allan S. Felsot, John B. Unsworth, Jan B.H.J. Linders, Graham Roberts, Dirk Rautman, Caroline Harris & Elizabeth Carazo, (2010). Agrochemical spray drift; assessment and mitigation—A review*[J], *Journal of Environmental Science and Health*, *Part B*, Vol.46, pp.1-23, US.

[2] Butler Ellis M. C., R. Alanis, A. G. Lane, C. R. Tuck, D. Nuyttens and J. C. van de Zande. (2017) Wind tunnel measurements and model predictions for estimating spray drift reduction under field conditions[J].

[3] Gao J.M., Ma J.L., (2017). Design and test of low-frequency Hartmann atomization nozzle with stepped resonance tube [J]. (带阶梯型谐振腔的 Hartmann 低频超声雾化喷嘴设计及试验). *Transactions of the Chinese Society of Agricultural Engineering*, Vol.33(12), pp. 66-73, Beijing/China.

[4] Hewitt A.J., (2008). Droplet size spectra classification categories in aerial application scenarios[J]. *Crop Protection*, Vol.27(9), pp.1284 - 1288, UK.

[5] Hilz E., Vermeer A.W.P., (2013). Spray drift review: the extent to which a formulation can contribute to spray drift reduction [J]. *Crop Protection*. Vol.44, pp.75-83, UK.

[6] Huang Y.B., Thomson S.J., Hoffmann W.C. et al, (2013). Development and prospect of unmanned aerial vehicle technologies for agricultural production management [J]. *International Journal of Agricultural & Biological Engineering*. Vol.6(3), pp.1-10, United States.

[7] He R., (2019). Development and Experiment Research of The Gas-Assisted Electrostatic Ultrasonic Atomizing Nozzle [D]. (气助式静电超声雾化喷头研制与试验). Jiangsu University. Jiangsu/China.

[8] Jiang C, (2019). Research on the mechanism of greenhouse cucumber application and equipment based on ultrasonic pneumatic atomisation technology [D]. (基于超声气力雾化技术的温室黄瓜施药机理以及装备研究). Yangzhou University. Jiangsu/China.

[9] Liu C., Hu J., Li Y., Zhang W., Li Q. (2023). Experiment on spray flow field characteristics and deposition performance of conical wind field anti-drift spray. *INMATEH - Agricultural Engineering*, Vol.69(1), pp. 559–568, Romania. DOI: https://doi.org/10.35633/inmateh-69-53

[10] Lu D.P., Lv X.L., Lei X.H., Zhang M.N., Yi Z.Y., (2017). Current research status of ultrasonic atomising nozzles and their application in agricultural engineering [J]. (超声雾化喷嘴的研究现状及在农业工程中的应用). *Jiangsu Agricultural Sciences*, Vol.45(21), pp. 255-258, Jiangsu/China.

[11] Maghsoudi H., Minaei S., Ghobadian B., Masoudi H, (2015). Ultrasonic sensing of pistachio canopy for low-volume precision spraying [J]. *Computers and Electronics in Agriculture*. Vol.112, pp.149-160, UK.

[12] Park J, Lee S-y, Choi L-y, Hong S-w, Noh H, Yu S-H. (2022) Airborne-Spray-Drift Collection Efficiency of Nylon Screens: Measurement and CFD Analysis[J]. *Agronomy*. Vol. 2(11):2865, Switzerland.

[13] Tian Z., Xue X., Duan F., Yao S., Ma W. (2022). Automatic system and method for improving aerial spray droplet penetration. *INMATEH - Agricultural Engineering*, Vol.68(3), pp.265–274, Romania.

[14] Wen S., Lan Y.B., Zhang J.T., Li S.H., Zhang H.Y., Xing H., (2016). Analysis and experiment on atomization characteristics of ultra-low-volume swirl nozzle for agricultural unmanned aviation vehicle[J]. (农用无人机超低容量旋流喷嘴的雾化特性分析与试验). *Transactions of the Chinese Society of Agricultural Engineering*, Vol.32(20), pp. 85-93, Beijing/China.

[15] Wu C.Q., Ye Z., Zhou Q., Huang W.J., Cao S.Y., (2021). Effect of atomizer structure on performance of ultrasonic atomization feed DMFC[J]. (雾化器结构对超声雾化供给 DMFC 的性能影响研究). *Chinese Journal of Power Sources*, Vol.45(7), pp. 841-843,876. Tianjin/China.

[16] Wu G.G., Wang P.F., Tian C. et al. (2021). Mathematical Model of SMD of Hydrodynamic Ultrasonic Atomizing Nozzle Based on Orthogonal Design. 22 April 2021, PREPRINT (Version 1) available at Research Square [*https://doi.org/10.21203/rs.3.rs-442908/v1*]

[17] Yan X.J., Chu S.H., Yang D.B., Yuan H.Z., (2021). Agriculture on the wings of science and technology: plant protection unmanned aerial vehicle (UAV) low-volume spraying technology reduces pesticide use and boosts control efficacy[J]. (给农业插上科技的翅膀：植保无人机低容量喷雾技术助力农药减施增效). *Journal of Plant Protection*, Vol.48(3), pp. 469-476, Beijing/China.

[18] Zhang J.T., Wen S., Jiang D.X., Zahng T.M., (2016). Prospects for ultrasonic atomisation in ultra-low volume sprays[J]. (超声雾化在超低量喷雾中的应用前景). *China Plant Protection*, Vol.34(10), pp.67-70, Beijing/China.

DISCRETE ELEMENT METHOD (EDEM) SIMULATION AND PARAMETER OPTIMIZATION: DESIGN AND TESTING OF A LOW-LOSS AND HIGH-EFFICIENCY CORN THRESHING DEVICE

/

离散元法（EDEM）仿真与参数优化： 低损高效玉米脱粒装置的设计与试验

Yaxiu HOU[1)], Shuqi SHANG, Xiang LI, Xiaoning HE, Haifeng ZHENG, Tongtong DONG, Xu LI, Zhixin LIU, Shuai YANG, Dongwei WANG*

[1)] Qingdao Agricultural University, College of Mechanical and Electrical Engineering / China;

Tel: +86-0532-58957391; E-mail: 200701031@qau.edu.cn

DOI: https://doi.org/10.35633/inmateh-71-16

Keywords: *low threshing efficiency, corn threshers, EDEM simulation, optimized design, test*

ABSTRACT

Aiming at the problems of low threshing efficiency and high damage rate of current threshing devices. In this study, the operational form of the threshing drum and the structure of the threshing element were innovated, and a new threshing drum with low damage and high efficiency was designed. Using EDEM software, flexible body modeling of corn kernels, cobs and whole ears was carried out. The dynamic analysis of the corn threshing process was completed and the simulation parameters were further optimized. The optimum operating parameters were analyzed by orthogonal rotational tests and response surface method with a speed of 800 r/min for the threshing drum, a clearance of 10 mm for the concave plate and 30 mm for the threshing drum. The radius of the round head of the threshing element was 5 mm. The height of the threshing element was 60 mm. The final threshing efficiency was 98.78% and the damage rate of threshing was 0.62%. The results show that the new threshing device can meet the requirements of low-loss threshing devices for corn combine harvesters and can provide a theoretical basis for the development of the theory and technical system of corn plot combine harvesters in the future.

摘要

针对现有脱粒装置脱粒效率低、损伤率高的问题。本研究对脱粒滚筒的工作形式和脱粒元件的结构进行了创新，设计出了一种低损伤、高效率的新型脱粒滚筒。利用 EDEM 软件对玉米籽粒粒、玉米芯和玉米果穗进行了柔性体建模。完成了玉米脱粒过程的动态分析，并进一步优化了模拟参数。通过正交旋转试验和响应面法分析了最佳运行参数，脱粒滚筒转速为 800 r/min，凹板间隙为 10 mm，脱粒滚筒间隙为 30 mm，脱粒元件圆头半径为 5 mm。脱粒元件的高度为 60mm。最终脱粒效率为 98.78%，脱粒损伤率为 0.62%。结果表明，新型脱粒装置能满足玉米联合收获机低损脱粒装置的要求，可为今后玉米小区联合收获机理论和技术体系的发展提供理论依据。

INTRODUCTION

As one of the most important food and feed crops in the world, maize has high production potential and economic benefits with edible, forage, and multiple industrial uses (*Yang et al., 2022*). However, there are many deficiencies in China's corn threshing technology, which seriously affect the development of China's corn industry (*Zhou et al., 2022*). Corn threshing is a key link in the corn harvesting process and the core technology of the corn combine. The structural design and threshing effect of the corn threshing device directly determine the operational performance of the corn combine (*Chen, 2022*). In recent years, in order to improve the effect quality of corn threshing equipment, domestic and foreign scholars have carried out systematic research from many aspects. Srison et al. used EDM to simulate the interaction characteristics of corn seeds, properly quantified the qualitative and directional information of particle flow (*Srison et al., 2016*). Pužauskas et al. created a mathematical model using finite element analysis to study the theory of the maize threshing process, and the relationship between the structural form of the threshing device and the rate of particle fragmentation was analyzed (*Pužauskas et al., 2016*). Zhao Wuyun et al. designed and manufactured a spiral plate tooth-type corn thresher, and established a mathematical model through tests to study and analyze the influence of factors on grain crushing rate during the threshing process and their interactions (*Zhao et al., 2012*).

Li Xinping et al. proposed the theory of "circumferential force circle" and designed a corn bionic machine based on the process of discrete corn kernels by chicken beaks (*Li et al., 2007)*. There is a lack of low-damage threshing devices for small-plot corn harvesting with different moisture content corn varieties, and most of the current simulation studies are based on a rigid model of corn, and establishing a flexible body model of corn is rarely applied in simulation analysis (*Zhou et al., 2021*). In order to analyze the damage of maize kernels during threshing, this paper uses the Hertz collision contact theory (*Wang et al., 2022*) as the basis for maize threshing simulation using the flexible body model, designs the structure of the new threshing element and the threshing device, screens the best working parameters using orthogonal tests, and optimizes the parameters by EDEM simulation, and finally determines the best parameters and verifies the validity of this study by comparing the test results before and after optimization (*Tang et al., 2022*). In this way, a more widely adaptable, high self-cleaning and low-damage plot corn harvester threshing device was designed.

MATERIALS AND METHODS

Determination of physical and mechanical properties related to the corn at maturity

In view of the easy damage of maize in the process of threshing, the mechanical characteristics of maize cob are studied, and several varieties are selected as research objects to establish EDEM flexible body simulation models with the mechanical characteristics of maize cob and maize kernel as indicators (*Li et al., 2021*). A further consideration is given to establish a model of the whole corn cob to simulate the threshing damage when the corn kernels are combined with the corn cob, so as to gain a more comprehensive and in-depth understanding of the threshing damage mechanism. In this experiment, corn kernel crushing rate and corn ear threshing rate were selected as test indexes, and the related physical and mechanical characteristics of corn ear and corn kernel were measured (*Zheng et al., 2020*). A simulation analysis model was created using the EDEM software to serve as a parameter basis for the investigation of the mechanical and physical characteristics of the corn cob. Further design of relevant threshing devices for corn varieties with 25%-35% (*Zhang et al., 2021*) moisture content, depending on the moisture content (*Gao et al., 2022*), and the average physical (*Zhang et al., 2015*) and mechanical characteristics, is shown in Table 1.

Table 1

Determination of the physical and mechanical properties of the components of maize

Parameters	Numerical value
Corn Poisson's ratio	0.40
Corn shear modulus	5.357×10^{7}
Corn density	1197 kg/m^3
Corn-corn recovery coefficient	0.70
Corn-corn static friction coefficient	0.30
Corn-corn rolling friction coefficient	0.04
Poisson's ratio of threshing drum	0.28
Threshing drum density	8000 kg/m^3
Shear modulus of threshing drum	2.93e+10
Corn-threshing drum recovery factor	0.70
Coefficient of static friction of corn-threshing drum	0.30
Coefficient of rolling friction of corn-threshing drum	0.04

Threshing drum element

Studies have shown that the adaptability of the plate teeth or finger plate teeth to the unevenly fed crop layer as well as the strong kneading effect of the grid concave plate with the cob and the obvious tapping and loosening effect on the grain-grass mixture facilitate the separation of the corn threshing material (*Hu et al., 2018*). The structural design of the threshing element with trapezoidal round-headed spike teeth in this study is a combination of the plate threshing drum and spike-tooth threshing drum concepts (*Di et al., 2018*), with the height of the trapezoidal spike teeth ensuring threshing efficiency and the rounded corners of the trapezoidal spike teeth reducing the damage rate of threshing, the general structure of which is shown in Fig.1 (*Yan et al., 2020*).

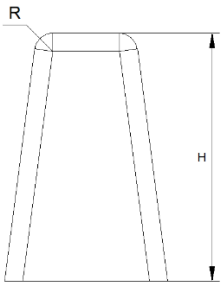


Fig. 1 – Trapezoidal round head nail teeth structure diagram

H: Thresher tooth height; R: The rounded corners of the thresher teeth

Overall structure design

The corn thresher is a longitudinal full-feed device connected with the feed port of the corn combine harvester. The main working parts are lower cover, upper cover plate, combined concave plate, threshing drum, motor and the overall structure is shown in Fig. 2.

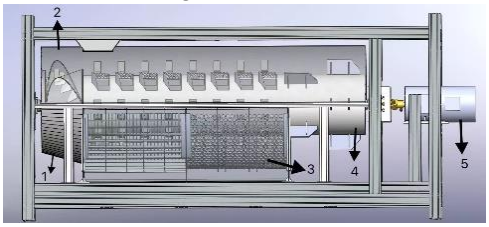
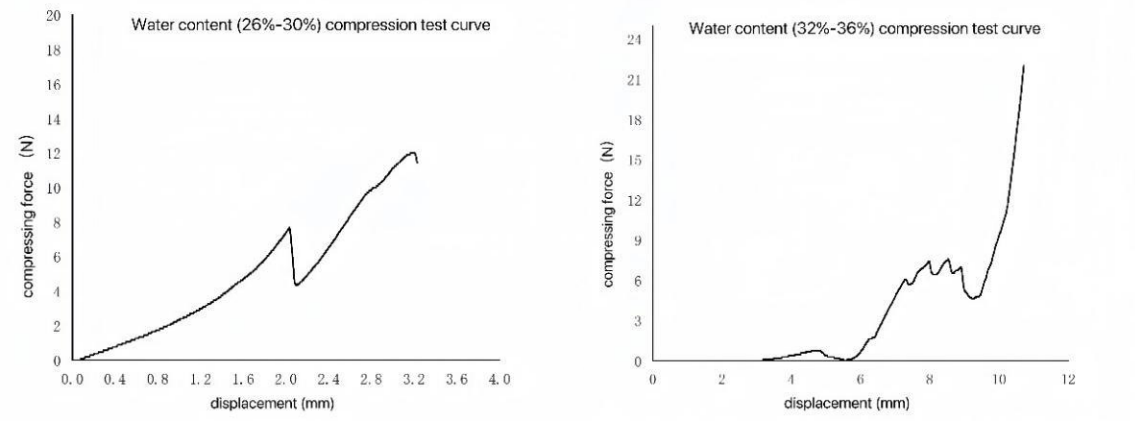


Fig. 2 – Corn threshing device

1. lower cover; 2. upper cover plate; 3. combined concave plate; 4. threshing drum; 5. motor

Compression test

In order to establish a flexible body model for corn, the critical crushing force of corn kernel is firstly determined by mechanical compression test, and then the possible damages during corn kernel threshing are theoretically analyzed based on the collision theory (*China Agricultural Science and Technology Press, 2007*). Since the corn kernel itself is a viscoelastic body, due to the existence of elastic deformation (*Xiao et al., 2021*), the contact centers of the two during the collision will produce displacements close to each other δ_z. The contact between the corn kernel and the threshing element can be regarded as a contact between a sphere and a plane (*Wang et al., 2018*), which leads to the radius of the contact, the distance of the displacement, and the amount of pressure on the contact area between the corn kernel and the threshing element. The results of the corn kernel compression test are shown in Fig. 3.



(a) *(b)*

Fig. 3 – The results of the corn kernel compression test

When the contact pressure F_0 between the corn kernels and the threshing element in contact with each other reaches the yield stress limit K of the corn kernels under one-way compression, a point under the surface of the contact area between the two reaches the limit of the elastic state, thus causing the corn kernels to crack or break.

Critical state of corn kernels without plastic deformation is:

$$F_0 = K \tag{1}$$

$$t = t^*, \delta_z = \delta_z^*, F = F^* \tag{2}$$

$$F_0 = \frac{3F}{2\pi ab} = \frac{3F}{2\pi\left(\frac{3p\,R_e}{4E^*}\right)^{\frac{2}{3}}} \tag{3}$$

The maximum contact force between the corn kernels and the threshing element is:

$$F_0^* = \frac{3F^*}{2\pi\left(\frac{3F^*\,R_e}{4E^*}\right)^{\frac{2}{3}}} \tag{4}$$

The maximum critical force of this variety of high moisture content corn kernels is 22.12 N, the maximum displacement is 10.72 mm, that is, when the contact force between the corn kernels and the threshing element reaches the critical force of the broken corn kernels, the relative speed of the two can be found as:

$$v_z = \left\{\frac{2\pi^5 K^5 22.12\,R_e^{\,3}}{60E^{*4}m}\right\}^{\frac{1}{2}} \tag{5}$$

Based on the measured data of the corn compression force, the force and stiffness are calculated by the formula :

$$K = \frac{P}{\delta} \tag{6}$$

Where: K is the stiffness; P is the force, (N); δ is the deformation, (N/m).

The magnitude of the force is taken as 22.12 N and the deformation is taken as 0.0076 N/m to obtain the parameters of the contact between the corn cob and the seed. The normal stiffness per unit area and the shear stiffness per unit area, so as to set the parameters of the Bond model in EDEM.

Bond modeling

Through mechanical compression test and formula calculation, the final Bond model parameters are determined, and the model is established by EDEM. T The model establishment of corn cob, corn kernel and corn ear is shown in Fig. 4, and the modeling parameters are shown in Table 2.



(a) *(b)* *(c)*

Fig. 4 – Bond model:
(a) Corn cob model; (b) Corn kernel model; (c) Corn ear model

Table 2

Parallel Bond Configuration

Parameters	Numerical value
Normal Stiffness per unit area	2.9e+11 N/m^3
Shear Stiffness per unit area	2.9e+11 N/m^3
Critical Normal Stress	3e+10 Pa
Critical Shear Stress	3e+10 Pa
Bonded Disk Radius	1.5 mm

PARAMETER OPTIMIZATION AND EDEM SIMULATION

Parameter optimization

The optimization of the threshing element includes the optimization of the radius of the round head of the threshing element and the height of the threshing element. As shown in Fig. 5 and Fig. 6, the threshing element parameters were imported into EDEM and the results were obtained as shown in Fig. 7, Fig. 8, and Fig. 9.



(a) *(b)* *(c)*

Fig. 5 – Comparison of round head radius design of threshing element:

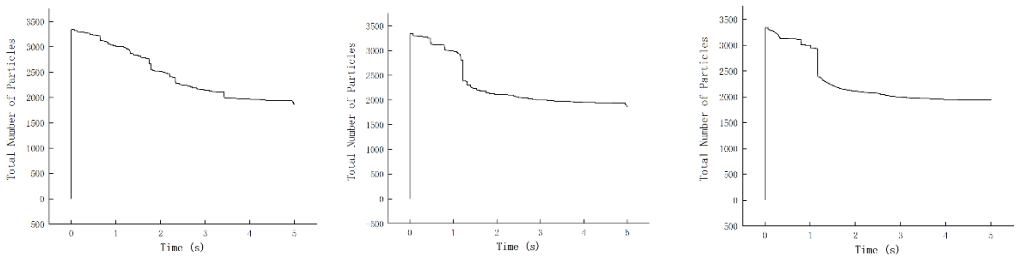
(a)R=3 mm; (b)R=5 mm; (c)R=8 mm



(a) *(b)* *(c)*

Fig. 6 – Comparison of height design of threshing elements

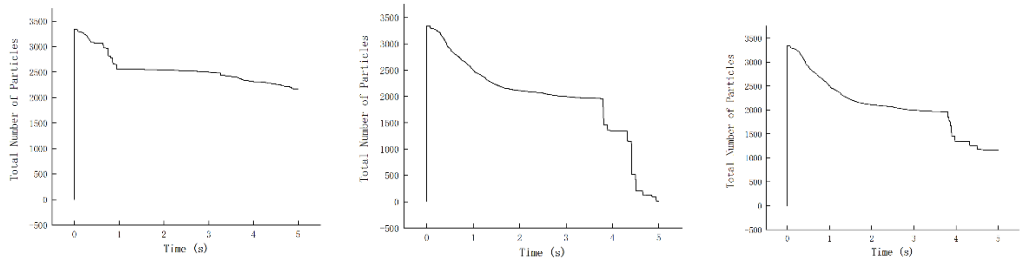
(a)h_t =50 mm; (b)h_t =60 mm; (c)h_t =70 mm



(a) *(b)* *(c)*

Fig. 7 – Contrast results of different heights with rounded corners of 3 mm

(a) R=3 mm, h_t =50 mm; (b) R=3 mm, h_t =60 mm; (c) R=3 mm, h_t =70 mm

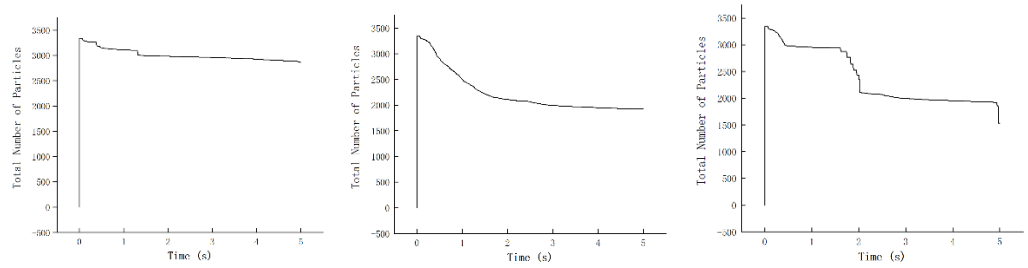


(a) *(b)* *(c)*

Fig. 8 – Contrast results of different heights with rounded corners of 5 mm

(a) R=5 mm, h_t =50 mm; (b) R=5 mm, h_t =60 mm; (c) R=5 mm, h_t =70 mm

(b)



(a) *(b)* *(c)*

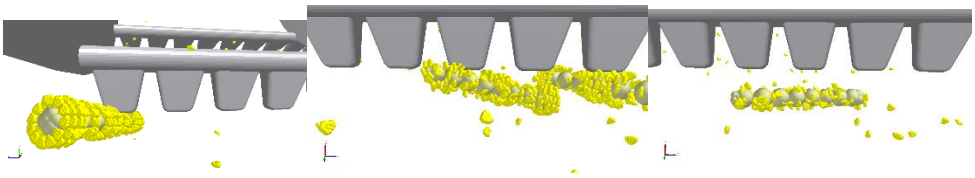
Fig. 9 – Contrast results of different heights with rounded corners of 6 mm

(a) R=6 mm, h_t =50 mm;(b) R=6 mm, h_t =60 mm;(c) R=6 mm, h_t =70 mm

The above threshing element is applied to EDEM, and the optimal parameters are finally determined as threshing element height is 60 mm and the radius of the threshing element head is 5 mm.

EDEM simulation

The following data were obtained from the simulation of the threshing drum by EDEM: the threshing rate of 98.78% was calculated using the number of bond breaks and the number of initial bond generation (*Yu et al., 2021*). The loss rate was obtained from the number of bond breaks of corn kernels and the total number of corn kernels (*Li et al., 2022*) to be about 0.32%. In summary, the overall threshing effect was good, but the threshing damage rate was still high, and the threshing rate increased from 96.27% to 98.78% and the threshing damage rate decreased from 2.65% to 0.62% compared with the conventional threshing device (*Qu et al., 2018*), while the designed segmented combined cylindrical threshing concave plate solved the problem of conventional gridded concave plate being blocked by corn cobs, reducing the seed harvesting. The design of the segmented cylindrical threshing concave solved the problem of conventional gridded concaves being clogged by corn bracts and reduced the plugging rate and entrainment losses during harvesting. Threshing simulation is shown in Fig. 10.



(a) (b) (c)

Fig. 10 – Threshing simulation

(a) Initial; (b) Middle; (c) End

TEST

Corn threshing bench test

The optimized device was machined out of pieces, and a test bed for corn threshing device was constructed for bench testing. The structure of the optimized test bench was shown in Fig. 11. This device adopts the back angle adjustment device and the replaceable threshing nail teeth on the threshing drum, which can carry out different kinds of test verification according to the new threshing nail teeth in the simulation, so that the test process is more convenient and efficient, and the test results can achieve the best effect. The final test result can completely take off the corn kernels and keep the integrity of the corn kernels, the optimal threshing effect of simulation is achieved and the test results are better.

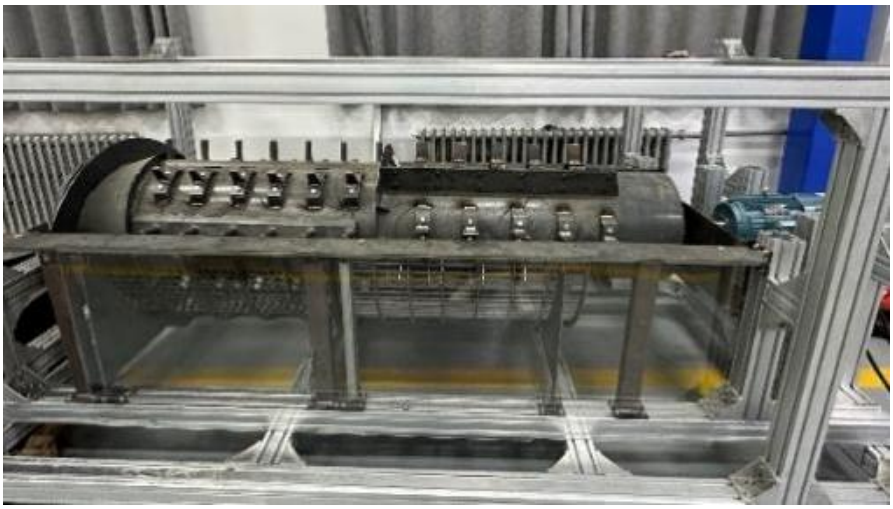


Fig. 11 – Corn threshing device test bench

Based on the experimental experience, the preliminary design of threshing device-related parameters was taken in the range of 9-11 mm for the concave clearance, 25-35 mm for the threshing clearance and 700-900 r/min for the threshing drum speed (*Chen et al., 2022*). The analysis of the orthogonal test was carried out using Design-expert software, and Box-Behnken Design was used for the calculation in order to reduce the number of tests. The factors and levels for orthogonal tests of threshing device parameters are shown in Table 3. The results of the orthogonal test for the parameters of the threshing device are shown in Table 4.

Table 3

Factors and levels for orthogonal tests of threshing device parameters

Level	Concave clearance A (mm)	Threshing clearance B (mm)	Threshing drum speed C (r/min)
-1	9	25	700
0	10	30	800
1	11	35	900

Table 4

Results of orthogonal tests on threshing device parameters

Test number	Concave clearance A (mm)	Threshing clearance B (mm)	Threshing drum speed C（r/min)	Threshing efficiency (%)	Threshing damage rate (%)
1	9	25	800	98.35	0.77
2	11	25	800	98.26	0.84
3	9	35	800	98.21	0.89
4	11	35	800	98.54	0.72
5	9	30	700	97.32	0.88
6	11	30	700	97.23	0.95
7	9	30	900	98.63	0.72
8	11	30	900	98.58	0.84
9	10	25	700	98.38	0.97
10	10	35	700	97.12	0.76
11	10	25	900	98.61	0.93
12	10	35	900	98.57	0.88
13	10	30	800	98.67	0.84
14	10	30	800	97.61	0.95
15	10	30	800	98.57	0.73
16	10	30	800	98.76	0.81
17	10	30	800	98.78	0.62

By comparing the results with the experiments conducted by other researchers, the final results of the threshing device in this paper were obtained to be better than the experimental results of other researchers (*Bi et al., 2015*). According to the results of the orthogonal test, the residuals of the test indexes were drawn (*Li et al., 2015*), and the reliability of the orthogonal test was analyzed. ANOVA was performed on threshing efficiency and threshing damage rate respectively to compare the significance of influencing factors, and the optimal combination of parameters was judged according to the significance effect, and the optimal parameters were finally determined. The ANOVA for threshing efficiency is shown in Table 5. The ANOVA of threshing damage rate is shown in Table 6.

Table 5

ANOVA of threshing efficiency

Source of variance	Mean square	Degrees of freedom	Sum of square	P value
Model	0.6213	9	0.0690	0.0277 < 0.05
A	0.0013	1	0.0013	0.0480 < 0.05
B	0.0032	1	0.0032	0.0457 < 0.05
C	0.2244	1	0.2244	0.0060 < 0.05
AB	0.0441	1	0.0441	0.1289
AC	0.0004	1	0.0004	0.8744
BC	0.0121	1	0.0121	0.3972
A2	0.1203	1	0.1203	0.0250
B2	0.1504	1	0.1504	0.0155
C2	0.0334	1	0.0334	0.1781
Residual	0.1042	7	0.0149	
Lack of fit	0.0423	3	0.0141	0.5108 > 0.1
Pure error	0.0619	4	0.0155	
Sum	0.7255	16		

Note:(P < 0.05 means the item is significant, P > 0.1 means the item is not significant)

Table 6

ANOVA of threshing damage rate

Source of variance	Mean square	Degrees of freedom	Sum of square	P value
Model	0.1206	9	0.0134	0.0005
A	0.0010	1	0.0010	0.0284 < 0.05
B	0.0084	1	0.0084	0.0123 < 0.05
C	0.0465	1	0.0465	0.0001 < 0.001
AB	0.0009	1	0.0009	0.3106
AC	0.0006	1	0.0006	0.3927
BC	0.0049	1	0.0049	0.0381
A2	0.0133	1	0.0133	0.0040
B2	0.0081	1	0.0081	0.0137
C2	0.0313	1	0.0313	0.0004
Residual	0.0053	7	0.0008	
Lack of fit	0.0043	3	0.0014	0.6300 > 0.1
Pure error	0.0010	4	0.0002	-
Sum	0.1259	16		-

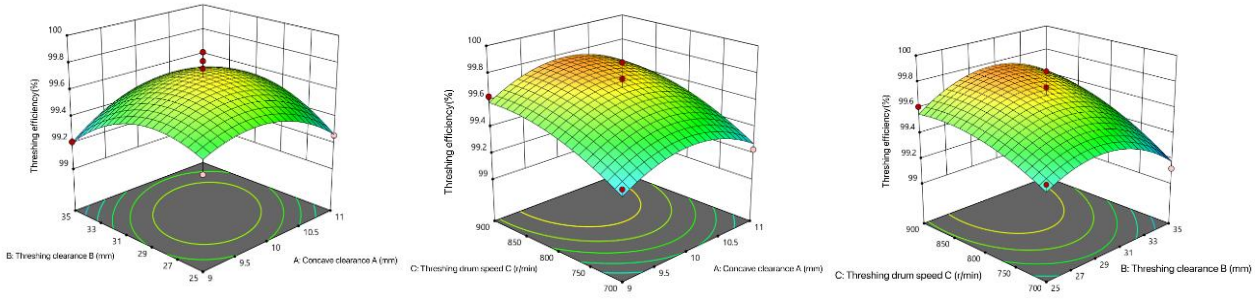
Note: (P < 0.05 means the item is significant, P < 0.001 means the item is highly significant, P > 0.1 means the item is not significant)

After analyzing the above two tables, it can be concluded that the effects of concave plate gap and threshing gap of threshing drum on threshing efficiency as well as threshing damage rate are significant (*Li et al., 2015*), especially the effect of threshing drum rotational speed on threshing efficiency and threshing damage rate is extremely significant.

RESULTS

Response surface analysis

The response surface analysis of threshing efficiency is shown in Fig. 12. The response surface of threshing clearance and concave clearance on threshing efficiency is shown in Fig. 12a. During the reduction of threshing clearance from 35 mm to 25 mm, the larger the concave clearance, the lower the threshing efficiency; when the concave clearance increased from 9 mm to 11 mm, the threshing efficiency increased with the increase of threshing clearance (*Zhang et al., 2022*). The response surface of threshing drum speed and concave clearance on threshing efficiency is shown in Fig. 12-b. The larger the concave clearance, the lower the threshing efficiency during the decrease of threshing drum speed from 900 r/min to 700 r/min; when the concave clearance increased from 9 mm to 11 mm, the threshing efficiency increased with the increase of threshing drum speed. The response surface of threshing drum speed and threshing clearance on threshing efficiency is shown in Fig.12-c. The larger the threshing clearance, the lower the threshing efficiency when the threshing drum speed decreases from 900 r/min to 700 r/min; when the threshing clearance increases from 25 mm to 35 mm, the threshing efficiency increases with the increase of threshing drum speed.

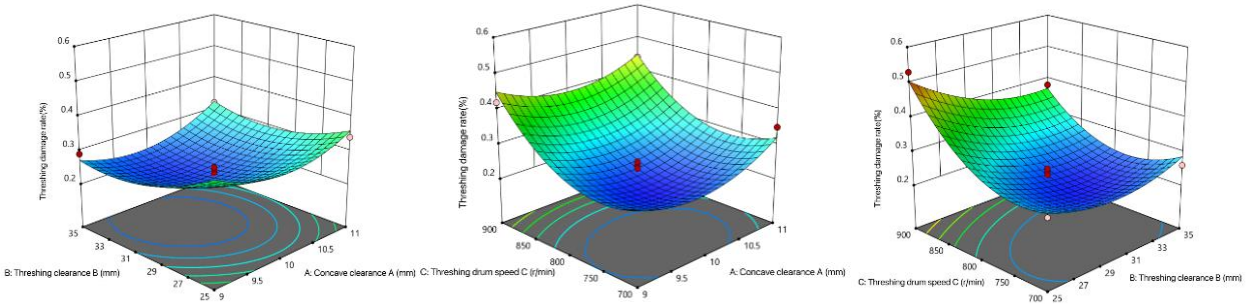


(a) *(b)* *(c)*

Fig. 12 - Response surface analysis of threshing efficiency

The response surface analysis of threshing damage rate is shown in Fig. 13 .The response surface of threshing clearance and concave clearance on threshing damage rate is shown in Fig. 13-a. When the threshing clearance decreases from 13 mm to 11 mm, the larger the concave clearance, the lower the threshing damage rate; when the concave clearance increases from 9 mm to 11 mm, the threshing damage rate decreases with the increase of threshing clearance.

The response surface of threshing drum speed and concave clearance on threshing damage rate is shown in Fig. 13-b. When the threshing drum speed decreased from 900 r/min to 700 r/min, the larger the concave clearance, the lower the threshing damage rate; when the concave clearance increased from 9 mm to 11 mm, the threshing damage rate increased with the increase of threshing drum speed. The response surface of threshing drum speed and threshing clearance on threshing efficiency is shown in Fig. 13-c. When the threshing drum speed decreased from 900 r/min to 700 r/min, the larger the threshing clearance, the lower the threshing damage rate; when the threshing clearance increased from 11 mm to 13 mm, the threshing damage rate increased with the increase of threshing drum speed.



(a) *(b)* *(c)*

Fig. 13 - Response surface analysis of threshing damage rate

The optimal parameters of the threshing drum were determined as follows: speed 800 r/min, concave clearance 10 mm, and threshing clearance 30 mm. After the optimization, the threshing efficiency of the threshing device increased to 98.78% and the damage rate of threshing decreased to 0.62%, which improved the overall performance of the threshing device compared with that before the optimization. It can also be concluded that the parameters affecting the threshing performance in the threshing device include not only the common threshing drum speed (*Wang et al., 2021*), concave clearance, and threshing clearance, but also the size and shape of the threshing elements have a great influence on the detachment effect.

CONCLUSION

(1) The optimized threshing device test bench has the characteristics of high efficiency and low loss. To some extent, it solves the problem of high damage rate of existing threshing devices.

(2) The critical force of grain crushing was determined by mechanical compression test and Herzen contact theorem, and the optimal working parameters were determined by EDEM simulation and optimization: threshing drum speed 800 r/min, concave clearance 10 mm, threshing clearance 30 mm.

(3) The bench test proved that when the rotating speed of the threshing drum was 800 r/min, the gap of the concave plate was 10 mm, the gap of the threshing was 30 mm, and the tilt angle of the test bench was 15 degrees, the corn threshing operation effect was the best. At this time, the threshing efficiency was 98.78%, and the threshing damage rate was 0.62%, which met the requirements of corn threshing operation.

ACKNOWLEDGEMENT

This research was funded by Shandong Province Key R&D Program (Major Science and Technology Innovation Project) Projects and High-performance seeding and harvesting key components and intelligent operation equipment creation (Grant NO.2021CXGC010813). Supported by Postgraduate Innovation Program of Qingdao Agricultural University.

REFERENCES

[1] Bi Quansheng. (2015). *Research on double roller differential speed corn threshing device with tooth spike* [D]. Anhui Agricultural University,

[2] Chen Weilin. (2022). Exploration on the promotion and application of mechanized corn harvesting technology [J]. *Farmers' Counselor*, (16):72-74.

[3] Chen Bingbing, Su Zhanke, Zhang Keping, Hou Chuankai, Sun Bugong, Zhang Peng. (2022). Design and simulation analysis of threshing device of intercropping pea harvester [J]. *Agricultural Equipment and Vehicle Engineering*, 60 (09): 20-25.

[4] China Academy of Agricultural Mechanization Sciences. (2007). *Agricultural Machinery Design Manual (Volume II)* [M]. Beijing: China Agricultural Science and Technology Press.

[5] Di Zhifeng, Cui Zhongkai, Zhang Hua, et al. (2018). Design and experiment of combined riffle block and spike tooth axial flow corn threshing roller [J]. *Journal of Agricultural Engineering*, 34(1): 28-34.
[6] Edvinas Pužauskas, Dainius Steponavičius, Eglė Jotautienė, et al. (2016). Substantiation of concave crossbar shape for corn ear threshing [J]. *Mechanika*, 22(6): 553-561.
[7] Fan C, Cui T, Zhang D, et al. (2019). Design of Feeding Head Spiral Angle Longitudinal Axis Corn Threshing Separation Device Based on EDEM[C]//2019 *ASABE Annual International Meeting. American Society of Agricultural and Biological Engineers*.
[8] Hu B.Y.,Li Y.M. (2018). Finite element simulation analysis of cob collision for corn seed threshing [J]. *Agricultural equipment technology*, 44(04):4-7.
[9] Li X.P., Gao L.X., Ma F.L. et al. (2007). Experiments on the impact damage of corn seeds [J]. *Journal of Shenyang Agricultural University*, (1): 89-93.
[10] Li Junzhong. (2021). *Research and development of key technology and equipment of corn seed direct harvesting based threshing device* [D]. Jilin University. DOI:10.27162/d.cnki.gjlin.2021.004964.
[11] Li X, Du Y, Liu L, et al. (2022). Research on the constitutive model of low-damage corn threshing based on DEM [J]. *Computers and Electronics in Agriculture*, 194: 106722.
[12] Li X, Du Y, Guo J, et al. (2020). Design, simulation, and test of a new threshing cylinder for high moisture content corn [J]. *Applied Sciences*, 10(14): 4925.
[13] Li Jicheng, Guo Lin, Zhang Tianhui. (2015). Analysis of dynamic characteristics of cross flow fan impeller of combine harvester based on fluid structure coupling [J]. *Research on Agricultural Mechanization*, 37 (09): 234-240. DOI: 10.13,427/j.cnki.njyi.2015.09.053.
[14] Qu Zhe. (2018). *Research on low damage combined corn threshing and separating device* [D]. China Agricultural University.
[15] Tang S.H., Jin C.K., Zhang G.H., Guo Hazel, Zhao Nan, Xu Bei. (2022). Research status of threshing and separating device of combine harvester in China [J]. *Agricultural Mechanization Research*, 44(03): 1-9+15. DOI:10.13427/j.cnki.njyi.2022.03.001.
[16] Waree Srison, Somchai Chuan-Udom et al. (2016). Effects of Operating Factors for an Axial-flow Corn Shelling Unit on Losses and Power Consumption [J]. *Agriculture and Natural Resources*, 50(5): 421-425.
[17] Wang Zhanbin, Wang Zhenwei, Zhang Yinping, Wei Xiuting, Liu Chengqiang, Li Lei.(2022). Simulation and experiment of hammer claw type corn threshing device [J]. *Agricultural Mechanization Research*, 44(12):140-147. DOI:10.13427/j.cnki.njyi.2022.12.028.
[18] Wang Meimei, Wang Wanzhang, Yang Liquan, Hou Mingtao. (2018). Research on corn kernel modeling method based on EDEM [J]. *Journal of Henan Agricultural University*, 52 (01): 80-84+103. DOI: 10.16445/j.cnki.1000-2340.2018.01.013.
[19] Wang S, Chen P, Ji J, et al. (2021). Design and experimental study of flexible threshing unit for Chinese cabbage seeds [J]. *INMATEH - Agricultural Engineering*, 65(3), pp.333-344. DOI: https://doi.org/10.35633/inmateh-65-35
[20] Xiao Jinlong, Zhao Jinbao. (2021). Research on virtual prototype of corn straw returning machine based on rigid flexible hybrid modeling [J]. *Agricultural Equipment and Vehicle Engineering*, 59 (05): 47-50.
[21] Yang Yalan, Li Yuliang, Li Ruishu, Chai Shuling, Wei Zhouxia, Hou Qirei. (2022). Thoughts on how to effectively improve the efficiency of corn breeding [J]. *Heilongjiang Grain*, (08): 39-41.
[22] Yan BX, Wu GW, Fu WQ, Gao NNA, Meng ZJ, Zhu P. (2020). Study on the factors influencing the bed position of corn precision seeding with high seed drop based on EDEM [J]. *Journal of Agricultural Machinery*, 51(S2):47-54.
[23] Yu Y, Li L, Zhao J, et al. (2021). Optimal design and simulation analysis of spike tooth threshing component based on DEM [J]. *Processes*, 9(7): 1163.
[24] Zhou Ke-chi, He Chang-an, Ji Chun-xue, Wang Hui, Zhang Heng.(2022). Research on corn breeding problems and countermeasures [J]. Heilongjiang Grain, (04): 64-66.
[25] Zhou Wenjing, Li Wenjuan, Guo Tao, et al. (2022). Effects of species and harvesting time on nutrient composition of silage corn [J]. *Grassland Science*, 39(07):1419-1428.
[26] Zhao Wuyun, Guo Kangquan. (2012). Optimization of working parameters of combined spiral plate tooth seed corn thresher [J]. *Journal of Agricultural Machinery*, 43(12): 56-61.
[27] Zhou Long. (2021). *Simulation analysis and experimental research of corn seed modeling and sowing process based on discrete element method* [D]. Jilin. DOI:10.27162/d.cnki.gjlin.2021.007542.
[28] Zheng Zhaohui. (2020). *Simulation study on seed collision characteristics of corn harvest clearing* [D]. Northeastern Agricultural University. DOI:10.27010/d.cnki.gdbnu.2020.000984.

[29] Zhang T., Li P., Zhang Y., Tang XL, Dai ZG, Li Y. (2021). Analysis of research progress on damage of corn harvesting machinery [J]. *Agricultural Technology and Equipment*, (01): 27-29.
[30] Zhang Xinwei, Yi Kechuan, Gao Lianxing. (2015). Analysis of contact mechanics during the collision between corn seeds and threshing components [J]. *China Agronomy Bulletin*, 31(14): 285-290.
[31] Zhang Longxiang. (2020). *Research and Design of Cleaning Device of Buckwheat Harvester Based on FLUENT-EDEM Coupling* [D]. Chengdu University. DOI: 10.27917/d.cnki.gcxdy.2020.000088.
[32] Zhang Hanzhong, Meng Wenjun, Wang Beibei. (2022). Research on gas-solid two-phase flow field of grab bucket discharge based on CFD-DEM coupling simulation [J]. *Mining Research and Development*, 42 (04): 166-172. DOI: 10.13,827/j.cnki.kyyk.2022.04.011.

PRELIMINARY RESEARCH REGARDING THE CREATION OF A CATEGORY OF COMPOSITE MATERIAL BASED ON A MUD MATRIX AND AGRICULTURAL WASTE AS FILLER MATERIALS

/

CERCETĂRI PRELIMINARE PRIVIND REALIZAREA UNUI MATERIAL COMPOZIT, BAZAT PE MATRICE DE NĂMOL ȘI DEȘEURI AGRICOLE, CA MATERIALE DE UMPLUTURĂ

Dana-Claudia FARCAȘ-FLAMAROPOL[1)], Elena SURDU[1*)], Radu I. IATAN[1)], Petru CÂRDEI[2*)], Ramona MARE[1)]

[1)]U.N.S.T "POLITEHNICA" of Bucharest, no. 313, Splaiul Independentei, sector 6, Bucharest, 060042, Romania

[2)] INMA Bucharest, Bd. Ion Ionescu de la Brad, No. 6 Romania, 013813

Tel: 0723213708; E-mail: elena.surdu@yahoo.com

Tel: 0726142837; E-mail: petru_cardei@yahoo.com

DOI: https://doi.org/10.35633/inmateh-71-17

Keywords: *composite, mud, waste, agricultural*

ABSTRACT

The article presents the results of preliminary experiments necessary for the foundation of an experimental method that ensures the design and manufacturing technology for a category of composite materials with a mud matrix and agricultural waste insertion. The resources and physico-chemical properties of the mud matrix as well as the resources and physical properties of potential agricultural waste constituents of the insertion in the composite material are presented. The technological variant for the manufacture of the finished product is also presented, consisting of a compression system of the composite mixture in a paste state until solidification with moisture removal (dehydration). From a large number of parameters characterizing the experimental system, few have been varied (insertion concentration in the material, height of the raw material column in the press, raw material density, pressing force), while the quality parameters of the process have only been considered for the capacity of dehydration and material densification. The statistical analysis of the results shows that for the capacity of dehydration and densification, the main input parameters that influence are the initial moisture and initial volume of raw material. Results are obtained that allow the development of a mathematical model for the technological process of manufacturing the composite material. The purpose of the research described in this article is to determine the feasibility and feasibility conditions of the material in its possible variations. This means identifying the insertion concentration and moisture intervals of the material before extrusion, possible. The upper and lower limits of these parameters are sought, so that the material exiting the die does not immediately, or over time, disintegrate, and at the same time, the extrusion process is possible with a reasonable energy consumption.

REZUMAT

Articolul prezintă rezultatele experimentelor preliminare necesare fundamentării unei metode experimentale care să asigure concepția și tehnologia de fabricație pentru o categorie de materiale compozite cu matrice de nămol și inserție de deșeuri agricole. Se prezintă resursele și proprietățile fizico-chimice ale matricii de nămol precum și resursele și proprietățile fizice ale deșeurilor agricole potențial constituente ale inserției în materialul compozit. Se prezintă și varianta tehnologică de fabricare a produsului finit constând într-un sistem de comprimare a amestecului compozit în stare de pastă până la solidificare cu eliminarea umidității (deshidratare). Dintr-un număr mare de parametri care caracterizează sistemul experimental, au fost variați puțini (concentrație de inserție în material, înălțimea coloanei de materie primă în presă, densitatea materiei prime, forța de presare) iar ca parametri de calitate ai procesului, deocamdată au fost considerați numai capacitatea de deshidratare și densificarea materialului. Analiza statistică a rezultatelor arată că pentru capacitatea de deshidratare și densificare, principalii parametri de intrare care influențează sunt umiditatea inițială și volumul inițial de materie primă. Se obțin rezultate care permit obținerea unui model matematic pentru procesul tehnologic de fabricare a materialului compozit. Scopul cercetărilor descrise în acest articol este stabilirea fezabilității și condițiilor de fezabilitate ale materialului in variantele posibile. Aceasta înseamnă identificarea intervalelor concentrației de inserție și umidității materialului înainte de extrudare, posibile. Se caută limitele superioară și inferioară ale acestor parametri, astfel încât materialul ieșit din matriță să nu se destrame imediat sau în timp și în același timp procesul de extruziune să fie posibil cu un consum rezonabil de energie.

INTRODUCTION

With the massive technological advancement of the industry, population growth, and climate change, a serious problem arises, namely the decrease of water resources due to pollution. Quick solutions are being sought to solve this problem.

As a result of water purification, a significant amount of sludge is produced, which contains inert and polluting substances, and its processing and valorisation is costly.

According to *(IRS SR 12702, 1997)*, sludge is a complex colloidal system resulting from the treatment of surface waters or the purification of wastewater, with a heterogeneous composition, containing water and suspended, colloidal, mineral, and organic particles, in which products of metabolic activities and/or raw materials, intermediate products, and finished products of industrial activities are incorporated.

One of the methods of valorising sludge is its use along with other filler materials to obtain composite materials to be used in different fields. The use of composite materials made from waste has the primary role of protecting the environment and increasing awareness of sustainability issues, which is very important. Composite materials can be self-recyclable and have high hardness, low density, good tensile strength, and low energy consumption.

To obtain bricks, a mixture of 45% cement and 55% sludge is centrifuged for 15 minutes until a homogeneous paste is obtained. This paste is poured into moulds and left to dry for 24 hours. To increase its strength, the brick is left in the open air for 3-4 days after being removed from the mould (*Pricop F. et al., 2017; Pop M., 2016*).

Another use of composite materials based on waste such as flakes, wood powder, and recycled plastic is for insulation panels, curb stones, frames, and plates (http://petbiocomp.ee.tuiasi.ro).

In a doctoral thesis by *Corbu O. in 2011*, a type of high-performance concrete made with waste glass aggregates was studied, followed by waste concrete and glass. In Brazil, briquettes were produced using dry sludge and vegetable oil, resulting in a calorific potential of 12.94 MJ/kg, slightly lower than coal but with a higher density (*Rocha S. et al., 2022*).

Dry sludge from wastewater treatment can also be used in brick production, mixed with clay in proportions of 0-40% of the brick's weight. The brick's surface is uneven, and its porosity is high, with specific weight and compressive strength decreasing as the sludge content increases (Matar M., 2008). Another type of brick results from mixing sludge with clay and shale, called bio-brick. It has the appearance and smell of ordinary bricks (*Allemanand J. E., 1984; Matar M., 2008*).

A state-of-the-art review on coir fibre-reinforced biocomposites is given in *(Hasan K.M.F.et al., 2021).* The preliminary feasibility analysis of braided tubular composites composed of natural fibres is another option for capitalizing on natural fibres, presented in (*Bruni-Bossio B., 2018).* Another variant of valorisation of natural materials in composites is that of mycelium composite construction materials from fungal biorefineries. A critical look at this type of materials is presented in *(Mautner at al., 2020).* Important concerns in the same direction can be found in *(Khalid M.Y., et al. 2021).*

Sludge can also be used in the production of ceramics and glass. Sludge ash contains silicates, the basic raw material in ceramics. Sludge ash is a fine powder that mixes easily with other components of ceramic paste. In other applications, sludge ash is transformed into a glass-like material (*Matar M., 2008; Șerbănoiu A., 2019*).

This article outlines the structure and manufacturing technology of the composite material with a sludge matrix and agricultural waste insertion, with the aim of formulating a systematic working technology that includes input, control (adjustment), and output parameters (including process quality parameters) in a series of future articles. The future articles will also provide results that express the dependence of the composite's quality parameters on the insertion concentrations and possible process parameters (starting moisture, maximum compression pressure, loading speed, temperature, etc.), as well as results regarding the behaviour of composite materials made under different moisture, temperature, and time conditions in the storage environment or the surrounding environment.

MATERIALS AND METHODS

2.1. Used component materials, description and properties

To utilize bio waste, bricks were made from dehydrated sludge with filling material of seed shells and sawdust (fig. 1).

Sunflower seed husks has been chosen because Romania is among the major producers of sunflower oil, and husks represent 21.1-29.8% of the seed quantity.

Sunflower seed husks contain: 21.85-22% lignin, 31% hemicellulose, and 34% cellulose, a composition very similar to that of wood *(Coșereanu C., 2015).* The physical properties to consider when using a woody or agricultural biofuel are: density, porosity, compactness, moisture content, and calorific value.

According to *(http://docplayer.org/73032490),* the calorific value is better the higher the lignin content, with sunflower seed husks having a superior calorific value of 16120 kJ/kg in the anhydrous state, while wood has a value of 15500 kJ/kg. Sunflower seeds have a porosity of approximately 55-75%.

The sludge resulting from water treatment are complex colloidal systems with heterogeneous compositions, containing colloid particles with a diameter smaller than 1 mm, dispersed particles with a diameter between 1 and 100 mm, aggregates, suspended material, etc., having a gelatinous appearance, and containing a lot of water (*Batali L. et al., 2015*).

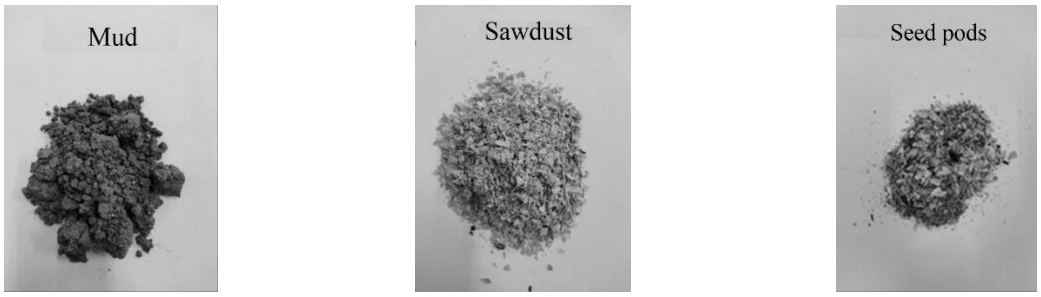


Fig. 1 - Utilized materials for obtaining composites with mud matrix and sawdust insert and/or seed husks

Moisture content (*Batali L. et al., 2015*): For materials retained on screens and grates: 60%; for fresh sludge: 95-97%; for excess activated sludge: 98%-99.5%; for precipitated sludge: 92%-95%. Specific density (*Batali L. et al., 2015*): raw primary sludge: 1.004-1.010 t/m^3; excess activated sludge: 1.001 t/m^3; after thickening: 1.003 t/m^3. According to technical literature data (*Batali L. et al., 2015; Arulrajah A., et al., 2011; Diliunas, J. et al., 2010*), there are also the following characteristics: density, r: 1.07-1.16 g/cm^3; upper plastic limit, wL: 100%-352%; lower plastic limit, wP: 49%-215%; compression index, Cc: 0.4-1.66; optimal Proctor moisture content, woc: 40%-53%; maximum dry density, gdmax: 8 kN/m^3.

Mechanical strength represents the capacity of biomass to resist internal tensions that occur in its structure as a result of external loads. The unit stress resulting from the application of an external load is normal stress (σ) and tangential stress (τ). In the case of simple stresses, such as compression or tension, they are determined by the ratio of the applied force (F) and the initial cross-sectional area of the specimen (S0) (*https://www.academia.edu/39766913/IRD_PROIECT; Panagiotis, 2011; Popescu I.N., 2014*). Simple stressors can be: axial (tension or compression); shear stresses; torsion stresses; bending stresses.

2.2. Granulometric analysis

In order to perform the granulometric analysis, the three materials, mud, seed shells, and sawdust, were thoroughly dried beforehand. The following equipment and instruments were used for determining the granulometric composition: analytical balance with a precision of ± 0.05 g (fig. 2); a vibrating sieve apparatus with a set of standardized sieves mounted in decreasing order of mesh size (fig. 3); a set of sieves with mesh sizes of: 1, 0.5, 0.315, and 0.125 mm.

Experimental procedure: 100 g of each material are weighed (fig. 4). The samples are loaded, one at a time, onto the top sieve, the lid is placed on, and the sieve set is fixed (fig. 5). The apparatus is set to a vibration level that allows particles to move across the sieve in a horizontal plane. The material is sieved for 10 minutes. The fixing system is removed, and the sieves are emptied, one at a time (fig. 6). Each granulometric fraction is weighed. The measurement tables are completed (Tables 1, 2, 3). The experimental results are processed by preparing the graphs (fig. 8, 9, 10). The minimum particle size is determined by interpreting the graphs.

The following notations will be used: ϕ for the sieve diameter in mm, R for the fraction retained on the sieve in g, and, T for the fraction passing through the sieve, in g.



Fig. 2 – Analytical balance

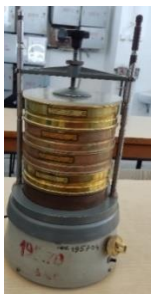


Fig. 3 - Vibration screening device

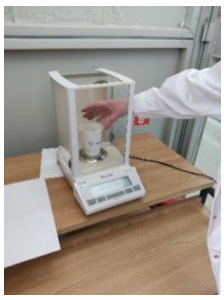


Fig. 4 - Weighing the sample



Fig. 5 - Powering the device



Fig. 6 - Emptying the sites

Analysing the diagrams from fig. 7 by interpolation, it is found that the average particle size has the value D_{med} = 0.463 mm for sludge particles. For the average diameter of the seed shell and sawdust particles, it was proceeded by extrapolation and the values 5.548 mm and 2.359 mm were obtained, respectively.

Table 1

Particle size measurements on sludge

ϕ, mm	R, g	T, g	$\sum q_i$, %	$1 - \sum q_i$, %
1.000	36.200	11.039	36.2	63.8
0.500	11.039	12.552	11.0	89.0
0.315	12.552	15.097	12.5	87.5
0.125	15.097	24.613	15.0	85.0
0.000	24.613	0.000	24.6	75.4

Table 2

Particle size measurements for seed shells

ϕ, mm	R, g	T, g	$\sum q_i$, %	$1 - \sum q_i$, %
1	91.370	4.547	91.3	8.7
0.5	4.547	3.295	4.5	95.5
0.315	3.295	0.811	3.2	96.8
0.125	0.811	0.000	0.8	99.2

Table 3

Particle size measurements on sawdust

ϕ, mm	R, g	T, g	$\sum R_i$, %	$100 - \sum R_i$, %
1	74.416	8.856	74.4	25.6
0.5	8.856	6.762	8.7	91.2
0.315	6.762	7.562	6.7	93.3
0.125	7.562	3.098	7.5	92.5
0	3.098	0.000	3.0	97.0

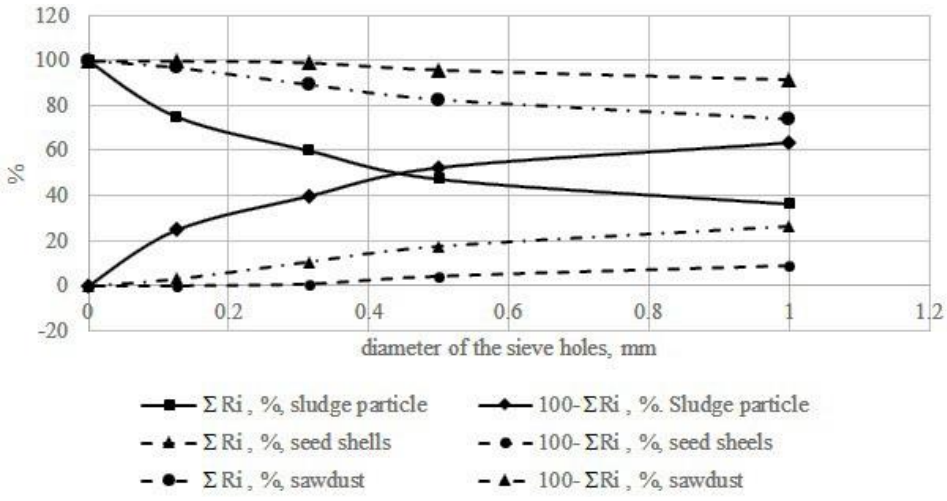
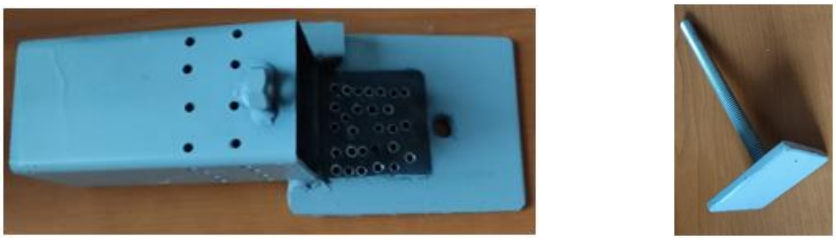


Fig. 7 - Processing of the mud results, the seed shells, and the sawdust results

2.3. Composite material preparation technology

The mould (fig.8a) is made of square pipe with dimensions of 45 x 45 x 2 mm and a height of 100 mm. The bottom is equipped with 2 mm diameter holes and is attached to the walls of the mould through a hinge that allows it to open for the removal of the pressed material. Two rows of holes of the same diameter were made on the walls of the mould to allow for the evacuation of excess water from the material. A piston pressed by weights was used to compact the material.

Experiment procedure: The concentrations of mud and additive material were determined: N100, N95S5, N90S10, N85S15, N80S20, N75S25, N70S30, N50S50, N95R5, N90R10, N85R15, N80R20, N75R25, N70R30, N65R35, N60R40, N50R50 (where N is the code for mud matrix, S is the code for seed coat insertion, and R is the code for sawdust insertion). Mixtures were made. 100 g of each type were weighed (using a digital kitchen scale). The moisture content of the materials was measured using a moisture meter, as shown in fig. 9.



a) b)

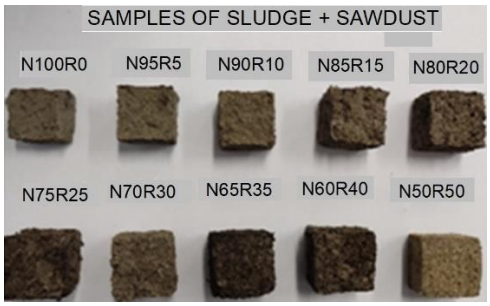
Fig. 8 - The mould for forming the composite material

a. matrix; b. plunger

The mixtures were pressed into the forming matrix, noting the initial dimensions of the sample, the pressing force, and time. After being removed from the matrix, the samples were measured and weighed. After two weeks, the samples are weighed and measured again (fig.10). The data is recorded in a table to study the evolution over time.



Fig. 9 - Moisture measurement



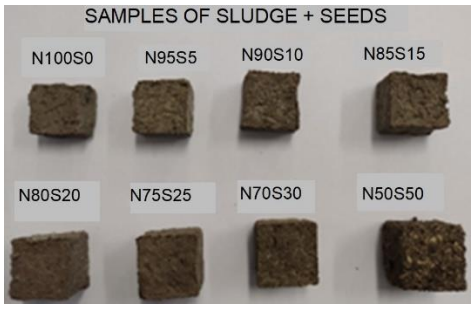


Fig. 10 - Samples of composite material after exiting the forming mould before pressing

RESULTS

In this chapter, quantified results of the prospective study of the manufacturing process of composite materials with mud matrix and seed shell insertion are presented. Technological parameters are those parameters of the composite material manufacturing process with mud matrix and insertion of various materials that characterize the product before and immediately after compression. For now, an exact list of the parameters of the technological system model used for composite manufacturing cannot be given. This is because some of the system parameters were kept constant during these initial experiments (initial material mass, compression time, compression matrix section dimensions, average particle size of the materials, physico-chemical parameters of the matrix material). Other parameters were varied too little for a complete study (initial moisture), or were not controlled (temperature). For the moment, it can be affirmed that the main input parameter considered was the insertion concentration in the composite material. In addition to this, the mass of material introduced into the mould, the initial volume, and its moisture are the main input parameters involved. Also, an important measure of the quality of the technological transformation process is the final density of the product.

If the variation of the final moisture (fig.11) and final density (fig.12) with the insertion concentration in the composite is graphically represented, it is observed that the obtained curves do not present significant peculiarities. However, they do show minima and maxima that cannot even be hypothetically explained at the current level of research. Under these conditions, it is more useful, at this stage, to perform a statistical analysis of the output parameters in relation to the experimentally varied input parameters.

For the moment, the input parameters with the largest variations are considered: insertion concentration in the composite material, c, pressing mass (which gives the pressing force), m_p, initial volume of the material in the mould, V_i, and material moisture before compression, u_i. Considering the final parameter as the final moisture of the composite product, u_f, a multivariate analysis based on multilinear regressions is used to obtain the dominant parameters that influence the final moisture.

In compliance with (*https://ro.kamiltaylan.blog/coefficient-of-determination*), a multilinear regression of the form is desired:

$$u_f = c_0 + c_1 c + c_2 m_p + c_3 V_i + c_4 u_i \quad (1)$$

where: $c_i, i = 0,1,2,3,4$ are coefficients of the free parameters (input). Taking into account the Pearson correlation matrix and the results of multiple regression analysis (*https://profs.info.uaic.ro/~val/statistica/StatGloss.htm#_Toc2658366*), the following relationship has been obtained:

$$u_f = 26.414253 - 283834.1917 V_i + 0.846478 u_i. \quad (2)$$

Input parameters c and m_p have been eliminated because they are correlated with V_i and u_i (see table 4). The Pearson correlation matrix can be observed in Table 4. Regression (2) corresponds to the determination coefficient R^2=0.603. The regression with three independent variables is indicated by the same analysis in relation (3):

$$u_f = 37.114209 + 0.976764 m_p - 406259.2635 V_i + 0.733969 u_i \quad (3)$$

with the determination coefficient, R^2=0.716.

The complete regression with 4 independent variables (the ones selected for analysis) is given in (4):

$$u_f = 16.648239 - 0.321762 c + 2.588281 m_p - 341411.5318 V_i + 0.841759 u_i \quad (4)$$

with the determination coefficient R^2=0.644.

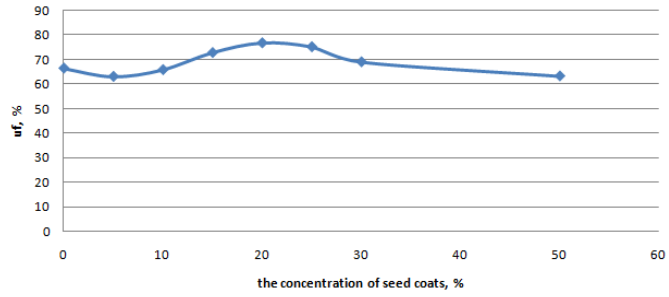


Fig. 11 - The dependence of the final moisture of the composite on the concentration of the insert

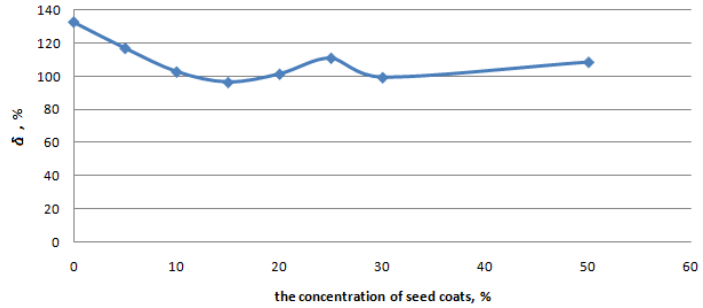


Fig. 12 - The dependence of the compression densification of the composite on the insertion concentration

Table 4

The Pearson correlation matrix for the case where the dependent variable is final density

	u_f	c	m_p	V_i	u_i
u_f	1	0.02035	0.0671116	-0.473602	0.533576
c	0.02035	1	0.982569	0.749836	0.460682
m_p	0.0671116	0.982569	1	0.667505	0.377645
V_i	-0.473602	0.749836	0.667505	0.995495	0.288896
u_i	0.533576	0.460682	0.377645	0.288896	1

The coefficient of determination, R^2, is a measure used to explain how much variability of one factor can be caused by its relationship with another related factor, according to (*https://en.wikipedia.org/wiki/Coefficient_of_determination; https://profs.info.uaic.ro/~val/statistica/StatGloss.htm#_Toc265836*)

This correlation, known as "goodness of fit," is represented as a value between 0.0 and 1.0. Regression equation (2) explains 60.3% of the variability of the final moisture content u_f, using only predictors (independent variables): V_i and u_i. Regression equation (3) explains 71.6% of the variability of the final moisture content u_f, using predictors: m_p, V_i si u_ii

The linear regression equation that depends on all the predictors considered in the model, (4), c, m_p, V_i and u_i, explains only 64.4% of the variability of the final moisture content u_f.

For the regression with the best performance, (3), the adjusted coefficient of determination is 0.603494, and the multiple correlation coefficient is R = 0.846629.

For the general regression, there is a right tail: F(2,5) = 6.327101, p-value = 0.046879 < 0.05, therefore the null hypothesis is rejected: H_0, which means that the linear regression is better than approximating with a constant value and hypothesis H_1 is accepted. Also, considering the variables that provide the best approximation, the analysis concludes that the variables c and m_p are not significant predictors for the dependent variable u_f. The multivariate analysis program notes that if any excluded variable is highly suspected to be related to the dependent variable (u_f), either theoretically or due to previous research, it is recommended to include the variable in the model, regardless of the p-value. To do this, the iteration setting must be modified according to the manual.

Linear regression assumes normality for residual errors. The p-value of the Shapiro Wilk test is 0.911. It is assumed that the data is normally distributed. Therefore, the test is validated regarding residual normality. The p-value of the White test is 0.596161 (F = 0.574642). It is assumed that the variance is homogeneous. Therefore, the test is validated regarding homoscedasticity (*https:// www.statskingdom.com/410multi_linear_regression.html*) and variance homogeneity. There is no multicollinearity problem since all VIF values are less than 2.5. The a priori power (regarding the model with all four predictors) must be calculated before running the regression. Although the testing power of the whole model is low: 0.1062, H_0 is rejected.

An alternative to linear regressions are power regressions, which in this case have the general form:

$$u_f = k \cdot c^{\alpha_c} \cdot {m_p}^{\alpha_{m_p}} \cdot {V_i}^{\alpha_{V_i}} \cdot {u_i}^{\alpha_{u_i}} \quad (5)$$

in which k, is a coefficient and α_c, α_{m_p}, α_{u_i} are exponents, all being determined from the experimental data through the method of least squares same as the coefficients of the linear regression (1). The synthesis of the results of the multivariate analysis for the form (5) of the regression is given in Table 5.

Table 5

The coefficients and exponents of the power-type regressions (homogeneous functions) for the final humidity

Solution's coefficient and exponents					R^2
k	α_c	α_{m_p}	α_{V_i}	α_{u_i}	
0.0209551	0.00170018	0.082028	-0.452973	0.840125	0.655
0.0176824	0	0.0842791	-0.467878	0.846776	0.741
0.0330896	0	0	-0.379778	0.933357	0.642

From table 5, it can be observed that the best solution is given by the dependence only on the variables m_p, V_i and u_i, therefore still an incomplete solution as in the linear regression. The statistics exclude the variable c from many formulas due to its closer correlation with the other independent variables (Table 4, the concentration row or column generally contains the highest values).

Table 6

The intercept and coefficients of linear regressions for final density

Solution's coefficient and exponents					R^2
Intercept	Coefficient c	Coefficient m_p	Coefficient V_i	Coefficient u_i	
2054.388894	2.319398	-77.322147	-2697596.046	1.41414	0.893
1906.861562	0	-65.705652	-2230146.274	2.191135	0.919
2062.103133	0	-64.434048	-2177807.476	0	0.932
1943.392501	0	-71.535244	0	0	0.939

The same type of statistical analysis is carried out further for the final density as the dependent parameter, considering the same four independent parameters. For linear regression, the general formula is the same as that given in (1), except that ρ_f appears instead of u_f.

Therefore, the load mass during pressing, m_p, explains 94% of the behaviour of the final density, making it the most accurate solution. This solution has, for the general regression, a right tail F(1,6) = 93.929532 and a p-value of 0.00000692232 < 0.05, hence the null hypothesis, H_0, is rejected as in the previous case.

The regression relationships can be written simply using Table 6, for example, the relationship with the highest coefficient of determination (R^2 = 0.94, R^2_{adj} = 0.93, F(1,6) = 93.93, p < 0.001) shows that the final density depends most strongly on the pressing mass, therefore on the force with which the forming composite is pressed in the mould.

Table 7

The Pearson correlation matrix for the case where the dependent variable is the final density

	ρ_f	c	m_p	V_i	u_i
ρ_f	1	-0.959894	-0.969514	-0.726446	-0.32719
c	-0.959894	1	0.982569	0.749836	0.460682
m_p	-0.969514	0.982569	1	0.667505	0.377645
V_i	-0.726446	0.749836	0.667505	0.995495	0.288896
u_i	-0.32719	0.460682	0.377645	0.288896	1

$$\rho_f = 1943.392501 - 71.535244 m_p. \quad (6)$$

The best power regression for final density is found in the same way as for final humidity, having the formula given by (7).

$$\rho_f = 33.394007 \cdot m_p^{-0.307592} \cdot V_i^{-0.458863} \quad (7)$$

All the power regression solutions given by (*https://profs.info.uaic.ro/~val/statistica/StatGloss.htm#_Toc2658366*), have coefficient given in table 8.

Table 8

The coefficients and exponents of the power regressions (homogeneous functions) for the final moisture content

Solution's coefficient and exponents					R^2_{adj}
k	α_c	α_{m_p}	α_{V_i}	α_{u_i}	
210.249096	0.00199632	-0.335184	-0.286420	-0.0477218	0.886
145.848877	0.0184161	-0.334727	-0.303509	0	0.914
33.394007	0	-0.307592	-0.458863	0	0.923

The composite material studied in these experiments proves to be possible to obtain through the proposed technological process. In these experiments, the authors aimed to vary some of the input parameters to verify the dependence of the output parameters (dependent variables) on predictors (input parameters) and the conditions of the technological process. The main input parameters considered in these experiments were: the concentration of the insertion in the composite material, the initial moisture content, the initial volume of the material, and the pressing mass, which actually means pressing force (by amplifying with gravitational acceleration) and ultimately compression pressure. The other important input parameters were kept constant for now (initial composite mass, cross-sectional dimensions of the matrix and insertion, compression temperature and time, and implicit compression speed), all of which could have significant influences in the compression process. Additionally, initial moisture content was slightly varied.

The parameters of particular interest in these experiments are the final moisture content (to estimate the intensity of dehydration in the technological process) and the final density (to evaluate the densification capacity of the technological process). Dehydration and especially densification are expected to have a significant influence on the mechanical and thermal properties of the final composite material.
In future studies, based on the conclusions from multivariate regression statistics, synthetic parameters of the composite material formation process will be formulated, such as a measure of dehydration.

$$\delta = \frac{u_i - u_f}{u_i} \tag{8}$$

A graphical representation of the dependence of dehydration (8) on initial moisture content, using linear regression relationships, is given in fig. 13.

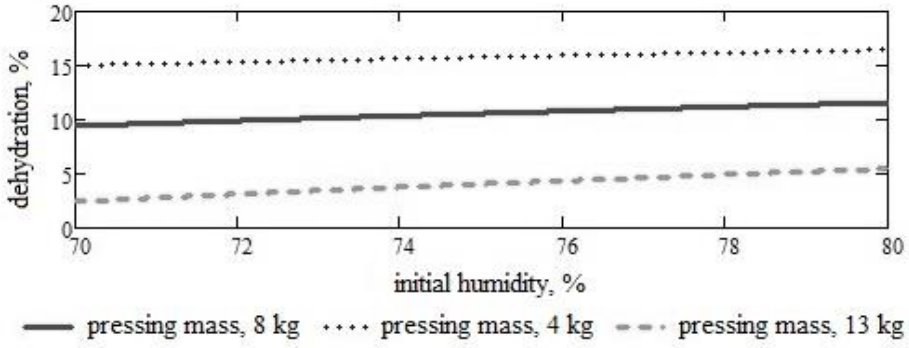


Fig. 13 - Variation of dehydration with the initial moisture content of the raw material from which the final composite is formed

CONCLUSIONS

C1) The experiments whose results are presented in this article demonstrate the feasibility of the proposed composite material using the described manufacturing process.

C2) The dependencies between the output and input parameters of the manufacturing process of the composite material with mud matrix and agricultural waste insertion are complex and can have a random character, as shown by the graphical representations of the final humidity and density as functions of the insertion concentration in the composite material. Currently, these studies are left for later, when more experimental results are accumulated, with more parameters being varied.

C3) Given the conclusion of C2, it has been opted for the statistical study of the experiments, which should give us some information on the connections between the output parameters (which represent the quality of the composite material at the output of the process and the quality of the manufacturing process) and the input parameters.

For this purpose, multivariate regression analyses were performed for the final humidity and density as output variables (dependents) and the insertion concentration in the material, pressing mass, initial volume, and initial humidity as independent variables (predictors).

The results show that:

- The final humidity depends most intensively on pressing mass (positive coefficient), initial volume (negative coefficient), and initial humidity (positive coefficient) in the case of multivariate linear regression, and on pressing mass (positive exponent), initial volume (negative exponent), and initial humidity (positive exponent);
- The final density depends most intensively on pressing mass (negative coefficient) in the case of multivariate linear regression, and on pressing mass (negative exponent) and initial volume (negative exponent) in the case of power multivariate regression.

In addition to the insertion concentration in the material and the initial moisture content, an attempt is made, if possible, to characterize the influence of other process parameters (matrix temperature, material pressing speed into the matrix, for example);

C4) The feasibility of the composite brick forming process also included the creation, at a low technical level, of the extrusion installation. This rudimentary installation was capable of producing variations of the desired composite material, with properties that make it further testable in various thermomechanical and acoustic trials.

Clearly, the improvement of the installation, possibly for standardized brick sizes, is a separate activity that cannot be done without preliminary research to demonstrate that the material can be obtained and has the required properties.

C5) The proposed regression relationships from the multivariate analysis are used to guide the choice of resolutions and intervals for input parameters in the manufacturing process and to form dimensionless input-output parameters that synthetically describe the quality of the material and process.

C6) It is clear that there are several future directions for this work. These include exploring additional input parameters beyond insertion concentration and humidity, as well as examining the effects of pressing force and loading speed. Additionally, it would be beneficial to increase the resolution of these parameters to gain a more detailed understanding of their impact. Finally, it is important to measure the quality of the resulting materials, specifically their mechanical resistance to compression, as well as their thermal and sound insulation properties.

REFERENCES

[1] Allemanand J. E. (1984), *Constructive Sludge Management: Biobrick*, *Journal of Environmental Engineering*, Vol. 110, No. 2, pp.301-311.

[2] Arulrajah, A., Disfani, M.M. et al. (2011), Select chemical and engineering properties of wastewater biosolids*, Waste management,* no.31, pp. 2522–2526

[3] Batali L. Carastoian A., (2015), The characterization, from a geotechnical point of view, of the sludge from the sewage treatment plants, with a view to their storage, *Construction Magazine,* no.117, pp.56-59

[4] Bruni-Bossio B. (2018), *Preliminary Feasibility Analysis of Tubular Braided Composites Composed of Natural Fibers*, PhD thesis, Department of Mechanical Engineering University of Alberta

[5] Corbu O. (2011), *Performance concretes*, PhD thesis, Technical University of Cluj-Napoca

[6] Coșereanu C. (2015), *Composites from recycled agricultural and industrial waste*, Rehabilitation thesis, Transilvania University of Brașov

[7] Diliunas, J., Dundulis, K. et al. (2010), Geotechnical and hydrochemical properties of sewage sludge, *Bulletin of Engineering Geology and Environment*, no.69, pp. 575–582

[8] Grammelis, Panagiotis (2011), Biomass Combustion Characteristics and Implications for Renewable Energy, *Process Biochemistry,* pp. 95 - 121

[9] Hasan K.M.F., Horváth P.G., Bak M., Alpár T. (2021), A state-of-the-art review on coir fiber-reinforced biocomposites, *RSC Advances*, no. 11, pp. 10548-10571

[10] Jones M., Mautner A., Luenco S., Bismarck A., John S. (2020), Engineered mycelium composite construction materials from fungal biorefineries: A critical review, *Materials & Design*, vol.187, pp. 1-16

[11] Khalid M.Y., Rashid A.A., Arif Z.U., Ahmed W. (2021), Natural fiber reinforced composites: Sustainable materials for emerging applications, *Results in Engineering*, Vol. 11, 100263

[12] Matar M. (2008), *Use of wastewater sludge in concrete mixes*, The Islamic University of Gaza

[13] Pricop, F., Chivoiu, A., Jianu, R., Moga, I. C. (2017*),* Innovative solutions for the treatment and recovery of sludge from industrial pretreatment stations, *AGIR Bulletin*, Bucharest, no. 3, pp. 50 - 54

[14] Pop, M. (2016), *Composite materials* , ed. UT Press, 142 p

[15] Popescu, I. N. (2014), *Composite materials*, Valahia University Press

[16] Rocha, S., Soares, P. & Maia, L. Rocha, S., Soares, P. & Maia, L. (2022), Briquettes from sludge in sewage treatment plant: calorific power, *Environ Sci Pollut Res*, Vol. 29, 91096–91104

[17] Șerbănoiu, A. A. (2019), *Management of the sustainable development of constructions from classic and ecological materials*, Master's thesis, Iași

[18] ***IRS SR 12702 (1997), *Sludges resulting from surface water treatment and wastewater treatment* http://petbiocomp.ee.tuiasi.ro

[19] http://docplayer.org/73032490-Furnizarea-de-biocombustibili-solizi-pentru-centralele-termice-de-putere- medie.html

[20] https://www.academia.edu/39766913/IRD_PROIECT
https://www.statskingdom.com/410multi_linear_regression.html

[21] https://ro.kamiltaylan.blog/coefficient-of-determination

[22] https://en.wikipedia.org/wiki/Coefficient_of_determination

[23] https://profs.info.uaic.ro/~val/statistica/StatGloss.htm#_Toc2658366

CALIBRATION OF WHITE RICE SIMULATION PARAMETERS BASED ON DISCRETE ELEMENT METHOD
/
基于离散元模拟的白米仿真参数标定

Biao XIE, Jinyin BAI, Jiagang YAN, Shibo ZHAO, Nian LIU, Qiang ZHANG*) [1]
College of Engineering, Huazhong Agricultural University, Wuhan / China;
Key Laboratory of Agricultural Equipment in Mid-lower Yangtze River, Ministry of Agriculture, Wuhan / China
Tel: +86 27 87282120; E-mail: zq604@mail.hzau.edu.cn
DOI: https://doi.org/10.35633/inmateh-71-18

Keywords: *white rice, discrete element method, angle of repose, parameter calibration*

ABSTRACT

Aiming at the lack of discrete element simulation models and parameters for rice polishing, grading, color sorting and other technologies and equipment, and the difficulty of guiding equipment design and optimization through simulation, this paper calibrates the simulation parameters of white rice based on angle of repose (AOR) test and simulation methods. Huanghuazhan and Dongnong 429 white rice were selected as research object. Numerical model of white rice was established by multi-sphere filling. According to physical test and references, the simulation parameter range of white rice particles was determined. Plackett-Burman test was used to screen parameters, and it was found that the particle-particle static friction coefficient and particle-particle rolling friction coefficient had significant effects on the AOR of white rice. The regression model between the AOR and the significance parameter was established according to the central composite design method. The simulation parameter combination that has significant influence on the physical AOR was determined through the optimization design, and verified by the simulation test. The simulation AOR was compared with the physical AOR, and the relative error of the two kinds of white rice was less than 3%. The results show that the calibration method proposed in this study can accurately simulate the physical AOR test, which can provide reference for discrete element simulation of white rice processing.

摘要

针对大米加工中抛光、分级和色选等技术和装备缺乏离散元仿真模型和参数，难以通过仿真指导装备设计与优化等问题，本文基于物理堆积试验和仿真方法对白米仿真参数进行标定。以黄华占和东农 429 两种白米为研究对象，采用多球填充建立了白米颗粒离散元数值模型；根据物理试验和参考文献确定了白米颗粒仿真参数范围；利用 Plackett-Burman 试验进行参数筛选，发现颗粒-颗粒静摩擦系数、颗粒-颗粒动摩擦系数对白米堆积角影响显著；并根据中心复合试验设计方法建立了堆积角与显著性参数间的回归模型；通过寻优设计确定对物理堆积角影响显著的仿真参数组合，并进行仿真试验验证，将仿真所得堆积角与物理试验值进行对比验证，两种白米的相对误差均小于 3%。结果表明，该研究提出的标定方法能准确模拟物理堆积试验，可为大米加工离散元仿真提供参考。

INTRODUCTION

Rice is one of the most important food crops in the world. Consumers are often influenced by psychology and perception when buying rice, so they preferentially choose rice with high appearance quality (*Zhao et al., 2023; Lu et al., 2019*). Rice is usually processed into commercial rice by drying, husking, milling, polishing, grading and color sorting (*Riaz et al., 2017*). Polishing, grading and color sorting are rice finishing, which can increase quality of rice and improve the competitiveness of rice products (*Ahmed et al., 2021*). The traditional rice finishing machinery design mainly relies on the processing experience, which is difficult to guide the optimization design of the processing equipment.

Discrete element method (DEM) reveals the motion characteristics and processing characteristics of the material from the particle scale, which has been widely used in agricultural material processing (*Zhao et al., 2021*), but there are few studies on rice finishing equipment by using the DEM. In order to improve the simulation accuracy, a large number of scholars have calibrated the parameters of dry and wet particle (*Zeng et al., 2021*).

[1] *Biao Xie, M.S. Stud. Eng.; Jinyin Bai, M.S. Stud. Eng.; Jiagang Yan, M.S. Stud. Eng.; Shibo Zhao, B.S. Stud. Eng.; Nian Liu, Prof. Ph.D. Eng.; Qiang Zhang, Prof. Ph.D. Eng.*

In this paper, the simulation parameter ranges of white rice were determined based on physical test and references. Taking the angle of repose (AOR) of physical test as the response value, the regression model between the response value and significant simulation parameters was established by Plackett-Burman (PB) test, steepest ascent test and central composite test design, and the white rice simulation parameters were obtained. The reliability of simulation parameters was verified by comparing the simulation AOR under the combination of optimal parameters with the physical AOR, so as to provide accurate and reliable simulation models and parameter calibration methods for rice polishing, grading, color sorting and other mechanized operations, and provide theoretical support for mechanical device design.

MATERIALS AND METHODS

Test materials

Indica Huanghuazhan and japonica Dongnong 429 rice varieties were selected in the test, among which the type of Huanghuazhan was long-grain and the type of Dongnong 429 was short-grain. The white rice for test was obtained by husking, milling and removing the broken rice. The moisture content of Huanghuazhan white rice (HWR) was 11.3%, and that of Dongnong 429 white rice (DWR) was 12.1%. The main materials of rice polishing, grading and color sorting machine were stainless steel. Therefore, the contact material of this research device was stainless steel.

Numerical model construction of white rice particle

One hundred grains of HWR and one hundred grains of DWR were randomly selected, and the triaxial dimensions (L, B, T) of the grains were measured with digital display vernier caliper (accuracy 0.01) (DL91150, Deli Office Technology Co., LTD., Ningbo, China). The Dimensional measurement diagram is shown in Fig. 1. To simplify the simulation model of white rice, white rice could be regarded as an axisymmetric ellipsoid (*Markauskas and Kačianauskas, 2011*). The length L was taken as the long axis D_L of the ellipsoid model, and the average value of the width B and thickness T were taken as the short axis D_S of the ellipsoid, as shown in Equations (1) and (2). In order to more directly reflect the differences between HWR and DWR, sphericity S_p was introduced for comparison (*Liu et al., 2018*). Sphericity (S_p) was calculated as shown in Equation (3). Results are shown in Table 1. Obviously, there was a clear difference in grain shape between the two types of white rice, and DWR possessed a higher S_p.

$$D_L = L \tag{1}$$

$$D_S = \frac{(B+T)}{2} \tag{2}$$

$$S_P = \frac{(LBT)^{\frac{1}{3}}}{L} \tag{3}$$

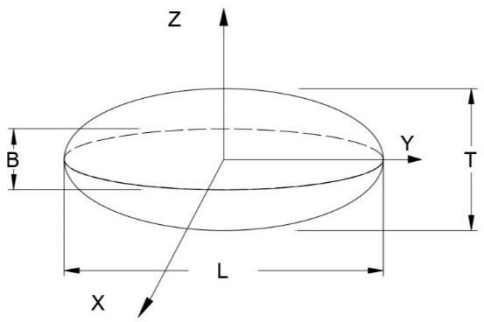


Fig. 1 - Dimensional measurement diagram

According to the simplified ellipsoid sizes of two kinds of white rice, three-dimensional model was established using SolidWorks 2018 (SolidWorks Inc., Concord, USA) software. The 3D model was imported into EDEM 2018 software (DEM Solutions Inc., Edinburgh, Britain) and filled with spheres. The white rice ellipsoid of HWR was filled with 9 spheres, and the white rice ellipsoid of DWR was filled with 7 spheres. The comparison between the discrete element model of white rice and the real rice was shown in Fig. 2, and the discrete element model of rice grain was close to the real shape.

Table 1

Triaxial dimensions and ellipsoid dimensions of white rice

	$L(D_L)$/mm	B/mm	T/mm	D_s/mm	S_p
HWR	6.83±0.26	1.98±0.10	1.70±0.07	1.98±0.08	0.44±0.01
DWR	5.59±0.20	2.61±0.12	1.88±0.10	2.45±0.08	0.54±0.02

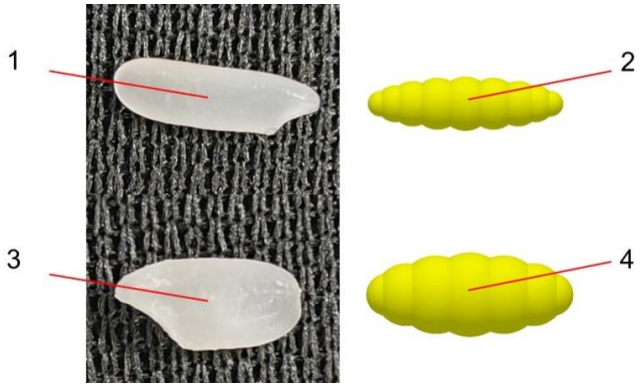
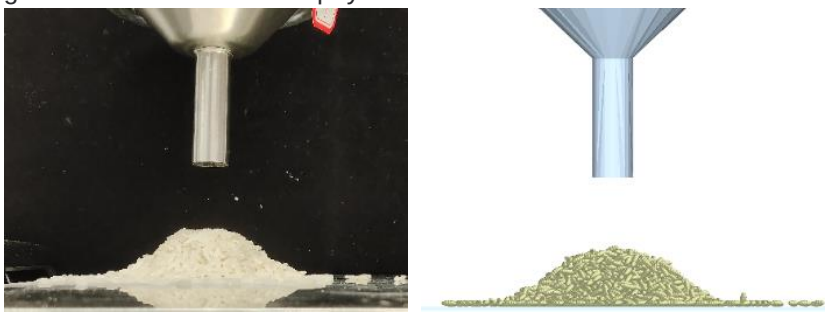


Fig. 2 - Comparison between the discrete element model and the actual condition
1-HWR; 2-model of HWR; 3-DWR; 4-model of DWR

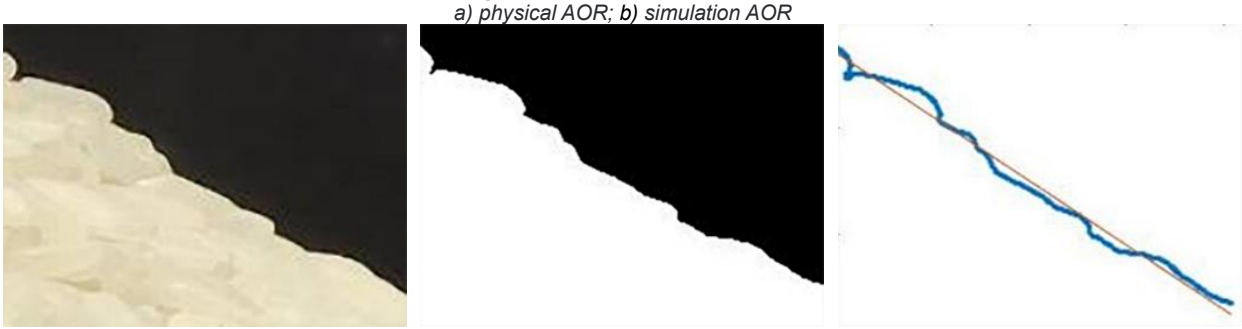
AOR test

The funnel method was used for AOR test of white rice to calibrate the simulation parameters of white rice (*Gong et al., 2021; Liu et al., 2020*). The physical test device was shown in Fig. 3(a), and the simulation test device was shown in Fig. 3(b). The tube length of the funnel was 50 mm, the inner diameter of the funnel outlet was 15 mm, and the distance between the funnel outlet and the stainless steel plate was 50 mm. 40 g white rice was poured into the funnel, and then the discharge port was opened. After white rice was still, the front view was photographed by the camera. Matlab R2018b (The Math Works Inc, Natick, Massachusetts, USA) was used to process the image, as shown in Fig. 4. Binarization, boundary extraction and boundary fitting were carried out in turn, and the slope of the fitting curve was the tangent value of the AOR. The test was repeated for 5 times, and the AOR of the left and right sides of the white rice pile were extracted in each test, and their average values were taken. The physical AOR of HWR was 32.38° and that of DWR was 33.46°.



a) *b)*

Fig. 3 - Measurement of AOR
a) physical AOR; b) simulation AOR



a) *b)* *c)*

Fig. 4 - Image processing
a) original image; b) binarization image; c) boundary fitting image

Intrinsic parameters of white rice

The Poisson's ratio, shear modulus and density intrinsic parameter ranges of white rice and stainless steel were determined through relevant literature (*Shitanda et al., 2002; Han et al., 2016; Zeng et al., 2017; Qiao et al., 2020*), as shown in Table 2.

Table 2

Material parameters obtained from literature

Parameters	Value	Source
White rice Poisson's ratio	0.2-0.3	(*Shitanda et al, 2002*)
Shear modulus of white rice/MPa	1-3.75	(*Han et al., 2016; Zeng et al., 2017*)
White rice density/(kg·m^{-3})	1350-1550	
Stainless steel Poisson's ratio	0.3	(*Qiao et al., 2020*)
Shear modulus of stainless steel/MPa	70000	
Stainless steel density/(kg·m^{-3})	7930	

Contact parameters of white rice

Restitution coefficient is a parameter to measure the deformation recovery ability of particles after collision. Free-fall test was used to measure the restitution coefficient. The test platform was shown in Fig. 5. With the coordinate paper as the test background, and the white rice fell stationary from 200 mm (H) each time and bounced after collision with the stainless steel. The maximum height (h) of the white rice bounced was recorded when the particle vertical upward trend. The test was repeated for 10 times, and the restitution coefficient was calculated by Equation (4). The range of particle-stainless steel restitution coefficient of HWR was 0.32 to 0.56. The range of particle-stainless steel restitution coefficient of DWR was 0.35 to 0.74.

$$e = \frac{v_2}{v_1} = \sqrt{\frac{2gh}{2gH}} = \sqrt{\frac{h}{H}} \tag{4}$$

where:

v_1 - The normal relative velocity of two objects before a collision;

v_2 - The normal relative velocity of two objects after a collision.

In this paper, white rice was arranged and pasted on the stainless steel plate as the contact bottom plate (*Li et al., 2022*) for the collision test. It was used to measure the restitution coefficient between white rice and white rice. The test method was the same as above. The range of particle-particle restitution coefficient of HWR was 0.28 to 0.54. The range of particle-particle restitution coefficient of DWR was 0.3 to 0.47.



Fig. 5 - Test platform for restitution coefficient

1-graph paper; 2-laptop; 3-stainless steel plate; 4-high-speed camera; 5-fill-in light

The inclined plane method was used to measure the particle-particle static friction coefficient and particle-stainless steel static friction coefficient. The test device was shown in Fig. 6. In order to prevent white rice from rolling, two grains were glued together. The angle of the stainless steel plate was changed by adjusting the height of the lifting platform. When the white rice began to slide, the angle of digital protractor was recorded. The static friction coefficient was calculated using the following Equation (5). Each group was repeated 20 times. The range of particle-particle static friction coefficient of HWR was 0.49 to 0.93, and the range of particle-stainless steel static friction coefficient was 0.38 to 0.54. The particle-particle static friction coefficient of DWR ranged from 0.47 to 0.83, and the particle-stainless steel static friction coefficient ranged from 0.35 to 0.55.

$$u_f = \tan\theta \tag{5}$$

where: u_f - static friction coefficient of white rice;

θ - the inclination angle.

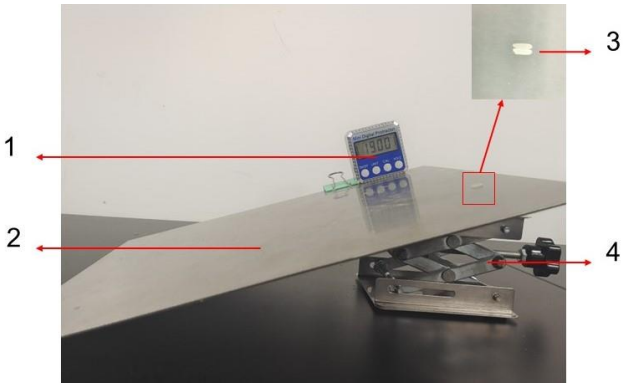


Fig. 6 - Test platform for static friction coefficient

1- digital protractor; 2- stainless steel plate; 3-whtie rice; 4- lifting platform

There is no standard method to measure the rolling friction coefficient at present. Through several simulation pre-tests and in combination with literature (*Han et al., 2014; Ma et al., 2022*), the range of particle-particle rolling friction coefficient is 0.001 to 0.15, and the range of particle-stainless steel rolling friction coefficient is 0.01 to 0.1.

RESULTS AND DISCUSSION

Analysis on the simulation results of PB test

In this study, the AOR of the physical test was used as the response value, and the PB test was designed by Minitab R20 (Pennsylvania State University, Commonwealth of Pennsylvania, USA). The parameters that significantly affected the AOR of HWR and DWR were screened out respectively. The 9 DEM parameters were represented by X_1~X_9, and each parameter was set at high (+1) and low (-1) levels. Each parameter range was determined based on the literature and the test and simulation pre-test in this paper. The same level values were used because the measurements of the two white rice varieties were not significantly different. The levels of PB test are shown in Table 3. The design and results of PB test are shown in Table 4. Table 4 shows that the AOR of white rice with different types are obviously different at the same parameters level, and the maximum difference in the AOR between two white rice varieties is 8.22°

Table 3

Factors and levels of PB test

Symbol	Parameters	Level	
		-1	+1
X_1	Poisson's ratio	0 .2	0.3
X_2	Density/kg·m^{-3}	1350	1550
X_3	Shear modulus/MPa	1	3.75
X_4	Particle-particle restitution coefficient	0.25	0.55
X_5	Particle-particle static friction coefficient	0.45	0.95
X_6	Particle-particle rolling friction coefficient	0.001	0.15
X_7	Particle-stainless steel restitution coefficient	0.3	0.6
X_8	Particle-stainless steel static friction coefficient	0.35	0.55
X_9	Particle-stainless steel rolling friction coefficient	0.01	0.1

Minitab R20 software was used to analyze the Significance of the PB test results. The analysis results of HWR and DWR are shown in Table 5. According to Table 5, the particle-particle static friction coefficient X_5 and particle-particle rolling friction coefficient X_6 have significant effects on the AOR of HWR and DWR. The remaining parameters have no significant effect on the AOR.

Table 4

Design and results of PB test

Number	X_1	X_2	X_3	X_4	X_5	X_6	X_7	X_8	X_9	HWR AOR β_i / (°)	DWR AOR β_j / (°)
1	1	-1	1	1	-1	-1	-1	-1	1	33.91	25.69
2	1	1	-1	1	1	-1	-1	-1	-1	32.31	28.58

Number	X_1	X_2	X_3	X_4	X_5	X_6	X_7	X_8	X_9	HWR AOR β_i / (°)	DWR AOR β_j / (°)
3	-1	1	1	-1	1	1	-1	-1	-1	50.25	45.58
4	-1	-1	1	1	-1	1	1	-1	-1	45.57	43.26
5	1	-1	-1	1	1	-1	1	1	-1	34.43	30.66
6	1	1	-1	-1	1	1	-1	1	1	50.27	46.90
7	1	1	1	-1	-1	1	1	-1	1	40.85	44.23
8	1	1	1	1	-1	-1	1	1	-1	30.99	28.72
9	-1	1	1	1	1	-1	-1	1	1	33.42	31.84
10	1	-1	1	1	1	1	-1	-1	1	51.75	44.21
11	-1	1	-1	1	1	1	1	-1	-1	49.30	45.70
12	1	-1	1	-1	1	1	1	1	-1	52.15	44.83
13	-1	1	-1	1	-1	1	1	1	1	42.69	41.56
14	-1	-1	1	-1	1	-1	1	1	1	36.05	31.94
15	-1	-1	-1	1	-1	1	-1	1	1	45.63	41.90
16	-1	-1	-1	-1	1	-1	1	-1	1	34.28	29.03
17	1	-1	-1	-1	-1	1	-1	1	-1	43.60	43.10
18	1	1	-1	-1	-1	-1	1	-1	1	32.75	28.42
19	-1	1	1	-1	-1	-1	-1	1	-1	31.02	29.57
20	-1	-1	-1	-1	-1	-1	-1	-1	-1	27.74	26.42

Table 5

Significance analysis of PB test for HWR and DWR

Parameters	Effect		Sum of squares		*P* value	
	HWR	DWR	HWR	DWR	HWR	DWR
X_1	0.706	-0.146	2.49	0.11	0.5184	0.7725
X_2	-1.126	1.006	6.34	5.06	0.3408	0.0678
X_3	1.296	0.760	8.40	2.89	0.2473	0.1530
X_4	0.104	-0.790	0.05	3.12	0.9234	0.1390
X_5	4.946	2.640	122.31	34.85	0.0009**	0.0003**
X_6	14.516	15.040	1053.57	1131.01	<0.0001**	<0.0001**
X_7	-0.084	0.456	0.04	1.04	0.9381	0.3753
X_8	0.154	0.990	0.12	4.90	0.8868	0.0716
X_9	0.424	-0.070	0.9	0.02	0.6962	0.8895

*Note: ** indicates highly significant (P<0.01), and * indicates significant (P<0.05), the same below.*

Analysis on the simulation results of steepest ascent test

Based on the results of PB test, significance parameters (X_5 and X_6) were selected for the steepest ascent test. The Particle-particle static friction coefficient was taken as 0.45-0.7. The Particle-particle rolling friction coefficient was taken as 0-0.075, and the remaining parameters were based on the average values in Table 3. The steepest ascent test design and results for HWR and DWR are shown in Table 6, respectively. The relative error (Y) between the AOR of simulation test (β) and the AOR of physical test (α) was calculated by Equation (6). When the relative error of AOR was the smallest, the adjacent steepest ascent test level was selected as the central composite optimization test parameter range.

$$Y = \frac{|\beta - \alpha|}{\alpha} \quad (6)$$

As shown in Table 6, the relative errors of the AOR of the steepest ascent test and the physical test decreased first and then increased. The relative errors of the AOR of the HWR steepest ascent test number 2 was the smallest, and the DWR steepest ascent test number 3 was the smallest. Therefore, the steepest

ascent test number 1 and number 3 of HWR were selected as low (-1) level and high (+1) level respectively for the subsequent central composite test design. Number 2 and number 4 of DWR were selected as low (-1) level and high (+1) level respectively for the subsequent central composite test design.

Table 6

Design and results of steepest ascent test of HWR and DWR

Number	X_5	X_6	Simulation AOR / °		Relative error / %	
			HWR / β_i	DWR / β_j	HWR/ Y_i	DWR/ Y_j
1	0.45	0	30.15	28.98	6.89	13.39
2	0.5	0.015	32.94	31.20	1.73	6.75
3	0.55	0.03	36.22	34.01	11.86	1.64
4	0.6	0.045	38.72	35.18	19.57	5.14
5	0.65	0.06	42.06	38.14	29.89	13.99
6	0.7	0.075	42.65	39.79	31.72	18.92

Analysis on the simulation results of central composite test

The central composite test was used to seek the optimal parameter combination of significance parameters such as particle-particle static friction coefficient and particle-particle rolling friction coefficient in the simulation test. The factor level ranges of particle-particle static friction coefficient and particle-particle rolling friction coefficient were obtained according to the steepest ascent test, and the factor levels of the central composite test are shown in Table 7. Design of central composite test was carried out by using Minitab R20 software. The design and results of central composite test are shown in Table 8. The mean values in Table 3 were used for the remaining parameters of the central composite test.

Table 7

Factors and levels of central composite test

Factor	level			
	-1		1	
	HWR	DWR	HWR	DWR
X_5	0.45	0.5	0.55	0.6
X_6	0	0.015	0.03	0.045

The regression models of AOR with particle-particle static friction coefficient (X_5) and particle-particle rolling friction coefficient (X_6) were established by binary regression fitting on the results of the central composite test. The regression equation of HWR is shown in Equation (7), and the regression equation of DWR is shown in Equation (8).

$$\beta_i = 33.446 + 0.722 X_{5i} + 2.549 X_{6i} - 1.794 X_{5i}^2 - 1.686 X_{6i}^2 + 0.062 X_{5i} X_{6i} \quad (7)$$

$$\beta_j = 34.327 + 0.43 X_{5j} + 2.511 X_{6j} + 2.133 X_{5j}^2 - 2.007 X_{6j}^2 + 0.157 X_{5j} X_{6j} \quad (8)$$

ANOVA was performed on the results of central composite test for HWR and DWR, and the results were shown in Table 8. The regression model of AOR of HWR and DWR are $P<0.0001$, and the P value of the lack of fit is greater than 0.05, indicating that the two models are extremely significant, and the lack of fit is not significant. The determination coefficient R^2 is 0.9753 and 0.9671 respectively, indicating that the two regression equations fit well and were reliable. The effect of X_{5i}, X_{6i}, X_{5i}^2 and X_{6i}^2 on the AOR of HWR and DWR was significant, while the effect of $X_{5i}X_{6i}$ on the AOR was not significant.

Table 8

Design and results of central composite test

Number	X_5	X_6	HWR AOR β_i / (°)	DWR AOR β_j / (°)
1	-1	-1	30.06	31.77
2	+1	-1	31.73	32.30
3	-1	+1	35.11	36.31
4	+1	+1	36.53	37.49
5	-0.5	0	32.69	34.49
6	+0.5	0	33.01	34.90

Number	X_5	X_6	HWR AOR β_i / (°)	DWR AOR β_j / (°)
7	0	-0.5	32.10	32.07
8	0	+0.5	35.34	35.25
9	0	0	33.60	34.87
10	0	0	33.61	34.11
11	0	0	33.36	33.96
12	0	0	33.22	34.70
13	0	0	33.96	34.55

Table 9

ANOVA of HWR and DWR for central composite test

Source	Degree of freedom	Sum of squares		Mean square		*P* value	
		HWR	DWR	HWR	*DWR*	*HWR*	*DWR*
Model	5	32.38	30.42	6.48	6.08	<0.0001**	<0.0001**
X_{5i}	1	2.35	0.83	2.34	0.83	0.0029**	0.0494*
X_{6i}	1	29.24	28.38	29.24	28.38	<0.0001**	<0.0001**
$X_{5i}X_{6i}$	1	0.02	0.10	0.02	0.10	0.7260	0.4396
X_{5i}^2	1	0.78	1.11	0.78	1.11	0.0362**	0.0289*
X_{6i}^2	1	0.69	0.98	0.69	0.98	0.0453**	0.0366*
Residual	7	0.82	1.03	0.12	0.15		
Lack of fit	3	0.50	0.43	0.16	0.14	0.2432	0.4990
Pure error	4	0.32	0.61	0.07	0.15		
Sum	12	33.21	31.45				

Verification test

Using the optimization design in Minitab R20 software, the AOR of HWR physical test 32.38° and the AOR of DWR physical test 33.46° were taken as the target values to substitute into their respective regression models for solution. The optimal combination of the significance parameters of HWR: the particle-particle static friction coefficient was 0.5 and particle-particle rolling friction coefficient was 0.0146. The optimal combination of significance parameters of DWR: the particle-particle static friction coefficient was 0.55 and particle-particle rolling friction coefficient was 0.0258. Other non-significant simulation parameters were averaged from Table 3. The DEM test was verified under the condition of optimal parameter combination, each group of tests was repeated 3 times. The comparison between simulated AOR and physical AOR is shown in Fig. 7. The AOR of HWR simulation test are 32.64°, 34.02° and 33.27°, respectively, and the relative error of AOR are 2.42%, 1.67% and 0.57%. The AOR of DWR simulation test are 33.29°, 32.70° and 33.36°, respectively, and the relative error of AOR are 0.51%, 2.25% and 0.29%. The relative error of the DEM test and physical test of the two varieties of white rice is less than 3%. The results of AOR test show that the DEM test have high similarity to the physical test, which indicates that the DEM parameters of HWR and DWR are accurate and reliable.

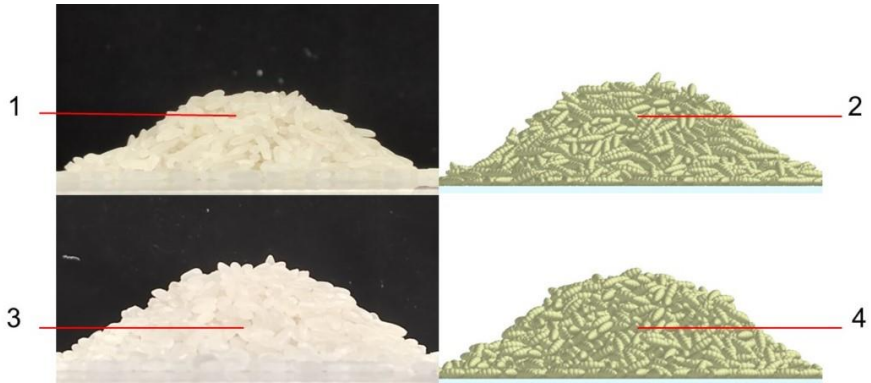


Fig. 7 - Comparison of AOR test of white rice

1-physical test of HWR; 2-simulation test of HWR; 3-physical test of DWR; 4-simulation test of DWR

CONCLUSIONS

In this paper, Huanghuazhan, an indica rice, and Dongnong 429, a japonica rice, were selected as the research objects. The DEM was used to calibrate white rice DEM parameters, and the accuracy and reliability of DEM parameter calibration were verified by physical AOR test. The conclusions are as follows:

(1) The triaxial dimensions of HWR and DWR were determined. Two kinds of discrete element models of HWR and DWR were established by multi-ball filling method. The DEM significance parameters and their optimal intervals of HWR and DWR were determined by PB test and steepest ascent test, respectively. The optimal range of significance parameters for HWR was as follows: the range of particle-particle static friction coefficient was 0.45 to 0.55, the range of particle-particle rolling friction coefficient was 0 to 0.015. The optimal range of significance parameters for DWR was as follows: particle-particle static friction coefficient was 0.5 to 0.6, particle-particle rolling friction coefficient was 0.015 to 0.045. Regression models of AOR and simulation parameters of HWR and DWR were established by central composite test. The coefficient of determination of HWR regression model and DWR regression model were 0.9753 and 0.9671 respectively.

(2) The AOR of physical test of HWR and DWR were taken as the target value to substitute into their respective regression models for solution. The optimal combination of significance parameters of HWR: the particle-particle static friction coefficient was 0.5 and the particle-particle rolling friction coefficient was 0.0146. The optimal combination of significant parameters of DWR: the particle-particle static friction coefficient was 0.55 and the particle-particle rolling friction coefficient was 0.0258. The relative error of the DEM test and physical test of the two varieties of white rice is less than 3%. The similarity of pile shape of HWR and DWR in simulation and physical test is high, which indicates that the DEM parameters are reliable. This calibration method can be used for discrete element calibration of related grains. It provides reference for the subsequent study on the adaptability of different varieties of machinery.

ACKNOWLEDGMENTS

The authors express their acknowledgment to the National Natural Science Foundation of China (Grant No. 32001423) and Natural Science Foundation of Hubei Province (Grant No. 2020CFB471) for financial support and all of the persons who assisted in this writing.

REFERENCES

[1] Ahmed, S.B., Ali, S.F., Khan, A.Z. (2021). On the frontiers of rice grain analysis, classification and quality grading: A review. *IEEE Access*, 9, 160779-160796. https://doi.org/10.1109/access.2021.3130472

[2] Gong, X., Bai, X., Huang, H., Zhang, F., Gong, Y., Wei, D. (2021). DEM parameters calibration of mixed biomass sawdust model with multi-response indicators. *INMATEH-Agricultural Engineering*, 65(3), 183-192. https://doi.org/10.35633/inmateh-65-19

[3] Han, Y., Jia, F., Tang, Y., Liu, Y., Zhang, Q. (2014). Influence of granular coefficient of rolling friction on accumulation characteristics (颗粒滚动摩擦系数对堆积特性的影响). *Acta Physica Sinica,* 63(17), 173-179. https://doi.org/10.7498/aps.63.174501

[4] Han, Y., Jia, F., Zeng, Y., Jiang, L., Zhang, Y., Cao, B. (2016). Effects of rotation speed and outlet opening on particle flow in a vertical rice mill. *Powder Technology*, 297, 153-164. https://doi.org/10.1016/j.powtec.2016.04.022

[5] Li, H., Zeng, R., Niu, Z., Zhang, J. (2022). A calibration method for contact parameters of maize kernels based on the discrete element method. *Agriculture*, 12(5), 664. https://doi.org/10.3390/agriculture12050664

[6] Liu, F., Li, D., Zhang, T., Lin, Z., Zhao, M. (2020). Analysis and calibration of quinoa grain parameters used in a discrete element method based on the repose angle of the particle heap. *INMATEH-Agricultural Engineering*, 61(2), 77-86. https://doi.org/10.35633/inmateh-61-09

[7] Liu, W., He, J., Li, H., Li, X., Zheng, K., Wei, Z. (2018). Calibration of Simulation Parameters for Potato Minituber Based on EDEM (基于离散元的微型马铃薯仿真参数标定). *Transactions of the Chinese Society for Agricultural Machinery,* 49(5), 12. https://doi.org/10.6041/j.issn.1000-1298.2018.05.014

[8] Lu, L., Fang, C., Hu, Z., Hu, X., Zhu, Z. (2019). Grade classification model tandem BpNN method with multi-metal sensor for rice eating quality evaluation. *Sensors and Actuators B: Chemical*, 281, 22-27. https://doi.org/10.1016/j.snb.2018.10.062

[9] Ma, Z., Traore, S. N., Zhu, Y., Li, Y., Xu, L., Lu, E., Li, Y. (2022). DEM simulations and experiments investigating of grain tank discharge of a rice combine harvester. *Computers and Electronics in Agriculture*, 198, 107060. https://doi.org/10.1016/j.compag.2022.107060

[10] Markauskas, D., Kačianauskas, R. (2011). Investigation of rice grain flow by multi-sphere particle model with rolling resistance. *Granular Matter*, 13, 143-148. https://doi.org/10.1007/s10035-010-0196-5

[11] Qiao, X., Jia, H., Wang, C., Wang, K., Yan, B., Guo, W. (2020). Design and experiment of ozone sterilizer device for organic matrix (有机基质臭氧消毒设备设计与试验). *Transactions of the Chinese Society for Agricultural Machinery*, 51(07), 138-145. https://doi.org/10.6041/j.issn.1000-1298.2020.07.016

[12] Riaz, M., Ismail, T., Akhtar, S. (2017). Harvesting, threshing, processing, and products of rice. *Rice Production Worldwide*, 419-453. https://doi.org/10.1007/978-3-319-47516-5_16

[13] Shitanda, D., Nishiyama, Y., Koide, S. (2002). Compressive strength properties of rough rice considering variation of contact area. *Journal of Food Engineering*, 53(1), 53-58. https://doi.org/10.1016/s0260-8774(01)00139-x

[14] Zeng, Y., Jia, F., Zhang, Y., Meng, X., Han, Y., Wang, H. (2017). DEM study to determine the relationship between particle velocity fluctuations and contact force disappearance. *Powder Technology*, 313, 112-121. https://doi.org/10.1016/j.powtec.2017.03.022

[15] Zeng, Z., Ma, X., Cao, X., Li, Z., Wang, Xi. (2021). Critical Review of Applications of Discrete Element Method in Agricultural Engineering (离散元法在农业工程研究中的应用现状和展望). *Transactions of the Chinese Society for Agricultural Machine*ry, 52(4), 1-20. https://doi.org/10.6041/j.issn.1000-1298.2021.04.001

[16] Zhao, H., Huang, Y., Liu, Z., Liu, W., Zheng, Z. (2021). Applications of discrete element method in the research of agricultural machinery: A review. *Agriculture*, 11(5), 425. https://doi.org/10.3390/agriculture11050425

[17] Zhao, L., Duan, X., Liu, H. (2023). Novel Grade Classification Tool with Lipidomics for Indica Rice Eating Quality Evaluation. *Foods*, 12(5), 944. https://doi.org/10.3390/foods12050944

DESIGN AND TEST OF INTELLIGENT YIELD MONITORING SYSTEM FOR PLOT COMBINE HARVESTER
/
小区联合收割机智能测产系统的设计与试验

Xiaoxiang ZHANG[1], Yingmei WANG, Renjie CHANG, Luxi ZHAO, Xin LI, Yinxing YAN, Wendong NIU, Shixing MA, Haiyan SONG*

College of Agricultural Engineering, Shanxi Agricultural University, Taigu / China

Tel: +86-0354-6288400 Email: haiyansong2003@163.com

DOI: https://doi.org/10.35633/inmateh-71-19

Keywords: *LabVIEW, plot breeding, single-chip microcomputer, yield monitoring system*

ABSTRACT

Traditional yield monitoring in breeding plots is manually conducted, which is labour-intensive and inefficient. To address this issue, a harvester-borne yield monitoring system that collects yield information during the harvesting in plots was designed. The system consists of a host computer and a slave computer. The slave computer used weight and moisture sensors to collect yield information of crops. The host computer used LabVIEW software to design a data management platform that displays and saves yield information and draws yield distribution maps for data visualization. The host and slave computers communicate data through 4G networks. By designing anti-interference measures, the dynamic experimental results showed that the maximum relative errors between the measured weight and moisture content by the system were 1.330% and 2.800%, which met the accuracy requirements of yield testing in plot breeding. The results indicated that the structure of the system is reasonable and can provide reliable yield monitoring tools for researchers in breeding plots.

摘要

传统的小区育种产量测试通过人工抽检完成，该方法劳动强度大、工作效率低。针对此问题，本文设计了一种在小区收获过程中采集产量信息的机载测产系统，该系统分为上位机和下位机两部分。下位机使用称重传感器与水分传感器采集小区作物的产量信息；上位机使用 LabVIEW 软件设计数据管理平台，对产量信息进行显示与保存，并绘制产量分布图，实现数据可视化；上下位机通过 4G 网络进行数据通信。通过对收割机进行抗干扰设计，动态实验结果显示测产系统重量与含水率测试的最大相对误差为1.330%和2.800%，均满足育种试验产量测试的精度要求。结果表明该系统结构设计合理，可以为小区育种科研工作者提供可靠的测产工具。

INTRODUCTION

Plot breeding is an important method for selecting superior varieties in agricultural research. In breeding experiments, the fundamental method for evaluating crop varieties is to use the actual yield of the variety in the same production environment, which requires breeders to monitor the yield every year. Compared with field operations, the advantages of plot breeding are many experimental varieties, small planting areas, and the harvesting and species examination of all plot crops can be completed in a shorter period, in which the influence of irrelevant factors on the experimental results is effectively reduced. At present, most breeding units rely on manual sampling for yield measurement, and the usual method is to use electronic scales and portable moisture loggers to measure the harvested grain in each plot and record the data manually (*Shuqi et al., 2021; Shuai et al., 2021*). This method leads to high labour intensity and low efficiency, and it is very likely to cause data confusion and affect the analysis of the results of breeding experiments.

Many types of yield monitoring systems for plot breeding experiments have been devised in some developed countries. For example, H2 Classic, H2 Stationary, and H2 High-Capacity yield monitoring systems produced by HM (HarvestMaster) in USA, and W1 and W1 plus weighing systems developed by Wintersteiger in Austria.

---

[1] *Xiaoxiang Zhang, As. M.S. Stud. Eng.; Yingmei Wang, As. M.S. Stud. Eng.; Renjie Chang, As. M.S. Stud. Eng.; Luxi Zhao, As. M.S. Stud. Eng.; Xin Li, As. M.S. Stud. Eng.; Yinxing Yan, As. M.S. Stud. Eng.; Wendong Niu, As. M.S. Stud. Eng.; Shixing Ma, As. M.S. Stud. Eng.; Haiyan Song* , Prof. Ph.D. Eng.*

All of them can accurately complete the one-time measurement of moisture, weight, and volumetric weight of the plot grain by cooperating with the harvester or thresher and analyse the data directly through software (*Campbell et al., 1996; Yan et al., 2011*). However, these yield monitoring devices are very expensive and must be used with supporting data analysis software, which discourages most breeding research units without enough budgets.

Yield monitoring, a crucial step in grain harvesting, has been studied extensively and advanced rapidly in the past decades. Currently, the mainstream yield monitoring methods primarily involve impact force measurement *(Fulton et al., 2018; Risius, 2014; Vlăduț et al., 2022)*. However, this method is not suitable for measuring yields in small areas. Another method involves the use of radiation, but the radiation sensors are restricted in many countries and regions *(Chosa et al., 2006*). The final approach is the design of weighing components to measure crops in blocks *(Bayano-Tejero et al., 2023; Mailander et al., 2010; Rosa et al., 2023)*. However, this method is susceptible to external influences during the monitoring process, leading to significant errors. Therefore, it is typically necessary to enhance measurement accuracy through improvements in both hardware and software. Most of the research on plot breeding yield monitoring equipment in China is only at the experimental stage, and no commercialized equipment has been developed. Zhao Liqing et al. of Qingdao Agricultural University designed a yield monitoring system for peanut based on plot breeding, which can achieve the monitoring of yield, water content and volumetric density of peanut (*Liqing, 2018; Liqing et al., 2015*). Zhang Hongmei et al. of Henan Agricultural University developed a plot yield monitoring system, which can measure yield at the plot experiments and realize the function of data recording and printing (*Hongmei et al., 2021; Yanzhong, 2019*). The above developed devices are only suitable for static measurements and are not suitable for using on plot harvesters, and do not enable simultaneous data collection.

To address the above problems, a yield monitoring system was designed for breeding experiments in plots. The system consists of a host computer data management platform and a slave computer data acquisition system. The slave computer collected yield information through sensors and transmitted the data to the host computer. A yield distribution map using this collected data was produced by the host computer. The system is relatively inexpensive and can significantly improve the efficiency of breeders in measuring crop yields, making it suitable for promotion during field harvest operations.

MATERIALS AND METHODS

Design of yield monitoring system for plot breeding

To avoid interference between different varieties during experimentation and facilitate field management, interval tracks is set up in the breeding area (as shown in Figure 1). The combine harvester will stop for about 10-20 seconds in the interval tracks to perform seed cleaning work to ensure that all crops harvested in the previous plot are loaded into the grain tank to prevent mixing. When the harvester stops at the edge of the interval track, the engine is in idle state. At this time, the yield date is collected and saved by the yield monitoring system. After the crop yield monitoring system finishes its work, workers will bag the harvested crops.

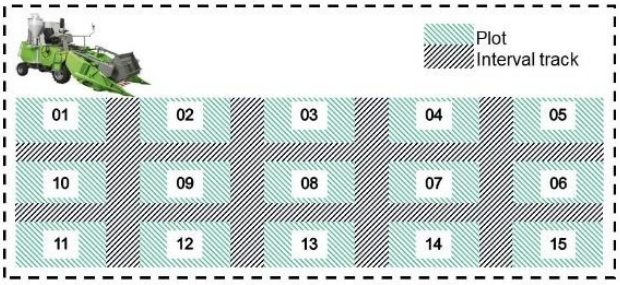


Fig. 1 - Plot operation

The intelligent yield monitoring system was designed according to the planting characteristics and harvest requirements of the breeding area. The system consists of two parts: the slave computer and the host computer (as shown in Figure 2). The slave computer was installed on the combine harvester and collected the production information of harvested crops; 4G-DTU transmission module was used to send production data to the host computer; the host computer was a computer installed with LabVIEW software which was used to design the data management platform to display and store production data, so that the date can be analysed more conveniently by researchers.

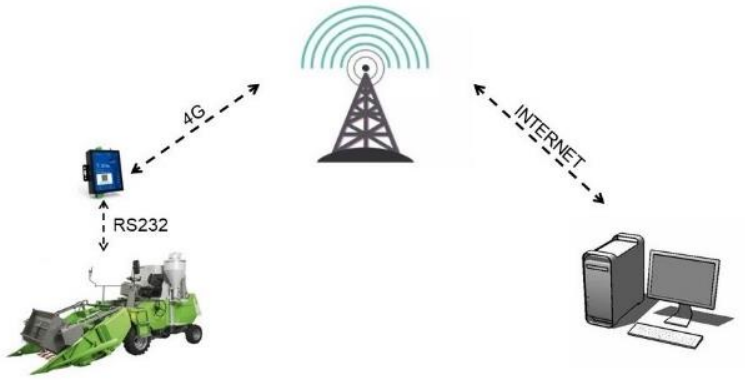


Fig. 2 - Overall flow chart for the yield monitoring system

Design of the slave computer

The slave computer was installed on the plot combine harvester and mainly used to collect yield information on crops in the plot. A main control module, weighing module, moisture content measurement module, data transmission module, and power supply module are included in the slave computer, whose composition diagram is shown in figure 3.

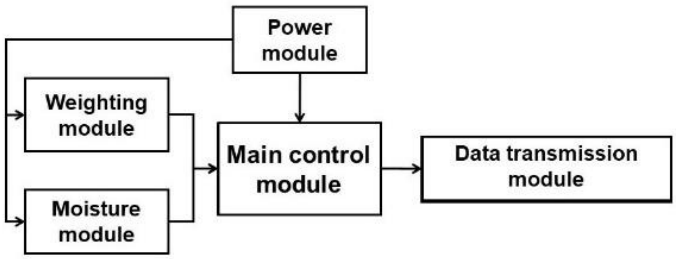


Fig. 3 - The slave computer composition system diagram

Main control module

The data collection and processing of various sensors was completed by the main control module, then the date was sent to the host computer through the data transmission module. The main control module of the yield monitoring system was designed using the STM32F103ZET6 chip produced by STMicroelectronics. This chip featured an ARM Cortex-M3 core (*Shuying et al., 2010*), which provided high data processing capability and running speed while consuming low power, making it suitable for the requirements of the yield monitoring system. The main performance parameters of the chip are shown in Table 1.

Table 1

Performance Parameters of Microcontroller

Project	Parameter
Controller size	100 × 100mm
Scale of printed circuit board	double-deck
Central processing unit	STM32F103ZET6
Maximum calculation speed	168 MHz
Memory size	64 KB
Disc size	1 megabyte
Input voltage	DC 9-28 V
Communication mode	RS-232，RS-485
Serial port	5
Working stability range	–40°C ~85°C

Yield monitoring module

Collecting information of plot crop yield is the most important part of the yield monitoring system, which includes the weight and moisture content of crops. To measure yield information in the plot experimental field, dynamic weighing method was chosen to obtain grain weight for the individual plot size (*Chung et al., 2016*), low yield, and the harvesting process cannot be continuous. In the method, weighing sensors were used to weigh grain tanks or grain conveying components in motion. A yield monitoring platform designed is shown in Figure 4. The grain was poured into the grain tank by the plot combine harvester through the feeding inlet, then the weight sensor and moisture sensor started measuring the weight and moisture content of the grain. When the measurement was completed, the grain was taken out through the collection box, and then the harvester would begin to work on the next plot.

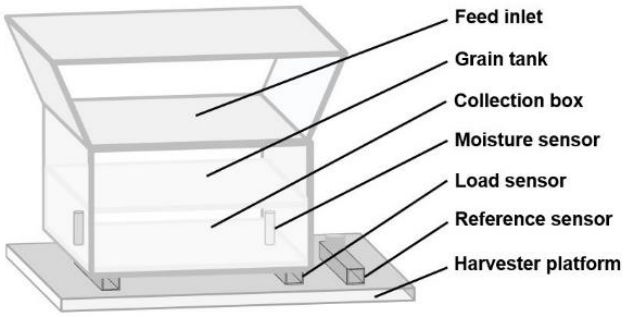


Fig. 4 - Weighing platform schematic

A strain gauge parallel beam weighing sensor (with a type of LC3151, range of 0~15kg and accuracy of 0.03%) was selected and installed at the bottom of the grain box. This sensor outputted weak differential voltage signals, amplified them and outputted voltage signals with an A\D conversion circuit. The main control module converted the voltage signal into the weight of the plot crops using a formula. The equivalent circuit of the weight sensor is shown in figure 5.

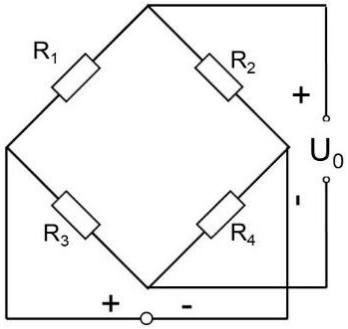


Fig. 5 - Equivalent circuit diagram for weighing sensor

The output voltage was calculated from the equivalent circuit diagram:

$$U_0 = \frac{R_1R_3 - R_2R_4}{(R_1 + R_2)(R_3 + R_4)}U \quad [v] \tag{1}$$

where R_1, R_2, R_3, R_4 is the resistance values of strain gauges, U_i is the DC power supply, U_O is the output voltage.

When the sensor was subjected to external pressure, the strain gauge underwent deformation, causing a change in resistance. The change in resistance for R_1 and R_3 due to tensile stress is ΔR_1 and ΔR_3. The change in resistance for R_2 and R_4 due to compressive stress is ΔR_2 and ΔR_4. The physical and electrical properties of the four strain gauges are identical, so $\Delta R_1=\Delta R_2=\Delta R_3=\Delta R_4=\Delta R$.

The output voltage of the sensor is:

$$U_0 = U_i \frac{\Delta R}{R} \quad [v] \tag{2}$$

where R is the resistance value of the four equivalent strain gauges, ΔR is the change in resistance value for all four strain gauges.

The output voltage of the formula (2) was converted into the weight of the measured grain after passing through the signal conditioning circuit (as shown in Figure 6). By utilizing SGM8424 and HX711 chips, a signal conditioning circuit for weighing sensors was designed. The SGM8424 chip's anti-aliasing circuit achieved hardware filtering, while the HX711 chip's amplification and A/D conversion circuits achieved high-precision signal conversion. Analog and digital wiring were separated and optocouplers were used for isolation to effectively avoid mutual interference caused by common impedance of ground wires between components. The sensor signal line was shielded and twisted together to reduce the influence of external electromagnetic fields on the circuit and effectively prevented the circuit from radiating electromagnetic energy outward.

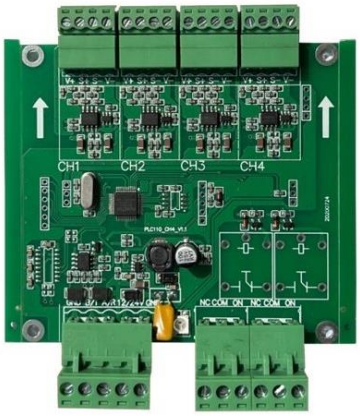


Fig. 6 - Signal conditioning

To improve the data acquisition accuracy and anti-interference ability of the yield monitoring system, a weight compensation device was designed, and software filtering algorithm was developed. An identical reference sensor was installed next to the weighing sensor, and a certain amount of iron block was fixed on the reference sensor as a counterweight. The reference sensor was only affected by the vibration of the harvester. The reference sensor and the weighing sensor were fixed in the same position, so the variation pattern of the vibration frequency and amplitude they received was synchronous. By using hardware differential circuit and microcontroller to process the weighing signal based on the reference signal, the interference of vibration can be reduced to some extent. The hardware circuit structure of a weighing sensor is shown in figure 7.

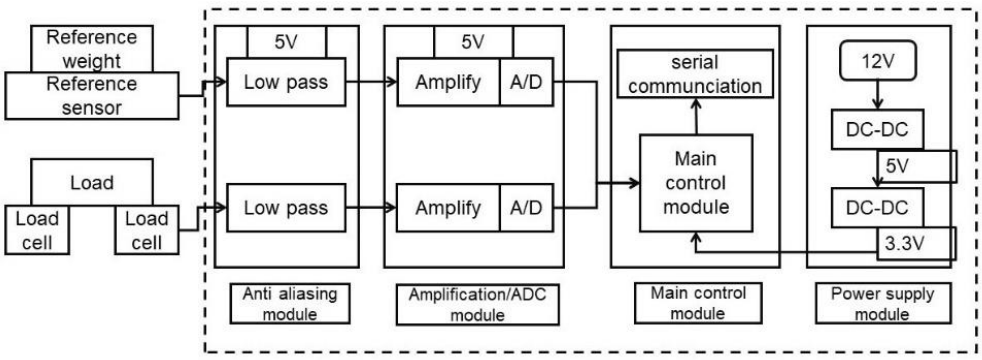


Fig. 7 - Hardware schematic for weighing module

Software filtering algorithms can also improve the anti-interference ability of measuring and producing systems. The voltage signal sampling values of weight sensor outputted, taken as a time sequence, were processed using a software algorithm that combined clipping filtering and recursive averaging filtering (*Qian et al., 2021; Pietrzak et al., 2014; Richiedei et al., 2018*), and errors caused by chance factors can be overcome, and periodic interference can be suppressed, significantly improving the repeatability and accuracy of the system's data acquisition.

The mathematical expression of the limit filtering algorithm is formula (3); and the mathematical expression of the recursive averaging filtering algorithm is formula (4).

$$Y_i = X_i \quad |X_i - x_{i-1}| \le A$$
$$Y_i = X_{i-1} \quad |X_i - x_{i-1}| \le A \tag{3}$$

$$Z_n = \frac{1}{N}\sum_{i=1}^{N-1} Z_{n-1} \tag{4}$$

In equation (3), X_i is the current sampling value, X_{i-1} is the previous sampling value, Y_i is the actual returned value, A is the maximum allowable error value. In equation (4), Z_n is the output after filtering the n(th) sampling value, Z_{n-1} is the unfiltered n-i(th) sampling value, n is the number of recursive averaging terms, that is, the arithmetic mean of the n(th) sampling's n, n-1, ..., n-N+1 sampling values.

The moisture sensor used for yield monitoring module was HM1500lf (accuracy ±3% RH, supply voltage 3.3 V). The sensor is small, has a built-in solid polymer, and can still work in harsh environments. Two sensors were installed at the bottom of the grain tank to calculate the moisture content of the crop in each plot by averaging the voltage. When comparing the yields of different varieties in experiments, it is necessary to convert them to the weight at the same moisture content using formula (5) (*Nelson et al., 1991; Rodrigues et al., 2020*).

$$M_i = M_k \frac{1-W_a}{1-W_b} \tag{5}$$

Where, M_i is the actual weight of crop in the (i)th plot, M_k is the weight of crop measured by the yield monitoring system, W_a is the moisture content of the crop measured by the yield monitoring system, W_b is the national standard moisture content of the crop.

Date transfer module

After the slave computer collected the information on the yield of the plots, it is necessary to transmit this data to the host computer. Due to the complexity of the field environment and problems such as long distances and difficult wiring in data transmission, wireless data communication was chosen for data transmission. 4G DTU (Data Terminal Unit) is a highly integrated data transmission unit that can conveniently convert serial port output data into IP information and send it to the server (*Su et al., 2021*). This method had fast transmission speed, long distance, stable communication during transmission, and low data loss.

The 4G DTU used the USR-781 designed by Jinan Youren Technology Co., Ltd. In the actual working process, the microcontroller converted the yield and location information into serial port data, which was sent through the RS232 circuit to the DTU module that communicated with the remote terminal. The received information was converted into IP information by DTU and sent through the base station. Finally, the server received the raw data, parsed it into yield information recognizable by the computer, saved it to the database for further processing, and the entire process achieved wireless data transmission. When transmitting data between the 4G DTU and the server, it is necessary to write a communication protocol. The collected data was packaged by the microcontroller and analysed by the remote terminal according to the communication protocol, which can ensure the smooth communication of the yield monitoring system. The communication protocol format is shown in Table 2.

Table 2

Coding Method

Data domain	Bytes
Header	1
Length	2
Mode	1
Identifying	2
Data	N（variable）
Checksum	1
End of frame	1

The communication protocol specified that each data frame consisted of seven parts: frame header, length, mode, identification, data, checksum, and frame footer. The frame header and footer were used to identify a data frame; length indicated the length of all data information from the frame header to the frame

footer. There were two modes, one was 0x01, indicating that the host computer sent instructions to the slave computer, including communication request, positioning request, and information acquisition, the other was 0x02, indicating that the slave computer sent data to the host computer, including weight and moisture content. The identification is used to identify data types. There were 0x8001, 0x8002 and 0x8003 to represent grain quality, grain moisture content, and instructions respectively. The checksum was the XOR checksum of a frame of data, used to verify if the received data was correct.

Power supply module

The slave computer module of the yield monitoring system needed to be powered when working in the field, using the self-contained battery of the harvester. The supply voltage of the STM32 main controller in the system was 3.3 V, and the supply voltage of the weight sensor and moisture sensor was 5 V. The voltage of the battery power supply was 12 V. Therefore, LM2596 chip and LM1117 chip were used to design a power-down circuit to reduce the 12 V voltage of the battery to a stable 5 V and 3.3 V for the main control module and various sensors. The designed power module is shown in figure 8.

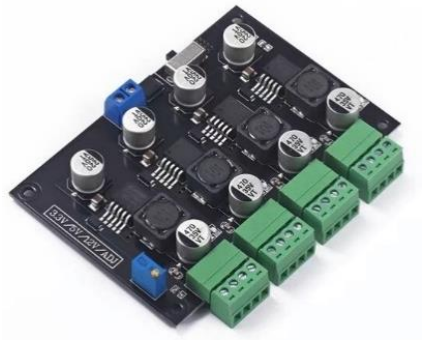


Fig. 8 - Power module

Host computer design

Based on the Windows 10 operating system, the host computer data management platform was designed using LabVIEW software. LabVIEW is a virtual instrument design software that uses graphical programming. It supports TCP data transmission and graphic drawing, and has obvious advantages in intelligent programming, processing capability, and cost-effectiveness *(Castillo-Ruiz et al., 2015; Purti et al., 2021; Voicea et al., 2011; Vlăduț et al., 2023)*. Using the built-in TCP serial port in LabVIEW can establish data communication with 4G DTU. The data sent by the slave computer was parsed according to the protocol and saved in the database created by Access, and then data management was performed by calling the database. The functions that the host computer needed to achieve include data display, storage, and drawing of yield information charts to help plot researchers further analyse data.

The designed data management platform is shown in the figure 9, including three interfaces for data acquisition, yield chart drawing, and data saving and querying. The data acquisition interface implemented functions such as network connection and data calibration. In the drawing interface, when comparing the yield of various plot crops, it is necessary to convert to weights at the same moisture content. In the data storage interface, the received data was parsed by protocol and stored in an established Access database in chronological order. The data display and table generation were achieved by writing a program which called the contents of the database, and can be queried historically.

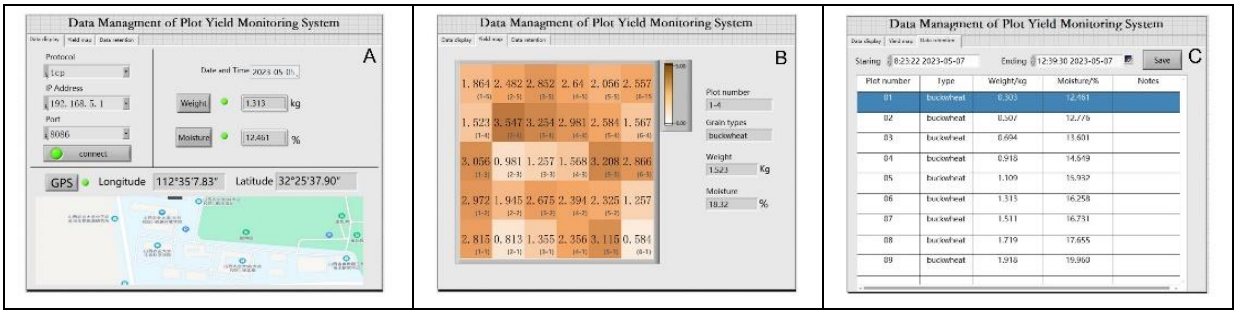


Fig. 9 – The yield monitoring system date management platform

a) Data acquisition interface; b) Yield chart drawing interface; c) Data storage and query

RESULTS AND DISCUSSION

Test of intelligent yield monitoring system

In order to verify the accuracy and stability of the intelligent yield monitoring system, the performance of the system for buckwheat was tested using a 4LZX-1.5 type plot combine harvester in the laboratory (as shown in figure 10).



Fig. 10 – Components diagram of the yield monitoring system

Before the test, the weighing sensor and moisture sensor were first calibrated. A standard weight was used to calibrate the weighing sensor and reference sensor respectively. After the calibration, ten samples of buckwheat (weight limit within 0-10 kg) using an electronic balance (range 0~20 kg, precision 0.01 g) were randomly taken, then they were put into the weighing tank in batches and the output voltage of the weighing sensor was recorded. The measurement was repeated three times, and the average value was taken each time. The experimental result is shown in figure 11, which indicated that there was a strong linear relationship between the output voltage of the weighing sensor and the weight of the buckwheat sample between 0-10 kg, and the y-axis intercept was 0.332 V, which was due to the weight of the sensor box, indicating that the output voltage of the sensor under no load was 0.332 V. Due to the influence of the volume of the tank and the range of the sensor, the maximum weight that could be measured each time didn't exceed 15 kg when the system was running. In actual field work, the yield of each small area will not exceed this value.

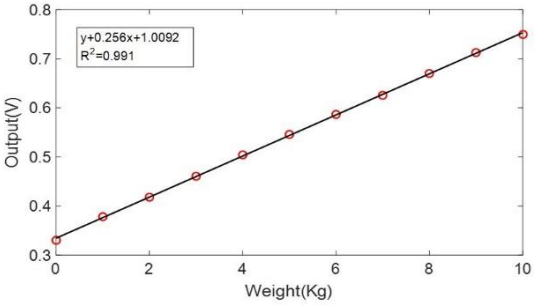


Fig. 11 – Weight calibration experimental results

The calibration of the moisture sensor was conducted in the laboratory. An electronic analytical balance (with an accuracy of 0.01g) was used to weigh a certain mass of buckwheat samples and they were placed in a sealed bag. Moisture content measurement samples were prepared ranging from 5% to 35% by adding distilled water. First, the moisture contents of the samples were measured by the drying method and taken as the actual values. Then, at different temperatures, the HM1500lf moisture sensor was inserted into the sealed bag for measurement. Five gradient temperatures were chosen: 14°C, 18°C, 22°C, 26°C, and 30°C for the measurements, repeated each experiment three times, and the average value was taken. The experimental result is shown in the table 3.

Table 3

Output voltage values of moisture sensors under different factors

Moisture contents /%	Temperatures /℃				
	14	18	22	26	30
6.01	0.937	0.950	1.011	1.135	1.209
10.93	1.424	1.474	1.554	1.678	1.750
15.14	1.699	1.756	1.845	2.041	2.101
21.28	2.180	2.341	2.392	2.464	2.526
27.83	2.589	2.701	2.747	2.777	2.882

The results showed that the output voltage of the moisture sensor had a clear pattern with the changes in moisture content and temperature. By performing regression analysis on the data, the optimal mathematical model is obtained as follows:

$$Y = 8.991 - 24.5002X_U{}^2 - 0.1666X_T{}^2 + 2.5004X_U + 0.5793X_T + 4.5071X_U X_T \quad (6)$$

where: Y is the moisture content of buckwheat samples, X_U is the voltage value of the humidity sensor, X_T is the sample temperature.

The mathematical model obtained through calculations was written in the C language and incorporated into the software equation of the system, and then the model was validated. 10 buckwheat samples with moisture content ranging from 5% to 35% were randomly prepared and the yield monitoring system was used to obtain measurement values, the results were finally compared with the actual values by drying method. The results are shown in figure 12.

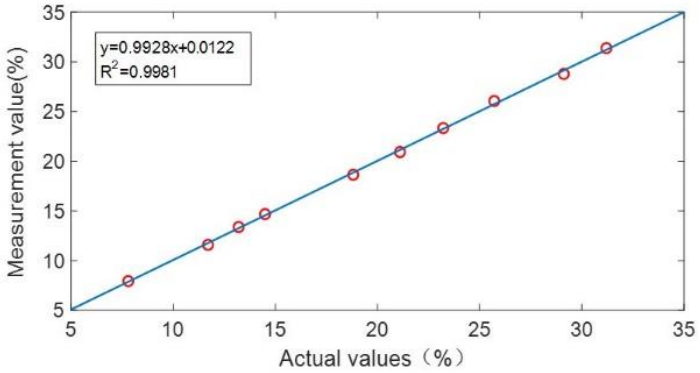


Fig. 12 – Model validation results

The calibrated results were written into the software program of the monitoring system, and the designed weighing platform was installed on a 4LZX-1.5 combine harvester. A data connection was established with the host computer to simulate field working conditions, where the engine of the harvester was idling (810 r/min). Different weight and moisture content buckwheat seeds were put into a weighing box, and the data collected by the intelligent yield monitoring system was recorded and analysed. The observation was made to see if the host computer could display the data and draw the yield diagram.

RESULTS

During operation, the yield monitoring system was affected by vibrations from the combine harvester. A test was conducted by pouring 2.5 kg of buckwheat seeds into a weighing tank and comparing the unprocessed data with compensated and filtered data. The table 4 showed that after compensation and software filtering, the maximum error decreased from 5.140% to 1.330%, and the average error decreased from 0.624% to 0.146%. This indicated that the designed compensation device and filtering algorithm effectively reduced data errors.

Table 4

The weight experiment result before processing and after compensation and filtering

Number	Without compensation device and filtering		After compensation device and filtering	
	Measurement value / kg	Relative error / %	Measurement value / kg	Relative error / %
1	2.606	4.256	2.526	1.050
2	2.372	-5.140	2.467	-1.330
3	2.581	3.230	2.522	0.875
4	2.597	3.882	2.526	1.037
5	2.446	-2.144	2.484	-0.625
6	2.526	1.040	2.512	0.465
7	2.479	-0.821	2.490	-0.415
8	2.622	4.885	2.528	1.118
9	2.406	-3.766	2.477	-0.925
10	2.521	0.822	2.505	0.214
Mean	2.516	0.624	2.504	0.146
Standard deviation	0.088	3.515	0.023	0.909
Range	0.251	10.025	0.061	2.448

During the moisture content testing experiment, ten samples with different moisture contents were prepared and poured into a grain tank in sequence. The moisture content test results from the computer were recorded and compared with the results obtained using the drying method. The results in table 5 showed that the maximum relative error between the actual and measured values in the moisture content test was 2.800%, the minimum relative error was 0.552%, and the average error was within the allowable range, meeting the requirements for monitoring crop yield.

Table 5

The Moisture content testing results

Sample number	Actual value/%	Measurement value/%	Relative error /%
1	12.230	12.461	1.889
2	12.570	12.418	-1.209
3	13.480	13.201	-2.070
4	14.250	14.649	2.800
5	15.620	15.332	-1.844
6	15.950	16.258	1.931
7	16.560	16.331	-1.383
8	17.080	17.550	2.752
9	17.570	17.407	-0.928
10	19.560	19.452	-0.552
Mean	15.487	15.506	0.139
Standard deviation	2.346	2.345	1.864
Range	7.330	7.03	4.870

Analysis of error sources in performance experiments may include the following aspects: inability to completely eliminate vibrations during weight measurement, failure to consider road excitation, and failure to consider changes in temperature and differences in particle gaps after grains fall into the grain tank during moisture content testing. To address these issues, corresponding measures had been taken to reduce their impact. Reducing the impact on harvesting machine vibrations and road excitation, algorithms with better filtering effects were developed and some limit devices were installed at the physical level. To address the error caused by the temperature difference and the grain gaps, a temperature measurement device was

designed, and temperature factors were incorporated into the process of measuring grain moisture content. To address the issue of uneven gaps between particles, the method of taking multiple measurements was employed and they were averaged.

Compared with other commercial monitoring systems (as shown in table 6), it was found that the designed system has a certain gap in date acquisition accuracy. The cost of our design is lower and the performance can basically meet the needs of plant breeding research, which has a high cost-performance ratio. Therefore, further research will be conducted to improve the collection accuracy based on the experimental results analysis, making it a potential alternative for commercial small-scale production measurement equipment.

Table 6

Performance index of yield monitoring system

Technical date	Wintersteiger W1	HM H2 Classic	INTELLIGENT YIELD MONITORING SYSTEM
Test Weight	±0.1 lbs (± 45g)	+/- 0.8 lb/bu (+/- 1 kg/hl)	0.909%(0 ~ 20kg)
Moisture	Accurate to ±1 %	+/- 0.5% for 0% to 27% moisture; +/-1.0% for 27% to 40% moisture	1.846% (for 10% to 30% moisture)

CONCLUSIONS

In this paper, a plot breeding yield monitoring system was described, which consists of a host computer and a slaver computer, achieving yield monitoring and wireless data transmission. It is proposed to improve the accuracy of data acquisition by combining a weighing compensation device with a software filtering algorithm to solve the problem of large measurement error of the yield monitoring system under dynamic conditions. The performance test results of the system showed that the maximum error between the measured value and the actual value in the weight test was 1.330%, and the standard deviation error was 0.909%. The maximum error between the measured value and the actual value in the moisture content test was 2.800%, and the standard deviation error was 1.864%. The host and slave computers can establish a stable data connection, resulting in high system stability which meets the requirements of yield monitoring in plot breeding experiments.

The system achieved synchronous yield monitoring during plot breeding experiments, improved efficiency, avoided data confusion, and was low-cost with good performance, providing breeders with cost-effective monitoring tools. Next, further research will be made to improve data collection accuracy.

ACKNOWLEDGEMENTS

This study was supported by the National Key R&D Program of China (2021YFD1600602-09), the Key R&D Program of Shanxi Province (2023CYJSTX07-22).

We extent our thanks to Haiyan Song, Yingmei Wang, Renjie Chang and their colleagues for their reading and helpful comments on this manuscript.

REFERENCES

[1] Bayano-Tejero, S., Márquez-García, F., Sarri, D., & Sola-Guirado, R. R. (2023). Olive yield monitor for small farms based on an instrumented trailer to collect big bags from the ground. *Precision Agriculture*.

[2] Campbell, R., Campbell, G., Christensen, C. (1996). *Grain weighing and measuring system*. US05487702A.

[3] Castillo-Ruiz, F.J., Pérez-Ruiz, M., Blanco-Roldán, G.L., Gil-Ribes, J.A., & Agüera, J. (2015). Development of a Telemetry and Yield-Mapping System of Olive Harvester. *Sensors* (Basel, Switzerland), 15, 4001 - 4018.

[4] Chosa, T., Shibata, Y., Kobayashi, K., Daikoku, M., Omine, M., Toriyama, K., Araki, K., & Hosokawa, H. (2006). Yield Monitoring System for a Head-Feeding Combine. *Japan Agricultural Research Quarterly*, 40(1), 37-43.

[5] Chung, S. O., Choi, M. C., Lee, K. H., Kim, Y. J., & Li, M. (2016). Sensing technologies for grain crop yield monitoring systems: a review. *Journal of Biosystems Engineering*, 41(4), 408-417.

[6] Fulton, J., Hawkins, E., Taylor, R., & Franzen, A. (2018). *Yield monitoring and mapping. In Precision Agriculture Basics*, 63–77.

[7] Hongmei Z., Yanzhong X., Kang L., Wanru L., Zheng Z., & Wanzhang W. (2021). Structure Design and Test of Corn Plot Yield Measurement System. *Journal of Agricultural Mechanization Research* (02),45-51. (in Chinese with English abstract)

[8] Liqing Z. (2018). *Research on Intelligent Integrated Test System of Moisture and Output in Peanut Experimental Plot* (Doctoral dispersion, Shenyang Agricultural University).

[9] Liqing Z., Ruichuan L., Linong G., Lianxing G., Sen G., & Yuanyuan Y. (2015). Study on Intelligent Yield Monitoring System of Peanut Combine Harvester. *Transactions of the Chinese Society for Agricultural Machinery* (11),82-87. (in Chinese with English abstract)

[10] Mailander, M., Benjamin, C., Price, R., & Hall, S. (2011). Sugar Cane Yield Monitoring System. *Applied Engineering in Agriculture*, 26(6), 965–969.

[11] Nelson, & S., O. (1991). Dielectric properties of agricultural products-measurements and applications. Electrical Insulation IEEE Transactions on Electrical Insulation.

[12] Pietrzak, P., Meller, M., & Niedzwiecki, M. (2014). Dynamic mass measurement in checkweighers using a discrete time-variant low-pass filter. *Mechanical systems and signal processing*, 48(1-2), 67-76.

[13] Purti, R. E., Yahya, A., Ju, O. Y., Isa, M. M., & Aziz, S. A. (2021). Portable wireless yield monitoring system on conventional rice combine. *Applied Engineering in Agriculture*, 37(1), 193-203.

[14] Qian, P., Lu, T., Shen, C., & Chen, S. (2021). Influence of vibration on the grain flow sensor during the harvest and the difference elimination method. *International Journal of Agriculture and Bioengineering* (005), 014. (in Chinese with English abstract)

[15] Richiedei, D., & Trevisani, A. (2018). Shaper-based filters for the compensation of the load cell response in dynamic mass measurement. *Mechanical Systems & Signal Processing*, 98(jan.1), 281-291.

[16] Risius, N. W. (2014). *Analysis of a combine grain yield monitoring system*. Diss. Iowa State University.

[17] Rodrigues, T. C., Carneiro, F. M., Brunini, R. G., Menezes, P., Bertonha, R. S., & Furlani, C. (2020). *Quality of reading among equipment for determining water content in corn kernels*. Universidade Estadual de Londrina (5).

[18] Rosa, U. A., Rosenstock, T. S., Choi, H., Pursell, D., Gliever, C. J., Brown, P. H., & Upadhyaya, S. K. (2011). Design and Evaluation of a Yield Monitoring System for Pistachios. *Transactions of the ASABE*, 54(5), 1555–1567.

[19] Shuai W., Zhihong Y., Wenjie Z., Lifang Y., Zexin Z., & Gele A. (2021). Review of Recent Advances in Online Yield Monitoring for Grain Combine Harvester. *Transactions of the Chinese Society of Agricultural Engineering* (17), 58-70. (in Chinese with English abstract)

[20] Shuqi S., Xiufeng W., Ranbing Y., Guoying L., Xiaolong Y., & Dongquan C. (2021). Research Status and Prospect of Plot-sowing Equipment and Technology. *Transactions of the Chinese Society for Agricultural Machinery* (02), 1-20. (in Chinese with English abstract)

[21] Shuying S., Zhijia C., & Chao K. (2010). The developing and application of the new generation of embedded MPU-STM32F103. *Next New Media Technology* (12), 59-63.

[22] Su, D., Qiu, T., Yin, Q., & Li, G. (2021). Research on Remote Monitoring and Early Warning System of New Energy Station Based on Multi-source Information Fusion. 2021 *6th Asia Conference on Power and Electrical Engineering (ACPEE)*. (in Chinese with English abstract)

[23] Vlăduț, N. V., Biriş, S. Ş., Cârdei, P., Găgeanu, I., Cujbescu, D., Ungureanu, N., Popa, L. D., Perişoară, L., Matei, G., & Teliban, G. C. (2022). *Contributions to the Mathematical Modeling of the Threshing and Separation Process in An Axial Flow Combine*. Agriculture (Switzerland), 12(10).

[24] Vlăduț, N. V., Ungureanu, N., Biriş, S. Ş., Voicea, I., Nenciu, F., Găgeanu, I., Cujbescu, D., Popa, L. D., Boruz, S., Matei, G., Ekielski, A., & Teliban, G. C. (2023). Research on the Identification of Some Optimal Threshing and Separation Regimes in the Axial Flow Apparatus. *Agriculture* (Switzerland), 13(4).

[25] Voicea, I., Pirnă, I., Vlăduț, V.N., Matache, M.G., & Bungescu, S. (2011). Experimental models of agricultural productivity maps obtained with the help of an information and satellite measurement system adaptable for different types of combines. *Proceedings of the 39 International Symposium on Agricultural Engineering "Actual Tasks on Agricultural Engineering*", 333-342.

[26] Yan L., Yingxiu W., Wenxin C., Qiqi Z., & Pingzhi Z. (2011). Development of Wintersteiger plot combine harvester and its application in wheat breeding. *Journal of Ningxia Agriculture and Forestry Science and Technology* (08), 15+18. (in Chinese with English abstract)

[27] Yanzhong X. (2019). *Design and experimental study of yield measurement system for maize plot breeding* (Master's dissertation, Henan Agricultural University). (in Chinese with English abstract)

RESEARCH ON DYNAMIC CHARACTERISTICS OF A DOUBLE-PENDULUM SUSPENSION FOR A BOOM SPRAYER
/
喷杆喷雾机双摆悬架动力学特性研究

Fang LI[1)], Xiaohu BAI*[2)]
[1)] School of Information and Control Engineering, Liaoning Petrochemical University, Fushun/China;
[2)] College of Engineering, Shenyang Agricultural University, Shenyang/China
E-mail: baixiaohu@syau.edu.cn
DOI: https://doi.org/10.35633/inmateh-71-20

Keywords: *dynamic model, passive suspension, active suspension, transient response, frequency response*

ABSTRACT
During the operation of a boom sprayer, various excitations can cause the boom to roll, yaw, or jolt, which can negatively impact the spray effect. In order to maintain the stability of the boom, it is crucial to incorporate a suspension between the vehicle body and the boom. This study established a dynamic model that describes the roll of a boom mounted on a double-pendulum suspension. The transfer function and frequency response function of the passive suspension were obtained, with the ground slope angle as input and the boom inclination angle as output. The analysis results showed that the passive suspension can partially isolate high-frequency disturbances but cannot follow low-frequency signals. For the active suspension, the transient and frequency responses were analyzed by numerical integration algorithm, the harmonic balance method and numerical solution. The results indicated that the active suspension can enable the boom to follow the ground slope, track low-frequency signals to a certain extent, and isolate high-frequency signals. The proposed mathematical model can be utilized to analyze the dynamic characteristics and provide guidance for the double-pendulum suspension design.

摘要
喷杆喷雾机田间作业时，各种激励会导致喷杆产生翻滚、偏转、振荡运动，对喷雾效果产生不利影响。为了保持喷杆稳定，在车体与喷杆之间安装悬架非常重要。本文建立了描述安装在双摆悬架上的喷杆翻滚运动的动力学模型。针对被动悬架，得出了以地面坡角为输入、喷杆倾角为输出的传递函数及频率响应函数，分析结果表明，被动悬架能在一定程度上隔离高频扰动，但不能跟踪低频信号。针对主动悬架，采用数值积分算法、谐波平衡法和数值解法分析了瞬态响应和频率响应。结果表明，主动悬架能使喷杆跟随地面坡角变化，可以在一定程度上跟踪低频信号，隔离高频信号。建立的数学模型可以用来分析双摆悬架的动力学特性，为喷雾机悬架设计提供参考。

INTRODUCTION

The effectiveness and efficiency of chemical spraying in agriculture is heavily influenced by the quality of plant protection equipment (*He, 2020*). Boom sprayers are commonly utilized due to their wide coverage and high productivity in applying chemical materials such as pesticides, herbicides, and fertilizers (*He, 2022; Qiu et al., 2015*). However, the motion of the boom caused by tractor vibration and uneven terrain can result in uneven distribution of the chemical agents. Rolling, yawing, and jolting are the primary types of motion that affect the boom in the vertical and horizontal planes. These motions will lead to harmful over-application or under-application of chemical agents (*Jeon et al. 2013; Langenakens et al.1999*). Although yawing and jolting have a greater impact on spray consistency, most boom sprayers are equipped with a vertical suspension to mitigate rolling (*Ramon et al., 1997; Cui et al., 2019*). Various types of vertical suspensions have been developed, including pendulum, trapezium, cable, and Douven suspensions (*Deprez et al., 2003*). Double-pendulum suspensions have gained popularity among manufacturers, with the first pendulum serving as a passive suspension and the second pendulum acting as an active suspension (*Tahmasebi et al., 2013*).

Fang Li, Lecturer, Ph.D.; Xiaohu Bai, Associate Prof., Ph.D.,Corresponding Author.

Theoretical investigations have been conducted for certain types of suspensions. O'Sullivan proposed mathematical models for both passive and active versions of a pendulum boom suspension, and simulated their transient and frequency responses (*O'Sullivan, 1986*). Experimental results confirmed the accuracy of the suspension models and demonstrated their usefulness in designing an appropriate pendulum suspension (*O'Sullivan, 1988*). Frost presented a mathematical model for an active twin-link boom suspension and its response to the rolling motion of the spray vehicle (*Frost, 1984*). Deprez et al. studied several suspension models, including a slow active pendulum suspension, a slow active trapezium suspension, a cable suspension, and a suspension based on following a curved profile, and found that they have the same mathematical model structure (*Deprez et al., 2002*). Anthonis et al. developed a parameterized mathematical model for the double pendulum suspension of the 39 m sprayer of John Deere, and optimized the distance to the rotation point of the damper and the appropriate damping value (*Anthonis et al., 2005*). Wu and Miao established a model with four spring-damper modules between the boom and the frame, and investigated the frequency response of the model under different excitation signals (*Wu et al., 2012*). Xue et al. added a hydraulic cylinder to the two-link trapezoidal spray boom passive suspension to obtain an active suspension, and simulated and analyzed its dynamic characteristics for controller design by MATLAB/SIMULINK (*Xue et al., 2018*). Cui et al. established a nonlinear dynamic model and geometric equation of the pendulum active and passive suspension system to design an adaptive robust controller (*Cui et al., 2020*). Zhuang designed a suspension with the combination of springs and dampers, and analyzed the dynamic and kinematic vibration characteristics of the boom by modal simulation and field tests (*Zhuang, 2020*). *Zhang, (2021),* designed an active and passive suspension based on the pendulum and isosceles trapezoid principle, established the dynamic model of the boom, and simulated the instantaneous response and frequency response by ADAMS vibration simulation technology. Yan et al. developed a geometric continuous model of spray boom vibration considering the influence of the boom sprayer body and boom suspension, and studied the dynamic behavior of the spray boom under step excitation (*Yan, 2021*). However, little research has been devoted to the effects of springs and dampers on the dynamic behavior of the double-pendulum suspension.

This paper presents a mathematical model for the double-pendulum suspension, which takes into account the influence of springs and dampers. The response of the boom is analyzed in both time and frequency domains for both passive and active suspensions. The aim of this study is to provide references for the design and parameter setting of the boom suspension.

MATERIALS AND METHODS

Structure and principle of the double-pendulum suspension

The double-pendulum suspension is comprised of two pendulum rods, height sensors, springs, dampers, and an actuator, as illustrated in Figure 1. The first pendulum rod is articulated to the frame and the second pendulum rod at O_1 and O_2, respectively. The boom is rigidly fixed to the second pendulum rod at G, the gravity center of the boom. A spring and a damper are connected between the first pendulum rod and the frame attached to the vehicle. An actuator is installed between the first and second pendulum rod.

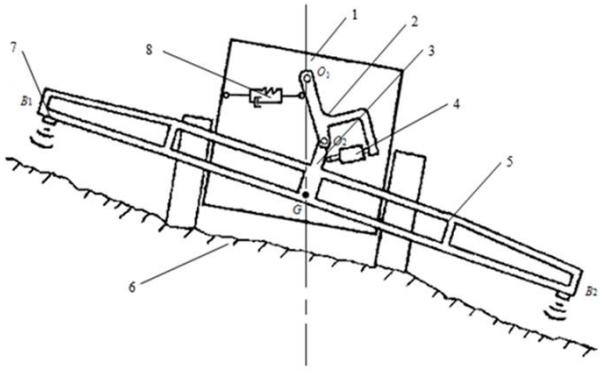


Fig. 1 - Structure of the double-pendulum suspension

1– frame; 2- first pendulum rod; 3- second pendulum rod; 4- actuator; 5- boom; 6- ground; 7- height sensor; 8- spring and damper

In the event that the power supply is deactivated and the actuator length remains constant, the suspension becomes passive, causing the boom to pivot only around O_1. A special case arises when the angle between the first and second pendulum rods is zero, indicating that the boom's balance position is horizontal, with its gravity center G below the hinge point O_1.

However, if the actuator length is either increased or decreased, the boom's gravity center will shift to the left or right, respectively, resulting in a non-horizontal equilibrium position. Consequently, by continuously regulating the actuator length, the suspension becomes active, enabling the boom to adapt to variations in ground slope.

Modelling of the Double-Pendulum Suspension

Passive Suspension

The suspension's parameters are presented in Figure 2.



Fig. 2 - Parameters of the double-pendulum suspension

The angles α, β, and γ represent the inclination of the ground to the horizontal, the inclination of the first pendulum rod to the vertical, and the inclination of the boom to the horizontal, respectively. The angle θ denotes the angle between the first and second pendulum rods. When θ remains constant at zero, the suspension becomes passive. For the generalized coordinate β, by applying the second Lagrange equation, the equation of the boom motion can be derived as:

$$\frac{d}{dt}\left(\frac{\partial E_k}{\partial \dot{\beta}}\right)-\frac{\partial E_k}{\partial \beta}=Q_\beta-\frac{\partial \psi}{\partial \dot{\beta}} \tag{1}$$

where, E_k represents the kinetic energy of the boom, N·m; Q_β represents the generalized force, N; ψ represents the dissipation function, N·m·rad/s.

The kinetic energy of the boom can be expressed as:

$$E_k=\frac{1}{2}I\dot{\beta}^2+\frac{1}{2}m\left[l_4{}^2\dot{\alpha}^2+(l_1+l_2)^2\dot{\beta}^2-2l_4(l_1+l_2)\dot{\alpha}\dot{\beta}\cos(\alpha-\beta)\right] \tag{2}$$

where, I represents the moment of inertia of the boom about the axis through G, kg·m^2; m represents the mass of the boom, kg; l_1 represents the length of the first pendulum, m; l_2 represents the length of the second pendulum, m; l_4 represents the distance between O_1 and the ground, m.

The generalized force can be expressed as:

$$Q_\beta=-mg(l_1+l_2)\sin\beta+k(\alpha-\beta)l_s{}^2 \tag{3}$$

where, k represents the stiffness coefficient of the spring, N/m; l_s represents the distance from the spring's installation position to O_1, m.

The dissipation function can be expressed as:

$$\psi=\frac{1}{2}c[l_d(\dot{\alpha}-\dot{\beta})]^2 \tag{4}$$

Where, c represents the damping coefficient of the damper, N·s/m; l_d represents the distance from the damper's installation position to O_1, m.

Assuming that α and β are small, ignoring the second-order terms, and substituting equations (2), (3) and (4) into equation (1), the equation of the boom motion can be stated in the following form.

$$\ddot{\beta}[I+m(l_1+l_2)^2]+\dot{\beta}cl_d{}^2+\beta[mg(l_1+l_2)+kl_s{}^2]=\ddot{\alpha}ml_4(l_1+l_2)+\dot{\alpha}cl_d{}^2+\alpha kl_s{}^2 \quad (5)$$

When the angle θ is equal to zero, the angle γ is equal to the angle β. Therefore, by performing the Laplace transform on equation (5) and rearranging the terms, the transfer function linking the inclination angle of the boom, γ, to the inclination angle of the ground, α, can be derived as:

$$H(s)=\frac{ml_4(l_1+l_2)s^2+cl_d{}^2s+kl_s{}^2}{[I+m(l_1+l_2)^2]s^2+cl_d{}^2s+mg(l_1+l_2)+kl_s{}^2} \quad (6)$$

Substituting $j\omega$ for s in equation (6), the frequency response function can be achieved as:

$$H(j\omega)=\frac{-ml_4(l_1+l_2)\omega^2+jcl_d{}^2\omega+kl_s{}^2}{-[I+m(l_1+l_2)^2]\omega^2+jcl_d{}^2\omega+mg(l_1+l_2)+kl_s{}^2} \quad (7)$$

Active Suspension

When the sprayer travels over undulating terrain, the actuator should be adjusted by extending or retracting it in order to maintain the boom parallel to the ground. This ensures that the suspension remains active. For the generalized coordinates β and γ, by applying the Lagrange equation of the second kind, the equations of the boom motion can be expressed as:

$$\frac{d}{dt}\left(\frac{\partial E_k}{\partial\dot{\beta}}\right)-\frac{\partial E_k}{\partial\beta}=Q_\beta-\frac{\partial\psi}{\partial\dot{\beta}} \quad (8)$$

$$\frac{d}{dt}\left(\frac{\partial E_k}{\partial\dot{\gamma}}\right)-\frac{\partial E_k}{\partial\gamma}=Q_\gamma-\frac{\partial\psi}{\partial\dot{\gamma}} \quad (9)$$

The kinetic energy of the boom can be expressed as:

$$E_k=\frac{1}{2}I\dot{\gamma}^2+\frac{1}{2}m\left[\dot{\alpha}^2l_4{}^2+\dot{\beta}^2l_1{}^2+\dot{\gamma}^2l_2{}^2-2\dot{\alpha}\dot{\beta}l_1l_4-2\dot{\alpha}\dot{\gamma}l_2l_4+2\dot{\beta}\dot{\gamma}l_1l_2\right] \quad (10)$$

The generalized force can be expressed as:

$$Q_\beta=-(mgl_1+kl_s{}^2)\beta+kl_s{}^2\alpha-Fl_3 \quad (11)$$

$$Q_\gamma=-mgl_2\gamma+Fl_3 \quad (12)$$

where, F represents the force exerted by the actuator, N; l_3 represents the distance between the installation position of the actuator and the point O_2, m.

Substituting equations (4), (10), and (11) into equation (8), and equations (4), (10), and (12) into equation (9), the equations of the boom motion can be stated in the following form.

$$-ml_1l_4\ddot{\alpha}+ml_1{}^2\ddot{\beta}+ml_1l_2\ddot{\gamma}+cl_d{}^2(\dot{\beta}-\dot{\alpha})+(mgl_1+kl_s{}^2)\beta-\alpha kl_s{}^2=-Fl_3 \quad (13)$$

$$(I+ml_2{}^2)\ddot{\gamma}-ml_2l_4\ddot{\alpha}+ml_1l_2\ddot{\beta}+mgl_2\gamma=Fl_3 \quad (14)$$

In order to enable the boom to follow ground undulations, the active suspension employs proportional control. This entails that the actuator velocity is directly proportional to the difference between the ground angle α and the boom inclination angle γ. The time delay caused by the sensor, signal processor, and actuator can be represented by an inertia loop. Therefore, the transfer function relating the actuator velocity to the difference between α and γ can be expressed as:

$$\frac{V(s)}{A(s)-R(s)}=\frac{K_p}{Ts+1} \quad (15)$$

Where,

$V(s)$, $A(s)$, and $R(s)$ represent the image functions of the actuator velocity v, the ground angle α, and the boom inclination angle γ in the frequency domain, respectively; K_p is the proportional coefficient of the inertia loop, $ms^{-1}rad^{-1}$; T is the time constant of the inertia loop, s.

The relationship between the velocity of the actuator and its displacement can be expressed mathematically as:

$$V(s)=sD(s) \quad (16)$$

From equations (15) and (16), the transfer function between *d* and (*α*-*γ*) can be derived as:

$$\frac{D(s)}{A(s)-R(s)}=\frac{K_p}{(Ts+1)s} \tag{17}$$

Through the application of inverse Laplace transformation, equation (17) can be changed to

$$T\ddot{d}+\dot{d}=K_p(\alpha-\gamma) \tag{18}$$

When *θ* is very small, the actuator displacement *d* is given by

$$d=l_3\theta=l_3(\gamma-\beta) \tag{19}$$

Substituting equation (19) into equation (18), the following equation can be obtained.

$$Tl_3\ddot{\gamma}-Tl_3\ddot{\beta}+l_3\dot{\gamma}-l_3\dot{\beta}-K_p\alpha+K_p\gamma=0 \tag{20}$$

The group of differential equations comprising equations (13), (14), and (20) describes the dynamic characteristics of the boom. If the ground angle *α* is known, the boom inclination angle and the actuator output can be calculated.

Assuming a step signal for the ground angle *α*, and defining the state variables, namely $x_1=\beta$, $x_2=\dot{\beta}$, $x_3=\gamma$, and $x_4=\dot{\gamma}$, the solution to equations (13), (14), and (20) can be converted into state equations as:

$$\begin{cases}\dot{x}_1=x_2\\ \dot{x}_2=\dfrac{1}{a+b}[\dfrac{b}{T}x_4-(\dfrac{b}{T}+cl_d{}^2)x_2+(\dfrac{K_pb}{Tl_3}-mgl_2)x_3-(mgl_1+kl_s{}^2)x_1+(kl_s{}^2-\dfrac{K_pb}{Tl_3})\alpha]\\ \dot{x}_3=x_4\\ \dot{x}_2=\dfrac{1}{a+b}[-\dfrac{a}{T}x_4+(\dfrac{a}{T}-cl_d{}^2)x_2-(\dfrac{K_pa}{Tl_3}+mgl_2)x_3-(mgl_1+kl_s{}^2)x_1+(kl_s{}^2+\dfrac{K_pa}{Tl_3})\alpha]\end{cases} \tag{21}$$

According to equation (21), the boom angle *γ* can be calculated by using the Runge-Kutta numerical integration algorithm and calling the ode45 function in MATLAB.

From equations (13), (14), and (20), it is difficult to obtain the frequency response function of the suspension with the ground angle α as the input and the boom angle γ as the output. Therefore, the harmonic balance method and numerical solution were adopted to calculate the frequency response (*Geng et al., 2013; Bai et al., 2000*).

Considering the first harmonic balance, $\alpha=\mathrm{A}_\alpha\sin(\omega t)$, $\beta=\mathrm{A}_\beta\sin(\omega t+\varphi_\beta)$, and $\gamma=\mathrm{A}_\gamma\sin(\omega t+\varphi_\gamma)$ can be set. Subsequently, the following nonlinear equations can be derived from equations (13), (14), and (20).

$$(mgl_2-b\omega^2)A_\gamma+(mgl_1+K-a\omega^2)A_\beta\cos(\varphi_\beta-\varphi_\gamma)-C\omega A_\beta\sin(\varphi_\beta-\varphi_\gamma)+[m(l_1+l_2)l_4\omega^2-K]A_\alpha\cos\varphi_\gamma-CA_\alpha\omega\sin\varphi_\gamma=0 \tag{22}$$

$$(mgl_1+K-a\omega^2)A_\beta\sin(\varphi_\beta-\varphi_\gamma)+C\omega A_\beta\cos(\varphi_\beta-\varphi_\gamma)-[m(l_1+l_2)l_4\omega^2-K]A_\alpha\sin\varphi_\gamma-CA_\alpha\omega\cos\varphi_\gamma=0 \tag{23}$$

$$Tl_3A_\beta\omega^2+(K-Tl_3\omega^2)A_\gamma\cos(\varphi_\gamma-\varphi_\beta)-l_3A_\gamma\omega\sin(\varphi_\gamma-\varphi_\beta)-K_pA_\alpha\cos\varphi_\beta=0 \tag{24}$$

$$-l_3A_\beta\omega+(K-Tl_3\omega^2)A_\gamma\sin(\varphi_\gamma-\varphi_\beta)+l_3A_\gamma\omega\cos(\varphi_\gamma-\varphi_\beta)+K_pA_\alpha\sin\varphi_\beta=0 \tag{25}$$

Equations (22), (23), (24), and (25) demonstrate the frequency response of the suspension. By solving these equations, the amplitude-frequency response of the active suspension can be determined, given a certain value for A_α.

RESULTS

Characteristics of Passive Suspension in Time Domain

When a sprayer works in a farm, the ground angle *α* may suddenly change due to the uneven terrain, which can be represented by a step signal (*Cui et al., 2019*). According to equation (6), the unit step response curves of the suspension can be acquired.

The suspension rotational damping coefficient is expressed as $C=cl_d^2$, while the suspension rotational stiffness coefficient is denoted as $K=kl_s^2$ (*Cui et al., 2017a*, *Cui et al., 2017b*). The parameters of the suspension were set as follows: m=67kg, I=110kg·m^2, l_1=0.45m, l_2=0.25m, l_4=0.96m (*O'Sullivan, 1988*).

When the value of K is equal to zero, the unit step response curves of the suspension with varying rotational damping coefficients are depicted in Figure 3.

When subjected to a unit step signal, the boom inclination angle initially rises from its starting point, subsequently decreases rapidly, and gradually returns to its state of equilibrium. The initial value of the boom inclination angle is irrelevant to the damper. Raising the rotational damping coefficient leads to a reduction in overshooting and settling time, as well as an increase in response speed. This is advantageous for quickly bringing the boom back to its stable state. However, as the rotational damping coefficient increases, the maximum value of the boom inclination angle also increases. This can result in the boom end coming into contact with either the crop or the ground.

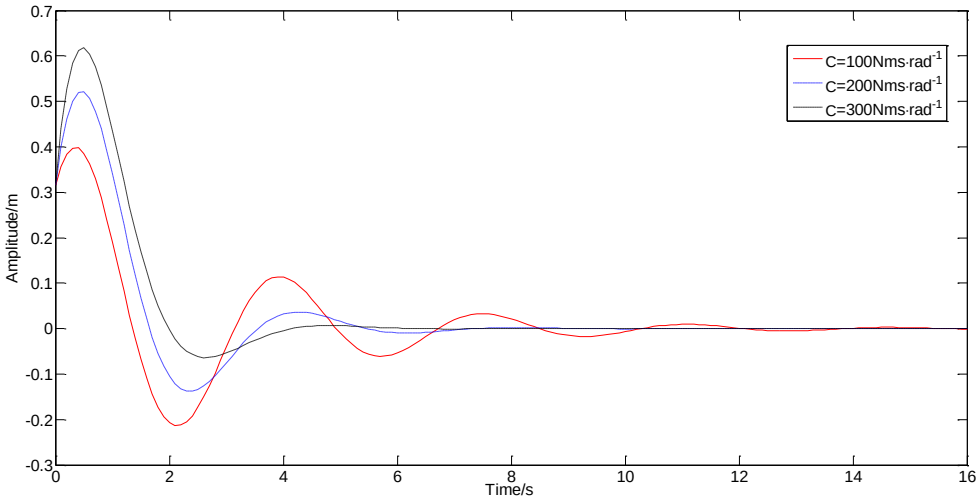


Fig. 3 - Unit step response curves with varying rotational damping coefficients

With C assigned a value of 300 Nms·rad^{-1}, the unit step response curves of the suspension with varying rotational stiffness coefficients are depicted in Figure 4.

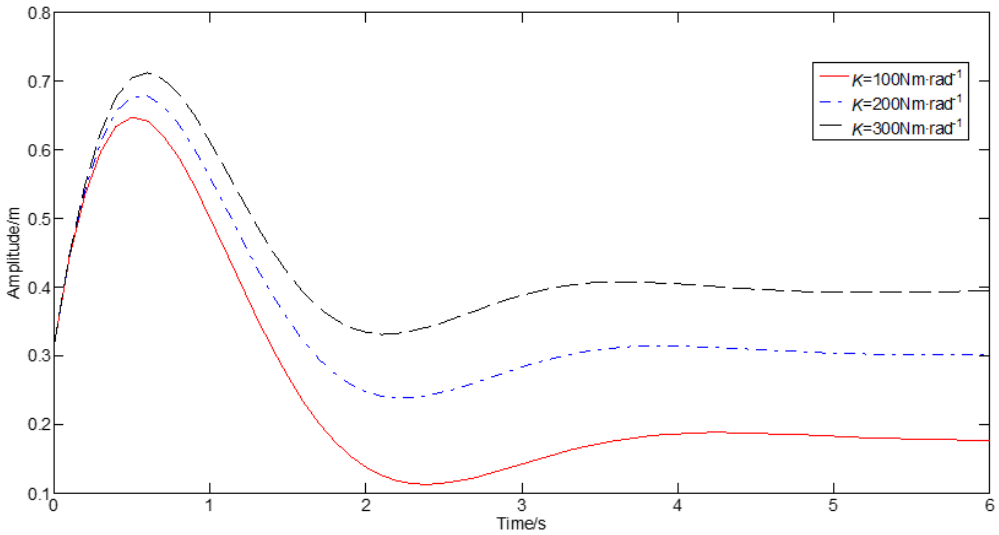


Fig. 4 - Unit step response curves with varying rotational stiffness coefficients

Characteristics of Passive Suspension in Frequency Domain

According to equation (7), the amplitude-frequency characteristic curves of the suspension can be acquired. When the value of K is equal to zero, the amplitude-frequency characteristic curves of the suspension with varying rotational damping coefficients are depicted in Figure 5.

The amplitude ratio of the boom angle *γ* to the ground angle *α* displays an initial increase in response to an increase in frequency, reaching its maximum value, and subsequently decreasing until it stabilizes at a constant value. When the excitation frequency matches the resonant frequency of the suspension, the amplitude ratio reaches its maximum value. The resonant frequency remains unaffected by the rotational damping coefficient. At this particular frequency, the amplitude ratio experiences a decline as the rotational damping coefficient increases. This suggests that an increase in damping can effectively mitigate the resonance between the suspension and the ground. Nevertheless, as damping increases, the suspension's ability to attenuate high-frequency excitation slows down.

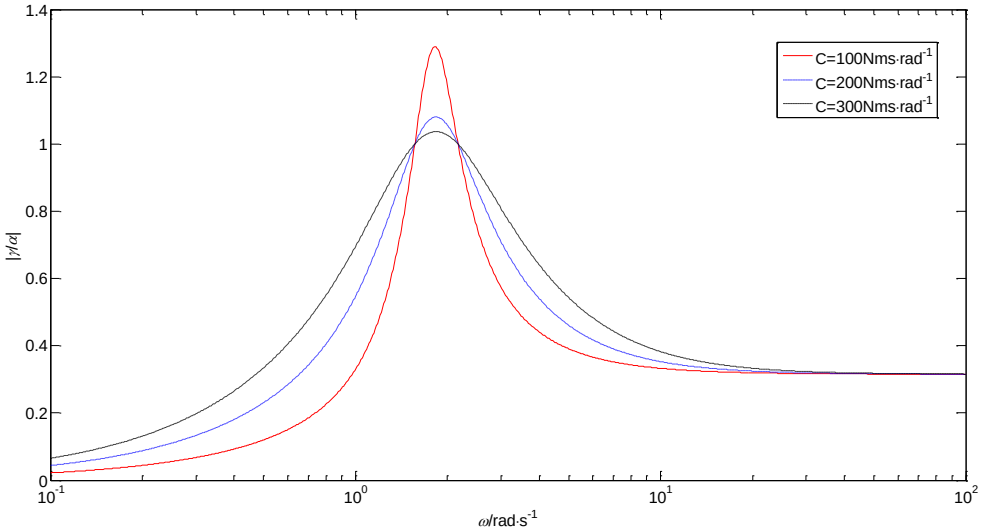


Fig. 5 - Amplitude-frequency characteristic curves with varying rotational damping coefficients

With *C* assigned a value of 300 Nms·rad^{-1}, the amplitude-frequency characteristic curves of the suspension with varying rotational stiffness coefficients are depicted in Figure 6.

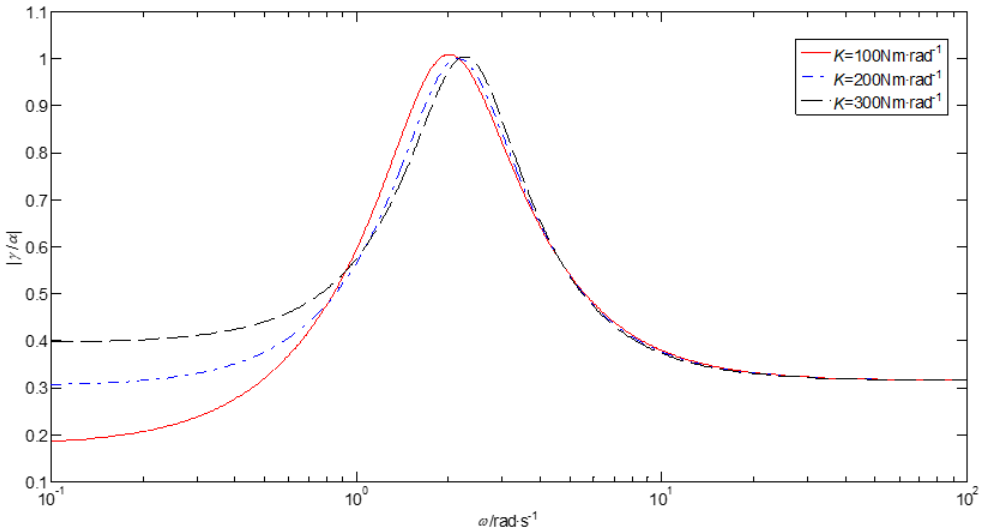


Fig. 6 - Amplitude-frequency characteristic curves with varying rotational stiffness coefficients

As the rotational stiffness coefficient increases, the resonant frequency also increases. This causes the ground disturbance to be easily transmitted to the boom across a wider frequency range. Consequently, the stability of the boom is compromised. At lower frequencies, an increase in the rotational stiffness coefficient leads to a rise in the amplitude ratio, which gradually approaches 1. This implies that an increase in the rotational stiffness coefficient is advantageous in making the boom follow the ground. The amplitude ratio of higher frequencies remains largely unaffected by an increase in the rotational stiffness coefficient.

Characteristics of Active Suspension in Time Domain

The ground angle α was established at 0.3 rad, considering the actual condition of hilly areas (*Cui et al., 2017a*; *Cui et al., 2017b*). The parameters for the boom were determined as m=67 kg, I=110 kg·m^2. Under the given conditions of l_1=0.45 m, l_2=0.25 m, l_3=0.2 m, K_p=0.3 ms^{-1}rad^{-1}, T=0.1 s, and K=0, the effect of rotational damping coefficients on the boom angle is demonstrated in Figure 7.

As the rotational damping coefficient of the suspension decreases, there is an increase in overshoot and settling time, resulting in a decline in stability. However, the response speed remains relatively unchanged. When utilizing the suspension parameters mentioned above and C is less than 90 Nms·rad^{-1}, the system will fail to converge and the boom will be unable to work normally.

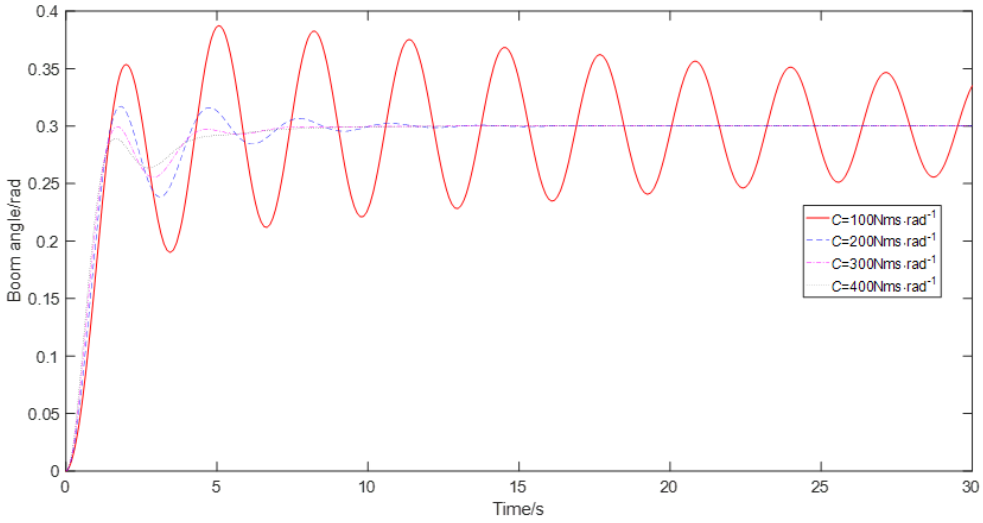


Fig. 7 - Effect of rotational damping coefficients on the boom angle

Under the given conditions of l_1=0.45 m, l_2=0.25 m, l_3=0.2 m, K_p=0.1 ms^{-1}rad^{-1}, T=0.1 s, and C=100 Nms·rad^{-1}, the effect of rotational stiffness coefficients on the boom angle is demonstrated in Figure 8.

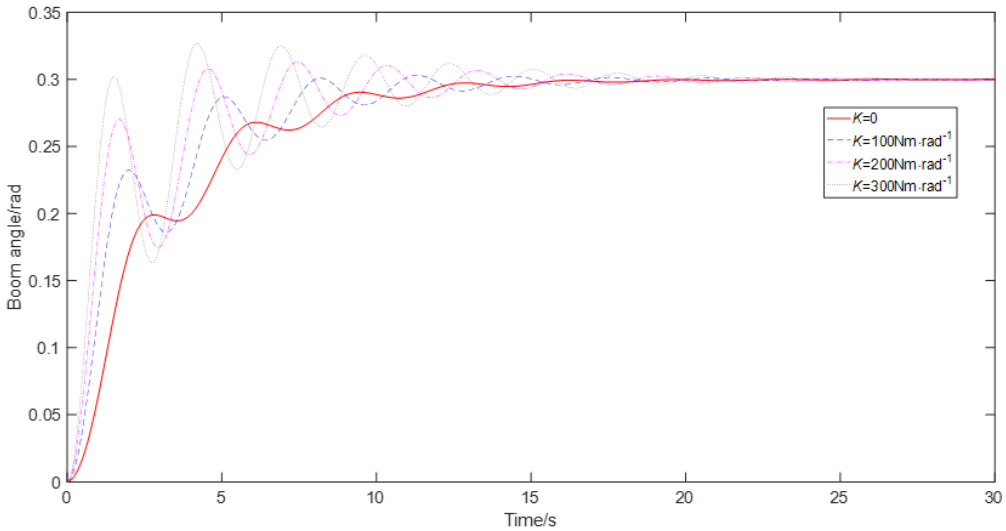


Fig. 8 - Effect of rotational stiffness coefficients on the boom angle

As the rotational stiffness coefficient of the suspension increases, the system exhibits a faster response and an increase in overshoot and settling time. In order to make the boom follow ground undulations quickly, the incorporation of springs through active suspensions can be effective. It is important to note, however, that the K value should not be excessively high as this may result in a prolonged settling time. Furthermore, if the proportional coefficient is large, an excessive K value may lead to system instability and hinder the proper functioning of the boom.

Characteristics of Active Suspension in Frequency Domain

The amplitude of the ground angle α was established at 0.3 rad. The parameters for the boom were determined as m=67 kg, I=110 kg·m^2. Under the given conditions of l_1=0.45 m, l_2=0.25 m, l_3=0.2 m, l_4=0.9 m, K_p=1 ms^{-1}rad^{-1}, C=100 Nms·rad^{-1}, T=0.1 s, and K=0, the amplitude-frequency response of the active suspension is shown in Figure 9.

At low excitation frequencies, specifically between point A and point B on the curve, the amplitude ratio of the boom angle γ to the ground angle α is approximately 1, which is a desirable outcome. The amplitude ratio experiences a slight decrease as it progresses from point B to point C, followed by a gradual increase from point C to point D. The maximum amplitude ratio is observed at point D, which corresponds to the resonant frequency of the active suspension. When the excitation frequency is greater than the resonant frequency, a swift decline in the amplitude ratio is observed, eventually stabilizing at a constant value. This phenomenon is similar to the frequency response of the passive suspension. As a result, a well-designed active suspension has the capability to effectively track low-frequency signals while attenuating high-frequency signals.

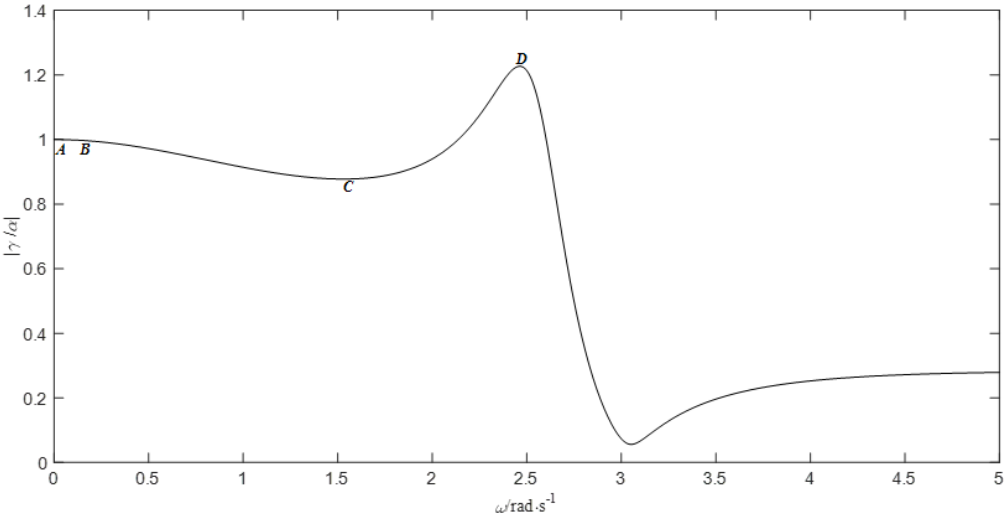


Fig. 9 - Amplitude-frequency response of the active suspension

CONCLUSIONS

The present study established a dynamic model that characterizes the roll of a spray boom equipped with a double-pendulum suspension, utilizing the second Lagrange equation. The transfer function and frequency response function of the passive suspension were derived with the ground slope angle as input and the boom inclination angle as output. The analysis results indicate that the passive suspension can partially attenuate high-frequency disturbances, but is unable to track low-frequency signals. Furthermore, the amplitude ratio of the boom inclination angle to the ground slope angle approaches a stable value beyond the resonant frequency as the frequency increases.

The transient response of the active suspension was analyzed through the utilization of a numerical integration algorithm. The frequency response was calculated using the harmonic balance method and numerical solution. The findings suggest that the active suspension, when equipped with suitable configuration and control parameters, can facilitate the boom's ability to track variations in the ground slope angle. At low frequencies, the amplitude ratio is approximately 1, but it declines sharply beyond the resonant frequency. This implies that the active suspension can effectively track low-frequency signals while partially isolating high-frequency signals.

The mathematical model presented in this paper has the potential to facilitate an analysis of the dynamic characteristics of the spray boom, thereby offering valuable insights for the design of its suspension.

ACKNOWLEDGEMENTS

This research was supported by talent scientific research fund of Liaoning Petrochemical University（No.2021XJJL-024）.

REFERENCES

[1] Anthonis, J., Audenaert, J., Ramon, H. (2005). Design optimization for the vertical suspension of a crop sprayer boom. *Biosystems Engineering*, 90(2), 153–160.

[2] Bai, H., Zhang, P., Huang, X. (2000). Study on the response computation method of a two degrees-of-freedom vibration absorber system with variable coefficient of sliding friction using optimum approximate technique (干摩擦动力吸振器简谐激励响应计算的最优化方法研究). *Journal of Vibration Shock*, 19(3), 43–46.

[3] Cui, L., Xue, X., Ding, S., Qiao, B., Le, F. (2017a). Analysis and test of dynamic characteristics of large spraying boom and pendulum suspension damping system (大型喷杆及其摆式悬架减振系统动力学特性分析与试验). *Transactions of the Chinese Society of Agricultural Engineering*, 33(9), 69–76.

[4] Cui, L., Xue, X., Ding, S., Gu, W., Chen, C, Le, F. (2017b). Modeling and simulation of dynamic behavior of large spray boom with active and passive pendulum suspension (双钟摆主被动悬架式大型喷雾机喷杆动力学仿真与试验). *Transactions of the Chinese Society of Agricultural Machinery*, 48(2), 82–90.

[5] Cui, L., Xue, X., Le, F., Mao, H., Ding, S. (2019). Design and experiment of electro hydraulic active suspension for controlling the rolling motion of spray boom. International *Journal of Agricultural and Biological Engineering*, 12(4), 72–81.

[6] Cui, L., Xue, X., Le, F., Ding, S. (2019). Design and evaluation method of testing bench for spray boom suspension systems (大型喷杆悬架系统测试平台设计与评价方法研究). *Transactions of the Chinese Society of Agricultural Engineering*, 35(16), 23–31.

[7] Cui, L., Xue, X., Le, F., Ding, S. (2020). Adaptive robust control of active and passive pendulum suspension for large boom sprayer (大型喷杆喷雾机钟摆式主被动悬架自适应鲁棒控制研究). *Transactions of the Chinese Society of Agricultural Machinery*, 51(12), 130–141.

[8] Deprez, K., Anthonis, J., Ramon, H. (2002). Development of a slow active suspension for stabilizing the roll of spray booms: part 1-Hybrid modelling. *Biosystems Engineering*, 81(2), 185–191.

[9] Deprez, K., Anthonis, J., Ramon, H. (2003). System for vertical boom corrections on hilly fields. *Journal of Sound Vibration*, 266(3), 613–624.

[10] Frost, A.R. (1984). Simulation of an active spray boom suspension. *Journal of Agricultural Engineering Research*, 30, 313–325.

[11] Geng, J., Zhao, Z. (2013). Analysis of amplitude-frequency response on steel wire rope shock absorber (钢丝绳减振器幅频特性研究). *Journal of Taiyuan University of Science and Technology*, 34(3), 233–237.

[12] He, X. (2020). Research progress and developmental recommendations on precision spraying technology and equipment in China (中国精准施药技术和装备研究现状及发展建议). *Smart Agriculture*, 2(1), 133–146.

[13] He, X. (2022). Research and development of efficient plant protection equipment and precision spraying technology in China: a review (高效植保机械与精准施药技术进展). *Journal of Plant Protection*, 49(1), 389–397.

[14] Jeon, H.Y., Womac, A.R., Gunn, J. (2004). Sprayer boom dynamic effects on application uniformity. *Transactions of the American Society of Agricultural Engineers*, 47(3), 647–658.

[15] Langenakens, J., Clijman, L., Ramon, H., Baerdemaeker, J.D. (1999). The effects of vertical sprayer boom movements on the uniformity of spray distribution. *Journal of Agricultural Engineering Research,* 74(3), 281–291.

[16] O'Sullivan, J.A. (1986). Simulation of the behavior of a spray boom with an active and passive pendulum suspension. *Journal of Agricultural Engineering Research*, 35(3), 157–173.

[17] O'Sullivan, J.A. (1988). Verification of passive and active versions of a mathematical model of a pendulum spray boom suspension. *Journal of Agricultural Engineering Research*, 40(2), 89–101.

[18] Qiu, B., Yan, R., Ma, J., Guan, X., Ou, M. (2015). Research progress analysis of variable rate sprayer technology (变量喷雾技术研究进展分析). *Transactions of the Chinese Society of Agricultural Machinery*, 46(3), 59–72.

[19] Ramon, H., Baerdemaeker, J.D. (1997). Spray boom motions and spray distribution: Part I-Derivation of a mathematical relation. *Journal of Agricultural Engineering Research*, 66(1), 23–29.

[20] Tahmasebi, M., Rahman, R.A., Mailah, M., Gohari, M. (2013). Active force control applied to spray boom structure. *Applied Mechanical Material*, 315, 616–620.

[21] Wu, J., Miao, Y. (2012). Dynamic characteristic analysis of boom for wide sprayer with different exciting sources (不同激励源下宽幅喷雾机喷杆的动态特性分析). *Transactions of the Chinese Society of Agricultural Engineering*, 28(4), 39–44.

[22] Xue, T., Li, W., Du, W., Mao, E. Wen, H. (2018). Adaptive fuzzy sliding mode control of spray boom active suspension for large high clearance sprayer (大型高地隙喷雾机喷杆主动悬架自适应模糊滑模控制). *Transactions of the Chinese Society of Agricultural Engineering,* 34(21), 47–56.

[23] Yan, J., Xue, X., Cui, L., Ding, S., Gu, W., et al. (2021). Analysis of dynamic behavior of spray boom under step excitation. *Applied Science*, 11(21), 10129.

[24] Zhuang, T. (2020). *Theoretical analysis and experimental research on boom vibration of large-scale high clearance sprayer* (大型高地隙喷雾机喷杆振动理论分析与试验研究) [Doctoral dissertation, Chinese Academy of Agricultural Mechanization Sciences].

[25] Zhang, X. (2021). *Design and research of spraying rod suspension device for sprayer* (喷杆式喷雾机喷杆悬挂架装置设计与研究) [Master dissertation, Shihezi University].

CALIBRATION OF DISCRETE ELEMENT PARAMETER OF SOIL IN HIGH-SPEED TILLAGE
/
高速耕作条件下土壤离散元参数标定

Shaochuan LI, Peisong DIAO*, Yongli ZHAO, Hequan MIAO, Xianghao LI, Hongda ZHAO
Shandong University of Technology, Collage of Agricultural Engineering and Food Science, ZiBo, China
*Tel: +86 13864306142 *) Corresponding author E-mail: dps2003@163.com*
DOI: https://doi.org/10.35633/inmateh-71-21

Keywords: *DEM, calibration of soil contact parameter, high-speed tillage, soil dynamic characteristic*

ABSTRACT
For the problem of lacking reliable values of soil parameters required for dynamic simulation analysis of soil under high-speed tillage, no-tillage soil was taken as the research object and its parameters were calibrated using the discrete element method in this study. The Edinburgh Elasto-Plastic Adhesion (EEPA) model was determined as the soil contact model by obtaining the loading force-deformation relationship through uniaxial sealing compression tests. The regression equation was established using Plackett-Burman test and quadratic orthogonal rotation test, and the interaction effects were analyzed. The measured values of the pile angle and strain were obtained through the pile angle test and the uniaxial seal compression test, and the optimal solution was carried out. Further, the simulated values and the measured values under the optimal parameters were compared and verified, the result showed that the error values were all less than 1%. Finally, the soil model was used for high-speed tillage simulation analysis, and the obtained soil particle displacement and groove width were compared with the measured values. It was found that the ditch width error value was 3.04% and the soil displacement was basically the same. This study proved that the contact model parameters were relatively reliable, which could provide theoretical reference for the dynamic characteristics of soil during high-speed cultivation of no-tillage soil.

摘要
针对进行高速耕作土壤动态仿真分析时所需土壤参数缺乏可靠性数值的问题，本研究以免耕土壤为研究对象，采用离散元方法对免耕土壤进行参数标定。通过单轴密封压缩试验获取加载力-变形量的关系确定 Edinburgh Elasto-Plastic Adhesion（EEPA）模型为土壤接触模型；利用 Plackett-Burman 试验和二次正交旋转试验建立回归方程，并进行交互效应的分析；通过堆积角试验和单轴密封压缩试验获取堆积角和应变的实测值并进行最优求解，将最优参数下的仿真值和实测值进行对比验证，发现误差值均小于 1%。最后以该土壤模型进行高速耕作仿真分析，将获取的土壤颗粒位移量和沟槽宽度与实测值进行对比，发现沟槽宽度误差值为 3.04%，土壤位移量基本一致。研究证明了接触模型参数较为可靠，可为免耕土壤高速耕作过程中土壤的动态特性提供理论参考。

INTRODUCTION

No-till operation can improve soil structure. However, no-till operation for a long time would cause soil compacted and show complex motion laws because of combined action of pressure, shear, and pull in soil-implement interaction (*Rusu, 2014; Cao et al., 2021; Bahrami, Naderi-Boldaji & Ghanbarian, 2020*).

The discrete element method has great advantages in revealing the soil movement characteristics in the process of agricultural machinery operation, which can not only simulate, but also predict the soil movement during the tillage process. Moreover, calibrating soil parameters in a DEM simulation is referential (*Fu & Chen, 2023; Dong, Zheng & Jia, 2022; Jan et al., 2019; Wang, Song & Zhou, 2022*). *Gao, Shang & Xu, (2022),* selected Hertz-Mindlin with JKR Cohesion model to calibrate straw-soil mixing model parameters, which provided reference and theoretical basis for studying key components of implement contacting soil in Huang Huai marine double cropping area. *Adajar et al., (2021),* used the discrete element method to calibrate five crop residues parameters and simulate interactions with soil, which proved the reliability of the discrete element method to simulate interactions. *Zhang et al., (2017),* used discrete element method consistent with soil particles characteristics to calibrate sand particles, and the dynamic behavior, velocity field, and force field of soil particles were studied based on discrete element method.

Chen et al., *(2013),* established soil particles with bonding effect using discrete element method to show soil cohesion, which could better predict soil disturbance characteristics, and calibrate the particle stiffness of different soils. *Milkevych et al., (2018),* used discrete element method to simulate tillage experiment, comparing particle displacement and soil disturbance index, and concluded that the discrete element model could accurately predict soil movement in the soil-tool interaction process under certain restrictive conditions. Discrete element method is a common way of studying soil flow in the soil-tool interaction process. *Qi & Chen, (2019),* established discrete element model to simulate soil flow process exploring soil particles flow characteristics and obtaining the sequential flow state of soil, which showed four distinctive stages: consolidating, releasing, settling, and static stages. *Fielke, Ucgul & Saunders, (2013),* established a soil discrete element model with plasticity, cohesion and adhesion according to the study of soil flow dynamic effect, which was verified by Angle of Repose, and the model effectiveness was proved through farming experiment further.

In this study, no-tillage soil model was constructed by discrete element method to study the soil motion laws and the soil particles motion characteristics in high-speed cultivation. The Elasto-Plastic model (EEPA) in EDEM software was used as the soil contact model (*Thakur, 2014*). Additionally, the repose angle and soil strain simulation test was carried out to verify the accuracy and effectiveness of soil discrete element model.

MATERIALS AND METHODS

Determination of soil basic parameters

Sandy loam soil samples (soil humidity 14.29%, volume 2×10^{-4} m^3) were collected at a depth of 10 cm using a ring knife according to the method reported by *Chen et al. (2013)*, as shown in Figure 1. The weight of soil measured using an electronic balance, and the soil wet density 1251 kg/m^3 through multiple measurements. The soil particle size was analyzed according to the particle size screening test (Figure 2) and the result showed that the soil particle size was > 4 mm 35.46%, < 4 mm 64.54%. The shape of the soil particles is represented as a single sphere to improve simulation efficiency and fit the soil shape extremely, the particles size larger than 5 mm are set to 5 mm while particles size smaller than 5 mm are set to 3 mm.



Fig. 1 - Ring knife test



Fig. 2 - Soil particle size screening test

Angle of repose and uniaxial seal compression test

Uniaxial sealing compression test is carried out on the soil to show the compaction state of no-till soil, which can better present the visco-plastic state and elastic-plastic of soil before and after compaction (*Le, Zhang & Liu, 2013; Bahrami, Naderi-Boldaji & Ghanbarian, 2020*), which is carried out at the rates of 8 mm/s, 32 mm/s and 50 mm/s respectively through a steel cylinder with a height of 200 mm and an inner diameter of 80 mm as shown in Figure 3.

Angle of repose (AOR) can directly reflect the soil mobility, which plays an important role in clarifying soil-implement interaction relationship in high-speed tillage (*Lajeunesse, Mangeney-Castelnau & Vilotte, 2004*). Therefore, a funnel with a height of 205 mm, lower diameter of 25 mm, and upper diameter of 240 mm is selected to be fixed on the iron frame, and the spacing between the funnel outlet and the plate is 95 mm (Figure 4). The funnel outlet should be opened to allow the soil to flow out naturally after the test soil poured into the funnel completely. Before that, the funnel outlet is blocked during experiment. The value of AOR is the average value after 5 measurements by protractor from different directions after the entire soil flows out and becomes static.



Fig. 3 - Uniaxial sealing compression test



Fig. 4 - Angle of repose test

The Plackett-Burman design screening test is applied to select the model parameters with influence on the test indexes significantly to avoid too many factors or some unvalued factors. The axial strain and AOR are taken as the response values in the later optimization test to study the fluidity and visco-plasticity of no-till soil in high-speed process.

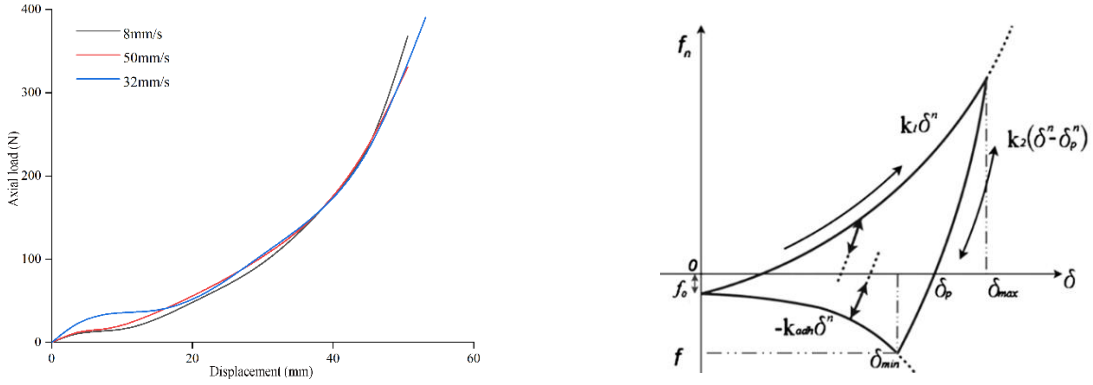
Soil particle contact model

The soil presented a free and discrete state naturally, however, the action of external forces changed the original soil structure due to the fact that soil particles bond and aggregate. The relationship between deformation and axial loading force is the same basically under different loading speeds as shown in Figure 5a. It is found that the EEPA soil particle contact model combining viscosity, elasticity and plasticity has similar mechanical properties compared with the loading process of soil uniaxial seal compression test (Figure 5b), which is consistent with the description of *Thakur et al., (2014)*. Therefore, the EEPA soil particle contact model is selected as the soil particle contact model of discrete element simulation. Notably, the normal contact force and displacement become linear when n=1.

The axial strain ε_n of the consolidated sample after the test is used to characterize the soil plasticity (*Xie, Wu & Wang, 2020*). ε_n is defined as follows (Equation 2):

$$\varepsilon_n = \frac{h_0 - h_1}{h_0} \tag{1}$$

where: h_0 - Initial height of soil sample in uniaxial seal compression test, [m]; h_1 - Final height of soil sample in uniaxial seal compression test, [m]. Therefore, the pressure plate is loaded at a constant rate selecting loading rate of 32 mm/s to save test time, and unloaded at the same rate when the axial pressure reaches 300 N. The height before loading is h_0, and the height after unloading is h_1.



(a) (b)

Fig. 5- (a) Axial load-displacement relationship (b) EEPA normal elastic force-normal overlap relationship

Plackett-Burman test

The EEPA contact model has 7 parameters, including collision recovery coefficient, static friction coefficient, dynamic friction coefficient, constant pulling force, surface energy, contact plastic deformation, loading branch index, bonding branch index, and tangential stiffness factor. Soil model is established according to the above parameters, and the test for calibration parameter influencing on soil AOR and axial strain is

carried out. According to the simulation settings, the impact recovery coefficient, static friction coefficient, dynamic friction coefficient, constant pull-out force, surface energy, contact plastic deformation, loading branch index, bonding branch index and tangential stiffness factor are selected as the influencing factors, and AOR and axial stress are taken as the response values.

In order to reduce the number of influential factors and calibration difficulty, the above test factors are selected preliminarily. The constant pull-out force is unconsidered in this study due to the constant existence among the soil particles. The loading fraction index is selected from 1 or 1.5 in EDEM software, and 1.5 is selected according to literature finally (*Xie, Wu & Wang, 2020*). Therefore, the test factors are set as collision recovery coefficient, static friction coefficient, dynamic friction coefficient, surface energy, contact plastic deformation, bond branch index and tangential stiffness factor. Then, the appropriate level for each factor is determined, combining with the parameter selection range of references, as shown in Table 1. Relevant parameters are set as follows: soil intrinsic parameter Poisson's ratio 0.38, shear modulus 1.3×10^6 Pa. Cylinder and funnel are made of stainless steel. The Poisson's ratio, density, and shear modulus is 0.3, 7850 kg/m^3, 7×10^{10} Pa respectively (*Barr et al., 2019; Tagar et al., 2014; Mohajeri & Rhee, 2021*). The Plackett-Burman screening test is designed as shown in Table 1. A center point is used to estimate the random error of the test, including 13 sets of tests in total.

Table 1 Experimental factors and levels

Parameter	Factor	Level	
		-1	1
M_1	Collision recovery coefficient e	0.2	0.6
M_2	Static friction coefficient u_s	0.3	0.8
M_3	Dynamic friction coefficient u_r	0.1	0.6
M_4	Surface energy $\triangle\gamma$ (J/m^2)	4	20
M_5	Contact plastic deformation λ_p	0.2	0.7
M_6	Bonding branch index X	1	2.5
M_7	Tangential stiffness factor K_{tm}	0.25	0.9

RESULTS

The results of Plackett-Burman test (Table 2) are analyzed to test the significance of each factor's influence on soil characteristics, and the results of variance analysis are shown in Table 3. The significance level of 0.05 is compared with the *P*-values of each factor. According to the variance analysis of AOR, the *P*-value of the regression model is 0.0245 < 0.05, indicating that the fitting model is significant. The *P* values of e and u_s are both less than 0.05, which confirms the influence of e and u_s on the AOR is significant. The *P* value of λ_P is less than 0.01, which indicates the influence of λ_P on the AOR is extremely significant. The *P* value of K_{tm} is less than 0.05, confirming the influence of K_{tm} on axial strain is significant, while the *P* value of $\triangle\gamma$ is less than 0.01, so the influence of $\triangle\gamma$ on axial strain is extremely significant. In summary, the contact plastic deformation ratio λ_P and surface energy $\triangle\gamma$ are the main factors affecting soil properties.

Table 2

Plackett-Burman test design and results

No.	Level								AOR / °	Axial strain
	M_1	M_2	M_3	M_4	M_5	M_6	M_7	M_8		
1	1	1	-1	1	1	1	-1	-1	36.33	36.03
2	-1	1	1	-1	1	1	1	-1	45.01	25.51
3	1	-1	1	1	-1	1	1	1	21.66	37.76
4	-1	1	-1	1	1	-1	1	1	41.99	44.84
5	-1	-1	1	-1	1	1	-1	1	34.65	5.37
6	-1	-1	-1	1	-1	1	1	-1	26.04	34.23
7	1	-1	-1	-1	1	-1	1	1	32.01	29.41
8	1	1	-1	-1	-1	1	-1	1	28.74	11.67
9	1	1	1	-1	-1	-1	1	-1	23.21	6.8
10	-1	1	1	1	-1	-1	-1	1	26.7	17.54
11	1	-1	1	1	1	-1	-1	-1	28.46	26.67
12	-1	-1	-1	-1	-1	-1	-1	-1	25.22	3.75
13	0	0	0	0	0	0	0	0	38.49	41.84

Table 3

Plackett-Burman test variance analysis

Index	Variance source	Sum of squares	Df	Mean square	F	P
AOR	model	580.69	8	72.59	14.74	0.0245
	e	71.05	1	71.05	14.42	0.0320
	u_s	95.99	1	95.99	19.49	0.0216
	u_r	9.43	1	9.43	1.92	0.2604
	$\triangle\gamma$	4.89	1	4.89	0.9926	0.3925
	λ_P	372.74	1	372.74	75.67	0.0032
	X	18.35	1	18.35	3.73	0.1491
	K_{tm}	8.04	1	8.04	1.63	0.2914
	Residual error	14.78	3	4.93		
	Sum total	649.56	12			
Axial strain	model	2072.50	8	259.06	9.71	0.0440
	e	24.37	1	24.37	0.9135	0.4097
	u_s	2.25	1	2.25	0.0845	0.7903
	u_r	135.21	1	135.21	5.07	0.1098
	$\triangle\gamma$	1093.67	1	1093.67	41.00	0.0077
	λ_P	262.08	1	262.08	9.83	0.0519
	X	38.74	1	38.74	1.45	0.3146
	K_{tm}	500.78	1	500.78	18.77	0.0227
	Residual error	80.02	3	26.67		
	Sum total	2469.87	12			

Orthogonal rotation combination experiment design

Quadratic orthogonal rotation combination test is designed based on the range of Plackett-Burman to obtain the values of λ_P and $\triangle\gamma$ corresponding to the measured values. The test level coding table is shown in Table 4, and the design and results of the test are shown in Table 5. In order to ensure the test effect, the middle values of Plackett-Burman test are taken for factors having little influence on soil characteristics: e=0.4 , u_s=0.55, u_r=0.35, X=1.75, K_{tm}=0.575.

Table 4

Horizontal code table

Level	$\triangle\gamma$	λ_p
1.414	20	0.7
1	16	0.575
0	12	0.45
-1	8	0.325
-1.414	4	0.2

Variance analysis is performed on the obtained AOR and axial strain. The *P* value of the fitting multiple regression model for AOR and axial strain is 0.0021 ($P < 0.01$), 0.0014 ($P < 0.01$) as shown in Table 6, confirming that the models fitted by each index are extremely significant. The determination coefficients of AOR fitting model are $R_1^2 = 0.901$, $R_{adj1}^2 = 0.83$, and the accuracy of central composite test is greater than 4. The determination coefficients of axial strain fitting model are $R_2^2 = 0.913$, $R_{adj2}^2 = 0.85$, and the accuracy of central composite test is greater than 4. Therefore, the results indicate that the fitting model is better and good predictive.

Table 5

Experimental scheme and results

Number	$\triangle\gamma$	λ_P	AOR	Axial strain
1	-1	-1	37.26	30.43
2	1	-1	32.72	11.29
3	-1	1	36.08	28.78
4	1	1	30.91	32.39

Number	$\triangle\gamma$	λ_P	AOR	Axial strain
5	-1.414	0	38.59	31.81
6	1.414	0	20.49	26.25
7	0	-1.414	29.64	9.84
8	0	1.414	37.93	19.05
9	0	0	20.45	21.13
10	0	0	20.21	23.94
11	0	0	20.84	21.13
12	0	0	20.23	22.53
13	0	0	20.89	23.94

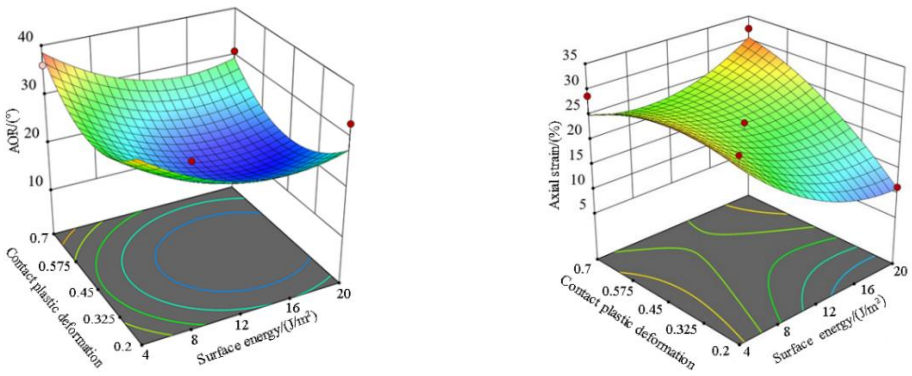
Table 6

Analysis of variance

index	Variance source	Sum of squares	D_f	Mean square	F	P
AOR	model	658.76	5	131.75	12.75	0.0021
	$\triangle\gamma$	155.83	1	155.83	15.08	0.0060
	λ_P	9.53	1	9.53	0.9225	0.3688
	$\triangle\gamma\lambda_P$	0.0992	1	0.0992	0.0096	0.9247
	$\triangle\gamma^2$	184.72	1	184.72	17.87	0.0039
	${\lambda_P}^2$	368.23	1	368.23	35.63	0.0006
	Residual error	72.35	7	10.34		
	Sum total	731.11	12			
Axial strain	model	546.75	5	109.35	14.67	0.0014
	$\triangle\gamma$	68.40	1	68.40	9.18	0.0191
	λ_p	131.83	1	131.83	17.69	0.0040
	$\triangle\gamma\lambda_p$	129.39	1	129.39	17.36	0.0042
	$\triangle\gamma^2$	125.31	1	125.31	16.82	0.0046
	${\lambda_p}^2$	64.64	1	64.64	8.67	0.0216
	Residual error	52.16	7	7.45		
	Sum total	598.91	12			

According to the experimental results and further analysis, the *P* values of the regression terms $\triangle\gamma$, $\triangle\gamma^2$ and ${\lambda_p}^2$ are all less than 0.01, indicating that they have significant influence on AOR. The significant influence degree of all items on the axial strain ranges from large to small as λ_p, $\triangle\gamma\lambda_p$, $\triangle\gamma^2$, $\triangle\gamma$, ${\lambda_p}^2$. The *P* values of the regression terms λ_p, $\triangle\gamma\lambda_p$ and $\triangle\gamma^2$ are less than 0.01, indicating that the influence on the axial strain is extremely significant, the P values of the regression terms $\triangle\gamma$ sum and ${\lambda_p}^2$ are less than 0.05, confirming that the influence on the axial strain is significant. The Design-Expert 12 software is used to refit to obtain the quadratic regression equation after removing nonsignificant items. The AOR and axial strain are represented by A and ε_n as shown in Equation 2, respectively:

$$\begin{cases} A = 20.52 - 4.41\Delta\gamma + 1.09\lambda_p + 5.15\Delta\gamma^2 + 7.28{\lambda_p}^2 \\ \varepsilon_n = 22.53 - 2.92\Delta\gamma + 4.06\lambda_p + 5.69\Delta\gamma\lambda_p + 4.24\Delta\gamma^2 - 3.05{\lambda_p}^2 \end{cases} \quad (2)$$



(a) (b)

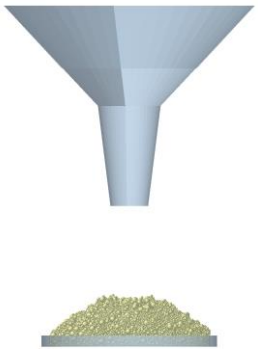
Fig. 6 - Effect of interaction on AOR and axial strain

The interaction of the contact plastic deformation ratio λ_p and surface energy $\triangle\gamma$ on AOR and axial strain is analyzed by the response surface, as shown in Figure 6. The response surface presents obvious slope (Figure 6a), indicating that the interaction effect of λ_p-$\triangle\gamma$ has a significant influence on the AOR, and the contours show large curvature, The response surface presents obvious slope (Figure 6b), indicating that the interaction effect of λ_p-$\triangle\gamma$ has a significant influence on the axial strain, and the contours show large curvature change.

The optimization function of Design-Expert 12 software is used to optimize the parameters, and the regression model is optimized by taking the measured stacking angle and axial strain as the target values. The actual test value shows that the angle of repose is 37.74° and the axial strain is 28.12%. At the same time, the importance of the two indexes is set. Setting the stacking angle as "+++" and axial strain as "++++".

The surface energy of soil particles is 7.32 J/m^2 and the contact plastic deformation ratio is 0.543. The parameters of the EEPA contact model are set as optimal values, and other parameters are set as intermediate levels, three simulation tests are carried out for AOR and axial strain respectively in EDEM. The results of AOR are 38.1°, 37.66° and 37.88°, and the errors with the measured values are all less than 0.95%.

The results of axial strain are 27.84%, 28.39%, 28.04%, and the errors of the measured values are all less than 1%. Further, the strain of the soil is calculated using the above formula, and the relation curve of axial stress-strain is shown in Figure 7. Based on the above analysis, it can be seen that the value simulation can match the actual value.



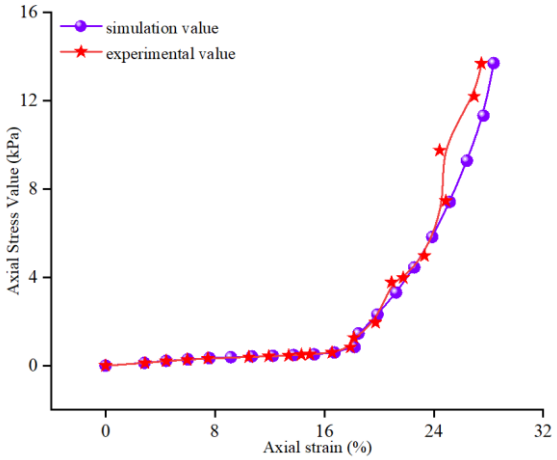
(a)

Fig. 7-(a) Angle of repose simulation test



(b)

Fig. 7- (b) Uniaxial seal compression simulation test



(c)

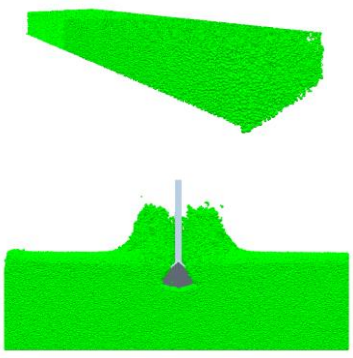
Fig. 7- (c) Axial stress-strain curve

Validation test

This experiment combined the real test and the discrete element test to further verify whether the optimized parameters of the discrete element soil model can truly reflect the soil mechanical properties in high-speed operation. The soil displacement values and ditch widths in simulation experimenting under different test speeds values are analyzed to verify the accuracy of the parameters using error indicators.



(a)



(b)

Fig. 8 - Field tillage test

Field tillage test is carried out in the soil sampling area to obtain the measured values. The tool, as shown in Figure 9a, is used to limit the maximum tillage depth to 60 mm. During the test, the tool is allowed to pass through the working area at a constant speed of 12 km/h, 13 km/h, 14 km/h, and the working distance is 4 m. The soil bin with length× width × height of 4000 mm×300 mm×200 mm is established by using EDEM software, and the soil bin is quickly generated by means of particle bed according to the calibrated discrete element parameters. The 3D model of tool, embedding basically with the real object, is imported into the EDEM software after the formation of the soil bin. The tillage depth is set to 60 mm and the speed is 12 km/h, 13 km/h and 14km/h, as shown in Figure 9b.



v=12km/h v=13km/h v=14km/h

Fig.9 - Measure ditch width

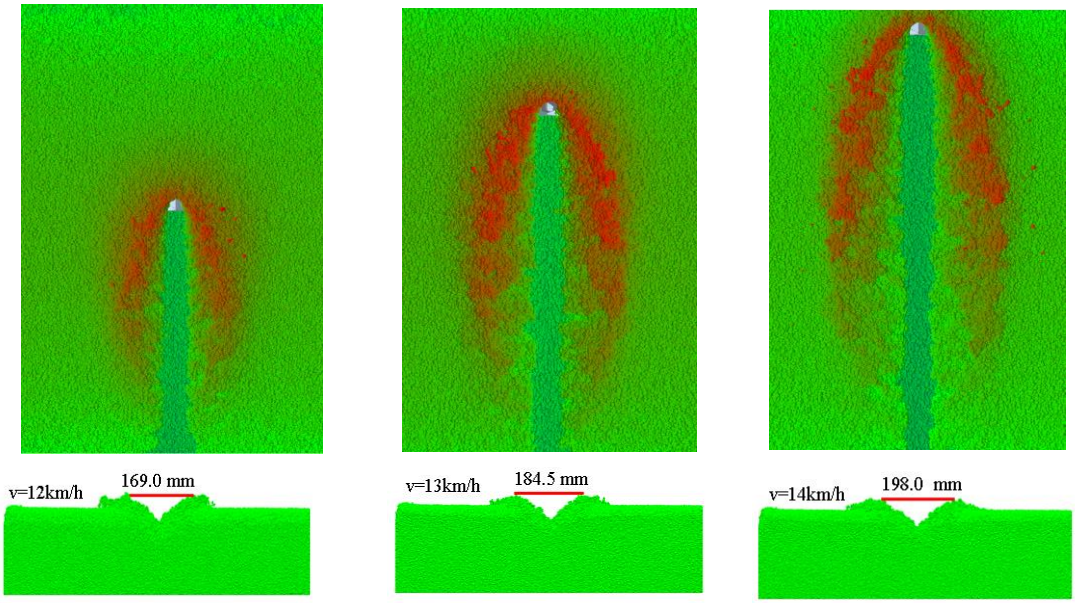


Fig. 10 - Ditch width simulation value

The measurement of ditch width, soil compaction and tillage will produce soil disturbance, affecting the physical properties of soil. The amount of soil disturbance can be represented by the ditch width. The virtual soil bin is tillage at different speeds to obtain the disturbance characteristics of the soil in the process of high-speed tillage. Five points are randomly selected to measure the ditch width after each tillage is completed, and the average value of 5 points is taken as the ditch width value, as shown in Figure 9. The field test results show that the ditch widths are 164.0 mm, 182.0 mm and 201.0 mm under the cultivation speed of 12 km/h, 13 km/h and 14 km/h respectively.

After the simulation of the tillage process is completed, the soil particles continue to calculate a certain time step, and the tool function of EDEM software is used to measure the ditch width under high-speed tillage, as shown in Figure 10.

The measured ditch widths at 12 km/h, 13 km/h, and 14 km/h are 169.0 mm, 184.5 mm, and 198.0 mm respectively. The error between experimental value and the simulation value is less than 3.04%, confirming that the simulation value is reliable. Soil particles obtain greater kinetic energy when the tool operates with larger speed, leading to the soil particles in contact with implement pressing on adjacent soil particles with a larger force, so a larger disturbance area and larger width of the ditch will be generated in the meantime.

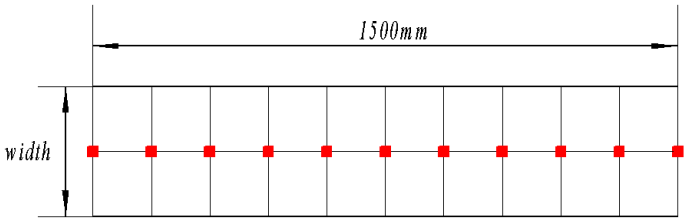


Fig. 11 - Schematic representation of Tracer distribution

Soil particle displacement can show the fluidity of soil-tool interaction, which is measured by tracer tracking method. The specific implementation plan is shown in Figure 11. An area with a working length of 1500 mm and a working width of 450 mm is selected in the middle of the working distance. A tracer is set every 150 mm, a total of 10 tracers being set, having the labels 1, 2, 3 to 10. The tillage direction is X direction, the width direction is Y direction, and the tillage depth direction is Z direction. After the tillage is completed, the displacement change of the tracer in the three directions is measured and the measurement results are shown in Figure 12.

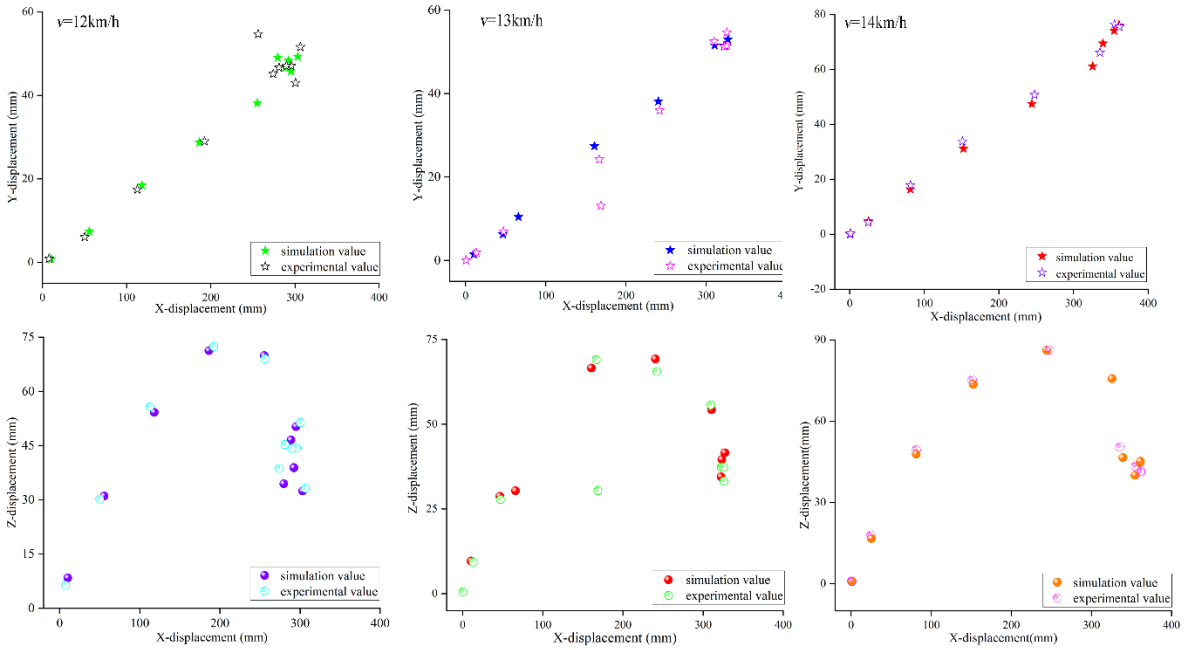


Fig. 12 - Soil displacement

The post-processing function in EDEM software is used to select ten regions and number them as 1-10 successively according to the actual tracer placement method. The displacement of particles in each region in three directions is obtained to ensure that the volume of the regions is consistent with the volume of the tracer, and the same number of soil particles in each region. It can be seen from Figure 12 that the simulation results are basically consistent with the experimental values, indicating that the model can better predict the soil displacement in high-speed cultivation process.

In order to further obtain the information of the soil-tool interaction, soil particles in the tillage area are selected as the research object of displacement. The value of the particle displacement in the X-axis direction, Y-axis direction and Z-axis direction are obtained. The time-displacement curves of particles at different speeds are obtained through data processing software, as shown in Figure 13.

It can be seen the soil particles have a large displacement in the three directions when the speed is 14 km/h. The difference in the change rate in the Z direction is significant, while the change rate in the X and Y directions is relatively small.

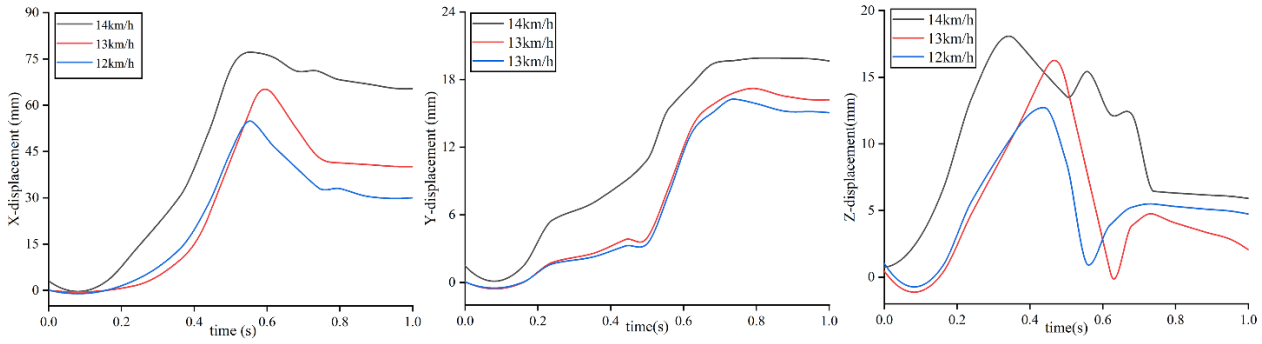


Fig. 13 - Soil average displacement in cultivation area

CONCLUSIONS

(1) The no-till soil was taken as the research object and the Edinburgh Elasto-Plastic Adhesion (EEPA) was chosen as contact model to calibrate the soil parameters using the discrete element method, which lays the foundation for the research on the soil dynamics properties and soil-tool interactions in the process of high-speed tillage.

(2) Plackett-Burman method was used to screen out that the plastic variable ratio λ_P and surface energy $\Delta\gamma$ had significant effects on AOR and soil strain. Quadratic orthogonal regression test was conducted according to the test result of Plackett-Burman method, the regression equation was established and the interaction effects of the factors were analyzed. The AOR test and uniaxial seal compression test were used to obtain the measured values of AOR and soil strain for optimal solution. After optimization, the plastic variation ratio λ_P is 0.543, and the surface energy $\Delta\gamma$ is 7.32 J/m^2.

(3) The optimized parameters were used for simulation tests. The error values were both less than 1% by comparing AOR and strain of simulation and experiment, and the stress-strain curves of simulation were basically consistent with the experiment, proving the reliability of the model. The error between the simulated value and the measured value of the ditch width was less than 3.04% after comparison, and the simulated value and the measured value of the soil displacement are basically the same. Therefore, the model predicts the soil dynamic characteristics in high-speed tillage.

ACKNOWLEDGEMENT

This paper was Supported by “the National Key Research and Development Program of China” (2021YFD2000401).

REFERENCES

[1] Adajar J., Alfaro M., Chen Y., Zeng Z., (2021), Calibration of discrete element parameters of crop residues and their interfaces with soil. *Computers and Electronics in Agriculture*, Vol.188, pp.106349.

[2] Bahrami M., Naderi-Boldaji M., Ghanbarian D., (2020), Dem simulation of plate sinkage in soil: calibration and experimental validation. *Soil & Tillage Research*, Vol.203, pp.104700.

[3] Barr J.B., Ucgul M., Desbiolles J., Fielke, J., (2019), Development and field evaluation of a high-speed no–till seeding system. *Soil & Tillage Research*, Vol.194, pp.104337.

[4] Cao X., Wang Q., Li H., (2021), Combined row cleaners research with side cutter and stubble clean disk of corn no-till seeder (玉米免耕播种机侧置切刀与拨茬齿盘组合清茬装置研究). *Transactions of the Chinese Society for Agricultural Machinery*, Vol.52, Issue 03, pp.36-44.

[5] Chen Y., Munkholm L.J., Nyord T., (2013), A discrete element model for soil–sweep interaction in three different soils. *Soil & Tillage Research*, Vol.126, pp.34-41.

[6] Dong X., Zheng H., Jia X., (2022), Calibration and experiments of the discrete element simulation parameters for rice bud damage. *INMATEH Agricultural Engineering*, Vol.68, Issue 03, pp.659-668. https://doi.org/10.35633/inmateh-68-65

[7] Jan D.P., Gemmina D.E., Verastegui F.R.D., Adam B., Cornelis W.M., (2019), Calibration of DEM material parameters to simulate stress-strain behaviour of unsaturated soils during uniaxial compression. *Soil & Tillage Research*, Vol.194, pp.104303.

[8] Fu M., Chen X., (2022), Parameters calibration of discrete element model for crushed corn stalks. *INMATEH Agricultural Engineering*, Vol. 69, Issue 01, pp. 399-408. https://doi.org/10.35633/inmateh-69-37

[9] Fielke J.M., Ucgul M., Saunders C., (2013), Discrete Element Modeling of Soil-Implement Interaction Considering Soil Plasticity, Cohesion and Adhesion. Kansas City, Missouri.

[10] Gao Z., Shang S., Xu N., (2022), Parameter calibration of discrete element simulation model of wheat straw-soil mixture in Huang Huai Hai production area (黄淮海产区小麦秸秆-土壤混合物的离散元仿真模型参数标定). *INMATEH Agricultural Engineering*, Vol.66, Issue 01, pp.201-210.

[11] Le V., Zhang J., Liu X., (2013), Ride comfort evaluation of vibratory roller under different soil ground (振动压路机用于不同土壤地面的平顺性评价). *Transactions of the Chinese Society of Agricultural Engineering*, Vol.29, Issue 9, pp.39-47.

[12] Lajeunesse E., Mangeney-Castelnau A., Vilotte J.P., (2004), Spreading of a granular mass on a horizontal plane. *Physics of Fluids*, Vol.16, Issue 7, pp.2371-2381.

[13] Milkevych V., Munkholm L.J., Chen Y., Nyord T., (2018), Modelling approach for soil displacement in tillage using discrete element method. *Soil & Tillage Research*, Vol.183, pp.60-71.

[14] Mohajeri M., Rhee C., (2021), Replicating cohesive and stress-history-dependent behavior of bulk solids: feasibility and definiteness in DEM calibration procedure. *Advanced Powder Technology*, Vol.32, Issue 5, pp.1532-1548.

[15] Qi L., Chen Y., (2019), Simulations of soil flow properties using the discrete element method (DEM). *Computers and Electronics in Agriculture*, Vol.157, pp.254-260

[16] Rusu T., (2014). Energy efficiency and soil conservation in conventional, minimum tillage and no-tillage. *International Soil & Water Conservation Research*, Vol.2, Issue 4, pp. 42-49.

[17] Thakur S.C., Morrissey J.P., Sun J., Chen J.F., Ooi J.Y., (2014), Micromechanical analysis of cohesive granular materials using the discrete element method with an adhesive elastoplastic contact model. *Granular Matter*, Vol.16, Issue 3, pp.383-400.

[18] Tagar A.A., Ji C., Adamowski J., Malard J., Abbasi, N.A., (2014), Finite element simulation of soil failure patterns under soil bin and field testing conditions. *Soil & Tillage Research*, Vol.145, pp.157-170.

[19] Wang W., Song J., Zhou G., (2022), Simulations and experiments of the seedbed straw and soil disturbance as affected by the strip-tillage of rowcleaner (带状耕作对种床秸秆清除率和土壤扰动的仿真与试验). *INMATEH Agricultural Engineering*, Vol.66, Issue 01, pp.49-61.

[20] Xie F., Wu Z., Wang X., (2020), Calibration of discrete element parameters of soils based on unconfined compressive strength test. *Transactions of the Chinese Society of Agricultural Engineering*, Vol.36, Issue 13, pp.39-47.

[21] Zhang R., Han D., Ji, Q., (2017), Calibration Methods of Sandy Soil Parameters in Simulation of Discrete Element Method (离散元模拟中沙土参数标定方法研究). *Transactions of the Chinese Society for Agricultural Machinery*, Vol.48, Issue 03, pp.49-56.

DESIGN AND EXPERIMENT OF CLAMPING-PULL-OFF APPLE PICKING ROBOT
/
夹持-拉断式苹果采摘机器人设计与实验

Shike GUO, Min FU*, Xiaoman CUI, Zijan WANG, Chengmeng WANG
Northeast Forestry University, College of Mechanical and Electrical Engineering, Harbin / China;
Tel: +86 15663688203; E-mail: fumin1996@163.com
DOI: https://doi.org/10.35633/inmateh-71-22

Keywords: *apple; picking robot; clamping-pull-off type; kinematic analysis; trajectory planning.*

ABSTRACT

For the standardized apple orchards in China, which are mainly dwarfed and densely planted, firstly, according to the spatial distribution characteristics of fruits within the tree canopy, a clamping-pull-off apple picking robot was developed by analyzing the parameters of apple cultivation and picking methods, in order to replace the manual harvesting operation. Then, the Denavit-Hartenberg (DH) method was used to establish the kinematic Equations of the apple-picking robot, the forward and inverse kinematic calculations were carried out, and the Monte Carlo method was used to analyze the workspace of the robot. Through the robot picking task planning and the simulation of the trajectory of the robotic arm, the scheme of the robot's picking strategy was given, and MATLAB software was applied to simulate the motion trajectory as well as to verify the feasibility of the trajectory planning scheme and the picking strategy. Finally, an apple-picking test bed was set up, the corresponding picking control system program was designed, and 45 apples were selected for picking tests. The results showed that during the robot's picking process, the average time for picking each fruit was 7.59 seconds, the fruit recognition success rate was 86.67%, and the picking damage rate was 5.13%.

摘要

针对以矮化密植为主的中国标准化苹果园，首先根据树冠内果实空间分布特征，通过苹果栽培参数及采摘方法分析，开发出一种夹持-拉断式苹果采摘机器人，以代替人工采收作业。然后，通过 D-H 方法建立苹果采摘机器人运动学方程，并进行了正、逆运动学计算，并采用蒙特卡罗法分析了机器人作业空间。通过对机器人采摘任务规划及机械臂轨迹仿真，进一步给出了整机采摘轨迹的方案，并应用 MATLAB 软件对整机运动轨迹进行仿真，验证了轨迹规划方案和采摘策略的可行性。最后，搭建了苹果采摘试验台，设计出相应的采摘控制系统程序，并选取了 45 个苹果进行采摘测试。结果表明，该机器人采摘每个果实的平均时间为 7.59s，果实识别成功率为 86.67%，采摘损伤率为 5.13%。

INTRODUCTION

Rich in minerals and vitamins, apples are one of the fruits that are consumed regularly. China is a large apple-producing country in the world, the apple planting area in China covered 2.32 million hectares, accounting for 17.9% of the global total planting area, with an annual output of about 43 million tons *(Bu et al., 2020)*. In order to timely, efficiently, and carefully harvest apples, annual orchards require a large seasonal manual labor for harvesting, with labor costs accounting for about 66% of total costs. With the expansion of the apple planting industry, the conventional manual picking method struggles to meet the current market demand. In the face of an escalating labor shortage, the development of efficient and adaptable apple harvesting robots holds significant practical value *(Lan et al., 2022)*.

With the rapid development of information technology, agricultural mechanization is moving to the next new development stage, namely, agricultural precision *(Hou, 2020)*. Scholars have conducted a series of studies on fruit and vegetable picking robots for apples *(Jia et al., 2020; Zhang et al., 2019)*, strawberries *(Mejia et al., 2023; Xiong et al., 2019),* kiwis *(He et al., 2023; Wang et al., 2023)*, citrus *(Sun et al., 2023; Yin et al., 2023)*, and tomatoes *(Feng et al., 2018; Wang et al., 2023).* Improving the picking efficiency and non-destructive picking of picking robots are hot research topics *(Jia et al., 2020)*, and related scholars have proposed their own solutions. For example, Zhao et al., *(2020)*, designed a pneumatic hybrid-driven apple-picking robot, in which after localizing the fruit coordinates through the vision system, the end-effector used flexible gripping to capture the fruits and separate the fruit stalks with a cutter. The hybrid use of both electric and pneumatic drives significantly improved the picking efficiency of the robot, and the average time required for harvesting each fruit was 7.81 s, with a successful harvest rate of 81.25%.

Williams et al., *(2019)*, developed a kiwifruit four-arm picking robot with four arms mounted in parallel on a robotic platform. The picking sequence of the robotic arms was coordinated by the control system during the picking operations, greatly improving the efficiency of the robot's picking. The average time required for harvesting each fruit was 5.5 s, with a successful harvest rate of 51%.

The end-effector is one of the critical components of the picking robot *(Chen et al., 2023).* Considering the growth characteristics and picking requirements of various types of fruits, different structural forms of end-effectors should be designed to achieve efficient picking *(Fu et al., 2015)*. For example, considering the growth characteristics of strawberries cultivated on ridges, picking requires high flexibility. Therefore, *Zhang et al., (2023)*, designed a six-degree-of-freedom clamping strawberry-picking end-effector with a clamping mechanism equipped with blades to harvest the fruit by clamping off the fruit stalks. Considering the fragile epidermis of tomato fruits, *Chen et al., (2021)*, developed a pneumatic suction-clamp integrated three-jaw picking end-effector that utilized a pneumatic system to regulate the clamping force and picked the fruits through a four-step action of adsorption, pull-back, clamping, and twisting. Due to the compressive nature of the gas, the end-effector had a certain buffering and protective effect, reducing the damage rate of tomato fruits. Addressing citrus and other spherical fruits, *Xu et al., (2018)*, designed a suction navel orange picking end-effector, using a suction cup to extract the fruit and then separating the fruit from the stalk with a cutter. The above research provides useful insights for the development of apple and other fruit and vegetable picking technology, but most of the current apple-picking end-effectors have certain limitations and are not adapted to picking fruits of different shapes, sizes, and various postures in any environment, i.e., the versatility is weak.

Given the above analysis, this paper focused on the typical standardized apple orchard working conditions in China and designed an apple-picking robot suitable for picking fruits of various shapes and sizes. Firstly, MATLAB software was performed to conduct forward and reverse kinematics analysis of the apple-picking robot, and the robot's workspace range was determined. Then, by planning the picking task and simulating the trajectory of the robotic arm, the picking strategy was formulated. Finally, an apple-picking test bed was established to verify the working efficiency of the apple-picking robot.

MATERIALS AND METHODS

Background

China’s standardized apple orchards feature dwarfed and densely planted trees with a high spindle shape, providing advantages such as a compact tree shape, open space in tree rows, good ventilation and light penetration, and ease of mechanized operations. As shown in Figure 1, the row spacing of fruit trees is about 3.0~4.0 m, with fruit tree heights generally ranging from 2.5~3.0 m, crown widths of 1.0~1.5 m, thicknesses of about 0.5~1.0 m, and a range of depths of fruit distributions of 0~0.4 m. Statistically, about 90% or more of the fruits are distributed at a height of 0.6-2.6 m *(Feng et al., 2023)*. According to the growth condition of dwarfed apple trees, it is determined that the target horizontal working space of the picking robotic gripper is 0~1.5 m, with a vertical working space of 0.5~2.8 m.

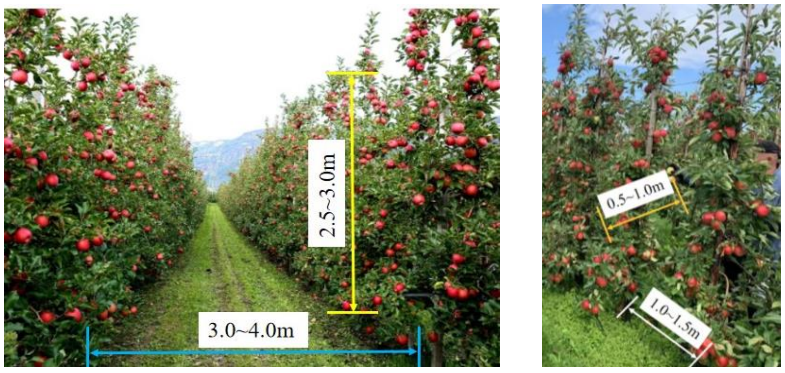


Fig. 1 - Dwarf and dense planting standard orchard

Fruit harvesting methods

During the process of picking apples, the end-effector first carries out the grasping action, targeting either the fruit or the fruit stalk. The main methods of capture include the clamping type and the suction type. After completing the gripping action, the fruits need to be separated from the fruit trees, with separation methods typically involving cutting, pulling, and twisting.

Following fruit picking, the primary methods of fruit collection include putting back, throwing down, and pipe collection. The specific analysis of the implementation of each stage is shown in Table 1.

Table 1

End-effector harvesting action methods

	Action	Principle	Characteristic
Capturing fruit method	Grab	Simulating the human hand to grab the fruits	Suitable for capturing fruits of all sizes
	Suck	Sucking the fruits, the end-effector by negative pressure	Suitable for capturing small shaped fruits
Separating fruit stalks method	Cut	Cutting the fruit stalks by means of cutters	Low damage to fruits and plants, but complicated control system
	Pull	Using external force to pull and break the fruit stalks	The operation is simple, but requires control of the force of pulling off the fruit stalks
	Twist	Using external force to twist off the fruit stalks	Rapidly twist off fruit stalks, but easily damages fruit skins
Collecting fruits method	Put back	Using a robotic arm to place fruits into a collection device	Reducing fruit damage but is time consuming
	Throw down	Releasing the fruit directly after picking it from the tree	Easy and convenient to operate, but easy to damage the fruit
	Pipeline	The fruit falls into the collection device through a pipeline	Fruits collection is efficient, but requires the design of piping to match the machine

After comparative analysis, grabbing is used to capture apples, pulling off to separate the stalks, and placing to collect the fruits. The geometric model of the apple-picking method is shown in Figure 2.

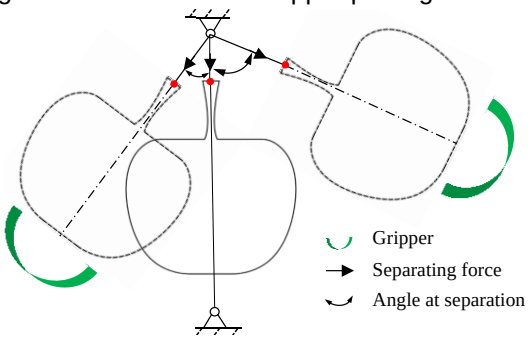


Fig. 2 - Geometric model of apple picking method

In manual harvesting operations, apples are picked in such a way that the stalks are pulled directly off the branches. The resulting tensile force pulls off the fruit stalks by tending to separate the fruit from the branch relative to each other. Inspired by the manual harvesting methods described above, the law of the separation of apple fruits from fruit stalks was investigated in a preliminary stage. From the study in reference *Chen et al., (2022)*, it can be observed that when the fruit stalk was separated from the branch at an arbitrary angle without damaging the fruit, the tensile force at separation increased with the increase of the apple diameter, within a range of 8.88 N to 39.6 N. Additionally, the maximum pressure an apple can withstand was found to be 15.35 N after an apple resistance test. Therefore, in this paper, to reduce the damage rate of the fruits during picking and to ensure the quality of the fruits, the clamping force when picking the fruits is set to 15.35 N, and the pulling force when separating the fruit stalks is set to 40 N.

Structure and working principle of the whole machine

The overall structure of the apple-picking robot is shown in Figure 3, mainly consisting of a robotic gripper, RGB-D camera, robotic arm, fruit collection box, support frame, navigation camera, and crawler chassis. While working, the robot first performs system initialization. Then, the robot localizes the fruit tree through the navigation system and stops when it reaches the position of the fruit tree. The RGB-D camera starts scanning the surroundings and, after recognizing the presence of apples nearby, the robotic arm carries the robotic gripper to hold the apples with the preset gripping force and uses a pulling and tugging method to pick the apples from the fruit tree. Finally, the robotic arm takes the robotic gripper and places the picked apples into the fruit collection box, completing the single-picking process.

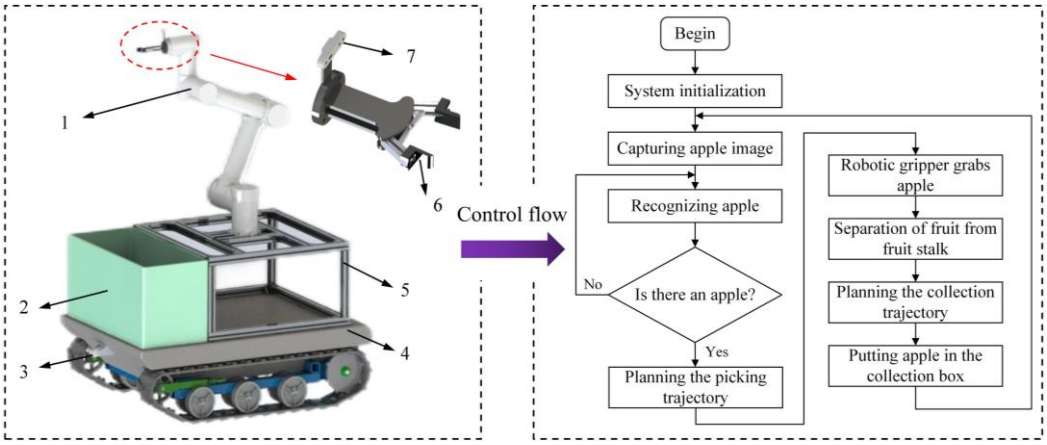


Fig. 3 - Structure and control flow of the apple picking robot

1. six-degree-of-freedom robotic arm 2. fruit collection box 3. navigation camera 4. crawler chassis 5. support frame 6. robotic gripper; 7. RGB -D camera

KINEMATIC ANALYSIS

Robot kinematics is primarily concerned with analyzing the relationship between the position of the end-effector and the joint variables of the robotic arm *(Wang et al., 2020)*. This chapter lays the foundation for the trajectory planning and picking strategy for robot by calculating the forward and inverse solutions of the robot kinematics and analyzing the workspace.

Forward kinematic analysis

The kinematic equations of the apple-picking robot were established using the Denavit-Hartenberg (DH) parameter method, and the connecting rod coordinates are shown in Figure 4. The D-H parameters for each joint were determined based on the connecting rod parameters and the relationships within the established coordinate system, as shown in Table 2.

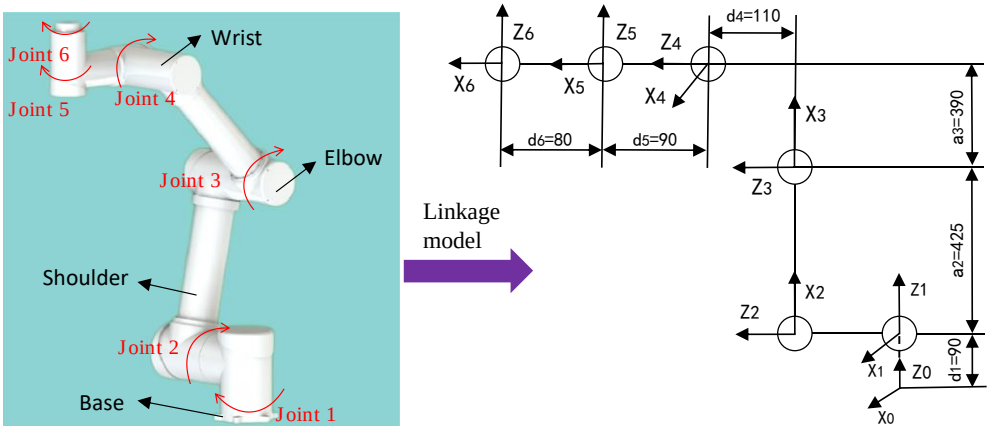


Fig. 4 - The connecting rod coordinate system

Table 2

Parameters of the apple-picking robot

i	α_i / (°)	a_i / mm	d_i / mm	θ_i/(°)	Variable Range
1	90	0	90	θ_1	-360~360
2	0	425	0	θ_2	-90~90
3	0	390	0	θ_3	-180~180
4	90	0	110	θ_4	-30~30
5	-90	0	90	θ_5	-90~90
6	0	0	80	θ_6	-90~90

where: i is the number of joints, α_i, is the rotation angle of the connecting rod, a_i is the length of the connecting rod, d_i is the offset distance of the connecting rod and θ_i is the joint angle. θ_1, θ_2, θ_3, θ_4, θ_5, and θ_6 are joint angle variables.

The transformation matrix between neighboring connecting rod coordinate systems is:

$$ {}^{i-1}_{i}T = \begin{bmatrix} cos\theta_i & -sin\theta_i cos\alpha_i & sin\theta_i sin\alpha_i & a_i cos\theta_i \\ sin\theta_i & cos\theta_i cos\alpha_i & -cos\theta_i sin\alpha_i & a_i sin\theta_i \\ 0 & sin\alpha_i & cos\alpha_i & d_i \\ 0 & 0 & 0 & 1 \end{bmatrix} \quad (1) $$

where:

${}^{i-1}_{i}T$ represents the Homogeneous transformation matrix of the connecting rod relative to the connecting rod $i-1$.

According to the principle of forward kinematics, each connecting rod transformation matrix can be obtained by substituting each connecting rod parameter from Table 2 into Equation (1).

Where the apple- picking robot equation of motion ${}^{0}_{6}T$ is expressed as the position of the end-effector with respect to the base coordinate system:

$$ {}^{0}_{6}T = {}^{0}_{1}T\,{}^{1}_{2}T\,{}^{2}_{3}T\,{}^{3}_{4}T\,{}^{4}_{5}T\,{}^{5}_{6}T = \begin{bmatrix} n_x & o_x & a_x & p_x \\ n_y & o_y & a_y & p_y \\ n_z & o_z & a_z & p_z \\ 0 & 0 & 0 & 1 \end{bmatrix} \quad (2) $$

Among them:

$$ \begin{cases} n_x = c_6\left(s_1s_5 + c_5c_1c_{234}\right) - s_6c_1s_{234} \\ n_y = c_6\left(c_5s_1c_{234} - c_1s_5\right) - s_6s_5s_{234} \\ n_z = c_5c_6s_{234} + s_6c_{234} \\ o_x = -s_6\left(c_5c_1c_{234} + s_1s_5\right) - c_6c_1s_{234} \\ o_y = -s_6\left(c_5s_1c_{234} - c_1s_5\right) - c_6s_1s_{234} \\ o_z = c_6c_{234} - c_5s_6s_{234} \\ a_x = -s_5c_1c_{234} + c_5s_1 \\ a_y = -s_5s_1c_{234} - c_1c_5 \\ a_z = -s_5s_{234} \\ p_x = 90c_1s_{234} + 110s_1 + 80\left(c_5s_1 - s_5c_1c_{234}\right) + 425c_1c_2 + 390c_1c_{23} \\ p_y = 90s_1s_{234} - 110c_1 - 80\left(s_5s_1c_{234} + c_1c_5\right) + 425c_2s_1 + 390s_1c_{23} \\ p_z = 90 - 90c_{234} + 425s_2 + 390s_{23} - 80s_5s_{234} \end{cases} \quad (3) $$

where:

c_i is an abbreviation of $cos\theta_i$, s_i is an abbreviation of $sin\theta_i$, $cos(\theta_i + \theta_j) = c_{ij}$, $sin(\theta_i + \theta_j) = s_{ij}$.

Inverse kinematic analysis

The kinematic inverse solution is that the angle of each joint is calculated by knowing the position and attitude of the robot's end-effector to achieve precise positioning and control of the robot. In this section, the matrix inverse multiplication analytic method was used to solve the kinematic inverse solution of the apple picking robot.

The values of the joint variables are solved in turn according to the analytic method as:

$$ \theta_1 = A\tan 2(80a_y - p_y, 80a_x - p_x) - A\tan 2\left(110, \pm\sqrt{(80a_y - p_y)^2 + (80a_x - p_x)^2 - 110^2}\right) \quad (4) $$

$$ \theta_2 = A\tan 2\left(\frac{(a_3c_3 + a_2)n - a_3s_3m}{a_2^2 + a_3^2 + 2a_2a_3c_3}, \frac{m + a_3s_3s_2}{a_3c_3 + a_2}\right) \quad (5) $$

$$ \theta_3 = \pm\arccos\left(\frac{m_2 + n_2 - a_2^2 - a_3^2}{2a_2a_3}\right) \quad (6) $$

$$ \theta_4 = A\tan 2\left(-s_6\left(n_xc_1 + n_ys_1\right) - c_6\left(o_xc_1 + o_ys_1\right), o_zc_6 + n_zs_6\right) - \theta_2 - \theta_3 \quad (7) $$

$$\theta_5 = \pm \arccos\left(a_x s_1 - a_y c_1\right) \tag{8}$$

$$\theta_6 = A\tan 2\left(\frac{n_x s_1 - n_y o_x}{s_5}, \frac{o_x s_1 - o_y c_1}{s_5}\right) \tag{9}$$

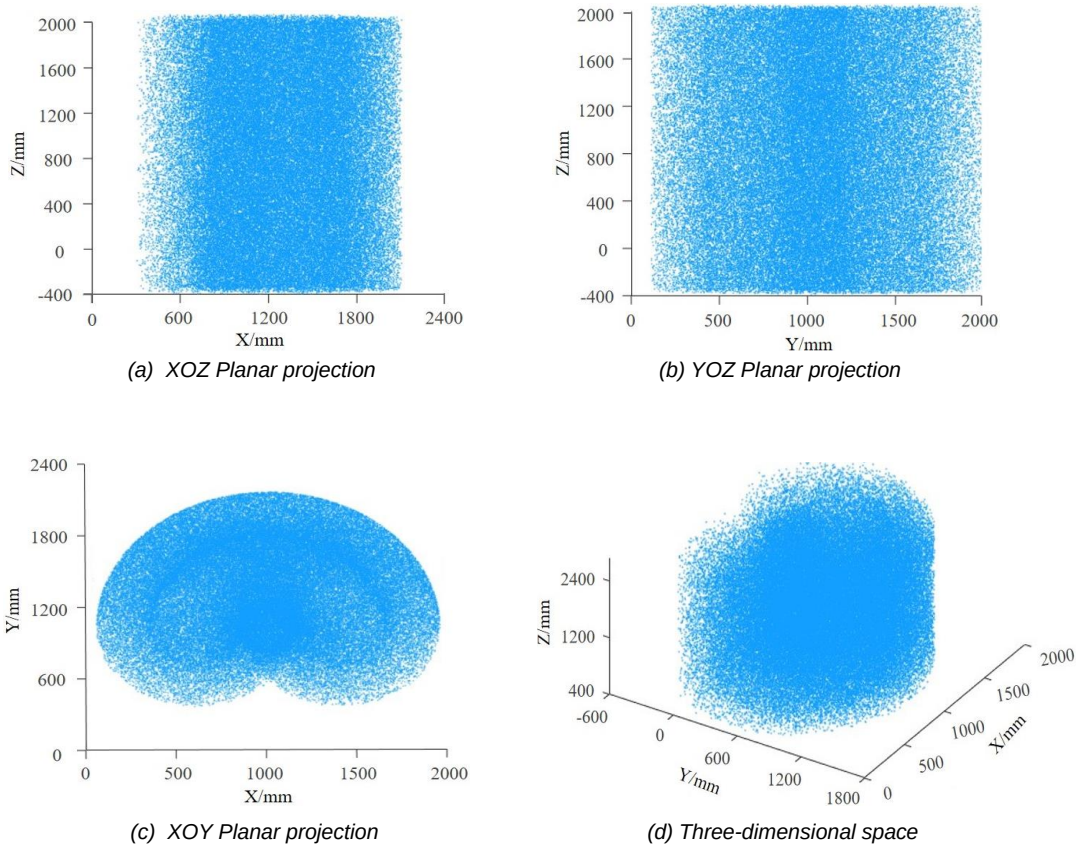
where:

$$\begin{cases} m = 90\left(s_6\left(n_x c_1 + n_y s_1\right) + c_6\left(o_x c_1 + o_y s_1\right)\right) - 90\left(a_x c_1 + a_y s_1\right) + p_x c_1 + p_y s_1 \\ n = p_z - 90 - 80a_z + 90\left(o_z c_6 + n_z s_6\right) \end{cases}$$

Workspace analysis

The workspace is the collection of spatial points that can be reached by the end-effector during the picking process of the robot, and its shape and size are the key factors that determine the robot's work performance. Based on the Robotics Toolbox in MATLAB software, the Monte Carlo method was used to solve the approximate solution in motion space *(Xu et al., 2018).*

Through the forward kinematics Equation (2), the position vector of the end-effector relative to the base was solved, and then multiple end position coordinate points were randomly generated by the Rand function to obtain the workspace as shown in Figure 5.



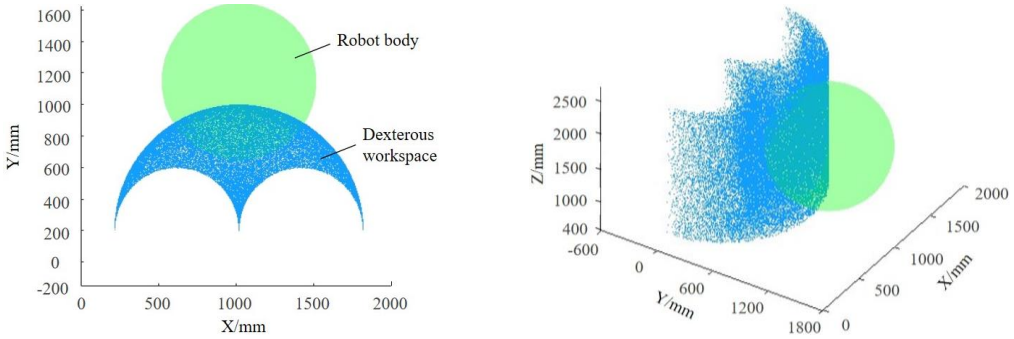
(a) XOZ Planar projection *(b) YOZ Planar projection*

(c) XOY Planar projection *(d) Three-dimensional space*

Fig. 5 -Workspace of the apple-picking robot

From Figure 5, the workspace of the apple-picking robot is a heart-like columnar space, X-direction travel is about 1.4 m; Y-direction travel is about 1.8 m; and Z-direction travel is about 2.0 m. The simulation results provide the foundation for the trajectory planning of the robotic arm and the design of the picking strategy in the subsequent section.

The dexterous workspace of the apple-picking robot is shown in Figure 6. The space avoids collisions between the robotic arm and the internal branches of the apple tree, as well as interference between the arm and the mechanics of the robot. During the actual picking task, the position of the picked apples should be within the dexterity workspace.



(a) XOY Planar projection *(b) Three-dimensional space*

Fig. 6 -Space for dexterous work

PICKING TRAJECTORY PLANNING

Picking task planning

When the robot has finished picking apple $i-1$ and will pick apple i, the picking motion can be divided into three phases:

(1) Leaving the apple $i-1$ place, avoiding branches and leaves.

(2) Moving within a safe area where there will be no collision with the branching vine, approaching the target apple i.

(3) Arriving at the target apple i, the robotic gripper performs the picking.

During the transfer of the picking target, it was necessary to ensure that the branches of the fruit tree don't interfere with the robot. During trajectory planning, a safety point H was added to split the motion of the second stage into two parts to ensure that the positional transitions of the robotic arm could take place in a safe area. As a result, each picking task involved the planning of four trajectory segments and five points, as shown in Figure 7.

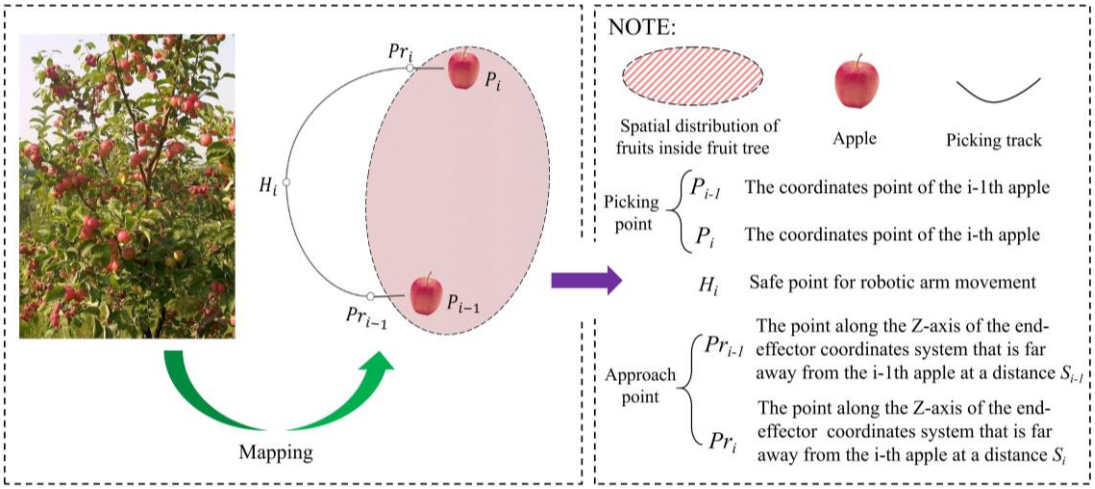


Fig. 7 - Trajectory planning node between two picks

When $i \neq 0$, the robot has just finished picking apple $i-1$ and will pick apple i. The path for trajectory planning is:

$$P_{i-1} \rightarrow Pr_{i-1} \rightarrow H_i \rightarrow Pr_i \rightarrow P_i$$

When $i = 0$, the robot has just started to work, the robot arm is in the zero position, and the coordinates' position of the end-effector is the point H at this time. The path for trajectory planning is:

$$H_0 \rightarrow Pr_0 \rightarrow P_0$$

Trajectory planning of the robotic arm

The purpose of robotic arm trajectory planning is to ensure that the position, velocity, and acceleration function curves of each joint variable are continuous and smooth during the completion of operational tasks *(Yang et al., 2020)*.

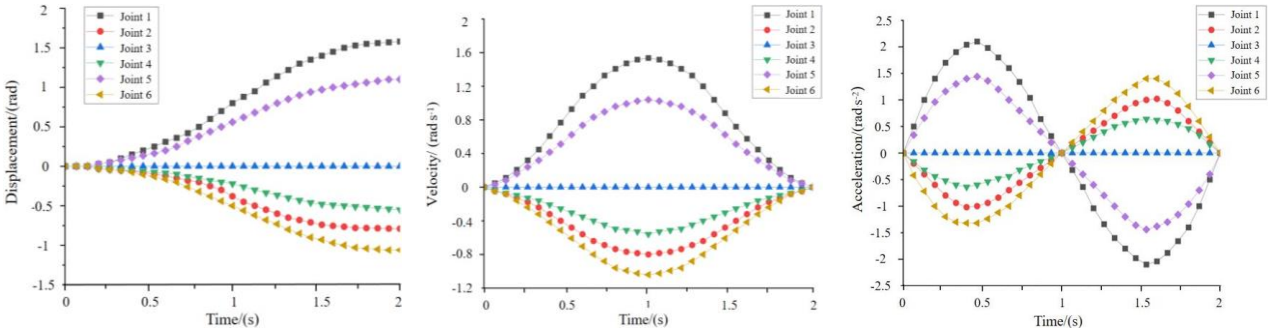
Common robot trajectory planning methods today include trapezoidal planning, S-planning, and polynomial planning. Among these, polynomial planning is the most commonly used, with a mature planning method that ensures the continuity of displacement, velocity, and acceleration in the planning process, allowing for smooth robot movement. Therefore, in this paper, the fifth-degree polynomial interpolation method was used, and the MATLAB Robotics toolbox was invoked to simulate joint space trajectory planning for any two points in the robot end-effector space.

A time-varying function is utilized to represent each joint variable during joint space trajectory planning, by which the process of trajectory change of the robot over a certain period of time is illustrated. The start point coordinate q_0 and end point coordinate q_1 of the robot are given. Utilizing the jtraj function, the call format is:

$$\begin{bmatrix} q & qd & qdd \end{bmatrix} = jtraj(q_0, q_1, t) \tag{10}$$

where: q stands for displacement; qd stands for velocity; qdd stands for acceleration; t stands for simulation time.

The $function\,jtraj$ is a fifth-degree polynomial interpolation, with default initial and final velocities set to zero. The simulation time was 2 s, and the jtraj function was called to observe the motion change process of each joint. The plot function was then used to generate the displacement, angular velocity, and angular acceleration curves of the robot, as shown in Figure 8.



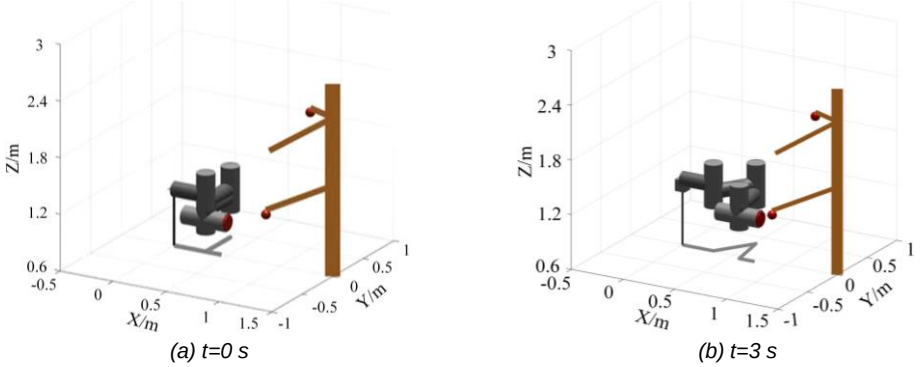
(a) displacement curve *(b) velocity curve* *(c) acceleration curve*

Fig. 8 - Dynamics of the joints over time

Figure 8(a) reflects the movement process of each joint over time. Figure 8(b) reflects the velocity variation of each joint over time, and they satisfy the requirement that the starting and ending velocities of the fifth-degree polynomial interpolation are all zero. The change in acceleration for each joint is depicted in Figure 8(c) and the curved motion is smooth without abrupt changes. Velocity and acceleration curves are smooth and excessive, without inflection points, interruptions, jumps, and other phenomena, indicating that the robot ran smoothly.

Dynamic simulation of picking trajectory

Based on kinematic forward and inverse solutions, as well as workspace analysis of the apple-picking robot, MATLAB simulation software was utilized to simulate the entire motion trajectory of the apple-picking robot. Two apples, positioned at different heights on an apple tree, were chosen as examples (the brown area represents the apple tree, and the red area represents the apples) to simulate the growing environment of apples in an orchard. The simulation results are shown in Figure 9.



(a) t=0 s *(b) t=3 s*

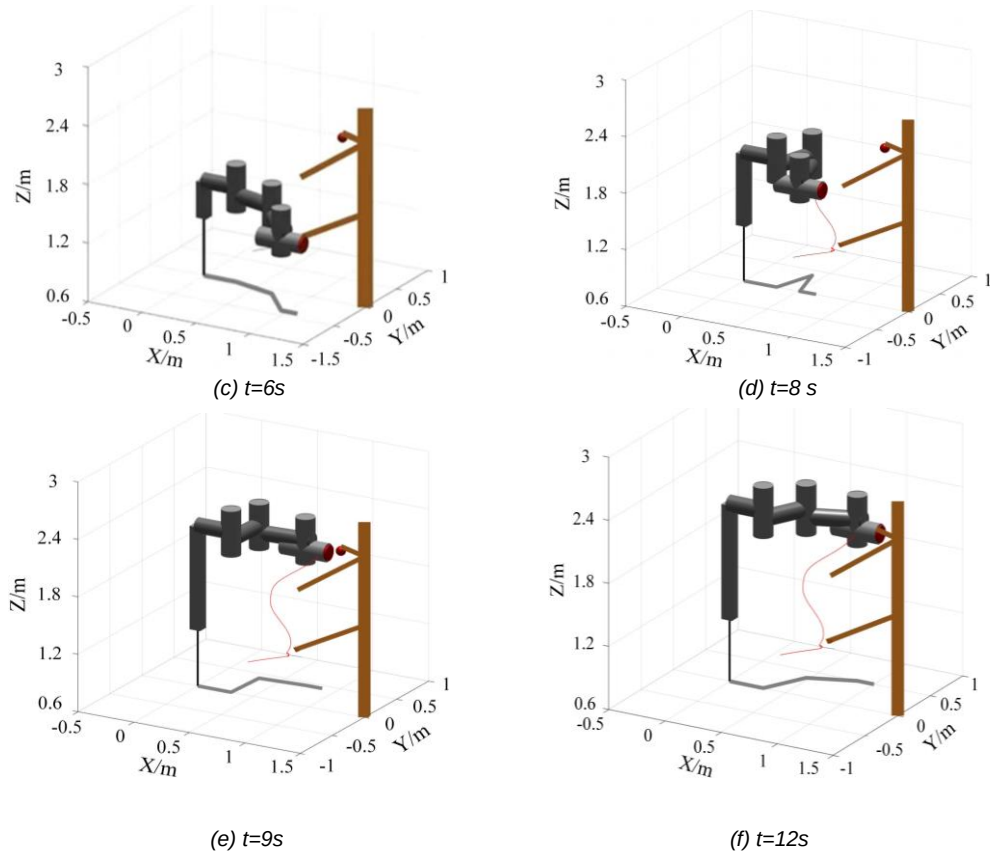


Fig. 9 - Dynamic simulation of the picking trajectory

The entire process took 12 s, starting from the recognition of the first apple to the completion of the second apple picking. At t = 0 s, the robot was in the initial state. From 1 to 3 s, the robot recognized the first apple and proceeded to pick it. Between 3 and 6 s, the robotic gripper successfully completed the picking of the first apple by clamping the fruit and pulling off the stalk. From 7 to 12 s, after navigating around branch obstacles, the robot recognized the second apple and completed the picking process. The simulation results showed that the robot took 6 s from the beginning of recognizing the first fruit to completing the picking, and then took 3 s to recognize the second fruit. During the fruit picking process, the entire picking trajectory of the machine met the requirements of the apple picking workspace, which verified the feasibility of the trajectory planning scheme and the picking strategy.

RESULTS

Control systems design

A picking test bed was set up in the laboratory environment for the apple picking test, and its hardware platform mainly includes robotic gripper, a robotic gripper, an RGB-D camera, an upper computer, and a control cabinet, as shown in Figure 10(a).

The upper computer is mainly responsible for running the main program of the control system, including acquiring and processing platform data and controlling platform equipment. The RGB-D camera is mainly responsible for providing real-time image data of scene objects and distance information included in the depth image data. The robotic gripper is mainly responsible for driving the robotic gripper to the designated position and cooperating with it to complete the corresponding action.

In addition, C+ + was used as the programming language in this paper, and MDK software was used for programming and debugging to design the picking control system program.

According to the working principle and operation flow of the robot, the visual recognition and localization module flow (see Figure 10(b)), the robotic gripper motion control module flow (see Figure 10(c)), and the robotic gripper motion control module flow (see Figure 10(d)) have been designed for controlling the hardware devices, such as the RGB-D camera, the robotic arm, and the robotic gripper.

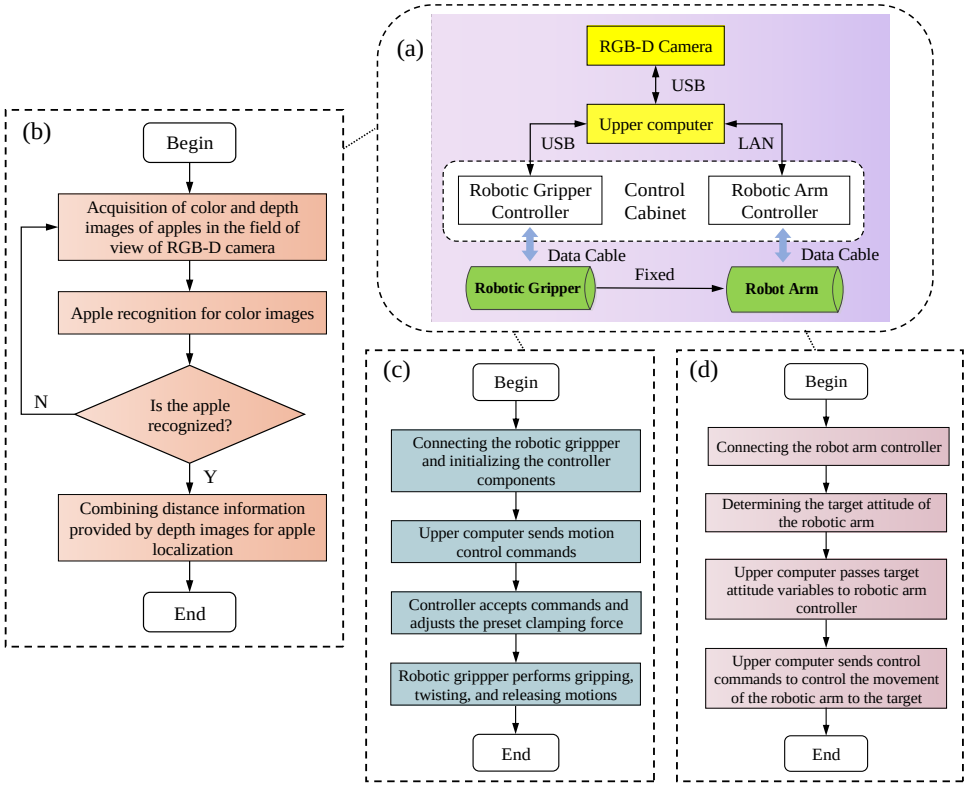


Fig. 10 - Hardware platform of the picking robot and the control flow of each module

(a). hardware platform; (b). control module of visual recognition and localization; (c). control module of the robotic gripper; (d). control module of the robotic arm

Results and analysis

The picking test was carried out on September 10, 2023, in a laboratory setting, as shown in Figure 11. Forty-five apples with an average fruit diameter of 72 mm were selected at the beginning of the test and placed at different heights of the fruit tree to verify the harvesting performance of the robot. During the work, the robotic arm was set to move at a speed of 1.5 m/s and separate the fruit stalks with a pulling force of 40 N, and the robotic gripper was set to hold the apples with a gripping force of 15.35 N. During the picking process, the robot first scanned the surroundings with an RGB-D camera, and after recognizing the apples, the robotic gripper gripped the apples with a preset gripping force. Then, the robotic arm carried the robotic gripper to pick the apples from the fruit tree in a pulling and tugging manner and carried the robotic gripper to put the picked apples into the collection box.

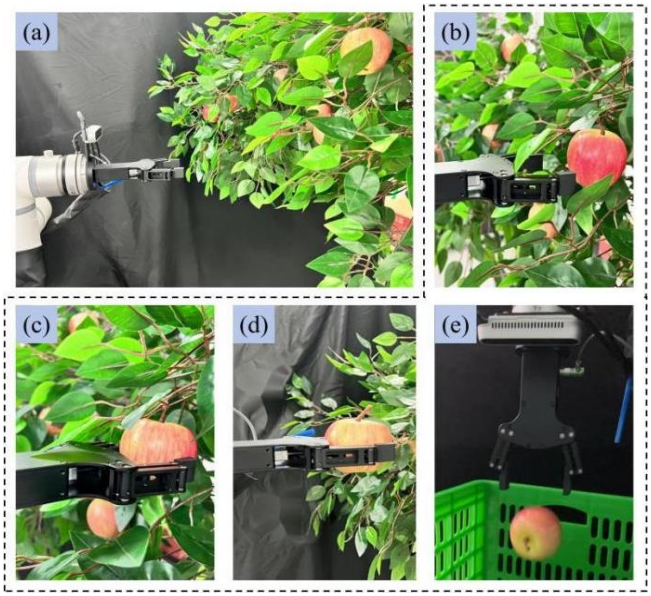


Fig. 11 - Apple picking process

(a). test Scenarios (b). recognizing apples (c). clamping apples at a preset clamping force (d). pulling off the stalks (e). collecting apples

Three picking tests were conducted from different angles of the fruit tree, and the results showed that the robot successfully recognized 39 fruits, with a recognition success rate of 86.67%. The robot collected 37 fruits without damage, resulting in a damage rate of 5.13%. The average time for picking each fruit was 7.59 seconds, of which the average time spent in the process of recognizing the fruits and moving to the picking stage was 3.26 seconds, while the average time spent in the process of picking and collecting the fruits was 4.33 seconds.

The reason for the failure of fruit picking in the test could be that some fruits were closer to the inner contour of the fruit tree and were obscured by branches and leaves, resulting in the RGB-D camera failing to recognize these fruits. In addition, the cause of fruit damage might be that when picking fruits that were too small in diameter, the preset gripping force exceeded the range of pressure that the fruit could withstand, resulting in the fruit being damaged by the robotic gripper.

CONCLUSIONS

(1) Taking Chinese dwarf anvil densely planted high spindle fruit trees as an object, a clamping-pull-off apple-picking robot was designed by analyzing apple cultivation parameters and picking methods. Firstly, the kinematic equations of an apple-picking robot were established by the D-H method, and forward and inverse kinematic calculations were performed. The robot reachable workspace and dexterous workspace ranges were solved using Robotics Toolbox in MATLAB software and the Monte Carlo method. Secondly, through the robot picking task planning and the simulation of the trajectory of the robotic arm, furthermore, the scheme of the robot's picking strategy was given. Finally, MATLAB was applied to simulate the motion trajectory of the apple-picking robot, validating the feasibility of the trajectory planning scheme and the picking strategy.

(2) An apple picking test bed was set up in the laboratory environment, and a corresponding picking control system program was designed based on the robot's working principle and workflow. Forty-five apples were selected and positioned at various heights on the fruit tree for picking tests. The results indicated that, during the robot's picking process, the average time for picking each fruit was 7.59 seconds, with a fruit recognition success rate of 86.67% and a picking damage rate of 5.13%.

ACKNOWLEDGEMENT

This paper was funded by the National Natural Science Foundation of China (Grant No.51975114).

REFERENCES

[1] Bu, L. X., Chen, C. K., Hu, G. R., Sugirbay, A., & Chen, J. (2020). Technological development of robotic apple harvesters: A review. *INMATEH-Agricultural Engineering*, 61(2), 151-164.

[2] Chen, K., Li, T., Yan, T., Xie, F., Feng, Q., Zhu, Q., & Zhao, C. (2022). A soft gripper design for apple harvesting with force feedback and fruit slip detection. *Agriculture*, 12(11), 1802.

[3] Chen, Q., Yin, C. K., Guo, Z. L., Wang, J. P., Zhou, H. P., & Jiang, X. S. (2023). Research status and development trend of apple picking robot key technology (苹果采摘机器人关键技术研究现状与发展趋势). *Transactions of the Chinese Society of Agricultural Engineering*, 39(04), 1-15.

[4] Chen, Z. W., Yang, M. J., Li, Y. W., & Yang, L. (2021). Design and test of tomato picking end-effector based on pneumatic non-destructive clamping control (基于气动无损夹持控制的番茄采摘末端执行器设计与试验). *Transactions of the Chinese Society of Agricultural Engineering*, 37(02), 27-35.

[5] Feng, C. C., Zhao, C. J., Li, T., Chen, L. P., Guo, X., Xie, F., et al. (2023). Design and testing of a four-arm apple picking robot system (苹果四臂采摘机器人系统设计与试验). *Transactions of the Chinese Society of Agricultural Engineering*, 39(13), 25-33.

[6] Fu, L., Zhang, F., Gejima, Y., Li, Z., Bin, W., & Cui, Y. (2015). Development and experiment of end-effector for kiwifruit harvesting robot (猕猴桃采摘机器人末端执行器设计与试验). *Transactions of the Chinese Society of Agricultural Machinery*, 46(3).

[7] Feng, Q., Zou, W., Fan, P., Zhang, C., & Wang, X. (2018). Design and test of robotic harvesting system for cherry tomato. *International Journal of Agricultural and Biological Engineering*, 11(1), 96-100.

[8] He, Z., Li, Z. X., Ding, X. T., Li, K., Shi, Y. G., & Cui, Y. J. (2023). Design and experiment of end effect for kiwifruit harvesting based on optimal picking parameters. *INMATEH-Agricultural Engineering*, 69(1).

[9] Hou, Z. (2020). Analysis of visual navigation extraction algorithm of farm robot based on dark primary colour. *INMATEH-Agricultural Engineering*, 62(3).

[10] Jia, W., Tian, Y., Luo, R., Zhang, Z., Lian, J., & Zheng, Y. (2020). Detection and segmentation of overlapped fruits based on optimized mask R-CNN application in apple harvesting robot. *Computers and Electronics in Agriculture*, 172, 105380.

[11] Jia, W., Zhang, Y., Lian, J., Zheng, Y., Zhao, D., & Li, C. (2020). Apple harvesting robot under information technology: A review. *International Journal of Advanced Robotic Systems*, 17(3), 1729881420925310.

[12] Lan, Y., Yan, Y., Wang, B., Song, C., & Wang, G. (2022). Current status and future development of the key technologies for intelligent pesticide spraying robots (智能施药机器人关键技术研究现状及发展趋势). *Transactions of the Chinese Society of Agricultural Engineering*, 38, 30-40.

[13] Mejia, G., de Oca, A. M., & Flores, G. (2023). Strawberry localization in a ridge planting with an autonomous rover. *Engineering Applications of Artificial Intelligence*, 119, 105810.

[14] Sun, Q., Zhong, M., Chai, X., Zeng, Z., Yin, H., Zhou, G., & Sun, T. (2023). Citrus pose estimation from an RGB image for automated harvesting. *Computers and Electronics in Agriculture*, 211, 108022.

[15] Wang, K., Zhang, W., Luo, Z. & Zhang, Y. (2020). Design and experiment of hitting pine cone picking robot (击打式松果采摘机器人设计与试验). *Transactions of the Chinese Society for Agricultural Machinery*, 51(8), 26-33.

[16] Wang, T., Du, W., Zeng, L., Su, L., Zhao, Y., Gu, F., Li, L., & Chi, Q. (2023). Design and Testing of an End-Effector for Tomato Picking. *Agronomy*, 13(3), 947.

[17] Wang, Y., He, Z., Cao, D., Ma, L., Li, K., Jia, L., & Cui, Y. (2023). Coverage path planning for kiwifruit picking robots based on deep reinforcement learning. *Computers and Electronics in Agriculture*, 205, 107593.

[18] Williams, H. A., Jones, M. H., Nejati, M., Seabright, M. J., Bell, J., Penhall, N. D., et al. (2019). Robotic kiwifruit harvesting using machine vision, convolutional neural networks, and robotic arms. *Biosystems Engineering*, 181, 140-156.

[19] Xiong, Y., Peng, C., Grimstad, L., From, P. J., & Isler, V. (2019). Development and field evaluation of a strawberry harvesting robot with a cable-driven gripper. *Computers and electronics in agriculture*, 157, 392-402. https://doi.org/10.1016/j.compag.2019.01.009

[20] Xu, L., Liu, X., Zhang, K., Xing, J., Yuan, Q., Chen, J., et al. (2018). Design and test of end-effector for navel orange picking robot (脐橙采摘机器人末端执行器设计与试验). *Transactions of the Chinese Society of Agricultural Engineering*, 34(12), 53-61.

[21] Xu, Z. B., Zhao, Z. Y., He, S., He, J. P., & Wu, Q. W. (2018). Improvement of Monte Carlo method for robot workspace solution and volume calculation (机器人工作空间求解的蒙特卡洛法改进和体积求取). *Optics and Precision Engineering*, 26(11), 2703-2713.

[22] Yang, C. G., Cheng, L., & Li, J. (2020). Robot control - kinematics, controller design, human-robot interaction and application examples (机器人控制–运动学、控制器设计、人机交互与应用实例). *Tsinghua University Press*: Beijing, China, pp.40-53.

[23] Yin, H., Sun, Q., Ren, X., Guo, J., Yang, Y., Wei, Y., Huang, B., Chai, X., & Zhong, M. (2023). Development, integration, and field evaluation of an autonomous citrus-harvesting robot. *Journal of Field Robotics*.

[24] Zhao, D., Wu, R., Liu, X., Zhang, X., & Ji, W. (2020). Design and Experiment of Apple Harvesting Robot Based on Gas-electric Hybrid Drive (气电混合驱动全天候苹果收获机器人设计与试验). *Transactions of the Chinese Society of Agricultural Machinery*, 51(2).

[25] Zhang, Y., Tian, Y., Zheng, C., Zhao, D., Gao, P., & Duan, K. (2019). Segmentation of apple point clouds based on ROI in RGB images. *INMATEH-Agricultural Engineering*, 58(3).

[26] Zhang, Y., Zhang, K., Yang, L., Zhang, D., Cui, T., Yu, Y., & Liu, H. (2023). Design and simulation experiment of ridge planting strawberry picking manipulator. *Computers and Electronics in Agriculture*, 208, 107690.

DESIGN AND EXPERIMENT OF AN END-EFFECTOR FOR HARVESTING SWEET PEPPER IN COMPLIANT OBSTACLE ENVIRONMENT
/
柔顺障碍环境下收获甜椒末端执行器的设计与试验

Yunting HUI[1#)], Yangyang LIAO[1#)], Decheng WANG[1*)], Xinxing LI[2*)], Zhiheng LU[3)], Yong YOU[1)], Hanchu JIA[1)]

[1)]College of Engineering, China Agricultural University, Beijing 100083, China;
[2)]College of Information and Electrical Engineering, China Agricultural University, Beijing 100083, China
[3)]Guangxi University, Nanning 530004, China;
** Correspondence: wdc@cau.edu.cn (D.W.). lxxcau@cau.edu.cn (X.L.).*
[#]These authors contributed equally to this work.
DOI: https://doi.org/10.35633/inmateh-71-23

Keywords: *sweet pepper picking; end-effector; mechanical properties; control system; experiment*

ABSTRACT

Picking sweet peppers by hand is often time-consuming and laborious. To overcome this, in the current study, we developed an end effector for mechanized and non-destructive harvesting of sweet pepper. The design includes grip modules, shear modules and control systems. Based on the establishment of an approximate mathematical model of sweet pepper fruit and the analysis of the biomechanical characteristics of sweet pepper fruit, a pinch finger was proposed. The proposed mechanism is able to successfully achieve non-destructive and stable fixation of sweet pepper and fruit bunches. Key parameters of peduncles cutting were obtained by the cutting test. A cutting mechanism was then designed to achieve efficient separation of the fruit and fruit stem. The designed end effector achieves precise control through a single-chip microcomputer and multi-sensor integrated control system to achieve mature target fruits. The test results showed that the picking success rate, damage rate and picking time of peppers were 93.3%, 1.6% and 5 seconds, respectively. The end effector designed for sweet pepper picking has a simple and reliable structure, which provides a reference for further research on sweet pepper picking robots.

摘要

手工采摘甜椒通常既费时又费力。为了克服这一点，在目前的研究中，我们开发了一种用于机械化和无损采摘甜椒的末端执行器。该设计包括夹紧模块、剪切模块和控制系统。在建立甜椒果实近似数学模型的基础上，结合对甜椒果实生物力学特性的分析，提出了夹指。所提出的机制能够成功地实现甜椒和果簇的无损稳定夹紧。通过对果穗的扦插试验，获得了果穗扦插的关键参数。然后设计了一种分离机构来实现果实和果柄的有效分离。所设计的末端执行器通过单片机和多传感器集成控制系统实现精确控制，获取成熟的目标果实。试验结果表明，辣椒的采摘成功率、损伤率和采摘时间分别为 93.3%、1.6%和 5s。所设计的甜椒采摘末端执行器结构简单可靠，为后续甜椒采摘机器人的研究提供了参考。

INTRODUCTION

Besides high vitamin A and C contents, sweet peppers are also rich in vitamin B and E, and minerals such as calcium, potassium, iron, and phosphorus (*Guo et al., 2016*). The content of many nutrients can increase up to five times following the maturity of sweet peppers (*Djurovic et al., 2015; Ferreira et al., 2016*). This vegetable also has a characteristic taste (*Lee et al., 2019*). The planting area of sweet peppers in China, which is second only to cabbage, accounts for 35% of the world's planting area of sweet peppers. In addition, Chinese sweet pepper production ranks first in the world (*Shi et al., 2017*). Picking is considered to be the most labor-intensive task in agricultural production (*Li et al., 2008; Graham et al., 2018*). The replacement of manual picking by robots has become a recent trend (*Chen et al., 2019*) following the popularization of agricultural technology (Kondo et al., 2009), the gradual reduction of rural labor and other related factors (*Fan et al., 2016; Bac et al., 2017*). As an integral component of fruit and vegetable picking robots, the end-effector is in direct contact with the fruit and plays an important role in improving the picking efficiency (*Song et al., 2006*) and operational stability of the picking robot (*Chiu et al., 2013; Jiang et al., 2017*).

Non-Chinese automatic sweet pepper picking robots have been developed over the past two decades, demonstrating great success in picking targets without affecting the environment of other crops (*Ji et al., 2014; Lehnert et al., 2017*). The grasping element of the "sweet pepper gripper" proposed by German crops team includes a passive adaptive FinRay finger, with a blade driven by the cylinder used to cut the sweet pepper from the plant (*Hemming J. et al., 2014*). The development of the end-effector is based on bionics and is able to protect the sweet pepper fruit.

Yet the bionic materials proved to be both difficult and expensive to process due to the complex structure of the gripping fingers, preventing the development of domestic promotion. Gauchel et al. designed a "lip-shaped end-effector" in 2012 that was placed close to the suction cup in order to stabilize the fruit without the requirement of holding fingers. However, the force exerted on the fruit during stalk cutting by the lip ring may break the fruit from the suction cup, while the large range of motion of the lip ring may damage the plant (*Bac et al., 2016*). FF Robotics, an Israeli company, simulated the manual picking process and designed a 3-degree-of-freedom Cartesian Coordinate Robot equipped with a telescopic three-finger underdriven end-effector, with the fingers coated with flexible material, which grasps the apple and rotates it by 90°, after which the robot arm retracts by a few inches, the fruit stalk is tugged and broken, and the end-effector lets go of the apple at the collection point to complete the picking of the apple (*Avigad et al., 2020*). Dogtooth Technologies in the UK designed an end-effector that utilizes a unique hooking of the strawberries by means of a broken shank gripping of the fruit stalk (*Robertson et al., 2020*). MetoMotion of Israel company designed a two-degree-of-freedom closed-chain string tomato stalk shear gripper for separating touching alibi bunches and gripping the target bunch tomato fruit stalks for robust and non-destructive harvesting (*Adi NIR et al., 2020*). LU RF developed a newly vacuum-based robotic apple harvesting system, using the twist-and-pull fruit picking method (*Renfu Lu et al., 2022*).

Despite the relatively limited research on fruit and vegetable picking robots in China (in the 1990s) (*Liu et al., 2017*), much progress has been made (*Lin et al., 2015*). For example, for low-destructive picking, a soft mechanism on the end-effector was set to achieve the constant output force required for low-destructive fruit clamping by Yubin Miao (*Miao et al., 2020*). Xinjiang currently employs self-propelled sweet pepper harvesters and Gansu uses traction sweet pepper pickers (*Liu, 2014*). Yi Wang et al. who simulated the head mechanism of snake designed an end-effector with the bite mode for citrus harvesting robot and suggested an optimization method of harvesting postures (*Wang et al., 2019*). Zhiguo Li et al. investigated the factors of affecting the human hand grasp type in picking tomato which provided theoretical basis for multi-finger end-effectors intelligent picking grasp planning algorithm (*Li et al., 2019*). However, studies on sweet pepper picking in China are limited, with marked differences in the methodology and results of existing research: (1) picking robot to separate pepper fruit clusters and fruit stalks of the influence of more factors, in the actual growth environment, the thickness of the fruit stalks, the degree of lignification is randomized, in addition to the plant in China planting methods, varieties, fruit maturity, fruit bunches and the distance between the branches and trunks of the fruit will have a direct impact on the effect of the separation of chili peppers and fruit stalks. (2) The skin of ripe chili peppers is brittle and easily damaged during mechanical picking, making it difficult to store. (3) Environmental problems of robotic operation. In the actual environment of the pepper plant, the distance between the main branches and lateral branches, the spatial distribution of the fruit, the weight of the fruit, the length of the fruit stalk, the leaf shade and other parameters change randomly, resulting in difficulty in identifying the specific cutting position of the fruit stalk.

The purpose of the current study was to design a flexible end-effector suitable for the reliable picking of sweet pepper while avoiding mechanical damage. The working environment of a picking robot is non-structural, while picking objects are generally tender and complex (*B et al., 2014; Fu et al., 2015; Yu et al., 2017*). Thus, end-effectors must be soft, stable during clamping, inexpensive and easy to control, and should consider the biological, physical and mechanical characteristics of the picking object (*Zhang, 2014; Shi et al., 2018; Xiong et al., 2018*). The aforementioned factors were considered to produce an end-effector prototype, which was then verified in order to provide technical support for the design of future sweet pepper picking robots.

MATERIALS AND METHODS

Sweet pepper fruit picking

In order to determine the most suitable robot sweet pepper picking method, the characteristics of several manual picking methods were tested in the field. In Fig. 1(a), the stem could be twisted with ease by simply rotating it, without pulling the target fruit; in Fig. 1(b), pulling the fruit straight down affected the machine vision positioning; in Fig. 1(c), the direct lifting of the fruit did not completely break the stalk; in Fig. 1(d), the target fruit was pulled down while rotating, with a relatively large motion range of the robotic arm and damage to surrounding plants; in Fig. 1(e), the fruit stem was cut to simulate artificial plucking. Fig. 1(f) proved to be suitable for the sweet pepper picking by the robot. Cutting the fruit peduncles directly avoided damage to surrounding fruits, stems, leaves, etc. The range of movement was also relatively small, greatly reducing the damage to the surrounding plants and resulting in minimal fruit stalk wounds. Therefore, the clamping and shearing method was employed to separate the fruits from the plants.



(a) Twisting without pulling (b) Pulling straight down (c) Direct lifting



(d) Rotating 90° while pulling downward (e) Manual picking (f) Shearing

Fig. 1 – Common sweet pepper picking methods

Robot end-effector structure

The principal components of the proposed end-effector were the mechanical parts (Fig. 2), control system (Fig. 3) and vision system, which were installed on the mechanical arm (Fig. 4). The end-effector adopted a two-finger clamping mechanism, which was composed of the clamping fingers, stepping motor, positive and negative screws, buffer material, timing belt and pulley, force sensor, stopper, coupling, etc. Two stepping motors were used as the power output. The sweet pepper picking process (Fig. 5) can be described as follows: 1) The machine vision recognized and located the target fruit. 2) The robotic arm drove the end-effector to the fruit location. 3) The control system sent out a clamping command to rotate the motor and generate a driving force that was transmitted to the gripping fingers. 4) The gripping fingers began to move closer to the sweet pepper fruit and subsequently clamp it. 5) The control system continuously monitored the force between the sweet pepper and the gripping finger measured by the force sensor within the gripping finger. Once the safety threshold set by the finger surface film force sensor was reached, the clamping finger stopped moving in the clamping direction and the clamping state was maintained. 6) The control system sent a message to the motor to start rotating the scissors. The output power was then transmitted to the scissors, closing them until the required position was detected by the stopper. 7) The motor controlling the gripping finger movement rotated in reverse, the gripping fingers and scissors moved to the outer limiter positions, the movement stopped, and picking was complete.

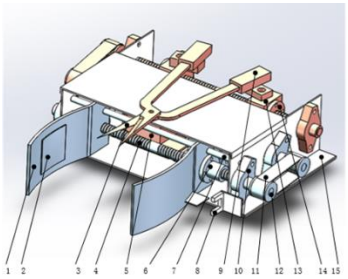


Fig. 2 – Overview of the end-effector structure

1. Clamping finger; 2. Force sensor; 3. Scissors; 4. Positive and negative screw; 5. Stepping motor; 6. Screw nut I; 7. Guide rod; 8. Stopper; 9. Scissors connector; 10. Bearing with seat; 11. Synchronous belt; 12. Pulley; 13. Nut seat; 14. Lead screw nut II; 15. Frame.

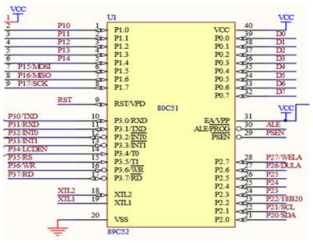


Fig. 3 – Microcontroller resource allocation

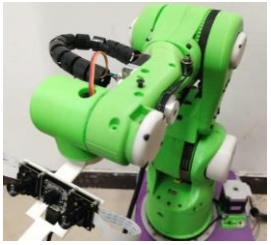


Fig. 4 - Mechanical arm

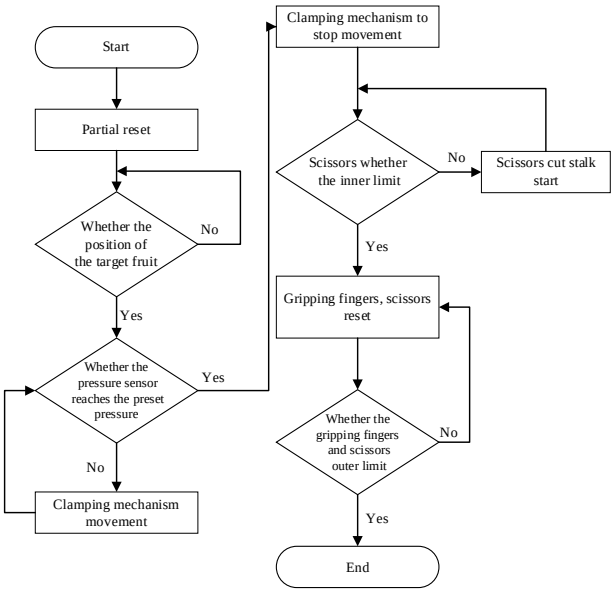


Fig. 5 – Flow diagram of sweet pepper picking

Sweet pepper mathematical model

Since the clamping mechanism was in direct contact with the fruit, the structural parameters of the clamping device were designed according to the physical size of the fruit (*Shi et al.,2018; Fengfeng et al., 2018*). "Rixwang 35132" was used as the experimental pepper fruit and was picked in the greenhouse of Lushou Green Garden in Luocheng, Shouguang, China. The appearance and size of this variety was taken as the design reference (Table 1). The fruit width range (the gap between the maximum and minimum values) was 39.22 mm, with multiple values of 79-83 mm; the thickness range was 32-90 mm, with multiple values distributed within 71-75 mm; and the fruit length range was 40-73 mm, with multiple values of 80-85 mm. The sweet pepper width and thickness direction ranges were observed to be smaller than that of the length direction. Thus, adjusting the clamping position via the width and thickness direction was more conducive to increasing the clamping success rate.

Table 1

Physical parameters of the Rixwang 35132 sweet pepper

Parameter	Max.	Min.	Average	Majority value	Extremums
Mass (g)	287.01	50.04	157.13	150-170	236.97
Width (mm)	102.54	63.32	80.06	79-83	39.22
Thickness (mm)	90.68	57.78	71.07	71-75	32.90
Fruit length (mm)	105.21	64.48	79.33	80-85	40.73
Length of fruit stalk (mm)	9.85	6.71	8.18	8.1-8.2	3.14

The sweet pepper fruit had the shape of an irregular cylinder with a larger diameter at the top than the bottom. The region of the fruit with the largest diameter was selected as the contact position between the sweet pepper and finger during clamping. Thus, the finger grip design was based on the largest diameter. Figure 6 presents a schematic diagram of a finger enveloped fruit. Compared with the straight grip, arc-shaped fingers are able to increase the contact point between the fingers and the fruit surface, improving the stability of the grip. In order to ensure the clamping effect, the circular curvature of the finger was less than the approximate circular minimum curvature of the sweet pepper fruit. The maximum fruit diameter corresponded to the minimum curvature. Measurement data reveals that the sweet pepper diameter did not exceed 110 mm. Thus, the approximate circle curvature of the sweet pepper fruit was greater than or equal to 0.018, and this value was used for the arc-shaped curvature of the finger.

The mechanism underlying the finger enveloping the target fruit was based on the sweet pepper fruit size in the longitudinal direction. In particular, a stable grasp of the sweet peppers requires a finger grip that is at least 50% larger than the fruit. The enveloping range of the gripping fingers was determined to be 55 mm and thus the arc length used to optimize gripping was set as 55 mm. Furthermore, the fruit height ranged within 64-106 mm. As the finger holding position was placed at the upper fruit region with the largest diameter, the finger height was able to meet the requirements when it reached half of the maximum fruit height. Thus, the finger height was set as 53 mm.

The final curved finger model was set as follows:

$$x^2 + y^2 = 3025\ (-27.5 \ll x \ll 27.5) \quad (1)$$

$$z = 53 \quad (2)$$

where x denotes the finger motion range, mm; y is the finger wrapped range; and z is the finger height, mm.

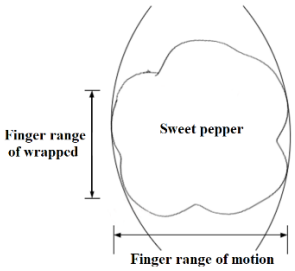


Fig. 6 – Diagram of the finger enveloping

Force analysis of gripping fingers

In order to demonstrate the wrapping of the fruit by the gripping fingers, the equatorial surface of the sweet pepper was taken as an example for force analysis (Figure 7). Due to the shape of the fruit, the force on the fruit can be considered to be concentrated in four points. The positive force of the fingers was denoted on the curved surface, the static friction force in the vertical direction, and the static friction force in the horizontal direction as Ni, fi and $f\,i'$, respectively.

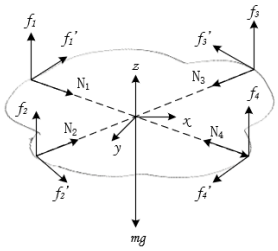


Fig. 7 – Mathematical model and stress analysis of sweet pepper

In Figure 7, fi is the static friction force in the vertical direction experienced by the i-th contact point, N; fi' is the static friction force in the horizontal direction experienced by the i-th contact point, N; Ni is the horizontal upward force experienced by the i-th contact point of the static friction force, N; and mg is the balance force of the sweet pepper, N. The balance force system in the horizontal direction is given as:

$$\sum_{i=1}^{n} N_i = F_x, \quad (3)$$

where N_i is the positive force of each point on the sweet pepper surface in contact with the gripping finger.

As the enveloping range of the fingers on both sides of the sweet pepper are approximately equal, the force-bearing area is approximately equal and the force in the horizontal direction can be considered symmetrical. More specifically, the magnitudes are equal while the directions are opposite. Therefore, in the horizontal direction, the resultant force F_x can be considered as zero.

When sweet pepper and the finger come into contact with the frictional point, the end-effector needs to hold the sweet pepper in a stable manner. The friction force generated by the clamping force must overcome the gravity of the sweet pepper, while the clamping force must avoid damage to the fruit (*Zhan et al., 2017*). These two requirements determine the size of the finger gripping force.

The resultant force of the static friction between the sweet pepper fruit and the gripping fingers in the vertical direction produced by the clamping force is greater than the gravity of the sweet pepper fruit:

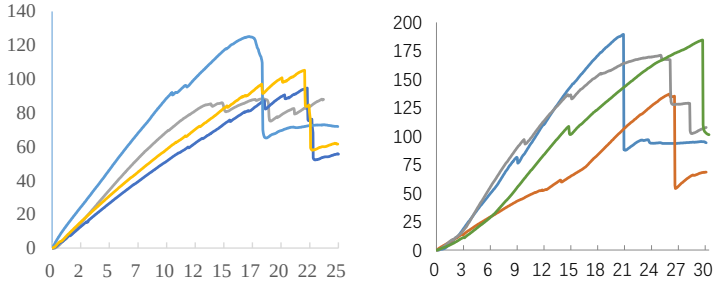
$$\mathrm{F_{Clamping}} \geq \mathrm{mg/2\mu} \quad (4)$$

$$\mathrm{F_{Clamping}} < \mathrm{F_{broken}} \quad (5)$$

where $F_{clamping}$ is the clamping force of the finger, N; μ is the friction coefficient between the silica gel and the sweet pepper fruit; m is the maximum mass of the sweet pepper fruit, kg; and g is the acceleration of gravity, which was taken as 9.8 m/s^2.

In order to determine the minimum positive force N min, the fruit quality was measured using Eq. (4), with a maximum fruit mass of approximately 287 g. Taking the variability of sweet pepper into account, taking 400 g fruits increases the margin coefficient of 28.25%, and the minimum positive force N_{min} was determined as 2.13 N. Furthermore, friction coefficient tests determined the friction coefficient between the silica gel and

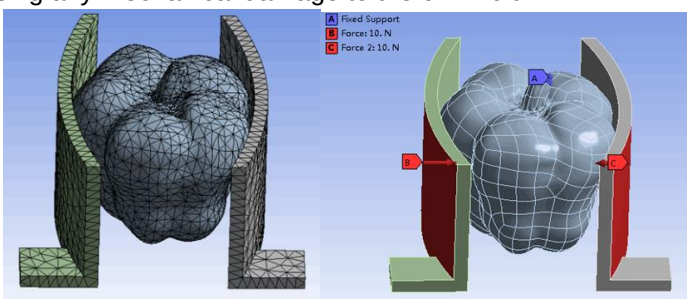
the sweet pepper fruit to be 0.92. In order to judge whether the positive force damages the biological tissues of the sweet pepper, a compression test was performed on the sweet pepper to determine the maximum positive force N_{min} for non-destructive picking. Eight randomly selected sweet pepper fruits were divided into 2 groups (4 in each group) and compressed horizontally and vertically to obtain the load displacement curves (Figure 8(a) and (b), respectively). The compression tests demonstrated that at a compression load less than 50 N, the load varied steadily with the displacement, and the sweet pepper was not damaged. The damage force of the sweet pepper was more than 50 N and thus the positive force ranged within 2.13-50 N.



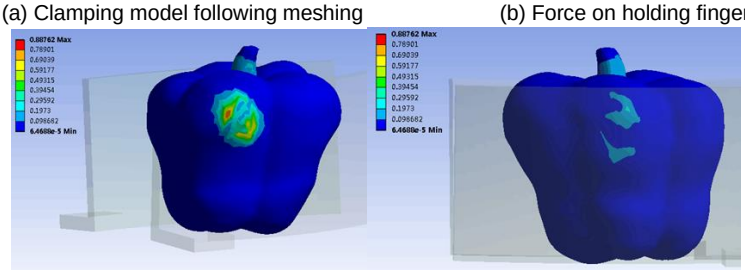
(a) Lateral compression (b) Longitudinal compression

Fig. 8 – Compressed displacement-load curve

The finite element analysis software ANSYS 17.0 was employed to simulate and analyze the clamping fingers in order to avoid damaging the target fruit. The mesh was divided into 21,735 nodes and 12,289 elements. Once the grid was divided, the loads and constraints were added to the gripping fingers and the red pepper. Previously, it was calculated that the appropriate range of gripping force for gripping fingers is 2.13-50 N. The clamping force of 5, 10, 15, 20, 25, 30, 35, 40, 45, and 50 N on sweet pepper skin was tested through preliminary experiments. The results of the pre-liminary experiments showed that the optimal clamping force was 10 N. During the clamping process, leftward and rightward pointing forces from the pepper and gripping fingers were added, respectively, and the rotation the gripping fingers was limited. Figure 9 presents the simulation analysis results. The maximum and rupture stress of the pepper fruit were determined as 0.375 MPa and 0.88762 MPa, respectively. This proved that the proposed clamping device had robust clamping performance without causing any mechanical damage to the chili fruit.



(a) Clamping model following meshing (b) Force on holding finger



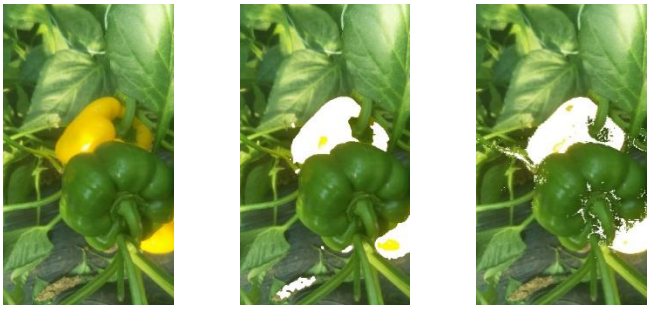
(c) Right-view of stress cloud diagram (d) Left-view of stress cloud diagram

Fig. 9 – Clamping stress analysis diagram

Image segmentation of sweet pepper

Immature sweet peppers of the experimental sample were green, while mature sweet peppers varied in color and were significantly different from the background (Figure 10(a)). Therefore, color, area and shape feature screening was employed to divide the sweet pepper image. The color image was converted from an RGB to HSV color space. The mature sweet peppers exhibited gray values in the H (hue) and S (saturation) components that were distinct to the gray values of the branches and leaves in the background. The differences

in gray values were used to apply a median filter to the H and S components. The segmentation threshold was then obtained through the Otsu automatic threshold segmentation (T). This threshold was adjusted based on the threshold determined from the image segmentation effect in order derive the segmentation thresholds in the H and S components as (0, 0.75T) and S (1.45T, 255), respectively. Figure 10(b) and (c) displays the segmentation effects in the H and S components, respectively. Noise within the image was removed using morphological opening and the holes were subsequently filled. The entire area was divided into different connected domains that were filtered according to the area and roundness of the pepper. The circular Hough transformation was applied to the occluded sweet pepper image, and the size was calculated and displayed in the form of a circumscribed rectangle. Figure 10(d) and (e) demonstrates the processing results.



(a) Original image (b) Segmentation of H component (c) Segmentation of S component



(d) Circular Hough transform (e) Processing results

Fig. 10 – Image segmentation of sweet pepper

Figure 11 compares the sweet pepper image segmentation effects of the H and S components. The threshold segmentation was optimal under the H component for greater occlusions in the image, and the connected domain was relative. The saturation of the leaves under strong light was similar to that of mature sweet peppers. The image segmentation in the S component was erroneous under this case. Thus, the H component of the HSV color space was selected for sweet pepper image segmentation.



(a) H component processing-1 (b) S component processing-1 (c) H component processing-2 (d) S component processing-2

Fig. 11 – Comparison of segmentation effects

Experimental implementation and results

Experimental implementation

The test materials included the end-effector prototype, a control box, an ASUS X550 laptop, and a tripod. The "Rixwang 35132" sweet pepper variety was picked in the Lushou Green Park greenhouse, Luocheng, Shouguang, China. The end-effector was supported by a height-adjustable tripod that was moved to the target fruit. The upper frame was removed during operation to facilitate debugging during testing. A total of 60 sweet peppers at 50% maturity or more were randomly picked. During the picking process, fruit that did not enter the gripping fingers, fallen fruit, uncut stalks, and broken sweet pepper were regarded as failures.



(a) Reset stage (b) Fruit is held

(c) Stalk is cut (d) Stem is cut

Fig. 12 – Picking process

RESULTS AND DISCUSSION

The growth environment of sweet peppers was shown in Figure 13. The picking target was "Rickswan 35132" normally growing sweet pepper fruit. The picking process consisted in the following operations: use the height to adjust the three tripod to support the end actuator; move the tripod to the target fruit; remove it during operation. Figures 2 and 3 are the picking process of different colors of pepper. From close to the plants, hold the fruit, cut the fruit handle, and cut.



Fig. 13 – Picking the field environment



Fig. 14 – The picking process of different colors of pepper

Table 2 reports the number of successful and failed fruit picking attempts. The experimental process of the developed device is shown in Figure 12. Sixty sweet pepper fruits were harvested using the developed device. The experimental results showed that 56 sweet pepper fruits were successfully picked (Figure 13), while 4 sweet pepper fruits were lost. The success rate of device picking was about 93.3%. Four failed cases include one fruit being pierced by scissors, one case where the handle failed to cut, and the other two cases where it failed to enter the grip area. The successful clamping of the target fruit by the designed clamping mechanism ensures that the end effector effectively separates the fruit and fruit stalks without damaging the target fruit. Therefore, this end effector can meet the current requirements for sweet pepper fruit picking.



Fig. 15 – Fruit picking effect

Table 2

Picking test results

Picking effect	Quantity
Successfully picked	56
Fruit did not enter the gripping fingers	2
Fruit stalk shear failure	1
Scissors pierced the fruit	1
Total	60

The fruit picking failures may be attributed to the following factors:

1) Some fruit had short and bent stems, resulting in stalks growing close to the end of the fruit. The gap between the fruit was very small and not wide enough to accommodate the scissors. Thus, the tip of the scissors may pierce the target fruit once the actuator is close.

2) In the greenhouse, the branches of the sweet peppers grow upward along the artificially pulled rope while the fruits and branches droop down due to gravity. These growth characteristics facilitate the clinging of individual sweet pepper fruits to the branches. This may result in the branches also entering the shear range of the scissors along with the sweet peppers, cutting off both the branches and fruit.

3) Two sweet peppers can grow from the same joint on the branch. In this case, when the end-effector approaches the target fruit from the front, the fingers also push the adjacent fruit, thereby moving the branch. This movement affects the target fruit, preventing it from entering the gripping region.

CONCLUSIONS

In the current study, a sweet pepper picking robot end-effector for the non-destructive picking of sweet peppers based on their biomechanical properties was designed. The device consists of a clamping module, a cutting module, and a control system. The clamping mechanism was able to successfully separate the fruit and fruit cluster, while the timely separation of the fruit and fruit stalk was achieved by the shearing mechanism. The control system integrated a single-chip microcomputer and multiple sensors. The proposed end-effector was centered around a single mechanical structure and multiple sensors. The picking and movement status was detected by the sensor and controlled by the single-chip microcomputer. The end-control principle was adopted to control the direction and pulse signals and enable the signal of the stepper motor driver to control the end-effector.

The proposed end-effector exhibits a simple structure and reliable performance. Test results demonstrate the ability of the end-effector to effectively realize the clamping of the fruit and the separation of the stalk, with a picking success rate of 93.3%, and an average picking time of 5 s per fruit. The proposed system was able to realize the non-destructive picking of the target fruit.

This study is based on the physical characteristics of sweet pepper fruit. In the structural design of the end effector, combined with machine vision, a testing device was successfully developed. The prototype was verified through picking experiments to meet the design requirements and achieve the functions of picking and positioning.

ACKNOWLEDGEMENT

This research was supported by the earmarked fund for China Agriculture Research System (CARS-34). The authors wish to thank the useful comments of the anonymous reviewers of this paper.

REFERENCES

[1] Bac, C.W., Hemming, J., Van Tuijl, B.A.J., Barth, R., Wais, E. and Van Henten, E.J. (2017). Performance Evaluation of a Harvesting Robot for Sweet Pepper. *J. Field Robot*., 34, 1123-1139.

[2] Bac, C.W., Roorda, T., Reshef, R., Berman, S., Hemming, J. and Van Henten, E.J. (2016). Analysis of a motion planning problem for sweet-pepper harvesting in a dense obstacle environment. *Biosyst. Eng*., 146, 85-97.

[3] Chen, K., Zou, X., Guan, Z., Wang, G., Peng, H. and Chongyou, W.U. (2019). Camera Calibration Method of Picking Robot Based on Shuffled Frog Leaping Optimization. *T. Chin Soc Agric Mach*., 50, 23-34.

[4] Chen, J., Wang, H., Jiang, H., Gao, H., Lei, W. and Dang, G. (2012). Design of end-effector for kiwifruit harvesting robot. *T. Chin Soc Agric Mach*., 43, 151-154.

[5] Chiu, Y.C., Yang, P.Y. and Chen, S. (2013). Development of the end-effector of a picking robot for greenhouse-grown tomatoes. *Appl. Eng. Agric*., 29, 1001-1009.

[6] Cosic, M., Djurovic, N., Todorovic, M., Maletic, R., Zecevic, B. and Stricevic, R. (2015). Effect of irrigation regime and application of kaolin on yield, quality and water use efficiency of sweet pepper. *Agric. Water Manage*., 159, 139-147.

[7] Fan, J., Xun, Y., Bao, G.J., Jun-Liang, W.U. and Yang, Q.H. (2016). Key techniques of Hangzhou white chrysanthemum picking robot. *J. Mech. & Ele. Eng*., 33, 909-914.

[8] Ferreira, R.D.C., Bezerra, R.D.S. and Rosa, J.Q.S. (2016). Effects of light intensity modification by reflective aluminized screenhouse on sweet pepper growth and yield. *Engenharia Agrícola*., 34, 626-635.

[9] Fu, L., Zhang, F., Gejima, Li, Z., Wang, B. and Cui, Y. (2015). Development and experiment of end-effector for kiwifruit harvesting robot. *Trans. T Chin Soc Agric Mach*., 46, 1-8.

[10] Graham, S.S., Zong, W., Feng, J. and Tang, S. (2018). Design and testing of a kiwifruit harvester end-effector. *Trans. ASABE*, 61, 45-51.

[11] Guo, X., Hao, X., Khosla, S., Kumar, K.G.S., Cao, R. and Bennett, N. (2016). Effect of LED interlighting combined with overhead HPS light on fruit yield and quality of year-round sweet pepper in commercial greenhouse. *Acta Horticulturae*, 1134, 71-78.

[12] Ji, W., Luo, D., Li, J., Yang, J. and Zhao, D. (2014). Compliance grasp force control for end-effector of fruit-vegetable picking robot. *Trans. Chin. Soc. Agric. Eng*., 30, 19-26.

[13] Jiang, Z., Hu, Y., Jiang, H. and Tong, J. (2017). Design and force analysis of end-effector for plug seedling transplanter. *PLOS ONE*, 12, e180229.

[14] Kondo, N., Yamamoto, K., Shimizu, H., Yata, K., Kurita, M., Shiigi, T., Monta, M. and Nishizu, T. (2009). A machine vision system for tomato cluster harvesting robot. *Eng. Agric. Environ. Food*., 2, 60-65.

[15] Lee, B., Kam, D., Min, B., Hwa, J. and Oh, S. (2019). A vision servo system for automated harvest of sweet pepper in Korean greenhouse environment. *Appl. Sci.-Basel*., 9, 2395.

[16] Lehnert, C., English, A., Mccool, C., Tow, A.W. and Perez, T. (2017). Autonomous sweet pepper harvesting for protected cropping systems. *IEEE Robot. Autom. Lett*., 2, 872-879.

[17] Li, Q., Hu, T., Wu C., Hu, X. and Ying, Y. (2008). Review of end-effectors in fruit and vegetable harvesting robot. *T. Chin Soc Agric Mach*., 39, 175-179

[18] Li, Z., Miao, F., Yang, Z., Chai, P. and Yang, S. (2019). Factors affecting human hand grasp type in tomato fruit-picking: A statistical investigation for ergonomic development of harvesting robot. *Comput. Electron. Agric*., 157, 90-97.

[19] Lin, H. and Xu, L. (2015). The development and prospect of agricultural robots in China. *Acta Agriculturae Zhejiangensis*, 27, 865-871.

[20] Liu, J. (2017). Research progress analysis of robotic harvesting technologies in greenhouse. *T. Chin Soc Agric Mach*., 048, 1-18.

[21] Liu, Z. (2014). Design of traction small pepper picker. *Farm Mach*., 124-125.

[22] Miao, Y. and Zheng, J. (2020). Optimization design of compliant constant-force mechanism for apple picking actuator. *Comput. Electron. Agric*., 170, 105232.

[23] Shi, N. and Hu, C. (2017). Current situation and breeding trend of pepper cultivation in China. Anhui *Agri. Sci. Bull*., 23(22).
[24] Shi, Y.G., Zhu, K.J., Zhai, S.H., Zhang, D.W., Liu, L., Zhao, J.Z., Long, Y. and Cui, Y.J. (2018). Design of an apple-picking end effector. Strojniski Vestn. *J. Mech. Eng.* 64, 216-224.
[25] Song. J., Zhang, T., Xu, L. and Tang, X. (2006). Research actuality and prospect of picking robot for fruits and vegetables. *T. Chin Soc Agric Mach*. 37, 158-162.
[26] Wang, Y., Yang, Y., Yang, C., Zhao, H., Chen, G., Zhang, Z., Fu, S., Zhang, M. and Xu, H. (2019). End-effector with a bite mode for harvesting citrus fruit in random stalk orientation environment. *Comput. Electron. Agric*. 157, 454-470.
[27] Wei, X.Q., Jia, K., Lan, J.H., Li, Y.W., Zeng, Y.L. and Wang, C.M. (2014). Automatic method of fruit object extraction under complex agricultural background for vision system of fruit picking robot. *Optik*., 125, 5684-5689.
[28] Xiong, J., He, Z., Lin, R., Liu, Z., Bu, R., Yang, Z., Peng, H. and Zou, X. (2018). Visual positioning technology of picking robots for dynamic litchi clusters with disturbance. *Comput. Electron. Agric*. 151, 226-237.
[29] Yu, H., Wang, S., Zhou, H., Yang, L. and Zhou, X. (2017). Research and Development of Ball-Picking Robot Technology. *ICIRA*. LNAI 10464,226-36
[30] Zhan, Z., Meng, Q., Hu, W., Ying, S., Fei, S. and Zhang, Y. (2017). Continuum damage mechanics based approach to study the effects of the scarf angle, surface friction and clamping force over the fatigue life of scarf bolted joints. Int. J. Fatigue 102, 59-78.
[31] Zhang, F. (2014). *Research and design of the nondestructive end-effector of kiwifruit*. Northwest A&F University. p. 68.
[32] Zhang, F.F., Wang J.S., Li, Y.F., Liu, Z.B. and Duan Y.Z. (2018). Design and test for clamping mechanism vegetable grafting robot. *J. Agric Mech Res*., 40, 135-138.

HEAT ENVIRONMENT STUDY OF PASSIVE SOLAR GREENHOUSE
/
被动式日光温室热环境研究

Zhouhua LIU [*1], Xin YOU [2], Penghui QIAO[2], Mengjun CHEN[2], Weiwei CHEGN[1]

[1] Shanxi Agricultural University, College of Urban and Rural Construction, Taigu/China
[2] Shanxi Agricultural University, College of Agricultural Engineering, Taigu/China
Tel: +86-0354-6287420; E-mail: lzh6175305@163.com
Corresponding author: Zhonghua LIU
DOI: https://doi.org/10.35633/inmateh-71-24

Keywords: *Passive solar greenhouse; Thermal environment; Cold, Low temperature and high latitude regions; Temperature change rate*

ABSTRACT

Passive solar greenhouses are developing rapidly in China and they can significantly increase crop yields. In order to promote the goal of temperature control in solar greenhouses in the high-latitude region of Shanxi, China, this paper conducted experiments to determine the three-dimensional thermal environment of solar greenhouses in the region, and the results showed that: regardless of the weather, the indoor temperature at the moment of midday exceeded 30°C; the temperature in the western region rose the fastest during the daytime, and declined the fastest in the eastern region during the nighttime. This research can provide theoretical support for the construction and management of solar greenhouses in low heat and water areas at high latitudes.

摘要

中国被动式日光温室发展迅速，被动式日光温室能够大幅提高作物产量。为促进中国山西高纬度地区日光温室的温度管控目标，本文对该地区的日光温室三维热环境进行试验测定，结果显示：无论何种天气，中午时刻室内温度都超过 30℃；白天西部区域温度上升最快，夜间东部区域下降速度最快。该研究可为高纬低热少水地区的日光温室建造和管理提供理论支撑。

INTRODUCTION

Solar greenhouses are a type of greenhouse unique to China and are built to accommodate the growth and development of vegetables in winter (*Panwar N.L. et al., 2011*), with passive solar greenhouses providing more than 30% of the total supply of vegetables and fruits (*Chao et al., 2019*). China's solar greenhouses mainly rely on solar energy absorption by the walls and ground during the day to store heat, and on heat dissipation by the walls at night to maintain indoor temperatures. Solar greenhouses can effectively increase crop yields and help maintain sustainable agricultural production. Temperature is one of the most important environmental factors in solar greenhouse production (*Shamshiri R.R. et al, 2018*). All biological and chemical processes throughout the life cycle of a crop must take place under certain temperature conditions. Nowadays, with the development of facility agriculture technology, the length and span of solar greenhouses are increasing and the space inside the greenhouse is gradually expanding, leading to uneven temperature distribution inside the greenhouse (*Wei et al., 2022*), which may affect the growth status of crops in different locations inside the solar greenhouse. The study of temperature variation patterns and distribution characteristics in solar greenhouses is of great significance for optimising solar greenhouses and thermal environment regulation.

A large number of studies have been conducted on the characteristics and change patterns of temperature distribution in solar greenhouse, and most researchers have used environmental monitoring sensors to obtain temperature data from solar greenhouse, and then used different methods to achieve prediction and control of the thermal environment in solar greenhouses. *Weiwei Cheng (2022)* analysed the three-dimensional thermal environment of a sunken solar greenhouse and found that the rate of change of the thermal environment along the vertical direction of the greenhouse was the greatest.

[1] *Zhonghua Liu, Asoc.Prof.Ph.D.Eng; Xin You, M.S.Eng; Penghui Qiao, M.S.Arg; Mengjun Chen, M.S.Arg; Weiwei Cheng, Ph.D. Eng.*

Jingjuan Hu (2014) used data analysis to analyse the characteristics of the changing thermal environment of a solar greenhouse in the Lishi district. *Jiangui Zhao (2019)* used the numerical filtering method to make an analysis of the environmental parameters of a solar greenhouse. At present, the most widely used software in solar greenhouse is Computational Fluid Dynamics (CFD). *Hongjun Xu (2019)* used CFD to simulate the wall temperature of a solar greenhouse and optimise its wall thickness. *Encai Bao (2018)* used CFD to simulate different rear wall ventilation in a solar greenhouse, providing a theoretical basis and experimental reference for the design of airflow circulation movement in the wall of an active thermal storage sunlight greenhouse; *Aohua Fan (2018)* used the solar greenhouse temperature field model for temperature regulation in solar greenhouses. However, due to the influence of various factors such as external meteorological conditions, wall structure parameters and production management methods on the simulation of the thermal environment in the greenhouse, there are still certain errors in the simulation of the thermal environment in the greenhouse, so other researchers use other methods to analyse the distribution of the thermal environment in the greenhouse. *Zhangyan Le (2018)* used the inverse distance weighting algorithm to model the temperature in the east-west direction of a large length solar greenhouse, and obtained the high and low value zones of the temperature in this solar greenhouse. *Junhua Zhang (2021)* used the kriging interpolation algorithm to model the canopy temperature field, obtained the temperature extrema by the differential evolution algorithm, and analysed the spatial and temporal variation patterns of the characteristic canopy temperature under different weather conditions. *Huihui Yu (2016)* used an improved particle swarm algorithm to optimize the LSSVM model for temperature prediction in a solar greenhouse.

This paper would use data analysis to study the temperature distribution and variation pattern of the solar greenhouse. The difference from previous studies was that in this experiment, a large number of temperature sensors, more intensive deployment and shorter acquisition intervals were used to study and analyse the thermal environment of the solar greenhouse. The study of the thermal environment of the solar greenhouse after intensive deployment will provide more effective information for the future deployment of temperature sensors in the solar greenhouse, contribute to the monitoring and control of temperature in precision agriculture and provide an important basis for the subsequent optimisation of the building model of the solar greenhouse.

MATERIALS AND METHODS

Experimental materials

The test solar greenhouse is a passive solar greenhouse located in Zhaozhuang Village, Zhaobi Township, Xiyang County, Jinzhong City, Shanxi Province, China, at latitude N: 37°30′, longitude E: 113°51′ and altitude 1549m above sea level. The area is located in the eastern part of Jinzhong City and the western foot of the Taihang Mountains, and belongs to the temperate and warm temperate semi-arid continental monsoon climate zone, with an annual average temperature of 9.3°C, an annual average frost-free period of 162 days, an annual average total sunshine hours of 2484.6 hours and an annual average precipitation of 572 mm.

The test solar greenhouse is a sunken solar greenhouse, sunken to a depth of 1.2m, facing south, 100m long, spanning 12m, with a back wall height of 5.6m, the back wall is a trapezoidal earth wall structure, the upper and lower widths are 2m and 8m respectively, the front roof is covered with polyethylene bottomless film, the solar greenhouse has no ventilation, the insulation is used to keep warm at night in spring and winter, and in winter the insulation is lifted at around 9:00am every day, and at 16:00pm. The insulation is lifted at around 9:00 am and dropped at around 16:00 pm.

The temperature inside the solar greenhouse is measured using the RC-5 temperature recorder from Jingchuang, with a temperature range of -30°C to 70°C.Temperature measurement accuracy: in the range of -20°C, -20°C, ± 0.5°C; other ranges of 1°C. Within the temperature range of -20°C to 40°C, the accuracy is ±0.5°C and the rest is ±1°C. U disk type temperature recorder using Jingchuang RC-5 temperature recorder usb automatic data temperature and humidity recorder, built-in wide-temperature CR2032 battery, set the recording interval of 12 minutes, can be recorded continuously for 3 months, regular replacement of the built-in battery, the temperature recorder continues to record the temperature.

Experimental methods

In this experiment, the temperature inside the solar greenhouse was measured using the spot measurement method. Three sections of the solar greenhouse were selected to measure the temperature in the east, middle and west sides of the crop area.

The distance between the indoor measurement line and the edge of the film on the south side of the greenhouse was 1.0m, 3.4m, 5.8m, 8.2m and 10.6m, and the distance between the measurement points on the same measurement line was 0m, 0.7m, 1.4m, 2.1m, 2.8m and 3.5m respectively. There were 28 measurement points in each section, a total of 84 measurement points, and the thermometer temperature collection time interval was set at 12 min, starting on 28 December 2021 and ending on 7 February 2022, with a total of 448,308 data.

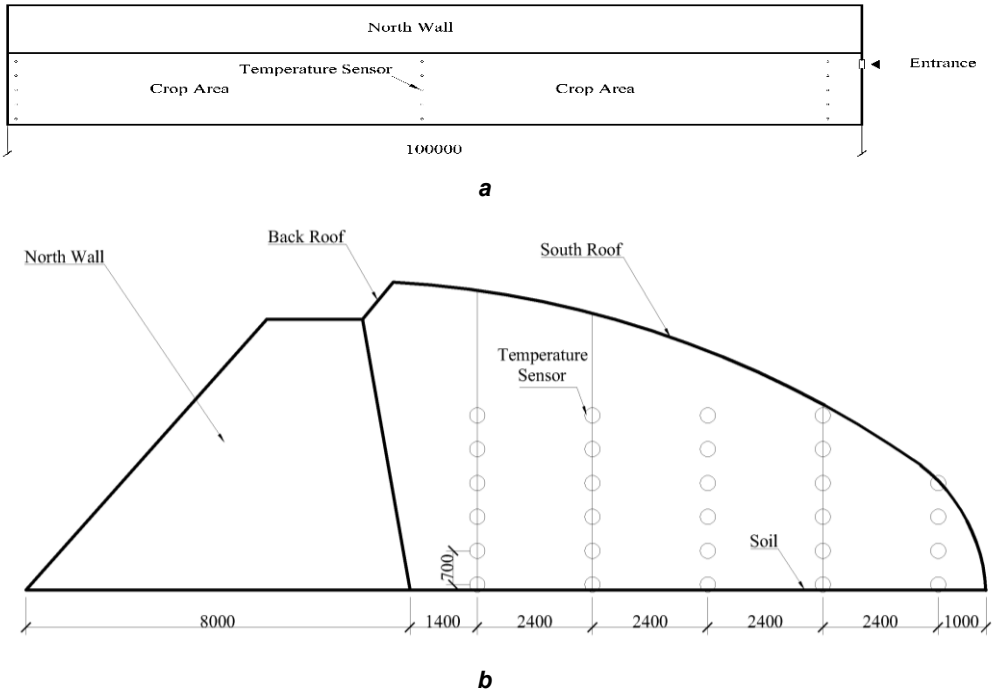


Fig. 1 - Distribution of solar greenhouse measurement points (a, plan view of solar greenhouse measurement points, b, cross-sectional view of solar greenhouse measurement points)

Data analysis

This experiment lasted 42 days, with 17 sunny days, 11 cloudy days, 8 cloudy days and 2 days of rain and snow. Since the insulation was not removed during the rainy and snowy days, the temperatures collected during the rainy and snowy days were ignored. The temperature data collected during the cloudy (January 2), sunny (January 3) and cloudy (January 4) days were collated and analysed to obtain the daily temperature change pattern and distribution characteristics of the solar greenhouse.

RESULTS

Indoor temperature

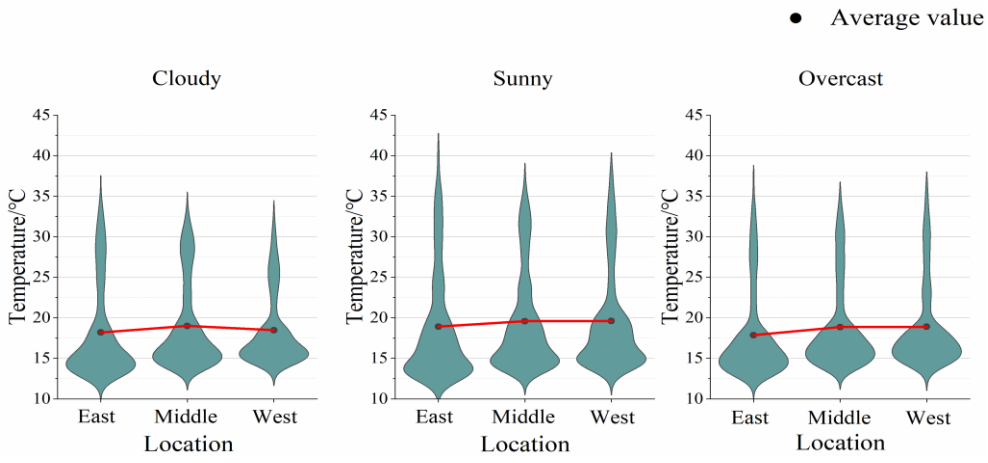


Fig. 2 - Overall analysis of solar greenhouse temperatures under different weather conditions

As shown in Figure 2, the temperature statistics for the sunroom on cloudy (2 January), sunny (3 January) and cloudy (4 January) days showed that the extremes of temperature in the sunroom occurred in the eastern part of the crop area under different weather conditions; regardless of the weather, the temperature was more concentrated around 14°C in the eastern part of the crop area, around 15°C in the central part of the crop, and around 15.5°C in the western part of the crop area. Table 1 showed the average temperatures and diurnal temperature differences at different locations in different weather conditions, and it could be seen that on the eastern side of the crop area, the diurnal temperature differences were the greatest in the solar greenhouse, and the maximum temperatures were above 30°C, which was not suitable for the growth of temperature-loving vegetable crops such as tomatoes. The main reason for this phenomenon is that the air in the room received solar radiation after the insulation curtain was removed, causing its temperature to rise rapidly, and with the gradual increase in the sun's altitude angle, the temperature only increased rather than decreased, reaching its maximum value at around 13:00 noon, before the temperature decreased afterwards.

Table 1

Temperature in different weather conditions

Weather conditions	Cloudy			Sunny			Overcast		
Position	East	Middle	West	East	Middle	West	East	Middle	West
Average temperature (°C)	18.20	18.99	18.47	18.91	19.58	19.59	17.85	18.85	18.89
Maximum temperature (°C)	39.4	36.3	34.4	42.9	38.7	39.6	38.4	36.5	37.5
Minimum temperature (°C)	11.1	13.2	12.7	11.2	13.1	12.5	11.7	13.3	12.2
Day and night temperature difference (°C)	28.3	23.1	21.7	31.7	25.6	27.1	26.7	23.2	25.3

Daily pattern of temperature change

In this experiment, a total of 84 temperature measurement points, 28 temperature measurement points per section, were laid out in the solar greenhouse to measure the temperature change characteristics at different locations in the solar greenhouse. Due to the large number of points laid out, the temperature data of each section was collated before analysing its daily temperature change pattern, and the temperature of each measurement point at different moments was calculated using the face-weighted average temperature method, with the formula as in (1), where T denotes temperature and S denotes area.

$$\bar{T} = \frac{\sum_{1}^{n} T_i S_i}{\sum_{1}^{n} S_i} (℃) \quad (1)$$

Face-weighted average temperature is a method of measuring temperature that involves distributing temperature over a specified face and weighting the temperature on that face by the weight of its relative position to obtain an average temperature. The main advantages of this algorithm are that it accurately reflects the distribution of temperature on a specified face, independent of boundaries; it also effectively provides accurate temperature data and is a more accurate predictor of temperature change.

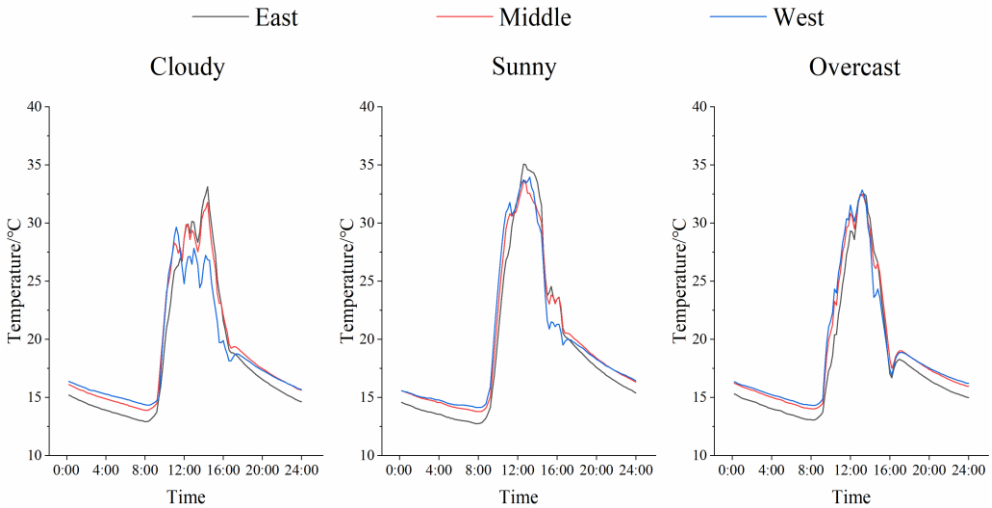


Fig. 3 - Graph of daily variation of temperature in the solar greenhouse

As shown in Figure 3, the indoor temperature reached its lowest value at around 8am, rising rapidly after the blanket was removed at 9am, slowing down after 11am, and then rising before falling gently after the blanket was put on at around 16pm; the night-time temperature in the solarium was much lower than the day-time temperature, and the highest and lowest temperatures of the day were found in the eastern part of the crop area of the solarium.

In cloudy weather, after the curtain was opened, the temperature showed a multi-peak change, the first time it reached the peak at around 11:00am, the temperature rise rate was west (7.5℃/h) > central (6.81℃/h) > east (6.46℃/h); after that, it was affected by cloudy weather, the received solar radiation was sometimes more and sometimes less, the temperature was also sometimes high and sometimes low, at around 14:30 pm On sunny days, the temperature basically showed a single peak change, and after the insulation curtain was opened at around 9:00am, the temperature rose rapidly, and by 11:00am, the rate of temperature rise was west (8.11°C/h) > central (7.76°C/h) > east (7.07°C/h), reaching its maximum at around 13:00 noon.

On cloudy days, the temperature showed multiple peak changes, reaching its peak at around 12:00 pm due to the “lower values of solar radiation on cloudy days, with the temperature growth rate in the west (5.64°C/h) > central (5.44°C/h) > east (5.39°C/h); the temperature reached its highest value at 13:00 pm. Analysis of the data showed that the temperature in this solar greenhouse rose fastest between 9am and 11am, as the sun first shone directly on the western wall after the curtain was lifted and some areas in the eastern part of the crop area were shaded by the eastern wall, resulting in a faster rise in temperature in the western part of the crop area than in the eastern part. After 12 noon, due to the change of the sun's altitude angle, the solar radiation received by the western part of the crop area gradually decreased, and at around 13:00, the temperature reached its highest value. After that, due to the decrease of the sun's altitude angle, the solar radiation received by the solar greenhouse also gradually decreased, and the temperature gradually decreased, as the western part of the crop area was shaded by the western hill wall, resulting in the fastest temperature decrease in this area, and by 16:00, the western part of the crop area ;By 16.00 pm, the temperature in the western part of the crop area had reached its lowest value compared to the other two areas, and after the insulation curtain was put on, the temperature in the solarium first rose slightly and then continued to decrease slowly.

In cloudy weather, from the afternoon when the curtains were covered to 8am the following day, the rate of temperature drop in the solarium was east of the crop zone (0.51°C/h) > central (0.48°C/h) > west (0.3°C/h); in sunny weather, from the afternoon when the curtains were covered to 8am the following day, the rate of temperature drop in the solarium was east of the crop zone (0.67°C/h) > central (0.62°C/h) > west (As the eastern part of the crop area is farther away from the eastern wall, it can only get a small amount of heat radiated from the eastern wall at night, while the western side of the crop area is near the western wall, the heat radiated from the western wall could effectively act on the western part of the crop area at night, slowing down the temperature drop in this area.

The graph also showed that the trend of temperature changes in the solarium varied from day to day due to varying weather conditions. In cloudy weather, the temperature in the solarium exceeded 30°C at 13:30-14:30, in sunny weather, at 10:30-14:30, and in cloudy weather, at 11:30-14:00.

Indoor temperature distribution on the coldest day

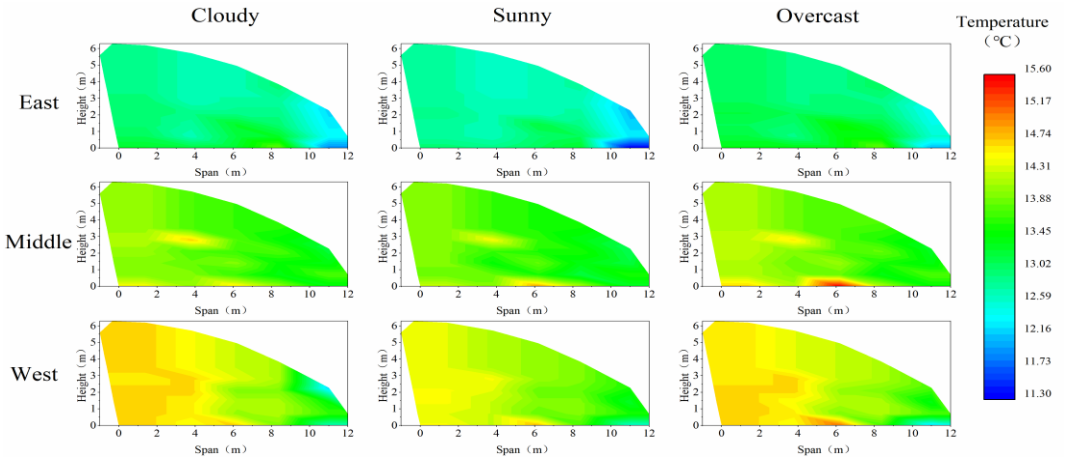


Fig. 4 - Cross-sectional temperature distribution of the solarium during extreme low temperatures

The indoor temperature reached its lowest value at around 8am and the cross-sectional temperature distribution is shown in Figure 5. As shown in Figure 4, the temperature distribution in this solar greenhouse is not uniform during extreme low temperatures. Under different weather conditions, the overall temperature in the crop area of the heliotrope at 8am showed a phenomenon of high temperatures in the west and low temperatures in the east. Along the span of the heliotrope, there was a basic trend of high temperatures in the north and low temperatures in the south, except for the ground temperature, with the lowest temperatures in the solar greenhouse located in the southernmost part of the eastern part of the crop area near the ground. It was obvious from the graph that the relationship between the magnitude of the temperature inside the solar greenhouse at the lowest temperature was cloudy > overcast > sunny. The difference in the minimum temperature of the next day was mainly due to the weather conditions of the previous day affecting the heat absorption values in the room, which is transferred to the solar greenhouse at night as the heat source of the solar greenhouse through radiation and convection, increasing the temperature inside the solar greenhouse. During the day, the heat absorbed by the solar greenhouse on a sunny day was greater than that absorbed on a cloudy day, so the temperature inside the solar greenhouse was higher on a cloudy day (4 January) than on a sunny day (3 January) and on a cloudy day (2 January) when the insulation had not been removed at 8am.

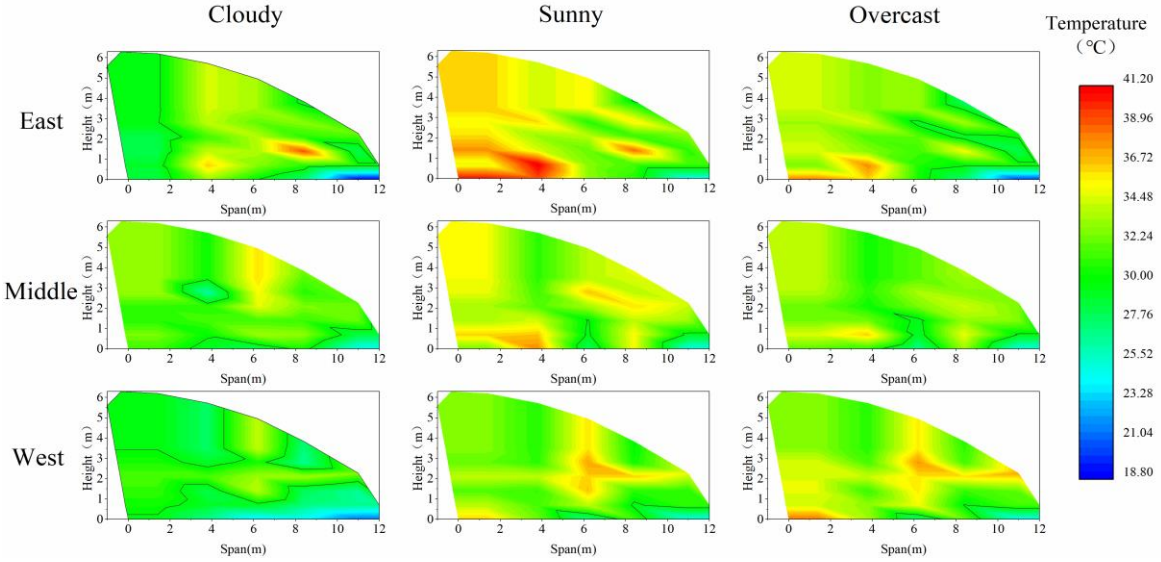


Fig. 5 - Cross-sectional temperature distribution of the solarium during extreme heat

The temperature in the solar greenhouse reached its highest value at around 13:00 in the afternoon on sunny and cloudy days, and at around 14:30 in the afternoon on cloudy days, with the cross-sectional temperature distribution shown in Figure 5. The lowest temperatures were located in the southern part of the crop area, near the ground, with the highest temperatures occurring in different sections of the crop area at different locations due to weather and location. In the western part of the crop area, the highest temperatures are in the middle of the solarium under different weather conditions: in the middle of the crop area. In sunny and cloudy weather, the maximum temperature is at ground level around 4 m near the back wall, and in cloudy weather the maximum temperature occurs in the middle of the solarium. In the eastern part of the crop area, on sunny and cloudy days, the maximum temperature was at ground level about 4 m near the back wall, and on sunny day there were small areas of high temperatures similar to those in cloudy weather, at a position 8 m from the back wall of the solar greenhouse; overall, the maximum temperature in the solar greenhouse was at a position 4 m near the back wall in the eastern part of the crop area. The main reason for this phenomenon is that from the morning after the uncovering of the curtain to 12 noon, as the sun's altitude angle gradually increases, the intensity of radiation also gradually increases, and the solar radiation received by the west wall gradually decreases, resulting in a gradual increase in temperature from west to east. At the same time, due to the large temperature difference between the inside and outside of the solarium, heat exchange occurs between the vicinity of the film and the outside world, making the temperature of the solarium high in the north and low in the south. Because of the uneven solar radiation received by the solar greenhouse during drizzly weather, the location of the highest temperatures differs from that of sunny and cloudy days. It can also be seen in Figure 5 that the temperature in most areas of the solarium exceeds 30°C in different weather conditions.

Discussions

The main object of this paper is to study a solar greenhouse in Xiyang County, Jinzhong City, Shanxi Province. By measuring its temperature and analyzing its daily temperature change pattern under different weather conditions and temperature distribution during extreme temperatures, we found that the rate of temperature rise, rate of temperature fall and temperature distribution in this solar greenhouse varied under different weather conditions in winter, and the maximum temperature exceeded 30°C, which would seriously affect the growth and development of temperature-loving crops. At this stage, most of the solar greenhouses in China are facing the problem of temperature increase and decrease.

At present, most of the solar greenhouses in China are facing the problem of low temperatures at night in winter, which leads to low-temperature disasters for vegetable crops, while the solar greenhouse studied in this paper has the problem of high daytime temperatures in winter, which is not suitable for the growth and development of temperature-loving vegetables. This is similar to the findings of *Lv Huanhuan (2021)*, both of which showed that high daytime temperatures in solar greenhouses may cause high temperature stress on vegetables and affect their yield. To address this problem, ventilation could be applied to this solarium according to different weather conditions. Proper ventilation could not only reduce the temperature in the solarium, but also effectively regulate the humidity and CO_2 concentration in the solarium to meet the requirements for normal crop growth in the solarium. If the ventilation is opened at around 10am on a sunny day, it can effectively reduce the rate of temperature rise in the solarium and lower the temperature in the solarium at the same time.

In this experiment, temperature data was only collected and analysed for the internal temperature of the solar greenhouse, which clearly showed the pattern of daily temperature changes and the distribution characteristics of the solar greenhouse, but to optimise the thermal environment of the solar greenhouse, the light intensity, humidity, soil and wall surface and internal temperature of the solar greenhouse should also be considered. In future studies, these data should be collected together with the temperature inside the solar greenhouse in order to obtain a more rational analysis of the thermal environment in the solar greenhouse and to better manage and optimize it.

CONCLUSIONS

In this paper, measurements of light were not covered in this article, and the coupling between light and temperature is not clearby. By selecting different weather conditions to analyse the trends of the thermal environment and the characteristics of temperature distribution in the solar greenhouse, the following conclusions were obtained:

Under different weather conditions, the maximum and minimum temperatures in this solarium were located in the eastern part of the crop area, and the maximum temperatures were all higher than 30°C, which was not conducive to the growth and development of temperature-loving vegetables.

The time to reach the maximum temperature in this solar greenhouse varied in different weather conditions, and the rate of change varied from location to location.

The maximum temperature in the solarium was around 4 metres from the back wall in the eastern part of the crop area and the maximum temperature exceeded 30°C in most areas of the crop area. periods, which were related to the indoor light and temperature.

ACKONWLEDGMENTS

I am very grateful to the College of Urban and Rural Construction for their help during the experiment and for the Shanxi Agricultural University Doctoral Start-up Fund(2023BQ06).

REFERENCES

[1] Aohua Fan (2018). Research on CFD simulation of winter solar greenhouse temperature field and uniform temperature regulation system（冬季日光温室温度场 CFD 模拟与均温调控系统研究）. *Northwest University of Agriculture and Forestry Science and Technology*, Xi′ an /China.

[2] Chao Chen, Nan Yu, Fengguang Yang et al (2019). Theoretical and experimental study on selection of physical dimensions of passive solar greenhouses for enhanced energy performance[J]. *Solar Energy*, Vol.191, pp.46–56, Beijing/China.

[3] Encai Bao, Zou Zhirong, Zhang Yong (2018). CFD simulation of heat transfer from rear walls of active thermal storage daylight greenhouses with different airflow directions（主动蓄热日光温室不同气流方向后墙传热 CFD 模拟）. *Journal of Agricultural Engineering*, Vol.34(22), pp.169-177, Xi′an /China.

[4] Hongjun Xu, Yanfei Cao, Yanrong Li et al (2019). CFD-based determination of the thickness of heat storage layer in sunlight greenhouse walls（基于 CFD 的日光温室墙体蓄热层厚度的确定）. *Journal of Agricultural Engineering*, Vol.35(04), pp.175-184, Xi′an /China.

[5] Jiangui Zhao, Zhiwei Li, Wenjun Li et al (2019). Testing and analysis of spatial and temporal distribution of environmental parameters in sunlit greenhouse tomato cultivation（日光温室番茄种植环境参数时空分布测试与分析）. *Shanxi Agricultural Science*, Vol.47(12), pp.2172-2176, 2181, Taiyuan/China.

[6] Jingjuan Hu, Guisheng Fan, Yanjuan Gao (2014). Experimental study on the characteristics of air temperature change in overwintering heliotrope greenhouses（越冬期日光温室空气温度变化特性的试验研究）. *Journal of Taiyuan Engineering*, Vol.45(04), pp.490-495, Taiyuan/China.

[7] Junhua Zhang, Kai-Cheng Shen, Dan-Yan Chen, et al (2021). Analysis of spatial and temporal variation of canopy temperature in a solar greenhouse based on the Internet of Things（大长度日光温室东西方向的温度变化特征）. *Journal of Agricultural Machinery*, Vol.52(07), pp.335-342, Xi′an /China /China.

[8] Lv Huanhuan, Niu Yuanyi, Zhang Man, et al (2021). Trend analysis of light intensity and air temperature and humidity in daylight greenhouses（日光温室光照强度与空气温湿度变化趋势分析）. *Journal of Agricultural Machinery*, Vol.52(S1), pp.410-417, Beijing/China.

[9] Panwar N.L., Kaushik S.C., Kothari S. (2011). Solar greenhouse an option for renewable and sustainable farming. *Renew Sustain Energy Rev*，Vol.15, pp.3934-3945, India.

[10] Shamshiri R.R., J. W. Jones, K. R. Thorp et al (2018). “Review of optimum temperature, humidity, and vapour pressure deficit for microclimate evaluation and control in greenhouse cultivation of tomato: a review,” *Int. agrophysics*, Vol.32(2), pp.287-302, United States.

[11] Weiwei Cheng, Zhonghua Liu (2022). Study on the change rate of the indoor temperature of a sunken solar greenhouse [J]. *INMATEH-Agricultural Engineering*, Vol.68 (3), pp. 119-126, Taiyuan/China.

[12] Yu H., Chen Y., Hassan S.G. et al (2016). Prediction of the temperature in a Chinese solar greenhouse based on LSSVM optimized by improved PSO[J]. *Computers and Electronics in Agriculture*, Vol.122，pp.94-102, Beijing/China.

[13] Zhangyan Le, Minghua Shi, Qucheng Wei, et al (2022). Characteristics of temperature variation in east-west direction of large-length daylight greenhouses[J]. *Guizhou Agricultural Science*, Vol.50(08), pp.94-102, Guizhou/China.

THE ELECTRIC TRACTION MOTORS BALANCING FOR LOAD TRANSFER EFFECTS COMPENSATION
/
ECHILIBRAREA MOTOARELOR ELECTRICE DE TRACȚIUNE PENTRU COMPENSAREA EFECTELOR TRANSFERULUI DE SARCINĂ

Mihail ANDREI [1)], Gabriel POPA[2)], Emil TUDOR [3*)], Paula ANGHELIȚA[3)], Mihai-Gabriel MATACHE[4*)])

[1)] Doctoral School of FIMM, National University of Science and Technology POLITEHNICA of Bucharest / Romania;

[2)] Railway Vehicles Department, National University of Science and Technology POLITEHNICA of Bucharest / Romania;

[3)] Renewable Sources and Energy Efficiency Department, National Institute for Research and Development in Electrical Engineering ICPE-CA, Bucharest / Romania;

[4)] National Institute for Research and Development in Machines and Installations Designed for Agriculture and Food Industry, INMA Bucharest / Romania;

Tel: +40755015614; E-mail: emil.tudor@icpe-ca.ro

DOI: https://doi.org/10.35633/inmateh-71-25

Keywords: *load transfer, traction characteristic, adhesion coefficient*

ABSTRACT

The individual drive of the axles of a vehicle produces a reduction of the axle adhesion, implicitly reducing the total traction force of the vehicle. The paper proposes eliminating load transfer effects by using an algorithm to redistribute the traction effort between the tractive axles equipped with electric traction motors. A case study is presented, using the balancing of the electric traction torque for an electric locomotive, using the load transfer effects compensation. The conclusions can be used to maximise the traction of all types of vehicles, such as trailers, hybrid tractors, large harvesters, and Diesel-electric locomotives.

REZUMAT

Acționarea individuală a axelor unui vehicul produce o reducere a aderenței axei, reducând implicit forța totală de tracțiune a vehiculului. Lucrarea propune eliminarea efectelor transferului de sarcină prin utilizarea unui algoritm de redistribuire a efortului de tracțiune între axele de tracțiune echipate cu motoare electrice de tracțiune. Este prezentat un studiu de caz, folosind echilibrarea cuplului de tracțiune electrică pentru o locomotivă electrică, folosind compensarea efectelor transferului de sarcină. Concluziile pot fi utilizate pentru a maximiza tracțiunea tuturor tipurilor de vehicule, cum ar fi autocamioane, tractoare hibride, utilaje agricole mari și locomotive diesel-electrice.

INTRODUCTION

Producing tractive torque at large vehicles implies the use of multiple tractive axles as a solution to overcome the limitations of the tractive effort due to the lack of adherence. Multiple tractive axles are used in trailers, hybrid tractors, large harvesters, and Diesel-electric locomotives. Because of the ease of control, for multiple traction, there is a preferred solution, consisting of independent electric motors for traction connected using a fixed single-gear transmission. A review regarding Electric Traction Motors for Battery Electric and Hybrid Vehicles presented the latest developments in electric traction motors and provided an efficient overview of the state-of-the-art motor designs, performances, technical limitations, as well as future concepts and trends (*Krings and Monissen, 2020*). The main topologies of the electric motors used for traction are the Direct-Current machines and the Alternative-current machines (*Nategh et al., 2020*). The AC machines are asynchronous machines and synchronous machines. Synchronous machines use permanent magnets PMSM or variable reluctance motors SRM (*Widmer et al., 2015*).

Regarding the independent tractive axle drive, a practical active traction control system is proposed, according to the wheel slip state of the front and rear axles, and the dynamic transfer of torque between axles is realised to maintain the vehicle propulsion power (*Wang et al., 2023*). From the papers involved in independent axle driving, it can be mentioned the analysis of *Nussupbek et al., (2023*), regarding a proposed phenomenon of redistribution of a 4x4 vehicle traction forces, by considering front and rear drive wheels separately as modular ones with reduction of all parameters to equation for each wheel separately.

The hydraulic system of the tractor hitch has the characteristics of a large load and complex working environment. A differential and integral sliding mode adaptive controller is designed for the hydraulic transmission system (*Liu et al, 2023*).

The dependence of the force of draft force on the square of the working speed is found in most of the literature (*Cardei et al., 2019*). The modelling of the running system pressure on the soil depending on the structural parameters of the tractors according to *Golub et al., (2023*) is important for the characterisation of the traction system of the vehicle, especially during the normal operation of agricultural vehicles while sliding on the soil.

When assessing the adherence of the tractive wheels to the ground (soil, road, rail), the adherence coefficient is a very important figure, which characterises the maximum possible torque which can be applied to the tractive axle. A new approach to estimating vehicle tire forces and road maximum adherence is presented by *Villagra et al., (2010*). A fast method for the computation of the wheel-rail forces, suitable for the investigations of problems regarding traction control and axle drive dynamics and their interaction with a vehicle's dynamic behaviour is presented in *Polach, (2001*). It is well-known that the adhesion coefficient between wheel and rail is widely variable, which has an influence on the running stability of vehicles, particularly the performance of driving and braking of the rail vehicles (*Zhao et al., 2018*). Prevention measures against adherence loss are necessary, and a new anti-slip control approach for four-wheel independent-drive electric vehicles based on the energy method is proposed, making full use of the distribution of motor energy between the body and the wheels during vehicle turning, being able to adjust the driving torque of each wheel (*Ci et al., 2023*).

Load transfer between tractive axles during traction is described in the comprehensive review of the current technologies in practice and future research trends in traction motors developed for high-speed railways, starting with Multiphysics design, including electromagnetic, mechanical, and thermal perspectives, with a special focus on understanding the use of the distributed traction system for high-speed railway system and related motor technology (*Paul et al., 2022*). The drive torque for each motor can be performed independently for the distributed drive, and the torque distribution can be optimised according to the axle load (*Gao et al., 2021*).

When speaking of multiplying the tractive force of a vehicle, the best example can be found in railway traction, where, based on the limited adherence of the wheel-to-rail system, multiple tractive axles must be used. A typical traction system consists of one or more locomotives and a train formed with several wagons. For locomotives, a two-bogie tractive solution with a total of 4 or 6 tractive axles is used. The Diesel-electric locomotives use the 4-tractive axle system and the all-electric locomotives use both 4-axle and 6-axle solutions. For large freight trains towing, multiple locomotives can be used according to *Sun et al., (2017*), in tandem operation, in independent operations and in "push-pull" operation. The experience was used, lately, in the Electric Multiple Units (EMU) passenger trains, where the traction system developed is located in the tractive coaches, similar to the underground trains. An example of improving the energy efficiency of rail vehicles equipped with multi-motor electrical traction when operating with partial load is shown in *Zarifyan et al., (2019*). Electronic control of multiple traction units used in modern AC high adhesion locomotives are very complex mechatronic systems and can be designed with two alternative traction topologies of either bogie or individual axle controls (*Spiryagin et al., 2017*). For proper acceleration or braking of the wheel, the driving torque should be kept near the adhesive level for the desired anti-slip control *(Isharat et al., 2016*). Depending on the type of drive system used, the distribution of the forces and moments generated by the drive equipment at the axles is different (*Arsene et al., 2018*).

The present paper will perform a case study for the two-axle bogie locomotive traction system, starting with an in-depth analysis of the axle load distribution, a study of the influence of load transfer on the traction characteristics of locomotives, pointing out the mechanical characteristics with limited grip for axle depending on the position of each axle. The original contribution of the authors is underlined by the presented algorithm of redistribution of the prescribed tractive force among the tractive axles for maximising the tractive force, applied for the case of torsion of the locomotive which generated a 15% unbalance between tractive axles.

MATERIALS AND METHODS

Calculation of axle load redistribution in the case of two-axle bogie vehicles

The case of a locomotive on two independent bogies having the *B0-B0* formula of axles will be analysed. Each of the two bogies transmits the traction forces to the box through a pivot. The calculation of the axle load redistribution is done in the following simplifying hypotheses:

- the bogie frame and the locomotive chassis are rigid assemblies that do not deform when the traction forces are applied or under their weight;
- traction motors generate equal traction forces;
- the forces of gravity and traction are evenly distributed on the bogies and the axles of the locomotive;

- the rolling resistance forces of the two bogies are neglected;

Symbol $F0$ represents the traction force at the locomotive hook and F represents the traction force corresponding to each axle.

In traction mode, two horizontal forces act on the locomotive:

- Traction force applied to the knuckle $F0$, to each driving axle having a force $F=F0/n$, $n = 4$ (number of driving axles);
- Resistant force T applied by the train to the traction hook.

These two forces form a torque that tends to unload the front axles and load the rear axles. In the absence of traction force, the axle load is $G/4$, and G is the total weight of the locomotive (equal in this case to the adherent weight).

In traction mode, due to the effect of the wiring torque, the loads on the four axles change, the values being denoted by: $G1$, $G2$, G_3 and $G4$. The variations of the axle loads will be equal to:

$$\Delta G_1 = \frac{G}{4} - G_1;\ \ \Delta G_2 = \frac{G}{4} - G_2;\ \ \Delta G_3 = \frac{G}{4} - G_3\ ;\ \ \Delta G_4 = \frac{G}{4} - G_4 \tag{1}$$

In the case of axle unloading, the ΔG values are positive, and in the case of overloading, the ΔG values are negative. The evaluation of the effect of the wiring torque is done by calculating separately the wiring of the box and the wiring of the bogies and then the total effect will be the sum of these two cumulative effects (superposition).

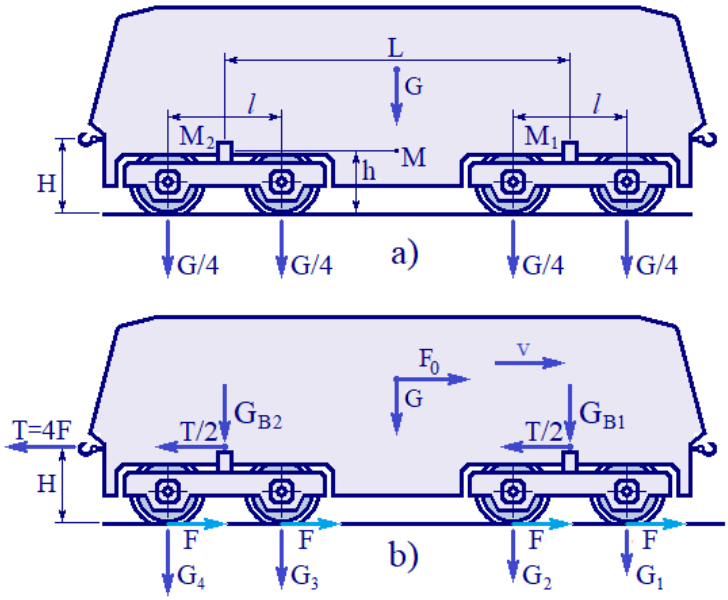


Fig. 1 - Forces acting on the motor vehicle in bogies

a) without traction; b) in traction mode

Two pairs of forces acting in equilibrium act on the locomotive box:

- The torque generated by the resistant force T (applied to the hook at height H above the upper rail level) and the two traction forces $T/2$ applied by bogies to the two pivots of the locomotive (forces applied at height h above the upper level of the rail). The torque generated by these forces tends to rotate the locomotive box in a counterclockwise direction;
- The torque generated by the two reactions at components G_{B1} and G_{B2} of the gravitational force G of the locomotive box applied to the supports of the pivots at a distance L. This torque tends to rotate the locomotive box in a clockwise direction;

Equating the moments of these two torques acting on the box, torques calculated concerning the point M located in the middle of the distance between the two pivots at the height h from the upper level of the rail, the equation is obtained:

$$T(H-h) = (G_{B2} - G_{B1}) \cdot \frac{L}{2} \tag{2}$$

This equation establishes the equality of the modules of the couples of those two moments of opposite directions. In the absence of traction, the two components of the weight force G are equal, the weight of the locomotive being evenly distributed over the two bogies.

In traction, a redistribution of the weight force occurs on the two bogies with the value ΔG_C.

$$G_{B1} = \frac{G}{2} - \Delta G_C \quad and \quad G_{B2} = \frac{G}{2} + \Delta G_C \tag{3}$$

Result:

$$\Delta G_C = \frac{G_{B2} - G_{B1}}{2} \tag{4}$$

From the equal relation of the moments of the couples acting on the box is obtained:

$$\Delta G_C = \frac{G_{B2} - G_{B1}}{2} = T \cdot \frac{H-h}{L} \tag{5}$$

The amount ΔG_C represents the effect of the box load transfer in the redistribution of loads on axles and bogies. By replacing the ΔG_C the expressions for the load of the box on the two bogies are obtained:

$$G_{B1} = \frac{G}{2} - T \cdot \frac{H-h}{L} \tag{6}$$

$$G_{B2} = \frac{G}{2} + T \cdot \frac{H-h}{L} \tag{7}$$

The evaluation of the load redistribution on the two axles of a bogie is made considering the two bogies loaded by the box with the loads G_{B1} and G_{B2} respectively. In traction mode, the loads on the four axles are G_{B1}, G_{B2}, G_{B3} and G_{B4}. For each bogie, the moment generated by the traction forces of the two axles is equal to the moment generated by the redistribution of the loads on the two axles:

$$\frac{T}{2}h = (G_2 - G_1)\frac{l}{2} \quad and \quad \frac{T}{2}h = (G_4 - G_3)\frac{l}{2} \tag{8}$$

Substituting in the equilibrium relation of the moments for each of the two bogies results:

$$\Delta G_{OB} = \frac{G_2 - G_1}{2} = \frac{G_4 - G_3}{2} = \frac{T}{2} \cdot \frac{h}{l} \tag{9}$$

Using G_B as the bogie's weight, in the absence of traction effort, the static load on the axle is:

$$G_0 = \frac{G}{4} + \frac{G_B}{2} \tag{10}$$

After applying the traction force T, the loads on the four axles will be:

$$G_1 = \frac{G_B + G_{B1}}{2} - \Delta G_{OB} \tag{11}$$

$$G_2 = \frac{G_B + G_{B1}}{2} + \Delta G_{OB} \tag{12}$$

$$G_3 = \frac{G_B + G_{B2}}{2} - \Delta G_{OB} \tag{13}$$

$$G_4 = \frac{G_B + G_{B2}}{2} + \Delta G_{OB} \tag{14}$$

Replacing expressions for ΔG_{OB}, G_{B1} and G_{B2} is obtained:

$$G_1 = \frac{G}{4} + \frac{G_B}{2} + \frac{T}{2} \cdot \left(-\frac{H-h}{L} - \frac{h}{l}\right) \tag{15}$$

$$G_2 = \frac{G}{4} + \frac{G_B}{2} + \frac{T}{2} \cdot \left(-\frac{H-h}{L} + \frac{h}{l}\right) \tag{16}$$

$$G_3 = \frac{G}{4} + \frac{G_B}{2} + \frac{T}{2} \cdot \left(+\frac{H-h}{L} - \frac{h}{l}\right) \tag{17}$$

$$G_4 = \frac{G}{4} + \frac{G_B}{2} + \frac{T}{2} \cdot \left(+\frac{H-h}{L} + \frac{h}{l}\right) \tag{18}$$

Unloading the 4 axles ΔG_i the index i representing the axle number ($i=1 \ldots 4$) is equal to:

$$\Delta G_i = G_0 - G_i \ (where\ i = 1 \ldots 4) \tag{19}$$

$$\Delta G_1 = \frac{T}{2} \cdot \left(+\frac{H-h}{L} + \frac{h}{l}\right) \tag{20}$$

$$\Delta G_2 = \frac{T}{2} \cdot \left(+\frac{H-h}{L} - \frac{h}{l}\right) \tag{21}$$

$$\Delta G_3 = \frac{T}{2} \cdot \left(-\frac{H-h}{L} + \frac{h}{l}\right) \tag{22}$$

$$\Delta G_4 = \frac{T}{2} \cdot \left(-\frac{H-h}{L} - \frac{h}{l}\right) \tag{23}$$

The forces generated by the motor-transmission system also contribute to the redistribution of axle loads and apply vertical forces Z on the drive axle, the values of which are given by the relations (24)-(26):

$$Z = F \cdot \frac{D}{2b} \quad \text{for the semi-suspended motor;} \tag{24}$$

$$Z = F \cdot \frac{D}{2b}\left(1 + \frac{1}{i}\right) \quad \text{for the suspended motor with the semi-suspended gear;} \tag{25}$$

$$Z = 0 \quad \text{for fully suspended motor and gear.} \tag{26}$$

where D is the diameter of the drive wheels, b is the distance in the horizontal direction between the axle axis and the point of support of the motor on the bogie frame and i is the gear ratio of the gear. These vertical forces produce a variation of the axle load due to the motor-reduction gear system equal to:

$$\Delta G_{OM} = Z \tag{27}$$

Expression of ΔG_{OM} can be written as:

$$\Delta G_{OM} = \pm F \cdot \frac{D}{2b} \cdot \lambda \tag{28}$$

where the coefficient λ depends on the type of motor suspension and gearbox:

$\lambda = 1$ for the semi-suspended motor; (29)

$\lambda = 1 + \frac{1}{i}$ for the suspended motor with the semi-suspended gear; (30)

$\lambda = 0$ for fully suspended motor and gear. (31)

The general expression of the load on the drive axles can be given in the form:

$$\Delta G_i = \frac{T}{2} \cdot \left(\pm \frac{H-h}{L} \pm \frac{h}{l} \pm \frac{D}{4b} \cdot \lambda \right) \quad (32)$$

This relationship highlights the three components that unload the axles of the locomotive in traction mode:

- the component represented by the term *+/-(H-h)/L* is the component given by the locking of the locomotive box. This term appears with the plus sign for the front bogie axles (bogie no.1) and with the minus sign for the rear bogie axles (bogie no.2);
- the component represented by the term *+/- h/l* represents the component given by the load transfer of the bogie under which the axle is mounted. This term appears with the plus sign if the axle is mounted in the front of the bogie (axles no.1 and no.3 respectively) and with the minus sign if the axle is mounted in the back of the bogie (axles no.2 respectively no.4).
- the component represented by the term *+/- D λ/4b* represents the component given by the force generated by the motor-reduction system. This term appears with the plus sign if the traction motor is placed in front of the axle (the axle is unloaded) and with the minus sign if the traction motor is behind the axle it drives (the axle is overloaded). In electric braking mode, the signs are reversed.

The influence of load transfer on the traction characteristics of locomotives

The redistribution of loads on the locomotive axles under the action of the coupling torques and the forces exerted on the drive axle by the traction gear have negative effects on the traction force that can be developed by the unloaded axles.

In the case of locomotives that have bogies in which the axles are operated in groups, (single-motor bogies) the traction force is automatically redistributed only between the axles of the same bogie. In this case, only the box wiring is manifested, which has a relatively low effect (max. 4% of the load on the bogies).

Locomotives with individual drive axles cannot make full use of the weight due to the tendency of the unloaded axles to skid.

The relationship gives the maximum traction force that a drive axle can develop:

$$F_{max} = \psi(v) \cdot (G_0 - \Delta G) \quad (33)$$

Where $\psi(v)$ is the speed-dependent axle adhesion coefficient.

The dependence of the velocity adhesion coefficient is approximated by parabola or hyperbola arcs, one of the commonly used formulas being:

$$\psi(v) = \frac{7.5}{v+44} + 0{,}161 \quad (34)$$

As previously shown, the unloading of an axle in traction or electric braking mode is given by the relation:

$$\Delta G = 2 \cdot F \cdot \left(\pm \frac{H-h}{L} \pm \frac{h}{l} \pm \frac{D}{4b} \cdot \lambda \right) = F \cdot \varphi \quad (35)$$

where:

$$\varphi = 2 \cdot \left(\pm \frac{H-h}{L} \pm \frac{h}{l} \pm \frac{D}{4b} \cdot \lambda \right) \quad (36)$$

For $\varphi > 0$ the axle is unloaded and $\varphi < 0$ the axle is overloaded.

By replacing the Φ result:

$$F_{max} = \psi(v) \cdot (G_0 - F_{max} \cdot \varphi) \quad (37)$$

$$F_{max} = \frac{\psi(v)}{1+\psi(v)\cdot\varphi} \cdot G_0 = \eta(v) \cdot G_0 \quad (38)$$

where:

$$\eta(v) = \frac{\psi(v)}{1+\psi(v)\cdot\varphi} \quad (39)$$

It is obvious that:

$\eta(v) < \psi(v)$ if $\varphi > 0$ (unloaded axle) (40)

$\eta(v) > \psi(v)$ if $\varphi < 0$ (overloaded axle); (41)

$\eta(v) = \psi(v)$ if $\varphi = 0$. (42)

The drive axle subjected to unloading behaves as if it were running with a low grip, and the overloaded axles behave as if they were running with an increased grip. In the graph in Figure 2, the family of curves was drawn $\eta(v)$ for the usual values of axle loads $(-0.20 \leq \varphi \leq 0.20)$.

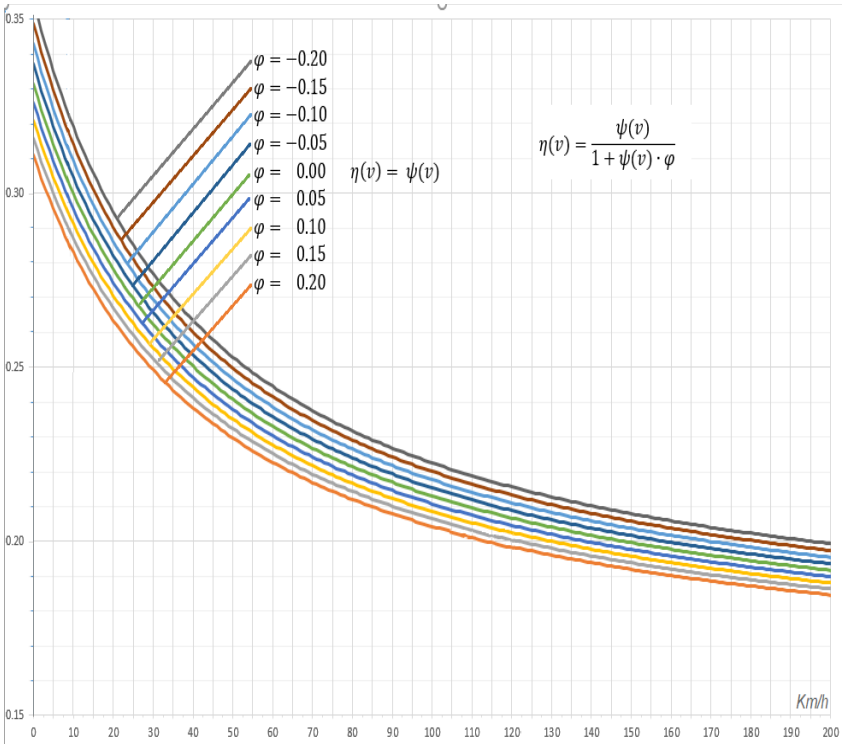


Fig. 2 - Calculation of adhesion limits according to the degree of unloading or loading the drive axle

In Figure 2 it can be observed that, in the absence of load transfer limitation measures, the limit of adhesion of the unloaded axles is considerably reduced, significantly diminishing the performance of the locomotive.

F(v) limited grip characteristics for drive axles depending on the position of each axle

Next, the traction characteristics $F(v)$ will be constructed for each drive axle affected by the wiring, depending on the position of the axle under the locomotives. For clarity, it will be exemplified on a locomotive with two bogies, each bogie having two axles, the example can be easily generalized for other types of locomotives.

Subsequently, based on the characteristics of each axle affected by the load transfer, the actual characteristic $F(v)$ of the locomotive will be constructed under the influence of the load transfer for different traction motor control systems.

The traction characteristic $F(v)$ for a single-drive axle has the following limits:

- On the right side it is limited by the maximum speed of the locomotive. This speed is mainly due to the maximum speed allowed by the rotors of the traction motors but also by a multitude of other factors such as suspension type, brake type, etc.
- The central part is limited by the maximum power that the traction motor can provide to the crankshaft;
- In the upper part the characteristic is limited by the adhesion and the adhesion is influenced by the load transfer ΔG_i.
- Taking into account the relations expressing the axle discharges ΔG_i calculated in the previous chapter and the fact that the values of the discharges given by the box load transfer are lower compared to the discharges given by the bogie load transfer, there is the following order of amplitude of these discharges:

$$\Delta G_4 < \Delta G_2 < 0 < \Delta G_3 < \Delta G_1 \quad (43)$$

Axles 1 and 3 will be unloaded and axles 2 and 4 will be overloaded. There will be the same order for the coefficients φ_i.

$$\varphi_4 < \varphi_2 < 0 < \varphi_3 < \varphi_1 \quad (44)$$

When constructing characteristic $F(v)$, the appearance of the adhesion limit curves in Figure 2 shall also be taken into account for the various values and signs of φ_i.

Using this demonstration, the characteristics $F(v)$ for each axle will have the appearance of Figure 3.

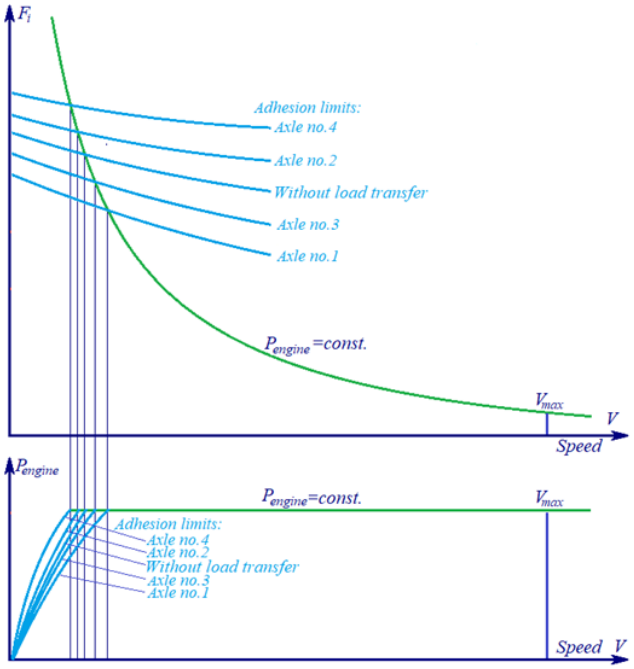


Fig. 3 - Characteristics F (v) and P (v) for each axle with the adhesion limits given by the wiring

In the case of locomotives for which the individual adjustment of the traction motors is performed, an algorithm of integral use of the adhesion will be proposed, even in the presence of load redistributions between the motor axles. The algorithm aims to compensate for the limitations caused by the unloading of the axles with the additional traction force available on the axles loaded as a result of the load transfer.

This is how the algorithm works:

- An order is given to increase the traction force of the locomotive. If no motor has slipped, it is further ordered to increase the traction effort.
- If a starting slip is detected on one of the motors, then that motor will enter the force limit at the grip limit. To compensate for the limitation of the traction force on the traction motor, the traction force is increased in the same way as for the other three motors which will uniformly take over the traction force deficit caused by the limitation produced by the traction motor.
- The traction force is further increased for non-slip axle.
- If another motor with a tendency to skid is detected, then it will also enter the force limitation and the traction force will be uniformly increased for non-slip axle.

The logic diagram for the implementation of this algorithm is shown in Figure 4.

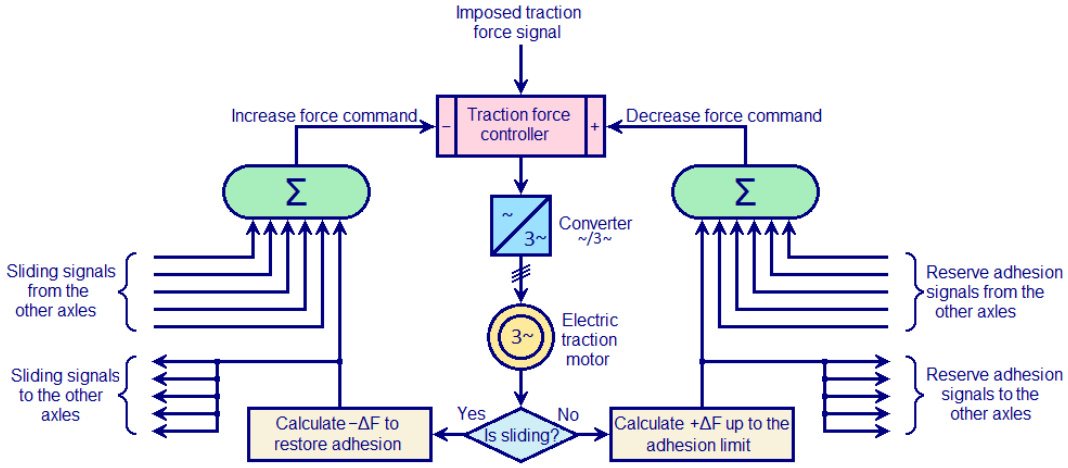


Fig. 4 - Scheme for the implementation of the algorithm for redistribution of traction forces on the loaded axles

For the efficient operation of this method in compensating the effects of load transfer, the redistribution of traction forces must be done equally on all non-slip axles. Any overloads to which the traction motors and the electric power equipment are subjected during this redistribution of traction forces will have minimum, tolerable values. Otherwise, there will be a risk of overcurrent or overvoltage protection coming into action, which will nullify these measures for the efficient use of locomotive adhesion.

RESULTS

Traction simulation software program under the influence of load transfer on locomotives

To visualize the traction characteristics under the influence of load transfer and how the load transfer influences the performance of the locomotive, a software code was written (named Sim Cabraj.exe) that simulates the behaviour of the drive axles and the locomotive as a whole, taking into account the negative effects of load transfer. The presented program calculates and represents graphically the traction characteristics of the locomotives taking into account the effect of the load transfer on the adhesion and the different solutions adopted to limit it.

The graphical representation of the traction characteristics starts from the calculation of the characteristics $F(v)$ for each axle. The calculation of the characteristics $F(v)$ of each axle is made according to the effects of the load transfer on each axle.

From the traction characteristics calculated for each axle, the traction characteristics of the locomotive are obtained by calculating the sum of the traction forces of the axles for a given speed. The calculation of these sums of the traction forces of the axles is made taking into account the limitations given by the constructive variant of the locomotive: the electrical diagram and the measures taken to reduce the load transfer and its effects.

The traction characteristics for the most used variants of locomotives were calculated and plotted:

- Locomotives with group adjustment of traction motors with anti-slip that act simultaneously on all axles;
- Locomotives with independent adjustment of traction motors, each axle having its anti-slip system;
- The variant proposed by the locomotive with independent adjustment of the traction motors, in which, in case of a slip, it achieves the automatic redistribution of the traction force on the other axles that have the adhesion ensured due to the load transfer (overloaded axles).

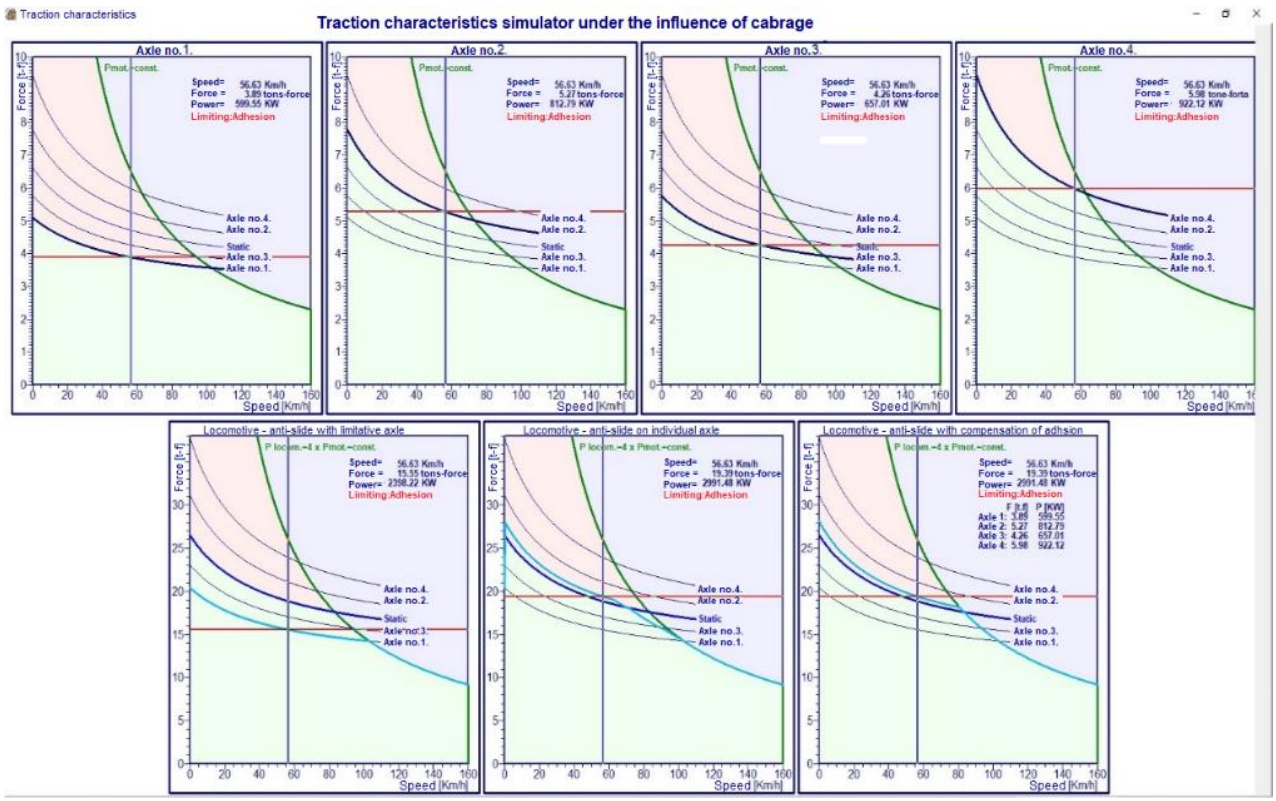


Fig. 5 - The main SimCabraj.exe application window.

After launching the program, two rows of diagrams are displayed in the main application window. The diagrams on the top row represent the traction characteristics for each driving axle of the locomotive. At the bottom row are three diagrams of traction characteristics for each of the three types of studied locomotives. The three variants of locomotives analysed can thus be easily compared, concluding their advantages and disadvantages. The following curves are drawn on each diagram:

- Constant power curve - green colour.
- Adhesion limit curve - dark blue, corresponding to the axle.

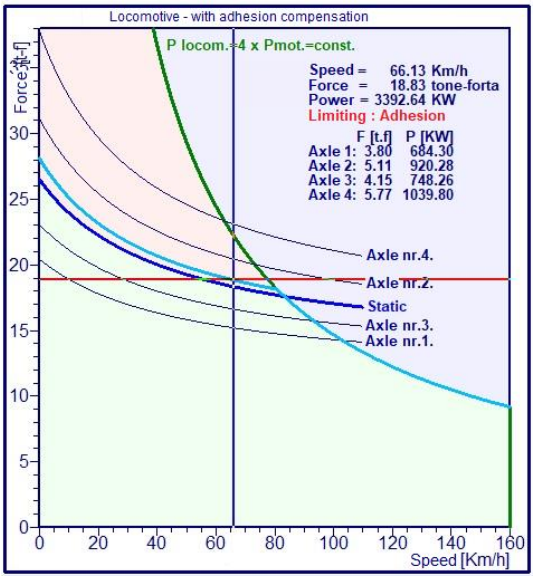


Fig. 6 - The Force-Speed characteristic after redistribution of traction efforts according to the algorithm

For comparison, the adhesion limits for all other axles were drawn with a thin line. With a thin blue line, the adhesion limit was represented in the absence of load transfer. For locomotives, (lower row) in light blue is the actual traction characteristic of the locomotive. The first two curves delimit three differently coloured areas:

- The light green area under these two curves is the area where the locomotive can operate normally;
- The red area above the grip curve is the slipping area;
- The blue area above the constant power curve is the overload operating area.

The values characteristic of the indicated cursor point (speed, traction force, power) are displayed in the upper right part of each diagram. By moving the cursors on different areas of the diagrams, following the way the traction characteristics are constructed and the implications of the three constructive variants on the performance of the locomotive can be evaluated.

CONCLUSIONS

The diagrams generated by the presented software show that this algorithm manages to avoid slipping the locomotive axles as a result of the balanced load transfer while keeping the traction characteristics of the locomotive unaltered. By applying this algorithm, the harmful effects of axle slipping are avoided and the power of the locomotive can be used in full. Using the proposed algorithm in controlling the torque commands for each independent drive, the unloaded axle motors will gradually enter the force limitation regime, and with the other motors, it will be possible to go beyond the normal adhesion limit, these being overloaded as a result of the load transfer. By doing so, it is theoretically possible to fully compensate for the load transfer, thus the locomotive operates practically with maximum adhesion.

ACKNOWLEDGEMENT

This work has been funded by the European Social Fund from the Sectorial Operational Programme Human Capital 2014-2020, through the Financial Agreement with the title "Training of PhD students and postdoctoral researchers to acquire applied research skills - SMART", Contract no. 13530/16.06.2022 - SMIS code: 153734. Part of the work was supported by MCID within Nucleu Program 42N / 2023, project number PN23140101, and by contract 25PFE/2021.

REFERENCES

[1] Arsene, S., Sebesan, I., Popa, G., Gheti, M.A., (2018), Considerations on studying the loads on the motor bogie frame, *IOP Conference Series: Materials Science and Engineering,* Volume 400, Issue 4, doi:10.1088/1757-899X/400/4/042003;

[2] Cardei P., Muraru S.L., Sfiru R., Muraru V, (2019) General structure of tillage draft force. Consequences in experimental and applicative researches, *INMATEH – Agricultural Engineering*, Vol. 59, No. 3 / 2019, ISSN 2068 – 2239, DOI:/10.35633/inmateh-59-28;

[3] Guangzong Gao; Jixin Wang; Tao Ma; Yunwu Han; Xihao Yang; Xuefei Li; (2021). Optimisation strategy of torque distribution for the distributed drive electric wheel loader based on the estimated shovelling load, *Vehicle System Dynamics*, Volume 60, 2022, Issue 6, Pages 2036-2054, DOI:10.1080/00423114.2021.1890153;

[4] Golub, G., Chuba, V., Achkevych, V., Krushelnytskyi, V., Tsyvenkova, N., (2023), Modelling of the running system pressure on the soil depending on the structural parameters of the tractors, *INMATEH - Agricultural Engineering*, Vol. 69, No.1 / 2023, https://doi.org/10.35633/inmateh-69-34;

[5] Ishrat, T., Ledwich, G., Vilathgamuwa, M., Borghesani, P., (2016), Wheel slip control based on traction force estimation of electric locomotives, *2016 Australasian Universities Power Engineering Conference (AUPEC)*, Brisbane, QLD, Australia, pp. 1-6, doi: 10.1109/AUPEC.2016.7749331;

[6] Krings, A., Monissen, C., (2020) Review and Trends in Electric Traction Motors for Battery Electric and Hybrid Vehicles, *2020 International Conference on Electrical Machines (ICEM)*, Gothenburg, Sweden, pp. 1807-1813, DOI: 10.1109/ICEM49940.2020.9270946;

[7] Changing LIU, Jinheng GU, Xin DU, Chengwen LIU, Yuefeng DU, Enrong MAO, Differential and integral sliding mode adaptive control algorithm for draft and position integrated control of electro-hydraulic hitch in agricultural tractor, *INMATEH – Agricultural Engineering*, Volume 70, No. 2 / 2023, ISSN 2068 – 2239, DOI:/10.35633/inmateh-70-36;

[8] Ci Longtao, Yan Zhou, and Dejun Yin, (2023) An Anti-Skid Control System Based on the Energy Method for Decentralized Electric Vehicles, *World Electric Vehicle Journal*, vol 14, no. 2: 49. DOI:10.3390/wevj14020049;

[9] Nategh, S., Boglietti, A., Liu, Yujing, Barber, D., Brammer, R., Lindberg, D., Aglen, O., (2020) A Review on Different Aspects of Traction Motor Design for Railway Applications, *IEEE Transactions on Industry Applications*, vol. 56, no. 3, pp. 2148-2157, DOI: 10.1109/TIA.2020.2968414;

[10] Nussupbek, Zh.T., Bekenov, T.N., Sattinova, Z.K., Beisenbi, M.A., Tassybekov, Zh.T., (2023) Substantiation of methods for calculation of traction forces redistribution indicators on modular front and rear wheels of the vehicle (4X4), *Transportation Engineering* Volume 13, September 2023, 100193, DOI:10.1016/j.treng.2023.100193;

[11] Paul S., Pil-Wan Han, Junghwan Chang, Yon-Do Chun, Jae-Gil Lee, (2022), State-of-the-art review of railway traction motors for distributed traction considering South Korean high-speed railway, *Energy Reports* 8 (2022) 14623–14642, DOI: 10.1016/j.egyr.2022.10.411

[12] Polach O., (2001), Influence of Locomotive Tractive Effort on the Forces Between Wheel and Rail, *Vehicle System Dynamics* Supplement 35, pp. 7-22, Zwets & Zeitlinger

[13] Spiryagin, M., Wolfs, P., Cole, C., Stichel, S., Mats B, Plöchl M., (2017), Influence of AC system design on the realisation of tractive efforts by high adhesion locomotives, *Vehicle System Dynamics*, DOI: 10.1080/00423114.2017.1308522

[14] Yannan Sun; Tong Zhang; Changxian Li, (2017), Study and construction of traction control system of EMUs, *36th Chinese Control Conference (CCC)*, Dalian, China, pp. 9972-9976, ISSN: 1934-1768, DOI: 10.23919/ChiCC.2017.8028948.

[15] Villagra J, d'Andréa-Novel B, Fliess M, Mounier H., (2010) A diagnosis-based approach for tire–road forces and maximum friction estimation, *Control Engineering Practice* Volume 19, Issue 2, Pages 174-184, ISSN: 0967-0661, https://doi.org/10.1016/j.conengprac.2010.11.005

[16] Zarifyan, A. Zarifyan, N. Grebennikov, T. Talakhadze, N. Romanchenko and A. Shapshal, (2019), Increasing the Energy Efficiency of Rail Vehicles Equipped with a Multi-Motor Electrical Traction Drive, *26th International Workshop on Electric Drives: Improvement in Efficiency of Electric Drives (IWED)*, Moscow, Russia, 2019, pp. 1-5, DOI: 10.1109/IWED.2019.8664283

[17] Kaihui Zhao, Peng Li, Changfan Zhang, Jing He, Yanfei Li, Tonghuan Yin, (2018), Online Accurate Estimation of the Wheel-Rail Adhesion Coefficient and Optimal Adhesion Antiskid Control of Heavy-

Haul Electric Locomotives Based on Asymmetric Barrier Lyapunov Function, *Journal of Sensors*, vol. 2018, Article ID 2740679, 12 pages. https://doi.org/10.1155/2018/2740679;

[18] Wang, Junnian, Gao, Shoulin, Lv, Siwen, Sun, Jie, Sun, Wen, Yang, Zhihua, (2023), Practical active traction control for independent-wheel-drive electric vehicle based on slip-ratio threshold determination, *Asian J Control* 25, pp. 3524–3540, ISSN1561-8625, DOI: 10.1002/asjc.3034;

[19] Widmer, J., Martin, R., Kimiabeigi, M., (2015) Electric vehicle traction motors without rare earth magnets, *Sustainable Materials and Technologies* 3, pp. 7–13, ISSN: 2214-9937, DOI: 10.1016/j.susmat.2015.02.001;

POROUS HOT AIR TEA DE-ENZYMING AND CARDING MACHINE UNDER GAS–SOLID COUPLING CONDITIONS: NUMERICAL SIMULATIONS AND PERFORMANCE TESTING
/
气固耦合条件下多孔热风式茶叶杀青理条机数值模拟与性能试验

Haijun BI[*1, 2)], Pengcheng JIA[1,2)], Kuan QIN[3,4)], Lei YU[5)], Chengmao CAO[3,4)], Dongsong XIA[3,4)], Xinliang GUO[1,2)], Yang LIU[3,4)], Bin CHEN[3,4)], Yuzhen BI[1,2)]

[1)] State Key Laboratory of Tea Plant Biology and Utilization, Anhui Agricultural University, Hefei, China
[2)] School of Tea and Food Science and Technology, Anhui Agricultural University, Hefei, China
[3)] School of Engineering, Anhui Agricultural University, Hefei, China
[4)] Anhui Intelligent Agricultural Machinery Equipment Engineering Laboratory, Hefei, China
[5)] Anji Yuanfeng Tea Machinery Co. Ltd, Huzhou, China
Corresponding author, Tel:+8613965131157; E-mail address: bihaijun@ahau.edu.cn
First author, Tel: +8613965131157; E-mail address: bihaijun@ahau.edu.cn
DOI: https://doi.org/10.35633/inmateh-71-26

Keywords: *tea processing, de-enzyming, carding machine, gas–solid coupling, gas–solid flow, numerical simulation, performance testing*

ABSTRACT
The gas–solid coupling of a porous hot-air tea de-enzyming and carding machine was studied by means of computational fluid dynamics and discrete element coupling. In the numerical model, the discrete phase of tea particles was simulated using Rocky-DEM software, while the gas phase was described by ANSYS Fluent software. A mathematical model of the movement characteristics of tea particles in air was established according to the principle of fluid mechanics, to carry out dynamic analysis of tea particles' movement process and derive how the motion of gas and tea particles is governed. Three sets of prototype tests were carried out on the basis of the design and simulation, and the average of their results taken. This showed that the hourly output of the test prototype was 3.89 kg/h, the bar-type rate was 89.14%, the de-enzyming moderation rate was 91.67%, and the average value of the measured effective operating temperature of the pot slot was 189 °C. The performance of the prototype was also tested and analyzed. After conducting a tea sensory evaluation expert appraisal, the sensory evaluation indices of the prototype-processed tea satisfied all current market requirements, being superior to those of the conventional de-enzyming and carding machine. The quality of the finished tea also met the agronomic standards and the operational requirements of the de-enzyming and carding machine.

摘要
通过计算流体动力学和离散元耦合的方法对多孔热风式茶叶杀青理条机的工作过程进行了气固耦合数值研究。在数值模型中，使用 Rocky-dem 软件模拟茶叶颗粒的离散相，ANSYS Fluent 软件描述气体相。通过研究并根据流体力学原理建立了茶叶颗粒在空气中运动特性的数学模型，以此来进行茶叶颗粒运动过程的动力学分析，分析气体和茶叶颗粒的运动规律。在设计与仿真的基础上，进行了三组样机试验，取 3 次试验结果的平均值，结果表明：试验样机的台时产量为 3.89 kg/h，成条率为 89.14%，杀青适度率为 91.67%，实测锅槽有效运行温度均值为 189°C；并在上述基础上对试验样机进行了性能测试与分析。经茶叶感官评审专家鉴定，加工后的茶叶感官评价指标均符合要求，各项指标均优于传统杀青理条机，制得的成品茶质量达到农艺标准，且满足杀青理条机的工作要求。

INTRODUCTION
Green tea is the main type of tea cultivated in China, ranked first in China's tea category, and it is the most common tea consumed by Chinese people (*You et al., 2023*). Both de-enzyming and carding play a vital role in tea processing; whether their joint effect is satisfactory or not directly impinges upon the appearance and quality of tea leaves (*Wang et al., 2022*).

De-enzyming refers to the use of an external high temperature to transfer heat to fresh tea leaves, to eliminate their oxidase activity. Doing so also vaporizes water, reducing the moisture content of parts of tea leaves, leaving them softer and easy to knead and shape, while also dispersing the smell of tea itself to produce a sweet aroma (*Cao et al., 2016*).

Carding is a method of processing tea leaves and turning them into strips, which facilitates subsequent processes, and it helps to promote the formation of desirable tea color, aroma, taste, and other qualities (*Yan et al., 2022*).

Currently, domestic and foreign researchers are mostly interested in the hot air roller de-enzyming process of the roller de-enzyming machine. Most of these studies compare the quality of de-enzyming leaves, by experience or by experiment, to investigate the most suitable parameters and equipment of tea de-enzyming process. For example, *Panchariya et al. (2002)* experimentally measured and studied the variation patterns of hot air temperature and air velocity with moisture content in the hot air-drying process of tea leaves. Later, with the help of Fluent software, *Xu et al. (2014)* revealed the heating condition during de-enzyming done by a leaf guide plate (segment design) when the angle of spiral rise is held constant. They verified whether the segmented design structure is effective at improving the de-enzyming quality. Employing an experimental approach, *Ye et al. (2014)* conducted a comparative study of the roller, steam heat, and steam heat-roller combination de-enzyming processes, assessing the sensory quality, tea composition, color, and aroma of the produced green tea.

Shi et al. (2015) used a coupled EDEM-Fluent technique to examine the effects of variation in roller speed, the number of leaf guides, the height of leaf guides, the width of leaf guides, and the structure of the hot air inlet on the de-enzyming quality during hot air de-enzyming process. Recently, *Yu et al. (2019)* applied Fluent-EDEM to the coupled simulation of an infrared de-enzyming machine and electric heating de-enzyming machine. They compared the temperature distribution of the flow field in the roller of two de-enzyming machines and the temperature distribution of flow field of tea particles after de-enzyming was completed. They concluded the de-enzyming efficiency, heat energy utilization, and de-enzyming effect of the infrared de-enzyming machine outperformed those of the electric heating de-enzyming machine. More recently, *Wang et al. (2022),* used CFD (Computational Fluid Dynamics) technology to simulate and analyze the temperature field of a trough-type de-enzyming and carding machine, aiming to solve the poor uniformity of temperature's distribution in the pot groove of the tea carding machine; their findings led to an idea to further improve the uniformity of temperature in the carding parts.

Porous hot air de-enzyming technology is a multi-component, multiphase thermal system composed of tea and hot air as its raw materials. In this paper, the 6CSL-800 tea de-enzyming and carding machine was selected as the research object. Tea was designated a discrete phase, while hot air was considered a continuous phase. Both discrete element software (Rocky-DEM) and fluid dynamics software (ANSYS Fluent) were used to carry out a joint simulation operation to analyze the coupling between the discrete field and flow field during de-enzyming and carding (*Li et al., 2021*). The operational process of the multihole hot air type tea de-enzyming and carding machine was studied, and this existing device prototype optimized and tested to achieve the goal of improving the tea de-enzyming quality and increasing the yield from leaves. However, relevant research based on the trough-type porous hot air de-enzyming technology is lacking, so further research work on that is necessary.

MATERIALS AND METHODS

General structure and working principle

As shown in Figure 1, the 6CSL-800 type tea de-enzyming and carding machine is mainly composed of a U-shaped multi-groove pot, a frame, an eccentric wheel, a crank slider mechanism, a hydraulic cylinder, a connecting rod, a motor, a fan, a gas heating device, a gas regulating valve, a gas conveying pipe, and other components (*Bi et al., 2022*). The over-all structure appears in Figure 1A. During its operation, the de-enzyming and carding machine delivers power to the U-shaped multi-groove pot via the belt drive and crank slider mechanism, realizing different changes in speed by altering the motor frequency to meet the needs of the tea processing process (Figure 1B).

The heating parts are distributed underneath the U-shaped multi-slot pot, which is driven by the crank slider mechanism for reciprocating linear motion.

The main technical parameters of the 6CSL-800 de-enzyming and carding machine presented in Table 1.

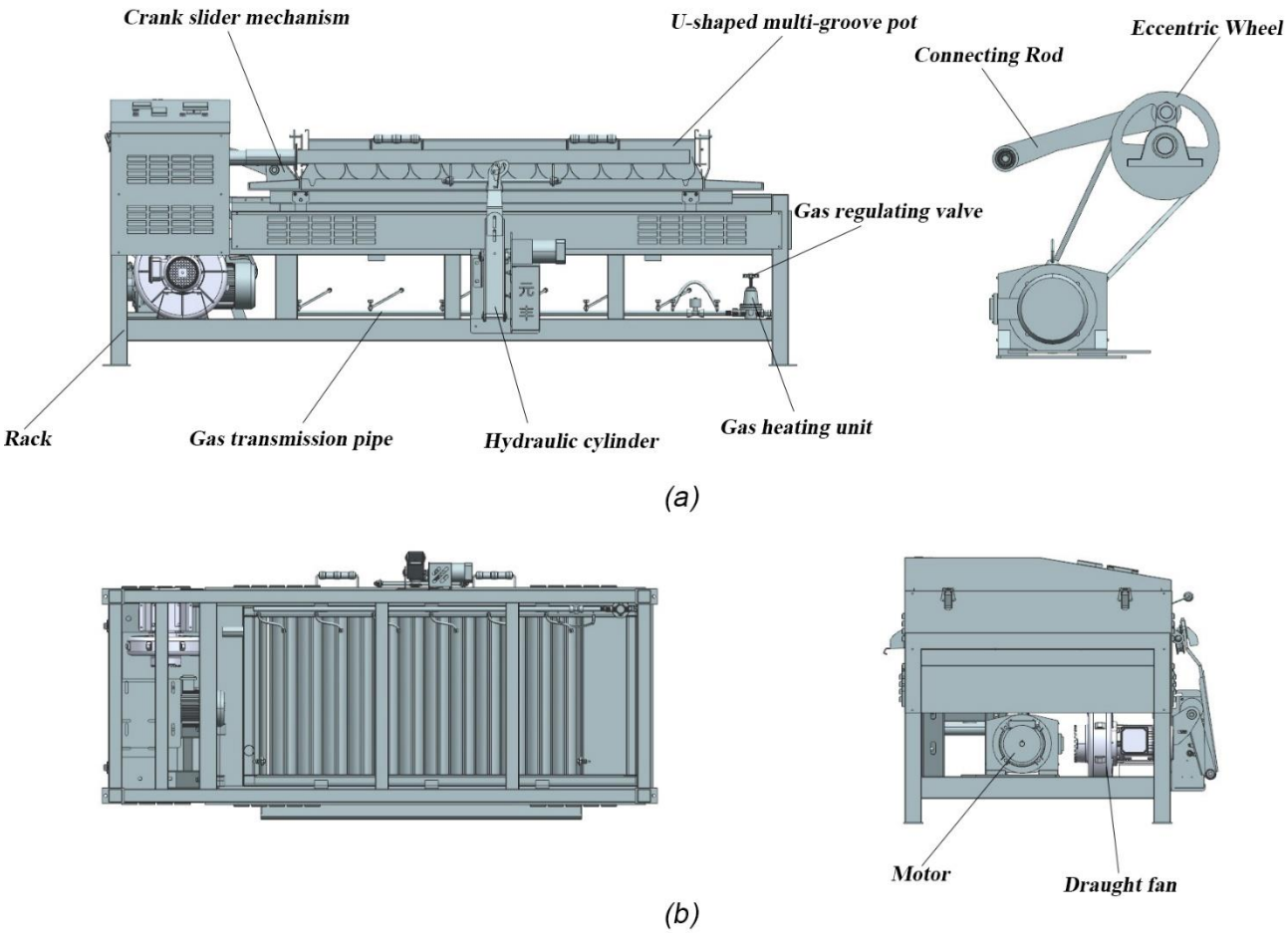


Fig. 1 - Schematic of the structure of the 6CSL-800 tea de-enzyming and carding machine
(a) Front view of the machine; (b) Upper and left view of the machine

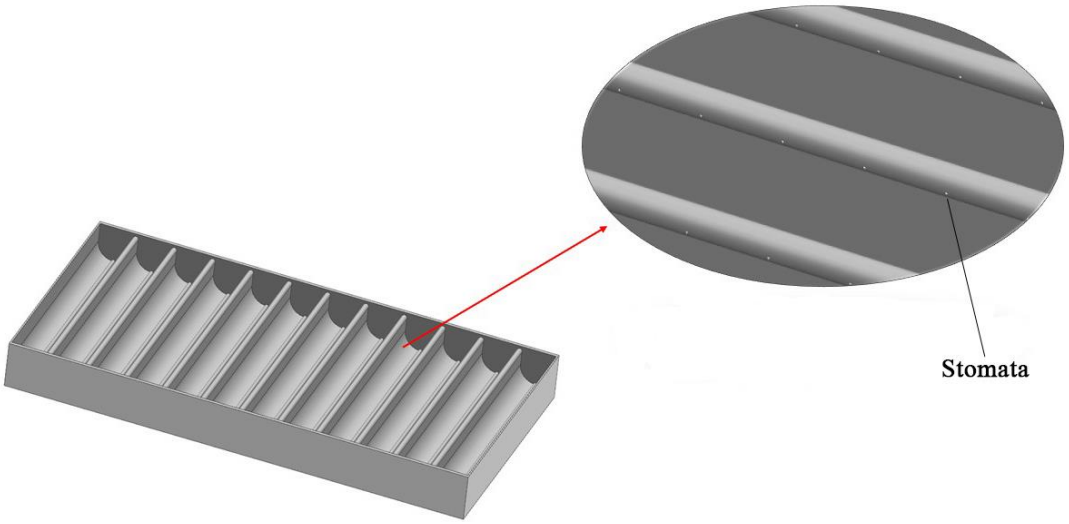
Table 1

Main working parameters of the tea carding machine

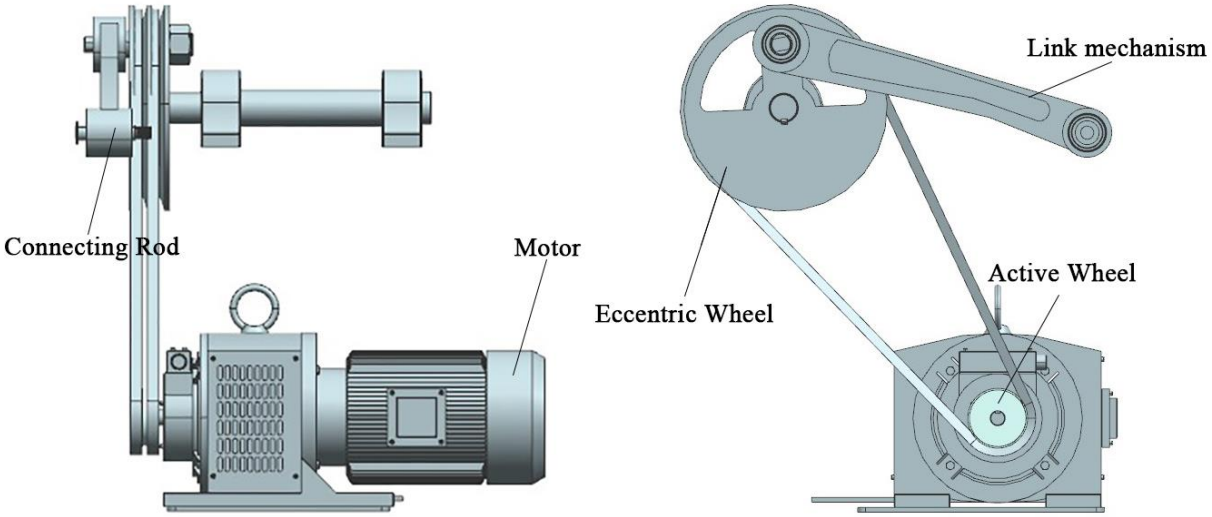
Major parameter	Value
Boundary dimension (mm)	2450 × 1100 × 950
Pot groove size (mm)	1000 × 600
Rated power (kw)	0.55
Working voltage (V)	380
Output per hour (kg/h)	≥ 3.5

Key component design

The 6CSL-800 machine's key parts are its U-shaped multi-groove pot and crank slider mechanism. The former is an important component, in that the depth size of the U-shaped slot, the width size of the pot, the size of the angle between the inner wall of the pot and horizontal surface, and other factors directly affect the efficacy of the tea de-enzyming and carding. As Figure 2A shows, there are air holes on the left and right sides of the inner wall of the U-shaped multi-groove pot, and the hot air discharged from the holes could alone release and disperse the green odor of the tea leaves and thereby prevent the phenomenon of 'water boredom' (*Wu et al., 2022*). As depicted in Figure 2B, the connecting rod mechanism of the crank slider mechanism is the key component of the machine's transmission, by implementing the reciprocating motion of the U-shaped groove by linking to the U-shaped groove. In the process of movement, the connecting rod applies a forward thrust and a downward pressure to the U-shaped multi-groove pot. The servo motor then propels the driving wheel to rotate, whose rotation could drive the slave wheel, eccentric wheel, and connecting rod in turn to perform reciprocating linear motion. When the connecting rod carries out this reciprocating linear motion, it causes the fixed pushing plate and carding plate to swing back and forth, achieving the purpose of evenly carding the tea leaves.



(a)



(b)

Fig. 2 - Structural diagrams of the key components

(a) Schematic diagram of the U-shaped multi-slot pot structure; (b) The crank slider mechanism

ANALYSIS OF THE MOVEMENT PROCESS OF TEA PARTICLES

The movement of tea particles in the pot groove is divided into three main stages. First, the tea particles move along the inner wall of the pot groove. Next, the tea particles leave the pot groove and undergo a throwing motion. Finally, the tea particles fall onto the pot groove' surface which entails collision movement. Ignoring the collision effect generated between tea particle and other particle, tea particle were treated as a single mass point, and a mathematical model of the motion characteristics of tea particle in air then established by following the principle of fluid dynamics; it was used to carry out a kinetic analysis of the motion process of tea particles (*Zhang et al., 2022)*.

Force analysis of the movement of tea particles along the inner wall of the pot groove

Here, a single tea particle was selected as the object of study, for which an absolute coordinate system was established on the ground and the motion process of tea particles along the inner wall of the pot trough was analyzed accordingly (*Wu et al., 2019*).

As illustrated in Figure 3, *AC* is the pot groove curve; point *B* is the location of the center of mass of the moving tea particle; *R* is the diameter of the tea particle, *n* is the normal vector of the mass point on the inner surface of the pot groove; *t* is the surface tangential vector of the mass point of the tea particle in the pot groove; and α is the angular acceleration.

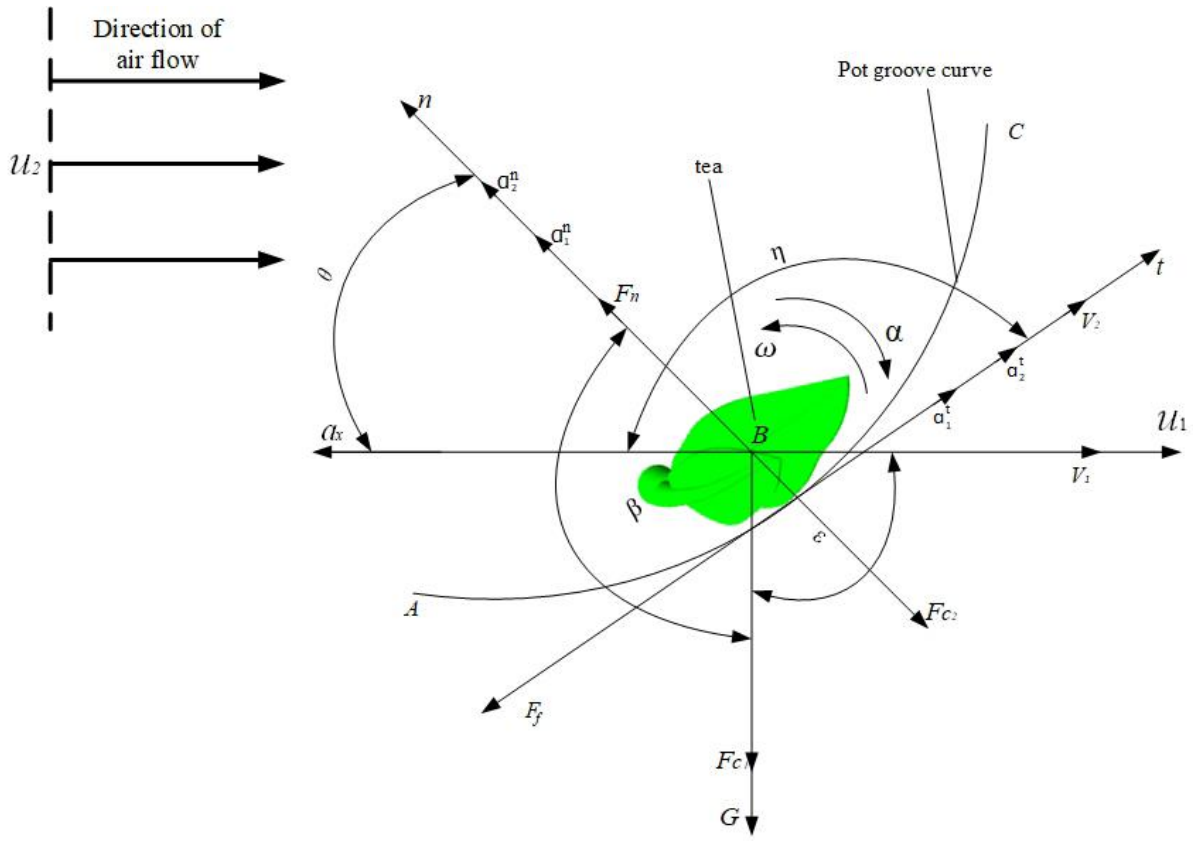


Fig. 3 - Force analysis diagram of tea particle tossing motion

As tea particles move along the inner wall of the pot trough under the action of the driving force, F_N<0, the relative average velocity of the friction force and tea particle's movement along the wall of the pot groove is in the opposite direction.

The Coriolis force acting on tea particles is as follows:

$$F_{c1} = -2m\omega \times V_1 = -2ma_{c1} \quad (1)$$

$$F_{c2} = -2m\omega \times V_2 = -2ma_{c2} \quad (2)$$

where:

ω is the angular velocity of tea particles (rad/s); V_1 is the velocity of reciprocating motion of the pot groove during operation (mm/s); V_2 is the relative velocity of the mass point when moving on the inner wall of the pot groove (mm/s); a_{c1} is the Koch acceleration of F_{c1} (mm/s^2); and a_{c2} is the Koch acceleration of F_{c2}.

According to their force analysis, the support force of the pot groove wall surface on the tea particles when they are moving along the curve of the pot groove is obtained as follows:

$$F_N = -(G + F_{c1})\cos\beta + ma_2^n + F_{c2} \quad (3)$$

The friction force on the wall of the pot groove facing the tea particles is given by:

$$F_f = (G + F_{c1})\cos\varepsilon + ma_2^t = \mu F_N \quad (4)$$

where:

F_N is the support force of tea particles (in newtons, N) on the pot groove's wall; F_f is the dynamic friction between the mass point and inner wall of the pot groove (N); G is the gravitational force (N) acting on tea particles (m is the mass, g is the acceleration of gravity, fixed at 9.81 m/s^2; $G = mg$); F_{c1} and F_{c2} is the Koch force generated by the mass point under the action of V_1 and V_2, respectively (N); β is the angle between the gravity G and the normal vector n (º); ε is the angle between the gravity G and the tangential vector t, (º); a_2^n and a_2^t are respectively the normal component and tangential vector of the absolute acceleration of the mass point in the direction of the pot groove's inner surface (mm); finally, μ is the friction coefficient of tea particles on the wall of the pot groove.

Analysis of the frictional and support forces affecting the tea particles leads to the following relationship between the tangential vector a_2^t and normal vector a_2^n of the absolute acceleration of tea particles on pot groove's inner wall:

$$ma_2^t = \mu[(G + F_{c1})\cos\beta - ma_2^n - F_{c2}] + (G + F_{c1})\cos\varepsilon \quad (5)$$

By analyzing the connection between vectors in Figure 2, the tangential vector a_x^t and normal vector a_x^n of tea particles' acceleration along the inner wall of the pot groove could be derived, as follows:

$$a_x^t = a_x \cos\eta \quad (6)$$

$$a_x^n = a_x \cos\theta \quad (7)$$

where: a_x is the acceleration of the pot groove under reciprocating motion (mm/s²); η is the angle between the acceleration of the pot groove's motion and the tangential vector t (º); and θ is the angle between the acceleration of the pot groove's motion and the normal vector n (º).

Given that the acceleration of tea leaves relative to the movement of the pot groove + acceleration of the inner wall of the pot groove = the absolute acceleration of tea particles, the latter could be obtained using a formula for point acceleration summation, as follows:

$$a_2^t = a_1^t + a_x^t \quad (8)$$

$$a_2^n = a_1^n + a_x^n \quad (9)$$

where: a_1^n and a_1^t are respectively the normal component and tangential vector of the mass point's acceleration in the direction of movement with respect to the inner surface of the pot groove (mm).

According to the force analysis diagram in Figure 3, the force acting on tea particles in the airflow when they move along the pot groove can be expressed this way:

$$u_1 = u_2 + V_1 - a_x \quad (10)$$

where: u_1 is the relative velocity of tea particles to the airflow (mm/s) and u_2 is the average velocity of the airflow (mm/s).

Force analysis of tea particles undergoing throwing and collision motion

A single tea particle was taken as the object of study, treating it as a mass point (*Zhang S. et al., 2020*). The absolute coordinate system is established on the ground, and the velocity direction of the tea particle and airflow is moving at an angle of θ with the horizontal direction, with no collision observed. The force analysis of the tea particle is presented in Figure 4.

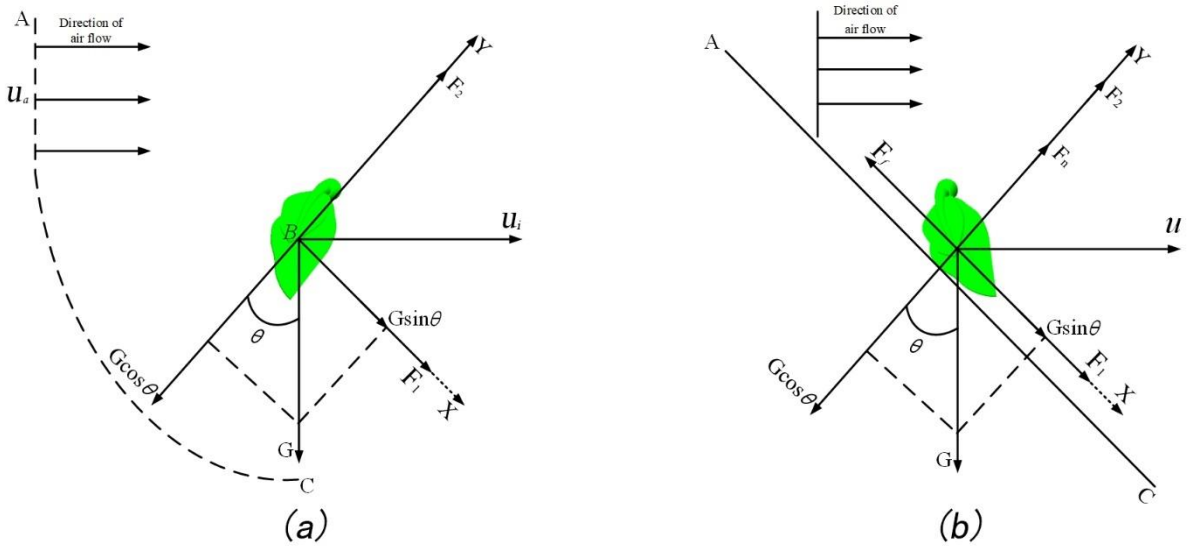


Fig. 4 - Force analysis diagrams of tea-particle throwing and collision motion

(a) Force analysis of the throwing motion of tea particles; (b) Force analysis of the collision motion of tea particles

As Figure 4 shows, *AC* is the pot groove curve, point *B* is the location of the moving tea particle's center of mass, and the left arrow points to the direction of airflow.

Assuming that the diameter of each tea particle is R, according to gas–solid two-phase flow theory, the force F_1 on the airflow from the equivalent tea particle diameter R_s is given as follows:

$$F_1 = k\ \rho\ S\ u_i^2 \tag{11}$$

According to Equation (11), it could be obtained as follows:

$$u_i = u_a - u_v \tag{12}$$

$$u_a = \frac{Q}{S_A} \tag{13}$$

where:

k is the resistance coefficient of a given tea particle; ρ is the density of air at room temperature under the machine's working conditions (kg/mm^3); S is the area of each tea particle facing the airflow (mm^2); u_i is the relative velocity of tea particles to airflow (mm/s); u_a is the average velocity of airflow (mm/s); u_v is the initial velocity of tea particles (mm/s); Q is the volume of airflow (mm^3/s); and S_A is the cross-sectional area of tea particle (mm^2).

According to the force analysis of tea particles, the following are obtained:

$$\begin{cases} F_x = F_2 - G\cos\theta \\ F_y = F_1 + G\sin\theta \\ G = mg \end{cases} \tag{14}$$

where:

F_x is the force acting on the tea particle along the vertical direction of motion (N); F_y is the force on the tea particles along the horizontal direction of motion (N); G denotes the force of gravity from the tea particles themselves (N); F_2 is the Magnus effect force (N); m is the mass of the tea particle, kg; and g is the acceleration of gravity of the tea particles (9.81 m/s^2).

The gravitational component force $G\cos\theta$ on the tea particles could be understood as the formation of differential pressure force with airflow vis-à-vis the Magnus effect force F_2 in reaching a phase equilibrium. The combined influence of various factors, such as airflow resistance F_1, and $G\sin\theta$, in the direction of motion of tea particles, could be derived using a set of differential equations for the motion of tea particle based on D'Alembert's principle, as follows:

$$\begin{cases} \dfrac{du_{vx}}{dt} = \dfrac{F_M}{m} - G\cos\theta \\ \dfrac{du_{vy}}{dt} = \dfrac{k\rho A\left(\dfrac{Q}{S_A} - u_v\right)^2}{m} + G\sin\theta \end{cases} \tag{15}$$

where:

u_{vx}, u_{vy} is the x, y direction of the tea particles speed, in mm/s.

Yet due to the constraints of certain factors, such as the angle between the groove wall and the pot groove's baffle, when the tea particles move they are bound to collide with the baffle. So, in addition to the above forces, they should also be subjected to the action of support force F_N and friction resistance F_f of the pot groove's inner wall. Applying D'Alembert's principle, the differential equations for the movement of tea particle is derived as follows:

$$\begin{cases} F_f = \mu F_N \\ \dfrac{du_{vx}}{dt} = \dfrac{F_M + F_N}{m} - G\cos\theta \\ \dfrac{du_{vy}}{dt} = \dfrac{k\rho A\left(\dfrac{Q}{S_A} - u_v\right)^2}{m} + G\sin\theta - \dfrac{\mu F_N}{m} \end{cases} \tag{16}$$

where: μ is the friction factor of the inner wall of the pot groove.

According to Equations (12-16), the acceleration of tea particles moving in the pot is influenced by the average velocity of airflow (u_a), the initial velocity (u_v) of tea particles, and the angle θ between the gravity of tea itself and the direction of the gravitational component of tea particles. Due to the action of airflow forces F_1 and F_2, the tea particles' acceleration when moving along the inner wall of the pot groove increases significantly, which causes them to bounce around when moving along the pot groove (*Luo, Cao, et al., 2022*). Because of the fixed diameter of tea particles (i.e., the cross-section area S_A of each tea particle is fixed), the average flow velocity u_a is greatly affected by the inlet flow rate, denoted by Q. Meanwhile, in the process of tea leaf carding, differences exist in the depth and width of different pot grooves, resulting in an inconsistency for the angle θ between tea particles and airflow velocity, which is influenced by not only the acceleration of tea leaves' own gravity in the vertical direction but also airflow disturbance. Moreover, the tea particles hit the inner wall of the pot groove, resulting in a smaller relative cross-sectional area of tea particles. Therefore, the average velocity of airflow u_a increases, which modifies the movement velocity of a given tea particle. The force analysis expounded above thus provides theoretical support for the subsequent simulation and experimental design (*Tang et al., 2021*).

DEM–FLUENT–BASED SIMULATION ANALYSIS

The Rocky-DEM's discrete elements, coupled with ANSYS Fluent's fluid dynamics software, were used here to simulate the operation process of a porous hot air type tea de-enzyming and carding machine (*Xue et al., 2022*). More specifically, the discrete element-based simulation software Rocky-DEM 2022 R1.2 was used to analyze the movement of tea particles in the pot groove, and ANSYS Fluent 2022 R1 was used to calculate the overall fluid dynamics of the model (*Geitani T. and Blais B., 2023*). The simulation parameters were set by Rocky-DEM software, with no adhesion presumed on the surface of tea particles. The Type C: Linear Spring Rolling Limit contact model was implemented for particle-to-particle interactions (*Tang et al., 2022*). The Hysteretic Linear Spring and Linear Spring Coulomb Limit contact force models were used for between the tea particles and walls of the pot groove, and the direction of gravitational acceleration was set. The basic parameters of tea particles and contact materials were set accordingly in the simulation test, whereas the contact parameters between tea particles and between them and the wall of the pot groove were set following the parameter-setting method proposed in literature (*Qin et al., 2022)*. These are listed in Table 2 *(Michiko et al., 2017)*.

Table 2

Basic parameter settings

Name	Parameter	Value
Tea particle	**Poisson's ratio**	0.38
	Density (kg·m^{-3})	562.4
	Shear modulus (Pa)	1×10^7
Pot groove	**Poisson's ratio**	0.3
	Density (kg·m^{-3})	7800
	Shear modulus (Pa)	7×10^7
Particle–particle	**Coefficient of restitution**	0.37
	Coefficient of static friction	0.5
	Coefficient of rolling friction	0.15
Particle–pot groove	**Coefficient of restitution**	0.4
	Coefficient of static friction	0.35
	Coefficient of rolling friction	0.1

Establishing the simulation model of tea particles

The Rocky-DEM software is able to render a real model of the particle shape on the basis of other 3D software. It can also use a custom polyhedron to import the particle model. Considering that the main purpose of the simulation process is to discern the movement track of tea particles in the pot groove and their full turnover in this groove, different shapes of tea particles could prolong the time required for the simulation's operation (*Wu et al., 2020*). Therefore, in practice, the axial length of tea particles should exceed their radial length of tea particles, so simplifying tea particles to spherical particles is inappropriate. Hence, in the present study, the tea particles were set as bar-type particles, with the bar-type tea particle model Straight Fiber built

on the basis of actual physical parameters of tea leaves (having a measured axial length of 24 mm and radial length of 2 mm). The ensuing shape of the tea particles after this modeling is shown in Figure 5.

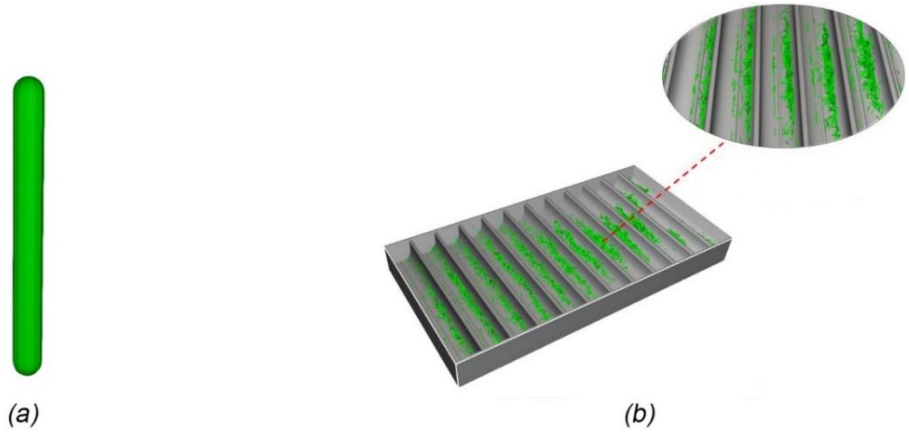


Fig. 5 - Tea particle simulation model

(a) Tea particle model; (b) Model of tea particles in the pot groove

Geometric model extraction and mesh generation in fluid domain

In this paper, using SolidWorks software, a 3D model of the whole structure of the porous hot air tea de-enzyming and carding machine was established. This model was appropriately simplified, by omitting those parts—such as the frame, gas appliances, and motor—not in direct contact with tea particles in the pot groove (*Luo et al., 2022*). Then, SolidWorks software was used to extract the fluid domain of the required simulation geometry model; the extracted fluid domain model was saved in an .iges format and imported separately into the ANSYS Fluent and Rocky-DEM software programs for the subsequent simulation operations (*Rakesh and Shibayan., 2023*), as illustrated in Figure 6. Structured meshing was presumed for the extracted fluid domain model; boundary conditions, such as INLET and OUTLET, were set; and the mesh was exported. The fluid domain mesh was imported to ANSYS Fluent software, the corresponding simulation parameters were set, and the k-epsilon (2 eqn) model was implemented for the turbulence model (*Xue et al., 2022*).

The working process of porous hot-air tea de-enzyming and carding machine was simulated by fluid dynamics. The air inlet connected to the fan at the bottom of the pot was set as the velocity inlet of the flow field, with the rate of air entering the fluid domain fixed (left unchanged). The airflow inlet was set to an 'Outflow' method, the inlet wind speed was set to 20 m/s (in accordance with the actual measured value), the inlet hot-air temperature was set to 350 K, the outlet pressure was set to 1 Pa, and the number of iterations was n = 1000. The specific simulation parameters are set out in Table 3. After all kinds of conditions and parameters were thus specified, the solving began (*Luo, Cao et al., 2022*).

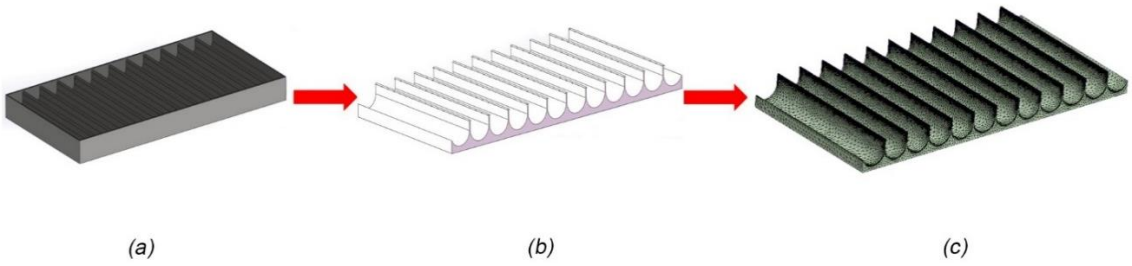


Fig. 6 - Fluid domain geometric model extraction and meshing

(a) Simplified model of pot groove; (b) The extracted fluid domain model; (c) Fluid domain meshing

Table 3

Fluent simulation parameter settings

PARAMETER	VALUE
Specific heat (K)	1006.43
Thermal conductivity (K)	0.0242
Velocity inlet (m/s)	20
Pressure outlet (Pa)	1
Backflow total temperature (K)	350
Number of iterations	1000

Coupling simulation process and result analysis

Coupling simulation process

After the solution for fluid motion was completed, it was post-processed by ANSYS Fluent software, to obtain the distribution nephogram and streamline diagrams of variable factors of the airflow field in the pot groove. As shown in Figures 7 and 8, the airflow was distributed into the pot groove via the inlet port on the bottom of the pot groove, and its velocity gradually decreased. After the airflow passed through a certain length, the airflow velocity gradually became stable. The airflow's speed at the airflow inlet of the pot groove was in a stage of deceleration, such that velocity of airflow in either section declined from the inside to the wall of the pot groove during deceleration. After airflow velocity is mostly stable, it is consistent on any section *(Qin et al., 2022*). When the airflow is in its deceleration stage, a pressure difference could appear on tea particles' surface, such that when they are propelled by airflow some of them could also be blown to pot groove's wall. When the tea particles are close to the wall of the pot groove, the airflow speed decreases, which leads to contact and even collision between the tea particles and wall.

As Figure 9 shows, after the post-processing of Fluent was completed, a Rocky workgroup was created in the ESSS module of the toolbox of ANSYS Workbench. After the coupling model was associated with the Rocky workgroup, 'Setup' was clicked to set relevant parameters. After doing so, the Setup of the Rocky workgroup was associated with the Solution of Fluent module, and then Setup was double-clicked to start Rocky for solving the coupling. Rocky-DEM and ANSYS Fluent were used for the coupling simulation analysis, and the movement trajectory of tea particles in the pot groove was then obtained, as depicted in Figure 10. When the tea particles move along the wall of the pot groove, they hit it many times, slowing their movement. Under the influence of airflow, the tea particles move at an accelerated speed, thus moving repeatedly until they complete the whole overturning process in the pot groove. Through the post-processing work of Rocky-DEM, the continuous distribution law of velocity and acting force between pot and tea particles in the differing motion stages under the condition of gas–solid coupling was obtained (Figure 11).

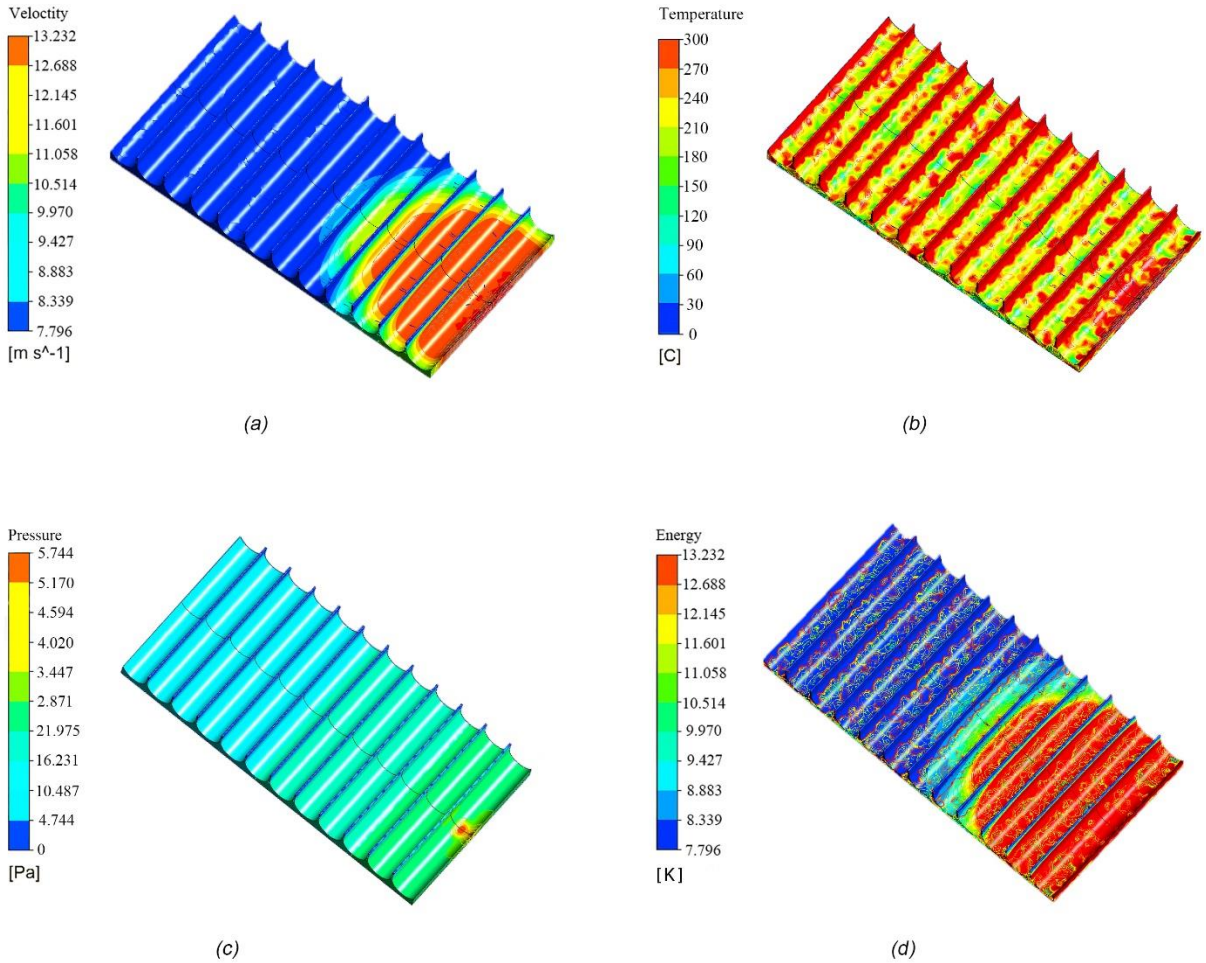


Fig. 7 - Fluid domain geometric model extraction and meshing

(a) Velocity cloud diagram; (b) Temperature cloud diagram; (c) Pressure cloud diagram; (d) Energy cloud diagram

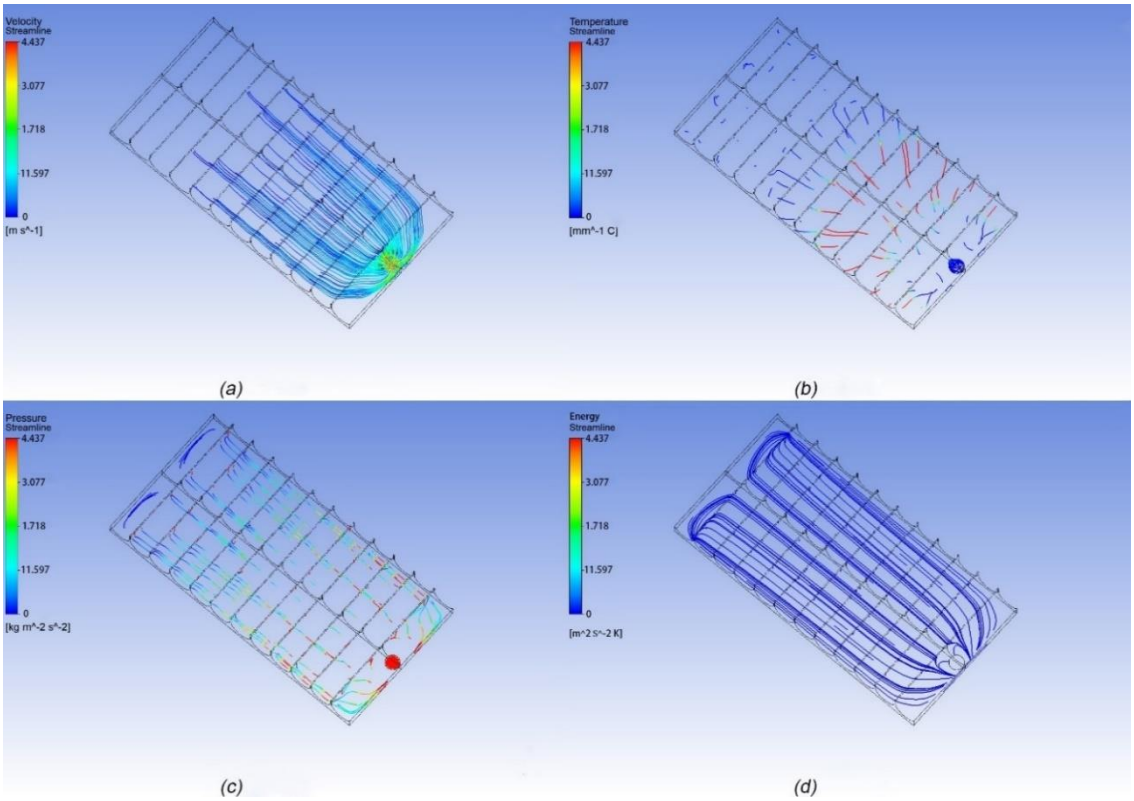


Fig. 8 - Streamline diagrams of the air flow field in the pot groove

(a) Velocity streamline diagram; (b) Temperature streamline diagram; (c) Pressure streamline diagram; *(d) Energy streamline diagram*

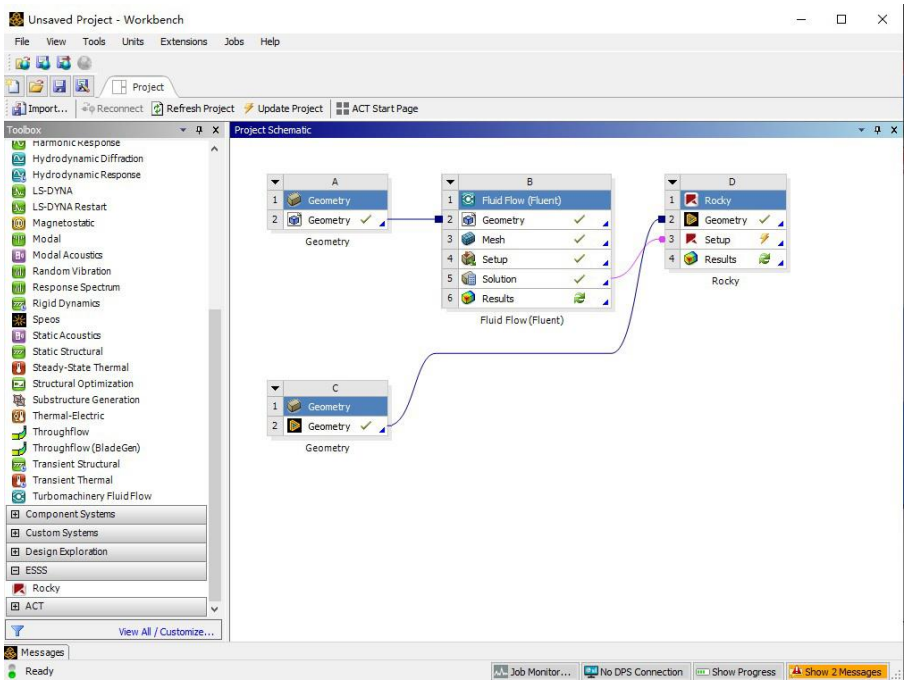


Fig. 9 - Co-simulation of Rocky-DEM and ANSYS Fluent

Simulation result analysis

In Rocky-DEM, the change condition of velocity, interaction force, and motion frequency between pot groove and tea particles under gas–solid coupling condition was analyzed using a block function (Figure 12). Under the same inlet wind speed, the movement speed and interaction force of tea particles gradually increase over time and then tended to stabilize. The force on the pot groove is mainly the interaction force generated by the collision with tea particles. Therefore, regardless of the influence of the interaction force between particles, its force is basically the same as the curve of the interaction force overtime generated by the tea particles' movement. As the pot groove moves in a reciprocating linear motion under the driving force of the motor, the motion frequency of the pot groove vis-à-vis the tea particles changes periodically. The pot groove,

however, is unaffected by any external torque; hence, its speed of reciprocating linear motion on the horizontal plane is a fixed value. When the inlet airflow velocity is constant, the movement speed of tea particles is basically the same at the same position in the groove.

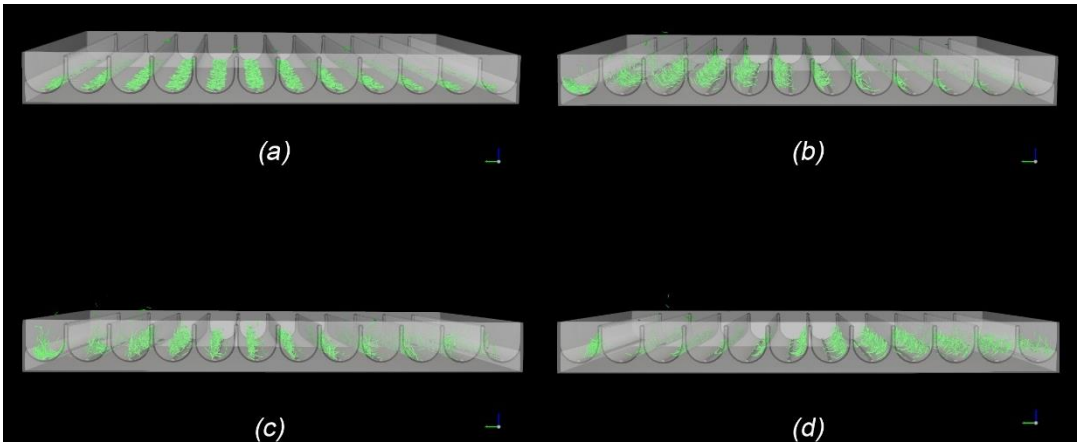


Fig. 10 - Movement trajectory of tea particles in the pot under the coupling condition

(a) The first stage; (b) The second stage; (c) The third stage; (d) The fourth stage

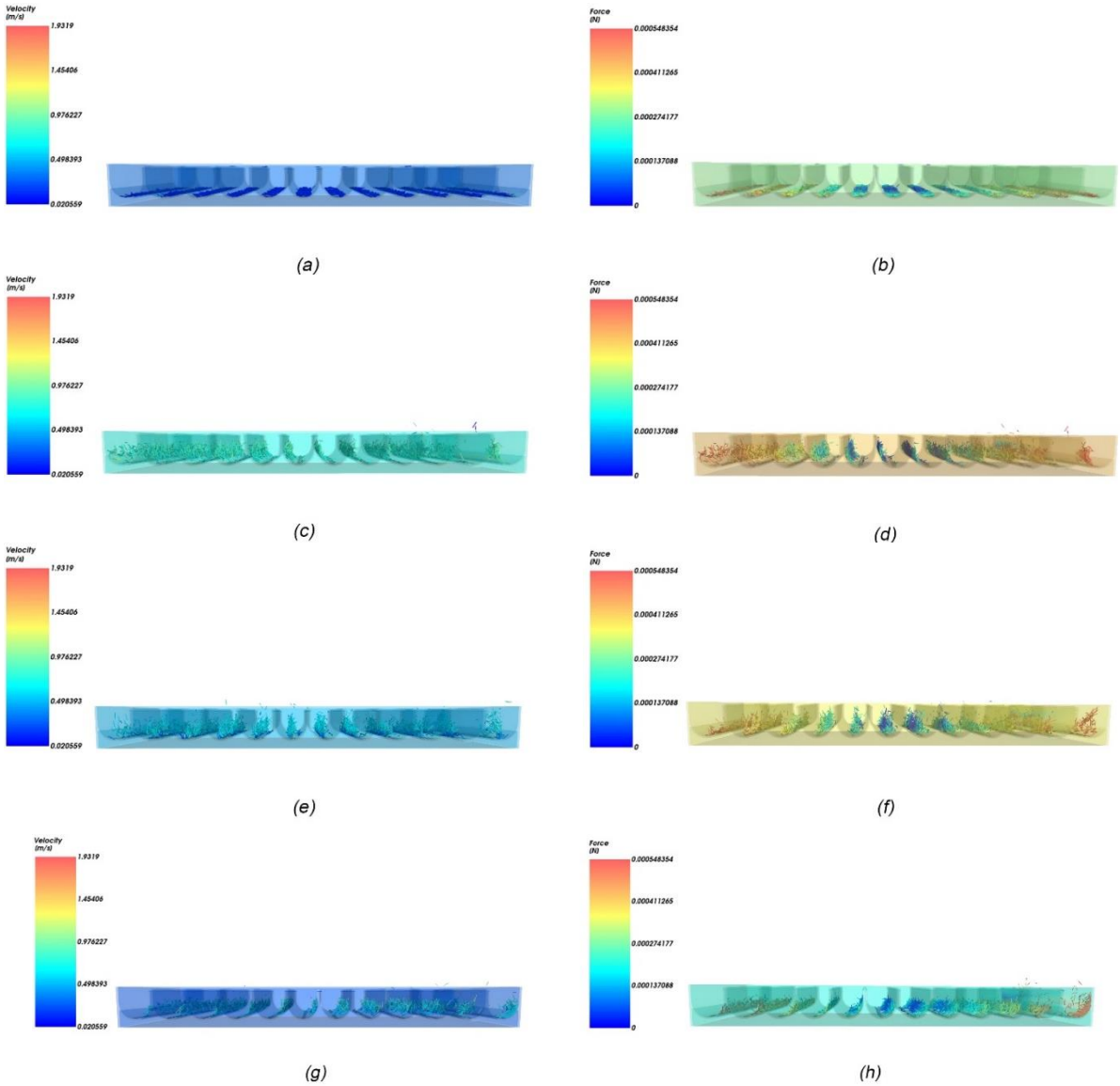


Fig. 11 - Continuous distribution of velocity and force in different stages of motion

(a) Continuous distribution of velocity in the first motion phase; (b) Continuous distribution of forces in the first motion phase; (c) Continuous distribution of velocity in the second motion phase; (d) Continuous distribution of forces in the second motion phase; (e) Continuous distribution of velocity in the third motion phase; (f) Continuous distribution of forces in the third motion phase; (g) Continuous distribution of velocity in the fourth motion phase; (h) Continuous distribution of forces in the fourth motion phase

Both Rocky-DEM and Fluent were used for the coupling simulation analysis. The distribution and motion state of tea particles in the pot groove were obtained, as were the changing curves for the speed, interaction force, and motion frequency of tea particles at differing positions of the groove under the same inlet airflow velocity. Collectively, these laid the foundation for the subsequent experimental design.

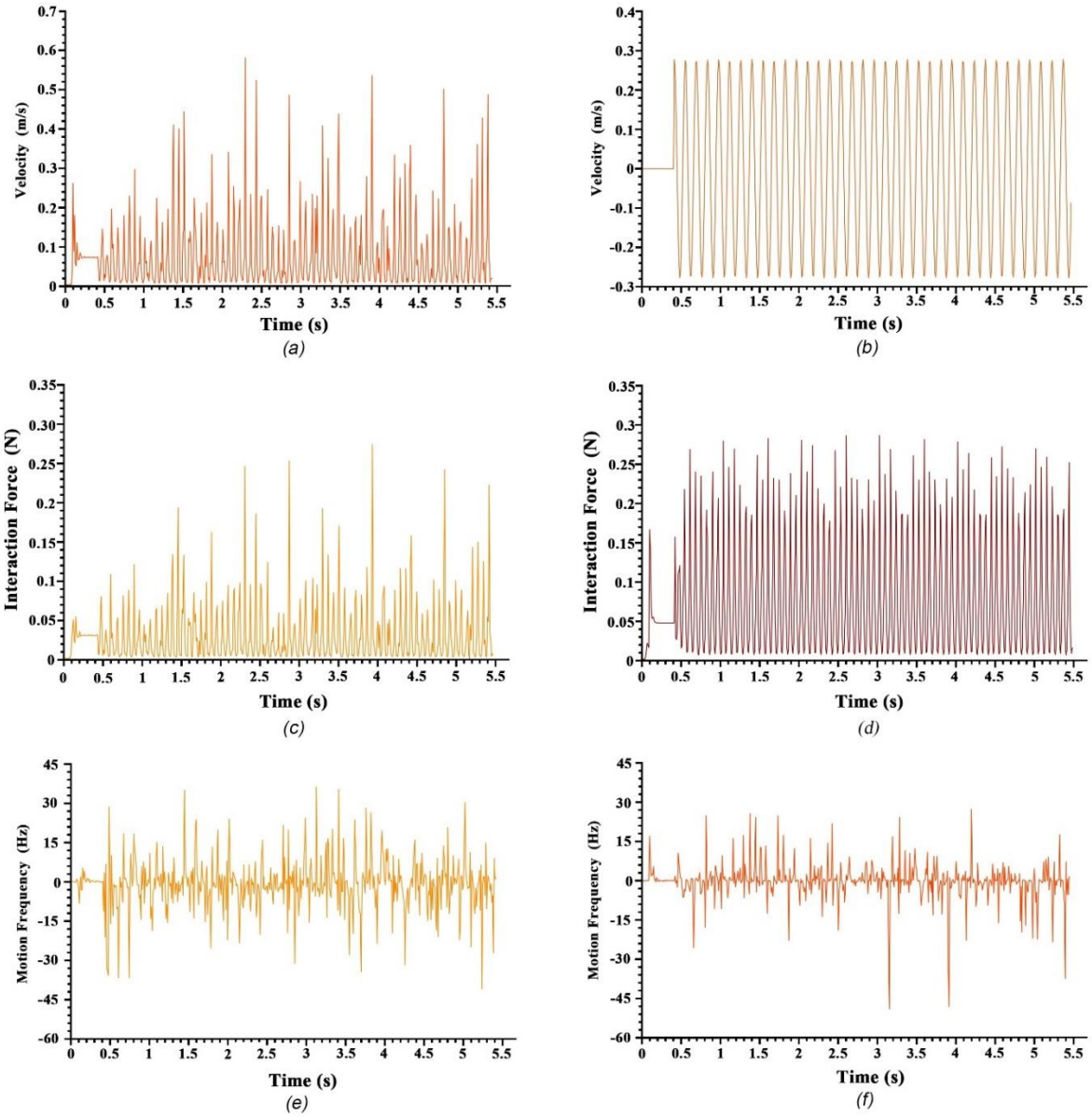


Fig. 12 - Simulation result analysis

(a) Motion speed of tea particles; (b) Kinematic velocity of the pot groove; (c) Interaction force between tea particles; (d) Pot groove interaction force; (e) Movement frequency of tea particles; (f) Movement frequency of pot groove.

RESULTS AND DISCUSSION

Performance test of porous hot air tea de-enzyming and carding machine

To verify the rationality of the designed parameters for the perforated hot-air tea de-enzyming and carding machine, the reliability of its working performance, and whether the quality of finished tea could meet current tea processing quality standards, a machine performance test was carried out in November 2022 in the workshop of Yuanfeng Tea Machinery Co., Ltd., Anji County, Huzhou City, Zhejiang Province. The tea sample used in the test was 'Anji Baiye No.1', and the test instruments and equipment included a stopwatch, an infrared temperature-measuring gun, an electronic platform weighing scale, an electronic balance, and a 6CSL-800 tea de-enzyming and carding machine. These test instruments and prototype are shown in Figure 13 (*Tang et al., 2022*).



Fig. 13 - Test instruments and equipment used

(a) Digital stopwatch; (b) Infrared temperature gun; (c) Electronic platform weighing scale; *(d) Electronic balance; (e) 6CSL-800 tea de-enzyming and carding machine*

Experimental design

The fresh leaves of local white tea cultivated in Anji County were selected as the experimental materials. The motor speed was set to approximately 240 r/min in the process of de-enzyming and 180 r/min for the carding phase; the total time of de-enzyming and carding was 10 min. The withered fresh tea leaves were poured into the pot, the performance of the prototype was tested thrice, and the average value of the three tests groups taken as the final test result. The actual empirical testing site is shown in Figure 14. Because no special test method and operation quality index are yet available for the performance of tea de-enzyming and carding machines in China, this test mainly refers to existing standards and requirements, specifically JB/T 10808—2007 “Tea Processing Equipment”, JB/T 12833—2016 “Tea Carding Machine”, and GB/T 23776—2018 “Tea Sensory Evaluation Method”. The test indices mainly included an output per hour, bar-type rate, de-enzyming suitability rate, pot groove surface temperature, and tea sensory evaluation index *(Zhang K. et al., 2020*).

(1) Output per hour: A stopwatch was used to record the time required for finishing one round of de-enzyming and carding, and the total quantity of tea at the end of the test was weighed. Hourly output is calculated this way:

$$P_1 = \frac{M_1}{t} \tag{17}$$

where: P_1 is the output per hour (kg/h); M_1 is the total mass of tea at the end of the experiment (kg); and t is the time required to complete a de-enzyming and carding (h).

(2) Bar-type rate: Of the processed dry tea, 100 g was taken; any excess impurities, such as broken tea, tea stems, and yellow leaves, were picked out, and the remainder divided into strip leaves and non-strip leaves accordingly. The sum of the two and their respective weights were measured, and then their average after

many experimental runs was taken. The percentage of strip and non-strip leaves in the dry tea samples was calculated by the weighing method, with bar-type rate determined as follows:

$$Y_1 = \frac{Q_1}{T_q} \times 100\% \quad (18)$$

where:

Y_1 is the bar-type rate (%;) Q_1 is the qualified quality of strip leaves (kg;) and T_q is the sum of the quality of strips leaves and the quality of non-strips leaves (kg).

(3) Following the requirements of the JB/T12833-2016 Tea Carding Machine, a prototype test was conducted in which the *de-enzyming suitability rate* served as the final evaluation index. At the end of the de-enzyming process, the dry tea sample was sampled (ca. 300 g). The weight of fresh leaves was measured on an electronic platform scale; the dry weight of fresh leaves per unit of time was calculated; and the red leaves, yellow leaves, burnt leaves, older leaves, and moderate leaves were selected and respectively weighed *(Liu et al., 2023*). The suitable degree of de-enzyming was determined by measuring the morphological characteristics and the content of its inclusions, including the selected de-enzymed moderate leaves for their green color and the sharp seedling-exposed strip-shaped leaves. By measuring the moisture content of fresh leaves of all grades, the de-enzyming suitability rate and the dry weight per unit area under the corresponding moisture content were each calculated. Using those values, the de-enzyming suitability rate was obtained as follows:

$$M_r = \frac{D_q}{M_1} \times 100\% \quad (19)$$

where:

M_r is the de-enzyming suitability rate (%); D_q is the quantity of dry tea that meets the requirements of de-enzyming quality (kg); and M_1 is the total mass of fresh leaves used in the experiment (kg).

(4) *Surface temperature of the pot groove*: The four diagonal positions on the pot groove's surface, the tea outlet, and the radial circumferential direction of the pot groove's inner wall were taken as three measuring points. The temperature of the measuring points within 10–15 cm from the surface of the pot groove was measured using an infrared thermometer. Each point was measured three times, and the average value of the sum of these three temperatures taken as the point temperature. Finally, the average value of the temperatures of the three measured point locations was taken as the effective working temperature of the pot groove.



Fig. 14 - Test site

Testing results

As presented in Table 4, by taking the average of the three machine tests, the hourly output of the test prototype was 3.89 kg/h and the bar-type rate was 89.14%, its de-enzyming suitability rate was 91.67%, with a measured average effective running temperature of the pot groove of 189 °C. Based on these, the performance of the test prototype was assessed and analyzed. As shown in Figure 15, the dry tea samples processed by the experimental prototype were then examined by tea sensory evaluation experts; the resulting evaluation indices met the color requirements for green tea. The sensory evaluation results after three tests are summarized in Table 5.

According to JB/T 10808—2007 Complete “Tea Processing Equipment”, JB/T 12833—2016 “Tea Carding Machine”, and GB/T 23776—2018 “Tea Sensory Evaluation Method”, the quality of the finished tea met the current agronomic standard and satisfied all the performance indices of the 6CSL-800 tea de-enzyming and carding machine. Notably, all the indices were superior to those of the traditional tea de-enzyming and carding machine.

Table 4

Test results

Parameter	First test	Second test	Third test	Mean value
Output per hour (kg·h^{-1})	3.81	3.79	4.08	3.89
Bar-type rate (%)	89.59	86.28	91.65	89.14
De-enzyming appropriate rate (%)	93.73	91.83	89.47	91.67
Surface temperature of the pot groove (°C)	180	210	178	189.3

Table 5

Tea sensory evaluation results

Group	Color	Bar-type	Liquor color	Appraisal result
First test	**Sap green**	**Flat vertical**	**Pale yellow**	**Qualified**
Second test	**Jade green**	**Slightly curved**	**Yellowish**	**Qualified**
Third test	**Green bloom**	**Flat vertical**	**Yellow green**	**Qualified**

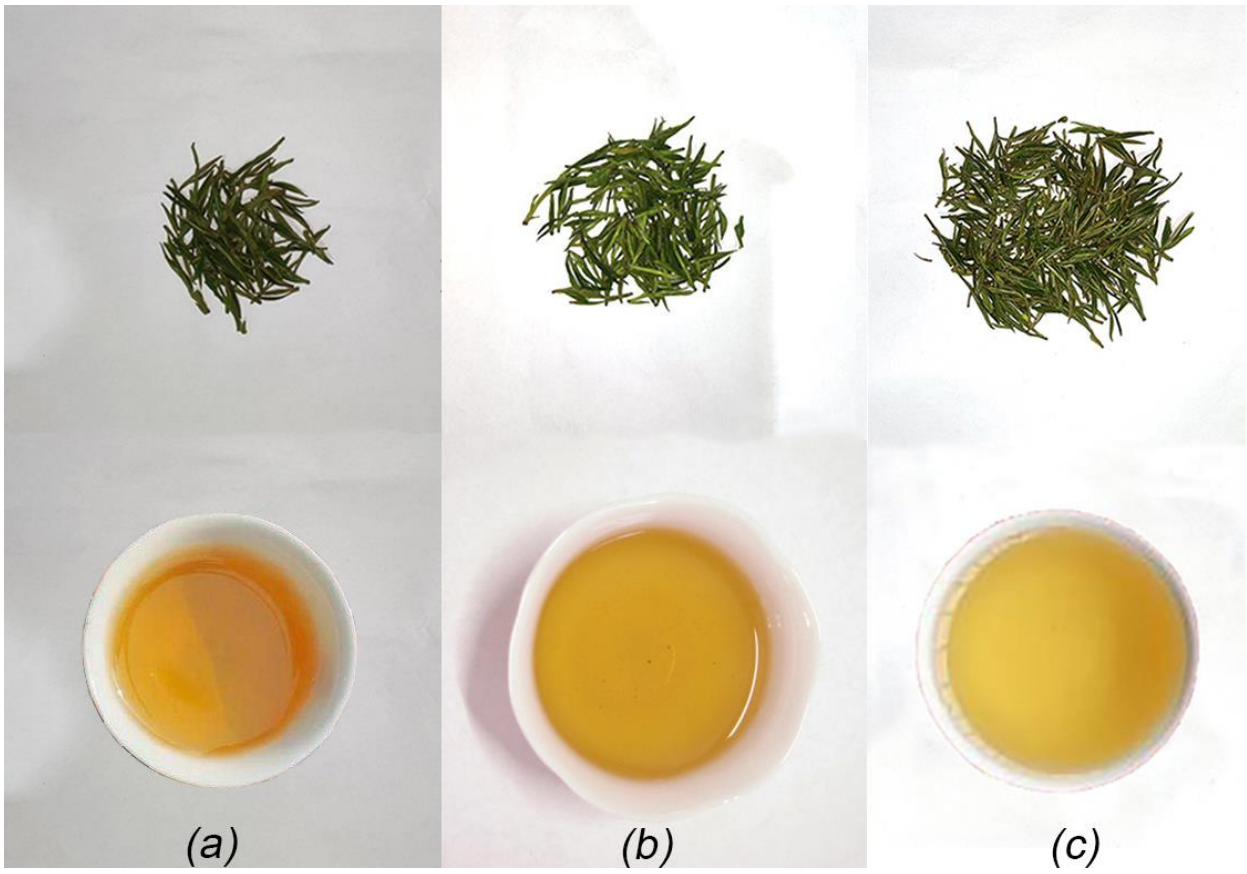


Fig. 15 - Tea evaluation results

(a) The first test; (b) The second test; (c) The third test

CONCLUSIONS

(1) By studying the working process of a porous hot-air tea de-enzyming and carding machine under a gas–solid coupling condition, it was established a mechanical model of tea particles’ movement characteristics through air following the principle of fluid mechanics. Using the coupling simulation method of Rocky-DEM and ANSYS Fluent, continuous and discrete-phase models were established, which verified the feasibility of measuring the movement process of tea in the pot groove on the basis of a gas–solid coupling simulation.

This simulation of tea movement's change process in the pot groove, based on the coupling of gas–solid two-phase flow, demonstrated high accuracy. Hence, it could provide a theoretical reference for the numerical simulation of the same type of tea processing equipment.

(2) The 6CSL-800 tea de-enzyming and carding machine was studied here. Due to numerous, intensive fluid dynamics calculations, a good convergence effect was not attained. Accordingly, the influence of changing the speed of the air inlet upon the coupling effect was not considered. Looking ahead, follow-up experiments could be carried out that alter the air inlet's speed, to further optimize and improve the porous hot air tea de-enzyming and carding machine.

ACKNOWLEDGEMENT

This work was supported by the National Natural Science Foundation of China (52205509), Anhui Provincial Natural Science Foundation Youth Fund Program (2208085QE155), Open Fund Program of State Key Laboratory of Tea Plant Biology and Utilization (SKLTOF20220118), and the Yuanfeng Tea Processing Technology Research and Quality Service Enhancement Enterprise Commissioning Project (KJ2022436).

REFERENCES

[1] Bi, H., Jia, P., Qin, K., Yu, L., Cao, C., and Bai, Y. (2022). Optimization design of pot slot structure of tea de-enzyming and carding machine. *Agronomy* [Basel]. 12: 2937. https://doi.org/10.3390/agronomy12122937.

[2] Cao, C., Wu, Z., Liang, S., and Ge Liangzhi. (2016). Design and experiment of double fuzzy control system for tea cylinder water-removing machine. *Transactions of the Chinese Society for Agricultural Machinery.* 47: 259-65. https://doi.org/11.1964/s.20160512.1031.008.

[3] Geitani El T., Blais, B. (2023). Solid-liquid rotary kilns: An experimental and CFD-DEM study. *Powder Technology*. 430: 119008. https://doi.org/10.1016/j.powtec.2023.119008.

[4] Li, Y., Liu, R., Liu, C., and Liu. L. (2021). Simulation determination and test of seed velocity coupling in the seed delivery tube of air-fed seed dispenser. *Transactions of the Chinese Society for Agricultural Machinery.* 52: 54-61+133.

[5] Liu, S., Cao, C., Ge, J., Zhao, C., Wu, Z., and Sun, Y. (2023). Design and simulation of a hot air drum killing machine with thermal energy circulation. *Journal of Agricultural Mechanization Research.* 45: 107-114. https://doi.org/10.13427/j.cnki.njyi.2023.10.032.

[6] Luo, K., Cao, C., Wu, Z., Zhang, X., and An, M. (2022). Optimization of roasted green tea winnowing via fluid–solid interaction experiments and simulations. *Foods.* 11: 3271. doi: 10.3390/foods11203271.

[7] Luo, K., Wu, Z., Cao, C., Qin, K., Zhang, X., An, M. (2022). Biomechanical characterization of bionic mechanical harvesting of tea buds. *Agriculture*. 12: 1361. https://doi.org/10.3390/agriculture12091361.

[8] Luo, K., Wu, Z., Cao, C., Qin, K., Zhang, X., and Zhong, H. (2022). Design and experiment of a combined pinch-and-cut picker for fresh tea leaves. *Transactions of the Chinese Society of Agricultural Engineering.* 38: 1-9.

[9] Michiko, S., Akiko, M., Stephen, H., Yasufumi, S., Naoki, F., Emiko, S., Kanae, A., Koichi M, I. (2017). EDEM Function in ERAD Protects against Chronic ER Proteinopathy and Age-Related Physiological Decline in Drosophila. *Developmental Cell.* 41: 652-664. https://doi.org/10.1016/j.devcel.2017.05.019.

[10] Panchariya, P., Popovic, D., Sharma, A. (2002). Thin-layer modelling of black tea drying process. *Journal of Food Engineering*. 52: 349-357. https://doi.org/10.1016/S0260-8774(01)00126-1.

[11] Qin, K., Zhang, Y., Shen, Z., Cao, C., Wu, Z., Ge, J., Fang, L., and Bi, H. (2022). Investigating the coupling effect of high pressure and hot air on external friction angle based on resistance reduction tests on subsoiling tillage tools for sandy clay loam. *Agronomy [Basel].* 12: 2663. https://doi.org/ 10.3390/agronomy12112663.

[12] Qin, K., Zhao, Y., Zhang, Y., Cao, C., and Shen, Z. (2022). Lateral stress and its transmission law caused by operation of a double-wing subsoiler in sandy loam soil. *Frontiers in Environmental Science.* 1873. https://doi.org/10.3389/fenvs.2022.986361.

[13] Rakesh, K., Shibayan, S. (2023). Erosion analysis of radial flow hydraulic turbine components through FLUENT-EDEM coupling. *Powder Technology*. 428: 118800. https://doi.org/10.1016/j.powtec.2023.118800.

[14] Shi, C., Zhang, X., Zhong, J., Qiao, X., Dai, H. (2015). Research on hot air killing process and structure optimization of killing machine based on multiphase flow coupling. *Journal of Mechanical & Electrical Engineering*. 32: 1050-1055.

[15] Tang, H., Xu, C., Qi, X., Wang, Z., Wang, J., Zhou, W., Wang, Q., and Wang, J. (2021). Study on periodic pulsation characteristics of corn grain in a grain cylinder during the unloading stage. *Foods.* 10: 2314. https://doi.org/10.3390/foods10102314.

[16] Tang, H., Xu, C., Xu, W., Xu, Y., Xiang, Y., and Wang, J. (2022). Method of straw ditch-buried returning, development of supporting machine and analysis of influencing factors. *Frontiers in Plant Science.* 13: 967838. https://doi.org/10.3389/fpls.2022.967838.

[17] Tang, H., Xu, C., Wang, Z., Wang, Q., and Wang, J. (2022). Optimized design, monitoring system development and experiment for a long-belt finger-clip precision corn seed metering device. *Frontiers in Plant Science.*13: 814747. https://doi.org/10.3389/fpls.2022.814747.

[18] Wang, P., Yi, W., Cheng, F., Wang, C., Zhou, Y., Deng, J. (2022). CFD-based experiments and optimization of tea baring components. *Journal of Chinese Agricultural Mechanization*. 43: 86-91. https://doi.org/10.13733/j.jcam.issn.2095-5553.2022.10.013.

[19] Wang, X., Wu, Z., Zhong, H., Huang, Y., Zhang, X., and Shi Z. (2022). Evaluation of the tea carding operation based on machine vision technology. *China Tea Processing.* 3: 40-45. https://doi.org/10.15905/j.cnki.33-1157/ts.2022.03.001.

[20] Wu, Z., Cao, C., Wang, E., Luo, K., Zhang, J., and Sun, Y. (2019). A method for tea selection based on morphological feature parameters. *Transactions of the Chinese Society for Agricultural Machinery.* 35: 315-21.

[21] Wu, Z., Huang, Y., Ouyang, T., Luo, K., Qin, K., Sun, Y. and Cao, C. (2022). Design and test of precise regulation system for process parameters of double-layer tea winnowing machine. *Agriculture.* 12: 1584. https://doi.org/10.3390/agriculture12101584.

[22] Wu, Z., Luo, K., Cao, C., Liu, G., Wang, E., and Li, W., (2020). Fast location and classification of small targets using region segmentation and a convolutional neural network. *Computers and Electronics in Agriculture.* 169: 105207. https://doi.org/10.1016/j.compag.2019.105207.

[23] Xu, H., Tan, H., Li, G., Xie, Chi., Li, J. (2014). Study on the spiral motion model of leaf guide plate of roller type tea killing machine. *Journal of Tea Science*. 34: 381-386. https://doi.org/10.13305/j.cnki.jts.2014.04.009.

[24] Xue, K., Gao, K., Kuang, F., Zhang, S., Liao, J., and Zhu, D. (2022). Machinery-plant-paddy soil coupling model based numerical simulation method of mechanical transplanting process of big rice seedling. *Computers and Electronics in Agriculture.* 198: 107053. https://doi.org/10.1016/j.compag.2022.107053.

[25] Ye, F., Gao, S., Gong, Z., Zhang, Q., Teng, J., Hou, W., Liang, B. (2014). Effect of different killing methods on the quality of green tea. *Journal of Sichuan Agricultural University*. 32: 160-164+171.

[26] Yan, J., Hu, D., Liu, Q., Yu, L., and Niu, S. (2022). Research progress of tea leaf striping technology and machinery. *Journal of Chinese Agricultural Mechanization.* 43: 75-83. https://doi.org/10.13733/j.jcam.issn.2095-5553.2022.02.011.

[27] You, Q., Shi, Y., Zhu, Y., Yang, G., Yan, H., Lin, Z., and Lv, H. (2023). Influence of different manufacturing processes on the key aroma-active compounds of green tea. *Food Science*. 1-14. https://doi.org/ 11.2206/TS.20221110.2102.022.

[28] Yu, W., Wu, R., Li, H., Pei, G., Jin, S., Huang, C., Zhu, R., Yang, P., Xiong, H. (2019). Numerical simulation of flow field inside the drum of tea infrared killing machine based on Fluent-EDEM coupling. *Food & Machinery*. 35: 104-109+120. https://doi.org/10.13652/j.issn.1003-5788.2019.08.020.

[29] Zhang, K., Wang, W., Zhao, X., and Liu, X. (2020). Design and test of a roller-type tea hot air re-drying machine. *Transactions of the Chinese Society for Agricultural Machinery.* 51: 377-86.

[30] Zhang, S., Tekeste, M., Li, Y., Gaul, A., Zhu, D., and Liao, J. (2020). Scaled-up rice grain modelling for DEM calibration and the validation of hopper flow. *Biosystems Engineering.* 194: 196-212. https://doi.org/ 10.1016/j.biosystemseng.2020.03.018.

[31] Zhang, Y., Tian, L., Cao, C., Zhu, C., Qin, K., and Ge, J. (2022). Optimization and validation of blade parameters for inter-row weeding wheel in paddy fields. *Frontiers in Plant Science.* 13: 1003471. https://doi.org/10.3389/fpls.2022.1003471.

DESIGN AND MANUFACTURE OF A SUPERCRITICAL CO_2 LIQUID EXTRACTION MACHINE FOR EXTRACTING BIOACTIVE COMPOUNDS

/

DESAIN DAN PEMBUATAN MESIN EKSTRAKSI SUPERKRITIS BERBASIS CO_2 CAIR UNTUK MENGEKSTRAKSI SENYAWA BIOAKTIF

Bambang Dwi ARGO*[1,2]; Adam SYECH[1]; Avial Yosua RIJADI[1]; Mochamad Bagus HERMANTO[1,2]; Wahyunanto Agung NUGROHO[1,2]

[1] Department of Biosystems Engineering, Faculty of Agricultural Engineering, Brawijaya University, Malang/ Indonesia

[2]Bioprocess Engineering, Department of Biosystems Engineering, Faculty of Agricultural Engineering, Brawijaya University, Malang / Indonesia

Tel: +6281232100465 ; E-mail: dwiargo@ub.ac.id

DOI: https://doi.org/10.35633/inmateh-71-27

Keywords: *extraction, supercritical, carbon dioxide, bioactive compound*

ABSTRACT

Bioactive compounds in animal and plant cells have many benefits for human health, such as antioxidants, antibacterial, anti-inflammatory, and anticancer. Extraction and separation of bioactive compounds from other compounds is an important step, and commonly, conventional methods are used, but these methods have disadvantages, like producing unwanted compounds. Alternative methods can be conducted using supercritical fluid extraction, but this equipment is expensive and has a small capacity. So, this study aims to produce functional and structural designs and manufacture supercritical fluid extraction machines using carbon dioxide solvents (CO_2) operating with a semi-continuous system. This research succeeded in designing and manufacturing a supercritical fluid extraction machine using carbon dioxide (CO_2) solvent that operates in a semi-continuous system for the extraction of bioactive compounds, with main components including cover frames, supercritical extractor chamber, low and high-pressure CO_2 tubes, compressors and boosters, pipelines, direct valves, manometers, heating, cooler, expanders, reservoirs and automatic control. Moreover, the preliminary simulation test studies revealed that the supercritical extractor chamber could withstand an absolute pressure of 1000 bar, a temperature of 300°C, and a work capacity of 1 L. It indicated that the supercritical CO_2 fluid extractor system was performing well for the conditioning of the extractor chamber, which is generated using a booster and controlled by a one-way valve. Then, the extract is transferred to the separation chamber to separate the CO_2 gas. Then, CO_2 gas is returned to the low-pressure CO_2 tubes for recycling and reuse for the following process.

ABSTRAK

Senyawa bioaktif pada sel hewan dan tumbuhan memiliki banyak manfaat bagi kesehatan manusia, sebagai antioksidan, antibakteri, antiinflamasi, dan antikanker. Ekstraksi dan pemisahan senyawa bioaktif dari senyawa lain merupakan langkah penting, dan biasanya dilakukan menggunakan metode konvensional, namun metode ini memiliki kelemahan seperti menghasilkan senyawa yang tidak diinginkan. Metode alternatif dapat dilakukan dengan ekstraksi fluida superkritis, tetapi peralatan ini mahal dan kapasitasnya kecil. Maka, penelitian ini bertujuan untuk menghasilkan desain fungsional dan struktural serta pembuatan mesin ekstraksi fluida superkritis menggunakan pelarut karbon dioksida (CO_2) yang beroperasi dengan sistem semi kontinyu. Penelitian ini berhasil merancang dan membuat mesin ekstraksi fluida superkritis menggunakan pelarut karbondioksida (CO_2) yang beroperasi dalam sistem semi kontinyu untuk ekstraksi senyawa bioaktif, dengan komponen utama meliputi rangka penutup, ruang ekstraktor superkritis, rendah dan tabung CO_2 bertekanan tinggi, kompresor dan boosters, saluran pipa, katup langsung, manometer, pemanas, pendingin, ekspander, reservoir dan kontrol otomatis. Selain itu, studi uji simulasi awal mengungkapkan bahwa ruang ekstraktor superkritis dapat menahan tekanan absolut sebesar 1000 bar, suhu sebesar 300°C, dan kapasitas kerja sebesar 1 L. Hal ini menunjukkan bahwa sistem pada ekstraktor cairan CO_2 superkritis bekerja dengan baik untuk pengkondisian ruang ekstraktor, yang dihasilkan menggunakan booster dan dikendalikan oleh katup satu arah, dan ekstrak dipindahkan ke ruang pemisahan untuk memisahkan CO_2. gas dari ekstrak (senyawa bioaktif). Gas CO_2 dikembalikan ke silinder CO2 bertekanan rendah untuk didaur ulang dan digunakan kembali untuk proses selanjutnya.

INTRODUCTION

The appropriate extraction method for bioactive compounds from various herbal plants has been widely studied. Conventional extraction methods are commonly used to extract bioactive compounds from these commodities. However, the disadvantage of this method is that it produces unwanted residues, and extract results can change because of the oxidation process during solvent separation (*Chen and Ling, 2000; Khanyile et al., 2022*). The extraction process using fluid at temperatures and pressures above the critical point is an alternative method to prevent the oxidative process of extraction results. Compared to conventional methods, such as liquid organic solvents, supercritical fluids have properties of a higher value of diffusivity and lower values of density, viscosity, surface tension, and the nature of the supercritical fluid can vary widely by regulating operating conditions (*Jha and Sit, 2021; Markom et al., 2012*), so that there is better flavor and fragrance obtained (*Dias et al., 2021*), and also conservation of its biological properties in their extracts *(Hämäläinen and Ruusunen, 2022; Tita et al., 2021*). Typically, carbon dioxide is a type of solvent used in supercritical fluid extractions due to the fact that the CO_2 gas has non-toxic and non-burned properties, is safe for the environment, has abundant material sources, has relatively low prices with high purity, and is suitable for extracting dangerous materials against low heat, low volatility, and polarity (*Santo et al., 2021*), and is easily separated from the material extracted (*Patil et al., 2021*). Carbon dioxide (CO_2) turns into a supercritical state when it is at critical pressure and temperature of 7.28 MPa and 304.1°K respectively *(Jin et al., 2021*).

The high-pressure gradients during pressure release can produce extracts free from living creatures and spores with a longer shelf life than the extract using standard solvents (*Santo et al., 2021*). The main drawbacks of Supercritical Fluid Extraction (SCFE) are the use of critical pressure that prevents system development for production scale, expensive equipment price, and low dielectric constants (*Fikri et al., 2022*). CO_2 and extractor storage tanks must be isolated correctly and equipped with a safety system. Supercritical CO_2 is nonpolar and lipophilic, whereas extraction capability is limited by polarity (*Dauber et al., 2022; Roy et al., 2022*). Co-solvent is recommended to improve the solubility of target compounds and or to increase extract selectivity by carrying out operations at lower pressure (*Pratiwi et al., 2018*). The decision of whether co-solvent can be considered a suitable companion solvent must be examined by cases. Supercritical Carbon Dioxide (SC-CO_2) shows good potential as a solvent to extract bioactive compounds from natural products *(Lefebvre et al., 2021*). However, until today, the scale of SC-CO_2 is still a small capacity, with a high price *(Larocca et al., 2023*). SC-CO_2, with a large capacity, needs to be adequately designed and manufactured with low operating costs to support the extraction of bioactive compounds from nature and their industrialization in the future. Therefore, this study developed a semi-continuous supercritical fluid extraction machine to reuse CO_2 solvents continuously and for the re-utilization of CO_2 in supercritical fluid extractions by flowing CO_2 gas and separating from the expander tube to the CO_2 tube at low pressure, with the hope of saving process time and producing high-quality extract materials.

MATERIALS AND METHODS

1. Basic Design of Machine

The design extraction machine is based on the theory of the supercritical method, where it is assumed that the solvent in supercritical conditions has high diffusivity so that the extract will have a very high purity value. In this case, the solvent to be used is carbon dioxide (CO_2). Carbon dioxide (CO_2) used in supercritical fluid extraction must be in supercritical conditions above the critical point (a specific temperature and pressure), so that it undergoes a phase change to become a gas. Carbon dioxide (CO_2) as a solvent has relatively moderate critical properties, around 31.1 °C for temperature and 73.8 bar for pressure (Laboureur et al., 2015). Thus, it is necessary to design a machine that can create supercritical conditions for carbon dioxide (CO_2), reacting carbon dioxide (CO_2) with materials, separating carbon dioxide (CO_2) from materials, and repeating the carbon dioxide (CO_2) cycle.

2. Engine Power Design

The supercritical reactor was built using a commercial compressor of the "lakoni" brand type "Imola 125", with electrical power specifications of 500 W for 2 hours (1 time supercritical CO2 production phase). The temperature controller uses the brand "Omron" type "e5scl" with electrical power of 3.5 W for 2 h for water heating and 2 h for 1 time supercritical CO_2 production. The heater uses the brand "Dernord" type "DN25", with electric power specifications of 750 W for 2 h for water heating and 2 h for 1 time supercritical CO_2 production phase. This study used 2 boosters, 2 temperature controls, and 2 heaters. So, the total engine power for 1 time of supercritical CO_2 generation was 2.507 kWh.

3. Design Calculation

3.1. Calculation of chamber capacity

The planning capacity for the extraction chamber was 1 L, and 37.5 liters for the separator. CO_2 cylinders use a capacity of 2 m^3 based on the following calculation:

$$P.V = n.R.T \quad (1)$$

$$V = \frac{n.R.T}{P} \quad (2)$$

$$V_1 = \frac{n.R.T}{P} \quad (3)$$

$$V_2 = \frac{n.R.T}{3P} \quad (4)$$

$$V_2 = \frac{1}{3}.\frac{n.R.T}{P} \quad (5)$$

$$V_2 = \frac{1}{3}V_1 \quad (6)$$

where: V_1 - volume of CO_2 gas cylinder (m^3); V_2 -volume of supercritical CO_2 cylinder (m^3);

Q - pressure; n - number of moles; R - common gas constant (8.31 J/mol.K); T - temperature (Kelvin)

3.2. Piping planning and calculation

The pipes used are made from SS304 stainless steel. The pipe used is calculated using the Barlow formula (Equation 7) to calculate the wall thickness of the pipe used (*Isaac and Sylvanus, 2022*).

$$t = \frac{P\ x\ D}{2\ x\ F\ x\ S\ x\ E} \quad (7)$$

where: P - pressure (kPa); S - minimum yield strength (kPa); t - pipe thickness (mm); D - pipe outside diameter (mm); F - design factor; E – magnitude of the longitudinal joint

3.2.1. Connecting pipe

The connecting pipe is used to connect the components of the supercritical extraction machine. The connecting pipe will be added with connectors such as tee, elbow, flange, and water nuts to connect components with a 0.5-inch or 21.34 mm in diameter. The data for the connecting pipe on the supercritical extraction machine are as follows: the pressure (P) of 12000 kPa, minimum yield strength (S) of 293000 kPa, outside diameter of the pipe (D) of 21.34 mm, and design factor (F) of 0.72 for pipes, and magnitude of longitudinal joints (E) of 1 for seamless pipes, and these data were calculated using Barlow Formulas as presented Equation 7 to get the pipe thickness. Based on the calculation, the pipe thickness is ≥ 0.607 mm. According to the *National Institute of Standards and Technology (NIST)* of stainless steel pipe thickness table (2023), the pipe thickness was equivalent to 1.65 mm.

3.2.2. Screw pipe

A screw pipe on the supercritical extraction machine is used to heat CO_2 gas and press it. The threaded pipe in supercritical extraction machines is 0.25 inch or 13.72 mm in diameter. The smaller pipe thickness will shorten the heating process. Screw pipe data on the supercritical extraction machine are as follows: the pressure (P) of 5000 kPa, minimum yield strength (S) of 293000 kPa, outside diameter of the pipe (D) of 13.72 mm, and design factor (F) of 0.72 for pipes, and magnitude of longitudinal joints (E) of 1 for seamless pipes, and these data were calculated using Barlow Formulas as presented Equation 7 to get the pipe thickness. Based on the calculation, the pipe thickness is ≥ 0.163 mm. Pipes with a thickness above 0.163 mm were categorized as pipes with schedule 10, namely SS304 pipes with a size of 0.25 inches.

3.3. Planning and calculation of the flow rate

The formula used in planning is the flow rate formula, then the Reynolds formula to determine the flow type. The data used in this study was a flow rate (Q) of 3.34 x 10^{-4} m^3/s, pipe diameter (D) of 0.0213 m, and π of 3.14. Then, the cross-sectional section (A) was found using Equation 8, and the average speed of the flow (v) was calculated using Equation 9, and the average flow speed was obtained at 9.382 m/s. After which, the Reynold number was calculated using Equation 10. Based on the calculation, the Reynolds number was 349,714.05, identified as turbulent (*Cantwell, 2019*).

$$A = \frac{\pi D^2}{4} \quad (8)$$

$$Q = A\ v \quad (9)$$

$$Re = \frac{D\ x\ v\ x\ \rho}{\mu} \quad (10)$$

Where:

Re: Reynolds number; ρ: fluid density 350 kg/m^3; μ : fluid viscosity= 2 x 10^{-5} kg/ m.s

RESULTS AND DISCUSSION

1. Working Principle of Machine

The supercritical fluid extraction process was carried out gradually, placing the raw material in the extractor chamber and filling pure CO_2 into a low-pressure tube. The compressor produced compressed air, and then the booster used the air to pump and compress CO_2 gas from a low-pressure tube to a high-pressure tube into a supercritical CO_2 fluid. Then the supercritical CO_2 fluid was flowed into the extract tube until reaching the supercritical condition and was left in a certain period of steady state to carry out the extraction process. After reaching a certain period, the pipe's faucet connecting the extractor tube and the separator tube was opened to move a mixture of supercritical fluid with extraction material into the separator. The air pressure in the separator chamber was controlled at 1 bar to change the CO_2 supercritical fluid phase to gas *(Alvarez-Henao et al., 2022; Salinas et al., 2020*). Followed by the separation between CO_2 fluids and extracted materials, CO_2 gas is returned, flowing into a low-pressure CO_2 tube to be reused. At the same time, the extract results are held in the separator chamber. The schematic of the working of the supercritical extraction machine is illustrated in Figure 1.

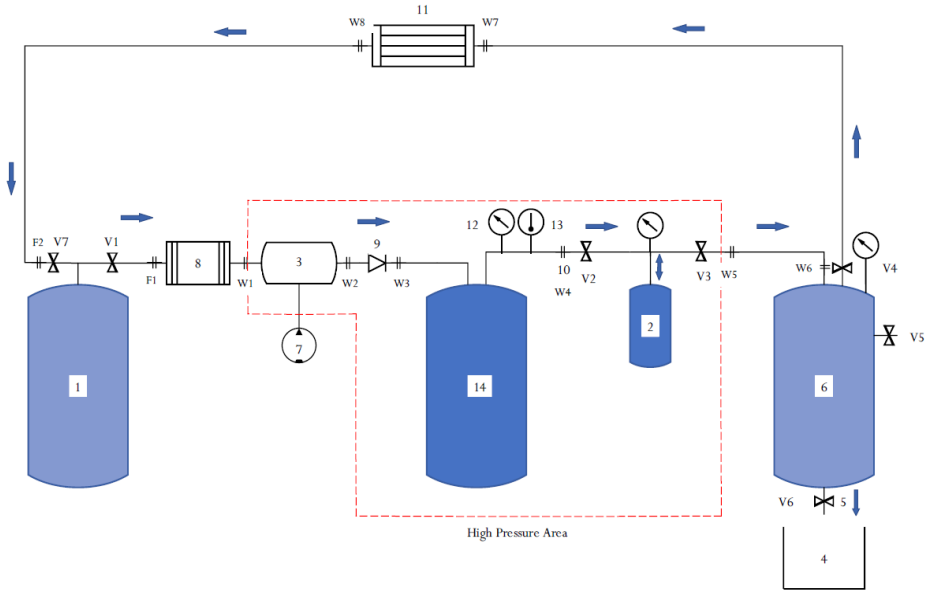


Fig. 1 - The schematic of the working of the Supercritical Fluid Extraction Machines

1. CO_2 tube; 2. extractor chamber; 3. Boosters; 4. Product output tank; 5. Valves (V1-V7); 6.Separator; 7. Compressor; 8. Heaters; 9. Check valves; 10. Water mur (W1-W8);11. Condenser; 12. Pressure gauges; 13. Thermometers; 14 Supercritical fluid storage tubes; 15.Flanges (F1-F2)

2. Functional and Structural Design and Realization

Functional design determines the layout and requirements of machine components and temperature control systems of supercritical fluid extraction. The functional design planning of the supercritical Fluid extraction machine, in the form of technical drawings, is presented in Figure 2. The specification from each component based on planning design and calculations is presented in Table 1, and also the construction realization of the supercritical CO_2 fluid extract machine is presented in Figure 3.

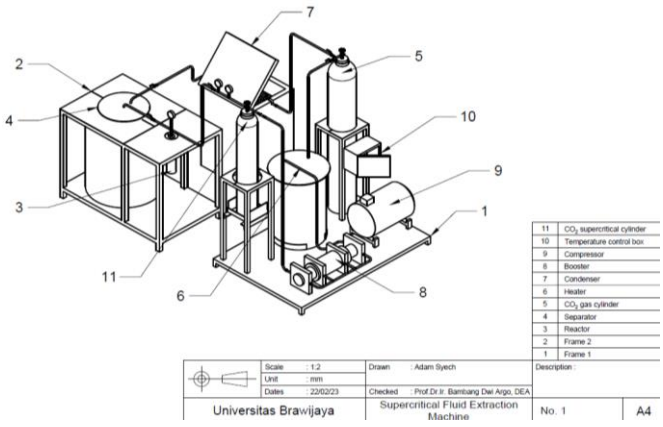


Fig. 2 - The Functional and Structural Design of Supercritical Fluid Extraction Machines

Table 1

Supercritical extraction machine specifications

Machine Component	Specifications
Supercritical extraction machine dimensions	1600 mm x 2600 mm x 1600 mm
Reactor	SS316, 1 L
Separator	SS316, 37.5 L
CO_2 gas tube	6000 mm^3
Supercritical CO_2 tube	2000 mm^3
Heater	90 L, module merk OMRON E5CSL
Condenser	Modified top-door refrigerator from “Midea” brand (commercial brand)
Framework 1 dimension	1400 mm x 970 mm x 900 mm
Framework 2 dimension	1080 mm x 680 mm x 860 mm
Compressor	Compressor brand "Lakoni" type Imola 125, with specifications of 1 hp, 145 L/min, 8 bar, 220 V/ 50 Hz
Thermometer`	100 °C
Pressure gauge	Diameter of 2,5 inches, 280 bars
Booster pump	Booster brand "suncenter" Type DGT40
Valve	Sankyo, SS304, 2,5 inches, max pressure 1000 WOG
Flange	SS304 JIS 10k dan ANCI 300 ½”
Water mur	SS304, 0.5 inches
Check valve	SS304, max pressure 250 bar, 0.5 inches

Based on Table 1, Figure 2 and Figure 3 showed that the supercritical CO_2 extractor has a maximum capacity of 1L and can retain the pressure up to 1000 bar using a semi-continuous system with extraction tube material, separator, and a piping system made of SS-316 material.

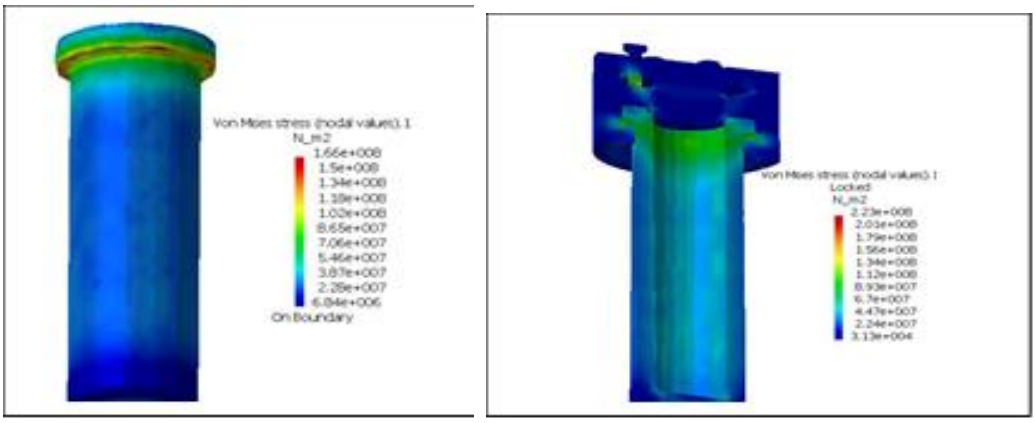


Fig. 2 - Supercritical fluid extraction machine realization

This extractor engine has a compression and booster capacity of 8 and 350 bar, respectively. Initial test results show that achieving supercritical fluid conditions requires a relatively long compression time of 2.5 h. Efforts to speed up the compression of supercritical fluids are carried out by manipulating the velocity of the airflow produced by the compressor or by increasing the ratio of high and low-pressure CO_2 tubes. In this study, the best ratio of CO_2 gas tube (high pressure) and supercritical CO_2 tube (low pressure) volumes was 3:1 (Table 1).

In addition, the compression speed of the supercritical fluid has an impact on increasing the capacity of the booster, which is 1:40, which means that an increase in pressure of 1 bar in the compressor will increase 40 bar in the booster. Furthermore, the release and termination of the supercritical fluid flow are still done manually using a faucet, which is installed between the CO_2 gas tube and the high-pressure CO_2 tube to ensure that the supercritical conditions in the extractor tube are according to the specified conditions. In the future automatic control is needed to ensure that supercritical conditions are appropriately achieved. However, one of the advantages of this machine is being able to recycle CO_2 gas coming from the separator tube to be accommodated in a low-pressure CO2 tube to be reused in the following process, thereby can reduce operational costs economically. Additionally, controlling the temperature of the CO_2 fluid in the cooling and heating unit on this machine uses an on-off control system, with the resulting control results according to the expected set point, with a deviation value in the range of 1°C than the specified reference value.

In this machine, a cylindrical extractor chamber (Figure 2 and Figure 3) made of SS-316 steel with a wall thickness of 2.5 cm can withstand pressure up to 1000 bar based on the simulation test in Figure 4. Figure 4 shows that the design of the supercritical extractor chamber structure can accept loads at high pressures of up to 1000 bar, indicating that the extractor chamber can be operated under CO_2 supercritical conditions, with a pressure and temperature of 73 bar and 31°C, respectively. The chamber extractor also has a safety factor of more than 14, which indicates that the supercritical fluid extraction machine is technically safe to operate.



(A) (B)

Fig 4 - The pressure distribution simulation in the outer chamber wall (A) and inner chamber wall (B) of the supercritical reactor lid

During the construction of the supercritical fluid extraction machine, there were many problems occurred, especially leakage in between pipe joints, as experienced by other researchers, such as (*Kwartiningsih et al., 2019)*, and various steps were taken to overcome them so that the supercritical extractor could function properly and safely during the extraction process. The list of problems and solutions for solved problems during construction are listed in Table 2.

At the end of the performance test, given the ongoing process of improving the design of the equipment, the supercritical extraction machine was successfully performed from 72.8 to 90.0 bar pressure and temperature of 31.1-35.5˚C, with a capacity of 1L with no leakage. However, reporting on research activities only extends to process simulation and tool design, then the process of separating bioactive compound components will be carried out in the next research phase.

Table 2

The list of problems and solutions for solved problems during construction

Problem	Solution
Leaks in the flange	To overcome the problem of joint leaks, it replaced flange-type connections with watermur seal rubber.
Inadequate installation and lack of Thread Seal Tape (TBA) provision	Ensuring that all installations are tight until the connection rotation is maximized and ensuring that there is a lot of TBA
Leaks at the joints due to damage to the seal rubber and leaks in the check valve	Changes with the new watermur seal rubber

CONCLUSIONS

This study was successful in designing and manufacturing a supercritical fluid extraction machine that uses carbon dioxide (CO_2) solvent and operates in a semi-continuous system for the extraction of bioactive compounds, with primary components such as frames, supercritical extractor chamber, low and high-pressure CO_2 tubes, compressors and boosters, pipelines, direct valves, manometers, heating, cooler, and expanders, and reservoirs and automatic control. Furthermore, the early testing simulation showed that the supercritical extractor chamber could resist an absolute pressure of 1000 bar, a temperature of 300°C, with a capacity of 1L.

The supercritical extraction machine performed well from 72.8 to 90 bar pressure and 31.1-35.5°C at the end of the preliminary performance test. The supercritical CO_2 fluid extractor system was working well for conditioning the extractor chamber, which is created by a booster and regulated by a one-way valve. The extract is then passed to the separation chamber, where the CO_2 gas is separated. The CO_2 gas is then recycled and reused in the following step by returning it to the low-pressure CO_2 cylinder.

ACKNOWLEDGEMENT

The study was funded by the Brawijaya University professor research grant program in 2022.

REFERENCES

[1] Alvarez-Henao, M. V., Cardona, L., Hincapié, S., Londoño-Londoño, J., & Jimenez-Cartagena, C. (2022). Supercritical fluid extraction of phytosterols from sugarcane bagasse: Evaluation of extraction parameters. *Journal of Supercritical Fluids*, *179*, 105427. https://doi.org/10.1016/j.supflu.2021.105427

[2] Cantwell, B. J. (2019). A universal velocity profile for smooth wall pipe flow. *Journal of Fluid Mechanics*, *878*, 834–874. https://doi.org/10.1017/jfm.2019.669

[3] Chen, Y. T., & Ling, Y. C. (2000). An overview of supercritical fluid extraction in Chinese herbal medicine: From preparation to analysis. *Journal of Food and Drug Analysis*, *8*(4), 235–247. https://doi.org/10.38212/2224-6614.2815

[4] Dauber, C., Carreras, T., Fernández Fernández, A., Irigaray, B., Albores, S., Gámbaro, A., Ibáñez, E., & Vieitez, I. (2022). Response surface methodology for the optimization of biophenols recovery from “alperujo” using supercritical fluid extraction. Comparison between Arbequina and Coratina cultivars. *Journal of Supercritical Fluids*, *180*, 105460. https://doi.org/10.1016/j.supflu.2021.105460

[5] Dias, A. L. B., de Aguiar, A. C., & Rostagno, M. A. (2021). Extraction of natural products using supercritical fluids and pressurized liquids assisted by ultrasound: Current status and trends. *Ultrasonics Sonochemistry*, *74*, 105584. https://doi.org/10.1016/j.ultsonch.2021.105584

[6] Fikri, I., Yulianah, Y., Lin, T. C., Lin, R. W., Chen, U. C., & Lay, H. L. (2022). Optimization of supercritical fluid extraction of dihydrotanshinone, cryptotanshinone, tanshinone I, and tanshinone IIA from Salvia miltiorrhiza with a peanut oil modifier. *Chemical Engineering Research and Design*, *180*, 220–231.

[7] Hämäläinen, H., & Ruusunen, M. (2022). Identification of a supercritical fluid extraction process for modelling the energy consumption. *Energy*, *252*, 124033. https://doi.org/10.1016/j.energy.2022.124033

[8] Isaac, S. O., & Sylvanus, C. A. (2022). Fundamental Principles and Mechanical Design Analyses of Oil and Gas Piping Systems: An Overview. *International Journal of Scientific & Engineering Research*, *13*(8), 840–851.

[9] Jha, A. K., & Sit, N. (2021). Comparison of response surface methodology (RSM) and artificial neural network (ANN) modelling for supercritical fluid extraction of phytochemicals from Terminalia chebula pulp and optimization using RSM coupled with desirability function (DF) and genetic. *Industrial Crops and Products*, *170*, 113769. https://doi.org/10.1016/j.indcrop.2021.113769

[10] Jin, W., Yang, J., Liu, D., Zhong, Q., & Zhou, T. (2021). Determination of inflammation-related lipids in depressive rats by online supercritical fluid extraction-supercritical fluid chromatography-tandem mass spectrometry. *Journal of Pharmaceutical and Biomedical Analysis*, *203*, 114210. https://doi.org/10.1016/j.jpba.2021.114210

[11] Khanyile, A. T., Andrew, J. E., Paul, V., & Sithole, B. B. (2022). A comparative study of supercritical fluid extraction and accelerated solvent extraction of lipophilic compounds from lignocellulosic biomass. *Sustainable Chemistry and Pharmacy*, *26*, 100608. https://doi.org/10.1016/j.scp.2022.100608

[12] Kwartiningsih, E., Sediawan, W. B., Hidayat, M., & Yuliansyah, A. T. (2019). Design of supercritical fluid extractor using dry ice as a supercritical solvent. *AIP Conference Proceedings*, *2097*, 030084. https://doi.org/10.1063/1.5098259

[13] Laboureur, L., Ollero, M., & Touboul, D. (2015). Lipidomics by supercritical fluid chromatography. *International Journal of Molecular Sciences*, *16*(6), 13868–13884.

[14] Larocca, V., Martino, M., Trupo, M., Magarelli, R. A., Spagnoletta, A., & Ambrico, A. (2023). Evaluation of carbon dioxide supercritical fluid extraction (CO2-SFE) on carotenoids recovery from red yeast cells. *Biomass Conversion and Biorefinery*. https://doi.org/10.1007/s13399-023-04434-z (In Press)

[15] Lefebvre, T., Destandau, E., & Lesellier, E. (2021). Sequential extraction of carnosic acid, rosmarinic acid and pigments (carotenoids and chlorophylls) from Rosemary by online supercritical fluid extraction-supercritical fluid chromatography. *Journal of Chromatography A*, *1639*, 461709. https://doi.org/10.1016/j.chroma.2020.461709

[16] Markom, M., Hassim, N., Anuar, N., & Baharum, S. N. (2012). Co-solvent Selection for Supercritical Fluid Extraction of Essential Oil and Bioactive Compounds from Polygonum minus. *ASEAN Journal of Chemical Engineering*, *12*(2), 19–26.

[17] Patil, P. D., Patil, S. P., Kelkar, R. K., Patil, N. P., Pise, P. V., & Nadar, S. S. (2021). Enzyme-assisted supercritical fluid extraction: An integral approach to extract bioactive compounds. *Trends in Food Science and Technology*, *116*, 357–369. https://doi.org/10.1016/j.tifs.2021.07.032

[18] Pratiwi, M. K., Masyrifah, L., Hawa, L. C., Dewi, S. R., Izza, N., Argo, B. D., Sucipto, S., & Wibisono, Y. (2018). Enhanced antibiofouling properties of chitosan-based membranes by coating and blending of Moringa Oleifera L extracts. *IOP Conference Series: Materials Science and Engineering*, *434*(1), 012191. https://doi.org/10.1088/1757-899X/434/1/012191

[19] Roy, S., Kr Saha, A., Panda, S., & Dey, G. (2022). Optimization of turmeric oil extraction in an annular supercritical fluid extractor by comparing BBD-RSM and FCCD-RSM approaches. *Materials Today: Proceedings*, *76*, 47–55. https://doi.org/10.1016/j.matpr.2022.09.039

[20] Salinas, F., Vardanega, R., Espinosa-Álvarez, C., Jimenéz, D., Muñoz, W. B., Ruiz-Domínguez, M. C., Meireles, M. A. A., & Cerezal- Mezquita, P. (2020). Supercritical fluid extraction of chañar (Geoffroea decorticans) almond oil: Global yield, kinetics and oil characterization. *Journal of Supercritical Fluids*, *161*, 104824. https://doi.org/10.1016/j.supflu.2020.104824

[21] Santo, A. T. do E., Siqueira, L. M., Almeida, R. N., Vargas, R. M. F., Franceschini, G. do N., Kunde, M. A., Cappellari, A. R., Morrone, F. B., & Cassel, E. (2021). Decaffeination of yerba mate by supercritical fluid extraction: Improvement, mathematical modelling and infusion analysis. *Journal of Supercritical Fluids*, *168*, 105096. https://doi.org/10.1016/j.supflu.2020.105096

[22] Tita, G. J., Navarrete, A., Martín, Á., & Cocero, M. J. (2021). Model assisted supercritical fluid extraction and fractionation of added-value products from tobacco scrap. *Journal of Supercritical Fluids*, *167*, 105046. https://doi.org/10.1016/j.supflu.2020.105046

NUMERICAL SIMULATION AND TEST OF HOT AIR FAN
/
热气流风机的数值模拟及试验

Guoliang YOU [1,2], Yaoming LI [*1,2], Hanhao WANG [1,2]
[1] Key Laboratory of Modern Agricultural Equipment and Technology, Jiangsu University, Zhenjiang, 212013/China
[2] School of agricultural equipment engineering, Jiangsu University, Zhenjiang, 212013/China
Tel: 13805283656; E-mail: ymli@ujs.edu.cn
DOI: https://doi.org/10.35633/inmateh-71-28

Keywords: *Combine harvest, Hot air fan, Orthogonal Experiments, CFD*

ABSTRACT
The value of high moisture content crops is higher and the planting area is wider. However, in the harvest process, due to the high moisture content, the cleaning loss is greater. In order to reduce the adhesion between the crop extraction mixtures and improve the cleaning performance, a method of hot air cleaning was proposed. By using the fan design theory and thermodynamics, the prototype design of the hot air fan was completed. Through orthogonal test, the most suitable parameter combination is 1445 r/min fan speed and 85℃ air inlet temperature. Computational fluid dynamics (CFD) was used to observe the air velocity and air temperature of the outlet under the optimal combination of parameters to check whether it meets the requirements of hot air cleaning. The reliability of numerical simulation was tested by bench test. Finally, a field experiment was carried out with the hot air fan to observe the difference between the cleaning effect and the fan under the optimal parameter combination, and compare the cleaning loss rate.

摘要
高含水率农作物的价值较高，种植面积较广。然而，在收获过程中，由于水分含量高，清选损失较大。为了减少农作物脱出混合物之间的粘附，提高清选性能，提出了热风清选方法。利用风机设计理论和热力学，完成了热气流风机的样机设计。通过正交试验，得出最合适参数组合为风机转速 1445r/min，进风口风温 85℃。采用计算流体力学(CFD)观察最佳参数组合下的出风口风速以及风温，检验其是否达到热风清选的要求。用台架试验检验数值模拟的可靠性。最后使用热气流风机进行田间试验，观察在最佳参数组合下的清选效果与普通风机的差别，并对比清选损失率。

INTRODUCTION

In the rape harvesting, a crucial link in the working process of the combine harvester is the cleaning process of the material. If the cleaning effect is not good, it is easy for the grain to adhere to the sieve. As a result, the effective working area of the cleaning device is reduced, the sieve was blocked and the material flow was blocked, and the impurity and loss rate of the cleaning device are generally high. The main function of the cleaning mechanism is to ensure that the impurity content and loss rate of the grain after cleaning meet the specified requirements. The short stalks, weeds and impurities in the extracted mixture after threshing were separated from the seeds. Cleaning device is an important working part of combine harvester, and its excellent performance is the guarantee of efficient operation of the whole machine *(Li et al., 2009; Cheng et al., 1998; Li et al., 2012; Du et al., 2007)*. The cleaning device of the combine harvester is mainly an air sieve cleaning device, which uses airflow and sieve to work together. The fans commonly used in the air sieve cleaning device include centrifugal fans, cross-flow fans, and combined multi-fans *(Li et al., 2020)*. The sieve includes a cylinder sieve and a vibrating sieve, etc. A vibrating sieve is usually composed of a multi-layer sieve, a commonly used sieve has a fish scale sieve, punching sieve, and braid sieve. Different sieves have different working characteristics and are suitable for cleaning different extrusions.

Yuko et al., (2012), studied the effect of the presence of straw in the removed mixture on the cleaning flow of the combine. The results show that the friction of the wall and the friction between the extruded particles are the important reasons for the energy loss of the cleaning air in the combine harvester. *Hyeon et al., (2015),* studied the influence of the combination of working parameters such as the installation Angle of the cleaning sieve, vibration frequency of the vibrating sieve, and speed of the cleaning fan on the cleaning effect of semi-feeding combine harvesting. The optimal combination of working parameters is obtained.

Liang et al., (2014), developed a grain loss monitoring sensor and established an adaptive fuzzy control system. Through the feedback signal of the loss monitoring sensor, the fan speed, the angle of the air distributor and the opening of the air intake can be adjusted in real time, which can effectively reduce the cleaning loss. *Casarsa et al., (2011),* studied the influence of volute wall position on the flow field distribution inside the fan by using numerical simulation methods and verified the reliability of the simulation results through tests. *Vasudeva et al., (2009),* studied the influence of radial spacing on the internal flow of the centrifugal fan, and obtained the first-rate radial spacing value. *Raftery et al., (2019),* used full-scale laboratory measurements of the airspeed generated by ceiling fans to predict indoor air movement. Thus, previous investigations have demonstrated the relationship between internal flow field of the impeller and the performance of the entire fan, but the impact of impeller on internal airflow field has not specifically been studied. *(Lee et al., 2016)* evaluated factors, such as inlet and outlet pressures, flow rate, torque and power, aiming at the optimal design of the centrifugal fan. Compared with most optimization studies, there are fewer studies examining outlet airflow distribution. The cleaning device of Yanma YH880(4LZ-3.5A) fully fed into the combine *(Gebrehiwot et al., 2010)* has the characteristics of wide width, multi-layer segment, secondary cleaning, etc. *Kwang et al., (2004),* selected several factors, such as the location of the blade cut-off, the radius of the cut off, expansion angle of scroll and impeller width, to optimize the velocity distribution of a centrifugal fan. *Cui Junwei et al., (2015),* designed a double-fan air sieve cleaning device. The front fan adopted a three-outlet structure, and the rear fan was placed in front of the miscellaneous auger, and the air generated was used to assist the discharge of short culm at the tail of the sieve. *Chai et al., (2020),* added a polytetrafluoroethylene coating to the surface of the vibrating screen to achieve the hydrophobic effect.

At present, most cleaning fans at home and abroad are simulated from the parameter and improved from the structure. Only the influence of air velocity and volume on the cleaning effect is studied. During cleaning, there is still a lot of residues on the vibrating sieve and shaking plate, resulting in sieve blockage. There is no further improvement of the fan, the cleaning effect has not been greatly improved, and the hot air technology is also mostly used for drying wet crops, without considering the combination with cleaning. At present, there are no hot air fan products at home or abroad. To improve the cleaning efficiency, reduce the cleaning loss rate, and reduce the problem of sieve plugging and material obstruction, the study and design of the hot air fan are presented. The air distribution, heat change, and air velocity change of the hot air in the fan, as well as the heat loss and air distribution in the cleaning room are studied. This helps to reveal the characteristics of the hot air fan and to improve the cleaning performance of the combine.

MATERIALS AND METHODS

The working principle of the hot air fan is that the heating device was installed at the inlet of the fan to provide hot air. The hot air is rotated by the fan, and the air at normal temperature is replaced by the hot air to complete the cleaning.

Electric heaters were used to provide imported heat. The action principle of the electric heater is mainly to use the thermal effect of electricity, the current passes through the heating element of the electric heater, so that it heats up so that the temperature of the liquid substance or other substances rises. The heating element of the electric heater can be a resistance wire, a metal sheet, or an electric heat pipe, etc., which can emit a lot of heat to heat the object. The working process is that the internal electric heating device was energized and heated, and the air was inhaled by the fan in front of the electric heating device. The air was heated by the electric heating device and discharged from the outlet to provide hot air.

The structure of the electric heater is shown in Figure 1.

The calculation formula of the heat emitted by the electric heater is:

$$Q = \Delta T \times \lambda \times \delta \times S \quad (1)$$

where:

Q represent heat dissipating capacity (W/m^2);

ΔT represent temperature difference (℃);

λ represent heat conductivity coefficient (W/mK);

δ represent thickness of thermal conductivity material (mm);

S represent heat radiating area (m^2).

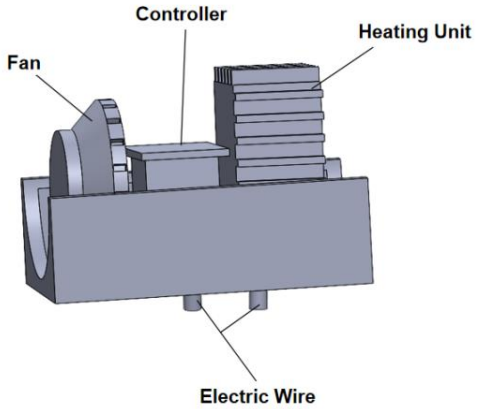


Fig. 1 - Internal structure of electric heater

Compared with the agricultural centrifugal fans commonly used now, the hot air fan can provide high heat flow without affecting the performance of the fan. The air temperature can be adjusted according to the humidity in the cleaning room so that the moisture extract with large material amount, high moisture content, and high grain content has a better separation effect without changing the structure or working parameters of the fan. It can meet or even improve the cleaning efficiency. The main improvement point is to change the original agricultural centrifugal fan into a hot air fan and connect the fan inlet with the electric heater. The optimized fan is installed on the Combine Harvester, which operates at a full load with an impeller speed of 1600 r/min.

The impeller structure parameters of the hot gas centrifugal fan are shown in Table 1, and in Figure 2.

Table 1

Structural parameters of four-blade centrifugal fan

Parameter	Number
Number of blades	4
Impeller outer diameter	556 mm
Impeller bore diameter	278 mm
Blade inlet mounting Angle	74°
Blade outlet mounting Angle	83°
Blade length	900 mm
Blade width	127 mm

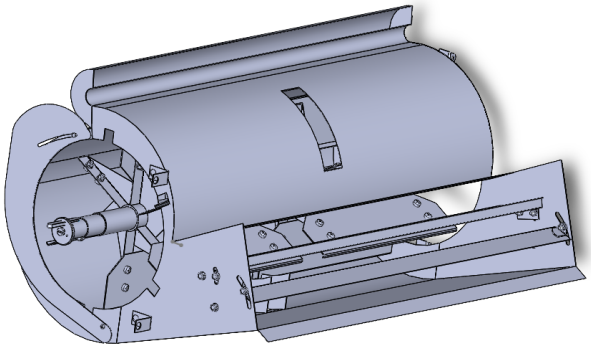


Fig. 2 - Fan model

Based on the designed 3D model, part module of SolidWorks software is used to model the simulated fluid domain, as shown in Figure 3. The flow field was numerically simulated by using FLUENT software. By analyzing the simulated air velocity and air temperature contour, it is verified whether the optimized fan can generate sufficient air velocity and temperature for separating the rape extraction mixture and whether the distribution of airflow is uniform and reasonable to ensure the cleaning effect.

The established model is imported into FLUENT software for preliminary treatment, tetrahedral unstructured Mesh is used in the mesh module to mesh the established airfield model, and all surfaces of thin-plate structures mesh to ensure that the average Element Quality of the mesh is above 0.8. The average distortion is less than 0.3. After partitioning, the model of the cleaning device generated a total of 20858413, 20957776 and 21039651 grids, respectively. The preparation work before calculation was carried out in the Setup module. The dynamic coordinate system method was adopted to set the fan impeller part in the airfield model as the dynamic coordinate system, and its center of rotation was the impeller axis.

The calculation model was selected as the Standard k-e model 23 with a wide range of applications, and the equation was solved by the SIMPLEC. The residual is set to 0.000 1 and the number of iteration steps is set to 20,000. This completes the preliminary treatment processing. Set the fan speed of 1445 r/min, the air inlet temperature of 85℃.

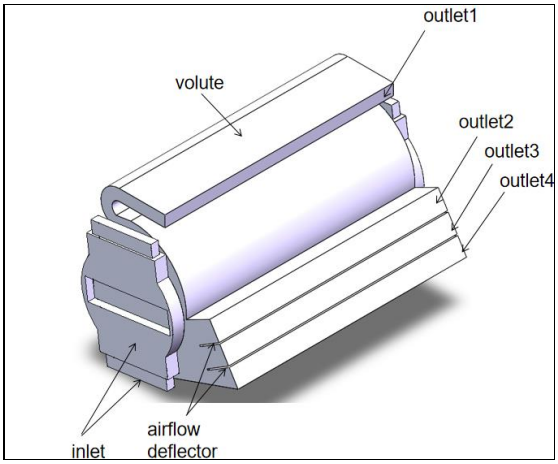


Fig. 3 - Airflow field model

A response surface analysis was conducted to examine the impact of fan speed, inlet air temperature, on the fan outlet air velocity and temperature.

A response surface analysis design was conducted using the Box–Behnken, the specific operations are as follows: first, Design-expert13 software was opened to set up the three-factor and three-level test *(Asad et al., 2021)*. Then, the air average velocity and average temperature at the upper and lower outlets were set as the response surface. Input the maximum and minimum values of the three factors.

The appropriate numerical combinations of factors were selected to verify their impact on cleaning performance.

RESULTS

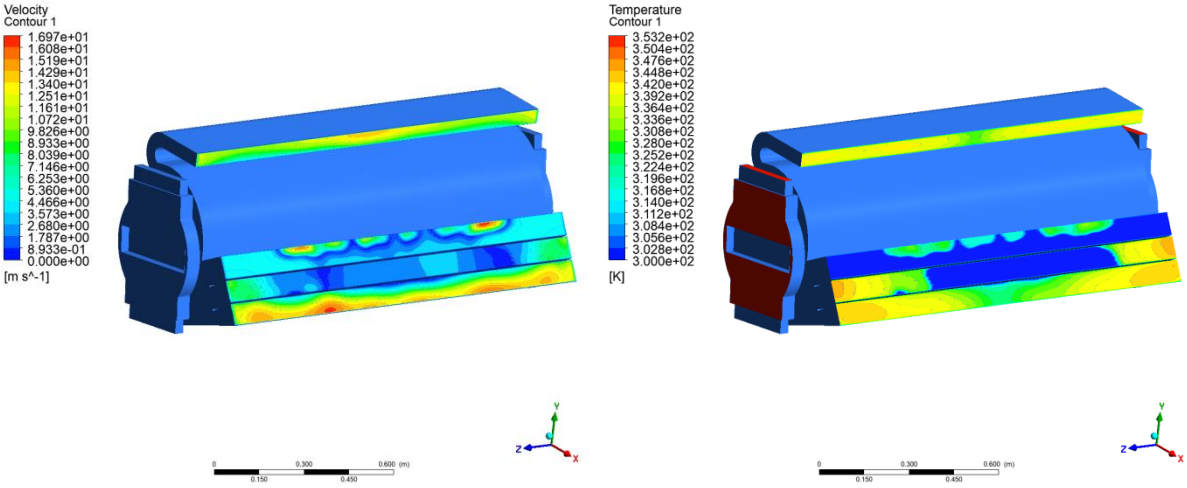
The response surface test table was obtained using Design-Expert13, and the experimental parameters satisfying the hot air cleaning were determined according to the simulation table. The experimental table is shown in the table 2.

Table 2

Test results of response surface of Hot-air fan cleaning performance.

	Fan speed	Inlet air temperature	Average air temperature at the upper outlet	Average air temperature at the lower outlet	Average air velocity at the upper outlet	Average air velocity at the lower outlet
	[rev/min]	[ºC]	[ºC]	[ºC]	[m/s]	[m/s]
1	1200	80	67.88	46.63	9.15	5.28
2	800	80	67.04	56.22	7.33	4.96
3	1200	80	67.88	46.63	9.15	5.28
4	1200	120	89.56	60.22	9.15	5.28
5	1200	80	67.88	46.63	9.15	5.28
6	1200	80	67.88	46.63	9.15	5.28
7	800	40	43.55	42.62	7.32	4.96
8	1200	80	67.88	46.63	9.15	5.28
9	1600	120	86.15	56.659	11.01	6.57
10	1600	80	55.65	41.22	11.01	6.57
11	1200	40	37.66	30.22	9.15	5.28
12	1600	40	30.69	26.64	11.01	6.57
13	800	120	97.46	72.31	7.32	4.96

The air velocity required for hot air cleaning is 7.6 m/s, and the air temperature is 60 °C *(Zhang et al., 2022)*. The optimal combination of parameters to satisfy the hot air cleaning is the fan speed of 1445 r/min, the air inlet temperature of 85 °C. The simulation results are shown in Figure 4.



a) Velocity Contour of at the outlet **b) Temperature Contour of at the outlet**

Fig. 4 - Simulation results

As can be seen from Figure 4, where the air velocity is higher, the air temperature is also higher. This is because the air velocity is larger, the hot air volume is also larger, so the air temperature is higher.

According to the simulation results, the average air temperature and average air velocity of each outlet are calculated to check whether the effect of hot air cleaning can be achieved. The air velocity and temperature of each outlet are shown in the Table 3.

Table 3

SIMULATION RESULTS

	Velocity [m/s]	Temperature [°C]
Outlet 1	10.6	65.2
Outlet 2	6.7	51.2
Outlet 3	5.3	57.6
Outlet 4	10.6	72.2

It can be seen from Table 3 that the average wind speed and wind temperature of the upper and lower outlet can meet the conditions of hot air cleaning. In particular, the air velocity and air temperature at outlet 1 and outlet 4 are large enough to effectively separate the impurity adhesion and improve the cleaning efficiency.

To verify the reliability of the numerical simulation, the fan speed is adjusted to 1435 r/min on the solid fan, the air inlet temperature is 88 °C. The average value of the sample points at the same position is compared with the numerical simulation, and the difference is observed. The experimental results are shown in the Figure 5.

It can be seen from Figure 5 that the changing trend of air velocity and temperature measured values of each outlet of the fan is generally the same as that of the numerical simulation values. The maximum error between the numerical simulation value of air velocity and temperature of each outlet and the measured value of the anemometer is <10%. On the one hand, the reason for the above measurement error is that the fan has only four blades, and the pressure pulsation occurs when the fan blades rotate, which makes the air velocity fluctuate periodically. In addition, due to the deviation of the boundary conditions used in the numerical simulation and the limitation of the calculation model, the error is further increased. Numerical simulation cannot completely replace the actual measurement to guide the design of the fan structure. Given the small difference between the numerical simulation results of air velocity and temperature of each outlet and the actual measurement results, it is reasonable to use the numerical simulation parameters to study the air distribution inside the fan.

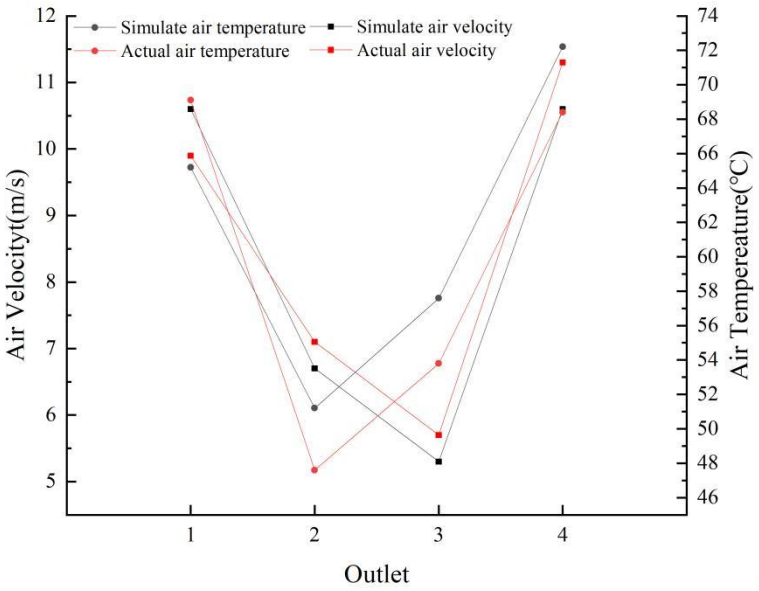


Fig. 5 - Simulation and bench comparison

The reliability of the numerical simulation was verified by bench test. A hot fan was installed on the harvester to harvest the rape. The cleaning effect of the specific heat airflow fan and the fan were tested in the field. In the process of harvesting, adjust the working parameter 1, Fan speed 1445 r/min for normal temperature wind harvesting, working parameter 2, Fan speed 1445 r/min, air inlet temperature 85℃. The model of the harvester is the Ward prime version, and the cleaning shoes are opened every 20 meters to compare the sieve surface blockage of the fan and the hot air fan. The test result is shown in Figure 6.



a. Cleaning shoes without hot air

b.



b. Cleaning shoes with hot air

Fig. 6 - Cleaning shoes comparison

As can be seen from Figure 6, the residual stems in the shoes cleaned by the hot air fan at A area are significantly less than that by the fan. At B area, the adhesion of wet crops to the screen surface was also significantly reduced. It can be seen that the hot air fan has a greater improvement in cleaning than the fan.

CONCLUSIONS

To improve the cleaning rate, different from changing the structure of the fan in the past, the fan is improved from the function for the first time. The heating device and fan type were selected, and a suitable fluid model was established.

The optimal parameters obtained by Design-expert are fan speed 1445 rev/min and inlet temperature 85 °C. The simulation was carried out with the best parameters, and the reliability of the simulation was verified by bench test.

The difference between the fan and the hot air fan is compared by field experiment. According to the observation of the cleaning shoes, the residual stem of the cleaning shoes of the hot air fan is less than that of the general fan cleaning shoes, and the adhesion of wet crops on the sieve surface is also less than that of the fan. The cleaning rate has been greatly improved.

ACKNOWLEDGEMENT

This research was financially supported by National Natural Science Foundation of China under Grant (31671590).

REFERENCES

[1] Asad M.F.A, Alam M.N, Tunç C, Sarker M.M. (2021), A Heat Transport Exploration of Free Convection Flow inside Enclosure Having Vertical Wavy Walls [J]. *Appl. Comput. Mech*. 2021, 7, 520–527.

[2] Casarsa L., Giannattasio P. (2011), Experimental study of the three-dimensional flow field in cross-flow fans [J]. *Experimental Thermal and Fluid Science*, 35(6):948-959.

[3] Chai X, Xu L, Sun Y, Liang Z, Lu E, Li Y. (2020), Development of a cleaning fan for a rice combine harvester using computational fluid dynamics and response surface methodology to optimise outlet airflow distribution [J]. *Biosyst. Eng*. 2020, 192, 232–244.

[4] Cheng F, Wang J. (1998), Experimental study on the main parameters of wind sieve type cleaning device[J]. *Journal of Agricultural Engineering*,1998(04):223-227

[5] Du W. (2007), *Numerical simulation and experimental research on airflow field of rape combine harvester clearing device* [D]. Wuhan: Huazhong University of Agriculture, 2007.

[6] Gebrehiwot M.G, De Baerdemaeker, J. & Baelmans, M. (2010), Effect of a cross-flow opening on the performance of a centrifugal fan in a combine harvester: *Computational and experimental study. Biosystems Engineering*, 105(2), 247-256.

[7] Goos, P. (2011). *Optimal design of experiments: A case study approach*.

[8] Hyeon J, Su C, Tae G K. et al. (2015), Study on performance improvement of a head-feeding rice combine for foxtail millet harvesting [J]. *Journal of Biosystems Engineering*. 40(1): 10-18.

[9] Kwang Y, K., & Seoung Jin, (2004), Shape optimization of forward-curved-blade centrifugal fan with Navier-Stokes analysis. *Journal of Fluids Engineering-Transactions of the ASME*, 126, 735-742.

[10] Li HX, Li YM, Ma, Z. (2020), Research status and development trend of scavenging fans in combine harvesters[J]. *Agricultural Machinery Chem Res*, 42(09):1-5.

[11] Lee Y T, Lim H C, Lund H, & Kaiser M J. (2016), Performance assessment of various fan ribs inside a centrifugal blower. *Energy*, 94, 609-622.

[12] Liang ZW, Li YM, Zhao ZZ. (2014), Method and sensor development for monitoring seed entrainment losses in longitudinal axial flow combine harvesters. *Journal of Agricultural Engineering*, 30(3): 18-26.

[13] Li H. (2012), *Research on the design theory and method of wind sieve type cleaning device* [D]. Wuhan: Nanjing Agricultural University, 2012.

[14] Li Y M, Tang Z, Li H C et al. (2009), Airflow field test on the sieve surface of wind sieve type cleaning device[J]. *Agricultural Mechanics Journal*, 2009, 40(12):80-83.

[15] Raftery P, Fizer J, Chen W, He Y, Zhang H, Arens E et al. (2019), Ceiling fans: predicting indoor air speeds based on full scale laboratory measurements. *Building and Environment*, 155, 210-223.

[16] Vasudeva Karanth K, Yagnesh Sharma N. (2009), CFD analysis on the effect of radial gap on impeller-diffuser flow interaction as well as on the flow characteristics of a centrifugal fan of unsteady flow in a centrifugal fan. *International Journal of Rotating Machinery*, 1e8.

[17] Yuko U., Masami M, Eiji I. et al. (2012), Turbulent flow characteristics of the cleaning wind in combine harvester [J]. *Engineering in Agriculture*, *Environment and Food*, 5(3): 102-106;
[18] Zhang T, Li Y, Xu L, Liu Y, Ji K, Jiang S. (2022), Experimental Study on Fluidization Behaviors of Wet Rice Threshed Materials with Hot Airflow [J]. *Agriculture*, 12, 601.

OPTIMIZING AND INTEGRATING ELECTROMECHANICAL ACTUATORS IN AGRICULTURAL EXCAVATOR BOOMS FOR ENHANCED EFFICIENCY AND BATTERY LONGEVITY

/

OPTIMIZAREA ȘI INTEGRAREA ACTUATORILOR ELECTROMECANICI ÎN BRAȚELE EXCAVATOARELOR AGRICOLE PENTRU EFICIENȚĂ ÎMBUNĂTĂȚITĂ ȘI LONGEVITATE A ACUMULATORILOR

Ioan Mihail SAVANIU[1)], Alexandru-Polifron CHIRIȚĂ*[2)], Ioana Aristia POPOVICI[1)], Oana TONCIU[1)], Magdalena CULCEA[1)], Ancuța NEAGU[1)], Robert BLEJAN[2),3)], Vasilica ȘTEFAN[4)]

[1)] Technical University of Civil Engineering Bucharest / Romania;
[2)] National Institute of Research & Development for Optoelectronics/ INOE 2000, Subsidiary Hydraulics and Pneumatics Research Institute / IHP / Romania;
[3)] National University of Science and Technology Politehnica Bucharest, Doctoral School of Power Engineering / Romania;
[4)] National Institute of Research and Development for Machinery and Installations for Agriculture and Food Industry – INMA Bucharest / Romania
** E-mail: chirita.ihp@fluidas.ro*
DOI: https://doi.org/10.35633/inmateh-71-29

Keywords: *electric propulsion, electromechanical actuator, mechatronics, energy-efficient farming.*

ABSTRACT

The research optimizes electric consumption in agricultural excavator booms by integrating electromechanical actuators and Power-by-Wire technologies. Utilizing a PID controller reduces electric motor peak current consumption, enhancing battery longevity. The research, carried out on a reduced-scale experimental stand, reveals the potential applications of the excavator arm equipment in agriculture, such as the precise location of irrigation systems, arrangement of terraces for orchards or vineyards, setting up greenhouses, and efficient unloading/loading of bulk materials. These applications signify the versatility and adaptability of electrically powered excavators in addressing diverse agricultural needs, emphasizing the significance of the developed mechatronic system for enhancing efficiency and sustainability in agricultural practices.

REZUMAT

Cercetarea optimizează consumul electric în brațele excavatoare agricole prin integrarea actuatorilor electromecanici și a tehnologiilor Power-by-Wire. Utilizarea unui controler PID reduce consumul maxim de curent al motorului electric, îmbunătățind durata de viață a acumulatorilor. Cercetarea, derulată pe un stand experimental la scară redusă, promite aplicații potențiale ale echipamentului brațului excavator în agricultură, precum localizarea sistemelor de irigații, amenajarea teraselor pentru livezi sau vie, înființarea serelor și încărcarea/descărcarea eficientă a materialelor vrac. Aceste aplicații semnifică versatilitatea și adaptabilitatea excavatoarelor electrice în abordarea diverselor cerințe din agricultură, subliniind importanța sistemului mecatronic dezvoltat pentru îmbunătățirea eficienței și durabilității în practicile agricole.

INTRODUCTION

In view of global and EU efforts through the European Green Pact *(*** The European Green Deal)* to reduce greenhouse gas emissions, agricultural equipment will in future be powered by electricity *(Soofi et al., 2022)*. Thus, electrically powered agricultural tractors are increasingly present on farms to carry out various specific activities.

As has recently been shown *(*** Research and Markets, 2023)*, the electric agricultural tractor market was valued at $98.7 million in 2022 and is projected to reach $234.0 million by 2028, growing at a CAGR of 14.06% between 2023 and 2028. The price of tractors in agricultural operations is influenced by the trend of electrification and automation of agricultural machinery.

Ioan Mihail Savaniu, PhD. Eng., Lecturer; Alexandru-Polifron Chiriță, PhD. Eng., Senior Research Scientist; Ioana Aristia Popovici, PhD. Eng., Lecturer; Oana Tonciu, PhD. Eng., Lecturer; Magdalena Culcea, PhD. Eng., Assist. Prof.; Ancuța Neagu, PhD. Eng., Lecturer; Robert Blejan, PhD. Student Eng., Research Assistant; Vasilica Ștefan, PhD. Eng., Senior Research Scientist

The electric agricultural tractor has seen an exponential increase in interest among farmers, manufacturers and researchers in the agricultural industry *(Mao et al., 2022; Scolaro et al., 2021; Troncon and Alberti, 2020; Mocera et al., 2023; Dhond et al., 2021)*, with electric vehicle (EV) sales reaching record highs. The presence of electric tractors on modern agricultural farms is also influenced by farmers' desire to use renewable sources to power them. The presence of electric tractors allows the introduction of modern technologies such as GPS guidance, automation of work processes, technologies that increase the productivity of agricultural activities.

Depending on the application, electric tractors can be classified into: tractors for light duty, tractors for medium duty, tractors for heavy duty. In the top position in the electric agricultural tractor market are light-duty tractors *(Khatawkar et al., 2019; Matache et al., 2020; Jia et al., 2018; Moreda et al., 2016)*, with a share of 50.98% in 2022. The high demand for light-duty electric agricultural tractors is due to their low mass, better battery performance and low cost compared to heavy-duty tractors *(*** Research and Markets, 2023; Matache et al., 2020)*. Also, in some countries there are increasingly strict regulations on the use of conventional tractors that do not meet new environmental standards. The world's leading manufacturers of electric agricultural tractors include Deere Company, Mahindra Group, Kubota Corporation, Yanmar, Massey Ferguson, Farmtac, Dongfeng, Kioti Tractor, New Holland, etc. *(*** IRB Tranding Market Insights, 2023)*.

In agriculture, the tractor is the basic equipment and for various agricultural activities various pieces of equipment (implements) are attached to it such as: ploughs; seeders; mowers; cultivators, etc. *(Magnusson and Pettersson, 2023; Varani et al., 2021; Un-Noor et al., 2022)*. Implements are accessories that help farmers to increase their productivity and to be able to perform several types of work with the same tractor *(*** Dataintelo)*. Implement manufacturers have developed a type of implement that turns the agricultural tractor into an excavator (see Fig.1). Generally, these implements are mounted at the rear of the tractor and are equipped with a boom, handle and bucket, turning the agricultural tractor into a mini-excavator. More and more farmers are using this type of equipment for small projects on a farm such as: transplanting trees, moving manure, proper excavation operations; moving agricultural soil, digging ditches, levelling small areas, precise location of irrigation systems, arrangement of terraces for orchards or vineyards, setting up greenhouses, efficient unloading/loading of bulk materials, etc. *(*** Holt Ag Solutions)*. This equipment is recommended to be used for short seasonal works, in which case it reduces labour costs and ensures greater safety in execution, but for large works this equipment cannot be used in place of classic excavators *(*** Victory Tractor Implements, 2022; *** Diamond B Tractors & Equipment)*.

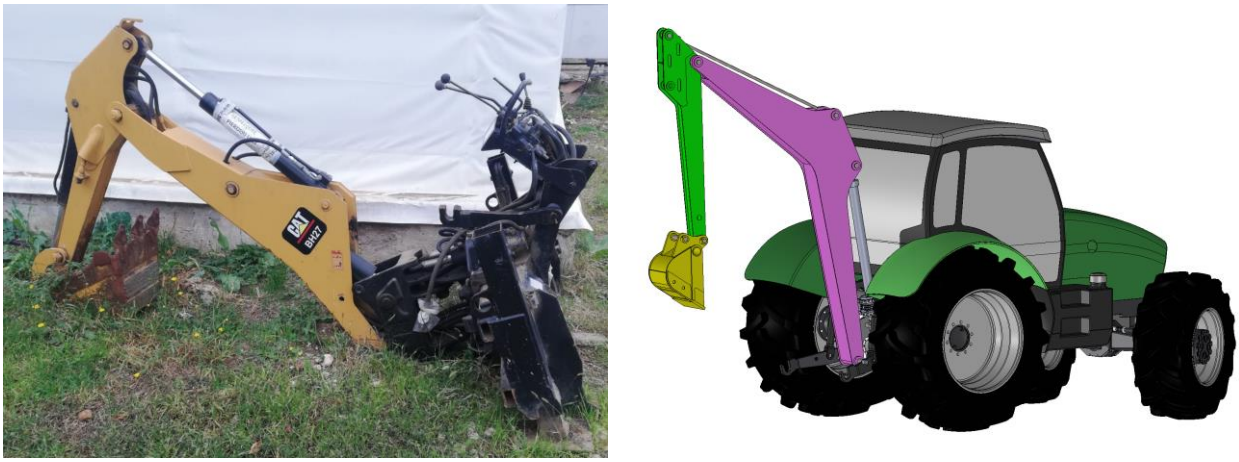


Fig. 1 - Excavator boom implement for an electric tractor

In the above context, there is a need for the development of couplings for electric agricultural tractors. While in the case of conventional tractors the tractor's hydraulic system or a power take-off is used to generate the energy needed to operate the hitch, in the case of electric tractors one wants to use the electrical energy from the tractor battery. The operation of the tractor battery for the coupling means, in the case of electrically operated couplings, to develop novel solutions for the operation of the coupling using electromechanical actuators.

PBW (power-by-wire) technologies, with distinctive design approaches, aim to extend the use of electromechanical actuators from aircraft control systems to the operation of various agricultural equipment. An electric actuator system using PBW technologies transports power between systems "through cables instead of traditional hydraulic lines, which improves performance.

Advantages of PBW actuators include: increased system safety and reliability due to the absence of flammable and hazardous hydraulic fluids; reduced weight, volume and complexity of power transmission; easier maintenance and lower associated costs due to the absence of hydraulic leakage; increased energy efficiency and improved dynamic characteristics *(Qiao et al., 2018)*. Another advantage of eliminating actuation of implements by electromechanical actuators for agricultural tractors is the elimination of the risk of soil or plant contamination from hydraulic oil leaks.

The field of electric tractor drive systems using electric power is a new field that is continuously developing. Like any new element, it has difficulties in implementing solutions on a large scale due to lack of experience and knowledge of drive solutions, energy storage, reliability and lack of trained technical staff to ensure maintenance work. The presented research examines the use of an electromechanical actuator in the actuation of a mini-excavator boom by testing it on a stand simulating digging activities.

MATERIALS AND METHODS

In order to study the actuation of implements using electromechanical actuators for electric tractors, the authors used an experimental stand to simulate digging processes for an excavator boom. The stand is built considering the geometry and the actuation mode of an excavator boom; the digging process is simulated by using weights that are placed at the boom level, as in Fig. 2. The experimental stand, shown in Fig. 3, is composed of four main subsystems: the boom, chassis metal structure subsystem; the actuation subsystem with electromechanical actuator; the actuator control subsystem; the motion and electrical energy monitoring subsystem.

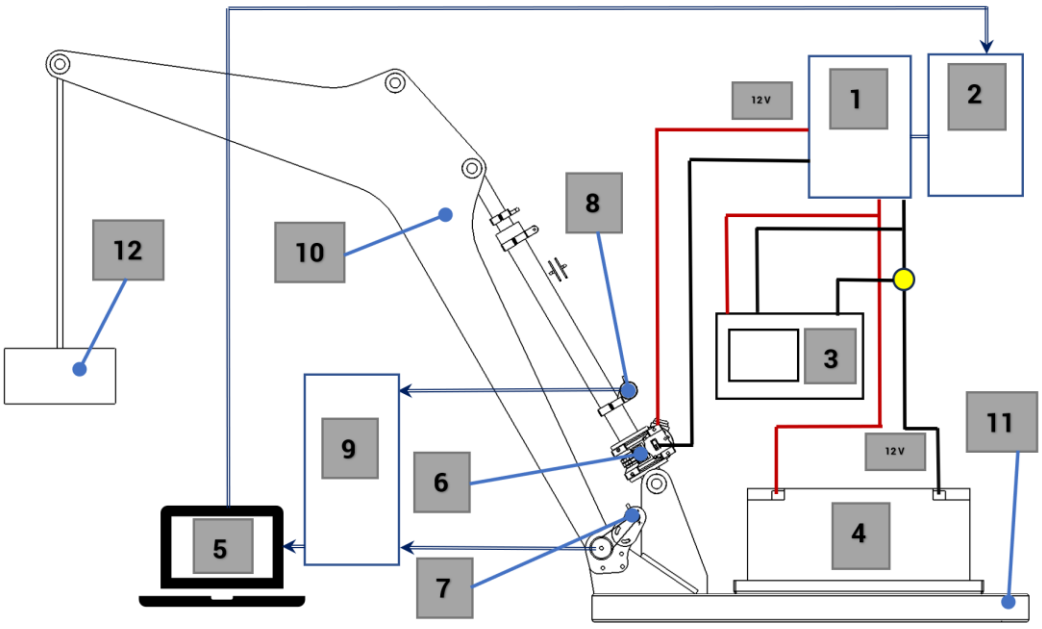


Fig. 2 - Experimental stand block diagram

Block diagram of the experimental stand, shown in Fig. 2, is composed of the following elements: 1 - relay block and PWM (Pulse-width modulation) 12 V /40 A; 2 - CONTROLINO MAXI 100-100-100 12 V controller; 3 - HIOKI PW 3198 electrical energy analyser; 4 - Deep Cycle Gel battery, voltage 12 V and 153 Ah; 5 - PC for control and data recording; 6 - electromechanical actuator powered at 12 V with 5000 N actuation force; 7 - rotary encoder E40S6-50-3-T-24 for determining the angular position of the boom; 8 - rotary encoder system E40S6-50-3-T-24 for measuring the speed of movement of the electromechanical actuator; 9 - data acquisition board - Arduino MEGA 2560 R3 (100 Hz experimental data acquisition frequency and 0.1 seconds plotting interval); 10 - excavator boom - welded metal structure; 11 - experimental stand chassis - welded metal structure; 12 - test weight.

The movement of the boom is achieved by the electromechanical actuator (Fig. 4) which is controlled by the PC via the Controlino PLC controller connected to the relay and PWM block (PWM DC Motor Speed Controller HHO-RC, 40 A continuous current and 2000 W maximum power).

The simulation of loads during digging is performed with the help of masses having different values (1.56, 6.25, and 12.5 kg), in total 20.31 kg. The PC control allows to change the direction of movement and speed of the electromechanical actuator with the help of relays. Movement monitoring is performed by means of two systems: a rotary encoder system mounted by means of a toothed belt transmission with a ratio of three on the excavator boom shaft, which records the angular position and angular speed of the excavator boom; a rotary encoder system mounted between the actuator rod and the actuator housing, which by means of a toothed belt measures the displacement and speed of the electromechanical actuator.

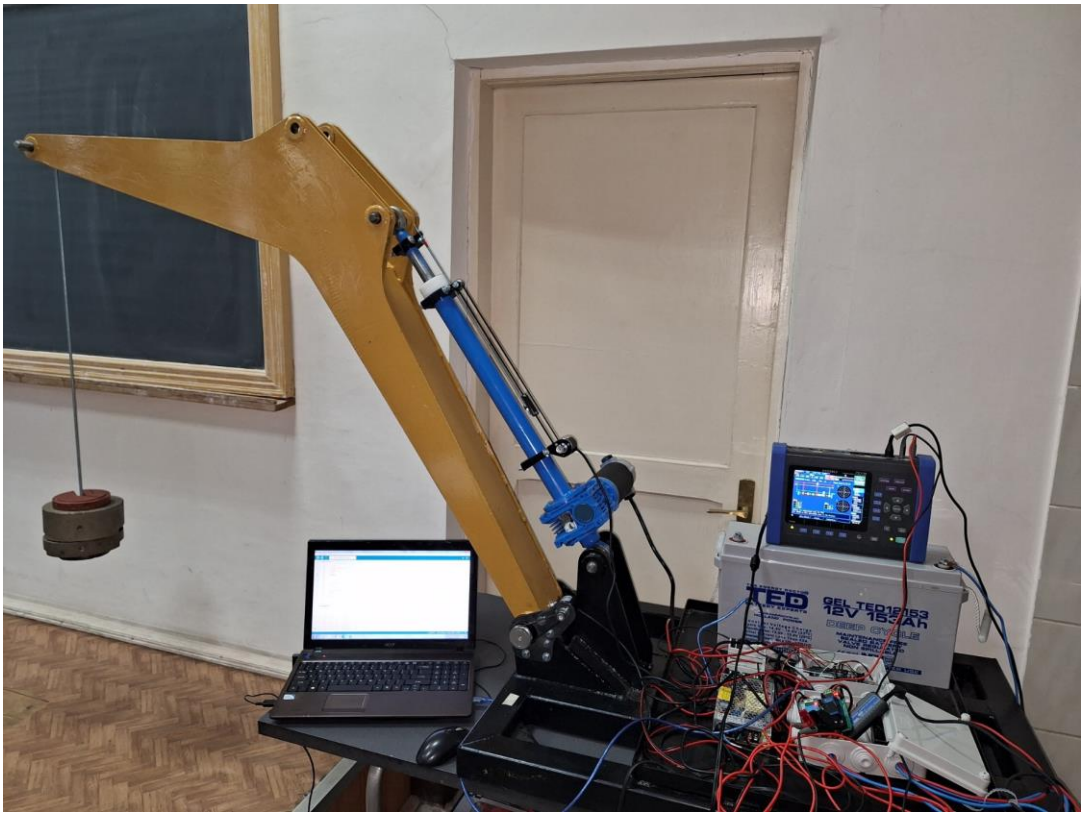


Fig. 3 - Experimental stand

The monitoring system of the electrical energy consumed by the electromechanical actuator is realized with the HIOKI PW 3198 current analyser. The HIOKI PW3198 power quality analyser has the measurement accuracy Voltage: ±0.1% of nominal voltage; Current: ±0.2% rdg. ±0.1 % f.s. + current sensor accuracy; Active power: ±0.2 % rdg. ±0.1 % f.s. + current sensor accuracy *(*** Hioki E.E. Corporation)*. The equipment, throughout the tests, collected data on supply voltage, current and electrical energy absorbed by the electromechanical actuator. The data stored in the storage medium of the equipment were analysed with the PQ ONE software which allows the presentation of the values of the electrical energy absorbed by the electromechanical actuator in graphical or tabular form *(*** Hioki E.E. Corporation, 2023)*.

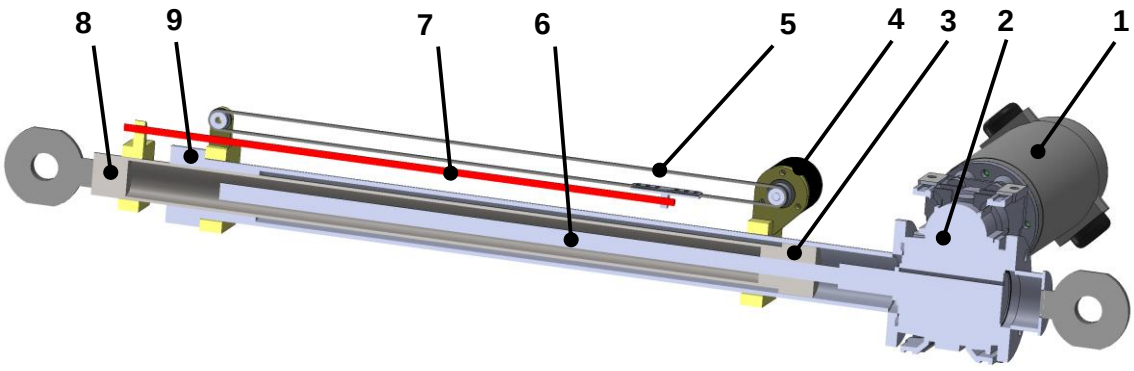


Fig. 4 - Electromechanical actuator section view

The electromechanical actuator (Fig. 4) consists of the following components: a 12 V / 250 W / 3000 rpm permanent magnet DC motor (PMDC Motor) (1), a PCM040U worm gear reducer (2) with a transmission ratio i = 60, a BSH 12 x 04 ball nut (3), an E40S6-50-3-T-24 rotary encoder (4), a 2GT-6 mm toothed belt transmission (5), and a C7 12 x 04 ball screw (6). The operation involves the electric motor transmitting rotational motion to the ball screw, subsequently converted into translational motion by the ball nut, connected to the actuator drive rod (8). The translational motion is monitored by a toothed belt transmission, transforming it into rotational motion at the encoder level. The encoder's rotation, with a pitch diameter of 12.22 mm, results in a 12.22 mm displacement of the actuator drive rod (8) relative to the fixed part of the actuator (9).

RESULTS

On the excavator boom with a 20.31 kg load attached, three experiments were conducted, that is 3 case scenarios were implemented. The first two result sets "1" and "2" comparatively illustrate the dynamic variations of various system parameters for constant control voltages with values of ± 12 V and ± 5 V, in intervals of 25 seconds with 5 second pauses. The two sets of dynamic variations of the parameters presented in Fig. 5 vary due to the control input (voltage); in the first case (”1”), the command is directly applied, while in the second case (”2”), a one-second delay (a ramp function) is employed. In the latter case, the command value gradually increases, reaching its maximum value after one second.

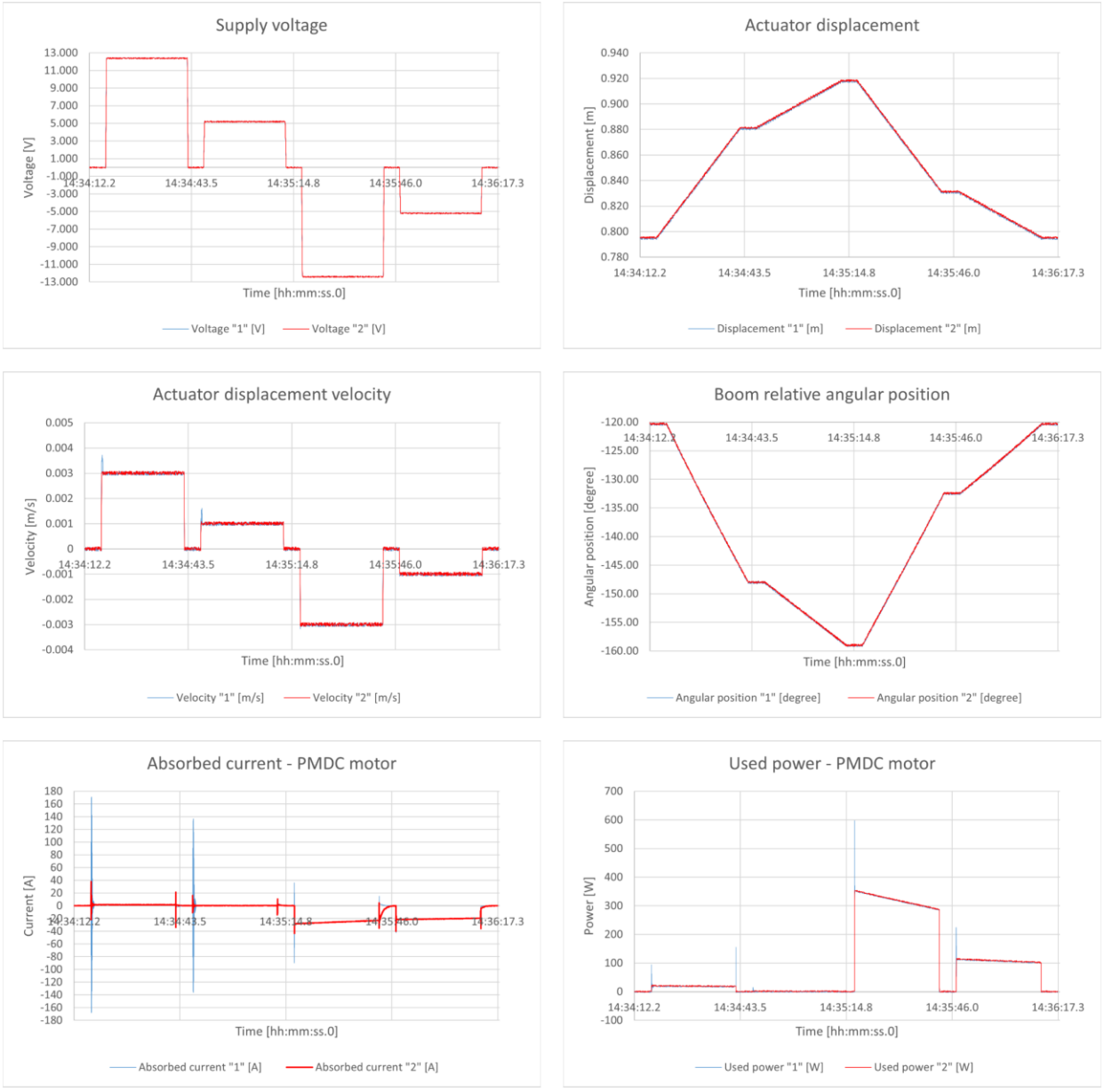


Fig. 5 - Dynamic variation of the system parameters corresponding to the experiments in cases no. "1" and "2"

In Fig. 5, one can notice how the ramp function used for system control voltage in case "2" has a positive influence on the system. Specifically, in comparison with the system in case "1", the graph depicting the instantaneous current absorbed by the PMDC motor shows that at system startup, the absorbed current is much lower, as is the case with the absorbed power. In the remaining graphs variations are negligible.

In the third experiment (case no. "3"), the system's power supply voltage was continuously controlled by a PID controller, tasked with regulating the rotation speed of the excavator boom. The PID controller was implemented in software using the "Arduino PID Library - Version 1.2.1" by Brett Beauregard *(Beauregard, 2017)*, and for plotting the graphs, the "Matplotlib 3.8.2" library *(*** Matplotlib 3.8.2 documentation)* was used.

The automatic control system's performances are depicted in Fig. 6, providing an overview of these performances in the top row graphs, where the control setpoint is compared with the relative angular velocity of the boom, on the left, while the instantaneous control error is presented on the right. Details of these variations are shown in the graphs below, revealing that the absolute control error of the automatic control system has a maximum value of 6.32%.

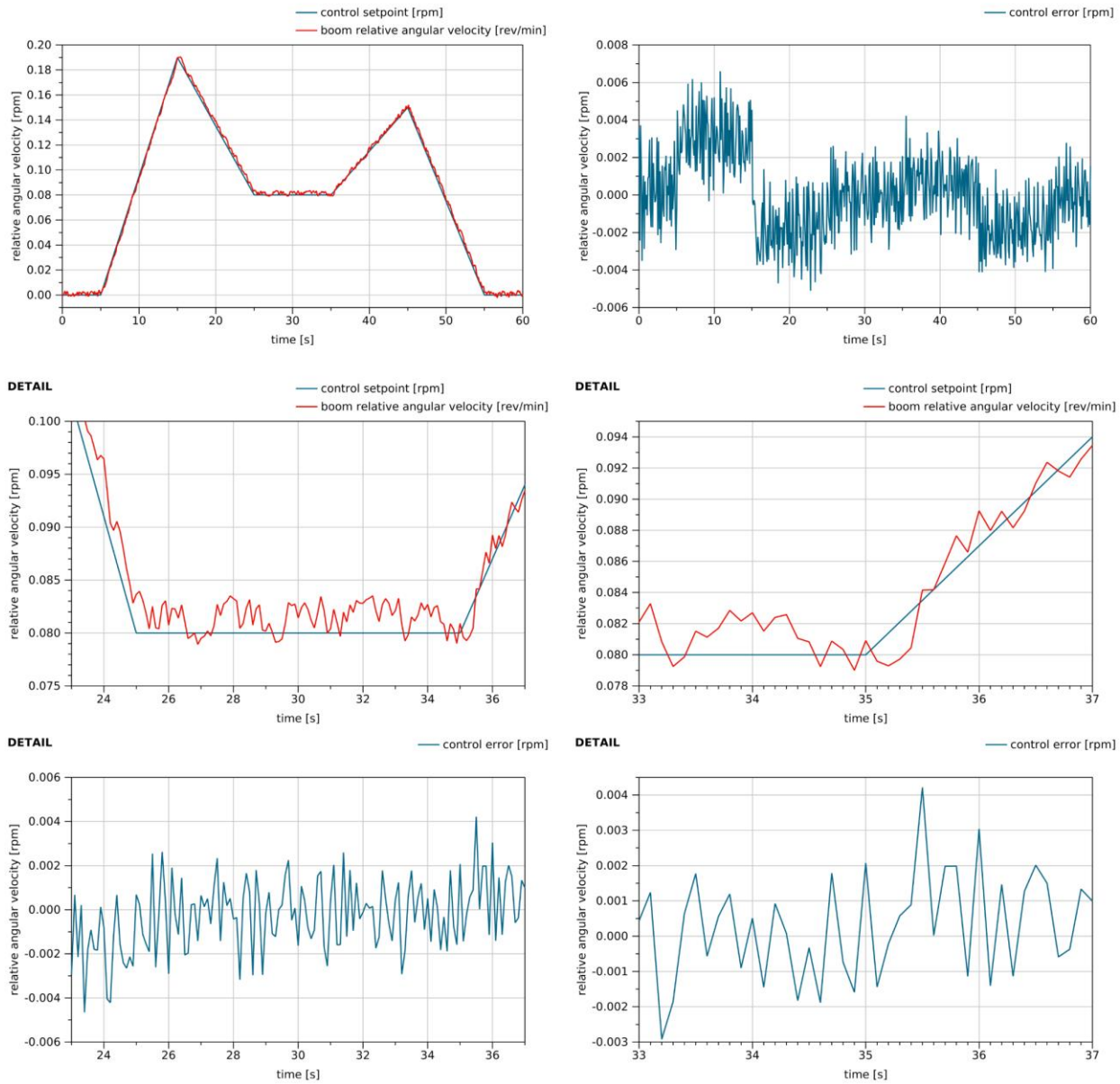


Fig. 6 - Dynamic performance of the system equipped with a PID controller - case no. "3"

Also, in Fig. 6, one can notice how the mechanical clearances within the mechatronic system controlling the excavator boom have a negative impact on the system's control performance.

These small mechanical clearances cause the error to asymmetrically oscillate around the 0 value, and the significant inertia of moving masses influences the control error, forcing it to briefly exceed the prescribed value.

The dynamic variation of the system parameters corresponding to the experiments in case no. "3" are presented in Fig. 7.

Moreover, in the graphs of Fig. 7, one can see how the control voltage continuously varies, except for the first and last 5 seconds when the voltage has low values and the current has high values, while the power consumed by the system has low values. This behaviour occurs when the PID controller tries to keep maintain system stability around the value of 0 for the displacement velocity and is caused by mechanical clearances and the inertia of moving masses. Such behaviour can potentially be avoided by implementing an automatic tuning of the PID controller and minimizing mechanical clearances.

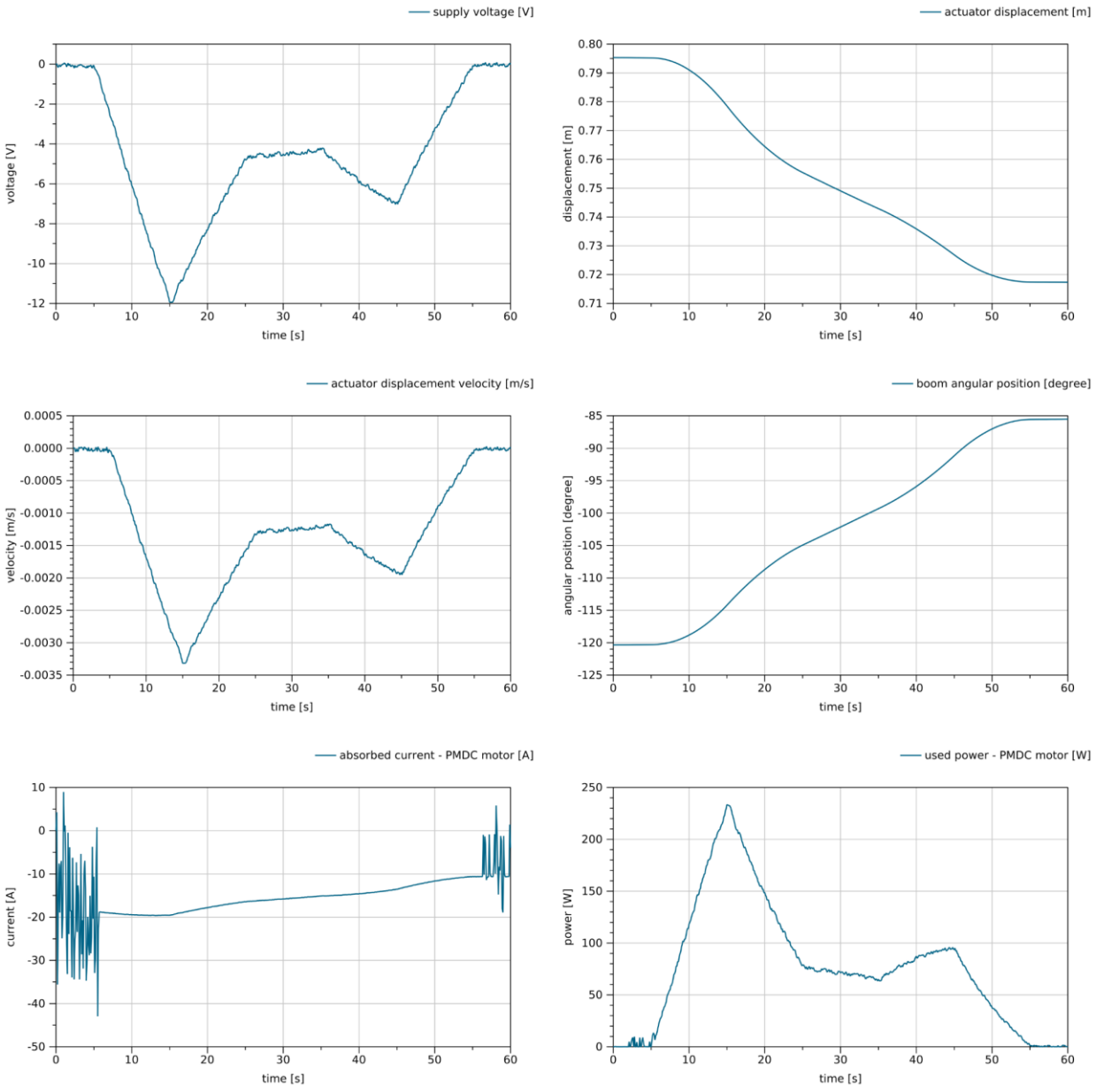


Fig. 7 - Dynamic variation of the system parameters corresponding to the experiments in case no. "3"

Also in Fig. 7, compared to Fig. 5, one can notice that the peak power consumed by the system has lower values, although a direct comparison cannot be made, and most importantly, the current absorbed by the electric motor no longer exceeds the value of 40 A, leading to an extension of the number of charge and discharge cycles of the battery.

Fig. 8 displays the energy used by the system in cases no. "1" and "2"; on this figure, one can see that the energy consumed by the system in the first two cases is virtually identical. Any small differences can be attributed to measurement errors and the slight influence of the ramp function on energy consumption.

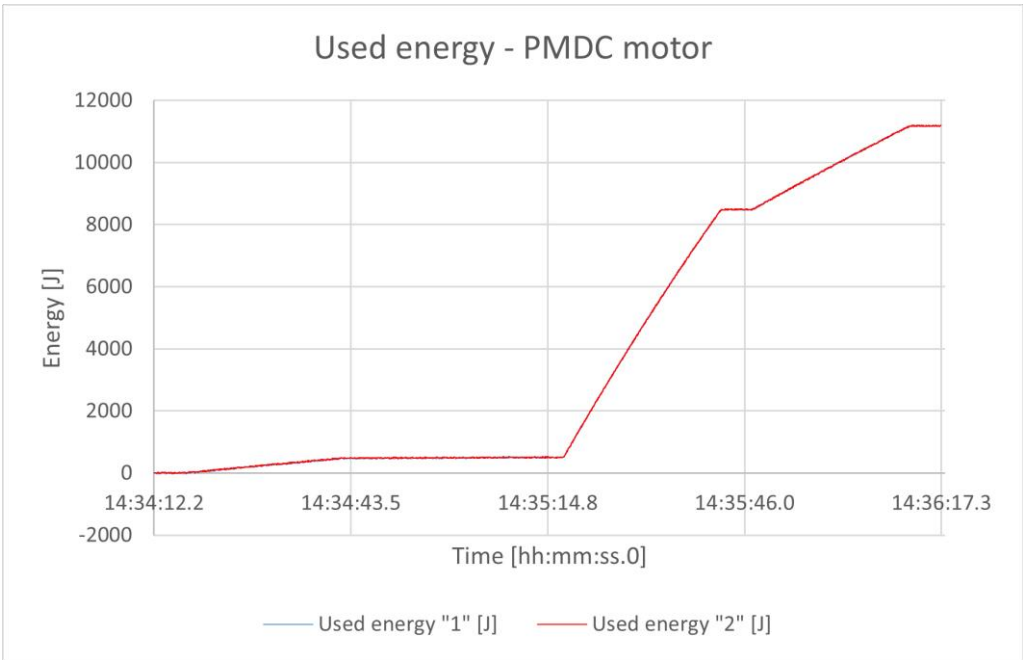


Fig. 8 – The energy used by the system in cases no. "1" and "2"

Fig. 9 displays the energy used by the system in case no. "3". Although the time variation of energy consumed by the system in this case is, on the right half of the graph, relatively similar to the time variation of energy consumed by the system in cases “1” and “2”, they cannot be compared because they have different operating cycles.

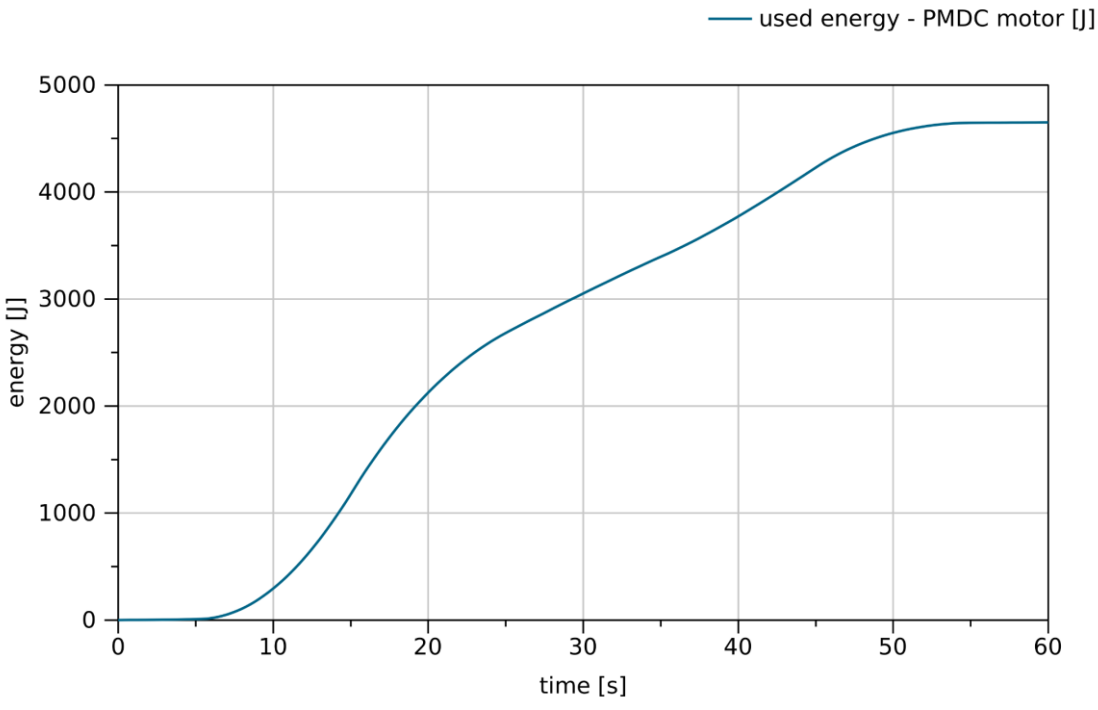


Fig. 9 – The energy used by the system in case no. "3"

CONCLUSIONS

The research highlights the feasibility of optimizing electric consumption in agricultural implements, specifically focusing on electrically powered excavator booms. By proposing and implementing an electric drive solution with electromechanical actuators, the article establishes a foundation for enhancing the efficiency of electrically powered agricultural machinery. The integration of Power-by-Wire (PBW) technologies, highlighted in the research, showcases the feasibility of using electromechanical actuators in agricultural equipment. The advantages of PBW, such as increased safety, reduced weight, and improved energy efficiency, show the feasibility of extending these technologies beyond aircraft control systems to enhance agricultural machinery.

Notably, the study reveals that the reduction in the current absorbed by the electric motor, particularly observed when utilizing a PID controller, contributes to improved battery longevity. The findings emphasize the crucial role of controlling the motor current in enhancing the overall efficiency and extending the lifespan of electric vehicle batteries.

In conclusion, the results presented in this article shed light on the dynamic performance of the mechatronic system controlling the excavator boom under various experimental conditions. The comparison of different control scenarios, including the direct application of commands and the use of a ramp function and a PID control revealed the impact of mechanical clearances and mass inertia on the system's control accuracy. The implementation of a PID controller demonstrated improvements in system stability, with potential benefits in terms of power consumption and the lifespan of the battery. However, challenges such as asymmetric oscillations and brief deviations from the setpoint were identified, underscoring the importance of automatic PID tuning and the reduction of mechanical clearances for enhanced system performance. These findings contribute valuable insights to the ongoing research in the field of mechatronic systems for electrically powered excavators and agricultural machinery, emphasizing the significance of addressing mechanical uncertainties for optimal control and energy efficiency.

ACKNOWLEDGEMENT

This research was funded by Internal Competition Programme for the financing of scientific research in UTCB (project acronym SOLUT, code UTCB-CDI-2022-016). This paper has also received financing under a project funded by the Ministry of Research, Innovation and Digitalisation through Programme 1—Development of the national research and development system, Sub-programme 1.2—Institutional performance—Projects financing the R&D&I excellence, Financial Agreement no. 18PFE/30.12.2021.

FUNDING

This article was funded by UTCB, grant number CNFIS-FDI-2023-F-0655.

REFERENCES

[1] Beauregard, B., (2017), br3ttb / *Arduino-PID-Library, Arduino PID Library* - Version 1.2.1. https://github.com/br3ttb/Arduino-PID-Library

[2] Dhond, R., Srivastav, U., Patil, B. T., & Vaishnav, H. (2021). Comparative Study of Electric Tractor and Diesel Tractor. *IOP Conf. Series: Materials Science and Engineering*, *1168*, 012003. International E-Conference on "Cutting Edges in Mechanical Engineering" (CEME 2020), 20th February 2021, Greater Noida, India. https://doi.org/10.1088/1757-899X/1168/1/012003

[3] Jia, C., Qiao, W., & Qu, L. (2018). Modeling and control of hybrid electric vehicles: A case study for agricultural tractors. *2018 IEEE Vehicle Power and Propulsion Conference (VPPC)*, Chicago, IL, USA, 1–6. https://doi.org/10.1109/VPPC.2018.8604997

[4] Khatawkar, D. S., Shaji James, P., & Dhalin, D. (2019). Modern trends in farm machinery-electric drives: A review. *International Journal of Current Microbiology and Applied Sciences*, *8*(1), 83–98. https://doi.org/10.20546/ijcmas.2019.801.011

[5] Magnusson, J., & Pettersson, E. (2023). *Electrifying Agricultural Implements*. *A study of design implications of electrification*. Jönköping University, School of Engineering, Sweden.

[6] Mao, Y., Wu, Y., Yan, X., Liu, M., & Xu, L. (2022). Simulation and experimental research of electric tractor drive system based on Modelica. *PLoS ONE*, *17*(11), e0276231. https://doi.org/10.1371/journal.pone.0276231

[7] Matache, M. G., Cristea, M., Găgeanu, I., Zapciu, A., Tudor, E., Carpus, E., & Popa, L. D. (2020). Small power electric tractor performance during ploughing works. *INMATEH - Agricultural Engineering*, *60*(1), 123–128. https://doi.org/10.35633/inmateh-60-14

[8] Mocera, F., Somà, A., Martelli, S., & Martini, V. (2023). Trends and future perspective of electrification in agricultural tractor-implement applications. *Energies*, *16*(18), 6601. https://doi.org/10.3390/en16186601

[9] Moreda, G. P., Muñoz-García, M. A., & Barreiro, P. (2016). High voltage electrification of tractor and agricultural machinery – A review. *Energy Conversion and Management*, *115*, 117–131. https://doi.org/10.1016/j.enconman.2016.02.018

[10] Qiao, G., Liu, G., Shi, Z., Wang, Y., Ma, S., & Lim, T. C. (2018). A review of electromechanical actuators for More/All Electrical aircraft systems. *Proceedings of the Institution of Mechanical Engineers, Part C: Journal of Mechanical Engineering Science*, *232*(22), 4128-4151. https://doi.org/10.1177/0954406217749869

[11] Scolaro, E., Beligoj, M., Perez Estevez, M., Alberti, L., Renzi, M., & Mattetti, M. (2021). Electrification of agricultural machinery: A review. *IEEE Access*, *9*, 164520–164541. https://doi.org/10.1109/ACCESS.2021.3135037

[12] Soofi, A. F., Manshadi, S. D., & Saucedo, A. (2022). Farm electrification: A road-map to decarbonize the agriculture sector. *The Electricity Journal*, *35*(2), 107076. https://doi.org/10.1016/j.tej.2022.107076

[13] Troncon, D., & Alberti, L. (2020). Case of study of the electrification of a tractor: Electric motor performance requirements and design. *Energies*, *13*(9), 2197. https://doi.org/10.3390/en13092197

[14] Un-Noor, F., Wu, G., Perugu, H., Collier, S., Yoon, S., Barth, M., & Boriboonsomsin, K. (2022). Off-road construction and agricultural equipment electrification: Review, challenges, and opportunities. *Vehicles*, *4*(3), 780-807. https://doi.org/10.3390/vehicles4030044

[15] Varani, M., Mattetti, M., & Molari, G. (2021). Performance evaluation of electrically driven agricultural implements powered by an external generator. *Agronomy*, *11*(8), 1447. https://doi.org/10.3390/agronomy11081447

[16] *** Dataintelo, Agricultural Equipment Attachments Market Research Report 2023-2031. Report ID: 103153. https://dataintelo.com/report/agricultural-equipment-attachments-market/

[17] *** Diamond B Tractors & Equipment, How to Choose the Perfect Tractor Attachment Backhoe. https://www.diamondbtractors.com/how-to-choose-the-perfect-tractor-attachment-backhoe/

[18] *** Hioki E.E. Corporation, (2023), PQ ONE. https://www.hioki.com/global/support/download/software/versionup/detail/id_562

[19] *** Hioki E.E. Corporation, Power Quality Analyzer PW3198. https://www.hioki.com/global/products/pqa/power-quality/id_5824

[20] *** Holt Ag Solutions, Different attachments and implements for farm equipment. https://www.holtags.com/different-attachments-implements-for-farm-equipment

[21] *** IRB Tranding Market Insights, (2023), Report on Electric Agricultural Tractor Market: Size & Share Analysis for 2031. https://www.linkedin.com/pulse/report-electric-agricultural-tractor-market-size/

[22] *** Matplotlib 3.8.2 documentation. https://matplotlib.org/stable/

[23] *** Research and Markets, (2023), Electric Farm Tractor Market - A Global and Regional Analysis: Focus on Product, Application, Adoption Framework, Startup, Patent, Value Chain, and Country-Wise Analysis - Analysis and Forecast, 2023-2028. https://www.researchandmarkets.com/report/electric-tractors?gad_source=1&gclid=CjwKCAiA0syqBhBxEiwAeNx9N_a0KgF25f9-UwMG43Ni_KMzwcM1fBgg-d42l6CUalskylP9PLuouxoCLyMQAvD_BwE

[24] *** The European Green Deal (Pactul verde european). https://commission.europa.eu/strategy-and-policy/priorities-2019-2024/european-green-deal_ro

[25] *** Victory Tractor Implements, (2022), Backhoe Attachment For Tractor — Key Things You Need To Know! https://etractorimplements.com/backhoe-attachment-for-tractor-key-things-you-need-to-know/

DISCRETE ELEMENT METHOD USED TO ANALYZE THE OPERATING PARAMETERS OF THE CUTTING TABLE OF CRAWLER SELF-PROPELLED REED HARVESTER
/
离散元法分析履带自走式芦苇收获机割台运行参数

Kuizhou JI [1)], Yaoming LI [1*)], Binbin JI[1,2)], Zhenwei LIANG [1)], Tuo DU[1)]
[1)] School of Agricultural Engineering, Jiangsu University, Zhenjiang, 212013, China
[2)] School of Mechanical Engineering, Nantong University, Nantong, 226019, China
Tel: 13805283656; E-mail: ymli@ujs.edu.cn
Corresponding author: Yaoming Li
DOI: https://doi.org/10.35633/inmateh-71-30

Keywords: *Discrete element, reed combine harvester, cutting table, multiple factors*

ABSTRACT
In this paper, the basic rigid unit and discrete element rigid model of reed stem and discrete element flexible model of reed stem were established by means of multi-spherical filling and other methods. Then, three-point bending test was carried out in EDEM software to complete the calibration of bonding parameters. Finally, simulation analysis was carried out with the loss rate as the index. The simulation results show that the optimal parameter combination is 46 r/min for the transverse transmission device, 53 r/min for the vertical clamping longitudinal transmission device, and 470 mm for the center distance of the drum. Finally, the initial field test verifies that the maximum parameter combination of the harvester header is 49 r/min for the transverse conveying device of the header, 51 r/min for the vertical clamping longitudinal conveyor and 1.1 m/s for the field forward speed of the reed harvester, and the loss rate of the harvester is 3.36%, and the optimal parameter combination is consistent with the simulation analysis results.

摘要
本文通过多球面体填充等方法建立了芦苇茎秆的基本刚性单元与离散元刚性模型以及芦苇茎秆的离散元柔性模型，随后在 EDEM 软件中开展了三点弯曲试验，完成了粘结参数的标定，最后以损失率为指标开展仿真分析，仿真结果表明最佳参数组合为横向拨送装置转速为 46r/min、直立夹持纵向输送装置转速为 53r/min、滚筒中心距为 470mm，最后通过初次田间试验验证了履带自走式芦苇收获机割台收获效果最大的参数组合为割台横向拨送装置工作转速为 49r/min、直立夹持纵向输送装置工作转速为 51r/min 和芦苇收获机田间前进速度为 1.1m/s 时，此时收获机割台的损失率为 3.36%，最优参数组合与仿真分析结果相符.

INTRODUCTION

Transverse transfer and longitudinal clamping of the whole reed stalk are the key technologies of the cutting table of crawler self-propelled reed harvester, and the working performance of the corresponding device directly affects the reed loss rate *(Jin et al., 2010, Liu et al., 2021)*. The first section is transverse transfer. After the reed stalk root is cut off, the transverse transfer device is transferred to the front end of the vertical clamping longitudinal transfer device. The second section is longitudinal conveying. The reed stalk is transported from the front end to the rear binding mechanism by the vertical clamping longitudinal conveying device. The connection of the two sections of conveying device is realized by the finger of the transverse transmitting device and the conveying roller.

At present, there are reed harvesters at home and abroad, they choose silage harvester headers to cut the reeds, and then the square baler pulled by the tractor collects and bales the broken reeds and sends them to the trailer for storage *(Luigi et al., 2016). Martelli et al* attached a header in front of the tractor, which contains a grinder to cut and crush the reeds *(Martelli et al., 2015). Ivan et al* designed a reed harvester capable of harvesting reed vegetation located at the edge of canals and lakes, consisting mainly of a floating harvesting device, a platform for conveying and storing reeds *(Ivan et al., 2017).* Jiangsu Binhai County Agricultural Mechanization Institute is designed to be 4GL-130 reed harvester on the basis of rice and wheat harvester, which is compact in structure, easy to hook, and adopts vertical header and manual lifting (*Yuan et al., 1987*). Ma Qingyong discussed and studied the position of the reed cutter table, and used the tracked chassis to solve the problem of heavy load on the front wheel of the harvester (*Ma et al., 2010*).

Yuan Chunfu improved the header device of the reed harvester in view of the problem of small cutting width of the reed harvester, and its cutting mechanism was composed of three cutters, which were respectively responsible for the cutting of the roots of the high-stem crop, the root of the high-pole crop and the cutting of the rattan on the side of the cutting surface (*Yuan et al., 2014*). *Ni et al* designed the reed harvester for the phenomenon that it is prone to lodging and jamming in the reed harvest process. Therefore, the multi-layer conveying chain is used to push the reed wheel and the moving tooth to drive the reed to move in the rotating direction of the chain (*Ni et al., 2021*).

In order to transport reed stalks neatly and orderly from transverse to longitudinal, this paper uses EDEM software to conduct discrete element simulation research on reed stalk transport process of crawler self-propelled reed harvester, establishes the rigid and flexible discrete element model of reed stalk, and constructs the transportation system simulation system of reed stalk from transverse conveying mechanism to vertical clamping longitudinal conveying mechanism. Discrete element method has been widely used *(Wang et al., 2010, Andrewg et al., 2011).* This method can provide information about the macroscopic and microscopic behavior of the particle system. *Lv et al., (2023),* verified the operation performance of their designed potato soil crushing and preparation combined operator by establishing a component-soil discrete element model. *Zhou et al., (2023),* established the root-tuber of Jerusalem artichoke at harvest time and calibrated its physical characteristics, thus laying a research foundation for the harvester.

The discrete element rigid model of reed stems was established by means of EDEM software polyhedron filling and layering. The discrete element flexible model of reed stems was established by Hertz-Mindlin with bonding contact model, and the parameters were calibrated by three-point bending test. The simplified discrete element model of the transversal conveyance and the longitudinal clamped conveyance was established, and the optimal rotation speed was obtained by dynamic analysis, which provided a theoretical basis for the selection of parameters in the subsequent field operation.

MATERIALS AND METHODS

Crawler self-propelled reed harvester cutting table device overall scheme design

Cutting table design scheme

The cutting platform of reed harvester designed in this paper integrates the functions of cutting, transverse transfer and longitudinal clamping, and can achieve low loss and high efficiency harvesting of the whole reed rod. The reed harvester cutting table device is mainly composed of the left and right dividing rod, cutting device, transverse transfer device, vertical clamping longitudinal conveying device and other working parts. The 3 D map is shown in Figure 1 (a), the physical diagram is shown in Figure 1 (b).

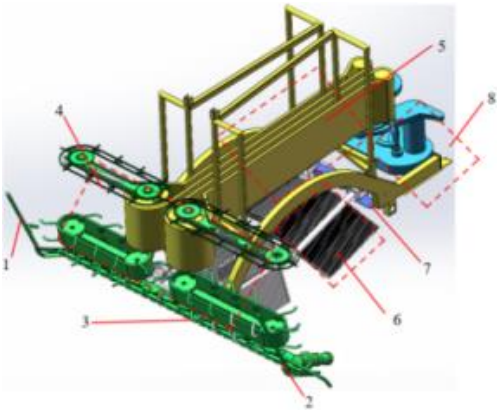


Fig. 1(a) - 3D illustration of header

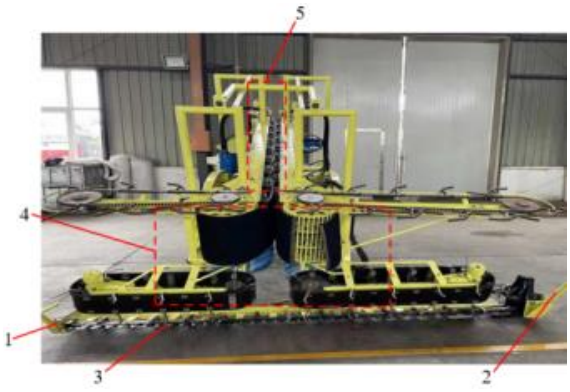


Fig. 1(b) - Real object of header

1-The right dividing rod of the cutting table; 2-cutting table left dividing rod; 3-cutting table cutting device; 4- cutting table transverse transfer device; 5-cutting table vertical clamping longitudinal conveying device; 6-cleaning device;7-bottom root device; 8-strapping device

Working principle of the cutting table device

When the crawler self-propelled reed harvester cutting platform device performs field harvesting operations, the hydraulic cylinder is responsible for controlling the lifting of the harvester cutting platform device, the reed plants are divided into ridges by the left and right dividers, and the reed plants are gathered and collected by the lateral transfer device. The reed stalks after cutting are transferred from both sides to the middle. The reed stalk is fed into the vertical clamping longitudinal conveying device by an active roller fitted with the high friction conveyor belt, and the reed stalk is finally transported by clamping at the entrance of the device to the binding place at the tail.

Discrete element analysis of transverse versus longitudinal conveying devices

Establishment of discrete element modeling

As shown in Fig.2, simplifying the three-dimensional model of the transverse and longitudinal gripper conveyer-device, leaving only the end of the transverse conveyer-device and the front end of the vertical gripper longitudinal conveyer-device affects the transition part of the tall reed stalk from the transverse conveyer-device to the longitudinal gripper conveyer-device.

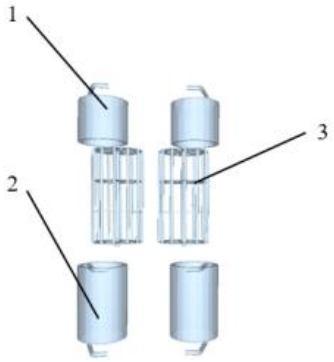


Fig. 2 - Simplified lateral and longitudinal conveying devices

1- Upper horizontal transfer mechanism; 2- Lower horizontal transfer mechanism; 3- Vertical clamping longitudinal conveyor

Definition of the reed stalk model

The Hertz-Mindlin with bonding contact model was used to construct the flexible model of reed culms *(Zhang et al., 2018).* The reed plants involved in this paper vary in length from 2.5-3 m and in diameter from 12-20 mm. In order to improve the simulation speed, the reed stalk model is simplified according to the physical characteristics of the reed stalk, and it is regarded as a hollow cylinder composed of rings composed of numerous particles and stacked with layers of rings. Basic parameters are shown in Table 1. It provides data basis for the establishment of reed stem discrete meta-model *(Bart et al., 2014).*

Table 1

Geometric dimensions of reed stalks

Parameter	Scope / mm	Mean value / mm
Culm length	2500~3000	2750
Stem wall thick	1.8~2.6	2.2
Stem diameter	12~20	16

Establishment of the Rigid model

The basic rigid element of reed stem was established by means of multi-spherical filling and layering *(Wang et al., 2020).* The specified particle coordinate rules (part) are shown in Fig.3 and Fig.4, and the discrete element rigid model of reed stalk established is shown in Fig.5.

	Position X (mm)	Position Y (mm)	Position Z (mm)	Physical Radius (mm)
4	2.03522	5.28128	-0.00130431	2.3
5	-5.27647	2.03485	-0.00184566	2.3
6	5.28165	-2.0304	0.000474478	2.3
7	-2.03004	-5.27683	-6.68751e-05	2.3

Fig. 3 - The polyhedron filling method

	Name	Particle Type	Position X (mm)	Position Y (mm)	Position Z (mm)
328	particle 337	New Particle 2	0	0	1546.3
329	particle 329	New Particle 2	0	0	1551
330	particle 330	New Particle 2	0	0	1555.7
331	particle 338	New Particle 2	0	0	1560.4
332	particle 339	New Particle 2	0	0	1565.1

Fig. 4 - Layered overlay method



Fig. 5 - Schematic diagram of discrete element rigid model of reed stalk

Establishment of the flexible model

In order to restore the deformation process of reed stems and improve the simulation accuracy, on the basis of the rigidity model of reed stems established by the multi-spherical filling method, the Hertz-Mindlin

with bonding contact model is used to bond each unit, and the force/moment between particles is set to 0 and updated gradually by Formula 1 *(Liu et al., 2018)*:

$$\begin{cases} \Delta F_{nb} = -v_n^{rel} k_{nb} A_b \Delta t \\ \Delta F_{tb} = -v_t^{rel} k_{tb} A_b \Delta t \\ \Delta M_{nb} = -\omega_n^{rel} k_{nb} J_b \Delta t \\ \Delta M_{tb} = -\omega_t^{rel} k_{tb} J_b \Delta t \end{cases} \quad (1)$$

The A_b cross-sectional area and polar moment of inertia J_b of parallel bonding bond are calculated as follows:

$$\begin{cases} A_b = \pi R_b^2 \\ J_b = \frac{1}{2}\pi R_b^4 \end{cases} \quad (2)$$

where ΔF_{nb} represents the increment of normal bonding force, [N], ΔF_{tb}represents tangential bonding force increment, [N], ΔM_{nb} increment of normal bonding moment is expressed, $[\mathrm{N \cdot m}]$, ΔM_{tb} represents tangential bonding moment increment, $[\mathrm{N \cdot m}]$, k_{nb} expresses normal bond stiffness, $[\mathrm{N/m^3}]$, k_{tb} denotes tangential bond stiffness, ω_n^{rel} represents the normal relative angular velocity, $[\mathrm{rad/s}]$, ω_t^{rel} tangential relative angular velocity, $[\mathrm{rad/s}]$, Δt indicating that the time is not long, [s], R_b denotes the bonding radius.

When the maximum normal stress σ_{max} and maximum tangential stress τ_{max} between particles exceed the predefined critical normal stress $\sigma_{critical}$ and critical tangential stress $\tau_{critical}$, the bonding bond between particles breaks:

$$\begin{cases} \sigma_{critical} < \sigma_{\max} = \frac{-F_{nb}}{A_b} + \frac{2M_{tb}}{J_b} R_b \\ \tau_{critical} < \tau_{\max} = \frac{-F_{tb}}{A_b} + \frac{2M_{nb}}{J_b} R_b \end{cases} \quad (3)$$

where F_{nb} represents the normal bonding force, $[N]$, F_{tb} represents the tangential bonding force, $[N]$, M_{nb} represents the normal bonding moment, $[\mathrm{N \cdot m}]$, M_{tb} Represents the tangential bond moment, $[\mathrm{N \cdot m}]$.

The state of reeds harvested by reed harvester can be judged by observing the stress of stalk model and the state of bonding bond.

Calibration of the bonding parameters

It is necessary to determine material parameters (density and Poisson's ratio, etc.), contact parameters (recovery coefficient and static friction coefficient, etc.) and bonding parameters (normal and tangential bonding parameters, etc.), and to calibrate the normal bonding strength k_n, tangential bonding strength k_s and radius between reed stalk particles by three-point bending test *(Gonzalez, et al., 2012; Hou et al., 2022).*

Three-point bending test

As shown in Figure 6, the geometric model of the support seat and indenter is established in EDEM software, and a force of 5N downward movement is applied to the indenter, and the loading speed is 10 mm/min. The time step is 5%, and the mesh is 3 times the particle *(Tong et al., 2022; Yidong et al., 2023).*

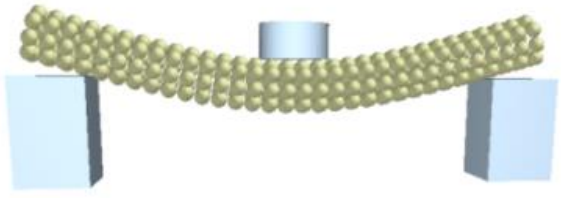


Fig. 6 - Three-point bending test in EDEM software

As shown in Table 2 and 3, the specific values of material parameters and contact parameters are given by referring to literature, and the bonding parameters mainly include: normal bonding strength, tangential bonding strength, bonding radius, critical normal stress and critical tangential stress.

Table2

Reed material parameters

Material	density（$\mathbf{kg \cdot m^{-3}}$）	Poisson ratio	Modulus of shearing（Pa）
Reed stalk	200	0.5	$4x10^6$
Loading parts	7800	0.3	$8x10^{10}$

Table3

Reed material parameters

Material	Recovery coefficient	Static friction coefficient	Sliding coefficient
Reed stalk-reed stalk	0.284	0.3	0.20
Reed stalk-Load piece	0.43	0.250	0.122

Test protocol and results

The test method of Box-Behnken using Design-Expert software, using the normal bond strength k_n, intensity of tangential bonding k_s and adhesion radius r as the test factors, and the bending strength as the test index. The test code is shown in Table 4:

Table4

Three-point bending test code list

Factor	Level		
	-1	0	1
Normal bond strength（N/m^3）	10^6	10^9	10^{12}
Intensity of tangential bonding （N/m^3）	10^6	10^9	10^{12}
Adhesion radius（mm）	1	3	5

The test index is the bending strength of reed stalk, and the calculation formula is as formula (4):

$$\delta_l = M_{\max} / W \tag{4}$$

where δ_l represents the bending strength of reed, [MPa], M_{max} represents the maximum bending moment, $[\mathrm{kNm}]$, W represents the cross-section coefficient, the cross section of reed stalk is:

$$W = \frac{\pi\varphi^3}{32}\left[1-\left(\frac{d}{\varphi}\right)^4\right] \tag{5}$$

where φ^3 represents the cross-section diameter of the reed stalk and d represents the inner diameter of the reed stalk. Three-factor three-level test performed using the Box-Behnken design test method of Design-Expert software. The results are shown in Table 5:

Table5

Analysis of three-point bending test results

Order	A: Normal bond	B: Intensity of tangential	C: Adhesion	δ_l（MPa）
1	1	0	-1	9.45
2	0	1	1	17.56
3	-1	0	-1	0.71
4	1	0	1	15.61
5	0	0	0	2.35
6	1	-1	0	5.41
7	0	-1	-1	1.44
8	1	1	0	18.62
9	0	0	0	2.37
10	0	0	0	2.39
11	0	0	0	2.38
12	0	-1	1	8.12
13	-1	1	0	7.62
14	0	1	-1	12.45
15	0	0	0	3.38
16	-1	0	1	6.44
17	-1	-1	0	0.35

The above results were fitted by quadratic polynomial regression, and the second-order regression model of the bending strength of reed stems, the normal and tangential bond strength and the bond radius was established, and the analysis of variance was carried out, as shown in Table 6.

Table 6

Analysis of variance of three-point bending test results

1	quadratic sum	free degree	free degree	F price	P price
model	572.75	9	63.64	358.65	<0.0001
A-k_n	144.25	1	144.25	812.91	<0.0001
B-k_s	209.41	1	209.41	1180.15	<0.0001
C-r	70.09	1	70.09	395.02	<0.0001
AB	8.82	1	8.82	49.71	0.0002
AC	0.046	1	0.046	0.26	0.6255
BC	0.62	1	0.62	3.47	0.1047
A^2	13.54	1	13.54	76.29	<0.0001
B^2	55.57	1	55.57	313.19	<0.0001
C^2	57.19	1	57.19	322.31	<0.0001
Residual	1.24	7	0.18		
Lack of Fit	0.43	3	0.14	0.70	0.5975
Pure Error	0.81	4	0.20		
Cor Total	573.99	16			

It can be obtained from the table that the model *P* value of the regression model 0.0001, and then it is known that the model is extremely significant. However, the P-value of the mismatch term was 0.5975> 0.005, which was not significant, indicating that the regression model fitted more reliably. The results of variance analysis show that the regression model of flexural strength of reed stems is reliable and can be used to predict flexural strength of flexible reed stems.

The regression equation of the regression model is as follows:

$$\delta = 2.57 + 4.25A + 5.12B + 2.96C + 1.48AB + 0.11AC - 0.39BC + 1.79A^2 + 3.63B^2 + 3.69C^2 \quad (1)$$

Using Design Expert software to solve the above model with the initial design point as the starting point, the optimal parameter combination of normal bond parameters, tangential bond parameters and bond radius can be obtained as follows:

1) The normal bond strength is 8.5×108 $\mathrm{N/m^3}$; 2) Tangential bond strength is 6.5×107 $\mathrm{N/m^3}$; 3) The bonding radius is 2.6 mm.

The three-point bending test was carried out again with the above parameter combination, and the bending strength of the reed stem was 2.43 MPa, which was 6.18% lower than that measured by the texture analyzer above (2.59 MPa), proving that the best parameter combination obtained can be used to establish the flexible reed stem model.

RESULTS

Experimental factors and indexes

This test mainly selects three main factors: the rotational speed of the transverse device, the vertical clamping speed and the center distance of the roller. The main evaluation index of the experiment was the loss rate of the transported reed stalk. In the EDEM software, Bond Status can determine whether the reed stalk has broken. As shown in Figure 7, the whole reed stalk is connected into a whole.

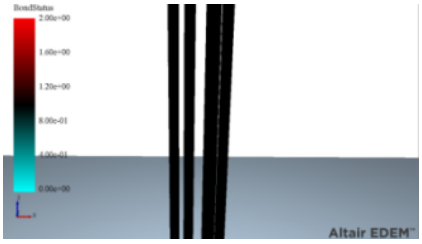


Fig. 7 – Bond Status of flexible reed stalks during EDEM analysis

Test protocol design

In this paper, Box-Behnken method was used to establish a mathematical model between the three factors of the transverse transfer device speed, the lower conveying speed and the active drum speed and the two evaluation indexes of reed stem loss rate, and the optimal parameter combination and the optimal response value were analyzed and found out. The test code table is shown in Table 7:

Table 7

Code list of discrete element simulation test of horizontal transfer and longitudinal clamping conveying device

Factor	Level		
	-1	0	1
A: The center distance of the drum (mm)	400	500	600
B: Transverse conveyor speed (r/min)	30	50	70
C: Upright clamping longitudinal conveyor speed (r/min)	30	50	70

A three-factor and three-level orthogonal test scheme was adopted in the experiment. The center distance of the drum A, the speed of the transverse transfer device B and the speed of the vertical clamping longitudinal transport device C were selected as the test factors. The loss rate of the flexible discrete element model of reed stalk was used as the test index.

Simulation sand analysis

As shown in Figure 8, at the beginning of the simulation, the particle factory generated a flexible reed stalk near the tooth, and the reed stalk continuously accelerated downward movement. Then move from both sides to the center. When the teeth move to the center position, the flexible reed stalk is transferred to the gripper conveyor belt behind the conveyor drum.

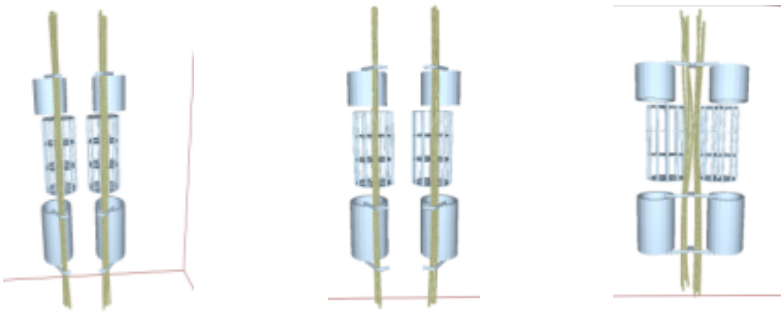


Fig. 8 - Simulation process analysis of transporting reed stalks with a device



Fig. 9 – Bond Status of flexible reed stalks during simulation

(a) Bond Status when there is no breakage (b) Bond Status when there is breakage

As shown in Figure 9 (a), when the reed stem is not in contact with the picking teeth, one rigid reed stem unit is bonded together by a bonding bond. When the reed stem is subjected to external forces, the surface of the reed stem skin will maintain a stable shape, which can effectively reduce the damage of external forces on the reed stem.

As shown in Figure 9 (b), when the flexible reed straw is too stressed in instantaneous time, the bond will be completely disconnected, and each rigid reed unit spreads under the influence of gravity. At this time, the reed straw is broken.

Analysis of the simulation results

In this test, the three-factor and three-level test protocol design was conducted by using the Box-Behnken test design method in Design-Expert *(Tumuluru et al., 2023)*. The response surface test protocol and results are shown in Table 8.

Table 8

Simulation analysis of transverse transfer and vertical clamping conveying process

Order number	A (mm)	B (r/min)	C (r/min)	Loss rate R (%)
1	1	0	1	5.9
2	0	1	1	7.2
3	0	0	0	4.8
4	1	0	-1	7.4
5	0	1	-1	7.8
6	0	-1	1	6.6
7	0	-1	-1	6.3
8	0	0	0	4.9
9	-1	-1	0	6.6
10	0	0	0	5.1
11	-1	0	-1	5.8
12	1	1	0	8.2
13	1	-1	0	6.8
14	0	0	0	5
15	-1	1	0	7
16	0	0	0	4.8
17	-1	0	1	5.6

Using Design-Expert software to fit the above results, the second-order regression model of the lateral transmission device speed, the vertical clip speed and the center distance of the roller was analyzed by variance, and obtained the results as shown in Table 9.

Table 9

Analysis of variance of simulation results

1	quadratic sum	free degree	mean square	F value	P value
model	18.84	9	2.09	41.21	<0.0001
A	1.36	1	1.36	26.80	0.0013
B	1.90	1	1.90	37.44	0.0005
C	0.50	1	0.50	9.85	0.0164
AB	0.25	1	0.25	4.92	0.0620
AC	0.42	1	0.42	8.32	0.0235
BC	0.20	1	0.20	3.99	0.0860
A2	2.15	1	2.15	42.38	0.0003
B2	9.66	1	9.66	190.29	<0.0001
C2	1.23	1	1.23	24.18	0.0017
Residual	0.36	7	0.051		
Lack of Fit	0.29	3	0.096	5.64	0.0641
Pure Error	0.068	4	0.017		
Cor Total	19.19	16			

From Table 9, the P value of the regression model =0.0001 <0.05, and the model is extremely significant, while the misfit term is 0.0641> 0.005, indicating a high degree of fit. The results of ANOVA showed that the regression model of reed stalk has high confidence in the prediction of flexible reed stalk.

The regression equation for this regression model is:

$$R=4.92+0.41A+0.49B-0.25C+0.25AB-0.33AC-0.22BC+0.71A^2+1.52B^2+0.54C^2 \quad (2)$$

Field testing

In order to verify the effect of crawler self-propelled reed harvester, this paper conducted a preliminary field test. In the field test map shown in Figure 10, the reed harvesting function was successfully divided, and there were few unharvested reed stalks in the process of dialing, and the whole cutting table device was not stuck or blocked. The best parameter combination of the test results is shown in Table 10.



Fig. 10 - Field test of crawler self-propelled reed harvester header

Table 9

Optimum parameter combination for the test results

Parameter	Optimal working speed of the header transverse toggle device (r/min)	The cutter holds the optimal longitudinal conveyor speed (r/min)	Minimum loss rate
value	49	51	3.6%

DISCUSSION

Figure 11 shows the response surface of the speed B of the transverse transfer device and the speed C of the vertical clamping longitudinal transfer device to the loss rate R when the center distance of the cylinder A is 500 mm. It can be seen from the figure that when the speed of the transverse transmission device B is fixed, under the speed condition of 30 ~ 42 r/min, the loss rate R decreases significantly with the increase of the speed of the vertical clamping longitudinal transmission device C, and maintains a low loss rate between 42 ~ 64 r/min, and then the loss rate rises slowly. When the vertical clamping longitudinal conveying device C is fixed, under the speed condition of 30 ~ 42 r/min, the loss rate R decreases significantly with the increase of the transverse transmitting device speed B, and maintains a low loss rate in 42 ~ 52 r/min, and then the loss rate rises slowly. It can also be seen from the figure that the influence of the speed of the transverse transfer device B on the loss rate is more significant than that of the vertical clamping longitudinal transmission device C.

Figure 12 shows the response surface of the cylinder center distance A and the vertical clamping longitudinal conveying device C to the loss rate R when the rotating speed of the transverse transfer device B is 50 r/min. It can be seen from the figure that when the center distance of the cylinder A is fixed, the loss rate R decreases significantly with the increase of the speed of the vertical clamping longitudinal conveying device C at the speed of 30 ~ 42 r/min, and maintains a low loss rate at 42 ~ 64 r/min, and then the loss rate slowly rises. When the speed of vertical clamping longitudinal conveying device C is fixed, the loss rate R increases significantly with the increase of the distance between the center of the cylinder and A under the condition of 400 ~ 420 mm, and maintains a low loss rate between 400 ~ 420 mm, and then the loss rate increases slowly. It is obvious from the figure that the impact of cylinder center distance A on the loss rate is more significant than that of the vertical clamping longitudinal conveying device speed C.

Figure 13 shows the response surface of the cylinder center distance A and the transverse transfer device speed B to the loss rate R when the speed of the vertical clamping longitudinal conveying device C is 50 r/min. As can be seen from the figure, when the center distance of the cylinder A is fixed, under the condition of 30 ~ 42 r/min, the loss rate R decreases significantly with the increase of the speed B of the transverse transmission device, and maintains a low loss rate between 42 ~ 52 r/min, and then the loss rate rises slowly. When the transverse transfer device B is fixed, the loss rate R increases significantly with the increase of the speed of the cylinder center distance from A at the speed of 400 ~ 430 mm, and maintains a low loss rate at 430 ~ 520 mm, and then the loss rate slowly rises. It can be seen from the figure that the impact of the loss rate R on the center distance of the cylinder A is more significant than that on the center distance of the cylinder.

In the experiment, the working speed of the transverse transfer device of the cutting table is 49 r/min, the working speed of the vertical clamping device of the cutting table is 51 r/min, and the field advance speed of the harvester is 1.1 m/s, which is consistent with the simulation analysis results in this paper. Finally, the reed harvester conducted field tests again to verify this parameter combination, and the loss rate of the reed

harvester cutting table device was measured to be about 3.6%, which verified the reliability of the parameter combination, and also verified that the crawler self-propelled reed harvester cutting table device designed in this paper can harvest reed crops with low loss and high efficiency.

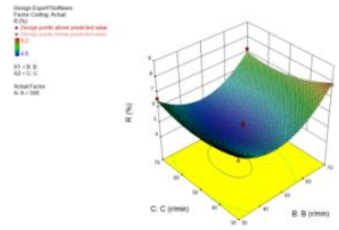


Fig. 11 - Influence of B and C on R when A is 500 mm

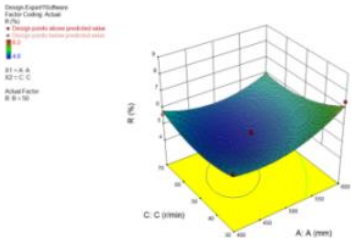


Fig. 12 - Influence of B and C on R when A is 500 mm

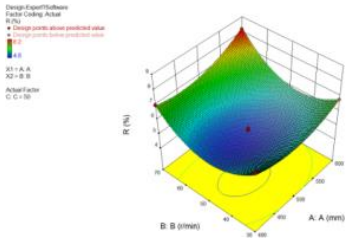


Fig. 13 - When C is 50 r/min, the influence of A and B on R

CONCLUSIONS

In this paper, the discrete element method was used to test the working speed of the transverse conveying device of the header, the working speed of the vertical clamping longitudinal conveyor and the field forward speed of the harvester, and the loss rate of the header of the reed harvester was used as the test index. The Box-Behnken orthogonal test method is used to establish the mathematical model of the above factors and indicators, and the optimal combination of parameters is obtained by multi-factor response surface analysis, and the specific conclusions are as follows:

(1) The basic rigid element and discrete element rigid model of reed stem were established by the method of multi-sphere filling and layering.

(2) Then the rigid flexible element is bonded into flexible element by Hertz-Mindlin with bonding contact model, and the discrete element flexible model of reed stalk is established.

(3) Then, a three-point bending test was carried out in EDEM software to complete the calibration of bond parameters necessary for the establishment of discrete element flexible model of reed stalk.

(4) The simulation results show that the optimal parameter combination is 46 r/min for the rotating speed of the transversal transmission device. The rotational speed of the vertical clamping longitudinal conveying device is 53 r/min. The center distance of the rollers is 470 mm.

(5) The results of the field test show that the working speed of the transverse transfer device of the cutting table is 49 r/min, the working speed of the vertical clamping device of the cutting table is 51 r/min, and the field advance speed of the harvester is 1.1 m/s. The optimal parameter combination is not much different from the simulation results in this paper. Finally, the reed harvester conducted field tests again to verify this parameter combination, and the loss rate of the reed harvester cutting table device was measured to be about 3.6%, which verified the reliability of the parameter combination, and also verified that the crawler self-propelled reed harvester cutting table device designed in this paper can harvest high-stalk reed crops efficiently. Due to time and environmental reasons, this paper has made a preliminary test of the reed harvester, but the feasibility of the scheme has been verified. In the future, this paper will continue to test, and further improve the performance of the harvester.

ACKNOWLEDGEMENT

This study was supported by the 2019 Jiangsu Provincial Science and Technology Plan Project (Key Project) (BE2019360), and each author helped me in my paper and experiment.

REFERENCES

[1] Andrewg, P., (2011). Development and validation of calibration methods for discrete element modelling. *Granular Matter*, Vol. 13(2), pp.127-132, America.

[2] Bart, L., Engelbert, T., Bart, D., Herman, R., Josse, D., & Wouter, S., (2014). Simulation of grain-straw separation by discrete element modeling with bendable straw particles. *Computers and Electronics in Agriculture*, Vol. 101, pp. 24-33, England.

[3] Ivan G., Ciupeca R., & Moise V., (2017). Kinematic scheme of equipment to reed harvesting machine MRS. *Engineering for Rural Development*, vol. 05, pp. 24-26, Latvia.

[4] Gonzalez, M., Fuentes, J., Ayuga, T., (2012). Determination of the mechanical properties of maize grains and olives required for use in DEM simulations. *Journal of Food Engineering*, Vol. 111(4), pp. 553-562, American.

[5] Hou, J., Xie, F., Wang, X., Liu, D., & Chen, Z., (2022). Determination of physical parameters of rice stalk contact and simulation calibration of discrete elements (水稻茎秆接触物理参数测定与离散元仿真标定). *Journal of Jiangxi Agricultural University*, Vol. 44(03), pp. 747-758, Jiangxi/China.

[6] Jin, J., (2014). Design and research of key components of reed harvesting vessels (芦苇收割船关键部件的设计与研究). *Agricultural University of Hebei*, Hebei/China.

[7] Liu, F., (2018). Discrete element modeling of wheat particles and short stalks in the cleaning device (清选装置中小麦颗粒和短茎秆离散元建模研究). *Northwest A & F University*, Shanxi/China.

[8] Lv, J., Liu, J., Zhao, Z., Yang, D., Li, J., & Sun, Q., (2023). Design and test of combined potato crusher and soil preparation machine (马铃薯碎土整地联合作业机设计与试验). *Journal of Agricultural Machinery*, Vol. 54 (08), pp. 19-29, Beijing/China.

[9] Luigi, P., Maria, D., Javier, S., (2016). Economic and energy analysis of different systems for giant reed. *Industrial Crops and Products*, Vol. 84, pp. 176-188, Holland.

[10] Liu, Y., (2021). *Design and testing of key components of chain cutting table for oil sunflower combine harvester (油向日葵联合收割机链切台关键部件的设计与试验). Huazhong Agricultural University*, Hubei/China.

[11] Ma, Q., Tian, L., & Wu, X., (2010). Design of 4WS2000 high pole reed harvester cutter table 4WS2000 (高杆芦苇收割机割台的设计). *Journal of Central South University of Forestry and Technology*, vol.30 (10), pp. 138-142, Han/China.

[12] Ni, Z., Ni, S., & Shen, Y., (2021). An elevated reed harvesting and baling device. CN214046684U, Jian gsu /China.

[13] Martelli R., Bentini M., Monti A., (2015). Harvest storage and handling of round and square bales of giant reed and switch grass, an economic and technical evaluation. *Biomass and bioenergy*, Vol. 83, pp. 551-558, England.

[14] Tumuluru, S., Armijo, B., Whitelock, P., (2023). Modeling and Optimization of High-Capacity Experimental Reclaimers to Minimize the Seed and Lint Loss during Roller Ginning of Upland and Pima Cotton. *Processes*, Vol. 11(10), pp.2868, Switzerland.

[15] Tong, S., Shao, M., Cao, M., & Zhao, J., (2023). Parameter calibration of corn stalk discrete element model based on DEM (基于 DEM 的玉米秸秆离散元模型参数标定). *China Agricultural Machinery and Chemical News*, 44(02), 69-75. Nanjing/China.

[16] Wang, G., Hao, W., Wang J., (2010). *Discrete cell method and its practice on EDEM (离散单元法及其在 EDEM 上的实践)*. Xian Polytechnic University Press, Xian/China.

[17] Wang, W., Liu, W., Yuan, L., Qu, Z., He, X., & Lv, Y., (2020). Wheat plant modeling and single longitudinal axial flow material movement simulation and experiment (小麦植株建模与单纵轴流物料运动仿真与试验). *Journal of Agricultural Machinery*, Vol. 51(S2), pp. 170-180, Beijing/China.

[18] Yuan, C., (2014). *High-rod crop harvester*. CN102652475B. Hunan /China.

[19] Yidong, X., Jordan, K., Tiasha, B., (2023). An experiment-informed discrete element modelling study of knife milling for flexural biomass feedstocks. *Biosystems Engineering*, Vol. 236, pp. 39-53, England.

[20] Yuan, W., Kuang, H., (1987) Type 4GL-130 reed harvester. *Agricultural machinery*, vol. 08, pp.17. Beijing/China.

[21] Zhou, J., Sun, W., Liang, Z., (2023). Construction of discrete flexible model during harvest (收获期菊芋根-块茎离散元柔性模型构建研究). *Journal of Agricultural Machinery*, Vol. 5, pp.1-16, Beijing/China.

[22] Zhang, T., Liu, F., Zhao, M., Ma, G., Wang, W., Fan, Q., & Yan, P., (2018). Measurement of contact physical parameters of corn stalk and discrete element simulation calibration (*玉米秸秆接触物理参数测定与离散元仿真标定*). *Journal of China Agricultural University*, Vol. 23(04), pp.120-127, Beijing/China.

TRIZ-AIDED DESIGN AND EXPERIMENT OF KIWIFRUIT PICKING END-EFFECTOR
/
TRIZ 辅助猕猴桃采摘末端执行器设计与试验

Min FU*, Shike GUO, Jianan CAI, Jiacheng ZHOU, Xiaoyi LIU
Northeast Forestry University, College of Mechanical and Electrical Engineering, Harbin / China;
Tel: +86 15663688203; E-mail: fumin1996@163.com
DOI: https://doi.org/10.35633/inmateh-71-31

Keywords: *kiwifruit; picking end-effector; multi-fruits envelope-cutting; TRIZ (Theory of Inventive Problem Solving)*

ABSTRACT

Currently kiwifruit picking process mainly leverages manual labour, which has low productivity and high human effort, meanwhile the existing kiwifruit picking machinery also has low picking efficiency and easily damages fruits. In this regard within this paper, a multi-fruit envelope-cutting kiwifruit picking end-effector was designed by applying TRIZ assistance. Firstly, a common kiwifruit picking end-effector was selected as the prototype system. The functional analysis method of TRIZ was applied to identify the functional defects of the system. TRIZ solution tools such as technical contradiction analysis, substance-field analysis, and trimming were utilized to improve and innovate the system, resulting in the design of a kiwifruit picking end-effector that recognizes fruits, envelops fruit clusters, cuts and separates fruit stalks, and is capable of picking kiwifruit in clusters. Then, simulation software ADAMS was applied to perform gait simulation of the end-effector picking action to verify the smoothness and coherence of the picking process. Finally, a kiwifruit picking test stand was set up to conduct picking tests in the form of fruit clusters. The results showed that the average time to pick each cluster of fruits was 8.8 s, the picking success rate was 89.3%, and the picking damage rate was 6.0%. All the indicators were better than the prototype and met the expected design requirements.

摘要

目前，在猕猴桃收获过程中多采用人工采摘作业，生产率低、劳动强度大，而现有的猕猴桃采摘机械也存在采摘效率低、易损伤果实等问题。对此，本文应用 TRIZ 理论辅助设计了一种多果包络切割式的猕猴桃采摘末端执行器。首先，选取一种常见的猕猴桃采摘末端执行器为原型，应用 TRIZ 的功能分析方法识别其存在的功能缺陷，并应用技术矛盾分析、物场分析、裁剪等 TRIZ 解题工具进行改进创新，设计了一种自动识别果实-包络果实簇-切割分离果梗的猕猴桃采摘末端执行器，可对猕猴桃成簇采摘。然后，应用仿真软件 ADAMS 对末端执行器的采摘动作进行步态仿真，验证采摘过程的平稳连贯性。最后，搭建猕猴桃采摘试验台，以果实簇的形式进行采摘试验。结果表明，该末端执行器采摘每簇果实平均用时为 8.8s，采摘成功率为 89.3%，采摘损伤率为 6.0%，各项指标均优于原型系统，符合预期设计要求。

INTRODUCTION

Kiwifruit is rich in nutritional value, known as the "king of fruit", and has a very large market demand. China is the world's largest agricultural country in terms of kiwifruit planting area and production, with its annual yield exceeding 3 million tons *(Fazayeli et al., 2019)*. The kiwifruit industry in China is still labour-intensive compared to developed countries, which especially manifests in the time-consuming and laborious harvesting process *(Yuan et al., 2020)*. With the scale-up of the kiwifruit planting industry, the traditional manual picking method is difficult to meet the current market demand. Therefore, the study of kiwifruit picking robots not only helps to reduce labour costs, and improve picking operation efficiency and kiwifruit high quality rate but is also of crucial importance for realizing the mechanization and standardization of the kiwifruit industry *(Guo et al., 2022; Li et al., 2022)*.

In recent years, scholars have conducted a series of studies on fruit and vegetable picking robots such as kiwifruit *(Williams et al., 2019; Williams et al., 2020)*, citrus *(Sun et al., 2023; Yin et al., 2023)*, apple *(Yan et al., 2021; Hu et al., 2022)*, cucumber *(Mao et al., 2020; Kim et al., 2023)*, tomato *(Feng et al., 2018; Wang et al., 2023)* and so on. However, improving fruit-picking efficiency and ensuring non-destructive fruit picking are two key criteria of fruit-picking robots, in which non-destructive picking is mainly ensured by the end-effector. For example, *Fu et al., (2015)*, designed a clamp-type kiwifruit picking end-effector in which the fruit was held by the clamping mechanism and automatically rotated to separate the fruit from the stalk.

Silwal et al. (2017), developed a clamping-type apple picking end-effector, consisting of three drivers and three fingers. After gripping the fruit with the three fingers, the base drove the fruit to rotate until it separated from the stalk. *Xu et al., (2018),* designed a suction-type navel orange picking end-effector, which utilized a suction cup to hold the fruit and a cutting blade to separate the fruit from the stalk. *Xiong et al. (2019),* designed a clamping-type strawberry picking end-effector, which separated the fruit from the stalk by pulling when the fruit was sucked. *Mu et al., (2020),* designed a clamp-type kiwifruit picking end-effector that used two bionic fingers to separate the fruit from the stalk by repeatedly bending the fingers after the fruit was clamped. *Xu et al., (2023),* designed a clamp-type broccoli picking end-effector to harvest broccoli by clamping-cutting method.

The above studies provide useful insights for the development of harvesting techniques for kiwifruit and other fruits and vegetables. However, the current kiwifruit picking end-effector is mostly of single-fruit clamping or sucking structure, which is prone to two problems during the fruit picking process: ① Picking kiwifruit by clamping or sucking is unstable when gripping the fruit, therefore leading to fruit loss. ② Approximately 87% of kiwifruit are distributed in clusters in the canopies *(Fu et al., 2018)*, and the use of single-fruit picking is highly possible to disturb neighbouring fruits, therefore leading to fruit drop.

TRIZ (Theory of Inventive Problem Solving) is a systematic and structured innovation methodology (*Altshuller et al., 1984*). The process of applying TRIZ to innovation design can be divided into four parts. Part I is problem description: The function, working principle, composition, and existing issues in the prototype system is described. Part II is problem analysis: TRIZ analytical tools such as functional analysis and cause analysis are utilized to find the functional deficiencies of the prototype system, and to explore the root causes of the problems. Then starting point can be caught to resolve these issues. Part III is problem- solving: problem-solving tools such as contradiction analysis and substance-field analysis are used to find innovative solutions. Part IV is scheme decision-making: all conceptual schemes are cross evaluated in terms of economy and implementability, etc, and the final implementation schemes are determined after selection and synthesis. It has been demonstrated in practice (*Yang et al., 2018; Azammi et al., 2018; Kang et al., 2022*), that TRIZ is applied to product design that can assist designers in triggering inspiration from different dimensions, finding solutions in a broader field, and improving the quality and efficiency of design.

Considering that the current kiwifruit picking robots lack design theory guidance in structure and usually have long design cycles as well as low product success rates, TRIZ was used to guide the conceptual design of a kiwifruit-picking end-effector. First, TRIZ tools were applied to analyse the problems of the prototype system and to improve and innovate it, and a multi-fruits envelope-cutting-type kiwifruit picking end-effector was designed. Then, ADAMS was applied to perform a gait simulation of the end-effector picking action to verify the effectiveness of the expected operation. Finally, a kiwifruit-picking test stand was set up to verify the working effect of the kiwifruit-picking end-effector.

MATERIALS AND METHODS

Background

Kiwifruit belongs to vine plants, and the trellis planting mode is mostly used in orchards, as shown in Figure 1. The fruit hangs down on the vine of the fruit tree in a clustered distribution, with a large bottom space and no interference from branches, leaves, etc., which is conducive to the implementation of the picking action *(Fu et al., 2015)*. The average lateral spacing of the trellis is 4 m, the longitudinal spacing is 2 m and the height is 2 m. The fruits are generally distributed within a spatial range of 1.5~1.8 m above the ground, with a cluster of 3~7 fruits.

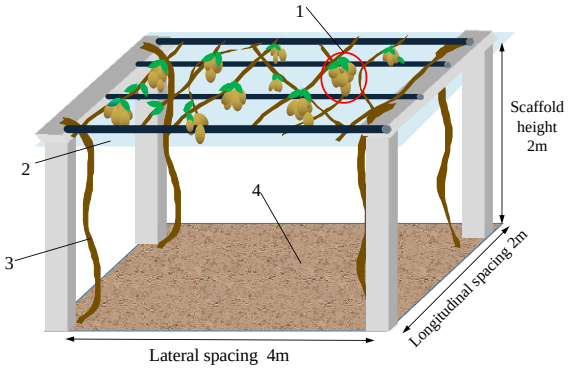


Fig. 1 - Equivalent model of trellis space

1. kiwifruit cluster; 2. trellis model; 3. kiwifruit tree; 4. ground level

According to the growth characteristics and planting environment of kiwifruit in the orchard, the expected picking indicator of the kiwifruit picking end-effector is a fruit picking speed of 7-10 s/cluster, with a success rate of over 90% and a fruit damage rate of less than 10%.

The kiwifruit-picking robot is mainly composed of an end-effector, a mobile device, a support device, and a collection device. During the robot working process, the end-effector plays a key role, which directly affects the picking efficiency and fruit damage rate of the picking robot. While the existing picking end-effector has the problem of low picking efficiency and easy fruit damage. To solve the above problems, a common kiwifruit picking end-effector was selected as a prototype in this paper, and TRIZ theory was applied to analyse the key structural defects and an improvement scheme was proposed.

Problems of the Prototype

1) Overall Structure: A common structure of clamped-type picking end-effector *(Rong et al., 2019)*, as shown in Figure 2, is mainly composed of a clamping support frame, drive screw, ball screw, fruit stalk clamping fingers, identification sensor, V-shaped gripper, stepper motor, frame.

2) Working Principle: First the position of the fruits is detected by the recognition sensor, and the V-shaped gripper is driven by the stepper motor to clamp the fruit with a preset clamping force. Then, the clamping stepper motor drives the fruit stalk clamping fingers to clamp the fruit stalk, and the linear stepper motor drives the clamping support frame forward by the drive screw (The fruit stalk clamping fingers are installed on the clamping support frame). Finally, the stalk is separated from the fruit by the pulling force of the fruit stalk clamping fingers and the fruit is picked completely.

3) Experimental indicators of the prototype *(Rong et al., 2019)*: The success rate of fruit picking is 86%, the fruit damage rate is 8%, and the average picking time of a single fruit is 17±0.5 s.

4) Existing problems: The pulling force on the fruiting stalk is excessive, which may easily damage the fruit. There are also problems during the picking process such as the weak ability to recognize fruits and the insufficient ability to clamp fruits.

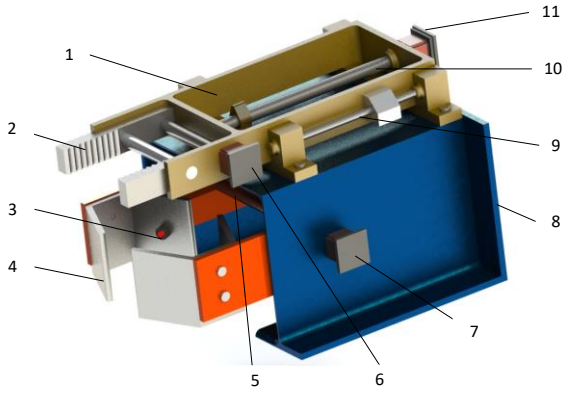


Fig. 2 - Clamp-type kiwifruit picking end-effector

1. clamping support frame; 2. fruit Stalk clamping fingers; 3. recognition sensor; 4.v-shaped gripper; 5. ball screw; 6. clamping stepper motor; 7. drive stepper motor; 8. frame; 9. guide rail slider; 10. drive screw; 11. linear stepper motor

TRIZ-Aided Design of End-Effector

The end-effector is installed at the front end of the robotic arm, and its main function is to pick fruit. It is mainly composed of three parts: a fruit clamping device, a fruit and stalk separation device and a recognition device.

System Function Analysis of the Prototype

System function analysis is one of the most important tools in TRIZ for analysing problems, where the interactions of system components are analysed for accomplishing function *(Fu et al., 2021).* In this paper, the system function model of the end-effector was established by the system function analysis, the functional relationship between the components in the system was clarified, and the functional defects of the end-effector were found, which provided the direction for the subsequent improvement and innovation.

Name of technical system: picking end-effector.

Function of the system: separation of the fruit from the stalk.

The objects of the system: fruit and stalk.

Components of the system: V-shaped gripper, recognition sensor, ball screw, drive stepper motor, fruit stalk clamping fingers, clamping stepper motor, clamping support frame, guide rail slider, linear stepper motor.

Components of super-system (Super-system is external components that exist outside the system and have an impact on the current system): Frame.

The functional relationship among functional objects, system components, and super-system components was analysed, and the system function model was established in Figure 3.

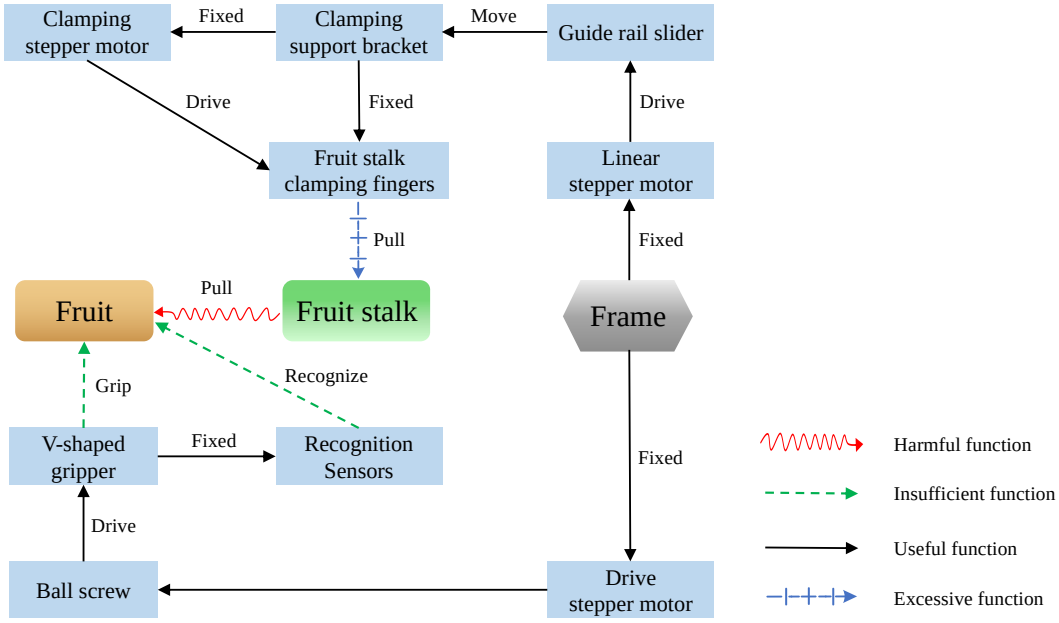


Fig. 3 - System function model of the prototype

As shown in Figure 3, the prototype has three functional defects: ① the V-shaped gripper has insufficient ability to grip fruits, which can easily cause fruit detachment. ② insufficient recognition of fruits by recognition sensors, resulting in low fruit-picking efficiency. ③ in the process of pulling off the stalk by the fruit stalk clamping fingers, the stalk can easily cause damage to the fruit skin.

Next, for the functional defect ① of the prototype, the technical contradiction analysis tool in TRIZ was applied to improve and innovate the design of the fruit clamping device; For the functional defect ②, the substance-field analysis tool in TRIZ was applied to improve and innovate the design of the recognition device; For the functional defect ③, the trimming tool in TRIZ was applied to improve the innovative design of the fruit and stalk separation device.

Design of Fruit Clamping Device

The technical contradiction analysis is one of the tools for problem-solving in TRIZ and refers to the contradiction where one parameter of a technical system is improved and causes another parameter to deteriorate. Technical contradictions are defined by TRIZ through 39 general engineering parameters and then the problem is solved according to the innovation principles recommended by the contradiction matrix table *(Fu et al., 2021)*.

For functional defect ①, the technical contradiction was defined: If the size of the V-shaped gripper was increased, then kiwifruits with different shapes could be adequately gripped, but it increased the weight of the end effector, which led to inconvenient movement and reduce fruit picking efficiency; If the size of the V-shaped gripper was reduced, then the weight was reduced, but it couldn't adequately grip various shapes of kiwifruit.

In this technical contradiction, the improved parameter is NO.35 (adaptability or versatility), and the deteriorated parameter is NO.1 (weight of moving object). Finding the contradiction matrix table to obtain the reference innovative principles: NO1 (Segmentation), NO6 (Universality), NO15 (Dynamicity), and NO8 (Counterweight). To address the lack of adaptability and versatility of the end-effector, valuable inventive principles were screened, and 2 conceptual solutions were proposed, as shown in Table 1.

Table 1

Analysis of valuable inventive principles

Serial number	Principle	Valuable content in detail	Conceptual solution
1	Universality	Enabling an object to perform many different functions	A device that could both adequately pick kiwi fruit of all shapes and assist in the collection of the fruit was installed to reduce the complexity of the mechanical system when picking the fruit.
2	Dynamicity	Increasing the motion of an object by turning its immobile parts into moving ones	Making the clamping device movable, and when picking kiwifruits of various shapes, the range of fruits surrounded could be adjusted by moving the clamping device.

From the above analysis, synthesizing conceptual solutions 1 and 2, a fruit clamping device was designed, as shown in Figure 5. The clamping device was designed as an envelope-type picking bin structure. During the picking process, the end effector moves upwards from the bottom of the kiwifruit, surrounding a cluster of fruits into the picking bin, achieving full clamping of the picked fruits. Meanwhile, a fruit collection end was added to the lower end of the picking bin, which could assist in the collection of fruits and improve the picking efficiency.

Design of Recognition Device

The substance-field analysis is one of the tools for problem-solving in TRIZ. The most basic substance field model is composed of three basic elements: S2 represents the tool (functional performer), S1 represents the object of action (functional receiver), and F is the interaction field between them. The problematic substance-field model is solved with 76 standard solutions from TRIZ *(Fu et al., 2021)*.

For the functional defect ②, the substance-field model of the problem was established, as shown in Figure 4(a). The light Field generated by S2 (the recognition sensors) couldn't adequately recognize S1 (the fruits). The TRIZ standard solution S2.1.2 was applied, and the substance-field model of the solution was shown in Figure 4(b).



(a) substance-field model of the problem *(b) substance-field model of the solution*

Fig. 4 - Substance-field analysis model

F-field, S1-object of action, S2-tool.

Conceptual solution 3 was proposed by the substance-field analysis: A colour detection sensor was installed on the baffle at the port of the picking bin and the detected colour was set to tan (the colour of the fruit is tan, and the colour of the fruit stalk is dark green). Meanwhile, two fruit recognition sensors were installed on the side panel of the picking bin, as shown in Figure 5. After the fruits were recognized by fruit recognition sensors, the end-effector moved upward to envelop the fruits into the picking bin. When the colour detection sensor detected that all the picked fruits had entered the picking bin, the end effector stopped moving.

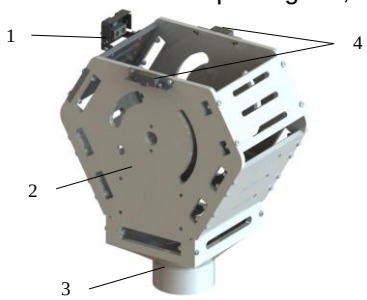


Fig. 5 - Structure of envelope-type picking bin

1. colour detection sensor; 2. envelope picking bin; 3. fruit collection end; 4. fruit recognition sensor

Design of Separation Device for Fruit Stalks

Trimming is one of the important tools for problem-solving in TRIZ. The principle of trimming is to optimize the functional structure of the system and improve the ideality by deleting or replacing the problematic components and redistributing the useful functions *(Fu et al., 2021)*.

For the functional defect ③, the TRIZ trimming tool was applied to analyse and solve the problem. In the process of pulling off the stalk by the fruit stalk clamping fingers, the stalk would pull on the fruit and cause damage to it. Therefore, the fruit stalk clamping fingers were identified as the trimming object, but their useful function needed to be retained. According to the trimming rule, "the function of the problematic component is replaced by the newly added component", a rotating cutter device was used to replace the fruit stalk clamping fingers to complete the useful function of pulling the stalk.

Conceptual solution 4 was proposed by the trimming tool as shown in Figure 6. The rotary cutter rotated clockwise at a preset speed to cut off the stalks of the fruits in the picking bin. Then, driven by the rotary stepper motor, the rotary cutter continued to rotate until it stopped at 180° from the initial position, waiting for the next picking. The rotary cutter device rotated one circle and could complete two cutting operations on the fruit stalks.

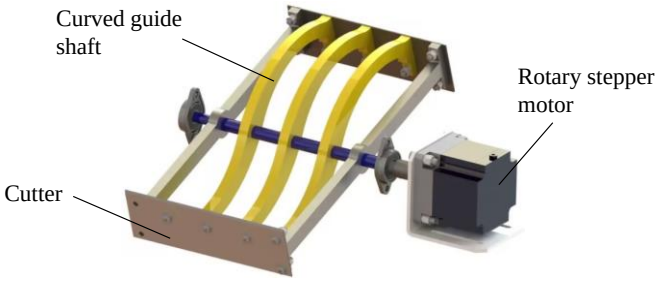


Fig. 6 - Schematic diagram of the rotary cutter structure

Structure and Working Principle of End-Effector

Synthesizing the above conceptual solutions, a multi-fruit envelope-cutting-type kiwifruit picking end-effector was designed, as shown in Figure 7. First, the end effector was delivered by the robotic arm to the appropriate kiwifruit picking area, then the recognition sensor started to scan the surrounding fruits. After recognizing the fruits, the robotic arm with the end-effector moved upward to envelop the fruit into the picking bin. Then, when the colour detection sensor detected that all fruits had entered the picking bin, the robotic arm stopped moving. The rotary cutter rotated clockwise to cut off the fruit stalks in the picking bin. Finally, the fruits slowly passed through the picking bin along the curved guide shafts and fell into the fruit collection end, completing a single picking process. The end-effector adopts the operation mode of enveloping the fruits - cutting the fruit stalks, it could realize the continuous picking of multiple fruits, improve the picking efficiency, and reduce the damage rate of the fruits.

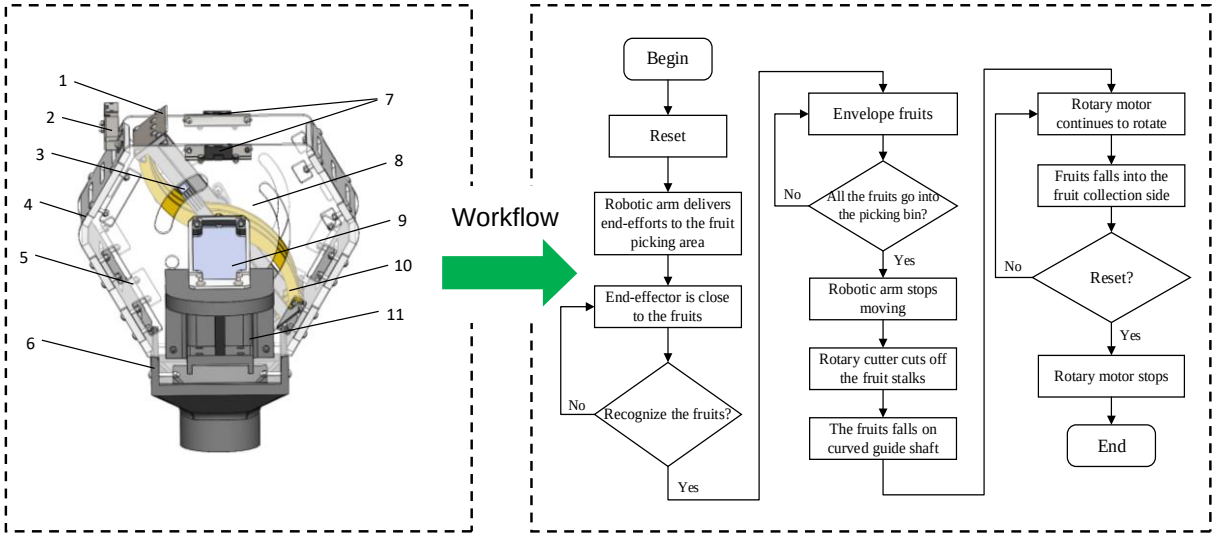


Fig. 7 - Schematic diagram of the end-effector structure and workflow

1. blade; 2. colour detection sensor; 3. hall sensor; 4. Baffle; 5. side plate; 6. fruit collection end; 7. fruit recognition sensor; 8. picking bin; 9. rotary stepping motor; 10. curved guide shaft; 11. connector.

The parameters of the kiwifruit-picking end-effector are shown in Table 2.

Table 2

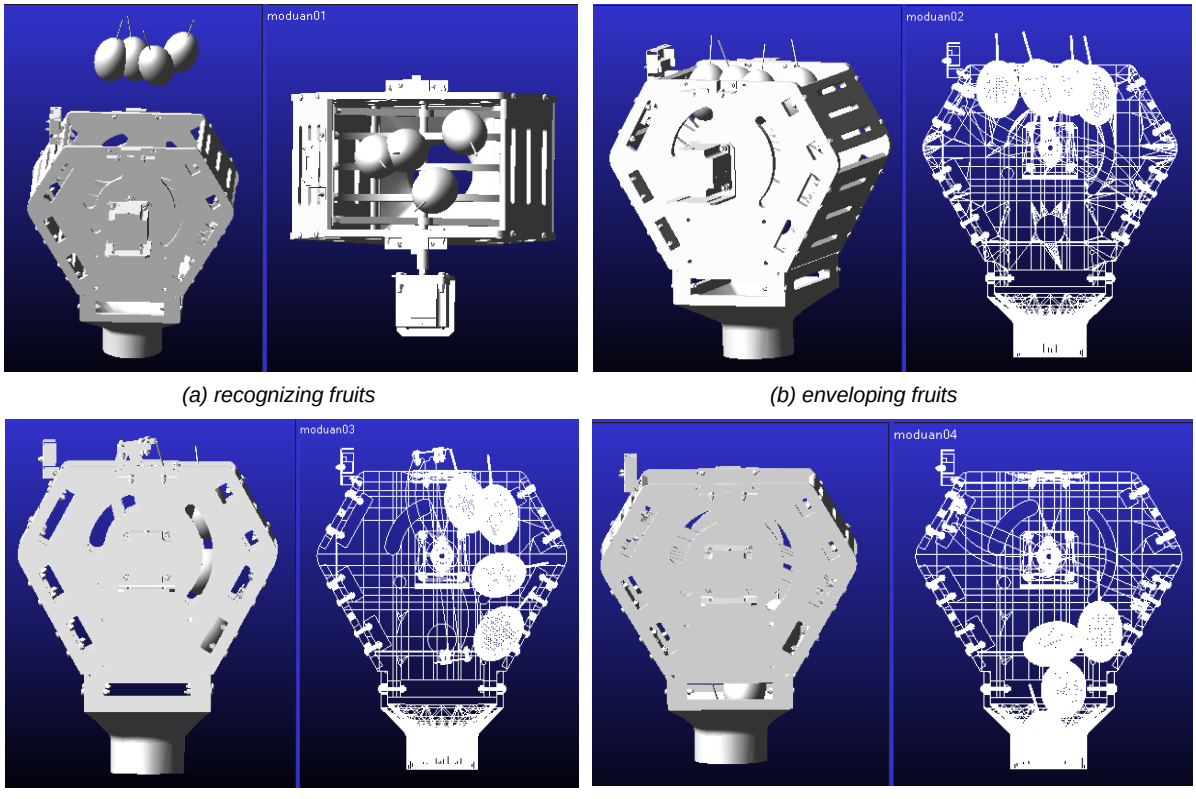
Parameters of the kiwifruit picking end-effector

Parameters	Numerical value
Weight of end-effector/kg	4
Lifting height of robotic arm/m	0~0.9
Operating speed of robotic arm/ (m.s-1)	1.5
Speed of stepper motor/(r.min-1)	6

RESULTS

Dynamics Simulation Analysis

To verify whether there is interference between the various mechanisms of the kiwifruit-picking end-effector and whether the picking action is smooth and coherent during the fruit-picking process, a fruit cluster of four kiwifruits was selected, with each kiwifruit having approximate dimensions of 65 mm in length, 52 mm in width, and 45 mm in thickness. ADAMS was used to simulate and analyse the picking action of the end-effector, including four motion gaits of identifying the fruits, enveloping the fruits, cutting off the fruit stalks and resetting the end-effector. The simulation results are shown in Figure 8.



(a) recognizing fruits *(b) enveloping fruits*

(c) cutting fruit stalks *(d) resetting the end-effector*

Fig. 8 - Simulation of end-effector picking action

STEP1: The end-effector recognized the kiwis by the fruit recognition sensors. STEP2: The robotic arm with the end-effector moved upward to envelop the fruits into the picking bin. STEP3: After the colour detection sensor detected that all fruits had entered the picking bin, the rotary cutter rotated clockwise to cut off the fruit stalks in the picking bin; STEP4: During resetting the end-effector, the fruits slowly passed through the picking bin along the curved guide shafts and fell into the fruit collection end. The simulation results showed that during the process of picking the fruit clusters, the various mechanisms of the end-effector were coordinated and non-interfering with each other, and the operation was smooth and coherent, which was in line with the expected design requirements.

Test Stand Set Up

A picking test stand was set up in a laboratory conducting picking trials as shown in Figure 9. The test stand mainly includes: the AUBO-E5 robotic arm test stand, trellis model, the kiwifruit picking end-effector and its control system, Lenovo R7000P portable computer, collection device, etc.

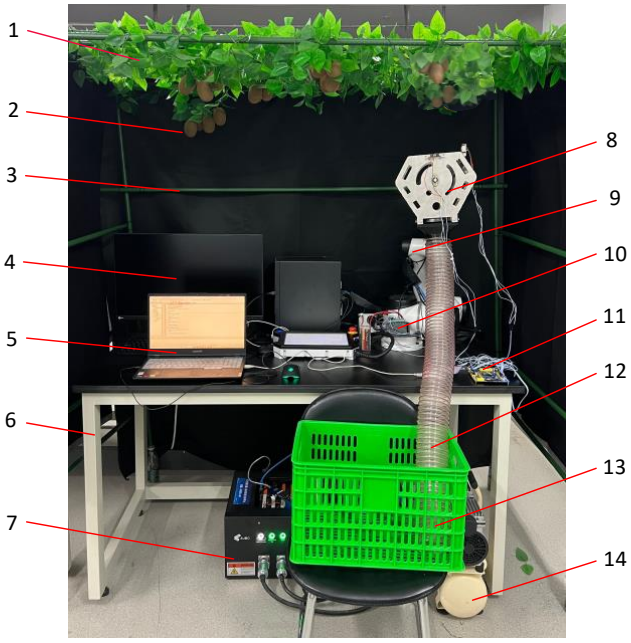


Fig. 9 - Kiwifruit picking test stand

1. vine; 2. kiwifruit; 3. trellis model; 4. upper computer; 5. portable laptop; 6. test stand; 7. control box; 8. end-effector; 9. robotic arm; 9. motor driver; 11. micro-controller control board; 12. hose; 13. fruit collection box; 14. compressed air pump

Test Method

The picking experiment was carried out on 20 July 2023. The AUBO-E5 robotic arm was used to support the end-effector for the picking operation, and the picking operation flow as shown in Figure 9, 75 kiwifruits of different shapes were selected for testing. The dimensions of the selected kiwifruit were measured to be a maximum of 72.7 mm and a minimum of 61.4 mm for the length, a maximum of 56.7 mm and a minimum of 49.5 mm for the width, and a maximum of 48.3 mm and a minimum of 44.6 mm for the thickness of the fruit. Based on the characteristics of kiwifruit clusters, 75 fruits were divided into 5 groups according to the number of fruits per cluster: 3, 4, 5, 6 and 7, and each group had 3 clusters with the same number of fruits. In this section, the picking success rate, average picking time per picking, and picking damage rate are used as the evaluation indexes for fast and non-destructive picking. The definitions are as follows:

$$T = \frac{t_0 - t_1}{c} \quad (1)$$

$$S = \frac{n}{h} \times 100\% \quad (2)$$

$$D = \frac{m}{n} \times 100\% \quad (3)$$

where: T - Average picking time, s;

S - Success rate, %;

D - Damage rate of fruits picked successfully, individual;

t_0 - Time of the start of picking, s;

t_1 - Time of the end of picking, s;

c - Number of fruit clusters, individual;

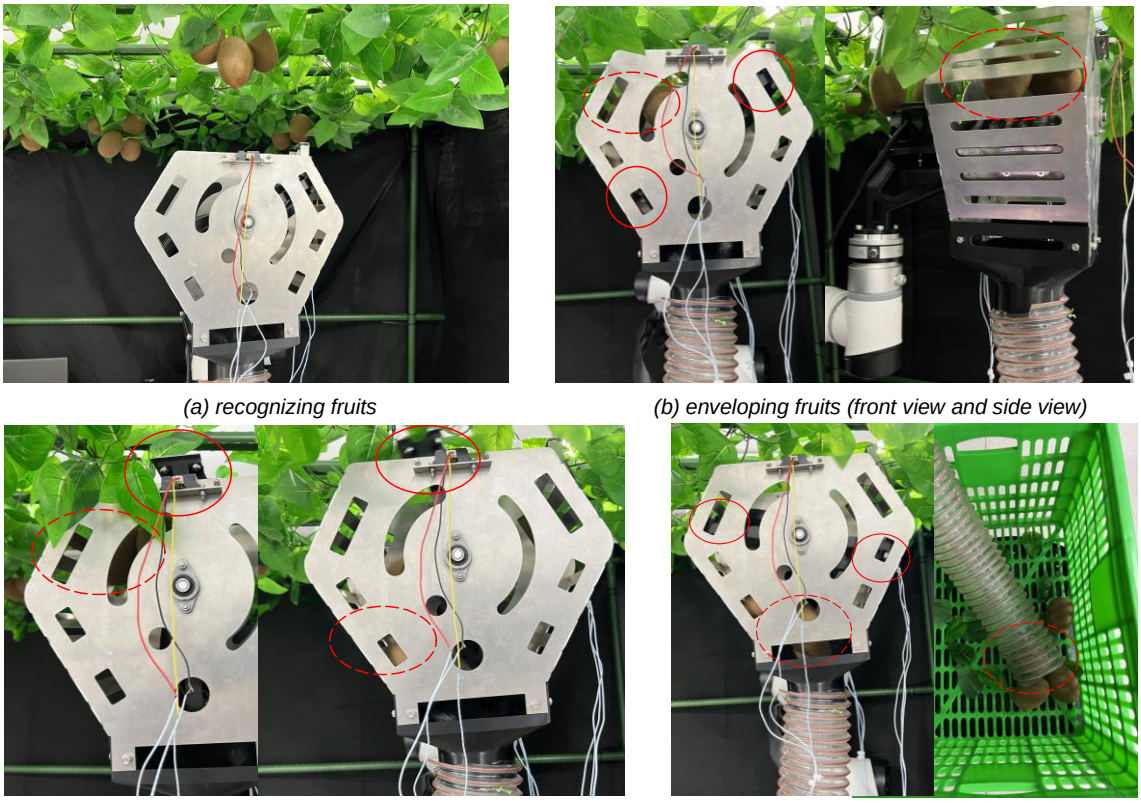
n - Number of fruits picked successfully, individual;

h - Total number of fruits, individual;

m - Number of damaged fruits, individual.

Analysis of Results

In this paper, picking experiments were carried out on 5 groups of 15 clusters of fruits respectively, as shown in Figure 10. The robotic arm first sent the end-effector to the area suitable for picking fruits, and after the fruits were recognized by the recognition sensor, the robotic arm carried the end-effector upwardly to envelope and pick the fruits, and the picked fruits fell into a fruit collection box through a hose.



(a) recognizing fruits *(b) enveloping fruits (front view and side view)*

(c) picking fruits (start of the picking and after the picking) *(d) collecting fruits (fruit falling into the collection hose and fruit falling into the collection box*

Fig. 10 - Kiwifruit picking process

where: Real-time status of rotary cutter

Real-time status of fruit position

During the above fruit-picking process, the robotic arm carried the end-effector picking operation at a speed of 1.5 m/s, and the stepper motor carried the rotary cutter at a speed of 6 r/min to separate the fruits from the fruit stalks, the results of the picking experiments being shown in Table 3.

Table 3

Results of picking experiments

Group	Number of fruits per cluster	Number of fruit clusters per group	Total number of fruits	Number of picking successes	Number of picking failures	Number of fruit damage	Picking success rate (%)	Fruit damage rate (%)	Average picking time per cluster (s)
1	3	3	9	9	0	0	100	0	6.5
2	4	3	12	12	0	0	100	0	7.3
3	5	3	15	14	1	1	93.3	14.3	8.5
4	6	3	18	15	3	1	83.3	13.3	10.2
5	7	3	21	17	4	2	81.0	17.6	11.5
	Total	15	75	67	8	4	89.3	6.0	8.8

According to Table 3, the average time for picking each cluster of fruits was 8.8 seconds, with a success rate of 89.3% and a damage rate of 6.0%. When the number of fruits picked in each cluster was 3~4, the picking success rate was 100%, and the fruit damage rate was 0. When the number of fruits picked in each cluster was 5~7, the more fruits picked in each cluster, the lower the picking success rate, and the higher the fruit damage rate.

The causes of fruit damage were analysed as follows:

① Fruit leaves interfered with the colour detection sensor, resulting in damage to one or more fruits by the rotary cutter before they reached the picking bin.

② During the picking or collection process, collisions between fruits could lead to damage to the skin of overripe fruits. (Note: Typically, when kiwifruit is picked in an orchard, the fruit is not yet fully ripe and is firmer, making the skin less likely to be damaged).

CONCLUSIONS

(1) For orchard scaffold-grown kiwifruit, TRIZ was applied to assist in the design of a new kiwifruit-picking end-effector. A multi-fruit picking method of automatically recognizing fruits - fully enveloping fruits - and Non-destructive separating fruit stalks was proposed for picking kiwifruit in clusters. The designed picking end-effector aggregates the fruit clusters into the picking bin by means of enveloping, separates the fruits and stalks using a rotating cutter and sets a curved guide shaft to buffer and guide the picked fruits.

(2) A kiwifruit picking test stand was established in a laboratory. Seventy-five fruits were selected and divided into five groups in the form of fruit clusters. The robotic arm was set at 1.5 m/s and the stepper motor at 6 r/min running speed for the picking test. The results showed that the average time to pick each cluster of fruits was 8.8 s, the picking success rate was 89.3%, and the picking damage rate was 6.0%. Compared with the picking experimental data of the prototype, the kiwifruit picking end-effector designed in this paper not only improved the fruit picking success rate and reduced the fruit damage rate, but also shortened the fruit picking time and thus improved the fruit picking efficiency.

ACKNOWLEDGEMENT

This paper was funded by the National Natural Science Foundation of China (Grant No.51975114).

REFERENCES

[1] Altshuller, G. S. (1984). Creativity as an exact science, the theory of the solution of inventive problems. *Gordon and Breach Science Publishers*: New York, USA, pp.5-25.

[2] Azammi, A. N., Sapuan, S. M., Ishak, M. R., & Sultan, M. T. (2018). Conceptual design of automobile engine rubber mounting composite using TRIZ-Morphological chart-analytic network process technique. *Defence Technology*, 14(4), 268-277.

[3] Fazayeli, A., Kamgar, S., Nassiri, S. M., Fazayeli, H., & de la Guardia, M. (2019). Dielectric spectroscopy as a potential technique for prediction of kiwifruit quality indices during storage. *Information Processing in Agriculture*, 6(04), 479-486.

[4] Feng, Q., Zou, W., Fan, P., Zhang, C., & Wang, X. (2018). Design and test of robotic harvesting system for cherry tomato. *International Journal of Agricultural and Biological Engineering*, 11(01), 96-100.

[5] Fu, L., Tola, E., Al-Mallahi, A., Li, R., & Cui, Y. (2019). A novel image processing algorithm to separate linearly clustered kiwifruits. *Biosystems Engineering*, 183, 184-195.

[6] Fu, L., Zhang, F., Yoshinori, G., Li, Z., Wang, B., & Cui, Y. (2015). Development and experiment of end-effector for kiwifruit harvesting robot (猕猴桃采摘机器人末端执行器设计与试验). *Transactions of the Chinese Society of Agricultural Machinery*, 46(3).

[7] Fu M. (2021). *Systematic Innovation Approach - TRIZ Practical Tutorial* (系统化创新方法 - TRIZ 实用教程). Northeast Forestry University Press: Harbin, China, pp.5-10.

[8] Hu, G., Chen, C., Chen, J., Sun, L., Sugirbay, A., Chen, Y., et al. (2022). Simplified 4-DOF manipulator for rapid robotic apple harvesting. *Computers and Electronics in Agriculture*, 199, 107177.

[9] Kang, C. Q., Ng, P. K., & Liew, K. W. (2022). A TRIZ-Integrated Conceptual Design Process of a Smart Lawnmower for Uneven Grassland. *Agronomy*, 12(11), 2728.

[10] Kim, S., Hong, S. J., Ryu, J., Kim, E., Lee, C. H., & Kim, G. (2023). Application of a modal segmentation on cucumber segmentation and occlusion recovery. *Computers and Electronics in Agriculture*, 210, 107847.

[11] Guo, L., Rui, S., Zhao, G., Gao, C., Fu, L., Shi, F., Dhupia, J., Li, R., & Cui, Y. (2022). Real-time detection of kiwifruit flower and bud simultaneously in orchard using YOLOv4 for robotic pollination. *Computers and Electronics in Agriculture*, 193, 106641.

[12] Li, C. E., Tang, Y., Zou, X., Zhang, P., Lin, J., Lian, G., & Pan, Y. (2022). A novel agricultural machinery intelligent design system based on integrating image processing and knowledge reasoning. *Applied Sciences*, 12(15), 7900.

[13] Mao, S., Li, Y., Ma, Y., Zhang, B., Zhou, J., & Wang, K. (2020). Automatic cucumber recognition algorithm for harvesting robots in the natural environment using deep learning and multi-feature fusion. *Computers and Electronics in Agriculture*, 170, 105254.

[14] Mu, L., Cui, G., Liu, Y., Cui, Y., Fu, L., & Gejima, Y. (2020). Design and simulation of an integrated end-effector for picking kiwifruit by robot. *Information Processing in Agriculture*, 7(1), 58-71.

[15] Rong H. (2019). *Development of kiwifruit picking end-effector based on fruit stem separation picking method* (基于果梗分离采摘方式的猕猴桃采摘末端执行器研制). [Thesis of Master, Northwest Agriculture and Forestry University]. China Campus Repository.

[16] Silwal, A., Davidson, J. R., Karkee, M., Mo, C., Zhang, Q., & Lewis, K. (2017). Design, integration, and field evaluation of a robotic apple harvester. *Journal of Field Robotics*, 34(6), 1140-1159.

[17] Sun, Q., Zhong, M., Chai, X., Zeng, Z., Yin, H., Zhou, G., & Sun, T. (2023). Citrus pose estimation from an RGB image for automated harvesting. *Computers and Electronics in Agriculture*, 211, 108022.

[18] Williams, H. A., Jones, M. H., Nejati, M., Seabright, M. J., Bell, J., Penhall, N. D., et al. (2019). Robotic kiwifruit harvesting using machine vision, convolutional neural networks, and robotic arms. *Biosystems Engineering*, 181, 140-156.

[19] Wang, T., Du, W., Zeng, L., Su, L., Zhao, Y., Gu, F., Liu, Li., Chi, Q. (2023). Design and Testing of an End-Effector for Tomato Picking. *Agronomy*, 13(03), 947.

[20] Williams, H., Ting, C., Nejati, M., Jones, M. H., Penhall, N., Lim, J., et al. (2020). Improvements to and large-scale evaluation of a robotic kiwifruit harvester. Journal of Field Robotics, 37(02), 187-201.

[21] Xiong, Y., Peng, C., Grimstad, L., From, P. J., & Isler, V. (2019). Development and field evaluation of a strawberry harvesting robot with a cable-driven gripper. *Computers and electronics in agriculture*, 157, 392-402.

[22] Xu, H., Yu, G., Niu, C., Zhao, X., Wang, Y., & Chen, Y. (2023). Design and Experiment of an Underactuated Broccoli-Picking Manipulator. *Agriculture*, 13(4), 848.

[23] Xu, L., Liu, X., Zhang, K., Xing, J., Yuan, Q., Chen, J., ... & Yu, C. (2018). Design and test of end-effector for navel orange picking robot (脐橙采摘机器人末端执行器设计与试验). *Transactions of the Chinese Society of Agricultural Engineering*, 34(12), 53-61.

[24] Yan, B., Fan, P., Lei, X., Liu, Z., & Yang, F. (2021). A real-time apple targets detection method for picking robot based on improved YOLOv5. *Remote Sensing*, 13(09), 1619.

[25] Yang, L., Yi, S., Mao, X., & Tao, G. (2018). Innovation design of fertilizing mechanism of seeder based on TRIZ theory. *IFAC-PapersOnLine*, 51(17), 141-145.

[26] Yin, H., Sun, Q., Ren, X., Guo, J., Yang, Y., Wei, Y., et al. (2023). Development, integration, and field evaluation of an autonomous citrus-harvesting robot. *Journal of Field Robotics*.

[27] Yuan J. (2020). Research progress analysis of robotics selective harvesting technologies (选择性收获机器人技术研究进展与分析). *Transactions of the Chinese Society of Agricultural Machinery*, 51(09), 1-17.

ENERGETICS OF PULLING FLAX STALKS WITH A DISC-BELT FLAX-PULLING APPARATUS

/

ЕНЕРГЕТИКА БРАННЯ СТЕБЕЛ ЛЬОНУ ДИСКОВО-ПАСОВИМ ЛЬОНОБРАЛЬНИМ АПАРАТОМ

Svitlana YUKHYMCHUK, Serhii YUKHYMCHUK*), Mykola TOLSTUSHKO, Igor TSIZ, Nataliya TOLSTUSHKO

Lutsk National Technical University, 75, Lvivska str., Lutsk, Ukraine;
*)*Tel: +380956447720; E-mail:* sergei-71@ukr.net
DOI: https://doi.org/10.35633/inmateh-71-32

Keywords: *pulling, flax stalks, disk-belt pulling apparatus, pulling stream, power, energy*

ABSTRACT

The article describes a new design of the disc-belt flax-pulling apparatus, which will increase the durability of the pulling belts and reduce the material consumption of the flax gleaning machine. The geometrical parameters of the pulling section of the disc-belt flax-pulling apparatus have been established. The energetics of the process of picking flax stalks, which are clamped in the curved longitudinal pulling stream of the disc-belt flax-pulling apparatus, have been theoretically investigated. The dynamics of changes in the components of pulling power when moving the flax stalk along the pulling stream were studied, depending on: the initial inclination of the flax stalk; from the forward speed of the flax harvester; from the angle of inclination of the pulling apparatus to the horizon. The energy per second of pulling and the value of its components are determined.

РЕЗЮМЕ

У статті дано опис нової конструкції дисково-пасового льонобрального апарата, яка дозволить підвищити довговічності бральних пасів та зменшити матеріаломісткість льонозбиральної машини. Встановлено геометричні параметри бральної секції дисково-пасового льонобрального апарата. Теоретично досліджено енергетику процесу брання стебел льону, які затискаються у криволінійному поздовжньому бральному рівчаку дисково-пасового льонобрального апарата. Вивчено динаміку зміни складових потужності брання при переміщенні стебла льону по бральному рівчаку в залежності: від початкового нахилу стебла льону; від поступальної швидкості льонозбиральної машини; від кута нахилу брального апарата до горизонту. Визначено секундну роботу брання та значення її складових.

INTRODUCTION

At all times in the centuries-old history of mankind, fibre flax has been grown by people to obtain fibre and seeds (*Karg, Sabine, 2022*). It also provides a third valuable product – shives. The distinctive feature of fibre flax is that the entire plant is used for human health (*Jhala and Hall, 2010*).

In the rapidly deteriorating environmental situation in the world, the population has realized the great importance of flax for health, the need to use environmentally friendly and healthy food, clothing, and a favourable living environment. Linen fabrics, linseed oil, and other products containing flax fibres are of great benefit to human health (*Omer et al., 2020*).

No other fibres can yet surpass the remarkable natural properties of flax, which creates comfortable conditions for the person wearing them. Developed methods for modifying flax fibre make it possible to use all the fibre contained in the stem, as well as waste from shaking and combing, to produce thin, cheaper household fabrics mixed with other fibres *(Yang et al., 2009*).

Even low-grade flax fibre is successfully used by foreign companies for reinforcing composites in the production of automobiles, as well as in aircraft, ship and carriage construction for sound, vibration and thermal insulation of passenger compartments, etc. (*Dudarev and Say, 2020*).

From flaxseeds, flaxseed oil is obtained for technical purposes and dietary medicinal food, which contains omega-3 fatty acids (*Zuk et al., 2015*). The latter provides a significant medicinal effect for various human diseases. Also, seeds are a source of protein, soluble polysaccharides, phenolic acids and flavonoids and other biologically active components.

The addition of flaxseeds and oil in the manufacture of bakery and confectionery products has a preventive effect on the human body (*Charney, 2014*).

Eco-friendly structural and thermal insulation materials are made from flax shives (*Yaghelyuk et al., 2020*). Structures with wall elements made from such materials have low heat loss and can be used in residential construction (*Jhala and Hall, 2010*).

Currently, Ukraine is dependent on cotton-growing countries for raw materials. Therefore, to ensure the economic and strategic independence of the country, it is extremely important to have domestic cellulosic fibrous raw materials to produce, for example, cotton wool, fabrics for the army, non-woven materials and threads for medicine, gunpowder and explosives from flax nitrocellulose (*Dudarev and Khomych, 2022*).

The quality and yield of flax varies greatly depending on weather conditions, soil type, varieties, cultivation techniques and other factors (*Lafond et al., 2008; Pisupati et al., 2021*). Fibre flax stems have a diameter of about 1.4–1.6 mm and a total height of up to 1.1–1.2 m (*Nag et al., 2015*) and one of the highest slenderness factor (i.e. the ratio between height and diameter of the stem) among botanical herbs and trees, which is about 365±33 (*Goudenhooft et al., 2019*). In the world, the yield of fibre flax straw is varied widely from 220 kg/ha to 4370 kg/ha depending on the country and weather conditions of cultivation (*Zając et al., 2012*). The seed yield is ranged from 270 kg/ha to 890 kg/ha/ (*Hall et al., 2016*). The seeds of the fibre flax contain 20–40% oil (*Zuk et al., 2015*).

For fibre flax, a seeding rate of 1800 seeds/m^2 is the better compromise long fibre yield, fibre mechanical performances and stem stability to lodging (*Bourmaud et al., 2016*).

The complex of flax harvesting operations begins with pulling the stalks out of the soil by the energying bodies of flax harvesters (*Abdel-Wahab et al., 2012*). Flax is harvested by pulling because the entire stalk is pulled from the soil and the productive part of the stalk, which contains fibre, is not lost with the stubble, which occurs during mowing (cutting) of flax (*Mańkowski et al., 2018*). When the streams of stalks are combined at the exit from the harvesters, a ribbon of flax stalks is formed (*Soucek et al., 2017*). All subsequent technological operations carried out on flax stalks in the field and during primary processing up to the separation of the fibre are carried out on the stalks in the ribbon. That is why, pulling flax and forming a ribbon is a technological operation where the parameters of the flax ribbon create the conditions for the efficient course of all subsequent technological operations (*Dudarev, 2020*).

Pulling apparatuses are used to pull flax stalks out of the ground during the mechanized harvesting of flax. Most often, these are belt and belt-disc pulling apparatuses (*Dudarev, 2015).*

In belt pulling apparatuses, the stalks are clamped between two pulling belts, which energy as belt transmissions, in which the working branch is tensioned. The belt covers the drive and driven pulleys, or the drive pulley and tension rollers.

In belt-disc pulling apparatuses, flax stalks are clamped between the pulling belt and the pulling disc. At the same time, the pulling disk rotates from contact with the pulling belt. That is, the belt is even more loaded than in the belt pulling apparatus.

Pulling belts are made of rubber reinforced with kapron threads and in the process of energy are stretched and need to be periodically tightened, and when worn, they need to be replaced.

In addition, these designs of pulling apparatuses are quite material-intensive. This is due to the use of pulleys, tension and support rollers, complex drive *(Dudarev et al., 2014).*

Therefore, it is urgent to develop such a design of the pulling apparatuses that would eliminate the mentioned shortcomings.

MATERIALS AND METHODS

We offer a new design of the disc-belt pulling apparatus (*Yukhymchuk et al., 2022*). In it, the drive is carried out directly on the pulling discs, and the passes press the flax stalks to the surface of the pulling discs. That is, the belt does not transmit torque from the driving to the driven pulleys, which means that it stretches less during operation. The pulling apparatus is tilted at an angle to the horizon.

Fig. 1 schematically shows the proposed disc-belt flax pulling apparatus.

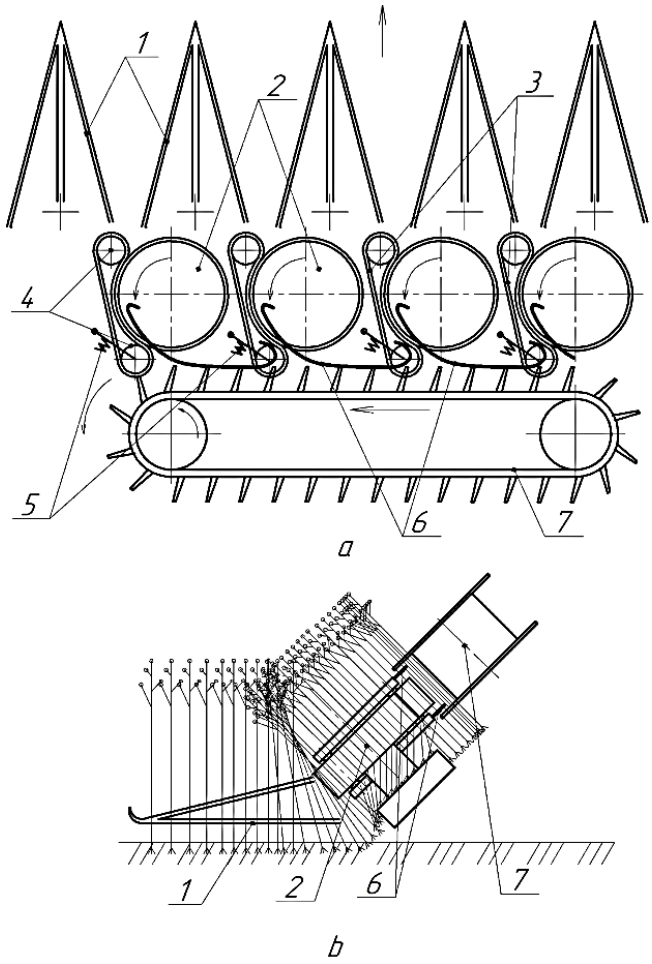


Fig. 1 - Disc-belt flax pulling apparatus

a – top view, b – side view

1 - dividers, 2 - pulling discs, 3 - pulling belts, 4 - rollers, 5 - spring-loaded fasteners, 6 - guide bars, 7 - transverse conveyor

The disc-belt flax pulling apparatus includes: a prefabricated frame (not shown in the figure); dividers *1*, pulling unit, which includes pulling disks *2*, pulling belts *3*, rollers *4*, spring-loaded fasteners *5*, guide bars *6*, transverse conveyor *7*.

The disc-belt flax pulling apparatus works as follows.

The drive of the pulling discs, which rotate in the same direction, is carried out from the frame crankcase. On the one hand, each pulling disk *2* is covered by a pulling belt *3*, which is put on rollers *4*. Due to the spring-loaded fastening *5* of the upper roller *4*, constant tension of the pulling belt *3* is ensured, which means the pressure in the pulling shaft.

When the machine moves along the surface of the field, the dividers 1 divide the flax stalks into separate strips and direct them to the mouths of the pulling streams. Further, the flax stalks are clamped between the contacting surfaces of the pulling discs 2 and pulling belts 3, pulled out of the ground and moved to the exit from the pulling streams, where they are captured by the fingers of the transverse conveyor 7 and, sliding along the surface of the guide rods 6, are moved to the exit from the disc-belt flax pulling apparatus. Later, depending on the type of flax harvesting machine, the stalk tape is either spread on the flax field, or fed to the following working bodies of the flax harvesting machine for combing the seed pods.

The pulling assembly contains fewer parts, so the proposed disk-belt flax pulling apparatus is less material-intensive compared to analogue ones. Due to the fact that the pulling belts do not transmit traction forces, but only clamp and hold the flax stalks, as well as the presence of spring-loaded upper rollers 4, the durability of the pulling belts is ensured.

For further studies of the new disc-belt flax pulling apparatus, it is necessary to conduct an energy analysis of the pulling process. Namely, to determine the dynamics of changes in the components of pulling power when moving the flax stalk along the pulling stream under different working conditions.

The geometric dimensions of the pulling section will be selected with the help of a sketch layout, using the Kompas computer program. Analogously to the existing four-handled pulling apparatuses, the width of one pulling section *B*=380 mm is considered (*Yukhymchuk et al., 2022*).

When choosing parameters, two conditions were taken into account. The first: the length of clamping the stalks in the pulling stream should be as long as possible to ensure the pulling of stalks of different characteristics (height, slope) and at different speeds of the unit. The second condition: the branches of the pulling belt, which is driven from the pulling disk, must not touch each other.

As a result of the graphic layout, the following geometric parameters of the pulling section were obtained (fig. 2): the distance between the centres of the pulling discs was 380 mm; radius of the rubberized pulling disc *R*=160 mm; the diameters of the belt transmission rollers were 80 mm, the thickness of the pulling belt was 10 mm; the gap between the pressing and overlapping branches of the belt, provided that there are no stalks in the grab rail, was 15 mm; the length of the belt was 1000 mm; the width of the pulling disc and the pulling belt, by analogy with the existing designs of belt pulling apparatuses, was 100 mm. The contact zone of the pulling disk and the pulling belt *AB* corresponds to the angle of reach of the pulling disk $\alpha = 80^o$, which in terms of the length of the reach zone is: $L = 2\pi R\frac{\alpha}{360^o} = 2\cdot 3.14\cdot 160\cdot\frac{80^o}{360^o} \approx 223$ mm. It is worth noting that when pulling flax, when there are flax stalks between the pulling disc and the pulling belt, this zone increases. So, if it is assumed that the stalks are pressed into one layer with a thickness of 1 mm, this zone will be characterized by an angle $\alpha = 86^o30^l$ and a length of $L \approx 241$ mm. And with a greater thickness of the stalk tape, the clamping zone will increase even more.

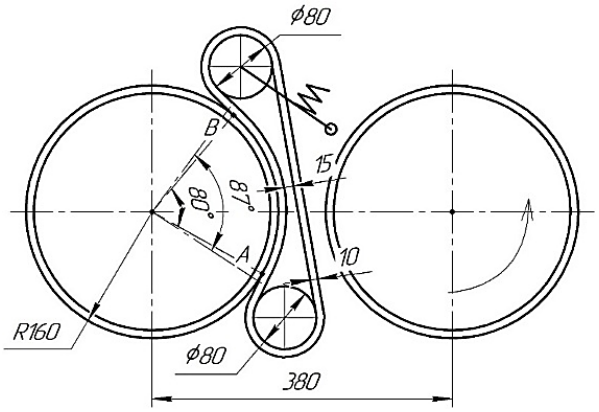


Fig. 2 - Structural diagram of the pulling section

The pulling apparatus performs two main functions - pulling flax stalks out of the ground and transporting them to the transverse conveyor. At the same time, the stalks clamped in the pulling streams carry out a complex movement, namely: relative movement under the action of the movement of the pulling belt and portable - during the movement of the machine.

Figure 3 shows a schematic representation of the frontal projection of the pulling apparatus in the Cartesian coordinate system *X′O′Y′*. The *O′Y′* axis is placed horizontally and directed to the right, and the *O′X′* axis is directed down.

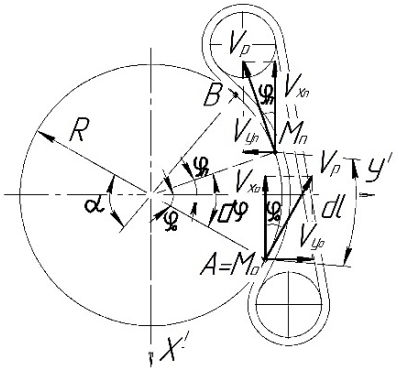


Fig. 3 - The scheme for determining the velocities of the stalk in the pulling stream

The flax stalk is conventionally marked by a material point M, which moves in the $X'OY'$ coordinate system along the curve AB. At the same time, the speed of the point M in the pulling stream Vp coincides with the circular speed of the pulling disk rim and the speed of the pulling belt movement (fig. 3). The velocity V_p forms a certain variable angle φ with the axis OY', depending on which the projection $V_{x'}$ acquires either positive or negative values. The projections of the velocity V_p on the axis OX' and OY' are equal:

$$\left.\begin{aligned} V_X &= V_p \cdot \cos\varphi; \\ V_Y &= V_p \cdot \sin\varphi. \end{aligned}\right\} \quad (1)$$

On the curvilinear sections of the pulling streams, the angle φ is equal to the acute angle between the radius of curvature drawn to the point M_n and the $O'X'$ axis (fig. 3), since the velocity V_p is directed tangentially to the curve and the vector V_p forms a right angle with the radius.

When moving along the pulling stream, the stalk of flax - point M_n will travel a distance dl in some time dt, which is equal to:

$$dl = V_p \cdot dt \quad (2)$$

This same path dl can be expressed in terms of the corresponding change in the angle $d\varphi$ as some length of the arc of a circle:

$$dl = R \cdot d\varphi \quad (3)$$

where R is the radius of the pulling disk.

Before that, the movement of the flax stalk was considered only under the influence of the rotation of the pulling disc, not taking into account the influence of the forward movement speed of the flax harvesting machine V_m. Under the influence of the last factor, the stalk also acquires a transfer speed V_m.

The process of harvesting flax stalks was considered in the $XYZO$ spatial coordinate system (fig. 4). The stationary coordinate axes OX, OY, OZ were placed in such a way that the OX axis is parallel to the speed of the machine movement V_m, the OY axis is parallel to the plane of the pulling apparatus and directed in the direction of movement of the clamped stalks, the OZ axis is perpendicular to the field surface and directed upwards. At the same time, the axis $O'X'$ of the frontal plane of the pulling apparatus forms an angle β with the OX axis - the angle of inclination of the pulling apparatus to the horizon, and the axis $O'Y'$ is parallel to the axis OY.

At the same time, the velocity V of the point M_n in the spatial coordinate system represents the vector sum of the projections V_x, V_y, V_z, where:

$$\left.\begin{aligned} V_x &= V_{px} + V_m = V_{x'} \cos\beta + V_m = V_p \cos\varphi \cos\beta + V_m, \\ V_z &= V_{pz} = V_{x'} \sin\beta = V_p \cos\varphi \sin\beta, \\ V_y &= V_{py} = V_{y'} = V_p \sin\varphi. \end{aligned}\right\} \quad (4)$$

With the known projections of the velocities V of the M_n point, find the projections on the OX, OY, OZ coordinate axis of the displacements dX, dY, dZ of the M_n point depending on the time dt:

$$\left.\begin{aligned} dX &= V_x dt, \\ dY &= V_y dt, \\ dZ &= V_z dt. \end{aligned}\right\} \quad (5)$$

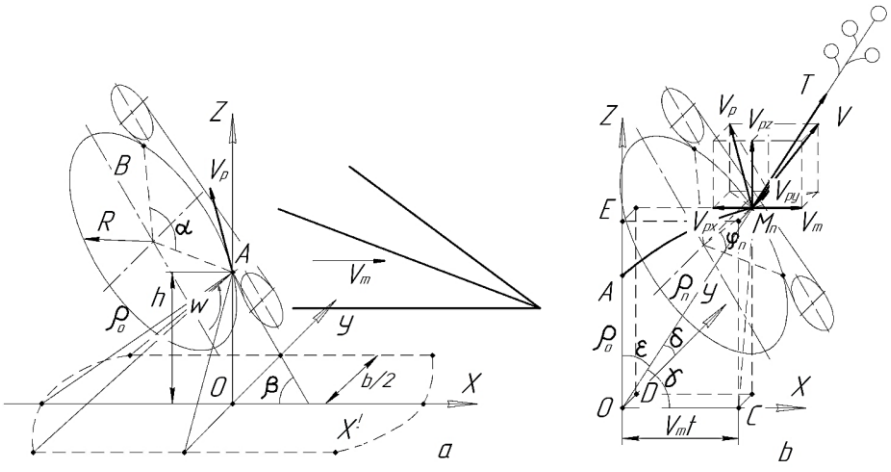


Fig. 4 - Calculation scheme of the stalk pulling process

Expressing the curved section *dt* in terms of $d\varphi$ and equating the right-hand sides of formulas (2) and (3), there is:

$$dt = \frac{R}{V_p} d\varphi \tag{6}$$

Integrating the system of equations (5), preliminarily substituting the velocity expressions from system (4) into the last one and replacing *dt* with the right-hand side of equation (6), it was found the equation for determining the coordinates of the point M_n at a certain time. In this case, the limits of integration for the curvilinear section of the pulling stream will be from φ_o to $\varphi_0 + \alpha$, i.e. $\varphi_n \in [\varphi_0; \varphi_0 + \alpha]$ (fig.3).

Finally, when the stalk of flax passes along the pulling stream, the coordinates of the point M_n are equal to:

$$\left.\begin{aligned} X_n &= R\left[\cos\beta\left(\sin\varphi_n - \sin\varphi_0\right) + {V_m}/{V_p}\left(\varphi_n - \varphi_0\right)\right] + X_0, \\ Y_n &= R\left(\cos\varphi_n - \cos\varphi_0\right) + Y_0, \\ Z_n &= R\sin\beta\left(\sin\varphi_n - \sin\varphi_0\right) + Z_0. \end{aligned}\right\} \tag{7}$$

In the equations of system (7), the quantities X_o, Y_o, Z_o are constants of integration and correspond to the coordinates of the point *A* of the beginning of the section of the *AB* curve considered in space.

As the origin of coordinates of the *XOYZ* spatial system, the point of placement of the flax stalk in the soil, which falls vertically into the mouth of the pulling stream (fig.4), was chosen. At the same time, the coordinates of point *A* are: X_0=0; Y_0=0; Z_0=*h*, where *h* - the height of the starting point of pulling.

Due to its design features, the pulling apparatus interacts with flax stalks during gleaning in such a way that the pass performs only part of the energy of pulling out the stalks. The rest of the energy is performed due to the portable translational movement of the machine.

The power used in this case is determined by the formula (*Yukhymchuk et al., 2021*):

$$N = N_p + N_m = TV_p \cos\left(\bar{T}, \bar{V}_p\right) + TV_m \cos\left(\bar{T}, \bar{V}_m\right) , \tag{8}$$

where: N_p and N_m - powers transmitted to the pulling disc and the machine for pulling the stalk out of the soil;

T - the force of pulling the flax stalk out of the ground;

$\bar{T}\bar{V}_p$ and $\bar{T}\bar{V}_m$ – the angles between the force vectors *T* and the speeds of the conveyor belt V_p and the aggregate V_m.

The force vector *T* is directed along the stalk in the direction of its extension (fig.4b).

The strength of *T* depends on many factors (properties of the soil, type of flax, characteristics of flax stalks, stalk density) and is determined experimentally. The value of this force *T* changes as the stalk root is pulled out of the soil. One of the most characteristic dependences of the force *T* on the length of the stalk extension $\Delta\rho$ is parabolic (*Yukhymchuk et al., 2021*), according to which the force *T* increases with an increase in $\Delta\rho$, reaches a maximum (T_{max}) and falls.

The formula for this dependence is as follows:

$$T = 4T_{\max}\frac{\Delta\rho}{a}\left(1 - \frac{\Delta\rho}{a}\right) \tag{9}$$

where *a* - the length of the path of force action (the length by which the stalk needs to be pulled out of the soil until the root is completely detached).

As stated earlier by *Yukhymchuk et al., (2021)* T_{max}=5 N, *a*=0.05 m. It is also made the assumption that the angle of inclination of the stalk during harvesting does not affect the value of $T_{max.}$

To ensure complete extraction of the flax stalk from the soil, the following conditions must be met:

$$\left.\begin{aligned} a &\le \rho_n - \rho_0, \\ \rho_0 &= \sqrt{\left(X_0 - X\right)^2 + \left(Y_0 - Y\right)^2 + Z_0^2}, \\ \rho_n &= \sqrt{\left(X_n - X\right)^2 + \left(Y_n - Y\right)^2 + Z_n^2}. \end{aligned}\right\} \tag{10}$$

where ρ_0 - the distance from the point $M_o(X_o; Y_o; Z_o)$ - the starting point of stalk pinching in the pulling stream ($M_o \equiv A$) to the point $O(X; Y; Z)$ - the location of the stalk root in the soil;

ρ_n - the distance from the point $M_n(X_n; Y_n; Z_n)$ the pinching point of the flax stalk when it is in the pulling stream, to the point $O(X; Y; Z)$.

Figure 4b shows the position of the pulling disk after some time *t*. During this time, the pulling apparatus moved to a distance equal to $V_m t$, and the pulling disc under the influence of the pulling pass turned to the angle $\varphi = V_p t / r$. At the same time, clamped at the point M_n with coordinates (X_n; Y_n; Z_n), the flax stalk forms the corresponding angles with the coordinate axes: angle γ with the *OX* axis, angle δ with the *OY* axis, and angle ε with the *OZ* axis.

The location in the soil of the root part of the stalk is determined by point *O* with coordinates (*X*; *Y*).

The following vectors emanate from the point M_n: *T*, *V*, V_m, V_p, where *V* is the vector of the absolute speed of movement of the point M_p in space $V=V_m+V_p$. The projections of the vector V_p onto the coordinate axes (fig. 4b) V_{px}, V_{py}, V_{pz} are based on the equations of system (4).

From fig. 4b, it can be seen that the vectors of these projections form the same angles with the flax stalk as the corresponding coordinate axes. Then equation 8 will take the form:

$$N = N_p + N_m = T\left(V_{px}\cos\gamma + V_{py}\cos\delta + V_{pz}\cos\varepsilon\right) + TV_m\cos\gamma \tag{11}$$

From the right-angled triangle OCM_n (fig.4, b) $OM_n = \rho_n -$ the distance from point M_n to point *O*, which is determined by the system of equations (10), and $OC=X_n - X$. From here:

$$\cos\gamma = \frac{OC}{OM_n} = \frac{X_n - X}{\rho_n} \quad . \tag{12}$$

Similarly, from the triangle ODM_n:

$$\cos\delta = \frac{OD}{OM_n} = \frac{Y_n - Y}{\rho_n} \quad . \tag{13}$$

And from the OEM_n triangle:

$$\cos\varepsilon = \frac{OE}{OM_n} = \frac{Z_n}{\rho_n} \quad . \tag{14}$$

By substituting expressions for their calculations (12), (13) and (14) into equation (11) instead of its corresponding elements, a system of equations for power calculation is obtained:

$$\left.\begin{aligned} N_P &= T\left(V_{px}\frac{X_n - X}{\rho_n} + V_{py}\frac{Y_n - Y}{\rho_n} + V_{pz}\frac{Z_n}{\rho_n}\right), \\ N_m &= TV_m\frac{X_n - X}{\rho_n}, \\ N &= N_p + N_m. \end{aligned}\right\} \tag{15}$$

According to equations (15), using formulas (9), (4), (7), (10) to find their elements, in order to quickly obtain the results of calculations based on various possible combinations of initial parameters, a computer program was developed in the computer system Maple algebras. This program allows you to monitor the change in power *N* and the distribution of its components N_p and N_m from the rotation of the pulling disc to the angle $\varphi_n \in [\varphi_0; \varphi_0 + \alpha]$ when pulling stalks with the corresponding *X*, *Y* coordinates of the points of the location of the roots. At the same time, it was taken into account that the stalk is picked under the condition:

$$0 \le \rho_n - \rho_o \le a \tag{16}$$

At $\Delta\rho > a$, the flax stalk is fully pulled out (*N*, N_p and N_m are equal to zero).

At the same time, the values of the parameters were as follows: the maximum value of the pulling force T_{max}=5 N; the length by which the stalk needs to be pulled out of the soil until the root is completely detached *a*=0.05 m; radius of the pulling disk *R*=0.16 m; the height of the starting point of harvesting *h*=0.2 m; the angle β of inclination of the receiver to the horizon was $\pi/3$, $\pi/4$ and $\pi/9$; angles $\varphi_0 = -\pi/6$, $\alpha = \pi/2$; circular speed of the pulling disk V_p=2.35 m/s; the speed of the car V_m was 1.18 m/s, 2.01 m/s and 2.47 m/s.

The resulting graphs of the component capacities using the Maple computer program were processed in another graphic computer program, Kompas. For clarity, using equation (3), it was changed from angular dimensions to linear dimensions, that is, along the abscissa axis, at the price of a division of 0.01 m, the length of the pulling stream zone *l*, which is involved in pulling the stalk, was set aside.

In this program, it is possible to find the energy, which goes to pulling the stalk - A, as well as the energy, which is performed by the pulling disc - A_p, and the energy, which is due to the traction force of the flax harvester - A_m. Graphically, the energy A, as well as its components A_p and A_m, are the areas of the figures formed by the corresponding curves of dependence N, as well as N_p and N_m and the abscissa axis (the length of the breech zone) divided by V_p. The formulas for calculating A, A_p and A_m are as follows:

$$\left.\begin{aligned} A &= \int_0^t N dt = \frac{1}{V_P}\int_0^l N dl, \\ A_P &= \frac{1}{V_P}\int_0^l N_P dl, \\ A_m &= \frac{1}{V_P}\int_0^l N_m dl. \end{aligned}\right\} \quad (17)$$

where t is the time during which the stalk is completely pulled out of the soil; l - the length of the pulling furrow zone, which is involved in pulling the stalk.

RESULTS AND DISCUSSION

In fig.4, the possible zone of the location of the roots of the stalks in the soil, which fall into the mouth of the pulling stream, is indicated by a dotted line. Let's consider three possible cases of stalks hitting the mouth of the pulling stream: when the stalk is tilted in the direction of movement of the flax pulling machine, when it is placed vertically, and when it is tilted in the direction opposite to the movement of the machine (fig.5). The central most inclined stalk has the X coordinate, which is $X = -h \cdot tg\beta = -0.2 \cdot tg60^0 = -0.341$ m.

For the stalk, which at the moment of clamping in the pulling stream was tilted in the direction of the flax pulling machine (coordinates of the location of its root in the soil were X=-0.341 m, Y =0 m (fig. 5a)) extraction from the soil occurs mainly according to due to the traction power of the machine N_m and only a small part is due to the drive power of the pulling disk N_p.

For the stalk, which was placed vertically at the time of being clamped in the grab rail (coordinates of the location of its root in the soil were X=0 m, Y =0 m (fig. 5b)), extraction from the soil occurs in the opposite way, mainly due to the power of the pulling disk N_p. and only a small part is due to the traction power of the N_m machine.

And for the stalk, which at the moment of being clamped in the pulling stream was tilted opposite to the direction of movement of the flax pulling machine (the coordinates of the location of its root in the soil were X=0.341 m, Y =0 m (fig. 5c)) extraction from the soil occurs only due to power of the drive of the pulling disk N_p, which is greater than the power N of pulling the stalk out of the ground, and the traction power of the machine N_m takes a negative value. That is, part of the power of the pulling apparatus through the stalk is spent on moving the machine - the so-called phenomenon of power circulation. Also from this fig. 5, it can be seen that for this stalk, the length of the pulling zone, which is involved in pulling the stalk, increases to 0.17 m.

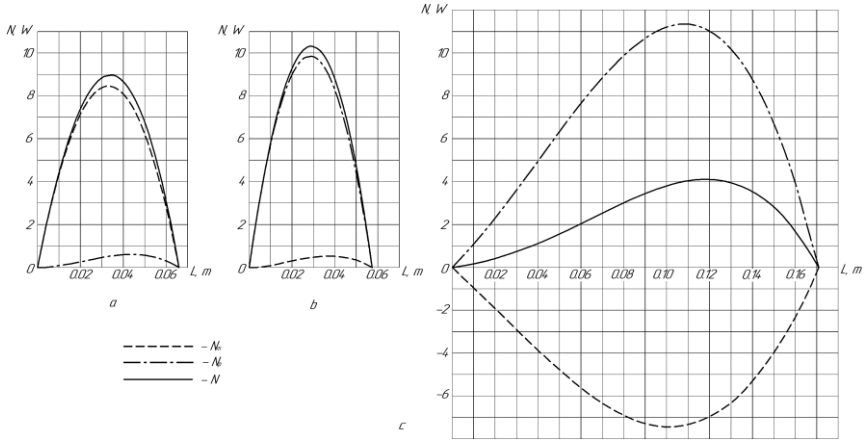


Fig. 5 - Power distribution during stalk pulling depending on the initial inclination of the flax stalk at V_m=2.01 m/s, $\beta = 60^0$

a – coordinates of the stalk root X=-0.341 m, Y =0 m, A_m=0.157 J, A_p=0.009 J, A=0.166 J;
b – coordinates of the stalk root X=0 m, Y =0 m, A_m=0.007 J, A_p=0.159 J, A=0.166 J;
c – coordinates of the stalk root X=0.341 m, Y =0 m, A_m=0.506 J, A_p=-0.340 J, A=0.166 J

The influence of the forward speed of the flax harvester on the distribution of the components of the power involved in pulling the stalk out of the ground was also analysed (fig. 6).

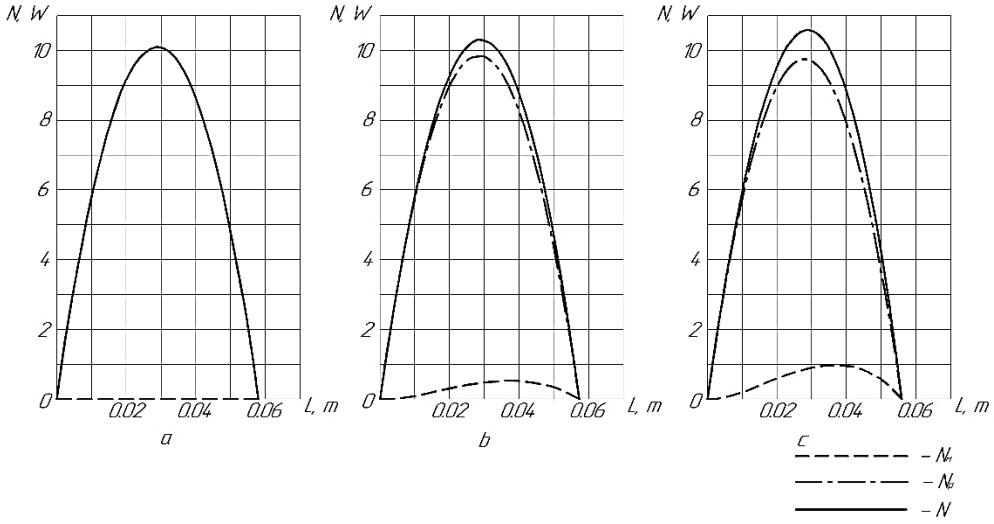


Fig. 6 - Power distribution during stalk pulling depending on the forward speed of the flax harvester at the stalk root coordinates X=0 m, Y =0 m

a – V_m=1.18 m/s, A_m=0 J, A_p=0.166 J, A=0.166 J;
b– V_m=2.01 m/s, A_m=0.007 J, A_p=0.159 J, A=0.166 J;
c – V_m=2.47 m/s, A_m=0.013 J, A_p=0.153 J, A=0.166 J

To do this, consider a stalk that enters the pulling stream vertically, that is, the coordinates of the root of the stalk *X*=0 m, *Y* =0 m (fig.6).

At the speed of the flax pulling machine V_m=1.18 m/s (fig.6a), the power *NM* from the movement of the machine is zero, and the graph of the power of the pulling disk N_p coincides with the graph of the power *N* for pulling the stalk out of the ground, that is, the stalk is pulled only under the action capacity of the pulling apparatus.

When the speed increases to V_m=2.01 m/s and to a speed of 2.47 m/s, it can be seen that when pulling the stalk out of the ground, the traction power N_m of the movement of the machine is already engaged and its share increases with the increase in the forward speed of the machine V_m.

Also, depending on the use of the pulling apparatus (installed on a flax winch or on a flax harvester), different angles of inclination of the pulling apparatus to the horizon are possible. Let's analyse how the angle of inclination of the pulling apparatus to the horizon affects the distribution of power when pulling the stalk out of the ground. To do this, consider a stalk that enters the pulling pit vertically, that is, the coordinates of the root of the stalk are *X*=0 m, *Y* =0 m. The speed of the machine is V_m=2.01 m/s, the angle of inclination of the pulling apparatus to the horizon is 60^0, 45^0 and 20^0 (fig.7).

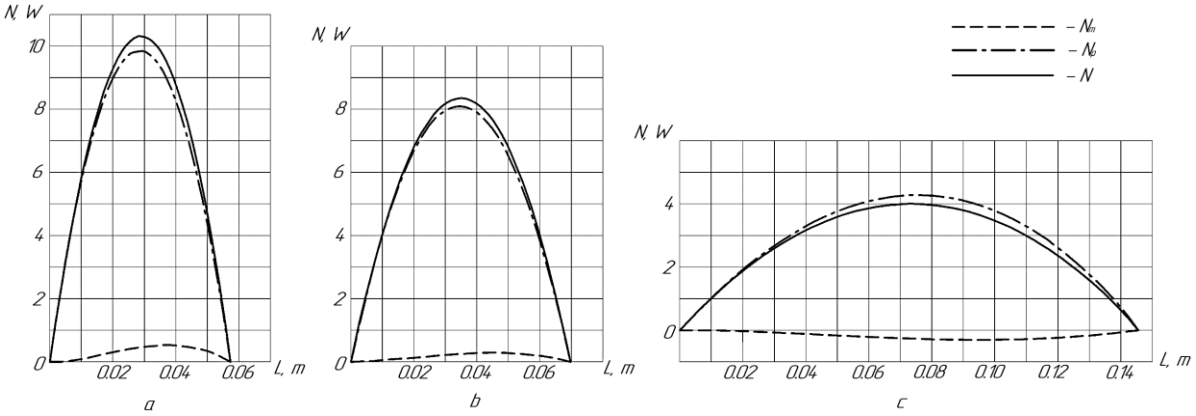


Fig. 7 - Power distribution when pulling a stalk depending on the angle of inclination of the pulling apparatus to the horizon with the coordinates of the root of the stalk *X*=0 m, *Y* =0 m, V_m=2.01 m/s

a – $\beta = 60^0$, A_m=0.007 J, A_p=0.159 J, A=0.166 J;

b – $\beta = 45^0$, A_m=0.005 J, A_p=0.161 J, A=0.166 J;

c – $\beta = 20^0$, A_m=-0.011 J, A_p=0.177 J, A=0.166 J

From the considered cases in fig.7, it can be seen that for the stalk that enters the picker vertically, it is pulled out of the soil mainly due to the power of the picker disk. When the angle of inclination of the harvester to the horizon is reduced, the share of traction power from moving the machine to pulling the stalk from the soil decreases. And for the case in fig.7c, it can be seen that the power takes negative values and part of the power of the pickup apparatus is spent on moving the machine - the phenomenon of power circulation described above. In addition, from the graphs in fig.7, it can be seen that when the angle of the pulling apparatus to the horizon is reduced, the length of the pulling stream zone, which is involved in pulling the stalk, increases from 0.057 m to 0.145 m.

As the calculations showed, the energy of pulling does not depend on the location of the stalks in the elementary bundle and in all cases is equal to A = 0.166 J.

In one second, the number of stalks n_s equal to:

$$n_s = B\ V_m\ t\ i \tag{18}$$

In our case, at B = 1.5 m, V_m= 2.01 m/s, t = 1 s, assuming i = 1600 stalks/m^2, it is obtained that J_c = 4824 stalks are selected in 1 second. Then the energy per second of pulling A_s will be equal to:

$$A_s = A \cdot n_s = 0.166 \cdot 4824 = 808.8 \text{ J}. \tag{19}$$

Flax stalks, which come to the pulling stream, are tilted by the side bars of the dividers in the direction of the machine, or as the central stalks are clamped vertically. If the power distribution graphs (fig. 4a, 4b) for an inclined and vertically standing stalk are considered, one can follow the following relationship: more inclined stalks are pulled out of the ground due to the traction power from the movement of the flax harvester, and less inclined stalks - under the action of the rotation of the pulling disc. Therefore, it can be assumed that in the general pulling of stalks, half of the power comes from the traction power of the movement of the flax pulling machine, and half - from the power of the pulling apparatus.

The spent energy was calculated: A_{ps}= 400 J; A_{ms} = 400 J.

CONCLUSIONS

The design of the disc-belt flax-pulling apparatus is proposed, which will increase the durability of the pulling belts and reduce the material consumption of the flax gleaning machine. The geometrical parameters of the pulling section of the disc-belt flax-pulling apparatus have been established. The energetics of the process of picking flax stalks, which are clamped in the curved longitudinal pulling stream of the disc-belt flax-pulling apparatus, have been theoretically investigated. The dynamics of changes in the components of pulling power when moving the flax stalk along the pulling stream were studied, depending on: the initial inclination of the flax stalk, the forward speed of the flax harvester, the angle of inclination of the pulling apparatus to the horizon. The energy per second of pulling and the value of its components are determined.

Graphical dependences of the distribution of pulling power between the loading of the disk-belt pulling apparatus and the traction force of the machine are given, depending on: the initial inclination of the flax stalk, the forward speed of the flax harvester, the angle of inclination of the pulling apparatus to the horizon. Calculations confirmed that the selected parameters of the apparatus fully satisfy the requirements of the pulling process. The pulling energy does not depend on the initial angle of inclination of the stalk and is equal to 0.166 J in all cases.

This design of the disc-belt pulling apparatus is at the design stage - drawings of assembly units and parts are being developed. This design is new, so the authors will be very grateful for comments and suggestions for its improvement.

REFERENCES

[1] Abdel-Wahab M. K., El-Sharabasy M. M. A. & El-Didamony M. I. (2012) Development and performance evaluation of a pulling flax machine. *Misr Society of Agricultural Engineering. (Farm machinery and power)* 29(3) Vol. 45, No. 3, 2012 pp. 973–992. https://www.academia.edu/105738184/Development_and_Performance_Evaluation_of_a_Pulling_Flax_Machine

[2] Bourmaud, A., Gibaud, M., & Baley, C. (2016). Impact of the seeding rate on flax stem stability and the mechanical properties of elementary fibres. *Industrial Crops and Products*, 80, 17-25. https://doi.org/10.1016/j.indcrop.2015.10.053

[3] Charney Madeleine (2014) Flax: Food and Fiber. *Journal of Agricultural & Food Information* Volume 15, 2014 - Issue 4 pp, 249-254. https://doi.org/10.1080/10496505.2014.952575

[4] Dudarev, I., Zabrodotska, L., Kirchuk, R., & Taraymovich, I. (2014) Reasoning on parameters of roller with spiral groove of flax pulling mechanism (Обґрунтування параметрів вальця з гвинтовим пазом льонобрального апарата). *INMATEH Agricultural Engineering*, 2014, 42(1), pp. 49–54. https://inmateh.eu/volumes/pdfs/8.pdf

[5] Dudarev I. (2015). *Theoretical bases for the modernization of flax production machines (Теоретичні основи модернізації машин для виробництва льону)***.** Monograph. Lutsk State Technical University, Lutsk, 268. Ukraine. ISBN 978-617-672-115-4 301

[6] Dudarev, I. (2020). A review of fibre flax harvesting: conditions, technologies, processes and machines. *Journal of Natural Fibers* (in press). http://doi.org/10.1080/15440478.2020.1863296

[7] Dudarev, I., & Say, V. (2020). Development of resource-saving technology of linseed harvesting. *Journal of Natural Fibers*, 17(9), pp. 1307-1316. https://doi.org/10.1080/15440478.2018.1558161

[8] Dudarev, I., & Khomych, A. (2022). Low-quality flax straw biomass harvesting for subsequent use as fuel: a review. *Agricultural Machines*, 48, 15-29. Ukraine. https://doi.org/10.36910/acm.vi48.779

[9] Goudenhooft, C., Alméras, T., Bourmaud, A., & Baley, C. (2019). The remarkable slenderness of flax plant and pertinent factors affecting its mechanical stability. Biosystems Engineering, 178, 1-8. https://doi.org/10.1016/j.biosystemseng.2018

[10] Hall, L.M., Booker, H., Siloto, R.M.P., Jhala, A.J., Weselake, R.J. (2016). Flax (Linum usitatissimum L.). *Industrial Oil Crops*, 157-194. https://doi.org/10.1016/B978-1-893997-98-1.00006-3

[11] Jhala, Amit J. & Hall, Linda M. (2010) Flax (*Linum usitatissimum L.*): Current Uses and Future Applications. *Australian journal of basic and applied sciences* 4(9):4304-4312

[12] Karg, Sabine. (2022) "Flax seeds from Neolithic and Bronze Age pile-dwelling sites in Europe" *Praehistorische Zeitschrift*, vol. 97, no. 1, 2022, pp. 90-109. doi.org/10.1515/pz-2022-2036

[13] Lafond, G. P., Irvine, B., Johnston, A. M., May, W. E., McAndrew, D. W., Shirtliffe, S. J., & Stevenson, F. C. (2008). Impact of agronomic factors on seed yield formation and quality in flax*. Canadian Journal of Plant Science,* 88, 485-500.

[14] Mańkowski, J., Maksymiuk, W., Spychalski, G., Kołodziej, J., Kubacki, A., Kupka, D. & Pudełko, K. (2018) Research on New Technology of Fiber Flax Harvesting. *Journal of Natural Fibers*. 2018. Vol. 15, Issue 1. pp. 53–61. doi: https://doi.org/10.1080/15440478.2017.1302390

[15] Nag, S., Mitra, J., & Karmakar, P. G. (2015). An overview on flax (Linum usitatissimum L.) and its genetic diversity. *International Journal of Agriculture, Environment and Biotechnology*, 8(4), 805-817.

[16] Omer, T. A., Amal, M. A. El-Borhamy, & Maysa, S. Abd. El-Sadek. (2020). Effect of harvesting dates and seeding rates on yield and yield components of some flax varieties. *Journal of Plant Production*, 11(12), 1501-1505. https://doi.org/10.21608/jpp. 2021.55272.1012

[17] Pisupati, A., Willaert, L., Goethals, F., Uyttendaele, W., & Park, C. H. (2021). Variety and growing condition effect on the yield and tensile strength of flax fibers. *Industrial Crops and Products*, 170, 113736. https://doi.org/10.1016/j.indcrop.2021.113 736

[18] Soucek, J., Sturc, T., Marecek, J. (2017). Analysis of linseed production with use of flax puller and combine harvester for its harvest. *Acta Univ. Agric. Silvic. Mendelianae Brun*, 65, 511-517.

[19] Yaheliuk, S., Didukh, V., Busnyuk, V., Boyko, G., & Shubalyi, O., (2020), Optimization on Efficient Combustion Process of Small-Sized Fuel Rolls made of Oleaginous Flax Residues. *INMATEH – Agricultural Engineering*, 62(3), pp. 361–368. Romania. https://doi.org/10.35633/inmateh-62-38/

[20] Yang, R.B., Li, X.J., Tan, S.L. (2009). Development survey and prospect of flax industry. *Modern Agricultural Sciences*, 4. http://en.cnki.com.cn/Article_en/CJFDTOTAL-NCSY200904121.htm

[21] Yukhymchuk, Sv., Yukhymchuk, S., Tolstushko, M., & Datsyuk, L. (2021). Energetics pulling of the flax stalks by pulling apparatus with rectlinear transversal streams (Енергетика брання стебел льону бральним апаратом з прямолінійними поперечними рівчаками). *Scientific notes (Наукові нотатки)*, Vol. 72, pp. 145-150, Ukraine. https://doi.org/10.36910/775.24153966.2021.72.21

[22] Yukhymchuk, Sv., Tolstushko, M., Yukhymchuk, S., & Datsyuk, L. (2022). Development of the design of a disc-belt flax-pulling device. (Розробка конструкції дисково-пасового льонобрального апарата) *Scientific notes (Наукові нотатки)*, Vol. 73, pp. 239-242, Ukraine. https://doi.org/10.36910/775.24153966.2022.73.35

[23] Zając, T., Oleksy, A., Klimek-Kopyra, A., & Kulig, B. (2012). Biological determinants of plant and crop productivity of flax (Linum usitatissimum L.). *Acta Agrobotanica*, 65(4), 3-14.

[24] Zuk, M., Richter, D., Matuła, J., & Szopa, J. (2015). Linseed, the multipurpose plant. *Industrial Crops and Products,* 75, Part B, 165-177. https://doi.org/10.1016/j.indcrop.2015.05.005

EVALUATION OF TRACTION CHARACTERISTICS OF TRACTOR TIRES ON LOOSE SOILS: SIMULATION AND EXPERIMENTAL RESEARCH
/
拖拉机轮胎在松软土壤上的牵引特性评价：仿真与试验研究

Jie WANG[1)], Lili SHANG[1)], Liangyuan XU[1,2)], Qiansheng TANG[1,2*)]
[1)] School of Engineering, Anhui Agricultural University, Hefei / China;
[2)] Anhui Intelligent Agricultural Machinery Equipment Engineering Laboratory, Hefei / China
E-mail: qiansh_tang@ahau.edu.cn
DOI: https://doi.org/10.35633/inmateh-71-33

Keywords: *bias-ply tire, tilled soil, Finite Element Analysis (FEA), traction characteristics*

ABSTRACT

In this study, a tire-soil rolling contact model based on the finite element method was established to determine the traction characteristics of the tire on the loose soil. Considering the soil parameters and tire parameters (loads, slip, inflation pressure and tread pattern), the influence of traction characteristics of the tire was obtained, taking tire sinkage and gross traction as evaluation indexes. The correctness of the tire-soil rolling contact model was verified by carrying out the soil bin-single wheel experiments. The results of the simulation and test showed that with the increase of load and sinkage of the tire, the gross traction tended to increase, thus enhancing the tire traction characteristics. With the increase of slip, the tire sinkage and gross traction increased, and the best tire traction characteristics were exhibited at a slip of 20%. Within the rated inflation pressure, as the inflation pressure increased, the tire sinkage decreased, the tire gross traction decreased and the traction characteristics of the tire were weakened. Under simulated working conditions, the traction characteristics of the tire first increased and then decreased with the increase of the number of tire lug pairs, and 15 tire lug pairs performed best. This paper presents a further study on the interaction between tires and soil under different influencing factors, and its findings provide an effective reference for predicting the traction performance assessment of tractor tires on working roads.

摘要

为了分析农用轮胎在松散土壤上的牵引特性，本研究以某型拖拉机轮胎为研究对象，综合考虑土壤参数、轮胎载荷、滑移、充气压力、胎面花纹等因素，以轮胎下沉量、轮胎总牵引力为指标来评价轮胎在土壤上的牵引性能。采用有限元方法建立了轮胎-土滚动接触模型，进行了轮胎-土沟槽试验。仿真与试验结果表明：随着载荷和轮胎下沉的增加，总牵引力呈增大趋势，从而增强了轮胎牵引特性。随着滑移量的增加，轮胎下沉量和总牵引力不断增大，在滑移量约为 20%时表现出最佳的轮胎牵引力特性。在额定充气压力范围内，随着充气压力的增大，轮胎下沉减小，总牵引力减小，轮胎的牵引力特性减弱。在模拟工况下，随着轮胎花纹数的增加，轮胎的牵引特性先增大后减小，存在最优值。本文深入研究了不同影响因素下轮胎与土壤的相互作用，其研究结果为预测拖拉机轮胎在工作道路上的牵引性能评估提供了有效参考。

INTRODUCTION

In recent years, an increasing number of large and medium-sized tractors have been used in agricultural production, and the rapid development and application of tractors have improved agricultural production efficiency to a certain extent. However, the increase in tractor power does not necessarily lead to an increase in production efficiency, since its driving ability also depends on the soil. The tire is the component in the closest contact with the soil, thus exploring the characteristics of the tire's movement on the soil is of great importance for improving the tire traction characteristics. The traction characteristics of tires on the soil have been investigated.

Wang et al. (2015) constructed a three-dimensional nonlinear finite element tire model with a detailed tread pattern and a smooth tread tire model for comparison. In these tire models, the tire-rim and tire-road interactions were considered and studied in the relationship between vertical loading and tire deflection, and the contact footprints, along with the pressure distribution achieved by the pressure-sensing pad experiment and the finite element tire modeling. *Sun et al. (2019)* established a finite element model for a 195/65R15 radial tire with the nonlinear analysis software ABAQUS, based on the tire structure and cord parameters.

[1] *Jie Wang, M.S. Stud. Eng; Lili Shang M.S. Stud. Eng; Qiansheng Tang, Ph.D. Eng.; Liangyuan Xu, Prof. Ph.D. Eng.*

Under constant tire pressure and load, the impact of velocity change on tire-cord stress during high-speed tire rolling was studied based on the finite element model to identify the relation between the cord stress and standing waves. *Wei et al. (2020)* proposed a finite element method for the analysis of the tire structure under the working conditions of assembly, with the help of ABAQUS software and the necessary evaluation of the finite element results of the loading condition, punching gas and loading, was also carried out. *Yamashita et al. (2018)* established a finite element model of wheel-soil interaction by using the multiplicative finite strain plasticity theory along with the capped Drucker-Prager failure criterion *(Drucker et al., 2013)*, investigated soil shaping, and analyzed the effects of tire-road friction, tire inflation pressure, vehicle velocity, and other factors on tire rolling radius and axle input torque.

Nakashima et al. (2009) analyzed the tractive performance of real automobile tires with two different tread patterns-smooth and grooved by FEA-DEM, to clarify the capabilities and limitations of the method for soil-tire interaction analysis. *El-Sayegh et al. (2020)* presented the coupling method of FEA-SPH to compute the interaction between an 8x4 off-road truck and gravelly soil (sand with gravel soil). The effect of gravelly soil compaction and truck loading on tire performance was discussed and investigated. *Zhao et al. (2019)* used the three-dimensional finite-discrete element method (FEM-DEM) for the simulation of tire-sand interactions, where the tire was discretized into hexahedron finite elements, and sand was modeled by using the discrete element method. *Zeng et al. (2019)* carried out the traction behavior research of an off-road tire on gravel terrain by the DEM-FEM coupling model with the calibrated microscopic input parameters mentioned.

Michael et al. (2015) proposed an efficient combination of the Discrete Element Method (DEM) and the Finite Element Method (FEM) to study the tractive performance of a rubber tire in interaction with granular terrain. *Bao et al. (2020)* analyzed the possibility of the wheels with wheel structure parameters and moving speed as experimental factors and designed a hydrostatic drive four-wheel vehicle. The values of wheel torque and rotational speed of each wheel in a wheel-soil contact simulation were confirmed to be consistent with actual values in the four-wheel vehicle. *Hu et al. (2021)* established an off-road tire steering model on sandy soil by using the discrete element method, the parameters of the sandy soil model were calibrated based on the triaxial compression test and inclined plate experiment. The influence of the steering radius, roll angle, and slip rate on the tire steering process was studied.

Huang et al. (2015) established a tractive trafficability predicted model through soil bin tests under light load, to study the tractive performance of lightweight vehicles on soft ground. Adopting the condition of light load with wheel load ranging from 30 to 90 N, the wheel sinkage, drawbar pull and tractive efficiency were taken as experimental indices, the wheel diameter, load and slip ratio were as experimental factors, and the regression orthogonal experiment scheme was designed. The effects of experimental factors on wheel tractive trafficability were also analyzed. Much literature focuses on rigid tires, sandy soils, and the strain behavior of soil, but relatively little on the comprehensive consideration of soil parameters, tire driving parameters, and the traction performance of bias-ply tires.

Therefore, this study focused on tractor tires and comprehensively took into consideration multiple factors related to tire forces and movement states, such as load, slip, inflation pressure, and the tire tread pattern to analyze the traction characteristics of agricultural tires on loose soil. In this paper, to address the above drawbacks, a new tractor tire-soil rolling contact finite element model is proposed, and simulation and experimental cases are investigated to verify the availability of the proposed model.

The main objectives of this paper were to (1) develop a tractor tire model and verify its correctness, (2) determine the physical parameters of loose soil, (3) establish a new finite element model of tire-soil contact, (4) construct soil bin-single wheel tester and analyze the influence of tire load, slip and inflation pressure on the traction characteristics of tractor tire, (5) investigate the influence of number of tread patterns on the traction characteristics of tractor tire by simulation further.

MATERIALS AND METHODS

Tire Modeling

An 11.2-24 8-ply rating bias-ply agricultural drive tire was simulated in this research. Considering the complex geometric structure of tires and rims, the tire-rim system was simplified into five parts including tread, belt plies, carcass, bead, and rim based on the requirements of tire structure and reliability. The tire design manual was used to obtain the tire-related parameters which were shown in Table 1. According to the tire parameters, a 3-dimensional (3D) model of the tire was constructed by using CATIA computer-aided design software (*Dassault Systèmes, Vélizy-Villacoublay, France*), as shown in Fig. 1.

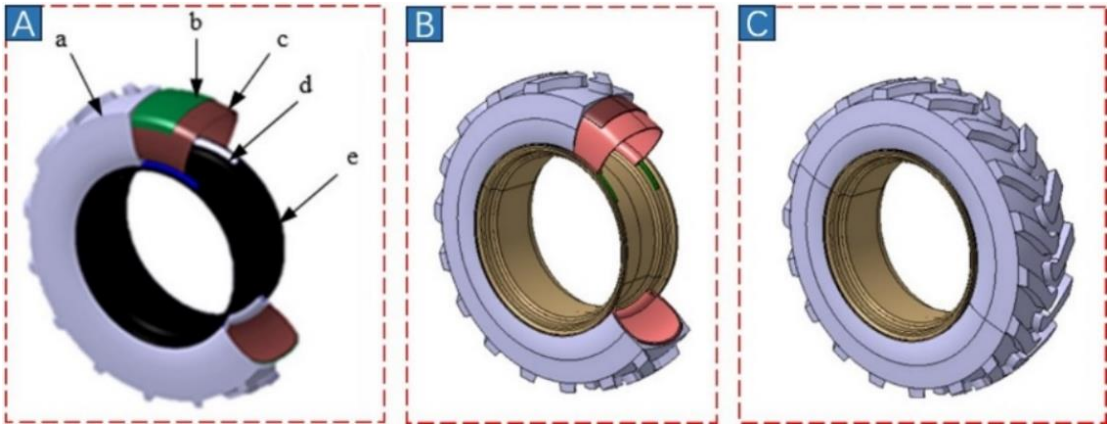


Fig. 1 – The tire 3D model

A is the structure of the tire schematic diagram (a – Tread; b – Belt ply; c – Carcass; d – Bead; e – Rim); B and C represent the tire 3D model in CATIA

Table 1

Tire-related parameters

Parameters	Overall diameter	Section width	Maximum inflation pressure	Maximum load
	[mm]	[mm]	[kPa]	[kg]
values	1105	285	240	1200

The 3D model of the tire was imported into the ANSYS Workbench finite element 118 analysis software (ANSYS, Inc., Canonsburg, PA), and correspondingly an appropriate material was assigned for each of the five tire components. Since the tread rubber material was highly non-linear and incompressible, the tread was simulated by the Yeoh constitutive model *(Li et al., 2016).* The carcass, Belt ply, and beads are the main load-bearing components of the tire. The materials of these tire components are composite materials that are composed of rubber materials and steel cords, and these tire components have the characteristics of anisotropic materials. Thus, these components were simulated with anisotropic materials in the process of modeling. The determined parameter values of the tread rubber material are shown in Table 2, and the defined parameter values of the tire carcass, Belt ply, and bead composite materials are shown in Table 3.

Table 2

Rubber material parameters

Component	Yeoh Material Ontology			Density (g/cm^3)
	C10	C20	C30	
Tread	2.3	-9.8	43.6	1.14

Table 3

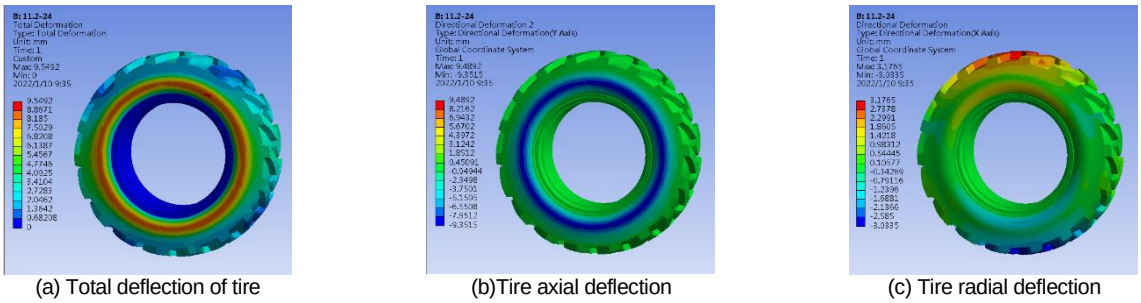
Anisotropic material parameters

Parameters		Belt ply	Carcass	Bead
Density (g/cm^3)		1.11	1.14	7.8
Poisson's ratio	U_{xy}	0.0034	0.004	0.3
	U_{yz}	0.49	0.49	0.49
	U_{xz}	0.0034	0.004	0.3
Elastic modulus (MPa)	E_x	80641	24.3	281
	E_y	55.7	24.3	281
	E_z	55.7	6.01	64.4
Shear modulus (MPa)	G_{xy}	14.28	6.01	64.4
	G_{yz}	19.24	8.2	93.5
	G_{xz}	14.28	6.01	64.4

Validation of tire model

In the tire-soil contact model, the correctness of the tire finite element model affects the reliability of the simulation results of the tire rolling on the soil. To verify the correctness of the tire model, the finite element simulation of the tire was performed with an inflated simulated tire. The tire-rim system was modeled in ANSYS Workbench, and a simulated 240 kPa standard inflation pressure was applied to the inside of the tire.

When the tire was inflated, the tire was deformed in section direction and the overall diameter direction; the tire side-wall part expanded outward, and the tire crown part moved upward. The deformation degree of the tire crown was lower than that of the tire sidewall, which was due to the softness and easy deformability of the sidewall material. The tire inflation simulation is shown in Fig. 2. According to the tire design requirements, the tire model can be considered correct when the maximum tire section width and overall diameter are less than the values specified by the tire manufacturer. The results of the tire inflation simulations show that the tire was inflated to an overall diameter of 1111.2 mm and a section width of 303.8 mm, both of which were less than the maximum deformation size, as shown in Table 4. Thus, the finite element model of the tire established in this paper is reliable and can be used for subsequent steady-state rolling simulations of the tire on the soil.



(a) Total deflection of tire (b)Tire axial deflection (c) Tire radial deflection

Fig. 2 - Tire deflections at the inflation pressure of 240 kPa (relative to standard atmospheric pressure)

Table 4

Tire inflation deformation volume compared with values specified by China National Standard (2017)

Dimension	After inflation simulation (mm)	Maximum allowable deformation after inflation (mm)
Overall diameter	1111.2	1135
Section width	303.8	308

Soil Modeling

The soil in contact with agricultural tires is mainly the soil at the plow layer (10 - 20 cm). The plow layer soil is affected by agricultural production activities, which makes the plow layer soil loose and unstable in physical properties. The mechanical properties of deep-layer soils with moderate water content and compact structure are hardly influenced by the external environment, thus deep-layer soil mechanical properties are excluded in this study. The modeling in this paper is based on the assumption that the soil is homogeneous, and the material of the soil is isotropic. In addition, in the process of modeling, the Drucker-Prager criterion is used to characterize the properties of soil materials. The Drucker-Prager criterion (DP criterion) is derived from the modification of the von Mises yield criterion, in which the yield strength-induced volume expansion is taken into consideration. DP criterion is expressed as follows (*Öztekin et al., 2016*):

$$\alpha I_1 + \sqrt{J_2} = K \tag{1}$$

where:

I_1 refers to the first invariant of the stress tensor; J_2 indicates the second invariant of the stress partial tensor; α and K are experimental parameters related to material properties and model selection, and they are determined by cohesion and internal friction angle. α and K are calculated according to the following formulae:

$$\alpha = \frac{2\sin\varphi}{\sqrt{3}\left(3-\sin\varphi\right)} \tag{2}$$

$$K = \frac{6C\cos\varphi}{\sqrt{3}\left(3-\sin\varphi\right)} \tag{3}$$

where: C is cohesion, (kPa); φ refers to angle of inter friction, (°).

The TSZ-2 full-automatic triaxial instrument (Nanjing soil instrument factory Co., LTD. China) was used in the triaxial experiment, which includes a pressure chamber, an axial compression system, a confining pressure loading system, and a software module.

The soil sample used in this experiment was yellow loose soil with a dry basis water content of 13.25% and the dry bulk density of 1.509 g/cm^3 (ρ). The diameter and height of the soil were 39.1 mm and 80 mm, respectively.

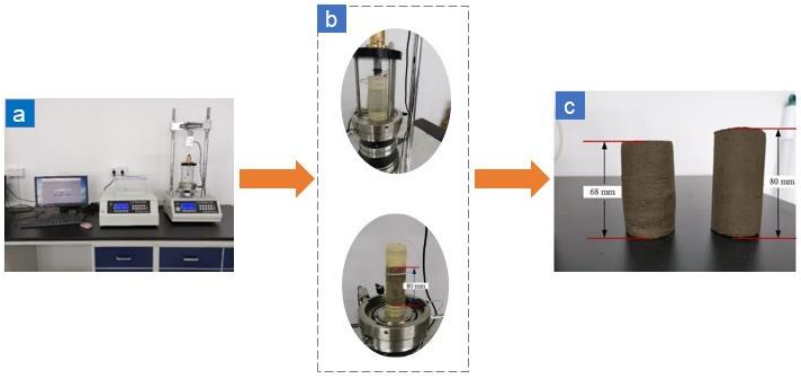


Fig. 3 - Soil triaxial instrument and deformation of soil sample at the end of the experiment

a – TSZ-2 full-automatic triaxial instrument; b –Soil loading; c – Experimental results.

In this paper, the mechanical properties of soil were measured by a triaxial experiment, and the process of the experiment is shown in Fig. 3. The experimental results are shown in Table 5.

Table 5

Loose soil parameters

Parameters	Density	Poisson's ratio	Shear modulus	Cohesion	Angle of internal friction
	[g/cm^3]	[%]	[MPa]	[kPa]	[°]
value	1.509	0.32	45	33.09	12.2

The wet bulk density and water content of undisturbed soil in the field were measured by using the cutting ring method on the samples from the surface layer (0 – 5 cm). To ensure the accuracy of the experiment, four measurement points were selected, among which three samples were taken from each point and the average value was taken as the measurement value of the point. The size and volume of the cutting ring in this experiment are Φ70×52 mm and 200 cm^3 respectively, as shown in Fig. 4. The wet bulk density of soil was obtained according to the following formulae:

$$\rho_0 = \frac{m_1 - m_2}{v} \tag{4}$$

where: ρ_0 is soil wet bulk density (g/cm^3), m_1 is the total weight of ring knife and soil, (g); m_2 is cutter weight, (g); v is ring cutter volume, (cm^3).



Fig. 4 - Soil wet bulk density and moisture determination experiment

a – Cutting ring; b – Self-weight of Aluminum box; c – Self-weight of soil; d – Weight of soil dried for 3 hours ; e – Drying oven; f – Constant weight of soil dried for 6 hours

The water content of the soil was obtained by drying the soil to constant weight in a drying oven, as shown in Fig. 4. The water content is then obtained according to the following formulae:

$$\omega = \frac{m_4 - m_5}{m_4 - m_3} \times 100\% \quad (5)$$

where:

ω is slip (per); m_3 refers to the self-weight of the Aluminum box (g); m_4 is the weight of soil and Aluminum box (g); m_5 indicates the constant weight of soil, (g).

The dry bulk weight of the field soil is then obtained according to the following formulae:

$$\rho = \frac{\rho_0}{1 + 0.01\omega} \quad (6)$$

where: ρ is dry bulk density of soil, (per).

The results of the density and water content experiment of the farmland soil are shown in Table 6:

Table 6

Test to get the bulk density and moisture content of farmland soil

Soil type	Measure point	Wet bulk density	Moisture content	Dry bulk density	Average wet bulk density	Average moisture content
		[g/cm³]	[%]	[g/cm³]	[g/cm³]	[%]
Loose soil	1	1.492	13.5	1.315	1.509	13.25
	2	1.504	13.3	1.327		
	3	1.523	13.4	1.343		
	4	1.515	12.8	1.343		

Tire-soil Contact Modeling

A tilled soil model was constructed with a length of 5 m, a width of 1 m, and a height of 0.8 m by using CATIA software. In terms of the characteristics of loose and soft soil, the soil was divided into two layers, namely, the tilled layer soil and the base layer. Based on the results of the triaxial experiment, the material parameters of the soil were added to ANSYS Workbench to determine the relevant parameters of the loose soil.

The establishment of the tire-soil contact model is the basis for the analysis of the interaction between the tire and the soil, and the contact state between the tire and the soil has a significant impact on the traction characteristics of the tire. In this study, a tire-soil rolling contact model was established by CATIA software (see Fig. 5A) and imported into ANSYS Workbench for simulation.

In this study, the tire sinkage, and gross traction were used as indexes to evaluate the traction characteristics of tires under the state of tire steadily rolling on the soil. The related indexes were calculated according to the following equations *(Zeng et al., 2019)*:

$$s = \frac{\omega r - v}{\omega r} \times 100\% \quad (7)$$

$$G_T = \frac{T}{r} \quad (8)$$

where: s is slip, (per); r refers to tire torque radius, (m); v is tire velocity, (m/s); T indicates input torque, (Nm); G_T is gross traction, (N).

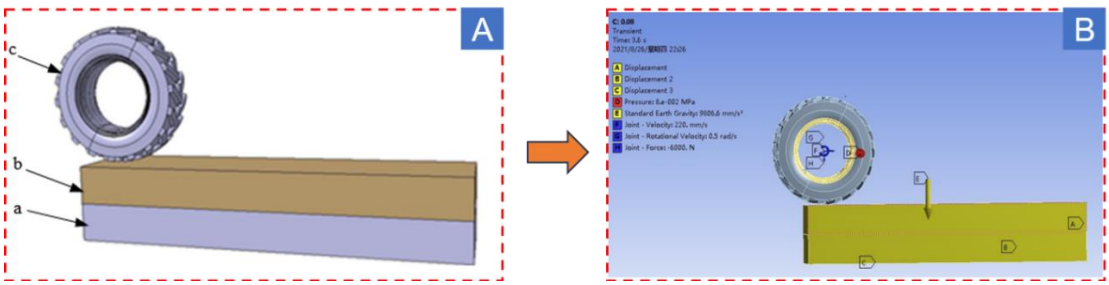


Fig. 5 - The tire-soil rolling contact model

a - The base layer; b -The tilled layer; c - Bias-ply tire

Firstly, the inflation pressure was applied to the tire in 0.02-0.34 s, and then the corresponding load was applied to the tire in 0.34-0.36 s. After the load on the wheel reached the target value, the tire was loaded with angular and horizontal velocity in 0.36-0.54 s. The simulation was performed by fixing the tire's angular velocity and changing the horizontal velocity of the tire to obtain different slips. The tire sinkage and tire traction were obtained by post-processing the simulation results, and the tire traction performance was studied by analyzing the results of the data on tire sinkage and tire gross traction (displacement was 0 mm, inflation pressure of tire was 8 kPa, the vertical load here was 6 kN). The tire-soil rolling contact model was shown in Fig. 5B. The mesh size in the tire-soil rolling contact simulation model was shown in Table 7.

Table 7

Mesh sizes used in the FEA model

Component	Tread	Belt ply	Carcass	Bead	Soil
Mesh size (mm)	32	32	32	28	20

A soil bin-single wheel tester composed of a soil bin, a single wheel test device, and a control and data acquisition system, was built to verify the accuracy of the numerical simulation results. The tire was mounted on the tire drive shaft of the soil bin tester. Firstly, a vertical load was applied to the tire and the magnitude of the vertical load was measured to a specified value by using a load cell and a screw jack. Secondly, the frequency conversion motor and servo motor were activated to pull the single wheel carriage assembly along the direction of travel to the specified speed with the tire being free-rolling, ensuring that the tire enters a stable driving state under a certain load. During the driving process, the torque sensor and the wire displacement sensor were used to record the values of the traction torque and sinkage of the tire, respectively. Then, the experiment curve of the traction torque and sinkage of the tire were obtained by using these values. Finally, the resultant values for the steady rolling condition of the tire were taken as the traction torque and sinkage of the tire under this load for subsequent calculations. The soil bin-single wheel tester was shown in Fig. 6.



Fig. 6 - Soil bin-single wheel tester

(a) Displacement sensors for the value of sinkage of the tire acquisition (b) Jack and load sensors (c) Laptop computer for data acquisition (d) Wheel input torque sensor (e) Traction motor unit to drive the wheel axle

RESULTS

Effect of Load

Because the soil resistance to the thrust and rolling of the tire is affected by the load on the tire, the traction characteristics of the tire are related to the load on the wheel. To explore the influence of on-wheel load on the traction characteristics of tire-soil contact, six groups of different on-wheel loads were simulated at a fixed slip rate of 20% and constant inflation pressure of 240 kPa. The six on-wheel load values were 0, 2000N, 4000 N, 6000 N, 8000 N, and 10000 N, respectively.

The cloud images of tire rutting imprint after the tire rolled under different loads were shown in Fig. 7, and the tire sinkage curve and traction curve were shown in Fig. 8. With the load on the wheel, the more obvious the rutting mark of the tire, the greater the soil deformation.

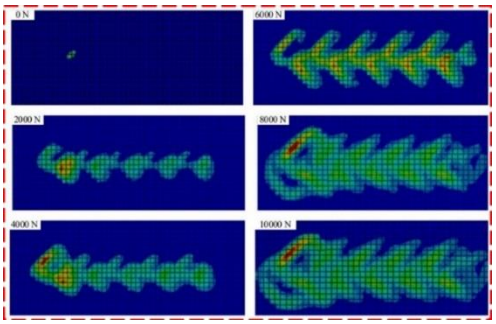
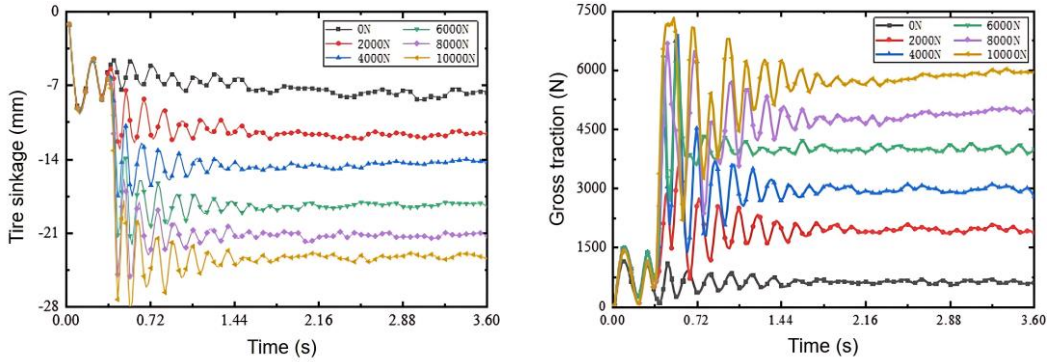


Fig. 7 - Comparison of tire rutting marks under different loads

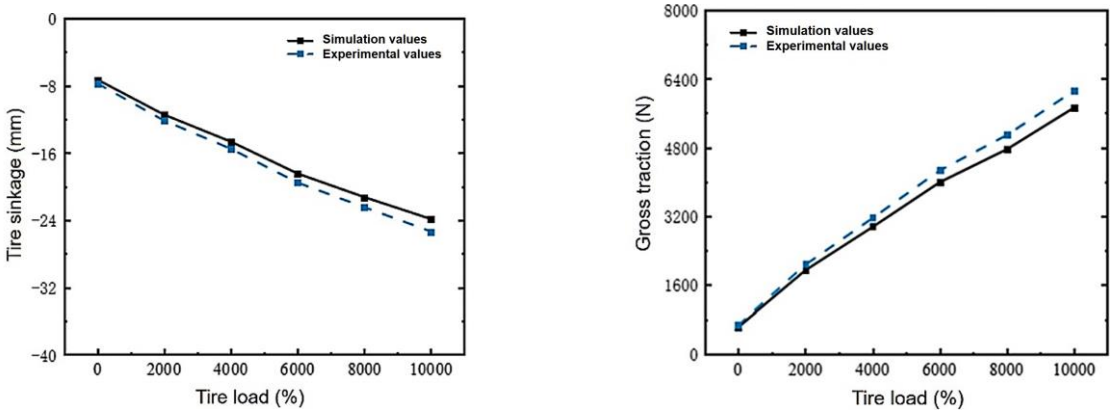


(a) Tire sinkage curve (b) Gross traction curve

Fig. 8 - The curve of the effect of different loads on the tire-soil contact action

In Fig. 8a and Fig. 8b, the tire was in the state of inflation, on-wheel loading, and speed loading during the first 0.54 s at the beginning of the simulation, and after 0.54 s, the tire was loaded to the corresponding horizontal speed and rotation speed. Due to the material nonlinearity of the tire and the soil, the geometric nonlinearity caused by the tire and soil deformation, and the contact nonlinearity during the rolling process, the corresponding values of variables such as sinkage and gross traction fluctuate, and then gradually become stable. The corresponding simulation results were obtained when the tire sinkage and gross traction values became stable during the tire rolling process. The relationship among tire sinkage, gross traction, and tire load was presented in Fig. 11.

As shown in Fig. 9a, the tire sinkage simulation value increased from 7.3 mm to 23.9 mm with the increase in tire load. In Fig. 9b, the tire gross traction simulation value increased 9.02 times with the increase in tire load. These results could be explained as follows: with the increase of tire load, the normal force of the tire on the soil increased, thus resulting in larger soil sinkage and a larger contact area between the tire and soil. In the case of the fixed ground adhesion coefficient, the larger the tangential reaction force of the soil on the tire, the larger the tire's gross traction, and the better the traction characteristics.



(a) Tire sinkage (b) Gross traction curve

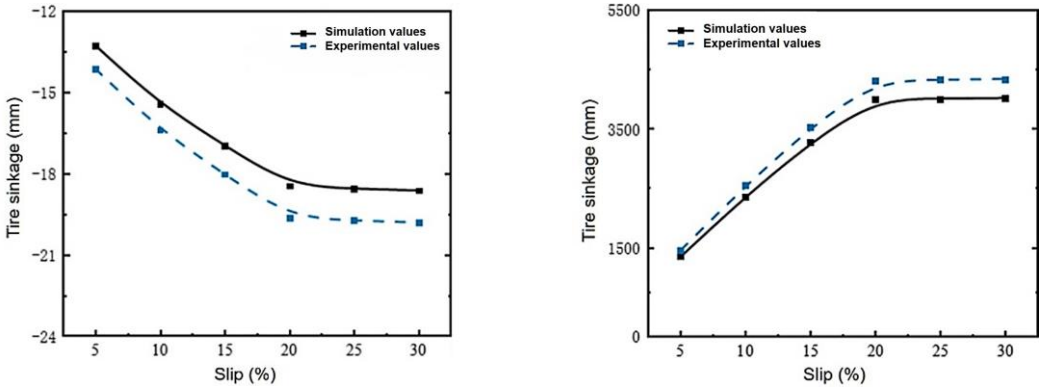
Fig. 9 - Effect of different loads on tire-soil contact interaction

Effect of Slip

The tire slip affects the shear deformation of soil and tire-soil contact surface, thereby affecting the tire traction characteristics. In this study, the tire slips were set as 5%, 10%, 15%, 20%, 25%, and 30%, respectively at a tire load of 6000 N and tire inflation pressure of 240 kPa. After the steady-state rolling results were processed, the values of tire sinkage, and tire gross traction under different tire slips were obtained to reveal the influence of different tire slips on tire traction characteristics (Fig. 10).

As shown in Fig. 10a, with the increase of the slip, the tire sinkage simulation value was firstly continuously increased, reaching the value of 18.47 mm at about 20% of the slip, and then the rate of growth tended to be stable. The gross traction increased as the slip increased, but there was a clear turning point for growth. As shown in Fig. 10b, when the slip increased from 5% to 20%, the increase in gross traction was greater; the trend in gross traction flattened out as the slip increased from 20% to 30%. When the slip reached 20%, the gross traction growth rate turned around indicating that the optimal tire traction characteristics were obtained.

As a result of the increase in slip, the shearing effect of the tire on the soil is enhanced, thus resulting in the enlarged soil shearing deformation and the increased tire sinkage. During the tire slipping process, the compaction of the soil is increased, thus soil deformation is reduced, and the tire sinkage is no longer increased. With the increase of slip, the soil is sheared to produce stacking. To ensure the normal driving of tires, tire gross traction is increased. When the tire slip intensifies to a certain extent, the soil compaction increases, and the shear force acting on the soil reaches the maximum and is limited by soil adhesion, thus the tire gross traction gradually becomes stable.

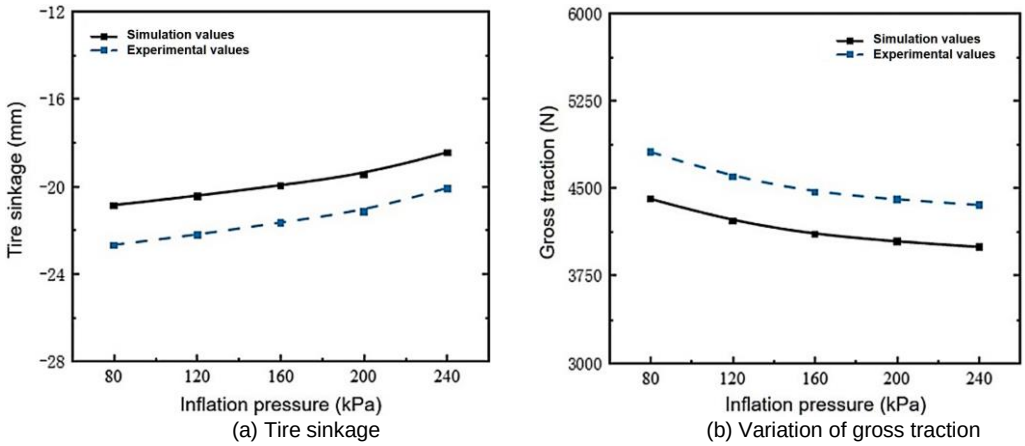


(a) Tire sinkage (b) Variation of gross traction

Fig. 10 - Effect of different slip on tire-soil contact interaction

Effect of Inflation Pressure

The change in the tire inflation pressure affects the stiffness of the tire which affects the adhesion of the tire to the soil. At the fixed tire slip of 20% and tire load of 6000 N, the influence of tire inflation pressure on tire traction characteristics was investigated under the inflation pressure conditions of 80 kPa, 120 kPa, 160 kPa, 200 kPa, and 240 kPa, respectively.



(a) Tire sinkage (b) Variation of gross traction

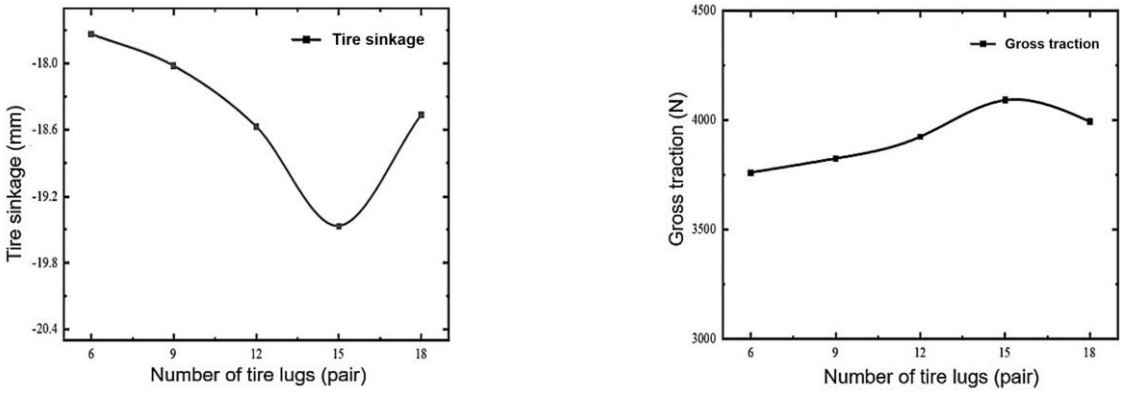
Fig. 11 - Effect of different inflation pressures on tire-soil contact interaction

As shown in Fig.11a, within the rated inflation pressure range (80 ~ 240 kPa), the sinkage of the tire decreases with the increase of inflation pressure, and when the rated inflation pressure reaches the maximum (240 kPa), the tire sinkage simulation value reaches a minimum of -18.47 mm. In Fig.11b, tire gross traction gradually decreases with the increase of tire inflation pressure, and the rate of gross traction reduction gradually decreases. When the inflation pressure reaches its maximum (240 kPa), the gross traction of the tire reduces by 8.5%.

With the increase of inflation pressure, the tread gradually deformed, the tire sidewall and crown parts expanded outward under the inflation pressure, and the tire stiffness increased. Under the same load, the contact area between the tread and soil under high inflation pressure was smaller than that under low inflation pressure, thus leading to the weakened shearing and compaction effects of tires on soil, eventually resulting in the decrease of tire sinkage and tire gross traction. Therefore, when the tractor works on the agricultural soil surface, the tire pressure should be reduced appropriately to improve the tire traction characteristics.

Effect of Number of pairs of lugs on the tire

The number of tread patterns affects the tire tread gap and the contact area between the tire and the soil. To investigate the effect of the contact area between tread and soil on tire traction characteristics, the finite element software was used to analyze the influence of the number of tread patterns on the traction characteristics of the tire, based on the traction characteristics under tire load, slip rate, and tire pressure that has been verified experimentally. The number of pairs of lugs on the tire was used to characterize the gap among tire patterns and tire-soil contact area, with the constant size of lugs on the tire. At the fixed tire slip of 20%, an inflation pressure of 240 kPa, and a constant wheel load of 6000 N, the effects of tire patterns on the tire sinkage, and tire gross traction were investigated by changing the number of pairs of lugs on the tire. (Fig. 12).



(a) Tire sinkage amount (b) Variation of gross traction

Fig. 12 - Effect of different tread densities on tire-soil contact interaction from simulation

As shown in Fig. 12a, the tire sinkage increases with the increase of the number of tire lug pairs. The tire sinkage reaches the maximum of -19.47 mm when the number of pairs of lugs on the tire increases to 15, and thereafter the tire sinkage decreases with the increase of the number of tire lug pairs. As shown in Fig. 12b, the gross traction force firstly increases and then decreases as the number of lug pairs increases. When the number of tire lug pairs increases to 15, the tire gross traction reaches the maximum of 4091 N, then the gross traction keeps decreasing.

Within a certain range, as the number of tire lug pairs increases, which results in the enhancement of the cutting effect on the soil and the increase of the shear slip surface, the soil sinkage and the gross traction increase, namely the enhancement of the traction characteristics of the tire. However, the excessive number of pairs of lugs on the tire will lead to a decrease in the gap between tread patterns, thus the tire gradually turns into a glossy tire, thereby weakening the shear effect of the tire on soil, namely, reducing gross traction to adversely affect tire traction characteristics.

The research content of this paper provides an effective reference value for the analysis of tractor tire-soil interaction using the finite element method. Its findings provide an effective reference for predicting the traction performance assessment of tractor tires on working roads.

CONCLUSIONS

In this study, a tire-soil rolling contact model was constructed using the finite element method, the tire-soil groove experiments were carried out, and the traction characteristics of the tire were analyzed based on multiple influencing factors such as the load, the slip, the inflation pressure, and the number of pairs of lugs on the tire.

The major conclusions were as follows:

(1) With the increase in on-wheel load, and the tire sinkage, gross traction showed an increasing trend, thus enhancing the traction characteristics.

(2) With the increase in the slip, the tire sinkage and the gross traction were continuously increased, reaching the growth rate turning point at the slip of about 20%, exhibiting the optimal tire traction characteristics.

(3) Within the rated inflation pressure range, as inflation pressure increased, the tire sinkage, and the gross traction decreased, thus the tire traction characteristics were weakened.

(4) Under the simulation conditions, with the increase of the number of tire lug pairs, the traction characteristics of the tire gradually increased and reached the maximum when the number of tire lug pairs was 15, and afterward decreased, thus 15 tire lug pairs performed best.

The research content of this paper provides an effective reference value for the analysis of tractor tire-soil interaction by using the finite element method. Its findings provide an effective reference for predicting the traction performance assessment of tractor tires on working roads.

ACKNOWLEDGEMENT

The authors thank Fund Project: National Key Research and Development Program and Technology Major Special Project and Anhui Province Engineering Laboratory of Intelligent Agricultural Machinery and Equipment and Anhui Agricultural University for their funding support.

REFERENCES

[1] Bao, Y. D., Yang, J., Zhao, Y. L., Liu, X. L., Guo, Y. L., Li, Z. P., & Xiang, J. Z. (2020). Design of the walking driving system for a blueberry harvester based on contact mechanical behavior of wheel-soil. *Transactions of the Chinese Society of Agricultural Engineering, China,* 36(07), 43-52. https://doi.org/10.11975/j.issn.1002-6819.2020.07.005

[2] Drucker, D. C., & Prager, W. (2013). Soil mechanics and plastic analysis or limit design. *q.appl.math, USA*, *10(2)*, 157-65. https://doi.org/10.1090/qam/48291

[3] El-Sayegh, Z., El-Gindy, M., Johansson, I., & Öljer, F. (2020). Development and validation of off-road tire-gravelly soil interaction using advanced computational techniques. *Journal of Terramechanics, Netherlands,* 91, 45-51. https://doi.org/10.1016/j.jterra.2020.05.004

[4] Hu, C., Gao, J., Diao, J., & Song, X. (2021). Numerical simulation of tire steering on sandy soil based on discrete element method. *AIP Advances, USA,* 11(1), 015015. https://doi.org/10.1063/5.0034585

[5] Huang, H., Li, J. Q., Wu, B. G., Zhang, G. Q., Xue, L., & Wang, Y. (2015). Construction and verification of lightweight vehicle wheel tractive trafficability model under light load. *Transactions of the Chinese Society of Agricultural Engineering, China,* 31(12), 64-70. https://doi.org/10.11975/j.issn.1002-6819.2015.12.009

[6] Michael, M., Vogel, F., & Peters., B. (2015). Dem–FEM coupling simulations of the interactions between a tire tread and granular terrain. *Computer Methods in Applied Mechanics and Engineering, Netherlands,* 289, 227-248. https://doi.org/10.1016/j.cma.2015.02.014

[7] Nakashima, H., Takatsu, Y., Shinone, H., Matsukawa, H., & Kasetani, T. (2009). FE-DEM analysis of the effect of tread pattern on the tractive performance of tires operating on sand. *Journal of Mechanical Systems for Transportation & Logistics, China,* 2(1), 55-65. https://doi.org/10.1299/jmtl.2.55

[8] Öztekin, E., Pul, S., & Hüsem, M. (2016). Experimental determination of Drucker-Prager yield criterion parameters for normal and high strength concretes under triaxial compression. *Construction and Building Materials, Netherlands, 112,* 725-732. https://doi.org/10.1016/j.conbuildmat.2016.02.127

[9] Sun, P. F., Huang, H. W., Zhou, S. T., Chiu, Y. J., Du, M., & Zhao, D. H. (2019). Experiment and analysis of cord stress on high-speed radial tire standing waves. *Shock and Vibration. USA*. https://doi.org/10.1155/2019/3607670

[10] Wang, W., Yan, S., & Zhao, Y. (2015). Numerical and experimental studies of a radial truck tire with tread pattern. *Simulation Transactions of the Society for Modeling & Simulation International, USA,* 91(11). https://doi.org/10.1177/0037549715608434

[11] Wei, L. J., Liu, H. O., Chen, H. Y., & Zhao, Z. Y. (2020). Finite element analysis of cross section of TBR tire. *Mechanics of Advanced Materials and Structures, USA,* 27(17). 1509-1517. https://doi.org/10.1080/15376494.2018.1517911

[12] Li, X. B., & Wei, Y. T. (2016). An improved Yeoh constitutive model for hyperelastic material. *Engineering Mechanics, China,* 33(12), 38-43. https://doi.org/10.6052/j.issn.1000-4750.2015.05.0388

[13] Yamashita, H., Jayakumar, P., Alsaleh, M., & Sugiyama, H. (2018). Physics-based deformable tire-soil interaction model for off-road mobility simulation and experimental validation. *Journal of Computational and Nonlinear Dynamics, USA,* 13(2), 021002. https://doi.org/10.1115/1.4037994

[14] Zhao, C. L., & Zang, M. Y. (2017). Application of the FEM/DEM and alternately moving road method to the simulation of tire-sand interactions. *Journal of Terramechanics, Netherlands,* 72, 27-38. https://doi.org/10.1016/j.jterra.2017.04.001

[15] Zeng, H. Y., Xu, W., Zang, M. Y., & Yang, P. (2019). Calibration of DEM-FEM model parameters for traction performance analysis of an off-road tire on gravel terrain. *Powder Technology, Netherlands,* 362, 350-361. https://doi.org/10.1016/j.powtec.2019.12.006

DESIGN AND OPTIMIZATION OF AN INTEGRATED EXCAVATION AND TRANSPLANTING DEVICE FOR TOBACCO
/
烟草打塘-移栽一体化装置的设计与优化

Zhiguo PAN[1)], Tianfeng SUN[1)], Xiaomeng WANG*[2)], Qiuqiang HOU[2)], Shiting LV[1)], Luming ZHANG[2)], Zhenfei YANG[2)], Xuehui ZHANG[2)]

[1)]College of Mechanical and Electrical Engineering, Qingdao Agricultural University, Qingdao, 266000, China;
[2)]Yunnan Tobacco Company Honghezhou Company, Honghezhou 652300, China;
DOI: https://doi.org/10.35633/inmateh-71-34

Keywords: *Tobacco Seedling Transplantation, Conical spiral blade, Discrete Element, Simulation optimization*

ABSTRACT

To overcome inadequate functional integration, irregular pits, and insufficient agricultural machinery and agronomy in tobacco seedling transplanting equipment under film, a digging transplanting integrated machine was built. The machine uses parallel four-bar mechanism. The excavation equipment uses conical spiral blades. Using the trajectory approach, the four bar mechanism's fundamental parameters can be reversed. This method meets the requirements for coordinated excavation and transplantation. Mechanical study of soil units determines upward movement characteristics. Additionally, spiral angle, spiral blade outer diameter, and spiral blade speed are quantified to affect soil movement. The range of factors is derived. Based on three factors binary regression orthogonal combination simulated optimization experiment, a discrete element analysis was performed to enhance parameters. Experimental factors optimized include a spiral angle of 19°, a spiral blade diameter of 378 mm, and a rotational speed of 258 rpm. The two optimized test indicators are: a 193 mm hole depth and 350 mm hole diameter. The improved results were verified by field validation studies using a 191 mm hole depth and 347 mm hole diameter. The simulation optimization results and field validation experiment results are very similar. This study provides a technical basis for tobacco farming concurrent drilling and transplanting research.

摘 要

针对目前烟苗膜下移栽装备功能集成度差、打塘不规整、农机农艺融合度较差等问题，设计了一种基于平行四杆机构的打塘-移栽一体式移栽机，其中打塘装置采用锥形绞龙结构。通过轨迹法反求出四杆机构的基本参数，满足打塘和移栽的同步同穴作业。通过力学分析，确定出土壤运动过程中的临界条件，计算出影响土壤运动的主要因素包括螺旋升角、钻头外径和钻头转速，并推导出因素的范围。为优化参数，进行了基于离散元的三因素二元回归正交组合仿真优化试验。优化后的试验因素为：螺旋升角为19°、钻头外径为378mm、钻头转速为258rpm。优化后的两项试验指标的结果为：穴孔的深度为 193mm，穴孔的直径为 350mm。为验证优化后的结果进行了田间验证试验，穴孔深度为191mm，穴孔直径为347mm。田间验证试验结果与仿真优化后的结果十分接近。本研究为烟苗打塘-移栽一体机的研发提供技术参考。

INTRODUCTION

Tobacco cultivation in the southern area of China involves the transplantation of tobacco plants into meticulously excavated deep trenches. Research conducted by agronomists has demonstrated that the practice of transplanting tobacco seedlings in deep pits yields several beneficial outcomes. These include an increase in temperature, enhanced resistance to drought, preservation of soil moisture, improved lighting conditions, enhanced soil fertility, reduced incidence of pests and diseases, and the provision of a conducive environment for the early growth of tobacco seedlings *(Chen et al., 2014; Wang et al., 2010)*.

Cui conducted a series of field tests aimed at investigating the influence of deep pit dimensions, specifically the diameter and depth, on tobacco development. Through these studies, Cui effectively demonstrated the significant role that pit size plays in determining the growth of tobacco plants *(Cui et al., 2018)*. Hence, the practice of excavating deep pits in tobacco transplanting operations has a clear correlation with the overall quality of tobacco transplantation and subsequent production. In order to tackle this critical process, scholars have conducted extensive research on devices for excavating deep pits. Academic researchers have drawn inspiration from spiral blades and undertaken comprehensive enhancements and optimization designs in order to fulfil the specifications pertaining to the diameter and depth of deep pits.

Jiang, *(1997)*, conducted a study to determine the critical speed of soil lifting motion for spiral blades. This investigation involved analysing the movement and stress experienced by individual soil units on the spiral surface of the drill bit. The aim was to investigate the relationship between the parameters of the spiral surface and the critical speed required for effective soil lifting. In accordance with this theoretical framework, scientists have developed a range of pond excavation apparatuses in order to meet the specific criteria pertaining to hole dimensions and functional objectives.

Liu et al., (2018), conducted an analysis of the operational mechanism of a portable hole forming machine and afterwards derived the structural parameters of the hole forming device based on the desired hole size. The effectiveness of the device's operation was then validated by field trials. A portable device has been developed for the purpose of facilitating tobacco transplantation in mountainous regions, specifically designed to create pond mouths. During the computation of structural characteristics, the soil is simplified as an isotropic elastic-plastic material, and the necessary aperture size is generated by means of a drilling tool *(Yu et al., 2018)*. The aforementioned studies address the issue of pre-transplanting digging in the context of tobacco cultivation. However, upon the completion of the digging device operation, mechanized transplanting becomes challenging due to problems such as ground wheel slip and unstable tractor forward speed. These issues hinder the ability of the transplanting machine to effectively plant seedlings into the pre-dug pits. Consequently, the process of manual transplantation is typically conducted subsequent to the mechanical excavation procedure.

The aforementioned issues serve as adequate examples to demonstrate the pressing need for resolving the integrated process of pit digging and transplanting in tobacco cultivation. Numerous academic investigations have been undertaken by scholars in relation to this subject matter. The duckbill transplanting mechanism is widely employed in dryland transplanting machines, making it the prevailing choice in this context. By manipulating the horizontal movement and speed of the duckbill mechanism, the machine can effectively control the forward speed and assure the proper alignment of the seedling during the direct planting process into the soil.

Xiong et al., (2020), designed the structural parameters of the duckbill planter based on the hole size, and optimized the motion trajectory through simulation, enabling the duckbill planter to squeeze out a hole in the soil while transplanting.

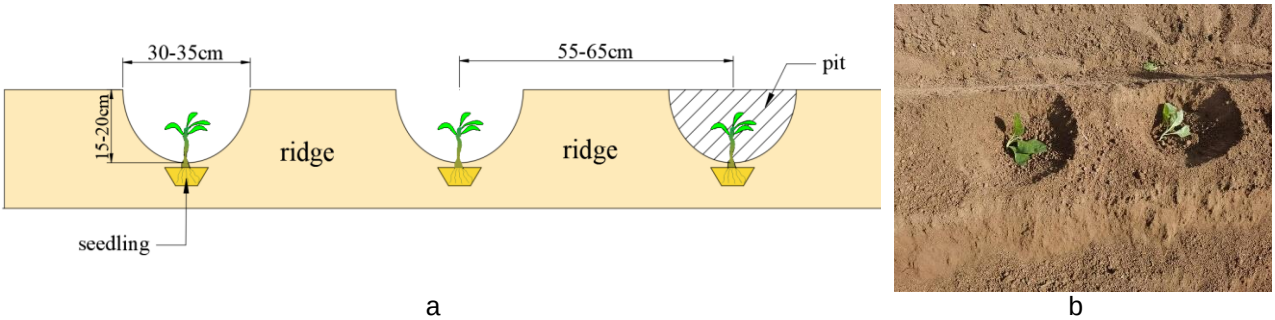
Fan et al., (2019), designed a self-propelled tobacco transplanting machine that uses a parallel four bar mechanism to control the duckbill planter for transplanting operations, forming a hole in the soil while transplanting. Despite the above researches demonstrated feasibility in hole digging and transplanting, it is crucial to acknowledge a notable limitation: the resulting holes are both small and irregular, posing challenges in meeting the agricultural demands for deep hole planting of tobacco seedlings.

In response to the above problems, this study combined the specific requirements of hole size and transplanting uprightness to design a multifunctional tobacco transplanter that integrates a digging mechanism and a transplanting mechanism, which realizes digging and transplanting simultaneously.

MATERIALS AND METHODS

Agronomic requirements

The tobacco seedlings were transplanted beneath a mulch film utilizing robust seedlings that were 35-40 days old and measured 5-8 cm in height *(Yao, 2017; Lu, 2015)*. As depicted in Figure 1, it is important to excavate pits prior to planting in order to provide an appropriate living environment for tobacco seedlings subsequent to transplantation. The deep pit has a top diameter ranging from 30 to 35 cm, a depth ranging from 15 to 20 cm, and a plant spacing of 55 to 65 cm.



a b

Fig. 1- Agronomy of tobacco seedling transplantation under film

Overall structure and working principle

A tobacco transplanting device based on a parallel four bar mechanism was designed to meet the requirements of agronomy while also achieving the integration of excavation and transplanting processes. The device consists of rotary tillage device, seedling feeding device, pond digging device, transplanting device, and transmission system. The ground wheel powers the movement of the seedling feeding device and the four bar mechanism device. Figure 2 depicts the overall structure.

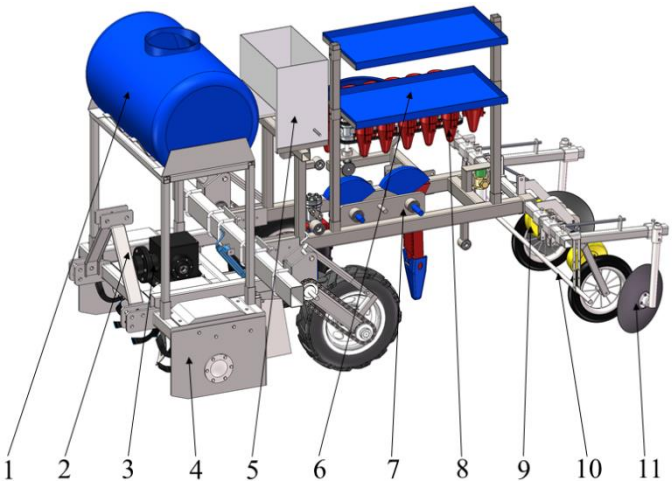


Fig.2-Structure diagram of the entire machine.

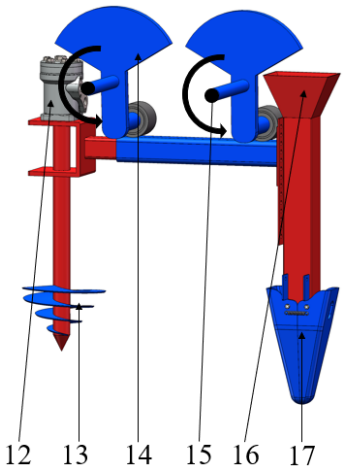


Fig.3-Structural diagram of the integrated mechanism for digging and transplanting.

1. Water tank; 2. Three point suspension device; 3. Reduction gearbox; 4. Rotary tillage device; 5. Fertilizer box; 6. Loading seedling trays; 7. Four bar mechanism; 8. Seedling feeding device; 9. Film pressing wheel; 10. Film covering device; 11. Earth cover wheel; 12. Hydraulic motor; 13. Spiral blades; 14. Counterweight block; 15. Rotation centre; 16. Falling seedling mouth; 17. Duckbill planter.

During the operational phase, the operator transfers the seedlings from the seedling tray and inserts them into the suspended cup of the seedling division device. The seedling division device and the four bar mechanism device exhibit simultaneous movement. When the seedling receiving aperture of the duck beak planter ascends to its highest position, the suspended cup initiates its opening mechanism, causing the tobacco seedlings to descend into the duck beak, so accomplishing the operation of seedling deployment. The completion of the works of digging and transplanting is facilitated by a device that combines a parallel four bar mechanism and is controlled by a transmission system. The duckbill planter is utilized to relocate tobacco seedlings to the precise location within the hole created by the digging mechanism.

Integrated operation device for digging and transplantation structural design

A digging transplanting mechanism has been devised, which utilizes a parallel four-bar mechanism to achieve integrated operation of digging and transplanting. The working principle and motion trajectory are depicted in Fig. 4. Two cranks exhibit a counterclockwise rotational motion around a shared centre of rotation, with both cranks rotating at an equivalent speed. Simultaneously with the rotation of the crank, the hydraulic motor propels the spiral blades of the excavation apparatus, causing them to rotate and create perforations on the ridge. The motion trajectory of the device is determined by four parameters, namely the length of the connecting rod, the forward speed of the implement, the speed of the crank, and the length of the crank. This can be observed from the working principle.

Parameters λ are typically provided to describe the composite motion that consists of both rotation and translation in the integrated process of excavation and transplantation.

In order to streamline the computation process, as demonstrated in equation (1), Fig 5 describes the law of influence on trajectory of the parameters λ.

$$\lambda = \frac{l\omega}{v} \tag{1}$$

Note: l is the length of the crank, (mm); ω is the crank speed, (rpm); v is the forward speed of the implement (m/min).

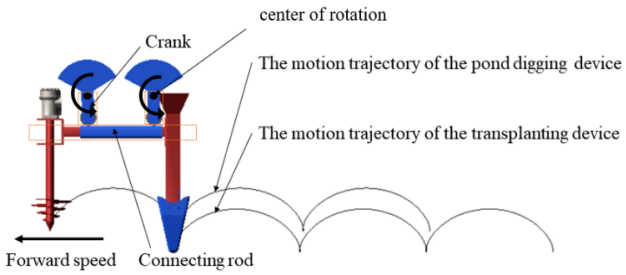


Fig. 4 - Motion trajectory diagram of the integrated mechanism for digging and transplanting

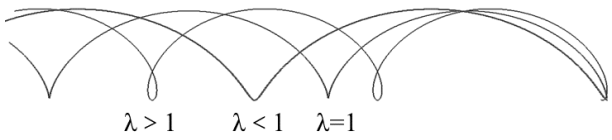


Fig. 5 - The law of influence on trajectory of the parameters λ

To ensure the vertical alignment of seedlings upon transplantation, it is imperative to maintain a value of λ equal to 1. The interdependence between the velocity of the implement and the speed at which planting occurs can be elucidated through the utilization of Formula 2, given that the implement is propelled by ground wheels.

$$\frac{v}{p} = d \tag{2}$$

Note: v is the forward speed of the implement, (m/min); p is the transplanting rate, (plants/min); d is the plant spacing, (m).

When determining the parameters for the connecting rod design, the distance between plants is selected as the intermediate value of 0.5 m. This implies that the length of the connecting rod is 0.5 m. According to the "*Operation Standards for Dryland Transplanters"*, it is stipulated that the operational efficiency of dryland transplanting machines must be equal to or greater than 35 plants per minute, although the upper limit of efficiency should normally not surpass 55 plants per minute. Hence, by supposing a constant rate of 45 plants per minute, the velocity of the machines may be determined as v=27 m/min. When the planting rate is 45 plants per minute, the angular velocity (ω) is equal to crank speed. By substituting the numerical value into equation (1), the resulting crank length is determined to be l=9.6 cm.

Designing parameters for spiral blades

During the excavation process, the soil is propelled upwards by the rotational movement of spiral blades, resulting in the formation of pits. Hence, throughout the soil displacement process, the motion of the soil can be categorized into two distinct phases. The initial phase involves the vertical displacement of the soil, wherein the dirt ascends in conjunction with the rotational motion of spiral leaves, so creating the essential depressions for the cultivation of tobacco seedlings. The subsequent phase involves the parabolic trajectory of the soil.

Factor analysis of soil lifting movement

The movement and stress of the soil at the interface between the outer edge of the spiral blade and the pit wall were investigated by researchers *(Xiao, 2010)*. The deduction made by the researcher states that when the relative velocity of the soil unit is zero (V_r=0), and the angle between the absolute velocity and the horizontal plane is zero (β=0), the critical speed formula for the rotation of the spiral blade, which allows the soil to rise, is as follows:

$$n_k = 9.6\sqrt{\frac{g\tan(\alpha+\varphi_1)}{(1-\frac{\tan\zeta}{\tan\alpha})^2 r_0 f_2}} \tag{3}$$

Note: g - Aacceleration of gravity; α- The spiral angle at the outer edge of the spiral surface, (°); φ_1- Friction angle between soil and spiral surface, (°); ξ- The angle between the velocity of soil particles at the outer edge of the spiral surface and the horizontal plane, (°); r_0- Drill radius, (mm); f_2- The internal friction coefficient of the soil, (N).

The relationship between the spiral angle and radius of the spiral blade and the critical speed of soil lifting motion can be observed from equation (3). Hence, it is imperative to ascertain the appropriate range of two variables in order to establish a factual foundation for subsequent simulation and optimization studies.

The range of outer diameter and helix angle for spiral blades

Figure 6 displays the three-dimensional representation of the spiral blade.

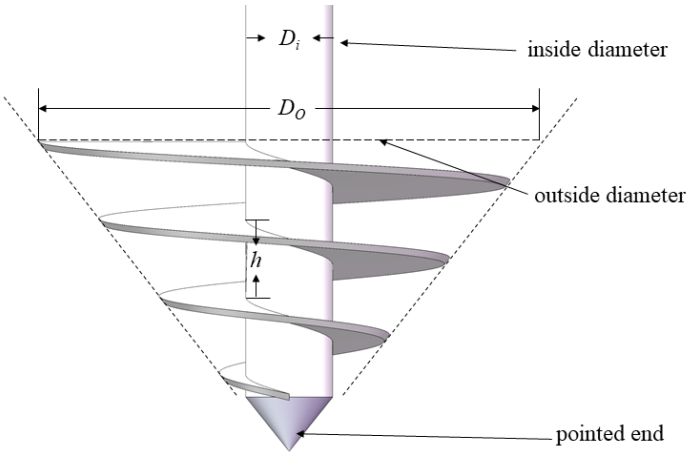


Fig. 6 - Three-dimensional view of spiral blades

h – Pitch, (mm); D_i- Diameter of central axis, (mm); D_O- Maximum diameter of spiral blade, (mm).

The diameter range of the pond mouth is determined by agricultural criteria, namely falling within the range of 350 mm to 400 mm. Additionally, the outer diameter D_0 of the drill bit must satisfy formula (4) *(Ba, 2022)*. Hence, the range of D_0 is determined to be 322 mm to 392 mm.

$$0.92D \le D_O \le 0.98D \tag{4}$$

Once the range of the outer diameter of the spiral blade has been established, the remaining structural parameter that needs to be determined is the spiral lift angle. The mathematical expression used to determine the spiral rising angle is as follows:

$$\gamma = \arctan\frac{h}{\pi D_i} \tag{5}$$

Note: γ is the spiral rising angle, (°).

The investigation conducted by researchers on the spiral rise angle has revealed that the design parameters for spiral rise angle must adhere to the constraints outlined in formula (6) *(Lu et al., 2022; Yang et al., 2020; Giuseppe et al., 2021)*.

$$\gamma \le 90^o - (\rho_1 + \rho_2) \tag{6}$$

Note: ρ_1 is the friction angle between soil and steel, (°); ρ_2 is the friction angle between the soil, (°).

Upon reviewing the related data, it was determined that the value of ρ_1 is 30°, whereas the value of ρ_2 is 40° *(Qin et al., 2016; Gao et al., 2015)*. Based on the given information, it can be inferred that the value of α is less than or equal to 20 degrees. Currently, the spiral rise angle of the excavated spiral blades is all above 15 °. Therefore, the range of spiral rise angles considered is limited to values between 15° and 20°.

The range of spiral blade speeds

Based on equation (3), it can be deduced that in the absence of contact between the spiral blade and the soil (ξ=0), the critical speed of the spiral blade is denoted as $n_k = 9.6g\tan(\alpha + \varphi_1)/r_0 f_2$.

However, it should be noted that the critical speed under these conditions does not hold any practical significance. The purpose of spiral blade rotation lies in generating upward motion force for soil displacement. Therefore, it is imperative to do kinematic and mechanical analyses on the soil unit within the context of soil flow. These analyses aid in determining the appropriate range of rotational speeds for the spiral blades.

Figure 7 depicts the force study conducted on the particles comprising the soil flow unit.

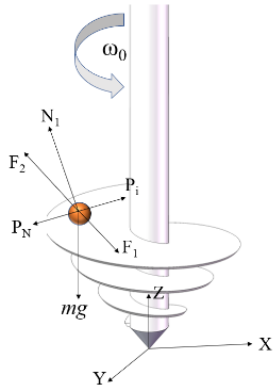


Fig. 7 - Force analysis of soil particle units

When the spiral blades undergo a consistent rotational velocity, the soil unit situated on these blades experiences many distinct forces. These forces consist of the gravitational force, denoted as mg, exerted on the soil unit due to gravity, as well as the positive pressure, labelled as f_1, exerted by the inner soil on the soil unit. Furthermore, there are other forces that are being exerted.

The supporting force (N_1) of spiral blades on soil units.

$$N_1 = mg\cos\gamma \tag{7}$$

The frictional force (F_1) of spiral blades on soil units.

$$F_1 = f_1 N_1 \tag{8}$$

The inertial centrifugal force (P_N) of the soil unit.

$$P_N = mr\omega_0^2 \tag{9}$$

Note: In the formula, r is the distance between the soil unit and the axis of rotation, (mm).

The positive pressure (P_i) of the outer soil on the soil unit.

$$P_i = P_N \tag{10}$$

The frictional force F_2 of the outer soil on the soil unit.

$$F_2 = f_2 P_i \tag{11}$$

After determining the force on soil particles, by calculating the acceleration and centrifugal force of the soil unit, one can directly assess the soil particles' motion status. The absolute acceleration of the soil unit can be determined as it is situated on the spiral surface of a uniformly rotating drill bit and moves in an upward direction with respect to the spiral surface.

$$a_a = a_e + a_r + a_k \tag{12}$$

Note: In the formula, a_e - implicated acceleration; a_r - relative acceleration; a_k Coriolis acceleration.

$$a_e = a_{en} + a_{e\tau} \tag{13}$$

$$a_r = a_{rn} + a_{r\tau} \tag{14}$$

$$a_{e\tau} = a_{r\tau} = 0 \tag{15}$$

Note: In the formula, a_{en} is the normal acceleration of the implicated motion; $a_{e\tau}$ is the tangential acceleration of the motion involved; a_{rn} is the normal acceleration of relative motion; $a_{r\tau}$ is the tangential acceleration of relative motion.

$$a_{en} = r\omega_0^2 \tag{16}$$

$$a_{rn} = \frac{v_r^2}{\rho} \tag{17}$$

Note: In the equation, ω_0 is the normal rotational speed, (rpm); v_r is the velocity of movement at the soil unit (mm/s); ρ is the curvature radius of the helix at the soil unit.

$$\rho = \frac{r}{\cos^2\gamma} \tag{18}$$

$$a_k = 2\omega_0 v_r \sin(90^o + \gamma) = 2\omega_0 v_r \cos\gamma \tag{19}$$

On the basis of equations (12) to (19), the absolute acceleration of the soil unit is calculated as follows:

$$a_a = r\omega_0^2 + \frac{v_r^2 \cos^2\gamma}{r} - 2\omega_0 v_r \cos\gamma \tag{20}$$

Because of $v_r\ cos\gamma$, it is the projection of v_r on the horizontal plane v_{rx}, so the absolute acceleration of the soil unit is:

$$a_a = r\left(\omega_0 - \frac{v_{rx}}{r}\right)^2 \tag{21}$$

From this, it can be determined that the soil unit's centrifugal force F_c is:

$$F_c = mr\left(\omega_0 - \frac{v_{rx}}{r}\right)^2 \tag{22}$$

The following equation is obtained by projecting the forces operating on the soil unit onto the X, Y, and Z axes:

$$f_2 P_i - f_2 F_3 - f_1 N_1 - mg\sin\gamma = 0 \tag{23}$$

$$N_1 - mg\cos\gamma = 0 \tag{24}$$

$$P_i - F_3 - P_N = 0 \tag{25}$$

Combining formulations (23) through (25) leads to the conclusion that:

$$mr\left(\omega_0 - \frac{v_{rx}}{r}\right)^2 = \frac{mg\left(f_1\cos\gamma + \sin\gamma\right)}{f_2} \tag{26}$$

The critical speed of the spiral blade is achieved when the soil unit remains stationary in relation to the blade's rotation. Hence, as equation (26), the critical angular velocity of the spiral blade can be determined.

$$\omega_0 = \sqrt{\frac{g\left(f_1\cos\gamma + \sin\gamma\right)}{rf_2}} \tag{27}$$

The critical speed of the spiral blade is:

$$n_0 = \frac{30}{\pi}\omega_0 = 9.6\sqrt{\frac{g\left(f_1\cos\gamma + \sin\gamma\right)}{rf_2}} \tag{28}$$

Note: In the formula, f_1 is the friction coefficient between the soil and the spiral surface, and f_2 is the friction coefficient between soil particles.

By integrating the data on spiral blade diameter and spiral angle, it can be determined that the critical speed falls between the range of 138.36 rpm to 188.22 rpm. To ensure the proper upward movement of the soil, the simulation test requires a minimum speed that is determined by calculating the highest critical value theoretically. This value is found to be 188.22 rpm.

In the drilling procedure, it is imperative to implement measures that prevent the soil ejected during drilling from infiltrating the pre-existing well, as depicted in Fig 8. The distance at which soil is ejected is directly influenced by the centrifugal force imposed on soil particles by the spiral blades. Therefore, the optimal rotational speed of the spiral should be determined by the rotational speed at which the soil particles no longer fall into the prepared pit.

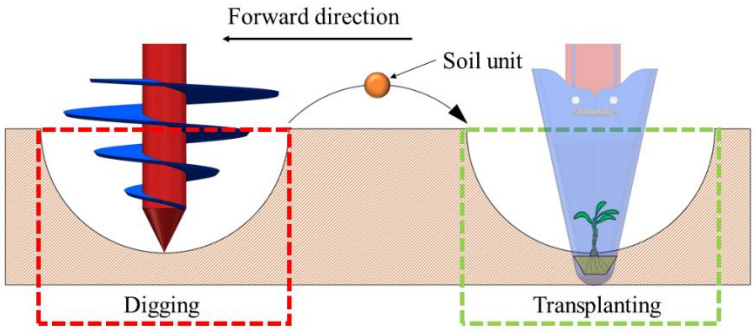


Fig. 8 - Schematic diagram of soil flowing into other pits

When doing theoretical calculations, it is imperative to take into account the minimum distance at which soil can infiltrate a previously excavated pit. By integrating the design parameters of pit size and plant spacing, a minimum distance of 250 mm can be determined. According to the data presented in Figure 9, the forces experienced during soil ejection encompass the influence of gravity as well as the forces exerted by spiral blades. Consequently, the trajectory of soil particles during ejection can be regarded as a form of oblique projectile motion. By utilizing equation (22), it is determined that the distance covered during soil ploughing is 250 mm when the rotational speed is 373.7 rpm.

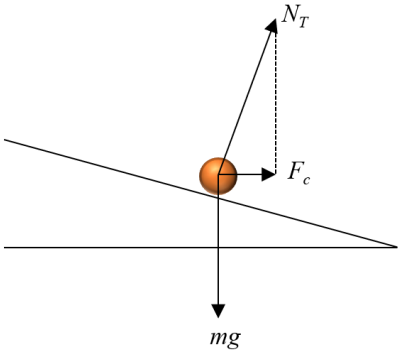


Fig. 9 - Force analysis of soil particles at the moment of being thrown out

N_T represents the force exerted by the spiral blade on soil particles at the moment when the soil is thrown out

Discrete element simulation optimization

Based on the aforementioned theoretical study, it has been ascertained that the primary factors influencing the dimensions of the pit are the spiral angle z_1 (x_1), the outer diameter z_2 (x_2) of the spiral blade, and the rotating speed z_3 (x_3) of the spiral blade. The experiment involves two indicators, specifically the depth of the hole (y_1, measured in millimetres) and the diameter (y_2, also measured in millimetres). Table 1 displays the experimental factors and corresponding levels.

Table 1. Experimental factors and levels

Factors / Levels	Spiral rising angle z_1 (°)	Spiral blade outer diameter z_2 (mm)	Spiral blade speed z_3 (rpm)
1	15	322	188.22
2	17.5	357	280.96
3	20	392	373.70

The present study utilizes a three factors binary regression orthogonal combination design and incorporates three zero point tests (m_0=3), resulting in an obtained r^2=1.831 *(Li et al., 2005; Li et al., 2005)*. Prior to conducting the experiment, it is imperative to encode the natural elements *(Zhuang et al., 1992; Zheng, 2004; He, 2013)*, as illustrated in Table 2.

Table 2. Test factor coding table

$x_j(z_j)$	z_1	z_2	z_3
$r(z_{2j})$	20	392	373.70
$1(z_{0j}+\Delta_j)$	19.3477	382.8684	349.504
$0(z_{0j})$	17.5	357	280.96
$-1(z_{0j}-\Delta_j)$	15.6523	331.1316	212.416
$-r(z_{1j})$	15	322	188.22
$\Delta_j=(z_{2j}-z_{1j}).(2r)^{-1}$	1.8477	25.8684	68.5440
$x_j=(z_j-z_{0j}).(\Delta_j)^{-1}$	$0.5412(z_1-17.5)$	$0.0387(z_2-357)$	$0.0146(z_3-280.96)$

Numerous academics have undertaken research on the intrinsic and contact properties of soil and steel in the extant body of literature. Hence, by the examination of relevant literature, the parameters utilized in the discrete element simulation are identified and shown in Table 3 *(Song et al., 2022; Tekeste et al., 2018; Sun et al., 2022)*.

Table 3. Basic simulation parameter settings

Parameter			Value
Intrinsic parameter	Soil	Density/(kg.m^{-3})	2679
		Shear modulus/(Pa)	1.2e+5
		Poisson's ratio	0.36

Parameter			Value
	Spiral blade	Density/(kg.m^{-3})	7810
		Shear modulus/(Pa)	2.07e+11
		Poisson's ratio	0.3
Contact parameter	Soil-soil	Restitution coefficient	0.2
		Static friction coefficient	0.4
		Rolling friction coefficient	0.3
	Soil- spiral blade	Restitution coefficient	0.5
		Static friction coefficient	0.5
		Rolling friction coefficient	0.3

The simulation process is represented in Fig. 10, and the pits following the simulation operation are displayed in Fig. 11.

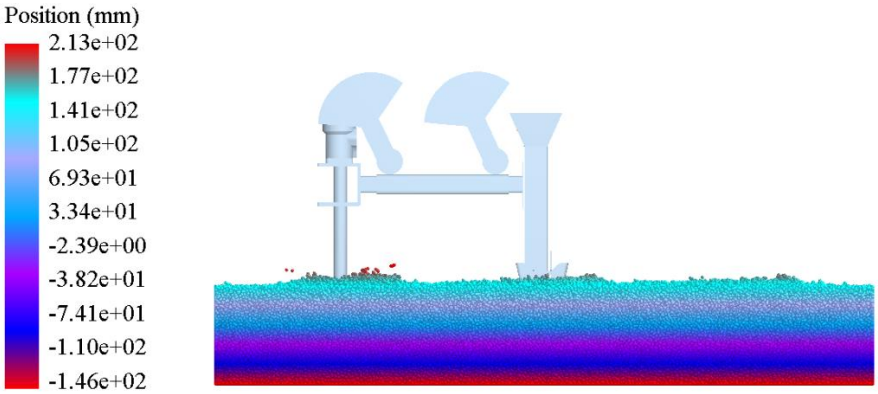


Fig. 10 - Simulation test process

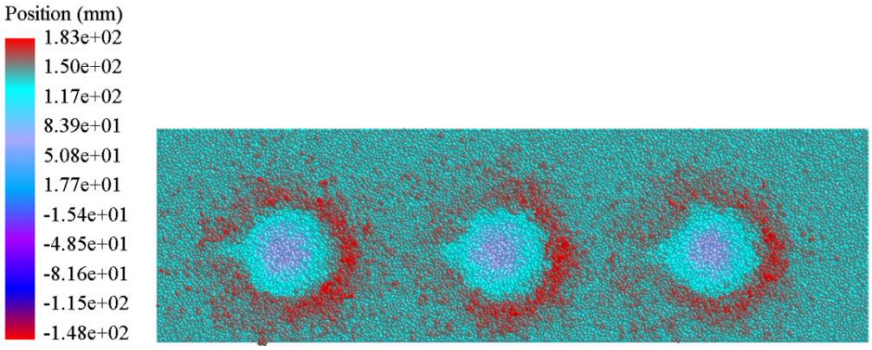


Fig. 11 - Simulation test effect

RESULTS AND DISCUSSION

Test results

The test results are presented in Table 4.

Table 4. Design of experiments results

Test	x_1	x_2	x_3	x_1x_2	x_1x_3	x_2x_3	x_1^2	x_2^2	x_3^2	y_1	y_2
1	-1	-1	-1	1	1	1	1	1	1	135	260
2	1	-1	-1	-1	-1	1	1	1	1	170	308
3	-1	1	-1	-1	1	-1	1	1	1	169	310
4	1	1	-1	1	-1	-1	1	1	1	188	342
5	-1	-1	1	1	-1	-1	1	1	1	162	306
6	1	-1	1	-1	1	-1	1	1	1	187	345
7	-1	1	1	-1	-1	1	1	1	1	181	343
8	1	1	1	1	1	1	1	1	1	198	380
9	$-r$	0	0	0	0	0	r^2	0	0	140	286
10	r	0	0	0	0	0	r^2	0	0	187	349
11	0	$-r$	0	0	0	0	0	r^2	0	164	287
12	0	r	0	0	0	0	0	r^2	0	194	348
13	0	0	$-r$	0	0	0	0	0	r^2	158	285
14	0	0	r	0	0	0	0	0	r^2	189	349
15	0	0	0	0	0	0	0	0	0	180	328
16	0	0	0	0	0	0	0	0	0	180	328
17	0	0	0	0	0	0	0	0	0	180	328

The depth and diameter of pits were acquired by a three factors binary regression orthogonal combination experiment, conducted under various parameter combinations. Fig.12 illustrates the juxtaposition of the test value curves and fit value curves of two regression models. The blue line corresponds to the measured value of the test, whereas the red line shows the value obtained from fitting the sample. It is evident that these two groups of numbers exhibit a high degree of proximity.

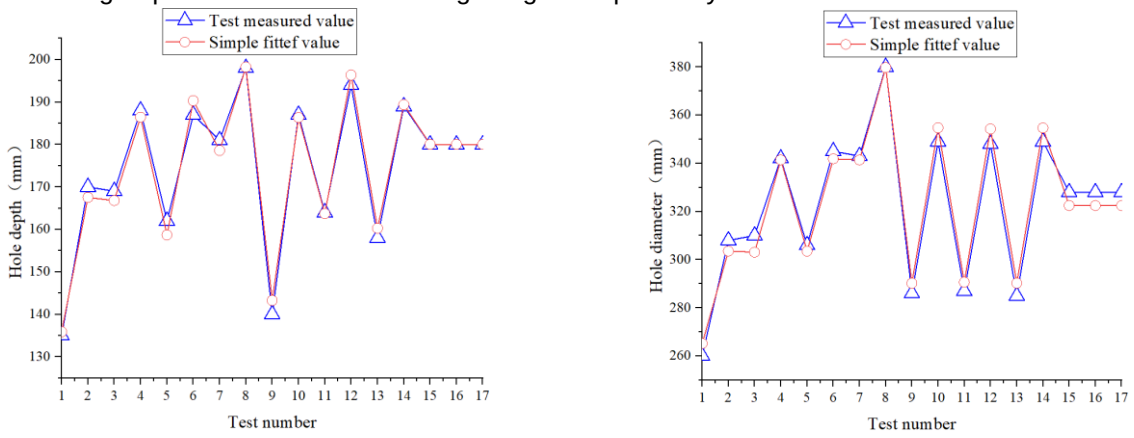


Fig. 12 - Comparison of measured and fitted values

According to the findings presented in Table 5, the P-values for both models are below the threshold of 0.01. This suggests that the models exhibit a high level of statistical significance, suggesting their ability to effectively predict the values of pit depth and pit diameter. The determination coefficients R^2 for the two models are 0.9659 and 0.9740, respectively. These values suggest that the regression models are able to account for 96.59% and 97.4% of the observed cases, respectively. The coefficient of variation (C.V.) for the two data sets is 1.48% and 1.65%, respectively. The aforementioned pair of primary values signifies a substantial level of concordance between the projected values of the regression equation and the observed measured values.

After removing insignificant factors, the binary regression equation for pore depth and pore diameter is obtained as follows:

$$y_1 = -1820.9436 + 128.45z_1 + 2.84z_2 + 1.3531z_3 - 0.097z_1z_2 - 0.0024z_2z_3 - 2.4345z_1^2 - 0.0006z_3^2 \quad (30)$$

$$y_2 = -325.7619 + 12.9034z_1 + 0.9098z_2 + 0.3474z_3 \quad (31)$$

Based on equation (30), there exists a positive linear relationship between the depth of the hole (y_1) and the spiral angle (x_1), the outer diameter of the spiral blade (x_2), and the rotational speed of the spiral blade (x_3). Based on equation (31), there exists a positive linear relationship between the hole diameter y_2 and the spiral angle x_1, the outer diameter x_2 of the spiral blade, and the rotational speed x_3 of the spiral blade. This phenomenon can be attributed to the three components theory, wherein it is seen that a greater spiral angle has the potential to enhance the soil's fluidity, hence facilitating its expulsion from the hole. There is a positive correlation between the outer diameter of the spiral blade and the diameter of the drilled hole. The depth of a hole is determined by the angle of repose of soil particles when the hole diameter is bigger. The upward lifting force exerted by the spiral blade is directly proportional to the rotational speed of the spiral blades. Hence, an increase in rotating speed results in an augmented vertical and horizontal displacement of the soil, as well as a deeper excavation. This finding aligns with the research outcomes of Meng and Gao *(Gao. 2018; Meng. 2007)*.

Table 5. Analysis of hole related data

Source	Hole depth				Hole diameter			
	Sum of Squares	Mean Square	*F* Value	*P*-Value	Sum of Squares	Mean Square	*F* Value	*P*-Value
Model	5063.27	562.59	86.00	< 0.01**	15087.08	1676.34	54.54	< 0.01**
x_1	2243.60	2243.60	342.96	< 0.01**	5024.54	5024.54	163.47	< 0.01**
x_2	1284.63	1284.63	196.37	< 0.01**	4896.33	4896.33	159.30	< 0.01**
x_3	1021.91	1021.91	156.21	< 0.01**	5012.34	5012.34	163.07	< 0.01**
x_1x_2	72.00	72.00	11.01	0.0128*	40.50	40.50	1.32	0.2887
x_1x_3	18.00	18.00	2.75	0.1411	2.00	2.00	0.0651	0.8060
x_2x_3	60.50	60.50	9.25	0.0188*	18.00	18.00	0.5856	0.4691
x_1^2	321.15	321.15	49.09	< 0.01**	46.60	46.60	1.52	0.2580
x_2^2	0.2295	0.2295	0.0351	0.8567	46.60	46.60	1.52	0.2580
x_3^2	36.60	36.60	5.59	0.0499	55.06	55.06	1.79	0.2226
Residual	45.79	6.54			215.15	30.74		
Lack of Fit	45.79	9.16			215.15	43.03		
Pure Error	0	0			0	0		
	R^2=0.9659; C.V.=1.48%				R^2=9740; C.V.=1.65%			

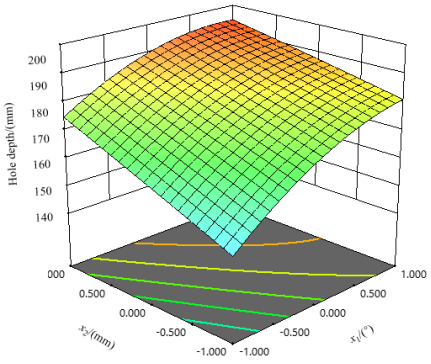
*Note: 0.01 < p < 0.05 (significant, *); 0.001 < p < 0.01 (highly significant, **).*

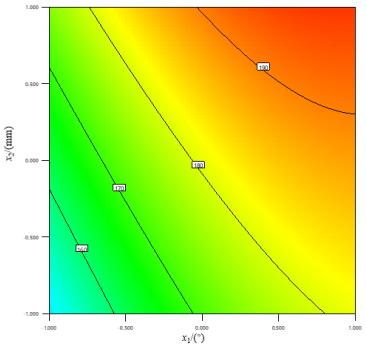
Table 5 demonstrates the significant influence of various factors on the depth of the hole. Firstly, the spiral angle (x_1) exhibits a highly significant impact on the depth of the hole (y_1) (P<0.01). Secondly, the outer diameter of the spiral blade (x_2) also displays an extremely significant influence on y_1 (P<0.01). Additionally, the helical blade speed (x_3) significantly affects the depth of the hole (y_1) (P<0.01). Furthermore, the interaction term x_1x_2, representing the combined effect of the spiral rising angle and the outer diameter of the spiral blade, significantly impacts y_1 (P<0.05). Similarly, the interaction term x_2x_3, representing the combined effect of the outer diameter of the spiral blade and the drilling speed of the spiral blade, significantly influences the depth of the hole (y_1) (P<0.05). Moreover, the square term x_1^2, representing the squared value of the spiral rise angle, significantly affects y_1 (P<0.01). However, it is worth noting that the remaining experimental factors do not exhibit a significant impact on the depth of the hole (y_1). Upon disregarding the negligible factors, the examination of the F-value reveals that the relative impact of each significant factor on the depth of pores follows the sequence $x_1>x_2>x_3>x_1^2>x_1x_2>x_2x_3$. This observation aligns with the functioning of the spiral blades of the excavator as investigated by Guo *(Guo et al., 2003)*. The spiral angle (x_1) exhibits a statistically significant effect on the pore diameter (y_2) with a p-value less than 0.01. Similarly, the outer diameter (x_2) of the spiral blade demonstrates an extremely significant influence on the hole diameter (y_2) with a p-value less than 0.01. Additionally, the helical blade speed (x_3) also exhibits an extremely significant impact on the hole diameter (y_2) with a p-value less than 0.01. Upon disregarding the negligible components, it becomes evident through a comparison of the F value that the three primary terms exhibit a very similar influence on the pore diameter. This finding aligns with the research outcomes of scholars investigating the interplay between conical spiral drills and soil *(Jin, 2022)*.

Response surface analysis

Based on the analysis of the response surface depicted in Fig 13, it is evident that the hole depth exhibits a positive correlation with the spiral angle x_1 when the drilling speed of the spiral blade is 280.96 rpm. Furthermore, the rise of this correlation follows a non-linear pattern, characterized by an initial increase, followed by a subsequent decrease. There is a positive correlation between the increase in diameter x2 of the spiral blade and the rising trend observed in the depth of the hole. When the spiral angle (x_1) is equal to 20 degrees and the outside diameter of the spiral blade (x_2) measures 392 mm, the depth of the hole (y_1) is determined to be 187 mm. The hole depth (y_1) exhibits a positive correlation with the spiral angle (x_1) as the outside diameter (x_2) of the spiral blade increases to 357 mm. There is a positive correlation between the increase in the outer diameter (x_2) of the spiral blade and the corresponding rise in the hole depth (y_1). When the helix angle (x_1) is equal to 17.5 degrees, the depth of the hole (y_1) measures 192 mm. There is a positive correlation between the increase in the outer diameter (x_2) of the spiral blade and the corresponding rise in the hole depth (y_1). An rising trend in hole depth (y_1) is observed when the rotational speed (x_3) of the spiral blade increases. When the outside diameter (x_2) of the spiral blade measures 392 mm and the rotating speed (x_3) of the spiral blade is 373.7 rpm, the depth (y_1) of the hole is 186 mm. The contour plot reveals the presence of a non-linear relationship between the spiral angle (x_1) and the outer diameter (x_2) of the spiral blade. This suggests a notable interaction between these two variables. When the helix angle (x_1) is 20° and the helix blade speed (x_3) is 373.7 rpm, the depth of the hole (y_1) is 183 mm. A discernible circular arc can be shown between the spiral rising angle (x_1) and the spiral blade speed (x_3), suggesting that the interaction between these two variables is not substantial. A notable interaction is observed between the outer diameter (x_2) of the spiral blade and its rotating speed (x_3), as evidenced by the presence of a non-parallel line segment.

Lead angle(x_1) and
Spiral blade outer diameter (x_2)
(x_3=280.96 rpm)





Lead angle(x_1) and Spiral blade speed (x_3) (x_2=357 mm)

Spiral blade outer diameter (x_2) and Spiral blade speed (x_3) (x_1=17.5°)

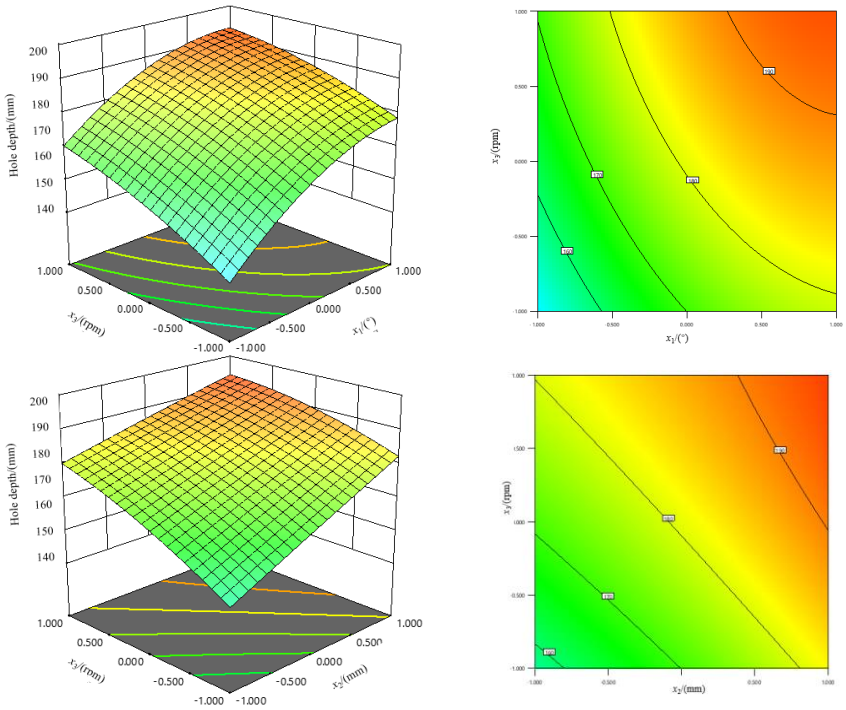


Fig. 13 - 3D response surface and 2D contour maps of hole depth

Parameter optimization

The regression equations for the two indicators are accompanied by a description of their maximum and lowest values, as presented in Table 6. The data presented in Table 8 reveals that the depths of the holes are consistently below 200 mm. The regression equation yields a minimum pore diameter value of 303.575 mm and a maximum pore diameter value of 374.26 mm, as indicated by the data.

Table 6 Maximum and minimum values in the regression equation

Test indicators			Test Factors		
			z_1	z_2	z_3
Hole depth	max	197.036	18.658	377.811	225.812
	min	134.443	16.013	336.189	197.036
Hole diameter	max	374.260	18.987	377.811	336.104
	min	303.575	18.987	336.189	225.816

During the pre-transplantation excavation process, it is imperative to create a hole of maximum size within the agronomic parameters to guarantee ample development space for tobacco seedlings. Hence, the optimization objectives were determined to be a hole depth of 200 mm and a hole diameter of 350 mm. According to the data presented in Table 6, the hole maximum depth measures 197.036 mm. Consequently, the optimization objective for the simulation experiment was determined to be the maximum value of the hole regression equation. The optimization target for the hole diameter is chosen to be 350 mm, and the relevant values for the factors are presented in Table 7.

Table 7. Optimization objectives

Optimization objectives and values		Test Factors		
		z_1	z_2	z_3
Hole depth (mm)	197.036	18.658	377.811	197.036
Hole diameter (mm)	350	18.987	375.158	257.818

Table 7 provides an overview of the range of intervals that have been optimized for three parameters. However, it is necessary to further optimize these three intervals by determining three specific values. The regression equation reveals that the coefficients associated with the three main terms are all positive, indicating a positive relationship between the value of the regression equation and the growth in the three components. Hence, the approach involves identifying the highest value within the specified range of factors and utilizing an integer as the precise value for the purpose of optimization, as depicted in Table 8. Based on the integration of the regression equation, it can be inferred that the optimal hole depth is 193 mm, while the hole diameter measures 350 mm.

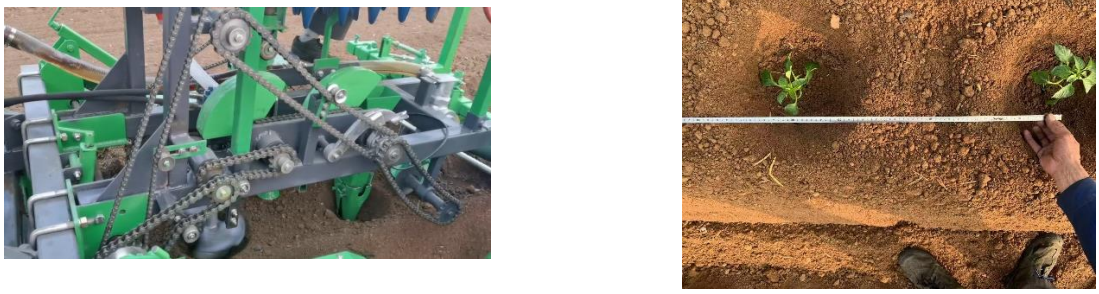
Table 8. Specific values after optimization

Test Factors			Test indicators	
z_1(°)	z_2(mm)	z_3(mm)	Hole depth (mm)	Hole diameter (mm)
19	378	258	193	350

Field validation test

In order to validate the outcomes of simulation optimization, a prototype was manufactured based on the parameters that were optimized through simulation trials. Subsequently, field experiments were carried out to assess the performance of the prototype.

The location of the experimental site is situated in Honghe Prefecture, in Yunnan Province, China. The soil composition at this site is characterized as sandy loam. The test site is depicted in Figure 14. Choose seedlings that have the age of 38 days and have favourable growth characteristics, namely seedling heights that fall within the range of 50 mm to 80 mm. Prior to conducting the experiment, a rotary tiller is employed in order to thoroughly pulverize the soil. Following the transplantation of 300 seedlings, it is imperative to gather pertinent data pertaining to the hole.



a. Test site **b. After transplanting**

Fig. 14 - Field experiment

The primary data acquired include measurements of hole depth and hole diameter. The mean depth and diameter of holes obtained from field testing were 191 mm and 347 mm, respectively. The numerical value closely approximates the outcome of the simulated optimization.

CONCLUSIONS

(1) The present study developed a tobacco planting device utilizing a parallel four-bar mechanism, which combines the advantageous characteristics of a spiral blade for hole excavation and a duckbill transplanting device for substrate seedling transplantation. To achieve simultaneous execution of excavation and transplanting procedures, the crank length is established as 9.6 cm, while the connecting rod length is set to be 50 cm. These measurements are calculated through the utilization of trajectory technology and theoretical calculations, taking into account the spatial separation between plants. This apparatus integrates the processes of excavation and transplantation to achieve the mechanical operation of tobacco planting.

(2) The present study involved an examination of the relationship between the spiral blades and the soil, with a focus on identifying the primary factors influencing the formation of holes. These factors encompassed the spiral lift angle, the maximum outer diameter of the spiral blades, and the rotational speed at which the blades operated. The calculation of the range of the three parameters was conducted in order to satisfy the agronomic prerequisites for tobacco cultivation. The values provided encompass a range of measurements: 15-20° for angles, 322-392 mm for lengths, and 188.22-373.30 rpm for rotational speeds.

(3) A simulation test was conducted using the discrete element method to investigate the effects of a three factors three-level regression orthogonal design. The test factors were optimized for the experiment. The findings of the optimization analysis indicate that a spiral lift angle of 19°, a maximum spiral blade diameter of 378 mm, and a rotational speed of 258 rpm result in the desired outcome for the pit. The depth of the hole is 193 mm, while its diameter measures 350 mm.

REFERENCES

[1] Ba, L. Z. (2022). *Design and experiment of orchard fertilizer digging machine*. Shanxi Agricultural University; DOI: 10.27285/d.cnki.gsxnu.2022.000647.

[2] Chen, X., Shi, L., Yuan, K., Wang, K. P. (2014). Discussion on the technology of flue-cured tobacco seeding transplant under plastic film. *Journal of Agriculture Sciences*, 1963-1964+1972. DOI: 10.13989/j.cnki.0517-6611.2014.07.068.

[3] Cui, Z. Y., Guo, X. B., Yang, Q. X., Zhao, X., Qi, B. Q. (2018). Effects of roasted tobacco well-cellar transplanting on temperature, root vigor, growth and development, and yield quality in well-cellar. *Anhui Agricultural Science Bulletin*. 38-39+64. DOI: 10.16377/j.cnki.issn1007-7731.2018.14.018.

[4] Fan, Y. Y., Li, J. H., Yao, J. (2019). Research on a self-propelled tobacco transplanter. *Anhui Agricultural Science Bulletin*. 2019, 25, 121-122. DOI: 10.16377/j.cnki.issn1007-7731. 21.044.

[5] Gao, W. J. (2018). Design and analysis of integrated digging and tree planting equipment. *Forestry Machinery & Woodworking Equipment*. 2018,46,12-16. DOI: 10.13279/j.cnki.fmwe.2018.0047.

[6] Gao, Z. C., Li, L. J., Yang, H. J., Zhu, Q., Zhou, Y., Min, S. H. (2015). Design and test of forward and reverse screw type soil amendment lime spreader. *Transactions of the Chinese Society of Agricultural Engineering*. 2015, 31. DOI: 10.11975/j.issn.1002-6819.2015.10.006.

[7] Giuseppe B., Itai E. (2020). The mechanics of brittle granular materials with coevolving grain size and shape[J]. *Proceedings of the Royal Society A*, 2021, 477(2249). DOI: 10.1098/RSPA.2020.1005.

[8] Guo, G. S., Gao, M. X., Guo, K. Q., Dang, G. R. (2003). Study of screw auger parameters of mounted hole digger on the basis of MATLAB. *Journal of Northwest A & F University (Natural Science Edition).* 3, 179-182. DOI: 10.13207/j.cnki.jnwafu.2003.03.042.

[9] He, Y. P. (2013). *Experimental design and analysis*; Chemical Industry Press: Beijing, China.

[10] Jiang, K. S. (1997). Study on the theory of trencher's bit ascension--debate on the critical speed of the bit. *Journal of Central South University of Forestry & Technology*. 3. DOI: 10.14067/j.cnki.1673-923x.1997.03.014

[11] Jin, C. (2022). Dynamics simulation and experimental investigation of earth auger bit-soil based on EDEM. Fujian, *Fujian Agriculture and Forestry University*. DOI: 10.27018/d.cnki.gfjnu.2022.000429.

[12] Li, Y. Y., Hu, C. R. (2005*). Experimental design and data processing*; Chemical Industry Press: Beijing, China, 2005.

[13] Li, Z. H., Luo, P. (2005). *SPSS for Windows Statistical Analysis Tutorial*; Electronic Industry Press: Beijing, China, 2005.

[14] Liu, G. H., Yu, L. H., Chen, X., Zhang, F. G., Fu, D. L., Huang, H. G., Wu, X. M. (2018). Design and experiment of knapsack deep planting hole forming machine for large den. *Jiangsu Agricultural Sciences*, 46, 263-267. DOI: 10.15889/j.issn.1002-1302.2018.21.066.

[15] Liu, Z. C., Jiao, A. S., Jin, H. J. (2022). Structural design and test of auger crusher of 5TH shellless gourd seed picker. *Journal of Machine Design*. 39, 119-122. DOI: 10.13841/j.cnki.jxsj.2022.08.003.

[16] Lu, C. L. (2015). *Research and design of tobacco transplanting machine*; Jiangxi Agricultural University. 2015.

[17] Meng, Q. H. (2007). *Research on simulation and mathematical interpretation of dynamic process to earth auger for tree deep planting*. Northeast Forestry University.

[18] Qin, K., Ding, W. M., Fang, Z. C., Du, T. T., Zhao, S. Q., Wang, Z. (2016). Design and experiment of plowing and rotary tillage combined machine. *Transactions of the Chinese Society of Agricultural Engineering*. 2016, 32, 7-16. DOI: 10.11975/j.issn.1002-6819.2016.16.002.

[19] Song, Z. H., Li, H., Yan, Y. F., Tian, F. Y., Li, Y. D., Li, F. D. (2022). Calibration method of contact characteristic parameters of soil in mulberry field based on unequal-diameter particles DEM theory. *Transactions of the Chinese Society for Agricultural Machinery*. 2022,53,21-33. DOI: 10.6041/j.issn.1000-1298.2022.06.002.

[20] Sun, J. B., Liu, Q., Yang, F. Z., Liu, Z. J., Wang, Z. (2022). Calibration of discrete element simulation parameters of sloping soil on loess plateau and its interaction with rotary tillage components. *Transactions of the Chinese Society for Agricultural Machinery*. 2022, 53, 63-73. DOI: 10.6041/j.issn.1000-1298.2022.01.007.

[21] Tekeste, Z. M., Balvanz, R. L., Hatfield, L. J., Ghorbani, S. (2018). Discrete element modeling of cultivator sweep-to-soil interaction: Worn and hardened edges effects on soil-tool forces and soil flow [J]. *Journal of Terramechanics*, 2019, 82. DOI: 10.1016/j.jterra.2018.11.001.

[22] Wang, F. F., Xu, R., Wang, B., Yang, J., Liu, L., Yang, Y.J., Yu, H. Y. (2010). Advantages and main technologies of standardized cultivation of roasted tobacco under the film. *Modern Agricultural Science and Technology*. 5, 52. DOI: 10.3969/j.issn.1007-5739.2010.05.031.

[23] Xiao, W. B. (2010). *Design and experimental study of tobacco transplanting machine*; Hunan Agricultural University.

[24] Xiong, J., Yang, Y. F., Pan, X. F., Yuan, F. X., Fang, G. (2020). Design of tobacco transplant duckbill digging machine. *China Southern Agricultural Machinery*. 51, 78-79+84. DOI: 10.3969/j.issn.1672-3872.2020.15.033.

[25] Yang, W. W., Fang, L. Y., Luo, X. W., Li, H., Ye, Y. Q., Liang, Z. H. (2020). Experimental study of the effects of discharge port parameters on the fertilizing performance for fertilizer distribution apparatus with screw. *Transactions of the Chinese Society of Agricultural Engineering*. 36(17):1-8.

[26] Yao, R. K. (2017). *Study on the key technology of pit type transplanting in Flue-cured Tobacco*. Hunan Agricultural University.

[27] Yu, L. H., Liu, G. H., Zhang, F. G., Wu, X. M., Hu, C. S. (2018). Test and analysis for performance on the knapsack well-cellar making machine for seeding transplanting. *Journal of Agricultural Mechanization Research*. 40, 141-145. DOI: 10.13427/j.cnki.njyi.2018.03.028.

[28] Zheng, S. H., Jiang, F. H. (2004). *Experimental design and data processing*; China Building Materials Industry Press: Beijing, China.

[29] Zhuang, C. Q., Wu, Y. S. (1992). *Fundamentals of Applied Mathematical Statistics*; South China University of Technology Press: Guangzhou, China.

STUDY ON VIBRATION ADSORPTION CHARACTERISTICS OF SMALL-PARTICLE-SIZE SEEDS BASED ON DEM
/
基于 DEM 的小粒径种子振动吸附特性研究

Wenxue DONG[1)], Na LI[1)], Fei LIU[*1)], Xuan ZHAO[1)], Lihe WANG[1)], Dezheng XUAN[1)], Wendong ZHONG[1)], Hengtong HU[1)], Xiang KONG[1)], Xinyu MENG[1)], Mingyi LI[1)], Zhijiang DUAN[1)]

[1)] College of Mechanical and Electrical Engineering, Inner Mongolia Agricultural University, Hohhot 010010, China;

Tel: 13238446338; E-mail: dong18403045597@163.com; afei2208@imau.edu.cn

DOI: https://doi.org/10.35633/inmateh-71-35

Keywords: *vibration; discrete element method; air-suction seed metering; seed-suctioning performance*

ABSTRACT

In order to explore the effect of vibration on the adsorption characteristics of small particle size seeds, based on the discrete element method, the changes in the variance of the average tangential force of seeds under different amplitudes were analyzed. The variance of the average tangential force of the seeds increases exponentially with the amplitude. It is inferred that the vibration will change the intensity of the population disturbance. This reduces the seed transient tangential force i.e. transient seed internal friction. To improve the adsorption characteristics of small-sized seeds, the adsorption characteristics at different amplitudes were verified with bench tests. Increasing the amplitude can improve the adsorption characteristics of small-sized seeds. To determine the optimal operating parameters, based on the Box–Behnken test principle, response surface tests were carried out using rotational speed, negative pressure, and amplitude as test factors and seed suction compliance and leakage rate as evaluation indexes. The optimum operating parameters were determined as: rotational speed of 12.05 r/min, negative pressure of 0.89 kPa, and amplitude of 5.75 mm. At this time, the seed suction pass rate was 95.1% and the leakage rate was 2.1%. which is in line with the standard requirements.

摘要

为探究振动对小粒径种子吸附特性的影响，基于离散元法，分析不同振幅下种子平均切向力方差的变化。种子平均切向力方差随振幅呈指数增加，据此推断振动会改变种群扰动强度，从而降低种子瞬态切向力即瞬时种子内摩擦力，以此提高种子吸附特性；通过台架试验验证不同振幅下的吸附特性，增大振幅可改善吸种特性。基于 Box-Behnken 试验原理，以转速、负压和振幅为试验因素，以吸种合格率和漏吸率为指标，进行响应面试验，确定最佳工作参数为：转速为 12.05 r/min，负压为 0.89 kPa，振幅为 5.75 mm，此时吸种合格率为 95.1%，漏吸率为 2.1%，符合标准要求。

INTRODUCTION

Air-suction seed-metering devices have high seeding precision and are widely used for crop seeding *(Zhang K. et al., 2017)*. A functioning seed dispenser causes vibrations that significantly affect the motion state of the seed population inside the seed chamber, while the motion state and degree of dispersion of the seed population directly affect the seed dispenser's seed-suctioning performance, which, in turn, affects the sowing accuracy *(Arzu Y. et al., 2014; Shi S. et al., 2015; Karayel D., 2022)*. Vibration during the sowing operation causes the seed population to have a certain speed, which leads to the phenomena of leakage and multiple sucking in the seed-sucking process and increases the variability of the seed sucking, affecting the seeding quality *(Yazgi A. et al., 2007; Ku s et al., 2021; Sakaguchi E. et al., 2001; Emrah Kus., 2021)*. When the vibration is larger, the seed population is more discrete, and the internal friction between seeds is smaller; however, due to the rapid movement of the population, the seeds are difficult to be adsorbed, resulting in a high leakage rate. Conversely, when the vibration is smaller, the seed population is less discrete, the internal friction between seeds is larger, the movement of the seed population is smaller, and the mobility of the seed population is poor, resulting in a high leakage rate. With an appropriate vibration, the seed population can reach the leakage rate of a relatively low state of "boiling" *(Liao Y.T. et al., 2022; Aliiev E. et al., 2019 ; Muhammad D. et al., 2021; Igor S. et al., 2021)*.

Vibration can cause the population to enter a "boiling" state due to the arrangement defects between the seeds in the population. The intensity of the vibration affects the "boiling" state of the seed population and, thus, the performance of seed adsorption. Medium-frequency vibration can make the seed population produce a "boiling" movement conducive to seed suctioning, wherein a low negative suction pressure can realize a high suction rate of qualified seeds *(Cujbescu D. et al., 2021; Zheng J. et al., 2023; Zhao X. et al., 2023; Wang B. et al., 2023)*.

One of the most common methods used to study the seeding process is DEM simulation analysis *(Lysych M.N. et al., 2021; Guzman L.J., 2020; Sharaby N.N. et al., 2020)*. *Chen et al. (2011)* further investigated the effects of different frequencies, amplitudes, and seed layer thicknesses on the spatial distribution of populations using EDEM software and determined the range of seed layer thicknesses favorable for the population's "boiling". *Hu et al. (2014)* analyzed the effects of vibration frequency and amplitude on the population movement pattern and seed supply performance based on the discrete element method, verifying them using high-speed photography technology and bench tests, and the simulation results coincided with the actual results. *Lu et al. (2016)* simulated and analyzed the homogenization process of a vibratory homogenizing device using the discrete element method and carried out experimental verification, and the verification results had a relatively small error with the simulation results, further confirming the discrete element method's high feasibility and accuracy.

Although the study determined the effect of vibration on the pneumatic seed discharger law, this law mainly applies to corn, rice, and other large-particle-size seeds. While quinoa and other small-particle-size (with an average diameter of less than 3 mm) pneumatic seed dischargers are the subjects of less relevant research. Quinoa is recognized as one of the world's most nutritious food crops with strong international market demand. Therefore, the effect of vibration on the stress and adsorption properties of small-particle-size populations should be studied using quinoa seeds as an example. In this paper, a quinoa seed contact model was developed based on the EDEM discrete element method. The force on quinoa seeds in the seed discharger under vibration was simulated and analyzed. The simulation results were verified using an indoor bench. In addition, a response surface test was designed using Design-Expert software. The optimal combination of working parameters was determined.

MATERIALS AND METHODS

Seed discharger structure and working principle

The seed discharger comprised a seed discharge shaft, air chamber, air chamber pressure plate, bushing, seed disk and shell, and other components, as shown in Figure 1. In this case, there were 18 clusters of suction holes distributed around the circumference of the seed disk, and each cluster contained four suction holes with a diameter of 0.8 mm for the adsorption of seeds. The seed tray was fixed to the seed discharge shaft and rotated in synchronization with the seed discharge shaft. The seed tray and the housing formed a seed chamber for storing the seeds.

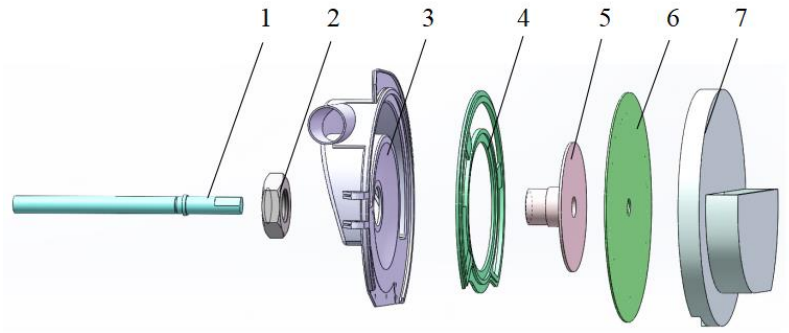


Fig. 1 - Structural diagram of air-suction seed metering

1. seed dispenser shaft; 2. fixing nut; 3. air chamber; 4. air chamber platen; 5. assortment tray; 6. assortment tray; 7. clamshell

The seed discharge device functions as follows: the seed discharge tray operates with the seed discharge axis under synchronous rotation. With the air chamber located outside the wind machine, when the vacuum in the air chamber reaches a certain negative pressure value, the seeds in the air chamber by the seed tray suction hole under the adsorption force overcome their own gravity and the friction between the seeds, and are ultimately adsorbed through the seed tray suction hole into the seed tray.

Due to the small size of the suction hole and the rotation of the seed tray, the suction hole can only carry out the stabilized adsorption of one seed, rather than using part of the suction hole as in the case of multiple suction. In a multi-suction situation, only one seed is stably adsorbed, and the adsorption force acting on the other seeds is less than their own gravity, which causes them to fall back into the seed chamber. Meanwhile, the adsorbed seed in the seed disk travels through the seed-carrying area to reach the seeding area, where the adsorption force disappears, and the seed falls into the ridge along the seed-guiding tube to complete the precise amount of seed discharge, as shown in Figure 2.

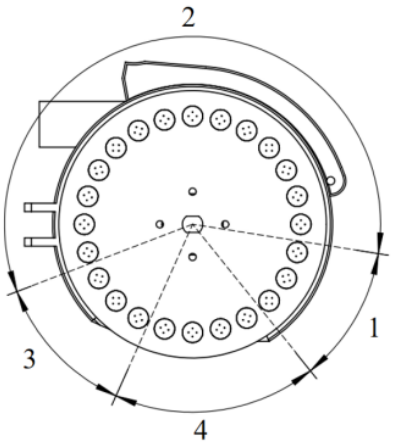


Fig. 2 - Working principle diagram of seed metering

1. seed dispersal area; 2. seed-holding area; 3. seed-dispensing area; 4. transition area.

Particle contact motion analysis

(1) Contact model

The discrete element method is used to simulate the collision process between particles, and these particles generate a contact force during the collision process. The contact force of soft-particle contact, an important contact model in the discrete element method, can be calculated according to the overlap between particles and the tangential relative displacement between particles, and the contact force between particles is closely related to internal friction. Therefore, this paper adopted the soft-particle contact model to simulate seed contact. Since there is no adhesion on the surfaces of quinoa seeds, the Hertz–Mindlin no-slip contact model was selected in this paper.

The damped motion of a spring oscillator was utilized to describe the contact process between the seeds, as shown in Figure 3, with the following equation of motion:

$$m\frac{d^2x}{dt^2} = -kx - \gamma\frac{dx}{dt} \quad (1)$$

where: x is the displacement from the equilibrium position, mm; m is the oscillator mass, g; k is the coefficient of spring elasticity; and γ is the spring damping factor.

In the normal direction, couplers are set to indicate seed contact without introducing any force, and sliders are set to achieve tangential sliding between seeds.

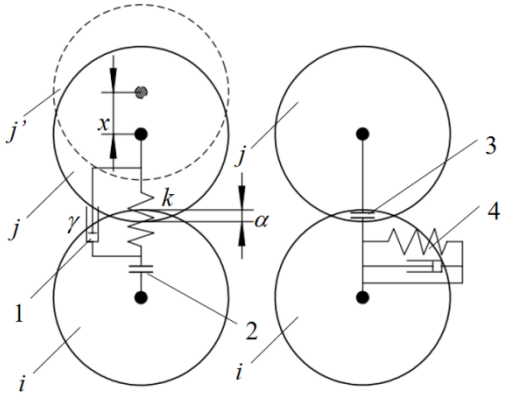


Fig. 3 - Soft-particle contact reduction model

1. shock absorbers; 2. coupler; 3. sliders; 4. spring; α is the normal overlap; γ is the spring damping factor; 2. k is the coefficient of spring elasticity; x is the displacement from the equilibrium position; and i and j are the seeds.

(2) **Contact force calculation** shows the force diagram of the seed contact process. In addition to its own gravity, a seed is also subjected to the normal and tangential forces generated by its contact with other seeds.

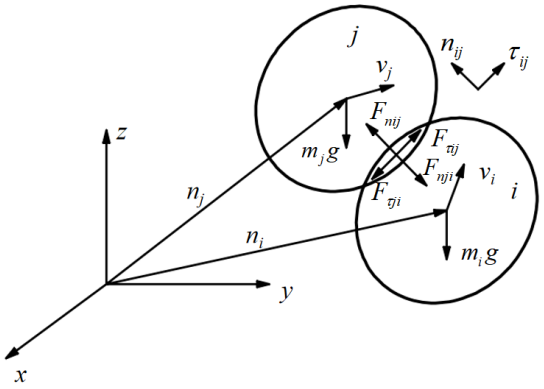


Fig. 4 - Seed contact process stress diagram

F_{nij} is the normal force on seed j; F_{nji} is the normal force on seed i; $F_{\tau ij}$ is the tangential force on seed j; $F_{\tau ji}$ is the tangential force on seed i; m_jg is the gravitational force on seed j; m_ig is the gravitational force on seed i; v_j is the velocity of seed j; v_i is the velocity of seed i; n_j is the center vector position of seed j; and n_i is the center vector position of seed i.

The normal force F_{nij} is the combined elastic and damping force acting on seed i by the spring and the normal damper. For three-dimensional spherical particles, according to the Hertz contact theory, F_{nij} is expressed as:

$$F_{nij} = (-k_n \alpha^{\frac{3}{2}} - \gamma_n v_{ij} \cdot n)n \tag{2}$$

where:

k_n is the normal elasticity coefficient; γ_n is the normal-phase damping factor; n is the unit vector from the sphere center of seed i to the sphere center of seed j; and v_{ij} is the velocity of seed i relative to seed j, m/s.

The tangential force is expressed as:

$$F_{\tau ij} = -k_\tau \delta - \gamma_\tau v_{\gamma\tau} \tag{3}$$

where:

K_τ is the tangential elasticity coefficient; δ is the tangential displacement of the point, m; γ_τ is the tangential damping coefficient; and $v_{\gamma\tau}$ is the contact slip speed, m/s.

When slip occurs on seed i, the following relationship exists:

$$\left|F_{\tau ij}\right| > \mu \left|F_{nij}\right| \tag{4}$$

At this point, the tangential force is:

$$\left|F_{\tau ij}\right| = -\mu \left|F_{nij}\right| n_\tau \tag{5}$$

where:

μ is the seed friction factor, and n_τ is the tangential unit vector.

Equation (5) is Cullen's friction law *(Li H.C. et al., 2011; Zhao Y.M. et al., 2006; Maroues F. et al., 2016)*, it can be seen from Eq.5 that the tangential force on the seed is the internal friction between the seeds. The tangential force on the seeds is the main factor that prevents the seeds from moving relative to each other or having a tendency to move relative to each other. Its magnitude is determined by the seed friction factor and normal force. The seed friction factor is a unique property. It remained essentially the same under the same test conditions. Therefore, in this paper, the internal friction between seeds is measured by the tangential force $F_{\tau ij}$.

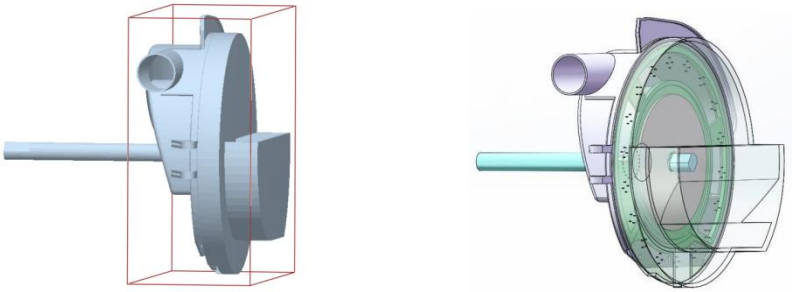
Air-suction seed metering are subject to airflow disturbances during the seed filling process. A coupled gas-solid two-phase flow (DEM-CFD) simulation method is usually used for such systems where airflow and particles coexist. For CFD (fluid dynamics methods), vibration causes the airflow to change in size and direction. This change affects the simulation test results. And in the physics experiment, the vibrations did not change the size or direction of the airflow.

Shi et al. (2015) found that the airflow disturbance factors could be approximated as being at the same level at the time of the test by a one-factor comparison. Therefore, in this paper, the airflow disturbance factors are approximated to be controlled at the same level. In this way, the effect of perturbation intensity with different amplitudes on the adsorption characteristics of small-sized seeds was investigated.

Test materials and equipment

(1) Simulation modeling

The seed dispenser was modeled using SolidWorks software and imported into EDEM as shown in Figure 5.



(a) SolidWorks model (b) EDEM model

Fig. 5 - Three-dimensional model of seed dispenser

In this paper, the seeds of Meng quinoa No. 1 were selected for the test, as shown in Figure 6(a). The simulation assumed that the external dimensions of the seeds were all the same due to the small size of the seeds and the low variability between the seeds. Firstly, the quinoa seeds were scanned and sampled with a Teng Yue intelligent industrial-grade 6.3 million-industrial-grating automatic 3D stereo scanner to obtain the quinoa seed model, as shown in Figure 6(b), which was imported into the EDEM simulation software to be filled to obtain the quinoa seed model close to the real quinoa seed model, as shown in Figure 6(c).



(a) Quinoa seed (b) Scanned model (c) Mesh fill model

Fig. 6 - Quinoa seed model

(2) Parameter setting

The parameters of the simulation were determined based on the results of previous work *(Wu Y.S. et al., 2017; Li D.P., 2020; Xu X.M. et al., 2019)*, as shown in Table 1. The Hertz-Mindlin contact model was chosen for the simulation. Simulate the Riley Time Ministerial Percentage setting of 20%. Mesh size was 2 mm. The simulation set the number of seeds at 20000 seeds. The total simulation time was 2 s, and the data were recorded every 0.01 s.

Table 1

Discrete element simulation parameters

Parameter	Numerical Value
Quinoa Poisson's ratio	0.25
PLA Poisson's ratio	0.36
Young's modulus of quinoa (MPa)	390.00
Young's modulus of PLA (MPa)	2350.00
Density of quinoa (g/cm^3)	0.87
Density of PLA (g/cm^3)	1.23
Quinoa–quinoa crash recovery factor	0.38
Quinoa–PLA crash recovery factor	0.50
Quinoa–quinoa static coefficient of friction	0.47
Quinoa–PLA static coefficient of friction	0.49
Quinoa–quinoa rolling coefficient of friction	0.12
Quinoa–PLA rolling coefficient of friction	0.11

To investigate the pattern of variation in the tangential forces on the seeds at different amplitudes, simulations were conducted with amplitude as the test factor and the vibration frequency of the seed discharger set at 10.7 Hz, the rotational speed of the seed discharger at 15 r/min, and the amplitude of the seed discharger at 0, 2, 4, 6, 8, and 10 mm *(Liu Y.Q., 2017)*.

Bench test conditions

The test seeds were selected from "Mengqua 1" grown in Ulanchab, Inner Mongolia, China. Vibration bench tests were carried out using the JPS-12 computer vision seed dispenser test rig manufactured by Harbin Bona Technology Co Ltd in China and the LKD-P absorbing electromagnetic shaker produced by Guangdong Lijia Industry Co, as shown in Figure 7.



Fig. 7 - Seeding performance test bench

1. vibrating stand; 2. seed dispenser stand; 3. air-aspirated quinoa seeder; 4. Electromagnetic shaker; 5. JPS-12 computer vision seed arranger test bed.

The bench test took the qualified rate of seed adsorption and the leakage rate as the evaluation index, 250 data were recorded continuously, and each group of tests was repeated three times to obtain the average value. As per the relevant standard, the quinoa precision hole sowed 3~5 seeds per hole. During sowing, it was assumed that all the seeds adsorbed by the suction pore clusters fell into the hole of the monopoly and that the seeds adsorbed by each suction pore cluster fell into the same hole. Each suction hole group was set up with 4 suction holes. When the number of seeds adsorbed by a suction hole group was less than 3, it was classified as leakage, and when each suction hole group stably adsorbed 3-5 seeds, it was classified as qualified adsorption. The leakage rate and qualified rate were calculated based on this standard.

$$M = \frac{n_1}{N} \times 100\% \tag{6}$$

$$Q = \frac{n_2}{N} \times 100\% \tag{7}$$

where:

M is the qualified rate, %; Q is the leakage rate, %; n_1 is the number of pore groups qualified for adsorption, pcs; n_2 is the number of suction hole clusters with leakage suction, pcs; and N is the total number of recorded suction pore clusters, pcs.

Bench test

A one-factor test was performed to verify the accuracy of the simulation results. The speed of the vibrating seed discharger seed disk was set as 15 r/min, the vibration frequency of seed discharger as 10.7 Hz, the negative pressure as 1 kPa, and the amplitude as 0, 2, 4, 6, 8, and 10 mm. To find the optimal combination of operating parameters, the designing of the experiments was carried out using Design-Expert software, and the factor coding is shown in Table 2.

Table 2

Discrete element simulation parameters

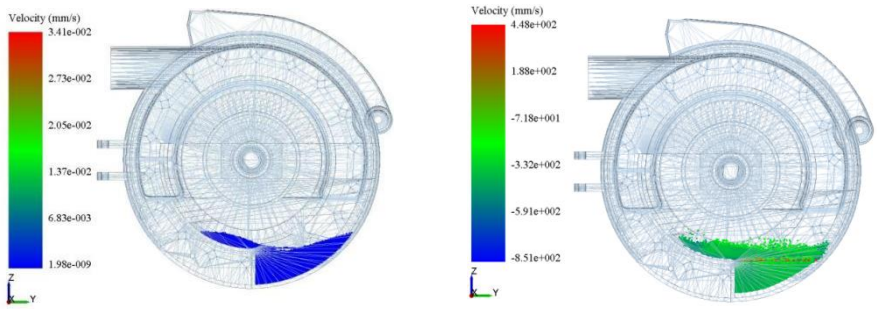
Level	Test Factors		
	Speed A (r/min)	Negative pressure B (kPa)	Amplitude C (mm)
1	10	0.8	4
0	12.5	1.0	6
-1	15	1.2	8

RESULTS

Simulation test results

(1) Population movement state analysis

The population movement state map is shown in Figure 8. Without vibration, the population was close to the wall inside the seed chamber, the internal friction between seeds was high, and the seed-suctioning performance was relatively poor. With vibration, the seed population began to show a throwing motion, and with the increase in amplitude, this throwing motion became gradually more obvious, and the seed population appeared to be in a "boiling" state. In this state, with the fluctuation in the normal force on the seeds and the change in the internal friction between the seeds, the seed-suctioning performance could be improved.



(a) Stationary stock (b) Population in boiling state

Fig. 8 - Population movement state map

(2) Normal force on seeds of different amplitudes

Using the EDEM software to output the total number of seeds, the total number of contacts, and the contact average normal force for each step, the average normal force f_{nt} applied to each seed at time t was:

$$f_{nt} = F_{nt} \frac{N_t}{N_{ct}} \tag{8}$$

where: F_{nt} is the average value of the contact normal force at time t, N; N_t is the total number of seeds at time t, grain; and N_{ct} is the total number of contacts at time t, grain.

Combine with equation (5) to calculate the average tangential force on the seed. The mean tangential force applied to the seeds at different amplitudes is shown in Figure 9. With vibration, the mean tangential force applied to the seeds appears to fluctuate irregularly, and the magnitude of the fluctuation increases with the increase in the amplitude.

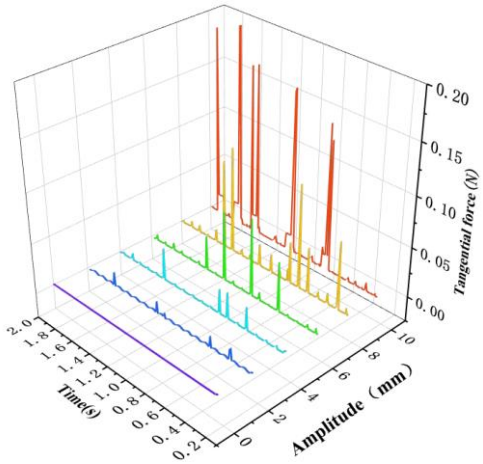


Fig. 9 - Average tangential force on seeds at different amplitudes

To quantitatively describe the fluctuation in the mean tangential force on the seeds, the variance formula is introduced with the following expression:

$$S^2 = \frac{1}{N_T} \sum (f_\pi - \frac{M_T}{N_T}) \tag{9}$$

$$M_T = \sum f_\pi \tag{10}$$

where:

S^2 is the variance; N_T is the total number of output data, N_T = 20000 grain; and M_T is the seed mean tangential force sum, N.

Figure 10 shows the pattern of the effect of amplitude on the seed tangential force. The seed mean tangential force variance increased exponentially with the amplitude, and when the variance was larger, the tangential force fluctuation was more discrete, and the fluctuation in the internal friction between seeds was larger, which improved the seed adsorption performance. The variance was highest when the amplitude was 10 mm, when the seeds were "boiling" violently in the seed chamber, which is unfavorable for seed adsorption. Therefore, an appropriate amplitude can change the internal friction between seeds, which, in turn, improves the seed-suctioning performance.

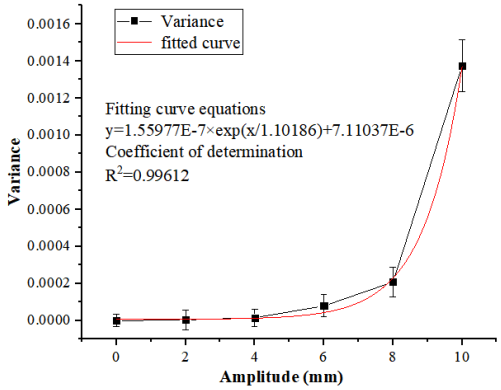


Fig. 10 - Effect of amplitude on variance in tangential force

Results and analysis of single factor test

The effect of amplitude variation on the seed adsorption performance is shown in Figure 11. As demonstrated in the figure, with the increase in the amplitude, the qualified rate of seed suctioning first shows a rising and then a falling trend. The leakage rate first shows a falling, then rising, falling, and, finally, sharply rising trend. Theoretically, the leakage rate at an amplitude of 4 mm should be less than at 6 mm. The phenomenon shown in Figure 11 may be due to variations in the number of seeds within the species chamber and experimental errors. When the amplitude was small, the effect of vibration on the population was small, and the internal friction between species was relatively large, which was not conducive to the population "boiling". With the increase in the amplitude, the effect of vibration on the population increased, and the friction between the species decreased, which was conducive to the population "boiling". As such, the leakage rate gradually decreased, thereby improving the seed-suctioning performance. However, the population "boiling" intensified with the further increase in the amplitude, so the seed speed at the suction hole was faster, and the original adsorption of seeds via the intense "boiling" of seed collisions fell, resulting in an increased leakage rate.

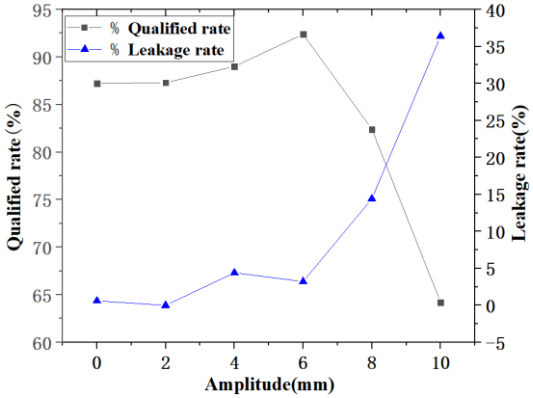


Fig. 11 - Seed adsorption performance curves at different amplitudes

Response surface test results and analysis

The experimental design was carried out using Design-Expert software, and the experimental protocol and results are shown in Table 3.

Table 3

Experimental design program and results

Test Number	Test Factors			Test Indicators	
	A	B	C	Qualified Rate Y_1 (%)	Leakage Rate Y_2 (%)
1	0	-1	1	84.7	12.6
2	1	1	0	85	12.4
3	0	0	0	93.4	2.2

Test Number	Test Factors			Test Indicators	
	A	B	C	Qualified Rate Y_1 (%)	Leakage Rate Y_2 (%)
4	-1	0	-1	86.3	3.6
5	0	1	-1	86.1	5.2
6	1	-1	0	88.6	4.1
7	-1	-1	0	90.5	6.2
8	1	0	1	81.9	15.3
9	-1	1	0	91.2	3.1
10	1	0	-1	81.1	8.1
11	0	1	1	83.6	12.7
12	-1	0	1	81.2	13.4
13	0	-1	-1	90.3	3.2
14	0	0	0	95.1	2.4
15	0	0	0	94.6	3.6

The regression analysis of the test results by Design-Expert software is shown in Table 4.

Table 4

Analysis of variance table of test results

Source of Variance	Qualified Rate Y_1 (%)					
	Sum of Squares	Freedom	Mean Square	F-Value	P-Value	Significance
Model	327.53	9	36.39	41.31	0.0004	**
A	19.85	1	19.85	22.53	0.0051	**
B	8.41	1	8.41	9.54	0.0272	*
C	19.22	1	19.22	21.82	0.0055	**
AB	4.62	1	4.62	5.25	0.0706	
AC	8.70	1	8.70	9.88	0.0256	*
BC	2.40	1	2.40	2.73	0.1596	
A_2	82.00	1	82.00	93.07	0.0002	**
B_2	4.99	1	4.99	5.66	0.0632	
C_2	200.15	1	200.15	227.18	＜0.0001	**
Residuals	4.41	5	0.88			
Fail to fit	4.15	3	1.38	10.63	0.0872	
Error	0.26	2	0.13			
Total	331.94	14				
Source of Variance	**Leakage Rate Y_2 (%)**					
	Sum of Squares	**Freedom**	**Mean Square**	**F-Value**	**P-Value**	**Significance**
Model	310.26	9	34.47	70.96	＜0.0001	**
A	23.12	1	23.12	47.59	0.0010	**
B	6.66	1	6.66	13.71	0.0140	*
C	143.65	1	143.65	295.68	＜0.0001	**
AB	32.49	1	32.49	66.87	0.0004	**
AC	1.69	1	1.69	3.48	0.1212	
BC	0.90	1	0.90	1.86	0.2311	
A_2	26.83	1	26.83	55.23	0.0007	**
B_2	3.85	1	3.85	7.92	0.0374	*
C_2	80.55	1	80.55	168.81	＜0.0001	**
Residuals	2.43	5	0.49			
Fail to fit	1.28	3	0.43	0.75	0.6164	
Error	1.15	2	0.57			
Total	321.69	14				

e, 0.05 < P < 0.1; ** indicates highly significant, P < 0.01.

As demonstrated in the variance results, the rotational speed and amplitude of the two indicators were highly significant, the negative pressure had a significant effect on the leakage suction rate, some of the factors had a two-by-two interaction, the regression model fit of the two evaluation indicators was highly significant, and the misfit term P was > 0.05, which indicates that there were no other factors affecting the evaluation indicators. The regression model after removing insignificant factors was:

$$Y_1 = 92.64 + 1.92A + 2.39C + 1.48AC - 5.75A^2 - 5.01C^2 \quad (11)$$

$$Y_2 = 5.68 - 3.83A - 0.73B - 5.88C + 2.58AB + 5.39A^2 + 0.77B^2 + 3.71C^2 \quad (12)$$

Using the regression coefficient test, it was concluded that the factors affecting the pass rate were amplitude, rotational speed, and negative pressure in order of predominance, and the factors affecting the leakage suction rate were amplitude, rotational speed, and negative pressure in order of predominance.

Based on the regression equation, a surface plot of the effects of factors with significant two-by-two interactions on the evaluation indicators was drawn. As shown in Figure 12, the qualified seed suction rate was higher when the rotational speed was 11.9-12.3 r/min, the negative pressure was 0.89-0.94 kPa, and the amplitude was 5.7-6.1 mm. As shown in Figure 12, with the increasing rotational speed, the qualified seed suction rate first rose and then decreased. When the rotational speed is low, the seed travels via the suction hole through the suction zone for a longer time, and there is a hole in the case of multiple suctioning. While the rotational speed is high, the seed via the suction hole travels through the west central zone for a shorter time, and part of the seed is not adsorbed via the suction holes into the suction zone, resulting in a high suction leakage rate. With the increase in negative pressure, the qualified rate first rose slowly after a slow decline because the negative pressure range selected for the test was favorable for seed suctioning, so the negative pressure on the qualified seed suction rate was small. However, the leakage rate significantly impacted the suction rate, whereby the negative pressure was small when the leakage rate was high, and the negative pressure was large when the leakage rate was lower, and the suctioning hole phenomenon increased. With the increase in amplitude, the qualified seed suction rate first rose and then fell. An appropriate amplitude can change the amount of internal friction between seeds, which, in turn, improves the seed-suctioning performance.

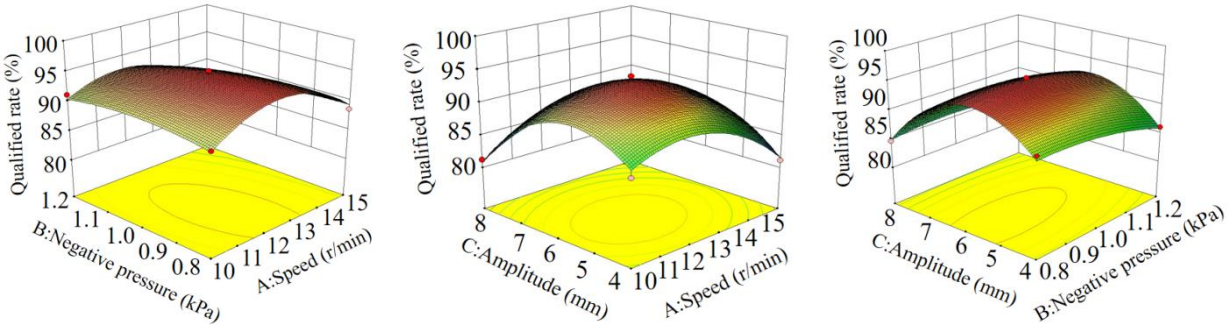


Fig. 12 - Effect of interaction on qualified rate

To obtain the best working parameters, a multi-objective optimization analysis was carried out using the Design-Expert software with a larger qualified rate and a smaller leakage suction rate as the objective function and the following objective function and constraints:

$$\begin{cases} \max Y_1(A,B,C) \\ \min Y_2(A,B,C) \\ \text{s.t.} \begin{cases} 10 \text{ r/min} \le A \le 15 \text{ r/min} \\ 0.8 \text{ kPa} \le B \le 1.2 \text{ kPa} \\ 4 \text{ mm} \le C \le 8 \text{ mm} \end{cases} \end{cases} \quad (13)$$

The optimal working parameters were calculated as follows: when the rotational speed of the seed discharger was 12.05 r/min, the negative pressure was 0.89 kPa, the amplitude was 5.75 mm, the qualified seed suction rate was 95.1%, and the leakage rate was 2.1%.

DISCUSSION

EDEM simulation was used to analyze the effect of vibration on the tangential force exerted on the seeds in the seed discharger. *Shi et al. (2015)* found that the airflow disturbance factors could be approximated as being at the same level at the time of the test by a one-factor comparison. It shows that the effect of airflow on the simulation results is acceptable.

In this study, the effect of airflow on seed tangential force was ignored during numerical simulation tests. The simulation results show that the average normal force on the seeds was stable and constant without vibration, resulting in relatively large inter-seed friction. As vibration causes seeds to produce a throwing motion, during the throwing process, the normal force between the seeds decreases and thereby reduces the internal friction between the seeds, which is favorable for seed suctioning. When the throwing process is over, the seeds in the bottom layer of the seed chamber collide with the seed chamber, and the seeds in other seed layers collide with each other, and the normal force increases instantly, i.e., the raised point of the curve in Fig. 10. The duration of this state is very short so it does not significantly affect the suctioning performance. When the vibration is too large, the seed throwing movement is intense, and the seeds pass through the suction hole at a faster speed, which is not conducive to seed suctioning. This agrees with the findings of *Lai et al. (2016)*.

The effects of different amplitudes on the seed adsorption performance are as follows: when the amplitude is small, the vibration of the population is small, and there is relatively high friction between the seeds, which is not conducive to the population "boiling". When the amplitude is large, the population "boiling" intensifies so the seed speed at the suction hole increases, and the original adsorption of the seeds via the intense "boiling" seed collision falls, resulting in an increased leakage rate. An appropriate amount of vibration can effectively reduce the internal friction between seeds and thus improve the qualified suction rate and reduce the leakage rate. If the vibration can be effectively reduced, it can be used to reduce the leakage rate. This is consistent with the findings of *Liao et al. (2022)*.

The results of the bench test show that the seed discharger worked with an amplitude within the range of 5.7-6.1 mm, and the seed suction pass rate was high, which is consistent with the results of the study by *Zhang et al. (2016).* Therefore, it is recommended that vibration be utilized to improve the seed-suctioning performance of small-particle-size air-aspirated seed dischargers.

CONCLUSIONS

In this study, the population movement was simulated using EDEM software, and the results were analyzed using the seed mean normal force variance as an indicator. It was concluded that proper vibration can reduce the internal friction between seeds and thus improve the seed-suctioning performance.

Taking the qualified seed suction rate and the leakage rate as indicators, a one-factor test was conducted on the amplitude, and the results obtained were consistent with those of the simulation analysis, which verified the correctness of the constructed contact model and the feasibility of using the discrete element method to simulate population movement.

A response surface test was used to analyze the rotational speed, negative pressure, and vibration, as well as some of the factors' two-by-two interactions with the indicators, to determine the optimal combination of operating parameters, detailed as follows: a rotational speed of 12.05 r/min, negative pressure of 0.89 kPa, amplitude of 5.75 mm, of the qualified seed suction rate of 95.1%, and suction leakage rate of 2.1%.

In subsequent studies, vibration can be used to improve seed-suctioning performance by adding excitation or damping devices, damping when the operating amplitude is large, and adding excitation when the operating amplitude is small. According to the optimal seed adsorption performance with the population movement and the size of the seed normal force, seed-stirring devices suitable for quinoa and other small-sized seeds can be designed so that the populations favor seed adsorption in a "boiling" state to improve the seed adsorption performance.

ACKNOWLEDGEMENT

This work was supported by the National Natural Science Foundation of China (32060418).

REFERENCES

[1] Aliiev, E., Gavrilchenko, A., Tesliuk, H. et al. (2019). Improvement of the sunflower seed separation process efficiency on the vibrating surface. *APTEFF*. 2019, 50, 1-352. DOI: https://doi.org/10.2298/APT1950012A.

[2] Arzu, Y., Adnan D. (2014). Measurement of seed spacing uniformity performance of a precision metering unit as function of the number of holes on vacuum plate. *Measurement*. 56, 128-135. DOI:10.1016/J.MEASUREMENT.2014.06.026.

[3] Chen, J., Zhou, H., Zhao, Z. et al. (2011). Analysis of Rice Seeds Motion on Vibrating Plate Using EDEM. *Transactions of the Chinese Society of Agricultural Machinery*. 42, 79-83+100.

[4] Cujbescu, D., Găgeanu, I., Persu, C. et al. (2021). Simulation of Sowing Precision in Laboratory Conditions. *Appl. Sci.* 11, 6264. https://doi.org/10.3390/app11146264.
[5] Emrah, K. (2021). Field-scale evaluation of parameters affecting planter vibration in single seed planting. *Measurement*. 184,109959. DOI:10.1016/J.MEASUREMENT.2021.109959.
[6] Guzman, L.J., Chen, Y., Landry, H. (2020). Discrete element modeling of seed metering as affected by roller speed and damping coefficient. *Transactions of the ASABE*. 63(1):189-198.
[7] Hu, J.P. Guo, K. Zhou, C.J. et al. (2014). Simulation and Experiment of Supplying Seeds in Box of Magnetic Precision Cylinder-seeder. *Transactions of the Chinese Society of Agricultural Machinery*. 45, 61-65.
[8] Ibrahim, E.J., Elfadil, A.D., Abdallah, A.D. (2022). Laboratory and Field Investigation Comparison for Seed Distribution Accuracy of a Multi-Rows Pneumatic Plate Metering Device. *Asian Journal of Agriculture and Food Sciences*. Volume 10-Issue 2. DOI:10.24203/ajafs.v10i2.6942.
[9] Igor, S., Elchyn, A., Gintas, V. et al. (2021). Modeling Separation Process for Sunflower Seed Mixture on Vibro-Pneumatic Separators. *Mechanika*. Volume, 27(4):311-320.
[10] Karayel, D., Güngör, O., Šarauskis E. (2022). Estimation of Optimum Vacuum Pressure of Air-Suction Seed-Metering Device of Precision Seeders Using Artificial Neural Network Models. *Agronomy* 12,1600. https://doi.org/10.3390/agronomy12071600.
[11] Ku, S.E. (2021). Field-scale evaluation of parameters affecting planter vibration in single seed planting. *Measurement*. 184,109959. DOI:10.1016/J.MEASUREMENT.2021.109959.
[12] Li, D.P. (2020). Discrete element analysis and performance test of pneumatic precision metering device for quinoa. *Inner Mongolia Agricultural University*.
[13] Lu, F.Y., Ma X., Qi L. et al. (2016). Parameter optimization and experiment of vibration seed-uniforming device for hybrid rice based on discrete element method. *Transactions of the Chinese Society of Agricultural Engineering*. 32,17-25. Doi:10.11975/j.issn.1002-6819.2016.10.003.
[14] Li, H.C., Li Y.M., Tang, Z. et al. (2011). Numerical simulation and analysis of vibration screening based on EDEM. *Journal of Agricultural Engineering*. 27, 117-121. Doi:10.3969/j.issn.1002-6819.2011.05.019.
[15] Liao, Y.T., Qi, T.X., Liao, Q.X. et al. (2022). Vibration characteristics of pneumatic combined precision rapeseed seeder and its effect on seeding performance. *Journal of Jilin University (Engineering Edition)*. 52, 1184-1196. Doi:10.13229/j. cnki. jdxbgxb20210001.
[16] Liu, Y.Q. (2017). Study on vibration characteristics of air suction no-tillage planter and its effect on seed metering performance. *Inner Mongolia Agricultural University*.
[17] Lysych, M.N., Chernyshev, V.V., Nagaytsev, V.M. (2021). Design and simulation of seed metering device for aerosowing of forest pelleted seeds. *Journal of Physics: Conference Series*. 2032,012062. DOI:10.1088/1742-6596/2032/1/012062
[18] Maroues, F., Flores, P., Claro, J. et al. (2016). A survey and comparison of several friction force models for dynamic analysis of multibody mechanical systems. *Nonlinear Dynamics*. 86, 1407. Doi:10.1007/S11071-016-2999-3.
[19] Muhammad, D., Rozzaq H.A., Makbul H. (2021). Multiobjective Optimization of Vibro-Pneumatic Separator Using Full Factorial Design. *Advances in Biological Sciences Research*. 19, 380-386. Doi:10.2991/absr.k.220305.059.
[20] Sakaguchi, E., Suzuki, M., Favier, J. F. et al. (2001). Numerical simulation of the shaking separation of paddy and brown rice using the discrete element method[J]. *Postharvest Technology*, 79(3): 307-315. DOI:10.1006/JAER.2001.0706.
[21] Sharaby, N. N., Doroshenko, A.A., Butovchenko, A. V. (2020). Simulation of Sesame Seeds Outflow in Oscillating Seed Metering Device Using DEM. *Inzhenerernyye tekh- nologii i sistemy = Engineering Technologies and Systems*. 30(2):219-231. DOI: https://doi.org/10.15507/2658-4123.030.202002.219-231.
[22] Shi, S., Zhang, D.X., Yang, L. et al. (2015). Simulation and verification of seed-filling performance of pneumatic-combined holes maize precision seed-metering device based on EDEM. *Transactions of the Chinese Society of Agricultural Engineering*. 31, 62-69. Doi: 10.3969/j.issn.1002-6819.2015.03.009.
[23] Wang, B., Liao, Q., Wang, L. et al. (2023). Design and Test of Air-Assisted Seed-Guiding Device of Precision Hill-Seeding Centralized Seed-Metering Device for Sesame. *Agriculture.* 13, 393. https://doi.org/10.3390/agriculture13020393.

[24] Wu, Y.S., Guo, Z.B., Du, W.L. et al. (2017). Study of the Material Properties on the Quinoa Threshed Mixture. *Journal of Agricultural Mechanization Research*. 39, 184-189. Doi:10.13427/j.cnki.njyi.2017.09.036.

[25] Xu, X.M., Li, F.X., Li, Y.X. et al. (2019). Design and Experiment of Quantitative Variable Pitch Screw. *Transactions of the Chinese Society of Agricultural Machinery*. 50, 89-97. Doi:10.6041/j.issn.1000-1298.2019.12.010.

[26] Yazgi, A., Degirmencioglu, A. (2007). Optimisation of the seed spacing uniformity performance of a vacuum-type precision seeder using response surface methodology. *Biosyst*. Eng. 97, 347–356. DOI:10.1016/J.BIOSYSTEMSENG.2007.03.013.

[27] Zheng, J., Liao, Y.T., Qi, T.X. et al. (2023). Effect of vibration on performance of pneumatic rapeseed precision metering device. *Journal of Huazhong Agricultural University*. 42, 233-242. DOI : 10.13300/j.cnki.hnlkxb.2023.02.029.

[28] Zhang K.; Yi S.J. (2017). Simulation and experimental optimization of seed filling performance of air-absorbing drum type corn seed discharger. *Transactions of the Chinese Society of Agricultural Machinery*. 48, 78-86. Doi: 10.6041/j.issn.1000-1298.2017.07.010 .

[29] Zhang, T., Liu, F., Zhao, M.Q. et al. (2016). Movement law of maize population in seed room of seed metering device based on discrete element method. *Transactions of the Chinese Society of Agricultural Engineering*. 32, 27-35. Doi:10.11975/j.issn.1002-6819.2016.22.004.

[30] Zhao, X., Zhang, T., Liu, F. et al. (2023). Sunflower Seed Suction Stability Regulation and Seeding Performance Experiments. *Agronomy.* 13, 54. https://doi.org/10.3390/agronomy13010054.

[31] Zhao, Y.M., Zhang, S.G., Jiao, H.G. et al. (2006). Simulation of discrete element of particles motion on vibration plane. *Journal of China University of Mining and Technology*. 586-590.

DESIGN AND EXPERIMENT OF NO-TILLAGE PLANTER FOR HIGH AND LOW BORDERS WHEAT
/
高低畦小麦免耕播种机设计与试验

Shandong YANG[1)], Chuang MA[1)], Baochang Zhang*[1)], Yinping ZHANG[1)], Jinchang YANG[2)]

[1)]School of Agricultural and Food Science, Shandong University of Technology, Zibo (255000), China;
[2)]Shandong Qingyun Yiyuan Agricultural Machinery Manufacturing Co., Ltd, Zibo (255000), China;
DOI: https://doi.org/10.35633/inmateh-71-36

Keywords: *Wheat seeder, High and low borders, simulation research, ship-type ridging device*

ABSTRACT

Aiming at the problems of low land utilization and serious water waste in the existing wheat planting pattern, a two-high and two-low wheat high-low border spaced apart planting mode was proposed, and a high and low borders wheat no-till planter that can finish stubbing, fertilization, border construction, seeding and other tasks was designed. The design and analysis of the ship-type ridging device were carried out, and the construction process was simulated to determine the optimal parameters. A field test was carried out, the average sowing depth was 3.17 cm, the qualification rate was 95%, the standard deviation was 0.38 cm, and the coefficient of variation was 12.06%. The average value of the width of the seedling belt was 9.40 cm, the qualification rate was 91.67%, the standard deviation was 0.29 cm, and the coefficient of variation was 3.09%. The average height difference between the high and low borders was 9.26 cm, the pass rate was 100%, the standard deviation was 0.35 cm, and the coefficient of variation was 3.83%. The average width of the borders was 52.18 cm, the qualified rate of the border width was 100%, the standard deviation was 1.00 cm, and the coefficient of variation was 1.93%. The differences between each index and the theoretical design are small and meet the agronomic requirements.

摘要

针对现有小麦种植模式土地利用率低、水资源浪费严重的问题，本文提出了一种两高畦两低畦间隔分布的小麦高低畦种植模式，并设计了一种可一次性完成灭茬、施肥、构畦、播种等工作的高低畦小麦免耕播种机。对船式构畦器进行了设计和分析，并对构畦过程进行了仿真，确定了最优参数。田间试验表明，播种深度的平均值为 3.17cm，合格率为 95%，标准差为 0.38cm，变异系数为 12.06%；苗带宽度的平均值为 9.40cm，合格率为 91.67%，标准差为 0.29cm，变异系数为 3.09%；高低畦的高度差平均值为 9.26cm，合格率 100%，标准差为 0.35cm，变异系数为 3.83%；畦面宽度平均值为 52.18cm，合格率是 100%，标准差是 1.00cm，变异系数是 1.93%，各项指标与理论设计差异较小且符合农艺要求。

INTRODUCTION

Wheat is one of the major grain crops in China, accounting for about 20% of the current total grain crop production in China *(Yang, 2008; Li, 2006)*. With the deepening of the structural reform of the agricultural supply side, as well as the promotion of the implementation of the seasonal fallow system in some areas, the sowing area of wheat has been reduced. This has led to a reduction in the total area of planted wheat in China, and the increase in yields showed a downward trend *(Qi, 2020; Gao, 2020)*. As to how to improve wheat yield, academician Songlie Yu proposed the technology of wide precision sowing of wheat. He believes that when the width of the seedling strip is within the range of 80~100 mm, wheat can fully utilize photosynthesis, which increases yield *(Yu, 1980)*. The planting pattern of the wheat-wide seedling belt on a high-low border is distributed between high and low borders *(Song et al., 2021)*. As shown in Fig. 1, two rows of wheat are planted in the raised borders and two rows in the low borders, and when the water is irrigated in the low ridge, the high ridge will have ensured the water required for germination due to water infiltration. This model can be used in rotation with corn, planted on the sloped side of the high borders, which also saves water. Compared with the traditional border planting mode, this planting mode can effectively save water and improve wheat acre yield. Therefore, this paper designs a no-tillage wheat seeder for the high-low border, which can simultaneously complete the stubbing, fertilization, border construction, seeding, suppression, and other tasks, realizing the combination of agronomy and agro-machinery.

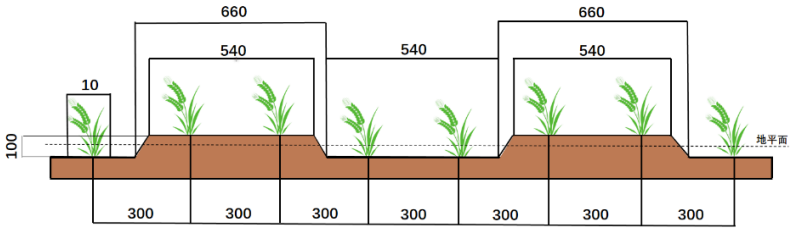


Fig. 1 - High and low borders planting mode

MATERIALS AND METHODS

The structure and working principle

The overall structure of a high-low border wheat no-till planter is shown in Fig. 2, which is mainly composed of a frame, rotary stubble device, fertilizer device, ridging device, profiling seeding device, and transmission part, and the main technical parameters of the whole machine are shown in Table 1.

The high-low border wheat no-till planter is connected to the tractor through a three-point suspension. Part of the fertilizer discharged from the fertilizer dispenser is spread to the ground through the fertilizer board. The power output shaft at the rear of the tractor connects with the main transmission through the universal joints to transfer the power to the rotating stubble device, and the stubble cutter shaft rotates at a high speed to mix the fertilizer with the soil. Driven by the tractor, the fertilizer device under the drive of the tractor, the fertilizer device, and the border construction device enter the soil in turn. The fertilizer device discharges the fertilizer into the fertilizer furrow through the chisel furrow opener to realize the function of deep fertilization. The border construction device extrudes and spreads the treated soil to both sides to form the border between high and low. The imitation sowing device imitates the shape according to the formation of the high and low borders. The seed dispenser discharges the wheat seeds into the underground seeding furrow to complete the seed dispensing operation through the double-disk wide seedling belt opener under the drive of the pressure wheel. The pressure wheel is installed at the back of the imitation sowing device and floats with the sowing unit to realize the suppression of wheat seeds.

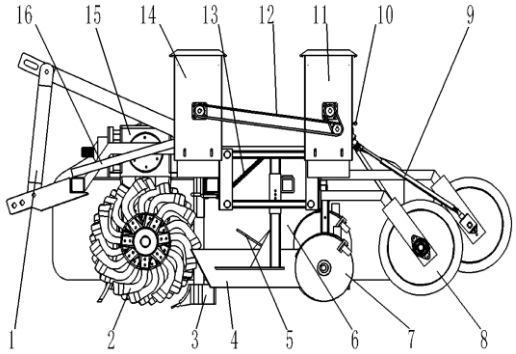


Fig. 2 - Structure diagram of the no-tillage planter for high and low borders wheat

1. Frame; 2. Rotary stubble device; 3. Fertilizer device; 4. Border framer; 5. Soil scraper; 6. Side plate; 7. Double disk wide seedling belt opener; 8. Pressure wheel; 9. Shaft drive; 10. Sowing volume adjustment gearbox; 11. Seed box; 12. Chain drive; 13. Tension spring; 14. Fertilizer box; 15. Main gearbox; 16. Fertilizer spreading plate.

Table 1

Technical parameters of the no-tillage planter for high and low-border wheat

Items	Parameters
Hook mode	Trifilar suspension
Working width /cm	240
Seeding rows	8
Seeding row spacing /cm	30
Planting depth /cm	2~4
Belt width /cm	10
Fertilization method	Deep fertilize and spread fertilizer

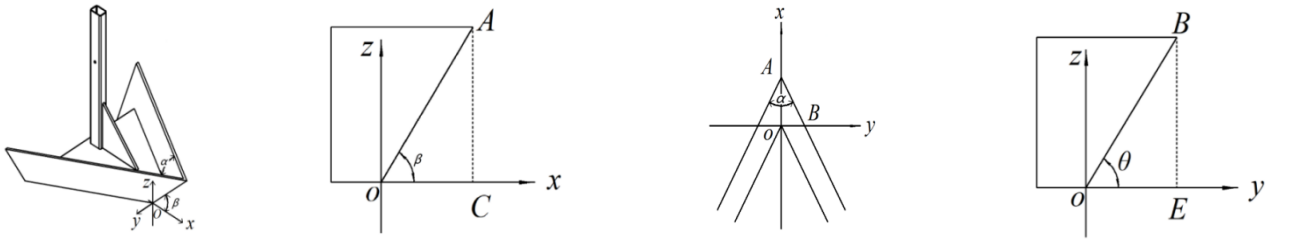
Critical Component Design

Design of ridging devices

(1) *Structural design of ridging device*

In this paper, a ship-type ridging device is designed, which mainly consists of a soil divider, a fascia plate, and a connecting handle. During operation, the stubble device first treats the plot, cuts off the stubble, and throws the soil from the low-border position to the high-border centrally. Then the ship-type ridging device trellis builder squeezes and throws the soil particles so that the soil in the low-border can be fully transferred to the high-border position. It solidifies the high border surface, reduces the natural slide of soil particles, and lays the foundation for subsequent sowing process.

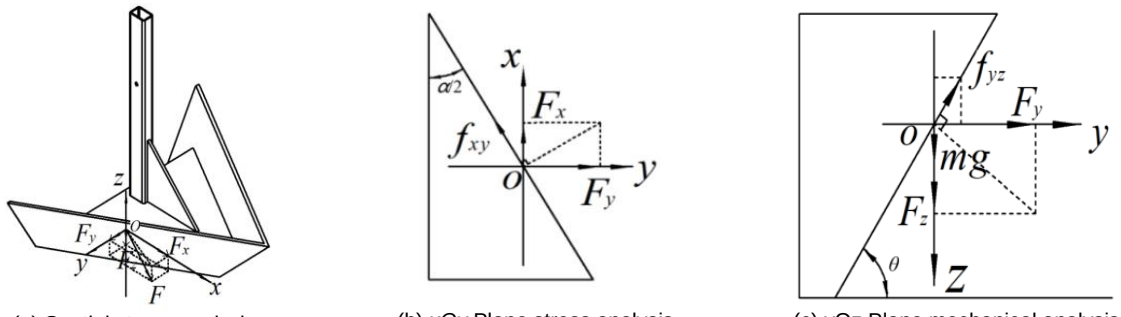
The upper front end of the ship-type ridging device is tilted forward to allow for easy access over the straw residue in the field, preventing it from collecting in the front of the implement and causing congestion. The sides of the ridging device are gradually tilted outward from low to high, squeezing the passing soil to both sides, creating a sloping surface for the high and low borders, and squeezing and spreading the soil particles from the low borders to the high borders *(Gou et al., 2012; Liu et al., 2021)*. According to the agronomic requirements, the width of the low border is 540 mm, and the height of the border is 100 mm. Because of the consideration of the return of soil at the end of the construction process and the compaction of the compaction wheels, the value range of the soil dividing angle α is 55~65°, the value range of the front inclination angle β is 55~65°, the width of the bottom of the ridging device is 550 mm, and the height of the ridging device is 200 mm in the vertical direction. The spatial coordinate system shown in Fig. 3(a) was established to analyse the structural parameters of the ridging device, and the forward direction of the ridging device was taken as the positive direction of the x-axis.



(a) space coordinates system (b) *xOz* plane geometry analysis (c) *xOy* plane geometry analysis (d) *zOy* plane geometry analysis

Fig. 3 - Geometry analysis of ridging device

The process of border construction can be regarded as an inclined plane acting on the soil, the soil particles to the two sides of the process of extrusion, selected any point on the side plate of the soil particles of the mass point o as the object of study *(Liu et al., 2017; Liu et al., 2019)*, the establishment of the mechanics of the spatial coordinate system as shown in Fig. 4, is still the direction of the forward direction of the ridging device for the x-axis positive direction, the forward speed of, the ridging device on the side of the soil particles of the instantaneous pressure for F. The process of border construction can be regarded as an inclined plane acting on the soil, the process of extrusion to the two sides of the soil particles.



(a) Spatial stress analysis (b) *xOy* Plane stress analysis (c) yOz Plane mechanical analysis

Fig. 4 - Mechanics analysis of point squeezing of soil particles

Kinetic equations for the soil particle plasmas along the x, y, and z axes are:

$$\begin{cases} F_x + f_{xy}\cos\dfrac{\alpha}{2} = ma_x \\ F_y + f_{yz}\cos\theta - f_{xy}\sin\dfrac{\alpha}{2} = ma_y \\ F_z - f_{yz}\sin\theta + mg = ma_z \\ f_{xy} = \tan\varphi\sqrt{F_x^2 + F_y^2} \\ f_{yz} = \tan\varphi\sqrt{F_y^2 + F_z^2} \\ F_x = F_y\tan\dfrac{\alpha}{2} \\ F_z = F_y\cot\theta \\ F = \sqrt{F_x^2 + F_y^2 + F_z^2} \end{cases} \quad (1)$$

where: m - soil particle quality, (kg);

g - gravity acceleration, (N/kg);

F_x - the texture of the soil grain is subjected to the component force of the instantaneous pressure in the X-axis direction at the O point, (N);

F_y - the texture of the soil grain is subjected to the component force of the instantaneous pressure in the Y-axis direction at the O point, (N);

f_{xy} - the friction force on a particle in the *xOy* plane, (N);

f_{yz} - the friction force on a particle in the *zOy* plane, (N);

φ - soil friction angle, (°);

a_x - acceleration of a particle in the X-axis direction, (m/s^2);

a_y - acceleration of a particle in the Y-axis direction, (m/s^2);

a_z - acceleration of a particle in the Z-axis direction, (m/s^2);

It is obtained from formula (1)

$$\begin{cases} a_x = \dfrac{F\left(\tan\dfrac{\alpha}{2} + \tan\varphi\right)}{m\sqrt{1+\tan^2\dfrac{\alpha}{2}\left(\dfrac{1+\tan^2\beta}{\tan^2\beta}\right)}} \\ a_y = \dfrac{F\left[1+\tan\varphi\tan\dfrac{\alpha}{2}\left(\dfrac{1-\tan\beta}{\tan\beta}\right)\right]}{m\sqrt{1+\tan^2\dfrac{\alpha}{2}\left(\dfrac{1+\tan^2\beta}{\tan^2\beta}\right)}} \\ a_z = \dfrac{F\left(\dfrac{\tan\dfrac{\alpha}{2}}{\tan\beta} - \tan\varphi\right)}{m\sqrt{1+\tan^2\dfrac{\alpha}{2}\left(\dfrac{1+\tan^2\beta}{\tan^2\beta}\right)}} \end{cases} \quad (2)$$

From equation (2), it can be seen that the force on the soil particle mass point is related to the soil parting angle α, the front inclination angle β, and the soil friction angle φ. By Newton's third law, the force is mutual, so it can be seen that the forward resistance of the bordering device is also related to the soil parting angle α, the front inclination angle β, and the soil friction angle φ. In addition, according to the rational formula of the traction resistance of the plough, it is known that the forward speed v of the bedding device is also one of the factors affecting the forward resistance of the bedding device:

$$R = R_1 + R_2 + R_3 = fG + kab + \varepsilon abv^2 \quad (3)$$

where: R - drag resistance of plough, (N);

f - combined friction coefficient, f =0.3~0.5;

k - coefficient of resistance to deformation of soil, (N/cm^2);

a - tilling depth, (cm);

b - working width, (cm);

ε - dynamic drag coefficient, (Ns^2/m^4);

v - the forward speed of the plough, (m/s^2);

(2) *Design of structural parameter optimization test scheme*

The Box-Behnken design experimental design in Design Expert software was used to analyse a 3-factor, 3-level response surface test for the soil splitting angle α, forward tilt angle β, and forward speed of the unit v. In the test, the forward resistance Q (N) and the width of the low border W (mm) were used as the test indexes for the response (*Asaf et al., 2007; Mak et al., 2012; Shmulevich et al., 2010*), and Table 2 shows the coding of the established test factors.

Table 2

Factors and coding of the experiment

Numbers	Factors		
	Factor A: Partition angle α / (°)	Factor B: top rake β / (°)	Factor C: Unit forward speed *v* / (km·h^{-1})
-1	55	45	7
0	60	60	8
1	65	75	9

Based on the above test factor coding table, the design of the test protocol was carried out with a total of 17 sets of tests, of which 12 sets were used as analytical factorization points 5 sets were used as nulls, and the null tests were repeated several times to estimate the experimental error. The experimental protocol and results are shown in Table 3. The forward resistance variance and low-border width variance were also analysed based on the experiments *(Choudhary et al., 1985)*.

Table 3

Response surface analysis and test results

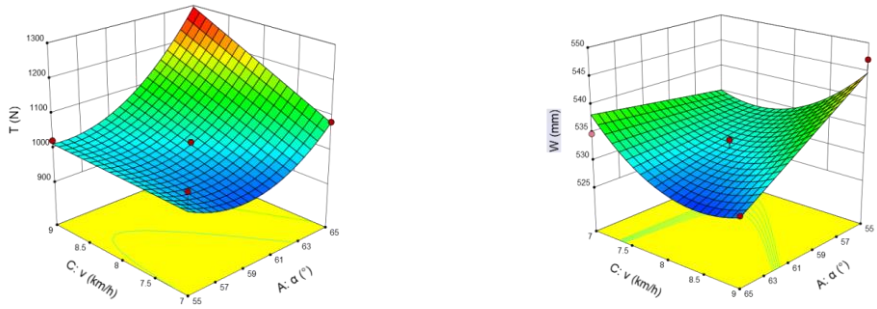
Numbers	Factor X1	Factor X2	Factor X3	Forward resistance T / (N)	Low border width W / (mm)
1	1	-1	0	1234.8	532.32
2	1	1	0	1181.1	526.78
3	0	0	0	981	533.16
4	1	0	-1	1082.8	534.8
5	0	0	0	981	533.16
6	0	-1	-1	990.4	536.92
7	0	1	1	1045.8	532.9
8	0	0	0	981	533.16
9	-1	0	1	1022.6	547.08
10	0	0	0	1021.3	529.3
11	-1	1	0	923.8	533.8
12	0	0	0	1021.3	529.3
13	-1	0	-1	1052.1	533.86
14	0	-1	1	1184	539.04
15	1	0	1	1254.1	529.08
16	-1	-1	0	1025	534.02
17	0	1	-1	924.5	540.18

By analysing the forward resistance ANOVA and low border width ANOVA. The results show that only the interaction of model X_1X_3 has a significant effect on forward resistance as well as low-border width, so the response surface analysis was performed. When the front inclination angle β is 60°, the relationship between the soil dividing angle and the forward speed of the unit and the forward resistance and the width of the low border is obtained as:

$$T = 16171.608 - 458.374X_1 - 545.313X_3 + 10.04X_1X_3 + 3.302X_1^2 \quad (4)$$

$$W = 441.91 + 6.932X_1\text{-}0.947X_1X_3 + 5.066X_3^2 \quad (5)$$

The specific rule of change is shown in Fig. 5(a). When the front inclination angle β is 60°, the forward resistance of the ridging device decreases with the forward speed of the unit, and the decrease in the soil dividing angle shows a decreasing and then slightly increasing trend. According to the plough's traction resistance rational formula, it can be seen that the smaller the forward speed of the unit, the forward resistance of the ridging device decreases. However, when the soil dividing angle is too small, the length of the ridging device will increase to satisfy the low-border width agronomical requirements. This leads to an increase in the force area in the forward direction of the unit, thus its forward resistance shows a slightly increasing trend. For the change of the width of the low border, the width of the low border needs to be maintained at about 54 cm. From Fig. 5(b), it can be seen that the width of the low border tends to decrease and then increase as the angle of parting decreases and the forward speed of the unit increases. The throwing distance of the soil particles in the forward direction of the unit is not enough to affect the bordering operation of the ridging device. Through the structure design of the ship-type ridging device, the low border's width is relatively increased, which meets the corresponding agronomic requirements.



(a) (b)

Fig. 5 - The response surface of the soil dividing angle and the forward speed of the unit to the forward resistance and the low border width

From the above response surface analysis, it can be seen that the three factors of soil parting angle, forward tilt angle, and forward speed of the unit will have interactive effects on the forward resistance and the width of the low border, therefore, the regression model was solved by applying Design-Expert software to optimize the regression model under the objective to obtain the best combination of parameters, and the optimization constraints are:

$$\begin{cases} \min T \\ 538\text{mm} \le W \le 542\text{mm} \\ s.t. \begin{cases} 55° \le \alpha \le 65° \\ 45° \le \beta \le 75° \\ 7\text{km/h} \le v \le 9\text{km/h} \end{cases} \end{cases} \quad (6)$$

The optimal parameter combinations were calculated as follows: 61.46° dividing angle, 64.98° forward tilt angle, 7.01 km/h forward speed of the unit, 923.80 N forward resistance, and 538.08 mm width of the low borders, which were rounded off to take the dividing angle of 61°, the forward tilt angle of 65°, and the forward speed of the unit of 7 km/h.

Layout of ridging device and stubble removal device design

To reduce the number of implements in the ground, the ridging device is set to construct two raised borders, one low border, and two half-low borders at a time. Install a soil scraper in the middle of the centre border builder and in the middle of the side border builder to level the surface of the high borders. The specific structure of the ridging device is shown in Fig. 6 (a).

To prevent the throwing of soil to bury the completed sowing rows during the process of rotary tillage and stubble removal, the direction of the rotary ploughing curved knives is rearranged. The rotary ploughing curved knives in the low borders are bent in the direction of the high borders and the straight knives are used in the high borders, to mix the stubble with the soil sufficiently and not throw the soil particles out of the outside of the machine tool, which can reduce the energy consumption. The specific structure is shown in Fig. 6 (b).



(a) (b)

Fig. 6 - Ridging device layout diagram and structure drawing of rotating tillage stubble removal device

Field experiment

Test conditions

Test prototype in Shandong Qingyun Yiyuan Agricultural Machinery Manufacturing Co., Ltd. trial, the test site for the Zibo Aimin Seed Industry Yellow River Beach test base, the use of "Kaite Shenzhou red 1804" tractor as supporting power, Figure 7 for the field test photos.



Fig. 7 - Prototype field test diagram

Test methods and contents

According to the national standard GB/T 20865-2007 "No Tillage Fertilization Seeder", this article tested the testing indicators for the sowing quality of wheat no tillage seeders and the requirements for high and low borders wheat planting modes. The main equipment used includes electronic scales, tape measure, board ruler, small shovel, plastic bags, etc. The wheat variety used in the test was blue wheat developed by Aimin Seed Industry, and the sowing rate of 187.5 kg/hm^2 was set in the test; the fertilizer was compound fertilizer, and the fertilizer application rate was 675 kg/hm^2*(Liu et al., 2011)*. The sowing speed was 7km/h.

(1) *Machine passability*

The tractor will pass if it operates at a predetermined speed and makes one round trip with the previous crop covered with straw without heavy blockage.

(2) *Seeding depth and seedling strip width*

The tractor was operated at a predetermined speed, 3 rows of raised borders and 3 rows of low borders were randomly selected, and 5 points were taken from each row within a 100 cm area, the soil layer was peeled back to measure the depth of wheat seeding as well as the width of seedling belt, and the data were recorded.

(3) *Height difference between high and low borders and width of borders*

The planter was operated at a predetermined speed, 3 rows of high borders and 3 rows of low borders were randomly selected, and the length of each row was randomly selected as a test area of 5 m. The width of the borders as well as the difference in height between the high and low borders were randomly measured in 5 places in the test area.

RESULTS

After the planter completed the operation, the seeding depth, seedling strip width, height difference between high and low borders, and border width were measured and recorded according to the test method, and the specific data are shown in Table 4.

Table 4

Test result				
Detection area	**Sowing depth /cm**	**Belt width /cm**	**High and low borders height difference / cm**	**Border width / cm**
1	3.00	9.47	9.38	52.54
2	3.50	9.44	9.14	52.30
3	3.19	9.27	9.56	51.96
4	3.03	9.39	9.18	52.30
5	3.17	9.33	8.96	51.90
6	3.14	9.49	9.32	52.06
Average	3.17	9.40	9.26	52.18
Qualified rate /%	95.00	91.67	100.00	100.00
Standard deviation /cm	0.38	0.29	0.35	1.00
Variable coefficient /%	12.06	3.09	3.83	1.93

The experimental results show that the seeding depth qualification rate of this planter is high, but the double disk opener itself has the characteristic of soil return, resulting in the seeding depth of some positions of the seedling belt changing. The coefficient of variation is larger; the effect of soil return on the width of the seedling belt is also smaller, so the coefficient of variation is smaller. The height difference between the high and low borders and the width of the borders are high, and the coefficients of variation are small, which are in line with the relevant agronomic requirements and standards.

The specific seedling emergence situation is shown in Fig. 8, the wheat seedling emergence results are good and the height difference between high and low borders meets the test requirements. After harvesting wheat, the yield of the traditional border wheat planting pattern was 9732 kg/hm^2, and the yield of the high and low border wheat planting pattern was 10745 kg/hm^2, which was up to 10.4%, and the effect of yield increase was obvious. The irrigation area was smaller than that of traditional border cropping, and the water saving could be up to 40%.



Fig. 8 - The emergence of wheat

CONCLUSIONS

(1) Aiming at the problems of low land utilization and serious waste of water resources in the existing wheat planting pattern, a two-high and two-low wheat high-low border planting pattern was proposed, and a no-tillage sowing machine for high and low borders was designed, which integrates stubbing, fertilizer application, border construction, and seeding.

(2) A ship-type ridging device was designed, the main influencing factors affecting the border construction resistance and the width of the low border were determined. The simulation test was carried out on the border construction process, and the optimal parameters were obtained after data processing. When the dividing angle α of the trellis is 61°, the forward inclination angle β is 65°, and the forward speed v of the unit is 7 km/h, the resistance of the ridging device is minimized under the condition of satisfying the width of the low border. The rotating stubble device was designed so that based on the completion of the stubbing operation, it can concentrate the soil of the low-border border towards the high-border border to reduce the resistance of the border construction.

(3) A field test was conducted, and the test data were analysed. According to national standards, the planter made three round trips within the 60 m test operating area without any serious blockage, and the machine had good passability. The average value of the sowing depth of the no-tillage wheat planter in the high and low borders was 3.17 cm, the qualification rate was 95%, the standard deviation was 0.38 cm, and the coefficient of variation was 12.06%. The average value of the width of the seedling belt was 9.40 cm, the qualification rate was 91.67%, the standard deviation was 0.29 cm, and the coefficient of variation was 3.09%. The average height difference between the high and low borders was 9.26 cm, the pass rate was 100%, the standard deviation was 0.35 cm, and the coefficient of variation was 3.83%. The average width of the borders was 52.18 cm, the qualified rate of the border width was 100%, the standard deviation was 1.00 cm, and the coefficient of variation was 1.93%. Finally, the differences between each index and the theoretical design are small and meet the agronomic requirements.

REFERENCES

[1] Asaf Z, Rubinstein D, Shmulevich I., (2007). Determination of discrete element model parameters required for soil tillage [J] (Shmulevich I. Determination of discrete element model parameters required for soil tillage) *Elsevier BV*, no.1, pp.227-242.

[2] Chiming Qi., (2020). Analysis of domestic wheat market situation [J] (国内小麦市场形势分析). China's national conditions and national strength, no. 10, pp. 60-62;

[3] Choudhary M.A., Yu Guo-Pei, Baker C.J., (1985). Seed placement effects on seedling establishment in direct-drilled fields [J] (Seed placement effects on seedling establishment in direct-drilled fields). *Elsevier BV*, no.1, pp. 79-93;

[4] Deping Song, Wei Li, Mingjun Li et al., (2021). Design and experiment of wheat high-low-border wide-seedling belt planter [J] (小麦高低畦宽苗带播种机设计与试验). *Journal of Chinese Agricultural Mechanization*, vol.42, no.3, pp. 1-6;

[5] Han X.M., Wang H.Y., (2005). The Analysis and Dynamic Emulation of the Cam Mechanism Based on ADAMS/View [J] (基于 ADAMS/View 机心凸轮机构分析与动态仿真). *Mechanical Engineer*, no.10, pp. 97-99;

[6] Jiancang Yang., (2008). *Study on the Development of Wheat Production and the Support of Science and Technology in China* [D] (我国小麦生产发展及其科技支撑研究). Chinese Academy of Agricultural Sciences.

[7] Jinbao Liu, Qingchao Li, Xuan Zheng et al., (2012). Research Status of Drag Reduction Technology for Soil Tillage Components [J] (土壤耕作部件减阻技术研究现状). *Xinjiang Agricultural Mechanization*, vol.37, no.6, pp. 25-28;

[8] Kaituo Fang, Hailang Ge, Yunyang Shi et al., (2019). Optimization and simulation of profile spraying mechanism based on ADAMS [J] (基于 ADAMS 的果树仿形施药机构优化设计与仿真分析). *Journal of Chinese Agricultural Mechanization*. vol.40, no.10, pp. 58-63;

[9] Lite LI., (2006). The opportunity for the development of China's wheat industry lies in the modernization of traditional staple food (中国小麦产业发展的机遇在于传统主食现代化). *Grain Processing*, no.4, pp.5-8;

[10] Liu L., Liu Z., Yang X. et al., (2011). Design and test on pneumatic no-till wheat planter [J] (气流输送式小麦免耕播种机设计和试验). *Transactions of the Chinese Society for Agricultural Machinery*, vol.42, no.2, pp. 54-57;

[11] Mak J., Chen Y.,Sadek M.A., (2012). Determining parameters of a discrete element model for soil–tool interaction [J] (Determining parameters of a discrete element model for soil–tool interaction) *Elsevier BV*, pp. 117-122;

[12] Shan Gao., (2020). Present situation and development countermeasures of wheat industrialization in China [J] (中国小麦产业化现状与发展对策). *Agricultural development and equipment*, no.3, pp. 25-26;

[13] Shmulevich I., (2010). State of the art modeling of soil–tillage interaction using discrete element method [J] (State of the art modeling of soil–tillage interaction using discrete element method). *Elsevier BV,* no.1, pp. 41-53;

[14] Shuhong Zhao, Enchen Jiang, Yixun Yan, et al., (2013). Design and motion simulation of opener with bidirectional parallelogram linkage profiling mechanism on wheat seeder [J] (基于 ADAMS 的播种机仿形机构运动仿真). *Transactions of the Chinese Society of Agricultural Engineering*, vol.29, no.14, pp. 26-32;

[15] Songlie Yu., (1980). High-yield cultivation of winter wheat by fine sowing [J] (冬小麦精播高产栽培). Journal of Shandong Agricultural College, no.2, pp. no.3, pp. 25-26;

[16] Wen Gou, Rongchao Ma, Wenyu Yang et al., (2012). Design of opener on no-till wheat seeder. *Transactions of the Chinese Society of Agricultural Engineering* [J], vol.28, no.S1, pp. 21-25;

[17] Wenyan Yao, Dianbao Zhao, Guangfei Xu et al., (2020). Design and experiment of non-blocking device for no-tillage seeding of maize with active strip-to-row [J] (条带对行主动式玉米免耕播种防堵装置设计与试验). *Transactions of the Chinese Society for Agricultural Machinery*, vol.51, no.S2, pp. 55-62+71;

[18] Xiaopeng Liu, Wenli Xiao, Lei Ma et al., (2017). Design and Ditching Quality Experiment on Combined Ship TypeOpener of Direct Rapeseed Seeder [J] (油菜联合直播机组合式船型开沟器设计与开沟质量试验). *Transactions of the Chinese Society for Agricultural Machinery*, vol.48, no.11, pp. 79-87; (in Chinese with English abstract)

[19] Xiaopeng Liu, Qingsong Zhang, Lichao Liu, et al., (2019). Surface Optimization of Ship Type Ditching System Based on Differential Geometry and EDEM Simulation [J] (基于微分几何与 EDEM 的船型开畦沟装置触土曲面优化). *Transactions of the Chinese Society for Agricultural Machinery*, vol.50, no.8, pp. 59-69; (in Chinese with English abstract)

[20] Xiaobing Fan, (2016). Research on corn no-tillage planner and its key components in wheat stubble fields [D] (麦茬地玉米免耕播种机及其关键部件的研究). *Nanjing Agricultural University*.

[21] Zhen Ji, Zhigang Liu, Jiannan Yu, et al., (2021). Design and simulation analysis of copying mechanism of shrub stubble machine [J] (灌木平茬机仿形机构的设计及仿真分析). *Machinery Design and Manufacture*, no.8, pp. 70-74;

[22] Zhuang W.D., Wang C., Wang X., (2006). The Analysis and Operating Setup for Flexi-Coil's Variable Planter [J] (Flexi-Coil 变量播种机使用设置的分析). *Journal of Agricultural Mechanization Research*, vol.60, no.3, pp. 56-57.

HARVEST LOSS TEST AND OPTIMISATION OF KEY COMPONENTS OF OILSEED RAPE CUTTING TABLES
/
油菜割台关键部件收获损失试验与优化

Jia YAO, Guohai ZHANG*), Xin WANG, Jitan LIAN, Minghao LIU, Xipeng QIAN, Yihu WANG, Peng LIU [1]
College of Agricultural Engineering and Food Science, Shandong University of Technology, Zibo 255000, China
Tel: +86-15965534882; E-mail: guohaizhang@163.com
Corresponding author: Guohai Zhang
DOI: https://doi.org/10.35633/inmateh-71-37

Keywords: *oilseed rape, mechanized harvesting, loss of headers, orthogonal test, parameter optimization*

ABSTRACT
Aiming at the problem of high loss of oilseed rape combine harvesting cutting platform, this paper combines the biological characteristics of oilseed rape, analyses the way and reason of oilseed rape loss, selects the harvester's forward speed, transverse cutter cutting height and longitudinal cutter cutting speed three factors to influence the loss rate of the cutting platform to carry out the study on the significance of the order of significance of the following: cutting speed > forward speed > cutting height. Through the response surface analysis method, the interaction between the factors was obtained. Through the regression model of the factors affecting the loss rate, the parameter optimisation was carried out with the objective of the lowest loss rate, and the optimal parameter combinations being obtained as follows: the forward speed was 5 km/h, the cutting speed was 1.5 m/s, and the cutting height was 50 cm. Finally, the results of the model were obtained to be reliable through the experimental validation.

摘要
针对油菜联合收获割台损失高的问题，本文结合油菜生物特性，对油菜产生损失的方式和原因进行分析，选择收获机前进速度、横向切割器切割高度和纵向切割器切割速度三项因素对割台损失率进行影响显著性研究，其显著性顺序为：切割速度>前进速度>切割高度；通过响应面分析法得到各因素之间两两存在交互作用；通过损失率影响因素回归模型，以损失率最低为目标进行参数优化，求得最优参数组合为：前进速度为 5km/h，切割速度为 1.5m/s，切割高度为 50cm；最后，经试验验证得到模型结果可靠。

INTRODUCTION
Rapeseed is the main oilseed crop in China, and its planting area and output are among the top in the world, which has an important position in China's agricultural production. In the rapid development of agricultural mechanisation today, compared with rice, wheat, corn and other bulk crops, rapeseed in all aspects of ploughing, planting, management, harvesting, breeding of fine varieties still has more room for development. In terms of biological control of oilseed rape, some scholars have experimented intercropping oilseed rape with wheat and intercropping with alfalfa to explore the attractiveness of natural enemies of aphids and the effect of biological control and crop yield (*Hatt et al., 2019; Tajmiri et al., 2017*); in terms of ploughing management, it is important to explore the effects of different ploughing methods on the growth of oilseed rape and its yield, and to combine the oilseed rape agronomic techniques to achieve the optimal management of oilseed rape (*Jankowski et al., 2023; Kristó et al., 2021; Bečka et al., 2021*). In addition, fertiliser application method (*Miersch et al., 2016*), planting density (*Khan et al., 2018; Zhang et al., 2017*), variety and sowing date (*Zorzenoni et al., 2019; Crnobarac et al., 2015*) have also become the focus of research on the full growth cycle of oilseed rape. In terms of mechanised harvesting of oilseed rape, the high rate of seed loss is an important reason restricting its development at present, the average loss rate of oilseed rape combined harvesting reaches 8.54%, and the loss of seed mainly originates from the disturbance of the cutting platform and separation and cleaning and other subsequent work processes, of which the loss generated by the cutting platform accounts for more than half of the total loss (*Wei, 2021; Kendall et al., 2017*). This leads to not only high harvest losses in the development of oilseed rape, but also environmental impacts that cannot be ignored.

[1] *Jia Yao, MAg. Stud. Eng.; Guohai Zhang, As. Ph.D. Eng.; Xin Wang, M.S. Stud. Eng.; Jitan Lian, MAg. Stud. Eng.; Minghao Liu, M.Sc. Stud. Eng.*

Firstly, the special biological nature of oilseed rape is an important reason for its high harvest losses. During the harvesting period, oilseed rape plants are tall, with many branches and inconsistent growth heights, and the upper part of the angiosperms are intertwined with each other, making it difficult to divide the harvest (*Yiren, 2021*). The lower part of the stalks are thick and tough, the lateral cutter will have impact on the stalks during operation, resulting in the upper part of the angular fruit being subjected to mutual extrusion pressure, and the current widely planted oilseed rape varieties with poor resistance to cracking angle, by vibration, beat, extrusion and other interferences are very easy to blow pods, resulting in oilseed rape drop grain loss; wrapped in the angular fruit, with the colour of the rapeseed being close to the colour of the soil, it is difficult to distinguish and pick up those fallen on the soil (*Yang, 2020; Wu and Wu, 2018; Zhang et al., 2021*). In addition, the low degree of agro-mechanical and agronomic adaptation is also a key cause of oilseed rape losses. At present, most of the cutting platforms used for harvesting oilseed rape are improved on the basis of rice and wheat cutting platforms by lengthening the cutting platforms, adding longitudinal cutters, and adjusting the working parameters and positions of the paddle wheels, and there are no special cutting platforms for oilseed rape. Researchers and scholars at home and abroad select and cultivate excellent varieties of oilseed rape, and at the same time explore the structural parameters and working parameters of each component of the cutting platform and the working parameter relationship between the components (*Frid et al., 2017*), with a view to taking measures to reduce the harvesting losses of oilseed rape from two important aspects of agro-mechanics and agronomy.

MATERIALS AND METHODS

Analysis of the main working parts of the cutting table

Harvesting Paddle Wheel

The paddle wheel is one of the most common paddles, mainly composed of paddle wheel and paddle bullet teeth, its function is to paddle the oilseed rape to be cut to the cutting platform, support the crop crooked stalks, so that the oilseed rape to achieve the state of easy cutting. Its structure sketch is shown in Fig.1.

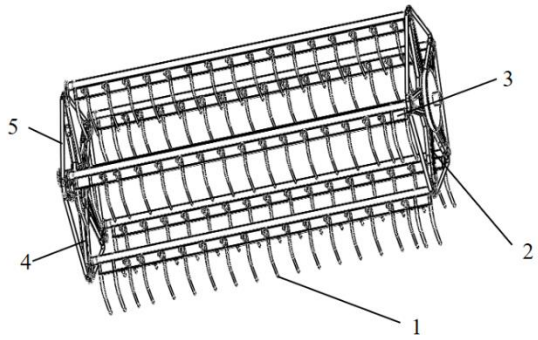


Fig. 1 - Sketch of the structure of the paddle wheel

1 - Bullet teeth; 2 - Eccentric wheel; 3 - Wheel axle; 4 – Spokes; 5 - Tension bar

The motion of the paddle wheel consists of the forward speed of the harvester and the rotary motion of the paddle wheel itself, the trajectory of which is shown in Fig.2.

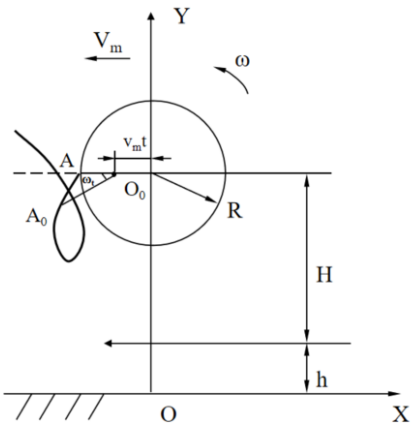


Fig. 2 - Movement trajectory of the plucking wheel

The motion trajectory equation is shown in Equation (1), and in order to ensure that the paddle wheel can play the role of paddle, the necessary condition is the ratio of the circumferential speed V_b of the paddle wheel and the forward speed V_m of the harvester, i.e., the paddle speed ratio λ>1, so that the motion trajectory of the paddle wheel as a co-cycloid (*Xiao et al., 2020*).

$$\begin{cases} x = V_m t + R\cos\omega t \\ y = H - R\sin\omega t + h \end{cases} \quad (1)$$

where:

V_m - Harvester forward speed, [m/s]; t - rasp wheel working time, [s]; R - radius of the paddle wheel, [m]; ω - Angular speed of rotation of the paddle wheel, [rad/s]; H - Vertical distance between the centre axis of the paddle wheel and the main cutter, [m]; h - height of the main cutter above ground, [m]

Through a large number of experimental studies by scholars at home and abroad, it is indicated that in the optimisation of the structure of the paddlewheel, the selection of eccentric paddlewheel, paddlewheel flexible elastic teeth, and elastic teeth into the harvesting method of slanting insertion is most suitable for the harvesting of oilseed rape because the growth of oilseed rape angular fruits is disordered and seriously entangled with each other, and the method of slanting insertion of harvesting is better adapted to the biological characteristics of oilseed rape, and it is able to reduce the loss of falling grains caused by insertion of elastic teeth into the inner part of the angular fruits (*Zhou et al., 2023*). In the optimisation of the working parameters of the paddlewheel, most of the scholars carried out optimisation tests in terms of the paddlewheel speed ratio, the horizontal position of the paddlewheel relative to the cutter, the vertical position of the paddlewheel and the paddlewheel rotational speed, and the optimisation of the parameters was carried out with the objective of reducing the loss rate.

Cutter

As one of the key components of the cutting platform, the cutting effect of the cutter has an important impact on the harvesting quality of the harvester. At present, the cutter used in oilseed rape harvester is reciprocating cutter, which mainly consists of reciprocating cutter and fixed support part, and its structure sketch is shown in Fig. 3.

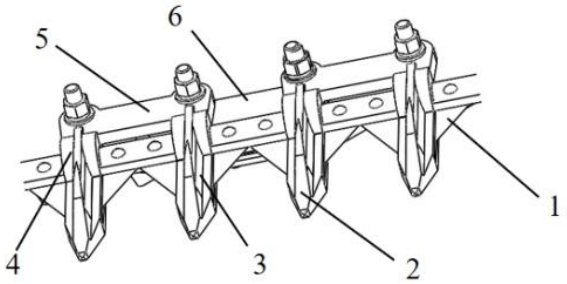


Fig. 3 - Schematic diagram of the structure of the reciprocating cutter

1 - Dynamic blade; 2 - Fixed blade; 3 – Presser; 4 – Shield; 5 - Shield beam; 6 - Tool holder

The working principle of the reciprocating cutter is that when the knife bar makes reciprocating movement, the moving blade and the fixed blade form a shear, which cuts off the oilseed rape stalks (*Wu Shouyi, 1992*). At present, the reciprocating cutter is mainly divided into three types: standard type, low cutting type and double knife pitch stroke type, the main difference is the relationship between the linear motion stroke s of the moving blade and the installation spacing t between the adjacent moving blade and the installation spacing t_0 between the adjacent fixed blade.

The structural dimension relationship of the standard reciprocating cutter is s=t=t_0=76.2 mm. This type of cutter has a faster cutting speed, is more adaptable to crop stalks, and is the most widely used cutter at present. Its structural shape is shown in Fig.4. Low-cutting type reciprocating cutter structure size for s=t=2t_0=76.2 mm, due to the two fixed blades between the fixed blade and a fixed blade, blade spacing is small, the crop stalks of the transverse skew amount is small, the cut stubble is lower, but prone to plugging the knife phenomenon. The structural dimension relationship of the double blade spacing stroke type reciprocating cutter is s=2t=2t_0=152.4 mm, which is characterized by lower cutting speed and small inertia force, but the cutting load on the cutting edge of the cutter is not uniform.

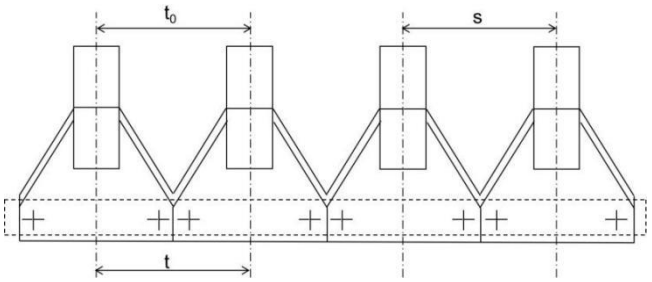


Fig. 4 - Standard Type II reciprocating cutter

Due to the serious entanglement and difficulty in dividing the upper end of the rape horn, the use of ordinary branching devices has a pulling force on the rape horn, resulting in the loss of thin and crispy horn pods and grains drop. The oilseed rape cutting table therefore needs to be fitted with a transverse cutter, which cuts the stalks, and a longitudinal cutter, which cuts the oilseed rape cuticle and acts as a branch. In the optimisation of the cutter structure, the main research is on the cutting mode of the cutter, the selection of the three types as well as the shape, number and angle of the blades; in the optimisation of the cutter's working parameters, the main optimisation is on the cutting height of the transversal and longitudinal cutters, the cutting speed and its ratio to the forward speed of the harvester (cutting speed ratio).

Field trials

Test device and conditions

The experiment was carried out in the experimental field of Weiyuan Town, Mutual Aid County, Haidong City, Qinghai Province, the experimental oil-seed rape variety is "Qingyou 331", the test oil-seed rape has already reached the optimal harvesting period, and the specific parameters are shown in Table 1.

Table 1

Test rapeseed parameters

Parametric	Unit (of measure)	Numerical value
Plant height	cm	163~178
Branching height	cm	45~58
Thousand-grain weight	g	4.0
Capacity	g/L	685
Seed moisture content	%	12
Stalk moisture content	%	17
Mean cuticle diameter	cm	33
Average cuticle thickness	cm	62

The harvester used for the test was a Dongfeng 4LZ-5.2AJ(G4) full-feed combine harvester, with the specific parameters shown in Table 2, and the other test supplies were electronic scales and catch tanks.

Table 2

Dongfeng 4LZ-5.2AJ(G4) fully fed combine harvester parameters

Sports event	Unit (of measure)	4LZ-5.2AJ(G4)
Overall dimensions (L*W*H)	mm	5100*2530*2850
Motive force	kW	92
Overall quality	kg	3730
Cutting table working width	mm	2200

Sports event	Unit (of measure)	4LZ-5.2AJ(G4)
Minimum Ground Clearance	mm	315
Feed rate	kg/s	5.2
Efficiency of production	hm^2 /h	0.35~0.75
Cutter type	/	Standard II
Wheel type	/	Toothed

Test scheme and loss rate measurement method

Regional division of test fields

The cutting width of the harvester is 2.2 m, so the width of the test area is selected to be 3 m, and the length of the test area is 25 m, of which, the per-harvesting stage is 5 m, the test harvesting stage is 20 m, the 20 m test area is divided into the normal harvesting area and the actual loss rate measurement area, and the test is finished when the cutter reaches the end of the test area at the position of 25 m, and the position of 4.5 m away from the end of the test is selected to be the lot for the measurement of actual loss rate of the cutter. The distribution map of the test field is shown in Fig. 5.

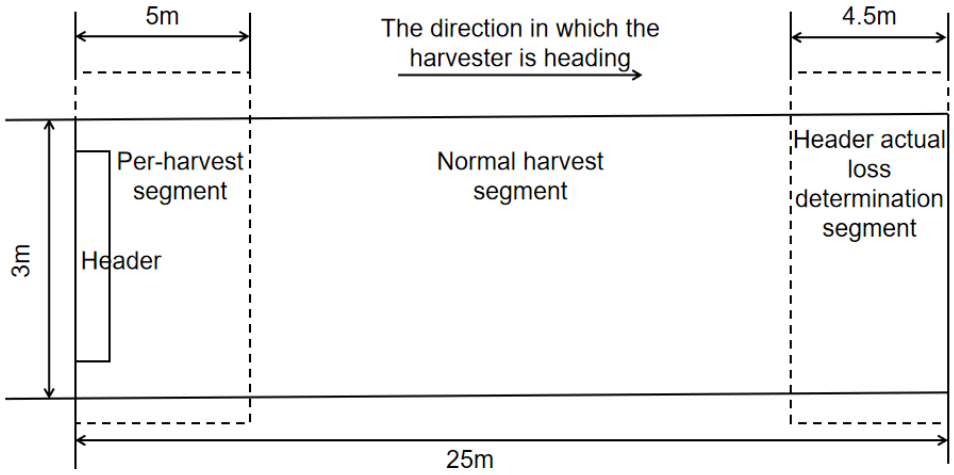


Fig. 5 - Distribution Map of Experimental Field Area

By analysing the biological characteristics of oilseed rape, the working principle and movement trajectory of the key components such as the paddle wheel and the cutter, combined with the review and summary of a large number of literature and books and other information, the cutting height of the transverse cutter, the longitudinal cutter's cutting speed and the forward speed of the harvester were selected as three factors to select five levels for the single-factor test, and the adjustment ranges of the test factor's working parameters are shown in Table 2.3. Among them, the cutting height of the transverse cutter was realized by adjusting the height of the cutting table. The results of the single-factor test were analysed and summarized, and the better three levels of each factor were selected for the orthogonal test to analyse the significance of the effect of each factor on the loss rate of the cutting table, explore the interaction between the factors through the response surface analysis method, and obtain the regression model of the factors and the loss rate of the cutting table, and obtain the optimal parameter combination with the lowest loss rate of the cutting table as the goal.

Table 3

Range of operating parameters of test factors

Parametric	Unit (of measure)	Adjustment range
Harvester forward speed	km/h	3~7
Cross cutter cutting height	cm	40~60
Longitudinal cutter cutting speed	m/s	1~2

Loss rate measurement method

According to the agricultural machinery promotion appraisal syllabus "oilseed rape combine harvester" (DG/T057), the test loss rate determination method is as follows: before the test to make three 2.5 m × 0.1 m × 0.06 m thin steel plate receiving sample groove, groove padded with flannel. In the measurement area, take three measurement points at equal spacing, choose the appropriate oilseed rape plant spacing at each measurement point, vertical operation direction across the width of the prototype operation to eradicate the corresponding flat-bottomed grooves with the sampling groove, and the sampling groove lying in which the groove is flush with the ground (*MOA, 2006; SAC, 2008*). When placing the sampling groove, one end of the sampling groove should be flush with the uncut rape end, and the other end, which exceeds the cutting width of the prototype, should be placed on the side of the vertical side cutter, to ensure that it can pick up the loss of rapeseed grain splash caused by the side vertical cutter, and the specific distribution is shown in Fig. 6.

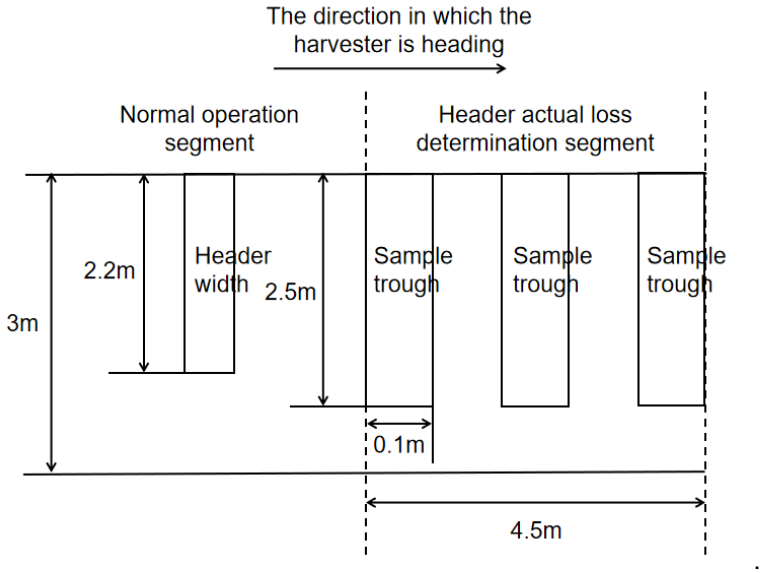


Fig. 6 - Sample slot distribution diagram

The loss rate of cuttings is calculated as shown in Equation (2). That is, the ratio of the actual loss of the cutting table in the measurement area to the total weight of the grains in the reception area is expressed as a percentage.

$$S = \frac{W(B \times L)}{M} \times 100\% \quad (2)$$

where:

S - Cutting table loss rate, [%];

W - Actual losses per square meter of the cutting table, [g];

B - Average actual cutting width, [m];

L - Length of the measurement area, [m];

M - Total weight of seeds caught in the catchment area, [g]

RESULTS

Analysis of single-factor test results

The effect of forward speed on the header loss rate

Test conditions: to ensure that the other components of the harvester working parameters remain unchanged, the forward speed is increased from 3 km/h to 7 km/h, and the change in the loss rate of the cutting deck is shown in Fig. 7. As can be seen from the figure, in the case of other factors remaining unchanged, the loss rate of the cutting platform with the increase in forward speed shows a trend of first decrease and then increase, and the magnitude of the change is larger, the loss rate is the lowest in the forward speed of 5 km/h, which can be shown that the forward speed of the cutter has a greater impact on the loss rate of the cutting platform. Forward speed is too slow, the paddle wheel will repeatedly slap the rape horn fruit, forward speed is too fast, the cutter cutting is not timely, the horn fruit leakage phenomenon appears, and the vibration frequency is accelerated. Therefore, too fast or too slow forward speed will increase the harvest loss.

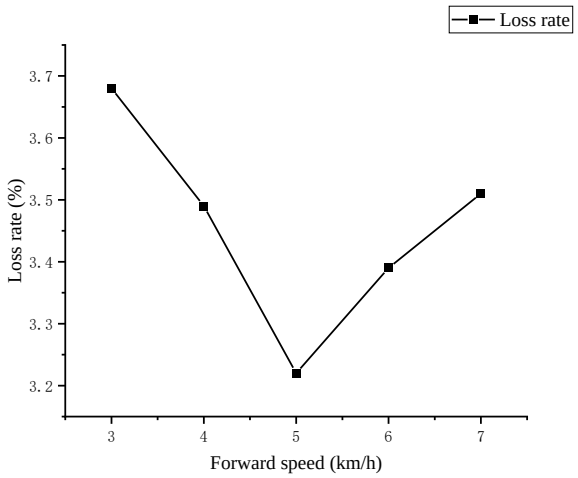


Fig. 7 - Forward velocity single-factor test results

Effect of cutting speed on header loss rate

Test conditions: to ensure that the other components of the harvester working parameters remain unchanged, the cutting speed is increased from 0.9 m/s to 2.1 m/s, and the change in the loss rate of the cutting platform is shown in Fig. 8. As can be seen from the figure, in other factors work parameters remain unchanged, gradually increase the cutting speed of the vertical cutter knife, the cutter loss is the first to decrease and then increase, when the cutting speed is 1.5 m/s, the lowest loss rate of the cutter is 3.22%. The curve changes in the image show that the cutting speed has a significant impact on the cutter loss rate. The reason is that the cutting speed is too low, and the forward speed of the harvester is not enough to match when the harvester is moving forward, the cutter is too late to cut, and the resulting vibration and angular fruit perturbation increases, increasing the loss of the cutting platform; when the cutting speed is too fast, the vibration frequency accelerates, and there is a repeated cutting phenomenon, so the seed splash is serious.

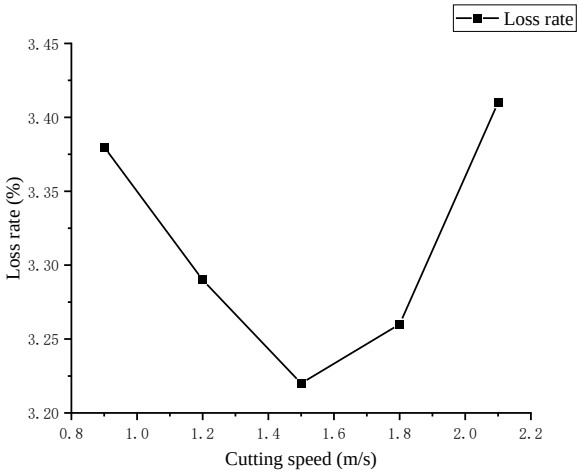


Fig. 8 - Single factor test results of cutting speed

Effect of cutting height on header loss rate

Test conditions: ensure that the working parameters of other parts of the harvester remain unchanged, the cutting height is increased from 40cm to 60cm, and the change of the loss rate of the header is shown in Fig. 9. As can be seen from the figure, when the working parameters of other factors remain unchanged, the cutting height is adjusted, and when the cutting height is 50 cm, the loss rate of the header is the lowest. When the cutting height is between 40 to 50 cm, the loss rate changes very little. When the cutting height is higher than 50cm, the loss rate of oilseed rape header shows a significant increase trend, indicating that the cutter is gradually close to the centre of the rapeseed horn and fruit layer, and the number of rapeseed stalks cut by the cutter decreases and the number of rape pods increases, which will definitely cause the loss of grain drop.

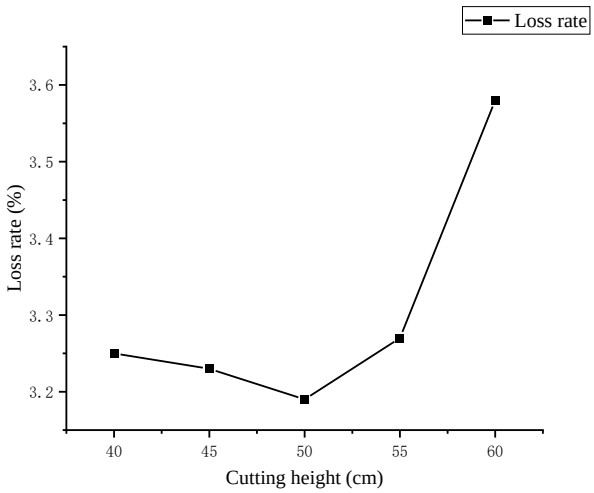


Fig. 9 - Single factor test results of cutting height

Analysis of multivariate test results

To further investigate the order of significance of each factor effect on the loss rate of the cutting table and the interaction between the factors, a three-factor, three-level quadratic regression orthogonal test was conducted on the influencing factors, and the levels of the relevant factors are shown in Table 4, and the results of the test are shown in Table 5.

Table 4

Encoding Table of Factors for Header Loss Rate Test Level

Level (of achievement etc.)	Considerations		
	Forward speed/(km/h)	Cutting speed/(m/s)	Cutting height/(cm)
	x_1	x_2	x_3
-1	4	1.2	45
0	5	1.5	50
1	6	1.8	55

Table 5

Results of Header Loss Rate Test

Test No.	Experimental factors			
	Forward speed / (km/h)	Cutting speed / (m/s)	Cutting height / (cm)	Cutting table loss rate / (%)
	x_1	x_2	x_3	y
1	-1	-1	0	3.45
2	1	-1	0	3.47
3	-1	1	0	3.52
4	1	1	0	3.55
5	-1	0	-1	3.32
6	1	0	-1	3.35
7	-1	0	1	3.31
8	1	0	1	3.41
9	0	-1	-1	3.27
10	0	1	-1	3.48
11	0	-1	1	3.46
12	0	1	1	3.41
13	0	0	0	3.15
14	0	0	0	3.13
15	0	0	0	3.14
16	0	0	0	3.09
17	0	0	0	3.11

The interaction of factors affecting the loss rate of the cutter was analysed with the help of response surface analysis and the regression equation was obtained using ANOVA and the results are shown in Table 6.

Table 6

Analysis of variance result

Source	SS	DF	MS	F-value	p-value
Modelling	0.39	9	0.043	80.16	<0.0001
x_1	0.00405	1	0.00405	7.57	0.0284
x_2	0.012	1	0.012	22.45	0.0021
x_3	0.003612	1	0.003612	6.75	0.0355
x_1x_2	0.000025	1	0.000025	0.047	0.8350
x_1x_3	0.001225	1	0.001225	2.29	0.1740
x_2x_3	0.017	1	0.017	31.59	0.0008
${x_1}^2$	0.11	1	0.11	196.47	<0.0001
${x_2}^2$	0.20	1	0.20	365.49	<0.0001
${x_3}^2$	0.018	1	0.018	33.76	0.0007
Residual	0.003745	7	0.000535		
Lost proposal	0.001425	3	0.000475	0.82	0.5472
Inaccuracies	0.00232	4	0.00058		
Aggregate	0.39	16			

Based on the ANOVA results, the p-value of the model < 0.01 indicates that the model is highly significant and the p-value of the misfit term > 0.05 is not significant, indicating that the model is reliable and well-fitted. The p-value of the primary term x_2, interaction term x_2x_3, and secondary terms x_1^2, x_2^2, and x_3^2 is $<$ 0.01 indicating that the effect on cutter loss rate is highly significant, the p-value of the primary terms x_1, $x_3<$ 0.05 indicating that the effect on cutter loss rate is significant and other factors are not significant. Comparing the p-values, the order of significance of the effects can be determined as follows: cutting speed x_2 > forward speed x_1 > cutting height x_3, and after removing the insignificant terms the fitted equation of the loss rate of the cutting table is obtained as follows:

$$y = 3.12 + 0.23x_1 + 0.039x_2 + 0.021x_3 - 0.65x_2x_3 + 0.16{x_1}^2 + 0.22{x_2}^2 + 0.66{x_3}^2 \quad (3)$$

Interaction analysis

The response surface of the effect of each test factor on the cutting table loss rate is shown in Fig.10, when the cutting height is located at the centre level of 50 cm, keeping the cutting speed constant, the loss rate of the cutting table tends to decrease and then increase with the increase of the forward speed; when keeping the forward speed constant, gradually increasing the cutting speed, the loss rate of the cutting table decreases first and then increases.

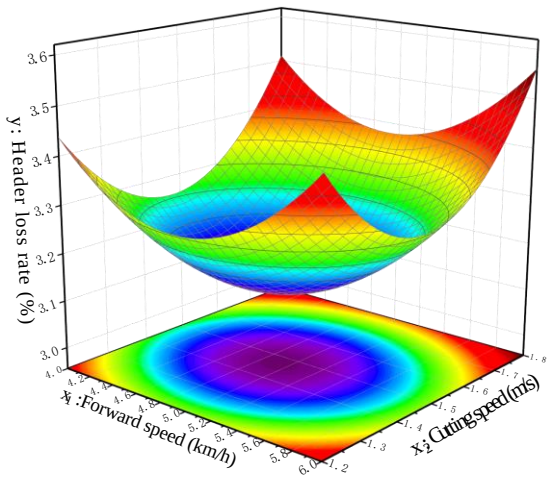


Fig. 10 - Influence of forward speed and cutting speed on the loss rate of the cutting table

From Fig. 11, it can be seen that when the cutting speed is at the centre level of 1.5 m/s, keeping the cutting height unchanged, the loss rate of the cutting table has a tendency to decrease and then increase with the increase of the forward speed, and the magnitude of the change is large; when keeping the forward speed unchanged, the loss rate of the cutting table increases with the increase of the cutting height, and the loss rate decreases and then increases, but the magnitude of the change is relatively small.

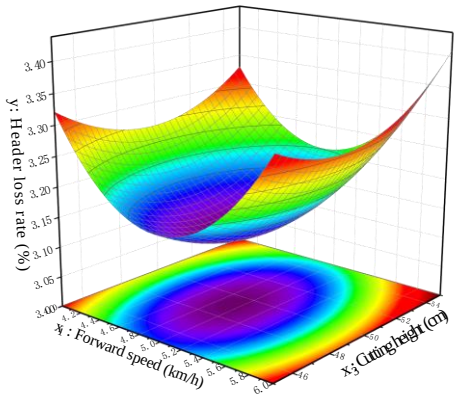


Fig. 11 - Influence of forward speed and cutting height on the loss rate of the cutting table

From Fig. 12, when the forward speed is at the centre level of 5 km/h, keep the cutting height unchanged, the loss rate of the cutting table tends to decrease and then increase with the increase of cutting speed; keep the cutting speed unchanged and gradually increase the cutting height, the loss rate of the cutting table has a small change, and the overall view shows an upward trend.

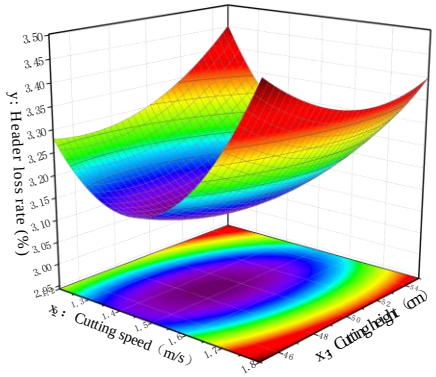


Fig. 12 - Influence of cutting speed and cutting height on the loss rate of the cutting table

CONCLUSIONS

To improve the effect of oil-seed rape harvesting, it is necessary to control the influencing factors in the optimal combination of parameters for harvesting operations, through the single-factor, multi-factor test and the analysis of the interaction between the factors, with the lowest loss rate of the cutting platform as the goal, the regression model in the range of the level of each factor test to optimize the solution, and get the optimal combination of working parameters as follows: the forward speed of 5 km/h, the cutting speed of 1.5 m/s, the cutting height of 50 cm, the loss rate of the cutting platform of 3.12%, the cutting speed ratio of 1.08. To further verify the reliability of the model, three tests were carried out in the experimental field using the above parameter combination results, and the test results are shown in Table 7, which shows that the error between the test results and the optimization results is less than 5%, indicating that the model is reliable.

Table 7

Comparative test results

Parametric	Cutting table loss rate (percent)	Cutting speed ratio
Optimal value	3.12	1.08
Test average	3.17	1.05
Relative error	0.05	0.03

The high gloss of oil-seed rape combined harvesting is an important reason restricting the development of oilseed rape mechanization, and the loss of the cutting platform accounts for a large proportion of the loss of the whole machine, and the investigation of the influence of the key components of the cutting platform on the loss rate is a key step to reduce the loss of oilseed rape harvesting.

The high loss of combined harvest of rapeseed is an important reason restricting the development of rapeseed mechanization. The loss of the header accounts for a large proportion of the loss of the whole machine, so exploring the influence of the key components of the header on the loss rate is a key step to reduce the harvest loss of rapeseed. In this paper, by reviewing a large number of literatures and books, combined with the summary of the biological characteristics of rapeseed, this paper analysed the ways and causes of rapeseed loss. The main forms of loss are grain splash loss, cut miss loss, and rapeseed drop loss due to cracking of rapeseed pods. The main reason is that the thin and brittle nature of rape pods can easily lead to cracking of rape pods, which increases the difficulty of separating crops. In addition, the low degree of agronomic matching of agricultural machinery is also an important reason. The three factors of forward speed, cutting height and cutting speed were selected to study the significant impact on the loss rate of the header, and the interaction between the factors was analysed. By establishing a regression model of the influencing factors of the loss rate, the parameters were optimized with the goal of the lowest loss rate, and the optimal combination of parameters was obtained, and the results of the model were verified by experiments to be reliable.

ACKNOWLEDGEMENT

The work was supported by the High Efficiency and Low Loss Single Longitudinal Axial Flow Threshing and Separation Technology and Development of Intelligent Flexible Threshing Device, (Grant No.2021YFD200050204), and the Development of Intelligent Multifunctional Wheat Corn Grain Combine Harvester, (Grant No.2016YF026).

REFERENCES

[1] Bečka D., Bečková L., Kuchtová P., Cihlář P., Pazderů K., Mikšík V., Vašák Jan, (2021). Growth and yield of winter oilseed rape under strip-tillage compared to conventional tillage. *Plant Soil Environ*, Vol. 67, No. 2, pp. 85-91, Czech Republic.

[2] Crnobarac J, Marinković B, Jeromela-Marjanović A, Balalić I, Jaćimović G, Latković D, (2015). The effect of variety and sowing date on oilseed rape yield and quality. *Agriculture and Food*, Vol.3 pp.241-245, Switzerland.

[3] Fríd M., Dolan A., Celjak I., Filip M., Bartos P, (2017). Harvest of cereals and oilseeds rape by combine harvesters New Holland CX 8090 and New Holland CR 9080. *Poljopr. Teh.*, Vol.42, pp.19–24, Czech Republic.

[4] Hatt, S., Xu, Q., Francis, F., & Chen, J, (2019). Intercropping oilseed rape with wheat and releasing Harmonia axyridis sex pheromone in northern China failed to attract and support natural enemies of aphids. *Biotechnology, Agronomy and Society and Environment*, Vol. 23(3), pp. 147–152, Belgium.

[5] Jankowski K J, Sokólski M, Załuski D, (2023). Winter oilseed rape: Agronomic management in different tillage systems and energy balance, *Energy*, Vol. 277, Denmark.

[6] Kendall S.L., Holmes H., White C.A., Clarke S.M., Berry P.M., (2017). Quantifying lodging-induced yield losses in oilseed rape. *Field Crops Research*, Vol. 211, ISSN. 0378-4290, pp. 106-113, Australia.

[7] Khan, S., Anwar, S., Kuai, J., Noman, A., Shahid, M., Din, M.; Ali, A., Zhou, G., (2018). Alteration in yield and oil quality traits of winter rapeseed by lodging at different planting density and nitrogen rates. *Sci. Rep*, Vol. 8, pp. 1–12, Britain.

[8] Kristó, I., Jakab, P., Irmes, K., Rácz, A., Vályi-Nagy, M., Tar, M., (2021). The effect of soil tillage process on soil physical parameters, yield of oil seed rape and profitability of production. *Research Journal of Agricultural Science*, Vol. 53(1), Hungary.

[9] Miersch, S., Gertz, A., Breuer, F., Schierholt, A., Becker, H.C, (2016). Influence of the semi-dwarf growth type on seed yield and agronomic parameters at low and high nitrogen fertilization in winter oilseed rape. *Crop Sci*, Vol. 56, pp.1573–1585, America.

[10] MoA, (2006), *NY /T 1231-2006 Technical Specification for Quality Evaluation of Oil-seed Rape Combined Harvester* (中华人民共和国农业部.NY /T 1231-2006 油菜联合收获机质量评价技术规范), China.

[11] Qing Yiren, (2021) *Research on angular resistance and plant structure of rapeseed carob and plucking mechanism for low-loss mechanized harvesting* (面向低损失机械化收获的油菜角果抗裂角性和株型结构与拨禾机理研究). Doctoral thesis, Jiangsu University, Jiangsu/China.

[12] SAC, (2008), *GB /T8007-2008 Test Methods for Harvesting Machinery Combine Harvester* (中国国家标准化管理委员会.GB /T8007-2008 收获机械联合收割机试验方法), China.

[13] Tajmiri, P., Fathi, S. A. A., Golizadeh, A., & Nouri-Ganbalani, G. (2017). Strip-intercropping canola with annual alfalfa improves biological control of Plutella xylostella (L.) and crop yield. *International Journal of Tropical Insect Science*, Vol. 37(03), pp. 208–216, England.

[14] Wei Junyi, (2021). *Analysis of the effect of vibration of rapeseed combines harvester on the structure of the cutting platform and grain loss* (油菜联合收获机振动对割台结构及落粒损失影响分析). Master's thesis, Huazhong Agricultural University, Hubei/China.

[15] Wu Shouyi, (1992). *Agricultural Mechanics (Next)* (农业机械学(下)). China Agricultural Machinery Press, Beijing, pp.48-56, ISBN. 7-111-03328-0.

[16] Wu Wenjie, Wu Chongyou, (2018). Research status of oil-seed rape combines harvester cutting table (油菜联合收割机割台研究现状). *Jiangsu Agricultural Science*, Vol.46, No. 07, pp. 5-11, Jiangsu/China.

[17] Xiao Yangyi, Yang Rui, Li Hang, Xu Hongmei, Tian Peng, (2020). Design and Kinematic Simulation of a Combine Harvester's Cutting Head Harvesting Device (联合收获机割台拨禾装置的设计与运动学仿真). *Journal of Huazhong Agricultural University*, Vol. 39 (04), pp. 156-162, Hubei/China.

[18] Yang Yi, Li Yaoming, Qing Yiren, (2020). Analysis and test on the trajectory of harvesting wheel of rapeseed combine harvester (油菜联合收获机拨禾轮的入禾轨迹分析与试验). *Agricultural Mechanization Research*, Vol. 42, No. 10, pp. 189-194, Heilongjiang/China.

[19] Zhang Xiaoyuan, Jiang Manxia, Li Zeliang, Yang Linchu, (2017) Effects of planting density on important agronomic traits and harvest index of rapeseed (种植密度对油菜重要农艺性状与收获指数的影响). Anhui Agricultural Science, Vol.45, No. 04. 19-20, Anhui/China.

[20] Zhang Yanan, Dong Hailong, Zhang Peng, (2021). Force analysis and damage evaluation of rapeseed grains in combined harvesting (油菜联合收获籽粒受力分析及损伤评价). *Forestry Machinery and Woodworking Equipment*, Vol.49, No. 02, pp. 41-43+48, Heilongjiang/China.

[21] Zhou Yujiao, Luo Bin, Liu Dingwei, Liu Dan, Qiu Yu, (2023). Design and experiment of rapeseed cutting table for 4LZ-4.0 grain combine harvester (4LZ-4.0 谷物联合收获机油菜割台设计与试验). *China Journal of Agricultural Machinery Chemistry*, Vol. 44 (09), pp. 22-27+35, Nanjing/China.

[22] Zorzenoni, T.O., de Andrade, A.P., Higashibara, L.R., Cajamarca, F.A., Okumura, R.S., Prete, C.C, (2019). Sowing date and fungicide application in the agronomic performance of oleaginous brassica for the biodiesel production. *Rev. Ceres,* Vol. 66, pp. 257–264, Brazil.

HOT AIR DRYING, IMPACT OF INFRARED DRYING, AND COMBINED HOT AIR-INFRARED DRYING ON ALFALFA DRYING QUALITY AND PERFORMANCE
/
热风干燥、红外干燥以及热风-红外联合干燥对苜蓿干燥质量和干燥性能的影响

Xihang SUN, Ziwen GUO, Guanghui WANG*), Chen CAI, Zhiqin WANG [1]
Department of Agricultural Engineering, College of Engineering, China Agricultural University, Beijing, China;
Tel: +86-18851128998; E-mail: 97554@cau.edu.cn
Corresponding author: Guanghui Wang
DOI: https://doi.org/10.35633/inmateh-71-38

Keywords: *Alfalfa, Combined drying, Drying characteristics, Drying quality*

ABSTRACT

This study analyzes the drying of alfalfa using hot air, infrared and combined drying techniques at different temperatures, irradiation heights and radiant powers. Different temperatures, radiation heights, radiation power and wind speed are used as control factors, and drying time, color, crude protein and specific energy consumption are used as evaluation indicators. After assigning weights to each indicator, the comprehensive evaluation index is calculated. Test results and data analysis show that the drying performance is optimal when the hot air flow velocity is 1.5 m/s, the hot air temperature is 62.1°C, the radiation distance is 10 cm, the radiation power is 1200 w, and the material thickness is 20 mm, it has the best drying performance; its coefficient of determination R^2 is 0.9995. The comprehensive evaluation index of alfalfa drying after combined drying is between 1.00 and 1.30, which is overall higher than hot air drying and infrared drying. Combined drying technology can effectively improve the efficiency and quality of the alfalfa drying process.

摘要

本研究分析了在不同温度、辐照高度和辐射功率下使用热风、红外和组合干燥技术对苜蓿进行干燥的情况。以不同温度、辐射高度、辐射功率和风速为控制因素，以干燥时间、色泽度、粗蛋白和比能耗为评价指标。对各指标赋予权重后，计算综合评价指数。测试结果及数据分析表明，当热风流速为 1.5m/s、热风温度为 62.1℃、辐射距离为 10cm、辐射功率为 1200w、物料厚度为 20mm 时，具有最佳干燥性能；其决定系数 R^2 为 0.9995。联合干燥后苜蓿干燥的综合评价指数在 1.00～1.30 之间，总体高于热风干燥和红外干燥，组合干燥技术可以有效提高苜蓿干燥过程的效率和质量.

INTRODUCTION

Alfalfa (*Medicago sativa L.*) is a highly nutritious leguminous plant with low leaf fiber content and high content of nutrients such as protein and carotenoids. Nitrogen fertilization is rarely required during planting, but the dry matter at maturity can have an average protein content of 17%, 60% digestible nutrients, and 23% fiber. The water content of freshly harvested alfalfa grass is more than 75% and is easy to rot and deteriorate after harvest, leading to a severe decrease in actual yield and loss of nutrients. Therefore, the treatment of harvested alfalfa is essential to prolong its storage time and reduce quality loss during storage. There are many ways to achieve material dehydration, hot air drying (*Vega-Gálvez et al., 2012*), infrared drying (*Huang, Li, Wang & Wan, 2021*), and a combination of various drying methods *(Bai-Ngew, Therdthai, Dhamvithee & Zhou, 2015; Wang, Li, Han, Ni, Zhao & Hao, 2019*) have been within the field of agricultural and sideline products such as research and application for many years. But, the mechanism research and application of new drying technology and combined drying are less.

Due to the robust adaptability of infrared drying, it is easy to combine with hot air to exert a synergistic effect (*Onwude, Hashim & Chen, 2016*). Mesery et al. studied the performance of infrared-hot air combined drying of apples and concluded that combined drying can produce lower specific energy consumption and higher thermal efficiency (*Hany S. El-Mesery & Gikuru Mwithiga, 2016*). Wang et al. attributed the reduction in infrared-hot air combined drying time of shiitake mushrooms to the rapid heating of infrared radiant energy that increases the moisture migration rate (*Hongcai Wang et al, 2014*).

[1] *Xihang Sun, M.S. Stud. Eng.; Ziwen Guo, M.S. Stud. Eng.; Guanghui Wang, Prof. Ph.D. Eng.; Chen Cai, M.S. Stud. Eng.; Zhiqin Wang, A.P. Ph.D. Eng.*

Zhang et al. studied the infrared convection drying of luffa and found that the drying time decreases with the increase of infrared intensity and the decrease of radiation distance, but too high infrared intensity and too low radiation distance will cause the material to be scorched (*Zhang et al., 2020)*. Different drying methods and conditions will affect dried products' nutritional value and sensory characteristics, and a large amount of energy consumption in drying will also lead to high costs. Therefore, it is necessary to determine the optimal drying method and process parameters for alfalfa.

MATERIALS AND METHODS

Materials

The material was fresh alfalfa, which was collected from Shangzhuang Experimental Station of China Agricultural University. The samples with good appearance and no damage were selected. After cleaning, the samples were evenly cut into 5 cm segments, put into sealed bags, and refrigerated at 4°C for the experiment. The moisture content of alfalfa was measured with ASAE Standard and the initial moisture content was 77.55±0.50% (wb).

Drying equipment

A schematic diagram of the drying test bench is shown in Fig. 1. Drying apparatus is mainly composed of a heating system and a control system. The experimental parameters were set via the control system. During hot air drying experiments, the air heater is the primary heating source and the temperature reaches the predetermined value. The infrared heating plate is mainly used for radiation heating samples and also is the heating source to heat the air during infrared drying as well. A thermocouple was plugged in the drying chamber to monitor the inside temperature. The air temperature was controlled in a stable range since the temperature data were transferred to the control system. The material tray is connected with an electronic balance to measure the mass change of the material in real-time during drying.

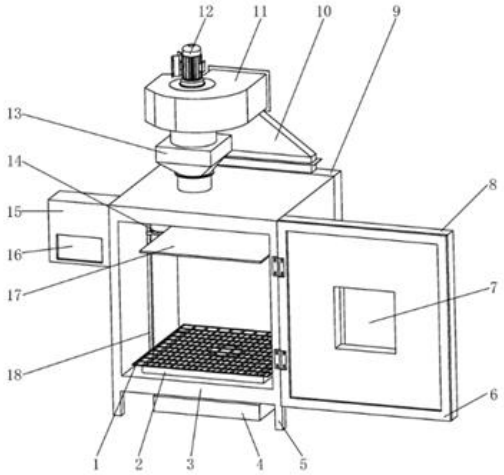


Fig. 1 - Structure diagram of infrared-hot air combined drying test bench

1. Mesh tray; 2. Uniform outflow plate; 3. Air distribution room; 4. Electronic balance; 5. Support frame; 6. Sealing gasket; 7. Observation window; 8. Door; 9. The back hollow wall; 10. Air channel; 11. Centrifugal fan; 12. Motor; 13. Air heater; 14. Slider bracket; 15. Control cabinet; 16. Touch screen; 17. Infrared heating plate; 18. Slide table

Experimental methods

In order to compare the effects of different drying conditions on the drying effect of alfalfa, a thin layer drying test was carried out. The experimental design was shown in Table 1. Since each drying test was repeated three times, the design did not express the repeated tests. The equipment adopts a hot air circulation design. When combined drying, the air was heated by the infrared plate, which kept the temperature constant. Therefore, the hot air temperature changed with different infrared parameters.

Table 1

The experimental design

Drying method	Experiment No.	Air velocity (m/s)	Air temperature (℃)	Material layer thickness (mm)	Radiant power (W)	Radiation heights (cm)
Hot air drying	1	1.0	55	15	---	---
	2	1.5	55	15	---	---
	3	2.0	55	15	---	---

Drying method	Experiment No.	Air velocity (m/s)	Air temperature (℃)	Material layer thickness (mm)	Radiant power (W)	Radiation heights (cm)
	4	1.5	45	15	---	---
	5	1.5	65	15	---	---
	6	1.5	55	10	---	---
	7	1.5	55	20	---	---
Infrared drying	8	1	---	15	1200	20
	9	1.5	---	15	1200	20
	10	2	---	15	1200	20
	11	1.5	---	10	1200	20
	12	1.5	---	20	1200	20
	13	1.5	---	15	600	20
	14	1.5	---	15	1800	20
	15	1.5	---	15	1200	10
	16	1.5	---	15	1200	30
Combined drying	17	1	70.5	15	1200	20
	18	1.5	61.8	15	1200	20
	19	2	55.4	15	1200	20
	20	1.5	62.1	10	1200	20
	21	1.5	61.5	20	1200	20
	22	1.5	51.2	15	600	20
	23	1.5	72.3	15	1800	20
	24	1.5	61.8	15	1200	10
	25	1.5	61.8	15	1200	30

Drying parameters

Moisture content

$$M_t = \frac{m_t - m_0}{m_0} \quad (1)$$

where:

M_t is the dry base moisture content of alfalfa at time t, (g water/g dry matter);

m_t is the mass of alfalfa at time t, g; and m_0 is the dry matter mass of alfalfa, g.

Moisture rate

$$MR = \frac{M_t}{M_0} \quad (2)$$

where MR is the moisture rate of alfalfa at time t, and M_0 is the initial dry base moisture content of alfalfa, (g water/g dry matter).

Drying rate

$$DR = \frac{M_t - M_{t+\Delta t}}{\Delta t} \quad (3)$$

where DR is the dry rate of alfalfa at time t, (g water/g dry matter·min); $M_{t+\Delta t}$ is the dry base moisture content of alfalfa at time $t+\Delta t$, (g water/g dry matter) and Δt is the interval time, min.

Water diffusion coefficient

$$MR = \frac{8}{\pi^2} exp\left(-\frac{\pi^2 D_{eff}}{4L_m^2} t_{dry}\right) \quad (4)$$

where D_{eff} is the effective water diffusion coefficient of alfalfa, m²/s; L_m is the half of alfalfa layer thickness, m; t_{dry} is the drying time, s.

$$D_{cal} = \frac{L_m^2}{60\alpha} = D_{eff} \cdot R_g \quad (5)$$

where D_{cal} is the estimated water diffusion coefficient, m²/s; R_g is a parameter related to geometric size.

Drying curve fitting based on the Weibull function

$$MR = \exp\left[-\left(\frac{t}{\alpha}\right)^{\beta}\right] \quad (6)$$

where α is the scale parameter, min; β is the shape parameter, and t is the drying time, min.

Color measurement

The fresh alfalfa served as a control. The dried alfalfa samples were crushed and passed through a 40-meshes sieve. The color was measured by using a LabScan XE type colorimeter (HunterLab, USA). The results were presented as averages of three determinations (*Xiao, Law, Sun & Gao, 2014*).

Crude protein

Crude protein content was determined by the Kjeldahl method. The KT8000 type Kjellott nitrogen analyzer was used for detection, and the final nitrogen content was multiplied by 6.25 to obtain the crude protein content (*Wang, Jiang & Shen, 2020*). The results are expressed as an average of the three measurements.

Energy Consumption

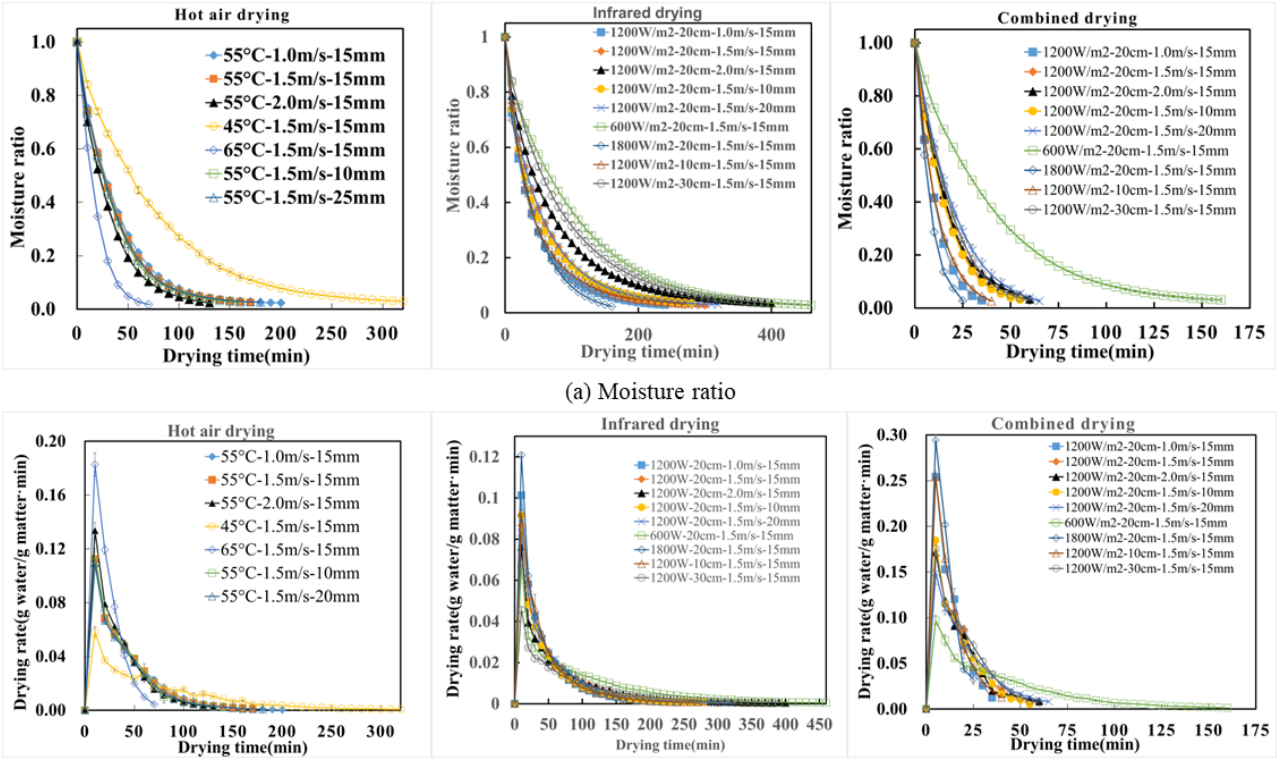
Since the total energy consumption of the equipment is the energy consumed by the entire pallet area (the drying bench is fully loaded), the specific energy consumption of drying materials in the test is calculated as follow *(Chauhan, Singh, Dhar & Powar, 2021*):

$$SEC = \frac{3.6E}{m_{\text{loss}}} \times \frac{A_s}{A_t} \tag{7}$$

where SEC is the specific energy consumption of alfalfa drying, MJ/kg; E is the total energy consumption of the drying test bench, kW·h; m_{loss} is the mass of evaporated water in drying, kg; A_s is the contact surface area between material layer and tray, m^2; A_t is the surface area of the tray, m^2.

RESULTS AND DISCUSSION

Effects of different drying conditions on drying dynamic



(a) Moisture ratio

(b) Drying rate

Fig. 2 - Drying curves of alfalfa under different drying conditions

The effects of three different drying conditions on the moisture content and drying rate of alfalfa are shown in Fig. 2. The effects of different drying conditions on the alfalfa's moisture ratio and drying rate during hot-air drying were shown in Fig. 2. In the same environment, the increasing temperature can reduce the steam pressure of air, which is far less than the material surface's steam pressure and accelerates the outward migration of water from inside of the materials. In addition, the high drying temperature can accelerate the convective heat transfer rate, which makes the temperature of samples rise rapidly and improves the water migration rate. The drying rate of materials reached the maximum in the early stage and then decreased gradually. At the same drying temperature, increasing the airspeed can increase the heat flux of air per unit time and reduce the thickness of the material drying boundary layer (*Wang et al., 2017*), which can improve

the heat transfer efficiency and speed up the evaporation rate of water on the material surface. Fig. 2 showed that when the air velocity was 2.0 m/s, the drying rate of alfalfa decreases rapidly in the middle and late periods. In addition to the decreased moisture ratio, another important reason is that the high temperature and high-speed air accelerates the drying rate and leads to tight fiber structure and hardened material surface (*Namkanisorn & Murathathunyaluk, 2020*), which impedes the migration of moisture inside the material to the surface.

The infrared drying time was longer than the hot air drying time, and the drying rate was low compared to hot air drying. The infrared radiation mode in the drying process was continuous radiation. To avoid the excessive temperature caused by the continuous accumulation of heating, the ambient air was inhausted into the drying chamber and took away the heat of the material, which decreased the drying rate and increased the drying time. At the same infrared power, the decrease of radiation intensity will weaken the infrared penetration, reduce the activity of water molecules, and lead to the extension of drying time. The moisture ratio slowed down with the increase of air velocity, and the drying time was prolonged, which was consistent with the research results of Adak et al. *(Adak, Heybeli & Ertekin, 2017*). The effect of hot air velocity on drying rate in combined drying was different from that in hot air drying. In the combined drying, infrared radiation is the primary heat source. While hot air brings in heat, it will also take away the heat generated by infrared radiation and reduce the drying temperature of materials. However, the hot air still heats the material. With the function of hot air, the heat loss of the material is much smaller than that of ambient temperature air. Therefore, the impact of changes in hot air speed in combined drying was greater than that of ambient air speed in infrared drying. It can be seen from Fig. 2 that the maximum drying rate variation between different material layer thicknesses is less than 3%. Under the same drying condition, the moisture ratio has no significant difference with the increase of the material layer thickness.

Drying characteristics based on the Weibull distribution function

Table 2

Calculation parameters of drying process under different drying conditions

Drying method	Experiment NO.	D_{eff} ($\times 10^{-9}$ m^2/s)	D_{cal} ($\times 10^{-8}$ m^2/s)	R_g	α	β	R^2
Hot air drying	1	7.49	2.43	3.25	38.5709	0.9585	0.9985
	2	8.55	2.63	3.08	36.8514	0.9611	0.9990
	3	11.13	3.07	2.75	30.5799	0.9680	0.9993
	4	4.29	1.25	2.91	75.0529	0.9400	0.9990
	5	22.68	5.02	2.21	18.6696	0.9954	0.9989
	6	4.02	1.19	2.97	34.9082	0.9720	0.9987
	7	14.19	4.40	3.10	37.8952	0.9539	0.9988
Infrared drying	8	5.40	2.39	4.43	39.2568	0.7755	0.9990
	9	4.60	1.83	3.98	51.1746	0.7694	0.9993
	10	3.04	1.40	4.60	66.9974	0.7511	0.9989
	11	1.91	0.89	4.64	47.0266	0.7370	0.9993
	12	7.23	3.20	4.42	52.1263	0.7885	0.9990
	13	3.00	0.96	3.21	95.0237	0.8016	0.9982
	14	8.59	2.41	2.80	35.1246	0.7532	0.9977
	15	4.94	2.24	4.53	41.8499	0.7561	0.9965
	16	3.15	1.11	3.51	84.3887	0.8277	0.9995
Combined drying	17	3.91	8.65	2.21	10.8356	1.0703	0.9995
	18	2.44	5.72	2.35	16.3963	1.0418	0.9993
	19	2.12	5.49	2.58	17.0910	1.0098	0.9992
	20	1.09	2.63	2.42	15.8270	1.0273	0.9995
	21	3.72	8.33	2.24	20.0190	1.0485	0.9998
	22	0.85	2.32	2.72	40.3655	1.0060	0.9995
	23	5.40	11.25	2.09	8.3329	1.1509	0.9998
	24	3.42	8.19	2.40	11.4457	1.0065	1.0000
	25	2.29	5.09	2.23	18.4089	1.0784	0.9992

Table 2 shows the drying process parameters under different drying conditions. Alfalfa's porous nature allows hot air to penetrate the material layer, promoting external water evaporation and making the shape parameter β less sensitive to layer thickness. In hot air drying, β ranged from 0.9 to 1.0, indicating the significant impact of external water evaporation. Unlike solid materials, convective drying in alfalfa mainly occurs on the

outer surface, influenced by thickness more than temperature. Infrared drying exhibited β values of 0.73 to 0.83, smaller than for solid materials. The main heat source in infrared drying is radiation, with internal moisture migration driven by infrared radiation. The β of infrared-hot air combined drying was greater than 1.0. It indicated that no matter how the radiation power and space changed in combined drying, the total drying process was determined by internal and external moisture diffusion, and was consistent with its drying principle (*Huang, Li, Wang & Wan, 2021*). The α in infrared drying was positively correlated with material layer thickness, air velocity, and radiation height and negatively correlated with radiation power.

For alfalfa, the effective water diffusion coefficient range under different drying methods was (1.91~ 54.0)×$10^{-9}$$m^2$/s, which was within the normal range of agricultural and sideline products (10^{-12}~10^{-8} m^2/s)(*Çağlar, Toğrul & Toğrul, 2009*). The estimated moisture diffusivity was (1.19~ 11.3)×$10^{-8}$$m^2$/s. Overall, compared to hot air and infrared drying, the moisture diffusion coefficient is high in infrared-hot air combined drying, which is more favorable for drying. In addition, the geometric parameter *Rg* of alfalfa ranges from 2.09 to 4.64, with an average value of 3.37, which was different to the geometric parameter 13.1 proposed by *Marabi et al.* (*Marabi, Livings, Jacobson & Saguy*, *2003*). There are a lot of gaps between alfalfa material layers, through which the air can flow to carry out heat exchange with materials inside the material layer. And the mechanism of heat transfer and moisture transfer is quite different from that of material slicing. Therefore, for porous media layers of materials, their geometric parameters should not be simply reduced to flat materials.

Effects on the color and crude protein of dried alfalfa

Fig. 3 showed the images of alfalfa under different drying conditions. The stems of alfalfa after hot-air drying yellowed, and the leaves showed obvious shrinkage, dark color, and high fragmentation degree, which were unavoidable problems in hot-air drying (*Huang et al., 2021*). After infrared drying, the alfalfa stems were yellow, but the leaves were intact, and the overall effect was similar to that of hot air drying. The leaves of alfalfa were best preserved after combined drying.

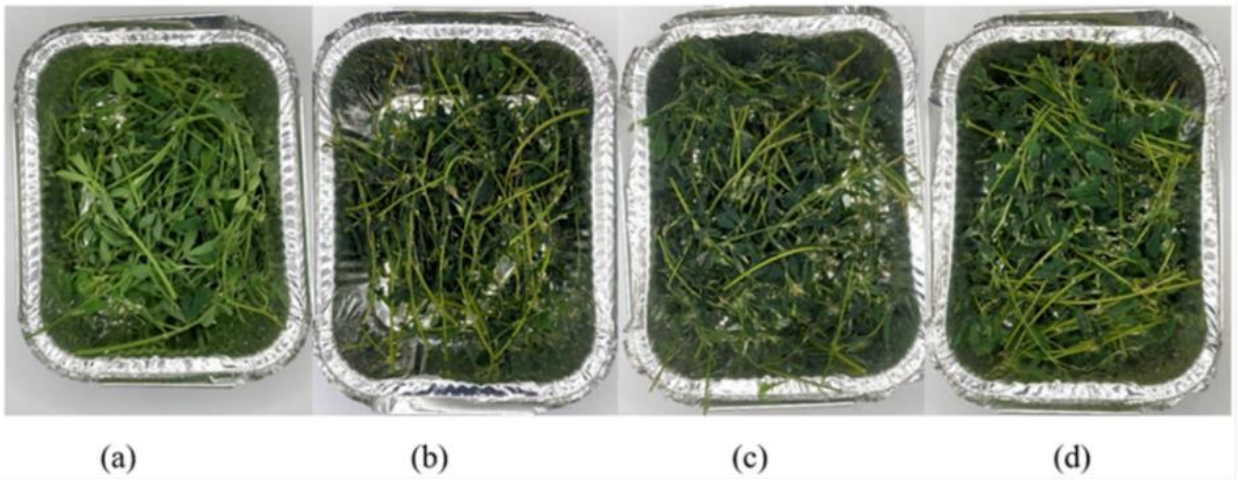


Fig. 3 - Photographic views of alfalfa under different drying conditions

Table 3

Color of alfalfa and crude protein content of alfalfa under different drying conditions

Drying method	Experiment No.	L^*	a^*	b^*	ΔE	Crude protein (%)
Fresh samples		32.14±1.28^{n}	-7.73±0.71^{n}	14.20±1.19^{bcdef}	---	19.08±0.35a
Hot air drying	1	42.15±0.70^{cd}	-6.02±0.10^{abc}	13.08±0.42^{j}	10.22±0.61^{cd}	16.29±0.25^{jk}
	2	41.13±0.40^{defg}	-6.09±0.07^{bc}	13.76±0.59^{defghij}	9.17±0.34^{defg}	16.74±0.01^{ghi}
	3	40.33±1.27^{fghi}	-6.21±0.03^{cde}	13.72±0.82^{defghij}	8.38±1.17^{fghi}	17.08±0.09^{cdefg}
	4	42.29±1.74^{bc}	-5.99±0.13^{abc}	14.60±0.70^{abc}	10.34±1.72^{bc}	16.46±0.02^{ij}
	5	40.00±0.35^{hi}	-6.15±0.04^{cd}	13.59±0.28^{efghij}	8.05±0.31^{hi}	17.26±0.22^{bcde}
	6	40.87±0.76^{efgh}	-6.36±0.06^{def}	13.75±0.77^{defhij}	8.88±0.77^{efgh}	16.75±0.02^{ghi}
	7	41.63±0.64^{cde}	-5.79±0.25^{a}	13.06±0.27^{j}	9.77±0.59^{cde}	16.80±0.01^{fghi}

Drying method	Experiment No.	L^*	a^*	b^*	ΔE	Crude protein (%)
Infrared drying	8	40.58±1.25^{efghi}	-6.39±0.07^{defg}	14.06±0.33^{cdefghi}	8.55±1.20^{fghi}	16.89±0.12^{efghi}
	9	41.63±0.26^{cde}	-6.21±0.19^{cde}	14.62±0.19^{abc}	9.62±0.27^{cde}	16.54±0.08^{hij}
	10	43.29±0.23^{ab}	-6.09±0.10^{bc}	14.87±0.19^{ab}	11.29±0.23^{ab}	15.89±0.02^{kl}
	11	41.42±0.46^{cdef}	-6.40±0.11^{efg}	14.32±0.15^{bcde}	9.38±0.45^{cdef}	16.47±0.12^{ij}
	12	41.97±0.11^{cd}	-5.98±0.09^{abc}	14.60±0.35^{abc}	9.99±0.13^{cd}	16.53±0.08^{hij}
	13	43.73±1.47^{a}	-6.08±0.04^{bc}	13.03±0.27^{j}	11.78±1.41^{a}	15.77±0.08^{l}
	14	40.20±0.89^{ghi}	-6.49±0.09^{fg}	13.12±0.37^{j}	8.25±0.85^{ghi}	16.94±0.06^{efgh}
	15	40.77±0.56^{efgh}	-5.85±0.12^{ab}	13.36±0.42^{hij}	8.88±0.54^{efgh}	16.76±0.06^{fghi}
	16	43.35±1.10^{ab}	-6.53±0.11^{fgh}	15.19±0.25^{a}	11.33±1.11^{ab}	16.01±0.10^{kl}
Combined drying	17	37.99±0.76^{kl}	-6.92±0.09^{klm}	13.42±0.24^{ghij}	5.96±0.77^{kl}	17.02±0.01^{efg}
	18	38.62±0.52^{jk}	-6.83±0.15^{jkl}	13.61±0.34^{efghij}	6.58±0.56^{jk}	17.54±0.35^{b}
	19	39.57±0.71^{ij}	-6.77±0.12^{hijk}	14.10±0.95^{cdefgh}	7.56±0.73^{ij}	17.20±0.28^{bcdef}
	20	38.22±0.30^{k}	-6.61±0.07^{ghij}	13.52±0.44^{fghij}	6.23±0.25^{k}	17.50±0.07^{bc}
	21	38.82±0.81^{jk}	-6.96±0.30^{klm}	14.15±0.47^{bcdefg}	6.77±0.83^{jk}	17.47±0.05^{bcd}
	22	40.08±0.44^{ghi}	-6.78±0.30^{ijkl}	13.33±0.41^{ij}	8.05±0.41^{hi}	16.94±0.14^{efgh}
	23	36.26±0.43^{m}	-7.13±0.10^{m}	14.16±0.19^{bcdefg}	4.17±0.41^{m}	16.46±0.17^{ij}
	24	37.09±0.97^{lm}	-7.01±0.24^{lm}	13.49±0.41^{fghij}	5.07±0.91^{lm}	17.30±0.03^{bcde}
	25	40.55±0.55^{efghi}	-6.58±0.14^{fghi}	14.46±0.22^{abcd}	8.50±0.56^{fghi}	17.05±0.12^{defg}

Note: Different letters within the same column indicate significant differences in the results.

Table 3 shows the significant impact of three different drying methods on alfalfa color difference (ΔE). As hot air temperature increased from 45°C to 65°C, ΔE decreased by 22.15%, indicating that high temperature can reduce the color change of alfalfa during hot air drying, which is contrary to the results of Xiao et al.*(Xiao et al., 2014*). But it is consistent with other references *(Tello-Ireland, Lemus-Mondaca, Vega-Gálvez, López & Di Scala, 2011; Zia & Alibas, 2021*). The reduction in color difference at higher temperatures is attributed to the occurrence of Maillard and non-enzymatic browning reactions, favored in dehydration under high temperatures and low humidity conditions. In infrared drying, radiation power significantly affects ΔE.

In infrared drying, the radiation power had the most significant effect on the color difference ΔE of alfalfa due to shortening the drying time. Based on the study of Chua et al. (*Chua, Chou, Mujumdar, Ho & Hon, 2004*), the longer time of infrared radiation leads to more drastic changes in color. The relationship between the radiation height and air speed and the color difference of alfalfa is consistent with the radiation power. The reason is that the smaller radiation height and air speed can effectively improve the drying efficiency of materials and reduce the exposure time of materials under infrared radiation. Combined drying yields smaller color differences than infrared and hot air drying. It shortens alfalfa's exposure to high-temperature environments, mitigating pigment oxidation and browning reactions. Thermal convection compensates for drying rate decreases, resulting in limited color changes.

In hot air drying, crude protein loss in alfalfa decreases with higher hot air temperature and speed. However, excessive heat, particularly above 60°C (*Chen et al., 2017*), leads to protein denaturation and inactivation. Prolonged exposure to high temperatures or prolonged low-temperature drying can both result in protein loss. In infrared drying, radiation power has the most significant effect on crude protein loss due to its impact on drying rates. The increase in air speed and radiation height reduces the accumulation of heat in the alfalfa material layer, allowing it to remain within the suitable temperature range for microbial activity for a long time during drying, resulting in protein loss. In combined drying, the radiation power controlled the hot air temperature. Although the flowed air could limit the heat inside the material, the higher hot air temperature kept the drying at a high temperature. When the radiation power was 1800 W, the hot air temperature was 72.3°C. Obviously, the denaturation of protein was intensified under this drying condition, and the rapid inactivation in a short period of time resulted in a significant decrease in the retention of crude alfalfa protein after drying. The change of hot air velocity and radiation height can change the drying time and temperature and increase the protein inactivation or decomposition rate, consistent with the change of crude protein loss caused by radiation power.

Overall, all three drying methods (hot air drying, infrared drying, and combined drying) cause significant crude protein loss in alfalfa, with combined drying showing the highest protein retention, followed by hot air drying, and then infrared drying.

Effects of different drying methods on drying time and energy consumption

The changes in drying time and energy consumption of alfalfa under different drying conditions were shown in Table 4. The infrared drying had the longest drying time, while the combined drying had the shortest drying time. This is in contrast to the fact that infrared drying can greatly reduce drying time and energy consumption as mentioned by Yang et al. *(Huang, Yang, Tang, Luo & Sunden, 2021*) , which is caused by different drying parameters, and the continuous normal temperature air in infrared drying reduces the heat inside the material and reduces the drying temperature, thereby increasing drying time and energy consumption.

Table 4

Drying time and energy consumption of alfalfa under different drying conditions

Drying method	Experiment No.	Drying time (min)	Energy consumption (kW·h)	Specific energy consumption (MJ/kg)
Hot air drying	1	200	2.77 ± 0.23^{hi}	42.31 ± 3.38^{h}
	2	170	3.45 ± 0.25^{fg}	51.49 ± 2.19^{fg}
	3	130	3.18 ± 0.11^{gh}	46.60 ± 2.75^{gh}
	4	320	3.71 ± 0.18^{f}	57.93 ± 3.56^{f}
	5	70	2.05 ± 0.15^{jk}	30.26 ± 2.87^{i}
	6	160	3.20 ± 0.18^{gi}	57.92 ± 1.27^{f}
	7	180	3.56 ± 0.25^{fg}	45.76 ± 1.32^{gh}
Infrared drying	8	240	6.27 ± 0.13^{e}	96.02 ± 1.06^{e}
	9	300	8.25 ± 0.16^{bc}	126.35 ± 7.29^{c}
	10	400	11.20 ± 0.20^{a}	185.62 ± 4.58^{a}
	11	280	7.96 ± 0.15^{c}	153.91 ± 4.72^{b}
	12	320	8.63 ± 0.14^{b}	111.35 ± 1.24^{d}
	13	460	7.41 ± 0.13^{d}	111.84 ± 1.42^{d}
	14	160	6.58 ± 0.13^{e}	101.06 ± 1.00^{e}
	15	270	7.29 ± 0.11^{d}	115.73 ± 3.40^{d}
	16	390	10.82 ± 0.15^{a}	184.76 ± 1.55^{a}
Combined drying	17	35	1.02 ± 0.06^{n}	16.03 ± 1.09^{l}
	18	55	1.56 ± 0.06^{lm}	25.49 ± 1.19^{ij}
	19	60	1.60 ± 0.05^{lm}	25.76 ± 0.71^{ij}
	20	55	1.57 ± 0.07^{lm}	29.94 ± 1.76^{i}
	21	65	1.84 ± 0.10^{kl}	24.40 ± 1.74^{ijk}
	22	160	2.45 ± 0.12^{ij}	38.84 ± 2.02^{h}
	23	25	1.06 ± 0.05^{n}	16.93 ± 0.60^{kl}
	24	40	1.21 ± 0.06^{mn}	19.61 ± 0.78^{jkl}
	25	60	1.75 ± 0.08^{kl}	27.21 ± 1.47^{ij}

Note: Different letters within the same column indicate significant differences in the results.

Among the three drying methods, the energy consumption ranging from large to small was infrared drying, hot air drying, and combined drying, which kept consistent with the changing trend of drying time. The infrared heating plate was continuous heated, and its power consumption is proportional to the drying time. In the combined drying, the heat in the hot air came from the heat dissipated by infrared radiation when drying materials, which improved the energy utilization rate and shortened the drying time. But in hot air drying and infrared drying, the drying time increased first and then decreased with the increase of air velocity and radiation power, respectively. In hot air drying, increasing the hot air flow rate could reduce the heating time of air and the rate of convection heat transfer. Consequently, the overall energy consumption increased. In addition, the change of feeding layer thickness in the three drying modes has no significant effect on the dryer's energy consumption.

Although the tray area is normalized, the maximum load of the test bench has not been reached. Hence, the specific energy consumption of the test bench is still large, and the unit energy consumption has a significant correlation with the change in material thickness.

Analysis of optimal parameters based on SWARA-EM

Evaluate the optimal drying method through the hybrid weight method of SWARA-EM. The fuzzy weight of SWARA was corrected by the EM method, and the final correction weight was obtained and shown in Table 5.

Table 5 Indicator weights based on SWARA-EM

Evaluation indicators	Objective weight (ξ_j)	Fuzzy weight (ω_j)	Fixed weight (λ_j)
Specific energy consumption (MJ/kg) A_1	0.28	0.30	0.33
Crude protein (%) A_2	0.27	0.30	0.32
The color difference value A_3	0.19	0.21	0.15
Drying time (min) A_4	0.26	0.18	0.19

The final weight corresponding to specific energy consumption (A_1), crude protein (A_2), color difference value (A_3), and drying time (A_4) were 0.33, 0.32, 0.15, and 0.19, respectively. The normalized data were used for calculation. The comprehensive evaluation index of alfalfa under different drying conditions was obtained, as shown in Fig. 4.

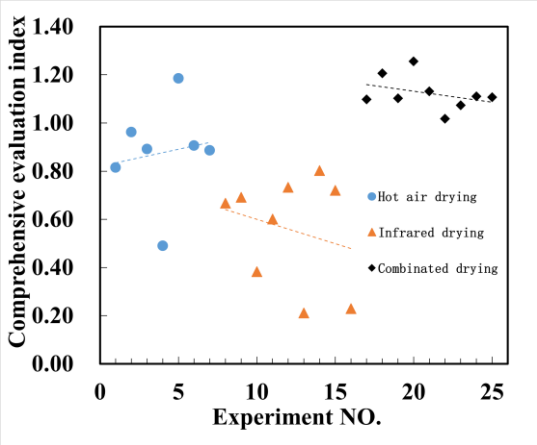


Fig. 4 - Comprehensive evaluation index based on SWARA-EM method

As can be seen from Fig. 4, the comprehensive evaluation index of alfalfa drying after combined drying is between 1.00 and 1.30, which is overall higher than hot air drying and infrared drying. The comprehensive evaluation index of hot air drying has a larger span, between 0.40 and 1.20. Under optimal drying conditions, the effect is even higher than some of the combined drying, but the overall effect is still lower than the combined drying; the comprehensive evaluation index of infrared drying is between 0.20 and 0.90, and the overall effect is lower than hot air drying and combined drying. Therefore, among the three drying methods compared, infrared-hot air combined drying has the potential to dry alfalfa with high efficiency and high quality.

The comprehensive evaluation index of Experiment NO.5 is better than that of the partial combined drying method. This is due to the higher hot air temperature shortening the drying time and reducing energy consumption. Compared with enzymatic browning and Maillard reaction caused by temperature changes, significantly reducing drying time has a more significant impact on color; it also reduces the time the material is exposed to high temperature environments, thereby improving the retention of crude protein. Therefore, the comprehensive evaluation index of test 5 is better than that of partial combined drying.

CONCLUSIONS

This study delved into the thin-layer drying characteristics of various methods applied to alfalfa. Remarkably, the combined drying method efficiently reduced the moisture content of alfalfa from 77.55% to less than 10% within a mere 25 minutes. Comparing these three drying methods, combined drying incurred minimal overall color loss in alfalfa, with the lowest color difference value recorded at 4.17, while infrared drying caused the most significant color loss, with a maximum color difference value of 11.78. Under varying drying parameters in the combined drying approach, the overall crude protein loss in alfalfa remained minimal, with a mere 1.54 percentage point reduction, surpassing the performance of hot air and infrared drying methods. In line with the Multi-Criteria Decision-Making analysis, it is evident that combined infrared-hot air drying technology holds promise in enhancing both the efficiency and quality of alfalfa drying processes.

REFERENCES

[1] Adak, N., Heybeli, N., & Ertekin, C. (2017). Infrared drying of strawberry. *Food chemistry*, *219*, 109-116.

[2] Bai-Ngew, S., Therdthai, N., Dhamvithee, P., & Zhou, W. (2015). Effect of microwave vacuum drying and hot air drying on the physicochemical properties of durian flour. *International Journal of Food Science & Technology*, *50*(2), 305-312.

[3] Çağlar, A., Toğrul, 0. T., & Toğrul, H. (2009). Moisture and thermal diffusivity of seedless grape under infrared drying. *Food and bioproducts processing*, *87*(4), 292-300.

[4] Chauhan, A., Singh, S., Dhar, A., & Powar, S. (2021). Optimization of pineapple drying based on energy consumption, nutrient retention, and drying time through multi-criteria decision-making. *Journal of Cleaner Production*, *292*, 125913.

[5] Chen, X., Lu, J., Li, X., Wang, Y., Miao, J., Mao, X., Zhao, C., & Gao, W. (2017). Effect of blanching and drying temperatures on starch-related physicochemical properties, bioactive components and antioxidant activities of yam flours. *LWT - Food Science and Technology*, *82*, 303-310.

[6] Chua, K.J., Chou, S.K., Mujumdar, A.S., Ho, J.C., Hon, C.K. (2004). Radiant-convective drying of osmotic treated agro-products: effect on drying kinetics and product quality. *Food control*, *15*(2), 145-158.

[7] El-Mesery H S, & Mwithiga G. (2015) Performance of a convective, infrared and combined infrared-convective heated conveyor-belt dryer[J]. Journal of Food Science and Technology, 52(5), 2721-2730.

[8] Huang, D., Yang, P., Tang, X., Luo, L., & Sunden, B. (2021). Application of infrared radiation in the drying of food products. *Trends in food science & technology*, *110*, 765-777.

[9] Huang, X., Li, W., Wang, Y., & Wan, F. (2021). Drying characteristics and quality of Stevia rebaudiana leaves by far-infrared radiation. *LWT*, *140*, 110638.

[10] Marabi, A., Livings, S., Jacobson, M., & Saguy, I. S. (2003). Normalized Weibull distribution for modeling rehydration of food particulates. *European food research and technology*, *217*(4), 311-318.

[11] Namkanisorn, A., & Murathathunyaluk, S. (2020). Sustainable drying of galangal through combination of low relative humidity, temperature and air velocity. *Energy Reports*, *6*, 748-753.

[12] Onwude, D. I., Hashim, N., & Chen, G. (2016). Recent advances of novel thermal combined hot air drying of agricultural crops. *Trends in food science & technology*, *57*, 132-145.

[13] Tello-Ireland, C., Lemus-Mondaca, R., Vega-Gálvez, A., López, J., & Di Scala, K. (2011). Influence of hot-air temperature on drying kinetics, functional properties, colour, phycobiliproteins, antioxidant capacity, texture and agar yield of alga Gracilaria chilensis. *LWT - Food Science and Technology*, *44*(10), 2112-2118.

[14] Vega-Gálvez, A., Ah-Hen, K., Chacana, M., Vergara, J., Martínez-Monzó, J., García-Segovia, P., Lemus-Mondaca, R., & Di Scala, K. (2012). Effect of temperature and air velocity on drying kinetics, antioxidant capacity, total phenolic content, colour, texture and microstructure of apple (var. Granny Smith) slices. *Food chemistry*, *132*(1), 51-59.

[15] Wang H., Zhang M., & Mujumdar A.S. (2014) Comparison of Three New Drying Methods for Drying Characteristics and Quality of Shiitake Mushroom (Lentinus edodes). *Drying Technology*, 32(15), 1791-1802

[16] Wang, J., Fang, X., Mujumdar, A. S., Qian, J., Zhang, Q., Yang, X., Liu, Y., Gao, Z., & Xiao, H. (2017). Effect of high-humidity hot air impingement blanching (HHAIB) on drying and quality of red pepper (Capsicum annuum L.). *Food chemistry*, *220*, 145-152.

[17] Wang, Q., Li, S., Han, X., Ni, Y., Zhao, D., & Hao, J. (2019). Quality evaluation and drying kinetics of shitake mushrooms dried by hot air, infrared and intermittent microwave–assisted drying methods. *LWT*, *107*, 236-242.

[18] Wang, Z., Jiang, H., & Shen, Y. (2020). Forage production and soil water balance in oat and common vetch sole crops and intercrops cultivated in the summer-autumn fallow season on the Chinese Loess Plateau. *European journal of agronomy*, *115*, 126042.

[19] Xiao, H., Law, C., Sun, D., & Gao, Z. (2014). Color Change Kinetics of American Ginseng (Panax quinquefolium) Slices During Air Impingement Drying. *Drying technology*, *32*(4), 418-427.

[20] Zhang, Y., Zhu, G., Li, X., Zhao, Y., Lei, D., Ding, G., Ambrose, K., & Liu, Y. (2020). Combined medium- and short-wave infrared and hot air impingement drying of sponge gourd (Luffa cylindrical) slices. *Journal of food engineering*, *284*, 110043.

[21] Zia, M. P., & Alibas, I. (2021). Influence of the drying methods on color, vitamin C, anthocyanin, phenolic compounds, antioxidant activity, and in vitro bioaccessibility of blueberry fruits. *Food Bioscience*, *42*, 101179

CRYOGENIC FREEZING OF SOME BERRY SPECIES USING AN EXPERIMENTAL MODEL OF MULTI-FUNCTIONAL QUICK-FREEZING EQUIPMENT
/
CONGELAREA CRIOGENICĂ A UNOR SPECII DE FRUCTE DE PĂDURE UTILIZÂND UN MODEL EXPERIMENTAL DE ECHIPAMENT MULTIFUNCȚIONAL DE CONGELARE RAPIDĂ

Cristian Marian SORICĂ[1*)], Nicolae-Valentin VLĂDUȚ[1)], Andreea Iulia GRIGORE[1)], Mario CRISTEA[1)], Elena SORICĂ[1)], Remus Marius OPRESCU[1)], Alexandru IONESCU[1)], Laurențiu Constantin VLĂDUȚOIU[1)], Lucian DUMITRESCU[2)]

[1)]INMA Bucharest, 6 Ion Ionescu de la Brad Blvd., Bucharest, Romania

[2)] ICDIMPH HORTING Bucharest/Romania

**E-mail: cri_sor2002@yahoo.com*

DOI: https://doi.org/10.35633/inmateh-71-39

Keywords: *preservation methods, cryogenic freezing, quick-freezing, liquid nitrogen, berry species*

ABSTRACT

For the preservation of horticultural products, the best results in keeping the attributes and quality at a level as close as possible to that of the fresh product are obtained when artificial cold (refrigeration, freezing) is used, unlike other methods. Among the existing freezing methods, freezing with cryogenic agents allows obtaining average linear freezing rates superior to the other methods. The fastest procedure for cooling food products involves the use of liquid nitrogen, which comes into direct contact with the surface of the food product that needs to be frozen. The paper analyzes the quick freezing process of three species of berries, namely blueberries, strawberries and raspberries, using an experimental model of multifunctional quick-freezing equipment - ICR, developed by INMA Bucharest as part of a national research programme. Total times and average linear freezing rates, as well as liquid nitrogen consumptions for each of the three species subjected to freezing, were tracked. Following the analysis of the experimental data, there were found the following: the minimum total freezing time, 498 s, was recorded for blueberries and the maximum total freezing time, 773 s, was recorded for strawberries; for blueberries and strawberries the average linear freezing rates recorded values of 6.32 cm/h and 6.29 cm/h corresponding to a very fast freezing process and for raspberries the average linear freezing rate recorded a value of 1.62 cm/h corresponding to a fast freezing process; liquid nitrogen consumption recorded a minimum value of 6.90 kg for blueberries and a maximum value of 7.20 kg for raspberries. In the case of blueberries, at the end of the freezing process, cracks and fissures of the epidermis and pulp were observed as a result of the thermal shock induced during the very rapid freezing process.

REZUMAT

Pentru conservarea produselor horticole, cele mai bune rezultate în păstrarea atributelor și calității la un nivel cât mai apropiat de cel al produsului proaspăt se obțin atunci când se utilizează frigul artificial (refrigerare, congelare), spre deosebire de alte metode. Dintre metodele de congelare existente, congelarea cu agenți criogenici permite obținerea unor viteze medii de congelare superioare celorlalte metode. Cel mai rapid procedeu destinat răcirii produselor alimentare presupune utilizarea azotului lichid, care ajunge în contact direct cu suprafața alimentul ce necesită a fi congelat. Lucrarea analizează procesul de congelare rapidă a trei specii de fructe de pădure, respectiv afine, căpșune și zmeură, utilizând un model experimental de echipament multifuncțional de congelare rapidă – ICR, dezvoltat de INMA Bucuresti, în cadrul unui program național de cercetare. S-au urmărit timpii totali și vitezele medii liniare de congelare, precum și consumurile de azot lichid pentru fiecare din cele trei specii supuse congelării. În urma analizei datelor experimentale s-au constatat următoarele: timpul total minim de congelare, 498 s, a fost înregistrat în cazul afinelor, iar timpul total maxim de congelare, 773 s, a fost înregistrat pentru căpșune; pentru afine și căpșune vitezele medii liniare de congelare au înregistrat valori de 6,32 cm/h și 6,29 cm/h corespunzătoare unui proces de congelare foarte rapidă iar pentru zmeură viteza medie liniară de congelare a înregistrat o valoare de 1,62 cm/h corespunzătoare unui proces de congelare rapidă; consumul de azot lichid a înregistrat o valoare minimă de 6,90 kg pentru afine și o valoare maximă de 7,20 kg pentru zmeură. În cazul afinelor, la finalul procesului de congelare s-au observat fisuri și crăpături ale epidermei și pulpei ca urmare a șocului termic indus în timpul procesului de congelare foarte rapidă.

INTRODUCTION

Fruits and vegetables, although they have a much lower content of energy substances than products of animal origin, play a very important role in human nutrition through their intake of vitamins, mineral substances and antioxidants *(Cirillo et al., 2023; Gherghi, 1994; Hoffmann et al., 2014)*, contributing to the smooth running of metabolic processes in the human body. Fruits and vegetables contain water in proportion of 80–90% (*Khan et al., 2017*), favoring microbial activity and enzymatic reactions inside the cells, resulting in chemical degradation and loss of quality. Under these conditions, fruits and vegetables are highly perishable, often requiring preservation processes. Preservation technologies aim to lower the intensity of metabolic processes like respiration and transpiration and also the activity of pathogenic microorganisms which represent the main cause of decomposition processes.

In order to prolong the shelf life period of perishable products, a series of preservation procedures can be used (*Alhamdan et al., 2018a; Alhamdan et al., 2018b; Biglia et al., 2016; Bilbao-Sainz et al., 2019; Sousa-Gallagher et al., 2016; Ingeau et al., 2015*): lowering the water content of the product (concentration, dehydration); the use of high temperatures (sterilization, pasteurization); the use of inhibitors of deterioration phenomena (chemical preservatives, bacteriocins, natural antimicrobials, acidification, sugar addition etc.); the use of low temperatures (modified atmosphere, freezing, refrigeration); the use of non-conventional methods (high pressure, high voltage electrical pulses, ionizing radiation, non-ionizing radiation, ultrasound, photodynamics, ozone etc.). When artificial cold (refrigeration, freezing) is used to preserve horticultural products, unlike all other methods, the best results are obtained in keeping the attributes and quality at a level as close as possible to that of the fresh product (*Aghdam and Bodbodak, 2014; Cao et al., 2018; Jha et al., 2018; Gales et al., 2022*).

Freezing, as a preservation method, increases the admissible storage time of food products by more than 5...50 times compared to refrigeration *(Niculita, 1998)*. The increase in shelf life, achieved through freezing, is due to the effects of low temperatures to strongly slow down or completely inhibit the development of microorganisms, to reduce or stop the metabolic processes in the case of living products, and to reduce the chemical and biochemical reactions.

Taking into consideration the average linear freezing rate, *Wm*, the International Institute of Refrigeration (Institut International du Froid - IIF) indicates the next categorization of freezing methods: slow freezing (*Wm* = 0.5 cm/h); rapid freezing (*Wm* = 0.5...3 cm/h); very fast freezing (*Wm* = 3...10 cm/h); ultrafast freezing (*Wm* = 10...100 cm/h).

The regular freezing of products, throughout which their average temperature decreases below -10 °C in a duration that does not permit the unleashing of undesirable enzymatic and microbiological reactions, is featured by the adoption of average linear freezing rates of 0.1...0.5 cm/h. Quick-frozen products are obtained at average linear freezing rates greater than 0.5 cm/h.

If the temperature decrease is achieved slowly, a progressive formation of reduced number of large ice crystals is obtained, which can ruin the cellular structure of the food product and irremediably damage the tissues upon thawing (*Delgado and Rubiolo, 2005; Chaudhary, 2021; Kotwaliwale et al., 2012; Buggenhout et al., 2006; Parandi et al., 2022; Chassagne-Berces et al., 2009)*. If, on the contrary, these temperatures are quickly attained, crystallization can be evaded through the formation of an amorphous stage, characterized by the formation of small ice crystals *(Li and Sun, 2002; Zhu et al., 2020; Van der Sman et al., 2013; James et al., 2015)*, which favors the stability of the products during the following storage period *(Fellows, 2017; Kennedy, 2003)*, while limiting weight loss due to dehydration *(Mulot et al., 2019)*.

The most important techniques of freezing food products are: the use of chilled air; touching with cold metal areas; touching with intermediate cooling substances; using cryogenic fluids.

Among the methods listed above, freezing with cryogenic agents allows obtaining higher average freezing rates than the other methods. This consists in using both, the latent heat of vaporisation at atmospheric pressure of some cryogenic liquids and the sensible heat that the formed vapors soaks up rising their temperature from the very low point of vaporisation to a point near the temperature when the food product freezes. The cryogenic substances utilized within this situation are: liquid nitrogen, nitrogen oxide, carbon dioxide.

By comparison with usual freezing methods, the cryogenic technique possesses the following benefits: rapid freezing, reduction of bacterial growth, minimal dehydration, significant lowering of quantitative losses due to dehydration, optimum conservation of nutritional value, maintenance of the appearance and taste of food products, significant reduction of investment costs in production facilities.

The fastest procedure for cooling food products involves the utilization of liquid nitrogen, that directly touches the surface of the product needed to be frozen. Being a major constituent of the air, the Nitrogen is odorless, tasteless, colorless and inert, and is inoffensive to the food. At atmospheric pressure, liquid nitrogen has a temperature of -196 °C, its principal characteristic being the capacity to absorb a large amount of heat right at inferior temperature, enabling raised refrigeration efficiencies and heat transfer coefficients far superior to mechanical systems. In the case of nitrogen, 48 % of the total refrigerating capacity is represented by the latent heat of phase change, and the remaining 52 % is represented by the sensible heat of the vapor. The experimental research presented within this paper aims to determine the working qualitative indices and the energy indices in the cryogenic freezing of some berries species, using a multifunctional quick-freezing technical equipment with liquid nitrogen, having a discontinuous operation and an automatic working regime.

MATERIAL AND METHODS

The experimentations were carried out using three species of berries commercially purchased, respectively blueberries, strawberries and raspberries (fig. 1).



Fig. 1 - Species of berries used in the experimentation

For the quick-freezing of berries, an experimental model of multifunctional quick-freezing equipment, with discontinuous operation, using liquid nitrogen as a thermal cooling agent, developed by INMA within a national research programme, was used (fig. 2). Currently, the equipment is subject to a national patent application (CBI A-00054/07.02.2023) and a European patent application (EPC EP23020352.3/25.07.2023).



Fig. 2 - Experimental model of multifunctional quick-freezing equipment – ICR

The ICR equipment uses the latent heat of vaporisation at atmospheric pressure of liquid nitrogen, in order to reduce the temperature of the products to the frozen storage temperature. The technical equipment includes new solutions for the distribution of liquid nitrogen by using high precision nozzles and homogenising the exposure to the liquid nitrogen jets by driving in a continuous rotation movement of the rack with trays on which the products subjected to quick freezing will be positioned. The equipment also ensures the superior recovery of the "exhausted" coolant, by reusing the cold nitrogen vapor (-30 °C) discharged from the quick freezing room, when cooling an adjacent room for pre-cooling/temporary storage in frozen state. To prevent the formation of ice and facilitate the access to the freezing rooms at the end of the quick freezing/pre-cooling or temporary storage in frozen state process, the access doors are equipped with sealing gaskets accompanied by defrost resistors.

The experimental model is endowed with temperature probes that permit continuous monitoring and control of process parameters:

- Thermocouple (chromel–alumel), type K, with rod diameter φ = 1.5 mm, measurement domain -100 ºC...+30 ºC, performs temperature measuring in the center of the product;
- Thermocouple, type K, with temperature transmitting segment, measurement domain -100 ºC...+30 ºC, performs temperature measuring on the outer surface of the product;
- Type TTR Pt 100 thermal resistance, measurement domain -200 ºC...+30 ºC, performs temperature measuring within the freezing room.

The mass of each sample was 5000 *g*, 500 *g* on each of the 10 trays (fig. 3). The average mass of a berry was determined, for each sample, as the mean of five aleatory weighings from the mass of the product. The average height and maximum equatorial diameter of the berries corresponding to each sample of the three species were also measured. This was achieved as a mean of five random measurements from the product mass.



Fig. 3 - Preparation of samples for experimentation

Considering the geometric shapes of the three fruit species, the minimum distance between the thermal center and the external surface of the product was calculated. Assuming that the plant tissue of the respective product is homogeneous, having constant thermal properties throughout its mass, it is considered that the thermal center coincides with the center of the product mass.

When it comes to products having regular geometric shapes, the thermal center (*CT*) concures with their geometric center. The minimum distance between the thermal center *CT* and the external surface of the product is denoted by δ_0, this being a significant parameter to determine the average linear freezing rate (fig. 4). For blueberries, δ_0 was approximated by *h/2*, for strawberries it was approximated by *h/3* and for raspberries it was approximated by *h'/2*.

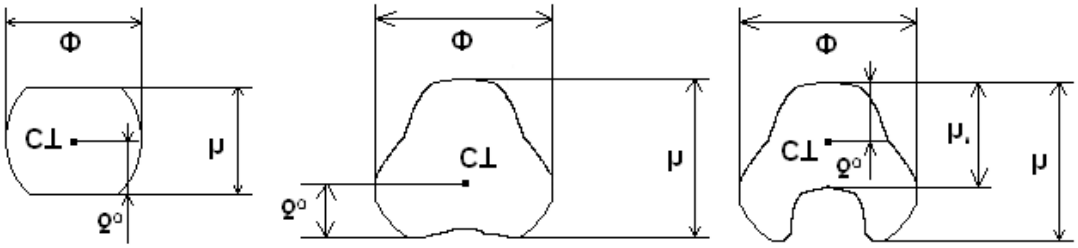


Fig. 4 - Dimensional characteristics according to the geometric shape of the analyzed product

When the temperature in the product thermal centre comes to -15 *ºC*, the freezing process is considered complete. During the freezing process there were followed the main parameters, such as:

- Freezing time from 0 *ºC* to -15 *ºC*;
- Temperature within the quick freezing room, at the end of the freezing process;
- Temperature on the surface of the product at the end of the freezing process;
- Temperature in the thermal center of the product, at the end of the freezing process;
- Total freezing time;
- Mass of the liquid nitrogen container used for freezing;

After processing the experimental data, the following indexes were determined:

- Average linear freezing rate;
- Liquid nitrogen consumption for a freezing cycle.

In order to classify a freezing process depending of cooling intensity, the average linear freezing rate is considered to be a suitable criterion and is defined by the relation:

$$w_m = \frac{\delta_0}{\tau_0}, \text{ [cm/h]} \quad (1)$$

where: δ_0 is the minimum distance between the thermal center and the external surface of the product, [cm];

τ_0 - the freezing time calculated starting from a uniform initial temperature of 0°C to the temperature to be achieved in the thermal centre, [h].

The variation in mass between the liquid nitrogen container before and after the completion of the freezing process, represents the liquid nitrogen consumption for a freezing cycle.

RESULTS

After the processing and interpretation of the experimental data, the following outcomes were achieved:

Table 1

The characteristics of the three species of berries used for experimentation

No.	Characteristic	UM	Value of parameters determined in the tests		
			Blueberries	Strawberries	Raspberries
1.	Sample mass	g	5000	5000	5000
2.	Average mass of a berry fruit	g	2.220	15.367	4.313
3.	Berries maximum equatorial diameter, Φ (average of 5 random measurements)	mm	17.2	35.2	23.1
4.	Berries average height, h	mm	13.3	40.5	h=18.8 / h'=4.1
5.	The minimum distance between the thermal center and the external surface of the product, δ_0	mm	6.65	13.50	2.05

The limit temperature within the quick freezing room was set to -30°C for all of the three species of berries used.

Process parameters, through the freezing process, can be read on the touch screen of the command and control panel or can be obtained by post-processing the data recorded on the SD memory card. Freezing times were obtained this way:

- the freezing time from 0°C to -15°C was calculated by substracting the recorded value when the temperature came to 0°C in the product's thermal centre, from the total timer recorded at the end of the freezing process (-15°C);

- the temperature within the quick freezing room, the temperature on the surface of the product and the temperature in the thermal center of the product, all measured at the end of the freezing process, were determined by directly reading the values indicated by the respective temperature sensors, at the end of the freezing process;

- the total freezing time was obtained by direct reading of the total timer recorded at the end of the freezing process.

Aspects during the experimentation are presented in figure 5.



Fig. 5 - Aspects during the experimentation

The followed parameters during the freezing process and the determined indexes are shown in Table 2.

Table 2

The parameters of the freezing process and the determined indexes

No.	Characteristic	U.M.	Value of parameters determined in the tests		
			Blueberries	Strawberries	Raspberries
1.	Freezing time from 0°C to -15°C	s	379	773	457
2.	Temperature within the quick freezing room, at the end of the freezing process	°C	-30	-32	-33
3.	Temperature on the surface of the product at the end of the freezing process	°C	-28	-30	-31
4.	Temperature in the thermal center of the product, at the end of the freezing process	°C	-15	-15	-15
5.	Total freezing time	s	498	965	603
6.	Average linear freezing rate for an operating cycle	cm/h	6.32	6.29	1.62
7.	Liquid nitrogen consumption for an operating cycle	kg	6.90	7.05	7.20

Total freezing time registered a minimum value for blueberries and a maximum for strawberries.

The average linear freezing rate registered values corresponding to a very fast freezing process for blueberries and strawberries, and corresponding value for a fast freezing process in the case of raspberries.

Liquid nitrogen consumption registered a minimum value for blueberries and a maximum for raspberries. The fact that the consumption of liquid nitrogen does not vary proportionally with the total freezing times for the three species of berries taken into account, may be a confirmation that the heat transfer from the product to the atmosphere inside the quick freezing room does not take place identically for all the three species and it depends on the composition and structure of the respective tissues, for some of them the thermal transfer is faster and for others slower, depending on the thermophysical characteristics of the respective product.

Aspect of the samples before and after freezing are presented in table 3.

Table 3

Aspect of the samples before and after freezing

Description	Samples aspect during the experimentation		
	Blueberries	Strawberries	Raspberries
Before freezing			
After freezing			

In the case of blueberries, following the visual analysis of the state of frozen products' outer surface, it was found that fissures and cracks appeared in fruit epidermis and pulp during freezing. Strawberry and Raspberry fruits reacted better, with no deterioration of the outer surface condition. *Allan-Wojtas et al. (1999)* stated that although rapid freezing was related to a better internal microstructure of individual berries, it may also cause a fissure on the berry skin as a result of thermal shock.

Although fast freezing is considered to be the best method to maintain the texture of frozen products, *Chassagne-Berces et al. (2009, 2010)* suggested that very fast freezing rates may lead to loss of firmness due to freeze cracking.

CONCLUSIONS

When artificial cold (refrigeration, freezing) is used to preserve horticultural products, unlike other methods, the best results are obtained in keeping the attributes and quality at a level as close as possible to that of the fresh product.

Among the existing freezing methods, freezing with cryogenic agents allows obtaining average linear freezing rates superior to the other methods.

The fastest procedure for cooling food products involves the use of liquid nitrogen, which comes into direct contact with the surface of the food product that needs to be frozen.

Although fast freezing is considered to be the best method to maintain the texture of frozen products, very fast freezing rates may lead to loss of firmness due to freeze cracking., as a result of thermal shock.

ACKNOWLEDGEMENT

This work was supported by the Romanian Ministry of Research, Innovation and Digitisation, through the NUCLEU Programme, Contract no. 5N/07.02.2019, Project code PN 19 10 01 04: ”Research on the superior valorization of some plant species newly cultivated in Romania”.

REFERENCES

[1] Aghdam M. S., Bodbodak S., (2014), *Food Bioprocess Technology*, Volume 7, Issue 1, pp. 37- 53, Springer US, p-ISSN 1935-5130, e-ISSN 1935-5149;

[2] Alhamdan A., Hassan B., Alkahtani H., Abdelkarim D., Younis M., (2018), Cryogenic freezing of fresh date fruits for quality preservation during frozen storage, *Journal of the Saudi Society of Agricultural Sciences*, Volume 17, Issue 1, pp. 9-16, ISSN 1658-077X, https://doi.org/10.1016/j.jssas.2015.12.001;

[3] Alhamdan A., Hassan B., Alkahtani H., Abdelkarim D., Younis M., (2018), Freezing of fresh Barhi dates for quality preservation during frozen storage, *Saudi Journal of Biological Sciences*, Vol. 25, Issue 8, pp.1552-1561, ISSN 1319-562X, https://doi.org/10.1016/j.sjbs.2016.02.003;

[4] Allan-Wojtas P., Goff H.D., Stark R., Carbyn S., (1999), The effect of freezing method and frozen storage conditions on the microstructure of wild blueberries as observed by cold-stage scanning electron microscopy, *The Journal of Scanning Microscopies - Scanning*, 21: 334-347. https://doi.org/10.1002/sca.4950210507;

[5] Biglia A., Combaa L., Fabriziob E., Gaya P., Aimoninoa D. R., (2016), Case studies in food freezing at very low temperature, *Energy Procedia,* Vol.101, pp. 305–312, ISSN 1876-6102, https://doi.org/10.1016/j.egypro.2016.11.039;

[6] Bilbao-Sainz C., Sinrod A., Powell-Palm M. J., Dao L., Takeoka G., Williams T., Wood D., Ukpai G., Aruda J., Bridges D. F., Wu V. C.H., Rubinsky B., McHugh T., (2019), Preservation of sweet cherry by isochoric (constant volume) freezing, *Innovative Food Science & Emerging Technologies*, Vol. 52, pp. 108-115, ISSN 1466-8564, https://doi.org/10.1016/j.ifset.2018.10.016;

[7] Cao X., Zhang F., Zhao D., Zhu D., Li J., (2018), Effects of freezing conditions on quality changes in blueberries, *Journal of the Science of Food and Agriculture*, Vol. 98, Issue 12, ISSN 0022-5142, e-ISSN 1097-0010, pp. 4673-4679;

[8] Chassagne-Berces S., Poirier C., Devaux M.F., Fonseca F., Lahaye M., Pigorini G., Girault C., Marin M., Guillon F., (2009), Changes in texture, cellular structure and cell wall composition in apple tissue as a result of freezing, *Food Research International*, Volume 42, Issue 7, pp. 788-797, ISSN 0963-9969, https://doi.org/10.1016/j.foodres.2009.03.001;

[9] Chassagne-Berces S., Fonseca F., Citeau M., Marin M., (2010), Freezing protocol effect on quality properties of fruit tissue according to the fruit, the variety and the stage of maturity, *LWT - Food Science and Technology*, vol. 43, Issue 9, pp. 1441–1449, https://doi.org/10.1016/j.lwt.2010.04.004;

[10] Chaudhary K., (2021), A review on effect of freezing on food, fruit and vegetable texture, *International journal of creative research thoughts*, Vol.9 (5), pp.217–221;

[11] Cirillo A., Magri A., Petriccione M., Di Vaio C, (2023), Effects of cold storage on quality parameters and nutraceutical compounds of pomegranate fruits (cv. Acco), *Advances in Horticultural Science*, Volume 37, Issue 1, pp. 15–23, https://doi.org/10.36253/ahsc-13850;

[12] Delgado A.E., Rubiolo A.C., (2005), Microstructural changes in strawberry after freezing and thawing processes, *LWT - Food Science and Technology*, Vol. 38, Issue 2, pp. 135-142, ISSN 0023-6438, https://doi.org/10.1016/j.lwt.2004.04.015;

[13] Fellows P. J., (2017), *Food Processing Technology (Fourth Edition): Principles and Practice*, Woodhead Publishing Series in Food Science, Technology and Nutrition, pp. 885-928, e-ISBN 9780081005231;
[14] Gales O., Jones J., Swarts N., (2022), An analysis on the impacts of cryogenic freezing on raspberry quality, *Advances in Horticultural Science*, Vol.36(4), pp.293–301, https://doi.org/10.36253/ahsc-13824;
[15] Gherghi A., (1994), *Technology of horticultural products valorisation. Keeping horticultural products fresh (Tehnologia valorificării produselor horticole. Păstrarea produselor horticole în stare proaspătă)*, vol. I, II, U.I. "Titu Maiorescu" F.I.H.A., Bucharest;
[16] Hoffmann K., Boeing H., Dufour A., Volatier J.L., Telman J.,Virtanen M., Becker W., De Henauw S., (2002), Estimating the distribution of usual dietary intake by short-term measurements, *European Journal of Clinical Nutrition*; 56(Suppl. 2): S53 – 62, https://doi.org/10.1038/sj.ejcn.1601429;
[17] Ingeaua M., Prisecaru T., Pirnă I., Sorică C., (2015), Analysis of a convective drying process of plums, *INMATEH Agricultural Engineering*, Vol.46, no.2, pp. 115 – 124;
[18] James C., Purnell G., James S. J., (2015), A Review of Novel and Innovative Food Freezing Technologies, *Food and Bioprocess Technology*, Pages 1616 – 1634, ISSN 1935-5149, https://doi.org/10.1007/s11947-015-1542-8;
[19] Jha P. K., Xanthakis E., Chevallier S., Jury V., Le-Bail A., (2018), Assessment of freeze damage in fruits and vegetables, *Food Research International*, Volume 121, Pages 479-496, ISSN 0963-9969, https://doi.org/10.1016/j.foodres.2018.12.002;
[20] Kennedy C., (2003), *Food Preservation Techniques*, Woodhead Publishing Series in Food Science, Technology and Nutrition, Pages 228-240, ISBN-10: 9781855735309, ISBN-13: 978-1855735309;
[21] Kotwaliwale N., Curtis E., Othman S., Naganathan G.K., Subbiah J., (2012), Magnetic resonance imaging and relaxometry to visualize internal freeze damage to pickling cucumber, *Postharvest Biology and Technology*, Volume 68, Pages 22-31, ISSN 0925-5214, https://doi.org/10.1016/j.postharvbio.2011.12.022;
[22] Li B., Sun D.W., (2002), Novel methods for rapid freezing and thawing of foods – a review, *Journal of Food Engineering*, Volume 54, Issue 3, Pages 175-182, ISSN 0260-8774, https://doi.org/10.1016/S0260-8774(01)00209-6;
[23] Mulot V., Benkhelifa H., Pathier D., Ndoye F-T., Flick D., (2019), Measurement of food dehydration during freezing in mechanical and cryogenic freezing conditions, *International Journal of Refrigeration*, Volume 103, Pages 329-338, ISSN 0140-7007, https://doi.org/10.1016/j.ijrefrig.2019.02.032;
[24] Niculiță P., (1998), *Refrigeration technique and technology in agri-food fields*, Didactic and Pedagogical Publishing House R.A, Bucharest, ISBN 973-30-5719-3;
[25] Parandi E., Pero M., Kiani H., (2022), Phase change and crystallization behavior of water in biological systems and innovative freezing processes and methods for evaluating crystallization, *Discover Food*, Volume 2, Issue 6, ISSN 2731-4286, https://doi.org/10.1007/s44187-021-00004-2;
[26] Sousa-Gallagher M. J., Tank A., Sousa R., (2016), *The Stability and Shelf Life of Food (Second Edition)*, Woodhead Publishing Series in Food Science, Technology and Nutrition, Pages 399-430, p-ISBN 9780081004357, e-ISBN 9780081004364;
[27] Van Buggenhout S., Messagie I., Maes V., Duvetter T., Van Loey A., Hendrickx M., (2006), Minimizing texture loss of frozen strawberries: effect of infusion with pectinmethylesterase and calcium combined with different freezing conditions and effect of subsequent storage/thawing conditions, *European Food Research and Technology*, Volume 223, Issue 3, Pages 395–404,ISSN 1438-2385, https://doi.org/10.1007/s00217-005-0218-4;
[28] Van der Sman R.G.M., Voda A., Van Dalen G., Duijster A., (2013), Ice crystal interspacing in frozen foods, *Journal of Food Engineering*, Volume 116, Issue 2, Pages 622-626, ISSN 0260-8774, https://doi.org/10.1016/j.jfoodeng.2012.12.045;
[29] Zhu Z., Luo W., Sun D.W., (2020), Effects of liquid nitrogen quick freezing on polyphenol oxidase and peroxide activities, cell water states and epidermal microstructure of wolfberry, *LWT*, Volume 120, 108923, ISSN 0023-6438, https://doi.org/10.1016/j.lwt.2019.108923.

THREE-DIMENSIONAL PATH PLANNING OF APPLE HARVESTING ROBOT BASED ON IMPROVED GENETIC ALGORITHM

/

基于改进遗传算法的苹果收获机器人三维路径规划

Zeyuan YAN[1)] *, Ming SUN[1)]

[1)] Xinxiang Vocational and Technical College, 453006, Xinxiang, Henan, China

*E-mail: yanzeyuan@xxvtc.edu.cn

Corresponding author: Dr. Zeyuan Yan

DOI: https://doi.org/10.35633/inmateh-71-40

Keywords: *harvesting robot, apple harvesting, path planning, improved genetic algorithm, three-dimensional space*

ABSTRACT

In recent years, the problem of "rural labor shortage" in China has become increasingly serious, with a large number of young laborers going out to work, leading to an increasing amount of idle rural land. With the intensification of population aging and the reduction of agricultural labor force in China, resulting in an urgent demand for agricultural robots. With the rapid development of agricultural machinery and automation technology, agricultural robots have been continuously developing. They can better adapt to the development of biotechnology in agriculture, and traditional harvesting methods may undergo significant changes, with an increased focus on the cultivation of crops. Therefore, this paper introduces a new encoding scheme on the basis of traditional genetic algorithm (GA) and proposes an improved double encoding GA. This new encoding scheme is used on the crossover link, whereas the path node sequence encoding scheme is still used on the mutation link. The selection operation is placed after the mutation, and the merging sorting and elitist selection are performed on the parent population, crossover population, and mutation population before selection, thereby accelerating the convergence speed. On the basis of the improved GA, the three-dimensional path of the apple harvesting robot is designed and planned, with the addition of adaptive adjustment function during the progress. The experimental simulation results show that the three-dimensional path planning of the apple harvesting mobile robot based on the improved GA can minimize the number of paths and loops and well meet the operational requirements of the harvesting robot.

摘要

近年来，我国"农村劳动力短缺"问题日益严重，大量年轻劳动力外出务工，导致农村闲置土地数量不断增加。随着中国人口老龄化的加剧和农业劳动力的减少，对农业机器人的需求迫切。随着农业机械及其自动化技术的快速发展，农业机器人也在不断发展。它们可以更好地适应农业生物技术的发展，传统的收获方法可能会发生重大变化，越来越注重作物的种植。因此，本文在传统遗传算法（GA）的基础上引入了一种新的编码方案，并提出了一种改进的双编码 GA。这种新的编码方案用于交叉链路，而路径节点序列编码方案仍用于变异链路。变异后进行选择操作，选择前对亲本种群、交叉种群和变异种群进行合并排序和精英选择，从而加快收敛速度。在改进遗传算法的基础上，设计并规划了苹果收获机器人的三维路径，并在过程中加入了自适应调整功能。实验仿真结果表明，基于改进遗传算法的苹果收获移动机器人三维路径规划可以使路径和回路的数量最小化，很好地满足收获机器人的操作要求。

INTRODUCTION

China is the world's largest producer of apples. With the accelerated pace of urbanization in China, a large number of young people have migrated to cities for work, resulting in a shortage of labor in rural areas. This phenomenon has led to a lack of labor for apple harvesting, and manual apple harvesting is faced with challenges, such as large workload and low efficiency. The transformation of agricultural production towards automation and intelligence is becoming urgent *(Alavi A. et al., 2011)*. With the rapid development of information technology, microelectronics, and agricultural mechanization, research on agricultural robots has achieved significant breakthroughs and been applied in various production fields, thereby promoting the development of agricultural production towards automation and intelligent integration. Harvesting is one of the most important processes in fruit and vegetable cultivation.

Fruits and vegetables generally have a short harvest period, large harvesting tasks, and high requirements, which all result in significant physical exhaustion for harvesters *(Chen M. et al., 2020)*. Currently, manual labor is mainly relied upon for fruit and vegetable harvesting in China, thus leading to high economic costs and low harvesting quality and directly affecting the economic income of fruit farmers *(Cheng X. Y. et al., 2019)*. With the gradual maturity of robot technology, China has begun to increase investment in the research of agricultural robots to achieve automation in the harvesting process. This action is of great significance for liberating rural labor and improving harvesting efficiency and quality *(Erhui L. et al., 2017)*. Path planning is the most important part of the operation of harvesting robots. The intelligence and automation of harvesting robots are mainly reflected in the planning of their motion range and workspace *(Geng X. et al., 2021)*. Apple orchards generally have complex terrains, and harvesting robots require good path planning techniques to navigate through them to save time and optimize the three-dimensional path calculation during the operation. By utilizing environmental models, collision simulations can be performed to successfully avoid obstacles and achieve optimal motion paths for fruit and vegetable harvesting robots.

The use of robots to harvest fruit was first proposed by Schertz and Brown in the 1960s. Since then, harvesting robots have undergone over 50 years of development, from the earliest robots that took dozens of seconds to harvest fruit to those that can do it within 10 seconds today. Research on fruit-picking robots in China has mainly focused on three aspects: apple image processing, robotic action control, and harvesting path planning.

First, two studies on apple image processing have been conducted. Satyam et al. (2021) applied dynamic threshold segmentation based on OTSU to the apple fruit image, used the information correlation between images to reduce the target fruit processing area, and finally employed a fast and mean-free correlation algorithm to track and recognize the target fruit *(Satyam P. et al., 2021)*. Haiying et al. (2018) used the red-green color difference method to segment out apples and extract their centers and radii and then established a matching strategy on the basis of area features combined with polar geometry to achieve fruit matching and positioning by using binocular vision. In the two studies, ordinary RGB images were only processed, and they had high complexity *(Haiying B. et al., 2018)*. Luo et al. (2017) transformed the problem of apple harvesting path planning into that of 3D apple harvesting robot control. They combined binocular camera images with the apple's position information to propose an improved genetic algorithm (GA) that solved local convergence issues and increased harvesting efficiency. However, this algorithm did not consider obstacles in the actual harvesting situation, making it less suitable for complex environments, in which fruit trees grow in real-world situations *(Luo L. F. et al., 2017)*. Wang et al. (2017) used a Kinect camera to provide color and 3D shape information and employed an efficient point cloud-based algorithm to achieve high apple recognition rates with a positioning accuracy of less than 10 mm. This approach can simultaneously recognize and process images of 20 apples in less than 1 second. Although this approach employed a depth camera for fast recognition and positioning, it did not consider path planning to improve apple harvesting efficiency *(Hu Z. et al., 2022)*.

Second, control issues related to robotic action have become a hot research topic in the field of intelligent control *(Jiang C. et al., 2021) (Kangkang M. et al., 2023) (Lee Y. et al., 2020) (Mahi Ö. K. M. et al., 2015) (Mas A. et al., 2020)*. Research on apple-picking robots based on deep reinforcement learning (DRL) architecture has emerged as a topic among scholars, but no mature theoretical framework for controlling apple-picking robots based on DRL architecture has appeared yet. Therefore, DRL-based apple-picking robots remain at an exploratory stage domestically and internationally. Li et al. (2019) proposed a trajectory planning method for apple-picking robots on the basis of stepwise transfer strategies. This method utilized the idea of transfer learning to transfer optimal strategies for trajectory planning from obstacle-free scenarios to scenarios with single obstacles, and then to scenarios with mixed obstacles, thereby improving the training efficiency and network performance of DRL algorithms *(Li S. Y. et al., 2019)*. Although relatively few direct achievements related to DRL apple-picking robots were gained since the advent of DRL algorithms, some theoretical explorations have been conducted on DRL fruit-picking robots with similar content. For example, Tang et al. (2020) proposed a path planning method for orchard robotics with fast collision-free path generation on the basis of DRL for watermelon harvesting *(Tang Y. et al., 2020)*. Cao et al. (2019) proposed a path planning method for virtual orchard robotics on the basis of DRL with obstacle avoidance capabilities. This method can achieve fast trajectory planning for a large number of harvesting tasks, and it is suitable for tasks where the positions of obstacles are unknown or change over time. The approach achieved an average success rate of over 96.7% in virtual orchard scenarios with variously placed obstacles *(Cao X. et al., 2019)*.

Third, research on path optimization for fruit-picking robots has mainly focused on methods, such as topological methods *(Paull M. L. et al., 2018)*, visibility graphs *(Perveen K. et al., 2023)*, grid-based methods *(Mohanasundaram S. et al. 2021),* and potential fields methods *(Ratta Q. et al., 2021)*. Progress has been made in research on path planning for mobile robots in terms of algorithms for global path planning and obstacle avoidance techniques *(Swetha K.et al., 2021)*. However, path optimization is a key factor in determining harvesting efficiency *(Mousavi S. M. et al., 2017)*, and it remains an understudied area. GAs have been widely used to solve optimization problems, such as two-dimensional path planning *(Sarangapani C. et al., 2016)*.

In the present paper, GAs were applied to optimize three-dimensional paths for apple picking. An improved GA that updates information based on limited domain information and adaptive updating rules were present to enhance convergence speed and solve issues, such as premature convergence and local optima solutions. A code for the path optimization algorithm was written, and its performance in three-dimensional path planning for apple picking was validated using both basic GAs and the improved GA approach *(Castro. et al., 2020)*.

MATERIALS AND METHODS

In general, the three-dimensional path optimization problem for apple picking robots can be described as follows: An apple picking robot needs to pick n apples, and the distance between the picked apples is known. If the apple picking robot only picks each picking object once, the shortest path for the apple picking robot starts from a certain picking point and ultimately returns to the starting point. The sequence numbers of n picking objects is recorded to form a set, and the circuit that the apple picking robot passes through after picking *n* picking points is recorded.

$$P = \{p_1 \to p_2 \to \cdots \to p_n \to p_1\} \tag{1}$$

where $p_i \in N$, $p_i \neq p_j (i \neq j)$, $i = 1, 2, 3, \cdots, n$, if the distance matrix between picking points is $D = (d_{ij})_{n \times n}$, then the mathematical model of the three-dimensional path optimization problem of the apple picking robot can be expressed as follows:

$$minf(P) = \sum_{i=1}^{n-1} d_{p_i, p_{i+1}} + d_{p_n, p_1} \tag{2}$$

Among them $f(P)$, represents the total path length of the apple picking robot's walking path.

Genetic algorithm

GA was proposed by Professor J. Holland in the 1970s, and it is commonly referred to as traditional GA or standard GA *(Xiaoming Y. et al., 2017)*. It simulates and draws inspiration from the phenomena of gene inheritance, crossover, and mutation in the process of natural biological evolution and designs the three main stages of individual selection, crossover, and mutation in the population from an algorithmic perspective. The retained and inherited individuals are those that have been evaluated as optimal through adaptability, reflecting the mechanism of “survival of the fittest, survival of the fittest” in the biological world. They continue to iterate and evolve in accordance with this until a certain convergence condition is met *(Xiaoqiang S. et al., 2019)*. GA is a probability search algorithm with global optimization capabilities, high universality, parallelism, and robustness. It has been successfully applied to solve path optimization problems, and its basic steps are as follows:

(1) The gene encoding scheme and set algorithm parameters are determined. The gene encoding scheme is designed on the basis of the feasible solution characteristics of the optimization problem, and its encoding structure and values are usually used for the path optimization problem of apple picking robots, which is based on nonrepeating sequence encoding of path nodes. The algorithm parameters mainly include population size, number of iterations, crossover probability, and mutation probability.

(2) The population is initialized, that is, a group of individuals is generated in accordance with the requirements of the genetic encoding scheme and the size of the population.

(3) The quality of individual populations is evaluated using fitness functions. Among them, the fitness function is usually constructed on the basis of the objective function of the optimization problem.

(4) Selection operation refers to selecting a sufficient number of individuals in accordance with a certain strategy on the basis of their fitness to form an offspring population. The better the individual’s fitness, the greater the probability of being selected. The commonly used selection strategies include roulette wheel strategy, elite strategy, and ranking optimization strategy.

(5) Cross operation refers to the random pairing of individuals in the offspring population, where genes are randomly exchanged on the basis of crossover probability. This step gives individuals the opportunity to obtain more excellent genes, thereby enhancing the diversity of the offspring population and maintaining strong search and optimization abilities.

(6) Mutation operation refers to randomly selecting some offspring individuals, changing certain gene loci of the individual based on the probability of mutation, and causing them to mutate into new individuals, thereby expanding the search and optimization scope.

(7) Steps (3)–(6) are repeated until the genetic evolution operation reaches the termination condition of the iteration. Traditional GAs have a universal algorithm framework with clear steps, and they allow for self-designed processes. However, they also have drawbacks, such as slow convergence speed or premature convergence, leading to local optima. Therefore, improving the above steps has always been the main direction for improving algorithm performance.

Dual Encoding Improved GA

When GA is used to solve the path optimization problem of apple picking robots, the most commonly used genetic encoding scheme is the sequence encoding of path nodes composed of each picking point. Its advantages are intuitiveness, strong correspondence, and easy-to-calculate individual fitness. The disadvantage is that if individuals directly cross operate, it can easily lead to duplicate genes or gene deletions between two individuals, thereby becoming illegal individuals. This article proposes a reproducible natural number encoding with a one-to-one mapping relationship with the sequence encoding of path nodes. Therefore, in this paper, this new encoding scheme is introduced on the basis of traditional Gas, and a dual encoding improved GA is proposed. This new encoding scheme is adopted in the crossover stage, whereas the path node sequence encoding scheme is still used in the mutation stage. The selection operation is placed after the mutation, and the parent population, the crossover population, and the mutated population are merged, sorted, and selected by elites before selection to accelerate the convergence speed. The following are specific instructions for each step of the algorithm in this article.

The sequence encoding of path nodes is the encoding corresponding to equation (1), which is usually represented by non-repeating natural number encoding. In actual coding, the starting point picking point number at the end of equation (1) can be removed. For example, when n=6, both sequences are valid encodings:

$$P_1=\{2,5,3,1,4,6\},P_2=\{3,2,5,6,4,1\}$$

The basic idea of repeatable natural number encoding is to uniquely map the sequence encoding of path nodes to repeatable natural number encoding, as follows:

$$f: P \to Q$$

$$P=\{p_n, p_{n-1},\cdots, p_2, p_1\}$$

$$Q=\{q_n, q_{n-1},\cdots, q_2, q_1\}$$

The mapping rule is: equal to the number of codes on the left side of the code with a value of *i* in *P* (denoted as) that are smaller than that value. To facilitate code generation and conversion

$$t_j=\begin{cases}1, p_j < p_k, j=n, n-1,\cdots, k+1\\ 0, else\end{cases} \quad (3)$$

The calculation formula for then is

$$q_i=\sum_{j=k+1}^{n} t_j, i=1,2,\cdots,n. \quad (4)$$

For example, mapping the above encoding results in: because in the encoding, the number of codes on the left side of code 6 that are smaller than it is 5, and the other numbers are also similar. Similarly, encoded mapping codes. Analyzing the mapping code *q*, it can be found that it has the following characteristics:

$$q_1 \equiv 0, 0 \leqslant q_i < i \quad (5)$$

Therefore, the mapping code q can also remove bits and be represented as:

$$q=\{q_{n-1},\cdots, q_2, q_1, 0 \leqslant q_i \leqslant i\} \quad (6)$$

In summary, the encoding q can be obtained from the mapping of encoding p in accordance with Equations (5) and (6), or it can be directly randomly generated according to equation (6).

Therefore, the second encoding scheme has the characteristics of simple mapping rules, flexible generation methods, and repeatable codes. It can be highly utilized in solving the problem of apple picking robots by using GAs. For the convenience of GA calls, the following is an algorithm for converting these two codes to each other.

According to the design concept of improving GA with dual encoding, genetic evolution will be completed in the order of "crossover mutation selection". During this period, only reproducible natural number encoding is used in the crossover stage, whereas path node sequence encoding is still used in the remaining stages, so that individual fitness calculation and mutation operation are not affected. Due to the lower complexity of encoding conversion than crossover operation, using two encoding conversions to complete one round of crossover operation is worthwhile for genetic evolution operations. Therefore, the initial population of the algorithm in this article is initialized on the basis of the sequence encoding of path nodes (excluding the return starting point at the end). For example, when the number of picking points n = 6, the gene encoding of each individual in the population is a sequence encoded by natural numbers. The task of constructing fitness functions with random nonrepeating permutations of 1–6 is to evaluate the quality of individual populations. For the path optimization problem of apple picking robots, the shorter the circuit of the apple picking robot is, the better the individual. Therefore, this algorithm takes the objective function as the fitness function of the algorithm, that is, for any individual P in the population, its fitness is:

$$fit(P) = \sum_{i=1}^{n-1} d_{p_i, p_{i+1}} + d_{p_n, p_1} \tag{7}$$

The crossover operator of GAs attempts to retain more excellent genes and improve individual fitness. Usually, the crossover operator needs to consider the sequence of genes and the content of genes themselves. In this regard, the crossover strategy designed by the algorithm in this article is based on the second encoding method, which selects the following three operators, in turn, to perform crossover operations on individual populations:

(1) Two-point crossing refers to randomly generating two gene points and exchanging the genes at the corresponding positions of two individuals.

(2) Fragment crossing refers to the random generation of two gene points, where the gene fragments between two individuals are exchanged as a whole.

(3) Consistent crossover refers to the exchange of each corresponding gene point between two individuals based on the probability of crossover.

The above three crossover operators gradually increase the degree of modification of individual excellent genes, and their effect on the fitness of new individuals after crossover increases in turn. By taking turns using them, the degree of evolution of population genes can be reasonably controlled, making the crossover effect of the algorithm more significant. Before the above crossover operator is executed, the "*p* to *q*" algorithm of encoding conversion must be called first to convert the path node sequence encoding *p* into a repeatable natural number encoding *q*. After the crossover operation is completed, the "*q* to *p*" algorithm is called to convert the encoding q into encoding p.

In genetic algorithm, mutation operator is mainly used to maintain population diversity and ensure the local optimization ability of the algorithm, especially in the late stage of genetic evolution. Because the designed crossover operator has significant crossover effect on individual populations and plays a part in evolution. Therefore, the mutation strategy of the algorithm can avoid damaging the cross effect. That is, one of the following four mutation operators is directly selected to make the parental population mutate a single population:

(1) Gene transposition refers to the direct exchange of genes at two random locations in an individual to be mutated.

(2) In gene reverse order, a random gene fragment is placed in reverse order from the individual to be mutated.

(3) In gene right shift, a random gene segment in the mutated individual is rotated to the right once.

(4) In gene left shift, a random gene segment in the mutated individual is rotated to the left once.

The above four mutation operators can have a significant effect on individual genes, causing changes in the path of apple picking robots and thereby increasing population diversity. Therefore, their comprehensive application could improve the mutation effect of the algorithm.

By selecting operators, GAs can evolve towards ideal solutions. Traditional selection operators, such as roulette strategy and tournament strategy, fully embody the "survival of the fittest" mechanism of GAs.

However, in situations where individual evolution efficiency is not high, the convergence speed is slow, and even premature convergence occurs. Considering the above factors, the crossover and mutation operators of the algorithm in this paper operate directly on the parent population, which can enable individuals to fully evolve. Therefore, the design of the selection operator mainly draws on the idea of elite individual selection. The specific approach is to merge the offspring population of the parent population and the mutated offspring population, calculate the individual fitness values of the merged population in ascending order, and select the top N (population size) individuals as the next-generation population directly. The above selection operator is executed after mutation operation. Compared with traditional selection operators, this selection operator combines the population of parents and children for selection, thus allowing individuals with sufficient evolution in various stages of inheritance to be selected and inherited into the next generation. Therefore, the convergence speed of inheritance is faster.

RESULTS

Experimental simulation and analysis were conducted from three aspects to test the performance and effectiveness of dual encoding improved GA. First, the population quality and diversity of the dual encoding improved GA and the traditional single encoding GA was compared. Then, the dual encoding improved GA, other GAs, and other intelligent heuristic algorithms were compared in terms of solution performance.

Experimental Environment and Parameter Settings

The experimental hardware environment is Intel Core i7-7200U CPU/8GB, the operating system is Windows 10, and the programming environment is Matlab2018a. The population size and iteration times of GA were set to N = 30 and G = 400, and those of the double coding improved GA were set to N = 50 and G = 800, respectively. The required crossover probability and mutation probability for the algorithm were set to Pc = 0.8 and Pm = 0.1, respectively. The node of the apple picking robot's operation area was set as 0, and its coordinate value is (0,0,0). The orchard has 29 picking points, represented by corresponding coordinates X, Y, and Z values. The number of each picking point is known (Table 1). The three-dimensional distribution of apple picking points is shown in Figure 1.

Table 1

Apple Picking Point Information Table

Picking point number	Coordinate X	Coordinate Y	Coordinate Z	Picking volume	Picking point number	Coordinate X	Coordinate Y	Outbound quantity	Picking volume
0	0	0	0	0	15	40	40	1.7	1
1	13	29	1.2	1	16	20	49	1.6	1
2	32	44	2.3	1	17	32	55	1.5	1
3	8	23	1.1	1	18	17	17	1.9	1
4	5	57	1.8	1	19	24	9	2.9	1
5	47	58	2.2	1	20	31	98	1	1
6	44	78	2.3	1	21	4	35	2.2	1
7	23	7	1.8	1	22	11	51	2	1
8	14	16	2.2	1	23	25	43	2.1	1
9	30	92	1.8	1	24	50	14	1.1	1
10	15	14	2.5	1	25	36	96	1.3	1
11	5	91	2.8	1	26	49	79	2.3	1
12	9	0	1.1	1	27	38	71	2.7	1
13	50	36	1.3	1	28	42	31	2.4	1
14	33	64	3	1	29	28	98	1.5	1

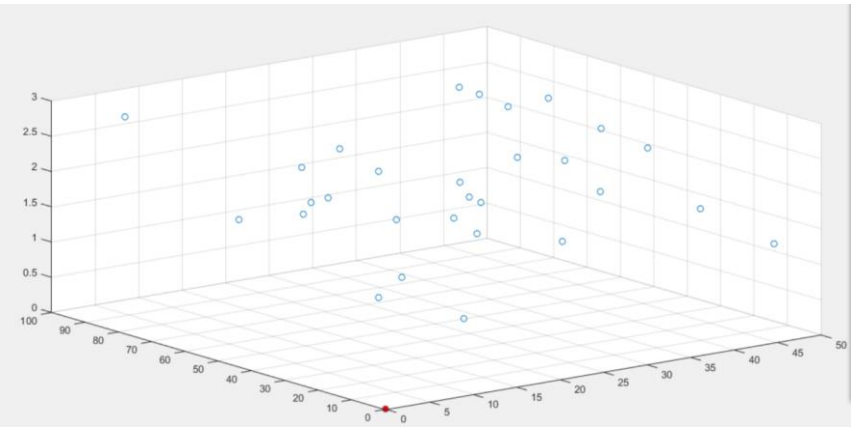


Fig. 1 - 3D Distribution of apple picking points

Experiment and Comparative Analysis

A dual coding improved GA was used to solve the three-dimensional path optimization model of apple picking and agricultural transportation robots, with a maximum iteration number of 2500 and a total travel distance as the objective function. A satisfactory solution can be obtained by solving the model, with a total travel distance of 1901.54 m for the robot. This algorithm took 61.62 seconds. The path map of the dual coding improved GA is shown in Figure 2, the convergence curve of the dual coding improved GA is shown in Figure 3, and the output result of the dual coding improved GA is shown in Figure 2.

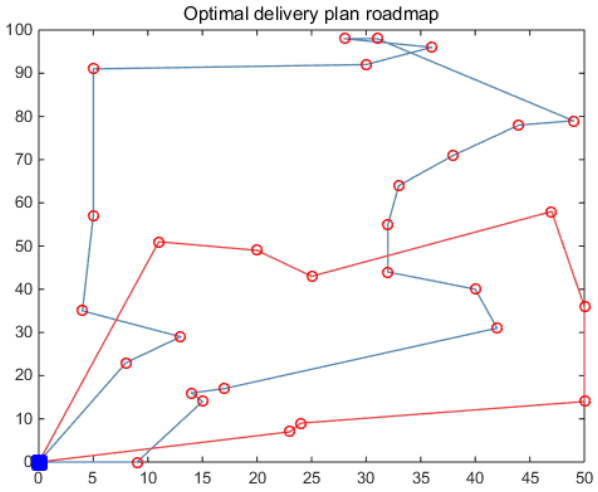


Fig. 2 - Path map of dual encoding improved genetic algorithm

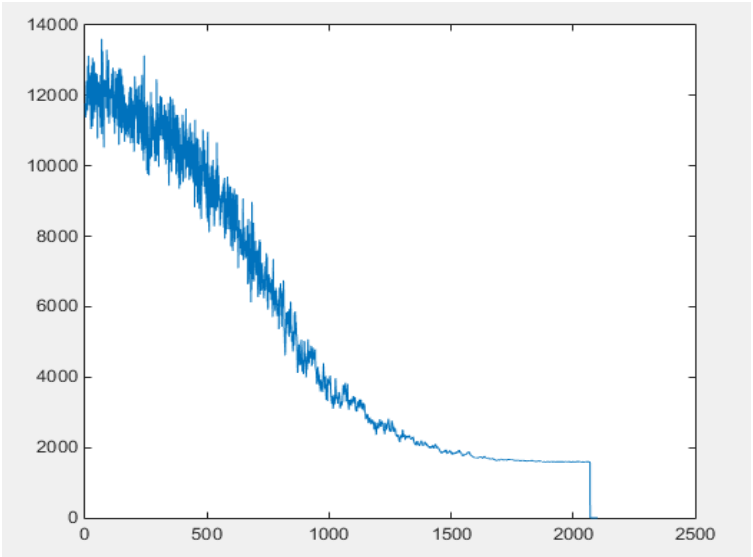


Fig. 3 - Convergence curve of dual encoding improved genetic algorithm

Table 2

Output results of double encoding improved genetic algorithm

Picking path	Total Distance	Algorithm convergence time
0→12→10→8→18→28→15→2→17→14→27→6→26→2 0→29→25→9→11→4→21→1→3→0	1901.54m	61.62s
0→7→19→24→13→5→23→16→22→0		

Table 2 shows the output results of the dual coding improved genetic algorithm. A traditional GA solution model was designed to further verify the effectiveness of the dual encoding improved G. With the initial cost and parameters unchanged, the total travel of the harvesting robot is 2226.61 m. The algorithm took 88.85 seconds. The path diagram of the traditional GA is shown in Figure 4, the convergence curve of the traditional GA is shown in Figure 5, and the output results of the traditional GA are shown in Table 3.

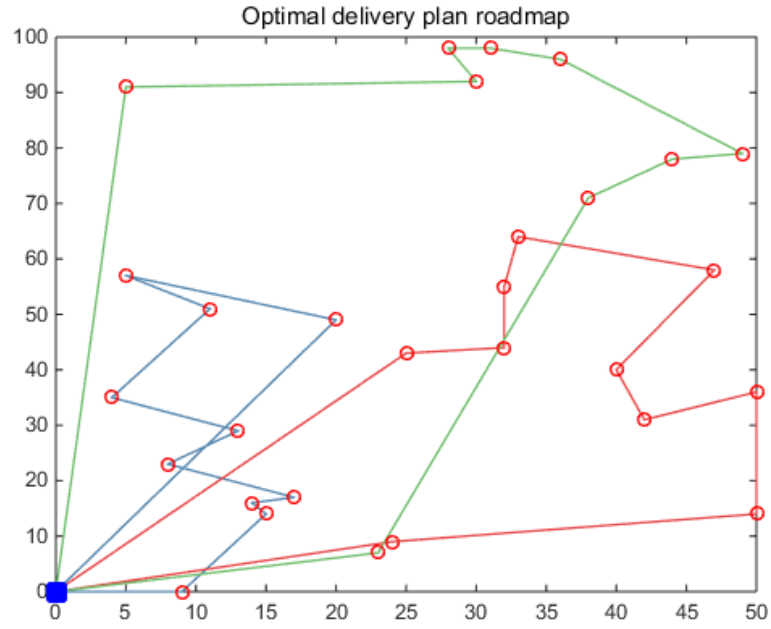


Fig. 4 - Traditional genetic algorithm path map

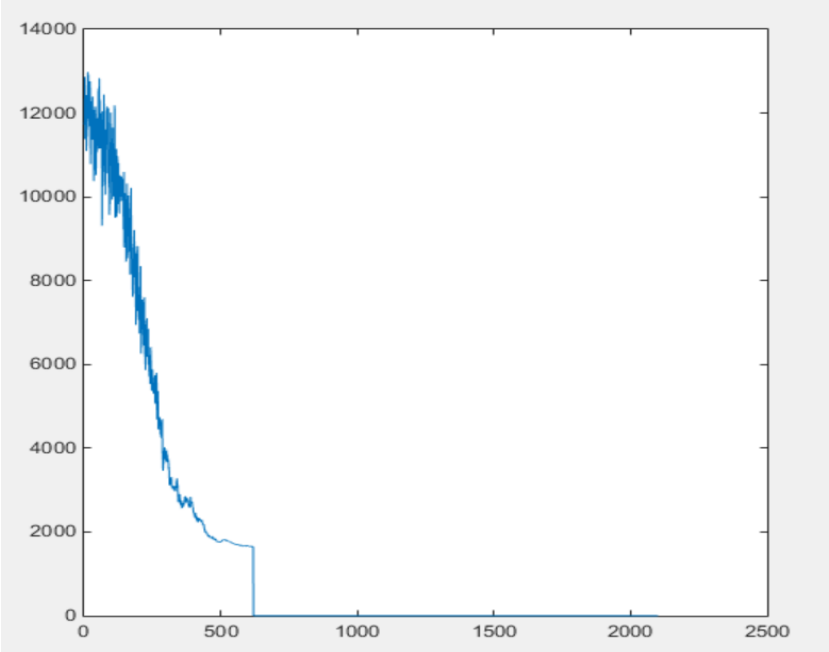


Fig. 5 - Convergence curve of traditional genetic algorithm

Table 3

Optimal Service Path

Picking path	Total Distance	Algorithm convergence time
0→12→10→8→18→3→1→21→22→4→16→0	2226.61m	88.85s
0→23→2→17→14→5→15→28→13→24→19→0		
0→7→27→6→26→25→20→29→9→11→0		

As shown in Table 3, the double coding improved GA has strong exploratory and convergent properties, and the value of the objective function is better than that in traditional GAs. The dual coding improved GA outperformed traditional GAs in terms of robot quantity, travel distance, and algorithm time. The traditional GA requires three paths to complete the apple picking task, whereas the dual coding improved GA only requires one path to complete the same task, thereby increasing the efficiency by 50%. In terms of the travel distance of the harvesting robot, the traditional GA has a total travel distance of 2226.61 m, whereas the double coding improved GA has a total travel distance of 1901.54 m to complete the same task. In terms of algorithm time, the traditional GA has a convergence time of 88.85 seconds, whereas the double coding improved GA has a convergence time of 61.62 seconds, which improves the algorithm efficiency by 30.64%.

CONCLUSIONS

In response to the problem of long walking paths and low efficiency of picking robots during the picking process, a three-dimensional optimal path planning for apple picking robots based on a dual coding improved GA was designed. The optimization problem of apple picking paths was transformed into a Travel Salesman Problem, local planning adjustments were made in real-time on the basis of the actual problems, and the optimal path was determined based on the number of robot turns. During the research process, MatLab was used for simulation experiments and analysis, and improvement plans were proposed to significantly improve the efficiency of robot operation. It enhances the stability during the operation process, saves considerable time and costs for fruit farmers, and confirms the reliability of the path planning scheme. Through algorithm research, software development and debugging, and simulation experiments, the following conclusions were drawn:

Under the general framework of GA, the optimization problem of apple picking path is transformed into a Travel Salesman Problem. A gene repeatable coding scheme is introduced for the optimization problem of apple picking path, making the design of crossover operators more flexible and convenient. This outcome not only avoids the generation of illegally encoded individuals but also greatly enhances the quality and diversity of the population. Compared with the time required for encoding conversion added in the algorithm, the experiments showed that this approach is worthwhile.

Selecting multiple crossover and mutation operators, in turn, and applying them to different individuals enhance the algorithm's local optimization ability, especially in the later stages of iteration, which helps the algorithm avoid premature convergence and jump out of local optima. These improvement ideas have positive significance in promoting the application and development of GAs. Combined with other strategies of GAs, they can even further effectively solve the optimization problem of large-scale apple picking paths, thereby providing more decision-making basis for production practice in the future.

REFERENCES

[1] Alavi A. H, Gandomi A. H. (2011). Prediction of principal ground-motion parameters using a hybrid method coupling artificial neural networks and simulated annealing. *Computers & Structures*, Vol. 89, Issue 23-24, pp. 2176–2194. England;

[2] Cao X., Zou X., Jia C., Chen M., Zeng Z. (2019). RRT-based path planning for an intelligent litchi-picking manipulator. *Computers and Electronics in Agriculture*, Vol. 156, pp. 105–118. England;

[3] Chen M., Zhang H., Wang X. (2020). Design of apple picking robot based on iterative learning PID algorithm. *Journal of Agricultural Mechanization Research*, vol. 42, Issue 6, pp. 83–86. China

[4] Castro D.R.G., Mar J.M., da Silva L.S. et al., (2020) Improvement of the bioavailability of Amazonian juices rich in bioactive compounds using glow plasma technique, *Food and Bioprocess Technology*, vol. 13, no. 4, pp. 670-679, America;

[5] Erhui L., Xifan Y. (2017). AGV path planning based on improved genetic algorithm and implementation platform. *Computer Integrated Manufacturing Systems,* Vol. 23, Issue 3, pp. 2017465-472. China;
[6] Geng X., Chen Z., Yang W., Shi D., Zhao K. (2021). Solving the traveling salesman problem based on an adaptive simulated annealing algorithm with greedy search. *Applied Soft Computing,* Vol. 11, Issue 4, pp. 3680–3689. Netherlands;
[7] Haiying B. (2018). Application of simulated annealing genetic algorithm in balance optimization of construction resources of hydropower projects. *Technical Supervision in Water Resources*, Vol. 5, pp. 108–112, 2018.
[8] Hu Z., Qin J., Wang Z. (2022). Robot Path Planning Based on Multi-strategy Improved RRT* Algorithm, 2022 6th International Conference on Automation. *Control and Robots (ICACR). IEEE,* pp. 17-24. China;
[9] Jiang C.; Fu J.; Liu W. (2021). Research on vehicle routing planning based on adaptive ant colony and particle swarm optimization algorithm. *International Journal of Intelligent Transportation Systems Research,* Vol. 19, Issue 1, pp. 83-91. Germany;
[10] Kangkang M., Lei W., Jingcao C. (2023). Robot path planning using fusion algorithm of ant colony optimization and genetic algorithm. *International Journal of Modeling, Simulation, and Scientific Computing,* 2341032. China;
[11] Lee Y., Yinman M. (2020). Adaptive interference suppression of phase-only thinned arrays via convex optimization. *IEEE Transactions on Antennas and Propagation*, Vol. 68, Issue 6, pp. 4583–4592. United States;
[12] Li S. Y, Huang N. (2019). High precision control simulation of spherical fruit picking robot. *Computer Simulation,* Vol. 36, Issue 10, pp. 302–306. China;
[13] Luo L. F., Zou X. J., Cheng T. C., Yang Z. (2017). Design of virtual test system based on hardware-in-loop for picking robot vision localization and behavior control. *Transactions of the Chinese Society of Agricultural Engineering,* vol. 33, Issue 4, pp. 39–46. China;
[14] Mahi Ö. K. M., Kodaz H. (2015). A new hybrid method based on particle swarm optimization, ant colony optimization and 3-opt algorithms for traveling salesman problem. *Applied Soft Computing,* Vol. 30, pp. 484–490. Netherlands;
[15] Mas A., Mori U., Sinapayen L., Maruyama N. (2020). Neural autopoiesis: organizing self-boundary by stimulus avoidance in biological and artificial neural networks. Artificial Life, Vol. 2020, Issue 4871, pp. 1–22. United States;
[16] Mohanasundaram S., Ramirez-Asis E., Quispe-Talla A., Bhatt M.W., Shabaz M., (2021) “Experimental replacement of hops by mango in beer: production and comparison of total phenolics, flavonoids, minerals, carbohydrates, proteins, and toxic substances”, *International Journal of System Assurance Engineering and Management*, vol. 13, France;
[17] Mousavi S.M., Imani S., Dorranian D., Larijani K., Shojaee M., (2017) “Effect of cold plasma on degradation of organophosphorus pesticides used on some agricultural products”, *Journal of Plant Protection Research*, vol. 57, pp. 25-35, Iran;
[18] Paull M. L., Seto J. J., Leonard, and Li H. (2018). Probabilistic cooperative mobile robot area coverage and its application to autonomous seabed mapping. *The International Journal of Robotics Research,* Vol. 37, Issue 1, pp. 21–45. England;
[19] Perveen K., Sanjay Kumar, Sahil Kansal, Mukesh Soni, Najla A. Alshaikh, Shanzeh Batool, Mehrun Nisha Khanam, Bernard Osei, (2023) "Multidimensional Attention-Based CNN Model for Identifying Apple Leaf Disease", Journal of Food Quality, vol. 2023, 1-12, Netherlands;
[20] Ratta P., Kaur A., Sharma S., Shabaz M., Dhiman G., “Application of Blockchain and Internet of Things in healthcare and medical sector: applications, challenges, and future perspectives”, Journal of Food Quality, vol. 2021, 1-20, 2021.Italy;
[21] Sarangapani C., Misra N.N., Milosavljevic V., Bourke P., Regan F.O’, Cullen P.J., (2016) “Pesticide degradation in water using atmospheric air cold plasma”, *Journal of Water Process Engineering*, vol. 9, pp.225-232, India;
[22] Satyam P., Satyam P., Ajay A., Davood K. (2021). Fuzzy tuned PID controller for envisioned agricultural manipulator. *International Journal of Automation and Computing*, Vol. 18, Issue 4, pp. 568–580. England;
[23] Swetha K., Venkataraman V., Sadhana G.D., Priyatharshini R., (2016) “Hybrid approach for anthracnose detection using intensity and size features”, in Proceedings of the 2016 *IEEE*

Technological Innovations in ICT for Agriculture and Rural Development (TIAR), pp. 28-32, Chennai, India;

[24] Tang Y., Chen M., Wang C. (2020). Recognition and localization methods for vision-based fruit picking robots: a review. *Frontiers of Plant Science,* Vol. 11, p. 510. Switzerland;

[25] Wei J., Liu G., Zhang Y. (2010). Particle swarm optimization based on simulated annealing for solving constrained optimization problems. *Systems Engineering and Electronics,* Vol. 32, Issue 7, pp. 1532–1536. China;

[26] Xiaoming Y., Sheng L., Jinqiu L., (2017). An ant colony algorithm with dynamic search strategy and its application in robot path planning. *Control and decision-making,* Vol. 32, Issue 3, pp. 552-556. China;

[27] Xiaoqiang S., Zhichao L., Xuan Z. (2019). Research on robot path planning based on improved adaptive ant colony algorithm, *2019 Chinese Control and Decision Conference (CCDC). IEEE,* pp. 506-510. China.

PATH PLANNING OF FRUIT AND VEGETABLE PICKING ROBOTS BASED ON IMPROVED A* ALGORITHM AND PARTICLE SWARM OPTIMIZATION ALGORITHM
/
基于改进 A*算法与粒子群算法的果蔬采摘机器人路径规划

Chen LI *
School of Applied Technology, Zhumadian Preschool Education College, Zhumadian, Henan, China
*E-mail: chenli6780@126.com
Corresponding author: Li Chen
DOI: https://doi.org/10.35633/inmateh-71-41

Keywords: agricultural robot, fruit and vegetable picking, path planning, A* algorithm, particle swarm optimization

ABSTRACT
Aiming at the suboptimal local path, slow convergence speed, and many inflection points in the path planning of fruit and vegetable picking robots in complex environments, a global planning method combining particle swarm optimization (PSO) algorithm and A algorithm was proposed. Firstly, Manhattan distance was taken as a heuristic function of global programming based on the A* algorithm. Secondly, the step size of PSO was adjusted to optimize the path, shorten the path length, and reduce the number of inflection points. Finally, the planned path of the fruit and vegetable picking robot was smoothed so that it could steadily move along a smoother driving path in real scenarios. The experimental results show that compared with the traditional PSO algorithm, the hybrid algorithm based on the improved A* algorithm and PSO algorithm achieves a smoother path and fewer folding points. In comparison with the PSO algorithm, moreover, this algorithm can guarantee the path generation efficiency and the global optimum. In the end, the effectiveness of the proposed method was verified by shortening the path length and reducing the accumulative number of inflection points.*

摘要
*针对复杂环境下果蔬采摘机器人路径规划中存在的局部路径次优、收敛速度慢、拐点多等问题，提出了一种基于粒子群优化算法和 A*算法相结合的全局规划方法。首先，基于 A*算法，将曼哈顿距离作为全局规划的启发式函数。其次，通过调整粒子群算法的步长来优化路径，缩短路径长度，减少拐点数量。最后，对果蔬采摘机器人规划路径进行平滑处理，使机器人能够在真实场景中平稳移动，使采摘机器人行驶路径更加平滑。实验结果表明，与传统的粒子群优化算法相比，基于改进 A*算法和粒子群算法的混合算法具有更平滑的路径和更少的折叠点。与粒子群优化算法相比，该算法能够保证生成路径的效率和全局最优性。通过缩短路径长度和减少累积拐点数量，验证了该方法的有效性。*

INTRODUCTION
With the development of machinery manufacturing industry in China, the popularization rate of agricultural machinery and fruit and vegetable machinery has gradually increased in recent years, accompanied by the elevated specialization level. Restricted by various factors, however, the automation degree of fruit and vegetable picking operations is very low, and a large quantity of manpower needs to be mobilized to collectively pick fruits and vegetables using picking tools like ladders, baskets, and scissors. Other picking methods have also been tried, e.g., picking the whole spurs of fruits and vegetables with long-handled garden shears or pulling down fruits and vegetables by rotating long-handled rubber claws, and even shaking fruits on the fruit tree in outdoor fruit and vegetable planting areas with the help of large-scale team and focusing on picking fruits falling to the ground. Meanwhile, picking robots have also been actively investigated by universities and research institutions in China *(Wang et al., 2012)*. Nevertheless, most of the current scientific picking methods fail to catch up with the flexibility and completeness of artificial picking in the current stage, so the actual popularization degree of intelligent fruit and vegetable picking remains to be improved.

Agriculture is one of the best scenarios for artificial intelligence to be put into practice. As an emerging field characterized by the deep integration of information technology and agriculture, intelligent agriculture has become an inevitable development trend through the organic combination of artificial intelligence and agriculture.

At present, picking environments have become complicated and diversified due to factors like the overlapping of fruit spurs in fruit trees, and the intelligence, automation, and mechanization levels of fruit and vegetable picking are relatively low *(Xu et al., 2014)*. Obstacles such as naturally growing branches and immature fruits bring difficulties to the picking path control design of picking equipment *(Gao et al., 2014)*. In order to improve the intelligence level of fruit and vegetable picking, liberate manpower, and improve the harvest quality and mechanization level, it is also necessary to improve the intelligent decision-making level of fruit and vegetable picking robots' dynamic trajectory planning in unstructured natural environments in addition to strengthening the standardized management of agronomy in the process of fruit tree planting *(Ji et al., 2011)*. Path planning is one of the most basic links for picking robots to realize autonomous navigation. It means that in the picking working environment with obstacles, the picking robot senses the picking environment by using the sensor device it carries, so as to continuously obtain information such as the size, position, distance, and obstacles of the working area to be picked. The parameters for picking robots to search for the optimal path should be planned, including the shortest, the safest, and collision-free path *(Liu et al., 2010)*. According to the understanding of the environment where the picking robot is located, path planning can be divided into two categories: global path planning with all the environment known and local path planning with environmental information partially known or unknown. The working environment of picking robots is generally known, so intelligent algorithms can be introduced to effectively improve the path planning efficiency of picking robots through the global-coverage path planning method.

STATE OF THE ART

In recent years, picking robots have attracted worldwide attention, and many research institutions and universities have successively carried out related research and development work, including mechanical structure design, visual system development, and intelligent algorithm research, and made some progress *(Grau et al., 2015)*. Satyam et al. designed a fruit and vegetable picking robot with seven degrees of freedom, which has accurate positioning ability with the picking success rate exceeding 80% *(Paul et al., 2021)*. Li et al. developed a fruit and vegetable picking robot, which acquired the contour of fruits and vegetables combining K-means clustering segmentation with Canny edge detection method, and then used the minimum circle wrapping method to extract the centre coordinates of fruits and vegetables. Finally, the spatial trajectory of the picking robot arm was drawn according to the quintic polynomial interpolation law to realize fruit and vegetable grabbing *(Li et al., 2019)*. Path planning is one of the key technologies of fruit and vegetable picking robots, which is mainly divided into global path planning based on known map environment and local path planning based on sensor information *(Orozco-Rosas et al., 2022)*. Global path planning mainly includes finding a path that connects the starting point and the target point while avoiding collision with obstacles. Therein, the path length, algorithm time, and spatial complexity are the main indexes to judge the performance of global path planning algorithms *(Tian et al., 2021)*. Commonly used global path planning algorithms are A* algorithm *(Chen et al., 2020)*, RRT algorithm *(Qureshi et al., 2021)*, and genetic algorithm (GA) *(Su et al., 2016)*. Among them, the RRT algorithm proposed by Sun et al. has complete probability, simple structure, and flexible search ability, making it suitable for path planning in various complex environments. Due to its random sampling mechanism, however, the RRT algorithm is subjected to such problems as low node utilization rate, high path complexity, and slow convergence *(Sun et al., 2019)*.

Local path planning focuses on the safety and real-time performance of the path, and the typical local path planning algorithms include A* algorithm *(Li et al., 2019)*, artificial potential field method *(Orozco-Rosas et al., 2019)*, and particle swarm optimization (PSO) algorithm *(Cao et al., 2019)*. In recent years, with the progress of sensor technology, scholars have made relevant research on path planning of agricultural robots based on machine vision *(Mondal et al., 2021)* or Lidar *(Ma et al., 2022)*. Wu et al. obtained crop row information from the camera, eliminated outliers based on the random sample consistency (RANSAC) algorithm, and extracted navigation paths using the least square method (LSM). The path detection rate can reach more than 90% *(Wu et al., 2020)*. Peng et al. improved the robustness and applicability of crop row extraction based on the automatic Hough transform-cumulative threshold method. Lidar sensors can accurately obtain environmental distance information along with strong anti-interference ability *(Peng et al., 2021)*. Meng et al. obtained the position of fruit trees using a laser scanner and planned the navigation path of agricultural machinery via LSM *(Meng et al., 2022)*. Ping et al. used two-dimensional Lidar to obtain the point clouds of vineyards, and proposed a vineyard path planning algorithm based on Support Vector Machine *(Ping et al., 2017)*.

Masumori et al. used 16-line Lidar to obtain three-dimensional point cloud information of maize, introduced confidence interval and K-means algorithm to cluster maize plants, and finally used the radial basis function path planning method to avoid plant trunks as much as possible.

The existing research mostly focuses on single plant or crop row detection, and the planned path is straight, which is convenient for robot control but not conducive to avoiding obstacles such as tree crowns and pedestrians between rows *(Masumori et al., 2020)*.

To sum up, the irregular crowns of fruit trees constitute one of the hidden dangers impeding the robot when doing fruit and vegetable picking operations. The traditional orchard planning paths are mostly straight lines, which is not conducive to avoiding obstacles such as crowns. In this study, taking fruit and vegetable picking as the research object, an improved artificial potential field method was proposed to optimize the robot navigation path between rows, specifically as follows: The A* algorithm was used to extract the ridge line and initial path, while the crowns of fruit trees and pedestrians were regarded as obstacles. Then, the initial path was optimized combining the PSO algorithm. Finally, a safe and reliable driving path for the picking robot was planned, expecting to provide technical reference for the picking path planning of mobile picking robots in orchards.

MATERIALS AND METHODS

Problem description

In an orchard, several fruit and vegetable picking robots were equipped to perform fruit and vegetable picking operations. In this study, the picking path of fruit and vegetable picking robots was studied, and the layout of the orchard is shown in Fig. 1. It is assumed that the fruit and vegetable picking robots could move vertically and horizontally in the orchard, which consisted of fruit trees, ridges, fruit and vegetable picking robots, and I/O starting points, where the I/O starting points were the starting and ending positions of the fruit and vegetable picking robots. It is assumed that the length of a single fruit tree in the orchard in the X direction is l, the width in the Y direction is w, the height is h, the ridge width is C, and the I/O starting point is rightly opposite to the first ridge. The orchard layout plan structure is as shown in Fig. 1.

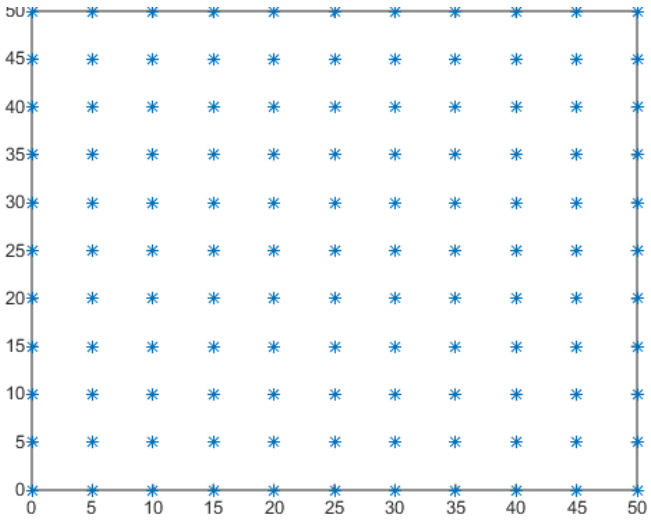


Fig. 1 - Orchard Layout Plan

In order to facilitate observation and calculation, every fruit tree in the orchard was arranged and distributed in the form of a grid. It is assumed that the system receives n orders in total, and the storage information of fruits and vegetables in each order is known. The maximum carrying weight of the fruit and vegetable picking robots is M, and the number of self-carried goods is Q, that is, the fruit and vegetable picking robots can carry at most Q fruits and vegetables in a single trip. On the premise that the fruit and vegetable picking robots met the double constraints of carrying capacity and container number, all the fruits and vegetables to be picked in the order were picked in batches, and the picking time of each batch was added. The optimization goal was to obtain the picking path with the least total time after addition.

Basic assumptions

Before establishing the mathematical model for picking path planning of fruit and vegetable robots, the following assumptions and parameters were set for fruit and vegetable picking robots and shelves:

(1) Each picking unit (Unit) in a picking task list of a picking robot corresponds to each fruit tree in the orchard;

(2) The number of Units in each fruit tree meets the number of orders selected;

(3) When the fruit and vegetable picking robot performs a certain action, it cannot perform other actions at the same time, and it will not interrupt the current action due to other factors, thus ensuring the continuity of picking operations;

(4) When starting to perform the picking task, the fruit and vegetable picking robot starts from the I/O starting point and needs to return to the I/O point after completing the picking task or reaching the constraint conditions;

(5) When the fruit and vegetable picking robot moves from one fruit tree to another, it needs to go through acceleration, uniform velocity, and deceleration stages. Assuming that the acceleration and decelerations of its horizontal movement are both under no-load and loaded conditions, the vertical velocity of the lifting platform in the vertical direction is the same as the falling velocity, which is set as v2.

Modelling

The path planning model for batched picking of fruit and vegetable picking robots was established as follows. Firstly, the symbols appearing in the optimization model are explained: *O* stands for the order set; S represents a set of fruit trees; B={0,1,2,.....,n} represents the set of picking points, where 0 is the starting point (sorting table); (x_i,y_i,z_i,m_i) presents the information on the Units to be picked on the order *O*, for example, (5,6,2,1) indicates the fruit trees of one Unit in Columns 5 and 6 in the orchard, with the height of 2 m and number of 1.

The picking time of fruit and vegetable picking robots for a complete order consists of 3 periods:

① the horizontal moving time between picking points, that is, the time T_1 required to move on the xoy surface;

② In the z-axis direction, the sum of the time needed by the lifting platform to rise and fall is T_2;

③ The picking and unloading time for Unit by fruit and vegetable picking robots is fixed, and the total time is T_3. The order picking time of fruit and vegetable picking robots is expressed as:

$$T=T_1+T_2+T_3 \tag{1}$$

Assuming that the horizontal moving distance of the picking robot is r_{ijs}.

To facilitate the path planning of picking robots, their horizontal trajectory r_{ijs} is divided into 3 stages:

(1) The horizontal distance from the I/O starting point to the first fruit and vegetable picking point *j*.

$$r_{ijs}=\begin{cases}(x_j-2)\times 1+(\dfrac{x_j-2}{2})\times c+y_j\times w, x_i \text{ is the starting point, } x_j\neq 1 \text{ or } 2, \text{and it's even}\\ (x_j-1)\times 1+(\dfrac{x_j-1}{2})\times c+y_j\times w, x_i \text{ is the starting point, } x_j\neq 1 \text{ or } 2, \text{and an odd number}\\ y_j\times w, x_i \text{ is the starting point, } x_j=1 \text{ or } 2\end{cases} \tag{2}$$

where both x_i and x_j represent the column positions of the picking point.

(2) The horizontal distance from the current fruit and vegetable picking point *i* to the fruit and vegetable picking point *j* to be picked, which is divided into two circumstances. When the fruit and vegetable picking points *i* and *j* are located at different ridges, namely, $x_i \neq x_j$. If the total numbers of rows at points *i* and *j* is smaller than *f*, the robot will choose to move out from the next ridge. Therein, *f* represents the number of rows of a single-column shelf in the y-axis direction.

$$r_{ijs}=\begin{cases}2l+c+(y_i+y_j)\times w, x_j-x_i=1, x_j \text{ is even}, y_i+y_j \le f\\ (x_j-x_i-1)\times l+(\frac{x_j-x_i-1}{2})\times c+(y_i+y_j)\times w, x_j-x_i>1, x_j \text{ is odd number}, y_i+y_j \le f\\ (x_j-x_i+1)\times l+(\frac{x_j-x_i+1}{2})\times c+(y_i+y_j)\times w, x_j-x_i>1, \text{odd number}, x_j \text{ is even}, y_i+y_j \le f\\ (x_j-x_i)\times l+(\frac{x_j-x_i}{2})\times c+(y_i+y_j)\times w, x_j-x_i>1, \text{it's even}, y_i+y_j \le f\end{cases} \quad (3)$$

If the total number of rows at points i and j is greater than f, the robot will move out from the last ridge.

$$r_{ijs}=\begin{cases}2l+c+(2f-y_i-y_j)\times w, x_j-x_i=1, x_j \text{ is even}, y_i+y_j>f\\ (x_j-x_i-1)\times l+(\frac{x_j-x_i-1}{2})\times c+(2f-y_i-y_j)\times w, x_j-x_i>1, \text{odd number}, x_j \text{ is odd number}, y_i+y_j>f\\ (x_j-x_i+1)\times l+(\frac{x_j-x_i+1}{2})\times c+(2f-y_i-y_j)\times w, x_j-x_i>1, \text{odd number}, x_j \text{ is even}, y_i+y_j>f\\ (x_j-x_i)\times l+(\frac{x_j-x_i}{2})\times c+(2f-y_i-y_j)\times w, \ x_j-x_i>1, \text{even}, y_i+y_j>f\end{cases} \quad (4)$$

Vegetable picking points i and j are in the same ridge.

(3) The horizontal distance from the last shelf picking point sorted by the picking robot in a single trip to the I/O starting point.

$$r_{ijs}=\begin{cases}(x_i-1)\times l+\frac{(x_i-1)}{2}\times c+y_i\times w, x_i \ne 0 \text{ and an odd number}, x_i=0\\ x_i\times l+\frac{x_i}{2}\times c+y_i\times w, x_i \ne 0 \text{ and it's even}, x_j=0\end{cases} \quad (5)$$

Assuming that the picking robot moves under the fruit and vegetable to the picked, the vertical moving distance of the lifting platform is d_1, expressed as follows:

$$d_1=\left|z_j-z_i\right|\times h \quad (6)$$

where z_i is the location of fruit and vegetable i; z_j is the location of fruit and vegetable j. The time T_1 of the picking robot in the horizontal direction depends on the maximum velocity and acceleration when moving. Assuming that the maximum velocity that the picking robot can reach when moving horizontally is v_1, it can be divided into two motion states: first, the velocity of the picking robot does not reach the maximum velocity v_1 during the movement on *xoy* plane, and then it makes uniform deceleration motion after uniform acceleration, that is, the moving distance of the picking robot is $s<\frac{v_1^2}{a}$; second, the velocity of the picking robot reaches the maximum velocity v_1 during the movement on *xoy* plane, and it moves at a uniform velocity later and then moves at a uniform deceleration, that is, the moving distance is $s<\frac{v_1^2}{a}$.

The driving time of the picking robot for the n^{th} time is calculated according to the horizontal moving distance r_{ijs} and whether the maximum velocity is reached, as below:

$$T_{1n}=\begin{cases}\left(\frac{r_{ijs}}{a}\right)^{\frac{1}{2}}, r_{ijs}<\frac{v_1^2}{a}\\ \frac{2v_1}{a}+\frac{r_{ijs}-\frac{v_1^2}{a}}{v_1}, r_{ijs}\geqslant\frac{v_1^2}{a}\end{cases} \quad (7)$$

The vertical rising and falling time of the picking robot's mechanical arm for the n^{th} time is T_{2n}, expressed as follows:

$$T_{2n}=d_{1n}/v_2 \quad (8)$$

Assuming that the loading time and unloading time spent by the picking robot when picking a single piece of fruit and vegetable are identical, being *s*, then the loading and uploading time spent by the picking robot in completing the picking of one batch of fruits and vegetables is:

$$T_3 = n \times s \tag{9}$$

According to the above description, the model for the picking robot's picking operation time can be expressed as below:

$$T_{min} = \sum_{n=1}^{n} \sum_{i=1}^{n} \sum_{j \neq i}^{n} (T_{1n} + T_{2n}) \times K_{ij} + T_3 \tag{10}$$

The constraint conditions are displayed as follows:

$$\sum_{i=1}^{Q} m_i \leqslant M, \ i=1,2,L,Q \tag{11}$$

$$q < Q \tag{12}$$

$$\sum_{i=1}^{n} \sum_{j \neq i}^{n} b_{ij} = n, b \in B; i=1,2,L,n; \ j=1,2,L,n \tag{13}$$

$$K_{ij} = \begin{cases} 1, \text{the selection point } i \text{ is selected, and then the} \\ \text{selection } j \text{ operation is carried out}, i, \ j=1,2,L,n \\ 0, \text{other} \end{cases} \tag{14}$$

$$m_j = m_i \times K_{ij} + 1 \tag{15}$$

$$\sum_{m} X_O^m = \sum_{m} X_{m+1}^O = X_O \tag{16}$$

Where:

Equation (10) indicates the optimization indexes for picking time; Equation (11) means that the weight of fruits and vegetables picked by the picking robot in a single trip cannot exceed *m*, or otherwise, it needs to return to the starting point first and upload for the next picking operation; Equation (12) represents the maximum number of grids of the picking robot, i.e., at most *Q* units can be accommodated in a single trip; Equation (13) reflects that all fruits and vegetables displayed in the order will be picked; Equations (14) and (15) represent the picking sequence of Units, and the continuity of the picking robot when picking a Unit is guaranteed; in Equation (16), X_O^m indicates that the picking robot returns to the starting point after Units are full loaded in the *m*-th trip or the weight reaches the upper limit, and X_{m+1}^O means that the picking robot starts from the starting point to pick up fruits and vegetables with empty load in the m+1-th trip, namely, the final full-loading position in the *m* -th trip equals the starting position in the *m* +1-th trip.

A* algorithm

The A* algorithm, a heuristic search method with high search efficiency, can solve the shortest and most effective path in static environments. In A*, the weight of each path is the sum of two costs, namely, the cost from the starting node to the current node and the heuristic distance. Searching in 8 directions from the starting point, the values of extension nodes are acquired using an evaluation function for comparisons, the minimum value is chosen as the next extension node, and this process is circulated until the end of the search, thus obtaining the final path. Since the node with the minimum estimated value is used as the next extension node in each search, the final cost is the lowest. The evaluation function is shown in Eq. (17):

$$f(n) = g(n) + h(n) \tag{17}$$

In Equation (17), $f(n)$ is the valuation function of node *n*; $g(n)$ represents the actual cost from the starting node to node *n*; $h(n)$ represents the estimated cost from node *n* to the ending node. The determination of the valuation function is closely related to the actual situation and will directly affect the result of the A* algorithm. Therefore, Manhattan distance is used as a heuristic function:

$$h(n) = |x_d - x_n| + |y_d - y_n| \tag{18}$$

In Equation (18), x_d is the x-coordinate of the target point; y_d represents the y-coordinate of the target point; x_n is the x-coordinate of node *n*; y_n is the y-coordinate of node *n*.

PSO algorithm

The idea of PSO comes from the study on birds' foraging behaviour, and birds can find the best destination through collective information sharing. The advantages of PSO mainly lie in its fast convergence speed, few parameters, simple algorithm, and easy implementation. Especially for high-dimensional optimization problems, it converges to the optimal solution faster and more efficiently than GA, but PSO can easily fall into a local optimal solution. In order to solve the above problems, therefore, an improved PSO algorithm was proposed in this study to solve the problem without affecting the search speed. The local and global particle search capability was enhanced. This algorithm is more conducive to solving the path planning problem of robots.

Steps of the hybrid algorithm

The basic A* algorithm uses a heuristic evaluation function to search, which is efficient and can realize the shortest path between two points. However, when the operation scene is large, the temporal and spatial complexity of the search increase exponentially. Therefore, the integrated longicorn search algorithm must be used for global path planning, which can not only realize local planning but also be suitable for large-scale environment. The concrete steps of the improved A* algorithm and PSO to realize robot path planning are as follows:

(1) A model diagram is constructed. Obstacles are randomly distributed according to the obstacle rate, the open list and close list are defined, to which initial values are assigned, and starting nodes are put into the lists.

(2) Real number encoding is adopted for particle swarm initialization. A particle swarm consisting of n particles is defined, followed by spatial search in the raster map. Particles have position attribute x and velocity attribute v, and a fitness function is defined as the optimization objective of path planning. The position of the i-th particle at time t is expressed as follows:

$$x_t^i=(x_t^{i1},x_t^{i2},L,x_t^{iD}) \quad i=1,2,L,n \tag{19}$$

The velocity of the i-th particle at time t is:

$$v_t^i=(v_t^{i1},v_t^{i2},L,v_t^{iD}) \quad i=1,2,L,n \tag{20}$$

where t represents the current number of iterations and D denotes the number of key points searched.

In this study, the path was mainly composed of searched key points connected with line segments, so Euclidean distance was selected as the fitness function of the algorithm, but there were obstacles in the map. The obstacles that the path passed through were taken as regular terms to realize obstacle-free path planning:

$$fit(x)=\sum_{i=1}^{D}\sqrt{(x_i-x_{i-1})^2+(y_i-y_{i-1})^2}+\lambda\times T \quad i=1,2,L,D \tag{21}$$

where x and y represent the grid positions corresponding to the real number codes of key points; λ is a penalty factor; T refers to the number of obstacles passed through by the current path.

(3) According to the environment selection strategy designed in this study, the particle swarm was divided into two categories: the selection, crossover, and mutation operators of GA* algorithm were embedded into the first category; the chemotactic operation of the BFO algorithm was embedded into the other category, and the parallel training comprehensively strengthened the local optimization ability of the particle swarm. The specific implementation of the environmental strategy is as follows: because the population updating mode in GA follows Darwin's evolution theory of natural selection, each population evolution is guided by the environment. The updating method of the bacterial foraging algorithm is to imitate the swimming, tumbling, staying, and other movement modes of individual bacteria when looking for food, and the movement of each step is controlled by the current nutritional gradient. When the two algorithms are used to solve the same target problem, because the update strategy is affected by different environments, the environment selected by the target individual is also different. Under the same environment, some potential individuals will be lost and the possibility of optimal solution will be reduced. In this study, the environmental coefficient Y_1 of GA and the environmental coefficient Y_2 of the bacterial foraging algorithm was calculated respectively. In GA, the population will be so affected by the environment s to produce selection, crossover, and mutation. In the bacterial foraging algorithm, the population is affected by the nutritional gradient.

Therefore, the Equations of Y_1 and Y_2 can be expressed as:

$$Y_1(x,i)=\sum_{i=1}^{n} mutate_{\beta} \times select_{\alpha}\left(\sum_{m=1}^{D} x_m\right)+cross_{\delta}(1\text{-}select_{\alpha})\times\left(\sum_{m=1}^{D} x_m\right) \tag{22}$$

$$Y_2(x,i)=\sum_{i=1}^{n}\left[-d_{atact}exp\left(-w_{atact}\sum_{m=1}^{D}(x_m-x_{im})^2\right)\right]+\sum_{i=1}^{n}\left[d_{repellant}exp(-w_{repellant}\sum_{m=1}^{D}(x_m-x_{im})^2\right] \tag{23}$$

In Equation (4), $mutate_{\beta}$, $select_{\alpha}$, and $cross_{\delta}$ represent the mutation, selection, and crossover probabilities of particles in GA, respectively. In Equation (23), d_{atact}, $d_{repellant}$, w_{atact}, and $w_{repellant}$ denotes the stress factors between individuals in the bacterial foraging algorithm, being the m-th element of the position attribute of the i-th particle. After the environmental coefficients of different algorithms are determined, the correlation between target individuals and different environments is solved through the Pearson correlation Equation, and individuals are subjected to optimization training according to associated environments selected. The calculation Equation for the individual environmental selection is:

$$\rho_{x,Y}=\frac{E((x-\mu_x)(Y-\mu_Y))}{\sigma_x\sigma_y} \tag{24}$$

Where μ_x and μ_Y represent the mean values of x and y, respectively; σ_x and σ_y denote the standard deviations of x and y, respectively. After the selection of the environmental strategy, the two kinds of particles are respectively subjected to selection, crossover, mutation of GA and chemotaxis of BFO. Among them, the selection, crossover, and mutation operations produce new particles as follows:

$$x_{t+1}^{i}=\eta x_t^j+(1-\eta)x_t^i;\ i,j=1,2,L,n,\ i\neq j \tag{25}$$

$$x_{t+1}^{j}=\eta x_t^i+(1-\eta)x_t^j;\ i,j=1,2,L,n,\ i\neq j \tag{26}$$

The new particles generated by the chemotactic operation are as follows:

$$x_{t+1}^{i}=x_t^i+C(i)\times\Phi(i)\quad i=1,2,L,n \tag{27}$$

where $C(i)>0$ represents the swimming step of forward particles; $\Phi(i)$ denotes a unit direction vector randomly selected after rotation.

(4) The two parallel particle swarm branches are fused to judge whether the optimal solution of the current particle swarm meets the set target threshold. If not, the update Equation of the improved PSO algorithm is executed. In this study, corresponding improvements were made according to the update Equation of the basic PSO algorithm. After the parallel optimization of GA and bacterial foraging algorithm, the mixed particle swarm reaches two global optimums. To integrate the optimization ability of the two algorithms, the two global optimal parameters were both introduced into the update Equation of particles, the updating of particles would be affected by G_{GA_best}, G_{BFO_best}, and P_{best}, and the improved update Equation of the PSO algorithm is as follows:

$$v_{t+1}^{i}=\omega\times v_t^i+c_1\times random(0,1)\times(P_{best\,t}^{i}-x_t^i)+c_2\times random(0,1)\times(G_{GA_best\,t}^{i}-x_t^i)+ c_3\times random(0,1)\times(G_{BFO_best\,t}^{i}-x_t^i) \tag{28}$$

$$x_{t+1}^{i}=x_t^i+v_{t+1}^i \tag{29}$$

where ω is the inertia weight, which decides the influence of historical velocity on the current velocity; c_1, c_2, and c_3 are learning factors; G_{GA_best} represents the global historical optimal solution obtained by genetic optimization in the hybrid particle swarm; G_{BFO_best} stands for the global historical optimal solution obtained by bacterial foraging optimization in the hybrid particle swarm; P_{best} is the historical optimal value of single particles in the search process. After particle swarm updating is completed, whether the optimal fitness function value of the particle swarm meets the set target threshold is judged again. If yes, the algorithm is ended; if not, Steps (2)-(5) are executed once again.

RESULTS

In this study, the number of picking points of fruit and vegetable picking robots in the orchard was assumed to be 40, and their position was represented by the corresponding *X*-coordinate and *Y*-coordinate values. The traveling speed of the fruit and vegetable picking robots was known, and the coordinates and picking quantity of 40 inspection points are shown in Table 1.

Table 1

Coordinates and picking quantity of picking points

Picking point	Coordinate (*X*)	Coordinate (*Y*)	Picking quantity (units)	Picking point (units)	Coordinate (*X*)	Coordinate (*Y*)	Picking quantity (units)
1	5	0	1	21	30	30	2
2	15	10	3	22	30	40	3
3	0	10	1	23	30	50	3
4	0	15	2	24	35	25	3
5	5	20	2	25	35	30	3
6	5	30	1	26	40	20	2
7	5	40	2	27	40	5	3
8	10	45	1	28	40	10	3
9	10	5	3	29	40	25	1
10	10	15	3	30	40	30	1
11	15	5	2	31	40	35	3
12	15	15	3	32	40	40	3
13	20	35	2	33	40	45	3
14	20	5	1	34	40	50	2
15	25	25	1	35	45	30	1
16	25	30	3	36	45	5	2
17	25	35	3	37	45	50	1
18	25	40	3	38	35	15	3
19	25	45	3	39	35	45	3
20	15	45	3	40	50	50	2

In this study, experiments were carried out on Intel i7 processor using Matlab2014a, and the optimization model of inspection path of agricultural robots was solved by the improved A* + PSO hybrid algorithm. The relevant parameters were set as follows: the number of particles was m=50; the inertia constant was w=0.5; the acceleration constant was c_1=c_2=c_3=2; the maximum flight velocity of particles generally did not exceed 10%-20% of the maximum velocity.

The path record table was Table=zeros (m, n); the maximum number of iterations was iter_max=100; the optimal path of each generation was Route_best=zeros(iter_max,n); the length of the best path of each generation was Length_ best =zeros (iter_max,1); the average path length of each generation was Length_ave= zeros(iter_ max,1). Simulation tests were carried out through the improved A* + PSO hybrid algorithm, respectively, and the corresponding calculation results were obtained.

In order to eliminate the influence of various random factors and verify the advantages and disadvantages of the improved A* + PSO hybrid algorithm designed in this study, the path optimization problem of fruit and vegetable picking robots was run 100 times by using the improved A* + PSO hybrid algorithm.

The convergence curve of the improved A* + PSO hybrid algorithm is shown in Fig. 2, and the optimal travel path of the agricultural inspection robots is shown in Fig. 3.

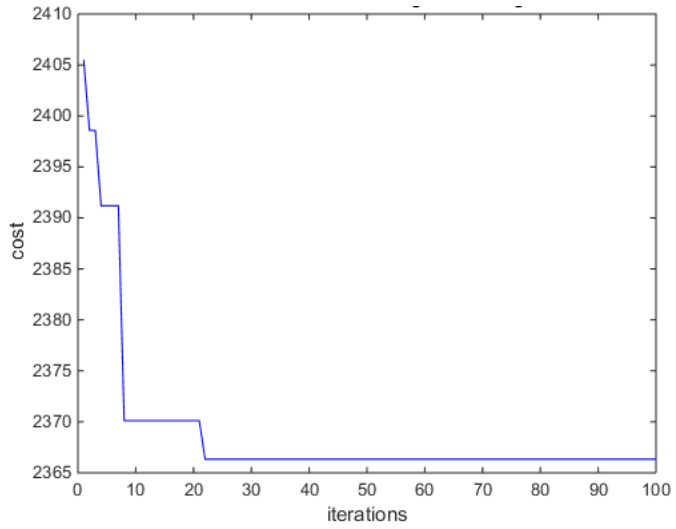


Fig. 2 - Convergence curve of improved algorithm and PSO algorithm

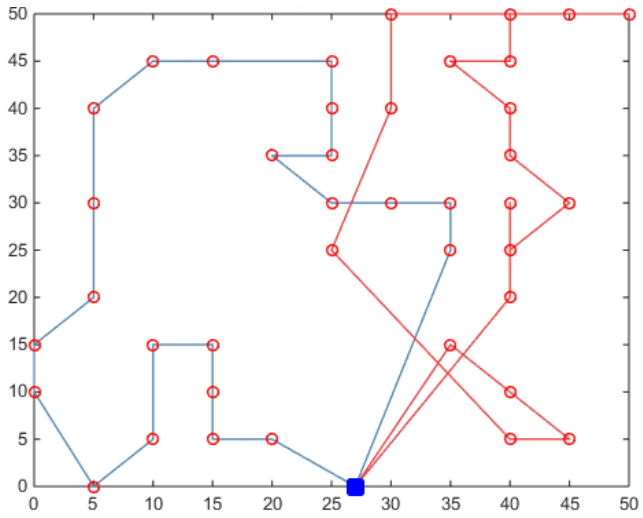


Fig. 3 - Optimal driving path of fruit and vegetable picking robots

In order to verify the effectiveness of the model and algorithm, the traditional PSO algorithm was used on the same platform, and the optimization model proposed in this study was solved with the same parameters. To achieve more scientific and effective experimental results, the maximum number of iterations of the traditional ant colony algorithm was also set to 100. The convergence curve of the traditional PSO algorithm is shown in Fig. 4, and the optimal path of fruit and vegetable picking robots is exhibited in Fig. 5.

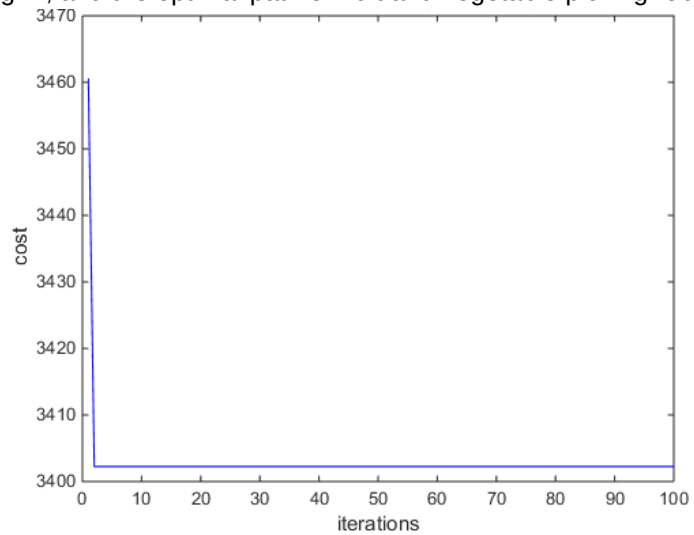


Fig. 4 - Convergence curve of the traditional PSO algorithm

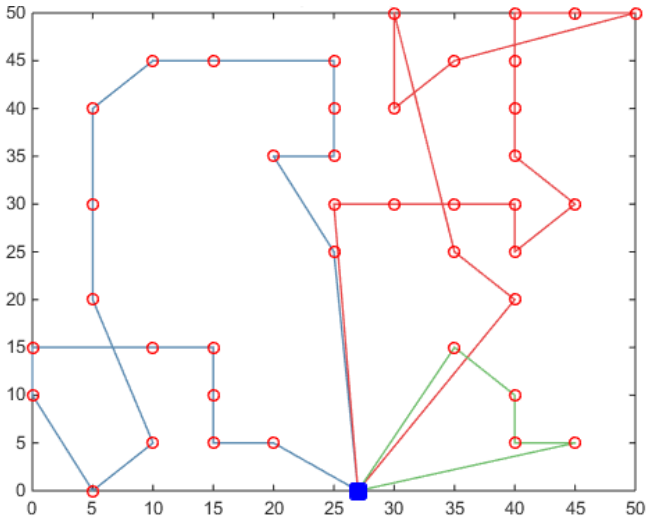


Fig. 5 - Optimal driving path of fruit and vegetable picking robots

The improved A* + PSO hybrid algorithm was compared with the traditional PSO algorithm in inspection path, total distance travelled by fruit and vegetable picking robots, and convergence time of the algorithm, and the comparison results are listed in Table 2.

Table 2

Comparison of improved A*+ PSO algorithm and traditional PSO algorithm

Algorithm	Inspection path	Robot	Distance (m)	Convergence time (s)	Total cost (yuan)
Improved A*+ PSO algorithm	0→14→11→2→12→10→9→1→3→4→5→6→7→8→20→19→18→17→13→16→21→25→24→0	2	366.34	100.17	2366
	0→26→30→29→35→31→32→39→33→34→40→37→23→22→15→27→36→28→38→0				
Traditional PSO algorithm	0→14→11→2→12→10→4→3→1→9→5→6→7→8→20→19→18→17→13→15→0	3	393.41	118.26	3402
	0→16→21→25→30→29→35→31→32→33→34→37→40→39→22→23→24→26→0				
	0→38→28→27→36→0				

It could be seen from Table 2 that the optimization ability and convergence of both A* algorithm and PSO algorithm were stronger than those of the traditional PSO algorithm. From the convergence curve of the algorithm, it could be intuitively seen that in terms of the driving distance of picking agricultural robots, the optimal path length obtained by the improved A* algorithm and particle swarm optimization algorithm was better than that obtained by the traditional ant colony algorithm. Compared with the traditional GA, the total inspection distance acquired through the improved ant colony algorithm was shortened by 27.07 m with a reduction rate of 6.88%. From the number of picking robots, the improved A* + PSO hybrid algorithm used 2 picking robots, while the PSO algorithm needed three; as for the convergence time, the traditional PSO algorithm spent longer convergence time than the improved A* + PSO hybrid algorithm. The convergence time of the improved A* + PSO hybrid algorithm was 18.09 seconds shorter (by 15.30%) than that of the traditional PSO algorithm.

CONCLUSIONS

In order to improve the efficiency of path planning and the accuracy of global coverage planning in the process of automatic navigation of picking robots, the improved A* + PSO hybrid path planning method was introduced into the path planning model of picking robots, and the efficiency of path planning was improved by optimizing the distance of path planning. The path planning algorithm of picking robots was simulated under the planting environment of large-scale plots.

Aiming at the multi-objective and batch picking path planning problem of picking robots in fruit and vegetable gardens, a three-dimensional path planning model that could pick Units in the order in turn was established by constructing three-dimensional spatial coordinates in this study and then solved by designing the improved A* + PSO hybrid algorithm. The experimental results show that, compared with other heuristic algorithms, the improved A* + PSO hybrid algorithm has a faster convergence speed under the same parameters, which can effectively prevent the algorithm from falling into the local optimum and get a solution with higher accuracy. In conclusion, the improved A* algorithm + PSO hybrid algorithm can effectively improve the path search accuracy of the PSO algorithm and then improve the efficiency of picking robots.

To sum up, the picking robot model and the improved A* + PSO hybrid algorithm constructed in this study reach a good fitting effect in fruit and vegetable picking, which can effectively improve the overall fruit and vegetable picking efficiency. In this study, however, only the order picking path planning under the single-instruction picking background of picking robots was investigated, that is, the picking robots started from the starting point, moved along the planned path to the row and column where the fruits and vegetables were to be picked, and returned to the starting point after picking the fruits and vegetables in batches. Therefore, the path planning of picking robots in multi-instruction operations will be deeply explored in the future.

REFERENCES

[1] Cao X., Zou X., Jia C., Chen M., Zeng Z. (2019), RRT-based path planning for an intelligent litchi-picking manipulator, *Computers and Electronics in Agriculture*, Vol. 156, ISSN 0168-1699, pp. 105-118, England;

[2] Chen M., Zhang H., Wang X., Li X. (2020), Design of apple picking robot based on iterative learning PID algorithm (基于迭代学习 PID 算法的苹果采摘机器人设计), *Journal of Agricultural Mechanization Research*, Vol. 42, no. 6, ISSN 1003-188X, pp. 83-86, China;

[3] Grau J., Grosse I., Keilwagen J. (2015), PRROC: computing and visualizing precision-recall and receiver operating characteristic curves in R, *Bioinformatics*, Vol. 31, no. 15, ISSN 1367-4803, pp. 2595-2597, England;

[4] Gao H., Wang H., Chen J. (2014), Research and design of kiwi fruit picking robots (猕猴桃采摘机器人的研究与设计), *Journal of Agricultural Mechanization Research*, Vol. 29, no. 2, ISSN 1003-188X, pp.75-79, China;

[5] Ji C., Feng Q., Yuan T., Tan Y., Li W. (2011), Development and performance analysis on cucumber harvesting robot system in greenhouse (温室黄瓜采摘机器人系统研制及性能分析), *Robot*, Vol. 33, no. 6, ISSN 1002-0446, pp. 726-730, China;

[6] Li S, Huang N. (2019), High precision control simulation of spherical fruit picking robot (球形水果采摘机械手的高精度控制仿真), *Computer Simulation*, Vol. 36, no. 10, ISSN 1006-9348, pp. 302-306, China;

[7] Liu J., Li P., Ni Q., Li Z. (2010), Design and test of the vacuum suction device for tomato harvesting robot (番茄采摘机器人真空吸盘装置设计与试验), *Transactions of the Chinese Society for Agricultural Machinery*, Vol. 41, no. 10, ISSN 1000-1298, pp. 170-173, 184, China;

[8] Meng B H., Godage I S., Kanj I. (2022), RRT∗-Based path planning for continuum arms, *IEEE Robotics and Automation Letters*, Vol. 7, no. 3, ISSN 2377-3766, pp. 6830–6837, United States;

[9] Mondal S C., Marquez P L C., Tokhi M O. (2021), Analysis of mechanical adhesion climbing robot design for wind tower inspection, *Journal of Artificial Intelligence and Technology*, Vol. 1, no. 4, ISSN 2766-8649, pp. 219-227, United States;

[10] Masumori A., Sinapayen L., Maruyama N., Mita T., Ikegami T. (2020), Neural autopoiesis: organizing self-boundary by stimulus avoidance in biological and artificial neural networks, *Artificial Life*, Vol. 2020, no. 4871, ISSN 1064-5462, pp. 1-22, United States;

[11] Ma N., Wang J., Meng Q H. (2022), Conditional generative adversarial networks for optimal path planning, *IEEE Transactions on Cognitive and Developmental Systems*, Vol. 14, no. 2, ISSN 2379-8920, pp. 662-671, United States;

[12] Orozco-Rosas U., Montiel O., Sepúlveda R. (2019), Mobile robot path planning using membrane evolutionary artificial potential field, *Applied Soft Computing*, Vol. 77, ISSN 1568-4946, pp. 236-251, Netherlands;

[13] Orozco-Rosas U., Picos K., Pantrigo J.J., Montemayor A.S., Cuesta-Infante A. (2022), Mobile robot path planning using a QAPF learning algorithm for known and unknown environments, *IEEE Access*, Vol. 10, ISSN 2169-3536, pp. 84648-84663, United States;
[14] Paul S., Arunachalam A., Khodadad D., Andreasson H., Rubanenko O. (2021), Fuzzy tuned PID controller for envisioned agricultural manipulator, *International Journal of Automation and Computing*. Vol. 18, no. 4, ISSN 2731-538X, pp. 568-580, China;
[15] Peng J., Gao X., Long H., Zhou C. (2021), A parameter measurement method for autonomous-rail rapid tram based on four-view stereo vision (基于四目立体视觉的智轨电车参数测量方法与系统), *Journal of Chongqing University*, Vol. 44, no. 4, ISSN 1000-582X, pp. 29-36, China;
[16] Ping X., Liu Y., Dong X., Zhao Y., Zhang Y. (2017), 3-D reconstruction of texture less and high-reflective target by polarization and binocular stereo vision (基于偏振双目视觉的无纹理高反光目标三维重构), *Journal of Infrared and Millimeter Waves*, Vol. 36, no. 4, ISSN 1001-9014, pp. 432-438, China;
[17] Qureshi A H., Miao Y., Simeonov A., Yip M C. (2021), Motion planning networks: bridging GAp between learning-based and classical motion planners, *IEEE Transactions on Robotics*, Vol. 37, no. 1, ISSN 1552-3098, pp. 48-66, United States;
[18] Sun J., Liu G., Tian G., Zhang J. (2019), Smart obstacle avoidance using a danger index for a dynamic environment, *Applied Sciences*, Vol. 9, no. 8, ISSN 1454-5101, pp. 1589, Romania;
[19] Su Y., Yang L., Song X. (2016), Design and experiment of intelligent mobile apple picking robot (智能移动苹果采摘机器人的设计及试验), *Journal of Agricultural Mechanization Research*, Vol. 2016, no. 1, ISSN 1003-188X, pp. 159-162, China;
[20] Tian Y., Zhu X., Meng D., Wang X., Liang B. (2021), An overall configuration planning method of continuum hyper-redundant manipulators based on improved artificial potential field method. *IEEE Robotics and Automation Letters*, Vol. 6, no. 3, ISSN 2377-3766, pp. 4867-4874. United States.
[21] Wang H., Mao W., Liu G., Hu X., Li S. (2012), Identification and location of fruit and vegetable robot based on visual combination (基于视觉组合的苹果作业机器人识别与定位), *Transactions of the Chinese Society for Agricultural Machinery*, Vol. 43, no. 12, ISSN 1000-1298, pp. 165-170, China;
[22] Wu K., Wang H., Esfahani M A., Yuan S. (2020), Achieving real-time path planning in unknown environments through deep neural networks, *IEEE Transactions on Intelligent Transportation Systems*, Vol. 23, no. 3, ISSN 1524-9050, pp. 1-10, United States;
[23] Xu M., Deng R. (2014), Comparison of domestic and foreign facilities in agricultural development (国内外设施农业发展的比较), *Journal of Beijing University of Agriculture*, Vol. 29, no. 2, ISSN 1002-3186, pp. 75-79, China.

AUTOMATED QUALITY ASSESSMENT OF APPLES USING CONVOLUTIONAL NEURAL NETWORKS
/
EVALUAREA AUTOMATĂ A CALITĂȚII MERELOR CU AJUTORUL REȚELELOR NEURONALE CONVOLUTIVE

Adrian IOSIF [1], Edmond MAICAN[1], Sorin BIRIȘ[1], Lucretia POPA[2]
[1] Faculty of Biotechnical Systems Engineering, U.N.S.T POLITEHNICA of Bucharest / Romania
[2] INMA Bucharest / Romania

E-mail: aiosif@yahoo.com
DOI: https://doi.org/10.35633/inmateh-71-42

Keywords: *apple quality assessment, convolutional neural networks, automated fruit sorting, image classification, deep learning applications in agriculture*

ABSTRACT
Quality assessment of apples is a pivotal task in the agriculture and food industries, with direct implications for economic gains and consumer satisfaction. Traditional methods, whether manual, mechanical or electromechanical, face challenges in terms of labor intensity, speed, and quality control. This paper introduces a solution using machine learning algorithms – specifically, Convolutional Neural Networks (CNNs) – for a more nuanced and efficient apple quality assessment. Our approach offers a balance between the high-speed capabilities of electromechanical sorting and the detailed recognition achievable with human evaluation. A dataset consisting of over 2000 apple images, labeled as 'Good' or 'Damaged', was compiled for training and validation purposes. The paper investigates various architectures and hyperparameter settings for several CNN models to optimize performance metrics, such as accuracy, precision, and recall. Preliminary evaluations indicate that the MobileNet and Inception models yield the highest levels of accuracy, emphasizing the potential of machine learning algorithms to significantly enhance apple quality assessment processes. Such improvements can lead to greater efficiency, reduced labor costs, and more rigorous quality control measures.

REZUMAT
Evaluarea calității merelor este o sarcină esențială în industriile agricole și alimentare, cu implicații directe asupra câștigurilor economice și a satisfacției consumatorilor. Metodele tradiționale, fie manuale, mecanice sau electromecanice se confruntă cu provocări în ceea ce privește efortul considerabil de muncă, viteza și controlul calității. Această lucrare propune o soluție care utilizează algoritmi de învățare automată – mai exact, rețele neuronale convolutive (CNN) – pentru o evaluare mai fină și mai eficientă a calității merelor. Abordarea noastră oferă un echilibru între capacitățile de sortare cu viteză mare ale metodelor electromecanice și recunoașterea detaliată realizabilă cu evaluarea umană. A fost compilat în scopuri de antrenare și validare un set de date compus din peste 2000 de imagini cu mere, fiecare măr fiind etichetat ca 'Bun' sau 'Stricat'. Lucrarea investighează diverse arhitecturi și configurări ale hiperparametrilor pentru mai multe modele de CNN în scopul optimizării indicatorilor de performanță (acuratețea, precizia, recall-ul). Evaluările preliminare indică faptul că modelele MobileNet și Inception oferă cele mai înalte niveluri de acuratețe, subliniind potențialul algoritmilor de învățare automată de a îmbunătăți semnificativ procesele de evaluare a calității merelor. Astfel de îmbunătățiri pot conduce la o eficiență mai mare, reducerea costurilor de muncă și tehnici de control al calității mai riguroase.

INTRODUCTION

The agriculture and food industries are among the most critical sectors not only for economic stability but also for ensuring human health and safety. One of the key steps in the food supply chain is the assessment of product quality, especially for fruits like apples, which constitute a significant portion of global fruit consumption. Quality assessment serves multiple purposes, such as grading for market pricing, segregating products for different usage scenarios (e.g., fresh consumption, juice extraction, or processed foods), and ensuring the overall safety and quality of the food. It is a complex but essential activity that is usually the intersection of human expertise, mechanical sorting technologies, and now, emerging computational methods.

In the context of automated quality assessment of apples, it is crucial to recognize the range of issues that can impact apple quality. Among parasitic diseases, Gray Mold, caused by the fungus Botrytis spp., manifests as a grayish fuzzy mold and can occur both in the field and during storage. Blue Mold, attributed to Penicillium expansum Thom, results in soft, water-soaked lesions covered with blue-green spores, commonly manifesting post-harvest. Lenticel Rot, due to the fungus Pezicula malicorticis Jacks Naum., affects the lenticels of apples, leading to dark lesions and a degradation in fruit quality (*Jamwal et al., 2002*).

Equally significant are non-parasitic diseases and damages. Superficial Scald is a physiological disorder that causes brown or dark patches on the apple's skin during long-term cold storage. Jonathan Spot appears as small, dark spots on the fruit's skin and is often associated with mineral imbalances or environmental stress factors. Internal Browning is another post-harvest disorder where the internal tissues of the apple turn brown, often due to storage conditions. Soft Scald is similar to Superficial Scald but results in soft, water-soaked lesions on the skin. Lastly, Soggy Breakdown makes the internal tissue of the apple turn water-soaked and spongy, often as a result of improper storage conditions (*Srivastava et al., 2021*). By understanding these parasitic and non-parasitic diseases and damages, the accuracy and reliability of automated quality assessment systems in categorizing and grading apples can be enhanced (*Nataraj et al., 2018*).

Despite its critical importance, the traditional methods employed for apple quality assessment have significant limitations. Manual sorting and grading are labor-intensive, time-consuming, and prone to human error. On the other hand, mechanical methods, although faster, often lack the nuanced understanding of 'quality,' as they primarily rely on size and weight as the determinant factors. These methods may overlook other essential quality metrics such as skin defects, color uniformity, and internal qualities that are important for grading and consumer satisfaction.

Recent advances in computer vision and machine learning have opened new avenues for automating quality assessment tasks. Convolutional Neural Networks (CNNs) have shown particular promise in image recognition challenges, extending their applicability to the agriculture sector (*Li et al., 2021*). Existing research has explored CNN-based approaches for defect detection in various fruits, vegetable classification, and even crop disease prediction. However, most of these studies have either focused on different fruits or have been limited to smaller datasets. Commercial solutions have begun to integrate machine learning but are often constrained by proprietary algorithms and high operational costs.

In the realm of automated apple sorting, *Kavdir and Guyer (2002*) utilized backpropagation neural networks (BPNNs) for sorting Empire and Golden Delicious apples based on surface quality. They employed both pixel gray values and texture features derived from apple images as inputs to their neural network classifiers. Their study explored two distinct classification scenarios: a 2-class classification, separating apples as either 'defective' or 'good,' and a 5-class classification that included various sub-categories of defects. Interestingly, they found that reducing the image resolution did not adversely affect classification accuracy, thereby offering a faster training and testing phase. Moreover, spectral bands were identified as effective indicators for distinguishing specific surface characteristics, such as bruising, leaf roller defects, and puncture marks. In terms of performance, the 2-class classifier achieved a classification success ranging from 89.2% to 100%. For the 5-class scenario, classification success varied between 89.7% and 100%, depending on the apple variety and the features used. Importantly, the research indicated that BPNN classifiers generally outperformed other methods when using pixel intensity as features, as opposed to extracted texture features. They concluded that neural networks could effectively capture the non-linear relationships between input features and output classes, and that spectral bands beyond 1000 nm improved defect identification in specific apple varieties. Despite the publication date of 2002, this work remains significantly relevant and pioneering in the field of using neural networks for apple sorting. Even in today's context, the findings and methodologies of Kavdir and Guyer stand out for their innovative approach in applying neural networks to agricultural tasks. Their use of BPNNs in this area laid an important work for subsequent research and developments, and the results they achieved continue to be pertinent in contemporary applications.

Yu et al. (2023) investigates the potential of Convolutional Neural Networks (CNNs) for the task of apple variety classification. Using a total of 7,439 apple images that represent 13 different apple classes, the study employs various deep learning architectures, namely AlexNet, VGG-19, ResNet-18, ResNet-50, and ResNet-101. The study employed two different dataset configurations to test the models, revealing that dataset balance plays a crucial role in classification performance. Specifically, all tested models achieved an accuracy above 96.1% when trained on a dataset with a training-to-testing ratio of 2.4:1, as compared to 89.4–93.9%

accuracy on a dataset with a ratio of 1:1. The VGG-19 model stood out, achieving a perfect 100% accuracy on the first dataset and 93.9% on the second. The study further delves into the impact of network architecture and depth on model size, accuracy, and computational time. It was found that as the number of layers in a model increased, so did its size, accuracy, and the time required for training and testing. Additionally, the authors employed techniques like feature visualization, strongest activations, and Local Interpretable Model-Agnostic Explanations (LIME) to interpret how different models understand and classify apple images. It was discovered that while series networks like AlexNet and VGG-19 focus on apple contours or shapes for classification, Directed Acyclic Graph (DAG) networks like ResNets focus on the entire apple region. The work not only confirms the applicability of CNNs in apple recognition but also contributes to the understanding of their interpretability, thereby providing a foundation for future agricultural applications of deep learning. This article is well-aligned with the broader scope of present research, as it similarly investigates the application of Convolutional Neural Networks (CNNs) for fruit classification, focusing particularly on apple varieties. The insights from this study provide a foundational understanding for the current research, particularly regarding the influence of dataset configuration and model architecture on classification performance. Acknowledging the shortcomings of existing methods, the present paper aims to explore the feasibility of machine learning algorithms, specifically Convolutional Neural Networks (CNNs), for an automated, efficient, and nuanced apple quality assessment. A thorough evaluation of various CNN architectures is conducted to ascertain the most effective in terms of accuracy, precision, and recall metrics. Additionally, this research introduces a custom CNN architecture, uniquely designed for apple sorting, and compares its performance with established models.

Wan and Goudos (2020) offer a refined framework that uses an advanced version of the Faster R-CNN algorithm, specifically designed for multi-class fruit identification tasks. Distinctive in their approach is the development of an extensive image dataset gathered from real-world outdoor orchards, featuring 4,000 images of fruits such as apples, mangoes, and oranges. To augment this dataset and improve model generalizability, they apply various data augmentation strategies. Their architectural enhancements, particularly the alterations made to the convolutional and pooling layers of the Faster R-CNN model, serve dual objectives: they accelerate the fruit detection process and enhance accuracy. Benchmarking studies corroborate the superiority of their method, showing that it surpasses existing models like YOLO, YOLOv2, YOLOv3 and Fast R-CNN in both speed and detection precision. Specifically, the modified Faster R-CNN model significantly outperforms these alternatives and demonstrates a mean Average Precision (mAP) exceeding 91% for multiple fruit types. This work represents a significant stride forward in the automation of agricultural processes. Its practical relevance lies in its potential applications for robotic harvesters, providing them with the capability to detect multiple types of fruits with high accuracy and speed.

Li et al. (2021) present a Convolutional Neural Network (CNN) model specialized for apple quality identification. The model successfully navigates the complexities associated with apple images, particularly when the background resembles the apple's surface. The authors compared their CNN-based approach with Google's Inception v3 and traditional image processing techniques that use features such as Histogram of Oriented Gradient (HOG) and Gray Level Co-occurrence Matrix (GLCM), paired with a Support Vector Machine (SVM) classifier. The CNN model showcased unparalleled training and validation accuracies, peaking at 99% and 98.98% respectively. Further, the model surpassed its competition in an independent test set, demonstrating an accuracy rate of 95.33%. Additionally, the CNN model proved to be more time-efficient, completing its training in just 27 minutes. The study reveals the potential of the proposed CNN model in complex apple quality assessment scenarios, outperforming existing models in both speed and accuracy. The authors plan to extend this model to gauge various apple attributes like color, size, ripeness, and even physiological disorders. They also envision expanding its utility to classify other fruits and integrate it into real-time sorting machinery.

Liu (2020) focuses on the role of deep learning in fruit classification, which is crucial for automating self-checkout and packaging systems in supermarkets. The study introduces a deep convolutional neural network model, called Interfruit, designed to handle the complexities inherent in fruit classification, such as category similarities. A unique dataset of 40 fruit categories was developed to train and test the Interfruit model. The study also uses an improved stack model that integrates the strengths of AlexNet, ResNet, and Inception. Interfruit achieved an overall test accuracy of 92.74%, surpassing other leading models in the domain. The model obviates the need for manual feature extraction and employs various network parameters and data augmentation strategies to bolster its predictive capabilities. Such high performance indicates the robustness and technical validity of the Interfruit model. The study concludes that Interfruit offers a promising and

comprehensive solution for automatically identifying and classifying fruits in supermarkets, aiding in quick retrieval of pricing and other identification information.

Zhang et al (2019) present an innovative paper that addresses the critical need for effective and efficient fruit detection in agricultural robots. Their approach leverages an advanced multi-task cascaded convolutional network (MTCNN) for high-accuracy, real-time performance. One of the contributions of this paper is the introduction of an improved image augmentation method, known as "fusion augmentation," designed to further elevate the performance of the fruit detector. To validate their model, the authors created a robust dataset that includes images from apple orchards as well as additional images from the Internet and ImageNet. The system was not only successful in detecting apples but also showed promising results when extended to other fruits like strawberries and oranges. In terms of efficiency, the system processed 100 images in under 80 seconds, closely approximating real-time performance. Given these results, this study's fruit detection system holds significant promise for broader applications, particularly in automating various agricultural tasks like sorting, grading, and yield estimation.

Keresztes et al. (2018) explore real-time fruit detection for proximal imaging, typically done using tractor-mounted cameras in orchards and vineyards. Their method is a two-step process that combines geometrical pre-processing with deep neural network (DNN) classification. The geometric pre-processing step, which employs a radial Hough-like operator, quickly narrows down probable regions where fruits may be located, making the subsequent DNN classification more efficient. The system was rigorously tested on grapes and apples, with encouraging outcomes that show high correlations with manual counting methods — up to 0.96 for grapes and 0.85 for apples. Moreover, the technology leverages an intelligent camera system, which is both cost-effective and easily adaptable to existing agricultural machinery like tractors. The camera system allows for the acquisition of large datasets while maintaining controlled lighting conditions for consistent fruit detection. This approach not only proves its efficacy in fruit detection but also offers valuable insights into agronomic parameters that could be crucial for advancing precision agriculture. Thus, the method holds potential not just for improving current farm management strategies but also for contributing to the development of more sophisticated decision-support tools in the future.

The Table 1 offers a summarized overview of the state-of-the-art research in the field of automated fruit sorting and classification, with a specific focus on apple sorting and quality assessment. This area of study has seen significant advancements, thanks to machine learning algorithms, particularly Convolutional Neural Networks (CNNs), and other data-driven methodologies. The table categorizes research papers by their authors and key contributions, outlines the methods and algorithms employed, and encapsulates their performance metrics or findings.

Another contribution to the field of automated fruit grading is the review of *Seema et al. (2015).* Their paper delves into the critical role of computer vision in agricultural automation, specifically focusing on fruit grading and sorting. They argue that while traditional human-operated methods are prone to errors and inefficiencies, computer-vision systems offer a more accurate and efficient alternative. The review identifies that the most commonly employed features for computer vision-based sorting are color, texture, and morphological characteristics. These features are typically used to assess factors like diseases, maturity, and overall quality of the fruit. Among the various machine learning techniques explored, Support Vector Machines (SVMs) were found to deliver high accuracy rates. However, Adaptive Neuro Fuzzy Interference Systems (ANFIS) provided the best overall performance. On the color modeling front, the HIS (Hue, Saturation, Intensity) model was highlighted as particularly effective due to its alignment with human perception. The review concludes that machine vision systems hold the potential to significantly improve the efficiency and accuracy of fruit grading, thereby making a strong case for their broader adoption in the agricultural sector.

Table 1

Overview of the state-of-the-art research in the field of automated fruit sorting and classification

Paper	Methods and Algorithms Used	Key Contributions	Performance and Findings
Kavdir and Guyer	Backpropagation Neural Networks (BPNNs)	Surface quality classification into 2 and 5 classes. Explores pixel gray values and texture features.	89.2% to 100% classification success depending on apple variety and features.
Fanqianhui Yu, Tao Lu, Changhu Xue	CNNs (AlexNet, VGG-19, ResNet-18, ResNet-50, ResNet-101)	Focuses on apple variety using deep learning. Explores dataset configurations and model architectures.	Accuracy > 96.1% with a balanced dataset. VGG-19 achieved 100% accuracy.

Paper	Methods and Algorithms Used	Key Contributions	Performance and Findings
Shaohua Wan and Sotirios Goudos	Modified Faster R-CNN	Extensive real-world dataset and architectural enhancements for multi-class fruit detection.	mAP > 91% for multiple fruit types, outperforming YOLO and Fast R-CNN.
Li, Feng, Liu, Han	CNNs	Specialized for apple quality. Compares CNN-based approach with Inception v3 and traditional methods.	Training and validation accuracies peaked at 99% and 98.98%.
Wenzhong Liu	Interfruit (Deep CNN)	Designed for self-checkout and packaging systems. Uses a unique dataset of 40 fruit categories.	Test accuracy of 92.74%, outperforming leading models.
Li Zhang et al.	Multi-Task Cascaded Convolutional Networks (MTCNN)	High-accuracy, real-time performance for agricultural robots. Introduces "fusion augmentation."	Processes 100 images in < 80 seconds, showing real-time performance.
Barna Keresztes et al.	Radial Hough-like operator + DNNs	Two-step process for real-time fruit detection using tractor-mounted cameras.	High correlation with manual counting: up to 0.96 for grapes and 0.85 for apples.

MATERIALS AND METHODS

The prevailing trend in automated fruit sorting research leans toward intricate classification schemes that involve complex feature sets and multiple quality metrics. While such approaches have merit, they often bypass a critical, foundational decision point in the agricultural supply chain: the initial binary classification of fruit as either acceptable or subpar for consumption or sale. The importance of this primary bifurcation cannot be overstated, as it serves as an essential presorting step for more granular quality evaluations, packaging, distribution, and other downstream processes.

The integration of a binary classification system as a presorting stage prior to multi-class classification offers a multitude of advantages. One of the immediate benefits is the quick filtration of subpar produce, enabling only quality apples to proceed to the more resource-intensive multi-class classification stage, thereby enhancing its accuracy and effectiveness. This method is computationally efficient, as it ensures that the greater computational resources required for multi-class classification are expended only on apples that have already passed a basic quality threshold. This initial classification also addresses the issue of class imbalance, which can otherwise disproportionately skew the performance of multi-class classifiers. The binary filter removes low-quality apples from the outset, mitigating this problem. Moreover, multi-class classifiers frequently encounter boundary issues that a preliminary binary sort can effectively alleviate by widening the distinctions between 'damaged' and 'good' classes, thereby improving the efficiency and accuracy of the multi-class system. In addition, this binary presorting technique enables a modular approach to fruit grading. It can function as a stand-alone unit that feeds into more specialized multi-class systems, offering greater flexibility in deployment and scalability. Training machine learning models for multi-class classification often takes longer; however, this initial binary sort streamlines the process by reducing the data set size and complexity, potentially accelerating training times. Furthermore, the simplicity of a binary model lowers the risk of overfitting compared to more complex multi-class models, serving as a regularization technique that enhances the generalization performance of subsequent models. Troubleshooting is also simplified; when errors occur, it is easier to determine whether they originated during the binary or multi-class classification stage. Finally, this presorting stage yields financial benefits by reducing both computational and labor costs, as fewer apples need to pass through the resource-intensive multi-class classification process. Overall, the use of a binary presorting stage substantially optimizes the apple grading process, rendering subsequent multi-class classifications more efficient, accurate, and cost-effective.

The current study addresses this often-overlooked area by introducing a robust method for this initial categorization. By establishing a reliable and efficient binary classification system, the research lays the groundwork for subsequent, more nuanced quality assessments. This initial filtration stage can have substantial implications for the agricultural supply chain, including the potential for reduced labor costs and minimized error rates in later stages of quality assessment.

The dataset initially comprises a total of 2468 apple images, all of which were personally captured in a single apple orchard. To improve the dataset's robustness and diversity, the original set of 2468 images was augmented, expanding the total number of images to 4200. The advantage of sourcing all images from the same area lies in the consistency it brings to the data. The dataset was collected during the peak harvest season to ensure representative sampling. Variability due to different lighting conditions, apple varieties, and background interference is minimized, thereby allowing the model to learn more efficiently and accurately. The

images are divided into two categories: ”Good” apples and ”Damaged” apples. These categories were created by manually inspecting each apple, ensuring a reliable and consistent labeling process.

In the orchard from which the apples used in this dataset were harvested, various cultivars were present, each exhibiting unique characteristics, most notably in the color of their skin when fully matured. These cultivars included the Golden Delicious, the Jonathan, and the ”Rabbit's Snout” (”Bot de iepure” in Romanian). The aim of this study was not to discriminate between these cultivars, but rather to conduct binary classification without taking skin color into account. While the inclusion of multiple cultivars with different mature skin colors undoubtedly complicates the classification task and may inhibit achieving high accuracy, this approach was intentionally chosen. The objective was to evaluate the efficacy of an apple sorting process that is cultivar-agnostic and does not rely on the specific hue of the skin at maturity for classification. This sets the groundwork for a more universally applicable sorting algorithm that can handle apples from diversified sources.

For easier data processing and model training, the images are organized into two separate folders corresponding to these categories. The original resolution of each image is 3648x2736 pixels. However, for computational efficiency and to facilitate faster training, these images were resized to a uniform shape of 150x150 pixels with 3 color channels (RGB). The input shape for the Convolutional Neural Network was set to (150, 150, 3), corresponding to the height, width, and the number of color channels of the resized images. An exception was the MobileNet network, for which the input shape was 224x224x3. The choice of image size is a trade-off between computational efficiency and model performance. Smaller images like 128x128 are faster to process and require less memory, but they might lack detail that could be important for classification. Larger images retain more detail but are computationally more expensive to process and may require more memory. With a larger number of pixels, the model might learn noise or insignificant variations in the data, rather than truly relevant features. This can lead to overfitting, especially if the training dataset is relatively small. During training, a tendency towards overfitting was observed, which led to the decision to use the 150x150 format, except for the MobileNet network (*Simonyan and Zisserman, 2015; Pen at al., 2023; Ke et al., 2023; Abdo et al., 2023*).

In our dataset, a class distribution where 55% of the apples fall under the ”Good” category and 45% are categorized as ”Damaged” can be observed. While the classes are not perfectly balanced, the distribution is relatively even, with only a 10% difference between the two categories. Such a slight imbalance is generally not substantial enough to significantly bias most machine learning algorithms. Given the near-balanced nature of our dataset, the question arises whether resampling methods are necessary or not. In cases with severe class imbalance, resampling is often recommended to create a more balanced dataset, thereby improving model performance. However, in this case, the 10% disparity between the classes is quite minimal, so the need for resampling methods like under-sampling or over-sampling becomes less pressing.

For a binary classification task like distinguishing between “Good” apples and “Damaged” apples, a 150x150 image size may be sufficient if the damage is usually large-scale and easily visible. However, if the types of damage are subtle or require high-resolution to spot, using larger images could be beneficial. Optimal image size in convolutional neural networks is influenced by computational resources, the subtlety of features in the data, risks of overfitting with smaller datasets (sometimes using larger images can lead to overfitting, especially if the dataset is small), and compatibility requirements with advanced architectures. Empirical determination of the most appropriate image size for this specific classification problem was achieved through training the convolutional neural network models on multiple image dimensions. Through experimentation, aided by available computational resources, an optimum image size was identified for yielding the best performance metrics for this particular application (Simonyan and Zisserman, 2015). The dataset employed for this study exhibits a well-balanced distribution between the two classes, “Good” and “Damaged” apples. This balance enhances the reliability of the model's predictions and mitigates the risk of class bias, thereby improving the generalizability of the findings.

Figure 1 offers selected samples from the dataset utilized in this study, showcasing the marked visual differences between the “Good” apples and the “Damaged” apples. The depicted apples belong to two distinct varieties, underlining the study's diversity. The first two images present apples from the “Good” apples category. These samples demonstrate a consistent color distribution, smooth skin texture, and an absence of discernible defects. In contrast, the following two images represent the “Damaged” apples category. Both of these apples display characteristics of a common fungal infection, evident through dark spots and altered skin texture. This specific infection is prevalent in the dataset. It is worth noting that the dataset did not feature apples with noticeable insect damage.



Fig. 1 - Samples from the dataset

These images serve to highlight the key distinguishing features that the convolutional neural network model aims to learn for accurate classification.

Choosing the optimal convolutional network architecture for evaluating apple quality depends on a variety of elements, such as the complexity of the visual cues in the dataset, the computational resources that can be allocated, and the urgency for real-time inference (*Ke et al., 2023; Abdo et al., 2023; Theng et al., 2023*).

LeNet, one of the foundational architectures in Convolutional Neural Networks, was introduced by Yann LeCun in the 1990s and played a pivotal role in the proliferation of deep learning in image recognition tasks. Its architecture is designed with a series of convolutional and subsampling layers followed by fully connected layers, setting the stage for many subsequent CNN designs (*Simonyan and Zisserman, 2015*). It is particularly well-suited for straightforward visual tasks. Given its design simplicity and relatively fewer parameters compared to modern networks, LeNet can be efficient and less prone to overfitting on smaller datasets. Therefore, it could be an excellent fit if the apple dataset does not possess overly complex features (see mode used in fig. 2).

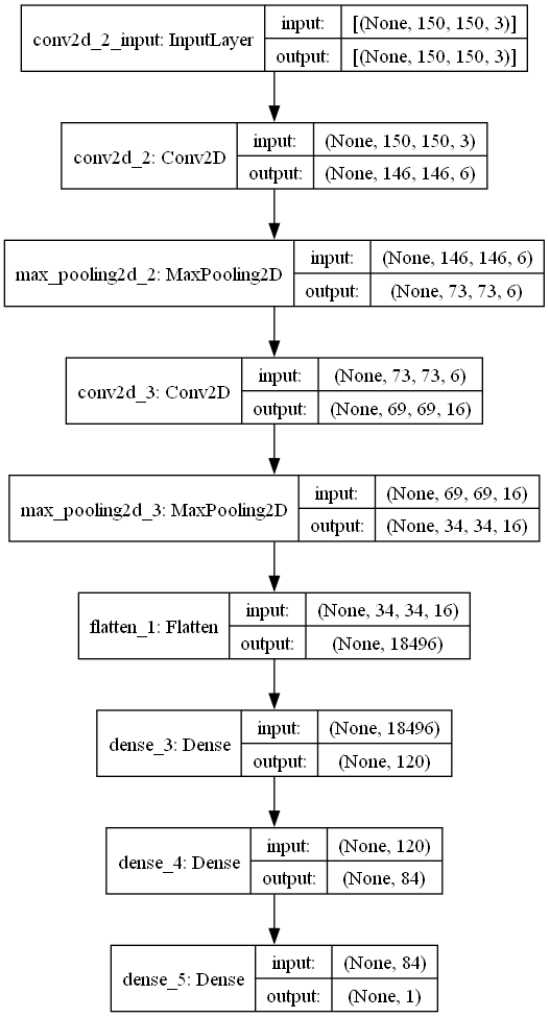


Fig. 2 – LeNet Implementation

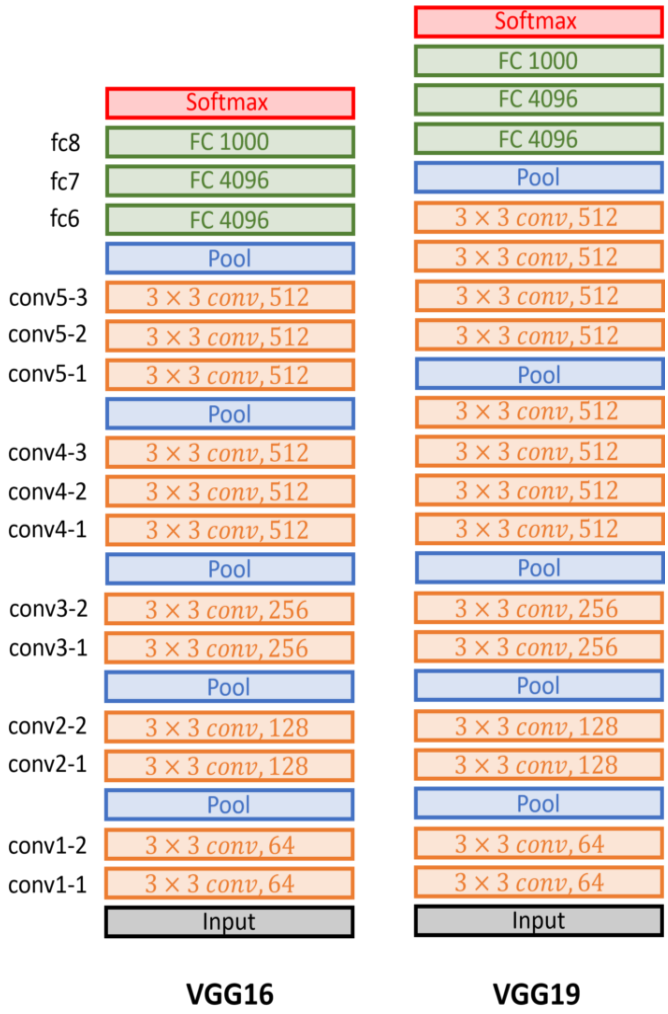


Fig. 3 - VGG16 and VGG19 Implementation

The VGG (Visual Geometry Group) architectures, specifically VGG16 and VGG19, are convolutional neural networks developed by the Visual Geometry Group at the University of Oxford. They were designed to be simple yet highly effective for a wide range of image recognition tasks. The primary attribute that distinguishes VGG architectures is their depth—specifically, the number of weight layers in the network. VGG16 and VGG19 have 16 and 19 weight layers, respectively. VGG16 consists of 13 convolutional layers, 5 max-pooling layers, and 3 fully connected layers. Each convolutional layer employs a small receptive field using 3x3 kernels, which is a key innovation contributing to the model's effectiveness. Max-Pooling layers are interspersed among the convolutional layers and utilize 2x2 kernels with a stride of 2 to reduce the spatial dimensions. Three Fully Connected layers are used at the end, the first two having 4096 channels and the final one having 1000 channels corresponding to the number of classes in the ImageNet dataset. ReLU (Rectified Linear Unit) is used as the activation function throughout the model (fig. 3). VGG19 is very similar to VGG16 but has 3 additional convolutional layers, increasing the depth to 19 weight layers. This makes VGG19 slightly more complex and computationally intensive but also offers a modest improvement in performance. Like VGG16, it also uses 3x3 convolutional kernels, max-pooling layers with 2x2 kernels and stride of 2, and fully connected layers toward the end of the architecture *(Nguyen et al., 2022; Ong et al., 2023; Anuar et al., 2023; Abdo et al., 2023*).

The Inception architecture, particularly its third version, InceptionV3, is a product of Google's research and has been one of the standout models for image classification tasks. Built on the foundational idea of 'network within a network', InceptionV3 employs multiple kernel sizes in parallel, rather than in series, to capture various spatial hierarchies of features within an image (fig. 4). This unique design choice facilitates the extraction of both local features using smaller convolutions and more global features with larger convolutions. Furthermore, the model incorporates techniques like factorization and efficient grid size reduction to keep the computational cost manageable. These sophisticated configurations ensure that the architecture learns a wide array of features at different scales. As such, InceptionV3 offers a versatile and robust approach, making it particularly apt for the multi-feature quality assessment in apples, where varied scales of features may be crucial (*Ong et al., 2023; Abdo et al., 2023*).

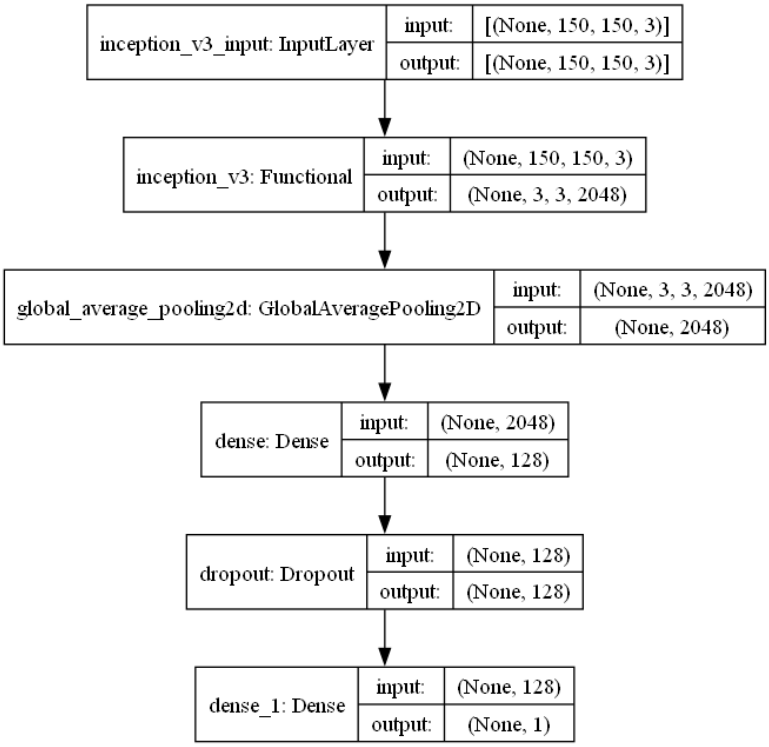


Fig. 4 - Inception Implementation

MobileNet, developed by Google, is specifically designed for mobile and embedded vision applications, striking a balance between computational efficiency and model performance. Utilizing depthwise separable convolutions, it factors standard convolutions into depthwise and pointwise operations, thereby significantly reducing the number of parameters and computational overhead without sacrificing the ability to capture meaningful features.

This design choice enables MobileNet to run efficiently even on devices with limited computational resources. Its architecture is not only compact but also modular, allowing for varying levels of granularity based on the application's requirements. If the computational budget is limited or rapid inference is required, MobileNet emerges as the prime choice. Its lightweight and fast processing characteristics make it suitable for real-time applications or environments where latency is a concern (*Khazalah et al., 2023*). However, like many efficient models, there might be a trade-off in accuracy when compared to larger, more resource-intensive networks (fig. 5).

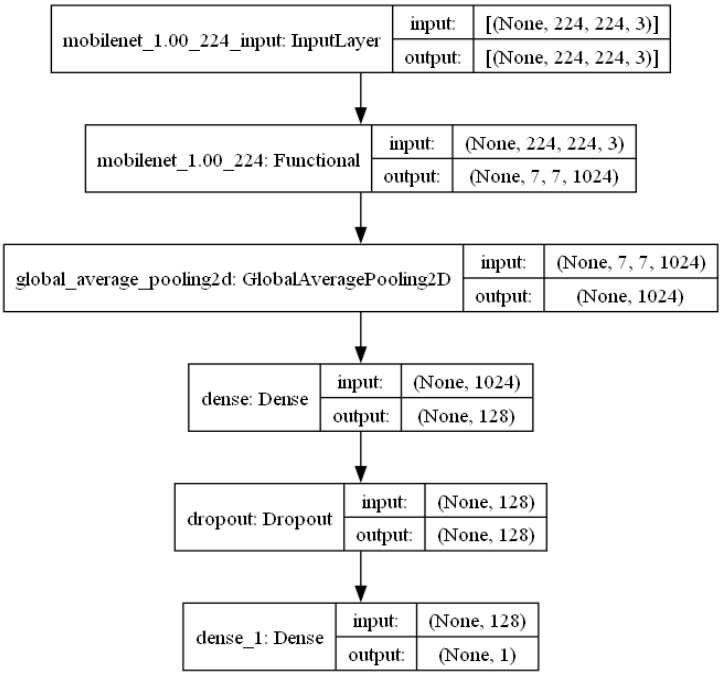


Fig. 5 - MobileNet Implementation

EfficientNet, designed by Google researchers, rethinks the way network scaling is done by proportionally adjusting depth, width, and resolution. This unique, coordinated scaling ensures improved performance with fewer parameters (*Tan and Le, 2019*). Born from an optimization process, its base model sets a foundation, which can be expanded based on computational needs. EfficientNet balances computational efficiency with performance, making it a prime choice in scenarios where both factors are vital (figure 6).

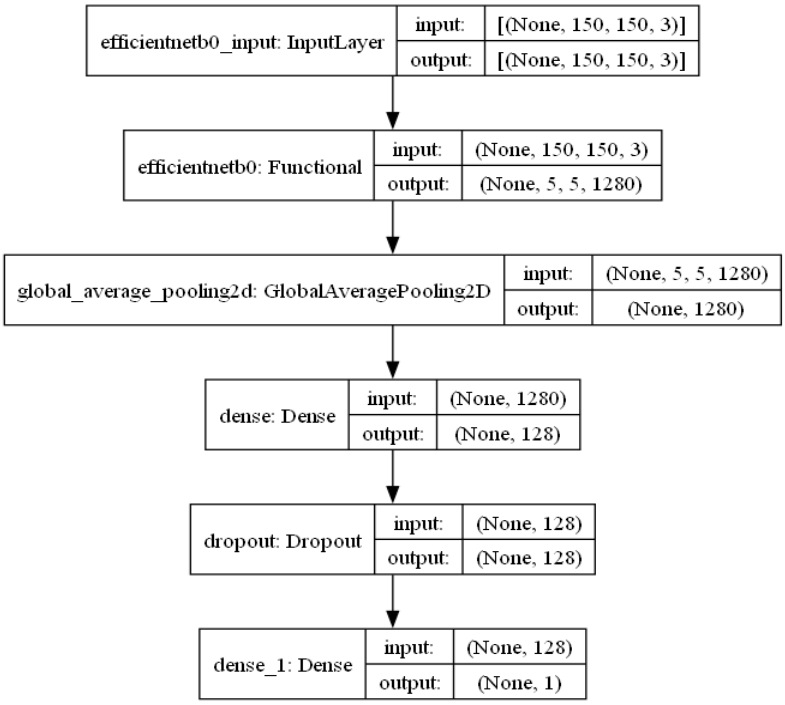


Fig. 6 - EfficientNet Implementation

For the unique demands of apple quality assessment, a custom CNN architecture may offer the most direct approach to achieving good performance (table 2). For example, a heightened emphasis on texture differentiation might necessitate a greater number of convolutional layers, while color-sensitive assessments could benefit from an increased number of filters in the initial convolutional layers (*Ong et al., 2023; Ke et al., 2023; Abdo et al., 2023; Anuar et al., 2023*).

All of these architectures were tested, as much as possible, under similar conditions, initially on the original dataset and then on the augmented dataset (batch size of 32, 30 training epochs, binary cross-entropy as the loss function, and the Adam optimizer with a learning rate of 0.0001).

Table 2

Custom CNN Model Implementation

Layer (type)	Output Shape	Param #
conv2d_6 (Conv2D)	(None, 148, 148, 32)	896
activation_10 (Activation)	(None, 148, 148, 32)	0
max_pooling2d_6 (MaxPooling2)	(None, 74, 74, 32)	0
conv2d_7 (Conv2D)	(None, 72, 72, 64)	18496
activation_11 (Activation)	(None, 72, 72, 64)	0
max_pooling2d_7 (MaxPooling2)	(None, 36, 36, 64)	0
conv2d_8 (Conv2D)	(None, 34, 34, 128)	73856
activation_12 (Activation)	(None, 34, 34, 128)	0
max_pooling2d_8 (MaxPooling2)	(None, 17, 17, 128)	0
flatten_2 (Flatten)	(None, 36992)	0
dense_4 (Dense)	(None, 64)	2367552
activation_13 (Activation)	(None, 64)	0
dropout_2 (Dropout)	(None, 64)	0
dense_5 (Dense)	(None, 1)	65
activation_14 (Activation)	(None, 1)	0

Total params: 2,460,865

Trainable params: 2,460,865

The primary metric used for assessing the performance of the binary classification models in this study is Accuracy, defined as:

$$\text{Accuracy} = \frac{Number\ of\ Correct\ Predictions}{Total\ Number\ of\ Predictions} \quad (1)$$

or

$$\text{Accuracy} = \frac{TP+TN}{TP+TN+FP+FN} \quad (2)$$

where:

TP = true positive (the items that were correctly identified as belonging to the positive class),

TN = true negative (the items that were correctly identified as belonging to the negative class),

FP = false positive (the items that were incorrectly identified as belonging to the positive class when they actually belong to the negative class - in many contexts, this is known as a "type I error" or a "false alarm"),

FN = false negative (the items that were incorrectly identified as belonging to the negative class when they actually belong to the positive class - this is sometimes referred to as a "type II error" or a "miss").

This metric is well-suited for binary classification tasks where the classes are approximately balanced. It gives us a simple, interpretable measure of the model's overall performance (*Seema et al., 2015*).

In addition to accuracy as the primary metric, the F1 score was also employed as a supplementary evaluation measure. For binary classification tasks such as ours, the F1 score is especially pertinent because it provides a balanced harmonic mean of precision and recall. This ensures that both false positives and false negatives are taken into account, making it a more comprehensive metric than accuracy alone, especially in situations where class imbalances exist (*Larner, 2023*). The F1 score is defined as:

$$F1 = 2 \times \frac{precision \times recall}{precision + recall}, \quad (3)$$

where:

precision = $\frac{TP}{TP+FP}$ (the number of correct positive results divided by the number of all positive results), and

recall = $\frac{TP}{TP+FN}$ (the number of correct positive results divided by the number of positive results that should have been returned).

In this analysis, the Binary Cross-Entropy (BCE) loss function is utilized, which is particularly suited for binary classification tasks. Binary Cross-Entropy quantifies the difference between two probability distributions: the true distribution and the predicted distribution. It measures the "distance" between the ground truth and our predictions, aiming to minimize this distance as the model learns. The rationale behind employing BCE for binary classification lies in its ability to handle probabilistic predictions. When predicting the two classes, it is essential not only to classify but also to measure the confidence of the model in its prediction. Binary Cross-Entropy penalizes the model significantly when it is confident and wrong, and to a lesser extent when it is unsure. This makes it particularly effective in driving the model towards making more accurate predictions with higher confidence *(Larner, 2023*).

Mathematically, the Binary Cross-Entropy loss for a set of predictions p with respect to true labels y is given by:

$$BCE = -\sum_{i=1}^{n} y_i \log(p_i) + (1 - y_i)\log(1 - p_i), \quad (4)$$

where:

n is the number of samples, y_i is the true label (0 or 1), p_i is the predicted probability of the sample belonging to class 1.

By optimizing this loss during the training process, the model endeavors to improve its binary classification performance, generating predictions that align closely with the ground truth.

To ensure robustness and generalization capabilities, it is essential to prevent overfitting in neural network models. Overfitting occurs when a model excels on the training data but struggles to generalize effectively to unseen or new data, capturing the noise and specificities of the training set rather than the general patterns. To address this challenge, L1 and L2 regularization techniques are applied across the convolutional and fully connected layers. These techniques introduce penalties to the loss function, acting as constraints that discourage the model from fitting too closely to the peculiarities of the training data.

The underlying principle of L1 and L2 regularization is the penalization of large values of model weights. While L1 regularization encourages sparsity by driving certain weights to zero, thereby leading to feature selection, L2 regularization aims to shrink weights towards zero without making them exactly zero, ensuring the values remain small and distributed.

Mathematically, the regularization term added to the loss function can be defined as:

$$Regularization\ Term = \lambda_1 \sum|w| + \lambda_{12} \sum w^2 \quad (5)$$

Here:

λ_1 and λ_2 represent the regularization coefficients for L1 and L2, respectively, and w signifies the model weights.

Incorporating these regularization terms in neural network training ensures a balance between adequately fitting the training data and retaining the capability to generalize to new instances. By incorporating these regularization terms, it is ensured that our models achieve a balance between fitting the training data and retaining their ability to generalize to new dataIn initial training sessions. Early Stopping was employed to halt training when the validation performance ceased to improve. It was observed that Early Stopping acted for all models up to the 30th epoch. As a result, subsequent training sessions were adjusted to have a fixed number of epochs set at 30, streamlining the training process and preventing overfitting.

The learning rate is adaptively adjusted during training using a "Reduce On Plateau" strategy. When the validation loss reaches a plateau, the learning rate is reduced by a factor, facilitating the model to escape local minima and potentially leading to better generalization (*Ke et al., 2023; Larner, 2023*).

RESULTS

The application of various Convolutional Neural Network (CNN) architectures for the binary classification of apples produced diverse outcomes in terms of accuracy and F1 score across both training and validation datasets (Table 3). The results elucidate the potential and limitations of each model with respect to their performance metrics.

Table 3

Performance Metrics of Various CNN Architectures (%)

Architecture	Train Accuracy	Train F1 Score	Validation Accuracy	Validation F1 Score
Custom CNN	0.91	0.91	0.92	0.90
LeNet	0.96	0.96	0.95	0.95
VGG16	0.91	0.91	0.91	0.91
VGG19	0.90	0.90	0.90	0.90
MobileNet	0.98	0.98	0.99	0.99
InceptionV3	0.98	0.98	0.98	0.99
EfficientNet	0.48	0.52	0.50	0.66

The following subsections provide a visual representation of the performance metrics for each CNN architecture (figures 7-13).

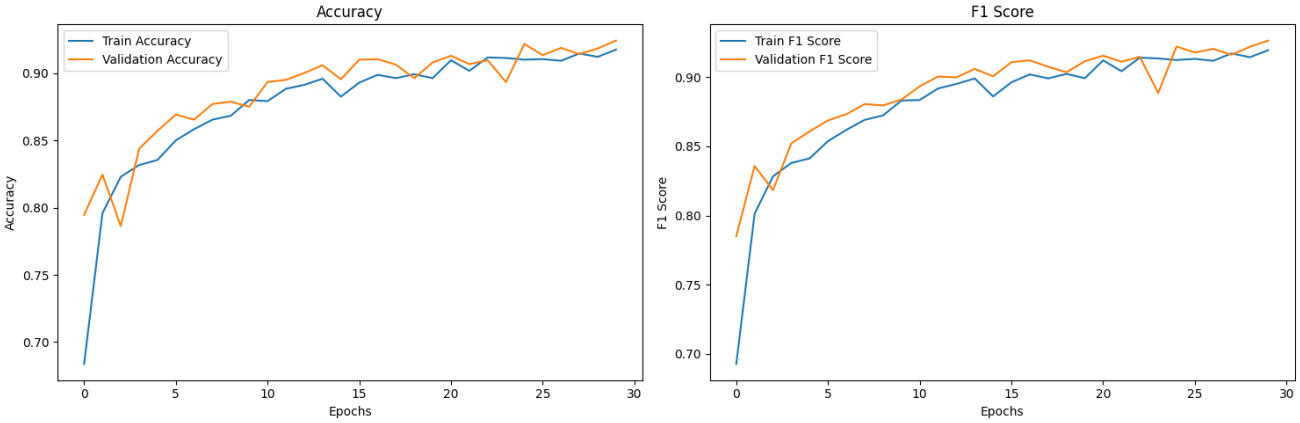


Fig. 7 - Custom CNN Architecture Performance Metrics: Accuracy and F1 Score

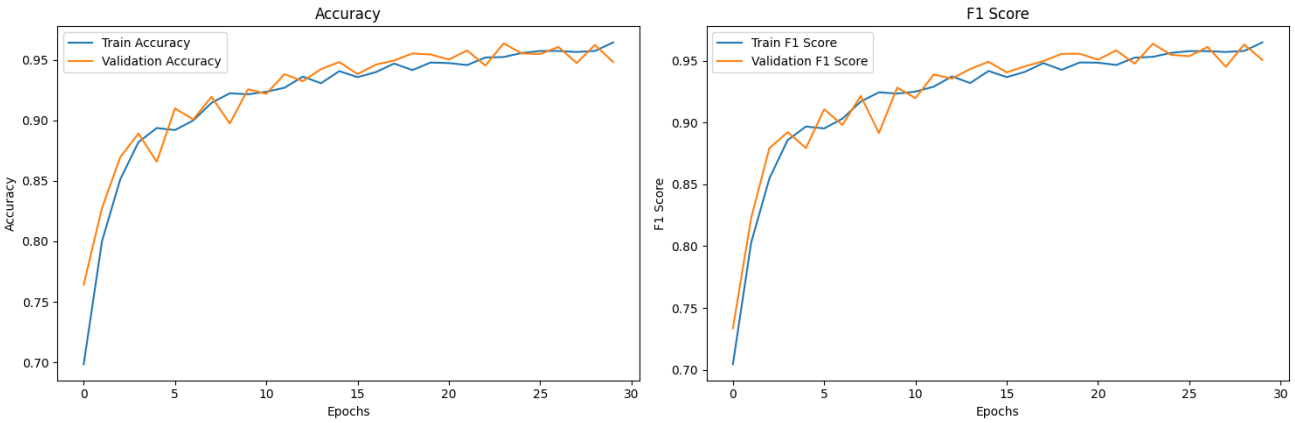


Fig. 8 – LeNet Architecture Performance Metrics: Accuracy and F1 Score

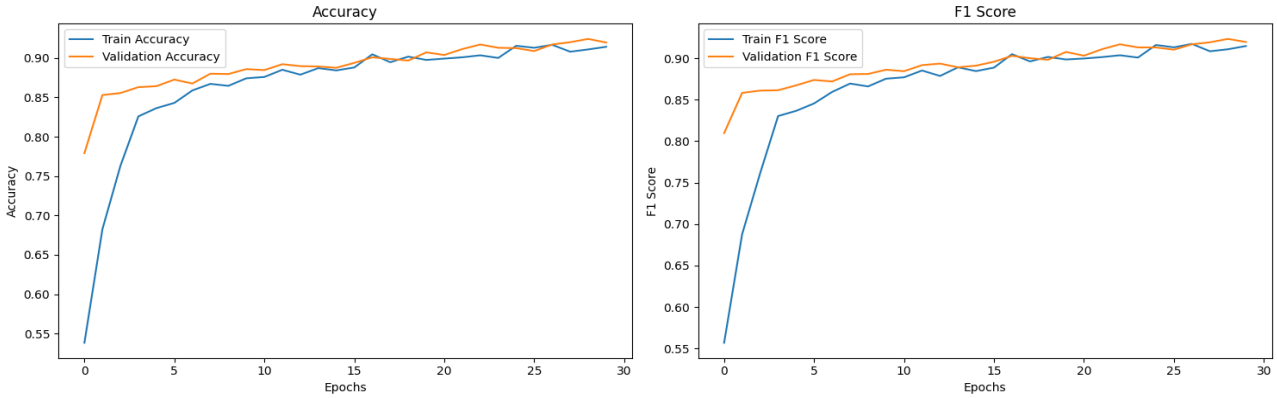


Fig. 9 - VGG16 Architecture Performance Metrics: Accuracy and F1 Score

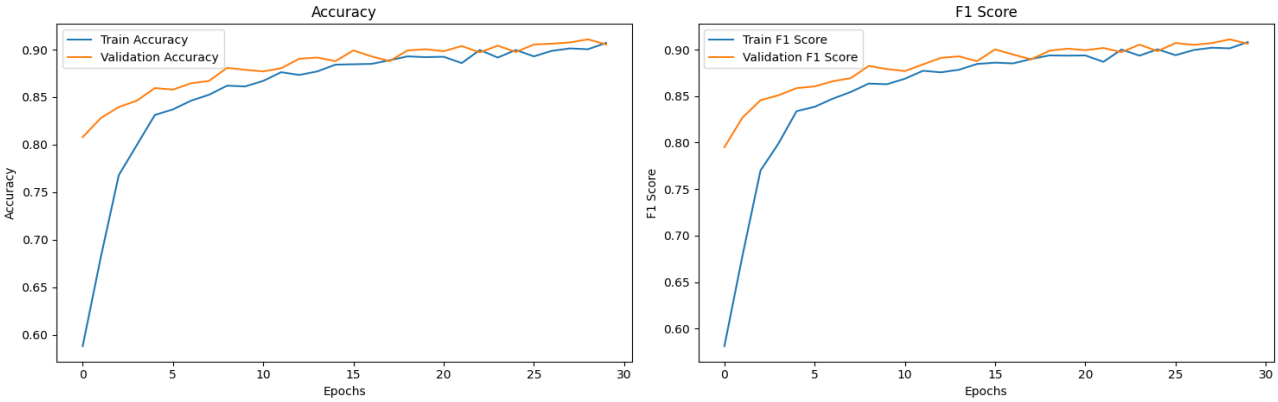


Fig. 10 - VGG19 Architecture Performance Metrics: Accuracy and F1 Score

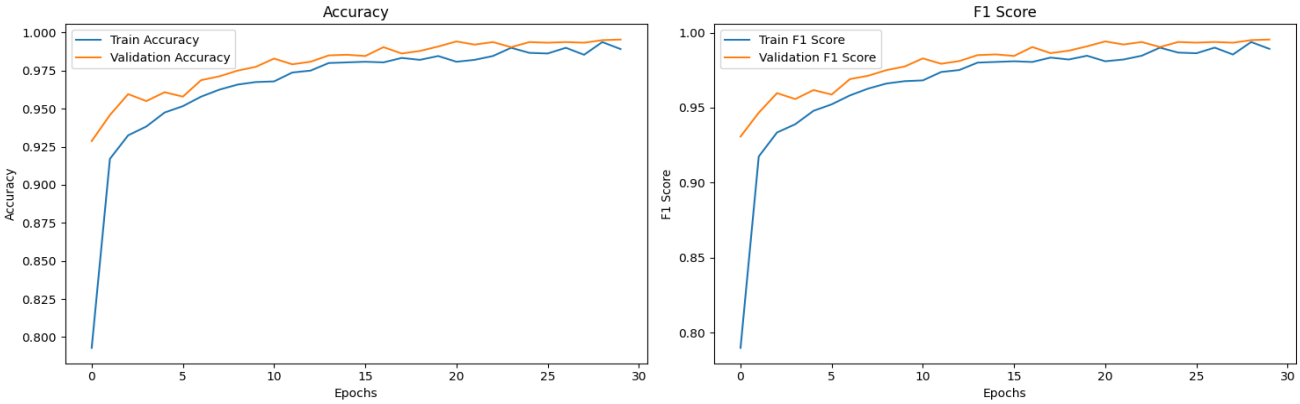


Fig. 11 – MobileNet Architecture Performance Metrics: Accuracy and F1 Score

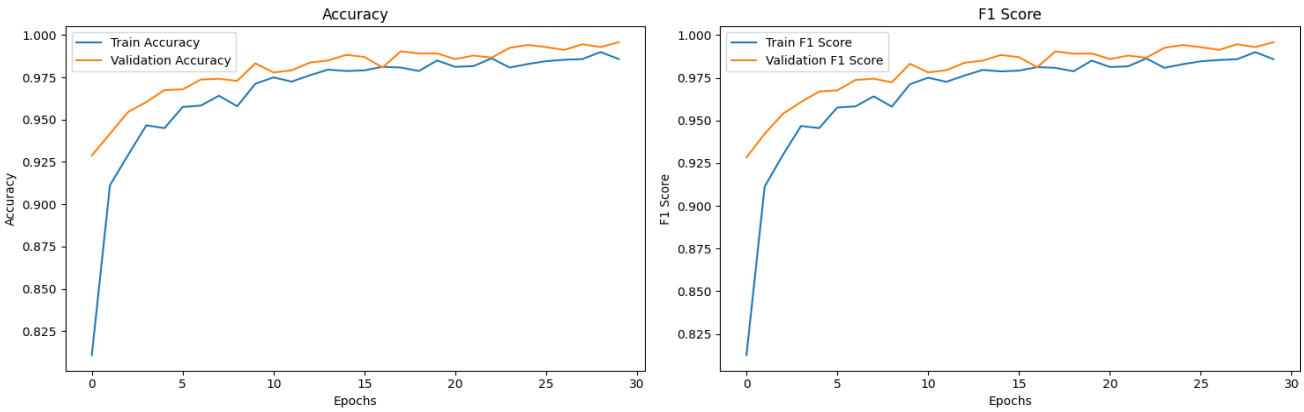


Fig. 12 - InceptionV3 Architecture Performance Metrics: Accuracy and F1 Score

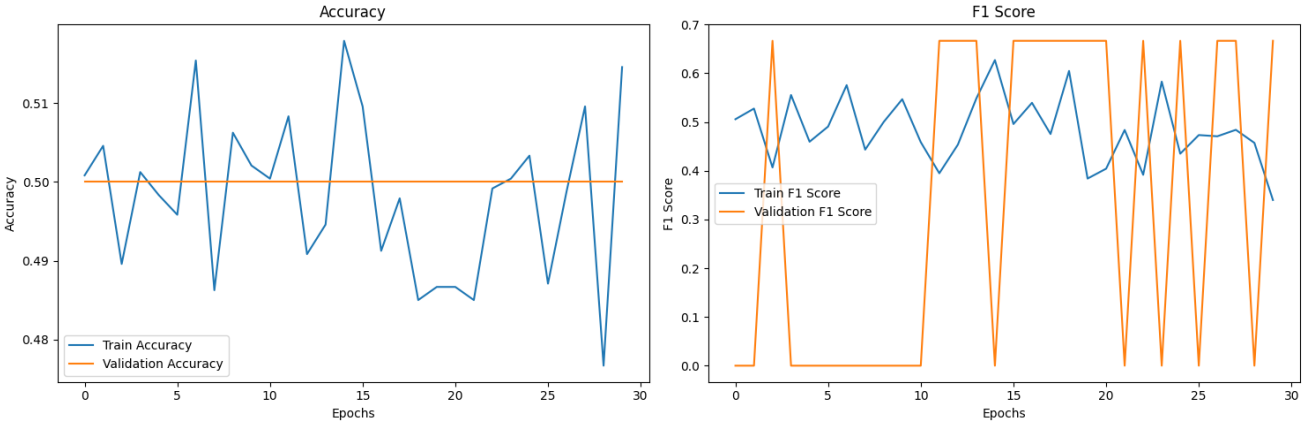


Fig. 13 – EfficientNet Architecture Performance Metrics: Accuracy and F1 Score

Each figure provides a visual trajectory of how the respective models performed across epochs, allowing for a comprehensive understanding of the models' learning patterns and stability. The results obtained provide a foundation upon which the subsequent conclusions are drawn, aiming to comprehend the practical applicability and limitations of the explored CNN architectures in the context of apple sorting through binary classification.

CONCLUSIONS

The empirical exploration of different Convolutional Neural Network (CNN) architectures has provided a basic understanding of their potential applicability in the binary classification of apples for sorting purposes.

Analyzing the data, it is evident that different architectures have offered various levels of performance, with MobileNet and InceptionV3 indicating a relatively high proficiency in this particular application, as opposed to the less consistent results derived from EfficientNet. The underperformance of EfficientNet might be attributed to various factors, such as potential misalignment between network configurations (like width, depth, and resolution scaling) and the particularities of the dataset, or possibly a deficiency in the volume or diversity of training data to adequately leverage the model's capabilities.

Interestingly, LeNet also demonstrated commendable performance, achieving 95% accuracy in validation. LeNet, one of the earlier and simpler CNN architectures, has often been acclaimed for its efficiency and lightweight nature, which can be particularly advantageous in scenarios where computational resources are limited or optimization is pivotal. Its relative simplicity, compared to more complex networks like InceptionV3 and MobileNet, allows for easier implementation and can often be less prone to overfitting when dealing with smaller datasets. This architecture, despite its age and simplicity, illustrates that enhanced complexity is not always synonymous with superior performance and underscores the importance of aligning the network architecture with the specific application and dataset.

On the other hand, while MobileNet and InceptionV3 have demonstrated higher metrics, particularly in validation accuracy, extending these results to wider or differing contexts requires additional scrutiny and validation. Employing networks that have achieved over 98% in validation accuracy, such as MobileNet and InceptionV3, brings with it both merits and challenges. Their high performance in this study indicates a capability to adeptly handle the specific classification problem, potentially offering reliable and accurate sorting in practical deployments. However, it is vital to consider possible limitations, such as a risk of overfitting due to their model complexity and depth, or the computational demands for deploying these networks, especially in scenarios where resources are limited, or optimization is crucial. The variation in results among the different CNN models implies that there is no one-size-fits-all solution, and choosing an appropriate model requires a balance between accuracy, computational cost, and implementation complexity. Additionally, it is crucial to consider that despite the quantitative results obtained, practical implementation in a real-world scenario encompasses a multitude of other variables that may affect performance, such as lighting conditions, apple varieties, and computational resources available.

This preliminary investigation into employing various CNN architectures for apple sorting in the agricultural sector provides an initial step and preliminary insights into a potentially broader application. While the performance metrics varied among the models tested, these discrepancies underscore the importance of continued research and development to refine these technologies for practical, field-based applications. The

findings from this study present an intriguing initial viewpoint for forthcoming research. Nevertheless, while these results offer a noteworthy starting point, the authors intend to further refine the system by conducting additional testing on an operational conveyor belt tasked with sorting apples, to further evaluate and enhance its practical application. Looking forward, the authors intend to expand the database with a larger and more diverse set of images and venture into more intricate classification challenges, exploring the realm of multiclass classification to provide a more comprehensive and nuanced sorting mechanism within the agricultural domain.

ACKNOWLEDGEMENT

Mr. Oprea Daniel, from Fundeni, Buzau County, to whom the authors extend their appreciation, has showcased a notable willingness to support our study. His provision of access to his apple orchard proved beneficial for obtaining essential photographs for our dataset. We additionally express our gratitude for his continued support, as he has kindly offered to assist with forthcoming data collection efforts.

REFERENCES

[1] Abdo, A., Hong, C.J., Kuan, L.M., Pauzi, M.M., Sumari, P., Abualigah, L, Zitar, R.A., Oliva, D. (2023). Markisa/Passion Fruit Image Classification Based Improved Deep Learning Approach Using Transfer Learning. In L. Abualigah (Ed.), *Classification Applications with Deep Learning and Machine Learning Technologies* (pp. 143-190). Springer. doi:10.1007/978-3-031-17576-3

[2] Anuar, N.A., Muniandy, L., Bin Jaafar, K.A., Lim, Y., Sabeeh, A.L., Sumari, P., Abualigah, L., Abd Elaziz, M., Alsoud, A.R.,Ahmad MohdAziz Hussein, A.M. (2023). Rambutan Image Classification Using Various Deep Learning Approaches. In L. Abualigah (Ed.), *Classification Applications with Deep Learning and Machine Learning Technologies* (pp. 23-44). Springer. doi:10.1007/978-3-031-17576-3

[3] Jamwal, A., Srivastava, J.N., Dutta, U. (2022). Important Diseases of Apple (Malus domestica L.) and Their Management. In J. S. Srivastava, *Diseases of Horticultural Crops: Diagnosis and Management* (Vol. I, pp. 31-60). Apple Academic Press.

[4] Kavdir, I., Guyer, D.E. (2002, November). Apple Sorting Using Artificial Neural Networks and Spectral Imaging. *Transactions of the ASAE. American Society of Agricultural Engineers, 45*(6).

[5] Ke, C., Weng, N.T., Yang, Y., Yang, Z.M., Sumari, P., Abualigah, L., Kamel, S., Ahmadi, M., Al-Qaness, M., Forestiero, A., Alsoud, A.R. (2023). Mango Varieties Classification-Based Optimization with Transfer Learning and Deep Learning Approaches. In L. Abualigah (Ed.), *Classification Applications with Deep Learning and Machine Learning Technologies* (pp. 45-66). Springer. doi:10.1007/978-3-031-17576-3

[6] Keresztes, B., Abdelghafour, F., Randriamanga. D., da Costa, J.-P., Germain, C. (2018). Real-time Fruit Detection Using Deep Neural Networks. *14th International Conference on Precision Agriculture.* Montréal. Retrieved from https://hal.science/hal-02518559

[7] Khazalah, A., Prasanthi, B., Thomas, D., Vello, N., Jayaprakasam, S., Sumari, P., Abualigah, L., Ezugwu, A.E., Hanandeh, E.S., Khodadadi, N. (2023). Image Processing Identification for Sapodilla Using Convolution Neural Network (CNN) and Transfer Learning Techniques. In L. Abualigah (Ed.), *Classification Applications with Deep Learning and Machine Learning Technologies* (pp. 108-128). Springer. doi:10.1007/978-3-031-17576-3

[8] Larner, A. (2023). *The 2x2 Matrix. Contingency, Confusion and the Metrics of Binary Classification.* Springer. doi:10.1007/978-3-030-74920-0

[9] Li, Y., Feng, X., Liu, Y., Han, X. (2021). Apple quality identification and classification by image processing based on convolutional neural networks. *Nature (Scientific Reports), 11*. doi:10.1038/s41598-021-96103-2

[10] Liu, W. (2020). Interfruit: Deep Learning Network for Classifying Fruit Images. *bioRxiv*. doi:10.1101/2020.02.09.941039

[11] Nataraj K. B, Manohar M., Poornima K., Niharika, U. (2018, February). Automated System for Detection of Apple Purity and Its Grading. *International Journal on Future Revolution in Computer Science & Communication Engineering, IV*(2), 100-103.

[12] Nguyen, T.-H., Nguyen, T.-N., Ba-Viet Ngo, B-V. (2022). A VGG-19 Model with Transfer Learning and Image Segmentation for Classification of Tomato Leaf Disease. *AgriEngineering*(4), 871–887. doi:10.3390/agriengineering4040056

[13] Ong, S.-Q., Nair, G., Al Dabbagh, R.D., Aminuddin, N.F., Sumari, P, Abualigah, L, Jia, H., Mahajan, S., G. Hussien, A.G., Abd Elminaam, D.S. (2023). Comparison of Pre-trained and Convolutional Neural Networks for Classification of Jackfruit Artocarpus integer and Artocarpus heterophyllus. In L. Abualigah (Ed.), *Classification Applications with Deep Learning and Machine Learning Technologies* (pp. 129-142). Springer. doi:10.1007/978-3-031-17576-3

[14] Pen, L.Z., Xian, K.X., Yew, C.F., Hau, O.S., Sumari, P., Abualigah, L., Ezugwu A.E., Al Shinwan, M., Gul, F., Mughaid, A. (2023). Artocarpus Classification Technique Using Deep Learning Based Convolutional Neural Network. In L. Abualigah (Ed.), *Classification Applications with Deep Learning and Machine Learning Technologies* (pp. 1-22). Springer. doi:10.1007/978-3-031-17576-3

[15] Seema, Kumar, K., Gill, G.S. (2015). Automatic Fruit Grading and Classification System Using Computer Vision: A Review. *Second International Conference on Advances in Computing and Communication Engineering* (pp. 598-603). Dehradun: IEEE. doi:10.1109/ICACCE.2015.15

[16] Simonyan, K., Zisserman, A. (2015). Very Deep Convolutional Networks. *ICLR 2015.* Retrieved from https://arxiv.org/abs/1409.1556v6

[17] Srivastava, J.N., Singh, A.K., Sharma, R.K. (2021). Diseases of Apples and Their Management. In G. A. Chand, *Diseases of fruits and vegetable crops: recent management approaches* (pp. 19-40). Apple Academic Press.

[18] Tan, M., Le, Q. v. (2019). EfficientNet: Rethinking Model Scaling for Convolutional Neural Networks. *Proceedings of the 36th International Conference on Machine Learning*, Long Beach, California, PMLR 97. Retrieved from arXiv:1905.11946v5 [cs.LG] 11 Sep 2020

[19] Theng, L.W., San, M.M., Cheng, O.Z., Shen, W.W., Sumari, P., Abualigah, L., Zitar, R.A., Izci, D., Jamei, M., Al-Zu'bi, S. (2023). Salak Image Classification Method Based Deep Learning Technique Using Two Transfer Learning Models. In L. Abualigah (Ed.), *Classification Applications with Deep Learning and Machine Learning Technologies* (pp. 67-106). Springer. doi:10.1007/978-3-031-17576-3

[20] Wan, S., Goudos, S. (2020). Faster R-CNN for multi-class fruit detection using a robotic vision system. *Computer Networks, 168*(107036). doi:10.1016/j.comnet.2019.107036

[21] Yu, F., Lu, T., Xue, C. (2023, December). Deep Learning-Based Intelligent Apple Variety Classification System and Model Interpretability Analysis. *Foods, 885*. doi:10.3390/foods12040885

[22] Zhang, L., Gui, G., Khattak, A.M. (2019). Multi-Task Cascaded Convolutional Networks Based Intelligent Fruit Detection for Designing Automated Robot. *IEEE Access, 7*. doi:0.1109/ACCESS.2019.2899940

IMPROVED YOLOv8-BASED AUTOMATED DETECTION OF WHEAT LEAF DISEASES
/
基于改进 YOLOv8 的小麦叶片病害自动检测

Na MA, Yanwen LI, Miao XU, Hongwen YAN*[1]
College of Information Science and Engineering, Shanxi Agricultural University, Taigu/China
Tel: +86-0354-6288165; E-mail: yhwhxh@126.com
DOI: https://doi.org/10.35633/inmateh-71-43

Keywords: *wheat leaf, disease detection, YOLOv8, CBAM attention mechanism*

ABSTRACT
Stripe rust, leaf rust, and powdery mildew are important leaf diseases in wheat, which significantly affect the yield and quality of wheat. Their timely identification and diagnosis are of great significance for disease management. To achieve convenient identification of wheat leaf diseases based on mobile devices, an improved YOLOv8 method for wheat leaf disease detection is proposed. This method incorporates the CBAM (Convolutional Block Attention Module) attention mechanism module into the feature fusion network to enhance the network's feature expression ability. Experimental results show that the improved YOLOv8 model has an accuracy, recall rate, and mean average precision (mAP) of 95%, 98.3%, and 98.8% respectively for wheat leaf disease detection, with a model memory usage of 5.92 MB. Compared with the Faster R-CNN, YOLOv5, YOLOv7, and YOLOv8 models, the mAP has been improved by 66.76, 48, 13.2, and 1.9 percentage points respectively, and it also has the lowest model memory usage. The research demonstrates that the improved YOLOv8 model can provide an effective exploration for automated detection of wheat leaf diseases.

摘要
小麦条锈病、叶锈病和白粉病是小麦叶部重要病害，严重影响小麦的产量和品质，其及时识别和诊断对于病害管理具有重要意义。为实现基于移动端的小麦叶部病害图像便捷识别，提出一种改进的yolov8 小麦叶部病害检测方法。该方法在特征融合网络中加入 CBAM 注意力机制模块以提高网络的特征表达能力。实验结果表明，改进的 yolov8 模型对小麦叶片病害检测的精确率、召回率和平均精度均值（Mean average precision，mAP）分别为 95%、98.3% 和 98.8%，模型内存占用量为 5.92MB。对比 Faster R-CNN、YOLOv5、YOLOv7 和 YOLOv8 模型，平均精度均值 mAP 分别提升了 66.76、48、13.2、1.9 个百分点，模型内存占用量方面也最优。研究表明改进的 YOLOv8 模型能够为小麦叶片病害实现自动化检测提供有效探索。

INTRODUCTION
Wheat is an important cereal crop and the second most consumed grain globally, second only to rice. It is a staple food for over one-third of the world's population. The yield of wheat is influenced by various factors such as climate, temperature, soil, pests, bacteria, and other biotic and abiotic factors *(Li et al., 2023; Sereda et al., 2023)*. Then, diseases also have a significant impact on the yield and quality of wheat (*Chai et al., 2022).* Most wheat diseases occur on the leaves, with powdery mildew, leaf rust, and stripe rust being the most common ones. All of these are fungal diseases that can cause significant yield losses in wheat *(Khan et al., 2022; Kartikeyan et al., 2021)*. However, due to the small size and difficult observation of early-stage diseases, farmers lacking professional knowledge, timely prevention and control of wheat diseases is not possible. Therefore, achieving accurate identification of wheat diseases and providing guidance for agricultural production in an efficient manner is one of the key factors for the development of modern agriculture.

The rapid and accurate identification of wheat disease types using computer vision technology has important application value in the prevention and control of wheat diseases. Traditional computer vision recognition of crop diseases usually involves multiple steps, such as preprocessing of disease images, lesion segmentation, feature extraction and selection, and classification using classifiers such as Support Vector Machine (SVM) and neural networks. *Sahu et al.* proposed a novel Hybrid Random Forest Multi-Class SVM (HRF-MCSVM) method for detecting plant leaf diseases *(Sahu et al., 2023)*.

Rahmanet et al. used the Gray-Level Co-occurrence Matrix (GLCM) algorithm to calculate 13 different statistical features of tomato leaves. The obtained features were classified into different diseases using Support Vector Machine (SVM) *(Rahmanet et al., 2023)*.

[1] *Na MA, As. Lect. M.S. Eng.; Yanwen LI, Lect. M.S. Eng.; Miao XU, Lect. M.S. Eng.; Hongwen Yan*, Prof. Ph.D. Eng.*

Kumar et al. used median filtering technique for preprocessing rice leaf diseases. The proposed prototype achieved an accuracy of approximately 98.8% in detecting and classifying rice leaf diseases *(Kumar et al., 2022)*. However, with the popularity of large-scale cultivation and the accelerated spread of crop pathogens, traditional methods of manually extracting features for input into classifiers are gradually being eliminated *(Thakur et al., 2022)*. Firstly, they are highly dependent on the quality of the original disease images, and the selection of the most appropriate preprocessing and segmentation methods depends on the nature of the dataset. Secondly, manual selection of features requires strong agricultural expertise and a limited number of selected features, in the face of massive data, then it is difficult to effectively construct the appropriate model using these traditional machine learning methods, which will greatly limit the progress of disease identification.

In recent years, with the generation of large-scale labelled data and the rapid improvement of computer processing power, deep learning technology has developed rapidly. Classification, target detection, image segmentation and other deep learning methods have become the latest technology for automatic detection of crop diseases *(Orchi et al., 2021; Chen et al., 2020)*. Agarwal et al. utilized convolutional neural networks to detect and classify diseases on tomato leaves. The average accuracy of the proposed model was 91.2% *(Agarwal et al., 2020)*. Jiang et al. proposed an improved VGG16 model and a multi-task transfer learning approach that can simultaneously identify diseases on rice leaves and wheat leaves, providing a reliable method for identifying leaf diseases in multiple plants *(Jiang et al., 2021)*. Parasa et al. designed an optimized framework based on ant-lion for YOLOv-5, which can generate images affected by diseases without impacting the original image *(Parasa et al., 2023)*. Fang et al. combined residual modules and initial modules to construct a lightweight multi-scale CNN model. They incorporated CBAM and ECA modules into the residual modules to increase the model's focus on diseases and reduce the impact of complex backgrounds on disease recognition. The proposed method achieved an accuracy rate of 98.7% in wheat disease identification *(Fang et al., 2023)*.

The above research shows that deep learning can achieve certain effects in crop and plant disease detection methods. However, existing models have the following issues: most methods with high detection accuracy have high model computational complexity and slow detection speed, while methods with low model computational complexity and fast detection speed have lower detection accuracy. YOLOv8 is the latest version of YOLO series of target detection algorithms, and compared to the previous version, YOLOv8 has a faster inference speed, higher accuracy, and is easier to train and adjust. Therefore, for the problem of wheat leaf disease, adopting the latest YOLOv8 model as the base model and improving it to be better applied to wheat leaf disease detection, realize efficient automated disease detection, improve detection accuracy, reduce prevention and control costs, and be able to ensure the quality and safety of agricultural products, is of great application prospect and social significance, and provides technical support for the development of intelligent identification system of wheat disease based on mobile terminal.

MATERIALS AND METHODS

Data acquisition and pre-processing

The experimental data was collected from the wheat experimental field of Shanxi Agricultural University, from 2020 to 2023. A total of 825 images of three types of wheat leaf diseases, including powdery mildew, stripe rust, and leaf rust, were collected using the vivo Z3i smartphone in complex natural environments. Among them, 306 images of powdery mildew, 320 images of leaf rust, and 304 images of stripe rust were collected. The data collection is shown in Figure 1.

a.powdery mildew



b.stripe rust

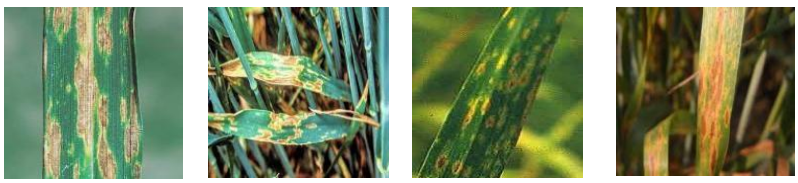




Fig.1 - Partial Data Collection

Due to the insufficient sample size of the wheat disease dataset to achieve convergence during model training, data augmentation techniques were employed to improve the training effectiveness of the network model and enhance its generalization ability. In this study, various data augmentation methods, including Gaussian blur, horizontal flip, vertical flip, non-uniform scaling, random translation, perspective transformation, and random cropping, were randomly combined to augment the dataset. Through data augmentation, a total of 1530 images of powdery mildew on wheat leaves, 1600 images of wheat leaf rust, and 1520 images of wheat stripe rust were obtained.

Use LabelImg to annotate the wheat leaf disease image dataset and save the annotations in .txt format. Label the disease regions on wheat leaves and set the labels as wheat powdery mildew, leaf rust, and stripe rust. A total of 2200 were annotated for wheat powdery mildew, 1725 for leaf rust, and 2070 for stripe rust.

Improved YOLOv8 model

Collecting wheat leaves in natural environments is challenging as they are prone to branch and leaf obstructions, which can decrease the accuracy of wheat leaf disease detection. In 2023, Ultralytics released an updated version of YOLO, the YOLOv8 model, which has higher accuracy *(Hussain et al., 2023)*. Therefore, this study adopts the YOLOv8 model to achieve automatic detection of wheat leaf diseases. To improve the accuracy and speed of wheat leaf disease detection, the YOLOv8 model will be further improved to obtain an optimal model that can be deployed for applications.

YOLOv8 model

The YOLOv8 model is divided into two parts: the Backbone network and the Head network. YOLOv8 incorporates the excellent features of previous generations of networks. The Backbone network and Neck part follow the idea of CSP, replacing the C3 module in YOLOv5 *(Xu et al., 2023)* with a more feature-rich C2f module. The convolution structure in the upsampling stage of PAN-FPN in YOLOv5 is removed. The features outputted from different stages of the Backbone are directly fed into the upsampling operation. The model provides different-sized models of N/S/M/L/X scales, which can meet the needs of different industries and domains.

The process of YOLOv8 detection is as follows:

The input image is passed through a backbone network to extract features.

The feature map is refined and fused through multiple downsampling and upsampling layers.

The feature map is then used for prediction, generating predicted bounding boxes and class probabilities for each grid cell.

Finally, post-processing operations such as non-maximum suppression (NMS) and threshold filtering are applied to obtain the final object detection results.

The improvements in YOLOv8 are as follows:

1. Backbone: YOLOv8 still follows the concept of CSP (Cross Stage Partial) used in YOLOv5, but replaces the C3 module with the C2f module, achieving further lightweight design. YOLOv8 also utilizes the SPPF (Spatial Pyramid Pooling Fusion) module used in YOLOv5 architecture.

Figure 2 shows the C3 structure diagram, while Figure 3 shows the C2F structure diagram. In Figure 3, the input Tensor of each Bottleneck has only half the number of channels compared to the previous level, resulting in a significant reduction in computational complexity. On the other hand, the increase in gradient flow can also noticeably improve the convergence speed and effectiveness.

2. PAN-FPN: YOLOv8 still employs the PAN (Path Aggregation Network) concept, but removes the convolutional structure in the upsampling stage of PAN-FPN used in YOLOv5. Additionally, the C3 module is replaced with the C2f module in YOLOv8.

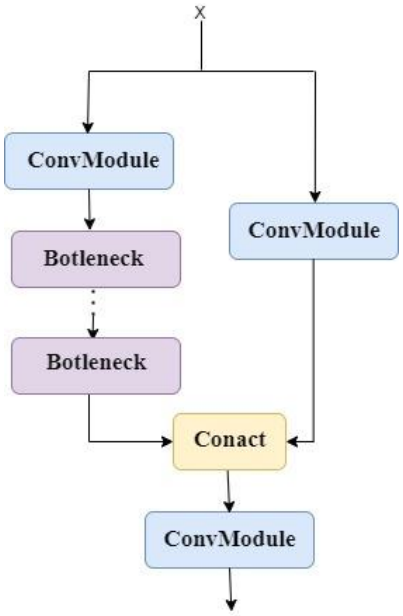


Fig. 2 - C3 model

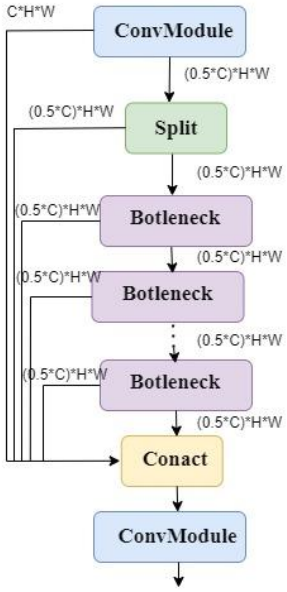


Fig. 3 - C2F model

3. Head changes: The most significant change in the Head part is that it transforms from the previous coupled head to a decoupled head, and it goes from Anchor-Based in YOLOv5 to Anchor-Free in YOLOv8. The head structure of YOLOv5 is shown in Figure 4, and the head structure of YOLOv8 is shown in Figure 5. From the figures, it can be observed that YOLOv8 no longer has the objectness branch as in the previous version. It only consists of decoupled classification and regression branches. Additionally, its regression branch utilizes the integral representation proposed in the Distribution Focal Loss.

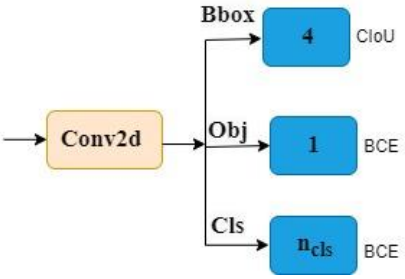


Fig. 4 - Yolov5 coupled head

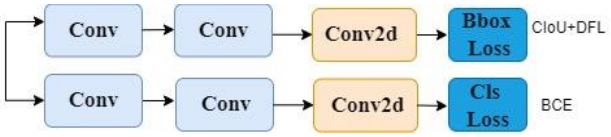


Fig. 5 - Yolov8 decoupled head

4. Loss function: YOLOv8 uses the VFL (Varifocal Loss) as the classification loss and combines DFL (Distribution Focal Loss) with CIOU (Complete Intersection over Union) Loss as the regression loss.

5. Sample Matching: YOLOv8 discards the previous IOU matching or unidirectional proportion assignment approach and instead uses the Task-Aligned Assigner matching method.

CBAM Attentional Mechanisms

CBAM (Convolutional Block Attention Module) attention mechanism is a module used for image recognition tasks. It introduces two sub-modules, channel attention and spatial attention, into convolutional neural networks to enhance the capturing ability of key features, as shown in Figure 6. The channel attention module adjusts the channel weights of feature maps by learning the relationships between channels, in order to extract the most representative features. This module first obtains the global features of each channel through global average pooling layer, and then calculates the channel weights through a fully connected layer. Finally, the channel weights are applied to the feature maps to adjust the importance of each channel.

The spatial attention module adjusts the spatial weights of feature maps by learning the relationships in the spatial dimension, in order to extract the most representative spatial information. This module first generates spatial feature maps through a convolutional layer, and then calculates the weights for each spatial position through a fully connected layer. Finally, the spatial weights are applied to the feature maps to adjust the importance of each spatial position.

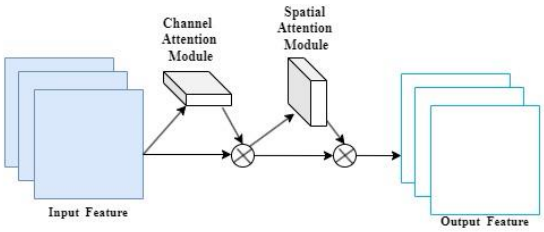


Fig. 6 - CBAM channel attention module

Improved YOLOv8

CBAM can enhance the feature capturing capability of the YOLOv8 model. By introducing two sub-modules, channel attention and spatial attention, CBAM can adjust the channel weights and spatial weights of the feature map to extract the most representative features and spatial information. By embedding the CBAM module in the YOLOv8 network, the detection accuracy and performance of the model can be improved.

Incorporating CBAM into the backbone layer of YOLOv8, the network architecture is shown in Figure 7.

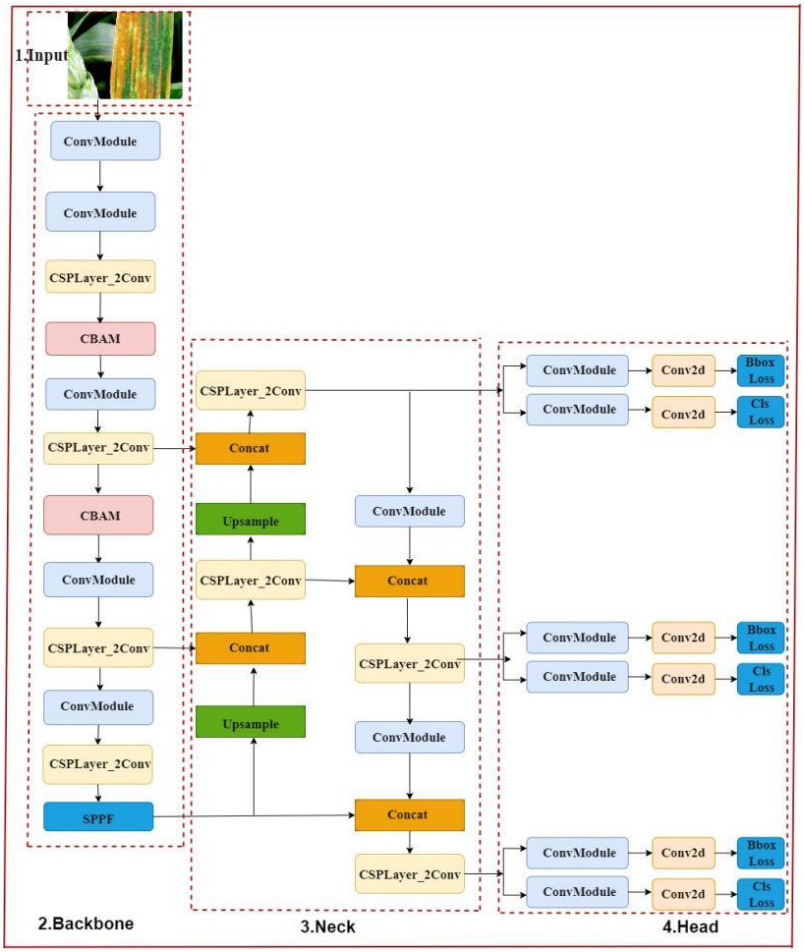


Fig. 7 - Improved YOLOv8 network structure

Model Evaluation Metrics

In this study, Precision (P), Recall (R), Average Precision (AP), and Mean Average Precision (mAP) are used to evaluate the performance of wheat leaf disease detection. The calculations are as follows:

$$\text{Precision} = \frac{\text{TP}}{\text{TP} + \text{FP}} \tag{1}$$

$$\text{Recall} = \frac{\text{TP}}{\text{TP} + \text{FN}} \tag{2}$$

where:

TP (True Positive) represents the number of correct predictions as positive samples.

FP represents the number of incorrect predictions as positive samples.

FN represents the number of incorrect predictions as negative samples.

Average Precision (AP): It is calculated by computing the precision-recall curve and taking the area under the curve (AUC). AP represents the average precision across all recall levels.

Mean Average Precision (mAP): It is the average of AP values calculated for each class or category. mAP provides an overall evaluation of the detection performance across different classes.

RESULTS

The operating system used for the experiment is Windows 10. The CPU model is Intel(R) Core(TM) i7-13700F @2.10GHz. The GPU model is NVIDIA GeForce RTX 4080. The system has 32GB of RAM and a 1TB mechanical hard drive. The programming language used is Python 3.9. The deep learning framework used is PyTorch 2.0.1. GPU acceleration libraries used are CUDA 11.8 and CUDNN 8.8.0.

The annotated data mentioned above is randomly divided into a training set and a test set in an 8:2 ratio. The improved YOLOv8 algorithm is used to evaluate the test set, which consists of 306 wheat leaf powdery mildew images, 320 wheat leaf rust images, and 304 wheat leaf stripe rust images. Among these images, there are 440 annotated wheat leaf powdery mildew instances, 345 annotated wheat leaf rust instances, and 414 annotated wheat leaf stripe rust instances.

In this study, the input image size is set to 640*640 pixels. The frozen training approach is used, with an initial learning rate of 0.0001, a momentum of 0.9, a batch size of 16, and a total of 100 iterations.

Detection results of different wheat diseases under the improved YOLOv8 model

To evaluate the performance of the improved YOLOv8 model, the wheat disease leaf samples in the test set were tested and the detection results, including TP, FP, and FN values, are shown in Table 1. From the table, it can be observed that out of the 440 marked wheat powdery mildew leaf samples, 440 were correctly detected as wheat powdery mildew, while 20 were falsely detected. Out of the 345 marked wheat leaf rust samples, 327 were correctly detected, 29 were falsely detected, and 18 were mistakenly detected as wheat leaf rust. As for the 414 marked wheat stripe rust samples, 414 were correctly detected as wheat stripe rust, while 11 were falsely detected.

Table 1

TP, FP, and FN values for different disease detection

Disease	TP	FP	FN
Wheat Powdery Mildew	440	20	0
Wheat Leaf Rust	327	29	18
Wheat Stripe Rust	414	11	0

Therefore, according to the precision, recall, and Mean Average Precision (mAP) calculation formulas, the detection results of different wheat leaf diseases by the algorithm in this paper are shown in Table 2. From Table 2, it can be observed that the average precision of the algorithm in this paper (mAP) can reach 98.8%, with the Precision of 95% and the recall of 98.3%.

Table 2

Detection results of different wheat leaf diseases

Disease	Precision [%]	Recall [%]	AP [%]
Wheat Powdery Mildew	95.7	1	99.5
Wheat Leaf Rust	91.9	94.8	97.7
Wheat Stripe Rust	97.4	1	99.1
Average	95.0	98.3	98.8

Partial detection examples are shown in Figure 8. From Figure 8, it can be seen that the algorithm proposed in this paper can accurately detect various types of wheat diseases. Figures 8(a)(b)(c) show that the algorithm can detect the targets well, whether it is with or against the light, in single leaf without obstruction.

Figures 8(d)(e)(f) show that the algorithm can also accurately detect wheat disease leaves in the case of multiple targets and obstructions. In summary, the improved YOLOv8 model can accurately detect different types of wheat disease leaves, and it has good detection performance for single targets, multiple targets, obstructions, and lighting effects.



Fig. 8 - Partial detection results

a *- leaf rust single target + backlit,* ***b*** *- powdery mildew single target + backlit,* ***c*** *- stripe rust single target + frontlit,* ***d*** *- leaf rust multiple targets + frontlit,* ***e*** *- powdery mildew multiple targets + frontlit;* ***f*** *- stripe rust multiple targets + backlit*

Comparison of improved YOLOv8 model and YOLOv8 model for wheat disease detection results

For each type of wheat leaf disease detection, the TP value represents the number of correctly detected instances of that disease, while the FP value represents the number of incorrectly detected instances of that disease. The comparison of TP/FP in wheat disease leaf detection results between the improved YOLOv8 model and YOLOv8 model is shown in Figure 9, where a represents the detection results of improved YOLOv8 algorithm for wheat powdery mildew, b represents the detection results of YOLOv8 algorithm for wheat powdery mildew, c represents the detection results of improved YOLOv8 algorithm for wheat leaf rust, d represents the detection results of YOLOv8 algorithm for wheat leaf rust, e represents the detection results of improved YOLOv8 algorithm for wheat stripe rust, and f represents the detection results of YOLOv8 algorithm for wheat stripe rust. It can be seen that for wheat powdery mildew and leaf rust, the improved algorithm in this study has an increase of 4 and 7 in TP values, and the decrease of 8 and 27 in FP values, respectively. Although the improvement in TP values is not significant, there is a significant difference in FP values, which highlights the advantage of the improved algorithm in this study.

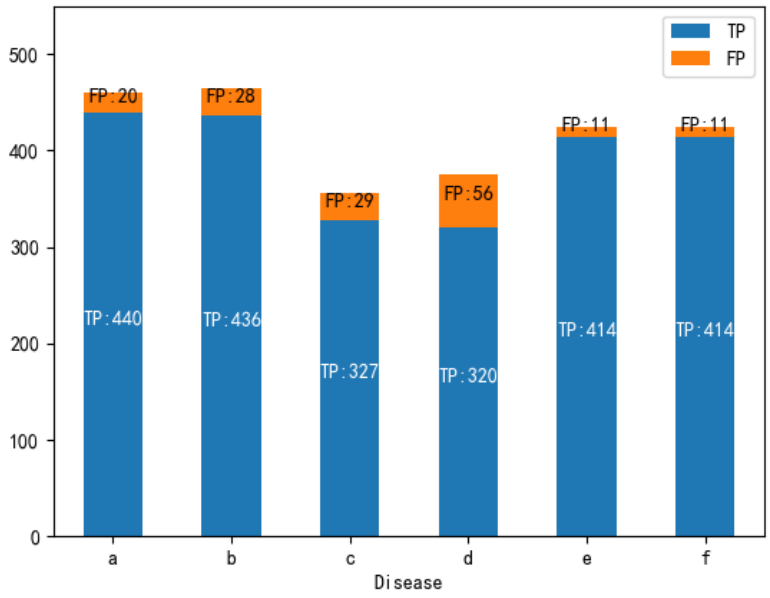


Fig. 9 - Comparison of TP/FP values for different algorithms

The detection results of improved YOLOv8 model and YOLOv8 model for different wheat leaf diseases are shown in Table 3. It can be observed that the improved algorithm in this study has improved precision and recall for wheat powdery mildew and leaf rust, and has also improved the AP values for all three wheat diseases. The mAP value for wheat disease detection has increased from 0.969 to 0.988, showing a 1.9% improvement.

Table 3

Detection Results of Improved YOLOv8 Model and YOLOv8 Model

	Disease	Precision[%]	Recall[%]	AP[%]
YOLOv8	Wheat Powdery Mildew	94	99.1	99.3
	Wheat Leaf Rust	85.1	92.8	92.4
	Wheat Stripe Rust	97.4	1.00	99.0
	average	92.2	97.3	96.9
Improved YOLOv8	Wheat Powdery Mildew	95.7	1	99.5
	Wheat Leaf Rust	91.9	94.8	97.7
	Wheat Stripe Rust	97.4	1	99.1
	average	95	98.3	98.8

Analysis of Comparative Results of Different Object Detection Networks

To qualitatively evaluate the detection results of the improved YOLOv8 model, the improved model was compared with the Faster R-CNN model *(Ren et al., 2015)*, YOLOv5 model *(Jiang et al., 2022)*, YOLOv7 model *(Wang et al., 2023)*, and the original YOLOv8 model on the test set of wheat leaf disease images. The detection results of the 5 models are shown in Table 4. It can be seen that the improved YOLOv8 algorithm in this paper achieves the best detection results for three types of wheat leaf diseases, and the model size is relatively small.

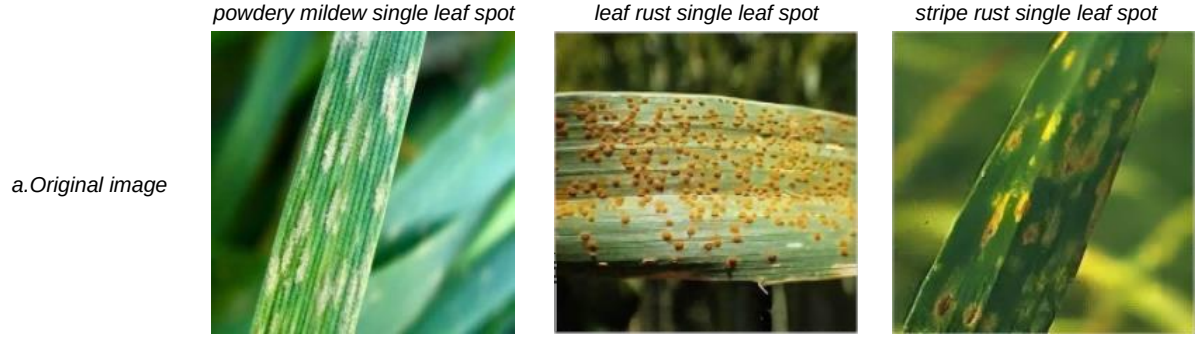
Table 4

Detection Results of Different Models

Model	AP [%]			mAP [%]	Size of the Weight Files (MB)
	Wheat Powdery Mildew	Wheat Leaf Rust	Wheat Stripe Rust		
Faster R-CNN	0.28	0.42	0.27	32.04	108
Ylov5	0.357	0.956	0.212	50.8	14.3
Yolov7	0.957	0.629	0.982	85.6	71.3
Yolov8	0.993	0.924	0.990	96.9	5.92
Improved Yolov8	0.995	0.977	0.991	98.8	5.92

In order to further demonstrate the detection results of five different object detection models for wheat leaf disease, detection on three types of wheat leaf diseases in the test set was conducted.

The comparison of the detection results is shown in Figure 10 and Figure 11.



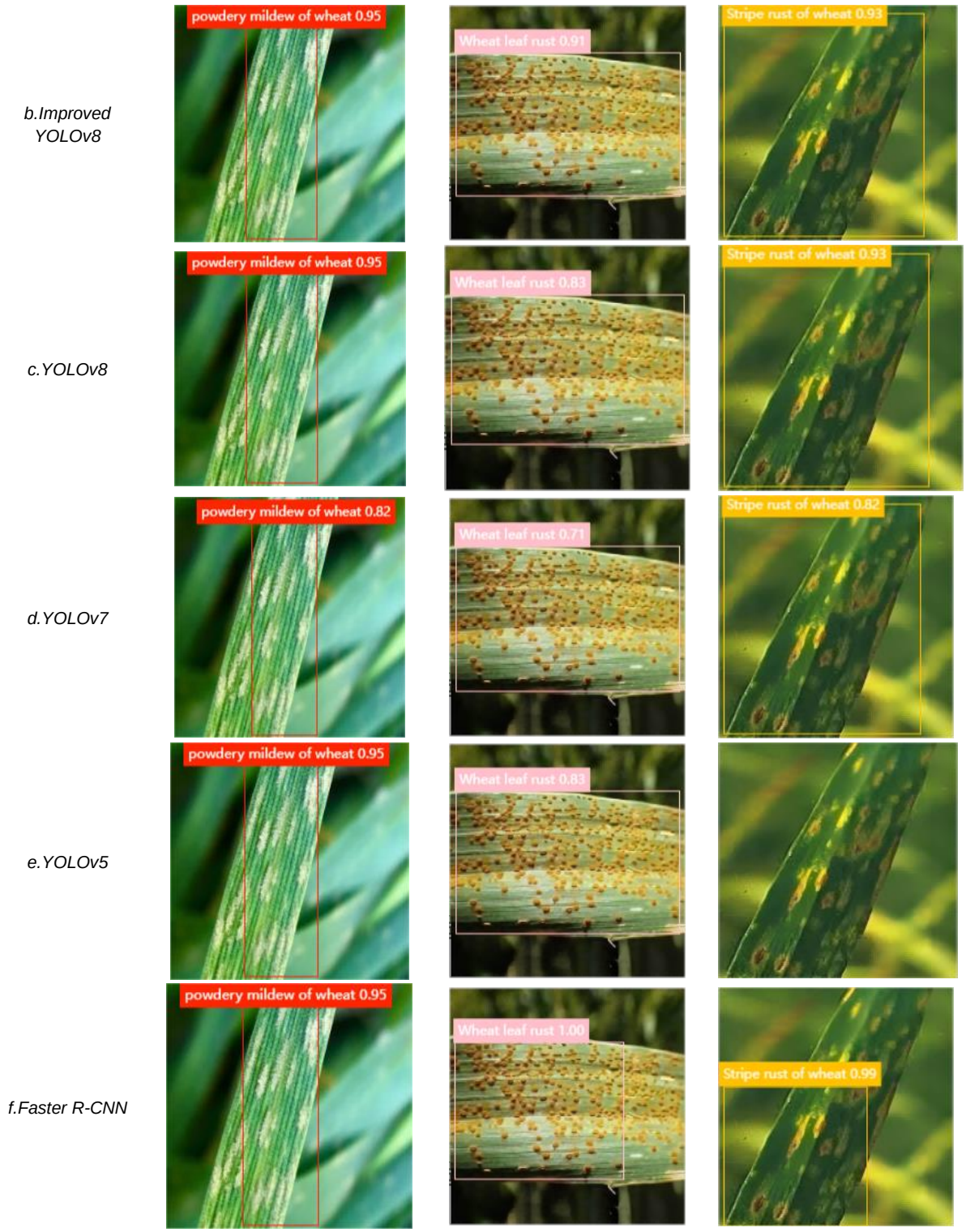
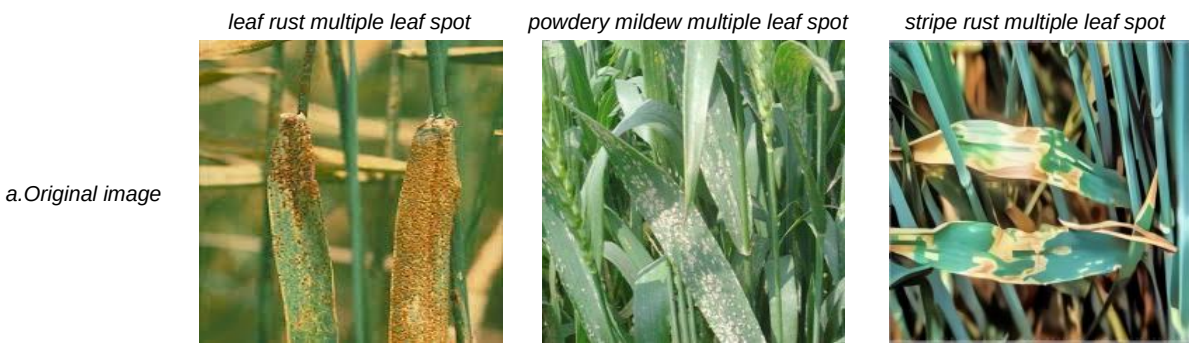


Fig.10 - Single-target prediction results of five models



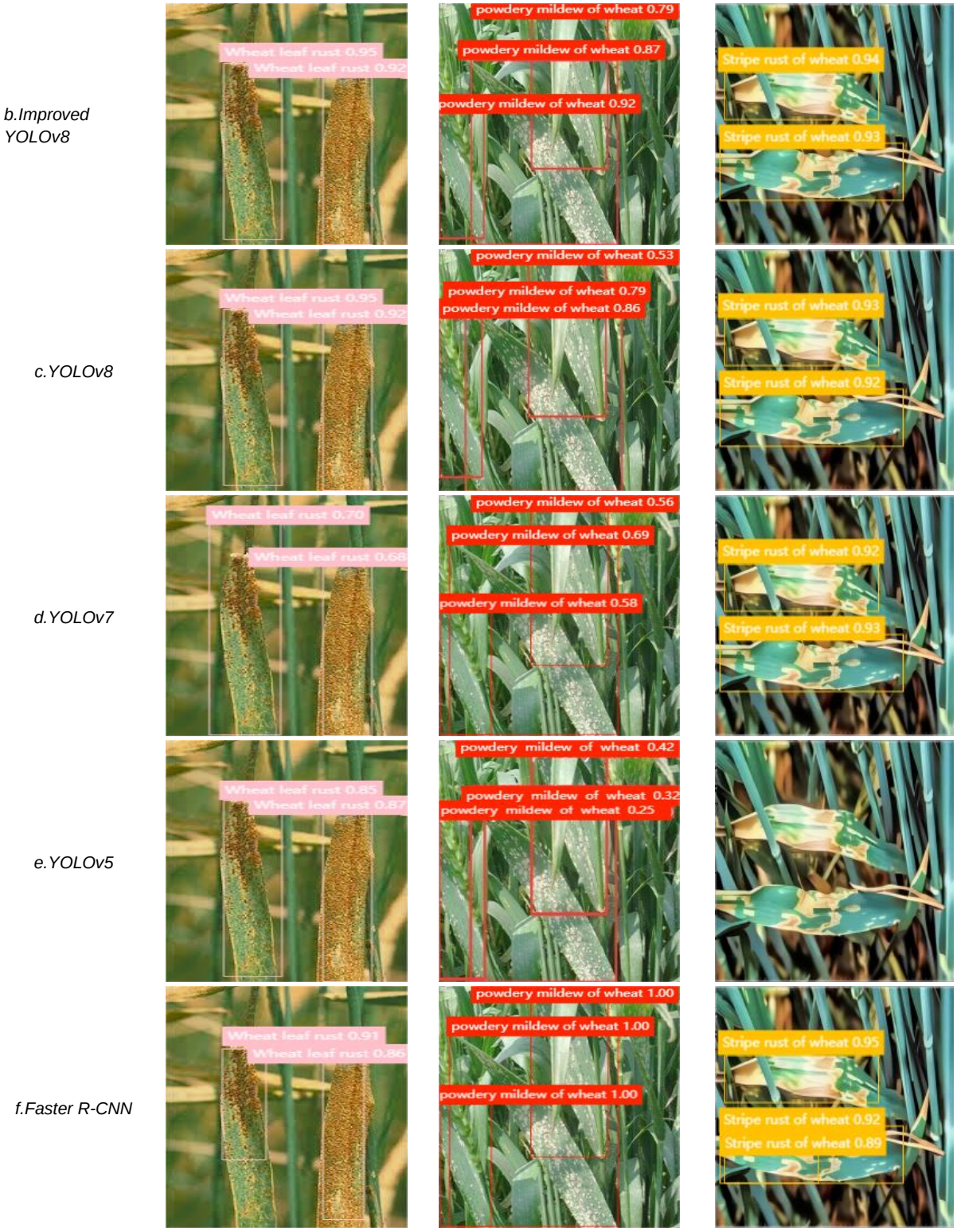


Fig.11 - Multi-target prediction results of five models

From the recognition results of the improved YOLOv8 model in Figure 10(b) and 11(b), it can be seen that the improved YOLOv8 model can accurately detect diseases in single-object, multi-object, and occluded scenarios, with high detection accuracy. From the YOLOv8 recognition results in Figure 10(c) and 11(c), it can be observed that the YOLOv8 model can detect disease leaves in both single-object and multi-object scenarios, but in some cases, the recognition rate is not as high as the improved YOLOv8 model. From the YOLOv7 recognition results in Figure 10(d) and 11(d), it can be seen that the YOLOv7 model can detect wheat disease targets in single-object detection, but with low recognition accuracy. In multi-object detection, there are cases of misjudgment.

From the YOLOv5 recognition results in Figure 10(e) and 11(e), it can be seen that the YOLOv5 model has missed detections in both single-object and multi-object detection. From the Faster R-CNN recognition results in Figure 10(f) and 11(f), it can be seen that the Faster R-CNN model has inaccurate detection ranges in both single-object and multi-object detection, and there are cases of repeated detections in multi-object detection. In conclusion, the improved YOLOv8 model in this paper has the best detection performance for wheat leaf disease.

CONCLUSIONS

(1) This study focuses on powdery mildew, leaf rust, and stripe rust of wheat leaves and proposes an improved YOLOv8 model for wheat leaf disease detection. The CBAM attention mechanism is introduced into the YOLOv8 model to improve its detection performance.

(2) To evaluate the performance of the improved YOLOv8 model, this paper compares the detection results of the original YOLOv8 model and the improved YOLOv8 model on the three types of wheat leaf diseases. The quantitative analysis of the detection results shows that the improved model increases the mAP value of wheat leaf disease detection from 0.969 to 0.988, with an improvement of 1.9 percentage points.

(3) Under the same experimental conditions, compared with the Faster R-CNN, YOLOv5, YOLOv7, and YOLOv8 models, the improved model achieves better results on the wheat leaf disease dataset, with an average precision (mAP) improvement of 66.76, 48, 13.2, and 1.9 percentage points, respectively. The experiments fully demonstrate that the improved YOLOv8 model has good performance in wheat disease detection.

The wheat leaf disease detection based on the improved YOLOv8 model has the advantages of small size, high accuracy, and fast recognition speed. It is convenient for deployment on machines for real-time detection, lightweight, and portable, providing a good reference for the application of wheat disease recognition on mobile devices. However, since there are very few samples in the collected data with multiple diseases simultaneously, further research is needed for the simultaneous detection of multiple wheat diseases.

ACKNOWLEDGEMENT

This research, titled “Improved Yolov8-based automated detection of wheat leaf diseases”, was funded by the Basic Research Program of Shanxi Province (202103021223241), the Youth Scientific Research Foundation of Shanxi Agricultural University(2020QC17).

REFERENCES

[1] Agarwal, M.; Singh, A.; Arjaria, S.; Sinha, A.; Gupta, ToLeD S. (2020). Tomato leaf disease detection using convolution neural network [J]. *Procedia Computer Science*, 167: 293-301. https://doi.org/10.1016/j.procs.2020.03.225

[2] Chai, Y.; Senay, S.; Horvath, D.; Pardey, P. (2022). Multi-peril pathogen risks to global wheat production: A probabilistic loss and investment assessment [J]. *Frontiers in Plant Science*, 13: 1034600. https://doi.org/10.3389/fpls.2022.1034600

[3] Chen, J.; Chen, J.; Zhang, D.; Sun, Y.; Nanehkaran, Y. (2020). Using deep transfer learning for image-based plant disease identification [J]. *Computers and Electronics in Agriculture*, 173: 105393. https://doi.org/10.1016/j.compag.2020.105393

[4] Fang, X.; Zhen, T.; Li, Z. (2023). Lightweight Multiscale CNN Model for Wheat Disease Detection. *Applied Sciences ,13*(9): 5801. https://doi.org/10.3390/app13095801

[5] Hussain, M. (2023). YOLO-v1 to YOLO-v8, the Rise of YOLO and Its Complementary Nature toward Digital Manufacturing and Industrial Defect Detection [J]. *Machines*, *11*(7): 677. https://doi.org/10.3390/machines11070677

[6] Jiang, Z.; Dong, Z.; Jiang, W.; Yang, Y. (2021). Recognition of rice leaf diseases and wheat leaf diseases based on multi-task deep transfer learning [J]. *Computers and Electronics in Agriculture*, 186: 106184. https://doi.org/10.1016/j.compag.2021.106184

[7] Jiang. P.; Ergu, D.; Liu, F.;Cai, Y.; Ma, B. (2022). A Review of Yolo algorithm developments[J]. *Procedia Computer Science*, 199: 1066-1073. https://doi.org/10.1016/j.procs.2022.01.135

[8] Kartikeyan, P.; Shrivastava, G. (2021). Review on emerging trends in detection of plant diseases using image processing with machine learning[J]. *International Journal of Computer Application*, 975: 8887. https://doi.org/10.5120/ijca2021920990

[9] Khan, H.; Haq, I.; Munsif, M.; Mustageem. (2022). Automated wheat diseases classification framework using advanced machine learning technique [J]. *Agriculture*, *12*(8): 1226. https://doi.org/10.3390/agriculture12081226

[10] Kumar, K.; Kannan, E. (2022). Detection of rice plant disease using AdaBoostSVM classifier[J]. *Agronomy journal*, *114*(4): 2213-2229. https://doi.org/10.1002/agj2.21070

[11] Li, Z.; Fang, X.; Zhen, T.; Zhu, Y. (2023). Detection of Wheat Yellow Rust Disease Severity Based on Improved GhostNetV2. *Applied Sciences, 13*(17), 9987. https://doi.org/10.3390/app13179987

[12] Orchi, H.; Sadik, M.; Khaldoun, M. (2021). On using artificial intelligence and the internet of things for crop disease detection: A contemporary survey [J]. *Agriculture*, *12*(1): 9. https://doi.org/10.3390/agriculture12010009

[13] Parasa, G.; Arulselvi, M.; Razia, S. (2023). An Intelligent Optimization Based Yolov5 Framework to Detect the Rice Leaf Disease[C].*2023 3rd Asian Conference on Innovation in Technology (ASIANCON). IEEE*, 1-4. https://doi.org/10.1109/ASIANCON58793.2023.10270771

[14] Rahman, S.; Alam, F.; Ahmad, N.; Arshad, S. (2023). Image processing based system for the detection, identification and treatment of tomato leaf diseases [J]. *Multimedia Tools and Applications*, *82*(6): 9431-9445. https://doi.org/10.1007/s11042-022-13715-0

[15] Ren, S.; He, K.; Girshick, R.; Sun, J. (2015). Faster r-cnn: Towards real-time object detection with region proposal networks[J]. *Advances in neural information processing systems*, 28. https://github.com/rbgirshick/fast-rcnn

[16] Sahu, S.; Pandey, M. (2022). An optimal hybrid multiclass SVM for plant leaf disease detection using spatial Fuzzy C-Means model [J]. *Expert Systems with Applications*, 214: 118989. https://doi.org/10.1016/j.eswa.2022.118989

[17] Sereda, I.; Danilov, R.; Kremneva, O.; Zimin, M. (2023). Development of Methods for Remote Monitoring of Leaf Diseases in Wheat Agrocenoses. *Plants*, *12*(18), 3223. https://doi.org/10.3390/plants12183223

[18] Thakur, P.; Khanna, P.; Sheorey, T.; Ojha, A. (2022). Trends in vision-based machine learning techniques for plant disease identification: A systematic review [J]. *Expert Systems with Applications*, 118117. https://doi.org/10.1016/j.eswa.2022.118117

[19] Wang, C.; Bochkovskiy, A.; Liao, H. (2023). YOLOv7: Trainable bag-of-freebies sets new state-of-the-art for real-time object detectors[C]. *Proceedings of the IEEE/CVF Conference on Computer Vision and Pattern Recognition*, 7464-7475. https://doi.org/10.48550/arXiv.2207.02696

[20] Xu, B.; Cui, X.; Ji, W.; Hao, Y.; Wang, J. (2023). Apple grading method design and implementation for automatic grader based on improved YOLOv5 [J]. *Agriculture*, *13*(1): 124. https://doi.org/10.3390/agriculture13010124

LIGNIN UTILIZATION FOR THE REMOVAL OF MICROPLASTIC PARTICLES FROM WATER
/
UTILIZAREA LIGNINEI PENTRU ÎNDEPĂRTAREA PARTICULELOR DE MICROPLASTIC DIN APĂ

Iuliana GĂGEANU[1)]; Florbela CARVALHEIRO*[2)]; Adam EKIELSKI*[3)]; Luis C. DUARTE[2)]
[1)] INMA Bucharest / Romania;
[2)]LNEG – Laboratório Nacional de Energia e Geologia, Unidade de Bioenergia e Biorrefinarias, Lisboa / Portugal;
[3)] Warsaw University of Life Sciences / Poland
E-mail: florbela.carvalheiro@lneg.pt; adam_ekielski@sggw.edu.pl
DOI: https://doi.org/10.35633/inmateh-71-44

Keywords: *microplastic removal, Miscanthus sp., OFMSW - Organic Fraction of Municipal Solid Wastes, Organosolv lignin, pine bark, solid anaerobic digestates, wastewater treatment*

ABSTRACT
The focus of the research was to evaluate the use of lignin from different sources as an agent for the removal of diverse types of microplastics when present in wastewater. Organosolv lignin was obtained from three different sources (Miscanthus sp., pine bark and solid anaerobic digestates from Organic Fraction of Municipal Solid Wastes) by an ethanol-based organosolv treatment carried out in a pressurized stirred-tank reactor. The lignins obtained were evaluated as an adsorbent for diverse types of microplastics: High-density polyethylene (HDPE), Polystyrene (PS), Expanded Polystyrene (EPS), and Polypropylene (PP). All lignins used had the capacity to capture plastic particles from all plastic types, but a differential absorbance potential was found both for plastic types and lignin samples. EPS was the least adsorb type for all lignin sources, with the remaining plastics presenting equivalent results. Pine bark lignin was the best adsorbent among the tested feedstocks, always presenting the best performance for all plastic types. The direct utilization of organosolv hydrolysates, avoiding lignin recovery presented a similar behaviour. These results open the possibility to develop new natural, plant-based, adsorbents for microplastic removal from contaminated wastewater.

REZUMAT
Scopul cercetării a fost evaluarea utilizării ligninei din diferite surse ca agent pentru îndepărtarea diferitelor tipuri de microplastic atunci când sunt prezente în apele uzate. Lignina a fost obținută prin metoda organosolv din trei surse diferite (Miscanthus sp., scoarță de pin și digestat anaerob solid din fracțiunea organică a deșeurilor solide municipale) printr-un tratament pe bază de etanol, realizat într-un reactor sub presiune cu agitare. Lignina obținută a fost evaluată ca adsorbant pentru diverse tipuri de microplastic: polietilenă de înaltă densitate (HDPE), polistiren (PS), polistiren expandat (EPS) și polipropilenă (PP). Toate tipurile de lignină au avut capacitatea de a capta particule de plastic din toate tipurile de plastic, dar a fost observant un potențial de absorbție diferențiat atât pentru tipurile de plastic, cât și pentru mostrele de lignină. EPS a fost tipul cel mai puțin captat pentru toate sursele de lignină, materialele plastice rămase prezentând rezultate echivalente. Lignina din scoarța de pin a fost cel mai bun adsorbant dintre materiile prime testate, prezentând cea mai bună performanță pentru toate tipurile de plastic. Utilizarea directă a hidrolizatelor de organosolv, evitând recuperarea ligninei a prezentat un comportament similar. Aceste rezultate deschid posibilitatea de a dezvolta noi absorbanți naturali, pe bază de plante, pentru îndepărtarea microplasticului din apele uzate contaminate.

INTRODUCTION
Plastic production has so far exceeded 348 million tonnes per year and despite the great efforts to reduce its use, the production is expected to double by 2035. Since it will take hundreds of years for some of the polymers in plastics to fully mineralize 3-5 hundreds of years for the majority of plastic materials), plastics cause serious pollution due to their cumulative and persistent properties (*Geyer et al., 2017*). (*Moharir & Kumar, 2019; Kyrikou & Briassoulis, 2007*).

Iuliana Găgeanu, Researcher; Florbela Carvalheiro, Researcher; Adam Ekielski, Professor; Luis Duarte, Researcher

Plastics are made from various combinations of over 5,000 different polymers and other chemicals. In general, the origin of microplastic (MP) particles can be divided into two sources: primary and secondary. Primary microplastic particles are produced as such to be used in the manufacture of larger objects, or e.g. directly in cosmetic products such as facial scrubs and toothpaste, or in abrasive blasting (e.g. to remove varnish). Secondary microplastic particles are formed from the breakdown of larger plastic products (*Zhang & Zhang, 2021*).

Several definitions of Microplastics (MP) are present in the literature. Generally, polymer particles with a diameter of 1 µm to 1 mm are called microplastics (*Bayo et al., 2020; Kefer et al., 2021*), but the most common adopted definitions define MP as fragments of any type of plastic less than 5 mm in length (*Bergmann et al., 2015; Koelmans et al., 2019; Crawford & Quinn, 2016, 2016; Collignon et al., 2014, Morioka et al., 2023*).

This diversity in size, is followed by a diversity in shapes, such as microspheres, fragments, foil foam granules, and fibres, to name just a few. Most synthetic particles are plastic fibres (*Belioka and Achilias, 2023).*

As previously mentioned, the most common definition of microplastics is defined as particles with a longest diameter of less than 5 mm. Plastic particles fall into two categories: primary microplastics, which are developed for industrial use, and secondary microplastics, which are produced when plastic products and things break down. Practically speaking, the size range that has been established has been accepted as it is thought to be the range at which many biota species take food. On the other hand, nanoplastics, which fall under the conventional definition of microplastics, are described as plastic particles with a size between 0.001 and 0.1 µm (*Lusher et al, 2017)*.

In recent years, significant attention has been drawn to the widespread presence of microplastic particles in nature and the potential threat posed by their ingestion by living organisms and their accumulation over the trophic system (*Ziani et al, 2023*). However, reliable, easy, cost-effective and reproducible ways to minimize these constraints still remain an important issue to be solved. As plastics degradation, e.g. by **biological means** is a challenge, due to their **hydrophobic nature,** a number of methods have been developed to remove microplastics from water. These include i) filtration, ii) froth flotation, iii) microbial transformation/dissimilation; iv) electrostatic separators, v) microplastics aggregation; vi) biological aggregation and vii) use of organosilanes.

1. **Filtration is the** simplest method, although it is limited to the efficiency of the filtration process. Filter-based technologies such as biofilter (*Liu et al., 2020*), ultrafiltration (UF) (*Tadsuwan & Babel, 2022*), rapid sand filter (RSF) (*Sembiring et al., 2021*), among others, have achieved the best performance in removing microplastics. Among them, the RSF technology ensures quick and effective removal of microplastics.
2. **The froth flotation method** - is a physicochemical separation based on the differences in surface properties of materials. The principle behind this method is that hydrophobic plastics are picked up by air bubbles and rise to the surface, where they are collected and separated from hydrophilic plastics (*Wang et al., 2015; Crawford & Quinn, 2017; Kokkilic et al., 2022*).
3. **Microbial transformation/dissimilation –** consists on plastic decomposing by microorganisms, involving (a) microbial adhesion to the polymer's surface, (b) the polymer's use as a carbon source, and (c) polymer degradation. Besides being difficult, this process also takes a long time.
4. Electroseparation is another possibility, in which the recovery rate of microplastics is almost 99%, making it an effective and promising technique for density separation (*Felsing et al., 2018*).
5. **Aggregation, e.g., flocculation** using chemical or biological substances is one of the promising methods for plastic separation. In this process flocs interacted with microplastics through hydrogen bonding, van der Waals forces or electrostatic forces (*Duan and Gregory, 2003; Lapointe et al., 2020*).
6. **Biological agglomeration,** is another method of purifying wastewater from microplastics is the use of bioreactors. A bioreactor system removes microplastics mainly through microbial uptake and sludge aggregate formation. In particular, domestic activated sludge likely promoted the accumulation of microplastics in wastewater treatment plants. The deposit containing microplastics is removed during the subsequent secondary deposition process (*Jeong et al., 2016*).
7. **Treatment with organosilanes**. The interaction of the organic group of organosilanes with the surface of microplastics leads to their attachment to the surface of the microplastic being collected in agglomerates in the first stage of the fixation process. The disadvantage of this method is the need to remove organosilane residues from the water.

Although the methods described above are suitable for purifying water from plastic in the vicinity of the source of contamination, they also present some drawbacks as: high costs for reactors of complex systems, the need to perform additional operations to remove some of the added compounds from the treated water, the use of chemical substances, etc.

As alternative to the former processes, the use of lignin for microplastic extraction from water is starting to be discussed and investigated, as it could represent a natural and safe manner to clean wastewaters that does not involve additional equipment or special reactors/tanks for processing the wastewater.

It has been proven in many publications that lignin can be used as an absorbent of metal ions. The factor that is responsible for the sorption function of lignin, free phenolic hydroxyl group and abundant vacant ortho- or para-sites, is able to absorb the heavy metal ions (Gupta et al.,2021). Therefore, due to the hydrophobic nature of plastics (PE, HDPE), it is possible for plastic microparticles to attach to lignin particles and form micro agglomerates.

Lignin is a complex natural polymer that represents up to one-third of the lignocellulosic biomass content whose structure depends on the origin source and on the method of obtaining it. Lignin can be extracted from many lignocellulosic biomass residues and byproducts. In industry it is typically extracted using alkaline or sulphite-base processes, producing kraft lignin, or lignosulfonates, which are byproducts of the pulp and paper industry (Ekielski and Mishra, 2021). Other types of lignin are those obtained as biorefinery by-products, i.e. after steam explosion or acid hydrolysis pre-treatments (*Martins et al., 2022, Gosselink, 2011*), but the purity of those lignins is typically low. High pure lignins, i.e., more reactive, and containing a low carbohydrate and ash content, can be obtained through the pre-treatment of biomass with organic solvents, i.e., alcohols, organic acids, or ketones, called organosolv processes (*Zhang et al., 2016*). Organosolv covers a broad range of solvents but the most used is ethanol due to its low cost and low boiling point, which allow an easy recovery. Furthermore, it also allows an efficient delignification (*Carvalheiro et al., 2022*).

MATERIALS AND METHODS

Biomass feedstocks

Mischantus sp. biomass was purchased from Comgoed (NL) by TU Delft and distributed by the Dutch Organization for Applied Scientific Research (TNO) within the consortium of the Brisk 2 project. The feedstock was supplied as pellets and was stored in plastic containers at room temperature. Pine bark (Maritine Pine, *Pinus pinaster*) was kindly provided by a Portuguese processor (Alfarroxo, Figueira da Foz, Portugal). The feedstock was supplied as chips and was stored in plastic containers at room temperature. Anaerobic solid digestate obtained from the Anaerobic Digestion of the organic fraction of municipal solid wastes (OFMSW) was kindly provided by Tratolixo (Abrunheira, Portugal). The feedstock was supplied as a slurry, and upon reception it was dried at 80º C until constant weight, screened for the removal of plastics by visual inspection, and then stored at room temperature. Figure 1 presents their typical morphology. All materials were milled to pass a 4 mm screen before use.

Organosolv process and lignin recovery

Lignin was obtained by an organosolv extraction using a 2-liter stainless steel, pressurized reactor (Parr Instruments Company, Moline, IL, USA) (Figure 2). The organosolv process was carried out using a liquid-to-solid ratio (LSR) of 7 (for *Miscanthus sp.* and pine bark) and a LSR=3 for the digestate, dry basis. A solvent ethanol:water (50:50 w/w) solution was used. The process was run under non-isothermal conditions heating up to 190ºC followed by a rapid cooling to room temperature.



Fig. 1 - Sources for obtaining lignin used for experiments



Fig. 2 - Laboratory equipment for extracting lignin

The liquid obtained from the process containing dissolved lignin was then treated to precipitate lignin using cold acidified water (distilled water brought to pH = 2 using H_2SO_4). After incubation (2 h, 30ºC, 150 rpm), the precipitated lignin was recovered after centrifugation in a benchtop centrifuge (at 5000 *g*, 20 min, room temperature).

After drying (45ºC, 48 h), the lignin thus obtained was intended to be used as a capturing agent for microplastics. Another approach was to use water contaminated with microplastics to precipitate lignin, analysing in the end both the precipitated lignin and the supernatant obtained.

Microplastic particles preparation

The types of plastic used were high-density polyethylene (HDPE), polypropylene (PP), polystyrene (PS) and expanded polystyrene (EPS), collected from waste commercial packaging materials. Large pieces of plastic were used to obtain microplastic by sanding the plastic pieces using sand paper with a medium grit P40 (ISO 6344). Plastic samples thus obtained were mixed with water at a 1:20 ratio (Figure 3).

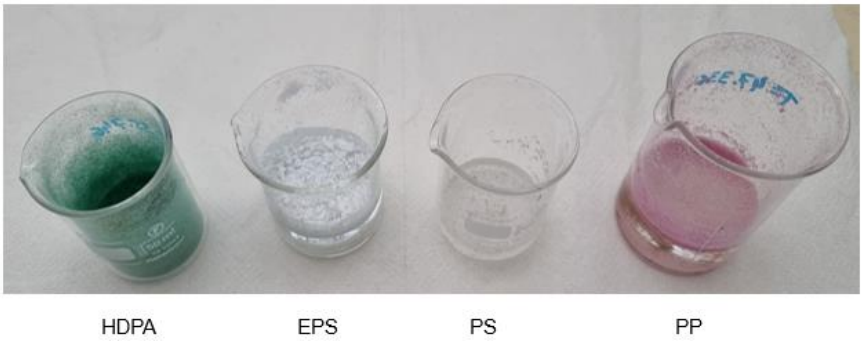


Fig. 3 - Plastic samples used for experiments

Microplastic particles characterization

A Brightfield OPTIKA B-50 microscope equipped with camera was used to determine the size of the different types of microplastics. The plastic-water solution was mixed and samples were placed on microscope slides and then observed using the 40x objective, taking pictures. Reference size images were taken using a 100 μm wide object subjected to microscope observation (Figure 4). The images were processed using ImageJ.JS software version 11.

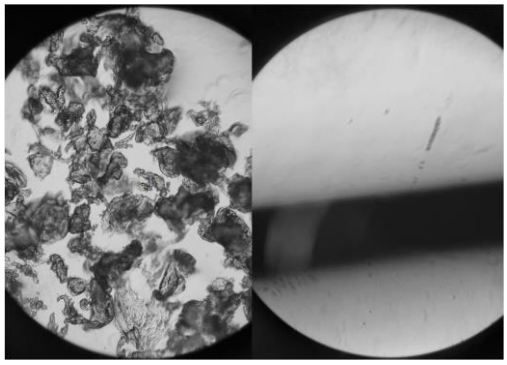


Fig. 4 - Plastic size analysis

Left – Microscopic view of the Microplastic water solution microscopic; right – reference size picture

Microplastics removal by lignin assays

To determine the possibility of removing microplastic from water using lignin, microscope slides were covered with 0.5 g of the three types of lignin obtained, dried, and weighed (Figure 5). The microscope slides were submerged in the plastic-water suspension (contained 1 g of plastic in 500 ml demineralized water), prepared for each type of plastic and left inside the mix for two hours, in circular containers with 60 mm diameter, next creating a water current at 50 rpm using a magnetic agitator, in order for the plastic particles to flow through the solution. The slides were then removed, weighed and let to dry.

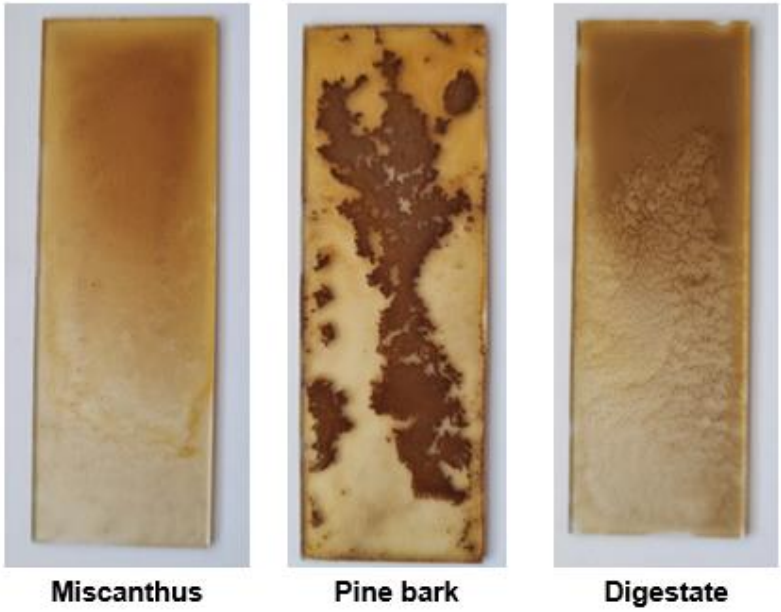


Fig. 5 - Slides covered with lignin samples

The dried slides were observed using the microscope to determine if the plastic particles adhered to the lignin particles for each type of plastic and each type of lignin separately.

A second test using the hydrolysate obtained directly from organosolv treatment which contained soluble lignin, was also carried in order to evaluate both lignin and plastic co-precipitation. For this method, 50 ml capacity falcons were used, adding 6.5 g of lignin solution (organosolv hydrolysate) to the falcon and 26 g of plastic containing-water 1:20 solution. The filled falcons (Figure 6) were set in the incubator at 30 ^{o}C for 2 h.



Fig. 6 - Falcons containing organosolv and plastic-water solution:
Left – before centrifugation; right – after centrifugation

After incubation, the suspension was centrifuged as described above. The supernatant) was removed and weighed and the falcon with pellet was dried in oven (45^{o} C, 48 h) and then weighed.

RESULTS

Plastic particle size analysis

Using the particle size analysis software, 50 measurements were taken, the results being presented in Table 1.

Table 1

Plastic particle size analysis results

	Area	Mean	StdDev	Min	Max	Perim.	Angle	Circ.	Median	Skew	AR	Round	Solidity	Length
No.	µm²	µm²		µm	µm	µm	°		µm					µm
1	2634	118	37	55	202	546	-34	0	116	-0	0	0	NaN	546
2	1947	142	42	54	214	400	-37	0	151	-0	0	0	NaN	400
3	2451	137	28	102	195	506	-29	0	131	-0	0	0	NaN	506
4	1214	61	14	38	96	248	-49	0	58	-0	0	0	NaN	248
5	1947	104	33	38	200	404	-49	0	101	-0	0	0	NaN	404
6	2290	96	32	47	184	472	-40	0	94	-0	0	0	NaN	472
7	2588	26	27	0	170	538	-39	0	22	-0	0	0	NaN	538
8	2954	58	18	26	142	615	-140	0	51	-0	0	0	NaN	615
9	1351	87	22	51	136	278	-48	0	85	-0	0	0	NaN	278
10	2359	97	27	34	152	490	-116	0	100	-0	0	0	NaN	490
11	1351	93	39	37	186	276	-99	0	82	-0	0	0	NaN	276
12	412	101	18	68	132	84	-31	1	105	-0	0	0	NaN	84
13	2290	90	18	57	140	475	-118	0	85	-0	0	0	NaN	475
14	1443	83	32	44	166	298	-37	0	69	-0	0	0	NaN	298
15	2107	109	38	48	184	435	-66	0	104	-0	0	0	NaN	435
16	962	107	34	57	187	195	-152	0	103	-0	0	0	NaN	195
17	1305	110	39	51	187	268	-90	0	102	-0	0	0	NaN	268
18	802	110	32	59	211	163	-58	0	102	-0	0	0	NaN	163
19	412	119	20	86	163	82	-126	1	118	-0	0	0	NaN	82
20	389	138	32	87	199	77	-150	1	145	-0	0	0	NaN	77
21	802	111	39	55	204	163	-118	0	109	-0	0	0	NaN	163
22	2061	72	23	39	171	427	-56	0	63	-0	0	0	NaN	427
23	1534	95	28	59	185	315	-138	0	91	-0	0	0	NaN	315
24	1512	119	47	37	206	310	-9	0	113	-0	0	0	NaN	310
25	1008	168	20	119	204	206	3	0	170	-0	0	0	NaN	206
26	2267	89	23	51	153	467	-43	0	85	-0	0	0	NaN	467
27	2886	84	26	36	153	597	-74	0	83	-0	0	0	NaN	597
28	916	108	15	85	136	187	-90	0	102	-0	0	0	NaN	187
29	5451	64	29	34	187	1132	-163	0	53	-0	0	0	NaN	1132
30	4191	69	24	34	161	870	5	0	64	-0	0	0	NaN	870
31	916	132	26	68	184	185	-53	0	132	-0	0	0	NaN	185
32	847	73	16	51	117	172	2	0	70	-0	0	0	NaN	172
33	2863	84	26	35	136	595	-77	0	85	-0	0	0	NaN	595
34	2657	70	28	34	156	552	-142	0	61	-0	0	0	NaN	552
35	1672	102	32	51	187	345	2	0	100	-0	0	0	NaN	345
36	1351	101	37	34	187	278	-94	0	91	-0	0	0	NaN	278
37	1992	166	35	85	213	410	-138	0	172	-0	0	0	NaN	410
38	2473	95	35	39	187	512	-48	0	91	-0	0	0	NaN	512
39	1145	115	29	53	175	235	-27	0	113	-0	0	0	NaN	235
40	1328	135	32	68	203	272	10	0	134	-0	0	0	NaN	272
41	756	149	29	101	212	152	-13	0	150	-0	0	0	NaN	152
42	2176	100	36	39	181	449	129	0	98	-0	0	0	NaN	449
43	2107	141	32	74	204	434	-14	0	136	-0	0	0	NaN	434
44	1374	72	23	46	153	282	-40	0	70	-0	0	0	NaN	282
45	1328	86	24	51	149	272	-64	0	86	-0	0	0	NaN	272
46	2451	99	32	51	204	505	-62	0	91	-0	0	0	NaN	505
47	1099	121	32	60	185	225	-27	0	117	-0	0	0	NaN	225
48	1947	115	42	47	216	404	-174	0	114	-0	0	0	NaN	404
49	802	120	37	56	186	163	-152	0	114	-0	0	0	NaN	163
50	618	109	32	60	161	123	-39	1	107	-0	0	0	NaN	123

Regardless of the plastic type, it was found that the minimum length of plastic particles was 77 µm, the smallest total area of 389 µm² and the maximum length was 1132 µm with an area of 5451 µm. The average length was 362 µm with a total area of 1755 µm.

Plastic removal

The dried slides covered with lignin and then submerged in plastic-water solution were observed under the microscope and the images taken were analysed (Figure 7), showing that the smaller plastic particles adhered to the lignin particles, which could mean that there is good potential for using lignin as water cleaning agent for water contaminated with microplastic.

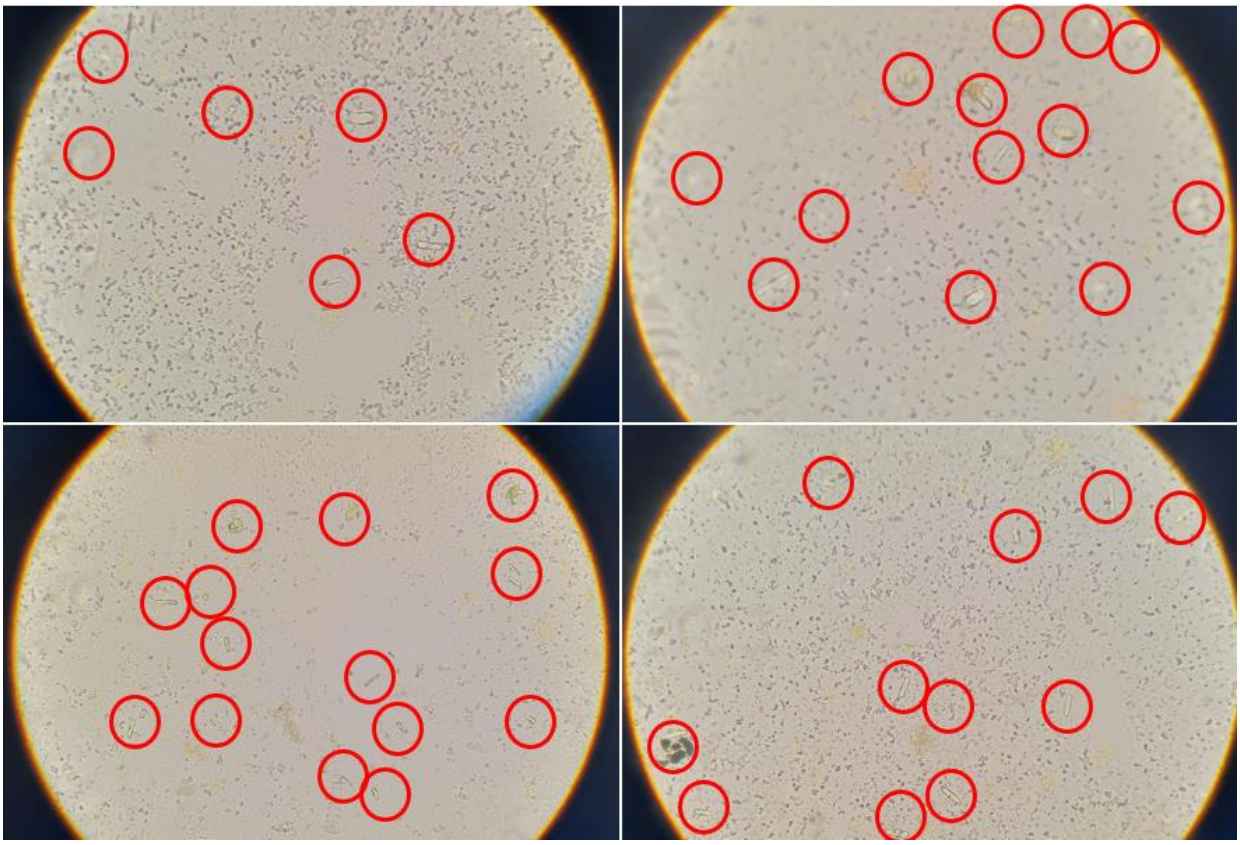


Fig. 7 - Plastic captured in lignin solution

The results from calculating the percentage of plastic removed from the plastic-water solution using lignin as a capture agent are shown in Figure 8.

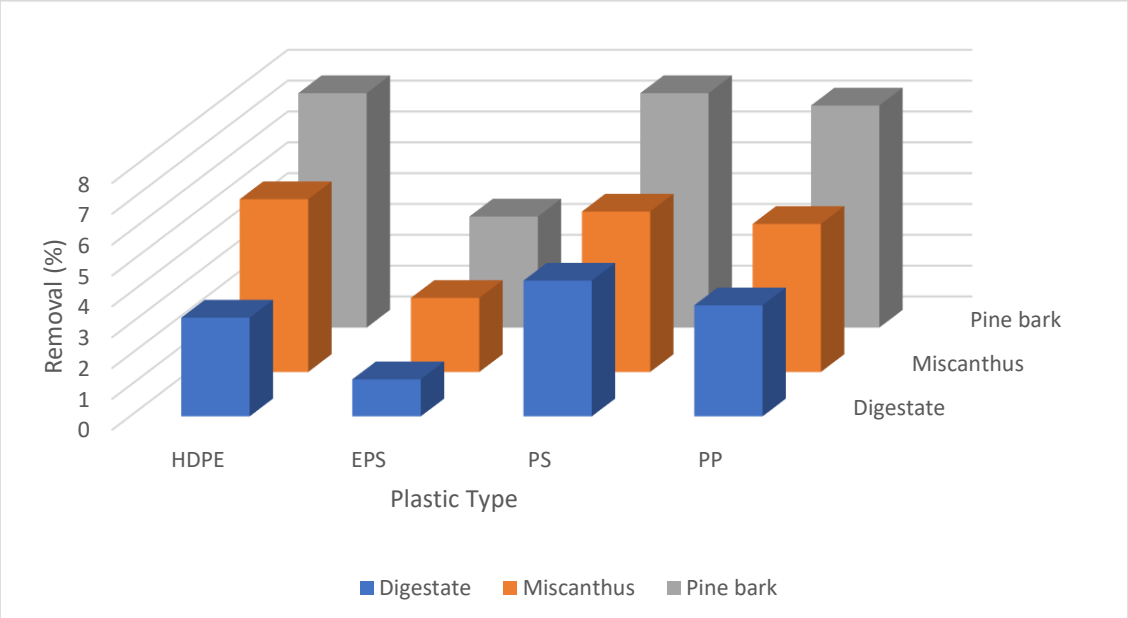


Fig. 8 - Microplastic removal as a function of plastic type and lignin origin

Analysing the data in Figure 8, it was found that the best results were obtained in the case of pine bark lignin and the weakest plastic removal was in the case of digestate lignin, for all the types of plastics used. Also, expanded PS adhered the least to the lignin surface for all types of lignin.

The results from calculating the amount of plastic captured in the lignin by using the plastic-water solution to precipitate the lignin are shown in Table 2 and figure 9.

Table 2

Results from calculating the amount of plastic captured in the lignin after precipitation

Lignin types	Plastic types	Falcon	Organosolv	Plastic water solution	Filled falcon	Supernatant	Falcon + precipitate	Plastic captured in the precipitated lignin	Percentage of plastic captured
		g	g	g	g	g	g	g	%
Miscanthus sp.	HDPA	13.76	6.51	26.05	46.32	26.13	20.19	0.076	5.80
	PS	13.93	6.51	26.05	46.49	26.09	20.40	0.036	2.80
	PS	13.75	6.5	26.04	46.29	26.11	20.18	0.069	5.29
	PP	13.75	6.62	26.04	46.41	26.11	20.30	0.075	5.75
Pine bark	HDPA	13.92	6.51	26.05	46.48	26.14	20.34	0.089	6.80
	PS	13.81	6.51	26.06	46.38	26.10	20.28	0.038	2.90
	PS	13.78	6.5	26.05	46.33	26.13	20.20	0.080	6.14
	PP	13.81	6.51	26.05	46.37	26.16	20.21	0.108	8.30
Digestate	HDPA	13.84	6.52	26.06	46.42	26.07	20.35	0.014	1.10
	PS	13.84	6.51	26.04	46.39	26.05	20.34	0.007	0.55
	PS	13.76	6.52	26.05	46.33	26.07	20.26	0.020	1.55
	PP	13.74	6.51	26.04	46.29	26.05	20.24	0.008	0.65

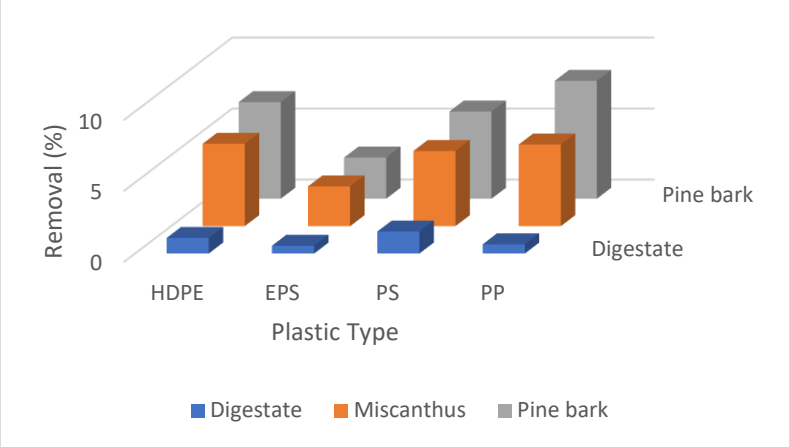


Fig. 9 - Microplastic removal from the lignin after precipitation

Analysing the data in Table 2 and Figure 9, it was found that the best results were obtained again in the case of pine bark and *Miscanthus sp.* lignin and the weakest plastic removal was in the case of digestate lignin, for all the types of plastics used. Also, expanded PS adhered the least to the lignin surface for all types of lignin. An explanation for which the percentages of plastic captured in the digestate lignin is even lower than in the case of lignin covered slides is because the digestate had a lower lignin content than *Miscanthus sp.* and pine bark, therefore, the organosolv used for precipitation had less lignin in which the plastic could be captured.

Overall, from the experiments performed to evaluate how plastic particles adhere to lignin, it was found that lignin had the capacity to capture plastic particles both in the solid lignin part after precipitation and centrifugation, but also in the supernatant obtained, leading to the conclusion that contaminated water can be used for lignin precipitation, reducing clean water consumption for obtaining lignin.

As microplastic removal using lignin has only been researched using lignin to form larger flocs that need to be subsequently removed (*Sacco et al., 2023*), the method proposed in this paper represents a novel approach for wastewater treatment and additional research is needed to further explore the effectiveness of lignin to capture microplastic particles from wastewater.

CONCLUSIONS

Microplastic poses a real threat to both humans and animals, because it can be easily ingested. Microplastic presents in wastewater or even water that is considered fresh is difficult to capture because of its size and floatability. The paper proposed a preliminary study on the possibility to use lignin as an agent for capturing microplastic particles from water by using two methods: the use of lignin as a passive filter for plastic contaminated water and the use of plastic contaminated water to precipitate lignin.

Lignin from three types of sources (*Miscanthus sp.*, pine bark and digestate) was used and the experiments were conducted using water contaminated with four types of plastic (high-density polyethylene, polypropylene, polystyrene and expanded polystyrene).

Both methods showed good preliminary results, plastic being captured in the lignin for both methods in all the samples examined, leading to the conclusion that lignin has potential for removing microplastic particles from wastewater.

ACKNOWLEDGEMENT

This work was partially supported under the BRISK2 project that has received funding from the European Union's Horizon 2020's Research and Innovation Programme under Grant Agreement number 731101, and by the Romanian Ministry of Research Innovation and Digitalization, through Programme 1 - Development of the national research-development system, Subprogramme 1.2 - Institutional performance - Projects for financing excellence in RDI, Contract no. 1PFE/30.12.2021. The work was partially carried out at the Biomass and Bioenergy Research Infrastructure (BBRI), funded by the BBRI-LISBOA-01-0145-FEDER-022059 project that is supported by the Operational Programme for Competitiveness and Internationalization (PORTUGAL2020), by Lisbon Portugal Regional Operational Programme (Lisboa 2020) and by North Portugal Regional Operational Programme (Norte 2020) under the Portugal 2020 Partnership Agreement, through the European Regional Development Fund (ERDF).

REFERENCES

[1] Bayo, J.; Olmos, S.; López-Castellanos, J. (2020). Microplastics in an urban wastewater treatment plant: The influence of physicochemical parameters and environmental factors. *Chemosphere, 238*, 124593, https://doi.org/10.1016/j.chemosphere.2019.124593.

[2] Belioka, M.-P.; Achilias, D.S. (2023). Microplastic Pollution and Monitoring in Seawater and Harbor Environments: A Meta-Analysis and Review. *Sustainability, 15,* 9079. https://doi.org/10.3390/su15119079.

[3] Bergmann, M.; Gutow, L.; Klages, M. (2015). Marine Anthropogenic Litter. Springer. ISBN 978-3-319-16510-3, DOI 10.1007/978-3-319-16510-3.

[4] Carvalheiro, F.; Duarte, L.C.; Pires, F.; Van-Dúnem, V.; Sanfins, L.; Roseiro, L.B.; Gírio, F. (2022). Effective Mild Ethanol-Based Organosolv Pre-Treatment for the Selective Valorization of Polysaccharides and Lignin from Agricultural and Forestry Residues. *Energies, 15,* 5654. doi.org/10.3390/en15155654.

[5] Collignon, A.; Hecq, J.-H.; Galgani, F.; Collard, F.; Goffart, A. (2014). Annual variation in neustonic micro- and meso-plastic particles and zooplankton in the Bay of Calvi (Mediterranean–Corsica), *Marine Pollution Bulletin Volume 79, Issues 1–2*, 293-298.

[6] Crawford, C.B.; Quinn, B. (2016). Microplastic Pollutants (first ed.), *Elsevier Science. Volume 79, Issues 1–2*, 293-298, ISBN: 9780128104699https://doi.org/10.1016/j.marpolbul.2013.11.023.

[7] Crawford, C.B.; Quinn, B. (2017). Microplastic separation techniques, *Microplastic Pollutants*, 203-218, https://doi.org/10.1016/B978-0-12-809406-8.00009-8.

[8] Danso, D.; Chow, J.; Streit, W.R. (2018). Plastics: Environmental and biotechnological perspectives on microbial degradation. *Appl. Environ. Microbiol., 85 (19),* e01095-19, https://doi.org/10.1128/AEM.01095-19.

[9] Ekielski, A; Mishra, P.K. Lignin for Bioeconomy: The Present and Future Role of Technical Lignin. Int. J. Mol. Sci. 2021, 22, 63. https://doi.org/10.3390/ijms22010063.

[10] Felsing, S.; Kochleus, C.; Buchinger, S.; Brennholt, N.; Stock, F.; Reifferscheid, G. (2018). A new approach in separating microplastics from environmental samples based on their electrostatic behavior. *Environ. Pollut. 234:* 20-28. doi: 10.1016/j.envpol.2017.11.013.

[11] Geyer, R.; Jambeck, J.R.; Law, K.L. (2017) "Production, Use, and Fate of All Plastics Ever Made. *Science Advances 3, no. 7*: e1700782, https://dx.doi.org/10.1126/sciadv.1700782.
[12] Gosselink, R. J. A. (2011). Lignin as a renewable aromatic resource for the chemical industry. *Doctoral Thesis*, Wageningen University, Wageningen, NL.
[13] Gupta A, Sharma V, Sharma K, Kumar V, Choudhary S, Mankotia P, Kumar B, Mishra H, Moulick A, Ekielski A, et al. A Review of Adsorbents for Heavy Metal Decontamination: Growing Approach to Wastewater Treatment. Materials. 2021; 14(16):4702. https://doi.org/10.3390/ma14164702
[14] Jaiswal, S.; Sharma, B.; Skukla, P. (2020). Integrated approaches in microbial degradation of plastics. *Environmental Technology & Innovation, Volume 17*, 100567, https://doi.org/10.1016/j.eti.2019.100567
[15] Jeong, C.B.; Won, E.J.; Kang, H.M.; Lee, M.C.; Hwang, D.S.; Zhou, B.; Souissi, S.; Lee, S.J; Lee, J.S. (2016). Microplastic Size-Dependent Toxicity, Oxidative Stress Induction, and p-JNK and p-p38 Activation in the Monogonont Rotifer (Brachionus koreanus), *Environ. Sci. Technol., 50, 16*, 8849–8857, https://doi.org/10.1021/acs.est.6b01441.
[16] Kefer, S.; Miesbauer, O.; Langowski, H.-C. (2021). Environmental Microplastic Particles vs. Engineered Plastic Microparticles—A Comparative Review. *Polymers, 13(17)*, 2881; https://doi.org/10.3390/polym13172881.
[17] Koelmans, A.A.; Nor, N.H.M.; Hemrsen, E.; Kooi, M.; Mintenig, S.M.; De France, J. (2019). Microplastics in freshwaters and drinking water: Critical review and assessment of data quality. *Water Res. 155*: 410–422. doi: 10.1016/j.watres.2019.02.054.
[18] Kokkilic, O.; Mohammadi-Jam, S.; Chu, P.; Marion, C.; Yang, Y.; Waters, K. (2022). Separation of plastic wastes using froth flotation – An overview, *Advances in Colloid and Interface Science Volume 308*, 102769, https://doi.org/10.1016/j.cis.2022.102769.
[19] Kyrikou, I.; Briassoulis, D. (2007). Biodegradation of Agricultural Plastic Films: A Critical Review. *J Polym Environ 15*:125–150, DOI 10.1007/s10924-007-0053-8.
[20] Liu, F.; Nord, N.B.; Bester, K.; Vollertsen, J.; (2020). Microplastics Removal from Treated Wastewater by a Biofilter. *Water, 12(4),* 1085; https://doi.org/10.3390/w12041085.
[21] Lusher, A.; Hollman, P.; Mendoza-Hill, J. (2017). Microplastics in fisheries and aquaculture - Status of knowledge on their occurrence and implications for aquatic organisms and food safety. Food and Agriculture Organization of the United Nations, Rome, ISBN 978-92-5-109882-0.
[22] Martins, M. M.; Carvalheiro, F.; Gírio, F. (2022). An overview of lignin pathways of valorization: from isolation to refining and conversion into value-added products. *Biomass Convers. Bior*. doi.org/10.1007/s13399-022-02701-z.
[23] Moharir, R.V.; Kumar, S. (2019). Challenges associated with plastic waste disposal and allied microbial routes for its effective degradation: A comprehensive review, *Journal of Cleaner Production, Volume 208*, 65-76, https://doi.org/10.1016/j.jclepro.2018.10.059.
[24] Morioka, T.; Tanaka, S.; Yamada, Y.; Yukioka, S.; Aiba, F. (2023). Quantification of microplastic by particle size down to 1.1 μm in surface road dust in an urban city, Japan, *Environmental Pollution, Vol. 334,* 122198, https://doi.org/10.1016/j.envpol.2023.122198.
[25] Rochman, C., Hoh, E., Kurobe, T.; The, S.J. (2013). Ingested plastic transfers hazardous chemicals to fish and induces hepatic stress. *Sci Rep 3*, 3263. https://doi.org/10.1038/srep03263.
[26] Sembiring, E.; Fajar, M.; Handajani, M. (2021). Performance of rapid sand filter – single media to remove microplastics, *Water Supply 21 (5): 2273–2284*, https://doi.org/10.2166/ws.2021.060.
[27] Sturm, M.T.; Horn, H.; Schuhen, K. (2021). Removal of Microplastics from Waters through Agglomeration-Fixation Using Organosilanes—Effects of Polymer Types, Water Composition and Temperature. *Water, 13,* 675. https://doi.org/10.3390/w13050675.
[28] Tadsuwan, K.; Babel, S. (2022). Microplastic abundance and removal via an ultrafiltration system coupled to a conventional municipal wastewater treatment plant in Thailand. *Journal of Environmental Chemical Engineering, Volume 10, Issue 2*, 107142, https://doi.org/10.1016/j.jece.2022.107142.
[29] Wang, C.; Wang, H.; Fu, J.; Liu, Y. (2015). Flotation separation of waste plastics for recycling—A review. *Waste Management Volume 41,* 28-38, https://doi.org/10.1016/j.wasman.2015.03.027.
[30] Zeenat Elahi, A.; Bukhari, D. A.; Shamim, S.; Rehman, A.; (2021). Plastics degradation by microbes: A sustainable approach, *Journal of King Saud University – Science, Volume 33, Issue 6*, 101538, https://doi.org/10.1016/j.jksus.2021.101538.

[31] Zhang, Z.; Harrison, M. D.; Rackemann, D. W.; Doherty, W. O. S.; O'Hara, I. M. (2016). Organosolv pretreatment of plant biomass for enhanced enzymatic saccharification. *Green Chem. 18, (2),* 360-381.
[32] Zhang, C., Zhang, D. (2021). Microplastics. In: Cui, W., Fu, S., Hu, Z. (eds) Encyclopedia of Ocean Engineering. Springer, Singapore. https://doi.org/10.1007/978-981-10-6963-5_318-1.
[33] Ziani, K.; Ioniță-Mîndrican, C.B.; Mititelu, M.; Neacșu, S.M.; Negrei, C.; Moroșan, E.; Drăgănescu, D.; Preda, O.T. (2023). Microplastics: A Real Global Threat for Environment and Food Safety: A State of the Art Review. *Nutrients. Jan 25;15(3):617*. doi: 10.3390/nu15030617.

EXPERIMENTAL STUDY ON NAVIGATION FOR WHEAT SEEDLING ROOT CUTTING BASED ON DEEP LEARNING
/
基于深度学习的麦苗断根导航实验研究

HaiBo LIN [*1,2], Chenhe XU [1,2], Yuandong LU [3] [1]
[1] School of Mechanical & Automotive Engineering, Qingdao University of Technology, Qingdao 266520, China
[2] Key Lab of Industrial Fluid Energy Conservation and Pollution Control (Qingdao University of Technology), Ministry of Education, Qingdao 266520, China
[3] Shandong Lingong Construction Machinery Co., Ltd., Shandong 016000, China
Email: linhaibo@qut.edu.cn; 871306176@qq.com; 1214398056@qq.com
DOI: https://doi.org/10.35633/inmateh-71-45

Keywords: *Deep learning, Agricultural machinery navigation line, Field experiment, Complex conditions, Algorithm robustness.*

ABSTRACT
In response to the automatic extraction of navigation lines for wheat root cutting, this paper conducted field experiments and analyses on the navigation line extraction algorithm, based on the improved YOLOv5 algorithm. Firstly, based on the characteristics of wheat seedling rows during the wheat rejuvenation period, the YOLOv5 algorithm was improved by using rotation detection box labels, and navigation lines were extracted by fitting the detection boxes using clustering methods. Then, an experimental system was established to conduct field experiments on the algorithm: (1) Tests were conducted at three speeds of 0.5 m/s, 1.0 m/s and 1.5 m/s respectively, and the position error of the root cutter was measured and analyzed, indicating that the actual navigation path position error increased with the speed. The best navigation performance was observed at 1 m/s, with an average positional error of 18.56 mm, meeting the requirements for wheat root cutting. (2) Robustness analysis of the algorithm was conducted using data collected from 2019 to 2022. Comparative tests were conducted from four aspects: different years, different time periods, different environments, and different yaw angles. The results showed that the algorithm proposed in this paper has stronger robustness and higher accuracy.

摘要
针对小麦断根导航线自动提取的问题，本文在改进 YOLOv5 算法的基础上，对导航线提取算法进行了田间实验测试和分析。首先，针对小麦返青期麦苗行的特点，用旋转检测框标识对 YOLOv5 算法进行改进，通过聚类方法对检测框拟合进行导航线的提取；然后，搭建实验系统对算法进行田间实验：（1）分别在 0.5m/s、1.0m/s、1.5m/s 三个速度下进行测试，测量分析断根刀的位置误差，表明实际导航路径位置误差随行进速度的增加而变大，1m/s 时导航效果最好，位置误差平均值为 18.56mm，满足小麦断根要求；（2）利用 2019-2022 年采集数据对对算法的鲁棒性进行实验分析，从不同年份、不同时段、不同环境及不同偏航角四个方面进行对比测试，结果表明本文算法鲁棒性更强、准确性更高，能够满足作业实时性要求。

INTRODUCTION
As one of the main food crops in China, the increase in wheat production is of great significance for the security of food in our country *(Jiang et al., 2021)*. As early as the 1960s and 1970s, *Yu et al (1985)* from Shandong Agricultural University studied the methods of increasing the yield of winter wheat and found that deep tillage and root-cutting operation during the rejuvenation period of winter wheat could promote the development of wheat roots and increase the yield significantly. Later, *Lv et al, (2006),* developed a set of small wheat root-cutting machine, which showed that mechanical root-cutting measures could increase the yield by 9.96%-11.4%. However, the machine needs to continuously adjust its posture during the operation process, ensuring that the wheels do not press against the wheat seedlings, while also preventing the root cutter from damaging the wheat seedlings, which is time-consuming and laborious for manual operation, and has low production efficiency. Therefore, it is necessary to develop a root cutting machine that can automatically navigate the wheat seeding line.

[1] *Lin Haibo, PhD, Lecturer; Xu Chenhe, MS; Lu Yuandong, MS*

At present, agricultural machinery in precision agriculture mainly uses satellite navigation systems such as Beidou and GPS for navigation and positioning *(Dhruba et al., 2018)*. However, the use of satellite navigation will face problems such as high equipment prices and unstable systems *(Sevilla et al., 2021)*. Moreover, the accuracy of satellite navigation is suitable for field operations, but it is not suitable for precision navigation of roots cutting. In recent years, machine vision and image processing technology has developed rapidly, and it has begun to be applied in various aspects such as field agricultural machinery navigation, variable spraying and weed identification (*He et al., 2021; Yun et al., 2021; Jeon et al., 2021; Li et al., 2021*). However, the application of this technology in the early wheat field navigation is less and not suitable, mainly because the wheat field environment is complex and diverse: (1) variations in lighting due to time differences and weather changes; (2) the shape of wheat seedlings in different growth periods was different; (3) the wheat field was affected by weeds, leaves and other debris; (4) shadows caused by agricultural machinery, power poles, and trees; (5) in the process of agricultural machinery operation, there is a certain yaw angle in the camera during the image acquisition process due to uneven ground or mechanical vibration. Therefore, how to provide a visual navigation line with strong robustness and high accuracy in a complex environment has become the hot sport of current research.

In recent years, deep learning has begun to be applied to the agricultural field, which has a wide range of applications in crop detection, but there are few reports on wheat field navigation applications. In this paper, a method of wheat seedling navigation line extraction based on deep learning was proposed, and field experiments were carried out to verify the reliability of the algorithm through field tests *(Liu et al., 2020; Pang et al., 2020; Khan et al., 2021; Liu et al., 2020; Villacrés et al., 2023; Amrani et al., 2023; Yadav et al., 2023)*.

MATERIALS AND METHODS

In response to the complexity of wheat field environments *(Jiang et al., 2016)*, this paper adopts the YOLOv5 algorithm model in deep learning to detect wheat seedlings and avoid the interference of weeds and other environmental background factors. Object detection algorithms have found widespread use in crop detection. However, there are not many studies on it used to detect crop rows, mainly because the algorithm usually uses a horizontal detection box to identify the target, and the crop rows in the image have a certain length and tilt angle. If the crop rows are marked in the whole column, it will inevitably lead to more soil background areas in the box and include other row crops, which is not conducive to the training of the model. In this regard, this paper uses a rotatable detection box to identify the position of wheat rows. It adds angle parameters to the horizontal detection frame, which is responsible for detecting the rotation of the frame.

Algorithm Improvement

Because the detection boxes with larger length and width are more sensitive to the angle change, the current main angle regression prediction method has the problem of boundary discontinuity. This will cause the loss value of the model to surge at the boundary, resulting in the detection accuracy of the algorithm is low at the boundaries *(Yang et al., 2019)*. In this paper, the angle prediction for object detection boxes is treated as a classification problem. To enhance the tolerance for errors between adjacent angles, a circular smooth label (CSL) *(Yang and Yan, 2020)* is introduced, tailored to the wheat field scene. This approach aims to improve the robustness of angle prediction within detection boxes.

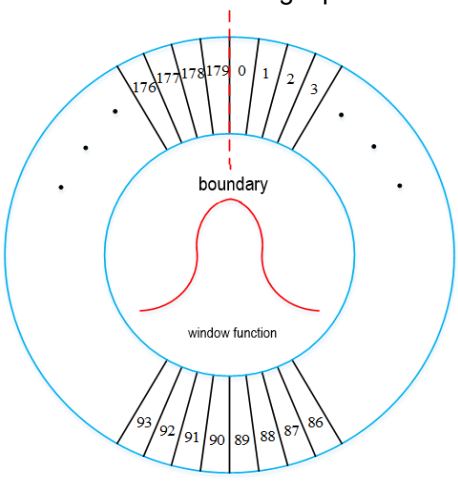


Fig. 1 - CSL schematic

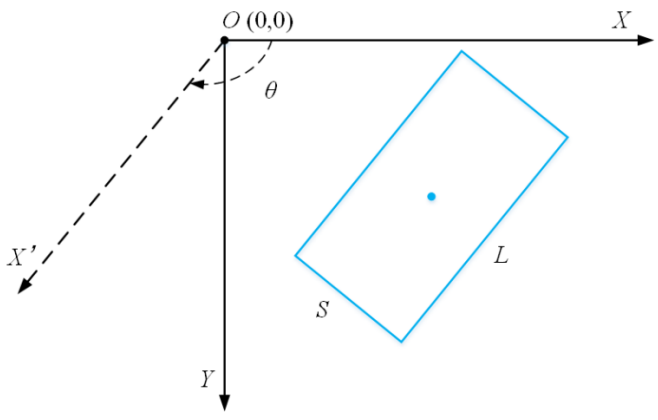


Fig. 2 - The schematic of rotation angle definition

The CSL schematic is shown in Figure 1, and the CSL is calculated as follows:

$$CSL(x)=\begin{cases} g(x) & \theta-r<x<\theta+r \\ 0 & \text{otherwise} \end{cases} \tag{1}$$

$$g(x)=ae^{-\frac{(x-b)^2}{2c^2}} \tag{2}$$

where, $g(x)$ represents the window function, here is the Gaussian function; r is the radius of the window function, which is taken here as 6; θ is the rotation angle of the detection box; a, b, and c are constants.

The angle range of CSL here is [0º, 180º). In Figure 1, 0º coincides with 180º, so only one of them is chosen. The parameters of the rotating detection box are expressed as (r_x, r_y, L, S, θ), where r_x and r_y are the horizontal and vertical coordinates of the center point of the box respectively, L is the long side of the box, and S is the short side of the box, the definition of the rotation angle θ is shown in Figure 2, which is the angle rotated by clockwise rotation along the X-axis direction to parallel with the long side of the detection box. To assess the effectiveness of angle prediction, a binary cross-entropy loss function, BCE With LogitsLoss, is employed to compute the angle loss. The formula for calculating the loss is as follows:

$$\begin{cases} loss(z,y)=\text{mean}\{l_0,\cdots,l_{N-1}\} \\ l_n=\text{sum}\{l_{n,0},l_{n,1},\cdots,l_{n,179}\} \\ l_{n,i}=-\left[y_{n,i}\ln\left(\delta\left(z_{n,i}\right)\right)+\left(1-y_{n,i}\right)\ln\left(1-\delta\left(z_{n,i}\right)\right)\right] \\ y_{n,i}=CSL(x) \end{cases} \tag{3}$$

where: N represents the number of samples; $i\in[0,180)$, divided into 180 categories; δ is the sigmoid function; $Z_{n.i}$ represents the probability of the i^{th} angle when predicting the n^{th} sample, when the value is 1, that is, the predicted value; $y_{n,i}$ represents the label value (true value) of the i^{th} angle calculated in $CSL(x)$ for the n^{th} sample. By substituting the predicted value of each rotation angle of the N^{th} sample and the true value into $l_{n,i}$, the 180 angle results of the N^{th} sample are obtained by summation, find the average of the calculated results of N samples, that is the loss value of the predicted angle. After adding the angle prediction branch, the number of channels in the output feature map becomes (1+4+a+180)×3.

Navigation line extraction

The R-YOLOv5 algorithm model in this paper identifies the whole row of wheat seedlings, that is, one row of wheat seedlings outputs one detection box. But in the actual output result, there may be multiple detection boxes corresponding to one row of wheat seedlings, so it is necessary to cluster detection boxes belonging to the same wheat seedlings. This paper proposes an adaptive clustering method for detection boxes of peer wheat seedlings. The specific steps are as follows:

Step 1: Define a data set $Data=\left\{Box_1\left(r_x^1,r_y^1,L^1,S^1,\theta^1\right),\cdots,Box_n\left(r_x^n,r_y^n,L^n,S^n,\theta^n\right)\right\}$ to store the parameters of the output detection box, where $r_x^i,r_y^i,L^i,S^i,\theta^i$ respectively represent the horizontal coordinate of the center point, the vertical coordinate of the center point, the long side, the short side and the rotation angle, n represents the number of detection boxes of an image output;

Step 2: Randomly select a detection box from the data set *Data* Box_i, add it to the data set, and $Class_1$ delete it from the data set;

Step 3: According to the parameters of the detection box Box_i to find out the center point of the box and parallel to the long side of the line equation $l_i: y=-\tan\theta^i x+r_y^i+\tan\theta^i r_x^i$, and then randomly select the detection box Box_j from the data set Data, calculate the distance between the center point of the box and the line l_i $d_{ij}=\left|\frac{\tan\theta^i\left(r_x^j-r_x^i\right)+r_y^j-r_y^i}{\sqrt{1+\left(\tan\theta^i\right)^2}}\right|$. If $d_{ij}<\frac{S^j}{2}$, then the detection box Box_j is deleted from the data set Data, and the data set is added into $Class_1$,otherwise, no operation is performed;

Step 4: Repeat step 3 to complete all the boxes in the data set Data, and finally get the data set that belongs to the wheat seedling detection box in the same row $Class_1$;

Step 5: Repeat step 2-3, finally get the data set $Class_1$,..., $Class_m$, m represents the number of rows of wheat seedlings.

The adaptive clustering results of the wheat seedling detection frame are shown in Figure 3. Figure 3(1) is the detection frame output by the R-YOLOv5 algorithm model before clustering. At this time, each detection frame is relatively independent. Figure 3(2) shows that after the adaptive clustering method is adopted, the detection boxes belonging to the same row of wheat seedlings are divided into one class, and the detection boxes belonging to the same row of wheat seedlings are set to the same color. The center line of the detection box in the same cluster is the row line of wheat seedlings.



(1) detection boxes before clustering (2) detection boxes after clustering

Fig. 3 - The adaptive clustering result of detection box

Experimental Platform

In this paper, field experiments are conducted to verify the navigation line fitting performance of the algorithm.

The experiment in this paper is based on the experimental platform of automatic row control system for wheat root-cutting fertilization developed by the author's project team, as shown in Figure 4. The mechanical device mainly consists of two parts: traction device and wheat root-cutting fertilization device.



Fig. 4 - Experimental platform mechanical device

The traction device of the experimental platform is an 80hp KAI WO 804 tractor, and the wheat root-cutting fertilization device is connected by a three-point suspension device. The wheat root-cutting fertilization device is shown in Figure 5. The device is equipped with multiple root-cutter, and their distance is 30 cm according to the planting spacing design.

Each root cutter is welded with a small round tube at the back and connected with a white plastic tube for spreading fertilizer and preventing fertilizer from splashing outside; the camera is installed on the upper end of the second root cutter, which is circled blue in the figure, the camera is about 50 cm from the ground, the pitch angle is set to 45°, the yaw angle is set to 0°, and the pixel is 1920×1080; the root cutters can move left and right driven by the motor device.



Fig. 5 - Partial structure of wheat root cutting fertilization device

The control system is composed of industrial computer, control board, motor and motor driver. After the wheat seedling images are collected by the camera, the industrial computer extracts the wheat seedling navigation line, then, calculates the deviation, and sends the deviation information to the control board. The control board outputs the corresponding control signal to the motor to drive the motor to navigate the line.

Experimental Process

The field experiment of this paper was conducted at the "Intelligent Root Cutting and Layered Fertilization Technology and Equipment Experimental Demonstration Base for Wheat" in Jiaonan, Qingdao, Shandong Province. In the process of the experiment, the manual driving tractor provided the power, and the automatic alignment of the wheat root-cutting fertilization device pulled behind was completed by the control system based on the algorithm in this paper, as shown in Figure 6. In addition, due to the complex environment of the wheat field, it is difficult to subdivide various single cases, so the navigation performance of the proposed algorithm is verified by controlling different forward speeds of the experimental platform instead of conducting specific test analysis in a single case. In order to simplify the test and facilitate the measurement, fertilization is not carried out during the traveling process.



Fig. 6 - The field test

As for the measurement of the position error of the actual navigation path, the position error was measured by two people every 0.5 m, and the average value was taken. The experimental platform is installed with 4 root cutters. Since the distances between root cutters and wheat planting are both 30 cm, the position error of the traveling path of one root cutter is only needed to be measured. The path corresponding to the root cutter equipped with a camera is selected for measurement in this test.

The position error measurement method of the actual path is shown in Figure 7, where A represents the soil area before the root cutting, B represents the wheat seedling area, C represents the soil area after the root cutting, l_1, l_2 respectively represents the accurate wheat seedling line, and l_3, l_4 respectively represents the line at the top of the protruding sides of the ditch cut by the root cutter. The specific measurement steps are as follows:

Step 1: Measure the distance between l_1, l_2 each position, and find the midpoint o_1 of the distance between the two rows of wheat seedlings, which is the accurate position;

Step 2: Measure the distance between l_3, l_4 the corresponding position, find the middle point o_2 of the top of the protrusion on both sides of the ditch, the point is the actual position of the cutter;

Step 3: Measuring the distance between o_1, o_2 the two points in the vertical wheat seedling line direction, that is, the position error of the root cutter traveling at the position point;

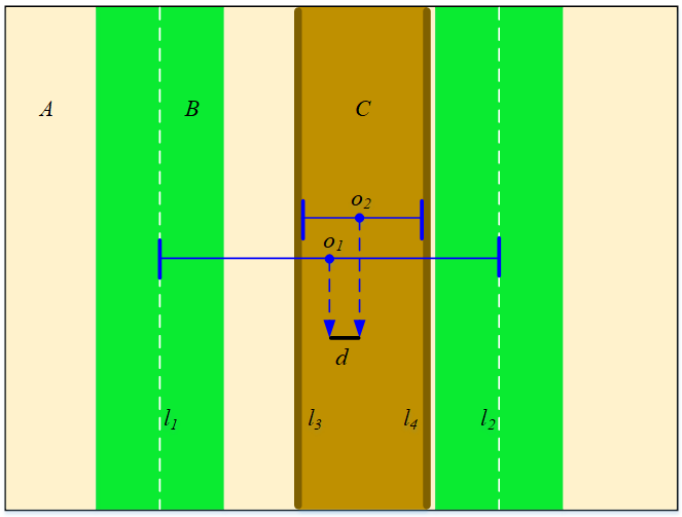


Fig. 7 - The schematic of position error measurement method

According to the papers of *Huo et al., (2004); Li and Zhu, (2006)*, the traveling speed of wheat root-cutting machine is usually 1.7 5 km/h (about 0.47-1.39 m/s), so the experiment set the forward speed of the platform in this paper as 0.5 m/s, 1.0 m/s and 1.5 m/s respectively. In each group of experiments, the distance of the platform at the set speed is about 30 m. Since the speed of the platform at the starting point and the end is unstable, select the middle section with a stable speed and a length of 20 m to measure the position error of the path of the root cutter. According to the position error measurement method, the error of 20 position points is measured in each group, as shown in Figure 8.

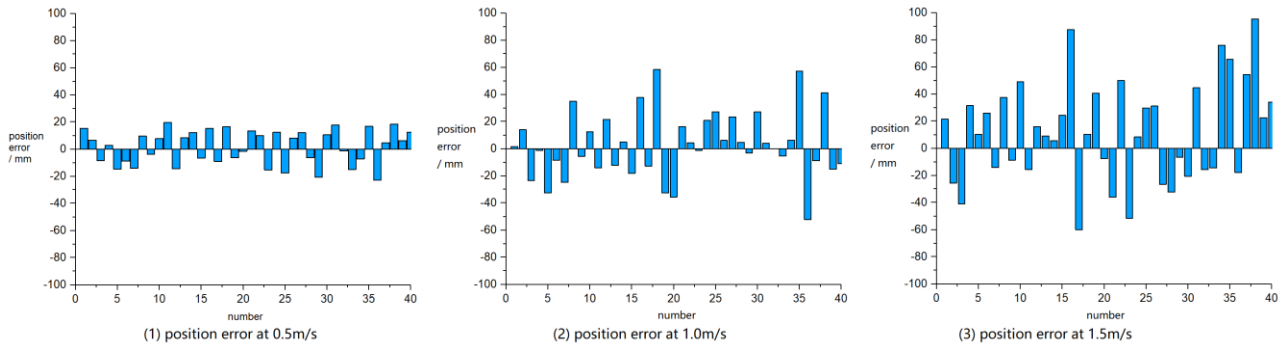


Fig. 8 - Position errors at different speeds

The maximum, average, and standard deviation of the navigation path position error at 0.5 m/s, 1.0 m/s, and 1.5 m/s were calculated. Based on the measurement results, when the traveling speed of the experimental platform is 0.5 m/s, the maximum, average and standard deviation of the position error are 22 mm, 11.27 mm and 2.32 mm, respectively. When the traveling speed of the experimental platform is 1.0 m/s, the maximum, average and standard deviation of the position error are 58 mm, 18.56 mm and 3.96 mm, respectively. When the traveling speed of the experimental platform is 1.5 m/s, the maximum, average and standard deviation of the position error are 95 mm, 31.9 mm and 4.72 mm, respectively.

The measurement results of the root cutters of the platform at different speeds show that the average and standard deviation of the actual navigation path position error increase with the speed during the platform moving. This phenomenon indicates that the faster speed, the more unstable the navigation effect. When the platform travels at a fast speed, it is subject to the calculation time of the upper computer and the response time of the lower computer of the control system. The positions of the root cutters cannot be corrected in time, resulting in a large position deviation.

Usually, the distance between the accurate path and the root of the wheat seedling on both sides is about 10 cm, and the maximum position error of the algorithm in the experiment is 95 mm. By observing the path of the root cutter, it is found that the wheat seedling is not accidentally injured. Therefore, the visual navigation provided by the algorithm for the automatic row control system of wheat root cutting meets the requirement that the root cutter does not hurt the seedling. Based on the experiment in this paper, it is also found that the navigation effect is best when the system operates at 1 m/s. When the navigation speed is lower than this speed, although the navigation accuracy is high, the operation efficiency is relatively low; when above this speed, the navigation accuracy decreases.

RESULTS

In order to verify the robustness and real-time navigation of the proposed algorithm, relevant images were selected from the accumulated data from 2019-2022, comparing the effects of the proposed algorithm and the improved algorithm from four aspects: different years, different periods of rejuvenation, different environments and different yaw angles. It was analyzed by combining distance error and angle error.

Comparative analysis of robustness of the algorithm

Since the wheat seedling lines involved in navigation line extraction usually pass through the upper and lower edges of the image, the algorithm proposed previously only targets at the wheat seedling lines that pass through the upper and lower edges of the image at the same time. Here, only the distance error and angle error of the wheat seedling line are counted, which are the same as the above conditions.

Comparison of wheat seedling line extraction in different years

In the wheat fields of different years, the soil moisture content will be different, and the growth state of wheat seedlings will be different, so the influence of wheat seedling images of different years on the two algorithms is analyzed here.

As shown in Figure 9, the images were respectively collected in March 2019-2022. It can be seen from the figure that the color of wheat seedlings and soil background in different years are quite different. Among which the soil moisture content in 2019 is relatively small, and the wheat seedlings have more dead leaves. Judging from the effect of wheat seedling line extraction, the two algorithms can obtain relatively accurate wheat seedling line. The algorithm in this paper can also extract the wheat seedling line on both sides of the image, but its accuracy is not as high as that in the middle of the image.

Fifty images were randomly selected for testing in each year, and the distance error and angle error were counted, as shown in Table 1. It can be seen from the table that each algorithm has little difference in various statistical indicators of the four years, indicating that the two algorithms have certain adaptability to wheat seedling images of different years. In addition, by comparing the two algorithms, it can be found that the distance error and angle error of the proposed algorithm are both smaller than that of the previous algorithm, which indicates that the proposed algorithm is more robust than the previous algorithm.

Table 1

The evaluation statistics of wheat seedling lines in different years under two algorithms

Algorithm	Categories	Range error / pixel	Angle error / °
Textual algorithm	In 2019	10.61	0.86
	In 2020	8.26	0.61
	In 2021	9.80	0.67
	In 2022	11.15	0.83
	Average	9.95	0.74
Previous algorithm	In 2019	19.55	1.64
	In 2020	15.37	1.43
	In 2021	23.62	1.79
	In 2022	15.86	1.56
	Average	18.60	1.60

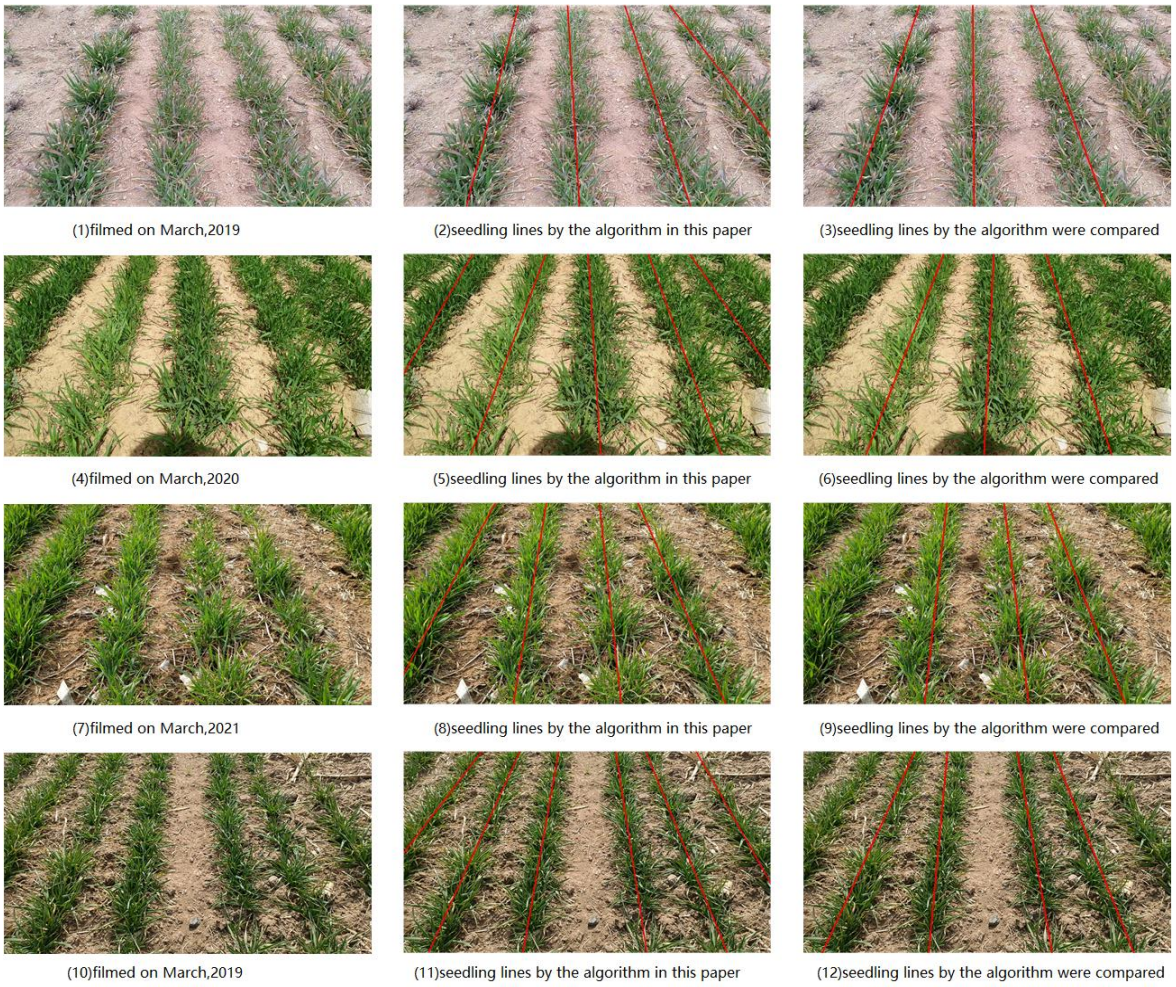


Fig. 9 - The wheat seedling lines in different years obtained by two algorithms

Wheat seedling line extraction and comparison in different periods of rejuvenation stage

The wheat that entered the rejuvenation stage began to grow and develop.

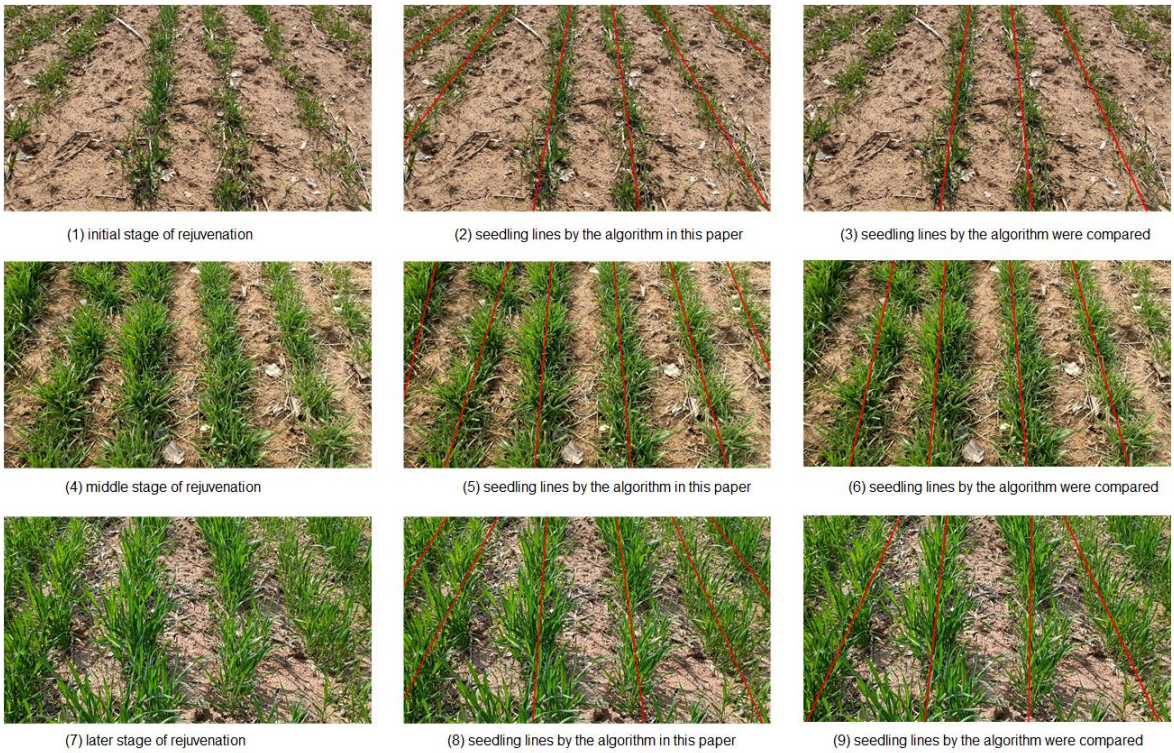


Fig. 10 - The wheat seedling lines at different time in rejuvenation period obtained by two algorithms

In Figure 10(1), the wheat seedlings in the early rejuvenation stage were collected at the end of February, when the wheat seedlings were sparse; in Figure 10(2), the wheat seedlings in the middle of the rejuvenation stage were collected in mid-March, when the wheat seedlings were flourishing; in Figure 10(3), the wheat seedlings at the later stage of rejuvenation were collected at the beginning of April, at which time the wheat seedlings began to joint, which showed a big difference in their appearance morphology. Therefore, the influence of wheat seedlings in different time periods of the rejuvenation period on the two algorithms is analyzed here. In the figure, the wheat seedlings in each time period obtained by the algorithm in this paper are more accurate, while the wheat seedlings in the late rejuvenation period obtained by the previous algorithm are slightly less accurate.

Table 2

The evaluation statistics of wheat seedling lines at different time under two algorithms

Algorithm	Categories	Range error / pixel	Angle error / °
Textual algorithm	Initial stage	10.52	1.06
	Middle stage	9.36	0.89
	Later stage	13.61	1.15
	Average	11.16	1.03
Previous algorithm	Initial stage	22.67	1.79
	Middle stage	16.34	1.53
	Later stage	31.64	3.06
	Average	18.5	2.12

Table 2 shows the evaluation statistics of 50 wheat seedling images at different time periods in the rejuvenation stage. As can be seen from the table, the extraction accuracy of the proposed algorithm is significantly better than that of the previous algorithm, especially in the late period of rejuvenation.

The distance error and angle error of the previous algorithm are twice as much as that of the proposed algorithm. In addition, the phenomenon of wheat seedling line leakage exists in the previous algorithm, which indicates that the robustness of the previous algorithm is not strong enough. The table also indicates that both methods exhibit relatively smaller errors in wheat seedling images from the mid-rejuvenation phase, indicating that the navigation lines extracted during this period are more accurate and suitable for wheat root-cutting by automatic row method.

Comparison of wheat seedling line extraction under different environmental backgrounds

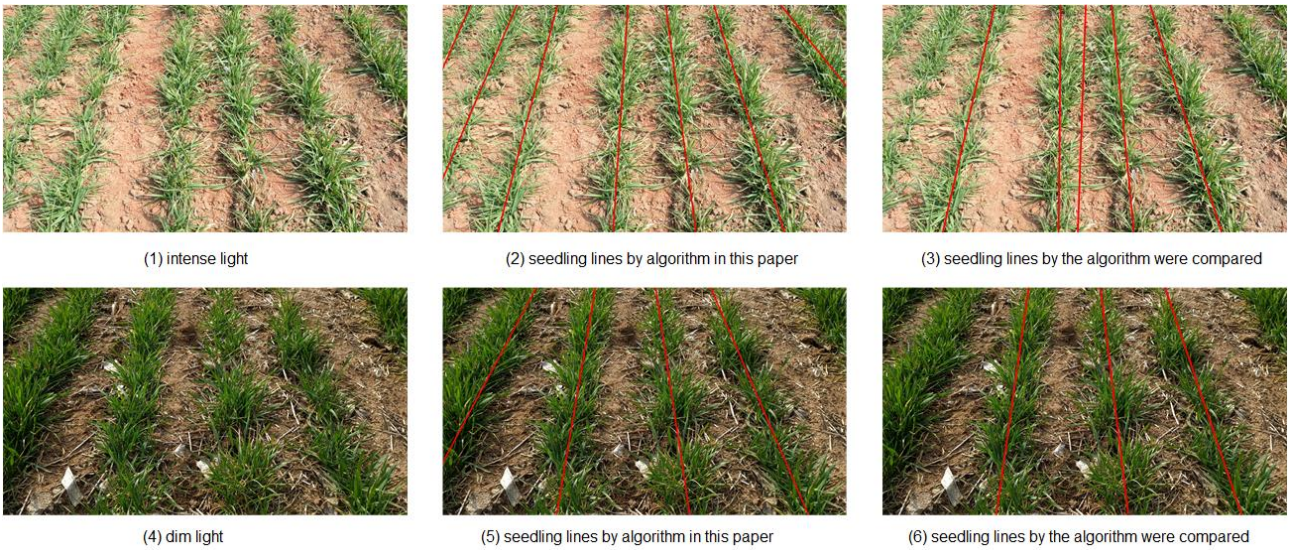


Fig. 11 - The wheat seedling lines under different illumination obtained by two algorithms

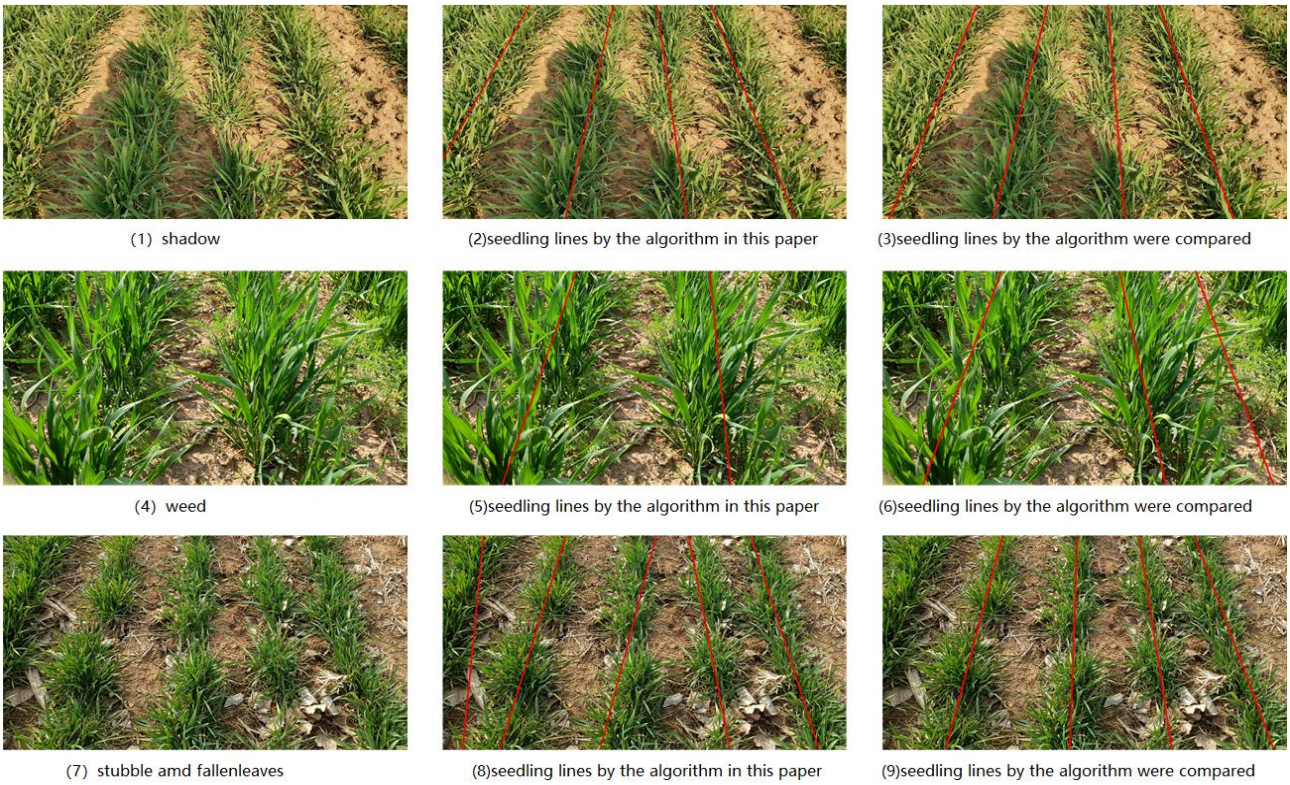


Fig. 12 - The wheat seedling lines under shadows, weeds, stubble and leaves obtained by two algorithms

To compare the performance of the two algorithms under different environmental backgrounds, 30 wheat seedling images each were selected from the dataset that had varying conditions such as strong light, low light, shadows, weeds, stubble, and fallen leaves. As can be seen from Figure10, light has little influence on the extraction effect of the proposed algorithm, but has some influence on the previous algorithm. As shown in Figure 10(3), strong light will increase the vertical projection value. Once the value exceeds the preset threshold, it is considered that there may be wheat seedling rows in the area. Therefore, when the light is strong, the previous algorithm will extract the wheat seedling line excessively, and when the light is dark, it will miss to extract the wheat seedling line.

Figure 11 shows the extraction effects of the two algorithms under the background of shadows, weeds, stubble and fallen leaves. As can be seen from the figure, the algorithm in this paper is less affected by shadow and weed environment, while more affected by stubble and fallen leaves. Through analysis, it is found that more corner points are detected in the stubble and fallen leaves area in the figure. Due to their irregular distribution in the image, sometimes the error of the extracted wheat seedling line is large. As for the previous algorithm, it is little affected by shadow, stubble and fallen leaves, but it is affected by weeds, and it is easy to misidentify the weeds between the rows as wheat seedlings.

Table 3

The evaluation statistics of wheat seedling lines in different background environment under two algorithms

Algorithm	Categories	Range error / pixel	Angle error / °
Textual algorithm	Intense light	9.06	0.87
	Dim light	10.69	0.95
	Shadow	11.54	0.94
	Weed	14.75	1.23
	Stubble and fallen leaves	19.58	1.69
Previous algorithm	Intense light	23.77	1.96
	Dim light	20.23	1.85
	Shadow	18.51	1.72
	Weed	28.94	2.90
	Stubble and fallen leaves	18.84	1.66

Table 3 shows the evaluation statistics of the two algorithms under different environmental backgrounds. As can be seen from the table, the extraction effect of the proposed algorithm is still better than the previous algorithm in terms of error. But the extraction accuracy is relatively low in the background of weeds, stubble and fallen leaves. In addition, the extraction accuracy of the previous algorithm is worse in the background of weeds.

Comparison of wheat seedling line extraction under different yaw angles

During real-world agricultural machinery operations in the fields, the uneven ground, mechanical vibration and crop line bending and other problems will inevitably lead to a certain yaw angle of the camera for image acquisition. Therefore, a robust crop row extraction method should be equally applicable to images captured with a non-zero yaw angle. In order to study the influence of yaw angle on the algorithm in this paper, 30 images with small yaw angle and 30 images with large yaw angle were selected from the wheat seedling data set respectively. In this paper, small yaw angle refers to less than 30°, and large yaw angle refers to greater than 30°. As shown in Figure 13, it can be seen that the wheat seedling line extracted by the algorithm in this paper has a higher accuracy, while the previous algorithm has a lower accuracy.

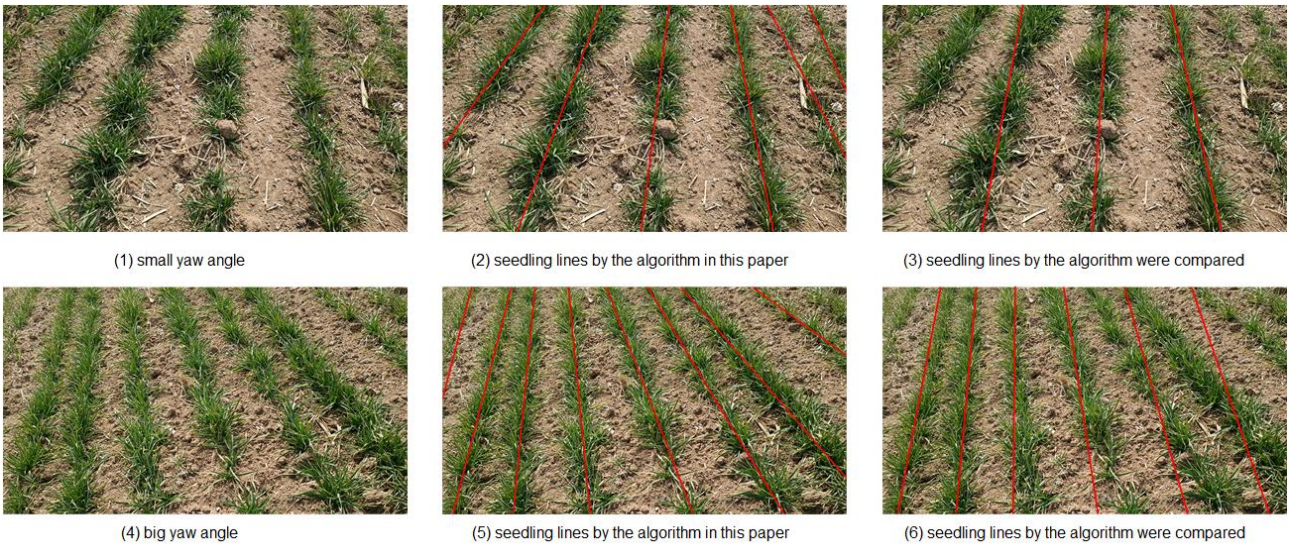


Fig. 13 - The wheat seedling lines at different yaw angles obtained by two algorithms

Table 4 shows the statistics of evaluation results of the two algorithms under different yaw angles. As can be seen from the table, the algorithm in this paper is less affected by yaw angle, while the previous algorithm is more affected by yaw angle, especially when the yaw angle is larger, its angle error can reach 8.46°.

Table 4

The evaluation statistics of wheat seedling lines at different yaw angles under two algorithms

Algorithm	Categories	Range error / pixel	Angle error / °
Textual algorithm	Small yaw angle	10.27	0.97
	Big yaw angle	13.54	1.18
Previous algorithm	Small yaw angle	42.61	3.89
	Big yaw angle	77.84	8.46

Based on the analysis of the above aspects, the wheat seedling line obtained by the algorithm in this paper is less than the previous algorithm in terms of distance error and angle error, and it has strong robustness under various environmental conditions.

Comparative analysis of real-time performance of the algorithm

In the above test process, the running time of the two algorithms for each image was recorded, and the average running time under each specific classification was calculated, as shown in Table 5. From the table, it can be observed that for wheat seedling images of size 1920×1080 pixels, the average runtime of the proposed algorithm for extracting wheat row lines ranges from 67 ms to 71 ms, while the previous algorithm's average runtime for the same task ranged from 50 ms to 55 ms. Therefore, the textual algorithm is 12 ms-21 ms slower than the previous algorithm. However, this time difference has no great impact on the field experiment, and it can still meet the real-time requirements of the job.

Table 5

Running time statistics of two algorithms

Items	Specific classification	Textual algorithm	Previous algorithm
Different years	2019	67.44 ms	52.23 ms
	2020	68.73 ms	51.65 ms
	2021	69.68 ms	52.94 ms
	2022	67.82 ms	53.61 ms
Different period of rejuvenating	Initial stage	68.99 ms	51.29 ms
	Middle stage	69.42 ms	52.47 ms
	Later stage	68.37 ms	52.67 ms
Different environmental background	Intense light	68.81 ms	52.19 ms
	Dim light	69.03 ms	51.42 ms
	Shadow	68.61 ms	51.00 ms
	Weed	68.33 ms	50.76 ms
	Stubble and fallen leaves	70.11 ms	52.98 ms
Different yaw angles	Small yaw angle	67.25 ms	53.44 ms
	Big yaw angle	68.43 ms	54.76 ms

CONCLUSIONS

This paper addresses the extraction of navigation lines for wheat root cutting and proposes a deep learning algorithm based on an improved YOLOv5 model. The algorithm's performance is tested and analyzed through field experiments, leading to the following key conclusions: (1) The measurement of the position error of the navigation line at different speeds shows that the average and standard deviations of the actual position error of the navigation path increase with the speed. The navigation effect is the best when the system operates at 1 m/s, and the maximum, average and standard deviation of the position error are 58 mm, 18.56 mm and 3.96 mm, respectively. (2) The improved algorithm and the original algorithm were tested by using the collected data from 2019-2022, and compared from four aspects: different years, different periods of rejuvenation, different environments and different yaw angles. The improved algorithm is superior to the original algorithm and has strong robustness under various circumstances.

ACKNOWLEDGEMENT

The research of this paper is funded by Natural Science Foundation of Shandong Province (ZR2021MF096). During the project, the help of Qingdao Zongsen Agricultural Machinery Research Institute and Qingbao Agricultural Machinery Station is greatly appreciated.

REFERENCES

[1] Amrani, A., Sohel, F., Diepeveen, D., Murray, D., Jones, M. G. K. (2023) Deep learning-based detection of aphid colonies on plants from a reconstructed Brassica image dataset. *Computers and Electronics in Agriculture,* Vol. 205. February 2023, 107587. England.

[2] Dhruba, N., Abhishek, S., Kshetrimayum, T. C. (2018). Multipurpose GPS Guided Autonomous Mobile Robot. *Progress in Advanced Computing and Intelligent Engineering*, Vol.564, pp. 361-372. Springer Singapore.

[3] He, J., Zhang, Y., Luo, X., Zhao, R., He, J. et al (2021). Visual detection of rice rows based on Bayesian decision theory and robust regression least squares method. *International Journal of Agricultural and Biological Engineering,* Vol. 14(1), pp. 199-206. China.

[4] Huo, W. G., Lv, Z. Q., Shao, J. (2004). Design of multi-functional root cutting machine for winter wheat (手扶式冬小麦多功能断根机设计). *Shandong Agricultural Machinery,* 2004(06), pp.11-13. *Shandong/China.*

[5] Jeon, C.-W., Kim, H.-J., Yun, C., Gang, M., Han, X. (2021). An entry-exit path planner for an autonomous tractor in a paddy field. *Computers and Electronics in Agriculture,* Vol.191, December 2021, 106548. England.

[6] Jiang, G. Q., Wang, X. J., Wang, Z. H., Liu, H. M. (2016). Wheat rows detection at the early growth stage based on Hough transform and vanishing point. *Computers and Electronics in Agriculture*, Vol. 123, pp. 211-223. England.

[7] Jiang, Y., Zhang L. L., Xue, P., Wang X. D. (2021). Development Status of Wheat Industry in China and International Experience for Reference (我国小麦产业发展情况及国际经验借鉴). *Journal of Agricultural Science and Technology*, Vol. 23(07), pp. 1-10. Beijing/China.

[8] Khan, S., Tufail, M., Khan, M. T., Khan Z. A., & Anwar, S. (2021). Deep learning-based identification system of weeds and crops in strawberry and pea fields for a precision agriculture sprayer. *Precision Agriculture,* Vol. 22(6), pp. 1-17. Netherlands.

[9] Li, C. Z., Zhu, G. Y., (2006). Design and research of a new type of winter wheat root cutting machine (一种新型冬小麦断根机的设计研究). *Farm Machinery*, Vol. 2006(22), pp. 80-81. *Beijing/China.*

[10] Li, X. G., Zhao, W., Zhao, L. L. (2021). Extraction algorithm of the center line of maize row in case of plants lacking. *Transactions of the Chinese Society of Agricultural Engineering (Transactions of the CSAE)*, Vol. 37(18), pp. 203-210. Beijing/China.

[11] Liu, F.C., Yang, Y., Zeng, Y.M., Liu Z. Y. (2020). Bending diagnosis of rice seedling lines and guidance line extraction of automatic weeding equipment in paddy field. *Mechanical Systems and Signal Processing,* Vol. 142(C), pp. 106791-106791. England.

[12] Liu, G., Nouaze, J. C., Mbouembe, P. L. T., Kim, J. H. (2020). YOLO-tomato: A robust algorithm for tomato detection based on YOLOv3. *Sensors,* Vol. 20(7), pp. 2145-2145. Switzerland.

[13] Lv, Z. Q., Li, R. Z., Dong, Q. Y., Yin, K. R., Yu, S. L. (2006). Mechanical root-cutting models for increasing the yield of winter wheat (冬小麦增产技术中机械断根方式的研究). Transactions of the Chinese Society of Agricultural Engineering, Vol. 2006(04), pp. 103-106. Beijing/China.

[14] Pang, Y., Shi, Y., Gao, S. C., Jiang, F., Veeranampalayam-Sivakumar, A., Thompson, L., Luck, J., Liu, C. (2020). Improved crop row detection with deep neural network for early-season maize stand count in UAV imagery. *Computers and Electronics in Agriculture,* Vol. 178, pp. 105766. England.

[15] Sevilla, M. F. de, Gutiérrez, Ó., Gómez, J., Tayebi, A., Álvarez, Á., Adana, F. S. de. (2021). On the application of radio planning tools in open environments for the improvement of autoguidance systems used in precision agriculture. *Computers and Electronics in Agriculture*, Vol. 187, August 2021, 106258. England.

[16] Villacrés, J., Viscaino, M., Delpiano, J., Vougioukas, S., Cheein, F. A. (2023). Apple orchard production estimation using deep learning strategies: A comparison of tracking-by-detection algorithms. *Computers and Electronics in Agriculture,* Vol. 204, January 2023, 107513. England.

[17] Yadav, P. K., Thomasson, J. A., Hardin, R., Searcy, S. W., Braga-Neto, U., Popescu, S. C., Martin, D. E., Rodriguez, R., Meza, K., Enciso, J., Diaz, J. S., Wang, T. (2023) Detecting volunteer cotton plants in a corn field with deep learning on UAV remote-sensing imagery. *Computers and Electronics in Agriculture*, Vol. 204, January 2023, 107551. England.

[18] Yang, X., Yan. J. (2020). Arbitrary-Oriented Object Detection with Circular Smooth Label. *European Conference on Computer Vision.* 2020, pp. 677-694. Springer: Cham.

[19] Yang, X., Yang, J., Yan, J., Zhang, Y., Zhang, T., Guo, Z., Xian, S., Fu, K. (2019). Scrdet: towards more robust detection for small, cluttered and rotated objects. *2019 IEEE/CVF International Conference on Computer Vision. South Korea: IEEE*, 2019, pp. 8232-8241. South Korea.

[20] Yu, S. L., Qi, X. H., Liu, X. Y., Dong Q. Y., Xu, Y. M. (1985). Studies on The Effect on Yield Increase by Deep Cultivation Root Cutting in Winter Wheat (冬小麦深耘断根增产作用的研究). *Scientia Agricultura Sinica*, Vol. 1985(04), pp. 30-35. Beijing/China.

[21] Yun, C., Kim, H.-J., Jeon, C.-W., Gang, M., Lee, W. S., Han, J. G. (2021). Stereovision-based ridge-furrow detection and tracking for auto-guided cultivator. *Computers and Electronics in Agriculture*, Vol. 191, December 2021, 106490. England.

SIMULATION TEST AND VERIFICATION OF MATERIAL CONVEYING FOR SMALL AND MEDIUM-SIZED AIR SUCTION JUJUBE PICKING MACHINE BASED ON CFD-DEM COUPLING

/

基于CFD-DEM 耦合中小型气吸红枣捡拾机物料输送仿真试验与验证

Fengkui ZHANG[1,2,3], Wenxi SHAO[1)], Shijie ZHAO[1,2,3)], Jikui ZHU[1,2,3)], Ping LI [1,2,3*]

[1)] College of Mechanical and Electrical Engineering, Tarim University, Alar 843300, Xinjiang, China;

[2)] Modern Agricultural Engineering Key Laboratory at Universities of Education Department of Xinjiang Uygur Autonomous Region, Tarim University, Alar 843300, Xinjiang, China

[3)] Key Laboratory of Tarim Oasis Agriculture (Tarim University), Ministry of Education, Tarim University, Alar 843300, Xinjiang, China

**Corresponding Author: Li Ping, Email: lpdyy716@163.com*

DOI: https://doi.org/10.35633/inmateh-71-46

Keywords: *Jujubes, Transportation, CFD-DEM coupling, Numerical simulation*

ABSTRACT

To improve the quality of air suction jujube picker, the CFD-DEM coupled method is used to numerically simulate the conveying process of jujube particles and explore the motion state, particle collision and energy loss of jujube particles in the pipeline. The erosion rate is selected as an evaluation index to discuss the influence of wind velocity, bending angle and diameter on the conveying process. The simulation results show that the collisions between jujubes, as well as the collisions between jujubes and pipe wall have an impact on the conveying performance, and the latter is more significant. The erosion rate is positively correlated with the wind velocity, negatively correlated with the pipe diameter, and the bending angle first decreases and then increases. The influence degree of factors on the erosion rate is: wind velocity > bending angle > pipeline diameter. The optimal parameter combination is a wind velocity of 28 m·s-1, a bending angle of 105 °, and a pipe diameter of 130 mm. At this time, the value of erosion rate is the lowest and the number of collisions and energy loss between jujube particles are reduced by 37.3 % and 13.87 % year-on-year, and those between jujube particles and pipe wall are reduced by 17.45 % and 17.61 % year-on-year, respectively. The test results show that the conveying pipe with optimized structural parameters can reduce the jujube skin damage rate by 2.06 %. The results of this study can provide a reference for the design and optimization of the air suction jujube picker.

摘要

中小型气吸式红枣捡拾机利用负压吸送原理完成红枣果实的输送作业，但因红枣与红枣、红枣与管壁碰撞等问题造成红枣表皮轻微损伤，为提高气吸式红枣捡拾机作业质量，利用 CFD-DEM 耦合的方法对输送管输送红枣颗粒过程进行数值模拟，探究红枣颗粒在管路内的运动状态、颗粒碰撞及能量损失情况，并以侵蚀速率为评价指标讨论风速、弯管角度和直径对输送过程的影响。仿真结果表明，红枣与红枣、红枣与管壁两种碰撞均对输送性能有影响，且后者更为显著；侵蚀速率与风速呈正相关，与管路直径呈负相关，与弯管角度则呈现先减小后增大；各因素对侵蚀速率的影响程度为风速>弯管角度>管路直径，最优参数组合为风速 28m•s-1，弯管角度 105°，管路直径 130mm，此时侵蚀速率值最低且枣间颗粒碰撞次数和能量损失同比降低 37.3%和 13.87%，红枣颗粒与管壁碰撞次数和能量损失同比降低 17.45%和 17.61%。验证试验结果表明，结构参数优化后的输送管对红枣表皮损伤率降低 2.06%。该研究结果可为气吸式红枣捡拾机的设计与优化提供参考。

INTRODUCTION

The research on mechanized harvesting equipment of jujubes mainly focuses on small and medium-sized air suction jujube picker *(Yuan et al., 2021; Yuan et al., 2022; Zhang et al., 2019)*. Its main function is to complete the tasks such as picking and conveying *(Zhang et al., 2020; Zhang et al., 2021)*, and separating and removing impurities of jujubes lying on the ground *(Du et al., 2022; Shi et al., 2022a)*. Because its selling price meets the cost demand of fruit farmers for harvesting, it is widely used in southern Xinjiang region, such as Kashgar, Aksu, Hotan and other places.

Fengkui Zhang, Master, Lecturer; Wenxi Shao, Graduate student; Shijie Zhao, Graduate student; Jikui Zhu, Lecturer; Ping Li, PhD, Professor.

The conveying process of small and medium-sized air suction jujube picker is mainly through the conveying pipeline of the picking device. In its negative pressure suction conveying process, the main flow is gas-solid two-phase. In actual production, it is found that the structure of conveying pipeline has a significant impact on the quality of the whole machine, especially on the jujube skin caused by a slight damage, which is not conductive to preservation and sale.

The discrete element method *(Basu et al., 2021; Jayasundara et al., 2022; Brandt et al., 2023; Carr et al., 2023)* and computational fluid dynamics numerical simulation techniques *(Nijssen et al., 2023; Rakesh and Shibayan, 2023; Weaver et al., 2023)* have become important tools for studying multiphase flow and structural optimization. The experimental method based on Computational Fluid Dynamics-Discrete Element Method (CFD-EDM) coupling is widely used to study the motion state between particles, as well as between particles and shells, and the characteristics in the airflow field *(Lewis et al., 2022; Ponzini et al., 2021; Hesse et al., 2023; Dustin et al., 2023)*. The method has also been used in the field of agricultural engineering to study the state of particles in the shell under the action of airflow, as well as to optimize the operation and structural parameters of key devices *(Leno et al., 2023; Kim et al., 2019; Qin et al., 2023)*. After optimization, the quality of mechanical equipment can be improved, such as small nut harvesting, grain sorting and seeder, et al. *(Ren et al., 2023; El-Emam et al., 2021; Hou et al., 2023)*.

The objectives of this study are: (1) the CFD-DEM coupling method is used to numerically simulate the conveying process of jujube particles in the conveying pipe of the small and medium-sized air suction jujube picking machine, so as to obtain the motion characteristics of jujube particles during the conveying process, the characteristics of airflow field distribution, as well as the relationship between the number of collisions and energy loss and the structural parameters of the conveying pipe; (2) through analyzing the movement state of jujubes in the conveying process, the distribution law in airflow field and the relationship between the collision and energy loss and the structural parameters of the conveying pipe is analyzed, and the optimization scheme of the conveying pipe structure is proposed; (3) the feasibility of the simulation results are verified, aiming to provide a reference for the design and optimization of small and medium-sized air suction jujube picking machine.

MATERIALS AND METHODS

Structure and Working Principle of the Picking Device

The picking device of the small and medium-sized air suction jujube picking machine (Fig. 1) includes a conveying pipe, separation and impurity removal box, unloading device and centrifugal fan and other more. Its working principle is to generate negative pressure inside the separation and impurity removal box through the centrifugal fan. Due to the pressure difference, the external airflow enters the mouth of the conveying pipe, and then the jujubes are picked and conveyed to the separation and debris removal box. The separation of materials and impurities, as well as the collection of materials, can be achieved through the separation and removal box and discharge device.

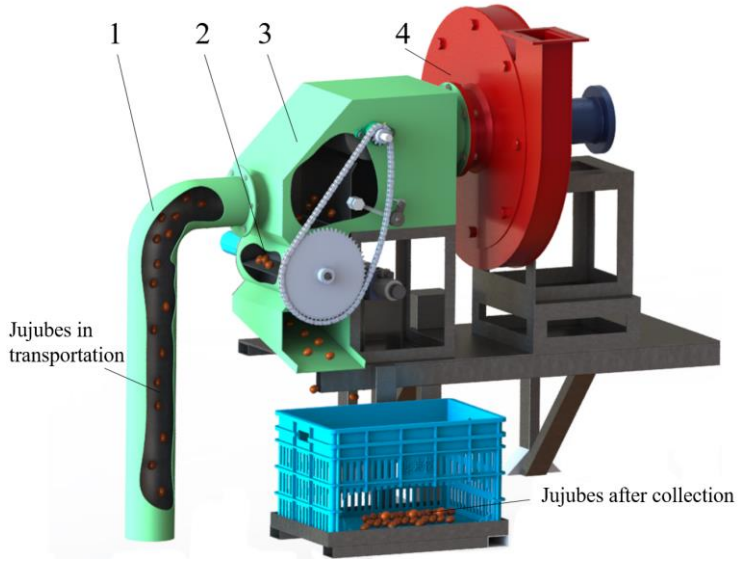


Fig. 1 - Picking device

1. Conveying pipe; 2. Unloading device; 3. Separation and debris removal box; 4. Centrifugal fan

A conveying pipe usually consists of a section of 90° metal elbow and a PU corrugated ventilation pipe with the same inner diameter as the outer diameter of the elbow connected through a stain less steel throat hoop. The flange plate welded at the outlet of the metal elbow can be connected to the flange bolt at the inlet of the separation and impurity removal box, ensuring that the working quality of the suction jujube picker cannot be reduced due to air tightness during the conveying process. According to the requirements of coupled numerical simulations, the grid size needs to be slightly larger than the material size. The cell grid size of the ANSYS Wrokbench in the ICEM module is set to 30 mm, and the pipeline is divided into grids using the swept method. The grid is quadrilateral, with a vertical section height of 700 mm, a horizontal section length of 200 mm, an elbow diameter of 130 mm, and a total number of grids of 2544. Its minimum cell mass, maximum cell mass and average mass are 0.618, 0.977 and 0.875, respectively. The grid quality meets the simulation requirements. After setting, the divided grid is shown in Fig. 2

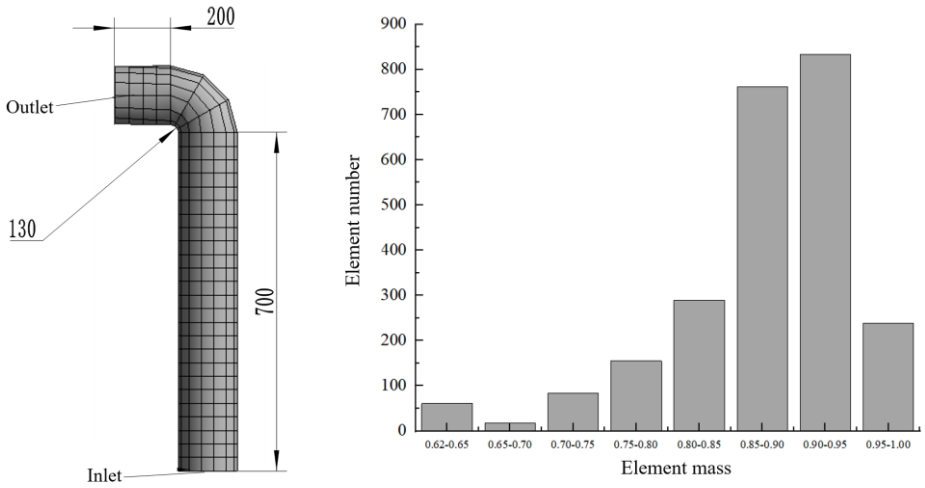


Fig. 2 – Grids of the conveying pipe

CFD-DEM coupled model construction

Fluent fluid model

Due to the high airflow velocity (which is generally greater than the suspension velocity of jujubes) during the transportation of jujube particles in the fluid, the void rate between jujubes is large, which belongs to the rarefied-phase pneumatic conveying. The Eulerian coupling model is used in the coupling, and the Wen & Yu model selected the traction model, which has the characteristics of adapting to large void rate and more meets the actual situation of jujube particle transportation process.

The Eulerian coupling model is used to simulate the transportation process of jujube particles, and the fluid volume fraction term and the differential equation of fluid motion are expressed as follows *(Weng et al., 2022)*:

$$\frac{\partial_{\varepsilon\rho}}{\partial_t}+\nabla(\rho\varepsilon\mu)=0 \tag{1}$$

$$\frac{\partial_{\varepsilon\rho}}{\partial_t}+\nabla(\rho\varepsilon\mu v)=-\nabla P+\nabla(\rho\varepsilon\nabla v)+\rho\varepsilon g-S \tag{2}$$

where t is the time; ε is the fluid volume fraction term; v is the flow velocity; g is the gravitational acceleration; ρ is the fluid density; S is the momentum source term; μ is the coefficient of viscosity; P is the pressure on the fluid microelement, and ∇ is the Hamiltonian differential operator.

The momentum source term S is the sum of the airflow resistance of the airflow acting inside the cell grid *(Hu et al., 2020)*.

$$S=\frac{\sum_{i=1}^{n}F_i}{V} \tag{3}$$

where V is the cell grid volume, and F_i is the resistance of the i-th particle to the airflow.

DEM solid particle contact and collision model

The contact mechanical behavior and interaction force between particle mechanical models are simulated and analyzed in EDEM software.

Since the velocity between the particles changes with the contact force, the jujubes are mainly subject

to rolling friction and air flow in the gas-solid two-phase flow, with no adhesion on the surface of jujubes. The Hertz-Mindlin no-slip contact model and the soft-sphere dry contact model are selected *(Wiacek, 2016)*, and the motion equations of the *i*-th particle are obtained according to Newton's second law *(Hamed et al., 2023)*:

$$m_i \frac{dV_i}{d_t} = m_i g + P = \sum_{j=1}^{n_i} \left(F_{n,ij} + F_{t,ij} \right) \quad (4)$$

$$I_i \frac{d\omega_i}{d_t} = \sum_{j=1}^{n_i} \left(T_{n,ij} + T_{t,ij} \right) \quad (5)$$

where g is the gravitational acceleration; P is the interaction force on the particles when they move in the airflow; I_i and m_i are the rotational moment of inertia and mass of particle i, respectively; V_i and ω_i are the velocity and angular velocity of particle i, respectively; $F_{t,ij}$ is the tangential component force; $F_{n,ij}$ is the normal component force; $T_{r,ij}$ is the rolling friction torque, and $T_{t,ij}$ is the tangential force torque.

According to the linear three-equation functional model of elastic damping, each force is simplified in the form of a combination of spring, damping, and slider form *(Xiong et al., 2019)*:

$$F_{n,ij} = -k_n \delta_n - n_n V_{n,ij} \quad (6)$$

$$F_{t,ij} = -k_t \delta_t - n_n V_{n,ij} - \frac{f_s |F_{n,ij}| \delta_t}{|\delta_t|} \quad (7)$$

$$T_{t,ij} = L_{ij} n_{ij} \times F_{t,ij} \quad (8)$$

$$F_{r,ij} = -k_r a - n_r \omega_{ij} - \frac{f_r |F_{n,ij}| a}{|a|} \quad (9)$$

where V is the velocity of motion of particles; δ is the displacement deformation between particles; a is the torsional deformation; k is the stiffness coefficient; f is the friction coefficient; η is the damping coefficient, and L is the amount of overlap. ij is between particles i and particles j, t is tangential, n is normal, s is sliding, and r is circumferential or rolling.

The interaction force P that particles are subjected to in the gas stream is expressed as follows:

$$P = k_g \rho A v^2 = k_g \rho A (v_q - v_w)^2 \quad (10)$$

where ρ is the density of the airflow; k_g is the drag coefficient, which is related to the shape of the material structure, surface characteristics and Reynolds number, etc. A is the area of the material facing the wind; v_w is the velocity of the material; v is the relative velocity of the material in the airflow; and v_q is the velocity of the airflow.

As shown in Table 1, the average equivalent diameter of jujube is 26.23 mm, and the particles are simplified to equivalent sphere. 26mm sphere particles are taken as the model of jujube particles, as shown in Fig. 3.

Table 1

Basic material parameters of jujube particles

Parameters	Work unit	Maximum values	Minimum value	Average value
Mass	g	8.12	2.91	4.87
Volumetric	ml	14	6	9.46
Densities	g·cm^{-3}	0.604	0.473	0.534
Equivalent diameter	mm	29.89	22.53	26.23

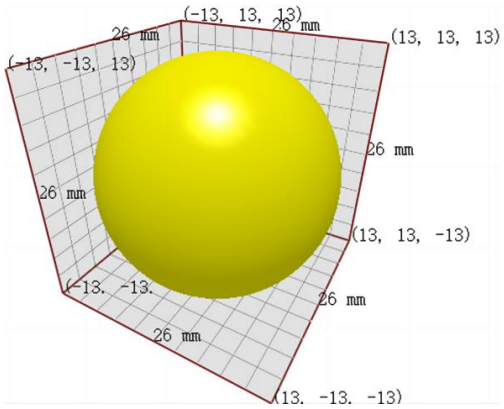


Fig. 3 - Jujube particle model

Performance evaluation index selection for CFD-DEM coupled conveying process

In response to the current simulation state of jujube conveying process in the conveying pipe, the erosion rate is taken as an evaluation index. Its principle is to simulate the erosion corrosion caused by particles in the fluid on the inner wall of the pipeline. The erosion rate is affected by wind velocity, pipe diameter, bending angle and other factors. To explore the effects of wind velocity, pipe diameter, bending angle and other factors on the conveying process, the control variables method is used to ensure that the other conditions have the same parameters in the simulation of jujube conveying process. Taking the erosion rate as an index, the influence of each factor on the erosion of the pipeline is determined. The orthogonal test method is used to further study the influence of factor interaction on the performance of jujube conveying process.

The main measurement index for the working performance of the conveying pipe of the picking device of the air suction jujube picker is the jujube skin damage rate *E*. *E* is thus selected as the evaluation index of the working performance for the optimization and verification of the conveying pipe.

$$E=\frac{M_1}{M}\times 100\% \quad (11)$$

where M_1 is the number of jujubes that pass through the outlet with damaged epidermis during the verification test and *M* is the total number of exported jujubes during the verification test.

Numerical simulation parameterization

The mass, volume and density of jujube particles are measured by balance and cylinder method. The frictional contact parameters between jujubes and pipe wall are measured by the inclined plate test. The recovery coefficient between jujubes and pipe wall is measured by the collision method *(Zhang et al., 2018)*. The relevant parameters are obtained through the pre-test of relevant material parameters and relevant literatures as shown in Table 2 *(Shi et al., 2022b; Wang et al., 2021)*.

EDEM parameter settings

The specific parameters of the materials used in EDEM are shown in Table 2. The particle radius is random, with a range of 0.85 to 1.15. 200 particles are generated per second, with an initial velocity of 0.5 m·s^{-1}. The simulation time step is 1e-05 s, and storage is performed every 0.01 s.

Table 2

Related parameters and contact coefficients of particles and materials

Parameters	Items	Numerical values
Jujube particles	Poisson ratio	0.248
	Shear modulus (MPa)	0.06
	Densities (kg·m^{-3})	534
Pipeline	Poisson's ratio	0.319
	Shear modulus (MPa)	1139
	Density (kg·m^{-3})	1380
Particles - pipe wall	Crash recovery factor	0.75
	Coefficient of static friction	0.25
	Coefficient of rolling friction	0.03
Particles	Crash recovery factor	0.77
	Coefficient of static friction	0.48
	Coefficient of rolling friction	0.04

Fluent parameter settings

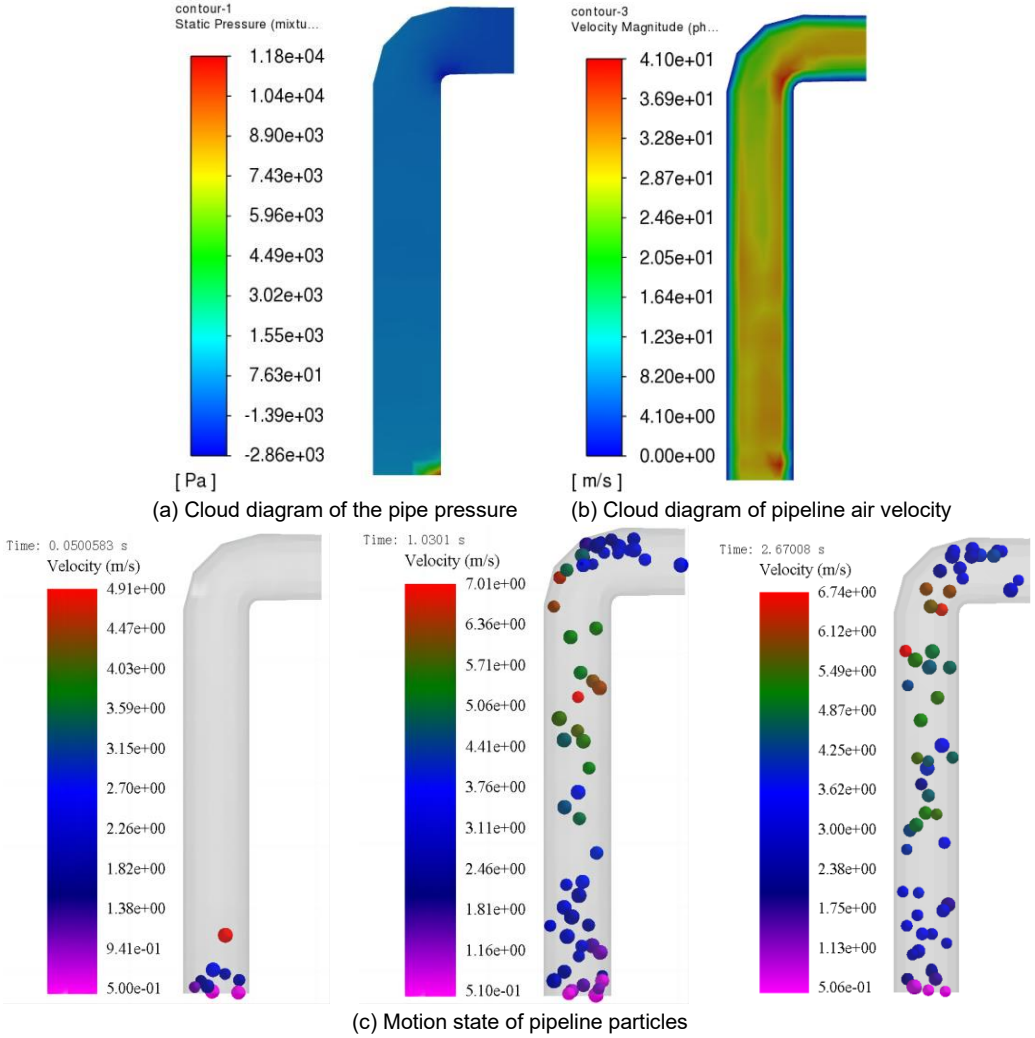
The Realizable k-ε model, no relative slip pipe wall, is adopted. The air is a fluid medium, with an inlet wind velocity of 28 m·s^{-1}, a turbulence intensity of 5% and a return intensity of 2.5% in Fluent. The control equations adopt Couple pressure equations, and the momentum term, turbulent kinetic energy and dissipation rate are all in second-order windward format. The residuals are set to 1e-06; the time step is 0.01 and the number of steps is 300.

RESULTS AND DISCUSSION

Dynamic Pressure, Airflow Velocity Distribution and Particle Motion in the Conveying Pipe

During the simulation, the particle plant is added at the inlet of the pipeline, and the number of particles generated per second is 200 for a total of 3 s. Fig. 4 (a) and (b) show the movement of particles in the elbow pipe at t=1.5 s.

It can be seen that the gas pressure in the horizontal and vertical sections of the pipeline is negative. The pressure from the outlet to the inlet of the material increases gradually, and the velocity of the gas in the pipe at this time is stable in 20.5-32.8 m·s^{-1}.



(a) Cloud diagram of the pipe pressure (b) Cloud diagram of pipeline air velocity

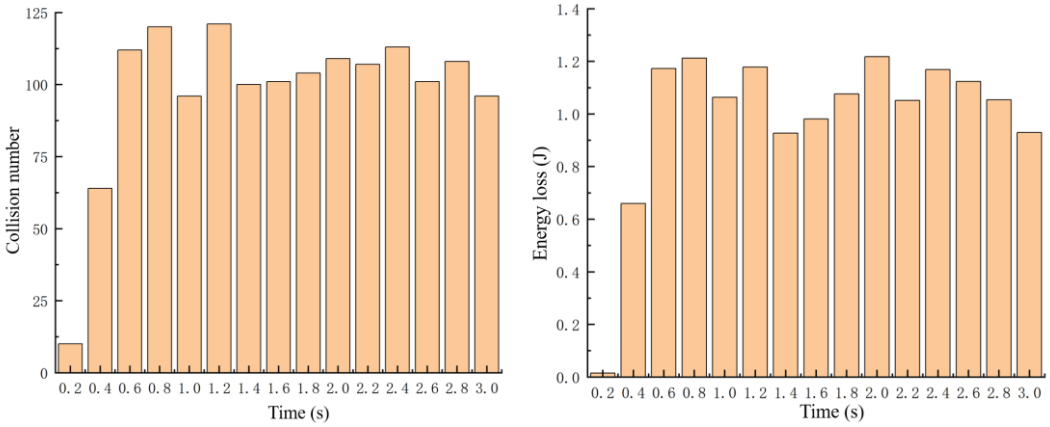
(c) Motion state of pipeline particles

Fig. 4 - Dynamic pressure, airflow velocity and particle motion in the conveying pipe

Fig. 4 (c) shows that jujube particles enters into the pipeline from the inlet, with an initial particle velocity of 0.5 m/s. Particles enter into an accelerated state through the vertical airflow, with most particles having a velocity of 3~4 m·s^{-1}, and a maximum velocity of 6~7 m·s^{-1}. In this stage, the closer the particle position, the faster the acceleration. The particles entering the elbow pipe are subjected to centrifugal force and collide with the outer wall of the elbow pipe, resulting in accumulation of jujube particles in the upper part of the elbow pipe and the phenomenon of particle bundles. In this stage, the particle velocity drops sharply to 2.41-3.71 m·s^{-1}. Subsequently, jujube particles enter the horizontal section under the pressure of the pipeline. In the horizontal section, the slightly larger jujube particles are located near the bottom of the horizontal pipeline in their own gravity, and small particles are mostly located above the large particles. According to the analysis of the overall motion state of particles, it can be seen that the distribution of particles in the three regions of the subsection are high on axis surrounded by low and granular bundles, and layered distribution, respectively.

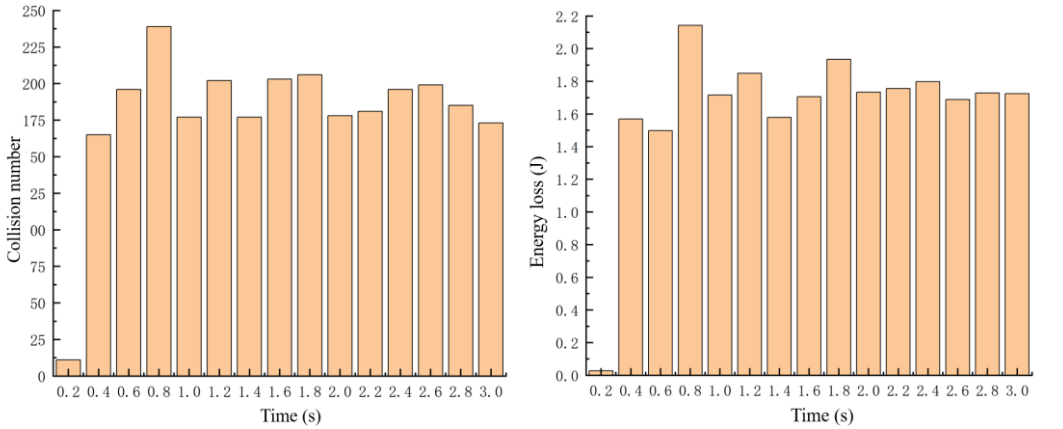
Date particle collision and energy loss

There are two situations where jujube particles collide under the centrifugal force of airflow and pipeline: collisions between jujubes, and collisions between jujube particles and pipeline. Energy loss will occur as the collision at the same time. This energy loss will reduce the velocity of jujube particles, increase the energy consumption in the air suction conveying process, and is not conducive to jujube conveying. As shown in Fig. 5, the collision of jujube particles in the vertical section is less. After 0.3 s, there is a large amount of particle accumulation at the elbow, and the particle collisions and energy loss also increase accordingly. In this stage, the number of collisions per 0.2 s is about 104 times, with an average energy loss of 1.06 J.



(a) Number of particle collisions between jujubes (b) Energy loss of particle collision between jujubes

Fig. 5 - Number of collisions and energy loss between jujubes



(a) Number of collisions between jujube particles and pipeline (b) Energy loss between jujube particles and pipe

Fig. 6 - Number of collisions and energy loss between jujube particles and pipe

It can be seen from the number of collisions and energy loss between particles and pipeline (Fig. 6) that, the collisions between the jujube particles and pipeline also occur mostly at the elbow, about 191 times, and the energy loss is 1.74 J.

According to the particle collision and energy loss during the overall movement of particles, it can be seen that the number of collisions between particles, as well as between particles and pipeline before the simulation time of 0.2 s are less. This is due to the scattered initial distribution of the material in the vertical section, with fewer particles in contact with each other and the pipeline. The majority of particles accumulate at the elbow, resulting in a large number of collisions and energy losses. Through data comparison, it can be found that there are certain differences in energy loss and collision frequency in each statistical interval. The number of collisions between particles and pipeline is 1.84 times that between particles, and the energy loss is 1.64 times. Therefore, the collision between jujube particles and the collision between jujube particles and pipeline particles simultaneously affect the conveying performance of jujubes. Particularly, the collision between jujube particles and pipeline has a more significant effect on the conveying performance.

Effect of wind velocity, bending angle and pipe diameter on erosion rate

Effect of wind velocity on erosion rate

The control variable method is used to explore the impact of different wind velocities on the erosion rate of the pipeline, and the test results are shown in Table 3. The test selects the wind velocities of 23, 28, 33, 38, and 43 $m \cdot s^{-1}$, a diameter of the elbow pipe of 130 mm, and a bending angle of 90° to simulate the erosion rate. The erosion efficiency under the five groups of wind velocities are 2.17e-7 $kg \cdot m^{-2} \cdot s^{-1}$, 3.62e-7 $kg \cdot m^{-2} \cdot s^{-1}$, 5.54e-7 $kg \cdot m^{-2} \cdot s^{-1}$, 7.8 4e-7 $kg \cdot m^{-2} \cdot s^{-1}$, and 1.03e-6 kg·m-2·$s^{-1}$, respectively.

Table 3

Pipe erosion rates under different wind velocities

Clusters	Wind velocity / m·s^{-1}	Erosion rates / kg·m^{-2}·s^{-1}
1	23	0.000000217
2	28	0.000000362
3	33	0.000000554
4	38	0.000000784
5	43	0.000001030

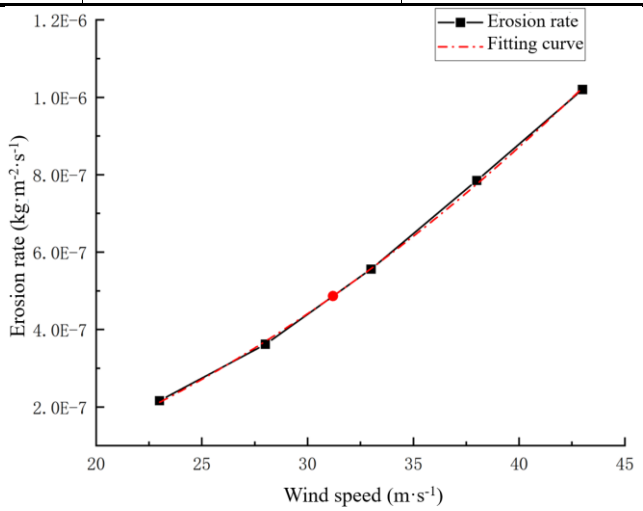


Fig. 7 - Relationship curve between the inlet wind velocity and the erosion rate

The relationship between the wind velocity and erosion rate of the pipeline is shown in Fig. 7, and its fitting curve function is: y = 6.09 e -10*x2+4.54 e-10*x-1.2e-7(R2=0.99957). It can be seen from Fig. 7 that the erosion rate increases linearly as the wind velocity increases. The increase of erosion rate is lower than 2e-7 in the interval of 23-38 m·s^{-1}, and that higher than 2e-7 in the interval of 43 m·s^{-1} or above.

Effect of bending angle on erosion rate

To investigate the effect of different bending angles on the erosion rate, only the bending angle is changed for a single factor test. Its wind velocity is 28 m·s^{-1}; the pipe diameter is 120 mm, and the bending angles are 90°, 97.5°, 105°, 112.5° and 120°, respectively. The test results are shown in Table 4.

Table 4

Erosion rates at different piping angles

Clusters	Bending angle (°)	Erosion rates / kg·m^{-2}·s^{-1}
1	90	0.000000373
2	97.5	0.000000369
3	105	0.000000362
4	112.5	0.000000365
5	120	0.000000372

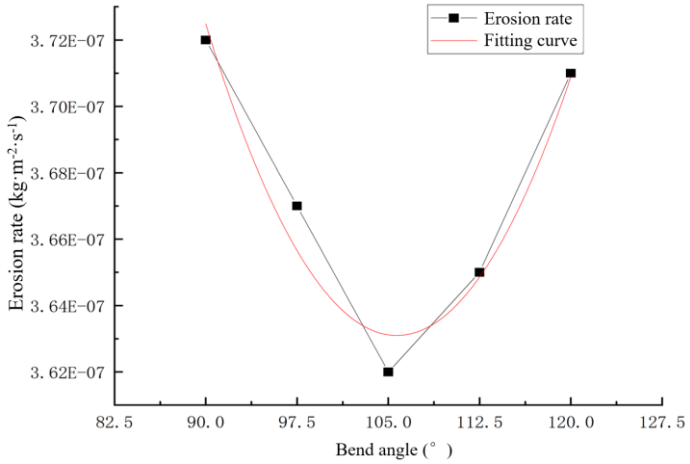


Fig. 8 - Relationship curve between the bending angle and erosion rate

The relationship between the bending angle and the erosion rate is shown in Fig. 8, and its fitting curve function is: y =3.81e-11*x2-8.05e-9*x+7.89e-7 (R2= 0.95211). The effect of the bending angle on the erosion rate of the law is that when the angle is in the range of 90-105°, the erosion rate continues to decrease and drops to the lowest point at 105 °, and then increases. Based on the experimental data and actual working conditions, 97.5-112.5° is selected as the reference factor range for orthogonal test.

Effect of the pipe diameter on the erosion rate

To determine the effect of the pipeline diameter on the erosion rate, the wind velocity is selected as 28 $m \cdot s^{-1}$, the bending angle as 90 °, and the diameters of the pipeline as 100 mm, 110 mm, 120 mm, 130 mm, and 140 mm, respectively. Three tests are carried out for each group, and the obtained data is shown in Table 5.

Table 5

Erosion rates at different bend diameters

Clusters	Pipe Diameter / mm	Erosion rates / $kg \cdot m^{-2} \cdot s^{-1}$
1	100	0.000000573
2	110	0.000000432
3	120	0.000000362
4	130	0.000000325
5	140	0.000000310

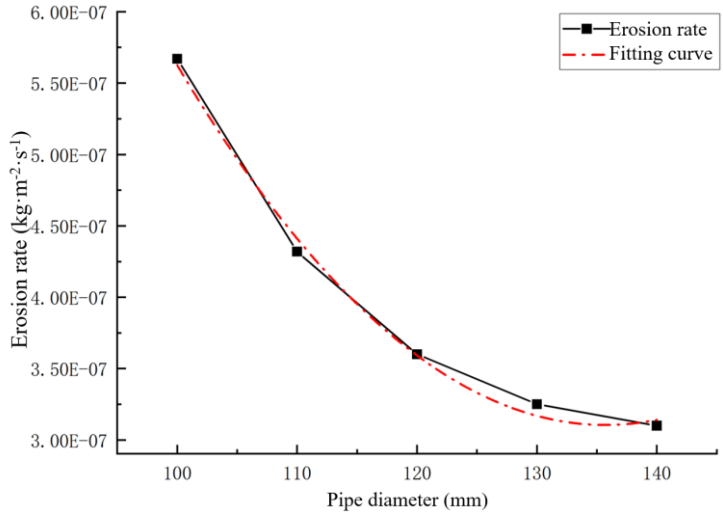


Fig. 9 - Relationship curve between the elbow diameter and the erosion rate

The relationship curve between the pipe diameter and the erosion rate is shown in Fig. 9. It shows that the erosion rate decreases as the pipe diameter increases. The decrease is large when the pipe diameter is in the range of 100-120 mm, and gradually reduced after 120 mm. It can be seen that the pipe diameter in the range of 120 -140 mm is more appropriate. A quadratic polynomial is used for fitting, and the fitted curve function is: y= -5.36957e -8*x2+1.97857e-10*x+ 3.95357e-6 (R2=0.99579).

Optimization simulation and analysis of the pipeline structural parameters

Determination of test factor levels

According to the test results of the wind velocity, bending angle, pipe diameter on the erosion rate, the wind velocity and erosion rate is positively correlated. Since the suspension velocity of jujubes needs to be greater than 28 $m \cdot s^{-1}$, 28~38 $m \cdot s^{-1}$ is selected as the factor level range of the orthogonal test according to the actual working conditions. Three levels: 28 $m \cdot s^{-1}$, 33 $m \cdot s^{-1}$, and 38 $m \cdot s^{-1}$ are selected. The bending angle and erosion rate first decrease and then increase, and the erosion rate is the smallest at 105 °. As such, 97.5 °, 105 ° and 112.5 ° are selected as the factor levels of the orthogonal test. The pipe diameter is negatively correlated with the erosion rate and the reduction rate decreases after 130 mm. 120 mm, 130 mm, and 140 mm are selected as the factor levels of the orthogonal test.

Orthogonal test and result analysis

Without considering the interaction of factors, $L_9(3^4)$ orthogonal test is designed to study the effect of test factors such as wind velocity (A), bending angle (B), and diameter of pipeline (C) on the erosion rate.

To obtain the optimal combination of pipeline structural optimization parameters through the polar analysis of data obtained from orthogonal test. The factor level coding of the orthogonal test is shown in Table 6.

Table 6

Experimental factors and corresponding level coding

Level	Considerations			
	Air velocity A (m·s-1)	Bend angle B (°)	Pipe Diameter C (mm)	Blank column
1	28	97.5	120	1
2	33	105	130	2
3	38	112.5	140	3

The orthogonal test results and polar analysis is shown in Table 7. The greater the polar difference between the factors, the greater the impact of the factors on the error. The polar analysis shows that the impact extent of factors on the erosion rate is: wind velocity > bending angle>pipe diameter. The smaller the erosion rate of the test indexes, the more in line with the actual working needs. Therefore, the optimal test combination is the smallest K value of each factor, and then A1B2C2 is the optimal test combination. Since the table does not include the group of tests, the combination of tests is verified that the erosion rate is 2.33E-7, which is the lowest in the 10 groups of tests. The optimal parameter combination is obtained as a wind velocity of 28 $m \cdot s^{-1}$, a bending angle of 105 °, and a pipe diameter of 130 mm.

Table 7

Orthogonal test results and extreme variance analysis

Serial number	Factor A	Factor B	Factor C	Blank column	Erosion rates
1	1	1	1	1	3.72E-07
2	1	2	3	2	2.48E-07
3	1	3	2	3	3.24E-07
4	2	1	3	3	4.05E-07
5	2	2	2	1	3.40E-07
6	2	3	1	2	5.64E-07
7	3	1	2	2	6.96E-07
8	3	2	1	3	6.27E-07
9	3	3	3	1	7.22E-07
K1	9.44E-07	1.47E-06	1.56E-06	1.43E-06	
K2	1.31E-06	1.22E-06	1.36E-06	1.51E-06	
K3	2.05E-06	1.61E-06	1.38E-06	1.36E-06	
k1	3.15E-07	4.91E-07	5.21E-07	4.78E-07	
k2	4.36E-07	4.05E-07	4.53E-07	5.03E-07	
k3	6.82E-07	5.37E-07	4.58E-07	4.52E-07	
Extremely poor	1.11E-06	3.95E-07	2.03E-07		
Optimal solution	A1	B2	C2		

Simulation of optimized pipeline

The optimal piping parameters are couple and simulated and remaining parameters are unchanged. The number of collisions and energy losses are as shown in Table 8.

Table 8

Coupling test results of the optimized pipe

Norm	Number of collisions			Energy loss		
	Pre-optimization	Post-optimization	Degree of optimization	Pre-optimi-zation	Post-optimization	Degree of optimization
Between jujubes	2330	1461	37.3%	14.83	12.77	13.87%
Between jujube and pipe wall	2688	2219	17.45%	24.45	20.14	17.61%

As shown in Table 8, the number of collisions and energy loss between jujubes after pipeline optimization are reduced by 37.3 % and 13.87 % year-on-year, respectively, and those between jujubes and pipe wall are reduced by 17.45 % and 17.61 % year-on-year, respectively. The reduction effect is obvious.

Test Verification for Optimized Pipeline

To test the feasibility of the simulation and optimization results of the conveying pipeline of the air suction jujube picker, it is verified through the test device. The test material was gray jujubes, and 500 red jujubes with intact skin were selected for test. Under the fixed wind velocity of 28 m/s of the conveying pipe, five tests were carried out on the un-optimized conveying pipeline and the optimized conveying pipeline respectively, so as to obtain the reduction values of jujube skin damage rate. After the completion of each group of tests, jujubes with cracked epidermis and exposed pulp were selected as epidermal damage, and the test results are shown in Table 9.

Table 9

Optimization test results

Test number	Reduction values of epidermal damage rate / %
1	2.2
2	1.8
3	2.6
4	1.6
5	2.1

According to the verification of the simulation test results by the test device, it can be seen that, the average epidermal damage rate of the pipeline after optimization is reduced by 2.06 %. This can reduce the damage of the pipe wall to the jujube epidermis to a certain extent, indicating that the optimized pipeline design is feasible.

CONCLUSIONS

(1) The CFD-DEM coupling method is used to simulate the movement process of jujube particles in the conveying pipeline, and the pipeline pressure, airflow distribution and the movement state of jujube particles in different parts of the pipeline are analyzed. According to the statistics of the number of collisions and energy loss between jujubes, as well as between jujubes and pipeline, it is found that these two kinds of collisions have a certain impact on the performance of conveying pipeline. The number of collisions and the energy loss between jujube particles and pipeline is large, and the impact on the conveying performance is more significant.

(2) Taking the erosion rate as the performance evaluation index, the wind velocity, bending angle and pipe diameter as the test factors, a single-factor test is carried out to determine the influence degree of each factor on the erosion rate. The orthogonal test method is used to further study the influence degree of each factor on the erosion rate, and the results show that wind velocity>bending angle>pipe diameter. The optimal parameter combination of the pipeline is a wind velocity of 28 $m \cdot s^{-1}$, a bending angle of 105 °, and a pipeline diameter of 130 mm.

(3) The verification results show that the number of collisions and energy loss between jujubes of the optimized pipeline are reduced by 37.3 % and 13.87 % year-on-year, and those between jujube particles and pipe wall are reduced by 17.45 % and 17.61 % year-on-year, respectively. The simulation test results verify that the average skin damage rate of optimized pipeline is reduced by 2.06 %, confirming that the optimizing the pipeline structural parameters can reduce the jujube skin damage to a certain extent.

ACKNOWLEDGEMENTS

This work was financially Supported by Bingtuan Science and Technology Program (Grant No. 2021CB018), and the Master Talent Project of the Tarim University Presidents Fund (Grant No. TDZKSS202110) for supporting this research. The authors are grateful to anonymous reviewers for their comments.

REFERENCES

[1] Basu, S., Chakrabarty, A., Nag, S., Behera, K., Bandyopadhyay, B., Grima, A. P., Ghosh, P. (2021). Design modification of iron ore bearing transfer chute using discrete element method. *Engineering Computations*, Vol. 38, No. 9, pp. 3590-3607.

[2] Brandt, V., Grabowski, J., Jurtz, N., Kraume, M., Kruggel-Emden, H. (2023). A benchmarking study of different DEM coarse graining strategies. *Powder Technology*, Vol. 426, 118629.

[3] Carr, M. J., Roessler, T., Robinson, P.W., Otto, H., Richter, C., Katterfeld, A., Wheeler, C. A. (2023). Calibration procedure of Discrete Element Method (DEM) parameters for wet and sticky bulk materials. *Powder Technology*, Vol. 429, 118919.

[4] Du, X.H., Han, C.J., Sheng, J.J., Diao, H.W., Song, D.l., Zhang, S.X. (2022). Optimized design and test of jujube picker（红枣捡拾机优化设计与试验）. *Chinese Journal of Agricultural Mechanical Chemistry*, Vol. 43, pp.43-50. (in Chinese)

[5] Dustin, S.W., Sanja, M. (2023). An Analysis of CFD-DEM with Coarse Graining for Turbulent Particle-Laden Jet Flows. *Fluids*, Vol. 8(7), 215.

[6] El-Emam, M. A., Zhou, L., Shi, W., Han, C. (2021). Performance evaluation of standard cyclone separators by using CFD–DEM simulation with realistic bio-particulate matter. *Powder Technology*, Vol. 385, pp. 374-394.

[7] Hamed, H., Behrad E., Reza. Z., Rahmat S.G., Navid, M. (2023). Comparative CFD-DEM study of flow regimes in spout-fluid beds. *Particuology*, Vol. 85, pp. 323-334.

[8] Hesse, R., Lösch, P., Antonyuk, S. (2023). CFD-DEM analysis of internal packing structure and pressure characteristics in compressible filter cakes using a novel elastic–plastic contact model. *Advanced Powder Technology*. Vol. 34, 104062.

[9] Hou, J.L., Ma D.X., Li H., Zhang Z.L., Zhou J.L., Shi, S. (2023). Design and experiments of a pneumatic centrifugal combined precision seed metering device for wheat (气力离心组合式小麦精量排种器设计与试验). *Journal of Agricultural Machinery*,
Available online: https://kns.cnki.net/kcms/detail/11.1964.S.20230731.1034.002.html (in Chinese)

[10] Hu, K., Dai, Y., Wang, Y. (2020). Research status and development trend of pneumatic direct seeding device for rice and oil (稻油兼用型气力式直播排种装置研究现状和发展趋势). *Agricultural Engineering*, Vol. 10(10), pp.8-11. (in Chinese)

[11] Jayasundara, C. T., Zhu, H. P. (2022). Impact energy of particles in ball mills based on DEM simulations and data-driven approach. *Powder Technology*, Vol. 395, pp. 226-234.

[12] Kim, J., Chung, M.Y. (2019) CFD-DEM Simulation of the Fluidized-bed Granulation of Food Powders. *Biotechnology and Bioprocess Engineering*, Vol. 24(1), pp. 569-578.

[13] Leno, G., Ying, C., Hubert, L. (2023). Coupled CFD-DEM Simulation of Seed Flow in Horizontal-Vertical Tube Transition. *Processes*, Vol. 11(3), pp. 909-909.

[14] Lewis, S., Antonia, B., Alberto, R.D., Mojtaba, G. (2022). Application of coarse-graining for large scale simulation of fluid and particle motion in spiral jet mill by CFD-DEM. *Powder Technology*, Vol. 411, 117926.

[15] Nijssen, T. M. J., Padding, J. T. J., Ottens, M. (2023). Hydrodynamics of expanded bed adsorption studied through CFD-DEM. *Chemical Engineering Science*, Vol. 280, 119027.

[16] Ponzini, R., Vià, R. D., Bnà, S., Cottini, C., Benassi, A. (2021). Coupled CFD-DEM model for dry powder inhalers simulation: Validation and sensitivity analysis for the main model parameters. *Powder Technology*, Vol. 385, pp. 119-226.

[17] Qin, M., Jin, Y., Luo, W., Wu, F., Shi, L.L., Gu, F.W., Cao, M.Z., Hu, Z.C. (2023). Measurement and CFD-DEM Simulation of Suspension Velocity of Peanut and Clay-Heavy Soil at Harvest Time. *Agronomy*, Vol. 13(7), 1735.

[18] Rakesh, K., Shibayan, S. (2023). Erosion analysis of radial flow hydraulic turbine components through FLUENT-EDEM coupling. *Powder Technology*, Vol. 428, 118800.

[19] Ren, D.Z., Yu, H.L., Zhang, R., Li, J.Q., Zhao, Y.B., Liu, F.B., Zhang, J.H., Wang, W. (2023). Measurement and CFD-DEM Simulation of Suspension Velocity of Peanut and Clay-Heavy Soil at Harvest Time. *Agronomy*, Vol. 12 (12), 2115.

[20] Shi, G.K., Li, J.B., Ding, L, P., Kan, Z. (2022a). Design and test of inertial airflow type jujube cleaning system（惯性气流式红枣清选系统设计与试验）. *Journal of Agricultural Machinery*, Vol. 53, pp.167-176.

[21] Shi, G.K., Li, J.B., Ding, L.P., Zhang, Z.Y., Ding, H.Z., Li, N., Kan, Z. (2022b). Calibration and Tests for the Discrete Element Simulation Parameters of Fallen Jujube Fruit. *Agriculture*, Vol.12, pp. 38.

[22] Wang, C.X. (2021). Experimental Study and Parameter Optimization of Comb-Brush Roller Type Picking Device of Ground Jujube; *Shihezi University*: Xinjiang, China.

[23] Weaver, S.D., Mišković, S. (2023). An Analysis of CFD-DEM with Coarse Graining for Turbulent Particle-Laden Jet Flows. *Fluids*, Vol. 8(7), pp. 215.

[24] Weng, X.X., Chen, C.Q., Wang, G., Wei, Z.B., Jiang, L., Hu, X.R. (2022). Numerical Simulation of Leaf Gathering Process of Fresh Leaf Collecting Pipeline Based on CFD-DEM (基于CFD-DEM的机采鲜叶管道集叶过程数值模拟研究). *Journal of Agricultural Machinery*, Vol. 53(11), pp. 424-432. (in Chinese)

[25] Wiacek, J. (2016). Geometrical parameters of binary granular mixtures with size ratio and volume fraction: experiments and DEM simulations. *Granular Matter*, Vol.18, pp. 42.

[26] Xiong, P. Y., Xue M.J., Wang Y., Zhang, H.X., Xue, X.Q., Li, Z.L., Hu, W.Q. (2019). Simulation analysis and test of air suction oil tea seed shell kernel cleaning device. *Journal of Zhongkai Agricultural Engineering College*, Vol. 32(01), pp. 35-40+45.

[27] Yuan, P.P., Li S.F., Han C.J., Zhang, J., Xu Y. (2021). Design and test of hydraulic system of sweeping-air suction type date picker（清扫—气吸式红枣捡拾机液压系统设计与试验）. *China Agricultural Machinery Chemical Journal*, Vol. 42, pp. 28-33. (in Chinese)

[28] Yuan, Y.W., Bai, S.H., Niu K., Zhou, L.M., Zhao, B., Wei, L.G., Xiong, S., Liu, L.J. (2022). Advances in mechanized harvesting technology and equipment for forest and fruit（林果机械化采收技术与装备研究进展）. *Journal of Agricultural Engineering*, Vol. 38, pp. 53-63.

[29] Zhang, F.K., Ran, J.H., Li, Z.J., Wang, D.W., Li, P. (2021). Air-suction landing jujube picker operating parameters optimization（气吸式落地红枣捡拾机作业参数优化）. *Fruit Tree Journal*, Vol. 38, pp. 1190-1200. (in Chinese)

[30] Zhang, F.K., Yu, F.F., Li, Z.J., Zhang, H., Lan, H.P., Li, P., Zhang, C.J. (2020). Design and experiment of air-suction landing jujube picker（气吸式落地红枣捡拾机的设计与试验）. *Acta Pomologya Sinica*, Vol. 37, pp. 278-285. (in Chinese)

[31] Zhang, T., Liu, F., Zhao, M.Q., Ma. Q., Wang, W., Fan, Q., Yan, P. (2018). Determination of physical parameters of corn stover contact with discrete element simulation calibration（玉米秸秆接触物理参数测定与离散元仿真标定）. *Journal of China Agricultural University*, Vol. 4, pp.120-127. (in Chinese)

[32] Zhang, X.J., Bai, S.H., Jin W., Yuan, P.P., Yu, M.J., Yan, J.S., Zhang, C.S. (2019). Development of pneumatic pick-up machine for low density cultivation of jujubes（气力式矮密栽培红枣捡拾机研制）. *Journal of Agricultural Engineering*, Vol. 35, pp.1-9. (in Chinese)

ANALYSIS ON PATH OPTIMIZATION OF AGRICULTURAL HANDLING ROBOTS BASED ON ANT COLONY-IMPROVED ARTIFICIAL POTENTIAL FIELD METHOD

/

基于蚁群-改进人工势场法的农业搬运机器人路径规划分析

Hexia CHU*
Department of Mathematics Education, Zhumadian Preschool Education College, Zhumadian, Henan, China
*E-mail: hexia_chu@163.com
Corresponding author: Hexia Chu
DOI: https://doi.org/10.35633/inmateh-71-47

Keywords: agricultural robots, handling path, path planning, ant colony algorithm, improved artificial potential field method

ABSTRACT

Aiming at the problems of low efficiency and slow function convergence of the ant colony algorithm in path planning of agricultural transport robots, a fusion algorithm combined with the artificial potential field method was proposed. Firstly, the function of each parameter was analyzed according to the mathematical model of the traditional ant colony algorithm, followed by the simulation analysis of the optimal parameters through grid map modeling in MATLAB and data recording. Secondly, the deficiency of the classical artificial potential field method in agriculture, i.e., it could not arrive at the endpoint or realize local locking, was improved by introducing the intermediate point and the relative distance of the target. Finally, the features of the two algorithms were combined and the improved artificial potential field method was integrated with the traditional ant colony algorithm so that the improved artificial potential field method could play a dominant role in the initial path planning stage of agricultural transport robots while the ant colony algorithm exerted the main effect in the later stage with the increase in the pheromone concentration. It was verified through simulation analysis, it was verified that the fusion algorithm of ant colony algorithm and improved artificial potential field method outperforms traditional ant colony algorithm in terms of farthest path, optimal path, running time, and iteration number.

摘要

*针对蚁群算法在农业运输机器人路径规划中效率低、函数收敛慢等问题，提出了一种与人工势场法相结合的融合算法。首先，根据传统蚁群算法数学模型对各参数的函数进行分析，并在 MATLAB 中通过栅格图建模对最优参数进行仿真分析，并记录数据。其次，通过引入中间点和目标相对距离的方法，改善了经典人工势场法在农业中无法到达终点和无法进行局部锁定的问题;最后，结合两种算法的特点，将改进的人工势场法与传统的蚁群算法相结合，使改进的人工势场法在农业运输机器人路径规划的初始阶段发挥主要作用，蚁群算法在后期随着信息素浓度的增加发挥主要作用。*通过仿真分析验证了将蚁群算法与改进的人工势场法相融合算法在最远路径、最优路径、运行时间、迭代次数各项数据都优于传统蚁群算法。

INTRODUCTION

With the development of society and the maturity of artificial intelligence technology, robots have gradually developed from industrial robots to intelligent agricultural handling robots, contributing to more convenient life *(Zhu et al., 2010)*. Agricultural handling robots involve the knowledge of various fields such as sensor technology, computer, automatic control, and communication technology. When located in an unknown environment, robots obtain external environmental information through external sensors and process it to realize their own positioning. Usually, the position and direction of the robot are controlled by real-time positioning and mapping of the surrounding environment *(Zhao et al., 2018)*. Generally speaking, agricultural handling robots use lidars, cameras, and inertial measurement devices as external sensors. These sensors integrate the advantages of small size, light weight, low cost, and rich image information. Vision sensors have been developing continuously *(Teng et al., 2018)*. At present, robot positioning generally includes ultrasonic navigation and positioning technology, visual navigation and positioning technology, and light reflection navigation and positioning technology of agricultural handling robots, GPS global positioning technology, etc. Robot positioning in indoor environments is the key and difficult point of

robot systems *(Wei et al., 2023)*. Because the positioning signal blocked by buildings is weakened, the outdoor lidar positioning cost is high, and the positioning signal of wireless sensors is easy to be attenuated, the positioning accuracy is affected by the navigation problem of robots, making it necessary for robots to plan an optimal collision-free path from the starting point to the endpoint in the environment according to the predetermined target *(Zhang et al., 2023)*. Before navigation, robots need to establish a map of the surrounding environment. Path planning is implemented in an unknown environment, and meanwhile, the obstacle avoidance ability of robots is also indispensable.

The working environment layout of agricultural handling robots is complex, which brings certain challenges to their path planning task. The traditional path planning algorithm has some shortcomings, such as low planning efficiency and poor operation safety of handling robots. For the identification and feature extraction of the surrounding environment during the movement of handling robots, therefore, the map of the surrounding environment is constructed, and the path planning of the handling robots is performed by using the artificial potential field method improved by ant colony, which will improve the path planning accuracy and speed up the learning efficiency of agricultural handling robots. It also provides accurate data for the operation of the robots in the process of movement. In this study, the global path planning and local path planning of agricultural transport robots were explored, and the low efficiency and poor security of transport robot planning algorithms were solved. Aiming at the low efficiency of transport robots, the path smoothing algorithm was studied. To solve the path tracking and control of handling robots, the path tracking research was carried out. The above work will provide certain reference significance and value for the path planning task of agricultural handling robots.

STATE OF THE ART

With the emergence of intelligent agriculture in recent years, agricultural handling robots have been widely studied and applied in the fields of industrial automation and intelligent factories. In the aspect of intelligent agricultural warehousing management, more efficient intelligent warehousing has gradually become the new direction of warehousing operation and development. How to plan the fast and energy-saving agricultural robot handling path is an important link to optimize the storage operation. As a typical engineering problem, the path planning of agricultural handling robots has great exploration space in improving robot positioning and mapping accuracy. Chinese and foreign experts and scholars have conducted extensive research from different angles, which can be roughly divided into two categories: traditional algorithms and bionic intelligent algorithms. Traditional algorithms, e.g., artificial potential field method, A* algorithm, and Dijkstra algorithm *(Das et al., 2016)*, have certain advantages in solving the path planning problem of agricultural handling robots in ideal environments. However, the artificial potential field method is easily disturbed by the external environment, accompanied by such problems as the increasing path length and the number of inflection points *(Mo et al., 2015)*. The real-time performance of the A * algorithm is poor, and the search efficiency of the algorithm is low due to the increase in the number of path nodes *(Tharwat et al., 2019)*. The Dijkstra algorithm is subjected to some problems such as low efficiency and high computational complexity *(Das et al., 2016)*. Moreover, the limitations of traditional algorithms often lead to local optimization and poor real-time performance in the path planning of agricultural transport robots. By observing the habits of natural creatures, bionic algorithms simulate the biological characteristics of group members, reduce the dependence on mathematical models, and exhibit strong global optimization and adaptability *(Zeng et al., 2016)*. Compared with the traditional path planning algorithm, therefore, intelligent optimization algorithms have higher efficiency and robustness in solving large-scale path planning problems. At present, swarm intelligence algorithms have been widely used in the field of path planning, among which the common ones are genetic algorithms, particle swarm optimization, and the ant colony algorithm. When used for path planning, genetic algorithms are easily influenced by the size of environmental grids, which leads to the long optimal path length, many inflection points, and slow convergence *(Ames et al., 2015)*. The Particle Swarm Optimization algorithm has a fast convergence speed in the initial iteration, but it is easy to fall into local optimization in the later iteration, which results in the unsmooth path and a large number of turns on the optimal path *(Yang et al., 2012)*. The ant colony algorithm is too random in the early iterative search, which gives rise to the low efficiency of the algorithm, and consequently, it will stagnate in the later centralized search, so the algorithm runs for a long time and is not suitable for large and complex maps *(Zhou et al., 2021)*. Therefore, the path planning problem of agricultural handling robots in complex

environments and how robots can rapidly and effectively complete cargo transportation tasks have become the current research hotspots.

In the global path planning environment, there are mainly grid-based A* algorithm *(Yan et al., 2021)* and traditional Dijkstra algorithm *(Javidrad et al., 2017)*, which are mainly used for path search, with higher efficiency and smaller calculated quantity. Among the traditional reinforcement learning, the Q-learning algorithm *(Wang et al., 2020)* has been widely used. Xu et al. combined the lazy line of sight algorithm with distance transformation for path planning. The path planned by this algorithm is more robust and smoother, yet the running time is longer *(Xu et al., 2019)*. Sombolestan et al. regarded the robot as a point and connected it with the vertex, starting point, and endpoint of the convex obstacle to form an intuitive and accessible view that does not intersect with the obstacle area *(Sombolestan et al., 2019)*. If the robot can plan the path in any environment, path planning can be implemented using the ant colony algorithm and genetic algorithm, which can greatly improve the search efficiency *(Zhu et al., 2021)*. In order to realize the multi-robot cooperative work of handling robots in dynamic environment, Ma et al. adopted the ant colony algorithm to realize the multi-robot cooperative work task *(Ma et al., 2013)*. Kyaw et al. put forward an algorithm based on mixed ant colony and bee colony, which is suitable for complex mine environments and enables the robot to effectively carry out path planning in complex environments *(Kyaw et al., 2020)*. Duan et al. proposed a cooperative path planning method for multiple UAVs based on the improved particle swarm optimization algorithm, which solved the path planning problem of UAVs in three-dimensional space *(Duan et al., 2020)*.

To sum up, common global path planning algorithms include A* algorithm, ant colony algorithm, genetic algorithm, and particle swarm optimization algorithm, while common local path planning algorithms include artificial potential field method, speed barrier method, and dynamic window algorithm *(Radwan et al., 2016)*. Among them, the ant colony algorithm integrates the merits of high stability, reliability, and independence. However, low search efficiency, long running time, and low convergence speed of the algorithm will be caused in case of a large search range and low pheromone concentration in the initial stage given its high dependence on pheromones. The artificial potential field method has the advantages of a simple mathematical model and fast response, but near the starting point, the repulsive force is ignored due to the excessive gravity, the intelligent vehicle collides with obstacles, and the target is unreachable, resulting in the local minimal point. Combining the characteristics of ant colony algorithm and artificial potential field method, the ant colony algorithm was firstly subjected to modeling and simulation analysis to obtain the optimal parameters, and the local minimum of the artificial potential field method was improved by introducing the relative target distance. Integrating the advantages of the ant colony algorithm and artificial potential field method, the improvement effect of the fusion algorithm was verified through mathematical modeling, theoretical analysis, and simulation experiments.

MATERIALS AND METHODS

Grid map modeling

According to the degree of obstacle information acquisition, the path planning of agricultural handling robots can be divided into local planning and global planning. In this study, global planning was discussed. In this study, the grid method was used to simulate the working environment of the robot, and the handling environment of the agricultural robot was decomposed into a series of equally-sized network units. The size of the unit depended on the size of the detection robot. Assuming that the inspection environment was a regular site with a length of L and a width of *w*, the environment was divided into m×n grids with a length of 1 and a width of *w*, respectively, each small grid is represented by N_{xy}, and the whole environment space is denoted as Φ, which is expressed by Equation (1).

$$\Phi = \sum N_{xy} | (x \in [1, m], y \in [1, n]) \tag{1}$$

The presence/absence of obstacle information in each grid is expressed by Equation (2).

$$N_{xy} = \begin{cases} 0, No\ barriers \\ 1, Barriers \end{cases} \tag{2}$$

Where: N_{xy} is the state information of each grid, N_{xy}=0 indicates that the obstacle-free area can be passed freely, and N_{xy}=1 means that the obstacle-containing area is forbidden to pass. By reference to the layout of substations in reality, multiple binary grid arrays were established to form the inspection environment for robots, and meanwhile, small grids (1×1) were set, as shown in Fig. 1.

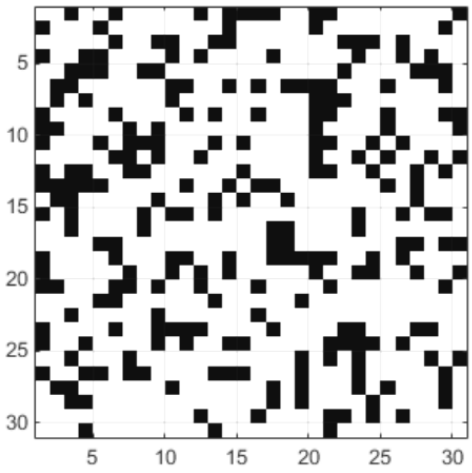


Fig. 1 - Grid map modeling

The grid method met the octree search strategy adopted in this study, that is, the robot could move between adjacent grids in eight directions in the search process.

Establishment of the path planning model

In the path planning process of agricultural robots, the position coordinates updated by each iteration of the algorithm were set to represent a moving route of agricultural robots. In the optimization algorithm of the agricultural robot handling path, the optimal path from the starting point to the target point was found from the two-dimensional grid map. The constraint conditions were set as follows:

(1) Map boundary and obstacle constraints. The moving path of the agricultural robot must be limited within the grid map boundary, and the moving path of the agricultural robot is forbidden to cross the obstacle node in the movable area.

(2) Path continuity condition. It is necessary to avoid path overlap and detour when the agricultural robot moves in the traffic area. Assuming that the position coordinates of the agricultural handling robot at time t are (x_t,y_t), the position coordinates (x_{t+1},y_{t+1}) of the agricultural handling robot at the next time need to meet $x_{t+1} \succ x_t$ or $y_{t+1} \succ y_t$.

(3) The shortest path condition. In order to realize path planning, the agricultural handling robot needs to find the shortest path from the starting point to the target point on the basis of satisfying the boundary constraints and path continuity conditions. Taking the Euclidean distance of the path as the fitness function of the algorithm, the path with the least fitness is the optimal path. The path length is calculated as shown in Equations (3) - (4).

$$L=S+L(i)+F \tag{3}$$

$$\begin{cases} S = X(1)-1 \\ L(i) = \sum_{i=2}^{c} (\sqrt{(X(i)-X(i-1))^2+1}) \\ F = X(end)-c \end{cases} \tag{4}$$

Where L is the length of the robot's moving path, $X(1)$ is the position of the first node of the path, X(end) is the position of the last node of the path, and c is the number of columns of the grid map.

ALGORITHM DESIGN

Ant colony algorithm

The ant colony algorithm is implemented mainly depending on pheromone concentration, with its principle displayed in Fig. 2. Under the fixed concentration of pheromones released by ants and the fixed volatilization rate of pheromones, if the ant colony starts from point *A* to the endpoint *E* and the path from point *C* to point *F* is blocked, there are two paths—*ABCED* and *ABFDE*—for the ant colony from point *A* to point *E*. Given a fixed quantity of ant colonies, *BC*=*CD*=2 and *BF*=*FC*=2. When the experiment starts, therefore, the quantity of ants passing through the two paths was basically identical, but with the lapse of time, the quantity of ants on *ABFDE* gradually increased. This is because this path is short, the concentration of pheromones released by ant colonies grows within certain time, and thus ant colonies are inclined to this path.

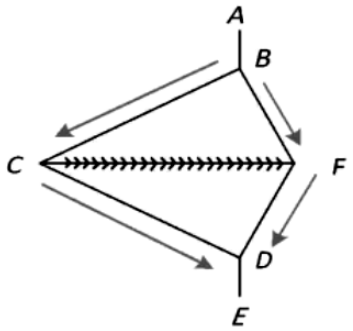


Fig. 2 - Principle of ant colony algorithm

By establishing the mathematical model of the ant colony algorithm to analyze the influence of various parameters on the algorithm, the following assumptions can be made for the ant colony search path: firstly, it is assumed that M ants participate in path search, the initial pheromone concentration of each path equals a constant *C*, and then the pheromone concentration *C* from X to Y can be expressed as $\tau_{AB}(0)=C$ (*C* is a constant). The *k*-th ant (*k*=1, 2, 3...., M) moves for t steps, and the probability for it to move from point X to point Y can be expressed as follows:

$$P_{XY}^{k}(t)=\begin{cases}\dfrac{\tau_{XY}^{a}(t)\eta_{XY}^{\beta}(t)}{\sum_{S\in a_k}\tau_{AS}^{a}(t)\eta_{XS}^{\beta}(t)}, B\in a_k \quad a_k=\{1,2,...,M\}-tabu(k)\\ 0, else\end{cases} \tag{5}$$

Where $\tau_{XY}^{a}(t)$ denotes the pheromone concentration on the path from *X* to *Y* at time t; a_k represents the set of places that the ant can reach at the next time; *tabu(k)* stands for the place previously passed by the ant; $\eta_{XY}^{\beta}(t)$ is the heuristic function from point *X* to point *Y*, which is an important parameter characterizing the probability for the ant to move from point *X* to point *Y* and can be expressed as below:

$$\eta_{XY}(t)=1/d_{XY} \tag{6}$$

Where d_{XY} indicates the distance between places. It is not difficult to see that a greater d_{XY} leads to the smaller distance and the smaller $P_{XY}^{k}(t)$; the greater the $\tau_{XY}^{a}(t)$, the smaller the $P_{XY}^{k}(t)$. The probability for ants to move from *X* to *Y* is negatively correlated with the distance between the two and positively correlated with the pheromone concentration.

From the beginning to the end of the ant colony, both the released pheromone $\Delta\tau_{XY}(t)$ and the volatilized pheromone should be considered. Assuming that the volatility coefficient is $\rho(0<\rho<1)$, the pheromone concentration can be updated as follows:

$$\tau_{XY}(t+1)=(1-\rho)\tau_{XY}(t)+\Delta\tau_{XY}(t) \tag{7}$$

$$\Delta\tau_{XY}(t)=\sum_{M}^{k=1}\Delta\tau_{XY}k(t) \tag{8}$$

According to Equation (8), the pheromone concentration update is equal to the volatilized pheromone concentration plus the newly added pheromone concentration, and the volatility coefficient ρ is negatively correlated with the pheromone concentration. In practical application, if the coefficient is too large, the pheromone concentration is volatilized at an accelerated speed, accompanied by the degraded global search ability of the robot and the slower algorithm convergence. When the coefficient is too small, the pheromone volatilization slows down, and the probability for the robot to choose different paths is reduced, which is not good for finding the optimal path.

$\Delta\tau_{XY}(t)$ is the pheromone released by the ant k from *X* to *Y*, which is expressed as follows:

$$\Delta\tau_{XY}^{M}=\begin{cases}\dfrac{Q}{L_k}, & the\ k^{th}ant\ is\ on\ the\ path\ XY\\ 0, else\end{cases} \tag{9}$$

L_k represents the distance of *XY*. Pheromone concentration *Q* refers to the total pheromone concentration after completing a cycle. After each iteration, the pheromones on all paths found by ants will be updated, which leads to the too rapid accumulation of pheromones and the local optimum of the

algorithm. An appropriate pheromone concentration is the precondition ensuring the global search ability of the ant colony algorithm.

Artificial potential field method

The artificial potential field method is a common algorithm for robot local path planning. Its basic principle is to use artificial potential field to create a kind of attraction and repulsion, and use the physical principle of "like charges repel each other, unlike charges attract" to describe the effect generated by the target point and obstacles in the movement process of agricultural robots. Therein, attraction is the direction from agricultural robots to the target point and repulsion indicates the direction from obstacles to agricultural robots. The resultant force borne by agricultural robots in the potential field is the direction of forward motion.

Assuming that the attraction and repulsion borne by robots on the potential field are U_{att} and U_{rep}, respectively, the resultant force borne by robots can be expressed as follows.

$$U=U_{att}+U_{rep} \tag{10}$$

The attraction field function can be denoted as below.

$$U_{att}(X)=\frac{1}{2}K_{att}(X-X_g)^2 \tag{11}$$

Where X_g indicates the position of the target, X represents the current position of the agricultural handling robot, and K_{att} is an attraction constant. Then, the attraction borne by the robot can be expressed as follows.

$$\vec{F}_{att}=-grad[U_{att}(X)]=K_{at}d(X,X_g)\overrightarrow{e_g} \tag{12}$$

Where $d(X,X_g)$ is the distance between the endpoint and the agricultural handling robot, which is a unit vector with the direction from the agricultural handling robot to the endpoint. It can be obtained that the attraction is positively correlated with the distance from the robot to the target point. The attraction field intensity declines with the decrease in the distance between the robot and the target point until the robot reaches the target point when the attraction potential field is zero. The repulsion field function of the agricultural handling robot can be expressed as follows.

$$U_{rep}(X)=\begin{cases}\frac{1}{2}K_{rep}(\frac{1}{d(X,X_0)}-\frac{1}{d_0})^2, d(X,X_0)<d_0\\ 0, \qquad\qquad d(X,X_0)\geqslant d_0\end{cases} \tag{13}$$

Where d_0 indicates the farthest distance between the agricultural handling robot and the obstacle. If the distance between the robot and the obstacle is greater than d_0, the effect of repulsion can be omitted. The repulsion borne by the robot in the repulsion field can be acquired through the negative gradient operation of the repulsion field function, expressed as follows.

$$F_{rep}=-grad[U_{rep}(X)]=\begin{cases}K_{rep}(\frac{1}{d(X,X_0)}-\frac{1}{d_0})\frac{1}{d^2(X,X_0)}\overrightarrow{e_0}, d(X,X_0)<d_0\\ 0, \quad d(X,X_0)\geqslant d_0\end{cases} \tag{14}$$

Therefore, the resultant force borne by the agricultural handling robot in the potential field can be expressed as below.

$$\vec{F}_{tol}=\vec{F}_{att}+\vec{F}_{rep} \tag{15}$$

It can be concluded from the above analysis that the artificial potential field method has many advantages. But there are also some problems in some specific situations, specifically as follows:

(1) Target inaccessibility. When the agricultural robot draws close to the endpoint, the repulsion may be greater than attraction so that the target point cannot be reached;

(2) Local minimum. The direction in which the agricultural robot bears the resultant force in the potential field determines the moving direction. If the resultant force received by the agricultural handling robot is zero at a certain point, that is, the attraction is equal to the repulsion, the agricultural robot cannot move, or wander about.

Improved artificial potential field method

(1) Target inaccessibility. When the agricultural handling robot reaches one point, it fails to reach the target point since the repulsion is greater than the attraction. By introducing the relative distance $d(X,X_g)$ of the target point, the new target point can add attraction to the agricultural handling robot so that the direction of the resultant force borne by the agricultural handling robot will change. The repulsion field function is redefined as follows.

$$U_{rep}(X)=\begin{cases}\frac{1}{2}K_{rep}(\frac{1}{d(X,X_0)}-\frac{1}{d_0})^2 d(X,X_g)^n, d(X,X_0)<d_0\\ 0, \quad d(X,X_0)\geqslant d_0\end{cases} \tag{16}$$

The following can be acquired through the negative gradient operation of the repulsion field function (16).

$$\vec{F_{rep}}=\begin{cases}\vec{F_{rep1}}+\vec{F_{rep2}}, d(X,X_0)<d_0\\ 0, \quad d(X,X_0)\geqslant d_0\end{cases} \tag{17}$$

In Equation (17).

$$\vec{F_{rep1}}=K_{rep}[\frac{1}{d(X,X_0)}-\frac{1}{d_0}]\frac{1}{d^2(X,X_0)}d(X,X_g)^n\vec{e_0} \tag{18}$$

$$\vec{F_{rep2}}=\frac{n}{2}K_{rep}[\frac{1}{d(X,X_0)}-\frac{1}{d_0}]^2 d^{n-1}(X,X_g)\vec{e_g} \tag{19}$$

In Equation (18), the direction of the unit vector $\vec{e_0}$ is from the obstacle to the robot, which is the direction of the repulsion borne by the agricultural handling robot. In Equation (19), the unit vector $\vec{e_g}$ is the direction in which the robot points to the target point and the direction of the attraction borne by the agricultural handling robot. Therefore, $\vec{F_{rep1}}$ denotes the repulsion borne by the agricultural handling robot and $\vec{F_{rep2}}$ represents the component of the attraction borne by the agricultural handling robot.

By introducing the relative distance of the target point, the attraction borne by the agricultural handling robot grows, the direction of the resultant force changes, and the robot can continue to move towards the target point. In this case, the direction of the resultant force borne by the agricultural handling robot can be expressed as below.

$$\vec{F}_{tol}=\vec{F}_{att}+\vec{F}_{rep1}++\vec{F}_{rep2} \tag{20}$$

(2) Local minimum. When the robot is unable to move due to the force balance in the potential field, the method of obstacle transfer can be used to make the robot get rid of the current situation that the attraction is greater than the repulsion. The specific operation steps are as follows:

Step1: When the robot can't move, the robot is connected into a line after confirming the positions of the robot and the target point;

Step2: Taking the path from the agricultural handling robot to the target point as the bottom, a perpendicular line is drawn through the obstacle, and the point *P* nearest to the obstacle on the perpendicular line is marked;

Step3: The robot is connected to point *P*, and this path is namely the path temporarily passed by the agricultural handling robot.

Artificial potential field method combined with ant colony algorithm

(1) The basic principle of the algorithm. In the initial stage of path planning, the improved artificial potential field method is used to avoid the inaccessibility of the target point and the local minimum, and the early-stage blind search of the ant colony algorithm is improved. Meanwhile, the improved fusion algorithm increases the pheromone concentration difference. As the pheromone concentration increases, the effect of the artificial potential field method is weakened, and the effect of the ant colony algorithm is fully exerted so that the agricultural handling robot can achieve the global optimal path within the shortest time.

In the traditional ant colony algorithm, the probability of ant k to move from point *X* to point *Y* can be expressed as.

$$P_{XY}^k(t)=\begin{cases}\frac{\tau_{XY}^a(t)\eta_{XY}^\beta(t)}{\sum_{S\in a_k}\tau_{AS}^a(t)\eta_{XS}^\beta(t)}, B\in a_k\\ 0, else\end{cases} \tag{21}$$

In Equation (21), the heuristic factor is $\eta_{XY}(t)=1/d_{XY}$, which represents the probability for the ant to move from point X to point Y and is negatively correlated with the distance. Another factor is then introduced so that the heuristic factor is correlated with the resultant force borne by the agricultural handling robot and the number of iterations, expressed as follows.

$$\eta_{Ftol} = \frac{D_{\max}}{D_{\max} \times a^{F_{tol}\cos\theta}} \tag{22}$$

In Equation (22), D represents the current number of iterations of the ant colony; $D_{\max}$ stands for the maximum number of iterations of the ant colony; $\cos\theta$ is the cosine value of the included angle between the movable direction of the agricultural handling robot and the direction of the resultant force borne.

In this case, the probability for the ant k to move from point X to point Y can be expressed as below.

$$P_{XY}^{k}(t) = \begin{cases} \dfrac{\tau_{XY}^{a}(t)\eta_{XY}^{\beta}(t)\eta_{F_{tol}}^{\gamma}}{\sum_{s\in a_k}\tau_{XS}^{a}(t)\eta_{XS}^{\beta}(t)\eta_{F_{tol}}^{\gamma}}, Y \in a_k \\ 0, else \end{cases} \tag{23}$$

In Equation (23), γ is the regulatory factor. It is not difficult to find that in case of a small number of iterations in the early stage, this factor exerts a great effect on the path planning of the agricultural handling robot, and the artificial potential field plays a dominant role. In the above equation, the resultant force is:

$$\vec{F}_{tol} = \vec{F}_{att} + \vec{F}_{rep1} + + \vec{F}_{rep2} \tag{24}$$

(2) In the fusion algorithm, the stress analysis of the agricultural handling robot in the grid map and the possible movement direction analysis of the robot are described as follows: in case of no external force, the robot can move towards eight directions. When the mobile robot bears a resultant force of F_{tol}, the robot may move leftward or lower leftward. According to the relationship of the cosine value of the included angle between the direction of the resultant force and the movable direction with η_{Ftol}, it can be known that the robot will move towards a direction with a smaller angle, namely, it will move bottom leftward.

RESULTS

Example simulation

The improved fusion algorithm was subjected to the simulation experiment via MATLAB2014B. In general, parameter optimization is realized through expert experience or repeated experiments, and the control variable method is adopted to optimize the ant number M, pheromone influencing factor, heuristic information influencing factor β, volatility coefficient ρ, and pheromone strength Q. ditu.qishi=[1,1], ditu.mubiao=[30,28], ditu.daxiao=30. It was acquired through repeated simulations in the preceding part that when the ant number M was set to 100, pheromone factor to 1.5, heuristic factor β to 3.0, volatility coefficient ρ to 0.5, and pheromone constant Q to 1, the simulated trajectory diagram acquired based on the ant colony-improved artificial potential field method is as shown in Fig. 3.

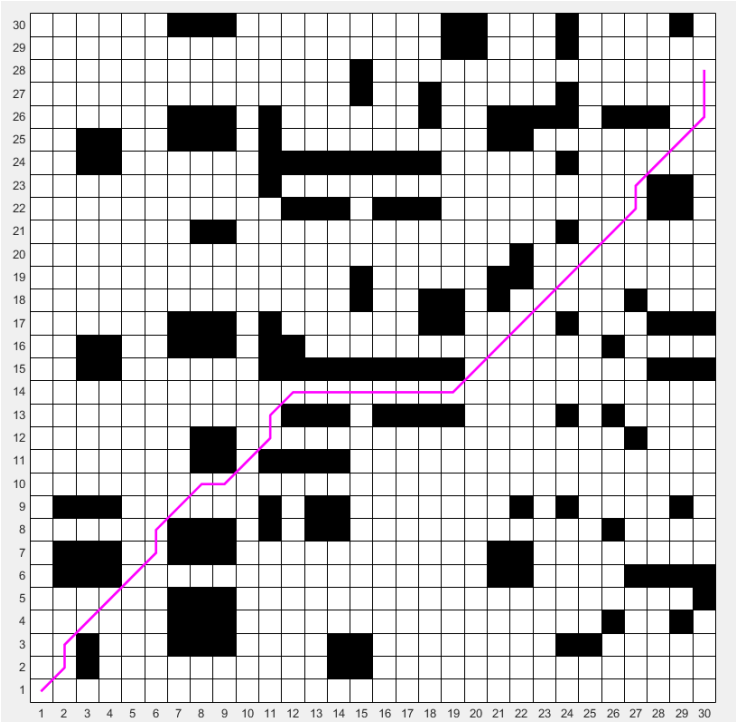


Fig. 3 - Simulated motion trajectory obtained through ant colony-improved artificial potential field method

Discussion of results

In this chapter, the problems of target inaccessibility and local minimum in the local path planning of the agricultural handling robot were mainly solved. The repulsion function was improved by adding an adjustment factor to the repulsion field function so that the target point became the lowest potential field and the target inaccessibility of the robot could be solved. The agricultural handling robot was prevented from local minimum by applying an external force towards another direction. When the agricultural handling robot encountered a dynamic obstacle in the dynamic environment, an improved repulsion field function was adopted to make the repulsion field function change with the local environment of the robot. Then, the feasibility of the improved algorithm was verified through experimental simulations. Next, the improved artificial potential field algorithm was combined with the ant colony algorithm. This mixed algorithm not only had the global path planning ability but also it was capable of avoiding temporary obstacles and dynamic obstacles in local path planning. In addition, the mixed algorithm achieved the shortest path and exhibited the stronger obstacle-avoiding ability.

CONCLUSIONS

In this study, a path planning model for the agricultural handling robot based on ant colony and improved artificial potential field method was established. By introducing the relative distance of the target and the intermediate point method, the repulsion field function of the agricultural handling robot was improved, and the problems of target inaccessibility and local minimum encountered by the artificial potential field method were solved. Moreover, the advantages and disadvantages of the ant colony algorithm were analyzed through grid map modeling and simulation. The improved potential field function was introduced based on the traditional ant colony algorithm, and a complex function containing the potential field factor and pheromone concentration was reconstructed. In addition, the slow search speed and local optimum of the ant colony algorithm were solved. Finally, the feasibility of the ant colony-improved artificial potential field method was further verified via MATLAB simulation analysis.

(1) The ant colony-improved artificial potential field algorithm can solve the local minimum and target inaccessibility of the robot. Local path planning is implemented using the artificial potential field method. The path is a random point in the environment instead of coordinate points on the environmental map. When road stiffness planning is carried out through the improved artificial potential field method, the robot will joggle on individual paths due to the defects of the artificial potential field method itself. With limited ability to process external environmental information, the artificial potential field method is generally applicable to local path planning, local environmental information processing, and decision-making.

(2) When working in a dynamic environment, the agricultural handling robot will encounter temporary stacking obstacles, which will hinder the robot's forward movement, that is, the object that suddenly blocks the robot appears on the working path of the robot. Under this circumstance, the robot needs to avoid dynamic obstacles through local path planning, followed by local path planning once again so as to complete the remaining path planning.

REFERENCES

[1] Ames B, Beveridge A, Carlson R, Djang C, Isler V, Ragain S, Savage M., (2015), A leapfrog strategy for pursuit-evasion in a polygonal environment, *International Journal of Computational Geometry and Applications*, vol. 25, no. 2, ISSN 0218-1959, pp. 77-100, Singapore;

[2] Das P. K, Behera H. S, Das S, Tripathy H. K, Panigrahi B. K, Pradhan S. K., (2016), A hybrid improved PSO-DV algorithm for multi-robot path planning in a clutter environment, *Neurocomputing*, vol. 207, ISSN 0925-2312, pp. 735-753, Netherlands;

[3] Duan W, Gu J, Wen M, Zhang G, Ji Y, Mumtaz S., (2020), Emerging technologies for 5G-IoV networks: applications, trends and opportunities, *IEEE Network*, vol. 34, no. 5, ISSN 0890-8044, pp. 283-289, United States;

[4] Javidrad F, Nazari M., (2017), A new hybrid particle swarm and simulated annealing stochastic optimization method, *Applied Soft Computing*, vol. 60, ISSN 1568-4946, pp. 634-654, Netherlands;

[5] Kyaw P. T, Paing A, Thu T. T, Mohan R. E, Le A. V, Veerajagadheswar P., (2020), Coverage path planning for decomposition reconfigurable grid-maps using deep reinforcement learning based travelling salesman problem, *IEEE Access*, vol. 8, ISSN 2169-3536, pp. 225945-225956, United States;

[6] Mo H, Xu L., (2015), Research of biogeography particle swarm optimization for robot path planning, *Neurocomputing*, vol. 148, ISSN 0925-2312, pp. 91-99, Netherlands;
[7] Ma X, Xu Y, Sun G, Deng L, Li Y., (2013), State-chain sequential feedback reinforcement learning for path planning of autonomous mobile robots, *Journal of Zhejiang University Science C*, vol. 14, no. 3, ISSN 2095-9184, pp. 167-178, China;
[8] Radwan A, Huq K. M. S, Mumtaz S, Tsang K. F, Rodriguez J., (2016), Low-cost on-demand C-RAN based mobile small-cells, *IEEE Access*, vol. 4, ISSN 2169-3536, pp. 2331-2339, United States;
[9] Sombolestan S. M, Rasooli A, Khodaygan S., (2019), Optimal path-planning for mobile robots to find a hidden target in an unknown environment based on machine learning, *Journal of Ambient Intelligence and Humanized Computing*, vol. 10, no. 5, ISSN 1868-5137, pp. 1841-1850, Germany;
[10] Tharwat A, Elhoseny M, Hassanien A. E, Gabel T, Kumar A., (2019), Intelligent Bézier curve-based path planning model using chaotic particle swarm optimization algorithm, *Cluster Computing*, vol. 22, no. 4, ISSN 1386-7857, pp. 1-22, United States;
[11] Teng Z, Lv J, Guo L, Xu Y., (2018), An improved hybrid grey wolf optimization algorithm based on Tent mapping (一种基于 Tent 映射的混合灰狼优化的改进算法), *Journal of Harbin Institute of Technology*, vol. 50, no. 11, ISSN 0367-6234, pp. 40-49, China;
[12] Wang B, Liu Z, Li Q, Prorok A., (2020), Mobile robot path planning in dynamic environments through globally guided reinforcement learning, *IEEE Robotics and Automation Letters*, vol. 5, no. 4, ISSN 2377-3766, pp. 6932-6939, United States;
[13] Wei Y, Jin F, Dong K, Song J, Mo W, Hui Y., (2023), Improved Global Path Planning A* Algorithm Based on Node Optimization (基于节点优化的改进全局路径规划 A*算法), *Computer Measurement & Control*, vol. 1, ISSN 1671-4598, pp. 13-16, China;
[14] Xu H, Wang N, Zhao H, Zheng Z., (2019), Deep reinforcement learning-based path planning of underactuated surface vessels, *Cyber-Physical Systems*, vol. 5, no. 1, ISSN 2333-5785, pp. 1-17, England;
[15] Yan Q, Ma R, Ma Y, Wang J., (2021), An adaptive simulated annealing particle swarm optimization algorithm(一种自适应模拟退火粒子群优化算法), *Journal of Xidian University*, vol. 48, no. 4, ISSN 1001-2400, pp. 120-127, China;
[16] Yang W, Wang H, Wang J., (2012), Research on path planning for mobile robot based on grid and hybrid of GA/SA, *Advanced Materials Research*, vol. 479-481, ISSN 1022-6680, pp. 1499-1503, Germany;
[17] Zhu D, Yan M., (2010), Survey on technology of mobile robot path planning (移动机器人路径规划技术综述), *Control and Decision*, vol. 25, no. 7, ISSN 1001-0920, pp. 961-967, China;
[18] Zhu K, Zhang T., (2021), Deep reinforcement learning based mobile robot navigation: a review, *Tsinghua Science and Technology*, vol. 26, no. 5, ISSN 1007-0214, pp. 674-691, China;
[19] Zeng N, Zhang H, Chen Y, Chen B, Liu Y., (2016), Path planning for intelligent robot based on switching local evolutionary PSO algorithm, *Assembly Automation*, vol. 36, no. 2, ISSN 0144-5154, pp. 120-126, England;
[20] Zhao X, Wang Z, Huang C, Zhao Y., (2018), Mobile Robot Path Planning Based on an Improved A* Algorithm (基于改进 A*算法的农业搬运机器人路径规划), *Robot*, vol. 40, no. 6, ISSN 1002-0446, pp. 903-910, China;
[21] Zhang Y, Gong P, Hu W., (2023), Improved artificial potential field method for smart vehicle path Planning (改进人工势场法的智能车路径规划), *Mechanical Science and Technology for Aerospace Engineering*, ISSN 1003-8728, https://doi.org/10.13433/j.cnki.1003-8728.20230066. China;
[22] Zhou Z, Mu P, Zhang R., (2021), Application of PSO optimization algorithm in smooth path planning (PSO 优化算法在平滑路径规划中的应用), *Software Guide*, vol. 20, no. 3, ISSN 1672-7800, pp. 67-72, China.

EVALUATION OF THE THERMAL BEHAVIOR OF PLANTS IN THE MICROGREENHOUSE WITH MICROBOLOMETRIC IMAGE SENSORS
/
EVALUAREA COMPORTARII TERMICE A PLANTELOR IN MICROSERA CU SENZORI DE IMAGINE MICROBOLOMETRICI

George IPATE [*1)], Constantin Daniel COTICI[1)], Alina-Daiana IONESCU [1)], Viorel FATU[1)], Iuliana GAGEANU[2)], Dan CUJBESCU[2)], Ana Maria NICOLAU[3)]

[1)] National University of Science and Technology "POLITEHNICA" of Bucharest / Romania.
[2)] National Institute of Agricultural Machinery Bucharest / Romania
[3)] National University of Science and Technology "POLITEHNICA" of Bucharest, Faculty of Aerospace Engineering / Romania;
Tel: 0766445321; E-mail: george.ipate@upb.ro
DOI: https://doi.org/10.35633/inmateh-71-48

Keywords: *thermal stress, Kalanchoe blossfeldiana, imagine camera*

ABSTRACT

In this research, the data from temperature measurements obtained with the InfiRay T2S+ device, an infrared thermal imaging camera have been checked to monitor plant thermal behaviour. Plant leaf temperature is a parameter frequently used as representative for stomatal conductance, as stomatal confinement results in attenuated transpiration, and consequently leads to increased plant temperature. Also, to identify the stress of the plant, indices of thermal and modified stress have been calculated. The results obtained show that the Kalanchoe blossfeldiana species chosen for this study, when exposed to extreme values of temperature or water requirements, presented significant changes in the infrared electromagnetic wave spectra.

REZUMAT

În această cercetare, au fost examinate datele din măsurătorile de temperatură obținute cu dispozitivul InfRay TS2+, o cameră de imagine termică în infraroșu pentru a monitoriza comportamentul termic al plantei. Temperatura frunzelor plantei este un parametru folosit în mod obișnuit ca identificator pentru conductanța stomatelor, deoarece închiderea stomatelor conduce la o transpirație redusă, care, la rândul său, conduce la o creștere a temperaturii plantei. De asemenea, pentru a identifica stresul plantei, au fost calculaţi indicii de stres termic modificat. Rezultatele obținute arată că specia Kalanchoe blossfeldiana aleasă pentru acest studiu, atunci când a fost expusă la valori extreme ale cerințelor de temperatură sau de apă, a prezentat modificări semnificative în spectrele undelor electromagnetice infraroșii.

INTRODUCTION

During the process of growth and development of crops, they are met by situations in which the structures of plants or leaves change, mainly due to the disturbances of environmental factors. Although in the specialized literature can be found described countless methods of research on the evolution of plants under conditions of environmental stress, the method of analysing the behaviour of plants in microgreenhouses with the help of the infrared electromagnetic spectrum (3-14 μm) is not sufficiently known and implemented, perhaps because of the reluctance regarding the costs that are somewhat high. Water stress is an essential abiotic factor that drastically affects plant development (*Cazacu A.C, 2015*). Lack of water, but to the same extent water in excess, presents serious challenges for the survival of crops, because it affects plant growth and reduces productivity. Plants have developed various mechanisms to respond to different environmental stressors (*Shabala S. and Shabala L., 2011*).

The thermal properties of plant leaves are influenced by a complex heterogeneous internal structure that contains a certain amount of water per unit area. This is a solid argument in the decision to conduct research with thermal remote sensing equipment, to which is added the ease of operation, precision and high resolution of infrared thermography (*Ishimwe R., Abutaleb K. and Ahmed F., 2014*). *Buitrago et al (2016)* investigated the stress response in the thermal infrared spectrum of two plant species and found that it had substantial impacts on the long-term thermal spectrum of plants, both in the mid-IR waveband (3–6 μm) as well as in the long wave band (6–16 μm). At the same time, they showed that thermal and water stress led to the change in the emissivity of the two species, but in different directions.

To understand these contrasting remarks, they determined leaf water capacity and the protective layer covering the epidermis thickness as the main factors contributing to the emissivity of the leaves. *Lee A.Y. et al. (2019)* tested a thermographic method capable of accurately measuring the temperature of the leaves of a peach, for measuring the water stress index of the culture. They showed that water stress on the crop, which occurs under water deficit conditions, produces an increase in the temperature of the leaves, which can be established by the proposed thermal imaging technique. The outcomes published by them demonstrate that the infrared images of leaf temperature distribution obtained in a time interval are meaningfully connected to the physiological parameters of culture that are unprotected to water deficiency. The degree or intensity of heat of the plant leaves was exactly extracted from the infrared images to investigate the water content. *Stoll and Jones (2007)*, in their research on mature vines, demonstrated that infrared thermography can be applied as a first step in identifying the onset of plant stress due to changes in stomatal opening. The measurements made can provide precise and sensitive indications of leaf temperature and, consequently, stomatal conductance can be determined. They also suggested that the application of infrared thermography has the potential to contribute to improving the management practices of a wine farm.

Pineda et al. al. (2020) present in their research a comprehensive review of works in which plant and crop thermography is applied to establish water content and discover plant stress. They estimate that in the near future infrared thermography, implemented in high-capacity facilities, will become a tool in plant genetic engineering for the creation of mutant varieties with resistance to pathogens or phenotypes, with much better results established in conditions well determined by abiotic stress. In this way, thermography has a major contribution to the development of the crops of the next generation, of Agriculture 5.0 (*Ragazou K., Garefalakis A., Zafeiriou E. and Passas, I., 2022*).

Ribeiro da Luz and Crowley (2010) state that emissivity is not the product of the reciprocity between solar energy and pigments, even so it represents the efficiency in the release of thermal radiation by the leaf surface. This signify that electromagnetic radiation in the infrared spectrum can include valuable knowledge concerning the leaf biochemistry and the fine structure of simple culture.

The non-invasive thermal inspection method can be used in all processes and for all agricultural products where there is heat transfer. Thermal imaging has grown rapidly and plays a predominant role in many area of agriculture, ranging from nursery observing, supply of water to land, soil pollution stress detection, plant disease diagnosis, yield evaluation, full growth assessment, and fruit and vegetable injury detection (*Ali M.M., Hashim N., Aziz S.A., Lasekan O., 2020*). However, accurate thermal estimation is influenced by the environmental conditions, who influence the thermal properties of the harvest under observation. Therefore, calibrating images according to specific environmental conditions is necessary to compare data from images obtained during different measurement periods and growing seasons (*Ishimwe R., Abutaleb K. and Ahmed F., 2014*).

The main goal of the work is to highlight an approach to the use of thermal images in precision agriculture in general, with a particularity in the assessment of the condition of plants in a micro greenhouse. A second objective is to use the most commonly used long-wave infrared thermal parameters (normalized plant or leaf temperature and crop water stress index) to measure the repercussion of environmental characteristics on the temperature of healthy houseplants.

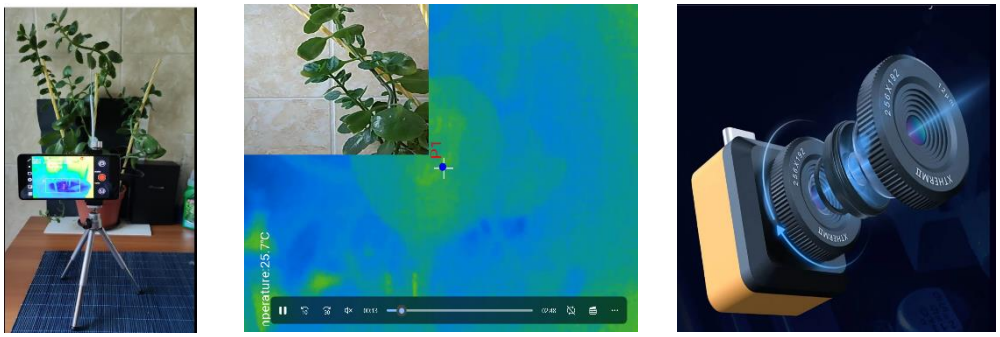
MATERIALS AND METHODS

An uncooled microbolometric technology device incorporate an optical package, a focal plane sensor array and an electronic processing circuit. The microbolometer run by captivating infrared radiation which determine a temperature-induced fluctuate in the resistance of the material. This change in resistance is settled as a variation in voltage while a direct current deviation is applied (*Grimming R., 2020*).

For this study, a species cultivated as an apartment plant (with beautiful flowers that usually appear in spring, but also with glossy leaves that give the plant a pleasant appearance) was chosen, especially due to its ability to manage with excessive conditions such as reduced temperature and drought. Therefore, it is expected that this plant has its own mechanism to survive with environmental stress regime, similar to the structural changes in the leaves, if the stress regime has an extensive duration (*Ştefîrţă A., Leahu I., Toma S., 2015*).

Kalanchoe spp. is a bush-like plant, with heights varying between 30-50 cm. The leaves are green and juicy, and the flowers are small in the form of beautifully coloured stars in red, pink, orange or yellow. Some species are perennial, others are annual or biennial.

Development of the experimental stand. Investigating the thermal radiation characteristics of Kalanchoe blossfeldiana, a small plant suitable for a small space that likes to be watered often, was complicated due to its high thermal reflection (fig.1-left). To make the measuring equipment, materials were chosen to eliminate the reflected and emitted disruptive radiation, the most suitable being those with low reflectance and low emissivity. Another aspect that requires special attention is the minimization of thermal radiation due to the surrounding environment (*Falsetti C., Kapulla R., Paranjape S., Paladino D., 2021*). A black curtain of material was placed at the rear of the pot containing the plant both for better contrast between the plant and its background on the thermal picture, but also to eliminate occasional heat emissions from the surroundings. An additional source of radiation is the thermal chamber that heats up during operation and which must also be avoided (*Wan Q., Brede B., Smigaj M., Kooistra L., 2021*).



a) b)..... .....c)

Fig. 1 – The experimental measuring stand and InfiRay thermographic camera T2S+

Image capture and analysis. The plant is grown in a simple pot, and the camera was placed on a support that integrates perfectly into any minimalist decor, and directed towards significant areas of interest. The temperature measurement took place under normal laboratory conditions. Thermal images of plant leaves were taken with the thermal camera “InfiraRay T2S+ Thermal Camera for Smartphone” (InfiraRay, P.R. China) which has a sensitivity of ±2°C or ±2% of the measurement range (whichever is greater). In figure 1c, it can be seen the "InfiraRay T2S+" camera. Its technical details are showed in Table 1.

Table 1

Technical specifications of the InfiraRay thermal camera T2S+ (from datasheets)

• Sensor: number of pixels: 49152 elements (256x192), uncooled microbolometer;	• Sensitivity: Average ≤ 60mK@25℃; F0.68;
• Spectral sensitivity: 8μm...14μm;	• Optical date: f=40mm; F #1.0;
• Optical angle: FOV 44.9°×33.4°;	• Measurement range: -20ºC +450ºC (without filter);
• Output: composite video signal (CVBS) (50 fields);	• Control: protocols Cam (USB type C);
• Operating temperature: -20ºC up to 50ºC;	• The frame rate of the image: 25 Hz.
• Dimensions 26×26×24.2mm	• Supported operating system: Android, Harmony OS, iOS

The images and recordings were made with the thermal camera's own software, the Xtherm Android application provided by the manufacturer, which can be downloaded for free from the Google Play store. Using the software, images can be recorded and saved in Live View Stream, and can be simultaneously added up to 3x different temperature measurement fixed points, a temperature spectrum line and a Region of Interest box, also known as ROI boxes, which best characterize the surface temperature (Fig.1b).

Based on the temperature distribution of the foliage, the temperature difference between the leaf and the air and the modified CWSI crop stress index, the thermographic effects of the ambient conditions on the plants can be analysed, such as the thermal state of the plants before or after irrigation. The leaf-air temperature difference ΔT is given by the relation:

$$\Delta T = Tl - Ta \ \ [°C] \quad (1)$$

where: Tl - the measured temperature of the leaf; Ta – temperature of the surrounding air.

The modified plant stress index, CWSI, was calculated from the relationship proposed by *Jones et al. (2002)* based on captured thermographic images (*Nagy A., 2015*):

$$CWSI = \frac{Tc-Tw}{Td-Tw} \quad (2)$$

where: Td - the maximum reference temperature of the foliage (minimum transpiration); Tw - the minimum reference temperature of the foliage (maximum transpiration); Tc - actual temperature values for each pixel.

Measurement conditions. Light is an important factor for the growth and flowering of Kalanchoe. This plant must not be deprived of light, the lack of light slows down growth and prevents the emergence of new shoots. But the interactive effects of light and soil radiation reflection on leaf temperature can have a negative effect on plant health, causing excessive absolute temperatures. Corresponding images are taken looking perpendicular to the plant structure showing the unshaded and naturally lit parts.

The ambient environment (air temperature and relative humidity, atmospheric pressure, VOC concentration) was continuously monitored with an IoT system consisting of a Bosch BMP680 digital environmental sensor and a Raspberry Pi B3+ development board, the data being saved, visualized and analysed on the Thingspeak IoT cloud platform (https://thingspeak.com/channels/1539770/private_show) made available by the creators of the MATLAB program, Mathworks Inc. - US.

Thermal long-wave infrared (TIR) cameras are calibrated sensors capable of recording emitted radiation in the wavelength range between 8–14 µm and providing images representing the temperature values per pixel (*Leblanc G., Kalacska M., Arroyo- Mora J.P., Lucanus O. and Todd A., 2021*). Thermal imaging allows detailed information about the surface temperature distribution (*Vollmer M. and Möllmann K.P., 2018*). A significant physiological trait for plant growth and development is stomatal activity, having a decisive role in carbon and water balance by permanently checking photosynthesis and transpiration (*Brendel O., 2021*). Consequently, stomatal water conductance is associated with productivity and tolerance to environmental stress and is closely correlated with leaf temperature (*Pineda M., Barón M. and Pérez-Bueno M.L., 2020*).

RESULTS

The thermal sensor generates an image depending on the different amounts of thermal energy it detects. By using a wide palette of different colours to display temperature differences (fig.2), objects and very slight changes in temperature can be detected despite low contrast conditions. In this way, the thermal patterns in an image can be represented using a very large and specific data set. Therefore, this approach allows a complex analysis of a large area of a plant in an image, performing the calculation of the mean temperature or the incidence distribution of temperatures on chosen areas.

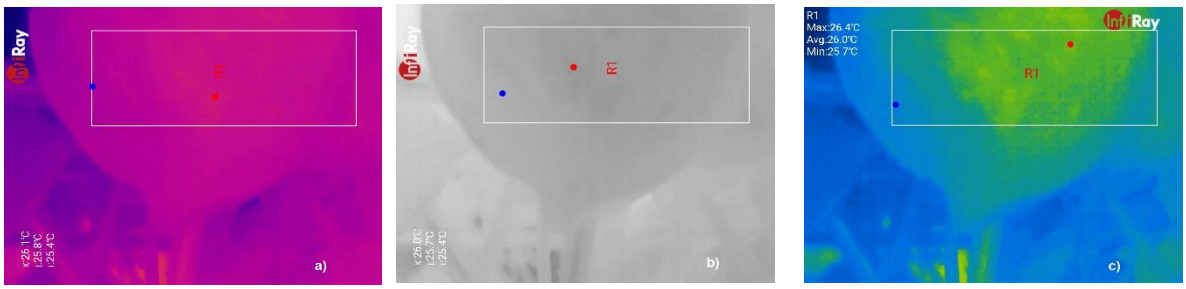


Fig. 2 - The corresponding thermal images (a-c) taken in the afternoon of June 17, 2023

Such image analysis was done with a general-purpose Iron palette (fig. 2a) that quickly identifies thermal anomalies and object heat. In this palette, hot objects are displayed in warm, light colours, while cooler objects are in dark, cool colours. Fig. 2b illustrates the different plant temperature distribution in the Black Hot colour palette. This palette is the inverted version of the White Hot palette, displaying warmer objects in black and cooler objects in white in a clear and realistic image. The Rainbow colour palette (fig. 2c) works well to detect minor temperature differences in a scene despite low contrast conditions. Warm colours illustrate the hottest part of the image and cool colours depict the frosty areas, but add more colours to the mix. It is a very good model for identifying objects in environments with slightest heat dissimilarity.

For the analysis, a region is outlined within the thermal image (rectangles - regions of interest ROI), where the maximum and minimum temperatures are tracked (fig.2).

The ROI box data can also be used as reference data for the temperature histogram. The ROI feature is a perfect tool for analysing different regions of a single thermal image. Each ROI is scalable and movable and can be sized and moved within the live view stream area. In the region of interest selected in figure 2, where the leaf has a low emissivity, it can be seen now that it has a maximum temperature of 26.4 °C, while the average value is just below 26.1°C, almost 0.4 degrees warmer than the environment.

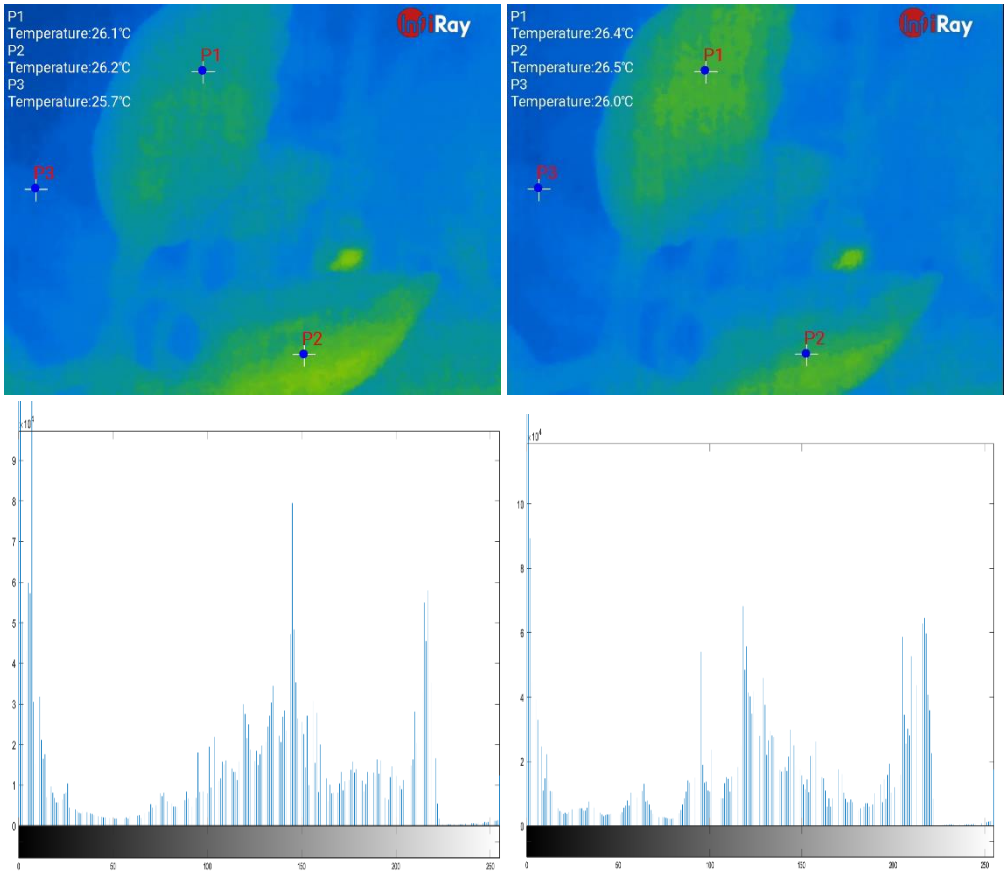


Fig. 3 - The thermal images corresponding to the effects of irrigation on the absolute temperature of the plant

The plant is watered with water at room temperature, differently depending on the periods of growth and rest. From spring to autumn, when the Kalanchoe grows and blooms, it needs a larger amount of water. Watering is done when the soil on the surface is a little dry. The effect of a soil watering operation on the absolute temperature of the plant leaf is shown in figure 3. During the measurements in the afternoon of June 24, a day when the temperature in the external environment reached extreme values of 39°C and the alerts were issued on meteorological conditions of severe weather, no significant change was observed in the absolute temperature of the leaves before and after watering the plant. In Figure 3-right, where the leaf is more heated, the core with high emissivity is at a higher temperature (26.5°C), only 0.5°C higher than the ambient environment, an increase that can be attributed to the acceleration of the process of transpiration of the leaf. The result is in agreement with the one obtained by *Buitrago et. al. (2016)* for beech leaves, who observed that an increase in the moisture content of the leaf increases the emissivity of the leaves.

During the rest period, watering is done with a smaller amount of water, because the Kalanchoe is a plant with juicy leaves and it can withstand the lack of water (for a short period of time). This period of water stress can lead the plant to have: smaller sizes and an earlier flowering (*Petcu E., Terbea M., Lazar C., 2007*).

At the bottom of figure 3 - the two graphs of the histogram of the images made in the Matlab R2022b program are displayed. The input image being an indexed image, the histogram shows the distribution of pixel values depending on the number of colours of the colour map. For the grayscale image, 256 intervals were used by default.

The n intervals of the histogram are each half-open intervals of width $\mathrm{A}/(n-1)$. In particular, the p-th interval is the half-open interval.

$$\frac{A(p-1.5)}{n-1} - B \leq x < \frac{A(p-0.5)}{n-1} - B \tag{3}$$

where: x is the intensity value. The scale factor A and offset B depend on the image class type.

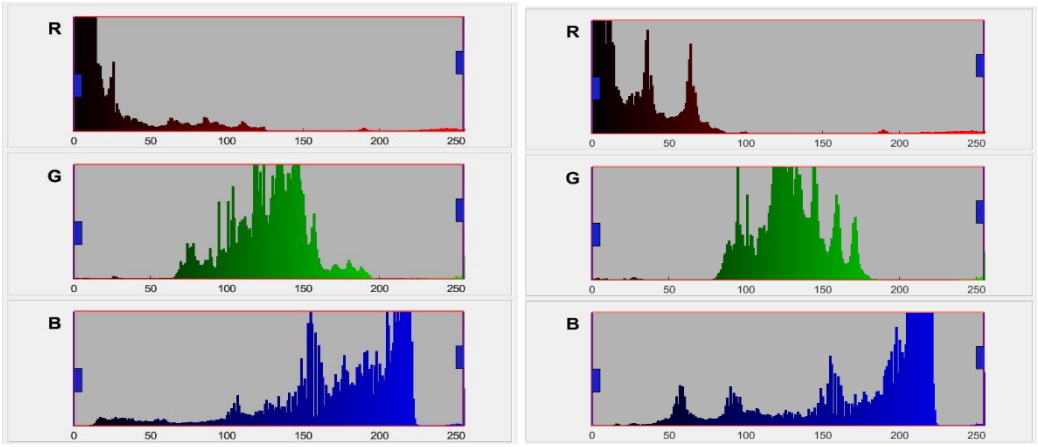


Fig. 4 - Colour histogram of RGB images corresponding to the effects of irrigation on plant temperature

The difference in measured temperature can be visualized much better by calculating the colour histograms of the RGB images (as can be seen in fig. 4). The number of intervals (for each colour component) is entered by the user, being the same for R, G and B colours. The output histogram can be un-normalized or normalized. The temperature increase of the leaves, of approx. 0.4°C, is highlighted by the increase in the frequency of occurrence of the intensity of the colour red - R, simultaneously with the decrease of the frequency of occurrence of the colour blue - B, while the frequency of occurrence of the intensity of the colour green - G remains constant.

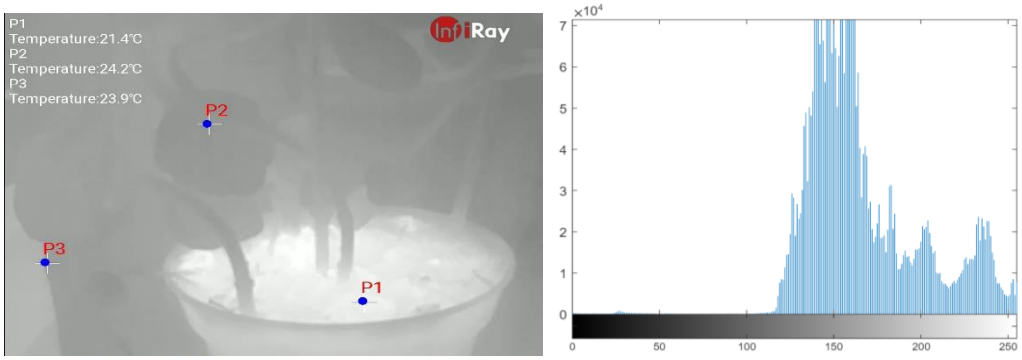


Fig. 5 - Thermographic image of the plant after watering and its histogram from 30.06.2023

In the evening of June 26, the plant was significantly cooler compared to the unstressed vine. No significant temperature difference was found between the leaves and the surrounding air (figure 5). The measurements indicate that the temperature difference ΔT was on average 0.3 °C, lower than that of the plant in the period before watering. Alternatively, it is possible that the irrigation operation affects the structure of the plant and, consequently, increases the reflection of radiation from the ground and thus increases the temperature of the leaves. In the presented thermal image, it can be seen that the soil temperature of 21.4°C is approx.2.8°C lower than the leaf temperature and 2.5°C lower than the air temperature.

The difference between the average leaf temperature and the air temperature was +1.67°C for the period without watering, but it was +0.53 °C for the period following watering. Thus, the effect of irrigation could also be detected on the fruit in addition to the foliage by using thermography. Based on the measurements, the existence of a high risk of water stress was not found. The average values of the modified stress index of the plant were 0.389±0.095 which means that the values were above the threshold value of 0.25. The optimal temperature for the growth and flowering of Kalanchoe varies between 15-25°C. In summer, the plant must be protected from direct sunlight and it is recommended to spray water on the leaves. There is clear evidence in the specialized literature that the plant is very sensitive to low temperatures, it can die if it is kept at temperatures varying between 0-10°C.

Thermal imaging as a non-invasive remote sensing method appears to be a suitable tool for studies where the temperature values of plant foliage, flowers or fruits can be reproduced with greater efficiency and precision than can be achieved with other methods. The choice of the measurement method used depends largely on the architecture of the plants and the availability of exposed flowers or fruits.

One of the main advantages of infrared thermography is that it covers a variety of different positions on the plant structure, which can hardly be achieved using the thermocouple method. In addition, by combining various optical devices and sensors with the performance of a deep learning neural network used for object detection, without applying image enhancement algorithms or excessive processing of measurement data, much-needed information about the condition of plants can be obtained in various weather conditions, such as clear sky, fog and rain, at different intervals.

CONCLUSIONS

The temperature differences observed during the study of the behaviour of the plant subjected to different operations/situations are encouraging for the application of the thermal image as a useful tool to make a correct assessment in the event of water stress states or to take advantage of the application of this methodology in the management of plant growth, or even more precisely, in the realization of irrigation control applications, which ensure an optimal water regime.

The productivity and quality of plant development are strongly influenced by the limiting abiotic conditions (thermal and water stress) manifested during the experimental period. Reducing the drastic effects of water stress can also be achieved by accumulating osmoprotectors, maintaining turgor, leading to a decrease in the rate of transpiration and the closing of stomata.

The processed thermal image can be displayed in a certain colour spectrum by using colour palettes. The cost vindication for implementing the thermography method increases as the prices of electronic elements decrease. Nowadays, infrared thermal devices provide up to 16 times the quality of image of devices used in decade past, for nearly the same cost.

REFERENCES

[1] Ali, M.M., Hashim, N., Aziz, S.A., Lasekan, O. (2020). Emerging non-destructive thermal imaging technique coupled with chemometrics on quality and safety inspection in food and agriculture *Trends in Food Science & Technology*, Vol. 105, November, pp. 176-185. https://doi.org/10.1016/j.tifs.2020.09.003

[2] Brendel, O., (2021). The relationship between plant growth and water consumption: a history from the classical four elements to modern stable isotopes. *Annals of Forest Science* (2021) 78: 47. https://doi.org/10.1007/s13595-021-01063-2

[3] Buitrago, M.F., Groen, T.A., Hecker C.A., Skidmore A. K. (2016). Changes in thermal infrared spectra of plants caused by temperature and water stress. *ISPRS Journal of Photogrammetry and Remote Sensing*, 111, pp. 22–31.

[4] Cazacu, A.C. (2015). *Research on the resistance to water stress of some wheat genotypes in pedoclimatic conditions at SCDA Turda (Cercetări privind rezistenţa la stresul hidric a unor genotipuri de grâu în condiţiile pedoclimatice de la SCDA Turda)* [Doctoral thesis]. University of Agricultural Sciences and Veterinary Medicine of Cluj-Napoca.

[5] Falsetti, C., Kapulla, R., Paranjape, S., Paladino, D., (2021). Thermal radiation, its effect on thermocouple measurements in the PANDA facility and how to compensate it. *Nuclear Engineering and Design*, Volume 375, 15 April, https://doi.org/10.1016/j.nucengdes.2021.111077

[6] Grimming, R., (2020). *Uncooled Microbolometer Imaging Systems for Machine Vision*. Electronic Theses and Dissertations. University of Central Florida. https://stars.library.ucf.edu/etd2020/1379

[7] Ishimwe, R., Abutaleb, K. and Ahmed, F. (2014). Applications of Thermal Imaging in Agriculture—A Review. *Advances in Remote Sensing*, 3, 128-140. http://dx.doi.org/10.4236/ars.2014.33011.

[8] Leblanc, G., Kalacska, M., Arroyo-Mora J. P., Lucanus, O., Todd, A., (2021). A Practical Validation of Uncooled Thermal Imagers for Small RPAS. *Drones* 2021, 5(4), 132; https://doi.org/10.3390/drones5040132

[9] Lee, A.Y., Kim S.Y., Hong S.J., Han Y.H., Choi Y., Kim M. Yun S.K., Kim G. (2019). Phenotypic Analysis of Fruit Crops Water Stress Using Infrared Thermal Imaging. *Journal of Biosystems Engineering*, 44: 87–94, https://doi.org/10.1007/s42853-019-00020-2

[10] Melucă, C. Cernat, S., Nistor T., (2011). Behavior of winter wheat varieties under water and heat stress conditions of burnas plain. AN. I.N.C.D.A. Fundulea, VOL. LXXIX, no. 2, *Genetica şi Ameliorarea Plantelor*, Electronic (Online) ISSN 2067–7758, www.incda-fundulea.ro

[11] Nagy, A., (2015). Thermographic evaluation of water stress in an apple orchard. *Journal of Multidisciplinary Engineering Science and Technology* (JMEST),Vol. 2 Issue 8, 2210 - 2215.

[12] Petcu, E., Terbea, M., Lazar, C., (2007). Research in the field of field plant physiology at Fundulea (Cercetari in domeniul fiziologiei plantelor de camp la Fundulea.) AN. I.N.C.D.A. Fundulea, Vol. LXXV, 2007, *Tribute volume - Physiology of Plants*

[13] Pineda, M., Barón, M., Pérez-Bueno, M.L., (2020). Thermal Imaging for Plant Stress Detection and Phenotyping. *Remote Sens*. 2021, 13(1), 68; https://doi.org/10.3390/rs13010068.

[14] Ragazou, K., Garefalakis, A., Zafeiriou, E. and Passas, I., (2022). Agriculture 5.0: A New Strategic Management Mode for a Cut Cost and an Energy Efficient Agriculture Sector. *Energies* 2022, 15(9), 3113; https://doi.org/10.3390/en15093113.

[15] Ribeiro da Luz, B., Crowley, J.K. (2010). Identification of plant species by using high spatial and spectral resolution thermal infrared (8.0–13 lm) imagery. *Remote Sens. Environ*. 114, 404–413.

[16] Shabala, S., Shabala, L., (2011). Ion transport and osmotic adjustment in plants and bacteria. *Biomol Concepts*. Oct 1:2(5):407-19. https://doi: 10.1515/BMC.2011.032.

[17] Ştefîrţă, A., Leahu, I., Toma, S., (2015). The specific and non-specific response of plants to the action of water and thermal stress: interactive relationships between water status and antioxidant protection (Răspunsul specific şi nespecific al plantelor la acţiunea stresului hidric şi termic: relaţiile interactive dintre status-ul apei şi protecţia antioxidant). *AŞM Bulletin. Life Sciences*, No. 1(325), 29-46.

[18] Stoll M., Jones H.G. (2007). Thermal imaging as a viable tool for monitoring plant stress. *J. Int. Sci. Vigne Vin*, 2007, 41, no.2, 77-84.

[19] Van Linden, V., Vereycken, R., Bravo, C., Ramon, H., and De Baerdemaeker, J. (2003). Detection Technique for Tomato Bruise Damage by Thermal Imaging. Proc. Postharvest Unltd Eds. B.E. Verlinden et al*., Acta Hort.* 599*, ISHS 2003*

[20] Vollmer, M., Möllmann, K.P., (2018). *Infrared Thermal Imaging, Second Edition*. Wiley-VCHVerlag GmbH&Co. KgaA

[21] Wan, Q., Brede, B., Smigaj, M., Kooistra, L., (2021). Factors influencing temperature measurements from miniaturized thermal infrared (TIR) cameras: A Laboratory-Based Approach. *Sensors* 2021, 21, 8466. https://doi.org/10.3390/s21248466

[22] *** Datasheet-t2s-t2l-thermal-camera-for-smartphone (2023). https://www.infiray.com/products/t2s-t2l-thermal-camera-for-smartphone.html

[23] *** MATLAB - Mathworks Help Center. (2023). *Image Processing and Computer Vision*. https://uk.mathworks.com/help/images/ref/imhist.html?s_tid=doc_ta

EVALUATION OF THE THERMAL BEHAVIOR OF PLANTS IN THE MICROGREENHOUSE WITH MICROBOLOMETRIC IMAGE SENSORS
/
EVALUAREA COMPORTARII TERMICE A PLANTELOR IN MICROSERA CU SENZORI DE IMAGINE MICROBOLOMETRICI

George IPATE [*1)], Constantin Daniel COTICI[1)], Alina-Daiana IONESCU [1)], Viorel FATU[1)], Iuliana GAGEANU[2)], Dan CUJBESCU[2)], Ana Maria NICOLAU[3)]

[1)] National University of Science and Technology "POLITEHNICA" of Bucharest / Romania.
[2)] National Institute of Agricultural Machinery Bucharest / Romania
[3)] National University of Science and Technology "POLITEHNICA" of Bucharest, Faculty of Aerospace Engineering / Romania;
Tel: 0766445321; E-mail: george.ipate@upb.ro
DOI: https://doi.org/10.35633/inmateh-71-48

Keywords: *thermal stress, Kalanchoe blossfeldiana, imagine camera*

ABSTRACT

In this research, the data from temperature measurements obtained with the InfiRay T2S+ device, an infrared thermal imaging camera have been checked to monitor plant thermal behaviour. Plant leaf temperature is a parameter frequently used as representative for stomatal conductance, as stomatal confinement results in attenuated transpiration, and consequently leads to increased plant temperature. Also, to identify the stress of the plant, indices of thermal and modified stress have been calculated. The results obtained show that the Kalanchoe blossfeldiana species chosen for this study, when exposed to extreme values of temperature or water requirements, presented significant changes in the infrared electromagnetic wave spectra.

REZUMAT

În această cercetare, au fost examinate datele din măsurătorile de temperatură obținute cu dispozitivul InfRay TS2+, o cameră de imagine termică în infraroșu pentru a monitoriza comportamentul termic al plantei. Temperatura frunzelor plantei este un parametru folosit în mod obișnuit ca identificator pentru conductanța stomatelor, deoarece închiderea stomatelor conduce la o transpirație redusă, care, la rândul său, conduce la o creștere a temperaturii plantei. De asemenea, pentru a identifica stresul plantei, au fost calculaţi indicii de stres termic modificat. Rezultatele obținute arată că specia Kalanchoe blossfeldiana aleasă pentru acest studiu, atunci când a fost expusă la valori extreme ale cerințelor de temperatură sau de apă, a prezentat modificări semnificative în spectrele undelor electromagnetice infraroșii.

INTRODUCTION

During the process of growth and development of crops, they are met by situations in which the structures of plants or leaves change, mainly due to the disturbances of environmental factors. Although in the specialized literature can be found described countless methods of research on the evolution of plants under conditions of environmental stress, the method of analysing the behaviour of plants in microgreenhouses with the help of the infrared electromagnetic spectrum (3-14 μm) is not sufficiently known and implemented, perhaps because of the reluctance regarding the costs that are somewhat high. Water stress is an essential abiotic factor that drastically affects plant development (*Cazacu A.C, 2015*). Lack of water, but to the same extent water in excess, presents serious challenges for the survival of crops, because it affects plant growth and reduces productivity. Plants have developed various mechanisms to respond to different environmental stressors (*Shabala S. and Shabala L., 2011*).

The thermal properties of plant leaves are influenced by a complex heterogeneous internal structure that contains a certain amount of water per unit area. This is a solid argument in the decision to conduct research with thermal remote sensing equipment, to which is added the ease of operation, precision and high resolution of infrared thermography (*Ishimwe R., Abutaleb K. and Ahmed F., 2014*). *Buitrago et al (2016)* investigated the stress response in the thermal infrared spectrum of two plant species and found that it had substantial impacts on the long-term thermal spectrum of plants, both in the mid-IR waveband (3–6 μm) as well as in the long wave band (6–16 μm). At the same time, they showed that thermal and water stress led to the change in the emissivity of the two species, but in different directions.

To understand these contrasting remarks, they determined leaf water capacity and the protective layer covering the epidermis thickness as the main factors contributing to the emissivity of the leaves. *Lee A.Y. et al. (2019)* tested a thermographic method capable of accurately measuring the temperature of the leaves of a peach, for measuring the water stress index of the culture. They showed that water stress on the crop, which occurs under water deficit conditions, produces an increase in the temperature of the leaves, which can be established by the proposed thermal imaging technique. The outcomes published by them demonstrate that the infrared images of leaf temperature distribution obtained in a time interval are meaningfully connected to the physiological parameters of culture that are unprotected to water deficiency. The degree or intensity of heat of the plant leaves was exactly extracted from the infrared images to investigate the water content. *Stoll and Jones (2007)*, in their research on mature vines, demonstrated that infrared thermography can be applied as a first step in identifying the onset of plant stress due to changes in stomatal opening. The measurements made can provide precise and sensitive indications of leaf temperature and, consequently, stomatal conductance can be determined. They also suggested that the application of infrared thermography has the potential to contribute to improving the management practices of a wine farm.

Pineda et al. al. (2020) present in their research a comprehensive review of works in which plant and crop thermography is applied to establish water content and discover plant stress. They estimate that in the near future infrared thermography, implemented in high-capacity facilities, will become a tool in plant genetic engineering for the creation of mutant varieties with resistance to pathogens or phenotypes, with much better results established in conditions well determined by abiotic stress. In this way, thermography has a major contribution to the development of the crops of the next generation, of Agriculture 5.0 (*Ragazou K., Garefalakis A., Zafeiriou E. and Passas, I., 2022*).

Ribeiro da Luz and Crowley (2010) state that emissivity is not the product of the reciprocity between solar energy and pigments, even so it represents the efficiency in the release of thermal radiation by the leaf surface. This signify that electromagnetic radiation in the infrared spectrum can include valuable knowledge concerning the leaf biochemistry and the fine structure of simple culture.

The non-invasive thermal inspection method can be used in all processes and for all agricultural products where there is heat transfer. Thermal imaging has grown rapidly and plays a predominant role in many area of agriculture, ranging from nursery observing, supply of water to land, soil pollution stress detection, plant disease diagnosis, yield evaluation, full growth assessment, and fruit and vegetable injury detection (*Ali M.M., Hashim N., Aziz S.A., Lasekan O., 2020*). However, accurate thermal estimation is influenced by the environmental conditions, who influence the thermal properties of the harvest under observation. Therefore, calibrating images according to specific environmental conditions is necessary to compare data from images obtained during different measurement periods and growing seasons (*Ishimwe R., Abutaleb K. and Ahmed F., 2014*).

The main goal of the work is to highlight an approach to the use of thermal images in precision agriculture in general, with a particularity in the assessment of the condition of plants in a micro greenhouse. A second objective is to use the most commonly used long-wave infrared thermal parameters (normalized plant or leaf temperature and crop water stress index) to measure the repercussion of environmental characteristics on the temperature of healthy houseplants.

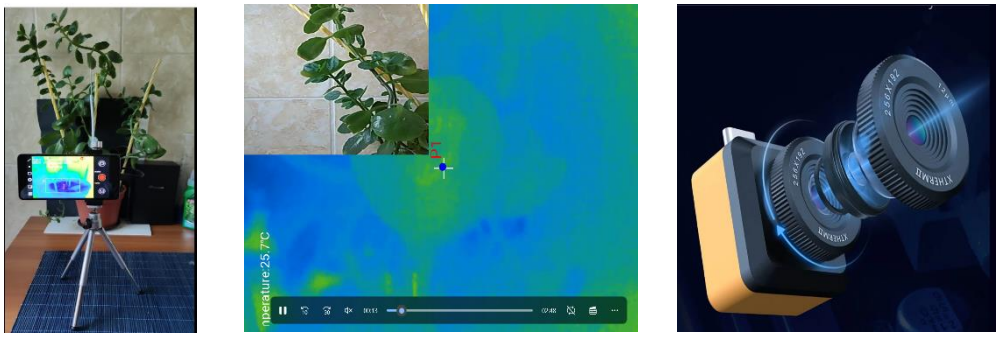
MATERIALS AND METHODS

An uncooled microbolometric technology device incorporate an optical package, a focal plane sensor array and an electronic processing circuit. The microbolometer run by captivating infrared radiation which determine a temperature-induced fluctuate in the resistance of the material. This change in resistance is settled as a variation in voltage while a direct current deviation is applied (*Grimming R., 2020*).

For this study, a species cultivated as an apartment plant (with beautiful flowers that usually appear in spring, but also with glossy leaves that give the plant a pleasant appearance) was chosen, especially due to its ability to manage with excessive conditions such as reduced temperature and drought. Therefore, it is expected that this plant has its own mechanism to survive with environmental stress regime, similar to the structural changes in the leaves, if the stress regime has an extensive duration (*Ştefîrţă A., Leahu I., Toma S., 2015*).

Kalanchoe spp. is a bush-like plant, with heights varying between 30-50 cm. The leaves are green and juicy, and the flowers are small in the form of beautifully coloured stars in red, pink, orange or yellow. Some species are perennial, others are annual or biennial.

Development of the experimental stand. Investigating the thermal radiation characteristics of Kalanchoe blossfeldiana, a small plant suitable for a small space that likes to be watered often, was complicated due to its high thermal reflection (fig.1-left). To make the measuring equipment, materials were chosen to eliminate the reflected and emitted disruptive radiation, the most suitable being those with low reflectance and low emissivity. Another aspect that requires special attention is the minimization of thermal radiation due to the surrounding environment (*Falsetti C., Kapulla R., Paranjape S., Paladino D., 2021*). A black curtain of material was placed at the rear of the pot containing the plant both for better contrast between the plant and its background on the thermal picture, but also to eliminate occasional heat emissions from the surroundings. An additional source of radiation is the thermal chamber that heats up during operation and which must also be avoided (*Wan Q., Brede B., Smigaj M., Kooistra L., 2021*).



a) b)..... .....c)

Fig. 1 – The experimental measuring stand and InfiRay thermographic camera T2S+

Image capture and analysis. The plant is grown in a simple pot, and the camera was placed on a support that integrates perfectly into any minimalist decor, and directed towards significant areas of interest. The temperature measurement took place under normal laboratory conditions. Thermal images of plant leaves were taken with the thermal camera “InfiraRay T2S+ Thermal Camera for Smartphone” (InfiraRay, P.R. China) which has a sensitivity of ±2°C or ±2% of the measurement range (whichever is greater). In figure 1c, it can be seen the "InfiraRay T2S+" camera. Its technical details are showed in Table 1.

Table 1

Technical specifications of the InfiraRay thermal camera T2S+ (from datasheets)

• Sensor: number of pixels: 49152 elements (256x192), uncooled microbolometer;	• Sensitivity: Average ≤ 60mK@25℃; F0.68;
• Spectral sensitivity: 8μm...14μm;	• Optical date: f=40mm; F #1.0;
• Optical angle: FOV 44.9°×33.4°;	• Measurement range: -20ºC +450ºC (without filter);
• Output: composite video signal (CVBS) (50 fields);	• Control: protocols Cam (USB type C);
• Operating temperature: -20ºC up to 50ºC;	• The frame rate of the image: 25 Hz.
• Dimensions 26×26×24.2mm	• Supported operating system: Android, Harmony OS, iOS

The images and recordings were made with the thermal camera's own software, the Xtherm Android application provided by the manufacturer, which can be downloaded for free from the Google Play store. Using the software, images can be recorded and saved in Live View Stream, and can be simultaneously added up to 3x different temperature measurement fixed points, a temperature spectrum line and a Region of Interest box, also known as ROI boxes, which best characterize the surface temperature (Fig.1b).

Based on the temperature distribution of the foliage, the temperature difference between the leaf and the air and the modified CWSI crop stress index, the thermographic effects of the ambient conditions on the plants can be analysed, such as the thermal state of the plants before or after irrigation. The leaf-air temperature difference ΔT is given by the relation:

$$\Delta T = Tl - Ta \ \ [°C] \tag{1}$$

where: Tl - the measured temperature of the leaf; Ta – temperature of the surrounding air.

The modified plant stress index, CWSI, was calculated from the relationship proposed by *Jones et al. (2002)* based on captured thermographic images (*Nagy A., 2015*):

$$CWSI = \frac{Tc-Tw}{Td-Tw} \quad (2)$$

where: Td - the maximum reference temperature of the foliage (minimum transpiration); Tw - the minimum reference temperature of the foliage (maximum transpiration); Tc - actual temperature values for each pixel.

Measurement conditions. Light is an important factor for the growth and flowering of Kalanchoe. This plant must not be deprived of light, the lack of light slows down growth and prevents the emergence of new shoots. But the interactive effects of light and soil radiation reflection on leaf temperature can have a negative effect on plant health, causing excessive absolute temperatures. Corresponding images are taken looking perpendicular to the plant structure showing the unshaded and naturally lit parts.

The ambient environment (air temperature and relative humidity, atmospheric pressure, VOC concentration) was continuously monitored with an IoT system consisting of a Bosch BMP680 digital environmental sensor and a Raspberry Pi B3+ development board, the data being saved, visualized and analysed on the Thingspeak IoT cloud platform (https://thingspeak.com/channels/1539770/private_show) made available by the creators of the MATLAB program, Mathworks Inc. - US.

Thermal long-wave infrared (TIR) cameras are calibrated sensors capable of recording emitted radiation in the wavelength range between 8–14 µm and providing images representing the temperature values per pixel (*Leblanc G., Kalacska M., Arroyo- Mora J.P., Lucanus O. and Todd A., 2021*). Thermal imaging allows detailed information about the surface temperature distribution (*Vollmer M. and Möllmann K.P., 2018*). A significant physiological trait for plant growth and development is stomatal activity, having a decisive role in carbon and water balance by permanently checking photosynthesis and transpiration (*Brendel O., 2021*). Consequently, stomatal water conductance is associated with productivity and tolerance to environmental stress and is closely correlated with leaf temperature (*Pineda M., Barón M. and Pérez-Bueno M.L., 2020*).

RESULTS

The thermal sensor generates an image depending on the different amounts of thermal energy it detects. By using a wide palette of different colours to display temperature differences (fig.2), objects and very slight changes in temperature can be detected despite low contrast conditions. In this way, the thermal patterns in an image can be represented using a very large and specific data set. Therefore, this approach allows a complex analysis of a large area of a plant in an image, performing the calculation of the mean temperature or the incidence distribution of temperatures on chosen areas.

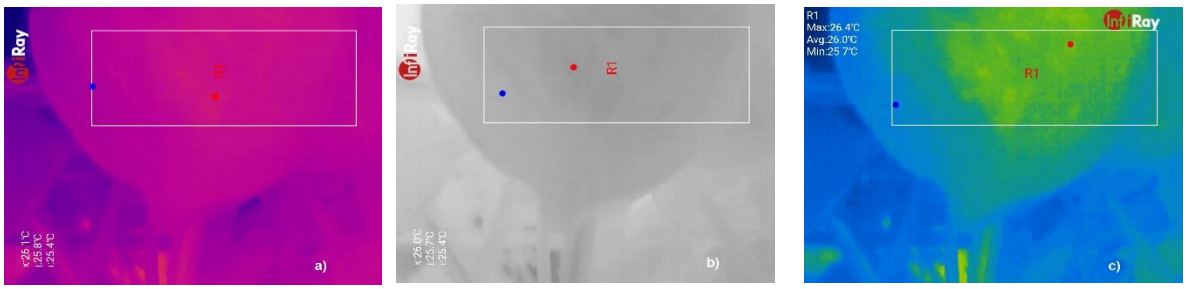


Fig. 2 - The corresponding thermal images (a-c) taken in the afternoon of June 17, 2023

Such image analysis was done with a general-purpose Iron palette (fig. 2a) that quickly identifies thermal anomalies and object heat. In this palette, hot objects are displayed in warm, light colours, while cooler objects are in dark, cool colours. Fig. 2b illustrates the different plant temperature distribution in the Black Hot colour palette. This palette is the inverted version of the White Hot palette, displaying warmer objects in black and cooler objects in white in a clear and realistic image. The Rainbow colour palette (fig. 2c) works well to detect minor temperature differences in a scene despite low contrast conditions. Warm colours illustrate the hottest part of the image and cool colours depict the frosty areas, but add more colours to the mix. It is a very good model for identifying objects in environments with slightest heat dissimilarity.

For the analysis, a region is outlined within the thermal image (rectangles - regions of interest ROI), where the maximum and minimum temperatures are tracked (fig.2).

The ROI box data can also be used as reference data for the temperature histogram. The ROI feature is a perfect tool for analysing different regions of a single thermal image. Each ROI is scalable and movable and can be sized and moved within the live view stream area. In the region of interest selected in figure 2, where the leaf has a low emissivity, it can be seen now that it has a maximum temperature of 26.4 °C, while the average value is just below 26.1°C, almost 0.4 degrees warmer than the environment.

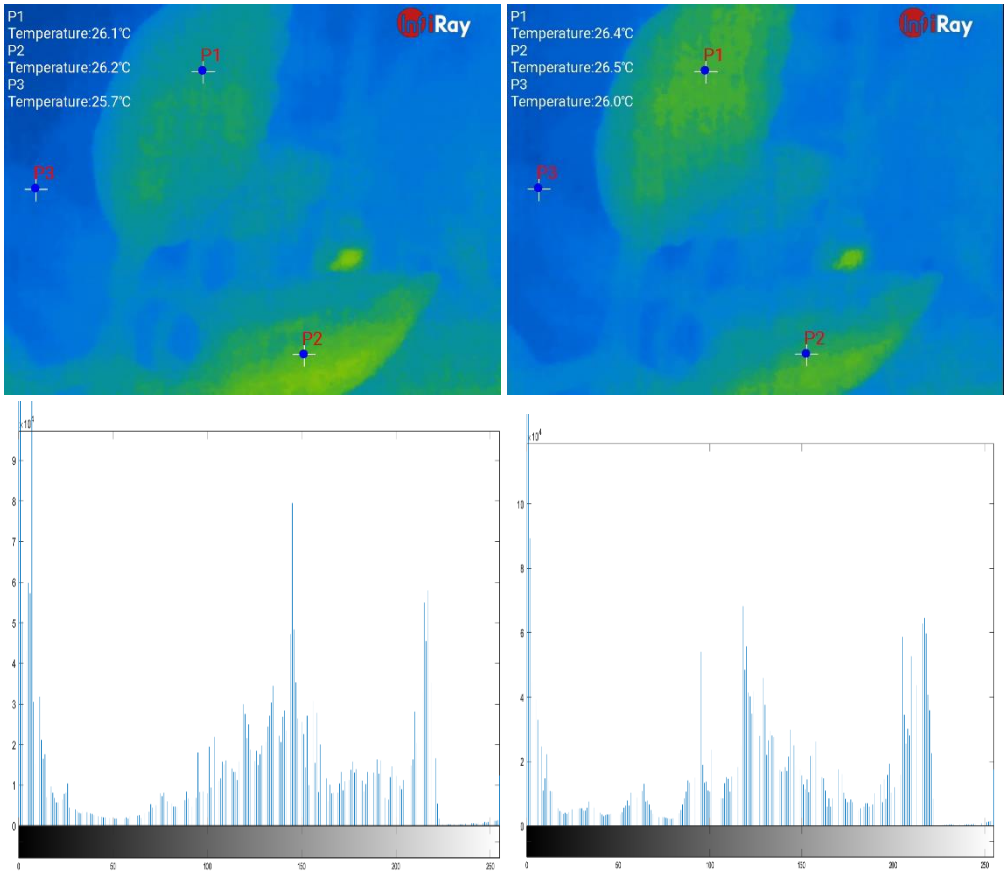


Fig. 3 - The thermal images corresponding to the effects of irrigation on the absolute temperature of the plant

The plant is watered with water at room temperature, differently depending on the periods of growth and rest. From spring to autumn, when the Kalanchoe grows and blooms, it needs a larger amount of water. Watering is done when the soil on the surface is a little dry. The effect of a soil watering operation on the absolute temperature of the plant leaf is shown in figure 3. During the measurements in the afternoon of June 24, a day when the temperature in the external environment reached extreme values of 39°C and the alerts were issued on meteorological conditions of severe weather, no significant change was observed in the absolute temperature of the leaves before and after watering the plant. In Figure 3-right, where the leaf is more heated, the core with high emissivity is at a higher temperature (26.5°C), only 0.5°C higher than the ambient environment, an increase that can be attributed to the acceleration of the process of transpiration of the leaf. The result is in agreement with the one obtained by *Buitrago et. al. (2016)* for beech leaves, who observed that an increase in the moisture content of the leaf increases the emissivity of the leaves.

During the rest period, watering is done with a smaller amount of water, because the Kalanchoe is a plant with juicy leaves and it can withstand the lack of water (for a short period of time). This period of water stress can lead the plant to have: smaller sizes and an earlier flowering (*Petcu E., Terbea M., Lazar C., 2007*).

At the bottom of figure 3 - the two graphs of the histogram of the images made in the Matlab R2022b program are displayed. The input image being an indexed image, the histogram shows the distribution of pixel values depending on the number of colours of the colour map. For the grayscale image, 256 intervals were used by default.

The n intervals of the histogram are each half-open intervals of width $\mathrm{A}/(n-1)$. In particular, the p-th interval is the half-open interval.

$$\frac{A(p-1.5)}{n-1} - B \leq x < \frac{A(p-0.5)}{n-1} - B \tag{3}$$

where: x is the intensity value. The scale factor A and offset B depend on the image class type.

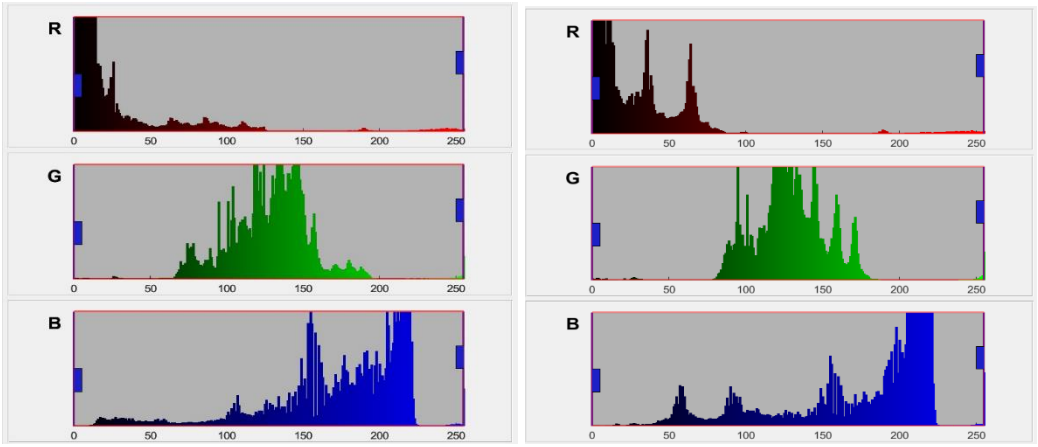


Fig. 4 - Colour histogram of RGB images corresponding to the effects of irrigation on plant temperature

The difference in measured temperature can be visualized much better by calculating the colour histograms of the RGB images (as can be seen in fig. 4). The number of intervals (for each colour component) is entered by the user, being the same for R, G and B colours. The output histogram can be un-normalized or normalized. The temperature increase of the leaves, of approx. 0.4°C, is highlighted by the increase in the frequency of occurrence of the intensity of the colour red - R, simultaneously with the decrease of the frequency of occurrence of the colour blue - B, while the frequency of occurrence of the intensity of the colour green - G remains constant.

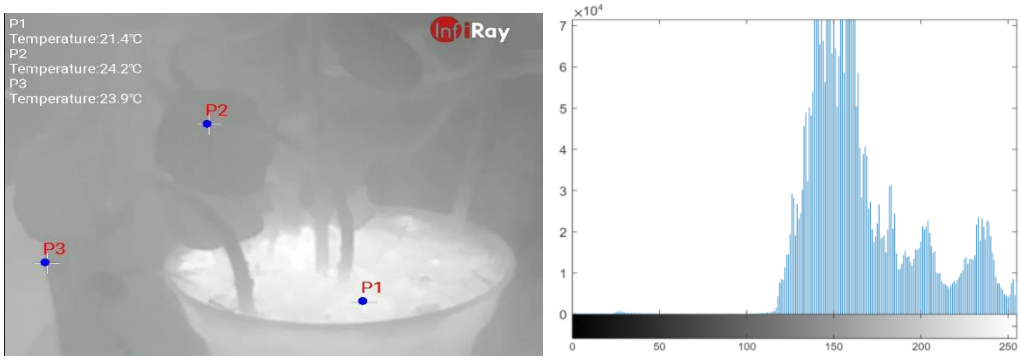


Fig. 5 - Thermographic image of the plant after watering and its histogram from 30.06.2023

In the evening of June 26, the plant was significantly cooler compared to the unstressed vine. No significant temperature difference was found between the leaves and the surrounding air (figure 5). The measurements indicate that the temperature difference ΔT was on average 0.3 °C, lower than that of the plant in the period before watering. Alternatively, it is possible that the irrigation operation affects the structure of the plant and, consequently, increases the reflection of radiation from the ground and thus increases the temperature of the leaves. In the presented thermal image, it can be seen that the soil temperature of 21.4°C is approx.2.8°C lower than the leaf temperature and 2.5°C lower than the air temperature.

The difference between the average leaf temperature and the air temperature was +1.67°C for the period without watering, but it was +0.53 °C for the period following watering. Thus, the effect of irrigation could also be detected on the fruit in addition to the foliage by using thermography. Based on the measurements, the existence of a high risk of water stress was not found. The average values of the modified stress index of the plant were 0.389±0.095 which means that the values were above the threshold value of 0.25. The optimal temperature for the growth and flowering of Kalanchoe varies between 15-25°C. In summer, the plant must be protected from direct sunlight and it is recommended to spray water on the leaves. There is clear evidence in the specialized literature that the plant is very sensitive to low temperatures, it can die if it is kept at temperatures varying between 0-10°C.

Thermal imaging as a non-invasive remote sensing method appears to be a suitable tool for studies where the temperature values of plant foliage, flowers or fruits can be reproduced with greater efficiency and precision than can be achieved with other methods. The choice of the measurement method used depends largely on the architecture of the plants and the availability of exposed flowers or fruits.

One of the main advantages of infrared thermography is that it covers a variety of different positions on the plant structure, which can hardly be achieved using the thermocouple method. In addition, by combining various optical devices and sensors with the performance of a deep learning neural network used for object detection, without applying image enhancement algorithms or excessive processing of measurement data, much-needed information about the condition of plants can be obtained in various weather conditions, such as clear sky, fog and rain, at different intervals.

CONCLUSIONS

The temperature differences observed during the study of the behaviour of the plant subjected to different operations/situations are encouraging for the application of the thermal image as a useful tool to make a correct assessment in the event of water stress states or to take advantage of the application of this methodology in the management of plant growth, or even more precisely, in the realization of irrigation control applications, which ensure an optimal water regime.

The productivity and quality of plant development are strongly influenced by the limiting abiotic conditions (thermal and water stress) manifested during the experimental period. Reducing the drastic effects of water stress can also be achieved by accumulating osmoprotectors, maintaining turgor, leading to a decrease in the rate of transpiration and the closing of stomata.

The processed thermal image can be displayed in a certain colour spectrum by using colour palettes. The cost vindication for implementing the thermography method increases as the prices of electronic elements decrease. Nowadays, infrared thermal devices provide up to 16 times the quality of image of devices used in decade past, for nearly the same cost.

REFERENCES

[1] Ali, M.M., Hashim, N., Aziz, S.A., Lasekan, O. (2020). Emerging non-destructive thermal imaging technique coupled with chemometrics on quality and safety inspection in food and agriculture *Trends in Food Science & Technology*, Vol. 105, November, pp. 176-185. https://doi.org/10.1016/j.tifs.2020.09.003

[2] Brendel, O., (2021). The relationship between plant growth and water consumption: a history from the classical four elements to modern stable isotopes. *Annals of Forest Science* (2021) 78: 47. https://doi.org/10.1007/s13595-021-01063-2

[3] Buitrago, M.F., Groen, T.A., Hecker C.A., Skidmore A. K. (2016). Changes in thermal infrared spectra of plants caused by temperature and water stress. *ISPRS Journal of Photogrammetry and Remote Sensing*, 111, pp. 22–31.

[4] Cazacu, A.C. (2015). *Research on the resistance to water stress of some wheat genotypes in pedoclimatic conditions at SCDA Turda (Cercetări privind rezistenţa la stresul hidric a unor genotipuri de grâu în condiţiile pedoclimatice de la SCDA Turda)* [Doctoral thesis]. University of Agricultural Sciences and Veterinary Medicine of Cluj-Napoca.

[5] Falsetti, C., Kapulla, R., Paranjape, S., Paladino, D., (2021). Thermal radiation, its effect on thermocouple measurements in the PANDA facility and how to compensate it. *Nuclear Engineering and Design*, Volume 375, 15 April, https://doi.org/10.1016/j.nucengdes.2021.111077

[6] Grimming, R., (2020). *Uncooled Microbolometer Imaging Systems for Machine Vision*. Electronic Theses and Dissertations. University of Central Florida. https://stars.library.ucf.edu/etd2020/1379

[7] Ishimwe, R., Abutaleb, K. and Ahmed, F. (2014). Applications of Thermal Imaging in Agriculture—A Review. *Advances in Remote Sensing*, 3, 128-140. http://dx.doi.org/10.4236/ars.2014.33011.

[8] Leblanc, G., Kalacska, M., Arroyo-Mora J. P., Lucanus, O., Todd, A., (2021). A Practical Validation of Uncooled Thermal Imagers for Small RPAS. *Drones* 2021, 5(4), 132; https://doi.org/10.3390/drones5040132

[9] Lee, A.Y., Kim S.Y., Hong S.J., Han Y.H., Choi Y., Kim M. Yun S.K., Kim G. (2019). Phenotypic Analysis of Fruit Crops Water Stress Using Infrared Thermal Imaging. *Journal of Biosystems Engineering*, 44: 87–94, https://doi.org/10.1007/s42853-019-00020-2

[10] Melucă, C. Cernat, S., Nistor T., (2011). Behavior of winter wheat varieties under water and heat stress conditions of burnas plain. AN. I.N.C.D.A. Fundulea, VOL. LXXIX, no. 2, *Genetica şi Ameliorarea Plantelor*, Electronic (Online) ISSN 2067–7758, www.incda-fundulea.ro

[11] Nagy, A., (2015). Thermographic evaluation of water stress in an apple orchard. *Journal of Multidisciplinary Engineering Science and Technology* (JMEST),Vol. 2 Issue 8, 2210 - 2215.

[12] Petcu, E., Terbea, M., Lazar, C., (2007). Research in the field of field plant physiology at Fundulea (Cercetari in domeniul fiziologiei plantelor de camp la Fundulea.) AN. I.N.C.D.A. Fundulea, Vol. LXXV, 2007, *Tribute volume - Physiology of Plants*

[13] Pineda, M., Barón, M., Pérez-Bueno, M.L., (2020). Thermal Imaging for Plant Stress Detection and Phenotyping. *Remote Sens*. 2021, 13(1), 68; https://doi.org/10.3390/rs13010068.

[14] Ragazou, K., Garefalakis, A., Zafeiriou, E. and Passas, I., (2022). Agriculture 5.0: A New Strategic Management Mode for a Cut Cost and an Energy Efficient Agriculture Sector. *Energies* 2022, 15(9), 3113; https://doi.org/10.3390/en15093113.

[15] Ribeiro da Luz, B., Crowley, J.K. (2010). Identification of plant species by using high spatial and spectral resolution thermal infrared (8.0–13 lm) imagery. *Remote Sens. Environ*. 114, 404–413.

[16] Shabala, S., Shabala, L., (2011). Ion transport and osmotic adjustment in plants and bacteria. *Biomol Concepts*. Oct 1:2(5):407-19. https://doi: 10.1515/BMC.2011.032.

[17] Ştefîrţă, A., Leahu, I., Toma, S., (2015). The specific and non-specific response of plants to the action of water and thermal stress: interactive relationships between water status and antioxidant protection (Răspunsul specific şi nespecific al plantelor la acţiunea stresului hidric şi termic: relaţiile interactive dintre status-ul apei şi protecţia antioxidant). *AŞM Bulletin. Life Sciences*, No. 1(325), 29-46.

[18] Stoll M., Jones H.G. (2007). Thermal imaging as a viable tool for monitoring plant stress. *J. Int. Sci. Vigne Vin*, 2007, 41, no.2, 77-84.

[19] Van Linden, V., Vereycken, R., Bravo, C., Ramon, H., and De Baerdemaeker, J. (2003). Detection Technique for Tomato Bruise Damage by Thermal Imaging. Proc. Postharvest Unltd Eds. B.E. Verlinden et al*., Acta Hort.* 599*, ISHS 2003*

[20] Vollmer, M., Möllmann, K.P., (2018). *Infrared Thermal Imaging, Second Edition*. Wiley-VCHVerlag GmbH&Co. KgaA

[21] Wan, Q., Brede, B., Smigaj, M., Kooistra, L., (2021). Factors influencing temperature measurements from miniaturized thermal infrared (TIR) cameras: A Laboratory-Based Approach. *Sensors* 2021, 21, 8466. https://doi.org/10.3390/s21248466

[22] *** Datasheet-t2s-t2l-thermal-camera-for-smartphone (2023). https://www.infiray.com/products/t2s-t2l-thermal-camera-for-smartphone.html

[23] *** MATLAB - Mathworks Help Center. (2023). *Image Processing and Computer Vision*. https://uk.mathworks.com/help/images/ref/imhist.html?s_tid=doc_ta

STUDY ON THE INFLUENCE OF MOISTURE CONTENT AND COMPRESSION RESISTANCE CHARACTERISTICS OF CORN GRAIN ON THRESHED BREAKAGE RATE

/

玉米籽粒含水率及抗压特性对脱粒破碎率的影响研究

Yinping ZHANG[1)], Zehua HAO[1)], Lihang JIAO[1)], Qinghua LUAN[*2)], Hua ZHOU[*1)], Meizhou CHEN[1)]

[1)]School of Agricultural and Food Science, Shandong University of Technology, Zibo (255000), China;

[2)]Agricultural machinery business service center of Zichuan, Zibo (255100), China.

DOI: https://doi.org/10.35633/inmateh-71-49

Keywords: *corn, moisture content, compression resistance characteristics, breakage rate, mechanical grain harvesting*

ABSTRACT

High breakage rate is the bottleneck that restricts corn grain mechanical harvesting in double-cropping area in China. The moisture content and compression resistance characteristics of corn grain have important effects on the breakage rate at threshing. In this paper, 5 corn varieties planted in double cropping area were selected and the effects of grain moisture content and compression resistance characteristics on threshed breakage rate were studied. Results showed that both the grains moisture content and the compression resistance characteristics had effects on the threshed breakage rate. The lower the moisture content, the greater the force required for breakage, and the more difficult it was to break. Meanwhile the breakage rate was also related to the displacement during pressing. The smaller the displacement, the lower the breakage rate, but if the displacement was too small, the corn was a silty variety and the breakage rate was still high. When the moisture content was 33%±1%, the threshing verification test showed that the average breakage rate of DH605, LY296 and KN21 was 5.39%, 5.02% and 7.13%, respectively, which was not suitable for grain mechanical harvesting under high moisture content (moisture content higher than 30%). However, the average breakage rate of LK868 and LD6018 was 4.76% and 4.25% respectively, which was suitable for grain mechanical harvesting under high moisture content. This research could provide a reference for corn varieties selection suitable for mechanical kernel harvesting in double cropping area.

摘要

脱粒破碎高是制约中国两熟区玉米机械粒收的瓶颈，玉米籽粒的含水率及抗压特性对脱粒破碎率有重要影响。本研究选取两熟区种植较多的5 个夏玉米品种，研究籽粒含水率及抗压特性对脱粒破碎率的影响。结果表明，籽粒含水率及抗压特性均对脱粒破碎率产生影响，籽粒含水率越低，破碎时所需的力越大，越不易破碎;同时破碎率也与破碎时的位移有关，位移越稳定，破碎率越低，但位移太小时，玉米可能为粉质品种，破碎率仍较高。在含水率为33%±1%时，进行脱粒验证试验，得到DH605、LY296 和KN21 的平均破碎率分别为5.39%、5.02%和7.13%，不适宜高含水率（含水率大于30%）机械粒收；LK868 与LD6018 的平均破碎率分别为4.76%和4.25%，适宜高含水率机械粒收。本研究为两熟区筛选适宜机械粒收的玉米品种提供了参考。

INTRODUCTION

Corn is one of the main food crops in the world. With the large-scale circulation of land and the reduction of rural labor force, corn mechanical harvesting is an effective way to reduce labor intensity and improve harvesting efficiency (*Liu et al, 2013; Wang et al., 2021*). At present, the high breakage rate in mechanical harvesting in China's double-cropping area has become a bottleneck that restricts grain mechanical harvesting (*Wang et al, 2017*). It is of great significance to research the influence of moisture content and compression resistance characteristics on the breakage rate at threshing, select varieties suitable for grain mechanical harvesting, and reduce the breakage rate at threshing during harvest, which will promote the mechanization process of corn production and ensure food security.

Scholars had done more research on corn grains moisture content at harvest. *Zhang Wanxu et al.* (*2018a; 2018b*) found that moisture content had a significant effect on grain breakage rate, and the difference was significant among different varieties. *Waelti (1967)* studied the response of grain crushing rate of different varieties to the change of drum speed in the range of grain moisture content between 20% and 31%, and found that the water content with the lowest crushing rate was different in different varieties during mechanical harvest.

Brass (1970) believed that when the grain water content was higher, the grain crushing rate increased rapidly with the increase of the roller speed. *Plett (1994)* found that the breakage rate was the lowest when the moisture content was 16.70% ~ 22.10%.

According to *Hall et al., (1970)*, the yield breakage rate was the lowest when the grain water content was 20%-23%. *Chowdhury et al. (1978),* believed that the mechanical damage rate was the lowest when the moisture content was 23%. *Li Lulu et al., (2017)* pointed out that when the moisture content was lower than 26.92%, the grain breakage rate was less than 8%. *Kang Yunyou et al., (2019),* found that the breakage rate was less than 5% when the moisture content did not exceed 25%. Using the fitting equation, *Chai Zongwen et al. (2017)* predicted that the breakage rate was less than 5% when the grain moisture content was about 19%. *Dutta, (1986),* believed that the rate of harvesting machinery damage increased sharply when the grain moisture content exceeded 20%. It is generally believed that high moisture content was the main factor to grain breakage, but there was few researches on the effect of grain compression resistance characteristics on breakage rate.

In this paper, the moisture content and compression resistance characteristics of different corn varieties were studied, and the effects of moisture content and compression resistance characteristics on the breakage rate at threshing were analyzed. The results could provide reference for the selection of varieties suitable for corn grain mechanical harvesting.

MATERIALS AND METHODS

Test materials

Five corn varieties, Denghai 605(DH605), Liyuan 296(LY296), Laike 868(LK868), Ludan 6018(LD6018) and Kono 21(KN21), were picked from Yueyang Agricultural Cooperative of Taian City, Shandong Province (117°E, 36°N), and different varieties were sown in one day.

Test methods

(1) Moisture content measurement

The sampling started from the disappearance of milk line of kernel on September 29. Samples were taken at 5:00 PM in 10 consecutive days, with 15 ears picked each time and kept in sealed storage. During the test, proper number of grains were hand-threshed and weighed in an aluminum box and recorded as wet weight WS. After weighing, the grains were dried at 105℃±3℃ for 480 min. After taking out the sample, the grains were weighed and recorded, and then continued to be dried for 60 min. If the difference in drying quality between the two times before and after is less than 0.02 g, recorded as dry weight Wg. The grains moisture content was calculated as Hy=(WS-WG)/ WS×100%.

(2) Determination of compression resistance characteristics

To measure the compression resistance characteristics, 10 corn grains were randomly selected from the hand-threshed grains. The breakage was mainly because by the threshing elements which stroke on the top of grains (*Zhang et al, 2012; Zhang et al, 2015*). As shown in Figure 1, a universal testing machine was used to press the top of the grain (*Yang et al, 2008*) and the grains was placed in the center of the compression fixture plate.

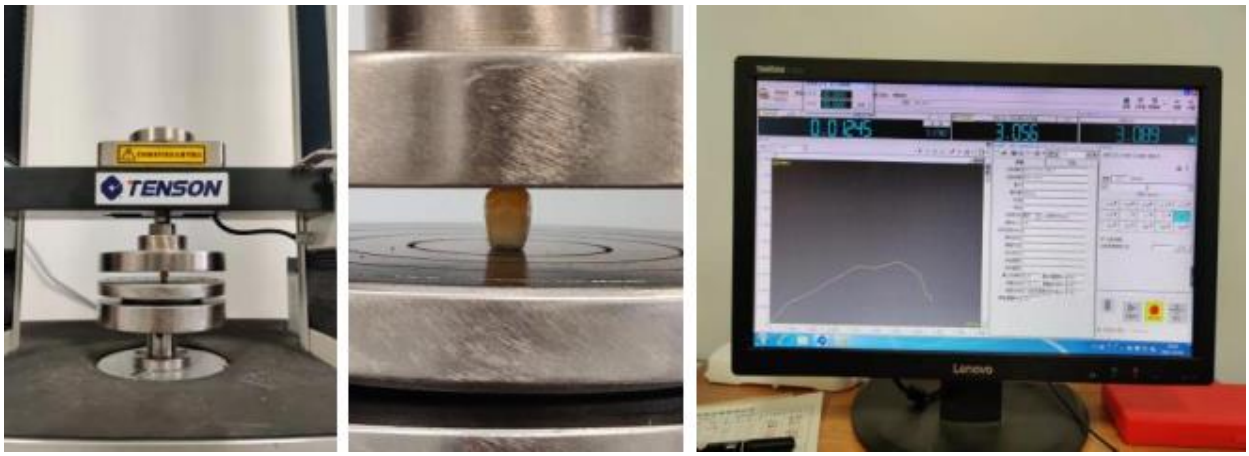


Fig. 1 - Test of grain compression resistance characteristics

The initial rise speed of the beam was set at 12 mm/min, and the clearing contact force was set at 5 N, that is, the upper beam touched the corn kernel. After the contact force with the grain exceeded 5 N, the universal testing machine entered the compression test state. After that, the rising speed of the test beam was set at 4 mm/min. The computer recorded the "force-displacement" curve of the compression test and stored the data. When the compression force reached 75% of the maximum breaking compression force, the beam stopped moving and the test ended.

Data Processing

Microsoft Excel 2016 was use for data analysis and processing.

RESULTS AND ANALYSIS

Figure 2 shows the change curve of grain moisture content of different corn varieties over time. Generally, the moisture content of different corn varieties at the beginning of physiological maturity was 41%-43%, the difference was not significant, and then all showed a downward trend. Comparing the changes of moisture content of different varieties of corn grains after entering the physiological maturity stage, it could be seen that the moisture content of LY296 and LD6018 decreased rapidly in the early stage and dropped below 36% on the third day after physiological maturity, while the moisture content of DH605, LY296 and KN21 decreased slowly in the early stage, and was still 36% to 40% on the third day. The moisture content exceeds 30% was high moisture content, LY296 was reduced to below 30% on the 7th day, LD6018 and LK868 was reduced to below 30% on the 8th day, and DH605 and KN21 was still above 30% on the 10th day. Therefore, it was preliminarily determined that DH605 and KN21 was in slow dehydration speed and were not suitable for grain mechanical harvesting.

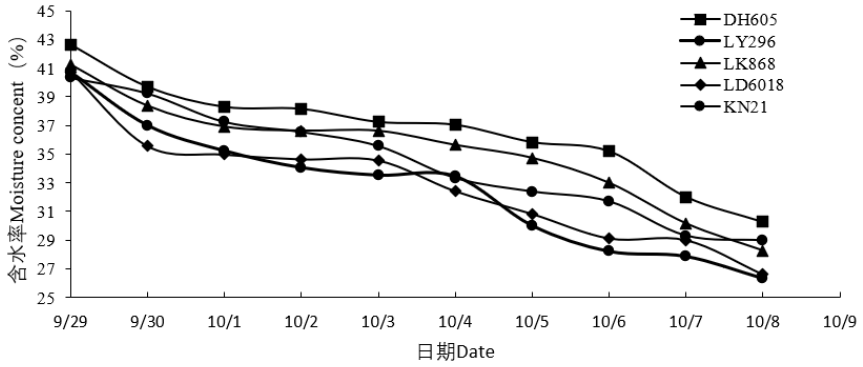
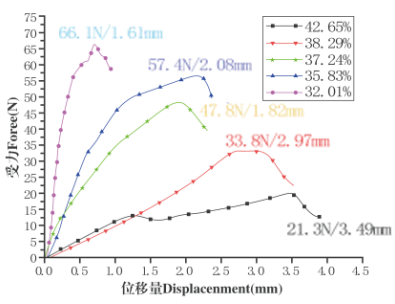


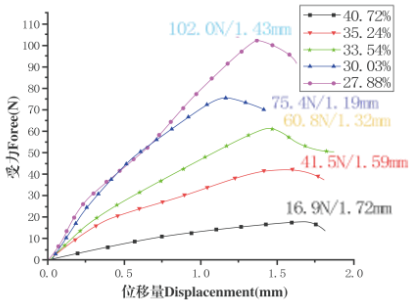
Fig. 2 - Curve of moisture content with time

Displacement and deformation would occur after compression (*Volkovas et al, 2006; Babiic et al, 2013; Mohamed et al., 2019; Zhang et al, 2012*), the maximum force and displacement deformation values when grains breakage reflected the compression resistance characteristics of corn grains.

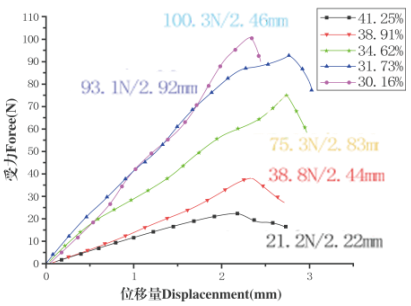
Figure 3 showed the force and deformation of corn grains in the process of the grains being compressed. Abrupt change points appear in the curve and the compression drops abruptly, indicating that the grain was broken at this time, the horizontal coordinate of the mutation point represented the maximum displacement at grains breakage and the ordinate indicated the maximum compression on the grain when it was broken.



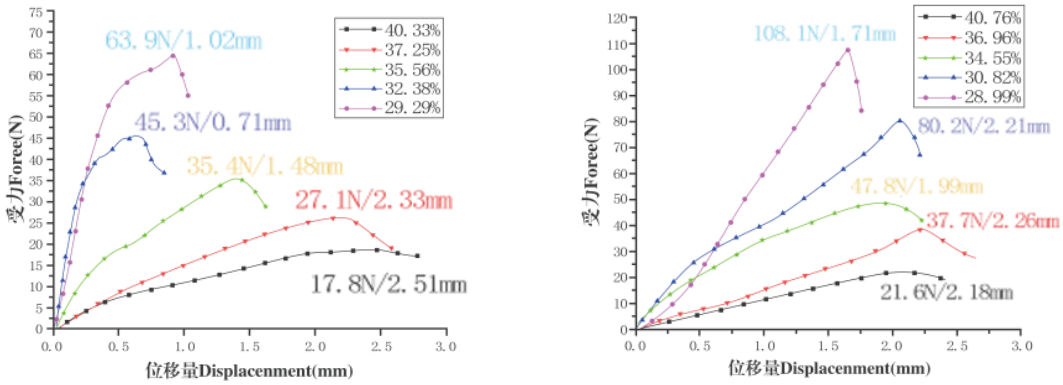
DH605



LY296



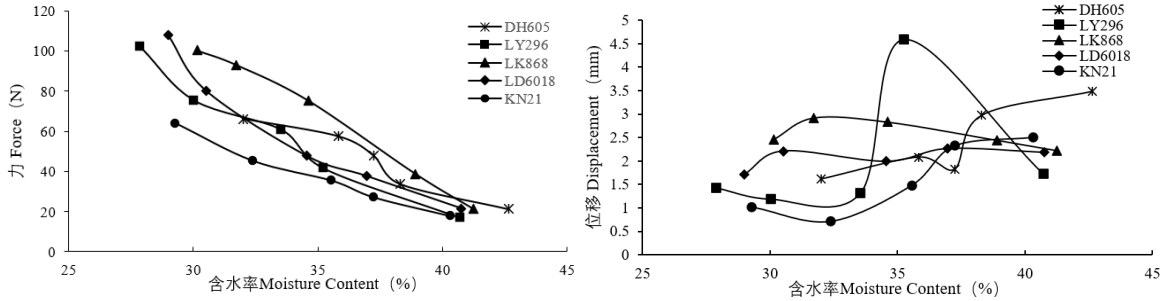
LK868



LD6018 KN21

Fig. 3 – Change curve of compression resistance characteristics of different varieties under different moisture content

Figure 4 shows the relationship between force and displacement of grain breakage and moisture content. According to Figure 4 (a), the force of the five varieties were increased with the decrease of moisture content, indicating that the lower the moisture content, the greater the force required for grain breakage and the more difficult it was to break. Comparing the breakage forces of different varieties with the same moisture content, it could be seen that when the moisture content exceeded 35%, the maximum force of the five varieties was small, indicating that the grain mechanical harvesting was not suitable. When the moisture content was 30% ~ 35%, the force of LK868 was much greater than of the other four varieties, which indicates that LK868 was suitable for grain mechanical harvesting when the moisture content was 30 ~ 35%. When the moisture content was 30% ~ 32%, the force of LY296 and LD6018 was greater than of DH605 and KN21, and there was a large upward trend, indicating that LY296 and LD6018 can perform grain mechanical harvesting when the moisture content was 30% ~ 32%, while DH605 and KN21 were not suitable for grain mechanical harvesting when the moisture content exceeded 30%. It was generally believed that the corn varieties that could have the grains harvested when the moisture content exceeded 30% were varieties suitable for grain mechanical harvesting (*Wang, 2016; Zhao et al, 2019*), but it can be seen that DH605 and KN21 were not suitable for grain mechanical harvesting.



(a) The relationship between force and moisture content (b) The relationship between displacement and moisture content

Fig. 4 - Relationship between grain compression resistance characteristics and moisture content

FIG. 3 and FIG. 4 (b) showed that with the decrease of moisture content, the displacements of the broken grains of the five varieties was in decreasing trend overall, indicating that with the decrease of moisture content, corn grains became compact. Under different moisture content conditions, the displacements during the breakage of LK868 (was between 2 ~ 3 mm) and LD6018 (was between 1 ~ 2 mm) were in small change range, and moisture content had no significant effect on the displacement of LK868 and LD6018 which indicated that the displacement of LK868 and LD6018 grains during breakage were not affected by moisture content. While DH605 (was between 1.5 ~ 3.5 mm), LY296 (was between 1 ~ 3.5 mm), and KN21 (was between 0.5 ~ 2.5 mm) were in a larger change range, and moisture content had significant effect on them. That indicated LK868 and LD6018 were stable and suitable for grain mechanical harvesting. As mentioned in the previous analysis, LY296 and LD6018 could be grain mechanical harvesting when the moisture content was 30% ~ 32%, but the maximum displacement of LY296 can withstand in this moisture content condition was small, only about 1mm, indicating that LY296 was a silty variety, easy to break, so that even if the moisture content met the requirements, it still couldn't for grain mechanical harvesting.

Based on the analysis of the force and displacement of different corn varieties, it could be preliminarily determined that DH605, LY296 and KN21 were not suitable for grain mechanical harvesting, LK868 and LD6018 were suitable, and LK868 could be harvested under the condition of the moisture content of 30% ~ 35%, LD6018 could be harvested under the condition of the moisture content of 30% ~ 32%.

Bench experiments

The results of laboratory experiment showed that the moisture content alone couldn't determine whether a corn variety was suitable for grain mechanical harvesting, and the compression resistance characteristics of the variety should be considered at the same time. In order to verify the influence of grains compression resistance characteristics on the breakage rate, the threshing bench experiment was carried on with a moisture content of 33%±1%. The threshing equipment shown in FIG 5 was self-made as in the paper of *Wang et al. (2020)*. Before the test started, the clearance of the concave plate was adjusted to 40 mm and the rotating speed of the drum to 400 r/min, and after the roller run stable, the corn ear was put into the ear elevator according to the variety and it was sent into the feeding inlet. When all the grains fell from the concave screen, the threshing device was turned off and the grains were collected. The test was repeated three times, the average breakage rate of corn grains was obtained, and the results were statistically analyzed.

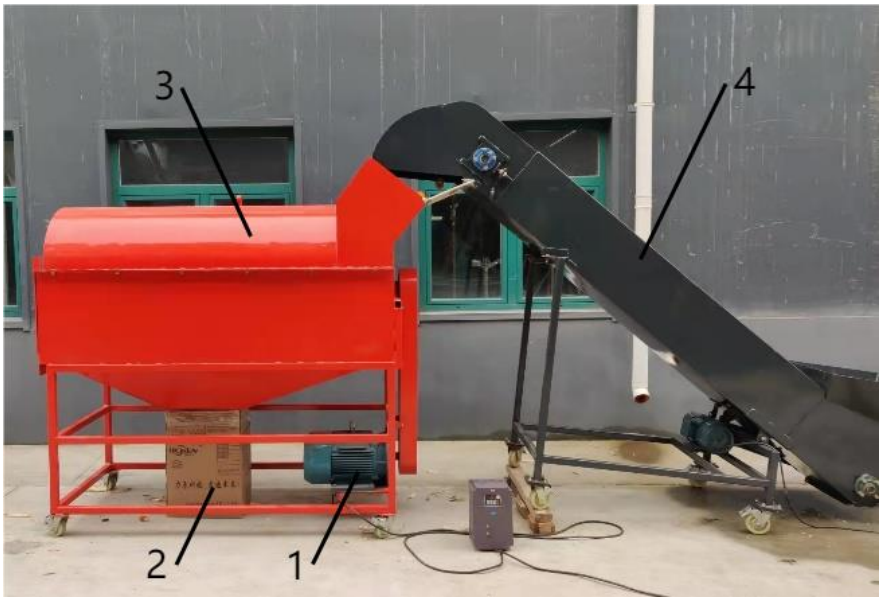


Fig. 5 - Threshing test site

1. Electrical machinery; 2. Grain collection box; 3. Corn threshing device; 4.Ear elevator

After the end of each group of experiments, all the collected grains were weighed, and the corn grains with visible cracks or broken skins were manually picked out and weighed too. Then the breakage rate was calculated. The grains after threshing were shown in Figure 6, and the results were shown in Table 1.

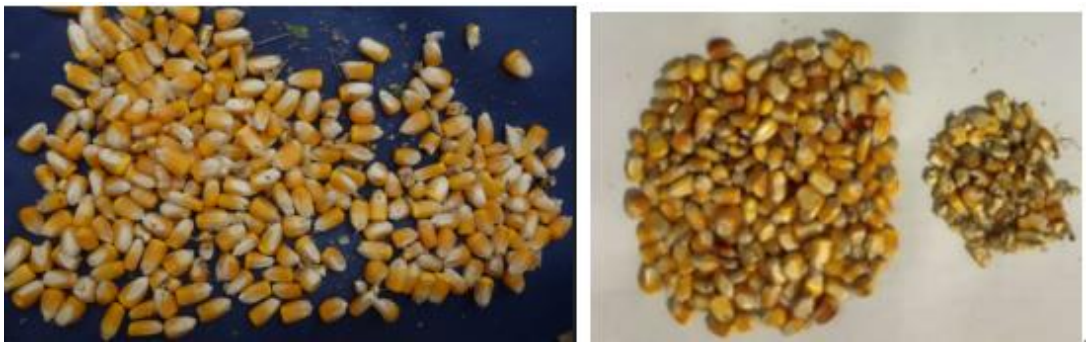


Fig. 6 - Threshing test results

Table 1

Grain breaking rate of different varieties

Corn varieties	DH605	LY296	LK868	LD6018	KN21
Breakage rates %	5.91	5.16	5.17	4.17	6.41
	5.02	4.98	4.31	3.96	7.74
	5.24	4.92	4.80	4.62	7.24
Average breakage rates%	5.39	5.02	4.76	4.25	7.13

As can be seen from Table 1, when the moisture content was 33%±1%, the average breakage rates of DH605, LY296 and KN21 were 5.39%, 5.02% and 7.13%, and 4.76% and 4.25% of LK868 and LD6018, respectively. According to "Agricultural Machinery Test Conditions", the breakage rate of grain mechanical harvesting was required to be less than 5%, indicating that DH605, LY296 and KN21 were not suitable for grain mechanical harvesting when the moisture content was 33%±1%, while LK868 and LD6018 were suitable. This is consistent with the previous analysis results.

CONCLUSIONS

(1) By analyzing the influence of grain compression resistance characteristics on the threshing breakage rate of five corn varieties with different moisture content, it was found that the force that the grain could withstand during compressing was negatively correlated with the moisture content. The lower the moisture content, the greater the force that the grain could withstand and the more difficult it was to break. The maximum displacement was not related to the moisture content, but mainly to the variety.

(2) The analysis of water content and compression resistance characteristics and threshing test showed that DH605, LY296 and KN21 had high average grain breakage rate and were not suitable for grain mechanical harvesting, while LK868 and LD6018 were suitable with low average grain breakage rate. This research provides a reference for the corn varieties selection of grain mechanical harvesting.

ACKNOWLEDGEMENTS

This work was supported by the Major agricultural technology in Shandong Province (No. SDNYXTTG-2023-01) and the Modern Agricultural Industrial System of Shandong Province (SDAIT-02-12).

REFERENCE

[1] Babić L.J., Radojèin M., Pavkov I. et al., (2013). Physical properties and compression loading behaviour of corn seed [J]. *International Agrophysics*, Vol. 27(2), pp.119－126. Poland.

[2] Brass R W. (1970). *Development of a low damage corn shelling cylinder* [D]. Ames: Iowa State University.

[3] Chai Zongwen, Wang Keru, Guo Yinqiao, et al., (2017). Current status of maize mechanical grain harvesting and its relationship with grain moisture content (玉米机械粒收质量现状及其与含水率的关系). *Scientia Agricultura Sinica*, Vol. 50(11), pp.2036-2043. Beijing/China.

[4] Chowdhury M.H., Buchele W. F. (1978). The nature of corn kernel damage inflicted in the shelling crescent of grain combines[J]. *International Journal for Engineering Modelling*, 21(4):610－614. Austria.

[5] Dutta P K. (1986). *Effects of grain moisture, drying methods, and variety on breakage susceptibility of shelled corns as measured by the Wisconsin Breakage* Tester[D]. Ames: Iowa State University.

[6] Gao Lianxing, Li Fei, Zhang Xinwei et al., (2011). Mechanism of moisture content affect on corn seed threshing (含水率对种子玉米脱粒性能的影响机理). *Transactions of Agricultural Machinery*, Vol. 42(12), pp.92-96. Beijing/China.

[7] Hall G.E, Johnson W.H. (1970) Corn kernel crackage induced by mechanical shelling. *Transactions of the ASABE*, 13(1): 51-55.

[8] Kang Yunyou, Zhang Daolin, Lu Xiufeng et. al., (2019). Experimental Study on Mechanized Directly Harvesting Technology and Machinery for Corn Grain [J]. (玉米籽粒机械化直收技术与机具试验研究). *Journal of Agricultural Mechanization Research,* Vol. (04), pp.176-181. Heilongjiang/China.

[9] Liu Fenghe, Wang Keru, Li Jian, et al, (2013). Factors Affecting Corn Mechanically Harvesting Grain Quality (影响玉米机械收粒质量因素的分析). *Crops*, Vol. (04), pp. 116~119. Beijing/China.

[10] Li Lulu, Lei Xiaopeng, Xie Ruizhi et al (2017). Analysis of influential factors on mechanical grain harvest quality of summer maize[J] (夏玉米机械粒收质量影响因素分析). *Scientia Agricultura Sinica*, Vol. 50(11), pp. 2044-2051. Beijing/China.

[11] Mohamed A F, Abdel M., (2009). Mechanical properties of corn kernels[J]. *Misr Journal of Agricultural Engineering*, Vol. 26(4), pp.1901-1922. USA.

[12] Plett, S., (1994). Corn kernel breakage as a function of grain moisture at harvest in a prairie environment[J]. *Canadian Journal of Plant Science*, Vol. 74(3), pp.543-544. Canada.

[13] Steele J.L., Saul R.A., Hukill W.V. (1967) Deterioration of shelled corn as measured by carbon dioxide production. *American Society of Agricultural Engineers*, 12(5): 685-689.

[14] Volkovas V, Petkevičius S, špokas L., (2006). Establishment of maize grain elasticity on the basis of impact load. *Mechanika*, Vol. 6(62), pp. 64-67. Lithuania.

[15] Wang Lei, (2016). *Screening and Demonstration of Maize Varieties with Early Maturing, Dense Tolerance and Machine Harvest Suitable Traits (早熟耐密宜机收玉米品种筛选与示范)*. Northwest A&F University. Yangling/China.

[16] Wang Keru, Li Lulu, Lu Zhensheng et al., (2021) Mechanized grain harvesting quality of summer maize and its major influencing factors in Huanghuaihai region of China (黄淮海夏玉米机械化粒收质量及其主要影响因素). *Transactions of the Chinese Society of Agricultural Engineering*, Vol. 37(7), pp.1-7. Beijing/China.

[17] Wang Keru, Li Shaokun, (2017). Progresses in research on grain broken rate by mechanical grain harvesting[J] (玉米籽粒机械收获破碎率研究进展). *Scientia Agricultura Sinica*, Vol. 50(11), pp.2018-2026. Beijing/China.

[18] Wang Zhanbin, Wang Zhenwei, Zhang Yinping, et al.,(2020).Design and Test of Longitudinal Axial Flexible Hammer-claw Corn Thresher[J](纵轴流柔性锤爪式玉米脱粒装置设计与试验). *Transactions of the Chinese Society for Agricultural Machinery*, Vol. 51(S2), pp.109-117. Beijing/China.

[19] Yang Yufen, Zhang Yongli, Zhang Benhua, et al., (2008). Experimental Study on Static Pressing Typical Corn Seed Kernel (典型玉米种子籽粒的静压破损试验研究). *Journal of Agricultural Mechanization Research*, Vol. (07), pp.149-151. Heilongjiang/China

[20] Zhang Wanxu, Wang Keru, Xie Ruizhi, et al., (2018a).Relationship Between Maize Grain Broken Rate and Moisture Content as well as the Differences among Cultivars (玉米机械收获子粒破碎率与含水率关系的品种间差异). *Journal of Maize Sciences*, Vol. 26(4), pp. 74-78. Jilin/China.

[21] Zhang WanXu, Ming Bo, Wang KeRu, et al, (2018b). Analysis of Sowing and Harvesting Allocation of Maize Based on Cultivar Maturity and Grain Dehydration Characteristics[J](基于品种熟期和籽粒脱水特性的机收粒玉米适宜播期与收获期分析). *Scientia Agricultura Sinica*, Vol. 51(10), pp.1890-1898. Beijing/China.

[22] Zhang Xinwei, Li Xinping, Yang Dexu, et al., (2012). Micromechanism of lnner Mechanical Cracks Generation and Expansion of Corn Seed Kernel (玉米种子内部机械裂纹产生与扩展的微观机理). *Transactions of the Chinese Society for Agricultural Machinery*, Vol. 43(12), pp.72-76. (in Chinese)

[23] Zhang Xinwei, Yi Kechuan, Gao Lianxing, (2015). Contacting mechanics analysis during impact process between corn seeds and threshing component (玉米种子与脱粒部件碰撞过程中的接触力学分析). *Chinese Agricultural Science Bulletin*, Vol. 31(14), pp.285－290.

[24] Zhao Rulang, Wang Yonghong, Li Shaokun et al., (2019). Screening of maize cultivars suitable for mechanical kernel harvest in Ningxia (宁夏宜机收玉米品种的初步筛选) *Journal of Maize Science*, Vol. 27(1), pp.130-135. Jilin/China.

EFFECTS OF INSULATION COVER MEASURES ON THE TEMPERATURE ENVIRONMENT OF CHINESE SOLAR GREENHOUSE
/
不同保温覆盖措施对日光温室温度环境的影响

Qian SUN [1)], Yang SONG [1)], Zhigang YANG [2)], Xiaorui LIU [2)], Shimao CUI *[1)]
[1)] Inner Mongolia Agricultural University, College of Horticulture and Plant Protection, Huhhot / China
[2)] Inner Mongolia Academy of Agricultural and Animal Husbandry Sciences, Institute of Vegetables and Flowers, Huhhot / China
Tel: +86-13514718505; E-mail: cuishimao@sina.com
Correspondent author: Shimao CUI
DOI: https://doi.org/10.35633/inmateh-71-50

Keywords: *Chinese solar greenhouse; Insulation cover measure; Thermal performance; Temperature environment; Solar radiation*

ABSTRACT

Chinese solar greenhouses (CSGs) are the important agricultural building facility with highly efficient and sustainable utilization of solar energy. In order to improve the thermal insulation performance and reduce the heat loss, different insulation cover measures were applied to Chinese solar greenhouses. In this study, a solar greenhouse with an internal insulation blanket (SG1), a greenhouse with an internal blanket and an internal plastic film (SG2) and a greenhouse with an external blanket, an internal blanket and an internal plastic film (SG3) were chosen as experimental objects to analyze their indoor temperature environment. The results indicated that the differences of solar radiation interior among three greenhouses were similar, which was not the main reason that caused the differences of the temperature environment in the three greenhouses. During the tests, the nighttime average temperature was increased by 2.1-3°C by adding the cover materials, and the duration of nighttime temperature greater than 8°C was increased by 33.5%-38.2%. In addition, the cost is increased by adding the insulation cover materials, but it will be beneficial for greenhouse production to reduce additional energy consumption.

摘要

日光温室是中国重要的农业设施，它能高效可持续的利用太阳能。为了改善温室保温性能从而减少热损失，研究了不同覆盖方式对日光温室温度环境的影响。该研究对单被内保温日光温室（SG1），单被双膜内保温日光温室（SG2）以及双被双膜内保温日光温室（SG3）进行了温度环境测试。研究结果表明：三座温室内太阳辐射的差异较小，而它们的温度环境的差异并非由所获得太阳辐射差异所造成。在测试期间，通过增加保温覆盖物，可使夜间平均温度增加 2.1～3°C，而且相较于 SG1，夜间温度大于 8°C 的持续时长也能够提升 33.5%～38.2%。此外，尽管增加保温覆盖使得成本上升，但是对于长期温室生产并减少额外供热是有利的。

INTRODUCTION

The greenhouse is an essential building facility for plant growth (*Irfan et al., 2021*). Under the situation that fossil energy is increasingly exhausting, and the environmental pollution caused by fossil fuel burning is inevitably getting worse, energy saving in agricultural greenhouses has become a key issue (*Gennadii et al., 2023*). The applications of solar energy in greenhouses have provided the renewable and clear energy for the needs of greenhouse heating (*Gorjian et al., 2021*). Chinese solar greenhouses (CSGs) are widely promoted in China because of their energy savings, improved efficiency, reduced energy consumption and low cost. Although frequently facing the harsh environmental conditions in cold winters, they had achieved notable economic and social benefits (*Tong et al., 2022)*.

CSGs are generally enveloped by the walls, the roof and its cover materials. The rear wall plays an important role to absorb and store solar energy projecting on it. The roof is covered with a fixed and transparent plastic film for lighting during daytime, and a rolled thermal insulation blanket covers the roof for heat preservation at night (*Cao et al., 2019; Tong et al., 2013*). However, there was approximately more than 60% of the total heat loss lost through the roof (*Xu et al., 2017*). In recent decades, multi-layered composite materials blankets were developed and widely used for the greenhouses to reduce the heat loss *(Qiao et al., 2008*).

Qian Sun, Ph.D; Yang Song, Assoc.Prof. Ph.D; Zhigang Yang, Assoc. Prof. Ph.D; Xiaorui Liu, Ph.D; Shimao Cui, Prof.Ph.D.

Hu et al., (2014), compared the insulation performance of three composite blankets having the same thickness, but the quality was different. The results showed that the insulation performance of the heaviest and porous blanket was the best than that of the compact blanket, and the lightweight blanket was not recommended to use in windy areas because of its poor windproof. *Liu et al., (2015),* analyzed the impact factors of the insulation performance by comparing various kinds of composite blankets. The insulation performance of blankets increased with their thickness in a certain weight. Although many materials, such as PE foam, spray-bonded cotton, waterproof fabric etc., have been used in blankets and the optimum applications need to be further investigated.

To improve the thermal environment performance of the greenhouses, different insulation cover measures was used for insulation. Thermal screens were drawn over the crop decreasing the heat loss by 35-60% at night (*Bailey, 1981*). Thermal curtains resulted in energy savings of about 28.7% in a double-layered plastic greenhouses at night (*Hyung-Kweon et al., 2018*). The external insulation system was applied to the multi-span greenhouse reducing by 36% of the glass roof heat loss (*Chen et al., 2023*).

Qu et al., (2004), designed and used a thin internal thermal screen in a solar greenhouse. The results showed that the nighttime air temperature inside the greenhouse covered with the screen increased by 0.7-1.0 °C. The energy saving effect of thermal screen used in solar greenhouse was poorer than that used in multi-span greenhouses. However, it was non-negligible that the internal insulation system had a significant impact on reducing the heat loss through the roof. In high latitude and cold regions, the insulation cover measures, represented by multi-cover system which integrated the internal insulation and the external insulation, could improve the thermal performance of solar greenhouses (*Liu et al., 2022*). The Chinese researchers' studies indicated that the insulation cover measures improved the thermal performance of solar greenhouses and decreased the energy consumption (*Bai et al., 2022; Wu et al., 2015*).

Because of the complex and diverse climate conditions in different regions of China, which are many types of solar greenhouses, it is crucial to select a suitable type of solar greenhouse to ensure optimum light and thermal performance based on the local environment. In this study, three solar greenhouses with different insulation cover measures were tested to analyze the interior temperature environment in Baotou, Inner Mongolia, China (40.6°N, 110°E). Comparing the experimental results, their temperature performance was evaluated. The study can provide an effective choice for greenhouse producers to reduce energy consumption.

MATERIALS AND METHODS

Tested solar greenhouses

In this study, SG1, SG2 and SG3 are chosen for testing. As shown in Figure 1, three solar greenhouses have basically the same structure which is double-layer steel frame structure. The orientation, the span, the length from east to west, the rear wall height, the ridge height and the wall thickness are 5° south to west, 10 m, 100 m, 4.2 m, 5.7 m and 1.5 m, respectively. SG1 is a greenhouse with single film and single internal thermal insulation. SG2 is a greenhouse with double film and single internal insulation. SG3 is a greenhouse with double film and double insulation. Other parameters are shown in Table 1. Moreover, both the air vents of SG1 and SG2 locate at the bottom of the south roof and the rear roof, and the air vent of SG3 locates at the bottom and top of the south roof due to the covered external insulation.

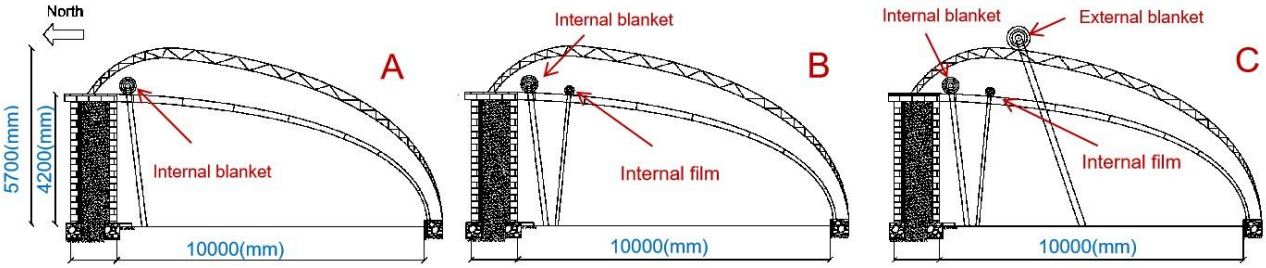
During the tested period, the opening and closing times of thermal blankets were 9:00 to 16:00. Tomato was cultivated in these greenhouses. Drop irrigation was used for improving the water efficiency. Other managements were consistent. To reduce the heat losses and energy consumption, there was no extra heating and ventilation in these greenhouses.

Experimental device and method

The data measurement planes were the 1/3 and 2/3 of east-west length direction of the greenhouse. Indoor temperature and solar radiation were measured by using the Farmland Microclimate Observation System (DZN1, Tianjin Meteorological Instrument Factory, China) which was placed in the middle of the span with the height of 1.5 m. Outdoor tested points were placed 1.5 m above the open ground. The measurement range of temperature was -40°C to 80°C with an uncertainty of 0.2°C, and the measurement range of solar radiation was 0 to 1400 W/m^2 with an uncertainty of 5%. The data collecting interval was 15 min.



(a)



(b)

Fig. 1 - Photo and schematic diagrams of tested solar greenhouses
(a) photos; (b) sectional view

A – a solar greenhouse with an internal blanket (SG1); B – a solar greenhouse with an internal blanket and an internal plastic film (SG2);
C – a solar greenhouse with an external blanket, an internal blanket and an internal plastic film (SG3).

Table 1

Specific parameters of different greenhouses

Number	Type	Cover materials		Insulation materials	
		External film	Internal film	Internal blanket	External blanket
SG1	External film and internal insulation	PO film (0.15 mm)	N/A	Expandable PE foam (13 mm)	N/A
SG2	Double film and internal insulation	PO film (0.15 mm)	PE film (0.03 mm)	Expandable PE foam (13 mm)	N/A
SG3	Double film and double insulation	PO film (0.15 mm)	PE film (0.03 mm)	Expandable PE foam (13 mm)	Waterproof and recycled cotton (25 mm)

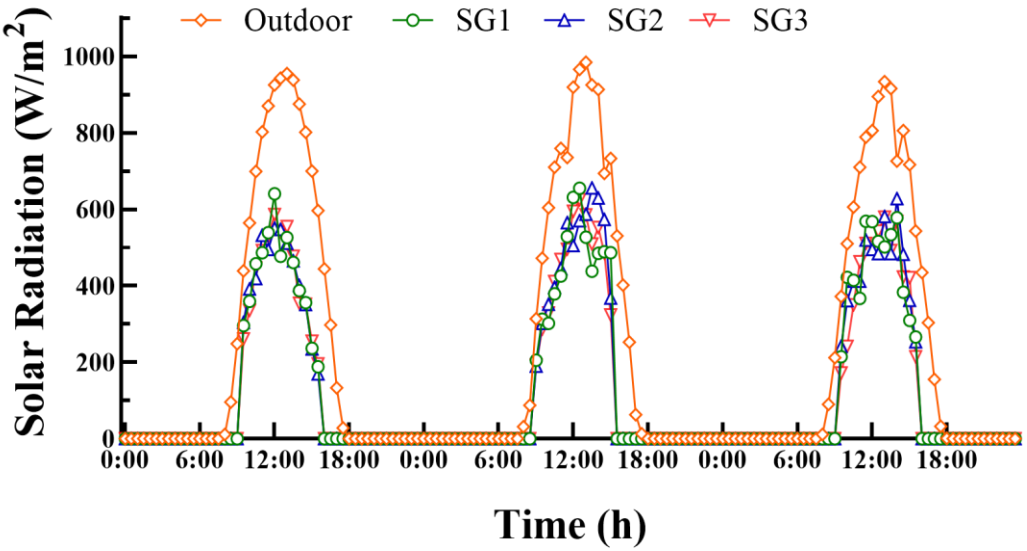
RESULTS AND DISCUSSION

Influence of solar greenhouse structure on the transmitted solar radiation

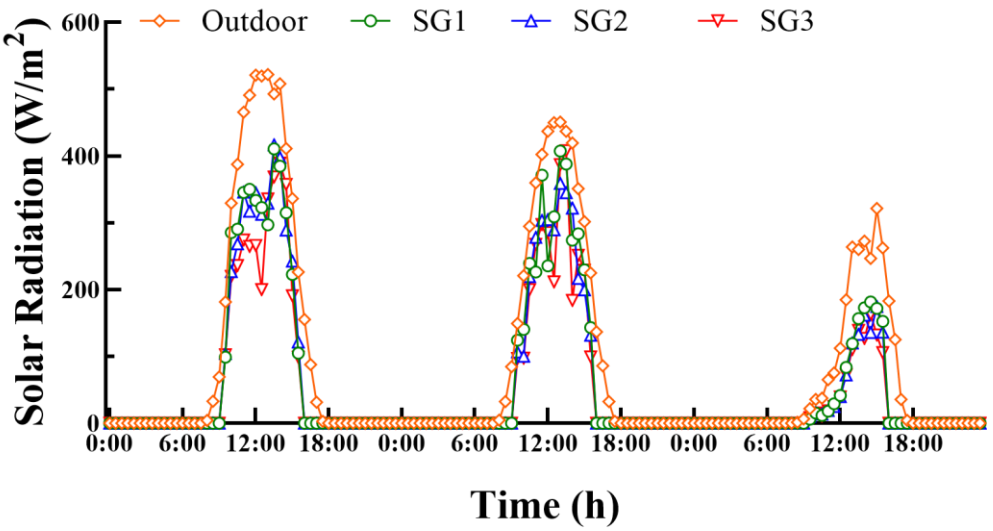
Solar radiation directly affects the light demand of crops and the heat demand in the solar greenhouse. During testing, December to February are the cold months for greenhouse production, and January is the coldest one with low temperature, freezing damage occurring frequently. Therefore, the transmitted solar radiation in January directly reflects the lighting and heat storage of the greenhouse, thereby affecting the thermal insulation performance. In order to describe the solar radiation of different greenhouses under different weather conditions more accurately, the solar radiation data of consecutive sunny days and consecutive cloudy days were selected to analyze (Jan 4 to 6 and Jan 20 to 22).

Figure 2 presents the solar radiation variations of three greenhouses under different weather conditions that vary with the solar radiation outdoor. In consecutive sunny days, the diurnal average solar radiation intensity of SG1, SG2 and SG3 were 428.3 W/m^2, 436.8 W/m^2 and 422.4 W/m^2 during lighting period, respectively. In consecutive cloudy days, the diurnal average solar radiation intensity of SG1, SG2 and SG3 were 212.9 W/m^2, 204.1 W/m^2 and 187.1 W/m^2, respectively. The solar radiation of three greenhouses on sunny and cloudy days presented consistent trends with minor differences. Therefore, the light performance of three greenhouses is consistent under same structure and weather conditions.

The differences of the temperature environment in three greenhouses are not mainly caused by the differences of transmitted solar radiation. However, they highly depend on the exterior solar radiation to ensure sufficient solar energy to provide a suitable environment for crop growth. Hence, it is crucial to take effective measures for thermal insulation to reduce the heat loss through the south roof in harsh winters.



(a)



(b)

Fig. 2 - Variations of indoor and outdoor solar radiation in different solar greenhouses
(a) consecutive sunny days; (b) consecutive cloudy days.

Influence of different insulation cover measures on the greenhouse temperature environment

Stability of the temperature environment

The crop growth relies on the congenial environment inside greenhouses. The temperature is significantly affected by greenhouse structures and heat preservation measures. The indoor and outdoor temperature variations of 31 days (December 15 to January 15) of three greenhouses were analyzed in Figure 3. During the period, the indoor temperature variations of three greenhouses indicated the insignificant differences at daytime (with the thermal insulation blankets rolled up at 9:00 a.m.) and its opposite at nighttime (with the thermal insulation blankets rolled down at 16:00 p.m.), while the nighttime outdoor temperature was lower. It was showed that effective insulation measures can ensure a relatively stable thermal environment with temperature changed sluggishly for the greenhouses during nighttime.

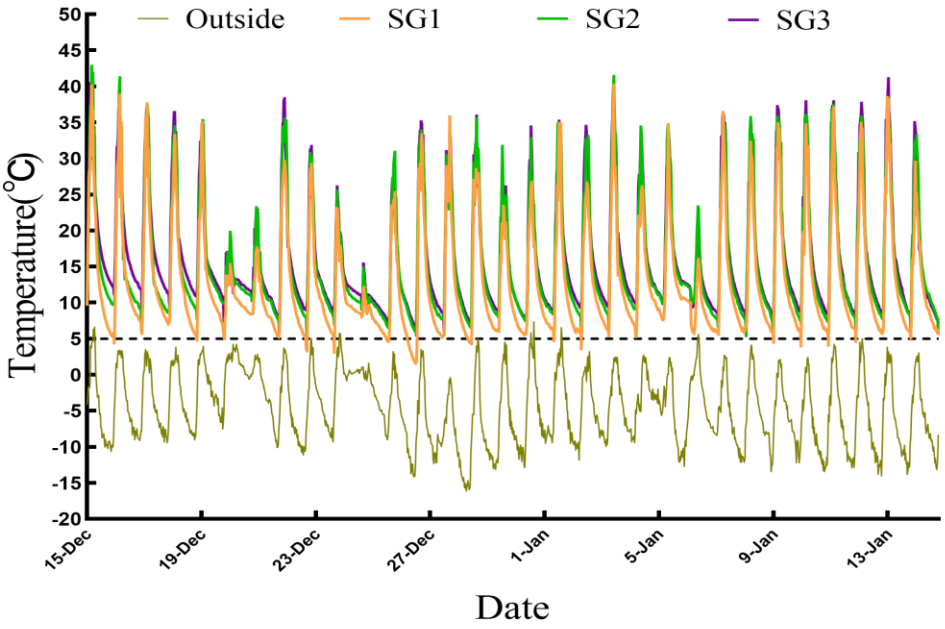


Fig. 3 - Variations of indoor and outdoor air temperature in different solar greenhouses for 31 days

Weather adaptability of solar greenhouses with insulation cover measures

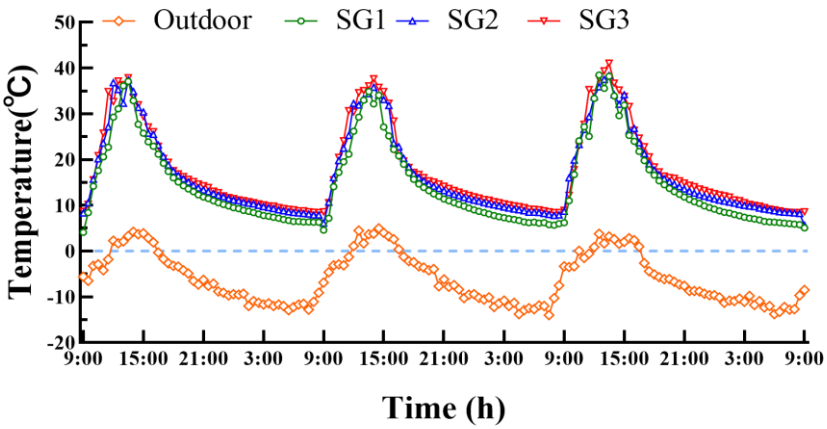
To further evaluate the temperature environment of three greenhouses, the representative continuous nice and bad days were selected, as shown in Figure 4.

On sunny days (January 11 to January 14), the indoor temperature increased rapidly with sunlight entering through the south roof of three greenhouses. When the indoor temperature reached the maximum temperature at 13:00 to 14:00, then it was gradually decreasing.

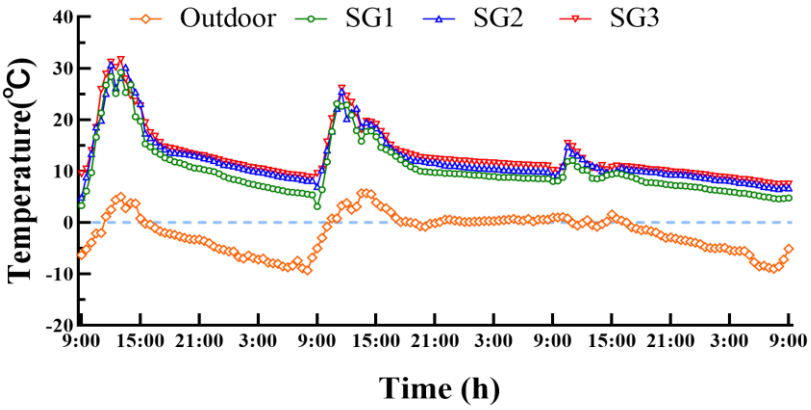
The average daytime indoor temperature of three greenhouses and the average daytime outdoor temperature were 14.6°C, 16.6°C, 17.4°C and -5.9°C, respectively, and the average temperature differences between indoor and outdoor were 20°C of SG1, 22.5°C of SG2 and 23.3°C of SG3, respectively.

The average nighttime indoor temperature of three greenhouses and the average nighttime outdoor temperature were 10.5°C, 12.4°C, 13.1°C and -8.5°C, respectively, and the average temperature differences between indoor and outdoor were 19°C of SG1, 20.9°C of SG2 and 21.6°C of SG3, respectively. On cloudy or overcast days, because of less solar radiation, the daytime indoor temperature rose slowly in three greenhouses, and this situation had not improved under bad weather conditions.

The average daytime indoor temperature of three greenhouses and the average daytime outdoor temperature were 10.4°C, 12.3°C, 13.1°C and -1.9°C, respectively, and the average temperature differences between indoor and outdoor were 12.3°C of SG1, 14.2°C of SG2 and 15°C of SG3, respectively. The average nighttime indoor temperature of three greenhouses and the average nighttime outdoor temperature were 8.5°C, 10.4°C, 11.1°C and -3.1°C, respectively, and the average temperature differences between indoor and outdoor were 11.6°C of SG1, 13.5°C of SG2 and 14.2°C of SG3, respectively.



(a)

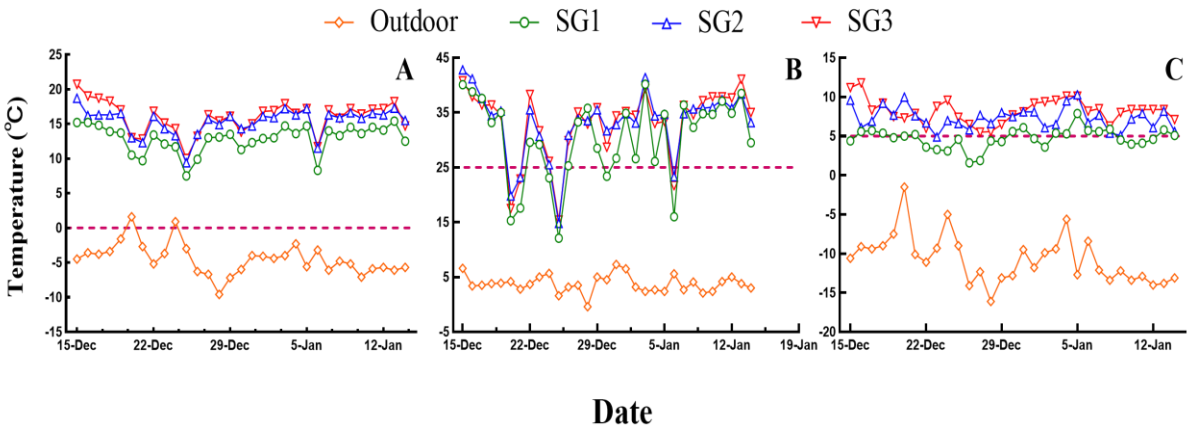


(b)

Fig. 4 - Variations of temperature in different solar greenhouses in different weather condition (a) sunny days; (b) cloudy or overcast days.

Nighttime temperature enhancement and time distribution

During the 31 days, as shown in Figure 5(a), the average daily temperature of SG1, SG2 and SG3 were 12.9°C, 15.3°C and 16°C, respectively, which were greater than 5°C. The average daily maximum temperature of SG1, SG2 and SG3 were 30.4°C, 33.2°C and 33.2°C, respectively. The average daily minimum temperature of SG1, SG2 and SG3 were 4.7°C, 7.3°C and 8.2°C, respectively. The nighttime minimum outdoor temperature ranged from -0.81°C to -15.9°C, and there were 18 days which the nighttime minimum outdoor temperature was below -10°C. And the days were 28 that the nighttime minimum outdoor temperature was below -5°C.



(a)

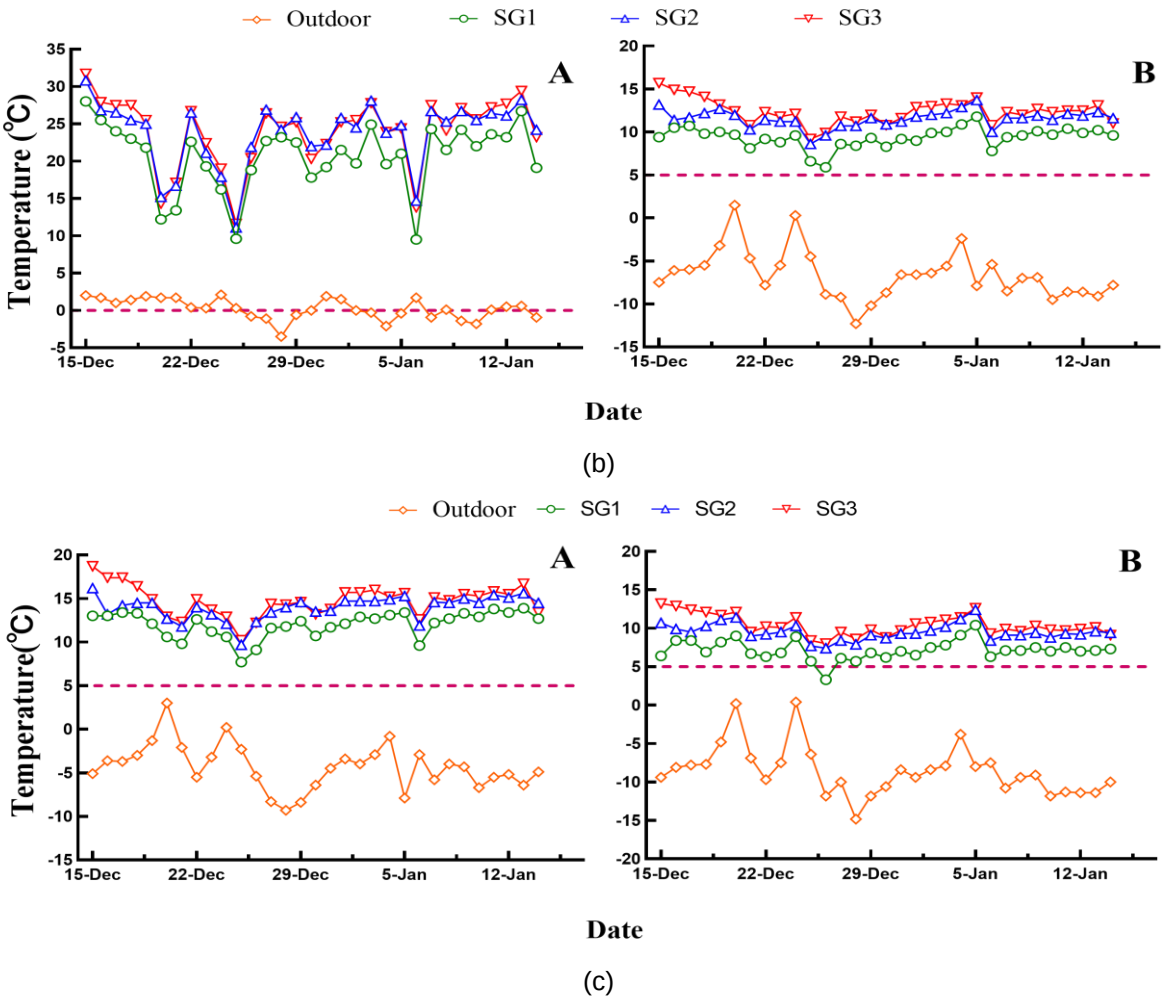


Fig. 5 - Comparison of air temperature in different solar greenhouses

(a) variations of average daily air temperature (A), average maximum air temperature (B) and average minimum air temperature(C); (b) variations of average daytime air temperature (A, 9:00-16:00) and average night air temperature (B, 16:00- next 9:00); (c) variations of night air temperature in different solar greenhouses (A, the first half of the night 16:00-0:00; B, the second half of the night 0:00-next 9:00).

At that time, there were 16 days in SG1 with the average daily minimum temperature below 5°C, while there were 1 day and 0 days in SG2 and SG3, respectively. Comparing with SG2 and SG3, the thermal environment stability of SG1 was worse than that of SG2 and SG3, which the insulation measure was not well meet the thermal insulation demand to effectively reduce heat loss through the south roof.

The nighttime average temperature is one of crucial factors to evaluate the thermal performance indoor. In Figure 5(b), the nighttime average temperature of SG1, SG2 and SG3 were 9.4°C, 11.5°C, and 12.4°C, respectively, which were greater than 5°C. The nighttime average temperature in SG2 and SG3 was increased by 2.1-3°C at least, comparing with SG1. It means that these three greenhouses can provide a suitable thermal environment for warm vegetables without auxiliary heating, while the thermal environment of SG3 is better than SG1 and SG2.

Figure 5(c) presented the variation of the nighttime temperature in the three greenhouses. The nighttime average temperature of SG1, SG2 and SG3 from 16:00 to 0:00 (the first half of the night) were 7.3°C, 9.4°C and 9.1°C, respectively, which were greater than 5°C. The nighttime average temperature of SG1, SG2 and SG3 from 0:00 to 9:00 (the second half of the night) were 7.1°C, 9.5°C and 10.4°C, respectively, which were greater than 5°C except that there was 1 day below 5°C in SG1.

Vegetables (such as tomato) are extremely affected by low-temperature, though they can bear for a short time. If the low-temperature environment continues for a long time, the growth of vegetables will suffer the cold damage. In Table 2, the duration of nighttime indoor temperatures less than 5°C was a total of 17 hours during 31 days in SG1, while it was only 1 hour in SG2 and 0 hour in SG3. The duration of nighttime indoor temperatures between 5°C and 8°C was a total of 204.25 hours during 31 days in SG1, while it was 43.5 hours in SG2 and 20.25 hours in SG3.

The temperatures less than 5°C was mainly distributed from 6:00 to 9:00 in SG1, which was defined as nighttime because the thermal blankets being not rolled up. The duration of nighttime temperatures greater than 8°C accounts for 58% in SG1, 91.5% in SG2 and 96.2% in SG3, respectively. At that times, with no heating supplement, a pure internal insulation blanket was not enough to meet the demands of heating preservation in harsh weather conditions. The decline of nighttime indoor temperature was reduced in SG1, but not obvious than that in SG2 and SG3. The internal plastic film under the internal blanket has effectively reduced the convection through the crevices of blanket which reduced the heat loss through the internal insulation in SG2. However, the air between external plastic film and internal blanket inside the greenhouse was irregularly disturbed by wind exterior. To achieve optimum insulation effect, the combination of external and internal insulation was used as insulation measure in SG3, reducing the heat loss caused by air flow between external plastic film and internal blanket. During 31 days, the nighttime indoor temperatures were greater than 5°C. Therefore, different insulation cover measures can improve the thermal performance of the solar greenhouse, and the combination of external and internal insulation was a more-effective measure than the others.

Table 2

Time distribution of low temperature in the greenhouses during 31 days

Duration	SG1			SG2			SG3		
	>8°C	5-8°C	<5°C	>8°C	5-8°C	<5°C	>8°C	5-8°C	<5°C
	[hour]			[hour]			[hour]		
16:00 -17:00	31	0	0	31	0	0	31	0	0
17:00-18:00	31	0	0	31	0	0	31	0	0
18:00-19:00	29	2	0	31	0	0	31	0	0
19:00-20:00	29	2	0	31	0	0	31	0	0
20:00-21:00	28.5	2.5	0	31	0	0	31	0	0
21:00-22:00	28	3	0	31	0	0	31	0	0
22:00-23:00	27.25	3.75	0	31	0	0	31	0	0
23:00-0:00	24.5	6.5	0	31	0	0	31	0	0
0:00-1:00	20.5	10.5	0	31	0	0	31	0	0
1:00-2:00	17.25	13	0.75	31	0	0	31	0	0
2:00-3:00	10.75	19.25	1	30.75	0.25	0	31	0	0
3:00-4:00	7.5	22.5	1	29.25	1.75	0	31	0	0
4:00-5:00	7	23	1	28	3	0	30	1	0
5:00-6:00	4.75	25.25	1	27.5	3.5	0	29.5	1.5	0
6:00-7:00	4	24.75	2.25	24	7	0	27.25	3.75	0
7:00-8:00	3	24	3	20.25	10.75	0	25.5	5.5	0
8:00-9:00	2.75	21.25	7	12.75	17.25	1	22.5	8.5	0

Cost evaluation

As shown in Table 3, the total cost of SG1, SG2 and SG3 were 284.7 RMB/m^2, 293.4 RMB/m^2 and 317.7 RMB/m^2, respectively. The total cost mainly includes basic construction cost and cover materials cost. The basic construction cost was the same for the three greenhouses. The cost of cover materials in SG2 increased by 8.7 RMB/m^2, which represented the internal plastic film and its control system. The internal plastic film, external blanket and their control system increased by 33 RMB/m^2 in SG3. For the long-term perspective in greenhouse production, the increasing cost of cover materials maintained the average nighttime temperature above 10°C, ensuring the suitable thermal environment for promoting vegetables maturation. Besides, compared with SG1, the tomato yield per unit area in SG2 and SG3 increased by 0.71 Kg/m^2 and 1.09 Kg/m^2, respectively. Considering that the wholesale price of tomatoes will rise to 14.0 RMB/Kg in winter, SG2 and SG3 can increase income by 9.94 RMB/m^2 and 15.26 RMB/m^2, respectively. Therefore, choosing SG2 or SG3 to plant vegetables can both generate significant benefits for farmers.

Table 3

Expenses of different solar greenhouses

Greenhouse	Construction		Cover materials				Other costs [RMB/m²]	Total [RMB/m²]	The increase of tomato yield [Kg/m²]
	Steel frame [RMB/m²]	Walls [RMB/m²]	Internal blanket [RMB/m²]	External blanket [RMB/m²]	External film [RMB/m²]	Internal film [RMB/m²]			
SG1	55.0	180.9	27.0	0.0	3.5	0.0	18.3	284.7	--
SG2	55.0	180.9	27.0	0.0	3.5	2.0	25.0	293.4	0.71
SG3	55.0	180.9	27.0	16.0	3.5	2.0	33.3	317.7	1.09

DISCUSSIONS

The enhancement of the thermal insulation performance in solar greenhouse is mainly attribute to effective insulation cover measures, because the coverings reduce the convection and radiation heat transfer between the greenhouse interior and exterior. However, under the continuous and extreme cold weather conditions, with no sufficient heat supplement, it is crucial to optimize the insulation cover measures. In addition, to meet the heat demand, it is essential to optimize the passive or active heating system. The combination of insulation measures and heating system will benefit to improve the thermal performance of the greenhouses.

CONCLUSIONS

In this study, three different insulation coverage measures solar greenhouses were designed and built in Baotou area. To evaluate the thermal insulation performance inside the greenhouses, the indoor temperatures under different weather conditions were experimentally measured. Based on the experimental results, the conclusions were as follows:

(1) The average transmitted solar radiation through SG1, SG2 and SG3 were 428.3 W/m^2, 436.8 W/m^2 and 422.4 W/m^2 during lighting period in consecutive sunny days, and those were 212.9 W/m^2, 204.1 W/m^2 and 187.1 W/m^2 in consecutive cloudy days. Therefore, the differences of the temperature environment in three greenhouses are not mainly caused by the differences of transmitted solar radiation.

(2) During 31 days, the nighttime average temperature of SG1, SG2 and SG3 were greater than 5°C. By adding insulation coverage materials, the nighttime average temperature was increased by 2.1-3°C, and the duration of nighttime temperature greater than 8°C was increased by 33.5%-38.2%. The insulation cover measures have effectively improved the thermal insulation performance of the greenhouses.

(3) The increase of cost was mainly ascribable to the insulation cover materials, however, the greenhouse will benefit from improving the indoor environment and reducing energy consumption in long term production. Meanwhile, it is beneficial for greenhouse production to increase yield and income.

ACKNOWLEDGEMENT

This work was supported by the National Key Research and Development Program of China (2023YFD2000601, 2023YFD2000602), the National Natural Science Foundation of China (31860573) and Inner Mongolia Scientific and Technological Achievements Transformation Project (CGZH2018039).

REFERENCES

[1] Ardiansah I, Bafdal N, Bono A, et al., (2021). Impact of Ventilations in electronic Device Shield on Micro-climate Data Acquired in a Tropical Greenhouse. *INMATEH-Agricultural Engineering,* 63(1), 397-404. DOI: https://doi.org/10.35633/inmateh-63-40

[2] Bai, G., Zhuang, W., (2022). Thermal Environment Simulation of Multi-layer Covered Integrated Solar Greenhouse Based on CFD (基于 CFD 的多层覆盖一体式日光温室热环境模拟）*Journal of Agricultural Mechanization Research*, 10, 218-221, 227.

[3] Bailey, B.J., (1981). The reduction of thermal radiation in glasshouses by thermal screens. *Journal of Agricultural Engineering Research*, 26(3), 215-224.

[4] Cao, K., Xu, H., Zhang, R., et al., (2019). Renewable and sustainable strategies for improving the thermal environment of Chinese solar greenhouses. *Energy and Buildings*, 202.

[5] Chen, F., Sun, W., Yu, W., et al., (2023). Analyzing light and thermal environment and insulation performance of a multi-span greenhouse with external insulation.（外保温连栋温室光热环境及保温性能分析）*Transactions of the Chinese Society of Agricultural Engineering*, 39(6), 194-203.

[6] Golub, G., Kepko, O., Pushka, O., et al., (2023). Modeling of Substrate and Air Temperature Dynamics in the Mushroom Greenhouse. *INMATEH-Agricultural Engineering*, 69(1), 315-324. DOI: https://doi.org/10.35633/inmateh-69-29

[7] Gorjian, S., Calise, F., Kant, K., et al., (2021). A review on opportunities for implementation of solar energy technologies in agricultural greenhouses. *Journal of Cleaner Production*, 285, 124807.

[8] Hu, Y., Li, J., Wu, S., (2014). Heat Preservation Test of Several Kinds of Thermal Insulation Quilt for Solar Greenhouse（几种日光温室保温被的保温性研究）. *Journal of Agricultural Mechanization Research*, 10, 218-221,227.

[9] Hyung-Kweon, K., Geum-Choon, K., Jong-Pil, M., et al., (2018). Estimation of Thermal Performance and Heat Loss in Plastic Greenhouses with and without Thermal Curtains. *Energies*, 11(3), 578.

[10] Liu, C., Ma, C., Wang, P., et al., (2015). Theoretical analysis and experimental verification of heat transfer through thick covering materials of solar greenhouse.（日光温室保温被传热的理论解析及验证）*Transactions of the Chinese Society of Agricultural Engineering*, 31(2), 170-176.

[11] Liu, X., Wu, X., Xia, T., et al., (2022). New insights of designing thermal insulation and heat storage of Chinese solar greenhouse in high latitudes and cold regions. *Energy*, 242.

[12] Qiao, Z., Zou, Z., Zhang, L., et al., (2008). Laboratory test of four kinds of heat preservation quilts for solar greenhouse（4 种日光温室保温被室内的试验性能测试） *Journal of Northwest A & F University (Natural Science Edition)*, 36(6), 153-158.

[13] Qu, M., Chen, Q., Song, S., (2004). Experimental analysis of the insulation performance of thermal screens in sunlight greenhouse（日光温室内保温幕保温性能测试分析）. *Journal of Huazhong Agricultural University*, 35(z2), 48-52.

[14] Tong, G., Chen, Q., Xu, H., (2022). Passive solar energy utilization: A review of envelope material selection for Chinese solar greenhouses. *Sustainable Energy Technologies and Assessments*, 50.

[15] Tong, G., Christopher, D.M., Li, T., et al., (2013). Passive solar energy utilization: A review of cross-section building parameter selection for Chinese solar greenhouses. *Renewable and Sustainable Energy Reviews*, 26, 540-548.

[16] Wu, H., Cui, S., Sun, Q., et al., (2015). Study on properties of inner thermal insulation solar greenhouse.（内保温日光温室的性能的研究）*Journal of Inner Mongolia Agricultural University,* 37(4), 33-41.

[17] Xu, H., Zhang, Y., Li, T., et al., (2017). Simplified Numerical Modeling of Energy Distribution in a Chinese Solar Greenhouse. *Applied Engineering in Agriculture*, 33(3), 291-304.

RESEARCH ON DAMPING PERFORMANCE OF ORCHARD FRUIT THREE-STAGE DAMPING TRAILER BASED ON ADAMS
/
基于 ADAMS 的果园果品三级减振拖车减振性能研究

Yifan WANG[1)], Nan AN[1)], Jiaxin LU[1)], Zhihong ZHAO[1)], Xiahui FU[1)], Qingliang CUI[1,2)], Juxia WANG*[1,2)]
[1)]College of Agricultural Engineering, Shanxi Agricultural University, Shanxi Taigu 030801 / China
[2)]Key Technology and Equipment of dry farming agricultural machinery Shanxi Key Laboratory, Shanxi Taigu 030801 / China
Tel: +86-18634418916; E-mail: wangjuxia79@163.com
DOI: https://doi.org/10.35633/inmateh-71-51

Keywords: *orchard transport trailer, D-level pavement, Vibration-damping system, simulation*

ABSTRACT

To enhance the vibration-damping performance of orchard transport trailers and reduce the damage rate during fruit transportation, a D-level simulation pavement was constructed, trailer's vibration-damping system was analyzed and two kinds of three-stage vibration-damping transport trailers were designed and optimized. The vibration mechanical properties of Fuji apples were experimentally evaluated, revealing a positive correlation between damage rate and vibration acceleration. By utilizing vibration acceleration as a vibration-damping parameter, the trailer's vibration-damping performance was simulated by Adams software. The results demonstrated that the three-stage trailer with rubber vibration-damping pads in the horizontal direction exhibited superior vibration-damping effectiveness compared to existing trailers.

摘要

为了提升果园运输拖车的减振性能，降低果品运输的损伤率，本文构建了 D 级仿真路面，对拖车减振系统进行分析，优化设计了两种三级减振果园运输拖车；以富士苹果为研究对象进行了振动力学特性试验，研究获得果品损伤率和振动加速度呈正相关关系；并以振动加速度作为减振参数，运用 Adams 软件对拖车的减振性能进行仿真分析，结果表明水平方向采用橡胶减振垫进行减振的三级减振拖车，相较于现有拖车具备更为优异的减振效果。

INTRODUCTION

In the northwest China, orchards have long sunshine hours, four distinct seasons and a rich variety of fruit trees. Because of the terrain conditions, the transport of orchard fruit mainly rely on human back or the trailer that was hooked up to the tractor. In recent years, the cost of manpower transport has been on the rise due to the continuous decline in the rural labor force; and the vibration-damping performance of current utilization trailer is relatively poor, which resulted in significant damage to a large quantity of fruit during transportation and diminished the economic value of the fruit. However, how to effectively optimize the vibration-damping structure of fruit trailers in orchards is of great significance in reducing fruit damage and improving fruit economic efficiency.

The vibration-damping system of vehicles was generally divided into active vibration-damping *(Teng, 2017; Bai et al., 2018; Yuan, 2022; Ma et al., 2023)* and passive vibration-damping *(Li et al., 2019; Yuan et al., 2020; Yang et al., 2021; Zhao et al., 2019)*, and scholars at home and abroad have carried out some researches on the vibration-damping structure of vehicles and achieved better results. Dong *(Dong, 2022)* constructed a two-stage vibration-damping model of vehicle passive and active suspensions and performed simulation analysis, and found that active vibration-damping had better smoothing performance than passive vibration-damping. Zhou *(Zhou et al., 2021)* executed simulation of vehicle active air suspension and discovered that its vibration-damping performance was better compared to passive air suspension. Chi *(Chi et al., 2017)* designed a hydraulic vibration-damping system, and the simulation results showed that the performance of damping system was improved by 27% compared with the traditional passive damping system in terms of z-direction acceleration and tire deformation.

[1] *Yifan Wang, M.S. Stud. Eng.; Nan An, M.S. Stud. Eng.; Jiaxin Lu, M.S. Stud. Eng.; Zhihong Zhao, M.S. Stud. Eng.; Xiahui Fu, M.S. Stud. Eng.; Qingliang Cui, Prof. Ph.D. Eng.; Juxia Wang, A.P. Ph.D. Eng.*

Zhong *(Zhong, 2020)* designed a three-stage vibration-damped active suspension, and the simulation analysis obtained that the vibration-damping performance of this suspension system was improved by 56.81% and 14.03% compared to the two-stage and one-stage active suspensions, respectively. Shen *(Shen et al., 2016)* designed an ISD suspension structure and indicated that the vibration-damping performance was superior to that of the passive suspension. Suo *(Suo et al., 2021)* proposed a unidirectional coupled oil-air suspension and found that this suspension structure has better vibration-damping performance than the conventional single cylinder oil-air suspension. Qi *(Qi et al., 2023)* designed a tertiary vibration-damping structure after improving the traditional secondary vibration-damping tracked transporter. When driving on C and D road surfaces, the structure improved the vibration-damping effect in the z-direction by 6.4% and 19.6% respectively, and in the x-direction by 18.4% and 17.7% respectively, compared with the secondary vibration-damping structure.

When fruit is harvested in orchards, it is often necessary to attach a trailer due to the limited carrying capacity of the primary vehicle. However, the attached trailer typically employed primary or secondary vibration-damping methods, which exhibited subpar performance in reducing vibrations and consequently resulted in significant fruit damage. In order to minimize fruit damage during transportation in orchards, there is an urgent need to optimize the body's vibration-damping structure of the trailer. In view of this, this paper designed a three-stage vibration-damping trailer for unmanned vehicle hookups in orchards, and determined the relationship between fruit damage rate and vibration acceleration through fruit biomechanical tests; then took the vibration acceleration as the vibration parameter and made a comparison with the existing trailer structure through the simulation analysis of the three-stage vibration-damping trailer. The purpose of the design was to determine that the vibration-damping performance was further optimized and that the three-stage vibration-damping trailer could significantly reduce the damage rate of the fruit and improve the economic benefits of the fruit.

MATERIAL AND METHODS

Model Construction

Orchard pavement model construction

There are five main methods currently used for pavement modeling: harmonic superposition, filtered white noise, inverse Fourier transform and time series modeling *(Shi et al., 2018)*. The method of filtering white noise is a process of fitting the pavement spectrum through a hypothetical transformation when the white noise meets certain conditions. It has the advantages of a complete theoretical basis, few modeling parameters and convenient real-time online simulation, so it is widely used *(Azizi et al., 2022; Qin et al., 2022)*. In this paper, the method of filtered white noise was used to simulate the pavement roughness.

Table 1

Grading standard of pavement roughness

Grade of pavement	Roughness coefficient of pavement $G_q(n_0)$ x 10^{-6} [m^3]		
	upper limit	lower limit	geometric mean
A	32	—	16
B	128	32	64
C	512	128	256
D	2048	512	1024
E	8192	2048	4096
F	32768	8192	16384
G	131072	32768	65536
H	—	131072	262144

Generally, the pavement roughness can be categorized into eight levels (as shown in Table 1). According to the national standard GB/7031-87, the displacement power spectral density of the pavement roughness can be fitted by the power spectral density criterion of single-channel displacement, the formula of power spectral density was defined as:

$$G_q(n) = G_q(n_0)\left(\frac{n}{n_0}\right)^{-w} \quad (1)$$

where:

$G_q(n)$ is displacement power spectral density; $G_q(n_0)$ is roughness coefficient of pavement, [m^3];
n_0 is reference spatial frequency, [n_0=0.1m^{-1}]; W is frequency index, [W=2];
n is spatial frequency of pavement spectrum, [m^{-1}].

Xu *(Xu et al., 2018)* utilized a measuring system to conduct field test measurement and analysis on the pavement roughness of orchards and revealed that the grade of orchard soft and solid dirt pavements in orchards was just between C and D. The fruit trailer designed in this paper was hooked up to an unmanned orchard vehicle for harvesting and transportation of orchard fruits, therefore the Class D pavement was chosen as the simulation pavement model. Based on the filtered white noise method, the Simulink module of MATLAB was used to simulate the pavement roughness simulation, and by changing the speed of the orchard unmanned transport vehicle and the pavement roughness coefficient, the pavement roughness time-domain model of the relevant pavement was obtained, as shown in Fig. 1. The time domain model of filtered white noise pavement roughness is shown as follows *(Yin et al., 2017)*:

$$Z_g(t) = -2\pi n_1 u z_g(t) + 2\pi n_0 \sqrt{G_q(n_0)u}\,\omega(t) \quad (2)$$

where: $Z_g(t)$ is displacement of pavement roughness, [m]; n_1 is cutoff spatial frequency under pavement roughness, [n_1=0.01m^{-1}]; u is vehicle speed, [m/s]; n_0 is reference spatial frequency, [n_0=0.1m^{-1}]; $G_q(n_0)$ is pavement roughness coefficient, [m^3]; $\omega(t)$ is Gaussian white noise, [$\omega(t)$=1].

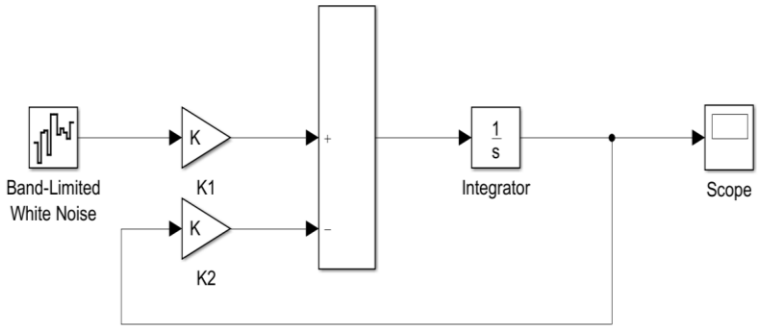


Fig. 1 – Time domain simulation model of pavement roughness

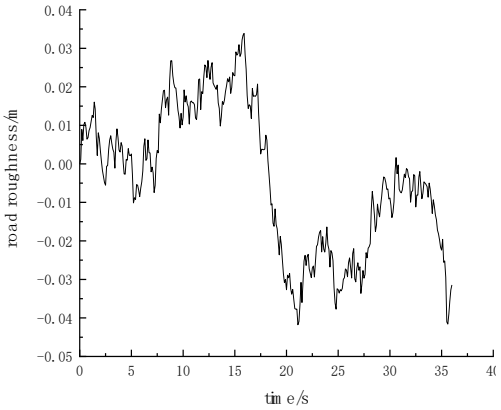


Fig. 2 – Road roughness of Class D pavement

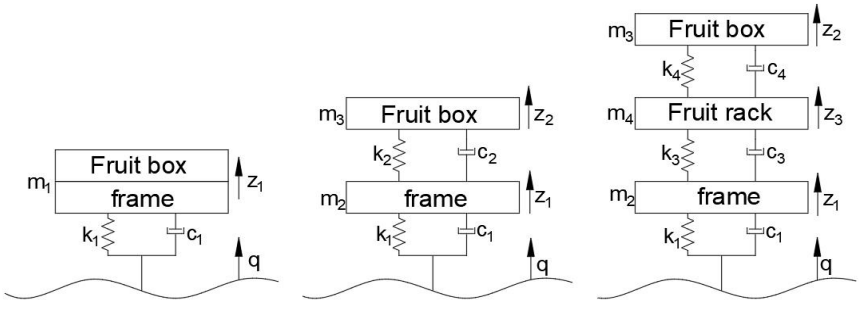
As can be seen in Figure 1, the gain modules were defined as:

$$K1 = 2\pi n_0 \sqrt{G_q(n_0)u}\,\omega(t) \quad (3)$$

$$K2 = 2\pi n_1 u \quad (4)$$

The time-domain model of the pavement roughness of the orchard unmanned transport vehicle was constructed at a vehicle speed of 1 m/s, and the resulting data of pavement roughness were shown in Fig. 2. As can be seen in Fig. 2, the highest value of this pavement roughness data was 0.0339 m and the lowest value was 0.0418 m. These data were used to construct a Class D pavement for subsequent trailer simulation pavement.

Modeling of vibration-damping system



(a) ***(b)*** ***(c)***

Fig. 3 – (a) One-stage vibration-damping system; (b) Two-stage vibration-damping system; (c)Three-stage vibration-damping system

At present, the existing orchard fruit trailers usually use one-stage or two-stage of vibration-damping, and its model simplified diagram of quarter structure is shown in Fig. 3. If the mass and stiffness of the wheel and the deformation of the wheel during travel were neglected, the displacement of the wheel in the z-direction was equal to the pavement roughness. In Fig. 3(a), the equation of the one-stage of the vibration-damping system was defined as:

$$m_1\ddot{Z}_1 + c_1\dot{Z}_1 + k_1Z_1 = c_1\dot{q}_1 + k_1q \tag{5}$$

where: m_1 is mass of transport trailer frames and fruit boxes, [kg]; Z_1 is displacement of the frame by ground excitation, [mm]; k_1 is stiffness of the damping structure between the frame and the axle, [N/mm]; c_1 is damping of damping structures between frame and axle, [N·s/mm]; q is pavement roughness function.

In Fig. 3(b), the equations for the two-stage of vibration-damping system were defined as:

$$\begin{cases} m_3\ddot{z}_2 + c_2\dot{z}_2 + k_2z_2 - c_2\dot{z}_1 - k_2z_1 = 0 \\ m_2\ddot{z}_1 + (c_1 + c_2)\dot{z}_1 + (k_1 + k_2)z_1 - k_2z_2 - c_2\dot{z}_2 = c_1\dot{q} + k_1q \end{cases} \tag{6}$$

where: m_2 is quality of transport trailer frame, [kg]; m_3 is quality of fruit boxes in transportation trailers, [kg]; Z_2 is displacement of a fruit box by ground excitation, [mm]; k_2 is stiffness of the damping structure between the fruit box and the frame, [N/mm]; c_2 is damping of the damping structure between the fruit box and the frame, [N·s/mm].

Because the pavement roughness function changed over time irregularly, it belonged to a non-periodic function. Therefore the pavement roughness function q could be regarded as the action of a series of instantaneous impulses, which might superimpose the system's response to each impulse excitation. Finally the system's response to the pavement roughness excitation was obtained. The system response to impulse excitation could reflect the vibration characteristics of the system.

At moment zero, the response of the system under unit pulse excitation was defined as:

$$h(t) = \frac{1}{m\omega}e^{-\xi\omega_n t}\sin\omega_d t \tag{7}$$

where: $\omega_n = \sqrt{\frac{k}{m}}$, $\xi = \frac{c}{2\sqrt{km}}$, $\omega_d = \omega_n\sqrt{1-\xi^2}$; m is quality of system components, [kg]; k is stiffness of the damping system, [N/mm]; c is damping of damping systems, [N·s/mm].

When the system reached the maximum overshoot M_p that is the 1st arrival at the extreme point, the time set as t_p. The formula of the time t_p was defined as:

$$t_p = \frac{\pi + arctan\frac{\sqrt{1-\xi^2}}{\xi}}{\omega_n\sqrt{1-\xi^2}} \tag{8}$$

The t_p magnitude reflected the speed of the system response and was closely related to the member of the instantaneous acceleration. The time t_p that reached the extreme point was getting longer, the acceleration response of fruit box was getting slower and the instantaneous acceleration was getting smaller. Therefore, in order to improve the vibration-damping performance of the transport trailer, the t_p can be increased by optimizing the structure of the fruit transport trailer. For a vibration-damping system, when the time that the system reached M_p was greater than the time that the pulse reached the peak excitation, a drastically changing signal could be changed into a flat signal.

Optimized design of vibration-damping system

Mathematical model of three-stage vibration-damping system

Existing trailers usually use one-stage or two-stage of vibration-damping, and the trailer vibration that was caused by ground excitation in the transport process was larger, causing serious damage to the fruit. Therefore existing trailers could not meet the requirements of the orchard fruit transport, the vibration-damping structure needed to be optimized for the existing trailer in order to enhance trailer performance and meet the requirements of actual production. Based on the technical requirements of the integration of intelligent unmanned vehicles and agronomy in orchards, a new optimization scheme was proposed for the existing trailer structure. According to the scheme, a three-stage vibration-damping trailer was designed.

The wheels were connected to the axle, the axle was connected to the frame, the frame was connected to the fruit box frame, and corresponding vibration-damping devices were added between the axle and the frame, the frame and the fruit box frame and the fruit box frame and the fruit box respectively.

The trailer adopted wheeled walking and was connected to the unmanned vehicle through the hitch device, and the power and braking of the trailer were provided by the unmanned vehicle, hence the trailer's power system took no account of the design process.

The quarter-structure model of the three-stage vibration-damping system is shown in Fig.3(c). The motion differential equations of the three-stage vibration-damping system model were defined as:

$$\begin{cases} m_3\ddot{z}_2 + c_4\dot{z}_4 + k_4 z_4 - c_4\dot{z}_3 - k_4 z_3 = 0 \\ m_4\ddot{z}_3 + (c_3 + c_4)\dot{z}_3 + (k_3 + k_4)z_3 - c_4\dot{z}_2 - c_3\dot{z}_1 - k_4 z_2 - k_3 z_1 = 0 \\ m_2\ddot{z}_1 + (c_1 + c_3)\dot{z}_1 + (k_1 + k_3)z_1 - k_3 z_3 - c_3\dot{z}_3 = c_1\dot{q} + k_1 q \end{cases} \quad (9)$$

where: m_4 is quality of fruit box frame for transportation trailers, [kg]; Z_3 is displacement of a fruit box frame by ground excitation, [mm]; k_3 is stiffness of the vibration-damping structure between the fruit box frame and the frame, [N/mm]; k_4 is stiffness of vibration-damping structures between fruit boxes and fruit box frame, [N/mm]; c_3 is damping of the damping structure between the fruit box frame and the frame, [N·s/mm]; c_4 is damping of vibration-damping structures between fruit boxes and fruit box frame, [N·s/mm].

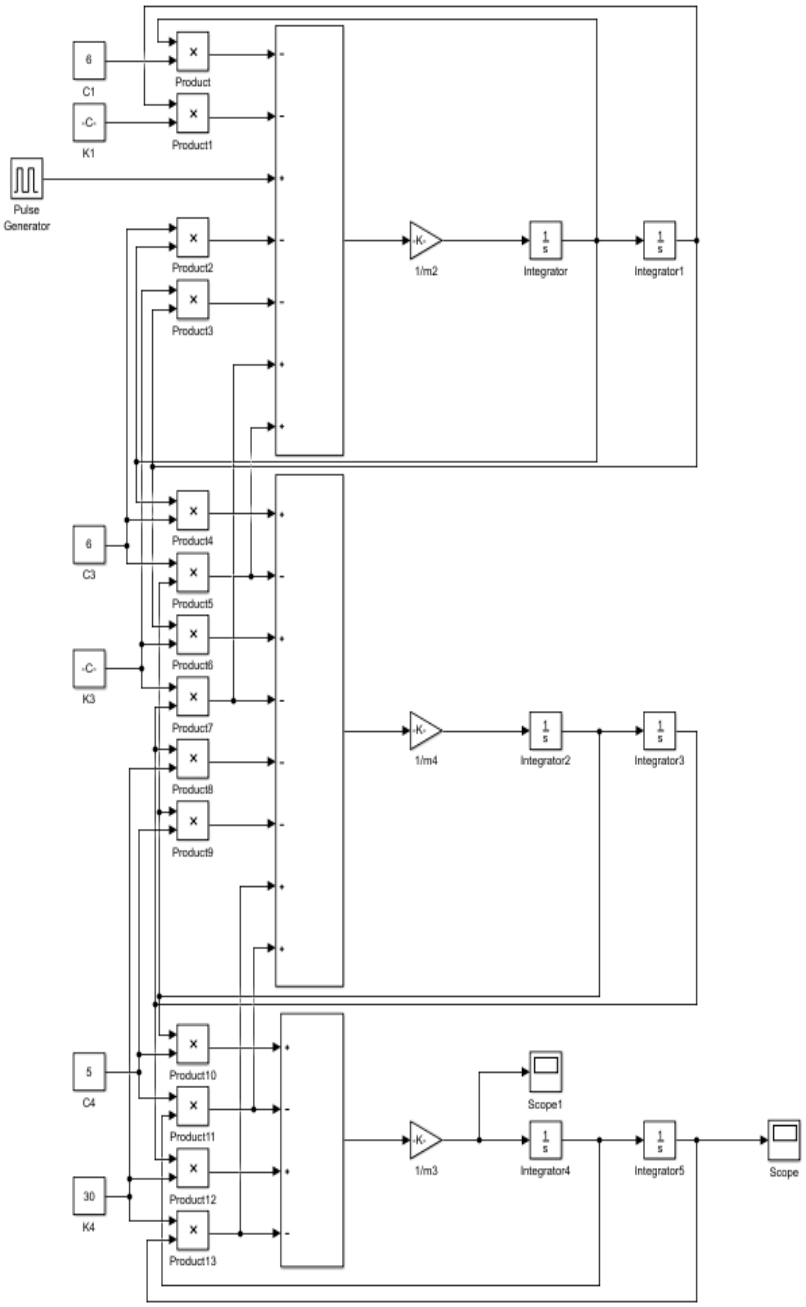


Fig. 4 – Simulink model diagram

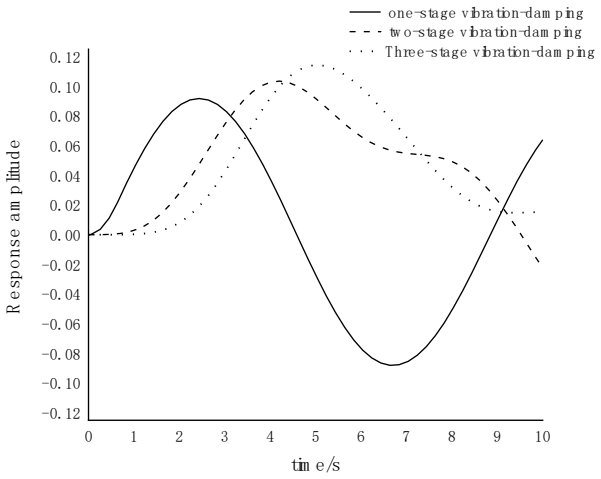
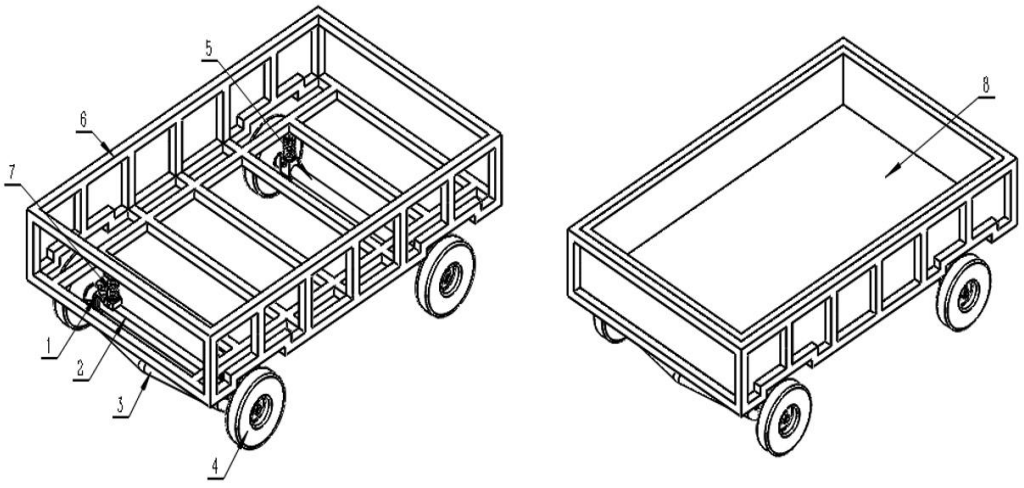


Fig. 5 – Response amplitude diagram of fruit box with different vibration reduction levels

As can be seen from Fig. 5, the t_p of the fruit box of the three-stage vibration-damping transportation trailer was larger than the t_p of the fruit box of the two-stage vibration-damping transportation trailer and was also larger than the t_p of the fruit box of the one-stage vibration-damping transportation trailer. At the same time, the larger the numerical value of t_p was, the slower the change in the amplitude response of the fruit box acceleration was, the smaller the acceleration was, and the smaller the stimulation of the fruits in the fruit box was subjected to. The above analysis expressed that the fruit damage rate that was caused by the three-stage vibration-damping transport trailer was lower than the fruit damage rate that was caused by both the two-stage vibration-damping transport trailer and the first-stage vibration-damping transport trailer under pulse excitation.

Optimized design of three-stage vibration-damping trailer structure

The structure of the one-stage and two-stage vibration-damping trailers for the orchard is schematically shown in Fig. 6. In Fig. 6(a), the one-stage of vibration-damped trailer was vibration-damped by a spring damper, which could reduce vibration-damping for the z-direction excitation that was perpendicular to the ground. Compared with the one-stage of vibration-damped trailer, the two-stage of vibration-damped trailer added rubber vibration-damping pads in the frame to further reduce vibration-damping, as shown in Fig. 6(b). In fact, the rubber vibration-damping pads further reduced the z-direction excitation that was perpendicular to the ground. When the trailer walked on the road, besides vibration excitation from the pavement in the z direction, the trailer also received vibration excitation in the x and y directions, therefore, based on the trailer structure of one-stage and two-stage vibration-damping, two structures of the three-stage vibration-damping trailer were designed (as shown in Fig. 7).

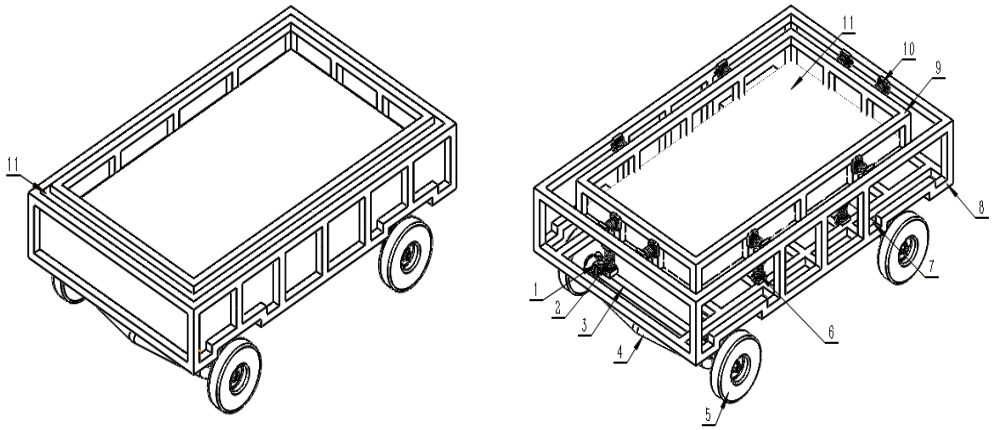


(a) *(b)*

Fig.6 – (a) Structure diagram of one-stage vibration-damping trailer;
(b)Structure diagram of two-stage vibration-damping trailer

1. Steering link 2. Front axle 3. Stabilizer rod 4. Wheels 5. Rear axle 6. Frame 7. Spring shock absorber 8. Rubber vibration pads

In Fig. 7(a), one kind of structure used the spring damper connection not only between the axle and the frame but also between the fruit box frame and the frame, added the rubber vibration-damping pads between the fruit box frame and the frame of the horizontal direction, and added the rubber vibration-damping pads inside the fruit box frame, which not only kept the rubber vibration-damping of the vertical direction unchanged but the vibration excitation of the horizontal direction was also reduced. In Fig. 7(b), another structure replaced the rubber vibration-damping pads between the fruit box frame and the frame with extension springs that had preload.



(a) *(b)*

Fig. 7 – Structure diagram of three-stage vibration-damping trailer

1. Steering link; 2. One-stage spring shock absorber; 3. Front axle; 4. Stabilizer rod; 5. Wheels; 6. Two-stage spring shock absorber; 7. Rear axle; 8. Frame; 9. Fruit box frame; 10. Stretch spring; 11. Rubber damping pad

Vibration mechanics property of fruits

Researches have shown that the transportation damage of fruit was one of the important causes of fruit loss, and fruit damage rate in the transportation process could reach 25%~45% *(Lu et al., 2009)*. Therefore, it is necessary to simulate the vibration of the fruit in the transportation process through the shaking table, observe the degree of damage and explore the relationship between the damage rate of the fruit and the vibration acceleration that was generated in the process of vehicle driving.

Test materials and instruments

Fuji apples, which grew in Shanxi Fruit Institute Academy of Agriculture Sciences, were picked in October 2022. In order to minimize the loss of water and other nutrients from the fruits, the picked apples were placed in the laboratory refrigerator at a storage temperature of 3~5℃ to complete the test as soon as possible; the sample fruits were uniformly shaped and sized, no pests and no mechanical damage in the experiment.

In order to simulate the vibration that was generated by the car travel on the pavement, the corresponding vibration excitation of the fruit box were provided by a vibration table (LongData, China); the transverse and longitudinal diameter of apples were measure by electronic vernier calipers with a measurement accuracy of 0.01 mm; the perimeter of apples at the equator was measured by a tape with a measurement accuracy of 1 mm.

Test methods

The 300 apples with undamaged surfaces were selected and weighed, the longitudinal and transverse diameters of the fruits were measured using electronic vernier calipers, the circumference of the fruit equator was measured by a tape and the measurement data were recorded respectively. The 300 fruit samples were divided into 15 groups, and the samples were numbered one by one for each group and loaded into a box measuring 25cm*25cm*25cm, and then the box was numbered.

During the actual transportation, when the pavement was in good condition, the vibration acceleration of the transport car was 0.2~1 g. Therefore vibration acceleration values were set to 0.2 g, 0.25 g, 0.5 g, 0.75 g, 1 g respectively in the simulation test. Considering that the long-distance transportation time of the fruit was generally more than 10 hours, combined with the actual situation, the actual transportation time of the simulation test was set to 15 hours. But in order to ensure the accuracy of the test simulation, based on the research of William and the specific situation of this laboratory, the actual vibration time of the test was reduced to 1/5 of the original, that is to say, the vibration time was 3 h *(Kipp et al., 2000)*.

Table 2

Vibration table debugging data

Sweep frequency [HZ]		20-200	10-500	10-55	10-500	5-80
Acceleration of vibration [g]		1	0.75	0.5	0.25	0.2
Upper limiting frequency (CD000) [HZ]		200	500	55	500	80
Lower frequency [HZ]	CD041	20	10	10	10	5
	CD080	20	10	10	10	5
Upper limit time (CD087) [s]		30	30	30	30	30
Lower limit time (CD088) [s]		30	30	30	30	30
Climbing speed (CD012) [s]		100	36.7	400	36.7	240
Rate of descent (CD013) [s]		100	36.7	400	36.7	240
Total time [s]	CD064	180	180	180	180	180
Amplitude setting [mmp-p]	CD003	58	70	30	60	35
	CD005	15	20	13	18	18

The vibration table adopted the frequency sweep mode, and the relevant debugging data are shown in Table 2. Fifteen boxes of apples were divided into 5 groups and each group carried out a vibration acceleration test (as shown in Fig. 8). At the end of the vibration test, each box of apples was labeled with the start and end time of the test. After the vibrated apples were placed for 24 hours, the damaged apples were selected, and then its damage diameter that was used to do damage grading was measured.

The damage classification method referred to the Agricultural Biomechanics and Agricultural Bio-electromagnetism edited by Sun et al *(Sun et al., 1996)*. Apples that have a damage diameter of less than 19 mm are considered as micro-injury, apples that have a damage diameter of more than 19 mm and less than 25.4 mm are considered as minor injury, apples that have a damage diameter of more than 25.4 mm and less than 31.75 mm are considered as moderate injury, and apples that have a damage diameter of more than 31.75 mm are considered as serious injury *(Sun et al., 1996)*. Therefore the test data were recorded according to the above classification.



Fig. 8 – Process diagram of vibration table test

RESULTS

Analysis of test results

The measurements showed that the mass of the apples ranged from 144 to 326 g, the transverse diameters ranged from 66.39 to 94.52 mm, the longitudinal diameters ranged from 57.78 to 84.48 mm, and the equatorial circumferences ranged from 218.1 to 290.5 mm. After grading the damaged apples in terms of damage diameter, the results obtained are shown in Table 3.

Table 3

Data obtained from grading damaged apples

Accelerated speed [g]	Box number	Number of slight damages	Number of minor damages	Number of moderate damages	Number of severe damages	Total number of damages	Damage rate [%]	Average damage rate [%]
0.2	1	3	2	0	1	6	30	23.33
	2	4	0	0	0	4	20	
	3	3	1	0	0	4	20	
0.25	4	4	1	0	0	5	25	26.67
	5	5	0	0	0	5	25	
	6	5	1	0	0	6	30	
0.5	7	6	0	0	0	6	30	31.67
	8	5	1	0	0	6	30	
	9	4	3	0	0	7	35	
0.75	10	6	2	0	0	8	40	36.67
	11	4	3	0	1	8	40	
	12	4	2	0	0	6	30	
1	13	8	4	0	0	12	60	50
	14	5	3	0	0	8	40	
	15	8	2	0	0	10	50	



(a) slight damage *(b) minor damages* *(c) severe damages*

Fig. 9 – Damage diagram of apples with different damage levels

As can be seen from Table 3, for the same vibration time, the higher the vibration acceleration, the higher the damage rate of apples. The damage grade of apples were mostly micro-injury, light injury, and very few were serious injury, which was consistent with the actual transportation condition. The damage situation of apples with different damage levels is shown in Fig. 9.

The unitary linear regression analysis of vibration acceleration and fruit damage rate was carried out by SAS software. The results showed that the determination coefficient of the regression model amounted to 0.9522, which indicated that the regression model had very high fitting accuracy and could be used as a response prediction. The regression equation is as follows:

$$y = 0.174 + 0.30126x \quad (10)$$

The relationship between the measured apple damage rate and the unitary linear regression curve is shown in Fig. 10. From Fig. 10, the vibration acceleration that was generated during vehicle traveling and the fruit damage rate presented positive linear correlation. Therefore the subsequent simulation tests could use vibration acceleration as a vibration-damping parameter to evaluate the vibration-damping performance of the designed three-stage vibration-damping trailer.

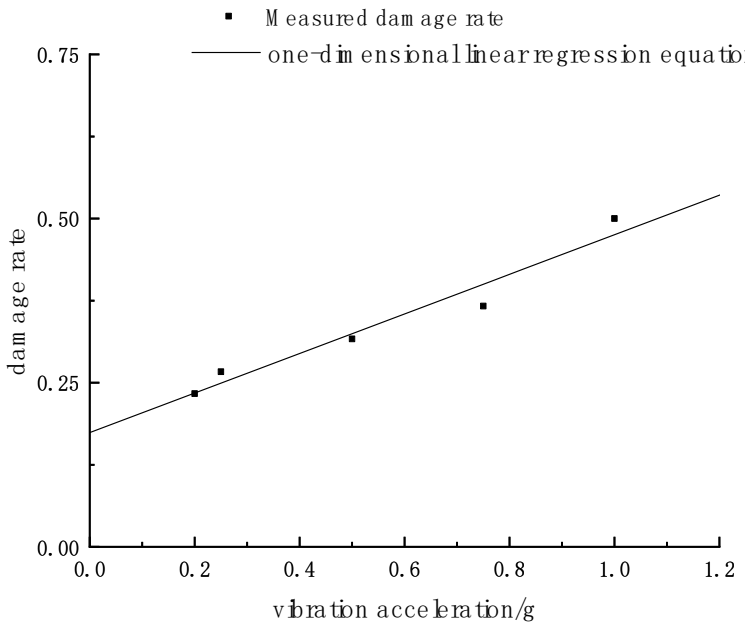


Fig. 10 – Relationship between measured fruit damage rate and unitary linear regression curve

Dynamics Simulation Analysis

Dynamic simulation analysis of the trailer structure was carried out using Adams software to test the vibration acceleration generated by the one-stage, two-stage and three-stage vibration-damped trailer when driving on Class D road surface, respectively. The relevant parameters of the trailer are shown in Table 4.

Table 4

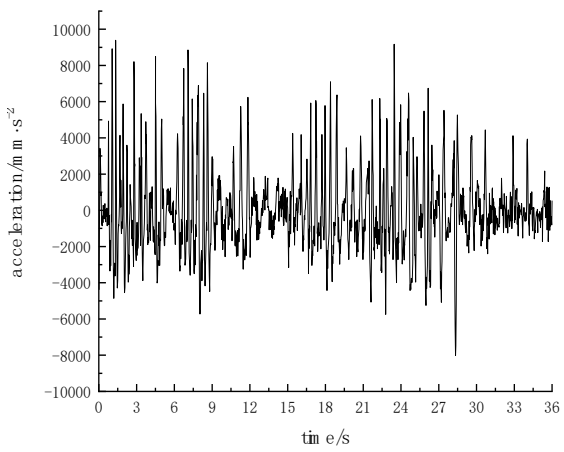
Values of trailer related parameters

Title	Symbolic representation	Numerical value	Unit
Frame quality	m_4	110	kg
Fruit box stand quality	m_2	70	kg
Fruit box quality	m_3	200	kg
First level vibration-dampening stiffness	k_1	42.06	N/mm
First level vibration-dampening damping	c_1	1.5	N s/mm
Second level vibration-dampening stiffness	k_3	34.11	N/mm
Second level vibration-dampening damping	c_3	1.5	N s/mm
Third level vibration-dampening stiffness	k_4	7.5	N/mm
Third level vibration-dampening damping	c_4	0.3	N s/mm
Tension spring stiffness	k_5	34.11	N/mm
Car speed	v	1	m/s

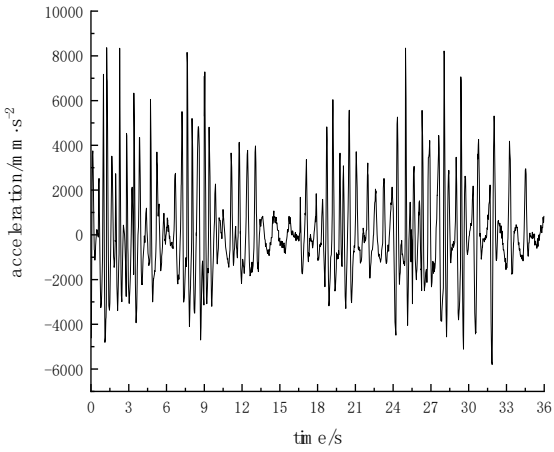
z-direction simulation results and analysis

The one-stage vibration-damped trailer, the two-stage vibration-damped trailer, and both structures' three-stage vibration-damped trailer each drove for 36 seconds on a D-class pavement at a speed of 1 m/s, and the acceleration response values of the fruit box were used as the simulation results.

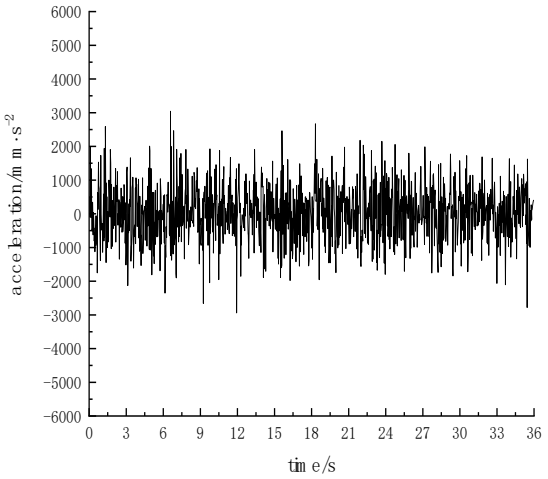
The acceleration response of the fruit box in the z-direction is shown in Fig. 11.



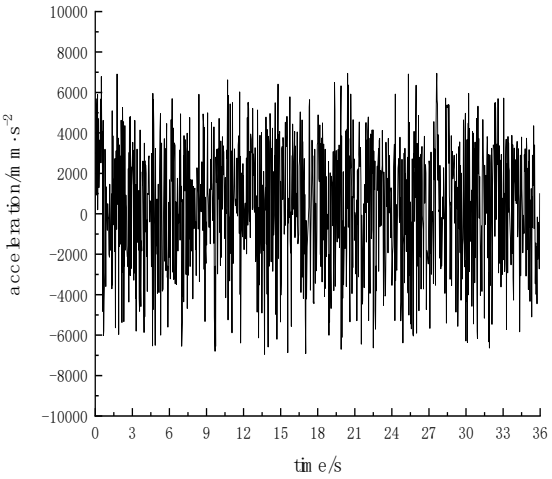
(a) acceleration response graph of one-stage vibration-dampening trailer in the z-direction



(b) acceleration response graph of two-stage vibration-dampening trailer in the z-direction



(c) acceleration response graph of three-stage vibration-dampening trailer Fig. 7(a) in the z-direction



(d) acceleration response graph of three-stage vibration-dampening trailer Fig. 7(b) in the z-direction

Fig. 11 – Acceleration response diagram in the z direction of the fruit box

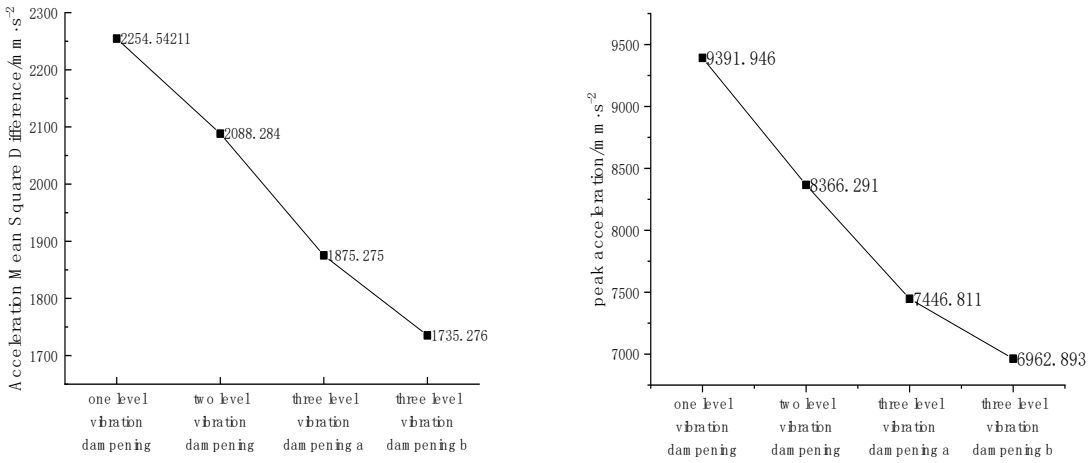
Based on Class D pavement, the z-direction acceleration optimization effect of the four structures of vibration-damped trailers is compared as shown in Fig.12.

From Fig.12, when the vibration-damped trailer was driving on the pavement of Class D, the acceleration mean square deviation of the two-stage vibration-damped trailer in the z-direction was optimized by 7.4% compared with that of the one-stage vibration-damped trailer and the acceleration peak value was optimized by 10.9%.

For the three-stage vibration-damped trailer rubber vibration-damping pads were utilized in the horizontal direction, the mean squared error of acceleration in the z-direction was optimized by 16.8% compared to the one-stage vibration-damped trailer and 10.2% compared to the two-stage vibration-damped trailer, and the peak acceleration was optimized by 20.7% compared to the one-stage vibration-damped trailer and 11.0% compared to the two-stage vibration-damped trailer.

For the three-stage vibration-damped trailer with tension spring in the horizontal direction, the mean squared error of acceleration in the z-direction was optimized by 23.0% compared to the one-stage vibration-damped trailer and 16.9% compared to the two-stage vibration-damped trailer, and the peak acceleration was optimized by 25.9% compared to the one-stage vibration-damped trailer and 16.8% compared to the two-stage vibration-damped trailer. The above analysis showed that the two kinds of three-stage vibration-damped trailers had better vibration-damping performance than the traditional one-stage and two-stage vibration-damped trailers in the z-direction.

The three-stage vibration-damped trailer that used tension spring for vibration-damping in the horizontal direction had better vibration-damping performance in the z-direction than the three-stage vibration-damped trailer that used rubber vibration-damping pads for vibration-damping in the horizontal direction.

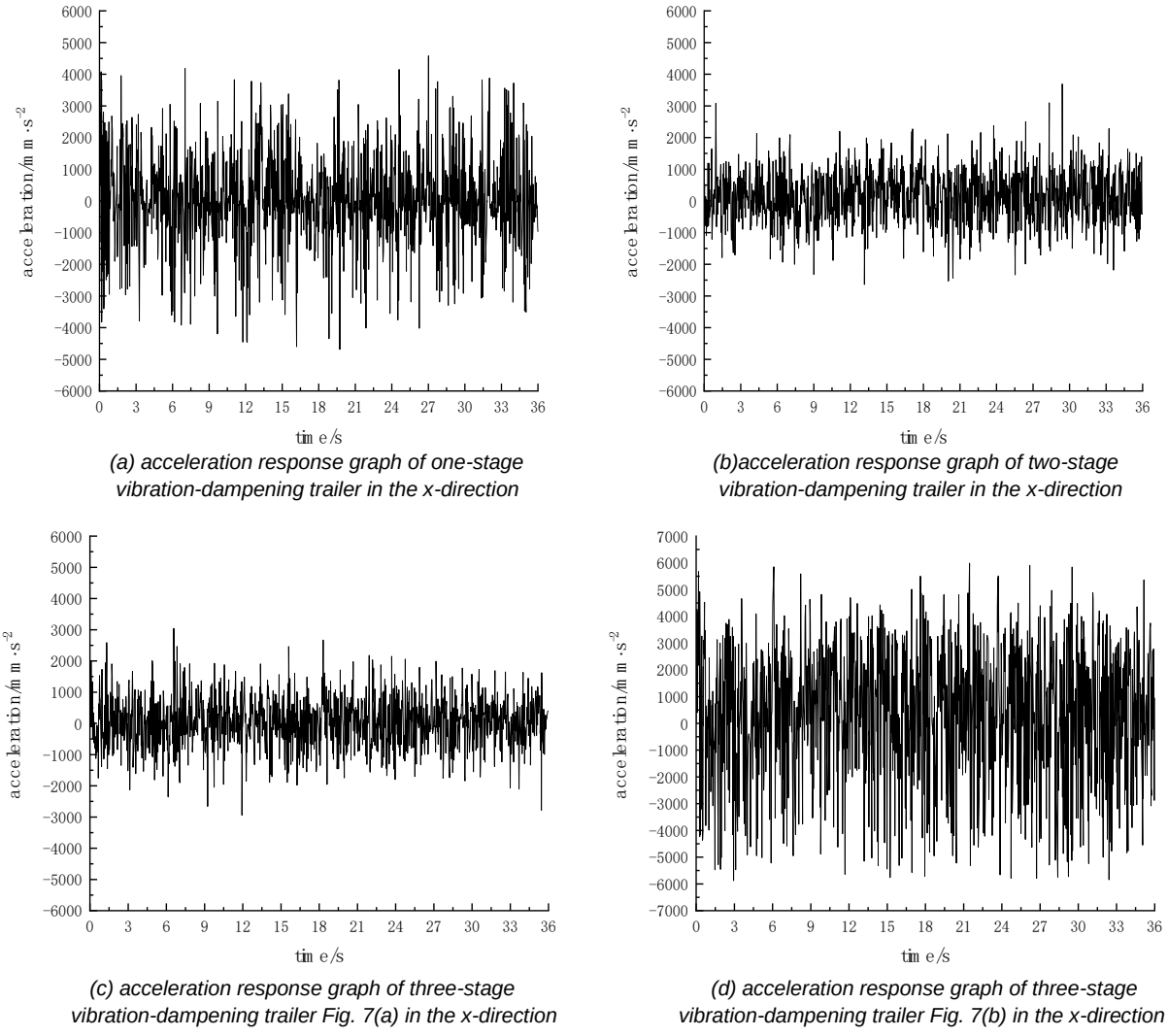


(a) z-direction acceleration mean square deviation *(b) Peak z-direction acceleration*

Fig. 12 – Comparison diagram of Z-direction optimization effect

x- and y-direction simulation results and analysis

When the trailer was in the process of driving, the fruit box would not only be excited by the vibration from the ground in the z-direction, but also by the vibration in the x-direction and y-direction. Therefore the vibration effect of the x-direction and y-direction needed to be simulated and analyzed. The acceleration response of the fruit box in the x-direction and y-direction are shown in Fig. 13 and Fig. 14, respectively.



(a) acceleration response graph of one-stage vibration-dampening trailer in the x-direction

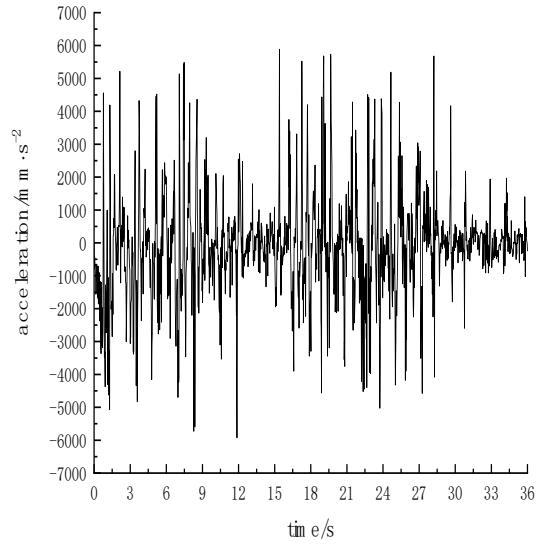
(b)acceleration response graph of two-stage vibration-dampening trailer in the x-direction

(c) acceleration response graph of three-stage vibration-dampening trailer Fig. 7(a) in the x-direction

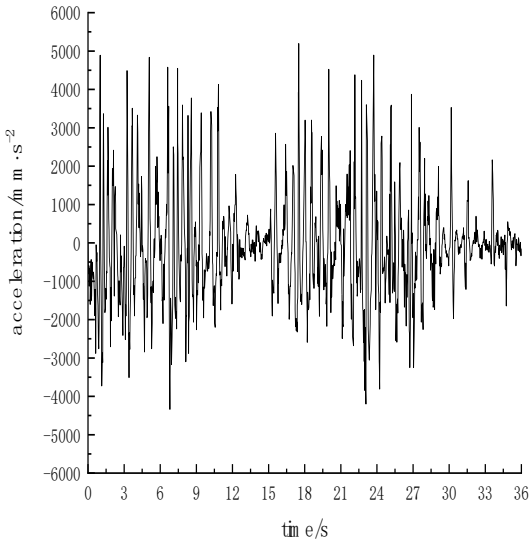
(d) acceleration response graph of three-stage vibration-dampening trailer Fig. 7(b) in the x-direction

Fig. 13 – Acceleration response diagram in the x direction of the fruit box

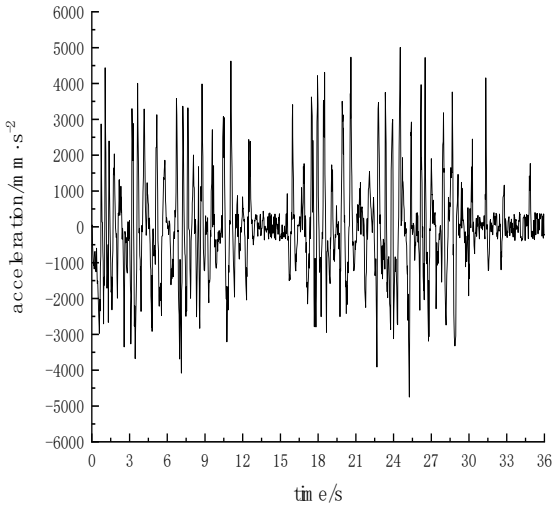
When the vibration-absorbing trailers of four structures were driving on the D-class road surface, the optimization effects of X-direction and Y-direction acceleration are compared in Fig.15 and Fig.16 respectively. From Fig. 15, the acceleration mean square deviation of the two-stage vibration-damped trailer in the x-direction was optimized by 41.2% and the peak acceleration is optimized by 19.4% compared with that of the one-stage vibration-damped trailer. For the three-stage vibration-damped trailer utilized rubber vibration-damping pads in the horizontal direction, its mean squared error of acceleration in the x-direction was optimized by 43.3% compared to the one-stage vibration-damped trailer and 3.5% compared to the two-stage vibration-damped trailer, and its peak acceleration was optimized by 33.5% compared to the one-stage vibration-damped trailer and 17.5% compared to the two-stage vibration-damped trailer. For the three-stage vibration-damped trailer with tension springs in the horizontal direction, the mean square deviation of acceleration in the x-direction increased by 73.7% compared with the one-stage vibration-damped trailer and 195.4% compared with the two-stage vibration-damped trailer, and the peak acceleration increased by 30.7% compared with the one-stage vibration-damped trailer and 62.2% compared with the two-stage vibration-damped trailer.



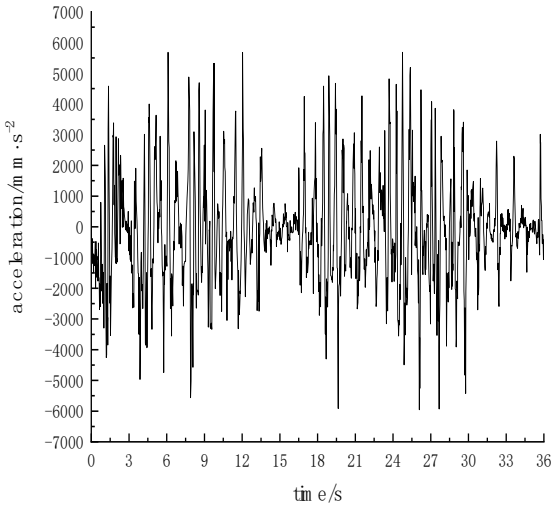
(a) acceleration response graph of one-stage vibration-dampening trailer in the y-direction



(b) acceleration response graph of two-stage vibration-dampening trailer in the y-direction



(c) acceleration response graph of three-stage vibration-dampening trailer Fig. 7(a) in the y-direction

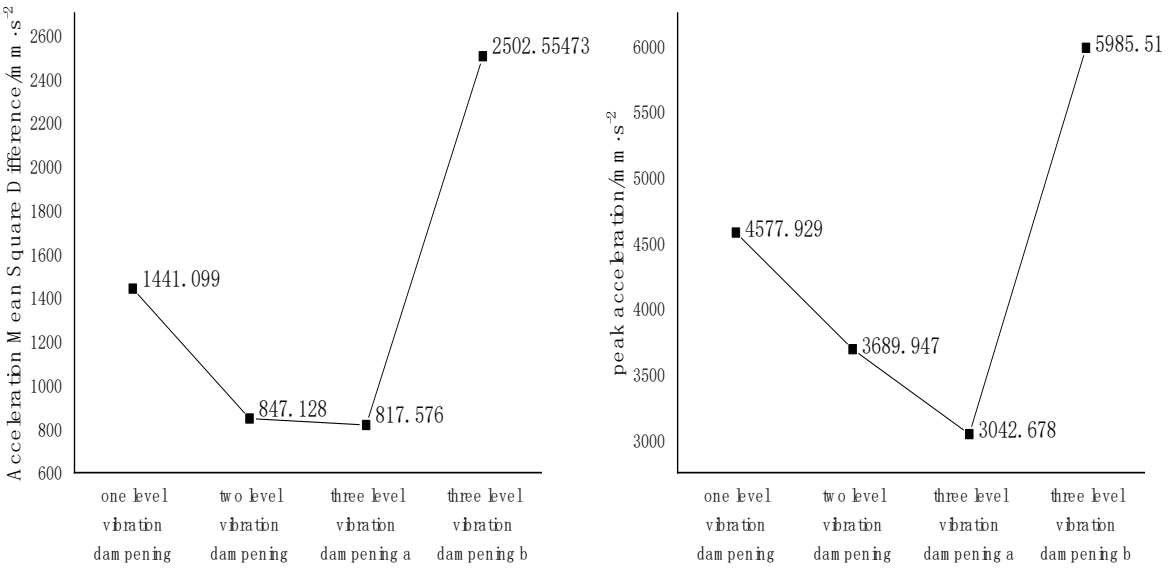


(d) acceleration response graph of three-stage vibration-dampening trailer Fig. 7(b) in the y-direction

Fig. 14 – Acceleration response diagram in the y direction of the fruit box

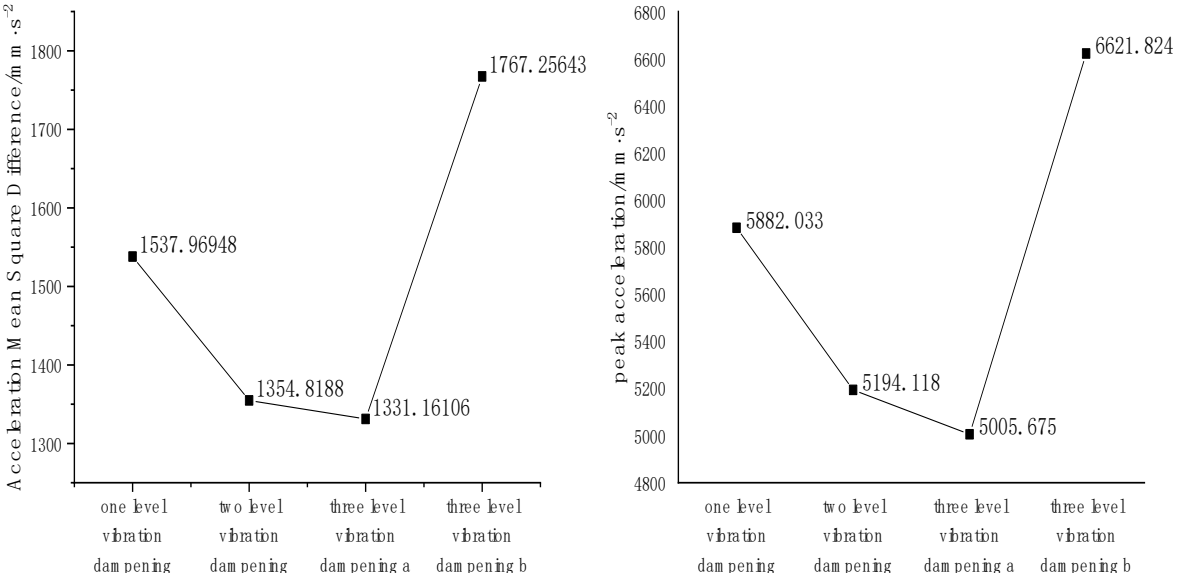
As can be seen from Fig. 16, the acceleration mean squared error of the two-stage vibration-damped trailer in the y-direction was optimized by 11.9% compared with the one-stage vibration-damped trailer, and the peak acceleration was optimized by 11.7%. For the three-stage vibration-damped trailer with rubber vibration-damping pads in the horizontal direction, the mean squared error of acceleration in the y-direction

was optimized by 13.4% compared to the one-stage vibration-damped trailer, 1.7% compared to the two-stage vibration-damped trailer, and the peak of acceleration optimized by 14.9% compared to the one-stage vibration-damped trailer and 3.6% compared to the two-stage vibration-damped trailer. Whereas, for the three-stage vibration-damped trailer with tensile springs in the horizontal direction, the mean squared error of acceleration in the y-direction was optimized by 14.9% compared to the one-stage vibration-damped trailer and 30.4% compared with the two-stage vibration-damped trailer, and the peak acceleration by 12.6% over the one-stage vibration-damped trailer and 27.5% over the two-stage vibration-damped trailer.



(a) x-direction acceleration mean square deviation *(b) Peak x-direction acceleration*

Fig. 15 – Comparison diagram of x-direction optimization effect



(a) y-direction acceleration mean square deviation *(b) Peak y-direction acceleration*

Fig. 16 – Comparison diagram of y-direction optimization effect

The above analysis showed that for the damping performance of the two designed three-stage vibration-damping trailers in the x and y directions, the three-stage vibration-damping trailer with rubber vibration-damping pads in the horizontal direction was better than the conventional one-stage vibration-damping trailer and two-stage vibration-damping trailer, while the three-stage damping trailer with tension springs in the horizontal direction had a worse vibration-damping performance than the conventional one-stage vibration-damping trailer and two-stage vibration-damping trailer in the x and y directions. Meanwhile, in the x and y directions, the three-stage vibration-damping trailer with rubber vibration-damping pads in the horizontal direction was better than the three-stage vibration-damping trailer with extension springs in the horizontal direction.

CONCLUSIONS

(1) Based on the pavement model of the orchard, the dynamics analysis of the vibration-damping system of the orchard transportation trailer was carried out, and two kinds of three-stage vibration-damping transportation trailers were designed; the results of the vibration mechanics test by the fruits showed that the damage rate of the fruits and the vibration acceleration were positively correlated, which provided a reference basis for the simulation test to evaluate the vibration-damping performance of the designed trailer.

(2) Taking the vibration acceleration as the vibration-damping parameter, the acceleration response diagram of the vibration-damping trailer that was driving at 1 m/s on the D-class road was generated by Adams simulation, and the results showed that compared with the one-stage and two-stage vibration-damping trailer, the optimization rates of the three stage vibration-damping trailer that had rubber vibration-damping pads of the horizontal direction were 16.8% and 10.2% respectively, and the optimization rates of the three stage vibration-damping trailer that had extension springs of the horizontal direction were 23.0% and 16.9% respectively.

(3) When driving on Class D pavement, for the three-stage transport trailer using a rubber vibration-damping pad in the horizontal direction, its vibration-damping optimization rates were 43.3% compared with the one-stage vibration-damping trailer in the x direction and 13.4% in the y direction, and its vibration-damping optimization rates are 3.5% compared with the two-stage vibration-damping trailer in the x direction and 1.7% in the y direction. For the three-stage vibration-damped trailer with tension springs in the horizontal direction, the vibration acceleration in the x- and y-directions was respectively increased by 73.7% and 14.9% compared to the one-stage vibration-damped trailer and by 195.4% and 30.4% compared with the two-stage vibration-damped trailer, and thus its vibration-damping performance in the x- and y-directions was worse than that of the existing trailer.

In short, the vibration-damping effect of the three-stage vibration-damping trailer that used rubber vibration-damping pads in the horizontal direction was the best, which could better achieve the purpose of improving the vibration-damping performance of a mountain orchard transportation trailer.

ACKNOWLEDGEMENT

The authors were funded for this project by the Key R&D Program of Shanxi Province (No.202102020101012), the National Natural Science Foundation of China (No.11802167) and science and the Applied Basic Research Project of Shanxi Province (No.201801D221297).

REFERENCES

[1] Azizi, A., (2018). Computer-Based Analysis of the Stochastic Stability of Mechanical Structures Driven by White and Colored Noise. *Sustainability* (10).

[2] Bai, R., Guo, D., (2018). Sliding-Mode Control of the Active Suspension System with the Dynamics of a Hydraulic Actuator. *Complexity*.

[3] Chi, Y., Ren, J., Wang, Y., Ji, X.Y., & Li, J.Q., (2017). Design and Simulation of Wheeled Tractor Hydraulic Active Suspension System (轮式拖拉机液压减振系统的设计与仿真分析). *Journal of Agricultural Mechanization Research* (09), 46-50, Haerbing/China.

[4] Dong, M.F., (2022). Modeling and Simulation of Different Vehicle Suspension Systems (车辆不同悬架系统的建模仿真分析). *Automobile Applied Technology* (21), 123-126, Xi'an/China.

[5] GB/T 7031－2005, Mechanical vibration—Road surface profiles—Reporting of measured data (机械振动 道路路面谱测量数据报告).

[6] Kipp, W.I., (2000). Vibration testing equivalence. *In ISTA Con,* Vol. 2006, No. 26, pp. 1-13.

[7] Li, X.P., Li, F.J., Cao, Z., & Yang, L.X., (2019). Vibration Performance of Two-Stage Vehicle Suspension with Inerters (含惯容器的两级汽车悬架振动性能). *Journal of Northeastern University (Natural Science)* (10), 1448-1453, Shenyang/China.

[8] Lu, L.X., Huang, X.F., & Hua, Y., (2009). Effect of packaging methods on vibration bruising of pear fruits by simulated transport tests (基于模拟运输条件的梨果实包装振动损伤研究). *Transactions of the Chinese Society of Agricultural Engineering* (06), 110-114, Beijing/China.

[9] Ma, T.G., Zeng, J.S., Feng, P.J., Yang, Y.Y., & Zhang, W.H., (2023). Research on hybrid damping semi-active vibration reduction control of secondary suspension of superconducting electric maglev train (超导电动磁悬浮列车次级悬挂混合阻尼半主动减振控制研究). *Journal of Mechanical Engineering* (10), 236-249, Beijing/China.

[10] Qi, D.Z., Ruan, X.S., Wu, Y.Z., Sun, Q., & Gao, W.Z., (2023). Optimal Design of Vibration Damping System for Transport Vehicles between Rows in Mountain Orchards (山地果园行间运输车减振系统优化设计). *Journal of Agricultural Mechanization Research* (10), 237-242, Haerbing/China.

[11] Qin, Y., Langari, R., Wang, Z., Xiang, C., & Dong, M. (2017). Road profile estimation for semi-active suspension using an adaptive Kalman filter and an adaptive super-twisting observer. *In 2017 American Control Conference* (ACC) pp. 973-978. IEEE.

[12] Shen, Y.J., Chen, L., Yang, X.F., & Yang, J., (2016). Improved design of dynamic vibration absorber by using the inerter and its application in vehicle suspension. *Journal of Sound and Vibration*.

[13] Shi, X.H., Jiang, X., Zhao, J., & Zhai, J.X., (2018). Research on vehicle-road coupling dynamic load on uneven pavement (不平路面车路耦合动载研究). *China Sciencepaper* (04), 408-413, Beijing/China.

[14] Sun, Y.Y., Yu, D.Y., (1996). Agri-biomechanics and agri-bioelectromagnetics (农业生物力学及农业生物电磁学). *China Agriculture Press,* Beijing/China.

[15] Suo, X.F., Jiao, S.J., Wang, G.F., Liu, S.M., & Zhang, Z.Y., (2021). Research on the Vibration Damping Performance of a Novel Single-Side Coupling Hydro-Pneumatic Suspension. *Tehnički vjesnik* (5).

[16] Teng, F.H., (2017). Study on optimization of suspension and Vibration reduction performance of tracked armored vehicle (履带式装甲车悬挂优化及减振性能研究). MD Dissertation, Zhongbei University, Shanxi/China.

[17] Xu, Z.F., Xue, X.Y., & Cui, L.F., (2017). Measurement and Analysis of Farmland Surface Roughness (农田地面不平度测量与分析). *Journal of Agricultural Mechanization Research* (01), 171-176, Haerbing/China.

[18] Yang, M., Zhang, J., & Luo, X.J., (2021). Research on New Types of Suspension Vibration Reduction Systems (SVRSs) with Geometric Nonlinear Damping. *Mathematical Problems in Engineering*.

[19] Yin, J., Chen, X.B., Wu, L.X., & Liu, Y.L., (2017). Simulation Method of Road Excitation in Time Domain Using Filtered White Noise and Dynamic Analysis of Suspension (滤波白噪声路面时域模拟方法与悬架性能仿真). *Journal of Tongji University (Natural Science)* (03), 398-407, Shanghai/China.

[20] Yuan, D.F., (2022). *Research on Semi-active control strategy of vehicle-mounted vibration isolation platform adopting continuously adjustable damper (基于连续可调半主动减振器的车载隔振平台控制策略研究).* MD Dissertation, Jilin University, Jilin/China.

[21] Yuan, J.Q., Zhou, Y.Q., Fan, J., & Lu, Z.X., (2020). Research on vibration characteristics of tractor driving on the farmland (农田行驶工况下拖拉机振动特性研究). *Journal of Chinese Agricultural Mechanization* (02), 127-134, Nanjing/China.

[22] Zhao, Y.Q., Xu, H., Deng, Y.J., & Wang, Q.W., (2019). Multi-objective optimization for ride comfort of hydro-pneumatic suspension vehicles with mechanical elastic wheel. Proceedings of the Institution of Mechanical Engineers, Part D: *Journal of Automobile Engineering* (11).

[23] Zhong, J.G., (2020). *Research on Modeling and Control of Three-stage Vibration Reduction Active Suspension (三级减振式主动悬架建模与控制研究).* MD Dissertation, Zhejiang Sci-Tech University, Zhejiang/China.

[24] Zhou, Y.Q., Li, L.Q., Sun, F.J., Wang, Y., Sun, M., & Li, H., (2021). Simulation Analysis of Active Air Suspension of Heavy-Duty Vehicle Based on Fuzzy PID Control (基于模糊 PID 控制重型汽车主动空气悬架仿真分析). *Automobile Parts* (05), 25-28, Guangzhou/China.

DESIGN AND EXPERIMENT OF OVERLOAD PROTECTION AND AUTOMATIC OBSTACLE AVOIDANCE MECHANISM FOR BIDIRECTIONAL PLOUGHING EQUIPMENT
/
双向犁耕防过载自动避障机构的设计与试验

Jinbao LIU[1)], Xuan ZHENG[*1)], Yanhui ZHANG[2)], Yuying SONG[2)], Zhihui TANG[1)]

[1)]Machinery Equipment Research Institute, Xinjiang Academy of Agricultural and Reclamation Science, Shihezi, 832000, China

[2)]College of Sciences, Shihezi University, Shihezi, 832000, China

Corresponding authors: Xuan Zheng, E-mail: jiazhengxuan@sohu.com

DOI: https://doi.org/10.35633/inmateh-71-52

***Keywords*: Agricultural engineering; Bidirectional ploughing; Overload protection; Automatic obstacle avoidance; Design; Experiments**

ABSTRACT

During the tillage of two-way ploughing equipment in rocky and barren soil, due to hard objects such as stones, the plough and the key working parts such as plough column are deformed and broken, thereby reducing the reliability and service life of machines and tools. As such, an anti-overload automatic obstacle avoidance mechanism for two-way ploughing is developed. The maximum obstacle avoidance height is 40 cm, and the obstacle avoidance angle α is designed. The rotation range is 4.6~51.5°, and the effective compression stroke of the spring after pre-tightening is 39.34 mm. The motion equation and quasi-static force equation of the mechanism are established. The ploughing resistance in the equilibrium state is 9.74 KN, and the required spring preload is 9.75 KN. Under the safety factor of 1.3, different spring elastic coefficients change with the rotation angle of the mechanism. The virtual prototype simulation model of the anti-overload automatic obstacle avoidance mechanism is established. The simulation results show that the mechanism can effectively perform the obstacle avoidance action. Bench test verifies that the mechanism can avoid obstacles according to the predetermined load. The field test shows that the stability coefficient of the ploughing depth of the mechanism is less than 8%. The results can effectively realize the obstacle avoidance function and ensure the farming quality, and provide an efficient and reliable anti-overload obstacle avoidance structure and parameter basis for the rocky land.

摘要

针对当前双向犁耕装备在多石贫瘠土壤耕作过程中，石块等坚硬物体使犁体以及犁柱等关键工作部件产生变形、断裂，降低了机具可靠性和使用寿命等问题，研制了双向犁耕防过载自动避障机构，对过载保护自动避障机构的结构和关键参数进行了设计，设计最大避障高度为 40cm，避障转角 α 转动范围为 4.6°~51.5°，弹簧预紧后的有效压缩行程为 39.34mm。分别建立了机构运动方程和准静态受力方程，得到平衡状态下犁耕阻力 9.74KN 对应所需的弹簧预紧力为 9.75KN，为提高机构可靠性设置安全系数为 1.3，分析了不同弹簧弹性系数随机构转角 α 的变化曲线。通过台架试验验证了机构能按照预定载荷进行避障动作，进行了田间试验，根据响应曲面设计法中 Box-Behnken Design 原理，试验结果表明，对耕深稳定性变异系数影响的贡献率由大到小依次为：耕速、耕深和弹簧弹性系数。机构耕深稳定性变异系数均小于 8%，能有效实现避障功能并能保证耕作质量，为多石地提供了高效可靠的防过载避障结构和参数依据。

INTRODUCTION

The farming soils in Xinjiang, West China are more barren, harder and more severely salinized than the black soils in Northeast China. Most farmlands are located at mountainous areas or valley basins, adjacent to grasslands, deserts and Gobi *(Wang et al., 2020; Gao et al., 2021)*. Consequently, the soils are rich in stones, fine sands and tree roots. In addition, agricultural machinery tillage will further compact the soil *(Mileusnić et al., 2022; Guilherme et al., 2021)*.

[1] *Jinbao Liu, Associate Researcher; Xuan Zheng, Researcher; Yanhui Zhang, Lecturer; Yuying Song, Postgraduate; Zhihui Tang, Researcher*

Studies have shown that straw manuring, ploughing & deep turning, and other mechanized tillage skills can improve salinized barren soils *(Zhang et al., 2020)*. The requirements for tillage modes and technical equipment have increased. When the existing tillage equipment contacts with hard objects, it will generate a larger load than the soils, resulting in deformation and fracture of the key parts of the plough and plough columns, reducing the working reliability of the whole machine and shortening the service life of the plough *(Li et al., 2021; Liu et al., 2021).*

The uneven resistance generated during ploughing *(Salavat et al., 2023; Kim, 2021, Kim, 2022a; Kim, 2022b)* will have a large impact on the implement *(Sheng et al., 2023; Mileusnić, 2022),* so does the traction performance of tractors *(Yeon et al., 2022; Mojtaba, 2023; Shafaei, 2021).* The anti-overload automatic obstacle avoidance mechanisms in agricultural machinery have been extensively studied. For instance, a bilateral working intra-row automatic obstacle avoidance weeder was designed, which can be used for effective intra-row weeding of grapes cultivated in trellis *(Ma et al., 2020).* An anti-overload flip plough consisting of an obstacle avoidance mechanism, an accumulator and an oil cylinder was designed *(Ma and Chang, 2020). Zhang (2021a)* designed an initiative obstacle avoidance and stubble cutting device for ploughing and stubble cutting in rocky desertification areas of Yunnan, which improved the service life and efficiency of stubble cutting devices. *Zhang et al. (2021b)* designed a boom manipulator obstacle detection system by integrating Beidou and LIDAR, which can acquire the position of obstacles. The two-way plough protectors in engineering applications are usually based on cutting bolts. When in contact with hard obstacles, the cutting bolts fracture and the plough body cannot work, which protects other parts of the plough from damage *(Wittke et al., 2022).* However, after the fracture of cutting bolts, the replacement is time-consuming and labour-intensive, and is more frequent in farmlands with stones, thereby largely reducing the working efficiency. The design of two-way plough equipment for anti-overload automatic obstacle avoidance mechanisms is rarely reported in China.

Herein, a two-way plough equipment with an anti-overload automatic obstacle avoidance mechanism is designed, aiming to solve the problem of rapid response and avoidance of stones when working in stone-rich barren soils. This design can rapidly restore after passing through stones, improving the reliability, adaptively and ploughing efficiency of ploughs. It can also offer a reference for other farming equipment to achieve anti-overload automatic obstacle avoidance, further improving the farming quality in barren soils, creating favourable seedbed conditions for crop growth.

MATERIALS AND METHODS

The anti-overload automatic obstacle avoidance mechanism of flip ploughs mainly consists of fixation boards, hinge shafts, connecting poles, plough column clamps, plough columns, plough body, elastic energy accumulator, supporting poles, and roller wheels. The structural installation is shown in Fig. 1, and the structure of the elastic accumulator is shown in Fig. 2.

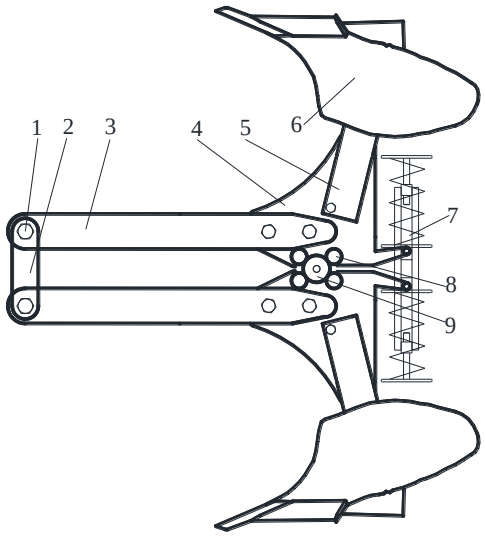


Fig. 1- Structure diagram of the overload protection mechanism

1. hinge shaft; 2. fixation board; 3. connecting pole; 4. plough column clamp; 5. plough column; 6. plough body; 7. elastic accumulator system;8. supporting pole;9. roller column

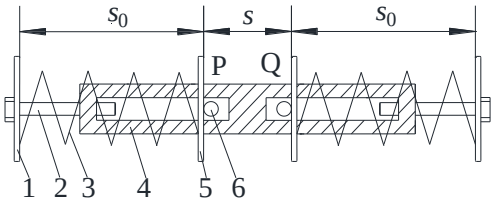
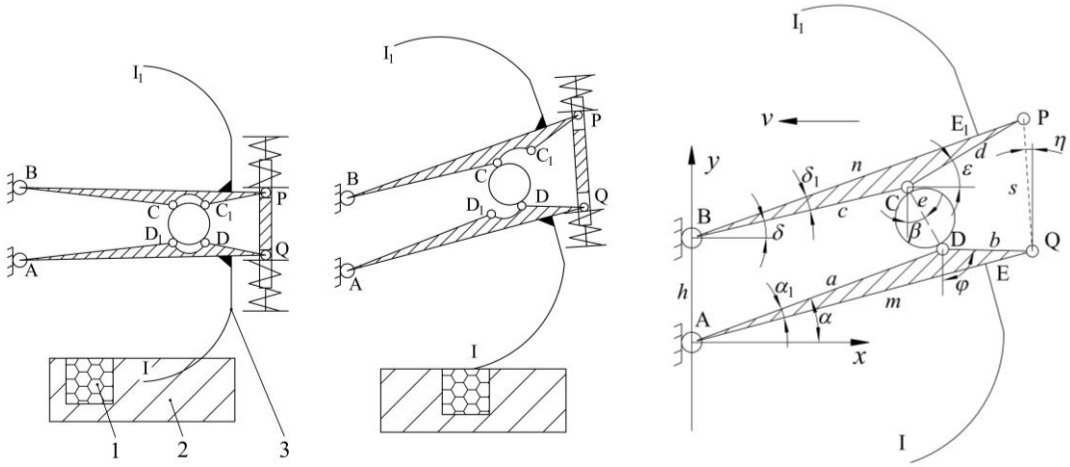


Fig. 2 - Structure diagram of the elastic accumulator

1. Upper seat of spring; 2. regulating pole; 3. spring; 4. spring frame; 5. lower seat of spring; 6. limit pins

For convenient design analysis, it can be taken as a multi-pole mechanism consisting of part 1 (AD1DQI), part 2 (CC1DD1), part 3 (BCC1PI1), part 4 (AB) and elastic accumulator PQ. The elastic accumulator PQ can impose pre-tightening forces at the points P and Q. Figures 3a and 3b shows the normal plough tillage status and the obstacle avoidance status when in contacting with stones respectively.



a. Plough tillage status *b. Obstacle avoidance status* *c. Diagram of the mechanism*

Fig. 3 - Diagram of overload protection automatic obstacle avoidance mechanism

1. Rock; 2. Soil; 3. Obstacle avoidance mechanism

In the xAy coordinate system (Fig. 3c), the vector equation in the closed vector polygon ABCDA is *(Naderi-Boldaji et al., 2023; Zhang et al., 2023) as follows:*

$$\left.\begin{aligned} c\cos\delta &= a\cos\alpha - e\sin\beta \\ h + c\sin\delta &= a\sin\alpha + e\cos\beta \end{aligned}\right\} \quad (1)$$

where a – the length of pole AD, mm;

c – the length of pole BC, mm;

e – the supporting diameter of roller, mm;

h – the length of frame AB, mm;

α – the included angle between pole AD and the horizontal direction, (°);

β – the included angle between pole CD and the vertical direction, (°);

δ – the included angle between pole BC and the horizontal direction, (°).

The coordinates of points P and Q are as follows:

$$\left.\begin{aligned} x_P &= n\cos(\delta + \delta_1) \\ y_P &= h + n\sin(\delta + \delta_1) \end{aligned}\right\} \quad (2)$$

$$\left.\begin{aligned} x_Q &= m\cos(\alpha - \alpha_1) \\ y_Q &= m\sin(\alpha - \alpha_1) \end{aligned}\right\} \quad (3)$$

where x_P, and y_P – the coordinates of point P in the xAy coordinate system;

x_Q, and y_Q – the coordinates of point Q in the xAy system;

m – the length of pole AQ, mm;

n – the length of pole BP, mm;

α_1 – the included angle between pole AD and pole AQ, (°);

δ_1 – the included angle between pole BC and pole BP, (°).

Specifically, the pole ADQ and pole BCP constitute a triangle:

$$\left.\begin{aligned}\alpha_1 &= \arccos\frac{a^2+m^2-b^2}{2am}\\ \delta_1 &= \arccos\frac{c^2+n^2-d^2}{2cn}\end{aligned}\right\} \quad (4)$$

where b is the length of pole DQ, mm; d is the length of pole CP, mm.

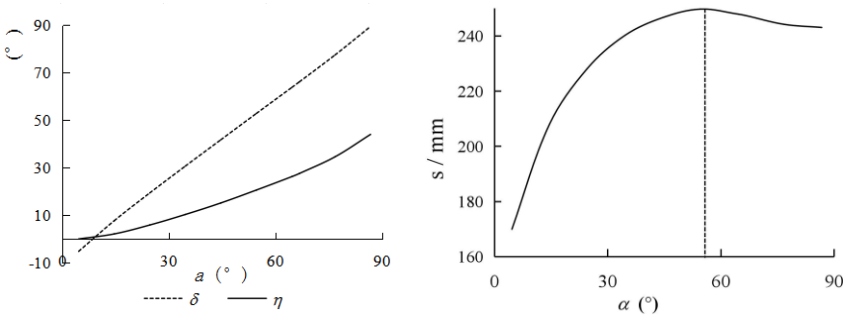
According to the coordinates of points P and Q, there is:

$$s = \left[(x_P - x_Q)^2 + (y_P - y_Q)^2\right]^{\frac{1}{2}} \quad (5)$$

$$\eta = \arctan\left(\frac{x_Q - x_P}{y_P - y_Q}\right) \quad (6)$$

where s is the distance between the upper and lower limit pins PQ, mm; η is the included angle between elastic accumulator PQ and the vertical direction, (°).

According to the structure of the flip plough, the obstacle avoidance mechanism is preliminarily set as a = 710 mm, b = 88.5 mm, c = 630 mm, d = 158 mm, h = 170 mm, m = 775 mm, n = 775 mm, α_1 = 4.6°, and δ_1 = 5.2°. The supporting diameter e of the roller wheel is 98 mm, and the central angle is θ. When the angle movement range α is 4.6°-90°, the relative changing curves of δ, η and s relative to α can be comprehensively known (Fig. 4).

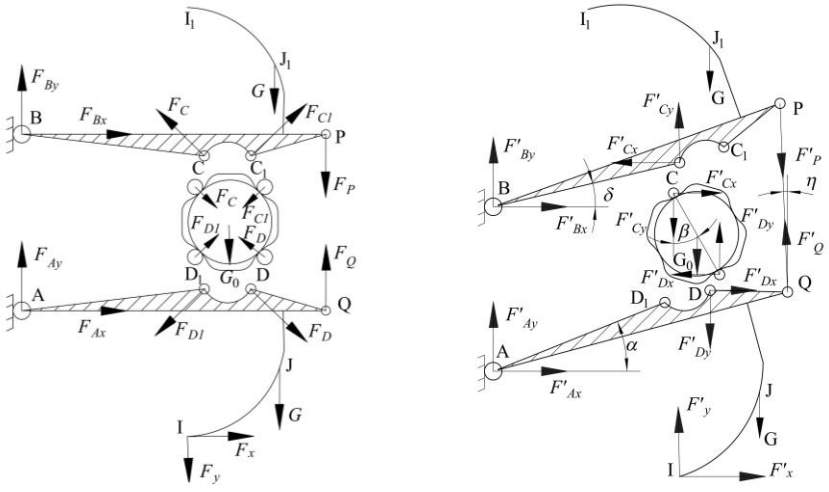


a. Changes of δ and η relative to α b. Changes of s relative to α

Fig. 4 - Change diagram of mechanism motion angle

The actual ploughing depth is usually 25-35 cm. Thus, the obstacle avoidance height is set as Δy_I=40 cm, ensuring the obstacles can be fully passed. Consequently, the angle rotation range is 4.6°-51.5°. The distance s of PQ is 170-248.68 mm. The effective compression stroke Δs of the pre-tensional spring are 39.34mm.

Its statical behaviours are analysed. Figs. 5 (a) and 5(b) show the normal ploughing state, and the anti-overload automatic obstacle avoidance state, respectively.



a. Plough tillage status b. Obstacle avoidance status

Fig. 5 - Static analysis diagram of mechanism

According to Figure 5b, the equilibrium equation 7 of the mechanism is obtained by applying force:

$$\left.\begin{aligned}
F'_{Ax}+F'_{Dx}+F'_{x}-F'_{Q}\sin\eta=0\\
F'_{Ay}-F'_{Dy}-F'_{y}-G+F'_{Q}\cos\eta=0\\
F'_{x}\,l\cos\lambda-F'_{y}\,l\sin\lambda-F'_{Dx}\,a\sin\alpha-F'_{Dy}\,a\cos\alpha+\\
F'_{Q}\cos\eta\cdot m\cos(\alpha-\alpha_1)+F'_{Q}\sin\eta\cdot m\sin(\alpha-\alpha_1)\\
-Gl_1\cos(\lambda_1-\alpha)=0\\
F'_{Cx}-F'_{Dx}=0\\
F'_{Dy}+G_0-F'_{Cy}=0\\
F'_{Dx}\,e\cos\beta-F'_{Dy}\,e\sin\beta+G_0\frac{e}{2}\sin\beta=0\\
F'_{Bx}-F'_{Cx}+F'_{P}\sin\eta=0\\
F'_{By}+F'_{Cy}-F'_{P}\cos\eta-G=0\\
F'_{Cx}\,c\sin\delta+F'_{Cy}\,c\cos\delta-F'_{P}\cos\eta\cdot n\cos(\delta+\delta_1)-\\
F'_{P}\sin\eta\cdot n\sin(\delta+\delta_1)-Gl_1\cos(\lambda_1+\delta)=0
\end{aligned}\right\} \quad (7)$$

where F_{Ax}, F_{Ay} – the support reaction forces at hinge point A, N;

F_{Bx}, F_{By} – the support reaction forces at hinge point B, N;

F_C – the support reaction force at supporting point C, N;

F_D – the support reaction force at supporting point D, N;

F_{C1} – the support reaction force at supporting point C1, N;

F_{D1} – the support reaction force at supporting point D1, N;

F_x, F_y – the resistance at centre-of-mass of the plough, N;

F_P, F_Q—the spring force of the elastic accumulator, N;

G – the gravity of upper and lower linkage plough, N;

G_0 – the gravity of roller wheel, N.

l – the distance from centre-of-mass I of the plough to hinge point A, mm;

l_1 – the distance from the assembly centre-of-mass J of the upper-lower linkage - plough to point A, mm;

λ - the included angle between l and the vertical direction, (°);

λ_1 – the included angle between l_1 and the horizontal direction, (°).

A three-dimensional model of the obstacle avoidance mechanism is built on SolidWorks. According to the preliminary parameter setting of the obstacle avoidance mechanism, the weights of part 1 (ADD1QI) and part 3 (BCC1PI1) are measured to be 995 N. When the mechanism is under normal ploughing state, the distance l_1 from the centre-of-mass of part *1* relative to point A is 767.4 mm; the included angle λ_1 relative to the horizontal direction is 27.36°; the distance l from the centre-of-mass I of the plough to hinge point A is 880 mm, and the included angle λ between l and the upright direction is 50°. Under the above conditions, when the ploughing resistance is known, the ranges of the spring initial pre-tightening force and the spring force during compression can be determined.

Based on the reported test methods, the resistance is measured using a developed plough-specific remote collector (Fig. 6). The remote collector connected the plough to the tractor.



Fig. 6 - Field experiments

1. Data collector; 2. Upper hanging sensor; 3. Lower hanging sensor

Figure 7 shows the variation of ploughing resistance in the normal tillage state.

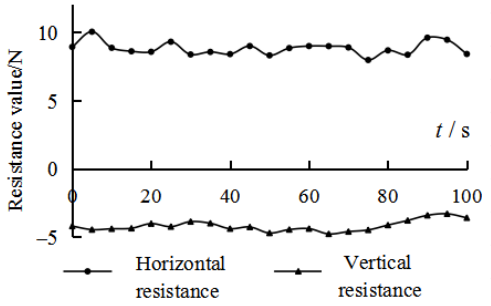


Fig. 7 - Structure and resistance of the plough

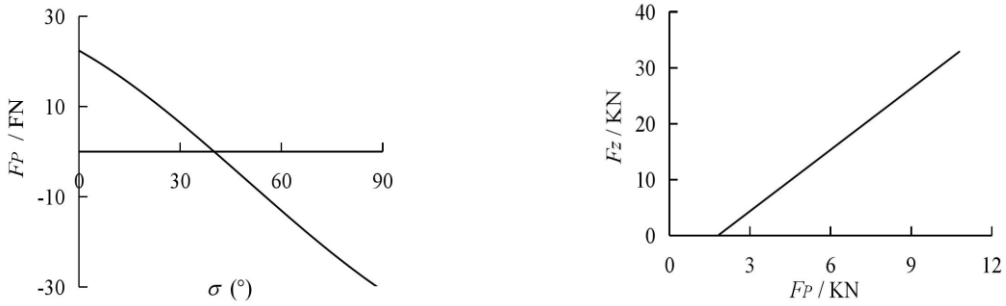
The test method at preliminary phase *(Liu et al., 2022)* is adopted, with a tillage speed of 12 km·h^{-1}, a tilling width of 0.42 m and a tillage depth of 0.35 m. The results show that the average horizontal resistance faced by the plough is 8.79 KN, and the average vertical resistance is 4.19 KN. Based on Eq. (7), it has F_P = F_Q = 9.75 KN. At this moment, the combined resistance F_z of the plough is 9.74 KN.

$$F_z = \sqrt{F_x^{\,2} + F_y^{\,2}} \tag{8}$$

The horizontal resistance F_x and vertical resistance F_y of the plough are determined by the plough structure and tillage conditions. The included angle σ between the two is as follows:

$$\tan\sigma = \frac{F_y}{F_x} \tag{9}$$

Based on Eq. (7), the average σ of the plough is 25.45°. The magnitude and direction of the horizontal resistance F_x and the vertical resistance F_y imposed on the plough are largely affected by the spring force F_P. The variation of the plough is shown in Fig. 8. When the combined resistance on the plough is known under the normal tillage state, as the angle σ gradually increases, the corresponding spring force decreases slowly. When σ is greater than 40.07°, the mechanism balance can be maintained only when the spring force direction changes. Thus, a reasonable plough structure cannot only generate minimal tillage resistance, but also require minimal spring force in an equilibrium state.



a. Effect of angle σ on spring force b. Relationship between the plough resistance and the spring pre-tightening force

Fig. 8 - Relationship between the plough body and the spring preload

According to the structure of the elastic accumulator, the upper and lower groups of springs are symmetrical, and the spring forces are equal between the two groups at any time. Hence, there is:

$$F_P = F_Q = k(s_1 - s_0) \tag{10}$$

where k – the elasticity coefficient of spring, KN/mm;

s_1 – the original length of spring, mm;

s_0 – the spring length after compression, mm.

After the initial pretension compression, the compression during obstacle avoidance is induced by the enlarged distance between the upper and lower limits. Hence, there is:

$$\frac{\Delta s}{2} = s_1 - s_0 \tag{11}$$

where Δs – the distance change between the upper and lower limit pins, mm.

Based on the preliminary parameter setting and the influence factors on the mechanism movement (auxiliary internal friction force), the safety factor is set as 1.3. The specific rigidity spring and variable rigidity spring are both analysed. The elastic coefficient of the specific rigidity spring is set as a constant. Fig. 9 shows the changes in the spring force with 4 levels of constant rigidity. As α gradually increases during the obstacle avoidance, the centre-of-mass height of the plough increases, and the spring force is enhanced. The smaller the elastic coefficient of the spring, the smaller the increase in spring force.

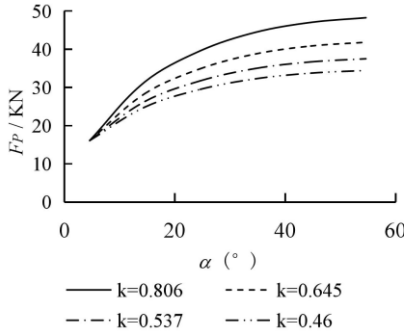
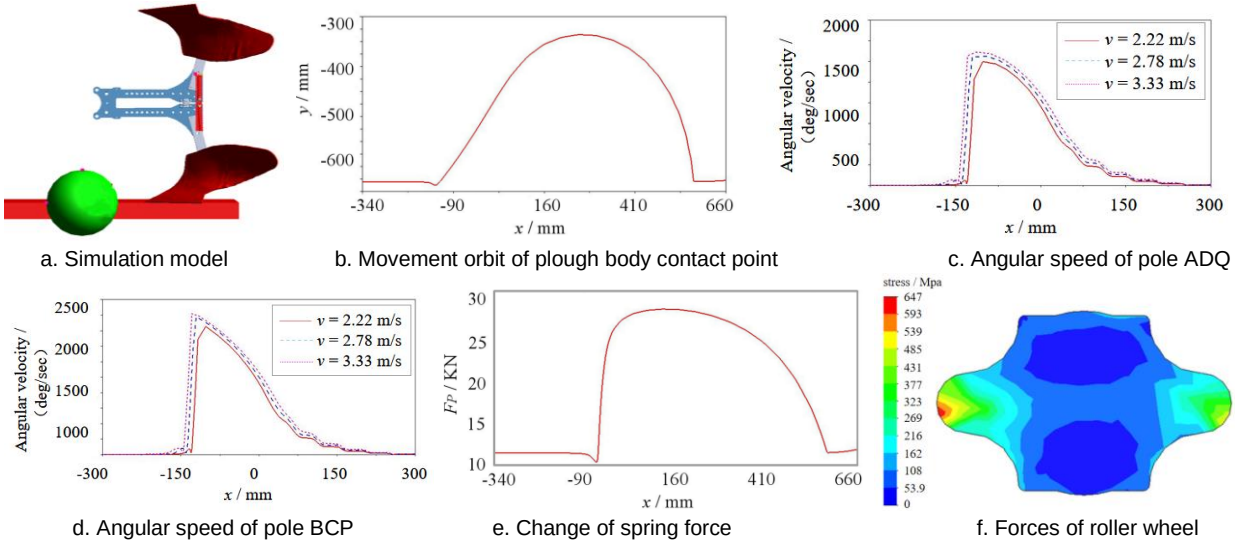


Fig. 9 - Change of spring force

RESULTS AND ANALYSIS

To avoid the effects of relevant structural parameters and motion parameters of the obstacle avoidance mechanism on tillage, the mechanism model is simplified to establish a 3D model on SolidWorks and imported it to ADAMS. Depending on how the parts are connected and moved, restraints are added between different parts (such as fixation pair, rotation pair, or mobile pair). The spring is added into the elastic accumulator, and the actual resistance is added to the centre-of-mass of the plough. During the simulation of obstacle avoidance, a contact force is added between the plough and ground, and the spheres are set on the ground to simulate rock obstacles. The height of the heaves above the ground is 30 cm. A straight-line movement drive is added onto the motion pair of the frame and ground, and the velocities are 2.22, 2.78, 3.33 m/s to simulate the actual working velocity and the mechanism movement from right to left (Fig. 10).



a. Simulation model b. Movement orbit of plough body contact point c. Angular speed of pole ADQ

d. Angular speed of pole BCP e. Change of spring force f. Forces of roller wheel

Fig. 10 - Mechanism simulation analysis

The motion obit of the plough contact point during obstacle avoidance is basically consistent with the contour of the obstacles. The mechanism can effectively avoid the obstacles (Fig. 10). Figs. 10c and 10d show the changes in the angular speeds of poles ADQ and BCP. Clearly, at a fast-working velocity, the obstacle avoidance rotation of the mechanism is fast. The angular speed of mechanism slightly fluctuates after the obstacle avoidance, indicating the working speed will affect the tillage stability to some extent. Moreover, the mechanism, after passing through the obstacles, can return quickly. The simulations show that the mechanism can simulate obstacle avoidance according to the contour of the obstacles. After passing the obstacles, it can restore rapidly, showing excellent obstacle avoidance performance.

The material of the trolley wheels is 40Cr, and the yield strength is 785 MPa. The results show that under a maximum impact load of 1.6 times the actual resistance, the maximum stress faced by the trolley wheels is 647 MPa, and the stress is concentrated on at the edge of contact with the supports.

A test bench is built up (Fig.11). The power supply of pulling force is the horizontal traction of the forklift. In the tests, a pulling force is applied through the forklift to simulate the actual resistance. A digital display pulling force meter is installed between the forklift and the mechanism, which can record the pulling force in real time. The spring coefficient is 0.46 kN/mm.



Fig. 11 – Anti-overload automatic obstacle avoidance test bench

1. Tensile power supply; 2. Digital display pulling force meter; 3. Spring; 4. Anti-overload automatic obstacle avoidance mechanism

The mechanical performance of the mechanism is validated by measuring the pulling force and connecting pole rotation angle on the bench. The tested data are listed in Table 1.

Table 1

Mechanism bench test data

No.	Pulling force /KN	Connecting pole rotation angle /(°)	
		Theoretical value	Tested value
1	15	0	0
2	16.3	0.5	0.2
3	24.8	10	9.5
4	29.5	20	19.7

Testing data comparison and theoretical analysis show that when the resistance is the same, the tested values of the connecting rod rotation angle and spring compression quantity are slightly smaller than the theoretical data. In actual conditions (Fig. 12), the revolving pair and spring seat connected to the connecting pole both generated slight frictional resistance at the hinge sites.



a. Obstacle avoidance rotation 1 *b. Obstacle avoidance rotation 2* *c. Obstacle avoidance limit positions*

d. Relocation dynamics 1 *e. Relocation dynamics 2* *f. Relocation dynamics 3*

Fig. 12 - Test movement process of obstacle avoidance mechanism

Conditions in the test site: the local soil generally contains rocks and gravels. In the 8th company, 164th regiment with rock-rich rocks, the average proportion of rocks in a 1 m^2 space with a tillage depth of 30 cm is 11.8%. The average residual stubble density is 3.6 kg/m^2, and the average water contents in soils with the depths of 0-10 cm, 10-20 cm, and 20-30 cm are 10.15%, 14.2% and 19.78%. The experiments were conducted in September 2021, and the auxiliary power supply was a John Deere 2204 wheeled tractor (Fig. 13).

Since the depth and speed of the plough tillage are the main factors that affect tillage resistance, according to the forces of the obstacle avoidance mechanism, the working stability and reliability of the mechanism shall be improved to make the obstacle avoidance mechanism adapt to different tillage depths and tillage speeds. Hence, the reliability of the machines and tools is determined according to the coefficient of variation of tillage depth stability.



Fig. 13 - Prototype field experiments

To study the effects of machine structure and working parameters on tillage, tillage depth stability is used to effectively reflect the stability of the mechanism under the normal working conditions. The tillage speed, tillage depth and spring elastic coefficient are selected as the testing factors. Taking the coefficient of variation of tillage depth stability as the evaluation index, the level of each factor is determined using the Box-Behnken Design of the response surface method software Design-Expert 8.0.6 (Table 2).

Table 2

Level of test factors

Level	Factor		
	Tillage speed /(m/s)	Tillage depth /cm	Spring elasticity coefficient/(KN/mm)
-1	2.22	25	0.415
0	2.78	30	0.460
1	3.33	35	0.535

Based on Box-Behnken Design, totally 17 groups of experiments were conducted. In each group, 20 measuring points were set and the average value was adopted. Then the variation coefficient of tillage depth stability in each group was determined. The results are shown in Table 3.

Table 3

Results of test

No.	Factor (code)			
	Tillage speed /(m/s)	Tillage depth/cm	Spring elasticity coefficient/(KN/mm)	variation coefficient of tillage depth stability /%
1	1	0	1	5.795
2	-1	0	1	5.135
3	0	1	1	5.021
4	0	0	0	5.97
5	0	0	0	5.755
6	1	0	-1	7.152
7	0	0	0	5.871
8	0	0	0	5.915
9	-1	-1	0	5.353
10	0	-1	1	6.002
11	0	-1	-1	7.125
12	-1	1	0	5.125
13	1	-1	0	6.915
14	1	1	0	5.893
15	0	0	0	5.756
16	-1	0	-1	5.522
17	0	1	-1	5.388

The testing data in Table 5 are sent to fitting and analysis of variance (ANOVA) on Design Expert 8.0.6. Then 2FI regression models of variation coefficient of tillage depth stability is established, and the significance tests of the models are shown in Table 4.

Table 4

Significant analysis of regression model of tillage depth stability

Source of variance	Sum of squares	Degree of freedom	F	P
Model	6.480	6	32.79	<0.01**
x_1	2.670	1	81.00	<0.01**
x_2	1.970	1	59.75	<0.01**
x_3	1.310	1	39.69	<0.01**
x_1x_2	0.157	1	4.79	0.054
x_1x_3	0.235	1	7.14	0.023*
x_2x_3	0.143	1	4.34	0.064
Residual	0.329	10		
Lack-of-fit term	0.293	6	5.29	0.065
Pure errors	0.037	4		
Sum	6.81	16		

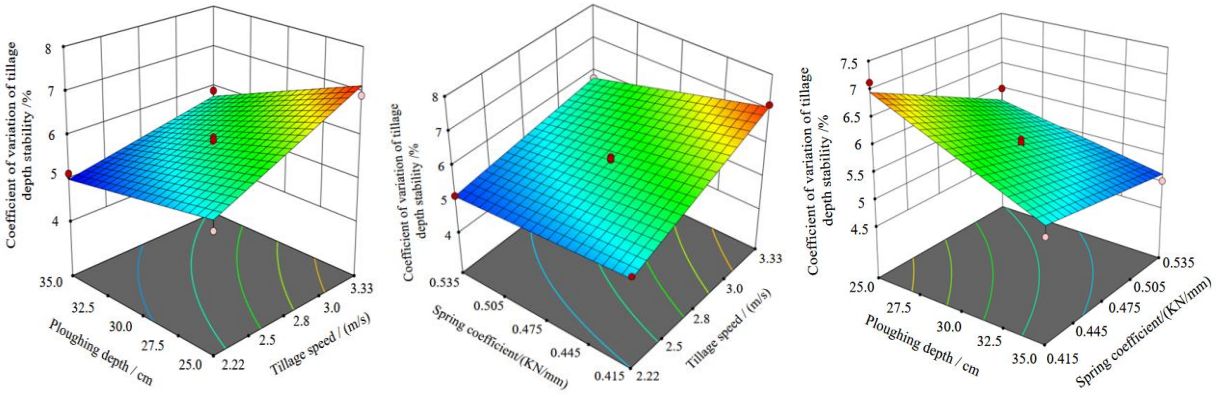
Note: ** very significant (P<0.01); * significant (P<0.05)

Analysis of the coefficient of variation of tillage depth stability shows (Table 4) that the pin of the regression model is < 0.01, indicating the model is extremely significant. Specifically, the coefficients of x1, x2, x3, and x1x3 are all significant (P<0.05), and other items are not. The regression equation of the coefficient of variation of tillage depth stability is as follows:

$$y = 5.864 + 0.578x_1 - 0.496x_2 - 0.404x_3 - 0.243x_1x_3 \quad (12)$$

Based on the regression equation, the response surface method (RSM) curves of the stability variation coefficient of tillage depth with respect to tillage speed, tillage depth and spring elastic coefficient are plotted on Design-Expert 12.0. The coefficient of variation of the tillage depth stability gradually increases as the tillage speed increases, and slightly decreases as the tillage depth and the spring elastic coefficient increase (Fig. 14). The contribution rates of different factors to the coefficient of variation of tillage depth stability rank as: tillage speed > tillage depth > spring elastic coefficient.

The experimental data show that in terms of the structural parameters of the obstacle avoidance mechanism, when the tillage speed, tillage depth and spring elastic coefficient are in the working ranges, the coefficient of variation of the tillage depth stability is less than 8%, meeting the design requirements.



(a) (b) (c)

Fig. 14 - Effect of interaction factors on tillage depth stability

a. Effects of the tillage depth and tillage speed on tillage depth stability

b. Effects of the spring elastic coefficient and tillage speed on tillage depth stability

c. Effects of the tillage depth and spring elastic coefficient on tillage depth stability

The results show that, when the tilling plough makes contact with hard objects, the mechanism can rapidly and effectively start the anti-overload automatic obstacle avoidance device to make the plough pass through hard obstacles. When the plough passes through the obstacles, it can immediately return to its working position, thereby avoiding missing tillage and stopping, and improving the reliability and working performance of the plough device.

CONCLUSIONS

A two-way plough equipment with anti-overload automatic obstacle avoidance mechanism is designed. Its aim is to achieve the anti-overload automatic obstacle avoidance function of a two-way plough equipment during tillage in rocky barren soils. The mechanism can rapidly respond and avoid obstacles such as rocks, and can immediately relocate after passing through the obstacles. Thus, it can improve the reliability, adaptivity and ploughing efficiency of the plough, and further improve the tillage quality in barren soils, creating excellent seedbed conditions for crop growth.

(1) The structure and key parameters of the anti-overload automatic obstacle avoidance mechanism are designed, and the obstacle avoidance motion process is analysed. Its motion equation and quasi-static forced equation are established, and its motion laws and force status are determined. At a safety factor of 1.3, the relation between spring pre-tightening force and plough resistance is clarified. The curves showing how the force of springs with different elastic coefficients changes with the rotation angle of the mechanism are plotted.

(2) A virtual prototype simulation model of the anti-overload automatic obstacle avoidance mechanism is constructed. The motion trajectory curves at the contact point of the plough, the changes in the angular speed of the chord parts during obstacle avoidance, and the changes of spring bounce before and after obstacle avoidance are obtained through ADAMS analysis. The forces of the trolley wheels are analysed. The simulations show that the mechanism can effectively perform obstacle avoidance actions.

(3) The site experiments validated that the mechanism can avoid obstacles at the preset load. Based on Box-Behnken Design of the response surface method, a three-factor scheme involving tillage speed, tillage depth and spring elastic coefficient was designed. The contribution rates of the test factors to the coefficient of variation of the tillage depth stability ranked as tillage speed > tillage depth > spring elastic coefficient. In the case of obstacle overloading, the mechanism can effectively perform obstacle avoidance actions, and the coefficient of variation of its tillage depth stability is less than 8%, meeting the design requirements.

FUNDING

This research was funded by the Xinjiang Corps Regional Innovation Plan (grant no. 2021BB015).

REFERENCES

1. Gao, Z., Fan, Q., Liu, Y., Wang, G., Yang, G., Shi, L., Wang, J., Zeng, S., Chen, Y. (2021). The Current Situation, Existing Problems, and Suggestions of the XPCC's Cultivated Land Quality Protection (兵团耕地质量保护现状、存在问题及建议). *Chinese Journal of Xinjiang Farm Research of Science and Technology*, Vol. *44* (6), pp. 1-5.
2. Guilherme, A.F. C., Renato, P. de L., Maurício, R. C., Ricardo, O. B., Mario, M. R., João, L.N. C., (2021). Machinery traffic in sugarcane straw removal operation: Stress transmitted and soil compaction. *Soil and Tillage Research*, Vol. (213), 105122.
3. Kim, W.S., Kim, Y.J., Park, S.U., Kim, Y.S. (2021). Influence of soil moisture content on the traction performance of a 78-kW agricultural tractor during plow tillage. *Soil and Tillage Research*. Vol. (207), 104851. https://doi.org/10.1016/j.still.2020.104851.
4. Kim, Y. J., Kim, W. S., Sim, T., Yi, S., Choi, Y. S. (2022a). Development of DEM-MBD coupling model for draft force prediction of agricultural tractor with plowing depth. *Computers and Electronics in Agriculture,* Vol. (202), 107405. https://doi.org/10.1016/j.compag.2022.107405.
5. Kim, Y.-S., Lee, S.-D., Baek, S.-M., Baek, S.-Y., Jeon, H.-H., Lee, J.-H., Siddique, M. A. A., Kim, Y.-J., Kim, Sim, W.-S., Yi, S., Choi, Y.-S. (2022b). Development of DEM-MBD coupling model for draft force prediction of agricultural tractor with plowing depth. *Computers and Electronics in Agriculture*, Vol. (202), 107405.
6. Li, Q.C., Zheng X., Meng X., Liu, J., Zhang, L., Liang, Y. (2021). Application status and improvement suggestions of mouldboard plough in the cornfield of Northern Xinjiang. *Journal of Chinese Agricultural Mechanization*, Vol. *42*(7), pp. 202-208.
7. Liu, J., Zheng, X., Meng, X., Tang, Z., Yang, H., Zhang, L. (2021). Current situation and prospect of research on plough surface (铧式犁犁体曲面研究现状与展望). *Journal of Chinese Agricultural Mechanization*, Vol. *42*(3), pp. 13-21+39.

8. Liu, J.B., Zheng, X., Meng, X.J., Yang, H.J., Zhang, L.Y., Li, Q.C. (2022). Analysis and experimental study on plough tillage resistance model（犁体耕作阻力模型仿真分析与试验研究）. *Agricultural Research in the Arid Areas*, Vol. *40* (1), pp. 264-274.
9. Ma, H., Chang, Y. (2020). Flipping plow with overload protection and its overload protection method. China Patent CN110637524A, 3 Jan 2020.
10. Ma, S., Xu, L., Yuan, Q., Niu, C., Wang, S., Yuan, X. (2020). Development of automatic obstacle-avoiding grapevine cold-proof soil cleaners (自动避障式葡萄藤防寒土清土机研制). *Transactions of the Chinese Society of Agricultural Engineering (Transactions of the CSAE)*, Vol. *36* (7), pp. 1-10.
11. Mileusnić, Z. I., Saljnikov, E., Radojević, R. L., Petrović, D. V. (2022). Soil compaction due to agricultural machinery impact. *Journal of Terramechanics*, Vol. (100), pp. 51- 60.
12. Mileusnić, Z.I., Saljnikov, E., Radojević, R. L., Petrović, D. V. (2022). Soil compaction due to agricultural machinery impact. *Journal of Terramechanics*, Vol. (100), pp. 51-60.
13. Naderi-Boldaji, M., Karparvarfard, S. H., Azimi-Nejadian, H. (2023). Investigation of the predictability of mouldboard plough draught from soil mechanical strength (cone index vs. shear strength) using finite element modelling. *Journal of Terramechanics*, Vol. (108), pp. 21-31.
14. Salavat, M., Yakov, L., Ildar, F., Eduard, K., Ildar, R. (2023). Justification of the soil DEM-model parameters for predicting the plow body resistance forces during plowing. *Journal of Terramechanics*, Vol. (109), pp. 37-44.
15. Shafaei, S.M., Loghavi, M., Kamgar, S. (2021). Profound insight into tractor energy dissipation through inevitable interaction inside wheel-soil interface for the period of plowing works. *Soil and Tillage Research*, Vol. (211), 104998.
16. Wang, W.X., Cao, Y.G., Su, R.Q., Qiu, M., Song, L., Zhou, W. (2020). Cultivated land protection policy in China: Background, Effect and future trends (我国耕地保护政策研究:基于背景、效果与未来趋势). *Chinese Journal of Agricultural Resources and Regional Planning*, Vol. *41*(10), pp. 40-51.
17. Wittke, M., Wolf, M., Weigert, F., Darnieder, M., Gerlach, E., Zimmermann, K., Theska, R. (2022). Investigations on a torque-compensating adjustment drive for mechanically sensitive device. European Society for Precision Engineering and Nanotechnology, Conference Proceedings - 22nd International Conference and Exhibition, EUSPEN 2022, Pages 81-82.
18. Zhang, M.Y., Qi, R.F., Wang, Q., Liu, F. (2021a). Design and performance test of obstacle detection system for boom manipulator (喷杆机械臂障碍物检测系统设计与性能测试). *China Agricultural Informatics*, Vol. *33*(2), pp. 49-56.
19. Zhang, S., Ren, W., Xie, B., Luo, Z., Wen, C., Chen, Z., Zhu, Z., Li, T. (2023). A combined control method of traction and ballast for an electric tractor in ploughing based on load transfer. *Computers and Electronics in Agriculture*, Vol. (207), 107750.
20. Zhang, W.F., Yang, S.Q., Lou, S., Jin, Y.H., Liu, P. (2020). Effects of tillage methods and straw mulching on the root distribution and yield of summer maize (耕作方式与秸秆覆盖对夏玉米根系分布及产量的影响). *Transactions of the Chinese Society of Agricultural Engineering (Transactions of the CSAE)*, Vol. *36*(7), pp. 117-124.
21. Zhang, W.K. (2021b). Study on Active Barrier Control System of Breaker Device Based on ADRC (基于 ADRC 的破茬装置主动避障控制系统研究). Kunming University of Science and Technology. (In Chinese)

DISTRIBUTION ROUTE OPTIMIZATION FOR MULTI-VEHICLE AGRICULTURAL MATERIALS CONSIDERING CARBON EMISSION COST
/
考虑碳排放成本的多车型农资配送路径优化研究

Li LI [1,2], Xuesong YANG [*1)]
[1)] School of Urban Design, Wuhan University, Wuhan, Hubei, China;
[2)] Teaching Affairs Department, Hubei Engineering University, Xiaogan, Hubei, China;
*E-mail: *E-mail: gygy88521@sina.com*
DOI: https://doi.org/10.35633/inmateh-71-53

Keywords: *Agricultural material logistics; Vehicle route; Improved ant colony algorithm; Differential updating; Chaotic disturbance*

ABSTRACT

Agriculture is the foundation of the national economy, and agricultural materials are the basis of agricultural development. As the three rural issues (agriculture, countryside, and farmers) become increasingly important, the distribution of agricultural materials attracts extensive attention. Given the slow development of rural logistics, the traditional agricultural material distribution process encounters many problems, such as cumbersome distribution links, high distribution costs, and low profit for enterprises, which in turn cause high production costs and low income for farmers. In consideration of soft time window constraints, this study adopted the agricultural material distribution route as the study object and established an optimization model of the agricultural material distribution route with fixed, transportation, energy consumption, time window penalty, and carbon emission costs as the objective functions. With regard to the algorithm, the operation of differential update and chaotic disturbance was innovatively enhanced and applied to the improved ant colony algorithm to simulate the model and obtain the optimal distribution route optimization model. Results show that the traditional ant colony algorithm improved by differential updating and chaotic disturbance has the advantages of low distribution cost, reasonable route, small number of activated vehicles, and short convergence time. Compared with the traditional ant colony algorithm, the improved ant colony algorithm can converge to the global optimum faster. This study provides guidance and suggestions on route selection and vehicle configuration to reduce costs and increase efficiency and offers certain theoretical support to alleviate urban traffic pollution and implement carbon trading policies in the future.

摘要

农业是国民经济的基础,而农业生产资料的支持是农业发展的基础，在"三农"问题愈发重要的今天，农业生产资料的配送问题也随之显得十分重要。由于农村物流发展缓慢,传统的农资配送过程中存在着配送环节过多、配送成本过高、企业获得利润过少的问题,同时也造成了农民生产成本过高、收入低的现象。基于此，本文以农资配送路径对象，以软时间窗约束为前提，以固定成本、运输成本、能耗成本、时间窗惩罚成本和碳排放成本为目标函数，建立了农资配送路径优化模型。在算法方面，创新性地改进了微分更新和混沌扰动的操作，将微分更新和混沌扰动应用于改进的蚁群算法对模型进行仿真求解，得到了最优分配路径优化模型。仿真结果表明：采用微分更新和混沌扰动对传统蚁群算法进行改求解模型，得到的分配成本更低，路线更好，激活车辆数量更少，算法收敛时间更短，并且与传统蚁群算法相比，改进蚁群算法可以更快地收敛到全局最优。研究结果也可以帮助企业对农资配送车辆路线的选择和车型配置决策提供指导和建议，帮助企业降本增效，并为未来缓解城市交通污染和碳交易政策的广泛实施提供一定的理论支持。

INTRODUCTION

As important agricultural inputs, agricultural materials are the bridge connecting industry and agricultural production and provide material guarantee and foundation for modern agriculture development (*Wang Xu et al., 2020*). Agricultural material logistics is an important link in the process of agricultural material sales, and in China, the distribution direction is from cities to the countryside, the distribution route is from trunk transportation to branch transportation, and the distribution scale is from large to small (diffused type). The different distribution types and obvious seasonality and regionality of agricultural material distribution increase the difficulty of the management, storage, and transportation of agricultural materials.

The problems of idle driving and secondary distribution also arise from improper planning and dispatching of agricultural material distribution vehicles (*Huo et al., 2017*). The relatively backward development of rural areas in China, the outdated infrastructures, the complex terrain, and poor traffic conditions have caused great difficulties in the distribution of agricultural materials (*Zhang, 2017*). Some distribution routes are unreasonable. Some problems, such as poor inventory management, untimely stocking, and information blocking of the strong demand for agricultural materials, also arise during busy farming seasons. As the main distribution tool, vehicles are particularly important and affect the circulation of agricultural materials (*Du and Chen, 2017*). Logistics distribution guarantees the smooth arrival of agricultural materials to farmers, and a discrepancy in it can affect the cultivation of crops and cause serious losses to farmers (*Wei et al., 2016*). This study qualitatively and quantitatively analyzed the problems in agricultural material logistics distribution, optimized the distribution route, and established an optimization model of agricultural material distribution. Moreover, the rural agricultural logistics distribution route was optimized, and distribution efficiency was enhanced. Through the optimization of the agricultural logistics distribution route, farmers can use reliable agricultural products at the minimum cost, enterprises can obtain increased profits, and vigorous and healthy agricultural development in China can be maintained. Exploring agricultural material logistics distribution is crucial to the development of agricultural material logistics and agriculture in China.

The construction of logistics facilities in China's rural areas is relatively backward, which is mainly reflected in the level of roads, means of transport, communication, and commodity storage. Compared with the total size of the road network mainly composed of rural roads, the density of rural roads in China is only about one-fifth that of the United States, 1/8 that of the United Kingdom, and 1/15 that of Japan. Currently, 184 townships and more than 50,000 administrative villages are still without roads. The number of agricultural materials storage facilities in China is seriously insufficient, and the existing storage facilities are not fully functional and cannot play their due functions, resulting in a great loss of agricultural materials in storage. The use of Internet information means to optimize the logistics and transportation routes of agricultural commodities, provide digital and shared agricultural logistics supply and marketing services for agricultural commodities transport warehouses, goods, vehicles, routes, and network resources, optimize the county and village three-level distribution system, and solve the problems of agricultural products up and farmers' livelihood and production means down.

State of the art

The logistics industry is highly developed in developed countries, such as those in Europe, the United States, Japan, and South Korea, and many research achievements in logistics have been obtained for urban and rural areas. Particularly, the rural land in America is highly intensive, and the distribution, inventory management, and information integration of rural agricultural materials are highly developed. Studies on rural logistics in China have focused on the optimization of distribution networks, the location of storage and distribution facilities, and logistics systems. *Mardaneh et al.* studied the factors that influence agricultural logistics and established an agricultural logistics system in accordance with the characteristics of rural logistics *(Mardaneh et al., 2016)*. Chaudhuri et al. reduced the logistics cost by optimizing the vehicle route and proposed a logistics transportation system *(Chaudhuri et al., 2018)*. *Ferrag* achieved a major breakthrough by combining multivehicle path optimization and game theory *(Ferrag et al., 2020)*. *Liu* solved multivehicle problems with time windows by using a genetic algorithm *(Liu et al., 2022)*. According to Chandra et al., fuel consumption is influenced by driving distance and the actual operation process of vehicles *(Chandra et al., 2014)*. *Lin* discussed the carbon emission of freight vehicle routing, especially the influence of vehicle speed on carbon emission *(Lin et al., 2021)*. *Luo* explored the influence of road gradient on vehicle fuel consumption in a reverse logistics recovery path *(Luo et al., 2016)*.

In addition, vehicle route optimization was also used in reverse logistics. With the development of the Internet, Çeken applied the positioning system to vehicle positioning and 2D code scanning technology to goods delivery *(Çeken et al., 2019)*. Remarkable breakthroughs in distribution center location and express delivery have been achieved in the United States where unified government management is implemented *(Marinaki et al., 2016)*. This management method breaks through the traditional system of departments in charge and contributes to the development of logistics effectively. In addition, increased attention has been devoted to the training system of logistics talents. The logistics talent system plays a crucial role in the logistics industry *(Badia-Melis et al., 2018)*.

Similar to the development model of the United States, the development model of Europe entails unified supervision and control of the government and independent operation of enterprises.

Advanced science and technology have considerably changed the development of the European logistics industry, and the continuous development of the Internet era has driven the coordinated progress of the logistics industry and promoted the rapid development of the European logistics industry *(Dulebenets et al., 2016)*. The development of the logistics industry in Japan mainly depends on the construction of strong domestic logistics infrastructure, and outstanding results have been achieved in logistics distribution specialization *(Braekers et al., 2016)*.

Many scholars have conducted studies on agricultural logistics. They qualitatively analyzed the concept and development of agricultural logistics from a macro perspective and quantitatively studied the optimization of site selection, route optimization, and the whole logistics network. *Ji et al.* improved the Baumol–Wolf model, proposed a 0-1 mixed integer programming model, and established a decomposition filtering model *(Ji et al., 2020)*. *Fazayeli* analyzed the logistics network system of agricultural resources in China and proposed the logistics supply network model of agricultural products *(Fazayeli et al., 2018)*.

Voutos discussed rural logistics distribution on the basis of the realization of the road network and improved the clustering algorithm to solve the distribution problem by dealing with the clustering center and edge points *(Voutos et al., 2019)*. *Leleń* combined the genetic algorithm and the Tabu Search algorithm to solve the vehicle routing problem *(Leleń et al., 2019)*. Bortolini effectively solved the vehicle routing problem with time windows by combining hill climbing and genetic algorithms *(Bortolini et al., 2016)*. *Hu* proposed a heuristic algorithm based on the Tabu Search algorithm and obtained the optimal solution of the vehicle routing problem *(Hu et al., 2020)*. *Olkhova* transformed dynamic problems into static problems by setting time periods and time points and proposed new ideas for solving dynamic vehicle routing problems *(Olkhova et al., 2017)*. *Lakshmanna* combined the best customer insertion rule with the genetic algorithm and embedded the fuzzy optimization program to verify the effectiveness of the model *(Lakshmanna et al., 2018)*. *Rajyalakshmi* studied the road network property of service facilities and changed the coding mode to obtain the genetic algorithm when the vehicle is not fully loaded *(Rajyalakshmi et al., 2022)*. *Liu* put forward a deterministic search method, which took less time and obtained more accurate results. Also, an efficient genetic operator was designed to solve the dynamic random shortest route problem by using the topological characteristics of the network *(Liu et al., 2023)*.

To sum up, energy conservation and emission reduction have become global concerns, and low-carbon technology and low-carbon economy have elicited extensive interest. With high fuel consumption and carbon emissions, the logistics industry needs to consume considerable energy to ensure product quality. Agricultural logistics serves rural areas. Given that the rural logistics network is imperfect, it has high energy consumption and carbon emission, and its effect on the environment is obvious. Therefore, the reduction of the energy consumption of logistics and the realization of green and sustainable development are essential. A review of previous studies on vehicle route optimization and vehicle evaluation in logistics shows that vehicle system evaluation has seldom been studied, and the studies on vehicle route optimization in logistics have focused on a single distribution center and a single model. Considering the economy and sustainability of vehicles, this study established a green multivehicle agricultural material distribution routing model under the background of logistics and designed and solved an improved ant colony algorithm. The feasibility and effectiveness of the proposed model and algorithm were verified by examples. The study can provide decision support and method guidance for distribution and management.

MATERIALS AND METHODS

Problem Description

After agricultural material distribution centers receive customers' demand orders, agricultural material distribution operation is performed by agricultural distribution vehicles, which are fully charged in distribution centers and deliver agriculture materials to different customers. However, each customer can accept the service of only one agricultural distribution vehicle. After an agricultural distribution vehicle completes the distribution, it returns to the starting point, namely, the distribution center. When a power warning is received by a distribution vehicle in the distribution process, it cannot reach the next distribution point and must replenish its battery power in a nearby fast-charging pile. Certain restrictions are imposed on the weight of goods distributed by agricultural distribution vehicles, so customers' total medical needs should not exceed the maximum load of agricultural distribution vehicles. The coordinates of customer points and the time window of the customer's request service are known.

This study did not consider road congestion and assumed that the road is smooth and that the agricultural distribution vehicle can reach customers' locations smoothly within the specified time window and complete the delivery service.

In this study, with K agricultural distribution vehicles in a distribution center as the study objects, the agricultural material distribution route to N customers was optimized. In consideration of green logistics and the timeliness of the agricultural material cold chain, this study assumed that the traditional vehicle routing optimization problem increases the time window penalty cost and the carbon tax cost.

(1) The distribution center has enough agricultural distribution vehicles, and the quality of each vehicle is known. The vehicles can run normally with the same constant power.

(2) The distribution center has sufficient agricultural material inventory, and customer demand, customer location, and delivery time are known. Every customer has been and can only be served by one agricultural distribution vehicle once.

(3) Each agricultural distribution vehicle starts from the distribution center. Once it receives its instruction, it does not accept other tasks and returns to the distribution center after completing the task.

(4) Every customer has a time window requirement for delivery time. Deliveries that are performed later or earlier than the delivery time result in a corresponding time window penalty cost.

Modeling

The objective function of multivehicle agricultural material distribution route optimization that considers the carbon emission cost includes the following aspects.

Fixed cost of vehicles

The fixed costs of agricultural material distribution include vehicle maintenance and depreciation costs. The distribution center has K agricultural distribution vehicles, and the fixed cost of each vehicle is F.

Therefore, the fixed cost of agricultural distribution vehicles is:

$$C_1 = \sum_{k=1}^{K} \sum_{j=1}^{N} F x_{0j}^{k} \tag{1}$$

where, x_{0j}^{k} is the decision variable, $x_{0j}^{k} = 1$ indicates that vehicle K leaves the distribution center to go to customer j, otherwise $x_{0j}^{k} = 0$; N is the number of customers.

Vehicle transportation cost

Vehicle transportation cost can be approximately regarded as positively related to mileage. Transportation cost C_2 can be expressed as:

$$C_2 = \sum_{k=1}^{K} \sum_{i=1}^{N} \sum_{j=1}^{N} C_{ij} Q_{ij} d_{ij} x_{ij}^{k} \tag{2}$$

where C_{ij} is the transportation cost per unit agriculture material and distance, Q_{ij} is the transportation volume from customer i to customer j, d_{ij} is the distance between customers i and j, and $x_{ij}^{k} = 1$ is the decision variable indicating that agricultural distribution vehicle K travels from customer i to customer j (otherwise, $x_{ij}^{k} = 0$).

Energy consumption cost in transportation process

Energy consumption cost: The first item is energy consumption during transportation. The energy consumption (B) of vehicle transportation is expressed as:

$$B = \alpha \sum_{i=0}^{N} \sum_{j=0}^{N} \sum_{k=1}^{K} d_{ij} x_{ij}^{k} \tag{3}$$

The total energy consumption cost during transportation is the product of vehicle transportation energy consumption and unit price δ of fuel.

$$C_3 = \delta B = \delta \alpha \sum_{i=0}^{N} \sum_{j=0}^{N} \sum_{k=1}^{K} d_{ij} x_{ij}^{k} \tag{4}$$

Time window penalty cost

Each customer has an acceptable service time range. Any delivery that exceeds this time range incurs a time window penalty cost. In accordance with customer satisfaction, time windows can be classified as hard, soft, and mixed. A hard time window requires the agriculture material to be delivered within the specified time, and early or late delivery is not allowed. A soft time window allows deliveries outside the specified time, but a penalty is imposed.

$$C_4 = \sum_{k=1}^{K}\sum_{i=1}^{N} H_i\left(t_i^k\right)\max\{\left(E_i - t_i^k\right),\left(t_i^k - L_i\right),0\}y_k^i \tag{5}$$

where: C_4 is the time window cost, and if the agricultural material delivery vehicle exceeds the customer's required time window, there will be a penalty cost;

$H_i\left(t_i^k\right)$ is the loss cost coefficient function caused by early or late delivery, which can be expressed as:

$$H_i(t_i^k) = \begin{cases} \infty, & t_i^k < e_i \cup t_i^k > l_i \\ \gamma, & e_i \le_i^k < E_i \\ 0, & E_i \le t_i^k \le L_i \\ \mu, & L_i < t_i^k \le l_i \end{cases} \tag{6}$$

where: L_i is the latest arrival time of agriculture material in the hard time window $[E_i, L_i]$, y_k^i means that customer i is served by vehicle k. $[e_i, l_i]$ represents the soft time window, which are the earliest and latest arrival time of agricultural material acceptable to customers. γ is the penalty cost of arriving earlier than the required time, and μ is the penalty cost of arriving later than the required time.

Carbon tax cost

Carbon emission cost = carbon tax price × carbon emission. Carbon emission = total energy consumption (B) × carbon dioxide emission coefficient (σ). Carbon tax cost is computed as:

$$C_5 = \omega\sigma B = \omega\sigma\alpha\sum_{i=0}^{N}\sum_{j=0}^{N}\sum_{k=1}^{K} d_{ij}x_{ij}^k \tag{7}$$

where, ω is the carbon tax price and σ is the carbon dioxide emission coefficient.

Optimization model setting

On the basis of the analysis of fixed, transportation, and fuel costs in the distribution process, time window penalty cost, and carbon tax cost, the following model is established:

$$minC = C_1 + C_2 + C_3 + C_4 + C_5 \tag{8}$$

The constraints are as below:

$$\sum_{k=1}^{\kappa} y_i^k = \begin{cases} 1, & i = 1,2,3,\cdots,N \\ k, & i = 0 \end{cases} \tag{9}$$

$$\sum_{k=1}^{\kappa}\sum_{j=1}^{N} x_{0j}^k = K \tag{10}$$

$$\sum_{k=1}^{K}\sum_{j=1}^{N} x_{0j}^k = N \tag{11}$$

$$\sum_{j=1} x_{0j}^k = \sum_{j=1} x_{j0}^k \,,,\ 1, k = 1,2,3,\cdots,k \tag{12}$$

$$\sum_{i=1}^{N}\sum_{j=1}^{N}\sum_{k=1}^{K}\gamma_i^k Q_{ij} \le Q \tag{13}$$

$$t_j^k = t_{ij} + max\{t_i^k, E_i\} + t_{si} \tag{14}$$

$$W,, Q_{ij} \le W_1 \tag{15}$$

where: Q is the maximum cargo capacity of agricultural distribution vehicles or the maximum transport capacity and W_1 is the minimum transport capacity.

Formula (8) yields the total cost of minimizing the objective function. Formulas (9) and (10) indicate that the number of refrigerated vehicles assigned by the distribution center does not exceed K, and each customer can only be served by one vehicle once. Formula (11) indicates that N customers accept service. Formula (12) shows that each agricultural distribution vehicle returns to the distribution center immediately after finishing the assigned task. Formula (13) indicates that the demand of N customers is less than or equal to the maximum cargo capacity of delivery vehicle K. Formula (14) presents the continuity of service time points for two customers. Formula (15) shows that the freight volume of the vehicle is greater than the minimum traffic volume and less than the maximum traffic volume.

ALGORITHM DESIGN

The location of goods was obtained using the scanning method, and polar coordinates represented the locations of goods. The area for warehouse entry and exit operations was selected as the starting point, and its angle was set to 0°. The equipment nodes were segmented with the maximum carrying capacity of the robot as the constraint condition, and several subregions that met the carrying capacity constraints were obtained.

Algorithm Improvement

(1) Improvement of the initial pheromone concentration. The initial pheromone concentration of the basic ant colony algorithm is similar in all routes. The first search of each iteration is blind search without direction guidance. As a result, the pheromone concentration of irrelevant routes is high, the search time is prolonged, and the algorithm is likely to be introduced into the local optimal solution. Therefore, in this study, the initial pheromone concentration was set as follows to guarantee the directionality of the algorithm at the initial search stage:

$$\tau_{ij}(0) = \frac{Q}{d_{0i} + d_{0j}}, i \neq j \tag{16}$$

where: Q is the total amount of pheromones released by ants for each search, d_{0i} is the actual distance between demand point i and the distribution center, and d_{0j} is the actual distance between demand point j and the distribution center.

(2) Improvement of the pheromone updating strategy (differential updating and chaotic disturbance). Pheromone update in the basic ant colony algorithm is likely to increase pheromone concentration errors in non-optimal routes, resulting in locally optimal solutions. This study used the ant cycle system in global route updating. In this system, after an iteration is completed, the selected route is given the same pheromone increment: the quotient of the total pheromone amount and total route length.

On this basis, the pheromone concentration is updated differently by highlighting the advantages and disadvantages of the route, that is:

$$\tau_{ij}(t+1) = (1-\rho)\tau_{ij}(t) + \Delta\tau_{ij} + \Delta\tau_{ij}^{*} \tag{17}$$

$$\Delta\tau_{ij} = \sum_{g=1}^{G} \Delta\tau_{ij}^{g} \tag{18}$$

$$\Delta\tau_{ij}^{g} = \begin{cases} \dfrac{Q}{L_g}, Z_g \text{ ,, } Z_{ave}, & (i, j) \text{ is the selected route} \\ 0, Z_g > Z_{ave} \end{cases} \tag{19}$$

$$\Delta\tau_{ij}^{*} = \begin{cases} \dfrac{Q}{L_{best}}, (i, j) \in \text{the points in the optimal route} \\ 0, (i, j) \notin \text{the points in the optimal route} \end{cases} \tag{20}$$

where: $\tau_{ij}(t)$ is the pheromone concentration on the route between demand points i and j in iteration t; ρ is the volatilization rate of the pheromone on the route after each iteration; $\Delta\tau_{ij}$ is the change amount of the pheromone between points i and j in each iteration; $\Delta\tau_{ij}^{g}$ is the value of the contribution of ants in group g to the pheromone changes of points i and j in the iteration; $\Delta\tau_{ij}^{*}$ is the extra reward to the optimal route, the pheromone on which is further strengthened; L_g is the total length of the route selected by the ants in group g;

L_{best} is the total length of the optimal route currently obtained; and G is the total number of ant groups. If the total distribution cost of the route selected by the ants in group g is less than the average distribution cost, the pheromone will be increased accordingly; otherwise, the value will be zero. The pheromone of the route that is worse than the average level of the iteration will decrease in this iteration because of pheromone-volatilization. $\Delta\tau_{ij}^{*}$ guarantees and emphasizes the pheromone concentration of the current optimal route.

However, as the number of iterations increases, the optimal route no longer changes, which means that the algorithm is trapped in a local optimal solution. Therefore, when the obtained optimal route does not change frequently, the chaotic disturbance mechanism is introduced to make the algorithm jump out of the current local optimal solution.

The settings are as follows:

$$\tau_{ij}(t+1) = (1-\rho)\cdot\tau_{ij}(t) + \xi F_{ij}(t) \quad (21)$$

$$F_{ij}(t+1) = \upsilon F_{ij}(t)[1-F_{ij}(t)] \quad (22)$$

where ξ is the adjustable coefficient, which is a constant; $F_{ij}(t)$ is the chaotic variable; υ is the control variable, the value of υ is in the range of [3.56, 4.0]. When υ =4 and $0 \le F_{ij}(t) \le 1$, the variable is in a chaotic state completely.

(3) Improvement of the transfer rule. The transfer rule of the basic ant colony algorithm only includes random search, which cannot highlight the best choice of pheromone and heuristic function to some extent, resulting in a low search speed. Therefore, this study combined deterministic search and random search to determine the choice of the next demand degree (j), and the specific settings are as follows:

$$j = \begin{cases} \arg\max\{\tau_{ij}^{\alpha}(t)\cdot\eta_{ij}^{\beta}(t)\}, q < q_0 \\ P_{ij}^{k}(t), q..q_0 \end{cases} \quad (23)$$

$$P_{ij}^{k}(t) = \begin{cases} \dfrac{\tau_{ij}^{\alpha}(t)\cdot\eta_{ij}^{\beta}(t)}{\sum_{s\,e\,allow_k}\tau_{is}^{\alpha}(t)\cdot\eta_{is}^{\beta}(t)}, & j \in allow_k \\ 0, & j \notin allow_k \end{cases} \quad (24)$$

where q, $q_0 \in (0,1)$, q_0 is a set constant, q is a random variable in the interval of (0,1), and α is the importance degree of pheromone concentration. The more important the pheromone concentration is, the greater its value is. b indicates the importance of the heuristic function, and $allow_k$ is the set of points that ants can go to when they are at point i. When random number $q < q_0$, a deterministic search is selected; when $q..q_0$, random search is used, and the next destination is selected in accordance with its probability.

Basic Steps of Algorithm

In this study, the improved ant colony algorithm was used to solve the minimum cost model of product distribution in distribution center. The approximate steps are as follows:

(1) Input related data matrix, parameter initialization, total iteration $TNC = 0$, ant group number $NC = 0$, pheromone concentration initialization, construct heurist function matrix;

(2) $NC=NC+1$, $k = 0$, place the NC group of ants in the distribution center;

(3) $k=k+1$, the k-th ant leaves and it delivers the products to stores according to the rules. Repeat (3) until the products have been delivered to all stores, and record relevant data;

(4) Return to (2) until $NC=NC_{max}$. Compare the results of NC group and update the pheromone concentration according to the rules;

(5) $TNC=TNC+1$, $NC=0$, return to step (2) until $TNC=TNC_{max}$. The optimal distribution route with the lowest distribution cost is obtained.

SIMULATION

Introduction to the Simulation

This study described an agricultural material logistics distribution model. The data of the case model used to test the validity of the proposed model and algorithm are shown in Table 1. The main contents are as follows. Agricultural distribution vehicles provide delivery services to 25 evenly distributed customer points with known time window constraints in a certain area, and every customer point can only be served by one delivery truck.

In the distribution process, various agricultural distribution vehicle models with different approved volumes are used. The information on the agricultural distribution vehicle is shown in Table 2. The following assumptions were applied: the fixed cost F of each agricultural distribution vehicle is 1,000 yuan/time, the vehicle speed is 40 km/h, the fuel consumption of the vehicle is 0.08 L/km without refrigeration, the unit transportation cost of unit goods is 2 yuan/(t·km), the waiting time for unloading is 1.5 h, the fuel price is 8 yuan/L, the penalty coefficient for early delivery is 5 yuan/h, the penalty coefficient for late delivery is 10 yuan/h, the carbon tax price is 0.3 yuan/kg, and the carbon dioxide emission coefficient is 2.3 kg/L.

Table 1

Customer information

Customer	Coordinate (X) km	Coordinate (Y) km	Demand volume (T)	Time window (min)	Service time (min)
0	40	50	0	(0,1236)	0
1	46	68	0.2	(912,967)	90
2	49	70	0.6	(825,870)	90
3	50	66	0.2	(65,146)	90
4	42	68	0.2	(727,782)	90
5	47	65	0.2	(15,67)	90
6	40	69	0.4	(621,702)	90
7	40	66	0.4	(170,225)	90
8	38	68	0.4	(255,324)	90
9	38	70	0.2	(534,605)	90
10	35	66	0.2	(357,410)	90
11	35	69	0.2	(448,505)	90
12	25	85	0.4	(652,721)	90
13	32	75	0.6	(30,92)	90
14	22	85	0.2	(567,620)	90
15	30	80	0.8	(384,429)	90
16	30	85	0.8	(475,528)	90
17	18	75	0.4	(99,148)	90
18	10	75	0.4	(179,254)	90
19	15	80	0.2	(278,345)	90
20	30	50	0.2	(10,73)	90
21	20	52	0.4	(914,965)	90
22	28	52	0.4	(812,883)	90
23	38	55	0.2	(732,777)	90
24	25	50	0.2	(65,144)	90
25	25	52	0.8	(169,224)	90

Table 2

Information on agricultural distribution vehicles

Truck model	Model 1	Model 2	Model 3	Model 4
Size	4000x2000x3000mm	4100x2040x3000mm	5600x2050x3000mm	8600x2050x3000mm
Self-mass	2t	3t	4t	5t
Number of tires	4	6	8	12
Swept volume	3000mL	3200mL	4000mL	4000mL
Fuel	#92	#92	#92	#92
Mileage	Unlimited	Unlimited	Unlimited	Unlimited
Rated load mass	3t	4t	6t	10t

The parameters involved in the algorithm were as follows: number of iterations MAXGEN = 100, number of ants m = 50, pheromone importance factor alpha = 1, heuristic function importance factor beta = 3, waiting time importance factor gamma = 2, time window span importance factor delta = 3, r0 is the parameter used to control the transfer rule and equals 0.5, pheromone volatilization factor rho = 0.85, and pheromone concentration update constant Q=5. MATLAB2022a was used to realize and run the algorithm, and the optimization model of the agricultural material distribution route that considers carbon emissions was solved in accordance with the specific data of the examples above.

RESULTS AND ANALYSIS

In this study, the route optimization model of agricultural material distribution was solved using the improved ant colony algorithm. The maximum number of iterations was set to 200, and the agricultural distribution vehicle start-up cost was 1,000 yuan. A satisfactory solution, that is, three agricultural distribution vehicles are needed to complete the agricultural material distribution task, was obtained by solving the model. The total travel distance of the agricultural distribution vehicle was 322.238 km, and the total cost was 3,322.215 yuan. The algorithm was run for 259.292 s. The improved ant colony algorithm route diagram is shown in Fig. 1. The convergence curve of the improved ant colony algorithm is shown in Fig. 2, and the calculation results are listed in Table 3.

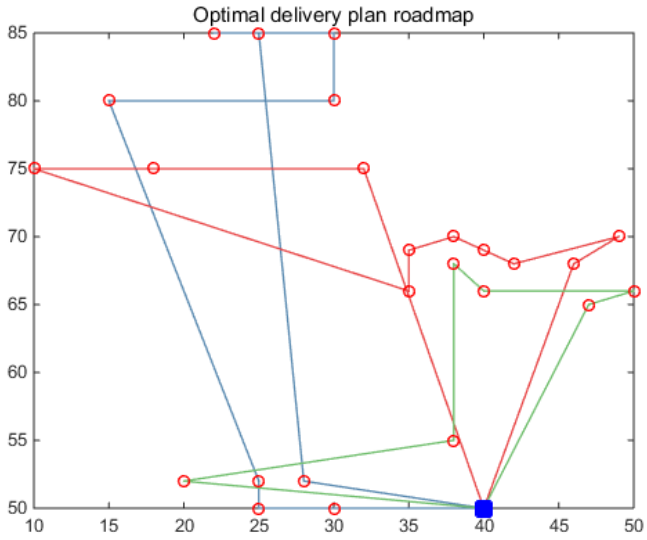


Fig. 1- Route diagram of improved ant colony algorithm

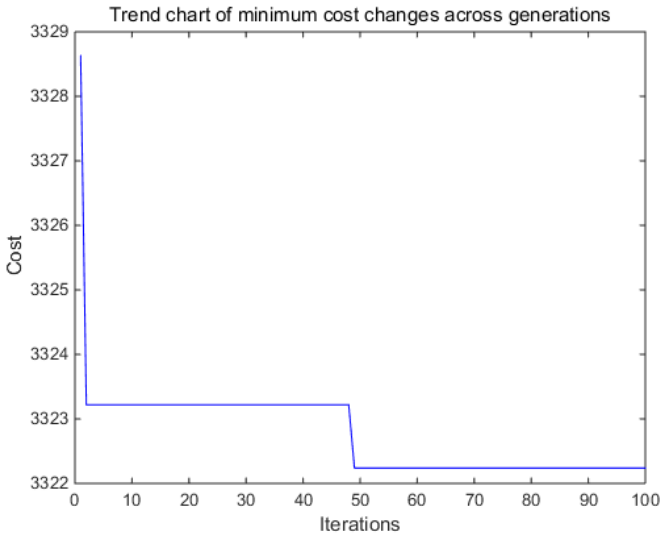


Fig. 2 –Convergence curve of improved ant colony algorithm

Based on the vehicle information in "Table 2 Information on agricultural distribution vehicles" and combined with the actual situation of optimizing the distribution path, select the vehicle. Here, a 4-ton vehicle with the lowest total cost was chosen to be used.

Table 3

Optimal service route

Service route	Model	Total distance	Convergence time	Total cost
0->20->24->25->19->15->16->14->12->22->0	4T	322.2386	259.292	3322.215
0->13->17->18->10->11->9->6->4->2->1->0	4T			
0->5->3->7->8->23->21->0	4T			

This study also designed a traditional ant colony algorithm solution model to further verify the effectiveness of the improved ant colony algorithm. Under the constant initial cost and parameters, four agricultural distribution vehicles were needed to solve the optimization model of the agricultural material route, and the total distance of an agricultural distribution vehicle was 346.048 km. The total cost was 4,346.109 yuan, and the algorithm was run for 304.661 s. The route diagram of the traditional ant colony algorithm is shown in Fig. 3, the convergence curve of the traditional ant colony algorithm is given in Fig. 4, and the calculation results are presented in Table 4.

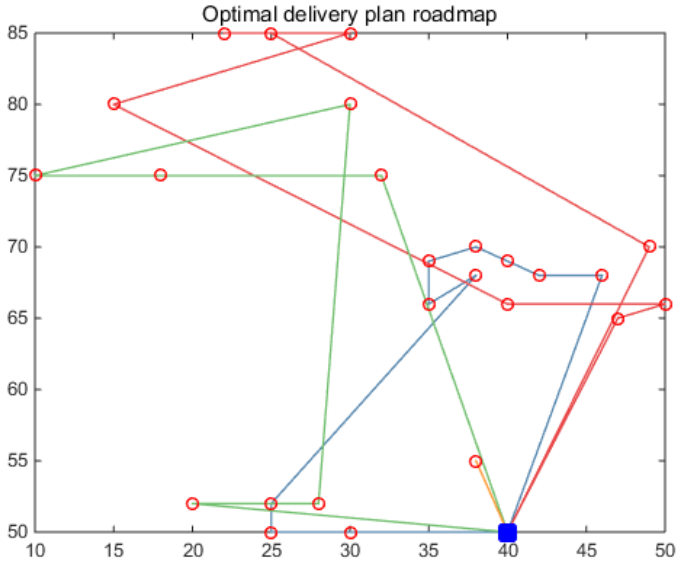


Fig. 3 - Route diagram of traditional ant colony algorithm

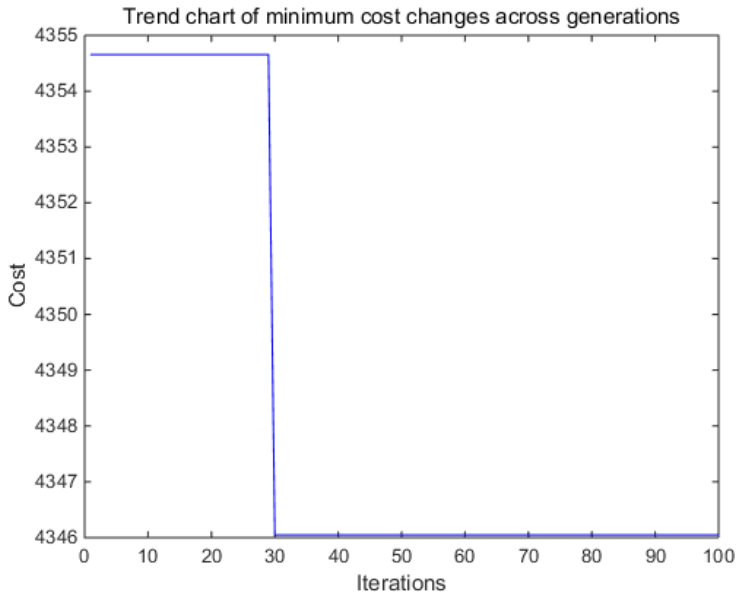


Fig. 4 - Convergence curve of traditional ant colony algorithm

Based on the vehicle information in "Table 2 Information on agricultural distribution vehicles" and combined with the actual situation of optimizing the distribution path, select the vehicle. Here, a 3-ton vehicle with the lowest total cost was chosen to be used.

Table 4

Traditional ant colony route

Service route	Model	Total distance	Convergence time	Total cost
0->20->24->25->8->10->11->9->6->4->1->0	3T	346.048	304.661	4346.109
0->5->3->7->19->16->14->12->2->0	3T			
0->13->17->18->15->22->21->0	3T			
0->23->0	3T			

The calculation results show that the improved ant colony algorithm has a lower distribution cost but more reasonable route compared with the traditional ant colony algorithm. The number of activated vehicles is small, and the convergence time of the algorithm is short. Compared with the traditional ant colony algorithm, the improved ant colony algorithm can converge to the global optimum faster with a lower distribution cost. In the multivehicle distribution route optimization model that considers carbon emissions, under the same conditions of driving distance, vehicle weight, traffic control, and others, the four-ton truck has obvious advantages, and it has the lowest total cost and the largest cost advantage. The existing agricultural material logistics distribution process is relatively complicated, and it involves many demand distribution points and freight types.

In terms of the total distance traveled by vehicles, the improved ant colony algorithm reduces by 7.39% compared to the traditional ant colony algorithm. In terms of algorithm convergence time, the improved ant colony algorithm improves by 17.50% compared to traditional ant colony algorithms. In terms of total cost, the improved ant colony algorithm reduces 30.82% compared to traditional ant colony algorithms. The traffic routes of vehicles are complex, and customers have strict requirements for agricultural material quality. Against the background of the market economy, competitive demands in the agricultural material market have increased. Therefore, for medical supplies with strict time requirements, the model that adopts a soft time window constraint and a loss function is suitable for actual situations. It decreases the cost resulting from transportation delays, improves customer satisfaction, and plays an important role in promoting the development of the modern logistics industry.

CONCLUSIONS

While ensuring the economic benefits of agricultural material distribution enterprises, it is also necessary to consider the environmental costs in the economic development of enterprises, in order to achieve a win-win situation between the logistics industry and ecological civilization development. This article mainly starts from the perspective of energy conservation and emission reduction, and takes into account the cost of converting low-carbon environmental protection into carbon emissions in the model. Under constraints such as vehicle load capacity and time window, the model considers the fixed cost of vehicle delivery, carbon emissions cost, vehicle transportation cost, and time window penalty cost as the objective functions for optimizing the agricultural material delivery path of multiple vehicle models. Using improved ant colony algorithm to study agricultural material enterprises with a single distribution center, the basic ant colony algorithm is improved from three aspects: initial pheromone concentration, pheromone update strategy, and transfer rules. By comparing the results under different parameter values, reasonable parameters are determined. And comparing the results of the improved ant colony algorithm with the basic ant colony algorithm, it is found that the improved ant colony algorithm has made some progress in the average value of the lowest delivery cost obtained. The research results of this article provide a reference for agricultural material distribution companies to propose multi vehicle logistics distribution path methods under the conditions of reducing energy consumption and increasing efficiency, making the company's development more suitable for the needs of building green logistics and developing green operations. The following conclusions were obtained from the analysis:

(1) Given the timeliness of some agricultural products, vehicle routing has a time limitation and a time constraint. A time window can be introduced to solve the multivehicle routing problem, and the traditional ant colony algorithm is usually adopted for the time constraint problem. Differential update and chaotic disturbance can be utilized to improve the traditional ant colony algorithm and make it conducive for future research on

multivehicle distribution under high agricultural demands. Such an improvement can avoid delays in the farming season and can boost the growth of crops.

(2) The improved ant colony algorithm has good sensitivity in solving large-scale calculation problems. In actual cases, the distribution from the distribution center to each demand point has good extensibility. The improved ant colony algorithm can be practically applied to the vehicle routing problem. In this study, the improved ant colony algorithm was compared with the traditional ant colony algorithm. The proposed algorithm shortens the response time and provides users with results faster compared with the traditional algorithm. With regard to the distribution route results, the distribution distance is short, and minimal fuel is consumed. The improved ant colony algorithm is environmentally friendly and decreases the transportation cost, thus benefiting farmers.

REFERENCES

[1] Badia-Melis R., Carthy U., Ruiz-Garcia L., Garcia-Hierro J., and Robla Villalba J. I., (2018), New trends in cold chain monitoring applications - a review, *Food Control*, vol.86, ISSN 0956-7135, pp.170-182, England;

[2] Bortolini M., Faccio M., Ferrari E., Gamberi M., and Pilati F., (2016), Fresh food sustainable distribution: cost, delivery time and carbon footprint three-objective optimization, *Journal of Food Engineering*, vol.174, no. 2, ISSN 0260-8774, pp.56-67, England;

[3] Braekers K., Ramaekers K., and Van Nieuwenhuyse I., (2016), The vehicle routing problem: state of the art classification and review, *Computers & Industrial Engineering,* vol.99, ISSN 0360-8352, pp.300-313, England;

[4] Çeken C., and Abdurahman D., (2019), Simulation modeling of an IoT based cold chain logistics management system, *Sakarya University Journal of Computer and Information Sciences*, vol.2, no.2, ISSN 1300-0632, pp.89-100, Sakarya/Turkey;

[5] Chandra A. A., and Lee S. R.,(2014), A method of WSN and sensor cloud system to monitor cold chain logistics as part of the IoT technology, *International Journal of Multimedia and Ubiquitous Engineering*, vol.9, no.10, ISSN 1975-0080, pp.145-152, United States;

[6] Chaudhuri A., Dukovska P. I., Subramanian N., Chan H. K., and Bai R., (2018), Decision-making in cold chain logistics using data analytics: a literature review, *The International Journal of Logistics Management*, vol.29, no.3, ISSN 0957-4093, pp.839-861, England;

[7] Cornillier F., Boctor F., and Renaud J., (2012), Heuristics for the multi-depot petrol station replenishment problem with time windows, *European Journal of Operational Research*, vol. 220, no. 2, ISSN 0377-2217, pp. 361-369, Netherlands;

[8] Deol G., Sunny J., and Naga O. R., (2021), Hadoop job scheduling using improvised ant colony optimization, *Turkish Journal of Computer and Mathematics Education*, vol. 12, no. 2, ISSN 1309-4653, pp. 3417–3424, Turkey;

[9] Du J., Chen L., (2017), Research on mobile agricultural material logistics distribution system based on ASD and LBS (基于 ASD 与 LBS 的移动农资物流配送系统研究), *Modern Electronics Technique*, vol.40, no. 1, ISSN 1004-373X, pp.167-170, China;

[10] Dulebenets M. A., Ozguven E. E., Ren M., and Ulak M. B., (2016), Intermodal freight network design for transport of perishable products, *Open Journal of Optimization,* vol.5, no. 4, ISSN 2325-7105 , pp.120-139, United States;

[11] Fazayeli S., Eydi A., and Kamalabadi I. N., (2018), Location-routing problem in multimodal transportation network with time windows and fuzzy demands: presenting a two-part genetic algorithm, *Computers & Industrial Engineering,* vol.119, ISSN 0360-8352, pp.233-246, England;

[12] Ferrag M. A., Shu L., Yang X., Derhab A., and Maglaras L., (2020), Security and privacy for green IoT-based agriculture: review, blockchain solutions, and challenges, *IEEE Access*, vol.8, ISSN 2169-3536 pp.32031-32053, United States;

[13] Huo H., Zang X.,Xu L., (2017), Research on the Cost Allocation Model of Agricultural Materials Joint Delivery (农资共同配送成本分摊模型问题研究), *Jiangsu Agricultural Sciences*, Vol.45, no.20, ISSN 1002-1302, pp.352-354, China;

[14] Hu X., Sun L., Zhou Y., and Ruan J., (2020), Review of operational management in intelligent agriculture based on the Internet of Things. *Frontiers of Engineering Management*, vol.7, Issue 3, ISSN 2095-7513, pp. 309-322, China;

[15] Ji B., Li Y., Cao D., Li C., Mumtaz S., and Wang D., (2020), Secrecy performance analysis of UAV assisted relay transmission for cognitive network with energy harvesting, *IEEE Transactions on Vehicular Technology,* vol.69, no.7, ISSN 0018-9545, pp.7404-7415, United States;
[16] Kanso B., Kansou A., and Yassine A., (2021), Open capacitated arc routing problem by hybridized ant colony algorithm, *RAIRO—Operations Research*, vol. 55, no. 2, ISSN 1290-3868, pp. 639–652, France;
[17] Lahyani R., Coelho C. L., Khemakhem M., Laporte G., and Semet F., (2015), A multi-compartment vehicle routing problem arising in the collection of olive oil in Tunisia, *Omega*, vol. 51, ISSN 0305-0483, pp.1–10, England;
[18] Lakshmanna K. and Khare N., (2018), Mining DNA sequence patterns with constraints using hybridization of firefly and group search optimization, *Journal of Intelligent Systems*, vol.27, no.3, ISSN 0334-1860, pp.349-362, Poland;
[19] Leleń P. and Wasiak M., (2019), The model of selecting multimodal technologies for the transport of perishable products, *Archives of Transport,* Vol.50, no.2, ISSN 2333-9721, pp.17-33, Poland;
[20] Lin X., Wu J., Mumtaz S., Garg S., Li J., and Guizani M., (2021), Blockchain-based on-demand computing resource trading in IoV-assisted smart city, *IEEE Transactions on Emerging Topics in Computing*, vol.9, no. 3, ISSN 2168-6750, pp.1373-1385, United States;
[21] Liu S. C., Zhang C., (2022), Optimization of Cold Chain Distribution Route with Mixed Time Window considering Customer Priority, *Computational Intelligence and Neuroscience*, Vol.2022, ISSN 1687-5265, pp.1-18. United States;
[22] Liu S.C., Zhang C., (2023), Robust optimization of agriculture products urban distribution path considering demand uncertainty, *Alexandria Engineering Journal*, vol. 66, ISSN 1110-0168, pp.155-165, Egypt;
[23] Luo H., Zhu M., Ye S., Hou H., Chen Y., and Bulysheva L., (2016), An intelligent tracking system based on internet of things for the cold chain, *Internet Research*, Vol.26, no.2, ISSN 1066-2243, pp.435-445, England;
[24] Mardaneh E., Lin Q., Loxton R., (2016), A heuristic algorithm for optimal fleet composition with vehicle routing considerations, *Optimization Methods and Software*, vol.31, no. 2, ISSN 1055-6788, pp.272-289, England;
[25] Marinaki M., and Marinakis Y., (2016), A glowworm swarm optimization algorithm for the vehicle routing problem with stochastic demands, *Expert Systems with Applications*, Vol.46, ISSN 0957-4174, pp.145-163, United States;
[26] Olkhova M., Davidich Y., Roslavtsev D., and Davidich N., (2017), The efficiency of transportating perishable goods by road and rail, *Transport Problems*, vol. 12, no. 4, ISSN 1896-0596, pp. 37-50. Poland;
[27] Ostermeier M. and Hübner A., (2018), Vehicle selection for a multi-compartment vehicle routing problem, *European Journal of Operational Research*, vol. 269, no. 2, ISSN 0377-2217, pp. 682–694, Netherlands;
[28] Rajyalakshmi V. and Lakshmanna K., (2022), A review on smart city - IoT and deep learning algorithms, challenges, *International Journal of Engineering Systems Modelling and Simulation*, vol. 13, no.1, ISSN 1755-9758, pp. 3-26. China;
[29] Srivastava S., Kumar S., and Garg R. K., (2021), A multi-objective optimization of TIG welding parameters using response surface methodology, *International Journal of Computer Aided Engineering and Technology*, vol. 14, no. 4, ISSN 1757-2657, pp. 575–590;
[30] Sv D. G. and Nalini T., (2021), Optimizing automated programming contracts with modified ant colony optimization, *Indian Journal of Computer Science and Engineering*, vol. 12, no. 1, ISSN 0976-5166, pp. 226–238, India;
[31] Voutos Y., Mylonas P., Katheniotis J., and Sofou A., (2019), A survey on intelligent agricultural information handling methodologies, *Sustainability,* vol.11, no.12, ISSN 2071-1050, pp.3278, Switzerland;
[32] Wang X., Gao B., An K., (2020), Research on Guizhou agricultural material logistics distribution mode from the perspective of new retail (新零售视角下贵州农资物流配送模式研究), *Logistics Sci-Tech*, vol.43, no. 01, ISSN 1002-3100, pp.45-47, China;

[33] Wei J., Chen T., Zhang C., (2016), Improved hybrid genetic algorithm and its application research to optimize agricultural distribution (改进混合遗传算法及其在农资优化配送中应用), *Computer Engineering and Applications*, vol.52, no. 02, ISSN 1002-8331, pp.234-238, China;

[34] Zhang Y., (2017), Discussion on Building a Modern Logistics and Distribution System for Agricultural Means of Production Commodities (浅谈构建农资商品现代物流配送体系), *China Circulation Economy*, Vol.11, ISSN 2096-3157, pp.17-19, China;

AGRICULTURAL UAV CROP SPRAYING PATH PLANNING BASED ON PSO-A* ALGORITHM

/

基于 PSO-A*算法的农业无人机作物喷洒路径规划

Lijuan Fan
Xinxiang Vocational and Technical College, Xinxiang, Henan, 453006, China.
**E-mail: fanlijuan@xxvtc.edu.cn*
Corresponding author: Fan Lijuan
DOI: https://doi.org/10.35633/inmateh-71-54

Keywords: *particle swarm optimization algorithm, A* algorithm, UAV, path planning, crop spraying operations*

ABSTRACT

Currently, drones have been gradually applied in the field of agriculture, and have been widely used in various types of agricultural aerial operations such as precision sowing, pesticide spraying, and vegetation detection. The use of agricultural UAVs for pesticide spraying has become an important task in the agricultural plant protection process. However, in the crop spraying process of agricultural UAVs, it is necessary to traverse multiple spray points and plan obstacle avoidance paths, which greatly affects the efficiency of agricultural UAV crop spraying operations. To address the above issues, traditional particle swarm optimization (PSO) algorithms have strong solving capabilities, but they are prone to falling into local optima. Therefore, this study proposes an improved PSO algorithm combined with the A algorithm, which introduces a nonlinear convergence factor balancing algorithm for global search and local development capabilities in the traditional PSO algorithm, and adopts population initialization to enhance population diversity, so that the improved PSO algorithm has stronger model solving capabilities. This study designs two scenarios for agricultural UAV crop spraying path planning: one without obstacles and one with obstacles. Experimental simulation results show that using the PSO algorithm to solve the obstacle-free problem and then using the A* algorithm to correct the path obstructed by obstacles in the obstacle scenario, the agricultural UAV crop spraying trajectory planning based on the PSO-A* algorithm is real and effective. This research can provide theoretical basis for agricultural plant protection and solve the premise of autonomous operation of UAVs.*

摘要

*目前，无人机已逐步应用于农业领域，并广泛应用于精密播种、农药喷洒、植被探测等各类农业空中作业。使用农业无人机喷洒农药已成为农业植保过程中的一项重要任务。然而，在农业无人机的作物喷洒过程中，需要穿越多个喷洒点并规划避障路径，这大大影响了农业无人机作物喷洒作业的效率。针对上述问题，传统的粒子群优化算法具有较强的求解能力，但容易陷入局部最优。因此，本研究提出了一种与 A*算法相结合的改进 PSO 算法，在传统 PSO 算法中引入了一种具有全局搜索和局部开发能力的非线性收敛因子平衡算法，并采用种群初始化来增强种群多样性，使改进的 PSO 算法具有更强的模型求解能力。本研究设计了两种农业无人机作物喷洒路径规划场景：一种是无障碍场景，另一种是有障碍场景。实验仿真结果表明，在障碍场景中，使用 PSO 算法解决无障碍问题，然后使用 A*算法校正障碍物遮挡的路径，基于 PSO-A*算法的农业无人机作物喷洒轨迹规划是真实有效的。该研究可以为农业植物保护提供理论依据，解决无人机自主运行的前提。*

INTRODUCTION

Science and technology are the primary productive forces and the key support for the high-quality development of agriculture. With the increase in agricultural scale and modernization level, traditional manual pesticide spraying can no longer meet the needs of field crops *(Aggarwal S. et al., 2021)*. In order to better meet the needs of farmers, drones have been widely used in the fields *(Al-Hourani A. et al., 2014)*. With the continuous advancement and application of drone technology, drones have become a mature tool in the fields and a new weapon for pesticide spraying *(Andreev A. S. et al., 2019)*. Compared with traditional manual spraying methods, drone pesticide spraying has the advantages of high speed, high efficiency, and large-scale operation *(Batliner M. et al., 2021)*. In terms of cost, time, and expenses, drone spraying significantly reduces labor costs, saves water, and increases pesticide utilization rate by more than 30%.

In addition to the significant improvement in efficiency, using drones for pesticide spraying can automate tasks without the need for manual intervention *(Bensafia Y. et al., 2018)*. It not only protects farmers from pesticide exposure but also prevents soil and ecosystem damage *(Eschmann H. et al., 2021)*. Using drones for spraying can reduce the labor pressure on farmers and improve the comfort and safety of their work *(Hasan S. F. et al., 2020)*. These drones are equipped with advanced navigation and sensing technologies, allowing for precise spraying of field crops *(Hassan R. et al., 2020)*. By controlling flight height, speed, and liquid dosage reasonably, the amount of pesticide used can be effectively reduced, waste can be minimized, and spraying accuracy can be improved *(Huang Y. et al., 2019)*. In the long run, it can also reduce labor costs and machinery losses, saving farmers a significant amount of expenses *(Keyvan M. et al., 2020)*.

With further technological advancements, drones will be able to respond more quickly to the pest control needs during crop growth and spray pesticides in a timely manner *(Khalilpour S. A. et al., 2020),* which helps ensure the quality and yield of agricultural products *(Li P. et al., 2018)*. Moreover, traditional pesticide spraying often leads to pesticide atomization and dispersion *(Li P. et al., 2018)*, causing air and water pollution. The application of drone pesticide spraying will further achieve and improve precise spraying, reduce pesticide usage and dispersion, and minimize environmental pollution *(Li X. et al., 2019)*. By improving agricultural productivity and reducing pesticide use, rural drone pesticide spraying can create more economic benefits for farmers and enhance agricultural comprehensive benefits *(Lv S. P. et al., 2019)*. Resolving the "agriculture, rural areas, and farmers" issues is a key focus of rural industrial revitalization. In the future, high-standard farmland construction will continue to be promoted across the country, modern technology-based farming methods will be widely adopted, and agricultural production will be mechanized and intelligent *(Ou M. et al., 2022)*. With the support of "drones +", farming will become easier and smarter, and a new form of "smart agriculture" will gradually unfold in the fields *(Peng H. et al., 2020).*

Currently, in order to adapt to the development trend of modern agriculture and efficient agriculture, the Ministry of Agriculture and Rural Affairs has actively responded to the call of the central government and accelerated the construction of high-standard farmland *(Pizarro L. A. O. et al., 2020).* It focuses on implementing the rural revitalization strategy, advancing land storage and technology storage, and making the improvement of grain production capacity a top priority. This indicates that the distribution of farmland will shift from dispersed to regular and concentrated development, and agricultural plant protection will face the demand for large-scale operations *(Ren B. et al., 2020)*. Only through modern agricultural machinery and equipment can this be effectively solved, creating broad application space for aerial plant protection represented by drones. Unmanned Aerial Helicopter (UAH) plays an important role in agricultural plant protection with its characteristics of large payload, long endurance, hovering, and vertical takeoff and landing *(Rubio J. et al., 2020)*. It will also become the development direction of new intelligent agricultural machinery and equipment.

Currently, UAH and rotary drones have been widely used in the prevention and control of pests and diseases in crops such as rice, cotton, and jujube *(Santos C. et al., 2020)*. However, there is still a long transition phase from "spraying" to "spray irrigation", and automatic or autonomous flight based on flight routes is one of the effective ways to improve agricultural plant protection efficiency. In previous studies, three commonly used spraying methods in irregular operating areas for plant protection were summarized, and a reasonable scanning route planning method based on graph theory was proposed to plan rational routes from the perspectives of route selection, waypoint collection, and obstacle avoidance, enabling UAH to operate autonomously *(Talak R. et al., 2019)*. However, most of the current research is based on the ideal route planning design of a single operating area. Considering the complex conditions of flight constraints, task constraints, and obstacle constraints in actual UAH flights, it is necessary to optimize the segmentation of large-scale regular rectangular plant protection areas to ensure the efficient flight of UAH in plant protection processes and meet practical operational requirements *(Wang F. et al., 2017)*. In view of this, this paper proposes a crop protection route segmentation method based on "spraying unit modules". Firstly, the full coverage operation mode of UAH is determined *(Wang G. et al., 2021)*, and then, the minimum spraying operation unit during plant protection operations is determined as the objective function based on the flight distance of the unmanned aerial vehicle in the non-flow spraying mode *(Wang H. et al., 2021)*. The concept of minimum module segmentation is adopted to optimize the rectangular farmland. Finally, the overall planning of the plant protection operation area and the optimization design of the operation route are achieved *(Welabo A. et al., 2020)*.

With the development of smart agriculture, computer vision has achieved good results in the field of agriculture *(Xu B. et al., 2015)*. For example, *You et al. (2021)* implemented an automatic weed identification system in a pasture with broadleaf weeds *(You X. et al., 2021)*. Zeng et al. (2019) proposed a cucumber leaf pest identification system *(Zeng Y. et al., 2019) (Zeng Y. et al., 2019)*. In addition, with the maturity of deep learning (DL) technology, it has been widely used in the field of agriculture in China *(Xu J. et al., 2018).* With the increase in the number of samples, deep learning technology has become more widely used and accurate in the classification and identification of crops and pests *(Yang F. et al., 2018)*.

However, there is relatively little research on how to achieve process automation after identification. Drones are gradually transitioning from the military field to the civilian field, and their combat strategies can be introduced to the agricultural sector *(Zhang F. et al., 2014)*. Drone trajectory planning is the basis of drone combat research and the basic guarantee of drone combat effectiveness. The model considers three different methods, covering most drone flight missions *(Zhao J. et al., 2020)*. Established a target function based on flight time and flight safety factors, used fuzzy technology to assess threat levels, and applied particle swarm optimization (PSO) search strategy to drone trajectory planning *(Zhao J. et al., 2021)*. Currently, swarm intelligence optimization algorithms are relatively popular in the field of drone trajectory planning, but swarm intelligence optimization methods are prone to local optima and cannot fundamentally solve the problem. Existing two-dimensional drone trajectory planning algorithms rarely consider the influence of obstacle space on trajectories.

In summary, an improved particle swarm optimization algorithm combined with the A* algorithm is proposed for drone trajectory planning in agricultural spraying operations. The PSO algorithm introduces the K-Means clustering algorithm to initialize the population to enhance population diversity, and nonlinear convergence factor to balance global search and local development capabilities, and the PSO algorithm's position update adjustment is introduced to avoid local optimization problems. The PSO algorithm is used to plan obstacle-free crossing trajectories for multiple marked spray tasks, and then the A* algorithm is used to locally avoid obstacles in the trajectory of the obstacle path.

MATERIALS AND METHODS

The fitness function can calculate the cost of the track and compare the cost values of different tracks to determine the quality of the track. This article comprehensively balances three factors: track length, obstacle collision, and height change, and models the fitness function:

$$F = \varphi_1 f_L + \varphi_2 f_C + \varphi_3 f_H \tag{1}$$

Among them: f_H represents the cost of height change, f_C represents the cost of obstacle collision, f_L represents the cost of track length, F represents the cost of track, φ_1 φ_2 φ_3 represents the weight values of different costs, and is a constant, and its proportion is related to the tasks performed by the drone.

(1) Track length cost. The length of the drone's flight path is one of the important indicators for evaluating the quality of the flight path. Considering the limited energy supply of the drone, the shorter the flight path, the less time and energy consumption, and the more advantageous it is for the drone. Assuming the number of trajectory nodes is n, and after smoothing through interpolation, the entire trajectory consists of N nodes. (x_i, y_i, z_i) and $(x_{i+1}, y_{i+1}, z_{i+1})$ represent the three-dimensional coordinates of the i-th node and the adjacent next node, respectively. Therefore, the cost of track length can be expressed as:

$$f_L = \sum_{i=1}^{N-1} \sqrt{\left(x_{i+1} - x_i\right)^2 + \left(y_{i+1} - y_i\right)^2 + \left(z_{i+1} - z_i\right)^2} \tag{2}$$

(2) Obstacle collision cost. When the flying altitude of the drone is lower than the height of the obstacle and the distance from the center point of the obstacle is less than the radius of the obstacle, a collision occurs. In order to maintain a certain distance between track nodes and obstacles, it is necessary to calculate the collision cost of obstacles:

$$f_C = \sum_{i=1}^{T} \sum_{j=1}^{N} C_{i,j}, C_{i,j} < R_{obsi} \tag{3}$$

$$C_{i,j}=\begin{cases}\sqrt{\left(x_i-x_j\right)^2+\left(y_i-y_j\right)^2}, & z_i \geq z_j \\ 0, & z_i \geq z_j\end{cases} \quad (4)$$

Among them, N is the total number of nodes after the smooth trajectory, T is the number of obstacles, R_{obsi} is the radius of obstacle i, and $C_{i,j}$ is the distance between the i-th obstacle and the j-th trajectory node.

(3) Highly variable costs. In order to prevent collisions with mountains or other obstacles and avoid radar search, drones must raise or lower their altitude, but repeated raising and lowering may also endanger the safety of drones. Therefore, it is necessary to constrain altitude changes, and the variance of track altitude can describe the stability of flight altitude as the cost of altitude changes:

(4) Highly variable costs. In order to prevent collisions with mountains or other obstacles and avoid radar search, drones must raise or lower their altitude, but repeated raising and lowering may also endanger the safety of drones. Therefore, it is necessary to constrain altitude changes, and the variance of track altitude can describe the stability of flight altitude as the cost of altitude changes:

$$f_H=\sqrt{\frac{1}{N}\sum_{k=1}^{N}\left(z_k-\frac{1}{N}\sum_{k=1}^{N}z_k\right)^2} \quad (5)$$

In the formula: z_k is the altitude value at the k-th track node, and N is the total number of track nodes.

A* Algorithm

The A* algorithm is a heuristic search method with high search efficiency, which can solve the shortest and most effective path in a static environment. In A*, the weight of each path is the sum of two costs, namely the cost and the heuristic distance from the starting node to the current node. Starting from the starting point, it is possible to search for 8 directions, use the evaluation function to obtain the values of the extension nodes for comparison, select the minimum value as the next extension node, and cycle this process until the search is completed. Finally, the final path was obtained. Because each search uses the lowest estimated node as the next expansion node, the final cost is the lowest. The evaluation function is shown in equation (6):

$$f(n)=g(n)+h(n) \quad (6)$$

In equation (1): $h(n)$ is the estimated cost from node n to the endpoint; $g(n)$ is the actual cost from the starting node to node n; $f(n)$ is the evaluation function of node n.

The determination of the valuation function is closely related to the actual situation and will directly affect the results of the A* algorithm. Therefore, the Manhattan distance is used as a heuristic function:

$$h(n)=\left|x_d-x_n\right|+\left|y_d-y_n\right| \quad (7)$$

In equation (2): x_n is the abscissa of node n; y_d is the ordinate of the target point; x_d is the abscissa of the target point; y_n is the ordinate of node n.

The A* algorithm is a heuristic search algorithm used to evaluate each search location during path planning, the evaluation function is shown in equation (8):

$$F(n)=G(n)+H(n) \quad (8)$$

In the formula: is the estimated cost of the optimal path from the n-th node to the target node. The actual cost from the starting point to the n-th node. The search process is identified through the OPEN table and the CLOSED table. The OPEN table records the nodes to be searched, the CLOSED table records the nodes that have been searched, and the OPEN table continuously rearranges according to the evaluation function to find the best node to achieve the search process.

Improved Particle Swarm Optimization Algorithm

The basic idea of the PSO algorithm is to seek the optimal solution through information sharing and mutual reference between individuals. Firstly, each particle represents a candidate solution in the PSO, and due to the randomness of the elementary particles, random solutions can be used to initialize them.

Secondly, by using a defined fitness function to evaluate particle state, individual optimal positions and global optimal positions can be obtained through comparison. Then, each iteration, the particles will reference and update their positions and velocities, and will also dynamically update. Through repeated iterations, the optimal solution is ultimately obtained. In this article, each particle represents a trajectory. Considering trajectory planning in three-dimensional space, assuming the number of trajectory nodes is n, for the k-th particle, equation (9) represents its position vector, and equation (10) represents its velocity vector.

$$P_k = \left[\left(P^x, P^y, P^z \right)_{(k,1)}, \cdots, \left(P^x, P^y, P^z \right)_{(k,n)} \right]^T \tag{9}$$

$$V_k = \left[\left(V^x, V^y, V^z \right)_{(k,1)}, \cdots, \left(V^x, V^y, V^z \right)_{(k,n)} \right]^T \tag{10}$$

If there are S particles in the particle swarm, there must be a single optimal position for the S particles, and for the entire particle swarm, there must also be a global optimal position, as shown in equation (11):

$$\begin{cases} p_{(k,best)} = [p_{(k,1,best)}, \cdots, p_{(k,n,best)}]^T \\ p_{best}^G \in [p_{(1,best)}, \cdots, p_{(S,best)}] \end{cases} \tag{11}$$

By substituting the position of particles into the fitness function F, the trajectory quality of particles can be evaluated. The higher the trajectory quality, the smaller the fitness function value F of the corresponding particle. For particle k, if the F-value after the t-th iteration is less than the value of the previous t -1st iteration, it will be updated. Otherwise, its historical best position will still be used, as shown in equation (12). Finally, among the historical optimal positions of S particles, choose the one with the lowest F-value as the global optimal position, as shown in equation (13):

$$P_{(k,best)}(t) = \begin{cases} P_{(k,best)}(t-1); & F\left(P_{(k,best)}(t-1)\right),, F\left(P_k(t)\right) \\ P_{(k,best)}(t); & F\left(P_{(k,best)}(t-1)\right) > F\left(P_k(t)\right) \end{cases} \tag{12}$$

$$F(P_{best}^G(t)) = \min[F(P_{(1,best)}(t)), \cdots, F(P_{(s,best)}(t))] \tag{13}$$

In the next iteration, the velocity and position of each particle are updated according to equation (14) as follows:

$$\begin{cases} V_k(t+1) = w \cdot V_k(t) + c_1 \cdot r_1 \cdot \left(P_{(k,best)} - P_k(t)\right) + c_2 \cdot r_2 \cdot \left(P_{best}^G(t) - P_k(t)\right) \\ P_k(t+1) = P_k(t) + V_k(t+1) \end{cases} \tag{14}$$

In the formula, w represents the inertia weight used to inherit the velocity of particles, and is the learning factor representing the learning ability to the best state of one's own history. The learning factor represents the learning ability of the optimal individual in the group, which is any random number between 0 and 1. It is also an arbitrary random number between 0 and 1.

The inertia weight w directly affects the search ability of particles. The larger the value, the better the particle inherits the original speed, resulting in higher speed and stronger global search ability. By dynamically changing the value of inertia weight w, it is convenient to adjust the global and local search capabilities of particles at different time periods. This article adopts an exponential form of inertia weight adjustment method to improve convergence speed:

$$w = (w_{\max} - w_{\min}) \cdot \exp\left[(1-t) \cdot \alpha\right] + w_{\min} \tag{15}$$

$$t \in \left[1, 2, \cdots T_{\max}\right] \tag{16}$$

In the formula (15), w_{min} is the minimum value of w, w_{max} is the maximum value of w, T_{max} is the maximum number of iterations, t is the current number of iterations, α is used to control the decay rate of inertia weight, and is a constant coefficient.

Traditional particle swarm optimization algorithms have poor population diversity. Introducing evolutionary operators such as crossover and mutation into its algorithm can effectively improve the diversity

of the population and avoid generating local optima. The commonly used mutation operators include Gaussian mutation (GM) and Cauchy mutation (CM). Due to the large range of random numbers and low peaks in the Cauchy distribution, introducing the Cauchy mutation operator in the PSO algorithm is more advantageous for particles to quickly jump out of local extremum and increase population diversity. If x satisfies the condition given in equation (17), it will become a Cauchy distribution.

$$f(x;x_0,\gamma)=\frac{1}{\pi}[\frac{\gamma}{(x-x_0)^2+y^2}] \tag{17}$$

$$x\in(-\infty,+\infty) \tag{18}$$

where: y is the width of x_0 related to half, and x_0 is the position of the maximum value of the function. When $x=1$, $x_0=0$ and x satisfy the condition of probability density function, equation (19) is its cumulative distribution function:

$$F(x;0,1)=\frac{1}{\pi}\arctan(x)+\frac{1}{2}, \tag{19}$$

$$x\in(-\infty,+\infty) \tag{20}$$

By performing an inverse transformation on equation (19), the inverse function can be obtained, and then the random numbers generated through uniform distribution can generate random numbers that follow the Cauchy distribution:

$$\begin{cases}\frac{1}{\pi}\arctan(CM)+\frac{1}{2}=Rand\\ CM=\tan\left[\pi(Rand-\frac{1}{2})\right]\end{cases} \tag{21}$$

In the equation, $Rand$ is any real number uniformly distributed within the range of (0,1), and CM is the Cauchy mutation operator.

Similar to inertia weights, the step size of Cauchy mutation also needs to be dynamically adjusted in order to generate certain large step size disturbances in the early stages of algorithm operation, causing particles to jump out of the current position and avoid local optima. In the later stage, convergence is accelerated in smaller steps, and the update rule for each particle in each iteration is:

$$P_k^{'}=P_k+P_k\cdot CM\cdot\exp\left[(1-t)\cdot\beta\right] \tag{22}$$

$$t\in\left[1,2,\cdots,T_{\max}\right] \tag{23}$$

In the formula, $P_k^{'}$ is the position of particle k after Cauchy mutation, T_{max} is the maximum number of iterations, P_k is the position of particle k, β is the current number of iterations, is a constant coefficient, used to control the speed of variation step size.

Algorithm Steps

In summary, the implementation steps of the 3D trajectory planning algorithm for agricultural drone spraying based on PSO-A* algorithm are as follows:

Step 1: Create an agricultural drone spraying environment based on the A* algorithm, and set the starting and ending points of the drone;

Step 2: Initialize the particle position and various parameters, including the total number of particles S, maximum number of iterations, maximum speed, number of track nodes n, maximum inertia weight, total number of track nodes n, minimum inertia weight, learning factors C1, C2, etc.

Step 3: Smoothing a trajectory containing only n trajectory nodes through cubic spline data interpolation to obtain a trajectory containing n trajectory nodes, which is used to calculate the fitness values of particles in equations (9) to (14);

Step 4: Find the individual and global optimal positions of each particle;

Step 5: Update the Cauchy mutation operator CM using equation (20), and obtain the particle position for the next iteration using equation (21); Update the inertia weight w using equation (17);

Step 6: Update particle velocity V_k and position P_k according to equation (16), where if V_k and P_k cross the boundary, take the boundary value;

Step 7: Repeat steps 3 to 6 until the final flight path for agricultural drone spraying is obtained.

RESULTS

Assuming the agricultural drone spraying operation area is T (L × W, where L is the horizontal length and W is the vertical length), under the same initial conditions (environmental factors, aircraft status, payload, etc.), the PSO algorithm, A* algorithm, and PSO-A* algorithm are used to achieve complete coverage of the target spray points.

PSO Algorithm for Obstacle-Free Trajectory Planning

The simulation experiment scene is set as a 700 m × 700 m agricultural drone spraying operation area. The specific distribution of the spray points in the operation area is shown in Table 1. The particle swarm algorithm is used to solve the path planning problem for multiple spray points in obstacle-free space. In the experiment, the parameters of the particle swarm optimization algorithm are set as follows: 50 particles, maximum iterations of 200 times, and learning factors C1 and C2 both set to 1.5. When the number of spray points is 30, the convergence curve of the PSO algorithm is shown in Figure 2, and the path planning of the PSO algorithm is shown in Figure 3. From Figure 2, it can be seen that the fitness curve of 30 task points in the PSO algorithm converges, and the optimal traversal path is found in the 98th iteration of the PSO algorithm. The PSO algorithm has good convergence effect, indicating that the PSO algorithm has strong modeling and solving capabilities.

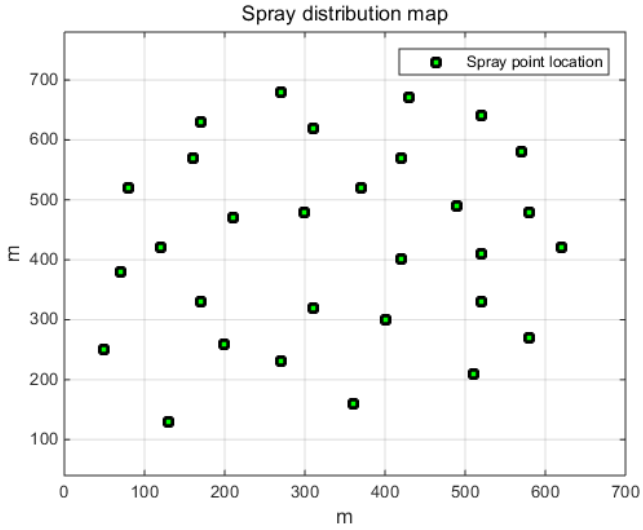


Fig. 1 - Operation area length and spraying point location coordinates (m)

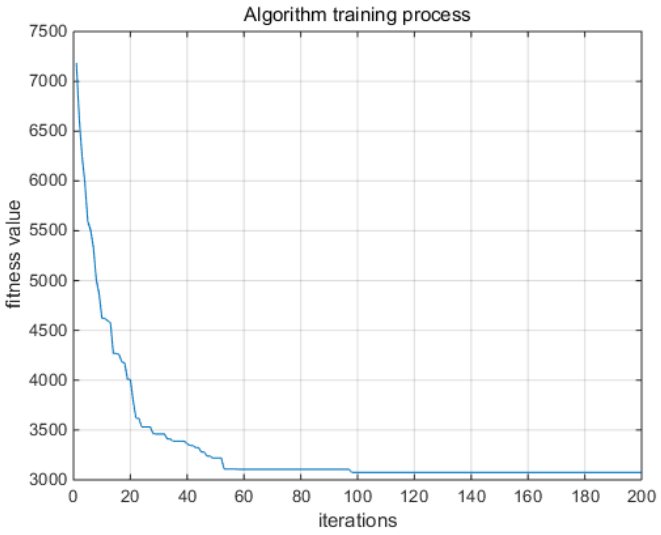


Fig. 2 - PSO algorithm convergence curve

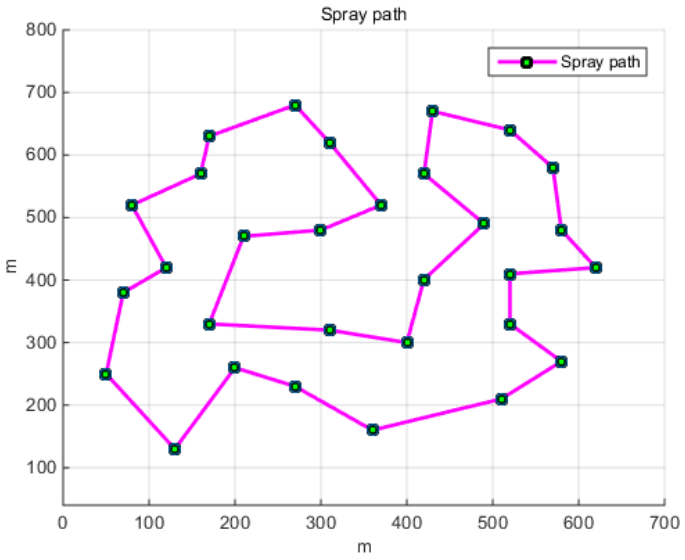


Fig. 3 - PSO algorithm track planning path

A* Algorithm Obstacle Avoidance Trajectory Planning

Obstacle avoidance trajectory planning based on A* algorithm, where the coordinates of building obstacles and spraying points are shown in Figure 4. Interactively mark obstacle areas to generate obstacle map masks. The obstacle area of the building is not accessible, and other areas are free to pass through.

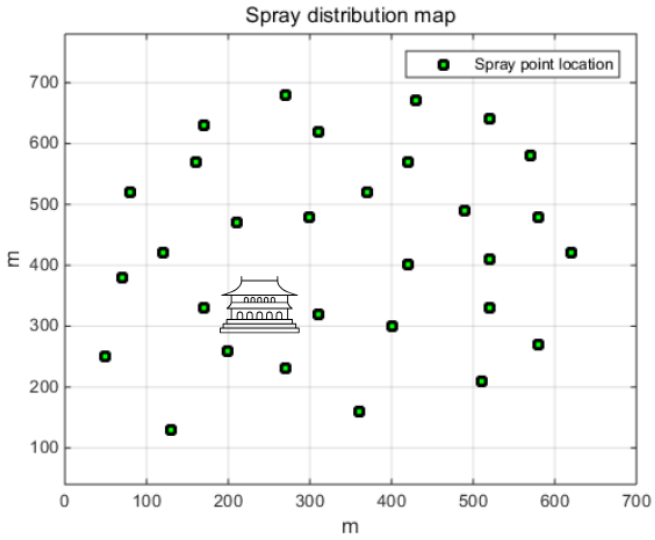


Fig. 4 - Coordinates of barrier buildings and spraying points (m)

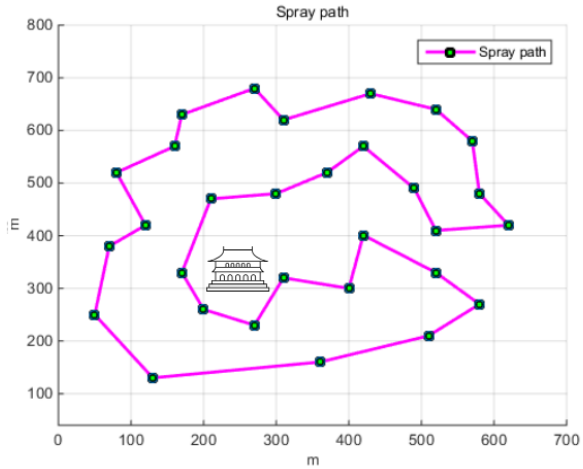


Fig. 5 - A* algorithm track planning path

Using the A* algorithm to avoid obstacles and plan the spraying trajectory of agricultural drones with obstacles at the work site. The trajectory planning effect is shown in Figure 5, and it can be seen from the figure that the A* algorithm has a good effect on obstacle avoidance trajectory planning. Taking into account the length and smoothness of the trajectory, the A* algorithm can be selected for obstacle avoidance trajectory planning.

Path Planning of Farmland Spraying Drones Based on PSO-A* Algorithm

Using PSO-A* algorithm to solve the trajectory planning problem of multiple spraying points in obstacle space. During the experiment, the parameters of the particle swarm optimization algorithm were set to 50 particle swarms, with a maximum number of iterations of 200, and learning factors C1 and C2 of 1.5. When the number of spraying points is 30, the convergence curve of the PSO-A* algorithm is shown in Figure 6, and the trajectory planning of the PSO-A* algorithm is shown in Figure 7. When agricultural drones spray in farmland areas, when obstacles are found in the planned trajectory from spraying point 16 to spraying point 9, the A* algorithm is used for obstacle avoidance secondary trajectory planning. The trajectory section starts at the coordinates of spraying point 16 and targets at the coordinates of spraying point 9 to correct this route. Figure 7 shows the A* algorithm's search for obstacle avoidance secondary correction effect trajectory, resulting in the trajectory planning results of unmanned aerial vehicles with multiple spraying points in farmland.

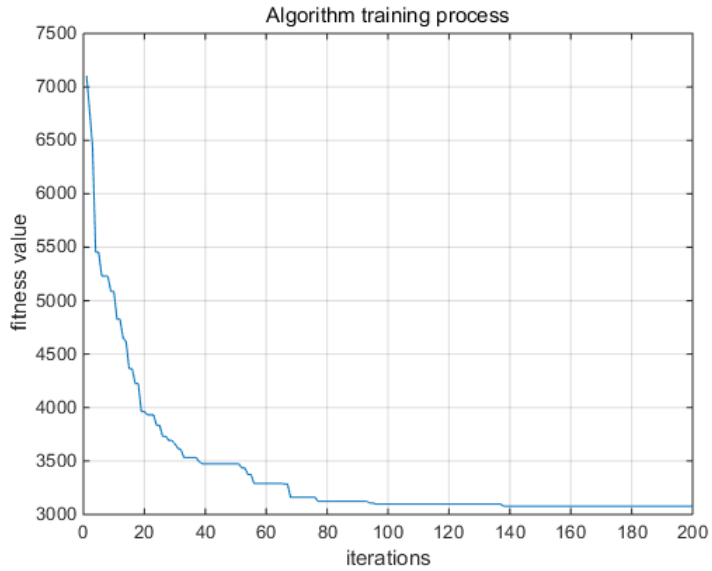


Fig. 6 - PSO-A* algorithm convergence curve

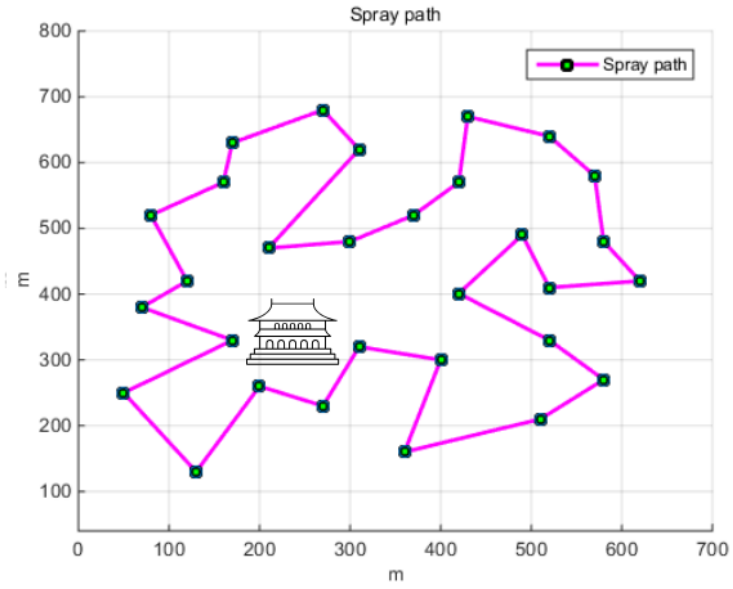


Fig. 7 - PSO-A* algorithm track planning path

CONCLUSION

This study proposed a field trajectory planning method for agricultural drones based on the PSO-A* algorithm. According to the actual requirements of agricultural drone field spraying, the multi-area operation trajectory problem was transformed into an optimization model of the particle swarm algorithm. Trajectory planning is a very complex optimization problem, and there is no absolute optimal solution in theory, only approximate optimal solutions can be obtained.

In addition to planning the flight trajectory of the drone, this study also optimized the low-altitude obstacle avoidance trajectory to better adapt to the requirements of low-altitude mission scenarios. The proposed trajectory planning algorithm for plant protection drones based on the PSO-A* algorithm can better find the approximate optimal trajectory of the plant protection drone in actual plant protection operations.

The PSO-A* algorithm has stronger capabilities in solving the trajectory planning model for drone spraying operations. The optimal traversal trajectory was found in the 98th iteration. The particle swarm algorithm has good convergence effect, indicating strong modeling and solving capabilities. In an environment with obstacles, the A* algorithm was used to avoid obstacles and plan the trajectory of agricultural drones in operational areas with obstacles. The A* algorithm has good performance in obstacle avoidance flight trajectory planning. Considering the length and smoothness of the trajectory, the A* algorithm can be used for obstacle avoidance flight trajectory planning.

In summary, the combination of the particle swarm algorithm and the A* algorithm not only improves the modeling and solving capabilities of the model, but also shortens the length of the trajectory planning. By fully considering the obstacle avoidance issues during low-altitude operations, dual trajectory correction can be performed to avoid collisions, which is beneficial to the implementation of unmanned aerial field spraying operations. This study did not consider how to determine the working task points. If machine vision and deep learning recognition processes are introduced, and the sample size is large enough, automatic extraction and classification of spray points (such as pest infested areas, weed areas, etc.) can be achieved, which can improve the autonomy of unmanned agricultural spraying operation systems and promote the development of smart agriculture.

REFERENCES

[1] Aggarwal S., Kumar N., Tanwar S. (2021). Blockchain-envisioned UAV communication using 6G networks: open issues, use cases, and future directions. *IEEE Internet of Things Journal,* Vol. 8, Issue 7, pp. 5416–5441. United States;

[2] Al-Hourani A., Kandeepan S., Lardner S. (2014). Optimal LAP altitude for maximum coverage. *IEEE Wireless Communications Letters*, Vol. 3, Issue 6, pp. 569–572. United States;

[3] Andreev A. S., Peregudova O. A. (2019). On output feedback trajectory tracking control of an omni-mobile robot. *IFAC-Papers OnLine*, Vol. 52, Issue 8, pp. 37–42. United States;

[4] Batliner M., Breitenecker F., Krner A. (2021). ARGESIM benchmark C11 'SCARA robot' with extended trajectory tracking control. *SNE Simulation Notes Europe*, Vol. 31, Issue 1, pp. 43–51. Germany;

[5] Bensafia Y., Ladaci S., Khettab K., Chemori A. (2018). Fractional order model reference adaptive control for SCARA robot trajectory tracking. *International Journal of Industrial and Systems Engineering*, Vol. 30, Issue 2, pp. 138–156. Netherlands;

[6] Eschmann H., Ebel H., Eberhard P. (2021). Trajectory tracking of an omnidirectional mobile robot using Gaussian process regression. *Automatisierungstechnik,* Vol. 69, Issue 8, pp. 656–666. Germany;

[7] Hasan S. F., Alwan H. M. (2020). Design of hybrid controller for the trajectory tracking of wheeled mobile robot with Mecanum wheels. *Journal of Mechanical Engineering Research and Developments*, Vol. 43, Issue 5, pp. 400–414. Malaysia;

[8] Hassan R., Bendary F., Elserafi K., Ghanem A., Soliman M. (2020). Comparative study methods of trajectory tracking control for robot manipulator (Dept. E). *Bulletin of the Faculty of Engineering Mansoura University*, Vol. 40, Issue 4, pp. 1–12, France;

[9] Huang Y., Mei W., Xu J., Qiu L., Zhang R. (2019). Cognitive UAV communication via joint maneuver and power control. *IEEE Transactions on Communications*, Vol. 67, Issue 11, pp. 7872–7888. United States;

[10] Keyvan M., Mohammad R. J., Abdollah H. K. (2020). A stable analytical solution method for car-like robot trajectory tracking and optimization. *IEEE/CAA Journal of Automatica Sinica*, Vol. 7, Issue 1, pp. 42–50. United States;

[11] Khalilpour S. A., Khorrambakht R., Damirchi H., Taghirad H. D., Cardou P. (2020). Tip-trajectory tracking control of a deployable cable-driven robot via output redefinition. *Multibody System Dynamics*, Vol. 16, Issue 4, pp. 1–28. Netherlands;
[12] Li P., Bao G., Fang X., Zhang L. (2018). Adaptive robust sliding mode trajectory tracking control for 6 degree-of-freedom industrial assembly robot with disturbances. *Assembly Automation*, Vol. 38, Issue 3, pp. 259–267. England;
[13] Li P., Xu J., (2018). Placement optimization for UAV-enabled wireless networks with multi-hop backhauls. *Journal of Communications and Information Networks*, Vol. 3, Issue 4, pp. 64–73. Germany;
[14] Li X., Xu J. (2019). Positioning optimization for sum-rate maximization in UAV-enabled interference channel, *IEEE Signal Processing Letters*, Vol. 26, Issue 10, pp. 1466–1470. United States;
[15] Lv S. P., Li D. H., Xian R. H. (2019). Research status of deep learning application in agriculture in China. *Computer Engineering and Applications*, Vol. 55, Issue 20, pp. 24-33. China;
[16] Ou M., Sun H., Zhang Z., Gu S. (2022). Fixed-time trajectory tracking control for nonholonomic mobile robot based on visual servoing. *Nonlinear Dynamics*, Vol. 108, Issue 1, pp. 251–263, United States;
[17] Peng H., Li F., Liu J., Ju Z. (2020). A Symplectic instantaneous optimal control for robot trajectory tracking with differential-algebraic equation models. *IEEE Transactions on Industrial Electronics*, Vol. 67, Issue 5, pp. 3819–3829. United States;
[18] Pizarro, L. A. O., Santibanez V., Garcia H. R., Chnin J. V. (2020). Sectorial fuzzy controller plus feedforward applied to the trajectory tracking of robot manipulators. *IFAC-Papers OnLine,* Vol. 53, Issue 2, pp. 9918–9923, United States;
[19] Ren B., Wang Y., Chen J. (2020). Trajectory-tracking-based adaptive neural network sliding mode controller for robot manipulators. *Journal of Computing and Information Science in Engineering*, Vol. 20, Issue 3, pp. 1–23. United States;
[20] Rubio J., Francisco P. C., García E., Juarez C. F., Lopez, G. J. (2020). Trajectory tracking of the robot end effector for the minimally invasive surgeries. *International Journal of Business Intelligence and Data Mining*, Vol. 16, Issue 1, pp. 66–88. China;
[21] Santos C., Espinosa F., Santiso E., Gualda D. (2020). Lyapunov self-triggered controller for nonlinear trajectory tracking of unicycle-type robot. *International Journal of Control, Automation and Systems,* Vol. 18, Issue 7, pp. 1829–1838. South Korea;
[22] Talak R., Karaman S., Modiano E. (2019). Optimizing information freshness in wireless networks under general interference constraints. *IEEE/ACM Transactions on Networking*, Vol. 28, Issue 1, pp. 15–28. United States;
[23] Wang F., Chao Z. Q., Huang L. B., Li H. Y., Zhang C. Q. (2017). Trajectory tracking control of robot manipulator based on RBF neural network and fuzzy sliding mode. *Cluster Computing,* Vol. 16, Issue 7, pp. 1–11. Germany;
[24] Wang G., Zhou J. (2021). Dynamic robot path planning system using neural network. *Journal of Intelligent Fuzzy Systems*, Vol. 40, Issue 2, pp. 3055–3063. Netherlands;
[25] Wang H., Li X., Jhaveri R. H., Gadekallu T. R. (2021). Sparse Bayesian learning based channel estimation in FBMC/OQAM industrial IoT networks. *Computer Communications*, Vol. 176, pp. 40–45. Netherlands.
[26] Welabo A., Tesfamariamr G. (2020). Trajectory tracking control of UR5 robot manipulator using fuzzy gain scheduling terminal sliding mode controller. *Journal of Mechatronics and Robotics*, Vol. 4, Issue 1, pp. 113–135. Japan;
[27] Xu B., Chen L. P., Tan Y. (2015). Research on the algorithm for minimum energy consumption path planning of multiple plant protection drones. *Journal of Agricultural Machinery*, 46 (11), pp. 36-42. Iran;
[28] Xu B., Chen L. P., Xu M. (2017). Algorithm for route planning of plant protection drones in multiple operation areas. *Journal of Agricultural Machinery*, Vol. 48, Issue 2, pp. 75-81. Iran;
[29] Xu J., Zeng Y., Zhang R. (2018). UAV-enabled wireless power transfer: trajectory design and energy optimization. *IEEE Transactions on Wireless Communications,* Vol. 17, no. 8, pp. 5092–5106. USA;
[30] Yang F., Xue Y. C., Li J. (2018). Path planning of traversal multi task target robots under static obstacles, *Journal of Tianjin University of Technology*, Vol. 37, no. 4, pp. 65-71. China.
[31] You X., Wang C., Huang J. (2021). Towards 6G wireless communication networks: vision, enabling technologies, and new paradigm shifts. *Science China,* Vol. 64, pp. 1–74. China;
[32] Zeng Y., Wu Q., Zhang R. (2019). Accessing from the sky: a tutorial on UAV communications for 5G and beyond, *Proceedings of the IEEE*, Vol. 107, Issue 12, pp. 2327–2375. United States;

[33] Zeng Y., Xu J., Zhang R. (2019). Energy minimization for wireless communication with rotary-wing UAV. *IEEE Transactions on Wireless Communications,* Vol. 18, Issue 4, pp. 2329–2345. United States;
[34] Zhang F., Wang L., Fu L. (2014). Recognition of cucumber leaf diseases based on support vector machine. *Journal of Shenyang Agricultural University*, Vol. 45, Issue 4, pp. 457-462. China;
[35] Zhao J., Huang J., Wang R., Peng H. R., Ji S. (2020). Investigation of the optimal parameters for the surface finish of k9 optical glass using a soft abrasive rotary flow polishing process. *Journal of Manufacturing Processes*, Vol. 49, pp. 26–34. United States;
[36] Zhao J., Huang J., Xiang Y. (2021). Effect of a protective coating on the surface integrity of a microchannel produced by microultrasonic machining. *Journal of Manufacturing Processes*, Vol. 61, pp. 280–295. United States;

CONSTRUCTION AND EVALUATION OF SIMULATION MODEL FOR THE GROWTH AND DEVELOPMENT OF MILLET IN ARID AREAS

/

干旱区谷子生长发育模拟模型的构建与评价

Yuzhi WANG [1)], Yaoyu LI [1)], Tengteng QU [1)], Siyu WANG [1)], Lili SUN [2)], Wuping ZHANG [1*)], Fuzhong LI [1*)]

[1)] College of Software, Shanxi Agricultural University, Taigu, Shanxi / China

[2)] College of Agricultural Engineering, Shanxi Agricultural University, Taigu, Shanxi / China

Corresponding authors: Tel: +8603546287093; Zhang Wuping; E-mail: zwping@126.com;

Li Fuzhong E-mail: sxaulfz@126.com

DOI: https://doi.org/10.35633/inmateh-71-55

Keywords: *Millet, Photosynthesis, Biomass allocation, Functional-structural plant model*

ABSTRACT

The establishment of crop growth models enables the simulation of the impacts of environmental changes on crop growth, providing theoretical guidance for exploring the relationship between environmental factors and crop growth. The model used the growth cycle (GC) as the simulation time step and was built upon four sub-models: topology, photosynthesis, biomass allocation, and geometric morphology. It was quantitatively utilized the concept of effective accumulated temperature (EAT) and parameters such as sink and expansion rate were used to explain the allometric growth relationships among different organs. The R2 values for the geometric morphological parameters such as leaf length, leaf width, leaf area, and internode volume ranged from 0.78 to 0.94, while the F-values for the regression equations ranged from 1533.53 to 13949.51. The R2 values for simulating leaf, internode, and earhead biomass were 0.62-0.94, 0.74-0.97, and 0.98, respectively, with RMSE values ranging from 0.02 to 0.13 g for leaf biomass, 0.03 to 0.13 g for internode biomass, and 1.71 g for earhead biomass. The results indicated that the model exhibited good performance and reliability in simulating the growth and development of leaves, internodes, and earheads. This provides a solid foundation for the development of a millet model with functional-structural feedback.

摘要

作物生长模型的建立可以模拟环境变化对作物生长的影响，为探索环境因子与作物生长的关系提供理论指导。模型以生长周期(GC)为模拟时间步长，建立了拓扑结构、光合作用、生物量分配和几何形态 4 个子模型。我们定量地利用了有效积温(EAT)的概念，并用库强和扩展率等参数来解释不同器官间的异速生长关系。叶长、叶宽、叶面积、节间体积等几何形态参数的 R^2 值为 0.78 ~ 0.94，回归方程的 f 值为 1533.53 ~ 13949.51。叶片、节间和穗生物量的 R^2 分别为 0.62 ~ 0.94、0.74 ~ 0.97 和 0.98，其中叶片、节间和穗生物量的 RMSE 分别为 0.02 ~ 0.13 g、0.03 ~ 0.13 g 和 1.71 g。结果表明，该模型对叶片、节间和穗的生长发育具有较好的模拟效果和可靠性。这为开发具有功能-结构相互作用的谷子模型提供了结实的基础。

INTRODUCTION

Millet is one of the staple foods grown in Asia, characterized by drought resistance, spine tolerance, and dual use of food and feed. Millet contains abundant dietary fiber and antioxidants, which are beneficial substances for the human body *(Muthamilarasan et al., 2016)*. At present, the genetic improvement of millet varieties is developing continuously, but it still faced the problem of the time-consuming and laborious breeding process *(Kapoor et al., 2022)*. Compared to field experiments, conducting a pre-experiment of crop growth through model simulation allows for earlier detection of potential issues in the experiment, thereby saving labor and financial costs.

Crop models have significant importance in agricultural intelligent decision-making systems, water and nutrient management, yield prediction, and other related areas. The crop growth model is based on light, temperature, water, and other conditions *(Chen et al. Y., 2022; Yu et al., 2022)*, which use computer and mathematical methods to simulate and predict the physiological and ecological processes of crops *(Adam et*

Yuzhi WANG, M.S. Stud. Eng.; Yaoyu LI, M.S. Stud. Eng.; Tengteng QU, M.S. Stud. Eng.; Siyu WANG, M.S. Stud. Eng.; Lili SUN, Ph.D. Eng.; Wuping ZHANG, Prof. Ph.D. Eng.; Fuzhong LI, Prof. Ph.D. Eng..

al., 2013). Most models require the adjustment of numerous parameters to complete the simulation process, and an accurate set of model parameters is an indispensable component of the model.

We have established four sub-models for millet growth and development based on field experimental data. These four models together form a functional-structural plant model for the entire growth cycle of millet. By programming in C++, the distribution and accumulation of biomass is simulated in different organs of millet and quantify the relationships between various parameters in the model. The aim is to construct a functional-structural feedback model for millet growth and development, thereby providing a better understanding of its growth and development processes.

MATERIALS AND METHODS

Field experiment design

Zhangzagu No.10 was used as the research object to conduct a field experiment at the experimental site (112°30'E, 37°26'N) in Wujiapu Village, Taigu District, Jinzhong City, Shanxi Province from May to October 2021. The characteristics of soil basic fertility in the test site are shown in Table 1.

Table 1

Soil nutrient content in the experimental site

Depth (cm)	**Alkali hydrolyzed nitrogen** (g/kg)	**Total nitrogen** (g/kg)	**Total phosphorus** (g/kg)	**Organic matter** (g/kg)
0~20	43.30	1.02	1.13	15.65
20~40	22.10	0.61	0.83	8.19

Data Collection

The morphological indexes of millet were measured manually with a straightedge, vernier caliper, protractor, and other tools, including leaf length, maximum leaf width, Angle between stem and leaf, length and diameter of stem and leaf joint. The growth state of millet plants in different periods was photographed by the digital camera, and leaf curvature and leaf area were extracted by image processing. Meteorological data were obtained from China Meteorological Data Network (http://data.cma.cn/), maximum, minimum and average temperature were used to calculate the daily effective accumulated temperature.

Model construction

Division of basic growth units

The leaf element in the model is the basic structural unit of the model. The internode of the millet and the leaf growing on the node are called leaf metamers *(Zhao et al., 2001)*. The growth interval of each leaf element is called a growth cycle, and the size of the growth cycle is determined by the morphological changes of the millet. The growth and development of millet obey the S-shaped curve. According to the analysis of field experiment data, the model takes the growth cycle as the step length to simulate the whole process of millet growth and development.

The relationship between leaf elements of millet and the effective accumulated temperature was analyzed to predict its growth and development. The effective accumulated temperature was calculated as follows:

$$GDD = \sum (T_{avg} - \mathrm{T}_0) \quad (1)$$

where:

GDD is the calculated effective product (℃ · d), T_{avg} is the daily average temperature (℃), and T_0 is the minimum temperature (℃) required by the growth of millet.

Simulation of geometric form

Suppose that in the N cycle of millet growth, $num(i,t,N)$ is the number of organs with type i and growth age t in millet individuals, and the biomass accumulated by various organs from their generation to the current cycle is $b(i,N)$. Then the geometric characteristics between leaves and nodes were calculated by the allometric change relationship between the cumulative biomass of the organ and the geometric size of the organ *(Zhang W. et al., 2018)*.

Leaf specific weight is one of the important physiological indicators reflecting the morphological characteristics of plant leaves *(Peng et al., 1993)*, and is also an important parameter for the simulation of many ecosystem processes. Leaf area was obtained by multiplying leaf biomass and leaf specific weight (Equation 2).

$$Leaf_Area(N,i,t) = \frac{Bio(i,N)}{\mathrm{LMA}} \quad (2)$$

where:

$Leaf_Area(N,i,t)$ is the leaf area (cm^2) in the N cycle. $Bio(i,N)$ is the biomass of leaf i at the N cycle. LMA represents the specific leaf weight of a leaf.

The green photosynthetic area of the internode is obtained by calculating the lateral surface area of the cylinder, which approximates the node as a cylinder. Through the analysis of experimental data, it can be seen that there is a linear relationship between internode surface area and biomass (Equation 3).

$$S_{node} = a * Bio_{node} + b \quad (3)$$

where:

S_{node} represents the photosynthetic area of the internode (cm^2); Bio_{node} is the cumulative biomass of the node; a and b are the parameters of a linear relationship.

Biomass production simulation

The photoresponse model of the rectangular hyperbola was used to describe the photosynthetic rate of green organs such as millet leaves and internodes (Equation 4).

$$P_n = \frac{\alpha \cdot I \cdot P_{max}}{\alpha \cdot I + P_{max}} \quad (4)$$

where P_n is the rate of photosynthesis (μmolCO^2 m^{-2}·s^{-1}); P_{max} is the maximum photosynthetic rate (μmolCO_2 m^{-2}·s^{-1}) in the assimilating organs (leaves and nodes) of millet at light saturation point. I is the photosynthetically active radiation intercepted by photosynthetic organs of millet (J m^{-2} s^{-1}); α is the initial quantum efficiency of the organ (gCO_2 m^{-2}·s^{-1}).

In this study, it is assumed that the organs of millet are not shielded from each other, so the photosynthetic active radiation I intercepted by all the green organs of individual millet is equal (Equation 5).

$$I = PAR \cdot k \cdot (1-r) \cdot exp\big(-k \cdot Surface(i,t,N)\big) \quad (5)$$

where *PAR* is the photosynthetically active radiation reaching the photosynthetic organs of millet (J m^{-2} ·s^{-1}).

The calculation method referred to; $Surface(i,t,N)$ is the photosynthesis area of the organ with type i and growth age *t* during the N structural growth cycle. r is the reflectance of green assimilative organs of millet.

The model calculated the PAR of photosynthetic active radiation reaching each green organ at different times of the day based on the latitude and sunshine duration of the crop growing place (Equation 6).

$$PAR = 0.5 \cdot Q \cdot \sin\beta \cdot (1.0 + 0.4 \cdot \sin\beta) \quad (6)$$

$$\sin\beta = \sin\delta \sin\varphi + \cos\delta \cos\varphi \cos\omega \quad (7)$$

where:

β is the altitude Angle of the sun; δ is the declination Angle; φ is the local latitude; ω is the solar hour angle, at the local 12 o 'clock is 0°, increasing 15° every hour; Q is the solar constant (1395 W/m^2).

Gauss three-point integral method was used to calculate the average daily photosynthesis rate of green organs of millet (Equation 8). According to the product of the photosynthesis area of each organ and its photosynthetic rate, the daily photosynthesis products of each organ were calculated.

$$\overline{P_n}(day) = \sum_{h=1}^{3} P_n[th(hh)] \cdot WT(hh) \cdot DL(day) \quad (8)$$

where: DL is day length; $WT(hh)$ is the weight value of the Gauss three-point integral method, and the values are $WT(1)$ =0.2778, $WT(2)$ = 0.4444, $WT(3)$ =0.2778. $\overline{P_n}(\mathrm{day})$ is the daily average daily photosynthetic organs photosynthetic rate (g CO2 m^{-2} s^{-1}).

Dark respiration of leaves and maintenance respiration of other plant organs also consume some photosynthesis products. The assimilation products consumed through daily maintenance growth activities of millet can be obtained by multiplying the newly added assimilate yield and the maintenance consumption coefficient of organs (and temperature correction coefficient). The growing consumption of each organ can be obtained by multiplying the newly added assimilate yield by the photorespiration consumption coefficient (and temperature correction coefficient) of the organ. Finally, the net assimilation amount was multiplied by the conversion coefficient to obtain the added biomass of millet under different growth cycles.

Biomass allocation simulation

Photosynthetic production accumulates to obtain the newly generated biomass for each growth cycle, and then each organ competes for the newly generated biomass based on the product of its sink strength and expansion rate, obtaining the biomass obtained by different types of organs at different growth stages (Equation 9). On this basis, the biomass obtained by the same organ in different growth cycles was accumulated to obtain the cumulative biomass value of the organ in different growth cycles, as shown in Equation 10:

$$\Delta b(i,t,N) = \frac{Sink(i) \cdot f(i,t) \cdot Q(N)}{\sum_i \sum_{t=1}^{N} num(i,t,N) \cdot Sink(i) \cdot f(i,t)} \quad (9)$$

$$b(i,N) = \sum_{i=1}^{N} \Delta b(i,t,N) \quad (10)$$

where:

$\Delta b(i,t,N)$ is the biomass (g) obtained by the organ type i and growth age t in the N growth cycle; $num(i,t,N)$ is the number of organs with type i and growth age t contained in the individual plant in the N growth cycle, which was obtained by the aforementioned millet structure module. $Sink(i)$ is the parameter of leaf metamers; $Q(N)$ is the available biomass of plants in the N^{th} growth cycle (g). $b(i,N)$ is the cumulative biomass obtained by an organ of type i in the N growth cycle (g).

The growth rate of various organs is characterized by the change rate of biomass during their growth and described by a normalized beta distribution curve (Equation 12), which involves three parameters related to organ types, namely $a(i)$, $b(i)$ and $T(i)$. The first two parameters control the shape of the curve. The third parameter represents the maximum number of expansion cycles of the biomass obtained from the growth of different organs. $a(i)$, $b(i)$ and $T(i)$ of various organs were obtained by analyzing the biomass changes of organs in different cycles.

$$f(i,t) = \frac{g(i,t)}{M} (1 \le t \le T(i)) \quad (11)$$

$$g(i,t) = (t-0.5)^{a(i)-1} \cdot (T(i)-t+0.5)^{b(i)-1} \quad (12)$$

$$M = \sum_{t=1}^{T(i)} g(i,t) \quad (13)$$

RESULTS AND ANALYSIS

Model Parameters

The parameters in the model can be divided into four categories: structural parameters, morphological parameters, photosynthetic parameters, and biomass allocation parameters. The structural parameters of the model can be determined by accumulated temperature. The effective accumulated temperature of millet from seedling emergence to mature harvest was 1489℃ day, and its development situation was shown in Fig. 1 (from heading stage to maturity stage, the number of leaf elements of millet did not change, and some of the generated organs would continue to grow. According to the relationship between leaf elements and accumulated temperature, the growth cycle calculated by accumulated temperature was used to describe the growth of millet).

According to its growth rate, one leaf element can be generated by the main stem of millet every accumulated temperature of 36.9℃ day. Therefore, the heat time of 36.9℃ day was defined as the growth cycle of a millet and expressed by variable N, so millet experienced 40 growth cycles in total. The effective accumulated temperature of millet from emergence to heading was about 800.5℃ day, so the millet went through 22 cycles before heading.

In the model, leaf Ⅰ, leaf Ⅱ, leaf Ⅲ were divided into three different types according to the different maximum expansion cycle (survival growth cycle) of each organ, so as to obtain seven different organs, namely leaf Ⅰ, leaf Ⅱ, leaf Ⅲ, node Ⅰ, node Ⅱ, node Ⅲ and earhead (Table 2). Meanwhile, for the sake of description, the first leaf and node that begins to grow is called leaf 1 or node 1, the second leaf and node is called leaf 2 or node 2, and so on to leaf 22 or node 22.

Table 2

Division of millet organs

	Leaf Ⅰ	Leaf Ⅱ	Leaf Ⅲ	Node Ⅰ	Node Ⅱ	Node Ⅲ	Earhead
Cycles	1-7	8-17	18-22	1-7	8-17	18-22	22-40
Maximum cycle	15	20	25	15	20	25	18

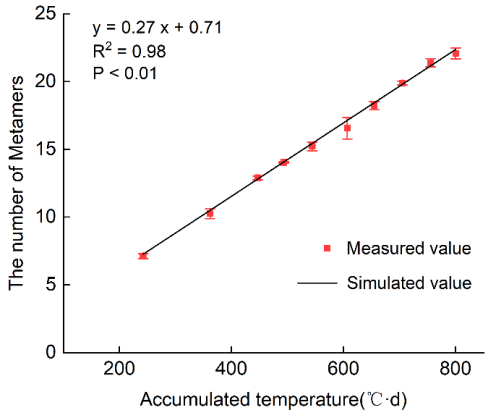


Fig. 1 - Effective accumulated temperature and number of Metamers

On this basis, through the operation of the model, the difference between simulated and measured values in each cycle was compared, and then the parameters were adjusted so that when the difference between simulated and measured values of biomass was less than 10%, the parameters were used as biomass production parameters in this study. The photosynthetic parameters of the organs were given based on the experimental data (Table 3).

Table

Model photosynthetic parameters

Symbol	Value	Parameters
P_{max}	37μ mol $CO_2 \cdot m^{-2} \cdot s^{-1}$	Maximum photosynthetic rate of a single organ
r	0.24	Blade reflectance
φ	37°	Latitude of test site

Based on the method described in section 2.3.3, the preset initial values were put into the model and the parameters of library strength and expansion rate of each organ of millet were obtained by gradient descent method, as shown in Table 3. From the perspective of different organs, the pool strength and expansion rate of leaves and internodes ranged from 0.01 to 0.08, 1.28 to 2.77 and 3.39 to 4.97, respectively, and the pool strength of leaves was greater than that of internodes. The distribution parameters of leaves would gradually decrease with the generation time (type change), and the expansion rate of internodes a tended to decrease with the generation time. The biomass allocation parameters of ear were different, and the reservoir strength and spread rate reached 5.57, 3.31 and 4.22, respectively. It is worth noting that the pool strength of ear is two orders of magnitude different from that of leaf and internode, and the expansion rate is also larger than that of leaf and internode.

Table 4

Biomass allocation parameters during millet growth

Type	Sink	Expand a	Expand b
Leaf Ⅰ	0.08	1.28	4.97
Leaf Ⅱ	0.03	1.48	4.13
Leaf Ⅲ	0.04	1.79	3.39
Node Ⅰ	0.02	2.77	3.43
Node Ⅱ	0.01	1.30	4.11
Node Ⅲ	0.02	0.73	3.53
Earhead	5.57	3.31	4.22

Parameter sensitivity analysis

This paper refers to the sensitivity analysis method of Zhang Ni et al. *(C. Zhang et al., 2019)*, and takes the photosynthetic parameters proposed in 3.1 (P_{max} =37, φ=37, r = 0.24) and changes each parameter by ±10% and ±30%, respectively. According to Formula 3, the dynamics change of cumulative biomass corresponding to the changes of different parameters in a given growth cycle were calculated, and the results were shown in Figure 2.

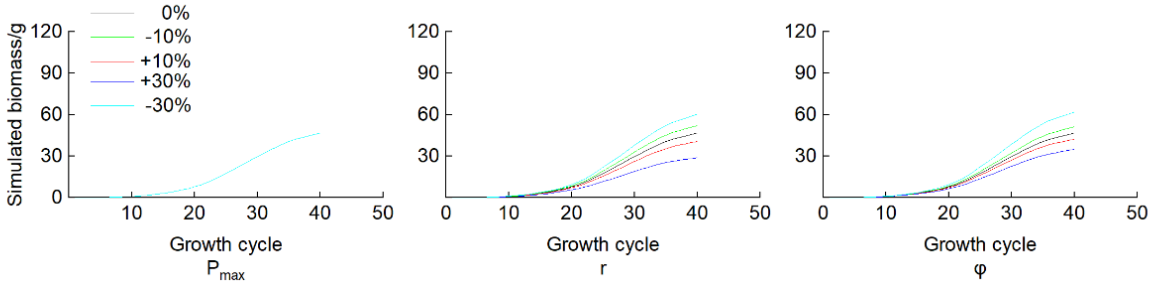


Fig. 2 - The impact of model parameter changes on biomass under different cycles

when:

P_{max} changes by ±10% (±30%), the variation range of biomass is always within 1%. The reflectance *r* and latitude *φ* have great influence on the biomass, and the influence degree gradually increases with the increase of the growth cycle. When *r* and *φ* vary by ±10% (± 30%), the biomass varies by ±10% (±33%) and ±13% (±38%), respectively. In general, the biomass simulated by this model is not sensitive to P_{max}, but more sensitive to *r* and *φ*.

Geometric form model simulation

The relationship between leaf length, leaf width, leaf area, internode volume, ear length and biomass of millet was analyzed, and the morphological structure parameters of millet organs and biomass were obtained, and the morphological structure model of millet was built. The geometric shape model of millet leaves is in Table 5. The R^2 values between biomass and leaf length, leaf width, leaf area, internode volume and ear length were 0.82, 0.78, 0.94, 0.82 and 0.89, respectively. The F value of the regression equation was between 69.09 and 3030.11, which proved the established model was valid and could be applied to the simulation of morphological parameters of various organs of millet.

Table 5

Parameters of millet morphological structure model

Parameter type	Regression equation	R^2	F
Leaf length	$y = 56.43 \cdot x^{0.44}$	0.82	1533.53
Leaf width	$y = 3.79 \cdot x^{0.38}$	0.78	2378.91
Leaf area	$y = 132.62 \cdot x$	0.94	13949.51
Node volume	$y = 8.19 \cdot x$	0.82	3030.11
Earhead length	$y = 3.84 \cdot \ln(x) + 17.93$	0.89	69.09

Biomass production model simulation

The photocontracting parameters listed in Table 4 were used to simulate the total biomass accumulated during each cycle of millet growth (Fig.3).

As can be seen from Figure 3, biomass accumulation basically accords with the "S" shaped curve of crop growth, and the determination coefficient R^2 and RMSE between simulated and measured values reached 0.95 and 4.48 g, indicating that the model can well describe above-ground biomass production of millet.

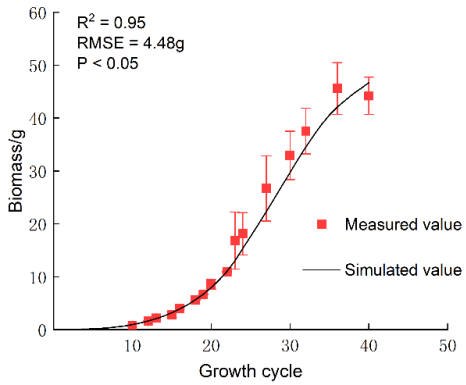


Fig. 3 - Comparison between measured and simulated values of millet biomass

Biomass allocation model simulation

Biomass allocation is a key component of the functional structural feedback mechanism and also a key component in constructing functional structural plant models. Based on the parameters obtained in the above biomass allocation model, the biomass of millet under 15 different leaf positions (leaf 7-leaf 21) was simulated, and the simulated values were compared with the measured values, as shown in Fig. 4. From the perspective of individual organs, the coefficients of determination R^2 between simulated values and measured values for 15 different leaf positions ranged from 0.62-0.94, and RMSE ranged from 0.03 g to 0.13 g. The simulation results of the middle part of 7-leaf 17 were more similar to the measured values, and the RMSE values were all less than 0.09 g.

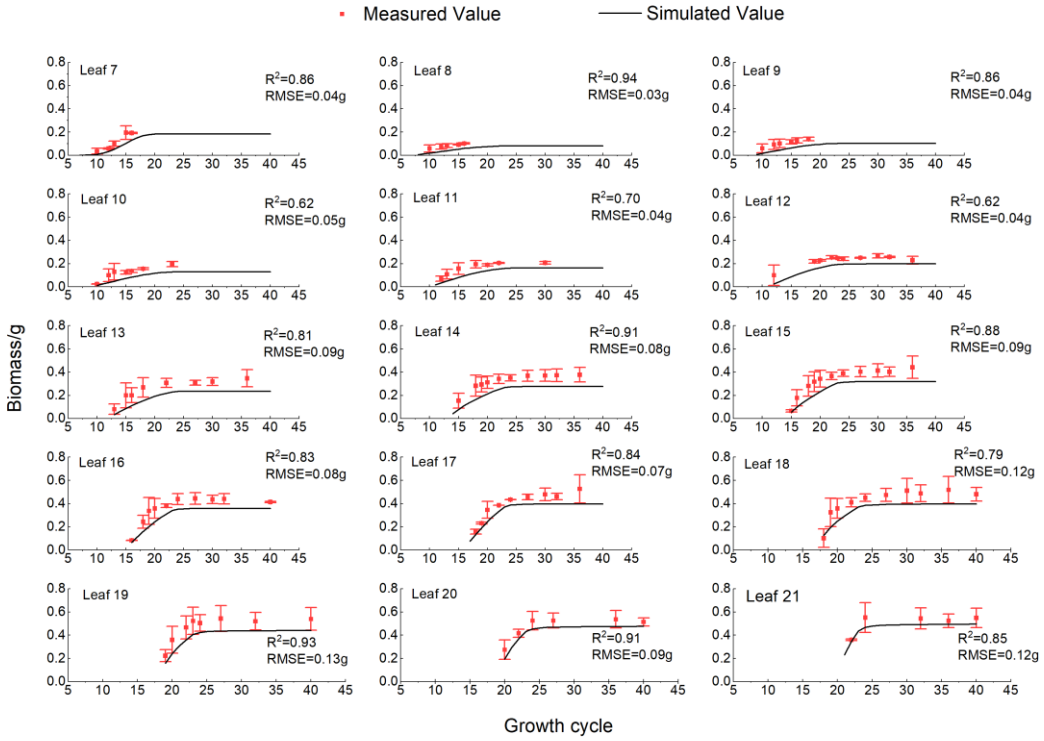


Fig. 4 - Comparison of simulated and measured cumulative biomass of different leaf positions in each cycle

The model simulated the biomass of millet under 15 different internodes (nodes 7-21), and compared the simulated value with the measured value. The results are shown in Fig.5.

As can be seen from the figure, the coefficient of determination R^2 of the simulated value and the measured value between 15 different nodes ranges from 0.74 to 0.97, and the RMSE ranges from 0.04 g to 0.12 g.

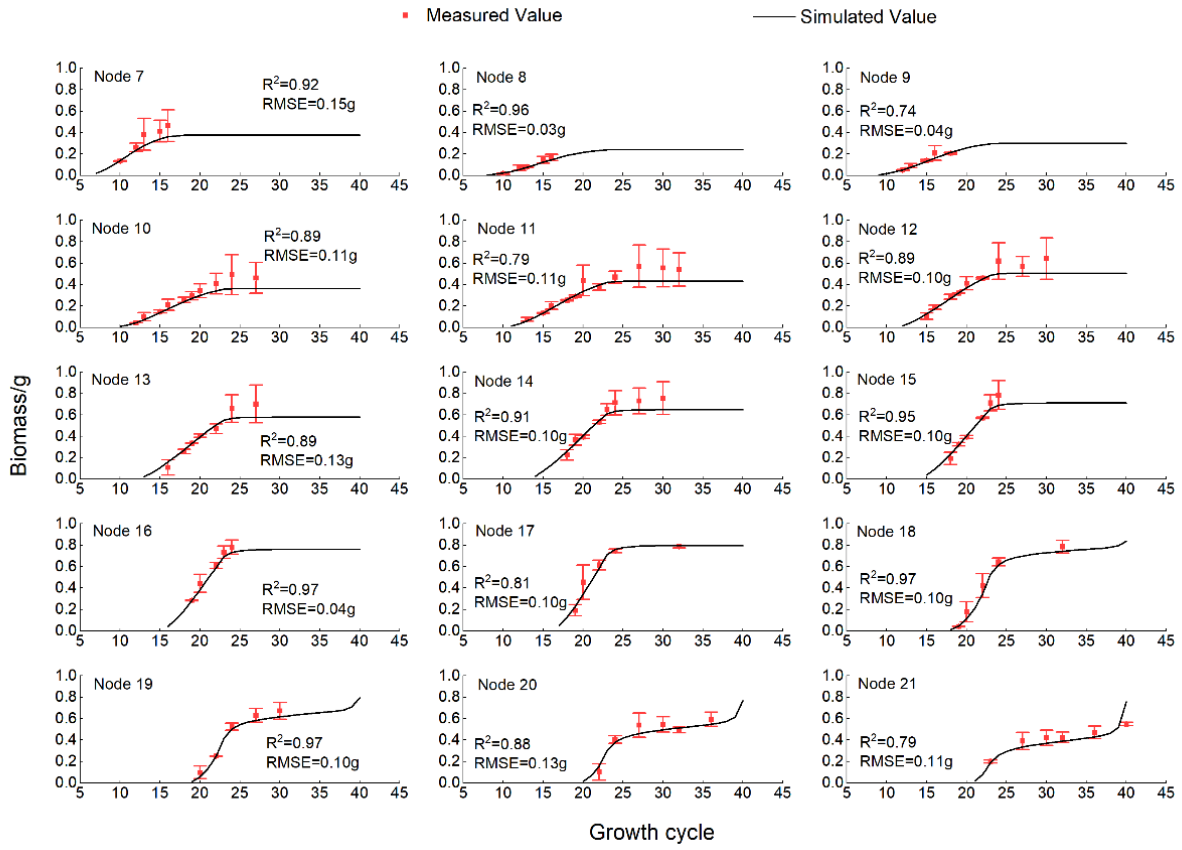


Fig. 5 - Comparison of simulated and measured cumulative biomass at different nodes and periods

The biomass of earhead is very important to yield *(Stein et al., 1997)*. The cumulative biomass of ear in each cycle is shown in Fig. 6. After the 22nd cycle, the proportion of new biomass allocated from millet plants to ear gradually increased, and reached the highest point around the 40th cycle. From the perspective of millet as a whole, the allocation of new biomass of whole millet plant after the 22nd cycle was significantly more inclined to ear. It can be seen from the figure that the simulated value is in high consistency with the measured value. The coefficient of determination R^2 reached 0.98 and the RMSE value was 3.17 g. It shows that the model has certain applicability.

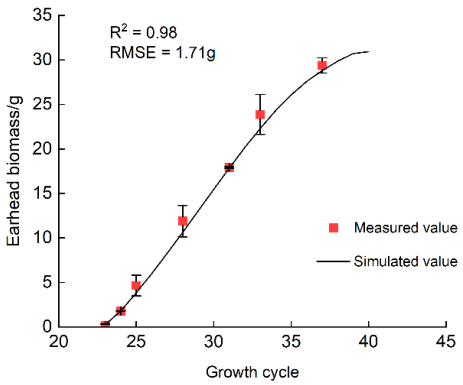


Fig. 6 - Comparison of simulated and measured cumulative biomass in each period of spike

Model verification

The first 5 samples of the experiment were used to build the model, and the last 5 samples were used to verify the biomass allocation results of the model. The accuracy of measured and simulated values is shown in Table 5. The root mean square errors of different leaf, stem and ear types were 0.03-0.11 g, 0.11-0.15 g and 1.71 g, respectively. The results showed that the model could be applied to simulate the growth of millet organs.

Table 6

Comparison between simulated and measured values of the model

Type	RMSE	MRE / %
Leaf Ⅰ	0.03	15.46
Leaf Ⅱ	0.06	20.67
Leaf Ⅲ	0.11	19.76
Node Ⅰ	0.15	26.79
Node Ⅱ	0.11	20.4
Node Ⅲ	0.07	16.7
Earhead	1.51	12.74

DISCUSSION

Under different cycles, photosynthetic parameter *r* affects the intercepted light and effective radiation (Equation 4), while latitude *φ* affects the photosynthetically active radiation reaching the leaves (Equation 7). Therefore, *φ* and *r* have a great influence on crop biomass, which is similar to the research results of *(J. Chen et al., 2018)*. Reflectance *r* is an important parameter to measure the photosynthetic performance of crops. It is important for the formation of the photosynthetic rate and biomass of leaves *(Luo et al., 2022)*. The maximum photosynthetic rate P_{max} had little effect on biomass simulation.

The geometric form model had a great influence on the simulation results of millet biomass, which was similar to the research results of *(Guo & Fritschi, 2020; Li et al., 2011)*, model comparing the relationship between leaf weight and biomass. The model simulated the morphological changes of various organs of millet, and the geometric morphological model built by this model had high simulation accuracy for leaf length, leaf width, leaf area, and internode volume of millet.

The simulation process of the photosynthesis of millet was simplified by using the Gaussian integral method. However, during the actual growth and development of crops, the light absorbed and reflected by different canopy layers was significantly different, and the fluctuation degree of the light environment of the lower leaves was greater than that of the upper leaves*(Ting et al., 2021)*. In the future, the accuracy of model simulation can be further improved by refining the accurate distribution of canopy illumination.

CONCLUSIONS

By analyzing the effective accumulated temperature, light and other environmental factors of millet growth, its growth model was established, which can be used to quantify the influence of different environmental factors on the growth and development process of millet, providing a scientific method for studying its growth and development law, and providing a theoretical basis for further exploring the relationship between its growth and the environment.

ACKNOWLEDGEMENT

The authors were funded for this project by the Major research and development Projects of Shanxi Province, China (2022ZDYF127), and the Basic Research Project of Shanxi Province (202103021224123).

REFERENCES

[1] Adam M., Wéry J., Leffelaar P. A., Ewert F., Corbeels M.,Van Keulen H. (2013). A systematic approach for re-assembly of crop models: An example to simulate pea growth from wheat growth. *Ecological modelling,* Vol. 250, 0304-3800. pp. 258-268. 10.1016/j.ecolmodel.2012.10.012

[2] Chen J., Chen S., Zhang Z., Fu Q., Bian J.,Cui T. (2018). Investigation on photosynthetic parameters of cotton during budding period by multi-spectral remote sensing of unmanned aerial vehicle. (无人机多光谱遥感反演花蕾期棉花光合参数研究). *Transactions of the Chinese Society for Agricultural Machinery,* Vol. 10, pp. 230-239. 10.6041/j. issn. 1000-1298.2018.10.026

[3] Chen Y., Chu C., He F.,Fang S. (2022). A mechanistic model for nitrogen-limited plant growth. *Annals of Botany,* Vol. 129, 0305-7364. pp. 583-592. 10.1093/aob/mcac018

[4] Guo Y.,Fritschi F. B. (2020). Influence of manganese availability on switchgrass and pearl millet biomass production. *Crop science,* Vol. 61, pp. 643-656. 10.1002/csc2.20310

[5] Kapoor C., Singh S. P., Sankar S. M.,Singh N. (2022). Enhancing drought tolerance in pearl millet

(Pennisetum glaucum L.): integrating traditional and omics approaches. *Euphytica,* Vol. 218, 0014-2336. pp. 104. https://doi.org/10.1007/s10681-022-03045-5

[6] Li X., Pan Z., Upadhyaya S., Atungulu G.,Delwiche M. (2011). Three-dimensional geometric modeling of processing tomatoes. *Transactions of the Asabe,* Vol. 54, pp. 2287-2296. 10.13031/2013.40642

[7] Luo J.-F., Xie C.-Q., Pan S.-L., Tang C.-L., Chen W., Yi H.-L., et al. (2022). A study of the spectral reflectivity of the osmanthus tree leaf and its spectral properties. *Journal of Quantitative Spectroscopy and Radiative Transfer,* Vol. 287, 0022-4073. pp. 108-228. 10.1016/j.jqsrt.2022.108228

[8] Muthamilarasan M., Dhaka A., Yadav R.,Prasad M. (2016). Exploration of millet models for developing nutrient rich graminaceous crops. *Plant Science,* Vol. 242, 0168-9452. pp. 89-97. 10.1016/j.plantsci.2015.08.023

[9] Peng S., García F., Laza R. C.,Cassman K. G. (1993). Adjustment for Specific Leaf Weight Improves Chlorophyll Meter's Estimate of Rice Leaf Nitrogen Concentration. *Agronomy journal,* Vol. 85, pp. 987-990. https://doi.org/10.2134/agronj1993.00021962008500050005x

[10] Stein A., Brouwer J.,Bouma J. (1997). Methods for comparing spatial variability patterns of millet yield and soil data. *Soil Science Society of America Journal,* Vol. 61, pp. 861-870. https://doi.org/10.2136/sssaj1997.03615995006100030021x

[11] Ting Z., Huixing K., Xinran K.,Yan Z. (2021). Dynamics of Photosynthetic Active Radiation and Photosynthetic Characteristics of Rice Leaves at Two Canopy Heights. (水稻冠层不同高度光合有效辐射动态与叶片光合作用特性研究). *Acta Scientiarum Naturalium Universitatis* Vol. 57, 0479-8023. pp. 723-732. 10.13209/j.0479-8023.2021.046

[12] Yu L., Liu Y., Liu T., Yu E., Bu K., Jia Q., et al. (2022). Coupling localized Noah-MP-Crop model with the WRF model improved dynamic crop growth simulation across Northeast China. *Computers and Electronics in Agriculture,* Vol. 201, 0168-1699. pp. 107-123. 10.1016/j.compag.2022.107323

[13] Zhang C., Ju X., Powlson D. S., Oenema O., Smith P.,Powlson D. (2019). environmental processes nitrogen surplus benchmarks for controlling n pollution in the main cropping systems of china nitrogen surplus benchmarks for controlling n pollution in the main. *Environmental Science & Technology,* Vol. 53, pp. 6678-6687. 10.1021/acs.est.8b06383

[14] Zhang W., Wang G., Han J., Li F., Zhang Q.,Doonan J. (2018). *A functional-structural model for alfalfa that accurately integrates shoot and root growth and development.* Paper presented at the 2018 6th International Symposium on Plant Growth Modeling, Simulation, Visualization and Applications (PMA).

[15] Zhao X., Reffye P. D., Xiong F. L., Hu B. G.,Zhan Z. G. (2001). Dual-scale automaton model for virtual plant development (虚拟植物生长的双尺度自动机模型). *Chinese Journal of Computers,* Vol. 24(6), pp.608-615

TOWARDS SUSTAINABLE SUBSISTENCE AGRICULTURE IN ROMANIA WITH LOW-COST IoT MODULES AND SOLUTIONS – PROOF OF CONCEPT

/

CĂTRE AGRICULTURĂ DE SUBZISTENȚĂ SUSTENABILĂ ÎN ROMÂNIA CU MODULE ȘI SOLUȚII IoT LOW-COST – PROOF OF CONCEPT

Ştefania-Adriana HOŢEI[1)], Cristina Ioana MARGHESCU[2*)], Rodica Cristina NEGROIU[2)], Andrei DRUMEA[2)]

[1)] Faculty of Electronics, Telecommunication and Information Technology, National University of Science and Technology POLITEHNICA of Bucharest;

[2)] Electronic Technology and Reliability Department, Faculty of Electronics, Telecommunication and Information Technology, National University of Science and Technology POLITEHNICA of Bucharest;

**Tel. +40 21 3169634, e-mail: cristina.marghescu@cetti.ro*

DOI: https://doi.org/10.35633/inmateh-71-56

***Keywords*:** *smart agriculture, IoT, low cost, ESP32*

ABSTRACT

Climate change is having a strong impact on agriculture. Smallholder farmers and those practicing subsistence agriculture are most affected. IoT monitoring tools enable real-time monitoring of crops to make decisions and better manage resources. For such tools to be attractive to smallholder and subsistence farmers, the system must be inexpensive and easy to use, preferably with interfaces with which the user is already familiar. The goal of the research was to develop a low-cost system with commercially available components and a familiar user interface. The system has successfully passed the first tests and is now being implemented.

REZUMAT

Schimbările climatice au un impact puternic asupra agriculturii, micii fermieri și cei care practică agricultura de subzistență fiind cei mai afectați. Instrumentele de monitorizare IoT permit monitorizarea în timp real a culturilor pentru a lua decizii și a gestiona mai bine resursele. Pentru ca astfel de instrumente să fie atractive pentru utilizatorii vizaţi, sistemul trebuie să fie ieftin și ușor de utilizat, de preferință cu interfețe cu care utilizatorul este deja familiarizat. Scopul cercetării a fost de a dezvolta un sistem ieftin cu componente disponibile comercial și o interfață familiară. Sistemul a trecut cu succes primele teste și este acum în curs de implementare.

INTRODUCTION

Romania has one of the highest percentages of rural population among the countries of the European Union, estimated at 44.51% in 2022 (*http://starea-natiunii.ro/index.php/ro/noutati/facts-figures/25-facts-figures/170-romania-si-agricultura-de-subzistenta*). At the same time, the percentage of the population working in agriculture is one of the highest, at 29.4% (as of 2014) (*https://highclere-consulting.com/agricultura-de-subzistenta-o-realitate-socio-economica-fara-viitor/*). In 2020, there were 2887 thousand agricultural holdings cultivating 12.8 million hectares of land. Of these, 54% were smaller than 1 ha. To put it another way, in 2010 (last known data), 86% of Romanian farms had an annual production of less than 4000 euros and could be considered subsistence farms (*https://highclere-consulting.com/agricultura-de-subzistenta-o-realitate-socio-economica-fara-viitor/*). Although the situation has changed since 2010 (most importantly, 1 million farms have been lost since then), there is still a significant number of subsistence farmers and small vegetable gardens next to houses. Against this backdrop and given the negative impact of climate change, it is important to find ways to improve production. Smart agriculture provides information to farmers and helps improve practices to increase production and protect crops. It is based on the IoT framework: sensors are used to collect data and the data is then processed to either guide a process or to improve understanding and enable prediction of various factors. The most commonly used sensors in agriculture are temperature, humidity, soil moisture, light dependent resistor (LDR), wind speed, RGB camera, hyperspectral camera, rainfall, NPK (Nitrogen Phosphorus Potassium) sensor (*Pathmudi et al., 2023*).

Ştefania-Adriana Hoţei, MSc. Student Eng.; Cristina Ioana Marghescu, Lect.Ph.D.; Rodica Cristina Negroiu, Lect.Ph.D.; Andrei Drumea, Assoc. Prof. Ph.D.

In the adoption of smart farming practices, the most common issues are related to initial investment costs, data volume, connectivity, and scalability (*Pathmudi et al., 2023*). Regarding the factors that facilitate the adoption of smart agriculture, the authors of Thomas and O'Hare, 2023 identified, based on a literature review, seven factors (positive impact on productivity, time and cost, information and knowledge gain, support for training, familiarity and market readiness, effective support for daily practice, accuracy and reliability, effective decision support, personalized and localized information, increased well-being) as well as six barriers (difficult or complex to use, infrastructure requirements for setup and use, lack of support, not adapted to farmers' needs, increased burden, perception of technology). In the Romanian context, initial investment costs, especially for those practicing subsistence agriculture, are perhaps the most important factor considered at the outset. The system should be easy to use and scalability is important from a sustainability perspective. With this in mind, a literature review of Low Cost Agricultural Systems was conducted. The results are summarized in Table 1 under the aspects of processing unit, sensors, communication and power supply. The keywords used were low cost & IoT& agriculture, and the databases queried were IEEE and ScienceDirect.

Table 1

Low cost monitoring systems

Reference	Sensors	Processing Unit	Communication	Power
Vijayaraja et al., 2022	Soil moisture	Node MCU	ADAFRUIT server, MQTT protocol	photo voltaic panels, battery
Mondal et al., 2017	Soil moisture	ATMEGA328P, RichDuino Board	Xbee	
Bhattacherjee et al., 2020	Soil moisture	Arduino pro mini	LoRA	3:7V Li-Ion 6V solar panel
Gill and Albaadani, 2021	Relative humidity and temperature, Soil Moisture Sensor, Soil Temperature Sensor, Light Intensity Sensor	NodeMCU	MQTT protocol	Lithium ion battery and solar panel
Kasama et al., 2019	illuminance, temperature, humidity, pressure, and concentration of carbon dioxide	a modified Atmega328P 8-bit 8-MHz RISC microcontroller board	RF24L01+, 2.4GHz ISM RF transceiver	Ultracapacitor and solar panel
Valenzuela et. al, 2018	Measure temperature, humidity, air pressure	tpanStamp AVR 2 module wireless abstract protocol (SWAP)	free ISM frequency .	AAA or AA batteries
John, 2016	Soil temperature and moisture	PIC16F877A	RF module	battery
Heble et al., 2018	Soil moisture Soil temperature Light intensity, relative humidity, and ambient temperature. Carbon dioxide Total solar radiation (TSR)	ATmega1281	802.15.4 compliant wireless mote which is developed in-house at the Wireless Networks (WiNet), LoRa	Solar panel, battery
Math and Dharwadkar, 2017	temperature and humidity – DHT22	ATmega328, Arduino Uno R3 Board	XBee	2 AA batteries
Mishra et al., 2023	Humidity and Temperature (DHT11) IR Sensor (LM393) PIR (ZRD09) Capacitive Soil Moisture		LoRa	
Dai and Sugano, 2019	photovoltaic temperature sensor STM431J provided by EnOcean	EnOcean sensor	LPWAN Sigfox	Energy harvesting
Kökten et al., 2020	SCD30 sensor	STM32 microcontroller	LoRa	

The most used sensors are soil humidity (*Vijayaraja et al., 2022; Mondal et al., 2017; Bhattacherjee et al., 2020; Gill and Albaadani, 2021; John, 2016; Heble et al., 2018; Math and Dharwadkar, 2017; Mishra et al., 2023*) and air temperature and humidity (*Gill and Albaadani, 2021; Kasama et al.,2019; Valenzuela et. al, 2018; Heble et al., 2018; Math and Dharwadkar, 2017; Mishra et al., 2023; Dai and Sugano, 2019*). XBee and LoRa are the most used communication protocols. Based on these findings a low cost IoT system for agriculture was developed.

MATERIALS AND METHODS

System description

A greenhouse or field is to be monitored using a network of sensors. The implementation of the system will consist of a number *n* of physical modules or nodes. The following requirements for the system have been defined: 1) It should measure soil moisture, air temperature, air humidity, and light intensity; 2) It should be powered either by easily replaceable batteries or be self-sufficient; 3) Data should be available online; 4) The user should be notified when certain thresholds are reached.

As stated, the proposed system targets home users who need to monitor key environmental factors by simplifying the access and use modalities. In simpler terms, in order to convince a user (a small to middle scale farmer) of the usefulness of such a solution, the resulting economic impact should be highlighted: fewer resources are consumed and the environmental impact is smaller by reducing water and thermal energy waste, maximization of production by extending the growing period, ease of automatic monitoring, which brings accurate and continuous data, and the possibility of continuous monitoring of the lot by reporting anomalies. The operation and implementation are simple, the maintenance is not very costly, only the battery needs to be changed, but with minimal cost and consumption. Light, air temperature, humidity and soil moisture sensors will be placed at key points, providing meaningful and general data about the condition of the area in question. The project will be modular so that additional sensors can be added for monitoring other environmental factors of interest, such as: soil pH, CO_2 concentration, solar radiation, etc. Low cost sensors have been chosen. The sensors used are presented in table 2.

Table 2

Sensors used

To be measured	Chosen sensor	
Air temperature and humidity	DHT11	Temperature range 0 °C and 50 °C
		Precision ± 2 °C
		Humidity range 20-80 %
		Precision ± 5 %
		Resolution 8 bits
		Sampling rate 1 Hz
	DHT22	Temperature range -40 °C and 80 °C
		Precision ± 0,5 °C
		Humidity range 0-100 %
		Precision ± 2 % and 5 %
		Resolution 16 bits
		Sampling rate 0.5 Hz
Soil humidity	Capacitive	Accuracy 2
	Resistive	Accuracy 2%, can corrode in time
Light	LDR	

From the point of view of the communication protocol, in order to make it easily accessible, aspects related to the reduction of complexity in use were considered. Romania has a population of **19.18 million** as of January 2021, and **15.49 million** internet users. Internet penetration in Romania stood at **80.7%** in January 2021. Here were **26.00 million** mobile connections in Romania in January 2021 (+0.9% vs January 2020). Smart phone ownership stands at 97% (*https://datareportal.com/reports/digital-2021-romania*).

For these reasons WiFI has been chosen. Another advantage is that its high data rates would allow the addition of a webcam. After the communication solution the ESP32-DevKit1 was chosen since it had integrated WiFi communication. ESP has been used before. A study (*Tao et al., 2021*) on communication technologies in agriculture for the period 2007-2021 identified 26 papers that used WiFi, 7 of which used this solution, published after 2020. The main components of the system can be seen in figure 1. To demonstrate the functionality, four types of nodes were designed: two simple nodes using batteries, and two complex nodes based on renewable energy.

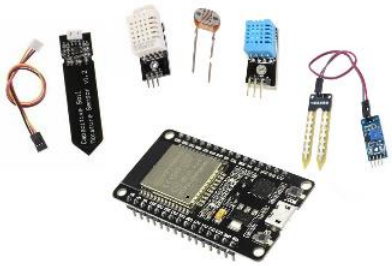


Fig. 1 - Main parts of the system

Since one problem of WiFi is its high energy consumption compared to other technologies (*Visconti et al., 2020*), it was decided to also test a renewable energy solution. There are three types of power blocks: power from a module with four AA alkaline batteries, power from photovoltaic panels, and energy stored in the Li-ion battery or in supercapacitors (ultracapacitors).

The collected data will be stored in an online Google Sheets file to facilitate its review and monitoring, avoiding mediation through a third-party cloud. Processing will consist of displaying the evolution of the collected data in the form of graphs to detect and report any anomalies.

When choosing the data storage method different IoT platforms were researched: ThingSpeak, Blynk, ThingsBoard MQTT and InfluxDB were considered but all had restriction in the free version. The best solution in the end was considered to be Google Sheets. In the case of the Google Sheets application, no additional account is required, only the Google account that most owners of a cell phone, tablet, laptop or PC with Internet access usually have. All the user has to do is connect directly to the spreadsheet where the data is to be stored from their phone or other device. From there, the code already implemented in the Google Script application for the spreadsheet takes over the entire process of receiving, retrieving, storing and displaying the data from the microcontroller. The account is free, keeping such a register is also free. And probably one of the most advantageous aspects is the fact that most people who own devices such as laptops or PCs are familiar with Microsoft's Office package, which includes Excel, which is similar to Google Sheets in its functionality and usage. The configuration possibilities of the functions are very extensive thanks to their scripting application, in which a Java Script-like code can be implemented to customize for each user.

The basic architecture of the system is presented in figure 2 and the diagram given in the figure 3 was created to illustrate the general operation of a node. It succinctly contains the main phases that a node continuously goes through in the system. To achieve effective data monitoring, the following steps must be performed: data acquisition from the sensors; data transmission via WiFi wireless communication protocol; storage of the collected data in a user-friendly app, in this case the free online application Google Sheets; putting the microcontroller into deep sleep to save energy until the next data acquisition from the sensors; and waking up the microcontroller via the internal RTC counter and restarting the cycle.

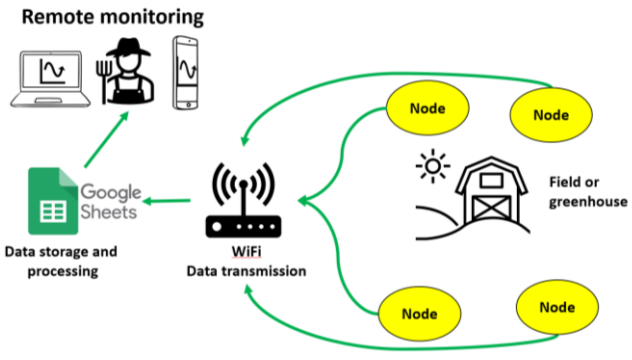


Fig. 2 - System architecture

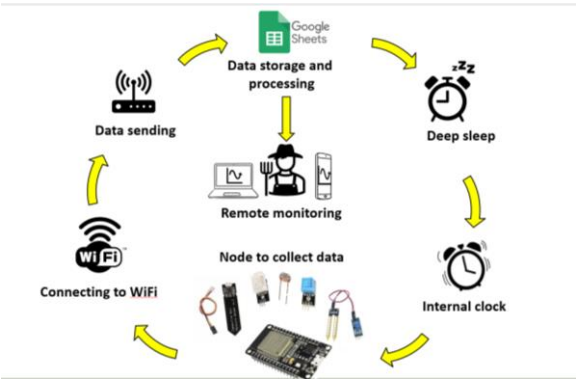
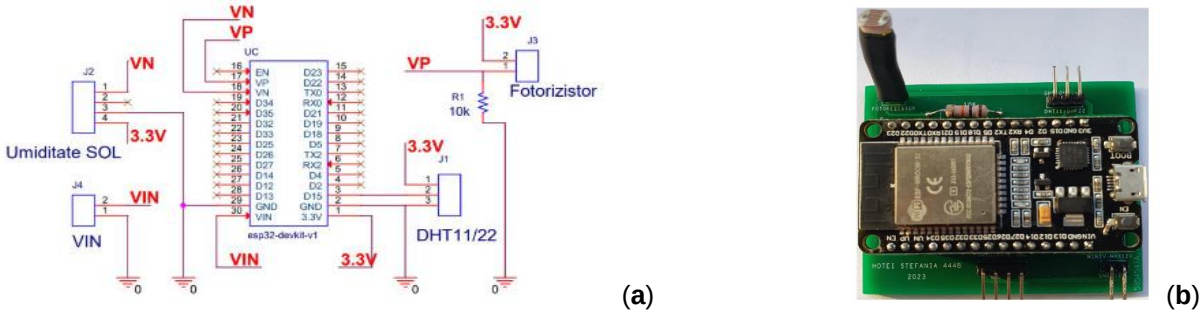


Fig. 3 - General operation

Hardware implementation

The nodes were built either on printed circuit board or perfboard. An overview is given below. The nodes were powered by battery (Node 1), solar panel and EDLC (Node 2), and LiPo Accumulator (Node 3).

The schematic and PCB for Node 1 is given in figure 4.



(a) (b)

Fig. 4 - Node 1, battery powered: schematic (a) and PCB (b)

For the renewable energy node that uses solar panels and supercapacitors the block diagram can be observed in figure 5 the schematic and PCB in figure 6. This node is also equipped with GPS and can be placed where it is needed.

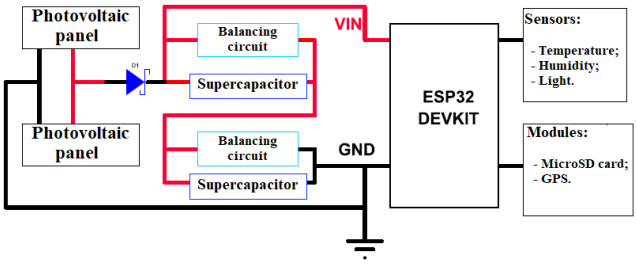
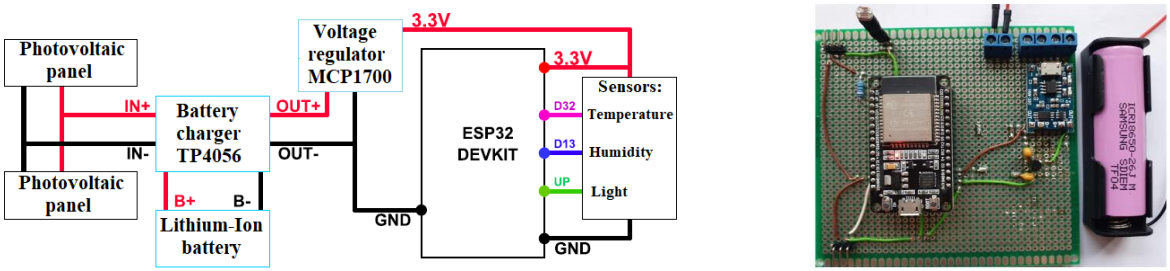


Fig. 5 - Node 3, photovoltaic panel and supercapacitors: block diagram



Fig. 6 - Node 3, photovoltaic panel and supercapacitors: PCB

The supercapacitor circuit was based on an earlier one researched by the authors (*Ionescu et al., 2016*). The last node (Node 4) used Li-Ion Accumulators.



(a) (b)

Fig. 7 - Node 4, block diagram (a) and perfboard (b)

An overview of the prices of the different components is given in Table 3.

Price (when purchased) overview **Table 3**

Part	Price in USD per piece
ESP DevKit	11.30
DHT11 DHT22	2.10 5.93
LDR	0.36
Soil humidity capacitive Soil humidity resistive	3.62 2.26
Solar panel	5.99
Supercapacitors	12.23
TP4056	1.77
MCP1700	1.15
Li-Ion	9.29
Other components	5.10
Perfboard	1.36

Node 1 had an approximate price of 17 USD, Node 2 21.21, Node 3 35.44 USD.

The power consumption per component is concentrated in Table 4.

Table 4

Power consumption

Part	Operating current
ESP DevKit - Deep sleep ultra-low power - RTC counter + RTC memory	240 mA 150 μA 10 μA
DHT11, DHT22	2.5 mA
Soil humidity - Resistive - Capacitive	 < 7 mA (maxim - 35 mA) 5 mA
SD Card	0,2 mA – 200 mA
GPS	45 mA

Source code and Google Sheets

The source code implemented on the microcontroller deals only with the data acquisition part from the sensors (figure 8), the management of the node activity, interpretation and implementation of alarms in case of anomalies is handled by the source code implemented in the Google Script application for several reasons. A first reason is the limited memory of the microcontroller, so only what is necessary is processed. Another reason is the large number of possibilities to implement the desired functions through the Java Script language adapted to Google Script.

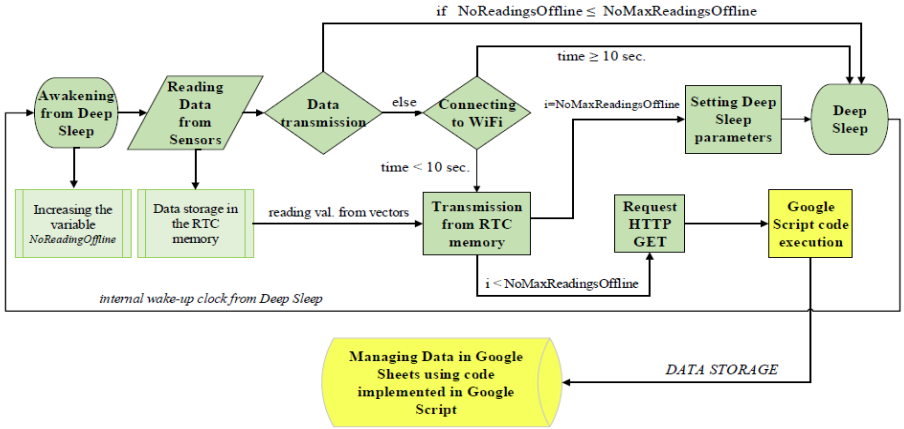


Fig. 8 - Microcontroller source code organigram

The process of retrieving data from the microcontroller is handled by the source code implemented in Google Script (figure 9). The language is based on JavaScript and provides a way to write custom scripts that can interact with Google services and supports event-driven programming, where scripts can be triggered automatically based on events such as form submissions, time-based triggers or changes in data spreadsheets.

The request made by the microcontroller, activates the doGet() method that takes the event e as a "string" of elements. In order to be able to enter the data to be monitored into a single computation register, but into spreadsheets for each node, the request must also contain a distinguishing feature for that node. So the first step after triggering the doGet() method is to check the source of the request. This is done in the "Verification no. Node" decision block, where, depending on the value entered in the "Node No=" parameter, the "sheetName" variable is assigned the name of the spreadsheet in which the values associated with the node in question are entered.

This procedure was necessary in order not to limit the user to the use of the network of nodes in a given space. Therefore, correlation of the obtained values should preferably be done in a separate spreadsheet. After deciding to which spreadsheet the values should be assigned the event containing the data is repeated and the values of interest are stored in a value buffer, each in the position it will physically occupy in the spreadsheet. After the "Extract values" action has been performed, the "Assignment in spreadsheet" step of these values follows.

Separately implemented methods were "Mark values below/above threshold" and "Format background colors". The first method takes the current vector of values and checks to see if each cell falls within the range of minimum and maximum thresholds that the user has selected in the table provided. If it does, nothing happens; if at least one of the values is out of range, the text "Attention!" is displayed in the last column of the table. The second method uses the same checking logic, but in case of mismatched values, this time of the whole worksheet, it colors the background of the mismatched cells bright red, so that the user can recognize them more easily and then make a decision.

The third implemented method deals with the part that sends a warning to the user when one of the examined parameters is out of the allowed range. The logic used only considers the number of selected transmissions. For example: the system has a complete cycle of 2 hours. This means that the microcontroller is brought out of deep sleep every 30 minutes to retrieve the data and transmits the data to the server on the fourth wake-up. This aspect drastically reduces the consumption, because the biggest consumer is the WiFi connection and the data transfer. Since the data in this example is sent in four sets, the method designed for "Send Alert!" does not check the first three sets of data, but only when the fourth is entered, it checks all the four datasets. If it detects irregularities, it sends the user an email with a warning that includes: the name of the node, the line(s) with the relevant parameter(s), the link to the node's worksheet, the graphics included in the worksheet. The process of data storage is performed in the block "Assignment in Spreadsheet" of the source code organization chart (Figure 9). At the end of the data transfer cycle, at least one new row is displayed in the spreadsheet on the node that transferred the data. After this block is executed, the data can be displayed in the spreadsheet.

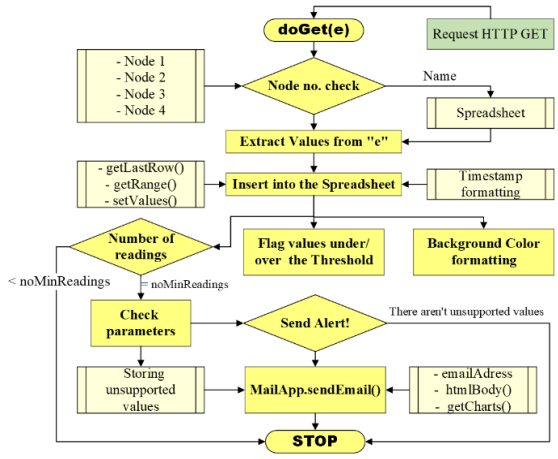


Fig. 9 - Google Script source code organigram

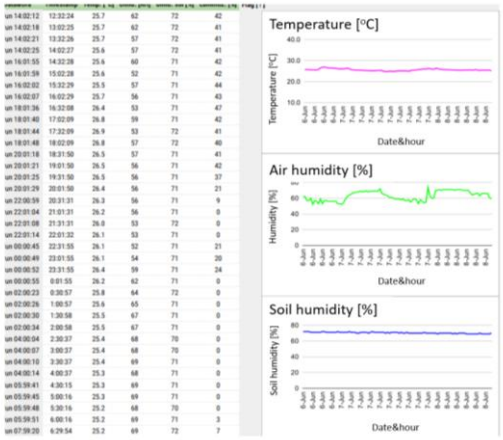


Fig. 10 - Received data displayed in table format as well as charts

The charts are displayed in real time and updated with each further iteration of the entered data and are available to the user at any time. They are displayed as seen in Figure 10. Each collected data set is assigned the exact time of collection. This is possible thanks to the RTC (Real Time Counter) module. There is also a column with the date and time when the iteration was inserted into the worksheet, to also track the process of automatic value insertion. Conveniently, monitoring from this point on can be done either by viewing the collected data or by using the worksheet that has the task of summarizing the data collected from all the nodes involved in the process; in the test case, all four nodes are monitored simultaneously in the "Total" worksheet (Fig.11).

Obtained results

Node no. 1			
Parameter	Min.	Max.	Mean
Temperature [°C]	24.5	26.7	25.45
Air humidity [RH]	40	62	29.29
Soil humidity [%]	70	90	73.16
Light intensity [%]	0	57	26.24
Alert no. [!]	1		

Node no. 2			
Parameter	Min.	Max.	Mean
Temperature [°C]	24.7	26.9	25.61
Air humidity [RH]	52	74	62.63
Soil humidity [%]	69	72	70.37
Light intensity [%]	0	51	25.57
Alert no. [!]	12		

Node no. 3			
Parameter	Min.	Max.	Mean
Temperature [°C]	24.8	27.1	25.24
Air humidity [RH]	42	66	51.11
Soil humidity [%]	28	74	69.14
Light intensity [%]	0	54	18.61
Alert no. [!]	2		

Node no. 4			
Parameter	Min.	Max.	Mean
Temperature [°C]	24.5	27.1	25.3
Air humidity [RH]	42	59	48.11
Soil humidity [%]	60	72	68.04
Light intensity [%]	0	56	12.89
Alert no. [!]	4		

Fig. 11 - Visualization of the summarized data of all nodes

In this worksheet, some Google Sheet-specific calculation formulas are implemented to take data from other worksheets and determine the minimum, maximum and average values of each parameter.

The downloaded file can also be stored in the cloud, which is also offered through Google services, but with the disadvantage that the corresponding storage space is limited in terms of memory size and cannot be the only option for long-term data storage. In this way, reports can be generated as often as the user wishes:

daily, weekly, monthly or yearly, emailed in the form of a .pdf file, and alerts are sent when the values exceed thresholds chosen by the user. This type of report is useful and necessary for long-term data monitoring. These data are related to the period of the agricultural season, the general environmental factors in the country, the type of crop and so on. Manual downloading of files can be done in several ways, depending on the needs of the user: Microsoft Excel, PDF, web page, CSV, TSV. They can be imported back into the online book at any time to correlate values or continue observations. A separate spreadsheet has been created in which the threshold values for each node are entered, so that the user has the possibility to change these parameters in real time according to his needs. Every node has a specific color to be easily distinguishable from other nodes and to complement the graphical interface the user interacts with.

RESULTS

In figure 12 the thresholds set can be seen, and non-compliant values were found for node number one when the values were inserted into the spreadsheet. This represents the worst case: The entire data collection and transmission cycle takes two hours, with data retrieved every half hour and all four captures transmitted, and the warning message is not sent until 90 minutes after the first deviation in values. This scenario was chosen to illustrate that a gradual decline in soil moisture values over the chosen time interval is not destructive. Certainly, a shorter cycle is required for "demanding" crops, and a longer cycle is possible for crops that are less sensitive to gradual changes over time.

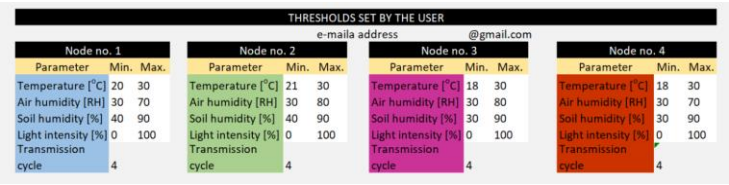


Fig. 12 - Thresholds chosen by the user (interface in Romanian with translation of the relevant parts)

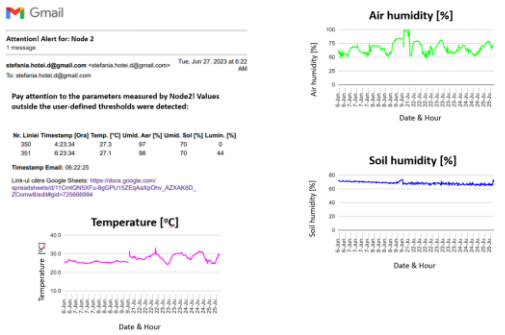


Fig. 13 - Example of alert mail received by the user

When the user receives the email on their phone, they can access the spreadsheet for that node to review the values and make decisions on how to proceed. An example of displaying non-compliant data can be the one that is described by the results shown in figure 13. If several parameters exceed the threshold at the same time, they are displayed in the same way: A warning "flag" is set in the last column of the table (regardless of whether only one or more values require a flag, only one is set), the background of the cell(s) is colored to highlight the out-of-bounds value(s), and the same email is sent with one or more rows, depending on the number of affected values. In this way, it can be seen the impact achieved by reducing quantity of the transmitted data to be stored in the database for monitoring.

A comparison of the nodes whose individual power block consists of four alkaline batteries of 1.5 V each is given in table 5.

Table 5

The comparison of the nodes

Cycle of continuous transmissions	Cycle of 4 transmissions
- once every 30 minutes. Data acquisition occurs every 30 minutes, and transmission occurs immediately thereafter, skipping the step of storing the data in RTC memory. Approximately 115 hours, 4.5 days of continuous operation.	- time between captures of 30 minutes, so data transmission occurs every 120 minutes, when the last iteration of data is captured, WiFi connection is established, and data packets are sent to Google Script. Approximately 240 hours, 10 days of continuous operation - node 1 second type of batteries approximately 120 hours, 5 days of continuous operation.

In this way, it can be seen the impact achieved with the help of reducing the number of connections to the access point and thus sending data to the stored database for monitoring.

As part of the analysis of the node powered by the supercapacitor battery, it was investigated how long the power block could withstand a long period of use, whether it was suitable to power the node at night or on less sunny days, and finally whether it was a supported choice in the current project.

The circuit was tested under shade charging conditions, where charging was slower, for a few hours over the course of a day. In the sun, the total charge requires about 0.5 hours of direct sunlight, with the two photovoltaic cells connected in parallel. The module built and tested is enough to cover the user's needs during a whole sunny or at least bright day. When it gets dark, the supercapacitors gradually and relatively quickly lose their stored energy. In one of the tests, collecting data every 30 minutes and transferring data every 2 hours (on the 4th transfer), only one data transfer was successful, but probably maxed out until the second, when reaching the operating threshold voltage of 4.4 V at the development board terminals after 3 hours. In another iteration of the tests, a continuous transmission of 75 minutes was achieved by immediate fetching and sending at 15 second intervals.

CONCLUSIONS

As mentioned at the outset, the system is aimed at subsistence farmers. In the testing process, different cases and scenarios of using the designed system were implemented. The general conclusion about the first two types of nodes implemented is that they offer a wide range of possible applications depending on the needs of the user. The system can be programmed to collect data at short intervals, which has the disadvantage of consuming batteries faster, but on the other hand, it can be scheduled to transmit as infrequently as possible. The overall operation of the two nodes is correct. However, in order not to invest too much money in batteries all the time, it was decided to test the operation of the system with renewable energy. This method did not prove to be particularly useful in terms of nighttime operation. In the case of the supercapacitor battery node, power cannot be maintained for more than 2 hours after the solar cells are turned off after dark. Therefore, this type of node is best suited for use outside the greenhouse, somewhere in the field or even in the garden outside the greenhouse, that is, in a place where monitoring is necessary during the day and not necessarily at night. The node works well under these conditions. It needs about 30 minutes of direct sunlight in the morning and then if it is a cloudy day to remain functional throughout the day. Transmission would occur each time it wakes from deep sleep so as not to risk losing power until the next iteration. In this way, only the time of day would be monitored, which in Romania is between 12 and 14 hours of light per day for the growing phase of most local crops.

The collected data can be analyzed at any time and using on any device and can be stored locally for future checks. For example, if the user has a record from the previous season, he can keep it locally and release the calculation book for the current season. Another method is to create a new online register to maintain consistency so that data obtained between seasons and physical harvest results can be automatically compared. This kind of automation of the process helps the user to better understand what they need for their crop, or even to generally adopt the data suggested by other studies and keep the environmental factors in the same register of values. To increase the covered area and if the nodes need to be placed further away from an Internet access point, it is possible to use a mesh network.

REFERENCES

[1] Bhattacherjee S. S., Shreeshan S., Priyanka G., Jadhav A. R., Rajalakshmi P., Kholova, J. (2020, March), Cloud based Low-Power Long-Range IoT Network for Soil Moisture monitoring in Agriculture, Proceedings of the *2020 IEEE Sensors Applications Symposium (SAS),* IEEE, Kuala Lumpur, Malaysia, pp. 1-5. doi: 10.1109/SAS48726.2020.9220017

[2] Dai J., Sugano, M. (2019, October), Low-Cost Sensor Network for Collecting Real-Time Data for Agriculture by Combining Energy Harvesting and LPWA Technology, Proceedings of the *2019 IEEE Global Humanitarian Technology Conference (GHTC),* IEEE, Seattle, WA, USA, pp. 1-4. doi: 10.1109/GHTC46095.2019.9033114

[3] Gill R., Albaadani A. N. H., (2021, October), Developing a Low Cost Sensor Node using IoT Technology with Energy Harvester for Precision Agriculture, Proceedings of the *2021 2nd International Conference on Smart Electronics and Communication (ICOSEC),* IEEE, Trichy, India, pp. 187-194. doi: 10.1109/ICOSEC51865.2021.9591849

[4] Heble S., Kumar A., Prasad K. V. D., Samirana S., Rajalakshmi P., Desai U. B., (2018, February), A low power IoT network for smart agriculture, Proceedings of the *2018 IEEE 4th World Forum on Internet of Things (WF-IoT),* IEEE, Singapore, pp. 609-614. doi: 10.1109/WF-IoT.2018.8355152.

[5] Ionescu C., Vasile A., Negroiu R., (2016, May), Investigations on balancing circuits for supercapacitor modules, Proceedings of the *2016 39th International Spring Seminar on Electronics Technology (ISSE)*, Pilsen, Czech Republic, pp. 521-526. doi: 10.1109/ISSE.2016.7563253

[6] John G. E., (2016, December), A low cost wireless sensor network for precision agriculture, Proceedings of the *2016 Sixth International Symposium on Embedded Computing and System Design (ISED),* IEEE, Patna, India, pp. 24-27. doi: 10.1109/ISED.2016.7977048

[7] Kasama T., Koide T., Bula W. P., Yaji Y., Endo Y., Miyake R., (2019, March), Low Cost and Robust Field-Deployable Environmental Sensor for Smart Agriculture, Proceedings of the *2019 2nd International Symposium on Devices, Circuits and Systems (ISDCS)*, IEEE, pp. 1-4. doi: 10.1109/ISDCS.2019.8719262

[8] Kökten E., Çalışkan B. C., Karamzadeh S., Soyak, E. G. (2020, October), Low-powered agriculture IoT systems with LoRa, Proceedings of the *2020 IEEE Microwave Theory and Techniques in Wireless Communications (MTTW)*, Vol. 1, IEEE, Riga, Latvia, pp. 178-183. doi: 10.1109/MTTW51045.2020.9244927

[9] Math R. K., Dharwadkar N. V., (2017, January), A wireless sensor network based low cost and energy efficient frame work for precision agriculture, Proceedings of the *2017 International Conference on Nascent Technologies in Engineering (ICNTE),* IEEE, Vashi, India, pp. 1-6. doi: 10.1109/ICNTE.2017.7947883

[10] Mishra S., Nayak S., Yadav R., (2023, January), An Energy Efficient LoRa-based Multi-Sensor IoT Network for Smart Sensor Agriculture System, Proceedings of the *2023 IEEE Topical Conference on Wireless Sensors and Sensor Networks*, IEEE, Las Vegas, NV, USA, pp. 28-31. doi: 10.1109/WiSNeT56959.2023.10046242

[11] Mondal A., Misra I. S.,Bose, S., (2017, April), Building a low cost solution using wireless sensor network for agriculture application, Proceedings of the *2017 International Conference on Innovations in Electronics, Signal Processing and Communication (IESC)*, IEEE, Shillong, India, pp. 61-65. doi: 10.1109/IESPC.2017.8071865

[12] Pathmudi V. R., Khatri N., Kumar S., Abdul-Qawy A. S. H., Vyas A. K. (2023), A systematic review of IoT technologies and their constituents for smart and sustainable agriculture applications, *Scientific African*. https://doi.org/10.1016/j.sciaf.2023.e01577

[13] Tao W., Zhao L., Wang G., Liang R., (2021), Review of the internet of things communication technologies in smart agriculture and challenges, *Computers and Electronics in Agriculture*, *189*, 106352, Vol. 189, 106352, ISSN 0168-1699. https://doi.org/10.1016/j.compag.2021.106352

[14] Thomas R. J., O'Hare G., Coyle, D., (2023) Understanding technology acceptance in smart agriculture: A systematic review of empirical research in crop production. *Technological Forecasting and Social Change*, 189, 122374. DOI: 10.1016/j.techfore.2023.122374

[15] Valenzuela A. A., Schwab M., Silnik A. A., Debattista A. F., Kiessling R. A., (2018, October), Low Power Wireless Sensor Node Platform for Agriculture Monitoring in Argentina, Proceedings of the *2018 International Conference on Cyber-Enabled Distributed Computing and Knowledge Discovery (CyberC)*, IEEE, Zhengzhou, China, pp. 101-1014. doi: 10.1109/CyberC.2018.00029

[16] Vijayaraja L., Dhanasekar R., Kesavan R., Tamizhmalar D., Premkumar R., Saravanan N., (2022, April), A Cost Effective Agriculture System based on IoT using Sustainable Energy, Proceedings of the *2022 6th International Conference on Trends in Electronics and Informatics (ICOEI)*, IEEE, Tirunelveli, India, pp. 546-549. doi: 10.1109/ICOEI53556.2022.9776726

[17] Visconti P., de Fazio R., Velazquez R., Del-Valle-Soto C., Giannoccaro N.I., (2020), Development of Sensors-Based Agri-Food Traceability System Remotely Managed by a Software Platform for Optimized Farm Management, *Sensors 20 (2020)* 3632. https://doi.org/10.3390/s20133632

EFFECT OF LOW-VOLTAGE -ELECTROSTATIC-FIELD (LVEF) ASSISTING REFRIGERATION ON PRESERVATION QUALITY OF STRAWBERRY
/
低压静电场辅助冷藏对草莓贮藏品质的影响

Huaming HOU [1,2,3]; Shuai CUI [1]; Dengming LI [1]; Zhigang LI [1]; Yisheng CHEN *[1]
[1)] College of Food Science and Engineering, Shanxi Agricultural University, Taigu 030801 / China;
[2)] College of Agricultural Engineering, Shanxi Agricultural University, Taigu 030801 / China;
[3)] Dryland Farm Machinery Key Technology and Equipment Key Laboratory of Shanxi Province, Taigu 030801 / China
Tel: +86-18404966321; E-mail: chenyisheng@sxau.edu.cn
DOI: https://doi.org/10.35633/inmateh-71-57

***Keywords:** Storage, Strawberry, electrostatic field, refrigeration*

ABSTRACT
In order to maintain the storage quality of strawberry after harvest and study the effect of low voltage electrostatic field (LVEF)-assisting refrigerated storage on strawberries quality, the study applied the low voltage electrostatic field (3kV 4±1 ℃ in LVEF group) to store strawberries in refrigeration environment, and setting refrigerated storage at 4±1°C as the control (CK group). The results showed that the freshness days of strawberries refrigerated by low voltage electrostatic field were twice as long as those of refrigerated group. The brightness and red-green degree of strawberries in LVEF group were 1.5 times and 2 times of those in CK group, respectively. The peak hardness of strawberry in LVEF group was 1.43 times of that in CK group, and the hardness decline range was 18.97% lower than that in CK group. The decreasing ranges of Total soluble solids (TSS), Titratable acids (TA) and Vitamin C(VC) in LVEF group were 43.91%, 60.01% and 46.17% lower than those in CK group, respectively. The increment of Malondialdehyde (MDA) of strawberries in LVEF group was 19.77% lower than that in CK group, and the activity peak of Superoxide dismutase (SOD) of strawberries in LVEF group was 1.22 times of that in CK group, and the decreasing range was 22.86% lower than that in CK group. After 10 days of storage, the weight loss rate and decay rate of strawberries in LVEF group and CK group were 16.69%, 15% and 70.65%, 59.45%, respectively. In conclusion, applying low voltage electrostatic field to refrigerated storage can effectively inhibit the quality deterioration of strawberries during refrigerated storage period.

摘要
为保持草莓采后贮藏品质。本研究采用冷藏环境中施加低压静电场（LVEF 组、3kV、4±1 ℃）方式贮藏草莓，以 4±1 ℃冷藏为对照（CK 组），探究低压静电场对草莓贮藏品质的影响。结果表明，低压静电场冷藏草莓保持新鲜的天数是冷藏组的 2 倍；LVEF 组草莓的亮度和红绿色度分别是 CK 组的 1.5 倍和 2 倍；LVEF 组草莓硬度峰值是 CK 组的 1.43 倍，硬度下降率较 CK 组低 18.97%；LVEF 组草莓的可溶性固形物、总酸、维生素 C 含量下降率分别较 CK 组低 43.91%、60.01%、46.17%；LVEF 组草莓的丙二醛(MDA)增量较 CK 组低 19.77%，LVEF 组草莓超氧化物歧化酶(SOD)活性峰值是 CK 组的 1.22 倍，其下降率较 CK 组低 22.86%；贮藏 10 d 时，LVEF 组和 CK 组草莓的失重率和腐烂率分别是：16.69%、15%和 70.65%、59.45%。由此可见，施加低压静电场可有效抑制草莓在冷藏过程中的品质劣变。

INTRODUCTION

After harvesting, strawberries have rapid physiological metabolism, and spoilage occurs when they are placed at room temperature for 1-2 days (*Barikloo et al., 2018*). In order to avoid postharvest loss of strawberries, it is urgent to take effective storage and preservation measures to maintain their edible quality and extend their shelf life. At present, the commonly used storage and preservation methods of postharvest strawberries include: refrigeration, modified atmosphere refrigeration, coating refrigeration, etc. The traditional refrigeration method is simple to operate, and the physiological metabolism of strawberries is inhibited by reducing the storage temperature, and the storage effect is improved with the decrease of the refrigeration temperature, but the storage cost also increases, and it may also cause cold injury loss (*Pott et al., 2020*).

[1] *As A.P. Ph.D. Eng. Huaming HOU; Yisheng CHEN, Prof. Ph.D. Eng.; Shuai CUI, M.S. Eng.*

Modified atmosphere refrigeration greatly inhibits the physiological metabolism of strawberries by adjusting the gas composition in the refrigerator room, but its equipment investment cost is high, and the modified atmosphere parameters need to be determined by experiments for different storage conditions, which has certain technical difficulties (*Wang et al., 1988*). The refrigeration method of coating film is often used to coat the surface of strawberry with multi-functional plant ingredient extract, and the effect of coating film on strawberry quality is still unclear and needs to be clarified. Electric field refrigeration acts on strawberries by applying different types of electric fields to the cold room, changing the activity of water molecules inside the strawberry, accelerating the rate of internal temperature drop, reducing heat loss, and inhibiting its metabolic activity (*Zhao et al., 2019*). Electric field refrigeration is increasingly used in the field of agricultural product preservation due to its non-contact and ion-free residue preservation.

Among different types of electric field refrigeration, low voltage electrostatic field (LVEF) assisted refrigeration is favored by the market due to its low voltage, good effect and low investment, and has been widely reported in the storage and preservation of fruits, vegetables and meat in recent years. The output voltage of low-voltage electrostatic fields is usually ≤3 kV, the current is ≤ 0.2 mA, and the power is ≤ 100 W, which has the characteristics of high safety, low equipment investment, energy saving and environmental protection (*Liu et al., 2023*). It has been reported that the low-voltage electrostatic field reduces the free energy of the repositioning of water molecules in agricultural products, reduces the migration of bound water to free water, and makes the water molecules form a more orderly cluster structure, as if building a moisture barrier for freshness in agricultural products.

In this study, an electric field generator was set up in the refrigerator to form a low-voltage electrostatic field, and the effects of electric field freezer refrigeration on the sensory quality, nutrient composition, cell membrane integrity and antioxidant activity of strawberry were explored, so as to provide a reference for the practical promotion of low-voltage electrostatic field-assisted refrigeration technology for agricultural products.

MATERIALS AND METHODS

Materials and Reagents

Within this study there have been used the following materials and reagents. Strawberries: Hongyan strawberries from Shanxi Nonggu Strawberry Industrial Park, picking fresh strawberries with uniform size, no pests and diseases and mechanical damage, eight ripe, packed into plastic hole pallet boxes after harvest, covered with PE plastic wrap, and transported back to the fresh-keeping laboratory immediately after harvest for storage tests. Reagents: Sodium hydroxide, trichloroacetic acid, thiobarbituric acid, phosphoric acid: analytical pure, Tianjin Damao Chemical Reagent Factory, ascorbic acid, potassium hydrogen phthalate, phenolphthalein: analytical pure, Tianjin Dengfeng Chemical Reagent Factory, anhydrous ethanol: analytical pure, Tianjin Fuyu Fine Chemical, red pheloline: analytical pure, Anhui Kuer Bioengineering Co., Ltd., ferric chloride: excellent pure, Tianjin Kemiou Chemical Reagent Co., Ltd., superoxide dismutase (Superoxide dismutase, SOD) assay kit: Nanjing Guangxin Biotechnology Co., Ltd.

Main instruments

Within this study there have been used the following main instruments. Electric field refrigeration unit. Electronic Balance: Type JY20002, Hunan Lichen Technology Instrument Co., Ltd. Digital Brix Meter: LC-DRT-94B, Hunan Lichen Science and Technology Instrument Co., Ltd. Potentiometric titrator: ZDJ-4A, Shanghai INESA Scientific Instrument Co., Ltd. Desktop high-speed refrigerated centrifuge: V-1200 type, Shanghai Mapped Instrument Co., Ltd. Portable Surface Colorimeter: CM-5 Type, Konica Corporation. Texture analyzer: TMS-PRO type, FTC Company. Visible spectrophotometer: 2100 type, Shanghai Da Nico Instrument Co., Ltd.

Methods

Construction of electric field refrigeration device

A low-voltage electrostatic field device is built, as shown in Fig. 1, which is mainly composed of an electric field generator, an electrostatic plate, a power cord, a wire, etc. The power cord is connected to the household circuit (220V), and after the action of the electric field generator, a 3kV voltage is formed on the electrostatic field plate, and the electrostatic field is released around the electrostatic plate. Fix the electrostatic plate on the back wall of the refrigerator, place fresh strawberries on the shelves of the refrigerator, and cover the strawberries with PE plastic wrap, as shown in Fig. 2.

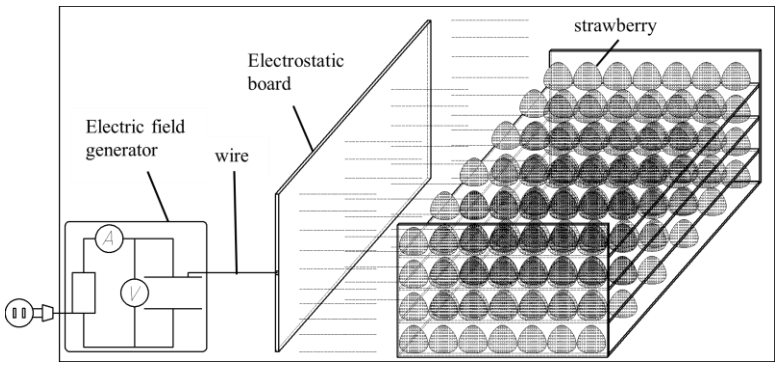


Fig. 1 - Schematic diagram of low-voltage electrostatic field device



Fig. 2 - Physical diagram of electric field refrigeration device

Sample handling

Strawberries were randomly divided into two groups: low-voltage electrostatic field refrigeration group (LVEF group) and refrigerated control group (CK group). The strawberries of the LVEF group were evenly placed on the shelf of the electric field refrigeration device and covered with PE plastic wrap, the voltage of the electrostatic plate was 3 kV, and the distance between the strawberries and the electrostatic plate was 30 cm. Arrange the strawberries of the CK group evenly on the shelves of the refrigerator and cover them with PE plastic wrap. In order to control the influence of electric field, the distance between the electric field refrigeration device and the refrigeration cabinet should not be less than 2 m. The refrigeration temperature of the strawberries in both groups was set at 4±1°C and the relative humidity was maintained at 90% ±5%. Strawberry quality indicators are measured by sampling every day.

Colorimetry

The brightness value (L*) and red-green value (a*) of strawberries in each treatment group during the storage period were measured daily by CM-5 portable surface colorimeter, and 10 strawberries were randomly selected during the measurement, and the measurement was repeated 3 times, and the average value was taken.

Hardness determination

The TMS-PRO texture analyzer was used to measure the hardness value of strawberries in each treatment group during the storage period every day, and a cylindrical measuring probe with a diameter of 3 mm was selected, and the loading speed was 100 mm/min, the unloading speed was 150 mm/min, the downward pressure distance was 5 mm, and the compression pause time was 2 s. During the measurement, 30 strawberries were randomly selected, and the measurement was repeated 3 times, and the average result was taken.

Weight loss rate determination

A total of 30 strawberries were selected in each treatment group, each of which was divided into small groups, and the weight loss rate of each group of strawberries during storage was measured daily using an analytical balance (accuracy 0.01 g), and the results were averaged. The weight loss rate M is calculated according to equation (1).

$$M = [(M_0 - M_n)/M_0] \times 100 \quad (1)$$

where: M is the weight loss rate of strawberry, [%]; M_o is the initial mass of strawberry, [g]; M_n is the mass of strawberries measured during storage, [g].

Determination of decay rate

Three groups of strawberries were fixed in each treatment group to measure the decay rate every day, and each group contained 30 strawberries, and the results were averaged. When the strawberry has shrunken,

has sap exudation, lesions or microbial colonies, etc., it is considered to have rotted, and the strawberry rot rate D is calculated according to equation (2).

$$D = (n/30) \times 100\% \quad (2)$$

where: D is the rate of decay, [%]; n is the number of rotten strawberries per measurement.

Soluble solids (TSS) content determination

Use a digital Brix meter to measure the TSS content of strawberries in each treatment group during the storage period every day, randomly take 12 strawberries, remove the calyx, mash them with a pestle, filter the juice with gauze, absorb the filtrate droplets on the refractive prism of the digital Brix meter, evenly cover the mirror, press the button to measure the TSS content, record the data after the screen display value is stable, repeat the measurement 3 times, repeat the sampling 3 times, and repeat the above operations, and the measurement results are averaged.

Total acid (TA) content determination

The ZDJ-4A automatic potentiometric titrator was used to measure the TA content of strawberries in each treatment group during storage every day, Set the pH of the acid-base titration end point of the instrument to 8.2 (*Chung et al., 2015*). Read and record the volume of the NaOH standard solution consumed. The TA content of strawberries was calculated according to equation (3), and the measurements were repeated 3 times, the samples were repeated 3 times, and the average value of the measurement results was taken.

$$X = [c \times (V_1 - V_2) \times k \times F]/m \times 100\% \quad (3)$$

where: X is the total acid content of strawberry, [%]; c is the concentration of NaOH standard solution, and the value is 1, [mol/L]; V_1 is the volume of NaOH standard solution consumed during titration, [mL]; V_2 is the volume of NaOH standard solution consumed during blank titration, [mL]; k is the conversion factor of acid, with a value of 0.067; F is the dilution factor of the test solution; m is the mass of the sample, [g].

VC content determination

The VC content of strawberries in each treatment group during the storage period was measured daily by spectrophotometry (*Shangjian et al., 2023*), and 12 strawberries were randomly ground into pulp for later use, and the measurement results were averaged by repeating the measurement 3 times and sampling 3 times.

Determination of malondialdehyde (MDA) content

The MDA content of strawberries in each treatment during the storage period was measured daily by spectrophotometry (*Wang et al., 2023*). 2 g of strawberry samples were weighed, 10 mL of 100 g/L trichloroacetic acid (TCA) solution was added, the homogenate was grinded, centrifuged at 4 °C at 10000×g for 20 min, 4.0 mL of supernatant was taken, 4.0 mL of 0.67% thiobarbituric acid (TBA) solution was added, mixed and boiled in a boiling water bath for 20 min, the absorbance values of the supernatant at 450 nm, 532 nm, and 600 nm wavelengths were determined, respectively. Repeated sampling measurements were taken 9 times ,the MDA content is calculated according to equation (4).

$$C = ((6.45 \times (OD_{532} - OD_{600}) - 0.56 \times OD_{450}) \times V)/(V_s \times m) \quad (4)$$

where: C is the MDA content, [μmol/kg fw]; OD_{450}, OD_{532} and OD_{600} are the absorbance values of the reaction mixture at 450 nm, 532 nm and 600 nm, respectively; V is the total volume of the sample extract, [mL]; V_s is the volume of the extracted liquid of the sample taken at the time of measurement, [mL]; m is the mass of the sample, [g].

Superoxide dismutase (SOD) activity assay

The SOD activity of strawberries in each treatment group during storage was measured daily using the SOD kit provided by Nanjing Jiancheng. The SOD activity of strawberries in each treatment group during the storage period was measured daily, 1 g of strawberry samples were taken, ground into a homogenate under ice bath conditions, and the reaction solution was prepared according to the operation steps of the kit , The absorbance values of the assay tube and the control tube were measured at a wavelength of 550 nm, the SOD activity (U/g) of strawberry was calculated according to the formula of the kit, the sampling was repeated for 9 times, and the results were averaged.

Statistical analysis of data

The data were processed using Excel 2019 software and were expressed as mean ± standard deviations. The Origin 2022 software was used to plot the statistical charts, the SPSS 26 software was used to analyze the significance and Duncan multiple means comparison (the difference was significant when $P<0.05$).

RESULTS AND ANALYSIS

Effect of low-voltage electrostatic field refrigeration on the appearance, color and hardness of strawberry

The appearance of the strawberries in the LVEF group and the CK group changed in Fig. 3, the appearance of the strawberries in the LVEF group remained rosy on the 10th day and still had commercial value, while the color of the strawberries in the CK group began to turn brown on the 4th day and lost their commercial value on the 5th day. The comparative analysis showed that the low-voltage electrostatic field could better maintain the appearance of strawberry, and the combination of low-voltage electrostatic field treatment and refrigeration had a synergistic effect on the sensory quality of strawberry. Compared with refrigerated storage, low-voltage electrostatic field refrigeration can extend the shelf life of strawberries by more than 1 time.

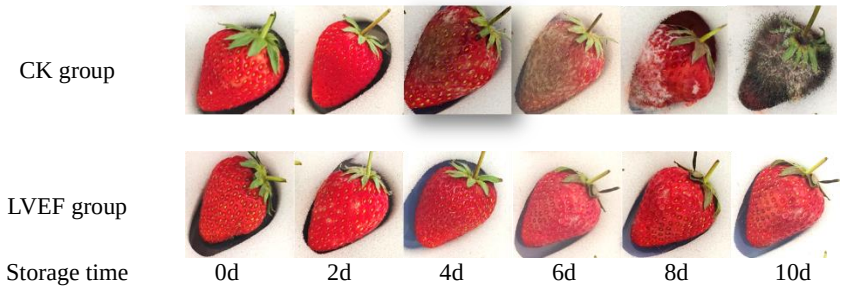
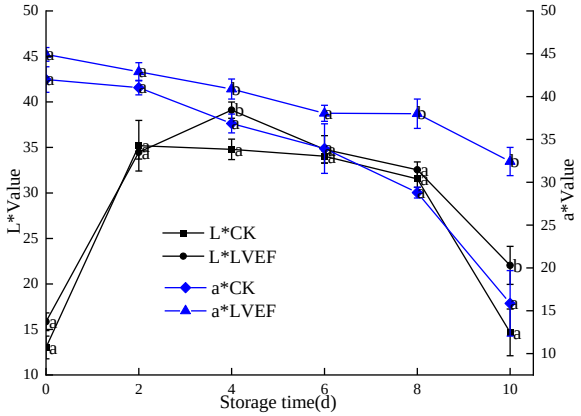


Fig. 3 - Changes in the appearance of strawberry during storage

The color of strawberries changes from white-green to dark red during ripening, and brown when overripe. As shown in Fig. 4, the L* value and red-green a* value of strawberry in the LVEF group were significantly higher than those in the CK group during storage, and the L* and a* values of strawberries in both groups showed a decreasing trend, and the L* value increased first and then decreased. On the 10th day, the L* and a* values of strawberry in the LVEF group were 22.04 and 32.42, respectively, which were 1.5 and 2 times higher than those of the CK group. The change of strawberry color is consistent with the change of its appearance. The change in color of strawberries is affected by moisture, anthocyanins, and respiration rate (*Kang et al., 2021*). The stability of anthocyanins is affected by the total acid content (*Ali et al., 2020*). It can be seen that the low-voltage electrostatic field can maintain the fresh color of strawberries for a long time by adjusting the total acid content of strawberries.



Different letters mean significant differences between groups (P< 0.05)

Fig. 4 - Effect of low voltage electrostatic field treatment on color change of strawberry

The hardness of strawberries in the LVEF group and the CK group during storage was shown in Fig. 5, and the hardness of strawberries in the LVEF group was significantly higher than that in the CK group during storage, and the hardness of strawberries in the two groups increased first and then decreased, and the hardness of strawberries in the LVEF group and the CK group reached the peak value of 0.86 N and 0.6 N, respectively, after 6 days of storage. It has been reported that the sudden change in ambient temperature and the rapid evaporation of water inside the strawberry lead to an increase in the hardness of strawberries (*Lin et al., 2020*). After the 6th day of storage, the hardness of strawberries in both groups began to decrease, and the results showed that the degradation of fruit cell wall, membrane material, and intercellular contact extrusion

would lead to the decrease of strawberry hardness (Khalifa et al., 2016). On the 10th day of storage, the hardness of strawberries in the LVEF group and CK group was 0.63 N and 0.4 N, respectively, and the hardness of strawberries in the LVEF group and CK group decreased by 26.74% and 33%, respectively, compared with the highest values. It was clear that the low-voltage electrostatic field is conducive to maintaining the commercial hardness of strawberries and delaying the decline rate of strawberry hardness.

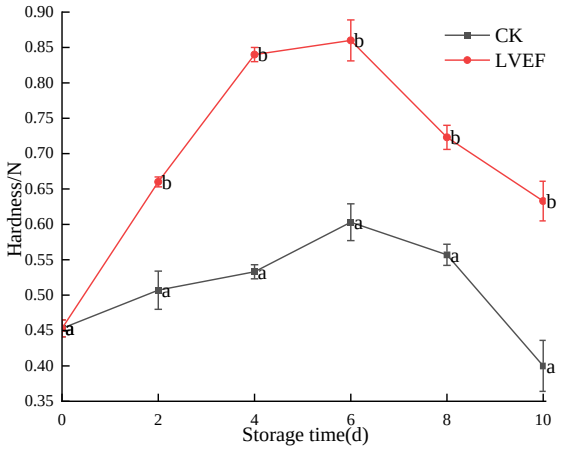


Fig. 5 - Effect of low voltage electrostatic field treatment on hardness of strawberry

Effect of low-voltage electrostatic field on weight loss rate and decay rate of strawberry

The changes of strawberry weight loss rate and decay rate during storage are shown in Fig. 6, and the weight loss rate and decay rate of strawberry in the CK group during storage were significantly higher than those in the LVEF group. On the first 8 days of storage, the increase rate of strawberry weight loss rate in the LVEF group was much lower than that in the CK group, and the weight loss rate of strawberry in the LVEF group and CK group were 3.17% and 57.32%, respectively. After 10 days of storage, the weight loss rate of strawberries in the LVEF group was 16.69%. Studies have shown that electric field treatment can inhibit the depletion of water and nutrients in fresh products (*Hu et al., 2021*). It was clear that the low-voltage electrostatic field is conducive to maintaining the moisture state and weight of strawberries. On the 7th day of storage, the decay rate of strawberries in the CK group reached 37.22%, which had lost its storage potential, and the decay rate of strawberries in the LVEF group was 11.39%. After 10 days of storage, the decay rate of strawberries in the LVEF group was 15%. Xu et al speculated that the electric field inhibited the growth of strawberry pathogens by ionizing the air to produce ozone and negative ion oxygen (*Xu et al., 2022*). Therefore, the low-voltage electrostatic field can effectively delay the decay of strawberries.

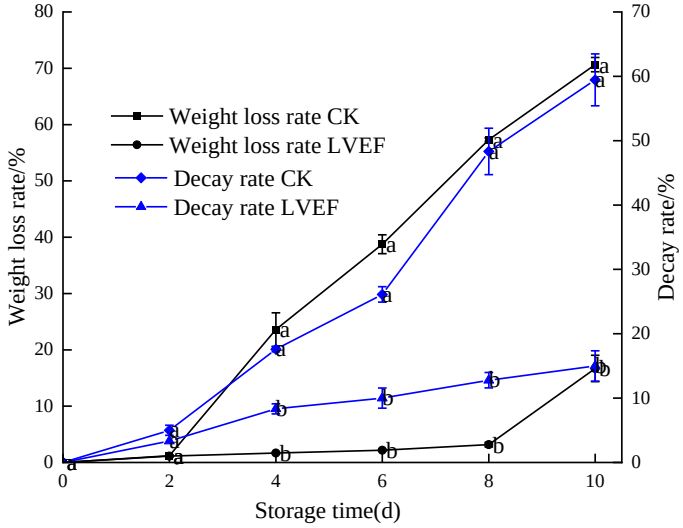


Fig. 6 - Effect of low-voltage electrostatic field treatment on weight loss and decay rate of strawberry

Effect of low-voltage electrostatic field on the contents of TSS, TA and VC in strawberry

The changes of TSS content in the LVEF group and the CK group during storage were shown in Fig. 7, and the TSS content of strawberries in the two groups increased first and then decreased. The TSS content of strawberries in the CK group reached the highest value of 11.47% on the 2nd day of storage, and then

decreased rapidly at a faster rate than that of the LVEF group, while the TSS content of strawberries in the LVEF group reached the highest value of 11.10% on the 4th day of storage, and the TSS content of strawberries in the LVEF group was significantly higher than that in the CK group. After 10 days of storage, the TSS content of strawberry in LVEF group and CK group was 9.07% and 7.73%, respectively, which decreased by 18.29% and 32.61% compared with the highest value of strawberry TSS content. Relevant studies have shown that the respiration and enzymatic effects of post-ripening strawberries in the early stage of storage promote the conversion of soluble acids and other substances into sugars. The TSS in the fruits in the middle and late stages of storage is consumed by respiratory metabolism (*Ito et al., 2014*). In conclusion, the low-voltage electrostatic field can inhibit the respiration intensity of strawberry and delay the occurrence of its respiratory peak, which is conducive to the preservation of soluble solids and sweet taste in strawberry.

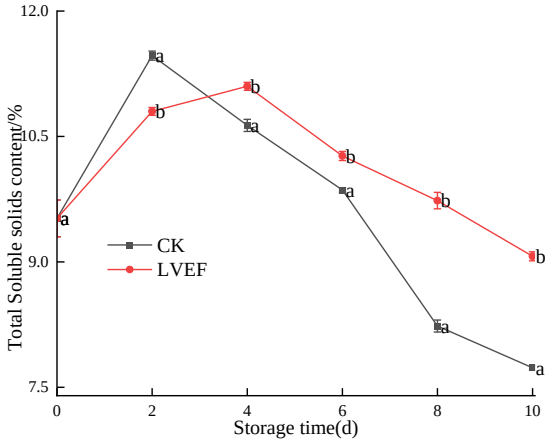


Fig. 7 - Effect of low-voltage electrostatic field treatment on TSS content of strawberry

Vitamin C is an indispensable nutrient in the human body for the prevention of iron deficiency anemia and has antioxidant effects (*Dawood et al., 2018*). The changes of TA and VC contents in the LVEF group and the CK group during storage are shown in Fig. 8 and Fig. 9, and the TA and VC contents of strawberries in the two groups showed a gradual decrease. During storage, the TA and VC contents of strawberries in the LVEF group were significantly higher than those in the CK group, and the decreasing rate of TA and VC contents was slower than that in the CK group. The initial TA and VC contents of strawberry were 0.88% and 73.53 mg/100g, respectively, and the TA contents of LVEF group and CK group were 0.78% and 0.63%, respectively, after 10 days of storage, down 11.36% and 28.41% respectively from the initial value. The VC contents of LVEF group and CK group were 61.17mg/100g and 50.57mg/100g after 10 days of storage, respectively, which decreased by 16.81% and 31.23% respectively compared with the initial values. It has been speculated that physiological metabolism such as respiration depletes fruit organic acids (*Chen et al., 2023*). The Moisture changes and enzymatic effects during storage lead to the oxidative decomposition of VC, leading to fruit senescence. In summary, the low-voltage electrostatic field can maintain the total acid and VC content of strawberry, maintain the sour taste and antioxidant capacity of the fruit by inhibiting metabolic activities such as respiration and water changes, and delay fruit senescence.

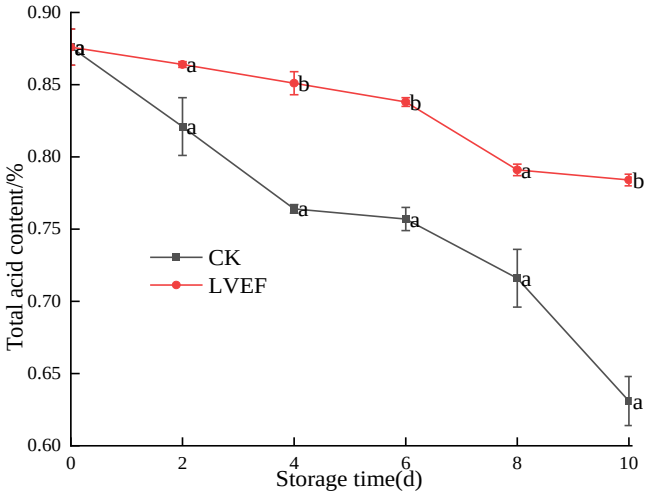


Fig. 8 - Effect of low-voltage electrostatic field treatment on TA content of strawberry

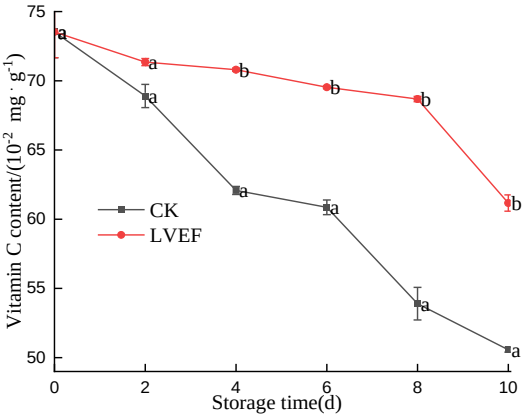


Fig. 9 - Effect of low-voltage electrostatic field treatment on vitamin C content of strawberry

Effect of low-voltage electrostatic field on MDA content and SOD activity in strawberry

Malondialdehyde (MDA) is one of the main products of lipid peroxidation in cell membranes when plants are stressed, and its content is often used to judge the degree of lipid peroxidation in cell membranes, and the higher the MDA content, the more serious the cell damage (*Lin et al., 2018*). The MDA content of strawberries in the LVEF group and the CK group during storage was shown in Fig. 10, and the MDA content of strawberries in the LVEF group and the CK group showed a gradual increase, and the MDA content of strawberries in the LVEF group was generally lower than that in the CK group during storage, and the increase rate was slower than that in the CK group. After 10 days of storage, the MDA content of strawberries in the LVEF group and CK group were 25.33 and 28.75μmol/kg, respectively, which were 24.64% higher than those in the LVEF group. Studies have shown that strawberry cells are destroyed by pathogenic microorganisms during storage to produce MDA (*Yuan et al., 2020*). In summary, the low-voltage electrostatic field had a certain inhibitory effect on the activity of strawberry pathogenic microorganisms, and reduced the degree of lipid oxidation in the strawberry cell membrane.

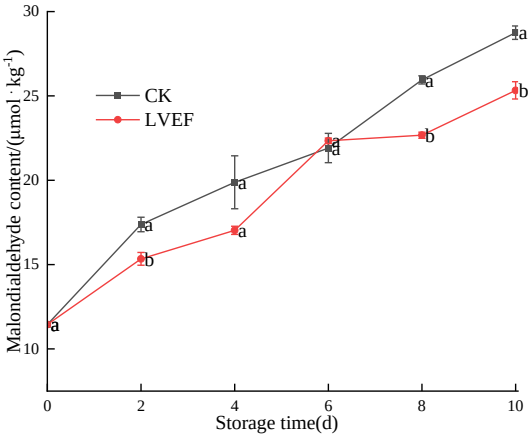


Fig. 10 - Effect of low-voltage electrostatic field treatment on MDA content of strawberry

SOD can scavenge reactive oxygen species *(Li-hui et al., 2019*) and play an important role in delaying plant senescence (*Wang et al., 2015*). The SOD activity of strawberries in the LVEF group and the CK group during storage was shown in Fig. 11, the SOD activity of strawberries in the two groups increased first and then decreased, and there was no significant difference in the SOD activity between the two groups after the first 4 days of storage, and the SOD activity in the LVEF group increased faster after the 4th day, which was significantly higher than that in the CK group, and reached the peak on the 6th day. The peak SOD activity of LVEF group and CK group was 1516.42 and 1243.45U/g, respectively, which was 21.95% higher than that of CK group, and then SOD activity began to decline, and the SOD activity of LVEF group and CK group decreased slower than that of CK group, and the SOD activity of LVEF group and CK group was 1124.88 and 827.24U/g after 10 days of storage, respectively .The results showed that the gradual increase of strawberry metabolic activity in the early stage of storage led to the increase of SOD activity, and the decrease of SOD activity caused by the senescence and biofilm destruction of strawberry in the middle and late stages of storage (*Li et al., 2018*). In conclusion, the low-voltage electrostatic field could induce the enhancement of strawberry SOD activity, reduce the oxidative damage of biofilm, and delay fruit senescence.

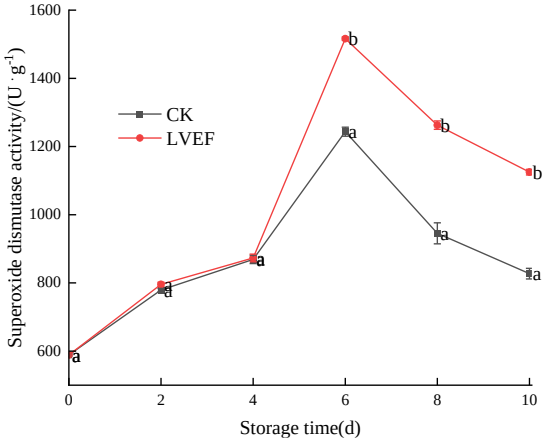


Fig. 11 - Effect of low-voltage electrostatic field treatment on SOD activity of strawberry

CONCLUSIONS

In this study, a low-voltage electrostatic field device suitable for strawberry storage was provided, which was simple in structure, reliable in principle and safe in operation. The results show that compared with traditional refrigerated storage, low-voltage electrostatic field assisting refrigeration is beneficial to maintain the appearance, color and hardness of strawberry, inhibit the respiratory and metabolic activity of strawberry, maintain the soluble solids, total acid and VC content of strawberry, maintain the sweet and sour taste of strawberry, inhibit the activity of strawberry pathogenic microorganisms, induce the enhancement of antioxidant enzyme activity of strawberry, maintain the integrity of strawberry biofilm, greatly reduce the weight loss rate and decay rate of strawberry, maintain the moist state of strawberry, delay fruit senescence, and prolong the shelf life of refrigerated strawberry by more than 1 time. Therefore, this study can lay a foundation for the popularization of low-voltage electric field-assisting refrigeration technology for strawberries.

ACKNOWLEDGEMENT

The authors are grateful for the financial support provided by the Shanxi Basic Research Program youth fund project (20210302124606), Science and technology innovation project of colleges and universities in Shanxi Province (2020L0161), Science and technology Innovation Fund project of Shanxi Agricultural University (2020BQ48), National Key Research and Development Program of China (2021YFD1600604), Shanxi Agricultural University High-Level Talent Project (2021XG013), Shanxi Scholarship Council of China (2021-068), Shanxi Postdoc Reward (SXBYKY2022001).

REFERENCES

[1] Ali L. M., Saleh S. S., Ahmed A. E.-R. a. E.-R., Hasan H. E.-S., Suliman A. E.-R. E., (2020), Novel postharvest management using laser irradiation to maintain the quality of strawberry, *Journal of Food Measurement and Characterization*, Vol. 14, ISSN:2193-4126, pp. 3615-3624, Egypt.

[2] Barikloo H, Ahmadi E., (2018), Shelf life extension of strawberry by temperatures conditioning, chitosan coating, modified atmosphere, and clay and silica nanocomposite packaging, *Scientia Horticulturae*, Vol. 240, ISSN:0304-4238, pp. 496-508.

[3] Chen W., Liu H., Chai Y., Guo C., Luo C., Chen D., Cheng X., Wang F., Huang C., (2023), Chitosan-pullulan films enriched with Artemisia annua essential oil: Characterization and application in grape preservation, *International Journal of Biological Macromolecules*, Vol.243, ISSN:0141-8130, pp.125216, Beijing/China.

[4] Chung H.-S., Kim H.-S., Lee Y.-G., Seong J.-H., (2015), Effect of deastringency treatment of intact persimmon fruits on the quality of fresh-cut persimmons, *Food Chemistry*, Vol.166, ISSN: 0308-8146, pp. 192-197, South Korea.

[5] Dawood M. a. O., Koshio S., (2018), Vitamin C supplementation to optimize growth, health and stress resistance in aquatic animals, *Reviews in aquaculture*, Vol.10, ISSN: 1753-5123, pp. 334-350, Japan.

[6] Hu F., Qian S., Huang F., Han D., Li X., Zhang C.J.L., (2021), Combined impacts of low voltage electrostatic field and high humidity assisted-thawing on quality of pork steaks, *LWT -- Food Science and Technology*, Vol. 150, ISSN: 0023-6438, pp. 111987, Beijing/China.

[7] Ito T., Kawamura T., Nakagawa A., Yamazaki S., Syuto B., Takaki K., (2014), Preservation of Fresh Food Using AC Electric Field, *Journal of Advanced Oxidation Technologies*, Vol. 17, ISSN: 1203-8407, pp. 249-253, Japan.

[8] Kang S., Xiao Y., Guo X., Huang A., Xu H., (2021), Development of gum arabic-based nanocomposite films reinforced with cellulose nanocrystals for strawberry preservation, *Food Chemistry*, Vol. 350, ISSN: 0308-8146, pp. 129199. Shaanxi/China.

[9] Khalifa I., Barakat H., El-Mansy H. A., Soliman S. A., (2016), Improving the shelf-life stability of apple and strawberry fruits applying chitosan-incorporated olive oil processing residues coating, *Food Packaging and Shelf Life*, Vol. 9, ISSN: 2214-2894, pp. 10-19. Egypt.

[10] Liu F., Xu Y., Zeng M., Zhang Y., Pan L., Wang J., Huang S. J. I. F. S., Technologies E., (2023), A novel physical hurdle technology by combining low voltage electrostatic field and modified atmosphere packaging for long-term stored button mushrooms (Agaricus bisporus), *Innovative food science & emerging technologies*, Vol. 90, ISSN: 1466-8564, pp. 103514, Wuxi /China.

[11] Lin D., Yang Y., Wang J., Yan W., Wu Z., Chen H., Zhang Q., Wu D., Qin W., Tu Z. J. I. J. O. B. M., (2020), Preparation and characterization of TiO2-Ag loaded fish gelatin-chitosan antibacterial composite film for food packaging, Vol. 154, ISSN:0141-8130, pp. 123-133, Sichuan /China.

[12] Lin Y., Chen M., Lin H., Lin M., Hung Y. C., Lin Y., Chen Y., Wang H., Ritenour M. A., (2018), Phomopsis longanae-induced pericarp browning and disease development of longan fruit can be alleviated or aggravated by regulation of ATP-mediated membrane lipid metabolism, *Food Chemistry*, Vol. 269, ISSN: 0308-8146, pp. 644-651, Fujian/China.

[13] Li-Hui Z., Yu Q., Ying Z., Xue-Ling C., Chao W., Jun W., Lan W., Li L., (2019), The preservation effect of eugenol sustained-release diatomite on strawberry, *Modern Food Science and Technology*, Vol.35, ISSN: 1673-9078, pp. 98-106, Hubei/China.

[14] Li M., Li X., Li J., Ji Y., Han C., Jin P., Zheng Y., (2018), Responses of Fresh-Cut Strawberries to Ethanol Vapor Pretreatment: Improved Quality Maintenance and Associated Antioxidant Metabolism in Gene Expression and Enzyme Activity Levels, *Journal of Agricultural and Food Chemistry*, Vol. 66, ISSN: 0021-8561, pp. 8382-8390, Nanjing/China.

[15] Pott D. M., De Abreu E. L. F., Soria C., Willmitzer L., Fernie A. R., Nikoloski Z., Osorio S., Vallarino J. G., (2020), Metabolic reconfiguration of strawberry physiology in response to postharvest practices, *Food Chemistry*, Vol. 321, ISSN: 0308-8146, pp. 126747, Malaga/Spain.

[16] Shangjian L., Jiajia C., Yuntong L., Qinhua Z., Weijian T., Xiaolin F., Kexin F., Wenzhong H., (2023), Application of cinnamaldehyde solid lipid nanoparticles in strawberry preservation, *Horticulturae*, Vol. 9, ISSN: 2311-7524, pp. 607, Zhuhai/China.

[17] Wang H. G., Gemma H., Oogaki C., (1988), Physiological characteristics and keeping quality of strawberry and kiwifruit during chilled storage, *Journal of the Japanese Society for Cold Preservation of Food* [Nippon Shokuhin Teion Hozogaku Kaishi], Vol. 14, pp. 8-14, Tsukuba/Japan.

[18] Wang Y., Zhang J., Wang D., Wang X., Zhang F., Chang D., You C., Zhang S., Wang X., (2023), Effects of cellulose nanofibrils treatment on antioxidant properties and aroma of fresh-cut apples, *Food Chemistry*, Vol. 415, ISSN: 0308-8146, pp. 135797, Xinjiang/China.

[19] Wang J., Sun G., Ji Q., Liu Z., Hao J., Wei Y. J. P., Machinery F., (2015), The role of active oxygen in harvested fruits and vegetables during senescence and its control, Journal of the science of food and agriculture, Vol. 33, ISSN: 0022-5142, pp. 51-54, Lleida/Spain.

[20] Xu C., Zhang X., Liang J., Fu Y., Wang J., Jiang M., Pan L., (2022), Cell wall and reactive oxygen metabolism responses of strawberry fruit during storage to low voltage electrostatic field treatment, *Postharvest Biology and Technology*, Vol. 192, ISSN: 0925-5214, pp. 112017, Wuxi/China.

[21] Yuan Z., Shi Y., Cai F., Zhao J., Xiong Q., Wang Y., Wang X., Zheng Y., (2020), Isolation and identification of polysaccharides from Pythium arrhenomanes and application to strawberry fruit (*Fragaria ananassa Duch*.) preservation, *Food Chemistry*, Vol. 309, ISSN: 0308-8146, pp. 125604, Huai'an/China.

Zhao Y. M., De Alba M., Sun D. W., Tiwari B., (2019), Principles and recent applications of novel non-thermal processing technologies for the fish industry-a review, *Critical Reviews in Food Science and Nutrition*, Vol. 59, ISSN: 1040-8398, pp. 728-742, Ireland.

ESTIMATION OF THE RANDOM INTENSITY OF THE SOIL TILLAGE DRAFT FORCES IN THE SUPPORTS OF THE WORKING BODIES OF A CULTIVATOR
/
ESTIMAREA INTENSITĂȚII ALEATORII A FORȚELOR DE TRACȚIUNE ÎN SUPORTURILE ORGANELOR DE LUCRU ALE UNUI CULTIVATOR

Petru CARDEI[1)], Nicolae CONSTANTIN[1)], Vergil MURARU[1)], Catalin PERSU[1)], Raluca SFIRU [*1)], Daniel LATEŞ[2)],
[1)*] INMA Bucharest / Romania;
[2)] "George Emil Palade" University of Medicine, Pharmacy, Sciences and Technology from Târgu Mureș / Romania
Tel: 0761.052.624; E-mail: raluca_sfiru@yahoo.com
DOI: https://doi.org/10.35633/inmateh-71-58

Keywords: *soil, draft, force, randomness, statistic, experimental, sequences*

ABSTRACT
The investigation on the unpredictability of the distribution of traction resistance forces on the working bodies of a specific type of MCLS complex cultivator is presented in the paper. The validation of the random character of the force that loads the active bodies is used to indicate the mathematical model that must be followed for the research of the soil processing system. Also, the research results elucidate some hypotheses issued in the conception and design of the machine: the more intense load for the working bodies located immediately after the tractor, the existence of working bodies that are constantly more intensively stressed and the causes. According to the literature, it is to be assumed that the forces that demand the working bodies, the supports, and the machine frame have a random nature. The conclusions of the descriptive, inferential statistical study (which do not quantify the random intensity) are explained together with the results. The experimental loads are compared to some of the most random strings to produce a quantitative estimate of the random intensity. As a result, processes that use random functions and the entirety of their approach are recommended in mathematical modelling for further research.

REZUMAT
În această lucrare este prezentată cercetarea cu privire la imprevizibilitatea distribuției forțelor de rezistență la tracțiune pe organele de lucru ale unui anumit tip de cultivator complex MCLS. Validarea caracterului aleator al forţei care încarcă organele active este utilizată pentru a indica modelul matematic care trebuie urmat pentru cercetarea sistemului de prelucrare a solului. De asemenea, rezultatele cercetării elucidează unele ipoteze emise în conceperea și proiectarea mașinii: sarcina mai intensă pentru organele de lucru situate imediat după tractor, existența unor organe de lucru care sunt solicitate în mod constant mai intens și cauzele. Conform literaturii de specialitate, se presupune că forțele care solicită organele de lucru, suporturile și cadrul mașinii au o natură aleatorie. Concluziile studiului statistic descriptiv, inferenţial (care nu cuantifică intensitatea aleatorie) sunt explicate împreună cu rezultatele. Încărcările experimentale sunt comparate cu unele dintre cele mai aleatorii șiruri pentru a produce o estimare cantitativă a intensității aleatorii. Ca urmare, procesele care folosesc funcții aleatoare și întreaga abordare a acestora sunt recomandate în modelarea matematică pentru cercetări ulterioare.

INTRODUCTION

The measurement of the soil tillage draft forces generated by the action of the working bodies in the soil in the agricultural machines intended for soil processing is a widely discussed problem in the literature. From the measurement with the dynamometer to complex measurements with force sensors or tensometric methods (simple or using complex tensometric frames), the authors tried to estimate the soil tillage draft forces during its processing, *(Askari M., et al., 2013; Carman K., et al., 2021; Rashidi M., et al., 2013; Afify M.T., et al., 2020; Abbaspour_Gilandeh Y., et al., 2020), (Abbaspour-Gillandeh M., et al., 2020; Markinos A., et al., Croitoru St., et al., 2016; Vlăduţ D.I., et al., 2017).* The resistance of the soil to deformation has a direct impact on energy usage and the effectiveness of agricultural work.

The parameters that influence the soil deformation resistance are, on the one hand, the mechanical and structural characteristics of the soil, its humidity, but also the geometry of the working bodies (working depth and width, orientation angles in relation to the direction of advance, shape and the quality of the contact surfaces) and their location on the load-bearing structure, the weight of the farm machinery, etc.

Elementary and complex statistical analyses are made in order to obtain formulas for the prediction of tensile strength. The operating speed, which is crucial to the energetics of soil processing, is another fundamental characteristic of the equipment designed for soil processing *(Mahmood H.F., et al., 2011).*

Estimating the soil tillage draft force per working body by tensometric means, using calibration techniques, is a simpler way, but with complex sources of errors in relation to classic measurements with the help of a dynamometer or some force doses. The tensometric signals recorded in the deformation sensors mounted on the supports of the working bodies of the cultivator have, at least at first glance, an irregular shape, they cannot be modelled with signals given by common laws used in the approximation of simple experimental functions. The need for a measurement procedure that is more practical than the traditional ones is just one reason why it is interesting to characterise the variation of resistance forces on the working body. Another reason is that mathematical modelling of the process can be used for practical purposes, such as predicting the intensity of the resistance force and designing safe and supple. Obviously, it is also about the optimization of load-bearing structures for the economy of material and the simplification of manufacturing technology. It is critical to ascertain if the loads the working body supports are deeply random or deterministic in light of these goals. Depending on the estimation results, the mathematical model usable in the prediction of aggregate dynamics and in the design of load-bearing structures will be a deterministic or a statistical one.

The literature is in agreement regarding the random nature of the physicochemical properties of the soil, (*Dharumarajan S., et al., 2017; Nia M.Z., et al., 2023; Wijiewardane N.K., et al., 2018; Amad M., et al., 2021; Wang Y.,et al., 2018; Cofie P., 2001; Ly H-B., et al., 2020; Liu K., et al., 2020; Garcia N.P., et al., 2016; Sadouki A., et al., 2013; Kumar V., et al., 2022; Sherkuziev D.Sh., et al., 2020)* in particular with the mechanical properties involved in the generation of resistance forces (*Cardei P., et al., 2021, Gill W.R., 1967; Zobeck T.M., et al., 1987; Obour A.K., et al.,2021).* Other authors simulate soils or mixtures of soil and rock with random characteristics, in order to predict their behaviour in various dynamic processes *(Gao W., et al.; 2021; Zhang J-Z., et al., 2022).* Under the name of spatial variability, the random nature of some soil properties is also studied and evaluated *(Delhome, J.P., 1979; ISSMGE-TC304, 2021; Mashalaba L., et al., 2020).* Interesting study examples for spatial variability are presented in (*Jurado C. S., et al., 2012; Tekeste M., et al., 2005; Uzielli M., et al., 2005),* and *(Pieczyńska-Kozlowska J., et al., 2021; Lu H., et al., 2022; Salgado R., et al., 2015; Zhang W., et al., 2015)* for a property used in the characterization of soil resistance, namely the cone penetrometer test. A large number of works describe the variability of the tensile strength of agricultural machines intended for soil processing (*Al_Neema K.A., et al., 2021; Al-Kheer A.Al-K.A., et al., 2011; Markinos A.).* The random nature of the forces generated by the action of the working bodies of the soil processing machines is primarily motivated by the inhomogeneous characteristics of the soil (density, granular composition, physical composition, humidity, chemical composition, etc.), also not infrequently, due to the irregular geometry.

However, there is no research that validates the random nature of the interaction process between the working bodies of agricultural machines intended for soil processing and which, based on the validation of the random nature of the stresses of such agricultural machines, recommends the approach to modelling work processes within the theory of random functions (*Hajek B., 2015; Knill O., 2009; Kobayashi H., et al., 2012; Leon-Garcia A., 2008).* More precisely, regarding the series of experimental recordings that form the subject of the analysis whose results are described in this article, they fall into the category of random vibration systems, for which specific approaches are recommended *(Meirovitch L., 1976; Buzdugan Gh., et al., 1982; Lalane Ch., 2002; Sireteanu T., et al., 1981).* In mechanized work processes in agriculture, vibration analysis has become very frequent, especially with the increase in the quality of agricultural working, with the emergence of precision agriculture and with automation, digitization and robotization in this field *(Gong Y., et al., 2023; Yue Y., et al., 2022; Biriş S.Şt., et al., 2022, Yanovych V., et al., 2022; Brăcăcescu C., et al. 2014, Geng C.X., et al., 2019; Samadi M., et al., 2019),* for example. Most of the specified authors work for prediction using descriptive statistical estimators, especially the mean value, and lately, inferential statistical analysis is used, especially based on linear regressions, (*Rogovskii I., et al., 2020; Colombi T., et al., 2019; Alonso A., et al. 2022; Al-Janobi A., et al., 2020).*

In this context, compared to the current and older literature, this work proposes an evaluation of some experimental data series for a quantified decision to approach the analysis through methods specific to deterministic phenomena or methods specific to random phenomena. At a higher level, the work aims to study the distribution of resistance forces on each working body, to confirm or refute some hypotheses.

For example, it will be appreciated if some working bodies are more loaded than others, if the most intense load remains on the same working body, and what the cause is. The hypothesis of the higher intensity of the resistance force on the working bodies in the line closest to the tractor is researched, and the result may show certain errors in the hypothesis and their causes.

MATERIALS AND METHODS

The subject of the research whose results are described in this article consists of one of the working configurations of a cultivator designed for research and farm exploitation. More precisely, the behaviour of the working bodies is targeted, in order to estimate the soil tillage draft forces that appear in the working process of the cultivator.

The agricultural equipment for which the analysis described in this article is made is one of the possible working configurations of the MCLS complex cultivator, capable of working in three variants, with different working widths (1 m, 2 m and 4 m). The description of this complex machine, fig. 1, intended for research and exploitation in the field of soil processing, can be found in *(Cardei P., et al., 2021; Cardei P., et al., 2021).*



Fig. 1 - The MCLS complex cultivator operating with an 80 HP tractor, in full configuration (working width of 4 m)

In this work, the statistical analysis of the experimental data is made only for the substructure formed by the left wing of the complex cultivator, having as a power source a 45 HP tractor, fig. 3. This is the 1 m working width configuration of the MCLS complex cultivator, intended for processing soils in narrow spaces (for example vineyards with narrow rows). In Fig. 2, the frame of the left wing of the cultivator is shown, with the working bodies together with the deformation sensors and the indices of the channels for collecting signals from the deformation sensors glued to the supports of the twelve working bodies.

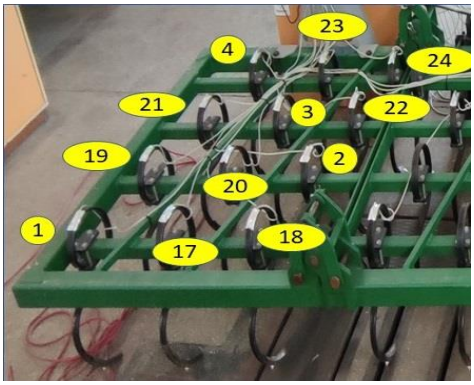


Fig. 2 - The left wing of the cultivator with the indexing of the data collection channels from the deformation sensors (working width 1 m).



Fig. 3 - The aggregate formed by the left wing of the cultivator in operation with a 45 HP tractor.

The acquisition of the experimental data was done exclusively with the help of the deformation sensors numbered as in Fig. 3, numbering that corresponds to the digital registration label in the computer. In Fig. 4, 6, 8 and 10 are graphically represented the finite time series collected during 40 s, in a work experiment,

grouped according to the four lines of working bodies successively positioned on the supporting frame, facing the back of the tractor. In the text or in the comments of the figures, the group of letters *ch* signifies the channel of the data acquisition channel from the sensor with the same number which is marked on the structure (Fig. 2).

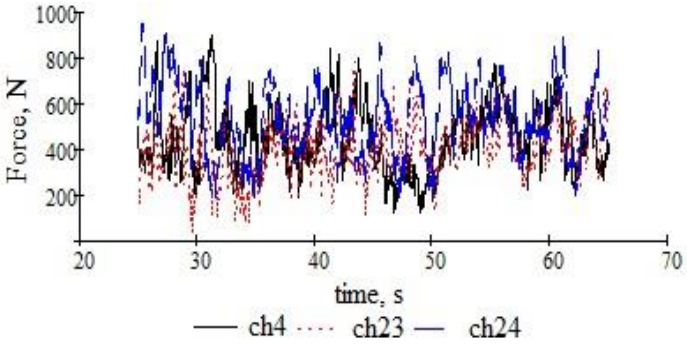


Fig. 4 - The graphs of the loads for the support of the working bodies of the first line after the tractor

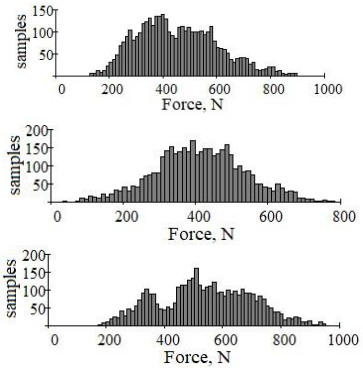


Fig. 5 - Histogram of the sequences: ch4, ch23, ch24

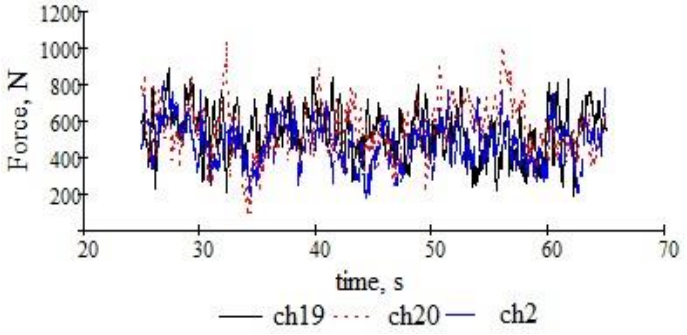


Fig. 6 - The graphs of loads of the supports of the working bodies in the second line after the tractor

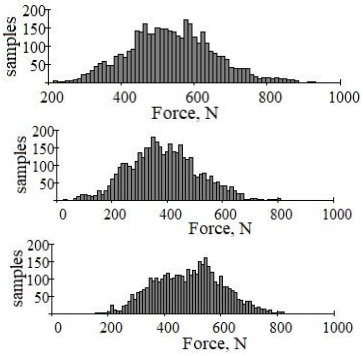


Fig. 7 - Histogram of the sequences: ch21, ch3, ch22

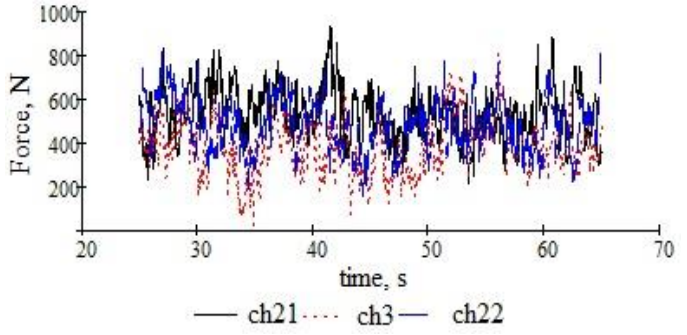


Fig. 8 - The graphs of loads of the supports of the working bodies in the third line after the tractor

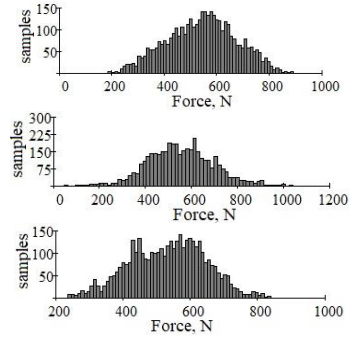


Fig. 9 - Histogram of the sequences: ch19, ch20, ch2

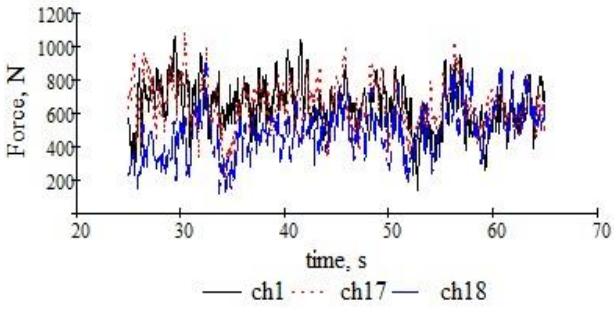


Fig. 10 - The graphs of loads of the supports of the working bodies in the last line of working bodies after the tractor

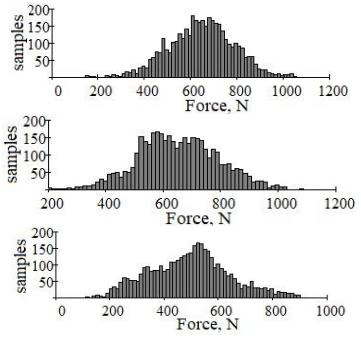


Fig. 11 - Histogram of the sequences: ch1, ch17, ch18

RESULTS

The results included in this chapter refer to the descriptive statistics of the time series collected from the supports of the twelve working bodies of the working variant with a working width of 1 m of the cultivator, signals represented graphically in Fig. 4, 6, 8, 10, and also to the analysis of the intensity of the random nature of these signals.

1. The basic and descriptive statistical analysis of the sequences of the loading of the working bodies' supports

A synthetic analysis of the experimental data gives first information about the random or deterministic character of the experimental data sequences registered for each support of the analysed structure. Estimators that characterize the basic statistics of the temporal series examined, according to *Wolfram Language, (2023*), are the minimum and maximum values, the average value of the standard deviation, variance, and median, which are given in Tables 1 and 2, for all sequences corresponding to the twelve working bodies, shown in Fig. 4, 6, 8 and 10 or as in Fig. 2. Also, the basic statistics contain also part of the quartile calculus presented in Tables 4 and 5 and the graphic, in Fig. 12. The descriptive statistics include also the estimators of Table 3: the asymmetry index (Skewness), the flattening index (Kurtosis*), (Clocotici V., 2023)* and the variation coefficient (CV), *(https://en.wikipedia.org/wiki/Coefficient_of_variation).*

Table 1

The minimum, maximum and average values of the sequences corresponding to the twelve working bodies of the cultivator

The minimum value, N			The maximum value, N			The average value, N		
125.72	32.35	172.7	897.83	784.96	952.14	453.12	410.58	537.52
212.62	23.03	154.4	930.94	808.89	819.48	536.51	385.6	483.49
187.09	45.99	235.69	888.56	1037.85	837.4	541.7	552.88	532.07
144.37	195.29	109.33	1057.49	1086.08	899.81	644.27	650.43	493.19

Table 2

The standard deviation, variance and median of the numerical sequences corresponding to the twelve working bodies of the cultivator

Standard deviation, N			Variance, N			Median, N		
149.5	124.46	158.34	22351.17	15490.2	25072.4	438.22	408.95	533.8
117.74	125.93	120.15	13863.58	15859.29	14434.94	533.04	379.44	488.24
131.68	145.76	112.19	17338.93	21245.42	12586.1	547.39	547.46	538.53
141.61	141.79	147.94	20054.74	20105.32	21887.41	647.45	645.22	498.41

Table 3

The values of the asymmetry index, the flattening index and the variation coefficient corresponding to the twelve working bodies of the cultivator.

Skewness			Kurtosis, N			CV		
0.41	0.02	0.04	-0.33	-0.08	-0.64	0.33	0.303	0.295
0.22	0.19	0.04	-0.02	-0.07	-0.48	0.219	0.327	0.248
-0.08	0.09	-0.08	-0.49	0.38	-0.43	0.243	0.264	0.211
-0.12	0.02	0.16	0.1	-0.07	-0.23	0.22	0.218	0.3

The statistical dependencies, expressed by the correlation coefficients between every two numerical sequences, are given in Table 6. The maximum value of the correlation coefficient between the numerical sequences coming from the supports of the twelve working bodies is 0.645. This value corresponds to the indexed sequences ch22 and ch24, i.e. the working bodies on the extreme right (in the forward direction of the machine), in the first two lines after the tractor. Therefore, the most intense dependence between the variations of the two numerical series is a weak one. Thus, there are no significant linear dependences between the sequences of the analysed forces.

Table 4

Characteristic values of the numerical sequences recorded on the supports of the working bodies on the first two lines of the cultivator, fig. 2

Estimator	channel4	channel23	channel24	channel21	channel3	channel22
Quartile 25%	339.273	327.172	428.674	455.728	299.328	392.892
Quartile 50% (average)	438.217	408.952	533.797	533.042	379.442	488.238
Quartile 75%	555.615	491.625	658.193	613.606	466.197	565.227
Minimum value	125.722	80.596	172.700	219.69	50.931	154.398
Maximum value	878.235	737.772	952.144	848.898	708.142	819.484

Estimator	channel4	channel23	channel24	channel21	channel3	channel22
Outliers	883.493	32.355	0	212.62	23.03	0
	884.456	40.473	0	213.598	25.838	0
	890.717	49.488	0	216.438	39.745	0
	891.415	72.519	0	852.363	717.214	0
	894.117	73.86	0	855.184	718.327	0
	896.248	75.725	0	856.582	718.479	0
	896.642	78.402	0	856.896	719.878	0
	897.831	741.669	0	857.943	720.053	0
	0	748.853	0	859.074	726.072	0
	0	749.196	0	859.23	728.523	0
	0	750.194	0	859.727	730.287	0

Table 5

Characteristic values of the numerical sequences recorded on the supports of the working bodies on the last two lines of the cultivator, fig. 2.

Estimator	channel19	channel20	channel2	channel1	channel17	channel18
Quartile 25%	447.741	453.983	447.364	549.359	553.246	387.216
Quartile 50% (average)	547.388	547.463	538.532	647.453	645.225	498.408
Quartile 75%	633.375	645.753	613.511	737.416	745.357	583.189
Minimum value	187.088	168.468	235.692	269.748	265.451	109.325
Maximum value	888.558	932.78	837.404	1017.000	1031.000	876.94
Outliers	0	45.992	0	144.373	195.285	878.22
	0	47.423	0	145.925	197.299	878.774
	0	54.576	0	148.274	199.931	884.484
	0	62.594	0	152.759	200.239	885.01
	0	68.012	0	157.282	205.016	886.038
	0	83.789	0	160.3	210.232	887.059
	0	94.841	0	163.122	218.006	887.376
	0	95.706	0	173.422	220.185	887.995
	0	98.932	0	186.968	223.329	889.027
	0	99.315	0	191.447	230.535	893.136
	0	103.517	0	212.417	236.918	893.692

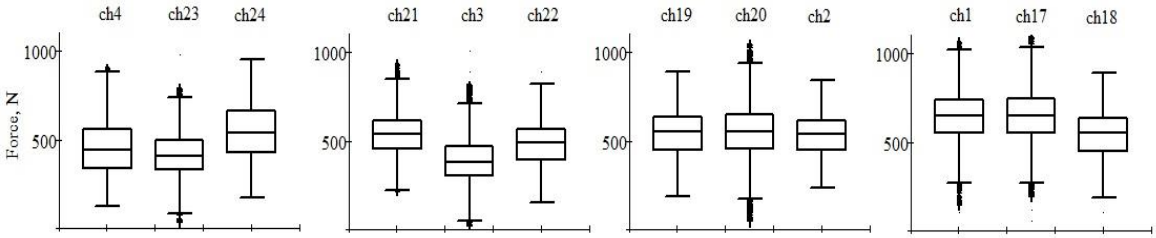


Fig. 12 - Statistical boxplot for the twelve numerical series

Table 6

The values of the correlation coefficient between the numerical sequences recorded from the supports of the 12 working bodies

	ch4	ch23	ch24	ch21	ch3	ch22	ch19	ch20	ch2	ch1	ch17	ch18
ch4	1	0.143	-0.053	0.317	0.210	0.006	0.101	0.170	0.024	0.072	0.105	0.064
ch23	0.143	1	0.323	-0.157	0.193	0.298	-0.031	0.192	0.204	-0.031	0.238	0.250
ch24	-0.053	0.323	1	-0.119	0.224	0.645	0.080	0.300	0.314	0.034	0.403	0.117
ch21	0.317	-0.157	-0.119	1	0.038	-0.038	0.409	0.035	0.161	0.370	0.149	0.071
ch3	0.210	0.193	0.224	0.038	1	0.241	0.123	0.434	0.213	0.007	0.145	0.062
ch22	0.006	0.298	0.645	-0.038	0.241	1	0.195	0.297	0.394	0.176	0.356	0.097
ch19	0.101	-0.031	0.08	0.409	0.123	0.195	1	0.043	0.091	0.502	0.171	-0.051
ch20	0.170	0.192	0.300	0.035	0.434	0.297	0.043	1	0.299	0.196	0.401	0.251
ch2	0.024	0.204	0.314	0.161	0.213	0.394	0.091	0.299	1	0.192	0.363	0.364
ch1	0.072	-0.031	0.034	0.370	0.007	0.176	0.502	0.196	0.192	1	0.404	0.092
ch17	0.105	0.238	0.403	0.149	0.145	0.356	0.171	0.401	0.363	0.404	1	0.320
ch18	0.064	0.250	0.117	0.071	0.062	0.097	-0.051	0.251	0.364	0.092	0.320	1

0.330	0.303	0.295
0.219	0.327	0.248
0.243	0.264	0.211
0.220	0.218	0.300

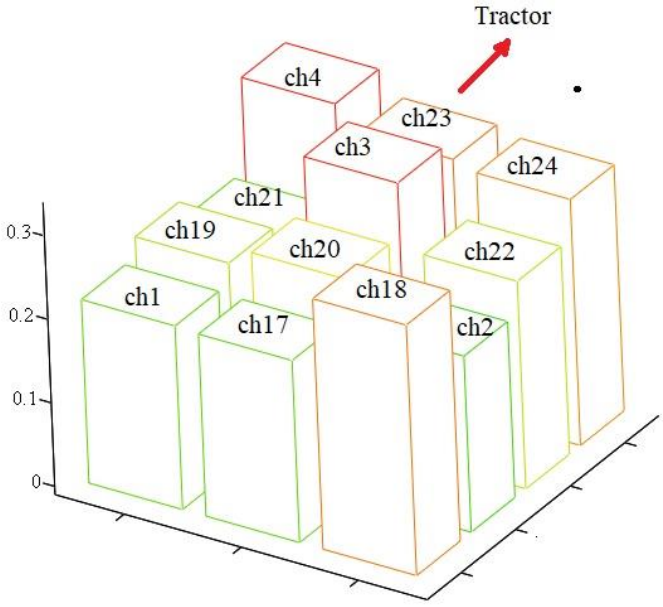




Fig. 13 - The distribution of the coefficient of variation (CV) on the twelve supports of the working bodies.

2. The migration of the maximum effort on the set of the supports of the working bodies

Although there is a global maximum of the load that is recorded throughout the experimental sequence, over all the working bodies (1057.49 N at the left rear body, respectively channel ch1, Table 1), a maximum of the loads exists at each time point of the recordings. An image related to the random intensity of the process can be given by the displacement or migration of this maximum load between the supports of the twelve working bodies. If the maximum load would not move or would oscillate between two, maximum three working bodies, then the information would raise the suspicion of a certain determinism, which could be explained either by constructive defects or by special structuring of the soil in which the work was done.

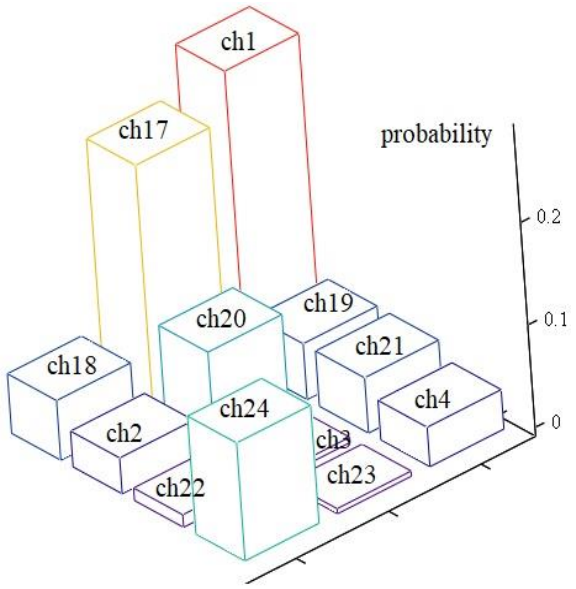


Fig. 14 - The probability of locating the maximum demand during the experiment

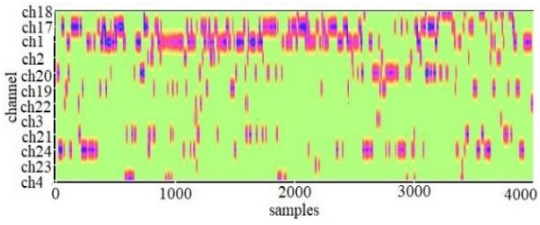


Fig.15 The migration of the maximum value of the stress on the set of supports of the working bodies.

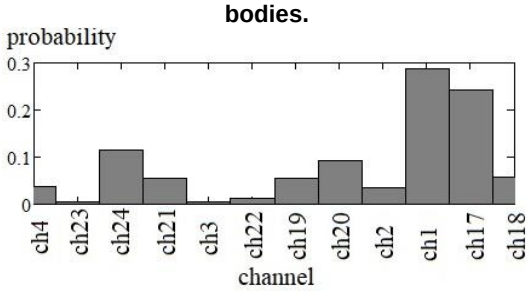


Fig. 16 - The probability of locating the maximum demand during the experiment

3. Analysis of the randomness of experimental data sequences

To estimate the random or deterministic character of the twelve strings of numerical data from the supports of the working bodies, relative entropy was used as a measure *(Cardei P., 2022).* The calculus of the relative entropy uses histograms of the 12 data series, similar to those in Fig. 5, 7, 9 and 11.

The histograms contain 200 classes each, in order to obtain the best possible precision. The obtained results are given in Table 7: the signal identified by the channel of origin, the number of classes required to reach the stopping criterion, n_h, the entropy value, E, of the maximum entropy, E_{max}, and of the relative entropy e_r. Also, in the last two columns, the coefficient of variation (see also fig. 13), CV, and the amplitude of the string values above the average value, SM, are given.

Table 7

Relative entropy values for the twelve numerical sequences, using two criteria for stopping the iterations, according to *Cardei (2022)*

	Discreet stopping criterion				Continuous stop criterion					
channel	n_h	E	E_{max}	e_r	n_h	E	E_{max}	e_r	CV	SM
4	85	6.043	6.443	93.790	84	5.997	6.392	93.818	0.330	2.974
23	80	5.779	6.358	90.894	84	5.812	6.392	90.920	0.303	3.038
24	85	6.106	6.443	94.765	83	6.038	6.375	94.721	0.295	2.618
21	79	5.744	6.340	90.597	84	5.795	6.392	90.650	0.219	3.350
3	87	5.840	6.476	90.189	84	5.761	6.392	90.118	0.327	3.361
22	81	5.911	6.375	92.726	84	5.928	6.392	92.742	0.248	2.797
19	82	5.986	6.392	93.648	84	5.986	6.392	93.648	0.243	2.693
20	80	5.598	6.358	88.056	84	5.630	6.392	88.076	0.264	3.477
2	81	5.950	6.375	93.338	84	5.968	6.392	93.356	0.211	2.721
1	83	5.738	6.409	89.531	84	5.721	6.392	89.506	0.220	3.530
17	86	5.818	6.459	90.064	84	5.750	6.392	89.951	0.218	3.209
18	80	5.930	6.358	93.268	84	5.963	6.392	93.287	0.300	2.748

According to the classification criteria proposed in *(Cardei P., 2022),* all the twelve numerical strings examined have an intensely random character, the relative entropies generally having values higher than 90%. For comparison, the string of the first 4000 prime numbers has an entropy value between 99.665% and 99.753%, calculated with histograms having 200 classes. It is found that the relative entropies obtained using two different criteria for stopping the iterations give similar results and hierarchies, the correlation coefficient between the two columns being 1. It is found that the strings of relative entropies in Table 7 are not correlated with the coefficient of variation, CV and are intensely anticorrelated with the series of amplitudes above the average, for the analysed experimental data sequences.

4 Cumulative probabilities

This subchapter presents the first applications in the analysis of numerical series as random strings, for the design of the supports of such working bodies.

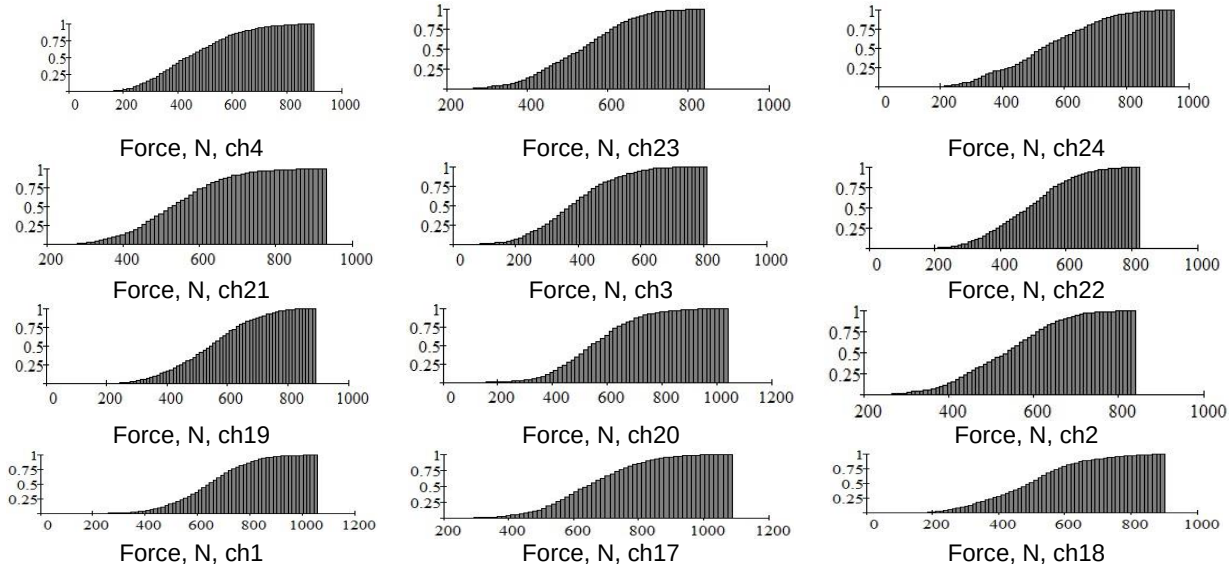


Fig. 17 - Cumulative probabilities for the twelve locations from which the signals were recorded with the deformation sensors

Starting from the histograms in Fig. 5, 7, 9, and 11, were calculated the cumulative probabilities which are plotted in Fig. 17. The cumulative probabilities thus calculated allow the determination by a convention of the resistance characteristics of the shape and material of the supports of the working bodies accepting a probability of the occurrence of an unwanted event (overload or reaching a limit value of the Von Mises stress in the measured or dangerous section).

The results given in Fig. 17 show that, for example, for the working body indexed ch1, the probability of registering load values lower than 1008 N is 99.5% or 0.995, and the probability of registering load values lower than 508 N is 18.2%. In other words, to cover 99.5 of the load cases at working body 1, it is necessary to design resistance to more than 1000 N.

These factors are taken into account for each working body during a later statistical analysis phase together with the determination of resistance to the relevant load and, given the presence of vibrations, resistance to fatigue.

Comments: The analysis of the results obtained for the experimental data series generated by the soil work process carried out with the 1 m width work variant of the MCLS, refers to those aspects examined in connection with the characterization of data randomness. All the statistics used for the analysis of the signals whose records are shown in Fig. 4, 6, 8, and 10, are used in aim to diagnose them as deterministic or random. Visual examination of the signals does not reveal the details necessary to decide whether the twelve signals are random or deterministic. The histograms (Fig. 5, 7, 9, and 11) show that the distribution of values of the experimental series does not fall, in general, between the classic ones used in statistics (normal, Gamma, exponential, Rayleigh, etc.). Many of the histograms of the twelve experimental series examined could be roughly approximated by the normal, Rayleigh, Poisson, Gamma, Beta or other distributions. However, such approximations do not help us in the random or deterministic characterization of the examined strings. There is a path of investigation in this direction, but it is being developed. However, it is important that between the twelve histograms, there are visible differences, not only in value but also in shape. Most show more than one maximum concentration of values, so an approximation with a normal or Poisson distribution cancels this information, for example. The differences between the characteristic histograms of the examined strings are the first piece of information that leans towards their random characterization.

Before examining the results of the basic and descriptive statistics, the results were arranged in Tables 1, 2 and 3, the statistical estimators were written in a matrix of four lines and three columns, corresponding to the placement of working bodies with supports on the resistance frame of the cultivator, fig. 2. It should be mentioned that the supports and the working bodies are not aligned in the direction of movement, but, to facilitate the passage of vegetable remains, they are slightly offset from each other.

The maximum values above 700-800 N and the minimum values, below 100 N, are excluded from the analysis of the quartiles in the representations in Fig. 12, where the specified values are declared outliers, according to *(MathSoft, Inc., 2000).* For practical purposes, it is observed that the average value over all the working bodies varies between 385.6 and 650.4 N, and the average value over all the working bodies has the value 518.4 N. The coefficient of variation of the average values over the twelve signals is 0.149 or 14.9%, which shows that the average variation is not very large, however, over 10% (a usual reference value). The standard deviation and the variance are implied in the comments about the estimators in Tables 1 and 3. The median is approximately equal to the average value for all twelve signals. These small differences affirm the central tendency of the examined experimental data and implicitly the small values of the asymmetry coefficient (skew). The asymmetry coefficient is still approximately null for each series of data, three of them with deviations to the right, the remaining nine with deviations to the left compared to the centre given by the average value.

The flattening index (or curvature coefficient, kurtosis) is zero for distributions with tails, generated by the presence of outliers. The distributions with thin and high peaks, having positive values of the buckling index, correspond to series with long tails and are called leptokurtic, and those with thick and small peaks, with negative values of the buckling index, have small tails and are called platykurtic. The distributions for which the vaulting index is zero are called mesokurtic *(Clocotici V., 2023).* In the case of the experimental strings examined in this article, there are two leptokurtic strings (channels 1 and 20, the rest being platykurtic). The data series collected on channels 1 and 20 have the most outliers, Fig. 12. The coefficient of variation, CV, allows the comparison of two series of experimental data from the point of view of the standard deviation. A small coefficient of variation indicates a better clustering around the mean value. From Table 3, it can be seen that the coefficients of variation are appreciable for all data series, higher for those with lower average loadings and lower for those with the highest average loadings.

The absolute size of the coefficients of variation and the differences between the coefficients of variation of the different signals are additional arguments for appreciating that the examined strings have a random character rather than a deterministic one. The value of the coefficient of variation over all the values of the CV matrix has the value 0.167 or 16.7%, which leads to the same conclusion of the randomness of the examined signals. Representations of the distribution of the coefficient of variation over the spatial distribution of the working bodies are given in Fig. 13. The graphic representation confirms the conclusions resulting from the examination of the numerical results in Table 3.

A numerical breakdown of the graphic representations in Fig.12 is given in Tables 4 and 5. Tables 4 and 5 also provide the values considered aberrant according to *(MathSoft, Inc., 2000)*, readers being able to see how many such values there are for each data string. It is found that there are four strings without outliers *(Nia M.Z., et al. 2023; Cardei P., 2022; Gill W.R., et al., 1967; Gao W., et al., 2021).*

Possible connections between the twelve strings (of a linear nature) can be detected by calculating the correlation coefficient. Table 6 presents the matrix of correlation coefficients in the rows of the set of experimental data examined. It was noticed that the dependencies are negligible, the highest value being 0.645, an insignificant value for linear dependency. This means that the twelve strings vary relatively independently, so another suggestion for the random characterization of the twelve strings.

The last test, which is specific to the estimation of the random character of a numerical sequence, proposed by *Cardei P., (2022),* clearly shows that the twelve strings are part of the first fourth of the strings with the most intense random character. For example, they are comparable to the randomness of the sequence of the first 4000 prime numbers, but below it.

In addition to the above, an important aspect in deciding the random character of the structure formed by the twelve working bodies is given by the migration of the maximum load over all the bodies, preferentially for some, but none excepted, which can be seen from the representations graphs from Fig. 14.



Fig. 18 - Photographic identification of one of the reasons that lead to the overloading of the working bodies on the last line of the cultivator

After the theoretical analysis, it was found through the analysis of the images (Fig. 18) taken during the experiments that one of the reasons why the working bodies from the rear of the cultivator are more intensively stressed. It is observed that the method of connecting to the tractor and maintaining the working depth is not able to eliminate the inclination of the supporting structure from the tractor to the back, so that the working bodies from the back of the structure work at a greater depth, in general than those in front of the cultivator.

CONCLUSIONS

The results presented in Chapter 3 and discussed in Chapter 4 show that posing the problem of the degree of randomness of the experimental data series makes sense, and has chances of solution and quantification.

The characterization of the intensity of the random character can be done first, even if only suggestively, through a series of estimators of descriptive and inferential statistics. Even if they do not quantify the randomness of a lot of experimental data, classical estimators can suggest the random character of the examined data as it was showed in the comments chapter.

The special estimator that is proposed as a quantifier of randomness (the degree of randomness or random intensity), the relative entropy, undoubtedly places all the data strings examined in the first quarter of the random strings, slightly below the randomness of prime numbers, but on par, in general, with pseudorandom strings generated by various methods.

In addition, as a confirmation of the decision given by means of relative entropy, it is worth mentioning the convergence of the assessment given by relative entropy with that obtained by using descriptive and inferential statistical estimators.

Consequently, it is recommended that the approach to the dynamics of such agricultural machinery be made as much as possible in terms of statistics and statistical dynamics. Thus, the stress sequences of the machines will be considered random sequences, given by random signals that must be treated in terms of reference to the theory of random signals. Also in these terms, the design of such machines must be done, especially their resistance structures.

The last conclusion refers to the fact of having already succeeded in using the MCLS complex cultivator to obtain some results and some consequences:

-for the soil that was worked with, there is no specific working body or a series of working bodies that are permanently the most stressed;

-the detection of a reason why the working bodies in the last line, counting from the tractor, due to the backward tilt given by the clamping system, register higher stress forces, this aspect also being noted on the photos.

The experimenters and designers of agricultural machines for soil processing know a number of physical reasons why the working processes of these machines are considered to have a random character: the anisotropy and inhomogeneity of the soil including the inhomogeneity of its moisture, the play in the joints of these machines, the deformations of the soil surfaces, the inclusions of plant residues, etc. This article brings in addition the possibility of quantifying the random character and the indication of the investigation of the problems of these machines using statistical dynamics, the theory of random functions.

As directions for the continuation of these researches, there are:

- mathematical modelling of the working process of agricultural machines intended for soil processing within the random systems theory;
- the inclusion of the working speed parameter in the mathematical modelling, although, in general, the critical speeds at which the component generated by the forward speed exceeds the static component of cutting the soil, are not reached (the desire for high productivity often leads to a decrease in the quality of the works);
- continuation of investigations in search of precise quantifications of the degree of randomness of some numerical strings.

ACKNOWLEDGEMENT

This research was supported by the Romanian Ministry of Research, Innovation and Digitalization, through Programme 1 - Development of the national research-development system, Subprogramme 1.2 - Institutional performance - Projects for financing excellence in RDI, Contract no. 1PFE/30.12.2021.

REFERENCES

[1] Abbaspour-Gillandeh M., Shahgoli G., Abbaspour-GillandehY.,Herrera-Miranda M.A., Hernandez-Hernandez J.L., Herrera_Miranda I., (2020). Measuring and Comparing Forces Acting on Moldboard Plow and Para-Plow with Wing to Replace Moldboard Plow with Para-Plow for Tillage and Modeling It Using Adaptive Neuro-Fuzzy Interface System (ANFIS), *Agriculture,* Vol. 10, No. 633, pp. 1-12.

[2] Afify M.T., El-Haddad Z.A., Lamia A.A.D., (2020). Modelling the Effect of Soil -Tool Interaction on Draft Force Using Visual Basic, *Annals of Agriculture Science, Moshtohor,* Vol. 58, No.2, pp. 223-232.

[3] Al_Neema K.A., Al-Jibouri M.A., Esmail E.L., (2021). The relationship between draft force and horizontal force acting on passive tillage tool in term of soil-tool interaction. A review, *IOP Conference Series: Earth and Environmental Science*, No. 735, pp. 1-6.

[4] Al-Janobi A., Al-Ahmed S., Aboukarima A., Almajhadi Y., (2020). Modeling of draft and energy requirements of a moldboard plow using artificial neural networks based on two novel variables, *Engeharia Agricola*, Vol. 40, No. 3, pp. 363-373.

[5] Al-Kheer A.Al-K.A., Eid M.Y., Aues Y., El Hami A., Kharamanda G., Mouazen A.M., (2011). Theoretical Analysis of the Spatial Variability in Tillage Forces for Fatigue Analysis of Tillage Machines, *Journal of Terramechanics,* Vol. 48, No. 4, pp. 285-295.

[6] Alonso A., Froidevaux M., Javaux M., Laloy E., Mattern S., Roisin Ch., Vanclooster M., Bielders Ch. (2022). A hybrid method for characterizing tillage-induced soil physical quality at the profile scale with fine spatial details, *Soi l& Tillage Research*, Vol. 216, pp. 1-12.

[7] Amad M., Ray R.P., (2021). Numerical study of random material properties within a soil specimen*, IOP Conference Series: Materials Science and Engineering,* Vol. 1141.

[8] Askari M., Khalifahamzehghasem S., (2013). Draft Force Inputs for Primary and Secondary Tillage Implements in a Clay Loam Soil, *World Applied Sciences Journal*, Vol. 21, No. 12, pp. 1789-1794.

[9] Biriş S.Şt., Constantin A-M., Anghelache D., Gageanu I., Cujbescu D., Nenciu F., Voicea I., Matei Gh., Popa L.D., Dutu M.F., Ungureanu N., Zelazinski T., Perisoara L., Fodorean G., (2022). Considerations regarding the vibrations transmitted to the operator by an axial flow harvester combine, *INMATEH-Agricultural Engineering,* Vol. 68, No. 3, pp. 747-756.

[10] Brãcãcescu C., Soricã C., Manea D., Guanxin Y., Constantin G.A., (2014). Theoretical contributions to the drive of cereal cleaning technical equipment endowed with non balanced vibration generating systems, *INMATEH-Agricultural Engineering*, Vol. 42, No. 1, pp. 69-74.

[11] Buzdugan Gh., Fetcu L., Radeş M., *Mechanical vibrations (Vibrații mecanice)*, Didactic and Pedagogical Publishing House, Bucharest, (1982).

[12] Cardei P., Biris S. S., Muraru S., Oprescu M., Consequences of modeling the draft tillage on the dynamics of the soil tillage agricultural machinery, *20th International Scientific Conference Engineering for Rural Development*, Jelgava, 2021.

[13] Cardei P., Constantin N., Sfiru R., Muraru V., Condruz P., (2021). Modular load-bearing structures for the study of interactions between the soil and working parts of agricultural machines, *Journal of Physics Conference Series*, Vol. 1781, No. 1, pp. 1-10, 012063.

[14] Cardei P., Nicolae C., Sfiru R., Muraru V., Muraru S.L., (2021). Structural analysis of a modulated load-bearing structure designed to investigate the interaction between soil and the working parts of agricultural machines, *Journal of Physics Conference Series*, Vol. 1781, No. 1, pp. 1-15, 012064.

[15] Cardei P., (2022). Randomness and determinism, is it possible to quantify these notions? *International Journal of Applied Sciences & Development,* Vol. 1, pp. 52-63. https://www.researchgate.net/publication/368527584_Randomness_and_Determinism

[16] Carman K., Marakoglu T., Taner A., Citil E., (2021). Prediction of Draft Force ad Disturbed Soil Area of a Chisel Tine in Soil Bin Conditions Using Draft Force and Its Comparison with Regression Model, *Selcuk journal of Agriculture and Food Sciences,* Vol. 35, No. 1, pp. 56-64.

[17] Clocotici V., (2023). Explanatory Dictionary of Statistics (Dictionar Explicativ de Statistica), https://profs.info.uaic.ro/~val /statistica/ StatGloss .htm, last accessed 24.01.2023

[18] Cofie P., (2001). *Mechanical properties of tree roots for soil reinforcement models*, Dissertation Wageningen University.

[19] Colombi T., Walder F., Buchi L., Sommer M., Liu K., Six J., van der Heijden M.G.A., Charles R., Keller T., (2019). On-farm study reveals positive relationship between gas transport capacity and organic carbon content in arable soil, *Soil,* Vol. 5, pp. 91-105.

[20] Croitoru St., Vladut V., Marin E., Matache M., Dumitru I., (2016). Determination of subsoiler's traction force influenced by different working depth and velocity, 15th *International Scientific Conference "Engineering for Rural Development*" Jelgava, Latvia, Proceedings, Vol. 15, pp. 817-825.

[21] Delhome J.P., (1979). Spatial variability and uncertainty in groundwater flow parameters: A geostatistical approach, Water Resources Research, *American Geophisical Union (AGU)*, Vol. 15, no.2, pp. 269-280.

[22] Dharumarajan S., Hedge R., Singh S.K., (2017). Spatial prediction of major soil properties using Random Forest techniques – A case study in semi-arid tropics of South India, *Geoderma Regional*, Vol.10, pp.154-162.

[23] Gao W., Yang H., Wang L., Hu R., (2021). Numerical Simulation of the Soil-Rock Mixture Mechanical Properties Considering the Influence of Rock Block Proportion by PFC2D, *Materials,* Vol. 14, No. 5442, pp.1-14.

[24] Garcia N.P., Rodriguez M.A.R., Anguas P.G., Cruz H.G., Fredlund D., Luis R.P., (2016). Compaction and mechanical properties of soils compacted in the gyratory compactor, *Revista Infrastructura Vial*, Vol. 18, No. 31/pp. 20-29.
[25] Geng C.X., Wang P., Qin P.L., Zhang W.B., Wang P.B., (2019). The optimal choice of the characteristic wavelengths in spectral imaging for cucumber downy mildew, *INMATEH-Agricultural Engineering*, Vol. 57, No. 1, pp. 29-36.
[26] Gill W.R., Vanden Berg G. E., (1967). Soil dynamics in tillage and traction, *Agricultural Research Service United States Department of Agriculture.*
[27] Gong Y., Ren L., Han X., Gao A., Jing Sh., Feng Ch., Song Y., (2023). Analysis of Operating Conditions for Vibration of a Self-Propelled Monorail Branch Chipper, *Agriculture*, Vol. 13, No. 1, pp. 1-22.
[28] Hajek B., *Random Processes for Engineers*, Cambridge University Press, 2015.
[29] Jurado C. S., Breul P., Bacconnet C., Benz-Navarrete M., (2021). Probabilistic 3D modelling of shallow soil spatial variability using dynamic cone penetrometer results and a geostatistical method, *Georisk: Assessment and Management of Risk for Engineered Systems and Geohazards*, Vol. 15, No. 2, pp. 139-151.
[30] Kim Y-S., Kim T-J., Kim Y-J., Lee S-D., Park S-U., Kim W-S., (2020). Development of a Real-Time Tillage Depth Measurement System for Agricultural Tractors: Application to the Effect Analysis of Tillage Depth on Draft Force during Plow Tillage, *Sensors,* Vol. 20, No. 3, pp. 1-16.
[31] Knill O., (2009) Probability Theory and Stochastic Processes with Applications, Overseas Press (India) PVT.LTD.
[32] Kobayashi H., Mark B.L., Turin W, Probability, (2012). *Random Processes*, and Statistical Analysis, Cambridge University Press.
[33] Kumar V., Malhotra J.S., Sharma S., Bhardwaj P., (2022) Soil Properties Prediction for Agriculture using Machine Learning Techniques, *Journal of Engineering Research and Sciences*, Vol. 1, No. 3, pp. 9-18.
[34] Lalane Ch., (2002). Mechanical Vibration&Shock, *Random Vibration*, vol. III, CRC Press.
[35] Leon-Garcia A., (2008). Probability, Statistics, and Random Processes for Electrical Engineering, Third Edition, Pearson Prentice Hall.
[36] Liu K., Yuan K-ze, Wu K., Effect of Water Content and Dry Density on Mechanical Properties of Compaction Loess, *IOP Conference Series: Materials Science and Engineering*, Vol 598, 2020.
[37] Lu H., Li H., Meng X., (2022). Spatial Variability of the Mechanical Parameters of High-Water-Content Soil Based on a Dual-Bridge CPT Test, *Water***,** Vol. 14, No. 343, pp. 1-17.
[38] Ly H-B., Pham B.T., (2020). Soil Unconfined Compressive Strength Prediction Using Random Forest (RF) Machine Learning Model, *The Open Construction & Building Technology Journal*, Vol. 14, No. 2, pp. 278-285.
[39] Mahmood H.F., Subhi Q.A., Hussein E.K., Comparison of Vibrations, (2011). Tillage Depth and Soil Properties for Moldboard and Disk Plows at Three Tillage Speed, *Asian Journal of Agricultural Research*, Vol. 5, No. 1, pp. 90-97.
[40] Markinos A., Gemtos Th., Kavalaris Ch., Karamoutis Ch., Soil Resistance to Ploughing Spatial Variability and Their Effects to Cotton Seed Yield Maps, *https://www.academia.edu/12684400 /Soil_Resistance_ To_Ploughing_Spatial_ Variability_And_Their*
[41] Mashalaba L., Galleguillos M., Seguel O., Poblete-Olivares J., (2020). Predicting spatial variability of selected soil properties using digital soil mapping in a rainfed vineyard of central Chile, *Geoderma Regional*, Vol. 22, No. E00289, 2020, pp. 1-18.
[42] MathSoft, Inc., (1999). Mathcad User's Guide, *Mathcad 2000 Professional.*
[43] Meirovitch L., (2001) Fundamentals of Vibrations, *Mc Graw Hill*, (first edition 1976).
[44] Nia M.Z., Moradi M., Moradi G., Taghizadeh-Mehrjardi R., (2023). Machine Learning Models for Prediction of Soil Properties in the Riparian Forests, *Land*, Vol. 12, No. 32, pp. 1-15.
[45] Obour A.K., Holman J.D., Simon L.M., Schlegel A.J., (2021). Strategic Tillage Effects on Crop Yields, Soil Properties, and Weeds in Dryland No-Tillage Systems, *Agronomy,* Vol. 11, No. 662, pp. 1-17.
[46] Salgado R., Prezzi M., Ganju E., (2015) Assessment of Site Variability from Analysis of Cone Penetration Test Data, *Joint Transportation Research Program Technical Report FHWA/IN/JTRP-2015/04*,
[47] Pieczyńska-Kozlowska J., Bagińska I., Kaea M., (2021). The Identification of the Uncertainty in Soil Strength Parameters Based on CPTu Measurements and Random Fields, *Sensors,* Vol. 21, No. 16, pp. 1-22.

[48] Rashidi M., Najjarzadeh I., Namin S.T., Naserzaeim F., Mirzaki S.H., Beni M.S., (2013). Prediction of Molboard Plow Draft Force Based on Soil Moisture Content, Tillage Depth and Operation Speed, *American-Eurasian Journal of Agriculture & Environment Science,* Vol. 13, No. 8, pp. 1057-1062.

[49] Rogovskii I., Titova L., Trokhaniak V., Trokhaniak O., Stepanenko S., (2020). Experimental study of the process of grain cleaning in a vibro-pneumatic resistant separator with passive weeders, Bulletin of the Transilvania University of Brasov, series II: Forestry, Wood Industry, *Agricultural Food Engineering*, Vol.13, No. 1, pp. 117-128.

[50] Sadouki A., Bouaricha L., Hdj Henn F.Z., Harichane Z., (2013). Investigation of soil parameters randomness effects on earthquake design forces, *International Conference on Earthquake Geotechnical Engineering:* Istanbul, Turkey.

[51] Salgado R., Prezzi M., Ganju E., Assessment of Site Variability from Analysis, Samadi M., Rostampour V., Abdollahpour Sh., (2019). The effect of mass flow rate of wheat solid particles on characteristics of acoustic signals in pneumatic conveying, *INMATEH-Agricultural Engineering*, Vol. 57, No. 1, pp. 187-198.

[52] Sherkuziev D.Sh., Aripov Kh.Sh., Alimov U.K., Maxmudova M.A., (2020), Research of agrochemical properties of soil processed with hydrogel, *IOP Conference Series: Materials Science and Engineering*, Vol 614.

[53] Sireteanu T., Gundisch O., Paraian S., (1981). *The random vibrations of automobiles (Vibratiile aleatoare ale automobilelor)*, Technical Publishing House, Bucharest / Romania.

[54] Tekeste M., Raper R.L., Schwab E.B., (2005). Spatial variability of soil cone penetration resistance as influenced by soil moisture on Pacolet sandy loam soil in the southeastern United States, *Southern Conservation Tillage Systems Conference Clemson University*.

[55] Uzielli M., Vannucchi G., Phoon K.K., (2005). Random field characterisation of stress-normalised cone penetration testing parameters, *Géotechnique,* Vol. 55, No. 1, pp. 3-20.

[56] Vlăduţ D.I., Vlăduţ V., Grigore I., Biriş S., (2017), Experimental research in qualitative indices of work for equipment for seedbed preparation in conservative system, *16th International Scientific Conference "Engineering for rural development",* Jelgava, Latvia, pp. 1174-1179.

[57] Wang Y., Li X., Zheng B., (2018). Experimental study on mechanical properties of clay soil under compression by ultrasonic test, *European Environmental and Civil Engineering*, Vol.22, No.6, pp. 666-685.

[58] Wijiewardane N.K., Ge Y., Wills S., Libohova Z., (2018). Predicting Physical and Chemical Properties of US Soils with a Mid-Infrared Reflectance Spectral Library, *Soil Science Society of America Journal,* Vol. 82, No. 3, pp. 722-731.

[59] Wolfram Language & System Documentation Center, last accessed 24.01.2023, https://reference.wolfram.com/language/tutorial/NumericalOperationsOnData.html#7135.

[60] Yanovych V., Honcharuk T., Honcharuk I., Kovalova K., (2018). Engineering management of vibrating machines for targeted mechanical activation of premix components, *INMATEH-Agricultural Engineering*, Vol. 54, No. 1, pp. 25-34.

[61] Yue Y., Tian H., Liu F., Zhang T., Li D., Wang D., (2022). Analysis of vibration characteristics for rubbing machine based on modal test, *INMATEH-Agricultural Engineering*, Vol. 68, No. 3, pp. 41-50. DOI: https://doi.org/10.35633/inmateh-68-04

[62] Zhang J-Z., Zhang D-M., Huang H-W., Phoon K.K., Tang C., Li G., (2022). Hybrid machine learning model with random field and limited CPT data to quantify horizontal scale of fluctuation of soil spatial variability, *Acta Geotechnica,* Vol. 17, No. 1148, pp.1129-1145.

[63] Zhang W., Pan Y., Bransby F., (2020). Scale effects during cone penetration in spatially variable clays, *Géotechnique*, pp. 1-13.

[64] Zobeck T.M., Onstad C.A., (1987). Tillage and rainfall effects on random roughness: A review, *Soil and Tillage Research,* Vol. 9, No. 1, pp. 1-20.

[65] *https://en.wikipedia.org/wiki/Coefficient_of_variation*

[66] *https://www.researchgate.net/publication/368527584_Randomness_and_Determinism*

[67] *ISSMGE-TC304 (2021), State-of-the-art review of inherent variability and uncertainty in geotechnical properties and models, International Society of Soil Mechanics and Geotechnical Engineering (ISSMGE) – Technical Committee TC304 'Engineering Practice of Risk Assessment and Management', 2021. DOI: 10.53243/R0001.*

RESEARCH ON THE PROCESS OF OBTAINING BUTTER IN LABORATORY CONDITIONS
/
CERCETĂRI PRIVIND PROCESUL DE OBȚINERE A UNTULUI ÎN CONDIȚII DE LABORATOR

Iuliana STANA[1)], Paula TUDOR[*1)], Alexandru CIRIC[*1)], Mihaela BEGEA[*1)], Gheorghe VOICU[*1)], Vasilica STEFAN[2)]
[1)]National University of Science and Technology Politehnica Bucharest, Faculty of Biotechnical Systems Engineering / Romania
[2)] INMA Bucharest / Romania
Tel: 0724715585; Email: ghvoicu_2005@yahoo.com
DOI: https://doi.org/10.35633/inmateh-71-59

Keywords: *butter process, artisan churn, stirring speed, concentration of the cream, yield in butter*

ABSTRACT
Optimizing the process of obtaining butter requires experiments in laboratory conditions, where some parameters need to be adjusted and monitored. For a low-capacity churn with a horizontal semi-helical paddle, the beating time was determined depending on the speed of the beater and the fat content of the cream. At a fat content of 30% in the cream, the butter percentage obtained at low speeds was 27.7%, while for a speed of 3000 rpm a butter percentage of only 21.3% was obtained. The paper also presents other results necessary for establishing the functional parameters of small churns.

REZUMAT
Optimizarea procesului de obținere a untului necesită experimente în condiții de laborator, în care unii parametri este necesar a fi reglați și monitorizați. Pentru un putinei de capacitate mică, cu o paletă orizontală semielicoidală, s-a determinat timpul de batere în funcție de turația bătătorului și conținutul de grăsime al smântânii. La un conținut de grăsime de 30% în smântână, procentul de unt obținut la trepte joase de turație a fost de 27,7%, în timp ce pentru o turație de 3000 rpm s-a obținut un procent de unt de numai 21,3%. Lucrarea prezintă și alte rezultatele necesare stabilirii parametrilor funcționali ai putineielor de capacități mici.

INTRODUCTION

Butter is a dairy product, composed of fat, water and non-fat dry matter, which is obtained through thermal and mechanical treatments of the cream. According to the Regulation 1308/2013, as well as the Romanian Order 524/2002, butter is defined as the product with a milk-fat content of not less than 80% but less than 90%, a maximum water content of 16% and a maximum dry non-fat milk-material content of 2%. In addition, according to the national legal regulations (Romanian Law 307/2022), butter is the product obtained exclusively from milk components, being a water-in-fat emulsion, with a fat content of at least 80%. It is obtained by processing the pasteurized cream, derived from milk, manufactured in compliance with technical quality conditions.

Cream, as raw material for butter, is the layer of fat that forms naturally on the surface of milk, through the slow agglomeration of fat globules that emulsify. It is removed from the surface of the milk by creaming or extracted from the milk by centrifugation in a cream separator and is characterized by a high fat content. Usually, for the cream used in the butter production, has at least 30% fat in weight percentage. From a physico-chemical point of view, cream is an oil-in-water emulsion, with the sizes of milk fat globules in the range of 0.1-15 μm (*Romanian Law 307/2022; Panchal et al., 2021*).

The methods used to make butter (the Fritz process and batch-wise churning) basically turns the cream into butter grains and buttermilk by agitation and by beating air into the cream. The microstructure of the butter grains as well as of the finished butter is characterized by a dispersion of water, air, fat crystals and fat globules in oil. The consistency of butter can be influenced to a large extent by temperature treatment of the cream (physical cream ripening) (*Amare, 2020*; *Frede and Buchheim, 2007*).

From technological perspective, butter is obtained through the churning of the cream, followed by the removing of the excess liquid phase (buttermilk).

It is a specific food matrix with a specific texture and flavour in particular defined mainly by the lipids, which have a significant impact on the texture (hardness, plasticity, adhesiveness and viscosity, as well as cuttability and spreadability) and rheology, as well as on the sensory properties such as the mouth-fullness and colour (*Wright et al., 2001; Matuszek, 2010; Pădureț, 2021; Chudy et al., 2022; Pavlova et al., 2022*).

From the point of view of colloidal physics, butter is a water/oil emulsion, compared to cream which is an oil/water emulsion (*Serdaroglu et al., 2015; Romanian Order 524/2002*). Its classification is done according to:

- the origin of raw material (milk cream, whey cream, buttermilk cream, frozen cream);
- the acidity of the cream (sweet or fermented);
- the added ingredients (salt, sugar, honey, vegetable fat);
- thermal and mechanical processing procedures (pasteurized or sterilized, melted, powdered, remixed, anhydrous fat from butter).

An important factor that determines the correct evolution of the churning process is the temperature of the cream which varies depending on the season (in the case of production facilities not having a strictly controlled environmental temperature) and the type of butter manufactured. The ripened and chilled cream is brought to the churn. The degree of filling of the churn is 40-50% in its total volume, if the fat content of the cream varies between 25% and 37%. During the first 3-5 minutes of churning, the churn stops 1-2 times and, through a special valve, gases which create an overpressure in the beater and can increase butter losses are evacuated from it (*Celik and Bakirci, 2000; Funahashi and Horiuchi, 2008; Fred and Buchheim, 2007; Lee and Martini, 2018; Kalla et al., 2016; Sun et al., 2008*).

The churning process takes 45-60 minutes and is influenced by several factors. The cream is churned until grains of butter with a diameter of 3-5 mm are obtained, then the churn stops and the buttermilk is removed - through a sieve or cheesecloth – draining it into the buttermilk collecting vessel. The moment when the butter grain achieves the desired size should be carefully observed. If the churning is stopped too early, the butter grain will be smaller and the buttermilk will be more difficult to separate, making also the washing process of the grain more difficult. If the churning is stopped too late, the butter grain will have a larger diameter, more buttermilk will be retained in the grain, the water content will be higher and the preservation of the butter will be reduced (*Frede and Buchheim, 2007; Vithanage et al., 2009*).

The fat content of the buttermilk must be 0.2-0.3% and the temperature must be 2-3°C higher than the temperature of the cream at the beginning of the churning. The butter grain is then washed to completely remove the buttermilk. The temperature of the washing water is determined according to the consistency of the butter. If the consistency of the butter grain is normal, the temperature of the washing water should be equal to the temperature of the buttermilk. If the consistency of the butter grain is soft, then the washing water with a temperature 1-2°C lower will be used and in the case of butter grain with a hard consistency the washing water with a temperature 1-2°C higher than that of buttermilk must be used.

The working parameters of the churn are set according to the consistency and temperature of the butter. The rotation speed of the churn is set at 7-10 rpm. The kneading temperature is set according to the strength of the butter and varies between 7-11°C in summer and 9-13°C in winter. It is regulated by sprinkling the churn with washing water. After 3-5 minutes from the start of the kneading process, the churn is stopped and the excess of water or buttermilk is removed, and the kneading is continuing afterwards.

The characteristics of the butter churning process are affected by the fat content of the cream, the flow rate of the cream and especially by the feeding temperature of the cream, which influences the water content of the butter (*Funahashi and Horiuchi, 2008*). An analysis of the churning process indicated that the water content of butter decreases with increasing the beater shear speed and, after reaching a minimum level, increases linearly. In addition, the way of feeding and the feed administered to dairy animals influences the physical properties of butter and affects its processing properties (*Avramis et al., 2003*).

At low speeds of the whipping arm (approx. 60 rpm), it is considered that the optimal parameters of the process of transforming cream into butter are obtained by stirring it at a temperature of 10°C (*Kalla et al., 2016*). The same authors specify that the stirring temperature, the stirring speed and their interaction have a significant effect on the stirring time and the quality of the butter, if the other parameters, such as acidity, fat percentage, temperature and ripening time, were kept constant (*Sinha et al., 2015*).

Previous experiments show that mixing camel milk with goat milk improves mixing efficiency and microbial quality of butter obtained at different mixing levels. Although butter can be made from pure camel milk, the stirring and fermentation time is longer (Asresie *et al., 2013*).

Also, organoleptic properties such as colour, aspect, taste and texture were optimized when butter samples were prepared from 35% fat cream at a stirring temperature of 10-12°C, compared to cream having 30% and 40% fat content (*Siddique et al., 2011*). Thus, the fat content of the cream and the mixing temperature affect the yield and quality of the butter, influencing the quality parameters.

A longer cream ripening time results in larger butter grains, higher viscosity and a higher solid fat content. Both ripening time and stirring time have an effect on the thermal behaviour of the cream. The stirring time decreases significantly with increasing ripening time, and the crystallization state that promotes partial coalescence (i.e., the aggregation of butter grains) is obtained in the first hour of cream ripening at 10°C (*Buldo et al., 2013*). Heat transfer is influenced by the size of the ripening vessel (a larger vessel results in slower latent heat transfer). Furthermore, the flow of fat globules during agitation is affected by the speed and type of impeller. Therefore, the crystallization time and thus the rate of partial coalescence of milk fat globules is different for different types of churn.

Cream ripening is an important process that influences the production time and the production of butter with a constant quality. The hardest butter was obtained from cream matured at 5°C with stirring at 240 rpm, respectively at 10°C with stirring at 40 rpm. A softer butter was obtained from cream matured at 10°C with stirring at 240 rpm, which also had the highest water content. Other researches (*Lee and Martini, 2018*) show that the hardness of the butter can be adapted by changing the ripening conditions of the cream, which can be ripened at higher temperature with low agitation without changing the hardness of the butter.

Therefore, the working conditions, the stirring time, the type of batter, the physico-chemical characteristics of the raw material such as temperature, are just a few elements to consider when making butter, regardless of the origin of the milk (*Lapcikova et al., 2022* ; *Mtibaa et al., 2021; Panchal et al., 2021; Tsedey et al., 2018; Pavlova et al, 2022*). For example, since the butter's functional properties are directly influenced by the crystallization of milk fat globules during maturation of cream, the type of cooling (e.g. rapid versus slow cooling) can contribute to a significant difference in butter firmness (*Panchal et al., 2021; Lapcikova et al., 2022*). By applying different procedures for obtaining butter, using manual or electric churns, it is possible to highlight the influence of various process parameters (such as speed of the paddle, temperature and fat content of the cream as raw material in the churning process) on the technological parameters such as the yield in butter (*Rønholt et al., 2012; Rønholt et al., 2014; Lapcikova et al., 2022*).

The objective of this work was to identify the influence of speed and stirring time on the butter yield and its physico-chemical characteristics when processing cow's milk cream with a fat content of approximatively 30%, 35%, and 40%.

MATERIALS AND METHODS

In the experiments performed, an electric churn was used, designed and made from a vessel of approx. 4 litres, to which a Fasco 50747-D500 7021-1641 motor was added, with nominal speed 3000 rpm, three-speed adjustable, 1/100 hp, 52 Amps, 115 Volts 60/50 Hz, with thermal protection.

The motor shaft is ϕ8 mm, and a rectangular, helically inclined beater paddle was attached to its end so that the cream has an up-down movement. The cream moves to the edge, up, out, and back to the centre in a small swirl. The engine was attached directly to the lid of the vessel. In order to have stability during the beating process, and the vessel was placed on a solid support.

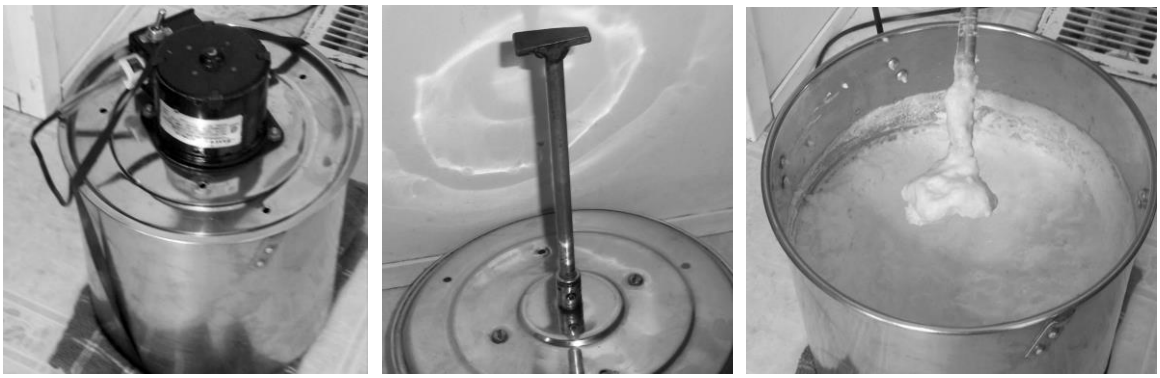


Fig. 1 - Electric churn used in the experiments: general appearance and the stirrer shaft with the stirring paddle

The determination of the dry matter content in cream was performed by the method ISO 6731:2010.

The determination of fat content in the samples of cream was performed by the acido-butyrometric method (*Gerber method*), using a Super Vario N centrifuge for butyrometers and specific butyrometers (*Funke-Gerber, Berlin, Germany*).

The determination of the acidity was performed by the titrimetric method (titration with a 0.1N sodium hydroxide solution in presence of phenolphthalein 1% solution in ethyl alcohol 96% vol.).

The determination of pH was performed using the potentiometric method.

The determination of the moisture content and the non-fat solids content in butter was performed by the method ISO 3727-1 and ISO 3727-2 respectively, and the fat content was calculated based on the method ISO 3727-3.

In each experiment, a quantity of 1.5 kg of cow's milk cream was used, from each category (mentioned in Table 1). The cream was procured from the local market, coming from the store of Pantelimon Dairy Farm.

The determinations were made in the laboratory of ICA Research & Development, both for the raw material and for the finished product.

To determine the physico-chemical characteristics of the raw material used in the experiments and presented in table 1, the following pieces of equipment were used: Mettler Toledo laboratory pH-meter, measurement range 0–14 pH units, 1% resolution; Kern 770 analytical balance, used for masic analysis in acidity, fat and dry matter determination, precision 0.0001 g, operating temperature 10-30°C; Super Vario N centrifuge, used to determine the fat content of cream and butter, 600-1130 rpm; Sanyo Owen OMT oven for the determination of dry matter, with a capacity of 60 litres and an adjustable temperature of 5–300 °C.

After pouring the cream into the laboratory designed churn, the electric motor was started (the speed setting being previously adjusted). At first the noise produced by the paddle was more intense, and as the butter grains began to form, the noise faded. The end of the churning process was visually assessed at the time of separating the butter beans from the buttermilk.

The formed butter was collected and washed three times using tap water, with the last wash adding ice to improve the consistency of the product. The remaining water was drained through a cheesecloth, and the butter was placed in the refrigerator (4-6°C), to be kept for laboratory testing.

The purpose of the experiments was to identify the influence of paddle speed and beating time on butter yield (finished product) at different fat content of cream, respectively determining the characteristics of the finished product (dry matter and fat content), taking into account the characteristics of the raw material.

RESULTS AND DISCUSSION

The determined values of the physico-chemical parameters of the raw material are presented in Table 1.

Table 1

Physico-chemical parameters of the cream used to obtain butter

Physico-chemical parameter	Cream, approx. 30% fat	Cream, approx. 35% fat	Cream, approx. 40% fat
pH	4.95	4.58	4.87
Acidity, (º Thorner)	57.90	50.94	58.47
Fat, (g / 100 g)	31.55	36.12	45.42
Total dry matter, (%)	35.53	40.92	49.87

The literature provides for the calculation of the probable amount of butter, the following calculation formula (1):

$$C_u = \frac{C_s+(G_s-G_m)}{G_u-G_m}\left(1-\frac{P_u}{100}\right) \quad (1)$$

where: C_u – amount of butter obtained (kg); C_s – amount of cream used (kg); G_s – fat content of the cream (%); G_m – fat content of the skimmed milk (%); G_u - fat content in butter (%); P_u - fat loss during manufacturing (%).

In general, the density of the cream after normalization fell within the limits prescribed by specialized literature, respectively: for cream with 8-10% fat – 1,024 g/cm^3, for cream with 20% fat – 1,018 s/cm^3, for cream with 35% fat - approx. 0.998 g/cm^3 .

From the experimental determinations carried out in the laboratory, the following results for the yield in butter were obtained for different types of cream and different blade spades (Table 2).

Table 2

Data obtained from experimental determinations

The type of cream	30% fat		35% fat		40% fat	
Blade speed, (rpm)	Time (min)	Resulting finished product (g)	Time (min)	Resulting finished product (g)	Time (min)	Resulting finished product (g)
1 – 1000 rpm (T1)	55	415	51	495	45	527
Step 2 – 2000 rpm (T2)	44	362	42	434	31	461
Step 3 – 3000 rpm min (T3)	30	320	28	396	17	423

Based on the results obtained, it can be underlined that the fat content of the cream used influences the beating time. This can be explained by the fact that closer fat globules join together faster and cause coalescence in a shorter time.

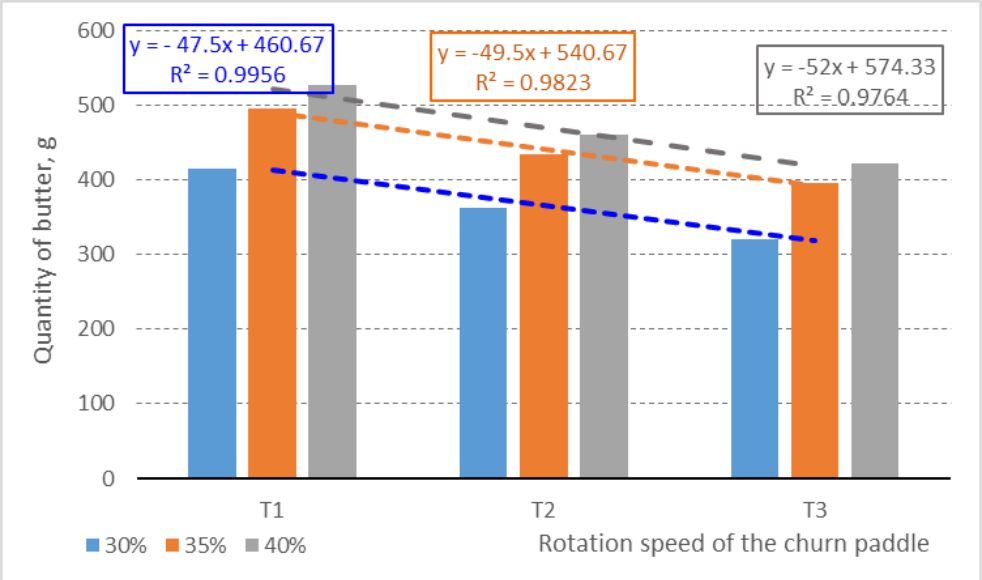


Fig. 2 - The variation of the amount of butter obtained, depending on the speed of the agitator

Figure 2 shows the variation of the amount of butter obtained during churning, depending on the speed of the agitator, for the three fat contents of the initial cream.

For the batch with a higher fat content, the churning time was shorter, comparing to the batch with a lower fat content (30%) for which a longer churning time was required to separate the butter from the buttermilk. However, it was demonstrated that when reducing the churning time, through the increase of the speed of the shaft with the agitator paddle, the amount of separated butter decreases, for the same fat concentration of the cream, and a large part of the fat remains in the buttermilk (and is considered as “lost”).

For the samples where a higher speed was used, there were higher losses of fat in the buttermilk, which caused a low butter yield of the process.

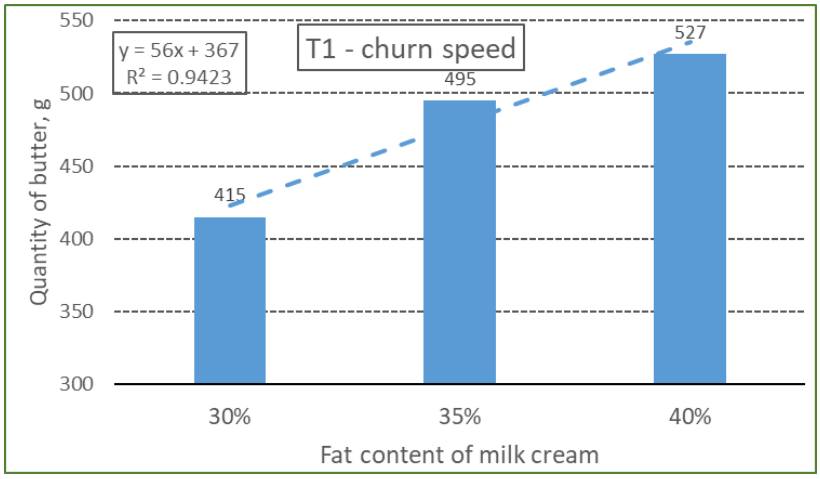
Figure 2 reveals that for different speed steps, increasing from 1000 to 3000 rpm, the amount of butter decreases linearly with the speed, presenting a correlation coefficient R^2 of 0.976, for a fat concentration of the cream of approx. 40% and 0.996, for an initial fat concentration of approx. 30%.

Making a different analysis of the data in table, a linear variation of the values of the butter quantity obtained through churning, for each speed of the mixer, is also found, depending on the fat content of the cream used as raw material.

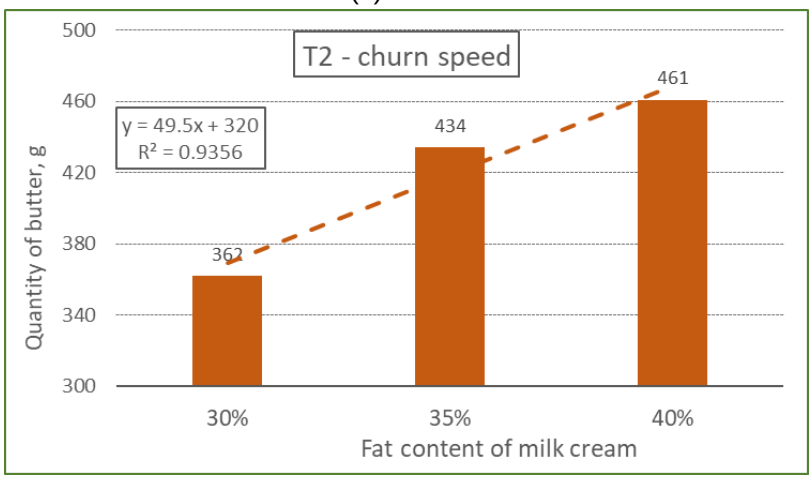
The correlation with the experimental data shows a correlation coefficient R^2 with decreasing values from low speed to high speed, with values between 0.942, for speed step T1 and 0.929 for speed step T3. This phenomenon is shown in Figure 3, (a,b,c).

It should be noted that *Lee and Martini* (*2018*) obtained the hardest butter when the cream was ripened at 5°C at a beater speed of 240 rpm, respectively at 10°C and a speed of 40 rpm, i.e. for cold cream and higher speed or for cream at a higher temperature and lower speed.

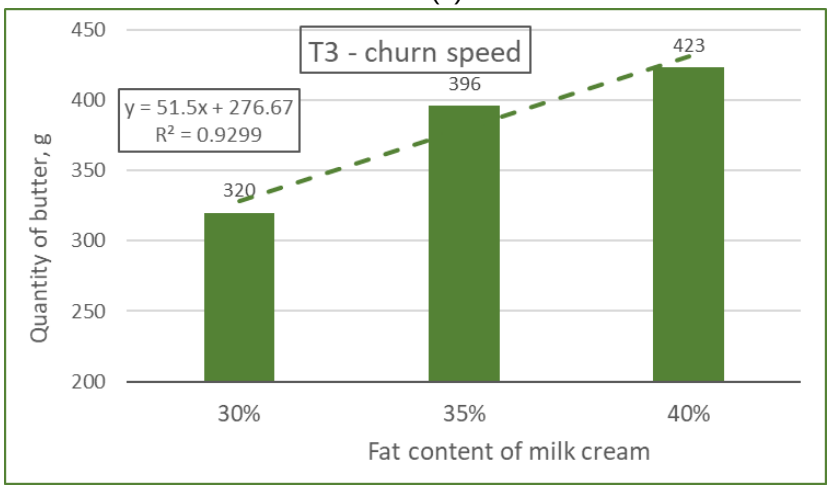
If the cream has higher temperature, and the churning speed is also higher, then a softer butter with a higher water content is obtained. The work of these authors shows that the hardness of the butter can be adapted by changing the ripening conditions of the cream, respectively by correlating it with the speed of the stirring paddle(s).



(a)



(b)



(c)

Fig. 3 - The variation of the amount of butter obtained during beating, depending on the fat content of the cream, for the three speeds of the mixer (a,b,c)

Therefore, the aging temperature of the cream and the convenient choice of the functional parameters of the cream are very important.

The cream ripening temperature and stirring speed have an effect on lipid crystallization and processing behaviour, respectively on butter hardness.

Figure 4 shows the variation of the beating time, in order to separate the butter, for the three speed steps of the agitator, from 1000 rpm to 3000 rpm , at the three fat contents of the cream.

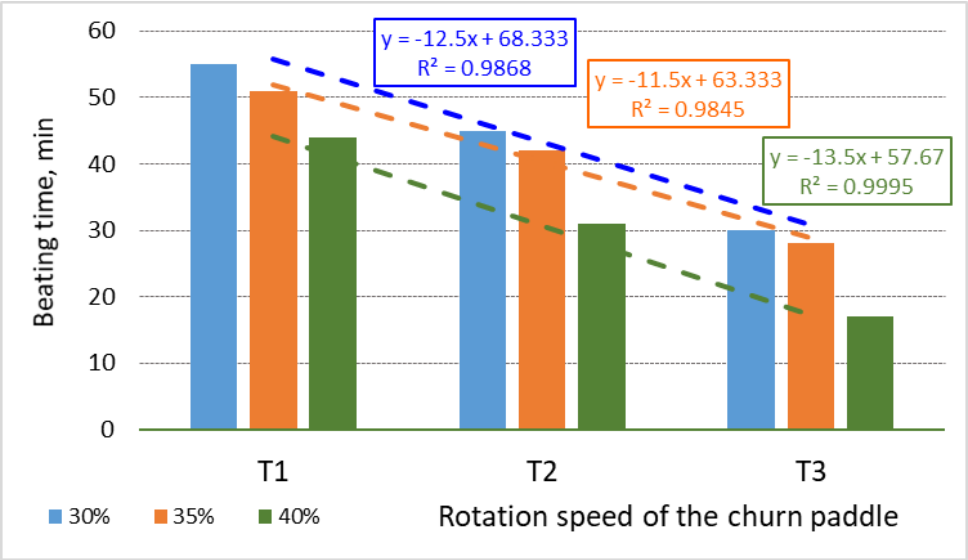


Fig. 4 - The variation of the churning time, depending on the fat content of the cream, for the three speeds of the mixer

As stated before, the churning time decreases with both the speed of the agitator and the increase of the fat concentration, showing a decreasing linear variation. For the three speed steps, increasing the correlation coefficient R^2 of the beating time with the speed of the agitator, also shows decreasing values from 0.987 for cream with a fat content of approx. 30% to 0.999 for cream with a fat content of approx. 40 % (Fig. 4).

It should be mentioned that all the cream used in the experiments was kept in the refrigerator overnight, and batches of 1.5 kg were taken from the total quantity of cream to perform each experiment, so that the cream subjected to the tests had a starting temperature of experiment of about 10 °C. This value supports the statement from the work of the authors *Kalla et al. (2016)*, who mention that the optimum parameters of stirring time and moisture content were obtained when the cream was stirred at a churning temperature of 10 °C. Using suitable conditions of temperature and speed, high quality butter can be produced also in domestic or laboratory conditions.

Table 3

Experimental parameters of electric potential

	Product 1		Product 2		Product 3	
The speed of the stirring paddle	Dry matter (%)	Fat (%)	Dry matter (%)	Fat (%)	Dry matter (%)	Fat (%)
Step 1	66.53	65.3	70.43	69.09	81.43	80.3
Step 2	66.84	64.44	69.84	68.54	80.84	79.31
Step 3 (3000 rpm)	67.02	63.19	69.02	67.81	80.52	78.81

From the works studied and from our observations, it was found that it is necessary to wash the butter with cold water, several times, after draining the buttermilk. The cleaner the butter is, the more resistant it becomes to usual storage conditions, not going rancid for a longer time, especially if it is well pressed. After that, the butter must be cooled and removed from the mold. Normally, from 100 litres of milk, 8 to 12 litres of cream can be obtained, respectively about 4 kg of butter and 5-6 litres of buttermilk, which can be bottled or further processed.

When analysing the dry matter and the fat of the resulting finished product, the following values were obtained.

The results obtained do not show significant differences, and the fat content of the finished product is different in the three samples because cream with different fat content was used, under different processing conditions.

For raw material with high fat content the water content of the butter decreases, and this aspect is important because the legislation takes into account only the non-fat dry substance for butter.

In this situation, it can be argued that the speed does not have a major impact on the physico-chemical parameters, but as can be observed, at higher speeds the losses are significant.

The determined values classify the obtained butter, according to the product standard, either as type A table butter, the first 2 products, or superior butter for the third one.

From the obtained result, at a fat content approx. 30% of the cream, the yield in butter obtained at low speeds of rotation was 27.7%, while for a rotation of 3000 rpm a yield in butter obtained was only 21.3 %. If the fat content of the cream is approx. 40%, then the yield in butter obtained also increases, so that its values become 35.1% for low speed and 28.2% for high churning speed.

CONCLUSIONS

In correlation with the research of other specialists in the field, the initial characteristics of the cream influence the physico-chemical characteristics of the butter. For the experimental tests presented in this paper, a manufactured electric churn with a single semi-helical stirring paddle, arranged horizontally at the end of a vertical shaft, was used. The speed of the agitator was adjustable in three steps, and the maximum speed specified on the electric motor was 3000 rpm.

The research carried out showed that the higher the speed of the stirring paddle is, the smaller the churning yield obtained, regardless of the initial fat content of the cream.

In addition, the functional parameters of the butter churn are very important for the final characteristics of the butter. Thus, the churning time decreases linearly with the increase of the speed of the mixer and with the increase of the fat content of the cream, until phase separation (butter grains from buttermilk).

For the samples where a higher speed was used, there were higher losses of fat in the buttermilk, which causes a low butter yield of the process.

REFERENCES

[1] Amare, G. (2020). Operational and User manual for Manually Operated Butter Churner, Bahir Dar, Ethiopia, *Technical Report*, 11 pages, DOI: 10.13140/RG.2.2.35915.82724.

[2] Asresie, A., Seifu, E., Kurtu, FY (2013). Churning efficiency and microbial quality of butter made from camel milk alone and blending it with goat milk, *Net Journal of Agricultural Science*, 1(3): 75-80, https://www.netjournals.org/pdf/NJAS/2013/3/13-029.pdf.

[3] Avramis, C.A., Wang, H, McBride, B.W., Wright, T.C., Hill, A.R. (2003). Physical and Processing Properties of Milk, Butter, and Cheddar Cheese from Cows EDF Supplement Fish Meal, *Journal of Dairy Science*, 86(8), 2568–2576, doi: 10.3168/jds.S0022-0302(03)73851-X.

[4] Bornaz, S., Fanni, J., Parmentier, M. (1995). Heat treatment of cream: A model of the butter textures response in relation with triglycerides composition. *Journal of the American Oil Chemists ' Society*, Vol. 72, pp. 163–169, https://doi.org/10.1007/BF02638894.

[5] Buldo, P., Kirkensgaard, JK, Wiking, L. (2013). Crystallization mechanisms in cream during ripening and initial butter churning, *Journal of Dairy Science*, 96(1): 6782-6791, https://doi.org/10.3168/jds.2012-6066.

[6] Celik S., and Bakirci I. (2000). A study on the physical and chemical properties of cookery-type butter, *Pakistan Journal of Biological Sciences*, Vol.3 Iss . 4 pp. 596-598, DOI: 10.3923/pjbs.2000.596.598.

[7] Chudy, S.M., Cais-Sokolińska, D., Tomaszewska-Gras, J. (2022). Physicochemical Characteristics and Consumers' Preferences for Milk Fat Products. *Applied Science*, *12*, 11986. https://doi.org/10.3390/app122311986

[8] Frede, E., Buchheim, W. (2007). Buttermaking and the churning of blended fat emulsions, International *Journal of Dairy Technology*, 47(1): 17 – 27, DOI: 10.1111/j.1471-0307.1994.tb01266.x.

[9] Funahashi, H., Horiuchi, J. (2008). Characteristics of the churning continuous butter manufacture and modeling using an artificial neural network, *International Dairy Journal*, Vol. 18, Iss. 3, 323-328, https://doi.org/10.1016/j.idairyj.2007.08.001.

[10] Kalla, A.M., Sahu C., Agrawal A.K., Bisen P., Chavhan B.B., Sinha G. (2016). Development and performance evaluation of frustum cones shaped churn for small scale production of butter, *J. Food Sci Technology*. 53(5): 2219–2226, https://doi.org/10.1007/s13197-015-2110-y.

[11] Lapcikova, B.; Lapcik, L.; Valenta, T.; Kučerová, T. (2022). Functional and quality profile evaluation of butters, spreadable fat, and shortenings available from Czech market, *Foods*, 11(21):3437, https://doi.org/10.3390/foods11213437.

[12] Lee, J., Martini S. (2018). Effect of aging cream temperatures and agitation on butter properties, *Journal of Dairy Science*, 101(9): 7724-7735, https://doi.org/10.3168/jds.2018-14725.

[13] Matuszek, T. (2010). Rheological Properties of Lipids. In Chemical and Functional Properties of Food Lipids; Eds. Sikorski, Z.E., and Kolakowska, A.; CRC Press: New York, NY, USA; pp. 61–79, https://doi.org/10.1201/9781003040392.
[14] Mtibaa, I.; Zouari, A.; Attia, H.; Ayadi, MA; Danthine, SM (2021). Effects of Physical Ripening Conditions and Churning Temperature on the Butter-Making Processor and the Physical Characteristics of Camel Milk Butter, Food and Bioprocess Technology, 14(2):1-11, https://doi.org/10.1007/s11947-021-02649-4.
[15] Panchal, B.; Truong, T.; Prakash, S.; Bansal, N.; Bhandari, B. (2021). Influence of Emulsifiers and Dairy Ingredients on Manufacturing, Microstructure, and Physical Properties of Butter, Foods, 10(5), https://doi.org/10.3390/foods10051140.
[16] Pavlova, T.A.; Dunaev, A.V.; Danilova, E.S. (2022). Technology of producing butter with long-term storage from goat milk. *IOP Conf. Ser. Earth Environ. Sci.,* 1, 12047, doi:10.1088/1755-1315/1052/1/012047.
[17] Pădureţ, S. (2021). The Effect of Fat Content and Fatty Acids Composition on Color and Textural Properties of Butter. *Molecules*, *26*, 4565. https://doi.org/10.3390/molecules26154565.
[18] Rønholt, S.; Kirkensgaard, J.J.K.; Pedersen, T.B.; Mortensen, K.; Knudsen, J.C. (2012). Polymorphism, microstructure and rheology of butter. Effects of cream heat treatment. *Food Chemistry,* 135, 1730–1739, https://doi.org/10.1016/j.foodchem.2012.05.087.
[19] Rønholt, S.; Madsen, A.S.; Kirkensgaard, J.J.K.; Mortensen, K.; Knudsen, J.C. (2014). Effect of churning temperature on water content, rheology, microstructure and stability of butter during four weeks of storage. *Food Structure,* 2, 14–26, https://doi.org/10.1016/j.foostr.2014.07.001.
[20] Serdaroglu, M., Öztürk, B., Kara, A. (2015). An Overview of Food Emulsions: Description, Classification and Recent Potential Applications. *Turkish Journal of Agriculture - Food Science and Technology*, 3, 430, https://doi.org/10.24925/turjaf.v3i6.430-438.336.
[21] Siddique, F., Khan, KS, Ahmad, A., Ahmed, A., Gulfraz M., Wattoo, F.H. (2011). Development and optimization of sweet cream butter from buffaloes at cottage scale, *African Journal of Biotechnology*, 10(75), 17265-17274, https://doi.org/10.5897/AJB11.2049.
[22] Sinha, G., Kalla, AM, Sahu, C., Agrawal, AK, Khare, A., Choudhary, KK, Shrivastava, A. (2015). Development and evaluation of improved small scale butter churn, *International Journal of Research Studies in Biosciences (IJRSB),* 54-59, https://www.researchgate.net/publication/292971424.
[23] Sun, J.F., Kitamur, Y., Satake, T. (2008). Application of Stirling cooler to food processing: Feasibility study on butter churning, *Journal of Food Engineering*, 84(1): 21-27, https://doi.org/10.1016/j.jfoodeng.2007.04.020.
[24] Tsedey, A., Bereket, Z., Genene T. (2018). Implications of introducing improved butter churner on churning time and butter making efficiency, *Research & Reviews*: *Journal of Food and Dairy Technology*, 6(2).
[25] Vithanage, C.R., Grimson, M.J., Smith, B.G. (2009). The effect of temperature on the rheology of butter, spreadable blend and spreads, *Journal of Texture Studies*, 40(3): 346 – 369, https://doi.org/10.1111/j.1745-4603.2009.00186.x.
[26] Wright, A.J., Scanlon, M.G., Hartel, R.W., Marangoni, A.G. (2001). Rheological properties of milkfat and butter. *J. Food Sci.,* 66, 1056–1071, https://doi.org/10.1111/j.1365-2621.2001.tb16082.x.
[27] *** Regulation (EU) No 1308/2013 establishing a common organisation of the markets in agricultural products, Romanian Law on milk and dairy products, 307/2022.
[28] *** Romanian Order 524 / 2002 for the approval of the Norm regarding the names under which they are sold, and the quality conditions of spreads intended for commercialization.
[29] *** International Organization for Standardization. (2010). *Milk, cream and evaporated milk - Determination of total solids content* (ISO 6731:2010) (Reference method)
[30] *** International Organization for Standardization. (2001). *Butter - Determination of moisture, non-fat solids and fat contents - Part 1: Determination of moisture content* (ISO Standard No. ISO 3727-1: 2001 / IDF 80-1) (Reference method).
[31] *** International Organization for Standardization. (2001). *Butter - Determination of moisture, non-fat solids and fat contents — Part 2: Determination of non-fat solids content* (Reference method). (ISO Standard No. ISO 3727-2: 2001 / IDF 80-2).
[32] *** International Organization for Standardization. (2003). *Butter - Determination of moisture, non-fat solids and fat contents - Part 2: Calculation of fat content*. (ISO Standard No. ISO 3727-3: 2003 / IDF 80-2)

DESIGN AND EXPERIMENTAL OPTIMIZATION OF ROTARY CUTTING SAFFLOWER HARVESTING END EFFECTOR

/

回转切割式红花采收末端执行器设计与试验优化

Puhang LI, Xinyue ZHANG, Hao ZHANG, Zeyu WANG, Shiwei WEN, Jun CHEN*
College of Mechanical and Electronic Engineering, Northwest A&F University, Yangling 712100/China
Tel: +86-13572191773; E-mail: chenjun_jdxy@nwsuaf.edu.cn
DOI: https://doi.org/10.35633/inmateh-71-60

Keywords: *safflower harvesting; rotary cutting tool; end effector; gear transmission; Fluent simulation*

ABSTRACT

Aiming at the problems of high damage rate and loss rate of the existing safflower harvesting equipment, this study designed a rotary cutting safflower harvesting end effector by combining the growth characteristics and mechanical properties. Through force analysis of the cutting tool, the key factors, which affects the harvesting performance, were clarified to be the blade inclination and the knife shaft speed. The Fluent software was used to analyze the flow field of the harvesting chamber, which aims to determine the appropriate wind speed. To improve the working performance of the rotary cutting safflower harvesting end effector, a three-factor, three-level orthogonal test was carried out with the blade inclination, knife shaft speed and wind speed as the influencing factors, and with the recovery rate, damage rate and loss rate as the response indexes. A regression model for the three-factor interaction was developed and optimized based on the results of the Box-Behnken test. The optimal parameter combination is: the blade inclination is 15°, the knife shaft speed is 1570, and the wind speed is 6 m/s. A test of the optimization results showed that the recovery rate was 91.47%, the damage rate was 7.51%, and the loss rate was 4.67%. This study can provide theoretical basis and technical reference for the mechanized harvesting of safflower.

摘要

针对现有红花采收装备存在损伤率高、采净率低等问题，该研究结合红花植株生长特点及力学特性，设计了一种回转切割式红花采收末端执行器。通过对刀具进行受力分析，明确了影响采收性能的关键因素为刀刃倾角和刀轴转速；利用Fluent软件对采收腔室流场进行分析，确定适宜的入口风速。为提升回转切割式红花采收末端执行器的工作性能，以刀刃倾角、刀轴转速和入口风速为影响因素，以花丝采净率、损伤率、掉落率为响应指标，进行三因素三水平正交试验。根据Box-Behnken试验结果建立了三因素交互作用的回归模型并对其进行优化，获得最优参数组合为：刀刃倾角15°，刀轴转速1570rpm，入口风速6m s^{-1}。对优化结果进行试验验证，结果表明，采净率为91.47%，损伤率为7.51%，掉落率为4.67%。该研究可为红花机械化采收提供理论依据和技术参考。

INTRODUCTION

Safflower is an important cash crop in China, with extremely high value in medical, food and economy (*Ren et al., 2017; Wang et al., 2006; Xue et al. and Li, 2005*). A survey shows that China's safflower planting area has reached 33,300 hectares, and its origin is mainly concentrated in Xinjiang, Yunnan, Gansu, Ningxia, Henan and other regions (*Zhou et al., 2021*).

Recently, the mechanized harvesting of crops has become a hot topic (*Hu et al., 2020, 2021, 2022; Joao et al., 2011; Jobbagy et al., 2021; Pu et al., 2023; Zhang et al., 2021*). In terms of safflower harvesting, scholars have carried out relevant research, and it mainly focus on the methods of pneumatic, pulling, combing, cutting and so on (*Zhang et al., 2019*). *Cao et al.* (*2019*) developed a comb-type safflower harvesting machine, which realized the plucked picking of filaments through the rotating action of the harvesting shaft. This way the mechanized blind harvesting was realized and the efficiency of safflower harvesting was improved, but it had a high rate of missed harvesting. *Zhang et al.* (*2020*) developed a portable roller-type safflower harvester, where the manual hand-held picking head was aligned with the filaments so as to feed the filaments into the rollers, and the pulling force generated by the high-speed rotation of the rollers picked the filaments, which was able to reduce labor intensity and improve the harvesting efficiency. *Zhang et al.* (*2022*) designed a three-finger pull-out safflower picking end effector, where the filaments were harvested by three harvesting fingers

using pulling. *Zhang et al.* (*2022*) designed a double-acting opposite direction cutting end effector for safflower harvester, which was driven by a cam to realize the low-speed clamping and cutting of filaments. It effectively reduced the damage rate in harvesting, and realized the low-damage rate of the filaments harvesting.

Above all studies, the damage to the structure of the filaments is the greatest weakness of the existing safflower harvesting devices. In this study, high recovery rate, low damage rate and low loss rate are the design objectives to improve the quality of mechanized safflower harvesting. This study combined the growth characteristics and mechanical properties of safflower to design a rotary cutting safflower harvesting end effector. The structural and motion parameters of the key components were theoretically analyzed. The factors of the performance indexes were determined and the prototype and the field test were carried out, which was intended to provide reference for the design and optimization of safflower harvester.

MATERIALS AND METHODS

Safflower characteristics

Physical properties of safflower are the basis for the design of safflower harvesting end effector. The measurement was carried out at Gongchuang Planting Specialized Cooperative, Yuanzhou District, Guyuan City, Ningxia Hui Autonomous Region, from July 20 to 30, 2023. The main varieties are Yu Hong No. 3, as shown in Figure 1. The five-point method was used for field sampling, and 20 safflower plants in full bloom were selected from each sampling point to obtain the main characteristics of safflower, as is shown in Table 1.

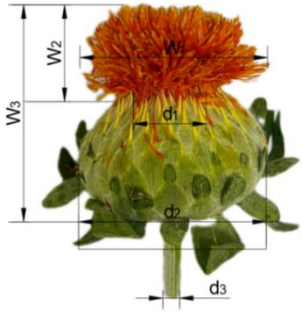


Fig. 1 - The schematic diagram of physical properties of safflower

Table 1

Physical characteristics of safflower

Type	Mean ± standard deviation	95% confidence interval	P value（S-W）
Filament banner(w_1/mm)	32.98 ± 3.7	31.92~34.04	0.38505
Filament length(w_2/mm)	19.12 ± 2.59	18.38~19.86	0.37784
Safflower height(w_3/mm)	40.68 ± 3.38	39.72~41.64	0.14341
Necking Diameter(d_1/mm)	7.54 ± 1.05	7.24~7.84	0.07363
Flower bulb diameter(d_2/mm)	30.58 ± 3.70	29.53~31.63	0.14108
Flower stem diameter(d_3/mm)	3.024 ± 0.41	2.91~3.14	0.77226

Overall structure and principle

As is shown in Figure 2, the safflower harvester is mainly composed of an electronic control system, binocular camera, three-axis robotic arm, rotary cutting safflower harvesting end effector, collection device and walking device.

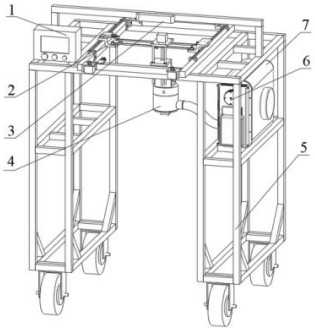


Fig. 2 - The safflower harvester structure schematic diagram

1 - electronic control system; 2 - three-axis robotic arm; 3 - binocular camera; 4 - rotary cutting safflower harvesting end effector; 5 - walking device; 6 - negative pressure fan; 7 - collection device

After the binocular camera acquires the spatial position information of the safflower, the electronic control system adjusts the three-axis robotic arm to align the end effector with the filaments for harvesting, and the cut filaments are collected to the filament collection device through the conveying pipeline under negative pressure fan.

Design and analysis of key components

- ***Rotary cutting end effector structural design***

The structure of the rotary cutting end effector is shown in Figure 3, which mainly consists of stepping motor, transmission gear set, filament feeding status monitoring device, cutting tool, conical feeding device, negative pressure pipeline, cutting disk and housing. Its working principle is: the suction force generated by the negative pressure fan sucks up the safflower filaments and keeps the vertical state. Then the safflower is fed into the feeding device. Meanwhile, the filament feeding status monitoring device real-time monitors the distance between the filaments and the device. When safflower arrives at the appropriate harvesting position, the stepping motor is controlled to start to drive the cutting tool rotating to achieve rotary cutting, so that the filaments and the ball of flower can be separated. Under negative pressure, the separated filaments are adsorbed to the filament collection box through the negative pressure pipeline. The collection of filaments is completed.

The rotary cutting tool is the key component of the filament harvesting mechanism. During operation, the three knives rotate under the motor drive, and the knives hold the filaments to cut them off. Under the adsorption force of the negative pressure fan, the filaments remain vertical and converge, which ensures the integrity of the cut filaments, reduces the damage rate of the filaments and improves the recovery rate. Based on the safflower characteristics, the parameters of the filament harvesting mechanism was designed, and the key factors affecting the recovery rate were determined by analyzing the force and speed of filaments under the action of the rotary cutting tool.

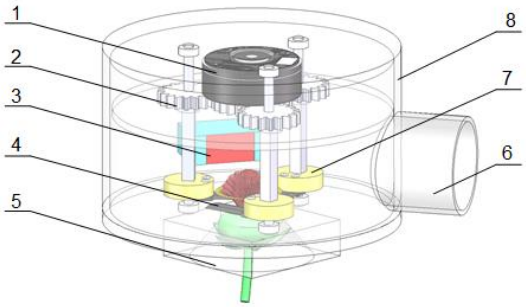


Fig. 3 - The diagram of the rotary cutting end effector

1 - stepping motor; 2 - transmission gear set; 3 - filament feeding status monitoring; 4 - cutting tool; 5 - conical feeding device; 6 - negative pressure pipeline; 7 - cutting disk; 8 - housing

The stepping motor is PM3505 head brushless motor, which is characterized by small size, high torque and light weight. This motor can effectively reduce the volume of the end effector and is more suitable for the field of safflower picking end effector. At the same time, the PM3505 motor is equipped with AS5600 encoder, which can be controlled by the controller to reset the motor after each cutting operation. This function can avoid blocking the flower feeding port, so as to ensure the smooth feeding of filaments for the next cutting. The transmission gear set is connected to the PM3505 head brushless motor, which can adjust the rotation speed of the cutting tool according to the operational requirements. During operation, three knives of the rotary cutting set rotate from the outside to the inside to cut the filament, which can expand the cutting radius of the rotary cutting set. The reset function of the motor and the filament feeding status monitoring device work together to change the saffron filament cutting effect.

- ***Filament clamping cutting analysis***

To avoid the filament sliding out along the blade due to the excessive tilt angle, which can result in uneven resistance to damage the filament *(Pang, 1982)*, the force state of the filament during the cutting process is analyzed to obtain the best cutting effect. As is shown in Figure 4, Take the necking center point *O* as the object of study, the particle *O* is subjected to positive blade pressure $F_{a,}F_{b,}F_{c}$ and blade friction $N_{a,}N_{b,}$ N_{c} of the three knives. Since the initial position angle between each two of the three knives is 120°, both the angle *α* and the angle *β* are 30° when all knives are tangent to the necking of the flower bulb (just when the filament begins to be cut). Since the rotation speeds of knife A, knife B and knife C are the same, the positive pressure on the cutting blades of the three are also equal, which means $F_a = F_b = F_c$.

According to the friction equation, the edge friction is shown in Equation (1).

$$N_i = F_i f \tag{1}$$

where: i - the number of knife (i =*a, b, c, corresponding to the knives A, B, C*);

f - friction coefficient of cutting tool on filament.

As the positive pressure F_a, F_b, F_c of the cutting blade are equal, so the blade friction N_a, N_b, N_c of the three are also equal. With the particle *O* as the origin, with the direction of the cutting blade curve and its normal for the *x*, *y* axis respectively to establish a coordinate system, Equation (2), (3) are as follows.

$$N_a \cos\alpha = N_b \cos\beta \tag{2}$$

$$N_a \sin\alpha + N_b \sin\beta = N_c \tag{3}$$

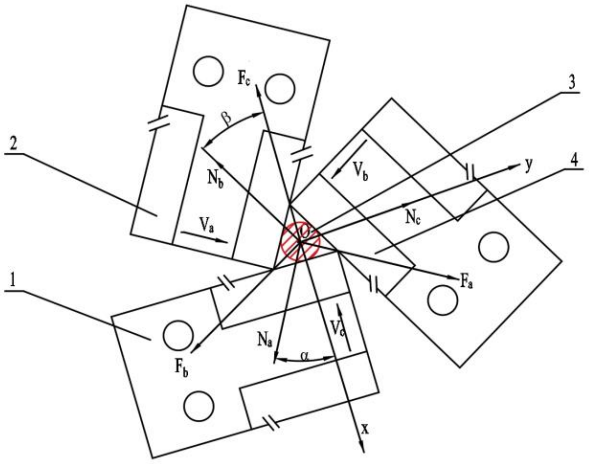


Fig.4 - Force analysis diagram for filament clamping and cutting

1 - knife C; 2 - knife A; 3 - flower bulb necking; 4 - knife B

Combined with the above analysis, the force on the particle *O* is in equilibrium, and the combined force generated by the positive pressure F_a, F_b, F_c and friction N_a, N_b, N_c is in the same straight line. The filaments will remain relatively stable during the cutting process, and will not produce the phenomenon of slippage.

- ***Analysis of cutting resistance of blade***

To reduce the filament damage and fragmentation caused by the impact of the knives, and to reduce the filament damage rate, the composition of the blade cutting resistance force system and the force situation were analyzed. To simplify the analysis model, the cutting force of the three knives is analyzed two by two.

The necking of the flower bulb is a collection of filaments wrapped in sepals, and when cutting filaments from the necking, it is analyzed as a whole unit. When cutting filaments, the cutting blade of the knives and the cutting surface are the main parts that cut off the filaments and withstand the cutting resistance. As is shown in Figure 5, at the moment of cutoff, the cutting resistance of the blade mainly includes: reaction force of the cut filament on the blade R_c, reaction force of the extruded filament on the lower blade R_{zg1}, reaction force of the extruded filament on the lower blade $R_{d1,}$ friction T_1 and pressure of the cutting filament on the upper blade surface *mg,* reaction force of the extruded filament on the upper blade $R_{zg2,}$ reaction force of the extruded filament on the lower blade $R_{d2,}$ friction T_2, just as the Equation (4)~(7) shows.

$$T_1 = fR_1 \tag{4}$$

$$R_1 = R_{zg1} \sin\delta + R_{d1} \cos\delta \tag{5}$$

$$T_2 = f(R_2 + mg\cos\delta) \tag{6}$$

$$R_2 = R_{zg2} \sin\delta + R_{d2} \cos\delta \tag{7}$$

where:

R_1 - reaction force of filaments on the lower blade, [N];

R_2 - reaction force of filaments on the upper blade, [N];

m - quality of filaments, [kg];

f - friction coefficient of blade to filaments.

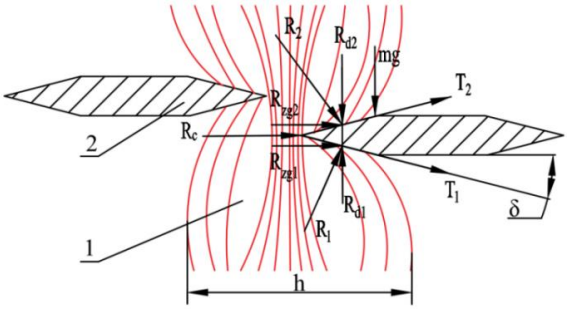


Fig. 5 - Cutting mechanics analysis of blade

1 - safflower filaments; 2 - blade

When extruded, the stress and strain of the filament conforms to the generalized Hooke's law, then the stress-strain relationship when the filaments are extruded by the blade is shown in Equation (8).

$$\varepsilon = \frac{h_{zg}}{h} \approx \frac{\sigma}{E} \tag{8}$$

where: ε- relative density of filaments;

h_{zg} - thickness of extruded filaments on one side of the knife, [mm];

h - total thickness of filaments on one side of the knife, [mm];

σ- extrusion stress on filaments, [Pa];

E - modulus of elasticity of filaments, [Pa].

Substitute equation (8) into equations (5) and (7), according to Pusytgin correlation theory (*Li, B., 2005*), R_{zg1} and R_{zg2}, R_{d1} and R_{d2} are approximately equal respectively. Integrate the unit width dh_{zg} and unit force dR_{zg1}, dR_{zg2} yields Equation (9).

$$R_{zg1} = R_{zg2} = \frac{E}{h}\tan\delta\int_0^{h_{zg}} h_{zg}dh_{zg} = \frac{E}{2h}h_{zg}^{\ 2}\tan\delta \tag{9}$$

The unit reaction force dR_{d1} caused by the lateral pressure of the blade is shown in Equation (10).

$$dR_{d1} = dR_{d2} = \mu\varepsilon E dh_{zg} \tag{10}$$

where: μ - filaments Poisson ratio.

$$R_{d1} = R_{d2} = \mu\frac{E}{h}\int_0^{h_{zg}} h_{zg}dh_{zg} = \mu\frac{E}{2h}h_{zg}^{\ 2} \tag{11}$$

To realize the cutting process, the cutting force P of the blade has to be satisfied with Equation (12)~(13).

$$P \geq R_c + R_{zg1} + R_{zg2} + T_1 + T_2 \tag{12}$$

$$R_c = \Delta l_2 \sigma_s \tag{13}$$

where: Δ- thickness of the blade, [mm];

l_2 - effective length of the blade, [mm].

Cutting resistance is maximized at the point where the neckdown is about to be completely severed, which means $h_{zg} = h$. The cutting force P can be obtained as Equation (14).

$$P = \Delta l_2\sigma_s + EH\left[\tan\delta + f(\sin\delta\tan\delta + \mu c\,\mathrm{os}\,\delta)\right] + mgf\cos\delta \tag{14}$$

According to the physical characteristics of filaments, the modulus of elasticity of filaments is 2.5×10^6Pa, and the Poisson ratio of filaments is 0.25. Substituting the characteristic parameters of filaments into Equation (14), it can be seen that the cutting force P increases with the increase of the inclination angle of the blade, and the trend of the increase is smaller when δ is satisfied with 10°≤ δ ≤20°. Combined with the above analysis, to reduce the cutting force required for separation and to reduce the harvesting damage rate, 10°≤ δ ≤20°was selected as the test factor for filament cutting performance.

- ***Analysis of cutting speed***

To effectively reduce the filament damage rate, the cutting speed of rotary cutting tool was analyzed (*Li et al., 2020*). Since the blade is straight, the radius of rotation at each point of the blade is different when the tool rotates to cut, so the linear velocity *v* is also different. During operation, the safflower was fed by the robotic arm to the appropriate position after the cutting tool rotates and cuts at high speed. The linear velocity *v* can be calculated by Equation (15).

$$v = 2\pi nr \tag{15}$$

where: n - knife rotational shaft speed, [rpm];

r - actual cutting tool radius, [mm].

Combined with the characteristics of safflower, the actual cutting radius of the tool *r* ranges from 26 to 40 mm. According to the previous test, knife shaft speed ranges between 1200-1800 rpm. With the Equation (15) for calculating, the blade linear velocity *v* is 3.27~7.54 $\mathrm{m\ s^{-1}}$. The larger the knife shaft speed *n* is, the larger the blade linear velocity *v* is. Comprehensive analysis of the above, the knife shaft speed *n* was selected as the key factor affecting the effect of harvesting, and the value range is rounded to 1200~1800 rpm.

- ***Design of filament feeding status monitoring device***

The precision of filament cutting position is the key to reduce filament breakage (*Zhang et al., 2022*). The current harvesting method is difficult to meet the demand for accurate positioning, which is easy to cause damage to filament. In this study, a method of infrared sensor to monitor the filament cutting position was proposed. The filament feeding status monitoring device is schematically shown in Figure 6, which consists of detection component, transmitting component and receiving component. According to the real-time monitoring of safflower filaments and infrared sensor distance, it is possible to determine whether the end effector has reached the proper harvesting position (*Zhang et al., 2022*).

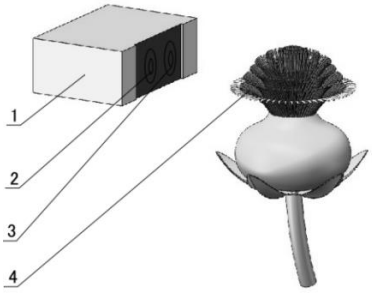


Fig. 6 - Schematic structure of filament feeding status monitoring device

1 - detection component; 2 - transmitting component; 3 - receiving component; 4 - safflower

- ***Simulation analysis of flow field in harvesting chamber***

The flow field generated by the negative pressure collection system is the key to the filament recovery rate. The flow field carries the lightweight filaments through the harvesting chamber and reaches the filament collection box through the conveying pipeline. Fluent software was used to analyze the flow field inside the harvesting chamber to find out the characteristics of the airflow inside the chamber, and the key factors affecting the filament harvesting effect were determined, which provides a theoretical basis for the optimization of the structural parameters of the rotary cutting end effector.

The wind speed is the key parameter that determines whether the filaments can be kept in a vertical state. It also influences whether the cut filaments can be transported to the collection box smoothly. The value is determined by the operating air volume of the negative pressure fan. According to the replacement principle *(Dai, 2008)*, the air volume of the fan should be the volume of the inner chamber of the harvesting device, as is shown in Equation (16).

$$V_f = \frac{Q}{STK} \tag{16}$$

Where: Q - rated air volume of fan, [$\mathrm{m^3}$];

S - inlet cross-section of feeding device, [$\mathrm{m^2}$];

T - the time it takes to cut a safflower down, [s];

K - coefficients that take into account the attenuation of the airflow and losses along the way (K=1.3~1.6).

It was experimentally determined that S = 0.1m^2 and T = 1s. Combined with Equation (16), the wind speed ranges from 3 to 7 $\mathrm{m\ s^{-1}}$.

According to the calculated wind speed, numerical simulation of the chamber flow field under the action of the negative pressure fan was carried out. The velocity distribution vector diagram of the chamber flow field was obtained, as shown in Figure 7. The airflow forms a high-speed area with a large area at the chamber entrance and chamber exit. Due to the existence of the guide port, the flow field layout is relatively straight, which is beneficial to the efficient collection of filaments. The analysis shows that the harvesting end effector chamber and the rotary cutting tool are the key structures affecting the distribution of the flow field for filament harvesting. The fluid motion characteristics inside the chamber is in line with the expected effect, which can realize the function of efficiently collecting safflower.

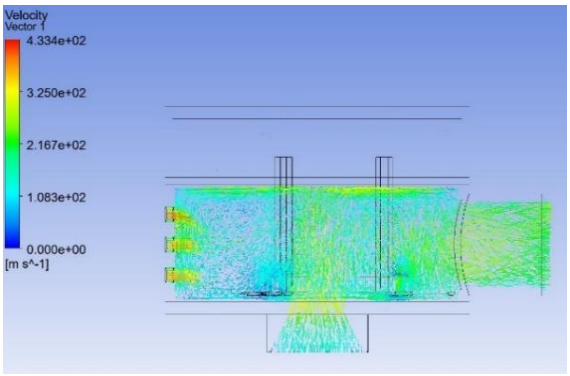


Fig. 7 - Vector diagram of flow field velocity in the harvesting chamber

Experimental materials and equipment

The orthogonal test of cutting end effector was carried out in July 2023 in the laboratory of Northwest Agriculture and Forestry University (NWAFU), and the test safflower was "Yu Hong No. 3" planted by Gongchuang Planting Specialized Cooperative, Yuanzhou District, Guyuan City, Ningxia Hui Autonomous Region. The test equipment is the designed rotary cutting end effector and the collection device, which consists of a centrifugal fan, a lithium battery, a collection box and a collection hose. The test instruments mainly include electronic balance (Suzhou Jutian Instrument and Equipment Co., Ltd., range: 0-3000g, precision 0.01g), SW-6234C tachometer (Speed Group Co., Ltd., range 2.5~99999rpm, precision 0.1rpm) and so on.

Experimental methods

- ***Determination of influencing factors***

Based on the previous analysis, combined with the structure and working parameters of the designed rotary cutting safflower harvesting end effector, the three key factors affecting the harvesting effect were selected as blade inclination, knife shaft speed and wind speed.

(1) Blade inclination: According to the preliminary calculations, the larger the blade inclination, the more unstable the cutting process, which is more likely to push down the filament and cause greater damage to the filament. On the contrary, the smaller the blade inclination, the service life of the cutting tool will be reduced, making the knife easy to break. According to the pre-test, the blade inclination selection range is more suitable within 10°~20°.

(2) Knife shaft speed: The knife shaft speed determines whether the filaments can be cut down smoothly. If the knife shaft speed is too high, the knife will cut the filaments excessively, which will cause some damage to the filaments and make the quality of the harvested filaments poor. If the knife shaft speed is too low, the filaments will be difficult to be cut down smoothly. According to the pre-test, the knife shaft speed is suitable in the range of 1200~1800 rpm.

(3) Wind speed: The higher the wind speed, the more the filaments will be kept in a vertical state into the harvesting chamber, so that the cutting tool will cut down the filaments completely. In this way, the filaments can be collected into the collecting device smoothly, so as to improve the quality of the filaments harvested. If the wind speed is too low, the filaments are more scattered, which will make the cut down filaments more fragmented. The filaments are prone to be retained in the chamber of the end effector, which will result in the loss of filaments, thus making the quality of the collected filaments poorer. According to the pre-test, the wind speed selection range of 3~7$\mathrm{m\ s^{-1}}$ is more appropriate.

- ***Response indicators***

$$y_1 = \frac{m_1}{m} \times 100\% \quad (17)$$

$$y_2 = \frac{m_2}{m_1} \times 100\% \quad (18)$$

$$y_3 = \frac{m_3}{m} \times 100\% \quad (19)$$

where, y_1 - recovery rate, is the percentage of the mass of filaments harvested to the total mass of filaments;

y_2 - damage rate, is the percentage of the mass of filaments that produced damage versus the mass of filaments that were harvested;

y_3 - loss rate, is the percentage of the mass of dropped filaments to the total mass of filaments;

m - the total mass of the filaments, [g];

m_1 - the filaments harvested, [g];

m_2 - the mass of filaments that produced damage, [g];

m_3 - the mass of dropped filaments, [g].

According to the working performance requirements of the rotary cutting safflower harvesting end effector, the test selected the recovery rate y_1, the damage rate y_2 and the loss rate y_3 as the evaluation indexes of the harvesting effect (*Zhang et al., 2022*), which can be obtained by Equation (17)~(19).

- ***Test design***

To analyze the effects of different blade inclination, knife shaft speed and wind speed of rotary cutting safflower harvesting end effector on the performance of safflower harvesting operation, and to find the optimal parameter combination, according to Box-Behnken test theory, three-factor and three-level analysis test was designed, which analyzes the values of test factors. The test factors and levels are shown in Table 2.

Table 2

Test factors and levels

Levels	Blade inclination x_1 (°)	Knife shaft speed x_2 (rpm)	Wind speed x_3 ($m\ s^{-1}$)
-1	10	1200	3
0	15	1500	5
1	20	1800	7

RESULTS

The test scheme and results are shown in Table 3, with a total of 17 groups of tests, including 12 analytical factors and 5 zero-point estimation errors, with groups 1 to 12 being analytic factorial design tests, and groups 13 to 17 being central design tests (*Wang et al., 2020*).

Test results and analysis

- ***Test program and results***

Table 3

Test results

number	blade inclination x_1	knife shaft speed x_2	wind speed x_3	recovery rate y_1	damage rate y_2	loss rate y_3
1	10	1200	5	90.62	9.11	5.8
2	20	1200	5	87.25	7.32	7.5
3	10	1800	5	91.93	10.21	5.4
4	20	1800	5	91.11	9.62	5.9
5	10	1500	3	90.35	9.44	7.2
6	20	1500	3	89.62	8.53	8.5
7	10	1500	7	92.63	8.72	4.7
8	20	1500	7	90.22	7.65	4.9
9	15	1200	3	86.71	7.72	8.3
10	15	1800	3	88.15	8.64	8.8
11	15	1200	7	86.84	6.46	7.5
12	15	1800	7	91.92	8.52	5.7

number	blade inclination x_1	knife shaft speed x_2	wind speed x_3	recovery rate y_1	damage rate y_2	loss rate y_3
13	15	1500	5	89.01	7.44	6.3
14	15	1500	5	89.24	7.85	6.2
15	15	1500	5	88.86	7.54	5.5
16	15	1500	5	89.07	7.41	5.9
17	15	1500	5	89.42	7.56	5.6

- ***Regression modeling and significance analysis***

The analysis of variance was performed by Design-Expert 8.0 software to establish the coded regression mathematical model of recovery rate, damage rate and loss rate on blade inclination, knife shaft speed and wind speed. Table 4 shows the analysis of variance and significance test of the test results.

As can be seen from Table 4, the fit of the regression model of each factor on recovery rate y_1, damage rate y_2 and loss rate y_3 was highly significant (P < 0.01). For the misfit term, the P value of the three models was greater than 0.05, which was not significant, indicating that the regression model was not misfit. After eliminating the insignificant factors, the regression model of each factor on recovery rate y_1, damage rate y_2 and loss rate y_3 was obtained as Equation (20)~(22).

$$y_1 = 89.12 - 0.92X_1 + 1.46X_2 + 0.85X_3 + 0.64X_1X_2 - 0.42X_1X_3 + 0.91X_2X_3 + 1.70X_1^2 - 0.60X_2^2 - 0.12X_3^2 \quad (20)$$

$$y_2 = 7.56 - 0.54X_1 + 0.80X_2 - 0.37X_3 + 0.30X_1X_2 - 0.040X_1X_3 + 0.28X_2X_3 + 1.13X_1^2 + 0.38X_2^2 - 0.10X_3^2 \quad (21)$$

$$y_3 = 5.90 + 0.46X_1 - 0.41X_2 - 1.25X_3 - 0.30X_1X_2 - 0.28X_1X_3 - 0.57X_2X_3 - 0.50X_1^2 + 0.75X_2^2 + 0.93X_3^2 \quad (22)$$

From the analysis of F value of each factor in Table 4, it can be seen that the three factors affecting the recovery rate are knife shaft speed, blade inclination, and wind speed in descending order of importance. The damage rate is affected by knife shaft speed, blade inclination, and wind speed in descending order of importance. And the loss rate is affected by wind speed, knife shaft speed, and blade inclination in descending order of importance.

Table 4

Analysis of variance of the test results

origin	recovery rate		damage rate		loss rate	
	F value	P value	F value	P value	F value	P value
model	55.30	<0.0001	70.78	<0.0001	15.56	0.0008
X_1	68.91	<0.0001	98.13	<0.0001	8.46	0.0168
X_2	175.26	<0.0001	210.13	<0.0001	8.86	0.0271
X_3	58.95	0.0001	45.84	0.0003	71.28	<0.0001
$X_1.X_2$	16.68	0.0047	14.87	0.0062	2.05	0.1950
$X_1.X_3$	7.24	0.0311	0.26	0.6230	1.73	0.2305
$X_2.X_3$	33.98	0.0006	13.42	0.0080	7.54	0.0287
X_1^2	125.40	<0.0001	221.05	<0.0001	6.00	0.0441
X_2^2	15.36	0.0058	24.78	0.0016	13.51	0.0079
X_3^2	0.61	0.4607	1.83	0.2185	20.54	0.0027
lost proposal	3.54	0.1267	0.53	0.6864	1.94	0.2650

highly significant ($P < 0.01$); insignificant ($P \geq 0.05$); X_i is the level value of x_i, i=1,2,3.

- ***Effect of interaction factors on response functions***

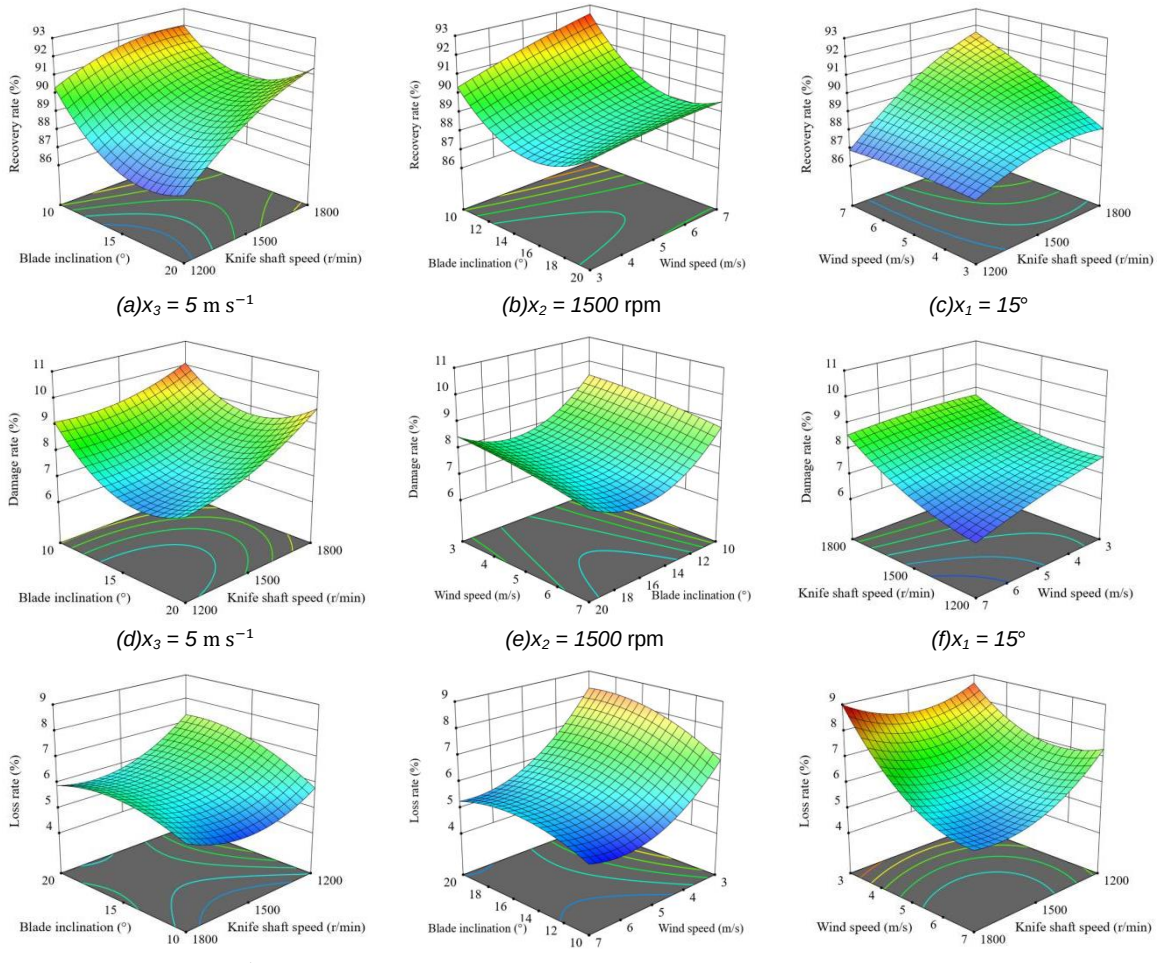
The effects of the three-factor interaction on the recovery rate are shown in Figure 8(a)~(c). From Figure 8(a), it can be seen that when the wind speed is fixed at 0 level (x_3 = 5 m s^{-1}), the response surface curve changes faster along the direction of the blade inclination, which means the effect of the blade inclination on the recovery rate is more significant. From Figure 8(b), it can be seen that when the knife shaft speed is fixed at 0 level (x_2 = 1500 rpm), the response surface curve changes faster along the direction of the blade inclination, which means the effect of the blade inclination on the recovery rate is more significant.

From Figure 8(c), it can be seen that when the blade inclination is fixed at 0 level (x_1 = 15°), the response surface curve changes faster along the direction of the knife shaft speed, which means the effect of the knife shaft speed on the recovery rate is more significant. Therefore, under the premise of meeting the requirements of the recovery rate, a higher knife shaft speed is selected.

The effects of the three-factor interaction on the damage rate are shown in Figure 8(d)~(f). From Figure 8(d), it can be seen that when the wind speed is fixed at 0 level (x_3 = 5 m s^{-1}), the response surface curve changes faster along the direction of the blade inclination, which means the effect of the blade inclination on the damage rate is more significant.

From Figure 8(e), it can be seen that when the knife shaft speed is fixed at 0 level (x_2 = 1500 rpm), the response surface curve changes faster along the direction of the blade inclination, which means the effect of the blade inclination on the damage rate is more significant. From Figure 8(f), it can be seen that when the blade inclination is fixed at 0 level (x_1 = 15°), the response surface curve changes faster along the direction of the knife shaft speed, which means the effect of the knife shaft speed on the damage rate is more significant. Therefore, under the premise of meeting the requirements of the damage rate, a smaller blade inclination is selected.

The effects of the three-factor interaction on the loss rate are shown in Figure 8(g)~(i). From Figure 8(g), it can be seen that when the wind speed is fixed at 0 level (x_3 = 5 m s^{-1}), the response surface curve changes faster along the direction of the knife shaft speed, which means the effect of the knife shaft speed on the loss rate is more significant. From Figure 8(h), it can be seen that when the knife shaft speed is fixed at 0 level (x_2 = 1500 rpm), the response surface curve changes faster along the direction of the wind speed, which means the effect of the wind speed on the loss rate is more significant. From Figure 8(i), it can be seen that when the blade inclination is fixed at 0 level (x_1 = 15°), the response surface curve changes faster along the direction of the wind speed, which means the effect of the wind speed on the loss rate is more significant. Therefore, under the premise of meeting the requirements of the loss rate, a higher wind speed is selected.



(a)x_3 = 5 m s^{-1} *(b)x_2 = 1500 rpm* *(c)x_1 = 15°*

(d)x_3 = 5 m s^{-1} *(e)x_2 = 1500 rpm* *(f)x_1 = 15°*

(g)x_3 = 5 m s^{-1} *(h)x_2 = 1500 rpm* *(i)x_1 = 15°*

Fig. 8 - Effect of interaction factors on response functions

Parameter optimization and validation

- ***Parameter optimization***

To ensure that the rotary cutting safflower harvesting end effector has better working performance, according to the objectives of high recovery rate, low damage rate and low loss rate, the structure and working parameters of the end effector were optimized.

The optimization solution was carried out by using the Optimization-Numerical module in Design-Expert 8.0. The objective function and constraints are shown in Equation (23).

$$\begin{cases} \max y_1(x_1, x_2, x_3) \\ \min y_2(x_1, x_2, x_3) \\ \min y_3(x_1, x_2, x_3) \\ 15 \le x_1 \le 20 \\ 1200 \le x_2 \le 1800 \\ 3 \le x_3 \le 7 \end{cases} \quad (23)$$

After optimization, the best parameter combinations of influencing factors were obtained as follows: blade inclination is 15.31°, knife shaft speed is 1566.63 rpm, wind speed is 6.13 $\mathrm{m\ s^{-1}}$. At this time, the model predicted that the recovery rate was 92.88%, the damage rate was 7.79%, and the loss rate was 4.88%.

- ***Verification test***

The test validation was carried out in July 2023 in Gongchuang Planting Specialized Cooperative, Yuanzhou District, Guyuan City, Ningxia Hui Autonomous Region, rounding the optimized parameter combinations to blade inclination of 15°, knife shaft speed of 1570 rpm, and wind speed of 6 $\mathrm{m\ s^{-1}}$. The test site is shown in Figure 9.



Fig.9 - Field trial validation

To eliminate random errors, the test was repeated 10 times under this parameter combination. And the results were averaged. The recovery rate was 91.47%, the damage rate was 7.51%, and the loss rate was 4.67%. The relative errors with the theoretical optimized values were 0.6%, 0.9%, and 1.5%, respectively, which indicated that the resulting optimal parameter combinations could satisfy the requirements of practical applications.

CONCLUSIONS

(1) Aiming at the problems of high damage rate and low recovery rate during safflower harvesting, this study designed a rotary cutting safflower harvesting end effector. After the filament feeding status monitoring device monitors that the filament arrives at the suitable cutting position, the motor drives the three knives to rotate to realize the cutting of the filament, which can effectively reduce the filament damage rate and improve the recovery rate.

(2) By establishing the mechanical model of tool-filament cutting, the dynamics of filament cutting process was analyzed. According to the theoretical analysis and calculation, it was determined that the blade inclination and the knife shaft speed were the key factors affecting the harvesting effect. Simulation was carried out to analyze the characteristics of the flow field inside the harvesting chamber, and the inlet wind speed was determined as the key factor affecting the harvesting effect.

(3) The Design-Expert software was used to analyze the effects of blade inclination, knife shaft speed and wind speed of the harvesting device on the recovery rate, damage rate and loss rate, respectively. A cubic regression model was constructed to optimize the structure and working parameters of the harvesting device, so as to obtain the optimal parameter combinations of blade inclination of 15 °, knife shaft speed of 1570 rpm and wind speed of 6 $\mathrm{m\,s^{-1}}$. The validation test was carried out in the field. The recovery rate, damage rate and loss rate are 91.47%, 7.51% and 4.67%, respectively, which can meet the requirements of parameter optimization of rotary cutting safflower harvesting end effector.

(4)

ACKNOWLEDGEMENT

The authors appreciate the financial support provided by the National Natural Science Foundation of China (32272001) and the Qinchuangyuan Project of Shaanxi Province (2023KXJ-016).

REFERENCES

[1] Cao, W., Yang, S., Li, S., Jiao, H., Lian, G., Niu, C., An, L. (2019). Parameter optimization of height limiting device for comb-type safflower harvesting machine (梳夹式红花采收机等高限位装置参数优化). *Transactions of the Chinese Society of Agricultural Engineering*, Vol.35, Issue 14:48-56;

[2] Dai, F. (2008). Selection and calculation of the blowing rate of air-assisted sprayers (风送喷雾机风量的选择与计算). *Plant Protection*, Issue 06:124-127;

[3] Hu, G., Bu, L., Chen, J. (2020). Simulation to determination of significant parameters on apple stress for combing harvesting in trellis trained trees. *Scientia Horticulturae*, Vol.274;

[4] Hu, G., Chen, C., Chen, J., Sun, L., Sugirbay, A., Chen, Y., Jin, H., Zhang, S., Bu, L. (2022). Simplified 4-DOF manipulator for rapid robotic apple harvesting. *Computers and Electronics in Agriculture*, Vol.199;

[5] Hu, G., Zhang, E., Zhou, J., Zhao, J., Gao, Z., Sugirbay, A., Jin, H., Zhang, S., Chen, J. (2021). Infield Apple Detection and Grading Based on Multi-Feature Fusion. *Horticulturae*, Vol.7, Issue 9;

[6] Jobbagy, J., Martin, D., Koloman, K., Patrik, B. (2021). Mechanized Grape Harvest Efficiency. *Applied Sciences-Basel*, Vol.11, Issue 10;

[7] Joao, P., Martins, D., Cunha, W. (2011). Operational performance of the mechanized and semi-mechanized potato harvest. *Engenharia Agricola,* Vol.31, Issue 4:826-834;

[8] Li, B. (2005). *Research on the One-Sheet Hyperboloid Cylindrical Cutter with Flat Surface and Straight Edge (单叶双曲面平板直刃滚筒式切碎器的研究)*. PhD dissertation, China Agricultural University, Beijing/China;

[9] Li, S. (2005). Safflower 2005' became popular (红花2005'走红). *Modern Chinese Medicine*, Issue 06:50;

[10] Li, T., Meng, Z., Ding, H., Hou, J., Shi G., Zhou K. (2020). Mechanical analysis and parameter optimization of cabbage root cutting operation (甘蓝切根作业力学分析与参数优化). *Transactions of the Chinese Society of Agricultural Engineering*, Vol.36, Issue 07:63-72;

[11] Pang, S. (1982). Slip Shear Theory and Selection of Slip Shear Angle (关于滑切理论与滑切角的选用). *Journal of Huazhong Agricultural College*, Issue 02:64-69;

[12] Pu, Y., Wang, S., Yang, F., Ehsani, R., Zhao, L., Li, C., Xie, S., Yang, M. (2023). Recent progress and future prospects for mechanized harvesting of fruit crops with shaking systems. *International Journal of Agricultural and Biological Engineering*, Vol.16, Issue 1;

[13] Ren, C., Wu, Y., Tang, X., Hu, J., Chen, J., Wu, Q., Pei, J. (2017). Safflower's origin and changes of producing areas (红花的起源与产地变迁). *China Journal of Chinese Materia Medica*, Vol.42, Issue 11:2219-2222;

[14] Wang, F., Wang, D. (2020). Design and test of 4TSQ-2 sugar beet top cutter (4TSQ-2型甜菜切顶机设计及试验). *Transactions of the Chinese Society of Agricultural Engineering*, Vol.36, Issue 02:70-78;

[15] Wang, J., Pang, X., Hu, Y. (2006). An analysis on ecological and climatic conditions for cultivation Carthamus tinctorius L in alar irrigated area (阿拉尔垦区红花栽培气候生态条件分析). *Agricultural Research in the Arid Areas*, Issue 03:42-44+53;

[16] Xue, X., Zhang, M. (2005). The main nutrients and utilization value of Xinjiang safflower (新疆红花的主要营养成分及利用价值). *Food and Nutrition in China*, Issue 12:40-42;

[17] Zhang, S., Chen, Q., Liu J., Chen, Y., Chen, J., Jin, H., Luo, T. (2021). Research on design and experiment of multifunctional vegetable filed machine. *INMATEH-Agricultural Engineering*, Vol.63 (1), 434-442;

[18] Zhang, T., Zhang, L., Ge, Y., Liu, G., Zhang, X. (2020). Development and Test of a Portable Roller-type Safflower Harvester (便携对辊式红花采收机的研制与试验). *Journal of Agricultural Mechanization Research*, Vol.42, Issue 03:76-81;

[19] Zhang, X., Ge, Y., Chen, F., Yu, P. (2022). Design of Three-Finger Pull-Out Safflower Picking End Effector (三手指拉拔式红花采摘末端执行器的设计). *Machinery Design & Manufacture*, Issue 01:145-149;

[20] Zhang, X., Zhang, H., Shi Z., Jin, W., Chen, Y., Yu, Y. (2022). Design and experiments of seed pickup status monitoring system for cotton precision dibblers (棉花精量穴播器取种状态监测系统设计与试验). *Transactions of the Chinese Society of Agricultural Engineering*, Vol.38, Issue 05:9-19;

[21] Zhang Z., Lv, Q., Ren, J., Han, C., Yuan, P., Zhang, X. (2019). Design of critical components for safflower harvesting machinery by rotary shear (旋转剪切式红花花丝采摘机械关键部件的设计). *Journal of Chinese Agricultural Mechanization*, Vol.40, Issue 07:1-6;

[22] Zhang, Z., Zhao, M., Xing, Z., Liu, X. (2022). Design and Test of Double-acting Opposite Direction Cutting End Effector for Safflower Harvester (红花采收机双动对切式末端执行器设计与试验). *Transactions of the Chinese Society for Agricultural Machinery*, Vol.53, Issue 12:160-170;

[23] Zhou, Y., Guo, J., Ma, X., Fan, X., Chen, Y., Lin, M. (2021). Research on Current Situation and Development Countermeasures of Xinjiang Safflower Production (新疆红花生产现状及发展对策研究). *Journal of Anhui Agricultural Sciences*, Vol.49, Issue 19:199-201+217.

THE EVOLUTION OF ROMANIAN AGRICULTURE MECHANIZATION DEGREE
/
EVOLUTIA GRADULUI DE MECANIZARE IN AGRICULTURA ROMANEASCA

Ancuta MARIN, Vili DRAGOMIR*, Ruxandra POP, Marian BUTU
Institute of Research for Agriculture Economy and Rural Development, Bucharest / Romania

Tel: +40733839694; E-mail: Dragomir.vili@iceadr.ro
DOI: https://doi.org/10.35633/inmateh-71-61

Keywords: *sustainable agriculture, regional disparities, technology imports, mechanisation*

ABSTRACT
Mechanization is a fundamental aspect of agricultural sector modernization, bringing with it both benefits and challenges. The purpose of this study was to evaluate the degree of mechanization of Romanian agriculture and identify the major trends that marked the evolution of this process in the last ten years. Regional differences in the degree of mechanization were also explored, highlighting the particularities and challenges of each region. This analysis will provide a comprehensive perspective on the impact of mechanization in agriculture in Romania and will serve as a basis for the formulation of appropriate agricultural policies for the sustainable development of the country's agricultural sector.

ABSTRACT
Mecanizarea reprezintă un aspect fundamental al modernizării sectorului agricol, aducând cu sine atât beneficii cât și provocări. Scopul acestui studiu a fost evaluarea gradului de mecanizare al agriculturii românești și identificarea tendințelor majore care au marcat evoluția acestui proces în ultimii zece ani. De asemenea, au fost explorate diferențele regionale în ceea ce privește gradul de mecanizare, evidențiind particularitățile și provocările fiecărei regiuni în parte. Această analiză va oferi o perspectivă cuprinzătoare asupra impactului mecanizării în agricultura din România și va servi drept bază pentru formularea politicilor agricole adecvate în vederea dezvoltării durabile a sectorului agricol din țară.

INTRODUCTION

Mechanization in agriculture is the use of modern equipment and technologies to automate and optimize agricultural processes. This practice has significantly transformed the agricultural sector, bringing with it numerous benefits and challenges. Increased efficiency is one of the most significant advantages of mechanization in agriculture. The use of modern equipment and technologies is transforming the way agricultural activities are carried out, contributing to better and more sustainable production (*Peng et al., 2022, Partal et al., 2023*). In general, mechanization has been reported to bring with it considerable advantages in terms of increased efficiency in agriculture *(Arun et al., 2019).* This not only facilitates agricultural processes, but also contributes to increased productivity and reduced costs, all of which have a positive impact on the economic performance of the agricultural sector. However, it is important that mechanization is applied responsibly, also taking into account environmental and societal aspects, to ensure sustainable and balanced agriculture (*Emami et al., 2018*).

Mechanization in agriculture has not only increased efficiency, but also led to a considerable reduction in human effort in agricultural activities (*Peng et al., 2022, Grzelak et al., 2019*). This transformation has a significant impact on work and working conditions in the agricultural sector, for example by reducing the risk of accidents, optimizing the work schedule, reducing the physical effort of agricultural workers *(Duckworth et al., 2019, Yiorgos et al., 2022*).

Also, the increase in the degree of mechanization in agriculture was a determining factor in the increase in agricultural production, ensuring a greater amount of agricultural products in an efficient and sustainable way. By using modern equipment and technology, farmers can successfully manage crops over larger areas, applying fertilizers and pesticides with precision and achieving higher yields (*Ștefan et al. 2019, Grzelak et al., 2019*). The work of ploughing, sowing, harvesting and processing crops became much faster and more efficient, leading to a significant increase in production. Moreover, with the help of mechanization, farmers can optimize resources such as water and energy, contributing to greater efficiency in the production process. From fertilizer application to irrigation and harvesting, mechanization provides greater control over agricultural variables (*Onwunde et. al., 2016; Popescu et al., 2017*).

However, mechanization in agriculture also comes with challenges, such as high costs for purchasing and maintaining equipment, reliance on fossil fuels, and the risk of job losses in agriculture. It is important to balance the benefits with the impact on the environment and society, and develop solutions that lead to more efficient and sustainable agriculture. Mechanization in agriculture is a key factor in the evolution and modernization of the agricultural sector in Romania. Over the decades, the use of technology and agricultural equipment has become increasingly significant, having a significant impact on the efficiency, yields and sustainability of Romanian agriculture and in ensuring food security (*Popescu et al., 2017; Bădan, 2017*).

In this context, the present article focuses on the analysis of the degree of mechanization in Romania, investigating the evolution of this process over a period of ten years. The purpose of this study is to assess the degree of use of modern agricultural equipment and technologies, as well as to identify trends and major changes that have marked this evolution. The analysis will address both the general aspects of mechanization in agriculture and the aspects related to the different categories of agricultural machinery. In addition, regional differences in the degree of mechanization will be explored, highlighting the particularities and challenges of each region *(Vittis et al., 2022).* This analysis will provide a comprehensive perspective on the impact of mechanization in Romanian agriculture and provide a solid framework for understanding future trends and formulating appropriate agricultural policies to increase the competitiveness and sustainable development of Romanian agriculture.

MATERIALS AND METHODS

To carry out this analysis on the evolution of agricultural machinery in Romania, the statistical data available from the National Institute of Statistics for the period 2013-2022 were used. The data collected has been carefully analysed to understand trends and changes in the country's agricultural industry. Data analysis tools were used to calculate rates of increase or decrease and to identify patterns in the data.

Data for different categories of agricultural machinery such as tractors, ploughs, power cultivators, power planters, power-driven sprayers and dusters, self-propelled grain harvesters, self-propelled forage harvesters, potato harvesters and machines, balers for straw and hay balers and windrowers for fodder, were collected and analysed separately to obtain a complete picture of the evolution of each machine category. The analysis also included a comparison between different development regions in Romania to identify regional variations in the purchase of agricultural machinery. Annual growth rates were calculated and graphs were made to highlight the evolution over time of the number of machines.

For further study, the imports of agriculture machinery over a five year period were analysed. The data were extracted from trade map, by selecting the harmonised codes for agricultural machinery for soil works and harvesting, as follows:

'843229 Harrows, scarifiers, cultivators, weeders and hoes for use in agriculture, horticulture
'843210 Ploughs for use in agriculture, horticulture or forestry
'843239 Seeders, planters and transplanters (excl. no-till machines)
'843242 Fertiliser distributors (excl. sprayers and manure spreaders)
'843221 Disc harrows for use in agriculture, horticulture or forestry
'843231 No-till direct seeders, planters and transplanters
'843241 Manure spreaders (excl. sprayers)
'843351 Combine harvester-threshers
'843359 Harvesting machinery for agricultural produce (excl. mowers, haymaking machinery, straw)
'843352 Threshing machinery (excl. combine harvester-threshers)
'843330 Haymaking machinery (excl. mowers)
'843360 Machines for cleaning, sorting or grading eggs, fruit or other agricultural produce
'843353 Root or tuber harvesting machines

RESULTS

Mechanization in agriculture is a key factor in the evolution and modernization of the agricultural sector in Romania. Over the decades, the use of technology and agricultural equipment has become increasingly significant, having a significant impact on the efficiency, yields and sustainability of Romanian agriculture and in ensuring food security.

AGRICULTURAL TRACTORS

The agricultural tractor was and is the emblem of agricultural mechanization. With more than 100 years of history, it has been improved every time it was needed, adapting to various needs and expanding its range of applications. Analysing the tractor fleet over the last 10 years, based on data collected from the National Institute of Statistics, a nationwide increase of 53,494 units (+27.96%) is observed. By development region, the most tractors were purchased in the North-West region, followed by the South-Muntenia and Centre regions (Figure 1).

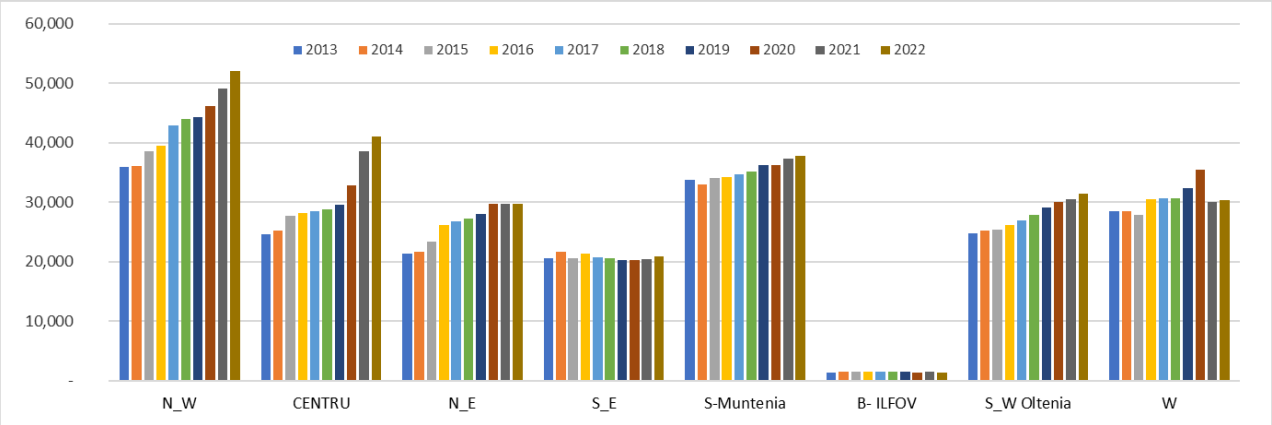


Fig. 1 – Endowments with tractors in Romania, during 2013-2022, by regions

At country level, the tractor fleet had an average of 215,672 units, during the analysed period, with a relatively homogeneous annual growth rate of +2.7776 per year.

PLOWS FOR TRACTOR

One of the most important works of the soil is ploughing, which has a quality directly proportional to that of the agricultural machinery used for this endeavour. Thus, the plough is the most needed work tool, ploughing consists of cutting and moving the furrow of land laterally, simultaneously with its overturning and shredding. This can be done at various depths, depending on the type of soil, the crop that is on it, the surface you have to plough. These aggregates can be attached to tractors or motor cultivators, having 2-5 furrows or even more, depending on the needs (*Petcu et al., 2023*).

Analysing the data available at the INS for the period 2013-2022, an increase, at the country level, of 9,969 pieces (+6.56%) is observed. By development region, in the North-West, the most ploughs for tractors were purchased, followed by the South-Muntenia and Central Regions, in the same order as that of tractors (Figure 2).

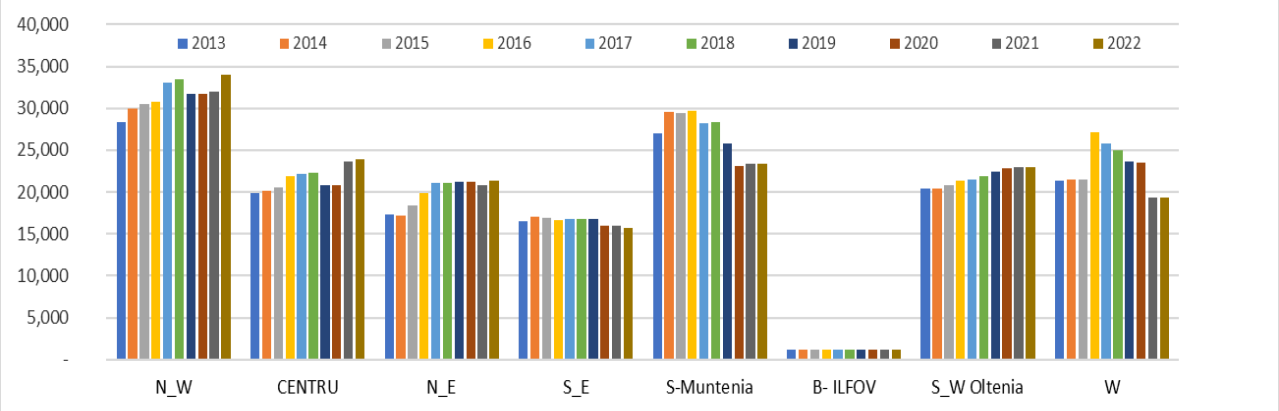


Fig. 2 – Endowments with ploughs for tractors in Romania, during 2013-2022, by regions

MECHANICAL CULTIVATORS

The cultivator is a special tool that prepares the soil for sowing and facilitates harvesting, simplifying manual work and saving time (*Stavytskyy et al., 2017*).

Analysing the data available at the INS for the period 2013-2022, the existence of two sub-intervals 2013-2020 and 2021-2022 can be observed. During the first interval, the number of mechanical cultivators, at the level of the farm, increased by 4,188 pcs (+14.16%), while during the second interval the decrease is accentuated, their number being reduced by 8,681 pcs (26%) compared to maximum. At the country level, the annual rate of decrease was -1.815 per year.

By development regions, growth rates between +0.257 and +2.114 per year were recorded in the Centre Region, the Bucharest-Ilfov Region and the South-West Oltenia Region. In the other regions of the country, the rates were decreasing, the values being between -0.357 and -6.451 per year, much more pronounced than the increases, so that at the country level there is a decrease in these machines (Figure 3).

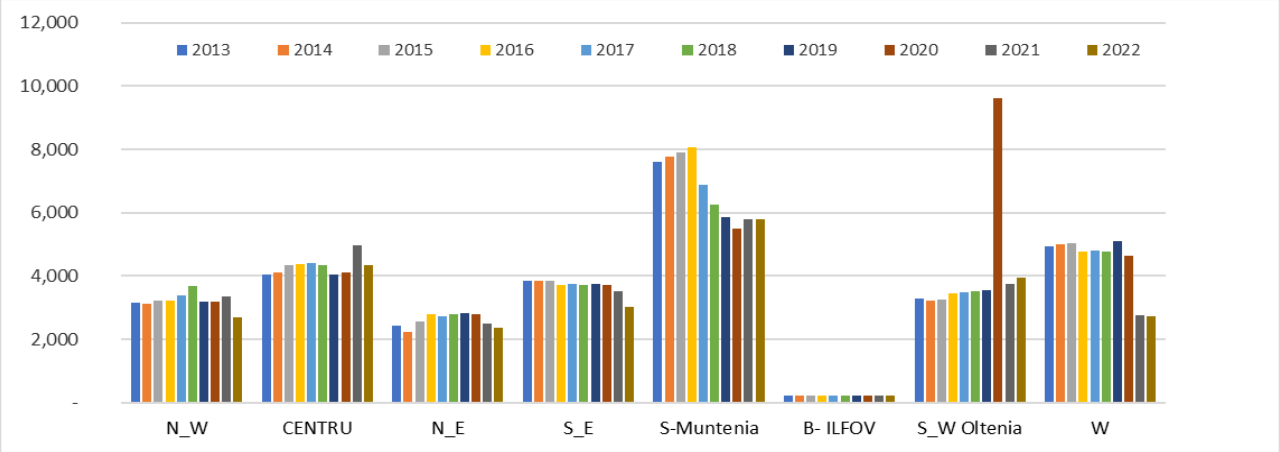


Fig. 3 – Endowments with mechanical cultivators, during 2013-2022, by regions

MECHANICAL SEEDERS

Mechanical seeders are devices that plant seeds for crops by measuring and placing them in the soil at equal distances and covering them to a certain depth. The use of mechanical seeders leads to an improvement in crop yield (seeds harvested/seeds planted) up to 9 times.

Analysing the data available at the INS for the period 2013-2022, the existence of two sub-intervals 2013-2016 and 2017-2022 can be observed. During the first interval, the number of mechanical seeders at field level increased by 6,450 pcs (+8.62%), while during the second the decrease is accentuated, their number decreasing by -11,549 pcs (-14.21%) compared to maximum. At the country level, the annual rate of decrease was -0.7814 per year (Figure 4).

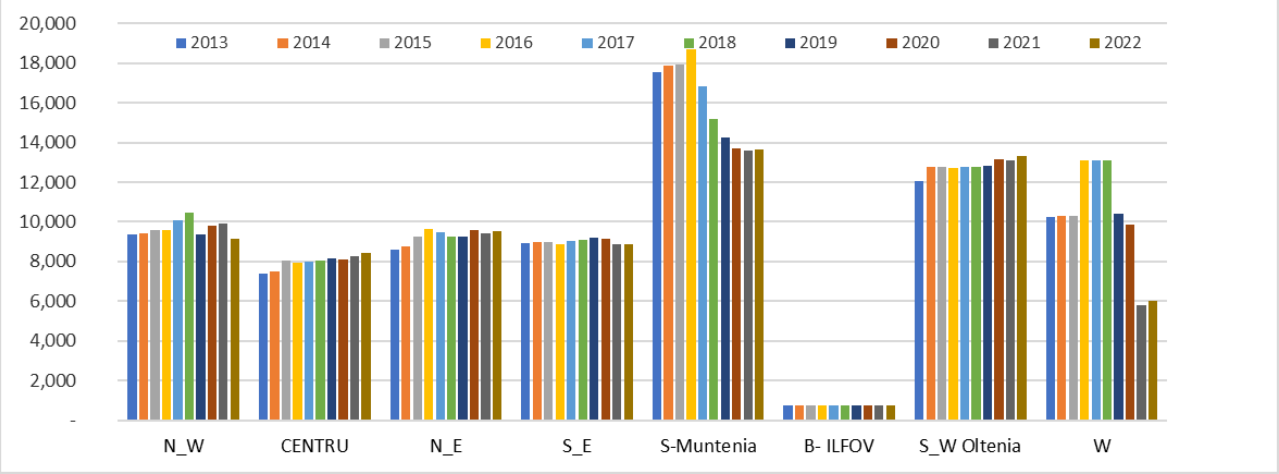


Fig. 4 – Endowments with mechanical seeders in Romania, during 2013-2022, by regions

SELF-PROPELLED COMBINES FOR HARVESTING CEREALS

Self-propelled combines for harvesting grassy cereals are used for direct harvesting of plants from the field and for split harvesting. In this case, the plants are harvested with windrowers and left in the furrows, the combine (equipped with a plant lifter) carrying out their lifting and threshing.

Analysing the data available at the INS for the period 2013-2022, it is observed that the number of self-propelled combines for harvesting grassy cereals decreased by -1,938 pieces (-7%) compared to the maximum recorded. At the country level, the annual rate of decrease was -0.0151 per year. (Figure 5).

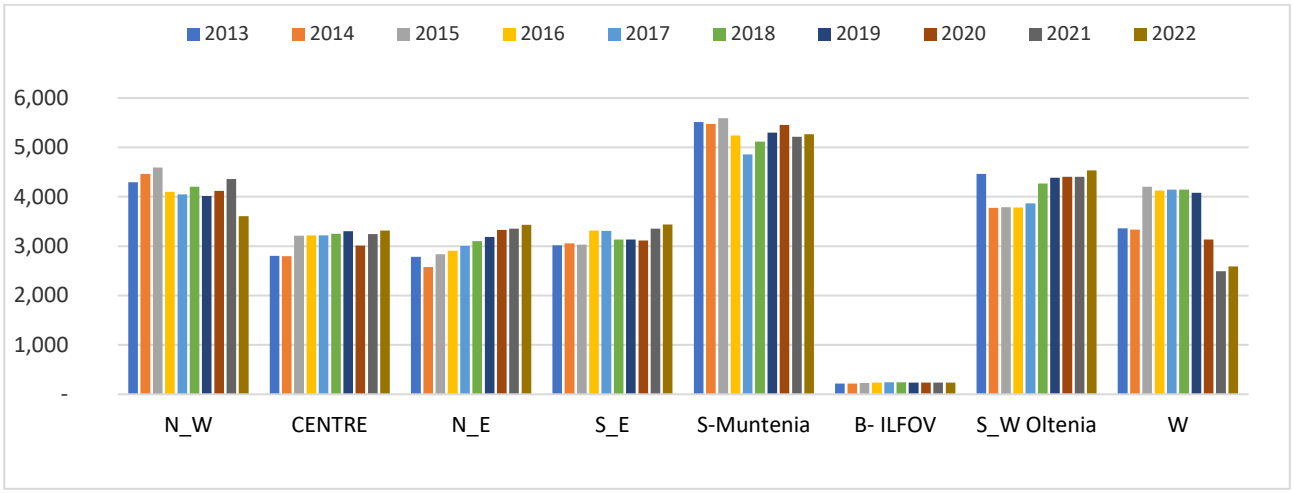


Fig. 5 – Endowments with p self-propelled combines for harvesting cereals in Romania, during 2013-2022, by regions

SELF-PROPELLED COMBINES FOR FORAGE HARVESTING

The self-propelled forage harvester is intended for the harvesting of silage forage plants, grasses and silage corn. It performs operations of cutting, chopping and loading the material into a means of transport. The combine is equipped with a grass harvesting equipment, a furrow gathering equipment and a corn silage harvesting equipment.

Analysing the data available at the INS for the period 2013-2022, there is an increase in the number of self-propelled forage harvesters by 374 units (+7%), followed by a slight decrease in 2022, by 57 units (4.75%) compared to the maximum registered. At country level, the annual growth rate was relatively homogeneous, of +3.6750 per year. By development region, the most self-propelled forage harvesters were purchased in the North-East, followed by the South-East and South-West Oltenia Region (Figure 6)

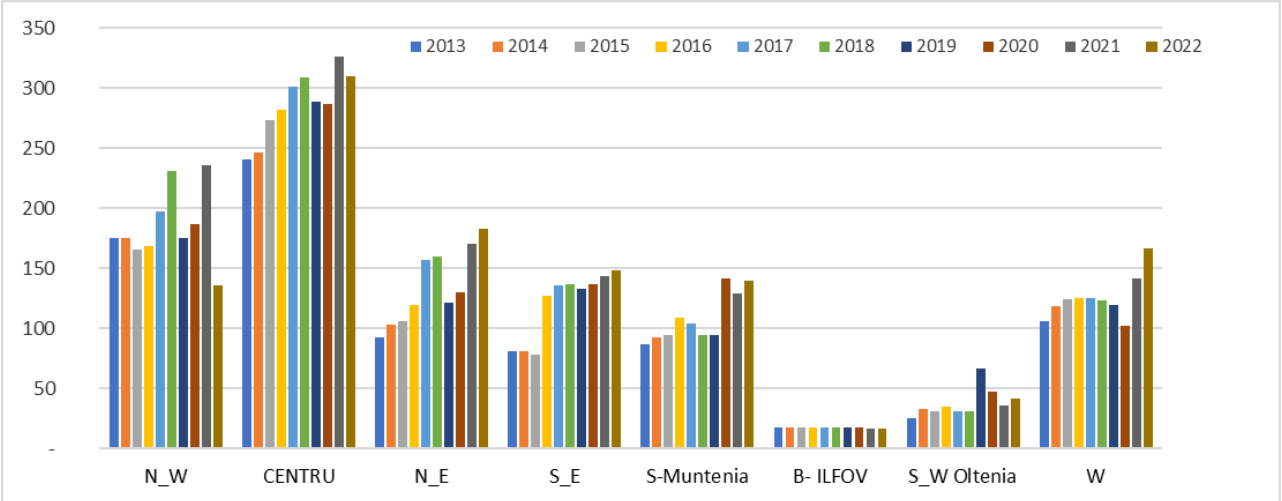


Fig. 6 – Endowments with self-propelled forage harvester in Romania, during 2013-2022, by regions

COMBINES AND MACHINES FOR HARVESTING POTATOES

Combines and potato harvesters are specially designed for digging up potatoes and their subsequent harvesting. These are machines aggregated by the tractor's power take-off cardan.

In order not to distort the analysis, only the areas of potato cultivation were taken into account, the southern regions being excluded. Analysing the data available at the INS for the period 2013-2022, it can be said that the situation of combines and machines for harvesting potatoes was relatively constant because the increase of 852 pcs (+16.14%) recorded in the period 2013-2020 was almost entirely annualized by the sharp decrease from 2021-2022, respectively – 810 pcs (-13.21%), the annual growth rate at the country level was +0.0881 per year (Figure 7).

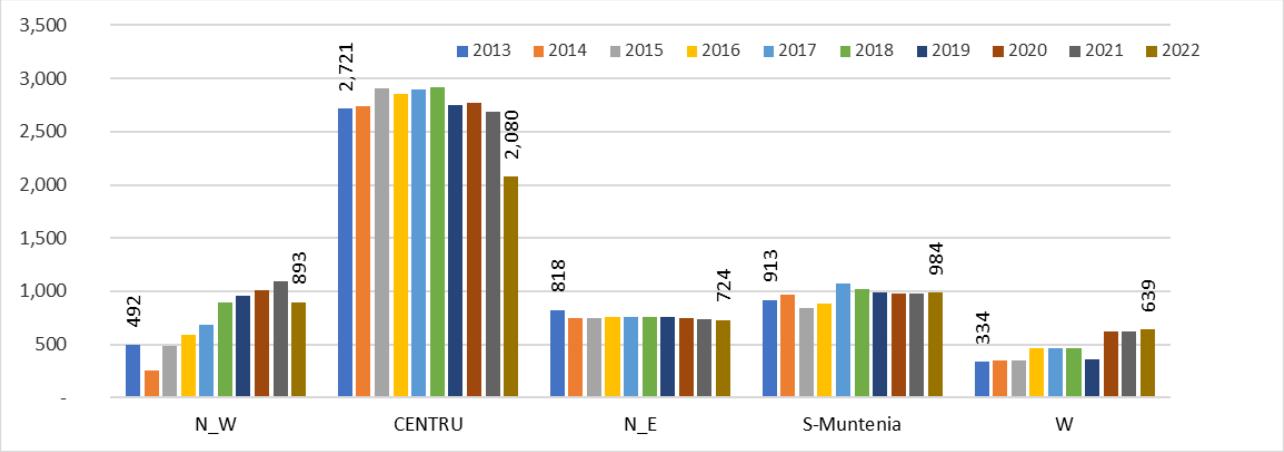


Fig. 7 – Endowments with combines and machines for harvesting potatoes ploughs for tractors in Romania, during 2013-2022, by regions

STRAW AND HAY BALING PRESSES

Straw and hay balers are agricultural machines capable of forming cylindrical or rectangular bales, very well compressed, making them very easy to handle, even manually. Straw and hay balers are equipped with automatic knotters, using twine for tying.

Analysing the data available at the INS for the period 2013-2022, a doubling of the number of presses for baling straw and hay, of 9,691 pcs (+94.77), can be observed at country level. By development region, the most straw and hay baling presses were purchased in the Central Region, followed by the North-West, South-West Oltenia and North-East Regions (Figure 8).

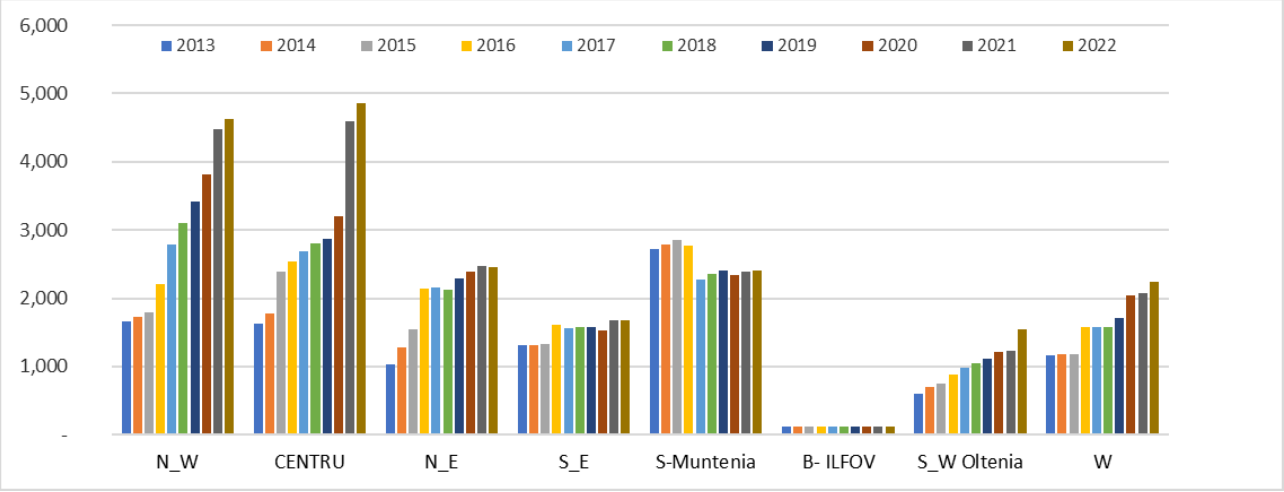


Fig. 8 – The quantitative situation of the baling presses for straw and hay, during 2013-2022, by regions

Although there is more and more talk about Agriculture 4.0 and digital and precision agriculture and data driven agricultural systems these concepts are more difficult to apply in the case of small and medium-sized farms due to limited resources and specific constraints.

Small and medium-sized farmers are often faced with an overload of human and financial resources, and these resources are often directed towards the basic needs of the agricultural operation, such as the purchase of seeds, fertilizers and crop treatments. Allocating funds for the purchase of precision agriculture equipment or technologies can be difficult, because they may not be seen as urgent or immediate investments (*Hadelan et al., 2022*). It is also important to mention that some small and fragmented agricultural lands can make it difficult to use technologies such as large tractors or agricultural combines. Moreover, access to technical expertise and consulting services for precision agriculture is limited in many rural areas, which can make it difficult to implement these technologies. Small and medium-sized farmers may face difficulties in finding and hiring qualified personnel to assist them in the adoption and efficient use of these technologies (*Zhang et al., 2022*). Despite these obstacles, there are initiatives aimed at making precision agriculture more accessible to small and medium-sized farmers, including through subsidies and financing for the purchase of equipment, training programs and consultancy, as well as collaborations between farmers to share costs and resources. With proper support and an attentive approach to the specific needs of these agricultural holdings, precision agriculture can become a reality for small and medium-sized farmers, bringing them significant benefits in terms of increasing productivity and efficiency, as well as reducing the impact on the environment.

Modern agricultural machinery is a crucial factor in increasing the efficiency, productivity and sustainability of Romanian agriculture. The import of agricultural machinery is motivated by the need to replace old and obsolete equipment, as well as to meet the new technological requirements of contemporary agriculture. For example, it is widely recognized that manure and other by-products can be effectively repurposed within soil-crop systems, serving as a valuable nutrient source while also enhancing the physical structure of the soil. It is imperative that land application is conducted with precision and care to minimize any adverse environmental impacts, and this is why manure spreaders are becoming so popular (*Ștefan et al, 2019*).

In Romania, imports of agricultural machinery in Romania cover a wide range of equipment, from tractors and agricultural combines to specialized machinery for agricultural work, such as seed drills, ploughs or irrigators. Imports of agricultural machinery are also an indicator of Romanian farmers' willingness to adapt to modern agricultural technologies and improve their farming practices. Most marketed harvesting machinery are the haymaking machinery (excluding mowers). Interesting is that in 2018, a peak of combine harvester-thresher imports was registered (over 15.000 units) compared to other years (8-900 units per years between 2019-2022) (Figure 9.)

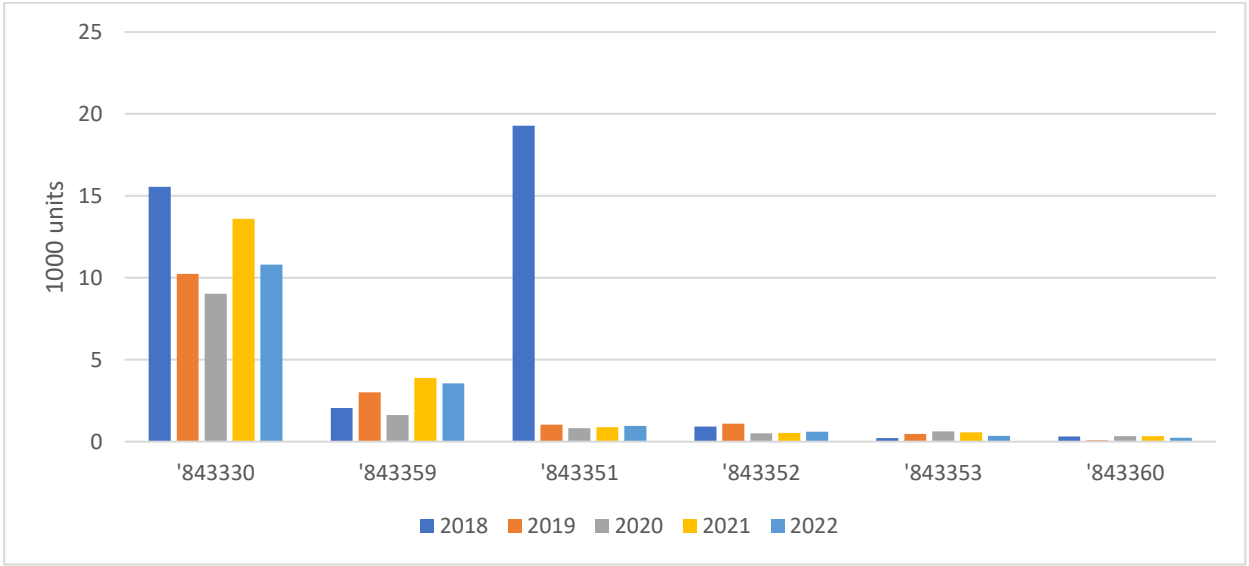


Fig. 9 - List of products imported by Romania detailed products in the following category:
8433 Harvesting or threshing machinery, incl. straw or fodder balers; grass or hay mowers; machines for cleaning, sorting or grading eggs, fruit or other agricultural produce

'843330 Haymaking machinery (excl. mowers); '843359 Harvesting machinery for agricultural produce (excl. mowers, haymaking machinery, straw; '843351 Combine harvester-threshers; '843352 Threshing machinery (excl. combine harvester-threshers); '843353 Root or tuber harvesting machines; '843360 Machines for cleaning, sorting or grading eggs, fruit or other agricultural products;

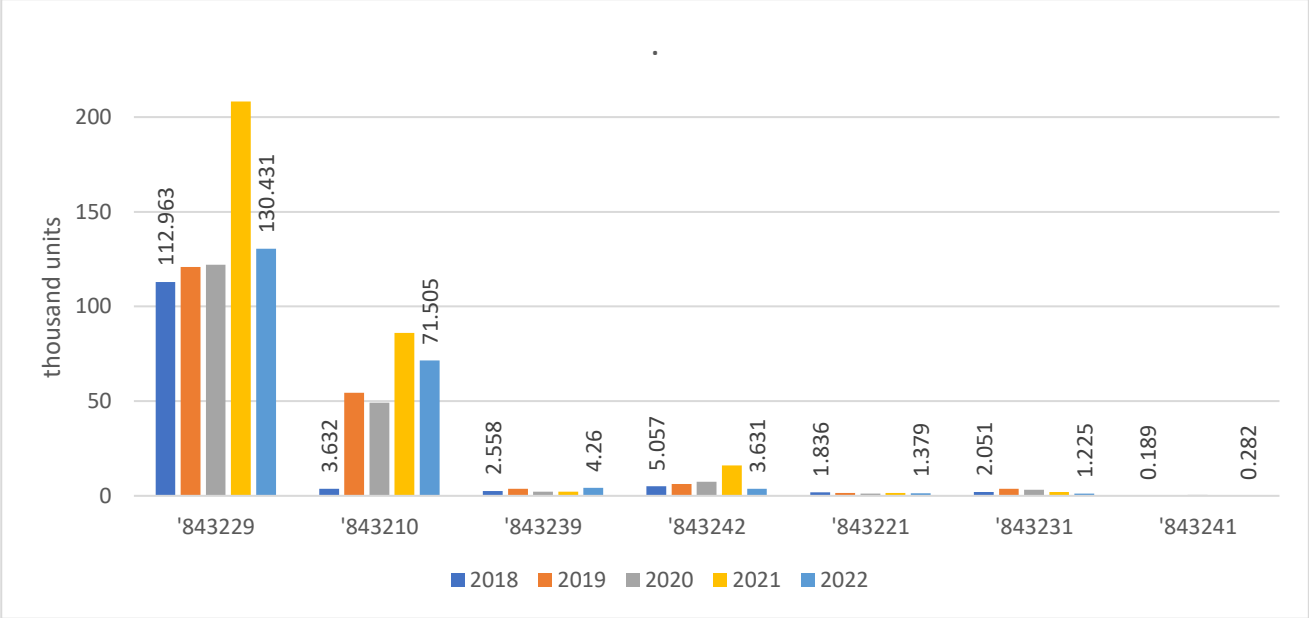


Fig. 10 - List of products imported by Romania, detailed products in the following category: 8432 Agricultural, horticultural or forestry machinery for soil preparation or cultivation (excl. sprayers and dusters); lawn or sports-ground rollers; parts thereof

'843229 Harrows, scarifiers, cultivators, weeders and hoes for use in agriculture, horticulture or forestry (excl. disc harrows); 843210 Ploughs for use in agriculture, horticulture or forestry; 843239 Seeders, planters and transplanters (excl. no-till machines); 843242 Fertiliser distributors (excl. sprayers and manure spreaders; 843221 Disc harrows for use in agriculture, horticulture or forestry; 843231 No-till direct seeders, planters and transplanters; 843241 Manure spreaders (excl. sprayers)

Romania imports agricultural machinery from several countries, each of them offering specific products and agricultural technologies. Among the main countries supplying agricultural machinery for Romania are: Germany, Italy, Poland and China (Figure 11).

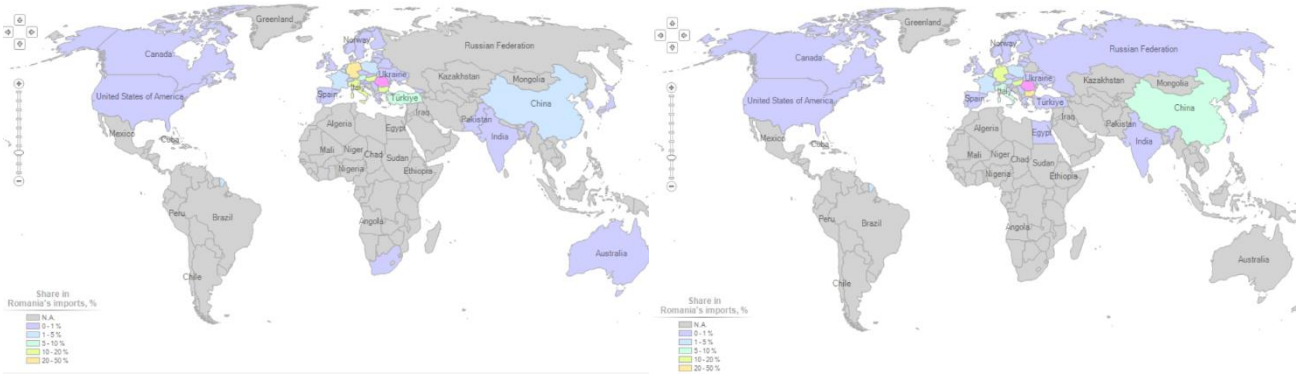


Fig. 11 - Romania's imports of agriculture machinery, by country (left -code 8433, right – code 8432)

Germany is a major supplier of tractors, agricultural combines, harvesters and other high-quality equipment. Italy is known for the production of precision agricultural machinery, including viticulture and horticulture equipment. Poland is an important supplier of tractors and agricultural equipment for the Romanian market. The Netherlands specializes in the production of precision agricultural machinery, including planting and harvesting machinery. These are just a few examples of countries supplying agricultural machinery for Romania. Imports of agricultural machinery from these countries reflect the needs and preferences of Romanian farmers and offer solutions for the modernization and development of the country's agricultural sector.

The level of endowment of Romanian agriculture has evolved significantly in the last decades, reflecting the efforts to modernize and adapt to European standards. Agriculture has remained an essential pillar of the Romanian economy, and investments in agricultural equipment and technologies have played an important role in increasing the efficiency and competitiveness of the sector.

However, there are still significant differences in the level of farm equipment, with large and medium-sized farms being better equipped with modern farm machinery and precision technology, while small farmers may experience difficulties in purchasing and using this equipment. Continued agricultural policy development and government support for technology accessibility and sustainable agricultural development remain essential to ensure that all farmers in Romania benefit from the appropriate level of equipment and technology to increase their efficiency and productivity.

CONCLUSIONS

In conclusion, the detailed analysis of the evolution of agricultural machinery in Romania reveals significant trends in the mechanization of the agricultural sector. The agricultural tractor, with over a century of history, has continued to evolve and adapt to the changing needs of agriculture. In the last 10 years, the number of tractors has increased significantly, reflecting an increase in efficiency and productivity in agriculture. Tractor ploughs also became more common, with an increase of 6.56%, indicating an improvement in soil preparation. In contrast, the number of mechanical cultivators has seen a significant decrease in the last two years. Mechanical seeders and power-driven sprayers and dusters also showed significant fluctuations over the same period. Self-propelled hay and forage harvesters saw slight declines, while straw and hay balers saw a significant increase of almost 95%. Forage windrowers had a relatively constant evolution with minor fluctuations. Overall, these data reflect the adaptability of farmers to the changing demands of the agricultural sector and the need to continue to explore technological innovations and improvements to increase the productivity and sustainability of Romanian agriculture.

ACKNOWLEDGEMENT

This research work was carried out with the support of Ministry of Agriculture and Rural Development, financed from Project ADER 22.1.1 *Designing technical-economic analysis models for the resilience and sustainability capacity of agricultural sector and the production processes optimization*.

REFERENCES

1. Arun, G.C., Yeo, Jun-Ho, Y., & Kiran, Ghimire. (2019). Determinants of Farm Mechanization in Nepal. *Turkish Journal of Agriculture - Food Science and Technology, 7(1), 87–91. https://doi.org/10.24925/turjaf.v7i1.87-91.2131*
2. Bădan, D. N. (2017). Analysis regarding the fleet and the farm equipment in Romania compared to the European Union. In *Agrarian Economy and Rural Development-Realities and Perspectives for Romania. 8th Edition of the International Symposium, November 2017, Bucharest* (pp. 69-73). Bucharest: The Research Institute for Agricultural Economy and Rural Development (ICEADR).
3. Duckworth, A. L., Quirk, A., Gallop, R., Hoyle, R. H., Kelly, D. R., & Matthews, M. D. (2019). Cognitive and noncognitive predictors of success. *Proceedings of the National Academy of Sciences*, *USA*, *116*(47), 23499–23504. https://doi.org/10.1073/pnas.1910510116
4. Emami, M., Almassi, M., Bakhoda, H. *et al.* Agricultural mechanization, a key to food security in developing countries: strategy formulating for Iran. *Agric & Food Secur* **7**, 24 (2018). https://doi.org/10.1186/s40066-018-0176-2
5. Grzelak, A., Guth, M., Matuszczak, A., Czyżewski, B., & Brelik, A. (2019). Approaching the environmental sustainable value in agriculture: How factor endowments foster the eco-efficiency. *Journal of Cleaner Production*, *241*, 118304.
6. Hadelan, L., Zrilić, M., Rogelj, M. J., & Sušac, M. Z. (2022). Enhancing the productivity of small farmers in Croatia through the agricultural fund for rural development. *Economics of Agriculture*, *69*(4), 1043-1059.
7. Onwude, D.I., Abdulstter, R., Gomes, C. and Hashim, N. (2016), Mechanisation of large-scale agricultural fields in developing countries – a review. *J. Sci. Food Agric., 96: 3969-3976. https://doi.org/10.1002/jsfa.7699*
8. Partal, E., Oltenacu, C. V., Paraschivu, M., Cotuna, O., Dima, M., & Contescu. (2023). Effects of different soil tillage on soil moisture, weed control, yield and quality of maize (Zea mays L.). *Number 40/2023, 1-8*
9. Peng J, Zhao Z and Liu D (2022) Impact of Agricultural Mechanization on Agricultural Production, Income, and Mechanism: Evidence from Hubei Province, China. *Front. Environ. Sci. 10:838686. doi: 10.3389/fenvs.2022.838686*

10. Petcu, V., Bubueanu, C., Casarica, A., Săvoiu, G., Stoica, R., Bazdoaca, C., ... & Horhocea, D. (2023). Efficacy of trichoderma harzianum and bacillus subtilis as seed and vegetation application combined with integrated agroecology measures on maize. *Romanian Agricultural Research*, (40).
11. Popescu A., Dinu T., Stoian E., Mituko Vlad I. (2017), Trends in agriculture endowment with machinery in Romania 2007-2015, *Scientific Papers Series Management, Economic Engineering in Agriculture and Rural Development Vol. 17, Issue 2, 2017, p. 291-300,* available at the address: http://managementjournal.usamv.ro/pdf/vol.17_2/Art40.pdf
12. Stavytskyy, A. and Prokopenko, O. (trans.) (2017) Investments in Agricultural Machinery and its Efficiency in Ukraine. *Ekonomika*, *96(1), pp. 113–130. doi:10.15388/Ekon.2017.1.10667.*
13. Ștefan, V., Cârdei, P., Popa, L., David, L., & Ciupercă, R. (2019). Influence of the manure spreading machines' working parameters on the qualitative performances of the fertilization process. *INMATEH-Agricultural Engineering*, *58*(2), 115-120.
14. Vittis,Y., Godfray, C., Obersteiner, M., et al. (2022). Agricultural mechanisation could reduce global labour requirements by hundreds of millions of agri-food workers, 22 February 2022, *Preprint (Version 1) available at Research Square [https://doi.org/10.21203/rs.3.rs-1344105/v1]*
15. Zhang, H., Li, J., Shen, J., & Song, J. (2022). Measurement of supply-and demand-side endowment effects and analysis of their influencing factors in agricultural land transfer. *Land*, *11*(11), 2053.

MECHANICAL PROPERTIES AND CONSTRUCTION OF CONSTITUTIVE MODEL FOR COMPRESSION AND STRESS RELAXATION OF CATTLE MANURE
/
牛粪压缩和应力松弛特性及其本构模型构建研究

Weisong ZHAO[1,2], Yongsheng CHEN[1,2], Weiqiang LIN[3], Zhenwei WANG[1,2], Qimin GAO[1], Hu XIE[1], Biao MA[1], Mingjiang CHEN[*1], Jingjing FU[*1,2]

[1] Nanjing Institute of Agricultural Mechanization, Ministry of Agriculture and Rural Affairs, Nanjing 210014, China;
[2] Western Research Institute, CAAS, Changji 831100, China;
[3] Zhongnong Guoke (Nanjing) Planning and Design Co., Ltd, Nanjing 210014, China;
Tel: +86 02584346161; E-mail: chenmingjiang@caas.cn; tutujing12@163.com
Correspondent authors: Mingjiang Chen, Jingjing Fu
DOI: https://doi.org/10.35633/inmateh-71-62

Keywords: *cattle manure; compression; intrinsic modeling; parameter fitting; stress relaxation*

ABSTRACT
In order to study the mechanical properties of compression and stress relaxation of manure under drainage conditions, the experiment was carried out with cattle manure as the object, and the constitutive models were improved to describe the stress-strain curves of compression and stress relaxation. The defined constitutive model was determined by parameter identification, and the influence laws of moisture content and filling mass on the compression and relaxation process were investigated. The results show that the improved Nishihara model and the five-component generalized Maxwell model can better describe the compression and stress relaxation properties of cattle manure, and the coefficients of determination of the parameters of the fitted intrinsic model are all greater than 0.9, with high fitting accuracy. The compression process was divided into three stages: exhaust, drainage, and viscoelastic-plastic deformation. The stress decay rate tended to change quickly and then slowly, and there was a negative correlation between the compressed mass, moisture content, and stress decay rate. Duncan's mean comparisons revealed that the differences in elastic modulus between different moisture content / compressed mass groups in the parameters of the cattle manure compression principal model were all significant (P<0.05). The differences in elastic modulus and coefficient of viscous attenuation between different moisture content groups in the parameters of the stress relaxation model were all significant. The study's results can provide the theoretical basis for the study and simulation of CM's compression and dewatering mechanism and provide support for the solid-liquid separator for livestock and poultry manure.

摘要
压缩过程中粪污的力学特性尚不清晰，严重制约固液分离机具的优化改进。为研究排水条件下牛粪压缩及应力松弛的力学特性，以牛粪为对象开展试验，分别采用改进西原模型和五元件广义 Maxwell 模型对压缩和应力松弛的应力应变曲线进行描述。通过定义的本构模型对不同含水率、压缩质量的牛粪力学试验数据进行参数辨识，确定相关模型参数，并探究各因素对压缩及松弛过程的影响规律。研究结果表明：改进西原模型、五元件广义 Maxwell 模型可以较好地描述牛粪压缩、应力松弛特性，拟合求解的本构模型参数决定系数均大于 0.9，拟合精度高。压缩过程分为排气、排水和粘弹塑性变形 3 个阶段；应力衰减速率呈先快后慢变化趋势，压缩质量、含水率与应力衰减速度呈负相关关系。Duncan 均值比较结果发现：牛粪压缩本构模型参数中不同含水率/压缩质量组间弹性模量差异均显著（P＜0.05）；应力松弛模型参数中不同含水率组间弹性模量和粘性衰减系数差异均显著（P＜0.05）。压缩与应力松弛力学特性的研究结果可为牛粪压缩脱水机理研究、仿真模拟提供理论依据，为畜禽粪便固液分离机具提供支撑。

INTRODUCTION
The annual production of livestock manure in China is 4 billion tons (*Wang et al.*, *2023*; *Yi et al.*, *2021*), which is vast. In China, the direct discharge of untreated livestock manure is prohibited, and the government encourages the utilization of livestock manure as a resource to achieve sustainable development of animal husbandry (*Bai et al.*, *2016*). The moisture content of livestock and poultry manure is generally above 80%, and solid-liquid separation (compression dehydration) is the critical common link in the pre-treatment of comprehensive utilization of manure (*Cârdei P. et al.*, *2019*; *Hjorth et al.*, *2010*).

After solid-liquid separation, dry solids and low-impurity liquids are obtained, facilitating subsequent management, disposal, and return to the field, reducing the cost of manure treatment and greenhouse gas emissions from farms (*Aguirre-Villegas et al.*, *2019*; *Guilayn et al.*, *2019*; *Husfeldt et al.*, *2012*). Currently, screw press or press auger is widely used in solid-liquid separation of livestock manure *(Guan et al., 2016; Zhao et al., 2017*). The machine mainly comprises a motor, screw, screen, and other components. In a screw press separator, the effluent is transported into a cylindrical screen with a screw. The liquid will pass through the screen and be collected. At the end of the axle, the DM-rich fraction will be pressed against the plate, and more liquid will be pressed out of the solid fraction. The solid phase will drop from the opening between the plate and the opening of the cylindrical mesh (*Stefan et al.*, *2021*; *Stefan et al.*, *2019*; *Zhao et al., 2017*). With the attenuation of water content, the dewatering of livestock and poultry manure produces a phase change process from liquid to solid, and the body change process further compresses the cake (solid). In the later stage of dewatering, the manure particles are deformed and rebound due to extrusion and friction, which makes the machine generally have the problems of high energy consumption, unstable operation performance (high or low moisture content of solids after dewatering), and mutual inhibition of processing efficiency and dewatering degree. In order to achieve the screw press dewatering, both presses dry and squeeze fast operating effect, the group designed a broken tooth screw, through the manure stress increase, release, and then increase, to achieve the principle of nonlinear compression dewatering of the alternating load, and experimental and simulation research (*Zhu et al., 2017*).

Livestock manure compression dewatering from the highly abstracted model point of view can be understood as the role of the external load (effective stress), the pore water between the manure particles through the porous media discharge, manure particles skeleton acts as a spring to produce deformation. However, the modulus of this "spring" will change with the change of effective stress, and the degree and speed of deformation are mainly related to the compression mode and the nature of fecal matter itself. In recent years, scholars have measured fecal matter's particle size distribution and nutrient content, studied fecal matter's rheological properties, and clarified the critical value of fecal matter as a Newtonian and non-Newtonian fluid (*Shi et al., 2014; Ehlers et al.*, *2012*). However, the manure's compression and stress relaxation characteristics under loading are not precise, and the constitutive model has yet to be established.

Therefore, the compression mechanical properties test is carried out in this study with cattle manure (CM) as the research object, and the compression and stress relaxation tests are carried out using a universal testing machine with the moisture content (MC) and filling mass (LM) as the test factors. The obtained stress-strain data were curve-fitted, the parameters of the defined constitutive model were identified, and then the compression mechanical properties of CM were studied. The results may provide theoretical information for studying manure compression and dewatering mechanism, simulation, and optimization design of solid-liquid separators.

MATERIALS AND METHODS

Test materials and equipment

Manure sample preparation

The manure used in the experiment was obtained from Hexing Dairy Farm, Haimen District, Jiangsu Province, China. The 9GY-16B Livestock Manure Solid-Liquid Separator developed by the Nanjing Institute of Agricultural Mechanization, Ministry of Agriculture and Rural Affairs, was used to separate fresh cow manure to obtain cow manure solids with a moisture content of about 70%. The moisture content of CM was regulated by the natural drying method and the addition of deionized water, and CM with a moisture content of 50%, 65%, and 80% were obtained and sealed in plastic boxes. The compression vessel was 252 mm in height, 108 mm in outer diameter, and 2 mm in wall thickness, made of 304 stainless steel, with small holes (2 mm in diameter) around the cylinder wall for drainage. Sequentially, 500 g, 750 g, and 1000 g of CM with 50%, 65%, and 80% moisture content were placed into the compression vessel with a pre-pressure of 5 N. The test samples with different moisture contents were numbered by filling in the mass-test number. Each set of tests was repeated three times, and 27 test samples were prepared.

Compression and stress relaxation test equipment and methods

The test equipment used is Jinan Chuanbai Instrument and Equipment Co., Ltd., production of a microcomputer-controlled electronic universal testing machine and self-made compression device, universal testing machine model WDW-20, grade 0.5 level. Self-made compression device including pressure rod, compression container, acrylic shell, faucet and base, and other components.

Other auxiliary instruments include the DGH30-1A electric heating blast drying oven produced by Nanjing Testing Instrument Factory and the YP300001D electronic scale (range 0-30 kg, accuracy 0.1g) produced by Shanghai Lichen Instrument Technology Co.

CM was considered a whole in the compression process, and the compression cross-sectional area and initial height were entered into the universal testing machine. Through the program control module, the movement speed of the compression bar is set to 50 mm/min, and the compression is stopped when the stress reaches 0.8 MPa. The computer software will measure the load value and deformation and transform them to get the stress-strain (compression) curve. After each group of compression tests stops loading, the compression rod does not move to keep the deformation of fecal matter, and the value of stress change is recorded by the universal testing machine. The test is ended after 120 seconds to get the change curve of stress with time (stress relaxation curve). The compression displacement and drainage mass when the compression stress reached the maximum value were recorded during the test.

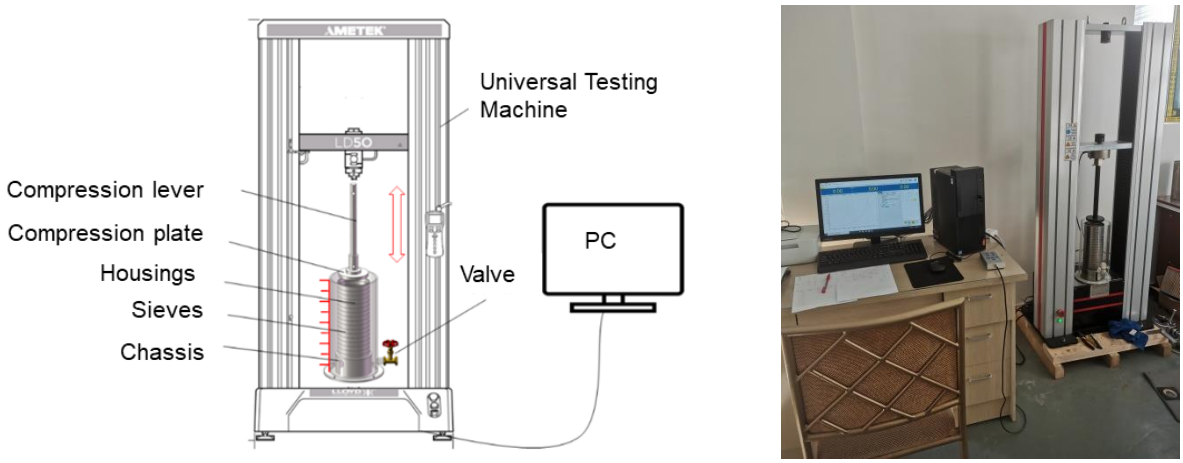


Fig. 1 - Compression test device

Methods of constructing the intrinsic model and determining the parameters of the intrinsic equations

Firstly, the stress-strain curves and stress-relaxation curves during compression of CM were obtained experimentally to study the compression and relaxation characteristics; secondly, the compression and stress-relaxation models of CM were constructed concerning the research methods of the previous researchers on related materials (e.g., soil, straw, seed cotton, etc.) (*Ding et al., 2023; Wang et al., 2021; Kong et al., 2021; Nona et al.*, *2014*). Then, series-parallel arithmetic rules were applied to solve the constitutive equations, and the experimental values were used as the target to test the difference between the calculated values obtained by the constitutive equation and the experimental values so that the proper constitutive model and equations could be determined; lastly, the parameter values of the constitutive equations corresponding to all the experiments were obtained by using the 1stOpt and Matlab software to solve the equations.

RESULTS

Analysis of compression test

The compression curves of 500, 750, and 1000 g FM at 50%, 65%, and 80% MC with a loading speed of 50 mm/min are shown in Fig. 2. As can be seen from Fig. 2, the characteristics of the stress-strain curves obtained from each group of repeated tests were the same, and the dispersion was not significant. Under different MC, the compression stress-strain curve of CM has the same trend. With the increase of strain, the stress shows a slow and then fast growth trend. The compactness of CM increased with the rise of stress, and the bulk modulus increased, indicating that the CM has compression hardness. However, it was also observed that MC and FM have an effect on the rate of change of the stress-strain curve. For example, for the same MC and strain conditions, the higher the FM, the higher the stress value of CM, and the difference in stress gradually increases with the decrease of MC. This indicated that CM has compression hardness (Yao et al., 2023), and the lower the MC, the better the compression hardness; the increase of MC will reduce the sensitivity of the FM to the stress-strain.

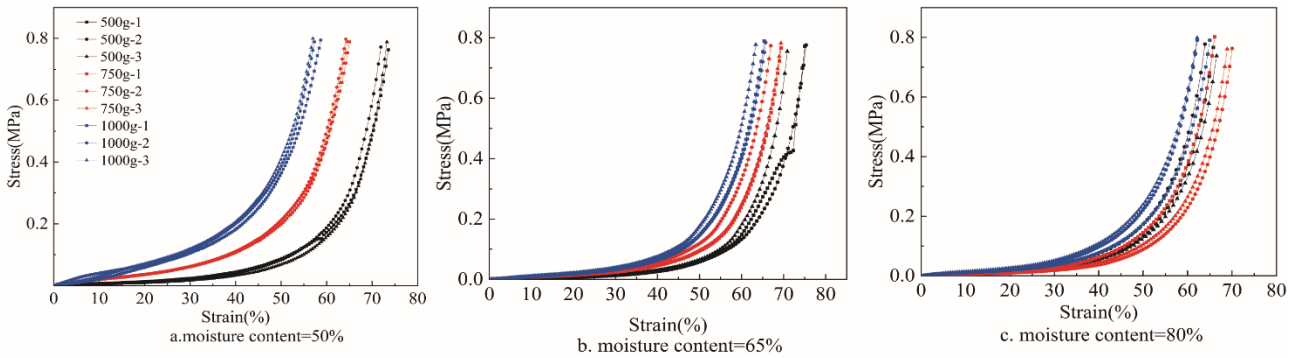


Fig. 2 - Compression stress-strain curve of CM with different MC

The mechanical changes of CM in the compression and dehydration process are more complicated, mainly manifested in viscoelastic properties. Through the observation of the test process and the analysis of the compression curve (Fig. 2), it is found that the stress growth rate in the initial stage of compression is slow. The curve is flat, probably because this stage is mainly exhausting, and the CM particles undergo misalignment and rearranging, which will be referred to as the exhausting stage. As compression proceeds, the growth rate of stress becomes faster, and the particles and moisture are compressed as the load-bearing body in this stage, which is drainage-based. Direct contact, slip, and deformation between particles occur, and this stage is called the drainage stage. After that, the stress increases significantly with the increase of strain, and this stage is mainly compressed CM particles, accompanied by a small amount of moisture overflow. The particle volume decreases significantly, the density increases and the particles undergo elastic or plastic deformation; this stage is the visco-elastic-plastic deformation stage.

Analysis of typical compression stress-strain curves of CM revealed that it showed prominent elastic characteristics in the initial and later stages of compression (Fig. 3), and the reason for this was analyzed to be probably related to the moisture content. In the venting stage, the stress change is small (0 to 0.04 MPa) in the extensive strain range (0 to 40%), and the curve as a whole is quasi-linear; in the draining stage (stress from 0.04 to 0.3 MPa), probably due to the fast draining speed and large draining volume of CM, the CM particles begin to deform plastically, and thus the modulus increases gradually; and in the late stage of dewatering (stress >0.3 MPa), there is only a tiny amount of moisture discharged In the late stage of dewatering (stress > 0.3 MPa), only a little water was discharged, and the moisture content of CM was in a relatively stable state. Although the stress increased exponentially, the stress-to-strain ratio was stable, indicating that CM had good elasticity characteristics at this stage.

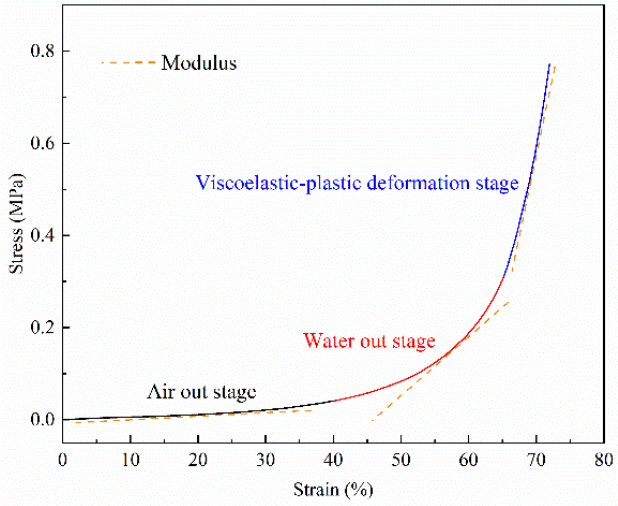


Fig. 3 - Typical stress response of the compression experiment

Analysis of stress relaxation tests

Figure 4 demonstrates the stress relaxation curves of CM with 500, 750, and 1000g FM at 50%, 65%, and 80% MC. It can be seen that the characteristics of the curves obtained from each group of repeated tests are the same, i.e., the rate of stress attenuation shows a tendency to change quickly and then slowly and finally tends to be stabilized, which is similar to the relaxation characteristics of agricultural materials, such as cotton and straw (*Kong et al., 2021; Ma et al., 2016*).

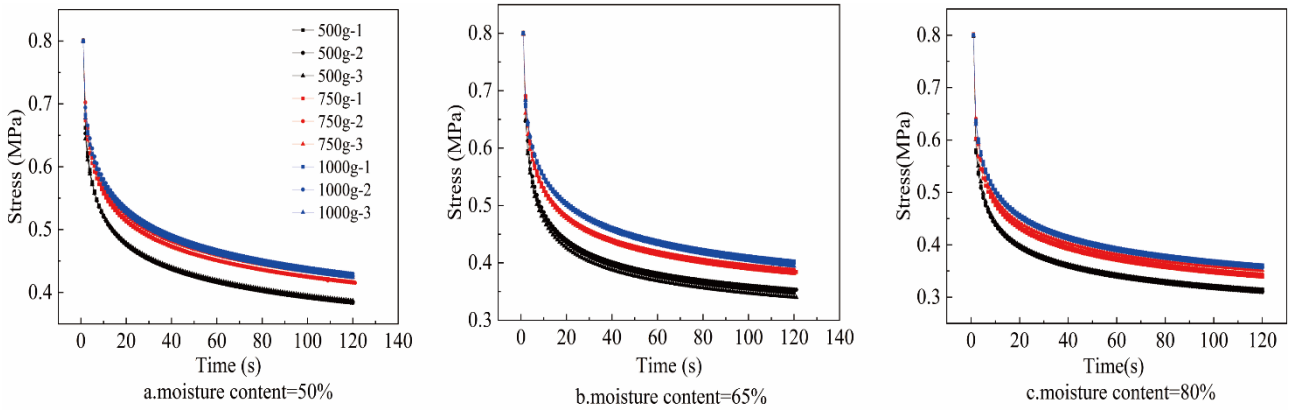


Fig. 4 - Stress relaxation curve of CM with different MC

Figure 4 shows that at the exact moment, the smaller the FM, the smaller the stress, indicating that the FM negatively correlates with the stress decay rate. In order to further observe the effect of MC on stress relaxation, the stress relaxation curves under 50%, 65%, and 80% MC are plotted with 750g FM for example (Fig. 5). Fig. 5 shows that at the same time, the greater the MC, the smaller the stress; the time required for the stress to decay from 0.8 MPa to 0.6 MPa (attenuation ratio is 25%) under 50%, 65%, and 80% MC corresponds to 6, 4, and 2 s, indicating a negative correlation between MC and stress decay rate. The reason may be that under the same FM, the higher the MC, the less the dry matter of CM, the smaller the particle contact surface, and the larger the pores, so the stress dissipation speed is faster after being compressed.

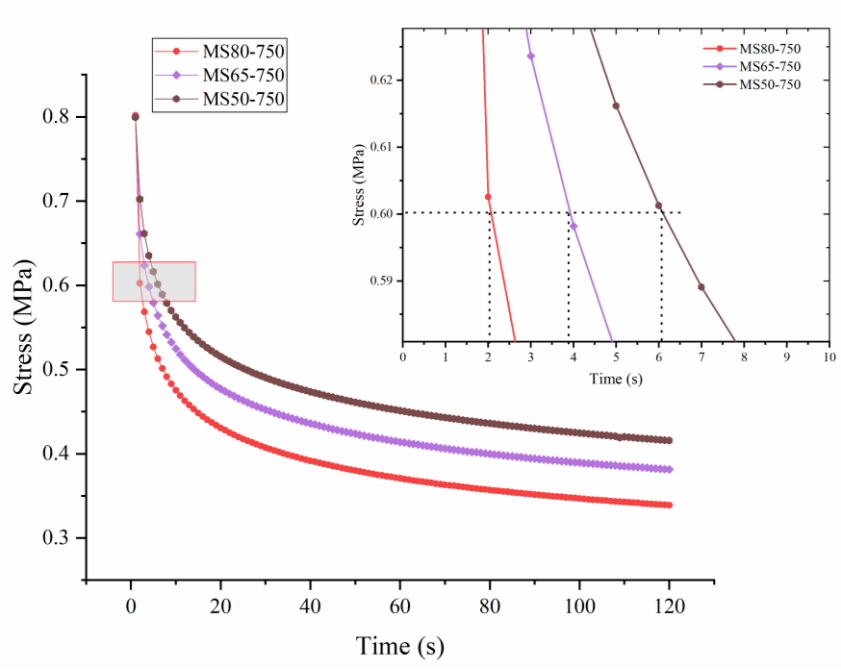


Fig. 5 - Effect of MC on the stress decay rate

Model Construction

Compression principal model

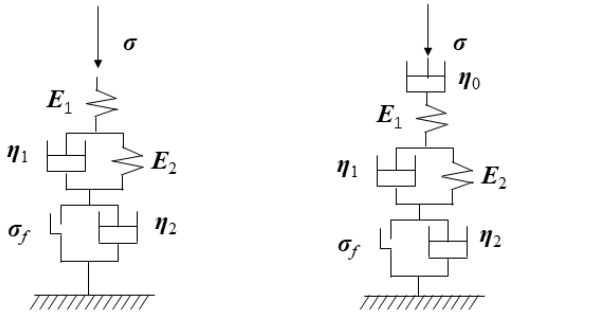
The Nishihara body model (*You W. et al., 2022*) (Fig.6a), which is composed of Hooke, Kelvin and viscoplastic bodies in series, is suitable for reflecting the compressive mechanical properties of soft materials, but it describes stage 1 as elasticity only. The intrinsic equations of the Westphalian body are:

$$\begin{cases} \frac{\eta_1}{E_1}\dot{\sigma} + \left(1 + \frac{E_2}{E_1}\right)\sigma = \eta_1\dot{\varepsilon} + E_2\varepsilon\left(\sigma < \sigma_f\right) \\ \ddot{\sigma} + \left(\frac{E_2}{\eta_1} + \frac{E_2}{\eta_2} + \frac{E_1}{\eta_1}\right)\dot{\sigma} + \frac{E_1E_2}{\eta_1\eta_2}\left(\sigma - \sigma_f\right) = E_2\ddot{\varepsilon} + \frac{E_1E_2}{\eta_1}\dot{\varepsilon}\left(\sigma \geq \sigma_f\right) \end{cases} \quad (1)$$

where σ is the total stress, MPa; $\dot{\sigma}, \ddot{\sigma}$ are the first and second order derivatives of the total stress with respect to time, respectively; $\dot{\varepsilon}, \ddot{\varepsilon}$ are the first and second order derivatives of the total strain with respect to time, respectively; E_1, E_2 are the elastic moduli of the Hooke body in the Hooker body element and the Kelvin body

element, MPa, respectively; η_1, η_2 are the viscous modulus of the Newtonian body in the Kelvin element and the visco-plastic body, MPa-s; σ_f is the initial stress of the Coulomb body in the visco-plastic body, MPa.

In order to better reflect the viscoelastic properties of the material, Fanting Kong et al. (*Kong. et al., 2021*) added one Newtonian body to obtain a modified Westfield body (Fig. 6b), established a model that uniformly reflects the three compression stages, and applied the tandem operation rule to derive the intrinsic equation of the modified Westfield body model, as shown in Eq. 2.



a. Nishihara model b. Improved Nishihara model

Fig. 6 - Compression mechanical model

σ is total stress, MPa; η_1 is viscosity modulus of tandem Newtonian body, MPa·s; E_1 is elasticity modulus of tandem Hookean body, MPa; E_2 is elasticity modulus of Hookean body in Kelvin body, MPa; η_2 is viscosity modulus of Newtonian body in Kelvin body, MPa·s; σ_f is initial stress of Cullen body, MPa; η_3 is viscosity modulus of Newtonian body in Viscoplastic body, MPa·s.

$$\begin{cases} \frac{\eta_1}{E_2}\ddot{\sigma} + \left(1 + \frac{E_2}{E_1} + \frac{\eta_1}{\eta_0}\right)\dot{\sigma} + \frac{E_2}{\eta_0}\sigma = \eta_1\ddot{\varepsilon} + E_2\dot{\varepsilon} & (\sigma < \sigma_f) \\ \frac{\eta_1}{E_1}\ddot{\sigma} + \left(1 + \frac{\eta_1}{\eta_2} + \frac{E_2}{E_1} + \frac{\eta_1}{\eta_0}\right)\dot{\sigma} + \left(\frac{E_2}{\eta_0} + \frac{E_2}{\eta_2}\right)\sigma - \frac{E_2}{\eta_2}\sigma_f = \eta_1\ddot{\varepsilon} + E_2\dot{\varepsilon} & (\sigma \geq \sigma_f) \end{cases} \quad (2)$$

The compression process of CM is constant velocity compression, so the first order derivative of strain with respect to time is constant and the second order derivative is zero, i.e., $\dot{\varepsilon}$= constant and $\ddot{\varepsilon}$= 0. Collating Eq. (2) yields the intrinsic equations of the visco-elastic-plastic model of CM compression as:

$$\begin{cases} \frac{\eta_1}{E_2}\ddot{\sigma} + \left(1 + \frac{E_2}{E_1} + \frac{\eta_1}{\eta_0}\right)\dot{\sigma} + \frac{E_2}{\eta_0}\sigma = C_1 & (\sigma < \sigma_f) \\ \frac{\eta_1}{E_1}\ddot{\sigma} + \left(1 + \frac{\eta_1}{\eta_2} + \frac{E_2}{E_1} + \frac{\eta_1}{\eta_0}\right)\dot{\sigma} + \left(\frac{E_2}{\eta_0} + \frac{E_2}{\eta_2}\right)\sigma - \frac{E_2}{\eta_2}\sigma_f = C_2 & (\sigma \geq \sigma_f) \end{cases} \quad (3)$$

With MC as 65%, the data of the first repeated test of 500 g FM were fitted, and the fitting effect is shown in Fig. 7. From the fitting curve, it can be seen that the coefficient of determination R^2 of the fit result of the Nishihara model is 0.926, and the coefficient of determination R^2 of the fitting result of the optimized Nishihara model is 0.974. The fitting curve is basically consistent with the test curve, indicating the fitting accuracy. The higher the value, the more accurate the fitting result. Therefore, the optimized Nishihara model was chosen to construct the constitutive model of CM compression stage.

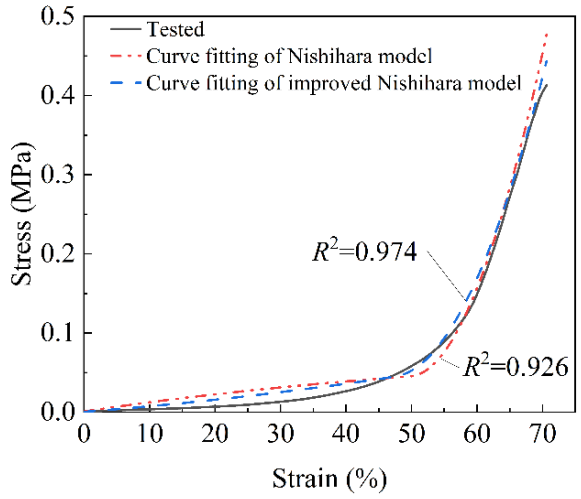


Fig. 7 - Curve fitting of compression model

Stress relaxation model

It can be seen from Fig. 4 that the stress relaxation curves of CM under different compression conditions have similar shapes and basically the same changing rules, so the same model can be used to describe them. Studies have shown that the stress relaxation characteristics are often described by the generalized Maxwell model, which can be divided into a three-element generalized Maxwell model (Fig. 8a) and a five-element generalized Maxwell model (Fig. 8b) according to the number of elements. The three-element generalized Maxwell model is composed of a Hooke element and a Maxwell model connected in parallel, and its stress relaxation stage equation is as follows:

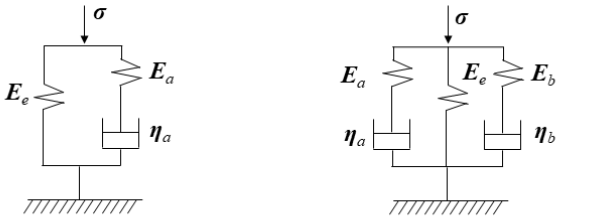
$$\sigma(t) = \varepsilon_i\left(E_a e^{-t/T_a} + E_e\right) \quad (4)$$

In the formula $\sigma(t)$ is the stress at time t, MPa; ε_i is the initial strain; t is time, s; T_a is the stress relaxation time of Maxwell element $T_a=\eta_a/E_a$, s; η_a is the viscosity modulus of Newton body, MPa·s.

The five-element generalized Maxwell models is a Maxwell model connected in parallel in the three-element generalized Maxwell model, and its stress relaxation stage equation is:

$$\sigma(t) = \varepsilon_0\left(E_a e^{-t/T_a} + E_b e^{-t/T_b} + E_e\right) \quad (5)$$

where ε_0 is the initial strain, %; E_a, E_b are the damping elastic moduli of the first and second Maxwell bodies, MPa; T_a and T_b are the stress relaxation times of the first and second Maxwell bodies, $T_a=\eta_a/E_a$, $T_b=\eta_b/E_b$, s; η_a, η_b are the attenuation viscosity coefficients of the first and second Maxwell bodies, respectively, MPa·s; E_e is the instantaneous elastic modulus, MPa.



a. Generalized Maxwell 3-element mechanical model

b. Generalized Maxwell 5-element mechanical model

Fig. 8 - Stress relaxation mechanical model

E_e is instant elastic modulus; E_a and E_b are decaying elastic modulus of the first and second Maxwell body, respectively; η_a and η_b are decay viscosity coefficients of the first and second Maxwell body, respectively; σ is real-time stress.

It can be seen from Eq. (4) that the three-element generalized Maxwell model contains only one stress relaxation time T_a; it can be seen from Eq. (5) that the five-element generalized Maxwell model contains two stress relaxation times, T_a and T_b. It can be seen from Fig. 4 that the stress relaxation process of CM tends to be fast first and then slow, and the five-element generalized Maxwell model has more advantages. The data of the third repeated test with a MC of 65% and 1000 g FM were used for fitting, and the fitting effect is shown in Fig. 9.

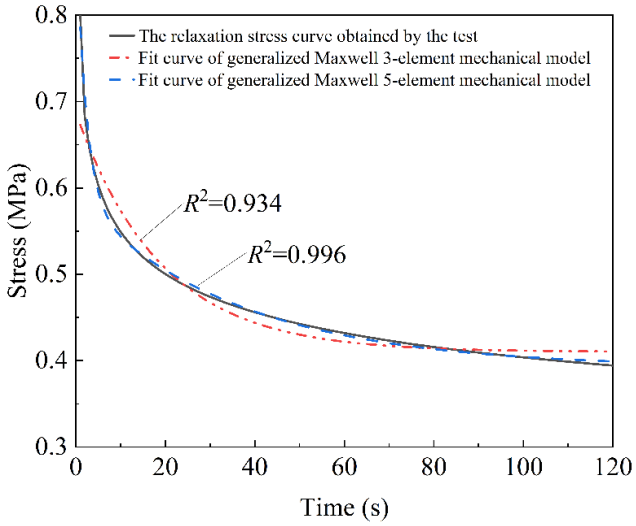


Fig. 9 - Fitting curve of stress relaxation model

The coefficient of determination R^2 of the fitting equation of the three-element generalized Maxwell model is 0.934, and the difference between the fitting curve and the test curve is large; the coefficient of determination of the fitting equation of the five-element generalized Maxwell model R^2 is 0.996, which indicates a high fitting accuracy. Therefore, the five-element generalized Maxwell model is chosen to construct the constitutive model in the relaxation stage.

Parameter determination and analysis

Parameter determination

The constitutive equation of the optimized Nishihara model was written into the 1stOpt software by programming, and the parameters of the compressive stress-strain curves of CM under the test conditions of 50%, 65%, 80% MC, and 500, 750, and 1000 g FM were respectively calculated. Fitting (a total of 27 groups) was solved to obtain six parameters to be determined in the constitutive equation, namely E_1, E_2, η_0, η_1, η_2, and σ_f. SPSS software was used to process the solved parameter values to obtain. The parameter values of the CM compressive model were compared and analyzed using the Duncan's mean multiple comparison method, and the results are shown in Table 1.

Table 1

Effects of moisture content and compression mass on the parameters of the CM compression constitutive model

	FM	E_1	E_2	η_0	η_1	η_2	σ_f	R^2
50%	500	112.7±12.64 aA	0.76±0.15a A	2.86E13±4.96E13 aA	4.42E4±3.12E3aB	2.90E14±5.02E14aA	0.11±0.01aA	0.93±0.03
	750	462±18.23a B	6.26±0.49 aA	4.09E12±7.07E9 aA	2.25E6±3.93E4aA	3.53E18±3.96E16aC	0.14±0.03bB	0.96±0.01
	1000	2203.33±115.47aC	49.03±13.05aB	2.18E13±5.77E11aA	1.26E8±1.16E7aB	4.59E16±1.01E16bB	0.17±0.003bC	0.94±0.03
65%	500	1.25E4±7.86E3bA	5.35E1±1.91E1bB	1.22E11±1.17E10aA	1.95E8±2.12E7bA	5.6E12±6.72E10aA	0.09±0.01aA	0.96±0.003
	750	2.41E7±2.26E6aB	6.99E1±3.55aC	2.69E17±5.47E16aB	1.93E12±2.31E11aB	5.24E15±1.65E15aB	0.04±0.03aA	0.928±0.03
	1000	2.20E5±2.31E4aA	3.48±0.29aA	2.96E10±1.09E9aA	8.35E8±2.88E7aA	1.92E11±1.99E10aA	0.08±0.03aA	0.94±0.01
80%	500	5.30E3±2.0E3abA	1.78E1±1.09E1aA	4.79E16±1.58E16bA	2.05E7±5.51E6aA	5.92E10±6.0E9aA	0.08±0.026aA	0.94±0.02
	750	9.23E13±1.95E13bB	1.54E3±2.01E2bC	8.91E29±9.36E28bB	1.11E20±2.89E19bB	4.11E21±9.02E20bB	0.06±0.04abA	0.92±0.02
	1000	5.97E10±5.51E9bA	1.05E3±9.82E1bB	1.75E20±2.99E19bA	3.73E16±7.01E15bA	4.17E17±3.46E16cA	0.15±0.07abA	0.93±0.01

Note: The results are compared by Duncan 's multiple comparisons, different letters on shoulder indicate significant difference among difference moisture content groups (lowercase letters) and difference compression quantity groups (uppercase letter) (P<0.05). The same below.

It can be seen from Table 1 that the coefficients of determination R^2 for fitting the compressive stress-strain curves of CM using the optimized Nishihara model are all greater than 0.92. The results show that the optimized Nishihara model can better describe the compressive mechanical properties of CM.

The elastic modulus reflects the strength of the elastic deformation ability of CM. The larger the value, the weaker the elastic deformation ability and the worse the softness of the inner tissue of CM. In each group of tests in Table 1, E_2 is smaller than E_1, indicating that in the CM compression constitutive model, the elastic deformation capacity of the series spring element E_1 is stronger than that of the spring element E_2 in the Kelvin body, and the flexibility of the former is better than that of the latter.

The viscosity coefficient reflects the strength of CM's anti-deformation viscous resistance. The larger the value, the stronger the anti-deformation viscous resistance and the worse the fluidity of the internal tissue of CM. In each group of tests in Table 1, η_0 and η_2 are close in size, and both are greater than η_1, indicating that in the CM compression constitutive model, the viscous resistance against deformation of the Maxwell body viscous element η_0 and the Coulomb body viscous element η_2 are close, and both stronger than Kelvin body viscous element η_1.

Construct the CM stress relaxation model with the five-component generalized Maxwell model and use the same method to fit and solve the model parameters of CM stress relaxation under different test conditions, namely ε_i, E_a, E_b, η_a, η_b and E_e; then the results were compared and analyzed by the Duncan's method of multiple comparison and are shown in Table 2.

It can be seen from Table 2 that the coefficients of determination R^2 for fitting CM stress relaxation curves using the five-element generalized Maxwell model are all greater than 0.99, and the results show that the optimization of the Nishihara model could describe the mechanical properties of CM stress relaxation.

Through secondary development, the optimized West Proton model, the five-element generalized Maxwell model, and their corresponding parameter values can be applied to software such as ANSYS or ABAQUS to obtain a simulation model that can accurately describe the mechanical properties of CM compression and stress relaxation. Carry out the simulation of CM compression, and dehydration under the operation of different mechanisms, shorten the development cycle of equipment and save the cost of prototype processing.

Table 2

Effects of MC and FL on parameters of CM stress relaxation constitutive model

MC	*FM*	ε_0	E_a	E_b	η_a	η_b	E_e	R^2
50%	500	0.07±0.02aA	5.36±0.80aAB	1.94±060aA	2.66±1.02aA	34.12±3.32aA	5.86±2.49aA	0.995±0.002
	750	0.04±0.001aA	7.63±0.48aB	2.02±0.48aA	4.32±0.08cA	35.59±1.94bA	9.85±0.21aA	0.996±0.001
	1000	0.067±0.03aA	5.06±1.90aA	1.87±0.29bA	3.16±1.04aA	35.99±1.16bA	7.03±2.332aA	0.995±0.001
65%	500	0.05±0.005aA	9.51±0.43bB	2.02±0.267aA	3.66±0.30aA	30.46±1.13aA	7.37±0.88aA	0.997±0.001
	750	0.07±0.02bA	5.02±1.21bA	2.24±0.38aA	2.52±0.57bA	33.41±1.43bB	5.33±1.14bA	0.996±0.001
	1000	0.07±0.05aA	5.89±2.88aAB	1.99±0.22bA	3.46±1.78aA	34.98±1.31bB	7.07±3.58aA	0.996±0.001
80%	500	0.08±0.044aA	8.70±2.25bB	1.59±0.67aA	2.65±1.14aA	29.86±3.16aA	4.88±2.32aA	0.995±0.003
	750	0.10±0.01cA	5.28±0.62bA	1.48±0.35aA	1.82±0.20aA	30.28±1.20aA	3.42±0.46cA	0.994±0.001
	1000	0.09±0.013aA	5.91±1.02aAB	1.38±0.03aA	2.30±0.38aA	30.23±0.38aA	4.27±0.66aA	0.994±0.001

The influence of various factors on the mechanical characteristics of compression

Moisture content

The influence of MC and FL on the parameters of the CM compression constitutive model was analyzed by using the Duncan mean value comparison method, as shown in Table 1. The results showed that the elastic modulus (E_1, E_2) of different MC groups were significantly different (P<0.05). With the increase of MC, the elastic modulus, especially the elastic modulus E_1 in Hooke's body, increased significantly. The reason may be that the hydrophilic group in CM particles absorbs water, making the cell wall stronger and maintaining better elasticity. The difference of viscosity modulus (η_0, η_1, η_2) among groups with different MC was significant (P<0.05), which may be due to the positive correlation between viscosity modulus η_0 and MC in CM, the higher the MC, the higher the viscosity modulus, the larger η_0 is. It is comprehensively shown that moisture content and compression quality have a significant influence on elastic modulus and viscous modulus.

Filling mass

Table 1 shows that the elastic moduli (E_1, E_2) of different FM groups were significantly different (P<0.05). When MC is 50%, the elastic modulus increases with the increase of FM, probably because the larger the FM, the longer the pressure transmission path, and the local stress generated by the contact and extrusion of CM particles increases, which increases the elastic modulus. When the MC is between 65% and 80%, the elastic modulus first increases and then decreases as the FM increases. The reason may be related to the significant interaction between MC and FM.

The viscous modulus (η_1, η_2) differed significantly among different FM groups (P<0.05), which may be due to the fact that FM affects the relative motion between CM particles, resulting in changes in internal friction, which in turn affects the viscous modulus. When MC was 50%, the difference in viscosity modulus η0 was not significant between groups, but the difference in viscosity modulus η0 was significant between 65% MC and 80% MC groups, and the viscosity modulus η_0 increased significantly with the increase of MC. The reason may be that when the MC is 50%, there is less water between the CM particles, the CM is basically in a discrete state, and the viscosity modulus η_0 is not significantly different under different masses.

Influence of various factors on stress relaxation characteristics

Moisture content (MC)

As shown in Table 2, the Duncan mean comparison results showed that the elastic modulus and viscosity attenuation coefficient were significantly different among different MC groups (P<0.05), which may be due to the interaction between CM particles and particles and between particles and liquid. Adhesion makes it difficult to disperse during the stress relaxation process, and the change of MC affects the adhesion between CM particles, so there is a significant difference. When FM is 500 g and 1000 g, the elastic modulus and viscous attenuation coefficient change with water content are basically the same between the two groups (basically showing a trend of rising first and then decreasing); when FM is 750 g, elastic modulus and viscous attenuation coefficient increase with water content and reduce. The reasons for the above phenomenon may include both the influence of MC on the adhesion force and the interaction between MC and FM.

Filling Mass (FM)

As shown in Table 2, the Duncan mean comparison results show that the elastic modulus E_a and the viscous attenuation coefficient η_b of different FM groups are significantly different (P<0.05), indicating that FM has an effect on the spring element E_a of the first Maxwell body and the spring element E_a of the second Maxwell body. The viscous element η_b has a greater influence. There were no significant differences in elastic modulus E_b, E_e, and viscosity attenuation coefficient η_a among different FM groups (P>0.05).

CONCLUSIONS

(1) The uniaxial compression test shows that the compression dehydration process of CM can be divided into three stages: degassing, drainage, and viscoelastic-plastic deformation, and the elastic characteristics are obvious in the early stage and late stages of compression. Multi-parameter fitting the coefficient of determination R^2 is greater than 0.92, indicating that the optimized West Proton model can accurately describe the stress-strain relationship of CM during the compression process.

(2) The results of the stress relaxation test show that the stress decay rate of CM is fast first and then slow, and it only takes 6 s at most for the stress to decay from 0.8 MPa to 0.2 MPa, and the stress decay rate has a negative correlation with FM and MC; The Maxwell model fits the stress relaxation curve of CM, and its coefficient of determination R^2 is greater than 0.99, indicating that the model can fully characterize the stress relaxation characteristics of CM.

(3) The fitting parameters of the CM compression test showed that the elastic modulus and viscous modulus were significantly different among different MC groups (P<0.05), and MC and FM had significant effects on the elastic modulus and viscous modulus. The results of stress relaxation fitting parameters showed that there were significant differences in elastic modulus and viscous attenuation coefficient among different MC groups (P<0.05). Under different FM, there were differences in the elastic modulus and viscous attenuation coefficient between groups with MC. It may not only include the influence of MC on adhesion but also be related to the interaction between MC and FM.

ACKNOWLEDGEMENT

This project study was supported by the Jiangsu Province Agricultural Science and Technology Independent Innovation Fund Project (project number: CX(22)3093), and the Key Research and Development program of Hebei Province(Grant No.20327313D).

REFERENCES

[1] Aguirre-Villegas H. A., Larson R. A., Sharara M. A. (2019), Anaerobic digestion, solid-liquid separation, and drying of dairy manure: measuring constituents and modeling emission. *Science of the Total Environment*, 696, 134059. DOI: 10.1016/j.scitotenv.2019.134059

[2] Bai Z., Ma L., Jin S., Ma W., Velthof G. L., Oenema O., Liu L., Chadwick D., Zhang F. (2016), Nitrogen, phosphorus, and potassium flows through the manure management chain in China. *Environmental Science & Technology*, 50(24), 13409-13418. DOI: 10.1021/acs.est.6b03348

[3] Cârdei P., Stefan V., Popa L., Ciupercă R. (2019), Statistical models for the working process carried out by the organic fertilizer spreading machine. *INMATEH Agricultural Engineering*, 58(2). DOI: 10.35633/inmateh-58-13

[4] Ding Q., Sun H., Li Y., et al. (2023), Establishment and verification of soil mechanical compaction prediction model in paddy field under intensive production conditions (集约化生产条件下稻田土壤机械压实预测模型构建与验证). *Transactions of the Chinese Society of Agricultural Engineering*, 39(3): 42-51. DOI:10.11975/j.issn.1002-6819.202210216

[5] Ehlers G. A. C., Wagachchi D., Turner S. J. (2012), Nutrient conditions and reactor configuration influence floc size distribution and settling properties. *Water Science and Technology*, 65(1), 156-163. DOI: 10.2166/wst.2011.849

[6] Guan Z., Xinzhi W., Xu Z., et al. (2016), Optimal design and experiment of screw extrusion solid-liquid separator for cow manure(牛粪污螺旋挤压式固液分离机优化设计与试验). *Transactions of the Chinese Society for Agricultural Machinery*, 47(11): 192-197. DOI:10.6041/j.issn.1000-1298.2016.11.026

[7] Guilayn F., Jimenez J., Rouez M., Crest M., Patureau D. (2019), Digestate mechanical separation: efficiency profiles based on anaerobic digestion feedstock and equipment choice. *Bioresource Technology*, 274, 180-189. DOI: https://doi.org/10.1016/j.biortech.2018.11.090

[8] Hjorth M., Christensen K. V., Christensen M. L., Sommer S. G. (2010), Solid—liquid separation of animal slurry in theory and practice. A review. *Agronomy for Sustainable Development*, 30(1), 153-180. DOI: 10.1051/agro/2009010

[9] Husfeldt A. W., Endres M. I., Salfer J. A., Janni K. A. (2012), Management and characteristics of recycled manure solids used for bedding in Midwest freestall dairy herds. *Journal of Dairy Science*, 95(4), 2195-2203. DOI: 10.3168/jds.2011-5105

[10] Kong F., Wu T., Chen C., et al. (2021), Mechanical properties and construction of constitutive model for compression and stress relaxation of seed cotton (籽棉压缩与应力松弛力学特性及模型构建). *Transactions of the Chinese Society of Agricultural Engineering*, 37(07): 53-60. DOI:10.11975/j.issn.1002-6819.2021.07.007

[11] Ma Y., Xuan C., Wu P., et al. (2016), Experiment on stress relaxation of corn stover during compression with assisted vibration (玉米秸秆振动压缩过程的应力松弛试验). *Transactions of the Chinese society of agricultural engineering*, 32(19): 88-94. DOI:10.11975/j.issn.1002-6819.2016.19.012

[12] Nona K. D., Lenaerts B., Kayacan E., Saeys W. (2014), Bulk compression characteristics of straw and hay. *Biosystems Engineering*, 118, 194-202. DOI: 10.1016/j.biosystemseng.2013.12.005

[13] Shi H., Lv T., Zhu H., et al. (2014), Rheological properties and apparent viscosity model of pig manure (猪粪流变特性与表观粘度模型研究). *Transactions of the Chinese society for agricultural machinery*, 45(02): 188-193. DOI:10.6041/j.issn.1000-1298.2014.02.031

[14] Stefan V., Cardei P., Popa L., David L., Ciuperca R. (2019), Influence of the manure spreading machines' working parameters on the qualitative performances of the fertilization process. *INMATEH Agricultural Engineering*, 58(2), 115-120. DOI: 10.35633/inmateh-58-12

[15] Stefan V., Zaica A., Iosif A. (2021), Research on the uniformity degree of solid organic fertilizers distribution. *INMATEH Agricultural Engineering*, 65(3), 495-504. DOI: 10.35633/inmateh-65-51

[16] Wang R., Yu J., Wang T., Wang T., Li X. (2021), Experimental study on molding technology for a mixture of corn straw and cow manure. *Bioresources*, 16(1), 1740-1756. DOI: 10.15376/biores.16.1.1740-1756

[17] Wang S., Lv R., Yin X., Feng P., Hu K. (2023), Effects of the ratio of substituting mineral fertilizers with manure nitrogen on soil properties and vegetable yields in China: a meta-analysis. *Plants*, 12(4), 964. DOI: 10.3390/plants12040964

[18] Yao Y., Zhu B., Liu L. (2023), Differential description of basic mechanical properties of different soils (不同类土的基本力学特性差异性描述). *Chinese Journal of Geotechnical Engineering*, 45(1): 33-46. DOI:10.11779/CJGE20220083

[19] Yi X., Yu L., Chang S., Yin C., Wang H., Zhang Z. (2021), The effects of China's organic-substitute-chemical-fertilizer (OSCF) policy on greenhouse vegetable farmers. *Journal of Cleaner Production*, 297, 126677. DOI: https://doi.org/10.1016/j.jclepro.2021.126677

[20] [20] Zhao W., Zhu D., Qu H., et al. (2017), Design and experiment of interrupted-whorl screw extrusion device (断齿式螺旋挤压装置设计与试验). *Journal of Agricultural Mechanization Research*, 39(8): 86-91. DOI:10.3969/j.issn.1003-188X.2017.08.018

[21] [21] Zhao W., Zhu D., Zong W., et al. (2017), Operation parameter optimization of interrupted-whorl screw dewatering device of solid-liquid separator for livestock and poultry manure(畜禽粪污固液分离机断齿螺旋脱水装置运行参数优化). *Transactions of the Chinese society of agricultural engineering*, 33(02): 25-31. DOI:10.11975/j.issn.1002-6819.2017.02.004

[22] Zhu D., Zhao W., Zong W., et al. (2017), Numerical simulation analysis of flow field in flow channel of internal interrupted-whorl screw separator (断齿式挤压脱水流道内流场数值模拟). *Transactions of the Chinese Society for Agricultural Machinery*, 48(10): 92-100. DOI:10.6041/j.issn.1000-1298.2017.10.011

STUDY ON THE CHARACTERISTICS OF *Cerasus humilis* FREE FALLING IMPACT / 钙果自由落体冲击平板特性研究

Shilei KANG[1,2], Yanshun XU[1], Jingpu ZHOU[1], Bin TONG[1], Junlin HE*[1,2]
[1]College of Agricultural Engineering, Shanxi Agricultural University, Taigu 030801, China;
[2]Dryland Farm Machinery Key Technology and Equipment Key Laboratory of Shanxi Province, Taigu 030801, China
Tel: +86-0354-6288400; E-mail: hejunlin26@126.com
Corresponding author: Junlin HE
DOI: https://doi.org/10.35633/inmateh-71-63

Keywords: *Cerasus humilis*, *free-fall impact, contact model, optimization*

ABSTRACT
The contact parameters between calcium fruit and comb teeth are the key to the virtual picking test. In this paper, the physical test of free-falling impacting plate on the self-built test bench and the centre rotation composite simulation test of rigid body dynamics were carried out. The relationship between the contact parameters and dynamic characteristics was obtained, and the contact model was optimized. The contact stiffness k=0.868, force index e=1.91 and damping C=5.56E-4 were obtained when the height of the free falling body was 500 mm. The model was applied to lower free-fall simulation test, and the obtained results were in good agreement with the physical test results. The contact model can be used in the subsequent picking simulation.

摘要
钙果与梳齿之间的接触参数是进行虚拟采摘试验的关键，本文通过自建试验台进行了自由落体冲击刚性板的物理试验与刚体动力学的中心旋转复合仿真试验。获得了接触参数与动态特征之间的关系，并通过优化得到了接触模型，自由落体高度 500 mm 时获得的接触刚度 k=0.868，力指数 e=1.91，阻尼 C=5.56E-4。并将模型应用到更低自由落体高度仿真试验中,得到的结果与物理试验结果一致性很高，该接触模型可以用于后续的采摘仿真。

INTRODUCTION
When *Cerasus humilis* is harvested, the comb teeth are used to comb it off by impact, the fruit gets kinetic energy from the comb teeth, and there is a tendency to splash away from the picking mechanism *(Liu et al., 2021)*. So, it is necessary to study the dynamic phenomenon of the fruit after impact. Physical test method and virtual test method are commonly used to study dynamic behaviour of fruits. Since the fruits on the branches are often very close *(He et al., 2018)*, the behaviour of combing is a group behaviour. The physical test method is difficult to record the trajectory and other parameters of each fruit, which cannot be studied in detail. However, virtual experiments can obtain a lot of information about each element, such as displacement, velocity, collision force, energy, etc. As a biomaterial, *Cerasus humilis* has complex mechanical properties, and collision is the main force form in the harvest process. In order to study the dynamic behaviour of fruit after being impacted, it is necessary to obtain the contact parameters of the interaction between comb teeth and fruits. The free-fall impact test is the closest method to the picking. This method has been widely used by previous researchers to study the impact damage sensitivity of fruits such as apples, pears and peaches *(Yu et al., 2014; De et al., 2015; Gancarz et al., 2016; Komarnicki et al., 2017; Surdilovic et al., 2018)*. Of course, the free-fall impact test also has defects, the impact point of the fruit and the direction of rebound can't be determined. *Lewis et al* similarly concluded that the drop test technique was the most realistic simulation of what actually happened, although it was difficult to control the point of impact *(Lewis et al., 2007)*.

It is generally believed that the deformation rate significantly affects the mechanical properties of fruits, so it has become a problem to be solved in engineering applications to study the mechanical properties of fruits under different impact velocities and establish corresponding dynamic mechanical models. The impact test of a single fruit is a good compromise between applying actual load and method with sufficient control parameters, which is repeatable and controllable, and is an important way to obtain the contact parameters of the fruit and comb *(Brusewitz et al., 1994)*.

[1] *Shilei KANG,As Lec.PhD. Eng; Yanshun XU,M.S. Eng; Jingpu ZHOU,M.S. Eng; Bin TONG,M.S. Eng; Junlin HE,Prof.Ph.D.Eng.*

In view of the advantages and disadvantages of the above physical tests and virtual tests, this study made a comparative analysis of the physical tests and virtual tests to reproduce the mechanical phenomena of the fruit in the virtual tests. In this process, the simulation parameters are constantly adjusted to achieve the above purpose, and the accurate contact parameters between the fruit and the plate are finally obtained.

MATERIALS AND METHODS

Physical test of plate impacted by free falling fruit

The material was "Nongda No. 4" *Cerasus humilis*, which was sampled one day later than the quasi-static test in the literature (*Shilei et al., 2023)*. The samples were taken from the same field and the same sample screening and processing methods were used, which can be regarded as a same batch.

This experiment adopts a self-made test bench, which is composed of force sensor, plate, signal acquisition card, transmitter, processing software, etc. The structure and simplified model are shown in Fig.1. The cylindrical pressure sensor (AR-DN331) is selected, the accuracy is 0.1% full scale, the response frequency is 15 kHz. According to the weight of the fruit and the height of the test, the approximate range of the impact force is preliminarily calculated by the momentum theorem, and the range is selected as 50 N. Transmitter can output 0 V to 5 V voltage signals. The signal acquisition card converts an analogue signal into a digital signal. The USB3200N 12-bit acquisition card is selected, and the sampling frequency is as high as 5 MHz. The response frequency of sensor and acquisition card is considered comprehensively, and the sampling frequency is set to 10 kHz. Software is installed in computer, which can display and record in real time. One end of the sensor is reliably connected to the plate, the other end is fixed to the table. The plate is made of steel with a diameter of 100 mm and a thickness of 3 mm. The column with a steel ruler on the surface is fixed on the table, and the tray is adsorbed on the surface of the steel ruler with a magnet, and its centre is facing the plate.

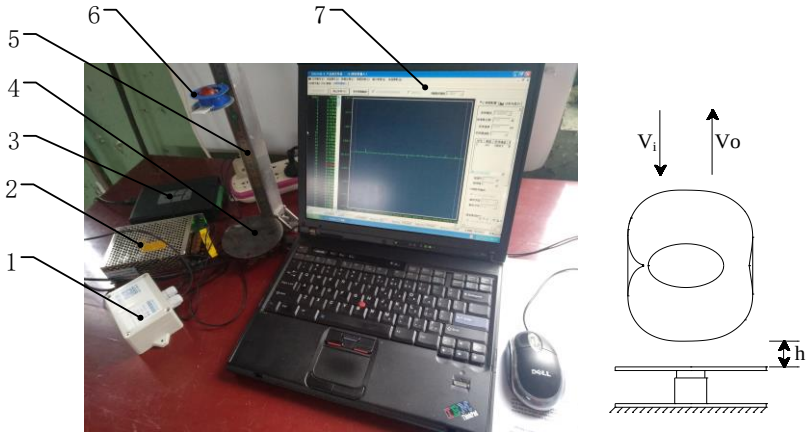


Fig. 1 - Free fall impact test device and the simplified model

1. Transmitter; 2. DC power supply; 3. Signal acquisition card; 4. Plate and force sensor; 5. Column; 6. Tray; 7. Software

The test device can obtain the time history data of the impact force. The force acting on the contact surface acts as a function of time depending on the mass of the fruit, the height it falls, and the contact radius of the fruit. The contact force acting as a function of time $F(t)$ can be easily obtained by computer-controlled data acquisition systems, and the method based solely on $F(t)$ would be highly desirable (*Meredith et al., 1990)*.

In the actual *Cerasus humilis* picking, the fruit is accelerated after comb, or can fall outside the comb tooth surface, then the impact speed should be limited to a certain range. When the fruit is in free fall, even if the height is only 500 mm, regardless of air resistance, its impact speed will reach 3.16 m/s, according to the previous picking experience with simple comb teeth, the collision at this speed is enough to make the fruit splash. In order to investigate the dynamic behaviour of fruits at different impact speeds, physical impact tests were carried out at the height of 100 mm, 200 mm, 300 mm, 400 mm and 500 mm, respectively.

When the fruit falls freely, its posture will be automatically adjusted, and the minimum cross-section will be perpendicular to the direction of gravity, so the cheek of the fruit will first contact with the target surface, which is why it was found in previous impact test studies that this part was the most severely damaged (*He et al., 2019)*. However, it is not certain when the height is low. Therefore, before the fruit falls, the cheek is turned down in advance, so that the first contact is made to that part.

Due to the uneven distribution of the external shape and internal mass of the fruit, the direction of fruit after the first contact with the plate is uncertain. Therefore, the point and angle of the second contact are not controllable, and it is likely to pop out of the range of the plate without obtaining complete data.

In the study, the samples with the first two impact points on the plate are considered to be valid, and at least 5 valid sample data are obtained for each height.

In any impact test device, the fruit does not impact directly on the sensor, but on the plate that is firmly connected to the sensor, and this is no exception. So, the signal received by the sensor is not only the impact force. It includes two parts: the gravity of the plate and the impact force of the fruit on it. The output signal of the sensor is a standard voltage signal with a range of 50 N and a signal amplitude of 5 V, then each voltage signal corresponds to a force value of 10 N, and the impact force value is calculated by formula (1):

$$F = (V_1 - V_0) \times 10 \quad (1)$$

where: V_1 - the measured voltage value, V_0 - static voltage signal value

The typical impact curve obtained from the impact test is shown in Fig.2, the drop height of which is 500 mm, these curves are obtained by subtracting the gravity portion of the plate. Three distinct impacts usually can be found in the data obtained from each sample, and the impact force gradually decreases. The first peak value of each curve is the fruit impact force value, and the three impact forces in the figure are 9.47 N, 4.22 N and 2.62 N respectively. When an increase in voltage is detected that exceeds the noise level of the force sensor, contact is initiated. There were difficulties in identifying the origin of the impact (*McGlone et al., 1997)*. When the value returns to the noise level of the sensor, it does not indicate that the fruit has separated from the plate, but that the vibration of the plate above the sensor has stopped.

The first peek is caused by the impact force in any curve. Since strain is the basis of force measurement, so when the fruit bounces off the plate, the plate will obtain a certain kinetic energy, damped free vibration occurs, then the strain material of the sensor has stiffness and damping. Previous researchers have described plates as being infinite mass and stiffness. In fact, no matter what form of sensor is used, there will be strain, there are plates between the force measuring element and the impact object, and the plate in order to ensure the reliability of the impact, generally relatively large, its weight can't be ignored. Some researchers have adopted a structure similar to this without considering this problem (*Lu et al., 2007)*. This is a problem introduced by the test device, the mechanical properties of the device will affect the response of the fruit collision, and must be considered.

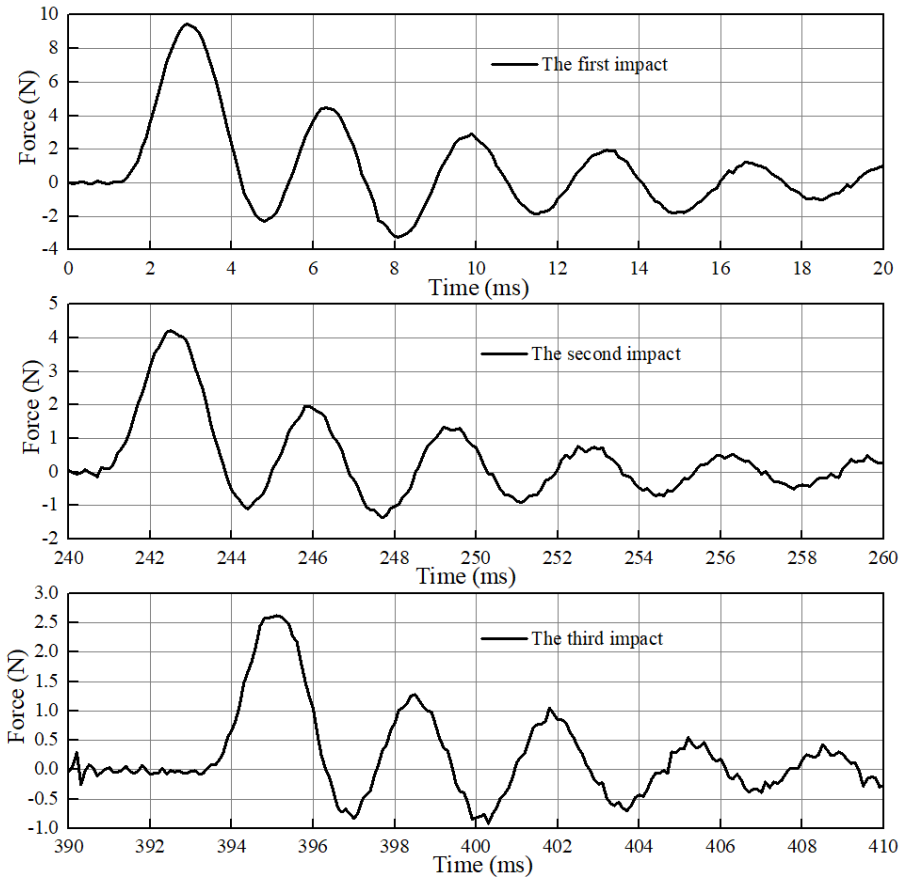


Fig. 2 - Typical impact force time history curve

Test the vibration characteristics of the device

Before studying the fruit impact test device, it must first be understood the vibration characteristics of the test device itself. Their height by the fall, each shock vibration between the peaks of vibration period statistics for T_d=3.5±0.1 ms. The second and third peaks of each shock are caused by the vibration of the test system itself. The smaller the impact force is, the greater the noise interference of the signal, the second and third peaks of the first impact are selected, and the attenuation coefficient is calculated to solve the damping ratio of the system, see formulas (2) and (3).

In theory, the ratio between the peaks of displacement is used to represent the degree of attenuation, but what is obtained in the test is the impact force. Under constant stiffness, the displacement is proportional to the impact force, so the impact force ratio is used here to calculate the attenuation rate.

- logarithmic decrement: $$\delta = \ln\frac{A_3}{A_2} = \frac{2\pi\xi}{\sqrt{1-\xi^2}} \quad (2)$$
- damping ratio: $$\xi = \sqrt{\frac{\delta^2}{\delta^2+4\pi^2}} \quad (3)$$

where: A_2, A_3 - the second and third peak forces formed by the first impact.

The average value and standard deviation of the damping ratio at each height of free falling body are shown in Table 1, and it can be found that they are very close. The accuracy of the test results and the stability of the device are confirmed. The overall average damping ratio is 0.073±0.008.

Table 1

The average and standard deviation of damping ratio respectively

Height of free fall（mm）	100	200	300	400	500	Overall average
Average damping ratio	0.069	0.074	0.075	0.076	0.068	0.073
Standard deviation	0.013	0.007	0.006	0.003	0.011	0.008

The vibration circular frequency of the test system is: $p_d = \frac{2\pi}{T_d} = 1797$ (4)

where p_d represents natural frequency of the damped system, which intrinsic dimension is 1, unit is 1.

T_d *is* the time between peaks, value is 3.5 ms in the text, which is obtained by test statistics

Then the stiffness of the test system is: $k = p_d^2 * m = 645842\ N/m = 645.8\ N/mm$ (5)

Where k is the system stiffness, N/mm, m is the mass of plate, 0.2 kg.

Damping: $$c = \xi * 2\sqrt{mk} = \xi * 2\sqrt{0.2 * 645842} = 0.073 * 721 = 52.47\ N \cdot s/m = 0.05247\ N \cdot s/mm \quad (6)$$

where c is the system damping.

Dynamic impact simulation of fruit

ADAMS is suitable for solving macroscopic mechanical dynamics problems. The collision and movement trajectory of *Cerasus humilis* in picking is a typical dynamic problem, so it is carried out in this platform. The contact parameters between fruit and comb are the key of virtual simulation. Therefore, the above physical experiments of fruit free-falling impacting plates are carried out. However, only physical tests have not been able to determine contact parameters. Perhaps this simple impact model can be calculated through theory, but our purpose is to study the picking process in the later stage, when the theoretical calculation will not be completed, so numerical simulation is adopted to find the contact parameters. Contact parameters such as contact stiffness and damping were calibrated in combination with physical experiments and numerical simulations *(Coetzee et al., 2016; 2017)*.

Preliminary calculation of contact parameters

Hertzian contact is the most commonly used contact theory. Its application has some basic assumptions, such as smooth and homogeneous contact objects, small elastic deformation, and only normal pressure on the contact surface. In fact, the impact test of the fruit has gone completely beyond the scope of the assumptions. However, the contact stiffness obtained by this theory is still valuable for reference, and can be used as a starting point for optimizing the search for equivalent contact parameters.

According to Hertz contact theory, the relevant formula is as follows (7, 8, 9, 10):

$$\frac{1}{R} = \frac{1}{R_1} + \frac{1}{R_2} \tag{7}$$

$$\frac{1}{E^*} = \frac{1-v^2}{E_1} + \frac{1-v^2}{E_2} \tag{8}$$

$$a = \left(\frac{3PR}{4E^*}\right)^{1/3} \tag{9}$$

$$\delta = \frac{a^2}{R} = \left(\frac{9P^2}{16RE^{*2}}\right)^{1/3} \tag{10}$$

where: a - contact radius; δ - contact depth; P - contact force at collision.

R_1 is defined as the fruit radius, with an average of 10 mm. R_2 is the radius of the plate, which is infinite. the equivalent radius R is calculated by formula (7) to be approximately equal to R_1 is 10 mm.

E_1 is defined as the elastic modulus of the fruit. Since the core is in the middle of the fruit and thicker pulp is separated from the plate during impact, the stiffness of the pulp is considered to be similar to that of the fruit. Therefore, E_1 is preliminarily set 1 MPa (*Shilei et al., 2023*), and E_2 is the elastic modulus of the plate, which is very large compared with the fruit, so the equivalent elastic modulus is shown in formula (11).

$$E^* = E_1/\left(1 - {v_1}^2\right) = 1.28\,MPa = 1.28\,N/mm^2 \tag{11}$$

According to the above formula (7, 8, 9, 10), the collision force calculation formula (12) can be obtained:

$$P = \left[\left(\frac{16RE^{*2}}{9}\right)^{1/2}\right]\delta^e \tag{12}$$

contact stiffness $$k = \sqrt{\frac{16RE^2}{9}} = 5.4\,N/mm$$

The prediction of contact dynamic behaviour largely depends on the choice of contact force model. The definition of contact generally includes two algorithms, namely collision function method and penalty function method. The most commonly used collision function method is actually implemented using the 'impact' function in the Adams solver.

The contact force is calculated as shown in formula (13).

$$F_{impact} = \begin{cases} 0 & q \geq q_0 \\ k(q_0 - q) - C\frac{dq}{dt} \cdot step(q, q_{0,} - \delta, 1, q_0, 0) & q \leq q_0 \end{cases} \tag{13}$$

where q_0 - initial distance; q- actual distance; dq/dt - distance rate; k corresponds to the contact stiffness; e stands for resilience index; δ is the penetration depth; C is damping.

Modelling in ADAMS

The geometric model of the fruit and plate are built in SolidWorks, which is better at building complex 3D models, and then import it into ADAMS *(Du et al., 2021)*. Set the weight of the fruit to 4.8 g, and adjust the height of the lower edge of the fruit to the test height. A spring is used to connect the plate to the earth, and an axial moving pair is set. The stiffness is set to 645.8 N/mm, and the damping is set to 0.05247 N.s/mm.

In order to reduce the number of contact parameters to be optimized, the effects of penetration depth on the contact force and the time between the first two collisions are first investigated. The contact parameters are set according to the above calculation, k is 5.4, e is initially set as 2, and C is 0.1% of k (5.4E-3). Simulation results show that the rebound height is much lower than the physical test, indicating that the model parameters are seriously deviated. If the rebound height is low, the energy loss is large, which has the greatest relationship with damping. If the damping is too large and too much energy is consumed, the damping is reduced, and the initial setting is 4E-4. The penetration depth is set to 0.1 mm, 0.01 mm and 0.001 mm respectively. Part of the results are shown in Table 2. The analysis shows that the coefficient of variation of the first impact contact force and the interval time between the first two impacts is small, and these indicators tend to be stable with the decrease of penetration depth. The penetration depth can be set to a smaller value of 0.001 mm to ensure that damping is involved in the calculation as early as possible.

Table 2

Impact forces and impact intervals at different penetration depths

Penetration depth（mm）	First impact force（N）	Interval between first two impacts（ms）
0.1	27	335
0.01	26.2	314
0.001	26.2	314
Average	26.5	321
Standard deviation	0.38	9.8
Variable coefficient	1.42%	3.06%

Orthogonal rotating centre composite virtual test

If the above Settings are used, the simulated first impact contact force will be much larger than the value of the physical test for comparison, regardless of the adjustment of other parameters. Because k is the factor that has the greatest influence on the contact force, its value is reduced, and the initial value range is 0.3 to 1 N/mm. In the selection principle of e, when k is low, the value is large, ranging from 1.5 to 3. If C takes the value of 4E-4 in the above test, its value range is appropriately expanded to 1E-4～6E-4.

A Central Composite Experiment Design (CCD) is done through Design Expert 8.0.6, and through the response surface optimization to find the optimal parameter combination. The contact parameters of each design point are input into the simulation model, and the corresponding target data is calculated, as shown in Table 3.

Table 3

Three-factor CCD experiment design

Run	Stiffness(A)	Force index(B)	Damping(C)	Force（N）	Interval（ms）
1	1	2.25	3.5E-4	14.9	334
2	0.44	1.8	2E-4	9.4	380
3	0.65	2.25	6E-4	11.8	275
4	0.86	1.8	5E-4	11.2	310
5	0.44	2.7	5E-4	13.6	282
6	0.65	2.25	1E-4	13.6	385
7	0.44	1.8	5E-4	7.6	276
8	0.3	2.25	3.5E-4	9.7	328
9	0.86	2.7	2E-4	18.3	334
10	0.86	2.7	5E-4	15.1	287
11	0.65	2.25	3.5E-4	13.1	326
12	0.44	2.7	2E-4	14.3	362
13	0.65	1.5	3.5E-4	8.4	323
14	0.65	3	3.5E-4	17.7	301
15	0.86	1.8	2E-4	12.4	372

RESULTS

Analysis of variance

The first contact force represents the maximum contact strength. The variance analysis of the contact force data is shown in Table 4. The model is extremely significant, with a coefficient of determination (CoD) R^2 of 0.978, is shown in formula 14, indicating a high correlation between the model and the experimental factors. The factor A, B and C all have extremely significant influence on the model. It can also be seen from the influence of all factors on the contact force in Fig.3 that the contact force varies greatly within the variation range of all factors.

Table 4

Variance analysis of the first contact force

Source	DF	SS	F-value	P-value	Sig
Model	3	135.74	160.46	<0.0001	**
A	1	31.82	112.84	<0.0001	**
B	1	96.70	342.95	<0.0001	**
C	1	7.22	25.59	0.0004	**
Residual	11	3.1			
Total	14	138.84			

*Notes: SS is the sum of squares, DF is degrees of freedom, Sig is significance, ** means P < 0.01, $F_{0.01}(1,11)=9.65$, $F_{0.01}(3,11)=6.22$.*

$$F_{max-1} = -3.79 + 7.33A + 5.97B - 4890C \quad (14)$$

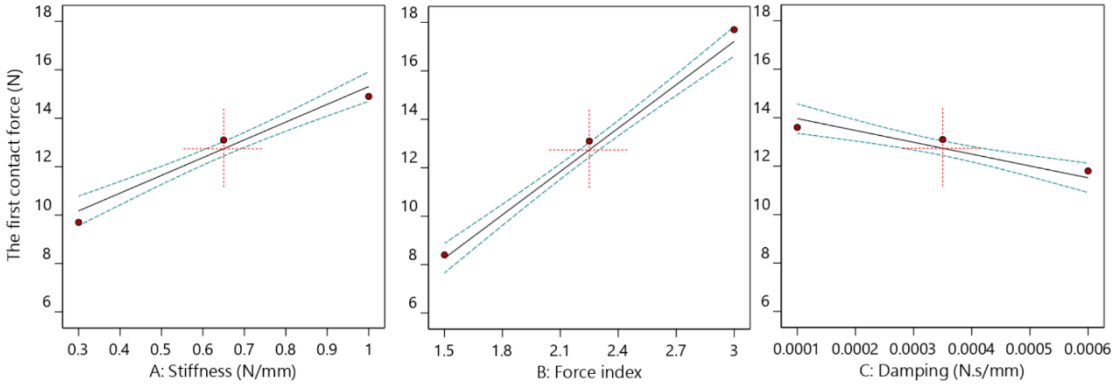


Fig. 3 - Single-factor relationship between first contact force and contact parameters

The interval between two contacts represents energy absorption. The variance analysis of the interval time data is obtained in Table 5. The model is extremely significant, and the CoD R^2 is 0.994, is shown in formula 15, indicating a high correlation between the model and the factors. The stiffness k is not significant to the model, e and C are extremely significant to the model, and the interaction terms AB, AC, BC and B^2 are extremely significant. It can also be seen from the influence of various factors on the contact force in Fig.4 that the contact force varies greatly within the variation range of B and C.

Table 5

Analysis of variance between two contact intervals

Source	DF	SS	F-value	P-value	Sig
Model	9	2750.33	158.17	<0.0001	**
A	1	12.55	0.7216	0.4237	
B	1	885.99	50.95	0.0002	**
C	1	16730.16	962.13	<0.0001	**
AB	1	300.12	17.26	0.0043	**
AC	1	703.13	40.44	0.0004	**
BC	1	190.13	10.93	0.0130	**
B^2	1	430.21	24.74	0.0016	**
Residual	7	17.39			
Total	14	138.84			

Notes: ** means P < 0.01, $F_{0.01}(1,7)=12.2$, $F_{0.01}(1,7)=6.72$.

$$t = 325.69 + 47.03B - 5.98 * 10^5 C - 66AB + 3.03 * 10^5 AC + 73539BC - 30.67B^2 \quad (15)$$

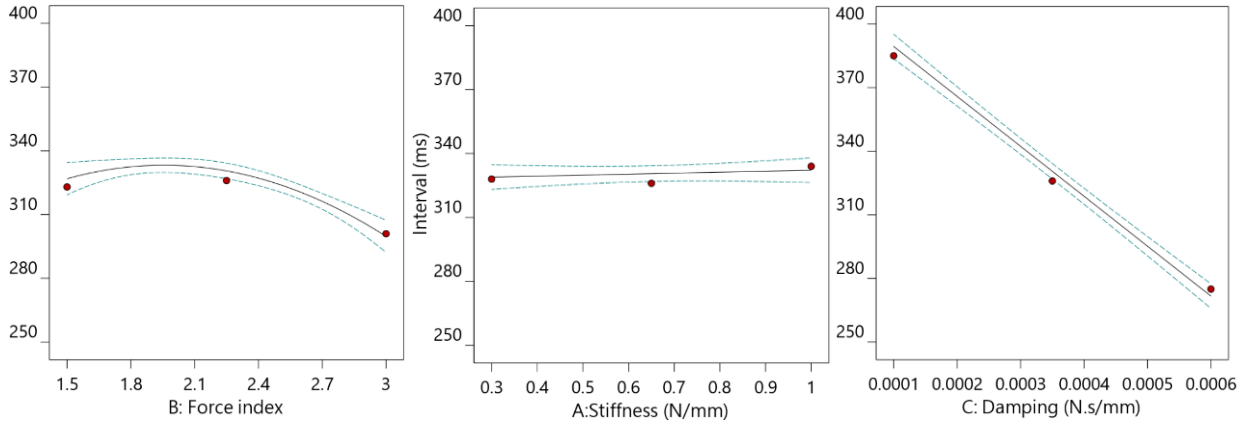


Fig. 4 - Single-factor relationship between two contact intervals and contact parameters

Contact model optimization

The sample data closest to the average value of 500 mm free-fall impact is taken as the optimization target. The first impact force of this sample is 11.3 N, the interval time of the first two impacts is 299 ms, and the appropriate error range is set. If the two results data of the above sample can be reproduced in ADAMS, The contact parameters are reasonable. The optimized parameters are k=0.868, e=1.91, C=5.56E-4.

This set of data is used to construct a contact model, and the corresponding collision results data is calculated and shown in Table 6 together with the physical test data. A difference of up to 2% can been seen.

Through experimental design and optimization, the optimal contact parameters are found accurately, and the physical test phenomenon reappear well in the simulation test. Previous studies have also verified the feasibility of finding contact parameters through optimization through standard rubber balls *(Tabatabaekoloor et al., 2013)*.

Table 6

Comparison of contact force and interval at free fall of 500 mm

	Force（N）	Interval（ms）
Physical test	11.3	299
Virtual test	11.4	293
Difference	0.1	6
Difference/Physical test	0.9%	2%

The contact parameters obtained above are input into the collision models of other free-falling bodies for simulation. The corresponding contact collision data are obtained. Compared with the sample data under the height of the falling body, the difference between the physical and simulation test results is only 7% at most. Due to space limitations, the data are not listed here. Therefore, the above contact model can be used to simulate the impact below the velocity corresponding to the height of the free-falling body.

CONCLUSIONS

(1) By analysing the time history data of the impact force, it is found that the impact force of each collision presents the phenomenon of damped free vibration attenuation, and the connection between the fruit plate and the earth is not rigid. Then, the vibration parameters are obtained by theoretical calculation.

(2) The influence of each contact parameter on the contact force and interval was obtained through a set of orthogonal rotating centre composite tests. The optimal contact model was obtained by using the optimization method by comparing with the physical test. The contact stiffness k=0.868, force index e=1.91 and damping C=5.56E-4 are obtained when the height of the free falling body is 500 mm. The model is applied to lower free-fall simulation test, and the obtained results are in good agreement with the physical test results. The contact model can be used in the subsequent picking simulation.

ACKNOWLEDGEMENT

This research, titled “Study on the Characteristics of *Cerasus humilis* Free Falling Impact”, was funded by project: “Science and Technology Innovation Fund of Shanxi Agricultural University (Grant No. 2017017)”, and was also supported by “Shanxi Basic Research Programme (Grant No. 202203021221174)”.

REFERENCES

[1] Brusewitz, G. H. (1994). Drop impact testing applications to fruit quality. *International agrophysics*, 8(3).

[2] Coetzee, C. J. (2016). Calibration of the discrete element method and the effect of particle shape. *Powder Technology*, 297, 50-70.

[3] Coetzee, C. J. (2017). Calibration of the discrete element method. Powder Technology, 310, 104-142.

[4] De Kleine, M. E., & Karkee, M. (2015). Evaluating a non-Newtonian shear-thickening surface during fruit impacts. *Transactions of the ASABE*, 58(3), 907-915.

[5] Du, X., Shen, T., Zhao, L., Zhang, G., Hu, A., Fang, S., & Yao, X. (2021). Design and experiment of the comb-brush harvesting machine with variable spacing for oil-tea camellia fruit. *International Journal of Agricultural and Biological Engineering*, 14(1), 172-177.

[6] Gancarz, M. (2016). Correlation between cell size and black spot of potato tuber parenchyma tissue after storage. *Postharvest Biology and Technology*, 117, 161-167.

[7] Goltsberg, R., Etsion, I., & Davidi, G. (2011). The onset of plastic yielding in a coated sphere compressed by a rigid flat. *Wear*, 271(11-12), 2968-2977.

[8] He, Y., He, J., Du, X., & Fang, D. (2018). Design and experimental study of the finger-type lifter test bench for Cerasus humilis branches. *INMATEH-Agricultural Engineering*, 56(3), pp.147-154.

[9] He Yongqiang, He Junlin, Fang Dawei, Du Xiaobin. (2019). Collision Injury Assessment of Mechanical Harvesting Cerasus humilis Fruit Based on Deformation Energy (基于变形能的机械采收钙果果实碰撞损伤评估). *Agricultural Engineering,* Vol.9, pp. 67-72, Beijing/China.

[10] Komarnicki, P., Stopa, R., Kuta, Ł., & Szyjewicz, D. (2017). Determination of apple bruise resistance based on the surface pressure and contact area measurements under impact loads. *Computers and Electronics in Agriculture*, 142, 155-164.

[11] Lewis, R., Yoxall, A., Canty, L. A., & Romo, E. R. (2007). Development of engineering design tools to help reduce apple bruising. *Journal of Food Engineering*, 83(3), 356-365.

[12] Liu, S., Junlin, H. E., & Wu, N. (2021). Design and experimental study of the comb-type harvesting test bench for *Cerasus humilis*. *INMATEH-Agricultural Engineering*, 63(1), pp.261-270. DOI: https://doi.org/10.35633/inmateh-63-26.

[13] Lu Lixin, Wang Zhiwei (2007). Dropping impact mechanical characteristics of apple (苹果跌落冲击力学特性研究). *Transactions of the CSAE*, Vol.23, pp. 254-258, Beijing/China.

[14] McGlone, V. A., Jordan, R. B., & Schaare, P. N. (1997). Mass and drop-height influence on kiwifruit firmness by impact force. *Transactions of the ASAE*, 40(5), 1421-1428.

[15] Meredith, F. I., Leffler, R. G., & Lyon, C. E. (1990). Detection of firmness in peaches by impact force response. *Transactions of the ASAE*, 33(1), 186-0188.

[16] Shilei, K. A. N. G., Jiaxuan, L. U., Huhu, Y. A. N. G., Yanxi, G. U. O., & Junlin, H. E. (2023). Mechanical model of *Cerasus humilis* established by uniaxial compression physical test and virtual simulation. *INMATEH-Agricultural Engineering*, 69(1), pp. 527-536. DOI: https://doi.org/10.35633/inmateh-69-50

[17] Surdilovic, J., Praeger, U., Herold, B., Truppel, I., & Geyer, M. (2018). Impact characterization of agricultural products by fall trajectory simulation and measurement. *Computers and Electronics in Agriculture*, 151, 460-468.

[18] Tabatabaekoloor, R. (2013). Engineering properties and bruise susceptibility of peach fruits (Prunus persica). *Agricultural Engineering International: CIGR Journal*, 15(4), 244-252.

[19] Yu, P., Li, C., Takeda, F., & Krewer, G. (2014). Visual bruise assessment and analysis of mechanical impact measurement in southern highbush blueberries. *Applied Engineering in Agriculture*, 30(1), 29-37.

DESIGN AND EXPERIMENT OF IMPELLER TYPE VARIABLE FERTILIZER DISCHARGER DEVICE BASED ON EDEM SIMULATION

/

基于 EDEM 仿真的叶轮式变量排肥器设计与试验

Bai-wei Wang [1,2], Gang Che[*1,2], Lin Wan [*1,2], Nai-chen Zhao [1], Zhan-nan Guan [1]
[1)]College of Engineering, Heilongjiang Bayi Agricultural University, Daqing/P.R.China
[2)]Key Laboratory of Intelligent Agricultural Machinery Equipment in Heilongjiang Province, Daqing / P.R.China
Tel：+86-459-13836961617;E-mile: chegang180@126.com;
Corresponding author: Gang Che
DOI: https://doi.org/10.35633/inmateh-71-64

Keywords: *impeller-type, fertilizer discharger device, EDEM, variable, experiment*

ABSTRACT

Aiming at the problem of poor uniformity and stability of fertilizer discharge caused by the operation of the fertilizer discharger device in the variable fertilization operation of rice, combined with the agronomic requirements of deep fertilization on the northeast side, an impeller type variable side deep fertilizer was designed. According to the change of the prescription map, the adjustment factors are changed to achieve reasonable fertilization. Based on EDEM simulation, using the fertilizer discharge stability and uniformity coefficient of variation as indicators, under different impeller blades, different impeller speeds and different fertilizer discharge port angles, a secondary orthogonal rotation combination test was carried out, using Design-Expert. V8.0.6.1 is analyzed and tested, the regression equation and the response surface diagram are obtained, the interaction between the influencing factors is analyzed, and the best combination is determined. It is concluded that the stability and uniformity coefficient of variation of fertilizer discharge have reached the quality evaluation index of fertilization machinery. According to technical specifications, the variation coefficient stability of is 0.67%~2.85%, and the variation coefficient of uniformity is 2.7%~16.4%. When the number of blades is 6, the fan angle of the fertilizer outlet is 35.7°, and the impeller speed is 18.85 r·min^{-1}, the minimum variation coefficient of stability is 0.67%, and the minimum variation coefficient of uniformity is 2.1%. The bench test results are basically consistent with the optimal combination of simulation, and meet the design requirements.

摘要

针对在水稻变量施肥作业中，排肥器运转导致排肥均匀性和稳定性较差的问题。结合东北侧深施肥农艺要求，设计了一种叶轮式变量侧深施肥器。根据处方图变化，改变调节因素来实现合理施肥。基于 EDEM 模拟仿真，以排肥稳定性、均匀性变异系数为指标，在不同叶轮叶片、不同叶轮转速和不同排肥口角度大小参数下，进行二次正交旋转组合试验，运用 Design-Expert.V8.0.6.1 进行分析检验，得到回归方程和响应曲面图，分析影响因素之间交互作用，确定最佳组合，得出：排肥稳定性和均匀性变异系数均达到了施肥机械质量评价指标技术规范要求，稳定性变异系数为 0.67%~2.85%，均匀性变异系数为 2.7%~16.4%。当叶片数为 6 片，排肥口扇面角度大小为 35.7°，叶轮转速为 18.85 r·min^{-1} 时，稳定性变异系数最小为 0.67%，均匀性变异系数最小为 2.1%。台架实验结果与仿真最优组合基本吻合，符合设计要求。

INTRODUCTION

As rice is an important part of my country's food supply, it is particularly important to increase rice yield *(Shi et al., 2020)*. Fertilization is one of the main factors to increase crop yield. How to apply fertilizer reasonably has become a problem that cannot be ignored. Variable side-depth fertilization can carry out precise fertilization according to soil fertility, and achieve fertilizer saving and other effects *(Yuan et al., 2011; Mirzakhaninafchi et al., 2021; Cao., 1984)*. It solves the problems of inaccurate fertilization amount and low fertilizer utilization rate in the process of quantitative fertilization of rice, and achieves a good effect of weight loss and yield increase. The most critical part of the variable side-depth fertilization device is the fertilizer discharge device.

[1]*Bai-wei Wang, master degree; Gang Che, Prof. Ph.D.; Lin Wan, Prof. Ph.D.; Nai-chen Zhao, Ph.D.; Zhan-nan Guan master degree;*

The stability of the fertilizer supply, discharge and fertilization of the fertilizer discharge device determines its performance *(Wen et al., 2019)*. At present, the mainstream fertilizer discharge device at home and abroad include horizontal shaft type, horizontal turntable type, vibration type et al. *Bao et al., (2002), Ishola et al., (2014), Jun et al., (2021)*, most of them rely on forced fertilizer discharge, which will cause pulsation and fertilizer sticking inside the fertilizer discharge device resulting in inaccurate stability and uniformity of fertilizer discharge. Japan's Yanmar, Kubota, and Iseki respectively adopt horizontal hole-disk fertilizer discharge devices and outer grooved wheel-type dislocation fertilizer discharge device, which largely solve the pulse phenomenon in the fertilizer discharge process and improve accuracy and uniformity, but the structure is complex and difficult to maintain *(Zha et al., 2020; Cheng et al., 2012).* Wang Jinfeng *(Wang et al., 2021)* designed the disc top-outside deep fertilization device for rice fields and Li Kai *(Li et al., 2017)* designed the dual-variable external groove wheel fertilizer discharge device. By adjusting the rotation impeller speed of the rotating shaft, the amount of fertilizer discharge can be changed, which improves the uniformity and stability of fertilization to a certain extent. However, in the process of work, pulsation occurs, resulting in inaccurate fertilizer application.

According to the agronomic requirements of side deep fertilization and the design technical requirements of fertilizer discharger device mechanism, the domestic side deep fertilization device has problems such as poor fertilization uniformity and stability. Combining with the characteristics of special granular fertilizer for side deep compound fertilizer commonly used in rice planting in Northeast China, an impeller-type variable side deep fertilizer is innovatively designed. Through the adjustment of fertilization amount, the fertilizer discharge device is studied by using EDEM software simulation, which provides a theoretical basis for the innovative development and optimization design of side deep fertilization equipment.

MATERIALS AND METHODS

Structure and working principle of fertilization device

The impeller-type variable fertilization device is shown in Fig. 1. It is mainly composed of a fertilizer box, an impeller-type fertilizer discharger device, a drive motor, an air delivery system, and a frame. The work flow chart of the whole machine is shown in Fig. 2.

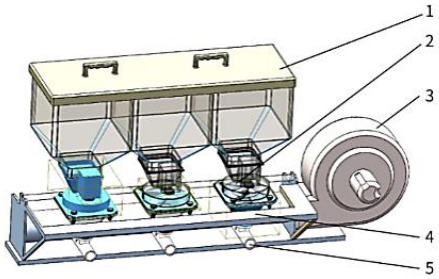


Fig. 1 - Wheeled variable fertilization device
1. Fertilizer box; 2. Impeller fertilizer discharge device ; 3. Fan; 4. Frame; 5: Venturi tube

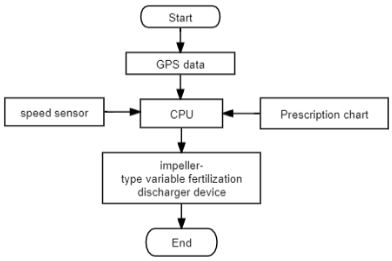


Fig. 2 - Work flow chart of the whole machine

The structure and working principle of the impeller type fertilizer discharger device

Impeller type fertilizer structure

The structure of the impeller type fertilizer discharger device mainly includes the upper casing, the impeller blade, the middle baffle, the lower casing, and the brush. The main components of the fertilizer discharger device structure are shown in Fig. 3.

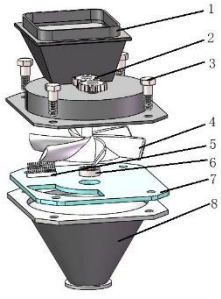


Fig. 3 - Three-dimensional drawing of the fertilizer discharger device component
1. Upper casing; 2. Transmission gear; 3. Fastening bolt; 4. Impeller blade; 5. Brush; 6. Bearing; 7. Middle baffle; 8. Lower casing

The working principle of fertilizer discharger device

When the fertilizer discharge device is in operation, fertilizers enter through the device inlet. The CPU, according to the prescription diagram information, converts PWM signals and transmits them to the discharge device motor. The discharge device motor achieves variable fertilization by adjusting the impeller speed, replacing different impellers, or adjusting the opening size of the central baffle in the fertilizer discharge port, in accordance with specified angles.

Granular Fertilizer Movement Analysis

Momentary Force Analysis of Fertilizer Particles Sliding During Fertilization

When the fertilizer falls to the fertilizer discharger device only the surface sliding on the impeller boss is considered. During the fertilizer filling process, the impeller rotates and the fertilizer fills the fertilizer discharger device cavity. Select a certain granular fertilizer A as the research object, and analyze it at a certain moment, assuming that the linear velocity of the fertilizer A is equal to the rotational linear velocity of the outer diameter of the blade, and taking the center of the impeller as the origin, a reference coordinate system OXYZ is established. The force analysis of granular fertilizer A is shown in Fig.4, the following relationship 1 is obtained:

$$F_A = G + F_N + F_f + F_c + F_e + F_b \tag{1}$$

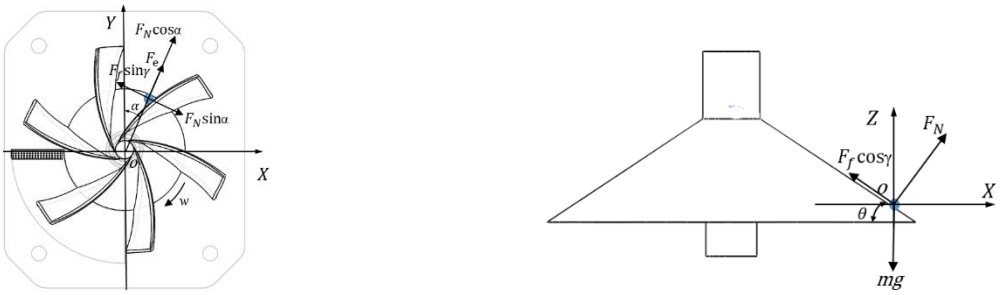
In the formula：$G = m_A g, F_f = \mu m_A g, F_C = 2 m_A \omega v_{rel}, F_e = m_A \omega^2 r$

where: F_A is the resultant force of granular fertilizer A, (N); G is the gravity of granular fertilizer A, (N); F_N is the support force of granular fertilizer A on the blade, (N); F_f is the friction force of granular fertilizer A on the impeller, (N) ; F_c is the Coriolis force, ((N); Fe is the traction centrifugal force, (N); m_A is the mass of the particle A, (g); ω is the angular velocity of the impeller, (r/min); r is the distance from the center of the impeller to the centroid of the fertilizer, (mm)；v_{rel} is the velocity relative to the boss, m/s.

The direction and magnitude of the interaction forces between granular fertilizers are constantly changing, but there is a mutual interaction force between the particles. At this point, an equilibrium state is reached, and the interaction force between the fertilizers is zero. During the sliding moment of granular fertilizer A, A is stationary relative to the convex surface, with v_{rel} being zero, meaning F_C is zero. At this moment, the resultant force acting on the fertilizer is described by the following equation:

$$F_A = G + F_N + F_f + F_e \tag{2}$$

At this time, it is assumed that the direction of the friction force received is opposite to the direction of motion. The angle between the friction force and the XOZ plane is set to γ, and the analysis shows that the larger the γ, the smaller the slip along the Z axis. The force analysis of granular fertilizer A is shown in Fig. 4.



（a） （b）

Fig. 4 - Instantaneous force analysis of fertilizer particles sliding during fertilization process

Analyzing the fertilizer particle A at the sliding instant equation is 3, 4, 5:

$$F_e + F_N \cos\alpha = 0 \tag{3}$$

$$F_N \sin\alpha - F_f \sin\gamma = 0 \tag{4}$$

$$F_f \cos\gamma \cos\theta + F_N \sin\theta - G = 0 \tag{5}$$

Simplified processing:

$$\gamma = \arctan\frac{r\omega^2 \sin\alpha \cos\theta}{g\cos\alpha - r\omega^2 \sin\theta} \tag{6}$$

where: θ is the bottom angle of the impeller boss, (°); α is the initial angle of fertilizer sliding, (°); γ is the angle between the friction force and the XOZ plane, (°)

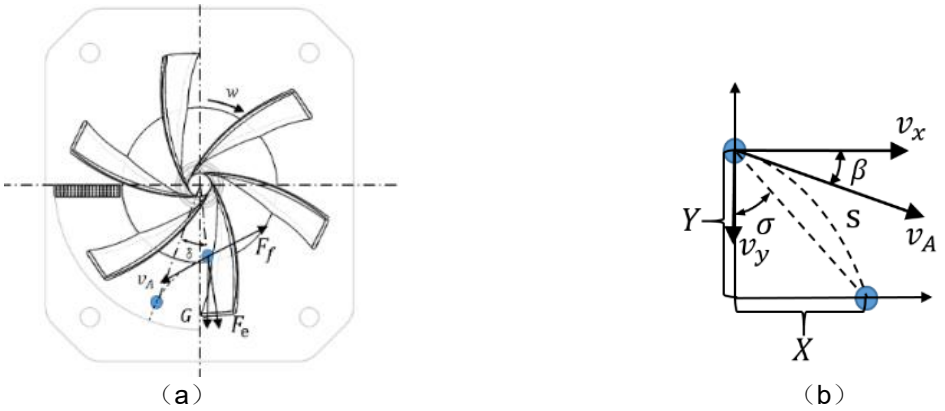
According to the kinetic energy theorem, analyze the possible maximum relative velocity, take the projection form of the particle center of mass motion differential equation on the coordinate axis, and establish the motion equation:

$$m\frac{d_v}{d_t} = mg\sin\alpha - \mu mg\cos\alpha \tag{7}$$

The larger the γ, the more parallel the fertilizer movement track is to the Y-axis direction, the easier it is to enter the fertilizer discharger device cavity, and the smaller the slippage along the Z-axis is. On the contrary, the greater the Z-axis slippage, the fertilizer will have slippage fluctuations, which will affect the filling factor. It can be seen from formulas 6 and 7 that γ is related to ω (impeller speed n), bottom angle θ of impeller boss, initial angle α when fertilizer begins to slide, and distance r from impeller center to fertilizer center of mass. Therefore, appropriately increasing the rotational impeller speed ω helps to improve the uniformity and stability of fertilization.

Momentary Force Analysis of Sliding Granular Fertilizer during Fertilizer Discharging

When the fertilizer reaches the fertilizer outlet of the middle baffle, the fertilizer moves flat and the impeller speed when it leaves the impeller is the impeller tangential fertilizer speed V_A, and falls to the lower casing under the joint action of its own gravity G, centrifugal force F_e and air resistance F_f, decompose V_A into V_X, V_y, and its horizontal displacement X and vertical displacement Y are shown in Fig. 5



（a） （b）

Fig. 5 - Analysis of fertilizer particle discharge port movement in fertilizer discharge process

$$\begin{cases} \mathrm{X} = v_x t \\ \mathrm{Y} = v_y t \\ \mathrm{Z} = \frac{1}{2} g t^2 \end{cases} \tag{8}$$

$$v_A = \omega r \tag{9}$$

$$v_x = v_A\cos\beta \tag{10}$$

$$v_y = v_A\sin\beta \tag{11}$$

Where: X is the x displacement of the fertilizer particle A in the horizontal direction, (m); Y is the y displacement of the fertilizer particle A in the horizontal direction, (m); Z is the z displacement of the fertilizer particle A in the vertical direction, (m); v_x is the movement of the fertilizer particle A in the horizontal direction. The velocity in the x direction per hour, (m/s); v_y is the velocity in the y direction of the fertilizer particle A when it is thrown flat, (m/s); g is the acceleration of gravity, (m/s^2); t is the time for the fertilizer particle A to do flat throwing motion, (s); ω is the angular velocity of the impeller blade, (rad/s); r is the distance from the center of the impeller to the center of mass of the fertilizer, (mm).

According to Newton's second law, when the fertilizer is thrown, the trajectory is a parabola, and the differential equation of motion is established:

$$\begin{cases} m\frac{d^2x}{dt} = 0 \\ m\frac{d^2}{dt} = mg \end{cases} \tag{12}$$

When t=0, X=0, $m\frac{d^2x}{dt} = v_x$; when t=0, y=0, $m\frac{d^2x}{dt} = 0$

According to the motion equations 8~12 of the granular fertilizer, the trajectory equation of motion is:

$$Z = \frac{g}{2v_x^2}x^2 \tag{13}$$

$$\delta = \arctan\frac{X}{Y+r} = arctan\frac{\omega r\cos\sqrt{\frac{2Z}{g}}}{\frac{s\omega}{\sigma}\sqrt{\frac{2Z}{g}}+r} \tag{14}$$

Where: δ is the starting and ending position rotation angle of the fertilizer, (°); σ is the offset angle of the fertilizer flat throwing, (°); s is the length of the fertilizer flat throwing trajectory, (mm).

The position of the fertilizer drop point is related to the rotation angle δ, and the rotation angle δ is related to the angular velocity ω, the fertilizer rotation angle σ, and the vertical displacement Z. When the fertilizer rotation angle σ and the vertical displacement Z are constant, as the rotational impeller speed n increases, the falling δ will also increase. The larger the δ, the easier it is for the fertilizer to accumulate and cause blockage. Therefore, appropriately increasing the impeller speed can improve the performance of fertilizer discharge.

EDEM simulation test analysis

The fertilizer used in this paper is domestic compound fertilizer, the raw material of the fertilizer discharger device is transparent PVC hard plastic, and the 3D printing material used in the test is PLA. Compared with PLA, PVC has a shorter service life and is prone to problems such as wear and aging, and 3D printing is more accurate and convenient. The brush is made of nylon 66. Through consulting the literature *(Tormi et al., 2022; Xing et al., 2019; Tai et al., 2020; Gao et al., 2019)* and related experiments, the size parameters of the fertilizer and the characteristic parameters of various materials are obtained as shown in Table 1.

The average length, width, and height of the compound fertilizer are 4.66 mm, 4.31 mm, and 3.92 mm, and the equivalent diameter is 4.28 mm. The average spherical rate is 95%, and the density is 1670 kg/m^3.

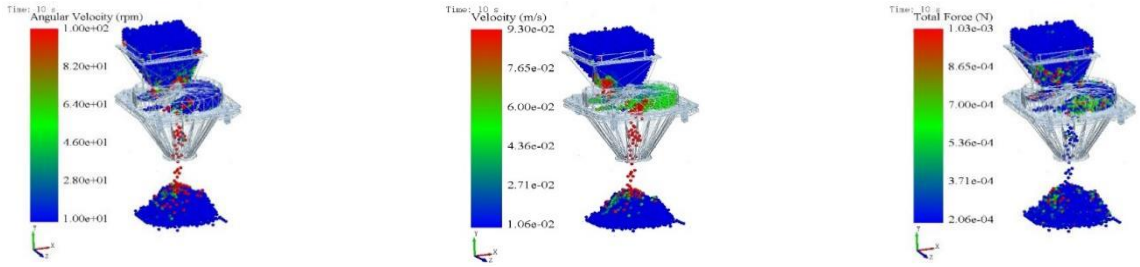
Table 1

Compound fertilizer and geometry simulation parameters

Item	Property	Value	Item	Property	Value
fertilizer	Poisson's ratio	0.25	Granules-Granules	rolling friction coefficient	0.28
	Shear modulus	1.0X10^7		static friction coefficient	0.48
	Density kg/m^3	1670		Recovery coefficient	0.52
PLA	Poisson's ratio	0.35	Fertilizer-PLA	rolling friction coefficient	0.18
	Shear modulus	4.0X10^8		static friction coefficient	0.23
	Density kg/m^3	1255		Recovery coefficient	0.51

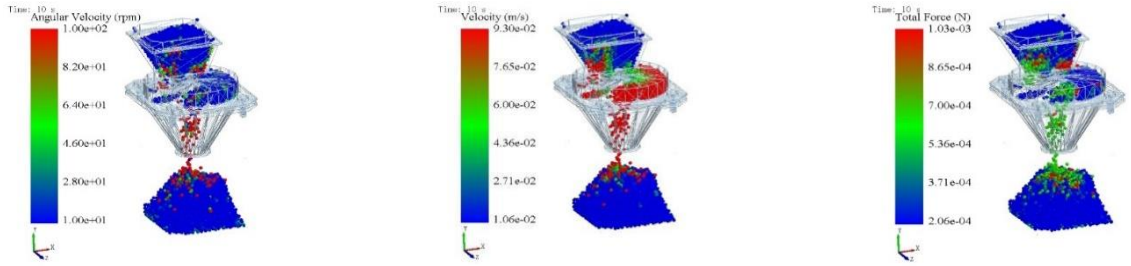
RESULTS

After importing the fertilizer discharge device into the EDEM software, an analysis was conducted on the fertilizer angular velocity, fertilizer velocity, and forces acting on the fertilizer for impeller speeds of 10 m/s and 20 m/s, respectively. The changing status can be visually observed through the color and data bars of the fertilizer, as depicted in Figures 6 and 7.



（a） （b） （c）

Fig. 6 - The angular velocity, velocity and force model of the fertilizer when the impeller speed is 10 r/min



（a） （b） （c）

Fig. 7 - The angular velocity, velocity and force model of the fertilizer when the impeller speed is 20 r/min

It can be seen from Figs. 6 and 7 that the angular velocity, velocity, and force of the fertilizer vary greatly when the fertilizer inlet contacts the impeller and when the impeller discharges the fertilizer from the fertilizer outlet, while the other places have no obvious variation range. According to the angular velocity model, with the increase of the impeller speed, the fertilizer angular velocity ranges from 10 ~ 100 r/min when the variation range is large. The fertilizer speed model shows that the fertilizer speed range of the large change is concentrated inside the fertilizer discharger device cavity. With the increase of the impeller speed, the speed of the fertilizer also increases, and the range is $1.06\times10^{(-2)}$ ~ $9.3\times10^{(-2)}$ m/s. According to the fertilizer force model, with the increase of the impeller speed, when the fertilizer inlet contacts the impeller and when the impeller discharges the fertilizer from the fertilizer discharge port, the greater change is in the range of $2.06\times10^{(-4)}$ ~ $1.03\times10^{(-3)}$ N. Compared with other rotational impeller speeds, the angular velocity, velocity, and force of the fertilizer have no major changes in places where the variation range is large. With the increase of the impeller speed, the angular velocity, velocity, and force of the fertilizer all increase.

Simulation experiment design and analysis

Use Setup Selections in Analyst to construct Grid Bin grid *(Wang et al., 2023; Dang et al., 2022),* refer to NY/T 1003-2006 "Technical Specifications for Quality Evaluation of Fertilizer Machinery" standard, design experiments, calculate the variation coefficient of fertilizer discharge stability and the uniformity variation of fertilizer discharger device coefficient.

Central Composite Design

Domestic compound fertilizers were selected to carry out three-factor five-level quadratic rotation combination design experiments, and the optimum working parameter combination was obtained through significance analysis. During the simulation process, without the influence of other environmental factors, according to the rice fertilization rate of 300-675 kg/ha, the number of leaves is selected to be 2~6 pieces, the fan angle of the fertilizer outlet is 30~70°, and the impeller speed is 5~25 r min^{-1}. The factor code table is Table 2, the test program design and results are shown in Table 3, X_1, X_2, X_3 in the table are the number of blades, the fan angle of the fertilizer discharge port and the code value of the impeller speed, Y_1, Y_2 are the coefficient of variation of fertilizer discharge stability and the fertilizer uniformity variation coefficient.

Table 2

Experiment factor coding

coding	factor		
	Number of blades X_1/[piece]	Fan angle of fertilizer outlet X_2/[°]	impeller Speed X_3/[r·min^{-1}]
1.682	6	70	25
1	5	60	20
0	4	50	15
-1	3	40	10
-1.682	2	30	5

According to the design of the test coding table, conduct a simulation test and fill in the test results in Table 3.

Table 3

Experimental design and results

coding	Number of blades X_1/[piece]	Fan angle of fertilizer outlet X_2/[°]	impeller Speed X_3/[r·min^{-1}]	Coefficient of variation Y_1 of fertilizer discharge stability [%]	Fertilizer uniformity variation coefficient Y_2 [%]
1	-1	-1	-1	0.85%	5.68%
2	1	-1	-1	1.72%	12.38%
3	-1	1	-1	1.34%	2.73%
4	1	1	-1	2.13%	16.44%
5	-1	-1	1	2.46%	4.72%
6	1	-1	1	1.72%	4.34%
7	-1	1	1	1.32%	8.82%
8	1	1	1	1.29%	3.13%
9	-1.68	0	0	1.01%	5.01%
10	1.68	0	0	2.84%	16.33%
11	0	-1.68	0	1.36%	4.40%
12	0	1.68	0	1.18%	3.19%
13	0	0	-1.68	0.82%	13.43%
14	0	0	1.68	3.29%	2.86%
15	0	0	0	1.56%	4.53%
16	0	0	0	1.76%	2.76%
17	0	0	0	2.36%	6.39%
18	0	0	0	1.25%	9.98%
19	0	0	0	3.09%	5.71%
20	0	0	0	1.23%	5.81%
21	0	0	0	1.75%	9.98%
22	0	0	0	3.78%	5.42%
23	0	0	0	1.54%	3.45%

Analysis of test results

The software Design-Expert.V8.0.6.1 was used to carry out multiple regression fitting analysis on the experimental results, and the regression equation between the factors and between the coefficient of variation of stability and the coefficient of variation of uniformity was established. The results of variance analysis and significance are shown in Table 4. For the stability coefficient of variation, the model significance test $p<0.01$ indicates that the model is statistically significant. The first-order item X_1, the second-order item $X_1 X_3$ have a very significant impact ($P<0.01$), the second-order item X_3^2 has a significant impact ($P<0.05$), and the lack-of-fit P value is 0.332>0.05, which is beneficial to the model, there is no lack of fit factor, and the fitting degree is good. For the coefficient of variation for homogeneity, the model significance test $p<0.01$, indicates that the model is statistically significant. The first-order items X_1, X_3, the second-order items $X_1 X_3$ have a very significant impact ($P<0.01$), and the second-order items X_1^2 has a significant influence ($P<0.05$), and the lack of fit P value is 0.4467>0.05, which is beneficial to the model. There is no lack of fit factor, and the degree of fitting is good. This regression equation can be used instead of the real point of the test to analyze the experimental results.

Table 4

Analysis of Regression Equations ANOVA

source of variance	stability coefficient of variation				uniformity coefficient of variation			
	sum of square	degrees of freedom	F	P	sum of square	degrees of freedom	F	P
Model	4.974E-004	9	4.57	0.0069	0.031	9	5.30	0.0037
X_1	1.524E-004	1	12.62	0.0035	8.167E-003	1	12.41	0.0037
X_2	1.832E-005	1	1.52	0.2400	2.829E-005	1	0.043	0.8390
X_3	1.183E-005	1	0.98	0.3404	8.460E-003	1	12.85	0.0033
X_1X_2	1.914E-005	1	1.58	0.2303	3.583E-005	1	0.054	0.8192
X_1X_3	1.148E-004	1	9.50	0.0087	8.762E-003	1	13.31	0.0029
X_2X_3	4.327E-005	1	3.58	0.0809	3.954E-005	1	0.060	0.8102
X_1^2	4.290E-005	1	3.55	0.0821	3.960E-003	1	6.02	0.0291

source of variance	stability coefficient of variation				uniformity coefficient of variation			
	sum of square	degrees of freedom	F	P	sum of square	degrees of freedom	F	P
X_2^2	7.232E-006	1	0.60	0.4529	1.158E-003	1	1.76	0.2075
X_3^2	8.675E-005	1	7.18	0.0189	7.444E-004	1	1.13	0.3069
Residual	1.570E-004	13			8.557E-003	13		
Lack of fit	7.219E-005	5	1.36	0.332	3.412E-003	5	1.06	0.4467
Pure error	8.486E-005	8			5.145E-003	8		
Sum	6.544E-004	22			0.040	22		

Note: * indicates significant impact (P <0.05) and ** indicates very significant impact (P <0.01).

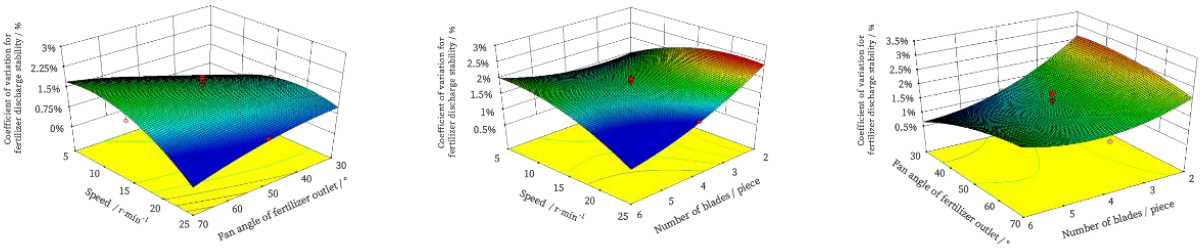
Carry out quadratic response surface regression analysis, remove insignificant factors, and obtain the following multivariate quadratic response surface regression model:

$$Y_1(\%) = 0.016 + 3.34 \times 10^{-3} X_1 + 3.79 \times 10^{-3} X_1 X_3 - 2.37 \times 10^{-3} X_3^2 \quad (15)$$

$$Y_2(\%) = 0.060 + 0.024 X_1 - 0.025 X_3 - 0.033 X_1 X_3 - 6.84 \times 10^{-3} X_1^2 \quad (16)$$

Response Surface and Interaction Analysis

The coefficient of variation of fertilizer discharge stability and the coefficient of variation of fertilizer discharge uniformity are important indicators to measure the fertilizer discharger device. The influence of the interaction of various factors on the stability coefficient of variation is analyzed, and the corresponding mathematical model is obtained. For example, Table 5 shows the interactive effects of various factors on the coefficient of variation of fertilizer discharge stability. Fig. 8 shows the response surface analysis diagram of each factor on the coefficient of variation of fertilizer discharge stability. Table 6 shows the interaction of various factors on the coefficient of variation of fertilizer discharge uniformity. Interaction effects, as shown in Fig. 9 is the response surface analysis diagram of each factor on the coefficient of variation of fertilizer uniformity.



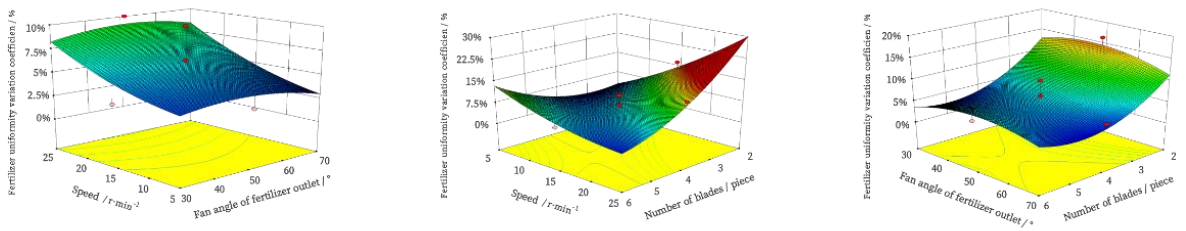
（a） （b） （c）

Fig. 8 - Effect of interactions on stability coefficient of variation

Table 5

Interaction of factors on coefficient of variation of fertilizer discharge stability

Coefficient of variation Y_1 of fertilizer discharge stability Y_1	Number of blades X_1/(piece)	Fan angle of fertilizer outlet X_2/(°)	impeller speed X_3/（r·min^{-1}）	Value range of Y_1min factor
decrease	4	increase	constant	50-X2-70°
decrease	4	constant	increase	15–X3-25 r·min^{-1}
decrease	increase	50	constant	4-X1-6 piece
decrease	constant	50	increase	15–X3-25 r·min^{-1}
decrease	increase	constant	15	4-X1-6 piece
increase	constant	increase	15	30-X2-50°



(a) (b) ©

Fig. 9 - The effect of interaction on uniformity

Table 6

Interaction of factors on coefficient of variation of fertilizer discharge uniformity

Coefficient of variation of uniformity Y_2	Number of blades X_1/(piece)	Fan angle of fertilizer outlet X_2/(°)	impeller speed X_3/（r·min^{-1}）	Value range of Y_2min factor
Decrease after increase	4	increase	constant	50-X_2-70°
increase	4	constant	increase	5–X_3-15 r·min^{-1}
increase	2-4	50	5-15	4-X_1-6 piece
decrease	5、6		15-25	15–X_3-25 r·min^{-1}
increase after decrease	increase	constant	15	3-X_1-5 piece
Decrease after increase	constant	increase	15	50-X_2-70°

Experimental optimization

Utilizing Design-Expert.V8.0.6.1 software for optimization, a mathematical model represented by equation (17) was established to determine the optimal combination of factors. Through calculations, it was found that when the number of blades is 6, the fan angle of the fertilizer outlet is 35.7°, and the impeller speed is 18.85 r·min^{-1}, the minimum coefficient of stability variation is 0.67%, and the minimum coefficient of uniformity variation is 2.1%.

$$\begin{cases} \min Y_1 \\ \min Y_2 \\ \text{s.t} \begin{cases} 2 \le X_1 \le 6 \\ 30° \le X_2 \le 70° \\ 5 \le X_3 \le 25 \\ 0 \le Y_1(X_1、X_2, X_3) \le 1 \\ 0 \le Y_2(X_1、X_2, X_3) \le 1 \end{cases} \end{cases} \quad (17)$$

Bench test

The experiment site is the seeding laboratory of Heilongjiang Bayi Agricultural Reclamation University, the fertilizer is Stanley compound fertilizer, and a self-made fertilizer discharge device is used. During the experiment, the fertilizer discharge device is installed on the test bench, and the test factors of the fertilizer discharge device adopt the optimal combination of simulation, the middle baffle and blades are 3D printed, and the motor speed is precisely controlled by a single-chip microcomputer. The fertilizer discharge performance test bench is shown in the Fig. 10.

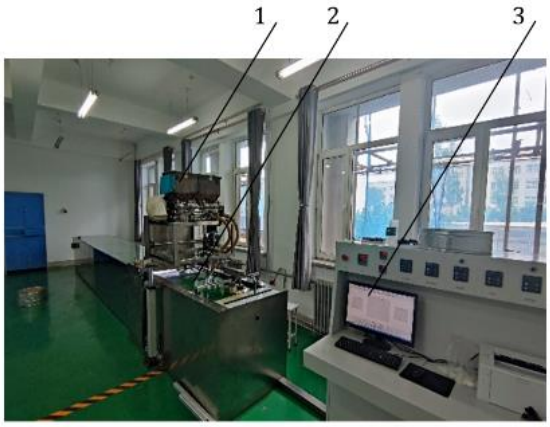


Fig. 10 - Test bench of impeller fertilization device

1. Seed-discharging performance test bench 2. Fertilizer device 3. Fertilizer collection belt

During the stability test, the conveyor belt does not rotate. The collection box below the fertilizer discharger device collects the fertilizer mass for 15 s, repeats 5 times, and takes the average value. Calculate the coefficient of variation for stability.

In the uniformity test, the conveyor belt speed of the test bench was 1 m·s^{-1}, and 30 continuous sections of 10 cm fertilizer mass were collected, repeated 5 times, and the average value was taken to calculate the uniformity coefficient of variation. The experimental results are shown in the table 7.

Table 7

Test results

Number of experiments	Coefficient of variation Y_1 of fertilizer discharge stability [%]	Fertilizer uniformity variation coefficient Y_2 [%]
1	1.56	4.65
2	0.89	7.32
3	2.65	6.55
4	3.28	5.23
5	2.11	4.98
average value	2.098	5.746

Bench test results show that the coefficient of variation of fertilizer discharger device stability is 2.098%, and the coefficient of variation of uniformity is 5.746%. The simulation results are basically consistent with the bench results and meet NY/T 1003-2006 "Technical Specifications for Quality Evaluation of Fertilizer Machinery" Standards to meet fertilization requirements.

CONCLUSIONS

In addressing the challenges of poor fertilizer uniformity and stability resulting from the operation of the fertilizer discharger device in variable-rate fertilization for rice, a blade-type variable-rate fertilizer discharger device was designed. The key component structural parameters of the blade-type discharger device and the instantaneous processes of filling and discharging fertilizer were analyzed to identify the factors influencing the discharger device's performance.

Through EDEM discrete element simulation, a Central Composite Design was employed to investigate the effects of impeller speed, fan angle of fertilizer outlet, and number of blades. Utilizing Design-Expert.V8.0.6.1 software for optimization analysis, both the stability and uniformity coefficients of variation for fertilizer discharge met the technical specifications required for the mechanical quality assessment of the fertilization equipment. The stability coefficient of variation ranged from 0.67% to 2.85%, while the uniformity coefficient of variation ranged from 2.7% to 16.4%.

Taking the number of blades, the fan angle of the fertilizer outlet, and the speed of the impeller as the influencing factors, the variation range of each factor is determined, and the regression equation is obtained through analysis. Combined with the change trend of the response surface method, after the optimization module is processed, it is obtained: when the number of blades is 6, the fan angle of the fertilizer outlet is 35.7° and the impeller speed is 18.85 $r \cdot min^{-1}$, the coefficient of variation of the stability is 0.67%, and the coefficient of variation of the uniformity is at least 2.1%. The bench test verification results are basically consistent with the simulation results and meet the design requirements.

ACKNOWLEDGEMENT

The authors were funded by the China Central Government's Special Project for Guiding Local Science and Technology Development (ZY20B05); the National Grassroots Agricultural Technology Promotion Project (NJ202105); and the Heilongjiang Provincial Natural Science Foundation Project (LH2022E098).

REFERENCES

[1] Bao, B.Q., Long-Ze, A. N., Feng-Ying, H.U. (2002). The rice field mechanization state in Japan, China and other countries (我国和日本等国水田机械发展概况). *Journal of Agricultural Mechanization Research.* Vol. 03, pp.23-25. Heilongjiang/China.

[2] Cao, R.D. (1984). Experimental research on disc fertilizer discharger device (盘式排肥器的试验研究). *Journal of Agricultural Machinery*, Vol. 03, pp.74-81. Jiangsu/China.

[3] Cheng, C.H., Xu, C.L., Bi, C.H., & Zhang, X.D. (2012). Research on side deep fertilization technology and device of rice transplanter (水稻插秧机侧深施肥技术及装置的研究). *Journal of Heilongjiang Bayi Agricultural Reclamation University*, Vol. 06, pp. 10-12+25. Heilongjiang/China.

[4] Dang, Y., Yang, G., Wang, J., Zhou, Z., & Xu, Z. (2022). A Decision-Making Capability Optimization Scheme of Control Combination and PID Controller Parameters for Bivariate Fertilizer Applicator Improved by Using EDEM. *Agriculture*, Vol. *12*(12), pp. 2100. Henan/China.

[5] Gao, G.B. (2019). *Design and experiment of key components of wind-driven rice side-deep fertilizer discharger device* (风送式水稻侧深施肥装置关键部件设计与试验), Master's thesis, Northeast Agricultural University. Heilongjiang/China.

[6] Ishola, T. A., Yahya, A., Shariff, A. R. M., & Aziz, S. A. (2014). A novel variable rate pneumatic fertilizer applicator. *Instrumentation Science & Technology,* Vol. 42(4), pp. 369-384. Malaysia

[7] Jun, L., Dequan, Z., Qilei, T., Congyang, Y., Tingjue, W., Kang, X., ... & Juan, L. (2021). Design and experiment of adjustable socket-wheel precision fertilizer apparatus for dry direct-seeding rice. *INMATEH-Agricultural Engineering*, Vol. 63(1), pp. 121-130. Anhui/China.

[8] Li, K. (2017). *Design and research of variable fertilization system* (变量施肥系统的设计与研究) Master's thesis, Shihezi University. Xinjiang/China.

[9] Mirzakhaninafchi, H., Singh, M., Bector, V., Gupta, O. P., & Singh, R. (2021). Design and development of a variable rate applicator for real-time application of fertilizer. *Sustainability*, Vol. 13(16), pp. 8694. India

[10] Shi, Y., Zhu, Y., Wang, X., Sun, X., Ding, Y., Cao, W., & Hu, Z. (2020). Progress and development on biological information of crop phenotype research applied to real-time variable-rate fertilization. *Plant methods*, Vol. 16, pp. 1-15, England.

[11] Tai, Q.L. (2020). *Design and experiment of adjustable socket wheel precision fertilizer discharger device* (可调窝眼轮式精量排肥器设计与试验), Master's thesis, Anhui Agricultural University. Anhui/China

[12] Tormi, I., Märt, R., Indrek, V., & Jüri, O. (2022). Feasibility analysis of fluted roller dispenser application for precision fertilization. *INMATEH-Agricultural Engineering*, Vol. 68(3), pp. 415-423. Estonia

[13] Wang, J.F., Shang, W.H., Weng, W.X., & Chen, X.S. (2021). Design and experiment of side-deep fertilization device for rice fields with disc ejector (圆盘顶出式水田侧深施肥装置设计与试验). *Journal of Agricultural Machinery*, Vol. 06, pp. 62-72. Heilongjiang/China.

[14] Wang, J.F., Fu, Z.D., Weng, W. X., & Yang, D.G..(2022). Design and experiment of double-row fertilizer for side-deep fertilization of rice fields with conical disc push plate (圆锥盘推板式水田侧深施肥双行排肥器设计与试验). *Journal of Agricultural Machinery*, Vol. 02, pp. 53-62+106, Heilongjiang/China.

[15] Wen, X., Ya.X.H. (2019). Design and parameter optimization of key components of organic fertilizer spreader (有机肥撒播机关键部件设计及参数优化). A*gricultural Machinery Use and Maintenance* Vol.06, pp. 25. Guangxi/China

[16] Xing, X.P. (2019). *Research on two-stage screw-driven fertilizer discharge and deep fertilizer discharger device in rice fields* (水田双级螺旋驱动的排肥与深施肥装置研究) Master's thesis, South China Agricultural University. Guangdong/China.

[17] Yuan, W.S., Mei, J., Chong you, W., Ti Giong, X. (2011). Development status and prospect of seed manure fertilizing mechanization in China (国内种肥施肥机械化发展现状及思考). *Journal of Agricultural Mechanization Research*, Vol. 12, pp.1-5, Heilongjiang/China.

[18] Zha, X., Zhang, G., Zhang, S., Hou, Q., Wang, Y., & Zhou, Y. (2020). Design and experiment of centralized pneumatic deep precision fertilization device for rice transplanter. *International Journal of Agricultural and Biological Engineering*, Vol. *13*(6), pp. 109-117. America

RESEARCH ON SEMANTIC SEGMENTATION OF GREENHOUSE ROAD IMAGE
/
温室大棚道路图像的语义分割研究

YongZheng YANG, HongBo WANG*, ZhiCheng XIE, JunMao LI, ZiLu HUANG
College of Mechanical and Electronic Engineering, Inner Mongolia Agricultural University, Hohhot / China
Tel: +86 13739981395; E-mail: wanghb@imau.edu.cn
DOI: https://doi.org/10.35633/inmateh-71-65

Keywords: *road detection, SETR, DeepLabv3+, semantic segmentation*

ABSTRACT
To realize the automatic driving of agricultural machinery in the greenhouse, this paper uses image acquisition equipment to collect road images in the greenhouse and makes data sets, builds SETR (SEgmentation TRansformer) model based on Transformer framework and DeepLabv3+ model based on convolution neural network for semantic segmentation of road images in the greenhouse, and verifies the semantic segmentation ability of the two models to road images in the greenhouse. Several groups of training periods are set as observation points to observe the semantic segmentation effect of the two models on the greenhouse road image, and the test set which has not been trained by the model is used as the prediction object to verify the performance of the two models on the semantic segmentation of greenhouse road image. The SETR model reached 94.64% PA (Pixel Accuracy) on the greenhouse road data set, and 82.72% mIoU (Mean Intersection over Union), DeepLabv3+ model reached 90.80% PA and 72.35% mIoU on the greenhouse road data set. Both models have excellent performance in semantic segmentation of greenhouse road images, and the performance of SETR model is slightly better than that of DeepLabv3+ model. The semantic segmentation performance of the two models for greenhouse road images can meet the needs of actual deployment.

摘要
为实现农业机械在温室大棚中的自动驾驶，本文使用图像采集设备采集温室大棚中道路图像并制作了数据集，搭建基于 Transformer 框架的 SETR 模型与基于卷积神经网络的 DeepLabv3+模型对温室大棚中道路图像进行语义分割，验证两种模型对温室大棚中道路图像语义分割能力。设置了多组训练周期作为观测点，观测两种模型对温室大棚道路图像的语义分割效果，以未投入过模型训练的测试集作为预测对象，验证两种模型对温室大棚道路图像语义分割的性能。SETR 模型在温室大棚道路数据集上达到了 94.64%的 PA、82.72%的 mIoU,DeepLabv3+模型在温室大棚道路数据集上达到了 90.80%的 PA、72.35%的 mIoU，两种模型在对温室大棚道路图像的语义分割上均有优异表现，SETR 模型的性能略高于 DeepLabv3+模型，两种模型对温室大棚道路图像的语义分割性能均满足在实际部署的需求。

INTRODUCTION
With the development of artificial intelligence, technologies such as autopilot and robot automatic cruise are gradually applied in various industries *(Yoon et al., 2022; Daduna, 2020)*. The autopilot of intelligent mechanical equipment in the greenhouse, open-air farm and other environments is one of the important development directions of intelligent agriculture. As one of the basic tasks of self-driving, semantic segmentation is an important support for the panoramic analysis of roads and the pixel-level classification of road environment. Based on the analysis of the visual navigation extraction algorithm of agricultural robot based on dark primary colour, *Zhongkun Hou, (2020*), proposed a method of farmland image preprocessing and edge detection based on dark primary colour, which provides some reference for the analysis of visual navigation extraction algorithm of field navigation robot based on dark primary colour.

With the development of deep learning technology, more and more models are used in the field of image semantic segmentation, which refers to the pixel-level classification of images *(Xiongi et al., 2021)*.

Yong Zheng YANG, M.S. Stud.; HongBo Wang, Professor, Correspondent author; ZhiCheng XIE, M.S. Stud.; JunMao LI, M.S. Stud.; ZiLu HUANG, M.S. Stud.

For example, the full convolutional network FCN *(Long et al., 2015)* which first applied deep learning technology to semantic segmentation, FCN uses convolutional encoder-decoder architecture to upsample the image to generate image features, and classifies the image at the pixel level in an end-to-end way. Impressive results have been obtained on datasets with PASCAL VOC and Cityscapes. With the brilliance of FCN in the field of image semantic segmentation, there are some models such as Mask R-CNN *(He et al., 2017)*, DeepLab *(Chen et al., 2018)* and BiSeNet *(Yu et al., 2018)* with VGG, ResNet, DensenNet and other frameworks as the backbone of the network, which have excellent performance in image semantic segmentation. *Yu et al. (2021)* further improved and designed a new BiSeNe V2 model for real-time semantic segmentation with higher precision and higher efficiency for BiSeNet, and introduced a new guided aggregation layer to combine features, so that BiSeNet V2 has a better performance for semantic segmentation of data sets such as Cityscapes. *Ren et al. (2023)* improved the BiSeNet network architecture by sharing the head of the two-branch network, eliminated parameter redundancy and improved the extraction of shallow features of the image, and verified that the algorithm has a significant improvement in real-time performance and accuracy on multiple data sets. *Chen et al. (2018)* proposed a new model DeepLabv3+, by combining the advantages of pyramid pooling module and encoder-decoder structure, and verified that the encoder-decoder network structure is faster and stronger on PASCAL VOC and Cityscapes data sets. The HRNet designed by *Wang et al. (2020)* realizes the parallel connection of convolutional streams from high resolution to low resolution and the exchange of repeated information across resolutions, so that the image maintains a high-resolution representation in the whole process of coding, and the features have more accurate spatial information and richer semantics. *Fan et al. (2021)* designed a new network structure STDC on the basis of BiSeNet, and did a number of experiments on CamVid data set and Cityscapes data set to verify the effect of the model, and finally realized 76.8% mIoU with 97.0FPS. *Hu (2020)* introduced a new efficient and lightweight neural architecture RandLA-Net to realize the semantic segmentation of large-scale point cloud images. RandLA-Net can process 1 million points at a time, and the speed is greatly improved, which surpasses many advanced speech segmentation models on Semantic3D and SemanticKITTI data sets.

Transformer was first used in natural language processing. Unlike CNN, which relies on convolution and recursion to obtain information *(Vaswani et al., 2017)*. Transformer is completely based on multiple attention mechanism to obtain global context information, surpassing RNN *(Yin et al., 2017)*, Deep RNNs *(Shi et al., 2017)*, BiRNN *(Johansen et al., 2017)* and other models with excellent performance in natural language processing at that time. Because Transformer has excellent performance in natural language processing and its framework is different from the traditional convolution neural network, many visual attempts of Transformer framework began to emerge. VIT *(Dosovitskiy et al., 2020)* ushered in the era of the application of Transformer to computer vision, and achieved better results in image classification tasks using multiple small and medium-sized data sets for image recognition benchmark testing with fewer computing resources. The subsequent DETR *(Carion et al., 2020)* algorithm completes the application of Transformer in the field of target detection, and has a very excellent effect compared with the target detection algorithm based on CNN in the same period. Therefore, Transformer is widely used in the field of computer vision, in which SETR *(Zheng et al., 2021)* and Segformer *(Xie et al., 2021)* are the representatives of Transformer in semantic segmentation algorithms. SETR regards image semantic segmentation as a sequence-to-sequence prediction task, uses Transformer global context modelling, provides a powerful semantic segmentation model, and has achieved excellent results on data sets such as Cityscapes. Segformer unifies Transformer and lightweight MLP decoder, which can output multi-scale features and achieve local and global attention at the same time, and has a more powerful representation. Segformer verifies its strong semantic segmentation ability on multiple data sets. *Jin et al. (2021)* designed a new semantic segmentation network TrSeg based on Transformer, which can adaptively capture global context information in multi-scale. Several groups of experiments show that TrSeg has better performance than other multi-scale models to obtain information. *Gu et al. (2022)* proposed a semantic segmentation model HRViT, which integrates high-resolution multi-branch architecture and ViT. This model reduces the redundancy in the linear layer and increases the attention blocks with enhanced expressiveness. Finally, it is proved that the model has great potential in semantic segmentation on multiple semantic segmentation data sets. *Lu et al. (2021)* adopted a different way of building semantic segmentation than the traditional way of building semantic segmentation, put encoder-decoder into pre-training, only put classifiers into meta-learning, and designed a new classifier: Classifier Weight Transformer (CWT). CWT can dynamically adjust the weight of the classifier in an inductive way when the support set is put into training, so as to adapt to each query image. Although the model is simple, its performance is much better than other models through experiments.

With the development of deep learning, the model of image semantic segmentation becomes more efficient and accurate, which provides technical support for autopilot and panoramic analysis of roads. In this paper, the road environment image in the greenhouse is used to prepare the data set, and SETR model, which is the most mature and leading semantic segmentation model in Transformer framework, and DeepLabv3+ model, which also has excellent performance in convolution neural network, are selected to segment the self-built greenhouse road data set, and the feasibility of semantic segmentation of greenhouse road is verified. It provides a theoretical basis for automatic driving of intelligent agricultural machinery in the greenhouse.

MATERIALS AND METHODS

Network framework of SETR

The design of encoder in SETR *(Zheng et al., 2021)* takes Transformer as the main body and is composed of layer Normalization, multi-head attention layer (Multi-head self-attention MSA) and multi-layer perceptron (Multilayer Perceptron MLP) blocks. Because Transformer accepts the input of one-dimensional sequence embedded by features (where L is the length of the sequence and C is the size of the hidden channel), the image of H × W needs to be segmented into grids containing multiple slices p of 16 × W hand 16, and each slice p is mapped into a sequence with dimension C through the linear projection (linear mapping) function. In order to encode the spatial information of the slice, the literature learns a specific embedded pi for each location I to get the final sequence as input $E = \{e_1 + p_1, e_2 + p_2, ..., e_L + p_L\}$.

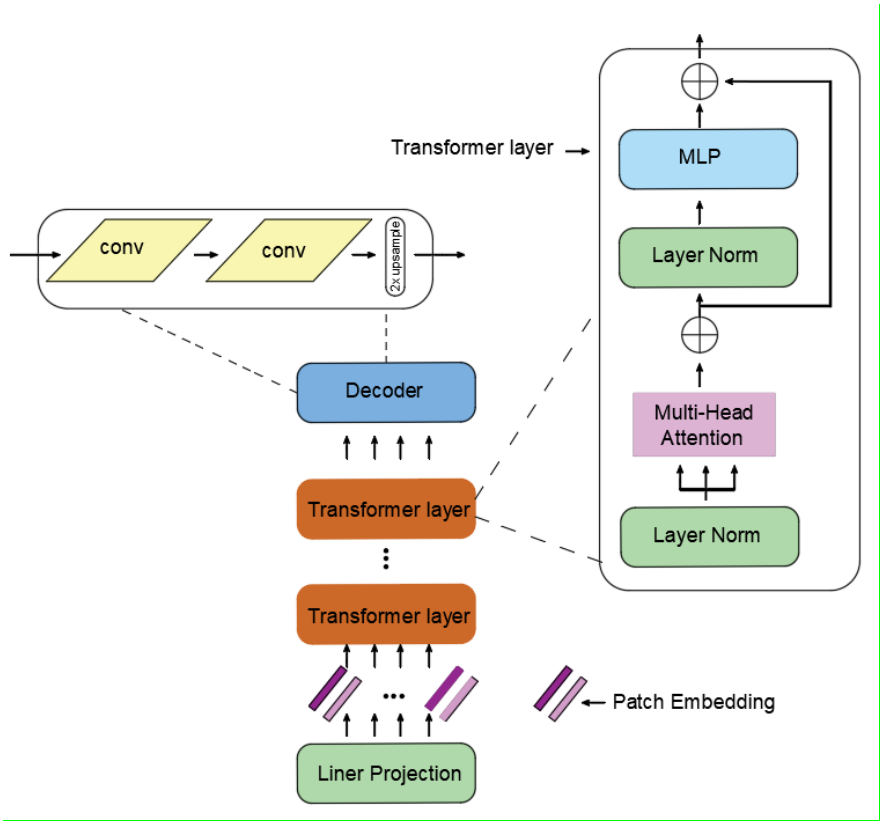


Fig. 1 - The structure of SETR Model

In reference *Zheng et al., (2021)*, three modules are designed for Decoder: Naive upsampling (Naive), Progressive UPsampling (PUP) and Multi-Level feature Aggregation (MLA). Among the three kinds of Decoder, the architecture of Naive is the simplest. Naive uses a two-layer network to map features to the number of target categories, and then directly uses bilinear upsampling to get the original image resolution. In order to avoid excessive noise, PUP returns to the original image resolution by gradually double up sampling. MLA uses a multi-level feature fusion strategy similar to the pyramid feature fusion strategy, and in order to enhance the interaction between different layers of features, it uses the method of down-to-down fusion (element-wise addition), and finally 4x bilinear up-sampling back to the original image resolution. The SETR model takes up more computing resources. Due to the limitations of the experimental hardware, this paper chooses Naive, which has the simplest architecture, as the Decoder of the SETR model. The structure of the SETR model is shown in Figure 1.

Network framework of DEepLabV3+

As a continuation of DeepLabv3 semantic segmentation model, Deeplabv3+ *(Chen et al., 2018)* has better ability to recover object edge information and takes up less computing resources. Deeplabv3+ uses Deeplabv3 as encoder, so DeepLabv3+ can use hole convolution (Atrous convolution) to extract deep convolution neural network to calculate features at any resolution, and obtain more informative features by changing the size of encoder output stride. Deeplabv3+ proposes a simple and efficient decoder. Firstly, the output features of the encoder are 4 times bilinear up-sampled and connected with the low-level features of the backbone network, and the training difficulty is reduced and the features are refined through multiple convolution layers. Finally, a simple 4-fold bilinear up-sampling is performed to return to the original image resolution. On the backbone network, Deeplabv3+ adopts Xception *(Chollet, 2018)*, which is faster and more effective in image classification, and replaces all the maximum pool layer (max pooling) in Xception with deep separable convolution layer (depthwise separable convolution). The structure of the Deeplabv3+ network is shown in Figure 2.

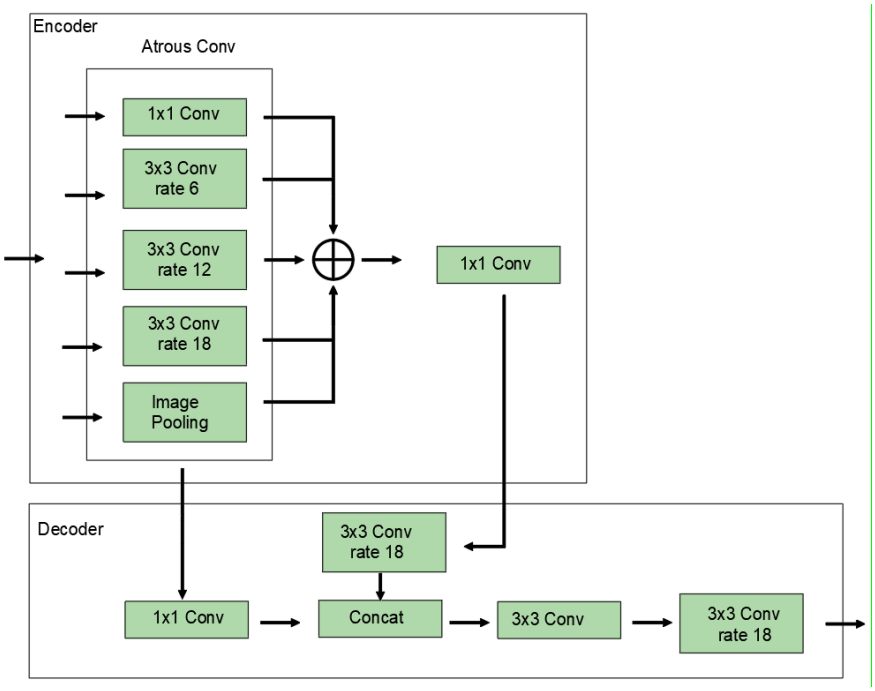


Fig. 2 - The structure of Deeplabv3+ Network

Image acquisition of datasets

The image of establishing the data set is collected in a tomato greenhouse in city of Hohhot. The captured image is shown in Figure 3.



Fig. 3 - Road images collected in greenhouse



Fig. 4 - Image acquisition equipment

The image is divided into a greenhouse corridor road and an inter-crop road. The tracked intelligent car used in the image acquisition equipment is equipped with an Astra Pro Plus camera, and the image acquisition equipment is shown in Figure 4. Control the image acquisition equipment to move in the greenhouse, simulate the moving road condition of intelligent agricultural machinery in the greenhouse, and record the road and around the road when moving in real-time. The images are collected repeatedly in multiple greenhouse corridors and roads among crops to enrich the data set. One image is extracted from the real-time recorded video every 12 frames, and a total of 1400 field road images are collected by manual screening, of which 1000 are used as a training set, 200 as verification set and 200 as a test set.

Image calibration of datasets

Using LabelMe tool to calibrate the collected data sets, the calibrated categories are: intercrop road-road1, greenhouse corridor-road2, greenhouse crops-crop, tomato-tomato on crops, plastic film-background1 in greenhouse, earthen wall in greenhouse-background2, brick wall in greenhouse-background3, which are divided into 7 categories, and the contours of all kinds of targets in the image are depicted. The calibrated image is generated into a label image, in which both the original image and the label image are RGB images, and the sizes of the three channels of each category are: road1 [128,0,0], road2 [128,128,128], crop [0,128,0], tomato [227,139,6], background1 [0,0,128], background2 [128,128,0], background3 [128,0,128]. The original image and its label image are shown in Figure 5. The calibrated training set and verification set are used in the model training, and the uncalibrated test set is not put into the model training to test the prediction ability of the model to the road in the greenhouse.

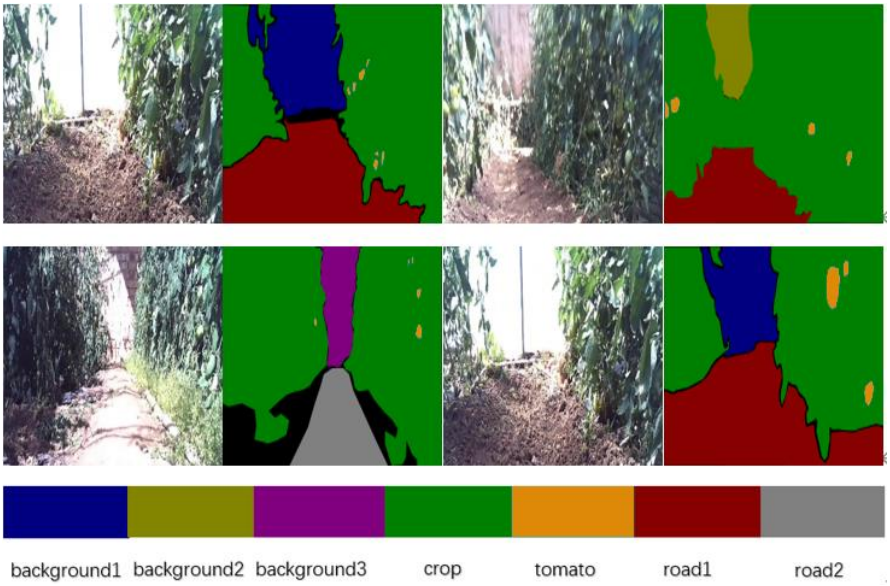


Fig. 5 - Road image and its label image

RESULTS

Experimental environment and evaluation indicators

In this paper, PyTorch deep learning framework is used to build SETR and Deeplabv3+ models, and the development language is Python3.9. Five NVIDIA Tesla V100 GPU 32GB were used to train the SETR and Deeplabv3+ models. In the training strategy, random gradient descent (SGD) is used as the optimizer, the initial learning rate is set to 0.001, the training cycle (epoch) is set to 500, and the learning rate decreases by 10% every 50 training cycles, and five images per batch (batch) are input into the model for training. The evaluation index selects pixel accuracy (Pixel Accuracy, PA) and average intersection ratio (Mean Intersection over Union, MIoU). The effect of the model is evaluated by the score of the two models on the two evaluation indexes. The evaluation index formula is as follows:

$$PA = \frac{\sum_{i=0}^{N} p_{ii}}{\sum_{i=0}^{N}\sum_{j=0}^{N} p_{ij}} \quad (1)$$

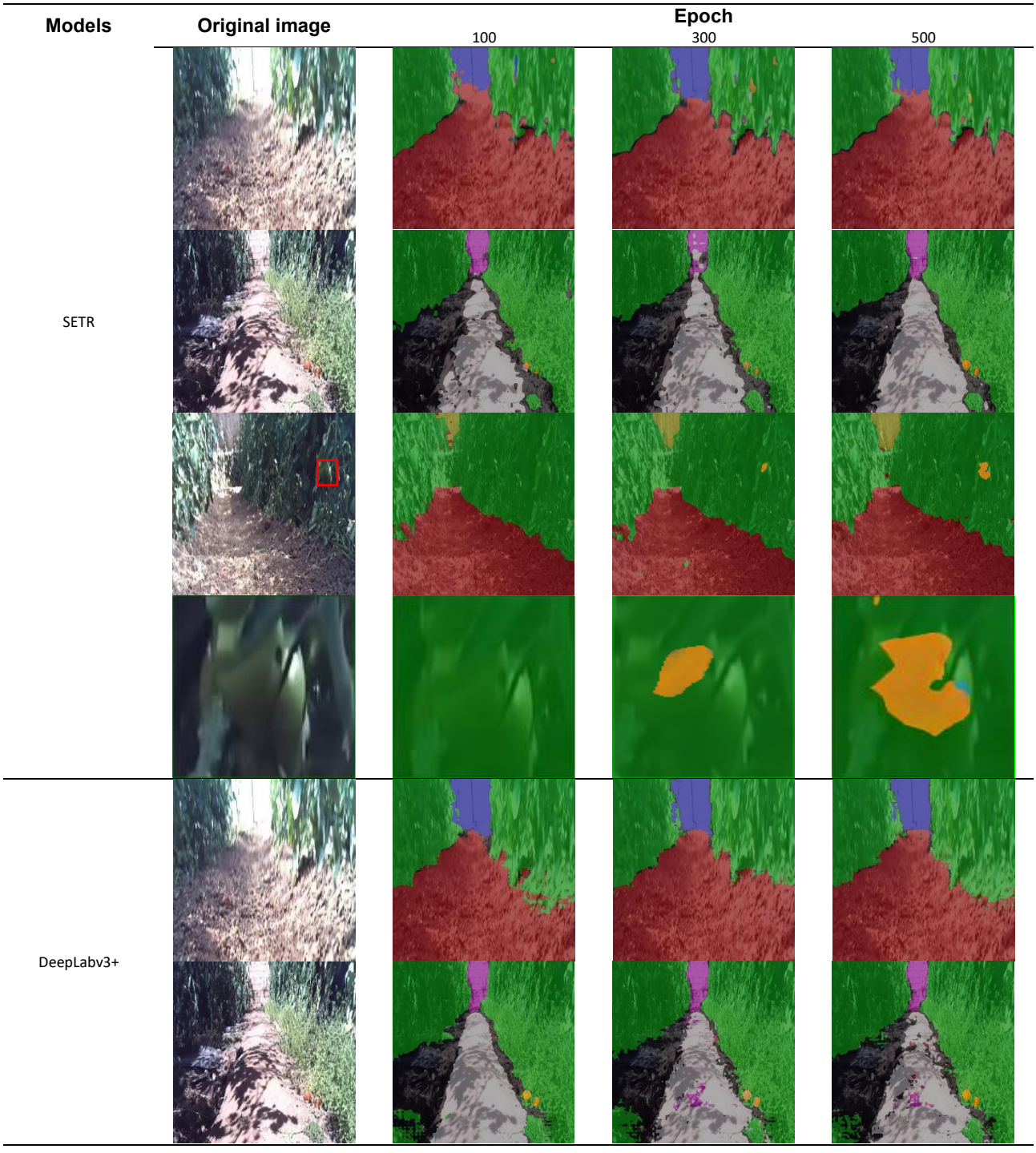
$$mIoU = \frac{1}{N+1}\sum_{i=0}^{N}\frac{p_{ii}}{\sum_{j=0}^{N}p_{ij}+\sum_{j=0}^{N}p_{ji}-p_{ii}} \quad (2)$$

In the formula N is the number of categories, p_{ii} is the real case, p_{jj} is the true negative case, p_{ji} is the false negative case, p_{ij} is the false positive case.

Analysis of the training effect of two models

The prepared training set and verification set are put into the built SETR model and DeepLabv3+ model for training, respectively, and the training effect of the model is observed at 100,300,500 epochs.

The semantic segmentation effect of the model under the three training cycles is shown in Figure 6. The training effect of the model is evaluated according to PA and mIoU evaluation indicators, as shown in Table 1.



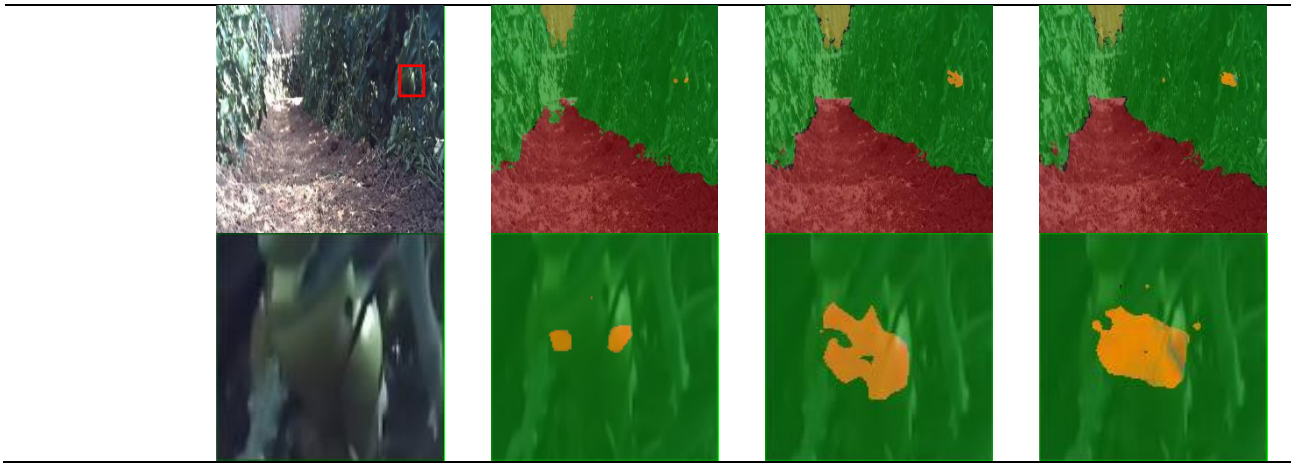


Fig. 6 - The Semantic Segmentation effect of each training epoch of the two models

According to the analysis of Figure 6, both SETR and DeepLabv3+ models can segment the semantics of each target in the greenhouse road image after 100 times of training, and the target contour is basically consistent with the actual contour, but there are many phenomena of segmentation errors, especially the edge between the targets is not well segmented, and the small target tomato in the greenhouse road image is not well segmented. After 300, 500 times of training, the semantic segmentation ability of SETR model to the field road image is gradually enhanced, and the segmentation error phenomenon is gradually reduced. After 500 times of training, the model can segment the edge of the target very well, and can complete the segmentation of small target tomatoes. After 300, 500 times of training, the semantic segmentation ability of DeepLabv3+ model for the greenhouse road image does not change much, especially for greenhouse corridor-road2, the semantic segmentation effect is poor, there are still big segmentation errors, the edge segmentation between multiple targets is not clear enough, and there is interference between targets, so the semantic segmentation of small target tomato can be completed. Although the two models can complete the semantic segmentation of tomatoes in the field road after 500 times of training, the segmented tomato contours are not completely consistent with the actual contours and some tomatoes cannot be recognized. It should be due to the small number of tomato targets in the image and too little semantic information of the tomato in the greenhouse road data set.

Table 1

Evaluation index scores of each training epoch of the two models

Models	Epoch					
	100		300		500	
	PA / %	mIoU / %	PA / %	mIoU / %	PA / %	mIoU / %
SETR	93.78	81.34	94.95	86.98	96.46	90.45
DeepLabv3+	92.71	80.69	93.37	82.55	93.34	81.55

The analysis of Table 1 shows that after 100, 300, 500 times of training, the PA and mIoU values of the SETR model are gradually increasing. Combined with the analysis of Figure 7, it shows that the semantic segmentation ability of the SETR model to the greenhouse road image is enhanced, and the PA and mIoU of the SETR model reach 96.46% and 90.45% respectively after 500 times of training. After 100, 300, 500 times of training in the DeepLabv3+ model, the values of PA and mIoU of the model did not change significantly, the PA of the model was about 93.3%, and the mIoU was about 81.5%, indicating that the DeepLabv3+ model did not improve its ability of semantic segmentation of field roads with the increase of training times, which was consistent with the analysis of Figure 7. In the case of 500 times of training of the two models, the two evaluation indexes of the SETR model were much higher than those of the DeepLabv3+ model, with PA 3.12% higher and mIoU higher by 8.9%.

To sum up, both SETR model and DeepLabv3+ model can complete the task of semantic segmentation of greenhouse road images after different times of training. SETR model has significantly improved the ability of semantic segmentation of greenhouse road images after different times of training, while DeepLabv3+ model has not significantly improved the ability of semantic segmentation of greenhouse road images after many trainings. And after 500 times of training, the semantic segmentation ability of SETR model is obviously better than that of DeepLabv3+ model.

Analysis of prediction results of two models

In order to test the generalization ability of the two models and whether there is a fitting phenomenon in the two models, the untrained test set is taken as the prediction object, and the trained SETR model and Deeplabv3 model are used to predict the test set. The semantic segmentation effect of the two models is shown in Figure 7, and the prediction ability of the model is evaluated by three evaluation indexes of PA, mIoU, as shown in Table 2.

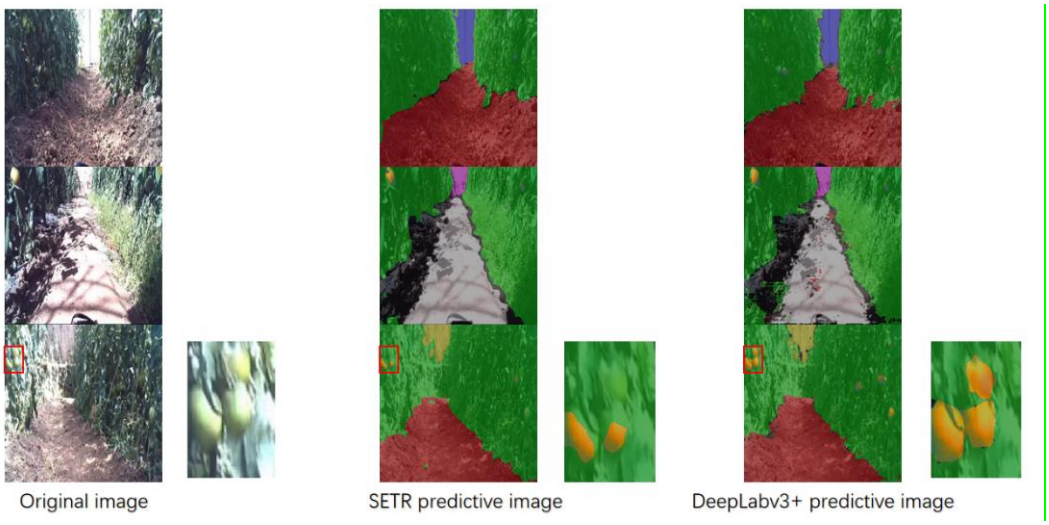


Fig. 7 - Semantic Segmentation effect of two models on Test set

Table 2

Evaluation Index score of semantic Segmentation of Test set by two models

Models	Evaluation index	
	PA/%	mIoU/%
SETR	94.64	82.72
DeepLabv3+	90.80	72.35

According to the analysis of Figure 7, SETR model and DeepLabv3+ model predict the test set, and realize the semantic segmentation of each target in the greenhouse road image. The target contours predicted by SETR model and DeepLabv3+ model is basically consistent with the actual contours of the target, but there are also some errors. Generally speaking, the effect of SETR model on image semantic segmentation is higher than that of DeepLabv3+ model. The image predicted by SETR model has fewer errors, the edges between targets are clearer, and the predicted target contours are more consistent with the actual contours of targets. However, the semantic segmentation effect of SETR model on small target tomatoes is slightly worse than that of DeepLabv3+ model.

It can be seen from Table 2 that SETR model and DeepLabv3+ model have high scores on the performance of semantic segmentation of greenhouse roads. Among them, the PA of SETR model reaches 94.64%, the PA of SETR model reaches 82.72%, the PA of DeepLabv3 + model reaches 90.80%, and the score of 72.35% SETR model is higher than that of DeepLabv3+ model in all indicators of semantic segmentation of greenhouse road data sets. Compared with Table 2 and Table 1, both SETR model and DeepLabv3 model have some overfitting in the semantic segmentation of greenhouse road data sets. Compared with the SETR model, the PA decreased by 1.82% and the MIoU decreased by 7.73%. Compared with the DeepLabv3+ model, the PA decreased by 2.54% and the SETR model decreased by 9.2%. The overfitting problem of the DeepLabv3 + model is slightly more serious than the DeepLabv3 + model. There is a certain overfitting problem in the two models, which should be caused by the insufficient number of images in the data set, and the images are subjective by manual calibration, and there is a certain deviation between the calibrated target contour and the real contour, thus affecting the semantic segmentation ability of the model to the image. According to the score of semantic segmentation of each excellent model in each open data set, the performance of semantic segmentation of greenhouse road data set by SETR model and DeepLabv3+ model can meet the requirements of actual deployment.

CONCLUSIONS

In order to realize the automatic driving of agricultural machinery in the greenhouse, it is necessary to analyse the road environment of the greenhouse. Semantic segmentation can achieve pixel-level classification of images and panoramic analysis of the environment, which is an important support for autopilot. Semantic segmentation of greenhouse road image can provide agricultural machinery with road information, crop information and other environmental information, which is an important support for agricultural machinery to perceive the changing greenhouse environment.

In this paper, according to the demand of automatic driving of agricultural machinery in the greenhouse, a tracked intelligent car with camera is used as image acquisition equipment and several images of greenhouse road are collected. After the manual calibration of the greenhouse image, a greenhouse road data set is established. Two models of SETR based on Transformer framework and DeepLabv3+ based on convolution neural network are built, and several groups of semantic segmentation experiments are carried out on the self-built greenhouse road data set. The two models have accomplished the task of semantic segmentation of greenhouse images. SETR model achieves PA94.64%, mIoU82.72%, DeepLabv3+ model achieves PA90.80%, mIoU72.35%, SETR model has higher semantic segmentation performance than DeepLabv3+ model in greenhouse road image. In terms of the semantic segmentation performance of the greenhouse road image, the two models can meet the deployment requirements of automatic driving of agricultural machinery in the greenhouse. This paper realizes the semantic segmentation of the road data set of self-built greenhouse through two semantic segmentation models of DeepLabv3+ and SETR, accomplishes one of the important tasks of automatic driving of agricultural machinery in greenhouse, and provides an important theoretical support for agricultural machinery to realize automatic driving of greenhouse.

REFERENCES

[1] Carion, N., Massa, F., Synnaeve, G., Usunier, N., Kirillov, A., Zagoruyko, S. (2020). End-to-end object detection with transformers. *In Computer Vision – ECCV 2020* (Springer International Publishing), Vol. 12346, pp. 213-229. https://doi.org/10.1007/978-3-030-58452-8_13

[2] Chen, L. C., Papandreou, G., Kokkinos, I., Murphy, K., Yuille, A. L. (2018). Deeplab: semantic image segmentation with deep convolutional nets, atrous convolution, and fully connected CRFs. *IEEE Transactions on Pattern Analysis and Machine Intelligence,* vol. 40 issue 4, pp. 834-848. https://doi.org/10.1109/tpami.2017.2699184

[3] Chen, L. C., Zhu, Y., Papandreou, G., Schroff, F., Adam, H. (2018). Encoder-decoder with atrous separable convolution for semantic image segmentation. *In Proceedings of the European conference on computer vision (ECCV)*, pp. 801-818. https://doi.org/10.1007/978-3-030-01234-2_49

[4] Chollet, F. (2017). Xception: Deep Learning with Depthwise Separable Convolutions. *2017 IEEE Conference on Computer Vision and Pattern Recognition (CVPR)*. https://doi.org/10.1109/cvpr.2017.195

[5] Daduna, J R. (2020). Automated and autonomous driving in freight transport-opportunities and limitations. *In Computational Logistics: 11th International Conference, ICCL 2020,* vol. 12433, pp. 457-475. https://doi.org/10.1007/978-3-030-59747-4_30

[6] Dosovitskiy, A., Beyer, L., Kolesnikov, A., Weissenborn, D., Zhai, X., Unterthiner, T., Houlsby, N. (2020). An image is worth 16x16 words: Transformers for image recognition at scale. *arXiv preprint arXiv:2010.11929*. https://doi.org/10.48550/arXiv.2010.11929

[7] Fan, M. Y., Lai, S. Q., Huang, J. S, Wei X. M., Chai Z. H., Luo J. F., Wei X. L. (2021). Rethinking BiSeNet for real-time semantic segmentation. *2021 IEEE/CVF Conference on Computer Vision and Pattern Recognition (CVPR)*, pp. 9716-9725. https://doi.org/10.1109/cvpr46437.2021.00959

[8] Gu, J., Kwon, H., Wang, D., Ye, W., Li, M., Chen, Y. H., Pan, D. Z. (2022). Multi-scale high-resolution vision transformer for semantic segmentation. In *Proceedings of the IEEE/CVF Conference on Computer Vision and Pattern Recognition* pp. 12094-12103. https://doi.org/10.1109/cvpr52688.2022.01178

[9] He, K., Gkioxari, G., Dollár, P., Girshick, R. (2017). Mask R-CNN. *In Proceedings of the IEEE international conference on computer vision*, pp. 2961-2969. https://doi.org/10.1109/iccv.2017.322

[10] Hu, Q., Yang, B., Xie, L., Rosa, S., Markham, A. (2020). RandLA-Net: Efficient Semantic Segmentation of Large-Scale Point Clouds. *2020 IEEE/CVF Conference on Computer Vision and Pattern Recognition (CVPR)*. pp. 11105-11114. https://doi.org/10.1109/cvpr42600.2020.01112

[11] Jin, Y, Han, D, Ko, H. (2021). TrSeg: transformer for semantic segmentation. *Pattern Recognition Letters*, vol. 148, issue 4, pp. 29-35. https://doi.org/10.1016/j.patrec.2021.04.024

[12] Johansen, A. R., Sønderby, C. K., Sønderby, S. K., & Winther, O. (2017). Deep recurrent conditional random field network for protein secondary prediction. *In Proceedings of the 8th ACM international conference on bioinformatics, computational biology, and health informatics,* pp. 73-78.

[13] https://doi.org/10.1145/3107411.3107489

[14] Long, J., Shelhamer, E., Darrell, T. (2015). Fully convolutional networks for semantic segmentation. In *Proceedings of the IEEE conference on computer vision and pattern recognition*, pp. 3431-3440. https://doi.org/10.1109/cvpr.2015.7298965

[15] Lu, Z., He, S., Zhu, X., Zhang, L., Song, Y. Z., Xiang, T. (2021). Simpler is better: Few-shot semantic segmentation with classifier weight transformer. *In Proceedings of the IEEE/CVF International Conference on Computer Vision,* pp. 8741-8750. https://doi.org/10.1109/iccv48922.2021.00862

[16] Ren, F. L., Yang, L., Zhou H., B., He X., Xu, W. X. (2023). Real-time semantic segmentation based on improved BiSeNet (基于改进BiSeNet的实时图像语义分割). *Optics and Precision Engineering*, vol. 31, issue 8, pp. 1217-1227. https://doi.org/10.37188/OPE.20233108.1217

[17] Shi, H, Xu, M, Li, R. (2017). Deep learning for household load forecasting – a novel pooling deep RNN. *IEEE Transactions on Smart Grid,* vol. 9, issue. 5, pp. 5271-5280. https://doi.org/10.1109/tsg.2017.2686012

[18] Vaswani, A., Shazeer, N., Parmar, N., Uszkoreit, J., Jones, L., Gomez, A. N., Polosukhin, I. (2017). Attention is all you need. *Advances in neural information processing systems*, arXiv:1706.03762. https://doi.org/10.48550/arXiv.1706.03762

[19] Wang, J., Sun, K., Cheng, T., Jiang, B., Deng, C., Zhao, Y., Xiao, B. (2020). Deep high-resolution representation learning for visual recognition. *IEEE transactions on pattern analysis and machine intelligence*, vol. 43, issue 10, pp. 3349-3364. https://doi.org/10.1109/tpami.2020.2983686

[20] Xie, E., Wang, W., Yu, Z., Anandkumar, A., Alvarez, J. M., Luo, P. (2021). SegFormer: Simple and efficient design for semantic segmentation with transformers. *Advances in Neural Information Processing Systems*, pp. 12077-12090. https://doi.org/10.48550/arXiv.2105.15203

[21] Xiong, W., Tong, L., Jin, J. Y., Wang, C. S., Wang, J., Zeng, C. Y. (2021). Research on semantic segmentation algorithm based on convolutional neural network (基于卷积神经网络的语义分割算法研究). *Application Research of Computers*, vol. 38, issue 4, pp. 1261-1264. https://doi.org/10.19734/j.issn.1001-3695.2019.12.0705

[22] Yin, W., Kann, K., Yu, M., Schütze, H. (2017). Comparative study of CNN and RNN for natural language processing. *arXiv preprint arXiv:1702.01923*. https://doi.org/10.48550/arXiv.1702.01923

[23] Yoon, J. Y., Jeong, J., Sung, W. (2022). Design and implementation of HD mapping, vehicle control, and V2I communication for robo-taxi services. *Sensors*, vol. 22, issue 18, pp. 7049. https://doi.org/10.3390/s22187049

[24] Yu, C., Gao, C., Wang, J., Yu, G., Shen, C., Sang, N. (2021). BiSeNet v2: Bilateral network with guided aggregation for real-time semantic segmentation. *International Journal of Computer Vision*, vol. 129, pp. 3051-3068. https://doi.org/10.1007/s11263-021-01515-2

[25] Yu, C., Wang, J., Peng, C., Gao, C., Yu, G., Sang, N. (2018). BiSeNet: Bilateral segmentation network for real-time semantic segmentation. In *Proceedings of the European conference on computer vision (ECCV),* pp. 325-341. https://doi.org/10.1007/978-3-030-01261-8_20

[26] Zheng, S. X., Lu, J. C., Zhao, H. S., Zhu, X. T., Luo, Z. K., Wang, Y. B., Fu, Y. W., Feng, J. F., Xiang, T., Philip, H. S. Torr, Zhang, L. (2021). Rethinking semantic segmentation from a sequence-to-sequence perspective with transformers. *In Proceedings of the IEEE/CVF conference on computer vision and pattern recognition,* pp. 6881-6890. https://doi.org/10.1109/cvpr46437.2021.00681

[27] Zhongkun, H. (2020). Analysis of visual navigation extraction algorithm of farm robot based on dark primary colour. *INMATEH-Agricultural Engineering*, *62*(3). https://doi.org/10.35633/inmateh-62-23

DESIGN AND SIMULATION OF THREE-DEGREE-OF-FREEDOM WRIST STRUCTURE OF PICKING MANIPULATOR
/
采摘机械手三自由度腕部结构设计及仿真

Junhui SUN [1)], Jinliang GONG [2*)], Yanfei ZHANG [1*)]
[1)]School of Agricultural Engineering and Food Science, Shandong University of Technology, Zibo/China
[2)]School of Mechanical Engineering, Shandong University of Technology, Zibo/China
Tel: +8618265338441; E-mail: 1392076@sina.com; gjlwing@sdut.edu.cn
DOI: https://doi.org/10.35633/inmateh-71-66

***Keywords**: underactuated, picking manipulator, cardan joint, optimised design, ANSYS*

ABSTRACT
*In order to solve the problem of poor flexibility of existing picking manipulators, a picking manipulator with a wrist joint has been designed, the wrist is capable of rotating 45° forward and backward around the x and y axes. Firstly, ANSYS was used to simulate the performance of different hoses under different conditions, and finally a 4*6mm PVC hose was selected to replace the internal cardan joint as the transmission component. Secondly, the wrist structure was optimized using genetic algorithm to reduce the tendon rope variation differences to 0.31mm and 0.24mm. Finally, the results of orchard picking experiments indicate that the end-effector rotation of 720° can ensure that the fruit stalks can be unscrewed, the time required to complete the picking is 1.6s, and the overall picking success rate was 100%. After 9 days of placing the harvested fruit, both the flesh and skin are intact, indicating that the manipulators can complete the non-destructive picking operation.*

摘要
*为了解决现有采摘机械手灵活性差的问题，设计了一种带有腕部关节的采摘机械手，其腕关节可绕 x 轴和 y 轴正负旋转 45°。首先，使用 ANSYS 对不同软管在不同工况下的性能进行了仿真，最终选择了 4*6mm 的 PVC 软管代替内部万向节作为传动部件。其次，利用遗传算法对腕部结构进行优化，将腱绳的变化量差值缩小到 0.31mm 和 0.24mm。最后，果园采摘实验结果表明，末端执行器旋转 720°可确保拧断果柄，完成采摘所需的时间为 1.6 秒，整体采摘成功率为 100%。采摘的果实放置 9 天后，果肉和果皮都完好无损，表明机械手可以完成无损采摘操作。*

INTRODUCTION
At present, the harvesting operation of fruit and vegetable products has the characteristics of concentrated cycle, large amount of labour and mainly manual operation *(Bao et al., 2013)*, The reduction of labour, the cost of labour increases to promote the development of mechanized harvesting *(Bu et al., 2020)*, the expansion of the scale of the standardized orchard, for the orchard intelligent, mechanization provides favourable conditions *(Li et al., 2021)*.and efficient picking robots can help to realize the automation of picking operation *(Chen et al., 2023)*, in which the picking manipulator as an actuator, and its performance determines the efficiency and quality of the picking operation.

Chen et al., (2021), designed a fully pneumatic suction-clamp integrated tomato picking end-effector, which completes the picking operation in four steps: adsorption, pull-back, clamping, and twisting. *Yu et al., (2022),* developed a tomato picking robot with autonomous recognition capability and soft three-finger gripping jaws capable of non-destructive picking. To evaluate the performance of end effectors used in soft tree fruit harvesting, *Goulart et al., (2023),* has defined a set of measurement standards. *Stevanović et al., (2023)*, designed a composite 6-DOF robot harvester with telescopic robot arm for plum farmyards, it can carry the picked fruits to the designated location. *Vítor et al., (2023)*, proposed a stackable 3 DoF SCARA manipulator for tomato harvesting. the manipulator was able to position itself very close to the target in less than 3 seconds, where an end-effector could adjust its position for the picking. *Boisclair et al., (2022)* designed a hand with 17 degrees of freedom with a manually operable thumb structure that allows the hand to have three different grasping postures.

[1] *Junhui SUN, M.S. Eng.; Jinliang GONG, A. Prof. Ph.D. Eng.; Yanfei ZHANG, Prof. Ph.D. Eng.*

Hohimer et al., (2019) and *Hua et al., (2023)* design of pneumatic flexible picking hand claw has little damage to the surface of fruits and vegetables. Flexible end-effector enables non-destructive picking operations, as shown by pulp damage studies conducted by *Bu et al., (2020)*. Pneumatic finger gripping is faster and has better adaptability compared to tendon-driven ones.

Various scholars have achieved remarkable results in the field of picking robots, but the current picking robots still have the following problems. The manipulator usually uses pulling *(Zhi et al., 2023)*, twisting, and cutting of fruit stalks to carry out picking operations. The picking method of pulling off the fruit stalk is relatively simple *(Wang et al., 2023)*, but it requires the robotic arm to provide a large pulling force as well as displacement, and it is also prone to cause the branch to sway, resulting in the dislodging of other fruits. The drive and end-effector of the picking manipulators designed in *Long et al., (2023)* and *Zhang et al., (2023)* cannot be separated, resulting in large size and weight. If the picking method of unscrewing the fruit stalk is used, the end-effector and driver need to be rotated together, which reduces the flexibility, and the picking space is narrow, and the large size is not conducive for the robotic arm to adjust the position of the end-effector.

In order to solve the problem of poor flexibility of the existing manipulator, this paper designs a rope-driven underactuated apple picking manipulator with three rotational degrees of freedom wrist joints based on the double cardan joint structure, which has higher flexibility, versatility, and can realise high-efficiency and non-destructive picking.

MATERIALS AND METHODS

Manipulator configuration analysis and design

Compared with fully actuated end-effector, underactuated end-effector has the advantages of simple structure and small size. At the same time, the adaptability of underactuated end-effector is more suitable for gripping objects of different shapes and sizes *(Wei et al., 2021)*. The rope-driven type has a simple structure and smaller size, and it meets the gripping force requirements of fruit and vegetable picking although the gripping force of the end-effector is smaller.

When the length of the finger is certain, the higher the number of knuckles, the better the envelope of the finger to a round object, but the stable grasping space of the finger will decrease, resulting in an increase in the force required for stable grasping. In contrast, a finger with 3 knuckle units has better envelopment and a larger stable grasping space. The gripping object of the manipulator is a spherical fruit, and 3 fingers can complete the gripping. Therefore, the end-effector selection of 3 circumferential uniform distribution of the fingers, the number of knuckles of each finger is 3.

There are three main ways for picking robots to pick apples: cutting, pulling and twisting the stalk. The direct pulling of apples by the robot will cause the branch to shake, which will result in branch damage and the shedding of the rest of the ripe fruits, and the pulling process requires a larger pulling force and stroke. If a blade is used to cut the stalk for picking, a force of 18-28 N is required to cut the stalk (Table 1), compared to the much less vigorous method of twisting the stalk, which requires only 2-5 N (Table 2) *(Deng et al., 2019)*.

Table 1

Apple stalk cutting force

Diameter/mm	58.33	64.2	72.5	82.1	90.5
Cutting force/N	18.2	21.3	23.3	25.2	27.8

Table 2

Apple stalk twisting force

Diameter /mm	62.1	71.6	77.8	83.5	88.4	91.3
Twisting force/N	2.34	3.24	3.55	3.86	3.99	4.21

Combining the above analyses, a rope-driven underactuated apple picking manipulator with rotary unscrewing of the fruit stalk as the picking method and a wrist structure with three rotational degrees of freedom was designed, as shown in Fig. 1.

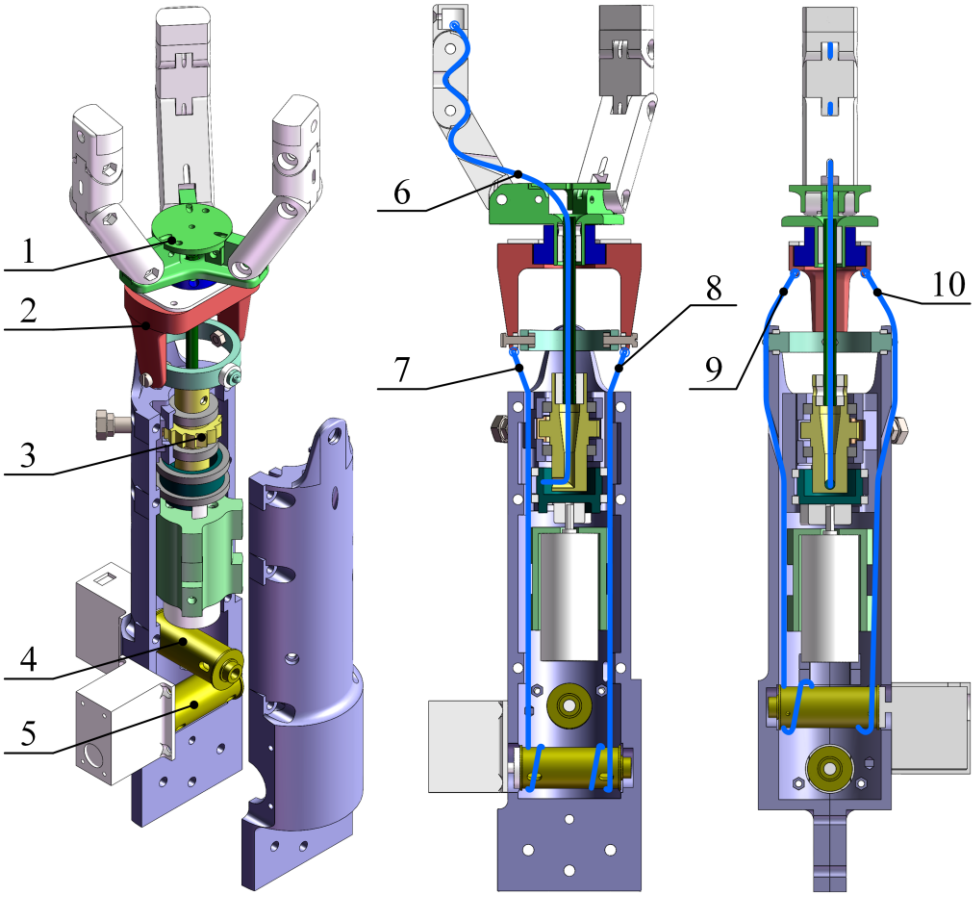


Fig. 1 – Rope-driven underactuatedn picking manipulator

1. End-effector; 2. Wrist module; 3. End-effector drive module; 4. Winding spool I; 5. Winding spool II; 6. Tendon rope I; 7. Tendon rope II; 8. Tendon rope III; 9. Tendon rope IV; 10. Tendon rope V

The manipulator includes an underdriven end-effector, a three rotational degrees of freedom wrist module and a drive module. The three fingers in the end-effector are uniformly distributed around the circumference, and are driven by a tendon rope to close it and torsion springs at the knuckle to open it. And the three fingers are ultimately driven by a tendon rope, so that the movement of the three fingers is synchronized. The end-effector drive module is responsible for controlling the opening and closing as well as the rotation of the end-effector. The wrist module can rotate 45° clockwise and counterclockwise around the *x* and *y* axes, and adopts a double cardan joint type structure with inner and outer nesting, as shown in Fig. 2., so that the end-effector can rotate continuously in a full circle while the wrist is deflected.

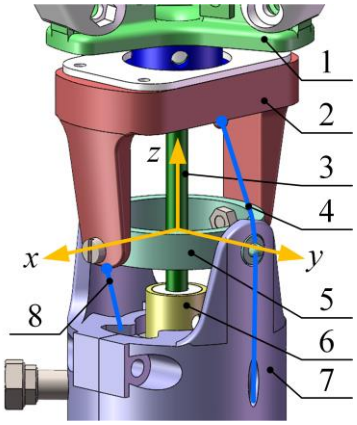


Fig. 2 – Three rotational degrees of freedom wrist structure

1. end-effector; 2. n-bracket; 3. Hose; 4. tendon rope V; 5. circular bracket; 6. output shaft; 7. Shell; 8. tendon rope II

The tendon rope II and III in the opposite direction wrapped in the winding spool II, the winding spool II rotation can make a tendon rope downward tightening at the same time upward relaxation of the other tendon rope, so as to drive the wrist around the y-axis rotation. When the wrist rotates around the y-axis, in order to avoid non-essential rotation of the wrist around the x-axis due to changes in the tension of the tendon cords

IV and V, it is necessary to ensure that the tendon cords IV and V pass through a point on the y-axis. So that the wrist around the y-axis rotation, tendon rope IV, V is always in a taut state.

Since the underdriven end-effector is remotely driven by a tendon rope, in order to avoid entanglement of the tendon rope I driving the end-effector with the output shaft during the end-effector rotation, it is necessary to ensure that the tendon rope I passes through the centre of the cardan joints, however, the existing standard parts of the cardan joints cannot satisfy this requirement. Moreover, when installing the inner and outer nested double cardan joint structure, it is necessary to ensure that the centres of the two cardan joints coincide, which requires high installation accuracy. In order to reduce the installation difficulty and the manufacturing cost of non-standard parts, a hose is used instead of the internal cardan joint as the transmission component.

Hose Simulation and Selection

The main function of the hose is to transmit the torque from the output shaft to drive the end-effector to rotate. There are three kinds of working conditions: transmitting torque in the vertical state, bending, and transmitting torque in the bending state. Using ANSYS to simulate three working conditions, and based on the simulation results, with the premise of meeting the harvesting requirements and the goal of excellent transmission efficiency, the selection of hoses is carried out.

In order to reduce the manufacturing cost of non-standard parts, the hose selects the common ones on the market, naming the different materials and specifications, see Table 3, and the properties of different materials are shown in Table 4.

Table 3

Hose Nomenclature

Inner Diameter*Outer Diameter (mm)	3*5	4*6	4*8	6*8	6*10	8*10	8*12
Silicone Hose	G-1	G-2	G-3	G-4	G-5	G-6	G-7
Rubber Hose	X-1	X-2	X-3	X-4	X-5	X-6	X-7
PVC Hose	P-1	P-2	P-3	P-4	P-5	P-6	P-7
TPU Hose	T-1	T-2	T-3	T-4	T-5	T-6	T-7

Table 4

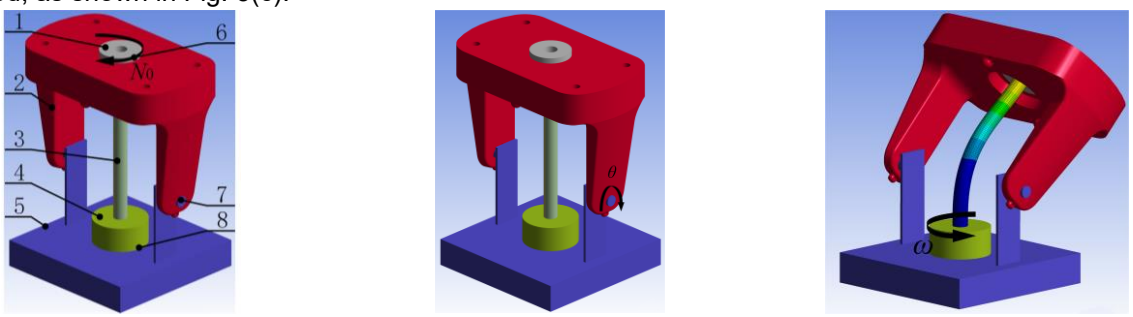
Table of material properties

Name	Young's modulus (GPa)	Densities (kg/m^3)	Poisson's ratio
Silicone Hose	0.12	1120	0.48
Rubber Hose	0.83	1343	0.45
PVC Hose	0.47	1020	0.41
TPU Hose	1.62	950	0.42

According to Table 2, it can be seen that the maximum torque required to unscrew the fruit stalk is about 0.2 N•mm. Considering the obstruction of branches during the rotation process, the load during the hose rotation process is set to 0.6 N•mm. When the wrist is in a vertical state, fix the revolute II and III, and apply a clockwise torque of 0.6 N•mm at the palm to simulate the deformation of the hose, which is the rotation angle S of the palm, as shown in Fig.3(a).

The torque N_1 required for bending the hose was simulated by rotating the n-bracket 45° clockwise with the revolute I and III fixed, as shown in Fig. 3(b).

After the n-type bracket is rotated 45° around the x-axis, the output shaft is made to rotate at a speed of 1 r/min at a constant speed for the whole circumference, and the required torque N_2 of the output shaft is simulated, as shown in Fig. 3(c).



(a) Torsion simulation in wrist vertical state (b) Wrist rotation simulation (c) Torsion simulation in wrist deflection state

Fig. 3 – Hose simulation under different working conditions

1. palm; 2. n-bracket; 3. Hose; 4. output shaf;t 5. Shell; 6. revolute I; 7. revolute II; 8. revolute III

Build an evaluation function as:

$$p = S + N_1 + N_2 \quad (1)$$

where: p is value of evaluation; S is rotation angle of the palm, [°]; N_1 is torque required for bending the hose, [N•mm]; N_2 is required torque of the output shaft, [N•mm].

The smaller value p of the evaluation function represents the higher transmission efficiency of the hose. The simulation results are shown in Table 5, The simulation results are shown in Table 5, G-1, G-2, G-4 and G-6 undergo large deformation during the simulation and cannot meet the design requirements. The hose with an inner diameter of 4mm, an outer diameter of 6mm and a material of PVC is finally selected.

Table 5

Hose simulation results

Name	S (°)	N_1 (N•mm)	N_2 (N•mm)	p	Name	S (°)	N_1(N•mm)	N_2(N•mm)	p
P-1	273.75	87.07	106.52	467.34	T-1	65.18	297.21	386.76	749.15
P-2	113.32	157.30	186.42	457.04	T-2	34.67	537.81	781.36	1353.84
P-3	31.39	597.77	684.73	1313.89	T-3	9.49	1325.43	1867.32	3202.24
P-4	42.54	290.76	342.16	675.46	T-4	12.84	904.03	1367.35	2284.22
P-5	13.85	1181.17	1422.30	2617.32	T-5	4.17	2063.98	2864.80	4932.95
P-6	20.18	659.99	936.27	1616.43	T-6	6.09	1569.40	2606.80	4182.29
P-7	7.25	1430.86	1923.60	3361.70	T-7	1.45	2965.34	4125.20	7091.99
G-1	314.08	22.34	Invalid		X-1	119.23	117.65	245.36	482.24
G-2	268.28	40.51	Invalid		X-2	64.93	194.46	398.62	658.01
G-3	127.38	152.54	209.38	498.30	X-3	17.85	732.61	1263.50	2013.96
G-4	155.57	Invalid			X-4	24.16	359.35	668.23	1051.74
G-5	56.17	306.10	389.46	751.73	X-5	7.86	1460.10	2036.50	3504.46
G-6	87.00	Invalid			X-6	11.46	445.85	1564.23	2021.54
G-7	29.40	403.30	559.78	992.48	X-7	2.74	2049.00	3698.24	5749.98

Optimization of wrist structure and building control models

The structural schematic diagram of the wrist rotating around the y-axis is shown in Fig. 4, and a polar coordinate system is established with the centre of rotation H of the circular bracket as the pole and the counterclockwise direction as the positive direction. In the figure, point I (l_{HI},-η) is the contact point between the tendon rope and the shell, and point J (l_{HJ},0) is the fixation point of the tendon rope on the circular bracket.

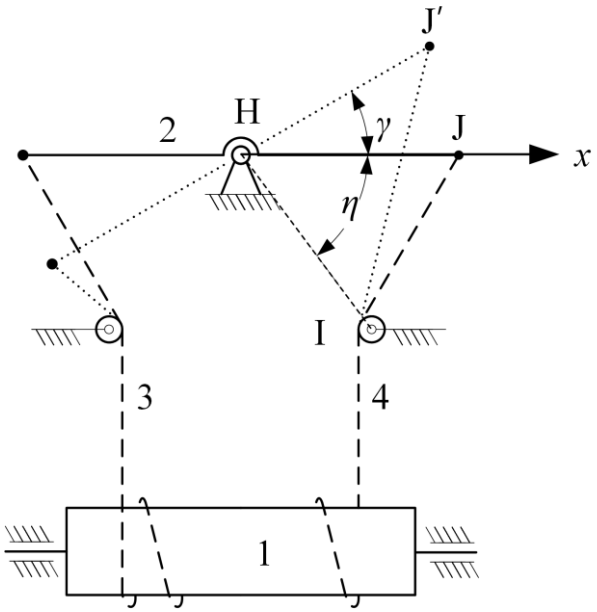


Fig. 4 – Wrist rotation around y-axis structure schematic diagram

1. winding spool II; 2. circular bracket; 3. tendon rope II; 4. tendon rope III

When the circular bracket is rotated counterclockwise by an angle γ, the length change of tendon rope III and tendon rope II is:

$$\Delta l_3 = \left| \sqrt{l_{HI}^{\ 2} + l_{HJ}^{\ 2} - 2\cos(\eta+\gamma) l_{HJ} l_{HI}} - l_{JI} \right| \tag{2}$$

$$\Delta l_2 = \left| \sqrt{l_{HI}^{\ 2} + l_{HJ}^{\ 2} - 2\cos(\eta-\gamma) l_{HJ} l_{HI}} - l_{JI} \right| \tag{3}$$

in which,

$l_{JI} = \sqrt{l_{HI}^{\ 2} + l_{HJ}^{\ 2} - 2\cos\eta l_{HJ} l_{HI}}$; $l_{HI} = \frac{22.2}{\cos\eta}$; l is the distance between two points, [mm]; γ is angle of rotation of circular bracket, [°]; Δl_3 is length change of tendon rope III, [mm]; Δl_2 is length change of tendon rope II, [mm];

The difference in the length change of tendon ropes II and III is:

$$\Delta l_{23} = f(\gamma) = \left| \Delta l_2 - \Delta l_3 \right| \tag{4}$$

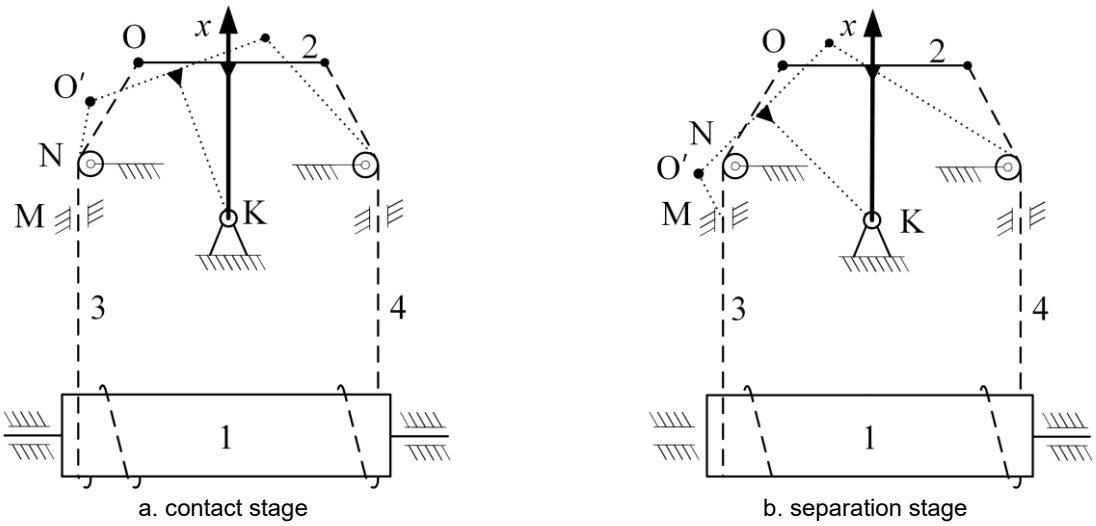
in which, Δl_{23} is difference in the length change of tendon ropes II and III, [mm].

Combining Equation (2), (3) shows that the difference in the length change of tendon rope is affected by η, γ and l_{HJ}.

$$\frac{df}{d\gamma} = \frac{\sin(\eta+\gamma) l_{HJ} l_{HI}}{\sqrt{l_{HI}^{\ 2} + l_{HJ}^{\ 2} - 2\cos(\eta+\gamma) l_{HJ} l_{HI}}} - \frac{\sin(\eta-\gamma) l_{HJ} l_{HI}}{\sqrt{l_{HI}^{\ 2} + l_{HJ}^{\ 2} - 2\cos(\eta-\gamma) l_{HJ} l_{HI}}} \tag{5}$$

Since Equation (5) is not constant to zero, the two tendon ropes do not change in length by the same amount during the rotation of the circular bracket.

The structural schematic diagram of the wrist rotation around the x-axis is shown in Fig. 5. A polar coordinate system is established with the *n*-bracket rotation centre K as the pole and the counterclockwise direction as the positive direction. The rotation process can be divided into two stages, the tendon rope and shell contact stage and separation stage. In the figure, the point N(l_{KN}, K) is the contact point between the tendon rope and the shell, the point M(l_{KM}, $\pi/2$) is the necessary point on the axis of the rotation axis of the *n*-bracket through which the tendon rope passes, and the point O(l_{KO}, ξ) is the fixation point of the tendon rope on the circular bracket.



a. contact stage b. separation stage

Fig. 5 – Wrist rotation around the *x*-axis structure schematic diagram

1. winding spool I; 2. n-bracket; 3. tendon rope IV; 4. tendon rope V

Points O, N and M are collinear when the *n*-bracket is turned counterclockwise by an angle ζ_0. The slopes of the line ON and the line NM are equal.

$$\frac{l_{KN}\sin\kappa - l_{KO}\sin(\xi+\zeta_0)}{l_{KN}\cos\kappa - l_{KO}\cos(\xi+\zeta_0)} = \frac{l_{KM} - l_{KN}\sin\kappa}{-l_{KN}\cos\kappa} \tag{6}$$

When the *n*-bracket is rotated counterclockwise by an angle ζ, the change Δl_4 in the length of the tendon rope IV is:

$$\Delta l_4 = \begin{cases} \left| \sqrt{l_{KO}^{\ 2} + l_{KN}^{\ 2} - 2\cos(\kappa - \xi - \zeta) l_{KO} l_{KN}} - l_{ON} \right| & \zeta \le \zeta_0 \\ \left| \sqrt{l_{KO}^{\ 2} + l_{KM}^{\ 2} - 2\cos(\frac{\pi}{2} - \xi - \zeta) l_{KO} l_{KM}} - l_{ON} - l_{NM} \right| & \zeta > \zeta_0 \end{cases} \quad (7)$$

where,

$$\kappa = \frac{\pi}{2} - \arccos\frac{30}{l_{KN}};\ l_{MN} = \sqrt{l_{KM}^{\ 2} + l_{KN}^{\ 2} - 2\cos(\frac{\pi}{2} - \kappa) l_{KN} l_{KM}};\ l_{ON} = \sqrt{l_{KO}^{\ 2} + l_{KN}^{\ 2} - 2\cos(\kappa - \xi) l_{KN} l_{KO}};$$

l is the distance between two points, [mm]; ζ is angle of rotation of *n*-bracket, [°]; Δl_4 is length change of tendon rope IV, [mm];

In order to make the change Δl_4 in the length of the tendon rope IV with the angle ζ of rotation similar in the two phases, let $l_{KN} = l_{KM}$.

The tendon rope V is always in contact with the shell and its length change Δl_5 is:

$$\Delta l_5 = \left| \sqrt{l_{KO}^{\ 2} + l_{KN}^{\ 2} - 2\cos(\kappa - \xi + \zeta) l_{KO} l_{KN}} - l_{ON} \right| \quad (8)$$

where, Δl_5 is length change of tendon rope V, [mm].

The difference Δl_{45} in the amount of change in the length of tendon ropes IV and V is:

$$\Delta l_{45} = g(\zeta) = |\Delta l_4 - \Delta l_5| \quad (9)$$

In which, Δl_{45} is difference in the length change of tendon ropes IV and V, [mm].

Combined with Equation (7)(8), known l_{KM} is 31, it can be seen that the difference in the length change of tendon ropes IV and V is affected by ζ, ξ and l_{KO}, and is also not constant to zero.

Establish a function for the maximum value of the difference in tendon rope changes during wrist rotation,

$$\begin{aligned} F &= \max(f(\gamma)), \gamma \in (0, 45) \\ G &= \max(g(\zeta)), \zeta \in (0, 45) \end{aligned} \quad (10)$$

In which, F is maximum value of difference in the length change of tendon ropes II and III, [mm]; G is maximum value of difference in the length change of tendon ropes IV and V, [mm].

The relationships between F and its parameters and between G and its parameters are shown in Fig. 6 and Fig. 7.

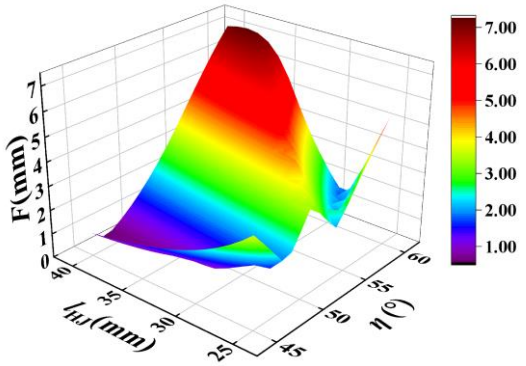


Fig. 6 – Plot of F against η and l_{HJ}

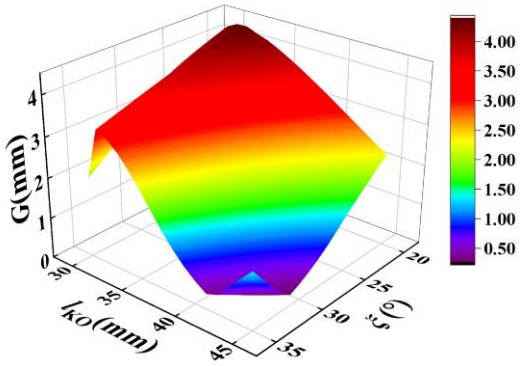


Fig. 7– Plot of G against ξ and l_{KO}

Use the genetic algorithm toolbox in Matlab to analyze and calculate the configuration parameters of the wrist to meet design requirements. Taking Equation (10) as the objective function, whose value is minimized as the optimization objective, η, l_{HJ}, ξ and l_{KO} are used as the design variables.

The range of values of $(\eta, l_{HJ}, \xi, l_{KO})$ is chosen to be [(45,25,20,30); (60,40,35,45)]. Setting an initial population size of 200, a crossover probability of 0.6, a variance rate of 0.007, a number of iterations of 5000. The outputs are η =60, l_{HJ} =25.5, ξ =31.2, l_{KO} =45, F =0.31and G =0.24.

During wrist rotation, although there is a difference in the amount of change in the length of the two tendon ropes, after optimization of the wrist configuration, the difference is minimized to a reasonable range. Constructing a wrist control model based on the amount of tendon rope change on the tightening side, according to Equation (3),(7) yields.

$$\theta_2 = \frac{\sqrt{l_{HI}^{\ 2} + l_{HJ}^{\ 2} - 2\cos(\eta - \gamma) l_{HJ} l_{HI}} - l_{JI}}{r_2} \tag{11}$$

where, θ_2 is the rotation angle of the winding spool II, r_2 is the radius of the winding spool II.

$$\theta_1 = \begin{cases} \dfrac{\sqrt{l_{KO}^{\ 2} + l_{KN}^{\ 2} - 2\cos(\kappa - \xi - \zeta) l_{KO} l_{KN}} - l_{ON}}{r_1} & \zeta \le \zeta_0 \\ \dfrac{\sqrt{l_{KO}^{\ 2} + l_{KM}^{\ 2} - 2\cos(\frac{\pi}{2} - \xi - \zeta) l_{KO} l_{KM}} - l_{ON} - l_{NM}}{r_1} & \zeta > \zeta_0 \end{cases} \tag{12}$$

where, θ_1 is the rotation angle of the winding spool I, r_1 is the radius of the winding spool I.

Equation (11)(12) construct a model for controlling the rotation angle of the wrist and clarify the relationship between the rotation angle of the wrist and the rotation angle around the spool.

RESULTS

Picking effect experiment

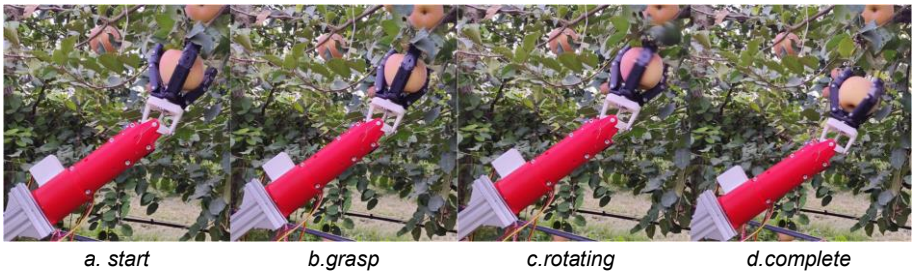
Produce a physical prototype of the manipulator and conduct field tests in the orchard. Through several picking tests and slow playback observation of the picking process, it is found that the end-effector rotation of 720° can ensure that the fruit stalks are unscrewed, and the time required to complete the picking is 1.6s.

The picking effect of the manipulator was tested under the wrist in the vertical state (Fig. 8) and the deflection state (Fig. 9). The experimental results showed that the success rate of picking by rotating the gripper was 90% under two different wrist states. Due to some fruits being placed between two thicker branches, the gripper was unable to rotate and pick them. The overall success rate was 100%, and no other fruits were detached during the picking process. The test results showed that the success rate of picking by rotating the end-effector under the two wrist states was 90%, which was due to the fact that some of the fruits were in between two thicker branches, which caused the end-effector to be unable to rotate for picking. Picking can be accomplished by pulling and tugging after the end-effector is grasped, with an overall success rate of 100%, and without causing the rest of the fruits to fall off during the picking process.



a. start *b.grasp* *c.rotating* *d.complete*

Fig. 8 – Picking process with wrist in vertical state



a. start *b.grasp* *c.rotating* *d.complete*

Fig. 9 – Picking process with wrist in deflection state

The surface of the fruit was intact after picking, and the fruit picked manually was used as a reference to observe the damage of the fruit flesh in the contact area with the manipulator. After 9 days of placement, the fruit flesh in both the finger contact area and the manipulator contact area were intact and free of damage injury, as shown in Fig. 10, indicating that the manipulator was capable of accomplishing non-destructive picking operations.

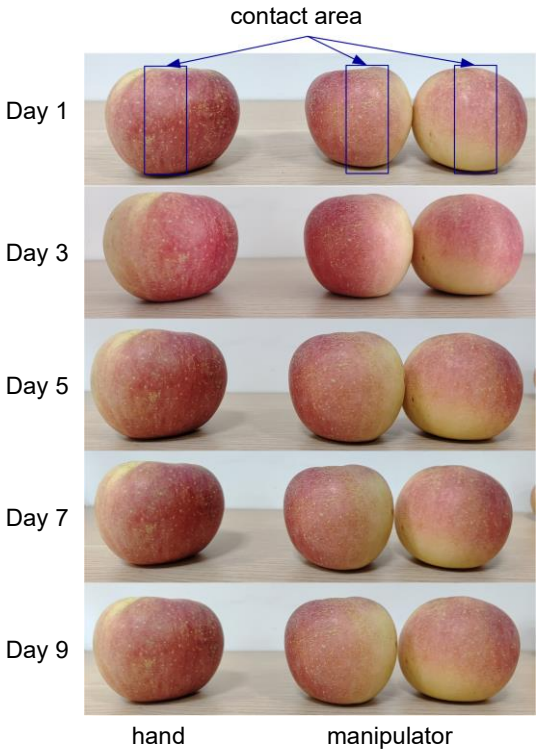


Fig.10 – Flesh damage test

CONCLUSIONS

The rope-driven underactuated picking manipulator designed in this paper has an internally and externally nested double gimbaled wrist structure, and the wrist can be rotated 45° positively or negatively around the x and y axes. The end-effector is able to rotate continuously in a full circle while the wrist rotates, dramatically increasing the flexibility of the manipulator.

Using ANSYS to simulate the performance of different specifications of the hose in different working conditions, the feasibility of the hose as a transmission component is verified, and the PVC hose of 4*6mm (inner diameter*outer diameter) is selected to replace the internal cardan joints to reduce the installation precision requirements and reduce the cost of non-standard parts manufacturing.

With the objective of minimizing the difference in the amount of tendon rope changes between the two sides, the wrist conformation parameters were optimized by genetic algorithm, which reduced the difference in the amount of tendon rope changes to 0.31 mm and 0.24 mm. Through geometric mathematical modeling, the relationship between the winding spool angle and the wrist angle was clarified, and the wrist angle control model was constructed.

The results of the field picking test in the orchard show that the end-effector rotation of 720° can ensure that the fruit stalk is unscrewed, and the time required to complete the picking is 1.6s. The picking operation could be carried out with the wrist in both the vertical and deflected states, with an overall success rate of 100%, and the picking process did not result in the dislodging of the rest of the fruit. The surface of the picked fruit was intact, and the flesh in the area in contact with the manipulator was intact after 9 days of placement, indicating that the manipulator is capable of accomplishing non-destructive picking operations.

ACKNOWLEDGMENT

This work was funded by the Top Talents Program for One Case One Discussion of Shandong Province, the Key Research and Development Program of Shandong Province (Major Innovative Project in Science and Technology) (2020CXGC010804), Shandong Provincial Natural Science Foundation (ZR2021MC026).

REFERENCES

[1] Bao G J, Zhang S B, Chen L, et al. (2013). Design of spherical fruit end-grasper based on FPA (基于气动柔性驱动器的球果采摘抓持器). *Transactions of the Chinese Society for Agricultural Machinery*. Vol.44, Issue 05:242-246.

[2] Bu L X, Chen C K, Hu G R, et al. (2020). Technological development of robotic apple harvesters: A review. *INMATEH-Agricultural Engineering*, Vol. 61, Issue 2:151-164.

[3] Bu L X, Chen C K, Hu G R, et al. (2020). Assessment of apple damage caused by a flexible end-effector[J]. *INMATEH-Agricultural Engineering*, Vol. 62, Issue 3:309-319.

[4] Boisclair, J., Laliberté, T., and Gosselin, C., 2022, On the design of an adaptable underactuated hand using rolling contact joints and an articulated palm. *Journal of Mechanisms and Robotics*, Vol. 15, Issue 5:051001.

[5] Chen Q, Yin C K, Guo Z L, et al. (2023). Current status and future development of the key technologies for apple picking robots (苹果采摘机器人关键技术研究现状与发展趋势). *Transactions of the Chinese Society of Agricultural Engineering*, Vol.38, Issue 4: 1-15.

[6] Chen Z W, Yang M J, Li Y W, et al. (2021). Design and experiment of tomato picking end-effector based on non-destructive pneumatic clamping control(基于气动无损夹持控制的番茄采摘末端执行器设计与试验). *Transactions of the Chinese Society of Agricultural Engineering*，Vol. 37, Issue 2:27-35.

[7] Deng X L, Luo Z Y, Pang J Q, et al. (2019). Design and experiment of bionic nondestructive handheld suction apple picker(仿生无损吸取式苹果采摘装置的设计与试验). *Journal of China Agricultural University*. Vol. 24, Issue 10:100-108.

[8] Goulart R, Jarvis D, Walsh K B. (2023). Evaluation of end effectors for robotic harvesting of mango fruit. *Sustainability*, Vol. 15, Issue 8:6769.

[9] Hohimer C J, Wang H, Bhusal S, et al. (2019). Design and field evaluation of a robotic apple harvesting system with a 3d-printed soft-robotic end-effector. *American Society of Agricultural and Biological Engineers*, Vol. 62, Issue 2:405–414.

[10] Hua H L, Song J, Zhao J B, et al., (2023), Sensor-Less Grasping Force Control of a Pneumatic Underactuated Robotic Gripper. *Journal of Mechanisms and Robotics*, Vol. 16, Issue 3:031005.

[11] Li T, Qiu Q, Zhao C J, et al. (2021). Task planning of multi-arm harvesting robots for high-density dwarf orchards(矮化密植果园多臂采摘机器人任务规划). *Transactions of the Chinese Society of Agricultural Engineering.* Vol. 37, Issue 2:1-10.

[12] Long Y L, Wang B L, Jin H J, et al. (2023). Variable stiffness actuator and variable stiffness flexible gripper based on differential gear train(基于差动轮系的变刚度执行器及变刚度柔性手爪). *Journal Of Mechanical Engineering*. Vol. 59, Issue 01:91-102.

[13] Stevanović I, Ilić U, Rodić A. (2023). Prototyping of robot harvester for plum farmyards–mechanical design. *Advances in Service and Industrial Robotics,* Vol.135, 470-477.

[14] Vítor T, Manuel F S, Filipe N S, et al. (2023). Design and control architecture of a triple 3 dof scara manipulator for tomato harvesting, *2023 IEEE International Conference on Autonomous Robot Systems and Competitions,* pp. 87-92,

[15] Wei B, He J Y, Shi Y, et al. (2021). Design and Experiment of Underactuated End-effector for Citrus Picking(欠驱动式柑橘采摘末端执行器设计与试验). *Transactions of the Chinese Society for Agricultural Machinery*, Vol. 52, Issue 10:120-128.

[16] Wang X, Kang H, Zhou H, et al. (2023). Development and evaluation of a robust soft robotic gripper for apple harvesting. *Computers and Electronics in Agriculture*, 204: 107552.

[17] Yu F H, Zhou C Q, Yang X, et al. (2022). Design and Experiment of Tomato Picking Robot in Solar Greenhouse[J]. *Transactions of the Chinese Society for Agricultural Machinery*. Vol. 53, Issue 01:41-49.

[18] Zhao Y W, Geng D X, Liu X M, et al. (2019). Kinematics analysis and experiment on pneumatic flexible fruit and vegetable picking manipulator(气动柔性果蔬采摘机械手运动学分析与实验). *Transactions of the Chinese Society for Agricultural Machinery*, Vol. 50, Issue 08:31-42.

[19] Zhi H, Li Z X, Ding X T, et al. (2023). Design and experiment of end effect for kiwifruit harvesting based on optimal picking parameters. *INMATEH-Agricultural Engineering*, Vol. 69, Issue 1:325-334.

CLOUD-SIDE COLLABORATION-BASED TASK ALLOCATION STRATEGY FOR AGRICULTURAL MACHINE FLEET
/
基于云边协同的农机群任务分配策略

Junzheng ZHAO[1)], Jinliang GONG [2*)], Yanfei ZHANG[1*)]
[1)]School of Agricultural Engineering and Food Science, Shandong University of Technology, Zibo/China
[2)]School of Mechanical Engineering, Shandong University of Technology, Zibo/China
Tel:+8615318571313; E-mail: junx1219@163.com; 1613484972@qq.com
DOI: https://doi.org/10.35633/inmateh-71-67

Keywords: *cloud robotics, genetic algorithm, farmland tasks, task allocation*

ABSTRACT
In order to rationally plan the amount of tasks and task areas for each agricultural robot in the farm, a cloud-side collaborative task allocation scheme is proposed. The cloud platform divides farm tasks based on field obstacles and extracts the center of gravity prime points for each farm task; plasmas as regional task target points through dynamic genetic algorithms for near-field aggregation, after accelerating the solution process by dynamic crossover and variational operators, the Metropolis criterion is introduced to eliminate the local optimal solution of the algorithm and obtain the globally optimal allocation solution. The simulation experiments demonstrate that the total cost of task execution is reduced by 9.21%, 5.66%, and 7.21% when using four agricultural machines compared to three, five, and six agricultural machines, respectively, and the feasibility of the algorithm is proved experimentally. Reasonable task allocation can improve the overall production efficiency of agriculture, which is informative for unmanned farms operating in large areas.

摘要
为合理规划农场中各个农业机器人任务量与任务区域，提出一种云边协同的任务分配方案。云平台依据田间障碍物划分农田任务，提取各个农田任务重心质点；质点作为区域任务目标点通过动态遗传算法进行近场聚合，经动态交叉、变异算子加速求解过程，引入 Metropolis 准则，剔除算法局部最优解，得到全局最优分配解。仿真实验表明，四台农机执行任务较三台农机、五台农机、六台农机执行任务总代价分别降低了 9.21%、5.66%、7.21%，并通过实验证明了算法的可行性。合理的任务分配，可提高农业整体生产效率，对无人农场大区域作业具有参考价值。

INTRODUCTION

Smart agriculture is the result of fully utilizing modern information technologies, leveraging agricultural data as a production factor, and integrating modern information technologies such as the Internet of Things, big data, and intelligent equipment across agriculture. With the large-scale popularization and application of cloud platform and driverless, the autonomous operation of intelligent farm machinery in unmanned farms has gradually become a mainstream development way (*Huang et al., 2022; Tanzilya. et al., 2021; Jeff, 2020*). Based on Cloud Edge Collaboration technology, according to the difference between the operation site and robot performance, the robots are divided into tasks within the farm, and the operation area is reasonably planned, which helps to utilize the advantages of group operation and improve the operation efficiency (*Nikitenko et al., 2018; Teslya et al 2020; Zhu et al, 2018*).

Cloud-side collaborative work is the process by which the cloud platform divides the area to be worked on and assigns it to a specific robot based on the performance of the swarm of robots within a known environment (*Ferrer et al., 2021*). Task assignment simplifies robotic swarm operations through discrete job scenarios, and is an important research direction for achieving collaborative group operations. At present, the research of cloud-side multi-machine collaboration is mainly in the field of aerospace drones (*Hu et al., 2020*), underwater exploration robots (*Jensen-Nau et al., 2021*), disaster search robots (*Haris et al., 2017*), etc. However, due to the complexity of the agricultural environment and the pressing need to address the issue of full coverage in agricultural machinery operations, there is a lack of research on cloud robot collaboration in

[1] *Junzheng ZHAO, M.S. Eng..; Jinliang GONG, A. Prof. Ph.D. Eng.; Yanfei ZHANG, Prof. Ph.D. Eng.*

the field of agriculture. *Xiangyin Zhang et al. (2023*) proposed a two-layer learning search with elite particles to improve the genetic algorithm and reduce the robot search and rescue time. *Fu-Zhen Zhang* and others *(2022)* obtained smoother multi-UAV trajectories on the basis of global cost minimization by establishing heterogeneous target cost matrices to solve the UAV trajectory model separately. *Wang et al., (2023)*, proposed a multi-objective optimization algorithm under multiple constraints with one-inflection point collaboration and introduced the binary crossover method to perturb the local search and verified the effectiveness of the algorithm. *Viraj et al., (2022),* illustrate the key components of a cloud robotics system through an architectural formulation that inspires how cloud robotics systems can be utilized to solve real-world problems. *Rahman et al., (2019)* offloaded multiple tasks to robots individually through a multilevel decision scheme with multilayer genetic algorithms for parcel picking and distribution applications in a 36-cell workspace warehouse scenario with a master robot completing the task flow of assigning 40 nodes. The above studies are mostly on industrial robot collaboration, but have a better guidance for carrying out swarm collaboration on farmland robots.

In this paper, an unmanned farm with smart farm machine collaboration is taken as a research context, where the unmanned farm is partitioned into several sub-areas due to field roads and farm obstacles. A near-field segmentation of the full field is performed by an improved genetic algorithm to obtain several different subsets of tasks to be operated, and the agricultural machines are scheduled to operate in different subsets of tasks in a discrete manner. The operation of different agricultural machines in close proximity to each other reduces the non-operational path loss of significant cross-area operations, reduces operating time, and effectively avoids accidental machine collisions when operating in different subsets of tasks.

MATERIALS AND METHODS

Cloud robotics architecture

Intelligent robots in unmanned farms offload complex issues such as task allocation, job scheduling, and path planning to cloud platforms and edge cloud platforms, and the robots only need to be equipped with basic sensors and basic network equipment to realize farmland operation tasks. As the decision-making layer of intelligent agricultural production, the cloud platform carries out regional segmentation based on the static map provided by the user, forms the operation plan in accordance with the algorithm of the task allocation model, schedules the robots to complete the farm operation tasks, and feeds the monitoring data back to the user in the process of the task execution to ensure the controllability and stability of the operation. The cloud robot architecture is shown in Fig. 1.

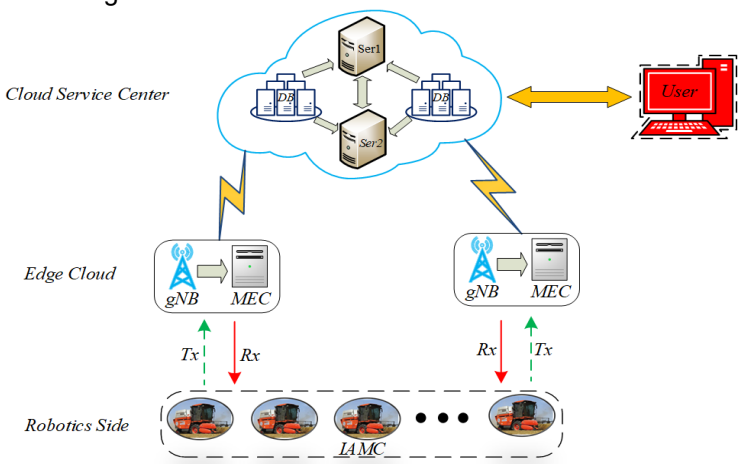


Fig. 1 - Cloud robot architecture

Job scenario analysis

Multi-machine cooperative task assignment is a process of assigning the sequence of operations and tasks to specific farm machines before operations. Take the collaborative harvesting machine scenario in unmanned farm as an example, decompose the irregular farmland geometric model into multiple triangles and calculate the center of gravity, connect the center of gravity to get a simplified graph, continue to solve the center of gravity of the farmland in a loop and use the center of gravity as a task chain traversing the prime points to plan the order of operation of agricultural machines, and the way of planning the center of gravity of the farmland is shown in Fig. 2. The harvester operates round-trip within the sequence of operations at the rated machine operating width, and the farm machinery operates as shown in Fig. 3.

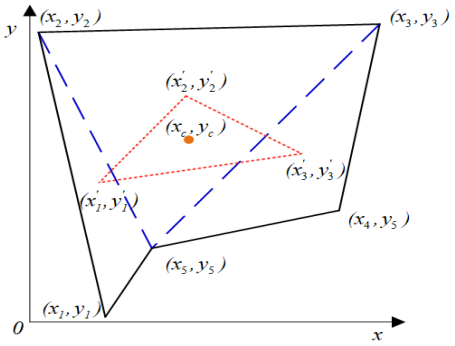


Fig. 2 - Farmland center of gravity planning

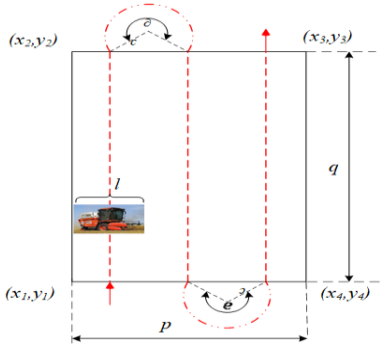


Fig. 3 - Agricultural reciprocating operations

The actual scenarios of group collaboration are complex and variable, in order to simplify the problem and facilitate the planning of mathematical models, the following assumptions are made based on the actual farm scenarios:

(1) The performance parameters and operational parameters of the robot are known; (2) Only one farm machine may operate on each task; (3) The operational path of the farm task is known; (4) Agricultural machines are allowed to duplicate parts of their paths during operations; (5) The mission is considered fully accomplished when all farm machinery returns to the mission rendezvous point.

R: Indicates the group of farm machinery to be assigned to the operation, r is the number of the machine in the fleet, R={1, 2, 3, …, r} and $t>1$.

T: indicates the total number of current job tasks, t is the assignment number, T={1, 2, 3, …, t} and $t>1$.

E: denotes the set of performance parameters of the first agricultural machine. $\mathrm{E}=\{\upsilon_i, v_i, \omega_i, w_i$ $l_i, c_i, \partial_i, \vartheta_i, \eta_i\}$, υ_i denotes the average speed of the operating state of the agricultural machinery (km/h), v_i denotes the average non-operational speed of the farm machine (km/h), ω_i denotes the power lost in the operating state of the agricultural machine (kW/h), w_i denotes the non-operational power loss of the farm machine (KW/h), l_i denotes the width of the agricultural machinery (m), c_i denotes the turning radius of farm machinery (m), ∂_i denotes the turning angle of the farm machine, ϑ_i denotes the operational efficiency of agricultural machinery (m²/h), η_i denotes the residual energy of the farm machinery (kW).

M: denotes the set of task parameters **M**={$a_t, (x_{1t}, y_{1t})(x_{2t}, y_{2t})(x_{3t}, y_{3t})(x_{4t}, y_{4t})(x_{ct}, y_{ct}), p, q, d$}, a_t denotes the size of the task area (m²), , $(x_{1t}, y_{1t})(x_{2t}, y_{2t})(x_{3t}, y_{3t})(x_{4t}, y_{4t})$ denotes the coordinates of the execution point of the task operation, p denotes the maximum horizontal width of the farmland (m), q denotes the maximum vertical length of the farmland (m), d denotes the distance between the centers of gravity of neighboring subregions (km).

Multitasking job cost function

According to Job Scenario Analysis, the task cost is generated during the operation of the agricultural machine, which is mainly composed of the total path traveled, the maximum task completion time and the total energy loss. Assuming that there are r agricultural machines, t operational tasks available in the environment, the following objective function can be defined:

$$f = \lambda \max(S_i) + \mu \sum_{i=1}^{r} L_i + \delta \sum_{i=1}^{r} Q_i + f_p \quad (1)$$

In the formula, f is the operational generation value, S_i is the total amount of time it takes for the farm machine to complete its task, L_i is the total path of agricultural machinery to accomplish a task, Q_i is the total energy loss of the farm machine to accomplish the task, λ, μ, δ is the weighting factor and λ, μ, $\delta \in [0,1]$, f_p is the penalty function in the task system.

Task assembly point $\Upsilon=(x_s, y_s)$ as point 0, the t subregions are the 1st to the points in order, therefore, the center of gravity distance matrix d between any two subregions in the farm is:

$$d = \begin{bmatrix} d_{00} & \cdots & \cdots & d_{0t} \\ \vdots & 0 & & d_{ji} \\ d_{ij} & & 0 & \vdots \\ d_{t0} & \cdots & \cdots & d_{tt} \end{bmatrix} \tag{2}$$

On the basis of the complete workload T, task subset partitioning of farmland based on operation-independent factors such as farm roads and non-operational farmland yields a set of neighboring aggregated tasks U_τ for continuous operations. Within the operation subset U_τ, the tasks are performed by the designated farm machine E_r^τ. The mathematical model is given in the following equation:

$$T = U_1 + U_2 + ... + U_\tau \tag{3}$$

$$U_\tau = M_i + ... + M_j \qquad i, j \in \{1, 2, \cdots t\} \tag{4}$$

$$\mathrm{E}_r^\tau \to U_\tau \tag{5}$$

The time S_i for a farm machine to complete a task consists of three parts: the time for the regional transition, the time for the task operation, and the time for the return trip, and the task time is calculated by the formula:

$$S_i = \sum_{t=1}^{\lceil U_\tau \rceil} \frac{d_{t-t+1}}{v} + \sum_{t=1}^{\lceil U_\tau \rceil} \left(\left\lceil \frac{p}{l} \right\rceil \frac{q}{\upsilon} + \frac{\partial c}{\upsilon} \left\lfloor \frac{p}{l} \right\rfloor \right) + \frac{d_{t-\Upsilon}}{v} \tag{6}$$

The distance L_i of the path of the farm machine to complete the task consists of three parts: the regional path transformation, the path of the farm machine operation, and the return path of the farm machine, and the total path of the task is calculated by the formula:

$$L_i = \sum_{i=1}^{r} \sum_{i=1}^{\lceil U_\tau \rceil} d_{i,i+1} + \sum_{i=1}^{r} \sum_{i=1}^{\lceil U_\tau \rceil} \left(\left\lceil \frac{p}{l} \right\rceil q + \partial c \left\lfloor \frac{p}{l} \right\rfloor \right) + \sum_{i=1}^{r} d_{k-\Upsilon} \tag{7}$$

The energy loss Q_i of the farm machine to complete the task consists of three parts: the energy loss of the farm machine adjacent to the task shift, the energy loss of the farm machine operation, and the energy loss of the farm machine return trip, and the energy loss is calculated by the formula:

$$Q_i = \sum_{i=1}^{\lceil U_t \rceil} \frac{d_{i-i+1}}{v} w_i + \sum_{t=1}^{\lceil U_\tau \rceil} \left(\left\lceil \frac{p}{l} \right\rceil \frac{q}{\upsilon} + \frac{\partial c}{\upsilon} \left\lfloor \frac{p}{l} \right\rfloor \right) \omega_i + \frac{d_{t-\Upsilon}}{v} w_i \tag{8}$$

After the initial task allocation scheme is formed, the feasibility of this scheme is evaluated by substituting the average operating efficiency of the agricultural machine as a parameter into the penalty function. The penalty function f_p is given in the following equation:

$$f_p = \sum_{i=1}^{t} a_i - \frac{\sum_{i=1}^{r} S_i}{r} \vartheta + \zeta \left(\frac{\sum_{i=1}^{t} a_i}{\vartheta r} - \frac{\sum_{i=1}^{r} S_i}{r} \right) \tag{9}$$

In the formula, the area of operation is predicted with the average operating time and operating efficiency of all agricultural machines of the program, and compared with the total area of the actual task. Second, depending on the complexity of the operating environment, the total working time in the ideal state is calculated and differed from the actual working time as a measure of the cost factor of energy consumption, and the parameter ζ is calculated as follows:

$$\zeta = \begin{cases} 1 & Q_i < \eta_i \\ \infty & Q_i \geq \eta_i \end{cases} \tag{10}$$

Genetic code

Traditional genetic algorithms have strong stochastic search ability and global optimization ability, but the random crossover and mutation methods are prone to premature emergence of local optimal solutions, which cause the algorithm to converge prematurely (*Alan et al., 2021; Wang et al., 2021*).

In order to ensure that the algorithm can find the optimal solution, the dynamically adjusted crossover operator and variation operator are designed; and the Metropolis criterion is introduced to enhance the ability of the algorithm to jump out of the local optimal solution.

The chromosome is encoded in three distributed segments, with the first segment representing the sequence of tasks, t tasks grouped in chaotic order from 1 to t, with a total of t positions. The second paragraph indicates the number of operating farm machinery, with 1 digit. The third segment indicates the number of the farm machine, corresponding to the intermittent tasks, respectively, with a total of r digits. Chromosomal gene coding is shown in Fig. 4.

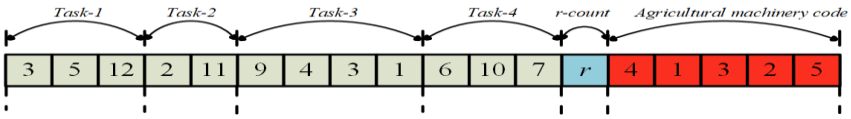


Fig. 4 - Chromosome gene coding map

Choice of operator

In this paper, roulette algorithm with elite retention strategy was chosen to design the selection operator. According to the encoding design in Figure 4, an initial population of C individuals is generated. By calculating the fitness of each individual using Formula 1, the fitness value of individual i in the population is obtained as f_{Ci}. Using the optimal value f_{max} of the population from each iteration as the evaluation criteria, $C1$ elite individuals are selected. Subsequently, the complementary population $C2$ is obtained by dynamically updating the crossover operator with the variation operator, and the population update process is as follows:

$$p_i = \frac{f_{Ci}}{f_{max}} \tag{11}$$

$$C1 = \left\lceil \frac{\sum_{i=1}^{C} f_{Ci}}{f_{max}} \right\rceil \tag{12}$$

$$C = C1 + C2 \tag{13}$$

Dynamic crossover, Variational operators

Gene crossover is the recombination of slices of genes at different locations on a chromosome, and gene mutation is the mutation of a gene at a random location on a chromosome. In order to accelerate the process of population evolution, the crossover probability P_C and mutation probability P_m are dynamically adjusted according to the relationship between the difference between the current individual fitness value of the population and the average fitness value of the population, as well as the elite retention of the population $C1$. The dynamic calculation formula is as follows:

$$P_c = \begin{cases} k_1 \cos[(\frac{f_{max} - f'}{f_{max} - \overline{f}})\frac{C - C1}{C}] & f' \geq \overline{f} \\ k_2 & f' < \overline{f} \end{cases} \tag{14}$$

$$P_m = \begin{cases} k_3 \cos[(\frac{f_{max} - f'}{f_{max} - \overline{f}})\frac{C - C1}{C}] & f' \geq \overline{f} \\ k_4 & f' < \overline{f} \end{cases} \tag{15}$$

In the formula, f_{max} is the maximum value of current population fitness, $\overline{f}$ is the mean value of population fitness, f' is the value of cross individual fitness, k_1, k_2 is the crossover coefficient, k_2 is the default coefficient of the crossover operator and $k_1 + k_2 = 1.0$, k_4 is the default coefficient of the variation operator and $k_3 + k_4 = 1.0$.

Improved genetic algorithm flowchart

Dynamic crossover, variational operators improve the ability to find local optima, but the algorithm is prone to terminate early and ignore the global optimum. Therefore, it is necessary to expand the search scope to jump out of the local optimal solution. The Metropolis criterion accepts floating solutions with a certain probability, which strengthens the fault tolerance of the algorithm and enables it to probabilistically jump out of the local optimal solution.

The probability p_s mathematical model is as follows:

$$p_s = \begin{cases} e^{-\frac{|f_{Ci}-\overline{f}|}{mx-0.95mf}} & 0.8\overline{f} \le f_{Ci} \le 1.2\overline{f} \\ 1 & f_{Ci} < 0.8\overline{f},\ f_{Ci} > 1.2\overline{f} \end{cases} \quad (11)$$

In the formula, mx is the maximum number of iterations of the algorithm, mf is the number of iterations of the current algorithm. The flow of the improved genetic algorithm is shown in Fig. 5.

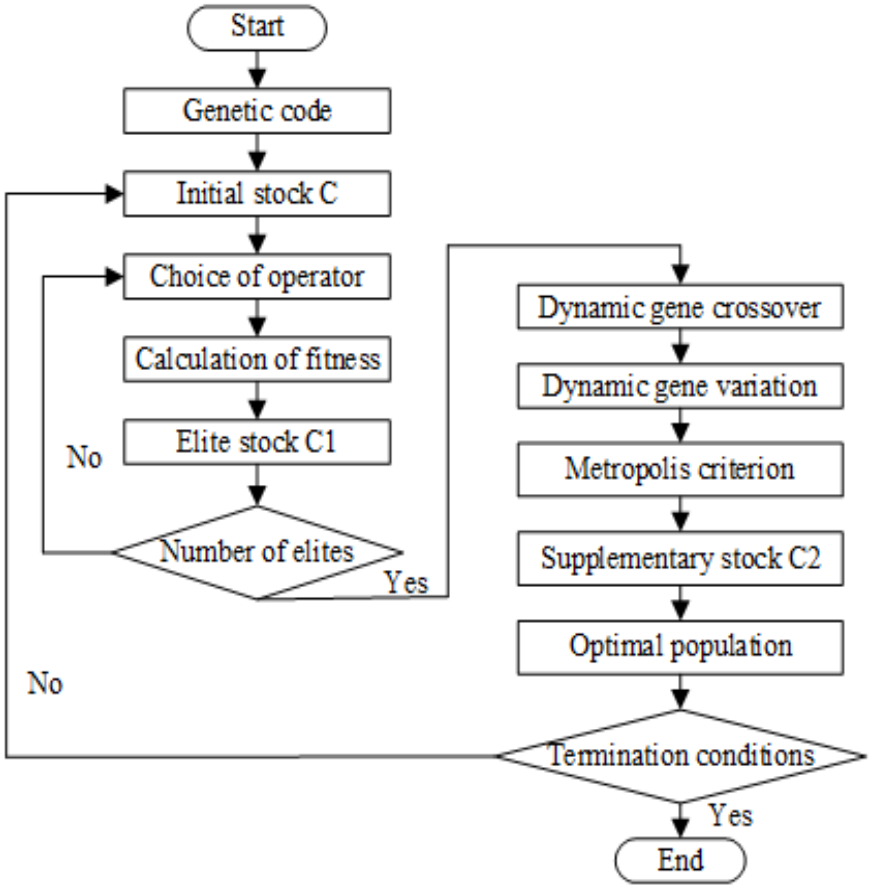
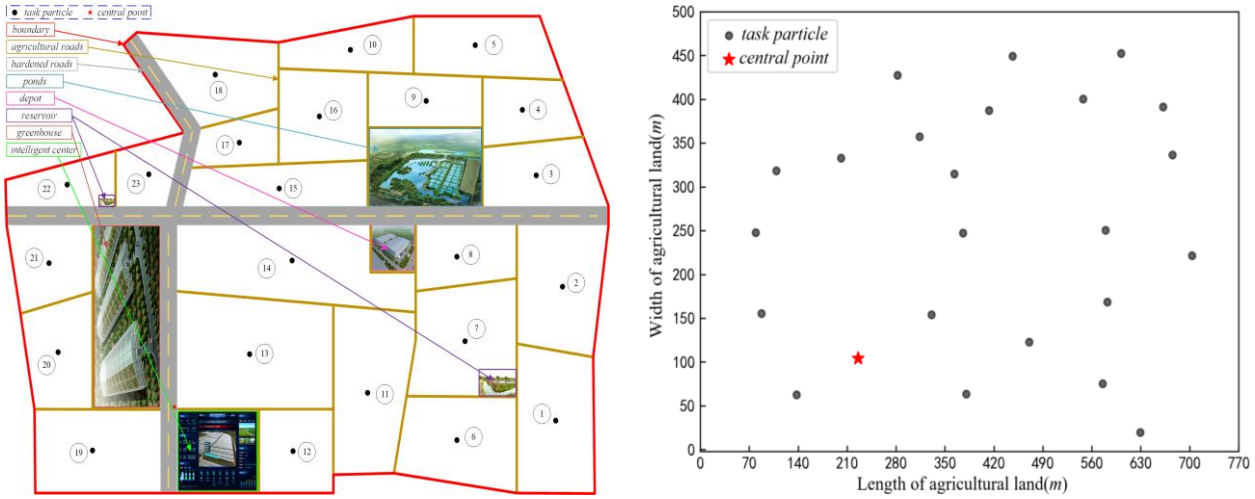


Fig. 5 - Improved genetic algorithm flowchart

RESULTS

Task preprocessing

In order to verify the feasibility and effectiveness of the allocation algorithm in this paper, simulation experiments are carried out in Windows 10 system based on python3.9 environment. Taking the unmanned farm as the experimental environment, after extracting the unmanned farm e-map, the unmanned farm is divided into multiple sub-regions based on multiple field obstacles, and the center of gravity of each sub-region is extracted as the task chain traversal prime point, and the farm e-map is shown in Fig. 6(a). The electronic map of the farm is converted into map feature information that can be recognized and stored by the computer, and the length and width of the farmland are used as the horizontal and vertical axes within the two-dimensional coordinate system to establish the farm task mass map, as shown in Fig. 6(b).



a) Map of the farm *b) Map of the center of gravity of farmland*

Fig. 6 - Farm map

Subset division of agricultural machinery tasks

The task chain formed by the elite ant colony algorithm is used as the basis for subset division. The partial parameters of the task plot obtained according to the task platform in the experiment are shown in Table 1, and the partial parameters of the performance of the six agricultural machines are shown in Table 2.

Table1

Parameters of the mission plots

Farmland serial number	Area (m^2)	Coordinate of the mass point	Farmland serial number	Area (m^2)	Coordinate of the mass point
1	16390.54	(698.4,96.4)	13	20707.13	(330.7,154.2)
2	16515.65	(703.2,221.7)	14	24085.33	(375.7,247.3)
3	14451.20	(675.1,336.4)	15	15577.27	(363.1,314.7)
4	12386.74	(661.7,391.4)	16	13387.69	(412.7,387.3)
5	14200.96	(601.8,452.3)	17	10947.88	(313.4,357.4)
6	16202.86	(575.4,75.2)	18	17078.69	(282.1,427.3)
7	16953.57	(582.3,168.7)	19	15452.15	(137.4,62.7)
8	11510.91	(579.7,250.3)	20	13575.37	(87.4,155.4)
9	11198.11	(547.6,400.2)	21	10572.52	(79.3,247.8)
10	13325.13	(446.7,449.1)	22	10760.20	(108.7,318.6)
11	17579.16	(470.4,122.8)	23	8695.74	(201.4,332.7)
12	11948.83	(380.4,63.4)			

Table 2

Performance parameters of agricultural machines

Farmland serial number	Operating rate (km/h)	Non-operating rate (km/h)	Operating loss (kW/h)	Non-operating loss (kW/h)	Average efficiency (m^2/h)	Energy (kJ)
1	4.60	9.7	57.81	29.78	6500	4617.324
2	4.50	10.2	60.13	29.41	5300	4958.424
3	4.30	9.6	57.61	28.97	5600	4849.956
4	4.10	9.7	59.12	29.45	6000	5063.112
5	3.90	9.8	58.21	30.51	6200	5009.292
6	4.60	10.1	59.34	28.98	5800	5356.224

Assuming that the operating state of the farm machine is exactly the same as the planning operating state of the algorithm, the initial population size of the improved genetic algorithm is 30, and the initial p_c=0.6, p_m=0.2, k_1=0.4, k_2=0.6, k_3=0.8, k_1=0.2. After 1000 iterations, the optimal solution for task assignment of different groups of agricultural machines is obtained, and the task operation flow is shown in Figs. 7 to 10.

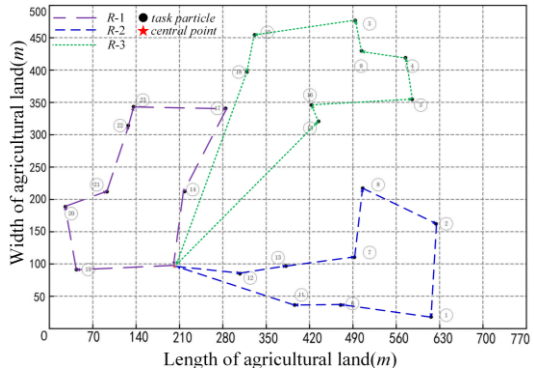


Fig. 7 - Three farm machines in operation

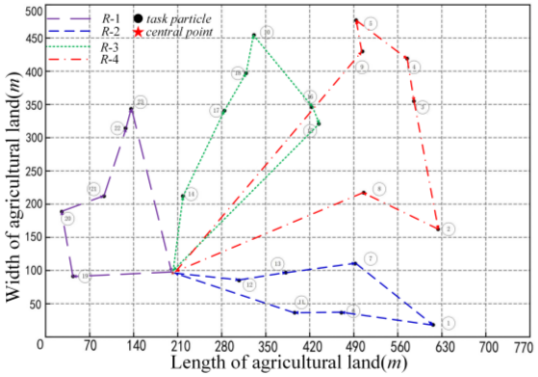


Fig. 8 - Four farm machines in operation

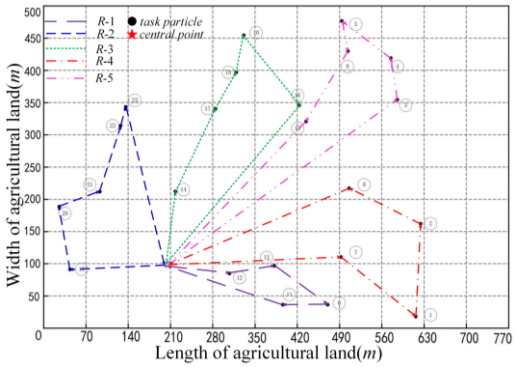


Fig. 9 - Five farm machines in operation

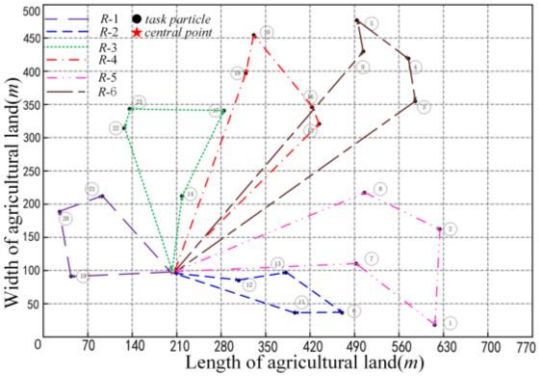


Fig. 10 - Six farm machines in operation

The unmanned farm is divided into 23 farmland tasks to be operated, and the improved genetic algorithm is used to plan the task area for farm machinery operation, and output the chromosome solution for task allocation, which is decoded to obtain the different farm machinery task sequences, and the farm machinery task sequences are shown in Table 3. In the allocation scheme, the task cost is analyzed by the task sequence of the agricultural machine and the performance parameters of the agricultural machine, and the maximum operating time of the agricultural machine, the total loss of task energy, the total path of the task and the penalty function are taken as the initial evaluation criteria, and the secondary evaluation is carried out based on the differences in the weighting ratio of the four and is taken as the total cost of the task, and the final task cost of the operation is shown in Table 4.

Table 3

Sequence of agricultural machinery tasks

Number of agricultural machines	Task ① Sequence	Task ② Sequence	Task ③ Sequence	Task ④ Sequence	Task ⑤ Sequence	Task ⑥Sequence
three	19→20→21→22→23→17→14	12→13→7→8→2→1→6→11	15→16→3→4→9→5→10→18			
four	19→20→21→22→23	12→13→7→1→6→11	14→17→18→10→16→15	9→5→4→3→2→8		
five	12→13→6→11	19→20→21→22→23	14→17→18→10→16	7→1→2→8	3→4→5→9→15	
six	19→20→21	12→13→6→11	14→17→23→22	15→16→10→18	8→2→1→7	9→5→4→3

Table 4

Cost of agricultural machinery tasks

Number of agricultural machines	Maximum operating time (h)	Energy loss (kJ)	Total path (km)	Non-operational path (km)	Penalty function	Aggregate consideration
three	18.98	11065.104	226.71	3.77	41.73	1171.39
four	14.82	10799.388	227.32	4.38	25.16	1127.23
five	12.25	10598.292	227.93	4.99	-18.04	1063.45
six	10.52	10927.62	228.45	5.51	33.27	1146.10

According to Table 4, the maximum operating time of the six farm machines is the smallest, and this option should be preferred when faced with tasks that are more agro-temporal. However, the operation of multiple farm machines causes an increase in the non-operational path and penalty function thereby increasing the total cost, and the penalty function in the table shows peaks and valleys with the increase in the number of farm machines. In this task allocation five farm machines were the most reasonable, the total cost of the task was reduced by 7.21% compared to six farm machines, but the operating time was increased by 16.44%, which was difficult to meet the requirements in the face of the task with strong agronomic nature. It can be seen that when faced with different agricultural tasks should be based on different operational needs to determine a reasonable allocation program to ensure the optimal global benefits.

Experimental verification

In the actual operation of the unmanned farm, the information collection robot can collect the growth conditions of crops at different growth stages in the farmland by traversing the farmland with the RMONCAM HD600 infrared camera. In this paper, the task assignment and field full traversal experiments were conducted by the farmland information collection robot built by Shandong University of Science and Technology in cooperation with Zibo Harvest Seed Industry Company, the experimental site was the south lawn of the library of Shandong University of Technology.

This paper collects the map of the experimental environment and transforms it into an electronic map to provide a basis for subsequent task allocation, simulates the actual agricultural production activities to divide the experimental site into 11 sub-areas, as shown in Fig. 11, and selects three information acquisition robots to carry out experimental verification. Some of the operational parameters of the three information-gathering robots are summarized in table 5.



a. Task segmentation **b. Robot field traversal**

Fig. 11 - Farm task operation

Table 5

Operational parameters of the information-gathering robot

Number of agricultural machines	Operating rate (m/s)	Non-operating rate (m/s)	Turning radius (m)	Operating width (m)
r-1	1.4	2.1	1.5	1.2
r-2	1.4	2.1	1.5	1.2
r-3	1.8	2.7	1.8	1.5

In this experiment, the sequence of tasks for each robot is r-1:4→3→2→1,r-2:5→6→7,r-3:8→9→10→11.The robot departs from the mission rendezvous point (the pentagonal labeled point in Fig. 11a), sequentially into the planning work area, and return to the mission rendezvous point upon completion of all tasks. The cloud platform counts the actual traversed area, area repetition rate, and the actual working time of each robot to complete the task, and monitors the execution of the whole task, designing the human-machine interaction interface as in Fig. 12, and the results of the operation data statistics are shown in Table 6.

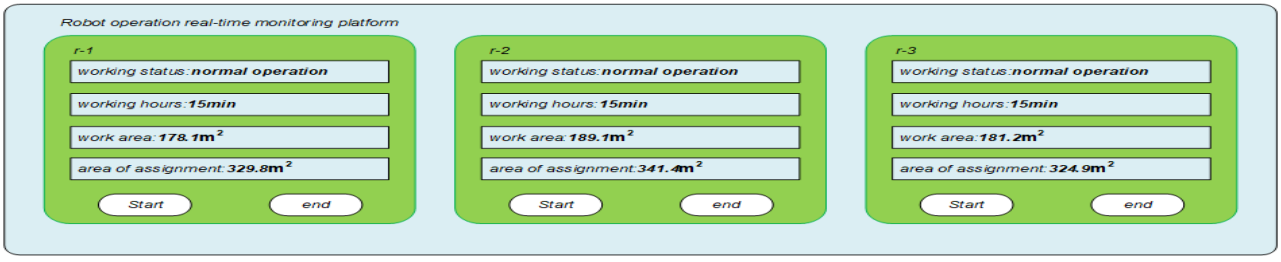


Fig. 12 - Human-machine interaction interface

Table 6

Machine operation data

Cloud data	r-1	r-2	r-3
operating area ($m^{2)}$	376.5	414.4	385.7
area repeatability	14.15%	21.4%	18.7%
operation time (min)	34.7	42.1	38.7

In this paper, the task allocation is based on the theoretical workload of each robot, and the farm operation is planned in a theoretically optimal way, so the path repetition rate is low when each robot traverses. As can be seen from Table 7, each of the participating robots is able to achieve 100% coverage of their respective work areas, and all of them are able to complete the traversal task within a short working time, which proves the effectiveness of the proposed algorithm.

CONCLUSIONS

The large-scale operation of unmanned farms is the direction for the development of smart agriculture. Compared to traditional manual labor, the operational capacity of unmanned agricultural machinery far exceeds the former. Based on the information of different agricultural lands and the performance parameters of agricultural machinery, this paper establishes an objective function to reasonably allocate tasks, ensuring the optimal use of resources. This has reference value for the large-scale operation of unmanned farms.

This paper establishes a multi-machine task cost model and maps the operation time, energy loss, and task path into the improved genetic algorithm. It analyzes task allocation schemes for different numbers of agricultural machinery to achieve optimal collaborative benefits among multiple machines. The results indicate that the optimal task allocation scheme is to deploy five agricultural machines, which reduces energy loss by 4.22%, 1.86%, and 3.01% respectively compared to operations with three, four, and six machines. Additionally, it lowers the total cost by 9.21%, 5.66%, and 7.21% in each scenario. The on-site operations demonstrate that the algorithm is capable of completing the assigned tasks with relatively low task costs.

ACKNOWLEDGEMENT

This work was funded by the Top Talents Program for One Case One Discussion of Shandong Province, the Key Research and Development Program of Shandong Province (Major Innovative Project in Science and Technology) (2020CXGC010804), Shandong Provincial Natural Science Foundation (ZR2021MC026).

REFERENCES

[1] Alan K., Edson R., Anderson, L., (2021). Multi-robot Task Allocation Using Island Model Genetic Algorithm [J]. *IFAC PapersOnLine*, 2021, Vol. 54(1).

[2] Ferrer A-J., Panadero J., Marques J-M., Jorba-Esteve J., (2021). Admission Control for Ad-hoc Edge Cloud [J]. *Future generation computer systems*, Vol. 114, pp. 548-562.

[3] Haris, B., Janusz, B., Shashank, G., Karol, M., Pawel, M., Daniel, S., Kostas, A., Roland, S., Geert, D., (2017). Integrated Data Management for a Fleet of Search-and-rescue Robots [J]. *Journal of Field Robotics*, Vol. 34, pp. 539-582.

[4] Hu, Y., Yao, Y., Ren, Q., Zhou, X., (2020). 3D multi-UAV cooperative velocity-aware motion planning [J]. *Future generation computer systems*, Vol. 102, pp. 762-774.

[5] Huang, C., Ke, Y., Hua, X., (2022). Current status and outlook of the application of edge computing in smart agriculture (边缘计算在智慧农业中的应用现状与展望) [J]. *Journal of Agricultural Engineering*, Vol.38, pp. 224-234.

[6] Jeff, C. (2020) Smart Agriculture Designs Tap IoT Technologies [J]. *Circuit cellar*, (358): pp. 42-49.

[7] Jensen-Nau, K., Hermans, T., Leang, K., (2021). Near-Optimal Area-Coverage Path Planning of Energy-Constrained Aerial Robots with Application in Autonomous Environmental Monitoring [J]. *IEEE transactions on automation science and engineering*, Vol.18, pp. 1453-1468.

[8] Nikitenko, A., Lavendelis, E., Ekmanis, M. (2018). Task allocation methods for homogeneous multi-robot systems: feed pushing case study [J]. *Automatic Control and Computer Sciences*, Vol. 52, pp. 371-381.

[9] Rahman, A., Jin, J., Rahman, A., Cricenti, A., Afrin, M., Dong, Y. (2019). Energy-efficient optimal task offloading in cloud networked multi-robot systems [J]. *Computer networks*, Vol. 160, pp. 11-32.

[10] Tanzilya, S., Svetlana, G., Dinka, M., (2021). Path of sustainable development of agricultural ecosystems in the context of digitalization [J]. *E3S Web of Conferences*, 262(a).

[11] Teslya, N., Smirnov, A., Ionov, A., (2020). Multi-robot coalition formation for precision agriculture scenario based on gazebo simulator [C], *Proceedings of 15th International Conference on Electromechanics and Robotics "Zavalishin's Readings",* pp. 329-341.

[12] Wang, F., Huang, Z., Han, M., (2023). Heterogeneous UAV cooperative multi-task allocation based on KnCMPSO algorithm (基于 KnCMPSO 算法的异构无人机协同多任务分配) [J]. *Journal of Automation*, Vol.49, pp.399-414.

[13] Wang, M., Zhao, B., Liu, Y., (2021). Static task allocation for multimachine cooperative operation based on multivariate grouping genetic algorithm (基于多变异分组遗传算法的多机协同作业静态任务分配) [J]. *Journal of Agricultural Machinery*, Vol. 52, pp. 19-28.

[14] Viraj. D., Girish. B, (2022). Building and evaluating cloud robotic systems: A systematic review [J].*Robotics and Computer-Integrated Manufacturing*, Vol. 73, pp. 102240.1-102240.14.

[15] Zhang, F., Zhu, Y., (2022). A task allocation method for multi-UAV cooperative reconnaissance in complex environments (复杂环境中多无人机协同侦察的任务分配方法) [J]. *Journal of System Simulation*, Vol. 34, pp. 2293-2302.

[16] Zhang, X., Xia, S., Zhang, T., (2023). Multi-UAV cooperative task allocation based on adaptive genetic learning particle swarm algorithm (基于自适应遗传学习粒子群算法的多无人机协同任务分配) [J]. *Control and Decision Making*, Vol. 38, pp. 3103-3111.

[17] Zhu, D., (2018). IOT and big data based cooperative logistical delivery scheduling method and cloud robot system [J]. *Future generation computer systems*, Vol. 86, pp. 709-715.

VIBRATION ASSESSMENT OF TRACTOR OPERATOR BASED ON VIBRATION SIGNALS
/
ΑΞΙΟΛΟΓΗΣΗ ΒΑΣΕΙ ΣΗΜΑΤΩΝ ΔΟΝΗΣΗΣ ΤΩΝ ΚΡΑΔΑΣΜΩΝ ΠΟΥ ΔΕΧΕΤΑΙ Ο ΧΕΙΡΙΣΤΗΣ ΤΟΥ ΕΛΚΥΣΤΗΡΑ

Christos I. DIMITRIADIS*[1)]; Dimitrios KATERIS[2)]; Panagiotis XYRADAKIS[3)]; Aspasia GIALAMA[4)]; Theodoros GIALAMAS[4)]

[1)] Department of Agriculture, International Hellenic University, 57400, Thessaloniki, Greece;
[2)] Institute for Bio-Economy and Agri-Technology (iBO), Centre of Research and Technology-Hellas (CERTH), 6th km Charilaou-Thermi Rd., 57001 Thessaloniki, Greece;
[3)] Department Of Agriculture, Crop Production & Rural Environment, University of Thessaly, 38446, Volos, Greece;
[4)] Department of Agriculture – Agrotechnology, University of Thessaly, 41500, Larissa, Greece.
Tel: +30 6973 009199; E-mail: dimchristos@hotmail.com
DOI: https://doi.org/10.35633/inmateh-71-68

Keywords: *mechanical vibration, permissible working hours, health effects, tractor operators*

ABSTRACT
Operator fatigue during work with agricultural machinery is a significant factor contributing to fatal accidents in Greece. Workers operating agricultural machinery, especially those working with tractors and off-road machines, constitute one of the most hazard-prone groups due to mechanical vibrations transmitted from the ground to the operators' seats. Operators of tractors and off-road machines are exposed to intense mechanical vibrations, underscoring the importance of cumulatively calculating permitted working hours. This work presents a study that was conducted at the Laboratory of Safety and Ergonomics of Agricultural Machinery, Department of Agriculture – Agrotechnology, Faculty of Agricultural Sciences, University of Thessaly, in order to evaluate the vibrations generated when operators work with agricultural tractors and off-road machinery. The results of the study showed that the highest levels of vibration occurred during disc harrowing operation, particularly when the disc harrow moved vertically or at an angle of 30° to the ploughing direction. For seed bed preparation, it is recommended to use tractors equipped with a suspension system for the operator's cabin and a seat with an adjustable range of perceived vibration. Additionally, to prevent fatigue or health problems for tractor operators, it is advisable to limit permitted working hours to fewer than 8 hours per day.

ΠΕΡΙΛΗΨΗ
Η κόπωση του χειριστή κατά τη διάρκεια της εργασίας με γεωργικά μηχανήματα είναι ένα σημαντικός παράγοντας ο οποίος συμβάλει στην πρόκληση πολλών θανατηφόρων ατυχημάτων στην Ελλάδα. Οι Χειριστές γεωργικών μηχανημάτων, ιδιαίτερα εκείνοι που χειρίζονται ελκυστήρες και μηχανήματα εκτός δρόμου, αποτελούν μια από τις πιο επιρρεπείς σε κινδύνους ομάδες χειριστών λόγω των μηχανικών κραδασμών που μεταδίδονται από το έδαφος στα καθίσματα τους. Οι χειριστές ελκυστήρων και μηχανημάτων εκτός δρόμου εκτίθενται σε έντονους μηχανικούς κραδασμούς, υπογραμμίζοντας τη σημασία του σωρευτικού υπολογισμού των επιτρεπόμενων ωρών εργασίας. Η εργασία αυτή παρουσιάζει μια μελέτη που διεξήχθη στο Εργαστήριο Ασφάλειας και Εργονομίας Αγροτικών Μηχανημάτων του Τμήματος Γεωπονίας – Αγροτεχνολογίας, της Σχολή Γεωπονικών Επιστημών του Πανεπιστημίου Θεσσαλίας και έχει σαν σκοπό την αξιολόγηση των δονήσεων που δημιουργούνται όταν οι χειριστές εργάζονται με γεωργικούς ελκυστήρες και οδικά μηχανήματα. Τα αποτελέσματα της μελέτης έδειξαν ότι τα υψηλότερα επίπεδα κραδασμών εμφανίστηκαν κατά την εκτέλεση εργασιών με την χρήση δισκοσβάρνας προσαρμοσμένης σε γεωργικό ελκυστήρα, ιδιαίτερα όταν η δισκοσβάρνα κινούνταν κάθετα ή υπό γωνία 30° ως προς την κατεύθυνση του οργώματος. Για την προετοιμασία της σποράς, συνιστάται η χρήση ελκυστήρα εξοπλισμένου με σύστημα ανάρτησης της καμπίνας του χειριστή και κάθισμα με ρυθμιζόμενο αντικραδασμικό σύστημα. Επιπλέον, για να αποφευχθεί η κόπωση ή τα προβλήματα υγείας των χειριστών του ελκυστήρα, συνιστάται ο περιορισμός των επιτρεπόμενων ωρών εργασίας σε λιγότερες από 8 ώρες την ημέρα.

INTRODUCTION

Agricultural workers operating tractors face exposure to whole-body vibrations, a challenge influenced by factors such as the type of mounted farm implements, tractor speed, and field conditions. These vibrations, characterized by multiaxis translational and rotational inputs affecting various body areas, traverse through the buttocks, torso, and spinal column (*Amari et al., 2015; Scarlett et al., 2007*). Operating in such an environment leads to fatigue, impacting ride comfort and contributing to health issues like metabolic disorders, cardiovascular problems, and nervous system complications (*Rahmatalla et al., 2023; Loutridis et al., 2011*).

Farmers dedicate many hours to agricultural activities throughout the year, with tractor usage reaching up to 14 hours on the busiest days (*Sorainen et al., 1998*). This prolonged engagement exposes them to work-related hazards, notably whole-body vibration *(Biriș et al., 2022; Singh et al., 2021; Vlăduţ et al., 2013*). Unlike the industrial sector, whole-body vibration exposure in tractor drivers is intricate due to variable factors during fieldwork (*Singh et al., 2018*). Tractor-mounted implements and interactions with the terrain contribute to the whole-body vibration experienced by drivers (*Singh et al., 2018; Kumar et al., 2001*). Vibrations are transmitted to the operator's body through points of contact such as the tractor floor, operational levers, seat pan, seat backrest, and steering wheel, potentially causing discomfort and health issues (*Cheng et al., 2022; Dmitrieva and Myakishev, 2019; Village et al., 2012*).

Modern tractors are equipped with specialized shock-absorbing systems, primarily integrated into the support bases of the control cabin and seat. The purpose of these systems is to absorb generated mechanical vibrations as much as possible, thereby minimizing their impact on the operator's body (Marsili et al., 2002). It is noteworthy that each part or organ of the human body has a range of natural resonance frequencies, and these frequencies inherently affect the permissible duration of exposure to mechanical vibrations.

Many studies (*Loutridis et al., 2011*) indicate that tractor drivers often experience vibration levels surpassing the exposure action value (0.5 m/s2) outlined in Directive 2002/44/EU (*E.U. Directive, 2002*). Elevated vibration exposure is closely associated with various health conditions, including musculoskeletal hazards (e.g., back pain) (*Griffin, 2007*), fatigue (e.g., muscle tiredness) (*Loutridis et al., 2011*), and nervous system problems (e.g., carpal tunnel syndrome) (*Goglia et al., 2003*).

Driver performance is also affected by tractor vibrations (Village et al., 2012). Research indicates that off-road situations expose individuals to more severe whole-body vibrations compared to on-road scenarios (*Adam et al., 2020*), potentially surpassing recommended health exposure limits (*ISO 2631-1, 1997*). Elevated whole-body vibration exposure is a significant occupational risk factor associated with lower back pain among tractor drivers (*Singh et al., 2019*). Furthermore, whole-body vibration can induce muscle elongation and shortening, leading to increased muscular tension and fatigue (*Ritzmann et al., 2010*). Of particular concern are low-frequency vibrations (1-10 Hz), which significantly impact tractor operators due to uneven terrain and imbalanced engine parts (*Nawayseh, et al., 2020*). The human body's sensitivity to low-frequency vibrations, coupled with extended exposures, results in rapid weariness, reduced functioning, and potential harm to the operator's health (*Singh et al., 2021*). Whole-body vibration directly affects driver attentiveness, increasing physical and mental strain, leading to fatigue and drowsiness (*Bhuiyan et al., 2022*).

Exposure of a body part or organ to high-level vibrations at their resonance frequencies can lead to extremely unpleasant symptoms, especially chronic health conditions.

The main physical characteristics of the mechanical vibrations measured during experimental tests include their intensity, measured in m/s², and their frequency, measured in Hz. It is crucial that the generated vibrations do not surpass specific permissible values. These values are established to safeguard operators and are determined in accordance with EU guidelines, specifically the ISO 2631/97/Amd 1:2010 standard and Directive 89/391/EEC (consolidated in 2008)!

Measures aimed at safeguarding operators from mechanical vibration include the installation of safety cabins on modern tractors, which are mounted on hydraulic shock absorbers. It is imperative that the seat is capable of damping vibrations and is in good condition to effectively protect the operator during work. The manner in which auxiliary agricultural machinery is connected to the tractor is a crucial factor, as it significantly influences the intensity of the generated vibrations. Other factors that significantly affect operator fatigue include the speed of movement during work, the condition of the ground, and the operator’s sitting posture. In modern tractors, in addition to adjusting the vibration range, there is the option to rotate the operator's seat 15° to the right and left. This feature assists operators when they need to turn their bodies to look backward and control the attached agricultural machinery (*Brienza et al., 1996*).

This study aimed to identify, record, and analyse the factors that contribute to tractor operator fatigue under real-time conditions. Additionally, the study sought to measure the magnitudes of mechanical vibrations and frequencies that occur in the control cabin of agricultural tractors during field movement.

MATERIALS AND METHODS

The experimental determination of whole-body vibrations on the operator's seat of agricultural tractors was conducted on uncultivated land containing straw remnants from previous cultivation. The moisture content of the soil was 20% (dry basis), and this level remained constant throughout the tests. The soil had a sandy-clay-loam (SCL) mechanical composition, and the ambient temperature during the experiments was 20°C.
For the experimental tests, the LAMBORGHINI Premium 950 tractor was used. This tractor boasts a power output of 70 kW and is equipped with a mechanical system for adjusting the seat's vibration range, hydrostatic steering, and 4-wheel drive (4WD). The speed was maintained within the range of 5.5 – 6.0 km/h throughout the tests. Ploughing was conducted prior to disc harrowing to prepare the seedbed. The disc harrow used for the experimental tests was a secondary tillage implement with a working width of 3.20 m, featuring a total of 33 discs, each with a diameter of 0.50 m, and operating at a depth of 0.11 m.

The study was focused on the whole-body vibrations generated during all agricultural operations carried out with the aforementioned agricultural tools on the operator's seat.

To determine the accelerations of mechanical vibrations within the control cabin of the tractor, experimental tests were conducted with a towed disc harrow attached. Sensors placed under the operator's seat recorded the impacts of mechanical vibrations. The results of the experimental tests were analysed to determine the magnitude of the interactions among all factors that cause unpleasant symptoms in operators and to establish the permitted working time.

The vibrations were captured using an electronic recording unit known as VIBROTEST 60 from Bruel & Kjaer Vibro Company. This unit is equipped with adjustable sensors secured under the operator's seat using magnets, capable of recording signals for all magnitudes of vibration. This is to ensure better visualization and assessment of the vibrations affecting the operator. Throughout the tests, the range of vibrations and the corresponding frequencies were recorded. The device was calibrated to record 1600 values, for each 250 m field stretch, capturing vibration accelerations in m/s² and frequencies in Hz ranging from 0 – 100 Hz at intervals of 0.3125 Hz. Three replicates were performed for each measurement. The experimental tests were conducted along three movement paths: a) parallel to ploughing, b) at an angle of 30° degrees to ploughing, and c) perpendicular to ploughing. From these measurements, the average was calculated and the maximum value of the averages was taken for each direction. The measurements were conducted according to international standards ISO 2631-1-5/1997, ISO 10326-2:2022 and ISO 8041-1:2017. These standards define the permissible limits for daily exposure to vibrations known as or A(8), which corresponds to a vibration acceleration of 0.50 m/s², and the vibration dose value (VDV) of 9.1 m/s^1.75.

The values obtained were analysed using a computer and specialized software designed to create graphs. The graphs depict vibration accelerations in units of m/s² versus frequencies in units of Hz.

Test measurements

The maximum vibration values were analysed in three axes: X (vibrations in the horizontal longitudinal axis in the direction of tractor motion), Y (vibrations in the horizontal transverse axis in the direction of tractor motion), and Z (vibrations in the vertical axis in the direction of tractor motion). Based on the experimental tests, the averages of the maximum values obtained in the three directions, X_{max}, Y_{max}, and Z_{max} were recorded, and the daily vibration dose was calculated.

Calculation of the daily vibration dose or A(8)

The calculation of the daily vibration dose (DVD), internationally denoted as A(8), is determined by taking the highest mean acceleration value of the three repetitions in the X, Y, and Z directions. This is shown in equations (1) to (3).

The highest value of DVD or A(8) in m/s² was taken into account during the calculation (*Griffin et al., 2006*) of the permissible daily working hours (PDWH).

$$A_x(8) = 1{,}4\, a_{wx} \sqrt{\frac{T_{\exp}}{T_0}} \quad [\text{m/s}^2] \tag{1}$$

$$A_y(8) = 1{,}4_{awy}\sqrt{\frac{T_{\exp}}{T_0}} \quad [m/s^2] \tag{2}$$

$$A_z(8) = 1{,}0_{awz}\sqrt{\frac{T_{\exp}}{T_0}} \quad [m/s^2] \tag{3}$$

where:

T_{exp} = 6 h the desired duration of daily work (ISO, 1997)

T_o = 8 h the duration of daily work,

α_{wx}, α_{wy}, α_{wz} = the maximum acceleration values (m/s²) in the x, y, and z axes, respectively.

The daily vibration dose was determined by the highest values of $A_x(8)$, $A_y(8)$, and $A_z(8)$. The daily vibration dose, A(8), is calculated from the root mean square (rms) values of the vibration accelerations in all directions. This value is proportional to the magnitude of the vibration acceleration and the square root of its duration. The highest daily vibration dose (DVD), denoted as A(8), is determined according to equation (4) (*Griffin et al., 2006*).

$$A(8) = \max\left[A_x(8), A_y(8), A_z(8)\right] \quad [m/s^2] \tag{4}$$

The accelerometers were placed in the same position as the operator, for example, under the operator's seat. Their orientation was aligned with the directions of the vibrations. The recording was continuous during the 6 hours of daily working time of exposure (T_{exp} = 6 h).

The calculation of the daily vibration dose or A (8) is given (*Griffin et. al., 2006*), by equation (5):

$$A_1(8) = k_l\sqrt{\frac{1}{8}a_{wl}^2 \times 6} = k_l\frac{\sqrt{3}}{2}a_{wl} \quad [m/s^2] \tag{5}$$

where:

a_{wl} = the maximum value of the averages of vibration accelerations (r.m.s.), in direction *i*, for a desired daily working duration (6 hours).

k_l = human sensitivity factor, equal to 1.4 for the x and y directions and 1.0 for the z direction.

Calculation of the operator's permitted daily working hours

The calculation of permitted working hours for agricultural tractor operators is based on guidelines provided by European Standard EN 14253: 2003 + A1: 2007 and ISO 2631-1-5/1997. According to these standards, the upper limit of the tolerable permissible acceleration of vibration at the operator's seat, above which personal protective measures are required for up to eight (8) hours of work, is determined as: A(8) = 0,50 m/s² for T_0 = 8 hours of work.

The calculations took into account the permissible vibration acceleration, which is lower than A(8) = 0,45 m/s² for T_0 = 8 hours of work eliminating the need for additional measures. Therefore, the calculation of permissible working hours is given by equation (6) and is a function of the permissible value of the daily vibration dose (A8), the desired working hours T_0 and the maximum value of the daily vibration dose. This maximum value is obtained from the maximum accelerations of the vibrations in each direction (x, y, and z) on the operator's seat (ISO, 2631-1-5: 1997).

$$T_e = \frac{A^2(8) \times T_0}{A^2_{\max}(8)} \quad [h] \tag{6}$$

where:

T_e was measured in hours

A^2_{max} (8) = m/s², the maximum value of the daily vibration dose from the three directions x, y, and z,

A^2 (8) = 0.45 m/s², the allowable daily vibration dose at which operator protection measures are not required.

T_0 = 8 hours

Te = allowed working hours/day

If the daily vibration dose is Ai (8) > 0.45 m/s², then additional measures must be taken to protect the operator's health.

RESULTS

Determination of the daily vibration dose A(8) and the operator's working hours with the Lamborghini premium 950 tractor with disc harrow was performed.

Test No.1 Lamborghini premium 950 tractor with disc harrow, 1st pass on ploughed ground, movement parallel to ploughing, Tractor speed = 8.0 km/h.

From Table 1, for movement parallel to ploughing (1st pass), it can be seen that the developed accelerations α_w = m/s² of the vibrations in the three directions X_{max}, Y_{max}, and Z_{max}, are at low levels <0.5m/s². Therefore, the permissible working hours can be more than 8 hours per day. The maximum value was observed in the Z direction, α_w = 0.326 m/s², and the value of the daily vibration dose (DVD) in the X direction is A(8) = 0.297 m/s².

Table 1

Values of the daily vibration dose (DDI) and the allowable working hours of agricultural tractor operators

Vibration axis	Max mean values	Frequencies	DDI values A(8)	Allowed working hours	Vibrations comparison	Vibration change percentage
	[α_w = m/s²]	[Hz]	[m/s²]	[h]		[%]
X	0.245	1.56	**0.297**	**>8**	X→Y	51.2*
Y	0.162	1.88	0.197	–	Z→Y	101.2*
Z	**0.326**	2.19	0.282	–	Z→X	33.0*

* The rates of change of the vibrations are obtained for the x-axis ((0.245-0.162)/0.162)*100 = 51.2, for the y-axis ((0.326-0.162)/0.162)*100 = 101.2, and for the z-axis ((0.326-0.245)/0.245)*100 = 33, respectively.

Test No.2 Lamborghini premium 950 tractor with disc harrow, 2nd pass on ploughed ground, movement parallel to the ploughing, Tractor speed = 8.0 km/h.

From Table 2, for movement parallel to the ploughing (2nd pass), it can be seen that the developed accelerations α_w = m/s² of the vibrations in the three directions X_{max}, Y_{max}, Z_{max}, are at low levels <0.5 m/s². Therefore, the permissible working hours can be more than 8 hours per day. The maximum value is found in the Z direction, α_w = 0.376 m/s², and the value of the daily vibration dose (DVD) in the Z direction is A(8) = 0.326 m/s².

Table 2

Values of the daily vibration dose (DDI) and the allowable working hours of agricultural tractor operators

Vibration axis	Max mean values	Frequencies	DDI values A(8)	Allowed working hours	Vibrations comparison	Vibration change percentage
	[α_w = m/s²]	[Hz]	[m/s²]	[h]		[%]
X	0.145	3.44	0.176	–	Y→X	37.3
Y	0.199	1.25	0.241	–	Z→Y	89.0
Z	**0.376**	2.19	**0.326**	**>8**	Z→X	159.3

Test No.3 Lamborghini premium 950 tractor with disc harrow, on dry ploughed ground, movement parallel to the ploughing, Tractor speed = 8.0 km/h.

From Table 3, for movement parallel to ploughing on dry soil, it is seen that the developed accelerations α_w = m/s² of the vibrations in the three directions X_{max}, Y_{max}, Z_{max}, are at high levels >0.5 m/s². Therefore, the permissible working hours not exceed 8 hours per day, specifically 4:07 hours. The maximum value is found in the Z direction, α_w = 0.729 m/s², and the value of the daily vibration dose (DVD) in the Z direction is A(8) = 0.631 m/s².

Table 3

Values of the daily vibration dose (DDI) and the allowable working hours of agricultural tractor operators

Vibration Axis	Max mean values	Frequencies	DDI values A(8)	Allowed working hours	Vibrations comparison	Vibration change percentage
	[α_w = m/s^2]	[Hz]	[m/s^2]	[h]		[%]
X	0.350	1.88	0.424	–	Y→X	40.3
Y	0.491	1.88	0.595	–	Z→Y	48.5
Z	**0.729**	2.50	**0.631**	**4:07**	Z→X	108.3

Test No.4 Lamborghini premium 950 tractor with disc harrow, on dry ploughed ground, movement perpendicular to the ploughing, Tractor speed = 8.0 km/h.

From Table 4, for movement perpendicular to the ploughing, it can be seen that the developed accelerations α_w = m/s2 of the vibrations in the three directions X_{max}, Y_{max}, and Z_{max}, are at high levels >0.5 m/s^2. Therefore, the allowable working hours must not exceed 8 hours per day, specifically 1:16 hours. The maximum value is found in the Z direction, α_w = 1.364 m/s^2, and the value of the daily vibration dose (DVD) in the Z direction is A(8) = 1.181 m/s^2.

Table 4

Values of the daily vibration dose (DDI) and the allowable working hours of agricultural tractor operators

Vibration axis	Max mean values	Frequencies	DDI values A(8)	Allowed working hours	Vibrations comparison	Vibration change percentage
	[α_w = m/s^2]	[Hz]	[m/s^2]	[h]		[%]
X	0.810	2.81	0.982	–	X→Y	10.6
Y	0.732	6.56	0.887	–	Z→Y	86.4
Z	**1.364**	2.19	**1.181**	**1:16**	Z→X	68.4

Test No.5 Lamborghini premium 950 tractor with disc harrow, on dry ploughed ground, driving at an angle of 30° degrees to the ploughing, Tractor speed = 8.0 km/h.

From Table 5, for movement at an angle of 30° degrees to ploughing, it was found that the developed accelerations α_w = m/s^2 of the vibrations in the three directions X_{max}, Y_{max}, Z_{max}, are at high levels >0.5 m/s^2. Therefore, the allowable working hours must be less than 8 hours per day, specifically 2:05 hours. The maximum value is observed in the Z direction, α_w = 1.364 m/s^2, and the value of the daily vibration dose (DVD) in the Y direction is A(8) = 0.990 m/s^2.

Table 5

Values of the daily vibration dose (DDI) and the allowable working hours of agricultural tractor operators

Vibration Axis	Max mean values	Frequencies	DDI values A(8)	Allowed working hours	Vibrations comparison	Vibration change percentage
	[α_w = m/s^2]	[Hz]	[m/s^2]	[h]		[%]
X	0.583	2.81	0.707	–	Y→X	40.2
Y	0.817	2.81	**0.990**	**2:05**	Z→Y	34.6
Z	**1.10**	2.19	0.953	–	Z→X	88.7

DISCUSSION

The threshold values that trigger action for daily vibration exposures are 1.15 m/s^2 for A(8) and 21 m/s^1.75 for VDV. Exceeding these levels of whole-body vibrations can pose risks to health and affect the operator's ability to operate the tractor (*Gialamas et al., 2007; Gialamas et al., 2009; Gravalos et al., 2009*). It is commonly reported that these vibrations cause or exacerbate injuries to the lower back and spine. Risks are highest when accelerations are high and when the duration of exposure is long. Additionally, the frequency of

the vibrations plays a significant role, as they can cause coordination issues with various body organs. Vibrations from agricultural machineries, particularly tractors, are known for their potential to induce fatigue and various other health issues in operators.

In the context of seedbed preparation using tractors, the utilization of tractors equipped with a suspension system for the operator's cabin and a seat with an adjustable vibration range is essential. This technological feature is instrumental in enhancing operator comfort and minimizing the potential health risks associated with prolonged exposure to vibrations during agricultural tasks.

The results in the tables above reveal distinct patterns in vibration levels during different tractor operations. Specifically, during disc harrowing when the tractor moved parallel to the ploughing direction, the recorded vibrations were at their lowest levels. This observation suggests that, under these circumstances, there is the potential to extend the permitted working hours beyond the standard 8 hours per day. This insight is crucial for operational planning, allowing for more flexible scheduling and increased efficiency in seedbed preparation.

Conversely, when disc harrowing occurred with the equipment moving vertically or at an angle of 30 degrees with the ploughing direction, the recorded vibrations were at their highest levels. This finding implies that, under such conditions, it is advisable to limit the permitted working hours to less than 8 hours per day. This precautionary measure is essential to prevent operator fatigue and minimize the risk of health issues associated with prolonged exposure to elevated vibration levels.

Considering the overall well-being of tractor operators, it is recommended that all modern tractors be equipped with shock-absorbing systems. These systems play a crucial role in preventing or reducing vibrations transmitted to the operator's seat and, consequently, minimize the impact on the body of the tractor operator. The implementation of shock-absorbing systems aligns with a proactive approach to occupational health and safety in agriculture. Operators of off-road machinery should be informed about possible adjustments, such as seat adjustments, to minimize the intensity of vibrations as much as possible.

CONCLUSIONS

This study presents an evaluation of the seat vibrations generated when operators work with agricultural tractors and off-road machinery. The study showed that the highest levels of vibration occurred during disc harrowing operation, particularly when the disc harrow moved vertically or at an angle of 30° to the ploughing direction. The choice of tractors with advanced features, strategic scheduling based on vibration levels during specific operations, and the integration of shock-absorbing systems are integral components in fostering a safer and more productive working environment for tractor operators engaged in seedbed preparation.

REFERENCES

[1] Adam, S.A., Abdul Jalil, N.A., Md. Rezali, K.A., & Ng, Y.G. (2020). The effect of posture and vibration magnitude on the vertical vibration transmissibility of tractor suspension system. *International Journal of Industrial Ergonomics*. 80:103014. https://doi.org/10.1016/j.ergon.2020.103014

[2] Amari, M, Caruel, E, Donati, PJE. (2015). Inter-individual postural variability in seated drivers exposed to whole-body vibration. Ergonomics. 58(7):1162–1174. doi:10.1080/00140139.2014.968633

[3] Bhuiyan, M.H.U., Fard, M. & Robinson, S.R. (2022). Effects of whole-body vibration on driver drowsiness: a review. *Journal of Safety Research*, 81:175–189. https://doi.org/10.1016/j.jsr.2022.02.009

[4] Biriș S.Șt., Constantin A-M., Anghelache D., Găgeanu I., Cujbescu D., Nenciu F., Voicea I., Matei Gh., Popa L.D., Duțu M.F., Ungureanu N., Żelaziński T., Perişoară L., Fodorean G. (2022). Considerations regarding the vibrations transmitted to the operator by an axial flow harvester combine, *INMATEH - Agricultural Engineering* 68 (3), pp. 747-756

[5] Brienza, D.M., Karg, P.E., & Brubaker, C.E. (1996). Seat cushion design for elderly wheelchair users based on minimization of soft tissue deformation using stiffness and pressure measurements. *IEEI Transactions on rehabilitation Engineering*. 4:320-327. doi:10.1109/86.547933

[6] Cheng, L., Wen, H., Ni, X., Zhuang, C., Zhang, W. & Huang, H.J.M. (2022). Optimization study on the comfort of human-seat coupling system in the cab of construction machinery. *Machines.* 11(1):30. doi:10.3390/machines11010030

[7] Council Directive 89/391/EEC of 12 June 1989 on the introduction of measures to encourage improvements in the safety and health of workers at work [2008] OJL183/1.

[8] Dmitrieva, E., Myakishev, A. (2019). Improving the design of the tractor seat. *Traktory i Sel Hozmashiny.* 86(4):50–53. doi:10.31992/0321-4443-2019-4-50-53.
[9] EN 14253:2003+A1:2007 - Mechanical vibration - Measurement and calculation of occupational exposure to whole-body vibration with reference to health - Practical guidance
[10] E.U. Directive 89/391/EEC of 12 June 1989 on the introduction of measures to encourage improvements in the safety and health of workers at work [2008] OJL183/1.
[11] E.U. Directive, G.E. Provisions, (2002). Directive 2002/44/EC of the European Parliament and the Council of 25 June 2002 on the minimum health and safety requirements regarding the exposure of workers to the risks arising from physical agents (Vibration) (sixteenth individual directive within the meaning of article 16 (1) of directive 89/391/EEC), Off. J. Eur. Communities L 117. 6–7.
[12] Gialamas, Th., Gravalos, I., Kateris, D., Xyradakis, P., Tsatsarelis, K. and Gemtos, Th. (2007). Experimental determination of vibrations in the control room of agricultural tractors. Proceedings of the 5th Panhellenic Conference on Agricultural Engineering. 79-86.
[13] Gialamas T., Gravalos I., Kateris D., Xyradakis P., Tsiropoulos Z., Tsatsarelis K., Moshou D. and Gemtos Th. (2009). Vibrations in the operator's seat during plowing with different tractors. *Proceedings of the 6th Panhellenic Conference on Agricultural Engineering*.
[14] Goglia, V., Gospodaric, Z., Kosutic, S., Filipovic, D. (2003). Hand-transmitted vibration from the steering wheel to drivers of a small four-wheel drive tractor. *Appl. Ergon.* 34:45–49. doi:10.1016/s0003-6870(02)00076-5
[15] Gravalos, I., Gialamas, Th., Kateris, D., Xyradakis, P., Tsiropoulos, T., & Moshou, D. (2009). Vibration measurements and analysis of agricultural tractors operating on traditional and electronic regulator. Proceedings of XXXIII CIOSTA - CIGR V Conference on Technology and Management to Ensure Sustainable Agriculture, *Agro Systems, Forestry and Safety*. 2:1511-1515.
[16] Griffin, M. J., Howarth, H. V. C., Pitts, P. M., Fischer, S., Kaulbars, U., Donati, P. M., Brereton, P.F. (2006). Advisory committee on safety and health at work. Guide to good practice on hand-arm vibration. In Non-binding guide to good practice with a view to implementation of directive 2002/44/EC on the minimum health and safety requirements regarding the exposure of workers to the risks arising from physical agents (vibrations). Luxembourg, European Commission, 61.
[17] Griffin, M.J. (2007). Discomfort from feeling vehicle vibration, *Veh. Syst. Dyn.* 45:679–698. https://doi.org/10.1080/00423110701422426
[18] ISO 2631-1:1997/AMD 1:2010 (2010). Mechanical vibration and shock — Evaluation of human exposure to whole-body vibration — Part 1: General requirements — Amendment 1
[19] ISO 2631-1-5:1997 (1997). Mechanical vibration and shock -- Evaluation of human exposure to whole-body vibration
[20] ISO 10326-2:2022 (2022). Mechanical vibration — Laboratory method for evaluating vehicle seat vibration — Part 2: Application to railway vehicles.
[21] ISO 8041-1:2017 (2017). Human response to vibration - Measuring instrumentation - Part 1: General purpose vibration meters.
[22] Kumar, A., Mahajan, P., Mohan, D., Varghese, M. (2001). IT—information technology and the human interface: tractor vibration severity and driver health: a study from rural India. *J. Agric. Eng. Res.* 80:313–328. https://doi.org/10.1006/jaer.2001.0755
[23] Marsili, A., Ragni, L., Santoro, G., Servadio, P. & Vassalini, G. (2002). Innovative Systems to reduce Vibrations on Agricultural Tractors. Comparative Analysis of acceleration transmitted through the driving Seat. Bios. Eng., Silsoe Research Institute. 81:35- 47. https://doi.org/10.1006/bioe.2001.0003
[24] Nawayseh, N., Alchakouch, A. & Hamdan, S. (2020). Tri-axial transmissibility to the head and spine of seated human subjects exposed to fore-and-aft whole-body vibration. *Journal of Biomechanics*. 109:109927. https://doi.org/10.1016/j.jbiomech.2020.109927
[25] Rahmatalla, S., Qiao, G., DeShaw, J., Kinsler, R. (2023). Quantifying supine human discomfort in off-road whole-body vibration. *Ergonomics.* 66(4):479–491. doi:10.1080/00140139.2022.2096261.
[26] Ritzmann, R., Kramer, A., Gruber, M., Gollhofer, A. & Taube, W. (2010). EMG activity during whole body vibration: motion artifacts or stretch reflexes? *European Journal of Applied Physiology*. 110:143–151. doi:10.1007/s00421-010-1483-x
[27] Scarlett, A.J., Price, J.S. & Stayner, R.M. (2007). Whole-body vibration: evaluation of emission and exposure levels arising from agricultural tractors. *Journal of Terramechanics*. 44:65–73. https://doi.org/10.1016/j.jterra.2006.01.006

[28] Singh, A., Singh, L.P., Singh, S., Singh, H., Prakash, C. (2018). Investigation of occupational whole-body vibration exposure among Indian tractor drivers. *Int. J. Hum. Factors Ergon*. 5: 151–165. https://doi.org/10.1504/IJHFE.2018.092240

[29] Singh, A., Nawayseh, N., Singh, L.P., Singh, S. & Singh, H. (2018). Whole body vibration exposure during rotary soil tillage operation: the relative importance of tractor velocity, draft and soil tillage depth. *IJAME.* 15(4):5927–5940. doi:10.15282/ijame.15.4.2018.15.0452.

[30] Singh, A., Nawayseh, N., Singh, L.P., Singh, S., Singh, H. (2019). Investigation of compressive stress on lumbar spine due to whole body vibration exposure in rotary tillage operation. *IJAME.* 16(2):6684–6696. doi:10.15282/ijame.16.2.2019.16.0503.

[31] Singh, A., Samuel, S., Singh, H., Kumar, Y. & Prakash, C. (2021). Evaluation and analysis of whole-body vibration exposure during soil tillage operation. *Safety.* 7:61. https://doi.org/10.3390/safety7030061

[32] Sorainen, E., Penttinen, J., Kallio, M., Rytkonen, E., Taattola, K. (1998). Whole-body vibration of tractor drivers during harrowing. *Am. Ind. Hyg. Assoc. J.* 59:642–644. https://doi.org/10.1080/15428119891010820

[33] Village, J., Trask, C., Chow, Y., Morrison, J.B., Koehoorn, M., Teschke, K. (2012). Assessing whole body vibration exposure for use in epidemiological studies of back injuries: measurements, observations and self-reports. *Ergonomics.* 55:415–424. https://doi.org/10.1080/00140139.2011.643243

[34] Vlăduţ V., Biriş S.Şt., Bungescu T., Herişanu N. (2013). The influence of vibrations on the operator in the grain harvesters, *Applied Mechanics and Materials*, Vol. 430, pp 290-296, Trans Tech Publications, doi: 10.4028/www.scientific.net/AMM.430.290

STUDY OF THE KEY COMPONENT PARAMETERS OF THE WINGED CHISEL PLOW ON SOIL-STRAW DISTURBANCE PATTERN
/
混秸带翼凿式犁关键部件扰动规律的研究

Kun CHEN[1)], Xianliang WANG[*1)], Jiangtao JI[2)], Xiangcai ZHANG, Xiupei CHENG[1)], Hua ZHOU[1)], Zhongcai WEI[1)] Lei LIU[1)], Mingyue BAI[1)], Shang GAO[1)],

[1)]School of Agricultural Engineering and Food Science, Shandong University of Technology, Zibo (255000), China;
[2)]College of Agricultural Equipment Engineering, Henan University of Science and Technology, Luoyang (471000), China
Tel: +86-18560168518; E-mail: 18560168518@163.com
Corresponding author: Xianliang Wang
DOI: https://doi.org/10.35633/inmateh-71-69

Keywords: *DEM, winged chisel plow, soil bin experiment, straw mixing rate, soil-straw displacement, draught force*

ABSTRACT
Understanding the soil-straw disturbance pattern of the key component parameters of the straw mixing winged chisel plow is the key to designing and optimizing the straw mixing winged chisel plow (a chisel plow for mixing and mulching straw). In this study, a straw-soil-winged chisel plow interaction model was established, and the working principle, key components of the winged chisel plow were determined based on soil bin experiment and theoretical analysis. Discrete element method (DEM) was used to study the influence of disturbance pattern of key components of the winged chisel plow on soil-straw displacement, straw mixing rate and draught force. The results show that the main components of the winged chisel plow that affect the operating efficiency of the implement are the soil lifting plate height, the wing mounting height and the wing width. The height of the soil lifting plate affects the efficiency of the winged chisel plow in secondary disturbance of soil-straw and its own performance in turning over soil, with an optimal range of 110 mm-170 mm. The installation height of the wing mounting mainly affects the position of the soil lifting plate in the soil layer. In order to achieve the best operating effect, the position of the soil lifting plate needs to meet the "lower lifting and upper turning" requirement. The optimal installation height of the wing mounting is 95 mm-145 mm. The width of the wing mainly affects the working width of the implement, and its optimal value is 180 mm-220 mm. The width of the wing mainly affects the working width of the implement, and its optimal value is 180 mm-220 mm. The established simulation relative error is within 12.60%, which can better study the disturbance pattern of soil-straw. This study may provide a reference for optimizing and designing wing-type chisel plows and subsoil shovels.

摘要
了解混秸双翼凿式犁关键部件参数对土壤-秸秆的扰动规律，是设计和优化混秸双翼凿式犁（一种覆混秸秆的凿式犁）的关键。本研究建立了秸秆-土壤-混秸双翼凿式犁相互作用模型，以土槽试验为基础，结合理论分析确定了混秸双翼凿式犁的工作原理与关键部件，并采用离散元法（DEM），研究了混秸双翼凿式犁关键部件的参数变化对土壤-秸秆位移、机具混埋效果以及机具牵引力的影响规律。结果表明：混秸双翼凿式犁影响机具作业效果的关键部件为抬土板高度、铲翼的安装高度与铲翼的宽度。抬土板高度影响带翼凿式犁二次扰动土壤-秸秆的效率与其本身翻转土壤的性能，最优取值范围为 110mm-170mm。铲翼安装高度主要影响抬土板在土层之中的位置，为了作业效果达到最佳状态，抬土板的位置需满足"下抬上翻"，铲翼安装高度的最佳取值为 95mm-145mm。铲翼宽度主要影响机具的作业宽度，其最佳取值为 180mm-220mm。建立的仿真相对误差在 12.60%内，能较好的研究土壤-秸秆的扰动规律。该研究可能为优化和设计翼式凿式犁和深松铲提供参考。

INTRODUCTION
In conservation tillage, large amounts of straw cover have been one of the main factors limiting crop yields, so effective straw handling is an important requirement for arable tools. At present, the main methods of straw return to the field in China include mulching return to the field, rotary plow return to the field, deep turning return to the field, and mulching and mixing return to the field *(Chen Q.C. et al., 2015).*

Deep turning and rotary plow for field return, using a moldboard plow and rotary tiller respectively, turn and break up the soil, leaving no residue on the soil surface, and have a high efficiency of straw return *(He J. et al., 2018)*, but long-term use of these two implements can damage soil structure and lead to a decline in soil nutrients, as well as increase the risk of soil erosion and runoff *(Yang L.Q. et al., 2018; Sun N.N. et al., 2018)*. In contrast, the use of chisel plows to cut the soil in mulching and returning to the soil does not completely bury the residual straw on the surface, part of the straw is stored on the surface to prevent wind and water erosion of the soil and the other part of the straw is buried with the soil to increase the organic matter of the soil and at the same time break up the compact soil layer of the soil, effectively improving the soil structure *(Guan W.D. et al., 2023)*. The chisel plow is one of the main supporting implements in mulching and mixing *(Wang H.N. et al., 2017)*. Many studies have been conducted on chisel plows by scholars at home and abroad. *Zhang C. et al., (2022),* took the chisel plow as a research object, used DEM to study the effect of soil disturbance and compared it with the deep pine shovel, and found that the chisel plow could significantly increase the effect of soil disturbance. *Salar R.S. et al., (2021),* studied a new type of winged chisel plow, conducted research on the performance of the wings, and found that the winged chisel plow can effectively improve soil loosening efficiency and retain some residues on the soil surface. *Zeng Z. et al., (2020),* analyzed the effects of chisel, wing, narrow and torque shovels on straw-soil disturbance in soil bin experiment and combined them with simulation experiments to illustrate the effects of different implements on soil-straw. Compared with the ordinary chisel plow, the winged chisel plow can effectively improve the mixing rate, soil loosening rate and working width, and it is a kind of excellent land preparation implement. Understanding the soil-straw disturbance pattern of the key components of the wing chisel plow is crucial for its design and optimization.

In plowing, the soil-straw-equipment interaction affects the surface straw movement while also determining the degree of surface straw mixing *(Zheng K. et al., 2016)*. Due to the difficulty of analyzing soil and straw movement states at the microscopic level in soil bin experiment and actual field tests, DEM has become the mainstream for dealing with particles-equipment interactions *(Guo Y.J et al., 2017)*. Scientists at home and abroad use DEM to establish particles-straw models and simulate their mutual movements, which can effectively and accurately observe the movement status of the particles. *Wang W.W. et al. (2022),* designed a vertical bionic stubble cleaning and anti-blocking device based on the multi-segmented serrated structure of mantis toe, and verified the high straw cleaning rate and seedbed uniformity of the machine through DEM analysis of the straw disturbance displacement and straw cleaning rate under the operation of the machine. *Song C.Y. et al., (2022),* established a soil-trencher model to analyze the microscopic disturbance behavior of soil at different depths and operating speeds. *Fan Z. P. et al., (2023),* explored the conveying mechanism of crushed corn stalks in a screw conveyor, and verified the feasibility of using discrete element simulation to analyze the conveying process of crushed corn stalks. *Ren D. Z. et al., (2022),* used DEM to determine the optimal structural parameters of the soil removal device for straw pickup and pelletizing machines. At present, the particles-machine model established by DEM is relatively perfect, and DEM can be used to analyze the microscopic movement of particles and some regular conclusions, however, most of the scholars rely on DEM to analyze most of the research on the machine, and most of the soil bin experiment carried out are used to validate the accuracy of the model, which is likely to cause the simulation test and the actual working conditions are not consistent with each other, which will lead to the actual results of the machine being not able to reach the best state. In this study, based on the soil trough test and theoretical analysis, the key components and their parameter ranges affecting the straw mulching and mixed effect of the winged chisel plow are obtained, which correspond to the actual working conditions. The winged chisel plow improves the effect of straw mulching on the basis of maintaining the original loosening effect of the chisel plow. Based on this, this paper investigates the perturbation pattern of the key components of the winged chisel plow, which is the key to designing and optimizing an efficient winged chisel plow.

In this study, a winged chisel plow is used to analyze the working principle of the machine based on soil bin experiment and to study the microscopic patterns using DEM. The objectives of this study were: (1) To study the soil and straw disturbance characteristics of the winged chisel plow through soil bin experiment and theoretical analysis, to explain the working principle of the machine, to compare it with the ordinary chisel plow, and to clarify the main working parts and parameter ranges of the machine. (2) The soil-straw-winged chisel plow interaction model was established by DEM, and the microscopic motion pattern of soil and straw, straw mixing rate and draught force during machine operation were investigated. (3) To analyze the pattern of influence of the variation of different key parameters (the soil lifting plate height, the wing mounting height, the wing width) on the disturbance characteristics of the machine. (4) Experimental data such as straw displacement, draught force and straw mixing rate were used to verify the accuracy of the simulation model.

MATERIALS AND METHODS

Winged chisel plow structure and parameters

The structure of the winged chisel plow consists of a shovel handle, shovel tip, tilling board, wings and soil lifting plate. The shovel handle of the chisel shovel is a rounded shovel handle, and the general structure of the implement is shown in Fig. 1. Among these, the outer contour line of the shovel tip is a straight section, and the tilling board is a curved section with a radius of curvature of 320 mm, and the straight section is tangent to the curved section. *Salar M.R. et al., (2013),* studied the mechanical characteristics of the winged chisel plow and found that the degree of soil fragmentation, area of disturbance and its resistance of the forward wing is greater than that of the rearward wing, and the role of the shovel wing is mainly to take up the lifting plate of the shovel wing and to increase the width of the operation, so the choice of the rearward wing reduces the resistance of the implement. *Aluko O.B and Seig D.A., (2000),* showed that the chisel plow produced the least traction at an entry angle of 30°, so the entry angle of the winged chisel plow was chosen to be 30°. The specific structural parameters of the chisel winged plow are shown schematically in Fig. 2.

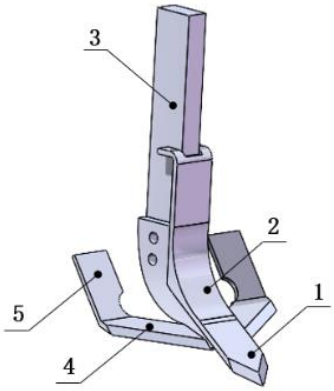
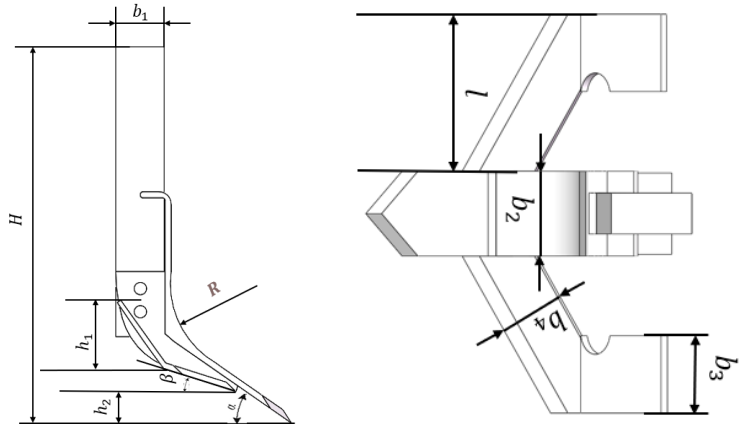


Fig. 1 - Winged chisel plow

1 – shovel tip; 2 – tilling board; 3 – shovel handle; 4 – wing; 5 – soil lifting plate



(a) (b)

Fig. 2 - Structure parameter diagram

(a) Side view; (b) Top view

Table 1

Winged chisel plow structural parameters

Parameter	Unit	Size
overall height H	mm	850
shovel handle width b_1	mm	90
shovel handle thickness t_1	mm	25
tilling board width b_2	mm	60
the radius of the tilling board R	mm	320
soil lifting plate width b_3	mm	60
Angle of entry of the shovel, α	degrees	30
Angle of entry of the wing, β	degrees	20

Soil bin experiment procedure and data acquisition

The trial was completed in July 2023 in an indoor soil bin at the Innovative Laboratory of Protected Tillage Technology and Intelligent Equipment, Shandong University of Technology. The soil in the soil bin was loam (72% sandy soil, 15% silt, and 13% clay). Using a cutting ring, soil samples were taken from 10 different locations with a sampling depth of 5 mm, 10 mm, and 15 mm. The average moisture content of the soil was measured to be 17.6% (dry basis) using a drying method, and the average bulk density of the soil was 1.51 g/cm^3. In the soil bin simulating the field where corn straw was crushed and returned to the field, the density of straw paving was 0.5 kg/m^2.

Mark five stalks as shown in Fig. 3a. The length of the five stalks is 7.5 cm and the radius is 1 cm. The third stalk is placed at the center of the implement operation, and the remaining stalks are placed horizontally with a horizontal distance of 4 cm. Mark a 500 mm x 100 mm work area A (Fig. 3a) using a marking ruler and chalk powder, and observe and record the position of the straw in area A after the work is completed using the marking ruler. The test machines were a winged chisel plow and a common chisel plow.

The draught force was measured during the test using a six-component force measurement instrument (Fig. 3b) on the frame of the electric inverter four-wheel drive tractor (TCC-2.1 model, Harbin Bona Technology Co., Ltd., Shanghai, China). The implement is installed on the frame of the tractor, which is connected to the frame using a three-point suspension and secured to the frame with U-bolts. The frame is equipped with a draught force load sensor and a data acquisition box to export the draught force during the implement's operation. The winged chisel plow has a penetration depth of 250 mm, allowing the tractor travel at a speed of 8 km/h. Record the movement trajectory of the five straws during work, find the final position of the straws, calculate the forward and horizontal displacement of the straws from the initial and final positions, and derive the traction force value recorded by the traction load sensor from the computer of the tractor.



(a) (b) (c)

Fig. 3 - Preparation for soil bin experiment
(a) Calibrated straw position; (b) Six-component force measurement instrument; (c) Winged chisel plow

Figure 4b shows the working effect of the winged chisel plow. To calculate the straw mixing rate after the work is completed, the binary method is used in Matlab to process the area A in Figure 3a and Figure 4b, and the result is shown in Figure 4c. The area of straw exposed to the surface is captured, and the percentage of straw on the soil surface is determined as the straw mixing rate *(Zeng Z. and Chen Y., 2018).*

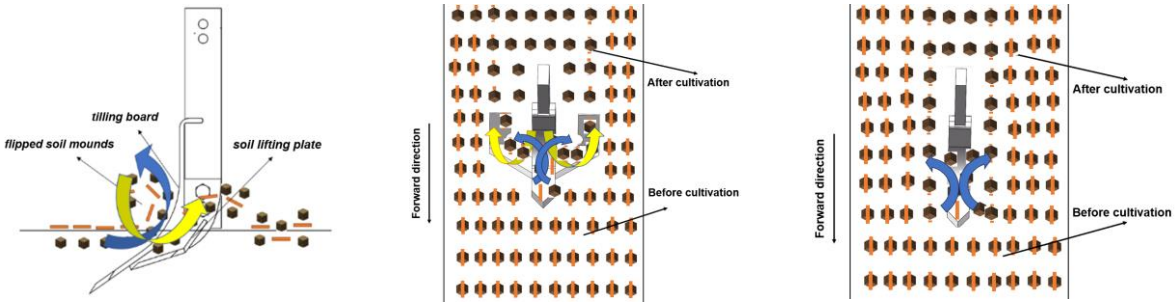


(a) (b) (c)

Fig. 4 - Straw cover
(a) Job effectiveness; (b) Area A after operation; (c) Binary processing.

Operating principle

The working principle of the winged chisel plow and the working process of each component were clarified through soil tank experiments. During the interaction between the winged chisel plow and the soil, it exerts cutting, squeezing, and other effects on the soil, causing soil fragmentation. This not only loosens the soil, but also turns it over, forming strip-shaped soil ridges that are turned over onto the surface (Fig. 5a), allowing the surface straw to be mixed into the soil. During forward operation of the machine, the tilling board pushes the soil-straw mixture to the sides. The more soil disturbance caused by tools, the higher the level of straw incorporation, and the lower the level of coverage remaining on the soil surface. The winged chisel plow is equipped with wings and soil lifting plates. The soil pushed to the sides falls onto the soil lifting plates on both sides, which perform secondary mixing of soil and straw. The ordinary chisel plow has a narrow working width and poor straw mixing effect (Fig. 5c). In contrast, the design of the wings and the soil lifting plates in the winged chisel plow greatly increases the working width of the chisel and the efficiency of straw mixing and burying.



(a) (b) (c)

Fig. 5 - Operating principle
(a) Soil-straw movement; (b) Winged chisel plow tillage effect; (c) Ordinary chisel plow tillage effect.

The design of the wing mounting height h_2

When the wing mounting height is 7 cm, 12 cm, and 17 cm, the position of the soil lifting plate is located in the soil tillage layer, between the soil surface and the tillage layer, and in the soil surface (Fig. 6). The wing mounting height not only affects the penetration performance and disturbance range of the implement, but also determines the mixing effect of the surface straw. When the wing height is 7 cm, the soil lifting plate is completely located in the soil, at which point the soil lifting plate will generate a large amount of resistance, causing the greatest disturbance to the soil. The surface soil will also be greatly disturbed due to the squeezing and pushing force of the wing on the cultivated soil layer. However, the soil lifting plate does not directly affect the surface straw, the actual mixing effect does not reach the ideal state. When the wing mounting height is 17 cm, the wing has a cutting effect on the soil surface layer of 0-5 cm. The soil lifting plate is completely located above the soil surface layer, at this time the disturbance of the wing to the soil is too small, and the loosened soil of the wing is too little to have a mixing effect on the straw above the surface layer. The machine relies solely on the tilling board for mixing, and the mixing effect is not good. When the wing mounting height is 12 cm, the soil lifting plate penetrates the soil surface and is located between the soil tillage layer and the surface layer. Due to its own angle of penetration, the soil lifting plate also has a turning effect on the soil, turning the soil and straw in front of itself. At the same time, the soil lifting plate located on the upper part of the topsoil can also disturb the soil and straw ahead of the tilling board, resulting in a secondary disturbance, which maximizes the soil mixing effect. In addition, the plow wing part has a large disturbance range on the surface soil, which solves the mechanical compaction problem of the surface soil.

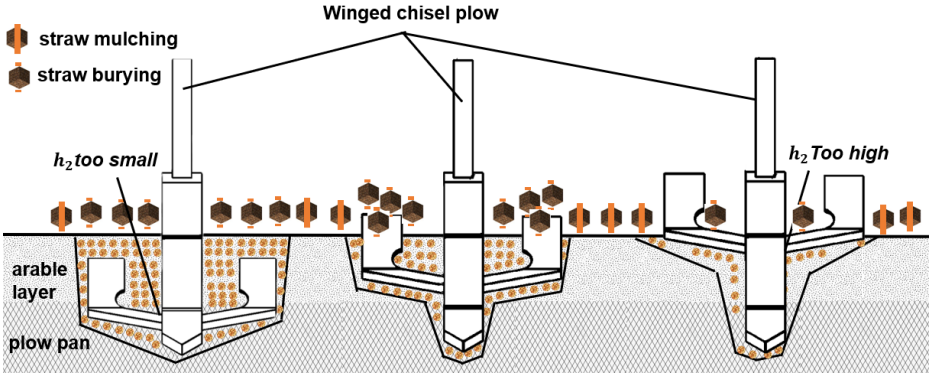


Fig. 6 - The influence of wing mounting height on soil-straw disturbance

The design of the soil lifting plate height h_1

Figure 7 shows the position of the soil lifting plate when it is 8 cm, 14 cm, and 20 cm, respectively. When the height of the soil lifting plate is 8 cm, the top of the soil lifting plate is located at the surface of the ground, and the soil lifting plate is completely located in the soil. Although its effective area can completely disturb the soil, due to the height limit, the disturbance of the surface straw at this time is basically caused by the extrusion and burial of the soil, and the soil lifting plate does not directly affect the surface straw. In actual working conditions, the tilling board turns the soil and straw in front of it by turning the soil, while pushing the soil and straw to the sides (Fig. 8). The soil lifting plate will have a secondary turning effect on it. If the height of the soil lifting plate is not enough, the secondary turning effect of the straw will be weakened, and the turned soil and straw will fall from above the soil lifting plate onto the ground behind it. When the soil lifting plate height is 20 cm, it reaches the maximum height for

turning the soil on the tilling board. However, due to the weight of the soil, when the soil moves in the direction of the soil lifting plate, it will inevitably displace downward, and the upper part of the soil lifting plate will not effectively contact the soil, so this part does not have a significant effect.

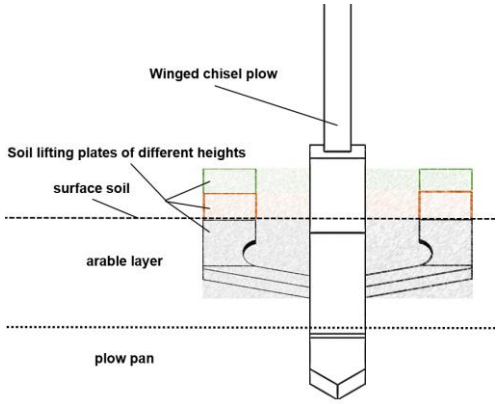


Fig. 7 - Soil lifting plates of different heights



Fig. 8 - Direction of soil-straw movement

The design of the wing width l

The function of the wing is to receive the soil lifting plate and cut the soil during operation. The width of the wing, (see Fig. 2), affects the actual working width and determines the position of the soil lifting plate. If the wing is too wide, the soil lifting plate cannot perform secondary mixing and burying of the soil and straw turned over by the tilling board. At the same time, the horizontal distance between the soil lifting plate and the tilling board is too large, it will also cause less disturbance to the soil and straw in between, and the soil lifted by the soil lifting plate and the tilling board will be squeezed in the middle, resulting in extremely uneven soil surface after the operation of the implement, leaving three soil ditches. If the wing is too narrow, it will directly affect the working width of the implement, and the soil lifting plate and the tilling board will have overlapping soil working areas. At this time, the resistance of the implement will not decrease significantly, but the operation efficiency will decrease.

To explore the optimal value of the width of the wing, it is necessary to understand the effective working width of the tilling board and the horizontal displacement distance of the soil-straw pushed by it. An ordinary chisel plow without wing was used for soil bin experiment, and the experimental process is shown in Figure 9a. The working effect of a common chisel plow is shown in Figure 9b. The overall working width is approximately 394 mm, and the actual measured disturbance widths on the left and right sides of the center of the soil ditch are 196 mm and 198 mm, respectively. Based on this, in order to make the soil lifting plate reach the working width of the tilling board, the soil lifting plate should be placed at a distance of 196-198 mm from the center of the implement. Due to the influence of the width of the soil lifting plate itself, the width of the wing should be between 170 mm and 230 mm. Within this range, the soil lifting plate can provide secondary disturbance to the soil and straw turned over by the tilling board, while achieving the optimal operating width.



(a) (b)

Fig. 9 - Common chisel plow soil bin experiment
(a) Experiment process of ordinary chisel plow; (b) Working width of ordinary chisel plow.

Establishment of discrete element simulation model

Set up a soil model in EDEM, with soil particles modeled as single particles with a radius of 5 mm, and the mechanical relationship between soil particles modeled as Hertz-Mindlin with Bonding contact model. The Bonding model can reflect the adhesion and elastic-plasticity between particles, and the bond radius of particles in the Bonding model can reflect the moisture content of soil, which can better simulate the breakage and deformation between soil particles. The deformation of straw can be neglected, and the effect of the winged chisel plow on straw is basically a disturbance. Therefore, the straw is set as a rigid model consisting of multiple particles stacked together. The mechanical relationship model between straw and soil and the winged chisel plow is a Hertz-Mindlin (no slip) contact model, which can better simulate the interaction between soil-straw-winged chisel plow. Corn straw was set up as a single pile of particles with a radius of 10 mm, the straw length is 75 mm. To simulate field straw mulching, the straw mulching density was set to 0.5 kg/m^2, resulting in a total of 1200 straws, which were randomly generated. After the generation is complete, five stalks are generated in the implement operation center at the same horizontal position as the soil bin experiment to record the forward and lateral displacement of the stalks. Geometric modelling of the winged chisel plow using SolidWorks 2022, the winged chisel plow is saved in step format and imported into the EDEM model, the material is 65Mn steel. The forward speed of the machine is 8km/h, and the penetration depth is 250 mm. The calibration test of material parameters for soil and straw was conducted, and the test process is shown in Figure 10 *(Wang X.L. et al., 2017; Tao C. et al., 2023; Fu M., 2023; Carlos M.et al.)*. The calibrated soil-straw parameters obtained are shown in Table 2.

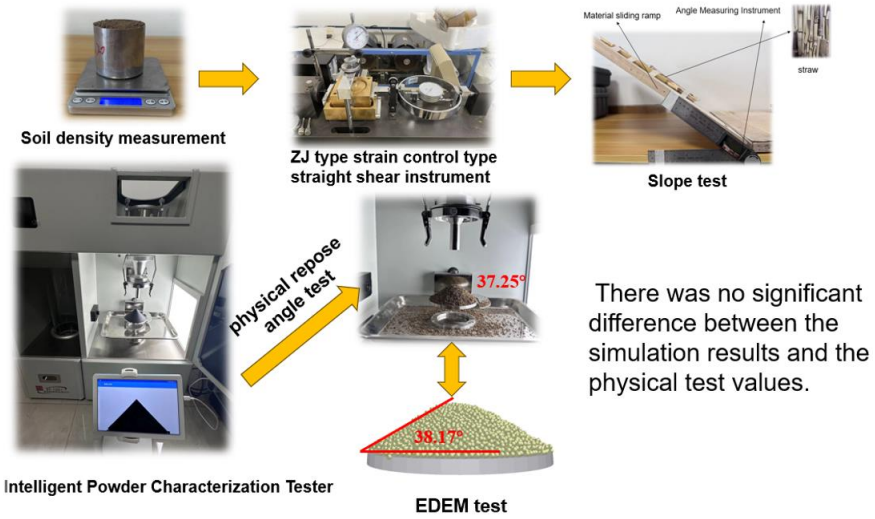


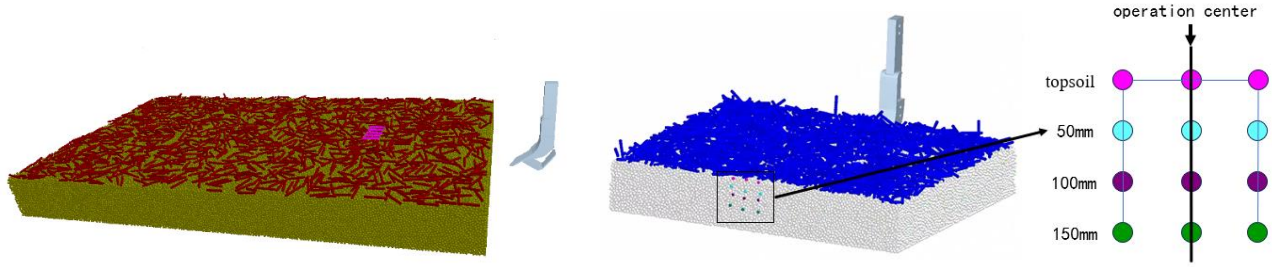
Fig. 10 - Calibration experiment

Table 2

Simulation parameter

Parameters	Value
Soil density/(kg·m^{-3})	1450
Soil Poisson's ratio	0.41
Soil shear modulus /MPa	1.24
Soil-Soil collision recovery coefficient	0.6
Soil-Soil static friction coefficient	0.36
Soil-Soil rolling friction coefficient	0.17
Straw density/(kg·m^{-3})	241
Straw Poisson's ratio	0.4
Straw shear modulus /MPa	1
Straw-Straw collision recovery coefficient	0.485
Straw-Straw static friction coefficient	0.213
Straw-Straw rolling friction coefficient	0.098
Straw-Soil collision recovery coefficient	0.6
Straw-Soil static friction coefficient	0.537
Straw-Soil rolling friction coefficient	0.16

Starting from the surface soil, mark four soil particles with a distance of 50 mm above and below the center of the work, and then mark a total of eight particles with a distance of 100 mm to the left and right (Fig. 11b). The focus is on clarifying the comprehensive disturbance of soil particles at the center of the chisel plow operation, the position of the wing, and the position of the soil particles on the surface under the action of the tilling board, shovel tip, and wing. Through the EDEM post-processing interface, the displacement of selected particles in the real-time longitudinal, horizontal, and vertical directions during the operation of the implement can be statistically analyzed. It is convenient for quantitative analysis of the disturbance of soil particles by winged chisel plow.



(a) (b)

Fig. 11 - Calibration experiment
(a) Calibrated straw position; (b) Calibrated soil position.

Simulation data acquisition

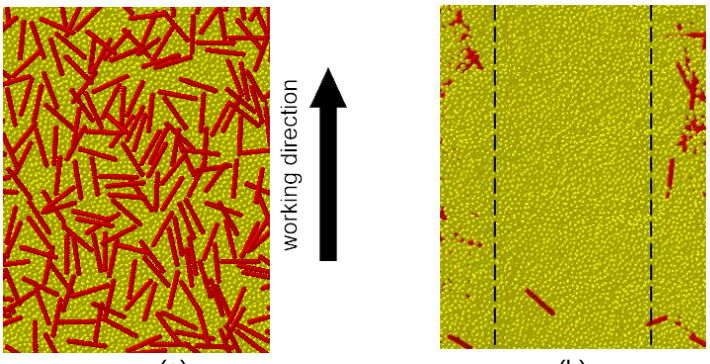
In the simulation experiment, the height of the soil lifting plate h_1, the width of the wing l, and the height of the wing mounting h_2 were used as variables, with four levels for each variable. To ensure the accuracy of the experiment, each group of experiment was repeated five times, and the average value of the obtained results was taken. In post-processing, the displacement changes in the X-axis and Y-axis directions of the marked soil and straw were derived as positive and lateral displacements, respectively, and the draught force of the winged chisel plow was evaluated to estimate the energy consumption generated by the implement.

Table 3

Parameters of key components of winged chisel plow

Variable	h_1/mm	l/mm	h_2/mm
1	80	160	70
2	110	180	95
3	140	200	120
4	170	220	145
5	200	240	170

In the simulation, the overall effect of straw burying is shown in Fig. 12. Fig. 12a shows the initial straw coverage, and Fig.12b shows the straw coverage after the work. The dotted line represents the trajectory of the implement. Generally speaking, the displacement of soil-straw closer to the implement is larger, and the straw mixing effect on the working path of the chisel is better than on both sides. The mixing rate of straw is determined by the ratio of straw area to total area. The mixing rate of straw is a key factor in determining the actual working performance of the implement, and can also be used as an experimental indicator to determine the optimal parameters of the implement.



(a) (b)

Fig. 12 - Calibration experiment
(a) Before the operation; (b) After the operation.

RESULTS

Comparison between ordinary chisel plow and winged chisel plow

The winged chisel plow has an innovative design for the shovel wing, which functions to increase the straw mixing rate and working width of the implement, resulting in a good straw mulching and mixing effect and meeting the requirements for returning straw to the field. To investigate the impact of winged chisel plows on the performance of agricultural machinery, the straw cover R, the working width W, and the draught force F of ordinary chisel plows and winged chisel plows were compared. In comparison to the ordinary chisel plow, although the average draught force of the implement increased by 532.92 N, the average straw mixing rate increased by 42.98%, and the working width increased by 41.86 cm (Table 3). Comparing the images in the figure 4a and figure 9b, it can be seen that the straw burying effect achieved by the tested chisel and wing plow was significantly improved, which was expected.

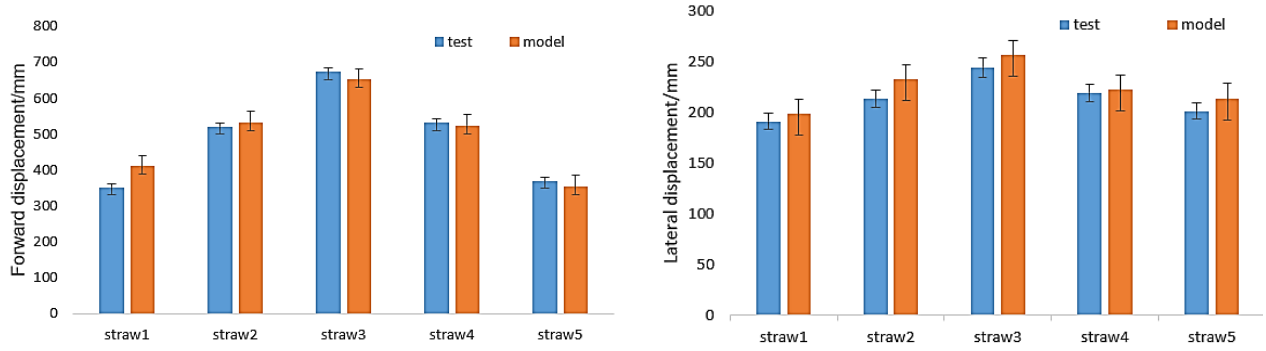
Table 3

Comparison of the two plows

Type	R / %	F / N	W / mm
Winged chisel plow	84.37	1603.24	39.47
Ordinary chisel plow	41.39	1070.26	81.33

Experimental verification

To verify the accuracy of the model, the model results were compared with the measured data from the soil bin experiment, including the positive and lateral displacement of the straw, the draught force, and the straw mixing rate, using relative error to evaluate consistency.



(a) (b)

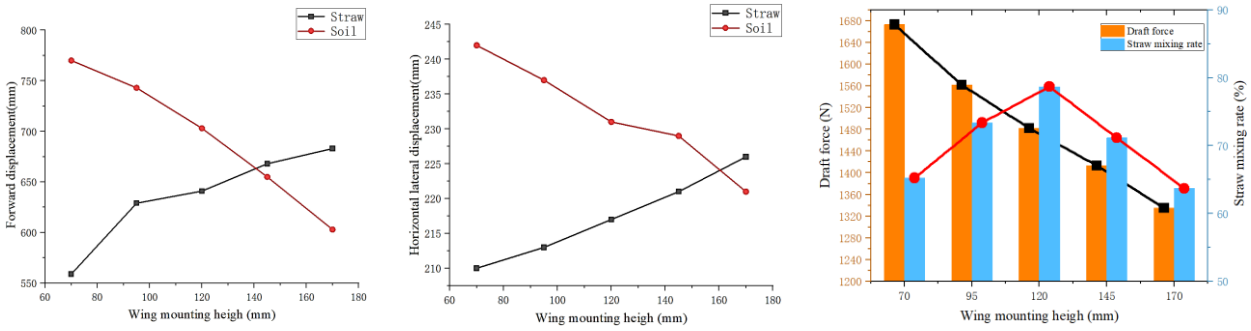
Fig. 13 –Simulation and practical experiment
(a) Forward displacement; (b) Lateral displacement;

The graphs of positive and lateral displacements of the five calibration straws were drawn and compared with the soil bin experiment results. The analysis of the test results shows that the straw3 located at the center of the implement operation has the greatest impact on the disturbance, and the straw displacement decreases as it moves away from the center. The positive displacement error of straw is between 1.67% and 5.45%; the lateral displacement error of straw is between 0.52% and 6.84%. The average straw mixing rate under simulation was 78.3%, while the average straw mixing rate in actual experiments was 81.9%. The error in straw mixing rate was between 2.54% and 6.37%. The average draught force of the implement when working stably under simulation is 1498.77 N, and the average draught force of the implement measured by a six-point measuring instrument during the soil bin experiment is 1603.24 N. The error of the tractive resistance of the implement is 5.29% to 12.60%, which is relatively small, and the variation trend of the test data is consistent with the simulation test. The soil bin experiment verified the accuracy of the discrete element simulation test and the feasibility of the discrete element simulation field test.

The influence of the wing mounting height

The simulation model was used to predict the impact of different wing mounting height on the displacement of straw and soil, as well as the straw mixing rate and draught (Fig.14). As the wing mounting height increases, the displacement of the wing on the straw gradually increases, and the disturbance on the soil gradually decreases. When the position of the soil lifting plate is closer to the soil surface, the effective disturbance area of the soil decreases, resulting in a decrease in the displacement of the soil,

and the draught force also decreases accordingly. The straw mixing rate first increases and then decreases, reaching a maximum of 79.3% at 120 mm. When the wing mounting height is too high, the soil lifted by the soil lifting plate will decrease, and there will not be enough soil to cover the straw, resulting in a decrease in the straw cover. When the height is less than 95 mm, the wing of the shovel cannot produce a turning effect on the soil and straw in front due to its low height.

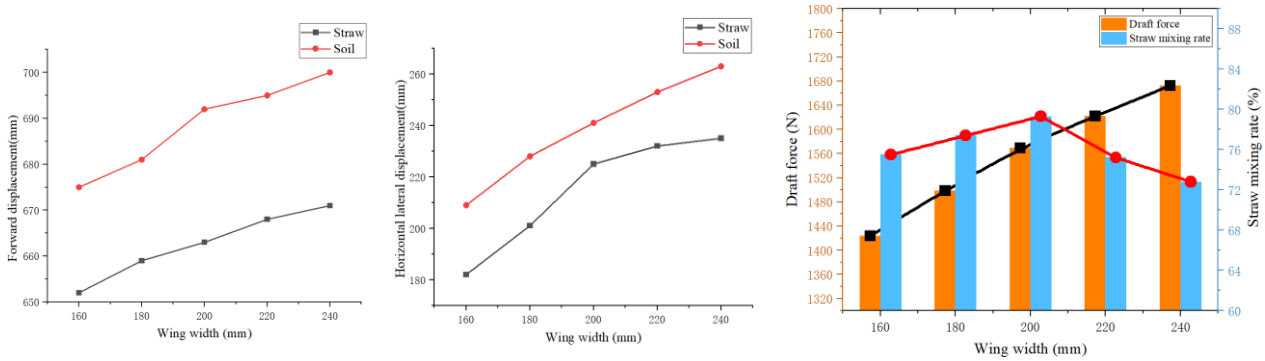


（a） （b） （c）

Fig. 14 – Simulation experiment results of the wing mounting height
(a) Forward displacement; (b) Lateral displacement; (c) Straw mixing rate

The simulation analysis results are consistent with the theoretical analysis results. In order to achieve the best operating effect of the plow, the installation height of the wing should be designed within 95 mm-145 mm.

The influence of the wing width



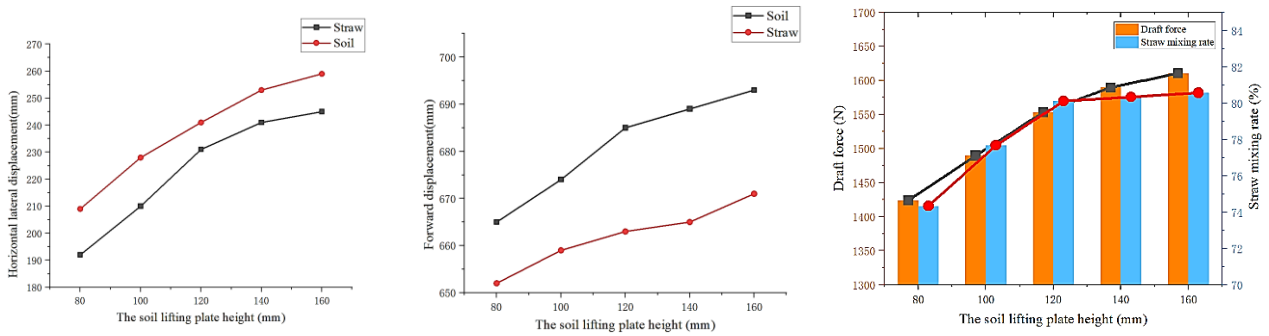
(a) (b) (c)

Fig. 15 – Simulation experiment results of the wing width
(a) Forward displacement; (b) Lateral displacement; (c) Straw mixing rate

The simulation model was used to predict the impact of different wing widths on the displacement of straw and soil, as well as on the straw mixing rate and draught force (Fig.15). The increase in the width of the wing will lead to an increase in the displacement of soil and straw. The increase in the width of the wing means that the width of the soil cut by the wing increases, the disturbance range of the soil is wider, and the draught force also increases. When the wing width is greater than 200 mm, the straw burying rate gradually decreases. The wing width affects the horizontal position of the soil lifting plate in the soil layer. When the wing is too wide, the distance between the soil lifting plate and the center of operation increases, and the effective area of the soil lifting plate for turning the soil and straw on the tilling board decreases, resulting in a reduction in straw mixing efficiency. When the wing is at 170 mm, the disturbance width is insufficient, the amount of soil cut by the wing is small, and the mixing effect cannot reach the optimal state. To sum up, the optimal value range of the wing is 180 mm-220 mm.

The influence of the soil lifting plate height

The simulation model was used to predict the impact of different lifting plate height on the displacement of straw and soil, as well as on the straw mixing rate and draught force (Fig.16). As the height of the soil lifting plate increases, the overall displacement of soil and straw gradually increases, and the traction resistance gradually increases. The soil lifting plate has a small amount of disturbance to the soil in the soil layer, and the impact on soil displacement is mostly due to the secondary turnover effect after the tilting board is turned over.



(a) (b) (c)

Fig. 16 – Simulation experiment results of the soil lifting plate height
(a) Forward displacement; (b) Lateral displacement; (c) Straw mixing rate

The height of the soil lifting plate restricts the maximum height of the mixed straw bale. Before the soil lifting plate reaches the maximum height of turning, the height of the turned soil and straw increases with the increase in the height of the soil lifting plate. When the height increases from 80 mm to 140 mm, the straw mixing rate of straw increases by 5.9%. When the height increases from 140 mm to 200 mm, the straw cover remains basically unchanged. The soil lifting plate reaches its highest value of turning soil and straw at 140 mm-200 mm, so the effective area of the upper part of the soil lifting plate decreases. If the height of the soil lifting plate is not sufficient, the secondary turning effect of the straw will be weakened, and the turned soil and straw will fall from the top of the soil lifting plate onto the rear surface. Therefore, the optimal value range of the soil lifting plate is 110 mm-170 mm.

CONCLUSIONS

Taking the designed winged chisel plow as the research object, through soil bin experiments, theoretical analysis, and simulation tests, the impact of key component parameters of the winged chisel plow on soil-straw disturbance was explored. The conclusions are as follows:

(1) The soil bin experiment found that the winged chisel plow can achieve secondary disturbance of straw-soil interaction, provided that the wing parameters are within the ideal range. Combining theoretical analysis, the key components affecting the secondary disturbance of the winged chisel plow are the wing mounting height, soil lifting plate height, and wing width.

(2) Compared to the conventional chisel plow, the degree of straw coverage achieved with the wing chisel plow, increased by 42.98%, the working width increased by 42.86 cm. The design of the winged chisel plow significantly improved the straw mixing effect.

(3)The wing mounting height determines the depth of the wing and soil lifting plate in the soil layer. When the mounting height is 95 mm-145 mm, the straw cover reaches its highest value. The height of the soil lifting plate determines the effective area of the secondary disturbance of soil-straw. Too low a soil lifting plate reduces secondary disturbance and is not conducive to straw mixing. Too high will cause the upper area to become ineffective. The experiment data shows that after reaching a height of 140 mm, the benefit of straw mixing becomes weak. The width of the wing mainly affects the working width of the winged chisel plow, provided that it is within the range of 160 mm-240 mm. Below this range, the straw mixing efficiency decreases; when it exceeds this range, the land after the operation will become extremely uneven.

(4) The simulation model established using soil-straw parameters obtained from calibration experiment and the experimental data obtained from soil bin experiment were compared. The model was able to predict the disturbance of the soil-straw by the machinery with good accuracy, with relative errors of 6.84%, 12.60%, and 6.37% for straw displacement, draught force, and straw cover, respectively.

ACKNOWLEDGEMENT

This research was supported by the National Natural Science Foundation of China (Grant No. 32101631)

REFERENCES

[1] Aluko O.B., Seig D.A., (2000). An experimental investigation of the characteristics of and conditions for brittle fracture in two-dimensional soil cutting. *Soil and Tillage Research, 57*:143–157.

[2] Carlos M., Miguel H., María L., et al. (2023). DEM computational simulation of the polishing of the tagua (PHYTELEPHAS AEQUATORIALIS) palm nuts. *INMATEH Agricultural Engineering*, vol.70, no.2, pp.299-308. DOI: https://doi.org/10.35633/inmateh-70-29.

[3] Ren D.Z., Bai X.W., Huang W.Y. et al., (2022). Simulation optimization of a conveying and soil-removing device for a corn stalks picking and pelletizing machine (秸秆捡拾制粒机输送除土装置仿真优化). *INMATEH Agricultural Engineering,* vol.68, no.3, pp.32-40. DOI: https://doi.org/10.35633/inmateh-68-03.

[4] Fan Z.P., Ma Z., Wang H.B. et al., (2023). Optimization of screw conveying of kneaded corn stalks based on discrete element method (基于离散元法的揉碎玉米秸秆螺旋输送的优化). *INMATEH Agricultural Engineering*, vol.69, no.1, pp.626-634. DOI: https://doi.org/10.35633/inmateh-69-60.

[5] Fu M., Chen X.Q., Gao Z.F. et al., (2023) Parameters calibration of discrete element model (碎玉米秸秆离散元模型参数标定). *INMATEH Agricultural Engineering*, vol.69, no.1, pp.399-408. DOI: https://doi.org/10.35633/inmateh-69-37.

[6] Gao W.S. (2007). Development trends and basic principles of conservation tillage (论保护性耕作技术的基本原理与发展趋势) [J]. *Scientia Agricultura Sinica, 40*(12):2702-2708. (in Chinese)

[7] Guo Y.J., Cao Z.F., Jiang S.S. et al. (2017). Experimental research on the core ploughshare furrow opener based on the discrete element method (基于离散元法芯铧式开沟器的试验研究) [J]. *Journal of Chinese Agricultural Mechanization, 38*(01):6-10.

[8] Guan W.D., Liu C.S., Qin Q. et al. (2023). The Application Status and Development Trend of Conservation Tillage in Black Soil Region (浅谈保护性耕作应用现状与发展趋势) [J]. *Modern Agriculture Research, 29(08)*:147-150.2023, 29(08):147-150.

[9] He J., Li H.W., Chen H.T. et al. (2018). Research Progress of Conservation Tillage Technology and Machinery (保护性耕作技术与机具研究进展) [J]. *Transactions of the Chinese Society for Agricultural Machinery, 49*(04): 1-19. (in Chinese)

[10] Sun N.N., Wang X.Y., Li H.W. et al. (2018). Performance of straw returning equipment under different mechanized straw returning pattern in northeast rice area (东北稻区不同秸秆还田模式机具作业效果研究) [J].*Transactions of the Chinese Society for Agricultural Machinery, 49(Supp)*: 68 -74, 154. (in Chinese)

[11] Salar M.R., Karparvarfard H.S, Askari M. et al. (2021). Forces and loosening characteristics of a new winged chisel plough [J]. *Research in Agricultural Engineering, 67*(1): 17-25.

[12] Song C.Y., Zhang X.C., Li H. et al. (2022). Effect of tine furrow opener on soil movement patterns using the discrete element method and soil bin study (基于 EDEM 仿真与土槽试验的移动式开沟器土壤扰动规律研究). *INMATEH Agricultural Engineering,* vol.68, no.3, pp.350-360.

[13] Tian X.L., Cong X, Qi J.T. et al. (2021). Calibration of Discrete Element Model Parameters for Corn Stalk-Soil Mixture in Black Soil Region (黑土区玉米秸秆-土壤混料离散元模型参数标定) [J]. *Transactions of the Chinese Society for Agricultural Machinery. 52*(10): 100-108+242.

[14] Tao C., Mo Z.Y., Lu F.Y. et al. (2023) Measurement of physical property parameters for green onion seeds (大葱种子物性参数测量及 DEM 参数仿真标定). *INMATEH Agricultural Engineering*, vol.70, no.2, pp.137-146. DOI: https://doi.org/10.35633/inmateh-70-13.

[15] Wang H.N., Wang X.C., Huang J. et al. (2017). Effect of straw incorporated into soil on reducibility in soil and root system and yield of rice (秸秆还田对土壤还原性和水稻根系生长及产量的影响) [J]. *Transactions of the CSAE, 33*(20):116-126. (in Chinese)

[16] Wang X.L., Hu H., Wang Q.J. et al. (2017). Calibration Method of Soil Contact Characteristic Parameters Based on DEM Theory (基于离散元的土壤模型参数标定方法) [J]. *Transactions of the Chinese Society for Agricultural Machinery. 48*(12):78-85. (in Chinese)

[17] Wang W.W., Song J.L., Zhou G.A. et al., (2022). Simulations and experiments of the seedbed straw and soil disturbance as affected by the strip-tillage of rowcleaner (带状耕作对种床秸秆清除率和土壤扰动的仿真与试验). *INMATEH Agricultural Engineering,* vol.66, no.1, pp.49-61.

[18] Yang L.Q., Gao Y.Y., Zhu J.F. et al. (2018). Conservation tillage technology and related equipment (保护性耕作技术与配套机具）[J]. *Journal of Agricultural Mechanization Research, 40*(4):263-268. (in Chinese)

[19] Zheng K., Chen W.Z., Yang H.W. et al. (2016). Current situation and prospect of straw returning mechanized technology (秸秆还田机械化技术研究现状和展望）[J]. *Jiangsu Agricultural Sciences, 44*(9):9-13. (in Chinese)

[20] Zeng Z., Chen Y. (2019). Simulation of straw movement by discrete element modelling of straw-sweep-soil interaction [J]. *Biosystems Engineering. 180*, 25–35.

[21] Zeng Z., Ma X., Chen Y. et al. (2020). Modelling residue incorporation of selected chisel ploughing tools using the discrete element method (DEM) [J]. *Soil & Tillage Research.197(C).*104-505.

[22] Zhang C., Fan X.H., Li M.S. et al. (2022). Simulation Analysis and Experimental Study of Chisel Plow Soil Disturbance Based on EDEM. (基于 EDEM 的凿式犁铲土壤扰动仿真分析与试验)[J]. *Transactions of the Chinese Society for Agricultural Machinery. 53*(02): 1000-1298. (in Chinese)

STUDY OF THE KEY COMPONENT PARAMETERS OF THE WINGED CHISEL PLOW ON SOIL-STRAW DISTURBANCE PATTERN
/
混秸带翼凿式犁关键部件扰动规律的研究

Kun CHEN[1)], Xianliang WANG[*1)], Jiangtao JI[2)], Xiangcai ZHANG, Xiupei CHENG[1)], Hua ZHOU[1)], Zhongcai WEI[1)] Lei LIU[1)], Mingyue BAI[1)], Shang GAO[1)],

[1)]School of Agricultural Engineering and Food Science, Shandong University of Technology, Zibo (255000), China;
[2)]College of Agricultural Equipment Engineering, Henan University of Science and Technology, Luoyang (471000), China
Tel: +86-18560168518; E-mail: 18560168518@163.com
Corresponding author: Xianliang Wang
DOI: https://doi.org/10.35633/inmateh-71-69

Keywords: *DEM, winged chisel plow, soil bin experiment, straw mixing rate, soil-straw displacement, draught force*

ABSTRACT
Understanding the soil-straw disturbance pattern of the key component parameters of the straw mixing winged chisel plow is the key to designing and optimizing the straw mixing winged chisel plow (a chisel plow for mixing and mulching straw). In this study, a straw-soil-winged chisel plow interaction model was established, and the working principle, key components of the winged chisel plow were determined based on soil bin experiment and theoretical analysis. Discrete element method (DEM) was used to study the influence of disturbance pattern of key components of the winged chisel plow on soil-straw displacement, straw mixing rate and draught force. The results show that the main components of the winged chisel plow that affect the operating efficiency of the implement are the soil lifting plate height, the wing mounting height and the wing width. The height of the soil lifting plate affects the efficiency of the winged chisel plow in secondary disturbance of soil-straw and its own performance in turning over soil, with an optimal range of 110 mm-170 mm. The installation height of the wing mounting mainly affects the position of the soil lifting plate in the soil layer. In order to achieve the best operating effect, the position of the soil lifting plate needs to meet the "lower lifting and upper turning" requirement. The optimal installation height of the wing mounting is 95 mm-145 mm. The width of the wing mainly affects the working width of the implement, and its optimal value is 180 mm-220 mm. The width of the wing mainly affects the working width of the implement, and its optimal value is 180 mm-220 mm. The established simulation relative error is within 12.60%, which can better study the disturbance pattern of soil-straw. This study may provide a reference for optimizing and designing wing-type chisel plows and subsoil shovels.

摘要
了解混秸双翼凿式犁关键部件参数对土壤-秸秆的扰动规律，是设计和优化混秸双翼凿式犁（一种覆混秸秆的凿式犁）的关键。本研究建立了秸秆-土壤-混秸双翼凿式犁相互作用模型，以土槽试验为基础，结合理论分析确定了混秸双翼凿式犁的工作原理与关键部件，并采用离散元法（DEM），研究了混秸双翼凿式犁关键部件的参数变化对土壤-秸秆位移、机具混埋效果以及机具牵引力的影响规律。结果表明：混秸双翼凿式犁影响机具作业效果的关键部件为抬土板高度、铲翼的安装高度与铲翼的宽度。抬土板高度影响带翼凿式犁二次扰动土壤-秸秆的效率与其本身翻转土壤的性能，最优取值范围为 110mm-170mm。铲翼安装高度主要影响抬土板在土层之中的位置，为了作业效果达到最佳状态，抬土板的位置需满足"下抬上翻"，铲翼安装高度的最佳取值为 95mm-145mm。铲翼宽度主要影响机具的作业宽度，其最佳取值为 180mm-220mm。建立的仿真相对误差在 12.60%内，能较好的研究土壤-秸秆的扰动规律。该研究可能为优化和设计翼式凿式犁和深松铲提供参考。

INTRODUCTION
In conservation tillage, large amounts of straw cover have been one of the main factors limiting crop yields, so effective straw handling is an important requirement for arable tools. At present, the main methods of straw return to the field in China include mulching return to the field, rotary plow return to the field, deep turning return to the field, and mulching and mixing return to the field *(Chen Q.C. et al., 2015).*

Deep turning and rotary plow for field return, using a moldboard plow and rotary tiller respectively, turn and break up the soil, leaving no residue on the soil surface, and have a high efficiency of straw return *(He J. et al., 2018)*, but long-term use of these two implements can damage soil structure and lead to a decline in soil nutrients, as well as increase the risk of soil erosion and runoff *(Yang L.Q. et al., 2018; Sun N.N. et al., 2018)*. In contrast, the use of chisel plows to cut the soil in mulching and returning to the soil does not completely bury the residual straw on the surface, part of the straw is stored on the surface to prevent wind and water erosion of the soil and the other part of the straw is buried with the soil to increase the organic matter of the soil and at the same time break up the compact soil layer of the soil, effectively improving the soil structure *(Guan W.D. et al., 2023)*. The chisel plow is one of the main supporting implements in mulching and mixing *(Wang H.N. et al., 2017)*. Many studies have been conducted on chisel plows by scholars at home and abroad. *Zhang C. et al., (2022),* took the chisel plow as a research object, used DEM to study the effect of soil disturbance and compared it with the deep pine shovel, and found that the chisel plow could significantly increase the effect of soil disturbance. *Salar R.S. et al., (2021),* studied a new type of winged chisel plow, conducted research on the performance of the wings, and found that the winged chisel plow can effectively improve soil loosening efficiency and retain some residues on the soil surface. *Zeng Z. et al., (2020),* analyzed the effects of chisel, wing, narrow and torque shovels on straw-soil disturbance in soil bin experiment and combined them with simulation experiments to illustrate the effects of different implements on soil-straw. Compared with the ordinary chisel plow, the winged chisel plow can effectively improve the mixing rate, soil loosening rate and working width, and it is a kind of excellent land preparation implement. Understanding the soil-straw disturbance pattern of the key components of the wing chisel plow is crucial for its design and optimization.

In plowing, the soil-straw-equipment interaction affects the surface straw movement while also determining the degree of surface straw mixing *(Zheng K. et al., 2016)*. Due to the difficulty of analyzing soil and straw movement states at the microscopic level in soil bin experiment and actual field tests, DEM has become the mainstream for dealing with particles-equipment interactions *(Guo Y.J et al., 2017)*. Scientists at home and abroad use DEM to establish particles-straw models and simulate their mutual movements, which can effectively and accurately observe the movement status of the particles. *Wang W.W. et al. (2022),* designed a vertical bionic stubble cleaning and anti-blocking device based on the multi-segmented serrated structure of mantis toe, and verified the high straw cleaning rate and seedbed uniformity of the machine through DEM analysis of the straw disturbance displacement and straw cleaning rate under the operation of the machine. *Song C.Y. et al., (2022),* established a soil-trencher model to analyze the microscopic disturbance behavior of soil at different depths and operating speeds. *Fan Z. P. et al., (2023),* explored the conveying mechanism of crushed corn stalks in a screw conveyor, and verified the feasibility of using discrete element simulation to analyze the conveying process of crushed corn stalks. *Ren D. Z. et al., (2022),* used DEM to determine the optimal structural parameters of the soil removal device for straw pickup and pelletizing machines. At present, the particles-machine model established by DEM is relatively perfect, and DEM can be used to analyze the microscopic movement of particles and some regular conclusions, however, most of the scholars rely on DEM to analyze most of the research on the machine, and most of the soil bin experiment carried out are used to validate the accuracy of the model, which is likely to cause the simulation test and the actual working conditions are not consistent with each other, which will lead to the actual results of the machine being not able to reach the best state. In this study, based on the soil trough test and theoretical analysis, the key components and their parameter ranges affecting the straw mulching and mixed effect of the winged chisel plow are obtained, which correspond to the actual working conditions. The winged chisel plow improves the effect of straw mulching on the basis of maintaining the original loosening effect of the chisel plow. Based on this, this paper investigates the perturbation pattern of the key components of the winged chisel plow, which is the key to designing and optimizing an efficient winged chisel plow.

In this study, a winged chisel plow is used to analyze the working principle of the machine based on soil bin experiment and to study the microscopic patterns using DEM. The objectives of this study were: (1) To study the soil and straw disturbance characteristics of the winged chisel plow through soil bin experiment and theoretical analysis, to explain the working principle of the machine, to compare it with the ordinary chisel plow, and to clarify the main working parts and parameter ranges of the machine. (2) The soil-straw-winged chisel plow interaction model was established by DEM, and the microscopic motion pattern of soil and straw, straw mixing rate and draught force during machine operation were investigated. (3) To analyze the pattern of influence of the variation of different key parameters (the soil lifting plate height, the wing mounting height, the wing width) on the disturbance characteristics of the machine. (4) Experimental data such as straw displacement, draught force and straw mixing rate were used to verify the accuracy of the simulation model.

MATERIALS AND METHODS

Winged chisel plow structure and parameters

The structure of the winged chisel plow consists of a shovel handle, shovel tip, tilling board, wings and soil lifting plate. The shovel handle of the chisel shovel is a rounded shovel handle, and the general structure of the implement is shown in Fig. 1. Among these, the outer contour line of the shovel tip is a straight section, and the tilling board is a curved section with a radius of curvature of 320 mm, and the straight section is tangent to the curved section. *Salar M.R. et al., (2013),* studied the mechanical characteristics of the winged chisel plow and found that the degree of soil fragmentation, area of disturbance and its resistance of the forward wing is greater than that of the rearward wing, and the role of the shovel wing is mainly to take up the lifting plate of the shovel wing and to increase the width of the operation, so the choice of the rearward wing reduces the resistance of the implement. *Aluko O.B and Seig D.A., (2000),* showed that the chisel plow produced the least traction at an entry angle of 30°, so the entry angle of the winged chisel plow was chosen to be 30°. The specific structural parameters of the chisel winged plow are shown schematically in Fig. 2.

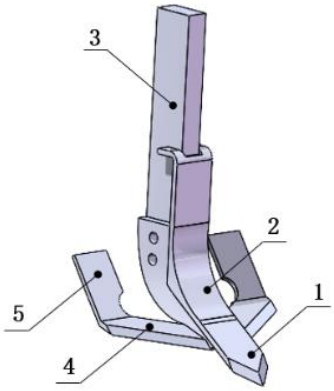
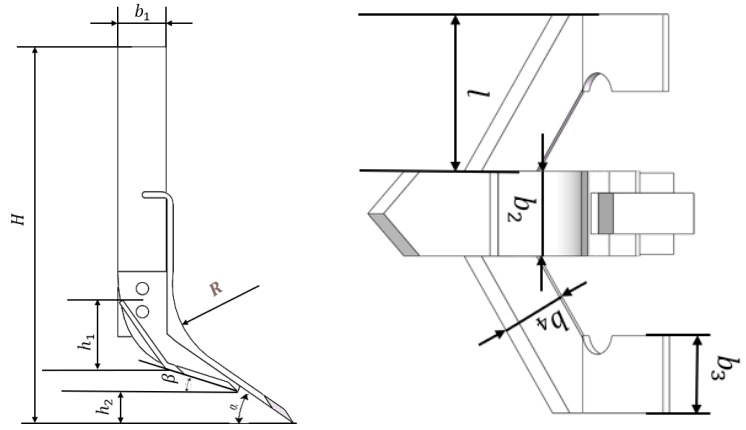


Fig. 1 - Winged chisel plow

1 – shovel tip; 2 – tilling board; 3 – shovel handle; 4 – wing; 5 – soil lifting plate



(a) (b)

Fig. 2 - Structure parameter diagram

(a) Side view; (b) Top view

Table 1

Winged chisel plow structural parameters

Parameter	Unit	Size
overall height H	mm	850
shovel handle width b_1	mm	90
shovel handle thickness t_1	mm	25
tilling board width b_2	mm	60
the radius of the tilling board R	mm	320
soil lifting plate width b_3	mm	60
Angle of entry of the shovel, α	degrees	30
Angle of entry of the wing, β	degrees	20

Soil bin experiment procedure and data acquisition

The trial was completed in July 2023 in an indoor soil bin at the Innovative Laboratory of Protected Tillage Technology and Intelligent Equipment, Shandong University of Technology. The soil in the soil bin was loam (72% sandy soil, 15% silt, and 13% clay). Using a cutting ring, soil samples were taken from 10 different locations with a sampling depth of 5 mm, 10 mm, and 15 mm. The average moisture content of the soil was measured to be 17.6% (dry basis) using a drying method, and the average bulk density of the soil was 1.51 g/cm^3. In the soil bin simulating the field where corn straw was crushed and returned to the field, the density of straw paving was 0.5 kg/m^2.

Mark five stalks as shown in Fig. 3a. The length of the five stalks is 7.5 cm and the radius is 1 cm. The third stalk is placed at the center of the implement operation, and the remaining stalks are placed horizontally with a horizontal distance of 4 cm. Mark a 500 mm x 100 mm work area A (Fig. 3a) using a marking ruler and chalk powder, and observe and record the position of the straw in area A after the work is completed using the marking ruler. The test machines were a winged chisel plow and a common chisel plow.

The draught force was measured during the test using a six-component force measurement instrument (Fig. 3b) on the frame of the electric inverter four-wheel drive tractor (TCC-2.1 model, Harbin Bona Technology Co., Ltd., Shanghai, China). The implement is installed on the frame of the tractor, which is connected to the frame using a three-point suspension and secured to the frame with U-bolts. The frame is equipped with a draught force load sensor and a data acquisition box to export the draught force during the implement's operation. The winged chisel plow has a penetration depth of 250 mm, allowing the tractor travel at a speed of 8 km/h. Record the movement trajectory of the five straws during work, find the final position of the straws, calculate the forward and horizontal displacement of the straws from the initial and final positions, and derive the traction force value recorded by the traction load sensor from the computer of the tractor.



(a) (b) (c)

Fig. 3 - Preparation for soil bin experiment
(a) Calibrated straw position; (b) Six-component force measurement instrument; (c) Winged chisel plow

Figure 4b shows the working effect of the winged chisel plow. To calculate the straw mixing rate after the work is completed, the binary method is used in Matlab to process the area A in Figure 3a and Figure 4b, and the result is shown in Figure 4c. The area of straw exposed to the surface is captured, and the percentage of straw on the soil surface is determined as the straw mixing rate *(Zeng Z. and Chen Y., 2018).*

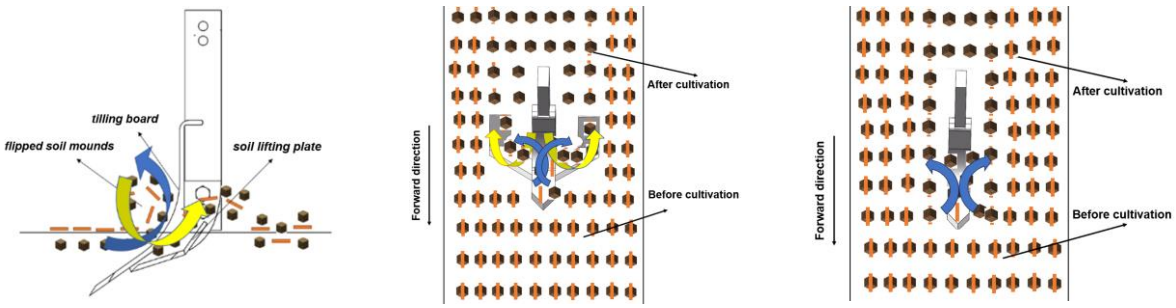


(a) (b) (c)

Fig. 4 - Straw cover
(a) Job effectiveness; (b) Area A after operation; (c) Binary processing.

Operating principle

The working principle of the winged chisel plow and the working process of each component were clarified through soil tank experiments. During the interaction between the winged chisel plow and the soil, it exerts cutting, squeezing, and other effects on the soil, causing soil fragmentation. This not only loosens the soil, but also turns it over, forming strip-shaped soil ridges that are turned over onto the surface (Fig. 5a), allowing the surface straw to be mixed into the soil. During forward operation of the machine, the tilling board pushes the soil-straw mixture to the sides. The more soil disturbance caused by tools, the higher the level of straw incorporation, and the lower the level of coverage remaining on the soil surface. The winged chisel plow is equipped with wings and soil lifting plates. The soil pushed to the sides falls onto the soil lifting plates on both sides, which perform secondary mixing of soil and straw. The ordinary chisel plow has a narrow working width and poor straw mixing effect (Fig. 5c). In contrast, the design of the wings and the soil lifting plates in the winged chisel plow greatly increases the working width of the chisel and the efficiency of straw mixing and burying.



(a) (b) (c)

Fig. 5 - Operating principle
(a) Soil-straw movement; (b) Winged chisel plow tillage effect; (c) Ordinary chisel plow tillage effect.

The design of the wing mounting height h_2

When the wing mounting height is 7 cm, 12 cm, and 17 cm, the position of the soil lifting plate is located in the soil tillage layer, between the soil surface and the tillage layer, and in the soil surface (Fig. 6). The wing mounting height not only affects the penetration performance and disturbance range of the implement, but also determines the mixing effect of the surface straw. When the wing height is 7 cm, the soil lifting plate is completely located in the soil, at which point the soil lifting plate will generate a large amount of resistance, causing the greatest disturbance to the soil. The surface soil will also be greatly disturbed due to the squeezing and pushing force of the wing on the cultivated soil layer. However, the soil lifting plate does not directly affect the surface straw, the actual mixing effect does not reach the ideal state. When the wing mounting height is 17 cm, the wing has a cutting effect on the soil surface layer of 0-5 cm. The soil lifting plate is completely located above the soil surface layer, at this time the disturbance of the wing to the soil is too small, and the loosened soil of the wing is too little to have a mixing effect on the straw above the surface layer. The machine relies solely on the tilling board for mixing, and the mixing effect is not good. When the wing mounting height is 12 cm, the soil lifting plate penetrates the soil surface and is located between the soil tillage layer and the surface layer. Due to its own angle of penetration, the soil lifting plate also has a turning effect on the soil, turning the soil and straw in front of itself. At the same time, the soil lifting plate located on the upper part of the topsoil can also disturb the soil and straw ahead of the tilling board, resulting in a secondary disturbance, which maximizes the soil mixing effect. In addition, the plow wing part has a large disturbance range on the surface soil, which solves the mechanical compaction problem of the surface soil.

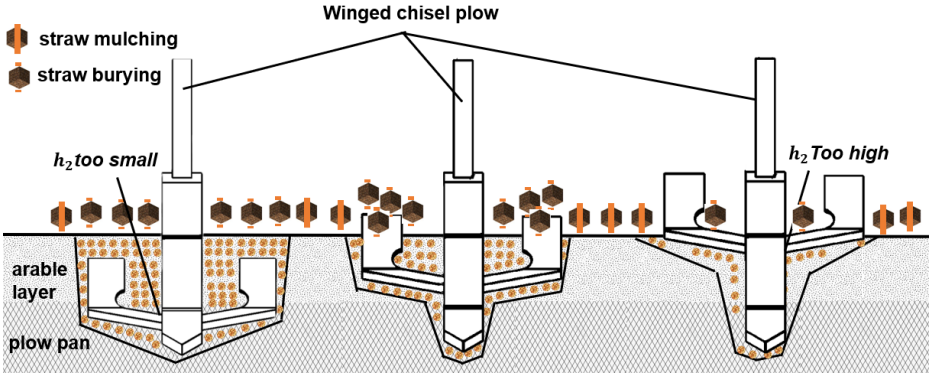


Fig. 6 - The influence of wing mounting height on soil-straw disturbance

The design of the soil lifting plate height h_1

Figure 7 shows the position of the soil lifting plate when it is 8 cm, 14 cm, and 20 cm, respectively. When the height of the soil lifting plate is 8 cm, the top of the soil lifting plate is located at the surface of the ground, and the soil lifting plate is completely located in the soil. Although its effective area can completely disturb the soil, due to the height limit, the disturbance of the surface straw at this time is basically caused by the extrusion and burial of the soil, and the soil lifting plate does not directly affect the surface straw. In actual working conditions, the tilling board turns the soil and straw in front of it by turning the soil, while pushing the soil and straw to the sides (Fig. 8). The soil lifting plate will have a secondary turning effect on it. If the height of the soil lifting plate is not enough, the secondary turning effect of the straw will be weakened, and the turned soil and straw will fall from above the soil lifting plate onto the ground behind it. When the soil lifting plate height is 20 cm, it reaches the maximum height for

turning the soil on the tilling board. However, due to the weight of the soil, when the soil moves in the direction of the soil lifting plate, it will inevitably displace downward, and the upper part of the soil lifting plate will not effectively contact the soil, so this part does not have a significant effect.

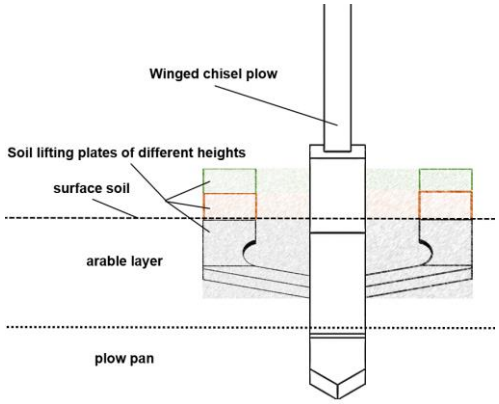


Fig. 7 - Soil lifting plates of different heights



Fig. 8 - Direction of soil-straw movement

The design of the wing width l

The function of the wing is to receive the soil lifting plate and cut the soil during operation. The width of the wing, (see Fig. 2), affects the actual working width and determines the position of the soil lifting plate. If the wing is too wide, the soil lifting plate cannot perform secondary mixing and burying of the soil and straw turned over by the tilling board. At the same time, the horizontal distance between the soil lifting plate and the tilling board is too large, it will also cause less disturbance to the soil and straw in between, and the soil lifted by the soil lifting plate and the tilling board will be squeezed in the middle, resulting in extremely uneven soil surface after the operation of the implement, leaving three soil ditches. If the wing is too narrow, it will directly affect the working width of the implement, and the soil lifting plate and the tilling board will have overlapping soil working areas. At this time, the resistance of the implement will not decrease significantly, but the operation efficiency will decrease.

To explore the optimal value of the width of the wing, it is necessary to understand the effective working width of the tilling board and the horizontal displacement distance of the soil-straw pushed by it. An ordinary chisel plow without wing was used for soil bin experiment, and the experimental process is shown in Figure 9a. The working effect of a common chisel plow is shown in Figure 9b. The overall working width is approximately 394 mm, and the actual measured disturbance widths on the left and right sides of the center of the soil ditch are 196 mm and 198 mm, respectively. Based on this, in order to make the soil lifting plate reach the working width of the tilling board, the soil lifting plate should be placed at a distance of 196-198 mm from the center of the implement. Due to the influence of the width of the soil lifting plate itself, the width of the wing should be between 170 mm and 230 mm. Within this range, the soil lifting plate can provide secondary disturbance to the soil and straw turned over by the tilling board, while achieving the optimal operating width.



(a) (b)

Fig. 9 - Common chisel plow soil bin experiment
(a) Experiment process of ordinary chisel plow; (b) Working width of ordinary chisel plow.

Establishment of discrete element simulation model

Set up a soil model in EDEM, with soil particles modeled as single particles with a radius of 5 mm, and the mechanical relationship between soil particles modeled as Hertz-Mindlin with Bonding contact model. The Bonding model can reflect the adhesion and elastic-plasticity between particles, and the bond radius of particles in the Bonding model can reflect the moisture content of soil, which can better simulate the breakage and deformation between soil particles. The deformation of straw can be neglected, and the effect of the winged chisel plow on straw is basically a disturbance. Therefore, the straw is set as a rigid model consisting of multiple particles stacked together. The mechanical relationship model between straw and soil and the winged chisel plow is a Hertz-Mindlin (no slip) contact model, which can better simulate the interaction between soil-straw-winged chisel plow. Corn straw was set up as a single pile of particles with a radius of 10 mm, the straw length is 75 mm. To simulate field straw mulching, the straw mulching density was set to 0.5 kg/m^2, resulting in a total of 1200 straws, which were randomly generated. After the generation is complete, five stalks are generated in the implement operation center at the same horizontal position as the soil bin experiment to record the forward and lateral displacement of the stalks. Geometric modelling of the winged chisel plow using SolidWorks 2022, the winged chisel plow is saved in step format and imported into the EDEM model, the material is 65Mn steel. The forward speed of the machine is 8km/h, and the penetration depth is 250 mm. The calibration test of material parameters for soil and straw was conducted, and the test process is shown in Figure 10 *(Wang X.L. et al., 2017; Tao C. et al., 2023; Fu M., 2023; Carlos M.et al.)*. The calibrated soil-straw parameters obtained are shown in Table 2.

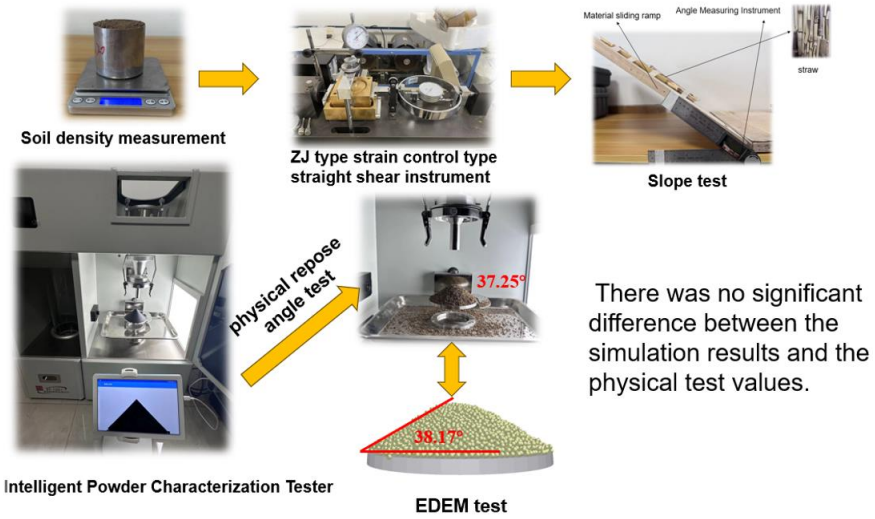


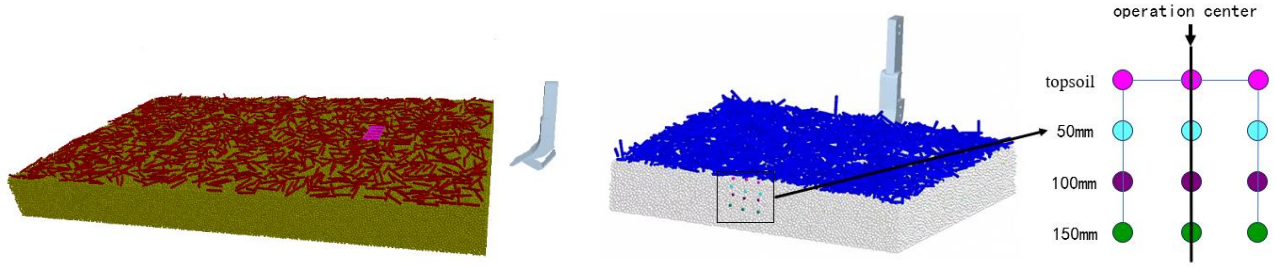
Fig. 10 - Calibration experiment

Table 2

Simulation parameter

Parameters	Value
Soil density/(kg·m^{-3})	1450
Soil Poisson's ratio	0.41
Soil shear modulus /MPa	1.24
Soil-Soil collision recovery coefficient	0.6
Soil-Soil static friction coefficient	0.36
Soil-Soil rolling friction coefficient	0.17
Straw density/(kg·m^{-3})	241
Straw Poisson's ratio	0.4
Straw shear modulus /MPa	1
Straw-Straw collision recovery coefficient	0.485
Straw-Straw static friction coefficient	0.213
Straw-Straw rolling friction coefficient	0.098
Straw-Soil collision recovery coefficient	0.6
Straw-Soil static friction coefficient	0.537
Straw-Soil rolling friction coefficient	0.16

Starting from the surface soil, mark four soil particles with a distance of 50 mm above and below the center of the work, and then mark a total of eight particles with a distance of 100 mm to the left and right (Fig. 11b). The focus is on clarifying the comprehensive disturbance of soil particles at the center of the chisel plow operation, the position of the wing, and the position of the soil particles on the surface under the action of the tilling board, shovel tip, and wing. Through the EDEM post-processing interface, the displacement of selected particles in the real-time longitudinal, horizontal, and vertical directions during the operation of the implement can be statistically analyzed. It is convenient for quantitative analysis of the disturbance of soil particles by winged chisel plow.



(a) (b)

Fig. 11 - Calibration experiment
(a) Calibrated straw position; (b) Calibrated soil position.

Simulation data acquisition

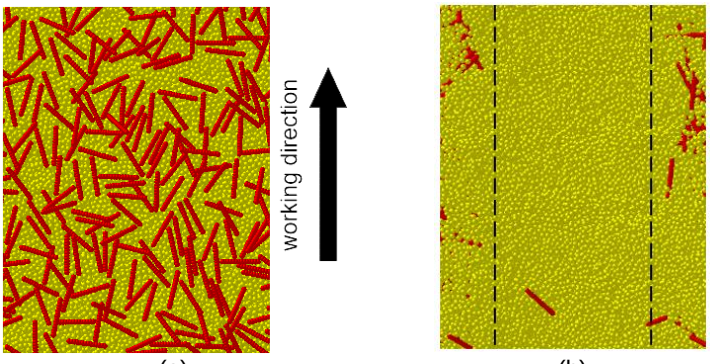
In the simulation experiment, the height of the soil lifting plate h_1, the width of the wing l, and the height of the wing mounting h_2 were used as variables, with four levels for each variable. To ensure the accuracy of the experiment, each group of experiment was repeated five times, and the average value of the obtained results was taken. In post-processing, the displacement changes in the X-axis and Y-axis directions of the marked soil and straw were derived as positive and lateral displacements, respectively, and the draught force of the winged chisel plow was evaluated to estimate the energy consumption generated by the implement.

Table 3

Parameters of key components of winged chisel plow

Variable	h_1/mm	l/mm	h_2/mm
1	80	160	70
2	110	180	95
3	140	200	120
4	170	220	145
5	200	240	170

In the simulation, the overall effect of straw burying is shown in Fig. 12. Fig. 12a shows the initial straw coverage, and Fig.12b shows the straw coverage after the work. The dotted line represents the trajectory of the implement. Generally speaking, the displacement of soil-straw closer to the implement is larger, and the straw mixing effect on the working path of the chisel is better than on both sides. The mixing rate of straw is determined by the ratio of straw area to total area. The mixing rate of straw is a key factor in determining the actual working performance of the implement, and can also be used as an experimental indicator to determine the optimal parameters of the implement.



(a) (b)

Fig. 12 - Calibration experiment
(a) Before the operation; (b) After the operation.

RESULTS

Comparison between ordinary chisel plow and winged chisel plow

The winged chisel plow has an innovative design for the shovel wing, which functions to increase the straw mixing rate and working width of the implement, resulting in a good straw mulching and mixing effect and meeting the requirements for returning straw to the field. To investigate the impact of winged chisel plows on the performance of agricultural machinery, the straw cover R, the working width W, and the draught force F of ordinary chisel plows and winged chisel plows were compared. In comparison to the ordinary chisel plow, although the average draught force of the implement increased by 532.92 N, the average straw mixing rate increased by 42.98%, and the working width increased by 41.86 cm (Table 3). Comparing the images in the figure 4a and figure 9b, it can be seen that the straw burying effect achieved by the tested chisel and wing plow was significantly improved, which was expected.

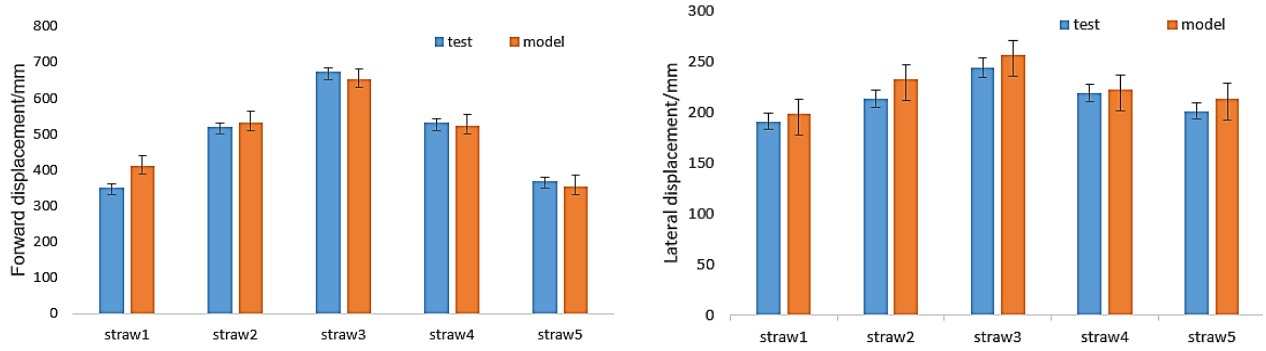
Table 3

Comparison of the two plows

Type	R / %	F / N	W / mm
Winged chisel plow	84.37	1603.24	39.47
Ordinary chisel plow	41.39	1070.26	81.33

Experimental verification

To verify the accuracy of the model, the model results were compared with the measured data from the soil bin experiment, including the positive and lateral displacement of the straw, the draught force, and the straw mixing rate, using relative error to evaluate consistency.



(a) (b)

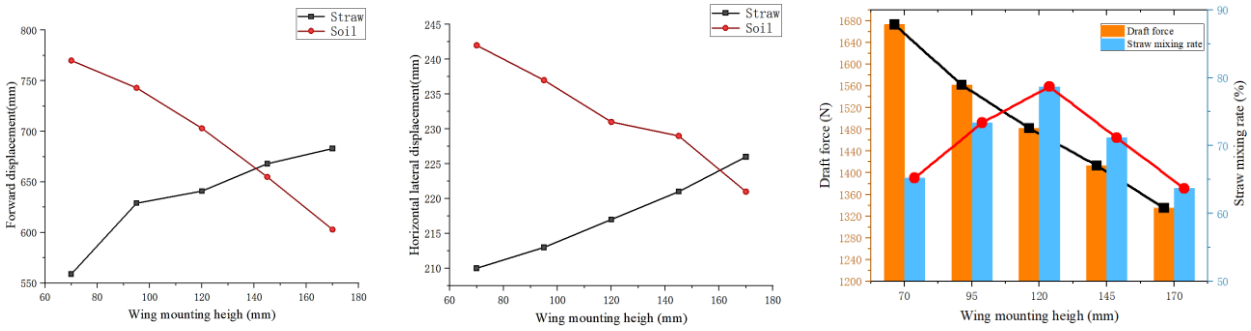
Fig. 13 –Simulation and practical experiment
(a) Forward displacement; (b) Lateral displacement;

The graphs of positive and lateral displacements of the five calibration straws were drawn and compared with the soil bin experiment results. The analysis of the test results shows that the straw3 located at the center of the implement operation has the greatest impact on the disturbance, and the straw displacement decreases as it moves away from the center. The positive displacement error of straw is between 1.67% and 5.45%; the lateral displacement error of straw is between 0.52% and 6.84%. The average straw mixing rate under simulation was 78.3%, while the average straw mixing rate in actual experiments was 81.9%. The error in straw mixing rate was between 2.54% and 6.37%. The average draught force of the implement when working stably under simulation is 1498.77 N, and the average draught force of the implement measured by a six-point measuring instrument during the soil bin experiment is 1603.24 N. The error of the tractive resistance of the implement is 5.29% to 12.60%, which is relatively small, and the variation trend of the test data is consistent with the simulation test. The soil bin experiment verified the accuracy of the discrete element simulation test and the feasibility of the discrete element simulation field test.

The influence of the wing mounting height

The simulation model was used to predict the impact of different wing mounting height on the displacement of straw and soil, as well as the straw mixing rate and draught (Fig.14). As the wing mounting height increases, the displacement of the wing on the straw gradually increases, and the disturbance on the soil gradually decreases. When the position of the soil lifting plate is closer to the soil surface, the effective disturbance area of the soil decreases, resulting in a decrease in the displacement of the soil,

and the draught force also decreases accordingly. The straw mixing rate first increases and then decreases, reaching a maximum of 79.3% at 120 mm. When the wing mounting height is too high, the soil lifted by the soil lifting plate will decrease, and there will not be enough soil to cover the straw, resulting in a decrease in the straw cover. When the height is less than 95 mm, the wing of the shovel cannot produce a turning effect on the soil and straw in front due to its low height.

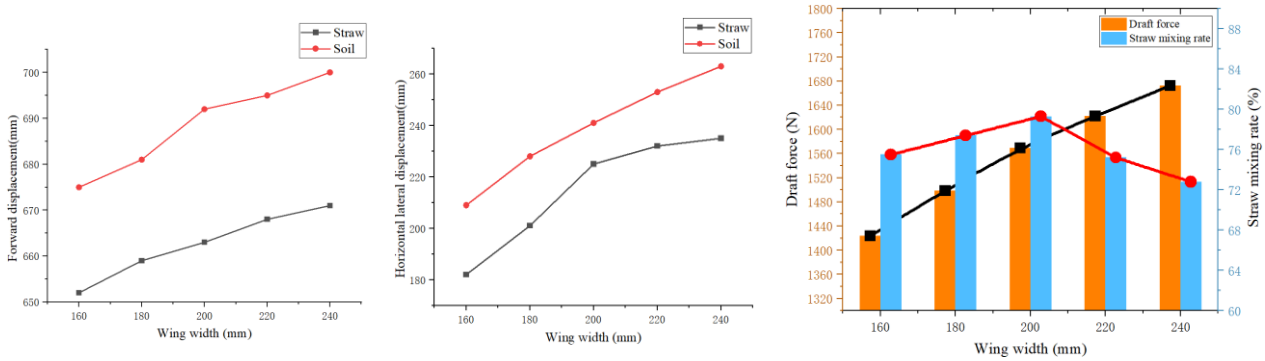


（a） （b） （c）

Fig. 14 – Simulation experiment results of the wing mounting height
(a) Forward displacement; (b) Lateral displacement; (c) Straw mixing rate

The simulation analysis results are consistent with the theoretical analysis results. In order to achieve the best operating effect of the plow, the installation height of the wing should be designed within 95 mm-145 mm.

The influence of the wing width



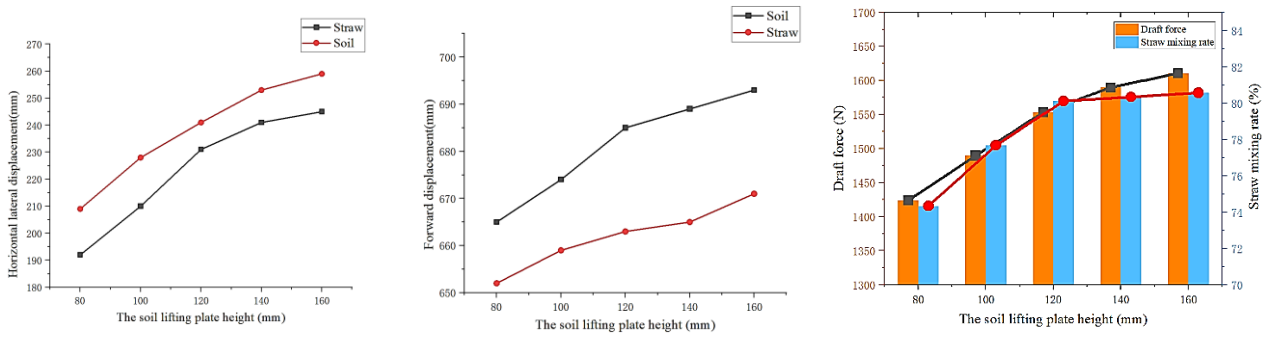
(a) (b) (c)

Fig. 15 – Simulation experiment results of the wing width
(a) Forward displacement; (b) Lateral displacement; (c) Straw mixing rate

The simulation model was used to predict the impact of different wing widths on the displacement of straw and soil, as well as on the straw mixing rate and draught force (Fig.15). The increase in the width of the wing will lead to an increase in the displacement of soil and straw. The increase in the width of the wing means that the width of the soil cut by the wing increases, the disturbance range of the soil is wider, and the draught force also increases. When the wing width is greater than 200 mm, the straw burying rate gradually decreases. The wing width affects the horizontal position of the soil lifting plate in the soil layer. When the wing is too wide, the distance between the soil lifting plate and the center of operation increases, and the effective area of the soil lifting plate for turning the soil and straw on the tilling board decreases, resulting in a reduction in straw mixing efficiency. When the wing is at 170 mm, the disturbance width is insufficient, the amount of soil cut by the wing is small, and the mixing effect cannot reach the optimal state. To sum up, the optimal value range of the wing is 180 mm-220 mm.

The influence of the soil lifting plate height

The simulation model was used to predict the impact of different lifting plate height on the displacement of straw and soil, as well as on the straw mixing rate and draught force (Fig.16). As the height of the soil lifting plate increases, the overall displacement of soil and straw gradually increases, and the traction resistance gradually increases. The soil lifting plate has a small amount of disturbance to the soil in the soil layer, and the impact on soil displacement is mostly due to the secondary turnover effect after the tilting board is turned over.



(a) (b) (c)

Fig. 16 – Simulation experiment results of the soil lifting plate height
(a) Forward displacement; (b) Lateral displacement; (c) Straw mixing rate

The height of the soil lifting plate restricts the maximum height of the mixed straw bale. Before the soil lifting plate reaches the maximum height of turning, the height of the turned soil and straw increases with the increase in the height of the soil lifting plate. When the height increases from 80 mm to 140 mm, the straw mixing rate of straw increases by 5.9%. When the height increases from 140 mm to 200 mm, the straw cover remains basically unchanged. The soil lifting plate reaches its highest value of turning soil and straw at 140 mm-200 mm, so the effective area of the upper part of the soil lifting plate decreases. If the height of the soil lifting plate is not sufficient, the secondary turning effect of the straw will be weakened, and the turned soil and straw will fall from the top of the soil lifting plate onto the rear surface. Therefore, the optimal value range of the soil lifting plate is 110 mm-170 mm.

CONCLUSIONS

Taking the designed winged chisel plow as the research object, through soil bin experiments, theoretical analysis, and simulation tests, the impact of key component parameters of the winged chisel plow on soil-straw disturbance was explored. The conclusions are as follows:

(1) The soil bin experiment found that the winged chisel plow can achieve secondary disturbance of straw-soil interaction, provided that the wing parameters are within the ideal range. Combining theoretical analysis, the key components affecting the secondary disturbance of the winged chisel plow are the wing mounting height, soil lifting plate height, and wing width.

(2) Compared to the conventional chisel plow, the degree of straw coverage achieved with the wing chisel plow, increased by 42.98%, the working width increased by 42.86 cm. The design of the winged chisel plow significantly improved the straw mixing effect.

(3)The wing mounting height determines the depth of the wing and soil lifting plate in the soil layer. When the mounting height is 95 mm-145 mm, the straw cover reaches its highest value. The height of the soil lifting plate determines the effective area of the secondary disturbance of soil-straw. Too low a soil lifting plate reduces secondary disturbance and is not conducive to straw mixing. Too high will cause the upper area to become ineffective. The experiment data shows that after reaching a height of 140 mm, the benefit of straw mixing becomes weak. The width of the wing mainly affects the working width of the winged chisel plow, provided that it is within the range of 160 mm-240 mm. Below this range, the straw mixing efficiency decreases; when it exceeds this range, the land after the operation will become extremely uneven.

(4) The simulation model established using soil-straw parameters obtained from calibration experiment and the experimental data obtained from soil bin experiment were compared. The model was able to predict the disturbance of the soil-straw by the machinery with good accuracy, with relative errors of 6.84%, 12.60%, and 6.37% for straw displacement, draught force, and straw cover, respectively.

ACKNOWLEDGEMENT

This research was supported by the National Natural Science Foundation of China (Grant No. 32101631)

REFERENCES

[1] Aluko O.B., Seig D.A., (2000). An experimental investigation of the characteristics of and conditions for brittle fracture in two-dimensional soil cutting. *Soil and Tillage Research, 57*:143–157.

[2] Carlos M., Miguel H., María L., et al. (2023). DEM computational simulation of the polishing of the tagua (PHYTELEPHAS AEQUATORIALIS) palm nuts. *INMATEH Agricultural Engineering*, vol.70, no.2, pp.299-308. DOI: https://doi.org/10.35633/inmateh-70-29.

[3] Ren D.Z., Bai X.W., Huang W.Y. et al., (2022). Simulation optimization of a conveying and soil-removing device for a corn stalks picking and pelletizing machine (秸秆捡拾制粒机输送除土装置仿真优化). *INMATEH Agricultural Engineering,* vol.68, no.3, pp.32-40. DOI: https://doi.org/10.35633/inmateh-68-03.

[4] Fan Z.P., Ma Z., Wang H.B. et al., (2023). Optimization of screw conveying of kneaded corn stalks based on discrete element method (基于离散元法的揉碎玉米秸秆螺旋输送的优化). *INMATEH Agricultural Engineering*, vol.69, no.1, pp.626-634. DOI: https://doi.org/10.35633/inmateh-69-60.

[5] Fu M., Chen X.Q., Gao Z.F. et al., (2023) Parameters calibration of discrete element model (碎玉米秸秆离散元模型参数标定). *INMATEH Agricultural Engineering*, vol.69, no.1, pp.399-408. DOI: https://doi.org/10.35633/inmateh-69-37.

[6] Gao W.S. (2007). Development trends and basic principles of conservation tillage (论保护性耕作技术的基本原理与发展趋势) [J]. *Scientia Agricultura Sinica, 40*(12):2702-2708. (in Chinese)

[7] Guo Y.J., Cao Z.F., Jiang S.S. et al. (2017). Experimental research on the core ploughshare furrow opener based on the discrete element method (基于离散元法芯铧式开沟器的试验研究) [J]. *Journal of Chinese Agricultural Mechanization, 38*(01):6-10.

[8] Guan W.D., Liu C.S., Qin Q. et al. (2023). The Application Status and Development Trend of Conservation Tillage in Black Soil Region (浅谈保护性耕作应用现状与发展趋势) [J]. *Modern Agriculture Research, 29(08)*:147-150.2023, 29(08):147-150.

[9] He J., Li H.W., Chen H.T. et al. (2018). Research Progress of Conservation Tillage Technology and Machinery (保护性耕作技术与机具研究进展) [J]. *Transactions of the Chinese Society for Agricultural Machinery, 49*(04): 1-19. (in Chinese)

[10] Sun N.N., Wang X.Y., Li H.W. et al. (2018). Performance of straw returning equipment under different mechanized straw returning pattern in northeast rice area (东北稻区不同秸秆还田模式机具作业效果研究) [J].*Transactions of the Chinese Society for Agricultural Machinery, 49(Supp)*: 68 -74, 154. (in Chinese)

[11] Salar M.R., Karparvarfard H.S, Askari M. et al. (2021). Forces and loosening characteristics of a new winged chisel plough [J]. *Research in Agricultural Engineering, 67*(1): 17-25.

[12] Song C.Y., Zhang X.C., Li H. et al. (2022). Effect of tine furrow opener on soil movement patterns using the discrete element method and soil bin study (基于 EDEM 仿真与土槽试验的移动式开沟器土壤扰动规律研究). *INMATEH Agricultural Engineering,* vol.68, no.3, pp.350-360.

[13] Tian X.L., Cong X, Qi J.T. et al. (2021). Calibration of Discrete Element Model Parameters for Corn Stalk-Soil Mixture in Black Soil Region (黑土区玉米秸秆-土壤混料离散元模型参数标定) [J]. *Transactions of the Chinese Society for Agricultural Machinery. 52*(10): 100-108+242.

[14] Tao C., Mo Z.Y., Lu F.Y. et al. (2023) Measurement of physical property parameters for green onion seeds (大葱种子物性参数测量及 DEM 参数仿真标定). *INMATEH Agricultural Engineering*, vol.70, no.2, pp.137-146. DOI: https://doi.org/10.35633/inmateh-70-13.

[15] Wang H.N., Wang X.C., Huang J. et al. (2017). Effect of straw incorporated into soil on reducibility in soil and root system and yield of rice (秸秆还田对土壤还原性和水稻根系生长及产量的影响) [J]. *Transactions of the CSAE, 33*(20):116-126. (in Chinese)

[16] Wang X.L., Hu H., Wang Q.J. et al. (2017). Calibration Method of Soil Contact Characteristic Parameters Based on DEM Theory (基于离散元的土壤模型参数标定方法) [J]. *Transactions of the Chinese Society for Agricultural Machinery. 48*(12):78-85. (in Chinese)

[17] Wang W.W., Song J.L., Zhou G.A. et al., (2022). Simulations and experiments of the seedbed straw and soil disturbance as affected by the strip-tillage of rowcleaner (带状耕作对种床秸秆清除率和土壤扰动的仿真与试验). *INMATEH Agricultural Engineering,* vol.66, no.1, pp.49-61.

[18] Yang L.Q., Gao Y.Y., Zhu J.F. et al. (2018). Conservation tillage technology and related equipment (保护性耕作技术与配套机具）[J]. *Journal of Agricultural Mechanization Research, 40*(4):263-268. (in Chinese)

[19] Zheng K., Chen W.Z., Yang H.W. et al. (2016). Current situation and prospect of straw returning mechanized technology (秸秆还田机械化技术研究现状和展望）[J]. *Jiangsu Agricultural Sciences, 44*(9):9-13. (in Chinese)

[20] Zeng Z., Chen Y. (2019). Simulation of straw movement by discrete element modelling of straw-sweep-soil interaction [J]. *Biosystems Engineering. 180*, 25–35.

[21] Zeng Z., Ma X., Chen Y. et al. (2020). Modelling residue incorporation of selected chisel ploughing tools using the discrete element method (DEM) [J]. *Soil & Tillage Research.197(C).*104-505.

[22] Zhang C., Fan X.H., Li M.S. et al. (2022). Simulation Analysis and Experimental Study of Chisel Plow Soil Disturbance Based on EDEM. (基于 EDEM 的凿式犁铲土壤扰动仿真分析与试验)[J]. *Transactions of the Chinese Society for Agricultural Machinery. 53*(02): 1000-1298. (in Chinese)

USING STATISTICAL ANALYSIS TO ASSESS THE EFFECTS OF FEEDING PELLETS ON FISH DIETARY PREFERENCES IN AN INTENSIVE POLYCULTURE SYSTEM

/

UTILIZAREA ANALIZEI STATISTICE PENTRU EVALUAREA EFECTELOR PELEȚILOR FURAJERI ASUPRA PREFERINȚELOR ALIMENTARE ALE PEȘTILOR ÎNTR-UN SISTEM INTENSIV DE POLICULTURĂ

Iulian VOICEA[1)], Petru CÂRDEI [1)], Vlad-Nicolae ARSENOAIA [2)], Nicoleta UNGUREANU [3)], Florin NENCIU [1)], Nicoleta VANGHELE *[1)]

[1)] Testing Department, National Institute of Research—Development for Machines and Installations Designed for Agriculture and Food Industry—INMA Bucharest, 013811 Bucharest, Romania;

[2)] Department of Pedotechnics, Faculty of Agriculture, Ion Ionescu de la Brad University of Agricultural Sciences and Veterinary Medicine, 700490, Iasi, Romania;

[3)] Faculty of Biotechnical Systems Engineering, National University of Science and Technology Politehnica Bucharest, 006042 Bucharest, Romania;

E-mail: vanghelelrc@gmail.com

DOI: https://doi.org/10.35633/inmateh-71-70

Keywords: *Nutrition Effects; Fish Diets; Aquaculture; Intensive Polyculture Systems;*

ABSTRACT

The paper proposes a statistical method for assessing the impact of multiple nutritional recipes on fish growth, raised in polyculture systems, a useful tool in selecting diets within small and medium-sized farms. After designing an experimental installation that produces pelletized feed, the study investigated the associations dependent on the feeder composition for three fish species involved in the experiment (Cyprinus carpio, Hypophthalmichthys nobilis and Carassius carassius). The fish relative mass and size variations have been used as performance parameters. The authors also issued hypotheses on the relations created between the studied species and determined the Feed Conversion Ratio.

REZUMAT

Articolul propune o metodă statistică pentru evaluarea impactului mai multor rețete nutritive asupra creșterii peștilor în sisteme de policultură, un instrument util în selectarea dietelor în cadrul fermelor de dimensiuni mici și medii. În urma proiectării unei instalații experimentale specializate pentru producția de furaje peletizate, studiul a investigat asocierile dependente de compoziția furajelor pentru trei specii de pești (Cyprinus carpio, Hypophthalmichthys nobilis și Carassius carassius). Pentru evaluarea performanței, s-au folosit ca parametrii masele relative și creșterea dimensiunii peștilor. Autorii au emis și câteva ipoteze cu privire la legătura creată între structura speciilor studiate și caracteristicile de bază ale dietelor lor preferate. și au calculat Rata de Conversie a Furajelor.

INTRODUCTION

Polyculture is the technology of growing a variety of aquatic species in the same pond, with the aim of improving overall production. This is accomplished by increasing the trophic and spatial niches, by raising different fish species that have complementary feeding preferences. Therefore, using polyculture practices, farmers could increase the production per unit area and successfully contribute to improving the aquatic environment. The presented results can be illustrated in the formulation of an experimental plan to study the dynamics of fish populations in aquaculture, following the systemic description of the phenomenon.

The paper considered a series of general aspects regarding fish feeding, that were presented in a research project (*Research Contract 5N/07.02.2019*), where the essential problems of fish feeding were also highlighted such as: the basic components (proteins, lipids, carbohydrates, vitamins, and minerals), and the connection between energy and proteins. Types of feeding, rate, frequency, and periods of feeding, automatic feeding systems were also addressed in (*Li, et al., 2013; FAO, 2016*).

A study that evaluated feed conversion and efficiency calculation (*Abdel-Twwab, et al., 2008*), corroborated the soundness of the feeding and growing systems, all of which are the main elements of the aquaculture management systems. The authors stated that most fish breeders use complete diets, usually made up of the following components and percentage ranges: protein, 18-50%; lipids, 10-25%; carbohydrates, 15-20%; ash, <8.5%; phosphorus, <1.5%; water, <10%; and traces of vitamins and minerals.

The problem of finding optimal diets for Israeli carp is presented in the paper of *Zahra, et al., (2015)* finally recommending a percentage of 40% proteins with 14% lipids. A research done by *Ali et al., (2022)* present the results of preliminary research on the optimal diet of carp. Since for the client the quality of the fish meat is highly important, the problem of the fish diet is also researched by the authors *Ljubojević, et al., (2022)*, who give several feeding recipes, including for carp. Similar problems were researched in other studies *(Shipton, et al., 2022; Al-Jader, et al., 2012; Fan, et al., 2015; Nandeesha, et al., 2000)*. The effects of feeding frequency on carp weight gain are presented in the work of *Ali, et al., (2022)*. The nutritional value of cereals in the diet of Common carp is the topic addressed by the authors *Sultana et al., (2001)*, considering that the local production of quality feeder can bring considerable benefits to the fish farming industry. A concentration of 99.3 g/kg of lipids is found optimal for breeding Crucian carp by the authors *Wang et al., (2014),* while other studies obtained similar results *(Przbyl, et al., 2004; Sun, et al., 2018)*. A research paper presents several problems with the Asian carp, associated with adaptation to the American continent (*Li, et al., 2013)*. The economic value generated by the Asian carp is emphasized, but so is the aggressiveness with which it imposes itself on the native carp. In *FAO, (2016),* several types of feeding for aquaculture fish are proposed. Among the nutritional components indicated by *FAO*, there are GOC, soybean meal, polished rice, fish meal, vegetable oil, vitamins, and minerals. The authors *Abdel-Twwab, et al., (2008*), discuss the effects of various protein diets on Nile tilapia. Effects of farm and commercial inputs on carp polyculture performance are analyzed in the paper of *Hernandez et al., (2022)*, considering the use of additives in feeder recipes.

The formulation of artificial diets for juvenile fish is significantly influenced by various factors, one of the most important being the larvae's capacity to effectively digest the essential nutrients *(Ali, et al., 2022)*. Several studies have undertaken a qualitative exploration of fish nutrition, analyzing in detail aspects related to the real efficiency of the feeder. For example, a research study that evaluated the effect of digestible protein levels in experimental diets for meagre (*Argyrosomus regius*) found that optimal digestible protein intake according to the ECR for rearing juvenile meagre was recorded in 0.8 g DP/100 g fish and day. A substantial literature on the problem of palletization and automation of feed administration in aquaculture systems can be found in various papers such as, *Gageanu, et al., (2019); Voicea, et al., (2021); Nenciu, et al., (2022); Matache, et al., (2021)*. Aquaculture developed under zero-waste conditions was addressed in *Nenciu, et al., (2022)*, where several innovative methods of sludge disposal and ecological food production were identified. The use of some aquaculture plants in fish-feeding diets is also a problem extensively addressed in the literature *(Voicea, et al., 2022)*. Other researchers have as objectives the optimal harvest ages of farmed fish. As an example, *Nguyen et al., (2001),* states that the common carp is optimally harvested at a mass between 0.3 and 0.7 kg. In the experimental process, the common carp was harvested at an average weight of 0.824 kg. In *Pitt et al., (2022)*, it is shown, for example, that carp is harvested at 200 g - 500 g or more (luxury specimens) in Indonesia and at 800 g in Japan, where it grows from April to autumn. The results of using vegetable diets, mixed diets, and synthetic diets are comparatively researched *(Ljubojević, et al., 2022; Byrd, et al., 2022; Kurćubić, et al., 2017; Dobrota, et al., 2022)*. The present study aims to explore the dietary preferences of three fish species (common carp, Asian carp, and Crucian carp) grown in an intensive polyculture system, using statistical analysis. The common challenge addressed involves the difficulty of quantifying the growth rate solely through fish measurements. This difficulty arises due to the varying feeding characteristics of different species and their distinct habitats within the basin. In addition, the introduction of varying numbers of fish from each species adds more complexity to the evaluation process.

MATERIALS AND METHODS

The experiments were conducted in the period 2019 - 2022 within INMA Bucharest institute, utilizing two fishing ponds of different sizes, employing a polyculture approach for fish farming. The large fishing pond, ICP 1 (Figure 1) is a construction made of reinforced concrete with a thickness of 300 mm, a width of 14.4 m, a length of 57 m, and a depth of 4.6 m.



Fig. 1 - Basin no. 1 (ICP1), covered pool and the location with details, the inside of the pool with water quality maintenance devices. The coordinates are 44º 30' 9.51'' N, 26º 4' 21.94'' E

The feeding system is composed of 3 feeders equipped with an auger and a pelletized feed disperser with a diameter between 2 and 10 mm, ensuring automated feeding by sequentially programming the dispersion on the surface of the pool. Two Osaga ORV Aerators were used to provide the optimum aeration-oxygenation level for the water in the fishing tank. The second pond (Figure 2) is an outdoor pilot basin, having a total capacity of 10,000 l. The basin was equipped with a supply system based on green energy (a hybrid wind-photovoltaic system).



Fig. 2 - Basin no. 2 (ICP 2), open fish-growing system

Fish species employed in the experiment and their dietary regime

Three species of fish were introduced into each of the two experimental basins: common carp (*Cyprinus carpio*), Asian carp (*Hypophthalmichthys nobilis*), and Crucian carp (*Carassius carassius*). The three fish species were raised together in the ponds. A total of 200 kg of juvenile fish from the three species has been introduced into each pool: 120 kg of common carp, 60 kg of Asian carp, and 20 kg of Crucian carp. At each such loading, one of the feeding diets D1, D2, D3, and D4 were administered separately, each consisting of 600 kg of pellets per pool, administered during four months of experimentation.

Feeder production using a simple pelletizing equipment

The production of the feeding pellets was carried out internally, using an extrusion equipment, designed and executed to be easily used by small and medium farms *(Nenciu, et al., 2022)*. Figure 3 presents the equipment used to pelletize fish feeder.

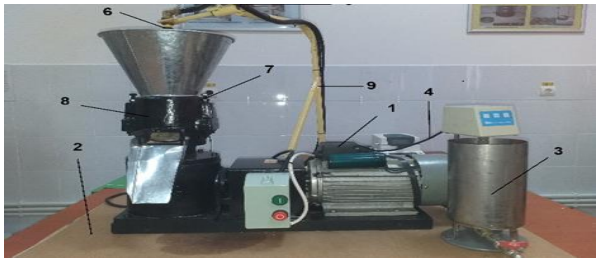


Fig. 3 - Development of a simple equipment design for pellet extrusion in fish feeder production

1 – steam generator; 2 – working stand; 3 – tank for storing blending solutions; 4 – mobile hose; 5 – pipe; 6 – adjusting nozzle; 7 – feeding hopper; 8 – electric heating belt; 9 – arm used to adjust the spraying position;

Four experiments were carried out in different time periods in the two pools, each of them starting with the same number of fish and administering the same amount of food, however in each experiment different type of diets were used: D_1, D_2, D_3, and D_4. The average initial and final masses for each experimental series were recorded. The length, height, and average thickness of the fish of each species have also been recorded. The four feeding recipes (diets) were structurally analyzed, with the data recorded in the sheets (energy value, ash content, moisture content, dry substance content, bulk density, unit density, crude fat content, and pellet durability obtained). The initial characteristics of the fish introduced into the pool, in each experiment, can be found in Table 1.

Table 1

Initial characteristics of fish

Fish species	Initial mass kg	Initial length cm	Initial height cm	Initial thickness cm
Common carp	0.200	16	6.40	1.10
Asian carp	0.150	20	4.20	1.60
Crucian carp	0.125	16	4.48	1.75

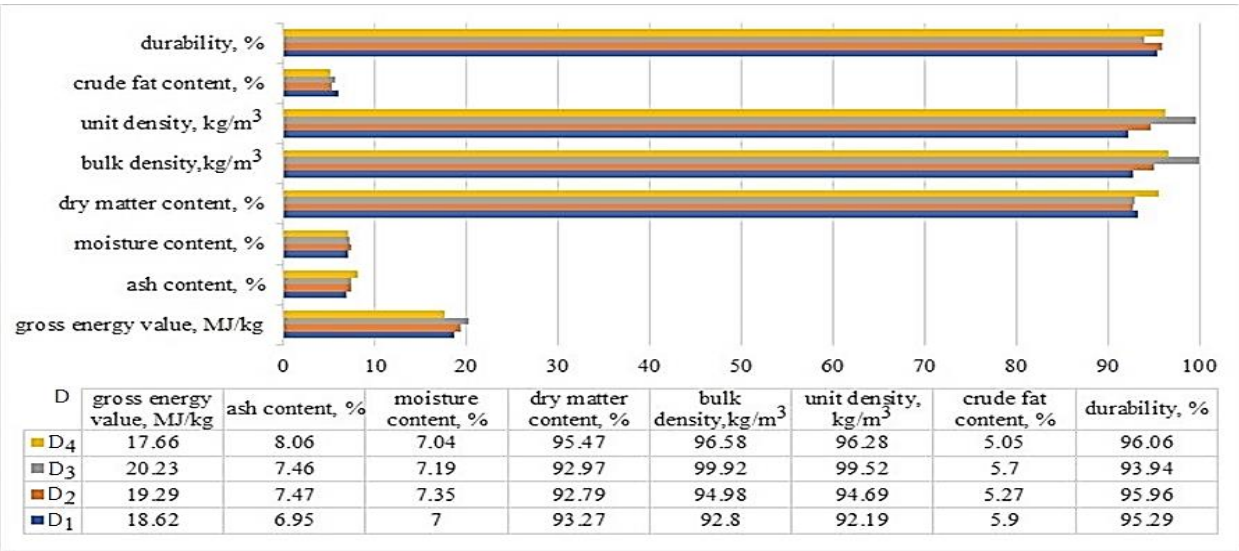
The characteristics of the fish determined at the end of the experiments can be found in Table 2, while the impact of the fish diets (for the four tested recipes) can be seen in Figure 4.

Table 2

Final characteristics of the fish in the two basins

Fish species	Basin	Diets	Mass kg	Length cm	Height cm	Thickness cm
Common carp	Basin 1	Diet 1	0.822	28	11.34	2.7
		Diet 2	0.785	27	10.94	2.5
		Diet 3	0.81	28	11.14	2.7
		Diet 4	0.705	26	10.4	2.65
	Basin 2	Diet 1	0.826	28	11.54	2.8
		Diet 2	0.782	27	10.81	2.72
		Diet 3	0.789	27	10.98	2.75
		Diet 4	0.698	25	9.85	2.57
Asian carp	Basin 1	Diet 1	0.48	48	10.08	1.89
		Diet 2	0.515	46	9.74	1.92
		Diet 3	0.544	47	9.98	1.97
		Diet 4	0.638	51	11.05	2.03
	Basin 2	Diet 1	0.48	48	10.1	1.91
		Diet 2	0.527	50	10.87	1.94
		Diet 3	0.566	51	11.08	1.99
		Diet 4	0.648	54	11.95	2.05
Crucian carp	Basin 1	Diet 1	0.403	22	5.94	2.26
		Diet 2	0.395	21	5.74	2.18
		Diet 3	0.426	23	6.21	2.28
		Diet 4	0.328	17	4.6	2.06
	Basin 2	Diet 1	0.421	23	6.04	2.28
		Diet 2	0.404	22	5.96	2.25
		Diet 3	0.45	23	6.01	2.32
		Diet 4	0.331	17	4.71	2.06

The main characteristics of the pellets in each of the four diets can be seen in figure 4.



D	gross energy value, MJ/kg	ash content, %	moisture content, %	dry matter content, %	bulk density,kg/m^3	unit density, kg/m^3	crude fat content, %	durability, %
D_4	17.66	8.06	7.04	95.47	96.58	96.28	5.05	96.06
D_3	20.23	7.46	7.19	92.97	99.92	99.52	5.7	93.94
D_2	19.29	7.47	7.35	92.79	94.98	94.69	5.27	95.96
D_1	18.62	6.95	7	93.27	92.8	92.19	5.9	95.29

Fig. 4 - The main characteristics of the pellets in each of the four diets

In the growing conditions described above and applying the described feeding diet, at the final measurement performed by random selection of a batch of fish, it was found that:

1) the fat content for the common carp species was 22.5% compared to the normal standard, which would be somewhere around 13-15% (with normal growth with controlled feeding, but also body growth would be lower by 10-12 % compared to what was obtained in the experiments referred to);

2) the fat content in Asian carp species was 12.5%, compared to the normal standard, which is 10% in a normal fish feed, but in this case, the body weight is 20% lower than what have been obtained in experimental

research. The Asian species have assimilated very well the intensive feeding without taking a large surplus of fat;
3) the crucian carp had a 20% higher fat intake than the normal standard, which would be somewhere around 10-12% of its body mass.
In essence, the carp and the crucian carp ate excessively and, as a result, at the evaluation, it could be seen that their livers were covered in fat. The working statistical evaluation method was based on the given equations (1)-(10). To highlight the performances of the four types of fish-feeding diets, the relative estimators have been be used:
- the average relative increase in fish mass:

$$\delta m_{rel}(p,b,R) = \frac{m(p,b,R) - m_0(p,b)}{m_0(p,b)} \cdot 100 \quad (1)$$

where $m(p,b,R)$ is the average final mass (after four months of growth) of the fish, *p* is the type of fish (common carp, Asian carp, and Crucian carp), b is the rearing pool (1 or 2), $m_0(p,b)$ is the average initial mass of the fish, and $\delta m_{rel}(p,b,R)$ is the relative average mass growth of the fish, which is expressed in percentages, R being the type of feeding diet used;
- the average relative increase in the length of the fish:

$$\delta L_{rel}(p,b,R) = \frac{L(p,b,R) - L_0(p,b)}{L_0(p,b)} \cdot 100 \quad (2)$$

where $L(p,b,R)$ is the average final length (after four months of growth) of the fish, $L_0(p,b)$ is the average initial length of the fish, and $\delta L_{rel}(p,b,R)$ is the increase in length relative to the average of all fish, expressed in percentages;
- the average relative increase in the height of the fish:

$$\delta h_{rel}(p,b,R) = \frac{h(p,b,R) - h_0(p,b)}{h_0(p,b)} \cdot 100 \quad (3)$$

where $h(p,b,R)$ is the average final height (after four months of growth) of the fish, $h_0(p,b)$ is the average initial height of the fish, and $\delta h_{rel}(p,b,R)$ is the increase in height relative average of the fish, which is expressed in percentages, R being the type of feeding recipe used;
- the average relative increase in the thickness of the fish:

$$\delta g_{rel}(p,b,R) = \frac{g(p,b,R) - g_0(p,b)}{g_0(p,b)} \cdot 100 \quad (4)$$

where $g(p,b,R)$ is the average final thickness (after four months of growth) of the fish, $g_0(p,b)$is the average initial thickness of the fish, and $\delta g_{rel}(p,b,R)$ is the increase in the average thickness relative to the fish, which is expressed in percentages.
A measure of the approximate volume growth of fish can be formulated, according to the following formula:

$$\delta V_{rel}(p,b,R) = \frac{V(p,b,R) - V_0(p,b)}{V_0(p,b)} \cdot 100 \quad (5)$$

where:

$$V_0(p,b) = L_0(p,b) \cdot h_0(p,b) \cdot g_0(p,b) \quad (6)$$

and

$$V(p,b) = L(p,b) \cdot h(p,b) \cdot g(p,b) \quad (7)$$

Similarly, the approximate density before the monitoring time interval can be defined according to the formula (8)

$$\rho_0(p,b) = \frac{m_0(p,b)}{V_0(p,b)} \quad (8)$$

respectively, the approximate density at the end of the experimental time interval (of treatment application or monitoring):

$$\rho(p,b,R) = \frac{m(p,b,R)}{V(p,b,R)} \quad (9)$$

A relative increase in density can be defined as follows:

$$\delta\rho(p,b,R) = \frac{\rho(p,b,R) - \rho_0(p,b)}{\rho_0(p,b)} \cdot 100 \quad (10)$$

Since in the two pools, the feeding recipes and medical treatments were identical, the study continued with the average values per pool. In this way, in formulas (1)-(10), the variable b disappears, and the functions become dependent on one or two variables, p (type of fish) and R (type of treatment).

RESULTS

The equations for calculating the increases in mass, length, height, and thickness, and, subsequent calculations of the density of the fish, allow some graphic representations that lead to some immediate conclusions. In Figure 5, the graphics depict the relative increases, in accordance with the experimental data and the defining equations (1)-(10), related to the type of diet (or recipe) administered. Diets are marked with D_1, D_2, D_3, and D_4. The calculations were performed by averaging over the two aquaculture basins.

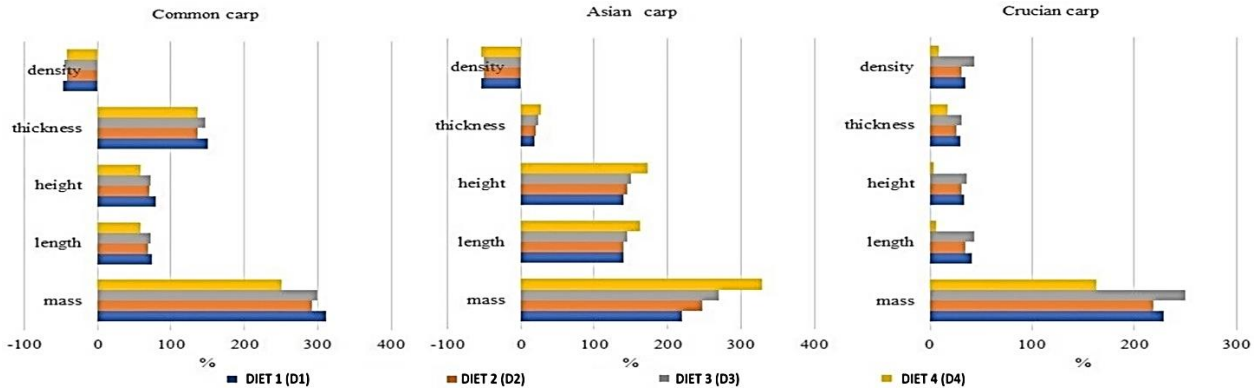


Fig. 5 - The relative increases in mass, length, height, width, and density of fish

From Figure 5, can be drawn the following results:

R1) the highest *relative mass increase* occurs as follows: in the common carp, it corresponds to the D_1 recipe and reaches the value of 312%; for the Asian carp, it corresponds to the D_4 diet and reaches the value of 329%; while for the Crucian carp, it corresponds to the D_3 diet and reaches the value of 250%;

R2) the highest value of the *relative increase in length* occurs as follows: for the common carp, it corresponds to the D_1 diet, with a value of 75% (with a small difference from the D_3 diet, with a value of 72%), for the Asian carp, it corresponds to the D_4 diet, with a value of 162.5%, and for the Crucian carp, it corresponds to the D_3 diet, with a percentage of 43.75%;

R3) the highest *relative increase in height* occurs in the common carp for the D_1 diet, with a value of 78.75%, for the Asian carp for the D_4 diet, with a value of 173.81%, and for the crucian carp for the D_3 diet, with a value of 36.38%;

R4) the *relative increase in width* (or *thickness*), with the highest intensity, occurs as follows: for the common carp for the D_1 diet, with a value of 150%, for the Asian carp for the D_4 diet, with a value of 27.5%, and for the Crucian carp for the D_3 diet, with a value of 31.43%;

R5) the *increase relative to the approximate density* of fish, with the highest magnitude, occurs as follows: for the common carp for the D_1 diet, with a value of -47.32%, for the Asian carp for the D_1 diet, with a percentage of -53.26% (a very small difference compared to the D_4 treatment, with the percentage of 53.22%), and for the Crucian carp for the D_3 diet, with a value of 43.67%.

R6) combining the performances of each diet for each category of fish, it can be observed that the best score is recorded: for common carp, diet D_1, Asian carp, diet D_4, and for Crucian carp, diet D_3.

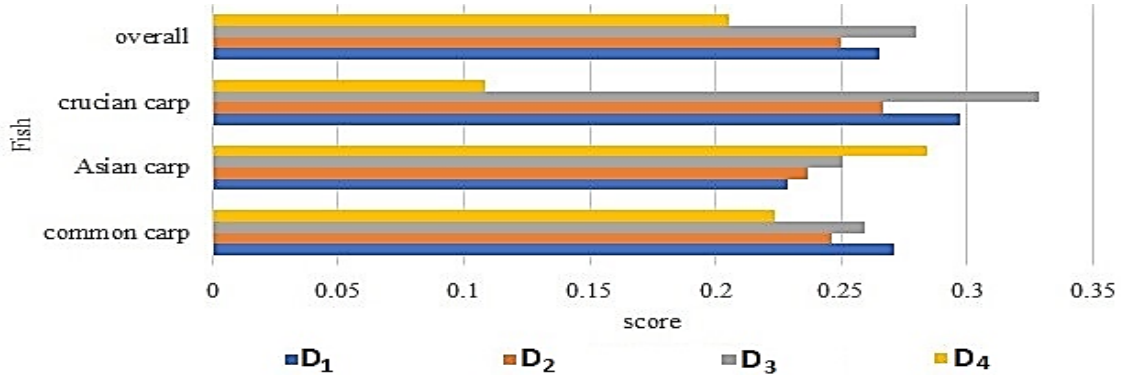


Fig. 6 - Graphic representations of the normalized scores recorded by the four diets for each fish category and globally (overall fish categories)

Investigating the dependence of the dietary preferences of fish on the food component

In order to obtain an assessment of the dependence of the dietary preferences of fish on the main characteristics of each diet, first are calculated the correlations between the scores of the diets for each fish species and the percentages of the components of the diets for the four types of diet. Table 4 gives the values and graphic representations for the main characteristics of the pellets in each diet. The correlations between the scores recorded for each fish species (including all types of fish) and the main characteristics of the four diets used in the experiment are given in Table 4.

Table 4

Correlations between the scores achieved by the three categories of fish and the average category, with each of the four feeding diets

Correlations	gross energy value	ash content	moisture content	dry matter content	bulk density	unit density	crude fat content	durability
Common Carp Score	0.583	-0.96	-0.052	-0.786	-0.222	-0.256	0.969	-0.6
Asian Carp Score	-0.511	0.936	-0.274	0.888	0.474	0.491	-0.723	0.229
Crucian Carp Score	0.859	-0.817	0.321	-0.939	0.066	0.04	0.827	-0.711
Overall score	0.863	-0.792	0.244	-0.891	0.141	0.111	0.858	-0.789

Table 5 shows the results of the univariate linear regression analysis *(Moineagu, et al., 1976; www.statistikindom.com)*. The main results are the coefficient of determination R^2 and the probability of rejecting the regression coefficients, *p* which show whether the respective independent variable (here, the characteristics of the feeding diets) is significant or not for the relative increases of the studied fish species or for all three species together.

Table 5

The main results of the study on the variation of the scores of the diets were applied to the main characteristics of the diets

Fish species	Common Carp		Asian Carp		Crucian Carp		Overall	
Features of the diet	R^2	p-value	R^2	p-value	R^2	p-value	R^2	p-value
gross energy value	0.34	0.417	0.26	0.489	0.74	0.141	0.74	0.137
ash content	0.92	0.04	0.88	0.064	0.67	0.183	0.63	0.208
moisture content	0.00	0.948	0.08	0.726	0.10	0.679	0.06	0.756
dry matter content	0.62	0.214	0.79	0.112	0.88	0.061	0.79	0.109
bulk density	0.05	0.778	0.22	0.526	0.00	0.934	0.02	0.859
unit density	0.07	0.744	0.24	0.509	0.00	0.960	0.01	0.889
crude fat content	0.94	0.031	0.52	0.277	0.68	0.173	0.74	0.142
durability	0.36	0.400	0.05	0.771	0.51	0.289	0.62	0.211

3.2. The average food consumption of all fish involved in the experiment, FCR calculation

An important parameter for raising fish in farms for any farm animals, is the Feed Conversion Ratio (FCR), defined, for example, in *(Wenk, et al., 1980; https://www.aquaneo-techna.com)*.

For the calculation of an estimated value of this performance parameter (quality) of the feeder, have been considered the following experimental data: 100 kg of fish were introduced into the basins at the beginning, whose average initial and final masses were 0.158333 kg and 0.772167 kg, respectively. Taking into account the initial average mass and the number of fish introduced into the basins, the result is an initial number of approximately 631 fish. The total amount of food administered in 120 days was 600 kg, and the estimated final mass of fish was 387.3288 kg. Dividing the amount of food by the final mass of the fish results in an average FCR of 1,549.

DISCUSSION

The results show that each of the three types of fish species registers maximum performance (increase in mass, length, height, and thickness as well as relative density), on one type of diet: *common carp* on diet D_1, *Asian carp* on diet D_4, and the *Crucian carp* on diet D_3. The D_2 diet does not determine maximum performance in any of the three types of fish.

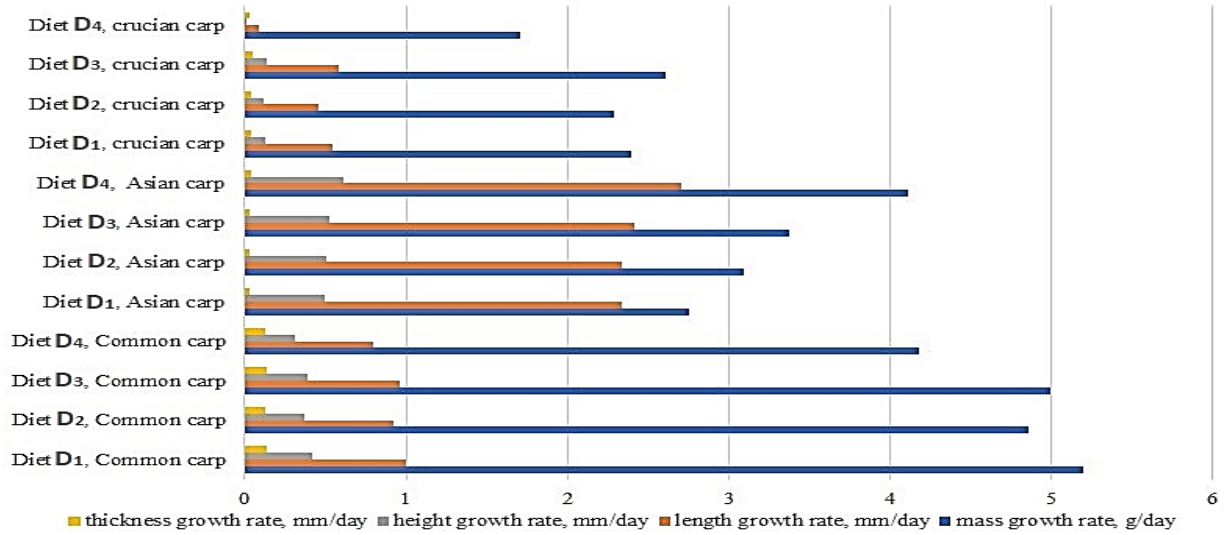


Fig. 7 – The mass growth rates and linear dimensions of the three fish species were monitored in the experiment

The average FCR value for all three species of fish involved in the experiment was 1,549, in accordance with the analyzed literature *(Singh, et al., 2011; Przbyl, et al., 2004; Saleh, et al., 2014)*. This FCR value is in accordance with the specialized literature for fish: Atlantic salmon, 1.0; tilapia, 1.5 to 4.6 for vegetable feeding; farmed salmon, 1.0; and Chinese and Asian carp, 4.9, with vegetable feeding, according to *(Saleh, et al., 2014; Sahzadi, et al., 2006)*. For the common carp, the authors *Przbyl, et al., (2004)*, who followed the evolution of FCR over time, indicate a minimum value of 2.07. The authors indicate that for common carp subjected to four diets, FCR values were between 1.43 and 1.5. For bream, the authors *Singh, et al., (2011)* use the term Feed Conversion Efficiency (FCE), calculated similarly to FCR, and indicate values between 0.37 and 0.76. For the pikeperch, *Dobrota, et al., (2022)* indicate FCR values between 1.56 and 2.55.

CONCLUSIONS

CG1. The tested feeding diets in the preferences of the different fish species is deduced from the scores achieved by each diet, for each of the three fish species and as a whole. Common carp prefer the D_1 diet, Asian carp prefer the D_4 diet, and Crucian carp prefer the D_3 diet. Overall, the preferences of the entire fish population go towards the D_3 diet.

CG2. From the analysis of the correlations between the dietary preferences of the fish (the scores recorded on the four diets) and the composition of the diets, it is observed that for the Common carp, the crude fat content and the energy value are the elements that best explain the growth of the fish both in mass and in length, width, and thickness.

CG4. The results obtained in the examined experiment regarding the cost of growth, used the FCR indicator. The values calculated from the experimental data for the FCR indicator fit very well with the results given in all the literature.

ACKNOWLEDGEMENT

This research was funded by MINISTRY OF AGRICULTURE AND RURAL DEVELOPMENT – ROMANIA - MADR – Sectoral Project ADER 25.2.2./18.07.2023 Vertical aquaponic farm adapted to current climate changes and Ministry of Research, Innovation and Digitalization, through Program 1 - Development of the national research-development system, Subprogram 1.2 - Institutional performance - Projects for financing excellence in RDI, Contract no. 1PFE/30.12.2021.

REFERENCES

[1] Aba, M., (2019), Criteria for choosing the best aquafeed for aquaculture, *Aquaculture in Africa*, https://www.aquacultureinafrica.com/?p=1901;

[2] Abdel-Twwab, M., Ahmad, M.H., Seden, M.E.A., (2008), The effect of feeding various dietary protein levels during growing on growth performance of *Nile tilapia, Oreochromis Niloticus L, 8th International Symposium on Tilapia in Aquaculture*;

[3] Al-Jader, F.A.M., (2012), Evaluation of common carp Cyprinus carpio l. performance fed at three commercial diets, *Mesopotamia Journal of Agriculture, 40, 4,* pp. 20-26;

[4] Ali, B., Rawal, Y. K., (2022), Evaluation of optimum dietary protein requirement for maximum growth of common carp (*Cyprinus carpio*) fingerlings, *Aquaculture Research*;
[5] Alvarez-González, C.A., Moyano-López, F.J., Civera-Cerecedo, R. et al., (2010), Development of digestive enzyme activity in larvae of spotted sand bass *Paralabrax maculatofasciatus* II: Electrophoretic analysis. *Fish Physiol Biochem 36,* pp. 29–37. https://doi.org/10.1007/s10695-008-9276-4;
[6] Byrd, G.V., Jha, B.R., (2022), Relative Growth of Lettuce (*Lactuca sativa*) and Common Carp (*Cyprinus carpio*) in Aquaponics with Different Types of Fish Food, *Water, 14, 3870*, pp. 1-13;
[7] Cârdei, P., Nenciu, F., Ungureanu, N., Pruteanu, M.A., Vlăduț, V., Cujbescu, D., Găgeanu, I., Cristea, O.D., (2021), Using Statistical Modeling for Assessing Lettuce Crops Contaminated with Zn, Correlating Plants Growth Characteristics with the Soil Contamination Levels. *Appl. Sci. 11, 8261*. https://doi.org/10.3390/app11178261;
[8] Ciobotaru, I.E., Nenciu, F., Vaireanu, D.I., (2013), The Electrochemical Generation of Ozone using an Autonomous Photovoltaic System. *Rev. Chim. 64,* pp. 1339–1342;
[9] Craig, S., Helfrich L., (2017), Understanding Fish Nutrition, Feeds, and Feeding, Virginia Cooperative Extension, *College of Agriculture and Life Sciences*, Virginia Tech;
[10] Davison, P., (2011), The specific gravity of mesopelagic fish from the northeastern Pacific Ocean and its implications for acoustic backscatter, *ICES Journal of Marine Science, 68 (10),* pp. 2064–2074;
[11] Dobrota, Gh., (2022), Reproduction and rearing of flounder (*Sander lucioperca, L.,)* in industrial aquaculture systems, Doctoral Thesis, Reproduction and rearing of flounder (Sander lucioperca, L., 1758) in industrial aquaculture systems, Doctoral Thesis*, University "Dunarea de Jos" from Galati*;
[12] Fan, Z., Li, J., Cheng, Z., Zhang, B., Qu, M., Sun, J., Bai, D., Qiao, X., (2015), Protein Sparing Effect of Lipid in Diets for Common Carp (*Cyprinus carpio*), *International Symposium on Energy Science and Chemical Engineering*, pp. 357-368;
[13] Fortes-Silva, R., Kitagawa, A.T., Vazquez, F.J.S., (2016), Dietary self-selection in fish: a new approach to studying fish nutrition and feeding behavior, *Teviewsin Fish Biology and Fisheries, 26 (1),* pp. 39-51;
[14] Găgeanu, I., Cârdei, P., Matache, M., Voicu, Gh., (2019), Researches on the statistical modelling of the process of pelleting biomass, testing classic powder compaction models, *INMATEH Agricultural Engineering Journal, 58, (3),* 119-124, DOI: 10.35633/INMATEH, pp. 59-13;
[15] Hernandez, M., Gasca-Leyva, E., Gressler, P., Krise, D., (2014), Effects of farm and commercial inputs on carp polyculture performance: participatory trial in an experimental field station, *Latin American Journal of Aquatic Research, 42 (3),* pp. 468-476;
[16] Imsland, A.K.D., Berg, M.S., Haugland, G.T., Eliasen, K., (2022), Comparing Body Density of Lumpfish (*Cyclopterus lumpus*) to Different Operational Welfare Indicators. *Fishes 7, 284*. https://doi.org/10.3390/fishes7050284;
[17] Kurćubić, V., Goran, Marković, G., Mašković, P., Miletić, N. Vučićević D., (2017), Basic parameters of the quality of fresh meat of different types of freshwater fish, *Acta Agriculturae Serbica, XXII, 43*, pp. 47-55;
[18] Li, D., Prinyawiwatkul, W., Tan, Y., Luo, Y., Hong, H., (2013), Asian carp: A threat to American lakes, a feast on Chinese tables, *Comprehensive reviews in food science and food safety*, pp. 1-23;
[19] Ljubojević, D., Ćirković, M., Novakov, N., Jovanović, R., Janković, S., Đorđević, V., Trbović, D., (2012). The impact of diet on meat quality of common carp, *Archiva Zootechnica, 15, (3),* 69-78;
[20] Luthada-Raswiswi, R., Mukaratirwa, S., O'Brien, G., (2020), Animal Protein Sources as a Substitute for Fishmeal in Aquaculture Diets: A Systematic Review and Meta-Analysis, Applied Sciences, 11 (9), pp. 1-16;
[21] Voicea, I., Fatu, V., Nenciu, F., Persu, C., Oprescu, R., (2022), Experimental research on bioinsecticide activity obtained by using an oleic extract from dwarf silver fir on some vegetable crops, *Scientific Papers-Series B-Horticulture*, Vol. 66I (1), pp. 575-580;
[22] Miao, W., and Lal, K.K., (2016), Food and Agriculture Organization of the United Nations (FAO) - Documentation of successful practices, Sustainable intensification of aquaculture in the Asia-Pacific region; *Regional office for Asia and the pacific food and agriculture organization of the United Nations Bangkok, (Ed.), Bangkok*, Thailand;
[23] Moineagu, C., Negură, I., Urseanu, V., (1976), *Statistics. Concepts, principles, methods,* Scientific and Encyclopedic Publishing House, Bucharest;

[24] Nandeesha, M.C., Gangadhara, B., Varghese, T.J., Keshavanath, P., (2000), Growth Response and Flesh Quality of Common Carp, *Cyprinus carpio* Fed with High Levels of Nondefatted Silkworm Pupae, *Asian Fisheries Science, 13,* pp. 235-242;

[25] Nenciu, F., Voicea, I., Cocarta, D., Vladut, V., Matache, M., Arsenoaia, V., (2022), Zero-Waste" Food Production System Supporting the Synergic Interaction between Aquaculture and Horticulture, *Sustainability, 14*, 13396;

[26] Nenciu, F., Voicea, I., Stefan, V., Nae, G., Matache, M.G., Milian, G., Arsenoaia, V., (2022), Experimental research on a feed pelletizing equipment designed for small and medium-sized fish farms, *INMATEH - Agricultural Engineering, 67(2),* pp. 374 – 383, DOI: https://doi.org/10.35633/inmateh-67-31;

[27] Nguyen, S.H., Bui, A.T., Le, L.T., Nguyen, T.T.T., de Silva, S.S., (2001), The culture-based fisheries in small, farmer-managed reservoirs in two Provinces of northern Vietnam: an evaluation based on three production cycles. *Aquaculture Research, 32,* pp. 975-990;

[28] Pang, M., Luo, W., Fu, B., Tong, J., (2018), Transcriptomic Profiles of Brain Provide Insights into Molecular Mechanism of Feed Conversion Efficiency in Crucian Carp (Carassius auratus), *International Journal of Molecular Sciences, 19 (3),* 858;

[29] Pitt, R.M., (2023), Carp Cultivation and the Highlands Aquaculture Development Centre, Aiyura, A report prepared for the project TCP/PNG/4503, *Re-establishment of Carp Fishing*, https://www.fao.org/3/R9972E/R9972E00.htm#TOC;

[30] Przbyl, A., (2004), Mazurkiewicz, J. Nutritive value of cereals in feeds for common carp (*Cyprinus carpio L.*), *Czech Journal of Animal Sciences, 49, 7,* pp. 307-314;

[31] Research Contract no.: 5N/07.02.2019PN 19 10 02 03: „ Research on the intensive breeding of fish in a polyculture system and the complex exploitation of aquatic bioresources (plants)", STAGE 1/Phase no. 1: Prospective study on the intensive growth of fish species in a polyculture system, 2019-2022, www.inma.ro;

[32] Sahzadi, T.M., Salim, M., Um-E-Kalsoom Shahzad K., (2006), Growth performance and feed conversion ratio (fcr) of hybrid fingerlings *(catla x labeo rohita*) fed on cottonseed meal, sunflower meal and bone meal, *Pakistan Veterinary Journal, 26, 4,* 163-166;

[33] Saleh, J-H, Al-Dubakel, A.Y., Taher M.M., (2014), Effects of feeding ratio on growth and food conversion rate of common carp Cyprinus carpio reared in floating cages, *Iraqui Journal of Aquaculture, 11 (1),* pp. 15-26;

[34] Shipton, T.A., (2021), Guidelines for feed use in carp and trout production systems in Central Asia and Eastern Europe, *FAO Fisheries and Aquaculture Circular No. 1224. Rome*, FAO. 2021 https://doi.org/10.4060/cb4640en;

[35] Singh, P., Maqsood S., Samoon Phulia V., Danish M., Chalal R.S., (2011), Exogenous supplementation of papain as growth promoter in diet of fingerlings of *Cyprinus carpio*, *International Aquatic Research, 3,* pp. 1-9;

[36] Sultana, S.M., Das, M., Chakraborty S.C. (2001). Effect of feeding frequency on the growth of common carp (Cyprinus carpio L.) fry, *Bangladesh Journal of Fisheries Research, 5 (2),* pp. 149-154;

[37] Sun, Y., Li, B., Zhang, X., Chen, M., Huijuan, T., Yu, X., (2018), Dietary available phosphorus requirement of crucian carp, *Carassius auratus*, *Aquaculture Nutrition,* 24, pp. 3-4;

[38] Velazco-Vargas, J., Tomás-Vidal, A., Hamdan, M., Moyano López, F.J., Jover Cerda, M., Martínez-Llorens S., (2014), Influence of digestible protein levels on growth and feed utilization of juvenile meagre Argyrosomus regius, *Aquaculture Nutrition 20 (5),* 520-531. https://doi.org/10.1111/anu.12105;

[39] Wang, A., Han, G., Lv, F., Yang, W., Huang, J., Yin, X., (2014), Effects of Dietary Lipid Levels on Growth Performance, Apparent Digestibility Coefficients of Nutrients, and Blood Characteristics of Juvenile Crucian Carp (*Carassius auratus gibelio*), *Turkish Journal of Fisheries and Aquatic Sciences, 14,* pp. 1-10;

[40] Wenk, C., Pfirter, H.P., Bickel, H., (1980), Energetic aspects of feed conversion in growing pigs, *Livestock Production Science, 7 (5),* pp. 483-495;

[41] Zahra, A., Jin, C., Sang-Min, L., (2015), Optimal Dietary Protein and Lipid Levels for Growth of Juvenile Israeli *Carp Cyprinus carpio, Fisheries and Aquatic Sciences, 18 (3),* pp. 265-271;

USING STATISTICAL ANALYSIS TO ASSESS THE EFFECTS OF FEEDING PELLETS ON FISH DIETARY PREFERENCES IN AN INTENSIVE POLYCULTURE SYSTEM

/

UTILIZAREA ANALIZEI STATISTICE PENTRU EVALUAREA EFECTELOR PELEȚILOR FURAJERI ASUPRA PREFERINȚELOR ALIMENTARE ALE PEȘTILOR ÎNTR-UN SISTEM INTENSIV DE POLICULTURĂ

Iulian VOICEA[1)], Petru CÂRDEI [1)], Vlad-Nicolae ARSENOAIA [2)], Nicoleta UNGUREANU [3)], Florin NENCIU [1)], Nicoleta VANGHELE *[1)]

[1)] Testing Department, National Institute of Research—Development for Machines and Installations Designed for Agriculture and Food Industry—INMA Bucharest, 013811 Bucharest, Romania;

[2)] Department of Pedotechnics, Faculty of Agriculture, Ion Ionescu de la Brad University of Agricultural Sciences and Veterinary Medicine, 700490, Iasi, Romania;

[3)] Faculty of Biotechnical Systems Engineering, National University of Science and Technology Politehnica Bucharest, 006042 Bucharest, Romania;

E-mail: vanghelelrc@gmail.com

DOI: https://doi.org/10.35633/inmateh-71-70

Keywords: *Nutrition Effects; Fish Diets; Aquaculture; Intensive Polyculture Systems;*

ABSTRACT

The paper proposes a statistical method for assessing the impact of multiple nutritional recipes on fish growth, raised in polyculture systems, a useful tool in selecting diets within small and medium-sized farms. After designing an experimental installation that produces pelletized feed, the study investigated the associations dependent on the feeder composition for three fish species involved in the experiment (Cyprinus carpio, Hypophthalmichthys nobilis and Carassius carassius). The fish relative mass and size variations have been used as performance parameters. The authors also issued hypotheses on the relations created between the studied species and determined the Feed Conversion Ratio.

REZUMAT

Articolul propune o metodă statistică pentru evaluarea impactului mai multor rețete nutritive asupra creșterii peștilor în sisteme de policultură, un instrument util în selectarea dietelor în cadrul fermelor de dimensiuni mici și medii. În urma proiectării unei instalații experimentale specializate pentru producția de furaje peletizate, studiul a investigat asocierile dependente de compoziția furajelor pentru trei specii de pești (Cyprinus carpio, Hypophthalmichthys nobilis și Carassius carassius). Pentru evaluarea performanței, s-au folosit ca parametrii masele relative și creșterea dimensiunii peștilor. Autorii au emis și câteva ipoteze cu privire la legătura creată între structura speciilor studiate și caracteristicile de bază ale dietelor lor preferate. și au calculat Rata de Conversie a Furajelor.

INTRODUCTION

Polyculture is the technology of growing a variety of aquatic species in the same pond, with the aim of improving overall production. This is accomplished by increasing the trophic and spatial niches, by raising different fish species that have complementary feeding preferences. Therefore, using polyculture practices, farmers could increase the production per unit area and successfully contribute to improving the aquatic environment. The presented results can be illustrated in the formulation of an experimental plan to study the dynamics of fish populations in aquaculture, following the systemic description of the phenomenon.

The paper considered a series of general aspects regarding fish feeding, that were presented in a research project (*Research Contract 5N/07.02.2019*), where the essential problems of fish feeding were also highlighted such as: the basic components (proteins, lipids, carbohydrates, vitamins, and minerals), and the connection between energy and proteins. Types of feeding, rate, frequency, and periods of feeding, automatic feeding systems were also addressed in (*Li, et al., 2013; FAO, 2016*).

A study that evaluated feed conversion and efficiency calculation (*Abdel-Twwab, et al., 2008*), corroborated the soundness of the feeding and growing systems, all of which are the main elements of the aquaculture management systems. The authors stated that most fish breeders use complete diets, usually made up of the following components and percentage ranges: protein, 18-50%; lipids, 10-25%; carbohydrates, 15-20%; ash, <8.5%; phosphorus, <1.5%; water, <10%; and traces of vitamins and minerals.

The problem of finding optimal diets for Israeli carp is presented in the paper of *Zahra, et al., (2015)* finally recommending a percentage of 40% proteins with 14% lipids. A research done by *Ali et al., (2022)* present the results of preliminary research on the optimal diet of carp. Since for the client the quality of the fish meat is highly important, the problem of the fish diet is also researched by the authors *Ljubojević, et al., (2022)*, who give several feeding recipes, including for carp. Similar problems were researched in other studies *(Shipton, et al., 2022; Al-Jader, et al., 2012; Fan, et al., 2015; Nandeesha, et al., 2000)*. The effects of feeding frequency on carp weight gain are presented in the work of *Ali, et al., (2022)*. The nutritional value of cereals in the diet of Common carp is the topic addressed by the authors *Sultana et al., (2001)*, considering that the local production of quality feeder can bring considerable benefits to the fish farming industry. A concentration of 99.3 g/kg of lipids is found optimal for breeding Crucian carp by the authors *Wang et al., (2014),* while other studies obtained similar results *(Przbyl, et al., 2004; Sun, et al., 2018)*. A research paper presents several problems with the Asian carp, associated with adaptation to the American continent (*Li, et al., 2013)*. The economic value generated by the Asian carp is emphasized, but so is the aggressiveness with which it imposes itself on the native carp. In *FAO, (2016),* several types of feeding for aquaculture fish are proposed. Among the nutritional components indicated by *FAO*, there are GOC, soybean meal, polished rice, fish meal, vegetable oil, vitamins, and minerals. The authors *Abdel-Twwab, et al., (2008*), discuss the effects of various protein diets on Nile tilapia. Effects of farm and commercial inputs on carp polyculture performance are analyzed in the paper of *Hernandez et al., (2022)*, considering the use of additives in feeder recipes.

The formulation of artificial diets for juvenile fish is significantly influenced by various factors, one of the most important being the larvae's capacity to effectively digest the essential nutrients *(Ali, et al., 2022)*. Several studies have undertaken a qualitative exploration of fish nutrition, analyzing in detail aspects related to the real efficiency of the feeder. For example, a research study that evaluated the effect of digestible protein levels in experimental diets for meagre (*Argyrosomus regius*) found that optimal digestible protein intake according to the ECR for rearing juvenile meagre was recorded in 0.8 g DP/100 g fish and day. A substantial literature on the problem of palletization and automation of feed administration in aquaculture systems can be found in various papers such as, *Gageanu, et al., (2019); Voicea, et al., (2021); Nenciu, et al., (2022); Matache, et al., (2021)*. Aquaculture developed under zero-waste conditions was addressed in *Nenciu, et al., (2022)*, where several innovative methods of sludge disposal and ecological food production were identified. The use of some aquaculture plants in fish-feeding diets is also a problem extensively addressed in the literature *(Voicea, et al., 2022)*. Other researchers have as objectives the optimal harvest ages of farmed fish. As an example, *Nguyen et al., (2001),* states that the common carp is optimally harvested at a mass between 0.3 and 0.7 kg. In the experimental process, the common carp was harvested at an average weight of 0.824 kg. In *Pitt et al., (2022)*, it is shown, for example, that carp is harvested at 200 g - 500 g or more (luxury specimens) in Indonesia and at 800 g in Japan, where it grows from April to autumn. The results of using vegetable diets, mixed diets, and synthetic diets are comparatively researched *(Ljubojević, et al., 2022; Byrd, et al., 2022; Kurćubić, et al., 2017; Dobrota, et al., 2022)*. The present study aims to explore the dietary preferences of three fish species (common carp, Asian carp, and Crucian carp) grown in an intensive polyculture system, using statistical analysis. The common challenge addressed involves the difficulty of quantifying the growth rate solely through fish measurements. This difficulty arises due to the varying feeding characteristics of different species and their distinct habitats within the basin. In addition, the introduction of varying numbers of fish from each species adds more complexity to the evaluation process.

MATERIALS AND METHODS

The experiments were conducted in the period 2019 - 2022 within INMA Bucharest institute, utilizing two fishing ponds of different sizes, employing a polyculture approach for fish farming. The large fishing pond, ICP 1 (Figure 1) is a construction made of reinforced concrete with a thickness of 300 mm, a width of 14.4 m, a length of 57 m, and a depth of 4.6 m.



Fig. 1 - Basin no. 1 (ICP1), covered pool and the location with details, the inside of the pool with water quality maintenance devices. The coordinates are 44º 30' 9.51'' N, 26º 4' 21.94'' E

The feeding system is composed of 3 feeders equipped with an auger and a pelletized feed disperser with a diameter between 2 and 10 mm, ensuring automated feeding by sequentially programming the dispersion on the surface of the pool. Two Osaga ORV Aerators were used to provide the optimum aeration-oxygenation level for the water in the fishing tank. The second pond (Figure 2) is an outdoor pilot basin, having a total capacity of 10,000 l. The basin was equipped with a supply system based on green energy (a hybrid wind-photovoltaic system).



Fig. 2 - Basin no. 2 (ICP 2), open fish-growing system

Fish species employed in the experiment and their dietary regime

Three species of fish were introduced into each of the two experimental basins: common carp (*Cyprinus carpio*), Asian carp (*Hypophthalmichthys nobilis*), and Crucian carp (*Carassius carassius*). The three fish species were raised together in the ponds. A total of 200 kg of juvenile fish from the three species has been introduced into each pool: 120 kg of common carp, 60 kg of Asian carp, and 20 kg of Crucian carp. At each such loading, one of the feeding diets D1, D2, D3, and D4 were administered separately, each consisting of 600 kg of pellets per pool, administered during four months of experimentation.

Feeder production using a simple pelletizing equipment

The production of the feeding pellets was carried out internally, using an extrusion equipment, designed and executed to be easily used by small and medium farms *(Nenciu, et al., 2022)*. Figure 3 presents the equipment used to pelletize fish feeder.

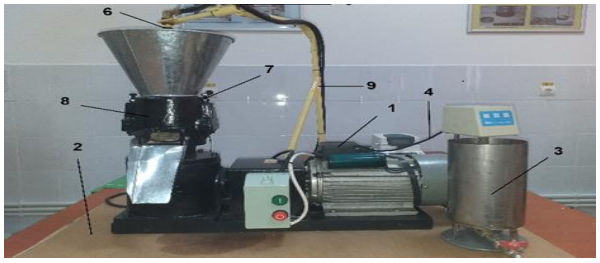


Fig. 3 - Development of a simple equipment design for pellet extrusion in fish feeder production

1 – steam generator; 2 – working stand; 3 – tank for storing blending solutions; 4 – mobile hose; 5 – pipe; 6 – adjusting nozzle; 7 – feeding hopper; 8 – electric heating belt; 9 – arm used to adjust the spraying position;

Four experiments were carried out in different time periods in the two pools, each of them starting with the same number of fish and administering the same amount of food, however in each experiment different type of diets were used: D_1, D_2, D_3, and D_4. The average initial and final masses for each experimental series were recorded. The length, height, and average thickness of the fish of each species have also been recorded. The four feeding recipes (diets) were structurally analyzed, with the data recorded in the sheets (energy value, ash content, moisture content, dry substance content, bulk density, unit density, crude fat content, and pellet durability obtained). The initial characteristics of the fish introduced into the pool, in each experiment, can be found in Table 1.

Table 1

Initial characteristics of fish

Fish species	Initial mass kg	Initial length cm	Initial height cm	Initial thickness cm
Common carp	0.200	16	6.40	1.10
Asian carp	0.150	20	4.20	1.60
Crucian carp	0.125	16	4.48	1.75

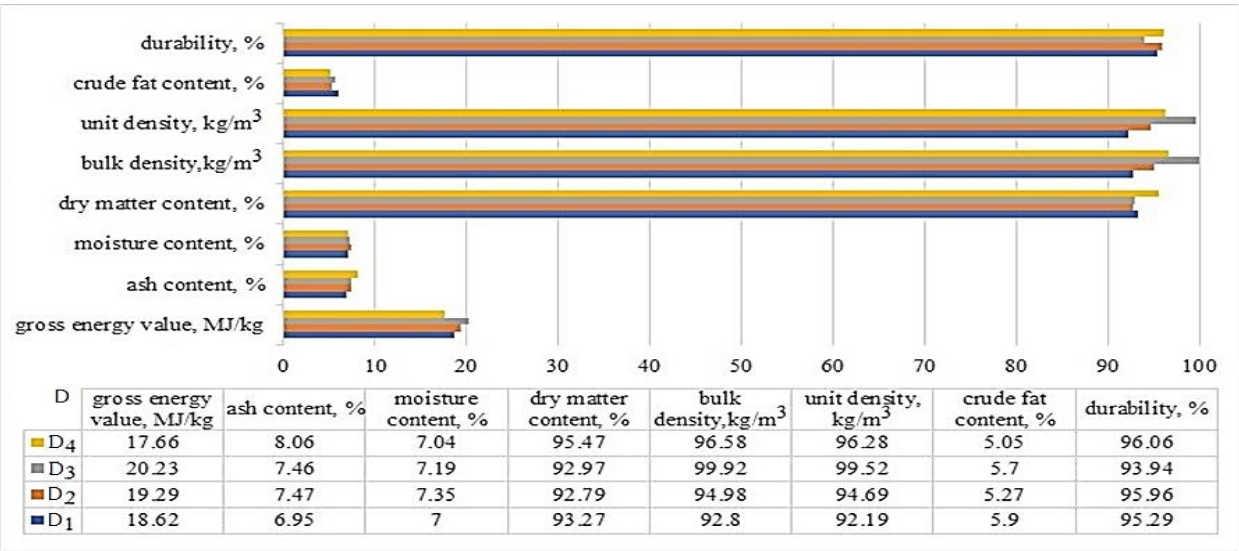
The characteristics of the fish determined at the end of the experiments can be found in Table 2, while the impact of the fish diets (for the four tested recipes) can be seen in Figure 4.

Table 2

Final characteristics of the fish in the two basins

Fish species	Basin	Diets	Mass kg	Length cm	Height cm	Thickness cm
Common carp	Basin 1	Diet 1	0.822	28	11.34	2.7
		Diet 2	0.785	27	10.94	2.5
		Diet 3	0.81	28	11.14	2.7
		Diet 4	0.705	26	10.4	2.65
	Basin 2	Diet 1	0.826	28	11.54	2.8
		Diet 2	0.782	27	10.81	2.72
		Diet 3	0.789	27	10.98	2.75
		Diet 4	0.698	25	9.85	2.57
Asian carp	Basin 1	Diet 1	0.48	48	10.08	1.89
		Diet 2	0.515	46	9.74	1.92
		Diet 3	0.544	47	9.98	1.97
		Diet 4	0.638	51	11.05	2.03
	Basin 2	Diet 1	0.48	48	10.1	1.91
		Diet 2	0.527	50	10.87	1.94
		Diet 3	0.566	51	11.08	1.99
		Diet 4	0.648	54	11.95	2.05
Crucian carp	Basin 1	Diet 1	0.403	22	5.94	2.26
		Diet 2	0.395	21	5.74	2.18
		Diet 3	0.426	23	6.21	2.28
		Diet 4	0.328	17	4.6	2.06
	Basin 2	Diet 1	0.421	23	6.04	2.28
		Diet 2	0.404	22	5.96	2.25
		Diet 3	0.45	23	6.01	2.32
		Diet 4	0.331	17	4.71	2.06

The main characteristics of the pellets in each of the four diets can be seen in figure 4.



D	gross energy value, MJ/kg	ash content, %	moisture content, %	dry matter content, %	bulk density,kg/m^3	unit density, kg/m^3	crude fat content, %	durability, %
D_4	17.66	8.06	7.04	95.47	96.58	96.28	5.05	96.06
D_3	20.23	7.46	7.19	92.97	99.92	99.52	5.7	93.94
D_2	19.29	7.47	7.35	92.79	94.98	94.69	5.27	95.96
D_1	18.62	6.95	7	93.27	92.8	92.19	5.9	95.29

Fig. 4 - The main characteristics of the pellets in each of the four diets

In the growing conditions described above and applying the described feeding diet, at the final measurement performed by random selection of a batch of fish, it was found that:

1) the fat content for the common carp species was 22.5% compared to the normal standard, which would be somewhere around 13-15% (with normal growth with controlled feeding, but also body growth would be lower by 10-12 % compared to what was obtained in the experiments referred to);

2) the fat content in Asian carp species was 12.5%, compared to the normal standard, which is 10% in a normal fish feed, but in this case, the body weight is 20% lower than what have been obtained in experimental

research. The Asian species have assimilated very well the intensive feeding without taking a large surplus of fat;
3) the crucian carp had a 20% higher fat intake than the normal standard, which would be somewhere around 10-12% of its body mass.
In essence, the carp and the crucian carp ate excessively and, as a result, at the evaluation, it could be seen that their livers were covered in fat. The working statistical evaluation method was based on the given equations (1)-(10). To highlight the performances of the four types of fish-feeding diets, the relative estimators have been be used:
- the average relative increase in fish mass:

$$\delta m_{rel}(p,b,R) = \frac{m(p,b,R) - m_0(p,b)}{m_0(p,b)} \cdot 100 \quad (1)$$

where $m(p,b,R)$ is the average final mass (after four months of growth) of the fish, *p* is the type of fish (common carp, Asian carp, and Crucian carp), b is the rearing pool (1 or 2), $m_0(p,b)$ is the average initial mass of the fish, and $\delta m_{rel}(p,b,R)$ is the relative average mass growth of the fish, which is expressed in percentages, R being the type of feeding diet used;
- the average relative increase in the length of the fish:

$$\delta L_{rel}(p,b,R) = \frac{L(p,b,R) - L_0(p,b)}{L_0(p,b)} \cdot 100 \quad (2)$$

where $L(p,b,R)$ is the average final length (after four months of growth) of the fish, $L_0(p,b)$ is the average initial length of the fish, and $\delta L_{rel}(p,b,R)$ is the increase in length relative to the average of all fish, expressed in percentages;
- the average relative increase in the height of the fish:

$$\delta h_{rel}(p,b,R) = \frac{h(p,b,R) - h_0(p,b)}{h_0(p,b)} \cdot 100 \quad (3)$$

where $h(p,b,R)$ is the average final height (after four months of growth) of the fish, $h_0(p,b)$ is the average initial height of the fish, and $\delta h_{rel}(p,b,R)$ is the increase in height relative average of the fish, which is expressed in percentages, R being the type of feeding recipe used;
- the average relative increase in the thickness of the fish:

$$\delta g_{rel}(p,b,R) = \frac{g(p,b,R) - g_0(p,b)}{g_0(p,b)} \cdot 100 \quad (4)$$

where $g(p,b,R)$ is the average final thickness (after four months of growth) of the fish, $g_0(p,b)$is the average initial thickness of the fish, and $\delta g_{rel}(p,b,R)$ is the increase in the average thickness relative to the fish, which is expressed in percentages.
A measure of the approximate volume growth of fish can be formulated, according to the following formula:

$$\delta V_{rel}(p,b,R) = \frac{V(p,b,R) - V_0(p,b)}{V_0(p,b)} \cdot 100 \quad (5)$$

where:

$$V_0(p,b) = L_0(p,b) \cdot h_0(p,b) \cdot g_0(p,b) \quad (6)$$

and

$$V(p,b) = L(p,b) \cdot h(p,b) \cdot g(p,b) \quad (7)$$

Similarly, the approximate density before the monitoring time interval can be defined according to the formula (8)

$$\rho_0(p,b) = \frac{m_0(p,b)}{V_0(p,b)} \quad (8)$$

respectively, the approximate density at the end of the experimental time interval (of treatment application or monitoring):

$$\rho(p,b,R) = \frac{m(p,b,R)}{V(p,b,R)} \quad (9)$$

A relative increase in density can be defined as follows:

$$\delta\rho(p,b,R) = \frac{\rho(p,b,R) - \rho_0(p,b)}{\rho_0(p,b)} \cdot 100 \quad (10)$$

Since in the two pools, the feeding recipes and medical treatments were identical, the study continued with the average values per pool. In this way, in formulas (1)-(10), the variable b disappears, and the functions become dependent on one or two variables, p (type of fish) and R (type of treatment).

RESULTS

The equations for calculating the increases in mass, length, height, and thickness, and, subsequent calculations of the density of the fish, allow some graphic representations that lead to some immediate conclusions. In Figure 5, the graphics depict the relative increases, in accordance with the experimental data and the defining equations (1)-(10), related to the type of diet (or recipe) administered. Diets are marked with D_1, D_2, D_3, and D_4. The calculations were performed by averaging over the two aquaculture basins.

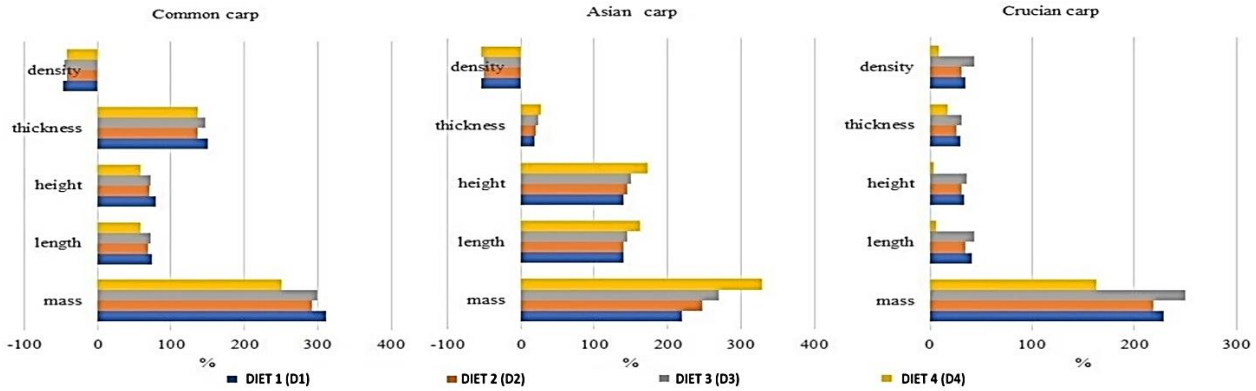


Fig. 5 - The relative increases in mass, length, height, width, and density of fish

From Figure 5, can be drawn the following results:

R1) the highest *relative mass increase* occurs as follows: in the common carp, it corresponds to the D_1 recipe and reaches the value of 312%; for the Asian carp, it corresponds to the D_4 diet and reaches the value of 329%; while for the Crucian carp, it corresponds to the D_3 diet and reaches the value of 250%;

R2) the highest value of the *relative increase in length* occurs as follows: for the common carp, it corresponds to the D_1 diet, with a value of 75% (with a small difference from the D_3 diet, with a value of 72%), for the Asian carp, it corresponds to the D_4 diet, with a value of 162.5%, and for the Crucian carp, it corresponds to the D_3 diet, with a percentage of 43.75%;

R3) the highest *relative increase in height* occurs in the common carp for the D_1 diet, with a value of 78.75%, for the Asian carp for the D_4 diet, with a value of 173.81%, and for the crucian carp for the D_3 diet, with a value of 36.38%;

R4) the *relative increase in width* (or *thickness*), with the highest intensity, occurs as follows: for the common carp for the D_1 diet, with a value of 150%, for the Asian carp for the D_4 diet, with a value of 27.5%, and for the Crucian carp for the D_3 diet, with a value of 31.43%;

R5) the *increase relative to the approximate density* of fish, with the highest magnitude, occurs as follows: for the common carp for the D_1 diet, with a value of -47.32%, for the Asian carp for the D_1 diet, with a percentage of -53.26% (a very small difference compared to the D_4 treatment, with the percentage of 53.22%), and for the Crucian carp for the D_3 diet, with a value of 43.67%.

R6) combining the performances of each diet for each category of fish, it can be observed that the best score is recorded: for common carp, diet D_1, Asian carp, diet D_4, and for Crucian carp, diet D_3.

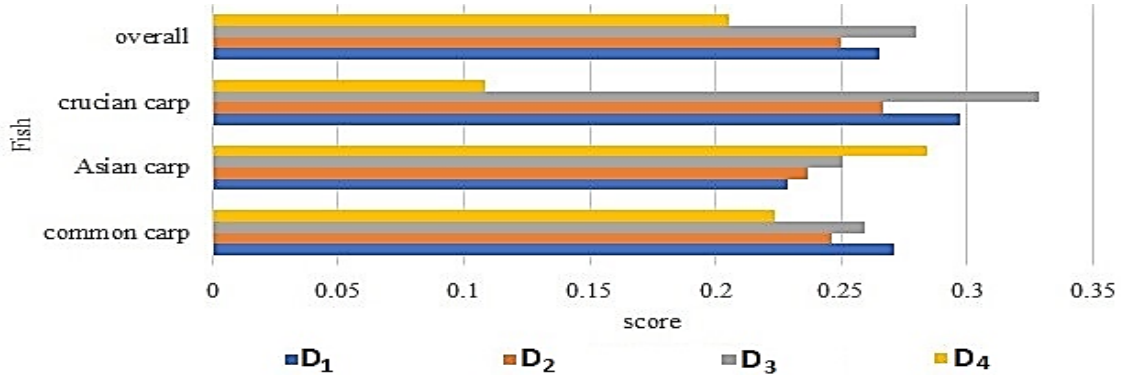


Fig. 6 - Graphic representations of the normalized scores recorded by the four diets for each fish category and globally (overall fish categories)

Investigating the dependence of the dietary preferences of fish on the food component

In order to obtain an assessment of the dependence of the dietary preferences of fish on the main characteristics of each diet, first are calculated the correlations between the scores of the diets for each fish species and the percentages of the components of the diets for the four types of diet. Table 4 gives the values and graphic representations for the main characteristics of the pellets in each diet. The correlations between the scores recorded for each fish species (including all types of fish) and the main characteristics of the four diets used in the experiment are given in Table 4.

Table 4

Correlations between the scores achieved by the three categories of fish and the average category, with each of the four feeding diets

Correlations	gross energy value	ash content	moisture content	dry matter content	bulk density	unit density	crude fat content	durability
Common Carp Score	0.583	-0.96	-0.052	-0.786	-0.222	-0.256	0.969	-0.6
Asian Carp Score	-0.511	0.936	-0.274	0.888	0.474	0.491	-0.723	0.229
Crucian Carp Score	0.859	-0.817	0.321	-0.939	0.066	0.04	0.827	-0.711
Overall score	0.863	-0.792	0.244	-0.891	0.141	0.111	0.858	-0.789

Table 5 shows the results of the univariate linear regression analysis *(Moineagu, et al., 1976; www.statistikindom.com)*. The main results are the coefficient of determination R^2 and the probability of rejecting the regression coefficients, *p* which show whether the respective independent variable (here, the characteristics of the feeding diets) is significant or not for the relative increases of the studied fish species or for all three species together.

Table 5

The main results of the study on the variation of the scores of the diets were applied to the main characteristics of the diets

Fish species	Common Carp		Asian Carp		Crucian Carp		Overall	
Features of the diet	R^2	p-value	R^2	p-value	R^2	p-value	R^2	p-value
gross energy value	0.34	0.417	0.26	0.489	0.74	0.141	0.74	0.137
ash content	0.92	0.04	0.88	0.064	0.67	0.183	0.63	0.208
moisture content	0.00	0.948	0.08	0.726	0.10	0.679	0.06	0.756
dry matter content	0.62	0.214	0.79	0.112	0.88	0.061	0.79	0.109
bulk density	0.05	0.778	0.22	0.526	0.00	0.934	0.02	0.859
unit density	0.07	0.744	0.24	0.509	0.00	0.960	0.01	0.889
crude fat content	0.94	0.031	0.52	0.277	0.68	0.173	0.74	0.142
durability	0.36	0.400	0.05	0.771	0.51	0.289	0.62	0.211

3.2. The average food consumption of all fish involved in the experiment, FCR calculation

An important parameter for raising fish in farms for any farm animals, is the Feed Conversion Ratio (FCR), defined, for example, in *(Wenk, et al., 1980; https://www.aquaneo-techna.com)*.

For the calculation of an estimated value of this performance parameter (quality) of the feeder, have been considered the following experimental data: 100 kg of fish were introduced into the basins at the beginning, whose average initial and final masses were 0.158333 kg and 0.772167 kg, respectively. Taking into account the initial average mass and the number of fish introduced into the basins, the result is an initial number of approximately 631 fish. The total amount of food administered in 120 days was 600 kg, and the estimated final mass of fish was 387.3288 kg. Dividing the amount of food by the final mass of the fish results in an average FCR of 1,549.

DISCUSSION

The results show that each of the three types of fish species registers maximum performance (increase in mass, length, height, and thickness as well as relative density), on one type of diet: *common carp* on diet D_1, *Asian carp* on diet D_4, and the *Crucian carp* on diet D_3. The D_2 diet does not determine maximum performance in any of the three types of fish.

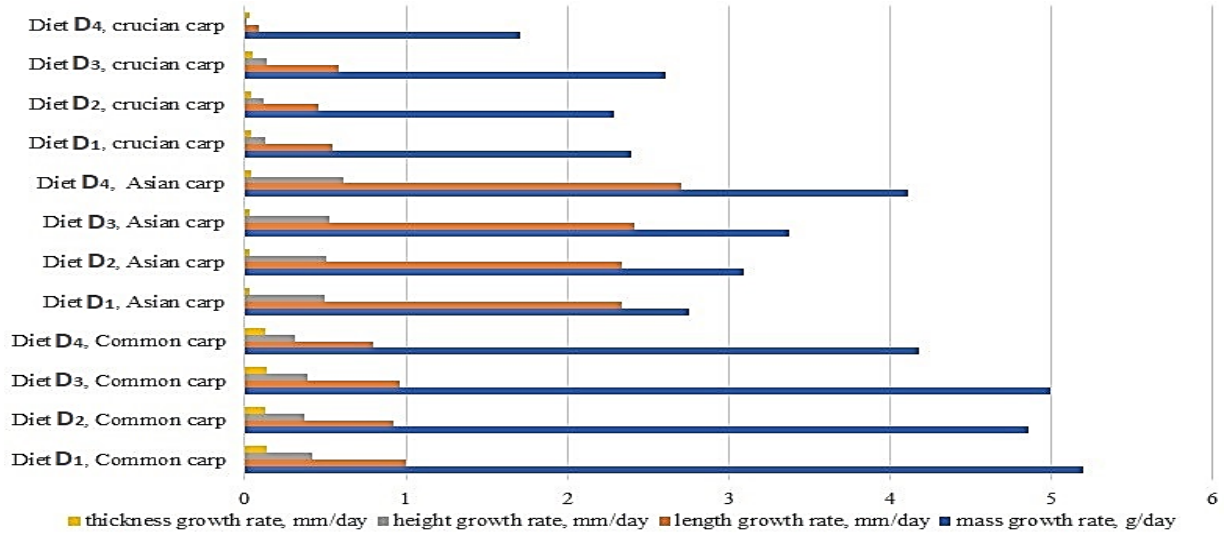


Fig. 7 – The mass growth rates and linear dimensions of the three fish species were monitored in the experiment

The average FCR value for all three species of fish involved in the experiment was 1,549, in accordance with the analyzed literature *(Singh, et al., 2011; Przbyl, et al., 2004; Saleh, et al., 2014)*. This FCR value is in accordance with the specialized literature for fish: Atlantic salmon, 1.0; tilapia, 1.5 to 4.6 for vegetable feeding; farmed salmon, 1.0; and Chinese and Asian carp, 4.9, with vegetable feeding, according to *(Saleh, et al., 2014; Sahzadi, et al., 2006)*. For the common carp, the authors *Przbyl, et al., (2004)*, who followed the evolution of FCR over time, indicate a minimum value of 2.07. The authors indicate that for common carp subjected to four diets, FCR values were between 1.43 and 1.5. For bream, the authors *Singh, et al., (2011)* use the term Feed Conversion Efficiency (FCE), calculated similarly to FCR, and indicate values between 0.37 and 0.76. For the pikeperch, *Dobrota, et al., (2022)* indicate FCR values between 1.56 and 2.55.

CONCLUSIONS

CG1. The tested feeding diets in the preferences of the different fish species is deduced from the scores achieved by each diet, for each of the three fish species and as a whole. Common carp prefer the D_1 diet, Asian carp prefer the D_4 diet, and Crucian carp prefer the D_3 diet. Overall, the preferences of the entire fish population go towards the D_3 diet.

CG2. From the analysis of the correlations between the dietary preferences of the fish (the scores recorded on the four diets) and the composition of the diets, it is observed that for the Common carp, the crude fat content and the energy value are the elements that best explain the growth of the fish both in mass and in length, width, and thickness.

CG4. The results obtained in the examined experiment regarding the cost of growth, used the FCR indicator. The values calculated from the experimental data for the FCR indicator fit very well with the results given in all the literature.

ACKNOWLEDGEMENT

This research was funded by MINISTRY OF AGRICULTURE AND RURAL DEVELOPMENT – ROMANIA - MADR – Sectoral Project ADER 25.2.2./18.07.2023 Vertical aquaponic farm adapted to current climate changes and Ministry of Research, Innovation and Digitalization, through Program 1 - Development of the national research-development system, Subprogram 1.2 - Institutional performance - Projects for financing excellence in RDI, Contract no. 1PFE/30.12.2021.

REFERENCES

[1] Aba, M., (2019), Criteria for choosing the best aquafeed for aquaculture, *Aquaculture in Africa*, https://www.aquacultureinafrica.com/?p=1901;

[2] Abdel-Twwab, M., Ahmad, M.H., Seden, M.E.A., (2008), The effect of feeding various dietary protein levels during growing on growth performance of *Nile tilapia, Oreochromis Niloticus L, 8th International Symposium on Tilapia in Aquaculture*;

[3] Al-Jader, F.A.M., (2012), Evaluation of common carp Cyprinus carpio l. performance fed at three commercial diets, *Mesopotamia Journal of Agriculture, 40, 4,* pp. 20-26;

[4] Ali, B., Rawal, Y. K., (2022), Evaluation of optimum dietary protein requirement for maximum growth of common carp (*Cyprinus carpio*) fingerlings, *Aquaculture Research*;
[5] Alvarez-González, C.A., Moyano-López, F.J., Civera-Cerecedo, R. et al., (2010), Development of digestive enzyme activity in larvae of spotted sand bass *Paralabrax maculatofasciatus* II: Electrophoretic analysis. *Fish Physiol Biochem 36,* pp. 29–37. https://doi.org/10.1007/s10695-008-9276-4;
[6] Byrd, G.V., Jha, B.R., (2022), Relative Growth of Lettuce (*Lactuca sativa*) and Common Carp (*Cyprinus carpio*) in Aquaponics with Different Types of Fish Food, *Water, 14, 3870*, pp. 1-13;
[7] Cârdei, P., Nenciu, F., Ungureanu, N., Pruteanu, M.A., Vlăduț, V., Cujbescu, D., Găgeanu, I., Cristea, O.D., (2021), Using Statistical Modeling for Assessing Lettuce Crops Contaminated with Zn, Correlating Plants Growth Characteristics with the Soil Contamination Levels. *Appl. Sci. 11, 8261*. https://doi.org/10.3390/app11178261;
[8] Ciobotaru, I.E., Nenciu, F., Vaireanu, D.I., (2013), The Electrochemical Generation of Ozone using an Autonomous Photovoltaic System. *Rev. Chim. 64,* pp. 1339–1342;
[9] Craig, S., Helfrich L., (2017), Understanding Fish Nutrition, Feeds, and Feeding, Virginia Cooperative Extension, *College of Agriculture and Life Sciences*, Virginia Tech;
[10] Davison, P., (2011), The specific gravity of mesopelagic fish from the northeastern Pacific Ocean and its implications for acoustic backscatter, *ICES Journal of Marine Science, 68 (10),* pp. 2064–2074;
[11] Dobrota, Gh., (2022), Reproduction and rearing of flounder (*Sander lucioperca, L.,)* in industrial aquaculture systems, Doctoral Thesis, Reproduction and rearing of flounder (Sander lucioperca, L., 1758) in industrial aquaculture systems, Doctoral Thesis*, University "Dunarea de Jos" from Galati*;
[12] Fan, Z., Li, J., Cheng, Z., Zhang, B., Qu, M., Sun, J., Bai, D., Qiao, X., (2015), Protein Sparing Effect of Lipid in Diets for Common Carp (*Cyprinus carpio*), *International Symposium on Energy Science and Chemical Engineering*, pp. 357-368;
[13] Fortes-Silva, R., Kitagawa, A.T., Vazquez, F.J.S., (2016), Dietary self-selection in fish: a new approach to studying fish nutrition and feeding behavior, *Teviewsin Fish Biology and Fisheries, 26 (1),* pp. 39-51;
[14] Găgeanu, I., Cârdei, P., Matache, M., Voicu, Gh., (2019), Researches on the statistical modelling of the process of pelleting biomass, testing classic powder compaction models, *INMATEH Agricultural Engineering Journal, 58, (3),* 119-124, DOI: 10.35633/INMATEH, pp. 59-13;
[15] Hernandez, M., Gasca-Leyva, E., Gressler, P., Krise, D., (2014), Effects of farm and commercial inputs on carp polyculture performance: participatory trial in an experimental field station, *Latin American Journal of Aquatic Research, 42 (3),* pp. 468-476;
[16] Imsland, A.K.D., Berg, M.S., Haugland, G.T., Eliasen, K., (2022), Comparing Body Density of Lumpfish (*Cyclopterus lumpus*) to Different Operational Welfare Indicators. *Fishes 7, 284*. https://doi.org/10.3390/fishes7050284;
[17] Kurćubić, V., Goran, Marković, G., Mašković, P., Miletić, N. Vučićević D., (2017), Basic parameters of the quality of fresh meat of different types of freshwater fish, *Acta Agriculturae Serbica, XXII, 43*, pp. 47-55;
[18] Li, D., Prinyawiwatkul, W., Tan, Y., Luo, Y., Hong, H., (2013), Asian carp: A threat to American lakes, a feast on Chinese tables, *Comprehensive reviews in food science and food safety*, pp. 1-23;
[19] Ljubojević, D., Ćirković, M., Novakov, N., Jovanović, R., Janković, S., Đorđević, V., Trbović, D., (2012). The impact of diet on meat quality of common carp, *Archiva Zootechnica, 15, (3),* 69-78;
[20] Luthada-Raswiswi, R., Mukaratirwa, S., O'Brien, G., (2020), Animal Protein Sources as a Substitute for Fishmeal in Aquaculture Diets: A Systematic Review and Meta-Analysis, Applied Sciences, 11 (9), pp. 1-16;
[21] Voicea, I., Fatu, V., Nenciu, F., Persu, C., Oprescu, R., (2022), Experimental research on bioinsecticide activity obtained by using an oleic extract from dwarf silver fir on some vegetable crops, *Scientific Papers-Series B-Horticulture*, Vol. 66I (1), pp. 575-580;
[22] Miao, W., and Lal, K.K., (2016), Food and Agriculture Organization of the United Nations (FAO) - Documentation of successful practices, Sustainable intensification of aquaculture in the Asia-Pacific region; *Regional office for Asia and the pacific food and agriculture organization of the United Nations Bangkok, (Ed.), Bangkok*, Thailand;
[23] Moineagu, C., Negură, I., Urseanu, V., (1976), *Statistics. Concepts, principles, methods,* Scientific and Encyclopedic Publishing House, Bucharest;

[24] Nandeesha, M.C., Gangadhara, B., Varghese, T.J., Keshavanath, P., (2000), Growth Response and Flesh Quality of Common Carp, *Cyprinus carpio* Fed with High Levels of Nondefatted Silkworm Pupae, *Asian Fisheries Science, 13,* pp. 235-242;

[25] Nenciu, F., Voicea, I., Cocarta, D., Vladut, V., Matache, M., Arsenoaia, V., (2022), Zero-Waste" Food Production System Supporting the Synergic Interaction between Aquaculture and Horticulture, *Sustainability, 14*, 13396;

[26] Nenciu, F., Voicea, I., Stefan, V., Nae, G., Matache, M.G., Milian, G., Arsenoaia, V., (2022), Experimental research on a feed pelletizing equipment designed for small and medium-sized fish farms, *INMATEH - Agricultural Engineering, 67(2),* pp. 374 – 383, DOI: https://doi.org/10.35633/inmateh-67-31;

[27] Nguyen, S.H., Bui, A.T., Le, L.T., Nguyen, T.T.T., de Silva, S.S., (2001), The culture-based fisheries in small, farmer-managed reservoirs in two Provinces of northern Vietnam: an evaluation based on three production cycles. *Aquaculture Research, 32,* pp. 975-990;

[28] Pang, M., Luo, W., Fu, B., Tong, J., (2018), Transcriptomic Profiles of Brain Provide Insights into Molecular Mechanism of Feed Conversion Efficiency in Crucian Carp (Carassius auratus), *International Journal of Molecular Sciences, 19 (3),* 858;

[29] Pitt, R.M., (2023), Carp Cultivation and the Highlands Aquaculture Development Centre, Aiyura, A report prepared for the project TCP/PNG/4503, *Re-establishment of Carp Fishing*, https://www.fao.org/3/R9972E/R9972E00.htm#TOC;

[30] Przbyl, A., (2004), Mazurkiewicz, J. Nutritive value of cereals in feeds for common carp (*Cyprinus carpio L.*), *Czech Journal of Animal Sciences, 49, 7,* pp. 307-314;

[31] Research Contract no.: 5N/07.02.2019PN 19 10 02 03: „ Research on the intensive breeding of fish in a polyculture system and the complex exploitation of aquatic bioresources (plants)", STAGE 1/Phase no. 1: Prospective study on the intensive growth of fish species in a polyculture system, 2019-2022, www.inma.ro;

[32] Sahzadi, T.M., Salim, M., Um-E-Kalsoom Shahzad K., (2006), Growth performance and feed conversion ratio (fcr) of hybrid fingerlings *(catla x labeo rohita*) fed on cottonseed meal, sunflower meal and bone meal, *Pakistan Veterinary Journal, 26, 4,* 163-166;

[33] Saleh, J-H, Al-Dubakel, A.Y., Taher M.M., (2014), Effects of feeding ratio on growth and food conversion rate of common carp Cyprinus carpio reared in floating cages, *Iraqui Journal of Aquaculture, 11 (1),* pp. 15-26;

[34] Shipton, T.A., (2021), Guidelines for feed use in carp and trout production systems in Central Asia and Eastern Europe, *FAO Fisheries and Aquaculture Circular No. 1224. Rome*, FAO. 2021 https://doi.org/10.4060/cb4640en;

[35] Singh, P., Maqsood S., Samoon Phulia V., Danish M., Chalal R.S., (2011), Exogenous supplementation of papain as growth promoter in diet of fingerlings of *Cyprinus carpio*, *International Aquatic Research, 3,* pp. 1-9;

[36] Sultana, S.M., Das, M., Chakraborty S.C. (2001). Effect of feeding frequency on the growth of common carp (Cyprinus carpio L.) fry, *Bangladesh Journal of Fisheries Research, 5 (2),* pp. 149-154;

[37] Sun, Y., Li, B., Zhang, X., Chen, M., Huijuan, T., Yu, X., (2018), Dietary available phosphorus requirement of crucian carp, *Carassius auratus*, *Aquaculture Nutrition,* 24, pp. 3-4;

[38] Velazco-Vargas, J., Tomás-Vidal, A., Hamdan, M., Moyano López, F.J., Jover Cerda, M., Martínez-Llorens S., (2014), Influence of digestible protein levels on growth and feed utilization of juvenile meagre Argyrosomus regius, *Aquaculture Nutrition 20 (5),* 520-531. https://doi.org/10.1111/anu.12105;

[39] Wang, A., Han, G., Lv, F., Yang, W., Huang, J., Yin, X., (2014), Effects of Dietary Lipid Levels on Growth Performance, Apparent Digestibility Coefficients of Nutrients, and Blood Characteristics of Juvenile Crucian Carp (*Carassius auratus gibelio*), *Turkish Journal of Fisheries and Aquatic Sciences, 14,* pp. 1-10;

[40] Wenk, C., Pfirter, H.P., Bickel, H., (1980), Energetic aspects of feed conversion in growing pigs, *Livestock Production Science, 7 (5),* pp. 483-495;

[41] Zahra, A., Jin, C., Sang-Min, L., (2015), Optimal Dietary Protein and Lipid Levels for Growth of Juvenile Israeli *Carp Cyprinus carpio, Fisheries and Aquatic Sciences, 18 (3),* pp. 265-271;

RESEARCH ON DETACHMENT PROCESS AND SEPARATION OF FROZEN SEA-BUCKTHORN FRUITS FROM BRANCHES
/
CERCETĂRI PRIVIND PROCESELE DE DETAȘARE ȘI SEPARARE A FRUCTELOR DE CĂTINĂ CONGELATE DE PE RAMURI

Radu CIUPERCĂ[1*)], Ana ZAICA[1)], Vasilica STEFAN[1)], Petruţa-PETCU[2)], Lucian DUMITRESCU[3)]
[1)]National Institute of Research- Development for Machines and Installations for Agriculture and Food Industry - INMA Bucharest/ Romania
[2)] National University of Science and Technology "POLITEHNICA" of Bucharest, Faculty of Aerospace Engineering / Romania;
[3)] ICDIMPH HORTING Bucharest/Romania
Tel: +40212693255; E-mail: ciupercaradu@yahoo.com
DOI: https://doi.org/10.35633/inmateh-71-71

Keywords: *sea-buckthorn, detachment process, separation, optimization*

ABSTRACT
Following the bibliographic and theoretical research carried out by the specialists of INMA Bucharest Institute, as well as the experience of sea buckthorn producers and processors, the experimental model of a high-performance equipment for separating frozen sea buckthorn fruits from the harvested mass (branches, fruits and leaves) was designed and made. Thus, the subject of this paper is the experimental research carried out on an improved equipment for detaching and separating frozen sea buckthorn fruits from the branches - ESFC. After an introduction in which the current state in the field was highlighted, the tested equipment was presented with the main functional parameters, adjustments necessary to obtain an optimal working regime suitable for the processed raw material. Following the experiments carried out, the main working indices of the equipment were determined, among which: the working capacity, the degree of separation of the fruits from impurities as well as the optimal functional regimes. Following the tests carried out, in two variants of arrangement of the paddle arms on the separation rotor, some conclusions were formulated, the most eloquent of which was that, for the equipment tested in Variant II equipped with the separation rotor, the highest values for the feed flow resulted for the angle of inclination of the paddle of 45^0 and the rotation speed of the rotor of 90 min^{-1} and a high degree of separation.

REZUMAT
În urma cercetărilor bibliografice şi teoretice realizate de specialiștii institutului INMA Bucureşti, dar și a experienței producătorilor și procesatorilor de cătină, s-a proiectat și realizat modelul experimental al unui echipament performant pentru separarea fructelor de cătină congelate, din masa recoltată (ramuri, fructe și frunze), astfel, subiectul acestei lucrării îl reprezintă cercetările experimentale efectuate asupra unui echipament îmbunătățit pentru desprindere și separarea fructelor congelate de cătină de pe crengi – ESFC. După o introducere in care s-a evidențiat stadiul actual in domeniu, s-a prezentat echipamentul experimentat cu principalii parametri funcționali, reglaje necesare pentru obținerea unui regim optim de lucru adecvat materiei prime procesate. In urma experimentărilor efectuate au fost determinați principalii indici de lucru ai echipamentului dintre care amintim: capacitatea de lucru, gradul de separare a fructelor de impurități precum si regimurile de funcţionale optime. In urma testărilor efectuare, in doua Variante de dispunere a brațelor cu palete pe rotorul de separare, au fost formulate unele concluzii dintre care cea mai elocventa a fost aceea ca, pentru echipamentul testat in Varianta II de echipare a rotorului de separare, au rezultat cele mai mari valori ale debitului de alimentare pentru unghiul de inclinare al paletei de 45^0 si viteza de rotaţie a rotorului de 90 min^{-1} si un grad ridicat de sortare.

INTRODUCTION

In the context of circular economy, the technical processing line follow the concept to use the entire plant/raw material harvested and processed, which means non-waste production (*Tkacz et al., 2021; Ivanišová et al., 2020).* This concept can be applied also on sea buckthorn frozen fruit technology, because the latest researches shown that the plant fractions are unconventional sources of potassium and calcium in leaves, but also the vegetative parts and seeds with endocarp have iron, copper and manganese.

So, the "morphological parts of sea buckthorn have the potential to produce food rich in high-antioxidant and anti-inflammatory components, such as phenolic compounds and triterpenes. *(Tkacz, et al., 2021).*

Nowadays researchers' results published by prestigious specialists, provide important quantities of information on a large number of sea buckthorn species established on different geographical areas over the world, in order to guide the sea buckthorn capitalization technological processes to produce good products for phyto-pharmaceutical and food industry (*Van der Sman, 2020)*. "In the future, it will be beneficial to analyse lipophilic components and formulations based on the sea buckthorn fraction in vivo studies" (*Tkacz et al., 2021).*

The product obtained from the sea buckthorn which is used as raw material in the food industry, pharmaceutical and cosmetic industry is needed to implement nutraceutical-rich applications *(Van der Sman, 2020).*

Some mathematical theoretical studies were made on dedicated sea buckthorn equipment (*Aan and Heinloo, 2014; Milea et al., 2020)* designed to process berries, but if it is taken into consideration the fact that the sea buckthorn surface has oval shape and the bark outer surface is waxy and covered with short hairs *(Vișan et al., 2019*), those models must be validated.

In recent scientific literature on freezing foods, the thermal processing is of actuality and due to high energy consumption and food quality, the technical process is revised and updated in order to integrate new technologies developed in this field.

Considering that the sea-buckthorn berries have complex antioxidant solutions in combination with sugars in different concentration (depending on the species and the origin of the culture), the rapid cooling during the freezing process may result in partial freeze concentration. So, during the separation process, the temperature of the fruits must be kept under observation, to avoid the multiple transitions that usually occur in the freezing-thawing process (freeze concentrations, vitrification, devitrification, recrystallization, and ice formation) *(Roos and Drusch, 2015)*.

From the point of view of the technologies used worldwide, in terms of harvesting and separating the buckthorn fruits from the harvested branches, it can be said that they are quite varied, incorporating technical equipment that generally have the same detachment and separation systems *(Vișan et al., 2019).*

Also, scientific works have been written that approach, from a theoretical point of view, the work process carried out by the different work systems within the mentioned technologies *(Milea et al., 2020; -Yu. Zubarev A. et al., 2022; Longsheng Fu et al., 2015; Jing Zhao et al., 2023; James C et al., 2015).*

In England, at Quellendolf Saxony-Anhalt, the fruits are pre-processed in a very short interval, i.e. about 2 h, where: the branches will be chopped and frozen with nitrogen and the fruits are detached from the branches and separated from the plant residues with the help of a vibrating system, and a ventilation system cleans them of leaves and other impurities (*https://www.youtube.com/watch?v=Spgc-REEUa4; https://www.mz-web.de/jessen/sanddornernte-in-seyda-tonnenweise-geballte-vitamine-24789988*).

In a technology used in Finland, after the branches are harvested, they are arranged on the conveyor belt that directs them to the back of the equipment where the brushes and metal beaters are positioned. The shaken branches are then left behind the equipment, and the fruits and leaves are transported to the front and pass through the sieves *(https://www.moz.de/landkreise/maerkisch-oderland/strausberg/artikel8/dg/0/1/975684/;http://www.nig-magdeburg.de/index.php?id=98&lang=2&hp=24)*.

In Hungary, there is a technology for the separation of frozen sea buckthorn fruits that was published in 2018. The operations that this technology carries out are: the frozen fruits are introduced into the equipment with circular sieves for separating the fruits from the branches, from this equipment the bare branches come out on one collector channel, and on the other collector sea buckthorn fruits + leaves, the latter are inserted into a sieve with a special semi-circular sieve, where large plant debris and damaged/dry grains/small grains are removed and only good grains and a small amount of plant debris are collected from this equipment. The processing flow is continued with a combined selector (vibrating sieves and air currents) to ensure a complete cleaning *(https://www.youtube.com/watch?v=s9VUmobIjeQ).*

In Italy, it is predominantly used a technology that includes several successive operations, such as: mechanized harvesting complemented by manual harvesting to reduce losses; unloading harvested material into transport containers and freezing; freezing raw material; drumming with vibrating systems, conveyors with rods; separation of fruits from plant residues with a sieve system; packaging for refreezing (*https://www.youtube.com/watch?v=xW5r7LZM2sI&feature=autoshare;http://www.weleda.co.nz/tuscany-italy/w3/i1039717/#.XIvI7ygzaUk; https://www.youtube.com/watch?v=NfZWwDSB3eI).*

In Asia, the BEYOND Company - Shanghai China, proposes a technological line adapted to the processing of sea buckthorn fruits. It developed this project (design, equipment manufacturing, installation and commissioning) and also took care of operator training.

The new technology developed by Shanghai realizes, first of all, the removal of vegetable remains (branches, leaves, etc.), from the material resulting from the detachment of the fruit from the branches *(https://www.china.cn/pic/3963705228_0.html; https://www.china.cn/pic/3963711516_0.html; https://french.alibaba.com/product-detail/grape-destemming-crushing-machine-grape-destemmer-and-crusher-grape-stem-removing-machine-60481359883.html?spm=a2700.8699010.normalList.76.4d4417d2lenuwr; https://www.china.cn/pic/ 3932550216_0.html; https://french.alibaba.com/product-detail/grape-destemming-crushing-machine-grape-destemmer-and-crusher-grape-stem-removing-machine-60481359883.html?spm=a2700.8699010.normalList.76.4d4417d2lenuwr).*

Considering the importance of sea buckthorn fruits for the economic environment, it follows that it is imperative to create a technology for separating the fruits from impurities that will provide an optimal raw material, from a qualitative point of view and obtained with as little costs as possible. Thus, this paper presents the technology elements that can be used to achieve the presented aspects.

MATERIALS AND METHODS

Experimental research activities presented in this paper are conducted on a technical equipment to separate the sea-buckthorn fruits from branches, symbolized ESFC, developed at INMA Bucharest, during an R&D project, respecting the frozen sea-buckthorn detachment process and separation used usually at international level, Fig. 1.

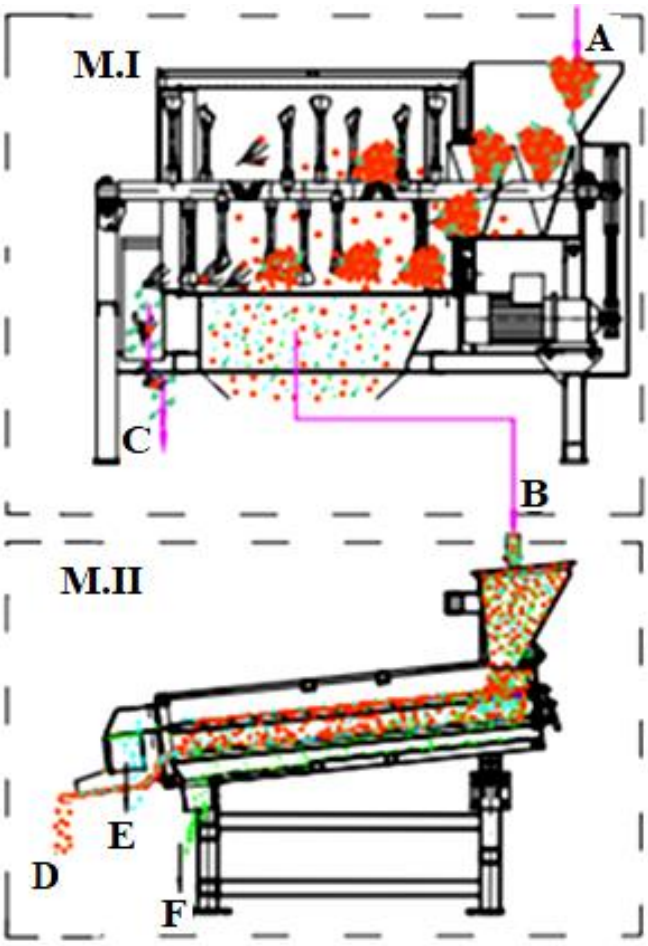


Fig. 1 –Technological process of frozen sea-buckthorn detachment and separation process designed for ESFC equipment (designed and manufactured technological process)

M.I - sea-buckthorn detachment module from branches; M.II –Sea-buckthorn separation; A – frozen raw material supply opening (fractions as: branches, leaves and fruits); B – separation material evacuation funnel (fruits + leaves/ impurity fractions); C – branches and twigs evacuation opening; D – sea-buckthorn evacuation opening; E – large and part of and light impurities evacuation trough; F – small and the other part of light impurities as well as heavy impurity evacuation trough;

The **M.I.** module represents the first process that must be made, respectively the module of frozen sea-buckthorn detachment from branches; this type of equipment is designed to separate the raw material in two main fractions wood fraction (branches and twigs) evacuated by C opening and vegetal fraction (fruits + leaves/impurity fractions) evacuated by B funnel, Fig. 1.

The working flow is longitudinal in order to increase the separation length and separation efficiency. Another special characteristic of **M.I** is the construction of fruit detached shaft that presents adjustable paddle (11*)* arms that are assembled in the main shaft (4) in several threaded sleeves in order to have variable geometries and working diameter, but also to adjust the paddles orientation angle and working regime. The detailed image and the components are shown in Fig. 2.

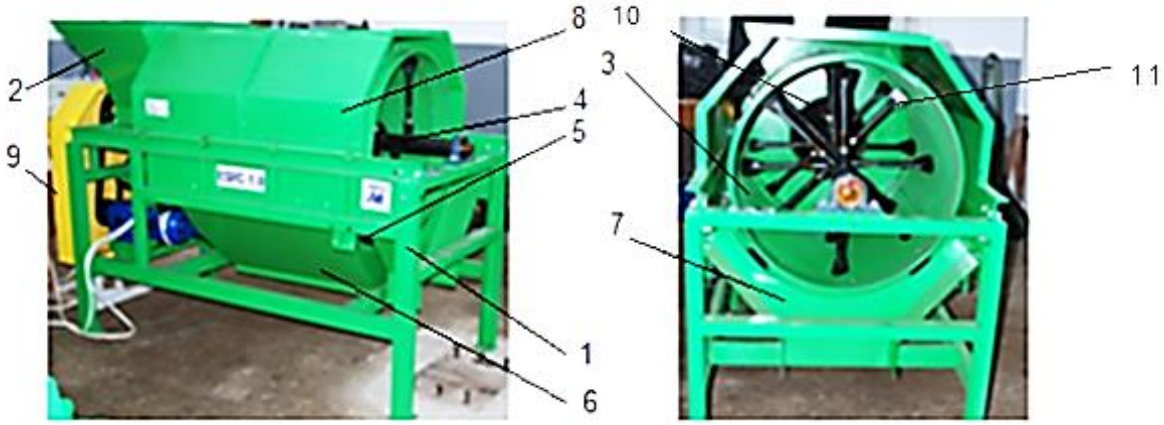


Fig. 2 – Module of sea-buckthorn detachment from branches (M.I)

1-metal support frame; 2- raw material supply opening; 3- cylindrical sieve; 4- fruit detaching shaft; 5- support and sieve roll; 6- vegetal material and small impurities evacuation funnel; 7- wood fraction and big impurities evacuation opening; 8- protection coverage; 9- belt drive transmission; 10 – helical winding; 11-adjustable paddle arms.

The main working part of the MI module, is the detachment rotor, shown in fig. 3. It is the active working body of the module and consists of a shaft (1), provided at the ends with axles for bearings (2, 3), on which some paddle arms are mounted, on a portion of its working length (6) in threaded bushings (4), secured by locknuts (7), and on the remaining portion of the shaft a helical coil (5) is welded.

The paddle arms can have adjustable working positions, both in terms of the working diameter and the angle of inclination of the paddle, thus influencing the working regime.

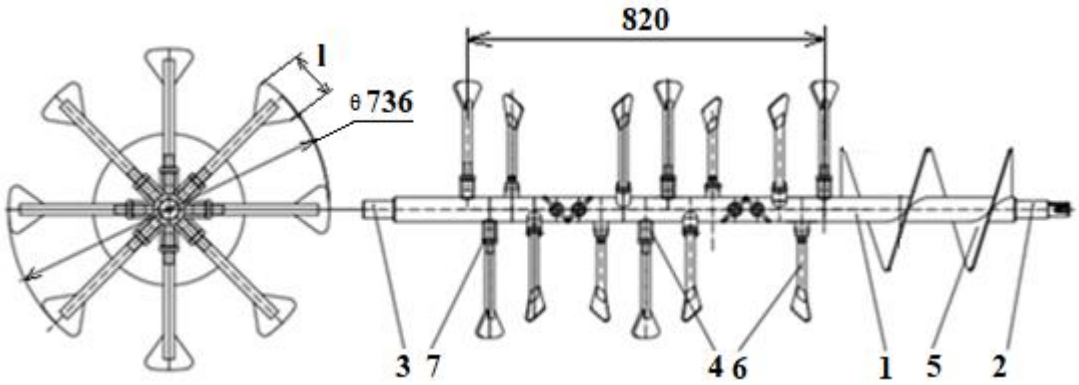


Fig. 3– The detachment rotor

1. Axle; 2, 3. Axle support; 4; Threaded bushing; 5. Spiral; 6. Paddle arm; 7. Locknut

The detachment rotor is composed of 17 paddle arms arranged on a propeller, whose pitch is 820 mm. The rotor propeller has a single step on which the paddle arms are arranged at equal distances, the propeller being of the discontinuous type, the material advances only when it is driven by the paddle. For this to happen, the paddles must be tilted at an angle that ensures the movement of the branches.

Starting from the imposed constructive and functional parameters, the working flow rate of the detachment rotor is determined according to relation (1).

$$Q = A \cdot \gamma \cdot \frac{p \cdot n_r}{60} \cdot k_v, kg/min \quad (1)$$

In which:

Q is the flow rate, [kg/min];

A – area of the section of the material supply chute of the paddle rotor, [m^2];

p – working step of a paddle, [m];

γ –volumetric mass of the separated material (buckthorn branches with fruits), [kg/m^3];

n_r – rotation frequency of the paddle rotor, [min^{-1}];

k_v – reduction coefficient of the axial speed of the material;

l – the maximum width of the rotor paddle, [m];

α – the angle of inclination of the rotor paddle, adjustable, [deg.].

To finalize the sea buckthorn fruit separation process, the material resulting from **M.I** must be passed through a sea buckthorn fruit separation Module, **M.II**, shown in Fig. 4, which has the role of separating sea buckthorn fruits from leaf debris and branch fractures resulting from the detachment module. The main components are shown in Fig. 4.

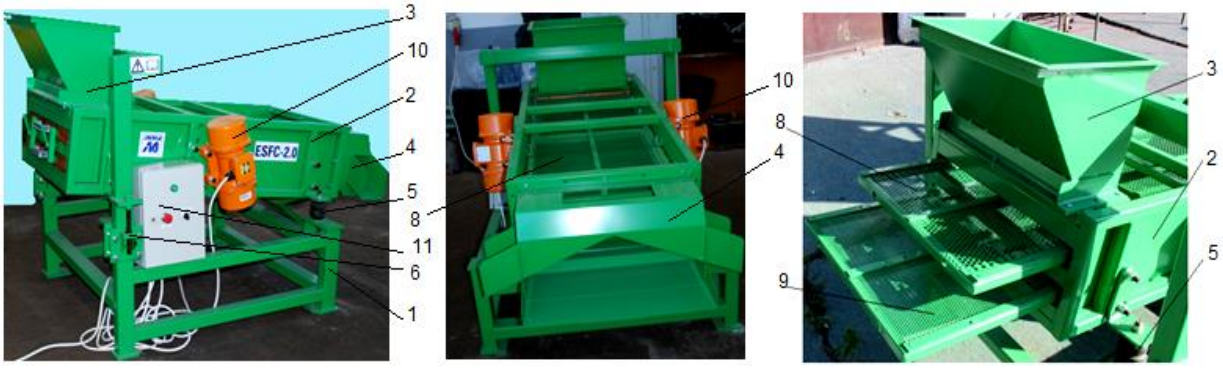


Fig. 4. Sea-buckthorn separation module (M II)

1-welded frame; 2- frame; 3- supply funnel; 4- fruit evacuation opening;5- vibration damping system;6- sliding system to support the mobile screens; 8- upper screen; 9- lower screen; 10- electric vibration generator; 11- electric panel to control the vibration frequency.

The main working parameters of the ESFC equipment are complex and largely influenced by the type of sea-buckthorn row material, fruit dimensions, fruit outer surface quality, life density, branches and twigs density, but also the thorn presence.

***M.I** working parameters:*

- fruit detaching shaft speed 256 rpm (motor power 3 kW);
- the active diameter dimension (paddle arms) max 750 mm;
- the longitudinal displacement of the raw material (the orientation paddles angle in accordance with longitudinal shaft axis) 1000 mm;
- the rotational speed of cylindrical sieve 108 rpm, installed power 3.55 kW (motor power 0.55 kW), the cylindrical sieve has a maximum diameter of 800 mm and a length of 1000 mm.

***M.II** working parameters*:

- adjustment of frame inclination angle in accordance with its longitudinal 5 ÷ 12 degrees;
- the length of the flat sieve is 1365 mm, the width is 590 mm, the adjustment of the maximum centrifugation force of the frame is 3.15 kN and its direction is generated by the electric vibration generator working frequencies and amplitude of 50 Hz;
- electrical power of vibrator motor 0.350 kW, maximum rotation 1000 rpm, the installed power is 2 x 0.350 kW.

For the technical solution of the machine, ESFC, a patent application registered with the number A-00398/2020 was submitted to OSIM (The Romanian State Office for Inventions and Trademarks).

The **main ESFC adjustments** are very important and are tailored for this modules that are working with perishable fruits. The frozen fruits must be very fast processed in order to avoid unfreezing and being damaged. This subject is part of the measuring methodology of the ESFC performance so:

The adjustments of the M.I working parameters are:

- the adjustment of the paddle rotor rotational speed, 111-56 min^{-1}- the optimum value is reached when the paddles impact force can detach the majority sea-buckthorn fruit from the branches without harming them and generate the raw material displacement. This parameter is designed to be adjusted using the electrical frequency converter;
- paddles working diameter 680 - 750 mm – the optimum value depends on the type of raw processing material respectively wood density (branches and twigs proportion) because in this way the M.I blocking can be prevented (phenomenon that usually happens in this type of equipment). Often, the paddles geometry has a helical profile;
- cylindrical sieve rotational speed is 108 rpm; this parameter reaches the optimum value when the fruit loses is smaller on *C* evacuation opening.

The adjustments of the M.II working parameters are:

- changing the inclination angle of plane sieve frames in accordance with longitudinal axis at 5…12 degrees;
- adjusting the centrifugal force direction of plane sieve frames by adjusting the position of electric oscillation generators (10), see Fig. 4. For tests, the electric vibrator is set to 80% of the maximum centrifugal force given by the producer.

The testing of ESFC equipment was drafted by INMA Bucharest researches, being an Experimental methodology under laboratory conditions in accordance with the specifications of its modules. The laboratory in which were made the experiments is placed near the freezing chamber from which is drawn out the sea-buckthorn raw material, and it is provided with electricity supply network to power both modules.

The work parameters and indices determined during the experiments were: work flow, productivity, fruit damaged degree; electric energy consumption; the fruit losses rate.

The measurement equipment underwent metrological verification and was calibrated, as further shown: digital multi-meter, OMEGA electronic thermometer - measurement range 0-50 ^{0}C; electric level indicator; Q338033 centrifugal tachometer – measurement range 60-24000 min^{-1}, watt-metric kit - measurement range 0-105 W, analytical balance.

The experimental researches were carried out for different values of the functional parameters in order to establish the optimal working regime for obtaining a quality final product with the lowest possible costs.

Thus, the constructive parameters of the ESFC equipment and the functional ones, used in the experiments, are:

- A = 0.0825 m^2;
- γ = cca.45 kg/m^3 ;
- p_{eI} = 0.054; 0.049; 0.042 m, achieved by tilting the paddle with the width of l_I = 0.060 m at angles $\alpha = 25^0; 35^0; 45^0$, Variant I;
- p_{eII} = 0.100; 0.090; 0.078 m, achieved by tilting the paddle with the width of l_{II} = 0.110 m at angles $\alpha = 25^0; 35^0; 45^0$, Variant II;
- n_r = 55; 70; 90; 110 min^{-1}, adjustable through the rotation frequency converter of the motor-reducer driving the paddle rotor;
- k_v - uncontrollable, because during operation it happens that some component parts of the branches (the tip of the branches or thorns) partially enter the holes of the rotating sieve, which covers the detachment rotor, or wrap around the paddle arms, situation in which it is difficult to move the branches. By conducting several tests, it was found that this phenomenon does not significantly depend on the speed of the rotor or rotational screen, and therefore a relationship cannot be formulated that expresses the coefficient of reduction of the axial speed of the material. In order to reduce this phenomenon, some paddle arms were removed, so that the axial distance between the arms was smaller than the minimum length of the sea buckthorn branches (approx. 150 mm), a situation that led to the reduction of the phenomenon of wrapping the branches on the arms. Thus, to determine the working flow, an average axial speed reduction coefficient of 0.55 was chosen;
- the working diameter of the extremity of the detachment rotor paddles of **M.I**, was 736 mm;
- n_s, cylindrical sieve rotation frequency of **M.II** = 108 min^{-1};
- the angle of inclination of the flat sieves of **M.II**, compared to the longitudinal axis, used in the tests, was 8 degrees;

- the equipment was tested using frizzing sea-buckthorn branches at -28^{0}C, with length between 300 ÷ 900 mm and bulkiness 3÷15 mm.

RESULTS

The results of the determinations for the working parameters of the ESFC equipment after the first separation module **M.I** and second passage through the **M.II** separation module, are presented in Table 1

Table 1

The working parameters of the ESFC equipment determined

No.	Working parameters	UM	Designed (Theoretical Value)	The measured parameters values (average)		
				First sorting, M.I		Second sorting, M.II
				Variant I	Variant II	
0	1	2	3	4	5	6
1	Working capacity of M.I	[kg/h]	500	348	450	
2	Consumed power of M.I, P_I	[kW]	3.55	2.7	3.3	
3	The rotational speed of the paddle rotor	min^{-1}		90		
4	Working capacity of M.II	[kg/h]	500			378
5	Consumed power of M.II, P_{II}	[kW]	0.7			0.62
6	Total consumed power of the process, P_t (line 2+5)	[kW]	4.25	3.32 Var.I; 3.92 Var.II		
7	Specific electricity consumption	[kWh/t]	8.5	9.41 Var.I ; 8.94 Var.II		

During operation, it was found that when entering the fruit detachment area, the branches sometimes jammed, making it difficult to advance the branches and often causing the detachment paddle rotor to jam.

Also, even if the angle of inclination of the paddles could be changed at the rotor paddles, the advance of the branches towards the exhaust mouth was very slow, a fact that greatly delayed the process and implicitly reduced the working capacity.

At the same time, due to the large number of detachment paddle arms, 17 pieces, the branches often wrapped around the rotor, which made it difficult to advance the branches and block the detachment process.

In such situations encountered, in order to eliminate or reduce the mentioned dysfunctions, the following changes were made in the technical and constructive documentation on the experimental model:

- the first three bushings where the paddle arms were mounted were removed from the rotor, in this way the entry space for the branches in the fruit detachment area was increased and the branches were no longer blocked;
- the width of the paddles was doubled by welding another paddle segment equal to the existing one, in this way the advance speed of the branches along the rotor was increased;
- to avoid wrapping the branches around the arms, the number of arms was reduced from 17 to 8.

The mentioned changes can be observed in fig. 5.

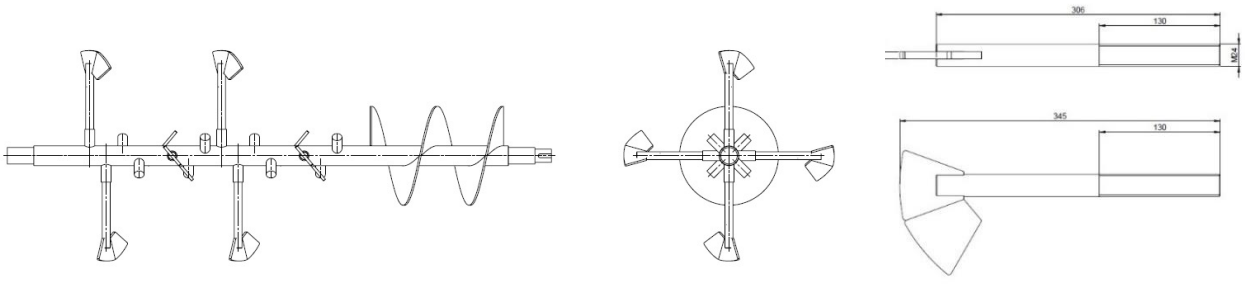


Fig. 5 - The detachment rotor - modified version

After making the mentioned changes of the detachment rotor "Modified version", in the Material and Method chapter and carrying out new tests, at the same speed of the detachment rotor, a visible improvement in the functionality of the equipment was found, in the area of detachment of sea buckthorn fruits, in the sense of reducing blockages with branches, simultaneously with the increase of their advance speed in the detachment drum by approx. 35 %.

In these conditions, the average feed flow increased by approx. 30%, under the conditions of a power consumption similar to the first variant.

At the same time, due to the fact that branch blockages in the detachment system were reduced, it increased by approx. 30% of the supply flow of the M II equipment and implicitly of its working capacity.

The variation of the working capacity of the **M.II** module depending on the inclination of the rotor arm paddle, in the constructive Variant II and its speed, is presented in Fig.6.

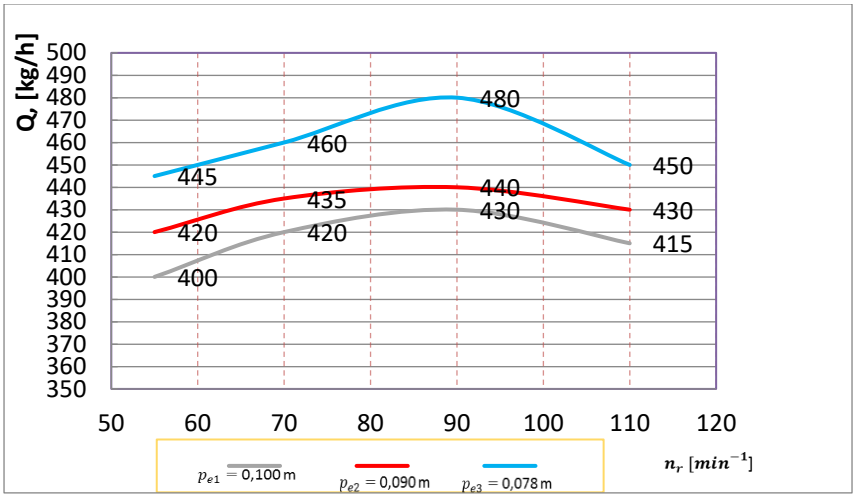


Fig. 6 - The variation of the working capacity of the M II module depending on the inclination of the rotor arm paddle, in the constructive Variant II and its speed

The qualitative indices of the resulting final product, are presented in table 2.

Table 2

The qualitative indices of the ESFC equipment determined

No.	Qualitative indices	UM	Designed (Theoretical) Value	The measured parameters values (average)	
				First sorting, M.I	Second sorting, M.II
1	The degree of fruit detachment from the branches of **M.I**	[%]	97-100	99.75	
2	Fruit damage rate in the detachment process of **M.I**, Gv	[%]	-	1.9	
3	Degree of sorting / screening, **M.II** for:	[%]			
	- large impurities, separated on the upper sieve, I_L		-	98.6	99.8
	- small impurities, separated on the upper and lower sieve, I_s		-	82.8	99.5
	- light impurities, smaller than the sea buckthorn fruits, I_l		-	92.5	99.8
4	Fruit loss rate in **M.II**, C_{fl}	[%]	-	0.8	0.55

The large impurities and some of the small ones can be manually sorted when the fruits come out of the **M.II**. The degree of separation of small and light impurities is reduced compared to the requirements of those who use the sorted fruits in the technological processes of the food or pharmaceutical industries, this is due to the fact that the impurities adhere to the surface of the fruits during the sorting process due to their moistening by the process of condensation, the material subjected to the process being frozen.

In order to finalize the process of separating small and light impurities from fruit, the product resulting from M.II it must be passed through a light impurities suction module after, beforehand, the material resulting from M II is dried, to obtain the purity of the fruits required by their beneficiaries.

In Fig. 7, 8 are presented some images from test made on ESFC equipment, respectively on **M.I** and **M.II**.



Fig. 7 - Images from the sea-buckthorn detachment module – M.I



Fig. 8 - Aspects from sea-buckthorn separating module -- M.II

CONCLUSIONS

- The technical equipment that separates the sea buckthorn fruit from the branches, works in designed parameters such as: the inclusion in the functioning regime of the active parts (rotation axis and oscillating sieve) but also the adjustments established in the project phase;
- From the point of view of energy consumption and working capacity, it can be stated that they are lower than the initial estimates, this fact being the cause of the lower supply flow with branches, compared to the estimated one;
- From the point of view of the quality parameters (such as: fruits not detached from the branches, crushed fruits, impurities in the final product), it can be concluded that the values obtained for these parameters are acceptable, with possibilities for improvement;
- The variation of the supply flow with branches, depending on the rotational speed of the paddle arm, for different angles of inclination of the paddles and implicitly of the pitch of the spiral achieved by the paddles, does not faithfully respect the theoretical relationship (1), this fact having as cause the non-uniformity of the material and the feed flow rate. For the equipment tested in Variant II equipped with the separation rotor, the highest values for the feed flow resulted for the angle of inclination of the paddle was 45^0 and the rotational speed of the rotor was 90 min^{-1}. The variation of the supply flow with branches can be seen in the diagram in Fig. 6.
- The degree of fruit detachment from the branches of **M.I**, was 99.75 %;
- Fruit damage rate in the detachment process of **M.I**, was 1.9%.

ACKNOWLEDGEMENT

This work was supported by:

Development of the national research-development system, Subprogramme 1.2 – Institutional performance – Projects for financing excellence in RDI, contract no. 16PFE. Project: PN 19 10 01 05 - Integrated management of work in farms, vineyards and orchards, contract no. 5/ 07.02.2019.

REFERENCES

[1] Aare Aan, MatiHeinloo, (2014), Dynamics of a Frozen Sea Buckhorn Berry Motion in a Separator, 25th DAAAM International Symposium on Intelligent Manufacturing and Automation, DAAAM, Procedia Engineering, pp.689 – 698, doi: 10.1016/j.proeng.2015.01.421.

[2] Ivanišová E., Meňhartová K., Terentjeva M., Harangozo L., Kántor A., Kačániová M., (2019), The evaluation of chemical, antioxidant, antimicrobial and sensory properties of kombucha tea beverage, *The Journal of Food Science and Technology*, pp.1840-1846. doi: 10.1007/s13197-019-04217-3.

[3] James C., Purnell G., James S.J. (2015) A review of novel and innovative food freezing technologies. *Food and Bioprocess Technology,* 8(8): pp.1616–1634.

[4] Jing Zhao, Zhihua Zhang, Hongdan Zhou,Zengfu Bai, Zengfu Bai, Kun Sun (2023) The Study on Sea Buckthorn (Genus Hippophae L.) *Fruit Reveals Cell Division and Cell Expansion to Promote Morphogenesis, College of Life Science*, Northwest Normal University, China 12(5), pp.1005, https://doi.org/10.3390/plants12051005.

[5] Longsheng Fu, Jun Peng, Qiang Nan, Yongjie Cui, (2015) Simulation of vibration harvesting mechanism for sea buckthorn, Engineering in Agricultural, *Environment and Food*, pp. 101-108, DOI:10.1016/j.eaef.2015.08.003.

[6] Milea D., Vișan A.-L., Ciupercă R., Păun A., Zaica Al., (2020), Mathematical modelling of plane sieve kinematic regime to optimize the separation process of frozen sea buckthorn berries, *International Symposium ISB INMA TEH*, pp. 15-20.

[7] R. G. M. van der Sman, 2020, Impact of Processing Factors on Quality of Frozen Vegetables and Fruits, Food Engineering Reviews 12, pp. 399–420, https://doi.org/10.1007/s12393-020-09216-1.

[8] Roos, Y.H.; Drusch, S., (2015), Phase Transitions in Foods, 2nd ed.; Academic Press: San Diego, CA, USA, pp. 366.

[9] Tkacz K, Wojdyło A., Turkiewicz IP., Nowicka P., (2021), Triterpenoids, phenolic compounds, macro- and microelements in anatomical parts of sea buckthorn (Hippophaë rhamnoides L.) berries, branches and leaves, *Journal of Food Composition and Analysis*, Volume 103, October 2021, 104107, https://doi.org/10.1016/j.jfca.2021.104107.

[10] Vișan A.L., Milea D., Ciupercă R., Bogdanof B.G., Păun A., Giurescu I., (2019), Post-harvest technology develop to separate the Romanian sea buckthorn fruits from the harvested branches, *Proceeding of 6th INTERNATIONAL SYMPOSIUM International Conference "Research People and Actual Tasks on Multidisciplinary Sciences*", pp.237-241, Lozenec/Bulgaria.

[11] Zubarev Yu. A., Gunin A. V., Panteleeva E. I., Vorobyeva A. V. (2022), Sea buckthorn cultivars promising for mechanized harvesting by cutting fruit-bearing branches, Proceedings on *Applied botany genetics and breeding* 183(2): pp. 43-50, DOI:10.30901/2227-8834-2022-2-43-50.

[12] ***https://www.youtube.com/watch?v=Spgc-REEUa4;

[13] ***https://www.mz-web.de/jessen/sanddornernte-in-seyda-tonnenweise-geballte-vitamine-24789988).

[14] ***https://www.moz.de/landkreise/maerkisch-oderland/strausberg/artikel8/dg/0/1/975684/;

[15] ***http://www.nig-magdeburg.de/index.php?id=98&lang=2&hp=24).

[16] ***https://www.youtube.com/watch?v=s9VUmobIjeQ

[17] ***https://www.youtube.com/watch?v=xW5r7LZM2sI&feature=autoshare;

[18] ***http://www.weleda.co.nz/tuscany-italy/w3/i1039717/#.XIvI7ygzaUk;

[19] ***https://www.youtube.com/watch?v=NfZWwDSB3eI

[20] ***https://www.china.cn/pic/3963705228_0.html;

[21] ***https://www.china.cn/pic/3963711516_0.html;

[22] ***https://french.alibaba.com/product-detail/grape-destemming-crushing-machine-grape-destemmer-and-crusher-grape-stem-removing-machine-60481359883.html?spm=a2700.8699010.normalList.76.4d4417d2lenuwr;

[23] ***https://www.china.cn/pic/3932550216_0.html

[24] ***https://french.alibaba.com/product-detail/grape-destemming-crushing-machine-grape-destemmer-and-crusher-grape-stem-removing-machine-60481359883.html?spm=a2700.8699010.normalList.76.4d4417d2lenuwr.

RESEARCH ON DETACHMENT PROCESS AND SEPARATION OF FROZEN SEA-BUCKTHORN FRUITS FROM BRANCHES
/
CERCETĂRI PRIVIND PROCESELE DE DETAȘARE ȘI SEPARARE A FRUCTELOR DE CĂTINĂ CONGELATE DE PE RAMURI

Radu CIUPERCĂ[1*)], Ana ZAICA[1*)], Vasilica STEFAN[1)], Petruţa-PETCU[2)], Lucian DUMITRESCU[3)], Oana Cristea[1)]

[1)]National Institute of Research- Development for Machines and Installations for Agriculture and Food Industry - INMA Bucharest/ Romania

[2)] National University of Science and Technology "POLITEHNICA" of Bucharest, Faculty of Aerospace Engineering / Romania;

[3)] ICDIMPH HORTING Bucharest/Romania

E-mail: ciupercaradu@yahoo.com

DOI: https://doi.org/10.35633/inmateh-71-71

Keywords: *sea-buckthorn, detachment process, separation, optimization*

ABSTRACT

Following the bibliographic and theoretical research carried out by the specialists of INMA Bucharest Institute, as well as the experience of sea buckthorn producers and processors, the experimental model of a high-performance equipment for separating frozen sea buckthorn fruits from the harvested mass (branches, fruits and leaves) was designed and made. Thus, the subject of this paper is the experimental research carried out on an improved equipment for detaching and separating frozen sea buckthorn fruits from the branches - ESFC. After an introduction in which the current state in the field was highlighted, the tested equipment was presented with the main functional parameters, adjustments necessary to obtain an optimal working regime suitable for the processed raw material. Following the experiments carried out, the main working indices of the equipment were determined, among which: the working capacity, the degree of separation of the fruits from impurities as well as the optimal functional regimes. Following the tests carried out, in two variants of arrangement of the paddle arms on the separation rotor, some conclusions were formulated, the most eloquent of which was that, for the equipment tested in Variant II equipped with the separation rotor, the highest values for the feed flow resulted for the angle of inclination of the paddle of 45^0 and the rotation speed of the rotor of 90 min^{-1} and a high degree of separation.

REZUMAT

În urma cercetărilor bibliografice şi teoretice realizate de specialiștii institutului INMA Bucureşti, dar și a experienței producătorilor și procesatorilor de cătină, s-a proiectat și realizat modelul experimental al unui echipament performant pentru separarea fructelor de cătină congelate, din masa recoltată (ramuri, fructe și frunze), astfel, subiectul acestei lucrării îl reprezintă cercetările experimentale efectuate asupra unui echipament îmbunătățit pentru desprindere și separarea fructelor congelate de cătină de pe crengi – ESFC. După o introducere in care s-a evidențiat stadiul actual in domeniu, s-a prezentat echipamentul experimentat cu principalii parametri funcționali, reglaje necesare pentru obținerea unui regim optim de lucru adecvat materiei prime procesate. In urma experimentărilor efectuate au fost determinați principalii indici de lucru ai echipamentului dintre care amintim: capacitatea de lucru, gradul de separare a fructelor de impurități precum si regimurile de funcţionale optime. In urma testărilor efectuare, in doua Variante de dispunere a brațelor cu palete pe rotorul de separare, au fost formulate unele concluzii dintre care cea mai elocventa a fost aceea ca, pentru echipamentul testat in Varianta II de echipare a rotorului de separare, au rezultat cele mai mari valori ale debitului de alimentare pentru unghiul de inclinare al paletei de 45^0 si viteza de rotaţie a rotorului de 90 min^{-1} si un grad ridicat de sortare.

INTRODUCTION

In the context of circular economy, the technical processing line follow the concept to use the entire plant/raw material harvested and processed, which means non-waste production (*Tkacz et al., 2021; Ivanišová et al., 2020).* This concept can be applied also on sea buckthorn frozen fruit technology, because the latest researches shown that the plant fractions are unconventional sources of potassium and calcium in leaves, but also the vegetative parts and seeds with endocarp have iron, copper and manganese.

So, the “morphological parts of sea buckthorn have the potential to produce food rich in high-antioxidant and anti-inflammatory components, such as phenolic compounds and triterpenes. *(Tkacz, et al., 2021).*

Nowadays researchers’ results published by prestigious specialists, provide important quantities of information on a large number of sea buckthorn species established on different geographical areas over the world, in order to guide the sea buckthorn capitalization technological processes to produce good products for phyto-pharmaceutical and food industry (*Van der Sman, 2020)*. “In the future, it will be beneficial to analyse lipophilic components and formulations based on the sea buckthorn fraction in vivo studies” (*Tkacz et al., 2021).*

The product obtained from the sea buckthorn which is used as raw material in the food industry, pharmaceutical and cosmetic industry is needed to implement nutraceutical-rich applications *(Van der Sman, 2020).*

Some mathematical theoretical studies were made on dedicated sea buckthorn equipment (*Aan and Heinloo, 2014; Milea et al., 2020)* designed to process berries, but if it is taken into consideration the fact that the sea buckthorn surface has oval shape and the bark outer surface is waxy and covered with short hairs *(Vișan et al., 2019*), those models must be validated.

In recent scientific literature on freezing foods, the thermal processing is of actuality and due to high energy consumption and food quality, the technical process is revised and updated in order to integrate new technologies developed in this field.

Considering that the sea-buckthorn berries have complex antioxidant solutions in combination with sugars in different concentration (depending on the species and the origin of the culture), the rapid cooling during the freezing process may result in partial freeze concentration. So, during the separation process, the temperature of the fruits must be kept under observation, to avoid the multiple transitions that usually occur in the freezing-thawing process (freeze concentrations, vitrification, devitrification, recrystallization, and ice formation) *(Roos and Drusch, 2015)*.

From the point of view of the technologies used worldwide, in terms of harvesting and separating the buckthorn fruits from the harvested branches, it can be said that they are quite varied, incorporating technical equipment that generally have the same detachment and separation systems *(Vișan et al., 2019).*

Also, scientific works have been written that approach, from a theoretical point of view, the work process carried out by the different work systems within the mentioned technologies *(Milea et al., 2020; -Yu. Zubarev A. et al., 2022; Longsheng Fu et al., 2015; Jing Zhao et al., 2023; James C et al., 2015).*

In England, at Quellendolf Saxony-Anhalt, the fruits are pre-processed in a very short interval, i.e. about 2 h, where: the branches will be chopped and frozen with nitrogen and the fruits are detached from the branches and separated from the plant residues with the help of a vibrating system, and a ventilation system cleans them of leaves and other impurities (*www.youtube.com/watch?v=Spgc-REEUa4; www.mz-web.de/jessen/sanddornernte-in-seyda-tonnenweise-geballte-vitamine-24789988)*.

In a technology used in Finland, after the branches are harvested, they are arranged on the conveyor belt that directs them to the back of the equipment where the brushes and metal beaters are positioned. The shaken branches are then left behind the equipment, and the fruits and leaves are transported to the front and pass through the sieves *(www.moz.de/landkreise/maerkisch-oderland/strausberg/artikel8/dg/0/1/975684/; www.nig-magdeburg.de/index.php?id=98&lang=2&hp=24)*.

In Hungary, there is a technology for the separation of frozen sea buckthorn fruits that was published in 2018. The operations that this technology carries out are: the frozen fruits are introduced into the equipment with circular sieves for separating the fruits from the branches, from this equipment the bare branches come out on one collector channel, and on the other collector sea buckthorn fruits + leaves, the latter are inserted into a sieve with a special semi-circular sieve, where large plant debris and damaged/dry grains/small grains are removed and only good grains and a small amount of plant debris are collected from this equipment. The processing flow is continued with a combined selector (vibrating sieves and air currents) to ensure a complete cleaning *(https://www.youtube.com/watch?v=s9VUmobIjeQ).*

In Italy, it is predominantly used a technology that includes several successive operations, such as: mechanized harvesting complemented by manual harvesting to reduce losses; unloading harvested material into transport containers and freezing; freezing raw material; drumming with vibrating systems, conveyors with rods; separation of fruits from plant residues with a sieve system; packaging for refreezing (*https://www.youtube.com/watch?v=xW5r7LZM2sI&feature=autoshare;http://www.weleda.co.nz/tuscany-italy/w3/i1039717/#.XIvI7ygzaUk; https://www.youtube.com/watch?v=NfZWwDSB3eI).*

In Asia, the BEYOND Company - Shanghai China, proposes a technological line adapted to the processing of sea buckthorn fruits. It developed this project (design, equipment manufacturing, installation and commissioning) and also took care of operator training.

The new technology developed by Shanghai realizes, first of all, the removal of vegetable remains (branches, leaves, etc.), from the material resulting from the detachment of the fruit from the branches *(www.china.cn/pic/3963705228_0.html; www.china.cn/pic/3963711516_0.html; https://french.alibaba.com/product-detail/grape-destemming-crushing-machine-grape-destemmer-and-crusher-grape-stem-removing-machine-60481359883.html?spm=a2700.8699010.normalList.76.4d4417d2lenuwr; www.china.cn/pic/ 3932550216_0.html; https://french.alibaba.com/product-detail/grape-destemming-crushing-machine-grape-destemmer-and-crusher-grape-stem-removing-machine-60481359883.html?spm=a2700.8699010.normalList.76.4d4417d2lenuwr).*

Considering the importance of sea buckthorn fruits for the economic environment, it follows that it is imperative to create a technology for separating the fruits from impurities that will provide an optimal raw material, from a qualitative point of view and obtained with as little costs as possible. Thus, this paper presents the technology elements that can be used to achieve the presented aspects.

MATERIALS AND METHODS

Experimental research activities presented in this paper are conducted on a technical equipment to separate the sea-buckthorn fruits from branches, symbolized ESFC, developed at INMA Bucharest, during an R&D project, respecting the frozen sea-buckthorn detachment process and separation used usually at international level, Fig. 1.

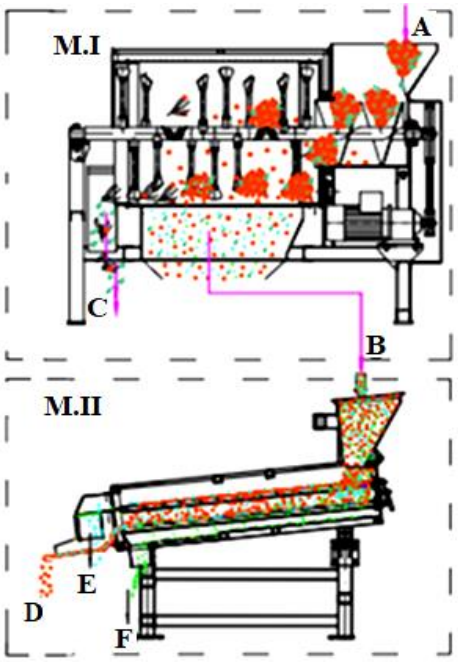


Fig. 1 –Technological process of frozen sea-buckthorn detachment and separation process designed for ESFC equipment (designed and manufactured technological process)

M.I - sea-buckthorn detachment module from branches; M.II –Sea-buckthorn separation; A – frozen raw material supply opening (fractions as: branches, leaves and fruits); B – separation material evacuation funnel (fruits + leaves/ impurity fractions); C – branches and twigs evacuation opening; D – sea-buckthorn evacuation opening; E – large and part of and light impurities evacuation trough; F – small and the other part of light impurities as well as heavy impurity evacuation trough;

The **M.I.** module represents the first process that must be made, respectively the module of frozen sea-buckthorn detachment from branches; this type of equipment is designed to separate the raw material in two main fractions wood fraction (branches and twigs) evacuated by C opening and vegetal fraction (fruits + leaves/impurity fractions) evacuated by B funnel, Fig. 1.

The working flow is longitudinal in order to increase the separation length and separation efficiency. Another special characteristic of **M.I** is the construction of fruit detached shaft that presents adjustable paddle (11*)* arms that are assembled in the main shaft (4) in several threaded sleeves in order to have variable geometries and working diameter, but also to adjust the paddles orientation angle and working regime. The detailed image and the components are shown in Fig. 2.

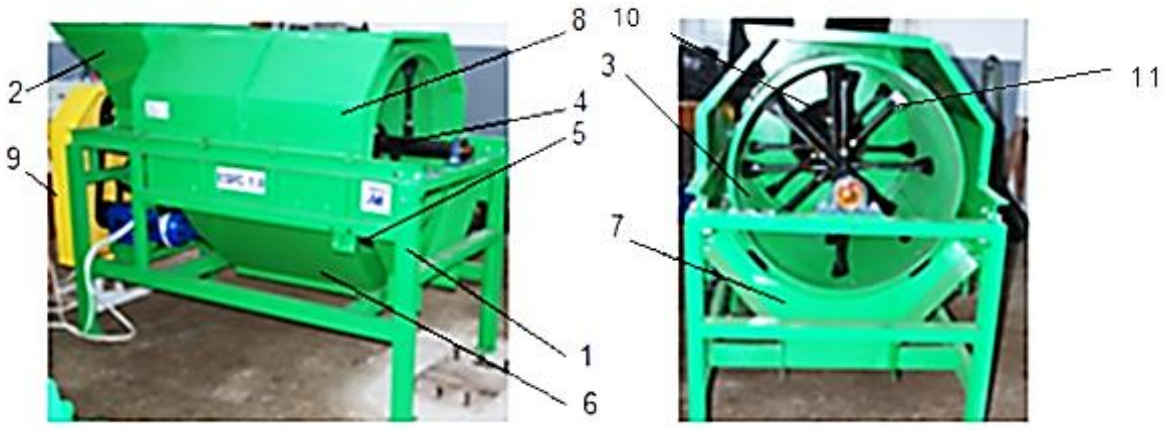


Fig. 2 – Module of sea-buckthorn detachment from branches (M.I)

1-metal support frame; 2- raw material supply opening; 3- cylindrical sieve; 4- fruit detaching shaft; 5- support and sieve roll; 6- vegetal material and small impurities evacuation funnel; 7- wood fraction and big impurities evacuation opening; 8- protection coverage; 9- belt drive transmission; 10 – helical winding; 11-adjustable paddle arms.

The main working part of the MI module, is the detachment rotor, shown in fig. 3. It is the active working body of the module and consists of a shaft (1), provided at the ends with axles for bearings (2, 3), on which some paddle arms are mounted, on a portion of its working length (6) in threaded bushings (4), secured by locknuts (7), and on the remaining portion of the shaft a helical coil (5) is welded.

The paddle arms can have adjustable working positions, both in terms of the working diameter and the angle of inclination of the paddle, thus influencing the working regime.

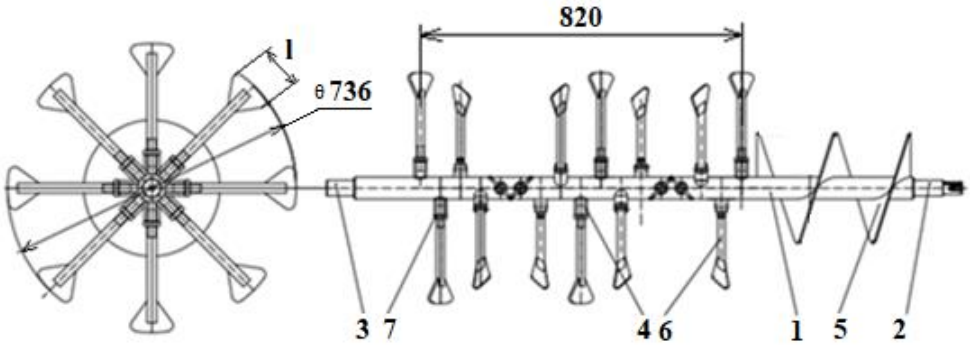


Fig. 3– The detachment rotor

1. Axle; 2, 3. Axle support; 4; Threaded bushing; 5. Spiral; 6. Paddle arm; 7. Locknut

The detachment rotor is composed of 17 paddle arms arranged on a propeller, whose pitch is 820 mm. The rotor propeller has a single step on which the paddle arms are arranged at equal distances, the propeller being of the discontinuous type, the material advances only when it is driven by the paddle. For this to happen, the paddles must be tilted at an angle that ensures the movement of the branches.

Starting from the imposed constructive and functional parameters, the working flow rate of the detachment rotor is determined according to relation (1).

$$Q = A \cdot \gamma \cdot \frac{p \cdot n_r}{60} \cdot k_v \quad (1)$$

In which:

Q is the flow rate, [kg/min];

A – area of the section of the material supply chute of the paddle rotor, [m^2];

p – working step of a paddle, [m];

γ –volumetric mass of the separated material (buckthorn branches with fruits), [kg/m^3];

n_r – rotation frequency of the paddle rotor, [min^{-1}];

k_v – reduction coefficient of the axial speed of the material;

l – the maximum width of the rotor paddle, [m];

α – the angle of inclination of the rotor paddle, adjustable, [deg.].

To finalize the sea buckthorn fruit separation process, the material resulting from **M.I** must be passed through a sea buckthorn fruit separation Module, **M.II**, shown in Fig. 4, which has the role of separating sea buckthorn fruits from leaf debris and branch fractures resulting from the detachment module. The main components are shown in Fig. 4.

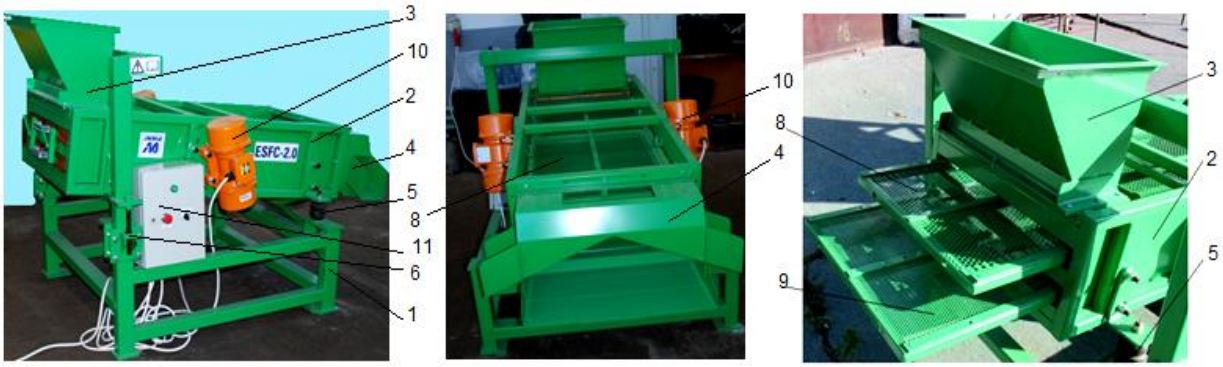


Fig. 4. Sea-buckthorn separation module (M II)

1-welded frame; 2- frame; 3- supply funnel; 4- fruit evacuation opening;5- vibration damping system;6- sliding system to support the mobile screens; 8- upper screen; 9- lower screen; 10- electric vibration generator; 11- electric panel to control the vibration frequency.

The main working parameters of the ESFC equipment are complex and largely influenced by the type of sea-buckthorn row material, fruit dimensions, fruit outer surface quality, life density, branches and twigs density, but also the thorn presence.

***M.I** working parameters:*

- fruit detaching shaft speed 256 rpm (motor power 3 kW);
- the active diameter dimension (paddle arms) max 750 mm;
- the longitudinal displacement of the raw material (the orientation paddles angle in accordance with longitudinal shaft axis) 1000 mm;
- the rotational speed of cylindrical sieve 108 rpm, installed power 3.55 kW (motor power 0.55 kW), the cylindrical sieve has a maximum diameter of 800 mm and a length of 1000 mm.

***M.II** working parameters*:

- adjustment of frame inclination angle in accordance with its longitudinal 5 ÷ 12 degrees;
- the length of the flat sieve is 1365 mm, the width is 590 mm, the adjustment of the maximum centrifugation force of the frame is 3.15 kN and its direction is generated by the electric vibration generator working frequencies and amplitude of 50 Hz;
- electrical power of vibrator motor 0.350 kW, maximum rotation 1000 rpm, the installed power is 2 x 0.350 kW.

For the technical solution of the machine, ESFC, a patent application registered with the number A-00398/2020 was submitted to OSIM (The Romanian State Office for Inventions and Trademarks).

The **main ESFC adjustments** are very important and are tailored for this modules that are working with perishable fruits. The frozen fruits must be very fast processed in order to avoid unfreezing and being damaged. This subject is part of the measuring methodology of the ESFC performance so:

The adjustments of the M.I working parameters are:

- the adjustment of the paddle rotor rotational speed, 111-56 min^{-1}- the optimum value is reached when the paddles impact force can detach the majority sea-buckthorn fruit from the branches without harming them and generate the raw material displacement. This parameter is designed to be adjusted using the electrical frequency converter;
- paddles working diameter 680 - 750 mm – the optimum value depends on the type of raw processing material respectively wood density (branches and twigs proportion) because in this way the M.I blocking can be prevented (phenomenon that usually happens in this type of equipment). Often, the paddles geometry has a helical profile;
- cylindrical sieve rotational speed is 108 rpm; this parameter reaches the optimum value when the fruit loses is smaller on *C* evacuation opening.

The adjustments of the M.II working parameters are:

- changing the inclination angle of plane sieve frames in accordance with longitudinal axis at 5…12 degrees;
- adjusting the centrifugal force direction of plane sieve frames by adjusting the position of electric oscillation generators (10), see Fig. 4. For tests, the electric vibrator is set to 80% of the maximum centrifugal force given by the producer.

The testing of ESFC equipment was drafted by INMA Bucharest researches, being an Experimental methodology under laboratory conditions in accordance with the specifications of its modules. The laboratory in which were made the experiments is placed near the freezing chamber from which is drawn out the sea-buckthorn raw material, and it is provided with electricity supply network to power both modules.

The work parameters and indices determined during the experiments were: work flow, productivity, fruit damaged degree; electric energy consumption; the fruit losses rate.

The measurement equipment underwent metrological verification and was calibrated, as further shown: digital multi-meter, OMEGA electronic thermometer - measurement range 0-50 ^{0}C; electric level indicator; Q338033 centrifugal tachometer – measurement range 60-24000 min^{-1}, watt-metric kit - measurement range 0-105 W, analytical balance.

The experimental researches were carried out for different values of the functional parameters in order to establish the optimal working regime for obtaining a quality final product with the lowest possible costs.

Thus, the constructive parameters of the ESFC equipment and the functional ones, used in the experiments, are:

- A = 0.0825 m^2;
- γ = cca.45 kg/m^3 ;
- p_{eI} = 0.054; 0.049; 0.042 m, achieved by tilting the paddle with the width of l_I = 0.060 m at angles α = 25^0; 35^0; 45^0, Variant I;
- p_{eII} = 0.100; 0.090; 0.078 m, achieved by tilting the paddle with the width of l_{II} = 0.110 m at angles α = 25^0; 35^0; 45^0, Variant II;
- n_r = 55; 70; 90; 110 min^{-1}, adjustable through the rotation frequency converter of the motor-reducer driving the paddle rotor;
- k_v - uncontrollable, because during operation it happens that some component parts of the branches (the tip of the branches or thorns) partially enter the holes of the rotating sieve, which covers the detachment rotor, or wrap around the paddle arms, situation in which it is difficult to move the branches. By conducting several tests, it was found that this phenomenon does not significantly depend on the speed of the rotor or rotational screen, and therefore a relationship cannot be formulated that expresses the coefficient of reduction of the axial speed of the material. In order to reduce this phenomenon, some paddle arms were removed, so that the axial distance between the arms was smaller than the minimum length of the sea buckthorn branches (approx. 150 mm), a situation that led to the reduction of the phenomenon of wrapping the branches on the arms. Thus, to determine the working flow, an average axial speed reduction coefficient of 0.55 was chosen;
- the working diameter of the extremity of the detachment rotor paddles of **M.I**, was 736 mm;
- n_s, cylindrical sieve rotation frequency of **M.II** = 108 min^{-1};
- the angle of inclination of the flat sieves of **M.II**, compared to the longitudinal axis, used in the tests, was 8 degrees;
- the equipment was tested using frizzing sea-buckthorn branches at -28^{0}C, with length between 300 ÷ 900 mm and bulkiness 3÷15 mm.

RESULTS

The results of the determinations for the working parameters of the ESFC equipment after the first separation module **M.I** and second passage through the **M.II** separation module, are presented in Table 1.

During operation, it was found that when entering the fruit detachment area, the branches sometimes jammed, making it difficult to advance the branches and often causing the detachment paddle rotor to jam.

Also, even if the angle of inclination of the paddles could be changed at the rotor paddles, the advance of the branches towards the exhaust mouth was very slow, a fact that greatly delayed the process and implicitly reduced the working capacity.

At the same time, due to the large number of detachment paddle arms, 17 pieces, the branches often wrapped around the rotor, which made it difficult to advance the branches and block the detachment process.

In such situations encountered, in order to eliminate or reduce the mentioned dysfunctions, the following changes were made in the technical and constructive documentation on the experimental model:

- the first three bushings where the paddle arms were mounted were removed from the rotor, in this way the entry space for the branches in the fruit detachment area was increased and the branches were no longer blocked;
- the width of the paddles was doubled by welding another paddle segment equal to the existing one, in this way the advance speed of the branches along the rotor was increased;
- to avoid wrapping the branches around the arms, the number of arms was reduced from 17 to 8.

Table 1

The working parameters of the ESFC equipment determined

No.	Working parameters	UM	Designed (Theoretical Value)	The measured parameters values (average)		
				First sorting, M.I		Second sorting, M.II
				Variant I	Variant II	
0	1	2	3	4	5	6
1	Working capacity of M.I	[kg/h]	500	348	450	
2	Consumed power of M.I, P_I	[kW]	3.55	2.7	3.3	
3	The rotational speed of the paddle rotor	min^{-1}		90		
4	Working capacity of M.II	[kg/h]	500			378
5	Consumed power of M.II, P_{II}	[kW]	0.7			0.62
6	Total consumed power of the process, P_t (line 2+5)	[kW]	4.25	3.32 Var.I; 3.92 Var.II		
7	Specific electricity consumption	[kWh/t]	8.5	9.41 Var.I ; 8.94 Var.II		

The mentioned changes can be observed in fig. 5.

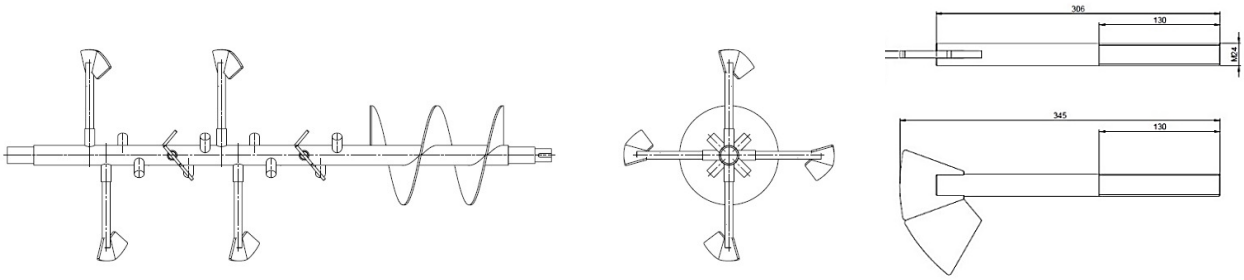


Fig. 5 - The detachment rotor - modified version

After making the mentioned changes of the detachment rotor “Modified version”, in the Material and Method chapter and carrying out new tests, at the same speed of the detachment rotor, a visible improvement in the functionality of the equipment was found, in the area of detachment of sea buckthorn fruits, in the sense of reducing blockages with branches, simultaneously with the increase of their advance speed in the detachment drum by approx. 35 %.

In these conditions, the average feed flow increased by approx. 30%, under the conditions of a power consumption similar to the first variant.

At the same time, due to the fact that branch blockages in the detachment system were reduced, it increased by approx. 30% of the supply flow of the M II equipment and implicitly of its working capacity.

The variation of the working capacity of the **M.II** module depending on the inclination of the rotor arm paddle, in the constructive Variant II and its speed, is presented in Fig.6.

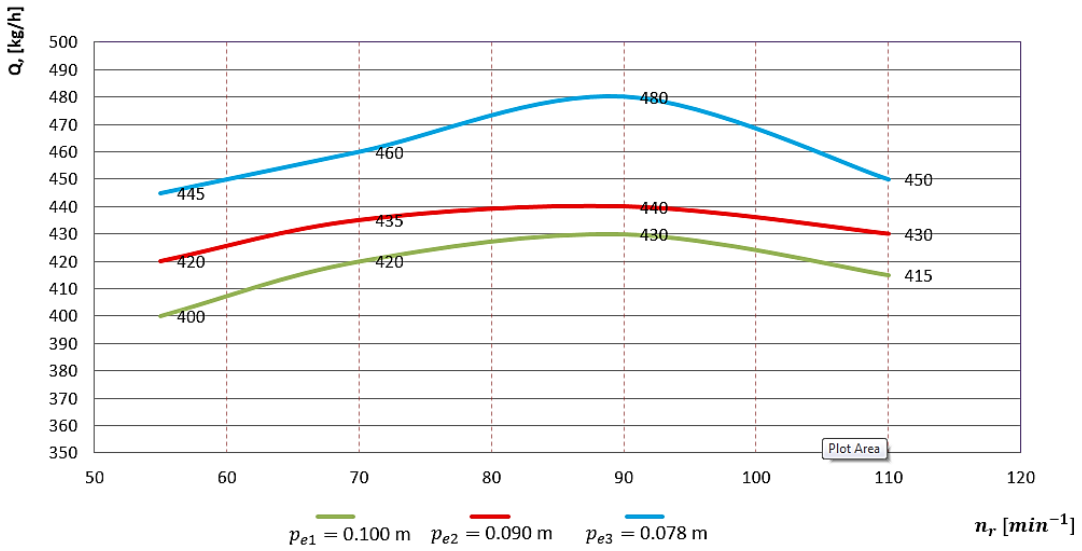


Fig. 6 - The variation of the working capacity of the M II module depending on the inclination of the rotor arm paddle, in the constructive Variant II and its speed

The qualitative indices of the resulting final product, are presented in table 2.

Table 2

The qualitative indices of the ESFC equipment determined

No.	Qualitative indices	UM	Designed (Theoretical) Value	The measured parameters values (average)	
				First sorting, M.I	Second sorting, M.II
1	The degree of fruit detachment from the branches of **M.I**	[%]	97-100	99.75	
2	Fruit damage rate in the detachment process of **M.I**, Gv	[%]	-	1.9	
3	Degree of sorting / screening, **M.II** for:	[%]			
	- large impurities, separated on the upper sieve, I_L		-	98.6	99.8
	- small impurities, separated on the upper and lower sieve, I_s		-	82.8	99.5
	- light impurities, smaller than the sea buckthorn fruits, I_l		-	92.5	99.8
4	Fruit loss rate in **M.II**, C_{fl}	[%]	-	0.8	0.55

The large impurities and some of the small ones can be manually sorted when the fruits come out of the **M.II**. The degree of separation of small and light impurities is reduced compared to the requirements of those who use the sorted fruits in the technological processes of the food or pharmaceutical industries, this is due to the fact that the impurities adhere to the surface of the fruits during the sorting process due to their moistening by the process of condensation, the material subjected to the process being frozen.

In order to finalize the process of separating small and light impurities from fruit, the product resulting from M.II it must be passed through a light impurities suction module after, beforehand, the material resulting from M II is dried, to obtain the purity of the fruits required by their beneficiaries.

In Fig. 7, 8 are presented some images from test made on ESFC equipment, respectively on **M.I** and **M.II**.



Fig. 7 - Images from the sea-buckthorn detachment module – M.I



Fig. 8 - Aspects from sea-buckthorn separating module - M.II

CONCLUSIONS

- The technical equipment that separates the sea buckthorn fruit from the branches, works in designed parameters such as: the inclusion in the functioning regime of the active parts (rotation axis and oscillating sieve) but also the adjustments established in the project phase;
- From the point of view of energy consumption and working capacity, it can be stated that they are lower than the initial estimates, this fact being the cause of the lower supply flow with branches, compared to the estimated one;
- From the point of view of the quality parameters (such as: fruits not detached from the branches, crushed fruits, impurities in the final product), it can be concluded that the values obtained for these parameters are acceptable, with possibilities for improvement;
- The variation of the supply flow with branches, depending on the rotational speed of the paddle arm, for different angles of inclination of the paddles and implicitly of the pitch of the spiral achieved by the paddles, does not faithfully respect the theoretical relationship (1), this fact having as cause the non-uniformity of the material and the feed flow rate. For the equipment tested in Variant II equipped with the separation rotor, the highest values for the feed flow resulted for the angle of inclination of the paddle was 45^0 and the rotational speed of the rotor was 90 min^{-1}. The variation of the supply flow with branches can be seen in the diagram in Fig. 6.
- The degree of fruit detachment from the branches of **M.I**, was 99.75 %;
- Fruit damage rate in the detachment process of **M.I**, was 1.9%.

ACKNOWLEDGEMENT

This work was supported by the Research, Innovation and Digitalization Ministry, "Development of the national research-development system", Subprogramme 1.2 – Institutional performance – Projects for financing excellence in RDI, contract no. 16PFE. Project: PN 19 10 01 05 - Integrated management of work in farms, vineyards and orchards, contract no. 5/ 07.02.2019.

REFERENCES

[1] Aare Aan, MatiHeinloo, (2014), Dynamics of a Frozen Sea Buckhorn Berry Motion in a Separator, 25th DAAAM International Symposium on Intelligent Manufacturing and Automation, DAAAM, Procedia Engineering, pp.689 – 698, doi: 10.1016/j.proeng.2015.01.421.

[2] Ivanišová E., Meňhartová K., Terentjeva M., Harangozo L., Kántor A., Kačániová M., (2019), The evaluation of chemical, antioxidant, antimicrobial and sensory properties of kombucha tea beverage, *The Journal of Food Science and Technology*, pp.1840-1846. doi: 10.1007/s13197-019-04217-3.

[3] James C., Purnell G., James S.J. (2015) A review of novel and innovative food freezing technologies. *Food and Bioprocess Technology,* 8(8): pp.1616–1634.

[4] Jing Zhao, Zhihua Zhang, Hongdan Zhou,Zengfu Bai, Zengfu Bai, Kun Sun (2023) The Study on Sea Buckthorn (Genus Hippophae L.) *Fruit Reveals Cell Division and Cell Expansion to Promote Morphogenesis, College of Life Science*, Northwest Normal University, China 12(5), pp.1005, https://doi.org/10.3390/plants12051005.

[5] Longsheng Fu, Jun Peng, Qiang Nan, Yongjie Cui, (2015) Simulation of vibration harvesting mechanism for sea buckthorn, Engineering in Agricultural, *Environment and Food*, pp. 101-108, DOI:10.1016/j.eaef.2015.08.003.

[6] Milea D., Vișan A.-L., Ciupercă R., Păun A., Zaica Al., (2020), Mathematical modelling of plane sieve kinematic regime to optimize the separation process of frozen sea buckthorn berries, *International Symposium ISB INMA TEH*, pp. 15-20.

[7] R. G. M. van der Sman, 2020, Impact of Processing Factors on Quality of Frozen Vegetables and Fruits, Food Engineering Reviews 12, pp. 399–420, https://doi.org/10.1007/s12393-020-09216-1.

[8] Roos, Y.H.; Drusch, S., (2015), Phase Transitions in Foods, 2nd ed.; Academic Press: San Diego, CA, USA, pp. 366.

[9] Tkacz K, Wojdyło A., Turkiewicz IP., Nowicka P., (2021), Triterpenoids, phenolic compounds, macro- and microelements in anatomical parts of sea buckthorn (Hippophaë rhamnoides L.) berries, branches and leaves, *Journal of Food Composition and Analysis*, Volume 103, October 2021, 104107, https://doi.org/10.1016/j.jfca.2021.104107.

[10] Vișan A.L., Milea D., Ciupercă R., Bogdanof B.G., Păun A., Giurescu I., (2019), Post-harvest technology develop to separate the Romanian sea buckthorn fruits from the harvested branches, *Proceeding of 6th INTERNATIONAL SYMPOSIUM International Conference "Research People and Actual Tasks on Multidisciplinary Sciences*", pp.237-241, Lozenec/Bulgaria.

[11] Zubarev Yu. A., Gunin A. V., Panteleeva E. I., Vorobyeva A. V. (2022), Sea buckthorn cultivars promising for mechanized harvesting by cutting fruit-bearing branches, Proceedings on *Applied botany genetics and breeding* 183(2): pp. 43-50, DOI:10.30901/2227-8834-2022-2-43-50.

[12] ***https://www.youtube.com/watch?v=Spgc-REEUa4;

[13] ***https://www.mz-web.de/jessen/sanddornernte-in-seyda-tonnenweise-geballte-vitamine-24789988).

[14] ***https://www.moz.de/landkreise/maerkisch-oderland/strausberg/artikel8/dg/0/1/975684/;

[15] ***http://www.nig-magdeburg.de/index.php?id=98&lang=2&hp=24).

[16] ***https://www.youtube.com/watch?v=s9VUmobIjeQ

[17] ***https://www.youtube.com/watch?v=xW5r7LZM2sI&feature=autoshare;

[18] ***http://www.weleda.co.nz/tuscany-italy/w3/i1039717/#.XIvI7ygzaUk;

[19] ***https://www.youtube.com/watch?v=NfZWwDSB3eI

[20] ***https://www.china.cn/pic/3963705228_0.html;

[21] ***https://www.china.cn/pic/3963711516_0.html;

[22] ***https://french.alibaba.com/product-detail/grape-destemming-crushing-machine-grape-destemmer-and-crusher-grape-stem-removing-machine-60481359883.html?spm=a2700.8699010.normalList.76.4d4417d2lenuwr;

[23] ***https://www.china.cn/pic/3932550216_0.html

[24] ***https://french.alibaba.com/product-detail/grape-destemming-crushing-machine-grape-destemmer-and-crusher-grape-stem-removing-machine-60481359883.html?spm=a2700.8699010.normalList.76.4d4417d2lenuwr.

INVESTIGATION OF THE ENERGY INDICATORS FOR THE SURFACE TILLAGE OF SOIL BY A HARROW WITH A SCREW-TYPE WORKING BODY

/

ДОСЛІДЖЕННЯ ЕНЕРГЕТИЧНИХ ПОКАЗНИКІВ ПОВЕРХНЕВОГО ОБРОБІТКУ ҐРУНТУ БОРОНОЮ З ГВИНТОВИМ РОБОЧИМ ОРГАНОМ

Volodymyr BULGAKOV[1)], Hryhorij KALETNIK[2)], Oleksandra TROKHANIAK[1)], Svitlana LUTKOVSKA[2)], Mykola KLENDII[3)], Semjons IVANOVS[4)], Lucretia POPA[5)], Vitalii YAROPUD[2)]

[1)]National University of Life and Environmental Sciences of Ukraine, Ukraine;

[2)]Vinnytsia National Agrarian University, Ukraine;

[3)]Separated Subdivision of National University of Life and Environmental Sciences of Ukraine, Berezhany Agrotechnical Institute, Ukraine;

[4)]Latvia University of Life Sciences and Technologies, Latvia;

[5)] National Institute of Research – Development for Machines and Installations Designed for Agriculture and Food Industry – INMA Bucharest / Romania

DOI: https://doi.org/10.35633/inmateh-71-72

Keywords: *tillage, machines, screw-type surface, tillage depth, work, power*

ABSTRACT

Restoration of the soil fertility is an important task for scientists and practitioners. Based on the constructed mathematical model of the surface of a screw-type working body, rotating around a fixed horizontal axis, there are determined the work and power of penetration of the screw-type working body into the soil, loosening the soil and overcoming the soil friction. It has been established that the cutting power is proportional to the square root of deepening of the working body ($a^{1/2}$), and the radius of the working body ($R^{1/2}$) is directly proportional to the speed of the unit V. On the basis of a complex of experimental studies, regression dependencies were derived to determine the traction resistance when cultivating the soil with a harrow, equipped with screw-type working bodies. It has been found that the dominant impact upon the value of the traction resistance P_x is exerted by the depth of tillage h, then by the angle of attack β of the battery of the screw-type working bodies, but the least impact is made by the change in the speed of the harrow V. The difference between the calculated and the experimental values of the traction resistance ranges from 9.6...11.2%.

АНОТАЦІЯ

Відновлення родючості ґрунту є важливим завданням для аграріїв України, серед яких зростає попит на застосування технології поверхневого обробітку ґрунту. На основі побудованої математичної моделі поверхні гвинтового робочого органу, який обертається навколо нерухомої горизонтальної осі, визначено роботу і потужність на врізання гвинтового робочого органу в ґрунт, розпушування ґрунту та на подолання тертя ґрунту. Встановлено, що потужність різання пропорційні кореню квадратному від заглиблення робочого органу ($a^{1/2}$) та радіусу робочого органу ($R^{1/2}$) прямо пропорційна швидкості руху агрегату V. На основі проведеного комплексу експериментальних досліджень, виведено регресійні залежності для визначення тягового опору, при обробітку ґрунту бороною із гвинтовими робочими органами. Встановлено, що домінуючий вплив на величину тягового опору P_x має глибина обробітку ґрунту h, далі кут атаки β батареї гвинтових робочих органів і найменше впливає зміна швидкості руху борони V. Різниця між розрахунковими та експериментальними значеннями величини тягового опору коливається в межах 9.6...11.2%.

INTRODUCTION

The present state of development of the transport and technological agricultural machines requires a search for new ways to improve the technological and operational parameters of the working bodies, which can increase productivity, improve the quality of the production processes, and also acquire new operational capabilities for restoration of the soil fertility (*Bularda et al., 2020; Croitoru et al., 2015; Vlăduţ D.I. et al., 2017*). The traction resistance of a tillage machine is a value that constantly changes during its operation. All the factors affecting the traction resistance of the machine may be classified into natural and climatic ones (the type and condition of the soil, the relief, rockiness, meteorological conditions); the structural (the type, shape and number of the working bodies, the material from which they are made, and the manufacturing technology, the machine weight, type and design of the running gear); the operational (technical condition of the machine, the correctness of adjustments, the degree of wear of the working bodies, etc.) *(Khaylis*, *1990*; *Lech, 2001; Croitoru et al., 2017; Vlăduţ D.I. et al., 2018; Vlăduţoiu et al., 2017; Xuanbin et al., 2019)*.

A number of works are devoted to the study of the functional and operational characteristics of the screw-type soil-cultivating working bodies and their interaction with the soil, in particular *Gevko and Rogatynsky, (1989), Pastushenko et al., (2020)*. In *Hevko et al., (2016), Pylypets et al., (2000) Klendiy and Pilipaka, (2016),* there are substantiated the design, kinematic and technological parameters of screw-type soil-cultivating working bodies in terms of their functional purpose. The theory of designing and constructing linear surfaces is reflected in *Klendii et al., (2016)*. The works *Wang, (2012),* theoretically substantiate the design of a soil-cultivating tool, in which helical surfaces in the form of a part of the unfolded helicoid are used as working surfaces.

The works *Manjula et al., (2017) Tripathi et al., (2015), Tian et al., (2018)* are devoted to the study of the impact of design and technological parameters of the developed variants of a harrow with screw-type working bodies upon the incorporation efficiency of the plant residues into the soil. The research of agrotechnological indicators of the quality of soil cultivated by a harrow with screw-type working bodies is considered in *Tsarenko et al., (2003), Yao et al., (2014)*.

However, the energy parameters of tillage by a harrow with screw-type working bodies have not yet been fully studied. So, the task of determining the work and power that must be consumed when tilling the soil with a harrow with screw-type working bodies is urgent.

The purpose of the work is to study the energy parameters for the soil cultivation by a screw-type working body of a transport-technological agricultural machine, depending on its parameters and operating modes.

MATERIALS AND METHODS

In order to determine the energy parameters of tillage by a harrow with screw-type working bodies, it will be considered in the form of an unfolded helicoid. Then the equation of the surface of the working body of the harrow with an axis parallel to the *Ox* axis has the following form:

$$\begin{aligned} X &= h\alpha - u\sin\varphi \\ Y &= p\sin\alpha - u\cos\varphi\cos\alpha \\ Z &= p\cos\alpha + u\cos\varphi\sin\alpha \end{aligned} \tag{1}$$

where: h – the screw helicoid parameter (ratio of helicoid pitch to full revolution), $h = \frac{b}{2\pi\cos\beta}$; β – the inclination angle of the axis of the cutting edge of the surface of the helicoid; φ – the elevation angle of the turning edge; u – the length of the rectilinear generatrix from the current point on the helix to the point on the surface; p – the diameter of the cylindrical shaft.

After turning the working body of the harrow at an angle β around axis *Oz* (Fig. 1) and taking into account its rotation around its own axis with an angular velocity ω, the trajectory of the movement of the arbitrary point on the surface of the working body will be written down as a function of time:

$$\begin{aligned} x(t) &= (h\alpha - u\sin\varphi)\cos\beta + (u\cos\varphi - p)\sin\beta\sin(\alpha+\omega) \\ y(t) &= (h\alpha - u\sin\varphi)\sin\beta - (u\cos\varphi - p)\cos\beta\sin(\alpha+\omega) \\ z(t) &= p\cos(\alpha+\omega) + u\cos\varphi\sin(\alpha+\omega) \end{aligned} \tag{2}$$

The speed of an arbitrary point on the surface is determined by differentiating dependence (2). There will be:

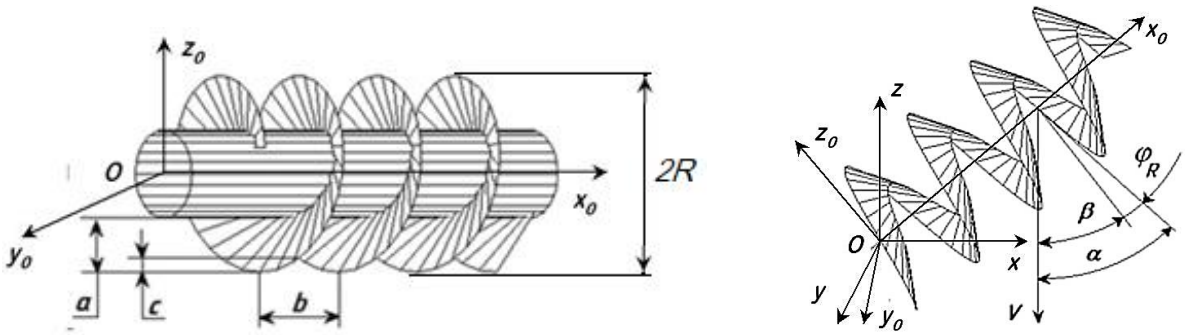
$$\overline{V} = \dot{x}(t)\cdot\bar{\imath} + \dot{y}(t)\cdot\bar{\jmath} + \dot{z}(t)\cdot\bar{k} \tag{3}$$

The relative speed of the soil movement at the entrance to the working area of the unit in the fixed coordinate system *OXYZ*, associated with the soil $V_0 = 0$, in the coordinate system of the aggregate will be equal to $V_2 = -\overline{V}$.

The relative speed of the movement V_{rel} of an arbitrary point of the screw-type working body relative to the soil will be equal to:

$$\overline{V_{rel}} = \overline{V} - \overline{\omega}\times\overline{r} \tag{4}$$

where $\overline{V}$ – the vector of the speed of the aggregate; $\overline{\omega}\times\overline{r}$ – the vector of the speed of the surface element of the working body with angular velocity $\overline{\omega}$ and the radius of rotation $\overline{r}$.



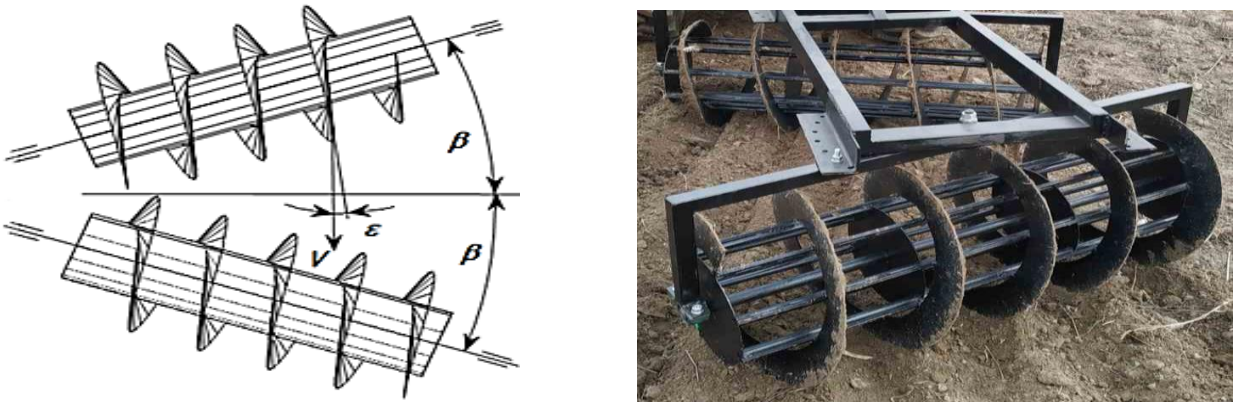
a b

Fig. 1 - Projections of the soil-cultivating helical surface of the screw-type working body

a – the depth of tillage, *c* – the height of the crests, *b* – the distance between the crests

In Fig. 2, on a scale, there are built the frontal and the horizontal projections of the screw-type working body for surface tillage to a depth of a = 0.10 m, with a pre-set distance between the ridges b = 0.2 m, with the designation of the rear angle ε. The design characteristics of this working body are: radii – R = 0.25 m, r = 0.15 m, the screw parameter – h = 0.0416. As a result of interaction with the soil, a reaction force arises, which will put pressure on the working surface of the coil.

The component of this force will try to shift the working body to the side, perpendicular to the direction of its movement. To balance this moment of force, it is advisable to arrange the aggregate in the form of two working bodies, as shown in Fig. 2. The surface of the second working body must have a turn rib with the opposite direction of winding and the direction of rectilinear generatrixes, as shown in Fig. 2. The cylindrical shaft for the tool is chosen taking into account the pre-set depth and tillage. Also, with this option it is possible to reduce the height of the ridges *c* and the distance *b* between the ridges (Fig. 4).



a) b)

Fig. 2 - A soil-cultivating harrow, consisting of two screw-type working bodies

a – a structural diagram; b – a general view

To avoid clogging of the inter-coil space with soil and plant residues, it is proposed to make the cylindrical shaft lattice.

The working body works like a disc soil-cultivating tool, that is, the profile of the cultivated field has ridges and depressions. At the moment of contact of the blade with the field surface, there are angles, similar to the angles of attack and roll for the disc tillage implements. It is possible to change the angle of roll by changing the inclination of the rectilinear generatrix of the surface with respect to its axis.

The developed working body has a simple design and low metal consumption. Unlike the disc tillage implements, it does not require individual bearing assemblies to mount individual tillage discs. Installation of one section of the screw tillage body is carried out using two bearing units, located at the ends of the section.

To determine the impact of the design, kinematic and technological parameters of the developed versions of the harrow with screw working bodies (independent factors (x_i) on the energy-power indicators of the aggregate displacement, experimental studies were used on the manufactured pilot plant, a general view of which is shown in Fig. 3.

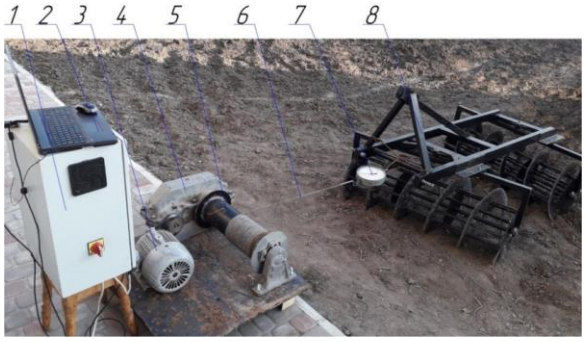


Fig. 3 - General view of the experimental setup and equipment for determination of the traction resistance of a harrow with screw-type working bodies

The harrow with a screw-type working body *8* was set in motion with the help of a cable *6,* which, in the process of moving, was wound on a drum *5*, fixed on a low-speed gearbox shaft *4*, driven by an electric motor *3*.

The Altivar 71-1 frequency converter and the Power Suite v.2.5.0 software, contained in PC 2, were used to start the engine and adjust its speed. The electric motor *3* and gearbox *4* are rigidly fixed at the beginning of the soil channel in order to be stationary, and only the harrow was movable.

After the completion of the process of moving the harrow with screw-type working bodies in the Power Suite window on the computer display, data were obtained about the change in torque and engine power over time. The scheme of the experiment: the implementation of the technological process by the aggregate for the purpose of surface loosening of the soil, closing moisture, planting seeds, destroying weeds, as well as for leveling the microrelief, created by pre-treatment. The number of repetitions is three. The minimum length of the path of the aggregate was 25 m. It was determined from the conditions that the permissible error does not exceed 2%, and the reliability is equal to 0.95.

In experimental studies, a planar method was used, which ensures the determination of the resulting force, acting between the electric motor with a gearbox and the harrow in one plane (longitudinal-vertical). Before each stage of the experiment the harrow with a screw-type working body was located in the extreme right position, the soil in the channel was preliminarily prepared according to the readings of the hardness tester.

The results of the research in the soil channel of the proposed harrow with a screw-type working body were illuminated in the computer display window.

Further, according to the peak values, the results obtained were recorded in tables.

RESULTS

To determine the loading parameters, the kinematics of turning of the working body will be considered, the axis of which is inclined at an angle β to axis OX of the fixed coordinate system $OXYZ$, associated with the soil, in which axis OY is directed in the direction of the movement of the aggregate, and axis OZ is directed vertically to the soil surface.

When the aggregate is moving at speed V, the passive working body is rolled with penetration into the soil to the tillage depth $h=a$, by the way, without slipping, a cylindrical surface with a radius r_0 will be rolled along a plane, buried from the soil surface to depth h_N :

$$r_0 = R - a + h_N \tag{5}$$

where R – the external radius of the screw-type spiral; h_N – the depth of the neutral layer $h_N < a$.

Accordingly, the angular speed of rotation of the screw-type working body, set at an angle β to the front of processing, is determined as:

$$\omega = \frac{V}{r_0 \cos\beta} \tag{6}$$

Therefore, each point of the working body with a radius less than $r<r_0$ will describe a curve called a shortened trochoid, and with radius $r>r_0$ – a curve called an elongated trochoid of this kind:

$$\begin{cases} y = r_0 - r\ sin\ \alpha\ cos\ \beta \\ z = r_0 - r\ cos\ \alpha \end{cases} \tag{7}$$

Fig. 4 shows the trajectory of the movement of the points of the screw-type working body during its rolling along the neutral layer ($z = 0$) in accordance with radius $r<r_0$ and $r>r_0$.

Since each point of the screw-type working body in its own coordinate system performs a plane-parallel movement, it is advisable to determine their speeds, using the method of the instantaneous center of velocities, which is located at a distance $z_C = r_0$ from the axis of the working body, and in plane yOz having coordinates C (y_C; z_C), where $y_C = 0$; $z_C = -r_0$. Determination of the speeds of the implement in relation to the mass of the cultivated soil is necessary to establish the nature of cutting and the distribution of forces on the surface of the implement.

The arm l_A of the arbitrary point A of the section of the helix, buried in the soil, the radial parameter and the angular α are determined according to the formula:

$$l_A = \sqrt{r^2 \cos^2 \alpha + (r \sin \alpha + z_0)^2} \quad (8)$$

For the points, placed on the cutting edge, $r = R$, arm l_{RA} will be equal to:

$$l_{RA} = \sqrt{R^2 + 2Rr_0 \sin \alpha + z_0^2}\ . \quad (9)$$

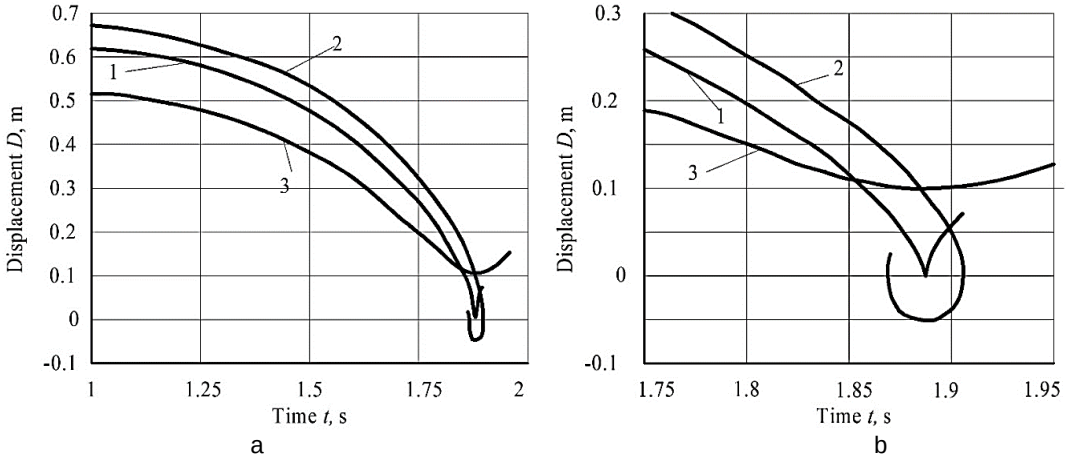


Fig. 4 - The trajectory of movement of the points of the screw-type working body during its rolling along the neutral layer ($z = 0$) of the soil (a) with the rolling radius

1 – r = 0.3 m, 2 – r = 0.2 m and 3 – r = 0.35 m

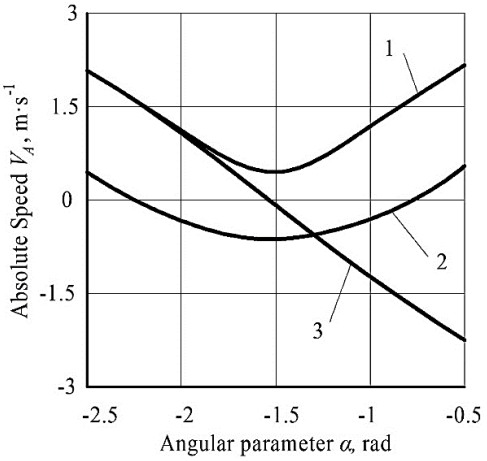


Fig. 5 - Change in the absolute velocity of point V_A at the edge of the screw with radius R = 0.28 m at the aggregate velocity V = 2 m s^{-1} from its angular parameter α

1 – absolute velocity V_A; 2 – projection V_A onto the axis of the system screw Oy_0; 3 – projection V_A onto the axis of screw Oz_0

Accordingly, the absolute speed V_A of the specified point in the fixed coordinate system $OXYZ$ will be $V_{Ay} = |\omega| l_{RA}$. Its projections on the Oy_0 axis and on the Oz_0 axis, respectively, will be equal to $V_{Ay} = |\omega| l_{RA}$. Its projections on axis Oy_0 and on axis Oz_0, respectively, will be equal to:

$$V_{Ay0} = \omega R \cdot \cos\alpha \quad (10)$$

$$V_{Az0} = -\omega(R \cdot \sin\alpha + r_0) \quad (11)$$

The change in speed and its components is shown in Fig. 5. In the coordinate system of the aggregate, the vertical component will not change, while the horizontal component will expand into the Oy and Oz axes (Fig. 6). In this connection:

$$V_{Ay} = \omega \cdot R \cdot \cos\alpha \cdot \cos\beta \quad (12)$$

$$V_{Az} = -\omega(R \cdot \sin\alpha + r_0) \cdot \sin\beta \quad (13)$$

Let us consider the speed components of the movement of the points of the cutting edge in the direction of the normal to the cutting surface and the tangent.

A normal direction is set by the radius of the vector, directed from an arbitrary point of the edge (point $A(R;\alpha)$) to the axis of rotation of the screw. The tangential component of the speed of point $A(R;\alpha)$ is directed along the tangential cutting surface in the direction of rotation and is directed perpendicular to the radius of the vector and the axis of rotation of the screw.

Accordingly, the indicated speed components of point $A(R;\alpha)$ are determined by the following dependencies:

$$V_{An} = V_{Ay} \cdot \cos(\alpha) + V_{Az} \cdot \sin(\alpha); \quad (14)$$

$$V_{At} = -V_{Ay} \cdot \sin(\alpha) + V_{Az} \cdot \cos(\alpha). \quad (15)$$

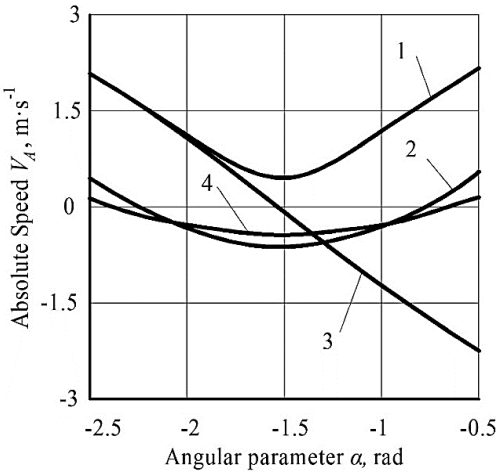


Fig. 6 - Change in the absolute velocity of point V_A on the edge of the propeller with radius R = 0.28 m at the aggregate velocity V = 2 m·s^{-1} from its angular parameter α

1 – absolute velocity V_A; 2 – the projection of V_A onto axis Oy; 3 – projection of V_A onto axis Oz; 4 – projection of V_A onto axis Ox

The change in speeds on the cutting edge is shown in Fig. 7 and Fig. 8.

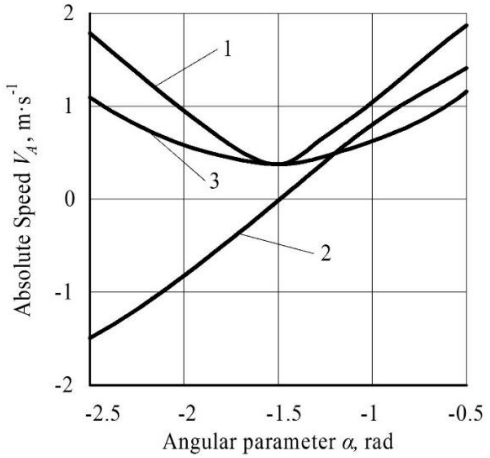


Fig. 7 - Change in absolute velocity V_A of the screw with radius R = 0.28 m at the speed of the aggregate V = 2 m·s^{-1} from α

1 – the absolute velocity V_A; 2 – the normal component V_{An}, perpendicular to the soil surface of the screw axis; 3 – the tangential component of V_{At}, tangential to the soil surface of the axis of the screw system

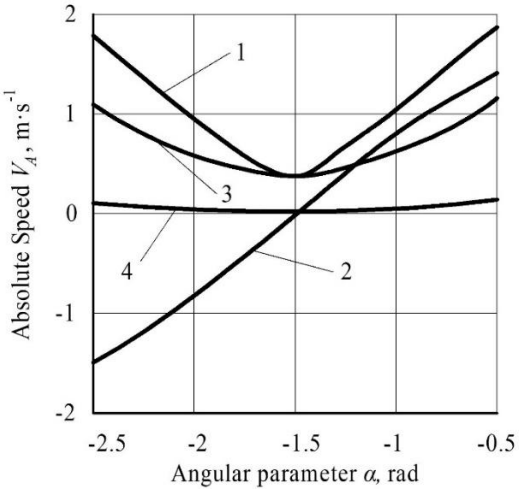


Fig. 8 - Change in the absolute speed V_A of the screw with a radius R = 0.28 m at an aggregate speed V = 2 m·s^{-1} from α to the line of the helical edge

1 – the absolute velocity V_A; 2 – the normal component V_{An} to the line of the screw-type edge; 3 – the tangential component $V_{A\tau}$ to the line of the screw-type edge; 4 – the binormal component V_{Ab} to the line of the screw-type edge

The tangential component of an arbitrary point $A(R; \alpha)$ is decomposed into a component in the direction of the blade (tangential to the edge line) $V_{A\tau}$ and a shear component along the soil (along the binormal to the edge line) V_{Ab}:

$$V_{A\tau} = V_{At} \cdot \cos(\varphi_R) \tag{16}$$

$$V_{Ab} = V_{At} \cdot \sin(\varphi_R) \tag{17}$$

Let us consider interaction of the passive screw-type working body with the soil. A screw with an outer radius R and an inner radius r_0 deepens into the soil to depth a, forming a submerged helical segment cut off by a plane $z=a$.

Area S of the section of the helical surface, buried by value a is defined as the integral over angle α in the coordinate system of the section y_0Oz_0, normal to the axis of the helix, running the value from $\alpha_1 = \pi + \arccos(1-a \cdot R^{-1})$ to $\alpha_2 = 2\pi - \arccos(1-a \cdot R^{-1})$. Considering the symmetry of the screw-type segment, the area of the recessed section will be equal to:

$$S = \int_0^{\arccos(1-a/R)} \left(R\sqrt{R^2+b^2} - \frac{R-a}{\cos\alpha}\sqrt{\frac{(R-a)^2}{\cos^2\alpha}+b^2} \right) d\alpha \tag{18}$$

The working helical surface is affected by the distributed pressure force directed along the normal and the corresponding friction forces from the mutual displacement of the soil relative to the helical surface, the direction of which is opposite to the relative force vector. Taking into account expression (1), the normal to the surface of the straight helicoid in vector form is defined as follows:

$$\bar{n}_{uv} = \sin\alpha_p \sin v\bar{i} - \sin\alpha_p \cos v\bar{j} + \cos\alpha_p \bar{k} \tag{19}$$

where $\alpha_p = arctg[T/(2\pi u)]$ – the elevation angle of the helix with a running radial parameter $u=r$; T–spiral step, T = 0.2 m.

The projections of the total forces from the normal pressure $p = p(r; \alpha)$ are equal, on plane y_0Oz_0 they are an integral part of the axial load onto the screw, and the projections on plane x_0Oz_0 are the component of the force that are turning the working passive body. Similarly, the projections of the contacting distributed forces $|\tau| = \mu|p|$ on these planes is the second component of the resulting forces. Here μ is the coefficient of friction of the working body to the soil surface.

Since it will be taken into account that tillage is carried out on the soil that has already been pre-treated, and in this case a relatively small depth of tillage is used, in the further study the distributed value of soil pressure will be replaced with its indirect value $p(r;\alpha) = p_c = \text{const}$.

Accordingly, the projections of the total forces on planes y_0Oz_0 and x_0Oz_0 will be equal:

$$P_{yOz} = p_c \cdot S_{yOz} \tag{20}$$

$$P_{xOz} = p_c \cdot S_{xOz} \quad (21)$$

where S_{yOz} and S_{xOz} – projections of the working area of the screw (screw segment) onto the corresponding coordinate planes of system $Ox_0y_0z_0$.

Next, S_{yOz} and S_{xOz} are defined. The surface of the helical segment onto plane y_0Oz_0 is projected into a circular segment, the arc of which is equal to l_α, and the chord, defining the boundary of the soil, is l_y. They will be respectively equal:

$$l_\alpha = R \cdot \alpha_r = 2R \arccos(1 - a \cdot R^{-1}) \quad (22)$$

$$l_y = \sqrt{2Ra - a^2} \quad (23)$$

The area of the circular segment S_{yOz} will be equal to:

$$S_{yOz} = R^2 arc\cos\left(1 - \frac{a}{R}\right) - (R - a)\sqrt{2Ra - a^2} \quad (24)$$

The surface of the helical segment onto plane x_0Oz_0 is projected into a segment, limited by a sinusoid and line $z=a$, the chord of which is equal to:

$$l_T = 2b \cdot \arccos(1 - a \cdot R^{-1}) \quad (25)$$

The area of the indicated segment S_{xOz} of the cosine wave is equal to:

$$S_{xOz} = 2R \cdot \cos[\arccos(1 - a \cdot R^{-1})] - 2b(R - a) \cdot \arccos(1 - a \cdot R^{-1}) \quad (26)$$

Dependencies (24) and (26) are inconvenient for engineering calculations, so they are simplified by applying them to the functions, describing the curves into which a helix is projected onto the indicated planes by expanding them into a Maclaurin series.

The helix (1) on the coordinate plane y_0Oz_0 is projected into a circle, the coordinate plane and x_0Oz_0 – in a cosine wave, the equations of which, respectively, will be equal to:

$$z_k = -\sqrt{R^2 - y^2} \quad (27)$$

$$z_c = -R\cos(y / b) \quad (28)$$

Let us expand the circle equation (27) as a function of $z_k(y)$ in the Maclaurin series:

$$Z_{KM} = -R + \frac{y^2}{2R} + \frac{y^4}{8R^3} \quad (29)$$

Figure 7 shows a graph of function (1), with which the equation of the circle (29) is replaced with a radius r = 0.25 m for the buried area of the soil, with a depth of a = 0.1 m.

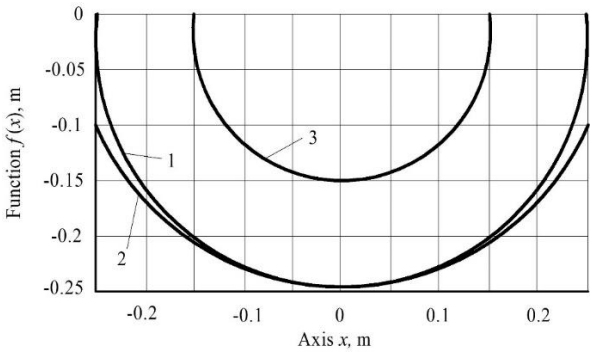
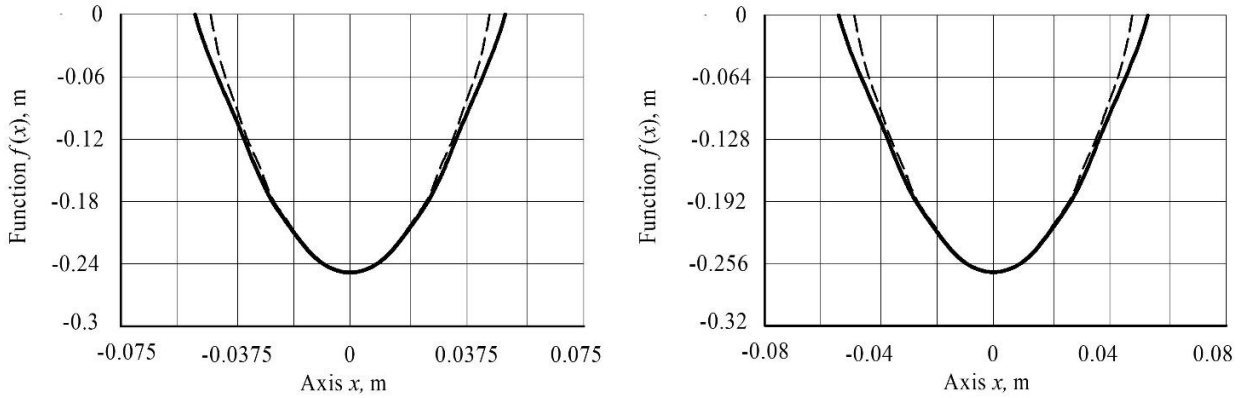


Fig. 9 - Graphs of functions, describing the outer circle with a radius R = 0.25 m – the projections of the helical surface onto the normal plane y_0Oz_0 (1), its approximation by a parabolic function in the Maclaurin series expansion (2), and the inner circle of the projection of the helix of the horizontal soil level line

The Maclaurin series expansion of the cosine equation (28) gives:

$$z_{cM} = -R + \frac{Ry^2}{2b^2} - \frac{Ry^4}{24b^4} + ... + O(y^6) \quad (30)$$

Fig. 10 shows a graph of function (29), with which will be replaced the cosine equation (30) for the working body with a radius of r = 0.25 m and a step of T = 0.2 m for a buried area with a depth of a = 0.1 m (Fig. 10 a), and a working body with a radius of r = 0.28 m and a pitch of T = 0.25 m (Fig. 10 b) for a recessed area with a depth of a = 0.12 m.



a) b)

Fig. 10 - Graphs of functions that describe a section of the sinusoid – a projection of the outer edge of the screw (helix) on the vertical longitudinal plane x_0Oz_0 (a solid line), its approximation by a parabolic function by expansion in the Maclaurin series (dashed line), and the horizontal line of the working body with an outer radius R = 0.25 m, step T = 0.2 m (a) and R = 0.28 m, step T = 0.25 m (b)

The analysis of dependences (29) and (30) shows that, with sufficient accuracy for practical calculations, one can restrict oneself to two terms of the expansion, thus approximating these dependences by square parabolas.

Accordingly, the chords of the projection of the helix onto planes y_0Oz_0 and x_0Oz_0 will be equal to:

$$l_{yM} = k_1\sqrt{Ra} \tag{31}$$

$$L_{xM} = k_2 b\sqrt{\frac{a}{R}} \tag{32}$$

where k_1 and k_2 – consolidated digital coefficients, respectively, for each of the projections.

Using the dependence to determine the areas that are limited by second-order parabolas, the dependences for the projection areas (24) and (26), respectively, will assume the form:

$$S_{xOzM} = \frac{4\sqrt{2}b}{3\sqrt{R}}a^{\frac{3}{2}} = 1,9\frac{b}{\sqrt{R}}a^{\frac{3}{2}} \tag{33}$$

$$S_{yOzM} = \frac{4\varepsilon\sqrt{2R}}{3}a^{\frac{3}{2}} = 1,7\sqrt{Ra}^{\frac{3}{2}} \tag{34}$$

In Fig. 11 and Fig. 12 there is shown correspondence of the curves with the dependences (24) and (33) for the projection onto plane y_0Oz_0 (Fig. 9) and dependences (26) and (34) for plane x_0Oz_0 – Fig. 12.

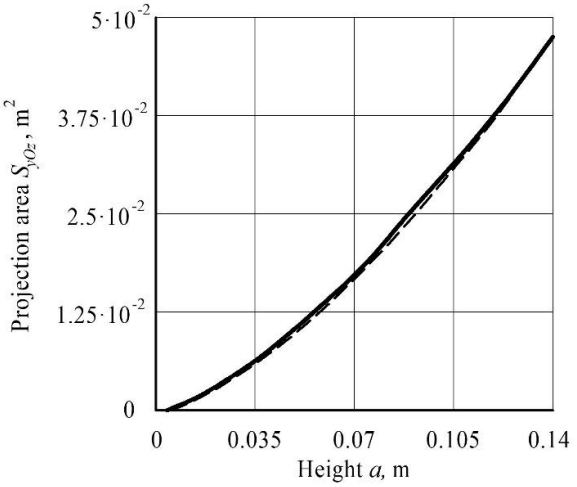


Fig. 11 - Dependence of the projection area S_{yOz} of the helical segment onto the normal coordinate plane y_0Oz_0 (solid line) upon height a and its approximation (dashed line) by dependence (33) for a screw with outer radius R = 0.28 m

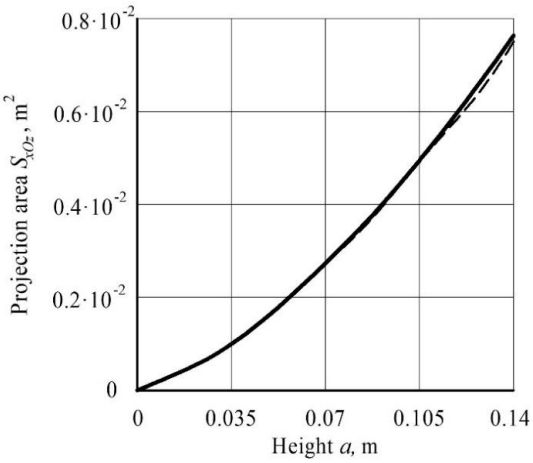


Fig. 12 - Dependence of the projection area S_{xOz} of the helical segment onto the longitudinal coordinate plane x_0Oz_0 (solid line) and its approximation (dashed line) by dependence (34) for a screw with outer radius R = 0.28 m, pitch T = 0.25 m

Accordingly, the chord of the screw segment, formed by the surface of the screw-type working body, immersed into the soil, will be equal to:

$$l_{\max M} = k_1 R \sqrt{1 + \frac{k_2^2 b^2}{k_1^2 R^2}} \cdot \sqrt{a} \tag{35}$$

The chord (34) is located in the plane, on which the projection of the helical sector area will be maximum:

$$S_{\max M} = \frac{2k_1}{3} \sqrt{1 + \frac{k_2 b^2}{k_1 R^2}} \cdot a^{\frac{3}{2}} \tag{36}$$

The indicated area projection practically corresponds to the area of the helical segment, immersed into the soil, and dependence (35) with an error of not more than 2% can be used to calculate the area instead of dependence (12).

When the helical section is inclined at an angle β to the front of the movement of the aggregate, the area of the helical segment, the area of which is determined by dependence (12) or approximated (36), is projected onto the frontal coordinate plane xOz of the coordinate system of the aggregate $Oxyz$ and, accordingly, plane xOz of the fixed coordinate system $OXYZ$, connected with the soil, into a paraboloid segment, the chord of which will be equal to:

$$l_{x\beta} = l_x \cos\beta + l_y \sin\beta = k_1 \sqrt{Ra} \sin\beta + k_2 b \sqrt{\frac{a}{R}} \tag{37}$$

Dependence (37) can be represented as:

$$l_{x\beta} = \frac{\sqrt{Ra}}{\sqrt{1 + \frac{k_2^2 b^2}{k_1^2 R^2}}} \sin\left(\varphi_\beta + \beta\right) \tag{38}$$

parameter, which is determined by the angle.

Accordingly, the area of the frontal surface of the working zone of the coil on plane XOZ, which has the shape of a paraboloid segment, will be equal to:

$$S_{XOZ} = \frac{2}{3} l_{x\beta} \cdot a = \sqrt{\frac{R}{1 + \frac{k_2^2 b^2}{k_1^2 R^2}}} \cdot a^{\frac{3}{2}} \sin\left(\varphi_\beta + \beta\right) \tag{39}$$

The cutting forces act upon the cutting edge of the helical surface. Their normal components, directed perpendicular to the edge in the plane of the helical working surface and directed towards its axis, are characterized by a load, distributed along the edge with intensity $q_n = q_n(\alpha)$, and the contacting components are characterized by a distributed load with intensity $q_t = q_t(\alpha)$, which are directed along the tangent to the edge and directed in the direction of rotation of the passive screw-type working body. Cutting into the soil passes along the leading edge of the helical segment, the arc length of which is determined according to

expression (15). Expanding this dependence $l_\alpha = l_\alpha(\alpha)$ into a descending Maclaurin series, a simplified approximate dependence l_α is obtained:

$$l_\alpha = 2(2a \cdot R)^{1/2} \cdot (1 + a \cdot (12R)^{-1}) \quad (40)$$

For the screw-type working bodies with a radius $R \leq 0.3$ m, dependence (22) with an error of less than 1% can be written as:

$$l_\alpha = 5.7(aR)^{1/2} \quad (41)$$

Considering that the edge of the screw-type working body cuts into the soil both in the normal and tangential directions and the speed of movement of the edge in these directions according to (14) – (16) is commensurate (Fig. 5, 6), then the cutting has a complex character with normal and tangential movement of the blade. Let us assume that the intensity of the distributed normal cutting components is constant and proportional to the value of the bearing resistance (hardness) of the soil σ_{lim}, $q_n = K_q \sigma_{lim} . V_{n.}$, where the resulting speed of the edge blade is given, which is 2/3 of the maximum value V_{An} determined by dependence (14). Here K_q depends on the sharpness of the edge blade. Then the power, consumed for cutting the cutting edge of the screw along the normal, taking into account its entire length of its cutting section will be equal to:

$$N_{p.n} = q_n l_\alpha V_{n.\sigma} = 2.85\, K_q \sigma_{lim}\, V_{n.\sigma} (aR)^{1/2} \quad (42)$$

The power from the tangential components of the cutting force of the edge blade is $N_{p.\tau} = \mu N_{p.n,}$ where μ is the coefficient of the soil friction along the edge.

Accordingly, the total power at the edge (blade) of the screw is:

$$N_{p.} = K_p \sigma_{lim} (1 + \mu) V_{n.\sigma} (aR)^{1/2} \quad (43)$$

where K_p – the integral cutting factor, K_p = 2.85 K_q.

The power, consumed for the resistance of the soil to its movement by the passive working body, is determined mainly by the friction forces along the helical surface since the normal speeds V_{Ab} are insignificant (Fig. 6), but the normal component forces are partially mutually compensated by the rotation of the passive working body.

Accordingly, the power to move the soil will be proportional to the area of the screw sector, the coefficient of friction *f* (taking into account the soil sticking to the working surfaces of the screw) and the hardness of the soil.

Taking into account (34), the power to move the soil will be written in the following form:

$$N_{n.} = K_n \sigma_{zp} V_{n.\tau}\, a^{1/2} \cdot a^{3/2} = K_n \sigma_{zp} V_{n.\tau}\, a^2 \quad (44)$$

where $V_{n.\tau}$ – the reduced value of the average speed of the screw moving relative to the soil, in the first approximation equal to 3/4 of value $V_{a\tau}$, determined from the dependence (16).

The analysis of dependences (42) and (43) shows that the cutting power is proportional to the square root of the deepening of the working body ($a^{1/2}$), and the radius of the working body ($R^{1/2}$) is directly proportional to the aggregation speed V. The power to move the soil is non-linearly proportional to the tillage depth ($a^{1/2}$), the radius of the working body ($R^{1/2}$) and is directly proportional to the aggregation speed V.

Since for the passive working bodies the analytical determination of the components of the load on the screw working body is laborious, in particular, it is difficult to determine the center of instantaneous speeds, then for preliminary calculations of the energy consumption for tillage by a harrow with screw-type working bodies, it is possible to carry out simplified calculations.

In particular, the integral work of displacement, cutting in and compaction can be determined from the displaced volume using Fink's formula:

$$dA_1 = p_{cp} \cdot \ln(1 + \varepsilon) dV_1 \quad (45)$$

where p_{cp} is the average pressure on the screw-type working body; ε – the linear soil compaction in the direction of movement of the aggregate up to 0.1; dV_1 – elementary volume undergoing compaction.

Accordingly, the power for moving, cutting in and compacting:

$$N_1 = p_{cp} \cdot (1 + \varepsilon) \cdot B \cdot h \cdot V \quad (46)$$

where B is the grip width; h – the processing depth; V – the speed of the aggregate.

The work, spent to provide kinetic energy to the soil particles by a screw-type working body at the loosening stage, is equal to:

$$dA = \rho_v \cdot v_v^2 \cdot dV_2 \quad (47)$$

where ρ_v – the bulk density of the soil; dV_2 – the elementary volume gaining speed V_2.

The power, spent for loosening and providing soil particles with kinetic energy, is equal to:

$$N = \rho_v \cdot k_v \cdot V_{2c}^2 \cdot B \cdot h \cdot V \quad (48)$$

where k_v – the coefficient of reduction of the particle velocities to the average k_v = 1.05…1.10.

The work, spent to overcome the friction of the soil against the screw-type working body, is equal to:

$$dA_3 = p_{cp} \cdot \mu \cdot l_w \cdot dS \quad (49)$$

where μ – the friction coefficient; dS – the surface element of the screw; l_w – the length of the movement (path) of the soil along the surface of the working body.

Accordingly, the power consumed to overcome the frictional resistance is equal to:

$$N_3 = \mu \cdot p_{cp} \cdot S_c \cdot V_{rel} \quad (50)$$

where S_c – the total area of the particle of the screw-type working body, buried in the soil; V_{rel} – relative speed of the movement according to (14).

The experimental research program included research into the change in the value of the horizontal component P_x of the resistance forces from the speed of the harrow V at various values of the angle of attack of the screw body β and the depth of processing h. To obtain the values of the studied quantity, there were used the peak (maximum) values, obtained from the data studies.

To determine the impact of the parameters of the technological and kinematic processing and the design parameters of a harrow with screw-type working bodies upon the traction resistance of the experimental version of the harrow (optimization parameter P_x), a full-factor experiment PFE-3^3 was performed, that is, determination of the dependence of the horizontal component P_x of the resistance forces on the changes in the three main speed factors of the harrow movement V, km·h^{-1}, angle of attack β of a battery of the screw-type working bodies, deg., and the processing depth h, m, i.e. $P_x = f(V, \beta, h)$. Since during the experiments the variable independent factors are heterogeneous and have different units of measurement, and the numbers, expressing the value of these factors, are of a different order, they were led to a unified system of calculations by moving from real values to encoded ones, presented in Table 1.

After coding the factors a plan-matrix of the corresponding multifactorial experiment of the PFE type 3^3 was compiled for the number of experiments $N = 3^3$. Experiments were performed with five-fold repeatability.

Table 1

The results of coding the factors and the levels of their variation in the study of the traction resistance of a harrow with a screw-type working body

Factors	Designation		Interval of variation	Levels of variation, natural/coded		
	Parameter value indicated as a code	Parameter value in the form of its natural value				
Speed of the harrow, *V*, km·h^{-1}	X_1	x_1	3	4/**–**1	7/0	10/**+**1
Angle of attack of the screw-type body, *β*, deg.	X_2	x_2	15	10/**–**1	25/0	40/**+**1
Depth of tillage, *h*, m	X_3	x_3	0.02	0.08/**–**1	0.1/0	0.12/**+**1

A general view of the regression equation of the traction resistance of a harrow with a screw-type working body, depending on the change in the speed of the harrow V, km·h^{-1}, the angle of attack β of the battery of the screw-type working bodies, deg., and the processing depth h, m, i.e. $P_x = f(V, \beta, h)$, has the form:

$$P_x = 423.64 + 821.58h + 219Vh + 0.296\beta^2 - 12.21\beta h + 46726h^2 \quad (51)$$

The obtained regression equation (51) may be used to determine the traction resistance of a harrow with a screw-type working body P_x, depending on the change in the speed of the harrow V, the angle of attack β of a battery of the screw-type working bodies and the tillage depth h, when tilling the soil.

Using the Statistica-6.0 software for the PC, a graphical reproduction of intermediate general regression models was built in the form of quadratic response surfaces and their two-dimensional sections of the traction resistance of a harrow with a screw-type working body P_x (force that acts in the horizontal plane) as a function of two variable factors $x_{i(1,2)}$ at a constant level of the corresponding third factor $x_{i(3)} = \text{const}$.

Graphical values of the results of the dependence of traction resistance, obtained by using Statistica-6.0, are shown in Fig. 13.

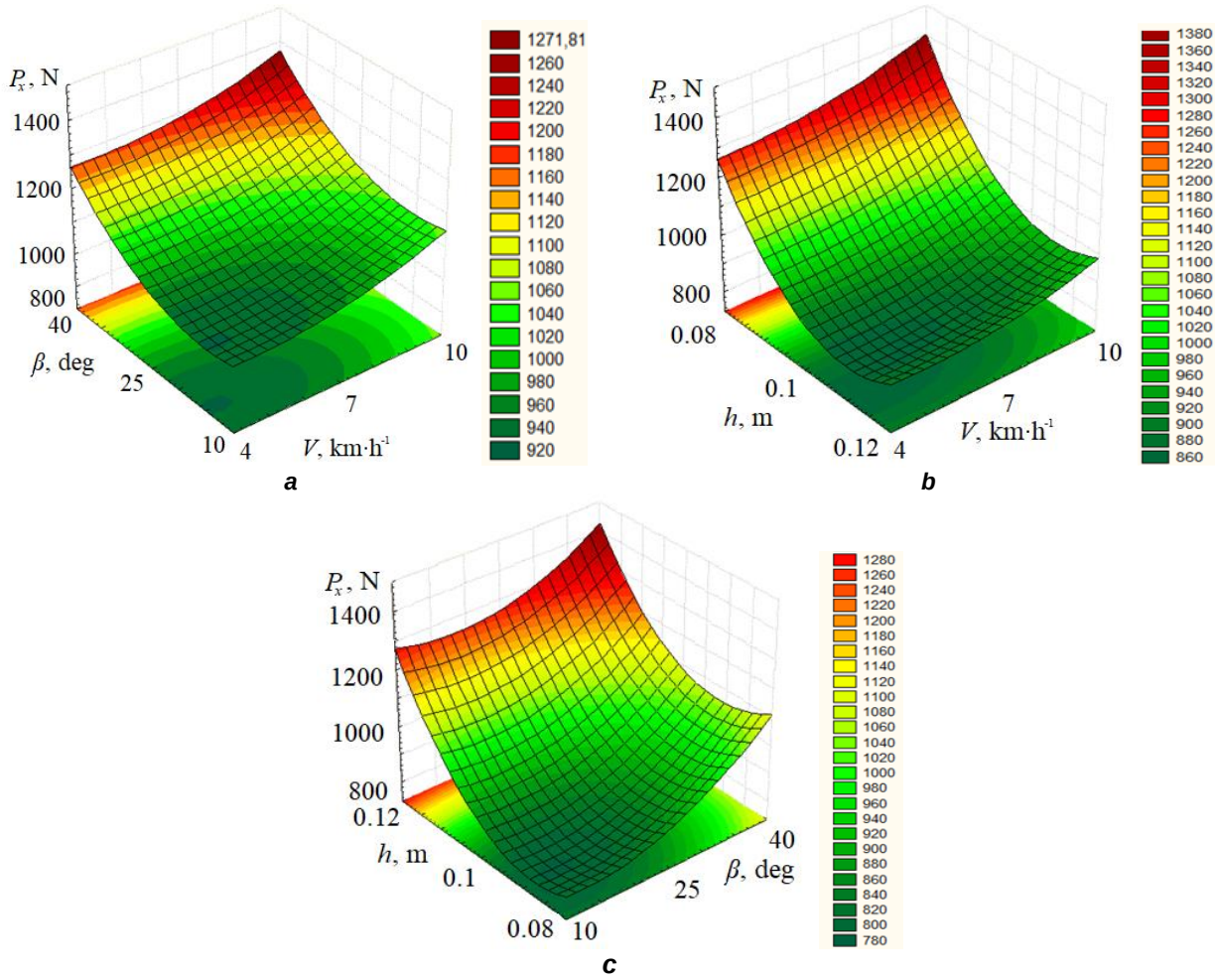


Fig. 13 - The response surface of the dependence of the traction resistance of a harrow with a screw-type working body, when tilling the soil: a – P_x (V, β); b – P_x (V, h); c – P_x (β, h)

Analysis of the regression equations shows that the following factors have the greatest impact upon the change in traction resistance: the depth of tillage h and the angle of attack β of a battery of screw-type working bodies. In general, an increase in traction resistance is caused by all factors: h, β and V. It is evident from Fig.13 that, with an increase in the factors h, β and V, the value of traction resistance increases. It has been found that an increase in the speed of the harrow V from 4 m·s^{-1} to 10 m·s^{-1} leads to an increase in traction resistance P_x by 9.8%. Increasing the angle of attack β from 10 deg. to 40 deg. leads to an increase in traction resistance P_x by 26.3%. An increase in the working depth h from 0.08 m to 0.12 m leads to an increase in traction resistance P_x by 29.8%. The angle of attack of a battery of screw-type working bodies β and the speed of the harrow V have a less significant effect.

CONCLUSIONS

From the analysis of the results obtained in the experimental research, the following conclusions were drawn:

1) It has been established that the cutting power of the soil by a screw-type working body of a transport-technological agricultural machine is proportional to the square roots of the penetration of the working body ($a^{1/2}$) and the radius of the working body ($R^{1/2}$) and is directly proportional to the speed V of the transport-technological agricultural machine. The power to move the soil depends on the depth of processing ($a^{1/2}$), the radius of the working body ($R^{1/2}$) and is directly proportional to the speed V of the machine.

2) Regression dependencies have been obtained to determine traction resistance when cultivating the soil a harrow with screw-type working bodies. It was found that the depth of tillage h has a dominant influence upon the value of traction resistance P_x, then angle of attack β of a battery of screw-type working bodies, but the change in the speed of the harrow V has the least impact. The constructed response surfaces of the dependence of traction resistance P_x during tillage by a harrow with screw-type working bodies, using the software "Statistica-6.0" for Windows, showed that an increase in the speed of the harrow V from 4 km·h^{-1} to 10 km·h^{-1} leads to an increase in traction resistance P_x by 9.8%. An increase in the angle of attack from 10 deg. to 40 deg. leads to an increase in traction resistance P_x by 26.3%. An increase in the tillage depth a from 0.08 m to 0.12 m leads to an increase in traction resistance P_x by 29.8%.

3) The difference between the calculated and experimental values of traction resistance ranges from 9.6...11.2%, which confirms the adequacy of the mathematical model.

REFERENCES

[1] Bularda M., Vişinescu I, Ghiorghe A., Vlăduţ V., Cujbescu D. (2020). The effect of conservative agricultural works on soil and field plants and optimized mechanization technologies, *INMATEH – Agricultural Engineering*, 61 (2), pp. 323-338, DOI: https://doi.org/10.35633/inmateh-61-35.

[2] Croitoru Şt., Marin E., Bădescu M., Vlăduţ V., Ungureanu N., Manea D., Boruz S., Matei Gh. (2015). Agrotechnical and energetic characteristics of new designed subsoiler, *Proceedings of the 43 International Symposium on Agricultural Engineering "Actual Tasks on Agricultural Engineering",* pp.165-176, 2015, Opatija-Croaţia.

[3] Croitoru Şt., Vlăduţ V., Voicea I., Gheorghe Gh., Marin E., Vlăduţoiu L., Moise V., Boruz S., Pruteanu A., Andrei S., Păunescu D. (2017). Structural and kinematic analysis of the mechanism for arable deep soil loosening, *Proceedings of the 43 International Symposium on Agricultural Engineering "Actual Tasks on Agricultural Engineering",* pp. 207-216, Opatija- Croaţia.

[4] Gevko B.M., Rogatynsky R.M. (1989). Screw feeders of agricultural machines. *Lvov. Great school.* 176 p.

[5] Hevko R.B., Rozum R.I., Klendiy O.M. (2016). Development of design and investigation of operation processes of loading pipes of screw conveyors. *INMATEH – Agricultural Engineering*, 50(3), 89-94.

[6] Khaylis G.A. (1990). Calculation of the working bodies of soil-cultivating machines: a tutorial. *Kyiv: UMK VO*, 83 p.

[7] Klendii M.B., Pilipaka S.F. (2016). An analytical model of the installation of spherical disks for the determination of geometric and technological characteristics. *Scientific Bulletin of the National University of Bioresources and Nature Conservation of Ukraine*, 241, 140–150.

[8] Klendii M.B., Klendii O.M. (2016). Interrelation between incidence angle and roll angle of concave disks of soil tillage implements. *INMATEH Agricultural Engineering*, 49(2), 13–20.

[9] Lech M. (2001). Mass flow rate measurement in vertical pneumatic conveying of solid. *Powder Technology*, 114(1–3), 55-58.

[10] Manjula E.V.P.J., Hiromi A.W.K., Ratnayake C. & Melaaen M.C. (2017). A review of CFD modelling studies on pneumatic conveying and challenges in modelling offshore drill cuttings transport. *Powder Technology*, 305, 782-793.

[11] Pastushenko S.I., Klendiy M.B., Klendiy M.I. (2020). The study of agrotechnological indications in the quality of soil processing by a harrow with screw working bodies. *Science bulletin TDATU.* 10(1), 1-12.

[12] Pylypets M.I., Gevko I.B., Pik A.I. (2000). Optimization of the working body with a spring shaft for flexible screw conveyors. *Bulletin of the National University "Lviv Polytechnic": "Optimization of manufacturing processes and technical control in machine-building and auxiliaries"*, 412, 84–91.

[13] Tian Y., Yuan P., Yang F., Gu J., Chen M., Tang J., Su Y., Ding T., Zhang K. & Cheng Q. (2018). Research on the principle of a new flexible screw conveyor and its power consumption. *Applied Sciences*, 8(7), article number 1038.

[14] Tripathi N., Sharma A., Mallick S.S. & Wypych P.W. (2015). Energy loss at bends in the pneumatic conveying of fly ash. *Particuology*, 21, 65-73.

[15] Tsarenko O.M., Voityuk L.M., & Shvayko M.V. (2003). Mechanical-technological properties of agricultural materials. *Kyiv: Meta*.

[16] Vlăduţ D.I., Vlăduţ V., Grigore I., Biriş S. (2017). Experimental research in qualitative indices of work for equipment for seedbed preparation in conservative system, *16th International Scientific Conference "Engineering for Rural Development"*, pp.1174-1179, Jelgava, Latvia.

[17] Vlăduţ D.I., Biriş S., Vlăduţ V., Cujbescu D., Ungureanu N., Găgeanu I. (2018). Experimental researches on the working process of a seedbed preparation equipment for heavy soils*, INMATEH – Agricultural Engineering*, 55 (2), pp.27-34.

[18] Vlăduţoiu L., Cârdei P., Vlăduţ V., Fechete L. (2017). Modern trends in designing and selecting the machine / equipment for soil deep tillage, *16th International Scientific Conference "Engineering for Rural Development*", pp.1415-1420, Jelgava, Latvia.

[19] Wang, D.-X. (2012). Research on numerical analysis and optimal design of the screw conveyor. *Univ. Technol.*, 27, 32-36.

[20] Yao, Y.P., Kou, Z.M., Meng, W.J., & Han, G. (2014). Overall performance evaluation of tubular scraper conveyors using a TOPSIS-based multi-attribute decision-making method. *Scientific World Journal*, 2014, article number 753080.

[21] Xuanbin B., Xiangyu Z., Jin H., Hongwen L., Qingjie W., Wenzheng L. (2019). Design and performance test of plowing and rotary tillage combined machine, *INMATEH – Agricultural Engineering*, 58(2), pp.213-222.

Basic parameters

Current number	Name of the parameter	Symbol of the parameter	Unit of measurement
1.	the screw helicoid parameter (ratio of helicoid pitch to full revolution)	q	m
2.	the inclination angle of the cutting edge axis of the helicoid surface	β	deg
3.	the elevation angle of the turning edge	φ	deg
4.	the length of the rectilinear generatrix from the current point on the helix to the point on the surface	u	m
5.	the diameter of the cylindrical shaft	p	m
6.	the angle of rotation of a point around the axis of the surface during its movement on a helical line located on a cylinder of radius *p*	γ	deg
7.	angular speed of the working body	ω	s^{-1}
8.	the depth of tillage	a	m
9.	the height of the crests	c	m
10.	the distance between the crests	b	m
11.	angle of attack of the working body	α	deg
12.	helix line elevation angle	φ_R	deg
13.	the vector of the speed of the aggregate	$\overline{V}$	$m \cdot s^{-1}$, $km \cdot h^{-1}$
14.	the relative speed of the movement of an arbitrary point of the screw-type working body relative to the soil	V_{rel}	$m \cdot s^{-1}$, $km \cdot h^{-1}$
15.	the tillage depth	h	m
16	the depth of the neutral layer	h_N	m
17.	cylindrical surface with a radius will be rolled along a plane, buried from the soil surface to depth h_N :	r_0	m
18.	external radius of the screw-type spiral	R	m
19.	the relative speed of the soil movement at the entrance to the working area of the unit	V_2	$m \cdot s^{-1}$
20.	spiral step	T	m
21.	the power, consumed for cutting the cutting edge	$N_{p.n}$	kW
22.	the power from the tangential components of the cutting force	$N_{p.\tau}$	kW
23.	the reduced value of the average speed of the screw moving relative to the soil	$V_{n.\tau}$	$m \cdot s^{-1}$
24.	the average pressure on the screw-type working body	p_{cp} –	MPa
25.	the linear soil compaction in the direction of movement of the aggregate up	ε	$MPa \cdot m^{-1}$
26.	the total area of the particle of the screw-type working body, buried in the soil; is the relative speed of movement according to	S_c	m^3
27.	the friction coefficient;	μ	-
28.	the length of the movement (path) of the soil along the surface of the working body	l_w	m
29.	the bulk density of the soil	ρ_v	$kg \cdot m^{-3}$
30.	consolidated digital coefficients	k_1 and k_2	-
31.	the grip width	B	m
32.	the coefficient of reduction of the particle velocities	k_v	
33.	force that acts in the horizontal plane	P_x	N
34.	the integral cutting factor	K_p	-
35.	the power for moving, cutting in and compacting	N_1	kW
36.	the power, spent for loosening and providing soil particles	N_2	kW
37.	the power consumed to overcome the frictional resistance	N_3	kW
38.	the work of displacement, cutting in and compaction	A_1	kJ
39.	the work, spent to provide kinetic energy to the soil particles	A_2	kJ
40.	the work, spent to overcome the friction	A_3	kJ

DESIGN AND TEST OF HIGH-SPEED FERTILIZER POINT-APPLIED DEVICE
/
高速穴施肥装置设计与试验

Xin DU, Tong WANG, Shufa CHEN, Qixin SUN, Zhihao XU, Changqing LIU*
School of Mechanical Engineering, Jiangsu Ocean University, Lianyungang 222005 / China
Tel: 0086-0518-85895322; E-mail: lyg_lcq@163.com
Corresponding author: Changqing Liu
DOI: https://doi.org/10.35633/inmateh-71-73

Keywords: *Fertilizer point-applied device; Root-zone fertilization; High-speed; Precision agriculture*

ABSTRACT
In order to improve the adaptability of the fertilizer point-applied device to the working speed, the key components of the high-speed fertilizer point-applied device were designed and simulated by numerical calculation in this study. The effects of working speed, discharging height and discharging mass on the distribution length of fertilizer particles were analyzed by a one-factor test, and a suitable range of factors was determined. The Box-Behnken test was conducted to investigate the interaction effect of the three factors on the distribution length of fertilizer particles, and the quadratic regression was fitted to the test results to establish the regression equations of working speed, discharging height and discharging mass on the distribution length of fertilizer particles, and the optimal combinations of the parameters of working speed, discharging height and discharging mass were obtained by solving the equations. Finally, the reliability and authenticity of the simulation analysis were verified by bench test.

摘要
为提高穴施肥装置对作业速度的适应性，本研究对高速穴施肥装置的关键部件进行了设计和数值计算模拟。通过单因素试验分析了作业速度、排肥高度和排肥质量对肥料颗粒分布长度的影响，并确定了合适的因素范围。通过 Box-Behnken 试验研究了三个因素对肥料颗粒分布长度的交互影响，并对试验结果进行了二次回归拟合，建立了作业速度、排肥高度和排肥质量对肥料颗粒分布长度的回归方程，求解得到作业速度、排肥高度和排肥质量的最佳参数组合。最后通过台架试验验证了仿真分析的可靠性和真实性。

INTRODUCTION

As most crops inter-root soil accounts for a low proportion of the total volume of farmland soil, the nutrients absorbed by the crop root system only come from the limited soil around the root system (*Zhang et al.*, 2020; *Gu et al.*, 2023), root zone fertilization can effectively improve the fertilizer utilization rate (*Jiang et al.*, 2018), compared with the conventional strip fertilization to reduce costs and increase efficiency is obvious (*Adu-Gyamfi et al.*, 2019). However, there are few research reports related to root zone fertilization machinery, and the lack of corresponding machinery and equipment restricts the promotion and application of root zone fertilization agronomy *(Ding et al., 2018; Li et al., 2019; Dimkpa et al., 2020)*.

As the core working part to realize the point application of fertilizer in the root zone, the performance of the fertilizer point-applied device directly affects the precision of fertilizer application and the utilization rate of fertilizer efficiency. By controlling the opening and closing of the flap, *Zhang et al., (2018),* intermittently distributed a continuous stream of fertilizer particles into the soil layer at a depth of 7-23 cm directly below the seeds. *Liu et al., (2018; 2021)*, used the spaced fertilizer cavity to take fertilizer in precise quantity, with positive pressure airflow to carry the fertilizer particles to be thrown out quickly, so as to realize the fertilization of the root zone hole application. *Wu et al., (2018),* used a rocker to control the opening and closing of a duckbill valve to achieve fertilizer burrowing. *Du et al.*, (*2023; 2022)*, used the Geneva intermittent mechanism to realize the root zone cavitation of fertilizer granules, which can effectively improve the fertilizer utilization and crop yield. *Dang et al., (2022),* proposes a novel optimization scheme for controlling fertilization rates in bivariate fertilizer applicators, utilizing EDEM for parameter acquisition and optimization algorithms for improved accuracy and adjustment time.

Xin Du, Lecturer Ph.D. Eng.; Tong Wang, MA. Eng. Stud.; Shufa Chen, Prof. Ph.D. Eng.; Qixin Sun, Prof. Ph.D. Eng; Zhihao Xu, B.S Stud.; Changqing Liu, Lecturer Ph.D. Eng.*

Zhang et al., (2020), use the DEM to solve the problem of fertilizer application in orchards, especially the problem of low uniformity. By proposing and simulating three fertilizer guiding mechanisms and analyzing the physical parameters, it was determined that the optimal radius of curvature of the mechanism is 600 mm, which can significantly improve the uniformity of fertilizer application by 49.02%. *Feng et al., (2021),* presented a deep fertilizer application mechanism with deformed gears and a corresponding test rig, where factors such as planetary carrier, spray hole size and pump pressure were optimized to meet the agronomic requirements. *Hu et al., (2020),* introduced a lightweight organic fertilizer distributor, which ensures the accuracy and uniformity of fertilizer application and reflects the stability and reliability of the control system by establishing a mechanical model and a mathematical model of fertilizer output.

Although experts and scholars have researched various principles and forms of point-applied fertilizer devices *(Hu et al., 2017),* generally the effect of fertilizer particles into points at high-speed operation is poor. Based on the high-speed centrifugal principle, a new type of fertilizer point-applied device is designed, which can effectively increase the working speed and improve the formation effect of fertilizer particle spot application. Taking the fertilizer point-applied device as a specific analysis object, the effects of working speed, discharge height and discharge mass on the distribution performance of fertilizer particles were explored by DEM simulation, and the interaction effects of each factor were obtained by Box-Behnken. This paper will provide equipment and technical reference for the development of efficient fertilizer application technology.

STRUCTURE AND KEY PARAMETERS

At present, fertilizers are generally applied synchronously at the time of planting, mainly relying on corn fertilizer planter for mechanized operation, the fertilizer system is its key component (shown in Figure 1), consisting of fertilizer box, fertilizer supply device, fertilizer supply pipe, fertilizer point-applied device, brushless motor, coupling, stepping motor and other components.

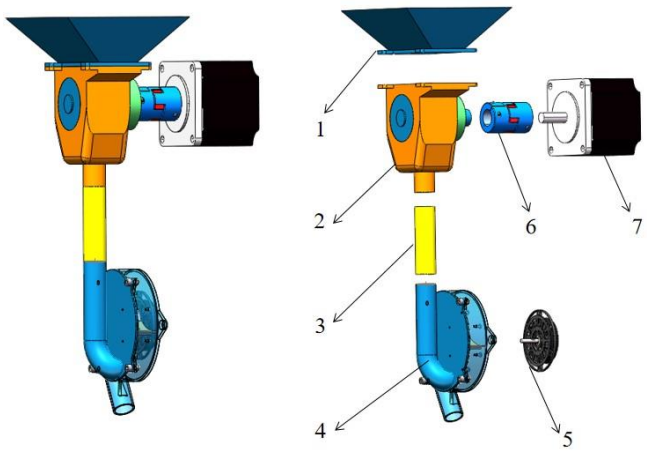


Fig. 1 – Fertilizer application system schematic

1. Fertilizer box; 2. Fertilizer supply device; 3. Fertilizer supply pipe;
4. Fertilizer point-applied device 5. Brushless motor 6. Coupling 7. Stepping motors

The main component of fertilizer point-applied device is shown in Fig. 2, which consists of screws, fertilizer feed tube, fertilizer discharge wheel, rubber push plate, fertilizer discharge tube, fertilizer discharger shell, nuts and bearings. Fertilizer discharge wheel rotates counterclockwise, and the fertilizer feed pipe continuously flows into the fertilizer particles stream. Fertilizer particles move counterclockwise under the joint action of the rubber push plate and the shell. When the fertilizer particles pass through the fertilizer discharge tube, they are thrown out at high speed by centrifugal force. With each revolution of the fertilizer discharge wheel, a heap of fertilizer granules is discharged.

MATERIALS AND METHODS

Simulation model construction

In this paper, the Stanley compound fertilizer (N-P_2O_5-K_2O 15-15-15) produced by Stanley Agricultural Group Co., Ltd. was selected as the research object. The average triaxial dimensions of the fertilizer particles were about 3.83 mm×3.62 mm×3.45 mm, which were randomly selected from 100 samples of fertilizer particles and measured with digital calipers (accuracy 0.01 mm).

The equivalent diameter and sphericity were 3.63 and 0.95, respectively. Their angle of repose, bulk density and water content were 31.6°, 984.6 kg/m^3 and 0.23%, respectively. Due to the high sphericity of the fertilizer particles, a single sphere with a diameter of 3.63 mm was used in the DEM simulation to model the fertilizer particle simulation (*Du*, *2023*).

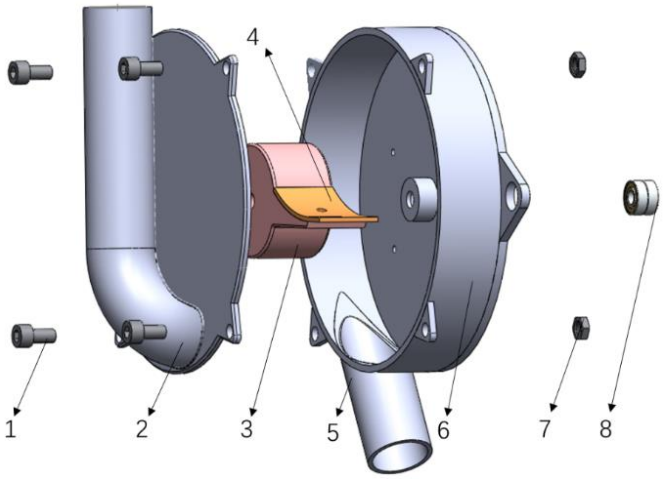


Fig. 2 – Structure of fertilizer grooved wheel

1. Screws; 2. Fertilizer feed tube; 3. Fertilizer discharge wheel; 4. Rubber push plate; 5. Fertilizer discharge tube; 6. Fertilizer discharger shell; 7. Nuts; 8. Bearings

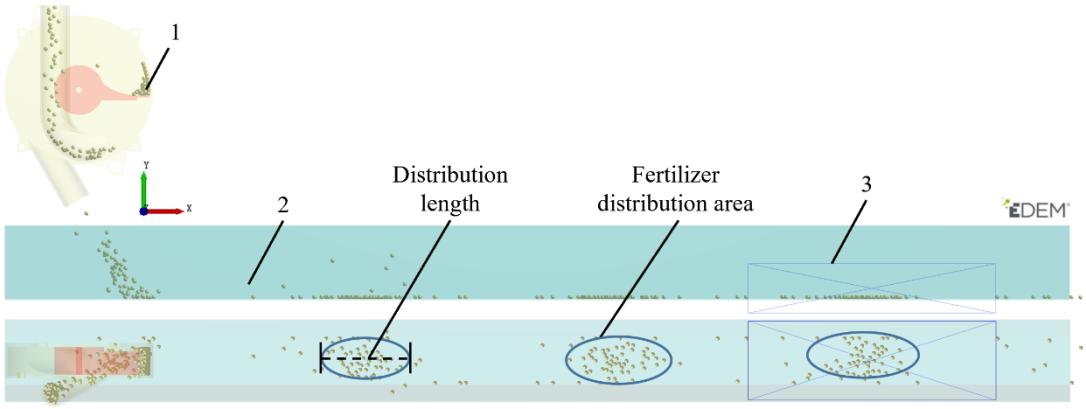


Fig. 3 – Schematic diagram of fertilizer particles distribution performance based on simulation

1. Fertilizer particles; 2. Conveyor belts; 3. Geometry bin

Modeling of the fertilizer point-applied device was carried out in the 3D drawing software SolidWorks 2016, which was saved in Step format and then imported into EDEM 2020, as shown in Fig. 3. The constitutive parameters and contact parameters of the coated fertilizer particles used in the simulation refer to related literature (*Du et al.*, 2021; *Du et al.*, 2022), and the values are shown in Table 1. The time step of the simulation in EDEM is 5×10^{-6} s, every 0.01 s the data is saved once, and the total simulation time is 6 s.

Table 1

Simulation parameters table

Parameters	Fertilizer granules	ABS	Conveyor belt
Poisson's ratio	0.225	0.394	0.350
True Density (kg/m^3)	2474	1060	1357
Shear modulus (Pa)	1.53×10^8	8.90×10^8	7.27×10^8
Coefficient of restitution	0.625	0.475	0.02
Coefficient of static friction	0.175	0.425	1.25
Coefficient of rolling friction	0.037	0.095	1.24

Test indicators

In order to study the fertilizer distribution effects of the fertilizer point-applied device, as shown in Fig. 3, set the fertilizer point-applied device stationary relative to the conveyor belt, add the Conveyor Translation movement for the conveyor belt in EDEM, and the fertilizer particles discharged from the fertilizer point-applied device fall onto the conveyor belt and then will move to the right relative to the fertilizer point-applied device. Set up the indicators to evaluate the fertilizer distribution effects of the point-applied device: fertilizer particle distribution length L, which are calculated as follows:

$$L_{fi} = X_{i\,first} - X_{i\,last} \tag{1}$$

L_{fi} is the distribution length of fertilizer particles in the i-th hole, mm. $X_{i\,first}$ is the x-direction displacement of the particles of the i-th hole fertilizer particles that first fall on the transmission belt, mm. $X_{i\,last}$ is the *x*-direction displacement of the last particle in the i-th hole fertilizer particle that falls on the transmission belt, mm.

The calculation method of the average particle distribution length of fertilizer is as follows:

$$L_f = \frac{\sum_{i=1}^{n} L_{fi}}{n} \tag{1}$$

where L_f is the average particle distribution length of fertilizer, mm; n is the number of fertilizer holes.

RESULTS

Working speed

When fertilizer discharging height and fertilizer discharging mass were 75 mm and 6.0 g, respectively, the operating speeds were set to 3.6, 5.4, 7.2, 9.0 and 7.2 km/h, the variation of the distribution length of the fertilizer particles with the working speeds was obtained as shown in Figure 4.

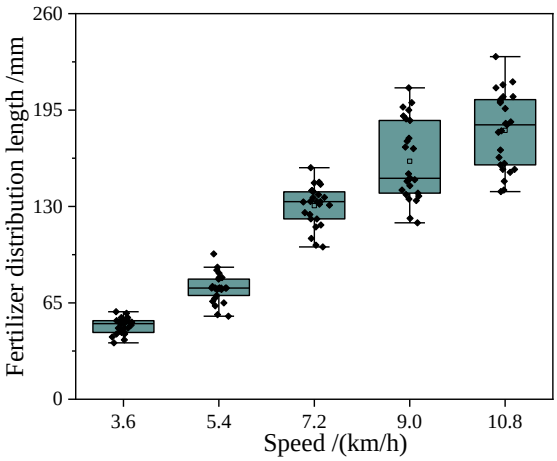


Fig. 4 – Variation of the performance of the fertilizer particles distribution with the working speed

From the box line plot, it can be seen that the median of the fertilizer particle distribution length increases gradually with the increase in operating speed, indicating that the fertilizer particle distribution length increases with the increase in operating speed. When the working speed is less than 7.2 km/h, the distance between the upper and lower boxes of the box plot is shorter, indicating that the distribution length of fertilizer particles is more concentrated, the coefficient of variation is smaller, and the working performance is more stable; on the contrary, when the working speed is greater than 7.2 km/h, the distribution length of fertilizer particles is more dispersed, which indicates that the performance of the fertilizer point-applied device is not particularly stable in high-speed operation.

Fertilizer discharging height

When working speed and fertilizer discharging mass were 7.2 km/h and 6.0 g, respectively, the fertilizer discharging height were set to 25, 50, 75, 100 and 125 mm, the variation of the distribution length of the fertilizer particles with the fertilizer discharging height was obtained as shown in Figure 5.

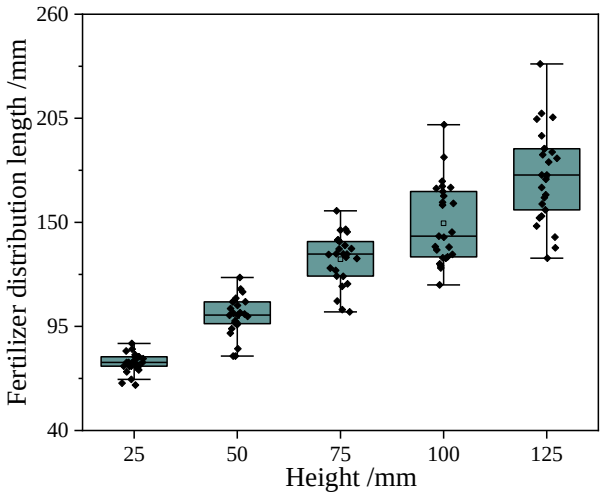


Fig. 5 – Variation of the performance of the fertilizer particles with the fertilizer discharging height

From the box line plot, it can be seen that the median of the fertilizer particle distribution length increases gradually with the increase in the fertilizer discharging height, indicating that the fertilizer particle distribution length increases with the increase in the fertilizer discharging height. When the fertilizer discharging height is less than 75 mm, the distance between the upper and lower boxes of the box plot is shorter, indicating that the distribution length of fertilizer particles is more concentrated, the coefficient of variation is smaller, and the working performance is more stable; on the contrary, when the discharging height is greater than 75 mm, the distribution length of fertilizer particles is more dispersed, which indicates that when the discharge height is larger, the performance of the point fertilizer application device is not particularly stable.

Fertilizer discharging mass

When working speed and fertilizer discharging height were 7.2 km/h and 75 mm, respectively, the fertilizer discharging mass were set to 3.0, 4.5, 6.0, 7.5 and 9.0 g, the variation of the distribution length of the fertilizer particles with the fertilizer discharging mass was obtained as shown in Figure 6.

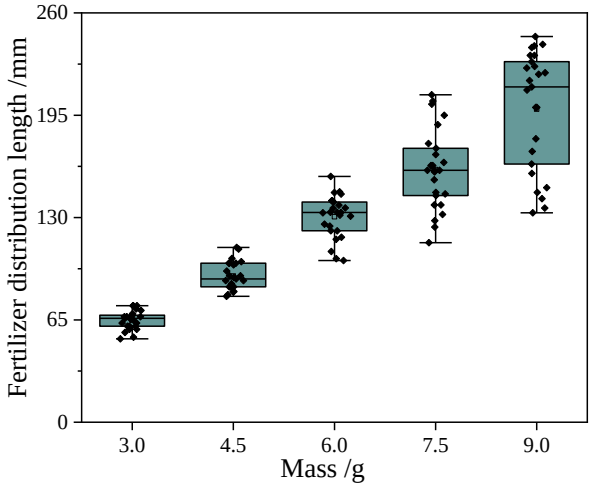


Fig. 6 – Variation of the performance of the fertilizer particles with the fertilizer discharging mass

From the box line plot, it can be seen that the median of the fertilizer particle distribution length increases gradually with the increase in the fertilizer discharging mass, indicating that the fertilizer particle distribution length increases with the increase in the fertilizer discharging mass. When the fertilizer discharging mass is less than 6.0 g, the distance between the upper and lower boxes of the box plot is shorter, indicating that the distribution length of fertilizer particles is more concentrated, the coefficient of variation is smaller, and the working performance is more stable; in contrast, the distribution length of the fertilizer particles was more dispersed when the mass of fertilizer discharged was greater than 6.0 g, suggesting that the performance of the fertilizer point-applied device was not particularly stable at larger masses of fertilizer discharged.

Interactions among the factors

The above analyses focused on considering the effect of a single factor on the target. In order to further analyze the pattern of the interaction between factors on the target results, a Box-Behnken test was designed with the working speed, fertilizer discharge height and fertilizer discharging mass as test factors, and fertilizer distribution length as test indicator. The test factors and levels are shown in Table 2. The test protocol and results using Design-Expert 8.0.6 are shown in Table 3.

Table 2

Test levels and factors

Test level	Speed v_m (m/s)	Height h (mm)	Mass m (g)
+1	10.8	125	9
0	7.2	75	6
-1	3.6	25	3

Table 3

Box-Behnken experiment design and results

No.	Speed v_m (m/s)	Height h (mm)	Mass m (g)	Length y (mm)
1	3.6	25	6	49
2	10.8	25	6	111
3	3.6	125	6	105
4	10.8	125	6	188
5	3.6	75	3	58
6	10.8	75	3	125
7	3.6	75	9	94
8	10.8	75	9	192
9	7.2	25	3	47
10	7.2	125	3	94
11	7.2	25	9	98
12	7.2	125	9	173
13	7.2	75	6	135
14	7.2	75	6	128
15	7.2	75	6	133
16	7.2	75	6	130
17	7.2	75	6	126

Multiple regression analysis was performed on the test results using Design-Expert 8.0.6 and Table 4 shows the results of the ANOVA of the regression model for the mean fertilizer particle distribution length.

From Table 4, it can be seen that the *P*-value of the quadratic regression model for the mean particle distribution length of fertilizer is less than 0.05 and the *P*-value of the lack of fit is greater than 0.05, which indicates that the model obtained from the regression is very significant and the regression equation does not suffer from the problem of unfitness. Therefore, the quadratic regression equation between each factor and the length of fertilizer particle distribution was obtained as follows:

$$y = -73.34 + 5.88v_m + 1.09h + 16.64m + 0.03v_m h + 0.72v_m m + 0.05hm - 0.11v_m^2 - 0.006h^2 - 1.30m^2 \quad (2)$$

The results of ANOVA showed that working speed, discharging height and discharging mass had a significant effect on the mean fertilizer particle distribution length, and the three factors had a significant effect on the mean fertilizer particle distribution length in the order of discharging height, working speed and discharging mass. The interaction terms working speed and fertilizer discharging mass, and fertilizer discharging height and fertilizer discharging mass had a significant effect on the mean fertilizer particle distribution length.

Table 4

Box-Behnken experiment design and results

Source of variance	Length *y* (mm)			
	Sum of square	Degree of freedom	*F*-value	*P*-value
Model	29211	9	108.47	<0.0001**
v_m	4458	1	148.99	<0.0001**
h	4563	1	152.50	<0.0001**
m	3400	1	113.64	<0.0001**
$v_m h$	110	1	3.68	0.0964
$v_m m$	240	1	8.03	0.0253*
hm	196	1	6.55	0.0376*
V_m^2	9	1	0.30	0.6034
h^2	1038	1	34.69	0.0006**
m^2	576	1	19.26	0.0032**
Residual	209	7		
Lack of Fit	156	3	3.92	0.1102
Pure Error	53	4		
Cor Total	29420	16		

Note: $P<0.01$ (highly significant, $**$); $P<0.05$ (significant, $*$).

In order to analyze the effect of the interaction term on the average particle distribution length of the fertilizer, a response surface was plotted as shown in Figure 7.

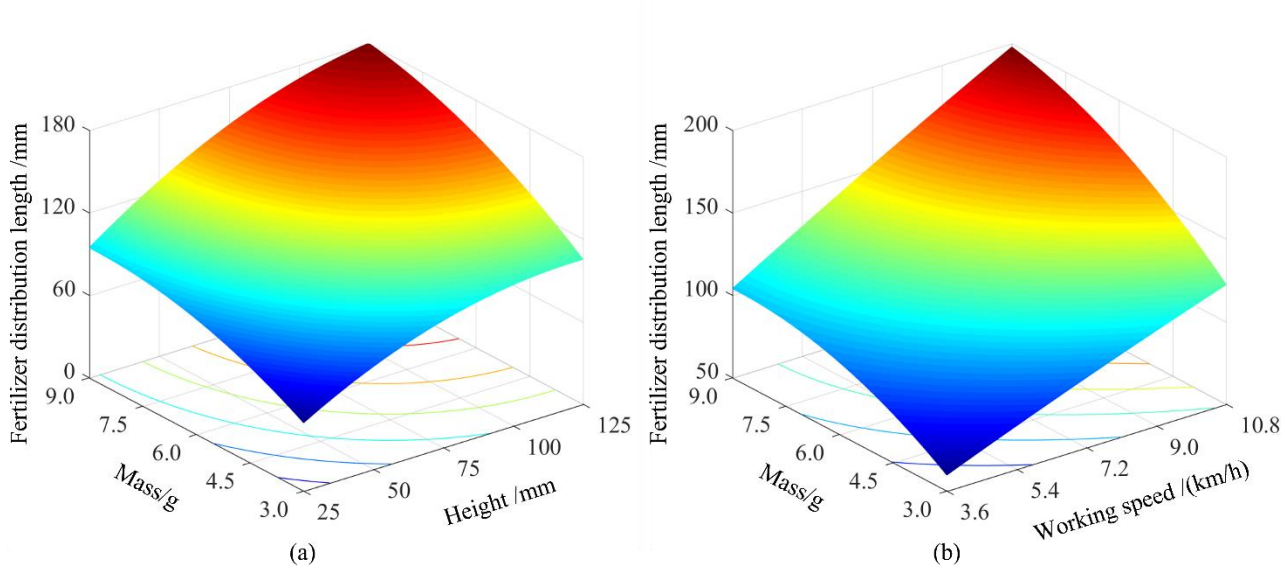


Fig. 7 – Response surface diagram

Fig. 7(a) shows the interaction effect of working speed and discharging mass on the distribution length of fertilizer particles. It can be seen that the distribution length of fertilizer particles increases with increasing discharging mass and working speed. Fig. 7(b) shows that the distribution length of fertilizer particles increases with increase in discharging mass and discharging height.

In order to solve the optimal combination of factors within the constraint range, the multi-objective optimization of fertilizer particle formation performance was carried out using the minimum distribution length as the evaluation index, and the optimization objective function and constraints are as follows.

$$y_{\min}(v_m,\ h,\ m)$$
$$\text{s.t.}\begin{cases}3.6\ \text{km/h} \le v_m \le 10.8\ \text{km/h}\\ 25\ \text{mm} \le h \le 125\ \text{mm}\\ 3\ \text{g} \le m \le 9\ \text{g}\end{cases} \quad (3)$$

After multi-objective optimization of the regression equation using Design-Expert 8.0.6, the fertilizer distribution length was 114.12 mm for the working speed, discharging height and mass of fertilizer at 4.05 km/h, 89 mm and 8.58 g. Repeating the numerical simulation three times in this condition, the fertilizer distribution length was 117.61 mm with the relative error of 3.06%, indicating that the regression equation is reliable.

Bench experiment

The key components of the fertilizer point-applied device were injection-molded by Tiertime UP 600 3D printer (accuracy 0.1 mm, ABS material). The operational performance of the fertilizer point-applied device was tested on the JPS-12 multifunctional seed metering test rig at the College of Engineering, China Agricultural University, as shown in Figure 8.

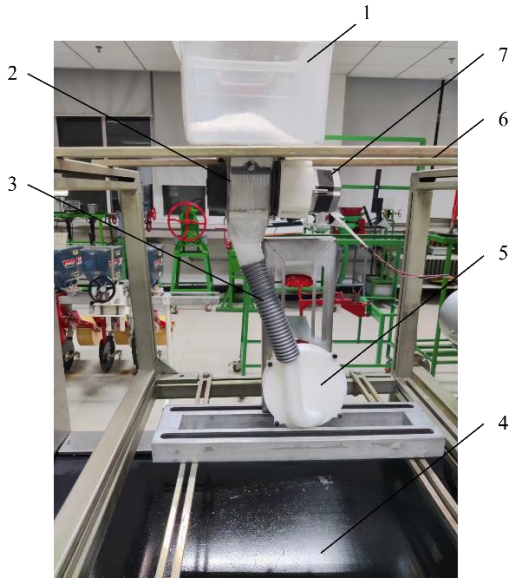


Fig. 8 – Schematic diagram of the fertilizer point-applied device

1. *Fertilizer box; 2. Fertilizer supply device; 3. Fertilizer supply pipe; 4. Conveyor belt; 5. Fertilizer point-applied device; 6. Mounting bracket; 7. Stepping motors*

In the three bench tests, the average distribution length of fertilizer particles was obtained to be 136 mm. Compared with the DEM simulation, the relative error was 19.17%. The small relative errors indicate that the overall accuracy of the established DEM simulation model is high.

CONCLUSIONS

In this study, the design and numerical calculation simulation of the key components of the high-speed fertilizer point-applied device were carried out. The effects of working speed, discharging height and discharging mass on the distribution length of fertilizer particles were analyzed by a one-factor test, and a suitable range of factors was determined. The interaction effect of the three factors on the distribution length of fertilizer particles was investigated by Box-Behnken test, and a quadratic regression was fitted to the test results to establish the regression equations of working speed, discharging height and discharging mass on the distribution length of fertilizer particles, and solved to obtain the smallest distribution length of fertilizer particles when the operating speed, discharge height and discharge mass were 4.05 km/h, 89 mm and 8.58 g, respectively. Finally, the reliability and authenticity of the simulation analysis were verified by bench test.

ACKNOWLEDGEMENT

This work was financially supported by Natural Science Foundation of the Jiangsu Higher Education Institutions of China (23KJB210007).

REFERENCES

[1] Adu-Gyamfi, R., Agyin-Birikorang, S., Tindjina, I., Manu, Y., Singh, U. (2019). Minimizing nutrient leaching from maize production systems in northern Ghana with one-time application of multi-nutrient fertilizer briquettes. *Science of the Total Environment*, *694*, 133667. DOI: 10.1016/j.scitotenv.2019.133667.

[2] Dang, Y., Yang, G., Wang, J., Zhou, Z., Xu, Z. (2022). A decision-making capability optimization scheme of control combination and PID controller parameters for bivariate fertilizer applicator improved by using EDEM. *Agriculture-Basel*, *12*(12), 2100. DOI: 10.3390/agriculture12122100.

[3] Dimkpa, C. O., Fugice, J., Singh, U., Lewis, T. D. (2020). Development of fertilizers for enhanced nitrogen use efficiency - Trends and perspectives. *Science of the Total Environment*, *731*, 139113. DOI: 10.1016/j.scitotenv.2020.139113.

[4] Ding, S., Bai, L., Yao, Y., et al. (2018). Discrete element modelling (DEM) of fertilizer dual-banding with adjustable rates. *Computers and Electronics in Agriculture*, *152*, 32-39. DOI: 10.1016/j.compag.2018.06.044.

[5] Du, X., Liu, C., Jiang, M., et al. (2021). Design and experiment of inclined trapezoidal hole fertilizer point-applied discharging device. *Transactions of the Chinese Society for Agricultural Machinery*, *52*(09), 43-53.

[6] Du, X., Liu, C., Jiang, M., Yuan, H. (2022). Design and development of fertilizer point-applied device in root-zone. *Applied Engineering in Agriculture*, *38*(3), 559-571. DOI: 10.13031/aea.14846.

[7] Du, X., Liu, C., Jiang, M., et al. (2022). Research on DEM calibration of contact parameters of coated fertilizer. *INMATEH - Agricultural Engineering*, *66*(1), 101-110. DOI: 10.35633/inmateh-66-10.

[8] Du, X., Liu, C. (2023). Research on the performance of particles distribution of fertilizer point-applied device in root-zone. *Journal of Applied Science and Engineering*, *26*(8), 1063-1072. DOI: 10.6180/jase.202308_26(8).0002.

[9] Du, X., Liu, C., Liu, C., Jiang, M., Yuan, H. (2023). Effect of controlled-release fertilizer on maize yield and nutrient uptake under a fertilizer one-time point-applied system. *INMATEH - Agricultural Engineering*, *69*(1), 673-680. DOI: 10.35633/inmateh-69-65.

[10] Feng, J., Yi, S., Li, Q. (2021). Design of deep-fertilization mechanism with deformed gears and performance tests. *INMATEH - Agricultural Engineering*, 321-332. DOI: 10.35633/inmateh-65-34.

[11] Gu, B., Zhang, X., Lam, S. K., et al. (2023). Cost-effective mitigation of nitrogen pollution from global croplands. *Nature*, *613*(7942), 77-84. DOI: 10.1038/s41586-022-05481-8.

[12] Hu, H., Li, H., Ma, S., et al. (2017). Design and testing of an inter-row hole-pricking granular fertilizer applicator for corn. *International Agricultural Engineering Journal*, *26*(1), 68-78.

[13] Hu, J., He, J., Wang, Y., et al. (2020). Design and study on lightweight organic fertilizer distributor. *Computers and Electronics in Agriculture*, *169*, 105149. DOI: 10.1016/j.compag.2019.105149.

[14] Jiang, C., Wang, H., Lu, D., et al. (2018). Single fertilization of urea in root zone improving crop yield, nutrient uptake and use efficiency in summer maize. *Transactions of the Chinese Society of Agricultural Engineering*, *34*(12), 146-153. DOI: 10.11975/j.issn.1002-6819.2018.12.017.

[15] Li, S., Lei, Y., Zhang, Y., et al. (2019). Rational trade-offs between yield increase and fertilizer inputs are essential for sustainable intensification: A case study in wheat–maize cropping systems in China. *Science of the Total Environment*, *679*, 328-336. DOI: 10.1016/j.scitotenv.2019.05.085.

[16] Liu, Z., Wang, Q., Liu, C., et al. (2018). Design and experiment of precision hole-fertilizing apparatus with notched plate. *Transactions of the Chinese Society for Agricultural Machinery*, *49*(10), 137-144. DOI: 10.6041/j.issn.1000-1298.2018.10.015.

[17] Wu, N., Lin, J., Li, B. (2018). Design and test on no-tillage planter precise hole fertilization system. *Transactions of the Chinese Society for Agricultural Machinery*, *49*(07), 64-72. DOI: 10.6041/j.issn.1000-1298.2018.07.008.

[18] Zhang, H. J., Li, Y. F., Xu, C. B., et al. (2020). Optimization research of fertilizer guiding mechanism based on the discrete element method. *INMATEH - Agricultural Engineering*, *60*(1), 275-286. DOI: 10.35633/inmateh-60-31.

[19] Zhang, J., Liu, H., Gao, J., Lin, Z., Chen, Y. (2018). Simulation and test of corn layer alignment position hole fertilization seeder based on SPH. *Transactions of the Chinese Society for Agricultural Machinery*, *49*(09), 66-72. DOI: 10.6041/j.issn.1000-1298.2018.09.007.

[20] Zhang, L., Song H., Chen, X., Lu, D., Wang, H. (2020). Primary study on nutrient migration under hole fertilization in Soils. *Soils*, *52*(06), 1145-1151. DOI: 10.13758/j.cnki.tr.2020.06.006.

[21] Zheng, Z., Wang, T., Liu, Z., et al. (2021). Study on filling performance of hole fertilization device and optimization of cavity. *INMATEH - Agricultural Engineering*, 64(2), 141-150. DOI: 10.35633/inmateh-64-13.

CONSIDERATIONS REGARDING THE EFFECTS OF SHOCKS AND VIBRATIONS ON OPERATORS OF SELF-PROPELLED AGRICULTURAL EQUIPMENT
/
CONSIDERATIII PRIVIND EFECTELE ŞOCURILOR ŞI VIBRAŢIILOR ASUPRA OPERATORILOR UTILAJELOR AGRICOLE AUTOPROPULSATE

Valentin VLĂDUŢ[1)], Sorin-Ștefan BIRIŞ[2)], Gigel PARASCHIV [2)], Nicoleta UNGUREANU[2*)], Sorin Tiberiu BUNGESCU[3)], Iulian VOICEA[1)], Dan CUJBESCU[1)], Iuliana GĂGEANU[1)], Evelin LAZA[1)], Lorena-Diana POPA[4)], Gheorghe MATEI[5)], Atanas ATANASOV[6)]

[1)]INMA Bucharest / Romania; [2)]NUST Politehnica Bucharest / Romania; [3)]USV "King Mihai I" Timişoara / Romania; [4)]ARDS Secuieni / Romania; [5)]University of Craiova / Romania; [6)]University of Ruse / Bulgaria

E-mail: nicoletaung@yahoo.com; aatanasov@uni-ruse.bg

DOI: https://doi.org/10.35633/inmateh-71-74

Keywords: *vibration, frequency, amplitude, shock, oscillation, human body*

ABSTRACT

Vibrations are part of the category of dynamic phenomena and are manifested in some environments as a consequence of an external excitation in the form of oscillations. These oscillations have negative effects on the environment in which they manifest. In the particular case where the environment is represented by the human body, the negative effects are felt at the level of its health, and the consequences are sometimes irreversible. In this context, it is necessary to study and know the effects that vibrations have on the human body. The main purpose of researches carried out in this field is to establish the limit up to which man can work in environments that generate vibrations, without the vibrations affecting his state of health.

REZUMAT

Vibraţiile fac parte din categoria fenomenelor dinamice și se manifestă în unele medii ca și consecință a unei excitaţii exterioare sub forma unor oscilaţii. Aceste oscilații au efecte negative asupra mediului în care se manifestă. În cazul particular în care mediul este reprezentat de corpul uman, efectele negative se resimt la nivelul sănătății acestuia, iar consecinţe sunt uneori ireversibile. În acest context, se impune necesitatea studierii şi cunoaşterii efectelor pe care le au vibraţiile asupra corpului uman. Scopul principal al cercetărilor realizate în acest domeniu este stabilirea limitei până la care omul poate lucra în medii generatoare de vibraţii, fără ca vibrațiile să îi afecteze starea de sănătate.

INTRODUCTION

Vibrations are dynamic phenomena that occur in elastic or quasi-elastic environment, after a local excitation; they behave as elastic oscillations as the excitation propagates throughout the environment (*Broch J.T., 1984*). The excitation, propagation, and radiation of an elastic wave can be studied if the environment has at least one geometric dimension big enough that the initial excitation can be regarded as local.

Vibrations are classified according to their direction, frequency, magnitude, and duration (*van Heuvelen et al., 2021*). The factors that influence the definition of the vibratory phenomenon allow for a broad classification of oscillations and elastic waves. Thus, depending on the dynamics of the phenomena, vibrations with low variation frequencies, such as those seen in mechanical structures, building structures, and seismic waves, exist alongside vibrations with high variation frequencies.

The physical nature of the environment determines how the oscillations propagate: in a solid environment, both transverse and longitudinal waves can propagate, whereas only longitudinal waves can propagate in a fluid environment (*Buzdugan Gh., 1982*).

In agriculture, the interaction between the tires of agricultural machines and the ground produces shocks and vibrations whose emission levels are significantly influenced by both the unevenness of the land and the nature of the agricultural work (*Pochi et al., 2022*), as well as by the constructive characteristics of the agricultural machine (*Nguyen and Inaba, 2011*; *Stojic et al., 2017*).

Vibrations are transmitted to the operator's body through various points of contact between him and the agricultural machine: steering wheel, seat, levers, pedals and especially the floor of the machine (*Biriș et al., 2022*).

Among the hazards to which operators of self-propelled agricultural machinery are subjected, the physical element arising from mechanical vibrations stands out (*Lima et al., 2023*). Researchers around the world have conducted extensive studies on the long-term exposure of agricultural machinery operators to shocks and vibrations (occupational exposure), which has negative consequences from the perspective of human health risks and from a socio-economic perspective (*Litchfield M.H., 1999*).

Many tractors emit vibrations above the exposure action value recommended by the Directive 2002/44/CE (by 0.5 m/s^2). Low frequency vibrations in the 1–10 Hz range are considered to have substantial adverse effects on human health (*Liang and Chiang, 2008*). Even vibrations with a frequency lower than 2 Hz can affect human health, to some extent or for short periods of time, because they cause motion sickness, felt by the operator of the agricultural machine as a discomfort that affects his working capacity (*Cutini et al., 2017*). The critical frequencies emitted by the moving tractor are usually in the range of 1–7 Hz, which are similar to the natural frequencies of different parts of the human body (*Kumar et al., 2001*).

Because of these critical frequencies, tractor operators are mainly at risk of developing musculoskeletal problems (*Punnett and Wegman, 2004*), the most affected being the lumbar region of the spine (*Prakash et al., 2013; Essien et al., 2018*). These spinal problems worsen when the operator works in difficult conditions (uncomfortable positions, non-ergonomic seats, repeated manual handling of weights, etc.) (*EU-OSHA, 2005*). The prolonged exposure of operators to vibrations in the 2–20 Hz range has been demonstrated to induce spinal degenerative diseases (*Okunribido et al., 2006*).

Some hand-held agricultural equipment creates high levels of vibrations, which are conveyed to the operators' arms, putting them at risk of developing hand and arm vibration syndrome, which affects the upper limb systems (musculoskeletal, neurological, and vascular) (*Bovenzi M., 1998*).

In addition to concerns for increasing the functional performance of agricultural machines, the designers and manufacturers of agricultural machines constantly make substantial efforts to limit the exposure of agricultural operators to vibrations (*Singh et al., 2022; Vlăduţ et al., 2013; Sorică et al., 2017)*. They are constantly looking for solutions to improve the comfort of the tractor operator, by designing and implementing ergonomic solutions such as active seats, front suspensions or cab suspension systems (*Cutini et al., 2017; Cârdei et al., 2023; Vlăduţ et al., 2014*).

These efforts are supported by standards and norms that regulate / establish certain limits regarding the exposure of the whole body to mechanical vibrations and repeated shocks (*SR EN ISO 13090-1*, *2002*; *ISO 5008*, *2002*; *SR EN ISO 10819:2013/A1, 2019*; *SR EN ISO 10819:2013/A2, 2023*; *ISO 2631-1, 2001*; *ISO 2631-5, 2018*).

MATERIALS AND METHODS

- **Vibration of the entire body**

The human body is a psychical and biological "system" of extraordinary complexity. It has a lot of linear and non-linear "elements" when seen as a mechanical system, and its mechanical qualities vary greatly from person to person.

From a biological standpoint, the situation is complicated, especially when psychical impacts are included. When considering the human response to vibrations and shocks, it is vital to consider both mechanical and psychical impacts (*Broch J.T., 1984*).

Because human body experiments are complex and time-consuming, the majority of available data has come from animal experiments. Of course, it is not always practical to compare the results of animal tests with the reactions predicted from humans, but such investigations frequently yield significant information.

At low vibration frequencies and levels, the human body, considered as a mechanical system, can be roughly approximated by a linear system of grouped parameters, as shown in Figure 1. The "thorax-abdomen" system appears to be one of the most essential parts of this system in terms of the impacts of vibrations and shocks.

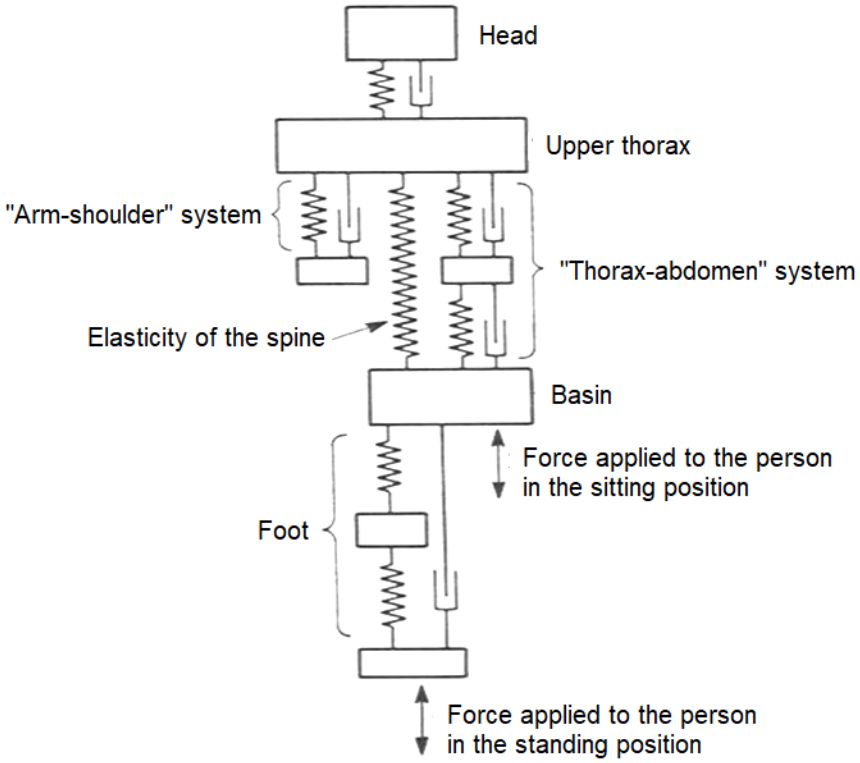


Fig. 1 – A simplified mechanical system which depicts the human body standing upright on a vertical vibrating platform

This is due to a specific resonance effect arising in the 3–6 Hz band (Figures 2 and 3), making effective vibration isolation when sitting or standing extremely challenging. Furthermore, the "head-neck-shoulder" system causes the resonance effect, which occurs between 20 and 30 Hz (Figure 3). The disturbances are also equivocal between 60–90 Hz, implying an eyeball resonance; between 100–200 Hz, a low resonance effect was discovered in the jaw-skull system.

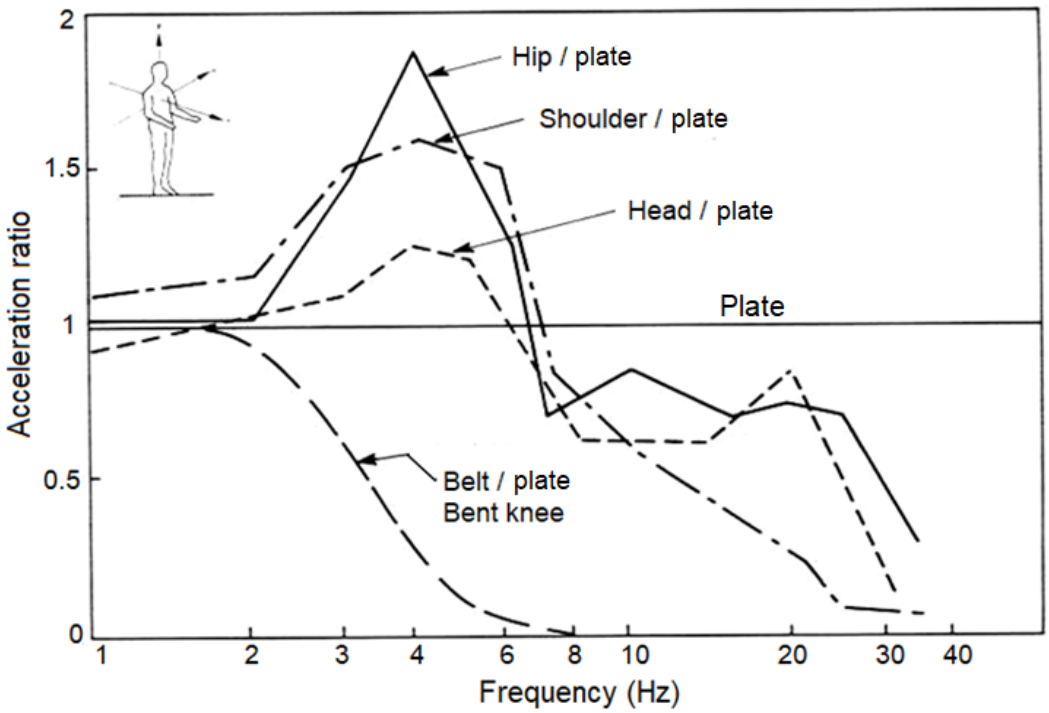


Fig. 2 – Transmission of vertical vibrations from the plate (platform) to different parts of the human body in the standing position, as a function of frequency

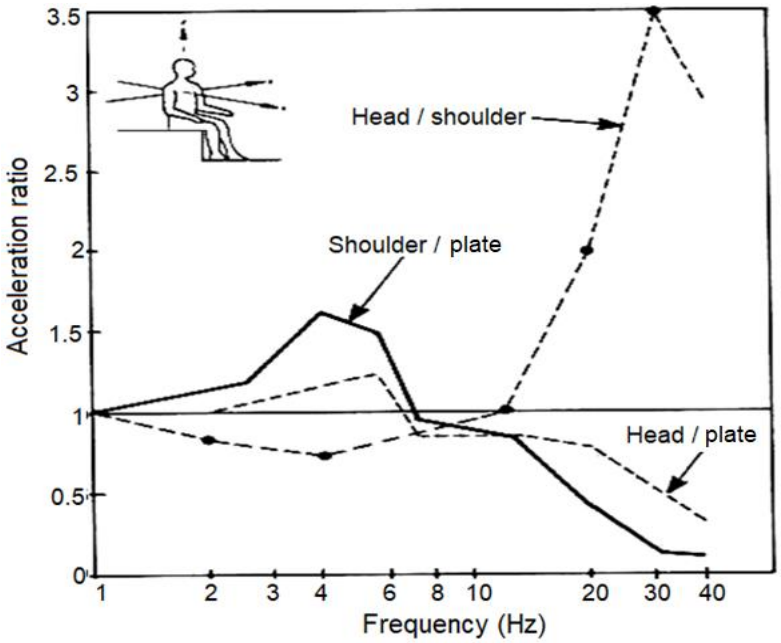


Fig. 3 – **Vertical vibration transmission from the plate (platform) into different parts of the body while in the seated position, as a function of frequency**

Above 100 Hz, the characteristics of the simple established models are similar to those given in Figure 1; however, they are not very useful. Continuous structural analysis methods, which can grow highly sophisticated, must be used. Such studies revealed the fundamental mode of vibration for the skull itself, which looks to be in the range of 300–400 Hz, with resonances for high modes about 600–900 Hz. Both signal (wave) theories must be utilized at calm high frequencies, in the form of the cut signal and the compression signal (sound signal).

The most important aspect of shock and vibration is tracking the peak of the low frequency string. Thus, some very interesting measurements were made, focused on the attenuation of vibrations along the human body (von Bekesy). Figure 4 depicts the data obtained at 50 Hz, as well as the attenuation from feet to head, which is on the order of 30 dB. Hand-to-head attenuation is approximately 40 dB.

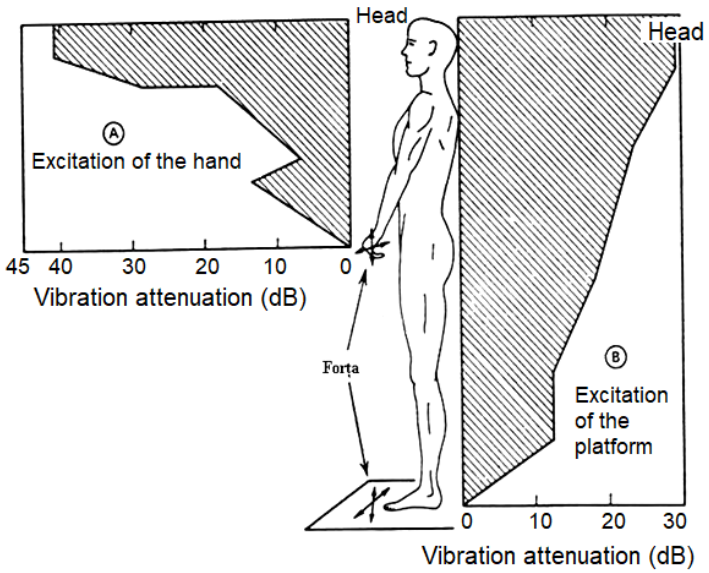


Fig. 4 – **Vibration attenuation at 50 Hz across the human body**

The attenuation is measured in decibels, beneath the value of the excitation point, when the hand (A) and platform (B) are excited on a subject that maintains the "standing" position. Recent research has focused on the perceived psychological impacts, discomfort, and pain. The majority of researches have focused on automotive drivers and airplane pilots, whose abilities to complete complicated tasks under adverse environmental conditions, such as vibration, are critical.

The available data is mainly used for subjects who are standing or seated. The ISO 2631-1:2001 and ISO 2631-5:2018 standards conveniently combine these data for a set of vibration curves for lateral and vertical vibrations spanning a frequency range of 1–80 Hz. These curves are depicted in Figure 5 (vertical accelerations – az) and Figure 6 (longitudinal accelerations – ax and transverse accelerations – ay), and are applied to vibrations conveyed to a person's torso when sitting or standing on the stated system's axis.

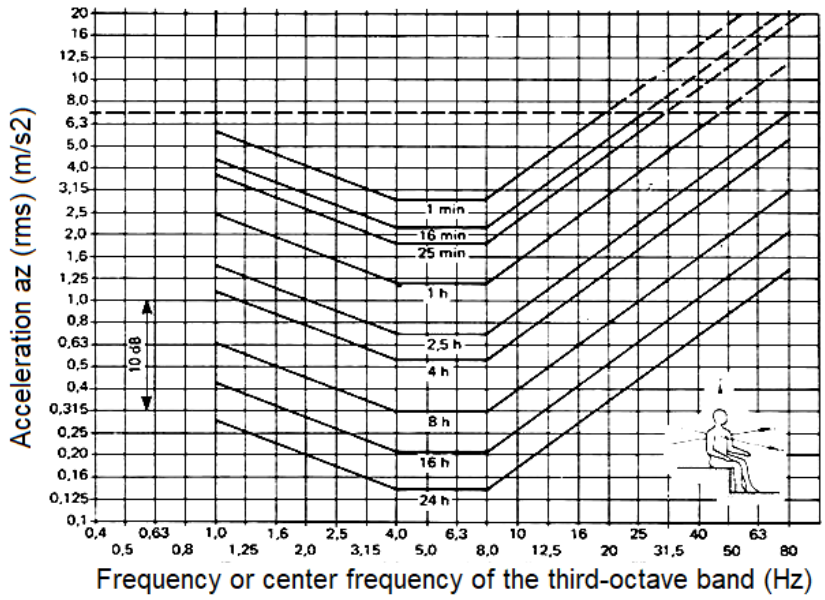


Fig. 5 – **The limit of vertical vibration exposure curves**

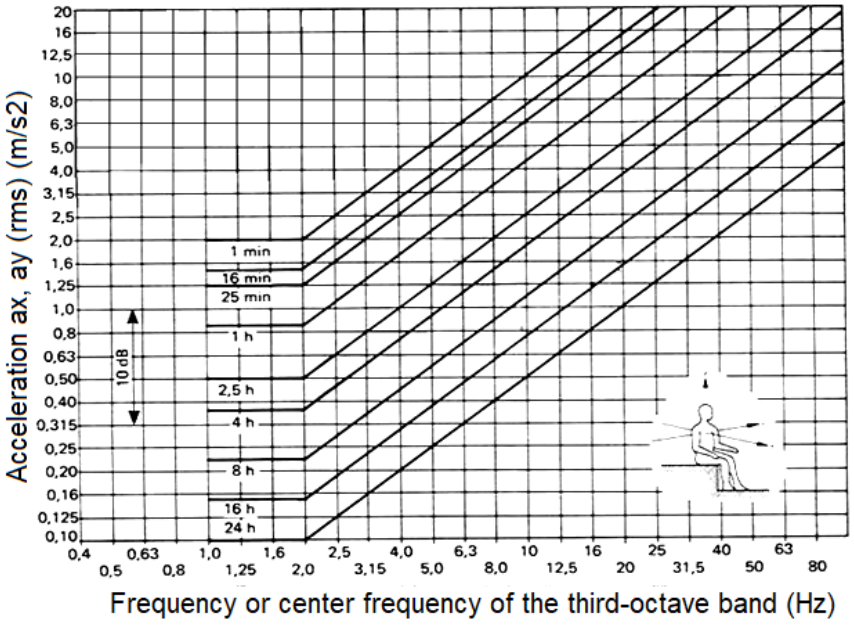


Fig. 6 – **The limit of exposure curves to longitudinal and transverse vibrations**

The upper part of the plate exposure limit is taken to be 2 times higher than the "fatigue reduction limit" shown in Figure 5, although the "reduced comfort limit" should be about a third of the specified levels. These criteria are provided as suggested guidelines or guideline curves, which is analogous to the quantitative classification of limits.

In Figure 7, the tolerance of the human subject to the acceleration pulsation of a single shock is indicated. The subjective reaction is expressed as a function of the maximum displacements of the original pulse over time. The number indicates the following reactions from the surfaces between the lines: I_a – the perception threshold; I_b – easy perceptions; I_c – strong, irritating perceptions; II_a – very uncomfortable perceptions, long exposures may pose a risk; II_b – extremely uncomfortable, very dangerous perceptions.

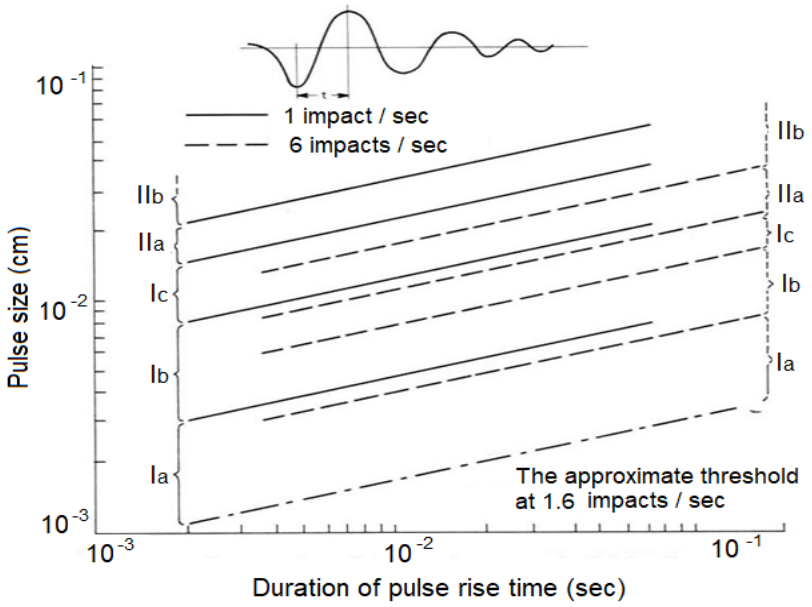


Fig. 7 – **Tolerance of the human subject, standing or lying down, to representative pulsations of repeated vertical impacts**

- **Arm vibration**

Arm vibration is the second big problem regarding the surface involved in the transmission to the human body. As a result, the challenges it poses differ from those raised by whole body vibration. Taking into account the vibration transmitted to the body while standing or sitting, the transmission of general problems such as: harmful movements, discomfort, reduced work efficiency, and so on, the vibration applied to the arm can also produce local physical damage if the level and exposure time are high enough.

When used for typical industrial durations, the vibration levels in many regularly used power tools are high enough to cause harm. ISO 5349-84 tries to collect common information about the appropriate form and to enable verdicts about the risk of harm from vibration exposure assessed in practice to be formed.

Figure 8 depicts suggested direction levels spanning the frequency range of 8 Hz to 1 kHz. Although exposure (presentation) curves for third-octave frequencies and octave bands are shown, when applied to the discrete spectrum frequency commonly encountered in hand rotation with tools, third-octaves are more stringent than octave bands.

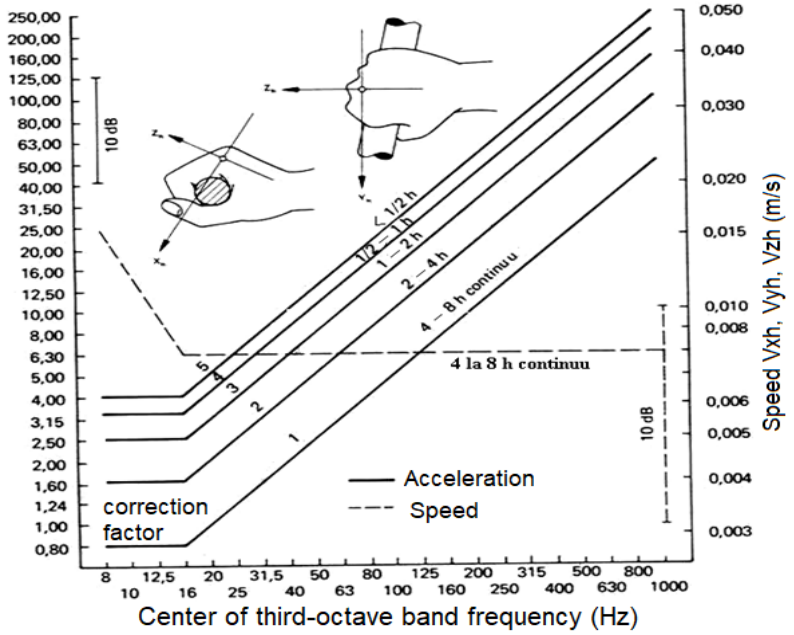


Fig. 9 – **The exposure guidelines for vibration transmitted to the hand**

RESULTS

- **Vertical vibrations' impact on the human body**

Most of the physical characteristics of the human body were obtained by analysing the experimental results, considering the human body as a passive and linear mechanical system. Of course, this is a valid hypothesis only in the case of very small amplitudes, and the presented results cannot be used in the study of mechanical tissue injuries. In reality, even well below the amplitudes required to produce injury, the response is nonlinear. This can be seen from the analysis of the experimental results, where the variation of the stiffness and resistance of the soft tissues is shown, depending on the elastic deformation.

The behaviour of bones is similar to that of solid bodies; in contrast, soft elastic tissues (muscles, tendons, connective tissues, etc.) behave similar to elastomers in terms of longitudinal modulus values and the S-shape of the stress-strain specific curve. These properties were investigated and connected with the quasi-static, pressure-volume connections of organs having internal cavities (such as the arteries, heart, and urinary bladder), taking linear behaviours into account while analysing dynamic responses. As a result, soft tissue can be represented phenomenologically as a viscoelastic environment; plastic deformations should be considered only if injuries occur.

Figure 9 depicts the mechanical impedance variation of a man standing or sitting on a platform that vibrates vertically. The body behaves as a unitary mass at frequencies less than about 2 Hz. The first resonance occurs between 4–6 Hz for the seated man, and the resonance peaks between 5–12 Hz for the standing human. The total energy transmitted to the person undergoing tests can be calculated using the numerical values of the impedance and the phase angle.

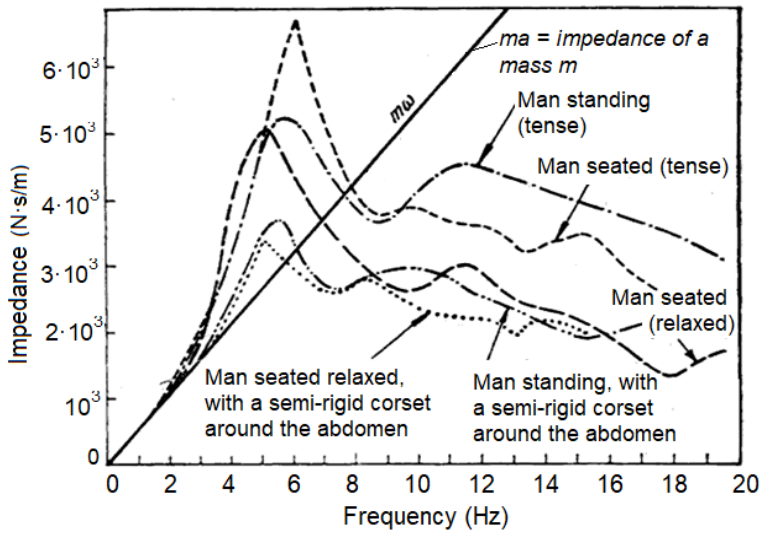


Fig. 9 – The mechanical impedance variation of a man standing or sitting on a vertically vibrating platform

The amplitudes of body motions caused by vibrations are smaller than the amplitudes of the vibrating plate at frequencies greater than 10 Hz and decrease continuously with increasing frequency. Figure 10 depicts the attenuation of vibrations transmitted from the vibrating plate to the skull. This attenuation is around 40 dB at 100 Hz.

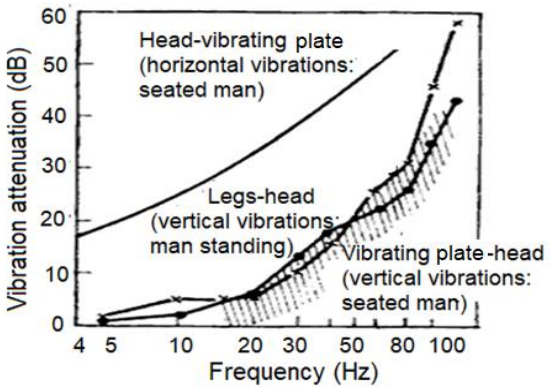


Fig. 10 – Attenuation of vibrations transmitted from the vibrating plate to the head

The effects of longitudinal vibrations on the human body

The thorax-abdomen system is one of the most significant subsystems of the body that is activated both in the sitting and seated (lying) positions. Because of the high flexibility of the diaphragm and the volume of air behind it, in the lungs, and in the chest cavity, the organs in the abdomen have enormous mobility. The abdominal mass vibrates inside and outside the thoracic cavity as a result of the trunk's longitudinal and transverse vibrations; therefore, vibrations occur in directions other than the longitudinal direction of excitation.

When the forces of inertia are directed towards the hips during the period of cycle, the abdominal wall is forced outwards and the abdomen appears dilated. Simultaneously, the deformation of the diaphragm towards the lower part of the body causes a decrease in the thoracic perimeter. In the second part of the cycle, the abdominal wall is forced inward, while the diaphragm is directed upward, and the chest circumference increases. The periodic movement of the abdominal organs has a strong resonance at frequencies of 3–3.5 Hz (Figure 11).

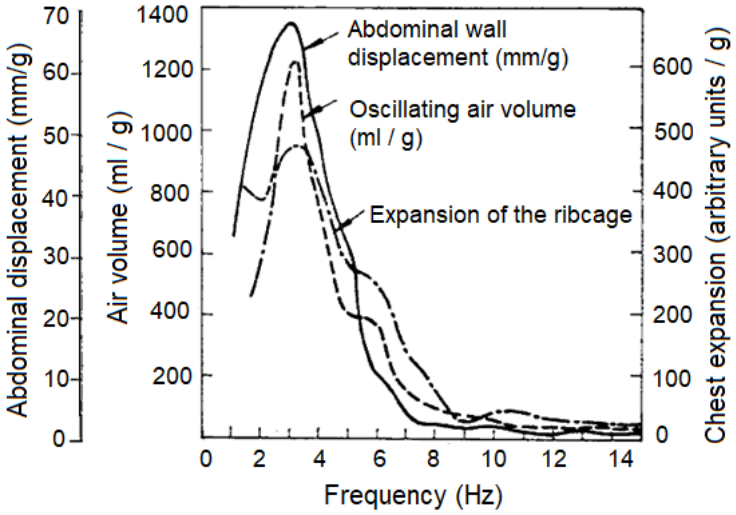


Fig. 11 – **The resonance domain for the abdominal organs**

In the mouth-thoracic cavity system, the oscillations of the abdominal mass are connected with the oscillations of the air. The measurement of the impedance of the latter system (by applying air at the level of the mouth with oscillating pressure) reveals that the abdominal wall and the front section of the chest cavity react to this pressure. Between 7–8 Hz, the impedance is low and the phase angle is zero.

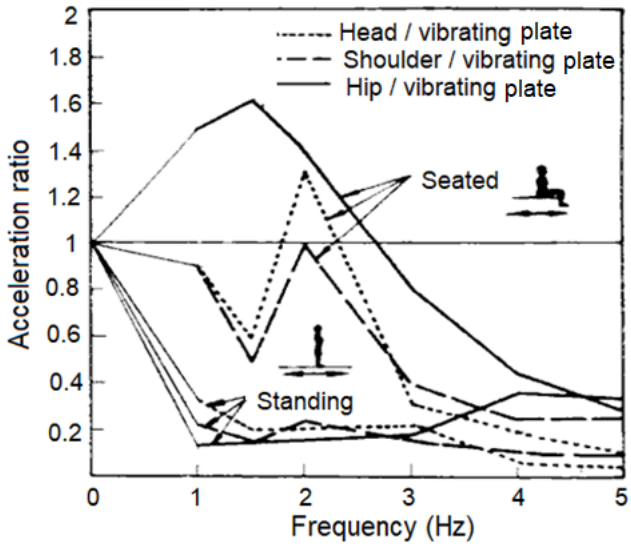


Fig. 12 – **Electrical circuit equivalent to the abdomen-chest-mouth system**

The abdominal wall responds best between 5–8 Hz, whereas the front region of the chest responds best between 7–11 Hz. The abdominal system's vibration, as a result of exposure to vibrations of a man standing or sitting, is easily determined from the modulation of the speed of an air current coming out of the mouth (Figure 11). Therefore, at high vibration amplitudes, speech can be modulated with the vibration frequency of the abdominal system. An electrical circuit equivalent to the abdomen-chest-mouth system is given in Figure 12.

- **The effects of transverse vibrations on the human body**

The human body's reaction to transverse vibrations - for example to horizontal vibrations, when it is in the normal, vertical position - is different from that corresponding to vertical vibrations. In this case, the forces act in a direction creating a right angle with the line of action of gravity's force. Because of this, the distribution of body mass along this line is of particular importance. Thus, the response to transverse vibrations of a seated and a standing body differs greatly, unlike the case of vertical vibrations, which correspond to the usual loading situation for the skeleton and spine, which usually take vertical loads.

Figure 13 contains experimental data regarding the transmission of vibrations at different levels along the body. In the case of a man standing, the amplitudes of the movements of the hip, shoulder and head are, at the frequency of 1 Hz, approximately 20–30% of the amplitude of the vibrating plate and decrease with increasing frequency.

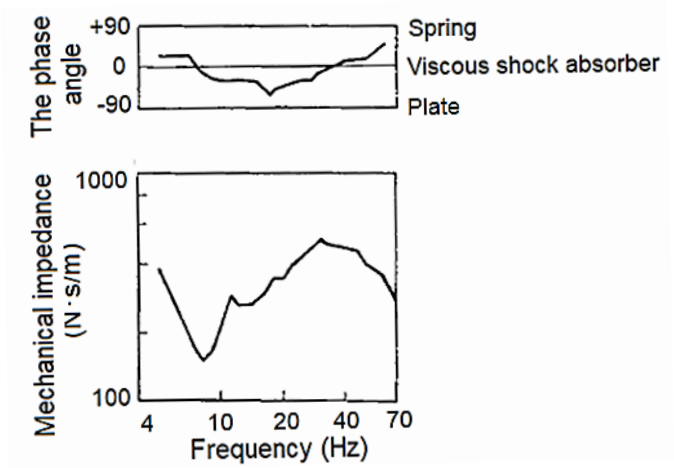


Fig. 13 – **Transmission of vibrations at different levels along the body**

At 2 and 3 Hz, the relative maximum values of the shoulder and head oscillation amplitudes occur. In the case of the man in the sitting position, an amplification of the oscillations of the hip at 1.5 Hz and of the head at 2 Hz is observed. All critical resonance frequencies are found between 1 and 3 Hz. The form of transverse body vibrations can be approximated to that of standing waves by comparing the body to a bar excited by transverse (bending) waves. As the excitation frequency increases, nodal points in the body move closer to the feet, because the phase shifts between the body elements and the vibrating plate increases continually with frequency. At the first frequency of resonance (1.5 Hz), the head of the seated person is 180° out of phase with the vibrating plate; between 2–3 Hz the phase shift is 360° (*Broch J.T., 1984*).

Apart from the transverse movements described in Figure 13 and analysed above, there are also longitudinal movements of the head, excited by the transverse vibrations.

Because of the architecture of the top vertebrae and the position of the head's centre of gravity, the human performs a forward-backward swaying movement of the head. At frequencies above 5 Hz, for a man either sitting or standing, the head movement occurs mainly in the vertical direction (with about 10–30% of the amplitude of the horizontal movement of the vibrating plate).

Vibrations emitted from hands

In connection with the studies on the use of vibrating hand tools, measurements were made regarding the transmission of vibrations from the hand to the arms and body.

Figure 14 depicts the mechanical impedance measured at the handle of a hand tool under representative working conditions. In the range of frequencies below 5 Hz, the impedance shows a maximum

probably determined by the natural frequencies between 1–3 Hz, of the human body subjected to transverse vibrations. A second strong maximum arises between 30–40 Hz, where the hand's effective mass (about 1 kg) is found in resonance due to the elasticity (estimated at 2 x 10^{-5} m/N) of the soft tissues in the palm bridge.

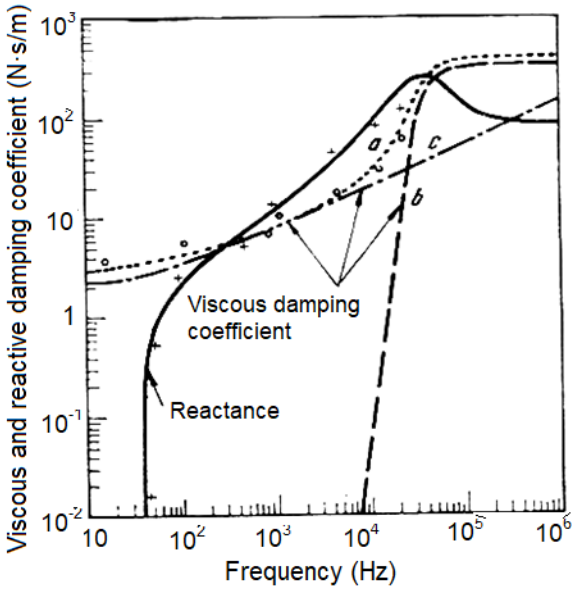


Fig. 14 – Mechanical impedance measured at the handle of a hand tool under representative working conditions

In the case of a manual tool that works at frequencies between 40–50 Hz, the amplitude of the vibration diminishes from the palm to the back of the hand by 35–65%. Other damping occurs at the elbow and shoulder joints.

- **Environment frequency domain**

In the frequency range above 100 Hz, simple models with concentrated parameters become less and less satisfactory for describing tissue vibration. At higher frequencies, the tissue must be viewed as a continuous environment through which vibrations travel.

Vibrations of the skull

The spectrum of skull vibrations is similar to that of a spherical elastic shell. According to the discovered nodal lines, the fundamental resonance frequency is between 300–400 Hz, and the resonances for higher modes of vibration occur at frequencies between 600–900 Hz.

The experimentally obtained ratio between the frequencies corresponding to the vibration modes is 1.7, while the theoretical ratio for the sphere is 1.5. The value of the elastic constant of the bones of the head, calculated according to the values obtained at the resonance) was considered the modulus of elasticity E = $1.4 \cdot 10^9$ N/m^2) corresponds quite well with the results of statistical tests, on samples from dry skulls, but it is somewhat lower than the one calculated from the data obtained during the static tests performed on the femur. The mechanical impedances of some small surfaces of the skull above the mastoid were measured, as well as the skin impedance in the auditory canal, the results being used in the studies on ear protection means.

A simple mass-spring system with a resonance frequency of 100–200 Hz in respect to the skull can describe the vibration of the lower jaw in reference to the skull.

Soft tissue impedance in the human body. Measurements were made of the impedance of the soft tissues of the human body on small surfaces (between 1–17 cm^2), with the help of vibrating pistons, whose frequency was between 10–20,000 Hz. At low frequencies, the impedance has the character of a high-value elastic reactance. As the frequency increases, the elastic reactance decreases, it cancels out at the mass resonance frequency if the frequency increases further (Figure 15).

These results cannot be explained based on a simple model with concentrated parameters, but require modelling based on a system with distributed parameters, including a viscoelastic environment. Because of the environment's high viscosity, several simplifying theoretical hypotheses, such as the hypothesis of an uniform, isotropic, and infinite environment, or the hypothesis that the vibrating element is a sphere and a

cylindrical piston, can be used. The results obtained based on these simplifications are consistent with the measured characteristics. Thus, absolute values can be assigned to the tangential viscosity and transverse modulus of soft tissue.

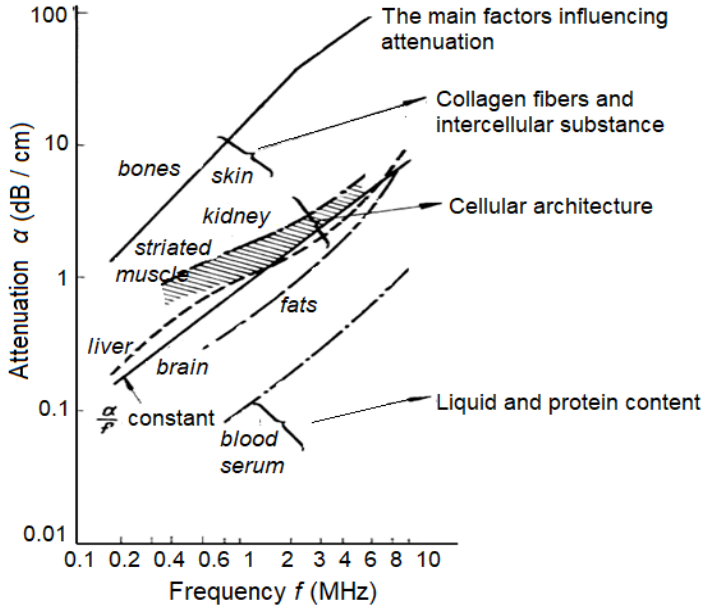


Fig. 15 – **The impedance of the soft tissues of the human body**

Both theory and measurements reveal that, in the audio frequency range, the majority of vibration energy spreads through tissue as transverse waves rather than longitudinal waves. At 200 Hz, the speed of transverse waves is around 20 m/s and grows roughly with the square root of the frequency. For comparison, the constant speed of sound (longitudinal waves) is about 1500 m/s. Surface waves, which have been observed optically, carry some of the energy along the body's surface. Their propagation speed is of a comparable order as that of transverse waves.

- **Effects of shocks and vibrations**

Movements and mechanical stresses caused by mechanical actions on the human body can have numerous impacts, including:

1. Movement can directly interfere with physical activity;
2. Mechanical damage or injury may occur;
3. Side effects (including subjective phenomena) might occur, causing changes in the body via biological receptors and transmission systems.

As for the thermal and chemical effects, they are usually negligible.

Mechanical influence

Of course, the methods of application and the effects of the forces on the body are different. Certain types of movements, speeds and accelerations (if they are high enough) can greatly disturb sensory and neuromuscular activities, such as: reading the indications of some devices, fine-tuning controls or body position, etc. Also, verbal communications can be made considerably more difficult.

Very little data is known regarding the size and type of movement that influences a certain type of activity. When there are such data, they are expressed only from the point of view of the human's ability to tolerate them, without disturbing the activity he submits. For example, the disturbance of visual acuity (Figure 16) that occurs due to body vibrations does not depend only on the frequency, but is approximately proportional to the amplitude of the vibration.

The disturbance can be limited by changing the frequency, by reducing the amplitude, or its influence can be reduced by reducing the requirements imposed to perform a certain operation. If they are of short duration and not repeated at very short intervals, most operations that man can perform are not directly influenced by the mechanical movement resulting from random shocks.

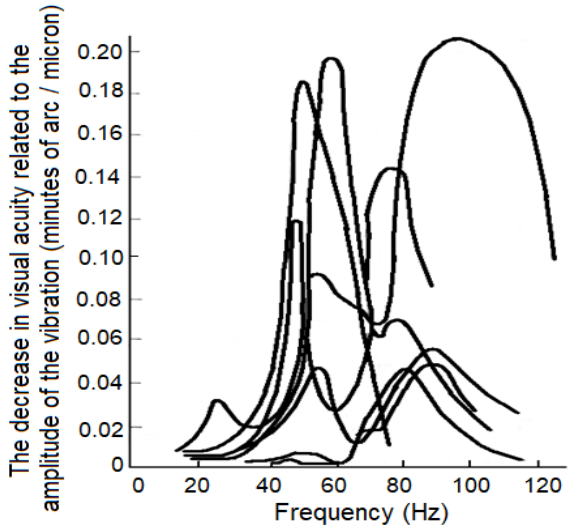


Fig. 16 – Disturbance of visual acuity due to body vibrations

In general, following the shock, the modification of the human working capacity occurs due to biological responses or mechanical injuries.

CONCLUSIONS

Given that prolonged vibrations and shocks are a problem for operators of self-propelled agricultural machinery working on uneven agricultural land, the imposition of time limits for uninterrupted work has become a priority, namely the identification of constructive solutions to reduce or minimize the harmful influence that they have an effect on the human body, as follows:

- at the European and international level (then taken over at the national level), standards have appeared that establish the general working conditions and limits for operators of agricultural machinery: SR EN ISO 13090-1: 2002; ISO 5008: 2002; SR EN ISO 10819:2013/A1: 2019; SR EN ISO 10819:2013/A2: 2023; ISO 2631-1: 2001; ISO 2631-5: 2018;
- constructive solutions were sought and identified to reduce vibrations at the main active parts of agricultural machines (especially the moving parts) that produce the greatest vibrations;
- new suspension systems and ergonomic seats have been developed that absorb the vast majority of vibrations so that the amplitude of those that reach the operator is minimal or reduced to zero, thus being able to work without health problems even 24 hours without interruption.

ACKNOWLEDGEMENT

This paper was supported by the Romanian Ministry of Education and Research, through the project of the Ministry of Research, Innovation and Digitalization through Programme 1 - Development of the national research-development system, Subprogramme 1.2 - Institutional performance - Projects for financing excellence in RDI, Contract no. 1PFE/30.12.2021.

REFERENCES

[1] Biriș S.Șt., Constantin A.M., Anghelache D., Găgeanu I., Cujbescu D., Nenciu F., Voicea I., Matei Gh., Popa D., Duțu M.F., Ungureanu N., Zelazinski T., Perișoară L., Fodorean G. (2022). Considerations regarding the vibrations transmitted to the operator by an axial flow harvester combine. *INMATEH – Agricultural Engineering*, 68(3), 747–756. DOI: https://doi.org/10.35633/inmateh-68-74

[2] Bovenzi M. (1998). Exposure-response relationship in the hand-arm vibration syndrome: an overview of current epidemiology research. *International Archives of Occupational and Environmental Health*, 7, 509–519. DOI: 10.1007/s004200050316

[3] Broch J.T. (1984). Mechanical vibration and shock measurements. Publishing House K. Larsen & Son A/S Bruel & Kjaer, ISBN 8787355345

[4] Buzdugan Gh. (1982). *Mechanical vibrations,* Didactic and Pedagogical Publishing House, Bucharest, Romania.

[5] Cârdei P., Constantin N., Muraru V., Persu C., Sfiru R., Vlăduţ N-V., Ungureanu N., Matache M., Muraru-Ionel C., Cristea O-D., Laza E-A. (2023). The random vibrations of the active body of the cultivators. *Agriculture*, 13(8), 1565. DOI: https://doi.org/10.3390/agriculture13081565

[6] Cutini M., Brambilla M., Bisaglia C. (2017). Whole-body vibration in farming: background document for creating a simplified procedure to determine agricultural tractor vibration comfort. *Agriculture*, 7(10), 84. DOI: https://doi.org/10.3390/agriculture7100084

[7] Essien S.K., Trask C., Khan M., Boden C., Bath B. (2018). Association between whole-body vibration and low-back disorders in farmers: a scoping review. *Journal of Agromedicine*, 23, 105–120. DOI: 10.1080/1059924X.2017.1383333

[8] Kumar A., Mahajan P., Mohan D., Varghese M. (2001). IT information technology and the human interface. *Journal of Agricultural Engineering Research*, 80(4), 313–328. DOI: https://doi.org/10.1006/jaer.2001.0755

[9] Liang C.-C., Chiang C.-F. (2008). Modelling of a seated human body exposed to vertical vibrations in various automotive postures. *Industrial Health*, 46(2), 125–137. DOI: 10.2486/indhealth.46.125

[10] Lima R.C.A., Minette L.J., Simões D., Rocha Q.S., Miyajima R.H., Fritz G.F., Schettino S., Soranso D.R., Nascimento G.S.P., Vieira M.P.L. (2023). Measurement time in the evaluation of whole-body vibration: the case of mechanized wood extraction with grapple skidder. *Forests*, 14(8), 1551. DOI: https://doi.org/10.3390/f14081551

[11] Litchfield M.H. (1999). Agricultural work related injury and ill-health and the economic cost. *Environmental Science and Pollution Research,* 6, 175–182. DOI: 10.1007/BF02987623

[12] Nguyen V.N., Inaba S. (2011). Effects of tire inflation pressure and tractor velocity on dynamic wheel load and rear axle vibrations. *Journal of Terramechanics*, 48, 3–16. DOI: https://doi.org/10.1016/j.jterra.2010.09.001

[13] Okunribido O.O., Magnusson M., Pope M.H. (2006). Low back pain in drivers: the relative role of whole body vibration, posture and manual materials handling. *Journal of Sound and Vibration,* 298, 540–555. DOI: https://doi.org/10.1016/j.jsv.2006.06.007

[14] Pochi D., Fornaciari L., Vassalini G., Grilli R., Fanigliulo R. (2022). Levels of whole-body vibrations transmitted to the driver of a tractor equipped with self-levelling cab during soil primary tillage. *AgriEngineering*, 4(3), 695–706. DOI: https://doi.org/10.3390/agriengineering4030044

[15] Prakash A., Manes G.S., Dixit A., Singh M. (2013). Performance status of rotavators being manufactured in Punjab. *Journal of the Institution of Engineers (India): Series A*, 94(1), 53–58. DOI: https://doi.org/10.1007/s40030-013-0038-7

[16] Punnett L., Wegman D.H. (2004). Work-related musculoskeletal disorders: the epidemiologic evidence and the debate. *Journal of Electromyography & Kinesiology,* 14, 13–23. DOI: https://doi.org/10.1016/j.jelekin.2003.09.015

[17] Singh A., Samuel S., Singh H., Singh J., Prakash C., Dhabi Y.K. (2022). Whole body vibration exposure among the tractor operator during soil tillage operation: an evaluation using ISO 2631-5 standard. *Shock and Vibration*, 2022, 6412120

[18] Sorică E., Vlăduţ V., Cârdei P., Sorică C., Brăcăcescu C. (2017). Comparative analysis of the noise and vibration transmitted to the operator by a brush cutter. *Proceedings of the XIVth International Conference „Acoustics and Vibration of Mechanical Structures – AVMS-2017*", 165–172, Timişoara, Romania. DOI: https://doi.org/10.1007/978

[19] Stojic B., Poznanovic N., Poznic A. (2017). Research and modelling of the tractor tire enveloping behaviour. *Journal of Vibration and Control*, 23, 290–304. DOI: https://doi.org/10.1177/1077546315576

[20] van Heuvelen M.J.G., Rittweger J., Judex S., Sañudo B., Seixas A., Fuermaier A.B.M., Tucha O., Nyakas C., Marín P.J., Taiar R., et al. (2021). Reporting guidelines for whole-body vibration studies in humans, animals and cell cultures: a consensus statement from an international group of experts. *Biology*, 10(10), 965. DOI: https://doi.org/10.3390/biology10100965

[21] Vlăduţ V., Biriş S. Şt., Bungescu T., Herişanu N. (2013). Influence of vibrations on the operator in the grain harvesters. *Applied Mechanics and Materials*, 430, 290–296. DOI: https://doi.org/10.4028/www.scientific.net/AMM.430.290

[22] Vlăduţ V., Pirnă I., Florea C., Popescu C., Brătucu Gh., Kabas O., Păunescu D. (2014). Influence of the vibration amplitude on the quality of shredded medicinal vegetal material subjected to sorting. *Proceedings of the 42nd International Symposium on Agricultural Engineering "Actual Tasks on Agricultural Engineering",* 273–282, Opatija, Croatia

[23] Directive 2002/44/EC of the European Parliament and the Council of 25 June 2002 on the minimum health and safety requirements regarding the exposure of workers to the risks arising from physical agents (vibration) (16th individual Directive within the meaning of Article 16 (1) of Directive 89/391/EEC). *Official Journal of the European Communities-Legislation*, 117(13), 6–7
[24] EU-OSHA - European Agency for Safety and Health at Work. (2005). Expert forecast on emerging physical risks related to occupational safety and health. European Agency for Safety and Health at Work: Bilbao, Spain, ISBN 92-9191-165-8
[25] ISO 5008. (2002). Agricultural wheeled tractors and field machinery-measurement of whole-body vibration of the operator
[26] ISO 2631-1. (2001). Mechanical vibration and shock. Evaluation of human exposure to whole-body vibration. Part 1: General requirements
[27] ISO 2631-5. (2018). Mechanical vibration and shock. Evaluation of human exposure to whole-body vibration. Part 5: Method for evaluation of vibration containing multiple shock
[28] SR EN ISO 10819:2013/A1. (2019). Mechanical vibrations and shocks. Hand-arm vibrations. Measurement and evaluation of the glove-to-palm vibration transmission factor. Amendment 1.
[29] SR EN ISO 13090-1. (2002). Mechanical vibrations and shocks. Indications regarding the security aspects of tests and experiments carried out with human subjects. Part 1: Whole body exposure to mechanical vibrations and repeated shocks
[30] SR EN ISO 10819:2013/A2. (2023). Mechanical vibrations and shocks. Hand-arm vibrations. Measurement and evaluation of the glove-to-palm vibration transmission factor. Amendment 2.

STUDIES ON THE DEVELOPMENT OF A RELIABILITY DIAGNOSIS FOR AGRICULTURAL TRACTORS GEARBOXES
/
STUDII PRIVIND DEZVOLTAREA UNUI DIAGNOSTIC DE MENTENANȚĂ LA CUTIILE DE VITEZE A TRACTOARELOR AGRICOLE

Alexandru-Vlad HELLER *); Nicolae FILIP; Teodora DEAC
Technical University of Cluj-Napoca, Department of Road Vehicles and Transport,
Bd. Muncii, Nr. 103-105, cod 400641, Cluj-Napoca / Romania;
Tel: +40264401779; E-mail: teodora.deac@auto.utcluj.ro
DOI: https://doi.org/10.35633/inmateh-71-75

Keywords: *reliability diagnosis, agricultural tractors, gearboxes, reliability indicators*

ABSTRACT
Faults and failures analysis involve a wide variety of engineering areas, so concepts and reliability indicators help us to determine the types of faults easier, their appearance in functioning and the mathematical relations for determining different failures. In this context, test stands help us to identify accelerated noises, vibrations and serious malfunctions that occur during operation and can lead to major equipment failure, thus helping engineers to quickly find optimal solutions in most cases. The current methods used to determine the reliability of the agricultural tractors gearboxes are those in open energy flow, as they best simulate the real operating conditions. An agricultural tractor gearbox test stand was designed to perform rapid noise and vibration diagnostics and reliability tests. Considering the working conditions of the gearbox and its possible failures, the stand was equipped with transducers and a data acquisition system for data collection.

REZUMAT
Defectele și analiza defectelor implică o mare varietate de domenii ale tehnicii, astfel conceptele și indicatorii de fiabilitate ne ajută să determinăm mai ușor diferitele tipuri de defecțiuni, apariția acestora în funcționare și relațiile matematice pentru determinarea diferitelor defecțiuni. În acest context, standurile de testare ne ajută să identificăm zgomotele accelerate, vibrațiile și defecțiunile grave care apar în timpul funcționării și pot duce la defectarea majoră a echipamentelor, ajutând astfel inginerii să găsească rapid soluțiile optime în majoritatea cazurilor. Metodele curente utilizate pentru determinarea fiabilității cutiilor de viteze ale tractoarelor Agricole, sunt cele în flux de energie deschis, acestea simulând cel mai bine condițiile reale de funcționare. Am proiectat un stand de testare a cutiilor de viteze ale tractoarelor agricole pentru realizarea de diagnostic și teste rapide de fiabilitate a zgomotului și vibrațiilor. Având în vedere condițiile de lucru ale cutiei de viteze și posibilele defecțiuni ale acesteia, standul a fost echipat cu traductoare și un sistem de achiziție de date pentru colectarea datelor.

INTRODUCTION

Reliability is an important part of the process of identifying safety problems that occur in the operation of equipment, devices and components. Reliability discipline is training top engineers in maintaining the technical condition of automotive equipment. The operation of a product is limited by the occurrence of a reduction in operating efficiency or a failure. Reliability is the ability of a product to function without failure. Mathematically, it is possible to estimate, with some degree of certainty, the behaviour of a product under certain conditions of use (*Filip, 2010*). Reliability is linked directly to the notion of quality of a product. To a certain extent, the notion of quality can be considered as the statistical learning of the operating conditions at a given time, while the notion of reliability is the dynamic learning of the operating conditions. (*Bosch, 2022*).

Reliability has a new role in engineering, in accordance with international standards: it forces the designers to learn to design in the new conditions of the quantitative specification of reliability from the conception phase. Reliability concerns also have the effect of eliminating the causes of systematic failure and reducing the probability of the occurrence of other defects, thus leading to "reliability improvement".

Experimental or laboratory reliability requires, in addition to special installations for reliability tests, the establishment of a correct test program to represent the conditions of use. This is difficult to achieve and in general the tests are carried out under conventionally established conditions. In this case, the problem arises of establishing the equivalence of the laboratory tests with that of the actual behaviour in use. (*Bonnick et al, 2005*).

Table 1

The main cases of reliability

Different concepts of reliability	Content
Forecast reliability (preliminary, predictive)	Is the reliability predetermined by calculation, by any previous trials. It is specific to the design stage of a product.
Experimental reliability (laboratory)	Reliability obtained through determinative tests in the laboratory on special stands, based on product samples. It is called: a) observed (estimated) - if it refers to the stage observed in the laboratory; b) extrapolation - if based on information from laboratory to make estimates by extrapolation of the length;
Operational reliability (exploitation)	Reliability determined based on the processing of operational information.
Rating reliability	The reliability prescribed in the technical documentation (standards, norms, contracts, etc.).
Intrinsic reliability	Determined based on the link between the applied stress and the stress resistance of the considered element.
Extrinsic reliability	Determined on the basis of sampling or analytical data processing with the help of reliability indicators.

Economic analysis of constructive solutions often shows that instead of a single product with a high reliability, high life and without need of maintenance or repair, it is more economical to use two or three products with a shorter life span and possibly repairable.

Basically, the automotive industry is able to produce a product with a high reliability, but unacceptable in terms of cost.

Analysing variations in cost depending on reliability and maintenance (Fig. 1.), it is found that there is an optimal economic zone (minimal cost) which corresponds to the optimum reliability (Ropt).

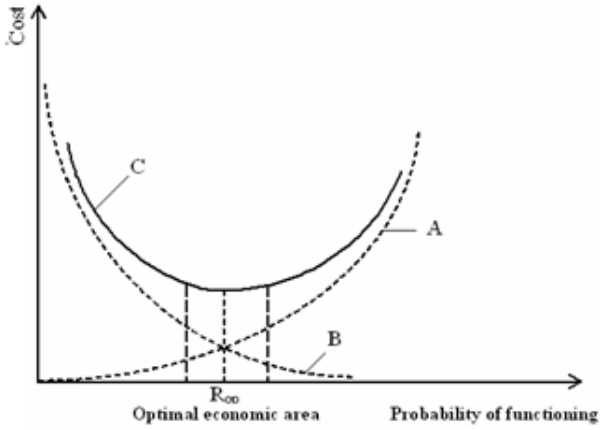


Fig. 1 – The relation between cost and reliability of a product

For a reliable R > Ropt, the investment cost is large in relation to the intended use. In many cases it should also be taken into account the damages caused by the lack of reliability.

In general, the value of Ropt is lower than the possible technical reliability. Therefore, a number of defects, not negligible, should be expected in order to ensure the most economical cost of operation. Thus, it is necessary to carefully schedule the appropriate maintenance.

In the end, the reliability which was adopted by the design solution represents a trade-off between reliability and maintenance cost.

The level of optimum reliability, Ropt, is different from one stage to another and from one use to another, depending on the effects and consequences.

Faults and failures is a vast domain of engineering. Quality control is not interested in the technical concept of defect, but "compliance" or "non-compliance" in relation to a set of circumstances. Later, at another level, the non-compliance found out is interpreted and treated as a defect in a technical sense, tracing the defects back to the conception phase.

Failure means the physico-chemical processes of degradation which has effect on malfunctioning. The defect is the event that occurs as a result of a failure. An item (simple element, component, entity, product, etc.), is not only an elementary part or component of a system, but also any product whose reliability is studied independently of the reliability of its components.

The item is characterized by a specific function that it has to fulfil.

During functioning, the component supports a certain stress that produces a cumulative deterioration, causing, after a random amount of time, the occurrence of an expected defect. This defect disrupts the functioning of the component (*Bertsche, 2008*).

The reliability of the component can be determined in two ways (*Cordos et al, 2000; Filip et al, 2020*):

a) The method is based on the assumption of a sample analysis. The general relations of reliability are determined considering a sample of elements working in the same conditions.

The number of defects that occur during functioning determines the variation in reliability over time. Reliability is defined on the basis of sample hypothesis and may also refer in this case to "intrinsic reliability" because the product is considered as a "black box" without considering the internal mechanism of the defect, and the reliability results from the behaviour of the item viewed from the exterior.

b) The method is based on physical mechanism of the degradation processes. It consists in the analysis of physical-chemical mechanism of the degradation process, the appearance of the defect and stochastic modelling. The forces applied and the stress resistance depending on operational time are considered random variables.

Stochastic modelling of the degradation process leads to the definition of the probability of occurrence of the faulty element and therefore to the definition of predictive reliability. This method of determination is based on the description of the internal mechanism of the defect.

MATERIALS AND METHODS

Considering the construction and operation mode of mechanical gearbox, with the variation of transmission ratio in steps, when testing them, the pursued objectives are: efficiency and power losses at different loads and speeds; the size, nature and position of the teeth footprint gears at the working under load; characteristic temperature (temperature regime of operation at different loads); noise and vibrations produced during operation; resistance to static request; durability of ball bearings; wear resistance of main parts; synchronizers quality and reliability; operation of the gearshift actuator; the reliability of a conventional gearbox expressed through the duration of operation until the first breakdown of the testing process or mechanism.

The project and the components of a stand intended for testing the reliability of a gearbox must ensure the possibility of reproducing the load regimes and operating speeds, which should be as close as possible to the operational operating conditions. This condition is necessary so that the obtained results come as close as possible, or coincide with the results obtained under real operating conditions. (Fig.2).

The measuring stand is designed to simulate, as faithfully as possible, the operation of the gearbox under working conditions (Fig.2).

The drive system is provided by a three-phase motor (*1*) with a power of 4 kw, which has an output shaft speed of 1500 rpm. The transmission of the moment from the drive motor to the gearbox is carried out by the planetary coupling (*2*). The gearbox (*3*) is fixed to the frame by an elastic coupling (4), thus it is isolated from unwanted vibrations during measurements. The transmission of the moment from the gearbox to the dynamic brake is accomplished with a planetary coupling (*5*) equipped with an elastic bush (*6*) and a low-frequency vibration attenuator (*7*). The dynamic brake (*8*) is a direct current motor, with a power of 4 kW, 220 V, used as a generator, which ensures the conversion of mechanical work into electrical energy, thus, making it possible to determine the power losses in the gearbox (*9*) (*Golgot et al., 2021*).

The working principle is the following: electrical energy is converted into mechanical work which is then converted back into electrical energy. This captured energy is used to charge the gearbox, by using high power resistors (*Heller et al., 2016; Mocanu, 2006*).

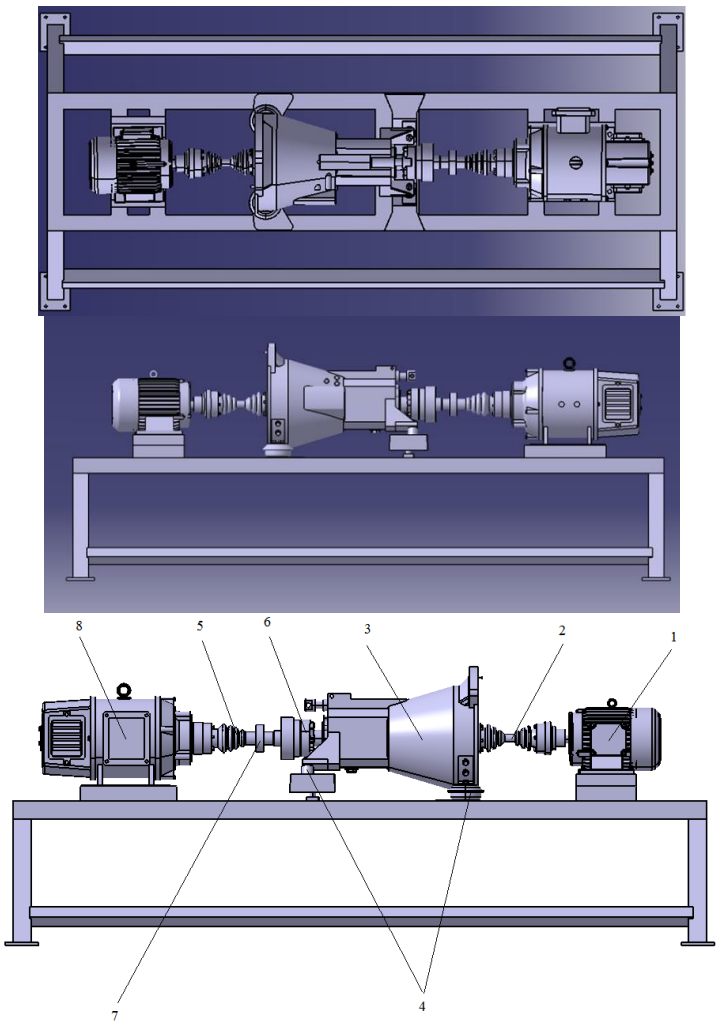


Fig. 2 - Gearbox test bench

1. Electric engine drive; 2. Planetary coupling; 3. Gearbox; 4. Elastic couplings; 5. Planetary coupling; 6. Elastic rubber flange; 7. Low- frequency vibration damper; 8. Brake dynamics

Method of testing in open energy flow

The method used for the gearbox's bench testing in the present paper is the method of testing in open energy flow (*Denton, 2006*). The testing bench must satisfy the following conditions:

- nominal power of the engine drive, must be at least equal to the power that the gearbox transmits during the operating conditions of the vehicle.
- the speed of the drive motor, must be at least equal to the nominal speed of the motor vehicle and can be changed continuously.
- the equipment should allow the measurement of torsion moment at the primary and secondary shafts using transducers (resistive or inductive);
- the brakes must be sized in terms of time and speed resulting from secondary shaft of gearbox, so they can absorb the power transmitted from the gearbox at all its ratios.

To measure the load applied to the gearbox, a Pico Ta009 direct current clamp meter (Fig.2) was used, a device that allowed precise monitoring of the current absorbed by the external consumers. Knowing the two parameters, the voltage and the intensity of the electric current, the degree of loading of the generator can be determined.

The adjustable rheostat was replaced by two light bulb panels, composed of 28 100 W (2800 W) light bulbs, 220 V supply voltage, each with a switch. This way, the amplitude of the signal was tracked by applying a progressive load to the gearbox.

For each position, three measurements were taken at three points, arranged at 90 degrees to each other. In each gear (3rd, 4th and 5th gear) 72 measurements were made at different loads and speeds. The determinations were made at the characteristic speeds (894 – 1482 revolutions per minute) with a load from 0% to 90% to be able to identify the proper vibration mode of the gearbox.

To perform the three measurements in three points arranged at 90 degrees to each other, the following procedure was followed: the piezoelectric sensor ai0 recorded the values in the vertical position of the three sections; the piezoelectric sensor ai1 recorded the values in the horizontal position of the three sections, by moving the position from point 1 to point 2. Each section was composed of two measurements at 90°, ai0(fixed)+ai1(left) A1, B1, C1 and ai0(fixed)+ai1(right) A2, B2, C2. Later, in the experimental data processing, these were extracted and compared in bands and frequency range.

RESULTS

After data collection, their processing consisted in the simultaneous determination of vibrations in three measuring points and for three sections. The results obtained after data processing are displayed in a wave chart, which is an interface component dedicated to displaying one or more graphical representations simultaneously, for which the variation over time is followed.

The analysis of the experimental results consisted in the development of the analysis in the frequency spectrum for the tests carried out *(Kloeden, 2008)*.

Figures 3a – 8a show the graph of the frequency bands of the measurements made at point A1, A2, B1, B2, C1, C2 at 0% load, and figures 3b – 8b show the graph of the frequency bands of the measurements made at the same points A1, A2, B1, B2, C1, C2 at the same load 0, the difference being that in the graphs marked with b the results are different due to the buffer that simulates the gearbox failure. From the analysis of the two graphs, in each analysed case it can be observed that the first harmonic F0 is approximately equal in both variants. The 8th harmonic is significantly higher in the case of the graph representing the measurements performed with a weakened buffer, i.e. figures 3b – 8b. The 25th harmonic is significantly higher in the case of the first graph, i.e. figures 3a – 8a representing the measurements performed with a tight buffer (*Upadhyay, 2020*).

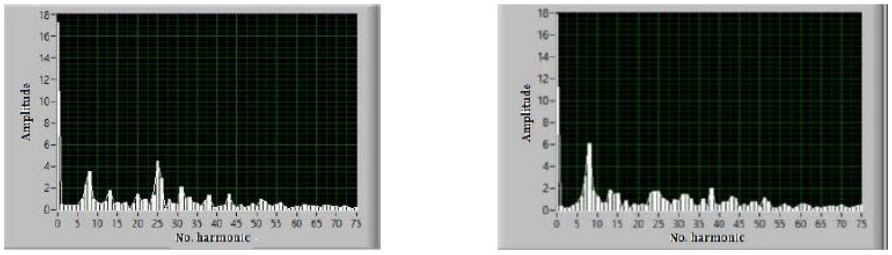


Fig. 3 - The graph of the frequency bands of the measurements made at point A1 at 0 % loading
a. T3 tight buffer A1 S0, b. T3 loose buffer A1 S0

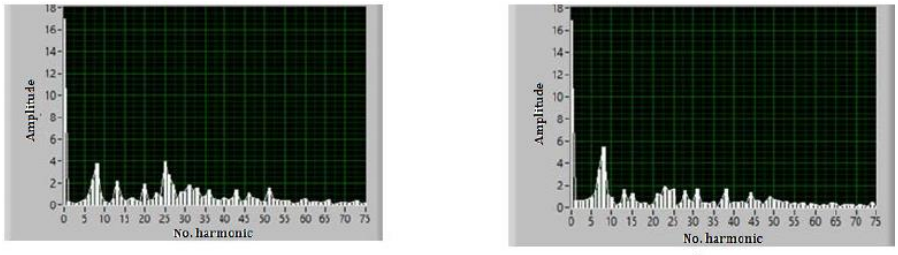


Fig. 4 - The graph of the frequency bands of the measurements made at point A2 at 0 % loading
a. T3 tight buffer A2 S0, b. T3 loose buffer A2 S0

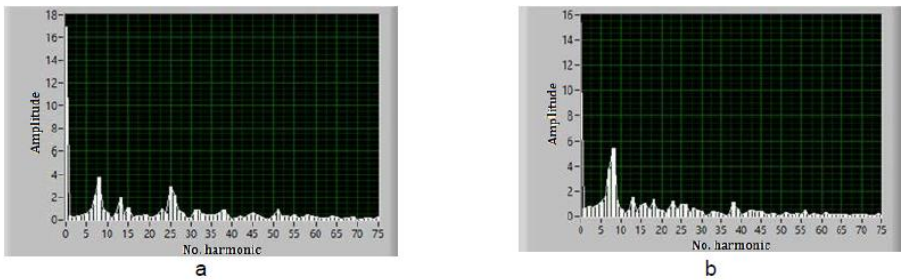
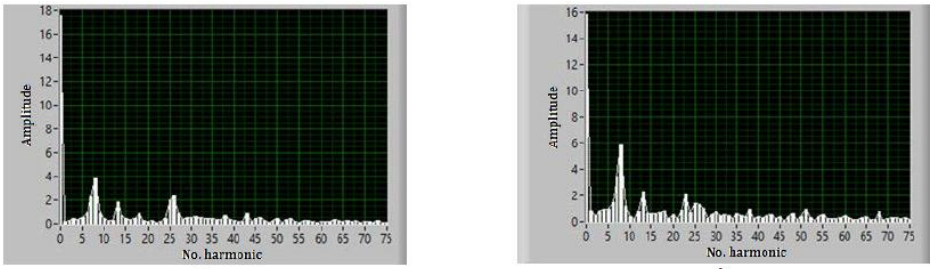


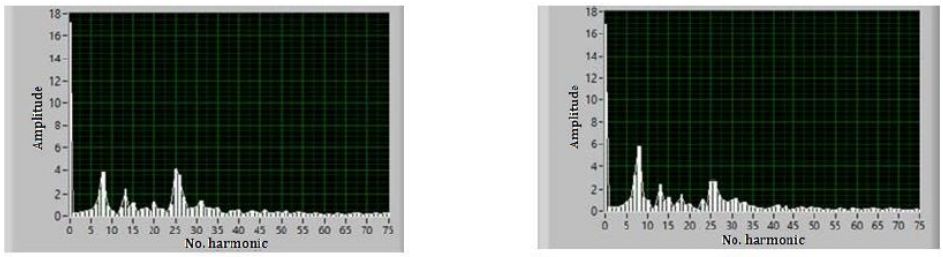
Fig. 5 - The graph of the frequency bands of the measurements made at point B1 at 0 % loading
a. T3 tight buffer B1 S0, b. T3 loose buffer B1 S0



a b

Fig. 6 - The graph of the frequency bands of the measurements made at point B2 at 0 % loading

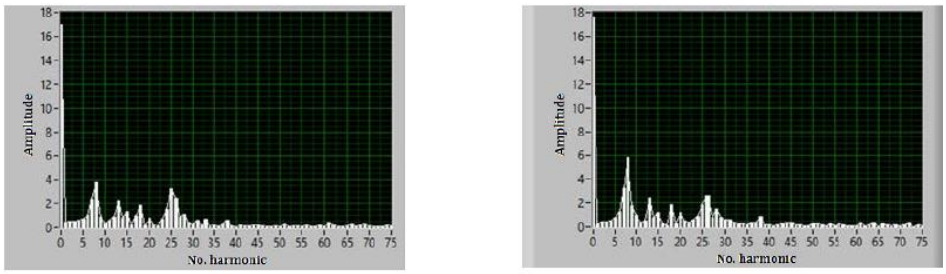
T3 tight buffer B2 S0, b. T3 loose buffer B2 S0



a b

Fig. 7 - The graph of the frequency bands of the measurements made at point C1 at 0 % loading

a. T3 tight buffer C1 S0, b. T3 loose buffer C1 S0



a b

Fig. 8 - The graph of the frequency bands of the measurements made at point C2 at 0 % loading

a. T3 tight buffer C2 S0, b. T3 loose buffer C2 S0

Similarly, the graphs of the frequency bands related to each measurement point without load and under load at 30%, 60%, 90% were made (*Dobre, 2018; Cardei et al., 2023*). The ratios of the dominant frequencies according to the load are presented in Table 1, and in Figs. 9-12. The dominant frequencies are represented according to the applied load.

Table 1

The ratio of the dominant frequencies as a function of the applied load

Loading [%]	Harmonic no.	Operating frequency f_a [Hz]	Dominant frequency f_d [Hz]	Ratio f_d / f_a					
				A1	A2	B1	B2	C1	C2
0	F7	24.78	13.58	0.547					
	F8		15.52	0.626					
	F25		48.5	1.956					
30	F7	24.73	13.58	0.549					
	F8		15.52	0.627					
	F25		48.5	1.961					
60	F7	24.55	13.58	0.553					
	F8		15.52	0.632					
	F25		48.5	1.975					
90	F7	24.45	13.58	0.555					
	F8		15.52	0.634					
	F25		48.5	1.983					

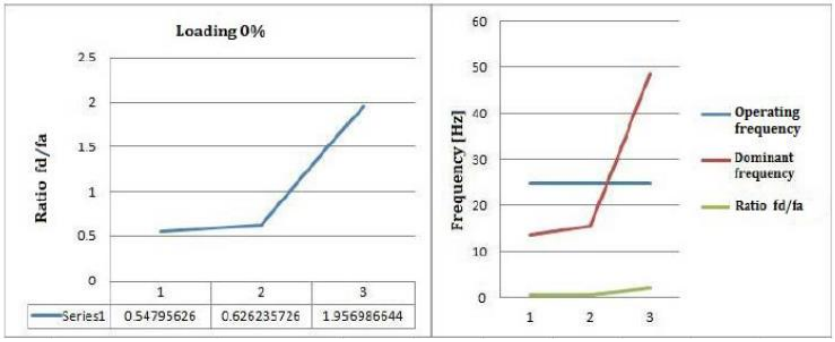


Fig. 9 - Dominant frequencies at 0 % loading

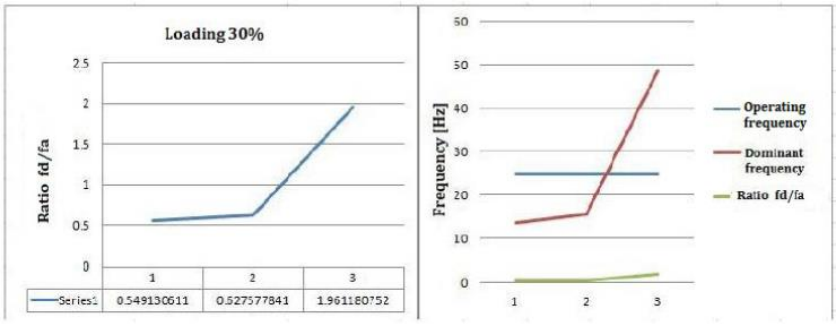


Fig. 10 - Dominant frequencies at 30 % loading

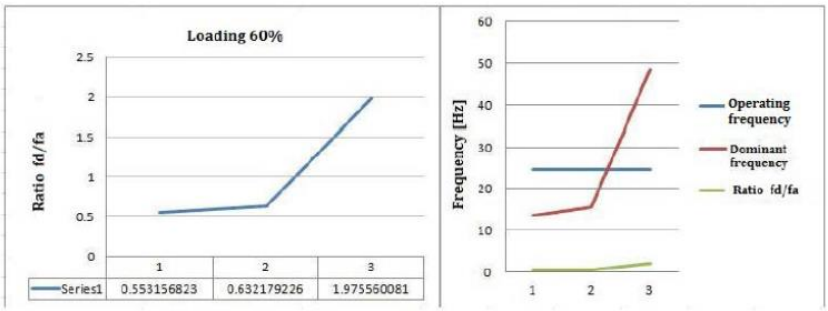


Fig. 11 - Dominant frequencies at 60 % loading

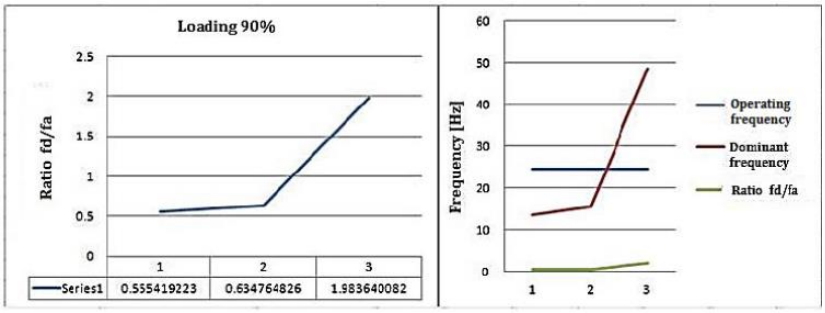


Fig. 12 - Dominant frequencies at 90 % loading

Following the analysis of the obtained experimental data, it was determined that although at 0% load the amplitudes of harmonics and automatic gearbox vibrations were approximately equal for both types of measurements with and without a buffer, with increasing load the value of the amplitude starts to increase in the case of measurements made with a buffer, reaching a significantly higher value (*Zhang et al., 2021*).

The functional parameters of gearboxes do not remain the same during their lifetime. This is explained by the fact that the parts that make up the gearbox wear out over time. The nature of parts wear is of two types: mechanical wear and chemical wear. Whatever the nature of the wear, it has the effect of altering the geometric shapes of the parts, which is finally reflected in the change of the dynamic parameters (gear noise, power losses, more pronounced heating of the components).

CONCLUSIONS

The study of vibration applied to reliability has the goal to improve gear ratio at different speeds to avoid critical resonance thresholds and can be applied for agricultural tractors.

Amplifying vibrations leads to rapid removal from operation of the elements (e.g., fatigue breaking shaft). Reducing vibrations extends the life cycle of the components of the gearbox.

The proposed stand can be used in practice in reliability tests. The stand has been designed to develop reliability testing based on acoustic and vibration measurements.

The vibro-acoustic analysis of the vibration mode of the gearbox is an effective way of evaluating its components. This type of analysis has the following advantages:

- the ability to quickly obtain information on failure mode and possible defects in agricultural tractors before gearbox failure.
- the investigation of the defect can be carried out without the need to dismantle the gearbox.
- the vibro-acoustic analysis technique is currently used in specialized centres around the world, but it is not yet used in our country.

The processing of the experimental results represented the analysis of 1024 values for each measurement point at the imposed speeds and load regime. The harmonics representing the contribution of the gearbox mounting pads to the vibration spectrum have been identified.

The developed stand can be used for the maintenance diagnosis of gearboxes of agricultural tractors. Thus, using the stand and the techniques of vibro-acoustic analysis, the defects in the gearbox components of agricultural tractors can be diagnosed, which leads to the extension of their life span.

REFERENCES

[1] Bertsche, B. (2008). *Reliability in automotive and mechanical engineering*. Springer, Berlin.

[2] Bonnick, A., Newbold, D., A. (2005). *Practical Approach to motor Vehicle Engineering and Maintenance*, Second Edition, Ed. Elsevier, Burlington.

[3] Cardei, P. et al. (2023). Superior inferential statistics of the experimental data of a complex experimental cultivator, *INMATEH Agricultural Engineering*, 71(3), 147-163, https://doi.org/10.35633/inmateh-71-12.

[4] Cordos, N., Filip N. (2000). *Reliability of Motor Vehicles (Fiabilitatea Autovehiculelor)*, Todesco Publishing House, Cluj-Napoca.

[5] Crișan, H., G., Heller, A., V. (2015). The graphical modeling, simulation and realization of an equipment with opto - reflective sensors for the management of urban public transport passengers, *Journal of Industrial Design & Engineering Graphics*, Special Issue, (10).

[6] Denton, T. (2006). *Advanced Automotive Fault Diagnosis*, Second Edition, Ed. Elsevier, United Kingdom.

[7] Dobre, A. (2018). The simulation of the dynamic behaviour for an elastic mechanical transmission of passenger car, *Automotive engineering (Ingineria automobilului),* 48, 23-25.

[8] Filip, N. (2010). *Road traffic engineering (Ingineria traficului rutier)*, Mediamira Publishing House, Cluj-Napoca.

[9] Filip, N., Popescu, G. (2020). *Reliability and maintainability with applications in vehicle and transport engineering (Fiabilitatea si mentenabilitatea cu aplicatii in ingineria autovehiculelor si trasporturilor),* UT PRESS Publishing House, Cluj-Napoca.

[10] Golgot, C., Filip, N. (2021). Exhaust noise analysis research for a single-cylinder diesel engine and evaluation of noise filtration by simulation, *INMATEH Agricultural Engineering*, 65(3), 203-2012, https://doi.org/10.35633/inmateh-65-21.

[11] Heller, A., V., Filip, N. (2016). The development of an experimental test stand for diagnosis of gearbox reliability, *Romanian Journal of Automotive Engineering*, RoJAE vol. 22(3)

[12] Kloeden, P., Platen, E. (2008). *Numerical solution of Stochastic Differential Equations*, Springer, Sydney

[13] Mocanu, F. (2006). *Material resistance (Rezistenta Materialelor)*. Vol. I, Tehnopress Publishing House, Iasi.

[14] Robert, Bosch, Gmbh. (2022). *Automotive Handbook*. 11th Edition, Wiley Publishing House, BRT9781119911906.

[15] Upadhyay, K. (2020). *Basics of Vibration and Condition Analysis*, Notion Press Publishing House, ISBN 9781648999635.

[16] Zhang, M. et al. (2021). Experimental study on air flow field characteristics of suction metering device, *INMATEH Agricultural Engineering*, 65(3), 57-66, https://doi.org/10.35633/inmateh-65-06.

THE RELATIONSHIP BETWEEN ENVIRONMENTAL PUBLIC PERCEPTION AND GREEN PRODUCT TRADE. THE MODERATING ROLE OF POLICIES AND LEGAL TEXT [1]

公众环境认知与绿色产品贸易的关系——政策法律文本的调节作用

Guoli HAN *[1)]; Shuming MA [2)]

[1)] College of Humanity and Law, Xinxiang Institute of Engineering, Xinxiang, Henan 453000 / China;
[2)] Commercial College, Henan Normal University, Xinxiang, Henan 453000 / China
E-mail: hanguoli5986@163.com
DOI: https://doi.org/10.35633/inmateh-71-76

Keywords: *environmental policy, emotional perception, green product trade, legal text*

ABSTRACT

In today's increasingly accelerating globalization, environmental protection and sustainable development have become the focus of common concern for all countries. Public environmental awareness, that is, the public's understanding and attitude towards environmental issues, has a significant impact on environmental protection work. Meanwhile, with the rise of green product trade, the market trading of green products is becoming increasingly active. As one of the means to regulate the relationship between public environmental awareness and green product trade, the role of policies and legal texts is increasingly prominent. This article will explore the relationship between public environmental awareness and green product trade and analyze the regulatory role of policies and legal texts in it. This article explores the impact of trade and environmental policies on the financial system through computer software. It constructs a theoretical hypothesis model to explore the moderating effect of policy and legal texts on the relationship between public emotional perception of environmental policies and green product trade. After empirical testing, all research hypotheses in this study have been supported. The results showed that at a test level of 0.01, consumers' perception of green efficacy, perceived green responsibility, green purchasing behavior, emotional arousal, and moderate values were significantly positively correlated. Among them, the R-value of perceived green efficiency and green purchasing behavior is 0.701, and the R-value of perceived green responsibility and green purchasing behavior is 0.638, indicating the degree of correlation between perceived green efficiency, perceived green responsibility, and green purchasing behavior. Green purchasing behavior is highly correlated. The conclusion indicates that the government has further increased export subsidies for the clean industry, implemented differentiated environmental tax policies, and emphasized the coordinated use of procedures, promoting the development of the clean industry and the upgrading of industrial structure.

摘要

在全球化日益加速的今天，环境保护和可持续发展已经成为各国共同关注的焦点。公众环境认知，即公众对环境问题的认识和态度，对环境保护工作具有重要影响。同时，随着绿色产品贸易的兴起，绿色产品的市场交易也日益活跃。政策法律文本作为调节公众环境认知与绿色产品贸易关系的手段之一，其作用日益凸显。本文将探讨公众环境认知与绿色产品贸易的关系，并分析政策法律文本在其中的调节作用。 本文通过计算机软件实现贸易和环境政策对金融体系的影响。本文构建了一个理论假设模型，探讨政策和法律文本对公众对环境政策的情感感知与绿色产品贸易之间关系的调节作用。经过实证检验，本研究的所有研究假设都得到了支持。结果显示，在 0.01 的检验水平下，消费者感知绿色功效、感知绿色责任、绿色购买行为、情绪唤醒和适度价值观显着正相关。其中，感知绿色效能与绿色购买行为的 R 值为 0.701，感知绿色责任与绿色购买行为的 R 值为 0.638，表明感知绿色效能、感知绿色责任与绿色购买行为之间的相关程度。 绿色购买行为高度相关。 结论表明，政府进一步加大对清洁产业的出口补贴，实行差别化的环境税收政策，注重程序的协调使用，促进了清洁产业的发展和产业结构的升级。

[1] *Guoli Han, Associated professor; Shuming Ma, Assistant professor*

INTRODUCTION

With the increasingly serious global environmental problems, the public's attention to environmental protection is constantly increasing. Meanwhile, with the continuous development of global trade, green product trade has gradually become an important part of global trade. The relationship between public environmental awareness and green product trade has become an important research issue. Public environmental awareness refers to the level and attitude of the public towards environmental issues. The growth of public environmental awareness has promoted the implementation of environmental protection actions, thereby promoting the implementation of environmental protection actions. In terms of green product trade, improving public environmental awareness can promote consumers' demand for green products, thereby promoting the development of green product trade. Policy and legal texts refer to a series of policies and regulations formulated by the government related to environmental protection. These policies and regulations can directly or indirectly affect public environmental awareness and green product trade. For example, the government can formulate environmental regulations to limit environmental pollution, which can increase public awareness of environmental protection. At the same time, the government can also encourage the development of green product trade through subsidies and other policies. Environmental problems are closely related to trade and economic development. Since the industrial age, the rapid growth of science and technology has promoted the rapid growth of the global economy, but it has also produced a series of environmental problems. As an important economic activity, international trade is destined to be closely linked with the natural environment from the moment it comes into being. Along with trade liberalization, in addition to the rapid economic growth, the ecological environment continues to deteriorate, and international trade disputes related to the environment are constantly emerging. With the increasing popularity of environmental protection in the world, the change in people's consumption concept and the enhancement of environmental protection consciousness, this traditional concept needs to be updated. Whether the product meets ecological protection requirements has become an important factor that must be addressed in product competitiveness. As an important engine to stimulate China's economic growth, changing the trade structure can drive industrial structure adjustment (*Cao et al., 2017*). For the current serious environmental pollution situation, the government should introduce policies at the macro level to support the clean industry with low energy consumption and low pollution and promote its export expansion to achieve green and healthy economic development by optimizing and upgrading the industrial structure.

Generally speaking, the paths of initiating and promoting behavior can be divided into rational and the emotional paths. Wang and others think that reason is not the motive of behavior but only the means to get happiness or avoid pain (*Wang et al., 2018*); Daviron believes that the individual's consumption decision results from the interaction between cognition and emotion. Because the individual's cognitive resources are limited, making a completely rational decision is impossible, and the individual's consumption decision has an obvious emotional preference. Emotion, as the information clue of individual preference, will directly impact the consumption decision (*Daviron et al., 2012*). Can et al. believe that under globalization, countries worldwide, especially developing countries, will take the initiative to lower their environmental regulatory standards to gain a competitive advantage in international competition to promote their economic growth (*Can et al., 2021*). Liu et al. concluded that the structural effect caused by international trade has a greater impact on the environment than the scale and technical effects (*Liu et al., 2017*). He took the per capita sulfur dioxide emissions as the environmental pollution index. The empirical results show that for every 1% increase in income caused by trade, the per capita sulfur dioxide emissions will decrease by 1.7%. Schwarz et al. think that the influence of business reputation on perceived risk is very important, and businesses must maintain their reputation (*Schwarz et al., 2019*). Alam et al. further explained the "green trust", the willingness to rely on sending some products, services or brands based on the beliefs or expectations brought by the reputation, good deeds and environmental performance of products, services or brands (*Alam et al., 2019*). Wu's research found that 30% of the respondents claimed to care about environmental issues, but less than 5% would turn positive pro-environment attitudes or motives into real actions (*Wu, 2017*); Chen et al. used the environmental input-output model to study the energy consumption and CO_2 emissions implied by import and export commodities in a country's foreign trade process (*Chen et al., 2019*). The results show that the CO_2 content of non-energy products exported by this country is far higher than that of imported products, and the exported products per unit output consume 40% more energy and emit 56% more CO_2 than the imported products per unit output.

China's rapid economic development, especially international and domestic trade, shows a leap-forward development momentum. However, the rapid expansion of international trade and domestic trade has also consumed many domestic natural resources, leading to many emissions of various pollutants, which has

caused great pressure on China's resources and environment (*Chang et al., 2017*). Under this background, it is particularly important to analyze the environmental pollution situation, the economic development situation and the characteristics of current international trade in China, study their interrelations, find a way to break through extensive and high resource consumption and adjust the industrial structure by developing clean industries with low energy consumption and low emissions. This paper chooses environmental participation, green purchasing attitude and environmental self-efficacy as cognitive factors, emotions as emotional factors, environmental participation as independent variables, green purchasing attitude and environmental self-efficacy as intermediary variables, and emotions as moderating variables to construct a structural equation model, so as to explore the influence of regulatory effects of policies and legal texts on green purchasing intention.

MATERIAL AND METHODS

Environmental pollution in an open economy

For a long time, China's export products have focused on earning foreign exchange, focusing on quantity, ignoring the quality and technical content of products and their environmental costs. Therefore, if our products want to meet these environmental standards and enter these countries' markets, a large part of the funds must be used for testing, certification and appraisal of environmental protection, as well as packaging and labeling of products and high certification and application fees, annual fees for the use of signs, etc. Members are allowed to take temporary environmental protection measures when the scientific basis is insufficient (*Sopranzetti, 2018; Díaz-DaPena et al., 2022*). Our country's enterprises need more and faster knowledge of foreign environmental standard change information, which seriously affects the enterprises' timely adjustment of competition countermeasures. When encountering green trade barriers, they can only do what they can.

Although various regions may have established various trade barriers for the sake of local protectionism, the resistance they face is much smaller than that of international trade. For the backward countries in the global market, domestic enterprises have to pay higher transaction costs in the process of entering international trade, and there is a big gap between them and the leading countries in terms of products and technologies. Therefore, for domestic enterprises, the cost of opening up the domestic market is much smaller than that of opening up the international market. In interregional trade, there is no comparison between import and export. From the perspective of supplier countries, there is no essential difference between interregional trade and international trade. They are both the stage for enterprises to realize their product value and the key step to maintain their survival and expand reproduction.

According to the traditional trade theory, the international trade of commodities is caused by different conditions or comparative interests of countries in production. The comparative interests of a country depend on the availability of factors of production relative to other countries and the investment requirements of various industrial sectors (*Gantman et al., 2018*). Comparative benefits exist based on the environmental differences in different regions. They constitute the internal contradiction between ecological functions. Determined by this contradiction, it will inevitably lead to the environmental problem of how to share scarcity, that is, the allocation problem. It is necessary to seek a combination to maximize the total utility of environmental functions to human beings.

Pollution tax is a policy tool that encourages businesses and individuals to reduce pollution emissions by increasing the cost of pollution through the collection of pollution taxes by the government. Emission costs refer to the expenses paid by enterprises or individuals to reduce or treat pollution. When pollution taxes increase, businesses or individuals need to pay higher emission costs. Emission intensity refers to the amount of pollution generated per unit of production or consumption activities. When pollution taxes increase, companies will reduce emission intensity by improving production efficiency and adopting clean production methods. Polluted products refer to goods or services that generate pollution. When the prices of these products increase, the cost of producing them will increase, including the resource cost of pollution control. Resource cost refers to the cost paid to obtain the resources required for production. In the production process of polluting products, resource costs may include the cost of measures taken to treat and reduce pollution. Common output indicates that three or more production or processes have similar or identical results in output. In this case, pollution may be the common output of three processes, such as X, Y, and Z, all of which produce pollution. Factor input refers to the production factors used in the production process, such as labor, capital, raw materials, etc. When considering pollution as a factor input, it means that pollution is considered a factor of production, which will affect the level and direction of production. Z level refers to the factors or parameters

that affect the production level, such as technical level, policy regulations, etc. In this model, production also changes as the Z level changes. When the pollution tax increases, the emission cost will increase, and the emission intensity will decrease. When the price of polluted products rises, the resource cost for pollution control will be higher, so the emission intensity will increase instead. If pollution is viewed as factor input, the production will change with the level of Z, and the relationship between them is no longer the only one. See Figure 1.

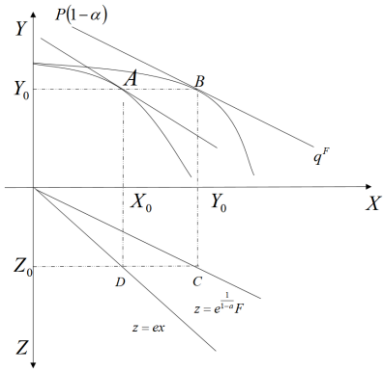


Fig. 1 - Production possibility curve of potential output and net output

In an economic system without pollution control, the maximum potential output of an industry is the possible production boundary. However, due to some resources being used for pollution control, the net output likelihood curve falls within the potential output likelihood curve. This may mean that as pollution control increases, the resources available for production decrease, resulting in a decrease in net output. In this case, e (potential output) and θ there may be a negative correlation between (net output). That is, with the θ the increase in pollution control may lead to a decrease in e. But this is only speculation based on existing information, and the specific situation may vary. Under different Y output conditions, an industry's maximum potential output is the possible production boundary of an economic system without pollution control. Because some resources are used for pollution control, the net output possibility curve is inside the potential output possibility curve. Then there is such a relationship between e, θ:

$$e = (1-\theta)^{\frac{1-a}{a}} \tag{1}$$

The pollution control cost is linked with the pollution discharge per unit output, and the cost brings low pollution discharge per unit output. Can be expressed in terms of price:

$$\theta = 1 - \left(\frac{ap}{\tau}\right)^{\frac{a}{1-a}} \tag{2}$$

It can be known that the proportion of factor resources invested in pollution control increases with the increase of pollution tax but decreases with the addition of product price.

Stimulated by government subsidies, enterprises in developing countries have increased the amount of pollution reduction, and their products have become closer and closer substitutes for those in developed countries. As a result, the price competition between enterprises in the two countries has intensified. To alleviate the intensified price competition, enterprises in developed countries will also increase pollution reduction (*Du et al., 2017; d'Amour et al., 2020*). Therefore, the marginal effect of developing countries' unilateral R&D subsidy on domestic enterprises' pollution reduction is greater than that of developed countries. Under the assumption that all products of the two countries are sold in developed countries, and the pollution discharge and damage caused are limited to developed countries, the social welfare of the two countries can be expressed as follows:

$$w^d = CS^d + \pi^d - D^d \tag{3}$$

$$w^f = \pi^f - s^f \gamma C(d^f) \tag{4}$$

In the given social welfare function, developed countries have relatively abundant capital elements, therefore they have a comparative advantage in the production of capital-intensive products. This means that developed countries have lower costs in producing capital intensive products, thereby gaining more consumer surplus and corporate profits in international trade. Among them, the social welfare in developed countries

consists of the surplus of $\theta \in [\theta^{l*}, 1]$ consumers plus the profit of enterprise minus the pollution damage $D^d$of two products.

According to the theory of comparative advantage, the capital factors in developed countries are relatively abundant, while developing countries have cheaper labor productivity. Compared with the endowment of labor factors, the endowment of capital factors has a relative comparative advantage.

Import low-pollution, labor-intensive products from developing countries, and the final result of the trade is that all trading countries can benefit from work, and the global total pollution emissions will be reduced. A government can strengthen environmental regulation by imposing an environmental tax on pollution-intensive products. It can achieve the purpose of environmental protection by re-optimizing resource allocation to reduce the production of pollution-intensive products.

Coordination between environment policy and trade of green products

International trade activities may aggravate market failures and worsen the environment. Economically, the fundamental cause of environmental degradation is market failure. Because the market can't correctly price environmental assets, external effects exist. In this way, under the action of market mechanism and guided by price signals, the effective allocation of environmental resources can be promoted, thus effectively protecting the environment. However, it isn't easy to internalize the environmental cost completely for various reasons. Due to the lack of a strong global environmental organization, it is difficult for a country to control its environmental pollution caused by other countries' production or consumption activities. At the same time, trade sanctions or restrictions can affect other countries' production or consumption activities and indirectly achieve the purpose of environmental protection.

For developing countries, the environmental effects of international trade are negative both in the short and long term, and international trade will further worsen the ecological quality. If a country implements higher environmental standards, it will relocate domestic enterprises; However, if a government implements lower environmental measures, it will attract enterprises to enter its production (*Oh, 2017*). Therefore, when an enterprise can choose its location independently, it will increase the distortion effect of environmental policy. As the application of strategic trade policy in new fields, the green trade policy comes into being along with the increasing attention developed countries in Europe and America paid to trade and environmental issues. It adopts green R&D to supplement financial resources and environmental pollutant discharge tax. The strategic effect of the environmental tax is greater than that of R&D technical subsidy; that is, under the same proportion, the former is more effective than the latter in enhancing market competitiveness and transferring strategic profits of enterprises. On the contrary, the effect of the last will be better.

Under price competition, improving low-tech enterprises' product quality reduces the difference, intensifying price competition. In contrast, enhancing high-tech enterprises' product quality increases the difference and eases price competition. Improving the pollution reduction of enterprises' products in developing countries reduces the difference and thus intensifies the price competition. In contrast, that of enterprises' products in developed countries increases the contrast and thus eases price competition. At the same time, improving the quality of high-tech industries reduces the profits of low-tech enterprises. Therefore, the governments of high-tech and low-tech enterprises are motivated to reduce the other enterprises' quality. Although the increase in product pollution reduction of enterprises in developing countries reduces the profits of enterprises in developed countries, it increases the surplus of consumers in developed countries, reduces environmental damage, and improves the overall social welfare of developed countries. Therefore, governments in developed countries still have the strategic motivation to encourage enterprises in developing countries to carry out R&D for pollution reduction.

Trade liberalization has expanded the scale of economic activities, which requires increasing input demand. Suppose the original technology is still used in output realization or sales. In that case, using natural resources and discharging pollutants will increase without effective environmental policy support, thus deteriorating the environmental quality. With the increase in income level, consumers will increase their willingness to buy products produced under stricter environmental standards. In addition, the rise in income level can give the government more financial resources for environmental protection and governance (*Qin et al., 2019*). Countries participating in free trade will more likely produce in sectors with comparative advantages. If a country has the advantage of natural resources, it will lead to specialized production of products with abundant resources. The general equilibrium model constructed in this paper is divided into six modules: production activity module, international trade module, institutional behavior module, investment and savings module, pollution control module and equilibrium module - Figure 2.

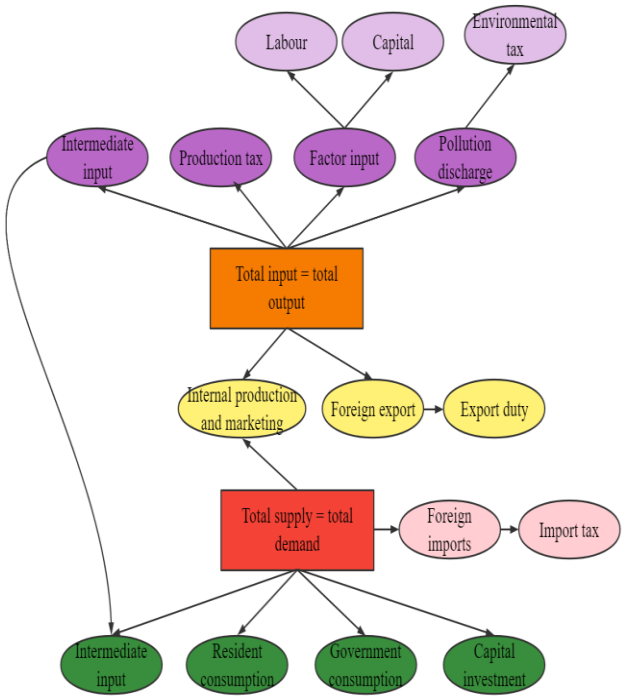


Fig. 2 - Model structure of coordination between environment policy and green product trade

The general equilibrium model studied in this paper is the open economy model, including residents, enterprises, government and foreign four economic subjects. Residents earn income through labor, capital factor income distribution, transfer payments from enterprises and the government, and foreign investment, and pay personal income tax to the government for consumption and savings. The import and export quantities of foreign markets have been determined by Armington conditions and CET (constant elastic transformation) function. In addition, foreign investors will earn income from investments in China's capital market *(Fernández et al., 2018)*.

Armington conditions and CET function have determined the import quantity and export quantity of foreign markets. In addition, foreign investors will earn income from investments in China's capital market (*Fernández et al., 2018*). Domestic products must also be optimally distributed between domestic sales and exports, determined by the relative prices and elasticity of imported and exported household products. The Armington equation is a model used to describe trade between countries, which considers the endowment of production factors and technological differences between countries. The CET function, which often replaces the elastic production function, describes the substitution relationship between production factors. In the study, these two models were combined to construct a general equilibrium model for the coordination of environmental policies and green product trade. In the general equilibrium model of the coordination between environmental policies and green products trade established in this paper, the Armington equation and CET function are chosen to describe it (*Singh et al., 2022*). First, take the logarithm of both sides of the first-order condition of the Armington equation, and you can get the formula:

$$\frac{QM_c}{QDC_c} = \left[\frac{PDC_c}{PM_c} * \frac{1-\delta_c^q}{\delta_c^q}\right]^{\frac{1}{1-\rho_c^q}} \tag{5}$$

$$ln\frac{QM_c}{QDC_c} = \frac{ln\frac{1-\delta_c^q}{\delta_c^q}}{1-\rho_c^q} + \beta\, ln\frac{PDC_c}{PM_c} \tag{6}$$

In the above formula, it is necessary to know four quantities, namely, the import quantity of the commodity sector C, the number of domestic products for domestic sales, and the price ratio of the two, and then estimate the coefficient of the standard logarithmic equation by using the least square method.

Assuming that each manufacturer only produces a single product, the number of products in both countries is also the number of manufacturers in both countries. Assume that policymakers maximize the utility W of the whole society by controlling the amount of pollution emissions that is:

$$W = S[u(C) - \delta D(Z)] \quad (7)$$

Assuming the total social consumption is S, the utility function is u, the pollution emissions are D, and the damage function is $D(Z)$, where Z is a factor that affects pollution damage. According to the title, the utility function u is a concave function of the import quantity of commodity sector C and the domestic product quantity sold domestically, while the damage function $D(Z)$ is a convex function of positive growth in pollution emissions. It can be seen that utility is a function of total social consumption S, utility function u, pollution emissions D, and damage function $D(Z)$. Among them, the concave function of total social consumption with increasing D, Z represents the damage caused by pollution discharge, and it is a positive and growing convex function about pollution discharge, representing the sensitivity coefficient of utility to pollution.

Because the more intensive the pollution discharge, the higher the utilization rate of human capital, thus producing more products and increasing the nominal factor price. Suppose the sensitivity of production cost per unit output to environmental policy is greater than that of R&D cost per unit output. In that case, the productivity increase will be greater than the wage increase. The marginal cost and price will drop when the environment is more relaxed. In the opposite direction, the appearance of new products will also produce an effect: the substitution effect caused by product diversity. When the variety of products is more, and the same income level can buy more kinds of products, the pollution-intensive products will have more opportunities to consume, worsening the environmental quality.

It can be further analyzed the relationship between domestic trade and environmental quality by examining the relationship between international trade and environmental quality. In contrast, the expansion of international trade is conducive to environmental improvement. Our theoretical model assumes that the substitution effect caused by product diversity is greater than the income effect caused by product diversity. Still, it is smaller than the total effect of the income and structure effects. Therefore, trade can promote environmental quality. This paper holds that the structural impact of international trade and the income effect caused by product diversity will promote the improvement of environmental quality. In contrast, the substitution effect caused by product diversity will worsen the environmental quality. The total effect of international trade on environmental quality depends on the interaction of the three outcomes.

When the enterprise's green R&D capability is high, if the government strategically raises the environmental tax, the enterprise will choose to reduce the output first because the income of green R&D investment at this time is not as cost-effective as temporarily decreasing the output to reduce the environmental tax burden. Because the possibility of successful R&D of its new technology is very small or the cost of success is extremely high, the tax burden reduced through green technology innovation cannot compensate the R&D cost. Therefore, when the government continuously raises the environmental tax, the enterprise chooses to reduce the output to reduce its environmental tax expenditure. In an extreme case, the enterprise decides to stop production completely.

Hypothesis of emotion-behavior regulation effect model of policy and legal texts

Green consumption behavior includes the dual purpose of satisfying self-demand and environmental protection demand. Individuals with negative emotions tend to underestimate the value of products, leading to a negative evaluation of products by consumers and then to negative purchase intention. Active consumers ignore environmental problems unconsciously, reducing their sensitivity to environmental issues and making purchasing green products difficult. Under the action of positive emotion, the individual opens up the thinking of solving problems and promotes his cognition and behavior, thus having a positive and far-reaching effect on the individual's future behavior and way of doing things. In the state of fear, human beings will have the consciousness of running away, and in the case of anger, they will tend to aggressive behavior. When an individual is in a negative emotional state, his thinking will focus on the cause and time of the emotional state, his review will become narrow, his vigilance will be enhanced, and he will be nervous easily. Influenced by positive emotions, individuals are more inclined to explore new things and take the initiative to care about the environment.

Generally speaking, consumer professional knowledge includes two modules: subjective knowledge and objective knowledge, in which factual knowledge is the information about products stored in consumers' memory, such as the types of products, the attributes that can be obtained, and the characteristics of evaluation criteria, etc. Performance-based purchasing behavior refers to a sustainable consumption behavior generated by consumers without consideration for protecting the environment and health. Consumers' emotional state

has a positive impact on consumers' purchasing behavior of green, energy-saving and environment-friendly household appliances. Therefore, the pleasant emotion brought by the purchased goods plays an important role in consumers' purchasing decisions. The value points out that there are differences between the perceived value of public emotion and the traditional dimension because the social value contained in the conventional perceived value has duality, specifically including the improvement of customers' image and the concern of the ecological environment, so the division of social value and green value is harmonious. In contrast, the division of the value of the image and environmental protection efficiency value is more specific.

The psychological trade barrier of consumers is a difficult index to quantify, and purchase intention plays an important role in the occurrence of purchase behavior, and it is a predictive index to promote the event of purchase behavior. Therefore, in the empirical analysis, this paper measures whether the psychological trade barrier of consumers exists through the perceived quality of foreign products and the purchase intention of foreign products. The standards recognized by this nation are universally applicable, and external groups need to refer to their standards and be consistent with themselves; that is, internal groups evaluate external groups and determine their standards. In the research field of consumer behavior, attitude affects consumers' buying behavior, but attitude does not directly influence consumers' buying behavior. Attitude often affects consumers' buying behavior through their willingness to buy certain products.

Therefore, this study assumes that green buying behavior can be divided into two basic dimensions: buying green products and resisting non-green effects, as shown in Figure 3. Compared with the simple dichotomy, this classification method makes a more detailed analysis of green buying behavior, which better describes the complex multidimensional characteristics of green buying behavior. Accordingly, the two-factor hypothesis of green buying behavior is put forward.

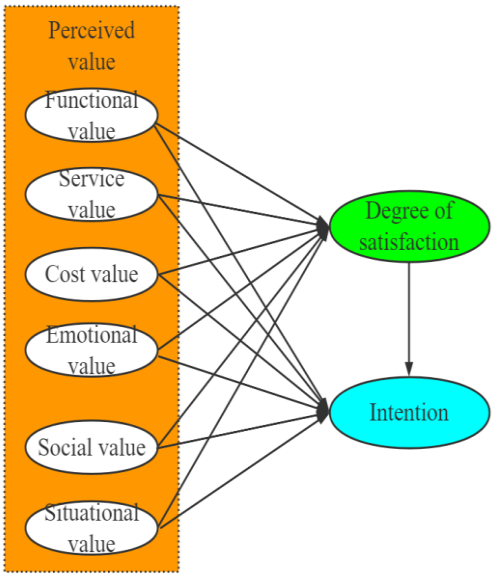


Fig. 3 - The hypothesis of the emotion-behavior dual-factor model of green purchase

Products can be divided into two categories according to their green degree. The first category is that the products consume less energy, resources, or environmental pollution, among similar products. When consumers know the green attributes of products and make conscious purchase decisions, the previous decision to resist non-green effects will positively impact this decision to buy green products. Therefore, this study puts forward the hypothesis.

Hypothesis 1: Resisting the behavior of non-green products has a significant positive impact on the behavior of purchasing green products.

Because consumers with positive environmental sentiments tend to ignore environmental problems and underestimate the environmental protection value of green products, they will not consider the importance and urgency of purchasing green products enough, resulting in positive environmental sentiments that are not conducive to forming the purchase intention of green products.

However, the poor brand image will make the customers who intend to make the original purchase change their purchase decisions and reconsider whether to buy the product or service or buy other similar brands. The perceptual point of view is that customers make purchasing decisions according to subjective criteria such as personal feeling and status, an intangible benefit that products give customers. These two

views show that products' tangible and intangible benefits can drive consumers' demand. Accordingly, the following assumptions are put forward:

Hypothesis 2: Negative emotions upward regulate the positive relationship between green buying attitude and green buying intention.

Purchase intention is the possibility for customers to buy a certain service or product, and customers will decide whether to accept the service or product after they have a certain objective understanding of the image of the service or product. In addition to considering consumers' perceived value of products when selling products, enterprises should also consider the reference group and other external factors that will affect consumers' purchase intention. Public emotional perception affects customer satisfaction first and then customer behavior tendency. Based on the research of scholars, this study thinks that the perceived value of public emotion can affect consumers' purchase intention and puts forward the following theoretical assumptions:

Hypothesis 3: Perceived value significantly impacts consumers' purchase intention.

Compared with the use of strategic environmental tax alone, the government will still adopt a higher balanced environmental tax rate under the policy combination of strategic environmental tax and green R&D subsidy, or the combination of green R&D subsidy policy can effectively improve domestic environmental standards. When people are aware of the importance of the environment, the consequences of environmental deterioration and their responsibility for improving the environment, they will actively develop a green circular economy. The sense of responsibility will affect consumers' green purchasing behavior and mediate the relationship between consumers' psychological factors and purchasing behavior. The greater the positive emotion is awakened, the stronger the individual's perception of green effectiveness and green responsibility will be, and the greater the possibility of the individual's green purchasing behavior will be. Therefore, the following assumptions are put forward:

Hypothesis 4: In the positive emotional state, policy and legal texts have a positive and significant impact on green buying behavior and play an intermediary role in the influence of positive emotional appeal on buying behavior.

International trade mainly affects environmental quality through structural effects, income effects caused by product diversity and substitution effects caused by product diversity. Therefore, in the analysis of this section, according to the mechanism of international trade and domestic trade on environmental quality, the following empirical model is constructed:

$$\begin{aligned} ln\,P\,ollu_{i,t} = \beta_0 + \beta_1\,ln\,I\,nter_{i,t} + \beta_2\,ln\,I\,ntra_{i,t} + \beta_3\,ln\,G\,DP_{i,t} + \beta_4\,ln\,P\,op_{i,t} - dens_{i,t} \\ + \beta_5\,ln\,F\,DI_{i,t} + \beta_6\,ln\,C\,om_{i,t} + \varepsilon_{i,t} \end{aligned} \quad (8)$$

Among them is the discharge of three pollutants in each province; $Inter$is the international trade of various areas; $Intra$is the domestic trade of each province; $GDP$is the economic scale of each province; $Pop - dens$is the population density of each province, the actual use of foreign direct investment in various provinces; Com represents the industrial structure of each province; $\varepsilon$is the error term.

RESULTS

Simulation analysis of coordination between trade policy and environmental policy

Free trade may prompt those polluting production and processing processes to move to those areas with relatively loose environmental regulatory policies. Therefore, there is no need to reduce consumption or increase pollution control. Rich countries can enjoy abundant consumption and a clean environment by importing pollution-intensive products from other countries. The world has been divided into two regions, the North and the South, and the countries in these regions jointly determine the world market price. Every region is made up of many identical countries. The only difference between the two regions is that the strictness of the pollution emission policies they implement is different. If the pollution emission policies between the two regions are the same, there will be no trade between them. At the same time, whether in the South or the North, the pollution emission policy may be looser or stricter than the optimal policy.

The trade policy of reducing export tax rebates is mainly aimed at economic behavior, which has a weak effect on improving the environment. The way of resource allocation is based on the optimization of economic output, which may increase pollutant emissions in the short term. In this section, it is proposed to simulate the coordinated use of the two policies, change the restrictions on the use of the policies alone, and study how to control pollution emissions while maintaining steady economic development.

Scenario 1: Increase the export tax rebate for lightly polluted industries from 5% to 7% of the benchmark tax rate. The environmental tax collection standards are chemical oxygen demand, ammonia nitrogen, sulfur dioxide and nitrogen oxides. The collection standards are 1.5 yuan/pollution equivalent, 1.3 yuan/pollution equal, 1.1 yuan/pollution equivalent and 1.1 yuan/pollution equivalent, respectively.

Scenario 2: Increase the export tax rebate for lightly polluted industries from 6% of the benchmark tax rate to 9%, and the environmental tax collection standard is the same as scenario 1.

From the simulation results, the coordinated use of trade policy and environmental policy greatly impacts the trade structure. Under the dual effects of the two approaches of polluting industries, the export is reduced, which is larger than that of the policy alone, and the import also begins to show positive changes. As shown in Table 1.

Table 1

Influence of coordination between environment and green product trade on import and export of various industries

Industry type	Scenario 1		Scenario 2	
	Export	Imported	Export	Imported
Severe pollution	-0.638	0.187	-1.207	0.336
Moderate pollution	-0.551	0.154	-0.966	0.215
Light pollution	0.408	-0.051	0.805	-0.095
Non-pollution	0.369	-0.122	0.548	-0.173

From the simulation of the coordinated use of environmental policy and green product trade, the result is better than that of policy alone. The measures of increasing export tax rebates for lightly polluted industries will help the export of clean industries to improve, and the change of domestic output will make the import also change, showing a positive trend. The author believes this is mainly due to the relative support of the two policies for developing clean industries, which are attributed to the heavily polluted industries. When the domestic demand cannot be met, the supply must be increased through imports, leading to the increase of importance of heavily polluted industries.

Through industrial wastewater, industrial solid waste, industrial waste gas, industrial smoke and dust, industrial powder and industrial sulfur dioxide, the regression analysis of mixed effect, fixed effect and random effect models of international trade, domestic trade and environmental pollution is carried out. First, all variables are described statistically, as shown in Table 2.

Table 2

Statistical description of variables

Variable	Mean	Standard deviation	Min	Max
Pollu	36031.21	9630.25	8036.71	18966.28
Inter	3506.71	2054.87	21.36	5058.96
Intra	9871.42	6625.89	1086.77	8806.91
GPD	3305.69	2861.24	2216.89	6328.72
Pop-dens	386.01	450.28	425.03	7524.86
FDI	30.06	44.12	42.16	251.47
Com	0.51	0.23	0.19	1.05

International trade hurts industrial wastewater and industrial solid waste, which shows that the development of international trade has inhibited the emissions of these two environmental pollution indicators and has a significant role in promoting environmental quality. The total effect of international trade on environmental quality depends on the comprehensive impact of these three effects. Therefore, among the four environmental pollution indicators, the substitution effect caused by product diversity is dominant. For domestic trade, the substitution effect caused by product diversity is far greater than the income effect caused by product diversity.

Using the cointegration system test based on VAR (Value at Risk) method, the following results are obtained in Table 3:

Table 3

Cointegration test of sulfur dioxide, dependence on foreign trade and support on foreign investment

Suppose	Eigenvalue	Statistic	5% key value	Probability
Assumption 1	0.3905	18.6523	35.5722	0.5825
Assumption 2	0.3877	10.6335	41.5923	0.5505
Assumption 3	0.1827	31.1362	13.7554	0.6582

The import and export trade and foreign direct investment increase in China's trade liberalization have always affected China's environmental quality. In the investigated period, foreign exchange is related to the discharge of environmental pollutants. Foreign direct investment also aggravates China's environmental load. The reason is that most foreign direct investment in China has a low level of investment. With the continuous increase of foreign investment, its production scale is also expanding, thus aggravating the pressure of environmental pollution.

The impulse response function test is mainly used to describe the system's dynamic characteristics, that is, the impact of the change or effect of each endogenous variable on itself and all other endogenous variables. GIRF (generalized impulse response function) is a commonly used method, so this method is used for the analysis below. The impact response period is set to 100, and the analysis results obtained after the simulation are shown in Figure 4.

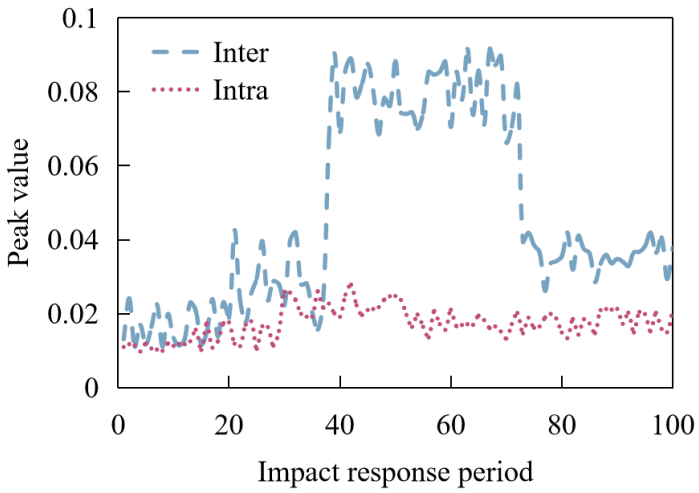


Fig. 4 - Impact response function diagram

For a new impact of foreign capital dependence in the current period, the response value of sulfur dioxide emissions in the first 20 periods was small. The sulfur dioxide emissions increased slowly, and the growth rate accelerated from the 40th period to the 50th period and then increased extremely slowly from the 80th period to the 90th period. There was a slight decline from the 90th to the 100th period, but the range was very small. On the whole, the change from the 50th to the 100th period was very small, which was relatively stable. From the cumulative response value of sulfur dioxide emissions caused by the impact of foreign trade dependence and foreign investment dependence in the whole response period, the influence of foreign trade dependence on pollution emissions is relatively large. In contrast, that of foreign investment dependence is much smaller.

It can be inferred that the increase in dependence on foreign trade will aggravate China's environmental pressure, and its negative effects are constantly increasing. Still, this trend is gradually slowing down in the later period. That is, the impact of foreign direct investment on environmental pollution is smaller than that of import and export trade. There is a long-term stable equilibrium relationship among the variables. The increase in imports can reduce the emission of industrial sulfur dioxide to a certain extent, which is beneficial to the environment. In contrast, the increase in exports will bring more industrial sulfur dioxide emissions, which will worsen our country's environment, consistent with our theoretical analysis.

Regulatory effect of legal text

According to the model fitness analysis and the preliminary hypothesis test results, the original model is adjusted to construct a reasonable model with fitness up to standard. The difference between the alternative and original models is that there is no direct relationship between environmental participation and green purchase intention in the optimized alternative model. The alternative model is a complete intermediary model composed of green purchase attitude and environmental self-efficacy as intermediary variables. On this basis, continue to analyze the relationship among environmental participation, green buying attitude, environmental self-efficacy and green buying intention in different groups. The analysis results are shown in Figure 5.

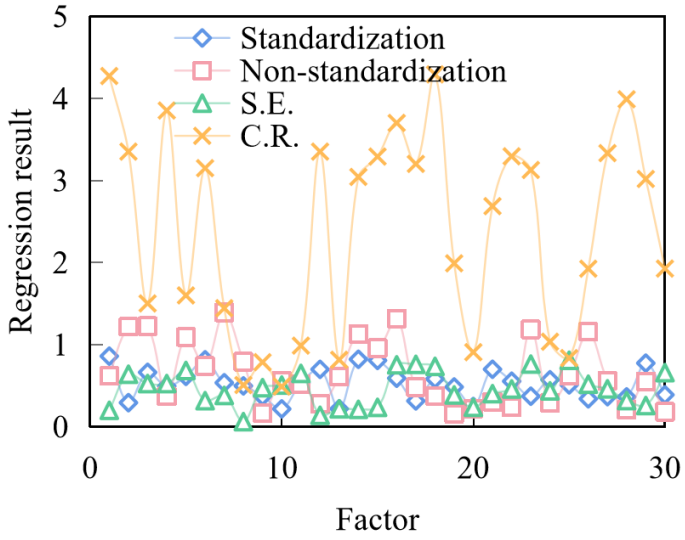


Fig. 5 - Regression analysis results

It can be seen that, without any emotional stimulation, environmental participation at the significance level of 0.05 has a significant positive impact on green purchasing attitude and environmental self-efficacy, green purchasing attitude has a positive impact on green purchasing intention, and environmental self-efficacy has a positive impact on green purchasing intention. The standardization effect of environmental participation on environmental self-efficacy indicates that positive emotions can regulate the positive relationship between environmental self-efficacy and green purchasing intention.

See Table 4 for a summary of the regulatory effects of legal texts on public emotional perception. As can be seen from Table 8, compared with negative emotions, positive emotions have a greater impact on green buying behavior, both in the two dimensions of buying green products and resisting non-green products.

Table 4

The moderating effect of legal texts on Public emotional Perception

Path description	Direct influence effect	Indirect influence effect	Total influence effect
Emotion → Buying Green Products	0.53575	0.00803	0.0684
Negative emotions → Buying green products	0.35919	0.01892	0.34878
Positive Emotion → Resist Non-Green Products	0.21096	0.00544	0.35766
Negative emotions → Resistance to non-green products	0.41975	0.03665	0.42338

This study holds that cognition is shallow, transient and low-involved, while emotion is profound, persistent and high-involved. It significantly regulates two paths: income positive emotion → buying green products and positive emotion → resisting non-green products.

Emotion is more conducive to expanding people's attention, cognition and behavior, enabling individuals to obtain and analyze information more effectively and make more appropriate action choices.

It also has the long-term and sustained effect of enhancing personal resources, such as strengthening people's physical strength, intelligence, psychological adjustment ability and social coordination. From a qualitative point of view, taking behavioral externalities as the criterion, buying green products can increase the positive externalities of behaviors, while resisting non-green effects can reduce the negative externalities of behaviors.

Regardless of the differences between different types of positive emotions, first examine consumers' general reaction to the overall positive emotions. Table 5 lists Pearson correlation coefficients of perceived green efficacy, perceived green responsibility, green buying behavior, emotional arousal and moderate values.

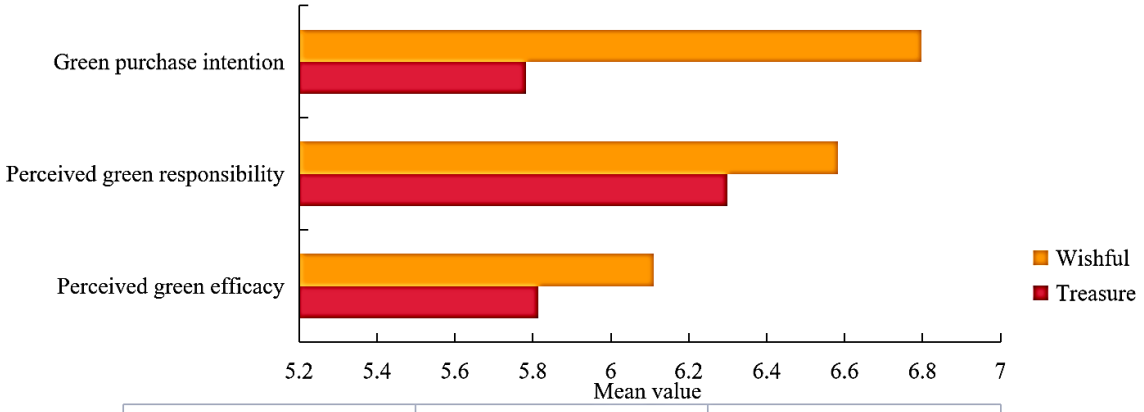
Table 5

Correlation test between different variables

	Mean value	Standard deviation	Perceived green efficacy	Perceived green responsibility	Green purchasing behavior	Emotional arousal degree	Mean values
Perceived green efficacy	5.67101	1.84112	1				
Perceived green responsibility	5.50558	1.40546	0.638	1			
Green purchasing behavior	5.20061	1.56629	0.701	0.668	1		
Emotional arousal degree	5.73771	1.82754	0.441	0.504	0.638	1	
Mean values	5.62312	1.59013	0.739	0.619	0.641	0.618	1

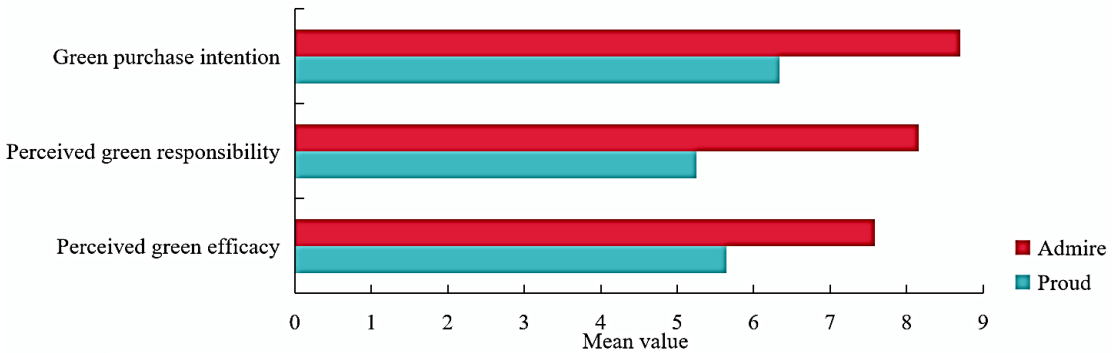
It can be found that under the test level of 0.01, consumers' perceived green efficacy, perceived green responsibility, green buying behavior, emotional arousal and moderate values are significantly positively correlated. Among them, the R value of perceived green effectiveness and green purchasing behavior is 0.701, and the R value of perceived green responsibility and green purchasing behavior is 0.638, which indicates that the degree of correlation between perceived green efficacy, perceived green responsibility and green purchasing behavior is highly correlated.

To sum up, there is no significant difference in the perceived green efficacy of different positive emotions, but there are substantial differences in perceived green responsibility and green buying behavior; hypothesis 1 is not true, and hypotheses 2 and 3 are true. See Figure 6 and Figure 7 for the comparison of specific intuitive mean values. Yearning is higher than the average of other positive emotions.



	Perceived green efficacy	Perceived green responsibility	Green purchase intention
Wishful	6.110369578	6.582291738	6.798130949
Treasure	5.81299005	6.300113234	5.78150635

Fig. 6 - Comparison of the mean values of different positive emotions



	Perceived green efficacy	Perceived green responsibility	Green purchase intention
Admire	7.587755674	8.16251902	8.703301996
Proud	5.646936213	5.252206136	6.335823994

Fig. 7 - Comparison of the mean values of different positive emotions

Pride and appreciation are the same in consumers' perceptions of green effectiveness. Still, there are substantial differences between pride and gratitude in the perception of green responsibility and green purchasing behavior. When analyzing the four positive emotions, different levels of emotional arousal will affect consumers' perception of green efficacy, green responsibility and green purchasing behavior; Compared with consumers with low arousal, consumers with high arousal can produce higher perceived green effectiveness, perceived green accountability and green purchasing behavior. That is to say, consumers with higher emotional arousal have higher perceived green energy, perceived green responsibility and green purchasing behavior, and differences in perceived green efficacy, perceived green responsibility, and green purchasing behavior can also be generated by different degrees of moderate values.

To show the influence of the relationship strength between nodes on the public conditional green purchasing behavior more straightforwardly, this section adds two modes: the relationship strength and the behavior potential difference for comparative analysis. In a random relational network, the relational power of all nodes in the network is randomly selected between (0,1). By analyzing the diffusion trend of public conditional green buying behavior and network equilibrium, it can be seen that in the consumption network under the weighted small-world network structure, using the potential difference priority mode to select the sender whose conditional green buying behavior diffuses with the receiver will make the conditional green buying behavior selection of all individuals in the network be optimized quickly.

According to the previous empirical results, the positive and negative moderating effects of the perceived effectiveness of environmental protection behavior on the three paths coexist, and the positive moderating effect is obviously higher than the negative moderating effect. As can be seen from Figure 8, at the initial stage of simulation, whether in random mode, intensity priority mode or potential difference priority mode, the average level of conditional green purchasing behavior in the network has increased slightly with the enhancement of the perception of the effectiveness of environmental protection behavior, but the network balance has deteriorated.

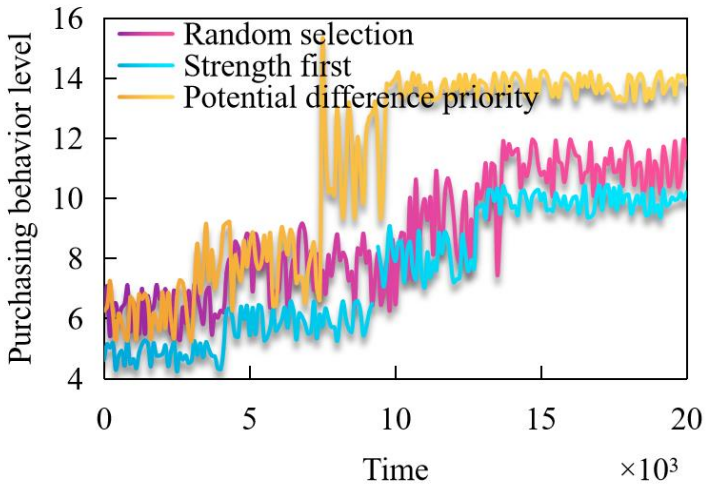


Fig. 8 - The changing trend of conditional green purchasing behavior under the intervention of environmental protection effectiveness perception

In addition, in the early stage of simulation, the variance of conditional green purchasing behavior of all nodes in the network in different modes drops rapidly. It enters a channel of steady decline in the middle and late stages. At the same time, the network balance begins to show signs of optimization, and the network balance in the strength priority mode and the potential difference priority mode is equivalent.

As can be seen from Figure 9, after the government's environmental protection investment intervention, the individual conditional green purchasing behaviors in the network all show a downward trend, and the network balance becomes worse. At the initial simulation stage, the growth rate of the potential difference priority mode is higher than that of the intensity priority mode. With the increase of the simulation step, the growth rate of the behavior of the two modes approaches and the number of individuals with "poor conditional green purchasing behavior" becomes smaller and smaller.

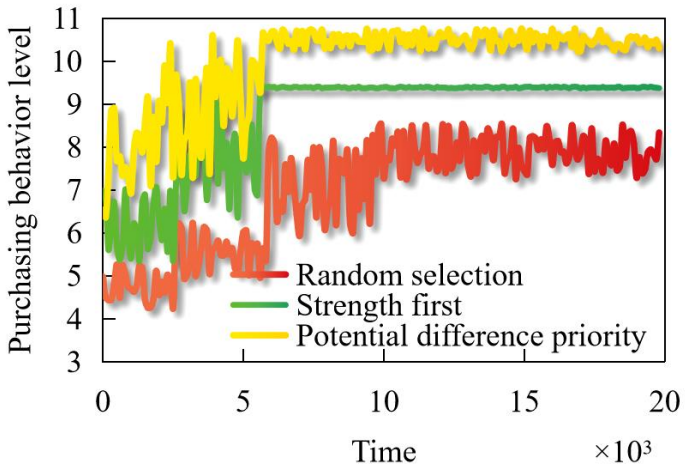


Fig. 9 - Change trend of conditional green purchasing behavior under the intervention of government environmental protection investment

From the increment of conditional green purchasing behavior in the simulation process, the diffusion of conditional green purchasing behavior in the potential difference priority mode is weakly interfered with by the government's environmental protection investment, and the network balance is relatively good. The network balance also worsens. At the middle and late stage of the simulation, the average conditional green purchasing behavior of all individuals in the network began to increase slightly. At the same time, in the initial simulation stage, the variance of conditional green purchasing behavior of all nodes in the strength priority mode and potential difference priority mode network decreased sharply. Still, the network balance became worse, And the random pattern is the smallest. From the variance of network nodes' conditional green purchasing behavior, under the potential difference priority mode, when the urban noise pollution takes the value of 7, the variance of all nodes' dependent green purchasing behavior decreases the most in the middle and late period, and the network balance is achieved as quickly as possible.

The level of consumer ethnocentrism and conformity psychology directly impact the purchase intention of foreign products. The total effects of consumer ethnocentrism, attitude towards foreign products, the impact of country of origin and conformity psychology on the purchase intention of foreign products have all passed the parameter significance test. The quality of consumers' perception of foreign products and their willingness to buy depend largely on the above three factors. The country-of-origin effect has the greatest influence on the perceived quality of foreign products. In addition, domestic enterprises should actively seek ways to establish joint ventures with developed countries while introducing alien advanced technology and learning from foreign advanced manufacturing technology and management experience to improve product quality and technical content.

A country's optimal strategic environmental tax rate is always lower than its domestic marginal environmental damage; the government is motivated to implement environmental dumping to help domestic enterprises make profits. Try to improve the comprehensive utilization rate of wastewater, gas and waste materials in enterprises, comprehensively utilize all kinds of construction and industrial wastes, and comprehensively consider the recycling of urban domestic sewage and the resource utilization of household wastes. Emotion is the psychological reaction of consumers. When consumers experience an intimate and pleasant experience in purchasing, they are more likely to stimulate their desire to buy. Therefore, green food manufacturers should communicate and communicate with consumers from the perspective of consumers when conducting related marketing activities. They can be more willing to pursue a healthier, more scientific and more civilized way of consumption. Therefore, when green products are given environmental protection characteristics, they are more able to meet consumers' needs, and they are willing to make green purchases.

CONCLUSIONS

This paper constructs a theoretical hypothesis model to explore the moderating effect of policy and legal texts on the relationship between public emotional perception of environmental policies and trade in green products. After an empirical test, all the research hypotheses of this study are supported. It is found that the development of international trade inhibits the emissions of these two environmental pollution indicators and has a significant role in promoting environmental quality.

The increase in dependence on foreign exchange will aggravate the pressure on China's environment, and its negative effects are constantly increasing. Still, this trend is gradually slowing down in the later period. This study holds that cognition is shallow, transient and low-involved, while emotion is profound, persistent and high-involved. From a qualitative point of view, taking behavioral externalities as the criterion, buying green products can increase the positive externalities of behaviors, while resisting non-green effects can reduce the negative externalities of behaviors. When the value of urban noise pollution is 7, the variance of conditional green purchasing behavior of all nodes decreases the most in the middle and late periods, and the network balance is achieved as soon as possible.

COMPETING OF INTERESTS

The authors declare no competing of interests.

AUTHORSHIP CONTRIBUTION STATEMENT

Guoli Han: Writing-Original draft preparation, Conceptualization, Supervision, Project administration.
Shuming Ma: Methodology, Software, Validation.

REFERENCES

[1] Alam, M. S., Selvanathan, E. A., Selvanathan, S., & Hossain, M. (2019). The apparel industry in the post-Multifiber Arrangement environment: A review. *Review of Development Economics*, *23*(1), 454–474.

[2] Can, M., Ahmed, Z., Mercan, M., & Kalugina, O. A. (2021). The role of trading environment-friendly goods in environmental sustainability: Does green openness matter for OECD countries? *Journal of Environmental Management*, *295*, 113038.

[3] Cao, B., & Wang, S. (2017). Opening up, international trade, and green technology progress. *Journal of Cleaner Production*, *142*, 1002–1012.

[4] Chang, S.-H., & Chang, C.-W. (2017). Tie strength, green expertise, and interpersonal influences on the purchase of organic food in an emerging market. *British Food Journal*, *119*(2), 284–300.

[5] Chen, K., Nie, H., & Ge, Z. (2019). Policy uncertainty and FDI: Evidence from national elections. *The Journal of International Trade & Economic Development*, *28*(4), 419–428.

[6] d'Amour, C. B., & Anderson, W. (2020). International trade and the stability of food supplies in the Global South. *Environmental Research Letters*, *15*(7), 074005.

[7] Daviron, B., & Voituriez, T. (2012). Reforming agricultural and trade policy in France: the limits of multi-actor coalitions. In Global Justice Activism and Policy Reform in Europe (pp. 186–212). Routledge.

[8] Díaz-DaPena, A., Grecco Zanon Moura, T., & Rubiera-Morollón, F. (2022). From the Local Economy to the Global Market. Municipal-Level Spatial Economic Modelling of International Trade for Brazil. *International Regional Science Review*, *45*(3), 352–379.

[9] Du, R., Wang, Y., Dong, G., Tian, L., Liu, Y., Wang, M., & Fang, G. (2017). A complex network perspective on interrelations and evolution features of international oil trade, 2002–2013. *Applied Energy*, *196*, 142–151.

[10] Fernández, Y. F., López, M. A. F., & Blanco, B. O. (2018). Innovation for sustainability: the impact of R&D spending on CO2 emissions. *Journal of Cleaner Production*, *172*, 3459–3467.

[11] Gantman, E. R., & Dabós, M. P. (2018). International trade and factor productivity as determinants of the real effective exchange rate. *Applied Economics Letters*, *25*(5), 331–334.

[12] Liu, N., An, H., Hao, X., & Feng, S. (2017). The stability of the international heat pump trade pattern based on complex networks analysis. *Applied Energy*, *196*, 100–117.

[13] Oh, C. H. (2017). How do natural and man-made disasters affect international trade? A country-level and industry-level analysis. *Journal of Risk Research*, *20*(2), 195–217.

[14] Qin, G., Tao, F., Li, L., & Chen, Z. (2019). Optimization of the simultaneous pickup and delivery vehicle routing problem based on carbon tax. *Industrial Management & Data Systems*, *119*(9), 2055–2071.

[15] Schwarz, J., Mathijs, E., & Maertens, M. (2019). A dynamic view on agricultural trade patterns and virtual water flows in Peru. *Science of the Total Environment*, *683*, 719–728.

[16] Singh, A., Ahuja, H., Bhadoria, V., & Singh, S. (2022). Control implementation of squirrel cage induction generator-based wind energy conversion system. *Journal of Scientific & Industrial Research*, *79*(4), 306–311.

[17] Sopranzetti, S. (2018). Overlapping free trade agreements and international trade: A network approach. *The World Economy*, *41*(6), 1549–1566.
[18] Wang, H., & Ang, B. W. (2018). Assessing the role of international trade in global CO2 emissions: An index decomposition analysis approach. *Applied Energy*, *218*, 146–158.
[19] Wu, C. (2017). Human capital, life expectancy, and the environment. *The Journal of International Trade & Economic Development*, *26*(8), 885–906.

ROMANIAN BIOMASS PELLET MARKET – TECHNO-ECONOMIC ANALYSIS
/
PIAȚA ROMÂNEASCĂ A PELETELOR DIN BIOMASĂ - ANALIZĂ TEHNICO-ECONOMICĂ

Georgiana MOICEANU[1)]; Mirela - Nicoleta DINCĂ*[1)]; Mihai CHIȚOIU[2)]; Gigel PARASCHIV[1)]; Oana-Diana CRISTEA[3)]

[1)] National University of Science and Technology POLITEHNICA Bucharest / Romania;
[2)] CENIT SRL / Romania;
[3)] National Institute for Research-Development of Machines and Installations Designed for Agriculture and Food Industry – INMA Bucharest/ Romania;
Tel: +40761938017; E-mail: mirela.dinca@upb.ro
DOI: https://doi.org/10.35633/inmateh-71-77

Keywords: *pellet industry, biomass, techno-economic analysis, profitability index, net present value*

ABSTRACT

Biomass is currently the most widespread form of renewable energy, and its exploitation is constantly increasing due to concerns about the major impact of fossil fuel consumption, in terms of climate change, global warming and their negative impact on the human factor. Biomass can be transformed using modern technologies into solid, liquid, and gaseous fuels. One of the most widely used biomass biofuels is wood pellets. Pellets obtained from woody biomass represent a very successful renewable energy source, due to their characteristics that include high density, high calorific value, low moisture content, but also ease of storage and transport. Romania's biomass pellet industry has recorded significant growth due to the increasing demand for green energy. Investment in modern technology improves production efficiency and enhances competitiveness in international markets. However, fluctuations in raw material prices such as biomass transportation costs and moisture content often affect profit margins. Improving infrastructure and continued investment in research and development are crucial to strengthening Romania's position in the global renewable energy market. In this context, the purpose of the article is to present an analysis for Romanian pellet market industry.

REZUMAT

Biomasa este în prezent cea mai răspândită formă de energie regenerabilă, iar exploatarea acesteia este în continuă creștere datorită preocupărilor legate de impactul major al consumului de combustibili fosili, în ceea ce privește schimbările climatice, încălzirea globală și impactul negativ al acestora asupra factorului uman. Biomasa poate fi transformată cu ajutorul tehnologiilor moderne în combustibili sub formă solidă, lichidă și gazoasă. Printre cei mai utilizați biocombustibili din biomasă sunt peletele din lemn. Peletele obținute din biomasă lemnoasă reprezintă o sursă de energie regenerabilă de mare succes, datorită caracteristicilor acestora care includ densitate ridicată, putere calorică mare, conținut de umiditate scăzut dar și ușurință în depozitare și transport. Industria peletelor din biomasă din România a înregistrat o creștere semnificativă datorită cererii tot mai mari de energie verde. Investițiile în tehnologii moderne îmbunătățesc eficiența producției și sporesc competitivitatea pe piețele internaționale. Cu toate acestea, fluctuațiile prețurilor materiilor prime, cum ar fi costurile de transport al biomasei și conținutul de umiditate, afectează adesea marjele de profit. Îmbunătățirea infrastructurii și investițiile continue în cercetare și dezvoltare sunt esențiale pentru consolidarea poziției României pe piața globală a energiei regenerabile. În acest context, scopul articolului este de a prezenta o analiză pentru industria românească a pieței peletelor.

INTRODUCTION

In the context of climate changes and their effect on the environment and the human factor, biomass has been promoted as an important resource for reducing greenhouse gas emissions through its conversion into biofuels (*Ilham, 2022*). The European Environment Agency has stated that to meet the global goal of reducing the carbon footprint by 50% by 2050, increasing the use of renewable energy is one of the most significant greenhouse gas reduction policies implemented by various countries of the EU (*Bui-Duy et al., 2023*).

Bioenergy, or energy derived from bio-based sources, represents a type of renewable energy that is environmentally friendly and economically viable. Thus, in the last decade, bioenergy production in the form of solid, liquid, or gaseous fuels has begun to play an important role in the global energy mix *(World Bioenergy Association, 2019; Jelonek et al., 2020).*

Biomass fuel pellets represent one of the most important energy sources that can be a promising substitute for fossil fuels (*Sarker et al., 2023*). At present, pellets are the most cost-effective technique to convert biomass into fuel and are a rapidly growing component of the energy sector *(Jelonek et al., 2020)*. According to Statista report and as it can be seen in Figure 1, the European demand for wood pellets is expected to grow to more than 38 million metric tons by 2025, thus Europe is expected to remain the most important target market for wood pellets through 2025. In 2020, the European Union led the world pellet production with 13 MMT (million metric tons), followed by North America with 11 MMT, China with10 MMT, South America with 4.4 MMT and Oceania with 0.8 MMT (*https://www.statista.com/statistics/243910/global-wood-pellet-consumption-outlook/*).

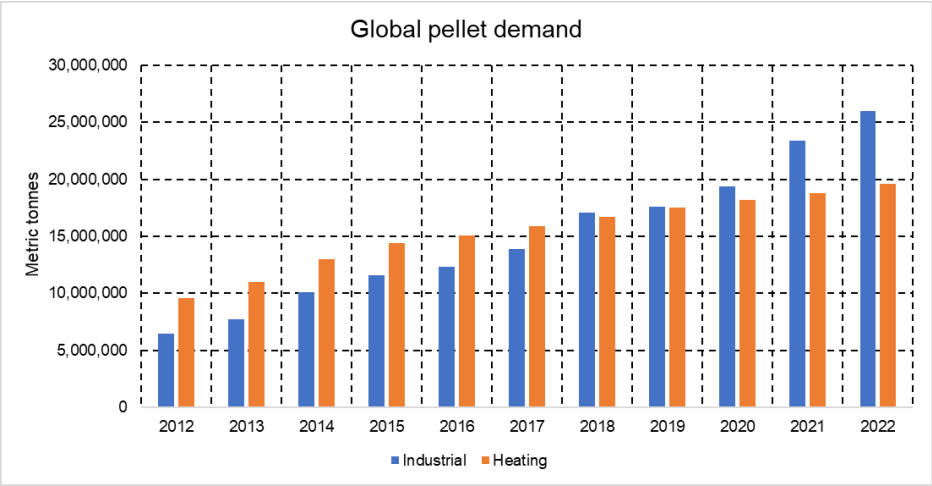


Fig. 1 – Global pellet demand for a 10-year timeframe *(TCPEL, 2022)*

The EN*plus* certification scheme defines three pellet quality classes, namely: EN*plus* A1, EN*plus* A2 and EN*plus* B (*European Pellet Council, 2015; Paraschiv et al., 2017*).

A1 quality class pellets (premium quality) are the most commonly used; pellets are obtained only from untreated wood residues, they are mainly used in the residential sector for burning in individual stoves and boilers, they produce the lowest amount of ash and have the highest calorific value.

A2 quality class pellets are obtained from raw materials with a high content of tree bark, they are used for combustion in larger installations and produce a larger amount of ash.

B quality class pellets (industrial class) are obtained from a wide range of raw materials, including chemically treated wood by-products, produce the highest amount of ash and have a significantly lower calorific value than that of class A2.

The most common biomass feedstocks used for pellets production are wood processing industry waste, agricultural and forest residues, and energy crops. The pellets produced from these biomass feedstocks have a high density and an extremely low moisture content (<10%), and a high energy conversion efficiency (about 75%) (*Paraschiv et al., 2017; Pradhan et al., 2018*).

Many works can be found in the literature focused on techno-economic analysis used to estimate the production cost of wood pellets. In their research, Ebadian et al. *(Ebadian et al., 2021)* have modelled an inter-continental agricultural pellet supply chain and estimated the production cost and price of agricultural pellets. In a recent study, Visser and co-workers *(Visser et al., 2020)* reviewed existing literature on pellet costs and performed a techno-economic analysis of the impact of different design variables on cost components (feedstock type, production location and pellet plant size). Schipfer et al. *(Schipfer et al., 2020)* carried out another study where the main objective was to establish a framework to test the European residential wood pellet market for competitive spatial equilibrium using modern trade theory.

Sarker et al., (2023) realised a techno-economic analysis of torrefied fuel pellet production from agricultural residue via integrated torrefaction and pelletisation process. The authors tested and compared two scenarios: scenario 1 - pelletisation of torrefied biomass with additives and scenario 2 - pelletisation of torrefied biomass without any external additives and they reported that the economic analysis suggests that both

scenarios are profitable. In their results highlighted that the lowest selling price of generated torrefied pellets was found to be $103.4 at the plant gate for scenario 1 and $105.1 per tonne for scenario 2. Furthermore, sensitivity analysis indicates that, in producing pellets for both scenarios, among all variable costs, labour cost has a greatest impact on net present value and minimum selling price. A similar study was carried out by *Manouchehrinejad et al., (2021)*, which investigated the techno-economic analysis of two integrated torrefaction and pelletisation systems: torrefaction before pelletisation and torrefaction after pelletisation configurations to produce torrefied wood pellets. The authors reported that the minimum selling price for torrefaction before pelletisation is $207 Mg^{-1} at the plant gate and $197 Mg^{-1} for the torrefaction after pelletisation configurations.

In the context of the current global focus on environmental protection and carbon dioxide emission reduction, the biomass pellet market has become an important part of the energy infrastructure of many European countries, including Romania. As the demand for renewable energy increases significantly, the pellet industry becomes even more important in providing clean and sustainable energy.

Europe has been a major player in the growth of the biomass pellet industry, having been at the forefront of the establishment of laws and policies that encourage the effective use of renewable energy sources. The pellet industry has changed dramatically during the 1990s as concerns over climate change and the high expense of fossil fuels have grown. Thanks to persistent efforts to establish favourable legal frameworks and to invest in cutting-edge technologies for the manufacture and use of pellets, several European nations, including Germany, Sweden, and Austria, have emerged as leaders in the production and consumption of biomass pellets. In figure 2, the top 5 countries that had the highest production in 2021 are presented.

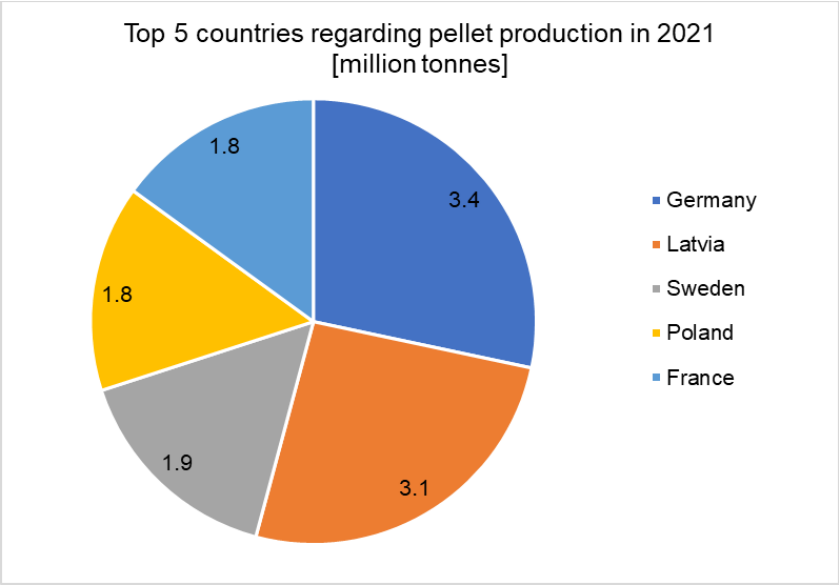


Fig. 2 – Top 5 countries in 2021 that had the highest pellet production
(adapted after Bioenergy Europe Statistical Report, 2021)

The Romanian market has evolved in a way that closely resembles European patterns over the past few decades, exhibiting gradual development. The Romanian government has encouraged the growth of the meat industry through a number of legislative and policy efforts, which has increased the quantity of biomass resources used and broadened the country's energy mix. Romania has the potential to dramatically improve its position on the biomass market by putting into practice efficient growth plans and investing in state-of-the-art technologies, even though it is currently in a relatively early stage of development in comparison to other European nations. The literature on the techno-economic analysis of Romanian pellet production is scarce. In this context, the main aim of this article is to present an analysis for Romanian pellet market industry.

MATERIALS AND METHODS

The economic assessment involves the computation of the net present value (NPV) and profitability index (PI) for the investment. The methodology for the economic analysis followed the model of the authors *Pantaleo et al*., which was used to analyse the market for pellets in Italy. Applying the prices currently used in Romania and the data available from different suppliers, the techno-economic analysis was possible.

Net Present Value (NVP) is defined as the total present value for the projected return on an investment that is offset by its initial outlay. NVP is used to determine initiatives or projects that will produce the greatest return in relevant time frames. In addition, NVP is used to verify that a business choice will last for a defined period of time by meeting its objective benchmark and demonstrating more viability in competition with alternatives. To determine NPV, the company's cumulative profits over a certain number of years are discounted using a marginal rate of return *(Alizadeh et al., 2023)*.

The NPV can be calculated based on Equation (1):

$$NVP = -\beta + \sum_{j=1}^{T} \frac{\emptyset_j}{(1+R)^j} \quad (1)$$

where β is the initial investment;

T is the project lifetime, [in years];

$\emptyset_j$ is the cash flow in each year (j).

The discount rate or cost of capital is shown by R in the above equation.

Profitability index (PI) is used to assess how much profit may come from a particular investment. The PI is calculated according to Equation (2) *(Pantaleo et al., 2020)*:

$$PI = \frac{NVP}{C_{Investment}} \quad (2)$$

where the cost of investment ($C_{Investment}$) is calculated according to Equation (3) *(Pantaleo et al., 2020)*:

$$C_{Investment} = C_{pell} + C_{dry} + C_{chip} + C_{store} + C_{inst} + C_{eng} \quad (3)$$

where:

C_{pell} - the cost of pelletizing the plant;

C_{dry} - the cost of drying the plant;

C_{chip} - the cost of pre-treatment processes;

C_{store} - the cost of storage;

C_{inst} - the cost of plant installation;

C_{eng} – the plant engineering cost.

Payback Time (PBT) is the time (in years) required for the capital invested in an asset to be repaid by the net cash flow it produces. A shorter PBT is preferable because it gives the investor a clear idea of how long the initial outlay will be at risk. PBT is the period of time in years that a project needs to pay back its initial investment (δ) through earnings after interest and taxes (μ) *(Alizadeh et al., 2023)*.

The equation for estimating PBT is presented in Equation (4):

$$PBT = \frac{\delta}{\mu} \quad (4)$$

Before starting to analyse the cost, a modelling process of the pelletization process was realized using the program for business process modelling ADONIS Communities. In Figure 3 the process is presented considering that the trigger is represented by the demand for pellets on the market.

Adonis Software offers a methodical approach to comprehend, record, and enhance the way that operations are carried out. For increasing productivity, effectiveness, and flexibility, modelling processes is an essential activity. It promotes a better knowledge and administration of company processes by providing a comprehensive perspective on how work is done.

The pelletizing process is adapted according to the raw material used, but usually includes the following stages: reception of the raw material, drying, grinding, pelletizing, cooling, packaging, as can also be seen in figure 3.

The size reduction of lignocellulosic biomass is an important step in the pelletization process. This influences a number of factors, such as compaction, the contact area between the particles, the friction forces between the pressed material and the die wall, but also the material flow. Biomass shredding is done with the help of hammer mills, which are chosen according to the feedstock type, the degree of humidity and the production capacity (*Whittaker and Shield, 2017*).

Water is a key parameter in the pelletization process, biomass moisture being one of the most important parameters that determine the durability of the pellets. The optimum moisture content differs depending on the type of biomass used, such as: for pine it is between 6–13%, straw 8–15% and Miscanthus 20–25%. Biomass drying is carried out with fully automated continuous flow dryers (*Whittaker and Shield, 2017*). In the pelletizing process, the optimum moisture content is considered to be between 10-15% (*Pradhan et al., 2018*).

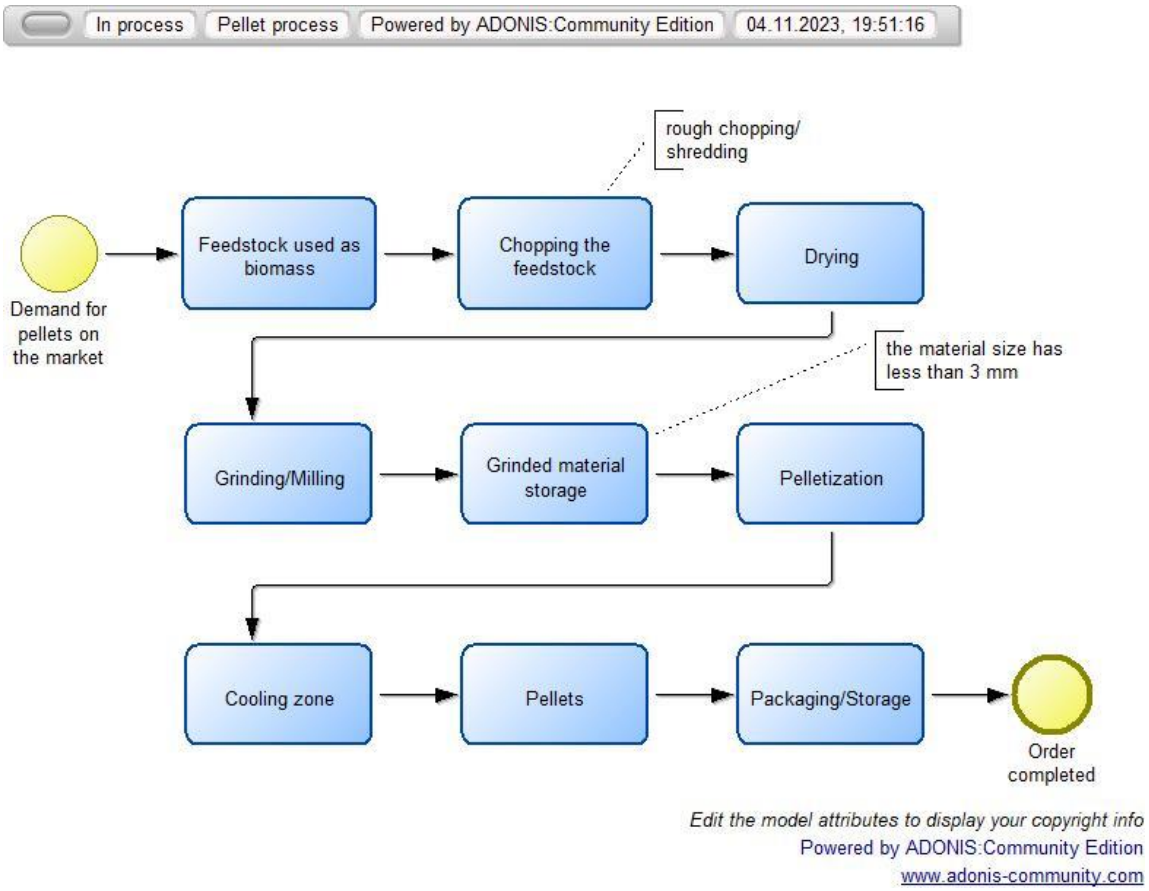


Fig. 3 – Modelling of the pelletization process

Pelletizing process represents the operation of transforming the biomass feedstock into fuel. The producing pellets process involves placing biomass under high pressure and forcing it through the cylindrical holes of a die. This process is known as extrusion (*Paraschiv et al., 2017; Ciolkosz, 2023*).

Cooling is the mandatory operation to be performed after pelletizing, due to the high temperature of the finished product when exiting the extrusion die. The outlet temperature can reach 90 - 100°C, there being a risk of damage to the finished product if it is further stored or packaged at this temperature (*Ciolkosz, 2023*).

Semi-automatic or fully automated machines are used to pack the pellets in plastic bags or special material bags. Pellets can be used for domestic use (ovens or home heating) or industrial use (gasification, pyrolysis and co-generation (*Paraschiv et al., 2017; Pradhan et al., 2018*).

RESULTS

Since European Union proposed a raise in renewable energy consumption by 2030, countries started analysing the current situation regarding the global demand for renewable energy and the investments necessary for achieving the proposed goal *(Council of the European Union, 2018).*

In paper *(Pantaleo et al., 2020),* the authors made inquiries and presented the pellet production industry. One of the main conclusions stated the necessity of an accurate techno – economic assessment *(Thek and Obernberger, 2012)*. Also, the studies demonstrated the influence of physico-chemical and mechanical characteristics of the biomass on the production process of pellets which implies an influence on the pellet market evaluation from the point of view of investments, operational and maintenance costs necessary for developing a pellet factory *(Junginger and Sikkema, 2008*; *Castellano et al., 2015)*.

Regarding the analysis conducted in the present article it is necessary to mention the fact that the pellet production line is experimental being a part of the Testing Department from The National Institute of Research – Development for Machines and Installations Designed for Agriculture and Food Industry – INMA Bucharest. Also, some of the parameters mentioned were determined through previous research and adapted for the economic evaluation proposed.

The economic viability assessment was done considering the economic model proposed by *Pantaleo et al., (2020)*, the calculations being done using the equations proposed by the authors.

Thus, in the following table (Table 1) the data held constant are presented. Regarding the Cost of transport $c_{transport}$ the value in the table was selected by analysing the existing transportation market for raw materials, considering a distance of 100 km and a load of 20 t.

Also, the drying coefficient was obtained considering a biomass moisture content of 30% that after drying process will have 10% moisture content. The electricity needed per t of pellet was experimentally determined by researchers from the institute while the maintenance coefficient was selected based on literature research *(Nolan et al., 2010).* Regarding the determination of the electricity needed, for experiments, the determination of power consumption, electricity consumption, and specific electricity consumption of equipment in the flow was determined for every equipment that is a part of the process. Thus, the means for the working capacity, power consumption and specific power consumption was considered. The mean of the parameters resulted after subjecting the equipment to 3 tests (*Chitoiu, 2011*).

Table 1

Technical and economic parameters remaining constant

Parameters	Unit	Value
Maximum production capacity Q_{max}	t/hour	0.15
Production load factor i_U	%	75
Hourly production capacity Q	t/hour	0.113
Number of daily shifts n_{shifts}	-	1
Number of annual production hours H	hours/year	2016
Annual pellet production Q_{pellet}	t/year	226.8
Pellet moisture content m_{pellet}	%	10
Cost of transport $c_{transport}$ (1)	lei/t/km	2
Drying coefficient k_{drying} (2)	-	0.015
Price of electricity $P_{electricity}$	lei/MWh	500
Electricity needed per t of pellet E_{pellet} (3)	MWh/t	0.03
Annual cost of personnel c_{unit}	lei/year/person	36000
Maintenance coefficient k_M (4)	%	10
Lifetime of the plant n	years	6
Real discount rate r	%	3
Pellet market value P_{pellet}	lei/t	1100

In table 2 the technical and economic parameters that can vary for obtaining different scenarios are presented. The biomass amount and biomass price considered for the analysis were obtained by conducting a market analysis regarding the present pellet industry. Also, the average distance was selected according to the most common distance used for transportation of raw materials and considering that the surroundings are mainly fields that can represent potential biomass suppliers. Electricity needed for chipping was experimentally determined by researchers from the institute and also by one of the authors in his dissertation paper.

Table 2

Technical and economic parameters that can be varied for obtaining different scenarios

Parameters	Unit	Value
Biomass amount	t/year	2100
Biomass price	lei/t	50
Moisture content	%	12
Average transportation distance	km	50
Electricity needed for chipping	MWh/t	0,01
Personnel units per shift	units	2

Knowing the technical and economical parameters presented in the tables above the costs of investments, operation and maintenance could be calculated and are presented in table 3.

Table 3

Investments, operation and maintenance costs

Investments costs	Value (lei)	Operation and maintenance costs	Value (lei)
C_{pell}	49700	$C_{Biomass}$	105000
C_{dry}		$C_{Transport}$	28232
C_{chip}		C_{Drying}	3150
C_{store}	20000	$C_{Electricity}$	13905.15
C_{inst}	6000	$C_{Personnel}$	72000
C_{eng}	4500	$C_{Maintanance}$	4920
TOTAL	**79700**	**TOTAL**	**227207.15**

Regarding the cost of plant installation and the cost of plant engineering cost were calculated based on the authors elaboration considering two technicians employed for 15 days and a cost of 200 lei/day and a net installation cost established on by the pellet market industry.

Based on values established, the financial analysis results could be calculated to see if the investment would be viable and how long it would take to recover the cost of an investment. The net present value (NPV), profitability index (PI) and payback time (PBT) are presented in the table below (Table 4).

Table 4

Results of the financial analysis.
PBT—payback time; NPV—net present value; PI—profitability index

Economic parameters	Unit	Value
Revenue	lei	249480
Cash Flow	lei	27192.85
PBT	year	2.93
NPV	lei	53299.17
PI	-	0.66

As it can be observed the investment would be recovered in 2.93 years which is comparable with other studies done by researchers *(Pantaleo et al., 2020; Uchezuba et al., 2019).*

CONCLUSIONS

For the Romanian market, it is important to identify and use low-cost raw materials with low moisture content in order to obtain pellets with high financial profitability, the analysis said. In addition, further analysis and optimization of the biomass supply chain, biomass processing, and final energy conversion should be conducted to better meet end-user needs. As it could be seen from the conducted analysis, the pellet industry market has potential, but further analysis is needed to assess which recipe would be the most profitable and competitive on the market. The biomass market in Romania is varied which allows companies an optimal development in the pellet industry. However, a thorough analysis of all the factors involved in the production of this type of renewable energy is necessary. Potential market segments in the industrial, residential, commercial and rural sectors should also be evaluated to determine the most suitable application, given the differences in pellet quality and cost. Therefore, in the Romanian pellet industry, supply chain optimization strategies and identification of potential market segments are crucial to ensure long-term financial viability.

Also, as it could be observed from the analysis conducted the investment in a pellet plant would be viable and could bring a plus to the fuel market in Romania. The technical and economic parameters in the paper, present the potential for Romanian use of agricultural and forestry solid biomass to produce clean energy and reduce greenhouse gas emissions. Although investments are still needed further investigation for both technical and economic aspects would require a close attention to the application of artificial intelligence in the manufacturing process for further optimization.

REFERENCES

[1] Alizadeh, P., Tabil, L. G., Mupondwa, E., Li, X., & Cree, D. (2023). Technoeconomic Feasibility of Bioenergy Production from Wood Sawdust. *Energies*, *16*, 1914. https://doi.org/10.3390/en16041914

[2] Bui-Duy, L., Thanh Le, L., Vu-Thi-Minh, N., Hoang-Huong, G., Bui-Thi-Thanh, N., & Nha Nguyen, P. (2023). Economic and environmental analysis of biomass pellet supply chain using simulation-based approach. *Asia Pacific Management Review*, *28*(4), 470-486. https://doi.org/10.1016/j.apmrv.2023.02.002

[3] Castellano, J. M., Gómez, M., Fernández, M., Esteban, L.S., & Carrasco, J. E. (2015). Study on the effects of raw materials composition and pelletization conditions on the quality and properties of pellets obtained from different woody and non woody biomasses. *Fuel*, *139*, 629–636. https://doi.org/10.1016/j.fuel.2014.09.033

[4] Chitoiu M. (2011). Research on the use of agricultural and forestry solid biomass to produce clean energy and reduce greenhouse gas emissions – Dissertation Thesis, University POLITEHNICA of Bucharest.

[5] Ciolkosz, D. (2023). Manufacturing fuel pellets from biomass. *Pennsylvania State Biomass Energy Center and Department of Agricultural and Biological Engineering*. https://extension.psu.edu/manufacturing-fuel-pellets-from-biomass

[6] Ebadian, M., Sokhansanj, S., Lee, D., Klein, A., & Townley-Smith, L. (2021). Evaluating the Economic Viability of Agricultural Pellets to Supplement the Current Global Wood Pellets Supply for Bioenergy Production. *Energies*, *14*, 2263. https:// doi.org/10.3390/en14082263

[7] Ilham, Z. (2022). Chapter 3 - Biomass classification and characterization for conversion to biofuels in Value-Chain of Biofuels, Eds. Suzana Yusup, Nor Adilla Rashidi, Value – Chain of Biofuels, pp. 69-87, Elsevier. https://doi.org/10.1016/B978-0-12-824388-6.00014-2

[8] Jelonek, Z., Drobniak, A., Mastalerz, M., & Jelonek, I. (2020). Assessing pellet fuels quality: A novel application for reflected light microscopy. *International Journal of Coal Geology*, *222*, 103433. https://doi.org/10.1016/j.coal.2020.103433

[9] Junginger, M., & Sikkema, R. (2008). The global wood pellet trade—markets, barriers and opportunities. Workshop Summary: Utrecht, The Netherlands.

[10] Manouchehrinejad, M., Ted Bilek, E. M., & Mani, S. (2021). Techno-economic analysis of integrated torrefaction and pelletization systems to produce torrefied wood pellets. *Renewable Energy*, *178*, 483-493. https://doi.org/10.1016/j.renene.2021.06.064

[11] Nolan, A.; Mc Donnell, K., Devlin, G. J., Carroll, J. P., & Finnan, J. (2010). Economic analysis of manufacturing costs of pellet production in the Republic of Ireland using non-woody biomass. *Open Renew. Energy J*, *3*, 1–11.

[12] Pantaleo, A., Villarini, M., Colantoni, A., Carlini, M., Santoro, F., & Hamedani S. R. (2020). Techno – Economic Modeling of Biomass Pellet Routes: Feasibility in Italy. *Energies*, *13*(7), 1636. https://doi.org/10.3390/en13071636

[13] Paraschiv, G. (coord.), Dincă, M., Ungureanu, N., Moiceanu, G., & Toma, L. (2017). Installations for waste recycling/ Instalaţii pentru reciclarea deşeurilor. Politehnica Press Publishing House, Bucharest, 289 p., ISBN 978-606-515-750-7.

[14] Pradhan, P., Mahajani, S. M., & Arora, A. (2018). Production and utilization of fuel pellets from biomass: A review. *Fuel Processing Technology*, *181*, 215-232. https://doi.org/10.1016/j.fuproc.2018.09.021

[15] Pradhan, P., Arora, A., Mahajani, & S. M. (2018). Pilot scale evaluation of fuel pellets production from garden waste biomass. *Energy for Sustainable Development*, *43*, 1–14. https://doi.org/10.1016/j.esd.2017.11.005

[16] Sarker, T. R., German, C. S., Borugadda, V. B., Meda, V., & Dalai, A. K. (2023). Techno-economic analysis of torrefied fuel pellet production from agricultural residue via integrated torrefaction and pelletization process. *Heliyon, 9*, e16359. https://doi.org/10.1016/j.heliyon.2023.e16359

[17] Schipfer, F., Kranzl, L., Olsson, O., & Lamers, P. (2020). The European wood pellets for heating market - Price developments, trade and market efficiency. *Energy*, 212, 118636. https://doi.org/10.1016/j.energy.2020.118636

[18] Thek, G., & Obernberger, I. (2012). The Pellet Handbook. The Production and Thermal Utilisation of Biomass Pellets; Routledge: London, UK.

[19] Uchezuba, D. I., Mbai, S., Zimmermann, I., & Bruwer, J. (2019). Investigating wood pellet torrefaction investment and its economic feasibility in the Krumhuk, Khomas region of Namibia. *SN Appl. Sci., 1*, 402. https://doi.org/10.1007/s42452-019-0390-y

[20] Visser, L., Hoefnagels, R., & Junginger, M. (2020). Wood pellet supply chain costs – A review and cost optimization analysis. *Renewable and Sustainable Energy Reviews*, *118*, 109506. https://doi.org/10.1016/j.rser.2019.109506

[21] Whittaker, C., & Shield, I. (2017). Factors affecting wood, energy grass and straw pellet durability – a review, *Renewable and Sustainable Energy Reviews*, *71*, 1-11. https://doi.org/10.1016/j.rser.2016.12.119

[22] *** Bioenergy Europe Statistical Report. (2021). Report Pellet. https://epc.bioenergyeurope.org/bioenergy-europe-pellet-report-2019/

[23] *** Council of the European Union. (2018). Directive of the European Parliament and of the Council on the Promotion of the Use of Energy from Renewable Sources; Council of the European Union: Brussels, Belgium.

[24] *** European Pellet Council – EPC. (2015). EN-plus Handbook *Part 3: Pellets Quality Requirements, Version 3.0*. https://enplus-pellets.eu/en-in/component/attachments/?task=download&id=103

[25] ***Statista, Wood pellets - global demand forecast through 2025. https://www.statista.com/statistics/243910/global-wood-pellet-consumption-outlook

[26] *** TCPEL. (2022). Pellet Production Profit Analysis: Is it a Profitable Business? https://www.tcpel.com/pellet-production-profit-analysis-is-it-a-profitable-business/

[27] ***World Bioenergy Association. (2019). *Global Bioenergy Statistics*. http://www.worldbioenergy.org/uploads/191129%20WBA%20GBS%202019_HQ.pdf

EXPERIMENTAL RESEARCH ON REED HARVESTING WITH "ERBA" ELECTRIC BOAT
/
CERCETĂRI EXPERIMENTALE PRIVIND RECOLTAREA STUFULUI CU AMBARCAȚIUNEA ELECTRICĂ "ERBA"

Vasilica ȘTEFAN[1)], Radu CIUPARCĂ[1)], Emil TUDOR[2)], Mihai MATACHE[1)], Ionuț VASILE[2)], Ion Cătălin SBURLAN[2)], Ana ZAICA[1)]

[1)] National Institute of Research – Development for Machines and Installations Designed for Agriculture and Food Industry – INMA Bucharest/ Romania;
[2)] National Institute for Research and Development in Electrical Engineering, ICPE-CA Bucharest, Romania
Tel: +40722245443; E-mail: valle_vali@yahoo.com
DOI: https://doi.org/10.35633/inmateh-71-78

Keywords: *reed, harvester, electric, autonomy, agricultural, aquatic vegetation, biomass*

ABSTRACT

The article presents the results obtained from experimental research conducted with an electric equipment (a watercraft) for harvesting aquatic biomass (reed, cattail, water lily, etc.), remote controlled, symbolized as ERBA. This equipment was designed and built in Romania by researchers from INMA Bucharest and ICPE-CA, at the level of experimental model. The purpose of this equipment is to develop a national system of machines for cleaning lakes, navigable canals, and specific areas of the Danube Delta Biosphere Reserve from excess biomass that needs to be removed for the proper functioning of aquatic ecosystems. The harvested biomass is used as raw material for the production of liquid and gaseous fuels, as well as biofertilizers, which can be utilized as inputs in the bioeconomy. The phenological characteristics of the harvested biomass, the structural and functional characteristics of the vessel, the laboratory experimental records, the nautical indices, the exploitation indices, and the energy consumption were measured under different working conditions and regimes, and with different types of biomass.

REZUMAT

Articolul prezinta rezultatele obținute in cadrul cercetărilor experimentale ale unui echipament electric (ambarcațiune) de recoltat biomasa acvatica (stuf, papura, zambila de balta, etc.), controlat de la distantă, simbolizat ERBA, echipament proiectat și realizat în Romania, de cercetătorii de la INMA București și ICPE-CA, la nivel de model experimental. Echipamentul a fost realizat in scopul dezvoltării pe plan național a sistemei de mașini destinată curățării lacurilor, canalelor navigabile și a zonelor specifice Biosferei Delta Dunării, de biomasa în exces care trebuie înlăturată pentru buna funcționare a ecosistemelor acvatice. Biomasa recoltată poate fi folosită ca materie prima pentru obținerea de combustibili lichizi, gazoși și biofertilizatori, produse care pot fi utilizate ca inputuri în bioeconomie. Au fost măsurate caracteristicile fenologice ale biomasei recoltate, caracteristicile constructive și funcționale ale ambarcațiunii, înregistrate la experimentările de laborator, indicii nautici, indicii de exploatare și consumul de energie, realizate in diferite condiții și regimuri de lucru și diferite tipuri de biomasă.

INTRODUCTION

Aquatic weed control is a critical aspect of maintaining the health and balance of aquatic ecosystems. There are studies about various methods and strategies for effectively managing and controlling aquatic weeds. These studies provide valuable insights into the challenges associated with aquatic weed control and offer potential solutions to mitigate their negative impacts.

One common approach discussed by *Siemering and Hayworth, (2005), and Hofstra and Clayton, (2001)* is the use of herbicides and surfactants for aquatic weed control. The paper evaluates the efficacy and environmental impacts of different herbicides, considering factors such as target weed species, application methods, and potential non-target effects. The research aims to identify herbicides that effectively control aquatic weeds while minimizing harm to non-target organisms and the aquatic ecosystem.

Another area of focus is the use of biological control methods for aquatic weed management exploring the use of natural enemies, such as insects or fish, to control the growth and spread of invasive aquatic weeds. The research investigates the effectiveness of different biological control agents, their impact on non-target species, and the long-term sustainability of such approaches. These studies provide valuable insights into the potential benefits and limitations of biological control as a strategy for aquatic weed management *(Torawane and Mookat, 2019)*.

Additionally, there is a discussion about the importance of integrated weed management approaches for effective and sustainable aquatic weed control. *Clayton (1996)* and *Lavergne and Molofsky, (2006),* emphasize the need to combine multiple control methods, such as mechanical removal, herbicide application, and biological control, to achieve optimal results. The research explores the effects of integrating different control strategies and assesses their long-term effectiveness in preventing weed resurgence and maintaining the ecological balance of aquatic ecosystems.

Reed, often considered a weed, has emerged as a valuable resource for biofuel production and is seen as a highly promising and sustainable option. Reed, also known as Phragmites communis, is a tall perennial grass that grows in wetlands and marshy areas. It has gained attention as a potential feedstock for biofuel production due to its high biomass yield and ability to grow in diverse environmental conditions *(Obreja et al, 2023; Sciuto et al, 2023).*

One of the key advantages of using reed as a source of biofuels is its abundance. It is widely available in various regions around the world, making it a readily accessible and cost-effective feedstock. This availability reduces the dependency on traditional fossil fuels and contributes to a more sustainable energy future *(Piccitto et al, 2022, Shahrukh et al, 2021).*

Furthermore, reed is a highly efficient plant in terms of biomass production. It has a rapid growth rate and can yield a significant amount of biomass per unit area. This makes it an attractive option for biofuel production, as it can provide a substantial feedstock supply without requiring excessive land use.

In addition to its high biomass yield, reed also offers environmental benefits. It has the ability to absorb and store large amounts of carbon dioxide during its growth, thereby acting as a carbon sink. By utilizing reed as a source of biofuels, greenhouse gas emissions can be effectively reduced and climate change impacts mitigated *(Ivan et al, 2016).*

Moreover, reed can be cultivated in marginal lands or areas unsuitable for traditional agriculture. This means that it does not compete with food crops for arable land, ensuring food security while simultaneously supporting biofuel production. This aspect makes reed a sustainable and socially responsible choice for biofuel feedstock.

Chao at al. investigates the physical and mechanical properties of mature reed stalks grown in the Yangtze River region. The experiments revealed various parameters, including stress resistance intensity, pulling resistance intensity, bending resistance intensity, shearing resistance intensity, and modulus of elasticity. The results showed that the reed stem material exhibited significant anisotropy and non-linearity, suggesting the need for an anisotropic constitutive relationship when establishing reed mechanical models.

Furthermore, the article presents the differences between the physical and mechanical properties of reed compared to other crops such as *Arundo donax L.,* ramie, and wheat. These differences indicate that traditional agricultural machines used for cutting and processing other crops may not be suitable for reed harvesting. Therefore, it is recommended the adoption of a new cutting technology that aligns with the specific physical and mechanical properties of reed.

In conclusion, reed holds great potential as a source of producing biofuels. Its abundance, high biomass yield, environmental benefits, and ability to grow in diverse conditions make it an attractive option for sustainable energy production. By harnessing the power of reed, the reliance on fossil fuels can be reduced, climate change can be mitigated, and a contribution to a greener future can be brought.

Aquatic reed harvesters are specialized machines designed for the efficient and sustainable harvesting of reeds from wetland areas. These machines are specifically engineered to navigate through water bodies, such as lakes, ponds, and marshes, where aquatic biomass typically grow *(https://headdredging.com;https://relong-tech.com;https://aquarius-systems.com/equipment/aquatic-weed-harvester/; Ștefan et al, 2022; Tudor et al., 2023).*

The modern harvesters are innovative machines that have been specifically designed to efficiently harvest biomass while incorporating sustainable practices such as utilization of renewable energy sources and electrically power, making them environmentally friendly alternatives to traditional harvesting methods. They are equipped with converters that efficiently convert renewable energy into usable electrical power.

With integrated converters and electric motors, these harvesters eliminate the need for additional external equipment, streamlining the harvesting process *(Tudor et al. 2022; Popovici et al., 2022).*

The primary purpose of aquatic reed harvesters is to collect reeds in a controlled and systematic manner. They are equipped with cutting mechanisms, typically in the form of rotating blades or sickle bars, which can efficiently cut the reeds at the desired height. The harvested reeds are then collected and stored on board the machine for further processing. One of the key advantages of using aquatic reed harvesters is their ability to minimize environmental impact. These machines are designed to operate with minimal disturbance to the surrounding ecosystem. They are equipped with low ground pressure tracks or pontoons, which distribute the weight of the machine evenly and prevent damage to the wetland habitat.

Aquatic reed harvesters also offer increased efficiency and productivity compared to manual harvesting methods. They can cover large areas in a relatively short period, allowing for faster and more cost-effective reed collection. Additionally, these machines are often equipped with advanced features such as GPS navigation and automated cutting systems, further enhancing their efficiency.

Huang et al, (2022), analyses the development and optimization of a reed harvester for efficient and effective reed harvesting. It highlights the current limitations of domestic reed harvesters, such as the lack of mature technology, versatility, and mass production. The study focuses on designing a reed harvester that integrates cutting and conveying processes, analyzing key components, and determining optimal working parameters. Through a quadratic orthogonal rotation combination test and regression mathematical modeling, the study identifies the optimal combination of operation parameters for the reed harvester. The results demonstrate that with a forward speed of 0.85 m/s, cutting speed of 1.40 m/s, and chain conveying speed of 1.33 m/s, the harvester achieves a failure rate of 4.17%, cutting efficiency of 44.21 plants/s, and conveying rate of 93.60%. These optimized parameters were further validated in field tests, where the relative errors with the optimized values were within an acceptable range.

Overall, the study provides a theoretical basis for controlling operating parameters and improving the design of reed harvesting implements. The developed reed harvester effectively addresses challenges such as uneven stubble, low cutting efficiency, and blockage during the conveying process. The optimized parameters ensure that the harvester meets the requirements for reed harvesting, with satisfactory performance in terms of failure rate, cutting efficiency, and conveying rate.

Due to the rising number of internal-combustion automobiles that rely on non-renewable conventional fuels, there has been a surge in energy-related concerns and environmental problems (*Tudor et al, 2022; 2023)*. Consequently, numerous countries have introduced electric vehicles as substitutes for traditional automobiles, aiming to decrease reliance on oil and mitigate the air pollution associated with conventional *vehicles (Wenbo et al, 2016; Hu etal, 2018; Calotă et al, 2022; Suvac et al, 2019, Culcea et al, 2023).*

Furthermore, the use of aquatic reed harvesters can contribute to the sustainable management of wetland ecosystems. By selectively harvesting reeds, these machines can help control the growth and spread of invasive species, maintain biodiversity, and promote the overall health of the wetland habitat.

The aquatic reed harvesters are specialized machines that play a crucial role in the efficient and sustainable harvesting of reeds from aquatic environments. Their ability to minimize environmental impact, increase productivity, and contribute to the sustainable management of wetland ecosystems make them valuable tools in the reed harvesting industry.

MATERIALS AND METHODS

The researchers are faced with a technical challenge in developing an electric vehicle harvester for aquatic vegetation. This challenge arises from the specific requirements of the harvester, such as the need for high torque at low speeds, maneuverability, high load capacity, low draught, and affordability. To address these requirements, the authors proposed an electro-hydraulic architecture that utilizes paddles driven by hydraulic motors for propulsion and auxiliary services, also powered by motors and hydraulic actuators.

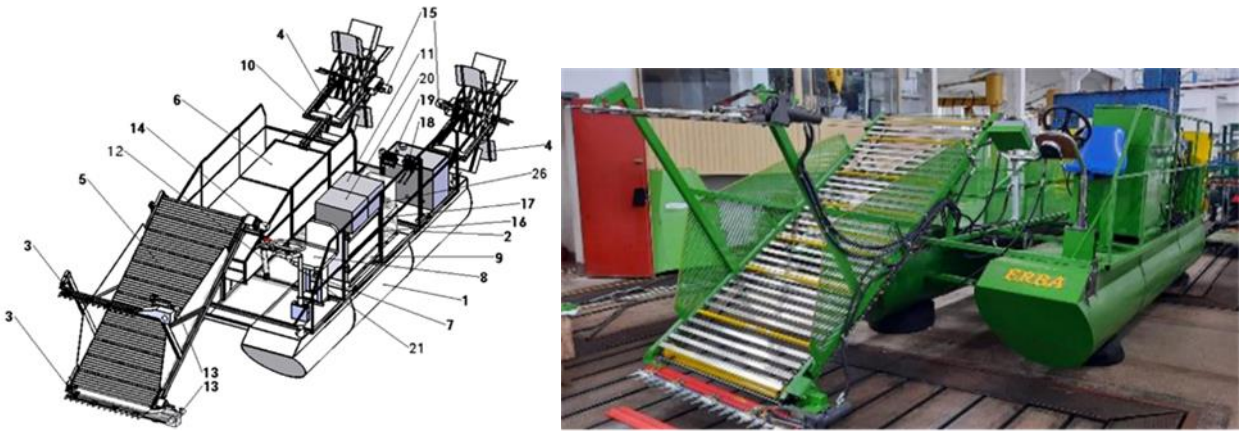
For conducting the tests, the ERBA electric equipment was used. This machine was developed within a larger research project that aimed to utilize the harvested biomass as a source of liquid biofuel. The equipment for harvesting aquatic biomass, ERBA (Fig.1 a, b), is a self-propelled device powered by a hydrostatic electric motor, remotely controlled.

It performs the cutting of the biomass, stores it in a collection bin, and transports it to the unloading area. The biomass is unloaded either into another aquatic transport vehicle or in a nearby temporary storage area.

The key components of the equipment presented in Fig.1a are identified as: *1* - assembled floats, *2* - welded frame, *3* - double-blade cutter bar, *4* - paddle wheel, *5* - conveyor, *6* - biomass collection bin,

7 - steering system with rudder, *8* - user seat, *9* - electric batteries, *10* - plate indexing, *11* - electrical elements, *12* - hydraulic actuator, *13* - hydraulic knife drive motor, *14* - conveyor chain drive hydraulic motor, *15* - paddle drive hydraulic motor, *16* - electric motor, *17* - double pump, *18* - Proportional distributor, *19* - sectional distributor, *20* - electronic control, *21* - remote control, *26* - converter.

For the energy source of the harvester, the authors have developed a system of 33 kWh Li-Ion batteries connected in parallel. These batteries supply an electronic converter and a 14.5 kW rated power electric motor, which in turn drives a hydraulic double-circuit pump. Additionally, this vehicle can be controlled remotely.



a) **b)**

Fig. 1 – Reed harvester experimental model (ERBA):
a) key components design b) manufactured equipment

The *float assembly* consists of two floats, each measuring 4.5 meters in length, with a diameter of 0.8 meters at the bottom and a straight section with a width of 0.7 meters at the top. Each float is made up of three sections, each measuring 1.5 meters in length, welded together with metal, and sealed tightly.

The *paddle wheel, two in number, provides* propulsion for the vessel. The active part of each paddle wheel consists of 8 curved blades arranged radially, driven by a hydraulic motor. The role of the paddle wheels is both for forward movement and for left/right turns. The control is achieved using a proportional distributor, which ensures independent operation of each paddle wheel and the variation of speed, depending on the need, by adjusting the oil flow transmitted to the hydraulic motor.

The equipment for harvesting aquatic biomass performs the cutting of aquatic biomass, especially reeds, in deep water conditions exceeding 1 m. The equipment for harvesting aquatic biomass is intended for the collection of aquatic biomasses, in the Danube Delta, as well as other areas of interest such as ponds, navigable canals, lakes, recreational areas, etc.

The *cutting system* is equipped with two double-blade cutting devices, with guide plates and triangular lamellar blades, which have an alternating rectilinear motion and are individually driven by a hydraulic motor. The guide plate cutting device includes a main bar, guides, guide plates, blade rail carriers, knife blades, and detachable assembly elements. The knife blades are riveted to the blade rail carriers and have two sharp, smooth edges. The aquatic biomass harvesting equipment, performs the cutting of low-lying biomass at water level using only the lower blade (Fig. 2b), while reeds, cattails, or other tall plants are cut into two fractions using both blades, with the upper blade positioned 1.5 m above the lower blade (Fig 2 a). The upper blade, which cuts the stem above the water, is positioned 100 mm horizontally in front of the lower blade, performing the first cut.

The harvested biomass is then taken up by the conveyor belt and discharged directly into the *collection bin area,* which is a fixed metal structure welded to a frame, with a useful volume of approximately 2.5 m^3. Both the walls and the floor of the bin are secured with self-drilling screws and made of perforated sheet metal to allow easy drainage of water.

The *hydraulic system* assembly provides the necessary hydrostatic energy for the equipment movement and the operation of all functional systems of the vessel. It consists of a dual gear pump that supplies two hydraulic circuits (the first circuit operates the flaps through two hydrostatic motors and the second circuit operates the hydrostatic motors that drive the conveyor, cutting blades, and the two hydraulic cylinders that lower and raise the conveyor).

The *electronic control* system assembly allows remote operation of the vessel or operation by an operator on board, depending on the control mode.

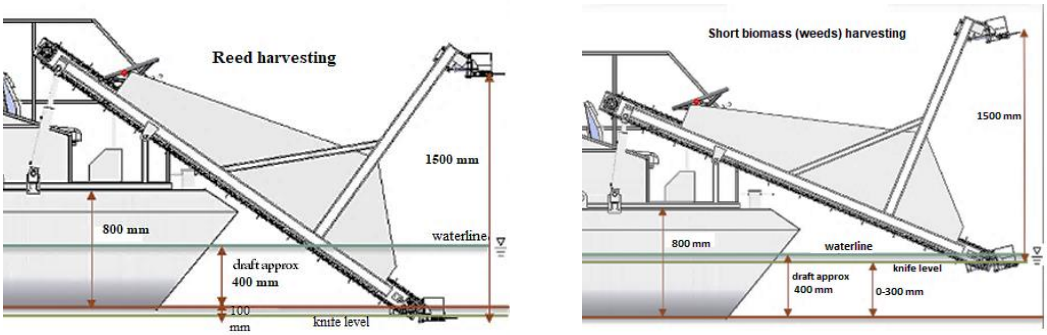


Fig. 2 – Biomass cutting possibilities for
a) tall biomass (reed); b) short biomass

When measuring a vessel, there are several nautical indices that are commonly measured to assess its performance, stability, and overall operational characteristics. Some of the key nautical indices include: draft, length overall, beam (maximum width), displacement, freeboard, speed, etc.

The total length *(L)* of the equipment is measured from its forwardmost point (bow) to its aftmost point (stern), including any extensions or overhanging parts. This measurement is used to quantify vessel size and is often a governing factor for regulations and restrictions.

Beam is the maximum width *(l)* of the vessel measured at its widest point. Beam provides an indication of a vessel stability and carrying capacity.

The experimental research focused on determining the state of buoyancy and equilibrium of the vessel, calculating the inertia at rest and determining the characteristics and operational indices of the vessel.

Buoyancy is defined as the tendency of a body to float or rise when submerged in a fluid. The resultant force acting on a submerged body by the fluid is called the *buoyant force.* For a boat to float in equilibrium, it is necessary that the weight of the displaced water be equal to the weight of the ship. If the body weighs more than the fluid - it sinks; if the body weighs less than the fluid - it floats.

Two forces act on the vessel floating on the water: the weight of the ship P and the weight of the volume of water displaced by the ship's body (floats) D, according to Archimedes' principle. Forces P and D are equal in magnitude, opposite in direction, and act along the same line normal to the basal plane. P has its point of application at center of gravity of the ship, and D has its point of application at center of gravity of the hull. The weight of water displaced by the ships body (floats) D is determined, according to equation of flotation, eq. (1).

$$D = \gamma \cdot V_s = P \tag{1}$$

where: P is the weight of the ship, including operator weight, (N); D is the weight of the volume of water displaced, (N); $\gamma = \rho \cdot g$ is the specific weight of water, (N/m^3), ρ is the density of water (kg/m^3), g is acceleration of gravity (9.81 m/s^2), V_s is the volume of the submerged part of the floats, (m^3).

Another nautical parameter that needs to be measured is the *draft (h).* Draft is represented by the vertical distance from the vessel waterline to the deepest part of its hull and is important for determining the vessel immersion level, load-carrying capacity, and maneuverability in shallow waters. The volume of fluid displaced can be estimated by multiplying the draft *(h)* by the cross-sectional area (A) of the submerged part of the vessel hull:

Working capacity, *W,* measures the proportion of reeds effectively harvested by the electric reed harvester. It takes into account factors such as the cutting mechanism, collection system, and overall design of the harvester. Higher harvesting efficiency indicates a more effective harvester.

Working capacity, W, is represented by the area harvested in a unit of time at a certain speed of travel established, according to relation (10).

$$W = \frac{v \cdot l_f \cdot t}{10^5} \tag{2}$$

where W is the work capacity, (ha/h); v is the boat speed, (km/h); l_f is the furrow width, (m); t is harvesting time, (h).

The energy efficiency has to be measured to evaluate the autonomy of the vessel, using the power consumption during various tests, including the trip using solely the paddlewheels, and the harvesting of various types of crops. The targeted autonomy of this vessel was 2 hours of harvesting within a 10 km trip.

For the different operation regimes of the vessel, maximum autonomy can be computed from the maximum available energy by dividing to the power level absorbed during that task.

$$A_{trip} = \frac{E_{max} - E_{min}}{P} \left[\frac{kWh}{kW}\right] \quad (3)$$

To compute the A_{trip} for various operations, it is necessary to know the storage capacity of the battery and the average power consumption during various modes of operation, like the power consumption during movement using only the paddlewheels, or during harvesting using knives, loader and paddlewheels.

The real autonomy computed is evaluated using the hourly consumption Q, which has to be determined in the same way the Electric Vehicles are used to, by measuring the initial and the final energy stored in the battery pack, by using the SOC (State of Charge) values, and the operating time t_{op}.

$$Q = \frac{E_{init} - E_{act}}{t_{op}} \left[\frac{kWh}{h}\right] \quad (4)$$

where E_{init} is the energy at the beginning of the daily trip, [kWh]; E_{act} is the actual remaining energy, [kWh] and t_{op} is the operating time, [hours]. The value of the hourly consumption, Q, is used to compare the efficiency of the drive and to compute the remaining time of operation, also called the autonomy of the vessel, A, [h]. The remaining range (expressed in operating hours) is an estimate based on reporting the remaining energy to average hourly consumption Q of that day.

$$A = \frac{E_{act} - E_{min}}{Q} [h] \quad (5)$$

where E_{act} is the actual remaining energy, expressed in kWh, E_{min} is the minimum energy (usually 20% of the total stored energy) in kWh and the average hourly consumption Q is expressed in kWh/h.

Test time and movement time are reported by the GPS tracking system. The initial and final energy levels were deducted from the battery pack voltages using the voltage state-of-charge dependency curve as measured in the laboratory. No temperature correction was used for the real storage capacity.

RESULTS

The experimental research in the real environment took place from February 2023 to April 2023 at the Fish Farm in the locality of Săbiești, Dâmbovița County, Romania. On this occasion, the equipment was launched into the water, and the first demonstrations in the real environment were conducted.

Before this, measurements were carried out at idle to verify the correspondence between the technical execution documentation and the physically constructed equipment within the execution department, recording its constructive characteristics. The constructive characteristics of the aquatic biomass harvesting equipment are shown in Table 1. The overall functional verification was checked to observe the proper operation without noises and vibrations, tightness of the hydraulic system and floaters or any unauthorized heating of moving components. All the necessary adjustments were performed and the equipment was prepared for the real environment tests.

Table 1

The constructive characteristics of ERBA harvester

Parameters	Values
Overall dimensions size (length×width×height) /mm×mm×mm	7800x2500x1800
Electric engine power/kW	14,5
Battery storage capacity/kW	33
Cutting width/mm	1100
Machine weight/kg	1880
Paddlewheel diameter/mm	1300
Float dimension (length×width×height) /mm×mm×mm	4500x800x750

The experimental research began with determining the buoyancy of the vessel, considering its own weight and then with various loads. The buoyancy and the depth of immersion (draft) are correlated and were determined taking into account the constructive characteristics shown in Table 1.

Under these conditions, the draft of the vessel (Fig. 3) could be observed, with its mass of 1880 kg (without load and people on board), being 0.35 m (out of the total 0.75 m float height, of which 0.40 m are above the waterline). The draft of the vessel with people on board is shown Fig. 4. *Draft* is the vertical distance measured from the baseline to the waterline.

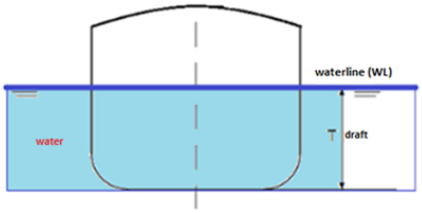


Fig. 3 – Draft measurement



Fig. 4 - Measuring the draft of the boat in different conditions

The correlation between equipment total mass (own mass+ load) and the deep of immersion (draft) is very important for the equipment not to sink. The obtained results can be read in Fig. 5. It is recommended that the overall mass does not exceed 80% of total load capacity, meaning a total maximal load of 1720 kg.

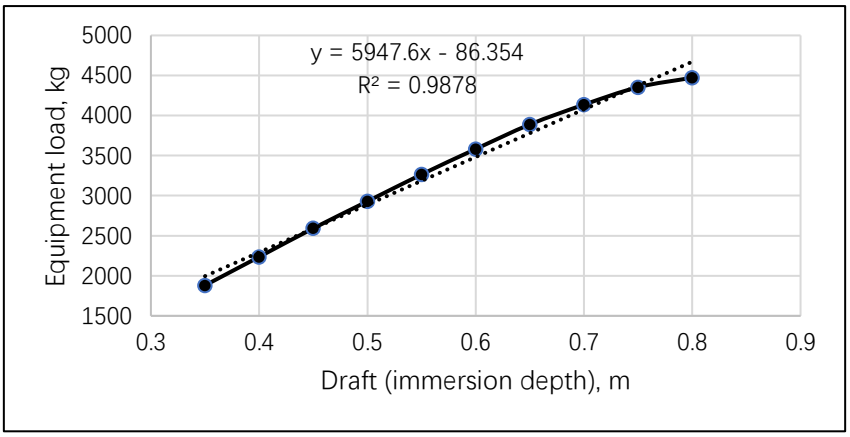


Fig. 5 - The correlation between equipment total mass and draft

It also has been measured the *turning circle* which refers to the path followed by a vessel when making a turn. It's a critical consideration for ship maneuverability, provides vital information about the ship's maneuverability and ability to navigate in narrow or crowded waters. It helps determining how much space a ship needs to execute turns safely and efficiently, which is critical for avoiding collisions and safely navigating through channels, and other confined areas. The nautical indices measured or calculated are presented in Table 2.

Table 2

Nautical indices

Parameters	Values			
	Test 1	Test 2	Test 3	Average
Buoyant force for equipment owns mass (1880 kg), N	18639	-	-	-
Buoyant force at the operating mass of the equipment (2500 kg), N	25702	-	-	-
Draft at its own mass (1880 kg), m	0.34	0.36	0.35	0.35
Draft at load and operators' mass (2500 kg), m	0.45	0.46	0.48	0.463
Inclination around the longitudinal axis without load, °	1 (towards the front)	1	1	1
Inclination around the longitudinal axis with load, °	1.5	1.5	1.5	1.5

Parameters	Values			
	Test 1	Test 2	Test 3	Average
Turning circle diameter with one propeller engaged (pivot turn), m	8	8	8	8
Duration of the pivot turn, s	21	19	20	20
Turning circle diameter with both propellers in operation, m	16	15.5	16.5	16
Duration of the turn with both propellers in operation, s	34	35	33	34

Inertia represents the ability of the vessel to continue its movement through water after a change in the regime of the ship propulsion, such as stopping or reversing. For example, if a ship is moving at full speed forward and the engines are suddenly stopped, the ship does not immediately come to a halt but continues to move due to its inertia. The characteristics of inertia are the distance traveled and the time taken to cover that distance. These can be determined when the moment of engine stoppage and the moment of the vessel final stop are known, and if the moment of changing the direction of travel is known, the distance and the time required to stop from that moment can be determined.

The time to stop the equipment with its own mass was t_1 = 2.76 s and with load and operators' mass was t_2=2.56 s, when the equipment speed was 7.46 km/h. These values help calculating the distance that the equipment is doing until the final stopping, being 2.09 m respectively 1.94 m.

During the tests, the speed of the vessel, from shore to the harvesting area, was determined and also the speed when the equipment was performing the harvesting. The average and maximum speed of the vessel was determined with a GPS application – (Strava), as shown in Fig. 6. Speed is critical for travel planning, fuel consumption analysis, and estimating time of arrival. A maximum speed of 12.5 km/h was reached, with an average speed of 4.2 km/h.

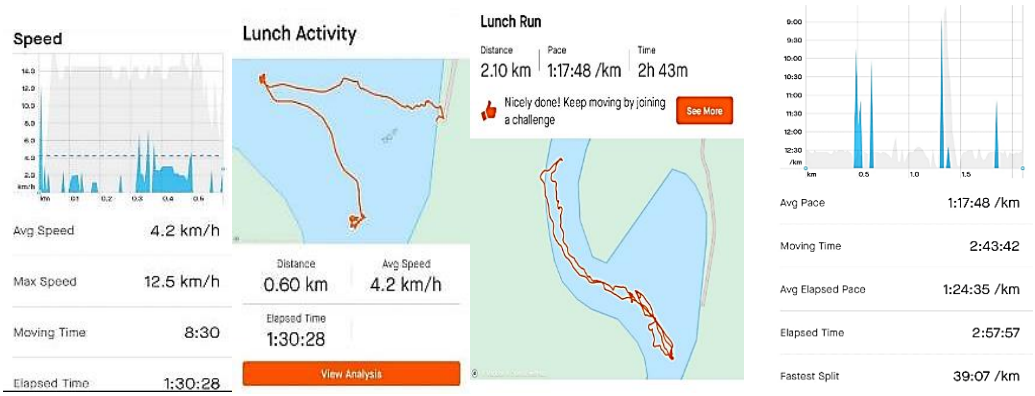


Fig. 6 - Travel speed and routes travelled

After the nautical tests were carried out, the exploitation indices were measured. These tests were done to determine the main qualitative working indicators.

The working capacity of the equipment is determined based on the results obtained during tests under operating conditions. During the determination of the working capacity, no adjustment is made to the machine. Three measurements are made for each sample.

The noise was determined using a sound level meter. The noise level is an important factor to consider for environmental impact, crew comfort, and potential disturbance to marine life.

The width of the harvested furrow, is measured in one pass with the harvesting equipment and the value is presented in Table 3. By knowing the width of the harvested furrow, it can be calculated how much area the harvester can cover in a given time, which is essential for planning and optimizing the harvesting process.

The working capacity was determined taking into account the following characteristics of the equipment and operating regimes: v = 1.51 and 3.05 km/h (minimum and maximum working speed); l_f = 1.03 m (furrow width).

Table 3

The working parameters of the equipment

Parameters	Values			
	Test 1	Test 2	Test 3	Average
Minimum working speed, km/h	1.5	1.52	1.51	1.51
Maximum working speed, km/h	3	3.05	3.1	3.05
Transport speed with the load and operators, km/h	7.1	7.5	7.8	7.46
Conveyor belt speed at 600 motor rpm, m/s	0.23	0.22	0.24	0.23
Conveyor belt speed at 1250 engine rpm, m/s	0.66	0.68	0.59	0.64
Furrow width, m	1.1	0.96	1.05	1.03
Minimum hourly working capacity, ha/h	0.1545	0.1545	0.1545	0.1545
Maximum hourly working capacity, ha/h	0.305	0.305	0.305	0.305
Noise level, dB	70.1	74.8	77.86	74.25

On the lake where the equipment was tested, two areas of biomass were identified, namely *sedge* (rest of rushes) with a maximum height above the water of 0.9 m and *reed* with a height of approx. 3 m above the water level. The reed was cut, in the first phase of the tests, from a depth of approx. 100 mm below the water level, to check the operation of the cutting knives. Later it was cut 400-500 mm below the water level. Some aspects during the experiments are presented in Fig. 7 a-e.



a - Harvesting reeds



b - Rush harvest



c - Noise level measurement



d) Reed stem



e) Typha stem

Fig. 7 - Some aspects during the experiments

Biomass samples were taken and laboratory measurements were done, the results of the phenological characteristics determined by the harvested biomass are recorded in Table 4.

Table 4

The phenological characteristics of biomass

Parameters	Numerical value Reed *(Phragmites communis)*	Numerical value Typha *(Typha latifolia)*
Stem thickness, mm	5-15	6-40
Crop height (from the root), mm	3500-4000	1250-1550
Steam length cut between bottom and the top blade, mm	1000-1500	200-900
Steam length cut above the top blade, mm	1200-1500	0
Volumetric mass, kg/m^3	58	56,4
Estimated biomass mass stored in the 2.5 m^3 bin, kg	145	141

The harvesting operation went normally, meaning that the electric systems operated according to the operator's commands, with three operational speeds available, using the electric motor adjusted to 600 rpm speed for normal operation, and switching at 1250 rpm when higher power is needed.

The hydraulic oil heating and functionality testing regime is carried out with the machine running and the speed set at the level of 300 rpm. The transition from the dock to the harvesting place can be completed with the Driving Mode which can imply a 600 rpm speed of the electric motor.

For harvesting, depending on the need, the speed for the electric motor can be selected to be 1250 rpm or 600 rpm, as appropriate, using the buttons located on the remote control. Thus, using two independent and linear power control over the two paddlewheels, high manoeuvrability of the vessel is obtained.

The temperature of the electric motor has not exceeded 104°C, compared to the maximum permissible value of 150°C. For safety reasons, the converter has a threshold for limiting the output power when the internal temperature of the electric motor is above 125°C. The temperature of the electric converter did not exceed 38.7 ºC, compared to the maximum allowable value of 100ºC, which is also the protection threshold for the power converter. The energy consumption is shown in Table 5.

Table 5

Energy consumption of each operated equipment, measured on the lake

Operation	Time	Pack voltage	Current consumption	Power consumption	Motor speed
	h.min	V_{dc}	A_{dc}	kW	r/min
Oil pre-heating	12.2	62.57	9.43	0.6	300
Lower cutter	12.49	62.47	21.45	1.3	600
Positioning actuator	12.49	62.47	11.32	0.7	600
Both paddle wheels	12.49	62.38	63	3.9	300
Both paddle wheels & Lower cutter & Conveyor on	13.27	62	140	8.7	1250
Both paddle wheels & both cutters & Conveyor on	13.31	61.9	80	5.0	600
Both paddle wheels & both cutters & Conveyor on	13.45	61.28	180	11.0	1250
Both paddle wheels & Lower cutter & Conveyor on	14.01	60.94	132	8.0	1250
Both paddle wheels	14.31	60.35	80	4.8	600
Both paddle wheels & Lower cutter & Conveyor on	15.01	60.11	180	10.8	600

During the tests performed on the lake, the initial State of Charge (SOC) was 98% of the available capacity. At the end of the tests, the measured State of Charge was 70%. As measured during the dry reed harvesting, the current absorbed from the batteries has values between 130 and 180 A_{dc}, values corresponding to an instantaneous energy consumption of about 7–12 kW.

For the different operation regimes of the vessel, maximum autonomy is computed from the maximum available energy by dividing by the power level absorbed during that task, using Equation 6 and values from Table 5 for the harvesting and the trip operation.

$$A_{harv} = \frac{E_{max} - E_{min}}{P_{harv}} \left[\frac{kWh}{kW}\right] = \frac{33-6.6}{12} = 2.2 \text{ [h]} \quad (6)$$

where E_{max} is the maximum stored energy in the three Li-Ion batteries, 33 kW, expressed in kWh, E_{min} is the minimum energy (20% of the total stored energy of 33 kWh) and for P_{harv} was used the maximum measured value of 12 kW.

For the trip, when only the two paddle wheels were used for propulsion, was measured a consumption P_{trip} of about 3.9 kW (see Table 5), for an average travel speed of 10 km/h.

$$A_{trip} = \frac{E_{max} - E_{min}}{P_{trip}} \left[\frac{kWh}{kW}\right] = \frac{33-6.6}{3.9} = 6.77 \text{ [h]} \quad (7)$$

The A_{trip} for movement using only the paddle wheels is 6.77 h, and during harvesting using both knives, loader and paddle wheels, is 2.2 h. Using the up results, it can be concluded that the maximum trip distance is 67 km, with the average speed of 10 km/h.

During the tests, the energy consumption from the batteries, the test duration, the real trip, as well as the average speed and maximum speed were measured. The data was collected over 6 test sessions, each one being presented in Table 6.

Table 6

Energy consumption during tests on the lake

Date	Initial energy E1	Final energy E2	DC initial voltage V_1	DC final voltage V_2	Test time t_g	Trip time t_{op}	Real trip dx	Average speed v_{med}	Max Speed v_{max}	Energy cons. CE_{21}	Remaining range t_{rem}
	kWh	kWh	V	V	h	h	km	km/h	km/h	kWh/h	h
01.03.23	32.44	32.13	65.48	64.40	1.50	0.15	0.60	4.0	12.5	2.09	12.21
08.03.23	32.12	31.06	64.40	63.70	1.78	0.36	0.93	2.6	13.6	2.94	8.31
20.03.23	31.06	30.44	63.70	63.35	1.33	0.38	1.28	3.4	12.5	1.62	14.76
20.03.23	30.44	29.04	63.35	62.60	0.68	0.27	0.72	2.7	9.6	5.17	4.34
10.04.23	29.04	28.05	62.56	62.26	1.08	0.22	0.81	3.7	10.4	4.50	4.77
10.04.23	27.98	23.17	61.9	60.11	1.05	0.45	3.20	7.1	10.5	10.71	1.55
Total	**32.44**	**23.17**	**65.48**	**60.11**	**7.42**	**1.83**	**7.54**	**4.1**	**13.6**	**5.07**	**3.27**

The energy efficiency was measured to evaluate the autonomy, as described in Eq. 4 and Eq. 5. The energy consumption is evaluated as the hourly consumption and was to be determined by measuring the initial and the final energy stored in the battery pack by using the SOC (State of Charge) values, and the operating time t_{op}.

$$Q = \frac{E_{init} - E_{act}}{t_{op}} = \frac{27.99 - 23.17}{0.45} = 10.71 \left[\frac{kWh}{h}\right] \quad (8)$$

The value of the hourly consumption Q, computed in the Equation 8, is the maximum value obtained durring harvesting the crop, and was used to compute the worst time of operation, also called the autonomy of the vessel. The remaining range (expressed in operating hours) is an estimate based on reporting the remaining energy to that day's average hourly consumption Q.

$$A = \frac{E_{act} - E_{min}}{Q} = \frac{23.17 - 6.60}{10.71} = 1.55\ [h] \quad (9)$$

where E_{act} is the actual remaining energy, expressed in kWh, E_{min} is the minimum energy (20% of the total stored energy of 33 kWh). Total autonomy, $A_{max,}$ can be computed using the maximum available energy and the maximum hourly consumption.

$$A_{max} = \frac{E_{max} - E_{min}}{Q} = \frac{33 - 6.60}{10.71} = 2.46\ [h] \quad (10)$$

The vessel has more than 2 h operating time at maximum load. In this autonomy estimations, the test time and movement time are reported by a GPS tracking system.

It was found that, for the first test trips, the energy consumption was small, but when thick reeds were intensively harvested, the measured consumption was 10.71 kWh/h, this value being very close to the maximum designed figure of 11 kWh. Under these conditions, the battery could maintain the harvest for 2.46 hours.

CONCLUSIONS

Following the testing of the experimental model of the *Aquatic biomass harvesting equipment*, symbolized as ERBA, the following conclusions were drawn:

1) The equipment fulfils the functional role for which it was designed, being autonomous equipment, electrically operated, and remote controlled. The presented equipment can be scaled in different sizes, both in length, installed power and predicted autonomy. Such of harvester provides an important link in aquatic biomass management, especially in old floating reed control, by contributing to the maintenance and clearance of navigation canals affected by the development of aquatic biomass in excess. The harvester can be used in fish lakes, canals, ponds, and the Danube Delta.

2) The working capacity of the equipment at the speed v = 1.51 and 3.05 km/h (minimum and maximum working speed) was 0.15 - 0.305 ha/h, the furrow width l_f was 1.03 m.

3) The ERBA harvester achieves autonomy of over 2.46 hours of working time in the maximum load scenario.

ACKNOWLEDGEMENT

This research was funded by a grant of the Romanian Research, Innovation and Digitalization Ministry, through Sectoral Plan, contract no. 1PS/2021.

REFERENCES

[1] Calotă, R., Savaniu, M., Girip, A., Năstase, I., Georgescu, M. R., Tonciu, O. (2022). Study on Energy Efficiency of an Off-Grid Vending Machine with Compact Heat Exchangers and Low GWP Refrigerant Powered by Solar Energy. *Energies,* 15(12), 4433. https://doi.org/10.3390/en15124433

[2] Cao Zhen, Jin Xin, Liao Qingxi (2011) Experimental research on physical and mechanical parameters of matured bottom stalk of the reed for harvester design. *International Journal of Agricultural and Biological Engineering,* vol. 4 no 2. pp. 36-42

[3] Clayton, J. S, (1996). Aquatic weed and their control in New Zeeland lakes. *Lake and Reserv. Management.* Vol 12(4):477-486.

[4] Culcea, M., Darie, E., Gheorghe, S., Pecsi, R., Savaniu, M.I., (2023). The influence of a DC-AC inverter used in a stand-alone vending machine equipped with photovoltaic panels, *IOP Conference Series: Earth and Environmental Science,* 1185 (1), 012003, DOI:10.1088/1755-1315/1185/1/012003.

[5] Hofstra, D.E., Clayton, J.S. (2001). Evaluation of Selected Herbicides for the Control of Exotic Submerged Weeds in New Zealand: I. The Use of Endothall, Triclopyr and Dichlobenil. *Journal of Aquatic Plant Management,* 39: 20-24.

[6] Hu, Z., Yuan, J. (2018). China's NEV market development and its capability of enabling premium NEV: Referencing from the NEV market performance of BMW and Mercedes in China. *Transportation Research Part A: Policy and Practice*, 118, 545–555. https://doi.org/10.1016/j.tra.2018.10.010

[7] Huang, J. C., Zhang, B., Tian, K. P., Liu, H. L., Shen, C. (2022). Design and optimization of the parameters of the key components for reed harvester. *Int J Agric & Biol Eng*., 15(6): 96–103.

[8] Ivan, Gh., Mircea, C., Brăcăcescu, C., Găgeanu, I. (2016) Considerations regarding reed harvesting technologies, *ISB INMATEH 2016 International Symposium*, pp.383-390.

[9] Lavergne, S., Molofsky, J., (2006). Control Strategies for the Invasive Reed Canarygrass (Phalaris arundinacea L.) in North American Wetlands: the Need for an Integrated Management Plan, *Natural Areas Journal* 26(2), 208-214, https://doi.org/10.3375/0885-8608(2006)26 .

[10] Obreja, C.D., Buruiana, D.L., Mereuta, E., Muresan, A., Ceoromila, A.M., Ghisman, V., Axente, R.E. Detection of reed using CNN method and analysis of the dry reed (phragmites australis) for a sustainable lake area. *Plant Methods 19,* 61 (2023). https://doi.org/10.1186/s13007-023-01042-w.

[11] Piccitto, A., Scordia, D., Corinzia, S.A., Cosentino, S.L., Testa, G. (2022). Advanced Biomethane Production from Biologically Pretreated Giant Reed under Different Harvest Times. *Agronomy*, 12, 712, https://doi.org/10.3390/agronomy12030712.

[12] Popovici, I.A., Savaniu, M., Tonciu, O., Culcea, M., Teodorescu, A., (2022). Various operation mode of construction machinery using energy obtained from renewable sources. *Proceedings of 2022 International Conference on Hydraulics and Pneumatics – HERVEX*, 86-98.

[13] Sciuto. L., Licciardello. F., Barbera. A.C., Cirelli. G. (2023). Giant reed from wetlands as a potential resource for biomethane production, *Ecological Engineering*, 190, 106947, ISSN 0925-8574, https://doi.org/10.1016/j.ecoleng.2023.106947.

[14] Shahrukh, N.A., Bhaskar, S., Abhishek G. (2021). Aquatic weed as a biorefinery resource for biofuels and value-added products: Challenges and recent advancements, *Cleaner Engineering and Technology*, 4, 100235, https://doi.org/10.1016/j.clet.2021.100235.

[15] Siemering, G., Jennifer, H. (2005). Aquatic Herbicides: Overview of Usage, Fate and Transport, Potential Environmental Risk, and Future Recommendations for the Sacramento-San Joaquin Delta and Central Valley. *White Paper for the Interagency Ecological Program.* SFEI Contribution 414. San Francisco Estuary Institute, Oakland, CA.

[16] Suvac, A., Cucu, L., Stoica, M., Savaniu, M. (2019). Development and optimization of a three-wheeled electric vehicle frame using structural materials. *In Journal of Physics: Conference Series*, 1297(1), 012021. IOP Publishing. DOI: 10.1088/1742-6596/1297/1/012021.

[17] Ștefan, V., Constantin, A.M., Popa, L., Tudor, E., Miron, C. (2022). Equipment used to harvest biomass from lake areas*, ISB INMATEH International Symposium* 2022, 544-553.

[18] Torawane, S., Mokat, D. (2019). Aquatic weed management and development through innovative ways. *ASM Group of Institutes*, 491-502

[19] Tudor, E., Matache, M.G., Vasile, I., Sburlan, I.C., Stefan, V., (2022). Automation and Remote Control of an Aquatic Harvester Electric Vehicle. *Sustainability 14*, (10), 6360, https://doi.org/10.3390/su14106360

[20] Tudor, E., Matache, M.G., Vasile, I., Sburlan, I.C., Stefan, V., (2023). Electric drive system powered by LI-ION batteries for aquatic biomass harvester, *INMATEH Agricultural Engineering*, 69 (1), 609-616, https://doi.org/10.35633/inmateh-69-58

[21] Wenbo, L., Ruyin, L., Hong, C. (2016). Consumers' evaluation of national new energy vehicle policy in China: An analysis based on a four-paradigm model. *Energy Policy 2016*, 99, 33–41.

WRITING INSTRUCTIONS

Article Types

Three types of manuscripts may be submitted:

1. **Regular articles:** These should describe new and carefully confirmed findings, and experimental procedures should be given in sufficient detail for others to verify the work. The length of a full paper should be the minimum required to describe and interpret the work clearly (max.10 pages, even number);
2. **Reviews:** Submissions of reviews and perspectives covering topics of current interest are welcome and encouraged (max.12 pages, even number).

Manuscripts should be written in English (American or British usage is accepted, but not a mixture of these) and submitted **electronically** at the following e-mail addresses: ***inmatehjournal@gmail.com***
Please be sure to include your full affiliation and e-mail address (see Sample manuscript)
The authors are responsible for the accuracy of the whole paper and references.
There are allowed 2 papers by each first author.
The text layout should be in single-column format. To avoid unnecessary errors it is strongly advised to use the "spell-check" and "grammar check" functions of your word processor.

Review Process

All manuscripts are reviewed by 2 members of the Scientifically Review Office. Decisions will be made as rapidly as possible and the journal strives to return reviewers' comments to authors in approx.3 weeks.
The editorial board will re-review manuscripts that are accepted pending revision.

NOTE:

Submission of a manuscript implies: that the work described has not been published before (excepting as an abstract or as part of a published lecture or thesis) that it is not under consideration for publication elsewhere.

1. REGULAR ARTICLES

- Manuscripts should be concise, in ***1.15 line spacing***, and should have 2 cm all over margins. The font should be ***Arial 10 pt.*** Ensure that each new paragraph is clearly indicated, using **TAB at 1 cm**.
- Title will be ***Arial 12 pt***. and explicit figures will be ***Arial 9 pt***.
- Text will be written in English.
- Chapters' titles are written by ***Arial 10 pt, Bold, Uppercase*** (e.g. **INTRODUCTION, MATERIALS AND METHODS**), between chapters is left a space for 10 pt. At the beginning of each paragraph, TAB of 1 cm.
- The paper body will be written in ***Arial 10 pt., Justify alignment***.

TITLE ***Arial 12 pt., Uppercase, Bold, Center*** *(in English language)* and ***Bold Italic*** *(in native language).*
Should be a brief phrase describing the contents of the paper. Avoid long titles; a running title of no more than 100 characters is encouraged (without spaces).

AUTHORS ***ARIAL 9, Bold, Centre alignment***
Under the paper's title, after a space (enter) 9 pt., write ***authors' names*** and ***affiliations (Arial 8 pt.-Regular)***
When the paper has more than one author, their name will be followed by a mark (Arabic numeral) as superscript if their affiliation is different. Less than 6 authors.
Corresponding author's name (next row), ***(Arial 8 pt.)***. Should be added also: phone, fax and e-mail information, for the paper corresponding author (***font: 8 pt., Italic***).

KEYWORDS ***(In English)*** about 4 to 7 words that will provide indexing references should be listed (title: ***Arial 10pt, bold italic,*** text ***Arial 10 pt., italic***).

A list of non-standard *Abbreviations* should be added. In general, non-standard abbreviations should be used only when the full term is very long and used often. Each abbreviation should be spelled out and introduced in parentheses the first time it is used in the text. Standard abbreviations (such as ATP and DNA) need not to be defined.
ABSTRACT ***(in English and Native language, Arial 10 pt.)***, the title *bold*; the text of abstract: *italic*) should be informative and completely self-explanatory, briefly present the topic, state the scope of the experiments, indicate significant data, and point out major findings and conclusions. The Abstract should be max.250 words. Complete sentences, active verbs, and the third person should be used, and the abstract should be written in the past tense. Standard nomenclature should be used and abbreviations should be avoided. No literature should be cited.
INTRODUCTION (***Arial 10 pt.)*** should provide a clear statement of the problem, the relevant literature on the subject, and the proposed approach or solution. It should be understandable to colleagues from a broad range of scientific subjects. We should refer to the current stage of researches performed in the field of the paper to be published, by quoting up-to-date specialty studies, preferably published after 2006, excepting certain referential specialty

books/studies, especially papers issued in magazines/journals/conferences/ISI quoted symposia or in other international data bases, which are well known and available.

MATERIALS AND METHODS (***Arial 10 pt.***) should be complete enough to allow experiments to be reproduced. However, only truly new procedures should be described in detail; previously published procedures should be cited, and important modifications of published procedures should be mentioned briefly. Methods in general use need not be described in detail.

RESULTS (***Arial 10 pt.***) should be clarity presented. The results should be written in the past tense when describing findings in the authors' experiments. Results should be explained, but largely, without referring to the literature. Discussion, speculation and detailed interpretation of data should not be included in the Results, but should be put into the Conclusions section.

CONCLUSIONS (***Arial 10 pt.***) The main conclusions drawn from results should be presented in a short Conclusions section. Do not include citations in this section.

Formulae, symbols and abbreviations: Formulae will be typeset in Italics (preferable with the Equation Editor of Microsoft Office 2003) and should be written or marked as such in the manuscript, unless they require a different styling. They should be referred to in the text as Equation (4) or e.g. (4). The formulae should be numbered on the right side, between brackets ***(Arial 10 pt.)***:

$$P = F \cdot v \tag{1}$$

Terms of the equation and the unit measure should be explained, e.g.

P is the power, [W];
F – force, [N];
v – speed, [m/s]

SI units must be used throughout.

Tables should be self-explanatory without reference to the text. The details of the methods used in the experiments should preferably be described in the legend instead of in the text. The same data should not be presented both in table and graph form or repeated in the text.
Table's title will be typed ***Arial 9 pt, Bold, Centered***
In the table, each row will be written Arial 9 pt, single-spaced throughout, including headings and footnotes.
The table should be numbered on the right side, ***Arial 10 pt.***

Figures ***(Arial 9 pt., Bold, Center)***should be typed in numerical order (Arabic numerals). Graphics should be high resolution (e.g.JPEG).Figure number is followed by what represent the figure or graph e.g.:

Fig.1 – Test stand

Legend: ***Arial 8 pt, Italic, Center,*** e.g.:
1 - plansifter compartments; 2- break rolls; 3 – semolina machines; 4 – reduction rolls; 5 – flour

ACKNOWLEDGMENTS (***Arial 10 pt.***) of people, grants, funds etc should be brief (*if necessarily*).

REFERENCES (***Arial 10 pt.***)
(In alphabetical order, in English and in the original publication language).
Minimum 10 references, last 10 years, minimum 3 references from the last 2 years

It can be used "*References*" tool from the *Word Editor*. **APA Style (American Psychological Association)**
https://apastyle.apa.org/style-grammar-guidelines/references/examples

All references must be provided in English
Authors are fully responsible for the accuracy of the references.

References should be **alphabetically**, with complete details, as follows:

Examples:
Books: https://apastyle.apa.org/style-grammar-guidelines/references/examples/book-references

Jackson, L. M. (2019). *The psychology of prejudice: From attitudes to social action* (2nd ed.). American Psychological Association. https://doi.org/10.1037/0000168-000
Kesharwani, P. (2020). *Nanotechnology based approaches for tuberculosis treatment*. Academic Press.
Sapolsky, R. M. (2017). *Behave: The biology of humans at our best and worst*. Penguin Books.

Torino, G. C., Rivera, D. P., Capodilupo, C. M., Nadal, K. L., & Sue, D. W. (2019). *Microaggression theory: Influence and implications*. John Wiley & Sons. https://doi.org/10.1002/9781119466642

In text:

- ***Parenthetical citations***: (Jackson, 2019; Sapolsky, 2017)
- ***Narrative citations***: Jackson (2019) and Sapolsky (2017)

Journal Article:

https://apastyle.apa.org/style-grammar-guidelines/references/examples/journal-article-references

Grady, J. S., Her, M., Moreno, G., Perez, C., & Yelinek, J. (2019). Emotions in storybooks: A comparison of storybooks that represent ethnic and racial groups in the United States. *Psychology of Popular Media Culture*, *8*(3), 207–217. https://doi.org/10.1037/ppm0000185

In text:

- ***Parenthetical citation***: (Grady et al., 2019)
- ***Narrative citation***: Grady et al. (2019)

Conference or Symposium:

https://apastyle.apa.org/style-grammar-guidelines/references/examples/conference-proceeding-references

Duckworth, A. L., Quirk, A., Gallop, R., Hoyle, R. H., Kelly, D. R., & Matthews, M. D. (2019). Cognitive and noncognitive predictors of success. *Proceedings of the National Academy of Sciences*, *USA*, *116*(47), 23499–23504. https://doi.org/10.1073/pnas.1910510116

In text:

- ***Parenthetical citation***: (Duckworth et al., 2019)
- ***Narrative citation***: Duckworth et al. (2019)

Dissertation / Thesis:

https://apastyle.apa.org/style-grammar-guidelines/references/examples/published-dissertation-references

Zambrano-Vazquez, L. (2016). *The interaction of state and trait worry on response monitoring in those with worry and obsessive-compulsive symptoms* [Doctoral dissertation, University of Arizona]. UA Campus Repository. https://repository.arizona.edu/handle/10150/620615

In text:

- ***Parenthetical citations***: (Kabir, 2016; Miranda, 2019; Zambrano-Vazquez, 2016)
- ***Narrative citations***: Kabir (2016), Miranda (2019), and Zambrano-Vazquez (2016)

https://apastyle.apa.org/style-grammar-guidelines/references/examples/unpublished-dissertation-references

Harris, L. (2014). *Instructional leadership perceptions and practices of elementary school leaders* [Unpublished doctoral dissertation]. University of Virginia.

In text:

- ***Parenthetical citation***: (Harris, 2014)
- ***Narrative citation***: Harris (2014)

Patents: Names and initials of authors, year (between brackets), patent title (Italic), patent number,country:

Grant, P. (1989). *Device for Elementary Analyses*. Patent. No.123456. USA.

Legal regulations and laws, organizations:

https://apastyle.apa.org/style-grammar-guidelines/references/examples/iso-standard-references

International Organization for Standardization. (2018). *Occupational health and safety management systems—Requirements with guidance for use* (ISO Standard No. 45001:2018). https://www.iso.org/standard/63787.html

Occupational Safety and Health Administration. (1970). *Occupational safety and health standards: Occupational health and environmental control: Occupational noise exposure* (OSHA Standard No. 1910.95). United States Department of Labor. https://www.osha.gov/laws-regs/regulations/standardnumber/1910/1910.95

In text:

- ***Parenthetical citations***: (International Organization for Standardization, 2018; Occupational Safety and Health Administration, 1970)
- ***Narrative citations***: International Organization for Standardization (2018) and Occupational Safety and Health Administration (1970)

Web references: The full URL should be given in text as a citation, if no other data are known. If the authors, year, and title of the documents are known and the reference is taken from a website, the URL address has to be mentioned after these data.

Citation in text

Please ensure that every reference cited in the text is also present in the reference list (and vice versa).

Do not cite references in the Abstract and Conclusions !.

Unpublished results, personal communications as well as URL addresses are not recommended in the references list.

Making personal quotations (one, at most) should not be allowed, unless the paper proposed to be published is a sequel of the cited paper. Articles in preparation or articles submitted for publication, unpublished, personal communications etc. should not be included in the references list.

Citations style

***Text**:* All citations in the text may be made directly (or parenthetically) as bellow.

- ***single author**:* the author's name (without initials, unless there is ambiguity) and the year of publication:
  "as previously demonstrated *(Brown, 2010)*".
- ***two authors**:* both authors' names and the year of publication: *(Adam and Brown, 2008; Smith and Hansel, 2006; Stern and Lars, 2009)*
- ***three or more authors**:* first author's name followed by "et al." and the year of publication: "As has recently been shown *(Werner et al., 2005; Kramer et al., 2000)* have recently shown ...."

Citations of groups of references should be listed first alphabetically, then chronologically.

Units, Abbreviations, Acronyms

- Units should be metric, generally SI, and expressed in standard abbreviated form.
- Acronyms may be acceptable, but must be defined at first usage.

2. REVIEWS

Summaries, reviews and perspectives covering topics of current interest in the field, are encouraged and accepted for publication. Reviews do not have the requirements for regular articles. However, should include: (*) an introductory chapter, (**) a careful and critical presentation of the relevant aspects of the topic approached and (***) emphasis of the aspects that aren't known and require further research to progress. Reviews should be concise (max. 12 pages).

Edited by: INMA Bucharest
6, Ion Ionescu de la Brad Blvd., sect. 1, Bucharest, ROMANIA
Tel: +4021.269.32.60; Fax: +4021.269.32.73
https:// inmateh.eu
e-mail: ***inmatehjournal@gmail.com***